JOURNAL
OF THE
PHYSICAL SOCIETY
OF JAPAN

Volume 10
1955

Published by the
PHYSICAL SOCIETY OF JAPAN

JOURNAL OF THE PHYSICAL SOCIETY OF JAPAN Vol. 10, No. 1, JANUARY, 1955

Contribution to the Theory of Upper and Lower Bounds in Boundary Value Problems

By Hiroshi FUJITA

Department of Physics, Faculty of Science,
University of Tokyo

(Received August 12, 1954)

In the present paper certain approximate methods concerning self-adjoint operators H of Hilbert spaces which can be expressed in the form $H=T^*T$ are developed. Some theorems are formulated with remarks and examples. They give a method of obtaining upper and lower bounds of the value of the solution, at each preassigned point, of a boundary value problem. As a numerical example we consider the following Poisson's equation, $-\triangle u=1$ in D, $u=0$ on C, where D denotes the square domain in the xy-plane with vertices at $(1, -1)$, $(1, 1)$, $(-1, 1)$, $(-1, -1)$ and C is the boundary of this square. Upper and lower bounds of the value of the solution u at the origin are calculated. The result of the second approximation is $0.2939 \leqq u(0, 0) \leqq 0.2953$.

In order to show that the results are applicable to many problems, several differential operators familiar in mathematical physics, for instance, Laplace's differential operators with different boundary conditions are reduced to the form T^*T.

Introduction

The present paper is intended to be a contribution to the theory of estimating the bounds of errors in certain approximate methods in boundary value problems. This method is based on the theory of self-adjoint operator H of Hilbert spaces which can be expressed in the form $H=T^*T$. An abstract theory of such operators has been developed by J. v. Neumann [11] and F. J. Murray [10], and a general theory of approximate solutions of linear equations and eigenvalue problems for such operators has been given by T. Kato [8], making use of the results of v. Neumann and Murray.

The purpose of the present paper is manifold. First, in § 1. we shall show by several examples how most of the linear operators of mathematical physics can be expressed in the form $H=T^*T$. The considerations in this section are the preliminaries of the succeeding sections as well as of other applications which we shall deal with in future. § 2. is devoted to give a formula for the calculation of upper and lower bounds of the value of a quadratic functional associated with a boundary value problem. § 3. concerns with the pointwise approximation of the solution of a boundary value problem. There we shall give a simplified proof of the fundamental theorem regarding the solution of linear equation $T^*Tu=f$. In the paper of Kato this theorem has been proved by making use of the results of v. Neumann and Murray; so it would be worth while to present here an independent elementary proof. Next, we proceed to consider in abstract manner how to improve the estimation and discuss the convergence of the approximation (§ 4.).

A numerical example will be given in § 5. The problem considered is the same as that of Greenberg [7], and the method is not essentially different, but use is made of different trial functions. It is seen that the covergence is much improved and a satisfactory result is obtained by the second approximation. In § 6. we refer to the intimate relation between the hypercircle method and our method. Indeed, it will be seen that our method is not essentially different from those proposed by authors of the hypercircle method and others. (See references [1, 2, 3, 4, 5, 7, 9, 12, 14, 15, 16, 18].) But it would seem that our method is mathematically convenient, in as much as there exist the fundamental theorems of v. Neumann and Murray. On the other hand, our method may be useful to determine the conditions imposed on trial functions.

Also we hope that our method is more es-

1551 63/20

sential in the eigenvalue problems, which are, however, not treated in this paper. We shall deal with the latter in a subsequent paper.

§ 1. Decomposition of an Operator into the Form T^*T

When T is a linear operator with its domain $\mathfrak{D}$ in a (real or complex) Hilbert space $\mathfrak{H}$ and its range in a second Hilbert space $\mathfrak{H}'$ ($\mathfrak{H}$ and $\mathfrak{H}'$ may be identical), T^*, the adjoint of T, is defined together with its domain $\mathfrak{D}^*$ in $\mathfrak{H}'$ by the condition that

$$(Tu,\ v)=(u,\ T^*v) \tag{1.1}$$

holds for any $u\in\mathfrak{D}$ and any $v\in\mathfrak{D}^*$ [13], [17]. In (1.1), the left and the right side represent the inner product in $\mathfrak{H}'$ and $\mathfrak{H}$ respectively. In general, T^*T is a self-adjoint operator in $\mathfrak{H}$. In order to apply our method to a given operator H, it is necessary to reduce H to the form T^*T. This section is devoted to illustrate this decomposition through several examples of differential operators. We begin with the following propositions.

(**I**) A self-adjoint operator H can be reduced to the form T^*T if and only if it is positive definite. In fact, if $H=T^*T$, then $(Hu,\ u)=(T^*Tu,u)=(Tu,\ Tu)\geq 0$, while if H is positive, then there exists $\sqrt{H}$, the positive square root of H, and $(\sqrt{H})^*=\sqrt{H}$.

However, it must be remarked that even if H is of a familiar type, $\sqrt{H}$ is usually so complicated that one can hardly deal with it in practice of the variational calculus. When H is not positive but semi-bounded, it is enough for the purpose of some applications to replace H by $\pm H+cI$ where I is the identity operator and double sign and real number c should be chosen suitably.

(**II**) Let H be as follows.

$$H=\sum_{k=1}^{n}H_k=H_1+H_2+\cdots+H_n,$$
$$H_k=T_k^*T_k,\ \mathfrak{D}_k=\mathfrak{D}\subset\mathfrak{H},$$
$$\mathfrak{D}_k^*\subset\mathfrak{H}'_k\ (k=1,\ 2,\dots,\ n).$$

Then T can be defined so that

$$Tu=(T_1u,\ T_2u,\dots,\ T_nu),\ u\in\mathfrak{D}.$$

This means that the range of T and the domain of T^* are contained in $\mathfrak{H}'=\mathfrak{H}_1'\times\mathfrak{H}_2'\times\cdots\times\mathfrak{H}_n'$ (cartesian product). We see that for $v=(v_1,\ v_2,\ \dots,\ v_n)$ $(v_k\in\mathfrak{D}_k^*)$, the following relation holds.

$$T^*v=T_1^*v_1+T_2^*v_2+\cdots+T_n^*v_n\,.$$

(**III**) When T is a differential operator, (1.1) is closely related to the so-called Green's identity. As for a differential operator it should be noted that even if it is linear in the usual terminology, it is not linear as an operator in a Hilbert space unless its boundary condition is homogeneous. In case of inhomogeneous boundary conditions, a device as shown in Example 6. is necessary.

(**IV**) When H is the gradient of a quadratic functional in the sense that $\delta J[u]=2(Hu,\ \delta u)$, where $J[u]=(Lu,\ Lu)$ and δ denotes the first variation, it is natural to take $T=L$.

Examples.

In the following examples, Hilbert spaces are assumed to be real for the sake of brevity. We shall treat only differential operators in 2-dimensional Euclidean space, but analogous procedures are applicable to more general cases, e. g. n-dimensional differential operators.

Several notations, which will occur also in succeeding sections, are introduced as follows.

D is a bounded domain in xy-plane with a sufficiently regular contour C. Let n be the outer normal to C. $\partial/\partial n$ is the differentiation in the direction of n, while v_n, where v is a vector function defined on C, means the component of v in the direction of n. ds is the line element of C.

All functions considered here belong to L^2 in its range of definition. $L^2(D:\rho)$, where ρ is a positive function, is the Hilbert space with the inner product which is the integral over D with the density function ρ. $L^2(D)$ is identified with $L^2(D:1)$. We use $\times$ to represent the cartesian product of Hilbert spaces.

$L^2(C:\sigma)$, where σ is a positive function of $L^2(C)$, is defined similarly.

$M_k(D)$ is the set of functions defined and continuous together with their derivatives of up to $(k-1)$-th order and provided with piecewise continuous k-th order derivatives. The set of functions belonging to M_k and vanishing on C together with their derivatives along n of up to $(k-1)$-th order is denoted by $\hat{M}_k$. When w belongs to M_0, w_C means the restriction of w to C.

u and v represent the general elements of $\mathfrak{D}$ and $\mathfrak{D}^*$ respectively.

Finally, we remark that from the strict point of view, T and T^* given below must be replaced by their closed extension [13].

Example 1. Let $\mathfrak{H}$ and $\mathfrak{H}'$ be $L^2(D)$. If $Tu=\Delta u$, $u \in \hat{M}_2$, where Δ means the Laplace's differential operator, then $T^*v=\Delta v$, $v \in M_2$, and $T^*Tu=f$ implies that

$$\Delta\Delta u=f \quad \text{in } D, \quad u=\frac{\partial u}{\partial n}=0 \quad \text{on} \quad C.$$

Example 2. $\mathfrak{H}=L^2(D)$, $\mathfrak{H}'=L^2(D)\times L^2(D)$.

If $Tu=\operatorname{grad} u$, $u\in\hat{M}_1$, then $T^*v=-\operatorname{div} v$, $v\in M_1\times M_1$ and $T^*Tu=f$ implies that

$$-\Delta u=f \quad \text{in } D, \quad u=0 \quad \text{on} \quad C.$$

Example 3. $\mathfrak{H}=L^2(D:r)$,

$$\mathfrak{H}'=L^2(D:p_1)\times L^2(D:p_2)\times L^2(D:q).$$

If $Tu=\left(\frac{\partial u}{\partial x}, \frac{\partial u}{\partial y}, u\right)$, $u \in \hat{M}_1$, then

$$T^*v=T^*(v_1, v_2, v_3)$$
$$=\frac{1}{r}\left\{-\frac{\partial}{\partial x}(p_1v_1)-\frac{\partial}{\partial y}(p_2v_2)+qv_3\right\}$$

$v\in M_1\times M_1\times M_0$,

and $T^*Tu=f$ implies that

$$-\frac{\partial}{\partial x}\left(p_1\frac{\partial u}{\partial x}\right)-\frac{\partial}{\partial y}\left(p_2\frac{\partial u}{\partial y}\right)+qu=rf$$
$$\text{in } D,\ u=0 \text{ on } C.$$

Example 4. Let $\mathfrak{H}$ and $\mathfrak{H}'$ be as in Example 2.

If $Tu=\operatorname{grad} u$, $u\in M_1$, then

$$T^*v=-\operatorname{div} v, \quad v\in M_1\times M_1, \quad v_n=0$$

and $T^*Tu=f$ implies

that $-\Delta u=f$ in D, $\frac{\partial u}{\partial n}=0$ on C.

Example 5. $\mathfrak{H}=L^2(D)\times L^2(C)$,

$$\mathfrak{H}'=L^2(D)\times L^2(D).$$

If $Tu=\operatorname{grad} w$, $u=(w, w_C)$, $w\in M_1$, then

$$T^*v=(-\operatorname{div} v, v_n), \quad v\in M_1\times M_1.$$

In this case $T^*Tu=f$, where $u=(w, w_C)$, $f=(\varphi, \psi)$, implies that

$$-\Delta w=\varphi \quad \text{in } D, \quad \frac{\partial w}{\partial n}=\psi \quad \text{on } C.$$

Example 6. $\mathfrak{H}=L^2(D)\times L^2(C)$,

$$\mathfrak{H}'=L^2(D)\times L^2(D)\times L^2(C).$$

If $Tu=T(w, w_C)=(\operatorname{grad} w, \sigma w)$, $w \in M_1$, then for $v=(v_1, v_2, v_3)$, $v_1\in M_1$, $v_2\in M_1$, $v_3\in L^2(C)$,

$$T^*v=(-\operatorname{div}(v_1, v_2), (v_1, v_2)_n+\sigma v_3).$$

Now, $T^*Tu=f$, where $u=(w, w_C)$ and $f=(\varphi, \psi)$, implies that

$$-\Delta w=\varphi \quad \text{in } D, \quad \frac{\partial w}{\partial n}+\sigma^2 w=\psi \quad \text{on } C.$$

§ 2. Bounds of Quadratic Functionals

In this section we consider the problem of obtaining upper and lower bounds to the value of a quadratic functional $J[u]$, where u is the solution of a boundary value problem. As for physical meanings of this problem, reference is made to Diaz [5].

Hilbert spaces are again assumed to be real, for it is almost immediate to modify the results so that they hold in complex spaces.

Lemma 1. If $(v_0, v_1-v_0)=(v_2, v_1-v_0)=0$, *then*

$$2(v_2, v_1)-\|v_2\|^2\leqq\|v_0\|^2\leqq\|v_1\|^2 \tag{2.1}$$

Proof. By virtue of $(v_0, v_1-v_0)=0$, $\|v_1-v_0\|^2\geqq 0$ yields $\|v_0\|^2\leqq\|v_1\|^2$. On the other hand, $(v_2, v_1-v_0)=0$ and $\|v_2-v_0\|^2\geqq 0$ give the inequality $2(v_2,v_1)-\|v_2\|^2\leqq\|v_0\|^2$.

Theorem 1. Let u_0 be a vector determined by the equation $T^*Tu_0=f$. For any u, v satisfying the conditions

$$u\in\mathfrak{D}, \quad T^*v=f, \tag{2.2}$$

the following inequality holds:

$$2(u, f)-\|Tu\|^2\leqq\|Tu_0\|^2\leqq\|v\|^2. \tag{2.3}$$

Proof. $T^*(v-Tu_0)=0$ ensures that

$$(Tu_0, v-Tu_0)=(Tu, v-Tu_0)=0$$

and we can substitute Tu_0, v, Tu for v_0, v_1, v_2 of Lemma 1 respectively.

Remark. A large class of boundary value problems in mathematical physics can be reduced to $T^*Tu=f$ as we have seen in § 1, and quadratic functionals in question are often $\|Tu\|^2$.

To apply (2.3) it is necessary to find u, v in accordance with (2.2), which is not difficult in cases of differential operators treated in § 1 if C and f are both sufficiently simple.

Example 1. Let u_0 be determined by

$$-\Delta u_0=f \quad \text{in } D, \quad u_0=0 \quad \text{on } C.$$
(Poisson's problem)

Let T, T^* be as in § 1. Example 2. Now u is a continuous and piecewise smooth function vanishing on C, and v, 2-component vector function, is chosen so that $-\operatorname{div} v=f$. Then (2.3) takes the following form;

$$2\int_D u f\,dxdy-\int_D |\mathrm{grad}\,u|^2\,dx\,dy$$
$$\leqq \int_D |\mathrm{grad}\,u_0|^2\,dxdy \leqq \int_D |v|^2\,dxdy.$$

Example 2. Let u_0 be determined by

$$-\Delta u_0=0 \quad \text{in } D, \quad \frac{\partial u_0}{\partial n}=\psi \quad \text{on } C.$$

(Neumann's problem)

The results of § 1. Example 5 are applicable, where we take $(0, \psi)$ as f and (u, u_C) as (w, w_C). u is any function belonging to M_1, that is, a continuous and piecewise smooth function.

In order to find a vector function $v=(v_1, v_2)$ such that $T^*v=(0, \psi)$, the following consideration may be useful.

Suppose $\bar{v}\in M_2$, then putting

$$v=\left(\frac{\partial \bar{v}}{\partial y},\ -\frac{\partial \bar{v}}{\partial x}\right),$$

we observe that

$$\mathrm{div}\, v=0, \quad v_n=\frac{\partial \bar{v}}{\partial s}.$$

Hence, for the construction of v, it is sufficient to find $\bar{v}$ satisfying the conditions

$$\frac{\partial \bar{v}}{\partial s}=\psi \quad \text{on } C, \quad \bar{v}\in M_2. \tag{2.4}$$

Now (2.3) gives the following inequality:

$$2\int_C u\psi ds-\int_D |\mathrm{grad}\,u|^2\,dxdy$$
$$\leqq \int_D |\mathrm{grad}\,u_0|^2\,dxdy \leqq \int_D |\mathrm{grad}\,\bar{v}|^2\,dxdy.$$

§ 3. Bounds of the Value at a Point of the Solution of a Boundary Value Problem

In the following consideration Hilbert spaces may be complex unless otherwise stated. We denote the real part of a complex number z by $\Re e(z)$.

Lemma 2. Let v_0, v_1, v_2 be any vectors of a Hilbert space such that

$$(v_1-v_0,\ v_2-v_0)=0. \tag{3.1}$$

Then for any vector h, the following inequalities hold.

$$\left|\left(v_0-\frac{v_1+v_2}{2},\ h\right)\right| \leqq \frac{1}{2}\|v_1-v_2\|\cdot\|h\|, \tag{3.2}$$

$$\left.\begin{array}{l} |(v_0-v_1,\ h)| \leqq \|v_1-v_2\|\cdot\|h\|, \\ |(v_0-v_1,\ h)| \leqq \|v_1-v_2\|\cdot\|h\|. \end{array}\right\} \tag{3.3}$$

Proof. By virtue of (3.1), we have

$$\begin{aligned} \|v_1-v_0\|^2+\|v_2-v_0\|^2 &= \|v_1-v_0\|^2 \\ &\quad +\|v_2-v_0\|^2 \pm 2\Re e(v_1-v_0,\ v_2-v_0) \\ &= \|(v_1-v_0)\pm(v_2-v_0)\|^2 \\ &= \|v_1-v_2\|^2=\|2v_0-(v_1+v_2)\|^2 \end{aligned}$$

and hence,

$$\left.\begin{array}{l} \left\|v_0-\dfrac{v_1+v_2}{2}\right\|=\dfrac{1}{2}\|v_1-v_2\| \\ \max(\|v_0-v_1\|,\ \|v_0-v_2\|)\leqq\|v_1-v_2\|. \end{array}\right\} \tag{3.4}$$

Thus we obtain

$$\left|\left(v_0-\frac{v_1+v_2}{2},\ h\right)\right| \leqq \left\|v_0-\frac{v_1+v_2}{2}\right\|$$
$$\cdot\|h\|=\frac{1}{2}\|v_1-v_2\|\cdot\|h\|$$

Similarly, using the latter of (3.4), we deduce (3.3).

From Lemma 2, we arrive immediately at our main theorem, which is slightly different from its original form given by Kato [8].

Theorem 2. Let u_0 be a vector determined by the equation $T^*Tu_0=f$. For a given vector g belonging to the range of T^* we set $\xi=(u_0, g)$. Let u, u', v, v' be any vectors satisfying the conditions:

$$u,\ u'\in\mathfrak{D};\quad v,\ v'\in\mathfrak{D}^* \text{ and } T^*v=f,\ T^*v'=g. \tag{3.5}$$

Then the following inequality holds.

$$\left|\xi-\frac{1}{2}(\alpha+\beta)\right| \leqq \frac{1}{2}\varepsilon\delta, \tag{3.6}$$

where

$$\alpha=(u, g)+(f, u')-(Tu, Tu'),\ \beta=(v, v')$$
$$\varepsilon=\|Tu-v\|, \qquad \delta=\|Tu'-v'\|. \tag{3.7}$$

Proof. (3.5) implies $(Tu-Tu_0, v-Tu_0)=(u-u_0, f-f)=0$, therefore, we can adopt Tu_0, Tu, v for v_0, v_1, v_2 in (3.2) respectively. Next, we substitute $v'-Tu'$ for h in (3.2).

Then (3.2) yields (3.6) because of the following relations.

$$\begin{aligned} (Tu_0,\ v'-Tu') &= (Tu_0,\ v')-(Tu_0,\ Tu') \\ &= (u_0,\ g)-(f,\ u'), \end{aligned}$$
$$\begin{aligned} (Tu+v,\ v'-Tu') &= (Tu,\ v')-(v,\ Tu') \\ &\quad -(Tu,\ Tu')+(v,\ v')=(u,\ g)-(f,\ u') \\ &\quad -(Tu,\ Tu')+(v,\ v'). \end{aligned}$$

Remark 1. Making use of (3.3), we can obtain

$$|\xi-\alpha|\leqq\varepsilon\delta. \qquad |\xi-\beta|\leqq\varepsilon\delta. \tag{3.8}$$

These inequalities also give estimations of ξ but are less sharp than (3.6).

Remark 2. (3.6) can be derived directly without Lemma 2.

For example, we introduce u_0' (assuming its existence) and $F(\varphi, \psi)$ such that $T^*Tu_0'=g$ and $F(\varphi, \psi)=\|T\varphi-\psi\|^2$, $\varphi\in\mathfrak{D}$, $\psi\in\mathfrak{D}^*$. And we set

$$\begin{aligned}A&=F(u_0+u_0',\ v+v'),\\ B&=F(u+u',\ Tu_0+Tu_0'),\\ a&=F(u_0-u_0',\ v-v'),\\ b&=F(u-u',\ Tu_0-Tu_0').\end{aligned}$$

Since A, B, a, b are non-negative,

$$|(a-b)-(A-B)|\leqq a+b+A+B.$$

while by an elementary calculation, we have

$$a+b+A+B=2(\varepsilon^2+\delta^2),$$

$$(a-b)-(A-B)=8\Re e\left(\xi-\frac{\alpha+\beta}{2}\right).$$

Consequently,

$$\left|\Re e\left(\xi-\frac{\alpha+\beta}{2}\right)\right|\leqq\frac{1}{4}(\varepsilon^2+\delta^2). \tag{3.9}$$

Obviously we can replace u_0, u, v respectively by those multiplied by k ($k>0$), and replace u_0', u', v' respectively by those multiplied by $e^{i\theta}/k$ (θ; real). Thereby we obtain

$$\left|\Re e\left(e^{-i\theta}\left(\xi-\frac{\alpha+\beta}{2}\right)\right)\right|\leqq\frac{1}{4}\left(k^2\varepsilon^2+\frac{1}{k^2}\delta^2\right) \tag{3.10}$$

(3.10) reduces to (3.6) under the suitable choice of k and θ.

On the other hand, when the spaces are real, we can calculate upper and lower bounds of $\|T(u_0+u_0')\|^2$ and $\|T(u_0-u_0')\|^2$ according to Theorem 1, and consequently those of their difference $4(Tu_0, Tu_0')=4(u_0, g)=4\xi$. The results thus achieved can be verified to be equivalent to (3.9).

Remark 3. The estimation of ξ given by (3.6) is good when ε and δ are small. This is one of the reasons why we prefer $v'-Tu'$ to v' as h in (3.2), since in most applications it is often difficult to find v' such that $T^*v'=g$ and $\|v'\|$ is small.

Remark 4. In particular, if $\mathfrak{H}$ is a function space, e.g. $L^2(D)$ in § 1, and g is δ_P, the Dirac's delta function singular at a preassigned point P, ξ will reduce to the value of u_0 at P.

Of course, this use of delta function requires a later justification, which can be carried out by certain routine of the limiting procedures. However, since in cases of differential operators the equation $T^*Tu_0'=\delta_P$ is formally satisfied by the Green's function (this fact is itself suggestive in finding v'), we can establish the validity of formal results rather easily by making use of Green's theorem. Furthermore, if we put, for instance,

$$g=-\frac{\partial\delta_P}{\partial x},$$

then ξ will reduce to

$$\left(\frac{\partial u_0}{\partial x}\right)_P.$$

Examples. To apply (3.6) to a boundary value problem, where T, T^* are already known, it is only necessary to find trial vectors in accordance with (3.5). Among differential operators in § 1, we take up only two of them to illustrate how to construct trial vectors, though the other ones in § 1 can be dealt with quite similarly. Let $P=(x_0, y_0)$ be the preassigned point in D and δ_P be as in Remark 4. The distance between (x, y) and P is denoted by r.

Example 1. Let u_0 be determined by

$$-\varDelta u_0=f \ \text{ in } D,\quad u_0=0 \ \text{ on } C.$$

T and T^* are given in § 1. Example 2.

1°. Let g be δ_P. Then $\xi=u_0(P)$. Trial vectors are chosen so that the following conditions hold.

$$\left.\begin{aligned}&u\in\hat{M}_1,\ v\in M_1\times M_1,\ -\operatorname{div}v=f,\\ &u'=\frac{1}{2\pi}\log\frac{1}{r}+\tilde{u}',\ \tilde{u}'\in M_1,\ u'=0\\ &\qquad\qquad\qquad\qquad \text{on } C,\\ &v'=\operatorname{grad}\left(\frac{1}{2\pi}\log\frac{1}{r}\right)+\tilde{v}',\\ &\quad\tilde{v}'\in M_1\times M_1,\ \operatorname{div}\tilde{v}'=0.\end{aligned}\right\} \tag{3.11}$$

We observe that $-\operatorname{div}v'=g$ and $\delta=\|Tu'-v'\|$ is finite.

2°. Let g be $-\dfrac{\partial\delta_P}{\partial x}$. Then $\xi=\left(\dfrac{\partial u_0}{\partial x}\right)_P$. In this case we assume that $\partial f/\partial x$ is piecewise continuous and trial vectors must satisfy certain subsidiary conditions in addition to (3.5) as follows:

$$\begin{aligned}&u\in\hat{M}_1,\ \frac{\partial u}{\partial x}\in M_1,\quad \frac{\partial v}{\partial x}=\left(\frac{\partial v_1}{\partial x},\ \frac{\partial v_2}{\partial x}\right)\\ &\qquad\qquad\in M_1\times M_1,\quad -\operatorname{div}v=f;\\ &u'=\frac{1}{2\pi}\frac{\partial\log r}{\partial x}+\tilde{u}',\ \tilde{u}'\in M_1,\ u'=0 \ \text{ on } C;\\ &v'=\operatorname{grad}\left(\frac{1}{2\pi}\frac{\partial\log r}{\partial x}\right)+\tilde{v}'\\ &\qquad\tilde{v}'\in M_1\times M_1,\ \operatorname{div}\tilde{v}'=0.\end{aligned}$$

Integrals appearing in α, β should be regarded as their principal values.

Example 2. Let u_0 be determined by

$$\Delta u_0=0 \quad \text{in } D, \quad \frac{\partial u_0}{\partial n}=\psi \quad \text{on } C$$

and

$$I_C(u_0)=\int_C u_0\, ds=0\,.$$

We use T, T^* defined in § 1. Example 5, restricting the domain of T to the set of functions satisfying $I_C=0$. Setting $g=(\delta_P, 0)$, we have $\xi=u_0(P)$. Noting $f=(0, \psi)$, we choose trial vectors so that the following conditions hold. $(u, u_C)\in\mathfrak{D}$ is identified with u.

$$\begin{aligned}
&u\in M_1, \quad I_C(u)=0, \\
&\qquad v\in M_1\times M_1, \quad \operatorname{div} v=0, \quad v_n=\psi \\
&u'=\frac{1}{2\pi}\log\frac{1}{r}+\tilde{u}', \quad \tilde{u}'\in M_1, \quad I_C(u')=0 \\
&v'=\operatorname{grad}\left(\frac{1}{2\pi}\log\frac{1}{r}\right)+\tilde{v}', \\
&\qquad \tilde{v}'\in M_1\times M_1, \quad \operatorname{div}\tilde{v}'=0, \quad v_n{}'=0.
\end{aligned}$$

In constructing v, v' the device referred to in § 2. Example 2 may be of use.

§ 4. Improvement of Bounds

When additional trial vectors satisfying certain conditions are available, we can improve the approximation given by (2.3) or (3.6). We will deal with (3.6) only, since similar and rather simpler discussions are possible concerning the latter.

Let $\mathfrak{R}$ and $\mathfrak{N}^*$ be the range of T and the 0-point set of T^* (the set of v satisfying $T^*v=0$) respectively. It is well known that $\overline{\mathfrak{R}}$ (the closure of $\mathfrak{R}$) and $\mathfrak{N}^*$ are mutually orthogonal and their direct sum is $\mathfrak{H}$. In other words,

$$\overline{\mathfrak{R}}\oplus\mathfrak{N}^*=\mathfrak{H}'\,. \tag{4.1}$$

Now, we consider some methods to make ε in (3.6) small.

Let $\{\varphi_i\}$, ψ_0, $\{\psi_i\}$ be as follows.

$$\left.\begin{aligned}
&\{\varphi_i\}=\{\varphi_1, \varphi_2,\cdots\}, \quad \varphi_i\in\mathfrak{D}, \\
&\{\psi_i\}=\{\psi_1, \psi_2,\cdots\}, \\
&\psi_0\in\mathfrak{D}^*, \quad T^*\psi_0=f \text{ and } \psi_i\in\mathfrak{N}^*. \\
&\qquad\qquad (i=1,\ 2,\ldots)
\end{aligned}\right\} \tag{4.2}$$

1°. Setting $u_n=\sum_{i=1}^n a_i\varphi_i$, $v_m=\psi_0+\sum_{k=1}^m b_k\psi_k$, we note that u_n, v_m satisfy (3.5). We determine the value of a_i, b_k by minimizing $\varepsilon^2=\|Tu_n-v_m\|^2$.

From the relation

$$\varepsilon=\|\psi_0-\textstyle\sum_{i=1}^n a_iT\varphi_i+\sum_{k=1}^m b_k\psi_k\|$$

we observe that, when optimum values of a_i, b_k are used, $\varepsilon\equiv\varepsilon(u_n, v_m)$ reduces to the norm of the projection of ψ_0 on the orthonormal complement of the subspace spanned by

$$\{T\varphi_1,\cdots, T\varphi_n, \psi_1,\cdots, \psi_m\}\,.$$

Further we notice that by virtue of (4.1), $\{a_i\}$ and $\{b_k\}$ can be determined separately. In fact, if $\{T\varphi_i\}$, $\{\psi_k\}$ are both orthonormal, a_i, b_k reduce to the "Fourier coefficients" of ψ_0, that is, $a_i=(\psi_0, T\varphi_i)$ $b_k=-(\psi_0, \psi_k)$. It is evident that, when $\{T\varphi_i\}$ and $\{\psi_k\}$ span $\mathfrak{R}$ and $\mathfrak{N}^*$ respectively, $\varepsilon(u_n, v_m)$ tends to 0 for any ψ_0 as $n\to\infty$, $m\to\infty$.

2°. The iterative method used by Greenberg [7] is generalized in the following form. Here we assume that spaces are real.

Trial vectors u_{n+1}, v_{n+1} at the $(n+1)$-th step are given in terms of u_n, v_n, φ_n and ψ_n.

$$\left.\begin{aligned}
&u_{n+1}=u_n+a_n\varphi_n, \quad v_{n+1}=v_n+b_n\psi_n \\
&\qquad\qquad\qquad (v_0=\psi_0) \\
&\text{where} \\
&a_n=-\frac{(Tu_n-v_n, T\varphi_n)}{\|T\varphi_n\|^2} \\
&\quad\ =\frac{(f, \varphi_n)-(Tu_n, T\varphi_n)}{\|T\varphi_n\|^2} \\
&b_n=\frac{(Tu_n-v_n, \psi_n)}{\|\psi_n\|^2} \\
&\quad\ =-\frac{(v_n, \psi_n)}{\|\psi_n\|^2}\,.
\end{aligned}\right\} \tag{4.3}$$

Though at each step the value of ε decreases, it can occur that ε does not tend to 0 as $n\to\infty$ even if $\{T\varphi_i\}$ and $\{\psi_i\}$ span $\mathfrak{H}'$ together. For instance, suppose that $(\psi_1, \psi_k)=0$, $(\psi_2, \psi_k)=0$ $(k=3, 4,\cdots)$. Then ε^2 is not less than the square of the component of Tu_2-v_2 in the plane spanned by ψ_1 and ψ_2. The component mentioned above is, in general, not zero unless ψ_1 and ψ_2 are orthogonal.

Analogous considerations concerning δ are omitted here.

§ 5. Numerical Example

As a numerical example of our results, we apply (3.6) to the same problem treated by Greenberg [7], which is also the one considered in § 3. Example 1, where $f\equiv 1$ and D denotes the square domain in the xy-plane with vertices at $(1, -1)$, $(1, 1)$, $(-1, 1)$, $(-1,$

$-1)$ and C is the boundary of this square.

In other words, we treat the Poisson's equation,

$$-\Delta u_0=1 \quad \text{in } D, \quad u_0=0 \quad \text{on } C. \tag{5.1}$$

Let the point P in § 3. Example 1. be the origin. Then ξ reduces to $u_0(0,\ 0)$. According to (3.11) and noting the statement in § 4. 1°, we set

$$u_n=\textstyle\sum_{i=1}^n a_i\varphi_i, \qquad v_n=\psi_0+\sum_{i=1}^n b_i\psi_i,$$

$$u_n'=\varphi_0'+\textstyle\sum_{i=1}^n a_i'\varphi_i'$$

$$v_n'=\psi_0'+\textstyle\sum_{i=1}^n b_i'\psi_i'$$

where

$$\psi_0=-\frac{1}{2}\boldsymbol{r}=-\frac{1}{2}(x,\ y),$$

$$\psi_0'=\operatorname{grad}\left(\frac{1}{2\pi}\log\frac{1}{r}\right)=-\frac{1}{2\pi}\frac{\boldsymbol{r}}{r^2}$$

$$\varphi_0'=\begin{cases}\dfrac{1}{2\pi}\log\dfrac{1}{r} & (r\leqq 1)\\[2ex] 0 & (r\geqq 1)\end{cases}$$

$$\varphi_1=\varphi_1'=(x^2-1)(y^2-1),$$

$$\varphi_2=\varphi_2'=(x^4-1)(y^4-1),$$

$$\psi_1=\psi_1'=\operatorname{grad}(\Re e(z^4)),$$

$$\psi_2=\psi_2'=\operatorname{grad}(\Re e(z^8)). \qquad (z=x+iy)$$

We use the optimum values of a_i, b_i, a_i' and b_i' stated in § 4. 1°. In calculation of quantities in (3.7), it is convenient to use the elimination algorithm*.

The results are shown below, where we introduce A, U, L and E_R defined by the relations

$A=(\alpha+\beta)/2=$ the approximating value of $u_0(0,\ 0)$,

$U=A+\varepsilon\delta/2=$ the upper bound,

$L=A-\varepsilon\delta/2=$ the lower bound,

$E_R=\varepsilon\delta/2A=$ the relative error.

	$n=0$	$n=1$	$n=2$
a_1		0.3125	0.2399
a_2			0.0529
b_1		0.0486	0.0453
b_2			−0.0013
a_1'		0.0220	−0.0388
a_2'			0.0443
b_1'		0.0111	0.0117
b_2'			0.0003
ε^2	0.667	0.00741	0.000338
δ^2	0.0175	0.00929	0.00475
U	0.339	0.2961	0.2953
A	0.284	0.2918	0.2946
L	0.229	0.2876	0.2939
E_R	20%	1.5%	0.23%

§ 6. Concluding Remarks

1. The fact that some differential operators in mathematical physics can be reduced to the form T^*T, where T and T^* are of familiar types, is much advantageous from the view point of applications of the general theory of Hilbert spaces. For instance, when T and T^* are those in § 1. Example 2, the relation (4.1), that is, $\mathfrak{R}\oplus\mathfrak{N}^*=\mathfrak{H}'$ corresponds to "Helmholtz's theorem" of vector functions. In the subsequent papers we will apply our T^*T-method to different subjects.

2. We have seen that some differential equations with inhomogeneous boundary conditions can be reduced to the problems of linear operators in suitable Hilbert spaces (§ 1. Example 5. 6.).

When we must treat such a problem as $\Delta u_0=0$ in D, $u_0=f$ on C, we can transform this problem to the one considered in § 1. Example 2. by a well-known method. An alternative way is to define suitable Hilbert spaces and decompose directly the operator in question but these spaces are of a different type and hence we have not introduced them in this paper.

3. In order to make clear the intimate relation between the hypercircle method [15] and our T^*T-method, it seems sufficient to indicate the correspondence between notions of the former method and those of ours. Notions and propositions in the hypercircle method are expressed with the terminology of the elastic theory, from which it had started and to which it was applied.

Some of the correspondence mentioned above are as follows.

Hypercircle method	T^*T-method
state vector S	vector v of $\mathfrak{H}'$
solution vector S_0	Tu_0 (in § 3.)
S satisfies the condition of the compatibility.	v belongs to the range of T.
stress equation	equation $T^*v=f$

4. Concerning the problem of § 3, some authors' results correspond to (3.8) rather than to (3.6). Furthermore, in their papers we observe a few different devices to avoid the difficulty stated in § 3. Remark 4. A related survey has been given by Maple [9].

---

* See P. S. Dwyer: Linear Computations, New York, (1951) p. 168.

In conclusion the author wishes to express his sincere thanks to Prof. T. Kato for his kind directions and advices in writing this paper as well as for his continual teaching in disciplines of mathematical physics.

References

1) P. Cooperman: Quart. Appl. Math. **10** (1953) 359.

2) J. B. Diaz and H. J. Greenberg: J. Math. Phys. **27** (1948) 193.

3) J. B. Diaz and A. Weinstein: J. Math. Phys. **26** (1947) 133.

4) J. B. Diaz and A. Weinstein: Amer. J. Math. **70** (1948) 107.

5) J. B. Diaz: Memoria publicada en Collectanea Mathematica **4** (1951).

6) G. Fichera: J. Math. Phys. **29** (1950) 59.

7) H. J. Greenberg: J. Math. Phys. **27** (1948) 161.

8) T. Kato: Math. Ann. **126** (1953) 253.

9) C. G. Maple: Quart. Appl. Math. **8** (1950) 213.

10) F. J. Murray: Trans. Amer. Math. Soc. **37** (1935) 301.

11) J. v. Neuman: Ann. of Math. **33** (1932) 294.

12) W. Prager and J. L. Synge: Quart. Appl. Math. **5** (1947) 241.

13) M. H. Stone: Linear Transformations in Hilbert Space. (1932).

14) J. L. Synge: Proc. Roy. Soc. **A 191** (1947) 447.

15) J. L. Synge: Quart. Appl. Math. **6** (1948) 15.

16) J. L. Synge: Proc. Roy. Irish. Acad. **A 53** (1950) 41.

17) B. v. Sz. Nagy: Spektraldarstellung linearer Transformationen des Hilbertschen Raumes. (1942).

18) K. Washizu: J. Math. Phys. **32** (1953) 118.

JOURNAL OF THE PHYSICAL SOCIETY OF JAPAN Vol. 10, No. 1, JANUARY, 1955

Formation Energy of Superlattice in Ni_3Fe (III).

Kinetics of the Superlattice at the Formation Stage with Long Range Order

By Shūichi IIDA

Department of Physics, Faculty of Science, University of Tokyo

(Received December 5, 1953)

The superlattice formation of Ni_3Fe in steady temperature annealings (at 500°C, 480°C and 460°C) was studied by direct observation of the heat of evolution and by measurement of specific heat on heating after each treatment. The multiple-step character of formation process of this superlattice disappeared gradually by lowering the temperature of anneal. All results are plotted on the same internal energy-temperature plane. The diagram is well explained by our theoretical treatment of the process which divides the process into two steps, with and without the long range order. But there was found a process of the third type, which remains after the second process has been completed. This becomes more distinct when the annealing temperature is lowered. For instance, when the disordered specimen was rapidly cooled to 460°C, and annealed at this temperature, it was observed that the development of order looks as though it reaches an apparent saturation after about 80 hours annealing. But, measurements of specific heat on heating of the corresponding specimen showed that the internal energy of the specimen is about 170 cal/atom higher than that of true equilibrium state at 460°C. This type of process, which has a relaxation time of the order of a month, will presumably be related to the antiphase problem. The nucleation and antiphase problems in superlattice are also discussed. The specimen which was quenched from 700°C shows an anomalous generation of heats between 230°C and 420°C on heating. This will be an important phenomenon for the formation process of this superlattice.

§ 1. Introduction

Since the suggestion of O. Dahl[1], many works has been done to prove the existence of superlattice Ni_3Fe. A detailed study of this alloy was given by S. Kaya[2]. He observed the time change of the electric resistivity at steady temperature annealings. The specimen alloy was first heated at a temperature sufficiently above the critical temperature and was cooled rapidly to the temperature just ten degrees below. Then the time change of the electric resistivity was observed until it reached its equilibrium value at this temperature. After that, the specimen was again cooled rapidly to the temperature ten degrees further below, and the time change of the electric resistivity was again observed. Starting from 550°C, the procedure was repeated to 440°C at every ten degrees. The results were as the followings;

(1) Above 490°C, time change of electric resistivity is hardly observed.

(2) At 490°C, the electric resistivity exhibits a drastic change and it continues for about 7 days at this temperature.

(3) Below 490°C, the necessary duration of annealing at each temperature to obtain the equilibrium is several ten hours.

The results show that the alloy has a typical A_3B type superlattice and the critical temperature is just above 490°C. However, about the relaxation characteristics of the variation of electric resistivity at 490°C, he found an unexpected phenomenon. Below 490°C the time change of electric resistivity at constant temperature was simple. It can be described by a single relaxation time constant. But, at 490°C, the variation seems to reach an apparent saturation after about 10 hours annealing. After that the rate of variation increases again gradually to reach its maximum at about 40 hours annealing and then gradually decreases to zero after about 7 days annealing.

This phenomenon was studied by the present author in paper I[3] of this study, by using calorimetric method. He measured the time change of internal energy of this alloy at 490°C annealing. It was shown that the variation of internal energy also exhibits the above mentioned anomalous multiple-step character. He also showed that the process can be divided into two processes. Then he assumed that the development of order consists of two steps, with and without long range order formation. He assumed further that the process A, development of order without long range order, has no critical temperature on cooling and will show a simple relaxation character during the annealing at a constant temperature. On the other hand the process B, the development of order with long range order, has a sharp critical temperature (just above 500°C)*, and comes into action only below the critical temperature. Further he concluded that the process A is of a cooperative nature. Namely, when a specimen was cooled slowly from high temperature to just below the critical temperature, the initial state of the specimen will be a state equal to an equilibrium state at just above the critical temperature which has no long range order. Though, by passing through the critical temperature, the equilibrium nature of this state without long range order is lost, it will still have some equilibrium property just like as super-cooled liquid. Therefore, the development of long range order must start with a small rate at the beginning. The rate increases gradually, reaches its maximum, and then decreases to zero.

He assumed that the main process at the critical temperature of this alloy is the process B. The observed existence of the process A is only due to the preceding rapid cooling. (10 degrees in Kaya's case, 100 degrees for the author's case.)

In the paper II[4] of this study, the process A was studied by measuring specific heat on cooling. It was shown that the development of local order without long range order begins already at 580°C on cooling, and have a relaxation time of hours at 510°C. As predicted by the theory[5], it has no critical temperature and shows a simple relaxation characteristic.

Now, below the critical temperature, the development of order will consist of two different types of processes A and B. In the paper I we showed that, at 490°C, these two types of processes could be separated clearly. The first problem to be studied in this paper is to answer the question how these two types of processes appear by changing the temperature of anneal.

§ 2. Development of Order Below the Critical Temperature

In the paper I, we made a number of measurements of specific heat to observe the associated change of internal energy in the annealing at 490°C. At the same time, direct measurements of heat of evolution of the specimen in the annealing at 490°C were carried out. The agreement of these two experiments was satisfactory. Therefore we use the latter method for the present study.

The specimen alloy and the apparatus used here were the same as those in the previous two papers. (74.59% Ni, 24.37% Fe, 0.71% Mn). Ordering behaviours were observed at 500°C, 480°C, and 460°C. The specimen was first heated in vacuum to 850°C, and after keeping thirty minutes at this temperature it was cooled rapidly to the annealing temperatures. After about thirty minutes at each of the annealing temperatures, we could start to observe the temperature difference $\Delta T(t)$ between the specimen and the surrounding copper wall. This temperature difference ΔT, which is required to keep the temperature of the specimen constant, is proportional to the rate of internal energy decrease $-dU/dt$, namely

$$-dU/dt = k\Delta T\ ,$$

where k is a proportionality constant. The observations were continued until the difference of temperatures ΔT became zero within the experimental error. Then the specimen was cooled rapidly in a furnace to the room temperature. After that the specimen was heated again and its specific heats on heating were observed from 100°C to 700°C.

The proportionality constant k is determined by assuming that the total heat evolved at annealing is equal to the difference of areas between the specific heat curve on heating after each measurement and the specific heat curve on cooling at each measurement. The specific heat curves on cooling were obtained by using the results of Fig. 4 of the paper II (there, the specific heats on cooling of the specimen with various rates of cooling were observed.). Fig. 1 shows the temperature-time histories of these measurements. Fig. 2 shows the specific heat-temperature curves on cooling during these experimental processes. As the total energy decrease at each annealing is large enough, the incorrectness of the estimation of each cooling curve causes no serious error. It will be noticed that the alloy has a ferromagnetic transformation at 575°C, and the main part of the anomaly shown in Fig. 2 is due to this transformation. The final results are shown in Fig. 3, Fig. 4, and Fig. 5. At 500°C, we could obtain almost perfect separation of the two types of process,

---

* The specimen used in the present study contains 0.7% Mn. It gives somewhat different values for critical temperature (just above 500°C) and relaxation times, compared with the results by S. Kaya.

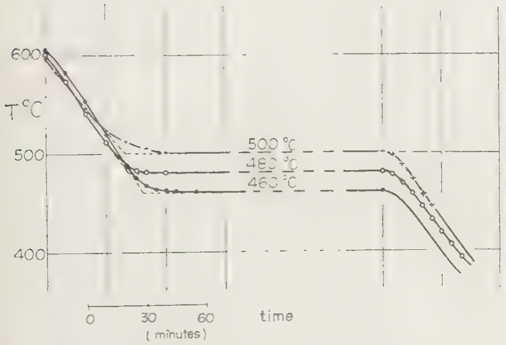

Fig. 1. Temperature-time histories of the three experiments. The total times annealed at 500°C, 480°C and 460°C are 52 hours, 50 hours, and 81 hours respectively.

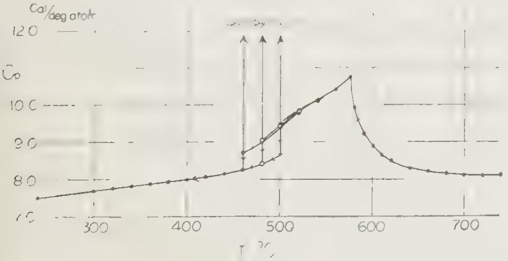

Fig. 2. Specific heats-temperature curves on cooling corresponding to the three experiments. The straight lines at 500°C, 480°C, and 460°C mean the specimen alloy was kept at these temperatures and there the heat of evolution was observed.

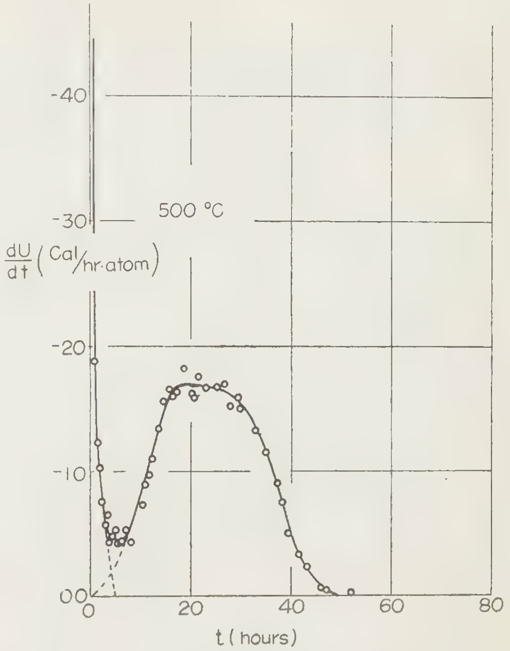

Fig. 3. The rate of the internal energy decrease plotted against the time of anneal at 500°C.

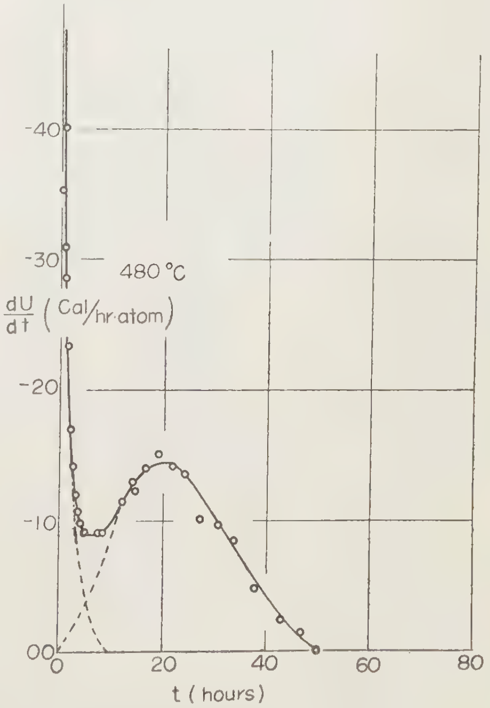

Fig. 4. The rate of the internal energy decrease plotted against the time of anneal at 480°C.

---

* The time interval of each neighbouring points in all specific heat curves on heating is always two minutes. In the measurements of specific heat, the specimen is heated with constantly supplied energy.

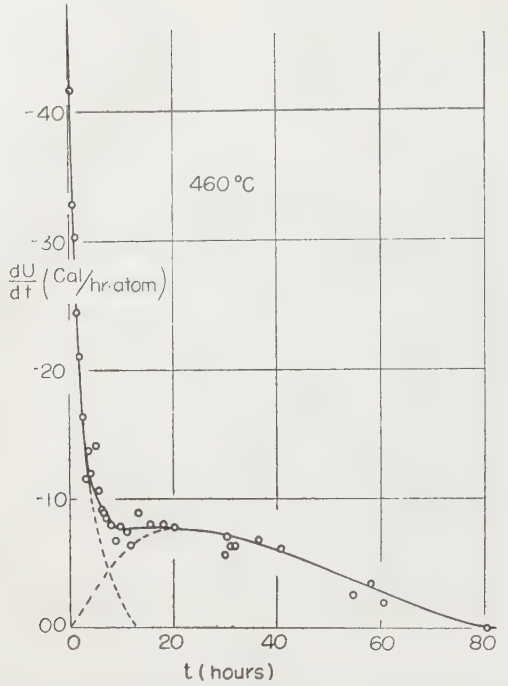

Fig. 5. The rate of the internal energy decrease plotted against the time of anneal at 460°C.

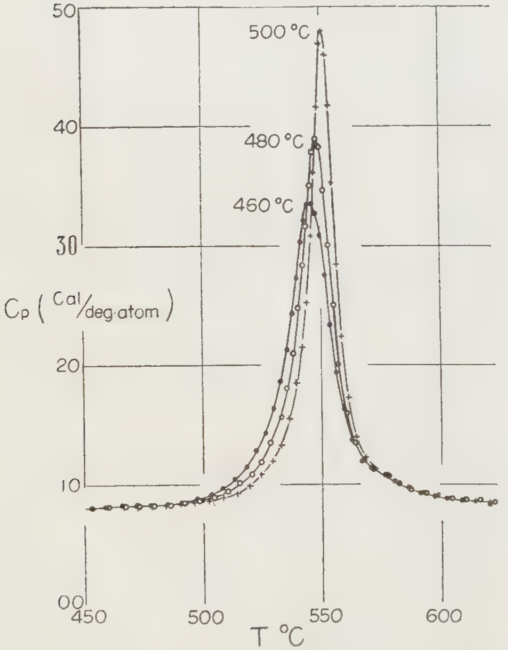

Fig. 6. Anomalous specific heat curves on heating after the annealings at 500°C, 480°C and 460°C.

and a clear form of the process B was observed. In Fig. 6 and Fig. 7, we show the specific heat curves on heating after the experiments.*

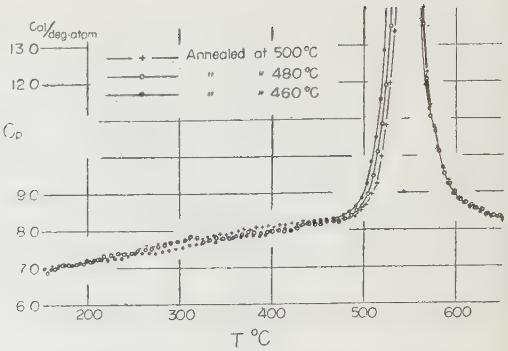

Fig. 7. Specific heat curves on heating in a normal temperature range after the annealings at 500°C, 480°C and 460°C.

The differences between the internal energy at room temperature of the specimen after annealing treatment and that of the specimen quenched from 600°C, are 578, 561, and 557 cal/atom for the annealing at 500°C, 480°C, and 460°C respectively. The values were calculated from the anomalies of specific heat on heating. Although the total amounts of internal energy decreased during the treatments were almost same for the three cases, the internal states of order seems to be quite different. By lowering the temperature of anneal, the order-disorder transformation on heating started at lower temperature as can be seen in Fig. 6, and Fig. 7.

More detailed information about the nature of the superlattice formation is obtained if the rate of the internal energy decrease are plotted against the amounts of energy which has been liberated by the time corresponding to that rate. These are shown in Fig. 8. In the figure, we can distinguish two types of formation process as shown by dotted lines in the figure.

In Fig. 9, the results are plotted on $\Delta U-T$ diagram. In the figure, the ordinate ΔU indicates a part of the internal energy decrease due to superlattice formation $U(T)-U_0(T)$, as in usual theoretical treatments. But in this case, the ferromagnetic transformation makes the definition of $U_0(T)$ (zero point of internal energy at each temperature) unclear. Therefore, we define $U_0(T)$ as the internal energy corresponding to the internal energy of perfectly disordered specimen at that temperature. The specific heat on cooling corresponding to this perfectly disordered state was already calculated in the paper II[4], as a limit case of cooling experiments with various rates of cooling. The results of the paper II, especially specific heat on cooling corresponding to various rates of cooling were fully used to construct the diagram. Straight lines corresponding to 500°C, 480°C, and 460°C indicate courses of the above three experiments. Upper circles show the internal energy of the initial states of the annealing and the lower circles that of the final states. The intermediate circles mean the states at which the process A just has completed. These are calculated from the results of Fig. 8. The circles at 510°C, showing the growth of local order, are taken from the paper II, and the circle at 490°C is the result of the paper I of this study corresponding to the annealing for 150 hours at 490°C. Other data used in this figure will be shown later. The curves shown by broad lines mean the internal energy-temperature relations for the equilibrium state of this alloy. They show a typical scheme of A_3B type superlattice. Here, as noticed already, not only the part of energy of lattice vibration but also the part of energy associated with ferromagnetic transformation are eliminated in the figure. Actually, there are some complications due to their coupling with the atomic ordering. The problem will be discussed later. The most significant results obtained from the diagram are a remarkable discrepancies between the energies corresponding to the true equilibrium states at each of the annealing temperatures and the energies obtained apparently as equilibrium. However, the discussion about this problem will be given later after the following several experiments. Here, only the observed variation characteristics of the processes A and B shown in Fig. 3, 4, and 5 are discussed.

Now, two different effects (a) and (b) are expected from the lowering of annealing temperature. The coefficient of atomic diffusion will decrease by lowering the temperature. It results in a decrease of the reaction rate and accordingly an increase of relaxation time. We call it the effect (a). Next, there will be a second effect originating from the temperature variation of cooperative character of the disorder-order transformation. The effect of this kind, which we call the effect (b), will be expected to be very different in the processes A and B, so that the detailed total effects will be discussed respectively hereafter.

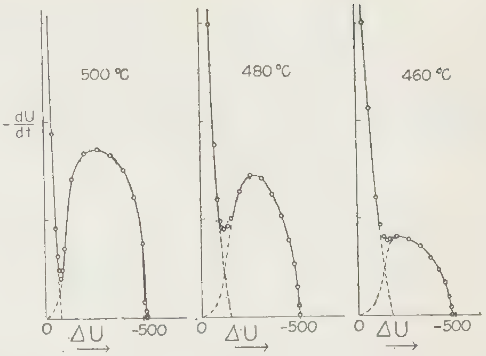

Fig. 8. The rate of the internal energy decrease as functions of the amount of energy liberated.

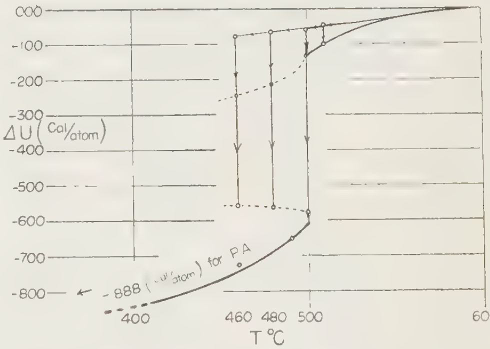

Fig. 9. Internal energy-temperature diagram of this Ni_3Fe superlattice.

(1) Process A, without long range order.

The total amount of energy decrease in this process will increase if the annealing temperature is lowered. (see Fig. 9.) This will make the initial rate of reaction larger and will counterbalance the tendency due to the effect (a). Thus, as the net result, the initial rate remains unchanged and only the time of reaction increases.

(2) Process B, with long range order.

The process of this type at the critical temperature has been concluded as one of the cooperative rate process characterized by a bell shaped curve in $(-dU/dt-t$ diagram. For convenience we define $\left|\frac{dU}{dt}\right|_M$, t_M, and t_T as the maximum value of $\left|\frac{dU}{dt}\right|$, the time of annealing t corresponding to this maximum value, and the total time of annealing. Then by the effect (a), t_M and t_T will increase and

$\left|\dfrac{dU}{dt}\right|_M$ will decrease. But the effect (b) will have a special influence on t_M. Namely, the degree of instability of initial state having no long range order will increase more and more by lowering the annealing temperature. The tendency will accelerate the formation of long range order to result in smaller t_M. These two effects will counterbalance, and the t_M becomes invariant as shown in the figures.

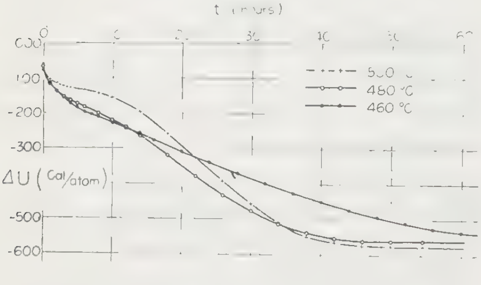

Fig. 10. The amounts of energy decrease are plotted against the times of anneal at 500°C, 480°C, and 460°C.

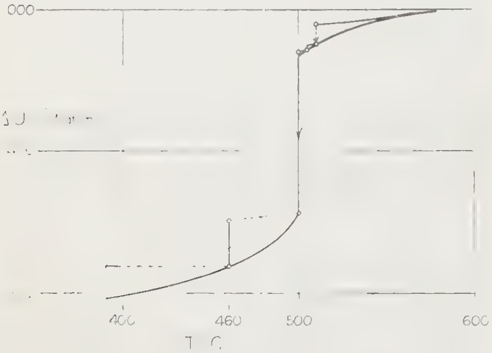

Fig. 11. Internal energy-temperature history in the multiple-step heat treatment.

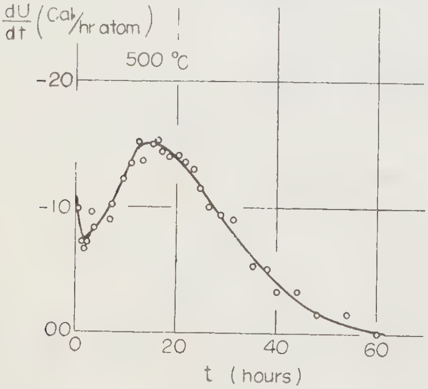

Fig. 12. The rate of the decrease in the internal energy plotted against the time of anneal at 500°C in the multiple-step heat treatment.

The actual curve of observation can be regarded as superpositions of the above two types of process A and B. When the temperature of annealing is lowered, the separation of two processes A and B becomes more and more obscure as expected from the above simple consideration. In Fig. 10, the total amount of energy decrease obtained by integrating the results of Fig. 3, Fig. 4, and Fig. 5 are plotted against the time of annealing.

The cooperative formation of long range order in the above sense will be a general character of disorder-order transformation in A_3B type superlattices, though there will be some differences about the nafure of cooperation for various alloys.[6),7),8),9)]

§ 4. Development of Atomic Order in a Multiple-step Heat Treatment

If the process A is a simple reaction of local ordering without long range order, the total amount of this type of ordering will decrease if the specimen has been annealed just above the critical temperature. Then, after this preannealing, the development of atomic order at a temperature just below the critical temperature will have an ideal form of the process B.

This was shown experimentally. Fig. 11 shows the procedure of the experiment. The specimen was first slowly cooled down to 510°C in vacuum, kept there for 5 hours which is sufficient to reduce the rate of internal energy decrease to zero, and then cooled down to 505°C, keeping there for 3 hours. After that the temperature of the specimen was lowered to 500°C and the evolution of heat was observed continually at this temperature by using the same method as before. The results are shown in Fig. 12.

After obtaining an equilibrium at 500°C, the specimen was cooled rapidly to 460°C, and again the evolution of heat was observed at this temperature. The results are shown in Fig. 13. After that, the specimen was cooled rapidly in a furnace and then the specific heat-temperature curve on heating was observed as before. It is shown in Fig. 17.

Now, in Fig. 12, we have a refined form of the process B. The process A is very much diminished in this experiment. But we note that the minimum rate of reaction which appears after about two hours anneal is rather high compared with the corresponding value of the previous experiment at 500°C (Fig. 3). The maximum rate appears at an earlier stage of annealing, compared with the latter. These effects are contradictory to the conclusion of simple mathematical treatments,[5),9)] according to which the development of long range order in these conditions must start more slowly. The discrepancy may be attributed to a certain nucleation process. If we assume that the nucleation difficulty is diminished to some extent by the development of local order, then our results can be understood.

The curve of Fig. 13 will be regarded as a further development of order in a crystal lattice which has a certain long range ordering. It shows again a simple rate process, The data are plotted in Fig. 14, against the amounts of the internal energy decrease, and the amounts of the internal energy decrease as functions of times of annealing are plotted in Fig. 15.

Now, a most important result obtained is a large discrepancy of internal energy between the state corresponding to the final state of the above experiment at 460°C and the state corresponding to the apparent final state of the previous experiment at 460°C. This is already shown in Fig. 9. There, the equilibrium curve below the critical temperature was obtained from the data of the paper I, and data of an experiment of perfect annealing which will be described in section 6. From Fig. 8, it will be quite clear that the final state of the previous experiment corresponds almost exactly to the final state of the process B. Therefore, the further development of order towards the equilibrium state must proceed with a sufficiently slow rate of reaction. Y. Sichijo[10)] found that when the alloy was annealed at 450°C, the specific resistivity of this alloy could not reach to its final value even after a month's anneal. This fact supports our results.

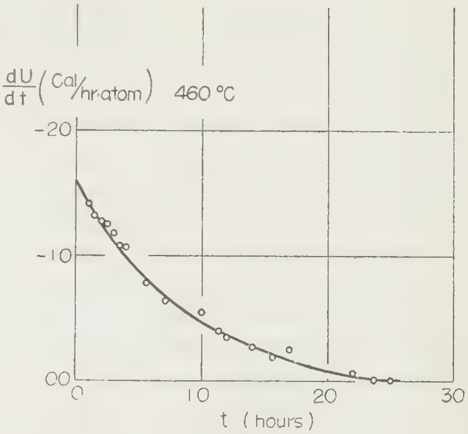

Fig. 13.

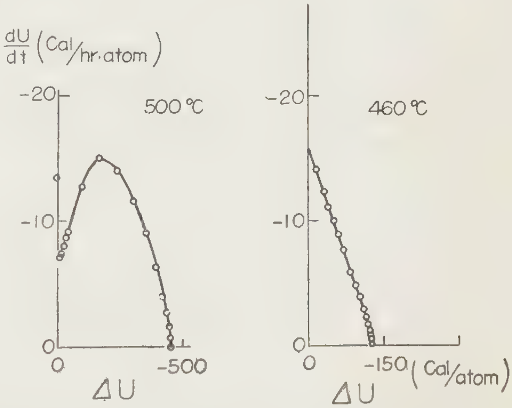

Fig. 14. The rate of the decrease in the internal energy as functions of the amounts of energy decrease at 500°C and 460°C respectively in the multiple-step heat treatment.

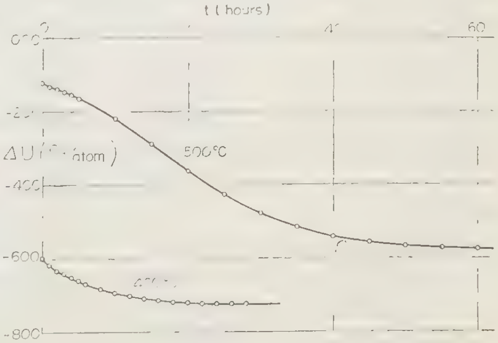

Fig. 15. The amounts of the internal energy decrease are plotted against the times of anneal at 500°C and 460°C in the multiple-step heat treatment.

The results can be explained by the nucleation and antiphase theory. According to the nucleation theory of superlattice, the stability of a superlattice nucleus is a function of its volume and temperature[11)]. The probability of generation of a nucleus is also a function of its volume, temperature, and the degree of order of the matrix. Just below the critical temperature the critical size of the stable nucleus is large and the probability will be small. In the multiple-step heat treatment, the specimen was first annealed at just below the critical temperature. At this temperature the probability of generation of stable nuclei will be small and therefore there will be less antiphases in the final state. Thus the further development of order at 460°C will be mainly due to the development of local order within the individual antiphases. Then, the development will be accomplished easier and there will be no complication about the antiphase problem. Boundary energy of the antiphase will have no serious contribution to the total energy. But, in the previous experiment of disorder-order transformation at 460°C, the starting state at 460°C was a nearly perfect disorder. Therefore, there will be a large probability of generation of nuclei. These nuclei will grow almost independently at first, then come to contact with each other and finally will become antiphase domains. The energy excess of about 180 cal/atom compared with the final equilibrium state will be left for the single phase reaction of these antiphase domains. The process must have a long relaxation time and makes the last stage of the disorder-order transformation of this alloy, which we had reported already as the fourth stage of the transformation in the paper I.

§ 5. Nucleation and Antiphase Problems

As described already, the anomalous parts of the results obtained seem to be related closely to the nucleation and antiphase mechanism. The problem will be discussed here from a general standpoint of superlattice theory.

We must first distinguish between the disorder-order transformation as a non-equilibrium process, and the temperature variation of order corresponding to the equilibrium states.

As to the equilibrium states, it will be possible to define sharply its long range order. In an equilibrium state there is no long range order above the critical temperature. Below that there is a definite long range order. The whole lattice is divided into several sublattices which are occupied by each kind of atoms only. There will be no antiphase at least in an idealized condition. Actually, there may be antiphases, but they will have sufficient sizes and will be bounded clearly with one another, just like a polycrystalline material. In the subboundaries and dislocations the situation will be complicated. But the volume of such parts will be sufficiently small. There is no ambiguity for the definition of long range order.

As to the non-equilibrium process, there are two different aspects to describe the transformation below the critical temperature. For simplicity, we consider only a case where the disordered alloy at a high temperature is rapidly cooled to some temperature below the critical temperature, and is annealed at this temperature. One is that there is uniform development of local order, but as the temperature is below the critical temperature, the arrangement gradually changes into an assembly of small antiphases and these antiphases gradually grow by the movement of antiphase boundary at expense of neighbouring small antiphases until they grow to sufficient sizes. The other is that there may be at first a uniform development of local order as before, but, if the temperature is lower than the critical temperature, there is some probability to produce highly ordered nuclei in the matrix, and, if the stable nucleus once appeared, they will grow and touch with one another. Here, we define a nucleus as a part of a crystal (1) which has a long range order and (2) has a fairly large size, so large that thermal agitation can not alter the phase of this long range order. Namely the change of the phase can only occur by movement of boundary of other nuclei.

The difference of the two aspects comes from the different view point for the possibility to distinguished the ordered nucleus from the surrounding disordered matrix. Then what is the driving force to create a long range order? So long as we consider the nearest neighour energy E_σ only, the situation seems to be in favour to the former theory and I. G. Edmunds and R. M. Hinde[12] asserted in their study of $AuCu_3$ superlattice that the formation of long range order is only a secondary effect of the development of short range order affected by a cooperative character of the ordering configuration, and the growth of antiphases will be more accidental in this alloy. But, there is a doubtless reason to indicate that other kinds of energy must play a fairly important rôle in the formation of superlattice. In fact, if we consider only the nearest neighbour energy E_σ, we can not have a superstructure with long range order at all in A_3B type superlattices which is a face-centered cubic lattice as Ni_3Fe.13),14) Since two of the nearest neighbours, of one atom can be nearest neighbours, there are infinite possibilities of configurations having no long range order and having maximum nearest neighbour energy. H. Sato emphasized the importance of the second nearest neighbour interaction in his study of Fe-Al and Fe-Si alloys.15),16)

Following the usual quantum mechanical treatment, the energy of an atom in the lattice must be related to the whole configuration of the neighbouring atoms. There is an evidence for such a kind of configurational energy to exist even in the temperature range above the critical temperature in CuPt superlattice17). We call these kind of energy, containing second or third nearest neighbour energies, the configurational energy E_c. The principal rôle of the energy E_c will be its strong tendency to develop long range order. In face centred-cubic lattices, the development of long range order will be mainly due to the existence of this configurational energy E_c.

Moreover, we have a certain reason to expect the existence of an other kind of energy E_s. According to a recent idea of Fermi energy of superlattice, there are some alloys in which the decrease of Fermi energy attained by a subdivision of the Brillouin zones will have a considerable contribution to their superlattice formation.16),18),19),20) The energy of this kind is undoubtedly related to long range order.

We may think that such kinds of energy E_c and E_s play a fairly important rôle in the last stage of Ni_3Fe superlattice. The observed large difference of energy at 460°C, which amounts to about 180 cal/atom and has been attributed to a single phase process of antiphases (section 4) will be understood only by these considerations.

Next, the geometrical stability of antiphases in this alloy will be discussed. Even in an initial stage of ordering, the whole atomic configuration can be regarded as a large assembly of many small antiphases. Therefore, the stability of antiphases must be in a close connection with the relaxation character of ordering not only in the final stage but also in the whole stages. The Ni_3Fe superlattice has four antiphases. We suppose the number four is necessary for this alloy to show a sufficient stability of antiphases. The reason is based upon topological consideration. In a map, four colours are necessary and sufficient to paint the lands separately, and three colours are almost sufficient. In three dimentions four colours will be almost sufficient. If there is only two antiphases as the case of β brass, there is no possibility of antiphase grains to exist except an unstable case where the antiphase is an island surrounded completely by the other phase. If it is an island, the need for the minimum in energy of boundary surface makes the antiphase shrink, and there would be no stable antiphase. Moreover, it is possible in this alloy that many antiphases coexist without changing its nearest neighbour energy E_σ. This can be easily seen from the fact that there are close packed atomic planes of Ni only in the perfectly ordered arrangement, like as (100) plane. The atomic plane of this kind can be a stable boundary surface of antiphases in such a configuration. Such a boundary is much like a twin boundary and its surface energy will be so low that it will be necessary to consider a special mechanism for the boundary displacement. We believe that the long relaxation time of superlattice formation in Ni_3Fe is partly due to these geometrical reasons.

Therefore, if we assume that the contribution of configurational energy E_c is somewhat smaller in Ni_3Fe superlattice than in other superlattices, then the smaller E_c will be directly connected with the mentioned geometrical stability of antiphase, the driving force to develop long range order will be rather small in this alloy, and the observed cooperatiev formation of long range order will be explained. Moreover, the observed anomalous stability of antiphases at 460°C and the large energy remained for a single phase process will also be understood by this assumption.

Finally we may mention the relationship between the lattice imperfection (impurities, defects, and dislocations) and the disorder-order transformation. Undoubtedly the imperfections play a principle rôle on the atomic diffusion and the formation process of order, especially for the nucleation problem and the

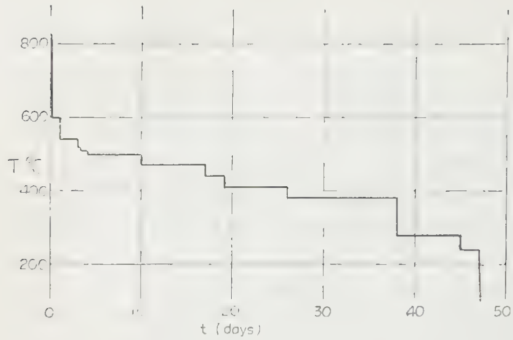

Fig. 16. Temperature-time history of the perfectly annealed specimen.

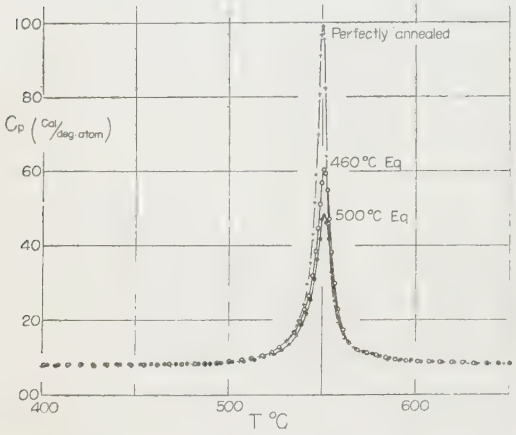

Fig. 17. Anomalous specific heat curves on heating for the three different heat treatments of long anneal. The curve for 500°C is equal to the corresponding curve of Fig. 6, and the curve for 460°C corresponds to the multiple-step heat treatment.

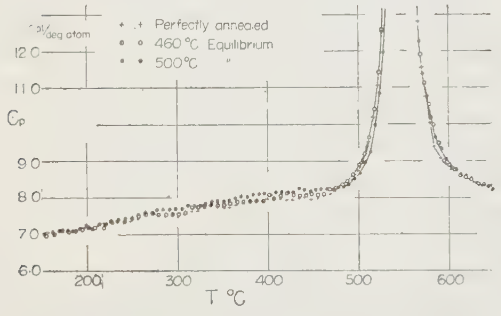

Fig. 18. Specific heat curves on heating after the three annealings of long duration.

Table I.

	Ni_3Fe	Bragg-Williams	Peierls
RTc/E_0	1.73	2.19	1.33
E_l/E_0	0.152	0.00	0.46
Q/E_0	0.535	0.218	0.36

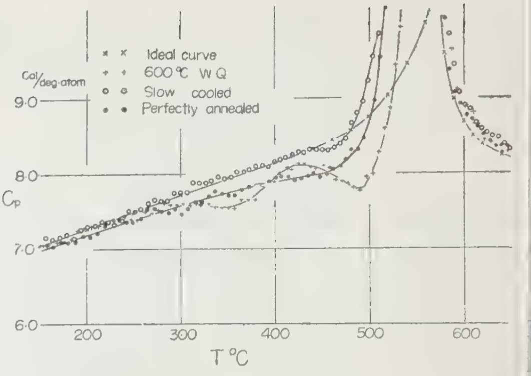

Fig. 19. Specific heat curves on heating for three different heat-treatments with an enlarged ordinate scale. The ideal curve corresponds to the infinite rate of cooling.

antiphase problem[21]. But the study of thi field is not enough developed to allow us detailed discussion of the mechanism. Yet we shall later come back to this problem.

§ 6. Specific Heat for the Perfectly Annealed Specimen

The specimen alloy was annealed carefull for 47 days to obtain a perfectly ordered state The temperature-time history of the treatmen is shown in Fig. 16. The specific heat-temperature curve on heating thus obtained i shown in Fig. 17 andFig. 18 with two curve obtained by the previous experiments (sectio 2).

The total decrease of internal energy refer ed to that in the disordered state was ca culated to 888 cal/atom. In Table I, the dat are compared with thoretical approximation for a A_3B type superlattice[23]. Where E_0 i the total energy of the disorder-order trans formation per gram atom, E_l is the energ associated with the local order just above th critical temperature and Q represents th latent heat. The data are obtained from Fig. 9. It must be noticed that Q/E_0 is fairl large. We believe that it means that th contribution of E_c and E_s cannot be neglected

In Fig. 19, the four curves of specific hea are shown with an enlarged scale. The curv for slowly cooled specimen corresponds to th data of Fig. 4 in the paper II. Here we not an interesting feature of the curves. In th figure, specific heats for the perfectly anneale specimen are a little lower than that of th slowly cooled specimen in the temperatur

Table II. Amounts of energy supplied to the specimen to heat it up for each temperature range are tabulated for 12 measurements of specific heat on heating after various heat treatments. The corresponding curves of specific heat are; (1), (2)—Fig. 21, (3)—Fig. 20, (8), (9), (10)—Fig. 7, (11), (12)—Fig. 18 of this paper and (4), (5), (6), (7)—Fig. 2 of the paper II. (cal/atom).

		100°–200°	200°–300°	300°–400°	400°–500°	500°–600°	600°–700°
(1)	700°C water quench	709	731	750	812	994	831
(2)	600°C water quench	706	744	762	801	973	832
(3)	Rapidly cooled in air	708	746	790	803	990	834
(4)	3.0 deg/min at 500°C	707	751	797	830	1023	832
(5)	1.8 deg/min at 500°C	703	749	793	834	1034	831
(6)	0.9 deg/min at 500°C	707	750	791	827	1062	834
(7)	0.4 deg/min at 500°C	706	749	793	832	—	—
	Mean of (4), (5), (6), (7)	706	749	793	832	—	—
(8)	500°C anneal	698	744	790	819	1517	833
(9)	480°C anneal	690	741	778	815	1503	837
(10)	460°C anneal	695	731	774	815	1498	830
(11)	500°C and 460°C anneal	689	738	778	809	1671	833
(12)	Perfext anneal	700	737	770	807	1834	832
	Mean of (8), (9), (10), (11), (12)	695	738	776	813	—	—
	Defference of two means	11	11	17	19	—	—

range below 500°C. It is quite generally observed that an alloy with long range order has the specific heat slightly smaller than that without long range order. This will be seen in Table II. Here, the amounts of energy supplied to the specimen to heat it up for each of the temperature ranges are tabulated for 12 measurements of specific heat on heating after various heat treatments. (4), (5), (6), and (7) correspond to the specimen cooled in furnace with various rates which will not have any long range order, and (8), (9), (10), (11), and (12) correspond to the specimen after various heat treatments of long duration which will certainly have long range order. (1), (2), and (3) will be discussed in the next section. The above mentioned tendency can be seen clearly from this table. The last line illustrate the mean difference of energy between the specimen with and without longe range order.

The difference must be emphasized, because, so long as we consider only the ordering energy, there is no reason why a perfectly annealed alloy has specific heats on heating smaller than those of disordered specimen. The phenomenon is explained by two mechanisms. One is an interaction between the lattice vibration and the atomic ordering. This phenomenon was studied theoretically by Y. Shibuya and others[24]. In an ordered state, each atom will situate in an more close packed position, so the freedom of its vibration will decrease and it results in a small decrease of specific heat due to lattice vibration. A temperature independent part in the decrease of specific heat of about 0.11 cal-deg.atom will be explained by this effect. The other mechanism is the interaction of the ferromagnetic spin ordering and the atomic ordering. It is a well known fact that the ferromagnetic curie temperature of this alloy increases with the development of long range order. (about 100°C) Therefore the specific heat on heating of ordered alloy due to the magnetic transformation will be lower than that of disordered alloy in a temperature range below the curie temperature of disordered alloy. It will be the origin of the temperature dependent part of the difference of specific heat in Table II.

§ 7. Anomalous Phenomenon Associated with Quenching

In the paper II, it was concluded that at the usual rates of cooling, the development of atomic order proceeds without long range order and the results obtained for various rates of cooling could be explained by the simple theory of disorder-order transformation. But, there was a serious difference between the specific heat curve on heating of a specimen quenched into water from 600°C and those of a specimen cooled with normal rates in furnace. In Fig. 19, we see anomalous decreases of specific heat in the temperature range 300∼400°C for the specimen quenched from 600°C into water. This phenomenon may be attributed to a mechanism different from that of the decrease of specific heat appeared in 450°C∼500°C which is easily understood as a simple reaction of atomic ordering activated by the increase of temperature. This phenomenon was already pointed out by T. Suzuki[25] and can be seen in the initial permeability-temperature curve on heating of permalloy obtained by G. W. Elmen[26]. Our specimen will be studied in some details as to this anomalous generation of heat at low temperature.

In Fig. 20, specific heat curves on heating of the specimen after cooling treatments with different rates are shown. The treatments used are (1) quenched into water from 600°C, (2) rapidly cooled in air, and (3) cooled in furnace. The curve (3) corresponds to the curve (b) of Fig. 3 in the paper II.

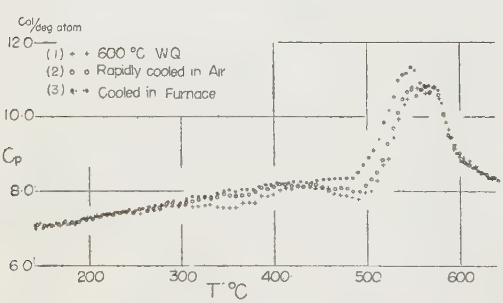

Fig. 20. Specific heats on heating for Ni_3Fe specimen. The preceding treatments are; (1) quenched into water from 600°C, (2) rapidly cooled in air, and (3) cooled in furnace.

In Fig. 21, a specific heat curves on heating of the specimen quenched from 700°C and 800°C are shown. A similar curve for the specimen quenched from 510°C was already shown in Fig. 10 in the paper II, and there was no anomaly in 200°∼450°C.

Specific heat curves on heating of a pure nickel specimen quenched into water from 1000°C, that of cooled in furnace and a curve on cooling of the same specimen were measured. In this case, the agreement of the three curves is satisfactory.

§ 8. Discussions about the Anomalous Generation of Heat

From our experimental results, we conclude that there exists an unknown reaction X for this specimen which prooeeds from about 700°C to 500°C in cooling. We further assume that the reaction X is not completed in a rapid cooling such as the quenching into water.

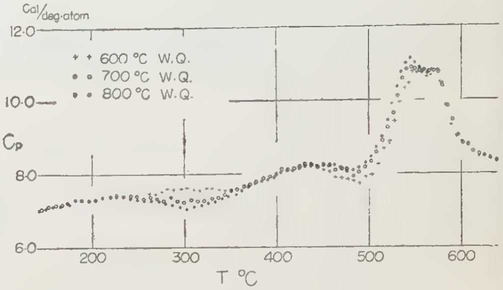

Fig. 21. Specific heats on heating for Ni_3Fe specimen quenched into water from 600°C, 700°C, and 800°C.

The reaction X will be separated from the usual ordering reaction of local order above the critical temperature. Because, the reaction seems to be independent on the local ordering reaction which begins from about 450°C on heating. In the treatment terminated by rapid cooling in air shown in Fig. 20 there will be no sufficient time to develop the local order, as will be seen from the specific heat curve above 450°C. But the reaction X seems to be finished even in this rate of cooling.

The energy change associated with this reaction X seems to be quite small as can be seen in Fig. 21. It is shown in this figure that when the quenching temperature is raised the specific heat in 230°∼420°C decreases and on the other hand, the specific heat in 440°C ∼570°C increases. As a result, the total amounts of heat to heat up the specimen from room temperature to 700°C are almost equal for these three cases. The situation can be seen in the Table II, where (1), (2) and (3) correspond to the above three experiments.

We believe the phenomenon must be related to the behaviour of imperfections in the crystal lattice and a rough explanation of these results will be as follows. In general, if a metal is cooled from high temperature, there will proceed a sort of structual changes in the crystal lattice. A configurational change of the assembly of various imperfections is a rough picture of such structural changes. In a superlattice alloy, this structural changes will be influenced greatly by the atomic ordering tendency and the interaction between imperfections and superlattice will begin already well above the critical temperature on cooling. In our specimen, if we assume that these structural changes begin appreciably from about 700°C and end at about 520°C on cooling, it will be identified with the reaction X. If the specimen was quenched from these temperature range, the high temperature state containing various imperfections will be quenched under a complicated interaction to the atomic order (it may have a freezing effect). In high temperatures, the crystal lattice will be in a state with a violent thermal agitation. Therefore, the higher the quenching temperature, the more unstable imperfections exist in the crystal at room temperature. Thus by increasing the quenching temperature the lattice structure becomes more unstable at room temperature. This unstable structure can easily change its configuration at the lower temperature on heating. This reaction will associate movements of atoms and the degree of order will increase as a result of these atomic movements. This accidental increase of the degree of order will be the origin of the anomalous generation of heats appeared from 230°C to 420°C on heating.

Here, we notice that our specimen contains 0.71% Mn. Ni$_3$Mn alloy also have a superlattice, and the specific heat-temperature curve on heating of Ni$_3$Mn alloy after quenched from 750°C shows anomalous decreases of specific heat from 250°C to 450°C. Moreover, a series of alloys Ni$_3$Fe$_{1-x}$Mn$_x$ have a superstructure which varies gradually from Ni$_3$Fe type to Ni$_3$Mn type which has no critical temperature. Thus undoubtedly the small content of Mn is playing a great rôle on this superlattice formation, especially on its relaxation characteristics. In general, by the addition of Mn, the critical ordering temperature increases, and the relaxation time of disorder-order transformation decreases. In the reaction X, we also believe that the Mn atoms play an important rôle. If we use a purely binary alloy of Ni$_3$Fe, what kind of change in the phenomenon associated with the reaction X will be expected? At present we have no answer to this. But we believe that the existence of reaction X is essential in disorder-order transformation of alloys and is not a consequence of small Mn added. M. Hirabayashi and others[28] observed the same phenomenon in CuAu and Cu$_3$Au superlattices. To give an answer to the above question, a further studies are needed in close cooperation with the theory of the atomic ordering and lattice imperfections.

From a preliminary study of Takahashi[3] on the effect of Mn added to Ni$_3$Fe, we had already substantiated that the two-step formation of long range order is an essential character of Ni$_3$Fe superlattice and is not a consequence of the small contents of Mn added. Moreover, a study of R. J. Wakelin and E. L. Yates[14] made for high purity Ni$_3$Fe alloys afforded a dependable answer to this problem. The measured points of specific resistivity in the annealings at 490°C and 480°C of Fig. 1 in their paper show definite deviations from the curves they drawed monotonously. This fact proves the existence of multiple-step transformation. We also mention here an interesting study made by Y. Yokoyama[29], who observed a polygonization phenomenon for this alloy, in an annealing at 490°C.

§ 9. Conclusions

In the first paper of this study[3], the formation stages of Ni$_3$Fe superlattice annealed at 490°C after quenched from 600°C are separated into four parts. The first stage of annealing of about 0~20 minutes at 490°C which have a large influence on the structure sensitive quantities was not explained at that time.

Now, we can say that the stage is evidently the process of structural change named as reaction X. The second stage is the development of local order without long range order. This stage was studied in the second paper[4], where we showed a good agreement of the experimental data with the simple relaxation theory of disorder-order transformation. The third stage, the development of order with long range order, was studied in this paper and deviation from the simple theory appeared in the initial and the final stages of the reaction. The reason of the deviations was attributed to nucleation and antiphase mechanisms. Thus, the forth stage is explained as the so-called single phase process of these antiphases. The all stages were explained at least in qualitatively.

All the questions which were raised in the present paper and which were left for further studies seem to be connected with imperfections of crystal lattice.

The writer expresses his true thanks to professor Seiji Kaya for his constant guidance.

References

1) O. Dahl: Z. f. Metallkunde **28** (1936) 133.
2) S. Kaya: J. Hokkaido Univ. **2** (1938) 29.
3) S. Iida: J. Phys. Soc. Japan **7** (1952) 373.
4) S. Iida: J. Phys. Soc. Japan **9** (1954) 346.
5) S. Iida: J. Phys. Soc. Japan unpublished.
6) G. J. Diens: J. Appl. Phys. **22, 8** (1951) 1020.
7) G. Borelius, K. E. Larrson and H. Selberg: Ark. Fys. **2** (1950) 161.
8) L. R. Aronin: J. Appl. Phys. **23, 6** (1952) 642.
9) Y. Takagi, T. Oguchi and G. Shirane: Bull. Tokyo Inst. Tech. **B 3** (1950) 225.
10) Y. Sichijo: unpublished.
11) J. C. Fisher, J. H. Hollomon and D. Turnbell: J. Appl. Phys. **19, 8** (1948) 775.
12) E. G. Edmunds and R. M. Hinde: Proc. Phys. Soc. **65, 393 B** (1952) 716.
13) F. E. Haworth: Phys. Rev. **56** (1939) 289.
14) R. F. Wakelin and E. L. Yates: Proc. Phys. Soc. **66, 399 B** (1953) 221.
15) H. Sato: Sci. Rep. RITU, **A 3** (1951) 13.
16) H. Sato: Sci. Rep. RITU, **A 4** (1952) 161.
17) C. B. Walker: J. Appl. Phys. **23** (1952) 118.
18) T. Muto: Sci. Rep. Inst. Phys. Chim. Res., Tokyo, **34** (1938) 377.
19) J. C. Slater: Phys. Rev. **84** (1951) 179.
20) J. F. Nicholas: Proc. Phys. Soc. **66, 399 A** (1953) 201.
21) D. Chipman and B. E. Warren: J. Appl. Phys. **21, 7** (1950) 696.
22) S. Kaya: Rev. Mod. Phys. **25** (1953) 49.
23) C. Nix and W. Schockley: Rev. Mod. Phys. **10** (1938) 1.
24) Y. Shibuya, Y. Fukuda and T. Fukuroi: Sci. Rep. RITU, **A 3** (1951) 183.
25) T. Suzuki: Theory of dislocation, Japan Inst. Metals (1951).
26) G. W. Elmen: J. Frank. Inst. **207** (1929) 606.
27) S. Kaya and M. Nakayama: Phys. Math. Soc. Japan, **3, 22** (1940) 126.
28) M. Hirabayashi, S. Nagasaki and H. Maniwa: J. Japan Inst. Metals, **B 14** (1950) 1.
29) T. Yokoyama: Rep. Yokohama Univ. **1** (1951) 23.

JOURNAL OF THE PHYSICAL SOCIETY OF JAPAN Vol. 10, No. 1, JANUARY, 1955

On the Mechanism of Aging in Aluminium-Silver Alloys, II. Nature of the Guinier-Preston Zone

By Ken-ichi HIRANO and Hiroto SAKAI*

Department of Physics, Tokyo Institute of Technology,
Oh-okayama, Meguro-ku, Tokyo

(Received June 25, 1954)

The process of the precipitation from supersaturated solid solution of aluminium containing from 5 to 53 weight % of silver, has been studied by the electrical resistance measurements. The discreteness between the low temperature- and the high temperature-aging has been reconfirmed. The nature of the Guinier-Preston zone, which is the product of the low temperature-aging, has been studied in detail and the correlated phenomena with it, such as the intermediate maximum observed in the isothermal low temperature-aging curve and the reversion phenomenon, have been satisfactorily interpreted in terms of the stability of the Guinier-Preston zone.

§ 1. Introduction

In the preceding paper[1], from the results of the calorimetric measurements, one of the authors has put forward and confirmed his view that the aging takes place in two discrete stages; at the temperature range of the low temperature-aging (*LT*-aging), the resulting property changes during the aging are attributable to the formation of the Guinier-Preston zone which is a segregation of silver atoms on the {111} planes of the matrix lattice, in this temperature range also the formation of the intermediate precipitate (γ' phase) which is coherent to the matrix and the equilibrium incoherent precipitate (γ phase) may take place, after lengthy aging treatment; on the other hand, at the high temperature aging range (*HT*-aging), the intermediate coherent phase is formed immediately when the supersaturated solid solution starts to decompose after the incubation period, and at a later stage this intermediate precipitate changes into the equilibrium incoherent precipitate accompanied by the recrystallization reaction. At the intermediate temperature between the *LT*- and *HT*-aging range, the first stage of the aging may involve the formation of the *G–P* zone in the matrix lattice which has the critical stable size at that aging temperature and the second stage may involve the formation and growth of the γ' phase, this stage may be regarded as a period during which nuclei of the γ' phase is formed directly in the matrix and grown with resolution of some part of the existing *G–P* zone.

Recently Dehlinger and Knapp[2] have pointed out in their paper, the theoretical explanation for the formation of the *G–P* zone (they named "Complex") and determined the upper limiting temperature of the stable *G–P* zone as a function of the silver content in the solid solution matrix, result of which coincides with the experimental works of Köster and his coworkers[14] and one of the authors[1] fairly well. Koda and Takeyama[3] have carried out the electron microscopic studies and have favoured the existence of a discreteness between the *G–P* zone and the γ' precipitation.

In a very recent paper Guinier and Walker[4] have re-examined the diffuse scattering with both low and high angle X-ray technique by 20 weight percent alloys and confirmed the interpretation of age hardening process offered by Guinier in 1939[5].

Though the high temperature-aging stage is clearly demonstrated to be the result of the formation of the platelets of the γ' phase[6], but the exact relation between it and the *LT*-aging stage cannot be considered as fully determined by the previous workers. To obtain further informations in this point of view, we have carried out the electrical resistance measurements subsequently to the calorimetric measurements.

---

* Hiroto Sakai: Now at Tokyo Research Laboratory, Mitsui Mining and Smelting Co., Shimomeguro, Meguro-ku, Tokyo.

Raynor and Wakeman[7], and Rotherham, and Larke[8] have reported the revised solvus curve of this alloy as shown in Fig. 1 which has been also reconfirmed by Hirano and Takagi[9] by the calorimetric measurements. The maximum solid solubility of silver in aluminium is about 55 weight % (about 24 atomic %) instead of previous 48 weight %[10], therefore we have carried out the experiment on the alloys, silver contents of which are from 5 to 53 weight %.

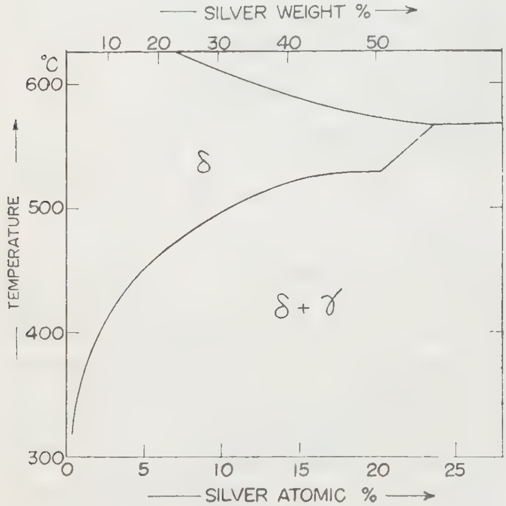

Fig. 1. Revised solvus curve.

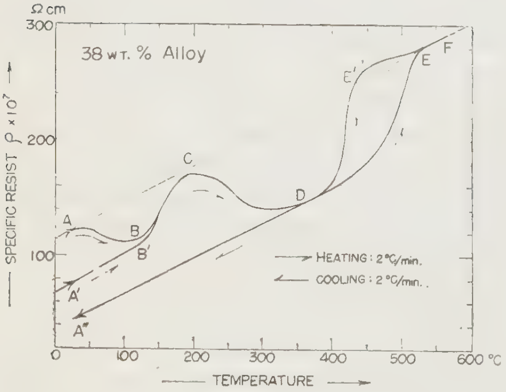

Fig. 2. $\rho-T$ curve for 38 weight % alloy.

§ 2. Specimens and Experimental Procedure

The preparation of the alloys has been described in the previous paper[1]. Alloys containing arranged silver were prepared from 99.99% aluminium and 99.99% silver using a similar procedure.

Square bars having dimension of about 0.2 cm thick, 0.3 cm wide and 10.0 cm long were used for the electrical resistance determination.

The solution heat treatment consisted in heating the specimens for 2 ~ 5 hours at 560°C followed by quenching in water of the room temperature. The aging treatment and heating treatment were conducted in an electric furnace.

The electrical resistance measurements were carried out by the potentiometric method. Two pairs of contactors were pressed to the specimen. One of them was for the current leads and the other was for the potential leads. The apparatus was set in vacuum to prevent oxidation.

§ 3. Experimental Results and Discussions

(1) *LT*- and *HT*-aging

In Fig. 2, the curve *ABCDEF* represents the electrical resistance versus temperature curve (ρ-T curve) for 38 weight % alloy (13 atomic %), obtained by reheating the specimen immediately after quenching. The curve *A'B'CDEF* was obtained by the same specimen after quenching followed by the *LT*-aging treatment at 100°C for 140 hours before reheating. The heating rate of the measurement was much the same as the calorimetric measurements, 2°C per minute. The curve *FEE'A"* represents the cooling curve obtained by cooling the specimen from the one phase region (temperature range above the solvus curve) down to the room temperature.

Comparing the results with those of the calorimetric measurements, it can be deduced that the first fall *AB* in the range at about 50°~150°C in the first curve is attributable to the formation of the *G–P* zone during the measurement and following rise *BC* at 150°~190°C is due to the resolution of it as the stability of it decreases with increasing temperature. The decreased value, *AA'*, at the starting point of the curve *A'B'CDEF* may be attributed to the existent *G–P* zone before reheating which must have been formed by 100°C-140 hours aging. The rise *B'C* is due to the resolution of it. At the point *C*, which lies nearly on the line *AEF* which represents the quenched state, the alloy returns to the quenched state. Above 190°C two curves meet each other and thereafter both show the second fall *CD*, which is attributable to the γ' phase precipitation. No effect of the *LT*-aging to the ρ-T curve above the temperature of the point *C* has been observed, this seems to be one of the characteristics come from the discreteness between the *LT*- and *HT*-aging processes.

With increasing temperature, metastable γ' phase may transform to the equilibrium γ phase, but because of its slow rate or few effect of it to the electrical resistance, accompanied electrical resistance change could not be observed by the heating rate of 2°C per minute.

The second rise *DE* is due to the resolution of the precipitated phase, accompanied by the increasing solid solubility of silver in aluminium with increasing temperature. The point *E* represents the two phase boundary in the equilibrium phase diagram.

The hysteresis between heating and cooling was observed, temperature difference between *E* and *E'* was about 90°C independently upon the cooling rate between 0.5° and 5°C per minute.

(2) **Effect of the heating rate**

We must notice that the shape of the ρ-T curve is not independent upon the heating rate. This can be seen in Fig. 3 (a) and (b) which were obtained by 53 weight % alloy (22 atomic %) for different heating rates immediately after quenching.

The general feature of the curves in Fig. 3 (a) is identical to the one mentioned in Fig. 2, but in this case because of the relative

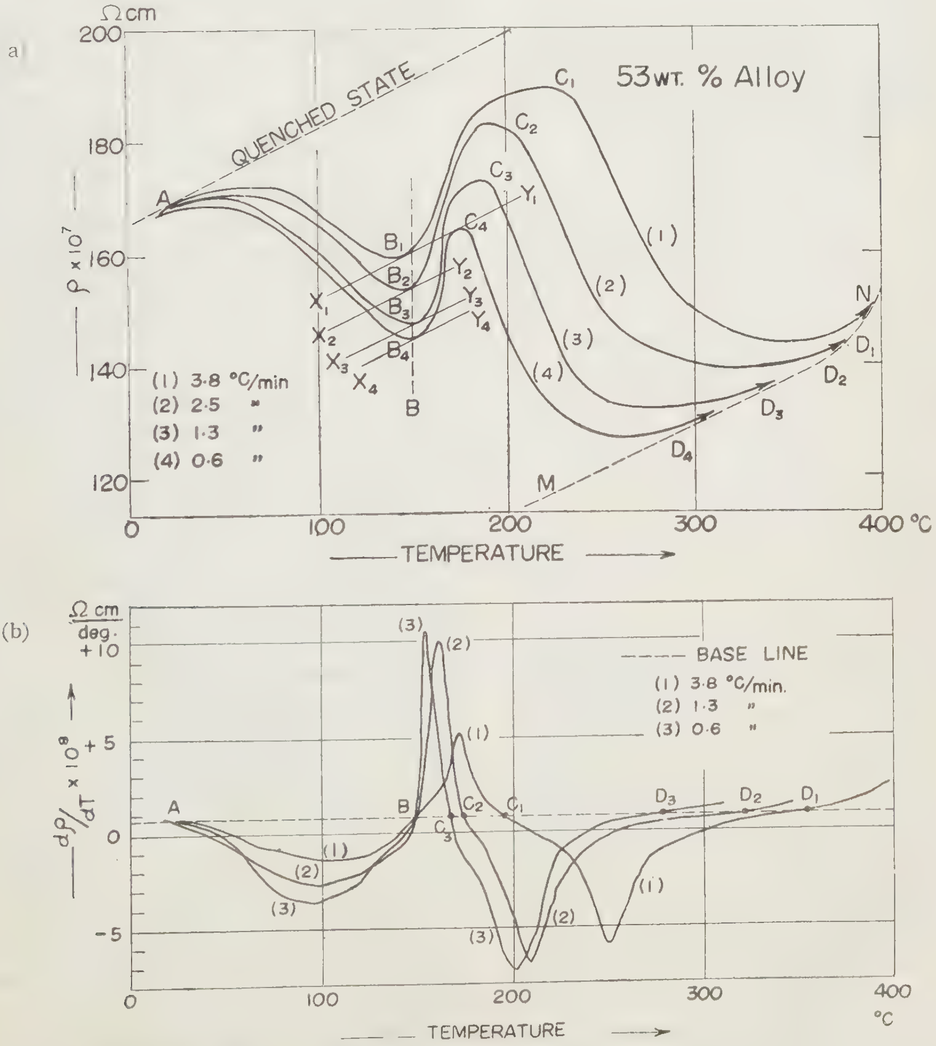

Fig. 3. (a) $\rho - T$ curves obtained by different heating rates.
(b) $d\rho/dT$ versus temperature curves derived from (a).

rapid rate of the γ' phase transformation, the decrease due to it superposes upon the increase due to the resolution of the *G-P* zone, then at the point *C* the curves do not return exactly on the *AE* line. This is clearly understood by the fact that the slower the heating rate is, the lower the temperature range of the decreasing resistance due to the γ' phase precipitation removes, as shown by C_1D_1, C_2D_2, C_3D_3 and C_4D_4 in Fig. 3 (a).

On the contrary to the fact that the heating rate affects to the location of the second decrease *CD* and not to the decreasing value (that is, the point D_1, D_2, D_3 and D_4 lie on the quilibrium state line marked by *MN* in the figure), it does not affect to the location of the first valleys (B_1, B_2, B_3 and B_4 which are the tangential points of the lines, X_1Y_1, X_2Y_2, X_3Y_3 and X_4Y_4, which are parallel to the quenched state line *AE*, to the ρ-T curves), but affects to the depth of them. From this fact it may be recognized that the heating rate affects quantitatively but not qualitatively to the formation of the *G-P* zone, while it affects qualitatively but not quantitatively to the γ' phase precipitation.

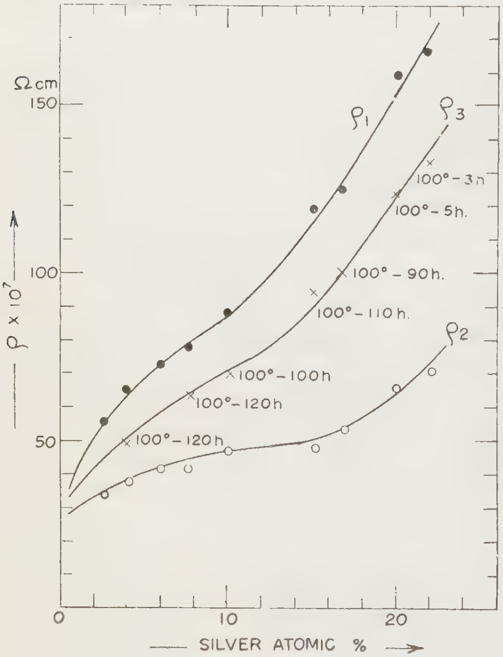

Fig. 4. Specific resistance versus silver content curves.

Fig. 3 (b) was obtained from (a), where $d\rho/dT$ is plotted against temperature. The curves resemble to the C_p-T curves as shown in Fig. 3 in the previous paper[1]. Decrease and increase of the electrical resistance correspond to the evolution and absorption of heat respectively. In Fig. 3 (b), different influences of the heating rate to the locations of the points *B* and *D* are clearly distinguishable.

(3) Specific Resistance and Silver Content

The specific resistances of the alloys containing various percents of silver measured at the room temperature are shown in Fig. 4 for three states respectively. ρ_1 is the value obtained immediately after quenching, ρ_2 is for slow cooled and ρ_3 is for the alloys which were low temperature-aged, the aging temperature and time are shown in the figure. The characteristic inclination of the curves must have some relations to the abnormal shapes of the solvus as shown in Fig. 1.

(4) Isothermal and Isochronal Aging Curves

The decrease of the specific electrical resistance during the isothermal aging is not monotone, particularly at the *LT*-aging temperature, as shown in Fig. 5 obtained with 53 weight % alloy, the general shape of which is much the same as that obtained on the alloys of the other silver contents by the previous investigators; Geisler, Barrett and Mehl[11] on 10, 20 and 30 weight % alloys, Köster and his coworkers[12] on 38 weight % alloy.

On aging at 100°C, the initial decrease which continues about 10 hours, is followed by a rise of the resistance to an intermediate maximum and then decrease begins again. On aging at 200°C, the decrease is monotone from the starting point and intermediate maximum is absent. The initial decrease at the lower temperature aging is attributable to the formation of the *G-P* zone and the second decrease is to the γ' phase precipitation. It is recognized that the former is concerned with the reversion phenomena which is observed when the specimen is brought to the temperature in the range of the *HT*-aging after the *LT*-aging treatment. As discussed later, this is attributable to the resolution of the *G-P* zone in to the matrix.

The monotonous decrease at the *HT*-aging and the second decrease at the *LT*-aging are attributable to the γ' phase precipitation, this has been confirmed by the *X*-ray investigations by Glocker, Köster, Scherb and Ziegler[13], and Guinier and Walker[4].

The origin of the intermediate maximum between two stages in the *LT*-aging curve has been remained as an open question, although Geisler, Barrett and Mehl[11] have discussed and put forward the mechanism in which it has been attributed to the effect of the coherency of the transitional precipitate with the matrix. The aging characteristics of the other properties other than the electrical resistance, such as the hardness[14], the elastic limit[14], the Young's modulus[15], and the thermo-electromotive force[12], and the phenomena of reversion can not be interpreted satisfactorily by their mechanism. It was found that this is interpreted satisfactorily, if we take into consideration the stability of the *G-P* zone as a function of the silver content of the remained matrix, the details of which will be described in the next section.

From Fig. 5, the isochronal electrical resistance versus temperature curves were obtained and shown in Fig. 6. Two valleys, characteristic to the *L-T* and *HT*-aging, are clearly distinguishable.

(5) Nature of the *G–P* zone

From the fact that the atoms in the *G-P* zone are remaining on the lattice sites of the parent matrix, it may be predicted that the stability and existent quantities of it should be sensitive to the silver concentration in the remained matrix.

Dehlinger and Knapp[2] have investigated theoretically and obtained a T_m-C curve, where T_m is the maximum temperature limit below which the *G-P* zone can be stable to exist and C is the silver content in the matrix. If the quenched alloy is aged at the temperature above T_m, the *G-P* zone can not be formed and the γ' phase must be formed from the starting, this is the *HT*-aging process. While below T_m, the precipitation sequence could not be simple, as an aggregation of solute atoms into the *G-P* zone precedes the formation of the platelet structure which is the beginning of the γ' phase precipitation, the mechanism of which will be demonstrated as followings.

In Fig. 7, T_m versus silver concentration curve is shown schematically, referring to the study of Dehlinger and Knapp. T_m decreases with decreasing C.

If the specimen, silver concentration of which is C_0, is homogenized at the temperature above the solvus, then quenched to the room temperature, and aged at the temperature T_a, which is lower than T_m, the first stage of the aging is the formation of the *G-P* zone. On annealing, these clusters grow in size both by absorption of the silver atoms not contained in the clusters and by coalescence of some of the clusters, then the number of the clusters decreases as the average size of them increases. The stability of these *G-P* zones may be represented by the temperature above which these become unstable and are resolved completely into the matrix when the specimen is heated after the aging. Then if $T_m > T_a$, the *G-P* zone is stable and vice versa. During the aging, silver content in the matrix can decrease from C_0 down to C_4, where C_4 is the equilibrium value at the aging temperature, that is, the solubility limit of silver in aluminium at that temperature, then T_m decreases down to T'_m in Fig. 7.

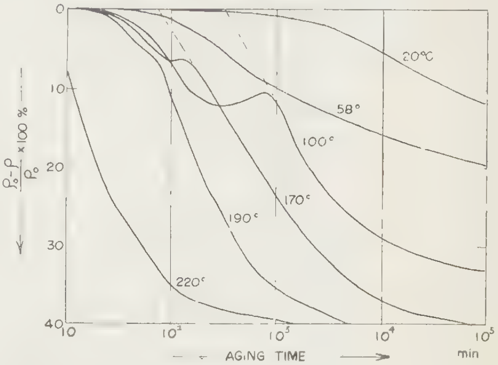

Fig. 5. Isothermal aging curves for 53 weight % alloy.

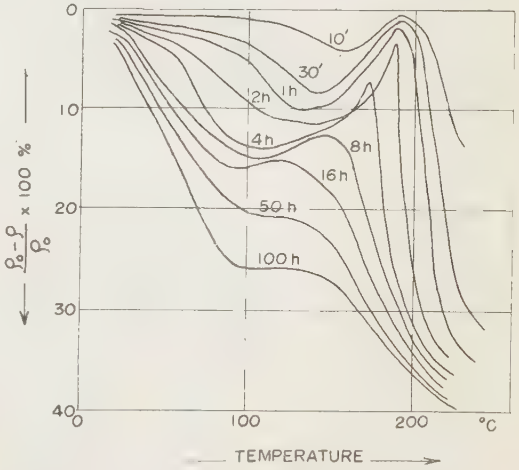

Fig. 6. Isochronal electric resistance versus temperature curves, obtained from Fig. 5.

In Fig. 8 (a), change of C during the aging is plotted against aging time and corresponding change of (T_m-T_a) is shown in Fig. 8 (b) schematically. It has been shown by the X-ray measurement that the decreasing silver content in the matrix due to the formation of the *G–P* zone, ΔC in Fig. 8 (a), is negligibly small except the adjacent region round the *G–P* zone. Furthermore from the C_p measurements it was found that the stability of the *G–P* zone increases very rapidly to a saturated value, therefore after aging for the time t_1, C and (T_m-T_a) reaches respectively to the saturated value as shown in the figures.

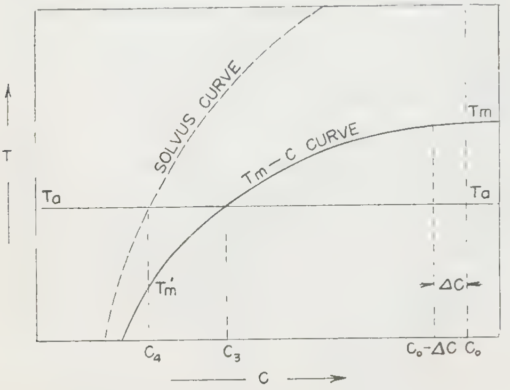

Fig. 7. Upper limit temperature of the G–P zone as a function of the silver concentration in the matrix.

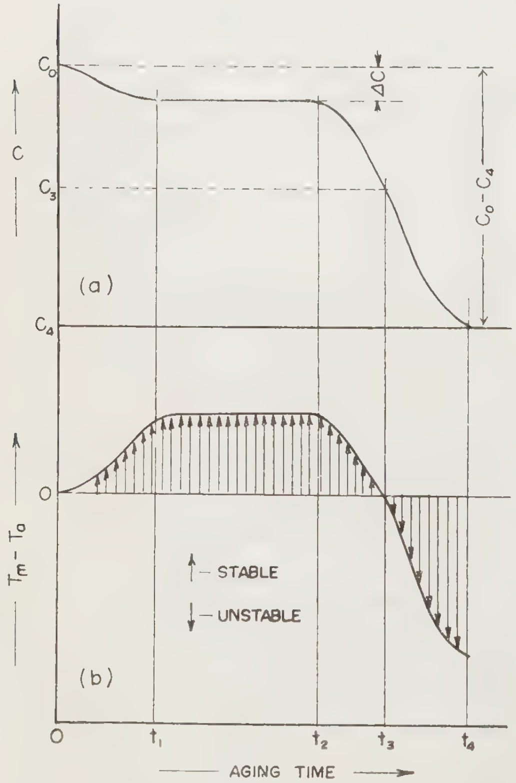

Fig. 8. (a) Time dependence of the silver concentration in the matrix during LT-aging.
(b) Change of the stability of the G–P zone during LT-aging.

With further annealing the γ' precipitates can be appeared directly from the matrix by the mechanism of nucleation and growth, which is same to the *HT*-aging process, the incubation time of which, t_2, must be identical with that calculated from the activation energy of the *HT*-aging. This has been confirmed as shown in (**6**) of this paper. The silver content in the matrix decreases by the γ' precipitation rather rapidly after the time t_2, then (T_m-T_a) decreases. After the time t_3, where $T_m=T_a$, the *G–P* zone becomes unstable.

(6) Interpretation of the Aging Curves

In Fig. 9 and Fig. 10, observed isothermal aging curves of the hardness and the electrical resistance are schematically illustrated, where the curve *AD* are shown as the summation

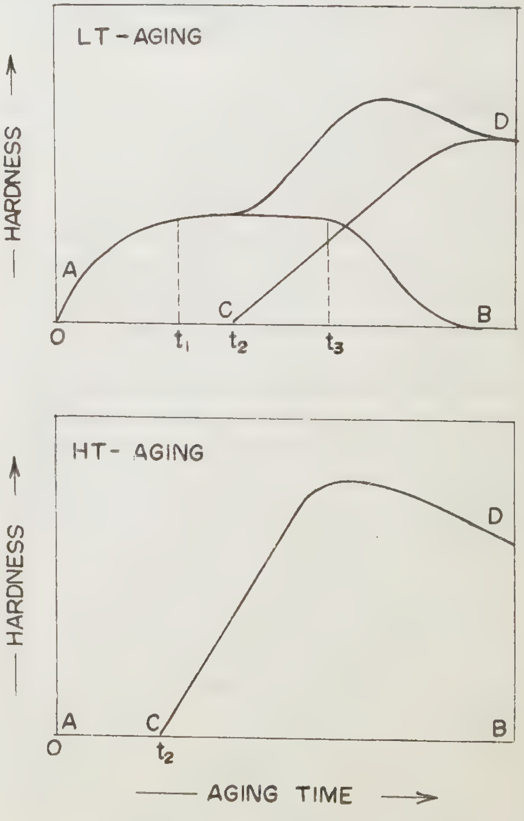

Fig. 9. Isothermal aging curves of hardness.

of two reactions come from the formation and resolution of the G–P zone, AB, and from the precipitation of the γ' phase, CD. The time denoted by t_1, t_2 and t_3 correspond to those in Fig. 8.

The possibility of the occurrence of the intermediate maximum in the electrical resistance curves is satisfactorily interpreted as shown in Fig. 10.

The time t_2 can not appear explicitly in the LT-aging curves, but it will be obtained by the extrapolation as shown in Fig 6 by the dashed lines. From our mechanism, it will be expected that the activation energy for the γ' phase precipitation which can be calculated using the time t_2 obtained from the LT-aging curves must be coincide with that calculated from the HT-aging curves. This was actually confirmed with 20 weight % alloy as shown in Fig. 11, where (log t_2) is plotted against $1/T$, t_2 was obtained from the electrical resistance curve and T is the absolute aging temperature. It may be noted that the extrapolation of the straight line obtained from the HT-aging curves passes exactly through the line obtained from the LT-aging curves, therefore from the slope of this line the same activation energy of about 22,000 cal/mol. was obtainable. The dashed line in Fig. 11 is the (log t'_2) versus $1/T$ line, where t'_2 is the aging time to produce a set of the central streaks which is a completely different type of scattering from that due to the G–P zone, obtained from the results of the X-ray investigation after Guinier and Walker[4]. They have suggested that this scattering must be attributed to the γ' precipitation, hence t'_2 must be regarded as the time required to produce the γ' phase of some constant size. The activation energy calculated from this line is also 22,000 cal/mol. which coincides with that obtained from t_2.

(7) Reversion Phenomenon

The phenomenon of reversion has been reported by Köster and his coworkers[12) 13)] with 38 weight % alloy as shown in Fig. 12 (a) and (b). This phenomenon is characteristic to the LT-aged alloys when they are reheated at the HT-aging temperature range for a short time. The HT-aged alloys do not show this phenomenon even when they are reheated at higher temperature. The upper

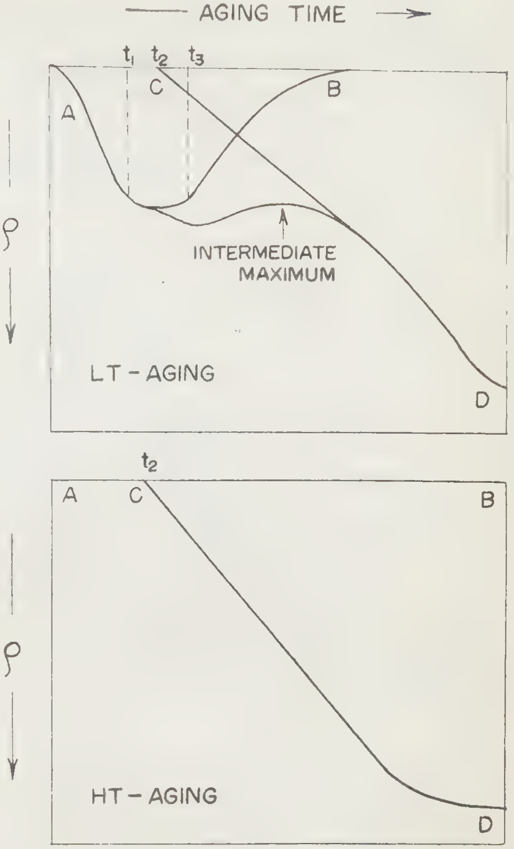

Fig. 10. Isothermal aging curves of electrical resistance.

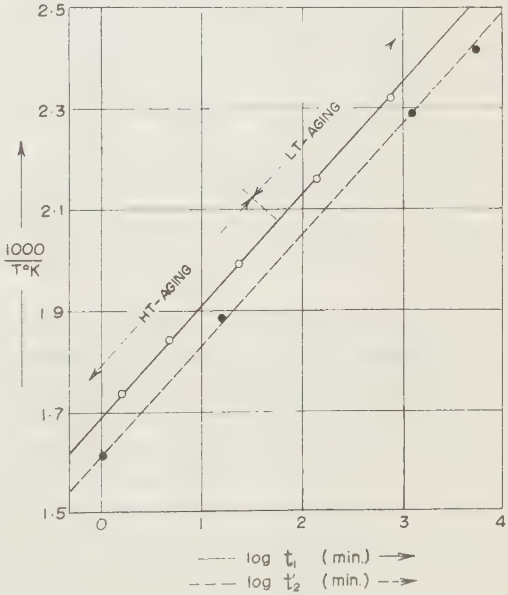

Fig. 11. t_2 versus $1/T$ line for 20 weight % alloy. Dashed line was obtained from the X-ray measurements *after* Guinier and Walker.

curves in Fig. 12 (a) and (b) represent respectively the change of the hardness and the electrical conductivity during 150°C-aging and lower curves represent the value obtained after the reversion treatment for 2 minutes at 220°C after each aging time as shown by the arrows in the figures. The effect from the γ' precipitation at 220°C during the reversion treatment may be disregarded because in 38 weight % alloy the incubation period for it at 220°C is more than 50 minutes.

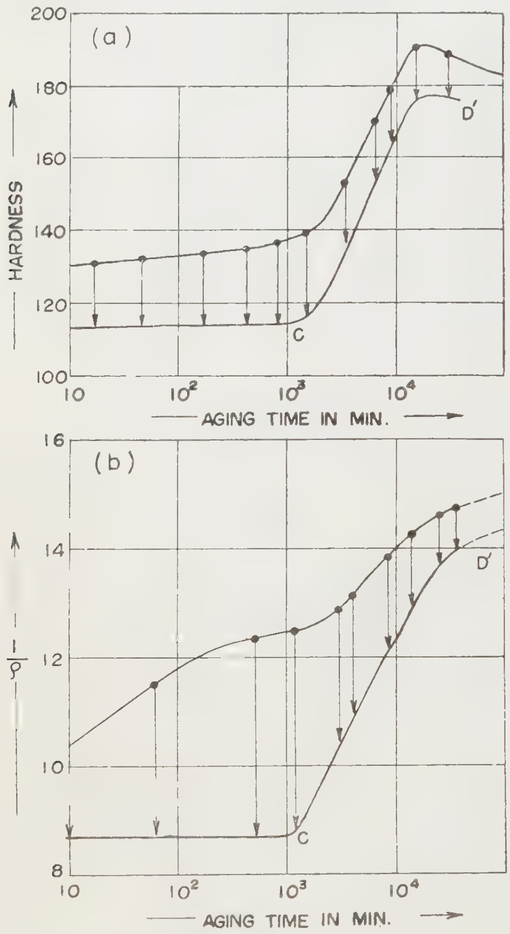

Fig. 12. (a) and (b) Reversion phenomena in 38 weight % alloy. *After* Köster and his coworkers.

Comparing Fig. 12 with Fig. 9 and Fig. 10, it was confirmed that the degree of the reversion is exactly same to the quantity due to the *G–P* zone in the aging curve, then remaining part after the reversion, *CD′* in Fig. 12, is much the same to the part of the curve *CD* in Fig. 9 and Fig. 10, which is a contribution of the γ' precipitation to the total *LT*-aging curve *AD*. No contribution of the γ' precipitate to the reversion was observed. Thus the reversion phenomenon has been interpreted as the dissolution of the existent *G–P* zone at that time.

Acknowledgments

The authors wish to express their sincere thanks to Professor Yutaka Takagi for his valuable discussions and to Professor Werner Köster (Max-Planck-Institute für Metallforschung) for his cordial letter in which he discussed our previous paper in comparison with his results. Also thank Mr. Hideyo Maniwa for his encouragements.

References

1) K. Hirano: Jr. Phys. Soc. Japan **8** (1953) 603.

2) U. Dehlinger and H. Knapp: Z. Metallkde. **43** (1952) 223.

3) S. Koda and T. Takeyama: Research Reports of Engineering Faculty of Hokkaido University No. **7** (1952) 250. (in Japanese)

4) C. B. Walker, and A. Guinier: Acta Metallurgica **1** (1953) 568.

5) A. Guinier: Ann. Phys. **12** (1939) 192.

6) A. H. Geisler: Phase Transformations in Solids (John Willey and Sons, Inc. 1951) pp. 387–544.

7) G. V. Raynor and D. W. Wakeman: Phil. Mag. **40** (1949) 404.

8) L. Rotherham and L. W. Larke: J. Inst. Metals **81** (1952–53) 68.

9) K. Hirano and Y. Takagi: J. Phys. Soc. Japan **9** (1954) 730.

10) M. Hansen: Z. Metallkde. **20** (1928) 217.

11) A. H. Geisler, C. S. Barrett and R. F. Mehl: Trans. AIMME. **152** (1943) 182.

12) W. Köster, H. Steiner and J. Scherb: Z. Metallkde. **43** (1952) 202.

13) R. Glocker, W. Köster, J. Scherb and G. Ziegler: Z. Metallkde. **43** (1952) 208.

14) W. Köster and F. Braumann: Z. Metallkde. **43** (1952) 193.

15) K. Tanaka, H. Abe and K. Hirano: J. Phys. Soc. Japan, will be published.

Note added in proof: The authors are recently informed of the work of B. Belbeoch and A. Guinier (Compt. rend., **238** (1954) 1003.) In this paper, new results of the X-ray study on "Relation between the structure and the mechanical properties during hardening of the Al–Ag alloys" have been reported. The development of the structure was followed by diffusion diagrams that have been shown to be of two types: ring diagrams characteristis of zones formed by the collecting of the Ag atoms in the solid solution; and distorted diagrams, due to the small precipitates of Al–Ag_2 in the form of lamellæ parallel to the (111) plane. They also showed that there is exact correspondence between the two stages of the structure and of the hardness.

JOURNAL OF THE PHYSICAL SOCIETY OF JAPAN Vol. 10, No. 1, JANUARY, 1955

Molecular Sound Velocity and Molecular Compressibility of Organic Halogen Compounds*

By Otohiko NOMOTO

Kobayasi Institute of Physical Research,
Kokubunzi, Tokyo

(Received August 3, 1954)

Molecular compressibility $W=(M/\rho)\beta^{-1/7}$ and molecular sound velocity $R=(M/\rho)V^{1/3}$ were computed for organic halogen compounds employing existing ultrasonic velocity data and the halogen increments were obtained, also making use of the values of the molecular sound velocity and the halogen increments given by Lagemann, Evans, and McMillan. (M= molecular weight, ρ=density of the liquid, V=sound velocity in the liquid, β=adiabatic compressibility of the liquid). The deviation from additivity rules with respect to the constitutive elements of the molecule is somewhat smaller for the molecular compressibility than for the molecular sound velocity, the percentage deviation for halogen increments of the molecular compressibility being about 1/2～2/3 as compared with the percentage deviation for halogen increments of the molecular sound velocity.

§ 1. Introduction

Rao's molecular sound velocity[1])

$$R=\frac{M}{\rho}V^{1/3}, \qquad (1)$$

and the molecular compressibility first introduced by Wada[2])

$$W=\frac{M}{\rho}\beta^{-1/7}, \qquad (2)$$

are known as quantities independent of the temperature for each organic liquid and satisfying additivity rules with respect to the constitutive elements of the molecule (atoms or bonds), although these rules for the molecular sound velocity begin to fail for halogen compounds, according to Lagemann, Evans and McMillan[3]). Here M means the molecular weight, ρ the density of the liquid, V the sound velocity in the liquid, and β the adiabatic compressibility, and it is customary to measure V in m/sec, and β in 10^{-12} cm^2/dyne, while ρ is measured in g/cm^3.

The present author[4]) noticed that the molecular compressibility of liquid mixtures is a linear function of concentration—molar fraction of one of the components—except in water-alcohol mixtures, while the molecular sound velocity of liquid mixtures deviates from linear dependency on molar fraction also in case when the density of the two component liquids are widely different each other, the molecular sound velocity *vs.* molar fraction curves becoming concave upwards in this latter case.

It seems, therefore, natural to suppose that the deviation from additivity rules in case of the halogen compounds is also smaller for the melocular compressibility than for the molecular sound velocity, because in this case the deviation from additivity rules is presumably due to the heavy halogen atoms contained in the molecules. The present paper deals with the elucidation of this problem and reports of the results of computations of the molecular sound velocity and the molecular compressibility of halogen compound liquids, performed by employing existing ultrasonic velocity data.

§ 2. Results

It was revealed that the fluctuations of the increments due to the halogen molecules I, Br, Cl and F obtained from the organic liquids containing these atoms are smaller for the molecular compressibility than for the molecular sound velocity.

Table I summarizes the result and shows the mean values of the halogen increments (bond-increments) of the molecular compres-

---

* The text in Japanese of this paper will be published in "Bulletin of the Kobayasi Institute of Physical Research".

Table III. Molecular sound velocity and molecular compressibility of organic halogen compounds.

Liquids	Chemical formula	ρ g/cm³	V m/sec	β 10^{-12} cgs	Molecular compressibility				Molecular sound velocity R							Author of the ultrasonic velocity data
					W_{exp}	W_{cal}	δW	X	R_{exp}	Bond additivity R_b	δR_b	x_b	Atomic additivity R_a	δR_a	x_a	
iodobenzene	C_6H_5I	1.8280	1114	44.08	64.96	63.80	1.16	20.92^{M}				280.2*			303.5^{*M}	L E M
n-butyl iodide	$CH_3CH_2CH_2CH_2I$	1.6144	971.5	65.63	62.69	62.36	0.33	20.09				259.5^{*m}			256.5^{*m}	L E M
methylene iodide	CH_2I_2	3.325	973.3	31.75	48.91	49.72	−0.81	19.06^{m}				304.0^{*M}			301.8*	L E M
methyl iodide	CH_3I	2.28	834	63.05	34.43	35.06	−0.63	19.13	586.0	569.6	16.4	300.4	573.4	12.6	298.5	S
ethyl iodide	C_2H_5I	1.9465	869	68.03	43.86	44.16	−0.30	19.46	764.6	764.3	0.3	284.4	768.4	−3.8	282.1	S
propyl iodide	C_3H_7I	1.747	929	66.31	53.38	53.26	0.12	19.88	950.3	958.9	−8.6	275.4	963.4	13.1	272.8	S
						mean C–I=19.76				mean C–I=284.0			mean I=285.9			
bromoform	$CHBr_3$	2.8904	931.2	39.90	51.65	52.26	−0.61	15.47	854.2*			253.0^{*M}			250.6_{*}	L E M
n-butyl bromide	$CH_3CH_2CH_2CH_2Br$	1.2741	1019	75.59	58.96	58.32	0.64	16.36	1082*			212.4*			209.5^{*m}	L E M
bromobenzene	C_6H_5Br	1.4953	1170	48.85	60.23	59.76	0.57	16.19	1107*			231.2*			254.5^{*M}	L E M
s-tetrabromoethane	$CHBr_2\cdot CHBr_2$	2.9666	1041	31.10	71.31	71.98	−0.67	15.59	1181*			246.6*			244.0*	L E M
ethylene bromide	$CH_2Br\cdot CH_2Br$	2.1777	1009	45.11	50.06	50.74	−0.68	15.22	865.3*			240.1*			237.6*	L E M
methylene bromide	CH_2Br_2	2.4843	963.2	43.38	40.84	41.64	−0.80	15.10^{m}	963.2*			250.5*			248.2*	L E M
propylene bromide	$CH_3\cdot CHBr\cdot CH_2Br$	1.9405	994.9	52.06	59.15	59.84	−0.69	15.21	994.9*			229.6*			227.0*	L E M
o-bromotoluene	C_7H_7Br	1.4237	1205	48.38	69.00	68.86	0.14	15.86	1278*			207.6^{*m}			230.5*	L E M
p-bromotoluene	C_7H_7Br	1.3934	1164	52.97	69.59	68.86	0.73	16.45^{M}	1291*			220.6*			243.5*	L E M
						mean C–Br=15.72				mean C–Br=232.4			mean Br=238.4			
carbon tetrachloride	CCl_4	1.5942	937.8	71.33	52.45	52.20	0.25	13.11				236.1*			233.6*	L E M
chloroform	$CHCl_3$	1.4870	1001	67.11	44.02	44.25	−0.23	12.97	803.2*			236.0*			233.6*	L E M
chlorobenzene	C_6H_5Cl	1.1042	1289	54.50	57.55	57.09	0.46	13.51	1110*			236.2*			259.5^{*M}	L E M
n-butyl chloride	$CH_3\cdot CH_2\cdot CH_2CH_2Cl$	0.8851	1140	86.96	55.24	55.65	−0.41	12.64	1093*			223.4*			220.5^{*m}	L E M
s-tetrachloroethane	$Cl_2HC\cdot CHCl_2$	1.5947	1170	45.81	60.58	61.02	−0.44	12.87	1109*			228.6*			226.0_{*}	L E M
ethylene chloride	$CH_2Cl\cdot CH_2Cl$	1.2524	1216	54.00	44.68	45.40	−0.72	12.69	843.7*			229.4*			226.8*	L E M
methylene chloride	CH_2Cl_2	1.336	1093	62.66	35.30	36.30	−1.00	12.55	654.9*			232.2*			229.9*	L E M
propylene chloride	$CH_3\cdot CHCl\cdot CH_2Cl$	1.1554	1162	64.10	53.96	54.50	−0.54	12.78	1028*			224.2*			221.4*	L E M
o-chlorotoluene	$C_6H_4\cdot CH_3\cdot Cl$	1.0826	1319	53.08	66.26	66.19	0.07	13.12	1282*			211.6^{*m}			234.5*	L E M
p-chlorotoluene	$C_6H_4\cdot CH_3Cl$	1.0697	1308	54.64	66.78	66.19	0.59	13.64	1294*			223.6*			246.5*	L E M
n-propyl chloride	C_3H_7Cl	0.8884	1091	94.56	46.14	46.55	−0.41	12.64	913.9	904.9	9.0	239.0	911.0	2.9	236.4	S
cyclohexyl chloride	$C_6H_{11}Cl$	1.000	1319	57.47	66.45	67.35	−0.90	12.15^{m}	1300	1298.5	1.5	227.3	1311	−11.0	222.5	S
benzyl chloride	$C_6H_5\cdot CH_2Cl$	1.098	1420	45.17	66.85	66.19	0.66	13.71^{M}	1295	1300.4	−5.4	224.6	1281	14.0	247.6	S
o-dichlorobenzene	$C_6H_4Cl_2$	1.305	1295	45.69	65.23	65.04	0.19	13.14	1227	1240.6	−13.6	223.2	1227	0.0	233.5	S

trichloro-ethylene	$CHCl:CHCl_2$	1.447	1049	62.80	50.26	49.93	0.33	13.16	922.6	914.2	8.4	232.8	923.0	−0.4	233.4	S
acetyl chloride	$CH_3CO \cdot Cl$	1.104	1060	80.61	37.49	37.18	0.31	13.36	724.8	705.6	19.2	249.0^M	715.0	9.8	233.3	S
pentachloroethane	$CCl_3 \cdot CHCl_2$	1.672	1113	48.28	69.54	69.25	0.29	13.11	1254	1248.0	−6.0	230.9	1280	−26.0	228.3	S
m-dichlorobenzene	$C_6H_4Cl_2$	1.287	1295	46.33	65.99	65.04	0.95	13.55	1243	1240.6	2.4	231.2	1227	16.0	241.5	S
1, 2, 4, trichlorobenzene	$C_6H_3Cl_3$	1.456	1301	40.58	73.44	72.99	0.45	13.20	1361	1375.4	14.4	225.2	1368	−7.0	231.2	S
tetrachloroethylene	$CCl_2:CCl_2$	1.614	1066	54.52	58.04	57.88	0.16	13.09	1049.5	1049.0	0.5	230.1	1064	−14.5	229.9	S
								mean C–Cl=13.05				mean C–Cl=230.0(229.9)			mean Cl=233.5	
hexadecafluoroheptane	C_7F_{16}	1.62027	444.0	313.07	105.20	104.12	1.08	6.99^M	1827	1834	−7	112.59	1830	−3	109.81	LWEU
bis(trifluoromethyl)-chlorononofluoro-cyclohexane	$C_6ClF_9(CF_3)_2$	1.79126	582.3	164.65	112.17	112.71	−0.54	6.88^m	1940	1959	−19	111.73^m	1957	−17	108.87^m	LWEU
bis(trifluoromethyl))-decafluorocyclohexane	$C_6F_{10}(CF_3)_2$	1.74636	513.1	217.50	106.20	106.72	−0.52	6.89	1834	1842	−8	112.50	1840	−6	109.63	LWEU
(trifluoromethyl)-undecafluoro-cyclohexane	$C_6F_{11}(CF_3)$	1.78751	577.6	167.69	94.21	93.98	0.23	6.94	1631	1612	19	114.38^M	1610	21	111.50^M	LWEU
								mean C–F≒6.92				mean C–F≒112.80 ≒113			mean F≒109.95 ≒110	

Remarks: The values with * are taken from Lagemann, Evans, and McMillan's paper. *M* means the maximum value, and *m* the minimum value.

sibility, and the bond-increments and atomic increments of the molecular sound velocity, together with the maximum values, minimum values, and the deviation. Also the existing values of these increments are also indicated in the table.

In this table the deviation indicates the ratio of the difference between the maximum and the minimum values to the average value. For example, the deviation of the bond increment of the molecular compressibility δX is defined by

$$\delta X = \frac{(X_i)_{\max} - (X_i)_{\min}}{(X_i)_{\mathrm{av}}}, \qquad (3)$$

where $(X_i)_{\max}$ denotes the maximum value, $(X_i)_{\min}$ the minimum value, and $(X_i)_{\mathrm{av}}$ the average value of the individual increments ($i=1, 2, 3, \ldots, n$) obtained from each of the liquids employed in calculation.

In obtaining the halogen increments, the values of the increments due to other constitutive elements (atoms or bonds) are assumed to be constant, the values of these increments employed in the calculation being indicated in Table II. In this table the bond increments of the molecular compressibility are the values given by Wada[2], the bond increments of the molecular sound velocity are the values given by Lagemann and Corey[7] (cf. also Lagemann and Dunbar[8]), and the atomic increments of the molecular sound velocity are taken from Rao's paper[9].

Table I indicates that the fluctuations of the halogen increments of the molecular compressibility are smaller than the fluctuations of the halogen increments of the molecular sound velocity. The ratios of the percentage deviations of the halogen bond-increments for the molecular compressibility δX to that of the bond-increments of the molecular sound velocity δx_b are also indicated in the table. They are 0.60 forC–I, 0.40 for C–Br, 0.74 for C–Cl, and 0.70 for C–F. Although there is no exact meaning in these figures, because these figures depend also on the number of the liquids employed in calculation and on the special nature of each substance employed, these figures indicate that the fluctuation of the halogen increments are of the order of 1/2∼2/3 for the increments of the molecular compressibility as compared with the increments of the molecular sound velocity. It is

Table I. Halogen increments of the molecular compressibility and the molecular sound velocity.

	Atoms or bonds	Existing results		Present result					
				mean	max	min	deviation	number of liquids	ratio of deviations
I. Halogen		(Wada)		X			δX		$\delta X/\delta x_b$
increments of the	C–I	19.65		19.76	20.92	19.06	9.4%	(6)	0.60
molecular	C–Br	15.54		15.72	16.45	15.22	7.8	(9)	0.40
compressibility	C–Cl	12.91		13.05	13.71	12.15	12.0	(20)	0.74
(bond-increments)	C–F	—		6.92	6.99	6.88	1.6	(4)	0.70
IIb. Halogen		(Lagemann)	(L E M)	x_b			δx_b		
increments of	C–I	—	281.2	284.0	304.0	259.5	15.7%	(6)	
the molecular	C–Br	—	232.4	(232.4)*	253.0	207.6	19.5	(9)	
sound velocity	C–Cl	230	228.1	230.0	249.0	211.6	16.2	(20)	
(bond-increments)	C–F	—	—	113	114.4	111.7	2.3	(4)	
IIa. Halogen		(Rao)	(L E M)	x_a			δx_a		
increments of	I	304	287.3	285.9	303.5	256.5	16.4%	(6)	
the molecular	Br	245	238.4	(238.4)*	254.5	209.5	18.9	(9)	
sound velocity	Cl	227	233.2	233.5	259.5	220.5	16.7	(20)	
(atomic-increments)	F	—	—	110	111.5	108.9	2.5	(4)	

* The values with asterisks indicate that these are not new results because they are based on the same liquids as employed in the calculations of Lagemann, Evans and McMillan.

Table II. The values of the increments of other atoms or bonds employed in calculation.

Bond increments of the molecular compressibility		Molecular sound velocity			
		bond increments		atomic increments	
C–H	5.10	C–H	95.2	H	92.5
C–C	−1.10	C–C	4.25	C	10
C=C	5.68	C=C	129	O	74
C=O	9.93	C=O	186	double bond	110
cyclic compound	4.80				

also to be noticed that the percentage deviation is very small for F-increments, which may, presumably be due to the small atomic weight, though the small number of the liquids employed in calculation is also a part of the reason of this small percentage deviation.

The mean values of the halogen increments here obtained are in agreement with existing results within 1.5%, although the atomic increments given by Rao are not in good agreement with our result.

Table III shows the results of calculation for individual liquids. There are indicated for each liquid the chemical formula, density, sound velocity and adiabatic compressibility at 20°C; experimental values of the molecular compressibility W_{exp} (i.e., the values obtained from the values of the density and the adiabatic compressibility according to equation (2)), the calculated value W_{cal}, and the deviation $\delta W = W_{\mathrm{exp}} - W_{\mathrm{cal}}$, and the halogen increments X; the experimental values of the molecular sound velocity R_{exp} obtained by equation (1), the calculated values R_b computed by employing bond additivity rule, the deviation $\delta R_b = R_{\mathrm{exp}} - R_b$, the halogen bond-increments x_b, the calculated values of the molecular sound velocity R_a obtained by employing the additivity rules of the atomic increments, the deviation $\delta R_a = R_{\mathrm{exp}} - R_a$, and the halogen atomic increments δR_a, and the authors of the sound velocity data. For some of the liquids containing I, Br and Cl, molecular sound velocity and the halogen increments are calculated by Lagemann, Evans and McMillan. These values are also indicated in Table III and are marked with asterisks.

Conclusion

It is known that the additivity rules of the molecular sound velocity with respect to the constitutive elements of the molecules begin to fail for halogen compounds. The deviation from additivity rule of the molecular compressibility is smaller in this case and the percentage deviation of the halogen increments of the molecular compressibility is about 1/2∼2/3 of the percentage deviation of the halogen increments of the molecular sound velocity if we ascribe all the deviations to the halogen atoms.

References

1) Rama Rao: Indian J. Phys. **14** (1940) 109.

2) Y. Wada: J. Phys. Soc. Japan **4** (1949) 280.

3) R. T. Lagemann, J. S. Evans and D. R. McMillan Jr.: J. Amer. Chem. Soc. **70** (1948) 2996.

4) R. T. Lagemann, W. E. Woolf, J. S. Evans and N. Underwood: J. Amer. Chem. Soc. **70** (1948) 2994.

5) W. Schaaffs: Zeits. Phys. Chem. **194** (1944) 66.

6) W. Schaaffs: Zeits. Naturforsch **3a** (1948) 396.

7) R. T. Lagemann and J. E. Corey: J. Chem. Phys. **10** (1942) 759.

8) R. T. Lagemann and W. S. Dunbar: J. Phys. Chem. **49** (1945) 428.

9) Rama Rao: J. Chem. Phys. **9** (1941) 682.

JOURNAL OF THE PHYSICAL SOCIETY OF JAPAN Vol. 10, No. 1, JANUARY, 1955

Interference Fringes in Electron Micrographs of Magnesium Oxide

By Tadatosi HIBI,

Research Institute for Scientific Measurements,
Tohoku University, Sendai, Japan

Kyozaburo KAMBE* and Goro HONJO

Physics Department, Tokyo Institute of Technology,
Oh-okayama, Meguro, Tokyo, Japan

(Received October 30, 1953)

The striations, or so called equal thickness fringes, appearing in electron micrographs of magnesium oxide, have been studied in detail. It was found that the spacing of the striations ranges from 50 to several hundred Ångstroms, depending on the index of reflexion, azimuth, and glancing angle. The explanation of the striations is given by the dynamical theory applied to a wedge-shaped crystal. Calculated spacings of the striations as a function of azimuth and glancing angle are compared with observed values, giving fairly good agreement. Some newly found crystal shapes other than cubic and the effect of simultaneous reflexions on the striations are also described.

§ 1. Introduction

It is well known that smoke particles of magnesium oxide are microcrystals having a clean cut cubic habit as revealed by the electron microscopy. It has been noted that electron micrographs of the particles frequently show parallel striations along their contours with uniform spacings[1)2)]. A theoretical explanation of these striations has been given, applying the dynamical theory of electron diffraction, that they appear as a result of Bragg reflexion of electron wave in the crystal[3)4)5)], and they are called "equal-thickness interference fringes."

Heidenreich and Sturkey[4)] (hereafter referred to as HS) have calculated the spacing

---

[*] Now at Electrotechnical Laboratory, Tanashi, Tokyo, Japan.

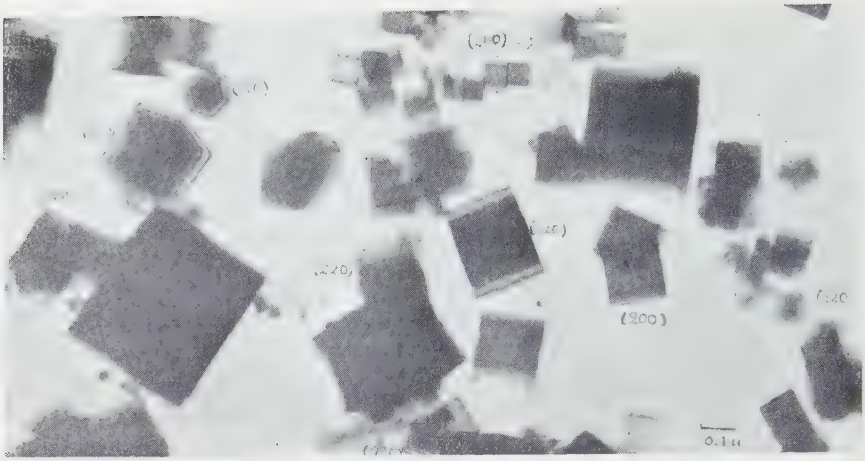

Fig. 1. Magnesium oxide crystals showing striations. Indices of Bragg reflexion are indicated.

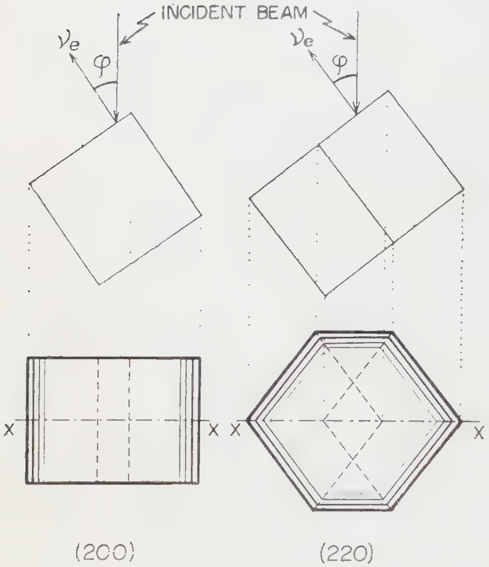

Fig. 2. Lower figures are sketches of the images of the crystal. We can see easily from the shape of these images that the reflecting net-planes are oriented parallel to the lines marked XX. In upper figures the crystals are viewed in the direction perpendicular to the reflecting net-planes, showing the orientation of the crystal with respect to the incident beam. The azimuth angle φ is indicated.

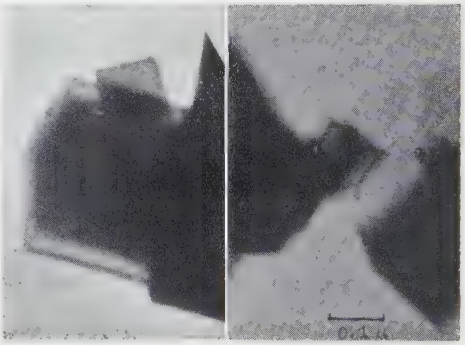

Fig. 3. Striations due to reflexions other than (200) and (220).

of the striations, using the formula of the dynamical theory given by MacGillavry⁽⁶⁾, and obtained a fair agreement with the observed values.

Hall⁽⁷⁾ has observed similar striations in dark-field micrographs. He measured the spacing of the striations and found that the spacing varies in a certain range, in accordance with Kinder⁽²⁾, and opposed to HS. Further he pointed out the fact that this phenomenon is closely related to the multiple diffraction spots found in usual electron diffraction⁽⁸⁾.

Kato⁽⁹⁾ has discussed this phenomenon by the dynamical theory developed for finite polyhedral crystals⁽¹⁰⁾, and concluded that the striations due to double refraction are observed in just-focused images, whereas in defocused images they are disturbed in the neighbourhood of the crystal edge by the effect of Fresnel diffraction.

One of the present authors⁽¹¹⁾ has obtained, in the course of the study of the resolving power of an electron microscope, a large number of micrographs of magnesium oxide with fairly high resolution. By a detailed inspection of these micrographs we found some properties of the striations. As they have not been reported before, it may be worth

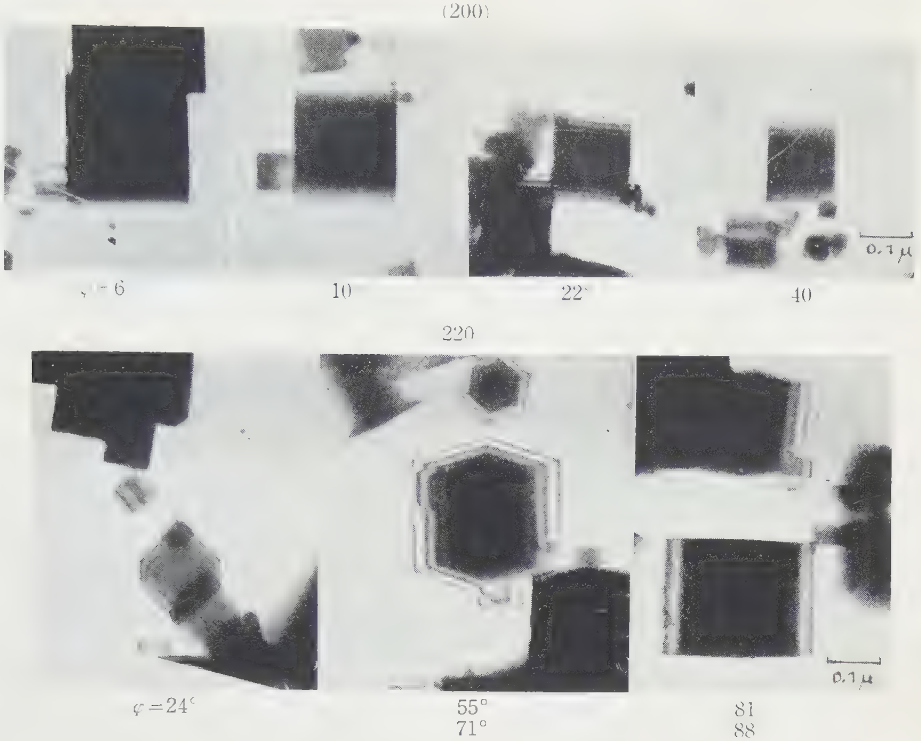

Fig. 4. (200) and (220) cases for various azimuths.

while to describe them here along with the result of a comparison with the theory.

§ 2. Experimental Observations

Fig. 1 shows an example of the micrograph of magnesium oxide smoke particles, in which the crystals showing the striations are comparatively numerous. The indices of Bragg reflexions responsible for the appearance of the striations can be known from the shape of the contour of the image, in virtue of the fact that the Bragg angles are very small. For instance, the contour of the images containing the striations due to (200) and (220) reflexions should be respectively a rectangle and a hexagon which is symmetric with respect to the diagonal which is parallel to the reflecting net-plane (Fig. 2).

It was found, as we see in Fig. 1, that the greater part of the striations can be attributed to (200) and (220), the strongest reflexions of magnesium oxide. The striations which correspond to other reflexions are usually faint, and comparatively rare (Fig. 3); on 25 plates picked up *at random*, there were 116 (200) reflexions, 105 (220) reflexions, and 51 others.

The spacing of the striations was measured for the images obtained with accelerating voltage 50 kV, and electron-optical magnification 7000. Only images of good focus were used. It was found that the spacing varies in a fairly wide range. For example, the spacing varies from about 50 to 200 Å in the case of (200).

The lower limit of about 50 Å seems to be brought about by the resolution limit of the microscope, because the contrast of the striations became very small when they had a small spacing and these striations could be found only in the plates of particularly high resolution. Fig. 7 shows an example of small spacing. The striations with small spacings are apt to be masked by the effect of absorption, so that it is possible that we have missed striations with spacings smaller than 50 Å.

The upper limit of about 200 Å for (200) seems to be characteristic of the index of reflexion. For (220) the upper limit is about 300 Å. For other reflexions, still larger values of the spacing are observed.

One of the causes of the variation of the spacing is certainly the variation of the azimuth, or the orientation of the crystal

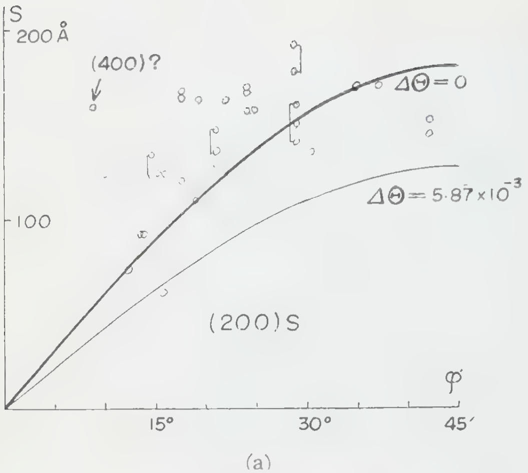

(a)

around the normal of the reflecting net-plane. The azimuth is known from the shape of the contour of the image, and represented by an angle φ, which we call azimuthal angle and define as follows: For (200), φ is the angle between the normal ν_e of one of the two front faces of the crystal and the direction of the electron beam (see Fig. 2). In this case φ is determined by measuring the ratio between the length and width of the rectangular image. For (220), φ is the angle between the direction of the electron beam and the normal ν_e of one of the front faces which is perpendicular to the reflecting net-plane (Fig. 2). φ is determined in this case from corner angles of the hexagonal contour.

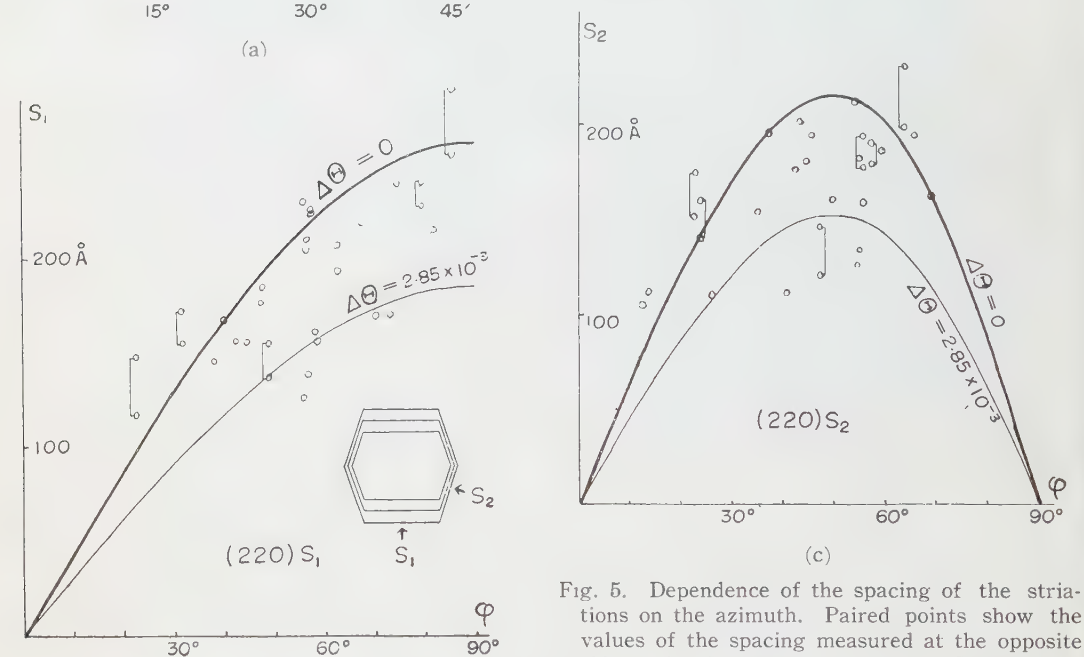

(b)

(c)

Fig. 5. Dependence of the spacing of the striations on the azimuth. Paired points show the values of the spacing measured at the opposite sides of the same crystal. Curves are theoretical.

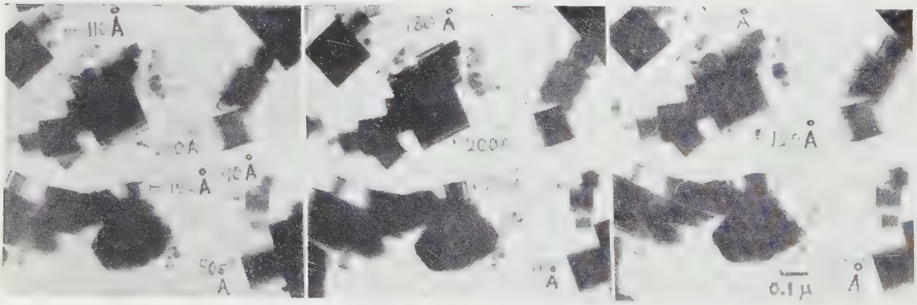

Fig. 6. A series of micrographs of the same area in a sample. The spacings are indicated.

As shown by the examples in Fig. 4, we can find the images of crystal containing the striations corresponding to various azimuths. In Fig. 5 the observed values of the spacing are plotted against the azimuth. We see that

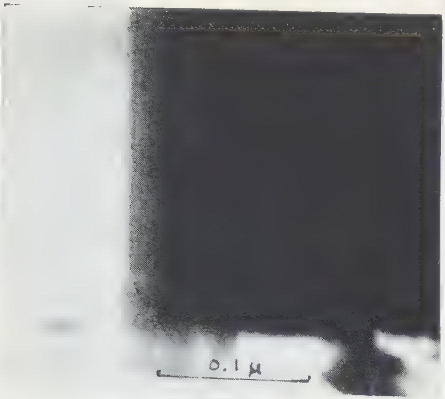

(2 0)

Fig. 7. An example of small spacing.

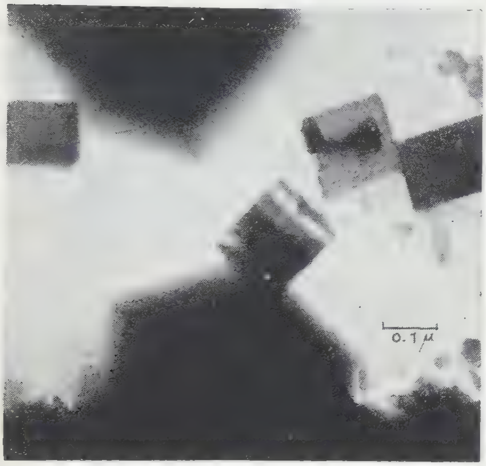

(400) ?

Fig. 8. An example of large spacing.

for a given index of reflexion and a given azimuth the spacing varies in a certain range. It is clearly exhibited in Fig. 6 which shows a series of micrographs of the same area in a sample. They were taken under almost the same condition except that the specimen was a little shifted arbitrarily, by moving the specimen holder perpendicularly to the electron beam, and the focusing was readjusted at each time. These adjustments are always accompanied by a small rotation of individual crystals. As indicated in Fig. 6, the spacing of the striations in the same crystal varies greatly from plate to plate, and this variation is far greater than can be expected from the slight change in the azimuth. We shall see later that this variation of the spacing is due to a small deviation of the glancing angle from the Bragg angle.

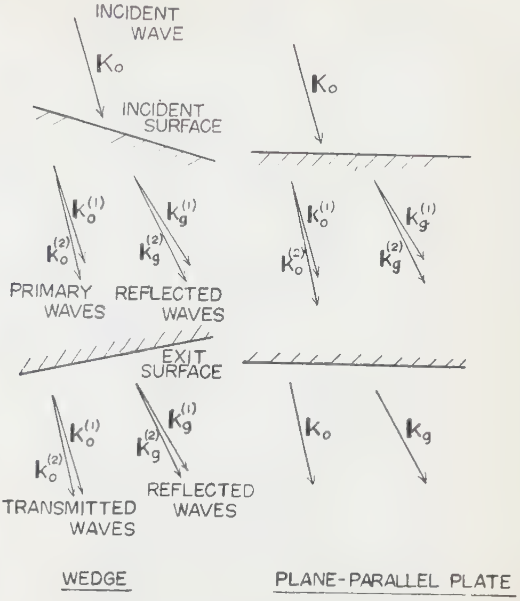

Fig. 9. Double refraction in a wedge-shaped crystal, compared with the case of a plate crystal.

Among the striations in the rectangular images, those with especially large spacing, exceeding greatly the ordinary values, have been observed at times (Fig. 5 and Fig. 8). They are usually faint, and as we shall see later, may be associated with a higher order reflexion of (200), say the (400) reflexion.

§ 3. Theory

The striations have been explained by Kossel[3], HS[4], and later by Kato[9], on the basis of the dynamical theory of electron diffraction due to Bethe[12] and developed by MacGillavry[6]. An important consequence of this theory which is used in the explanation is double refraction[13][14][15]. Let a parallel electron wave enter a wedge-shaped crystal through one surface (incident surface). (Fig. 9) When a Bragg reflexion takes place in the crystal, the double refraction occurs on the surface and the primary and reflected waves in the crystal are both divided into two. These waves are refracted again when they emerge from the crystal through another surface (exit surface), and come out in vacuum as a pair of transmitted waves and a pair of reflected waves.

In bright field micrographs, the reflected waves are cut out by an aperture in the objective lens, so that only the intensity distribution due to the two transmitted waves

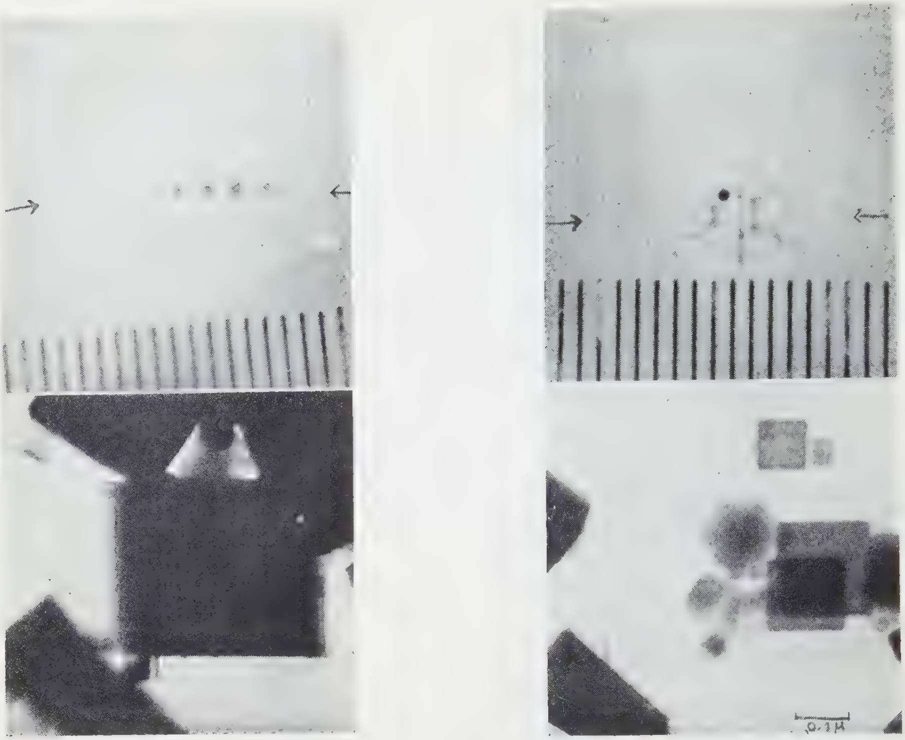

(200) (220)

Fig. 10. The multiple spots in diffraction photographs and the striations in electron micrographs. In (200), two pairs of diffraction spots correspond to the two sides which show the striations in micrographs. In (220), six pairs correspond to six sides. Arrows indicate the normal position of the Debye ring.

on the electron-optical object plane of the microscope is reproduced in the micrograph image4). The striations we are discussing in the present paper are nothing but the interference fringes made by these doubly refracted transmitted waves.

Similar striations in dark-field images as observed by Hall7) are the interference fringes of the two reflected waves. In usual diffraction photographs the pair of reflected waves are observed as a pair of spots. Several pairs corresponding to different wedge-shaped parts of a crystal constitute a multiple spot found in Debye rings14)16)17)18). (Fig. 10)

MacGillavry's dynamical theory6), which has been used by HS, is developed for the case of a plane-parallel plate, so that it is inadequate to be used in the explanation of the present phenomenon, because the striations appear only in wedge-shaped parts of a crystal. (In the case of a plate the doubly refracted waves are united again at the exit surface into one (Fig. 9).) Nevertheless, HS calculated the spacing of the striations using MacGillavry's formula, and obtained after some approximations a fair agreement with the observation. In fact, Kato9) has shown that even when we consider the double refraction by a wedge in a more proper way than HS, taking the finiteness of the crystal into account, the final result obtained after some approximations is essentially the same as that obtained by HS. We describe here the process of calculation following HS, considering its relation with the double refraction.

In the first place, Kato9) has shown that the finiteness of the crystal has an influence on the striations only in the out-focus micrograph images as a sort of Fresnel diffraction. So long as the in-focus images are concerned, we can consider that the surfaces of the crystal extend infinitely. Then the refraction of the waves occurs in such a way that the tangential component of the wave number vectors are connected continuously on the surfaces, as shown in Fig. 11.

As a *beat* between the waves which are represented by wave number vectors $\boldsymbol{k}_0^{(1)}$ and

$\boldsymbol{k}_0^{(2)}$, the intensity of the primary wave varies periodically in crystal as shown in the right side of Fig. 11. Its nodal planes are parallel to the incident surface. This intensity variation occurs in just the same way as in the case of a plate. According to MacGillavry[6], its period D_0, measured in the direction of $\boldsymbol{K}_0$ as shown in Fig. 11, is expressed as

$$D_0=\left[\frac{1}{\lambda^2}\left(\frac{V_{hkl}}{E}\right)^2+\left(\frac{\Delta\Theta}{d_{hkl}}\right)^2\right]^{-1/2}, \qquad (1)$$

Here, E is the accelerating voltage, λ is the wave length in vacuum corresponding to E, V_{hkl} is the Fourier coeffiicient of the inner potential for the reflexion concerned, d_{hkl} is the spacing of the reflecting net-plane, $\Delta\Theta$ is the deviation of glancing angle from the Bragg angle.

Thus when we consider the intensity of the primary wave on the exit surface, as shown in Fig. 11, it is expressed as a function of the effective thickness D_e (the thickness of the crystal measured in the direction of $\boldsymbol{K}_0$) as

$$I_{\text{prim.}}=I_0\cdot\frac{1}{\lambda^2}\left(\frac{V_{hkl}}{E}\right)^2 D_0^2\cdot\cos^2\left(\pi\frac{D_e}{D_0}\right). \qquad (2)$$

I_0 is the intensity of the incident wave. (The effect of absorption is neglected throughout the present calculation.) (2) shows that the intensity variation on the exit surface has its maxima where D_e is an integral multiple of D_0.

To calculate the spacing of the striations we must obtain the intensity variation on the object plane of the microscope made by the interference between $\boldsymbol{K}_0^{(1)}$ and $\boldsymbol{K}_0^{(2)}$. As we see in Fig. 11, the refraction on the exit surface occurs in such a way that the intensity variation of the striations can be obtained when the intensity variation on the exit surface, given by (2), is normally projected on the object plane. Hence we can consider that the striations in the image are the magnified reproduction of the intensity variation *on the exit surface*, and thus the spacing of the striations can be easily derived from D_0 when we can find from the image of the crystal how the incident and exit surfaces are oriented.

It must be mentioned that an appreciable deviation from HS's value appears when the angles between the wave vectors and the surfaces are fairly small. In the case of magnesium oxide, the electron beam enters into the crystal through three cube faces and emerges through three remaining cube faces.

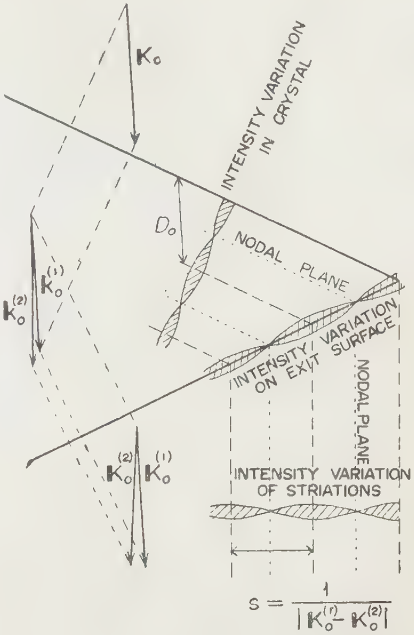
K_o
INTENSITY VARIATION IN CRYSTAL
D_o
NODAL PLANE
$K_o^{(1)}$
$K_o^{(2)}$
INTENSITY VARIATION ON EXIT SURFACE
NODAL PLANE
$K_o^{(2)}$ $K_o^{(1)}$
INTENSITY VARIATION OF STRIATIONS
$s=\frac{1}{|K_o^{(1)}-K_o^{(2)}|}$

Fig. 11. Wave number vectors are related by the continuity of tangential component. Interference of two slightly different waves gives the intensity variation (beat) in and behind the crystal perpendicular to the incident surface and incident wave respectively.

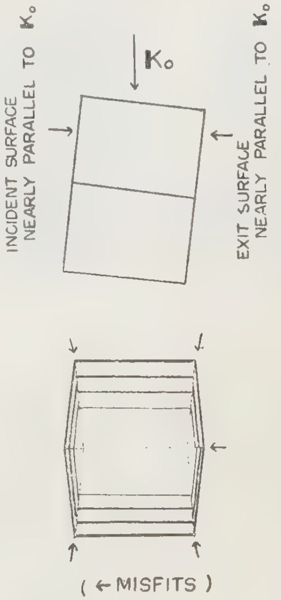
INCIDENT SURFACE NEARLY PARALLEL TO K_o
K_o
EXIT SURFACE NEARLY PARALLEL TO K_o
(← MISFITS)

Fig. 12. Illustration of the misfit of the spacing, which occurs on the images of the cube edges. The amount of misfit is exaggerated.

There are six wedge-shaped parts which have different combinations of these incident and exit surfaces. When one of the incident surfaces becomes almost parallel to the incident beam, it is possible that the value of D_0 is different for different wedge-shaped parts, or that for some wedges the spacing of the striations cannot be obtained directly from D_0 as described above. Then a detailed inspection of the striations might reveal that in the hexagonal image they do not make successive hexagons on account of the misfit of the spacing on the boundary of the cube faces, as illustrated in Fig. 12.

We have such cases for (220) when φ is very small or close to 90°. An estimation of the order of magnitude shows that, for example, the discrepancy of D_0 will exceed 10% when φ is smaller than about 10°. However, we could not find this phenomenon in our photographs, because at such azimuths the spacing itself became so small that we could not observe such details.

§ 4. Comparison with Experiment

Table I shows the value of D_0 at Bragg angle ($\Delta\Theta=0$) for the main reflexions of MgO, calculated by (1). ($E=50$ kV, $\lambda=0.0535$ Å)

Table I. Characteristic values for main reflexions of MgO (calculated).

hkl	d (Å)	V (volt)	$D_0(\Delta\Theta=0)$ (Å)	$\Delta\Theta_{1/2}(10^{-3}$ rad)
200	2.10	7.85	358	5.87
220	1.475	5.40	521	2.85
222	1.215	4.20	670	1.81
400	1.050	3.46	813	1.29
420	0.939	2.92	963	0.98
422	0.857	2.57	1094	0.78

The spacing s is derived from D_0 considering the orientation of the surfaces. In the present case the ratio between s and D_0 can be expressed as a function of the azimuthal angle φ defined in § 2. The spacing s is given as follows:

$$\text{for (200),}\quad s=\frac{\sin 2\varphi}{2}D_0\,,$$

$$\text{for (220),}\quad s_1=\frac{\sin\varphi}{2}D_0\,,$$

$$s_2=\frac{\sin 2\varphi}{2\sqrt{1+\cos^2\varphi}}D_0\,. \qquad (3)$$

According to (1) and (3), the spacing of the striations varies in fairly wide range depending on index of reflexion, azimuth, and deviation of glancing angle from the Bragg angle.

For a given reflexion, D_0 is largest when $\Delta\Theta=0$. The thick curves in Fig. 5 show the variation of the spacing with the azimuth for the maximum value of D_0 (Table I). These curves should be the upper limit of the spacing of the striations to be observed.

When $\Delta\Theta$ is not zero, the spacing becomes smaller, and the intensity of the striations must also become smaller. Eq. (2) shows that the amplitude of the sinusoidal variation of the intensity is proportional to the square of D_0. Thus, the amplitude becomes a half of its maximum value, when the spacing becomes $1/\sqrt{2}$ of its maximum value. The thin curves in Fig. 5 show these values of the spacing. The deviation angle $\Delta\Theta$ for this case, denoted by $\Delta\Theta_{1/2}$, is shown in Table I.

We expect that the observed points lie below the thick curve and most frequently above the thin curve. We find in Fig. 5 that this is satisfied fairly well for (220). In the case of (200), however, the distribution of the observed points is shifted to higher values, and corresponds to the value of V_{200} equal to about 5 volts, against the theoretical value of 7.85 volts. As the cause of this discrepancy we can consider the following effects.

1) The striations due to (400) or other reflexions may be erroneously taken in.

2) The effect of slight defocusing may cause an error in the measurement of the spacing and the length of the edges, accordingly in φ.

3) The existence of the crystals, whose three edges are not equal, leads to a wrong estimation of φ.

4) The effect of other weak reflexions occurring simultaneously with (200) may vary the spacing.

It is not certain, however, whether the present discrepancy is only caused by these secondary effects.

The intensity measurement of the striations has not been carried out. However, we could conclude by a visual inspection that for a given azimuth the intensity of the striation decreases with the decrease of the spacing, in qualitative agreement with the theory. The striations can be observed at the spacing down to almost half of the maximum value

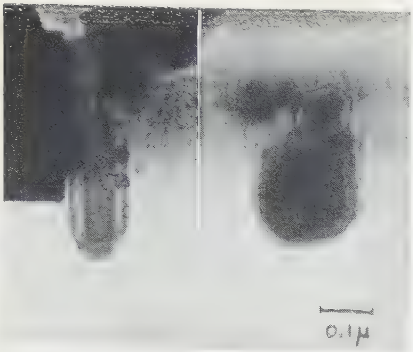

Fig. 13. Striations in irregularly shaped crystals.

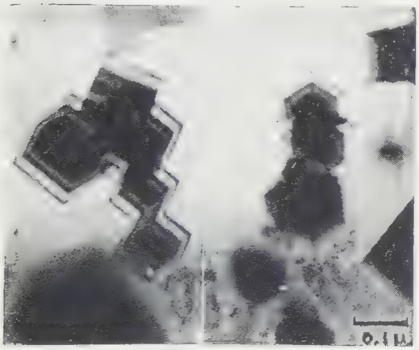

(a) (b)

Fig. 14. (a) Striations in connected crystals. (b) Striations in crystals merely in contact.

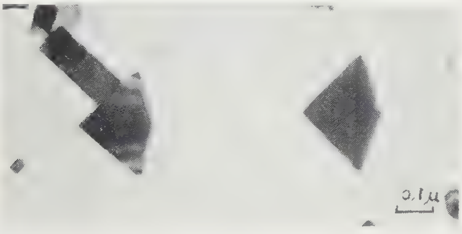

(a) (b)

Fig. 15. Striations in twinned crystals.

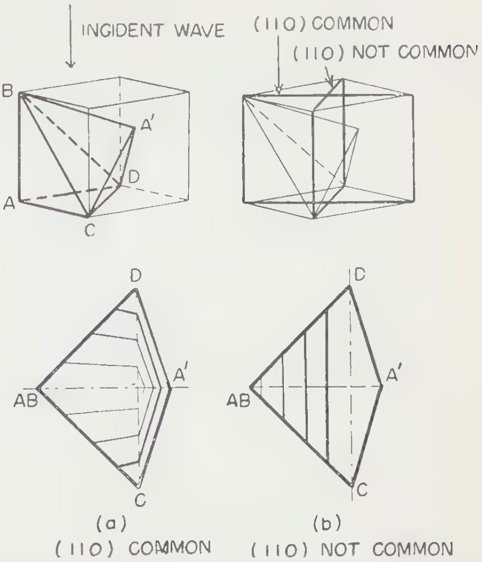

Fig. 16. Explanations of Fig. 15. The crystal is made up by combining a tetrahedron ABCD and its mirror image A'BCD at the (111) twinning plane BCD. The plane ACD lies perpendicular to the electron beam. Reflecting (110) net-planes both common and not-common are indicated.

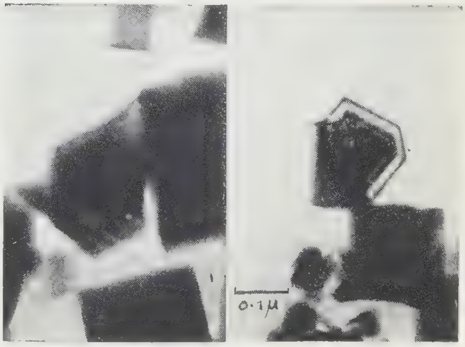

Fig. 17. Striations in crystals with extraordinary habit.

for a given azimuth. It seems that smaller spacings cannot be observed only because the contrast of the striations becomes too small.

It was observed that the striations due to stronger reflexions (larger V_{hkl} values) appear more frequently, as described in § 2. It can be explained from Eq. (2) that, though the amplitude of the sinusoidal intensity variation is equal at $\Delta\Theta=0$ for all reflexions, it decreases more rapidly with the increase of $\Delta\Theta$ for weaker reflexions, so that the angular allowance in the orientation of the crystal for the appearance of the striations is smaller for weaker reflexions. The value of $\Delta\Theta_{1/2}$ (Table I) multiplied by the multiplicity of the net-plane may serve as a measure for this angular allowance. For (200) and (220) it has roughly the same value. Actually, these reflexions appear with about the same frequency, as shown in § 2. However, the sum of its value over the remaining reflexions in Table I is larger than the value for (200), whereas, the total observed frequency is about a half of (200). This may be the result of the fact that the striations having wider spacings are apt to be missed in the frequency counting, because they are hidden by the effect of absorption.

It is frequently observed that the spacing

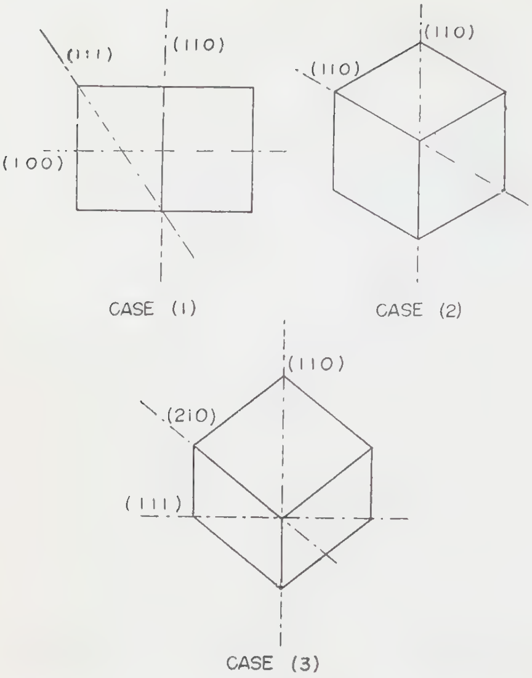

Fig. 18. Illustration of the images of crystal when simultaneous reflexions are occurring.

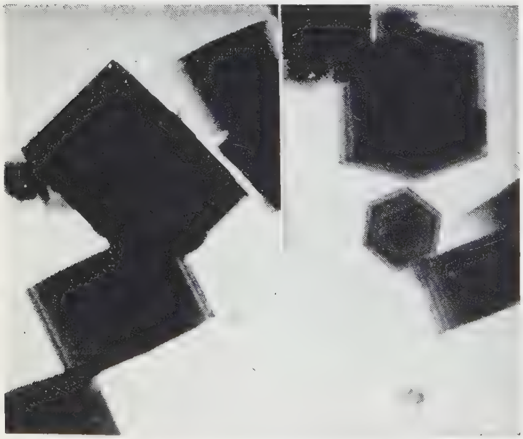

CASE (1) CASE (2)

Fig. 19. Anomalous striations caused by simultaneous reflexions.

of the striations is different at the two opposite sides of an image, as indicated in Fig. 5 by paired points. The cause of it is not clear. One cause may be the effect of accompanying weak reflexions.

§ 5. Further Experimental Observations

(a) *Crystals with extraordinary shapes*[19)]

We have observed not merely the crystals with cubic habit. Fig. 13 shows the examples of irregularly shaped crystals which show the striations apparently of the same origin as in the cube crystals.

The crystals shown in Fig. 14 (a) are considered that their crystal lattices are connected continuously on the boundary, so that the fringes go through the boundary continuously. On the other hand, if the two separate crystals are merely in contact with each other, fringes are superposed as shown in Fig. 14 (b).

An interesting example is given in Fig. 15. The crystals show contours as if they have tetrahedral habit, whereas, the fringes in them are not parallel to the contour and appear in different ways for two crystals. These can be explained by assuming that the crystals are twinned, as illustrated in Fig. 16. The fringes in Fig. 15 (a) are considered to be due to a (220) reflexion by a (110) net-plane that is common to the two twinned parts, while the fringes in Fig. 15 (b) are considered to be due to a (220) reflexion by a (110) net-plane that belongs only to the one part of the twin.

The crystals shown in Fig. 17 are also examples which have extraordinary habit.

(b) *Effect of simultaneous reflexions.*

Up to now we have considered that only a single reflexion is occurring, and calculations have been developed neglecting all other reflexions. Actually, however, other reflexions are not always negligibly weak, and their influence may appear more or less upon the spacing or the intensity of the striations. When the crystal is in a particular orientation, two or more reflections occur simultaneously, and their reflected waves have comparable amplitudes. In such a case, the transmitted wave is divided into three or more waves, and their beat takes a form considerably more complex than in the case of a single reflexion. We can consider three typical cases, where two or three relatively strong reflexions occur simultaneously. Fig. 18 illustrates how the image appears in these cases.

1) Azimuthal angle $\varphi=\pi/4$ for (200). It corresponds to $\varphi=\pi/2$ for (220). In this case (200), (220), and (222) reflexions occur simultaneously.

2) φ for (220) is specified by $\cos\varphi=1/\sqrt{3}$. In this case we have two (220) reflexions that

reflect simultaneously.

3) φ for (220) is specified by $\cos\varphi=\sqrt{2/3}$. In this case (220), (222), and (420) reflect simultaneously.

In each case the direction of the incident wave is nearly parallel to a certain principal zone-axis, so that the total effect of reflexions other than those considered above is not negligibly small. Consequently, we cannot discuss the problem quantitatively. Fig. 19 shows examples of the cases 1) and 2). The shape of contours indicates that these crystals are in the specified orientation, and we see clearly the striations with unusual features.

§ 6. Discussions

HS arrived at the conclusion that the variation of D_0 with $\Delta\Theta$ would not be observed, considering the two disturbances, namely, the effect of inelastic scattering and the effect of angular aperture in the incident beam. Our observation have shown however that the change of D_0 can be observed until it becomes about a half of its maximum value. In our case the accelerating voltage is 50 kV, so that the effect of inelastic scattering may not be quite different from HS's 65 kV. On the other hand, the existence of finite aperture in the incident beam introduces the variation of $\Delta\Theta$, and consequently of the spacing in a certain range, and makes the striations diffuse and indistinct. Hence in our case this aperture has been probably smaller than in the case of HS.

We have seen that the spacing varies sensitively with the variation of the direction of the electron beam. We must be always conscious of this effect when we try to observe quantitatively the effect of other conditions on the spacing, *e.g.* variation in the accelerating voltage or focusing.

Hall[7)] has observed the effect of accelerating voltage, using two voltages 65 kV and 40 kV. From equation (1) the spacing is proportional to the square of the accelerating voltage only when $\Delta\Theta=0$. The variation of the spacing with $\Delta\Theta$ seems to be the cause of the fact that they obtained the observed value 1.35 for the ratio of the spacing, against the calculated value 1.28.

Kato[9)] has discussed how the striations in defocused images are disturbed by the effect of Fresnel diffraction. Fig. 20 shows examples of defocused image. Observations of these images seem to agree qualitatively with Kato's calculations (see Kato[9)]). Here also the effect of the change in $\Delta\Theta$ should be taken in mind in the interpretation of the images.

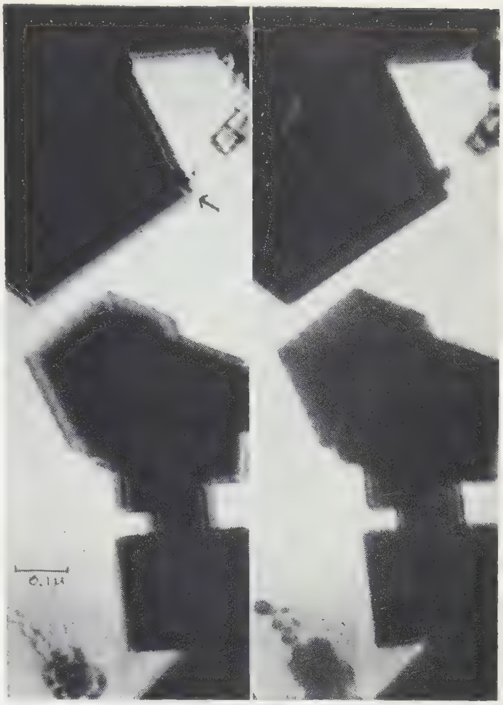

FOCAL-LENGTH TOO SMALL (OVER-FOCUS)

FOCAL-LENGTH TOO LARGE (UNDER-FOCUS)

Fig. 20. Striations in defocused images. (The arrow indicates a misfit of the spacing, occurring probably from the difference in the effect of Fresnel diffraction.)

To use an accelerating voltage as high as possible may be favourable in order to observe further detail of the striations, avoiding the effect of inelastic scattering, especially to observe those misfits of the spacing as described in the theory, or the effect of simultaneous reflexions as described in § 5 (b).

Acknowledgements

The authors wish to express their thanks to Prof. Ryoji Uyeda and Prof. Shizuo Miyake for their encouragement, to Dr. Norio Kato for valuable discussions, to Mr. Shoichi Takahashi for his elaborations in taking micrographs, and to Mr. Takuzo Ogawa for his assistance.

References

1) R. D. Heidenreich: Phys. Rev. **62** (1942) 291.
2) E. Kinder: Naturwiss. **31** (1943) 149.
3) W. Kossel: Naturwiss. **31** (1943) 323.
4) R. D. Heidenreich and L. Sturkey: J. App. Phys. **16** (1945) 97.
5) R. D. Heidenreich: J. App. Phys. **20** (1949) 993.
6) C. MacGillavry: Physica **7** (1940) 334.
7) C. E. Hall: J. App. Phys. **19** (1948) 198.
8) J. M. Cowley and A. L. G. Rees: Nature **158** (1946) 150.
9) N. Kato: J. Phys. Soc. Jap. **8** (1953) 350.
10) N. Kato and R. Uyeda: Acta Cryst. **4** (1951) 227.
N. Kato: J. Phys. Soc. Jap. **7** (1952) 397.
11) T. Hibi, S. Takahashi and K. Yada: J. Electronmicroscopy **1** (1953) 23.
12) H. Bethe: Ann. Phys. **87** (1928) 55.
13) M. v. Laue: *Röntgenstrahlinterferenzen*, Leipzig 1941, p. 331.
14) L. Sturkey: Phys. Rev. **73** (1948) 183.
15) N. Kato: Proc. Jap. Acad. **25** (1949) 41.
16) J. M. Cowley and A. L. G. Rees: Proc. Phys. Soc. **59** (1947) 287.
17) G. Honjo and K. Mihama: Acta Cryst. **4** (1951) 282, J. Phys. Soc. Japan **9** (1954) 184.
18) H. J. Altenhein, K. Molière and H. Niehrs: Naturwiss. **39** (1952) 447.
19) T. Hibi and T. Ogawa: J. Phys. Soc. Japan **9** (1954) 627.

Note added in proof. The authors have found, after this paper was put into print, that a theoretical work by H. Niehrs on the same problem has been published (H. Niehrs: Zeit. für Phys. **138** (1954) 570, *Ibid.* **139** (1954) 88). An experimental work by A.-M. D'Ans is referred to in his papers.

JOURNAL OF THE PHYSICAL SOCIETY OF JAPAN Vol. 10, No. 1, JANUARY, 1955

Integrated Intensities of the Diffracted and Transmitted X-rays due to ideally Perfect Crystal (Laue Case)

By Norio KATO

Kobayasi Institute of Physical Research, Kokubunji, Tokyo, Japan

(Received July 6, 1954)

The analytical expressions of the integrated reflecting power and transmitting power of X-rays for absorbing perfect crystals are obtained as follows:

The diffracted wave:

$$R_H{}^y = e^{-\mu_0 t}\cdot\frac{\pi}{2}\left[2\sum_{n=0}^{\infty} J_{2n+1}(2A)+I_0(h)-1\right] .$$

The transmitted wave:

$$R_T{}^y = e^{-\mu_0 t}\cdot(-2\pi)\left[\sum_{m=1}^{\infty} m\cos m\beta I_m(h)\right]-R_H{}^y .$$

In these formulae

$$h=2A\sqrt{k^2+g^2} \qquad \text{and} \qquad \beta=\tan^{-1}k/g .$$

J_m is the first kind Bessel function of m-th order and I_m is the modified Bessel function of m-th order, and the other notations are the same as those of Zachariasen's text-book on X-ray diffraction (1944). A practical method of obtaining the numerical values of $R_H{}^y$ and $R_T{}^y$, and calculated results are shown.

§ 1. Introduction

Since Borrmann observed[1] the effect that the apparent absorption coefficient of X-rays in crystals is greatly reduced at Bragg angles, detailed experiments have been reported[2] on behaviors of transmitted and diffracted beams in Laue cases (cf. Fig. 1). These experimental results can be understood[4)-7)] in principle on the basis of the dynamical theory of X-ray diffraction in which normal absorption as well as interaction between incident and scattered radiations are taken into account. According to the theory developed by Kohler³⁾, Laue⁴⁾, Hirsch⁵⁾ and Zachariasen⁶⁾, the intensities of transmitted and diffracted beams are expressed as functions of the glancing angle of incident beam relative to the crystal. Experimentally, however, only the integrated intensities can be measured accurately with less difficulties. Hirsch⁵⁾ has calculated graphically the numerical values of integrated transmitting and reflecting power for symmetrical Laue cases and compared with experimental results.

The purposes of this paper are to present the analytical expressions of integrated transmitting power and reflecting power and to give a practical method to obtain their numerical values.

§ 2. Fundamental Equations and Notations

According to the dynamical theory, when parallel monochromatic X-ray beams are reflected by a net plane with indices $H(h_1, h_2, h_3)$, the intensity ratios of the diffracted and transmitted beams to the incident beam are given as follows:

The diffracted wave:

$$\frac{I_H}{I_0}=|b|\frac{|q|}{|q+z^2|}e^{-\mu_0 t}\{\sin^2(av)+\sinh^2(aw)\}\ . \tag{1}$$

The transmitted wave:

$$\begin{aligned}\frac{I_T}{I_0}=\frac{1}{|q+z^2|}e^{-\mu_0 t}[&|q+z^2|\\ &+\{|q+z^2|+|z^2|\}\sinh^2(aw)\\ &-\{|q+z^2|-|z^2|\}\sin^2(av)\\ &\pm\tfrac{1}{2}|(|q+z^2|+|z^2|)^2-|q|^2|^{1/2}\sinh(2aw)\\ &\pm\tfrac{1}{2}|(|q+z^2|-|z^2|)^2-|q|^2|^{1/2}\sin(2av)]\ .\end{aligned} \tag{2}$$

Here, I_0, I_H, and I_T show the intensity of the incident, reflected and transmitted beams respectively. The other notations are the same as those used in Zachariasen's textbook, and summarised in Hirsch's paper⁵⁾. Their meanings are as follows:

$$q=K^2 b\psi_H\psi_{\bar{H}}\ . \tag{3}$$

$$z=\tfrac{1}{2}(1-b)\psi_0+\tfrac{1}{2}b\alpha\ . \tag{4}$$

$$a=\pi t_0/\lambda\gamma_0\ . \tag{5}$$

$$v+iw=(q+z^2)^{1/2}\ . \tag{6}$$

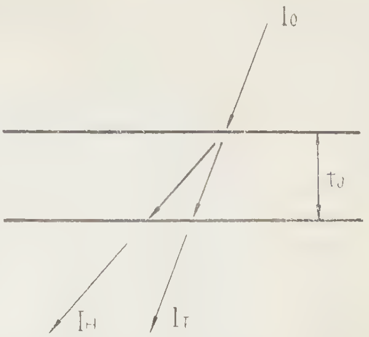

Fig. 1. Laue case for plane parallel plate crystal.
I_0: Incident wave. I_T: Transmitted wave.
I_H: Diffracted wave. t_0: Thickness of crystal.

$$b=\gamma_0/\gamma_H\ . \tag{7}$$

$$\alpha=2(\theta_B-\theta)\sin 2\theta_B\ . \tag{8}$$

$$t=\frac{t_0}{2}\left(\frac{1}{\gamma_0}+\frac{1}{\gamma_H}\right). \tag{9}$$

θ: The glancing angle of incidence at the net plane concerned.

θ_B: The Bragg angle (derived from the kinematical theory).

γ_0 and γ_H: The direction cosines of the incident and diffracted beams to the normal of the crystal surface.

λ: Wave length of X-rays.

K: Polarization factor; $K=1$ for normal component and $K=|\cos 2\theta|$ for parallel component.

μ_0: The usual linear absorption coefficient.

ψ_0' and ψ_H': The Fourier coefficient of index 0 and H of ψ' respectively*, where ψ' is the real part of 4π times of the polarizability of crystal.

ψ_0'' and ψ_H'': The Fourier coefficient of index 0 and H of ψ'' respectively*, where ψ'' is the imaginary part of 4π times of the polarizability of crystal.

The sign $\pm$ in Eq. (2) is determined by the following relations, where U represents $\{z+\sqrt{q+z^2}\}\sqrt{q}$.

For the coefficient of $\sinh(2aw)$,

$|U|>1$ corresponds to + sign,
$|U|<1$ corresponds to − sign.

For the coefficient of $\sin(2av)$,

$\arg U>0$ corresponds to + sign,
$\arg U<0$ corresponds to − sign.

---

* These definitions of ψ_0', ψ_0'', ψ_H' and ψ_H'' are the same as those of Zachariasen and not those of Hirsch, which can be used only when the crystal possesses an inversion centre.

It is convenient further to define the following parameter according to Zachariasen.

$$y\equiv\{\tfrac{1}{2}(1-b)\psi_0'+\tfrac{1}{2}b\alpha\}/K|\psi_H'||b|^{1/2}\ . \tag{10}$$

$$g\equiv\tfrac{1}{2}(1-b)\psi_0''/K|\psi_H'||b|^{1/2}\ . \tag{11}$$

$k\equiv\psi_H''/\psi_H'$ (when crystal has inversion centre) (12)

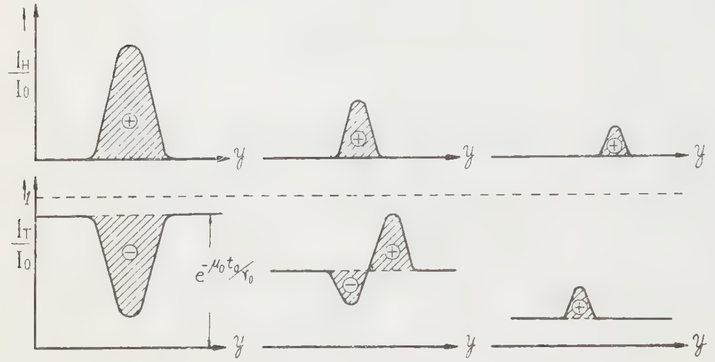

(a) t_0: small (b) t_0: middle (c) t_0: large

Fig. 2. Schematic diagrams of the diffracted and transmitted intensities.

$\equiv\{\psi_H\psi_{\bar{H}}-|\psi_H'|^2\}/2i|\psi_H'|^2$
(when crystal has no inversion centre) (12′)

These parameters are proportional to the following quantities respectively.

y: The deviation from the Bragg angle.

g: ψ_0'' which is related to the mean absorption coefficient μ_0 by the equation $\mu_0=-\dfrac{2\pi}{\lambda}\psi_0''$.

k: The imaginary part of $\psi_H\psi_{\bar{H}}$. When lattice has inversion centre, this is proportional to ψ_H'' or the H-th Fourier coefficient of the absorption coefficient $\mu_H\left(=-\dfrac{2\pi}{\lambda}\psi_H''\right)$.

A: The product of the structure factor and the thickness of the crystal.

Since $|k|\ll 1$ and $|g|\ll 1$ in most actual cases, the following approximations can be used.

$$|q+z^2|/|q|\simeq 1+y^2\ . \tag{14}$$

$$|z|/\sqrt{|q|}\simeq|y|\ . \tag{15}$$

$$av\simeq A\sqrt{1+y^2}\ . \tag{16}$$

$$aw\simeq\frac{A(k+yg)}{\sqrt{1+y^2}}\ . \tag{17}$$

Then, Eqs. (1) and (2) can be reduced to the following forms;

$$\frac{I_H}{I_0}\simeq\frac{|b|}{1+y^2}e^{-\mu_0 t}\{\sin^2(av)+\sinh^2(aw)\}\ . \tag{18}$$

$$\frac{I_T}{I_0}\simeq e^{-\mu_0 t}\Big\{1+\frac{1+2y^2}{1+y^2}\sinh^2(aw) -\frac{1}{1+y^2}\sin^2(av)+\frac{y\sqrt{1+y^2}}{1+y^2}\sinh(2aw)\Big\}\ . \tag{19}$$

The schematic diagrams of I_H/I_0 and I_T/I_0 against the parameter y are shown in Fig. 2 for various crystal thickness t_0 .

According to Zachariasen and Hirsch, the integrated power ratios in y-scale can be written as follows,

$$R_H{}^y=\frac{1}{|b|}\int\frac{I_H}{I_0}dy\ , \tag{20}$$

$$R_T{}^y=\int\Big\{\frac{I_T}{I_0}-e^{-\mu_0 t_0/\gamma_0}\Big\}dy^*\ . \tag{21}$$

The experimentally measured integrated power ratios, $R_H{}^\theta$ and $R_T{}^\theta$, can be obtained readily from $R_H{}^y$ and $R_T{}^y$ by multiplication of a constant factor; *i.e.*

$$R_H{}^\theta=\frac{|K\psi_H|}{\sqrt{|b|}\sin 2\theta_B}R_H{}^y\ , \tag{22}$$

$$R_T{}^\theta=\frac{|K\psi_H|}{\sqrt{|b|}\sin 2\theta_B}R_T{}^y\ . \tag{23}$$

Then, our purpose is to obtain the definite integrals of $R_H{}^y$ and $R_T{}^y$, with I_H/I_0 and I_T/I_0 given by Eqs. (18) and (19) respectively.

§ 3. Integrated Reflecting Power and Transmitting Power

The results of calculations are as follows;

$$R_H{}^y=e^{-\mu_0 t}\cdot\pi/2[\underbrace{2\sum_{n=0}^{n}J_{2n+1}(2A)}_{W}+I_0(h)-1]\ , \tag{24}$$

$$R_T{}^y=e^{-\mu_0 t}(-2\pi)[\sum_{m=1}^{\infty}m\cos m\beta I_m(h)]-R_H{}^y \tag{25a}$$

$$=e^{-\mu_0 t}(\pi h)[-\{I_1(h)+\cos\beta I_0(h)\} +2\sin\beta\cdot P]-R_H{}^y\ , \tag{25b}$$

where

$$P=\tfrac{1}{2}\sin\beta\cdot\exp\{\cos\beta\cdot h\}\int_0^h I_0(t) \times\exp\{-\cos\beta\cdot t\}dt\ . \tag{25c}$$

The details of the calculations are explained in Appendix A. In these formulae, J_m is the first kind Bessel function of m-th order and I_m is the modified Bessel function of m-th order. The parameter h and β are obtained by the formulae as follows;

---

* $e^{-\mu_0 t}$ is equal to the transmitting power when an incident beam deviates largely from the Bragg angle.

$$h=2A\sqrt{k^2+g^2}\,, \tag{26}$$

$$\beta=\tan^{-1} k/g\,. \tag{27}$$

This implies that h and β are formally the absolute value and the phase angle, respectively, of a vector whose x- and y-components are $2Ag$ and $2Ak$ as shown in Fig. 3. Because Ag is proportional to $t_0\psi_0''$ and Ak to $t_0\psi_H''$ (in the case that crystal has inversion centre) or t_0 × the imaginary part of $\psi_H\psi_{\bar{H}}/|\psi_H'|$ (in the case that crystal has no inversion centre), h implies the product of the effective path length through crystal slab and the absorption index in an extended sense (*cf.* the above explanation of k and g).

In $R_H{}^y$ of Eq. (24), W is the term calculated and discussed thoroughly by Waller[8]), and it corresponds to the integrated reflecting power of non absorbing crystal. This term is nearly equal to 1 for moderately strong reflexions, provided the crystal thickness is larger than say 1μ. Then in all practical cases

$$R_H{}^y=e^{-\mu_0 t}\cdot\pi/2\cdot I_0(h)\,. \tag{24'}$$

It may be worthy to note here that $R_T{}^y$ is not convergent in the usual meaning as shown in Appendix A and the above expressions of $R_T{}^y$ is the Cauchy's principal value, *i.e.* $\lim\limits_{a\to\infty}\int_{-a}^{+a}dy$. Therefore proper cautions are necessary to determine experimental values of $R_T{}^y$, especially in the case where intensity curve is asymmetric.

For certain special values of β the expressions of $R_T{}^y$ can be simplified as follows:

(i) Symmetrical Laue case.

Since $\gamma_0=\gamma_H$, g is always zero. Then $\beta=\pi/2$. In this case

$$R_T{}^y(g=0)$$
$$=e^{-\mu_0 t}(\pi h)[-I_1(h)+2\sum_{n=0}^{\infty}(-)^n I_{2n+1}(h)]-R_H{}^y \tag{28a}$$

$$=e^{-\mu_0 t}(\pi h)\left[-I_1(h)+2\int_0^h I_0(t)dt\right]-R_H{}^y\,. \tag{28b}$$

(see Appendix)

(ii) The cases $k=0$.

Since $\beta=0$ and π correspond to the cases >0 and $g<0$ respectively,

$$R_T{}^y\begin{pmatrix}k=0\\ g>0\end{pmatrix}=e^{-\mu_0 t}(\pi h)[-I_1(h)-I_0(h)]-R_H{}^y\,, \tag{29}$$

$$R_T{}^y\begin{pmatrix}k=0\\ g<0\end{pmatrix}=e^{-\mu_0 t}(\pi h)[-I_1(h)+I_0(h)]-R_H{}^y\,. \tag{30}$$

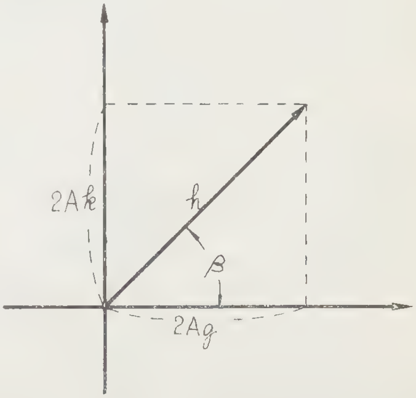

Fig. 3. Relations between the parameters h, β and A, g, and k. $h=2A\sqrt{g^2+k^2}$ and $\beta=\tan^{-1}k/g$. Since $R_H{}^y$ and $R_T{}^y$ are even functions of β, it suffices to consider the region $\pi\geqslant\beta\geqslant 0$.

§ 4. Approximate Formulae

(i) Thin crystals.

Using the decreasing power series of $I_n(h)$ for $h\ll 1$, the integrated power ratios for thin crystals are expressed by

$$R_H{}^y\simeq e^{-\mu_0 t}\cdot\pi/2\{1+\tfrac{1}{4}h^2+(1/64)h^4+\cdots\}\,, \tag{31}$$

$$R_T{}^y\simeq e^{-\mu_0 t}\cdot\pi\{-\cos\beta\cdot h-\tfrac{1}{2}\cos 2\beta\cdot h^2+\cdots\} -R_H{}^y\,. \tag{32}$$

If the terms of orders higher than the 3rd are omitted, Eq. (31) becomes the same one as Eq. (3.187) in Zachariasen's text-book*. For the limiting case $h\simeq 0$, $R_T{}^y\simeq -R_H{}^y$. This fact corresponds to the Bragg, James and Bosanquet's experiment[9]), where the transmitted intensity is reduced by the same amount as the diffracted intensity.

(ii) Thick crystals.

For thick crystals, we can obtain the asymptotic formulae of $R_H{}^y$ and $R_T{}^y$ as follows; (see Appendix B)

$$R_H{}^y\simeq e^{-\mu_0 t}\frac{\pi}{2}\frac{e^h}{\sqrt{2\pi h}}\left\{1+\frac{1}{8h}+\frac{9}{2(8h)^2}+\cdots\right\}\,, \tag{33}$$

$$R_T{}^y\simeq e^{-\mu_0 t}\cdot\pi\frac{e^h}{\sqrt{2\pi h}}\left\{D_0+\frac{D_1}{h}+\frac{D_2}{h^2}+\cdots\right\}\,, -R_H{}^y \tag{34}$$

---

* Of course h must be considered to be $2Ak$ in the Zachariasen's formulae, which can be applied only to the symmetrical case with $g=0$.

where

$$D_0=\frac{1}{2}\frac{1+\cos\beta}{1-\cos\beta}+\frac{1}{2}=\frac{1}{1-\cos\beta}$$

$$D_1=\frac{3}{4}\left\{1+\frac{1}{4}(1-\cos\beta)\right\}\frac{1+\cos\beta}{(1-\cos\beta)^2}+\frac{3}{4}\cdot\frac{1}{4}$$

$$D_2=\frac{3\cdot5}{8}\left\{1+\frac{1}{4}(1-\cos\beta)+\frac{3}{32}(1-\cos\beta)^2\right\}\times\frac{1+\cos\beta}{(1-\cos\beta)^3}+\frac{3\cdot5}{8}\cdot\frac{3}{32}$$

$$D_3=\frac{3\cdot5\cdot7}{16}\left\{1+\frac{1}{4}(1-\cos\beta)+\frac{3}{32}(1-\cos\beta)^2+\frac{5}{128}(1-\cos\beta)^3\right\}\frac{1+\cos\beta}{(1-\cos\beta)^4}+\frac{3\cdot5\cdot7}{16}\cdot\frac{5}{128}\,.$$

$$\cdots\cdots\cdots\,. \tag{35}$$

Eq. (34) is valid for $h(1-\cos\beta)\gg1$. The accuracy of these asymptotic expansions will be explained in detail in Appendix B. Especially, for symmetrical Laue case ($\beta=\pi/2$), Eq. (34) is reduced to

$$R_T{}^y\simeq e^{-\mu_0 t}\cdot\frac{\pi}{2}\cdot\frac{e^h}{\sqrt{2\pi h}}\left\{1+\frac{17}{8}\frac{1}{h}+5\frac{41}{128}\frac{1}{h^2}+18\frac{603}{1024}\frac{1}{h^3}+\cdots\right\}. \tag{34'}$$

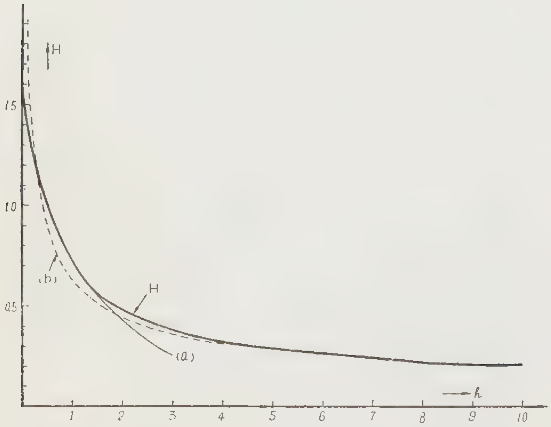

Fig. 4. Integrated reflecting power. Ordinate represents $H=R_H{}^y e^{(\mu_0 t-h)}$, abscissa h.
(a) corresponds to the Zachariasen's approximate formula for thin crystal.
(b) corresponds to the Hirsch and Zachariasen's approximate formula for thick crystal.

By an approximate calculation Hirsch and Zachariasen showed that

$$R_H{}^y\simeq R_T{}^y\simeq e^{-\mu_0 t}\sqrt{\frac{\pi}{16Ak}}e^{2Ak}, \tag{36}$$

when the crystal is large enough. This conclusion can be verified by taking the first term of Eqs. (33) and (34')*.

§ 5. Method of Numerical Calculation and Some Examples

(a) $R_H{}^y$.

According to Eq. (24'), $R_H{}^y$ is proportional to the product of the exponential term and the function $I_0(h)$. Since the good table of $I_0(h)$ is given in Watson's text-book on Bessel function[10], there is no difficulty in obtaining its numerical values. The results are shown in Fig. 4 and also in Fig. 5, where the ordinate is $H=R_H{}^y e^{(\mu_0 t-h)}$ instead of $R_H{}^y$ itself for the sake of convenience of description. From this figure, it is clear that the Hirsch and Zachariasen's asymptotic formulae of $R_H{}^y$ in Eq. (36) is good approximation for $h=2Ak\gtrsim4$.

(b) $R_T{}^y$.

Since $R_T{}^y$ are expressed by the infinite series of Bessel functions or the definite integral in Eq. (25a) and (25b), its numerical calculation is more complicated than $R_H{}^y$. The practical calculation is carried out as follows.

(i) The range $h\leqslant6$.

In the usual tables of Bessel function, the numerical values of I_n are given thoroughly in the range $h\leqslant6$ and $n\leqslant11$[11]. Then there is no difficulty in obtaining $R_T{}^y$ for all values of β*, by using Eq. (25a). For sufficient accuracy it is in general necessary to calculate up to the n term, where $n\simeq h$.

(ii) The range $h>6$.

In Eq. (25b), I_0 and I_1 can be calculated with a good approximation by using asymptotic expansions or the numerical tables of I_0 and I_1[10]. To calculate the values of P, it is convenient to distinguish the following two cases.

(1) $h(1-\cos\beta)\gtrsim5$.

In this case, P can be calculated by the asymptotic expansion given in Appendix B. Then $R_T{}^y$ can be approximated by the initial four terms of Eq. (34) within the errors of 5%.

(2) $h(1-\cos\beta)\lesssim5(h>6)$.

In this intervening region of h, it is most practical to calculate the definite integral P

---

* cf. footnote on p. 9.

* Since, from eq. (25a) $R_T{}^y$ is an even function of β, the integrated transmitting power is independent of the sign of k. Then it suffices to consider the range $0\leqslant\beta\leqslant\pi$.

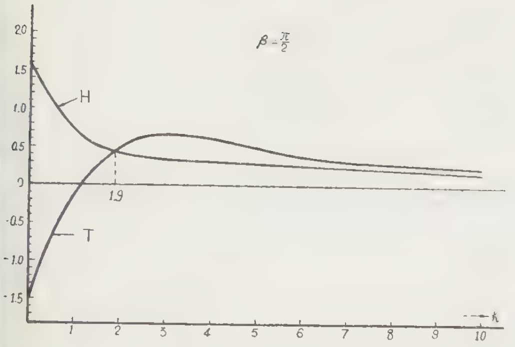

Fig. 5. Integrated reflecting power and transmitting power for $\beta=\pi/2$. $H=R_H{}^y e^{(\mu_0 t-h)}$ and $T=R_T{}^y e^{(\mu_0 t-h)}$.

n Eq. (25b) by graphical method using the able of $I_0(h)$.

The numerical results are given in Figs. 5 ind 6, where $T=R_T{}^y e^{(\mu_0 t-h)}$ is shown. In ig. 5, T for $\beta=\pi/2$ and also H are shown or comparison. It can be seen that the two curves of T and H coincides at $h=1.90$. For he larger values of h, T is always larger han H, but T becomes equal to H asympotically noted by Hirsch and Zachariasen for hick crystals. For thick crystals such as $i>10$, the accurate measurement of intensity y means of spectrometer is very difficult lue to the reduction of absolute intensity of X-rays. Usually, therefore the photographic methods are used to measure such a weak ntensity and the experimental errors can not e minimized less than about 10%. Then it loes not lead to incorrect conclusions to consider that $R_T{}^y \simeq R_H{}^y$ in the case of thick rystal, since this relation is accurate to 10% or $h>20$.

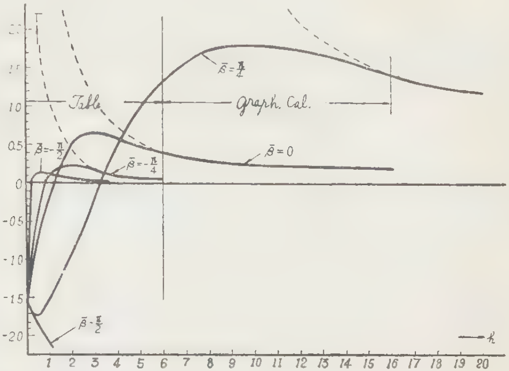

Fig. 6. Integrated transmitting power for a few values of $\beta\neq\pi/2$. The dotted lines are asymptotic expansions of each curve (*cf.* Eqs. (34) ane (35)). Ordinate represents $T=R_T{}^y e^{(\mu_0 t-h)}$. $\bar{\beta}=\beta-\pi/2$.

The numerical examples for $\beta\neq\pi/2$ are given in Fig. 6. It is clear that T shows different behaviors as function of the variable h for different values of β. Since ψ_0'' is always negative in Eq. (11), the sign of $\bar{\beta}=\beta-\pi/2$ is determined by the sign $(\gamma_0-\gamma_H)$. When the crystal is thick enough, it is expected that the transmitted intensity for $\gamma_0>\gamma_H$ is larger than the intensity for $\gamma_0<\gamma_H$.

Acknowledgements

It is the author's pleasure to express his sincere thanks to Professor R. Uyeda who very kindly took the trouble of reading through the manuscript before publication and giving the author many valuable advices. The author wishes also to thank Mr. Ootake for his assistance in numerical calculations.

Appendix A

ntegral calculation of $R_H{}^y$ and $R_T{}^y$.

a) $R_H{}^y$.

$R_H{}^y$ can be written as $R_H{}^y=e^{-\mu_0 t}J_H$, where

$$J_H=\int_{-\infty}^{+\infty}\frac{1}{1+y^2}\left\{\sin^2 A\sqrt{1+y^2}+\sinh^2\frac{A(k+gy)}{\sqrt{1+y^2}}\right\}dy\,.$$
$$=W+V$$

n this formula,

$$W=\int_{-\infty}^{+\infty}\frac{\sin^2 A\sqrt{1+y^2}}{1+y^2}\,dy=\pi\sum_{n=0}^{\infty}J_{2n+1}(2A)\,,\quad (cf.\ \text{Waller}^{8)})$$

$$V=\int_{-\infty}^{+\infty}\frac{1}{1+y^2}\sinh^2\frac{A(k+yg)}{\sqrt{1+y^2}}dy\,.$$

f we write

$$h=2A\sqrt{k^2+g^2}\,,\qquad \beta=\tan^{-1}k/g \quad\text{and}\quad y=-\cot\theta\,,$$

the term V can be calculated as follows

$$V=\frac{1}{2}\int_0^{\pi}[\cos h\{h\cos(\theta+\beta)\}-1]d\theta=\frac{\pi}{2}[I_0(h)-1]\,.\quad\text{(G. and M.}^{11)}\text{ p. 46)}\tag{A1}$$

(*b*) $R_T{}^y$.

It is more convenient to calculate $R_H{}^y+R_T{}^y$ instead of $R_T{}^y$ itself. $R_H{}^y+R_T{}^y$ can be written as

$$R_H{}^y+R_T{}^y\equiv e^{-\mu_0 t}J_{T+H}\,,\tag{A2}$$

where

$$J_{T+H}=\int_{-\infty}^{+\infty}\left\{\cosh(2aw)+\frac{y\sqrt{1+y^2}}{1+y^2}\sinh(2aw)-e^{2Ag}\right\}dy\,.$$

For large values of y, the integrand of J_{T+H} becomes

$$\{e^{2A(g+k/y)}-e^{2Ag}\}\sim e^{2Ag}\left\{\frac{k}{y}+\frac{1}{2!}\left(\frac{k}{y}\right)^2+\cdots\right\}.$$

Then the above integral is divergent in usual meaning of integral, but Cauchy's principal value can be obtained definitely.

Let
$$J_{T+H}=J_{T+H}{}^{(1)}+J_{T+H}{}^{(2)}\,,$$
where

$$J_{T+H}{}^{(1)}=\int_{-\infty}^{+\infty}\left\{\cosh\frac{2A(k+yg)}{\sqrt{1+y^2}}-\cosh 2Ag\right\}dy\,,$$

$$J_{T+H}{}^{(2)}=\int_{-\infty}^{+\infty}\left\{\frac{y\sqrt{1+y^2}}{1+y^2}\sinh\frac{2A(k+yg)}{\sqrt{1+y^2}}-\sinh 2Ag\right\}dy\,.$$

By using the same transformation in (a),

$$J_{T+H}{}^{(1)}=\int_0^{\pi}[\cosh\{h\cos(\theta+\beta)\}-\cosh\{h\cos\beta\}]\frac{d\theta}{\sin^2\theta}\,.$$

Since

$$\cosh\{h\cos\varphi\}=I_0(h)+2I_2(h)\cos 2\varphi+\cdots+2I_{2n}(h)\cos 2n\varphi+\cdots\quad\text{(G. and M.}^{11)}\text{ p. 42)}\,,$$

$$J_{T+H}{}^{(1)}=2\sum_{n=0}^{\infty}I_{2n}(h)\int_0^{\pi}\{\cos 2n(\theta+\beta)-\cos 2n\beta\}\frac{d\theta}{\sin^2\theta}$$
$$=-2\pi\sum_{n=0}^{\infty}(2n)\cos 2n\beta I_{2n}(h)\,.$$

In this derivation, we use the following relation.

$$\int_0^{\pi}\{\cos 2n(\theta+\beta)-\cos 2n\beta\}\frac{d\theta}{\sin^2\theta}=\lim_{\varepsilon\to 0}\int_{\varepsilon}^{\pi-\varepsilon}d\theta\qquad\text{(Cauch's principal value)}$$
$$=\int_0^{\pi/2}\{\cos 2n(\theta+\beta)+\cos 2n(\theta-\beta)-2\cos 2n\beta\}\frac{d\theta}{\sin^2\theta}$$
$$=-4\cos 2n\beta\int_0^{\pi/2}(\sin n\theta/\sin\theta)^2\,d\theta$$
$$=-2n\pi\cos 2n\beta\,.$$

By the similar procedures, we obtain

$$J_{T+H}{}^{(2)}=\int_0^{\pi}[\cos\theta\sinh\{h\cos(\theta+\beta)\}-\sinh\{h\cos\beta\}]\frac{d\theta}{\sin^2\theta}$$

$$=-2\pi\sum_{n=0}^{\infty}(2n+1)\cos(2n+1)\beta I_{2n+1}(h)\,.$$

$$\therefore J_{T+H}=-2\pi\sum_{m=0}^{\infty}m\cos m\beta I_m(h)\,. \tag{A3}$$

c) Another expression of J_{T+H}.

By the recurrence formulae of Bessel function

$$mI_m(h)=(h/2)\{I_{m-1}(h)-I_{m+1}(h)\}\,, \qquad \text{(G. and M.}^{11)}\text{ p. 20)}$$

we obtain

$$J_{T+H}{}^{(1)}=-2\pi\sum_{n=1}^{\infty}(2n)\cos 2n\beta I_{2n}(h)$$

$$=-\pi hI_1(h)+2\pi h\sin\beta\sum_{n=0}^{\infty}\sin(2n+1)\beta I_{2n+1}(h)$$

$$J_{T+H}{}^{(2)}=-2\pi\sum_{n=0}^{\infty}(2n+1)\cos(2n+1)\beta I_{2n}(h)$$

$$=-\pi h\cos\beta I_0+2\pi h\sin\beta\sum_{n=1}^{\infty}\sin 2n\beta I_{2n}(h)\,.$$

$$\therefore J_{T+H}=-\pi h[I_1(h)+\cos\beta I_0(h)]+2\pi h\sin\beta\cdot P\,, \tag{A4}$$

where

$$P=\sum_{m=0}^{\infty}\sin m\beta I_m(h)\,.$$

By another recurrence formulae of Bessel function

$$\frac{d}{dh}I_m(h)=\frac{1}{2}[I_{m+1}(h)+I_{m-1}(h)]\,, \qquad \text{(G. and M.}^{11)}\text{ p. 20)}$$

we obtain

$$\frac{\partial P}{\partial h}=\frac{1}{2}\sin\beta\, I_0+\cos\beta\cdot P\,. \tag{A5}$$

This is the differential formula which must be satisfied by P. Then, using that $P=0$ at $h=0$,

$$P=\frac{1}{2}\sin\beta\cdot\exp\{\cos\beta\cdot h\}\int_0^h I_0(t)\exp\{-\cos\beta\cdot t\}dt\,. \tag{A6}$$

Especially, for the case $\beta=\pi/2$

$$P=\frac{1}{2}\int_0^h I_0(t)dt$$

$$=\frac{1}{2}hI_0(h)+\frac{\pi}{4}h\{iI_1(h)\boldsymbol{H}_0(ih)-I_0(h)\boldsymbol{H}_1(ih)\}\,, \tag{A7}$$

where $\boldsymbol{H}_m$ is the Sturve's function of m-th order (Mc$^{12)}$ p. 49 and 71).

Appendix B

The asymptotic expansion of I_0, I_1 and P.

a) I_0 and I_1.

As shown in usual text-books, Bessel function I_n can be expressed by the asymptotic expansion as follows for large values of h;

$$I_n=\frac{e^h}{\sqrt{2\pi h}}\left\{1+\frac{(1-4n^2)}{1!(8h)}+\frac{(1-4n^2)(3^2-4n^2)}{2!(8h)^2}+\cdots+R_m{}^n\right\},\qquad \text{(G. and M.[11] p. 58)}$$

where $R_m{}^n$ is the remainders of the first m terms and can be estimated by

$$|R_m{}^n|=|I_n-S_m{}^n|\simeq\frac{A^n{}_{m+1}}{p^{m+1}}\qquad\text{for}\qquad h\geq p\,.$$

In this expression $A^n{}_{m+1}$ is the coefficient of $1/h^{m+1}$ in the above expansion of I_n, and $S_m{}^n$ is the sum of the first m terms (Watson[10] p. 199). Then, the expansion formulae of I_0 and I_1 are obtained readily,

$$I_0\simeq\frac{e^h}{\sqrt{2\pi h}}\left\{1+\frac{1}{8h}+\frac{9}{128h^2}+\cdots\right\}, \tag{A8}$$

$$I_1\simeq\frac{e^h}{\sqrt{2\pi h}}\left\{1-\frac{3}{8h}+\frac{15}{128h^2}+\cdots\right\}. \tag{A9}$$

(b) P.

Transforming P into g by the following relation, we obtain

$$g(h)=\frac{2}{\sin\beta}\sqrt{2\pi h}\,e^{-h}P\,,$$

$$g\left(1-\cos\beta-\frac{1}{2h}\right)+\frac{\partial g}{\partial h}=\sqrt{2\pi h}\,e^{-h}I_0(h)\,. \tag{A5$'$}$$

When h is large enough,

$$\sqrt{2\pi h}\,e^{-h}I_0(h)\simeq A_0+\frac{A_1}{h}+\frac{A_2}{h^2}+\cdots\,.$$

Now, we write formally

$$g\simeq B_0+\frac{B_1}{h}+\frac{B_2}{h^2}+\cdots\,,$$

and equating the coefficient of $1/h^i$ of both side in (A5′), we obtain

$$B_0=\frac{A_0}{1-\cos\beta}\,,\qquad B_i=\frac{A_i+(i-1/2)B_{i-1}}{1-\cos\beta}(i\geq 1)\,.$$

Then the general solution of (A5′) is

$$g\simeq C\sqrt{2\pi h}\,e^{-(1-\cos\beta)h}+\left\{B_0+\frac{B_1}{h}+\frac{B_2}{h^2}+\cdots\right\},$$

where C is an integral constant, which is shown to be equal 0, since

$$P=\frac{\sin\beta}{2}\frac{e^h}{\sqrt{2\pi h}}\frac{1}{1-\cos\beta}\,,$$

for large values of $h(1-\cos\beta)$. Then, we obtain

$$P=\frac{\sin\beta}{2}\frac{e^h}{\sqrt{2\pi h}}\left\{B_0+\frac{B_1}{h}+\frac{B_2}{h^2}+\cdots+E_m\right\}, \tag{A10}$$

where

$$B_0=1/1-\cos\beta\,,$$

$$B_1=\frac{1}{2}\left\{1+\frac{1}{4}(1-\cos\beta)\right\}\Big/(1-\cos\beta)^2,$$

$$B_2=\frac{3}{4}\left\{1+\frac{1}{4}(1-\cos\beta)+\frac{3}{32}(1-\cos\beta)^2\right\}\Big/(1-\cos\beta)^3,$$

$$B_3=\frac{5\cdot 3}{8}\left\{1+\frac{1}{4}(1-\cos\beta)+\frac{3}{32}(1-\cos\beta)^2+\frac{5}{128}(1-\cos\beta)^3\right\}\Big/(1-\cos\beta)^4$$

$$\cdots\cdots\cdots\cdot$$

E_m is the remainder of the first m terms and can be estimated by

$$|E_m|\simeq\frac{|A_{m+1}|+(m+1/2)|B_m|}{p^{m+1}}\qquad\text{for}\qquad h\geq p\,.$$

Eq. (A10) can be proved to be equal to the asymptotic expansion of Eq. (A7) in the case of $\beta=\pi/2$.

References

1) G. Borrmann: Phys. Z. **43** (1941) 157; Z. f. Phys. **127** (1950) 297.

2) H. N. Campbell: Acta Cryst. **4** (1951) 180; J. App. Phys. **22** (1951) 1139.

G. L. Rogossa and G. Schwarz: Phys. Rev. **86**, 421; **87** (1952) 995.

H. Yoshioka: The annual meeting of the Physical Society of Japan, 1952.

3) M. Kohler: Ann. d. Phys. **18** (1933) 265.

4) M. v. Laue: Acta Cryst. **2** (1949) 106.

5) P. B. Hirsch: Acta Cryst. **5** (1952) 176.

6) W. H. Zachariasen: *Theory of X-ray Diffraction in Crystals*, 1944. Proc. Nat. Acad. Sci. **38** (1952) 378.

7) G. N. Ramachandran: J. App. Phys. **23** (1952) 500.

8) I. Waller: Ann. d. Phys. **79** (1926) 261.

9) W. L. Bragg, R. W. James and C. H. Bosanquet: Phil. Mag. **42** (1921) 1.

10) G. N. Watson: *Bessel Function* 1922.

11) A. Gray and G. B. Mathews: *A Treatise on Bessel Functions and Their Applications to Physics* 1922.

12) N. W. Mc Lachlan: *Bessel Functions for Engineers* 1934.

JOURNAL OF THE PHYSICAL SOCIETY OF JAPAN Vol. 10, No. 1, JANUARY, 1955

Microwave Spectrum of $SPCl_3$, Theoretical

By Takashi ITOH

Department of Physics, Faculty of Science,
University of Tokyo, Tokyo

(Received July 20, 1954)

The quadrupole hyperfine structure of the $J=0\rightarrow1$ rotational spectrum of $SPCl_3$ is calculated by the method of Bersohn and Mizushima and Itoh. Spectrum of excited vibrational states as well as of the ground state is considered. The theoretical spectrum consists of four groups of lines corresponding to the isotopic species $SPCl_3^{35}$, $SPCl_2^{35}Cl^{37}$, $SPCl^{35}Cl_2^{37}$, and $SPCl_3^{37}$. Asymmetric rotor lines of $SPCl_2^{35}Cl^{37}$ and $SPCl^{35}Cl_2^{37}$, which may appear in the frequency region concerned, are also examined. Discussions are given of the experimental results of the following article.

§ 1. Introduction

Microwave spectrum of thiophosphoryl chloride $SPCl_3$ in 30,000 Mc region has been investigated by Williams, Sheridan, and Gordy[1)], who assigned the 10th, 11th, and 12th rotational lines. They determined the molecular structure from the results of their measurements, but obtained no information about quadrupole coupling of Cl nuclei. On the other hand, Tsukada[2)] studied the $J=0\rightarrow1$ rotational spectrum in 3,000 Mc region, where nuclear quadrupole effect is relatively important. The results of his measurements will be analyzed in this paper.

Quadrupole coupling in symmetric molecules of the type XYZ_3, where Z nuclei have coupling while X and Y have no coupling, have been investigated theoretically by Bersohn[3)] and by Mizushima and Itoh[4)]. The theoretical pattern for the $J=0\rightarrow1$ transition was given by Mizushima and Itoh, and it was used for the analysis of the microwave spectrum of bromoform $CHBr_3$ observed by Kojima, Tsukada, and Hagiwara[5)]. The same method is applied to $SPCl_3$ in this paper.

§ 2. Quadrupole Coupling

The first-order Hamiltonian of quadrupole coupling of nuclei in a rotating molecule is given by[6)]

$$H=\sum_i eQ_i\left\langle\left(\frac{\partial^2 V}{\partial z^2}\right)_i\right\rangle_{Av}\times\frac{3(\mathbf{J}\cdot\mathbf{I}_i)^2+\frac{3}{2}(\mathbf{J}\cdot\mathbf{I}_i)-\mathbf{J}^2\mathbf{I}_i^2}{2J(2J-1)I_i(2I_i-1)}, \tag{1}$$

where J is the rotational angular momentum of the molecule, I_i is the nuclear spin, eQ_i is the electric quadrupole moment of the nucleus, and $(\partial^2V/\partial z^2)_i$ is the second derivative of the electrostatic potential at the position of the nucleus with respect to the z axis fixed in space. The average is taken over the state with $M_J=J$.

It is obvious that for the rotational state $J=0$ the right hand side of (1) vanishes. In this case all the nuclear spin states are degenerate. Therefore, the hyperfine structure of the $J=0\rightarrow1$ spectrum arises solely from that of the state $J=1$.

The factor $\langle(\partial^2V/\partial z^2)_i\rangle_{Av}$ can be expressed in terms of the rotational quantum numbers J and K and of quantities fixed in molecule by eq. (8) of I. For $J=1$, $K=0$, we have

$$\left\langle\left(\frac{\partial^2 V}{\partial z^2}\right)_i\right\rangle_{Av}=-\frac{1}{5}\frac{3\cos^2\theta_i'-1}{2}\frac{\partial^2 V}{\partial a_i^2}, \tag{2}$$

where a_i is the axis along the ith bond and θ'_i is the angle between a_i and the principal axis of the least moment of inertia. The axis of the least moment of inertia coincides with the figure axis in symmetric molecules $SPCl_3^{35}$ and $SPCl_3^{37}$, but in asymmetric molecules $SPCl_2^{35}Cl^{37}$ and $SPCl^{35}Cl_2^{37}$ they do not coincide with each other, the deviation being about 8° and 6°30′ respectively.

In the following, quadrupole energies in symmetric molecules $SPCl_3^{35}$ and $SPCl_3^{37}$ and asymmetric molecules $SPCl_2^{35}Cl^{37}$ and $SPCl^{35}Cl_2^{37}$ are given under separate captions.

§ 3. XYZ_3 Type Molecules

In symmetric molecules $SPCl_3^{35}$ and $SPCl_3^{37}$, the coupling constants of three nuclei are equal to each other:

$$eQ_1\left\langle\left(\frac{\partial^2 V}{\partial z^2}\right)_1\right\rangle_{\rm Av}=eQ_2\left\langle\left(\frac{\partial^2 V}{\partial z^2}\right)_2\right\rangle_{\rm Av}=eQ_3\left\langle\left(\frac{\partial^2 V}{\partial z^2}\right)_3\right\rangle_{\rm Av}.$$

The matrix elements of the Hamiltonian for his case have been tabulated by Bersohn[3] as functions of J with nuclear spins $I_i=1$ and 3/2. Mizushima and Itoh[4],[5] calculated the hyperfine structure of the $J=1$ state. The results are given in Table I after correcting a few numerical errors involved in I and II. The symmetry of the spin functions and the multiplicities of the levels are also shown.

Table I. Energy of quadrupole coupling in XYZ$_3$ type molecules when $J=1$, $I_i=3/2$.

A_1		A_2		E	
$2F+1$	$\dfrac{E_Q}{eQ_1\left\langle\left(\frac{\partial^2V}{\partial z^2}\right)_1\right\rangle_{\rm Av}}$	$2F+1$	$\dfrac{E_Q}{eQ_1\left\langle\left(\frac{\partial^2V}{\partial z^2}\right)_1\right\rangle_{\rm Av}}$	$2F+1$	$\dfrac{E_Q}{eQ_1\left\langle\left(\frac{\partial^2V}{\partial z^2}\right)_1\right\rangle_{\rm Av}}$
12	0.750	6	−0.250	10	0.250
10	−2.000	4	1.000	8	0.250
8	2.331	2	−1.250	8	−1.000
8	−0.831			6	2.000
6	1.106			6	0.750
6	−1.356			6	−1.750
4	2.170			4	1.392
4	−2.420			4	−0.612
2	0.750			4	−2.280
				2	2.380
				2	−0.630

4. XYZ$_2$Z′ Type Molecules

In the asymmetric molecules SPCl$_2^{35}$Cl^{37} and PCl^{35}Cl$_2^{37}$, coupling constants of two nuclei e equal, but the third one differs from e others. The ratio of the coupling conants calculated by using (2) and the ratio $Q_{35}/Q_{37}=1.26878$[7] is as follows:

$$\frac{Q_{37}\left\langle\left(\frac{\partial^2 V}{\partial z^2}\right)_{37}\right\rangle_{\rm Av}}{Q_{35}\left\langle\left(\frac{\partial^2 V}{\partial z^2}\right)_{35}\right\rangle_{\rm Av}}=\begin{cases}-0.012 \text{ for SPCl}_2^{35}\text{Cl}^{37},\\ \ \ 0.245 \text{ for SPCl}^{35}\text{Cl}_2^{37}.\end{cases}$$

he coupling in SPCl$_2^{35}$Cl^{37} is very close to e case of two identical nuclei as treated by oley[8] and Myers and Gwinn[9], while the oupling in SPCl^{35}Cl$_2^{37}$ is fairly close to the se of one nucleus as treated by Bardeen d Townes[10]. It will be convenient to draw rves, which represent the energies of quadupole coupling, by connecting various limitg cases such as mentioned above. We ve drawn such curves for the case of $J=1$ d $I_i=3/2$. The results are shown in Fig. 1. hese curves give the energies of quadrupole oupling as functions of the ratio of coupling nstants x. The case of the preceding section rresponds to $x=1$. $x=0$ corresponds to the se treated by Foley and Myers and Gwinn. $1/x=0$ corresponds to the case treated by Bardeen and Townes. These limiting cases were connected according to the non-crossing rule of the energy levels. The derivatives of the curves at $x=1$, $x=0$ and $1/x=0$ were also utilized in drawing the curves.

§ 5. Theoretical Spectrum of SPCl$_3$

Using the above results we obtain the theoretical spectrum for the $J=0\rightarrow1$ rotational transition of SPCl$_3$ as shown in Fig. 3 of the following paper. In the calculation the quadrupole coupling constant of the PCl bond $eQ_i\times\partial^2V/\partial a^2_i$ was assumed to be −60 Mc (for Cl^{35}) on the basis of the empirical relation found by Gordy[11] between the coupling constant and the electronegativity difference of bonded atoms. The positions of the hypothetical unsplit rotational lines were calculated from the molecular dimensions determined by Williams, Sheridan, and Gordy[1], PCl=2.02 A, PS=1.85 A, ∠ClPCl=100.5°. The spectrum of excited vibrational states of the low frequency Cl-P-Cl bending mode $\nu=171\,\text{cm}^{-1}$ of e species was considered as well as that of the ground state. The shift of the spectrum due to vibration was neglected, but only the symmetry restriction on spin functions imposed by the exclu-

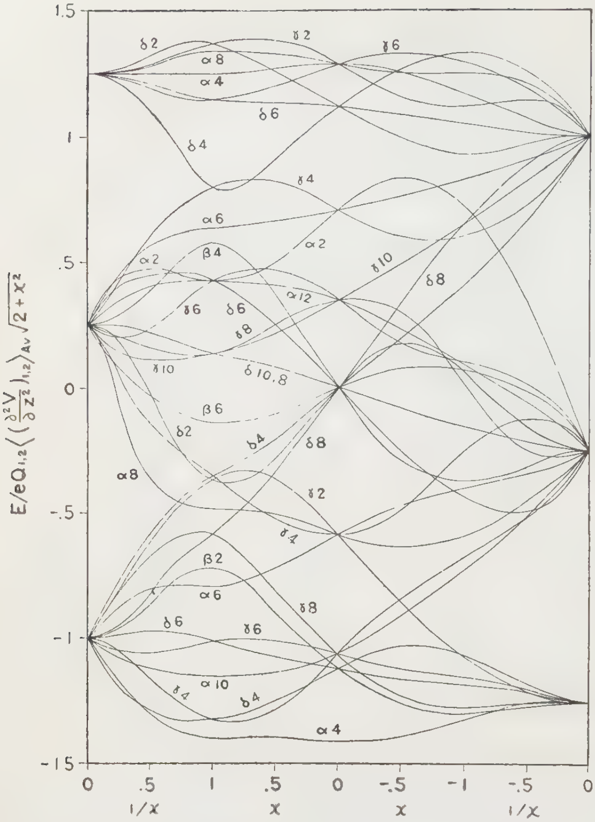

Fig. 1. Energy of quadrupole coupling in XYZ_2Z' type molecules when $J=1$, $I_i=3/2$. Parameter $x=eQ_3\left\langle\left(\frac{\partial^2 V}{\partial z^2}\right)_3\right\rangle_{Av}\Big/eQ_{1,2}\left\langle\left(\frac{\partial^2 V}{\partial z^2}\right)_{1,2}\right\rangle_{Av}$. α, β, γ, δ designate states which reduce to A_1, A_2, E_e, E_o respectively when $x=1$. The integer attatched to the curve is the multiplicity of the level $2F+1$.

sion principle was taken into account. The relative abundance of four isotopic molecules $SPCl_3^{35}$, $SPCl_2^{35}Cl^{37}$, $SPCl^{35}Cl_2^{37}$, and $SPCl_3^{37}$ was assumed to be 1:1:1/3:1/27, since the relative abundance of Cl^{35} and Cl^{37} is about 3:1. The intensity of each hyperfine component was taken proportional to $2F+1$. For the details of the method see reference II.

§ 6. Asymmetric Rotor Lines

Some of the asymmetric rotor lines of $SPCl_2^{35}Cl^{37}$ and $SPCl^{35}Cl_2^{37}$ may appear in the low frequency region concerned. This possibility is large since $SPCl_3$ is a nearly spherical top molecule, in which the rotational energy levels are very close together. Moreover since $SPCl_3$ is a heavy molecule, rotational levels with high J values are densely populated at room temperature. The maximum of the thermal distribution curve is at $J\approx 60$. Therefor
we must consider all the lines with $J\lesssim 10$
The most important lines are due to th
transitions $\Delta J=0$. Since there is a gre
number of lines of this type, it
practically impossible to calculate th
individual frequencies of them accuratel
However, the number and the intensi
of the lines, which fall into the measure
range, can be estimated approximate
by using formulas applicable to slight
asymmetric rotors.

One of the most important types
transitions is that for which $\Delta J=$
$\Delta K_{-1}=0$, $\Delta K_{+1}=-1$, that is, the trans
tion between the levels separated by th
asymmetric K-type doubling. If th
asymmetry of the molecule is sufficient
small, the frequencies of these lines ca
be estimated by Wang's formula[12]

$$\nu=\frac{a-c}{2}\,\frac{(J+K)!}{(J-K)!\,(K-1)!\,(K-1)!}\,\frac{\delta^K}{16^{K-1}\left(1-\frac{1}{2}\,\delta\right)^{K-1}}\,,$$

where $K=K_{-1}$ and $\delta=(b-c)/(a-c)$ a
a, b, c are the rotational constants ($a=h^2/8\pi^2$
etc.). For example, in $SPCl_2^{35}\,Cl^{37}$, $a=1,4$
Mc, $b=1,397$ Mc, and $c=1,375$ Mc. Then it
found that only a few lines of this type f
into the frequency range 2,600–2,900 Mc mea
ured by Tsukada. However, the intensit
of the individual lines are rather stro
The squares of the matrix elements of t
dipole moment summed over M and M' a
approximately given by[13]

$$(2J+1)\frac{K^2}{J(J+1)}\,\mu_a^{\,2}\ .$$

For lines with $J\approx 50$ and $K\approx J/3$, the inten
ties may be several times stronger than th
of the $J=0\rightarrow 1$ line.

Another type of transition is $\Delta J=0$, $\Delta K_{-1}=$
(and $\Delta K_{+1}=-1$ for $SPCl_2^{35}Cl^{37}$, 0, -2
$SPCl^{35}Cl_2^{37}$). The frequencies of the lin
corresponding to this type of transition a
approximately given by

$$\nu=\left(a-\frac{b+c}{2}\right)(2K+1)\ .$$

The frequencies fall into the 2,600–2,900
region when $K\approx 16$. There are many lin
corresponding to different J values grea

an K. The intensities of the lines are given y13)

$$(2J+1)\frac{J(J+1)-K^2}{2J(J+1)}(\mu_b^2+\mu_c^2)\,.$$

he intensities are small because of the small- ss of μ_b and μ_c. For $SPCl_2^{35}C^{37}$, $\mu_b^2=0.02$ ^{2} and $\mu_c^2=0$. However, the total intensity these lines will be considerably large as ere are so many lines of this type.

Thus, the intensity of the asymmetric rotor es seems to be quite appreciable in the equency range under consideration. Of urse, the above estimation is very rough, d the formulas (3) and (4) do not hold for rge values of J. However, the asymmetric tor lines will be at least as strong as to be servable, and they may obscure the $J=0\rightarrow1$ ectrum considerably.

. Discussion

The quadrupole hyperfine structure of the $=0\rightarrow1$ rotational spectrum of $SPCl_3$ was cal- lated theoretically assuming the coupling nstant to be −60 Mc (for Cl^{35}). The theo- tical spectrum consists of four groups of es corresponding to the isotopic species PCl_3^{35}, $SPCl_2^{35}Cl^{37}$, $SPCl^{35}Cl_2^{37}$, and $SPCl_3^{37}$, shown in Fig. 3 of the following paper, ere the last one is not shown since it is ry weak. The over-all quadrupole splitting about 10 Mc. The quadrupole effect is parently reduced by the averaging over the tational motion. The splitting will be some- at increased if we assume a larger value r the coupling constant.

The spectrum of excited vibrational states as considered, but the shift of the spectrum e to vibration was not taken into account, ce the shift is expected to be of the order 1 Mc or less. It is unconceivable that the brational shift would affect the general ture of the spectrum.

The observed spectrum presented in the lowing paper is in rough agreement with e theoretical one, but it shows a very wide read, which can neither be explained by adrupole effect nor by vibrational shift. The ason for this discrepancy will be partly due to the neglect of the second-order quadrupole effect, which arises from the matrix elements of the quadrupole Hamiltonian connecting different rotational levels. The second-order effect, which has not been taken into account in the preceding calculations, will be considerably large for $SPCl_3$, since the rotational levels with the same J and different K are very close together in this molecule. The magnitude of the second-order quadrupole energy is estimated to be of the order of 2∼3 Mc.

The main source of the wide spread of the observed spectrum, however, will probably be due to the appearance of the asymmetric rotor lines of $SPCl_2^{35}Cl^{37}$ and $SPCl^{35}Cl_2^{37}$ investigated in the preceding section. The intensity of the observed spectrum is much stronger than the theoretical intensity for the $J=0\rightarrow1$ transition. It is apparent, therefore, that some of the asymmetric rotor lines have merged with the $J=0\rightarrow1$ spectrum.

In conclusion, the author wishes to thank Profs. M. Kotani and S. Kojima for their interest and helpful discussions on this work.

References

1) Q. Williams, J. Sheridan and W. Gordy: J. Chem. Phys. **20** (1952) 164.

2) K. Tsukada: J. Phys. Soc. Japan **10** (1955) 60.

3) R. Bersohn: J. Chem. Phys. **18** (1950) 1124; thesis, Harvard University (1949).

4) M. Mizushima and T. Itoh: J. Chem. Phys. **19** (1951) 739, refered to as I in the text.

5) Kojima, Tsukada, Hagiwara, Mizushima, and Itoh: J. Chem. Phys. **20** (1952) 804, refered to as II in the text.

6) H. B. G. Casimir: *On the Interaction between Atomic Nuclei and Electrons* (Teyler's Tweede Genootschap, E. F. Bohn, Haarlem, 1936).

7) R. Livingston: Phys. Rev. **82** (1951) 289.

8) H. M. Foley: Phys. Rev. **71** (1947) 751.

9) R. J. Myers and W. D. Gwinn: J. Chem. Phys. **20** (1952) 1420.

10) J. Bardeen and C. H. Townes: Phys. Rev. **73** (1948) 97.

11) W. Gordy: J. Chem. Phys. **19** (1951) 792.

12) S. C. Wang: Phys. Rev. **34** (1929) 243.

13) P. C. Cross, R. M. Hainer and G. W. King: J. Chem. Phys. **12** (1944) 210.

JOURNAL OF THE PHYSICAL SOCIETY OF JAPAN Vol. 10, No. 1, JANUARY, 1955

Microwave Spectra of SPCl$_3$, Experimental

By Kineo TSUKADA

Department of Physics, Tokyo University of Education

(Received July 20, 1954)

The microwave spectra of thiophosphoryl chloride, SPCl$_3$, were studied within the frequency region from 2,600 Mc to 2,900 Mc with the cavity spectrometer, of which minimum detectable absorption coefficient was about $5 \times 10^{-9}\,\mathrm{cm}^{-1}$. Several absorption lines of the rotational transition of the symmetric and asymmetric top molecules were observed and their temperature effect examined.

§ 1. Introduction

In the wave-length region of 10 cm, microwave spectra have been observed only for a few molecules, because of small absorption coefficients which are theoretically expected to be proportional to the 2nd power of the frequency. The rotational spectra of low-J transitions of symmetric top molecules, of which three corner atoms are I, Br or Cl with nuclear quadrupole moment, for example, CHI$_3$, CHBr$_3$ and SPCl$_3$, exist in this region. Their theoretical analysis was given by Bersohn[1] and by Mizushima and Itoh[2], and their spectra seemed to be very complex except for low-J transition. Among these molecules, bromoform was the first observed and analysed one[3], whose rotational spectra of $J=0\rightarrow1$ were measured at 2,400 Mc to 2,650 Mc. The rotational spectra of $J=0\rightarrow1$ of SPCl$_3$ were estimated to exist at wave-length of about 11 cm.[4] The present paper describes the results of the measurement of the spectra of SPCl$_3$* in the 2,600 Mc to 2,900 Mc range and their analysis. In the course of our preliminary experiment[5], Williams, Sheridan and Gordy[6] reported about the 10th to 12th rotational spectra of S^{32}PCl$_3^{35}$, S^{32}PCl$_3^{37}$ and S^{34}PCl$_3^{35}$. When each molecule of SPCl$_3$ contains three Cl atoms which belong to the same isotope Cl^{35} or Cl^{37}, it is a symmetric top molecule. If those three Cl atoms consist of two kinds of isotopes, Cl^{35} and Cl^{37}, the molecule is an asymmetric rotor, having rather large asymmetry, so the spectra are very complex. These spectra are very much sensitive to the molecular structure. All lines have a spread of several Mc arising from the hyperfine structure due to the nuclear electric quadrupole moment of the Cl nuclei. Besides these complex spectra of asymmetric rotors and hyperfine structures, there is splittir due to vibrations of molecules. Relative inte sities of the splitted lines depend on temper ture and their rotational states.

In the preliminary experiment, the absor tion cell of the transmission type, which w made by the circular wave guide, 9 m length and 9.1 cm in diameter, was used. C measuring, there were some difficulties. On was the mode contour of output power the frequency-modulated klystron. Becau of the small absorption coefficient, rather hig pressure of gas was necessary, so the li width became broad and the hyperfine lin were overlapping. Then, at least 10 Mc the frequency-sweep range was necessar But width of the mode contour was about Mc. To a certain extent, this difficulty w avoided by the double crystal balancing, whi demanded very much tedious adjustme Other one was the ghost due to reflections the windows of the absorption cell, who periods were several Mc. Cone-type windows instead of plane glass windows, and an we matched attenuator placed just behind t window of input side of the cell were efficie to eliminate the ghost. Any way, narrowne of the frequency-sweep range made th method to be of little value. In the limit complete saturation of spectral lines, t maximum power absorbed is proportional square of frequency. So dimensions of t absorption cell must become larger as fr quency becomes lower. Generally, the Sta or Zeeman modulation seems to be difficu because of larger dimensions of the cell lower frequency. Using the cavity resonat as the cell, it was rather easy to get t

---

* The author wishes to thank Mr. Mash Yamaha for his offer of this sample.

ectrometer, of which minimum detect-ble absorption coefficient was 5×10^{-9} n^{-1}, without troublesome ghosts and ode contour. But in this frequency gion, the half width of resonance curve the cavity was much narrower than ose of spectral lines. So, it was much borious to search the spectra. In this periment, difference between Q's of the vity filled with gas and that was mped off was plotted point-by-point at ch frequency. It would be desirable record the spectra continuously. It ay be achieved by changing frequency the oscillator and cell synchronously. In is it is noteworthy that, at changing equency, irregular variations of Q of the vity and output power of the oscillator must much smaller than that due to absorption gas.

2. The Experimental Apparatus and Procedure

The cavity resonater was first filled with e gas and then pumped off, and the varia-on of loaded Q, ΔQ, was observed. Then e absorption coefficient α_g of the gas was ven by (1).

$$\alpha_g=(2\pi/\lambda Q^2)\Delta Q \text{ cm}^{-1}. \qquad (1)$$

e cylindrical cavity made by copper had mensions of 65 cm in length and 16 cm in ameter, and had shortening plunger backed mixture of carbon and paraffin for mode-mping, the clearance between the cavity all and plunger being about 1 mm. The indows were slits of 15×2 mm (wall thick-ss 2.5 mm) and covered by thin mica. The ode of the cavity was TE_{01n}, n being 4 to and its Q was about 4×10^4.

The apparatus is shown in Fig. 1. The ystron was equipped with a tunable wave ide resonater. The frequency sweep of the odulation was carried out at 1 kc with a w tooth generator. The range of frequency eep was about 1.5 Mc. The power trans-itted through the cavity was detected by e crystal detector and amplified. The ampli-r was the low-cut audio amplifier of 4 stages ith gain of about 130 db. The third stage lve had zero grid bias and the forth stage lve was given about −180 v bias by cells. he output signal of the amplifier was recti-fied by 6H6. This was also biased by cells of 150 v and time constant was enough large to indicate the height of Q curve of the cavity. As input power to the crystal detector was small and its characteristic was in the square law region, the output voltage of the amplifier was proportional to the input power to the crystal detector. A fraction $4Q^2/Q_1Q_2$ of power from the oscillator flows out through the cavity, Q_1 and Q_2 being the external Q's of the input and output windows respectively. So relative variation $\Delta V/V$ of the output of the peak voltmeter is equal to $2\Delta Q/Q$. The minimum detectable $\Delta Q/Q$ was about 1/2,600. This value was limited chiefly by fluctuation of output power of the klystron and noise of the crystal. By this value and formula (1), minimum detectable absorption coefficient α_{gmin} was roughly 5×10^{-9} cm^{-1}. When the cavity was filled with gas, following two phenomena were observed. One was shift of resonance frequency of the cavity due to change of the dielectric constant. This shift was about 16 kc at 1 mmHg of $SPCl_3$. If steep region of the klystron's mode-contour was used or if the wave-form of the modulation-voltage and the characteristic of the amplifier were inadequate, this shift changed the output of the peak voltmeter. The other was constant decrease** of Q, which corresponds to $\tan\delta$ of about 1×10^{-7}/mmHg. When the cavity was filled with $OPCl_3$, which has the same order of dipole moment as $SPCl_3$ and whose rotational spectra of $J=0\rightarrow1$ where at about 4,000 Mc, similar decrease

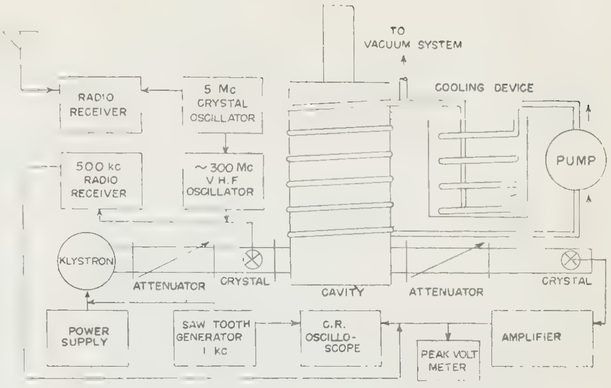

Fig. 1. Diagram of the spectrometer.

** This constant decrease may be due to many weak lines of asymmetric top molecules. See § 4. See, also, reference 7.

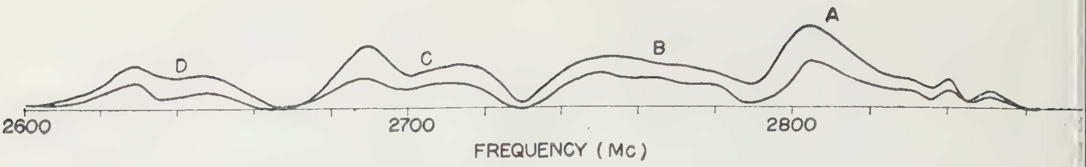

Fig. 2. Absorption curves of $SPCl_3$. The pressure is 1.2 mm Hg. The upper curve is at +4°C and the lower at +45°C.

was observed and about 60 to 70% of that.

Measurements were made every 2 Mc between 2,600 Mc and 2,850 Mc and at several points between 2,850 Mc and 2,900 Mc.

In order to measure the temperature effect of the spectra due to vibration, the cavity was cooled or heated. For this purpose, as Fig. 1 shows, the copper pipe was wound around the cavity, dimensions of the pipe being 17 m in length and 0.48 cm in inner diameter. Hot water or alcohol cooled by dry ice were circulated through this pipe, and the temperature of the cavity was varied from −40°C to +45°C. The measurement was carried out at +4°C and +45°C.

The frequency was measured as follows: the output power of the klystron was mixed with that of the frequency-calibrated V.H.F. oscillator by the crystal and the beat was amplified by the radio receiver. The beat was observed, if following relation was satisfied,

$$F-nf=\pm R.$$

F, f, and R were frequencies of the klystron, V.H.F. oscillator and radio receiver, respectively. For suitable values of R and the range of frequency sweep, two beats were observed at the same time on the oscilloscope and these were of use for measurement of Q. The value of f was about 300 Mc, so $n=9$, and R was about 500 kc. The calibration of the V.H.F. oscillator was made by comparison of the output or its higher harmonics with those of the 5 Mc quartz oscillator, which was calibrated by the standard waves from the broadcasting station. Thus f was plotted every 5 Mc, 5/2 Mc and 5/3 Mc.

§ 3. Results of Measurements

The measured absorption spectra of $SPCl_3$ in the region between 2,600 Mc and 2,900 Mc are shown in Fig. 2. The pressure was 1.2 mmHg. Back ground, whose value was about 40% of the maximum intensity of the spectra, was substracted from the measured variati of Q, ΔQ, caused by filling up the cavity wi gas. The back ground was obtained fro the lowest level of the change of Q. T intensity of absorption lines increased rapid with falling temperature, but the distributi of the spectra was little changed. In t figure, the upper curve shows result at +4° and the lower at +45°C. The back grou also changed with temperature and increas by about 60% at +4°C from that at +45°C

The spectra consisted chiefly of four part A, B, C and D. In addition to these, the were some weak lines between 2,820 Mc a 2,860 Mc. The central frequencies, relati intensities and ratios of the intensities +4°C to that at +45°C, of these four pa are shown in Table I.

These parts are perhaps composed of ma unsplit lines. These lines can not be reso ed at such pressure, but the absorption cur is not always smooth.*** The absorpti coefficient of A, the maximum of all, w about 7×10^{-8} cm^{-1} per mmHg at +4° This value is much larger than the theore cal one. The reason is not clear. It is po sible that the high-intensity lines due to asyr metric rotors may be superposed each oth and the estimated absorption coefficient m

Table I. Relative intensity is that at +4°C. Rat is the intensity at +4°C divided by that +45°C.

group	central frequency	relative intensity	ratio
A	2805 Mc	10	1.8
B	2760 Mc	7	1.6
C	2710 Mc	6	1.8
	2689 Mc	8	1.8
D	2647 Mc	4	1.6
	2629 Mc	6	1.7

*** In the preliminary experiment, there we large fluctuations due to instability of the circu in measuring $\Delta Q/Q$, so very rugged curve w obtained.[5]

be too large.

4. Discussion

There are two kinds of isotopes of chlorine, Cl^{35} and Cl^{37}, whose relative abundance is 3 o 1, and also four kinds of isotopes of sulphur, among which amounts of S^{32} and S^{34} are 95 and 4% respectively. So there are many combinations of these isotopes for $SPCl_3$. Among these, only molecules containing S^{32} are possible to be observed, and relative abundances of $S^{32}PCl_3{}^{35}$, $S^{32}PCl_2{}^{35}Cl^{37}$, $S^{32}PCl_2{}^{35}$-$Cl_2{}^{37}$ and $S^{32}PCl_3{}^{37}$ are 1:1:1/3:1/27. The spectra of $S^{32}PCl_3{}^{35}$ and $S^{32}PCl_3{}^{37}$, of the 10th, 11th and 12th rotational lines, were observed by Williams, Sheridan and Gordy⁶⁾ at about 30,000 Mc and their results were as follows: $B_0=1,402.64\pm0.05$ Mc, $1,355.72\pm0.05$ Mc, $d_{P\text{-}S}=1.85\pm0.02$ A, $d_{P\text{-}Cl}=2.02\pm0.01$ A, $\angle ClPCl=100.5\pm1.0°$. So the rotational spectra of $J=0\rightarrow1$ of these symmetric top molecules are estimated to be 2,805 Mc and 2,711 Mc respectively. The frequency of the group A corresponds to that of $S^{32}PCl_3{}^{35}$. The intensity of the line corresponding to $S^{32}PCl_3{}^{37}$ is 1/27 of that of $S^{32}PCl_3{}^{35}$, so this cannot be observed.

Because $SPCl_3$ molecules are nearly spherical top molecules, those which have two kinds of chlorine isotopes have rather large asymmetry. The Ray's asymmetric parameters⁸⁾ κ of $S^{32}PCl_2{}^{35}Cl^{37}$ and $S^{32}PCl^{35}Cl_2{}^{37}$ are -0.52 and -0.41 respectively. The spectra of 0_{00} to 1_{01}, due to these asymmetric rotors are estimated to be at 2,772 Mc and 2,741 Mc respectively. The group B seems to correspond to these two lines. The different line-shapes and relative intensities of A and B may be due to different types of splitting of the hyperfine structure or superpositions of lines with other origins.

As the origins of the remainder of the observed lines, C and D, the following two cases may be supposed: the Q branch of the rotational spectra of the asymmetric rotors, and the excited vibrational lines. Many intensive lines in the Q branch, due to the splitting of the paired levels⁷⁾⁸⁾⁹⁾¹⁰⁾ with the same K values and the J values more than about 13, exist at 2,700 Mc region. The Boltzmann factor is about one half at $J=60$, so rather high-J lines may be observed. Values of the squared direction cosine matrix elements⁹⁾ of several lines summed over the three directions of space and over all values of M and M' are one or more, so the intensities of these lines are comparable to or more than those of the symmetric top molecules, so far as we take no account for the relative abundance. Frequencies of those lines cannot be estimated exactly. The back ground of the spectra is perhaps due to these rotational lines⁷⁾ of the asymmetric rotors.

If the excited vibrational lines are far from those of the ground state, they exhibit series of equally spaced lines, whose intensities decrease gradually with decreasing frequency. The relative intensities of these lines are sensitive to the temperature, so that it is possible to distinguish whether the lines are excited vibrational ones or not, by measuring at different temperatures. Table II showes the relative intensities of the excited vibrational lines to the ground state ones in case of the vibrational frequency of 171 cm⁻¹.

Table II. Relative intensity of the excited vibrational line. The vibraional frequency is 171 cm⁻¹.

n	relative intensity at +4°C	at +45°C
0	1	1
1	0.82	0.92
2	0.51	0.63
3	0.28	0.39
4	0.14	0.23
5	0.07	0.12

The absolute intensity of the ground vibrational lines is also sensitive to the temperature. If the change of the line width is neglected and the pressure is kept constant, α_{gmax} is proportional to

$$T^{-7/2}\{1-\exp(-h\nu/kT)\}^2$$

for the transition of $J=0\rightarrow1$. This is the case in which the hyperfine splitting is comparable to or slightly more than the line width. The calculated ratio at the ground state of α_{gmax} at +4°C to that at +45°C is estimated to be 1.9. If all the vibrational lines coinside, the ratio will be 1.6. Though, because of rather poor accuracy of the observed ratio in Table I, the discrimination is difficult, all lines seem to have the same temperature dependence (ratios are all about 1.7) and none of these seems to belong to excited

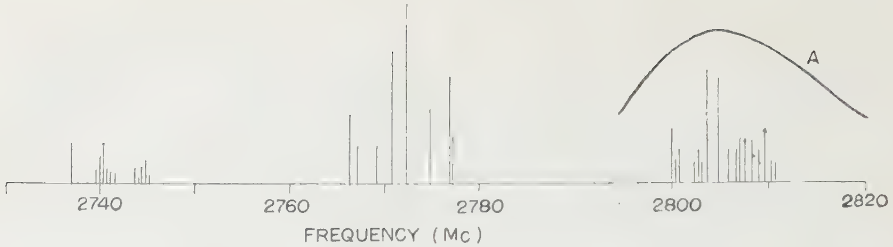

Fig. 3. Calculated result. $d_{P-Cl}=2.02$ A, $d_{P-S}=1.85$ A, $\angle Cl-P-Cl=100.5$[5)] and $(eQq)_{35}=-60$ Mc. The second-order effect is neglected. The curve A shows measured result (see Fig. 2.).

vibrational levels. So C and D are thought to be lines due to the asymmetric rotors.*

In addition to these complexity, each line is splitted by the nuclear electric quadrupole interaction of chlorine nuclei. The theoretical calculation shows that the maximum separation $\Delta\nu_h$ of the hyperfine splitting of the $SPCl_3^{35}$ or $SPCl_3^{37}$ spectra is given by the following equation[2)7)].

$$\Delta\nu_h=0.173|eQq_{zz}|\ \text{Mc}, \qquad (2)$$

where eQq_{zz} is the quadrupole coupling constant of the chloine nucleus referred to the Cl-P axis. At deduction of this formula, the separation of the inversion doublet is small and the second-order nuclear quadrupole interaction is neglected. The second-order effect makes the splitting larger (by about 2∼3 Mc)[7)]. Fig. 3** shows the calculated result of the hyperfine structures (H.F.S.) of rotational transitions of $J=0\rightarrow1$ of $S^{32}PCl_3^{35}$ and of $J=0_{00}\rightarrow1_{01}$ of $S^{32}PCl_2^{35}Cl^{37}$ and $S^{32}PCl^{35}Cl_2^{37}$, and also, shows measured curve of the group A. In the calculation, eQq_{zz} was assumed to be −60 Mc for Cl^{35}.*** As seen in the figure, even for the transition of $J=0\rightarrow1$, H.F.S. of the asymmetric rotors, especially $SPCl^{35}Cl_2^{37}$, are different from H.F.S. of the symmetric ones.

To discuss characters of the asymmetric top molecules more deeply, it is necessary to make measurement over wide frequency range and analyse this result.

Acknowledgement

The author should like to express cordial gratitude to Professor S. Kojima for his guidance during this work. The author also wishes to acknowledge the help of Mr. Shigeo Hagiwara with construction of the spectometer.

References

1) R. Bersohn: J. Chem. Phys. **18** (1950) 1124.
2) M. Mizushima and T. Itoh: J. Chem. Phys. **19** (1951) 739.
3) S. Kojima, K. Tsukada, S. Hagiwara, M. Mizushima and T. Itoh: J. Chem. Phys. **20** (1952) 804.
4) M. Kotani: Kagaku **19** (1949) 482.
5) S. Kojima, K. Tsukada and S. Hagiwara: Summary of Symposium of Moleculer Physics, Nikko, Sept., 1953, p. 52.
6) Q. Williams, J. Sheridan and W. Gordy: J. Chem. Phys. **20** (1952) 164.
7) T. Itoh: J. Phys. Soc. Japan **10** (1955) 56.
8) G. W. King, R. M. Hainer and P. C. Cross: J. Chem. Phys. **11** (1943) 27.
9) P. C. Cross, R. M. Hainer and C. W. King: J. Chem. Phys. **12** (1944) 210.
10) R. M. Hainer, R. C. Cross and C. W. King: J. Chem. Phys. **17** (1949) 826.
11) R. Livingston: Phys. Rev. **82** (1951) 289 L.
12) R. Livingston: See *"Microwave Spectroscopy"* (1953) by Gordy, Smith and Trambarulo.

---

* Temperature dependence of the asymmetric rotor's line is slightly different from that of symmetric one, because of different energy value of the rotational level in the Boltzmann factor.

** This figure is indebted by Dr. T. Itoh. For the calculation, see reference 7.

*** The pure nuclear quadrupole spectrum of chlorine of solid $SPCl_3$ could not be observed at the liquid air temperature. The observed spectra of solid $OPCl_3^{35}$ [10)] and PCl_3^{35} [11)] yielded the coupling constants of 58 Mc and 52 Mc, respectively. Generally eQq_{zz} of gaseous state is several per cent greater than that of solid state.

JOURNAL OF THE PHYSICAL SOCIETY OF JAPAN Vol. 10, No. 1, JANUARY, 1955

Development of Emulsions due to Self Nucleation

By Hiromu WAKESHIMA

The Kobe University of Mercantile Marine

(Received June 8, 1954)

Based on the formulae for the absolute rate of self-nucleation in condensed systems and also for the growth of droplets derived by the author, the process of development of emulsions in solutions supersaturated with dissolved liquid, when the meta-stable state is broken by self-nucleation, is approximately treated, in a way similar to that given previously[1]. The relations giving such as the threshold condition for the appearance of turbidity and the number density of droplets are obtained.

§ 1. Introduction

So far as the author is aware of, we have no satisfactory theory of the development of emulsions by self-nucleation in solutions supersaturated with dissolved liquid, though the phenomenon is interesting as it is relatively simple among similar phenomena. S. Ono[2], discussing the allied phenomena, i.e., the sedimentation in a solution, derived from the stand point of Becker's rate of nucleation[3], a formula which was successful in explaining qualitatively the experimental law given by Weimarn[3]. But this result concerns rather with a rough estimation of the general tendency of the sedimentation and does not allow the quantitative confirmation of experimental results. D. Turnbull and J. C. Fisher[5], on the other hand, gave an expression for the absolute rate of nucleation in condensed systems. They derived it on the basis of the nucleation theory developed by Volmer[6], Becker and co-workers and also on the basis of the absolute reaction rates, first introduced by Eyring[7]. Before their result be verified by experiment, the whole process of some phenomena involving self-nucleation, to which only their result is applicable, should be clarified theoretically.

In the following we will discuss from the same point of view the phenomenon of the development of emulsion in a liquid mix when the solubility is lowered by lowering the temperature and the droplets of one component develop in the solution by self-nucleation; particulary we take up the case where water droplets develop on cooling benzene containing water in consequence of the lowering of mutual solubility. First the rate of self-nucleation in condensed systems will be discussed and then we proceed to the rate of droplet growth. Using these results the process of nucleation will be treated in a way similar to that in the preceding papers. The result of this treatment gives the number density of solute droplets appearing in the solution after the break of meta-stable state of supersaturation due to self-nucleation. This number density, together with the total amount of solute separated, determines the size of the droplets developed. These, as well as the rate of development of emulsion, will be compared with experimental data.

§ 2. The Rate of Self-Nucleation in Condensed Systems

Results similar to those given by D. Turnbull and J. C. Fisher[5] can simply be obtained modifying Frenkel's derivation[8] of the rate of nucleation in vapors.

Let ϕ_A and ϕ_B be the bulk free energy per molecule of the solute in phase A (dissolved state) and B (separated state) respectively and μ a constant proportional to the interfacial free energy between the two liquids, reduced per solute molecule at the interface. Then the free energy change $\Delta\phi$ accompanying the formation of a droplet of phase B out of g molecules in phase A can be expressed as $\Delta\phi=(\phi_B-\phi_A)g+\mu g^{2/3}$. At the top of the free energy barrier in the embryo-nucleus transition, i.e., for the critical droplet corresponding to $g=g^*$, we have $d(\Delta\phi)/dg=\phi_B-\phi_A+(2/3)\mu g^{*-1/3}=0$ and therefore $\Delta\phi^*\equiv(\phi_B-\phi_A)g^*+\mu g^{*2/3}=(1/3)\mu g^{*2/3}$. Now put $\chi\equiv-d^2\cdot(\Delta\phi)/dg^2=(2/9)\mu g^{-4/3}$ and $\chi^*\equiv(2/9)\mu g^{*-4/3}$. As shown by Frenkel[8], the stationary rate of nucleation ν per unit volume per unit time is approximately given by

---

* A similar relation holds between the rate of nucleation given by Becker and Döring and that obtained by Frenkel.

$$\nu = N^* D_*^* (\chi^*/2\pi kT)^{1/2} , \tag{1}$$

where N^* denotes the equilibrium number of critical droplets per unit volume, D_*^* the probability with which a critical droplet captures a molecule in unit time.

According to the theory of absolute rate of reaction[7]. D_*^* can be expressed as

$$D_*^* = a g^{*2/3} (kT/h) \exp(-\Delta f_*^*/kT) . \tag{2}$$

Here h denotes Planck's constant, $a g^{*2/3}$ the average number of dissolved solute molecules in contact with a critical droplet and Δf_*^* the free energy of activation for the embryo-nucleus transition, i.e., for the capture of one solute molecule by a critical droplet.

As

$$N^* \doteqdot N \exp(-\Delta\phi^*/kT)\ ^{9)}, \tag{3}$$

where N gives the number of solute molecules in phase A per unit volume of the solution, we have, using (1), (2) and (3)

$$\nu = (n^*/g^{*2/3}) \cdot (\mu/9\pi kT)^{1/2} \cdot (NkT/h) \cdot \exp\{-(\Delta\phi^* + \Delta f_*^*)/kT\}, \tag{4}$$

where $n^* \equiv a g^{*2/3}$. This is a formula which is the same as that given by D. Turnbull and J. C. Fisher[5] except for the factor $g^{*2/3}$ in the denominator*. The factor $(n^*/g^{*2/3})(\mu/9\pi kT)^{1/2}$ in Eq. (4) is in many cases of the order of magnitude of 1~10, so that we have

$$\nu \simeq (NkT/h) \exp\{-(\Delta\phi^* + \Delta f_*^*)/kT\} , \tag{4a}$$

which is the approximate formula given by D. Turnbull et al[5]. However, the factor mentioned above differs sometimes much from 1 and in such cases (e.g., the actual case mentioned previously) we have to use Eq. (4) instead of (4a).

If we assume, for simplicity, the molecules to be spheres of a diameter δ, $a g^{2/3}$ can be expressed approximately as $a g^{2/3} \doteqdot \pi(\delta g^{1/3})^2 \cdot \delta N$, whence we have $a = 6 N v_B$, where v_B is the volume of a solute molecule in phase B. Further, substituting σ for μ in (4), σ being the interfacial free energy per unit area ($\sigma = \mu/\pi\delta^2$), (4) can be transformed into

$$\nu = (2 v_B \delta/h) \cdot (\sigma kT)^{1/2} \cdot N^2 \cdot \exp\{-(\Delta\phi^* + \Delta f_*^*)/kT\}. \tag{4b}$$

As for Δf_*^*, it is difficult to make a rigorous evaluation of it, but it would not be unnatural to suppose that Δf_*^* can be replaced, to a rough approximation, by the mean of the two quantities Δf_{dif} and Δf_{vis}, Δf_{dif} being the free energy of activation for the diffusion of a solute molecule in the solvent and Δf_{vis} the free energy of activation for self-diffusion of the solute or the corresponding quantity for viscocity. This is because Δf_*^* refers to the jump of a solute molecule over the interface between the solute liquid and the solvent, while Δf_{dif} refers to the jump of a solute molecule in the solvent and Δf_{vis} to that in the solute.

Furthermore, according to the theory of absolute rate of reaction[10], there exists a relation between the coefficient of diffusion D and the free energy of activation for diffusion Δf_{dif}, such that $D = (\lambda^2 kT/h) \cdot \exp(-\Delta f_{dif}/kT)$ or $\Delta f_{dif} = -kT \ln Dh/\lambda^2 kT$. There exists also a relation $D_s = (\lambda_s^2 kT/h) \cdot \exp(-\Delta f_{vis}/kT)$ or $\Delta f_{vis} = -kT \ln D_s h/\lambda_s^2 kT$ where D_s means the coefficient of self-diffusion for the solute liquids; λ and λ_s are the distances between the successive equilibrium positions through which a solute molecule is transported in each jump in the course of diffusion as well as of self-diffusion. They may be replaced by the diameter of a solvent molecule δ' and that of a solute molecule δ respectively, without committing a great error. Using these equations we get

$$\exp(-\Delta f_*^*/kT) = (h/kT)(D D_s)^{1/2}/\delta'\delta . \tag{5}$$

§ 3. Growth of a Droplet

In calculating the rate of growth of a droplet we assume, as in the previous case[1], that the growth of each droplet is independent of the growth of other droplets, i.e., we assume that the effect of collision and other mutual influences between droplets can be neglected.

The number of solute molecule captured by a droplet of radius r on its unit surface per unit time can be expressed as bN_r where N_r is the number density of the solute molecule in the solution near the surface and b denotes the ratio of the number of the molecules captured by a droplet on its unit surface per unit time to the number of dissolved molecules in unit volume of the solution; b is approximately equal to $(\delta kT/h) \cdot \exp(-\Delta f_*^*/kT)$ corresponding to the rate of nucleation given by (4b).

The number of the molecules liberated from unit surface of the droplet per unit time, assumed to be independent of the surrounding condition, can be expressed approximately as bN_∞, where N_∞ denotes the number density of the molecule in the saturated solution. This can be derived from the condition of equilibrium between the droplet and the solution, neglecting the change in N_∞ which might be appreciable for very small droplets (e.g., $r < 10^{-6}$ cm). Thus the time rate of increase of the radius of a droplet is given by $dr/dt = v_B b(N_r - N_\infty)$.

If we assume the net capture of the dissolved solute molecules by a droplet to be supplied by a stationary diffusion of the molecule in the surrounding solution, it is easy to show that the relation $N - N_r = (r/D)b(N_r - N_\infty)$, holds, where N denotes the number of solute molecules per unit volume of the solution at a point sufficiently distant from the droplet. Therefore we have as before, $dr/dt = v_B b\cdot(N - N_\infty)/(1 + br/D)$. H. L. Frisch and F. C. Collins[11] recently obtained this equation by a more elaborate treatment. Now D is of the order of magnitude 10^{-5} cm^2.sec^{-1} and b, 10^2 cm.sec^{-1}. Therefore, neglecting 1 compared to br/D, we have

$$dr/dt = v_B D(N - N_\infty)/r\,, \tag{6}$$

which is the formula obtainable by the usual treatment of considering diffusion of the solute molecule only.

§ 4. Nucleation Process

Consider, to make the matter concrete, the case where the solubility decreases as the temperature of a solution falls, as in the case of the development of emulsion in benzene supersaturated with water. When the temperature of the supersaturated solution is lowered at a constant rate, the nucleation will become appreciable practically at a certain instant, and thereafter the rate of nucleation will rise because of the decrease in solubility. As the time goes on the nucleation and the growth of droplets will gradually cancel the rise of the degree of supersaturation produced by the decrease in solubility; the increase of the rate of nucleation will diminish by and by and the rate, after passing over a maximum, will fall rapidly down to zero. Then the number of droplets remains practically constant, though each of them will continue to grow further as long as the solubility is kept decreasing. After an elapse of a certain time interval, the degree of supersaturation will become always nearly equal to 1. As the process in question is of such a complexity, we shall here content ourselves with only an approximate treatment of it.

Before we enter the details of the treatment, it would be better to emphasize that, as one sees from (4b), the change in N as well as in T have a remarkable influence on the rate of nucleation, even in the case where they have only little effect on the rate of droplet's growth given by (6). In view of this nature of the function $\nu(N, T)$, the rate of growth dr/dt of a droplet of radius r, will be assumed to be constant and be given always by

$$dr/dt = v_B D(N_0 - N_\infty)/r\,, \tag{6a}$$

so far as we are in the time interval during which the rate ν is of considerable magnitude. Here N_0 denotes the initial number density of the solute molecule in the solution, D as well as N_∞, refers to the time origin which will be taken at the instant when the rate of nucleation attains its maximum value. Furthermore, as a substitute for the accurate but complicated function $\nu(N, T)$ given by (4b) in the vicinity of $\nu_0(N_0, T_0)$, we make use of an approximate formula of the form similar to that given previously[1],

$$\nu = \nu_0 (N/N_0)^{\phi_{N_0}} (T/T_0)^{-\phi_{T_0}} \tag{7}$$

where

$$\phi_{N_0} = 2(1 + 2\pi r_0^{*3}/3v_B)$$

and

$$\begin{aligned} -\phi_{T_0} = [&(T_0/2\sigma - 4\pi r_0^{*2}/k)(d\sigma/dT)_0 \\ &+ 1/2 + \Delta f_*^*/kT_0 + (4\pi r_0^{*2}/k)\{\sigma_0/T_0 \\ &- (kr_0^*/3v_B)(dN_\infty/dT)_0 T_0/N_{\infty 0}\}]\,. \end{aligned}$$

Here r^* denotes the radius of a critical droplet and values of all quantities in the above expressions with a subscript $_0$ refer to those at the time origin. Eq. (7) can be derived as follows. From the general expression for the rate of self-nucleation $\nu = CN^{K_1}T^{K_2}\exp[f(N, T)]$ with constants C, K_1 and K_2 we have

$$\begin{aligned} \nu/\nu_0 = &(N/N_0)^{K_1}(T/T_0)^{K_2} \\ &\cdot\exp[f(N, T) - f(N_0, T_0)]\,. \end{aligned}$$

Neglecting small quantities of higher orders in $N/N_0 - 1$ as well as in $T/T_0 - 1$,

$$\begin{aligned} &\exp[f(N, T) - f(N_0, T_0)] \\ &\quad = \exp[(N\cdot\partial f/\partial N)_0(N/N_0 - 1) \\ &\qquad + (T\cdot\partial f/\partial T)_0(T/T_0 - 1)]\,. \end{aligned}$$

Also $\exp(N/N_0-1)$ and $\exp(T/T_0-1)$ can be replaced by N/N_0 and T/T_0. Thus we get the following relation from which (7) will be obtained,

$$\nu/\nu_0=(N/N_0)^{(K_1+N\cdot\partial f/\partial N)_0}(T/T_0)^{(K_2+T\cdot\partial f/\partial T)_0}. \tag{7}$$

Now $(T/T_0)^{-\phi_{T_0}}$ can be written as a function of time t. It is equal to $(1-\alpha/T_0\cdot t)^{-\phi_{T_0}}$, where α means the time rate of temperature fall and t the time elapsed since the time origin. As $|\alpha/T_0\cdot t|\ll 1$ in the time interval we are considering for nucleation, $(T/T_0)^{-\phi_{T_0}}$ can be approximated as

$$\exp(\alpha/T_0\cdot\phi_{T_0})\equiv\exp(\phi_2 t) \text{ with } \phi_2\equiv\alpha/T_0\cdot\phi_{T_0}.$$

As for the factor $(N/N_0)^{\phi_{N_0}}$, we have to calculate

$$-dN/dt=4\pi/v_B\cdot\int_0^{r_m} f\cdot(dr/dt)\cdot r^2 dr\,,$$

where $f\cdot dr$ denotes the number density of droplets, with radiu between r and $r+dr$, and r_m the radius of the largest droplet at the instant t. According to the assumption (6a), the time of growth θ, for a droplet of radius r, since its nucleus is generated, can be looked upon as time-independent and so the relation $f=\partial\theta/\partial r=\nu/(dr/dt)$ is approximately valid. Therefore we have

$$-dN/dt=(4\pi/v_B)\int_0^{r_m} r^2\nu dr\,, \tag{8}$$

where ν refers to the time $t-\theta$. Now as the first approximation to ν, we take, as in the former case[1], such a value of ν at each moment that one would have when one takes off the solution the quantity of solute molecules, sufficient to make up the decrease in the number of molecules due to nucleation and also due to the growth of droplets. Thus we replace ν in (8) by, ν', satisfying

$$\nu'\equiv\nu_0(T/T_0)^{-\phi_{T_0}}\equiv\nu_0\exp\{(\alpha/T_0)\cdot\phi_{T_0}(t-\theta)\}.$$

Using this and the integration of (6a), $r^2=2v_B D(N_0-N_\infty)\cdot\theta$, $-dN/dt$ can be shown to be

$$-dN/dt=(4\pi\nu_0/v_B)e^{\phi_2 t}\int_0^{r_m} r^2\exp(-\phi r^2)dr\,,$$

with

$$\phi=(\alpha/T_0)\phi_{T_0}/2v_B D(N_0-N_\infty)\,.$$

We may not commit a great error if we replace the upper limit of this integration by ∞, because the integrand becomes negligibly small for larger r. Thus we have

$$-\frac{dN}{dt}\fallingdotseq\frac{4\pi\nu_0}{v_B}e^{\phi_2 t}\int_0^\infty r^2 e^{-\phi r^2}dr$$
$$=\frac{\pi\nu_0}{v_B}e^{\phi_2 t}\frac{1}{\phi}\sqrt{\frac{\pi}{\phi}}\,. \tag{8a}$$

As $N\fallingdotseq N_0$ at $t=-\infty$, we get, integrating the above equation

$$N_0-N\fallingdotseq(\pi\nu_0/v_B\phi)\cdot(\pi/\phi)^{1/2}\cdot\phi_2^{-1}\cdot\exp(\phi_2 t)$$

or

$$\left(\frac{N}{N_0}\right)^{\phi_{N_0}}\fallingdotseq\left[1-\frac{\pi\nu_0}{v_B N_0\phi}\sqrt{\frac{\pi}{\phi}}\cdot\frac{1}{\phi_2}\cdot\exp(\phi_2 t)\right]^{\phi_{N_0}}\equiv\phi_1(t)\,, \tag{9}$$

and finally the relation

$$\nu=\nu_0\phi_1(t)e^{\phi_2 t}\,. \tag{10}$$

At the time origin the rate of self-nucleation attains its maximum, therefore we have $\phi_1'(0)=-\phi_2\cdot\phi_1(0)$ or

$$\phi_2=\frac{\pi\nu_0}{v_B N_0\phi}\sqrt{\frac{\pi}{\phi}}(1+\phi_{N_0})\,. \tag{11}$$

This is the condition which determines the origin, i.e., the nucleation peak. And using this, Eq. (9) can be expressed as

$$\phi_1(t)=\left[1-\frac{1}{1+\phi_{N_0}}e^{\phi_2 t}\right]^{\phi_{N_0}}. \tag{9a}$$

Numerical or graphical integration of the equation

$$n=\nu_0\int_{-\infty}^{+\Theta}\phi_1(t)e^{\phi_2 t}dt\,. \tag{12}$$

gives us the number density of solute droplets in the solution. The final average size of the droplet can easily be found from this quantity n and the total amount of solute separated.

§ 5. Results of the Numerical Computation

Numerical computation was carried out for the case where an emulsion appear in benzene saturated with water at 40°C. As far as the author is aware of, we have no reliable experimental data of the diffusion coefficient D of water in benzene. So we calculated it using the formula

$$D=(\lambda^2/v_f^{1/3})(kT/2\pi m)^{1/2}\exp(-\Delta E_{vap}/nRT)$$

given by Eyring et al.[12], notation being the same as in their text. In view of the general discrepancy between the calculated and the observed values of the diffusion coefficient as is shown in their text[13]), the calculated value of D was multiplied by the average ratio of these two mentioned in their table. Thus we obtain for the value of D at 280.5°K $D=4.21\times 10^{-5}\,\text{cm}^{-2}.\text{sec}^{-1}$. D_s is computed using the formula[14]) $D_s=\lambda_1 kT/\lambda_2\lambda_3\eta$ given in that text, the result being $D_s=3.22\times 10^{-5}\,\text{cm}^{-2}.\text{sec}^{-1}$. at the same temperature. Using these values we get from Eq. (5) $\exp(-\varDelta f_*^*/kT)=2.944\times 10^{-3}$ for 280.5°K. In calculating the factor for other temperatures, $\varDelta f_*^*$ was assumed to be constant.

Solubility s of water in benzene, in weight percent, is computed using the formula $s=(1.85\times 10^6/T)\exp(-3.40\times 10^3/T)$, which the present author derived from the data given in the International Critical Tables.

The following table shows the rate of self-nucleation calculated from Eq. (4b), the number density N of dissolved water molecule being assumed to be that which corresponds to saturation at 40°C. We see from this table that the increase in ν_0 with lowering temperature is conspicuous, as mentioned already.

Temp.	40°	35°	30°	25°	20°C
ν_0	0	1.74×10^{-108}	1.09×10^{-7}	2.27×10^{11}	6.24×10^{17}

The next table gives the temperature T_0 corresponding to values of α chosen arbitrarily.

α deg.sec.$^{-1}$	1	0.1	0.01
T_0°C	26.8°	27.5°	28.1°

We see from this table that α, the time rate of temperature fall, has little effect upon the temperature which corresponds to the maximum rate of self-nucleation, but its decrease causes the temperature to rise somewhat as will be expected.

The following graph shows the relation between the time and the rate of self-nucleation $\nu=\nu_0\phi_1(t)e^{\phi_2 t}$. Also $\phi_1(t)$ and $\exp(\phi_2 t)$ for $\alpha=0.1$ is given.

The number density of droplets n obtained through graphical integration of the above curves and the corresponding average radii $\bar{r}$ of droplets at 20°C is given in the next table.

α deg.sec^{-1}.	1	0.1	0.01
n	2.79×10^6	1.04×10^5	$3.77\times 10^3/\text{cm}^3$
r	3.40×10^{-4}	1.02×10^{-3}	3.06×10^{-3} cm

We see from this table that the number density n differs much when the rate of temperature fall differs.

§ 6. Discussion

We have neglected the liberation or absorption of the heat of solution accompanying the growth of a droplet. This effect can be taken into account[1]) approximately replacing the diffusivity D by the effective diffusivity D_e which satisfies $D_e=D/\{1+D\lambda_*(dN_\infty/dT)/\kappa\}$, where λ_* denotes the heat of solution per molecule and κ the thermal conductivity of the solution. But this replacement causes no essential change in what has been discussed above, because

$$(D-D_e)/D=1-1/\{1+D\lambda_*(dN_\infty/dT)/\kappa\}\simeq 10^{-4}$$

for the present case.

In the above treatment of the problem, we have assumed that the rate of nucleation is always the stationary one corresponding to the surrounding condition at each moment, in spite of the changing circumstances. Namely, we have neglected the effect of time lag in the self-nucleation. To what extent is this simplification admissible?

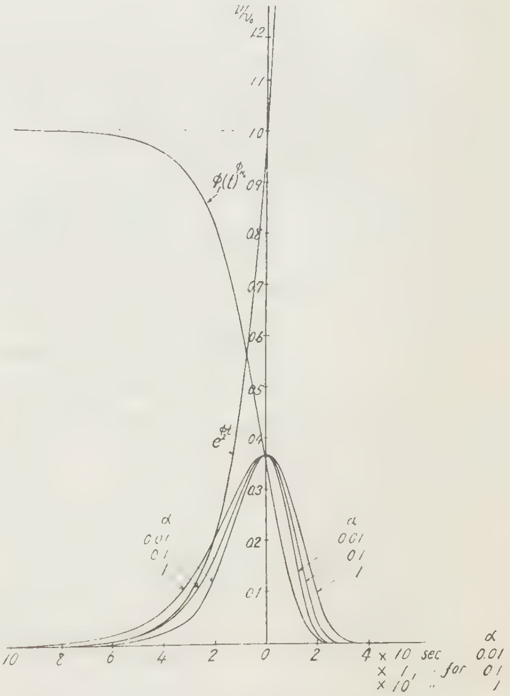

Fig. 1.

According to Frenkel[8]), the net number of embryos $I(g)$ increasing in size from $g-1$ to g per unit time per unit volume, satisfies $-I=D_*\partial f/\partial g+D_*/kT\cdot f\cdot\partial\varDelta\phi/\partial g$, where $f(g)$ denotes the number of embryos of various size, per unit volume in non-equilibrium state.

From this equation we have the following partial differential equation satisfied by $f(g)$,

$$\frac{\partial f}{\partial t}=\frac{\partial}{\partial g}\left(D_*\frac{\partial f}{\partial g}\right)+\frac{1}{kT}\frac{\partial}{\partial g}\left(D_* f\frac{\partial \Delta\phi}{\partial g}\right).$$

In our case $D_*=(ag^{2/3}kT/h)\exp(-\Delta f_*{}^*/kT)$, corresponding to Eq. (2). Now most relevant to the problem of nucleation in question is the value of f and its gradient with respect to g in the region $g\simeq g^*$ where the equation

$$\begin{aligned}\frac{\partial f}{\partial t}&=\frac{\partial}{\partial g}\left(D_*\frac{\partial f}{\partial g}\right)+\frac{1}{kT}\frac{\partial}{\partial g}\\&\quad\cdot\left\{D_* f\left(\frac{\partial^2\Delta\phi}{\partial g^2}\right)^*(g-g^*)\right\}\\&\doteqdot\frac{\partial}{\partial g}\left(D_*\frac{\partial f}{\partial g}\right)+\frac{D_*}{kT}\left(\frac{\partial^2\Delta\phi}{\partial g^2}\right)^* f,\end{aligned}\tag{13}$$

is approximately valid, as $\partial\Delta\phi/\partial g=0$ at $g=g^*$ and $D^*f\gg(g-g^*)\cdot\partial(D^*f)/\partial g$. $I(g)$ remains constant throughout all g after the stationary state is established and it is equal to ν, the stationary rate of nucleation. And we have

$$D^*\partial f_\infty/\partial g+(D_*/kT)(\partial\Delta\phi/\partial g)f_\infty=-\nu\,,\tag{14}$$

where f_∞ expresses the stationary value for f. Because the major part of the time lag would be contained in the period comming near to the stationary state, $\partial(D_*\partial f/\partial g)$ in Eq. (13) may be replaced by $\partial(D_*\partial f_\infty/\partial g)$, which can be expressed as $-(D_*/kT)(\partial^2\Delta\phi/\partial g^2)\cdot f_\infty$ from Eq. (14), when a rough estimation of time lag matters. Then we have from Eq. (13)

$$\begin{aligned}\frac{\partial f}{\partial t}&=\frac{D_*}{kT}\left(\frac{\partial^2\Delta\phi}{\partial g^2}\right)^*(f-f_\infty)\\&=-\frac{2}{9}\mu\frac{D_*}{kT}g^{*-4/3}(f-f_\infty)\\&\equiv-\mathcal{E}(f-f_\infty),\end{aligned}\tag{15}$$

and its solution

$$f=f_0e^{-\varepsilon t}+f_\infty(1-e^{-\varepsilon t})=f_\infty+(f_0-f_\infty)e^{-\varepsilon t}\,,$$

where f_0 denotes the initial value of $f(g)$ for $t=0$.

The rate of nucleation ν_t in the transient period satisfying $\nu_t=(D_*\partial f/\partial g)^*$, can easily be calculated, and the result is

$$\nu_t=\nu[1+\{\partial(f_0-f_\infty)/\partial g/(\partial f_\infty/\partial g)\}e^{-\varepsilon t}].\tag{16}$$

If we take for the time lag τ the time corresponding to $f_0{}^*=0$ and $\nu_t/\nu=1-1/100$, then we get the relation

$$\tau=4.6/\mathcal{E}\ \text{sec.}\,.\tag{17}$$

R. F. Probstein[15) has calculated more rigorously the time lag in the self-nucleation of a supersaturated vapor and has obtained results rather involved. The simple formula (17) given above, when applied to the case considered by him, gives right order of magnitude for τ as will be seen from the next table showing the nearly corresponding quantities.

Case	water vapor	nitrogen
Prob.	5×10^{-6} sec	3×10^{-8} sec
Wake.	8×10^{-6} sec	5×10^{-8} sec

Now $\mathcal{E}$ for water embryos in benzene, critical, e.g., at 27.9°C as considered before, is about 3×10^{6} sec^{-1} and the time lag τ is estimated to be 1.5×10^{-6} sec. Therefore the previous simplification can be justified.

So far we have assumed that the interfacial free energy between the droplet and the solution is constant. But this might be questionable in the case where the minute droplet, critical to nucleation, are concerned, i.e., those of radius $r^*\simeq10^{-7\sim8}$ cm. We expect that comparison between the present theory and experiment will throw light on this point.

The author is grateful to Prof. I. Uhara of Kobe University for his helpful discussion. His thanks are also due to Prof. T. Nagamiya of Osaka University for his kind criticism.

References

1) H. Wakeshima: J. Phys. Soc. Japan **9** (1954) 400.

2) S. Ono: Mem. Facal. Eng. Kyushu Univ. **4** (1943) 191 (in Japan.)

3) R. Becker: Ann. Phys. **32** (1938) 128.

4) D. v. Weimarn: Chem. Rev. **2** (1925) 217.

5) D. Turnbull and J. C. Fisher: J. Chem. Phys. **17** (1949) 71.

6) M. Volmer and A. Weber: Z. Phys. Chem. **119** (1926) 227.

R. Becker and W. Döring: Ann. Phys. **24** (1935) 719.

8) S. Glasstone, K. J. Laidler and H. Eyring: The Theory of Rate Processes, p. 195.

9) J. C. Fisher, J. H. Hollomon and D. Turnbull: J. App. Phys. **19** (1948) 775.

10) S. Glasstone, K. J. Laidler and H. Eyring: The Theory of Rate Processes, P. 524.

11) H. L. Frisch and F. C. Collins: J. Chem. Phys. **21** (1953) 2158.

12) S. Glasstone, K. J. Laidler and H. Eyring: The Theory of Rate Processes, P. 525.

13) ibid., P. 527.

14) ibid., P. 519.

15) R. F. Probstein: J. Chem. Phys. **19** (1951) 619.

JOURNAL OF THE PHYSICAL SOCIETY OF JAPAN Vol. 10, No. 1, JANUARY, 1955

On the Radio Wave Propagation in a Stratified Atmosphere

By Ryozo YAMADA

Electrical Communication Laboratory

(Received January 12, 1954)

This paper deals with the development of Weber's functions, and applying them the solution of the radio wave propagation is expressed in the form of the residue series[1], in the case when the modified index of refraction varies with height as $a+bh+ch^2$.

§ 1. Introduction

Since the phenomena of the radio duct was discovered, the theory has been developed by many investigators chiefly on the basis of the W.K.B. approximation method[2], applying to the arbitrary shape of the modified index profile.

In this paper we deal with this ploblem in the case when the modified index of refraction varies with height as $a+bh+bh^2$. This seems the simplest case to explain the phenomena due to the "single surface duct." In this case the solution of the electromagnetic field involves Weber's function, so the asymptotic expansions of Weber's function is developed by the method of the steepest descent, and then the field is calculated.

§ 2. The Field from a Dipole

The electromagnetic field from a vertical electric (magnetic) dipole near the earth can be calculated by finding a suitable solution of the scalar equation

$$\nabla^2\psi+k^2N^2\psi=0\ .$$

Here ψ is the z component of a electric (magnetic) Hertzian vector Π which has the z component alone.

The known solution is given by[3]

$$\psi=\int_0^\infty \kappa J_0(\kappa r)v(z,\ \kappa)d\kappa\ , \tag{1}$$

where r and z are the cylindrical coordinates of the field point and

$$v=\frac{2}{W}\left[\frac{u_1'(0)-pu_1(0)}{u_2'(0)-pu_2(0)}-\frac{u_1(z_1)}{u_2(z_1)}\right]u_2(z_1)u_2(z)$$
$$z\geqslant z_1\ , \tag{2}$$

$$v=\frac{2}{W}\left[\frac{u_1'(0)-pu_1(0)}{u_2'(0)-pu_2(0)}-\frac{u_1(z)}{u_2(z)}\right]u_2(z_1)u_2(z)$$
$$z\leqslant z_1\ . \tag{3}$$

The symbols used in the expression have following meanings;

1. z_1 is the height of the dipole. (The dipole is located at $r=0$ $z=z_1$).

2. $N(z)$ is the modified index of refraction, k and k_2 are the propagation factors of the vacuum and the earth respectively.

3. u_1 and u_2 are such solutions of the equation

$$\frac{d^2v}{dz^2}+[k^2N^2(z)-\kappa^2]v=0\ , \tag{4}$$

which for sufficiently large z represent the waves traveling in the direction of decreasing and increasing z respectively; W is the Wronskian of u_1 and u_2.

4. p is the function of κ that depends upon the polarization. For a vertical electric dipole

$$p=p_e=\frac{k^2N^2(0)}{k_2^2}\sqrt{\kappa^2-k_2^2}\ .$$

For a vertical magnetic dipole

$$p=p_k=\sqrt{\kappa^2-k_2^2}\ .$$

The radicals are to indicate the root with the positive real part. The time factor is taken as $\exp(-i\omega t)$. In our case the modified index of refraction varies with height as

$$k^2N^2(z)=k_0^2\{1+b^2(z-z_0)^2\}\ . \tag{5}$$

If this relation is inserted in Eq (4) and the independent variable is changed from z to $x=(z-z_0)/H$, we obtain

$$\frac{d^2v}{dx^2}+\left(\gamma+\frac{x^2}{4}\right)v=0\ , \tag{6}$$

where

$$H=(2k_0b)^{-1/2}\ , \tag{7}$$

$$\gamma=(k_0^2-\kappa^2)H^2\ . \tag{8}$$

The solutions u_1 and u_2 are expressed in terms of Weber's function as

$$u_1(x,\ \gamma)=e^{-(\gamma-i/2)\pi/4}D_{-i\gamma-1/2}(xe^{i\pi/4})\ , \tag{9}$$

$$u_2(x,\ \gamma)=e^{-(\gamma+i/2)\pi/4}D_{i\gamma-1/2}(xe^{-i\pi/4})\ . \tag{10}$$

§ 3. The Expansions of Weber's Function

a) Whittaker's expression in Kummer's function.[4] This expression is useful when both x and γ are small.

b) The asymptotic expansion of Whittaker[4]. This expansion is useful when $|x| \gg |\gamma|$.

c) Both x and γ are large excluding the region $\gamma+i/2 \sim -\frac{x^2}{4}$. Whittaker's integral representation gives[4][5]

$$D_{-i\gamma-1/2}(e^{i\pi/4}x) = \frac{-e^{(\gamma-i/2)\pi/2}}{\sqrt{2\pi}} \int_{\infty}^{-\infty}\left[\exp\left(i\frac{x^2}{4}+e^{i3\pi/4}xt-\frac{t^2}{2}\right)\right] (-t)^{-i\gamma-1/2}dt \tag{11}$$

$$D_{i\gamma-1/2}(e^{-i\pi/4}x) = \frac{-\Gamma(i\gamma+1/2)}{2\pi i} \int_{\infty}^{(0+)}\left[\exp\left(i\frac{x^2}{4}+e^{i3\pi/4}xt-\frac{t^2}{2}\right)\right] (-t)^{-i\gamma-1/2}dt\,. \tag{12}$$

We make the transformation

$$\gamma+i/2=\frac{x^2}{4}\sinh^2 w_0 \equiv \frac{x^2}{4}\sinh^2(\alpha+i\beta)$$

$$t=x\exp(w-i\pi/4)\,,$$

where x is positive real and α, β are real. There is a one-one correspondence between $\alpha+i\beta$ and $\gamma+i/2$ if we suppose that $\alpha>0$ and β is restricted to lie between $-\pi/2$ and $\pi/2$. Then the integral to be investigated becomes

$$\int\left[\exp\left(i\frac{x^2}{4}+e^{i3\pi/4}xt-\frac{t^2}{2}\right)\right](-t)^{-i\gamma-1/2}dt = e^{(3i-10\gamma)\pi/8}\int e^{-x^2 f(w)}dw\,, \tag{13}$$

where $f(w) \equiv -i(1/4+e^w+e^{2w}/2-w/4\cdot\sinh^2 w_0)$. In order to obtain the suitable expansions from this, we use the method of steepest descent[6]. The stationary points w_A and w_B, where $df(w)/dw=0$, are determined by $\exp w_A=\sinh^2 w_0/2$ and $\exp w_B=\sinh^2(w_0+\pi i)/2$.

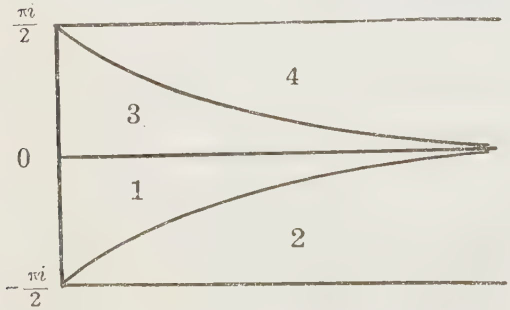

Fig. 1. w_0-plane. $\Psi_1(w_2)$ is negative in 4 and is positive in 1, 2 and 3. $\Psi_1(w_2-2\pi i)$ is negative in 2 and is positive in 1, 3 and 4.

Among the values of w_A and w_B we choose w_1 and w_2 which satisfy $|\arg w_1|<\pi$, $0<\arg w_2<2\pi$ respectively. Then all the stationary points are given by $w_1+2n\pi i$ and $w_2+2m\pi i$, where n and m assume all integral values. If we write $\Psi_1(w)=\mathrm{Im}\{f(w)-f(w_1)\}$, $\Psi_2(w)=\mathrm{Im}\{f(w)-f(w_2)\}$, the contours of the integration that pass through w_1 and w_2 are determined by $\Psi_1(w)=0$, $\Psi_2(w)=0$ respectively.

We divide the domain of values of complex $w_0 \equiv \alpha+i\beta$ into 4 subdomains according as the signs of $\Psi_1(w_2)$, $\Psi_1(w_2-2\pi i)$, which will be named 1, 2, 3, 4 as are indicated in Fig. 1.

For these subdomains, the contours of the integration take the shapes as are shown in Fig. 2. (rigid lines)

By the method similar to that of the Bessel function[6], the integral (13) along the contours that pass through w_1, $w_1+2\pi i$, and w_2, which we denote as (w_1), $(w_1+2\pi i)$ and (w_2), can be calculated in the following forms

$$(w_1)=-\sqrt{\frac{2\pi}{2\cosh w_0}}\exp\{-5\pi(\gamma-i/2)/4\} \cdot\exp\left[\frac{ix^2}{4}\left\{\mathrm{cooh}\, w_0+\frac{1}{2}\sinh^2 w_0 -\left(\sinh^2 w_0-\frac{2i}{x^2}\right)\log x\sinh^2\frac{w_0}{2}\right\}\right] \times\left\{1+\frac{i}{24x^2}\cdot\frac{8\cosh^2 w_0-11\cosh w_0+5}{\cosh^3 w_0\cdot\sinh^2 w_0/2} -\cdots\cdots\right\}.$$

$$(w_1+2\pi i)=-\sqrt{\frac{2\pi}{x\cosh w_0}} \times\exp\{-5\pi(\gamma-i/2)/4\} \cdot\exp\left[\frac{ix^2}{4}\left\{\cosh w_0+\frac{1}{2}\sinh^2 w_0 -\left(\sinh^2 w_0-\frac{2i}{x^2}\right)\log x\sinh^2\frac{w_0}{2} -i2\pi\sinh^2 w_0\right\}\right] \times\left\{1+\frac{i}{24x^2}\cdot\frac{8\cosh^2 w_0-11\cosh w_0+5}{\cosh^3 w_0\cdot\sinh^2 w_0/2} +\cdots\cdots\right\},$$

$$(w_2)=\sqrt{\frac{2\pi}{x\cosh w_0}}\exp\{-5\pi(\gamma-i/2)/4\} \cdot\exp\left[\frac{ix^2}{4}\left\{-\cosh w_0+\frac{1}{2}\sinh^2 w_0\right.\right.$$

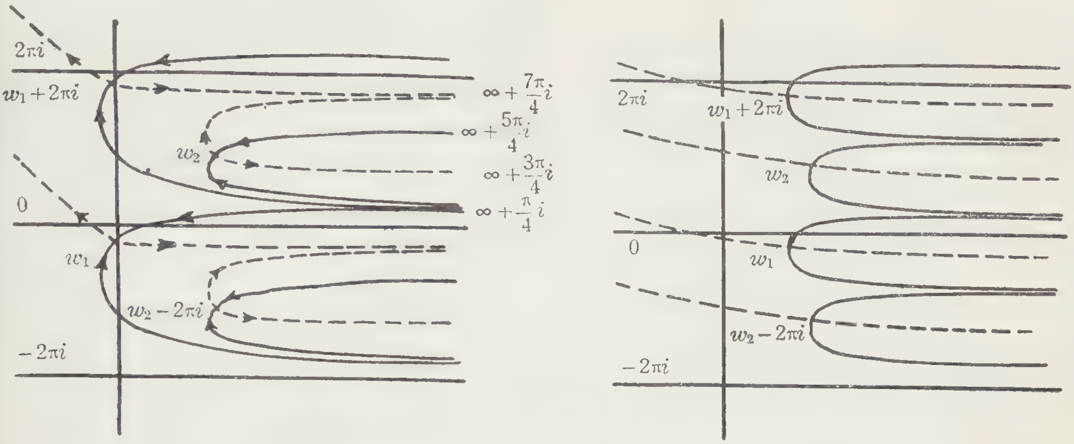

w_0 is in subdomain 1. in subdomain 2.

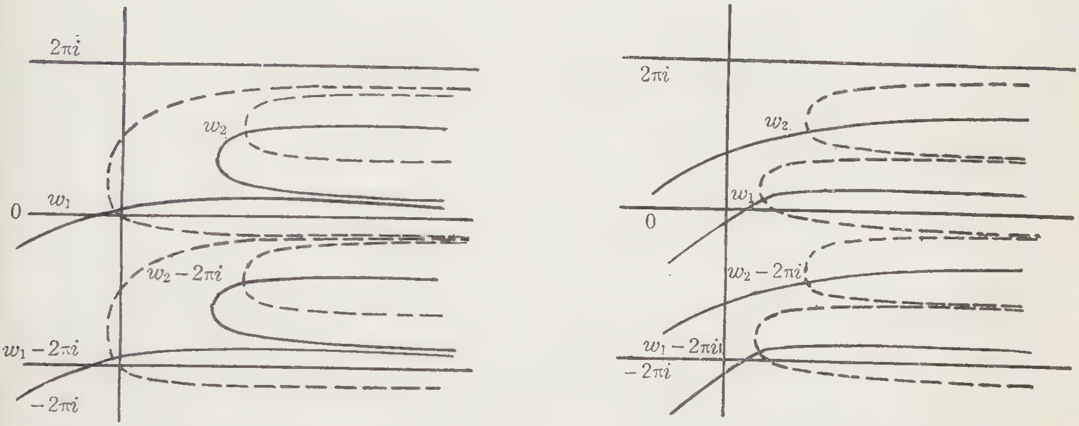

in subdomain 3. in subdomain 4.

Fig. 2. w-plane.

$$-\left(\sinh^2 w_0-\frac{2i}{x^2}\right)\log x\cosh^2\frac{w_0}{2}$$

$$-i\pi\sinh^2 w_0\Big\}\Big]$$

$$\times\left\{1+\frac{i}{24x^2}\cdot\frac{8\cosh^2 w_0+11\cosh w_0+5}{\cosh^3 w_0\cdot\cosh^2 w_0/2}\right.$$

$$\left.+\cdots\cdots\right\}.$$

Considering the integral representation (11) (12) and the end points of contours, we can construct the tables of $D_{-i\gamma-1/2}$, $D_{i\gamma-1/2}$ in terms of (w_1) $(w_1+2\pi i)$, and (w_2) when (α, β) lies in the subdomain named 1, 2, 3 and 4 given by Table I. When x is negative, $D_{-i\gamma-1/2}(-x\exp i\pi/4)$, $D_{i\gamma-1/2}(-x\exp i\pi/4)$ are connected with $D_{-i\gamma-1/2}(x\exp i\pi/4)$, $D_{i\gamma-1/2}(x\exp -i\pi/4)$ by the circuit relations;

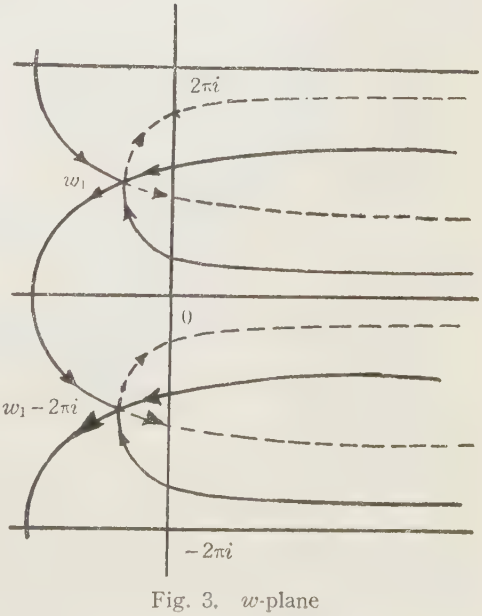

Fig. 3. w-plane

$$D_n(-e^{i\pi/4}x)=e^{-n\pi i}D_n(e^{i\pi/4}x)$$
$$+\frac{\sqrt{2\pi}}{\Gamma(-n)}e^{-i(n+1)\pi/2}D_{-n-1}(e^{-i\pi/4}x)$$
$$D_{-n-1}(-e^{-i\pi/4}x)=\frac{\sqrt{2\pi}}{\Gamma(n+1)}e^{-n\pi i/2}D_n(e^{i\pi/4}x)$$
$$-e^{-n\pi i}D_{-n-1}(e^{-i\pi/4}x)\,.$$

d) Both x and γ are large but $\gamma+1/2\approx -x^2/4$ 6). We write $\gamma+i/2=-x^2/4+\varepsilon$, then the integral (13) becomes $e^{-\pi(10\gamma-4i)/8}x^{-i\gamma-1/2}\int e^{-x2f(w)-i\varepsilon w}dw$, where $f(w)\equiv -i(1/4+e^{w}+e^{2w}/2+w/4)$. The stationary points of $f(w)$ are given by $w_1+2n\pi i$, if we write $w_1=-\log 2+\pi i$. Here n assumes all integral values. The contous of the integration are shown in Fig. 3. Then the integral representations (11) (12) become

$$D_{-i\gamma-1/2}(e^{i\pi/4}x)=\left(\frac{2}{3}\right)^{1/6}\pi^{1/2}x^{-i\gamma-1/6}e^{(i\log 2+\pi/4)(-x2/4+\varepsilon)-\frac{ix2}{8}-i\frac{2\pi}{3}}$$
$$\times\left\{\left(\frac{v}{2}\right)^{1/3}H^{(2)}_{1/3}(v)-i\left(\frac{3}{2}\right)^{1/3}x^{-2/3}\left(\frac{v}{2}\right)^{2/3}H^{(2)}_{-2/3}(v)+\cdots\cdot\right\},$$

$$D_{i\gamma-1/2}(e^{-i\pi/4}x)=\Gamma\left(i\gamma+\frac{1}{2}\right)(12)^{-1/6}x^{-i\gamma-1/6}e^{(i\log 2-\pi/4)(-x2/4+\varepsilon)-\frac{ix2}{8}+i\frac{2\pi}{3}}$$
$$\times\left\{\left(\frac{v}{2}\right)^{1/3}H^{(1)}_{1/3}(v)-i\left(\frac{3}{2}\right)^{1/3}x^{-2/3}\left(\frac{v}{2}\right)^{2/3}H^{(1)}_{-2/3}(v)+\cdots\cdot\right\},$$

$$D_{-i\gamma-1/2}(-e^{i\pi/4}x)=\left(\frac{2}{3}\right)^{1/6}\pi^{1/2}x^{-i\gamma-1/6}e^{(i\log 2-3\pi/4)(-x2/4+\varepsilon)-\frac{ix2}{8}+\frac{i2\pi}{3}}$$
$$\times\left\{\left(\frac{v}{2}\right)^{1/3}H^{(1)}_{1/3}(ve^{-i\pi})+i\left(\frac{3}{2}\right)^{1/3}x^{-2/3}\left(\frac{v}{2}\right)^{2/3}H^{(1)}_{-2/3}(ve^{-i\pi})+\cdots\cdot\right\}.$$

$$D_{i\gamma-1/2}(-e^{-i\pi/4}x)=\Gamma'(i\gamma+1/2)(12)^{-1/6}x^{-i\gamma-1/6}e^{(i\log 2-5\pi/4)(-x2/4+\varepsilon)-\frac{ix2}{8}+\frac{i2\pi}{3}}$$
$$\times\left\{\left(\frac{v}{2}\right)^{1/3}H^{(1)}_{1/3}(ve^{-i\pi})+i\left(\frac{3}{2}\right)^{1/3}x^{-2/3}\left(\frac{v}{2}\right)^{2/3}H^{(1)}_{-2/3}(ve^{-i\pi})+\cdots\cdot\right\},$$

where $v=4\varepsilon^{3/2}/3x$.

The Wrouskian of $u_1(x,\gamma)$ and $u_2(x,\gamma)$ is shown to be

$$u_1\cdot\frac{du_2}{dx}-u_2\cdot\frac{du_1}{dx}=i\,.$$

§ 4. Calculation of the Field

If the variable of integration is changed from κ to γ by Eq. (8), the solution (1) becomes

$$\psi=\frac{i}{H}\int_{k^2H^2}^{-\infty}J_0(k_0r\sqrt{1-4b^2H^2\gamma})\,v(\gamma)d\gamma\,,\qquad(14)$$
$$v(\gamma)=\left[\frac{u_1'(x_0)-Hpu_1(x_0)}{u_2'(x_0)-Hpu_2(x_0)}-\frac{u_1(x)}{u_2(x)}\right]$$
$$\times u_2(x_1)u_2(x)\qquad x_1\geqslant x\,,$$

where $\sqrt{1-4b^2H^2\gamma}$ means the root with the positive real part.

Since $v(\gamma)$ has no pole in the half plane above the real axis as shown in Appendix I, and $\int_\infty H_0{}^{(2)}(k_0r\sqrt{1-4b^2H^2\gamma})\,v(\gamma)d\gamma=0$ as is shown in App. II, where $\int_\infty$ means the integration over the half circle of infinite radius lying in the upper half plane, ψ can be expressed as

$$\psi=\frac{i}{2H}\int_\infty^{-\infty}H_0{}^{(1)}(k_0r\sqrt{1-4b^2H^2\gamma})v(\gamma)d\gamma\,.\qquad(15)$$

This path of integration is deformed into a half circle of infinite radius in the lower half plane plus loops around the poles and the branch point as indicated in Fig. 4. Since the integral over the half circle is zero as is shown in App. II, Eq. (15) becomes

$$\psi=-\frac{\pi}{H}\sum_{m=1}^{\infty}R_m+\frac{i}{2H}\int_B H_0{}^{(1)}(k_0r\sqrt{1-4b^2H^2\gamma})$$
$$\times v(\gamma)d\gamma\,,\qquad(16)$$

where $\sum R_m$ means the sum of residues at all the poles of $v(\gamma)$ lying in the lower half plane and the integral is along the branch cut.

Since u_1 and u_2 are integral functions of γ, the only branch point γ_p is the branch point of p, and the simple poles designated by γ_m are determined by

$$u_2'(x_0, \gamma)-Hpu_2(x_0, \gamma)=0\,. \tag{17}$$

Then we can write Eq. (16) in the form

$$\begin{aligned}\psi=i\pi/H\cdot\sum_{m=1}^{\infty}&H_0^{(1)}(k_0r\sqrt{1-4b^2H^2\gamma_m})\\ &\times\frac{u_1(x_0, \gamma_m)-Hp_m u_1(x_0, \gamma_m)}{\left[\dfrac{\partial}{\partial\gamma}\left\{u_2'(x_0, \gamma)-Hpu_2(x_0, \gamma)\right\}\right]_{\gamma=\gamma_m}}\\ &\times u_2(x_1, \gamma_m)u_2(x, \gamma_m)\\ &+\frac{i}{2H}\int_B H_0^{(1)}(k_0r\sqrt{1-4b^2H^2\gamma})v(\gamma)d\gamma\,. \end{aligned}\tag{18}$$

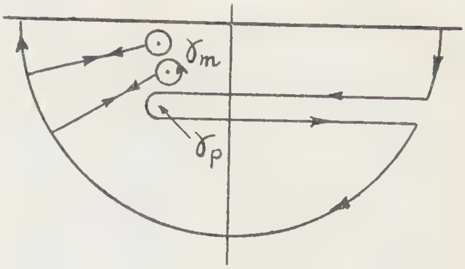

Fig. 4. γ-plane.

When k_0r is large, we use for $H_0^{(1)}$ the first term of the asymptotic expansion after Hankel, and assume $1\gg 4b^2H^2|\gamma_m|$, then Eq. (18) becomes

$$\begin{aligned}\psi\approx i\sqrt{\frac{4\pi b}{r}}\,&e^{ik_0r-i\pi/4}\sum_{m=1}^{\infty}e^{-ib\gamma_m r}U_m(x_1)U_m(x)\\ &+\frac{i}{2H}\int_B H_0^{(1)}(k_0r\sqrt{1-4b^2H^2\gamma})v(\gamma)d\gamma\,,\end{aligned}\tag{19}$$

where

$$U_m(x)=\frac{u_2(x, \gamma_m)}{\sqrt{\dfrac{u_2'(x_0, \gamma_m)}{Hp_m}\left[\dfrac{\partial}{\partial\gamma}\left\{u_2(x_0, \gamma)-Hpu_2(x_0, \gamma)\right\}\right]_{\gamma=\gamma_m}}}\,,$$

i) Calculation of the residue series.

We first discuss the limiting case; $Hp=\infty$. n this case Eq. (17) is reduced to $u_2(x_0, \gamma)=0$, and $u_2(x, \gamma)$ can be expressed by the proper expansion of $D_{i\gamma-1/2}(x\exp -i\pi/4)$ or $D_{i\gamma-1/2}$ $-x\exp -i\pi/4)$ according to the value of x_0. f x_0 and γ are positive large, we use the expansion represented in Table I. $D_{i\gamma-1/2}$ $x_0\exp -i\pi/4)$ has the zero points in the subdomain 2 of w_0, and in this subdomain u_2 can be expressed approximately as

$$\begin{aligned}u_2(x_0, \gamma)\approx&\{x_0^2+4(\gamma+i/2)\}^{-1/4}\\ &\cdot\exp[\{i\gamma\log(\gamma+i/2)-(\pi+i)(\gamma+i/2)\}/2]\\ &\times\cos\left\{\frac{x_0}{4}\sqrt{x_0^2+4(\gamma+i/2)}\right.\\ &+\gamma\log\frac{x_0+\sqrt{x_0+4(\gamma+i/2)}}{2}\\ &-\frac{\gamma}{2}\log(\gamma+i/2)-i\frac{\pi}{2}(\gamma+1/2)\,.\end{aligned}$$

Then γ_m is given approximately by the following equation

$$\begin{aligned}x_0/4\cdot&\sqrt{x_0^2+4(\gamma+i/2)}\\ &+\gamma\log\{x_0+\sqrt{x_0^2+4(\gamma+i/2)}\}\\ &-\frac{\gamma}{2}\log 4(\gamma+i/2)-\frac{i\gamma\pi}{2}+\frac{\pi}{4}\\ &=\left(n+\frac{1}{2}\right)\pi\end{aligned}\tag{20}$$

where n assumes all integral values.

By the similar process as above, γ_m can be calculated for different values of x_0, and is shown in Fig. 5.

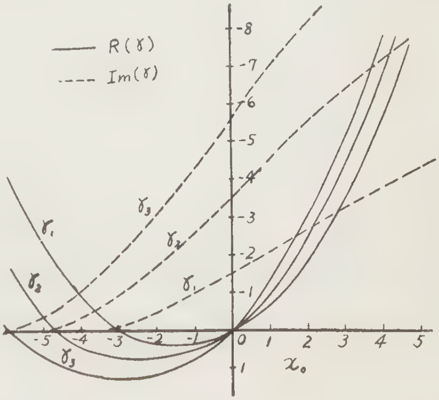

Fig. 5.

$U_m(x)$ can be calculated by the proper expansion according to the values of x, γ_m. Among $U_m(x)$, $U_1(x)$ and $U_2(x)$ are shown in Fig. 6 for $x_0=0$, $x_0=-3.07$, $x_0=-4.68$.

When the value of Hp is taken in account the value of γ_m is determined by Eq. (17).

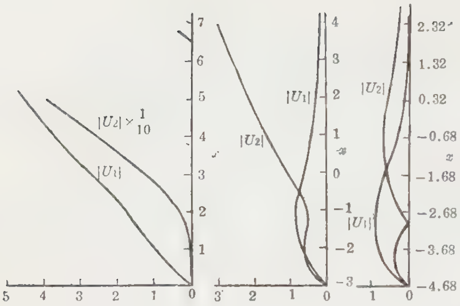

Fig. 6.

If x_0 and γ are large, we use the expansion represented in Table I. Then we can derive the next equation from Eq. (17)

$$\tan M(x_0, \gamma) = -\left[\frac{Hp}{\partial M/\partial x}\right]_{x=x_0} \tag{21}$$

where $M(x_0, \gamma)$ denote the left hand side of Eq. (20).

The value of $|Hp_e|$ is smallest for dry land, and $|Hp_h|$ takes its smallest value for sea water. For dry land at $\lambda=0.09$ m $(k_2^2/k_0^2)=2+i1.62$, and for sea water $(k_2^2/k_0^2)=69+i39$. The value of b is of the order of $10^{-4}\sim10^{-5}$. From these values we conclude the smallest values of $|Hp_e|$ and $|Hp_e|$ are of the order of 10^3. This values of $|Hp|$ are very great compared with $\partial M/\partial x$, Eq. (21) can be written approximately as $M(x_0, \gamma)\approx(n+1/2)\pi$.

ii) Calculation of the integral along the branch cut.

We calculate this integral by the method developed by A. Sommerfeld discussing his "Raumwellen"7). Using for v the expression as $(A-4)(A-5)$, this integral is calculated as

$$\frac{i}{2H}\int_B H_0^{(1)}(k_0 r\sqrt{1-4b^2H^2\gamma})v(\gamma)d\gamma$$

$$\approx \frac{2i}{r^2}\,\frac{k_0^2}{k_2^2-k_0^2}\exp i\{k_2 r-(z_1+z)\sqrt{k_0^2-k^2_2}\}$$

for vertical electric dipole.

$$\approx \frac{2i}{r^2}\,\frac{k_2^2}{k_2^2-k_2^2}\exp i\{k_2 r-(z_1+z)\sqrt{k_0^2-k_2^2}\}$$

for vertical magnetic dipole. This integral becomes very small when r and z_1+z are large.

§ 5. Approximation of the Actual Profile of Modified Index

As the quadratic form used in the theory does not represent at great heights the actual profile of modified index, it is necessary to determine the range of z, within which the quadratic representation may be a good approximation. According to the phase integral method, κ_m is determined by the equation $\int_0^{z_3}\sqrt{k^2N^2(z)-\kappa^2{}_m}\,dz=v_m$, where $k^2N^2(z_3)=\kappa^2{}_m$. That is, κ_m is determined by $N(z)$ for the values of z lying between 0 and $|z_3|$.

To determine this range of z, we first assume z_3', and in the range $0<z<z_3'$ we approximate the actual profile with the quadratic form $k^2N^2(z)=k_0^2\{1+b^2(z-z_0)^2\}$. For these values of k_0, b and z_0, we can determine the value of $\gamma_m(\equiv k_0^2H^2-\kappa_m^2H^2)$ by Fig. 6, and calculate the value of z_3 that satisfies $k^2N^2(z_3)=\kappa_m^2$. Then z_3' must be larger then $|z_3|$.

§ 6. Conclusion

When kr is large, the integral along the branch cut is small and the residue series converges very rapidly the field can be calculated by a few terms of the series of Eq (19). And Fig. 5 shows that if the value of x_0 is smaller than -3, the γ's for the first few modes are essentially real; i.e. the exponential attenuation with range is almost zero. This explains the strong field beyond the horizon (radio-duct phenomena).

When kr is small, the convergence of this series becomes slow. In this case, to calculate the field and to discuss the convergence, divergence, of rays due to the homogeneity of the atmosphere, we must rely on the method of the geometrical optics and it will be discussed in the Part II of this paper.

Appendix I. The Proof of Im $(\gamma_m)<0$

We write $\gamma_m=\xi_m+i\eta_m$ Eq. (6) is

$$d^2u^2/dx^2+(\gamma_m+x^2/4)u_2=0 \tag{A-1}$$

The conjugate complex of this equation is

$$d^2\tilde{u}_2/dx^2+(\tilde{\gamma}_m+x^2/4)\tilde{u}_2=0 \tag{A-2}$$

(A-1)×$\tilde{u}_2$−(A-2)×u_2 is

$$\tilde{u}_2\cdot d^2u_2/dx^2-u_2\cdot d^2\tilde{u}_2/dx^2=-2i\eta_m u_2 u_2$$

We integrate this equation, and obtain

$$\left[\tilde{u}_2 du_2/dx-u_2\cdot d\tilde{u}_2/dx\right]_{x_0}^{x}=-2i\eta_m\int_{x_0}^{x}|u_2|^2 nx \tag{A-3}$$

where $x\gg|\gamma_m|$

Since γ_m satisfies Eq. (17)

Table I.

	1	2	3	4
$-\sqrt{2\pi}e^{-\pi(\gamma+i/2)/2}D_{-i\gamma-1/2}(e^{i\pi/4}x)$	(w_2)	(w_2)	(w_2)	$(w_1)+(w_2)$
$-\frac{2\pi i}{\Gamma(i\gamma+1/2)}D_{i\gamma-1/2}(e^{-i\pi/4}x)$	$-(w_1+2\pi i)$	$(w_2)-(w_1+2\pi i)$	$(w_1)-(w_1+2\pi i)$	$(w_1)-(w_1+2\pi i)$

$$\Big[u_2\cdot du_2/dx-u_2\cdot du_2/dx\Big]_{x_0}^{x}$$
$$=-2i\,\mathrm{Im}\,(Hq)|u_2(x_0)|^2$$

m (Hp) is negative in the half plane above he straight line through γ_p and parallel to he real axis. By the asymptotic expansion f Whittaker we obtain

$$[\quad]^x=2ix^{-2\eta_m}\,.$$

Then Eq. (A-3) becomes

$$2ix^{-2\eta_m}-2i\,\mathrm{Im}\,(Hp)|u_2(x_0)|^2$$
$$=-2i\gamma_m\int_{x_0}^{x}|u_2(x)|^2dx\,.$$

Since the left hand side of this equation is ositive pure imaginary, η_m must be negative.

Appendix II. The proof of

$$\int_{\infty}H_0^{(2)}(k_0r\sqrt{1-4b^2H^2\gamma})v(\gamma)d\gamma=0$$

We prove it in the case x_0, x_1 and x positive, $Hp=\infty$. On the contour of this integration is in the domain 4 of w_0, using the expanion in Table I, u_1 and u_2 can be written as

$$u_1\sim(4\gamma)^{-1/4}[\exp\{i(\gamma+i/2)/2-i\gamma/2\cdot\log(\gamma+i/2\}]$$
$$\times\{\exp(-ix\gamma 1/2)+i\exp(ix\gamma^{1/2}-\pi\gamma)\}\,. \tag{A-4}$$

$$u_2\sim(4\gamma)^{-1/4}[\exp i\{x\gamma^{1/2}-(\gamma+i/2)/2+\gamma/2$$
$$\cdot\log(\gamma+i/2)\}]\,. \tag{A-5}$$

when γ becomes large.

Then the integrand becomes

$$\frac{1}{\sqrt{2\pi R}}\frac{e^{-R\gamma 1/2+i\pi/4}}{\gamma^{3/4}}\{\exp i(x_1+x-2x_0)\gamma^{1/2}$$
$$-\exp i(x_1-x)\gamma^{1/2}\}\,,$$

where $R=r/H$.

Since this integrand becomes 0 exponentially as $\gamma\to\infty$, this integral becomes 0. By the similar process we can prove

$$\int_{\infty}H_0^{(1)}(k_0r\sqrt{1-4b^2H^2\gamma})v(\gamma)d\gamma=0\,.$$

References

1) G. N. Watson: Proc. Roy. Soc. **A 95** (1918) 83–99.

2) C. L. Pekeris: J. Appl. Phys. **17** (1946) 1108–1124.

H. G. Booker: Meteorological Factors in Radio-wave Propagation, Proc. Phys. Soc. (London) (1947) 80–127.

H. Bremmer: Philips Research Reports Vol. 3 (1948) 102–120.

3) J. E. Freehafer: Propagation of Short Radio Waves (M.I.T. Vol. 13) 58–112.

4) Whittaker and Watson: Modern Analysis 4th ed. 347.

5) E. H. Rydbeck: Trans. Chalmers University of Technology **34** (1944).

6) T. Inui: Sherical Functions, Cylindrical Functions, Hypergeometric Functions 384, 405.

G. N. Watson: Theory of Bessel Functions (1922) 262–268.

7) A. Sommerfeld: Ann. Physik. **28** (1909) 665.

Short Notes

J. Phys. Soc. Japan **10** (1955) 78~79

Study of the Second Order Transition Temperature of High Polymer by the Photoelastic Method

By Motozo Kaneko, Rokuro Murai,
Kei Kishi and Dai Mori
Faculty of Science, Hokkaido University

(Received August 21, 1954)

It is attempted to measure the second order transition temperature of high polymers by means of the temperature dependency of photoelasticity. It is well known that the rubber-like materials show a characteristic birefringence under the state of tension[1]. If the second order transition temperature is assumed to correspond to the changing point from amorphous solid region to rubber-like region, the characteristic change of birefringence may appear at that point.

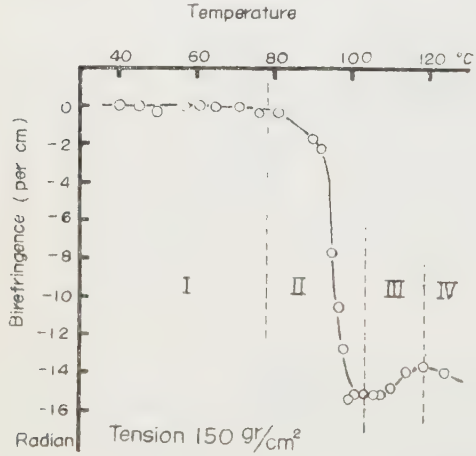

Fig. 1. Temperature dependency of birefringence of polystyrence under 150 gr/cm² tension.

In the present work, the films of commercial polystyrene and P.V.C. were used. These films were cast from solutions of the materials, benzene solution for polystyrene and nitrobenzene solution for P.V.C.. Then they were carefully dried. From a part of uniform thickness of these films, strips were cut out, 1.5^{cm} wide and 3.5^{cm} long. Their thickness was 0.05^{mm} for polystyrene and 0.25^{mm} for P.V.C.. The strip was hung in a little furnace with two windows and was put under constant tensile load. The birefringence of the strip was measured by the Sivessy-Dierkesmann compensation method, through the windows as increasing the temperature of the furnace. The rate of the increase of the temperature was 0.5°C/min. As the source of light, $\mathbf{D}_{\mathrm{Na}}$ was used.

The results of polystyrene at 150 gr/cm² tension and P.V.C. at 200 gr/cm² tension are graphed in Fig. 1 and Fig. 2. These figures indicate to be divided into four regions. In the first region (I), the absolute value of birefringence is small and almost independent of temperature, in the second region (II) the absolute value of birefringence abruptly increases with temperature, in the third region (III) the absolute value of the birefringence decreases with increasing temperature. In the last region (VI) the absolute value of the birefringence increases again with temperature. These four region seem to correspond to solid-like region, transition region, rubber-like region and flowing region respectively. If the transition point is assumed to be as the inflexion point of the second region, it becomes 95°C for polystyrene under 150 gr/cm² tension, and 70°C for P.V.C. under 200 gr/cm² tension. Under the condition of lower tension, the corresponding transition temperature becomes higher, and is 103°C for polystyrene at 100 gr/cm² and 74°C for P.V.C. at 100 gr/cm². For polystyrene, the transition point thus determined shows a little higher value than the one estimated by means of specific volume. These phenomena seem to agree with the result of the elastic measurement[2].

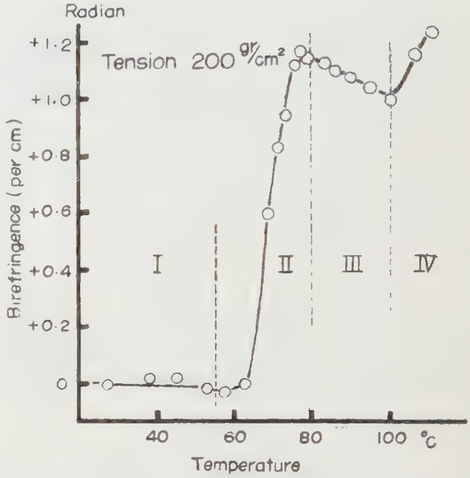

Fig. 2. Temperature dependency of birefringence of P.V.C. under 200 gr/cm² tension.

It is reported that the rubber-like stage does not appear in polystyrene[3], but in our experiment polystyrene also seems to show the rubber-like stage. This may be due to the fact that as the amount of tension was not sufficiently large in our experiment, the cross linkage by second bond was still effective.

The authors wish to thank Professor J. Furuichi for his kind advice and encouragement.

References

1) R. Kubo: "Rubber Elasticity" Kawade Book Comp. (1952) (in Japanese).

2) L. Nielsen and K. Buchdahl: J. Appl. Phys. **21** (1950) 488.

3) R. Klein and E. Jenkel: Z. Naturforschung **7a** (1952) 800.

J. PHYS. SOC. JAPAN **10** (1955) 79

Measurement of the Complex Permeability of Carbonyl Iron Powders at 4000 Mc/s

By Atsuo NISHIOKA and Hiroshi OKAMOTO

Electrical Communication Laboratory,
Musashino, Tokyo, Japan

(Received August 25, 1954)

Polyiron, which is widely used as a microwave high resistance attenuator, is composed of spherical carbonyl iron powders, few microns in diameter, dispersed in some insulating material such as polystyrol. But the skin effect is to be taken into account in the microwave region on such metal powders, and then their permeability should depend upon their particle sizes. To confirm this effect, we have measured four kinds of particle sizes of carbonyl iron powders at 4000 mc/s and found the remarkable skin effect on this powder.

The grades and average diameters of the powders are as follows in the Table I.

Table I. The grades and average diameters of carbonyl iron powder.

Grades	TH	E	HP	L
Diameter in microns (Weight Average)	5	8	10	20

Each grade of powder is dispersed in polystyrol, with the weight percents of 40, 60, 70, 75 and 80, and moulded in the form of wave guide section. Then we have measured the open and short circuit inpedances of the specimen by the standing wave method developed by B. Oguchi[1] which is similar to that of J. B. Birks[2]. We calculated the complex permeability from this data and extrapolated to the concentration of 100% by the empirical formula found by Birks as follows;

$$\log|\mu| = v\log|\mu_f|$$
$$\tan\delta_\mu = v\tan\delta_{\mu_f}\ ,$$

where

$|\mu|$: absolute value of the apparent permeability of the specimen
$|\mu_f|$: absolute value of the permeability of iron powder
$\tan\delta_\mu$: magnetic loss tangent of the specimen
$\tan\delta_{\mu_f}$: magnetic loss tangent of iron powder
v: volume fraction of iron powder.

As the variance of the observed values is not small, the extrapolated value of μ_f and $\tan\delta_{\mu_f}$ is not very accurate, but the larger the particle size, the smaller the permeability become. The $\tan\delta_{\mu_f}$ is not so much depending upon the size. This fact seems to contradict to the expectation that the large skin effect should lower the loss tangent. This is probably due to the contact of the particles. The extrapolated value of μ_f and $\tan\delta_{\mu_f}$ are given in Table II. This shows that the permeability of Grade TH does not show the tendency of saturation, that is, the skin effect is active until this order of size. So we will continue this experiment to the size of about 3 microns.

Table II.

Grade	TH	E	HP	L
μ_f	23	17	13	12
$\tan\delta_{\mu_f}$	1.4	1.4	1.4	1.5

Our results of Grade TH are in well accordance with that of J. B. Birks[3] who has measured on the particles about 5.5 microns in diameter.

References

1) B. Oguchi: Lectured at the meeting of the Institute of Electrical Engineers of Japan (1951).

2) J. B. Birks: Proc. Phys. Soc. **60B** (1948) 282.

3) J. B. Birks: Phys. Rev. **74** (1948) 843.

J. PHYS. SOC. JAPAN **10** (1955) 79~81

Supplementary Note to my Paper "An Approximate Study on the Detached Shock Wave in front of a Circular Cylinder and a Sphere"

By Kinzo HIDA

Department of Applied Physics,
Faculty of Engineering, Naniwa University

(Received September 20, 1954)

In a recent paper[1], the present writer has studied approximately the detached shock wave in front of a circular cylinder and a sphere by making use of the assumption that the flow behind a shock wave can be expressed by a rotational flow of an incompressible fluid. The shape, the location and the strength of a shock wave as well as the vorticity distribution, which at first were defined by four unknown parameters λ, b, U and k, were determined so as to satisfy suitable shock conditions in the close vicinity of the nose of the shock. From the magnitude and the direction of a streamline immediately behind the shock wave were derived three of such shock conditions, while the fourth condition was related to the entropy change from streamline to streamline. In the previous paper this fourth condition has remained to be unclear in some respects since a stream function for an incompressible fluid was used.

Here we shall show an alternative condition which is more lucid in its derivation and is given in terms of Crocco's stream function[2]. As is well known, Crocco's stream function designated here by Ψ_c is defined by the following formulae:

$$\left.\begin{aligned} y^\kappa u(1-w^2)^{1/(\gamma-1)} &= (\Psi_c)_y , \\ y^\kappa v(1-w^2)^{1/(\gamma-1)} &= -(\Psi_c)_y , \end{aligned}\right\} \tag{1}$$

where $\kappa=0$ for two-dimensional cases and $\kappa=1$ for axisymmetrical cases, and γ is the adiabatic exponent of a fluid. w is the magnitude of velocity, and u and v are the velocity components along x- and y-axes and these are all referred to the limit velocity. The fundamental equation for determining Crocco's stream function is written in the form:

$$\begin{aligned}\left(1-\frac{u^2}{a^2}\right)(\Psi_c)_{xx} - \frac{2uv}{a^2}(\Psi_c)_{xy} + \left(1-\frac{v^2}{a^2}\right)(\Psi_c)_{yy} \\ -\kappa\frac{(\Psi_c)_y}{y} = y^{2\kappa}(1-w^2)^{(\gamma+1)/(\gamma-1)} \\ \times\left(\frac{w^2}{a^2}-1\right)f(\Psi_c) .\end{aligned} \tag{2}$$

Here, a is the sonic speed referred to the limit velocity and $f(\Psi_c)$ is a function of Ψ_c only which is related with the increase of specific entropy of the fluid, ΔS, in passing through the shock, by the formula:

$$f(\Psi_c) = \frac{\gamma-1}{2\gamma\mathfrak{R}}\frac{d(\Delta S)}{d\Psi_c} , \tag{3}$$

where $\mathfrak{R}$ is the gas constant.

Taking the symmetrical nature of flow pattern into account, we can assume this function for smaller values of Ψ_c in the form:

$$f(\Psi_c) = \begin{cases} -k\Psi_c & \text{for two-dimensional cases,} \\ -kU/2 & \text{for axisymmetrical cases.} \end{cases} \tag{4}$$

Now, it should be noted that the stream function itself is small in the vicinity of the symmetrical axis. Hence, to a first approximation we can neglect u, v and w in comparison with a and unity. Then, substituting Eq. (4) for $f(\Psi_c)$, the basic Eq. (2) for Ψ_c is reduced to the same form as the corresponding equation in the previous paper, that is, Eqs. (15) and (24) in reference 1, and the velocity is given by

$$y^{2\kappa}w^2 = (\text{grad } \Psi_c)^2 ,$$

With these simplifications we can develop the analysis in the same way as in the previous paper and we have four shock conditions as before. As already mentioned, the first three conditions given in Eqs. (19) and (26) in reference 1 remain unchanged, while the fourth condition becomes in the form:

$$\begin{aligned}\frac{2(1-2\lambda)^2(M_1{}^2-1)^2}{\{1+(\gamma-1)M_1{}^2/2\}\{2\gamma M_1{}^2-(\gamma-1)\}} \\ = kF^2(U/a_s)^2 \quad \text{for a circular cylinder,} \\ = \tfrac{1}{2}kG(U/a_s)^2 \quad \text{for a sphere,}\end{aligned} \tag{5}$$

where M_1 is the Mach number of the undisturbed flow at infinity upstream and suffix s is referred to the stagnation point. F and G are certain functions defined in Eqs. (18) and (27) in reference 1 respectively.

These four equations can be easily solved as in the previous paper, but we shall here show an improved solution for the case of a circular cylinder.

Table I. Case of a circular cylinder.

M_1	1/b	
	Present note	Ref. 1
1.10	0.140	0.140
1.30	0.331	0.332
1.40	0.396	0.398
1.60	0.490	0.492
1.80	0.553	0.556
2.00	0.597	0.601
2.40	0.656	0.661
3.00	0.703	0.710
∞	0.791	0.810

Table II. Case of sphere.

M_1	1/b	
	Present note	Ref. 1
1.10	0.317	0.317
1.17	0.420	0.420
1.30	0.541	0.542
1.50	0.648	0.649
1.81	0.733	0.735
2.08	0.775	0.777
2.40	0.806	0.807
3.00	0.838	0.839
∞	0.893	0.894

In the previous paper we have expanded the functions F, which was defined by the modified Bessel functions, in power series of k and retained only the first few terms of k, but this approximation will be seen to be unnecessary.

At first, in place of Eq. (21) in reference 1, we can find the value*

$$\sqrt{k}\,b=\frac{3(\gamma+1)M_1(M_1^2-1)^2}{2(3M_1^2-1)\{1+(\gamma-1)M_1^2/2\}\sqrt{\gamma M_1^2-(\gamma-1)/2}}\equiv C\,. \tag{6}$$

Then, using the auxiliary constant D defined by

$$\frac{b}{F}\frac{\partial F}{\partial b}=1+\frac{3(M_1^2-1)^2}{(3M_1^2-1)\{1+(\gamma-1)M_1^2/2\}}\equiv D\,, \tag{7}$$

and substituting the complete form for the function F, we have

$$\frac{K_1(\sqrt{k})}{I_1(\sqrt{k})}=\frac{CK_1'(C)-DK_1(C)}{CI_1'(C)-DI_1(C)}\,. \tag{8}$$

This equation determines the numerical value of $\sqrt{k}$ and in conjuction with Eq. (6) we can finally find the distance b of the nose of the shock from the centre of a circular cylinder.

Numerical values of $1/b$ for the cases of a circular cylinder and a sphere are shown in Tables I and II together with the corresponding values in reference 1. As was expected, the difference between two series of values is very small.

In conclusion, the writer wishes to express his cordial thanks to Professor S. Tomotika for his continual guidance and kind inspection of the manuscript.

References

1) K. Hida: J. Phys. Soc. Japan **8** (1953) 740.
2) L. Crocco: Z.A.M.M., **17** (1937) 1.

---

* There is unfortunately some misprint in reference 1. Eq. (21) there should be read as:

$$\sqrt{k}\,b=\frac{3(M_1^2-1)^2}{(3M_1^2-1)\{1+(\gamma-1)M_1^2/2\}}\equiv C\,.$$

J. Phys. Soc. Japan **10** (1955) 81~82

Layer Growth of Artificial Graphite

By Takurō TSUZUKU
Technical Research Laboratory,
Tōkai Electrode Mfg. Co. Ltd.,
Fujisawa-City
and Tsutomu KOMODA
Central Research Laboratory,
Hitachi Co., Ltd., Kokubunji, Tokyo

(Received September 27, 1954)

Pyramidal layer growth has been observed on artifical monocrystals of graphite. Typical patterns shown in the accompanying electron micrograph (a) and (b), although the resolution of their centre parts are not quite clear, suggest concentric loops to be taken as the double-ended spirals expected when two screw dislocations of opposite signs emerge on the crystal surfaces[1].

Recently Horn[2] has recognized similar hexagonal spirals by means of optical techniques on a certain natural graphite of special origin. On the contrary it is emphasized that our sample is artificial graphite prepared as follows[3]; some quantity of carbon black seast 116 was packed loosely in small graphite crucibles and heat-treated to about 2500°C.

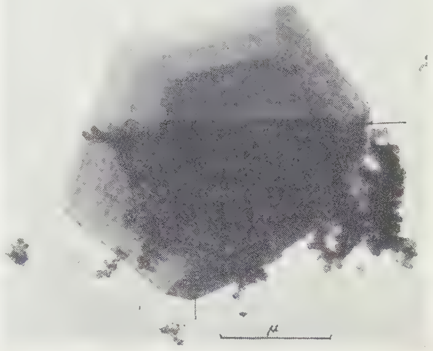

(a)

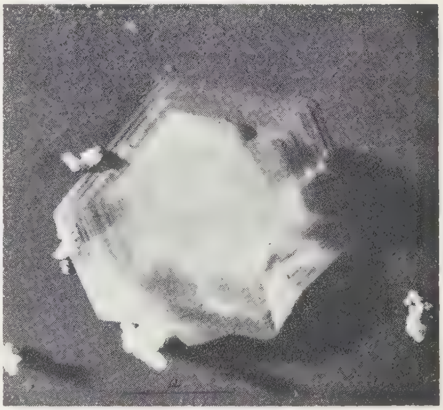

(b)

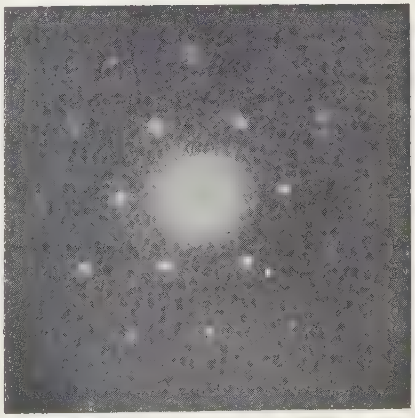

(c)

in a graphitizing furnace. The usual sprinkling method was employed for preparation of microscopy specimens, and some were slightly shadow-cast with germanium. Appearance of the preceeding grown crystals with hexagonal patterns was not so frequent that there were observed only two or three in each grid-mesh, and the particles surrounding them presented little growth in diameter, as shown in every photograph, by heat-treatment from the original size of about 300 A. in average. Electron diffraction, photographed for the identification at the same time, gave clear net patterns as shown in photograph (c) for the grown crystals.

Dimension of the pyramidal monocrystals was 500–800 $m\mu$ in heights and 1–5 μ in diameter. Bending lines like those of folded paper as indicated by arrows in (a) have been often observed which suggest the flexible structure probably owing to dislocations lying in them[4]. The step-heights of the layer hills roughly estimated by stereographic analysis of the germanium shadows vary from 150 A. to 350 A.; for instance that shown in (b) is about 220 A., thirty times as large as the interatomic spacing in $[00l]$ direction. This may indicate that, in terms of dislocation theory, scores of screw dislocation of the same sign are crowded in the core of each basal lamina. It is supposed that the density and configuration of those dislocation lines in the crowded area may be closely related with critical conditions on laminar nuclei formation which enable to initiate the spiral growth.

More detailed account will be published later.

The authors express sincere thanks to Dr. B. Tadano for his kind guidance, and to Mr. Y. Sasaki for providing the sample and useful discussion.

References

1) F. C. Frank: Disc. Farad. Soc., No. 5, (1949) 48.

2) F. H. Horn: Nature, **170** (1952) 581.

3) Y. Sasaki: Electric conductivity of carbon black in relation to bulk density, to be published in Tōkai Tech. Jour., Vol. 15, No. 2.

4) T. Tsuzuku: Kagaku, **23** (1953) 32. Chem. Abst., **47** (1953) 3648-d.

Errata

Hall Effect and Electrical Conductivity of Lead Selenide

By Eiji HIRAHARA and Miyuki MURAKAMI

J. Phys. Soc. Japan **9** (1954) 671, 681

1) Fig. 4 and Fig. 9 should be interchanged.

2) P. 674, right column, Eq. (8) and Eq. (10) should be read:

$$1/\mu = 1/\mu_I + 1/\mu_a + 1/\mu_0 = a \cdot T^{-3/2} + b \cdot T^{3/2} + c(e^{\Theta/T} - 1)^{-1}\,, \tag{8}$$

$$1/\mu_h = 0.38 \cdot T^{-3/2} + 4 \times 10^{-7} \cdot T^{3/2} + 5.8 \times 10^{-3}(e^{\Theta/T} - 1)^{-1}\,, \tag{10}$$

P. 675, left column, line 21, the equation should be read:

$$f(E) = [1 + \exp\{(E - \zeta)/kT\}]^{-1}\,,$$

P. 676, left column, lines 10, 9, and 2 from the bottom, the equations should be read:

$$A = \frac{1}{3} e^{-E_2/kT}$$

$$B = \frac{1}{6}[\cdots\cdots]$$

$$x_2 = \omega \sqrt[3]{-q + \sqrt{q^2 - p^3}} + \omega^2 \sqrt[3]{-q - \sqrt{q^2 - p^3}}\,.$$

P. 676, right column, line 11, should be read: $\pi \geqq \varphi \geqq 0$.

P. 677, left column, Eq. (19′) should be read:

$$n_t = \frac{1}{2} \alpha_h \cdot e^{(E_1 - E_2)/kT} \cdot \left\{ \sqrt{1 + \frac{4N_A}{\alpha_h \cdot \exp\{(E_1 - E_2)/kT\}}} - 1 \right\}\,.$$

P. 677, left column, lines 11 and 2 from the bottom, $(E_3 - E_2)/2$ and $(e \cdot h_t \cdot \mu_h)$ should be read $(E_3 - E_1)/2$ and $(e \cdot n_t \cdot \mu_h)$, respectively.

P. 677, right column, the equations in the lines 15, 16, and 17 should have the number of equation (29).

P. 679, right column, line 1, should be read: $n_h = \cdots\cdots$

P. 679, right column, Eq. (33) should be read:

$$\eta^3 + P \cdot \eta^2 - Q \cdot \eta / \alpha_h{}^0 - R \cdot 1/\alpha_h{}^0 = 0\,,$$

P. 680, left column, line 3 from the bottom, the equation should be read:

$$3\eta^2 \cdot \frac{\partial \eta}{\partial \alpha_h{}^0} + 2P \cdot \eta \cdot \frac{\partial \eta}{\partial \alpha_h{}^0} + \cdots\cdots\,,$$

P. 680, right column, line 8, E_2, E_3, E_A should be read E_2, E_3, N_A.

PROGRESS OF THEORETICAL PHYSICS

(Founded by H. Yukawa in 1946)

Published for the

Research Institute for Fundamental Physics

The Physical Society of Japan

Progress of Theoretical Physics Vol. 12, No. 3, 1954

A Formulation of the Theory of Alpha Particle Decay from Time-independent Equations .... R. G. THOMAS....253

A Hydrodynamical Description of Many Bose Particle System .... Toshiyuki NISHIYAMA....265

Many-body Problem in Quantum Field Theory, II.............Kazuhiko NISHIJIMA....279

Wave Fields in de Sitter Space ....Ken-iti GOTO....311

Kinematical Investigations of Meson-nucleon Reactions .... Satio HAYAKAWA, Masaaki KAWAGUCHI and Shigeo MINAMI....355

Mass Spectrum of Elementary Particles, II ....Hiroshi ENATSU....363

Vapour Pressures of He^3–He^4 Mixtures ....S. M. BHAGAT and P. K. KATTI....380

On the Time Reversal in the Quantized Field Theory .... Hiroomi UMEZAWA, Susumu KAMEFUCHI and Shō TANAKA....383

Letters to the Editor:

On the Direct Interaction in Nuclear Reactions .... S. HAYAKAWA and T. SASAKAWA....401

Potential in Quantum Field Theory ....T. IMAMURA....402

An Empirical "Charge Dependence" Relation to the Rest-masses of Elementary Particles ....S. YOSHIKAWA and T. HASEBE....403

Excitation of Metal Electrons by an Energetic Primary Particle ....T. SHINDO....406

Price $ 1.25 per copy
$ 15.00 per year (postage inclusive)
Annual dues for foreign members (individual subscribers)
$ 12.00 (postage inclusive)
〃 for foreign members of the Physical Society of Japan
$ 10.00 (postage inclusive)

Application for members, subscriptions and orders for back mumbers should be sent, directly or through book-dealers, to

The Publication Office
in
Yukawa Hall, Kyoto University, Kyoto, Japan

Journal of the Physical Society of Japan Vol. 10, No. 2, February, 1955

On the Halogen Nuclear Magnetic Resonance of Some Metal Halides I

By Teinosuke Kanda

Department of Physics, Kobe University

(Received August 14, 1954)

Chemical shifts of chlorine, bromine and iodine nuclear magnetic resonance of some metal halides were measured. The results indicates that the origin of the large shift is the second-order paramagnetism due to the halogen atom covalently bonnded to the neighbouring metal atoms in the crystal. The degree of covalency estimated from the shift has a reasonable order of magnitude. Spin-lattice relaxation times of LiBr, AgBr and TlBr were also measured and it was revealed that they have direct correlation to the shift. From this we concluded that the mechanism of T_1 of these crystals is the quadrupole coupling caused by the covalent bonding of the bromine atom.

§ 1. Introduction

Nuclear magnetic resonance studies of alkali halides had been performed by a few authors. Watkins and Pound[1,2] studied T_1 and the resonance figure of the halogen magnetic resonance of single crystals of LiF, KBr and KI. One of the striking conclusions of their experiment was that the apparent electric field gradient at the halogen nucleus in the crystal was about ten times larger than that due to the pure ions of alkali and halogen atoms, and they suggested some of its origins. Gutowsky and McGarvey[3] measured the chemical shift of Rb and Cs nuclear magnetic resonance of respective halides and they expected the origin of the shift to be the covalent bonding in the crystals. We measured the chemical shift of chlorine, bromine and iodine magnetic resonance of some metal halides and estimated the degree of covalent bonding in those crystals which have larger chemical shift. Existence of the covalent bonding should cause a large electric field gradient q at the nucleus as shown by Townes and Dailey[4]. Although all the crystals in our experiment have the cubic symmetry and q is cancelled out in the mean, the thermal vibration will break the symmetry and will make a large contribution to the spin-lattice relaxation mechanism.

§ 2. Experimental Procedure

The samples of NaBr and AgBr are single crystals while the others are powders. Details of the method to measure the shift were reported previously and will be omitted here[6]. Most of the experiment was performed by a permanent magnet of 6220 gauss, while, for the purpose of confirming the shift to be the "chemical shift", an electromagnet of about 3000 gauss was used. Measurement of T_1 was made by the saturation method using an autodyne detector. The intensity of the signal was calibrated by a "calibrator" developed by Watkins[2] and the radio frequency voltage across the sample coil was measured by a three stages r.f. amplifier loosely coupled to the detector coil as shown by Fig. 1. The magnetic field was modulated at 60 c.p.s. and the resonance was displayed on the recorder as a derivative of the absorption curve. The relation between the maximum deflection D_{ex} and the saturation factor $s=H_1^2\gamma^2T_1T_2$ is given in B.P.P.[5] for the case where the absorption curve is Lorentzian. Since the absorption curves of bromine resonance of LiBr, AgBr and TlBr were nearly Gaussian rather than Lorentzian, we calculated the theoretical saturation curve for the Gaussian type for the

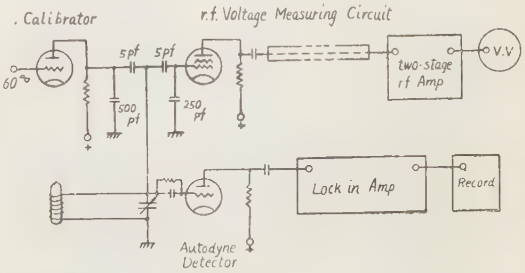

Fig. 1. Circuit diagram of T_1 measurement.

case I and case II of B.P.P. The results are shown in Fig. 2 (a) together with those of B.P.P. Although these four curves are very different in their analytical expression, the curves almost agree with each other when the abscissa is multiplied by an appropriate factor. Consequently we cannot determine whether our experimental curve belongs to the case I or to the case II but the saturation broadening factor b (ratio of the line width at high r.f. voltage to that at negligible voltage) is of use for the identification in some cases. Fig. 2 (b) shows the relation between b and s for the case I and case II, where curves are calculated ones, solid circles are experimental values for TlBr considered as belonging to the case I of Gaussian type and crosses are those for TlBr considered as belonging to the case II of Gaussian type. For TlBr, case I fitted better than case II while for AgBr, experimental saturation broadening was by some unknown reasons far less than the calculated values both for case I and case II and we could not identify it. Keeping this point in mind, we arbitrarily calculated T_1 of AgBr and LiBr from the curve for case I, as well as T_1 of TlBr.

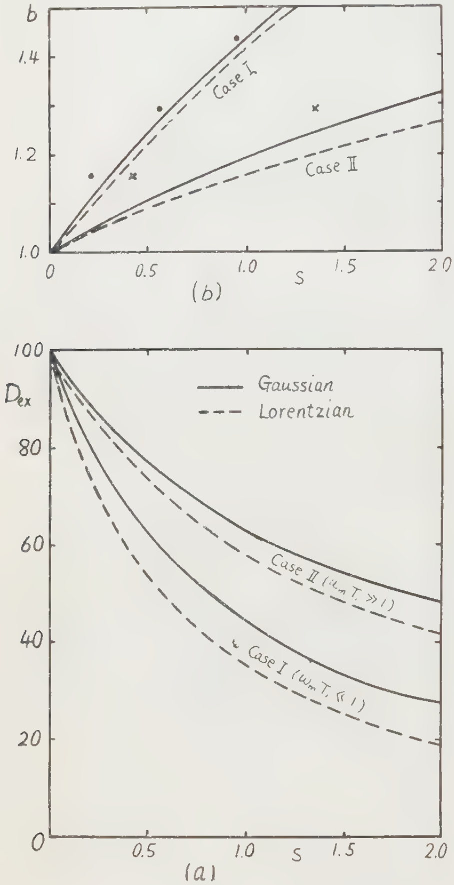

Fig. 2. Saturation curves for the absorption of Lorentzian and Gaussian type and for the case I and case II.

(a) D_{ex} versus saturation factor $s = H_1^2\gamma^2T_1T_2$.

(b) Saturation broadening factor b versus s.

§ 3. Experimental Results and Discussion

I. Chemical Shift

Measured chemical shift of various metal halides is shown in Fig. 3 where the horizontal line across each solid circle indicates the error estimated from the line width and the intensity of absorption. Shift is expressed as $\sigma = (H_{\text{sample}} - H_{\text{ref}})/H_{\text{ref}}$ where H_{sample} is the resonance field of the sample and H_{ref} is that of the reference sample both at the constant frequency. Negative shift corresponds to the paramagnetic one. The reference samples were the aqueous solutions of NaCl, NaBr and KI. It is already known[6] that the frequency of the halogen magnetic resonance of the solutions of various alkali-halides does not depend on concentration nor on the sort of alkali atoms. The results of Fig. 3 are summarized as follows:

(i) Many crystals are included irregularly in the range of $\pm 0.3 \times 10^{-4}$.

(ii) Large shifts are all in the paramagnetic region and the shift increases as the electro-

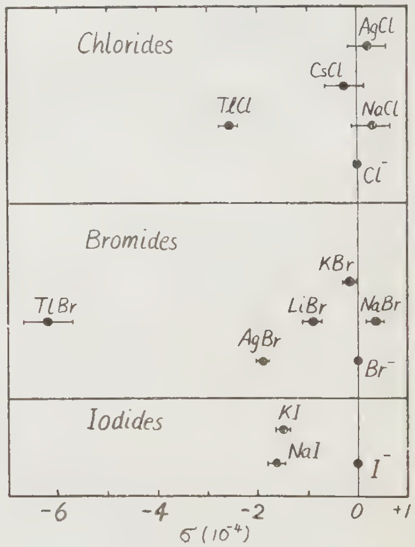

Fig. 3. Chemical shift of halogen nuclear magnetic resonance of some metal halides.

Table I. Chemical shift and estimated covalency of some metal halide crystals.

Crystal	$\left\langle \frac{a_0^3}{r^3} \right\rangle_p$	assumed ΔE	σ_{cal} for $\lambda^2=1$	σ_{exp}	λ^2
TlCl	7.16	8 eV	8.33×10^{-4}	2.51×10^{-4}	30%
LiBr	13.55	7	18.4	0.896	5
AgBr				1.89	10
TlBr				6.2	35
KI	18.0	6	28.5	1.48	5

negativity difference between metal and halogen atoms decreases.

(iii) For the crystals with the same metal atom, shift increases with the atomic number (Cl→Br→I).

According to the theory of chemical shift developed by Ramsey[7], the origin of the shift is classed into two, namely (i) diamagnetism and (ii) second-order paramagnetism. Diamagnetism of one valence electron of bromine atom was calculated to be about 1×10^{-5}. Experimental results and the smallness of the calculated diamagnetism make us conclude that the large shift cited above is due to the second-order paramagnetism caused by the covalent bonding in the crystal. A valence p-electron of the halogen ion will momentarily make a covalent bonding with one of the neighbouring metal ions and this deviation from the closed shell configuration will cause a paramagnetic shift as pointed out by Saika and Slichter[8]. When the covalency is small enough to permit us to consider each pair of atoms in covalent bonding as an isolated system, the shielding constant is the same as that of a molecule rotating at random and is given by

$$\sigma=-\lambda^2\frac{2e^2\hbar^2}{3m^2c^2}\frac{1}{\Delta E}\left\langle\frac{1}{r^3}\right\rangle_p$$

Here λ^2 is the total degree of covalency ($1-\lambda^2$ is the degree of ionicity), ΔE the mean energy of the excited state and $\langle 1/r^3\rangle_p$ the mean of $1/r^3$ of the valence p-electron. The nearest excited state allowed for the magnetic moment transition is the p-type excited state which is forbidden for the optical transition, and hence ΔE is not known. On the other hand, the excited state will lie between the s-type excited state (which is optically excitable and is known to be 7.7 eV for NaCl above the full band) and the conduction band (which is about 9.4 eV for NaCl above the full band). From the consideration above and of the approximate nature of the calculation, we take ΔE as 8 eV for the chlorides, 7 eV for the bromides

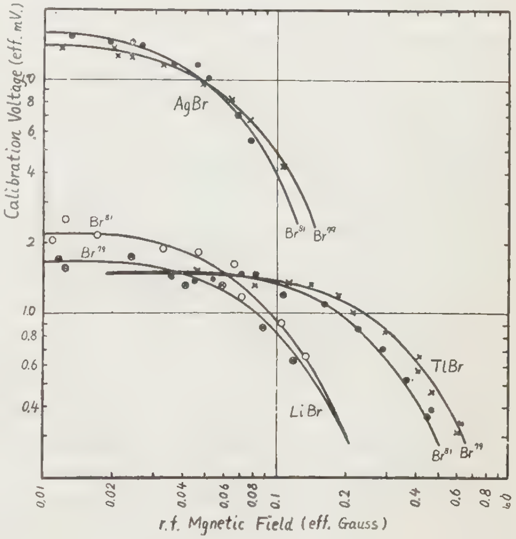

Fig. 4. Experimental saturation curves for LiBr, AgBr and TlBr.

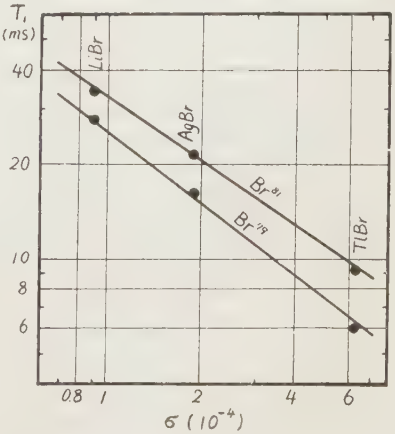

Fig. 5. Relation between T_1 and chemical shift of LiBr, AgBr and TlBr.

and 6 eV for the iodides. Using for $\langle 1/r^3\rangle_p$ the values given by Barnes and Smith⁹⁾ not corrected for relativistic correction, the degrees of covalency are estimated as listed in Table I.

II. Spin-Lattice Relaxation Time

Saturation curves for LiBr, AgBr and TlBr are shown in Fig. 4. As stated in a previous section, T_1 was estimated from the curve of case I of Gaussian type. T_1 values are 28 and 34 milliseconds for LiBr, 16 and 22 ms. for AgBr, 6.0 and 9.2ms. for TlBr, the former being for Br^{79} and the latter for Br^{81}. These values are shown in Fig. 5 with their relation to the chemical shift from which we conclude as follows:

(i) There is a remarkable correlation between T_1 and σ, suggesting that they might have the common origin. Experimental results seem to show $1/T_1$ to be proportional to σ though there are some ambiguities about the estimation of T_1.

(ii) Ratio of T_1 for Br^{81} to that for Br^{79} is 1.21, 1.38 and 1.53 for LiBr, AgBr and TlBr respectively. For purely quadrupolar relaxation, the ratio should be equal to the inverse square of the ratio of nuclear quadrupole moments, i.e. about 1.4. Considering various sources of error in the experiment, we may conclude that the relaxation of these crystals are purely quadrupolar.

(iii) T_1 value decreases as the distance between the nearest neighbours in the crystal increases.

As quoted in § 1, Pound and Watkins found that the electric field gradient at the halogen nucleus in the crystals of KBr and KI is much larger than the value calculated by dealing the lattice points as pure ions, and they suggested several origins for this amplification of the field gradient. We can point out the covalent bonding in crystals as an origin of the field gradient in the metal halides of lower ionicity. In the perfect lattice, even if the halogen atom is in a covalently bonded state, the electric field gradient is cancelled out owing to the cubic symmetry, but the paramagnetic shift exists. Change in interionic distance arising from dislocations or thermal vibrations will alter the degree of covalency for each of the neighbours of a given halogen atom and the electric field gradient thus originated will cause the quadrupolar splitting or the quadrupolar relaxation.

The author is greatly indebted to Professor T. Nagamiya and Professor J. Itoh for their valuable advice and discussion and to Mr. S. Shibata who lent him single crystals of NaBr and AgBr. He is grateful also to Mr. Y. Masuda for his kind cooperation throughout this experiment. This work has been supported in part by the Scientific Research Expenditure of the Ministry of Education.

References

1) Watkins and Pound: Phys. Rev. **89** (1953) 658.
2) Watkins, Thesis: Harvard Univ. (1952).
3) Gutowsky and McGarvey: J. Chem. Phys. **21** (1953) 1423.
4) Townes and Dailey: J. Chem. Phys. **17** (1949) 782.
5) Bloembergen, Purcell and Pound: Phys. Rev. **73** (1948) 679.
6) Masuda and Kanda: J. Phys. Soc. Japan **9** (1954) 82.
7) Ramsey: Phys. Rev. **78** (1950) 699; Phys. Rev. **86** (1952) 243.
8) Saika and Slichter: J. Chem. Phys. **22** (1954) 26.
9) Barnes and Smith: Phys. Rev. **93** (1954) 95.

JOURNAL OF THE PHYSICAL SOCIETY OF JAPAN Vol. 10, No. 2, FEBRUARY, 1955

Inversion Spectrum of Ammonia

By Tetsuji NISHIKAWA and Koichi SHIMODA
Department of Physics, Faculty of Science, University of Tokyo
Tokyo, Japan

(Received August 20, 1954)

The inversion spectrum of ammonia has been studied in the frequency range between 20 and 12 kMc/sec. 29 lines have been found and 33 lines remeasured. Observed frequencies are compared with the calculated values from Costain's formula and their deviations are discussed. The magnetic hyperfine splittings due to the proton spins for $K=1$ and $J=5, 6, 7, 8, 9$ lines have been resolved and measured. The observed splittings are in good agreements with the theoretical results.

§ 1. Introduction

The inversion spectrum of ammonia is the bestknown spectrum in the microwave spectroscopy. However, many uninvestigated ploblems are still involved in the spectrum. Before our study, 64 lines of $N^{14}H_3$ and 35 lines of $N^{15}H_3$, which correspond to different rotational quantum numbers, J and K, have been found between 17 and 40 kMc/sec1). The following empirical formula for the frequencies of the lines was given by Costain2);

$$\nu=\nu_0 \exp(AJ(J+1)+BK^2+CJ^2(J+1)^2 \\ +DJ(J+1)K^2+EK^4). \qquad (1)$$

Taking $A=-6.36996\times10^{-3}$, $B=8.88986\times10^{-3}$, $C=8.6922\times10^{-7}$, $D=-1.7845\times10^{-6}$, $E=5.3075\times10^{-7}$, and $\nu_0=23{,}785.88$ Mc/sec, this formula gave an rms. error of 2.9 Mc/sec for the observed lines of $N^{14}H_3$ except for $K=3$ lines.

The anomaly in the frequencies of the $K=3$ lines was explained by Nielsen and Dennison3) in terms of the interactions of vibrations with rotations, which lift the K-type degeneracy of the symmetric top molecule when $K=3, 6, 9, \cdots$. The deviations from Eq. (1) become appreciably large when $K=3$, and is expressed in the form

$$\Delta\nu=A'\mathrm{F}(J) \qquad (2)$$

where

$$\mathrm{F}(J)=(-1)^J[J(J+1)][J(J+1)-2] \\ [J(J+1)-6]/720\,. \qquad (2')$$

Costain gives $A'=0.252$ to fit the lines with $K=3$ and $J=3, 4, 5, 6, 7$. Eq. (2) shows that the anomalous deviations become considerably large for larger J lines which fall into the lower frequency region. Therefore, it is interesting to extend the observed range to low frequency region.

Recently, Gunther-Mohr and others4) have found new hyperfine splittings on the lines of ammonia and explained them on the basis of the interactions of the magnetic moments of the protons with the molecular rotational magnetic moment and the magnetic moment of nitrogen nucleus. For lines with $K\neq1$, these hyperfine splittings are so small that they could not be resolved*. But the doublings of lines with $K=1$ were observed for $J=2, 3, 4$ to be from 70 to 150kc/sec increasing with J. The magnetic interaction matrix has the off-diagonal elements which connect two states with K differing by two and, therefore, lift the degeneracy between $K=1$ and $K=-1$ states. The lines with J values larger than 5 fall into the lower frequency region than 20 kMc/sec. The intensities are weaker but the doublet separations increase roughly proportional to $(2J+1)$.

We have observed the inversion spectrum of ammonia including these lines in the frequency range between 12 and 20 kMc/sec by an ordinary source or Stark modulation method**. A X-band Stark waveguide cell three meters in length has been used.

§ 2. Observed Frequencies

We have found 26 lines of $N^{14}H_3$ and 3 lines of $N^{15}H_3$ in the range between 17 and 12 kMc/sec. They have J values larger than 8 and K values smaller than 12. Observed

---

* J. P. Gordon, H. J. Zeiger, and C. H. Townes have resolved the splittings by a molecular beam method when $J=3$, $K=3$ and $J=2$, $K=2$. (private communication.)

** The preliminary results in the frequency range between 15 and 17 kMc/sec are given by the authors in Journ. Phys. Soc. Japan **8** (1953) 426.

Table I. Inversion Spectrum of Ammonia below 16500 Mc/sec.

	Assign.		Frequency (Mc/sec)		Error	Intensity	
	J	K	Obs.	Calc.	(Mc/sec)	Obs.	Calc. (cm^{-1})
$\mathrm{N^{14}H_3}$	11	4	11947.14 ± 0.06	11965.26	-18.12	*MW*	2.0×10^{-7}
	10	1	12010.26 ± 0.12	12032.46	-22.20	*WW*	3.0×10^{-8}
	12	6	12251.46 ± 0.06	12270.93	-19.47	*M*	3.9×10^{-7}
	10	2	12332.72 ± 0.06	12350.52	-17.80	*MW*	1.3×10^{-7}
	11	5	12923.10 ± 0.06	12937.00	-13.90	*MW*	4.3×10^{-7}
	14	9	12951.32 ± 0.06	12973.90	-22.58	*W*	1.4×10^{-7}
	13	8	13297.49 ± 0.10	13314.87	-16.83	*W*	1.8×10^{-7}
	10	3	13296.37 ± 0.06	13332.07	-35.70	*M*	7.6×10^{-7}
	9	1	13612.08 ± 0.04	13620.37	$-\ 8.29$	*W*	1.1×10^{-7}
			13612.36 ± 0.04		$-\ 8.01$	*W*	
	10	4	13700.96 ± 0.06	13710.30	$-\ 9.34$	*M*	8.1×10^{-7}
	12	7	13719.51 ± 0.08	13731.20	-11.69	*MW*	4.2×10^{-7}
	9	2	13974.54 ± 0.08	13981.87	$-\ 7.33$	*MW*	4.9×10^{-7}
	11	6	14224.74 ± 0.06	14234.17	$-\ 9.43$	*MS*	1.8×10^{-6}
	9	3	14376.56 ± 0.06	14373.30	$+\ 3.26$	*MS*	2.5×10^{-6}
	10	5	14822.70 ± 0.06	14829.01	$-\ 6.31$	*MS*	1.7×10^{-6}
	16	12	15193.54 ± 0.10	15211.04	-17.50	*WW*	4.9×10^{-8}
	15	11	15195.98 ± 0.10	15210.58	-14.60	*W*	6.6×10^{-8}
	8	1	15233.12 ± 0.04	15236.94	$-\ 3.82$	*MW*	3.6×10^{-7}
			15233.36 ± 0.04		$-\ 3.58$	*MW*	
	14	10	15268.24 ± 0.06	15280.11	-11.87	*MW*	1.7×10^{-7}
	13	9	15412.52 ± 0.06	15422.09	$-\ 9.57$	*M*	8.2×10^{-7}
	9	4	15523.96 ± 0.06	15527.93	$-\ 3.97$	*S*	3.0×10^{-6}
	12	8	15632.88 ± 0.08	15640.14	$-\ 7.26$	*M*	9.1×10^{-7}
	8	2	15639.84 ± 0.06	15642.88	$-\ 3.04$	*MS*	1.6×10^{-6}
	11	7	15933.32 ± 0.06	15938.51	$-\ 4.19$	*MS*	1.9×10^{-6}
	10	6	16319.38 ± 0.04	16322.92	$-\ 3.54$	*S*	7.4×10^{-6}
	8	3	16455.13 ± 0.04	16460.53	$-\ 5.22$	*S*	8.8×10^{-6}
$\mathrm{N^{15}H_3}$	8	3	15589.75 ± 0.06	—	—	*W*	3.0×10^{-8}
	9	5	15908.53 ± 0.10	—	—	*WW*	2.2×10^{-8}
	8	4	16475.23 ± 0.06	—	—	*W*	3.4×10^{-8}

frequencies which were measured by a sort of frequency multiplier controlled by the standard frequency broadcast, JJY, are given in Table I. Assignments have been done using Costain's formula. Table II shows remeasured lines between 17 and 20 kMc/sec which were formerly observed less accurately by Sharbauch and others⁵⁾.

Calculated frequencies using Eq. (1) and Eq. (2) with the values of coefficients which were given by Costain are also given in these tables with their deviations from the experimental results. It is obvious that the errors of Costain's fomula systematically increase with increasing J and decreasing K, except for $K=3$. Therefore, in order to get a better fit, it is necessary to revise his formula introducing the higher order terms. Calculations of a revised formula by the method of least squares are now being carried out and the results will be published shortly.

The coefficient A' in Eq. (2) seems to be a little larger than 0.252 which was given by Costain. Nielsen and Dennison calculated $A' = 0.258\pm10$ percent. Though the precise determination of A' also depends on the calculations of a revised formula, it is probable that Nielsen and Dennison's theory on the

Table II. Remeasured Lines of the Ammonia Spectrum below 20000 Mc/sec.

	Assign.		Frequency (Mc/sec)		Error	Intensity	
	J	K	Obs.	Calc.	(Mc/sec)	Obs.	Calc. (cm^{-1})
$N^{14}H_3$	9	5	16798.22±0.04	16800.34	−2.12	*S*	6.4×10^{-6}
	7	1	16840.95±0.04	16842.25	−1.30	*MW*	1.1×10^{-6}
			16841.16±0.04		−1.09	*MW*	
	7	2	17291.54±0.04	17292.42	−0.88	*S*	4.8×10^{-6}
	8	4	17378.14±0.04	17379.28	−1.14	*S*	9.9×10^{-6}
	7	3	18017.42±0.04	18017.09	+0.33	*S*	2.6×10^{-5}
	12	9	18127.32±0.04	18129.56	−2.24	*S*	4.2×10^{-6}
	11	8	18162.54±0.04	18164.19	−1.65	*S*	4.2×10^{-6}
	13	10	18177.99±0.06	18180.82	−2.83	*MS*	9.8×10^{-7}
	10	7	18285.55±0.04	18286.68	−1.13	*S*	7.9×10^{-6}
	14	11	18313.80±0.06	18317.06	−3.26	*M*	4.3×10^{-7}
	6	1	18391.46±0.04	18391.75	−0.29	*M*	2.9×10^{-6}
			18391.65±0.04		−0.10	*M*	
	9	6	18499.28±0.04	18500.12	−0.84	*S*	2.7×10^{-5}
	15	12	18535.16±0.08	18538.36	−3.20	*MW*	3.5×10^{-7}
	8	5	18808.56±0.04	18808.79	−0.23	*S*	2.1×10^{-5}
	16	13	18842.76±0.10	18845.73	−2.97	*W*	6.8×10^{-8}
	6	2	18884.76±0.04	18884.76	0.00	*S*	1.3×10^{-5}
	7	4	19218.36±0.04	19218.52	−0.16	*S*	2.9×10^{-5}
	6	3	19757.40±0.04	19757.57	−0.17	*S*	6.9×10^{-5}
	5	1	19838.26±0.02	19838.26	0.00	*MS*	7.1×10^{-6}
			19838.41±0.02		+0.15	*MS*	
$N^{15}H_3$	7	3	17097.38±0.06	—	—	*W*	8.8×10^{-8}
	9	6	17548.42±0.08	—	—	*W*	9.3×10^{-8}
	8	5	17855.57±0.08	—	—	*W*	7.2×10^{-8}
	6	2	17943.45±0.10	—	—	*WW*	4.4×10^{-8}
	7	4	18259.15±0.08	—	—	*W*	1.0×10^{-7}
	6	3	18788.25±0.06	—	—	*MW*	2.4×10^{-7}
	5	2	19387.53±0.06	—	—	*W*	1.1×10^{-7}
	8	6	19701.99±0.06	—	—	*MW*	3.1×10^{-7}
	9	7	19708.24±0.04	—	—	*MW*	1.0×10^{-7}
	7	5	19793.45±0.06	—	—	*MW*	2.2×10^{-7}
	10	8	19810.86±0.06	—	—	*W*	6.0×10^{-8}
	6	4	19984.75±0.06	—	—	*MW*	2.8×10^{-7}
	11	9	20010.05±0.08	—	—	*W*	6.7×10^{-8}
	4	1	20131.53±0.12	—	—	*WW*	5.5×10^{-8}

K-type splitting fails to explain such large anomalous deviations of larger *J* lines as 100 ~500 Mc/sec.

§ 3. Intensities

The absolute intensities have not been measured, but the relative values have been observed and are given by *S*, *M* and *W* in the tables.

The peak intensities as a function of *J* and *K* are given approximately by

$$\alpha=2\times10^{-13}\nu^2\left[\frac{K^2}{J(J+1)}\right]g(2J+1)$$

$$\exp[-0.0475J(J+1)+0.0174K^2] \qquad (3)$$

for $T=300°\mathrm{K}$, where

$$g=2 \quad \text{for} \quad K=3,\ 6,\ 9,\cdots$$

and

$$g=1 \quad \text{for} \quad K=1,\ 2,\ 4,\ 5, \cdots$$

In this formula a line width parameter $\Delta\nu$ of 26 Mc/sec for 1 mm Hg pressure is assumed and its dependence on J and K is neglected. Costain pointed out that a better approximation may be given when the value calculated from Eq. (3) is multiplied by $\left[\dfrac{4K^2}{3J(J+1)}\right]^{-1/4}$.⁶⁾ Calculated intensities using Eq. (3) are given in Table I and II.

§ 4. Magnetic Hyperfine Structures

As shown in the tables, the doublings of centre lines arising from the magnetic interactions have been observed for $J=5$, 6, 7, 8, 9 and $K=1$. Intensities of two component lines are nearly equal in such large J lines. Observed splittings are given in Table III with calculated values from the theoretical formula given on page 1189 in reference 4 (a)*. Our calculations have been carried out only for the stronger components corresponding to the transitions $\Delta J=0$, $\Delta F_1=0$, and $\Delta F=0$. Thus the equation is simplified and the separations of the doublet lines are given by

$$\Delta\nu=(-1)^J[2B\mathfrak{G}(J,\ F_1,\ F) + 2D_2\mathfrak{F}(J,\ F_1,\ F)] \qquad (4)$$

Definitions of $\mathfrak{G}(J,\ F_1,\ F)$ and $\mathfrak{F}(J,\ F_1,\ F)$ are given in reference 4. The best fitted value for B is determined as -14.4 kc/sec** by Gunther-Mohr and others while $D_2=10.8$ kc/sec is calculated from the molecular constants of ammonia. Calculated values are in good agreement with our experimental results.

Table III. Splittings of the hyperfine doublings of the $N^{14}H_3$ spectrum. Comparison of theory and experiment. Observed values are accurate to about ±0.02 Mc/sec.

J, K	9, 1	8, 1	7, 1	6, 1	5, 1
Obs. spl. (Mc/sec)	0.28	0.24	0.21	0.19	0.15
Cal. spl. (Mc/sec)	0.27_3	0.24_4	0.21_5	0.18_6	0.15_6

$J=10$ and $K=1$ line was so weak that the doublet structure could not be resolved by our spectrometer. The satelite lines due to the nuclear quadrupole moment of the nitrogen nucleus were too weak to be observed in the measured lines.

Acknowledgement

The authors wish to express their hearty thanks to Prof. C.H. Townes and to Dr. C.C. Costain for their kind informations of their works. The authors also express their thanks to Mr. T. Itoh for his advice on calculations and to Mr. S. Sekino for his help in measurements and computations.

References

1) P. Kisliuk and C. H. Townes: *Molecular Microwave Spectra Tables, National Bureau of Standards Circular,* **518**, June 23, 1952.
2) C. C. Costain: Phys. Rev. **82** (1951) 108.
3) H. H. Nielsen and D. M. Dennison: Phys. Rev. **72** (1947) 1101.
4) (a) G. R. Gunther-Mohr, R. L. White, A. L. Shawlow, W. E. Good, and D. K. Coles: Phys. Rev. **94** (1954) 1184. (b) G. R. Gunther-Mohr, C. H. Townes and J. H. Van Vleck: Phys. Rev. **94** (1954) 1191.
5) A. H. Sharbaugh, T. C. Madison and J. K. Bragg: Phys. Rev. **76** (1949) 1529.
6) private communication.

---

* The third term in the equation should read $\left(1-\dfrac{3K^2}{J(J+1)}\right)$ instead of $\left(1-\dfrac{3}{J(J+1)}\right)$. Eq. (16) in reference 4 (b) should also read

$$f=\frac{1}{2}\left\{\frac{3}{2}\langle v|r^{-3}\sin^2\beta|v\rangle\times\frac{2g_Ng_H\mu_0{}^2}{F_1(F_1+1)}\boldsymbol{F}_1\cdot\boldsymbol{I}\Omega_2(\boldsymbol{J},\ \boldsymbol{I}_N) + \frac{(\rho-\alpha)}{2}\frac{(\boldsymbol{F}_1\cdot\boldsymbol{I})(\boldsymbol{F}_1\cdot\boldsymbol{J})}{F_1(F_1+1)}\right\}.$$

** Sign of B is incorrect on page 1190 in reference 4 (a).

JOURNAL OF THE PHYSICAL SOCIETY OF JAPAN Vol. 10, No. 2, FEBRUARY, 1955

Methods of Calculating the Crystalline Electric Field

By J. KANAMORI, T. MORIYA, K. MOTIZUKI
and T. NAGAMIYA

Department of Physics, Osaka University

(Received August 30, 1954)

Two convenient methods are developed for calculating the coefficients of expansion of the crystalline potential in spherical harmonics. One consists in extending Evjen's elementary method of obtaining Madelung's constant, dividing the lattice into multipoles, and summing their contributions in an elementary way, and the other is an extension of Bertaut's Fourier method of obtaining the electrostatic lattice energy of a point-charge lattice and that of a point-dipole lattice. For the latter, two slightly different methods are proposed. Applications to NaCl-type and CsCl-type lattices and to FeF_2 and CoF_2 lattices are given, and the merits and dismerits of the methods are discussed.

§ 1. Introduction

The object of this paper is to examine and establish a number of mathematical methods convenient for calculating the electrostatic field around a lattice point in ionic crystals. We find, after practical applications to lattices of NaCl-type and CsCl-type and to FeF_2 and CoF_2 lattices of rutile type, that two methods are most convenient: an extension of Evjen's direct summation method of calculating the Madelung constant and an extension of Bertaut's Fourier method of calculating similar things. The merits and dismerits of these two methods and of other methods will be discussed after developing these two methods and of other methods will be discussed after developing these two methods. Numerical results for the mentioned cases will be given.

§ 2. Direct Summation Method

We first consider a lattice consisting of positive and negative point charges. Later we shall come to dipole and other multipole lattices. The electrostatic potential around a chosen ion, which we shall take as the origin of the coordinates, can be expanded in spherical harmonics

$$\varphi(\boldsymbol{r})=\sum_{l=0}^{\infty}\sum_{m=0}^{l} r^l P_l^m(\cos\theta)(c_{lm}\cos m\varphi + d_{lm}\sin m\varphi), \quad (2.1)$$

$$P_l^m(\cos\theta)=\sin^m\theta\frac{d^m}{(d\cos\theta)^m}P_l(\cos\theta),$$

provided the contribution from that ion is omitted. Our object is to calculate the coefficients c_{lm} and d_{lm}.

Evjen[1)] developed an elementary method of calculating c_{00}, or the Madelung constant. It consists in summing up e_j/R_j over all the charges j, where R_j is the distance of the j-th ion from the origin and e_j its charge. The lattice is divided into shells of the highest possible symmetry around the origin and the contribution from each shell is added successively. In this process, charges on the surface between two shells are counted to belong half to the inner shell and half to the outer shell, those on the edges one quarter to the inner shell and three quarters to the outer shell, and those at the corners 1/8 and 7/8, respectively. This is in some cases equivalent to dividing the lattice into neutral unit cells of the highest possible symmetry, arranging them in the highest possible symmetrical manner, and then summing the contributions from them. This way is most effective for the convergency of the sum, for the effect of a neutral symmetric unit cell at large distances is that of a point multipole of a high degree (2^4-pole in the case of a cubic lattice) and the effect of a symmetrical arrangement of them at large distances is that of a still higher multipole placed at infinity. (The unit is actually not necessary to be a unit cell but can be any unit into which the lattice can be divided.[2),3)]) We shall modify Evjen's summation method in this way.

Now, when we want to calculate c_{10}, we differentiate $\varphi(\boldsymbol{r})$ with respect to z, z being the coordinate along the polar axis, and put $\boldsymbol{r}=$

0. We may instead differentiate $-e_j/R_j$ with respect to the z-coordinate of the j-th charge, Z_j, and sum it over j:

$$c_{10}=-\sum_j{}' e_j(\partial R_j^{-1}/\partial Z_j)=\sum_j{}' e_j Z_j/R_j^3. \tag{2.2}$$

The prime attached to the summation symbol means the omission of $j=0$, namely the charge at the origin. The summation can be carried out by the modified Evjen method stated above. Then the convergency is even more rapid, but the sum vanishes when the origin is a centre of symmetry.

We can calculate the higher coefficients in a similar way. We differentiate (2.1) l times in the direction specified by θ, φ and put $r=0$; then we have

$$\left(\frac{\boldsymbol{r}}{r}\,\mathrm{grad}\right)^l \varphi(\boldsymbol{r})\Big|_{r=0}=(-1)^l\sum_j{}'\left(\frac{\boldsymbol{r}}{r}\,\mathrm{grad}_j\right)^l\frac{e_j}{R_j}$$
$$=l!\sum_{m=0}^{l}P_l^m(\cos\theta)(c_{lm}\cos m\varphi+d_{lm}\sin m\varphi)\,, \tag{2.3}$$

where grad_j means the gradient operator with respect to the coordinates of charge j. First we put $\theta=0$ in (2.3) and obtain

$$c_{l0}=\frac{1}{l!}(-1)^l\sum_j{}'\left(\frac{\partial}{\partial Z_j}\right)^l\frac{e_j}{R_j}\,. \tag{2.4}$$

To obtain other coefficients, we may do for instance as follows. We write $(\boldsymbol{r}/r)\,\mathrm{grad}_j$ as

$$\frac{\boldsymbol{r}}{r}\mathrm{grad}_j=\frac{1}{2}\sin\theta e^{i\varphi}\left(\frac{\partial}{\partial X_j}-i\frac{\partial}{\partial Y_j}\right)+\frac{1}{2}\sin\theta\, e^{-i\varphi}\left(\frac{\partial}{\partial X_j}-i\frac{\partial}{\partial Y_j}\right)+\cos\theta\frac{\partial}{\partial Z_j}\,,$$

and pick up from $((\boldsymbol{r}/r)\mathrm{grad}_j)^l$ terms with factor $e^{im\varphi}$:

$$\sum_\beta\frac{l!}{(\beta+m)!\,\beta!\,(l-2\beta-m)!}\left(\frac{1}{2}\sin\theta\right)^{2\beta+m}(\cos\theta)^{l-2\beta-m}e^{im\varphi}$$
$$\cdot\left(\frac{\partial}{\partial X_j}-i\frac{\partial}{\partial Y_j}\right)^{\beta+m}\left(\frac{\partial}{\partial X_j}+i\frac{\partial}{\partial Y_j}\right)^{\beta}\left(\frac{\partial}{\partial Z_j}\right)^{l-2\beta-m},$$

where $(l-m)/2\geqslant\beta\geqslant0$. Since $\left(\frac{\partial}{\partial X_j}-i\frac{\partial}{\partial Y_j}\right)^\beta\left(\frac{\partial}{\partial X_j}+i\frac{\partial}{\partial Y_j}\right)^\beta$ is equivalent to $(-1)^\beta\left(\frac{\partial}{\partial Z_j}\right)^{2\beta}$ when operated on e_j/R_j, in virtue of Laplace's equation, the above expression can be written as

$$\left[\sum_\beta\frac{l!(-1)^l 2^{-2\beta-m}}{(\beta+m)!\,\beta!\,(l-2\beta-m)!}(\sin\theta)^{2\beta+m}(\cos\theta)^{l-2\beta-m}\right]e^{im\varphi}$$
$$\cdot\left(\frac{\partial}{\partial X_j}-i\frac{\partial}{\partial Y_j}\right)^{m}\left(\frac{\partial}{\partial Z_j}\right)^{l-m}.$$

The expression in the square bracket is $P_l^m(\cos\theta)$ times $l!/(l+m)!$, so that we have from (2.3)

$$\frac{1}{2}(c_{lm}-id_{lm})=\frac{(-1)^l}{(l+m)!}\sum_j{}'\left(\frac{\partial}{\partial X_j}-i\frac{\partial}{\partial Y_j}\right)^m\left(\frac{\partial}{\partial Z_j}\right)^{l-m}\frac{e_j}{R_j}\,. \qquad (m>0) \tag{2.5}$$

Another way of obtaining c_{lm} and d_{lm} is to expand $\varphi(\boldsymbol{r})$ in spherical harmonics as follows:

$$\varphi(\boldsymbol{r})=\sum_j{}' e_j/|\boldsymbol{R}_j-\boldsymbol{r}|^{1/2}$$
$$=\sum_{l=0}^{\infty}r^l\sum_{m=-l}^{l}\frac{(l-|m|)!}{(l+|m|)!}P_l^{|m|}(\cos\theta)e^{im\varphi}\cdot\sum_j{}'\frac{e_j}{R_j^{l+1}}P_l^{|m|}(\cos\theta_j)e^{-im\varphi_j}\,,$$

where θ_j, φ_j are the polar and azimuthal angles of $\boldsymbol{R}_j$. Comparing this with (2.1) we obtain

$$c_{l0}=\sum_j{}'\frac{e_j}{R_j^{l+1}}P_l(\cos\theta_j), \tag{2.6}$$

$$\frac{1}{2}(c_{lm}-id_{lm})=\frac{(l-m)!}{(l+m)!}\sum_j{}' \frac{e_j}{R_j^{l+1}} P_l^m(\cos\theta_j)e^{-im\varphi_l}\,. \qquad (m>0) \tag{2.7}$$

It can be seen that (2.4), (2.5) and (2.6), (2.7) are respectively the same.

Examples of the above formulas for $l=2$, $m=0$, 2 and $l=4$, $m=0$, 2, 4 are:

$$\begin{aligned}
c_{20}&=\sum_j{}'\frac{e_j}{R_j^3}P_2(\cos\theta_j)=\sum_j{}'\frac{e_j}{2R_j^5}(3Z_j^2-R_j^2)\,,\\
c_{22}&=\frac{1}{12}\sum_j{}'\frac{e_j}{R_j^3}P_2^2(\cos\theta_j)\cos\varphi_j=\sum_j{}'\frac{e_j}{4R_j^5}(X_j^2-Y_j^2)\,,\\
c_{40}&=\sum_j{}'\frac{e_j}{R_j^5}P_4(\cos\theta_j)=\sum_j{}'\frac{5e_j}{8R_j^9}\left(7Z_j^4-6Z_j^2R_j^2+\frac{3}{5}R_j^4\right),\\
c_{42}&=\frac{4}{6!}\sum_j{}'\frac{e_j}{R_j^5}P_4^2(\cos\theta_j)\cos 2\varphi_j=\sum_j{}'\frac{e_j}{24R_j^9}(7Z_j^2-R_j^2)(X_j^2-Y_j^2),\\
c_{44}&=\frac{2}{8!}\sum_j{}'\frac{e_j}{R_j^5}P_4^4(\cos\theta_j)\cos 4\varphi_j=\sum_j{}'\frac{210\,e_j}{8!\,R_j^9}(X_j^4-6X_j^2Y_j^2+Y_j^4).
\end{aligned} \tag{2.8}$$

There are following relations:

$$\begin{aligned}
-\frac{1}{2}c_{20}+3c_{22}&=\sum_j{}'\frac{e_j}{2R_j^5}(3X_j^2-R_j^2)\\
\frac{3}{8}c_{40}-\frac{15}{2}c_{42}+105c_{44}&=\sum_j{}'\frac{5e_j}{8R_j^9}\left(7X_j^4-6X_j^2R_j^2+\frac{3}{5}R_j^4\right),\\
\frac{3}{8}c_{40}+\frac{15}{2}c_{42}+105c_{44}&=\sum_j{}'\frac{5e_j}{8R_j^9}\left(7Y_j^4-6Y_j^2R_j^2+\frac{3}{5}R_j^4\right).
\end{aligned} \tag{2.9}$$

These can conveniently be used to calculate c_{22}, c_{42} and c_{44}.

Next we consider a dipole lattice which may consist of point dipoles of moments $\boldsymbol{p}_j$ placed at points $\boldsymbol{R}_j$. We have only to replace e_j/R_j by $(\boldsymbol{p}_j\,\mathrm{grad}_j)R_j^{-1}$. So the potential around the origin can be written in two ways as follows:

$$\begin{aligned}
\varphi_D(\boldsymbol{r})&=\sum_{l=0}^{\infty}\sum_j{}'\frac{(-1)^l}{l!}(\boldsymbol{r}\cdot\mathrm{grad}_j)^l\cdot(\boldsymbol{p}_j\,\mathrm{grad}_j)\frac{1}{R_j}\\
&=\sum_{l=0}^{\infty}\sum_{m=0}^{l}{}'\; r^lP_l^m(\cos\theta)(c_{lm}\cos m\varphi+d_{lm}\sin m\varphi)\,.
\end{aligned} \tag{2.10}$$

Therefore we have, in place of (2.4) and (2.5),

$$c_{l0}=\frac{1}{l\,!}(-1)^l\sum_j{}'\left(\frac{\partial}{\partial Z_j}\right)^l(\boldsymbol{p}_j\,\mathrm{grad}_j)\frac{1}{R_j}\,, \tag{2.11}$$

and

$$\frac{1}{2}(c_{lm}-id_{lm})=\frac{(-1)^l}{(l+m)!}\sum_j{}'\left(\frac{\partial}{\partial X_j}-i\frac{\partial}{\partial Y_j}\right)^m\left(\frac{\partial}{\partial Z_j}\right)^{l-m}(\boldsymbol{p}_j\,\mathrm{grad}_j)\frac{1}{R_j}\,. \qquad (m>0) \tag{2.12}$$

Formulas for lattices of higher multipoles can be written down in a similar way.

§ 3. Fourier Method

This is an extension of the method given by Bertaut[4,5] for evaluating the electrostatic lattice energy of the point-charge lattice and that of the dipole lattice. As before, we first consider a point-charge lattice. We replace the point charges by spherical charge distributions which do not overlap with one another. For most cases it is convenient to adopt the same radius and the same radial distribution of this spherical charge distribution for all the point charges except for the sign of the density. There may be also cases where different distributions for different kinds of ions can more conveniently be adopted. For the sake of brevity, we shall here assume the same distribution for all the charges.

The charge density in the whole lattice can be expanded in a Fourier series:

$$\rho(\boldsymbol{x})=\frac{1}{V}\sum_{\boldsymbol{h}}\rho_{\boldsymbol{h}}\exp(-2\pi i\boldsymbol{h}\cdot\boldsymbol{x})\,, \tag{3.1}$$

where $\boldsymbol{h}$ is a reciprocal lattice vector and V the volume of the unit cell. The Fourier coefficient $\rho_{\boldsymbol{h}}$ is calculated by

$$\rho_{\boldsymbol{h}}=\int_{\text{unit cell}}\rho(\boldsymbol{x})\exp(2\pi i\boldsymbol{h}\cdot\boldsymbol{x})d\boldsymbol{x}\,. \tag{3.2}$$

The potential in the whole lattice is obtained by use of Poisson's equation, $\varphi(\boldsymbol{x})=-4\pi\rho(\boldsymbol{x})$, as

$$\varphi(\boldsymbol{x})=\frac{1}{V}\sum_{\boldsymbol{h}}\frac{\rho_{\boldsymbol{h}}}{\pi|\boldsymbol{h}|^2}\exp(-2\pi i\boldsymbol{h}\cdot\boldsymbol{x})\,. \tag{3.3}$$

Now, to calculate $\rho_{\boldsymbol{h}}$, we express $\rho(\boldsymbol{x})$ as

$$\rho(\boldsymbol{x})=\sum_{j}e_j\sigma(|\boldsymbol{x}-\boldsymbol{x}_j|),\qquad \int\sigma(|\boldsymbol{x}|)d\boldsymbol{x}=1\,, \tag{3.4}$$

where e_j and $\boldsymbol{x}_j$ are the charge and position of point charge j. (3.2) then becomes

$$\rho_{\boldsymbol{h}}=\sum_{j=1}^{n}e_j\exp(2\pi i\boldsymbol{h}\cdot\boldsymbol{x}_j)\cdot\int\sigma(|\boldsymbol{x}|)\exp(2\pi i\boldsymbol{h}\cdot x)d\boldsymbol{x}=F(\boldsymbol{h})\sigma_h\,, \tag{3.5}$$

with

$$F(\boldsymbol{h})=\sum_{j=1}^{n}e_j\exp(2\pi i\boldsymbol{h}\cdot\boldsymbol{x}_j) \tag{3.6}$$

and

$$\sigma_h=\int\sigma(|\boldsymbol{x}|)\exp(2\pi i\boldsymbol{h}\cdot\boldsymbol{x})d\boldsymbol{x}=\frac{2}{h}\int_0^R r\sigma(r)\sin 2\pi hr\cdot dr,\quad h=|\boldsymbol{h}|\,. \tag{3.7}$$

$F(\boldsymbol{h})$ is the *structure factor*, the summation over j from 1 to n being extended over the charges in a unit cell, R is the radius of the spherical distribution and h the magnitude of $\boldsymbol{h}$.

The converngence of (3.3) depends on the choice of R and on the functional form of $\sigma(r)$. The greater R, the better the convergence; the spheres are therefore to be taken so as to touch each other. The form of $\sigma(r)$ which we actually assume will be given later, but it may be remarked that a function which vanishes smoothly at $r=R$ gives a good convergence.

We have to calculate c_{lm} and d_{lm} from (3.3) with (3.5). There are a number of method for this purpose, but we shall give two convenient ones.

A. $\varphi(\boldsymbol{x})$ contains the contribution from the spherical charge distribution around the origin. We shall denote it as $\varphi_0(|\boldsymbol{x}|)$ and subtract it from $\varphi(x)$. Then, operating $(\boldsymbol{r}\cdot\text{grad})^l$ on $\varphi(\boldsymbol{x})-\varphi_0(|\boldsymbol{x}|)$, we have

$$\begin{aligned}&(\boldsymbol{r}\cdot\text{grad})^l[\varphi(\boldsymbol{x})-\varphi_0(|\boldsymbol{x}|)]\\&\quad=\frac{1}{V}\sum_{\boldsymbol{h}}\frac{F(\boldsymbol{h})\sigma_h}{\pi h^2}(-2\pi i)^l(\boldsymbol{r}\cdot\boldsymbol{h})^l\exp(-2\pi i\boldsymbol{h}\cdot\boldsymbol{x})-(\boldsymbol{r}\cdot\text{grad})^l\varphi_0(|\boldsymbol{x}|)\,.\end{aligned} \tag{3.8}$$

We might put $\boldsymbol{x}=0$ in this equation to obtain

$$l!\,r^l\sum_{m=0}^{l}P_l^m(\cos\theta)(c_{lm}\cos m\varphi+d_{lm}\sin m\varphi) \tag{3.9}$$

as in (2.3), but the following procedure gives a better convergence. By a well-known theorem of potential theory, the mean value of a solution of Laplace's equation over a spherical surface is equal to its value at the centre of this sphere. $\varphi(\boldsymbol{x})-\varphi_0(|\boldsymbol{x}|)$ satisfies Laplace's equation for $r<R$, and therefore (3.8) also does so. So we multiply (3.8) by a centrally symmetric function $\tau(|\boldsymbol{x}|)$ and integrate, to obtain (3.9). τ is supposed to satisfy the following normalization condition:

$$\int_0^R 4\pi\tau(r)r^2dr=1\,, \qquad \tau(r)=0 \quad \text{for} \quad r\geqslant R\,. \tag{3.10}$$

We then obtain

$$\frac{1}{V}\sum_{\boldsymbol{h}}\frac{F(\boldsymbol{h})\sigma_h}{h^2}(-2\pi i)^l(\boldsymbol{r}\cdot\boldsymbol{h})^l\tau_h-\int\tau(|\boldsymbol{x}|)(\boldsymbol{r}\cdot\mathrm{grad})^l\varphi_0(|\boldsymbol{x}|)d\boldsymbol{x}\,, \tag{3.11}$$

where

$$\tau_h=\int\tau(|\boldsymbol{x}|)\exp(-2\pi i\boldsymbol{h}\boldsymbol{x})d\boldsymbol{x}=\frac{2}{h}\int_0^R r\tau(r)\sin 2\pi hr\cdot dr\,. \tag{3.12}$$

The second term in (3.11) does not depend on the direction of $\boldsymbol{r}$, so that it contributes only to c_{00}. We also notice that

$$(\boldsymbol{r}\cdot\boldsymbol{h})^l=r^lh^l\cos^l\Theta_h=r^lh^l\left[\frac{2^l(l!)^2}{(2l)!}P_l(\cos\Theta_h)+\text{lower Legendre functions}\right],$$

where Θ_h is the angle between $\boldsymbol{r}$ and $\boldsymbol{h}$, and that the lower Legendre functions should vanish on substitution in (3.11). Writing the polar and azimuthal angles of $\boldsymbol{r}$ and $\boldsymbol{h}$ as θ, φ and θ_h, φ_h, (3.11) therefore becomes

$$r^l\frac{(-2\pi i)^l2^l(l!)^2}{\pi V\cdot(2l)!}\sum_{m=-l}^{l}\frac{(l-|m|)!}{(l+|m|)!}P_l^{|m|}(\cos\theta)e^{im\varphi}$$
$$\cdot\sum_{\boldsymbol{h}}F(\boldsymbol{h})\sigma_h\tau_hh^{l-2}P_l^{|m|}(\cos\theta_h)e^{-im\varphi_h}-\int\tau(|\boldsymbol{x}|)(\boldsymbol{r}\cdot\mathrm{grad})^l\varphi_0(|\boldsymbol{x}|)d\boldsymbol{x}. \tag{3.13}$$

Comparing (3.13) with (3.19), we obtain

$$c_{00}=\frac{1}{\pi V}\sum_{\boldsymbol{h}}F(\boldsymbol{h})\sigma_h\tau_hh^{-2}-\int\tau(|\boldsymbol{x}|)\varphi_0(|\boldsymbol{x}|)d\boldsymbol{x}\,, \tag{3.14}$$

$$c_{l0}=\frac{(-2\pi i)^l2^l\,l!}{\pi V\cdot(2l)!}\sum_{\boldsymbol{h}}F(\boldsymbol{h})\sigma_h\tau_hh^{l-2}P_l(\cos\theta_h)\,, \qquad (l>0) \tag{3.15}$$

$$\frac{1}{2}(c_{lm}-id_{lm})=\frac{(-2\pi i)^l2^l\,l!}{\pi V\cdot(2l)!}\,\frac{(l+m)!}{(l-m)!}\sum_{\boldsymbol{h}}F(\boldsymbol{h})\sigma_h\tau_hh^{l-2}P_l^m(\cos\theta_h)e^{-im\varphi_h}\,. \qquad (l\geqslant m>0) \tag{3.16}$$

(3.14) with $\sigma_h=\tau_h$ has been derived by Bertaut.[4)] The second term in it can be written as

$$-e_0\iint\frac{\tau(r)\sigma(r')}{|\boldsymbol{r}-\boldsymbol{r}'|}drdr'$$

where e_0 is the point charge originally found at the origin. This formula can further be written

$$-e_016\pi^2\int_0^R T(r)S(r)dr\,, \tag{3.17}$$

where

$$T(r)=\int_0^R\tau(r)rdr\,,\ S(r)=\int_0^R\sigma(r)rdr\,. \tag{3.18}$$

In practice, it is convenient to take $\sigma(r)=\tau(r)$.

B. Another method is to expand $\exp(-2\pi i\boldsymbol{h}\cdot\boldsymbol{x})$ in spherical waves:

$$\exp(-2\pi i \boldsymbol{h}\cdot\boldsymbol{x})=\sqrt{\frac{\pi}{2}}\sum_{l=0}^{\infty}(2l+1)(-i)^l\frac{J_{l+\frac{1}{2}}(2\pi hr)}{\sqrt{2\pi hr}}P_l(\cos\Theta_h)\,. \qquad (h=|\boldsymbol{h}|,\quad r=|\boldsymbol{x}|.)$$

Putting this into (3.3) we have

$$\varphi(\boldsymbol{x})=\frac{1}{V}\sum_{l=0}^{\infty}\sum_{m=-l}^{l}\frac{(l-|m|)!}{(l+|m|)!}(2l+1)(-i)^l P_l^{|m|}(\cos\theta)e^{im\varphi}\sum_{\boldsymbol{h}}\frac{F(h)\sigma_h}{\pi h^2}\frac{J_{l+\frac{1}{2}}(2\pi hr)}{\sqrt{2\pi hr}}P_l^{|m|}(\cos\theta_h)e^{-im\varphi_h}\,.$$

We compare this with (2.1) and obtain

$$c_{l0}=\frac{1}{V}(2l+1)(-i)^l\sum_{\boldsymbol{h}}\frac{F(\boldsymbol{h})\sigma_h}{\pi h^2}\frac{J_{l+\frac{1}{2}}(2\pi hr)}{2\sqrt{hr}\cdot r^l}P_l(\cos\theta_h),\quad (l>0) \tag{3.19}$$

$$\frac{1}{2}(c_{lm}-id_{lm})=\frac{1}{V}\frac{(l-m)!}{(l+m)!}(2l+1)(-i)^l\sum_{\boldsymbol{h}}\frac{F(\boldsymbol{h})\sigma_h}{\pi h^2}\frac{J_{l+\frac{1}{2}}(2\pi hr)}{2\sqrt{hr}\cdot r^l}P_l^m(\cos\theta_h)e^{-im\varphi_h}\,. \qquad (l\geqslant m>0) \tag{3.20}$$

Formula for c_{00} can be obtained by correcting (3.19) for the contribution from the charge cloud at the origin, and is

$$c_{00}=\frac{1}{V}\sum_{\boldsymbol{h}}\frac{F(\boldsymbol{h})\sigma_h}{\pi h^2}\frac{J_{\frac{1}{2}}(2\pi hr)}{2\sqrt{hr}}-e_0\int_r^R 4\pi\sigma(r)r\,dr-e_0\frac{1}{r}\int_0^r 4\pi\sigma(r)r^2dr\,. \tag{3.21}$$

It can be shown that the above fomulas follow as a special case of the method A by putting

$$\begin{aligned}\tau(r)&=C[1-(r/r_0)^2]^{l-1}\quad\text{for}\quad r\leqslant r_0\leqslant R\\ &=0\quad\text{for}\quad r>r_0\,,\end{aligned} \tag{3.22}$$

C being adjusted so as to satisfy (3.10), and r in (3.19), (3.20) and (3.21) replaced by r_0.

§ 4. Fourier Method applied to a Multipole Lattice

If we are dealing with a dipole lattice which has point dipoles $\boldsymbol{p}_j$ at points j, we have only to replace $e_j\sigma(|\boldsymbol{x}-\boldsymbol{x}_j|)$ by $-(\boldsymbol{p}_j\,\mathrm{grad})\sigma(|\boldsymbol{x}-\boldsymbol{x}_j|)$, provided σ vanishes on the spherical surface, as already has been pointed out by Bertaut⁽⁵⁾. We notice that

$$\int-(\boldsymbol{p}_j\,\mathrm{grad})\sigma(|\boldsymbol{x}|)\exp(2\pi i\boldsymbol{h}\boldsymbol{x})d\boldsymbol{x}=\int 2\pi i(\boldsymbol{p}_j\boldsymbol{h})\sigma(|\boldsymbol{x}|)\exp(2\pi i\boldsymbol{h}\boldsymbol{x})d\boldsymbol{x}\,,$$

so that, looking at (3.5) and (3.6), we see that we have only to replace $F(\boldsymbol{h})$ by

$$F_D(\boldsymbol{h})=2\pi i\sum_{j=1}^{n}(\boldsymbol{p}_j\boldsymbol{h})\exp(2\pi i\boldsymbol{h}\boldsymbol{x}_j)\,. \tag{4.1}$$

Now, if we had a dipole $\boldsymbol{p}_0$ at the origin which had to be replaced by $-(\boldsymbol{p}_0\,\mathrm{grad})\sigma(|\boldsymbol{x}|)$, it obviously should have affected the coefficients c_{lm} and d_{lm}. The correction from it to $\varphi(\boldsymbol{x})$ is

$$\int\frac{(\boldsymbol{p}_0\,\mathrm{grad}')\sigma(|\boldsymbol{x}'|)}{|\boldsymbol{x}-\boldsymbol{x}'|}d\boldsymbol{x}'\,,$$

therefore the correction to $\int\tau(|\boldsymbol{x}|)(\boldsymbol{r}\cdot\mathrm{grad})\varphi(\boldsymbol{x})d\boldsymbol{x}$ is

$$\iint\tau(|\boldsymbol{x}|)(\boldsymbol{r}\cdot\mathrm{grad})\frac{(\boldsymbol{p}_0\,\mathrm{grad}')\sigma(|\boldsymbol{x}'|)}{|\boldsymbol{x}-\boldsymbol{x}'|}d\boldsymbol{x}\,d\boldsymbol{x}'$$

or

$$-\iint\frac{(\boldsymbol{r}\cdot\mathrm{grad})\tau(|\boldsymbol{x}|)\cdot(\boldsymbol{p}_0\,\mathrm{grad}')\sigma(|\boldsymbol{x}'|)}{|\boldsymbol{x}-\boldsymbol{x}'|}d\boldsymbol{x}\,d\boldsymbol{x}'.$$

This integral is proportional to $(\boldsymbol{r}\boldsymbol{p}_0)$ and can be evaluated, for instance, by expanding $|\boldsymbol{x}-\boldsymbol{x}'|^{-1}$ in spherical harmonics. The result is

$$-\frac{16\pi^2}{3}(\boldsymbol{r}\boldsymbol{p}_0)\int_0^R \tau(r)\sigma(r)r^2dr\,. \tag{4.2}$$

Thus we have for $l=1$, instead of (3.15) and (3.16) with $F(\boldsymbol{h})$ replaced by $F_D(\boldsymbol{h})$

$$c_{10}=\frac{-2i}{V}\sum_{\boldsymbol{h}} F_D(\boldsymbol{h})\sigma_h\tau_h h^{-1}\cos\theta_h-\frac{16\pi^2}{3}p_{0z}\int_0^R \tau(r)\sigma(r)r^2dr\,, \tag{4.3}$$

$c_{11}=$(the same expression except that $\cos\theta_h$ is replaced by $\sin\theta_h\cos\varphi_h$ and p_{0z} by p_{0x}), (4.4)

$d_{11}=$(the same, $\cos\theta_h$ replaced by $\sin\theta_h\sin\varphi_h$ and p_{0z} by p_{0y}). (4.5)

Similar treatment can be made for lattices of higher multipoles, but the details may not need be reproduced here. Also, the B method described in the preceding section is contained in the above formulas as a special case, or it can directly be applied by writing $F_D(\boldsymbol{h})$ for $F(\boldsymbol{h})$.

§ 5. Application to NaCl and CsCl Lattices

As a test of the foregoing methods, we calculated the coefficients of cubical harmonics of the fourth and sixth degrees for the NaCl-type and CsCl-type lattices. The potential around a positive ion can be expanded as follows, if the contribution from this ion is omitted:

$$\varphi(\boldsymbol{r})=-\frac{e\alpha_M}{a}+\frac{e}{a}\left\{c_4\left(\frac{r}{a}\right)^4 Y_4+c_6\left(\frac{r}{a}\right)^6 Y_6+\cdots\right\}, \tag{5.1}$$

where

$$Y_4=P_4(\cos\theta)+\frac{1}{168}P_4{}^4(\cos\theta)\cos 4\varphi=-\frac{3}{2}+\frac{5}{2}\frac{x^4+y^4+z^4}{r^4}\,, \tag{5.2}$$

$$Y_6=P_6(\cos\theta)-\frac{1}{360}P_6{}^4(\cos\theta)\cos 4\varphi=1-\frac{21}{2}\frac{y^2z^2+z^2x^2+x^2y^2}{r^4}+\frac{231}{2}\frac{x^2y^2z^2}{r^6}\,. \tag{5.3}$$

We applied the direct summation method and the Fourier B method to obtain c_4 and c_6. In the latter we adopted the following form of the charge distribution:

$$\sigma(r)=(15/2\pi R^3)(1-r/R)^2. \tag{5.4}$$

The corresponding Fourier coefficients are

$$\sigma_h=\frac{60}{\gamma_h{}^4}\left(2+\cos\gamma_h-3\frac{\sin\gamma_h}{\gamma_h}\right),\quad \gamma_h=2\pi hR. \tag{5.5}$$

R was taken to be $a/4$ for the NaCl lattice and $\sqrt{3}\,a/4$ for the CsCl lattice, where a is the lattice constant. Results are summarized in Table I.

Table I.

method	NaCl-type		CsCl-type	
	c_4	c_6	c_4	c_6
Direct summation	−3.580	—	9.323	−4.298
Fourier B method	−3.58	—	9.31	−4.32
Bethe method	−3.58	−0.82	—	—
Least square	−3.75 (−3.22)	−1.73 (−0.80)	9.36	−4.38

The direct summation method is most convenient in the present case; it gives a good convergence. The Fourier method B does not give so good a convergence and moreover it demands a rather laborious calculation of the Bessel functions. It works better when applied to more complicated structures, as we shall see later.

Bethe's[6] calculation is based on the original Madelung's method of summing the Columb potential over a linear array of point charges, expressing the result as a series in Bessel functions, and summing it over all the linear chains in the crystal. He differentiated the result four times and six times to obtain c_4 and c_6. The convergence seems to be good in this method but it may not conveniently be applied to more complicated structures.

The method denoted as "least square" is due to Nagamiya[7], Nagamiya and Matsubara[8], and Nozawa[9]. The former two authors calculated values of the potential at a number of points in the neighbourhood of a lattice point by Ewald's formula and then determined the coefficients c_4 and c_6 by the method of least square. The last author employed the fact that the potential, including that due to the charge at the origin, vanishes on the planes which bisect the lines joining the origin to the neighbouring opposite charges. He determined the coefficients c_4 and c_6 through the requirement that the integral of the square of the potential, expressed as a linear combination of r^4Y_4 and r^6Y_6, over the polyhedron formed by these planes takes its minimum value. His values are quoted in parentheses.

§ 6. Application to Lattices of the Rutile Type

We further calculated the electric potential around a metallic ion in FeF_2 and CoF_2. Our object is obviously to investigate the electronic level splitting of these metallic ions in their crystals and to investigate the interesting antiferromagnetic properties of these crystals, but the result will be postponed to a next paper. We calculated the coefficients with $l=2$ and $l=4$, since these and only these are effective for the level splitting of Fe^{++} and Co^{++} in which outer electrons are in $3d$ orbits, provided the wave function is written in a product form.

The metallic ions constitute a body-centred tetragonal lattice and the fluorine ions are situated at

$$(\pm ua,\ \mp ua,\ 0) \quad \text{and} \quad (\pm a/2\mp ua,\ \pm a/2\mp ua,\ c/2)$$

if the body-centre is taken as the origin. We shall take the x-axis in the [110]-direction, the y-axis in the [$\bar{1}$10]-direction and the z-axis in the [001]-direction. The potential around the origin, which is orthorhombic, can then be expressed as

$$\varphi(\boldsymbol{r})=A(x^2-y^2)+B(3z^2-r^2)+D[(x^4+y^4+z^4)-(3/5)r^4]$$
$$+F[z^4-6(x^2+y^2)z^2+(3/5)r^4]+G[-x^4+y^4+6(x^2-y^2)z^2]\,, \tag{6.1}$$

where

$$A=3c_{22}\,,\quad B=\frac{1}{2}c_{20}\,,\quad D=420\,c_{44}\,,\quad F=\frac{5}{8}c_{40}-105\,c_{44}\,,\quad G=\frac{15}{2}c_{42}\,. \tag{6.2}$$

There is an electric field at the position of F^-, which directs from the F^- to the adjacent metallic ion. Therefore each F^- is polarized. This polarization in turn produces an electric field at the position of each F^-. We have therefore to determine this polarization of F^- in a consistent manner. We assume for the polarizablity of F^- the value given by Pauling[10] and alternatively the value given by Shockley[11]:

$$1.04\ \text{Å}^3\ \text{(Pauling)}, \qquad 0.759\ \text{Å}^3\ \text{(Shockley)}\,.$$

The coefficients A, B, D, F, G and the fluorine induced dipole-moment p were calculated by the direct summation method and the Fourier A method. p was assumed to be a point dipole moment. In the Fourier A method, it was assumed

$$\sigma(r)=\tau(r)=(15/4\pi R^3)[3(1-r/R)^2-2(1-r/R)^3]\,, \tag{6.3}$$

which is characterized by $\sigma'(0)=\tau'(0)=0$ and $\sigma'(R)=\tau'(R)=0$. The corresponding Fourier coefficient is

$$\sigma_h=\tau_h=\frac{90}{\gamma_h^4}\left[\cos\gamma_h-5\frac{\sin\gamma_h}{\gamma_h}+\frac{8}{\gamma_h^2}(1-\cos\gamma_h)\right].\qquad(\gamma_h=2\pi hR)\tag{6.4}$$

R was taken to be the same for all the positive and negative ions and its value was so determined that the adjacent spheres touch each other.

The results of the numerical calculation are summarized in Table II and III.

Table II. FeF_2; $a=4.670$ A, $c=3.297$ A, $u=0.31$.

	direct summation	Fourier A method
Field at F^- (e/A^2)	$0.029+0.11p$	$0.0251+0.1196p$
A (e/A^3)	$0.0359+0.2889p$	$0.0355+0.2929p$
B (e/A^3)	$-0.0157+0.2751p$	$-0.0160+0.2788p$
D (e/A^5)	$-0.1261-0.2968p$	$-0.1292-0.3042p$
F (e/A^5)	$0.0366+0.0625p$	$0.0381+0.0622p$
G (e/A^5)	$-0.0562+0.0073p$	$-0.0560+0.0078p$
p (eA) Pauling	0.034	0.0298
Shockley	0.024	0.0210

Table III. CoF_2; $a=4.69$ A, $c=3.19$ A, $u=0.31$.

	direct summation	Fourier A method
Field at F^- (e/A^2)	$0.0636+0.1268p$	$0.0657+0.1193p$
A (e/A^3)	$0.0227+0.2974p$	$0.0213+0.2975p$
B (e/A^3)	$-0.0135+0.2911p$	$-0.0141+0.2925p$
D (e/A^5)	$-0.1307-0.2888p$	$-0.1298-0.2946p$
F (e/A^5)	$0.04405+0.0555p$	$0.0438+0.0554p$
G (g/A^5)	$-0.0603+0.0203p$	$-0.0604+0.0214p$
p (eA) Pauling	0.0762	0.0780
Shockley	0.0534	0.0548

In the method of direct summation we determined the coefficients of x^2, z^2, x^4, y^4, z^4 from whose combination we could get A, B, D, F, G. All the contributions from the charges in a rectangular parallelpiped of edges of lengths $3a$, $3a$, $5c$ were taken into account, the next unit cells on the z-axis were added in calculating the coefficients of the second and fourth degrees, and the contributions from a few further cells in the xy-plane were added in calculating the field at F^-. In the Fourier method A, we determined A, B, D, G and $(2/5)D+(8/5)F=c_{40}$, and the summation was extended up to about $h=\sqrt{43}/a$. Tables II and III show that these two methods yield numerical results which agree within two or three effective figures. The Fourier method gives a better convergence when applied to the calculation of the field at F^- and to the coefficients of the second degree, while the direct summation method appears to give slightly more reliable data for the coefficients of the fourth degree.

§ 7. Merits and Dismerits of Various Methods

1. The direct summation method is excellent when applied to simple structures and to coefficients of higher degrees. The convergence is better for higher degrees and for higher symmetry of the structure. It may not be effective when the symmetry of the crystal structure is low and the degree of the coefficient is also low. It may also not be convenient when the crystal structure is complicated.

2. The Fourier method is powerful even when the structure is complicated, since it makes use of the structure factor. There is no fear of carelessly dropping out some of

the contributions or erroneously counting them; we actually at first committed error in applying the direct summation method to the crystal of FeF_2, by erroneously taking the sign of some of the fluorine dipole-moments, and later discovered this error by applying the Fourier method. The A method with $\sigma=\tau$ is simpler than the B method, and the distribution given by (6.3) can conveniently be used for the coefficients of degree four or lower. With a fixed distribution, the A method gives a worse convergence for higher coefficients, while the B method is applicable to any degree l. The latter is, however, more troublesome since it requires the calculation of the Bessel functions. If a detailed table of Bessel functions is available, it is as good a method. For simple structures of a high symmetry, the direct summation method leads faster to the result, but if one is concerned with coefficients of different degrees at the same time, there is an advantage in the Fourier A method in that one can use the same coefficients for all l in the series (3.14), (3.15) and (3.16).

3. The well-known Ewald method gives an excellent convergence. The formula contains an adjustable parameter, and one can test the correctness of the calculation by adopting two different values of it. On the other hand, it is sometimes troublesome to find a suitable value of the parameter. The formula consists of a Fourier-like series and a direct summation-like series, and its differentiated formulas, such as given by Kornfeld[12], consist of many terms. Therefore the method cannot conveniently be applied to crystals of complicated structures and to higher coefficients. We think that the chief merit of this method consists in its excellent convergence.

4. The least square methods referred to in § 5 avoids the trouble of differentiating the Ewald formula four or six times, but the accuracy is not great.

5. Bethe s method, also referred to in § 5, does not seem to be convenient when applied to complicated structures.

The present work has been supported by a Grant in Aid from the Ministry of Education.

References

1) H. M. Evjen: Phys. Rev. **39** (1932) 675.
2) F. C. Frank: Phil. Mag. **41** (1950) 1287.
3) T. Nagamiya and T. Kisi: *Busseiron-Kenkyu* **25** (1950) 35 (in Japanese); *Collected Papers from the Fac. Sci. Osaka Univ.* Ser. B **12** (1950) (abstract).
4) F. Bertaut: Journ. de Phys. et Radium **13** (1952) 499.
5) F. Bertaut: Phys. Rev. **91** (1953) 415.
6) H. Bethe: Ann. d. Physik **3** (1929) 137.
7) T. Nagamiya: Proc. Phys.-Math. Soc. Japan 3rd Ser. **24** (1942) 137.
8) T. Nagamiya and T. Matsubara: *Scientific Papers from the Osaka Univ.* No. 14. (1949).
9) T. Nozawa: *Busseiron Kenkyu* **20** (1949) 1. (in Japanese.)
10) L. Pauling: Proc. Roy. Soc. (London) **A 114** (1927) 191.
11) J. R. Tessman, A. H. Kahn and W. Shockley: Phys. Rev. **92** (1953) 890.
12) H. Kornfeld: ZS. f. Physik **22** (1924) 27.

JOURNAL OF THE PHYSICAL SOCIETY OF JAPAN Vol. 10, No. 2, FEBRUARY, 1955

Non-empirical Calculation of the Diamagnetic Anisotropy of Benzene

By Takashi ITOH, Kimio OHNO and Hiroyuki YOSHIZUMI

Department of Physics, Faculty of Science,
University of Tokyo

(Received September 17, 1954)

The large anisotropy of the diamagnetic susceptibility of benzene, which is considered to be due to the free migration of π-electrons, is calculated by the antisymmetrized LCAO-MO method. We have included all the configurations obtained by excitation of one or two electrons from the lowest configuration and we have retained all the many-center integrals. The calculated value of the diamagnetic anisotropy is about 50% of the experimental value. The effect of configuration interaction is not small enough to be neglected.

§ 1. Introduction

It is well known that the diamagnetic anisotropies of conjugated organic molecules are very large. For instance, the values of the diamagnetic susceptibilities of benzene in the directions perpendicular and parallel to the plane of the molecule are -91×10^{-6} and -37×10^{-6} per mole respectively.

About twenty years ago, Pauling[1] treated this phenomenon as due to the free migration of π-electrons and obtained a good agreement with experiment by the semi-classical calculation. Immediately after Pauling's treatment, London[2] calculated quantum-mechanically the ratios of the diamagnetic anisotropies of several different planar aromatic hydrocarbons to that of benzene and again obtained a satisfactory agreement with experiment. But, in his calculation all the overlap integrals, even that between adjacent atomic orbitals, were neglected and the value of resonance integral was chosen so as to fit the value of the diamagnetic anisotropy of benzene to the experimental value. A few years later, Brooks[3] improved on London's calculation, by taking the overlap integrals between adjacent orbitals into account and recently some modifications of the values of the overlap and other integrals were introduced by Wheland and Matlov[4]. Brooks[5] attacked the same problem by the valence bond method, but his result was not so good in spite of the complexity of his calculation.

The non-empirical calculation of the absolute value of the diamagnetic anisotropy of benzene was first tried, so far as we know, by Kambe[6]. He calculated the energy of the ground state of a benzene molecule in the external magnetic field by the LCAO-ASMO method[7], but neglected all three- and four-center integrals and the calculated value of the diamagnetic anisotropy was 30% of the experimental one. Fujii and Shida[8] tried the same calculation independently and they included almost all these integrals in their computation*.

On the other hand, the importance of the configuration interaction in the ASMO treatment has been emphasized by Craig[9] and others for the past three years. We, therefore, thought it interesting to recalculate the diamagnetic anisotropy of benzene non-empirically taking configuration interaction into account and to obtain a more precise result within the range of π-electron approximation.

§ 2. The Hamiltonian and the Wave Functions

The $2p\pi$ electrons of the benzene molecule, which are responsible for the large diamagnetic anisotropy, are assumed to be in the field of the benzene skeleton consisting of six carbon ions viz. carbon atoms stripped of their $2p\pi$ electrons. The potential V_ν of the benzene skeleton acting on the ν-th electron can be expressed as the sum of the contributions from each ion:

$$V_\nu=\sum_{k=1}^{6} V_{\nu k}\ ,$$

---

* Unfortunately there were some numerical errors in their paper. For example, the values of the second derivatives with respect to the magnetic field H of $\varepsilon_{\pm1}$ and γ_{11} in column C of their Table II are in error numerically, and after correcting them, the final value of the diamagnetic anisotropy becomes 61% instead of 74% of the experimental value.

where $V_{\nu k}$ is the mutual potential between the ν-th electron and the k-th ion.

In the presence of magnetic field, the hamiltonian of the system is expressed as

$$\mathscr{H}=\sum_{\nu=1}^{6}\left\{\frac{h^2}{8\pi^2 m}(i\nabla_\nu+\boldsymbol{\alpha}_\nu)^2+V_\nu\right\}+\sum_{\substack{\mu,\nu=1\\ \mu<\nu}}^{6}\frac{e^2}{r_{\mu\nu}}\,, \tag{1}$$

where $\boldsymbol{\alpha}_\nu$ is the value of the vector potential $\boldsymbol{A}_\nu$ at the position of the ν-th electron multiplied by $2\pi e/hc$. The vector potential $\boldsymbol{A}_\nu$ which represents an uniform magnetic field $\boldsymbol{H}$ is given by

$$\boldsymbol{A}_\nu=\tfrac{1}{2}\boldsymbol{H}\times\boldsymbol{r}_\nu\ .$$

The origin of the coordinate $\boldsymbol{r}_\nu$ in the expression of the vector potential is not determined uniquely. Correspondingly the wave function varies with the choice of the coordinate origin (gauge transformation). In our case, it is most convenient to take the origin at the center of the molecule. Then the atomic orbitals to be used have the form

$$\exp(i\boldsymbol{\alpha}_k\cdot\boldsymbol{r}_\nu)\chi_k(\boldsymbol{r}_\nu),$$

where $\boldsymbol{\alpha}_k$ is the vector potential at the k-th nucleus multiplied by $2\pi e/hc$, and $\chi_k(\boldsymbol{r}_\nu)$ is the atomic eigenfunction of the k-th atom when the origin is taken at the k-th nucleus.

From the six atomic orbitals the following six molecular orbitals can be formed

$$\phi_l(\boldsymbol{r}_\nu)=(6\sigma_l)^{-1/2}\sum_k\exp\{(2\pi i/6)lk+i\boldsymbol{\alpha}_k\cdot\boldsymbol{r}_\nu\}\times\chi_k(\boldsymbol{r}_\nu)\,, \tag{2}$$

with $l=0,\ \pm1,\ \pm2,\ 3,\ (6\sigma_l)^{-1/2}$ being the normalization factor. Since we are concerned with the case of an uniform magnetic field perpendicular to the molecular plane, $\boldsymbol{\alpha}_k$ is a circularly rotating vector around the center of benzene ring. Then, the above molecular orbitals belong to the irreducible representation of the point group C_{6h} instead of D_{6h}. The hamiltonian also has the symmetry of C_{6h}.

In the lowest configuration ϕ_0 and $\phi_{\pm1}$ are fully occupied, and the symmetry property of the whole wave function is A_g. Of the other configurations, therefore, we have only to consider those which have the same symmetry A_g. There are no such configurations obtained by the elevation of one electron from the lowest configuration. So, we take the eleven A_g configurations obtained by excitation of two electrons. Other configurations where more than two electrons are excited are neglected from energetical consideration. All twelve A_g wave functions considered are given in Table I.

Table I. A_g wave functions

A_{1g} configuration functions [a], [c]

$$\psi_1=(\phi_0^2\ \phi_1^2\ \phi_{-1}^2)$$

$$\psi_2=(\phi_0^2\ \overline{\phi_1\ \phi_{-1}}\ \overline{\phi_2\ \phi_{-2}})$$

$$\psi_3=\frac{2}{\sqrt{3}}(\phi_0^2\ \underline{\phi_1\ \overline{\phi_{-1}\ \phi_2}}\ \overline{\phi_{-2}})-\frac{1}{\sqrt{3}}(\phi_0^2\ \overline{\phi_1\ \phi_{-1}}\ \overline{\phi_2\ \phi_{-2}})$$

$$\psi_4=(\phi_0^2\ \overline{\phi_1\ \phi_{-1}}\ \phi_3^2)$$

$$\psi_5=(\phi_1^2\ \phi_{-1}^2\ \overline{\phi_2\ \phi_{-2}})$$

$$\psi_6=(\phi_1^2\ \phi_{-1}^2\ \phi_3^2)$$

$$\psi_7=\sqrt{\frac{1}{2}}(\phi_0^2\ \phi_1^2\ \phi_2^2)+\sqrt{\frac{1}{2}}(\phi_0^2\ \phi_{-1}^2\ \phi_{-2}^2)$$

$$\psi_8=\sqrt{\frac{1}{2}}(\overline{\phi_0\ \phi_1^2\ \phi_{-1}}\ \overline{\phi_2\ \phi_3})+\sqrt{\frac{1}{2}}(\overline{\phi_0\ \phi_1}\ \phi_{-1}^2\ \overline{\phi_{-2}\ \phi_3})$$

$$\psi_9=\sqrt{\frac{2}{3}}(\underline{\phi_0\ \phi_1^2\ \overline{\phi_{-1}\ \phi_2}}\ \overline{\phi_3})+\sqrt{\frac{2}{3}}(\underline{\phi_0\ \overline{\phi_1\ \phi_{-1}^2\ \phi_{-2}}}\ \overline{\phi_3})$$
$$-\sqrt{\frac{1}{6}}(\overline{\phi_0\ \phi_1^2\ \phi_{-1}}\ \overline{\phi_2\ \phi_3})-\sqrt{\frac{1}{6}}(\overline{\phi_0\ \phi_1}\ \phi_{-1}^2\ \overline{\phi_{-2}\ \phi_3})$$

A_{2g} configuration functions [b], [c]

$$\psi_{1'}=\sqrt{\frac{1}{2}}(\phi_0^2\ \phi_1^2\ \phi_2^2)-\sqrt{\frac{1}{2}}(\phi_0^2\ \phi_{-1}^2\ \phi_{-2}^2)$$

$$\psi_{2'}=\sqrt{\frac{1}{2}}(\overline{\phi_0\ \phi_1^2\ \phi_{-1}}\ \overline{\phi_2\ \phi_3})-\sqrt{\frac{1}{2}}(\overline{\phi_0\ \phi_1}\ \phi_{-1}^2\ \overline{\phi_{-2}\ \phi_3})$$

$$\psi_{3'}=\sqrt{\frac{2}{3}}(\underline{\phi_0\ \phi_1^2\ \overline{\phi_{-1}\ \phi_2}}\ \overline{\phi_3})-\sqrt{\frac{2}{3}}(\underline{\phi_0\ \overline{\phi_1\ \phi_{-1}^2\ \phi_{-2}}}\ \overline{\phi_3})$$
$$-\sqrt{\frac{1}{6}}(\overline{\phi_0\ \phi_1^2\ \phi_{-1}}\ \overline{\phi_2\ \phi_3})+\sqrt{\frac{1}{6}}(\overline{\phi_0\ \phi_1}\ \phi_{-1}^2\ \overline{\phi_{-2}\ \phi_3})$$

---

[a] These functions reduce to A_{1g} functions when magnetic field is removed.

[b] These functions reduce to A_{2g} functions when magnetic field is removed.

[c] Hooked lines connecting singly occupied orbitals show that the spins of electrons in these orbitals are paired. For example,

$$(\phi_1^2\ \phi_{-1}^2\ \overline{\phi_2\ \phi_{-2}})=\frac{1}{\sqrt{2}}(\phi_1\ \bar{\phi}_1\ \phi_{-1}\ \bar{\phi}_{-1}\ \phi_2\ \bar{\phi}_{-2})$$
$$-\frac{1}{\sqrt{2}}(\phi_1\ \bar{\phi}_1\ \phi_{-1}\ \bar{\phi}_{-1}\ \bar{\phi}_2\ \phi_{-2})$$

where bar denotes β spin.

Since these A_g wave functions reduce to A_{1g} and A_{2g} functions as soon as the magnetic field is removed, we have shown them in two groups in Table I. The two groups of wave functions will be called simply A_{1g} functions and A_{2g} functions respectively even in the presence of an external magnetic field so long as this leads to no ambiguity. Thus, there are nine A_{1g} functions and three A_{2g} functions.

The above classification is convenient because some differences between the two kinds of wave functions exist as follows. When we expand the wave functions in Table I in powers of magnetic field H, the following results are obtained. In the case of the A_{1g} wave functions, terms of even powers have the symmetry A_{1g} and terms of odd powers have the symmetry A_{2g}, while in the case of A_{2g} wave functions they are reversed. Furthermore similar expansion of the hamiltonian (1) shows that it has the same property as A_{1g} wave functions:

$$\begin{aligned}\psi_i(A_{1g})&=\psi_i^{(0)}(A_{1g})+\psi_i^{(1)}(A_{2g})\cdot H\\&\quad+\psi_i^{(2)}(A_{1g})\cdot H^2+\cdots,\\ \psi_{i'}(A_{2g})&=\psi_{i'}^{(0)}(A_{2g})+\psi_{i'}^{(1)}(A_{1g})\cdot H\\&\quad+\psi_{i'}^{(2)}(A_{2g})\cdot H^2+\cdots,\\ \mathscr{H}&=\mathscr{H}^{(0)}(A_{1g})+\mathscr{H}^{(1)}(A_{2g})\cdot H\\&\quad+\mathscr{H}^{(2)}(A_{1g})\cdot H^2+\cdots.\end{aligned} \tag{3}$$

Considering these relations, we find that the matrix elements of the hamiltonian among A_{1g} states or among A_{2g} states are even functions of H, and matrix elements between A_{1g} and A_{2g} states are odd functions of H. We will refer to this later.

§ 3. Calculation of Matrix Elements

The matrix elements of the hamiltonian can be expressed in terms of the integrals over molecular orbitals using the standard method. The integrals which appear in the calculation are the orbital energies,

$$\varepsilon_l=\int\phi_l^*(\boldsymbol{r}_\nu)\left\{\frac{h^2}{8\pi^2m}(i\boldsymbol{\nabla}_\nu+\boldsymbol{\alpha}_\nu)^2+V_\nu\right\}\phi_l(\boldsymbol{r}_\nu)d\tau_\nu\ ,$$

and the coulomb-exchange integrals,

$$\gamma_{ll'}=\iint\phi_l^*(\boldsymbol{r}_\mu)\,\phi_l(\boldsymbol{r}_\mu)\,\frac{e^2}{r_{\mu\nu}}\,\phi_{l'}^*(\boldsymbol{r}_\nu)\phi_{l'}(\boldsymbol{r}_\nu)d\tau_\mu d\tau_\nu\ ,$$

$$\delta_{ll'}=\iint\phi_l^*(\boldsymbol{r}_\mu)\phi_{l'}(\boldsymbol{r}_\mu)\,\frac{e^2}{r_{\mu\nu}}\,\phi_{l'}^*(\boldsymbol{r}_\nu)\phi_l(\boldsymbol{r}_\nu)d\tau_\mu d\tau_\nu\ ,$$

$$\bar{\zeta}_{pq}^{mn}=\iint\phi_m^*(\boldsymbol{r}_\mu)\,\phi_n(\boldsymbol{r}_\mu)\,\frac{e^2}{r_{\mu\nu}}\,\phi_p^*(\boldsymbol{r}_\nu)\phi_q(\boldsymbol{r}_\nu)d\tau_\mu d\tau_\nu\ .$$

When these integrals are decomposed into integrals over atomic orbitals, we have integrals such as

$$\iint\exp\{i(\boldsymbol{\alpha}_u-\boldsymbol{\alpha}_t)\cdot\boldsymbol{r}_\mu\}\chi_t^*(\boldsymbol{r}_\mu)\chi_u(\boldsymbol{r}_\mu)\frac{e^2}{r_{\mu\nu}}\exp\{i(\boldsymbol{\alpha}_w-\boldsymbol{\alpha}_v)\cdot\boldsymbol{r}_\nu\}\chi_v^*(\boldsymbol{r}_\nu)\chi_w(\boldsymbol{r}_\nu)d\tau_\mu d\tau_\nu. \tag{4}$$

Since they involve the vector potential in the integrand, the direct evaluation is very complicated. Thus many authors have used the approximation to replace $\boldsymbol{r}_\mu$ and $\boldsymbol{r}_\nu$ in the exponential factors by their mean values $(\boldsymbol{R}_t+\boldsymbol{R}_u)/2$ and $(R_v+R_w)/2$ respectively where R_t, R_u, R_v and R_w are the positions of the nuclei. Although this approximation may not be ensured from the strict point of view, we will also use it in this paper for simplicity of calculation. Then the above integral reduces to

$$\exp\{2\pi i(f_{ut}+f_{wv})\}\iint\chi_t^*(\boldsymbol{r}_\mu)\chi_u(\boldsymbol{r}_\mu)\,\frac{e^2}{r_{\mu\nu}}\,\chi_v^*(\boldsymbol{r}_\nu)\chi_w(\boldsymbol{r}_\nu)d\tau_\mu d\tau_\nu\ , \tag{5}$$

where $2\pi f_{wv}$ and $2\pi f_{wv}$ are given by

$$2\pi f_{21}=2\pi f_{31}=-(2\pi e/hc)(S/6)\equiv\eta\ ,\qquad 2\pi f_{41}=0\ ,$$

S being the area of the benzene ring.

Using this approximation we obtain the following formulas for the integrals over molecular orbitals in terms of integrals over atomic orbitals

$$\sigma_l=1+2S_{12}\cos\left(\frac{2\pi l}{6}+\eta\right)+2S_{13}\cos\left(\frac{4\pi l}{6}+\eta\right)+(-1)^lS_{14}\ ,$$

$$\varepsilon_l=W_{2p}'+\sigma_l^{-1}\left\{H_{11}+2H_{12}\cos\left(\frac{2\pi l}{6}+\eta\right)+2H_{13}\cos\left(\frac{4\pi l}{6}+\eta\right)+(-1)^lH_{14}\right\}\ ,$$

$$\bar{\zeta}_{pq}^{mn}=\frac{1}{6}(\bar{\sigma}_m\sigma_n\bar{\sigma}_p\sigma_q)^{-1/2}\sum C_{tuvw}(tu\,|\,vw)\ ,$$

where

$$C_{tuvw}=\frac{s_t}{8s_m}\left\{2\cos\left[\frac{2\pi}{6}(-mt+nu-pv+qw)+2\pi(f_{ut}+f_{wv})\right]\right.$$

$$
\begin{aligned}
&+2\cos\left[\frac{2\pi}{6}(-mt+nu+qv-pw)+2\pi(f_{ut}+f_{vw})\right]\\
&+2\cos\left[\frac{2\pi}{6}(nt-mu-pv+qw)+2\pi(f_{tu}+f_{wv})\right]\\
&+2\cos\left[\frac{2\pi}{6}(nt-mu+qv-pw)+2\pi(f_{tu}+f_{vw})\right]\\
&+2\cos\left[\frac{2\pi}{6}(-pt+qu-mv+nw)+2\pi(f_{ut}+f_{wv})\right]\\
&+2\cos\left[\frac{2\pi}{6}(-pt+qu+nv-mw)+2\pi(f_{ut}+f_{vw})\right]\\
&+2\cos\left[\frac{2\pi}{6}(qt-pu-mv+nw)+2\pi(f_{tu}+f_{wv})\right]\\
&+2\cos\left[\frac{2\pi}{6}(qt-pu+nv-mw)+2\pi(f_{tu}+f_{vw})\right]\Bigg\}\,.
\end{aligned}
$$

W_{2p}' means the energy of a $2p\pi$ electron of an isolated carbon atom in the magnetic field. s_l and s_m are the symmetry numbers defined by Parr, Craig and Ross10). $\gamma_{ll'}$ and $\delta_{ll'}$ are not given above, since they are special cases of ζ^{mn}_{pq}.

The basic integrals over atomic orbitals, appearing in the above formulas, are defined by

$$S_{tu}=\int\chi_t^*(\boldsymbol{r}_\nu)\chi_u(\boldsymbol{r}_\nu)d\tau_\nu\,,$$

$$(t:vw)=-\int U_t(\boldsymbol{r}_\nu)\chi_v^*(\boldsymbol{r}_\nu)\chi_w(\boldsymbol{r}_\nu)d\tau_\nu\,,$$

$$(tu|vw)=\iint\chi_t^*(\boldsymbol{r}_\mu)\chi_u(\boldsymbol{r}_\mu)\frac{e^2}{r_{\mu\nu}}\chi_v^*(\boldsymbol{r}_\nu)\chi_w(\boldsymbol{r}_\nu)\times d\tau_\mu d\tau_\nu\,,$$

$$H_{tu}=-\sum_{\substack{v=1\\ v\neq u}}^{6}[(v:tu)+(tu|vv)]\,,$$

where U_t is the potential of the neutral carbon atom t.

It must be noted that the atomic eigenfunctions of the atoms in the magnetic field are not the same as the eigenfunctions of the zero-field case. But since the difference is very small, we neglect it and merely use the atomic orbitals of the zero-field case. These atomic orbitals may, in turn, be approximated by the usual Slater type functions with the effective charge $Z=3.18$. Then all the necessary integrals over atomic orbitals are given in the paper by Parr, Craig and Ross10).

§ 4. Calculation of the Diamagnetic Anisotropy

In the absence of a magnetic field, the 12×12 secular determinant factors into 9×9 A_{1g} and 3×3 A_{2g} determinants, and the ground state wave function is obtained as a linear combination of nine A_{1g} functions:

$$
\begin{aligned}
\psi_g=\sum_{i=1}^{9}c_i\psi_i=\;&0.910\psi_1+0.210\psi_2+0.142\psi_3\\
&+0.052\psi_4-0.056\psi_5-0.059\psi_6-0.227\psi_7\\
&+0.204\psi_8+0.069\psi_9.
\end{aligned}
\tag{6}
$$

When magnetic field is applied, we must consider three A_{2g} configurations in addition to nine A_{1g} configurations. For the present, however, we neglect A_{2g} configurations, and consider the 9×9 A_{1g} secular equation. The energy of the system depends on the magnetic field through the coefficients as well as through the matrix elements of the hamiltonian. Since the coefficients and matrix elements are even functions of H, the energy of the state can be expressed as a power series in H^2. Furthermore, since in general the energy of an eigenfunction is stationary with respect to a small variation of the coefficients, the contribution to the energy from the variation of the coefficients is proportional to H^4, and is irrelevant to the diamagnetic susceptibility. Thus, we regard the coefficients as constant, and obtain the diamagnetic anisotropy

$$\Delta\chi_{\mathrm{I}}\ (\text{with } A_{1g}\ \text{C.I.})=-\left(\frac{\partial^2(W_g-W_0)}{\partial H^2}\right)_{H=0},$$

where

$$W_g=\sum_{i,j=1}^{9}c_i^*c_j\int\psi_i^*\mathscr{H}\psi_j d\tau\,,$$

and

$$W_0=6W_{2p}'\,.$$

The coefficients c_i can be taken from (6). The term W_0 gives the diamagnetic susceptibility parallel to the molecular plane. This term was subtracted from W_g to give the diamagnetic anisotropy. The result of calculation is given in Table II. The value of the diamagnetic anisotropy for the single configuration function ψ_1 is also given.

The effect of A_{2g} configuration can be treated by the second order perturbation method and the contribution to the diamagnetic anisotropy is given by

$$\Delta\chi_{\mathrm{II}} = -\left[\frac{\partial^2}{\partial H^2}\left(\sum_{i'=1'}^{3'} \frac{|(\psi_g|\mathscr{H}|\psi_{i'})|^2}{W_g - W_{i'}}\right)\right]_{H=0},$$

where $\psi_{i'}$ are the three A_{2g} configuration functions.

The total diamagnetic anisotropy $\Delta\chi$ of the benzene molecule is obtained by adding $\Delta\chi_{\mathrm{I}}$ and $\Delta\chi_{\mathrm{II}}$. The result is given in Table II. The effect of configuration interaction is, as can be seen, not large, but cannot be neglected. The experimental value of diamagnetic anisotropy is also given for the purpose of comparison.

Table II.

$\Delta\chi_{\mathrm{I}}'$ [a]	$-21.70\times\left(\frac{2\pi eS}{6hc}\right)^2$	64.0%
$\Delta\chi_{\mathrm{I}}$ [b]	-20.13	59.4%
$\Delta\chi_{\mathrm{II}}$ [c]	3.31	$-$ 9.8%
$\Delta\chi=\Delta\chi_{\mathrm{I}}+\Delta\chi_{\mathrm{II}}$	-16.82	49.6%
$\Delta\chi_{\mathrm{exp}}$	-33.9	100 %

[a] The value when only the ground configuration is considered.

[b] The value with configuration interaction among nine A_{1g} states.

[c] Contribution from three A_{2g} states.

§ 5. Discussions

As is seen in Table II, the final value is about 50% of the observed one.

In order to refine the calculation, the proper consideration of the following points will be necessary.

1. We used LCAO approximation and Slater type atomic orbitals. It is probable that these approximations are not suitable for the calculation of the diamagnetic susceptibility although they may be good for the energy calculation.

2. The approximation to the integrals containing the vector potential was introduced solely for simplicity of calculation. London[2] originally used this approximation for the case of the adjacent atoms, but we extended it to the non-adjacent atoms, although the approximation may not be so good for the latter case.

3. The σ-π interaction may contribute to the anisotropy to some extent. However, σ-electrons are expected to prevent the free migration of π-electrons along the benzene ring, in other words, if we include this interaction, the anisotropy will diminish.

4. The values of the many center integrals given in the paper by Parr, Craig and Ross[10] were calculated using the Sklar approximation[11]. As the contribution to the susceptibility from these integrals proved to be rather large, a small error in these integrals may affect the final result appreciably.

We express our hearty thanks to Prof. M. Kotani for his continued interest in the problem; to the members of Kotani Laboratory, Assistant Professors K. Kambe and K. Niira, and Dr. S. Fujii for valuable discussions. We are indebted to Prof. D. P. Craig who sent us the unpublished computations from his paper[10], and to Dr. M. Mizushima who read the manuscript.

References

1) L. Pauling: J. Chem. Phys. **4** (1930) 673.
2) F. London: J. de Phys. et Rad. **8** (1937) 397.
3) H. Brooks: J. Chem. Phys. **9** (1941) 463.
4) W. Wheland and S. L. Matlow: Proc. Nat. Acad. Sci. **38** (1952) 364.
5) H. Brooks: J. Chem. Phys. **8** (1940) 939.
6) K. Kambe: *Report of the University of Electro-Communication* No. 1 (1951) 143 (in Japanese).
7) M. G. Mayer and A. L. Sklar: J. Chem. Phys. **6** (1938) 645.
8) S. Fujii and S. Shida: Bull. Chem. Soc. Japan **24** (1951) 242.
9) D. P. Craig: Proc. Roy. Soc. (London), A **200** (1950) 474.
10) R. G. Parr, D. P. Craig and I. G. Ross: J. Chem. Phys. **18** (1950) 1561.
11) A. L. Sklar: J. Chem. Phys. **7** (1939) 984.

Journal of the Physical Society of Japan Vol. 10, No. 2, February, 1955

Dielectric Properties of Lead·Strontium Titanate

By Shoichiro Nomura and Shozo Sawada
Institute of Science and Technology, University of Tokyo

(Received August 26, 1954)

The dielectric and thermal properties and lattice dimensions of lead·strontium titanate were investigated, the solid solution being realized in the whole range of molar percentage. It was found that lead·strontium titanate is also ferroelectric as lead·barium titanate and barium·strontium titanate. As the content of Sr^{2+} increases, the lattice volume and tetragonality decrease. The Curie temperature decreases linearly with the increase of the content of Sr^{2+} and any other transition point was not observed. Curie-Weiss formula holds above Curie temperature, the value of Curie constant being $(3\sim9)\times10^4$°C.

§ 1. Introduction

The investigations of the solid solutions of titanates have been performed on barium·strontium titanate, barium·lead titanate, etc. and several reports have been already published1),2),3),4),5). As well known, barium titanate is ferroelectric below 120°C and has two other transitions at about 5°C and −70°C respectively. Lead titanate is ferroelectric below about 500°C and there does not exist any other transition point for this substance. Strontium titanate, on the other hand, is believed to be non-ferroelectric, although some authors insist that it becomes ferroelectric very near the absolute zero temperature6). In the case of barium·lead titanate, the Curie temperature moves to the higher temperature side, while 5°C and −70°C transitions to the lower side, and thus the tetragonal region extends, in proportion to molar ratio of lead titanate. In barium·strontium titanate the contrary effect is observed. Considering these situations, it seems to be interesting to investigate lead·strontium titanate as another example of $Me^{2+}TiO_3$. We investigated the dielectric and thermal properties for several samples of lead·strontium titanate; $PbTiO_3$ $(70Pb\cdot30Sr)TiO_3$, $(50Pb\cdot50Sr)TiO_3$, $(30Pb\cdot70Sr)TiO_3$, $(10Pb\cdot90Sr)TiO_3$, in the temperature range from liquid air temperature to 500°C. It is expected that the whole range solid solutions observed in both barium·lead titanate and barium·strontium titanate will be also realized in lead·strontium titanate, as the atomic radii of these cations are nearly the same.

§ 2. Preparation of Samples

Strontium and lead titanates ceramics (chemical pure) were prepared separately by our usual method2), firing temperature being about 1250°C and 1100°C respectively. On firing lead titanates an attention must be paid to prevent it from reduction and evaporation of PbO. As the evaporation of PbO begins at comparatively low temperature, the firing time must be rather short. Being pulverized, mixed in a necessary molar concentration and pressed into a disk, the mixture was refired at 1150°C∼1350°C for a few hours. As the content of lead titanate increases, sintered samples become brittle because of growth of crystals which are easily observed by the microscope and are very similar in their appearance to that of single crystals prepared by our method previously reported7).

§ 3. Permittivity

Our method of measurement of the dielectric constant is a tuning method, where the frequency is 1043 kc/sec. Samples were put into a vacuum vessel in order to avoid the influence of moisture. All measurements were carried out after heating the sample up to 150°C by a furnace in the vessel. Fig. 1 shows one series of permittivity of lead·strontium titanate with various molar concentration in the temperature range from −150°C to 300°C. The dielectric anomalies at room temperature, which were reported in our former letter8), were perhaps due to moisture. In the present case there is no humps on the permittivity-temperature curves near room temperature. As the content of strontium titanate increases, the absolute value of permittivity becomes larger, and the peak value of (70 Sr·30 Pb)TiO_3 becomes 4000. The relation between Curie temperature and molar ratio is a straight line, which is illustrated in Fig. 2. Curie-Weiss formula holds above Curie temperature,

that is $\varepsilon = C/(T-T_c)$

where C and T_c are constants to be determined experimentally for each molar percentage. Fig. 3 shows the variation of C with the molar ratio. The value of C is 3×10^4°C on the side of strontium titanate and approaches 9×10^4°C on the opposite side, these results being consistent with those obtained formerly in our studies on barium·lead titanate and barium·strontium titanate[2].

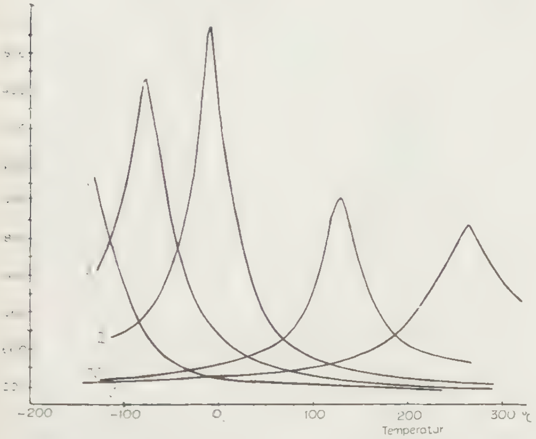

(I) (90Sr·10Pb)TiO_3 (II) (80Sr·20Pb)TiO_3
(III) (70Sr·30Pb)TiO_3 (IV) (50Sr·50Pb)TiO_3
(V) (30Sr·70Pb)TiO_3

Fig. 1. Permittivity vs. temperature.

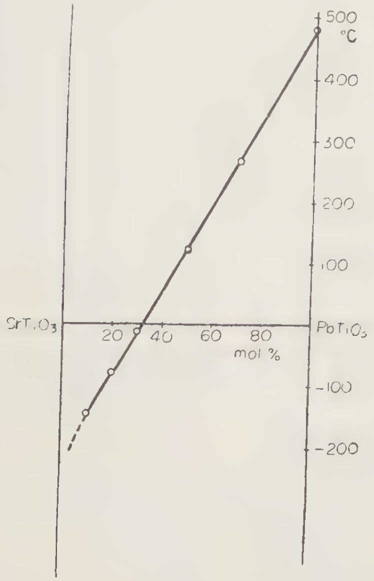

Fig. 2. Curie temperature vs. molar percentage.

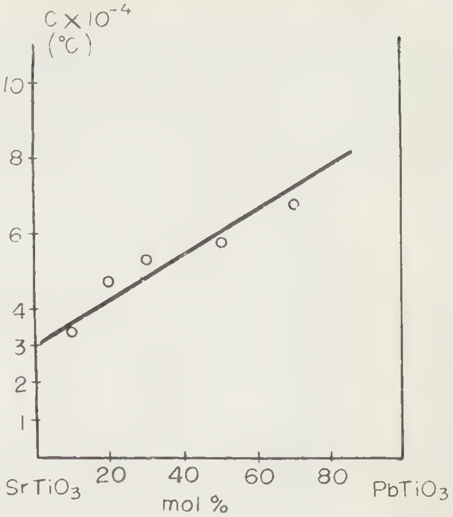

Fig. 3. Curie constant vs. molar percentage.

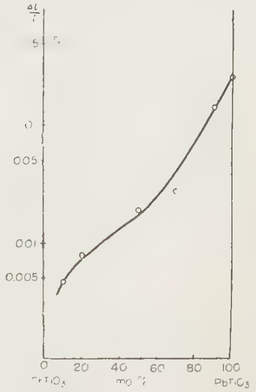

Fig. 4. Amount of thermal contraction vs. molar percentage.

§ 4. Thermal Expansion and Specific Heat

The linear thermal expansion were observed by the dilatometer used in our studies on barium titanate[9),10)], etc. In the case of $PbTiO_3$, a monotonous contraction is observed from room temperature, and its thermal expansion coefficient has a sharp negative peak, which amounts to -28×10^{-6} 1/deg, at the Curie temperature. As the content of strontium titanate increases, the value of linear thermal expansion coefficient in the ferroelectric region increases, and the value of the negative peak decreases. The value of the linear thermal expansion coefficient in the cubic region are 7∼10×10^{-6} 1/deg, the values of which are the same order with those of barium·lead titanate ceramics. Fig. 4 shows the change of $\Delta l/l$, that is the integrated relative contraction involved in the anomalous region, plotted against the molar ratio, where the vertical axis is measured with a logarithmic scale.

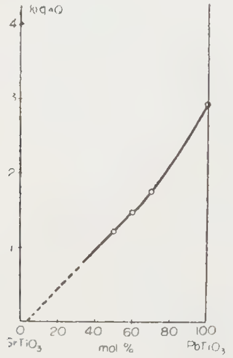

Fig. 5. Anomalous heat (cal/mol) vs. molar percentage.

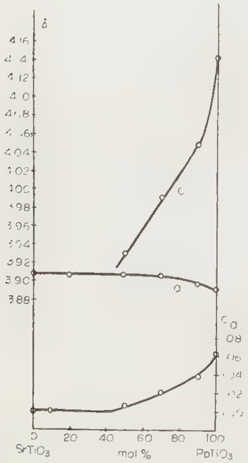

Fig. 6. Lattice constants vs. molar percentage.

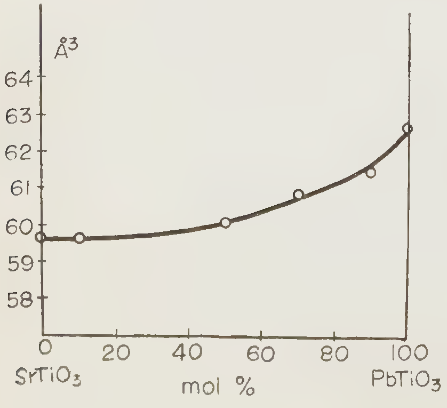

Fig. 7. Lattice volume vs. molar percentage.

The conduction calorimeter[10)] was used for the measurement of specific heat. Fig. 5 shows the relation between the anomalous heat and molar concentration, where 17 cal/mol for (50Pb·50Sr)TiO_3, 55 cal/mol for (70Pb·30Sr)TiO_3 and 900 cal/mol for $PbTiO_3$. In $PbTiO_3$, the anomaly of specific heat was observed to begin at 350°C and lasted to a high temperature about 50°C above Curie temperature, so that it is difficult to determine the accurate amount of anomalous heat, which has been reported as 1100 cal/mol by G. Shirane[11)].

§ 5. X-ray Analysis

The lattice constants at room temperature were determined by a back reflexion X-ray camera using Cu K_α beam. Assuming that the tetragonality of the crystals decreases as the content of strontium titanate increases, the obtained results are shown in Fig. 6, where the analysis was mainly performed by using the diffracted lines (510), (422) and (321). The change of the volume of unit cell with molar ratio derived from our above data, is shown in Fig. 7. This inclination is not inconsistent with the fact that the ionic radii of Pb^{2+} and Sr^{2+} are 1.32 Å and 1.27 Å respectively. It is supposed that the increase of the lattice volume at the right side in this figure is due to the ferroelectric strain, as in the cubic phase of the solid solutions any notable change of the lattice volume is not observed because of nearly equall ionic radii of Pb^{2+} and Sr^{2+} according to Wykoff.

§ 6. Conclusion

$PbTiO_3$ and $SrTiO_3$ make solid solution with each other in the whole range, in which the Curie temperature decreases as the content of $SrTiO_3$ increases. Except the Curie point where a phase transition occurs from a ferroelectric tetragonal structure to a non-ferroelectric cubic one, any transition point as in barium titanate was not discovered. It is notable, that the increase of the lattice volume in (Pb·Sr)TiO_3 is accompanied with the rise of the Curie temperature, while the relation is contrary in (Pb·Ba)TiO_3. This fact suggests that the anomalous properties of Pb^{2+} ion should be interpreted on the standpoint not

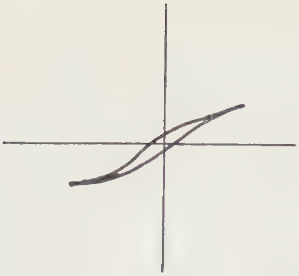

Fig. 8. Hysteresis loop $(10Pb\cdot 90Sr)TiO_3$.

only of the ionic radii but also of the atomic polarizability. The Santen & Jonker's formula¹⁾ related to the Curie constant C and the linear thermal expansion coefficient β, $\beta=1/C$, which is resulted from the assumption that the atomic polarizability does not change with temperature, seems to be not valid in the present case.

A large value of the spontaneous polarization P_s will be expected from the large amount of anomalous heat ΔQ according to the general relation $\Delta Q=\frac{1}{2}\gamma P_s^2$, where γ is a constant, but it is very difficult to estimate it from the $D\sim E$ hysteresis loop because of large coercive field. As a matter of fact, even in $(30\,Pb\cdot 70\,Sr)TiO_3$ the coercive field is over 10000 V/cm and any tendency of saturation in $D\sim E$ hysteresis loop is not observed for the applied a.c. field strength of 34000 V/cm. Just in $(10\,Pb\cdot 90\,Sr)TiO_3$, we observed a typical hysteresis loop as shown in Fig. 8, were the applied field strength is 20000 V/cm. The relation of the max. polarization with the applied a.c. field strength at liquid air temperature is illustrated in Fig. 9, where we see the spontaneous polarization is about 2μ Coulomb/cm², which is the same order as that of $[(10\sim20)Ba\cdot(90\sim80)Sr]TiO_3$. The value of the spontaneous polarization will increase more rapidly with the content of Pb^{2+} ion than substances in $(Ba\cdot Sr)TiO_3$.

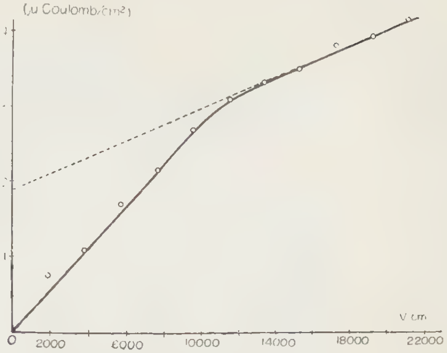

Fig. 9. Max. polarization vs. applied voltage $(10Pb\cdot 90Sr)TiO_3$.

References

1) J. H. van Santen and G. H. Jonker: Nature **159** (1947) 333.
2) S. Sawada and S. Nomura: Rep. Inst. Sci. and Tech., Univ. of Tokyo **4** (1950) 217.
3) A. von Hippel and co-workers: Ind. and Eng. Chem. **38** (1946) 1097.
4) G. Shirane and K. Suzuki: J. Phys. Soc. Japan **6** (1951) 274.
5) G. Shirane and A. Takeda: J. Phys. Soc. Japan **6** (1951) 329.
6) G. A. Smolenski: Doklaey Akad. Nauk. S. S. S. R. **70** (1950) 405.
7) S. Nomura and S. Sawada: Rep. Inst. Sci. and Tech., Univ. of Tokyo **6** (1952) 191.
8) S. Nomura and S. Sawada: J. Phys. Soc. Japan **5** (1950) 279.
9) S. Sawada and G. Shirane: J. Phys. Soc. Japan **4** (1949) 52.
10) S. Sawada and R. Ando: Rep. Inst. Sci. and Tech., Univ. of Tokyo **5** (1951) 143.
11) G. Shirane and E. Sawaguchi: Phys. Rev. **81** (1951) 458.

JOURNAL OF THE PHYSICAL SOCIETY OF JAPAN Vol. 10, No. 2, FEBRUARY, 1955

Dielectric Properties of Titanates Containing Sn^{4+} Ions I

By Shoichiro NOMURA

Institute of Science and Technology, University of Tokyo

(Received September 4, 1954)

Dielectric and thermal properties and lattice constants of the solid solutions of $Pb(Ti \cdot Sn)O_3$ and $Ba(Ti \cdot Sn)O_3$ were investigated, for the purpose of making clear the role of Y ion in the compounds of the perovskite type, XYO_3. In $Pb(Ti \cdot Sn)O_3$, according to the X-ray analysis, two phases seem to co-exist in the samples containing Sn^{4+} ions more than 75%, although the whole range solid solution might be expected from the standpoint of the "tolerance factor". The Curie point moves to the low temperature side with the increase of the content of $PbSnO_3$ and reaches 200°C in $Pb(20\%Ti \cdot 80\%Sn)O_3$. In $Ba(Ti \cdot Sn)O_3$, a rather steep decrease of the Curie temperature with the content of Sn^{4+} ions occurs and the whole range solid solution seems to be realized, although the X-ray analysis was not thoroughly made in this case. The dielectric constant $D \sim E$ hysteresis loop, thermal expansion and specific heat were observed. An anomalous hysteresis phenomenon was observed in $Pb(25\%Ti \cdot 75\%Sn)O_3$, which suggests that Ti^{4+} Ion and Sn^{4+} Ion respond differently to the external field in the ferroelectric state. Several speculations were mentioned with respect to this phenomenon.

§ 1. Introduction

Hitherto, miscellaneous ferroelectric substances, which are classifiable into three groups, namely, rochelle salt, potassium dihydrogen phosphate and barium titanate type, have been discovered by many investigators¹⁾. Among these, barium titanate type ferroelectrics have been studied most in detail, for the reason that their crystal structure, which is perovskite type²⁾, is simpler than those of the others. Lead titanate, lead zirconate, potassium niobate, sodium tantalate, etc. belong to this group.

In the perovskite type XYO_3 compounds, Y ion occupies the center of an octahedron composed of six oxygen ions. In ferroelectric or antiferroelectric states, the octahedron is distorted and the position of Y ion is moved from its center, that is the reason of the occurrence of spontaneously polarized state. The magnitude of the atomic displacement depends upon not only the attribute of Y ion but that of X ion and this is the cause of various change of the dielectric properties in solid solutions: $(Ba \cdot Pb)TiO_3$, $(Ba \cdot Sr)TiO_3$, $(Pb \cdot Sr)TiO_3$, $Ba(Ti \cdot Zr)O_3$ $Pb(Ti \cdot Zr)O_3$ etc.

Goldschmidt, Barth and Lunde found that in real perovskite structures the value of $(r_X+r_0)/\sqrt{2}(r_Y+r_0)$ lies between 0.77 and 0.99, and they called this ratio t as tolerance factor. Zachariasen made corrections due to coordination to the above formula by multiplying the numerator by 1.06 and the denominator by 0.95, and pointed out that the structure is precisely cubic, if t is equal to 1.0; the ilmenite structure is realized, if t falls below 0.9; neither perovskite nor ilmenite structure is realized for $t > 1.1$. Actually we obtain the value of t for several compounds of XYO_3 type as follows,

Substance	t
$BaTiO_3$	1.11
$BaSnO_3$	1.09
$PbTiO_3$	1.01
$PbSnO_3$	0.99
$PbZrO_3$	0.92

where we used the values of ionic radii, $r_{0^{2-}}=1.35Å$, $r_{Ba^{2+}}=1.35Å$, $r_{Pb^{2+}}=1.18Å$, $r_{Ti^{4+}}=0.60Å$, $r_{Sn^{4+}}=0.65Å$, $r_{Zr^{4+}}=0.80Å$.

Further, Matthias insisted that one of the necessary conditions for XYO_3 compound to be ferroelectric is that the electron configuration of Y ion is of innert gas-type³⁾. Really, the electron configuration of Ti^{4+} ion is the same with that of Ar atom and those of Zr^{4+} and Cb^{5+} are with that of Kr atom, although Ta^{5+} and W^{6+} have not, strictly speaking, innert gas-type electron configurations. We may consider, however, that the latter two ions behave as if having Xe like electron configuration, as long as we treat the chemical binding only, $4f$ electrons having orbits well inside the atom. Is the above mentioned restriction for Y ion is essential? Is there any possibility that XYO_3 compounds are ferroelectric or antiferroelectric when the electron configuration of Y ion is not of innert gas-type? To investigate this problem, we shall pay our attention to dielectric properties of stannates. Sn atom has the electron configuration of $(1s)^2(2s)^2(2p)^6(3d)^{10}(4s)^2(4p)^6(4d)^{10}(5s)^2(5p)^2$, so that the completely occupied $4d$ orbits is the outermost shell of Sn^{4+} ion. For the investigations of solid solutions of stannates, the whole range solid solution may be expected in the compounds of $Ba(Ti\cdot Sn)O_3$, $Ba(Zr\cdot Sn)O_3$, $Pb(Ti\cdot Sn)O_3$, $Pb(Zr\cdot Sn)O_3$, because the size of Sn^{4+} ion exists between those of Ti^{4+} ion and Zr^{4+} ion. These facts suggest that the investigations of the compounds containing Sn^{4+} ions are necessary and suitable to answer our questions stated above.

In this paper, we shall mention about the dielectric properties of the solid solutions $Pb(Ti\cdot Sn)O_3$ and $Ba(Ti\cdot Sn)O_3$, for the purpose of making clear the role of Y ion in the perovskite structures of XYO_3 compounds.

§ 2. Preparation of Samples

Barium titanate and barium stannate were prepared separately by our usual method[4)], firing temperature being about 1250°C. On firing lead titanate or lead stannate, attentions must be paied to prevent the reduction and the evaporation of PbO. Being pulverized, mixed in a needed molar concentration and pressed into a disk, the mixture was refired for a few hours at a little higher temperature than that in the first firing. The solid solutions $Pb(Ti\cdot Sn)O_3$ containing Sn^{4+} ion more than about 70%, were often cracked in the firing process. The quantitative chemical analysis of samples has not yet been made.

§ 3. Dielectric Properties

(a) Permittivity of Samples with Various Molar Percentages

Fig. 1 shows one series of the permittivity of $Pb(Ti\cdot Sn)O_3$ with different concentrations observed at 1043 KC/sec. As the content of $PbSnO_3$ increases, the absolute value of the permittivity becomes larger and the Curie temperature decreases linearly with the molar concentration up to about 75% Sn^{4+} ion. In the case of $Pb(25\%\ Ti\cdot 75\%\ Sn)O_3$, the permittivity at room temperature is about 200 and reaches 1000 at the transition temperature of about 220°C. The permittivity falls to very small value and its peak disappears, when the content of $PbSnO_3$ increases beyond

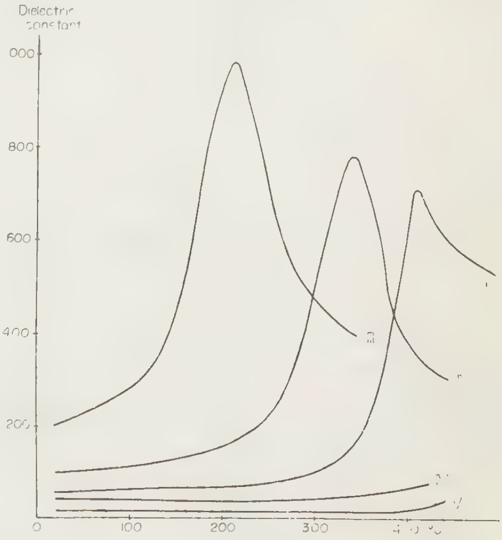

Fig. 1. Permittivity vs. temperature curve for $Pb(Ti\cdot Sn)O_3$.
(I) $Pb(70\%Ti\cdot 30\%Sn)O_3$ (II) $Pb(50\%Ti\cdot 50\%Sn)O_3$
(III) $Pb(25\%Ti\cdot 75\%Sn)O_3$ (IV) $Pb(10\%Ti\cdot 90\%Sn)O_3$
(V) $PbSnO_3$.

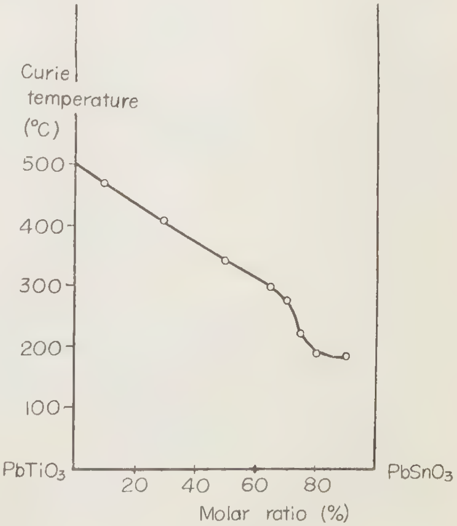

Fig. 2. Curie temperature vs. molar ratio for $Pb(Ti\cdot Sn)O_3$.

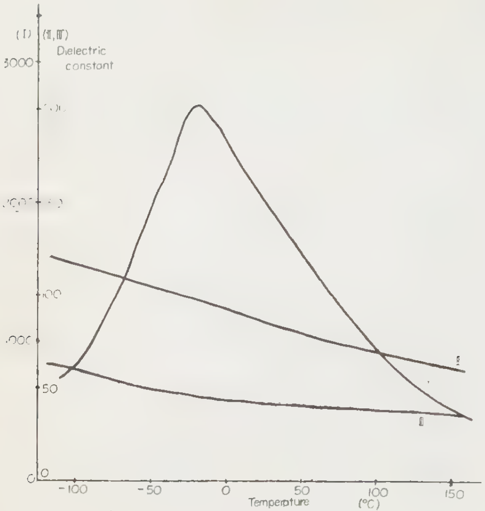

Fig. 3. Permittivity vs. temperature curve for $Ba(Ti \cdot Sn)O_3$.
(I) $Ba(85\% Ti \cdot 15\% Sn)O_3$ (II) $Ba(50\% Ti \cdot 50\% Sn)O_3$ (III) $Ba(30\% Ti \cdot 70\% Sn)O_3$.

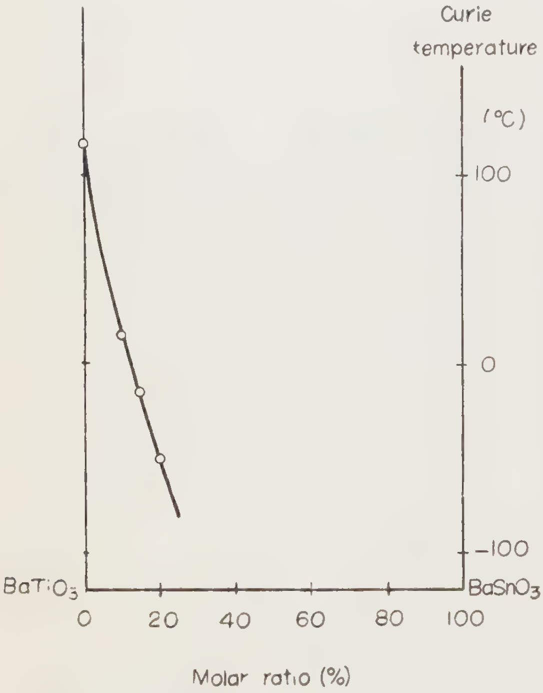

Fig. 4. Curie temperature vs. molar ratio for $Ba(Ti \cdot Sn)O_3$.

75%, as illustrated in Fig. 1, where $PbSnO_3$ itself has the value of permittivity as small as 16, which doesn't show any noticeable temperature dependence until a deceptive increasing of loss factor appears. Any anomaly was not observed in the sub-zero measurements down to liquid air temperature, where the samples were inserted into a vaccum vessel to prevent them from the effect of moisture. The relation between the Curie temperature and molar ratio is illustrated in Fig. 2, which shows a linear relation, up to 70 molar percent $PbSnO_3$.

Fig. 3 shows the permittivity versus temperature curves for $Ba(Ti \cdot Sn)O_3$. As the content of $BaSnO_3$ increases, permittivity decreases more rapidly than in the case of $Pb(Ti \cdot Sn)O_3$. The relation between the Curie temperature and the molar ratio is illustrated in Fig. 4. The dielectric anomalies at the second and third transition temperatures, which are 5°C and 70°C respectively in $BaTiO_3$ itself, disappear by adding only a few percent Sn^{4+} ion in place of Ti^{4+} ion. For $Ba(50\% Ti \cdot 50\% Sn)O_3$ and $Ba(30\% Ti \cdot 70\% Sn)O_3$, the permittivity at room temperature is about 85 and 40 respectively, and for $BaSnO_3$ itself it is only about 10, the magnitude of which does scarecely change from 100°C to 200°C.

(b) Hysteresis Loop

As well known the $D \sim E$ hysteresis phenomenon depens upon the electric domain structure and is an illustration of the existence of a spontaneous polarization. Its magnitude may be estimated from $D \sim E$ hysteresis loops. Of course, the effective value of the spontaneous polarization of ceramics is smaller than that of single crystals, because in the former the directions of domains are distributed at random.

Fig. 5 shows one typical $D \sim E$ hysteresis loop of $Pb(25\% Ti \cdot 75\% Sn)O_3$. Although its appearance is like that of $BaTiO_3$, the maximum polarization *vs.* field intensity curve, which may give the measure of the spontaneous polarization, has no tendency of saturation, as shown in Fig. 6. It is noteworthy that the more severe change of gradient of the curve is observed in the range of the applied

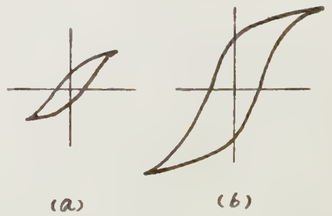

Fig. 5. Hysteresis loop of $Pb(25\% Ti \cdot 75\% Sn)O_3$.
(a) E = 8000 V/cm (b) E = 15000 V/cm

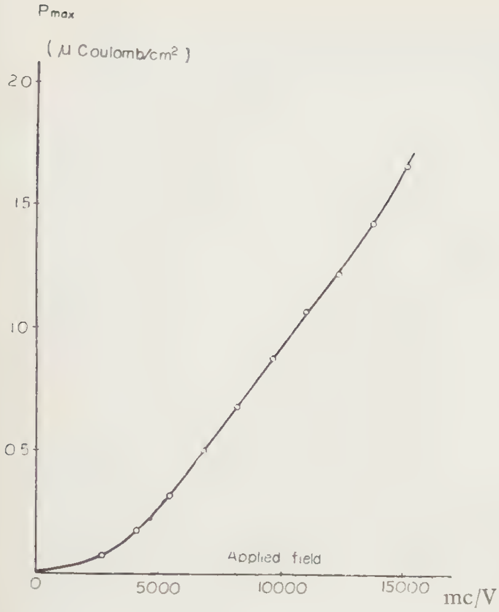

Fig. 6. P_{max} vs. field curve of $Pb(25\%Ti \cdot 75\%Sn)O_3$.

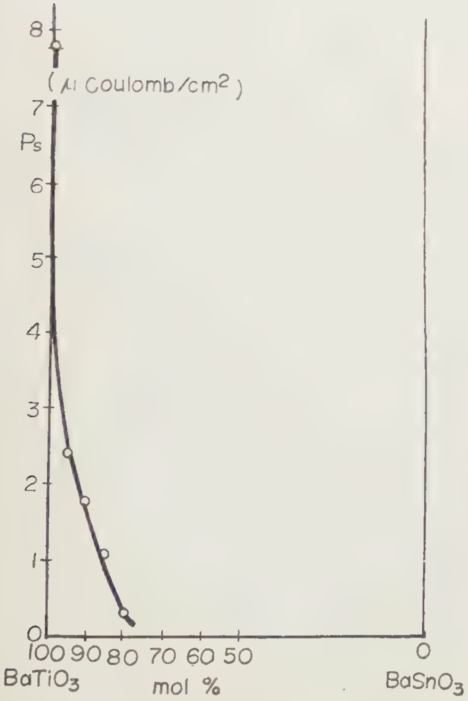

Fig. 7. Ps of $Ba(Ti \cdot Sn)O_3$ ceramics.

voltage within 4000 V/cm than that at the voltage above this value. The similar hysteresis loops were observed for the samples containing less than 75% Sn^{4+} ions but not for ones containing more than 80% Sn^{4+} ions.

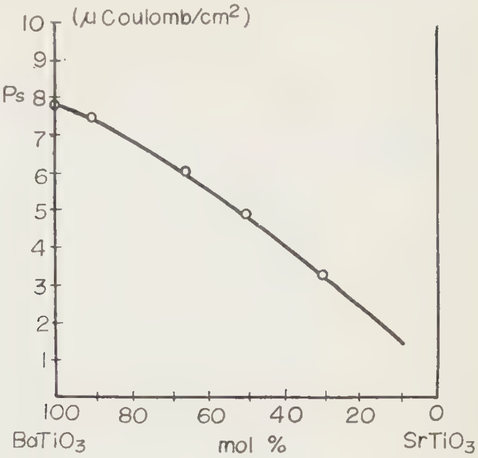

Fig. 8. Ps of $(Ba \cdot Sr)TiO_3$ ceramics.

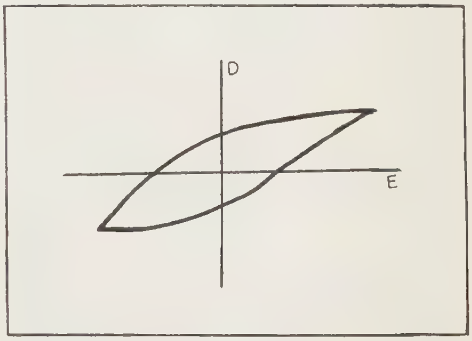

Fig. 9. Asymmetric hysteresis loop of $Pb(25\%Ti \cdot 75\%Sn)O_3$ E=5140 V/cm.

The magnitudes of the maximum polarization for $Pb(30\%Ti \cdot 70\%Sn)O_3$, $Pb(25\%Ti \cdot 75\%Sn)O_3$ and $Pb(10\%Ti \cdot 90\%Sn)O_3$ at the applied voltage of 10000 V/cm are 0.43, 0.9 and 0.09 μ coulomb/cm² respectively.

We can observe the similar dielectric hysteresis when Ti^{4+} ions are replaced by Sn^{4+} ions in $BaTiO_3$, Fig. 7 shows the spontaneous polarization of $Ba(Ti \cdot Sn)O_3$ of various molar percentages. It is interesting to compare it with Fig. 8, which shows the case of $(Ba \cdot Sr)TiO_3$ as an example of $(X_1 X_2)YO_3$ type compounds. The steep decrease of the magnitude of polarization for the former is apparently due to the peculiarity of Sn^{4+} ion. For the samples of $Pb(Ti \cdot Sn)O_3$, it is difficult to obtain similar figures from the $D \sim E$ relations. To examine this peculiarity, we observed the $D \sim E$ hysteresis loop for the sample which has accepted a so-called D.C. field treatment. After the sample ($Pb(25\% Ti \cdot 75\% Sn)O_3$ in this case) was cooled from 280°C to room

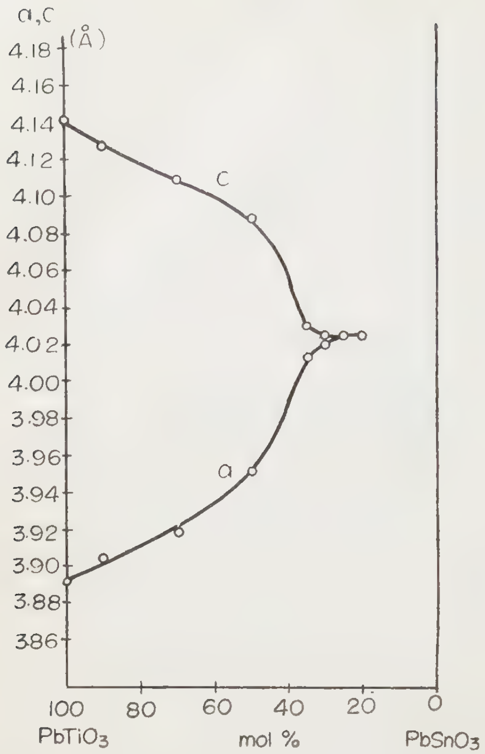

Fig. 10. Lattice constants vs. molar ratio ($Pb(Ti \cdot Sn)O_3$).

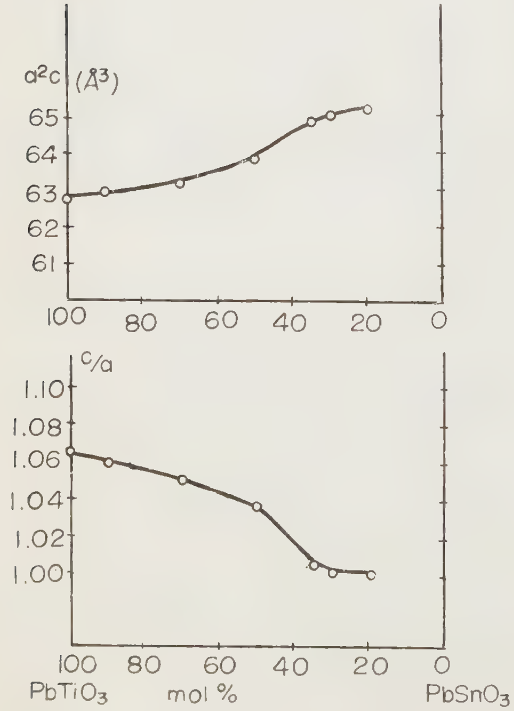

Fig. 11. Lattice volume and axial ratio vs. molar ratio ($Pb(Ti \cdot Sn)O_3$).

temperature during 1 hour, the D.C. field of about 5000 V/cm having been applied, an asymmetric hysteresis loop was observed, as shown in Fig. 9, but, when the sample was treated not at all or treated only at room temperature, only a symmetric one is observed. These fact suggest that the field responses of Ti^{4+} ion and Sn^{4+} ion are different in the ferroelectric state.

In the case of $Ba(80\% Ti \cdot 20\% Sn)O_3$, the distinct asymmetry was not observed, the reason of which will be discussed in Sec. 6.

§ 4. X-ray Analysis

We made the analysis of crystal structure by using the Debye-Scherrer's back reflection photograph to investigate the relation between dielectric properties and lattice constants. In the case of $Pb(Ti \cdot Sn)O_3$, we obtained the results of Figs. 10 and 11 at room temperature, which show that the tetragonality of the lattice decreases as the content of Sn^{4+} ion increases. The indices of diffraction (hkl), which were used in this analysis are (510), (422) and (321).

As the content of Sn^{4+} ion increases over 50% of total Y ions, the value of the ratio c/a at room temperature approaches 1 and is nearly equal to 1 in $Pb(25\% Ti \cdot 75\% Sn)O_3$, whose Curie temperature exists at about 220°C. And then, besides the main lines of perovskite structure, there appear extra lines those intensities increases with the amount of Sn^{4+} ions. It is unquestionable that the crystal structure of $PbSnO_3$ itself is not a simple one of perovskite type, although we have not yet studied it in detail. Naray-Szabo has reported in his recent paper[5] that it is a tetragonal structure which has eight $PbSnO_3$ molecules in a unit cell and its lattice constants are $a = 7.86$ Å, $c = 8.13$ Å, detailed atomic positions having not yet been known. It seems reasonable to suppose that such a rather complex structure may be more stable than a simple perovskite one in the region near $PbSnO_3$ and this one may co-exist with the perovskite one, in the intermediate region, although the whole range solid solution, as mentioned above, is expected from the standpoint of tolerance factor.

For $Ba(Ti \cdot Sn)O_3$, we have not thoroughly made the X-ray analysis. As $BaSnO_3$, however, has a perovskite structure ($a = 4.116$ Å), we may suppose that a continuous change of lattice constants will occur in this case, that is supported by the dielectric properties of $Ba(Ti\cdot Sn)O_3$, stated above.

§ 5. Thermal Properties

Anomalies of specific heat and thermal expansion were observed at the transition temperatures, and the amount of these anomalies varies with molar concentration. The specific heat was measured by the conduction calorimeter, which have been used formerly for WO_3, $PbTiO_3$ etc.[6], in our laboratory. The variation of the anomalous heat with the molar percentage, in the case of $Pb(Ti\cdot Sn)O_3$, is shown in Fig. 12, in which a little smaller anomaly than that of $BaTiO_3$ is seen for Pb(35% Ti·65% Sn)O_3, this amount being not unreasonable considering our results on lattice constants.

The remarkable thermal contraction observed at the Curie point in $PbTiO_3$ decreases its magnitude as the content of $PbSnO_3$ increases and any anomaly as well as any contaction is not observed in Pb(25% Ti·75% Sn)O_3.

§ 6. Discussion

According to our above investigations, we may suppose that Sn^{4+} ion behaves in a rather different manner from that of Ti^{4+} ion in the lattice. Using the values of ionic radii of O^{2-}, Ti^{4+}, Sn^{4+}, adopted in Sec. I, we obtain $2(r_{O^{2-}}+r_{Ti^{4+}})=3.90$Å and $2(r_{O^{2-}}+r_{Sn^{4+}})=4.00$Å respectively. The value of lattice constant a, on the other hand, is 3.95 Å, for instance, for Pb(50%Ti·50%Sn)O_3. Thus the displacement of Sn^{4+} ion from the center is expected to be smaller than that of Ti^{4+} ion and further the possibility of changing its direction of polarization for the former will differ from that for the latter, as easily seen from Fig. 13, where the dimensions are proportional to the actual ones. Although the domain structures are not yet known, we may suppose, from the standpoint of ionic radii, that the change of the direction of the polarization by the applied field occurs in the cells containing Ti^{4+} ion but hardly in those containing Sn^{4+} ion. Perhaps, this is the reason why the $D\sim E$ hysteresis loop for $Pb(Ti\cdot Sn)O_3$ doesn't show any inclination of saturation. When these samples are cooled from above Curie

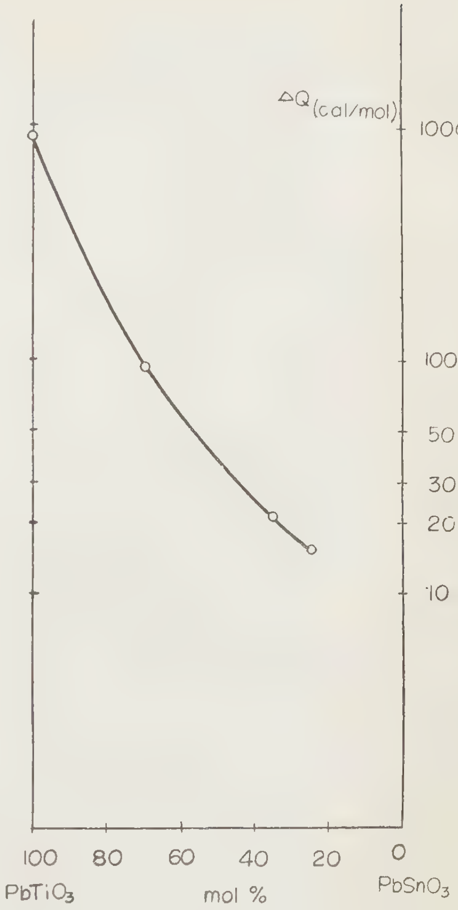

Fig. 12. Anomalous heat vs. molar ratio ($Pb(Ti\cdot Sn)O_3$).

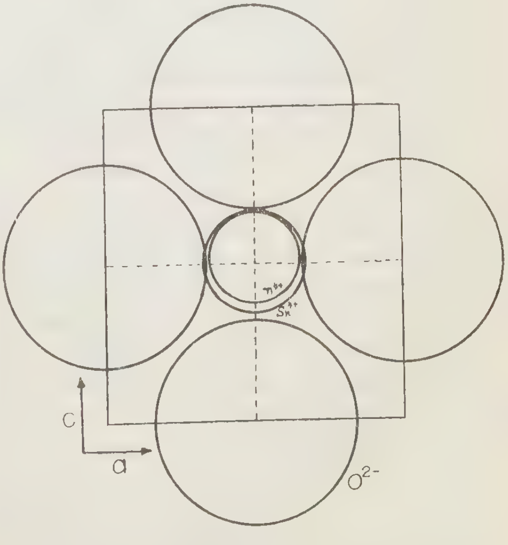

Fig. 13. Shematic atomic arrangement in Pb(50%Ti·50%Sn)O_3 lattice.

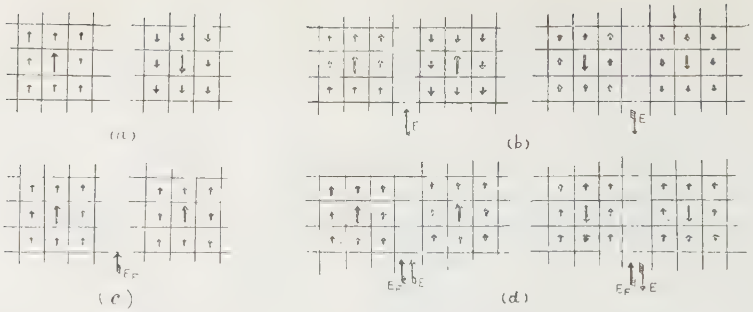

Fig. 14. Shematic model of Pb(Ti·Sn)O_3 lattice.

E applied field E_F Cooling field ↑ Ti^{4+} ion ↑……… Sn^{4+} ion

temperature in the external D.C. field, the undirectional distribution of Sn^{4+} ions, which cannot be removed by applying A.C. field, may be realized in the crystals, that is the reason for the appearance of asymmetric hysteresis loop. As the content of Ti^{4+} ion increases, the degree of the asymmetry in the hysteresis loop will be expected to become small, and if the lattice dimensions are larger than some critical values, the asymmetric hysteresis loop will be not observed. This case may correspond to the one of Ba(80% Ti·20% Sn)O_3.

In fact, these descriptions are too simple, and strictly speaking, may not be very much correct, because the conception of the ionic radii of the ion contains to some extent the nature of the chemical binding.

A speculated model for them is shown in Fig. 14, where (a) is for the natural state, (b) shows the change of (a) when the field is applied, (c) and (d) are the corresponding ones of (a) and (b), when accepted the field cooling*. In (a), we assume, that Sn^{4+} ion doesn't change its direction of displacement by applying field at room temperature, so that only partial saturation of the polarization may be attainable, while (a) turns to (c) when the field treatment (cooling) is done from above the Curie temperature. There are other possibilities of the displacement of Sn^{4+} ion in the crystal, the discussion stated above being only one speculation. One of them is that the displacement of Sn^{4+} ion dose not occur in the natural state and only do when the field cooling is given, because of the nature of Sn^{4+} ion electron configuration. Of course, we have not any sufficient evidence, to say which phenomenon is the real one in the crystal. But the characteristics, such as, the very low value of the spontaneous polarization, the nonsaturating $D \sim E$ relation and the D.C. field response of the permittivity, force us to think that the difference between the chemical binding of Sn^{4+} ion and Ti^{4+} ion in the crystal are essential to explain experimental facts. In order to clarify this point, it is desirable to investigate, in detail, the effects of the field treatment upon the dielectric behavior and the $D \sim E$ hysteresis phenomena.

As the saturation of $D \sim E$ hysteresis loops is not observed, we cannot estimate the magnitude of spontaneous polarization. It is possible. however, to know its order from the amount of anomalous heat at Curie point and the temperature dependence of dielectric constant above the Curie point, assuming the Devonshire's theory. Using $T_1 = 220°C$, $T_0 = 175°C$ and

$$\frac{X_0' T_1}{T_1 - T_0} = 0.0496\,,$$

we obtain $P_S = 2.8\,\mu$ coulomb/cm^2, for Pb(25% Ti·75% Sn)O_3, which is very small in comparison with that of $BaTiO_3$.

A concave characteristic in the maximum polarization *vs* field curve doesn't always mean that the dielectric constant will increase with D.C. applied field, because of the effects of the domain boundaries. The investigation of the effect of biasing field upon dielectric constant is now in progress.

The fact that the criterion of so-called tolerance factor for the XYO_3 compounds is not so effective in the case of Pb(Ti·Sn)O_3, shows that the electronic structure of the ion has also an influence on the phase diagram, and the electronic structure of Sn^{4+} ion, which is not of inert-gas type, is responsible to the anomalous dielectric behavior of $Pb(Ti\cdot Sn)O_3$. If we want to know the displacement of Sn^{4+} ion in the crystal, we must study the bonding energy of Sn-O etc. considering such electronic configuration of Sn^{4+} ion.

---

* Each halves of these figures correspond to (+) and (−) domains respectively.

In conclusion, the author wishes to express his sincere thanks to Assist. Prof. S. Sawada for his valuable discussion.

References

1) A. F. Devonshire: Adv. in Phys. **3** (1954) 85.
2) S. Miyake and R. Ueda: J. Phys. Soc. Japan **1** (1946) 32.
3) B. T. Matthias: Hel. Phys. Acta. **23** (1950) 167.
4) S. Sawada and S. Nomura: J. Phys. Soc. Japan **5** (1950) 231.
5) Naray Szabo: Muegy. Kozl. **1** (1947) 30.
6) S. Sawada, R. Ando and S. Nomura: Phys. Rev. **84** (1951) 1054.

JOURNAL OF THE PHYSICAL SOCIETY OF JAPAN Vol. 10, No. 2, FEBRUARY, 1955

The Steady Flow of Viscous Fluid past a Fixed Spheroidal Obstacle at Small Reynolds Numbers

By Tyûsei AOI

Osaka University of Engineering, Osaka

(Received September 20, 1954)

By making use of an exact solution of Oseen's equations of motion detailed theoretical discussion is made on the steady flow of an incompressible viscous fluid past a prolate or oblate spheroid, including a circular disc as a special case. The analytical exact solution of Oseen's equations are first obtained by the use of spheroidal functions, mathematical properties of which are also investigated separately in the writer's subsequent paper. The drag experienced by a spheroid is then computed and the general formula for the drag is obtained. Approximate formulae for the drags on a prolate and oblate spheroid and on a circular disc are also derived and some numerical results are obtained. Discussions on the pressure drag and the frictional drag experienced by a spheroid are made and it is thus found that these two drags contribute to the total drag in a definite ratio which is independent of the Reynolds number. Detailed analytical calculations are given only for the case of a prolate spheroid and the essential parts of the analysis for the case of an oblate spheroid are given in Appendix.

§ 1. Introduction

As is well-known, the steady flow of an incompressible viscous fluid past a solid obstacle can be discussed satisfactorily on the basis of Oseen's linearized equations of motion when the Reynolds number is fairly small. In previous papers [1~4] we have investigated in sequence the steady flow past a sphere, a circular cylinder and an elliptic cylinder including a flat plate, by making use of the exact analytical solutions of Oseen's equations. It has thus found that the actual flows observed in experiments can be deduced theoretically from the said solutions.

As far as we are aware, no detailed theoretical discussion based on the exact analytical solution of Oseen's equations seems to have been made in the case of the steady flow around an ellipsoid of revolution, that is, a prolate or oblate spheroid, which is so placed that the axis of symmetry is along the uniform stream, although an approximate calculation of the drag on a spheroid was carried out by Oseen [5] himself. The main object of the present paper lies in the derivation of the exact analytical solution of Oseen's equations in the case of the steady flow past a spheroid as well as in computing the drag experienced by the spheroid. The exact solution of Oseen's equations is obtained in the same manner as in the case of a sphere dealt with by Goldstein [6] as early as 1929 and the general expression for the drag on a spheroid is also derived. By the use of the said solution we can easily discuss, if desired, the flow patterns around the spheroid.

Discussions on the drag on a prolate or oblate spheroid has been made with special reference to the pressure drag and the frictional drag separately. Approximate formulae for the drags on a prolate and oblate spheroid and on a circular disc normal to the uniform stream are also derived.

In order to obtain the exact analytical solution of Oseen's equations for the present case, it is necessary to study on some mathematical properties of spheroidal functions. Such discussions are therefore made quite similarly to the case of the Mathieu functions and the results will be described in another paper [7].

Detailed analytical calculations are given only for the case of a prolate spheroid, since the analysis for the case of an oblate spheroid is quite similar to the former case. The essential parts of the analysis for the latter case are however given in Appendix.

§ 2. The General Solution

We consider a solid obstacle fixed in a steadily running uniform stream of an incompressible viscous fluid of infinite extent in every direction. Let (x, y, z) be the rectangular coordinates having the origin within the obstacle and the axis of x in the direction of the velocity U of the uniform stream. We denote $U+u$, v, w the components of the fluid velocity at any point, so that u, v, and w are the velocity of perturbation which become vanishingly small everywhere at a great distance from the obstacle. If terms of the second order in u, v, w are omitted, we get, from the Navier-Stokes equations of motion, the well-known linearized equations of Oseen,

$$U\frac{\partial}{\partial x}(u, v, w)=-\frac{1}{\rho}\left(\frac{\partial}{\partial x}, \frac{\partial}{\partial y}, \frac{\partial}{\partial z}\right)p + \nu\nabla^2(u, v, w) , \tag{1}$$

where p is the pressure, ρ the density, ν the kinematic viscosity, and ∇^2 stands for $\partial^2/\partial x^2 + \partial^2/\partial y^2+\partial^2/\partial z^2$. The fluid being assumed to be incompressible, the equation of continuity is then

$$\frac{\partial u}{\partial x}+\frac{\partial v}{\partial y}+\frac{\partial w}{\partial z}=0 . \tag{2}$$

If we put $k=U/2\nu$, these equations are, as Lamb† has shown, satisfied by

$$\left.\begin{aligned} u&=-\frac{\partial \phi}{\partial x}+\frac{1}{2k}\frac{\partial \chi}{\partial x}-\chi , \\ v&=-\frac{\partial \phi}{\partial y}+\frac{1}{2k}\frac{\partial \chi}{\partial y} , \\ w&=-\frac{\partial \phi}{\partial z}+\frac{1}{2k}\frac{\partial \chi}{\partial z} , \end{aligned}\right\} \tag{3}$$

and

$$p=\rho U\frac{\partial \phi}{\partial x} , \tag{4}$$

provided that

$$\nabla^2\phi=0 , \tag{5}$$

and

$$\nabla^2\chi-2k\frac{\partial \chi}{\partial x}=0 . \tag{6}$$

We consider that a prolate spheroid symmetrical with respect to its major-axis is so placed that its centre is at the origin of the coordinates and its major-axis is along the axis of x. Let the major- and minor-axes be of length $2a$ and $2b$ respectively. Then it is convenient to introduce the prolate spheroidal coordinates ξ, η defined by

$$x+i\tilde{\omega}=c\cosh(\xi+i\eta) ,$$

where $\tilde{\omega}=\sqrt{y^2+z^2}$ and $c=\sqrt{a^2-b^2}$. If we write t and μ for $\cosh\xi$ and $\cos\eta$, then it is rewritten as

$$x=ct\mu , \quad \tilde{\omega}=c\sqrt{t^2-1}\sqrt{1-\mu^2} . \tag{7}$$

Since the flow past the spheroid is symmetric about the axis of x and perturbations due to the presence of the obstacle vanish at infinity, the appropriate solution of equation (5) is given in terms of the Legendre functions $P_n(\mu)$ and $Q_n(t)$ as

$$\phi=cU\sum_{n=0}^{\infty}\alpha_n Q_n(t)P_n(\mu) , \tag{8}$$

where the α_n's are constants of integration.

To solve equation (6) we put $\chi=e^{kx}T(t)M(\mu)$, then the equation becomes separable in the variables and we are led to the set of two equations for $T(t)$ and $M(\mu)$. These equations take the same form as

---

† H. Lamb, 'Hydrodynamics', 6th ed., Cambridge 1932, § 342.

$$\frac{d}{dz}\left\{(1-z^2)\frac{dZ}{dz}\right\}+(\lambda+\kappa^2 z^2)Z=0\ , \qquad (9)$$

provided that κ stands for kc and $Z=T$ when $z=t$ while $Z=M$ when $z=\mu$.

For a discrete set of characteristic values of λ the solution† $M(\mu)$ which is regular at $\mu=\pm 1$, is expressed in series of the Legendre functions. Denoting it provisionally by $\mathrm{pe}_n(\mu)$, then

$$\left.\begin{aligned} \mathrm{pe}_{2n}(\mu)&=\sum_{r=0}^{\infty} A_{2r}^{(2n)} P_{2r}(\mu)\ ,\\ \mathrm{pe}_{2n+1}(\mu)&=\sum_{r=0}^{\infty} A_{2r+1}^{(2n+1)} P_{2r+1}(\mu)\ , \end{aligned}\right\} \qquad (10)$$

where the $A_r^{(n)}$'s depend on κ only and are expanded in powers of κ when κ is small.

Appropriate solutions $T(t)$ of equation (9) are found to be given as follows. The solution of the first kind as denoted here provisionally by $\mathrm{Re}_n(t)$ which diverges when its argument t is large is defined by the integral form:

$$\mathrm{Re}_n(t)=\frac{1}{\sqrt{2\pi}}\int_{-1}^{1} e^{\kappa t\mu} pe_n(\mu)d\mu\ , \qquad (11)$$

and is also expressed in series of the modified Bessel functions $I_{n+\frac{1}{2}}$, namely

$$\left.\begin{aligned} \mathrm{Re}_{2n}(t)&=\frac{1}{\sqrt{\kappa t}}\sum_{r=0}^{\infty} A_{2r}^{(2n)} I_{2r+\frac{1}{2}}(\kappa t)\ ,\\ \mathrm{Re}_{2n+1}(t)&=\frac{1}{\sqrt{\kappa t}}\sum_{r=0}^{\infty} A_{2r+1}^{(2n+1)} I_{2r+\frac{3}{2}}(\kappa t)\ , \end{aligned}\right\} \qquad (12)$$

Whilst the solution of the second kind as denoted here by $\mathrm{Se}_n(t)$ which vanishes as its argument t increases can be expressed in terms of the modified Bessel functions $I_{n+\frac{1}{2}}$ and $K_{n+\frac{1}{2}}$. Thus,†

$$\left.\begin{aligned} \mathrm{Se}_{2n}(t)&=\frac{2}{\kappa A_0^{(2n)}}\sum_{p=0}^{\infty} \nu_{2p} K_{p+\frac{1}{2}}\left(\frac{\kappa}{2}e^{\xi}\right) I_{p+\frac{1}{2}}\left(\frac{\kappa}{2}e^{-\xi}\right)\ ,\\ \mathrm{Se}_{2n+1}(t)&=\frac{24}{\kappa^2 A_1^{(2n+1)}}\cosh\xi\sum_{p=0}^{\infty} \nu_{2p+1} K_{p+\frac{3}{2}}\left(\frac{\kappa}{2}e^{\xi}\right) I_{p+\frac{3}{2}}\left(\frac{\kappa}{2}e^{-\xi}\right)\ , \end{aligned}\right\} \qquad (13)$$

where the ν_p's are constants involving only the $A_r^{(n)}$'s. These functions $Se_n(t)$ can be expanded in powers of κ when κ is small.

The appropriate general expression for χ is thus given by

$$\chi=Ue^{\kappa t\mu}\sum_{m=0}^{\infty}\beta_m \mathrm{Se}_m(t) pe_m(\mu)\ , \qquad (14)$$

where the β_m's are constants of integration.

The components u, v and w of the perturbation velocity and the pressure p at any point in the flow can be obtained by inserting the above general expressions for ϕ and χ into (3) and (4) respectively.

§ 3. Determination of the Constants of Integration α_n and β_m

The constants of integration α_n and β_m can be determined by the boundary conditions at the surface of the spheroid. To do this it is convenient to use, in place of u, v, w, the components of the perturbation velocity along t and μ increasing and denote them by v_t and v_μ respectively.

These components are given, in terms of ϕ and χ, by

$$\left.\begin{aligned} v_t&=-\frac{\sqrt{t^2-1}}{ch}\frac{\partial\phi}{\partial t}+\frac{\sqrt{t^2-1}}{2\kappa h}\frac{\partial\chi}{\partial t}-\frac{1}{h}\mu\sqrt{t^2-1}\,\chi\ ,\\ v_\mu&=\frac{\sqrt{1-\mu^2}}{ch}\frac{\partial\phi}{\partial\mu}-\frac{\sqrt{1-\mu^2}}{2\kappa h}\frac{\partial\chi}{\partial\mu}+\frac{1}{h}t\sqrt{1-\mu^2}\,\chi\ , \end{aligned}\right\} \qquad (15)$$

where

---

† Concerning the solutions of equation (9), namely spheroidal functions, used throughout this paper, reference should be made to the writer's another paper [7].

† The constant factors of (13) are slightly different from those in equation (28) in the writer's another paper [7].

$$h^2=\frac{1}{c^2}\left\{\left(\frac{\partial x}{\partial\xi}\right)^2+\left(\frac{\partial y}{\partial\xi}\right)^2+\left(\frac{\partial z}{\partial\xi}\right)^2\right\}=\frac{1}{c^2}\left\{\left(\frac{\partial x}{\partial\eta}\right)^2+\left(\frac{\partial y}{\partial\eta}\right)^2+\left(\frac{\partial z}{\partial\eta}\right)^2\right\}=t^2-\mu^2\ .$$

Substituting the expressions (8) and (14) for ϕ and χ into (15), we have, for the moment,

$$\left.\begin{aligned}v_t&=-\frac{U}{h}\sum_{n=0}^{\infty}\alpha_nQ_n^1(t)P_n(\mu)+\frac{U}{2\kappa h}\,e^{\kappa t\mu}\sum_{m=0}^{\infty}\beta_m\sqrt{t^2-1}\,\mathrm{pe}_m(\mu)\{\mathrm{Se}_m'(t)-\kappa\mu\,\mathrm{Se}_m(t)\}\ ,\\ v_\mu&=\frac{U}{h}\sum_{n=1}^{\infty}\alpha_nQ_n(t)P_n^1(\mu)-\frac{U}{2\kappa h}\,e^{\kappa t\mu}\sum_{m=0}^{\infty}\beta_m\sqrt{1-\mu^2}\,\mathrm{Se}_m(t)\{\mathrm{pe}_m'(\mu)-\kappa t\,\mathrm{pe}_m(\mu)\}\ ,\end{aligned}\right\}\tag{16}$$

where $P_n^1(\mu)$ and $Q_n^1(t)$ are both associated Legendre functions defined by

$$P_n^1(\mu)=\sqrt{1-\mu^2}\,P_n'(\mu)\qquad\text{and}\qquad Q_n^1(t)=\sqrt{t^2-1}\,Q_n'(t)$$

and dashes denote differentiation with respect to t or μ.

We now rewrite these expressions in the forms which are suitable for fitting the boundary conditions at the surface of the spheroid. For this purpose the right-hand side of equations are assumed to be expanded into the series of the Legendre functions $P_n(\mu)$ or that of the associated Legendre functions $P_n^1(\mu)$. Let us first introduce functions $F_{m,n}(t)$ and $G_{m,n}(t)$, such that

$$\left.\begin{aligned}\frac{1}{2\kappa}\,e^{\kappa t\mu}\sqrt{t^2-1}\,\mathrm{pe}_m(\mu)\{\mathrm{Se}_m'(t)-\kappa\mu\,\mathrm{Se}_m(t)\}&=\sum_{n=0}^{\infty}F_{m,n}(t)P_n(\mu)\ ,\\ \frac{1}{2\kappa}\,e^{\kappa t\mu}\sqrt{1-\mu^2}\,\mathrm{Se}_m(t)\{\mathrm{pe}_m'(\mu)-\kappa t\,\mathrm{pe}_m(\mu)\}&=\sum_{n=1}^{\infty}G_{m,n}(t)P_n^1(\mu)\ ,\end{aligned}\right\}\tag{17}$$

the derivation of which will be shown in later lines of this section. Then the expressions for v_t and v_μ become

$$\left.\begin{aligned}v_t&=-\frac{U}{h}\sum_{n=0}^{\infty}\left\{\alpha_nQ_n^1(t)-\sum_{m=0}^{\infty}\beta_mF_{m,n}(t)\right\}P_n(\mu)\ ,\\ v_\mu&=\frac{U}{h}\sum_{n=1}^{\infty}\left\{\alpha_nQ_n(t)-\sum_{m=0}^{\infty}\beta_m\,G_{m,n}(t)\right\}P_n^1(\mu)\ .\end{aligned}\right\}\tag{18}$$

Let the surface of the spheroid under consideration be specified by $t=t_0$, then the boundary conditions $u=-U$, $v=0$, $w=0$ become

$$v_t=-\frac{U}{h}\sqrt{t^2-1}\,\mu,\qquad v_\mu=\frac{U}{h}\,t\sqrt{1-\mu^2}\ ,$$

at $t=t_0$. Using the expressions (18) for v_t and v_μ these conditions yield immediately

$$\left.\begin{aligned}&\alpha_0Q_0^1(t_0)-\sum_{m=0}^{\infty}\beta_mF_{m,0}(t_0)=0\ ,\\ &\alpha_nQ_n^1(t_0)-\sum_{m=0}^{\infty}\beta_mF_{m,n}(t_0)=\begin{cases}\sqrt{t_0^2-1} & (n=1)\ ,\\ 0 & (n=2,\ 3,\ \cdots),\end{cases}\\ &\alpha_nQ_n(t_0)-\sum_{m=0}^{\infty}\beta_mG_{m,n}(t_0)=\begin{cases}t_0 & (n=1)\ ,\\ 0 & (n=2,\ 3,\ \cdots).\end{cases}\end{aligned}\right\}\tag{19}$$

Eliminating the α_n's from the second and third of these equations, we have

$$\sum_{m=0}^{\infty}\beta_m\{Q_n(t_0)F_{m,n}(t_0)-Q_n^1(t_0)G_{m,n}(t_0)\}=\begin{cases}Q_0^1(t_0) & (n=1)\ ,\\ 0 & (n=2,\ 3,\ \cdots)\ ,\end{cases}\tag{20}$$

with $Q_0^1(t)=-1/\sqrt{t^2-1}$ and the β_m's can be determined by solving this system of simultaneous linear algebraic equations.

In what follows we shall deal with the functions $F_{m,n}(t)$ and $G_{m,n}(t)$ appearing in (17).

The expressions of these functions can be given by using the well-known orthogonality and normalisation relations for a set of the Legendre functions $P_n(\mu)$, and we have, for the moment,

$$F_{m,n}(t)=\frac{2n+1}{2}\int_{-1}^{1}\frac{1}{2\kappa}e^{\kappa t\mu}\sqrt{t^2-1}\,\mathrm{pe}_m(\mu)\{\mathrm{Se}_m'(t)-\kappa\mu\,\mathrm{Se}_m(t)\}P_n(\mu)d\mu\ ,$$

$$G_{m,n}(t)=\frac{2n+1}{2n(n+1)}\int_{-1}^{1}\frac{1}{2\kappa}e^{\kappa t\mu}\sqrt{1-\mu^2}\,\mathrm{Se}_m(t)\{\mathrm{pe}_m'(\mu)-\kappa t\,\mathrm{pe}_m(\mu)\}P_n^1(\mu)d\mu\ .$$

For convenience we now introduce the functions $\sigma_{m,n}(t)$ defined by

$$\sigma_{m,n}(t)=\int_{-1}^{1}e^{\kappa t\mu}\mathrm{pe}_m(\mu)P_n(\mu)d\mu\ . \tag{21}$$

Then, after some reductions, we have

$$\left.\begin{aligned}F_{m,n}(t)&=\frac{2n+1}{4\kappa}\sqrt{t^2-1}\left[\sigma_{m,n}(t)\mathrm{Se}_m'(t)-\frac{\kappa}{2n+1}\{n\sigma_{m,n-1}(t)+(n+1)\sigma_{m,n+1}(t)\}\mathrm{Se}_m(t)\right]\ ,\\ G_{m,n}(t)&=\frac{2n+1}{4\kappa}\mathrm{Se}_m(t)\left[\sigma_{m,n}(t)-\frac{2\kappa t}{2n+1}\{\sigma_{m,n-1}(t)-\sigma_{m,n+1}(t)\}\right].\end{aligned}\right\} \tag{22}$$

Especially $F_{m,0}(t)$ can be reduced to a simple form. It is directly given by

$$F_{m,0}(t)=\frac{\sqrt{t^2-1}}{4\kappa}\{\sigma_{m,0}(t)\mathrm{Se}_m'(t)-\kappa\sigma_{m,1}(t)\mathrm{Se}_m(t)\}\ .$$

Noticing that

$$\sigma_{m,0}(t)=\sqrt{2\pi}\,\mathrm{Re}_m(t)\qquad\text{and}\qquad\sigma_{m,0}'(t)=\kappa\sigma_{m,1}(t)\ ,$$

we have, for the moment,

$$F_{m,0}(t)=\frac{\sqrt{2\pi}}{4\kappa}\sqrt{t^2-1}\{\mathrm{Re}_m(t)\mathrm{Se}_m'(t)-\mathrm{Re}_m'(t)\mathrm{Se}_m(t)\}\ .$$

The curly bracket on the right-hand side of the above equation gives, as is well-known, the Wronskian determinant composed of the two kinds of solutions $\mathrm{Re}_m(t)$ and $\mathrm{Se}_m(t)$ of equation (9), and therefore we have as usual

$$\mathrm{Re}_m(t)\mathrm{Se}_m'(t)-\mathrm{Re}_m'(t)\mathrm{Se}_m(t)=\frac{C_m}{t^2-1}\ ,$$

where C_m is a constant independent of t, which can be evaluated by assuming t to be large and replacing $\mathrm{Re}_m(t)$ and $\mathrm{Se}_m(t)$ by their asymptotic expressions, namely

$$\mathrm{Re}_m(t)\sim\frac{\mathrm{pe}_m(1)}{\sqrt{2\pi}}\frac{e^{\kappa t}}{\kappa t}\qquad\text{and}\qquad\mathrm{Se}_m(t)\sim\frac{e^{-\kappa t}}{\kappa t}\ . \tag{23}$$

Hence we have

$$C_m=-\frac{1}{\kappa}\sqrt{\frac{2}{\pi}}\,\mathrm{pe}_m(1)\ .$$

Thus we get finally

$$F_{m,0}(t)=-\frac{\mathrm{pe}_m(1)}{2\kappa^2}\frac{1}{\sqrt{t^2-1}}\ . \tag{24}$$

By the way, it is here to be mentioned that the function $\sigma_{m,n}(t)$ defined by (21) can be rewritten in series of the Legendre functions as:

$$\left.\begin{aligned}\sigma_{2m,n}(t)&=\sum_{r=0}^{\infty}\frac{2}{4r+1}f_{n,2r}(t)A_{2r}^{(2m)}\ ,\\ \sigma_{2m+1,n}(t)&=\sum_{r=0}^{\infty}\frac{2}{4r+3}f_{n,2r+1}(t)A_{2r+1}^{(2m+1)}\ ,\end{aligned}\right\} \tag{25}$$

where the $f_{n,r}(t)$'s are the coefficients of the following expansion:

$$e^{\kappa t\mu}P_n(\mu)=\sum_{r=0}^{\infty}f_{n,r}(t)P_r(\mu)\ ,$$

and are given by †

$$f_{n,r}(t)=(2r+1)\sum_{s=0}^{n}\frac{(2s)!(2n-2s)!(2r-2s)!}{(s!)^2(2n+2r-2s+1)!}\left\{\frac{(n+r-s)!}{(n-s)!(r-s)!}\right\}^2\varphi_{n+r-2s}(t),$$

with

$$\varphi_n(t)=(2n+1)\sqrt{\frac{\pi}{2\kappa t}}\,I_{n+\frac{1}{2}}(\kappa t)\ .$$

§ 4. The General Expression for the Drag

We shall next proceed to calculate the drag experienced by a prolate spheroid. As we have already mentioned in [1], two different methods are commonly used in calculating the drag on a solid body immersed in a stream of fluid. In one method the drag is obtained by summing up the viscous stresses exerted by the fluid upon the surface of the body, while in the other it is calculated by applying the theorem of momentum to an infinite mass of fluid surrounding the body.

If the analysis is based upon Oseen's equations, the first method gives the drag D on a solid obstacle in the form

$$D=-\rho U\iint\frac{\partial\phi}{\partial n}\,dS\ , \tag{26}$$

where the double integration is taken over the surface of the body and $\partial/\partial n$ denotes differentiation along the outward normal n to S. The second method gives

$$D=-\rho U\iint\frac{\partial\phi}{\partial n'}\,d\sigma\ , \tag{27}$$

where integration is taken round a large closed surface σ everywhere at a great distance from the obstacle and $\partial/\partial n'$ denotes differentiation along the outward normal n' to σ.

For the prolate spheroid, $t=t_0$, (26) becomes

$$D=-2\pi c\rho U(t_0^2-1)\int_{-1}^{1}\left(\frac{\partial\phi}{\partial t}\right)_{t=t_0}d\mu\ ,$$

whilst (27) gives

$$D=-2\pi c\rho U\int_{-1}^{1}\left[(t^2-1)\frac{\partial\phi}{\partial t}\right]_{t\to\infty}d\mu\ ,$$

σ being taken to be a large spheroidal surface confocal with the surface of the spheroid $t=t_0$. By making use of the expression (8) for ϕ either of the above two formulae gives one and the same value for the drag acting on the spheroid, namely

$$D=4\pi c^2\rho U^2\alpha_0\ . \tag{28}$$

By the aid of the first of equations (19), together with (24), α_0 can be written in the form

$$\alpha_0=\frac{1}{2\kappa^2}\sum_{m=0}^{\infty}\mathrm{pe}_m(1)\beta_m\ . \tag{29}$$

Thus we get the general expression for the drag in the form:

$$D=\frac{32\pi a^2\rho U^2}{R^2}\sum_{m=0}^{\infty}\mathrm{pe}_m(1)\beta_m\ , \tag{30}$$

where $R=2aU/\nu$ is the Reynolds number. Further, if we define the drag coefficient C_D by $D/(\frac{1}{2}\rho U^2\cdot\pi a^2)$, we have

$$C_D=\frac{64}{R^2}\sum_{m=0}^{\infty}\mathrm{pe}_m(1)\beta_m\ . \tag{31}$$

The general expression for the drag on an oblate spheroid with its face normal to a uniform stream can be also obtained in a similar manner and will be shown in Appendix.

§ 5. The Pressure Drag and the Frictional Drag

As mentioned previously [1], [4], the total drag on a solid obstacle can be analysed into the pressure drag D_p and the frictional drag D_f. As far as Oseen's approximation is concerned, these drags are given respectively by

$$\left.\begin{aligned}D_p&=-\rho U\iint l\,\frac{\partial\phi}{\partial x}\,dS\,,\\ D_f&=-\rho U\iint\left(m\frac{\partial\phi}{\partial y}+n\frac{\partial\phi}{\partial z}\right)dS,\end{aligned}\right\} \tag{32}$$

---

† See also equation (10) in [1].

where (l, m, n) are the direction cosines of the outward normal to the surface of the spheroid.

We deal with the particular case of the prolate spheroid and proceed to the computation of D_p, which is now given by

$$D_p=2\pi c\rho U(t_0^2-1)\int_{-1}^{1}\left\{(t_0^2-1)\mu^2\frac{\partial\phi}{\partial t}+t_0\mu(1-\mu^2)\frac{\partial\phi}{\partial\mu}\right\}d\mu\ .$$

Inserting the expression (8) for ϕ, we have, for the moment,

$$D_p=2\pi c^2\rho U^2\alpha_0(t_0^2-1)\int_{-1}^{1}\frac{\mu^2}{h^2}d\mu$$
$$-2\pi c^2\rho U^2(t_0^2-1)\sum_{n=1}^{\infty}\alpha_n\int_{-1}^{1}\{(t_0^2-1)Q_n'(t_0)\cdot\mu^2P_n(\mu)+t_0Q_n(t_0)\cdot\mu(1-\mu^2)P_n'(\mu)\}\frac{d\mu}{h^2}\ .$$

By applying some recurrence formulae for the Legendre functions $P_n(\mu)$ and $Q_n(t)$ and remembering that $h^2=t^2-\mu^2$, the second integral on the right-hand side becomes

$$\frac{n(n+1)}{2n+1}\int_{-1}^{1}\{P_{n-1}(\mu)Q_{n+1}(t_0)-P_{n+1}(\mu)Q_{n-1}(t_0)\}\frac{\mu d\mu}{t^2-\mu^2}\ .$$

By the way, making use of Neumann's formula[†] relating to the Legendre functions:

$$Q_n(t)=\frac{1}{2}\int_{-1}^{1}\frac{P_n(\mu)}{t-\mu}d\mu\ ,$$

we can easily show that

$$\frac{1}{2}\int_{-1}^{1}\frac{\mu P_n(\mu)}{t^2-\mu^2}d\mu=\begin{cases}Q_n(t) & \text{when } n \text{ is odd ,}\\ 0 & \text{when } n \text{ is even.}\end{cases} \tag{33}$$

Thus, the first integral in the above expression for D_p becomes

$$\int_{-1}^{1}\frac{\mu^2}{t^2-\mu^2}d\mu=2Q_1(t)\ ,$$

while the second integral vanishes for every value of n.

Therefore we get finally

$$\left.\begin{aligned}&D_p/D=(t_0^2-1)Q_1(t_0)\ ,\\ \text{and so}\quad &D_f/D=1-(t_0^2-1)Q_1(t_0)\ .\end{aligned}\right\} \tag{34}$$

This result shows that, if calculations are based upon Oseen's equations of motion, the total drag on the spheroid is divided into the pressure and frictional drags in a definite ratio, which is independent of the Reynolds number but dependent upon the shape of the spheroid.

The pressure drag obtained above can also be written in terms of elementary functions as

$$\frac{D_p}{D}=(t_0^2-1)\left\{\frac{t_0}{2}\log\frac{t_0+1}{t_0-1}-1\right\}\ , \tag{35}$$

where $t_0=1/\sqrt{1-(b/a)^2}$. The frictional drag is then given by $D_f/D=1-D_p/D$.

The similar result concerning the pressure and frictional drags on an oblate spheroid will also be given here. Let an oblate spheroid be placed in a uniform stream in such a way that its major-axis, i.e., the axis of symmetry, is along the stream and let the major- and minor-axes be of length $2a$ and $2b$ respectively. Then we have, (from the general expression for D_p given in Appendix),

$$\frac{D_p}{D}=(\tau_0^2+1)(1-\tau_0\cot^{-1}\tau_0) \tag{36}$$

with $\tau_0=(b/a)/\sqrt{1-(b/a)^2}$.

We can now deduce the results for some special cases. For a needle-like body placed along a uniform stream, we have, by putting $b=0$ in (35),

$$D_p=0\ ,\qquad D_f=D\ , \tag{37}$$

but it is evident physically that $D=0$ in this case. While for a circular disc set at right angles to a uniform stream we get, by putting $b=0$ in (36),

$$D_p=D\ ,\qquad D_f=0\ . \tag{38}$$

Further, in the case of a sphere $(a=b)$ we have, from either of (35) and (36),

---

[†] E. W. Hobson, 'The theory of spherical and ellipsoidal harmonics', Cambridge 1931, § 40.

$$D_p = \tfrac{1}{3}D\,, \qquad D_f = \tfrac{2}{3}D\,. \tag{39}$$

Thus, as we have already pointed out in [1], the pressure and frictional drags contribute to the total drag on the sphere in the ratio 1:2.

§ 6. An Approximate Expansion Formula for the Drag

In order to calculate numerically the values of the drag coefficient directly from the general expression (31) we must first determine the β_m's numerically by solving the system of simultaneous algebraic equation (20) for each given value of the Reynolds number; the work is thus rather cumbersome. It is therefore desirable to derive an approximate formula expanded in powers of the Reynolds number, which may be conveniently used for numerical computation of the values of the drag.

For this purpose we have to express β_m as well as $\mathrm{pe}_m(1)$ in powers of κ, or in powers of the Reynolds number R. To do this, we must expand the quantities $F_{m,n}(t_0)$ and $G_{m,n}(t_0)$ in (20) in powers of κ by using the series expressions for the coefficients $A_r^{(n)}$'s in $\mathrm{pe}_m(\mu)$ as well as the expansions for the function $\mathrm{Se}_m(t)$ and others in powers of κ[†]. Assuming R to be small it is thus found that $\beta_0, \beta_1, \beta_2, \cdots$ are of order $R, R^3, R^5, \cdots$ respectively, while it is seen that the quantity $\mathrm{pe}_m(1)$ is of order unity for any number of m.

Making use of the above estimated orders an approximate expansion formula for the drag coefficient for the case of a prolate spheroid is obtained correct to the order of R. The final result only will be given here. Thus,

$$C_D = \frac{64}{RS}\left[1 + \frac{1}{2S}R\right]. \tag{40}$$

where we have put for brevity

$$S = t_0\left\{(1+t_0^2)\log\frac{t_0+1}{t_0-1} - 2t_0\right\}.$$

with $t_0 = 1/\sqrt{1-(b/a)^2}$. Approximate expansion formulae correct to the higher orders of the Reynolds number R may be obtained in like manner, but it will be seen in later lines that the above formula will be sufficient for computing values of the drag coefficient when the Reynolds number is sufficiently small.

A similar approximate expansion formula for the drag coefficient is also obtained for the case of an oblate spheroids, namely

$$C_D = \frac{64}{RS}\left[1 + \frac{1}{2S}R\right]. \tag{41}$$

Although the same notation is used, S in this formula is different from that used in (40) and is defined as[†]

$$S = 2\sqrt{\tau_0^2+1}\,\{(1-\tau_0^2)\cot^{-1}\tau_0 + \tau_0\}$$

with $\tau_0 = (b/a)/\sqrt{1-(b/a)^2}$.

Approximate expansion formulae for the drag on a sphere and a circular disc can be readily obtained as limiting forms[††] of the above formulae (40) and (41). An approximate expansion formula for the drag on a sphere of diameter $d=2a$ can be obtained by tending t_0 to infinity in either of our preceding formulae (40) and (41). The result is

$$C_D = \frac{24}{R} + \frac{9}{2}\,, \tag{42}$$

where $R = Ud/\nu$ is the Reynolds number. As should be expected, this formula is in complete agreement with that obtained by Goldstein [6]. Next, if we put $\tau_0 = 0$ in (41), we get an approximate expansion formula for the drag on a circular disc of diameter $d=2a$ placed at right angles across the stream. Thus,

$$C_D = \frac{64}{\pi}\,\frac{1}{R} + \frac{32}{\pi^2}\,, \tag{43}$$

where, as before, the Reynolds number R is defined as $R = Ud/\nu$.

As mentioned before, Oseen [5] himself has calculated approximately the drags exerted on a prolate spheroid and an oblate spheroid including a sphere and a circular disc as special cases. Although the expressions and the notations are different, it is found after some reductions that out formulae are in com-

---

[†] For expansions of the spheroidal functions $\mathrm{pe}_m(\mu)$ and $\mathrm{Se}_m(t)$ necessary for our computation, reference should be made to the writer's another paper [7].

[†] For a prolate spheroid S can be written as

$$S = 2t_0\{(1+t_0^2)Q_0(t_0) - t_0\}$$

when $Q_0(t) = (1/2)\log((t+1)/(t-1))$; while, for the case of an oblate spheroid

$$S = 2\sqrt{\tau_0^2+1}\,\{(1-\tau_0^2)q_0(\tau_0) + \tau_0\}$$

and $q_0(\tau) = iQ_0(i\tau) = \cot^{-1}\tau$.

[††] A needle-like body is also a limiting case of a prolate spheroid, but, as mentioned above, the drag on such a body becomes evidently zero and is of no physical interest.

plete agreement with the corresponding Oseen's formulae.

By making use of our approximate formulae we shall now calculate numerically the values of the drag coefficient C_D for various spheroids, including a circular disc and a sphere at small Reynolds numbers.

Numerical values of C_D thus calculated are given in Table I. It is of some interest to note that the value of the drag coefficient of a sphere at any Reynolds number is always larger than the corresponding values for spheroids and a circular disc, each having the same length or the same cross-stream dimension as a sphere. We have already noticed in a previous paper [4] that such a curious property of the drag at small Reynolds numbers is also found in the group of a circular cylinder, an elliptic cylinder and a flat plate, provided that each of them has the same width across the stream.

Table I. *Values of* C_D.

Case *A*. Prolate Spheroid $(b/a=1/4)$
Case *B*. Prolate Spheroid $(b/a=1/2)$
Case *C*. Sphere
Case *D*. Oblate Spheroid $(b/a=1/2)$
Case *E*. Oblate Spheroid $(b/a=1/4)$
Case *F*. Circular disc

R	Case *A*	Case *B*	Case *C*	Case *D*	Case *E*	Case *F*
0.01	960	1446	2405	2176	2085	2040
0.05	192	291	485	438	420	411
0.1	96.6	146	245	221	212	207
0.2	48.7	73.9	125	112	107	105
0.4	24.7	37.7	64.5	58.0	55.4	54.2
0.6	16.7	25.7	44.5	39.9	38.1	37.2
0.8	12.7	19.7	34.5	30.8	29.4	28.7
1.0	10.3	16.1	28.5	25.4	24.2	23.6
2.0	5.51	8.85	16.5	14.6	13.8	13.4
3.0	3.91	6.45	12.5	—	—	—
4.0	3.12	—	—	—	—	—

Appendix

The case of an oblate spheroid

For completeness we shall give here, as an addendum, the results for the case of an oblate spheroid. For brevity only relevant parts of the analysis will be given and detailed calculations will be shown elsewhere.

The fundamental solution of Oseen's equations is given by ϕ and χ which satisfy equations (5) and (6) respectively. We consider an oblate spheroid which is situated in such a manner that its minor-axis, i.e., the axis of symmetry, is along a uniform stream. Let the major- and minor-axes be of length $2a$ and $2b$ respectively. Then it is convenient to introduce the oblate spheroidal coordinates defined by

$$x+i\tilde{\omega}=c\sinh(\xi+i\eta)\,,$$

or

$$x=c\tau\mu\,,\qquad \tilde{\omega}=c\sqrt{\tau^2+1}\sqrt{1-\mu^2}\,,$$

where $c=\sqrt{a^2-b^2}$ and $\tau=\sinh\xi$, $\mu=\cos\eta$.

The appropriate expression for the function ϕ is given by

$$\phi=cU\sum_{n=0}^{\infty}\alpha_n{}^*q_n(\tau)P_n(\mu)\,,$$

where the $\alpha_n{}^*$'s are constants of integration and $q_n(\tau)$ is ellipsoidal harmonics which is related to the Legendre function by $q_n(\tau)=i^{n+1}Q_n(i\tau)$.

If we assume the function χ in the form $\chi=e^{kx}T^*(\tau)M^*(\mu)$, then the functions $T_*(\tau)$ and $M^*(\mu)$ satisfy the equations:

$$\frac{d}{d\tau}\left\{(1+\tau^2)\frac{dT^*}{d\tau}\right\}-(\lambda+\kappa^2\tau^2)T^*=0\,,$$

$$\frac{d}{d\mu}\left\{(1-\mu^2)\frac{dM^*}{d\mu}\right\}+(\lambda-\kappa^2\mu^2)M^*=0\,,$$

where κ stands for *kc*. We denote the appropriate solution† regular at $\mu=\pm1$ of the second differential equation for $M^*(\mu)$ by $\mathrm{pe}_m{}^*(\mu)$ provisionally. Then these functions are connected formally with $\mathrm{pe}_m(\mu)$ by the relation $\mathrm{pe}_m{}^*(\mu;\,\kappa)=\mathrm{pe}_m(\mu;\,i\kappa)$ and are expressed in series of the Legendre functions as

$$\left.\begin{aligned}\mathrm{pe}_{2n}{}^*(\mu)&=\sum_{r=0}^{\infty}B_{2r}^{(2n)}P_{2r}(\mu)\,,\\ \mathrm{pe}_{2n+1}{}^*(\mu)&=\sum_{r=0}^{\infty}B_{2r+1}^{(2n+1)}P_{2r+1}(\mu)\,.\end{aligned}\right\}$$

The solution of the first kind of the first differential equation for $T^*(\tau)$ which diverges at infinity is given by

$$\mathrm{Re}_n{}^*(\tau)=\frac{1}{\sqrt{2\pi}}\int_{-1}^{1}e^{\kappa\tau\mu}\mathrm{pe}_n{}^*(\mu)d\mu\,,$$

and is expressed as

$$\left.\begin{aligned}\mathrm{Re}_{2n}{}^*(\tau)&=\frac{1}{\sqrt{\kappa\tau}}\sum_{r=0}^{\infty}B_{2r}^{(2n)}I_{2r+\frac{1}{2}}(\kappa\tau)\,,\\ \mathrm{Re}_{2n+1}{}^*(\tau)&=\frac{1}{\sqrt{\kappa\tau}}\sum_{r=0}^{\infty}B_{2r+1}^{(2n+1)}I_{2r+\frac{3}{2}}(\kappa\tau)\,.\end{aligned}\right\}$$

While, the solution of the second kind of the same equation which converges to zero when τ is large is given in the form

$$\left.\begin{aligned}\mathrm{Se}_{2n}{}^*(\tau)&=\frac{2}{\kappa B_0^{(2n)}}\sum_{p=0}^{\infty}\nu_{2p}{}^*K_{p+\frac{1}{2}}\left(\frac{\kappa}{2}e^{\xi}\right)I_{p+\frac{1}{2}}\left(\frac{\kappa}{2}e^{-\xi}\right),\\ \mathrm{Se}_{2n+1}{}^*(\tau)&=\frac{24}{\kappa^2B_1^{(2n+1)}}\sinh\xi\sum_{p=0}^{\infty}\nu_{2p+1}{}^*K_{p+\frac{3}{2}}\left(\frac{\kappa}{2}e^{\xi}\right)I_{p+\frac{3}{2}}\left(\frac{\kappa}{2}e^{-\xi}\right),\end{aligned}\right\}$$

where the $\nu_p{}^*$'s are dependent upon $B_r^{(n)}$.

Thus we find that the appropriate expression for the function χ is given by

$$\chi=Ue^{\kappa\tau\mu}\sum_{m=0}^{\infty}\beta_m{}^*\mathrm{Se}_m{}^*(\tau)\mathrm{pe}_m{}^*(\mu),$$

where the $\beta_m{}^*$'s are constants of integration.

The constants of integration $\alpha_n{}^*$ and $\beta_m{}^*$ in the above expressions for ϕ and χ can be determined by the boundary conditions at the surface of the spheroid which is specified by $\tau=\tau_0$. Thus, they are determined by solving the following system of simultaneous algebraic linear equations, namely:

$$\alpha_0{}^*q_0{}^1(\tau_0)-\sum_{m=0}^{\infty}\beta_m{}^*F_{m,0}{}^*(\tau_0)=0\,,$$

$$\alpha_n{}^*q_n{}^1(\tau_0)-\sum_{m=0}^{\infty}\beta_m{}^*F_{m,n}{}^*(\tau_0)=\begin{cases}\sqrt{\tau_0{}^2+1} & (n=1)\,,\\ 0 & (n=2,\,3,\,\cdots)\,,\end{cases}$$

---

† For the spheroidal functions relating to the oblate spheroidal coordinates reference should be made to Appendix of our paper [7].

$$\alpha_n^* q_n(\tau_0) - \sum_{m=0}^{\infty} \beta_m^* G_{m,n}^*(\tau_0) = \begin{cases} \tau_0 & (n=1)\,, \\ 0 & (n=2,\,3,\,\cdots)\,, \end{cases}$$

where $q_n^1(\tau)$ is an associated function of $q_n(\tau)$ defined as $q_n^1(\tau)=\sqrt{\tau^2+1}\,q_n'(\tau)$, and the functions $F_{m,n}^*(\tau)$ and $G_{m,n}^*(\tau)$ are given by

$$F_{m,0}^*(\tau) = -\frac{\mathrm{pe}_m^*(1)}{2\kappa^2}\frac{1}{\sqrt{\tau^2+1}}\,,$$

$$F_{m,n}^*(\tau) = \frac{2n+1}{4\kappa}\sqrt{\tau^2+1}\left[\sigma_{m,n}^*(\tau)\mathrm{Se}_m^{*\prime}(\tau) - \frac{\kappa}{2n+1}\{n\sigma_{m,n-1}^*(\tau)+(n+1)\sigma_{m,n+1}^*(\tau)\}\,\mathrm{Se}_m^*(\tau)\right],$$

$$G_{m,n}^*(\tau) = \frac{2n+1}{4\kappa}\,\mathrm{Se}_m^*(\tau)\left[\sigma_{m,n}^*(\tau) - \frac{2\kappa\tau}{2n+1}\{\sigma_{m,n-1}^*(\tau)-\sigma_{m,n+1}(\tau)\}\right],$$

with

$$\left.\begin{aligned} \sigma_{2m,n}^*(\tau) &= \sum_{r=0}^{\infty}\frac{2}{4r+1}f_{n,2r}(\tau)B_{2r}^{(2m)}\,, \\ \sigma_{2m+1,n}^*(\tau) &= \sum_{r=0}^{\infty}\frac{2}{4r+3}f_{n,2r+1}(\tau)B_{2r+1}^{(2m+1)}\,. \end{aligned}\right\}$$

Further, the β_m^*'s are determined by solving the following system of simultaneous algebraic linear equations

$$\sum_{m=0}^{\infty}\beta_m^*\{q_n(\tau_0)F_{m,n}^*(\tau_0) - q_n^1(\tau_0)G_{m,n}^*(t_0)\} = \begin{cases} q_0^1(\tau_0) & (n=1)\,, \\ 0 & (n=2,\,3,\,\cdots)\,, \end{cases}$$

where $q_0^1(\tau)=-\sqrt{\tau^2+1}$.

By making use of the above exact analytical solution of Oseen's equations we have calculated, as before, the general expression for the drag experienced by the oblate spheroid. By introducing the drag coefficient $C_D=D/(\frac{1}{2}\rho U^2\cdot\pi a^2)$ we get

$$C_D = \frac{64}{R^2}\sum_{m=0}^{\infty}\mathrm{pe}_m^*(1)\beta_m^*\,,$$

where $R=2aU/\nu$, as before.

The general expressions for the pressure and frictional drags D_p and D_f are given by

$$D_p/D = (\tau_0^2+1)q_1(\tau_0)\,,$$

$$D_f/D = 1-(\tau_0^2+1)q_1(\tau_0)\,,$$

with $q_1(\tau)=1-\tau q_0(\tau)$ and $q_0(\tau)=\cot^{-1}\tau$.

Acknowledgement

The writer wishes to express his cordial thanks to Professor S. Tomotika for his interest and invaluable advice throughout the series of investigations on the motion of viscous fluid and on allied subjects.

References

1) S. Tomotika and T. Aoi: Quart. J. Mech. and Applied Math., Oxford, **3** (1950) 140.
2) S. Tomotika and T. Aoi: Mem. Coll. Sci. Univ. of Kyoto, A, **26** (1950) 9.
3) S. Tomotika and T. Aoi: Quart. J. Mech. and Applied Math., Oxford **4** (1951) 401.
4) S. Tomotika and T. Aoi: Quart. J. Mech. and Applied Math., Oxford, **6** (1953) 290.
5) C. W. Oseen: 'Hydrodynamik', Leipzig 1927, § 18.
6) S. Goldstein: Proc. Roy. Soc. A **123** (1929) 225.
7) T. Aoi: J. Phys. Soc. Japan **10** (1955) 130.

Journal of the Physical Society of Japan Vol. 10, No. 2, February, 1955

On Spheroidal Functions

By Tyûsei Aoi

Osaka University of Engineering, Osaka

(Received September 20, 1954)

In this paper are investigated some mathematical properties of spheroidal functions satisfying the differential equation of the form:

$$\frac{d}{dz}\left\{(1-z^2)\frac{dZ}{dz}\right\}+(\lambda+\kappa^2z^2)Z=0\ .$$

One solution $\mathrm{pe}_n(z)$ regular at $|z|=1$, which has already been known as special case of the generalized spheroidal function $\mathrm{pe}_n^m(z)$, is developed into a Legendre expansion and its coefficients are obtained explicitly for several cases.

The solution of the first kind $\mathrm{Re}_n(z)$ and that of the second kind $\mathrm{Se}_n(z)$, which are valid especially when $z \gg 1$, are defined by the definite integrals and are also expressed in series forms in terms of the modified Bessel functions.

An alternative expression for $\mathrm{Se}_n(z)$, which is conveniently used even when z is not so large, is also defined in like manner as in the case of the derivation of the modified Mathieu function $\mathrm{FEK}_n(z)$ or $\mathrm{GEK}_n(z)$. Further, the asymptotic behaviours of these functions $\mathrm{Re}_n(z)$ and $\mathrm{Se}_n(z)$ are obtained.

Detailed calculations are developed for the case of a prolate spheroid. For the case of an oblate spheroid some essential parts only are given in Appendix.

§ 1. Introduction

As is well-known, in some boundary value problems in mathematical physics we deal with the so-called Helmholtz equation:

$$\frac{\partial^2 V}{\partial x^2}+\frac{\partial^2 V}{\partial y^2}+\frac{\partial^2 V}{\partial z^2}-k^2V=0\ , \qquad (1)$$

or,

$$\frac{\partial^2 V}{\partial x^2}+\frac{\partial^2 V}{\partial y^2}+\frac{\partial^2 V}{\partial z^2}+k^2V=0\ . \qquad (2)$$

For instance, the motion of a solid body in a viscous fluid and the scattering of electric waves by an obstacle are discussed on the basis of equations (1) and (2) respectively. In the former problem it is required to obtain a solution of exponential type of (1), while in the latter we require a solution of simple harmonic type of (2). In dealing with an ellipsoid of revolution, that is, a prolate or oblate spheroid, which is placed in a field symmetrical about the axis of revolution of the spheroid, it is convenient to introduce the prolate or oblate spheroidal coordinates in place of the Cartesian coordinates (x,y,z).

Confining ourselves to the discussion of equation (1) and to the problem relating to a prolate spheroid, we now introduce the prolate spheroidal coordinates (ξ,η) defined by

$$x+i\tilde{\omega}=c\cosh(\xi+i\eta)\ ,$$

where $\tilde{\omega}=\sqrt{y^2+z^2}$ and c is a constant depending upon the shape of the spheroid. Denoting $\cosh\xi$ by t and $\cos\eta$ by μ, we have

$$x=ct\mu\ , \qquad \tilde{\omega}=c\sqrt{t^2-1}\sqrt{1-\mu^2}\ . \qquad (3)$$

Assuming $V=T(t)M(\mu)$, we have two differential equations for determining $T(t)$ and $M(\mu)$, namely

$$\frac{d}{dt}\left\{(1-t^2)\frac{dT}{dt}\right\}+(\lambda+\kappa^2t^2)T=0\ , \qquad (4)$$

and

$$\frac{d}{d\mu}\left\{(1-\mu^2)\frac{dM}{d\mu}\right\}+(\lambda+\kappa^2\mu^2)M=0\ , \qquad (5)$$

where λ is a characteristic constant and κ stands for kc. These equations are both of the same form as

$$\frac{d}{dz}\left\{(1-z^2)\frac{dZ}{dz}\right\}+(\lambda+\kappa^2z^2)Z=0\ , \qquad (6)$$

and $Z=T$ when $z=t$ and $Z=M$ when $z=\mu$.

The main object of the present paper is to discuss the solutions of the above fundamental equation (6), i.e., the so-called spheroidal functions. The present investigation has been made in connection with the exact analytical solution of Oseen's equations for the motion of a prolate or oblate spheroid in a viscous fluid [1].

The investigations on the spheroidal functions seem to be rather few† and they are mainly concerned with the propagation of electric or sound waves on the basis of the solution of simple harmonic type of equation (2). In the present paper, however, we start from the equation of exponential type (1) and some new results are obtained which will also be applicable appropriately to the case of wave motion.

In cases when we deal with an oblate spheroid or when the equation (2) is dealt with, the respective fundamental equation takes a similar form to equation (6) except for the difference in signs and hence the analysis developed in the present paper will be readily applied to those cases. Some of the results relating to the solutions of exponential type for the case of an oblate spheroid are given in Appendix.

§ 2. Integral Representations of the Solutions

We shall apply the Laplace transformation to the fundamental equation (6). Thus we assume that this equation can be satisfied by

$$Z(z)=\int e^{\kappa z\zeta}w(\zeta)d\zeta\ , \qquad (7)$$

provided that a function $w(\zeta)$ and the limits of integration are properly chosen. Substituting (7) into (6) we have

$$\int e^{\kappa z\zeta}w(\zeta)\{\kappa^2z^2(1-\zeta^2)-2\kappa z\zeta+(\lambda+\kappa^2\zeta^2)\}d\zeta=0\ ,$$

which, by partial integration, can be reduced to

$$e^{\kappa z\zeta}(1-\zeta^2)\left(\frac{dw}{d\zeta}-\kappa zw\right)$$
$$-\int e^{\kappa z\zeta}\left[\frac{d}{d\zeta}\left\{(1-\zeta^2)\frac{dw}{d\zeta}\right\}+(\lambda+\kappa^2\zeta^2)w\right]d\zeta=0.$$

Thus the appropriate limits of integration are determined from the condition that when taken between the limits of integration, the integrated part vanishes, namely:

$$e^{\kappa z\zeta}(1-\zeta^2)\left(\frac{dw}{d\zeta}-\kappa zw\right)=0\ . \qquad (8)$$

While, a function $w(\zeta)$ is so determined that it satisfies the equation:

$$\frac{d}{d\zeta}\left\{(1-\zeta^2)\frac{dw}{d\zeta}\right\}+(\lambda+\kappa^2\zeta^2)w=0\ , \qquad (9)$$

which is of the same form as equation (6).

In the first place, we shall obtain a solution $Z(z)$ which is regular at $z=\pm1$. Such a solution is given by taking the integration from $\zeta=-1$ to $\zeta=1$ and by assuming w to be identical with Z. Thus, the required solution is given by

$$Z(z)=\omega\int_{-1}^{1}e^{\kappa z\zeta}Z(\zeta)d\zeta\ ,$$

provided that ω is connected with λ and is required to be one of a set of discrete characteristic values. Following Mölich††, we denote such a solution by $\mathrm{pe}_n(\mu)$ with a characteristic value ω_n, we have

$$\mathrm{pe}_n(\mu)=\omega_n\int_{-1}^{1}e^{\kappa\mu\zeta}\mathrm{pe}_n(\zeta)d\zeta\ , \qquad (10)$$

where again we have written μ for z. Thus it can be said that the spheroidal function $\mathrm{pe}_n(\mu)$ which is regular at $\mu=\pm1$ satisfies the homogeneous integral equation with the symmetric kernel (10). It is to be mentioned here that this spheroidal function reduces to the Legendre function $P_n(\mu)$ when the parameter κ becomes zero.

Next we shall proceed to find solutions of exponential type which can appropriately be used especially when $z\gg1$, and thus we take $t=\cosh\xi$ for z. Such solutions are classified into two kinds, namely the solution of the first kind which diverges when t is large and the solution of the second kind which vanishes when t tends to infinity. By taking the spheroidal function $\mathrm{pe}_n(\zeta)$ for $w(\zeta)$ in (7) and carrying out the integration from $\zeta=-1$ to $\zeta=1$, we defined the solution of the first kind, denoted provisionally by $\mathrm{Re}_n(t)$, as:

$$\mathrm{Re}_n(t)=\frac{1}{\sqrt{2\pi}}\int_{-1}^{1}e^{\kappa t\mu}\mathrm{pe}_n(\mu)d\mu\ . \qquad (11)$$

It will be seen later that this function is connected with the modified Bessel function of half-integral order $I_{n+\frac{1}{2}}$ as:

$$\mathrm{Re}_n(t)\to\frac{1}{\sqrt{\kappa t}}I_{n+\frac{1}{2}}(\kappa t)\ ,$$

when the parameter κ tends to zero.

---

† See, e.g., [2], [3] and [4].

†† Möglich [2] and Kotani [3] have discussed the generalized spheroidal function $\mathrm{pe}_n^m(\mu)$. Their $\mathrm{pe}_n{}^0(\mu)$ is equivalent to our $\mathrm{pe}_n(\mu)$.

The fundamental equation (6) remains unaltered when z is replaced by $-z$, so that

$$Z(z)=\int e^{-\kappa z\zeta}w(\zeta)d\zeta\ ,$$

becomes also a solution of (6) provided that the limits of integration are determined by the condition that when taken between the limits of integration,

$$e^{-\kappa z\zeta}(1-\zeta^2)\left(\frac{dw}{d\zeta}+\kappa zw\right)=0\ ,$$

and a function $w(\zeta)$ satisfies equation (9). As will be shown later in § 8, the solutions $Z(z)$, or $w(\zeta)$, have in general the asymptotic behaviour of two types when their argument z is large, namely $w(\zeta)\sim\frac{1}{\kappa\zeta}e^{\kappa\zeta}$ and $w(\zeta)\sim\frac{1}{\kappa\zeta}e^{-\kappa\zeta}$ for a large value of ζ. Hence, if for $w(\zeta)$ we take $\mathrm{pe}_n(\zeta)$ which is regular at $\zeta=1$, the integral can be taken from $\zeta=1$ to infinity, provided that $z>1$. Thus we define the solution of the second kind, denoted provisionally by $\mathrm{Se}_n(t)$, as:

$$\mathrm{Se}_n(t)=\sqrt{\frac{\pi}{2}}\int_1^{\infty}e^{-\kappa t\zeta}\mathrm{pe}_n(\zeta)d\zeta\ . \tag{12}$$

It will be seen later that this solution is related with the modified Bessel function of half-integral order $K_{n+\frac{1}{2}}$ as:

$$\mathrm{Se}_n(t)\to\frac{1}{\sqrt{\kappa t}}K_{n+\frac{1}{2}}(\kappa t)\ ,$$

when the parameter κ tends to zero.

§ 3. Series Expressions for $\mathrm{pe}_n(\mu)$

When the parameter κ is small, the spheroidal function $\mathrm{pe}_n(\mu)$ can be expanded in powers of κ. The generalized spheroidal functions $\mathrm{pe}_n^m(\mu)$ have been investigated by Kotani as early as 1933 and their expressions in some special cases have been given explicitly. In obtaining such series expansions we adopt here a procedure similar to that used in deriving the series expansions of the Mathieu function $\mathrm{ce}_n(z)$ or $\mathrm{se}_n(z)$. Thus we get series expressions for the spheroidal function $\mathrm{pe}_n(\mu)$ in concrete form. Our results are more extensive than Kotani's and hence it may be worth while to describe them in subsequent lines.

We assume that the parameter κ is small and that the function $\mathrm{pe}_n(\mu)$ and the corresponding characteristic constant λ_n are expanded in powers of κ as:

$$\begin{aligned}\mathrm{pe}_n(\mu)=P_n(\mu)&+f_2(\mu)\kappa^2\\&+f_4(\mu)\kappa^4+f_6(\mu)\kappa^6+\cdots\ ,\end{aligned} \tag{13}$$

and

$$\lambda_n=n(n+1)+\alpha_2\kappa^2+\alpha_4\kappa^4+\alpha_6\kappa^6+\cdots\ , \tag{14}$$

noticing that $\mathrm{pe}_n(\mu)$ and λ_n degenerate into $P_n(\mu)$ and $n(n+1)$ respectively when κ tends to zero, namely when a spheroid degenerates into a sphere. By starting from these expressions we can determine the functions $f_i(\mu)$ and the α_i's from the fundamental equation (6) or (5). The straightfoward calculation gives us the results required as described in the following.

$$\left.\begin{aligned}\alpha_2&=-\frac{1+(2n-1)(2n+3)}{2(2n-1)(2n+3)}\ ,\\ \alpha_4&=\frac{1}{2(2n+1)}\left\{\frac{n^2(n-1)^2}{(2n-3)(2n-1)^3}-\frac{(n+1)^2(n+2)^2}{(2n+3)^3(2n+5)}\right\}\ ,\\ \alpha_6&=-\frac{1}{(2n-1)(2n+1)(2n+3)}\left\{\frac{n^2(n-1)^2}{(2n-5)(2n-3)(2n-1)^4}-\frac{(n+1)^2(n+2)^2}{(2n+3)^4(2n+5)(2n+7)}\right\}\ ,\\ &\cdots\cdots\ .\end{aligned}\right\} \tag{15}$$

and

$$\left.\begin{aligned}f_2(\mu)&=-\frac{n(n-1)}{2(2n-1)^2(2n+1)}P_{n-2}(\mu)+\frac{(n+1)(n+2)}{2(2n+1)(2n+3)^2}P_{n+2}(\mu)\ ,\\ f_4(\mu)&=\frac{n(n-1)(n-2)(n-3)}{8(2n-5)(2n-3)^2(2n-1)^2(2n+1)}P_{n-4}(\mu)+\frac{n(n-1)}{(2n-5)(2n-1)^4(2n+1)(2n+3)}P_{n-2}(\mu)\\ &\quad-\frac{(n+1)(n+2)}{(2n-1)(2n+1)(2n+3)^4(2n+7)}P_{n+2}(\mu)\\ &\quad+\frac{(n+1)(n+2)(n+3)(n+4)}{8(2n+1)(2n+3)^2(2n+5)^2(2n+7)}P_{n+4}(\mu)\ ,\end{aligned}\right\} \tag{16}$$

$$\left.\begin{aligned}
f_6(\mu)=&-\frac{n(n-1)(n-2)(n-3)(n-4)(n-5)}{48(2n-9)(2n-7)(2n-5)^2(2n-3)^2(2n-1)^2(2n+1)}P_{n-6}(\mu)\\
&+\cdots\cdots\\
&+\frac{(n+1)(n+2)(n+3)(n+4)(n+5)(n+6)}{48(2n+1)(2n+3)^2(2n+5)^2(2n+7)^2(2n+9)(2n+11)}P_{n+6}(\mu)^{\dagger}\,,\\
\cdots&\cdots\cdots\,.
\end{aligned}\right\}$$

These expressions indicate that, when κ is small, we can express the spheroidal function $\mathrm{pe}_n(\mu)$ in terms of the Legendre functions $P_n(\mu)$ in the form:

$$\left.\begin{aligned}
\mathrm{pe}_{2n}(\mu)&=\sum_{r=0}^{\infty}A_{2r}^{(2n)}P_{2r}(\mu)\,,\\
\mathrm{pe}_{2n+1}(\mu)&=\sum_{r=0}^{\infty}A_{2r+1}^{(2n+1)}P_{2r+1}(\mu)\,,
\end{aligned}\right\}\tag{17}$$

the coefficients $A_r^{(n)}$'s being dependent upon the parameter κ. For some special cases we have

$$\left.\begin{aligned}
\lambda_0=&-\frac{1}{3}\kappa^2-\frac{2}{135}\kappa^4-\frac{4}{8505}\kappa^6+O(\kappa^8)\,,\\
&A_0^{(0)}=1\,,\\
&A_2^{(0)}=\frac{1}{9}\kappa^2+\frac{2}{567}\kappa^4-\frac{13}{127575}\kappa^6+O(\kappa^8)\,,\\
&A_4^{(0)}=\frac{1}{525}\kappa^4+\frac{4}{51975}\kappa^6+O(\kappa^8)\,,\\
&A_6^{(0)}=\frac{1}{72765}\kappa^6+O(\kappa^8)\,,\\
&A_8^{(0)}=O(\kappa^8)\,;\\
\lambda_1=&\,2-\frac{3}{5}\kappa^2-\frac{6}{875}\kappa^4+\frac{4}{65625}\kappa^6+O(\kappa^8)\,,\\
&A_1^{(1)}=1\,,\\
&A_3^{(1)}=\frac{1}{25}\kappa^2-\frac{2}{5625}\kappa^4-\frac{229}{15159375}\kappa^6+O(\kappa^8)\,,\\
&A_5^{(1)}=\frac{1}{2205}\kappa^4-\frac{4}{716625}\kappa^6+O(\kappa^8)\,,\\
&A_7^{(1)}=\frac{1}{405405}\kappa^6+O(\kappa^8)\,,\\
&A_9^{(1)}=O(\kappa^8)\,;\\
\lambda_2=&\,6-\frac{11}{21}\kappa^2+\frac{94}{9261}\kappa^4+\frac{21388}{44925111}\kappa^6+O(\kappa^8)\,,\\
&A_0^{(2)}=-\frac{1}{45}\kappa^2-\frac{2}{2835}\kappa^4+\frac{19}{1250235}\kappa^6+O(\kappa^8)\,,\\
&A_2^{(2)}=1\,,\\
&A_4^{(2)}=\frac{6}{245}\kappa^2-\frac{4}{132055}\kappa^4+\frac{15809}{757071315}\kappa^6+O(\kappa^8)\,,\\
&A_6^{(2)}=\frac{1}{4851}\kappa^4-\frac{4}{10696455}\kappa^6+O(\kappa^8)\,,
\end{aligned}\right\}\tag{18}$$

---

† The complete expression for $f_6(\mu)$ is not given here, since it is too lengthy. However, for special cases when $n=0, 1, 2$ and 3 the expression for $f_6(u)$ is shown indectly by (18).

$$\left.\begin{aligned}
&A_8^{(2)}=\frac{4}{4459455}\,\kappa^6+O(\kappa^8)\,,\\
&A_{10}^{(2)}=O(\kappa^8)\,;\\
\lambda_3=12-&\frac{23}{45}\,\kappa^2+\frac{3302}{1002375}\,\kappa^4-\frac{1572668}{26387521875}\,\kappa^6+O(\kappa^8)\,,\\
&A_1^{(3)}=-\frac{3}{175}\,\kappa^2+\frac{2}{13125}\,\kappa^4+\frac{251}{58471875}\,\kappa^6+O(\kappa^8)\,,\\
&A_3^{(3)}=1\,,\\
&A_5^{(3)}=\frac{10}{567}\kappa^2-\frac{4}{597051}\kappa^4+\frac{678641}{146292421275}\kappa^6+O(\kappa^8)\,,\\
&A_7^{(3)}=\frac{5}{42471}\,\kappa^4-\frac{4}{58482567}\,\kappa^6+O(\kappa^8)\,,\\
&A_9^{(3)}=\frac{4}{9386091}\,\kappa^6+O(\kappa^8)\,,\\
&A_{11}^{(3)}=O(\kappa^8)\,;
\end{aligned}\right\}$$

and so on.

Here it may be remembered that the above expressions can be obtained directly from the homogeneous integral equation (10) by a procedure similar to that used in obtaining the corresponding expressions for the Mathieu function $\mathrm{ce}_n(z)$ or $\mathrm{se}_n(z)$†.

§ 4. The Orthogonality and Normalisation Relations for $\mathrm{pe}_n(\mu)$

As mentioned above the spheroidal function $\mathrm{pe}_n(\mu)$ satisfies the homogeneous integral equation with the symmetrical kernel (10). Thus it can be immediately said that the family $\{\mathrm{pe}_n(\mu)\}$ forms a system of the orthogonal and normal functions for the range of the argument $|\mu|\leqq 1$, namely

$$\int_{-1}^{1}\mathrm{pe}_m(\mu)\mathrm{pe}_n(\mu)d\mu=\begin{cases}N_n & (m=n)\,,\\ 0 & (m\neq n)\,.\end{cases} \tag{19}$$

The norm N_n is easily determined by considering the expressions (17) for $\mathrm{pe}_n(\mu)$ and thus we have

$$N_{2n}=2\sum_{r=0}^{\infty}\frac{1}{4r+1}\{A_{2r}^{(2n)}\}^2\,,\qquad N_{2n+1}=2\sum_{r=0}^{\infty}\frac{1}{4r+3}\{A_{2r+1}^{(2n+1)}\}^2\,.$$

§ 5. The Series Expressions for $\mathrm{Re}_n(t)$ and $\mathrm{Se}_n(t)$

The spheroidal functions of exponential type $\mathrm{Re}_n(t)$ and $\mathrm{Se}_n(t)$, which are defined by the definite integrals (11) and (12) respectively, can be expressed in terms of the modified Bessel functions $I_{n+\frac{1}{2}}$ or $K_{n+\frac{1}{2}}$.

Taking into account that the spheroidal function $\mathrm{pe}_n(\mu)$ is connected with the Legendre functions as (17) and that the modified Bessel function $I_{n+\frac{1}{2}}$ is given by the integral form as

$$\sqrt{\frac{2\pi}{t}}\,I_{n+\frac{1}{2}}(t)=\int_{-1}^{1}e^{tz}P_n(z)dz\,, \tag{20}$$

we can immediately deduce from (11) that

$$\left.\begin{aligned}
\mathrm{Re}_{2n}(t)&=\frac{1}{\sqrt{\kappa t}}\sum_{r=0}^{\infty}A_{2r}^{(2n)}I_{2r+\frac{1}{2}}(\kappa t)\,,\\
\mathrm{Re}_{2n+1}(t)&=\frac{1}{\sqrt{\kappa t}}\sum_{r=0}^{\infty}A_{2r+1}^{(2n+1)}I_{2r+\frac{3}{2}}(\kappa t)\,.
\end{aligned}\right\} \tag{21}$$

---

† See E. T. Whittaker and G. N. Watson, 'A Course of Modern Analysis', § 19.3, 4th ed. Cambridge 1935.

Whilst the modified Bessel function $K_{n+\frac{1}{2}}$ is found to be related with the Legendre function as†

$$\sqrt{\frac{2}{\pi t}}\,K_{n+\frac{1}{2}}(t)=\int_1^\infty e^{-tz}P_n(z)dz\,, \tag{22}$$

and thus we obtain from (12)

$$\left.\begin{aligned}\mathrm{Se}_{2n}(t)&=\frac{1}{\sqrt{\kappa t}}\sum_{r=0}^{\infty}A_{2r}^{(2n)}K_{2r+\frac{1}{2}}(\kappa t)\,,\\ \mathrm{Se}_{2n+1}(t)&=\frac{1}{\sqrt{\kappa t}}\sum_{r=0}^{\infty}A_{2r+1}^{(2n+1)}K_{2r+\frac{3}{2}}(\kappa t)\,.\end{aligned}\right\} \tag{23}$$

These expressions for $\mathrm{Se}_n(t)$ are valid for a large value of κt.

§ 6. An Alternative Expressions for $\mathrm{Se}_n(t)$

The function $\mathrm{Se}_n(t)$, which is defined by (12) and expressed in the form (23), is, however, inadequate when its argument is fairly small, although it represents the characteristic properties in case when its argument is large. Thus it is desirable to deduce an appropriate expression for $\mathrm{Se}_n(t)$ which will be conveniently used when the parameter κ is small. Such an expression is deduced in a similar manner to the derivation of the expressions for the modified Mathieu function $\mathrm{FEK}_n(z)$ or $\mathrm{GEK}_n(z)$ [5].

The general solution $V(t,\mu)$ satisfying the Helmholtz equation (1) can be given by a linear combination of $T_n(t)\mathrm{pe}_n(\mu)$, provided that $\mathrm{Re}_n(t)$ or $\mathrm{Se}_n(t)$ is taken for $T_n(t)$. Thus, by making use of the orthogonality relation for $\mathrm{pe}_n(\mu)$ given by (19), we can write immediately

$$T_n(t)\backsim\int_{-1}^{1}V(t,\mu)\mathrm{pe}_n(\mu)d\mu\,, \tag{24}$$

and an appropriate solution can be obtained by adopting a known function $V(t,\mu)$ suitable for each purpose††.

We now intend to obtain the solution of the second kind and thus in (24) we put $V=\frac{1}{\sqrt{\kappa r}}K_{\frac{1}{2}}(kr)$ for $T_{2n}(t)$ and $V=\frac{1}{\sqrt{\kappa r}}K_{1+\frac{1}{2}}(kr)P_1(\cos\theta)$ for $T_{2n+1}(t)$. As is well-known, these are particuiar solutions of equations (1) when the spherical polar coordinates $x=r\cos\theta$, $\tilde{\omega}=r\sin\theta$ are employed.

Thus we put for the moment

$$\left.\begin{aligned}\mathrm{Se}_{2n}(t)&=\frac{\kappa^{2n+1}}{\sqrt{2\pi}\,A_1^{(2n)}}\int_{-1}^{1}\frac{1}{\sqrt{\kappa r}}K_{\frac{1}{2}}(kr)\cdot\mathrm{pe}_{2n}(\mu)d\mu\,,\\ \mathrm{Se}_{2n+1}(t)&=\frac{3\kappa^{2n+2}}{\sqrt{2\pi}\,A_1^{(2n+1)}}\int_{-1}^{1}\frac{1}{\sqrt{kr}}K_{1+\frac{1}{2}}(kr)P_1(\cos\theta)\cdot\mathrm{pe}_{2n+1}(\mu)d\mu\,,\end{aligned}\right\} \tag{25}$$

where again $T_n(t)$ has been replaced by $\mathrm{Se}_n(t)$.

In order to carry out these integrations it is necessary to rewrite the terms expressed in (r,θ) in terms of the spheroidal coordinates t and μ. For this purpose some preparations are made in the following lines. From Gegenbauer's addition theorem for the modified Bessel

---

† This can be deduced from the formula (G. N. Watson, 'Theory of Bessel functions,' Cambridge 1922, p. 172):

$$K_\nu(z)=\frac{\Gamma(\frac{1}{2})(\frac{1}{2}z)^\nu}{\Gamma(\nu+\frac{1}{2})}\int_1^\infty e^{-zt}(t^2-1)^{\nu-\frac{1}{2}}dt$$

by making partial integration and applying Rodrigues' formula for $P_n(z)$.

†† It is easily seen that when we adopt e^{kx} for V, $T_n(t)$ reduces to $Re_n(t)$. We can also take $\frac{1}{\sqrt{kr}}I_{n+\frac{1}{2}}(kr)P_n(\cos\theta)$ for V and then we get an expression of the solution of the second kind of $T_n(t)$.

function[†] we obtain directly

$$\frac{K_{n+\frac{1}{2}}(z)}{z^{n+\frac{1}{2}}}=\frac{(2n)!\sqrt{2\pi}}{2^{n+1}n!(\tau\sigma)^{n+\frac{1}{2}}}\sum_{p=0}^{\infty}(2n+2p+1)K_{n+p+\frac{1}{2}}(\tau)I_{n+p+\frac{1}{2}}(\sigma)C_p^{n+\frac{1}{2}}(\cos\phi)\,, \tag{26}$$

where z stands for $\sqrt{\tau^2-2\tau\sigma\cos\phi+\sigma^2}$ and $C_p^{n+\frac{1}{2}}(\cos\phi)$ is Gegenbauer's function, that is, the coefficient of α^p in the expansion of $(1-2\alpha\cos\phi+\alpha^2)^{-(n+1/2)}$ in ascending powers of α. Put $\tau=(\kappa/2)e^{\xi}$, $\sigma=(\kappa/2)e^{-\xi}$ and $\phi=\pi+2\eta$ we have $z=kr$. Further, taking into account that Gegenbauer's function can be expressed as[††]

$$C_p^{n+\frac{1}{2}}(\cos 2\eta)=\frac{n!}{(2n)!}\sum_{s=0}^{p}\frac{(-1)^{p+s}(2n+p+s)!}{s!(n+s)!(p-s)!}\cos^{2s}\eta\,, \tag{27}$$

we have

$$\frac{1}{(kr)^{n+\frac{1}{2}}}K_{n+\frac{1}{2}}(kr)=\frac{2^n\sqrt{2\pi}}{\kappa^{2n+1}}\sum_{p=0}^{\infty}\sum_{s=0}^{p}(-1)^s\frac{(2n+2p+1)(2n+p+s)!}{s!(n+s)!(p-s)!}$$
$$\times K_{n+p+\frac{1}{2}}\left(\frac{\kappa}{2}e^{\xi}\right)I_{n+p+\frac{1}{2}}\left(\frac{\kappa}{2}e^{-\xi}\right)\mu^{2s}\,.$$

From this we have, by putting $n=0$,

$$\frac{1}{\sqrt{kr}}K_{\frac{1}{2}}(kr)=\frac{\sqrt{2\pi}}{\kappa}\sum_{p=0}^{\infty}\sum_{s=0}^{p}(-1)^s\frac{(2p+1)(p+s)!}{(s!)^2(p-s)!}K_{p+\frac{1}{2}}\left(\frac{\kappa}{2}e^{\xi}\right)I_{p+\frac{1}{2}}\left(\frac{\kappa}{2}e^{-\xi}\right)\mu^{2s}\,,$$

and also when $n=1$, multiplying the both sides by $krP_1(\cos\theta)=\kappa t\mu(=kx)$, we have

$$\frac{1}{\sqrt{kr}}K_{1+\frac{1}{2}}(kr)P_1(\cos\theta)=\frac{2\sqrt{2\pi}}{\kappa^2}\cosh\xi\sum_{p=0}^{\infty}\sum_{s=0}^{p}(-1)^s\frac{(2p+3)(p+s+2)!}{s!(s+1)!(p-s)!}$$
$$\times K_{p+\frac{3}{2}}\left(\frac{\kappa}{2}e^{\xi}\right)I_{p+\frac{3}{2}}\left(\frac{\kappa}{2}e^{-\xi}\right)\mu^{2s+1}\,.$$

Substituting these expressions into the integrals (25) and carrying out the integrations, we obtain finally

$$\left.\begin{aligned}\mathrm{Se}_{2n}(t)&=\frac{2\kappa^{2n}}{A_0^{(2n)}}\sum_{p=0}^{\infty}\nu_{2p}K_{p+\frac{1}{2}}\left(\frac{\kappa}{2}e^{\xi}\right)I_{p+\frac{1}{2}}\left(\frac{\kappa}{2}e^{-\xi}\right)\,,\\ \mathrm{Se}_{2n+1}(t)&=\frac{24\kappa^{2n}}{A_1^{(2n+1)}}\cosh\xi\sum_{p=0}^{\infty}\nu_{2p+1}K_{p+\frac{3}{2}}\left(\frac{\kappa}{2}e^{\xi}\right)I_{p+\frac{3}{2}}\left(\frac{\kappa}{2}e^{-\xi}\right)\,,\end{aligned}\right\} \tag{28}$$

where the coefficients ν_p's are, after some reduction, given by

$$\nu_{2p}=(2p+1)\sum_{r=0}^{p}\sum_{s=r}^{p}(-1)^s\frac{2^{2r}(s+r)!}{(s-r)!\,(2s+2r+1)!}\frac{(2s)!(p+s)!}{(s!)^2(p-s)!}A_{2r}^{(2n)}\,,$$

$$\nu_{2p+1}=(2p+3)\sum_{r=0}^{p}\sum_{s=r}^{p}(-1)^s\frac{2^{2r}(s+r+1)!}{(s-r)!\,(2s+2r+3)!}\frac{(2s+1)!(p+s+2)!}{s!(s+1)!(p-s)!}A_{2r+1}^{(2n+1)}\,.$$

The above expressions can be conveniently used when the parameter κ is small, since the two series on the right-hand sides are rapidly convergent in such a case.

§ 7. Expansions of $\mathrm{Re}_n(t)$ and $\mathrm{Se}_n(t)$ in Powers of κ

It is sometimes convenient to express $Re_n(t)$ and $Se_n(t)$ in the forms of series expanded in powers of κ when κ is small.

For the function $\mathrm{Re}_n(t)$ we can easily write down the required series from (21) directly, by taking account of the expansion of the modified Bessel function $I_{n+\frac{1}{2}}$ as well as expansions of $A_r^{(n)}$'s given by (18). Thus we have

---

[†] G. N. Watson, ibid., § 11.41, equation (8).

[††] As far as we are aware, this formula seems to be new. The deduction of this formula is ommitted here, however.

$$\left.\begin{aligned}
&\sqrt{2\pi}\ \mathrm{Re}_0(t)=2+\frac{1}{3}t^2\kappa^2+O(\kappa^4)\ ,\\
&\sqrt{2\pi}\ \mathrm{Re}_1(t)=\frac{2}{3}t\kappa+\frac{1}{15}t^3\kappa^3+O(\kappa^5)\ ,\\
&\cdots\qquad\cdots\qquad\cdots\ .
\end{aligned}\right\}\tag{29}$$

In order to obtain an expansion for $\mathrm{Se}_n(t)$ it may be adequate to start from the series form (28) by making use of the expansions for the modified Bessel functions $I_{n+\frac{1}{2}}$ and $K_{n+\frac{1}{2}}$. However, we can also derive the required expansion directly from the integral form of $Se_n(t)$ given by (25). Using the expansion of $K_{n+\frac{1}{2}}$, we can expand $\frac{1}{\sqrt{kr}}K_{\frac{1}{2}}(kr)$ and $\frac{1}{\sqrt{kr}}K_{1+\frac{1}{2}}(kr)P_1(\cos\theta)$ in powers of κ. Thus, we have in terms of the prolate spheroidal coordinates (t,μ), we have

$$\frac{1}{\sqrt{kr}}\,K_{\frac{1}{2}}(kr)=\frac{1}{\kappa}\sqrt{\frac{\pi}{2}}\left\{\frac{1}{g}-\kappa+\frac{1}{2}g\kappa^2-\frac{1}{6}\,g^2\kappa^3+\frac{1}{24}\,g^3\kappa^4+O(\kappa^5)\right\}\,,$$

and

$$\frac{1}{\sqrt{kr}}K_{1+\frac{1}{2}}(kr)P_1(\cos\theta)=\frac{t\mu}{\kappa^2}\sqrt{\frac{\pi}{2}}\left\{\frac{1}{g^3}-\frac{1}{2}\,\frac{1}{g}\kappa^2+\frac{1}{3}\,\kappa^3-\frac{1}{8}\,g\kappa^4+O(\kappa^5)\right\}\,,$$

where for brevity we have put $g=\sqrt{t^2-1+\mu^2}$. Thus the integrands of (25) can be expressed in powers of κ if the expansion of $\mathrm{pe}_n(\mu)$ given by (13) is also used. The coefficients of the said expansion of $\mathrm{pe}_n(\mu)$ are the polynomials of the Legendre function $P_n(\mu)$ and hence it is necessary to evaluate the integral of the form

$$\int_{-1}^{1}\mu(t^2-1+\mu^2)^{m/2}P_n(\mu)d\mu\ ,$$

where m is a positive or negative integer. Remembering that $P_n(\mu)$ is expressed in series of μ, this integral becomes a sum of the integrals of the form:

$$\int_{-1}^{1}\mu^l(t^2-1+\mu^2)^{m/2}d\mu\ ,$$

where l is a positive integer.

Evaluating such integrals for various values of l and m, we have finally obtained the required expression for $\mathrm{Se}_n(t)$. The results for some special cases are given in the following.

$$\left.\begin{aligned}
&Se_0(t)=Q_0(t)-\kappa+\frac{1}{18}\{6t+(3t^2-4)Q_0(t)\}\kappa^2-\frac{1}{18}(3t^2-2)\kappa^3+O(\kappa^4)\ ,\\
&Se_1(t)=3Q_1,(t)-\frac{3}{50}\{(2+5t^2)+(8t-5t^3)Q_0(t)\}\kappa^2+\frac{1}{3}t\kappa^3+O(\kappa^4)\ ,\\
&Se_2(t)=\frac{45}{2}Q_2(t)+\frac{5}{392}\{3(-63t^3+40t)+(189t^4-183t^2-16)Q_0(t)\}\kappa^2+O(\kappa^4)\ ,\\
&\cdots\qquad\cdots\qquad\cdots\ .
\end{aligned}\right\}\tag{30}$$

$Q_n(t)$ being the Legendre function of the second kind.

It will easily be seen from the above expression that except for constant multipliers, $\mathrm{Se}_n(t)$ degenerates into $Q_n(t)$ as the parameter κ tends to zero.

§ 8. Asymptotic Behaviours of the Spheroidal Functions

Lastly, we shall deal briefly with the asymptotic properties of the spheroidal functions of exponential type for a large value of their argument.

It is readily found that the fundamental equation (6) has in general solutions of two kinds. One of them, that is, the solution of the first kind becomes asymptotically

$$Z(z) \sim \frac{C}{\sqrt{t^2-1}} e^{\kappa t} \sim C\frac{e^{\kappa t}}{t}\,, \tag{31}$$

when t is large, while the solution of the second kind becomes asymptotically

$$Z(z) \sim \frac{C}{\sqrt{t^2-1}} e^{-\kappa t} \sim C\frac{e^{-\kappa t}}{t}\,, \tag{32}$$

where the constant C is to be so determined that it satisfies each definition of spheroidal functions given before.

For the solution of the first kind $\mathrm{Re}_n(t)$ given by (11) and (21), we have, using the asymptotic form of the modified Bessel function,

$$\mathrm{Re}_n(t) \sim \frac{pe_n(1)}{\sqrt{2\pi}} \frac{e^{\kappa t}}{\kappa t}\,, \tag{33}$$

where $\mathrm{pe}_{2m}(1)=\sum\limits_{r=0}^{\infty} A_{2r}^{(2m)}$ and $\mathrm{pe}_{2m+1}(1)=\sum\limits_{r=0}^{\infty} A_{2r+1}^{(2m+1)}$. Similarly, the solution of the second kind $\mathrm{Se}_n(t)$ given by (12) and (23) has the asymptotic form as

$$\mathrm{Se}_n(t) \sim \sqrt{\frac{\pi}{2}}\, \mathrm{pe}_n(1) \frac{e^{-\kappa t}}{\kappa t}\,. \tag{34}$$

The asymptotic expression for $\mathrm{Se}_n(t)$ given in § 6 is also obtained. We start from the integral definition for $\mathrm{Se}_n(t)$ given by (25) and take into account that we can put κt and μ in place of kr and $\cos\theta$ respectively at a great distance from the origin of the coordinates, where the variable t is large. Then we have, for the moment,

$$\mathrm{Se}_{2n}(t) \sim \frac{\kappa^{2n+1}}{\sqrt{2\pi}\, A_0^{(2n)}} \frac{1}{\sqrt{\kappa t}} K_{\frac{1}{2}}(\kappa t) \int_{-1}^{1} \mathrm{pe}_{2n}(\mu) d\mu\,,$$

$$\mathrm{Se}_{2n+1}(t) \sim \frac{3\kappa^{2n+2}}{\sqrt{2\pi}\, A_1^{(2n+1)}} \frac{1}{\sqrt{\kappa t}} K_{1+\frac{1}{2}}(\kappa t) \int_{-1}^{1} \mu\, \mathrm{pe}_{2n+1}(\mu) d\mu\,.$$

Further we remember that both $K_{\frac{1}{2}}(\kappa t)$ and $K_{1+\frac{1}{2}}(\kappa t)$ become $\sqrt{\frac{\pi}{2}} \frac{e^{-\kappa t}}{\kappa t}$ asymptotically and that $\mathrm{pe}_n(\mu)$ in the above integrals is expressed in series of Legendre functions, and thus we have finally

$$\mathrm{Se}_n(t) \sim \kappa^{n+1} \frac{e^{-\kappa t}}{\kappa t}\,. \tag{35}$$

Here we only mentioned that this expression can also be derived directly from the series expression of $\mathrm{Se}_n(t)$ given by (28). The discrepancy between the constant multipliers in (34) and (35) is, of course, due to the slight difference in definitions of $\mathrm{Se}_n(t)$ and hence it is trivial.

Appendix

The case of an oblate spheroid

(i) The fundamental equations

It will be of use to give the essential results for the case when in place of the preceding prolate spheroidal coordinates we make use of the oblate spheroidal coordinates (t, μ) which are given by

$$x = ct\mu\,, \qquad \tilde{\omega} = c\sqrt{t^2+1}\sqrt{1-\mu^2}\,,$$

where $t=\sinh\xi$ and $\mu=\cos\eta$.

We start from the Helmholtz equation (1) and assume that $V=T(t)M(\mu)$. Then we have

$$\frac{d}{dt}\left\{(1+t^2)\frac{dT}{dt}\right\}-(\lambda+\kappa^2t^2)T=0\,, \tag{36}$$

and

$$\frac{d}{d\mu}\left\{(1-\mu^2)\frac{dM}{d\mu}\right\}+(\lambda-\kappa^2\mu^2)M=0\,. \tag{37}$$

These are the fundamental equations for the present case.

(ii) The series expression of $\mathrm{pe}_n{}^*(\mu)$

We denote the solution of the equation (37) by $\mathrm{pe}_n{}^*(\mu)$ which is regular at $\mu=\pm1$ when λ takes a characteristic value. By comparing the equation (37) with (5) we can easily see that there exists a relation between $\mathrm{pe}_n{}^*(\mu)$ and $\mathrm{pe}_n(\mu)$ as

$$\mathrm{pe}_n{}^*(\mu;\kappa)=\mathrm{pe}_n(\mu;i\kappa)\,. \tag{38}$$

The function $\mathrm{pe}_n{}^*(\mu)$ can be expanded in powers of κ or in series of the Legendre functions when the parameter κ assumes a small values. From the relation (38) we can immediately write down

$$\mathrm{pe}_n{}^*(\mu)=P_n(\mu)-f_2(\mu)\kappa^2+f_4(\mu)\kappa^4-f_6(\mu)\kappa^6+\cdots\,, \tag{39}$$

with

$$\lambda_n=n(n+1)-\alpha_2\kappa^2+\alpha_4\kappa^4-\alpha_6\kappa^6+\cdots\,, \tag{40}$$

where the $f_i(\mu)$'s and α_i's have been already given by (16) and (15) respectively. Further we can put

$$\left.\begin{aligned}\mathrm{pe}_{2n}{}^*(\mu)&=\sum_{r=0}^{\infty}B_{2r}^{(2n)}P_{2r}(\mu)\,,\\ \mathrm{pe}_{2n+1}{}^*(\mu)&=\sum_{r=0}^{\infty}B_{2r+1}^{(2n+1)}P_{2r+1}(\mu)\,.\end{aligned}\right\} \tag{41}$$

The coefficients $B_r{}^{(n)}$'s are given in powers of κ and these are connected with the $A_r{}^{(n)}$'s by the relations

$$B_r^{(n)}(\kappa)=A_r^{(n)}(i\kappa)\,. \tag{42}$$

(iii) The orthogonality and normalisation relations for $\mathrm{pe}_n{}^*(\mu)$

Since the function $\mathrm{pe}_n{}^*(\mu)$ satisfies the homogeneous integral equation with the symmetrical kernel as given by

$$\mathrm{pe}_n{}^*(\mu)=\omega_n{}^*\int_{-1}^{1}e^{\kappa\mu\zeta}\,\mathrm{pe}_n{}^*(\zeta)d\zeta\,, \tag{43}$$

it is immediately seen that the family $\{\mathrm{pe}_n{}^*(\mu)\}$ forms a set of the orthogonal and normal functions for the range $|\mu|\leqq1$, namely

$$\int_{-1}^{1}\mathrm{pe}_m{}^*(\mu)\,\mathrm{pe}_n{}^*(\mu)d\mu=\begin{cases}N_n & (m=n)\,,\\ 0 & (m\neq n)\,,\end{cases} \tag{44}$$

provided that the norms are given by

$$N_{2m}=2\sum_{r=0}^{\infty}\frac{1}{4r+1}\{B_{2r}^{(2m)}\}^2\,,\qquad N_{2m+1}=2\sum_{r=0}^{\infty}\frac{1}{4r+3}\{B_{2r+1}^{(2m+1)}\}^2\,.$$

(iv) The function $\mathrm{Re}_n{}^*(t)$

We denote the solution of the first kind of equation (36) by $\mathrm{Re}_n{}^*(t)$ which is defined by

$$\mathrm{Re}_n^*(t)=\frac{1}{\sqrt{2\pi}}\int_{-1}^{1} e^{\kappa t\mu}\,\mathrm{pe}_n^*(\mu)d\mu\,, \tag{45}$$

and is expressed as

$$\left.\begin{aligned}\mathrm{Re}_{2n}^*(t)&=\frac{1}{\sqrt{\kappa t}}\sum_{r=0}^{\infty} B_{2r}^{(2n)} I_{2r+\frac{1}{2}}(\kappa t)\,,\\ \mathrm{Re}_{2n+1}^*(t)&=\frac{1}{\sqrt{\kappa t}}\sum_{r=0}^{\infty} B_{2r+1}^{(2n+1)} I_{2r+\frac{3}{2}}(\kappa t)\,.\end{aligned}\right\} \tag{46}$$

When κ is small $\mathrm{Re}_n^*(t)$ can be expanded in powers of κ.

The asymptotic form of $\mathrm{Re}_n^*(t)$ is given by

$$\mathrm{Re}_n^*(t)\sim\frac{pe_n^*(1)}{\sqrt{2\pi}}\frac{e^{\kappa t}}{\kappa t} \tag{47}$$

when t is large.

(v) The function $\mathrm{Se}_n^*(t)$

Let us denote the solution of the second kind of equation (36) by $\mathrm{Se}_n^*(t)$, which corresponds to $\mathrm{Se}_n(t)$ given in § 6. This function is defined by

$$\left.\begin{aligned}\mathrm{Se}_{2n}^*(t)&=\frac{1}{\sqrt{2\pi}\,B_0^{(2n)}}\int_{-1}^{1}\frac{1}{\sqrt{kr}}K_{\frac{1}{2}}(kr)\cdot\mathrm{pe}_{2n}^*(\mu)d\mu\,,\\ \mathrm{Se}_{2n+1}^*(t)&=\frac{3}{\sqrt{2\pi}\,B_1^{(2n+1)}}\int_{-1}^{1}\frac{1}{\sqrt{kr}}K_{1+\frac{1}{2}}(kr)P_1(\cos\theta)\cdot\mathrm{pe}_{2n+1}(\mu)d\mu\,,\end{aligned}\right\} \tag{48}$$

and is expressed as

$$\left.\begin{aligned}\mathrm{Se}_{2n}^*(t)&=\frac{2\kappa^{2n}}{B_0^{(2n)}}\sum_{p=0}^{\infty}\nu_{2p}^*K_{p+\frac{1}{2}}\left(\frac{\kappa}{2}e^{\xi}\right)I_{p+\frac{1}{2}}\left(\frac{\kappa}{2}e^{-\xi}\right),\\ \mathrm{Se}_{2n+1}^*(t)&=\frac{24\kappa^{2n}}{B_1^{(2n+1)}}\sinh\xi\sum_{p=0}^{\infty}\nu_{2p+1}^*K_{p+\frac{3}{2}}\left(\frac{\kappa}{2}e^{\xi}\right)I_{p+\frac{3}{2}}\left(\frac{\kappa}{2}e^{-\xi}\right),\end{aligned}\right\} \tag{49}$$

where the coefficients ν_p^*'s are given by

$$\nu_{2p}^*=(2p+1)\sum_{r=0}^{p}\sum_{s=r}^{p}(-1)^{s+p}\frac{2^{2r}(s+r)!}{(s-r)!(2s+2r+1)!}\frac{(2s)!(p+s)!}{(s!)^2(p-s)!}B_{2r}^{(2n)}\,,$$

$$\nu_{2p+1}^*=(2p+3)\sum_{r=0}^{p}\sum_{s=r}^{p}(-1)^{p+s}\frac{2^{2r}(s+r+1)!}{(s-r)!(2s+2r+3)!}\frac{(2s+1)!(p+s+2)!}{s!(s+1)!(p-s)!}B_{2r+1}^{(2n+1)}\,.$$

When the parameter κ is small this function can be expanded in powers of κ and we have

$$\left.\begin{aligned}\mathrm{Se}_0^*(t)&=q_0(t)-\kappa+\frac{1}{18}\{6t+(3t^2+4)q_0(t)\}\kappa^2-\frac{1}{18}(3t^2+2)\kappa^3+O(\kappa^4)\,,\\ \mathrm{Se}_1^*(t)&=3q_1(t)-\frac{3}{50}\{(2-5t^2)+(8t+5t^3)q_0(t)\}\kappa^2+\frac{1}{3}t\kappa^3+O(\kappa^4)\,,\\ \mathrm{Se}_2^*(t)&=\frac{45}{2}q_2(t)+\frac{5}{392}\{3(-63t^3-40t)+(189t^4+183t^2-16)q_0(t)\}\kappa^2+O(\kappa^4)\,,\end{aligned}\right\} \tag{50}$$

and so on. $q_n(t)$ is an ellipsoidal harmonic, which is related to $Q_n(t)$ by $q_n(z)=i^{n+1}Q_n(iz)$, namely, $q_0(z)=\cot^{-1}z$ etc.

When the argument is large this function takes the asymptotic form as

$$\mathrm{Se}_n^*(t)\sim\kappa^{n+1}\frac{e^{-\kappa t}}{\kappa t}\,. \tag{51}$$

Acknowledgement

The writer wishes to express his cordial thanks to Professor S. Tomotika for his interest and stimulating advice during the present investigation.

References

1) T. Aoi: J. Phys. Soc. Japan **10** (1950) 119.
2) F. Möglich: Ann. d. Phys. **83** (1927) 609.
3) M. Kotani: Proc. Phys.-Math. Soc. Japan **15** (1933) 30.
4) M. Kotani: On wave functions relating to a prolate spheroid (in Japanese), Recent Problems in Physics, Iwanami, Tokyo (1948).
5) T. Aoi: On the solutions of the modified Mathieu equation (in Japanese), Preliminary Report No. **24**, Tomotika Lab., Univ. of Kyoto (1950).

JOURNAL OF THE PHYSICAL SOCIETY OF JAPAN Vol. 10, No. 2, FEBRUARY, 1955

Spontaneous Condensation in a supersonic Flow of Humid Air

By Hiromu WAKESHIMA

The Kobe University of Mercantile Marine

(Received September 24, 1954)

The problem of the spontaneous condensation of water vapor in a supersonic flow of moist air is approximately solved in a way similar to those given previovsly[1], on the basis of Becker-Döring's equation for the stationary rate of self-nucleation and also based on the law of droplet growth used before. Comparison of the theoretical prediction with experimental results given by Head[2] shows a considerably good agreement and thus it is revealed that major part of the delay of the appearance of condensation, from which some doubt has been cast over[3] the validity of Becker's formula in such cases, can be explained plausibly without the notion of time lag in the self-nucleation.

§ 1. Introduction

Spontaneous condensation of water vapor in the instantaneous expansion of humid air in a supersonic wind tunnel has attracted the attension of many investigators in recent years and yet the problem seems to remain still unsettled[3].

Oswatitsch[4] was the first to deal with the theoretical aspects of this phenomenon. He gave an equation for determining the location of the start of condensation, on the basis of Becker-Döring's equation and a law of droplet growth. But his equation contains an undetermined constant which should be calculated on the basis of experimental data. Charyk[5] assumed that the collapse of the supersaturated state takes place at a place where the degree of supersaturation is attained which corresponds to Becker-Doring's rate of self-nucleation ν of the order of magnitude $10^3/\mathrm{cm}^3$ sec. However, this choice of the value of ν, not only has no rational basis whatsoever, but also its conclusion showed an apparent contradiction to the experimental results given by Head[2] and by Eber-Wegener[6]. Namely in Head's experiments no condensation appeared where the theory had predicted it, while in Eber-Wegener's experiments condensation occurred later than was theoretically expected. In an effort to solve this contradiction between theory and experiment, Kantrowitz[7] imagined that a time lag, associated with reaching the stationary rate of self-nucleation assumed in the Becker-Doring's equation, might be responsible for the discrepancy mentioned above. Probstein[8] actually carried out an approximate computation of the self-nucleation in a non-stationary state under a simple initial condition and obtained a result that the time lag alone can hardly account for the existing discrepancy between theory and experiment. Similar result was also given by the author[9] who treated the problem of the time lag more generally.

Now the author previously presented a theory[1] dealing with the spontaneous development of fog or emulsions in a supersaturated vapor or liquid mixture, on the basis of the Becker-Döring's equation of nuleation and a law of droplet growth obtained by him. Similar treatment will be applied here to the problem of spontaneous condensation in a supersoic flow of humid air. To avoid much complication, we assume first that the change in pressure and in temperature of the air in the course of supersonic flowing corresponds to the flow without condensation and the nucleation will be calculated for this pressure and temperature change. The influence of nucleation thus obtained will be taken into account in the comparison of the theory with experiment.

§ 2. Rate of Self-Nucleation and Droplet Growth

We use in the following the equation of the rate of self-nucleation in a supersaturated vapor given in Frenkel's textbook[10], which is essentially the same as that of Becker-Doring's and is given by $\nu=N^*D_*^*(\chi^*/2\pi kT)^{1/2}$. Here N^* means the equilibrium number density of the critical droplets and D_*^* the probability with which a critical droplet captures a molecule per unit time. χ^* is a factor satisfying $\chi^*\equiv 2/9\,\mu g^{*-4/3}$ where μ denotes the surface free energy of the liquid per molecule and g^* the number of molecules containted in a critical droplet. Frenkel, assuming that all vapor molecules colliding with a droplet are captured by it, expressed D_*^* as $D_*^*=4\pi r^{*2}N(kT/2\pi m)^{1/2}$ where N denotes the number density of the vapor molecule and r^* the radius of a critical droplet. But as was mentioned already[1], it is possible that relatively small portion of the molecules making a collision with a droplet adhere to it. Therefore it will generally be legitimate to multiply the right-hand side of the above equation with a factor P, the so-called condensation coefficient. The value of P is considerably different according to observers[11] even in the macroscopic measurements. Later we will give a brief discussion about the effect of the choice of P which we assume to be a constant of the order of magnitude $1\sim10^{-2}$ for such small droplets as those of radius $10^{-6\sim8}$cm.

N^* is approximately equal to $N\cdot\exp(-4\pi r^{*2}\sigma/3kT)$[10], therefore ν can be expressed as

$$\nu=2v_B\sqrt{\frac{\sigma}{2\pi m}}\cdot N^2Pe^{-4\pi r^{*2}\sigma/3kT} \qquad (1)$$

where v_B denotes the volume of a molecule in a droplet and σ the surface tension of the liquid.

As pointed out already[1] the rate of self-nucleation $\nu(N,\ T)$ as a function of N and T, can approximately be represented by

$$\nu=\nu_0(N/N_0)^{\phi_{N_0}}(T/T_0)^{-\phi_{T_0}},$$

in the vicinity of $\nu_0(N_0,\ T_0)$, with

$$\phi_{N_0}=2(1+2\pi r_0^{*3}/3v_B)$$

and

$$-\phi_{T_0}=[(T_0/2\sigma-4\pi r_0^{*2}/k)(d\sigma/dT)_0+4\pi r_0^{*2}/k \cdot\{\sigma_0/T_0-kr_0^*/3v_B\cdot(dN_\infty/dT)_0T_0/N_{\infty0}\}].$$

Here N_∞ denotes the equilibrium number density of the molecule for a flat interface between the liquid and its arounding gas or solution. In these equations all quantities with a subscript $_0$ refers to the state corresponding to $(N_0,\ T_0)$. When we have to consider the time lag for the stationary rate of self-nucleation, we make use of the effective time lag τ_e defined previously[9], satisfying

$$\tau_e\equiv kT/2D_*^*\chi^* .$$

From the kinetic consideration of the condition of equilibrium between a droplet and its supersaturated surroundings and also on the assumption of a stationary diffusion of the molecule and of a stationary conduction of the heat of formation of the droplet out of separated molecules, a law of droplet growth was derived by the author previously[1], which is, in general, of the form

$$dr/dt=v_Bb(N-N_\infty e^{a/r})/(1+br/D_e) ,$$

where

$$a=2\sigma v_B/kT, \qquad b=P(kT/2\pi m)^{1/2}$$

and

$$D_e=D/\{1+D\lambda(dN_\infty/dT)/\chi\} .$$

D means here the diffusivity of the molecule in the surrounding medium, λ the heat of condensation or solution per molecule and κ the thermal conductivity of the surroundings. In a very short time interval of the order of 10^{-5} sec, available for droplet growth in our case, r does not exceed the order of 10^{-6} cm even for the rate of droplet growth $v_B bN$ which is of course larger than the actual rate. Considering that $b \sim 10^{4\sim 2}$ and $D_e \sim 10^{-1}$, br/D_e in the denominator of the above equation can be neglected as compared with 1, thus we have $dr/dt = v_B b(N - N_\infty e^{a/r})$. As will be seen from the original derivation[1]), this final result can also be directly deduced from the kinetic consideration alone, because a violent turbulent motion in the fluid would have the tendency of mixing up the air and thus provent the establishment of a gradient in the concentration of vapor molecules or in the temperature, around a droplet. Instead of this equation we can use

$$dr/dt = v_B b\{N - N_\infty(1 + a/r)\}\,, \qquad (2)$$

for droplets of radius $r > 10^{-7}$ cm and as will be seen later, in a state of large degree of supersaturation which actually is the matter in this case, a simple formula

$$dr/dt = v_B b(N - N_\infty) \qquad (2a)$$

suffices approximately for larger droplets mentioned above.

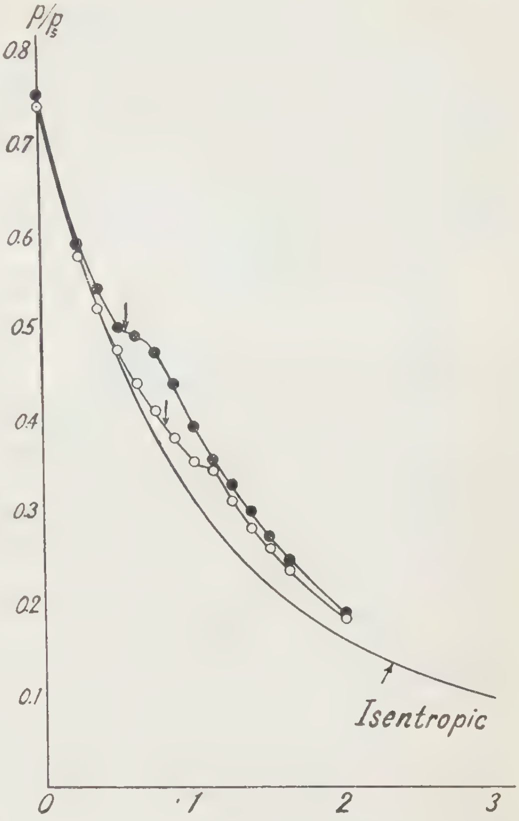

Fig. 1.

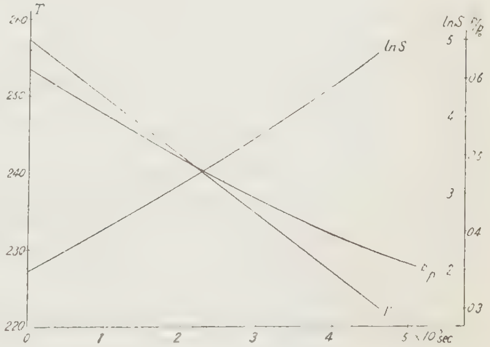

Fig. 2.

§ 3. Nucleation Process

Treatment of the nucleation process is similar to those in the previous papers[1]). To make the matter concrete, consider the actual case of a supersonic flow in a Laval nozzle performed by Head[4]). Fig. 1 gives an example of results of his measurements of pressure distribution shown in Fig. 6a of his thesis. In Fig. 2 is given the lowering of relative pressure p/p_s and temperature T as well as the rising in the degree of supersaturation S of the air in the course of a supersonic flow which was computed by the author from the isentropic curve in Fig. 1.

As will be seen from the comparison of these figures, principal nucleation begins rather suddenly and lasts only for a short period ($\sim 10^{-5}$ sec), though an appreciable amount of nucleation precedes and may follow the main part of nucleation. (For the time being, we assume that the time interval during which a remarkable increase in p/p_s over the isentropic change is observed, corresponds to the nucleation period; but we will see later that the latter is only a part of the former.) When we calculate using Eq. (1) and Eq. (2a) the rate of self-nucleation and the rate of droplet growth in the period during which nucleation is conspicuous (we will call such a period "nucleation period"), we see that the former increases by some thirty times while the latter decreases only 20 percent or so through this period. Therefore we assume as in the previous cases, that the rate of droplet growth is constant during the nucleation period and has the value corresponding to the state (N_0, T_0) at the time origin which we will take at the moment when the rate of self-nucleation attains its maximum. Other quantities such as a, b etc. that do not suffer a remarkable change during the nucleation period, like the rate of droplet growth, will also be treated as a constant.

Now T/T_0 in Eq. (1a) can be written as a function of t. Namely

$$T=T_0-\alpha t+(n-n_0)\lambda/c_e\rho$$

or

$$T/T_0=1-\alpha/T_0\cdot t+(n-n_0)\lambda/c_e\rho T_0$$

where α denotes the rate of the temperature fall, n the number density of condensed molecules, c_e the effective heat capacity per unit mass and ρ the density of the gas respectively. The last term on the right hand side of the above equation will be fully explained in § 5. As

$$1\gg\{\alpha/T_0\cdot t-(n-n_0)\lambda/c_e\rho T_0\},$$

in the nucleation period, we have, in approximation,

$$(T/T_0)^{-\phi_{T_0}}=\exp\{\phi_2 t-\phi_3(n-n_0)\}$$

with

$$\phi_2\equiv\alpha/T_0\cdot\phi_{T_0}$$

and

$$\phi_3\equiv\lambda\phi_{T_0}/c_e\rho T_0 \qquad (3)$$

In order that we can express $(N/N_0)^{\phi_{N_0}}$ in Eq. (1a) as a function of t, we have to calculate $-dN/dt$. The number density N decreases for three causes: First due to the pressure and temperature drop of the gas, second due to the nucleation and third, due to the droplet growth. The change due to the first cause can be expressed as

$$N_0 d/dt\cdot(1-\alpha t/T_0)^{1/(\gamma-1)},$$

because by the assumption of an adiabatic expansion of the gas we have

$$N/N_0=(p/p_0)^{1/\gamma}=(T/T_0)^{1/(\gamma-1)}$$

or

$$N=N_0(1-\alpha t/T_0)^{1/(\gamma-1)}.$$

If only the influence of this term is considered, then we get

$$(N/N_0)^{\phi_{N_0}}=(1-\alpha t/T_0)^{\phi_{N_0}/(\gamma-1)}$$
$$\doteqdot\exp\{-\alpha\phi_{N_0}t/T_0(\gamma-1)\}\equiv\exp(-K\phi_{N_0}t)$$

in the period concerned. The second term is $4\pi/3v_B\cdot r_G^3\nu_t$, where r_G means the radius of a just nucleated droplet, of which we will assume, with Probstein[8], the value corresponding to the number of molecules therein, $g_G=4/3\cdot g^*$. r_G will also be looked upon as a constant while ν_t, expressing the rate of nucleation at an instant t, varies during the nucleation period. For simplicity, we will substitute for ν_t, such a value of ν at each moment that one would have if the influence of decrease in N due to condensation is neglected, i.e.,

$$\nu_t=\nu_0\exp(\phi_2 t-K\phi_{N_0}t)\equiv\nu_0 e^{\phi_4 t}.$$

The third term can be, as in the former case[1], put into a form

$$4\pi/v_B\cdot\int_{rG}^{rm}r^2\nu_{t-\theta}\,dr$$

with r_m the radius of the largest droplet and ν_{t-0} the value of ν at the instant $t-\theta$, where θ means the time of growth for a droplet of radius r. We transform this, on the basis of a similar assumption as that of the second term and using Eq. (3), into

$$4\pi\nu_0 e^{\phi_4 t}/v_B\cdot\int_{r_G}^{r_m}r^2 e^{-\phi_4\theta}dr$$

The relation between θ and r can be obtained from the law of droplet growth (2). If we put

$$v_B b(N_0-N_\infty)\equiv\delta,$$

and

$$v_B b N_\infty a\equiv\varepsilon\,,$$

Eq. (2) becomes

$$dr/dt=\delta-\varepsilon/r$$

and, on integration, we have

$$\theta=\int_{r_G}^{r_m}\frac{dr}{\delta-\varepsilon/r}=(r-r_G)/\delta+\varepsilon/\delta^2\cdot\log\frac{r-\varepsilon/\delta}{r_G-\varepsilon/\delta}\,.$$

(1) Consider the case where P in Eq. (1) is of the order of magnitude 1. Then

$$\delta\simeq10^{-1}\quad\text{and}\quad\varepsilon\simeq10^{-9},$$

therefore the first term is much larger than the second on the right hand side of the above equation, and to neglect the latter term as compared with the former means that we adopt Eq. (2a) instead of Eq. (2). At any rate we have

$$\theta=(r-r_G)/\delta\,,$$

and using this relation, the integral in the third term mentioned above can be calculated as follows,

$$\int_{r_G}^{r_m} r^2 e^{-\phi(r-r_G)}dr \doteqdot \int_0^\infty (x+r_G)^2 e^{-\phi x}dx$$

$$=1/\phi^3\cdot(2+2r_G\phi+r_G{}^2\phi^2) \quad \text{with} \quad \phi=\phi_4/\delta\,.$$

If we denote

$$4\pi/3\cdot\{3/\phi^3\cdot(2+2r_G\phi+r_G{}^2\phi^2)+r_G{}^3\}\equiv\bar{v}\,,$$

the rate of increase in n can be expressed as

$$dn/dt=\bar{v}/v_B\cdot\nu_0 e^{\phi_4 t}.$$

Taking the effect of all these three causes into account and integrating the relation

$$-dN/dt=dn/dt+N_0 d/dt\cdot(1-\alpha t/T_0)^{1/(\gamma-1)},$$

we have

$$N_0-N=\bar{v}\nu_0/v_B\phi_4\cdot(\exp\phi_4 t-1)+N_0 Kt$$

or

$$N/N_0=1-\{\bar{v}\nu_0/v_B N_0\phi_4\cdot(\exp\phi_4 t-1)$$
$$+Kt\}\equiv\phi_1(t) \qquad (4)$$

Thus we finally obtain, in the first approximation, the function in the time t, of the rate of self-nucleation

$$\nu=\nu_0\phi_1(t)^{\phi_{N_0}}\cdot e^{\phi_2 t-\phi_3(n-n_0)} \qquad (5)$$

If we put this relation into the expression for the second term

$$4\pi/3v_B\cdot r_G{}^3\nu_t$$

and the third

$$4\pi/v_B\cdot\int_{r_G}^{r_m} r^2\nu_{t-\theta}dr\,,$$

we shall have a better approximation.

The number density of droplet n_* is obtained from the numerical or graphical integration of

$$n_*=\nu_0\int_{-\tau_1}^{\tau_2}\phi_1(t)^{\phi_{N_0}}\cdot\exp\{\phi_2 t-\phi_3$$
$$(n-n_0)\}\,dt \qquad (6)$$

where the upper and the lower limit of the integral should be taken at the instants when the rate of nucleation is vanishingly small.

Now we have selected the time origin satisfying $(d\nu/dt)_0=0$, whence we obtain

$$\phi_4=\bar{v}/v_B\cdot\nu_0(\phi_{N_0}/N_0+\phi_3) \qquad (7)$$

This relation determines the so-called threshold condition for the occurrence of spontaneous condensation when the coefficient P is of the order of magnitude 1.

(2) If $P\sim10^{-2}$, the rate of droplet growth is only few hundredths that of the above case and then no time is available for nucleated droplet to grow appreciably. Therefore, in a rough approximation, neglecting the growth of droplets, we have

$$-dN/dt=\bar{v}'/v_B\cdot\nu_0 e^{\phi_4 t}+N_0 d/dt$$
$$\cdot(1-\alpha/T_0\cdot t)^{1/(\gamma-1)}$$

with $\qquad \bar{v}'=4\pi/3\cdot r_G{}^3$

Integrating this, equations of the same form as above will be obtained.

Length of the nucleation period can be estimated as follows. Using Eq. (4) and Eq. (5), we have, in approximation,

$$\nu/\nu_0\doteqdot\exp[-\{(n-n_0)/N_0+Kt\}$$
$$\cdot\phi_{N_0}+\phi_2 t-\phi_3(n-n_0)]$$
$$=\exp[\phi_4 t-(\phi_{N_0}/N_0+\phi_3)\bar{v}/v_B\cdot\nu_0(e^{\phi_4 t}-1)/\phi_4]$$

which becomes from Eq. (7),

$$\nu/\nu_0=\exp(\phi_4 t-e^{\phi_4 t}+1)$$

If we assume $\nu/\nu_0=0.01$ for $t=-\tau_1$ and $+\tau_2$, then $-\tau_1$ and τ_2 are the solutions of the equation

$$-4.61=\phi_4 t-e^{\phi_4 t}+1$$

which gives $-\phi_4\tau_1=5.61$ and

$$\phi_4\tau_2=2.04$$

or

$$\tau=-\tau_1+\tau_2=7.65/\phi_4\,.$$

When we consider the relation

$$\phi_4=\alpha/T_0\cdot\{\phi_{T_0}-\phi_{N_0}/(\gamma-1)\}\,,$$

it can be seen from the above equation that length of the nucleation period depends on the time rate of temperature drop α and also on ϕ_{N_0}, ϕ_{T_0} and T_0, while it does not depend on the coefficient of condensation P.

§ 4. Transient Period in the Development of Fog

After the nucleation period is over, the number density of droplet n_* will practically remain constant, but the degree of supersaturation is still high and the rate of droplet growth large for a while. After an elapse of a certain time interval the degree of supersaturation will become nearly equal to 1, though droplets will grow further as long as the temperature is kept decreasing. We will call such a time interval a transient period in which the degree of supersaturation is large enough to maintain a large rate of droplet growth and a vivid liberation of heat through condensation. Let us assume, for simplicity, that all droplets have an average radius $\bar{r}$ in transient period and also $d\bar{r}/dt=v_B b(N-N_\infty)$. Then we have,

$$N_*-N=4\pi/3v_B\cdot n_*\bar{r}^3,$$

where N_* means the number density of molecule when no condensation has occurred.

Put

$$N_* - N_\infty = 4\pi/3 v_B \cdot n_* R^3,$$

then the following differential equation is obtained

$$d\bar{r}/dt = 4\pi n_* b/3 \cdot (R^3 - \bar{r}^3). \qquad (8)$$

It is difficult to solve this equation as R is a somewhat complicated function of the time t, (Namely in the actual case of very high degree of supersaturation $S \sim 10^{1\sim 2}$ we are considering, R^3 is practically proportional of N_* and N_* to p/T. By the assumption of an adiabatic expansion without condensation, we have approximately $N_* \infty T^{1/(\gamma-1)}$ or $R \infty T^{2 \cdot 5/3}$.) But we can draw some conclusions about the magnitude of the transient period. We obtained previously[1)] the following solution of the above equation when R is a constant.

$$\Theta = \frac{1}{8\pi n_* b R^2} [\log(1-\bar{r}_0/R)^2/(1-\bar{r}/R)^2$$
$$+\log(1+\bar{r}/R+\bar{r}^2/R^2)/(1+\bar{r}_0/R+\bar{r}_0^2/R^2)$$
$$+2\sqrt{3}\ \{\tan^{-1}(1+2\bar{r}/R)/\sqrt{3}$$
$$-\tan^{-1}(1+2\bar{r}_0/R)/\sqrt{3}\ \}] \qquad (9)$$

where $\bar{r}_0$ denotes the initial value of $\bar{r}$ and we will assume it to be $4\pi/3 v_B \cdot \bar{r}_0^3 n_* = n_e$, n_e denoting the value of n at the end of the nucleation period. Now Θ_1 which is obtained from the above equation using the constant value R_1 corresponding to the value of R at the end of the nucleation period (which we will take at the instant $\nu = 0.01\ \nu_0$), is smaller than the actual transient period Θ. This will be seen from the following comparison.

$$[d\bar{r}/dt + \partial(d\bar{r}/dt)/\partial R \cdot \delta R]/(d\bar{r}/dt)$$
$$= 1 + 3(\delta R/R)/(1-\bar{r}^3/R^3)$$
$$= 1 + (\delta R/R)/(1-\bar{r}/R)^3/(1+\bar{r}/R+\bar{r}^2/R^2)$$

while

$$(R+\delta R-\bar{r}_0)/(R-\bar{r}_0) = 1 + (\delta R/R)/(1-\bar{r}_0/R)$$

Therefore the relative decrease in the rate of droplet growth is larger than that in the corresponding range, for a small decrement δR, of R. On the contrary, Θ_2 obtained using R_2, corresponding to R at the instant Θ_2 after the end of the nucleation period, is larger than the actual transient period. The value of Θ depends, of course, on the choice of $\bar{r}/R$ and we will take this ratio to be 0.9 in the following numerical computation. In actuality Θ_1 is not much different from Θ_2 ($(\Theta_2 - \Theta_1)/\Theta_2 \lesssim 0.01$) and so we can make a rather accurate estimation of the length of the transient period.

§ 5. Condensation and the Change of Parameters in a Flaw

Consider a tube of stationary flow in a supersonic stream of air in which condensation takes place. Let a small quantity of heat dq is added per unit mass of the gas, as a result of condensation between two consecutive points ds distant along a stream line. Standard notation will be used except where noted.

From the equation of continuity $\rho u f =$ constant, we have

$$d\rho/\rho + du/u + df/f = 0 \qquad (10)$$

The equation of conservation of momentum can be expressed as

$$\rho u du = -dp \qquad (11)$$

Energy relation becomes in this case

$$udu = dq - 2ada/(\gamma-1), \qquad (12)$$

where $a^2 = \gamma p/\rho$. From these equations the following relations can easily be obtained.

$$du/u = -(\gamma-1)/a^2(M^2-1) \cdot dq$$
$$+1/(M^2-1) \cdot df/f \qquad (13)$$

$$dp/p = \gamma(\gamma-1)M^2/a^2(M^2-1) \cdot dq$$
$$-\gamma M^2/(M^2-1) \cdot df/f \qquad (14)$$

$$d\rho/\rho = (\gamma-1)/a^2(M^2-1) \cdot dq$$
$$-M^2/(M^2-1) \cdot df/f \qquad (15)$$

where M denotes the Mach number.

Consider the increase in the entropy for a change $p_1\mathbf{v}_1T_1 \to p_2\mathbf{v}_2T_2$, which we imagine as consists of the following two stages

$$p_1\mathbf{v}_1T_1 \xrightarrow{\text{isentropic}} p_1'\mathbf{v}_2T_1' \xrightarrow{\text{reversible}} p_2\mathbf{v}_2T_2,$$

then we have

$$\Delta s/c_v = \log(T_2/T_1') = \log(T_2/T_1)(T_1/T_1')$$
$$= \log(p_2/p_1)(v_2/v_1)^\gamma = \log(T_2/T_1)$$
$$+(\gamma-1)\log(v_2/v_1),$$
$$\therefore \quad (T_2-T_1)/T_1 = \log(p_2/p_1) + \log(v_2/v_1)$$
$$= \log(p_2/p_1) - \log(\rho_1/\rho_2).$$

Therefore we obtain from Eq. (14) and Eq. (15),

$$dT/T = (\gamma-1)(\gamma M^2-1)/a^2(M^2-1) \cdot dq$$
$$-(\gamma-1)M^2/(M^2-1) \cdot df/f \qquad (16)$$

The second terms on the right hand side of the equations (13), (14), (15) and (16) correspond to the isentropic change, while the first terms are of the similar form as that given by Head for the condensation shock, to which Head ascribed the phenomenon in question. Now when we consider the relation

$$T(\gamma-1)(\gamma M^2-\gamma)/a^2(M^2-1)=1/c_v\ ,$$

the rise in the temperature dT' due to heat addition by condensation dq, can be expressed as $dT'=dq/c_e$, with an effective heat capacity c_e per unit mass of the gas,

$$c_e=\gamma(M^2-1)/(\gamma M^2-1)\cdot c_v\ .$$

This is why we expressed the temperature change due to condensation as $(n-n_0)\lambda/c_e\rho$ before. $1/c_e$ varies with M and especially notably in the vicinity of $M=1$ where also the validity of all equations from Eq. (10) to Eq. (16) is lost. But except in this region c_e in Eq. (3) can approximately be treated as a constant with the value corresponding to that at the time origin, i.e., at the nucleation peak. Because conditions at the moment remote from the time origin would be irrelevant to the total amount of self-nucleation.

Now we see from Eqs. (10), (11) and (12) that where $M=1$ the following relation must hold

$$(\gamma-1)/a^2\cdot dq=df/f \qquad (17)$$

that is, the location corresponding to $M=1$ which is at the throat of the nozzle if the flow is isentropic, is shifted to the spot where the relation (17) is satisfied. Further from Eq. (14) and the relation

$$a^2=\gamma p/\rho=\gamma(\gamma-1)c_v T,$$

the following equation can be obtained, where c_v means the specific heat at constant volume of the gas

$$dp'/p=(\lambda/c_v\rho T)\cdot M^2/(M^2-1)\cdot dn \qquad (14a)$$

with dp', the pressure increase by heat addition due to condensation; this gives the relation between the heat liberated through condensation and the pressure change due to the heat addition. This pressure change is superposed on the pressure change corresponding to an adiabatic expansion of the gas without condensation and the resulting pressure change will be compared with experimental data.

§ 6. Results of Numerical Computation and Discussion

The numerical computation was carried out for two cases given in Head's report[2)]; one, (I), is the case of which the result of pressure distribution measurements is given in Fig. 6a and the other, (II), the case given in Fig. 6b in his thesis. Stagnation conditions of these are as follows;

Case	Stagnation pres.	Relative humid.	Stagnation temp.*
I	2790 mm Hg	74.4%	296.3°K
II	1520 mm Hg	43.8%	298.3°K

Physical constants necessary for the computation were taken from the same source when comparison with Head's calculation is the matter, otherwise they were taken from International Critical Tables.

The variation of surface tension of water droplet with its radius, which was given by Tolman[12)] some time ago, is not taken into account in the computation, for the reason reported previously[1)], but the effect of this change will be discussed later. Condensation coefficient P is assumed first to be 1.

Now as mentioned already, the change in pressure and in temperature of the gas corresponding to flow without condensation is computed and the nucleation at various stages of this pressure and temperature change as calculated using Eq. (1) is put into the right hand side of Eq. (7), together with other quantities obtainable from equations given above. The left hand side of Eq. (7) is also calculated for each stage of pressure and temperature change. From the coincidence of the value of both sides, following result is obtained as for the conditions at the time origin, i.e., at the nucleation peak.

	$(p/p_S)_0$	ν_0	S_0
I	0.45	1.3×10^{17}	39.6
II	0.36	2.3×10^{17}	74.5

The locations corresponding to the time origins are marked with arrows in Fig. 1. We see from this figure that the location where conspicuous condensation takes place in a supersonic flow nearly coincides with the regions corresponding to nucleation period mentioned previously.

---

* These values are computed by the author from graphs given in Fig. 1 and Fig. 6a, Fig. 6b of Head's dissertation.

To see the agreement between this theory and experiment more precisely, pressure rise in the vicinity of nucleation period, through the liberation of heat due to condensation $n\lambda/c_e\rho$, is computed using Eq. (4) and Eq. (14a) and given in Fig. (3), together with experimental values which express the distance, in terms of $\Delta p/p$ of observed points from the isentropic curve in Fig. 6a, of Head's report²⁾. Nucleation period and transient period are also given in the figure.

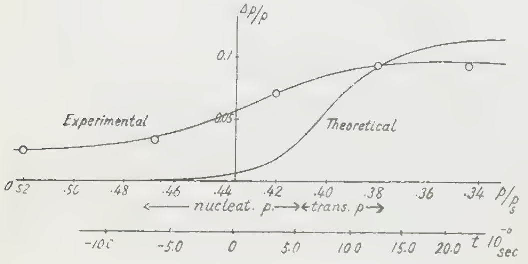

Fig. 3.

It can be seen from this figure that though the agreement between the calculated and the observed values is considerably good in view of the approximations adopted in the computation, it is still unsatisfactory when quantitative agreement, especially in the length of nucleation and trancient period is concerned. Effective time lag is to be considered in this case as it turns out to be of the order of magnitude $\tau_e \simeq 2\times10^{-6}$ sec.

When the condensation coefficient P is 0.01, nucleation peak (corresponding to $t=0$) does not appear, according to Eq. (7), until the location $p/p_S \simeq 0.20$ is reached. Moreover the effective time lag τ_e is of the order of 10^{-4} sec in this case. Therefore agreement with the experiment is out of question.

Should the variation of surface tension of water droplet with curvature of its surface be given by Tolman's formula¹²⁾, then the nucleation peak would have come to the location corresponding to $p/p_S \simeq 0.60$, the fact which is also contrary to the experimental result.

These arguments do not necessarily mean, however, that the surface tension of water droplet is strictly constant down to the smallest embryonic droplets and the coefficient P is always equal to unity. The surface tension possibly diminishes more or less with the radius of droplet, if not according to Tolman's formula which he himself did not claim to be valid down to the region concerned ($r \sim 10^{-8}$cm), and also possibly the coefficient of condensation P is considerably less then unity; the effect of these two factors may cancel each other and the nucleation peak appear in the vicinity of the location which one expects when these two effects are absent. It may even be probable when we consider the discrepancy between the above theory and the experiment concering the length of transient period. But the discrepancy may be due to the influence of turbulence which we have not taken into account. Therefore it would be difficult to determine the magnitude of these factors from such phenomena alone.

At any rate there seems to be no contradiction between the theory of self-nucleation and the phenomenon of the spontaneous condensation in a supersonic flow of humid air when we consider the whole process of fog development, on the basis of the law of droplet growth given by Eq. (2a).

In conclusion the author wishes to express his deepest gratitude to Prof. T. Nagamiya of Osaka University and to Prof. I. Imai of Tokyo University for their kind criticism on this work.

References

1) H. Wakeshima: J. Phys. Soc. of Japan **9** (1954) 400; J. Phys. Soc. of Japan **9** (1954) 407.
2) R. Head: "Investigation of spontaneous condensation phenomena," Guggenheim Aero. Lab. Calif. Inst. of Tech., Ph. D. Dissert. P. Wegener and R. Smelt: "Summary of NOL. research on liquifaction phenomena in hypersonic wind tunnels (NOL. 159)" NOL Memo. 10772 (Feb. 15 1950).
3) R. Head: loc. cit.
4) K. Oswatitsch: Z. A. M. M. **22** (1941) 1; Jahrbuch der L. F. F. (1941), 692.
5) J. V. Charyk: "Condensation phenomena in supersonic flow", Ph. D. Thesis, Calif. Inst. of Tech. (1946)
6) P. Wegener and R. Smelt: loc. cit.
7) A. Kantrowitz: Phys. Rev. **77** (1950) 572.; J. Chem. Phys. **19** (1951) 1097.
8) R. F. Probstein: J. Chem. Phys. **19** (1951) 619.
9) H. Wakeshima: J. Chem. Phys. **22** (1954) 1614.
10) J. Frenkel: Kinetic Theory of Liquid, pp. 397.
11) T. Alty and C. A. McKay: Proc. Roy. Soc. of London (A) **149** (1935) 104; J. Yoshida and H. Nakayama: Teionkagaku (in Japanese) **2** (1949) 159; W. Prüger: Z. Phys. **115** (1940) 202.
12) R. C. Tolman: J. Chem. Phys. **17** (1949) 333.

JOURNAL OF THE PHYSICAL SOCIETY OF JAPAN Vol. 10, No. 2, FEBRUARY, 1955

Piezoelectricity of Wood

By Eiichi FUKADA

Kobayasi Institute of Physical Research, Kokubunji, Tokyo

(Received September 3, 1954)

The direct and converse piezoelectric effects of wood have been studied. Assigning the z axis to the grain direction and the x and y axes to the radial and tangential direction of annual rings respectively, the piezoelectric effects corresponding to d_{14} and d_{25} were observed. When the shearing force is applied to the fibers in their oriented plane, the polarization occurs on the side planes of the fibers. The effect is symmetrical to the z axis, that is, the grain direction. The converse effects were observed by clamping together the wood specimen and a Rochelle salt crystal between metal frames, and measuring the output voltage of the Rochelle salt crystal when the alternating voltage at audio frequency is applied to the wood specimen. The value of the piezoelectric constants, $-d_{14}=d_{25}$, is in the order of 10^{-9} and about one twentieth of d_{11} of quartz. If we assume that the natural cellulose possesses the piezoelectricity in its crystalline state, that the cellulose micelle are oriented in only one direction namely z axis, in which the positive and negative direction of long axis of micelle are equally distributed and that micelle are arranged quite at random in the x y plane, the apparent piezoelectricity of wood are reasonably explained.

§ 1. Introduction

Piezoelectricity is usually attributed to the properties of crystalline materials. But we have only a few reports which describe the piezoelectricity of non-crystalline materials as rubber, paraffin, or glass1)2)3)4). Of particular interest are those which investigate the piezoelectricity of wool, human hair5), and wood6). These works were generally qualitative and do not seem to have drawn the proper attention. We have investigated quantitatively both the direct and converse piezoelectric effects of wood and confirmed that wood has the piezoelectric properties similar to the crystalline materials.

For convenience, three perpendicular axes were assigned for wood as shown in Fig. 1. z axis denotes the direction of grain, x axis the radial direction of annual ring and y axis the tangential direction of annual ring. This assignment has been adopted in the study of elastic properties of wood and the symmetry of rhombic order is concluded7).

At the initial stage of our experiment, square plates of wood cut perpendicularly to the grain were used. The thin silver foils were attached to the z planes by alcoholic solution of shellac. When the pressure was applied in the z direction, the considerable amount of charge was produced and the polarity of the charge was also found. But when the z planes were plated by evaporated silver in vacuum, the effects disappeared. The polarization might be due to the contact electricity between wood and silver foils. For a sample which the z direction is oblique to the square plane, the effect was slightly observed even when it was plated by the vacuum evaporation of silver. So it was predicted that the shearing force plays a role in producing polarization rather than the tension or compression.

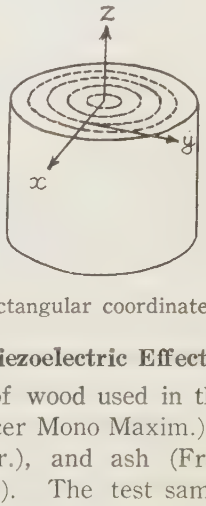

Fig. 1. Rectangular coordinates for wood.

§ 2. Direct Piezoelectric Effect

The kinds of wood used in the experiment are maple (Acer Mono Maxim.), spruce (Picea jezoensis Carr.), and ash (Fraxinus mandshurica Rupr.). The test samples were cut

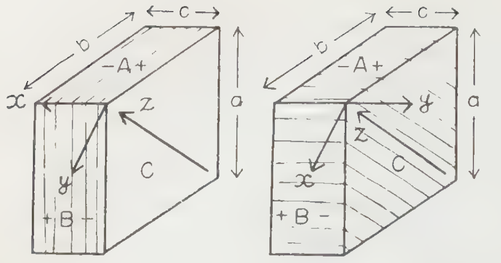

Fig. 2. The cuttings of sample which manifest the piezoelectric effect.

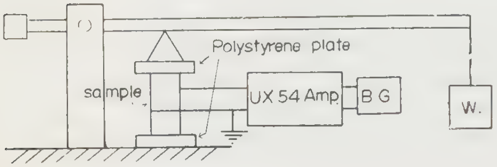

Fig. 3. The measuring apparatus for the direct piezoelectric effect.

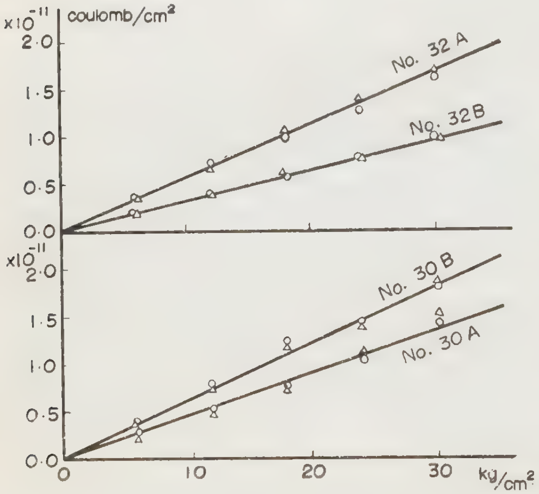

Fig. 4. The polarization vs. pressure relations of maple. NO. 32 and NO. 30 correspond d_{14} and d_{25} respectively.

as shown in Fig. 2 for convenience of applying the shearing force, which are the cases that manifest the piezoelectric effect. The dimensions of sample, *a*, *b* and *c*, are about 1.5 cm, 1.5 cm and 0.8 cm respectively The samples were dried for a few days in a decicater containing calcium chloride.

The measuring apparatus for the direct effect is shown schematically in Fig. 3. The pressure is applied to the wood specimen by a lever mechanism and the charge is led to the grid of the vacuum tube UX54 and measured by a ballistic galvanometer in the plate circuit.

Now consider samples cut out as in Fig. 2. When the pressure is applied on the plane A, the plane C is positively charged and the opposite plane of C is negatively charged. When the pressure is applied on the plane B, the sign of the charge on the plane C and the opposite plane of C is reversed. This means that the yz or xz shear produces the x or y polarization, so that the piezoelectric constants d_{14} and d_{25} are in the magnitude of measurable quantity. Fig. 4 shows examples of the charge-pressure relations of maple NO. 30 and NO. 32, which correspond d_{25} and d_{14} respectively. The circles denote the charge produced by applying pressure and the triangles the charge produced by removing pressure, the sign of the latter is reversed.

The piezoelectric constants were determined by comparing with a x-cut quartz crystal. Between the piezoelectric constant of wood d_w and the piezoelectric constant of quartz d_q the following relation holds:

$$\frac{d_w}{d_q}=\frac{2c}{a}\frac{\theta_w}{\theta_q}\cdot\frac{W_q}{W_w},$$

where θ_w represents the deflection of galvanometer, when the pressure W_w is applied on the wood, and θ_q, W_q are the corresponding quantities for the quartz crystal. *a* and *c* are the dimensions of sample shown in Fig. 2.

The piezoelectric constants which were determined by the direct effect are shown in Table I. In the crystallographical viewpoint eighteen different piezoelectric constants can exist which specify the nature of polarization and stress. In the results of our experiment only d_{14} and d_{25} were found to be finite. All other constants vanish within the precision of our experiment. It is interesting that d_{36} is equal to zero, contrary to the prediction of rhombic symmetry of elastic properties.

§ 3. Converse Piezoelectric Effect

The convincing proof of the piezoelectric effect is to verify the existence of the converse piezoelectric effect. For that purpose, a wood specimen and a Rochelle salt crystal are clamped together with a metal frame and the a.c. voltage was applied to the specimen. Then the wood becomes strained alternatively and transmits the oscillating force to the Rochelle salt crystal, the output voltage from which could be amplified to a measurable value. The actual apparatus is shown schematically in Fig. 5.

The Rochelle salt crystal is shielded within a metal case, on which the x-cut quartz crystal and the wood specimen, cut out as in Fig. 2 and sandwitched by the polystyrene plates, are placed and clamped together as shown in Fig. 5. First the a.c. voltage of about 600 c.p.s. is applied to the quartz crystal, at which frequency the amplifier has a maximum gain. Next, both plates of quartz are earthed and the a.c. voltage is applied between the plane C and the opposite plane of the wood specimen shown in Fig. 2 and the output of the Rochelle salt crystal is amplified by about 110 decibels. An example of the output current versus applied voltage relations for both cases is shown in Fig. 6. The sample is maple NO. 30B.

Comparing with the x-cut quartz crystal, the piezoelectric constant d_w of wood can be obtained from the following equation:

$$\frac{d_w}{d_q}=\frac{2c}{a}\,\frac{\theta_w}{\theta_q}\,\frac{V_q}{V_w},$$

where θ_w or θ_q denotes the reading of the output meter when the a.c. voltage V_w or V_q is applied on the wood or quartz respectively. The deduction of this formula is given in the appendix.

In the actual measurement the input voltage was divided by a fixed resistance r and a variable resistance R as shown in Fig. 5. By adjusting the variable resistance R, the output voltage from the Rochelle salt crystal becomes unaltered as a switch in Fig. 5 is turned to the either side. Then the ratio of two voltage which produce the same output voltage for both the wood and the quartz is calculated from the values of r and R, hence d_w is obtained. Further the null method was possible by applying the voltage on both the wood and the quartz at the same time and connecting the polarity of quartz so that the oscillating force of quartz cancel out that of wood.

The piezoelectric constants obtained from the converse effect are also shown in Table I, together with the value obtained from the direct effect. The agreement of both values is satisfactorily good. The values of spruce and ash are the mean values of a few samples.

Table I. The value of piezoelectric constants. (c. g. s. e. s. u.)

quartz	d_{11}	6.5×10^{-8}	
maple		direct effect	converse effect
NO. 32A	d_{14}	-2.6×10^{-9}	-2.4×10^{-9}
B	d_{14}	-1.5×10^{-9}	-2.6×10^{-9}
NO. 30A	d_{25}	2.8×10^{-9}	1.6×10^{-9}
B	d_{25}	3.9×10^{-9}	2.2×10^{-9}
NO. 34A	d_{14}'	-2.9×10^{-9}	-2.9×10^{-9}
B	d_{14}'	-3.4×10^{-9}	-2.0×10^{-9}
spruce	d_{14}	-5.0×10^{-9}	-2.3×10^{-9}
ash	d_{14}	-6.2×10^{-10}	-8.0×10^{-10}

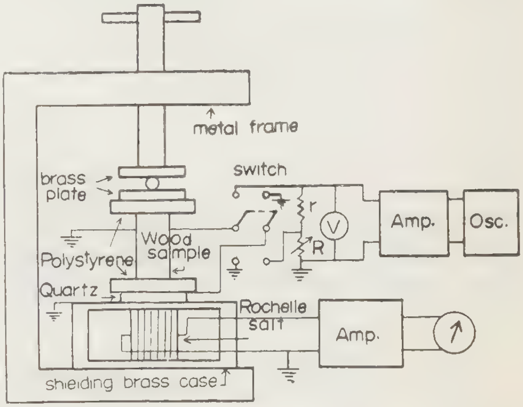

Fig. 5. The measuring apparatus for the converse piezoelectric effect.

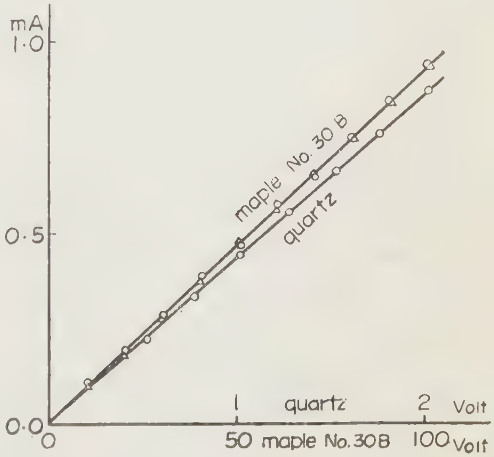

Fig. 6. The output current vs. applied voltage relations of maple NO. 30B and *x*-cut quartz crystal.

As is well known, in the converse piezoelectric effect the strain is proportional to the applied voltage, while in the electrostriction the strain is proportional to the square of the applied voltage. In order to ascertain that the effect is not due to the electrostriction, the applied voltage and the output voltage are led to the Braun tube oscillograph and made a Lissajous' figure. The figure shows a circle and confirms that frequency is not altered, so that the strain is proportional to the applied voltage. Further when the shielding of the Rochelle salt crystal is not complete, the induction voltage appears with no applied voltage on the sample. When the a.c. voltage is applied, the output increased or decreased from the induction voltage according to the different connection of the polarity of wood plate. This fact shows also the polarity of the effect.

§ 4. Discussion

In general we have the 18 different piezoelectric constants for the anisotropic materials, while in wood we could observe only two of them, d_{14} and d_{25}, in definite values, that is,

$$\begin{pmatrix} 0 & 0 & 0 & d_{14} & 0 & 0 \\ 0 & 0 & 0 & 0 & d_{25} & 0 \\ 0 & 0 & 0 & 0 & 0 & 0 \end{pmatrix}$$

If we make samples in which the x and y axes are rotated 45° and the z axis is unaltered, the observed piezoelectric constant d_{14}' is nearly the same with d_{14} as shown in Table I. Further the absolute values of d_{14} and d_{25} are equal within the limit of error of the present experiment. The piezoelectric effect is, therefore, symmetrical to the z axis.

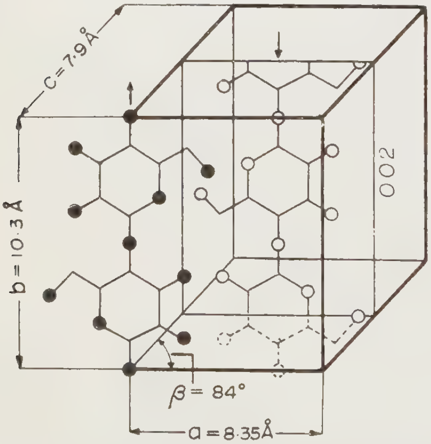

Fig. 7. The unit cell of the micell of natural cellulose. Circles represent oxygen, carbon and hydrogen are omitted.

If we take any plane of wood parallel to the z axis namely the grain direction and apply a shearing force in the direction of fibers clockwise in the plane, then the positive charge appears in the front side of plane and the negative charge on the back side.

Now the origin of the piezoelectricity of wood is entirely unknown, but it may be plausible that the effect is originated from the crystalline structure of natural cellulose fibers. The micell structure of natural cellulose is supposed to be as in Fig. 7[8)]. This belongs to the monoclinic symmetry, space groop C_2^2, and the possible piezoelectric constants are as follows:

$$\begin{pmatrix} 0 & 0 & 0 & d_{14} & d_{15} & 0 \\ 0 & 0 & 0 & d_{24} & d_{25} & 0 \\ d_{31} & d_{32} & d_{33} & 0 & 0 & d_{36} \end{pmatrix}$$

where x, y and z axes correspond to *a*, *c* and *b* in Fig. 7 respectively.

The arrangement of these micelle in the bulk structure of wood is very complicated. But it is known that the long axes of micelle are oriented parallel to the fiber axis in a fiber and the fibres have a fairly good orientation in the grain direction. So we assume that all these micelle are oriented parallel to the z axis, that the distribution of the positive and negative direction of z axis of each micell is at random and that in the x y plane the distribution of micelle is quite at random. It will correspond to the symmetry of D_∞. Then from the symmetry consideration, the resulting piezoelectric constants of the system are only d_{14} and d_{25}, and the relation $d_{14}=-d_{25}$ is also satisfied.

Therefore if we attribute the piezoelectric effect to the property of natural cellulose itself in its crystalline state, the apparent piezoelectric effect of wood is reasonably explained. We cannot, of course, neglect the complicated macroscopic structure of wood, especially the spiral structure of fibrils and their inclination to the grain direction. But if we consider the components of contribution of each micell, the above argument still remains to be valid.

It would not be too strange to deduce the piezoelectricity in natural cellulose if we notice that the single crystal of the cane sugar and that of the milk sugar have the 8 piezoelectric constants[9)] respectively, specified for the monoclinic symmetry C_2, of magnitude comparable with the quartz crystal.

The micellar structure of a number of high polymers have been already investigated by the x ray and electron diffraction methods. It is well known that their crystal symmetries are generally the monoclinic or the rhombic symmetry which are capable to be piezoelectric. Therefore there is a vast possibility that many high polymers other than the cellulose have the piezoelectricity also in their crystalline form, and it might not be too absurd to imagine the creation of the highly piezoelectric plastics which are artificially manufactured from linear high polymers.

The author wishes to express his hearty thanks to Dr. H. Kawai for his encouraging support throughout this work. He also wishes to thank Mr. M. Marutake for his valuable discussions and Mr. T. Uemura in the Government Forest Experiment Station, Ministry of Agriculture and Forestry, for his kindness in preparing the wood samples.

Appendix

For simplicity, let us consider a case that the wood and the quartz and the Rochelle salt crystal are clamped in series by the metal frame as in Fig. 8. When the voltage V_w is applied to the plates of wood separated by c_1, the wood deforms Δa_1 in the vertical direction, where a_1 is the vertical length of the wood specimen. The usual piezoelectric equation,

$$\Delta a_1 = \frac{a_1}{E_1}\frac{P}{A_1} + \frac{1}{2}d_w a_1 \frac{V_w}{c_1}, \tag{1}$$

holds, where P denotes the pressure, E_1 the Young's modulus of wood and A_1 the cross sectional area of specimen. The quartz deforms $\Delta a_2 - \Delta a_1$ by the pressure P, where a_2 denotes the thickness of the quartz plate. It stands:

$$\Delta a_2 - \Delta a_1 = \frac{a_2}{E_2}\cdot\frac{P}{A_2}, \tag{2}$$

where E_2, A_2 denotes the Young's modulus and the effective cross sectional area of the quartz respectively. As the Rochelle salt crystal is 45° x-cut, the equation similar to (1) holds,

$$\Delta a_3 - \Delta a_2 = \frac{a_3}{E_3}\frac{P}{A_3} + \frac{d_{14}}{2}\cdot a_3\cdot\frac{V_3}{c_3}, \tag{3}$$

where d_{14} is the piezoelectric constant of the Rochelle salt and V_3 is the output voltage. Other notations are similar to the former case. Finally the metal frame deforms $-\Delta a_3$, because now we assume that the total system does not deform,

$$-\Delta a_3 = \frac{a_4}{E_4}\cdot\frac{P}{A_4}, \tag{4}$$

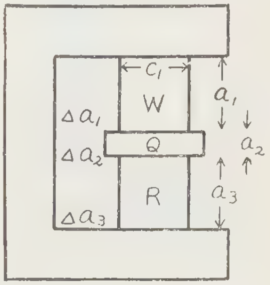

Fig. 8.

where a_4, E_4 and A_4 means the effective length, the Young's modulus and the effective cross section of metal frame respectively. Summing up from (1) to (4), we get,

$$0 = P\left(\frac{a_1}{E_1A_1} + \frac{a_2}{E_2A_2} + \frac{a_3}{E_3A_3} + \frac{a_4}{E_4A_4}\right) + \frac{d_w}{2}\frac{a_1}{c_1}V_w + \frac{d_{14}}{2}\frac{a_3}{c_3}V_3. \tag{5}$$

While between the pressure $\boldsymbol{P}$ and the output voltage V_3 of the Rochelle salt crystal it stands:[10)]

$$V_3 = f\frac{d_{14}}{\varepsilon_a}P = KP, \tag{6}$$

where f is the factor depending the dimension and ε_a is the dielectric constant of the Rochelle salt and K is a constant. From (5) and (6) we obtain,

$$\frac{d_w}{2}\frac{a_1}{c_1}V_w = -V_3\left[\frac{d_{14}}{2}\frac{a_3}{c_3} + \frac{1}{K}\left(\sum_i \frac{a_i}{E_iA_i}\right)\right] = \text{const.}\ \theta_w, \tag{7}$$

where θ_w denoted the reading of the output meter. In the case when the voltage is applied to the quartz crystal, we obtain the similar expression as follows:

$$d_q\frac{a_2}{a_2}V_q = \text{const.}\ \theta_q, \tag{8}$$

where V_q and θ_q denote the applied voltage and the reading of output meter respectively. Therefore we get the last equation,

$$\frac{d_w}{d_q} = \frac{2c_1}{a_1}\frac{V_q}{V_w}\cdot\frac{\theta_w}{\theta_q}. \tag{9}$$

References

1) W. G. Cady: Piezoelectricity, Mc Graw-Hill (1946) 234.
2) K. R. Brain: Proc. Phys. Soc. **36** (1924) 81.
3) H. F. Richards: Phys. Rev. **22** (1923) 122.
4) A. Shubnikov and B. Brunovskij: Bull. Acad. Sci. Leningrad (1928) 367.
5) A. J. P. Martin: Proc. Phys. Soc. **53** (1941) 186.
6) V. A. Bazhenov and V. P. Konstantinova: Doklady Akad. Nauk. S. S. S. R. **71** (1950) 283; Chem. Abst. **45** (1951) 2747.
7) R. Meredith: Mechanical Properties of Wood and Paper, Interscience (1953) 19.
8) K. H. Meyer and L. Misch: Helv. Chim. Acta. **20** (1937) 232.
9) W. F. Holmann: An. Phk. **29** (1909) 160.
10) H. Kawai: J. Phys. Soc. Japan **2** (1947) 113.

JOURNAL OF THE PHYSICAL SOCIETY OF JAPAN Vol. 10, No. 2, FEBRUARY, 1955

Der Zündmechanismus im Dieselmotor* (I)

Von Kunio TERAO
Technisches Laboratorium der Isuzu Motor A. G.

(Received September 18, 1954)

An experimental research in the mechanism of the ignition and the air-fuel mixture in the internal combustion engine was carried out. The fluctuating nature of the ignition-delay in the Diesel-engine was analysed statistically and we found that the probability of ignition in unit time of the liquid fuel, which was injected into the combustion-chamber, was nearly proportional to the time. For the explanation of these changes of ignition probability, the diffusion-phenomenon of fuel was discussed.

§ 1. Vorwort

Es ist in dem Forschungsgebiet des Verbrennungsmotors besonders wichtig, wie die Mischung des Brennstoffes und der Luft brennt.

Zur Entzündung des Brennstoffes in der adiabatisch gedrückten Luft, wie im Verbrennungsmotor, zu entzünden, hat man vielerlei Methoden, im Wesentlichen kann man aber von zwei verschiedenen Methoden sprechen, die schon von vielen Forschern untersucht worden sind. Die eine ist die, bei der man vorher eine Mischung des Brennstoffes und der Luft macht und dann entzündet, oder auch nach der adiabatischen Verdichtung, mittels Elektrofunken oder einer anderen thermischen Energie wie Ottomotor etc, entzündet. Die andere ist die, bei der man den flüssigen Brennstoff in die Hochtemperaturluft oder in die adiabatisch gedrückte Luft einspritzt und durch die Energie der Hochtemperaturluft entzündet, wie im Dieselmotor.

Wir finden jetzt viele ausgezeichnete Forschungen(1)(2)(3) der Verbrennung im technischen Schrifttum, sowhl beim Ottomotor als auch beim Dieselmotor und auch beim Bombe. Trotzdem bleiben immer noch viele Aufgaben der Zündung unerklärt.

Andrerseits wurden in der Neuzeit statistische Phänomene im physikalischen Gebiet von verschiedenen Physikern untersucht. Besonders hat Dr. Hirata, Professor der Fakulität der Naturwissenschaft der Tokyo Universität, gezeigt(4), dass man Phänomene, wie der Bruch, die sich von den mikroskopischen zu den makroskopischen vergrössern, nicht ohne Überlegung der Wahrscheinlichkeit erörtern kann, und seine Theorie wurde durch Forschungen vom Bruch des Glasses in seinem Laboratorium und andern bewiesen. Danach wandten er und einige andere Forscher(4) die Theorie im weiteren physikalischen Bereich an. Die Aufgaben des Zündmechanismus betreffend kann man so nachfolgende Annahmen machen.

Wenn man den flüssigen Brennstoff in die Hochtemperatur und Hochdruckluft einspritzt und dort entzündet, wie im Dieselmotor, zündet es gewöhnlich nach einer Weile Zündverzug. Ich untersuchte die Schwankungen dieser Zündverzüge im Dieselmotor und probierte mit statistischer Behandlung, wie schon erwähnt, die Wahrscheinlichkeit der Zündung zu bekommen und dadurch den Zündmechanismus zu erörtern.

§ 2. Versuchseinrichtung und Versuchsausführung

Ich prüfte mit einem Dieselmotor für Autowagen, dessen Hauptdimensionen folgende sind:

Bohrung	95 mm
Hub	120 mm
Brennkammer	
Hauptkammer	30 cc
Vorkammer	20 cc
Verdichtungsverhältnis	18.0
Einspritzpumpe	Bosch Typ
Einspritzdüse	Eindrosselloch-Nadeldüse
Einspritzdruck	100 kg/cm^2

Ich betrieb diesen Dieselmotor bei 600 U/min Leerlauf, mass die Druckänderung in der Vorkammer und Hubänderung der Nadeldüse, und dachte dadurch den Zündbeginn und den Einspritzbeginn messen zu können.

(Abb. 1) zeigt schematisch meine Versuchseinrichtung. Die Druck- und Hubänderungen wurden durch Elektrokapazität-Indikatore gemessen. Ich machte die Elektrokapazität C_H für den Hub der Nadeldüse und C_D für den Druck der Vorkammer, die in elektrische Strome verwandt wurden, die gleichzeitig beide durch zwei Elemente eines elektromagnetischen Oszillographes stromten. Beide Indikatore zeigen den Elektrostrom 30∼40 mA pro 1 μF, und die hier benutzten Elemente des Oszillo waren beide H Type, dessen Eigenfrequenz 1000 Hertz/Sek ist.

(Abb. 2) zeigt eines unserer Massergebnisse. Z ist die Zeit, deren Abstand von einem Punkt zu dem nächsten 1/100 Sek. ist, K bedeutet den Kurbelwinkel des Motors, D die Hubänderung der Einspritznadeldüse und V die Druckänderung in der Vorkammer. Die Hubänderung der Nadeldüse ist wie ersichtlich so klar, dass man beinahe genau die Anfangszeit der Erhöhung der Nadeldüse bestimmen kann. Ich sehe den Einspritzbeginn als diese Anfangszeit der Erhöhung der Nadeldüse an, denn der Brennstoff geht sobald aus, wie sich die Nadeldüse öffnet.

Man kann den Zündbeginn nicht ganz genau bestimmen, aber, hier, wie gewöhnlich, nahm ich dafür den Zeitpunkt an, wo der Druck in der Vorkammer rasch ansteigt. Die Zeit vom Einspritzbeginn bis zum Zündbeginn, betrachte ich als den sogenannten Zündverzug.

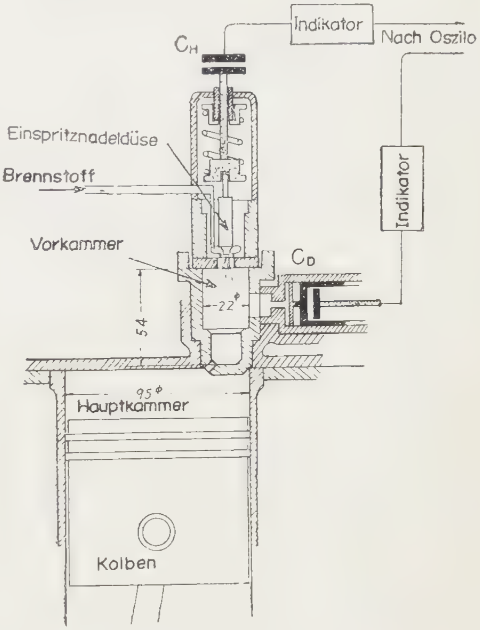

Abb. 1. Versuchseinrichtung.

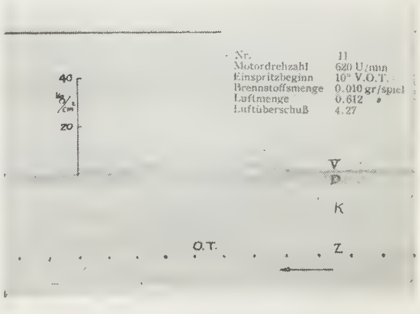

Abb. 2. Indikatordiagramm.

Ich machte drei verschiedene Versuche, nämlich zuerst wurde der Brennstoff auf 30° Kurbelwinkel vor O. T. eingespritzt, wo der Kolben gerade die oberste Stellung seines Weges einnimmt; beim zweiten Versuch wurde der Brennstoff auf 5° vor O.T. eingespritzt und beim dritten derselbe gerade auf O. T. Alle Versuche wurden jedes Mal auch unter Leerlauf bei 600 U/min gemacht, damit ich die drei Zustände miteinander bei verschiedener Temperatur und verschiedenem Druck prüfen konnte.

Auf einem Spiel kam dabei etwa 0.6 gr. Luft und 0.014 gr. Brennstoff. Das ist eine sehr grosse Masse Luft für den infragestehenden Brennstoff. Hier bekam ich bei einem Versuch hintereinander etwa 50 Spiele.

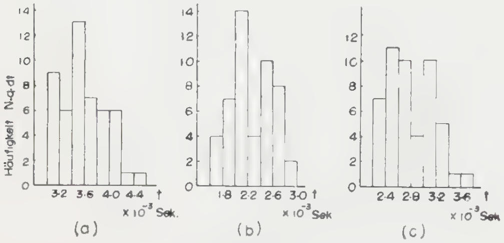

Zündverzug

Abb. 3.

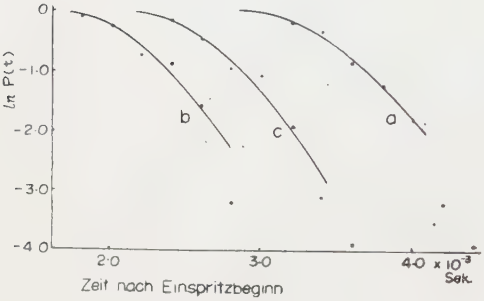

Abb. 4.

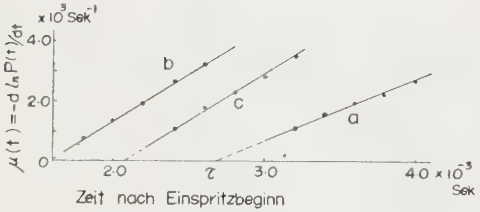

Abb. 5.

§ 3. Versuchsergebnis

Die Versuche haben gezeigt, dass die Zündverzüge jedes Mal schwanken. Abb. 3a, 3b und 3c zeigen die Häufigkeiten in Abhängigkeit von der Zündverzüge.

Stellen

$\mu(t)$: die Wahrscheinlichkeit der Zündung in Zeiteinheit

$P(t)$: die Wahrscheinlichkeit der Zündung, die es später als eine Zeit t geschieht

$q(t)$: das Häufigkeitsverhältnis der Zündung zwischen t und $t+dt$

dar, so bekommt man

$$P(t)=\int_{-\infty}^{\infty} q(t)\cdot dt \qquad p(0)=1$$

Und $P\cdot\mu\cdot dt$ ist die Wahrscheinlichkeit, dass die Zündung nicht stattfindet bis auf t, sondern während der nächsten dt, und dieselbe ist gleich $-dp$. So ist

$$P\cdot\mu\cdot dt=-dp$$

$$\mu\cdot dt=-dp/p\,,$$

und

$$\mu=-d(ln\cdot p)/dt$$

Sucht man $P(t)$ nach der Häufigkeiten in Abb. 3 und weiter davon $ln\cdot p$ und dann differenziert $ln\cdot p$ nach der Zeit nach Einspritzung, so bekommt man $\mu(t)$ wie in Abb. 5.

Wie diese zeigt, ist der Zusammenhang zwischen der Wahrscheinlichkeit $\mu(t)$ der Zündung in Zeiteinheit und der Zeit t beinahe geradlinig nach einer Zeit τ:

$$\mu(t)=K(t-\tau)$$

debei ist K konstant.

§ 4. Theoretische Betrachtung

Ich erörtere hier theroretisch und zwar qualitativ den Zündmechanismus des, wie im Dieselmotor, in die adiabatisch gedrückte Hochtemperatur- und Hochdruckluft eingespritzten Brennstoffes. Es gibt einige Arbeiten[5)6)], die vom Zündmechanismus eines in die Hochtemperaturluft im Ofen gestürzten flüssigen Brennstofftropfens, bzw, von der Verbrennung eines in stromender Luft bewegenden Brennstofftropfens sprechen. Aber bei meinen Versuchen wurden viele Brennstofftropfen nacheinander eingespritzt, deshalb muss man hier den Zündmechanismus von einem anderen Gesichtspunkt aus betrachten.

Nachdem der eingespritzte Brennstoff in vielen kleinen flüssigen Tröpfchen in die Luft geflohen ist, verdampfen allmählich alle Tröpfchen und erweitern sich in die Luft und dann stosst mit den Hochtemperatursauerstoff zusammen. Also vollzieht sich eine Mischung der Luft und des Brennstoffes.

Nun setze ich wie folgt voraus: In der Mischung fängt eine chemische Reaktion von einem oder einigen Orten an, wo nach einigen Kettenreaktionen die Zündung beginnt, und pflanzen sich die Flammen von dort fort. Wenn nämlich die chemische Reaktion in einem oder einigen Orten dieser Mischung einsetzt, entstehen da sogenannte Zündkerne, die sich anfangs allmählich vergrössern und von ihnen aus pflanzen sich die Flammen fort; der Druck in der Brennkammer steigt rasch auf, sowie die reagierende Masse so gross wird, dass die Reaktion sich rasch von der entstandenen Wärme zu der Nachbarmischung erweitern kann. Ich sehe hier den Zündverzug als die Zeit vom Einspritzbeginn des Brennstoffes bis zum Zeitpunkt, wo der Zündkern so gross wird, dass der Druck rasch aufsteigt.

Diese Zündkerne verlieren ihre anfangs entstandene Wärme durch die nachfolgend eingespritzten kalten Brennstoffe oder durch die Zylinderwand, wodurch einige von ihnen verschwinden, während andere diesen Verlust zu überwinden vermögen und verbrennen. Oder, wenn das Mischungsverhältnis zu dünn oder zu dick ist, pflanzen sich keine Flammen mehr fort und es zündet nicht, auch wenn die Zündkerne so gross werden. Deshalb können sich die Flammen nur von einem oder einigen wenigen Zündkernen fortpflanzen, die dabei leben bleiben können und ausserdem eine mässige Mischung haben. So kann man denken, dass es einem Zusammenhang zwischen der Zündverzugszeit und der Entstehung und Vergrösserung der Zündkerne geben müsse. Man kann auch den Zündmechanimus vom Gesichtspunkt des Zündverzuges aus erörtern.

Wie bereits gesagt, muss man das Phänomen mit Überlegung der Wahrscheinlichkeit betrachten, das sich vom mikroskopischen zum makroskopischen vergrössert. Nämlich zündet der Brennstoff unter einem bestimmten Zustand nicht bestimmt, sondern hat nur eine Wahrscheinlichkeit der Zündung. Je grössere Wahrscheinlickeit der Zündung er hat, desto zündbarer ist er. Bei der Zündung im Dieselmotor muss man auch an diese Wahrscheinlichkeit denken.

Nun denke ich an eine Wahrscheinlichkeit der Zündung in Zeiteinheit und zwar an zwei verschiedenen Möglichkeiten. Nämlich erstens, die Wahrscheinlickeit einer Entstehung der anfänglichen chemischen Reaktion und zweitens, diejenige der Vergrösserung der Reaktion.

Nun stellt man eine Wahrscheinlichkit der Zündung folgend dar:

$$\mu(t)=\alpha\cdot\beta \qquad (1)$$

$\mu(t)$: die Wahrscheinlichkeit der Zündung in Zeiteinheit.

α: die Wahrscheinlichkeit einer Enstehung der anfänglichen chemischen Reaktion.

β: die Wahrscheinlichkeit, dass sich die anfängliche Reaktion bis zum Kern vergrössert, von dem sich die Flamme sogleich fortpflanzen kann.

Ich will sie getrennt behandeln.

(i) *Die Wahrscheinlichkeit der Entstehung der anfänglichen chemischen Reaktion.*

Wenn die Moleküle des Brennstoffes und diejenigen des Sauerstoffes in der Luft zusammenstossen, entsteht es da eine Wahrscheinlichkeit der chemischen Reaktion. Deshalb kann man denken, dass die Wahrscheinlichkeit der Entstehung der Reaktion proportional der Stosszahl zwischen beiden Molekülen sei. Also:

$$\alpha\infty\nu_B\cdot\nu_S\cdot S_{B\cdot S}^2\sqrt{\frac{\pi}{h}\left(\frac{1}{m_B}+\frac{1}{m_S}\right)} \qquad (2)$$

ν_B: Molekulardichtigkeit des Brennstoffes

ν_S: Molekulardichtigkeit des Sauerstoffes

$S_{B\cdot S}$: Abstand zwischen den Zentren beider Moleküle beim Stoss.

m_B, m_S: Molekulargewichte beider Stoffe.

h: Planksche Konstante.

$S_{B\cdot S}^2\sqrt{\frac{\pi}{h}\left(\frac{1}{m_B}+\frac{1}{m_S}\right)}$ kann man als Konstante ansehen, weil es abhängig von dem Durchmesser und der Gewicht beider Stoffe ist.

So

$$\alpha\infty A\cdot\nu_B\cdot\nu_S \qquad (3)$$

$$A=S_{B\cdot S}^2\sqrt{\frac{\pi}{h}\left(\frac{1}{m_B}+\frac{1}{m_S}\right)} \qquad (4)$$

Andererseits ist diese Wahrscheinlichkeit proportional dem Volumen, das seine Dichtigkeiten beider Stoffe hat. Das Mischungsverhältnis, wo es sich relativ einfach zünden kann, ist in einer relativ kleiner Grenze, weil, wenn es zu dünn oder zu dick ist, die Reaktion nicht sich erweitern kann. Deshalb darf man zur Untersuchung der Wahrscheinlichkeit der Zündung nur diese Grenze berücksichtigen.

Man nehme an, dass

m: das Verhältnis der Luft im zündbaren Gebiet für diejenige, die unabhängig von der Diffusion ist,

λ: das durchschnittliche Mischungsverhältnis zwischen Brennstoff und Luft im zündbaren Gebiet,

ρ_l: die Dichtigkeit der Luft in dem Gebiet, das unabhängig von der Diffusion ist, sowie

Δv: das Volumen, dessen Zustand m sei,

so bekommt man:

$$\alpha \infty \sum A\cdot \rho_l^2\cdot m^2\cdot \lambda\cdot \Delta v \qquad (5)$$

weil $\nu_S \infty \nu_l$ (Molekulardichtgkeit der Luft im Diffusionsgebiet)$=\rho_l\cdot m$ und $\nu_B=\rho_l\cdot m\cdot \lambda$ ist.

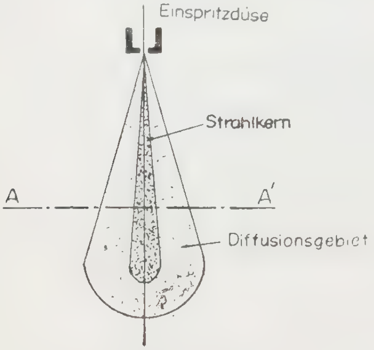

Abb. 6. Schematisches Bild von Einspritznebelsform.

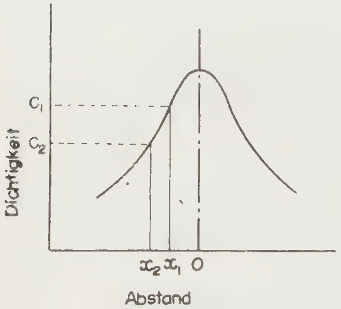

Abb. 7. Schematisches Bild von Dichtigkeit des Brennstoffes.

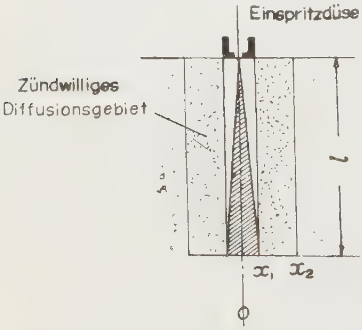

Abb. 8. Schematisches Bild von Diffusionsgebiet.

A, ρ_l, m, λ sind alle, wie schon gesagt, beinahe unabhängig vom Volumen des Diffusionsgebietes.

$$\alpha \infty A\cdot \rho_l^2\cdot m^2\cdot \lambda\cdot v$$

$$v=\sum \Delta v$$

v: das totale Diffusionsgebiet

Nun muss ich über das Diffusionsgebiet sprechen.

Die Einspritzform des flüssigen Brennstoffes in der Brennkammer bildet sich, wie in Abb. 6[1], eine Weile nach der Einspritzung. Wenn der ganze Brennstoff, von dem die Zündung abhängig ist, in einem Augenblick eingespritzt wird, ist der Zusammenhang zwischen der Dichtigkeit des Brennstoffes und dem Abstand von der Einspritzszentrallinie, falls eindimensional ist, wie folgt:

$$C=\frac{S}{2\sqrt{\pi Dt'}}\exp(-x^2/4Dt') \qquad (6)$$

C: die Dichtigkeit des Brennstoffes

D: der Diffusionsbeiwert

S: $\int_{-\infty}^{\infty} C\cdot dx$

t': Zeit nach dem Diffusionsbeginn

X: Abstand von der Einspritzszentrallinie

Abb. 7 zeigt das Verhältinis zwischen der Dichtigkeit des Brennstoffes und dem Abstand auf dem Ouerschnitt A-A' in Abb. 6.

Wenn man beispielsweise einfach die Form des Einspritznebels und des Diffusionsraumes als eine zylindrische ansieht wie in Abb. 8, ________, eine solche Form bildet bald nach Einspritzung ________, ist das Volumen des Diffusionsraumes wie folgt:

$$v=\pi l(x_2^2-x_1^2) \qquad (7)$$

l: die Länge des Einspritznebels.

x_1: der Abstand von der Zentrallinie, wo die Dichtigkeit des Brennstoffes C_l ist.

x_2: der Abstand von der Zentrallinie, wo die Dichtigkeit des Brennstoffes C_2 ist.

Ist D nicht so gross, so ist der Einfluss der Diffusion des später eingespritzten Brennstoffes im Gebiet des grossen x klein. Wenn es nicht so lange nach Diffusionsbeginn ist, ist im Gebiet des kleinen x der Brennstoff so dick und die Luft so mangelnd, dass die Zündfähigkeit sehr klein ist, wie bereits erwähnt, und vernachlässigen werden kann. Weiter, wenn die Haupteinspritzung eine Weile vor der Zündung endet, kann man annehmen, der Einfluss des anfangs eingespritzten Brennstoffes sei regulierbar. Wenn die Einspritzung nur einen Augenblick gemacht wird, so ist S in der Gleichung (6) konstant.

Von dieser Gleichung erhalten wir:

$$x_2^2-x_1^2=4Dt'ln\frac{C_1}{C_2}$$

deshalb sind

$$v=4\pi lDt'ln\frac{C_1}{C_2}$$

ist das durchschnittliche Mischungsverhältnis in dem Gebiet, wo die Dichtigkeit des Brennstoffes zwischen C_1 und C_2 ist, und bei einem bestimmten Zustand, wie schon erwähnt, beinahe konstant ist.

So ist

$$\alpha=K'\cdot A\cdot\rho_l^2\cdot m^2\cdot\lambda\cdot 4\pi\cdot l\cdot Dt'ln\frac{C_1}{C_2} \qquad (8)$$

K': Konstante

Man muss hier denken, durch welche Form es zu der Länge l kommt und wie die Abhängigkeit von der Zeit ist, aber man darf eine gewisse Zeit nach der Einspritzung diese Länge als konstant ansehen.

Wenn die Wahrscheinlichkeit der Entstehung der anfänglichen chemischen Reaktion nur von dem Diffusionsgebietvolumen beherrscht wird, wird der Zusammenhang zwischen der Zeit nach der Einspritzung und dieser Wahrscheinlichkeit wie in Abb. 9. Nämlich OA zeigt die Zeit, wo die Einspritznebelslänge nach dem Einspritzbeginn zu l wird, AB die Zeit, wo das Diffusionsgebiet gemacht wird und fast proportional der Zeit ist.

Eine Weile nach dem Ende der Einspritzung, wird der dickeste Teil, der sich im Zentralort befindet, allmählich durch die Diffusion dünner, und nachdem er dünner als die zündbareste Grenzdichtigkeit geworden ist, wird das zündbare Diffusionsgebiet mit der Zeit kleiner, wenn die Luft grossen Mangel an Brennstoff hat, nämlich die Luftüberschusszahl gross ist. BC in Abb. 9 zeigt diese Zeit. Nachdem die Mischung homogen geworden ist, muss das konstant werden, das an CD gezeigt wird.

In diesem Falle denke ich den Diffusionsbeiwert D, der abhängig von Temperatur und Druck ist, als konstant, weil die Diffusionszeit, die die Zündung beherrscht, nicht so lange und kürzer als 1.5×10^{-3} Sek. bei fast allen Fällen ist.

Ausserdem muss man andere Einflüsse, z. B. von den der Dichtigkeit der gedrückten Luft oder von den der Verdampfung des Brennstoffes, berücksichtigen.

Der Einfluss der Dichtigkeit der Luft ist quadratisch, falls er der Gleichung (8) folgt. Aber bei einem bestimmten anfänglichen Zustand sind die Differenzen zwischen dem frühesten Zündzeitpunkt und dem spätesten bei fast allen Fällen geringer als 1.5×10^{-3} Sek., und gewöhnlich, ausser anfänglichen Bedingungen, nicht so wichtig.

Die Verdampfung des Brennstoffes geschieht zusammen mit der Diffusion und man kann sie ruhig vernachlässigen. Die Verdampfungsgeschwindigkeit eines flüssigen Brennstofftropfens ist proportional dem Quadrat des Tropfensdurchmessers, falls die Temperatur und der Druck homogen und unveränderlich sind. Deshalb, wenn der Brennstoff als viele Tropfen in die heisse Luft eingespritzt wird, ist die Verdampfungsgeschwindigkeit anfangs schnell und allmählich langsamer, aber hier muss man denken, dass die Temperatur der Mischung durch Wärmeaustausch allmählich höher wird.

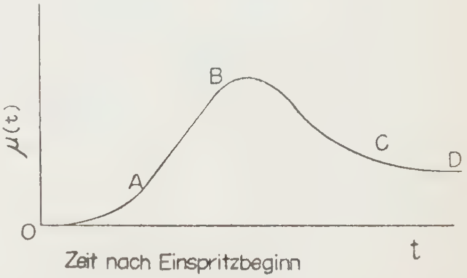

Abb. 9. Schematisches Bild des Zusammenhangs zwischen der Wahrscheinlichkeit der Zündung in Zeiteinheit und der Zeit nach Einspritzbeginn.

Wie bereits ausgeführt, trotzdem viele physikalische Ursachen vorherrschen, darf man sagen, dass die Wahrscheinlichkeit der Entstehung der anfänglichen chemischen Reaktion anfangs grösser von einer gewissen Zeit nach der Einspritzung an, und konstant wird und bleibt, wenn die Mischung ganz homogen wird.

(2) *Die Wahrscheinlichkeit, dass die anfängliche Reaktion ein Kern wird, wovon die Flamme sich bald fortpflanzen kann.*

Wie oben gesagt, kann es nicht zünden, wenn der Zündkern nicht so gross wird, dass die Flamme sich fortpflanzt. Nun sehe ich E als die sogenannte Aktivitätsenergie an, wodurch der Kern sich vergrössert und zündet, Dann muss β diese Wahrscheinlichkeit proportional $\exp(-E/RT)$ sein. (T: die absolute Temperatur der Mischung, R: die Gaskonstante). Wenn T konstant ist, ist β konstant, falls man E als Konstante annehmen kann. Man darf die Veränderung der Durchschnittstemperatur in der Brennkammer vernachlässigen, weil sie nicht so gross ist, während des Zündverzuges, aber T die Temperatur der Mischung am Zündort verändert sich durch den Wärmeaustausch und gewöhnlich wird mit der Zeit grösser. Deshalb muss β mit der Zeit grösser werden.

Da die Wahrscheinlichkeit der Zündung in Zeiteinheit proportional $\alpha\cdot\beta$ ist, und α und β anfangs nach Einspritzung sich mit der Zeit vergrössern, und nachher wegen gleichartiger Mischung konstant werden, so wird diese Wahrscheinlichkeit $\mu(t)$ anfangs grösser mit der Zeit und nachher konstant, auch wenn viele Bedingungen berücksichtigt werden müssen. Dies deckt sich mit meinen Experimentsergebnissen ausser für die Zeit, wo $\mu(t)$ fast Null ist.

Nach den obigen Überlengungen, hat dieZeit, wo die Wahrscheinlichkeit $\mu(t)$ fast Null ist, zwei Teile. Der eine ist derjenige, wo der Brennstoff sich fast nicht verdampft und es fast keine Wahrscheinlichkeit der Zündung gibt; der andere der, wo sich die chemische Reaktion bis zum Zündkern vergrössert. Im ersteren Falle wird die Zeit mit dem ansteigenden Druck länger und umgekehrt mit der ansteigenden Temperatur kürzer.

Aber die letztere ist umgekehrt proportional der Geshwindigkeit der chemischen Reaktion, da die Geschwindigkeit der chemischen Reaktion mit der Dichtigkeitvergrösserung schneller wird und mit Temperaturerhöhung der Mischung, wenn die Dichtigkeit und die Temperatur der Mischung hoch sind, muss die Zeit, wo die Wahrscheinlichkeit der Zündung fast Null ist, kürzer werden.

§ 5. Zusammenfassung

Wir müssen den Zündmechanismus vom Begriff der Wahrscheinlichkeit betrachten.

Im Fall, wo der in die adiabatisch gedrückte Hochtemperatur- und Hochdruckluft eingespritzte Brennstoff zündet, wie im Dieselmotor, erhielt ich von den Schwankungen der Zündverzüge die Wahrscheinlichkeit der Zündung in Zeiteinheit, die fast proportional der Zeit nach Einspritzung ist.

In dieser Arbeit wurde besprochen, warum diese Wahrscheinlichkeit solche Eigenschaft hat und verschiedene Bedingungen, die diese Wahrscheinlichkeit beherrschen, wurde angenommen. Nämlich der Einfluss der Diffusion ist grösst, aber Verdampfung, Temperatur, Dichtigkeit, Wärmeaustausch, usw haben auch einen relativ wichtigen Einfluss.

In der nächsten Arbeit will ich über viele Ergebnisse meiner Forschungen unter andern verschiedenen Bedingungen berichten. Dadurch werde ich erklären, wie meine Voraussetzungen und Überlegung mit den wirklichen Phänomenen übereinstimmt, und weiter, wieviele Zündpunkten es in der Zündung im Dieselmotor gibt.

Zum Schluss muss ich Herrn Dr. M. Hirata, Professor der Fakulität der Naturwissenschaften der Tokyo Universität und Herrn N. Terao vielen Dank sagen, die mir theoretisch und statistisch mit Rat und Tat beigestanden haben, und auch den Herren Professoren Dr. K. Hatta, T. Okazaki und Dr. S. Kumagai, der Technischen Fakulität derselben Universität, die während der meiner Forschungen mich leiteten und mir vielen guten Rat gaben

Auch danke ich herzlich Hrn. M.Ito, Direktor des technischen Laboratoriums der Isuzu Mortor A.G., der mir die Gelegenheit zu meiner Experimenten gab, sowie Herren T. Hori und N. Miyamoto, Ingenieure dieses Laboratoriums, die mir halfen.

Schrifttum

1) W. Jost: Explosions- und Verbrennungsvorgänge in Gasen (1939).

2) B. Lewis: Combustion, Flames and Explosions of gases (1951).

3) Fritz A. F.: Schmidt, Herbert H. Wolber: Zündverzug und Klopfen im Motor, VDI-Forschungsheft **392** (1938).
K. Neumann: Der Zündverzug in der Dieselmaschine, Forschung 10. Bd./Heft **1** (1939).

4) M. Hirata: Bull. Math. Stat. **3** (1949) 57. *Kikai no Kenkyu* **1** (1949) 182, 231; *Oyo-tokeigaku* (Die angewandte Statistik) 1949, 11.01.
N. Terao: J. Phys. Soc. Japan **7** (1952) 627.

5) The Oil Engine and Gasturbine: Vol. XXI. No. 245 November 1953.

6) Y. Tanazawa: Transaction of the Japan Society of Mechanical Engineers Vol. 15, No 52, 1949.

7) W. Jost: Diffusion in Solids, Liquids, Gases (1952).

* Ein Teil dieser Arbeit wurde schon in den Versammlung des JSEM am 26. Juni 1954 berichtet

Short Notes

J. PHYS. SOC. JAPAN **10** (1955) 161

On the Magnetic Ageing of Pure Iron

By Mitsuru ASANUMA and Shinji OGAWA
Institute of Physics, Hokkaido University

(Received October 18, 1954)

It has been known that the initial susceptibility of commercial pure iron varies remarkably on tempering in the vicinity of 130°C, and its origin has not yet been clarified.

In the past Y. Shimizu[1] at Tōhōku University explained that small amounts of sulphur in iron was responsible for its variation. According to his explanation, iron has little solubility to sulphur, which exists as inclusion of iron-sulphide. When the iron was heated up at about 130°C, the lattice parameter in c-axis of FeS varies and this variation might cause the variation of initial susceptibility. But his conclusion that this transformation is hindered by quenching is improbable, because this transformation is the second kind.

The commercial pure iron was used as specimen in our experiment. The specimens were annealed at 950°C for an hour and cooled down in the furnace to 350°C, and then quenched in water to keep out of the transformation of FeS. Then the initial susceptibilities of these specimens and of specimens which were tempered in the vicinity of 130°C for various tempering times after above-mentioned treatment were measured. The results are shown in fig. 1. Moreover the initial susceptibilities of the specimen which was annealed at 950°C in wet hydrogen atmosphere to remove the impurities were measured in the course of ageing as shown in Fig. 2. According to this result, any effect of ageing on initial susceptibility was not observed. Our specimens before and after hydrogen treatment contained 0.003 wt% and 0.002 wt% sulphur respectively, and that means that the sulphur content was hardly changed. Hence the sulphur is not responsible for the variation of the initial susceptibility.

In order to seperate the effects of carbon and nitrogen in iron, carbon or nitrogen was added to the specimens after hydrogen treatment and the initial susceptibilities were measured in the same way as mentioned above. Fig. 2 shows these results. The amounts of carbon and nitrogen in solid solution were determined by means of internal friction[2]. According to these results, the initial susceptibility of carburized specimen did not vary remerkably, but that of nitrided specimen varied exceedingly.

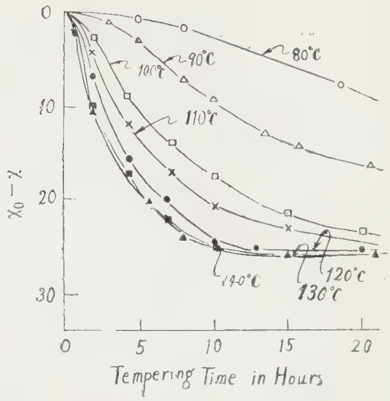

Fig. 1. The decreases of initial susceptibility *vs* tempering time.

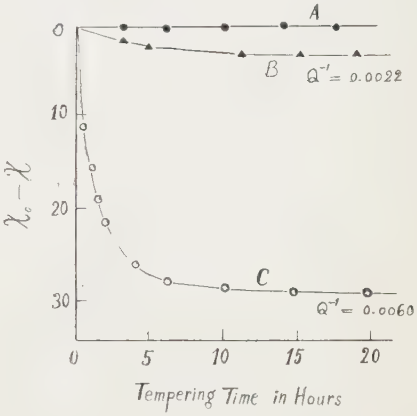

Fig. 2. The decreases of initial susceptibility *vs* tempering time. A: the specimen after hydrogen tretment. B: the specimen to which was added the carbon after hydrogen treatment. C: the specimen to which was added the nitrogen after hydrogen treatment. Ageing temperatures are 140°C.

From our experiment it was concluded that the precipitation of nitrogen and carbon is responsible for the variation of initial susceptibility and the influence of nitrogen is dominant, even if one takes the difference of the amounts of dissolved carbon and nitrogen in our specimens into account.

Recently, for the purpose of studying the precipitation of the carbon and nitrogen in α-iron, C. Wert[3] measured, independently on our work, the coercive forces of carburized and nitrided iron after ageing treatment. It seemes that his results also support our conclusion.

The details of our work will be publised in another paper. The authors were indebted to Professor S. Miyahara for his valuable advice.

References

1) Y. Shimizu: Jour. Japan Inst. Met. **5** (1941) 175. (in Japanese.)
2) T. S. Kē: Phys. Rev. **71** (1947) 533.
3) C. Wert: Act. Metal. **2** (1954) 361.

J. Phys. Soc. Japan **10** (1955) 162～163

Drift Mobility of Conduction Electron in KCl

By Hazimu KAWAMURA and Masami ONUKI
The Institute of Polytechnics,
Osaka City University

(Received November 22, 1954)

The Hall mobility of conduction electrons in alkali halide crystals have been recently measured by Redfield[1], Macdonald and Robinson[2]. The latter authors[2] found that the mobility for KBr is 12.5 cm²/volt-sec at room temperature which is near the Debye temperature of the crystal. It seems also interesting to measure the "drift" mobility at room temperature, since the extremely small mobility in this case is favorable to the measurement of the drift mobility rather than that of Hall mobility.

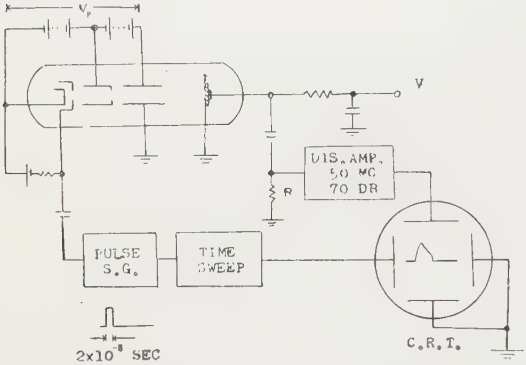

Fig. 1. Block diagram of the measuring equipment. V_p is the volage for accelerating the electron beam and V is for sweeping the scondary electrons in the crystal.

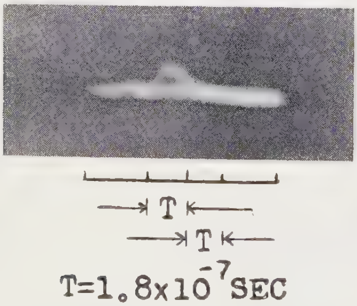

Fig. 2. Out put pulse due to the drift of secondary electrons. Time scale is determined by a delay line of a known constant.

Since the drift time of the electrons cannot exceed their life time in the crystal which is less than 10^{-7} sec in the alkali halide even for pure crystal, we must make the measurement of a phenomenon which occurs within such a short time interval as 10^{-7} sec. The block diagram of our equipment is shown in Fig. 1. The positive pulses of 2×10^{-8} sec width which are generated by a three-electrode trigger gap and coaxial cable are applied to the grid of an electron gun with the P.R.F. of 200 cycle. The pulsive electron beam bombarding the surface of KCl produces electron hole pairs in the crystal near the upper surface. The response due to the drift of the secondary electrons is picked up by the resistance R (800Ω) and amplified by a linear amplifier of distributed type whose band width was about 50 Mc and gain 70 db. The specimens were cut from pure KCl crystal which had no measurable hump in the absorption curve at the neighborhood of the absorption edge. The cleaved crystals were etched and grounded to about 2×10^{-2} cm thick. One of the photographs of the oscilloscope figures is shown in Fig. 2, which were taken at the moment of the switching-on of the electron sweeping field on the crystal, in order to avoid the space charge effect. The pulse duration of this figure reduced by the width of the pulse due to the initial electron beam was taken as the drift time of the electron. Varying the sweeping field, we measured the drift velocities as shown in Fig. 3. From the slope of this curve, the drift mobility was determined to be 3±1.5 cm²/volt-sec.

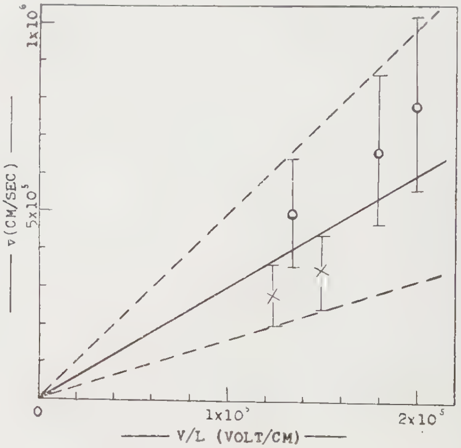

Fig. 3. The drift velocity v is plotted as the function of V/L (V: voltage applied on the crystal, L: crystal thickness).
×; for No. 2 sample, ○; for No. 3.

On the other hand, the theoretical value for KCl calculated from

$$\mu=(ea/\sqrt{2\hbar\omega m})(1/\varepsilon_\infty-1/\varepsilon)[\exp(\hbar\omega/kT)-1]$$

is ∼5 cm²/volt-sec at room temperature[3][4]. The fair agreement of the theory and experiment may be regarded as an accidental one, since in this case the perturbation theory is not applicable for the calculation of the electron mobility owing to a strong coupling of electrons and lattice vibration[3].

References

1) A. G. Redfield: Phys. Rev. **94** (1954) 537.
2) J. R. Macdonald and J. E. Robinson: Phys. Rev. **95** (1954) 44.
3) H. Fröhlich: Advances in Physics **3** (1954) 325.
4) D. J. Howarth and E. H. Sondheimer: Proc. Roy. **A 219** (1953) 53.

J. Phys. Soc. Japan **10** (1955) 163~164

Dependence on the Nature of the Electrode Surface of the Joshi Effect in Oxygen at Different Gas Pressures

By S. R. Mohanty, T. S. Nagarjunan, R. Srinivasan and G. Srinivasan

Physico-Chemical Laboratories, Banaras Hindu University, India

(Received December 7, 1954)

Mohanty and Kamath,[1] and Mohanty[2] have shown that the negative Joshi effect $-\Delta i$ in oxygen, under conditions of constant electrical excitation, *vis.*, at constant reduced potential $V_r=(V-V_m)/V_m$, where V is the potential applied and V_m that for breakdown, and at constant discharge current in dark i_D, increases initially with the gas pressure p to a maximum at $p_{-\Delta i\,\max}$ and diminishes thereafter. It is also known that *ceteris paribus* the *effect* is markedly sensitive to change in the nature of the electrode surface, *e.g.*, from blank (glass) to potassium chloride coated.[3] It was of interest therefore, to study the dependence on electrode contamination of the *effect* in oxygen at different p, and of $p_{-\Delta i\,\max}$.

The discharge vessel consisted of a carefully cleaned soft soda glass Siemens' tube containing finely powdered pure potassium chloride away from he discharge space (Fig. 1); its dimensions were: inner diameter of the outer tube, 17.0 mm; outer diameter of the inner tube, 9.7 mm; inter-electrode distance, 3.65 mm; thickness of glass walls, 1.2 mm; length of the discharge column, 18.3 cm. The high tension electrode consisted of a 10% solution of sodium chloride inside the inner tube. A helix of untarnished copper wire, the distance between two consecutive turns being uniform and sufficiently large to permit irradiation of the enclosed gas, wound on the outer tube constituted he low tension electrode. Pure oxygen, admitted into the Siemens' tube at different p in the range 100–450 mm Hg (29–31°C), was excited over 2–8 kV rms, 50 c/s). The *effect* was observed on a vacuum thermocouple (V.J.)—galvanometer (G) system (Fig. 1) with light from a 200 watt, 190 volt, tungsten filament (in glass) lamp placed at a distance of 12.5 cm from the discharge tube; the heat radiations from the lamp were cut off with an appropriate filter. Observations were repeated with the electrodes contaminated with potassium chloride by repeated tilting which left, after detachable particles were removed by tapping, a thin film of the substance on the electrodes.

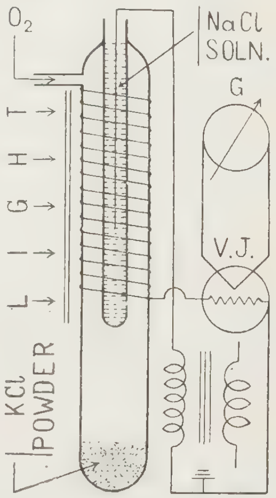

Fig. 1. Electrode contamination in the production of the Joshi effect in oxygen under ozonizer excitation.

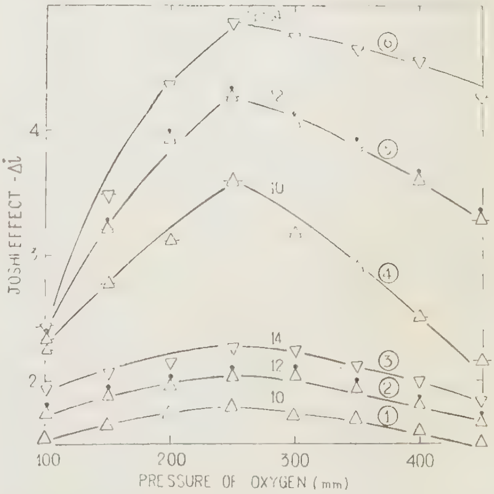

Fig. 2. Pressure variation of the Joshi effect in oxygen. [Curves 1, 2 and 3: Blank (glass). Curves 4, 5 and 6: KCl contaminated.]

The present investigations substantiate the existence of an optimum $p_{-\Delta i\,\max}$ at which, under conditions of constant electrical excitation, $-\Delta i$ is maximum (Fig. 2). Thus *e.g.*, at $i_D=12$, $-\Delta i$

with clean glass electrodes was 1.75 for 100 mm, increased to 2.05 at 250 mm, and diminished with further increase in p to 1.68 at 450 mm; the corresponding values of $-\Delta i$ under KCl contamination were respectively 2.35, 4.28 and 3.28. It is of interest that the rate of increase of $-\Delta i$ with p and that of the subsequent diminution are more pronounced for electrodes (KCl) contaminated than for those blank (glass). Furthermore, it would appear that $p_{-\Delta i\,\max}$ is not dependent upon the nature of the electrode surface. For the tube under investigation, $p_{-\Delta i\,\max}$ was 250 mm blank as also contaminated. It has been shown by Mohanty, Krishna Rao and Jayaraman[4] that $p_{-\Delta i\,\max}$ changes, on the other hand, with electrode separation.

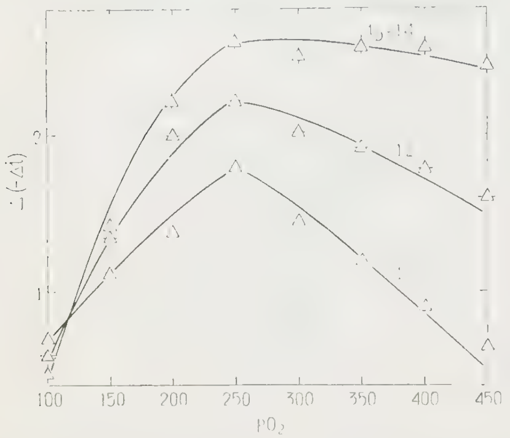

Fig. 3. The shift in the Joshi effect due to electrode contamination as a function of the gas pressure.

The significant rôle of the electrode surface in the production of the discharge[5] and the *effect*[6] has already been emphasized[3]. The change (enhancement) $\Delta(-\Delta i)$ in $-\Delta i$ with that in the nature of the electrode surface is maximum, like $-\Delta i$, at $p_{-\Delta i\,\max}$, *viz.*, 250 mm for the tube investigated (Fig. 3).

Grateful thanks of the authors are due to Prof. S. S. Joshi for his kind interest in the work.

References

1) S. R. Mohanty and G. S. Kamath: J. Indian Chem. Soc. **25** (1948) 405.
2) S. R. Mohanty: J. Indian Chem. Soc. **26** (1949) 553.
3) S. R. Mohanty: J. Phys. Chem. **58** (1954) 178.
4) S. R. Mohanty, G. V. G. Krishna Rao and J. Jayaraman: J. Sci. Industr. Res. **13 B** (1954) 583.
5) S. R. Mohanty: J. Chem. Phys. Under publication.
6) S. S. Joshi: Proc. Indian Sci. Congr., Presidential Address, Chem. Sec. (1943).
7) S. S. Joshi: Current Sci. **16** (1947) 19.

J. Phys. Soc. Japan **10** (1955) 164~165

Effect of Electron Bombardment on Secondary and Photo-electron Emission of Cesium-antimonide

By Kiyoshi Miyake

Electrical Communication Laboratory,
Nippon Telegraph and Telephon Cooperation,
Tokyo, Japan

(Received September 25, 1954)

The secondary electron emission of composite surfaces decreases with the duration of electron bombardment. There are, however, very few investigation into this cause. Since cesium-antimonide, according to Zworykin and others[1], is not only a good secondary electron emitter but also a high photo-sensitive one, the author has tried to study the change of both properties caused by electron bombardment.

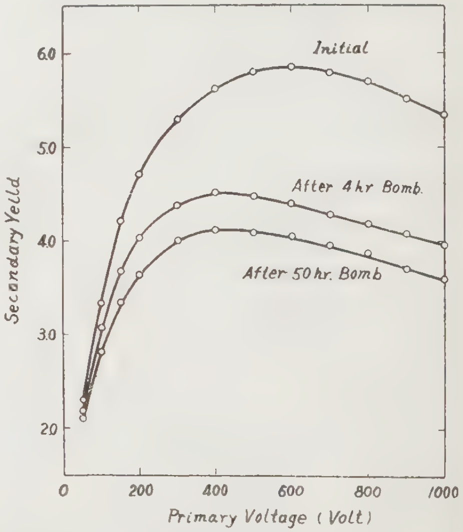

Fig. 1. Effect of electron bombardment on the secondary electron yield.

The experimental tube used consists of an electron gun and a collector for the measurement of secondary emission, and an anode mounted in a separate position for the measurement of photo-emission. A basket-shaped target made from thin nickel plate is able to slide along nickel stem towards the desired position. Cesium-antimonide surface was prepared on the basket after the usual process at a separate position for avoiding the contamination of electrodes. The secondary emission of such target was measured in the range of primary energy (V_p) from 50 V to 1000 V. The yeild is reproducible when the density of primary current (I_p) is small, and the maximum amounts to 4~6 at V_p=500 V~800 V. A typical yield curve is shown in Fig. 1 (Initial). The fatigue of yield is remarkable in the case of either high primary energy or large current density. The curves shown in Fig. 1 are obtained after the bombardment of a definite time at $V_p=200$ V, $I_p=98\ \mu$A (c.a. 200 μA/sq.cm). The decrease of secondary emission during the bombardment was shown in Fig. 2. As shown in the figure, the yield decreased from 4.6 at the initial state to 4.2 after about 2 hours and thenceforth varied very gradually. On the other hand, by bombarding of primary electron with $V_p=500$ V, $I_p=98\ \mu$A, the yield decreased rapidly from 5.1 at the begining to 3.8 after 6 hours.

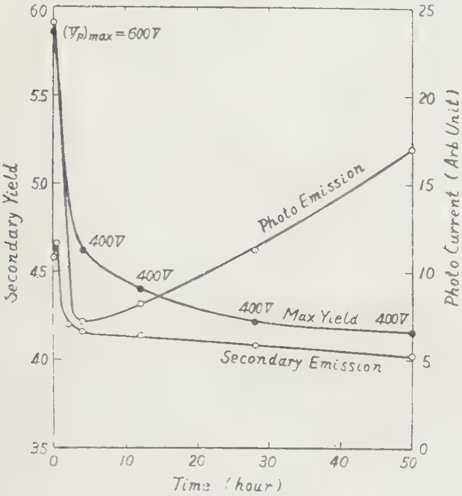

Fig. 2. The changes in secondary emission, photoemission and maximum secondary yield of cesium antimonide target, caused by continued electron bombardment at $V_p=200$ V, $I_p=98\ \mu$A.

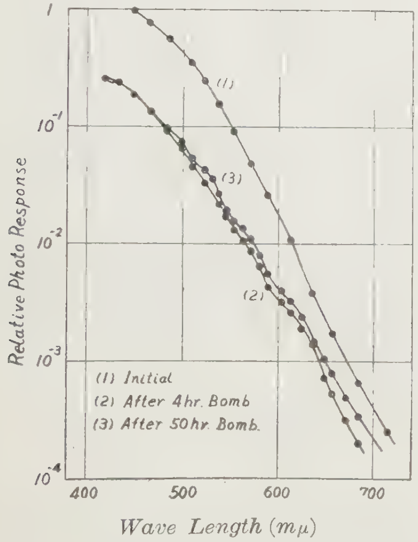

Fig. 3. The change in wave length characteristics.

The photo-response curve in Fig. 2, showing the total sensitivity for a tungsten filament lamp at 1900°K (color temp.), indicates that it is similar to the secondary emission one at first but increases considerably after long bombardment. Fig. 3 shows the effect of bombardment on the spectral photoelectric response, though the shift in the ordinate is uncertain. The initial response is a normal one, and a small hump near 600 mμ can be noticed. The effect of bombardment is to bring about several new humps near 610, 570, 530, 490 mμ, and two or more at shorter wave length.

It has been believed that the fatigue of secondary emission, for example, from BaO is due to dissociation of the compound or excess metallic layer near the surface. In the present case, however, the photoelectric data are suggestive of formation of color centers. And from this viewpoint the author would like to continue some more experiments on the fatigue of secondary emission.

The author wishes to express his hearty thanks to Dr. S. Yoshida for his sugestions and interests to this experiment, and Mr. S. Munesue for his helps in the measurement of spectral photoelectric response.

Reference

1) V. Zworykin and E. Ramberg: "Photo-Electricity and its Application" (John Wiley and Sons, Inc., New York 1949).

J. Phys. Soc. Japan **10** (1955) 165~166

On the Hall Effect of P-type Germanium in the Near Intrinsic Range

By Yasuo Kanai and Katsuhisa Furusyō
The Electrical Communication Laboratory, Tokyo, Japan

(Read Nov. 2, 1954; Received November 19, 1954)

Recently a number of experimental and theoretical studies have been made on the galvano-magnetic effect in semiconductors, and the Hall constant and the magneto-resistance constants are well studied especially. These constants are the coefficients of the 1st and 2nd terms of the electric current respectively, when it is expanded as an ascending series in the magnetic field strength, H.[1] The effects of the higher terms of H have been not so well investigated, since a strong magnetic field is necessary to observe such effects. But if the experiments are performed under such conditions that the effect of the 1st term vanishes, those of the higher terms of H could be detected easily. As is well known, the Hall constant, R, in the semiconductors which contain both electrons and holes is given, in the first approximation, by the formula[2];

$$R = -\gamma \frac{nb^2 - p}{(nb+p)^2}$$

where

n; number of electrons in c.c.
p; number of holes in c.c.
b; ratio of electron mobility to hole mobility.
γ; numerical factor which depends on the scattering mechanism of carriers.

and in the p-type germanium the condition $R=0$ is attainable in the near intrinsic range, so in this range the effects of the higher terms of H should be detected easily.

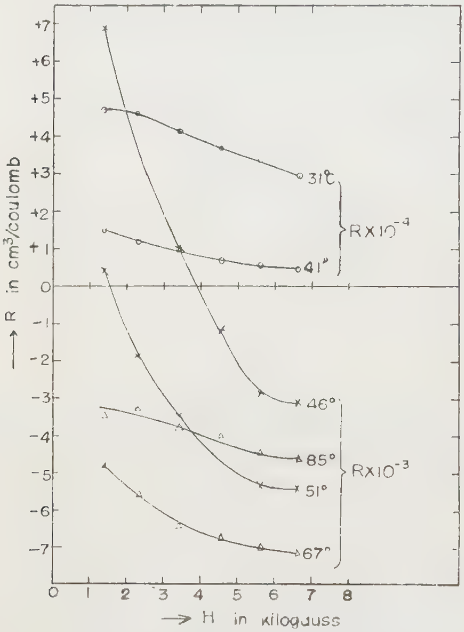

Fig. 1. The Hall constants of p-type germanium at various magnetic field strength in the near intrinsic range.

The H-dependence of R in the high purity and uniform p-type germanium was measured in the temperature range from about 20°C to about 85°C, in the magnetic field strength up to about 7 kilogauss. In these temperature ranges the temperature was kept constant in the accuracy of approximately ±0.1°C by the thermo-regulator. The specimen was shaped into thin slabs approximately 1 cm × 0.25 cm × 0.2 cm, and the Hall constants measured at low temperature indicated that the density of acceptor impurities was approximately 5.7×10^{13}/c.c. A typical result of our experiment is shown in Fig. 1 and it indicates a remarkable dependency of R on H.

Recently Madelung[3] has calculated numerically the dependence of R on H in the semiconductor which contained both electrons and holes. His calculations were based on the following assumptions:

(a) electrons which had one kind of effective mass and holes which had one kind of effective mass[4],
(b) spherical symmetry of energy surfaces for both carriers.
(c) energy independent mean free path.

According to his results R increases always with increasing H, while our experiment shows that the relation is reverse (Fig. 1). Thus our experimental results are not consistent with his calculations, so in the case of p-type germanium, any one of the above assumptions (probably assumptions (a) and (b)) should be incorrect[5].

References

1) For instance F. Seitz: Phys. Rev. **79** (1950) 372.
2) For instance W. Shockley, "Electrons and Holes in Semiconductors". (D. Van Nostrand Co., Inc. New York, 1950).
3) O. Madelung: Z. Naturforsch **8a** (1953) 791.
4) R. N. Dexter, H. J. Zeiger and B. Lax: Phys. Rev. **95** (1954) 557.
5) Recently, T. C. Harman, R. K. Willardson and A. C. Beer: (Phys. Rev. **95** (1954) 699.) were studied similar anomalous dependency of R on H in p-type germanium and concluded that the assumption (a) was incorrect.

JOURNAL OF THE PHYSICAL SOCIETY OF JAPAN Vol. 10, No. 3, MARCH, 1955

Beta-spectra of Ag110 and Sb124

By Toshio AZUMA

Phys. Dept. Naniwa University, Mozu, Sakai, Osaka

(Received June 23, 1954)

Beta-spectra of Ag110 and Sb124 have been measured with a double coil, magnetic lens spectrometer of about 2 percent resolving power and their Fermi plots were studied. For the decay of Ag110, it was found that the soft component of the continuous beta-ray spectrum could be analysed into three groups of allowed type with end points at 80–, 314–, and 530–kev. For Sb124, five beta-ray groups with end points at 2.39–, 1.68–, 1.07–, 0.63–, and 0.28–Mev are found, in which the group of the highest energy is infered as the first forbidden mixed interaction for ST or VA shape. The results for Sb124 agree with other observers.

§ 1. Introduction

For the decay of Ag110, three beta-ray groups with end points at 87-, 530-kev, and 2.86-Mev and many groups of gamma-rays have been reported.1)-8) The Fermi plot of the 530-kev beta-ray, which constitutes the main part of the continuous beta-spectrum, deviates from a straight line, and Siegbahn1) has suggested that this might indicate the presence of one or several beta-components of low intensities. But no satisfactory analysis or explanation has yet been given to it. In the present experiments, we have made a careful measurement of the beta-ray groups and have studied the Fermi plots making use of the correction factors for the first and second forbidden transitions. The results indicated the existence of soft beta-component of 314-kev of low intensity9).

For the decay of Sb124, considerable works have been done, especially with regard to the assignment of spin and parity changes in the decay scheme10)-21). It was concluded that the ground state of Sb124 → the first excited state of Te124 → the ground state of Te124 was 3(−)−2(+)−0(+), from the β-γ angular correlation experiments17). The curved Fermi plot of the highest energy beta-group was straightened by the first forbidden correction factor consistent with a general STP beta-interaction for spin change unity10). Such a beta-transition was, however, the first one observed hitherto. We have, therefore, re-investigated the Fermi plot with the correction factors calculated by Konopinski and Uhlenbeck22) for the single interactions and by Smith23) for the mixed interactions. The result confirmed the conclusion of previous authors.

§ 2. Experimental Method

The beta-rays and the conversion electrons from gamma-rays were investigated with the double coil, magnetic lens spectrometer of about 2 percent resolving power. The spectrometer was equipped with a set of aluminum baffles as those used by Van Atta *et al*24) to reduce the number of scattered beta-rays reaching the detector. The detector consisted of a side window G-M counter with a window of Zapon film of about 20 μg/cm^2 on the 50 mesh wire net.

The active material in solution, which was supplied from Oak Ridge, was applied on a Zapon film of about 30 μg/cm^2 and dried quickly under an infra-red lamp. A homogeneous thin source of 2 mm in diameter which had a surface density of not greater than 50 μg/cm^2 was obtained.

The efficiency of Zapon counter as a function of beta-ray energies was investigated for various pressure of the gas filling the counter, using the corrected Fermi plot of the 530-kev beta-ray from Cs137 25)26). The maximum energy, in which Zapon counter was used reliably, was estimated as 200-kev for the gas pressure of 25 mmHg27). The maximum energy rised gradually as the gas pressure increased. The soft beta-ray groups of energy lower than 200-kev were measured with such Zapon counter which is made to detect electrons of 5-kev and above. The other beta-rays were measured by the ordinary mica window G-M counter of 2.9 mg/cm^2. The spectrometer was calibrated using the internal conversion line of Cs137.

§ 3. Correction Factors

The measured beta-ray spectra have been investigated using the Fermi plot, namely, the plot of $(N/f(z, w))^{1/2}$ against the total energy, where N is the counts per minute of beta-rays per unit momentum, and $f(z, w)$ is the Fermi distribution function of transition probability and w is the energy of electron emitted in units of mc². A better approximation for $f(z, w)$, especially for large z, was given by Bethe and Bacher[28],

$$f(z, w)=f_N(z, w)[E^2(1+4\gamma^2)-1]^S ,$$

where

$$f_N(z, w)=(W^2-1)\frac{2\pi y}{1-e^{-2\pi y}} ,$$

and

$$S=(1-\gamma^2)^{1/2}-1 ,$$

$$\gamma=\begin{cases} \alpha z=z/137 , & \text{for } \beta^- \text{ emission} , \\ -\alpha z=-z/137 , & \text{for } \beta^+ \text{ emission} , \end{cases}$$

$$y=\gamma\cdot\frac{(1+\eta^2)^{1/2}}{\eta} ,$$

$$\eta=H\rho/1704 ,$$

$$W=(1+\eta^2)^{1/2} .$$

This approximation is accurate to about one percent for atomic numbers as large as $z=84$.

In order to determine the order of forbiddeness of the transition, a suitable correction factor C must be multiplied to $f(z, w)$ and the Fermi plot thus corrected, i.e. the curve of $(N/C\cdot f(z, w))^{1/2}$ plotted against the total energy must be examined to see if it lies on a straight line. The correction factors of the first and second forbidden transitions for five forms of interactions; scalar S, polar vector V, tensor T, axial vector A, and pseudoscalar P, has been given by Konopinski and Uhlenbeck[22]. Those of linear combinations have also been calculated by many authors,[23)29)30)] but those of Smith are convenient to use in our case.

The matrix elements which permit the transition 2—0 with the associated parity changes are shown in Table I. The notation of konopinski and Uhlenbeck's article are used here. The matrix elements of the linear combinations with the parity changes are shown in Table II, which are independent of the Fiertz interference term $1/W$.

The magnitudes of the nuclear matrix elements are not known, therefore, the correc-

Table I. The matrix elements which permit the transition 2—0 with parity changes.

Interaction	First Forbidden		Second Forbidden	
S			R_{ij}	no
V			R_{ij} A_{ij}	no
T	B_{ij}	yes	T_{ij} A_{ij}	no
A	B_{ij}	yes	T_{ij}	no
P			$\gamma_5 R_{ij}$	no

Table II. The matrix elements of linear combinations with parity changes.

Interaction	First Forbidden		Second Forbidden	
ST	$\int\boldsymbol{r}$, $\int\boldsymbol{\alpha}$	yes	$R_{ij}\,T_{ij}$, $R_{ij}\,A_{ij}$	no
VA	$\int\boldsymbol{\alpha}$, $\int\boldsymbol{\sigma r}$	yes	$R_{ij}\,T_{ij}$, $A_{ij}\,T_{ij}$	no
TP	$\int\boldsymbol{\sigma}\cdot\boldsymbol{r}$, $\int\gamma_5$	yes		

Table III. The correction factors.

Notation	Interaction	Shape of correction factor	Nuclear matrix element	Selection rule	Parity change
C_1	(ST), (VA), (TP).	$-\left(\frac{1}{3}KL_0+N_0\right)$	$\int\boldsymbol{r}^*\cdot\int\boldsymbol{\sigma}\times\boldsymbol{r}$ $\int\boldsymbol{\alpha}^*\cdot\int\boldsymbol{\sigma}\times\boldsymbol{r}$ $\int\boldsymbol{\sigma}\cdot\boldsymbol{r}^*\cdot\int\gamma_5$	0, ±1 (no 0–0) 0, ±1 (no 0–0) 0	yes yes yes
C_2	T, A.	p^2+K^2	B_{ij}	0, ±1, ±2 (no 0–0, 1–0,)	yes
C_3	T, A.	$p^4+K^4+\frac{10}{3}p^2K^2$	S_{ijk}	±2, ±3 (no 0–2)	no
C_4	(ST), (VA).	$\frac{1}{6}K^2(L_1-M_2)+\frac{3}{2}(L_2-M_2)$	$R_{ij}{}^*\cdot T_{ij}$	±2	no
C_5	(ST), (VA).	$\frac{1}{30}K^3L_0+\frac{1}{6}K^2N_0+\frac{1}{2}KL_1+\frac{3}{2}N_1$	$R_{ij}{}^*\cdot A_{ij}$, $A_{ij}{}^*$, T_{ij}	±2	no
C_6	T, A.	$\frac{1}{15}K^4\mp\frac{2}{5}K^3N_0+K^2(L_1+M_0)\mp 6KN_1+6L_2+9M_1$	T_{ij}	±2	no

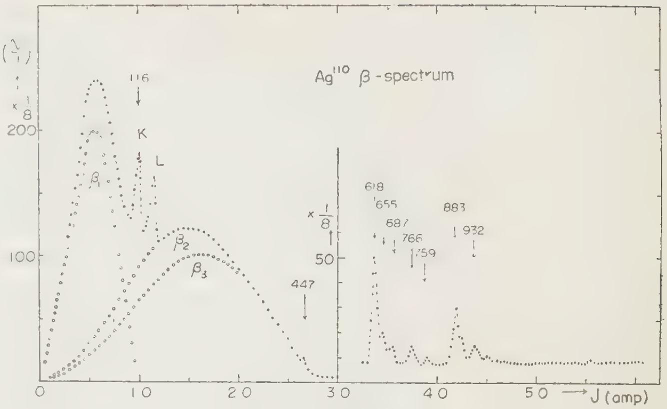

Fig. 1. The momentum plot of the beta-spectrum of Ag110. The black points show the measured values, and the open circles those constructed from the Fermi plot.

tion factors to be used must be considered in many combinations of them. But several cases are tried in this article.

In the first forbidden transitions, the simple cases, in which only one nuclear matrix element except B_{ij} exists, are energy independent owing to the predominant value of the term $(\alpha z/2\rho)^2$, where α is the fine structure constant and ρ is the nuclear redius in units of Compton wave length. Then the correction factor for B_{ij} was tried which was shown in Table III as C_2. The correction factors of Smith's article were tried also as shown in Table III, though the ratio of the nuclear matrix elements were not known.

In the second forbidden transitions, the correction factors which have single nonvanishing matrix elements S_{ijk} and T_{ij} were tried, and several cases of a linear combination of T_{ij} and A_{ij} in tensor interaction were investigated as shown in Fig. 7. Those of Smith's article were also tried in several cases.

The numerical calculations were performed on the assumption of $(\alpha z)^2 \ll 1$, which may be a fairly good approximation in our case.

The correction factors used in this article with the notation C_l are shown in Table III.

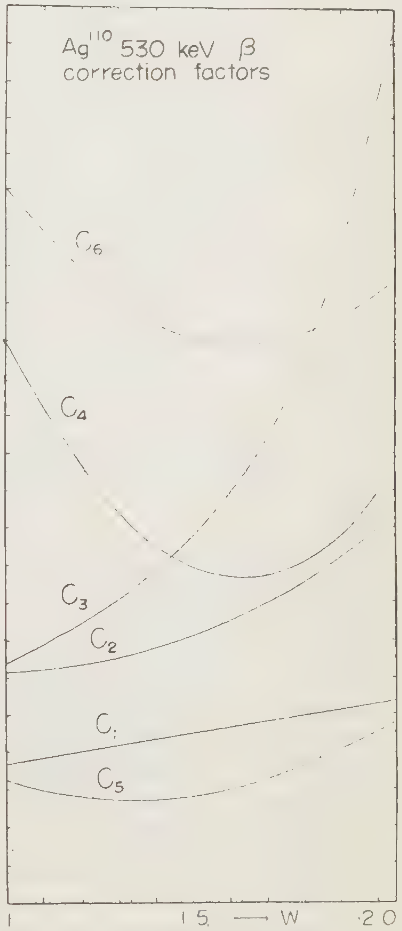

Fig. 2. The correction factors for the 530-kev beta-spectrum of Ag110.

§4. Ag110

In the present experiments, the measured spectrum consisted of two groups of soft beta-rays, and many groups of gamma-rays. The internal conversion lines are consisted with 116-, 447-, 618-, 655-, 687-, 760-, 759- 883-, and 932-kev gamma-rays, which were designated as strong and medium groups by Cork *et al*;[2] weak groups could not be detected because of the thin sample used in the present work. The momentum plot of the measured spectrum is shown in Fig. 1.

K/*L* ratio of the 116-kev gamma-ray is estimated as 1.2. This value is the same as those of the former authors, corresponding to the M_4-pole transition.

The uncorrected Fermi plot of the 530-kev beta-ray group is convex toward the energy axis as shown in Fig. 3. The numerical values of six correction factors calculated from Table III are shown in Fig. 2 in arbitrary units. The Fermi plots corrected with these factors are shown as curve 1 to 6 in Fig. 3, but none

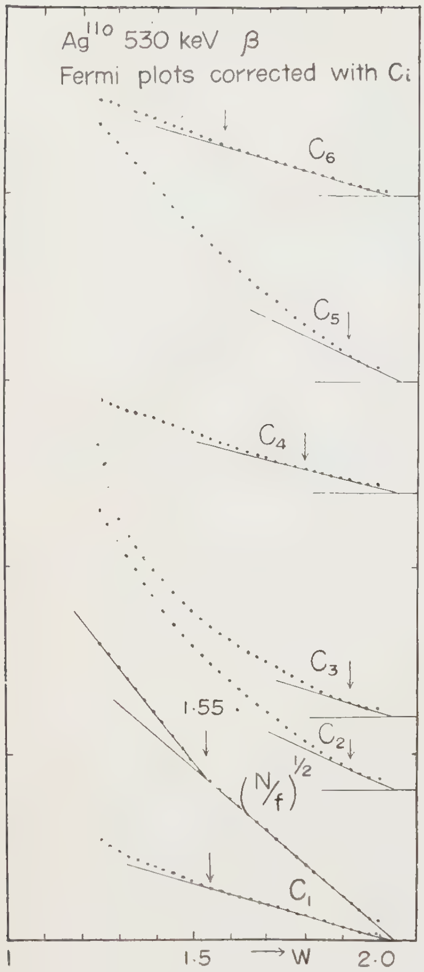

Fig. 3. The Fermi plots of the 530-kev beta-spectrum of Ag110, corrected with the correction factors (C_i).

of them give a straight line. Though the log(ft)-value of this beta-ray group is low, we have, further, examined it with a linear combination of A_{ij} and T_{ij} terms in the second forbidden of tensor interaction. At the various values of x^2 and y^2, where $x^2 = T_{ij}/A_{ij}$, and $y^2 = S_{ijk}/A_{ij}$, the corrected Fermi plots are tested, but the shapes of these curves are not sensitive to these ratio and no fit to a straight line could be obtained.

In this way we come to the conclusion that the 530-kev beta-ray spectrum may be complex, consisting, at least, of two groups. The best fit to the straight line is obtained for the uncorrected Fermi plot in the energy range of $1.60 \leqq W \leqq 2.038$. Extrapolating this part of the curve with a straight line, the full shape of the single 530-kev beta-ray group is constructed and is shown in Fig. 1 as the β_3-group.

The differences between the measured and constructed values at each energy give the second beta-ray group which fits a straight line in the Fermi plot in the energy range of $1.23 \leqq W \leqq 1.65$. The full shape of this group can also be constructed from the Fermi plot as shown in Fig. 1. The remaining soft beta-ray group which is shown as β_1-group in Fig. 1 fits fairly well a straight line in the Fermi plot with $W_0 = 1.157$.

Summarizing the results, we may conclude that the soft component of the continuous beta-ray spectrum of Ag110 can be analized into three groups of allowed type having the end points at 80-, 314-, and 530-kev respectively. The ratio of their intensities is measured as 10.7:3.2:15.3 from the area of the constructed momentum spectrum.

The values of log(ft) for these soft beta-ray groups are estimated from the table of Motzkowski[31] as 4.2, 6.0, and 7.0 for β_1, β_2, and β_3 respectively. The short half-life (24-seconds) of the excited state of Ag110 must be aboided. The soft beta-ray must certainly comes from the decay of the ground state of Ag110 (270-days).

§ 5. Sb124

The measured spectrum consists of two beta-ray groups and five internal conversion lines of 0.605-, 0.650-, 0.720-, 1.69-, and 2.10-Mev gamma-rays as shown in Fig. 4. Inset shows the K and L conversion lines of three gamma-rays.

K/L ratio of the 0.605-Mev gamma-ray is estimated as 6.7, which corresponds to E_2-pole transition.

The higher energy beta-component is studied using the Fermi plot. The numerical values of the correction factors are shown in Fig. 5 in arbitrary units. $C_1^{(1)}$ in Fig. 5 can be expressed as

$$C_1^{(1)} = G_T^2 \left| \int \beta \boldsymbol{\sigma} \times \boldsymbol{r} \right|^2 \left\{ \left[\frac{\alpha z}{2\rho}(1+x_i-y_i) + \frac{(1+x_i)}{3W} p^2 + (1-x_i)\frac{q}{3} \right]^2 + \left\{ \frac{(1+x_i)}{3W} p \right\}^2 + \frac{(1-2x_i)^2 p^2}{18} + \frac{(1+2x_i)^2 q^2}{18} + U \frac{p^2+q^2}{12} \right\},$$

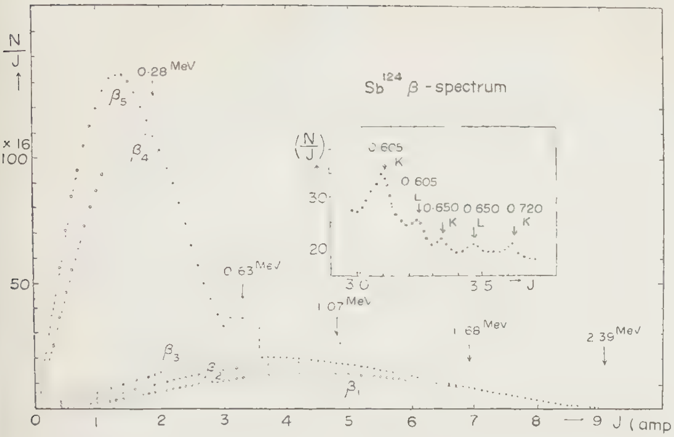

Fig. 4. The momentum plot of the beta-spectrum of Sb124, Black points show the measured values, and open circles those constructed from the Fermi plot.

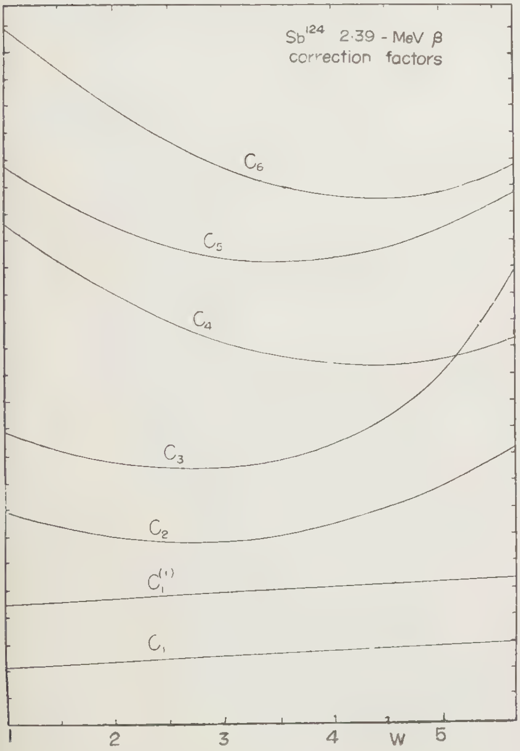

Fig. 5. The correction factors for the 2.39-Mev beta-spectrum of Sb124.

as regards to the notations, see references 10 and 32. In the present work, the numerical calculations are performed on the approximation of x_i and y_i are both equal to 1 and $U \ll 1$.

The Fermi plots corrected with C_4 and C_6 as shown in Fig. 6 lie on a straight line till W is equal to 3.25 and 3.55 respectively. But in this cases the plots deviate downward from the straight line at lower energies. Obviously the inner groups can not be constructed in such cases, then this must be aboided. Nakamura *et al*13) have tried to explain this spectrum with a linear combination of the terms T_{ij} and A_{ij}, considering the classification of the comparative half-life and taking account of the nuclear shell model.

A linear combinations of the terms S_{ijk}, T_{ij}, and A_{ij}, which have several values of $x^2=T_{ij}/A_{ij}$ and $y^2=S_{ijk}/A_{ij}$, have been tried in this article. But none of it gives the tendency of the correction factor C_1 as shown in Fig. 7.

Considering the energy levels of the nuclear gamma-rays, the best fits to the straight line are given by those of C_1 and $C_1^{(1)}$, both giving the same results. Then, the beta-transition of $\Delta I=1$, yes, is infered

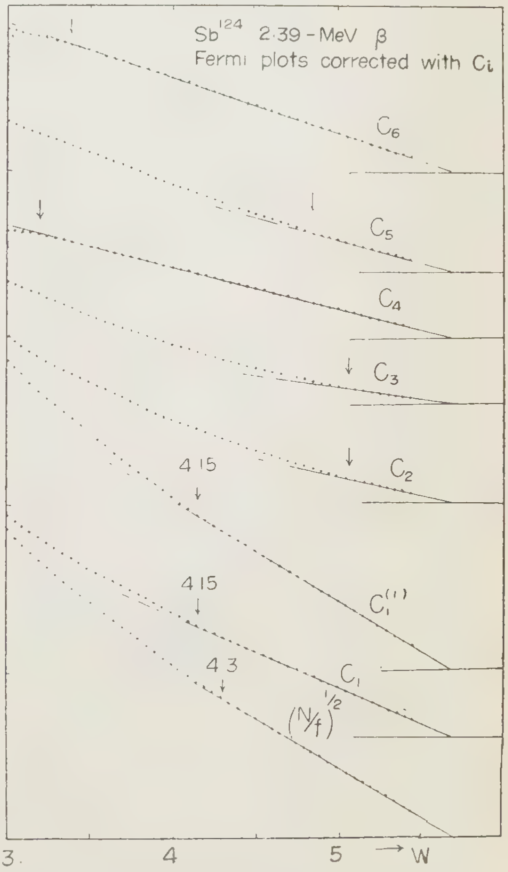

Fig. 6. The Fermi plots of the 2.39-Mev beta-spectrum of Sb124, corrected with the correction factors (C_i)

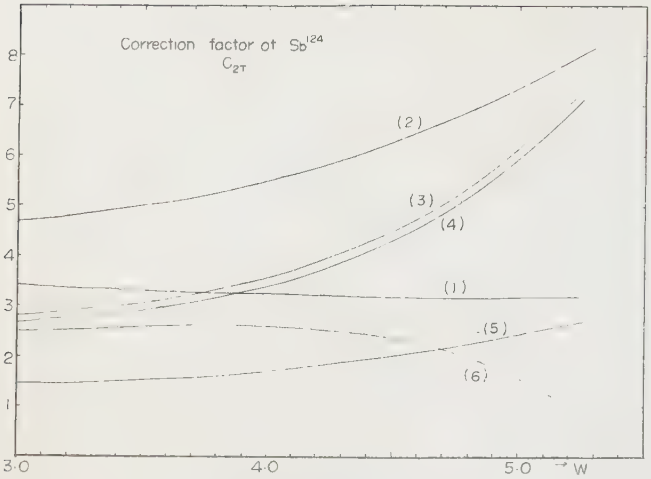

Fig. 7. Correction factors of Sb124.

(1) Correction factor which corrects the observed values on a straight line in the range of $3.0 \leq W \leq 5.4$.
(2) $C = C_{2T}$ with $x^2 = 15$, $S_{ijk} = 0$.
(3) $C = C_{2T}$ with $x^2 = 0$, $y^2 = 90$.
(4) $C = C_{2T}$ with S_{ijk}.
(5) $C = C_{2T}$ with A_{ij}.
(6) $C = C_{2T}$ with $y^2 = -1$, $x^2 = 15$.

to be the best fit to the data.

Further analysis of the beta-spectrum was completed assuming that the inner groups are of the allowed shape. This treatment of the beta-spectrum gives five beta-ray groups with end points at 2.39-, 1.68-, 1.07-, 0.63-, and 0.28-Mev respectively. Their intensity is computed as 22, 6, 4, 56, and 12 percent respectively from the area of the constructed momentum spectrum. These groups are shown in Fig. 4 with observed spectrum. These beta-ray analysis gives almost the same results as those of Langer *et al*, except the small differences between the end point energies and their intensities.

In conclusion, the author express his sincere gratitude to Professor K. Kimura of Kyoto University for his kind encouragement and discussions throughout the course of the work. Acknowledgement should also be made to Dr. K. Shinohara for his kind discussions and to Dr. S. Nakamura for his kind discussions on the correction factors, and also to Mr. K. Tsumori for his assistances with the operation of the spectrometer.

This work was financially supported by the special fund of the Ministry of Education.

References

1) K. Siegbahn: Phys. Rev. **75** (1949) 1277, **77** (1950) 233.
2) Cork, Rutledge, Branyan, Stoddard, Childs and LeBlanc: Phys. Rev. **80** (1950) 286.
3) F. Maienschein and J. L. Meem: Phys. Rev. **76** (1949) 899.
4) W. S. Emmerich and J. D. Kurbatov: Phys. Rev. **75** (1949) 1446.
5) W. Rall and R. G. Wilkinson: Phys. Rev. **71** (1947) 321.
6) W. C. Kelly: Phys. Rev. **85** (1952) 101.
7) Yu, Cheng and Kurbatov: Phys. Rev. **75** (1949) 1278.
8) M. Goldhaber and R. D. Hill: Rev. Modern Phys. **24** (1952) 179.
9) T. Azuma: Phys. Rev. **94** (1954) 638.
10) Langer, Lazar and Moffat: Phys. Rev. **91** (1953) 338.
11) D. R. Huchinson and M. L. Wiedenbeck: Phys. Rev. **88** (1952) 699.
12) F. R. Metzger: Phys. Rev. **86** (1952) 435, **90** (1953) 328.
13) Nakamura, Umezawa and Takeba: Phys. Rev. **83** (1951) 1273.
14) Langer, Moffat and Price: Phys. Rev. **79** (1950) 608.
15) C. S. Cook and L. M. Langer: Phys. Rev. **73** (1948) 1149.
16) Kern, Zaffarano and Mitchel: Phys. Rev. **73** (1948) 1142.
17) M. Morita and M. Yamada: Prog. Theor. Phys. **10** (1953) 111, 643.
18) Kloepper, Lennox and Wiedenbeck: Phys. Rev. **88** (1952) 695.
19) R. Stump: Phys. Rev. **86** (1952) 249.
20) D. T. Stevenson and M. Deutsch: Phys. Rev. **83** (1951) 1202.
21) E. K. Darby and W. Opechowski: Phys. Rev. **83** (1951) 676.
22) E. J. Konopinski and G. E. Uhlenbeck: Phys. Rev. **40** (1941) 308.
23) A. M. Smith: Phys. Rev. **82** (1952) 955.
24) Van Atta, Warshaw, Chen and Taimuty: Rev. Sci. Inst. **21** (1950) 985.
25) L. Langer and H. Price: Phys. Rev. **76** (1949) 641.
26) C. Peacock and A. Mitchel: Phys. Rev. **75** (1949) 197, 1272.
27) Langer, Moffat and Price: Phys. Rev. **76** (1949) 1725.
28) H. A. Bethe and R. F. Bacher: Rev. Modern Phys. **8** (1936) 194.
29) R. H. Good: Phys. Rev. **86** (1952) 620.
30) O. L. Pursey: Phil. Mag. **42** (1951) 1193.
31) S. A. Motzkowski: Phys. Rev. **82** (1950) 35.
32) H. M. Mahmoud and E. J. Konopinski: Phys. Rev. **88** (1952) 1266.

JOURNAL OF THE PHYSICAL SOCIETY OF JAPAN Vol. 10, No. 3, MARCH, 1955

Excitation Function for the Reaction ^{7}Li(γt)^{4}He up to 21 Mev

By Mitsuo MIWA

Department of Physics, Tokyo University of Education, Tokyo
Fulbright Research Scholar, University of Illinois,
Urbana, Illinois, 1953–54

(Received November 20, 1954)

The excitation function for the ^{7}Li(γt)^{4}He reaction up to 21 Mev has been studied by using betatron bremsstrahlung and nuclear emulsion, the statistics being much better than that of former workers. Resonance peaks were found at the excitation energies of 7.6, 8.6, 9.6, 11.7, (13.5) and 16.2 Mev, 9.6 and 16.2 Mev peaks being the most predominant. The results were in good agreement with those of Titterton and Brinkley in the general trend and the most predominant peaks of the excitation function.

§ 1. Introduction

The fine structure of the excitation function for the photodisintegration of light elements is now a favorite subject of many workers. Rather little, however, is known on the (γt) reaction of ^{7}Li. Stoll and Wächter[1] studied the problem by using a 15-Mev betatron and nuclear emulsion technique, finding resonances at the excitation energies of 5.25, 7.25 and 9.25 Mev. The number of events observed by them, however, was only about 100. Later Titterton and Brinkley[2] examined the reaction up to 24 Mev by the same techniques. They found resonance peaks at 9.3, 16.7, 21.5 and 23.5 Mev and an unresolved peak at about 13 Mev, the number of events observed being 338. The cross-section curve given by the latter is also quite different in the general trend from that of the former. The discrepancy between the two results may partly be attributed to the poorness of their statistics, especially that of the former workers.

Goldemberg and Katz[3] recently studied carefully ^{7}Li(γn)^{6}Li reaction by measuring photoneutron yield with boron counters and found resonances at the excitation energies of 9.6, 10.8, 14.0 and 17.5 Mev. Peaslee and Telegdi[4] argued that more individual levels should appear in (γn) than in (γt) reaction on light nuclei with $A=4n+3$, if the isotopic spin is a good quantum number (the charge independence of nuclear forces) and they concluded that experimental results on ^{7}Li cited above are in favor of the charge independence theory. More accurate result on the excitation function for ^{7}Li(γt)^{4}He reaction, therefore, seems to be desirable in the light of their discussion.

§ 2. Experimental Apparatus and Procedure

Lithium-loaded 200-micron Ilford E 1 plates have been exposed to the bremsstrahlung from the University of Illinois 22-Mev betatron. The beam was collimated by passing in turn through concrete and lead collimaters with tapered holes, as shown in Fig. 1. It was found that a thin filter of heavy element was very effective in reducing general fogging of nuclear emulsions. With a filter of 20 mil tungsten, for instance, about ten times more dose than without can be administered to the emulsion (300 r instead of 20 r at 21 Mev). A magnet system was interposed between the collimater and the nuclear plate, in order to turn away secondary electrons of lower energies. However this arrangement was not so effective in reducing the blackening of the nuclear emulsion. Slow neutrons, that would give spurious alpha-triton pairs originating from the ^{6}Li(nt)^{4}He reaction, were suppressed by placing the nuclear plate at the center of a long tube made of 1 mm cadmium sheets, with its axis parallel to the x-ray beam. The dose of x-rays administered to the nuclear emulsion was determined by a Victoreen chamber placed in an aluminium block behind the nuclear plate and ranged from 300 r at the running energy of 21 Mev to 100 r at 10 Mev.

The betatron was run at the energy of 21 Mev in most cases. The nuclear emulsions irradiated at such high energy, however, had many proton tracks and it was often found difficult to discriminate short proton tracks

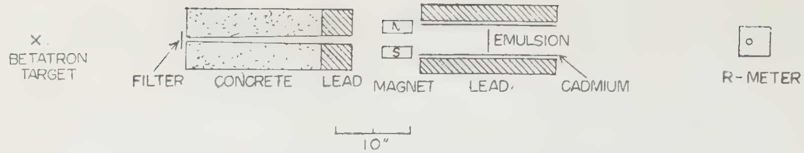

Fig. 1. Schema of the experimental arrangement.

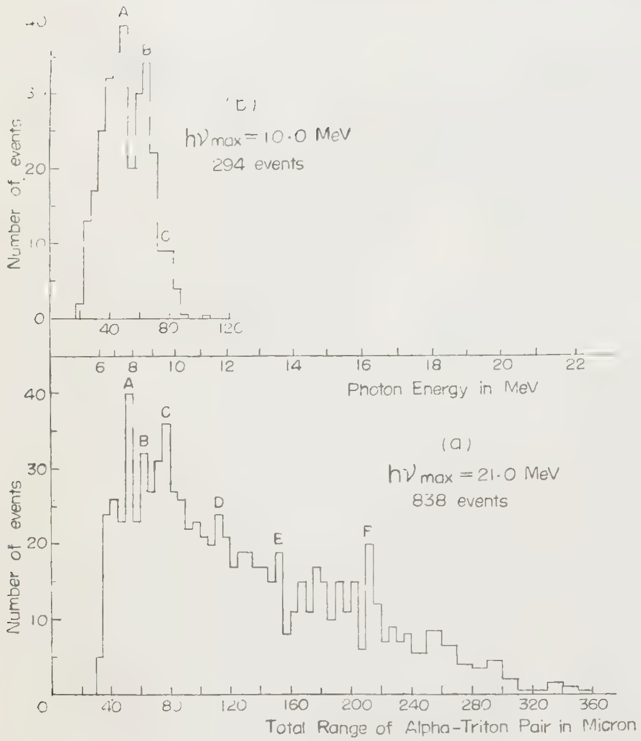

Fig. 2. Total range distribution.

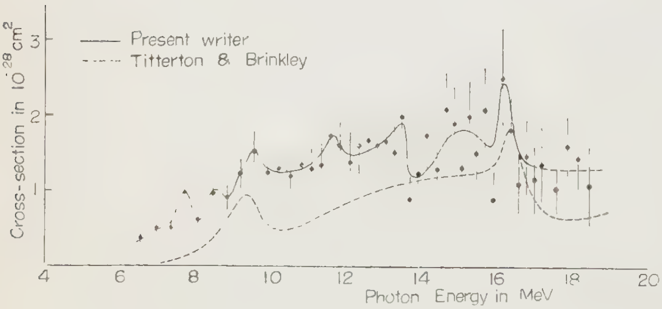

Fig. 3. Excitation function.

from alpha-triton pairs because of the inhomogeneity of the emulsion. A few nuclear plates, therefore, were exposed to 10 Mev x-rays, in order to reduce the number of such protons and to find more accurate information on the excitation function in lower energy region.

Irradiated nuclear emulsions were processed in the usual way, except that 30 per cent diluted normal amidol developer was used to achieve easier discrimination of the tracks of different kind.

838 and 294 events were found in the nuclear emulsions irradiated with 21 and 10 Mev x-rays respectively. Some of long triton tracks left the emulsion on the half way. The ranges of such tracks were estimated from the ranges of the partners on the basis of the observed alpha-triton range relation. As described above, it was difficult in some case to tell whether the short track observed was a proton or an alpha-triton pair. Low energy events, therefore, were checked by evaluating the ratio of ranges of the pair particles. Only those events within the reasonable range of the ratio were considered. Nevertheless, it seems likely that some of the events having total ranges below 50 and 40 microns in the emulsions irradiated at 21 and 10 Mev respectively are spurious.

§ 3. Results and Discussions

The total range distributions of the observed alpha-triton pairs are shown in the histograms of Fig. 2 (a) and (b). The corresponding excitation function was obtained by assuming tentatively Katz and Cameron's values[5] for the number of photons per unit dose and taking the difference between our absorber and theirs into consideration, and is shown in Fig. 3. The excitation function obtained by Titterton and Brinkley is also shown in the same figure for comparison, although they did not give absolute cross-section. The general trend of our excitation function is in good agreement with theirs. However, the absolute cross-sections for the excitation energies of 14.8 and 17.6 Mev, estimated later by them[6] on the basis of known cross-section for the $^{12}C(\gamma 3\alpha)$ reaction, are definitely lower than ours. The difference may partly be ascribed to the error in the cross-section for carbon and partly to the fact that Katz and Cameron used lucite block for establishing equilibrium of secondary electrons with primary x-rays, while we have used an aluminium one. However, the error due to this difference will certainly be less than 10 per cent.

Observed resonance peaks of the excitation function are given in Table I, together with those found by Stoll and Wächter and Titterton and Brinkley. The resonance levels found by Goldemberg and Katz on the (γn) reaction and the energy levels in the level scheme compiled by Ajzenberg and Lauritsen[7] are also shown for comparison. Again our result is in accord with that of Titterton and Brinkley in the predominant peaks, i.e. the peaks at 9.6 and 16.2 Mev. We have also found two minor peaks below 9.6 Mev and another two between 9.6 and 16.2 Mev, while they observed only one unresolved peak at about 13 Mev. We are sure about the three peaks at 7.6, 8.6 and 11.7 Mev, although they all are not very intense. The alpha-triton pair due to $^6Li(nt)^4He$ reaction has total range of 45 microns, well below the 7.6 Mev peak. Only few such tracks were found in the portion of nuclear emulsion, that was out of x-ray beam. The observed number of tracks given in Fig. 2 (b), therefore, was not corrected for such spurious tracks. In the case of 10 Mev run, the neutron yield is so low that the error due to this cause will be negligible. However, we are not quite certain of the peak at 13.5 Mev, because the peak almost dies out if we take the average of the values at the peak and the next point to the peak. The resonance peak corresponding to 4.6 Mev excited level given in the Ajzenberg and Lauritsen's scheme is out of our scope in the present study, because we did not consider tracks shorter than 25 microns in total range.

Table I. Energy Levels of ^7Li.

(γt) reaction			(γn)	Ajzenberg
Stoll and Wächter	Titterton and Brinkley	Present writer	reaction	and Lauritsen
				0.478 $J=\frac{1}{2}^-$
				4.61
5.25				*6.56 $(J=\frac{1}{2},\frac{3}{2}^+)$
7.25		7.6		7.46 $(J=\frac{5}{2}^-)$
		8.6		
9.25	9.3	9.6	9.6	
		11.7	10.8	
	(13)	(13.5)	14.0	
	16.7	16.2		
			17.5	
	21.5			
	23.5			

* Broad level

In conclusion, the writer wishes to express his sincere thanks to Dr. D. W. Kerst for his discussion and also to the other members of Physics Research Laboratory, University of Illinois, for the hospitality they have extended to the writer during his sojourn there.

References

1) P. Stoll and M. Wächter: Nuovo Cim. **10** (1953) 347.
2) E. W. Titterton and T. A. Brinkley: Proc. Phys. Soc. London A **66** (1953) 194.
3) J. Goldemberg and L. Katz: Phys. Rev. **95** (1954) 471.
4) D. C. Peaslee and V. L. Telegdi: Phys. Rev. **92** (1952) 126.
5) L. Katz and A. G. Cameron: Canad. Journ. Phys. **29** (1951) 518.
6) E. W. Titterton and T. A. Brinkley: Proc. Phys. Soc. London A **66** (1953) 579.
7) F. Ajzenberg and T. Lauritsen: Rev. Mod. Phys. **24** (1952) 321.

JOURNAL OF THE PHYSICAL SOCIETY OF JAPAN Vol. 10, No. 3, MARCH, 1955

Electrical Conductivity and Thermo-electric Motive Force in MgO Single Crystal

By E. YAMAKA and K. SAWAMOTO

Electrical Communication Laboratory, Tokyo

(Received July 3, 1954)

Electrical conductivities of MgO single crystals were measured by ac method from 650°C to 1000°C. Curves of log σ vs 1/T have the slope of 2.3 ev. Specific resistivities of magnesium-colored samples are smaller than those of uncolored and oxygen-colored samples, so that it may be concluded that charge carriers are originated from impurity levels of oxygen vacancies or interstitial magnesiums.

The measurements of sign of thermoelectric motive force showed that charge carriers are electrons in all samples. The values of T.E.M.F. are from 0.1 mV/deg. to 10 mV/deg. at various concentrations of excess magnesium.

§ 1. Introduction

Magnesium oxide is an useful material for studying electronic processes in divalent ionic crystals, since it has advantages of being available in large single crystals, of having a simple lattice structure and, moreover, of being well known for its fundamental properties. Although a few investigations[1),2)] were carried out in electrical conductivity, the detailed character of charge carriers is left unclarified. In the present work the measurements of electrical conductivity of uncolored and, magnesium-, and oxygen-colored single crystals were carried out by ac method in order to clarify the mechanism of conduction. Also thermo-electric motive force (T.E.M.F.) of single crystals was measured to decide the sign of charge carriers.

§ 2. Experimental Procedures

In order to avoid ionic current we carried out the measurements by ac method, but high frequency measurement is impossible because of high resistivity of samples. Also high resistivity compelled us to measure in nitrogen gas flow in order to avoid thermionic emission from the electrodes in high temperatures.

Fig. 1 shows the block diagram of the apparatus for electrical conductivity. The oscillator, attenuator, and amplifier are conventional ones. The measurements were done by attenuating the input voltage from the oscillator so as to keep the output voltage on the vacuum tube voltmeter constant, so that non-linearity of pre- and main-amplifier could be out of question and high accuracy was obtained by the accurate attenuator. Samples were held between Pt plates, as shown in Fig. 2. Temperatures of the samples were measured by Pt-Pt thermocouple, which was welded to one of Pt plates. The samples were heated by an electric furnace which covered a fused silica tube.

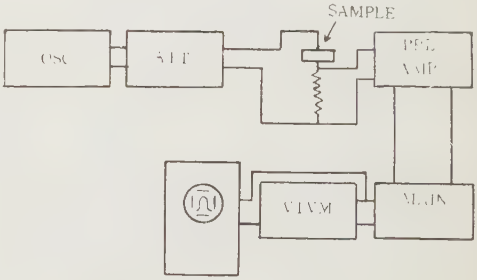

Fig. 1. Block diagram of the apparatus for electrical conductivity.

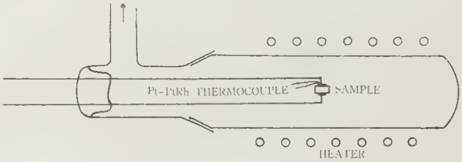

Fig. 2. Crystal mountaing for electrical conductivity.

T.E.M.F. was measured by a potentiometer and a galvanometer. Single crystal was held between *W* electrodes, whose temperatures were measured by two Pt-Pt Rh thermocouples respectively. The measurements were carried out in vacuum of 10^{-5} mmHg.

Single crystal samples were cleaved on the order of one-half millimeter thick and one-half centimeter square from large clear single crystals (MgO) supplied by the Norton Company. Samples were colored with magnesium by heating them in magnesium vapor in a closed vessel of stainless steel at temperatures of about 1250°C to 1300°C for an hour (Mg-MgO), and colored with oxygen by heating them in a stream of dry oxygen at temperatures of about 1300°C for two hours at a pressure of about one atmosphere (O-MgO). The measurements of optical absorption showed that; (1) MgO shows a considerable absorption in the ultraviolet region; (2) O-MgO shows a more intense absorption in that region; (3) Mg-MgO shows a very broad absorption in the vigible region. These absorption bands due to coloring with oxygen and magnesium are the some bands as Weber³⁾ observed. The typical absorption curves of three types of samples are given in Fig. 3 without corrections for surface reflection.

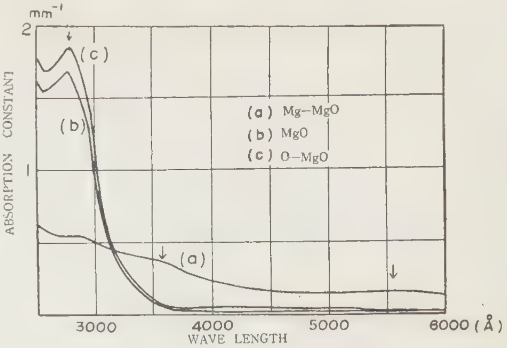

Fig. 3. Curves of optical absorption in MgO, Mg–MgO, and O–MgO.

§ 3. Result and Discussion

(a) Electrical Conductivity

The curves of log R vs $1/T$ in MgO, Mg-MgO, and O-MgO crystals have the same gradient as shown in Fig. 4. The deviation from the straight line occurred in high resistivity range. In order to ascertain the point whether the deviation is due to different impurity levels or to shunt capacity, the frequency of the oscillator was varried from 30 to 300 and 3000 CPS, the results also shown in Fig. 4. The resistivities in deviating range were calculated from a simple equivalent circuit in Fig. 5. The values obtained lay on a extrapolated part of the straight line as seen in Fig. 4. This indicated that the deviation was not due to different impurity levels, but to the shunt capacity.

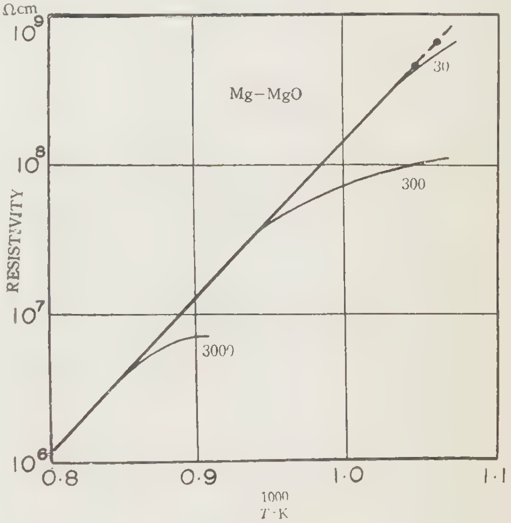

Fig. 4. Resistivities vs 1/T plot. The frequencies used were 30, 300 and 3000 CPS. A dark point shows the value calculated from resistivities at 30 and 300 CPS by using the equivalent circuit shown in Fig. 5.

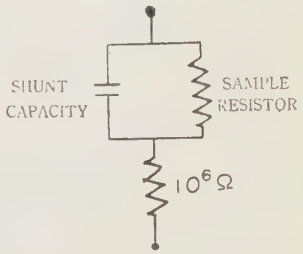

Fig. 5. Equivalent circuit for the measurements of electrical conductivity.

The work function in MgO, Mg-MgO and O-MgO crystals was the same value, being from 2.2 ev to 2.4 ev. However the specific resistivities of Mg-MgO were lower than those of MgO and O-MgO. The specific resistivities of three coloring types of samples at 977°C are tabulated in Table I. These facts may be interpreted as follows; (1) Impurity levels available to 2.3 ev work function are originated from excess magnesiums. (2) The fact that O-MgO samples have the same work function as Mg-MgO means that impurity levels originated from excess oxygens have a comparatively large work function and charge carriers from a small amount of excess magnesiums which exists even in O-MgO, play the major role at the temperatures at which the measurements

Table I. Specific resistivities at 977°C and activatian energies in MgO, Mg-MgO, and O-MgO samples.

	uncolored			O-colored		Mg-colored			
	a	b	c	a	b	a	b	c	d
Resistivity (Ω cm)	37	80	15	28	12	4	5.8	1.2	0.5
E (ev)	2.2	2.3	2.3	2.4	2.2	2.3	2.4	2.2	2.3

were carried out. (3) Furthermore the fact that difference of the specific resistivities between Mg-MgO and O-MgO is unexpectedly small, as shown in Table I, may be understood from our experimental conditions that the melting temperature (about 2500°C) is so much higher than our coloring temperatures (about 1300°C).

From our coloring conditions we expect that there are frozen-in impurity centers, so that we shall try to apply Nijboer's theory[2),4)] to our case. In the following we shall show that the work function measured does not correspond to half an activation energy ΔE for impurity centers, but to ΔE itself. Following Nijboer next formulas are obtained in the case that an impurity semiconductor has frozen-in impurity centers;

$$n=\frac{Ne}{N-Ne}\left\{\frac{2\pi mkT}{h^2}\right\}^{3/2}\exp\left(-\frac{\Delta E}{kT}\right) \qquad (n\ll N-Ne)\,, \tag{1}$$

$$n=Ne^{1/2}\left\{\frac{2\pi mkT}{h^2}\right\}^{3/4}\exp\left(-\frac{\Delta E}{2kT}\right) \qquad (n\gg N-Ne)\,, \tag{2}$$

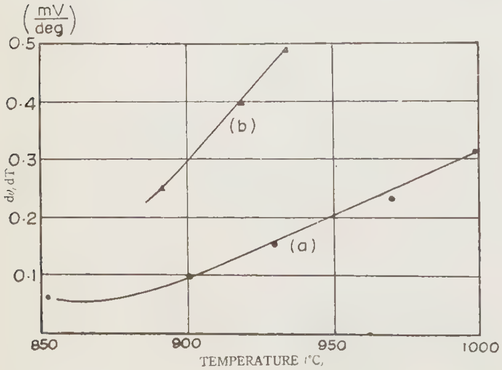

Fig. 6. T.E.M.F. vs T plot in Fg-MgO single crystal. Curve (a) shows the initial values. After heating at 1080°C for three minutes, curve (b) is obtained.

where N and Ne are the densities of impurity levels and electrons respectively. If we take the value of R as $10^7\ \Omega$cm at 977°C, then $n=6\times10^{11}\ \mathrm{cm}^{-3}$ by assuming mobility $\mu=1\ \mathrm{cm^2V^{-1}sec^{-1}}$. Then equation (2) gives $Ne\fallingdotseq 10^{22}\ \mathrm{cm}^{-3}$ for $\Delta E=4.6$ ev. This results is unreasonable, so that the work function may correspond to the activation energy itself.

Low work function in a range of 0.2 ev to 1.5 ev was often measured in the samples which were left in air for a long time, but after heating at about 1000°C such work function vanished. Although its origin was left uncertain, it seems to be due to surface absorption of gas.

(b) Thermo-electric Motive Force

The measurements of T.E.M.F. have been carried out in order to decide the sign of charge carriers. It indicated from signs that electron play major roles in three coloring types of samples. Values in Mg-MgO (~0.1 mV/deg.) were lower than those in O-MgO and MgO (~10mV/deg.). Their temperature dependence is shown in Fig. 6. Values of T.E.M.F. increased with temperature in the temperature range at which measurements were carried out. Yamashita[5)] pointed out the possibility of such behavoir when two different impurity levels are avilable to charge carriers. However only one activation energy was observed in the measurements of electrical conductivity, so that such unusual behavoir of T.E.M.F. is left unexplained.

§ 4. Conclusion

In the present work it is concluded from the sign of T.E.M.F. that charge carriers in our samples are electrons and originated from impurity levels (donor levels), which lie at 2.3 ev under the conduction band, due to excess magnesium.

Recently Day[6)] concluded from his measurements of photoconductivity that charge carriers released by irradiation with lights of absorption bands due to excess magnesium are not electrons but holes. This conclusion contradicts with ours. However his measurements were performed at the room temperature, while our measurements were at high temperatures, so that disagreements of conclusions might be due to difference of measuring temperatures. Mansfield[2)] said that magnesium oxide is a defect semiconductor containing a stoichiometric excess of oxygen and has an activation energy of 2 ev. Since impurity level of 2.3 ev activation energy is originated from excess magnesium in our samples, our impurity level has to be thought in different origin from his impurity level.

Finally we wish to thank Mr. O. Mikami for a grant for use of his spectro-photometer and also Mr. T. Ichimiya and Mr. T. Shindo for their interests in our work.

References

1) A. Lempicki: Proc. Phys. Soc. B **66** (1953) 281.
2) R. Mansfield: Proc. Phys. Soc. B **66** (1953) 612.
3) H. Weber: Z. Physik. **130** (1951) 392.
4) B. R. A. Nijboer: Proc. Phys. Soc. **51** (1939) 575.
5) J. Yamashita: Jou. Phys. Soc. Japan **4** (1949) 310.
6) H. R. Day: Phys. Rev. **91** (1953) 822.

JOURNAL OF THE PHYSICAL SOCIETY OF JAPAN Vol. 10, No. 3, MARCH, 1955

On the Resistivity and Crystal Structure of Binary Oxide of Nickel and Cobalt

By Tamio SAKATA

Research Laboratory, Ohkura Electric Company, Tokyo

Kimiko SAKATA

Institute of Science and Technology, University of Tokyo

and Kunihiko KIGOSHI

Department of Chemistry, Faculty of Science,
Gakushuin University, Tokyo

(Received October 2, 1954)

The solid solution MeO $(\mathrm{Me}=\mathrm{Ni}_1\mathrm{Co}_2)$ was prepared by quenching the specimens derived from mixture of nickel and cobalt carbonates from a temperature higher than 850°C. The resistivity measurement during the heat treatment provided a convenient measure of the phase change. MeO shows a high resistivity at room temperature and has a NaCl-type crystal structure with lattice parameter of 4.23_5 Å. We could lower its resistivity at our disposal through the definite heat treatment. The lowering of resistivity accompanied the shrinkage of lattice parameter and increase in oxygen content without appreciable change in crystal form. The conduction mechanism in MeO having low resistivity may be considered to be quite the same as in the case of black nickel oxide, except the degree of oxygen excess can amount to several percent in former case. The phase change in MeO, caused by the heat treatment was also investigated, in comparison with the case of pure cobalt and nickel oxides and the effect of *mixing* was discussed.

§ 1. Introduction

Mixed oxides of nickel, cobalt and manganese have been known as one of the oxide semiconductors. Since negative resistors made from these oxides are rather easily prepared with high reproducibility, they found various practical applications in electrical engineering as thermistors1),2),3).

At present, we cannot say much on the mechanism of electrical conductivity and the significance of mixing of metallic oxides, although, in practice, the resistivities and activation energies are controllable over wide range at our disposal by changing the mixing proportion of these three oxides.

To find the clue to clarify this mechanism was the main motive of the present experiment. The problem, however, contains so complicated physical natures that, it is of primary importance to grasp the change of properties with mixing ratio and to investigate the effect on electronic properties of the heat treatment about the specimen of definite composition.

The preliminary experiment along this line has been completed. The results are summarized in Fig. 1. The length of the bold line described at various points on the sides of the triangle represents the magnitude of the resistivity of the specimen having the corresponding composition, and the type of semiconduction is also inscribed as *p* and *n*, denoting *p*- and *n*-type respectively. In this experiment, specimens were all prepared through similar heat treatment, i.e., sintered at 1350°C for one hour in air, then slowly cooled. From this figure, we recognize a remarkable decrease in resistivity and activation energy in the mixed oxide of nickel and cobalt having proportion of 1 to 2 in atomic ratio (we denote such a mixed oxide as Ni_1Co_2 throughout this article). Only for this reason, we had an interest in the mixed oxide having this composition.

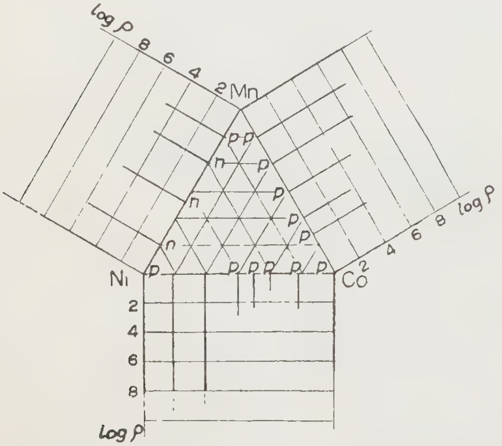

Fig. 1. Resistivities and signs of charge carrier in ternary oxide system Ni-Co-Mn. (*p* and *n* denote *p*-type and *n*-type respectively)

The present article describes the details of the experiment, which were carried out to examine the properties of the oxide Ni_1Co_2. The effects of heat treatment on this specimen were investigated in connection with the phase change. It was found out that the measurement of resistivity variation during heat treatment provided a sensitive measure of phase change$^{4)}$.

The significance of mixing nickel oxides with cobalt oxides should be clearly understood, when the results for the mixture are compared with those of pure nickel and pure cobalt oxides.

§ 2. The Preparation of the Specimens

The three kind of specimens were prepared.

Specimen-(a) The carbonates of nickel and cobalt were precipitated from the water solution of nickel and cobalt nitrate respectively, by adding ammonium carbonates. These carbonates were mixed with one to two in atomic ratio of metals concerned, i.e., Ni_1Co_2, then prefired at about 300°C to decompose carbonates.

After having been ground finely, a certain amounts of the black powder thus obtained, are moistened with several drops of lavender oil in order to be able to attach intimately to two stretched platinum wires (0.1 mm in dia. and clearance about 1 mm) set closely side by side. These wires served as the leads for resistivity measuring as well as a specimen support. The little bead-like specimen ($1.5 \times 1.5 \times 2\ mm^3$ approximately) with platinum leads thus obtained was dried in air-bath at about 180°C, and then served for experiments.

Specimen-(b) The pure cobalt specimen, prepared just like specimen-(a).

Specimen-(c) The pure nickel specimen, prepared just like above two.

§ 3. The Experimental Procedure

The electric furnace for the heat treatment is of air core type, made from the platinum ribbon wound (8 mm in dia., 40 mm in length). The heat capacity of this furnace is small enough to quench the specimens quickly, even when they are remaining in the furnace.

Therefore, the furnace, specimen supports and the Pt-PtRh thermocouple are mounted on a mica plate to fix the mutual position. The schematic diagram of the setout is shown in Fig. 2. The mica plate is then settled in a bell jar, in order to subject the specimen to heat treatment in appropriate atmosphere. Through leads wires drawn out of the bell jar, we can observe continuously what happens to the resistivity of the specimen during heat treatment.

The temperature of the furnace is recorded continuously by means of thermocouple. The time constant of cooling speed of the furnace is about 60 seconds in air.

After an appropriate heat treatment, we measured on a specimen at first its resistivity at room temperature, then it is ground finely so as to prepare powder specimens for X-ray analysis.

Using the iron anti-cathode under the tension of 30 KV and the electron current of 9 mA, the diffraction lines are recorded by means of Norelco recording spectrometer.

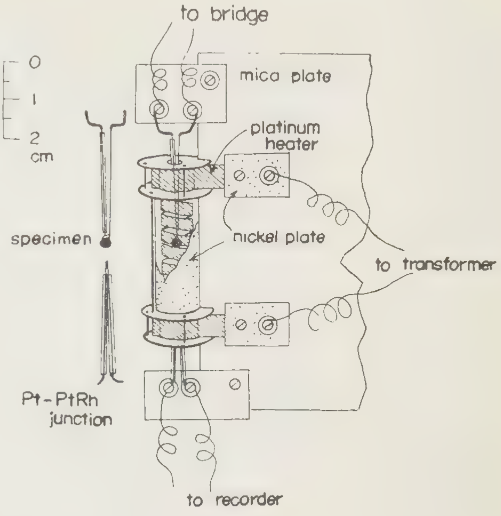

Fig. 2.

§ 4. The Effects of the Heat Treatments on the Variation of Resistivity with Temperature

To investigate the effect of heat treatment on the characteristics of the specimen, the observations of variation of resistivity with temperature are made on the three kinds of specimens mentioned in the preceeding section.

The case of mixed Ni_1Co_2

(1) The curve I in Fig. 3 shows the variation of resistivity with temperature in the course of heat treatment in air* to which the specimen-(a) is for the first time subjected. In this case resistivity decreases with the increase in temperature, up to 800°C., then suddenly starts to increase to a certain maximum value. But as the temperature rises further, it again slowly decreases. This curve distinguishes clearly three temperature regions as follows; the first from 250°C to 800°C, the second from 850°C to 1100°C and the third between them, that is the transition region. We refer to those, hereafter, as L-, H- and T-regions.

(2) The specimen quenched from a temperature of H-region shows the high resistivity at room temperature. The behaviour of the resistivity *vs.* temperature for such a specimen is shown in curve II in Fig. 3. We use hereafter such abbreviation as $(Ni_1Co_2)_H$ to denote the specimen of mixed oxide Ni_1Co_2 which has been quenched from a temperature in H-region.

(3) If the specimen $(Ni_1Co_2)_H$ is again subjected to heat treatment and then quenched from a certain temperature near the upper limit of the L-region—we denote such a specimen writing $(Ni_1Co_2)_{HL}$—it shows a very low resistivity at room temperature. Its variation of resistivity with temperature is shown in curve III in Fig. 3.

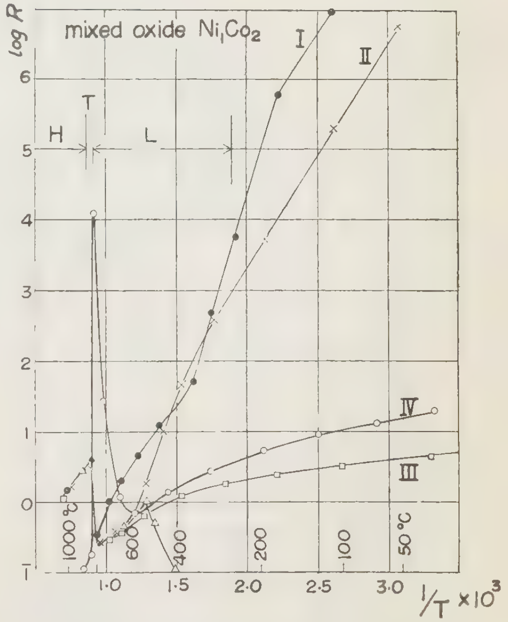

Fig. 3. Effects of heat-treatments on the variation of resistivity with temperature in the mixed oxide Ni_1Co_2.

(4) Curve IV in Fig. 3 shows the behaviour of the specimen $(Ni_1Co_2)_{HL}$, when the temperature is raised in vacuum. The anomaly of the resistivity takes place very rapidly, but

---

* Specimens were treated in air if not mentioned.

if compared to the case of curve I, we can see that the transition temperature shifts to lower side, and the maximum value of resistivity is much higher than that which curve I shows. Raising the temperature further, the resistivity falls again and finally the specimen is reduced to a metal. This fact suggests that the liberation of oxygens is taking place in T-region.

(5) Curve V shows the variation of resistivity with temperature in air for the specimen reduced to a metal. In low temperature region it actually behaves as a metal, but already in L-region it reverts to the oxide, and if quenched from a temperature of H-region, it is completely identified with $(Ni_1Co_2)_H$, having a high resistivity at room temperature.

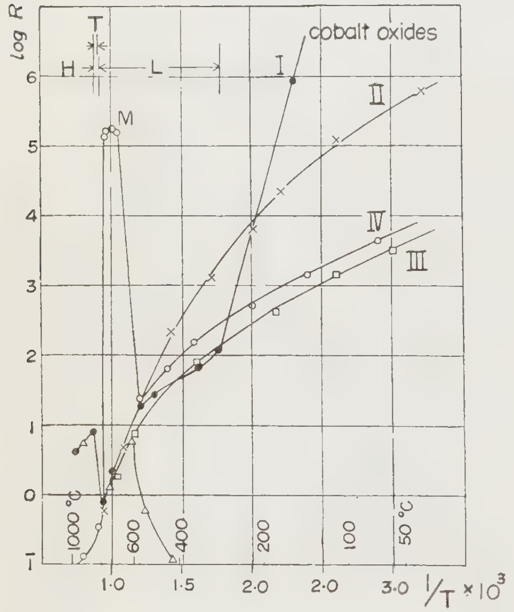

Fig. 4. Effects of heat-treatments on the variation of resistivity with temperature in the pure cobalt oxide.

(6) The resistivity *vs.* temperature curve of the specimen $(Ni_1Co_2)_{HT}$ appears between curves II and III, in L-region.

(7) The heat treatment below 250°C never affects the characteristics of specimens.

The case of pure cobalt oxide

(1) The curve I in Fig. 4 shows the variation of resistivity with temperature in the course of heat treatment in air to which the specimen-(b) is for the first time subjected. We see that the behaviour of the curve just corresponds to that of curve I in Fig. 3. But the three critical temperature regions are more or less deviating; H-region ranges from 860°C to 1100°C, T-region from 830°C to 860°C and L-region from 250°C to 830°C.

(2) The variation of resistivity with temperature for $(Co)_H$ and $(Co)_{HL}$ are shown in curves II and III in Fig. 4, respectively.

(3) When temperature is raised in vacuum, the variation of resistivity with temperature for the specimen such as $(Co)_H$ behaves like curve IV in Fig. 4. The general features for $(Co)_H$ are similar to those for $(Ni_1Co_2)_H$, but in the former, the maximum value of resistivity* is much higher than that of the latter, amounting to the order of magnitude of $10^5\Omega$, moreover, the temperature range corresponding to this maximum is rather wide, suggesting the existence of a stable phase in this range.—We denote this temperature range as M-region.—Further raise of temperature reduce the specimen to a metal.

(4) The variation of resistivity with temperature in air for the specimen which has been reduced to a metal is shown in curve V in Fig. 4. From this curve we can see that the oxidation begins to proceed already in L-region, and in T-region and H-region its behaviour is much the same as that of the oxide.

(5) $(Co)_{HM}$, which is obtained by quenching $(Co)_H$ in vacuum from a temperature of M-region, has a extremely high resistivity in air, and even at 300°C, its order of magnitude is still $10^6\Omega$.

The case of pure nickel oxide

(1) In this case, there is no similarity to those of (Ni_1Co_2) and pure cobalt oxide. The gradual decrease in resistivity is observed over the temperature range from 500°C to 1000°C, in the course of the initial heat treatment. The specimen quenched from about 1100°C has resistivity of more than $10^7\Omega$ in room temperature.

(2) The specimen is easily reduced to a metal, if it is brought to high temperature in vacuum.

---

* The word "resistivity" is used instead of resistance, because the measured resistance had the more definite significance, not affected by specimen size.

Table I. Various characteristics of the solid solution MeO (Me = Ni_1Co_2).

No.	heat treatment before quenching			crystal structure	lattice const.	resistance (room temp.)	activation energy
	temp.	time	resistance				
1	350°C	25 hr	7.3 Ω		Å	27 Ω	0.04_1 eV
2	380	51	1.9			7.2	0.04_1
3	410	0.1	9.0	NaCl	4.23_5	120	
4	440	2	1.5	NaCl	4.23_0	7.2	
5	440	10	1.3			5.5	0.04_2
6	440	23	1.1			4.4	0.04_1
7	500	19	0.98			4.7	0.04_5
8	510	6.5	0.95	NaCl	4.22_5	3.1	
9	540	20	0.81			5.5	0.03_8
10	550	25	0.68			6.8	0.06_6
11	620	3	0.36	NaCl (diffuse) spinel (weak)	(av.) 4.20_5 8.1_0	3.5	
12	640	24	0.3	NaCl spinel (strong)	4.19_8 8.0_9	21	
13	650	21	0.44			44	0.12
14	720	20	0.28			440	0.17
15	800	2.5	0.53	NaCl spinel (weak)	4.22_5 8.0_9	3.5×10^3	
16	820	0.1	2.4	NaCl spinel (very weak)	4.22_5 8.1_0	14×10^3	
17	1100	0.5	1.3	NaCl	4.23_5	$>10^7$	
18	1100	1		NaCl	3.53_5	metallic	

§ 5. The Change of Phase with Temperature

The case of mixed oxide Ni_1Co_2

It is assumed that any state of the specimen at a certain temperature is preserved to room temperature, when quenched rapidly from that temperature. This assumption is confirmed by the results of preceding section. We can guess, moreover, based upon the curve I in Fig. 3, how the change of phase is taking place with temperature.

The initial specimen—specimen-(a)—was identified by X-ray analysis to be a mixture of Co_3O_4 (spinel) and NiO (NaCl-type). Such phases are preserved throughout L-region.

In T-region, a transition of phase is taking place, i.e., the spinel patterns, existed in L-region begin to diffuse and a new NaCl-type patterns appear besides NiO patterns, which are identified with those corresponding to CoO.

In H-region, another phase appears. The diffraction patterns are identified with those

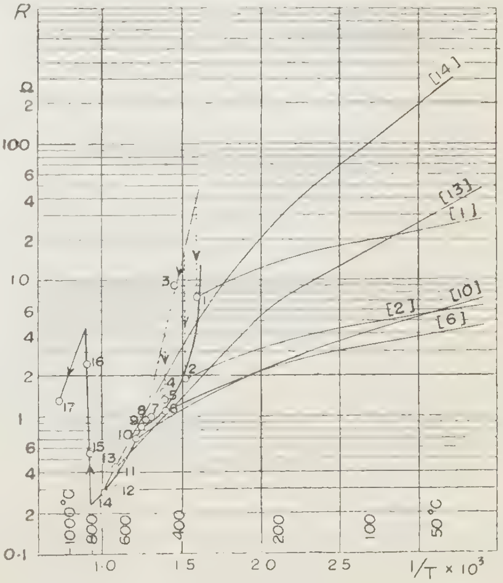

Fig. 5. The quenching conditions of the specimens listed in Table I.

of a single NaCl-type, having a lattice parameter of 4.23_5 Å. Such patterns have never been found in the lower temperature region.

Thus, in this phase, nickel oxides and cobalt oxides do not exist independently, but react with each other to form a definite solid solution, which may be regarded as MeO (Me= Ni_1Co_2) being isomorphous with NiO.

The results of X-ray analysis reveal that $(Ni_1Co_2)_{HLH}$, $(Ni_1Co_2)_{TH}$ as well as $(Ni_1Co_2)_H$ are identified with MeO, all having a lattice parameter of 4.23_5 Å. Thus, through the heat treatment in H-region we can bring any specimen of Ni_1Co_2 into a homogeneous MeO phase.

Using MeO as reference specimen, we studied its properties more closely. Results are summarized in Table I.

In L-region, the reaction rate of the oxide with oxygen is rather slow. Thus, the properties of the quenched specimen depends not only upon the quenching temperature, but also upon the time of duration kept at that temperature. The Fig. 5 illustrates the quenching conditions of the specimens listed in Table I. The numbers in this diagram corresponds to the specimen numbers, and small circles indicate that the specimens are quenched from such states. The bold line in Fig. 5 represents the quasi-equilibrium state* and the dotted lines illustrate the process of resistivity variation caused by the sudden change of temperature.

The characteristic curves of the resistivity variation with temperature for the several specimen are also included in this figure (curves [1], [2], [6], [10], [13] and [14]). It was found out that the characteristic curve for the specimen quenched from the quasi-equilibrium state is quite definite within the temperature range below its quenching temperature. This fact enabled us to determine the activation energy of the conduction, which is characteristic of the specimen.

In the temperature range from 300°C to 540°C, the crystal structure of MeO remains unchanged, but its lattice parameter seems to decrease with rise of temperature, accompanied by decrease in resistivity at room temperature (c.f. Nos. 3, 4 and 8). The chemical analysis shows qualitatively** that the oxygen content in the specimen increases with temperature. We can point out, moreover, that the activation energy of conductivity in the specimen heat-treated in this temperature range is very low and rather constant, as curves in Fig. 5 show.

In the temperature region from 540°C to 800°C, MeO gradually transforms itself to the spinel structure. The more develops the spinel structure with rise of temperature, the more becomes diffuse the diffraction patterns of MeO, while the lattice parameter of MeO decreases in the average. Thus, at 800°C, spinel patterns become very strong, and correspondingly the lattice parameter of MeO shrinks to 4.19_8 Å (No. 12). Such a state, in which the spinel is predominant, has higher resistivity and larger values of activation energy than in the state of MeO alone, even if the lattice parameter of MeO co-existing with the spinel is much smaller than that of the latter. It is, however, quite difficult to draw any conclusions from X-ray analysis, whether the spinel structure develops in the form of Me_3O_4+MeO or Co_3O_4+MeO.

In T-region (800°C−850°C), the spinel begins to fade away, while the patterns of MeO restore their strength, lattice parameter increasing with rise of temperature. In this region, the resistivity at room temperature increases as the decomposition of spinel into MeO proceeds.

Once the temperature reaches to H-region, the phase of MeO only is reproduced, and its lattice parameter recovers the original value of 4.23_5 Å.

The specimen reduced to a metal is found to be an alloy of Ni_1Co_2, having a NaCl-type structure with lattice parameter of 3.53_5 Å.

The cases of pure cobalt oxide and pure nickel oxide

The method applied is the same as in the foregoings. Before heat treatment, the diffraction patterns of specimen-(b) are identified with those of Co_3O_4 (spinel). $(Co)_H$ consists of Co_3O_4 and CoO (NaCl-type). When this is subjected to high temperature, spinels (Co_3O_4) gradually tend to prevail over NaCl-types (CoO), and at about 600°C there exist no CoO at all—the lattice parameter of Co_3O_4 is 8.08_5 Å in this case—.⁵⁾,⁶⁾,⁷⁾

---

* An equilibrium state is assured by no further drift of resistivity at the temperature. In the case of specimen No. 2, for example, the specimen was kept at 380°C. It was observed that the change of resistivity was negligible after 51 hours. Moreover, from the behaviour of the resistivity *vs.* time curve, we can expect that it takes about 50 hours for the further change of resistivity of 2 percent to occur. For this reason, we preferred the word quasi-equilibrium.

** In this experiment, there existed some difficulties in the quantitative chemical analysis.

$(Co)_{HM}$ consists solely of CoO with the lattice parameter of 4.26_3 Å.

Specimen-(c) is identified with NiO, having the lattice parameter of 4.18_2 Å.

§ 6. Discussions

The solid solution MeO is isomorphous in crystal structure with NiO, i.e., NaCl-type. The high resistivity of MeO suggests that the specimen is nearly stoichiometric in composition.

The behaviours of MeO in the temperature range up to 540°C are seen from specimens Nos. 1 to 9 in Table I. There seems to exist parallelism between lattice parameter and resistivity at room temperature. The decrease in resistivity may be attributed to the increase in metal deficit sites which comes out from absorption of oxygen atoms and subsequent diffusion of metal atoms in the same way as in the case of oxidation of nickel metal⁸⁾. Thus the higher is the quenching temperature and the longer is the time during which the sample is kept at that temperature, the resistivity decreases the more. 540°C may be considered as the critical temperature, because the spinel patterns though weak already appear in No. 10 which is quenched from 550°C. In No. 9, oxygen content takes the highest value possible to preserve NaCl-type structure, i.e., No. 9 is the state just before the appearance of spinel structure.

The excess of oxygen, therefore, in such a specimen may perhaps amount to several percent, which is overwhelming majority compared with that in black nickel oxide (about 0.5 percent)⁹⁾.

Comparison of the properties of MeO with those of cobalt oxide and nickel oxide, enables us to understand the roles that nickel atoms play in MeO.

$(Co)_H$ appears as a phase of mixed oxide composed of Co_3O_4 (spinel) and CoO (NaCl-type), in which CoO may be compared with MeO. CoO has a tendency to transform into Co_3O_4 (spinel) by oxidation from about 300°C. Thus, at about 600°C, CoO cannot exist at all, but appears as a uniform phase of Co_3O_4.

On the other hand, MeO can react with oxygen atoms from about 300°C, although it preserves the NaCl-type structure up to 540°C, resulting in non-stoichiometric compound with excess oxygen. The latter properties are rather similar to those of NiO, but the former is much more similar to that of CoO. Although such NaCl-type crystals of non-stoichiometric composition gradually turn to spinel type from 540°C, they are still able to co-exist with spinels even at about 600°C.

§ 7. Conclusion

(1) It was found out that the change of phase with temperature occurring in the specimens, is conveniently pointed out by singularity appeared in the variation of resistivity with temperature curve.

(2) We could prepare, irrespective of the history of specimens, the solid solution MeO (NaCl-type, $a=4.23_5$ Å) by quenching the specimens derived from mixture of nickel carbonate and cobalt carbonate from a temperature of H-region.

(3) The high resistivity of MeO may be attributed to the fact that its composition is nearly stoichiometric.

(4) On the other hand, low resistivity accompanied by the shrinkage of lattice parameter in specimens Nos. 3, 4 and 8, may be caused by high degree of oxygen excess, i.e., higher concentration of metal deficit sites.

(5) The conduction mechanism in MeO may be considered to be the same as in the case of black nickel oxides, except that the degree of oxygen excess can amount to several percent in the former, which is about 10 times as high as that in the latter.

(6) Our present knowledge on the MeO enable us to say about the mixing effect as follows; the above properties of MeO is considered to be of intermediate character between NiO and CoO, and its behaviour may be attributed partly to its NiO-like character and partly to its CoO-like one, i.e., the occurrence of a phase transition in MeO is suppressed to some degree by its NiO-like character, in

comparison with the case of pure CoO—CoO transforms into Co_3O_4 from a temperature as low as 300°C, while MeO persists in NaCl-type up to 540°C—. MeO possesses, on the other hand, much more stronger affinity with oxygen than in pure NiO, owing to its CoO-like character. Thus, without transforming its crystal structure, a state of the high degree of oxygen excess is realized in MeO.

(7) The chemical determination of the oxygen content in the specimens subjected to various heat treatment, seems to support above considerations, though qualitatively in this stage. The decrease in resistivity along the specimens Nos. 4, 5 and 6, thus, roughly corresponding to the increase of oxygen content. The quantitative analysis along this line is now proceeding.

In conclusion, the authors express their sincere appreciation to Dr. Y. Kakiuchi of the Institute of Science and Technology, University of Tokyo, for many discussions and encouragements during the experiment. They also thank Dr. T. Itoh and Mr. Y. Iitaka of University of Tokyo for facilities offered.

References

1) J. A. Becker, C. B. Green and G. L. Pearson: I.E.E. **65** (1946) 711.
2) E. J. W. Verwey, P. W. Haayman and F. C. Romeyn: Philips Tech. Rev. **9** (1947/48) 239.
3) Semi-conducteurs électroniques et complexes dérives: Collection Technique Du C.N.E.T. (1950) Paris.
4) T. J. Gray: Semi-Conducting Materials (1951) 180.
5) S. Holgersson and A. Karlsson: Z. anorg. allg. Chem. **183** (1929) 384.
6) J. Robin et J. Bénard: Compt. Rend. Acad. Sci. **234** (1951) 1830, **254** (1952) 734.
7) M. Le Blanc and G. Wehner: Z. physik. Chem. **168** (A) (1933) 59.
8) N. Cabrera and N. F. Mott: Rep. Prog. Phys. **12** (1948–49) 163.
9) C. A. Hogarth: Proc. Phys. Soc. London **B 64** (1951) 691.

JOURNAL OF THE PHYSICAL SOCIETY OF JAPAN Vol. 10, No. 3, MARCH, 1955

On the Precipitation Process in Aluminium-Zinc-Magnesium Alloys

Part I. Al–$Al_2Zn_3Mg_3$ System

By Ken-ichi HIRANO and Yutaka TAKAGI

Department of Physics, Tokyo Institute of Technology,
Oh-okayama, Meguro-ku, Tokyo

(Read July 11, 1954; Received Sept. 10, 1954)

When aluminium rich Al–Zn–Mg alloy containing 8 weight per cent zinc and 4 weight per cent magnesium is quenched from 450°C to the room temperature, a supersaturated solid solution is obtained, the breakdown of which on subsequent annealing at various temperatures has been studied by means of calorimetric and electrical resistance measurements and of X-ray photographs. The existing data have been incorporated with our new data to build up a more clear perspective as to the mechanism of precipitation. The existence of two separate processes has been confirmed, that is, the "Low Temperature-Aging" which is a stage of the formation of the Guinier-Preston zone and the "High Temperature-Aging" which involves the formation of the coherent precipitate and its transformation to the incoherent precipitate. This precipitation sequence is similar to those in the Al–Cu as well as in the Al–Ag binary alloys.

§ 1. Introduction

The construction of the Al-Zn-Mg system has been studied in detail by Köster, Wolf and Dullenkopf[1),2),3)]. They have confirmed the existence of the quasi-binary equilibrium between the alminium rich ternary solid solution (α phase) and the ternary metallic compound $Al_2Zn_3Mg_3$ (denoted by **T** phase in this paper) which has a body centered cubic structure[4)]. It has also been shown that the alloy containing 8 weight per cent zinc and 4 weight per cent magnesium is in the homogeneous state at 450°C, but, if the temperature is lowered, the **T** phase begins to precipitate at about 380°C which lies on the solvus surface in the ternary phase diagram.

Durer and Köster[5)] and Köster and Kam[6)] have investigated the precipitation process by means of the thermoelectric force, electrical resistance and hardness measurements and recognized the different effects of the low temperature-aging and the high temperature-aging.

Present paper records the results obtained from the calorimetric and electrical resistance measurements during heating the specimen after various aging treatments and the results obtained from the lattice spacing examination by the X-ray powder method during the aging.

§ 2. Experimental Procedure

The alloys were made from four-nine aluminium and high-purity metals. The metals were melted together in a graphite crucible and cast in an iron mold, then homogenized at 490°C for more than 70 hours after some cold working to disperse the casting structure.

The heat treatments for the aging were carried out in an electrical furnace in the air.

The specimens used for the specific-heat measurement were closed hollow cylinders having the external dimension: 2 cm in diameter and 3 cm in length. The electrical resistance specimens were square bars: 0.2 cm in thickness, 0.3 cm in width and 6.0 cm in length. The specimens for the powder X-ray examination were rods, 0.07 cm in diameter.

The measurements of specific-heat were made by means of an apparatus of the Nagasaki-Takagi type[7)]. The heating rate employed was about 3°C per minute. The electrical resistance were determined by a potentiometer method. The heating rate was the same as that used in the specific-heat measurement. The X-ray photographs were taken each time at the room temperature in a Debye-Scherrer camera, 7 cm in diameter, with K_α radiation of copper as quenched from various aging temperatures after various aging periods.

§ 3. Specific-heat Measurement

Fig. 1 represents the specific-heat *versus* temperature curves (*S-T* curves) obtained after various heat treatments. Using the values of C_p for pure Al, Zn and Mg, we have calculated the specific-heat of the alloy by the Kopp-Neumann rule and obtained the base line, ***XY*** in Fig. 1, which should be identical with the *S-T* curve of the alloy if it were not for any change in atomic configuration.

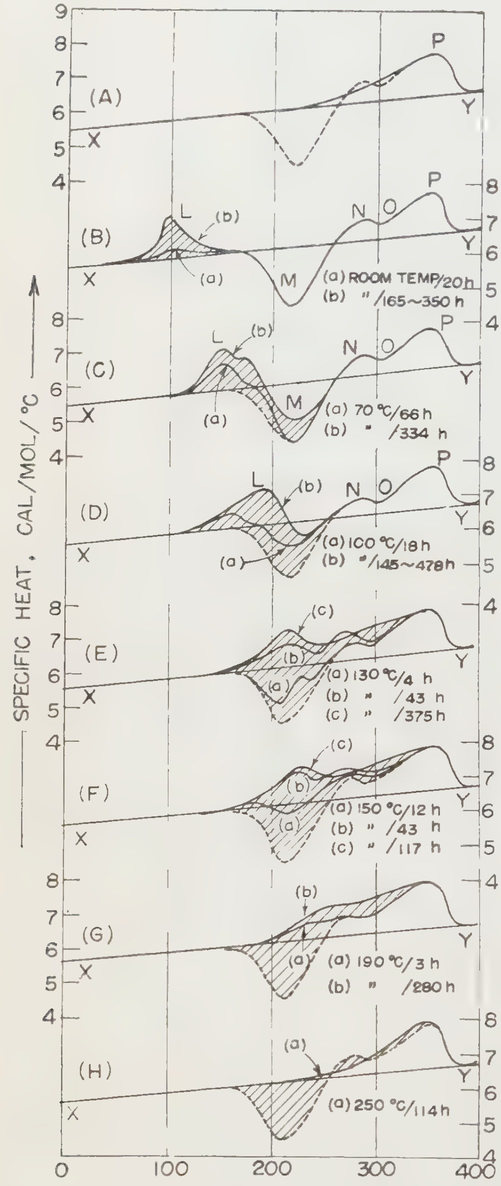

Fig. 1. *S*−*T* Curves for Various Heat Treatments.

In Fig. 1 (A), full-curve is the *S-T* curve of the alloy which was cooled to the room temperature from 450°C at the rate of 4°C per hour, which seems sufficiently slow to have a completely precipitated alloy. Up to about 240°C, the curve is in agreement with the base line ***XY***. Above 240°C, the curve diverges and shows a heat absorption ***P***. This heat is required to dissolve the precipitates which are going back into solution. Dashed curve in Fig. 1 is obtained by the alloy immediately after quenching. Heat evolution at 170°—260°C denoted by ***M*** is due to the precipitation of the **T** phase.

Fig. 1 (B)—(H) are the *S-T* curves of the alloy after quenching from 450°C to the room temperature and aged at the room temperature, 70°, 100°, 130°, 150°, 190° and 250°C for the time indicated in the figure, respectively.

In Fig. 1 (B), the *S-T* curves of the room temperature-aged alloy lie above the base line at temperatures up to about 180°C and the area denoted by ***L*** (heat absorbed), enclosed between the *S-T* curve and the base line increases with increasing aging time, but has a tendency to saturation. General feature of Fig. 1 (B) resembles the curves for Al-Cu8) and Al-Ag9) alloy which are obtainable after similar aging treatments.

Heat absorption ***L*** seems to be due to the dispersion of the Guinier-Preston zone (G-P zone) which is the clustering of solute atoms on the aluminium lattice, formed during the room temperature aging.

On the other hand, from 180°C onward, the *S-T* curves in Fig. 1 (B) coinside with the dashed curve and it has been observed that the heat evolution ***M*** is not affected appreciably by the room temperature aging. As the heat evolution ***M*** is attributable to the precipitation of the **T** phase during the measurement, it will be deduced from above fact that the precipitation of the **T** phase does not set in during the room temperature aging and only the formation of the G-P zone takes place.

Along ***NOP***, resolution of the precipitated phase is taking place but it will be noticed that the shape of the curve is quite different from that shown by the full curve in Fig. 1 (A). The additional minimum occurs at ***O*** after considerable resolution has taken place. In comparison with the results on Al-Cu[8] alloys, it will be shown that the first precipitation from the supersaturated solid solution is not the equilibrium **T** phase but an intermediate coherent phase (**T**′ phase) and the minimum ***O*** may be due to the breakdown of this intermediate phase into stable incoherent **T** phase.

On the aging temperature higher than 70°C, some complex curves have been obtained where the maximum ***L*** superposes itself on the minimum ***M*** and furthermore, in contrast with the room temperature aging, the area ***M*** itself decreases with aging time, this shows that the precipitation of the **T**′ or **T** phase takes place during the aging and they coexist with the G-P zone. Furthermore, the disappearance of the second minimum ***O*** has been confirmed after aging at rather higher temperatures as shown in Fig. 1 (E)—(H).

It will be noticed that after the aging at above 230°C, we could not observe the heat absorption ***L***, this shows that the formation of the G-P zone does not take place and only the precipitation of the **T** phase takes place during the aging at this temperature range.

For the low temperature-aging (LT-aging), it has been observed that after some aging time, further aging can not affect the shape of the S-T curve. It seems that the subsequent aging does not bring the alloy beyond a certain fixed state which depends upon the aging temperature. This fact has been confirmed by the measurements of lattice spacing and electrical resistance.

The temperature T_s where the heat absorption ***L*** attains its maximum is regarded as a measure of the stability of the existent G-P zone, saturated values of which have been obtained after sufficient aging time. Fig. 2 shows the aging temperature dependence of T_s. It will be indicated that the stability of the G-P zone increases linearly with the aging temperature.

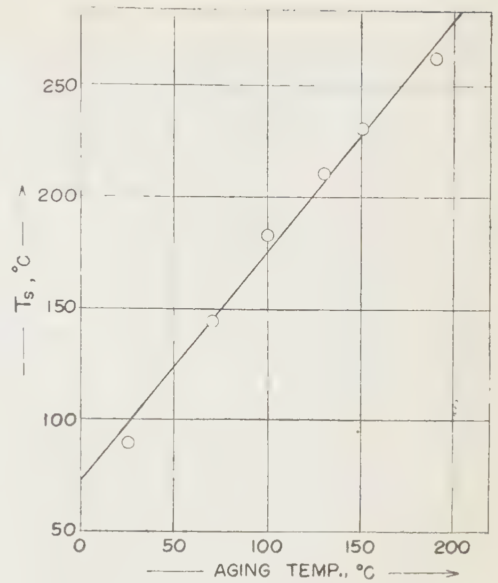

Fig. 2. Aging Temperature Dependence of T_s.

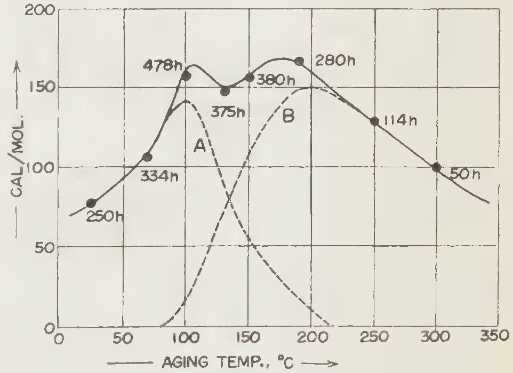

Fig. 3. Energy Difference between Aged Alloy and Quenched Alloy.

In Fig. 3, the energy difference between aged and as quenched alloy (the area enclosed between the S-T curves of them as shown hatched by the oblique lines in Fig. 1) is plotted against the aging temperature, which were obtained after sufficient aging time to attain the saturated value. Two maxima are clearly distinguished in Fig. 3. The curve seems to be constructed from two parts as shown by dashed curves, ***A*** and ***B***. The lower temperature part, ***A***, comes from the heat absorption due to the dispersion of the G-P zone (same heat must have been evolved during the aging) and the higher temperature part, ***B***, corresponds with the decrease of the heat evolution ***M***. From about 80°C onwards up to about 210°C, ***A*** and ***B*** superpose each other, then summation of them are observable instead of individual values. This indicates the coexistence of the G-P zone and the **T**′ or **T** phase.

§ 4. Electrical Resistance Measurement

In Fig. 4, the specific electrical resistance *versus* temperature curves (ρ-T curve) are

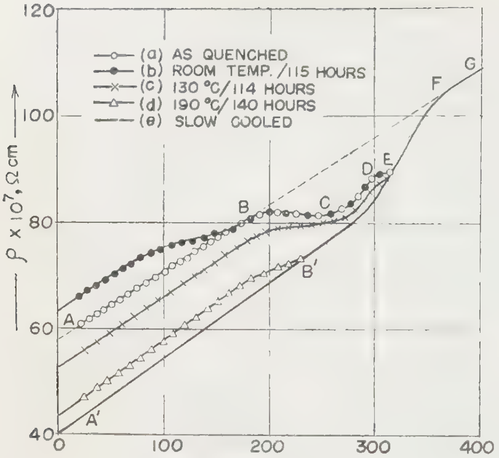

Fig. 4. $\rho - T$ Curves.

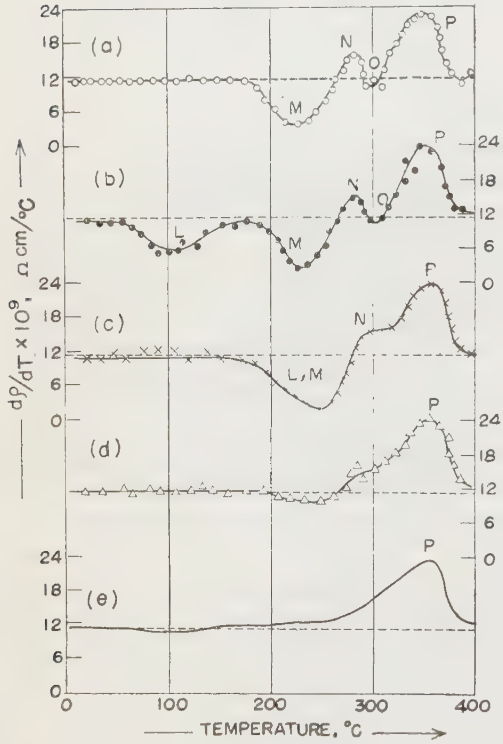

Fig. 5. $d\rho/dT$ *versus* Temperature Curves.

shown. Fig. 4 (a) was obtained by freshly quenched alloy and Fig. 4 (e) by slow cooled alloy. Fig. 4 (a) and (e) correspond respectively to the dashed curve in Fig. 1 and the full curve in Fig. 1 (A). The line ***ABC*** and the curve ***A′B′FG*** represent respectively the values for the supersaturated state and the precipitated equilibrium state.

From 220°C, the curve ***A′B′F*** begins to deviate upward and finally coincides with the line ***FG***. This must be correlated with the resolution of the precipitated phase into the solid solution.

In Fig. 4 (a), the drop ***BC*** indicates that the intermediate **T′** phase precipitates and some part of this resolutes into the matrix or transforms to the equilibrium **T** phase along ***CDE***, at the same time **T** phase may precipitates directly from the matrix. This corresponds to the appearance of the additional minimum ***O*** in Fig. 1. Along ***EF*** resolution is taking place as in the case of Fig. 4 (e).

Fig. 4 (b), (c) and (d) are the curves for the alloy quenched and aged at the room temperature for 115 hours, at 130°C for 114 hours, and at 190°C for 140 hours respectively. It has been confirmed that in contrast with the case of **T′** or **T** phase precipitation, the electrical resistance increases with the formation of the G-P zone.

In Fig. 5, $d\rho/dT$ is plotted against temperature, the values were derived from Fig. 4. Fig. 5 (a)—(e) correspond respectively with Fig. 4 (a)—(e). General shape of the curves in Fig. 5 resembles the S-T curves in Fig. 1 except that the minimum ***L*** in Fig. 5 corresponds with the maximum ***L*** in Fig. 1.

§ 5. Lattice Spacing Measurement

The lattice spacing of the matrix solid solution is plotted as a function of the aging temperature in Fig. 6. The aging time is described in the figure which seems to be long enough to give a saturated value. For comparison, the values for as quenched alloy, slow cooled alloy and for pure aluminium, are also shown in Fig. 6.

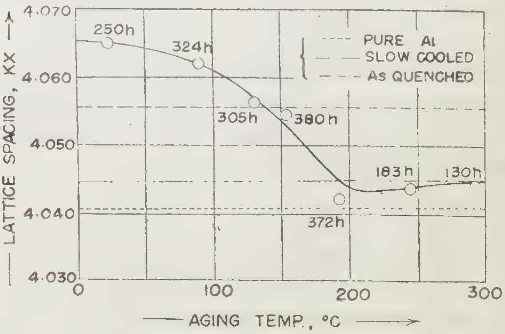

Fig. 6. Lattice Spacing of the Matrix.

The value of the slow cooled alloy is smaller than that of the freshly quenched alloy and nearer to the value of the pure aluminium. This shows that the decrease of solute atoms in the solid solution is accompanied with the **T** phase precipitation.

Comparison of Fig. 6 with Fig. 3 shows that the increase in the lattice spacing is caused by the formation of the G-P zone and the decrease by the **T** phase precipitation. It may be noticed that the decrease of solute atoms in the matrix does not take place during the formation of the G-P zone.

§ 6. Discussions

1. Retrogression Phenomena

In the previous work on Al-Ag alloys[10], we have shown that the retrogression phenomena is explainable with reference to the dispersion of the G-P zone. This effect in the present alloy has been observed by Köster and Kam[6] as shown in Fig. 7: an alloy partially hardened by the 20°C aging will soften on reheating for short periods at 150°, 175° and 200°C. Complete retrogression has not been obtained by 150° and 175°C, but by 200°C-reheating nearly perfect retrogression has been observed. This is in good agreement with our measurement (Fig. 3); at 150° and 175°C some extent of the G-P zone can remain stably while it can hardly remain at 200°C.

2. Stability of the G-P zone

We regard T_M which is the upper limit temperature of the existence of the G-P zone as the measure of the stability of it. Considering the discreteness between the formation of the G-P zone and the precipitation of the new phase and taking into account the dependence of T_M on the solute atom concentration in the matrix solid solution C, we have put forward a picture which can explain fairly well the precipitation sequence during the LT-aging in the Al-Ag[10] and Al-Cu[11] alloys.

Based on the X-ray examination, we need not take into account any change of C due to the formation of the G-P zone; the change of concentration should be attributed only to the precipitation of the new phase.

For the present alloy, assuming the relation between the T_M-C curve and the solvus as shown in Fig. 8 (A), we can explain the experimental results that after some aging period of the LT-aging, the alloy attains a certain saturated state, where the G-P zone and the **T** phase coexist, the amount of each being fixed by the aging temperature.

For comparison, the relation between the T_M-C curve and the solvus for Al-Ag alloy is shown schematically in Fig. 8 (B), detailes of which have been described in the previous paper[10],[11].

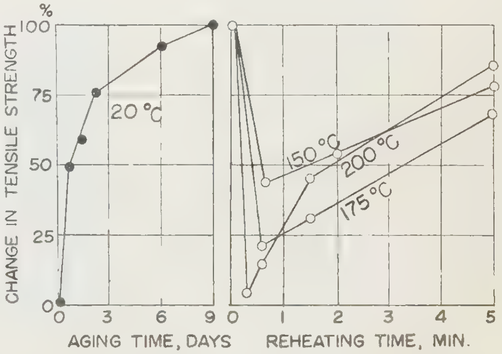

Fig. 7. Aging at Room Temperature, left; followed by Aging at Elevated Temperatures, right.

In Fig. 8 (A) and (B), the figure denoted by [1] represents the T_M-C curve in relation to the solvus in the equilibrium phase diagram. Characteristic feature of the T_M-C curve for the present alloy is that it intersects the solvus at the point corresponding to the temperature denoted by T_B.

The figure denoted by [2] represents the variation of C against the aging time, the aging temperature being chosen at T_A: after the incubation period, t_i, C_Q (the quenched value of C) begins to fall down due to the precipitation of the new phase, the final value C_R corresponds to the equilibrium state at the temperature, T_A, as shown in [1].

The figure denoted by [3] represents the change of the stability of the G-P zone against the aging time, which was derived from the figure [1] and [2], in the fashion as indicated by the dashed lines. If $T_M > T_A$, the G-P zone is stable, but if $T_M < T_A$, it is unstable. In the case of Al-Ag alloy, $T_M > T_A$ at the earlier stage of the LT-aging, but at the later stage it becomes that $T_M < T_A$, so the G-P zone must again disappear. Whilst, it will be noted that in the present alloy, if the aging temperature is lower than T_B, the G-P zone is stable evermore and can coexist indefinitely with the **T** phase, even at the final stage, since it holds always that $T_M > T_A$.

Similar examination has been carried out

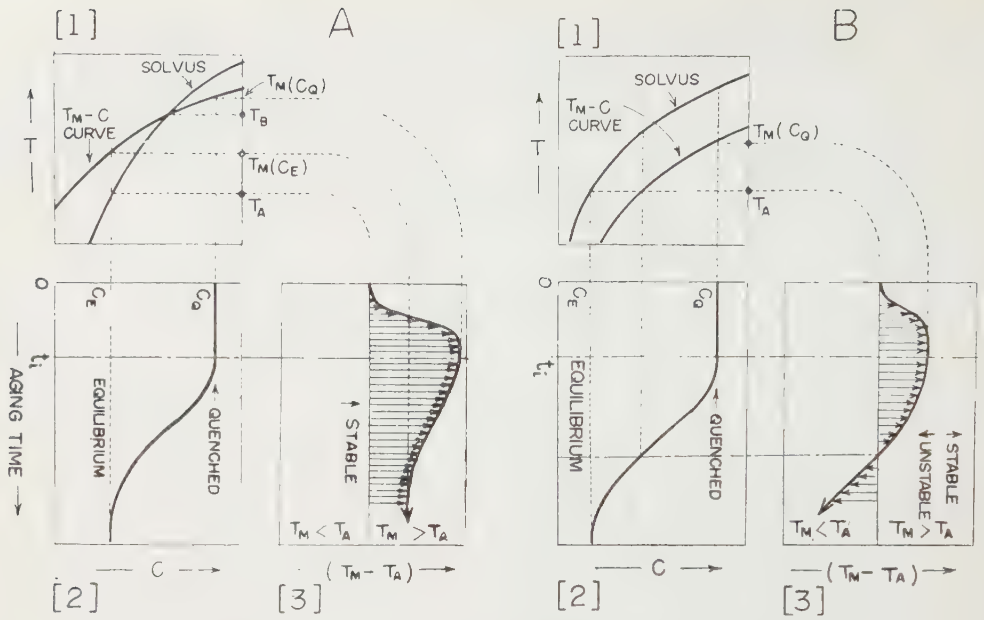

(A) Al–Zn–Mg (B) Al–Ag

Fig. 8. Change of the Stability of the G–P zone.

in magnesium rich Mg-Pb alloys[12]), the result reveals that the matter is just the same as in the present case.

Acknowledgements

The authors wish to express their cordial thanks to Mr. H. Maniwa and Mr. H. Sakai for helpful discussions.

The expense of this research has been defrayed from the Scientific Research Expenditure of Department of Education.

References

1) W. Köster and W. Wolf: Z. Metallkunde **28** (1936) 155.
2) W. Köster and W. Dullenkopf: ibid. **28** (1936) 309.
3) W. Köster and W. Dullenkopf: ibid. **28** (1936) 363.
4) F. Laves, L. Löhberg and H. Witte: Metallwirtschaft **14** (1935) 793.
5) A. Durer and W. Köster: Z. Metallkunde **30** (1938) 311.
6) W. Köster and K. Kam: ibid. **30** (1938) 320.
7) S. Nagasaki and Y. Takagi: J. Appl. Phys. Japan **17** (1948) 104.
8) N. Swindells and C. Sykes: Proc. Roy. Soc. **A 168** (1938) 237.
9) K. Hirano: J. Phys. Soc. Japan **8** (1953) 603.
10) K. Hirano and H. Sakai: J. Phys. Soc. Japan, **10** (1955), in press.
11) K. Hirano: *submitted to the* J. Inst. Metals, Japan.
12) K. Hirano, H. Maniwa and Y. Takagi: J. Phys. Soc. Japan, **10** (1955) 193.

JOURNAL OF THE PHYSICAL SOCIETY OF JAPAN Vol. 10, No. 3, MARCH, 1955

Precipitation from Solid Solution of Lead in Magnesium

By Ken-ichi HIRANO, Hideyo MANIWA
and Yutaka TAKAGI

Department of Physics, Tokyo Institute of Technology,
Oh-okayama, Meguro-ku, Tokyo

(Read October 19, 1953 and July 11, 1954; Received October 25, 1954)

The mechanism of precipitation from supersaturated solid solutions of lead in magnesium has been studied by means of calorimetric and electrical resistance measurements and of X-ray photographs with quenched and annealed alloys of various lead concentrations. The results reveal that the aging process is constituted from two discrete reactions. The first is the change in the matrix solid solution without decrease of the solute concentration, which corresponds to the formation of the *Complex* or the Guinier-Preston zone, and the second is the precipitation of the Mg_2Pb phase. It was concluded that the first is not the preparative one of the second. The upper limit temperatures of the existence region of the *Complex* were determined for various solute concentrations and shown in the phase diagram.

§ 1. Introduction

The solid solubility of Pb in Mg is rather less restricted. It decreases with decreasing temperature from about 7.75 atomic per cent at 465°C to about 5.20 atomic per cent at 400°C, 2.30 atomic per cent at 300°C and 0.5 atomic per cent at 200°C. This seems to be suitable for the study of the precipitation from supersaturated solid solution with the alloys of various solute concentrations.

Geisler, Barrett and Mehl[1] have studied the precipitation in this system and interpreted the results based on the simple nucleation and growth process. Recently the X-ray investigation has been carried out with single crystals by Nagashima and Nishiyama[2] and the presence of the platelets like the Guinier-Preston zone has been confirmed.

It seems that a further examination is required to see whether the G–P zone is the forerunner of the Mg_2Pb phase or not. We have carried out the calorimetric, electrical resistance and X-ray measurements and obtained some new data.

§ 2. Experimental Procedure

The alloys were made using high purity Mg with alloying additions of high purity Pb. Weighted quantities were melted together under KCl–NaCl (1:1) fluxes in a graphite crucible. After casting in an iron mold, the alloys were homogenized by annealing for about 50 hours at 500°C. The samples were solution-heat treated at 450°C for 2 hours at the end of which they were quickly quenched in the water of the room temperature. The slow cooled alloy was obtained by cooling the alloy at the rate of about 5°C per hour from 450°C to the room temperature. The methods of the measurements were described in the previous papers[3][4][5].

§ 3. Experimental Results

1. *S–T* Curves

In Fig. 1 (a), (b) and (c), the curves **D**, **E** and **F** show the specific heat *versus* temperature curves (***S–T*** curves) for 3.8 atomic per cent Pb alloy (about 25 weight per cent) after the aging treatments at 100°, 180° and 260°C respectively, the aging periods are described in the figure. The heating rate of the measurement was about 3°C per minute. **A** is the base line which has been calculated using the values of C_p for Mg and Pb assuming the alloy to be merely a mixture of them (Kopp-Neumann Rule). The **A**-line would be the ***S–T*** curve of the alloy if no change in atomic configuration were taking place. The curves **B** and **C** were obtained, respectively, with as quenched and slow cooled alloys. The curve **B** shows the heat evolution denoted by **X** at the temperature range between 180° and 280°C, which clearly is due to the precipitation of the Mg_2Pb phase. While at higher temperatures both **B** and **C** show the heat absorption denoted by **Y**, which is attributable to the resolution of the Mg_2Pb phase into the solid solution. The temperature where the heat absorption **Y** attains its maximum (in this case, 378°C), coincides fairly well with the value expected from the solvus curve proposed by Vosskühler[6], Foote and Jette[7], and Raynor[8].

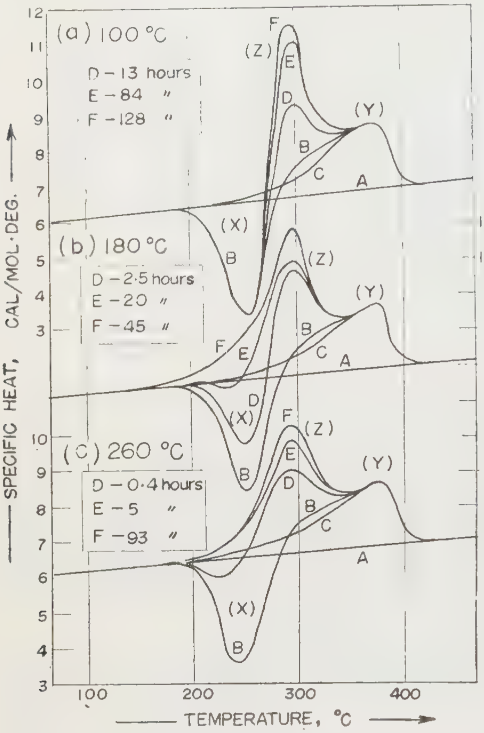

Fig. 1. Specific heat *versus* temperature curves for 3.8 atomic per cent Pb alloy.

D, **E** and **F** show additional heat absorption peaks denoted by **Z**, the maximum points of which lie at about 300°C. The quantity of this additional heat absorption increases with increasing aging period and shows the tendency to the saturation. In spite of the appearance of this additional heat absorption, about 340 cal./mol. at maximum, we could neither detect any corresponding change of the lattice spacing of the matrix nor find any additional lines due to a new phase by the X-ray powder method after 800 hours for 100°C-aging, 20 hours for 180°C-aging and 7 hours for 260°C-aging. Therefore, this additional heat absorption seems not to have its origin in the abnormality of the equilibrium solvus curve of the Mg_2Pb phase; if it were the case c-spacing of the matrix lattice should be decreased during the aging from 5,220 kX which is the value for as quenched alloy to less than 5.208 kX which is the equilibrium value at 300°C[9].

The additional heat absorption must be attributed to the dispersion of the ***Complex*** or the Guinier-Preston zone, which is the segregation of lead atoms in the matrix solid solution. This is rather similar to the observations in the low temperature-aged aluminium rich alloys such as Al–Ag[1], Al–Cu[10][11], Al–$Al_2Mg_3Zn_3$[5] and Al–$MgZn_2$[12] systems. For instance, in the low temperature-aged Al–Cu alloys, it has been recognized that Cu atoms segregate out on certain crystallographic planes of the parent crystal giving local Cu concentrations with local reduction of lattice spacing, although the mean lattice spacing remains unchanged[13][14][15].

2. ρ–T Curves

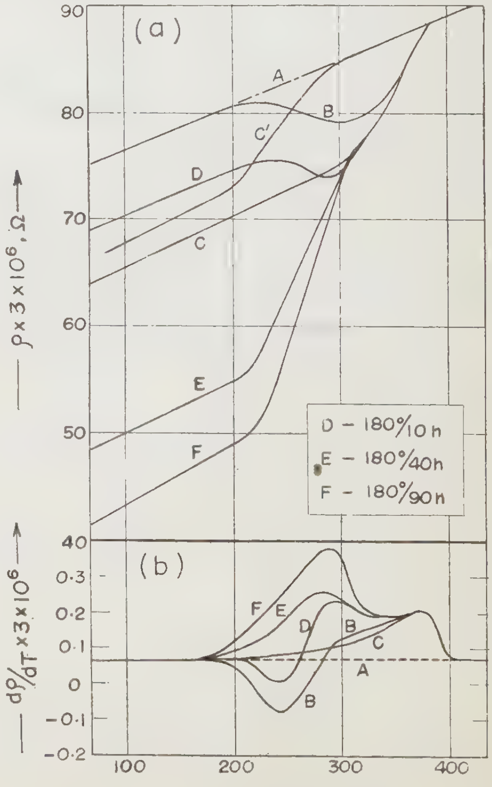

Fig. 2. Specific electrical resistance *versus* temperature curves.

Fig. 2 (a) represents the specific electrical resistance *versus* temperature curves obtained upon heating the same alloy as used in the case of Fig. 1, at the rate of 3°C per minute, after 180°C-aging. The aging periods are de-

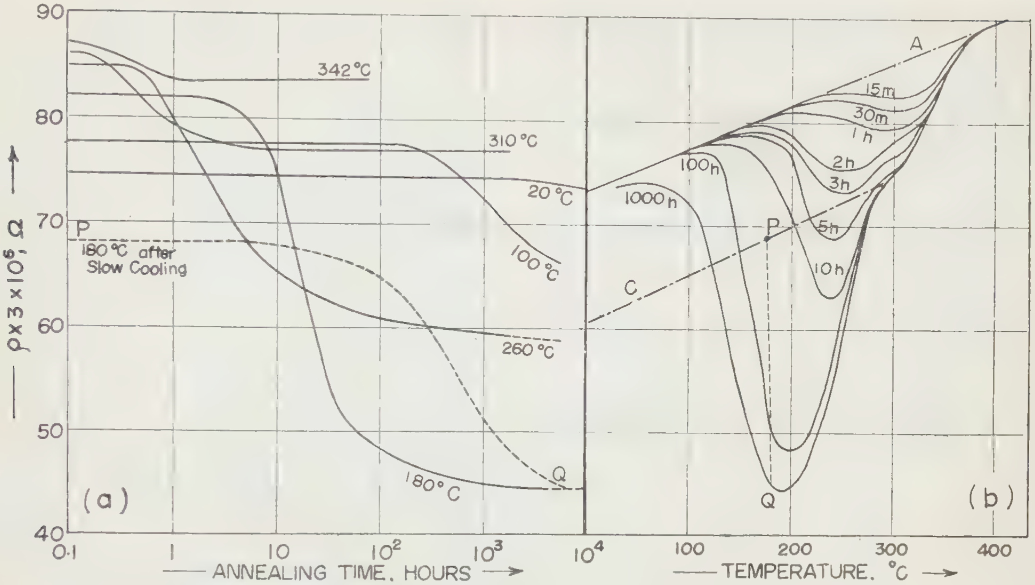

Fig. 3. (a) Isothermal aging curves. (b) Isochronal aging curves.

scribed in the figure which are somewhat different from those in Fig. 1 (b).

The curves **A, B, C, D, E** and **F** correspond respectively to the curves denoted by the same letters in Fig. 1 (b). The curve **C′** was obtained by cooling the alloy from 400°C at the rate of about 4°C per minute. A remarkable hysteresis between the curves **C** and **C′** was observed over the range between 400° and 240°C.

Fig. 2 (a) shows that both the formation of the *Complex* and the Mg_2Pb precipitation bring about the decrease of the electrical resistance of supersaturated solid solution, and that the effect of the former is more striking than that of the latter.

The values of $d\rho/dT$ were derived from the data shown in Fig. 2 (a) and were plotted against temperature in Fig. 2 (b). It may be noticed that a considerable similarity is existing between Fig. 1 (b) and Fig. 2 (b).

3. Isothermal Aging Curves

Fig. 3 (a) shows the isothermal aging curves of specific electrical resistance obtained by aging 3.8 atomic per cent Pb alloy at various temperatures. More or less, all curves show the tendency to decrease the value during the aging which may be attributed to the combined effect of the formation of the *Complex* and Mg_2Pb phase. To distinguish more clearly between the two effects, we have translate the data in Fig. 3 (a) into the isochronal curves showing electrical resistance *versus* temperature relations, as shown in Fig. 3 (b), where the nature of the two reactions is clearly distinguished. The outline of Fig. 3 (b) resembles that of Fig. 2 (a). The curves denoted by **A** and **C** in Fig. 3 (b), correspond respectively to the curves **A** and **C** in Figs. 1 and 2.

Using the values of the incubation period for lower aging temperatures, the activation energy for the formation of the *Complex* was estimated to be about 14600 cal./mol., on the other hand, we can roughly estimate the activation energy for the precipitation of Mg_2Pb in 20 weight per cent using the incubation periods determined by the X-ray work of Geisler, Barrett and Mehl, and the result obtained indicates that the value is about 28000 cal./mol.

4. Formation of the *Complex* in Slow Cooled Alloys

Fig. 4 shows the *S–T* curves of 2.8 atomic per cent (20 weight per cent) Pb alloy. The curve denoted by **A** was obtained by slow cooled alloy, while, further annealing the slow cooled alloy at 180°C for 1200 hours, we have obtained the curve denoted by **B**. Corresponding reaction in 3.8 atomic per cent Pb alloy was detected also by the electrical resistance measurement as shown by the dashed curve **PQ** in Fig. 3 (a) and by the dashed line **PQ** in Fig. 3 (b), where the electrical resistance of the slow cooled alloy decreases accompanied by the formation of the *Complex* during the subsequent prolonged annealing at 180°C. It has been recognized that the rate of the formation of the *Complex* in the slow cooled alloys is less than that in the quenched alloys and the incubation period in the former is more than 50 times longer than that in the latter.

Above fact may be an evidence for that formation of the *Complex* is not at all the preparative stage of the Mg_2Pb precipitation and the *Complex* can be formed in the matrix even after the Pb concentration of which decreases considerably due to the Mg_2Pb precipitation.

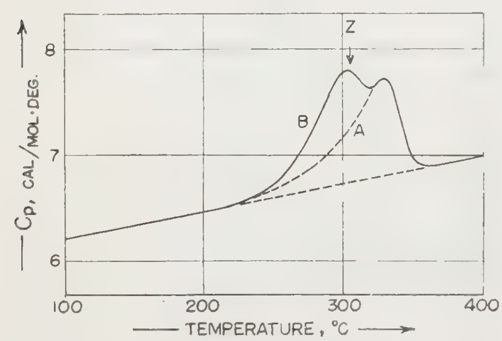

Fig. 4. Specific heat *versus* temperature curves for 2.8 atomic per cent Pb alloy.

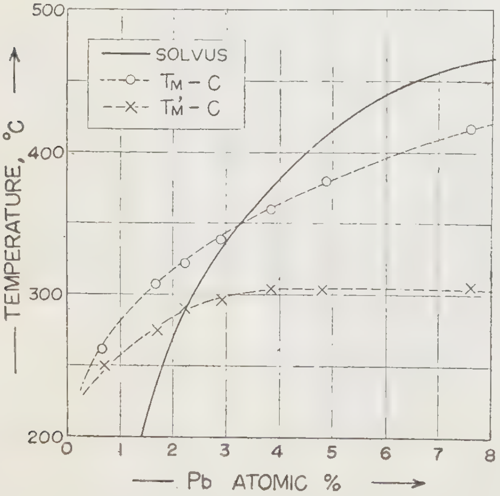

Fig. 5. Upper limit temperature of the existence region of the "Complex".

5. T_M-C Curve

We have carried out the calorimetric measurements on the alloys of various Pb concentrations and obtained the T_M-C curve as shown in Fig. 5, where T_M is the temperature where the additional heat absorption **Z** ends itself, which marks the upper limit temperature of the existence region of the *Complex*, and C is the solute concentration. It was detected that with the alloys containing more than about 4 atomic per cent of Pb, T_M increases up to the maximum value at the earlier period of aging, but at later stage of which T_M decreases accompanied by the precipitation of the Mg_2Pb phase. This show the sensitive dependence of T_M on the Pb concentration in the matrix solid solution. The maximum value of T_M among the observed values, for each alloy is shown plotted in Fig. 5. The solvus curve of the Mg_2Pb phase determined by Raynor and Vosskühler, is also shown in Fig. 5. It will be noticed that T_M-C curve intersects the solvus curve at the point which corresponds to about 3.3 atomic per cent of Pb and 350°C. Therefore, below about 350°C, in both as quenched and slow cooled alloys, the *Complex* may be always stable regardless of the existence or not of the Mg_2Pb phase.

In Fig. 5, T_M'-C curve is also shown, where T_M' is the temperature at which **Z** attains its maximum, this may be a measure of the stable size of the *Complex*.

§ 4. Remarks

Relating to other magnesium base alloys, it may be noted that Derge, Kommel and Mehl$^{16)}$ have shown that the mechanism of the high temperature aging is somewhat different from that of the low temperature aging, based upon the studies of the Widmanstätten structures of the quenched and annealed Mg-Sn alloys, the phase diagram of which is very similar to that of the present alloys$^{17)}$.

References

1) A. H. Geisler, C. S. Barrett and R. F. Mehl: Trans. A.I.M.E. **152** (1943) 201.
2) S. Nagashima and Z. Nishiyama: Memoirs of Inst. Sci. Ind. Res., Osaka University **11** (1954) 135.
3) K. Hirano: J. Phys. Soc. Japan **8** (1953) 603.
4) K. Hirano and H. Sakai: ibid, **10** (1955), in press.
5) K. Hirano and Y. Takagi: ibid, **10** (1955) 187.
6) H. Vosskühler: Z. Metallkunde **31** (1939) 109: Metall **4** (1950) 233.
7) F. Foote and E. R. Jette: Trans. A.I.M.E. **143** (1941) 124.

8) G. V. Raynor: J. Inst. Metals **66** (1940) 403.
9) G. V. Raynor: Proc. Roy. Soc. **A 180** (1942) 107.
10) N. Swindells and C. Sykes: Proc. Roy. Soc. **A 168** (1938) 237.
11) K. Hirano: Read at the Meeting of Phys. Soc. Japan at Osaka Univ., Oct. 31, 1954.
12) K. Hirano and Y. Takagi: Read at the Meeting of Japan Inst. of Metals at Ehime Univ. Oct. 24, 1954.
13) A. Guinier: Compt. rend. **206** (1938) 1641.
14) G. D. Preston: Proc. Roy. Soc. **A 167** (1938) 526.
15) J. M. Silcock, T. J. Heal and H. K. Hardy: J. Inst. Metals **82** (1954) 239.
16) G. Derge, A. R. Kommel and R. F. Mehl: Trans. A.I.M.E. **124** (1937) 367.
17) H. Vosskühler: Metallwirtschaft **20** (1941) 805; J. Inst. Metals, **66** (1940) 409.

JOURNAL OF THE PHYSICAL SOCIETY OF JAPAN Vol. 10, No. 3, MARCH, 1955

Crystal Structure and Phase Transition of Some Metallic Halides (III)

Structure Anomaly in α-Ag_2HgI_4

By Sadao HOSHINO

Tokyo Institute of Technology, Oh-okayama, Meguro, Tokyo, Japan

(Received October 20, 1954)

By a precise measurement by X-ray G–M spectrometer of reflexion intensities in α-Ag_2HgI_4, it was found that the relative intensity of Debye lines cannot be explained by zincblende type structure with disordered metallic atoms as was presumed previously by Ketelaar. The experimental result was explained by assuming the structure anomaly common to that has been proposed for certain other metallic halides (CuI, CuBr etc.) manifesting a similar peculiarity of line intensities. It was suggested that there may be correlation between the structure anomaly and the anomalously high ionic conductivity of this crystal.

§ 1. Introduction

It is well known that Ag_2HgI_4 crystal has two temperature modifications α and β with a phase transition at 52°C, and that the α-phase is accompanied by a large ionic conductivity. The phase transition and the crystal structures of this substance have been studied by Ketelaar[1]. He concluded that the phase transition would be of the order-disorder type analogous to the case of superstructures of alloys; that is, the β-phase has a pseudo-cubic tetragonal lattice with $a_0=c_0=6.32$Å, whereas the metallic atoms in the structure of the α-phase may be in a disordered state in such a way that one Hg and two Ag atoms are statistically distributed into four possible positions in a unit cell so that the structure as a whole becomes a cubic structure of zincblende type.

Frevel and North[2] recently observed a large number of weak extra Debye lines in the β-phase at room temperature, which suggested the presence of a superstructure with twice periods of both the a and c spacings. On the other hand, no reexamination has not been given concerning the crystal structure of the α-phase.

The present author performed the X-ray structure analysis on the α-phase of Ag_2HgI_4 by using powder samples, and obtained a slightly different result from that of Ketelaar. In this paper, the experimental result and discussions on certain kind of structure anomaly, which is noted to exist commonly in α-Ag_2HgI_4 and in some other metallic halide crystals, will be given.

§ 2. Sample

On the method of preparation of Ag_2HgI_4, it was pointed out[3] that a reaction in solution yields better results than solid state reaction. So, we applied the reaction by precipitation from aqueous solutions containing stoichiometric amounts of reactants as follows:

$K_2HgI_4aq.+2AgNO_3aq.\rightarrow Ag_2HgI_4\downarrow+2KNO_3aq.$

The solution of K_2HgI_4 was prepared from mercuric chloride and potassium iodide. The precipitate was repeatedly washed by hot water and desiccated, and then was formed in a plate of about 1 mm. thickness for X-ray measurement.

§ 3. Experiment

Debye photographs were taken at various temperatures covering the both phases of Ag_2HgI_4. Diagrams taken with a rod sample at room temperature showed that the lattice of β-Ag_2HgI_4 is body centered tetragonal with $a=a_0=6.32_4$Å and $c/a=2.00$, which is differing from either of those given by Ketelaar and by Frevel and North*. The higher the temperature in this phase region the weaker becomes the intensities of the super-structure lines. At 60°C in the α-phase region, the superstructure lines were no longer observed. The diagram showed that the structure of α-Ag_2HgI_4 has a face centered cubic lattice with $a=6.32$Å.

We have then performed a precise intensity measurement by a G-M X-ray spectrometer with a plate sample and a crystal-monochromated CuKα radiation. Plate sample and G-M tube were moved simultaneously so as to keep the position of symmetric reflexion. The observed intensity values, I_{obs}, of the several reflexion lines are given in Table I by a scale which makes the intensity of (111) equal to 1000. In this measurement accidental errors were about 3~5% for stronger lines and 10~20% for weaker lines.

§ 4. Interpretation of Experimental Result

In the first place, the structure of α-Ag_2HgI_4 proposed by Ketelaar — the structure of the zincblende type in which the metal atoms are thought to assume the completely disordered distribution — was reexamined by the present experimental result. In the calculation according to this model, $\frac{1}{3}(2f_{Ag}+f_{Hg})$ was used as a mean scattering factor of all of metal atoms. The result is shown by I_{cal} (1) in the third column in Table 1. There is noticed a disagreement between the observation and the calculation. Namely, the observed intensities of (200), (222) and (420) have larger values than the calculated ones. Similar kind of disagreement of line intensities has been formerly found also in the cases of CuI and CuBr, as was reported in Part I[4] and Part II[5] of this series. For CuI and CuBr this anomalous disagreement has been formally explained either by assuming different Debye temperature factors for iodine and metal atoms (the first assumption), or by supposing the presence of four metastable positions tetrahedrally surrounding every normal metal position ($\frac{1}{4}\ \frac{1}{4}\ \frac{1}{4}$ and its equivalent sites for the cubic ZnS type lattice) (the second assumption). Similar interpretations may be also applied in the case of α-Ag_2HgI_4.

Table I. The observed and calculated intensities for the several reflexions of α-Ag_2HgI_4.

hkl	I_{obs}	I_{cal} (1)	I_{cal} (2)	I_{cal} (3)	I_{cal} (4)
111	1000	1000	1000	1000	1000
200	28	9	25	25	116
220	613	780	543	555	941
311	294	476	279	300	331
222	13	2	11	12	21
400	47	126	49	46	102
331	68	215	76	63	100
420	16	3	18	23	22
422	75	369	97	92	233
511 333	26	161	35	26	50

By the first assumption of different Debye temperature factors $\exp[-M(\sin\theta/\lambda)^2]$ for the halogen and metal atoms, the best agreement of line intensities was obtained when we put $M_I=4$ and $M_{met}=9$, as shown in the fourth column ($I_{cal}(2)$) of Table I. We have next calculated the intensities according to the second assumption. It was assumed that $\delta=0.45$Å and $M_I=M_{met}=4$, and that every metallic atom occupys the four positions with an equal probability, where δ is the deviation of these positions from the ideal sites of metal atoms in the zincblende type structure (see Fig. 8 of Part I). It is seen that the result of this assumption ($I_{cal}(3)$ in the fifth column of Table I) gives an agreement as good as that due to the first assumption.

---

* Our detailed result will be published elsewhere.

Though a good agreement between the observation and the calculation was thus obtained, it must be noted that the above explanations of the intensity anomaly are only formal, and are by no means without objections. Namely, in the first assumption the use of very large temperature factor $M_{met}=9$ seems to be outside the scope of the Debye theory of temperature effect, which deals only with small thermal vibrations of atoms. Concerning the second assumption, it is not quite convincing whether the four stable positions of the metal atom assumed above may actually exist in the lattice. Moreover, the magnitude of 4 of Debye factor, chosen for iodine or metal atoms by both the assumptions to explain the rapid decrease of intensities with increasing scattering angle, is still large, though this may be explained as follows: since in the α-Ag_2HgI_4 there are only three metal atoms to fill the four equivalent positions, hence remaining positions are left vacant statistically, there might be provoked an irregular lattice distorsion, which results in a rapid intensity decrease with scattering angle in a manner similar to that due to the effect of thermal vibration.

Apart from these questionable points, we can point out the fact that the two assumptions are common in implying that the spatial distribution of metallic atom considered as spatial or time average has a finite extension arround the normal lattice sites, $\frac{1}{4}\,\frac{1}{4}\,\frac{1}{4}$ and its equivalent positions. This is the reason why the two assumptions resulted in the similar line intensities what are in agreement with observation. Then, the following assumption can also be another possible explanation of the anomaly. That is to assume an asymmetric anharmonic thermal vibration of metallic atoms which is especially vigorous towards four [111] directions, as was formerly suggested by Matsubara[6] in a theory of lattice energy and entropy change at the phase transitions of CuI crystal. According to this assumption, the mean position of metallic atom will deviate from the normal position at high temperatures, and hence the intensity anomaly will be explained as same as in the former cases. This explanation seems to be physically quite probable, though no decisive evidence can be given by the present X-ray data alone.

§5. Discussion

The X-ray intensity anomaly which can be explained by similar basis to the case of α-Ag_2HgI_4 has been formerly found in the many other metallic halides, for example, $\gamma\sim\alpha$-CuI[3], γ-CuBr[4], CuCl*, α-Cu_2HgI_4* (cubic ZnS type lattice), β-CuBr[4], β-AgI[7] (hexagonal ZnO type lattice) and α-CuBr[4], α-AgI[8] (body centered cubic or tetragonal lattice). As all of these substances are known to have anomalously high ionic conductivities at high temperatures, it may be reasonable to conceive that certain correlations exist between the ionic conduction of these crystals and their intensity anomalies.

We can tentatively suppose that there exist channels along which the metallic atoms may move more or less easily within the lattice; these channels may be along tetrahedral direction ([111] and its equivalents for cubic crystals) through the normal sites of metal atoms. This, then, amounts to assume that the potential for metallic atoms is comparatively flat in all portions along these channels, and which may be taken as an illustration of the assumption of the large asymmetric anharmonic thermal vibrations of metallic atoms as was proposed in the previous section to explain the intensity anomaly.

It has been sometimes supposed concerning some metallic halide crystals that their *averaged structures* having interstitial metallic atoms are essential to the high ionic conductivity. Krug and Sieg[9] has recently interpreted the X-ray intensity anomaly in CuI and CuBr by assuming the migration of metal atoms from the ideal position of the zincblende type lattice to interstitial sites corresponding to the NaCl type lattice sites with larger probabilities at higher temperatures. They considered that such averaged structure will intimately correlated with the high ionic conductivities of these crystals. If this is the case, the similar interpretation may probably be applied also in the present case of α-Ag_2HgI_4. We have calculated the intensity by this model, but the quantitative agreement with the observed intensities could not be obtained whatever proportion of the distribution of metal atoms to the NaCl lattice sites was assumed. The sixth column ($I_{cal}(4)$) of

---

* Unpublished results in our labolatory.

Table I illustrates an example of such calculation, where the contribution of metal atoms to the NaCl lattice sites is chosen as 20% of whole number of metal atoms and the temperature factors M_I and M_{met} are both chosen as 4.* There are also another presumable interstitial sites in the zincblende type lattice, namely the sites of CaF_2 type lattice, but such lattice sites can also not explain the anomalous intensity increase of (200), (222), (420) etc.

In spite of a close analogy between the structure of α-Ag_2HgI_4 and those of other metallic halides (CuI, CuBr etc.), it should be pointed out here that α-Ag_2HgI_4 (and also α-Cu_2HgI_4) is specially compared with other halides because of the presence of the positive ion vacancies in the lattice. Such vacancies might have some contribution to the ionic conduction of this crystal.

In conclusion the author wishes to express his best thanks to Prof. S. Miyake for his kind guidance in the course of the work.

This work was supported by a Grant in Aid for Fundamental Scientific Research from the Ministry of Education.

References

1) J. A. A. Ketelaar: Z. Krist., **80** (1931) 190; **87** (1934) 436. Z. physik. Chem. **B 26** (1934) 327. Trans. Faraday Soc. **34** (1938) 874.
2) L. K. Frevel and P. P. North: J. App. Phys. **21** (1950) 1038.
3) S. Miyake, S. Hoshino and T. Takenaka: J. Phys. Soc. Japan **7** (1952) 19.
4) S. Hoshino: J. Phys. Soc. Japan **7** (1952) 560.
5) L. Suchow and P. H. Keck: J. A. C. S. **75** (1953) 518.
6) T. Matsubara: Lecture in the Annual Meeting of the Phys. Soc. Japan held at Kyoto on Nov. 2, 1952.
7) L. Helmholz: J. Chem. Phys. **3** (1935) 740.
8) S. Hoshino: J. Phys. Soc. Japan **9** (1954) 295. L. W. Strock: Z. physik. Chem. **B 25** (1934) 441: **B31** (1936) 132.
9) J. Krug and L. Sieg: Z. fur Naturforschung **7a** (1952) 369; Private communication from J. Krug.

---

* We performed the intensity calculations by a similar model in the cases of CuCl, CuBr and CuI, but failed it in any cases in obtaining agreements between the calculated and the observed intensities in our experiments.

JOURNAL OF THE PHYSICAL SOCIETY OF JAPAN Vol. 10, No. 3, MARCH, 1955

Application of the Alternant Orbital Method to Benzene

By Takashi ITOH and Hiroyuki YOSHIZUMI
Department of Physics, Faculty of Science,
University of Tokyo, Tokyo

(Received October 12, 1954)

An improvement on the molecular orbital method is made by taking into account the correlation between the motions of electrons with opposite spin. For this purpose electrons with plus spin are assigned to orbitals which are somewhat localized at alternate atoms in molecules, while electrons with the minus spin are assigned to orbitals localized at the remaining atoms. With the use of these alternant orbitals the wave function with a given multiplicity and spatial symmetry can be constructed.

The method is applied to the π-electron system of the ground state of benzene and the results are compared with those obtained by the method of configuration interaction (C.I.). The energy depression obtained by the present method is 2.35 eV while that by C.I. is 2.7 eV. The inner product of these two wave functions is 0.985, which shows that the present method is a very satisfactory approximation to the C.I. calculation.

§ 1. Introduction

In many molecules the electronic wave function of the ground state is approximately given by a single determinant constructed from molecular orbitals each doubly occupied by electrons of opposite spin. The greatest shortcoming of such a determinantal wave function is found in its incapability of taking into account the correlation between the motions of different electrons, as has been discussed by many authors. There is some correlation between electrons of the same spin introduced by the exclusion principle, because it prevents the electrons of the same spin from being at the same place in any stationary state. But electrons of opposite spin move around in the field of the molecule independently of each other, and the influence of the electrostatic repulsion which tends to keep them apart is not incorporated in the ASMO wave function.

For example, in hydrogen molecule the single determinant constructed by assigning two electrons of opposite spin into the symmetric molecular orbital does not give a satisfactory approximation to the ground state wave function. Coulson and Fischer1) tried to remedy this defect by assigning the two electrons into different orbitals which are semi-localized on each hydrogen atom. The calculation was further somewhat modified by Mueller and Eyring2), who also applied the same method to hydrogen fluoride3). Hurley, Lennard-Jones, and Pople4) recently developed a theory of paired electron method, which is an extension of the semi-localized orbital method to the case of general polyatomic saturated molecules, in which the total wave function can be decomposed to wave functions for single bonds. Just the same method was applied by Schmid5) to the calculation of the cohesive energy of diamond which has a covalent structure.

In the case of non-localized bond such as in benzene, however, the semi-localized orbital method is not directly applicable, and some extension is necessary. Such an extension has been suggested by Löwdin6); he devised the so called *alternant orbital* method, which is applicable to metals, alternant hydrocarbons and any other alternant systems. In his method, electrons with plus spin are assigned to orbitals which have large amplitude at every alternate atom and small amplitude at the remaining atoms, while electrons with minus spin are assigned to orbitals whose amplitude change alternately but reversed to the former ones. In this way the tendency of electrons with opposite spin to keep apart from each other on account of the electrostatic force is incorporated in the wave function, and a better approximation to the true solution is attained.

In this paper, the alternant orbital method of Löwdin is applied to the simplest aromatic hydrocarbon, benzene. This molecule is particularly interesting since it is the representative of all the aromatic molecules. Furthermore, since an almost complete investigation of the C.I. has been performed for this molecule by Parr, Craig, and Ross⁷⁾, the degree of the success of the alternant orbital method can be measured by comparing our results with theirs.

§ 2. Alternant Orbital

We consider the alternant system in the sense of Coulson⁸⁾, that is, the alternant system is defined as a system in which all the atoms can be classified into two kinds such that neighbouring atoms always belong to different kinds. For example, aromatic hydrocarbons which contain no odd-membered rings and metals which have simple cubic or body-centered cubic lattices enter into this category.

As an example, we take a hypothetical cyclic hydrocarbon $C_{2n}H_{2n}$ which has recently been investigated by Moffitt⁹⁾ with the use of a simple molecular orbital method. We consider the $2p\pi$ orbitals of the $2n$ membered carbon ring, and construct the $2n$ mutually orthogonal orbitals

$$\phi_l=(2n\sigma_l)^{-1/2}\sum_{k=1}^{2n}\exp\frac{2\pi ilk}{2n}U_k$$
$$(l=1,2,\cdots\cdots,2n), \tag{1}$$

where U_k is the $2p\pi$ atomic orbitals at the kth carbon atom and $(2n\sigma_l)^{-1/2}$ is the normalization factor.

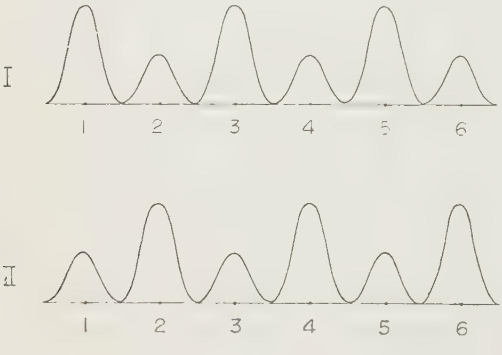

Fig. 1. Shapes of I- and II-type orbitals.

The above orbital functions have equal amplitude at all the carbon atoms. In order to take into account the correlation between orbitals of opposite spins, however, it will be adequate to assign electrons with plus spin into orbitals which are somewhat localized on every alternate atoms and electrons with minus spin into orbitals localized on the remaining atoms. Such orbitals have been constructed by Löwdin by taking the following linear combinations of the molecular orbitals:

$$\phi_{l\text{I}}=\cos\theta\,\phi_l+\sin\theta\,\phi_{l+n}\,, \tag{2a}$$
$$\phi_{l\text{II}}=\cos\theta\,\phi_l-\sin\theta\,\phi_{l+n}\,, \tag{2b}$$

in which θ is a parameter$\leq\pi/4$. These orbital functions have large and small amplitudes at the alternate atoms. They are called *alternant orbitals*. The maximum and minimum of amplitudes are reversed for I- and II-type orbitals. The amplitudes of these orbitals are illustrated schematically in Fig. 1.

Now we consider the special example, benzene. In this case $n=3$, and in the usual MO method, which corresponds to the choice $\theta=0$, the orbitals $l=0$, ±1 are assumed to be occupied in the ground state. We now assume that, in the ground state of the benzene molecule the orbitals $\phi_{0\text{I}}$, $\phi_{1\text{I}}$, and $\phi_{-1\text{I}}$ are occupied by three electrons with plus spin and the orbitals $\phi_{0\text{II}}$, $\phi_{1\text{II}}$, and $\phi_{-1\text{II}}$ are occupied by electrons with minus spin, θ being regarded as a variational parameter to be determined so as to minimize the energy of the system.

§ 3. Spin Coupling

The single determinantal wave function

$$\Psi_0(\theta)=\sum_{\text{P}}(-1)^{\text{P}}\text{P}\phi_{0\text{I}}(1)\phi_{1\text{I}}(2)\phi_{-1\text{I}}(3)$$
$$\times\phi_{0\text{II}}(4)\phi_{1\text{II}}(5)\phi_{-1\text{II}}(6)\chi_0\,, \tag{3}$$
$$\chi_0=\alpha_1\alpha_2\alpha_3\beta_4\beta_5\beta_6\,, \tag{4}$$

constructed by assigning three electrons with plus spin into three lowest I-type orbitals and three electrons of minus spin into three lowest II-type orbitals does not give a singlet state. Actually this wave function represents a mixture of a singlet and higher spin states.

The singlet functions can be constructed, for example, by the method of representation matrices of permutation group, or by the use of the spin operator method of Pratt¹⁰⁾ as extended by Löwdin¹¹⁾. The outline of the former method is given in the Appendix. There are five singlet states for the six electron system as shown in the branching diagram of Fig. 2. Of these five singlet states, (a), (b), and (c) belong to the spatial symmetry

A_{1g}, while (d) and (e) give rise to one A_{2g} and one B_{2u} states. It is interesting to note that these wave functions belong to the irreducible representations of the point group D_{6h}, in spite of the fact that the individual orbital functions do not.

Now there are three ${}^1A_{1g}$ states (a), (b), and (c). It would be interesting to see which one of these three singlets has the lowest energy, or to determine the best linear combination of them. But from a view point of the physical meaning, the state (a) is expected to be the best one on the following reason. The state (a) is a combination of two three-electron systems, each with spin 3/2, so that spins of three electrons in the I-type orbitals are parallel, and spins of three electrons in the II-type orbitals are also parallel. This means that the correlation between electrons in the same type orbitals is automatically introduced by the exclusion principle. Moreover the correlation between electrons in the I-type orbitals and electrons in the II-type orbitals are also taken into account by the semi-localization property illustrated in Fig. 1. Thus the correlations between every possible pair of different electrons are incorporated in this state, so that this is expected to yield the lowest energy. The spin function for this state is given by

$$\begin{aligned}\chi_a=&(1/2)\alpha_1\alpha_2\alpha_3\beta_4\beta_5\beta_6\\ &-(1/6)(\beta_1\alpha_2\alpha_3+\alpha_1\beta_2\alpha_3+\alpha_1\alpha_2\beta_3)\\ &\qquad\times(\alpha_4\beta_5\beta_6+\beta_4\alpha_5\beta_6+\beta_4\beta_5\alpha_6)\\ &+(1/6)(\alpha_1\beta_2\beta_3+\beta_1\alpha_2\beta_3+\beta_1\beta_2\alpha_3)\\ &\qquad\times(\beta_4\alpha_5\alpha_6+\alpha_4\beta_5\alpha_6+\alpha_4\alpha_5\beta_6)\\ &-(1/2)\beta_1\beta_2\beta_3\alpha_4\alpha_5\alpha_6\ .\end{aligned}\tag{5}$$

When the spin function χ_0 in (3) is replaced by χ_a, we have the total wave function $\Psi_a(\theta)$.

§ 4. Energy Depression

The Hamiltonian of the six π-electron system of benzene is

$$\mathscr{H}=\mathscr{H}_o+\mathscr{H}_r\ ,\tag{6}$$

where the orbital part

$$\mathscr{H}_o=\sum_{i=1}^{6}\left(-\frac{\hbar^2}{2m}\Delta_i+V_i\right),\tag{7}$$

and the inter-electronic repulsion part

$$\mathscr{H}_r=\sum_{i>j}^{6}\frac{e^2}{r_{ij}}\ .\tag{8}$$

The expectation value of energy is

$$\begin{aligned}E(\theta)&=\frac{\int\Psi^*(\theta)\mathscr{H}\Psi(\theta)d\tau}{\int\Psi^*(\theta)\Psi(\theta)d\tau}\\ &=\frac{\int\Psi^*(\theta)\mathscr{H}_o\Psi(\theta)d\tau}{\int\Psi^*(\theta)\Psi(\theta)d\tau}+\frac{\int\Psi^*(\theta)\mathscr{H}_r\Psi(\theta)d\tau}{\int\Psi^*(\theta)\Psi(\theta)d\tau}\\ &=E_o(\theta)+E_r(\theta)\ .\end{aligned}\tag{9}$$

$E_o(\theta)$ and $E_r(\theta)$ can be expressed in terms of one and two electron integrals as follows:

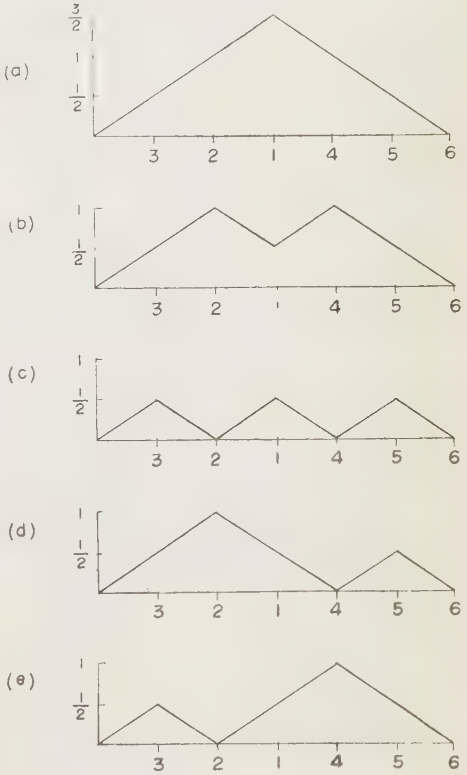

Fig. 2. Five singlet states for six electron system. (Spins of electrons are composed in the order 3, 2, 1, 4, 5, 6, since this order is most convenient from the view point of the spatial symmetry of of the orbitals.)

$$\begin{aligned}E_o(\theta)=\frac{1}{N}[&2(\mathcal{E}_0+2\mathcal{E}_1)(3+\cos 2\theta+2\cos^2 2\theta+2\cos^3 2\theta+\cos^4 2\theta+3\cos^5 2\theta)\cos^2\theta\\ &+2(\mathcal{E}_3+2\mathcal{E}_2)(3-\cos 2\theta+2\cos^2 2\theta-2\cos^3 2\theta+\cos^4 2\theta-3\cos^5 2\theta)\sin^2\theta]\ ,\end{aligned}\tag{10}$$

$$E_r(\theta)=\frac{1}{N}[\{4(\gamma_{00}+6\gamma_{01}+5\gamma_{11}-2\delta_{01}-\delta_{1-1})(1+\cos^4 2\theta)$$

$$
\begin{aligned}
&\quad +4(4\gamma_{01}+2\gamma_{11}-4\delta_{01}-2\delta_{1-1})(\cos 2\theta+\cos^3 2\theta)\\
&\quad +4(\gamma_{00}+4\gamma_{01}+4\gamma_{11})\cos^2 2\theta\}\cos^4\theta\\
&+\{4(\gamma_{03}+8\gamma_{12}+6\gamma_{02}+6\gamma_{13}-3\delta_{03}-6\gamma_{12}-2\delta_{02}-2\delta_{13}-2\delta_{1-2}-4\xi-4\eta-8\zeta^{01}_{23}-8\zeta^{02}_{13})\\
&\quad -8(\delta_{03}+2\delta_{12}+2\eta+4\zeta^{02}_{13})\cos^2 2\theta\\
&\quad -4(\gamma_{03}+8\gamma_{12}+6\gamma_{02}+6\gamma_{13}+\delta_{03}+2\delta_{12}-2\delta_{02}\\
&\quad -2\delta_{13}-2\delta_{1-2}-4\xi+4\eta-8\zeta^{01}_{23}+8\zeta^{02}_{13})\cos^4 2\theta\}\cos^2\theta\sin^2\theta\\
&+\{4(\gamma_{33}+6\gamma_{32}+5\gamma_{22}-2\delta_{23}-\delta_{2-2})(1+\cos^4 2\theta)\\
&\quad -4(4\gamma_{23}+2\gamma_{22}-4\gamma_{23}-2\delta_{2-2})(\cos 2\theta+\cos^3 2\theta)\\
&\quad +4(\gamma_{33}+4\gamma_{23}+4\gamma_{22})\cos^2 2\theta\}\sin^4\theta]\,, \qquad (11)
\end{aligned}
$$

$$N=3(1+\cos^2 2\theta+\cos^4 2\theta+\cos^6 2\theta)\,, \qquad (12)$$

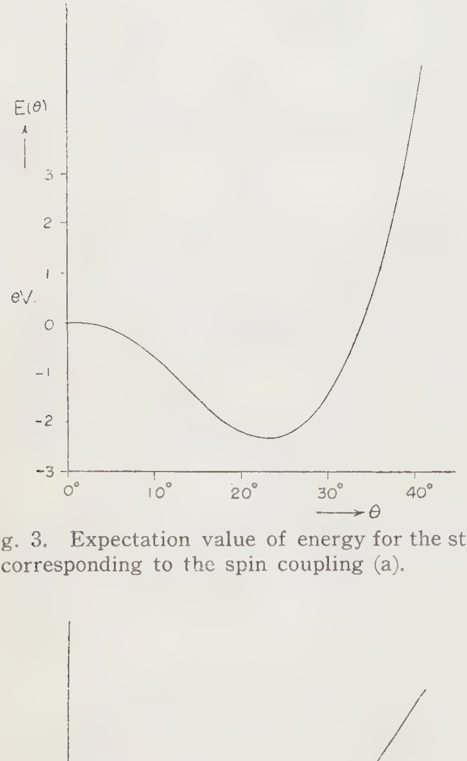

Fig. 3. Expectation value of energy for the state corresponding to the spin coupling (a).

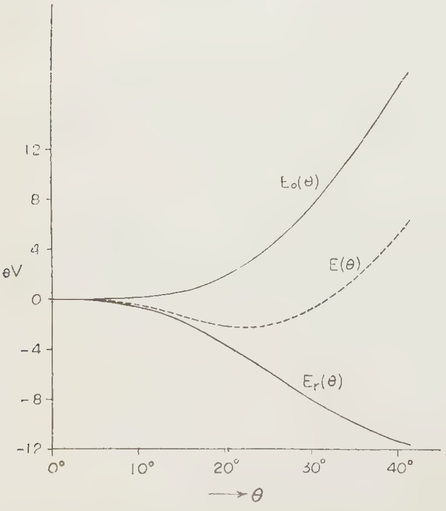

Fig. 4. Orbital part $E_o(\theta)$ and inter-electronic repulsion part $E_r(\theta)$ of the total energy $E(\theta)$.

where ε and γ, δ, ζ are one and two electron integrals defined and tabulated by Parr, Craig, and Ross[7].

The value of $E(\theta)$ is plotted in Fig. 3 as a function of θ. At $\theta=0$ the curve converges to a point which corresponds to the single determinant of usual molecular orbitals. The minimum of the curve lies at $\theta=23°$, where the energy depression, as compared to $\theta=0$, is 2.35 eV. The energy depression of 2.35 eV is a very satisfactory one, since the energy depression resulting from the extensive configuration interaction calculation performed by Parr, Craig, and Ross is 2.7 eV.

In Fig. 4 the orbital part $E_o(\theta)$ and the inter-electronic repulsion part $E_r(\theta)$ of the total energy $E(\theta)$ for the spin coupling (a) is plotted separately against θ, from which we can see that $E_r(\theta)$ decreases with θ, while $E_o(\theta)$ remains nearly constant up to $\theta=15°$ and then increases rapidly. This figure shows clearly how the inter-electronic repulsion energy is diminished by the use of alternant orbitals, which take into account the correlation between electrons with opposite spin.

§ 5. Relation to Configuration Interaction

It will be worth while to compare the wave function corresponding to the spin coupling (a), namely $\Psi_a(\theta)$, with the wave function obtained by C.I. For this purpose the former wave function was expanded as a linear combination of the usual configuration functions, the coefficients of which are shown in the second column of Table I. The values of coefficients for the optimum value of $\theta=23°$ are shown in the third column. The coefficients for the wave function of C.I. are also given in the fourth column for the sake of

Table I. Expansion of $\Psi_a(\theta)$ and $\Psi_{\text{C.I.}}$ in terms of configuration functions.

No.	${}^1A_{1g}$ configuration functions	$\Psi_a(\theta)$	$\Psi_a(23°)$	$\Psi_{\text{C.I.}}$
(1)	$\Psi_1=(\phi_0^2\phi_1^2\phi_{-1}^2)$	$\cos^6\theta\sigma(\theta)$ *	0.900	0.910
(2)	$\Psi_2=(\phi_0^2\overline{\phi_1\phi_{-1}}\,\overline{\phi_2\phi_{-2}})$	$\cos^4\theta\sin^2\theta\sigma(\theta)$	0.162	0.210
(3)	$\Psi_3=\frac{2}{\sqrt{3}}(\phi_0^2\underline{\phi_1\overline{\phi_{-1}\phi_2\phi_{-2}}})-\sqrt{\frac{1}{3}}(\phi_0^2\overline{\phi_1\phi_{-1}}\,\overline{\phi_2\phi_{-2}})$	$\sqrt{\frac{1}{3}}\cos^4\theta\sin^2\theta\sigma(\theta)$	0.094	0.142
(4)	$\Psi_4=(\phi_0^2\overline{\phi_1\phi_{-1}}\phi_3^2)$	0	0.000	0.052
(5)	$\Psi_5=(\phi_1^2\phi_{-1}^2\overline{\phi_2\phi_{-2}})$	0	0.000	-0.056
(6)	$\Psi_6=(\phi_1^2\phi_{-1}^2\phi_3^2)$	$-\cos^4\theta\sin^2\theta\sigma(\theta)$	-0.162	-0.059
(7)	$\Psi_7=\sqrt{\frac{1}{2}}(\phi_0^2\phi_1^2\phi_2^2)+\sqrt{\frac{1}{2}}(\phi_0^2\phi_{-1}^2\phi_{-2}^2)$	$-\sqrt{2}\cos^4\theta\sin^2\theta\sigma(\theta)$	-0.229	-0.227
(8)	$\Psi_8=\sqrt{\frac{1}{2}}(\overline{\phi_0\phi_1^2\phi_{-1}}\,\overline{\phi_2\phi_3})+\sqrt{\frac{1}{2}}(\overline{\phi_0\phi_1}\phi_{-1}^2\overline{\phi_{-2}\phi_3})$	$\sqrt{2}\cos^4\theta\sin^2\theta\sigma(\theta)$	0.229	0.204
(9)	$\Psi_9=\sqrt{\frac{2}{3}}(\underline{\phi_0\phi_1^2\overline{\phi_{-1}\phi_2\phi_3}})+\sqrt{\frac{2}{3}}(\underline{\phi_0\overline{\phi_1\phi_{-1}^2\phi_{-2}\phi_3}})$ $-\sqrt{\frac{1}{6}}(\overline{\phi_0\phi_1^2\phi_{-1}}\,\overline{\phi_2\phi_3})-\sqrt{\frac{1}{6}}(\overline{\phi_0\phi_1}\phi_{-1}^2\overline{\phi_{-2}\phi_3})$	$\sqrt{\frac{2}{3}}\cos^4\theta\sin^2\theta\sigma(\theta)$	0.132	0.069
(10)	Ψ_{10}	⋮	⋮	⋮
⋮	⋮	⋮	small	0
(22)	Ψ_{22}	⋮	⋮	⋮

* $\sigma(\theta)=2(1+\cos^2 2\theta+\cos^4 2\theta+\cos^6 2\theta)^{-1/2}$.

comparison. It can be seen that these two sets of coefficients are fairly close to each other. A measure of the resemblance is given quantitatively by the inner product

$$I(\theta)=\int\Psi_a^*(\theta)\Psi_{\text{C.I.}}d\tau\ , \tag{13}$$

where $\Psi_{\text{C.I.}}$ is the wave function in C.I. method. The value of $I(\theta)$ is plotted against θ in Fig. 5, which takes a maximum value at $\theta=21°$, the maximum value being about 0.985. For $\theta=0$, $I(0)=0.910$. Thus, the position of maximum of $I(\theta)$ is nearly coincident with the minimum position of $E(\theta)$, and $I(\theta)$ is very close to unity here. This result serves as a valuable check for the calculation.

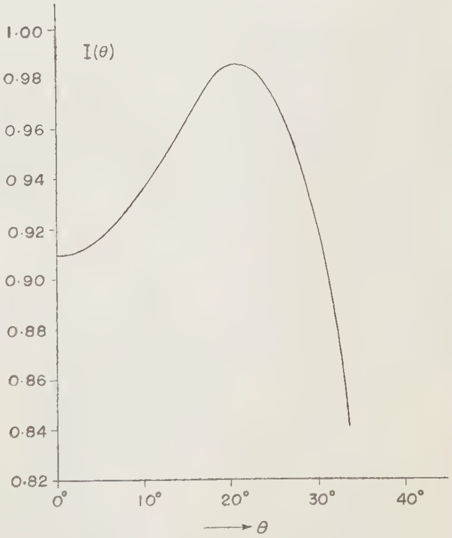

Fig. 5. Inner product between $\Psi_a(\theta)$ and $\Psi_{\text{C.I.}}$.

§ 6. Discussion

The alternant orbital method has been applied to the π-electron system in the ground state of the benzene molecule. It has been shown that the correlation between electrons of opposite spin can be satisfactorily taken into account by using alternant orbitals which are more or less localized on alternate atoms in the molecule. The merit of this method is that one can obtain a good approximation to a complete solution in the frame of simple orbital description without resorting to a complicated C.I. calculation. We hope to apply the present method to other molecules as well as their excited states in order to see whether it proves to be useful in these cases also. Comparison with a more complete solution will always be possible, when the result of C.I. is known.

The most interesting application of the present method will be to metals or crystals, where the C.I. calculation is practically impossible, since the selection of important configurations is difficult. Even in these cases, the alternant orbital method which involves only one variational parameter θ might improve the result obtained by the usual band approximation.

Finally we express our sincere thanks to Prof. M. Kotani for his kind guidance, to Prof. P.-O. Löwdin for his valuable correspondences, and to members of Kotani Laboratory, especially to Mr. Y. Mizuno, for helpful discussions.

Appendix: Method of Representation Matrix of Permutation Group

It is well known that the spin functions of an n electron system with a definite multiplicity form bases of an irreducible representation of the symmetric group $\mathfrak{S}_n$, and correspondingly on account of Pauli principle the spatial wave functions form bases of the irreducible representation which is contragradient to the direct product of the irreducible representation formed by the spin functions and the totally antisymmetric representation[12]. Let $U(P)\equiv\|U_{jk}(P)\|$ be the matrix of the representation formed by the spatial wave functions for the permutation

$$P=\begin{pmatrix} 1 & 2 & 3 & \cdots\cdots & n \\ p_1 & p_2 & p_3 & \cdots\cdots & p_n \end{pmatrix}.$$

Then the spatial wave function for this multiplicity is given by[13]

$$\left.\begin{aligned} \Psi_{jk}&=c\sum_P U_{jk}{}^*(P)P\Psi^0\,, \\ P\Psi^0&=\psi_1(p_1)\psi_2(p_2)\cdots\psi_n(p_n)\,, \end{aligned}\right\} \tag{14}$$

provided that the spatial wave function may be considered as constructed from a product $\Psi^0=\psi_1(1)\psi_2(2)\cdots\cdot\psi_n(n)$ of orbital functions. It has been shown by Kotani that when permutation Q is applied to the electrons, the above wave functions transform with the matrix $U(Q)$:

$$Q\Psi_{jk}=\sum_h U_{kh}(Q)\Psi_{jh}\,. \tag{15}$$

Thus the wave functions have the required transformation property. Furthermore, it has been shown that if Q_0 is the same permutation as Q applied to orbitals Ψ_{jk} transforms according to

$$Q_0\Psi_{jk}=\sum_h U_{jh}{}^*(Q)\Psi_{hk}\,. \tag{16}$$

In our special case of benzene molecule, the orbital functions ψ_1, ψ_2, ψ_3, ψ_4, ψ_5, ψ_6 should be identified with $\phi_{0\mathrm{I}}$, $\phi_{1\mathrm{I}}$, $\phi_{-1\mathrm{I}}$, $\phi_{0\mathrm{II}}$, $\phi_{1\mathrm{II}}$, $\phi_{-1\mathrm{II}}$. The representation matrices $U_{jk}(P)$ for the singlet state are explicity given in papers by R. Serber[14] and T. Yamanouchi[15], but it is convenient for the present purpose to take them in the following scheme:

$$U(12)=\begin{pmatrix} -1 & & & & \\ & \frac{1}{2} & -\frac{\sqrt{3}}{2} & & \\ & -\frac{\sqrt{3}}{2} & -\frac{1}{2} & & \\ & & & \frac{1}{2} & -\frac{\sqrt{3}}{2} \\ & & & -\frac{\sqrt{3}}{2} & -\frac{1}{2} \end{pmatrix} \qquad U(45)=\begin{pmatrix} -1 & & & & \\ & \frac{1}{2} & & -\frac{\sqrt{3}}{2} & \\ & & \frac{1}{2} & & -\frac{\sqrt{3}}{2} \\ & -\frac{\sqrt{3}}{2} & & -\frac{1}{2} & \\ & & -\frac{\sqrt{3}}{2} & & -\frac{1}{2} \end{pmatrix}$$

$$U(13)=\begin{pmatrix} -1 & & & & \\ & \frac{1}{2} & \frac{\sqrt{3}}{2} & & \\ & \frac{\sqrt{3}}{2} & -\frac{1}{2} & & \\ & & & \frac{1}{2} & \frac{\sqrt{3}}{2} \\ & & & \frac{\sqrt{3}}{2} & -\frac{1}{2} \end{pmatrix} \qquad U(46)=\begin{pmatrix} -1 & & & & \\ & \frac{1}{2} & & \frac{\sqrt{3}}{2} & \\ & & \frac{1}{2} & & \frac{\sqrt{3}}{2} \\ & \frac{\sqrt{3}}{2} & & -\frac{1}{2} & \\ & & \frac{\sqrt{3}}{2} & & -\frac{1}{2} \end{pmatrix}$$

$$U(23)=\begin{pmatrix} -1 & & & & \\ & -1 & & & \\ & & 1 & & \\ & & & -1 & \\ & & & & 1 \end{pmatrix} \qquad U(56)=\begin{pmatrix} -1 & & & & \\ & -1 & & & \\ & & -1 & & \\ & & & 1 & \\ & & & & 1 \end{pmatrix}$$

$$U(14)=\begin{pmatrix} \frac{1}{3} & -\frac{2\sqrt{2}}{3} & & & \\ -\frac{2\sqrt{2}}{3} & -\frac{1}{3} & & & \\ & & -1 & & \\ & & & -1 & \\ & & & & 1 \end{pmatrix}$$

Matrices for other transpositions and higher order permutations can easily be obtained by matrix multiplication. One can see that the matrices in this scheme take the reduced form for those permutations belonging to the subgroup $\mathfrak{S}_3 \times \mathfrak{S}_3$, and the five functions Ψ_{1k}, Ψ_{2k}, Ψ_{3k}, Ψ_{4k}, and Ψ_{5k} correspond to states (a), (b), (e), (d), (c) of Pratt's diagram, Fig. 2.

Matrix elements of Hamiltonian can be calculated by the formula

$$\left.\begin{aligned} \int \Psi_{ih}{}^{*} \mathscr{H} \Psi_{jk} &= \delta_{hk} \sum_{P} U_{ij}(P) H(P), \\ H(P) &= \int P \Psi^{0*} \mathscr{H} \Psi^{0} dv, \end{aligned}\right\} \tag{17}$$

and normalization-nonorthogonality matrix can be obtained by replacing $\mathscr{H}$ by unity; hence the secular equation is given as follows:

$$\det \left| \sum_{P} U(P) \{H(P) - E\Delta(P)\} \right| = 0 , \tag{18}$$

$\left(\Delta(P) \equiv \int P \Psi^{0*} \Psi^{0} dv\right)$. The energy corresponding to the function Ψ_{1k}, in which we are particularly interested, is given by taking the 1st row and column of this secular equation.

References

1) C. A. Coulson and I. Fischer: Phil. Mag. **40** (1949) 393.
2) C. R. Mueller and H. Eyring: J. Chem. Phys. **19** (1951) 1495.
3) C. R. Mueller: J. Chem. Phys. **19** (1951) 1498.
4) A. C. Hurley, J. Lennard-Jones and J. A. Pople: Proc. Roy. Soc. **A 220** (1953) 446.
5) L. A. Schmid: Phys. Rev. **92** (1953) 1373.
6) P.-O. Löwdin: Symposium on Molecular Physics, Nikko, Japan (1953) 13.
7) R. G. Parr, D. P. Craig and I. G. Ross: J. Chem. Phys. **18** (1950) 1561; Private communication.
8) C. A. Coulson and H. C. Longuett-Higgins: Proc. Roy. Soc. **A 192** (1947) 16.
9) W. Moffitt: J. Chem. Phys. **22** (1954) 320.
10) G. W. Pratt, Jr.: Phys. Rev. **92** (1953) 278.
11) P.-O. Löwdin: to be published.
12) B. L. van der Waerden: Die gruppentheoretische Methode in der Quantenmechanik, Leipzig (1932).
13) M. Kotani and M. Siga: Proc. Phys. Math. Soc. Japan **19** (1937) 471.
14) R. Serber: J. Chem. Phys. **2** (1934) 697.
15) T. Yamanouchi: Proc. Phys. Math. Soc. Japan **18** (1936) 623.

JOURNAL OF THE PHYSICAL SOCIETY OF JAPAN Vol. 10, No. 3, MARCH, 1955

Vibrational Relaxation in Polyatomic Gas (Methane)

By Takechiyo INOUE
Faculty of Engineering, Meiji University, Tokyo
and Takehito TAKAHASHI
Seizyo University, Setagaya, Tokyo

(Received August 23, 1954)

A method to obtain an expression of the intermolecular potential including internal coordinates is proposed. The potential is assumed to be the sum of interatomic ones. The calculation is carried out for CH_4-CH_4 interaction and the vibrational relaxation times for ν_4, ν_2 and ν_1 have been calculated. It is shown that ν_4 relaxation time corresponds to the value obtained by Eucken and Aybar and is the decisive one in the supersonic dispersion in accord with their experiment.

§ 1. Introduction

The energy transfer between translational and vibrational or rotational degrees of freedom in molecular collision was treated quantum-mechanically or semi-classically by Zener[1], Jackson and Mott[2], Takayanagi[3], Schwartz, Slawsky and Herzfeld[4], Massey and Burhop[5], Widom and Bauer[6] and many others. Aroeste[7] also investigated the collision between an atom and a plane polyatomic molecule limiting the motion in one plane. We intend to deal with the more general, though non-polar and chemically non-reactive, molecules.

The intermolecular potential in arbitrary configuration is of primary importance for collision problems, but there is no investigation made on theoretically firm ground except about that between hydrogen molecules[8]. In the case of polyatomic molecules the matter is so complicated that we must be content with a considerable approximation. The method of obtaining the intermolecular potential as the sum of potentials between constituent atoms has often been used, e.g. by Atoji and Lipscomb[9], Rowlinson[10], Takayanagi[3], Mizushima and Ohno[11], and others. Widom and Bauer[6] showed that the attractive potential played an important role with chemically reactive molecules, but when the molecules are non-reactive its contribution may be small. Schwartz and Herzfeld[12] discussed this point and introduced into their calculation a term taking account of the attractive part, but we omit it here.

It is the main aim of this paper to propose a method of treating more or less reasonably the normal coordinates of vibration in the collision between polyatomic molecules. Though the procedure may be very much simplified when the distance of closest approach is comparatively large, we develop a rather intricate method for wider adaptation. This method may also serve for the calculation of the intermolecular potential when vibration does not matter. We select CH_4-CH_4 interaction because on the one hand H-H interaction is known comparatively well and the repulsive potentials concerning carbon atoms may be neglected on account of their smallness, and because, on the other hand, we can compare the result with the experimental value obtained by Eucken and Aybar[13] and explain how the relaxation times for different normal vibrations are related to supersonic dispersion.

§ 2. Interaction Potential and the Normal Coordinates of Vibration

Let ρ_{ij} be the distance between two atoms i and j ($i=1,2,\cdots,N_1$; $j=1,2,\cdots,N_2$), atom i belonging to molecule (1) and atom j to (2). We assume that the interaction potential V_{ij} between the two atoms is a function ρ_{ij} only and the intermolecular potential W can be approximated by the sum of potentials between the atoms, i.e.

$$W=\sum_{ij} V_{ij}(\rho_{ij}) . \qquad (1)$$

We specify the positions of atoms i and j by the polar coordinates $(r_i\theta_i\varphi_i)$ and $(r_j\theta_j\varphi_j)$ with origins at the centers of gravity O_1 and O_2 of respective molecules, z axis being the line O_1O_2, and put

$$\cos\omega_{ij}=\cos\theta_i\cos\theta_j+\sin\theta_i\sin\theta_j\cos(\varphi_i-\varphi_j)\,, \tag{2}$$

then we have

$$\rho_{ij}{}^2=\rho^2+2\rho(r_j\cos\theta_j-r_i\cos\theta_i)+r_i{}^2+r_j{}^2-2r_ir_j\cos\omega_{ij}\,, \tag{3}$$

where ρ is the distance O_1O_2. We may accordingly expand $V_{ij}(\rho_{ij})$ with the surface harmonics of arguments $(\theta_i\varphi_i)$ and $(\theta_j\varphi_j)$. If we consider the rotations: $\boldsymbol{R}_i=(\theta_i\varphi_i\psi_i)$ and $\boldsymbol{R}_j=(\theta_j\varphi_j\psi_j)$ specified by Eulerian angles (ψ_i and ψ_j will be decided later on), the above surface harmonics can be regarded as the elements of representation matrices of these rotations. We denote the (h,k) element of the l-th unitary irreducible representation matrix by $D_{l,hk}(\boldsymbol{R}_i)$ and put

$$Y_{l,kh}(\boldsymbol{R}_i)=D_{l,hk}(\boldsymbol{R}_i)^*\,, \tag{4}$$

then we have

$$Y_{l,kh}(\boldsymbol{R}_i)=\exp(ik\psi_i+ih\varphi_i)P_{l,kh}(\theta_i)\,. \tag{5}$$

$P_{l,0h}(\theta_i)$ is related to Ferrers' associated Legendre function by the following formula[14)]

$$P_{l,0h}(\theta_i)=(-)^h\sqrt{\frac{(l-h)!}{(l+h)!}}\,P_l^{|h|}(\cos\theta_i)\,. \tag{6}$$

Thus we can expand V_{ij} as

$$V_{ij}(\rho_{ij})=V_{ij}(\rho)\sum_{l,l'\geq 0}\ \sum_{|k|\leq min(l,l')}A_{ll',k}(\boldsymbol{ij})\times Y_{l,0k}(\boldsymbol{R}_i)Y_{l',0-k}(\boldsymbol{R}_j)\,, \tag{7}$$

where the coefficient $A_{ll',k}(\boldsymbol{ij})$ is a function of r_i, r_j and ρ. We also write as

$$\frac{\partial}{\partial r_i}V_{ij}(\rho_{ij})=V_{ij}(\rho)\sum_{ll'}\sum_k D_{ll',k}(\boldsymbol{ij})Y_{l,0k}(\boldsymbol{R}_i)Y_{l',0-k}(\boldsymbol{R}_j)\,, \tag{8}$$

with the similar expansion for $\frac{\partial}{\partial r_j}V_{ij}(\rho_{ij})$.

If we denote the magnitude of a small displacement of atom $\boldsymbol{i}$ by $|\mathcal{E}_i|$, and the angle between this displacement and $\boldsymbol{r}_i$ by $\boldsymbol{\alpha}_i$, then we have a variation

$$\delta_i(A_{ll',k}Y_{l,0k}(\boldsymbol{R}_i))=D_{ll',k}Y_{l,0k}(\boldsymbol{R}_i)\mathcal{E}_i\cos\boldsymbol{\alpha}_i+A_{ll',k}\delta(Y_{l,0k}(\boldsymbol{R}_i)).$$

Let ψ_i be the angle which the $x'z'$ plane brought about by the rotation $\boldsymbol{R}_i$ makes with the plane decided by the displacement vector and $\boldsymbol{r}_i$, then $\delta(Y_{l,0k})$ is a variation due to a rotation about y' axis by an angle $\mathcal{E}_i\sin\boldsymbol{\alpha}_i/\boldsymbol{r}_i$. Hence we have[14)]

$$\delta(Y_{l,0k}(\boldsymbol{R}_i))=\frac{\sqrt{l(l+1)}}{2}(Y_{l,-1k}(\boldsymbol{R}_i)-Y_{l,1k}(\boldsymbol{R}_i))\frac{\mathcal{E}_i\sin\boldsymbol{\alpha}_i}{\boldsymbol{r}_i}\,.$$

$\mathcal{E}_i$ and $\boldsymbol{\alpha}_i$ can be expressed in terms of normal coordinates of vibration Q_λ as

$$\left.\begin{aligned}\mathcal{E}_i\cos\boldsymbol{\alpha}_i&=\frac{1}{\sqrt{N_1}}\sum_\lambda\eta_{\lambda i}\frac{Q_\lambda}{\sqrt{\boldsymbol{m}_i}}\cos\alpha_{\lambda i}\,,\\ \mathcal{E}_i\sin\boldsymbol{\alpha}_i&=\frac{1}{\sqrt{N_1}}\sum_\lambda\eta_{\lambda i}\frac{Q_\lambda}{\sqrt{\boldsymbol{m}_i}}\sin\alpha_{\lambda i}\,,\end{aligned}\right\} \tag{9}$$

where $\eta_{\lambda i}$ is the normalization factor.

If the orientation of molecule (1) as a whole is designated by the rotation $\boldsymbol{R}_1$, and that of atom i relative to this molecule by ω_i, $\boldsymbol{R}_i$ is the composite of ω_i and R_1 and $Y_{l,mk}(\boldsymbol{R}_i)$ can be expressed as

$$Y_{l,mk}(\boldsymbol{R}_i)=\sum_{h=-l}^{l}Y_{l,mh}(\omega_i)Y_{l,hk}(\boldsymbol{R}_1)\,. \tag{10}$$

Using these relations we have the following equations, assuming that V_{ij}, $\boldsymbol{m}_i$ etc. do not depend on i and j as in the case in our approximate treatment of CH_4-CH_4 interaction,

$$W+\delta W=V(\rho)\sum\left\{\begin{bmatrix}hh' & \\ ll' & k\end{bmatrix}+\sum_{\lambda\lambda'}\left(\begin{bmatrix}hh' & \\ ll' & k\lambda\end{bmatrix}\frac{Q_\lambda}{\sqrt{m}}+\begin{bmatrix}hh' & \\ ll' & k\lambda'\end{bmatrix}\frac{Q_{\lambda'}}{\sqrt{m}}\right)\right\}Y_{l,hk}(\boldsymbol{R}_1)Y_{l',h'-k}(\boldsymbol{R}_2)\,, \tag{11}$$

where $\boldsymbol{Q}_\lambda$ and $\boldsymbol{Q}_{\lambda'}$ are the normal coordinates of molecules (1) and (2), $\boldsymbol{m}$ is the mass of each atom and $\sum$ extends over all values of $|h|\leq l$, $|h'|\leq l'$, $|k|\leq min(l,l')$, $l\geq 0$ and $l'\geq 0$. Coefficients are defined, if all $\eta_{\lambda i}$'s are unity, as follows:

$$\begin{bmatrix}hh' & \\ ll' & k\end{bmatrix}=A_{ll',k}\left(\sum_{i=0}^{N_1}Y_{l,0h}(\omega_i)\right)\left(\sum_{j=1}^{N_2}Y_{l',0h'}(\omega_i)\right)\,, \tag{12}$$

$$\begin{bmatrix}hh' & \\ ll' & k\lambda\end{bmatrix}=\frac{1}{\sqrt{N_1}}\left\{D_{ll',k}\left(\sum_{i=1}^{N_1}Y_{l,0h}(\omega_i)\cos\alpha_{\lambda i}\right)+A_{ll',k}\frac{\sqrt{l(l+1)}}{2}\sum_{i=1}^{N_1}\frac{\sin\alpha_{\lambda i}}{r_i}(Y_{l,-1h}(\omega_i)-Y_{l,1h}(\omega_i))\right\}\times\left(\sum_{j=1}^{N_2}Y_{l',0h'}(\omega_j)\right)\,. \tag{13}$$

§ 3. Case of Methane

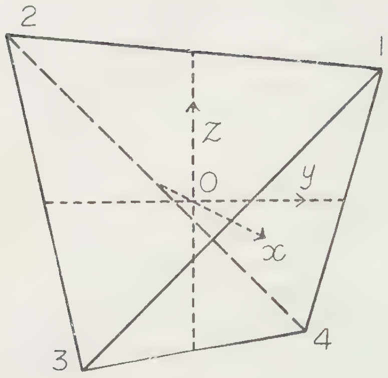

Fig. 1.

In the case of methane the intermolecular potential may be considered as the sum of H-H interactions because C-C and C-H interactions are small. We deal with the normal modes of vibration $A(\nu_1)$, $E(\nu_2)$ and $F'(\nu_4)$ neglecting $F(\nu_3)$. The structure of methane and its normal modes of vibration are well known[15)], and if the axis are taken as in Fig. 1 the angles defined in the previous section are easily calculated. They are given in Table I. Using these values we can calculate the coefficients in (12), (13), taking N_1 as 4, as follows:

$$\sum_{i=1}^{4} Y_{l,0k}(\omega_i)=\{1+(-)^k\}\left\{1+(-)^{l+k}\exp\left(-i\frac{k\pi}{2}\right)\right\}P_{l,0k}(\theta)\,, \tag{14}$$

Table I.

i	θ_i	φ_i	ψ_i				
			E_a	E_b	F_a'	F_b'	F_c'
1	θ	$\pi/4$	π	$5\pi/3$	π	$5\pi/3$	$4\pi/3$
2	θ	$5\pi/4$	π	$5\pi/3$	π	$2\pi/3$	$\pi/3$
3	$\pi-\theta$	$7\pi/4$	0	$2\pi/3$	π	$2\pi/3$	$4\pi/3$
4	$\pi-\theta$	$3\pi/4$	0	$2\pi/3$	π	$5\pi/3$	$\pi/3$

$\cos\theta=1/\sqrt{3}$ $\sin\theta=\sqrt{2/3}$

λ	$\cos\alpha_{\lambda i}$	$\sin\alpha_{\lambda i}$
A	-1	0
E	0	-1
F'	$\pm\sqrt{2/3}$	$1/\sqrt{3}$

i \ λ	singn of $\cos\alpha_{\lambda i}$		
	F_a'	F_b'	F_c'
1	−	−	+
2	−	+	−
3	+	−	−
4	+	+	+

$$\sum_{i=1}^{4}\cos\alpha_{\lambda i}Y_{l,0h}(\omega_i)=\begin{cases} -\sum_{i=1}^{4} Y_{l,0h}(\omega_i)\,, & (A)\\ 0\,, & (E)\\ -\sqrt{\frac{2}{3}}\{1+(-)^h\}\left\{\exp\left(i\frac{h\pi}{4}\right)-(-)^{l+h}\exp\left(-i\frac{h\pi}{4}\right)\right\}, & (F_a')\\ -\sqrt{\frac{2}{3}}\{1+(-)^h\}\left\{\exp\left(i\frac{h\pi}{4}\right)+(-)^{l+h}\exp\left(-i\frac{h\pi}{4}\right)\right\}, & (F_b')\\ \sqrt{\frac{2}{3}}\{1-(-)^h\}\left\{\exp\left(i\frac{h\pi}{4}\right)-(-)^{l+h}\exp\left(-i\frac{h\pi}{4}\right)\right\}, & (F_c') \end{cases} \tag{15}$$

$$\frac{2}{\sqrt{l(l+1)}}\sum_{i=1}^{4}\sin\alpha_{\lambda i}\{Y_{l,-1h}(\omega_i)-Y_{l,1h}(\omega_i)\}$$

$$=\begin{cases} 0\,, & (A)\\ \{1+(-)^h\}\left\{\exp\left(i\frac{h\pi}{4}\right)+(-)^l\exp\left(-i\frac{h\pi}{4}\right)\right\}\{P_{l,1h}(\theta)-P_{l,-1h}(\theta)\}\,, & (E_a)\\ -\{1+(-)^h\}\left\{\left[\exp\left(i\frac{3h-4}{12}\pi\right)-(-)^l\exp\left(-i\frac{3h+8}{12}\pi\right)\right]P_{l,1h}(\theta)\right. & \\ \qquad\left.-\left[\exp\left(i\frac{3h+4}{12}\pi\right)-(-)^l\exp\left(-i\frac{3h-8}{12}\pi\right)\right]P_{l,-1h}(\theta)\right\}, & (E_b)\\ \frac{1}{\sqrt{3}}\{1+(-)^h\}\left\{\exp\left(i\frac{h\pi}{4}\right)-(-)^l\exp\left(-i\frac{h\pi}{4}\right)\right\}\left\{P_{l,1h}(\theta)-P_{l,-1h}(\theta)\right\}, & (F_a') \end{cases} \tag{16}$$

$$\left|\begin{array}{l} -\frac{1}{\sqrt{3}}\{1-(-)^h\}\left\{\left[\exp\left(i\frac{3h-4}{12}\pi\right)-(-)^l\exp\left(-i\frac{3h-4}{12}\pi\right)\right]P_{l,1h}(\theta)\right. \\ \qquad\left.-\left[\exp\left(i\frac{3h+4}{12}\pi\right)-(-)^l\exp\left(-i\frac{3h+4}{12}\pi\right)\right]P_{l,-1h}(\theta)\right\}, \qquad (F_b') \\ -\frac{1}{\sqrt{3}}\{1-(-)^h\}\left\{\left[\exp\left(i\frac{3h-8}{12}\pi\right)-(-)^l\exp\left(-i\frac{3h+4}{12}\pi\right)\right]P_{l,1h}(\theta)\right. \\ \qquad\left.-\left[\exp\left(i\frac{3h+8}{12}\pi\right)-(-)^l\exp\left(-i\frac{3h-4}{12}\pi\right)\right]P_{l,-1h}(\theta)\right\}. \qquad (F_c') \end{array}\right.$$

$P_{l,\pm 1h}(\theta)$ can be evaluated by (6) and recurrence formulae

$$\sqrt{l(l+1)}\{P_{l,1k}(\theta)+P_{l,-1k}(\theta)\}=\sqrt{(l-k)(l-k-1)}P_{l-1,0k+1}(\theta)+\sqrt{(l+k)(l+k-1)}P_{l-1,0k-1}(\theta),$$

$$\sqrt{l(l+1)}\{P_{l,1k}(\theta)-P_{l,-1k}(\theta)\}=-\sqrt{(l-k)(l-k-1)}\cos\theta P_{l-1,0k+1}(\theta)$$
$$+2\sqrt{(l+k)(l-k)}\sin\theta P_{l-1,0k}(\theta)+\sqrt{(l+k)(l+k-1)}\cos\theta\, P_{l-1,0k-1}(\theta).$$

The values of the expressions in (14), (15) and (16) for $l=0, 1, 2, 3$ are listed in Table II (zero values are omitted). I, II, and III correspond to (14), (15) and (16) respectively.

Table II.

λ			A	E_a	E_b	F_a'		F_b'		F_c'	
l	h	I	II	III	III	II	III	II	III	II	III
0	0	4	-4								
1	0					$-4\sqrt{2}/3$	$4\sqrt{2}/3$				
	±1							$\pm4/3$	$\mp4/3$	$-i4/3$	$i4/3$
2	0			$4\sqrt{2}$	$-2\sqrt{2}$						
	±1							$i4/3$	$i4/3$	$\mp4/3$	$\mp4/3$
	±2				$2\sqrt{2}$	$\mp i4/3$	$\mp i4/3$				
3	0					$8\sqrt{2}/9$	$4\sqrt{2}/3$				
	±1							$\pm2\sqrt{6}/9$	$\pm\sqrt{2}/3$	$-i2\sqrt{6}/9$	$-i\sqrt{2}/3$
	±2	$\pm i2\sqrt{10}/3$	$\mp i2\sqrt{10}/3$								
	±3							$\mp2\sqrt{10}/9$	$\mp\sqrt{10}/3$	$-i2\sqrt{10}/9$	$-i\sqrt{10}/3$

§ 4. Repulsive Potential between Methane Molecules

H-H repulsive potential may be expressed as $V_{ij}(\rho_{ij})=A\exp(-a\rho_{ij})$. We use the values $a=3.666(A^{-1})$, $A=16\times10^{-11}(erg)$. We now calculate the coefficients $A_{ll',k}, D_{ll',k}$ in (7) and (8) for an appropriate values of ρ, say ρ_c, near the classical turning point when the temperature of gas is 382°K. If we adopt the values $\rho_c=3.281(A)$, we have $a\rho_c\simeq12$ and $ar\simeq4$ as the distance between C and H is known to be $r_i=r_j=r=1.094(A)$.

To calculate $D_{ll',k}$ we make use of the equation

$$\frac{\partial}{\partial r_i}\exp(-a\rho_{ij})=a\exp(-a\rho_{ij})(a\rho_{ij})^{-1}(a\rho\cos\theta+ar\cos\omega-ar), \tag{17}$$

where we write θ, θ' and ω instead of θ_i, θ_j and ω_{ij} for the sake of briefness. If we put

$$(a\rho_{ij})^2=(a\rho)^2-2a\rho\cdot\zeta\cos\psi+\zeta^2,$$

we have

$$\zeta=ar\{2(1-\cos\omega)\}^{1/2},$$

$$\cos\psi=(\cos\theta'-\cos\theta)\{2(1-\cos\omega)\}^{-1/2},$$

and we may use the formula[16)]

$$\frac{K_\nu(a\rho_{ij})}{(a\rho_{ij})^\nu}=2^\nu\Gamma(\nu)\sum_{m=0}^{\infty}(m+\nu)\frac{K_{m+\nu}(a\rho)}{(a\rho)^\nu}\cdot\frac{I_{m+\nu}(\zeta)}{\zeta^\nu}C_m{}^\nu(\cos\psi)\,, \tag{18}$$

where $C_m{}^\nu$ is a Gegenbauer's function. By the relations

$$C_m{}^{1/2}(\cos\psi)=P_m(\cos\psi)\,,$$

$$(2m-1)C_m{}^{-1/2}(\cos\psi)=P_{m-2}(\cos\psi)-P_m(\cos\psi)\,,$$

we obtain from (18)

$$\frac{\exp(-a\rho_{ij})}{\rho_{ij}}=\sum_{m=0}^{\infty}\frac{K_{m+1/2}(a\rho)}{(a\rho)^{1/2}}\cdot\frac{I_{m+1/2}(\zeta)}{\zeta^{1/2}}(2m+1)P_m(\cos\psi)\,, \tag{19}$$

$$\exp(-a\rho_{ij})=\sum_{m=0}^{\infty}\left\{\frac{K_{m-1/2}(a\rho)}{(a\rho)^{-1/2}}\frac{I_{m-1/2}(\zeta)}{\zeta^{-1/2}}-\frac{K_{m+3/2}(a\rho)}{(a\rho)^{-1/2}}\frac{I_{m+3/2}(\zeta)}{\zeta^{-1/2}}\right\}P_m(\cos\psi)\,. \tag{20}$$

Expanding $I_{m\pm 1/2}(\zeta)\zeta^{-m\mp 1/2}$ as series of Legendre polynomials and inserting them in (19) and (20), we have (see App. I)

$$\exp(-a\rho_{ij})(a\rho_{ij})^{-1}=\exp(-a\rho)\sum_{m=0}^{\infty}\sum_{n=0}^{\infty}b_{nm}P_n(\cos\omega)\{2(1-\cos\omega)\}^{m/2}P_m(\cos\psi)\,, \tag{21}$$

$$\exp(-a\rho_{ij})=\exp(-a\rho)\sum_{m=0}^{\infty}\sum_{n=0}^{\infty}a_{nm}P_n(\cos\omega)\{2(1-\cos\omega)\}^{m/2}P_m(\cos\psi)\,, \tag{22}$$

$$(1-\cos\omega)\exp(-a\rho_{ij})(a\rho_{ij})^{-1}=\exp(-a\rho)\sum_{m=0}^{\infty}\sum_{n=0}^{\infty}c_{nm}P_n(\cos\omega)\{2(1-\cos\omega)\}^{m/2}P_m(\cos\psi)\,. \tag{23}$$

We may also use the expansion (see App. II)

$$\{2(1-\cos\omega)\}^{m/2}P_n(\cos\omega)=\sum_{ll'k}p_{ll',k}(nm)Y_{l,0k}(\theta\varphi)Y_{l',0-k}(\theta'\varphi')\,. \tag{24}$$

If we expand (21), (22) and (23) in series of $Y_{l,0k}(\theta\varphi)Y_{l',0-k}(\theta'\varphi')$ the coefficients are obtained by (24) as

$$\left.\begin{aligned}A_{ll',k}&=\sum_{nm}a_{nm}p_{ll',k}(nm)\,,\\B_{ll',k}&=\sum_{nm}b_{nm}p_{ll',k}(nm)\,,\\C_{ll',k}&=\sum_{nm}c_{nm}p_{ll',k}(nm)\,,\end{aligned}\right\} \tag{25}$$

Using (17) and recurrence formula

$$(2l+1)\cos\theta\,P_{l,0k}(\theta)=(l-k+1)\sqrt{\frac{l+k-1}{l-k+1}}P_{l,0k}(\theta)+(l+k)\sqrt{\frac{l-k}{l+k}}P_{l-1,0k}(\theta)\,,$$

we obtain

$$\frac{1}{a}D_{ll',k}=a\rho\left\{\frac{\sqrt{l^2-k^2}}{2l-1}B_{l-1,l'k}+\frac{\sqrt{(l+1)^2-k^2}}{2l+3}B_{l+1,l',k}\right\}-arC_{ll',k}\,. \tag{26}$$

In the collision problem we may use the values of coefficients $A_{ll',k}$ and $D_{ll',k}$ for $\rho=\rho_c$. These are calculated by the help of Tables in Appendices, and some of them are listed in Table III. Finally we obtain the coefficients in (11) by (12) and (13) using the values in Tables II and III, and list them in Table IV. The values for $k=1,2,3$ are omitted because they are less important. The contributions from the terms for $l,l'>3$ may amount to about 10 percent, when averaged, as is shown below; but are neglected in the above calculation.

When we consider the transitions in vibrational states disregarding the rotational transitions we may use the root-mean-square of the coefficients averaged over the angle variables in the sense that

Table IV.

$\begin{bmatrix} hh' & 0 \\ ll' & \end{bmatrix} \div K$

l		0	3
l	$h \backslash h'$	0	±2
0	0	96	∓87.5i
3	±2	±87.5i	119

Table III.

	$A_{ll',0} \div K$		$D_{ll',0} \div aK$	
$l \backslash l'$	0	3	0	3
0	5.99	−10.38	3.50	− 5.31
1	14.08	−26.67	9.48	−21.55
2	14.73	−31.00	12.12	−24.50
3	10.38	−26.83	10.08	−30.33

$K = \exp(2ar)/4a\rho(ar)^2 = 3.881.$

$\frac{2}{\sqrt{5}} \begin{bmatrix} hh' & 0\lambda \\ ll' & \end{bmatrix} \div aK$

λ		A		E_a		E_b		F_a'		F_b'		F_c'	
	l'	0	3	0	3	0	3	0	3	0	3	0	3
l	$h \backslash h'$	0	±2	0	±2	0	±2	0	±2	0	±2	0	±2
0	0	−25.0	±20.0i										
1	0							−20.1	±26.5i				
	±1									±14.2	−18.7i	−14.2i	∓18.7
2	0			37.3	∓41.3i	−18.6	±20.7i						
	±1									32.9i	±40.5	∓37.9	40.5i
	±2					22.8	∓25.3i	∓37.9i	−40.5				
3	0							31.4	∓47.9i				
	±1									±13.6	−20.7i	−13.6i	∓20.7
	±2	∓38.7i	−60.3										
	±3									∓17.6	26.8i	−17.6i	∓26.8

Table V.

	$[(C/AK)c_{\lambda k}\cdot 10^{-2}]^2$				$\left[\frac{C}{AK}c_\lambda \cdot 10^{-2}\right]^2$
$\lambda \backslash k$	0	1	2	3	
0	1.473	0.006	0.040	0.000	1.519
A	0.123a^2	0.001a^2	0.004a^2	〃	0.128a^2
$E_{a,b}$	0.032a^2	0.001a^2	0.000a^2	〃	0.033a^2
$F'_{a,b,c}$	0.104a^2	0.003a^2	0.006a^2	〃	0.113a^2

$$\int Y_{l,km}(R) Y^*_{l',k'm'}(R)dR \Big/ \int dR = (1/2l+1)\delta_{ll'}\delta_{kk'}\delta_{mm'} .$$

In this case we have

$$W = C\exp(-a\rho)(1 + \sum_\lambda c_\lambda Q_\lambda/\sqrt{m} + \sum_{\lambda'} c_{\lambda'} Q_{\lambda'}/\sqrt{m}) , \tag{27}$$

where

$$C = A\left\{\sum_{ll'k} \frac{1}{(2l+1)(2l'+1)} \left|\begin{bmatrix} hh' & k \\ ll' & \end{bmatrix}\right|^2\right\}^{1/2} ,$$

$$c_\lambda = \sum_k c_{\lambda k} ,$$

$$c_{\lambda k}=\frac{A}{C}\left\{\sum_{ll'}\frac{1}{(2l+1)(2l'+1)}\left|\begin{bmatrix} hh' & k\lambda \\ ll' & \end{bmatrix}\right|^2\right\}^{1/2}.$$

The values are shown in Table V. ($\lambda=0$ corresponds to constant term, and $c_{0k}=c_0=1$.)

§ 5. Relaxation Times

We now proceed to the collision in which the energy transfer between the vibrational and the translational degrees of freedom occurs. We assume that the rotation of molecules plays no role in this energy exchange; this implies that the angles specifying the orientation of molecules in the potential function may be regarded as constants.

We begin with the one-dimensional treatment. We use the intermolecular potential given in (27). Eigenfunctions of the molecular vibration can be expressed as

$$Z_p Z_{p'}=\prod_{\lambda\lambda'} Z_{\lambda p}(Q_\lambda) Z_{\lambda' p'}(Q_{\lambda'})\,,$$

with the harmonic oscillator eigenfunction $Z_{\lambda p}$ and $Z_{\lambda' p'}$, p and p' being the total vibrational quantum numbers of respective normal modes of vibration. Expanding the wave function of the colliding system as

$$\Psi=\sum_{pp'} g(pp',x) Z_p Z_{p'}\,,$$

we have the Schroedinger equation, in the center of mass system,

$$\sum_{pp'} Z_p Z_{p'}\left(\frac{d^2}{dx^2}+k^2-\frac{2M}{\hbar^2}W\right)g(pp',x)=0\,, \tag{28}$$

$$k^2=\frac{2M}{\hbar^2}(E-E_p-E_{p'})\,,$$

where E_p and $E_{p'}$ are the energies of vibration of respective molecules and M is the reduced mass of the system.

Now we suppose that before collision the molecule (1) is in the first excited state of definite normal mode of vibration, say three-fold degenerate vibration F', the molecule (2) being in the ground state and after collision both are in the ground state. Then from (28) we have

$$\left.\begin{aligned}\left[\frac{d^2}{dx^2}+k_0^2-\frac{2M}{\hbar^2}W(p_0p_0'|p_0p_0')\right]g(p_0p_0')&=\frac{2M}{\hbar^2}W(p_0p_0'|pp_0')g(pp_0')\,,\\ \left[\frac{d^2}{dx^2}+k^2-\frac{2M}{\hbar^2}W(pp_0'|pp_0')\right]g(pp_0')&=\frac{2M}{\hbar^2}W(pp_0'|p_0p_0')g(p_0p_0')\,,\end{aligned}\right\} \tag{29}$$

where

$$k_0^2=\frac{2M}{\hbar^2}(E-E_{p_0}-E_{p_0'})\,,\qquad k^2=\frac{2M}{\hbar^2}(E-E_p-E_{p_0'})\,,$$

$$W(p_0p_0'|pp_0')=C\exp(-ax)\sum_{\lambda=F'}\frac{c_\lambda}{\sqrt{m}}\sum_{l,\mu}(1l\mu|Q_\lambda|000)$$

$$l=0,1\,,\qquad -l\leq\mu\leq l.$$

The matrix element for degenerate vibration $F_s'(s=a,b,c)$ is as follows[18]:

$$\left|\sum_{l\mu}(|l\mu|Q_\lambda|000)\right|^2=\frac{h}{8\pi^2\nu_4}\,.$$

By the well known Jackson and Mott solution, we obtain the transition probability per collision

$$p_{(4)}{}^{1\to0}=\frac{2^5\pi^4M^2\nu_4}{ha^4m}\left(\sum_{\lambda=F'}c_\lambda{}^2\right)\frac{\sinh\pi q_0\sinh\pi q}{(\cosh\pi q_0-\cosh\pi q)^2}\,,$$

$$q_0=\frac{2k_0}{a}\,, \qquad q=\frac{2k}{a}\,.$$

The relaxation time $\beta_{(4)}$ for ν_4-vibration is given by

$$\frac{1}{\beta_{(4)}}=\frac{2N}{V}D^2\left(\frac{2\pi\kappa T}{M}\right)^{1/2}P_{(4)}{}^{1\to 0}\,, \tag{30}$$

where

$$P_{(4)}{}^{1\to 0}=2\left(\frac{M}{2\kappa T}\right)^2\int_0^\infty p_{(4)}{}^{1\to 0}\exp\left(-\frac{Mv_0{}^2}{2\kappa T}\right)v_0{}^3dv_0\,,$$

and D is the collision diameter.

As no rigorous treatment can be performed in the three-dimensional case, we use quite the same procedure as developed by Schwartz and Herzfeld[12]. The difference lies in that whereas they employed a term taking account of the attraction we neglect the attractive potential because it may not contribute much.

Inelastic cross section is given by

$$Q_{(4)}=\int_0^\infty \frac{\pi}{k_0{}^2}\sum_{j=0}^{\infty}(2j+1)p_{(4)j}{}^{1\to 0}\exp\left(-\frac{Mv_0{}^2}{2\kappa T}\right)v_0{}^3dv_0\,.$$

We replace the sum over j by an integral and changing the variable v_0 to u_0 by the relation $u_0{}^2=v_0{}^2-\hbar^2 j(j+1)/(M^2\rho_c{}^2)$, obtain

$$Q_{(4)}=\frac{2^5\pi^5M^3\rho_c{}^2\nu_4}{ha^4m\kappa T}\left(\sum_\lambda c_\lambda{}^2\right)\int_0^\infty\frac{\sinh\pi q_0\sinh\pi q}{(\cosh\pi q_0-\cosh\pi q)^2}\exp\left(-\frac{Mv_0{}^2}{2\kappa T}\right)v_0dv_0\,,$$

where we write again v_0 instead of u_0 as an integration variable. In this case also we can evaluate the integral by the method of steepest descent with the result

$$\text{Integral}=\pi^{1/2}\exp(f(v_0{}^*))(-\tfrac{1}{2}f''(v_0{}^*))^{-1/2}v_0{}^*\,,$$

where

$$f(v_0)=-\frac{Mv_0{}^2}{2\kappa T}-\frac{4\pi^2M}{ah}(v_0-v)\,,$$

$$v_0{}^*=\left(\frac{4\pi^2\kappa T\nu_4}{aM}\right)^{1/3}\left[1-\frac{h\nu_4}{2M}\left(\frac{4\pi^2\kappa T\nu_4}{aM}\right)^{-2/3}\right].$$

The relaxation time is given by

$$\frac{1}{\beta_{(4)}}=\frac{2N}{V}\left(\frac{2\kappa T}{\pi M}\right)^{1/2}Q_{(4)}\,. \tag{31}$$

$\beta_{(2)}$ and $\beta_{(1)}$ can be obtained in a similar way.

With the values $M=1.338\times10^{-23}$ (g), $\nu_4=1306$ (cm^{-1}), $T=382$°K, $p=1$ atm., $a=3.666$ (A^{-1}), $r=1.094$ (A) and $D=3.8$ (A) (estimated from the zero of the mean intermolecular potential) we obtain the relaxation time for ν_4-vibration

from (30) $\qquad \beta_{(4)}=3.4\times10^{-6}$ (sec) ,

from (31) $\qquad \beta_{(4)}=7.6\times10^{-5}$ (sec) .

Using the matrix element of two-fold degenerate vibration, we get the corresponding values for ν_2-vibration

$$\beta_{(2)}=2.4\times10^{-4}\,(\text{sec})\,, \qquad \beta_{(2)}=6.7\times10^{-3}\,(\text{sec})\,.$$

The relaxation time for non-degenerate ν_1-vibration is much larger.

When there are more than one normal modes of vibration, it is a matter of interest whether the translational energy exchanges itself with the vibrational energy of one mode or with those of two or more modes in parallel. Schaefer19) discussed this point and showed that it was difficult from the mere dispersion data to decide which is the case. He gave the following equation for supersonic velocity u, when two vibrational modes were deactivated in parallel;

$$u^2=\frac{p}{\rho}\left[1+R\frac{U}{U^2+W^2}\right], \tag{32}$$

$$U=c_0+\frac{c_{s1}}{1+\beta_1{}^2\omega^2}+\frac{c_{s2}}{1+\beta_2{}^2\omega^2}, \qquad W=\frac{c_{s1}\beta_1\omega}{1+\beta_1{}^2\omega^2}+\frac{c_{s2}\beta_2\omega}{1+\beta_2{}^2\omega^2},$$

where β_1 and β_2 are relaxation times, c_{s1} and c_{s2} the molar heats of vibration, c_0 the sum of translational and rotational heats, ρ the density and ω the circular frequency of sound. Eucken and Aybar13) performed many accurate experiments and obtained for methane gas at 382°K, 1 atm., $\bar{\beta}=8.4\times10^{-7}$ (sec) with sound frequency $\omega/2\pi=6.04\times10^5$ (sec^{-1}). They inferred that the translational energy might not be transferred to more than one modes of vibration in parallel.

As $\beta_{(1)}$ and $\beta_{(3)}$ are out of the question, we use $\beta_{(4)}$ and $\beta_{(2)}$ as two relaxation times in (32) with the sound frequency above. It is clear that ν_2 vibration is quite negligible and the velocity dispersion depends effectively on one relaxation time in accordance with the view of Eucken and Aybar. $\beta_{(4)}$ should be compared with experimental value $\bar{\beta}$.

§ 6. Discussion

We developed a method of calculating the intermolecular potential including the internal coordinates of vibration assuming that it is a sum of interatomic potentials. This sort of assumptions seems to be inevitable in the present situation. According to our calculation the mean intermolecular potential is given by $A\left[{}^{00}_{00}0\right]\exp(-a\rho)$, which has the value 3.6×10^{-14} (erg) for $a=3.666$ (A^{-1}), $A=16\times10^{-11}$ (erg) (H-H interaction) and $\rho_c=3.281$ (A), while the Leanard-Jones potential20) gives 3.0×10^{-13} (erg) and the exponential-inverse-six-power potential21) gives 2.8×10^{-14} (erg). When the distance of closest approach is large, the potential including normal coordinates can be calculated much more simply, but such is not our case. When the constituent atoms are not alike the calculation becomes more complicated though not impossible. In calculating the relaxation times the three-dimensional treatment is, of course, superior in principle, but in regard to the method of approximation it is not easy to decide which should be the better. The result may be thought to be rather good in view of the assumptions made.

Appendix I

We use the expansion

$$\frac{I_{m+1/2}(\zeta)}{\zeta^{m+1/2}}=\sum_{n=0}^{\infty}\alpha_{nm}P_n(\cos\omega), \tag{A.1}$$

$$\alpha_{nm}=\frac{2n+1}{2}\int_{-1}^{1}\frac{I_{m+1/2}(\zeta)}{\zeta^{m+1/2}}P_n(\cos\omega)d(\cos\omega).$$

By the relation17)

$$\left(\frac{d}{d(\cos\omega)}\right)^i\frac{I_{m+\nu}}{\zeta^{m+\nu}}=(-)^i(ar)^{2i}\left(\frac{d}{\zeta d\zeta}\right)^i\frac{I_{m+\nu}(\zeta)}{\zeta^{m+\nu}}=(-)^i(ar)^{2i}\frac{I_{m+\nu+i}(\zeta)}{\zeta^{m+\nu+i}},$$

we have

$$\alpha_{nm}=\frac{2n+1}{2}\sum_{i=0}^{n}\frac{1}{(ar)^{2i+2}}P_n{}^{(i)}(1)\left\{\frac{(-)^{n+i}I_{m+1/2-i-1}(2ar)}{(2ar)^{m+1/2-i-1}}-\frac{1}{2^{m+1/2-i-1}\Gamma(m+\frac{1}{2}-i)}\right\}, \tag{A.2}$$

where

$$P_n^{(i)}(-1)=(-)^i P_n^{(i)}(1)=(-)^i \frac{(n+i)!}{(n-i)!\,i!\,2^i} .$$

If we put

$$K_{m+1/2}(a\rho)=f_{m+1/2}(a\rho)K_{1/2}(a\rho) ,$$

we have from (19), (21) and (A.1)

$$b_{nm}=(2m+1)(ar)^m f_{m+1/2}(a\rho)\sqrt{\frac{\pi}{2}}\alpha_{nm} , \tag{A.3}$$

and from (20), (21) and (22)

$$a_{nm}=a^2\rho r\left\{\frac{1}{2m+1}b_{n,m-1}+\frac{2}{2m+3}\left(b_{n-1,m+1}-b_{n,m+1}+\frac{n+1}{2n+3}b_{n+1,m+1}\right)\right\} , \tag{A.4}$$

$$c_{nm}=\frac{n}{2n-1}b_{n-1,m}-b_{nm}+\frac{n+1}{2n+3}b_{n+1,m} , \tag{A.5}$$

Thus we can calculate all the values α_{nm}, b_{nm}, a_{nm} and c_{nm}, among which we list a_{nm} in Table VI.

Table VI.

$$a_{nm}\div\sqrt{\frac{2}{\pi}}K$$

n \ m	0	1	2	3	4	5	6
0	5.9912	9.7617	8.1752	4.4187	3.0125	1.5236	0.7115
1	−9.0283	−12.965	−8.9246	−5.1547	−2.4934	−1.1067	−0.4423
2	4.0628	4.7705	3.0235	1.3355			
3	−0.5764	−0.8273					

Appendix II

We use the expansion in series of associated Legendre function

$$P_n(\cos\omega)\{2(1-\cos\omega)\}^{m/2}P_m(\cos\psi)=\sum_{l,l'\geq 0}\ \sum_{min(l,l')\geq k\geq 0} q_{ll',k}(nm)P_l^k(\cos\theta)P_{l'}^k(\cos\theta')\cos k\varphi . \tag{A.6}$$

By (24) and (6) we have

$$p_{ll',0}(nm)=q_{ll',0}(nm) ,$$

$$p_{ll',k}(nm)=\frac{1}{2}\sqrt{\frac{(l+k)!(l'+k)!}{(l-k)!(l'-k)!}}q_{ll',k}(nm) , \qquad (k\neq 0) . \tag{A.7}$$

Using the relation

$$(2l+1)\cos\omega P_l^k(\cos\omega)=(l-k+1)P_{l+1}^k(\cos\omega)+(l+k)P_{l-1}^k(\cos\omega) ,$$

we obtain the recurrence formula

$$\begin{aligned} q_{ll',k}(nm)=\frac{2m-1}{m}\Big\{&\frac{l-k}{2l-1}q_{l-1\,l',k}(n,m-1)+\frac{l+k+1}{2l+3}q_{l+1\,l',k}(n,m-1)\\ &-\frac{l'-k}{2l'-1}q_{ll'-1,k}(n,m-1)-\frac{l'+k+1}{2l'+3}q_{ll'+1,k}(n,m-1)\Big\}\\ &-\frac{2(m-1)}{m}\Big\{q_{ll',k}(n,m-2)-\frac{n+1}{2n+1}q_{ll',k}(n+1,m-2)-\frac{2}{2n+1}q_{ll',k}(n-1,m-2)\Big\} . \end{aligned} \tag{A.8}$$

Table VII. $(p_{lj,0}=(-)^m p_{jl,0})$

m	n	l	l'	
0	0	0	0	1
	1	1	1	1
	2	2	2	1
	3	3	3	1
1	0	1	0	1
	1	1	0	−1/3
		2	1	2/3
	2	2	1	−2/5
		3	2	3/5
	3	3	2	−3/7
		4	3	4/7
2	0	2	0	1
		1	1	−2
	1	3	1	3/5
		2	2	−2/3
		2	0	−2/3
		1	1	4/5
	2	4	2	18/35
		3	3	−12/25
		3	1	−18/25
		2	2	4/7
2	2	2	0	1/5
		1	1	−2/25
	3	4	4	−20/49
		4	2	−36/49
		3	3	8/15
		3	1	9/35
		2	2	−6/49
3	0	3	0	1
		2	1	−3
	1	4	1	4/7
		3	2	−4/5
		3	0	−1
		2	1	57/35
	2	4	3	−18/35
		4	1	−36/35
		3	2	20/21
		3	0	3/5
		2	1	−3/7
	3	4	3	62/77
		4	1	36/49
		3	2	−44/105
		3	0	−1/7
		2	1	9/245
4	0	4	0	1
		3	1	−4
		2	2	6
	1	4	2	−20/21
		4	0	−4/3
		3	3	6/5
		3	1	128/45
		2	2	−24/7
5	0	4	1	−5
		3	2	10
	1	4	3	1.71
		4	1	2.85
		3	2	−6.43
6	0	4	2	15
		3	3	−20
	1	4	2	−11.26
		3	3	14.94
7	0	4	3	−35
	1	4	3	23.1

$$q_{ll',0}(n,0)=\delta_{l-n,l'-n}\,,\qquad q_{ll',k}(n,0)=2\,\frac{(n-k)!}{(n+k)!}\,\delta_{l-n,l'-n}\,,\qquad (k\neq 0)\,. \tag{A.9}$$

Thus we can calculate the values of $p_{ll',k}(nm)$. Only $p_{ll',0}(nm)$ is shown (zero values omitted) in Table VII.

References

1) C. Zener: Phys. Rev. **37** (1931) 556.
2) J. M. Jackson and N. F. Mott: Proc. Roy. Soc. A **137** (1932) 703.
3) K. Takayanagi: Prog. theor. Phys. **8** (1952) 111, **8** (1952) 497, **9** (1952) 578.
4) R. N. Schwartz, Z. I. Slawsky and K. F. Herzfeld: J. Cnem. Phys. **20** (1952) 1951.
5) H. S. W. Massey and E. H. S. Burhop: *Electronic and Ionic Impact Phenomena* (1952).
6) B. Widom and S. H. Bauer: J. Chem. Phys. **21** (1953) 1670.
7) H. Aroeste: J. Chem. Phys. **21** (1953) 870.
8) H. Margenau: Phys. Rev. **64** (1943) 131.
9) M. Atoji and W. N. Lipscomb: J. Chem. Phys. **21** (1953) 1480.
10) J. C. Rowlinson: J. Chem. Phys. **20** (1952) 337.
11) M. Mizushima, K. Ohno and A. Ohno: J. Chem. Phys. **21** (1953) 2107.
12) R. N. Schwartz and K. F. Herzfeld: J. Chem. Phys. **22** (1954) 767.
13) A. Eucken und S. Aybar: Zeits. Phys. Chem. (B) **46** (1940) 195.
14) T. Takahashi: J. Phys. Soc. Japan **7** (1952) 307.
15) M. Born: *Optik* (1933) 553.
G. Herzberg: *Infrared and Raman Spectra of polyatomic Molecules* (1945) pp. 100, 307.
16) G. N. Watson: *Theory of Bessel Functions* (1922) p. 365.
17) G. N. Watson: ibid. p. 79.
18) H. H. Nielsen: Rev. Mod. Phys. **23** (1951) 90.
19) K. Schaefer: Zeits. Phys. Chem. (B) **46** (1940) 212.
20) R. B. Bird, E. L. Spotz and J. O. Hirschfelder: J. Chem. Phys. **18** (1950) 1395.
21) E. B. Mason and W. E. Rice: J. Chem. Phys. **22** (1954) 843.

Journal of the Physical Society of Japan Vol. 10, No. 3, March, 1955

On a Sodium Nitrate Polarization Prism and a Polarization Plate of a Scattering Type

By Tasaburô Yamaguti

Physical Institute, College of Arts and Sciences, Chiba University

(Read April 2, 1952; Received Octover 26, 1954)

Two types of polarizers are constructed, one being the "total reflection type" similar to the Feussner prism and the other is the "scattering type", in which the principle of Christiansen filter holding for the polarization. The former is made of a thin single crystal of sodium nitrate grown between two prisms of *SK5* glass or two glass plates which are cemented to two prisms of the same kind of glass by Canada balsam. No use of organic binders to attach the crystal to the glass remarkably simplifies the manufacturing process as well as protection of the polarizers from deteriorations due to the deliquenscence of the crystal.

The polarizer of the "scattering type" is constructed by binding directly two roughly ground surfaces of *SK5* glass plates with a thin single crystal of sodium nitrate. As *SK5* glass has the same refractive index with that of ordinary ray in sodium nitrate, and the orientation of the optical axis of the crystal is so chosen that it lies in the plane of the glass plate, the extraordinary ray is scattered at the boundaries between the crystal and glass, and only the ordinary ray proceeds in the direction of the incident light, when the natural light is incident upon it.

§ 1. Introduction

A polarizer of the total reflection type made of sodium nitrate was first made by Feussner early in 1884[1]. Although large single crystals of sodium nitrate are easily obtainable nowadays, there still remains some technical difficulties in the manufacture of polarizer due to the deliquescence and softness of the crystal. One of aims of the present work is to remove these difficulties.

For this purpose, the author made a polarizer by the use of a very thin single crystal grown between two prisms or plates of *SK5* glass, making use of the fact that the axis of the single crystal of sodium nitrate grown on mica sheet has a definite orientation[2]. The plates are further cemented to prisms of the same kind of glass with Canada balsam to form the polarizer. Thus we can obtain the polarizers without polishing the crystal and without using any organic binder to bind the crystal to the glass, hence we can protect them easily from the deliquescence by the use of some suitable coating materials.

The second type we have made is so called "scattering type"; as it acts as a polarizer by an effect of the scattering of light at the rough surface of a thin single crystal of sodium nitrate grown between ground surface of *SK5* glass plates.

§ 2. Methods of the Production and Characteristics of the Polarizers

By utilizing the fact that the single crystal of sodium nitrate grows on a mica sheet keeping its optical axis parallel to the normal of the sheet, we can obtain glass plates between which a single crystal of desired axis orientation being developed. That is, the orientation of the axis can be determined by cooling the melt of sodium nitrate containing the glass plates and a mica sheet gradually from the side of the mica sheet, the former were placed on the latter making a definite angle with it. For the present purpose, however, it is preferable to place the glass plates on the mica sheet so that the optical axis becomes parallel to the plate surface.

a) *The polarization prism*[3]. After removal of bubbles in the melt of sodium nitrate, glass plates of 32×10×1.3 mm were placed on the mica sheet keeping their surfaces parallel to the normal of the sheet. The plates then so pressed by a spring as to hold a very narrow gaps filled with the melt between them. When the temperature of the melt reached to about 370°C, the melt was cooled slowly from the mica side untill the gaps between the plates are filled with the crystal. Methods of removal of the crystal from the vessel and of annealings of the crystal are the same as described in the previous paper[4]. The plates then cleaved to form pairs of the plates connected with the thin single crystal. The optical axis of the crystal lies in the plane of the glass surface and is parallel to one of the edges, which was at right angles to the mica sheet when the crystal had grown. Each pair of the plates thus made was cemented with Canada balsam to two prisms of the glass of the angle of 23° as is shown in Fig. 1, which is a schematic diagram of the completed polarizer. Size of the polarizer is 10×12 mm in the entrance face of the light and 35 mm in the length. This polarization prism can be made also by direct growth of the thin single crystal in a narrow space between two glass prisms instead of the two plates. However, the polarizer made in such a way is apt to have strains and in consequence polarization is not always perfect.

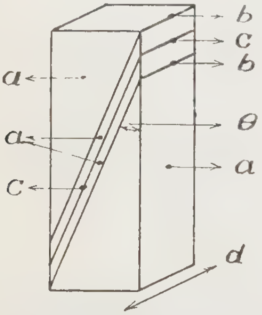

Fig. 1. The polarizer of the total reflection type. a: *SK5* glass, b: Canada balsam, c: single crystal of sodium nitrate, d: optical axis, and θ: the angle of the glass prism.

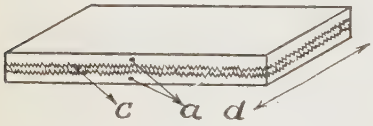

Fig. 2. The polarization plate of the scattering type.
a: *SK5* glass plates, c: single crystal of sodium nitrate, d: optical axis.

The refractive indices ω and $\mathcal{E}$ of sodium nitrate for the ordinary and the extraordinary ray are 1.5854 and 1.3369 respectively, while the index n of *SK5* glass is 1.5889. Calculation shows that the largest angle of refraction of the plane polarized light at the exit face of the present polarization prism is 15°36′ in the plane normal to the optical axis. Thus, the field of view of the present polarizer is as large as 31°, even when we limit the field symmetrically to the normal of the entrance face of the polarizer.

b) The polarizer of the scattering type[5]. Each one of the surfaces of plates of 35×35 ×1.4 mm *SK5* glass were ground by using carborundum of ♯400 to make it a rough surface. Then the plates are so placed in the melt as each roughly ground surface faces each other and at the same time they are perpendicular to the mica sheet. Then, by the same method as described before, we can made the "scattering type" polarizer made of two glass plates and a very thin single crystal grown between their ground surfaces. Fig. 2 shows a schematic representation of it, the optical axis of which is parallel to one of its edges.

Due to the facts that the contact surfaces of the glass and the crystal are rough, and n is nearly equal to ω, whereas it deviates remarkablly from $\mathcal{E}$, one of the component of the incident ray, vibrating in the principal plane, is scattered at the surface, while the other component passes through the surface without scattering, thus the plate acts as polarizer.

The reason why the type, in which the crystal is sandwiched between two roughly ground surfaces, is selected lies in the fact that it strengthen the binding force of the plates by the crystal as well as it gives the same degree of polarization whatever the direction of the incident light may be. However, as the result of investigation with a polarizer in which the crystal is grown between two surfaces, one of which is roughly ground and the other is polished, it was known that there is no difference with respect to the direction of the incident rays. This shows that the polarization effect is due to the scattering or the refraction at the boundary surfaces between the rough glass and the crystal: the same effect with that of the Christiansen filter, and is not due to the total reflection at minute planes composing the boundary.

Fig. 3 shows a photograph of a section paper lying 3 cm below a glass plate, on which

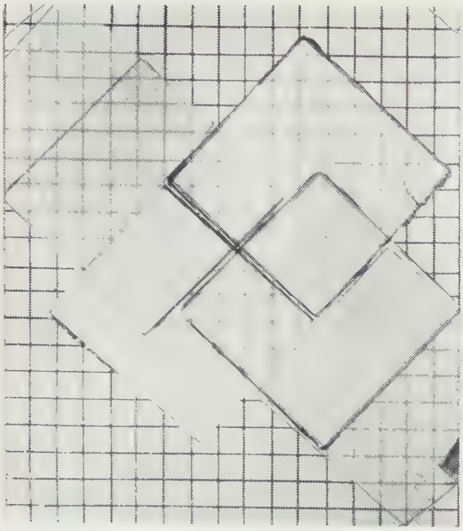

Fig. 3. Sights through the polarization plates: A single plate and two plates overlapped in the parallel positions are transparent, ones in the crossed positions being not transparent.

many polarization plates of this type are put in the crossed or parallel positions. We can see from the photograph that the functions of the polarization plates are satisfactory.

The present polarization plate is superior to ones of the old absorption type, as the former is highly transparent to all colours. Therefore, if we use it, for example, to see stereopictures of the natural colours, the pictures are seen to be very light and natural.

In conclusion the author's thanks are due to the Educational Department for financial support, to Mr. I. Makino of the Hitachi Works for his assistance and also to Mr. T. Wakabayashi for his advices.

References

1) K. Feussner: Z. f. Instrk. **4** (1884) 41.
2) T. Yamaguti: J. Phys. Soc. Japan **7** (1952) 113.
3) T. Yamaguti: Japanese Government patent No. 203619.
4) T. Yamaguti: J. Phys. Soc. Japan **7** (1952) 113; J. College. Art. Sci. Chiba Univ. **1** (1952) 13. (In Japanese).
5) T. Yamaguti: Japanese Government patent No. 204117.

JOURNAL OF THE PHYSICAL SOCIETY OF JAPAN Vol. 10, No. 3, MARCH, 1955

The Flow due to Impulsive Motion of a Wedge and its Similarity to the Diffraction of Shock Waves

By Akira SAKURAI

Tokyo Electrical Engineering College

(Received October 18, 1954)

After some general discussion, an analysis is performed to clarify the non-uniform region of the air flow caused by impulsive motion of a wedge with small vertex angle. It is shown that the present problem is quite similar to the well-known problem of the interaction of a shock wave and the wedge. By use of this similarity, some cases of wedges having not small vertex angles are discussed.

§ 1. Introduction

When a body is suddenly set in motion a transient flow occurs in the surrounding air and this flow brings about a reaction on the body.

As one of the most typical and simplest case of the problem, we shall consider the flow of gas generated by an infinite wedge which moves impulsively from rest at a finite and constant velocity u_0 (Fig. 1).

At any instant t, we may always have a region where the effect of the apex O has not yet reached, since the propagation velocity of a disturbance is finite. In this region, each of the flows generated by the two walls of the wedge is simple and equivalent to the flow which would be generated when an infinite plane rigid wall moves obliquely, as shown in Fig. 2 for the case of the upper surface.

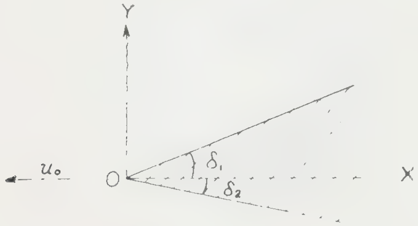

Fig. 1.

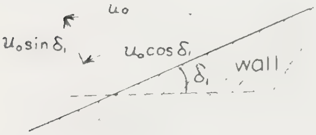

Fig. 2.

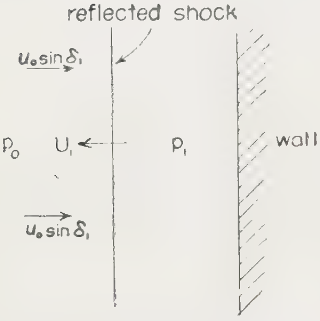

Fig. 3.

This flow is the same as that due to a wall moving normal to the surface at a constant velocity $u_0 \sin \delta_1$, since the motion of the wall parallel to its surface has no influence on the air. Further, when observed from the wall, the state of affairs is equivalent to the case of the reflection of a plane shock wave on the wall, more precisely, to that of a progressive plane shock front which is followed by the gas with the velocity $u_0 \sin \delta_1$ behind it and is reflected as shown in Fig. 3. The gas between the wall and the shock front is at rest and the propagation velocity U_1 of the reflected shock front is given by the relations[1)]

$$\left.\begin{aligned} &(U_1 - u_0 \sin \delta_1)^2 + (1/2)(\gamma+1) u_0 \sin \delta_1 \\ &\qquad \times (U_1 - u_0 \sin \delta_1) - c_0^2 = 0\ , \\ \text{and} \qquad &U_1 - u_0 \sin \delta_1 < 0\ , \end{aligned}\right\} \qquad (1)$$

where c_0 is the sound velocity of undisturbed region and γ is the ratio of the specific heats. Similar relations hold for the lower surface. Moreover, the pressures p_1 and p_2 in the region between the shock wave and the wall are obtained from the relations:

$$\frac{p_i}{p_0} = \frac{2\gamma}{\gamma+1}\left(\frac{U_i - u_0 \sin \delta_i}{c_0}\right)^2 - \frac{\gamma-1}{\gamma+1}\ , \quad (i=1,\ 2). \tag{2}$$

Accordingly, if we observe the phenomenon from the coordinate system O–XY fixed to the wedge (Fig. 1), it will be seen that in the regions at appropriate distances from the apex O two plane shock waves parallel to the walls of the wedge are propagating with velocity U_1 and U_2 respectively and the gas between the shock wave and the wall flows parallel to the wall with the uniform velocity $u_0 \cos \delta_1$ for the upper and $u_0 \cos \delta_2$ for the lower surface respectively.

Then, how are the circumstances in the region of flow field affected by the motion of the apex O? To clarify it we shall first consider, in § 2, the simple case of a wedge with small vertex angle and find that the problem is quite similar to the well-known discussion on the interaction between a plane shock wave and a wedge[2)3)]. Using this similarity, we shall give, in § 3, some discussions for the case in which δ_1 and δ_2 are not so small.

It is to be remarked here that the transient flow of our present problem has the nature of pseudo-stationariness and hence the flow field is represented by two independent variables X/t and Y/t.

Lastly, it should be added that the case $M > 1$; δ_1, $\delta_2 \ll 1$ has already been considered by Strang[4)] with the aid of a method which is quite different from ours.

§ 2. The Case of a Wedge with Small Vertex Angle

Since the disturbance generated by the wedge is small in this case, the entire flow field is represented by the linearized equation and the shock front can be treated as a sound wave; in particular the deviation of pressure p' from the undisturbed one p_0 is determined by the wave equation as:

$$\frac{\partial^2 p'}{\partial t^2} = c_0^2 \left(\frac{\partial^2 p'}{\partial X'^2} + \frac{\partial^2 p'}{\partial Y'^2}\right), \tag{3}$$

where X', Y' are coordinates fixed to the space and initially coincident with X, Y, namely,

$$X' = X - c_0 t\,, \quad Y' = Y.$$

According to the remark in § 1, p' must be a function of X/t and Y/t: thus we put

$$X'/(c_0 t) = x, \quad Y'/(c_0 t) = y, \quad p'/(c_0 \rho_0 u_0) = p. \tag{4}$$

Hence we have from (3)

$$(1-x^2)\frac{\partial^2 p}{\partial x^2} - 2xy\frac{\partial^2 p}{\partial x \partial y} + (1-y^2)\frac{\partial^2 p}{\partial y^2} = 2\left(x\frac{\partial p}{\partial x} + y\frac{\partial p}{\partial y} \right). \tag{5}$$

If p has been determined from (5), the velocity field can be obtained by any two of the following equations;

$$x\frac{\partial p}{\partial x} + y\frac{\partial p}{\partial y} = \frac{\partial u}{\partial x} + \frac{\partial v}{\partial y}\,,$$

$$x\frac{\partial u}{\partial x} + y\frac{\partial u}{\partial y} = \frac{\partial p}{\partial x}\,,$$

$$x\frac{\partial v}{\partial x} + y\frac{\partial v}{\partial y} = \frac{\partial p}{\partial y}\,, \tag{6}$$

where $(u_0 u,\ u_0 v)$ are $(X',\ Y')$ components of velocity[3]. In this coordinate system the apex O corresponds to $x = -u_0/c_0 \equiv -M,\ y = 0$.

Equation (5) is exactly the same as the so-called conical flow equation of Busemann. At first, we must distinguish between the two cases of $M < 1$ and $M > 1$ corresponding to subsonic and supersonic velocities of the wedge.

In the case $M < 1$, the apex O is situated in the bounding circle $x^2 + y^2 = 1$ (Fig. 4 a) and the region affected by the apex O is confined in the circle. On the assumption that $\delta \ll 1$ (where for simplicity we assume $\delta_1 = \delta_2 = \delta$), the shock wave propagating from the wall of the wedge mentioned in § 1 is now reduced to a sound wave s_0 and the pressure p behind the wave is given by (1) and (2). From (1), we have

$$U_1 - u_0 \sin \delta_1 = c_0 + \{(\gamma+1)/4\} u_0 \delta\,.$$

Inserting this into (2) gives

$$p = \delta\,. \tag{7}$$

Further, p has a singularity at the apex O, because of the fact that the vertical component of velocity v along the x-axis jumps from O to $\pm\delta$ there. In view of the third equation of (6), p must satisfy the relation:

$$\lim_{y \to \pm 0} \int_{-M-c}^{-M+c} \frac{\partial p}{\partial y}\, dx = \mp M\delta\,, \tag{8}$$

where c is an arbitrary positive small constant.

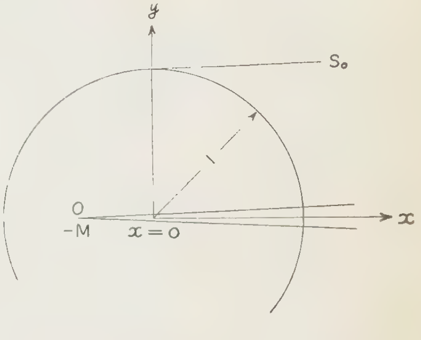

(a) $M < 1$

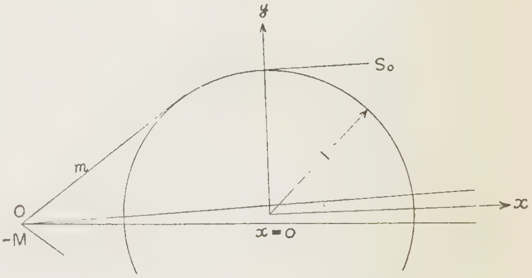

(b) $M > 1$

Fig. 4.

In the case of $M > 1$, on the other hand, the apex O falls outside the circle (Fig. 4 b) and the region affected by it now extends up to the Mach wave m, but, in the domain bounded by m and the circle, the state is uniform and the pressure p is readily given as:

$$p = M(M^2-1)^{-1/2}\delta\,. \tag{9}$$

To determine the flow field in the circle $x^2 + y^2 = 1$, we introduce ξ, η in place of x, y by the Busemann transformation as:

$$\left.\begin{aligned} &\xi + i\eta = Re^{i\theta}\,, \quad x + iy = re^{i\theta}\,, \\ &R = (1-\sqrt{1-r^2})/r\,. \end{aligned}\right\} \tag{10}$$

Then, equation (5) is reduced to the Laplace equation:

$$\frac{\partial^2 p}{\partial \xi^2} + \frac{\partial^2 p}{\partial \eta^2} = 1\,. \tag{11}$$

The condition (8) for the case of $M < 1$ is now transformed into

$$\lim_{\eta \to \pm 0} \int_{\xi_0 - c}^{\xi_0 + c} \frac{\partial p}{\partial \eta}\, d\xi = \mp \frac{M\delta}{\sqrt{1-M^2}}\,, \tag{12}$$

where $\xi_0 = -(1-\sqrt{1-M^2})/M$ corresponds to the apex $x = -M$.

Accordingly, our present problem is reduced to that of finding a harmonic function which takes on the given value on the unit circle

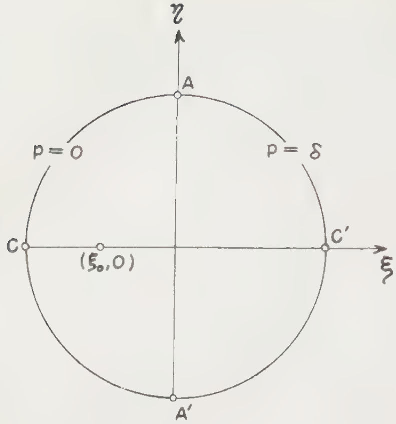

(a) $M<1$

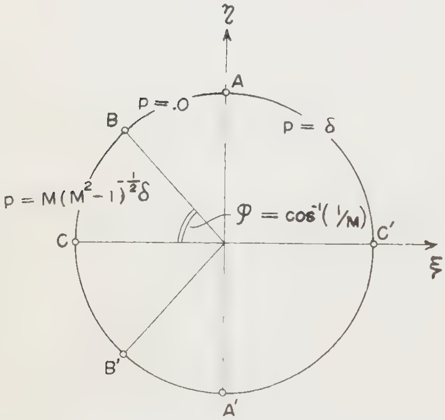

(b) $M>1$

Fig. 5.

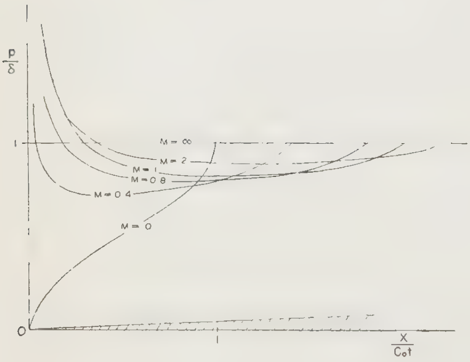

Fig. 6.

and moreover, in the case of $M<1$, a given singularity (12) at the point $(\xi_0, 0)$. These conditions are shown in Fig. 5.

The solution p in the case of $M>1$ is the sum of two harmonic functions p_1 and p_2 ($p_1 = \delta$ on $\widehat{AC'A'}$ and O on $\widehat{ACA'}$; $p_2 = M(M^2-1)^{-1/2} \times \delta$ on $\widehat{BCB'}$ and O on $\widehat{BC'B'}$) or,

$$p = p_1 + p_2 \quad (M>1)\,. \tag{13}$$

p_1 and p_2 are readily found as:

$$p_1 = \frac{\delta}{\pi}\left(\arg\frac{\zeta - i}{\zeta + i} - \frac{\pi}{2}\right), \tag{14}$$

$$p_2 = \frac{\delta}{\pi}\frac{M}{\sqrt{M^2-1}}\left(\arg\frac{\zeta_{B'}-\zeta}{\zeta_B-\zeta} - \varphi\right), \tag{15}$$

where $\zeta = \xi + i\eta$ and ζ_B, $\zeta_{B'}$ correspond to B, B' respectively,

$$\begin{aligned} \zeta_B &= -1/M + i(1-1/M^2)^{1/2}\,, \\ \zeta_{B'} &= -1/M - i(1-1/M^2)^{1/2}\,. \end{aligned} \tag{16}$$

The solution p for $M<1$ can be obtained as the sum of p_1 as given by (14), and a certain harmonic function p_3 which has a singularity (12) at $\zeta = \xi_0$ and vanishes on the circle, thus

$$p = p_1 + p_3 \quad (M<1)\,. \tag{17}$$

To determine p_3, we first consider a function which satisfies (12) near $\zeta = \xi_0$:

$$\mathrm{Re}\,[-(\delta/\pi)M(1-M^2)^{-1/2}\log(\zeta - \xi_0)]\,.$$

Then, p_3 can be easily constructed by the method of images. Thus

$$p_3 = \mathrm{Re}\left[\frac{\delta}{\pi}\frac{M}{\sqrt{1-M^2}}\log\frac{\xi_0\zeta - 1}{\zeta - \xi_0}\right]. \tag{18}$$

Now, the following formulae can be readily verified:

$$\left.\begin{aligned} &\lim_{M\to+1} p_2 = \lim_{M\to-1} p_3 = \mathrm{Re}\left[\frac{\delta}{\pi}\frac{1-\zeta}{1+\zeta}\right], \\ &\lim_{M\to\infty} p = \lim_{M\to\infty}(p_1+p_2) = p_1 + \lim_{M\to\infty} p_2 = \delta\,, \\ &\lim_{M\to 0} p_3 = 0\,. \end{aligned}\right\} \tag{19}$$

By using (14)–(19), the pressure distributions p/δ along the surface of the wedge have been computed, for various Mach numbers M, and the result is shown in Fig. 6.

We shall now compare Fig. 4 with Fig. 7 which shows the well-known configuration occurring when a plane shock wave is diffracted by a thin wedge; it will be seen that there is some similarity between them, especially in the region affected by the apex O. Moreover, comparing Fig. 6 with the corresponding ones in the previous works on the diffraction of shock waves[2)3)], we shall also find the similarity.

This similarity is not merely apparent, but is due to the fact that our present problem

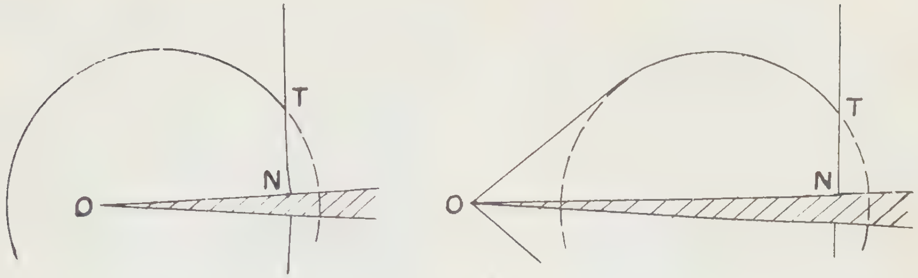

Fig. 7.

is essentially concerned with the interaction between the wedge and a shock wave which has the same form as the wedge and initially approaches the wedge as shown in Fig. 8 (such a shock wave is of course fictitious).

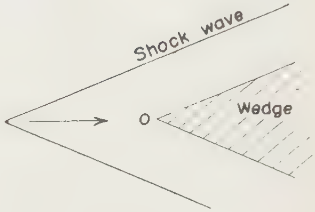

Fig. 8.

Accordingly, discussions on our problem proceed almost parallel to that of the diffraction of a shock wave. Moreover, using this similarity, we may estimate the effect of impulsive motion of a wedge on the surrounding air by means of the experiment of interaction of a shock wave and a wedge, although it is not quantitatively equivalent. For, the presence of shock wave TN in the circle in Fig. 7 whould give rise some effects on the flow field.

§ 3. The Case of a Wedge having not Small Vertex Angle

We have seen in § 2 that two different configurations appear according as $M<1$ or $M>1$ as shown in Fig. 4, namely, the disturbance from the apex O is advancing to the front for $M<1$, while receding along the wall for $M>1$. The same result will hold for the present case of a wedge having not small vertex angle, except that the characteristic value is not M in this case. As shown in Fig. 9, if δ_1 and δ_2 are larger than the critical shock detachment angle δ_0 for a given M, we may have a shock wave s propagating from the apex O to the front; on the other hand, for δ_1, δ_2 smaller than δ_0, we may have an attached shock wave s' and a curved shock waves*.

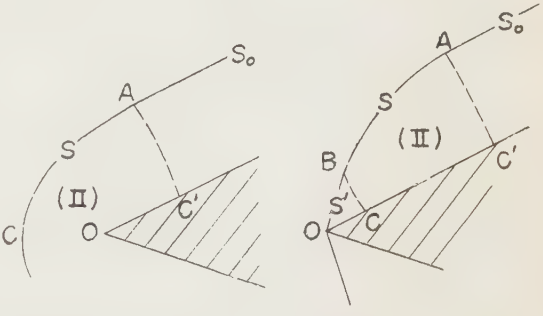

(a) δ_1, $\delta_2>\delta_0$ (b) δ_1, $\delta_2<\delta_0$

Fig. 9.

In the region behind s' the state will be uniform, at least near the apex O. Behind a border line AC', the state is uniform as mentioned in § 1.

It is in general difficult to determine the non-uniform field in the region (II) together with the form of its boundary, but we have some tractable special cases. In the following subsections (A), (B) and (C), we shall consider these cases.

(A) *The case:* $M\ll 1$

In this case, the problem is reduced to the acoustic theory and the solution is well known and almost the same as that in § 2. But it is interesting for us to compare it with the corresponding problem on the diffraction of a very weak shock around a wedge²⁾ and to find that there also exists the similarity between them which was discussed above. Their configurations are shown in Fig. 10.

Shock waves s_0 and s in Fig. 9 a are now sound waves and s is a part of the circle with center at O. The deviation of pressure p' from p_0 which is assumed to be small and satisfied by the wave equation takes the values $\gamma p_0 M$

---

* We are not concerned here with the cases: $\delta_1<\delta_0$, $\delta_2<\delta_0$; etc.

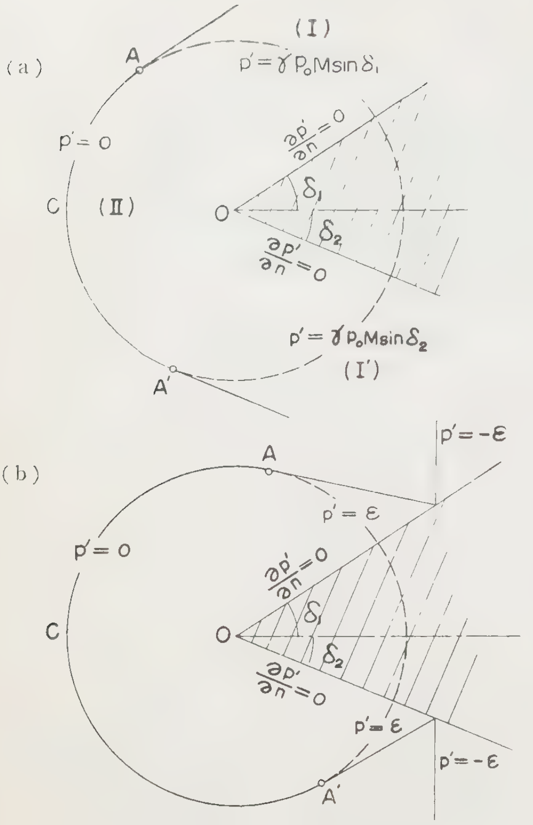

(a) Impulsive motion (b) Diffraction of Shock

Fig. 10.

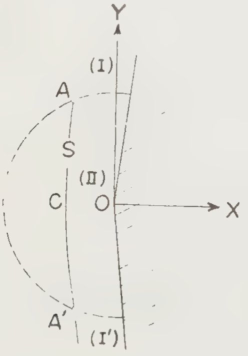

Fig. 11.

$\times \sin \delta_1$, $\gamma p_0 M \sin \delta_2$ in regions (I), (I′), derived from Eqs. (1), (2). Accordingly the problem of determining p' in (II) is a boundary value problem in a sector as shown in Fig. 10 a. On the other hand, corresponding boundary values for the problem of the diffraction of shock are shown in Fig. 10 b, where ε is a small quantity. Both problems are the same if $\delta_1=\delta_2$: therefore the solutions are completely similar to each other in this case. Further, it may be expected that the solution in the case $\delta_1 \fallingdotseq \delta_2$ is not very different in nature from the case $\delta_1=\delta_2$.

(*B*) *The case:* $\delta_1, \delta_2 \approx \pi/2$

Now, the corresponding problem in the case of diffraction of shock has been discussed by Lighthill[3]. As in the case (*A*), the above-mentioned similarity is also complete in the non-uniform region. The reason is, in brief, that their states are both not far different from that generated by a head-on encounter of a plane shock wave with a wall as in Fig. 3.

In the case of head-on encounter, the propagation velocity U of the reflected wave, the pressure $p^{(0)}$ and the sound velocity $c^{(0)}$ behind it are given by (1) and (2), on putting $\delta_1=\pi/2$, as

$$\left.\begin{aligned} &(U-u_0)^2+(1/2)(\gamma+1)u_0(U-u_0)-c_0{}^2=0\ , \\ &\qquad\qquad U-u_0<0\ , \\ &\frac{p^{(0)}}{p_0}=\frac{2\gamma}{\gamma+1}\left(\frac{u_0-U}{c_0}\right)^2-\frac{\gamma-1}{\gamma+1}\ , \\ &\left(\frac{c^{(0)}}{c_0}\right)^2=\frac{p^{(0)}}{p_0}\,\frac{p_0+p^{(0)}(\gamma-1)/(\gamma+1)}{p^{(0)}+p_0(\gamma-1)/(\gamma+1)}\ . \end{aligned}\right\} \tag{20}$$

Returning to our present problem, the wedge and the oncoming shock wave shown in Fig. 8 are now approximately plane and, after encounter the states in (I), (I′) and (II) (Fig. 11) have only a small perturbation from that represented by (20).

Then, in these regions, the pressure deviation p' is small and satisfied by the wave equation:

$$\frac{\partial^2 p'}{\partial t^2}=c^{(0)2}\left(\frac{\partial^2 p'}{\partial X^2}+\frac{\partial^2 p'}{\partial Y^2}\right).$$

If we put

$$X/(c^{(0)}t)=x,\ \ Y/(c^{(0)}t)=y,\ \ p'/(\rho^{(0)}c^{(0)})=p, \tag{21}$$

the above equation is reduced to equation (5). The (X, Y)-components of velocity (u, v) in (I), (I′), (II) are also satisfied by Eq. (6) and the region affected by O is confined in the circle $x^2+y^2=1$ as in § 2. The uniform states in the regions (I) and (I′) can be found as:

$$\left.\begin{aligned} &U_1,\ U_2=U\ , \\ &u=0,\quad v=u_0\varepsilon_1\,(\mathrm{I})\ ;\quad v=-u_0\varepsilon_2\,(\mathrm{I}')\ , \\ &p=0\ , \end{aligned}\right\} \tag{22}$$

by using the arguments in § 1 and taking account of the smallness of ε_1, ε_2, where $\varepsilon_1=\pi/2-\delta_1$, $\varepsilon_2=\pi/2-\delta_2$.

In view of the pseudo-stationariness and the relations (21), the shock wave s may be assumed to have the form

$$x=-k_0+f(y), \tag{23}$$

where $f(y)$ is unknown but of small magnitude and $k_0=U/c^{(0)}<1$ which is readily verified, considering that the flow is always subsonic behind the normal shock wave.

After some calculations using shock conditions and (23), we have u, v and p immediately behind the shock wave (23) as:

$$\left.\begin{aligned} u&=\frac{c^{(0)}}{\gamma+1}\frac{(3-\gamma)u_0+4U}{u_0+U}(f-yf'),\\ v&=u_0f',\\ p&=-\frac{4}{\gamma+1}\frac{\rho_0}{\rho^{(0)}}U(f-yf'), \end{aligned}\right\} \tag{24}$$

from which f can be eliminated to give

$$u=A_0p\,,\quad y\cdot\partial v/\partial y=B_0\cdot\partial p/\partial y\,, \tag{25}$$

where

$$\begin{aligned} A_0&=-\frac{(3-\gamma)u_0+4U}{4(u_0+U)}\frac{\rho^{(0)}}{\rho_0}\frac{c^{(0)}}{U}\,,\\ B_0&=\frac{\gamma+1}{4}\frac{u_0}{U}\frac{\rho^{(0)}}{\rho_0}\,. \end{aligned} \tag{26}$$

Since we neglect quantities of $O(\varepsilon_1^2)$ and $O(\varepsilon_2^2)$, both wall and shock in the circle may be approximated by straight segments, which are $x=0$ and $x=-k_0(x^2+y^2<1)$ respectively. Thus the region (II) of non-uniform flow in Fig. 11 is approximately $0>x>-k_0$, $x^2+y^2<1$ (Fig. 12). On the boundary of this region, we have the following conditions: on $x=0$, $u=0$; on the circular arc $\widehat{AC'}$, $\widehat{AC''}$, the results (22) hold; on $x=-k_0$ the relations (25) hold.

Thus, the problem of finding the field in (II) is reduced to solving a boundary value problem. As we have remarked above, it is readily seen that this problem is exactly the same as that which appears in the corresponding case in the diffraction[2], except that the values of A_0 and B_0 are different from their corresponding values. Further discussion on the problem is, therefore, omitted here.

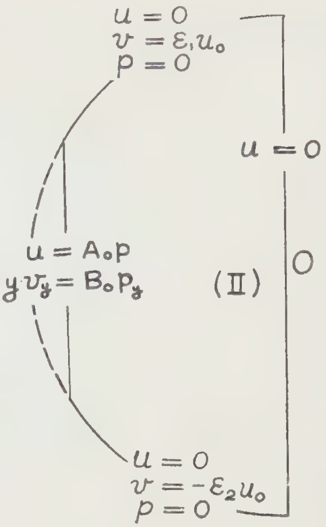

Fig. 12.

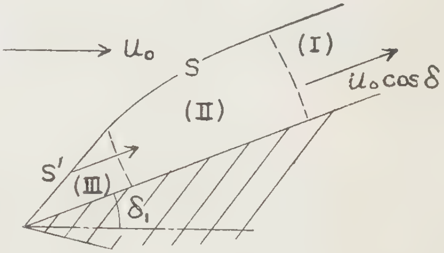

Fig. 13.

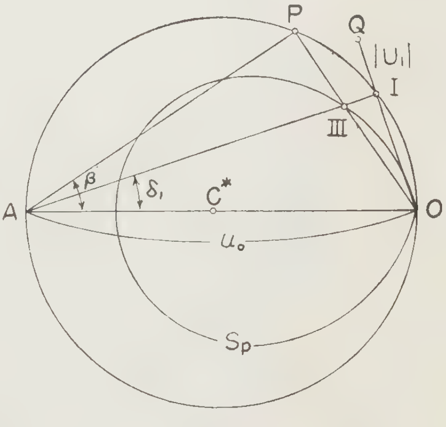

Fig. 14.

(*C*) *An approximate treatment for* δ_1, $\delta_2<\delta_0$

Since the flow along the upper and lower surfaces do not interact with each other in this case and can be determined separately, we shall consider only the upper part of them.

Now, if there happens the case that both states in regions (I) and (III) (where they are uniform) in Fig. 13 are almost the same, then the non-uniform state in (II) will be also approximately uniform and may be treated by a linear equation concerning its perturbation from the state (I) or (III). Ordinarily, such a case is not special. To see this, we shall compare, for example, the velocities in (I) and (III). Their directions are the same and parallel to the wall; as for their magnitudes, we have $u_0 \cos\delta_1$ in (I), while the value in (III) has not a simple analytic form but can be conveniently represented on the shock polar diagram. In Fig. 14, AO is u_0 and s_p is the shock polar, and the velocity in (III) is represented by $AIII$. Since the velocity in (I) is $u_0\cos\delta_1 = AI$, the difference between the velocities in (I) and (III) is $III\,I$, so that usually it can be considered to be small compared with AI. Further, the velocity component normal to and observed from the shock wave is $PO = u_0 \sin\beta$ for (III) and $QO = U_1 + u_0\sin\delta_1$ for (I) ($|U_1|/u_0 \sin\delta_1 \rightarrow (\gamma-1)/2$, as $M \rightarrow \infty$). Since the pressure behind the shock wave is determined by the above-mentioned normal component of velocity, the difference between the pressures in (I) and (III) is also small as we can see from Fig. 14.

Concerning the diffraction of shock wave by a wedge having not small vertex angle, Munakata$^{5)}$ has presented quite recently an approximate method in which the non-uniform field is approximated by a perturbation from some definite state.

In view of the above mentioned similarity in § 2, it may be expected that his method will also be applicable to our present problem.

The author wishes to express his gratitude to Professor Isao Imai for his invaluable advice and encouragement. The author is also indebted to Mr. H. Hasimoto for stimulating discussions.

References

1) Courant-Friedrichs: Supersonic Flow and Shock Waves (Interscience Publishers, 1948), pp. 152-153.
2) H. F. Ludloff: Advances in Applied Mechanics **III** (1953) 109.
3) M. J. Lighthill: Proc. Roy. Soc. London **A 198** (1949) 454; **200** (1950) 554.
4) G. Strang: Proc. Roy. Soc. London **A 195** (1948) 245.
5) K. Munakata: J. Aero. Sci. **21** (1954) 501.

JOURNAL OF THE PHYSICAL SOCIETY OF JAPAN Vol. 10, No. 3, MARCH, 1955

A New Graphical Solution of Ordinary Linear Differential Equation of the Second Order

By Isao OSHIDA

Kobayasi Institute of Physical Research, Kokubunji, Tokyo

(Read November 2, 1954. Received November 12, 1954)

A new graphical solution applicable to linear differential equations of second order was presented. This method is simpler in construction but is of higher accracy than the older methods. Two examples were given and it was shown that the error is very small in practice. The derivative dy/dx, as well as the solution $y(x)$ itself, is obtained simultaneously. Accordingly, this method can be conveniently applied to classical vibration problems, quantum-mechanical collision problems, eigenvalue problems in one dimension, and so forth.

§ 1. Introduction

To have the solution of ordinary differential equation of the second order, with which we meet frequently in phisical problems, many numerical and graphical methods have been developed$^{1)}$. But if we confine ourselves to linear equations, they are unnecessarily complicated or else too bad approximation. As for the numerical method, the author has presented a simpler method$^{2)}$. In this paper, a graphical method with simpler procedures was shown, the course of which can also be followed by numerial calculation.

§ 2. Transformation of the Differential Equation

We deal solely with the normal form

$$\frac{d^2y}{dx^2} + f(x)y = 0 , \qquad (1)$$

because any linear differential equation of the second order can be written in this form.

Equation (1) is equivalent to the following two simultaneous differential equations of the first order;

$$\frac{dy}{dx}=z\ , \tag{2A}$$

$$\frac{dz}{dx}=-f(x)y\ . \tag{2B}$$

For graphical solution, as well as numerical solution, it is more convenient to make use of the approximate *difference* equations in place of these *differential* equations. It can be done by putting

$$\frac{dy}{dx}\fallingdotseq\frac{1}{h}(y_{i+1}-y_i)\ , \tag{3A}$$

$$\frac{dz}{dx}\fallingdotseq\frac{1}{h}(z_{i+1}-z_i)\ . \tag{3B}$$

Here h is the pitch of x, that is, $x_i=x_0+ih$ $(i=1,2,3,\ \ldots.)$ and the corresponding values of y and z are y_i and z_i respectively. Substituting (3) into (2), we have

$$y_{i+1}\fallingdotseq y_i+hz_i\ , \tag{4A}$$

$$z_{i+1}\fallingdotseq z_i-hf(x_i)y_i\ . \tag{4B}$$

If a set of initial values of y and z, say, y_0 and z_0, is given, we can find y_1 and z_1 from (4A) and (4B), then y_2 and z_2, y_3 and z_3, and so on.

Unfortunately this procedure has too low accuracy, because (3A) and (3B) are only the first approximation and (4A) and (4B) are correct only to the first power of h. The accuracy can, however, be enhanced easily by taking, in place of (3A) and (3B), more accurate forms

$$\left(\frac{dy}{dx}\right)_{i+1/2}\fallingdotseq\frac{1}{h}(y_{i+1}-y_i)\ , \tag{5A}$$

$$\left(\frac{dz}{dx}\right)_i\fallingdotseq\frac{1}{h}\,z_{i+1/2}-z_{i-1/2}\ , \tag{5B}$$

and substituting them in (2), which lead to

$$y_{i+1}\fallingdotseq y_i+hz_{i+1/2}\ , \tag{6A}$$

and

$$z_{i+1/2}\fallingdotseq z_{i-1/2}-hf(x_i)y_i\ , \tag{6B}$$

or

$$z_{i+3/2}\fallingdotseq z_{i+1/2}-hf(x_{i+1})y_{i+1}\ . \tag{6B$'$}$$

The formulas are correct to the order of h^3, as is easily verified by expansion. Accordingly the use of (6) instead of (4) greatly improves the accuracy of the calculation.

§ 3. Initial Conditions

In most cases, a set of values of y and z, say, y_0 and z_0, is given as the initial condition. But, to make the use of (6), we have to know, for instance, y_0 and $z_{1/2}$ in order to have the succeeding values y_1, $z_{3/2}$, y_2, $z_{5/2}$, y_3, ... employing (6A) and (6B) alternatively. However, if we know y_0 and z_0, $z_{1/2}$ can be calculated to the second order of h, as shown in the following.

$$\begin{aligned}z_{1/2}\fallingdotseq z_0&+\frac{h}{2}\left(\frac{dz}{dx}\right)_0+\frac{1}{2}\left(\frac{h}{2}\right)^2\left(\frac{d^2z}{dx^2}\right)_0\\ &=z_0-\frac{h}{2}f(x_0)y_0-\frac{h^2}{8}\left\{\frac{d}{dx}\left(\frac{d^2y}{dx^2}\right)\right\}_0\\ &=z_0-\frac{h}{2}f(x_0)y_0-\frac{h^2}{8}\left[\frac{d}{dx}\{-f(x)y\}\right]_0\\ &=z_0-\frac{h}{2}f(x_0)y_0\\ &\qquad+\frac{h^2}{8}\left\{\left(\frac{df}{dx}\right)_0y_0+f(x_0)\left(\frac{dy}{dx}\right)_0\right\}\ .\end{aligned}$$

That is, according to (2A),

$$\begin{aligned}z_{1/2}\fallingdotseq&\left\{1+\frac{h^2}{8}f(x_0)\right\}y_0\\ &-\frac{h}{2}\left\{f(x_0)-\frac{h}{4}\left(\frac{df}{dx}\right)_0\right\}z_0\ .\end{aligned} \tag{7}$$

If the region of x extends to infinity and the condition is given at the point of infinity, we have to use the solution in series which is valid near the point at infinity in order to calculate the starting values of y and z, corresponding to an appropriate, finite value of x.

§ 4. Method of Graphical Construction

The procedure of the graphical method is as follows; the proof is given in the next section.

Draw two, parallel lines ***a*** and ***b***, the distance between them being D. According to the nomenclature of nomography, they are the supports of y and z respectively. y_i is given by the point Y on ***a***, the distance OY from the origin O being equal to y_i; similarly $z_{i+1/2}$ is given by Z on ***b***, QZ being equal to $z_{i+1/2}$. Draw two more parallel lines, ***r*** and s_{i+1}, as shown in Fig. 1, and let the distance between ***r*** and ***a*** be equal to

$$\frac{h}{1-h}D\ , \tag{8}$$

while that between s_{i+1} and ***b*** be equal to

$$\frac{hf(x_{i+1})}{1-hf(x_{i+1})}D\,. \tag{9}$$

If this value is negative, s_{i+1} comes to the same side with r with respect to b[3].

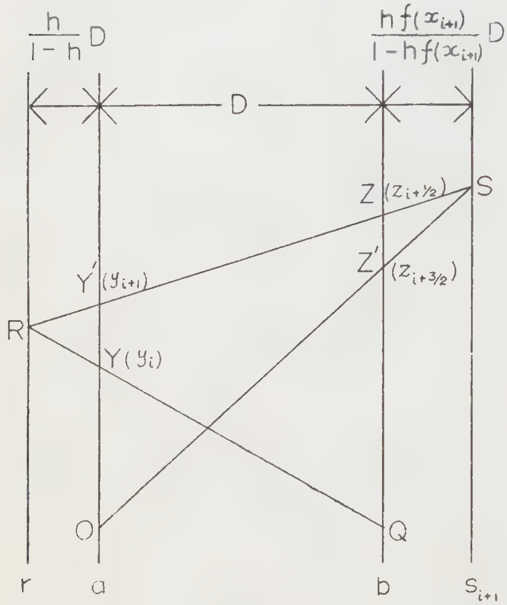

Fig. 1.

Now combine Q and Y, extend to R, the point where QY meets with r. Draw the line RZ, and find the point Y' where RZ meets with a, then Y' gives the next y-value, namely y_{i+1}.

To have $z_{i+3/2}$, which is necessary to calculate y_{i+2}, the similar procedure is applicable. That is, to get the point S, where $Y'Z$ meets with s_{i+1}, to combine O and S, and to find the intersection Z' of OS with b. Then QZ' gives the value $z_{i+3/2}$.

Starting from an initial values, y_0 and $z_{1/2}$, and repeating the procedure above, we have the values y_1, $z_{3/2}$, y_2, $z_{5/2}$, ... and so on, and consequently can obtain the solution on the graph.

§ 5. The Proof

The proof is very easy, as is deduced from elementary geometry.

$$YY':QZ=\frac{h}{1-h}D:\frac{h}{1-h}D+D=h:1\,.$$

Since QZ is equals to $z_{i+1/2}$, YY' is to $hz_{i+1/2}$. Hence, according to (6A),

$$OY'=OY+YY'=y_i+hz_{i+1/2}=y_{i+1}\,.$$

Similarly,

$$ZZ':Y'O=\frac{hf(x_{i+1})}{1-hf(x_{i+1})}D:\frac{hf(x_{i+1})}{1-hf(x_{i+1})}D+D$$
$$=hf(x_{i+1}):1\,.$$

Accordingly,

$$ZZ'=hf(x_{i+1})y_{i+1}\,,$$

and by (6B′),

$$QZ'=QZ-ZZ'=z_{i+1/2}-hf(x_{i+1})y_{i+1}=z_{i+3/2}\,,$$

which was to demonstrated.

§ 6. Example I

As an example, the equation of simple harmonic motion with the frequency 1/2, i.e.

$$\frac{d^2y}{dx^2}=-\pi^2y\,, \tag{10}$$

is taken, the solution of which is well known and serves for checking the accuracy of our method. The equation (10) can be devided into

$$\frac{dy}{dx}=z\,, \tag{11A}$$

and

$$\frac{dz}{dx}=-\pi^2y\,, \tag{11B}$$

following the programme shown above, since, however, the coefficients in the right hand side of (11A) and (11B) are so much differ as 1 to π^2, the line s_{i+1} gets so far as the construction becomes inconvenient, or, we have to adopt too small h, that also puts us to trouble. The better division is, clearly,

$$\frac{dy}{dx}=\pi z\,, \tag{12A}$$

$$\frac{dz}{dx}=-\pi y\,, \tag{12B}$$

This notice is also useful in general case of (2A) and (2B), for which we adopt

$$\frac{dy}{dx}=kz\,,$$

$$\frac{dz}{dx}=-\frac{1}{k}f(x)y\,,$$

with a proper constant k, such that k and $f(x)/k$ are as near as possible over the region of x in question.

As for the pitch h, it is convenient in practice, to adjust to such value that (8) and (9) amount to 0.1—0.5, if possible. In the present case, we put $h=0.05$, since (8) and (9) are both equal to $\pi h/(1-\pi h)=0.186$ with this value of h.

If the initial conditions are $y=0$ and $z=1$ for $x=0$, the exact solution is $y=\sin \pi x$. To have the graphical solution, we have to know $z_{1/2}=z(0.025)$ first. It can be done with (7), giving $z_{1/2}=0.997$. Starting with these two values, y_0 and $z_{1/2}=0.997$, we have the values of $y_1, y_2, \ldots$ and $z_{3/2}, z_{5/2}, \ldots$ according to the present method. The construction is shown in Fig. 2, while the numerical values read on the graph compared with the exact value $y=\sin \pi x$ are as follows. The agreement is fairly good. For example, at $x=0.5$, which is the final point of the integration, the error is only 0.4%.

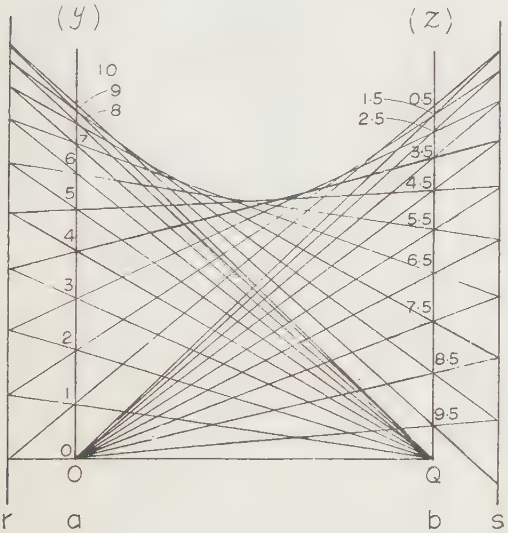

Fig. 2.

x	y (graphical)	y (exact)
0	(0)	0
0.05	0.168	0.156
0.1	0.306	0.309
0.15	0.449	0.454
0.2	0.580	0.588
0.25	0.700	0.707
0.5	0.800	0.809
0.35	0.880	0.891
0.4	0.940	0.951
0.45	0.980	0.988
0.5	0.996	1.000

§ 7. Example II

Next we deal with the following equation,

$$\frac{d^2y}{dx^2}=-xy\ , \tag{13}$$

$$y=1 \quad \text{and} \quad \frac{dy}{dx}=0\ , \quad \text{for} \quad x=0\ .$$

(13) is devided into two simultaneous differential equations,

$$\frac{dy}{dx}=z\ , \qquad \frac{dz}{dx}=-xy\ .$$

Fig. 3 shows the construction of the graphical solution, putting $h=0.2$. For this example, and it is also true in general, (9) varies with x, and accordingly s_{i+1} varies with x_{i+1}. The graphical starting values are $y_0=y(0)=1$ and $z_{1/2}=z(0.1)=-0.005$ and the results compared with the analytical solution

$$y=3^{-1/3}\Gamma(2/3)x^{1/2}J_{-1/3}(2x^{3/2}/3)\ ,$$

are given in the following. Here the agreement is satisfactory again; the errors do not exceed 0.01

x	y (graphical)	y (analytical)
0	(1.000)	1.000
0.2	0.997	0.999
0.4	0.992	0.989
0.6	0.969	0.964
0.8	0.920	0.916
1.0	0.842	0.839
1.2	0.737	0.728
1.4	0.591	0.582
1.6	0.413	0.405
1.8	0.210	0.202
2.0	−0.011	−0.015

§ 8. Remarks

The accuracy of this method can compare with that of a differential analyser, and the time needed is not so long. For instance, once the preliminary construction is over, it takes some fifteen minutes or so to draw an solution under given initial condition. Therefore this method is effective to find the integral of second-order equations when extraordinary accuracy is not requested. Even when the high accuracy is demanded, the present method can be used to find the first approximation.

For eigenvalue problems, with which we meet frequently in quantum mechanics as well as in classical vibration problems, we have to rely upon the trial-and-error method. That is, to start with presumed eigenvalue and given boundary condition at one end and to adjust the eigenvalue so as to fit the boundary condition at another end. Here this intuitive and handy method has much advantage again.

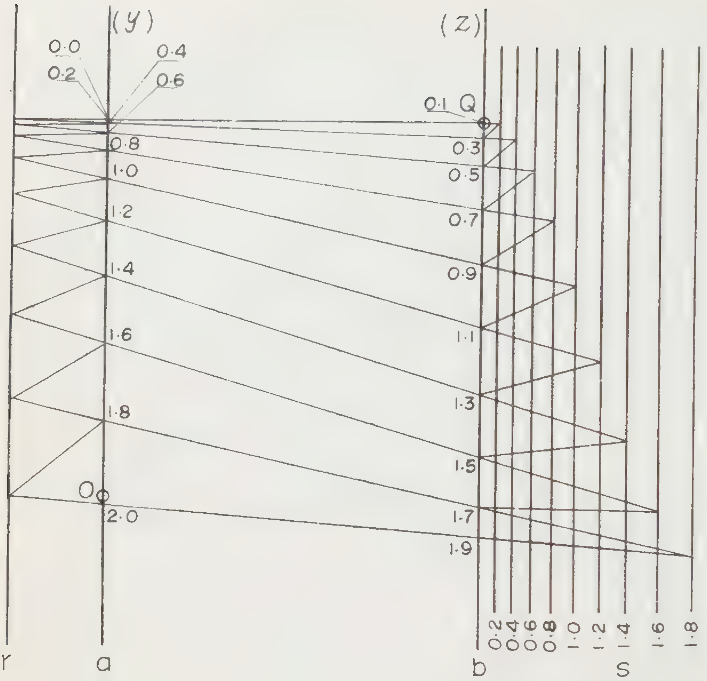

Fig. 3.

References

1) For the older methods, see e.g. H. von Sanden: "*Practische Analysis*", 2. ed, Leipzig and Berlin, 1923. For nomographic methods recentry developed, see K. Morita and Y. Simokawa: Memoirs of the Faculty of Technology, Kanazawa University **1** (1953) 1–13.

2) I. Oshida and H. Ichikawa: Research Report, Faculty of Engineering, Nagoya University **3** (1950) 9–12 (Japanese), Kagaku **20** (1950) 423–4 (in Japanese).

3) For the calculation of (8) and (9), the use of the following table is very convenient. Marcel Boll: "*Tables Numeriques Universelles*„, Paris 1947, pp. 190–5.

Short Notes

J. PHYS. SOC. JAPAN **10** (1955) 233~234

On the Blocking Layer of Selenium Rectifier (I)

By Jiro YAMAGUCHI, Tadao KANAZAWA,
Tôru MATOZAKI and Kazuji HIRAI
Faculty of Engineering, Osaka University

(Received September 18, 1954)

In this report the property of blocking layer of selenium rectifiers is investigated by compairing the characteristics of the ordinary Se-rectifier with that of the Se-rectifier with insulating film in the blocking layer, which is made as follows: the film of lacquer or silicon resin of 50~2000Å, which is previously spread over the distilled water, is put on the metallic Se layer on the steel plate, electroplated by nickel. Then on the resin film is covered cadmium as one electrode. Fig. 1 shows the constitution of this rectifier. The thickness of film is measured by the silica gauge[1] with the interference color[2] method.

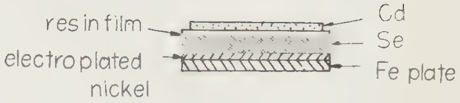

Fig. 1. Constitution of specimen used.

The electrostatic capacity of the Se-rectifiers with or without resin film is measured by the Wien-bridge at 5,000 cycle per sec under the d. c. bias voltage to the hard flow direction. From the experimental results we find that the inverse square of electrostatic capacity is proportional to the d. c. bias voltage, and this relation is in accordance with the theoretical prediction involved in Eq. (1). Moreover, the relation of electrostatic capacity versus film thickness is found to be expressed at Fig. 2.

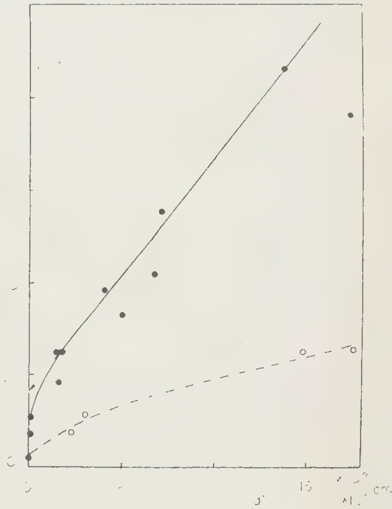

Fig. 2. Square of resin film thickness (d) versus inverse square of electrostatic capacity at room temp., when d. c. bias voltage is zero.
[Upper scale of absissa is for curve (1), lower for curve (2).]

In Fig. 3, let

C, C_0 and C_{00}: electrostatic capacity of barrier per unit area, that of zero bias voltage and the value of C_0 when exterpolating d to zero respectively,

d: thickness of resin film,

e: electronic charge,

L: (length of barrier)—d,

N: volume density of the space charge in semiconductor,

U: impressed voltage on barrier, which is nearly equal to the applied voltage to the rectifier, when it is to the hard flow direction,

ΔE: energy gap between conduction band and impurity level in semiconductor,

ϕ: work function of metal,

χ: electron affinity of semiconductor,

χ_0: difference between affinity of resin film and that of semiconductor,

ε_1 and ε_2: dielectric constant of resin film and semiconductor,

the theoretical consideration shows[3]

$$\frac{1}{C^2}=\frac{d^2}{\varepsilon_1^2}+\frac{2}{eN\varepsilon_2}\left(\frac{\phi-\chi}{e}-\frac{\Delta E}{2e}-U\right) \qquad (1)$$

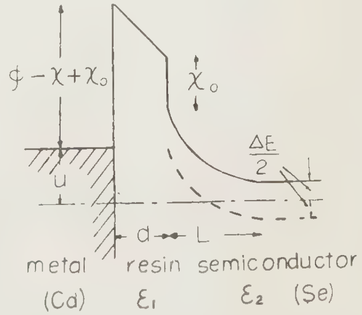

Fig. 3. Energy level diagram of compound blocking layer when negative bias voltage is impressed.

or
$$\frac{1}{C_0^2}=\frac{d^2}{\varepsilon_1^2}+\frac{2}{eN\varepsilon_2}\left(\frac{\phi-\chi}{e}-\frac{\Delta E}{2e}\right) \qquad (2)$$

and
$$\phi-\chi-\frac{\Delta E}{2}=-\frac{e}{C_{00}}\left[dU\Big/d\left(\frac{1}{C^2}\right)\right]. \qquad (3)$$

The experimental results are expressed by Eq. (1) when ε_2 is assumed to be 10 and $N=6\times10^{15}$, and they also agree well with the relation of Eq. (3) except for $d\gtrsim1000$Å. Extrapolating the results to $d=0$ as Fig. 2 and applying them to Eqs. (2) and (3), it is estimated that

$\varepsilon_1=2.5$ for lacquer resin film,

$\varepsilon_2=3.0$ for silicon resin film,

and $\phi-\chi-\Delta E/2=1.5\sim1.6$ eV . (4)

From the analysis of the experimental results of the Se-rectifier without resin film by the similar method, we found:

$N=(8\sim9)\times10^{15}$ (When ε_2 is assumed to be 10 as before)

and $\phi-\chi-\Delta E/2=0.7\sim0.8$ e.V. (5)

The difference of values in (4) and (5) suggests that CdSe exists in the blocking layer of the rectifier in the latter case.

In order to study the property of the resin film in the blocking layer the electron-diffraction method is used its wave length being 0.066Å. The resin film of the specimen is of lacquer, on which thin cadmium film is depositted from the standpoint of the experimental procedure.

Above the film thickness of 800Å, the diffraction patterns of Cd and Se are found in each side of the lacquer resin but those of CdSe can not be recognized.

In the case of the Se-rectifier without resin film i.e. the ordinary Se-rectifier, it is ascertained that Cd, CdSe and Se exist[4] one after another.

When the thickness of lacquer film is 20, 100, 130, 200, 430 or 500 Å, CdSe is found in both side of the resin film, that is, the patterns of Cd and CdSe are obtained at the side of depositted Cd and those of Se and CdSe are obtained at the place where Cd and resin film were taken oft.

From these observations[5] by electron diffraction, in the lacquer film less than 500 Å, there are many holes, through which Cd and Se combine chemically and CdSe is found in the interface. Above the thickness of 800 Å, the film is so dense that the chemical reaction does not take place. In the case of silicon resin, the singular border of thickness is nearly 1000 Å.

Thus we find that the difference of $(\phi-\chi-\Delta E/2)$ according to the existence or deficit of resin film, is due to the existance of CdSe layer in the blocking layer. Therefore in the Se-rectifier, CdSe layer plays the important role in the rectification.

The authors express their sincere thanks to Dr. S. Nagata for his experimental helpness on electron diffraction method.

References

1) H. Yoshinaga: J. A. P. Japan **12** (1943) 11 (in Japanese).
K. B. Blodgett: R. S. I. **12** (1941) 10.
2) H. Kubota: J. A. P. Japan **18** (1949) 139 and 247 (in Japanese) and J. O. S. A. **41** (1951) 1.
3) J. Yamaguchi and T. Miyauchi: Technical paper of Faculty of Engineering, Osaka University. **4** No. 113 (1954).
4) J. Yamaguchi and S. Katayama: J. Phys. Soc. Japan **5** (1950) 389.
S. Nagata and K. Agata: Phys. Soc. Japan **6** (1951) 523.
5) J. Yamaguchi, T. Kanazawa and T. Miyauchi: read before the meeting of Phys. Soc. of Japan at April, 1953.

J. Phys. Soc. Japan **10** (1955) 234~236

On the Blocking Layer of Selenium Rectifier (II)

By Jiro Yamaguchi

Faculty of Engineering, Osaka University

(Received September 18, 1954)

In the blocking layer of selenium rectifiers the selenides of covered metal, which is the ternary alloy of cadmium, tin and bismuth, have been observed by X-ray diffraction patterns[1]. If on the selenium layer is depositted cadmium instead of the ternary alloy, the rectifying property remains unchanged and cadmium selenide of about 10^{-4} cm thick is found in the blocking layer[2]. The rectification has been found in the layer between Cd

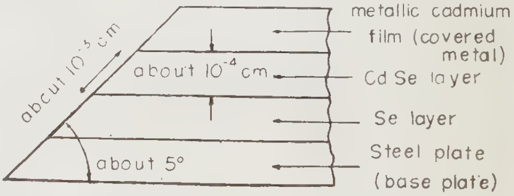

Fig. 1. Sectional view of the specimen.
(In this paper, each substance from upper to lower in the figure is denoted briefly as Cd, CdSe, Se and Fe respectively.)

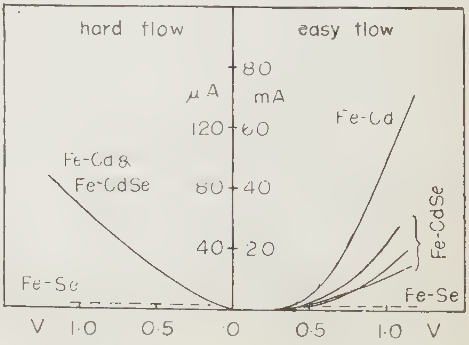

Fig. 2. Volt-Ampere characteristics for Fe electrode at room temp.

and Se, but whether the rectifying action is in the interface of Cd-CdSe or CdSe-Se, is not yet known. (Recently, this problem has been investigated by A. Hoftmann and F. Rose[3]), whose results accord with what will be shown in this paper.)

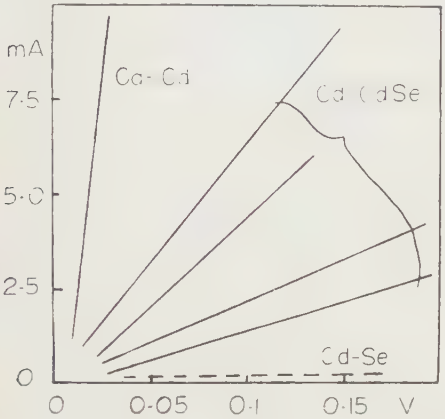

Fig. 3. Volt-Ampere characteristics for Cd electrode at room temp.

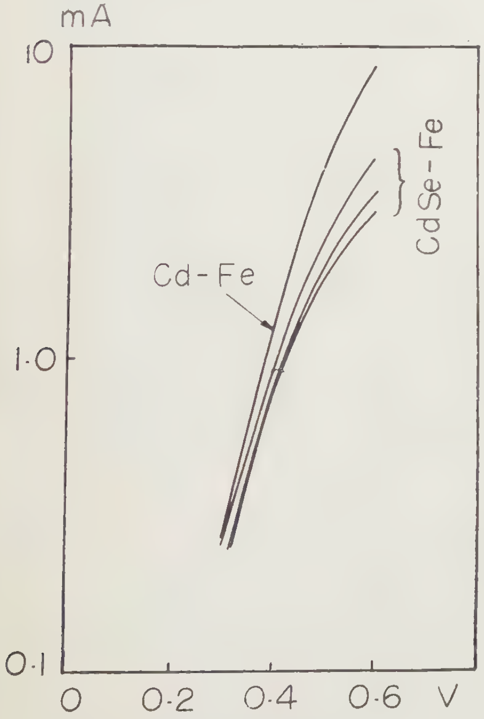

Fig. 4. The forward current at room temp. versus applied voltage.

When the selenium rectifier is obliquely ground, the angle of inclination being small (about 5°) as Fig. 1, CdSe is exposed and its width may be estimated to be about 10^{-3} cm.[4]) The specimen used in this report is such as mentioned above.

In the following experimental procedure, Cd or Fe in Fig. 1 is used as one electrode and the needle of $0.1\sim0.2$ mm diameter of several kinds of metal (i.e. W. Cd. Pt or Ni.), its tip being electro-polished, is as another electrode, touching on various places in Fig. 1 at the diameter of $(1.7\sim2)\times10^{-3}$ cm and the depth of about 1×10^{-3} cm. This is ascertained by the microscope in touching with metallic. Se. On probing by the needle electrode the position of CdSe is assumed to be in the boundary of Cd and Se, because CdSe layer could not be observed by naked eye.

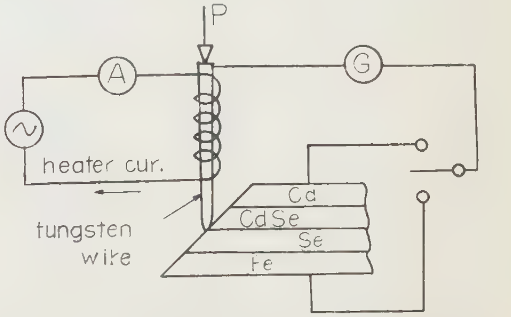

Fig. 5. Measuring apparatus of thermoelectric currents.

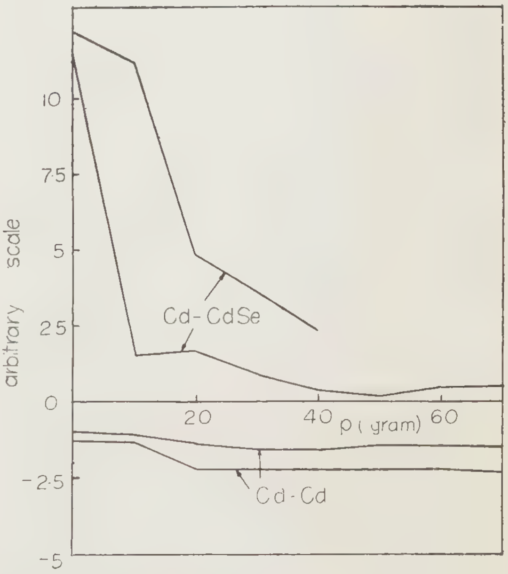

Fig. 6. Galvanometer deflection versus pressure of needle electrode.
(In the case of Fe–Se, the galvanometer deflection is very large and its direction shows Se being P-type semiconductor.)

The experimental results of rectification are shown in Figs. 2 and 3. In these figures the easy flow direction is defined as the polarity of needle electrode to be negative and the hard flow direction is reverse of that.

Although the bulk or spreading resistance in CdSe is large and different from each other, the resistance between Cd and CdSe is ohmic and the rectifying action is found between CdSe and Se or Fe. These characteristics do not vary, even if the ternary alloy is used as the covered metal or any kind of material is adopted as the needle electrode. Between Se and Cd or Fe, the resistance is so high that the current does not almost pass.

Fig. 4 shows the relation of the forward current versus the impressed voltage. It expresses that the slopes of these curves are nearly equal and about 13 V^{-1}.

The thermoelectric current is obtained by the measuring apparatus of Fig. 5, using Cd or Fe as one electrode. When the needle of tungsten, which is put on CdSe or Se, is heated by the electric current, the deflection of galvanometer expresses whether the semiconductor is P-type or N-type[5].

As shown in Fig. 6, the experimental results indicate that CdSe is N-type semiconductor, expressing the different property with Cd, and Se is P-type.

Consequently it is concluded that the rectifying action of selenium rectifier exists in the boundary of CdSe and Se and not of Cd and CdSe. Moreover CdSe is N-type semiconductor, Se being P-type.

The author expresses his sincere thanks to Mr. H. Kitama, Mr. T. Arakawa and Mr. F. Tomita for their helpness on experimental works.

References

1) J. Yamaguchi and T. Miyauchi: Electrotechnical paper of I. Elect. Eng. Japan **3** (1951) 5.

2) J. Yamaguchi and S. Katayama: J. Phys. Soc. Japan **5** (1950) 385.
S. Nagata and K. Agata: J. Phys. Soc. Japan **6** (1951) 523.

3) A. Hoffmann and F. Rose: Zeits. f. Phys. **136** (1953) 152.

4) J. Yamaguchi, S. Nagata and Y. Matsuo: J. Phys. Soc. Japan **6** (1951) 521.

5) J. W. Granille and C. A. Hogarth: Phys. Soc. Sec. B **64** (1951) 488.
M. Kikuchi and T. Onishi: Bullten of Electrotechnical Laboratry **16** (1952) 764 (in Japanese).

J. Phys. Soc. Japan **10** (1955) 236~237

Some Effects of Infrared Irradiation on ZnCdS Phosphors with Copper Activators

By Ken-ichi NAKAMURA

Shizuoka University, Oiwa-machi, Shizuoka-city, Japan

(Recieved November 11, 1954)

Luminescence phenonena of ZnS phosphors with copper (Cu) activators have been interpreted by Schön[1], Klasens[2] and Kallmann[3] etc. Their explanations are, however, discrepant. We have obtained the information of a new property of ZnCdS with Cu activators, and in the interpretation it may be assumed that traps caused by Cu have particular properties.

Five samples of hex-ZnCdS (NaCl 2%) phosphors with copper in concentrations from 0 to 5 parts per million are prepared.

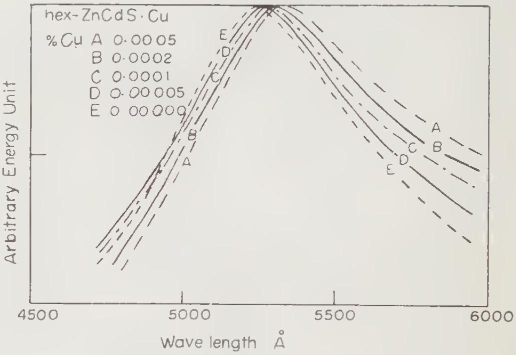

Fig. 1. Emission spectra for hex-ZnCdS: Cu during excitation by λ 3650 A at room temperature. The emission band is not shown which appears at the long wavelengths by copper activators.

They consist of 60% ZnS and 40% CdS in mol ratio, and are fired at 1000°C. The peak of the emission band appears at 5250 A in the phosphor without copper. As the concentration of copper is increased, the original emission band remains fixed in position (Fig. 1.) but a new emission band is observed with the peak near 6500 A, though the intensities of the new band are not measured quantitatively. In consequence, the emission during excitation shifts from green to orange by increasing the concentration of Cu activators. When they are irradiated by infrared (filter: Matsuda 1R–D1) during the decay period, the stimulating and the quenching effects are observed. The radiation is emitted with the emission band different from one of the phosphorescence. The reason may be attributed to the fact that the radiation in copper luminescence centers is predominant in the phosphorescence and the emisson due to infrared irradiation is caused in other centers as well. In the present investigation, the effects that infrared irradiation gives to those centers have been inquired. At first the decay characteristics both at the shorter wavelengths and at the longer wavelengths, of the two components of the emission band under the excitation of λ 3650 A or x-ray have been investigated at room temperature. In order to measure the intensity of luminescence, a photomultiplier tube (Sb–Cs photocathode) is used, combined with a blue filter (Matsuda v–B3(A)) or an orange filter (Matsuda v–O2(A)). The decay of phosphors at the longer wavelengths is always slower than that at the shorter wavelengths. The former becomes slower by increasing the concentration of copper, whereas the latter is little affected. Experimental results of the stimulating and the quenching effects are shown in Fig. 2.

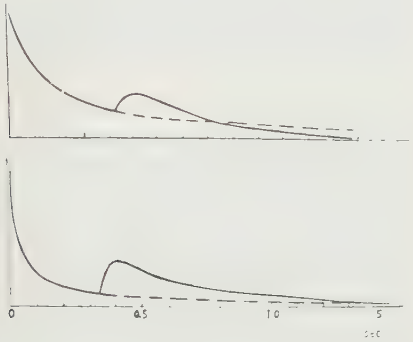

Fig. 2. Stimulating and quenching effects under infrared irradiation during the decay period. The upper part shows at the longer wavelengths, the lower at the shorter wavelengths and the dotted lines show the normal decay curves.

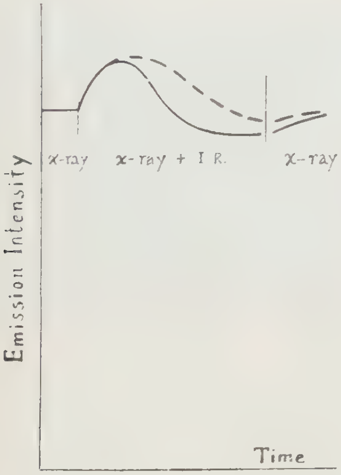

Fig. 3. Emission intensities *versus* time under infrared irradiation added to x-ray excitation. The dotted lines show them at the shorter wavelengths.

It is noticeable that the decay curve during infrared irradiation, at the longer wavelengths, crosses the normal decay curve after the short time, whereas at the shorter wavelengths, it does not cross during the longer time of the observation. These effects are observed in the four samples with Cu activators. The phosphor without Cu shows predominantly the quenching effect.

Another experiment has been tried, although not quantitatively. Infrared irradiation is added to the above phosphors under steady x-ray excitation. Emission intensities *versus* time are shown in Fig. 3.

After a while of adding infrared the decreasing of intensities is more remarkable at the longer wavelengths. In any case, however, the decreasing (quenching effect) is always observed.

In the explanation of the above results, it may be assumed that electron traps produced with Cu activators are deeper than those before they are incorporated[4]; and that electrons in those traps may make a direct coupling[3] with copper luminescence centers and the probability of the coupling is larger than that of raising up to conduction band at room temperature. If the cross sections of all luminescence centers are approximately equal for electrons in conduction band, they will give the same effects on all luminescence centers in emitting. Therefore, electrons from the copper traps into the conduction band with infrared irradiation may bring the additional radiation to the original one during the decay period, whereas the temporary radiation and thereafter the decreasing of the emission intensities of copper emission band (at the longer wavelengths) may occur. At the same time experimental results show the dissipation of energy in all luminescence centers under infrared irradiation.

We wish to express our hearty thanks to Assist. Prof. K. Takahashi, College of General Education, Tokyo University, for his encouragement. We are also indebted much to Mr. T. Kikuchi, Electro-Technical Laboratory, Department of Commerce, in the experiment. This research is carried out by the Scientific Research Grant of the Ministry of Education.

References

1) M. Schön: Z. Phys. **119** (1942) 463.
2) H. A. Klasens: Nature **158** (1946) 483.
3) H. Kallmann and B. Kramer: Phys. Rev. **87** (1952) 91.
4) R. H. Bube: Phys. Rev. **80** (1950) 655.

J. Phys. Soc. Japan **10** (1955) 238～240

Electron Bombardment Conductivity in Alkalihalide Crystals I

By Chiyoe Yamanaka and Tokuo Suita
College of Engineering, Osaka University

(Received December 27, 1954)

We have got some information concerning the motion of electrons and holes in single crystals of potassium chloride by bombarding a crystal with a pulse beam of electrons. Up to date, to measure the conductivity in alkalihalide crystals at room temperature is much affected by the space charge effects which cause distortion of the inner electric field in specimens. Now we concentrate our attentions on these space charge effects. With a field applied across a crystal in one direction the electrons which are excited to the conduction band at one end of the crystal will move to the another end. With the reverse field the excited holes will tend to move across the crystal. From the measurement of the induced conductivity, we can deduce the behaviors of electrons and holes, and also the space charge effects.

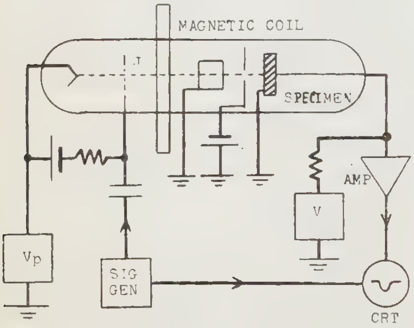

Fig. 1. Experimental Arrangement.

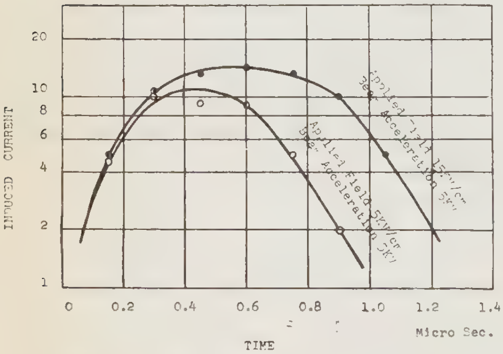

Fig. 2. Induced Current Patterns.

The experimental arrangement is shown in Fig. 1. A conventional X-ray tube attaching a control grid, accelerating plate and suppressor was used as an electron gun. The electron beam was focused by the magnetic coil. The suppressor plate was coated by a fluoresence substance enables us to check the collimation of the electron beam. The kinetic pumping system was used for vacuum which was about the magnitude of 10^{-6} mm Hg. The electron beam current was about 1 micro ampere. The accelerating voltages were up to 10,000 volts. The electron beam was controlled by the square signal which was generated by the discharge of a delay line. The beam form is shown in Plate 1 and its duration is about 0.2 micro sec. The applied field of specimens was up to 15,000 volts per cm. The induced current was amplified by a wide band amplifier, the properties of which were maximum gain 10^5 and upper half power frequency 10 MC. The specimens were illuminated by a tungsten light.

The dimensions of potassium chloride specimens were $10\times10\times0.5$ mm^3. Thin gold electrodes were attached by the evaporation. These specimens were annealed very carefully.

Since the experimental results were heavily affected by the space charge effects, we used two methods to evaluate them. At first, to minimize these effects, we bombarded specimens by a continuous electron beam under applying alternating field and then hit the specimen by a pulsed electron beam under an appropriate static field. The induced current patterns for electron and hole currents were shown in Plate 3 and 4 respectively. The static applied field was 12,500 volts per cm and the beam accelerating voltage was 5,000 volts. When we used several repeating pulses almost every second, we could see the decay of induced electron currents in each succesive bombardment and its magnitude tended to a final steady value. The hole induced current was extremely small and decayed steeply. The second, to accumulate the space charge, we bombarded the specimens by a continuous electron beam under a static field and then took off the static field and hit the specimens by a single beam. The induced current patterns under the inner space charge fields, which were the reversed directions of the previously applied fields, were shown in Plate 5 and 6 for electron and hole currents respectively. These current patterns were completely died out after several succesive bombardments. From these results we can conclude that under such fields, one fifth of the breakdown strength, trapping for excited electrons and holes is very strong and these charge carriers never traverse the whole crystal length. In fact, the crystals were colored by trapped carriers.

To evaluate the mean free time of an electron, τ, we measured the induced electron current under

Plate 1

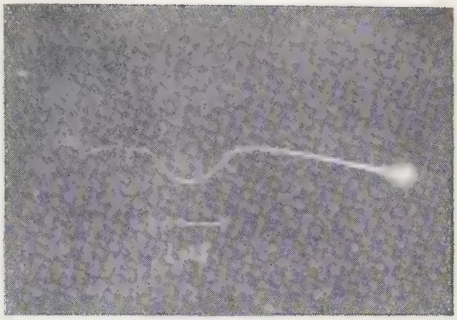

Plate 2

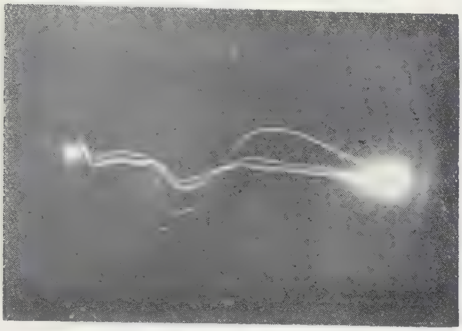

Plate 3

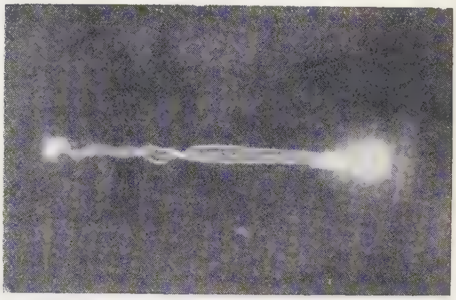

Plate 4

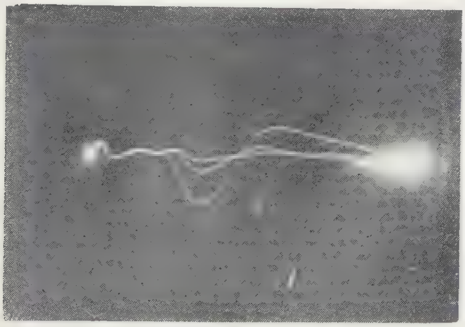

Plate 5

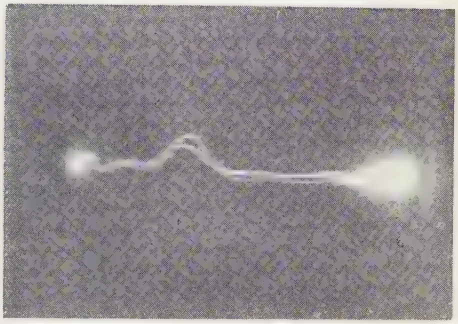

Plate 6

Oscillograph traces showing induced conductivity and electron beam; sweep duration 5 u sec, repetition frequency 1 c/sec.

the so-called space charge free condition. The current pattern at beam acceleration 5,000 volts, applied field 15,000 volts/cm is shown in Plate 2. The induced current[1] is

$$i(t)=\begin{cases}\dfrac{ebV\tau\delta}{L^2}[1-\exp(-t/\tau)]\,, & 0\leq t\leq t_a\,,\\ \dfrac{ebV\tau\delta}{L^2}[\exp(t_a/\tau)-1]\exp(-t/\tau)\,, & t_a\leq t\,,\end{cases}$$

where J is the amplitude of the electron beam, δ is the secondary yield, τ is the mean free time of excited electrons, b is the mobility, L is the length of crystal, t_d is a duration of the beam and V is the applied voltage for specimen. If we draw a current pattern in semilog plots, we can estimate the mean free time, τ, of electron from the derivatives of the curves, that is about 0.15 micro sec. In our experiments electrons nevertraversed the whole specimen length[2]. If we assume the electron mobility as 10 cm^2/volt-sec, according to Macdonald's results[3], the depth of the trapped space charges from the bombarded surface will be 10^{-2} cm. Assuming the trap cross-section σ as 10^{-16} cm^2, thermal velocity of a free electron v as 10^7 cm/sec, the density of traps $N_t=1/\tau\sigma v$ will be 10^{16} per cm^3.

The space charge effects have an essential role to clarify the behaviers of electrons and holes in alkalihalide crystals. Judging from the current patterns,[4] the maximum space charge field in the crystal seems to be the same order of the externally applied fields.

References

1) L. P. Smith: Semi-conducting Materials 114, 1951 London.
2) K. G. Makay: Phys. Rev. **74** (1948) 1606.
3) J. R. Macdonald, J. E. Robinson: Phys. Rev. **95** (1954) 44.
4) C. Yamanaka and T. Suita: Read before the Annual Meeting of Phys. Soc. of Japan (1954).

J. PHYS. SOC. JAPAN **10** (1955) 240~241

Microwave Spectrum of Methyl Mercaptan (I)

By Takeshi KOJIMA

Department of Physics, Faculty of Liberal Arts University of Toyama

and Tetsuji NISHIKAWA

Department of Physics, Faculty of Science, University of Tokyo

(Received December 8, 1954)

The microwave spectrum of methyl mercaptan has been studied in the frequency range between 16 and 26 kMc/sec. About eighty lines have been observed. Their frequencies and orders of the Stark effect are listed in Table I. Among them, we have found a series of lines which corresponds to a transition, $\Delta J=0$, $\Delta K=\pm 1$, $\Delta(K+\tau)=0$, where J and K are the usual rotational quantum numbers and τ $(=1, 2, 3)$ is the quantum number of the hindered rotation. The member lines of the series exhibit first-order Stark effect patterns and are marked in Table I.

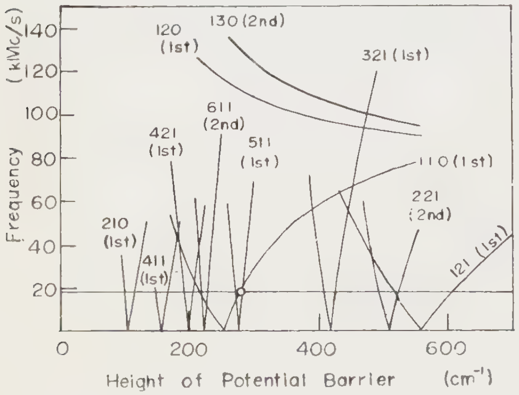

Fig. 1. Frequencies of $K, \tau, n \longleftrightarrow K-1, \tau+1, n$ transitions for $n=0$ and $n=1$ The orders of Stark effects are indicated in parentheses.

Table I. Microwave Spectrum of Methyl Mercaptan.

Frequency Mc/sec	Stark-effect	Rel. Int.	Frequency Mc/sec	Stark-effect	Rel. Int.
16057.0	1	*W*	21865.5	1	*M*
16059.8	2	*W*	21877.1	1	*MW*
17320.4	1	*M*	○21901.0	1	*M*
18039.4	2	*M*	21943.5	2	*W*
18257.8	1	*MW*	21973.2	1	*WS*
○18396.0	1	*MW*	○22269.4	1	*M*
18431.8	1	*M*	22329.8	1	*MW*
○18446.3	1	*W*	22560.2	1	*W*
18494.1	2	*MW*	○22661.4	1	*MW*
18499.7	1	*W*	22780.1		*WW*
○18509.7	1	*W*	22827.3	2	*MW*
○18586.1	1	*W*	23073.8	1	*W*
○18675.6	1	*W*	○23078.2	1	*MW*
○18778.6	1	*W*	23230.3	1	*M*
18806.4	1	*MW*	23257.0	2	*M*
○18895.7	1	*W*	23339.2	1	*W*
18991.8	1	*W*	23494.4	1	*W*
○19027.1	1	*W*	○23520.4	1	*MW*
○19173.0	1	*MW*	23566.6	2	*W*
19273.6		*WW*	23617.3	2	*M*
○19334.0	1	*MW*	23773.8	1	*W*
○19510.4	1	*MW*	23801.8	1	*M*
19568.3	2	*W*	○23989.0	1	*MW*
○19702.9	1	*MW*	24067.5	1	*M*
○19912.2	1	*MW*	○24485.0	1	*M*
19999.5	2	*W*	24988.5	1	*W*
20052.6	1	*MW*	○25009.0	1	*W*
○20138.6	1	*MW*	25121.4	1	*W*
20241.9	1	*MW*	25127.	2	*W*
○20383.3	1	*MW*	25142.2	2	*M*
○20646.4	1	*MW*	25143.7	2	*M*
○20928.9	1	*MW*	25154.9	2	*M*
21057.4	2	*W*	25206.8	2	*MS*
21131.1	1	*W*	25219.7	2	*MS*
○21231.7	1	*MW*	25290.8	2	*MS*
21519.9	1	*W*	25291.8	2	*MS*
○21555.5	1	*MW*	○25562.0	1	*W*
21734.6	1	*W*	25659.7	2	*M*
21766.6	1	*W*			

The accuracy of the frequencies is considered to be ±0.1 Mc/sec.

Since the molecule is very similar to methyl alcohol, the theory of Dennison and others[1] may be applicable. Using the molecular constants determined by Solimene and Dailey[2], starting points of several series which may fall into the microwave frequency range have been calculated as functions of the height of potential barrier which hinders the internal rotation. The results are shown in Fig. 1.

From this figure the observed series has been tentatively assigned to the transition, $\Delta J=0$, $K=0\rightarrow 1$, $\tau=2\rightarrow 1$, in the ground state of torsional vibration, $n=0$. If this assignment is correct, the height of potential barrier is estimated to be $280 \pm 50\ \mathrm{cm}^{-1}$. This value is also supported by the measurement of the intensities of the first excited torsional state lines relative to those of the ground state lines for the $J=0\rightarrow 1$ transition. These lines were assigned by the earlier investigators[2][3], while the assignment of the second excited torsional state lines in reference 2 seems to be incorrect.

The authors express their thanks to Prof. K. Shimoda for his advice and encouragement.

References

1) J. S. Koehler and D. M. Dennison: Phys. Rev. **57** (1940) 1006.
   D. G. Burkhard and D. M. Dennison: Phys. Rev. **84** (1951) 408.
   E. V. Ivash and D. M. Dennison: J. Chem. Phys. **21** (1953) 1804.
2) N. Solimene and B. P. Dailey: Phys. Rev. **91** (1954) 464.
3) T. M. Shaw and J. J. Windle: J. Chem. Phys. **19** (1951) 1063.

J. Phys. Soc. Japan **10** (1955) 241~242

Influence of External Radiation on an A-Hg Discharge Tube

By Tsunesaburo ASADA, Toshizo NAKAYA and Tetsuo MAMURO

Department of Physics, Osaka University

(Received December 22, 1954)

Irradiation of faint ultra-violet ray or visible light from a light source into the discharge space of low pressure A-Hg discharge tubes, has been found to remarkably increase the starting potential.

The requisite for this effect is the existence of relatively high wall temperature of 40–90°C (i.e. high concentration of Hg atoms) and relatively high pressure of argon gas (at least higher than a certain lower limit, a few mm Hg).

So long as the illumination is meager, the starting potential (Vsr) under irradiation rises almost in proportion to Log(intensity), but when the intensity of illumination exceeds a certain value, which varies with the kind of light sources, the starting potential (Vsr) shows a somewhat saturated constant voltage (Vsr)sat. Furthermore, strong irradiations of a light, whether its source is incandescent lamp, neon light, argon light or even scattering day-light through windows, give the same value in the saturated voltage as the case of mercury light.

One example given in Fig. 1 where D.C. source is used with a tube of a hot cathode (inner diameter 23 mm, electrode separation 30 cm, argon pressure 4 mm Hg with the wall made of λ2537 transmitting glass), sufficiently illustrates these behaviours of the starting potentials with and without irradiation.

1) It is seen that $_2$Vsr$=_4$Vsr$=_5$Vsr$=$(Vsr)sat. in all region of wall temperature.

2) In the region lower than 63°C, the effect of irradiation in raising the starting potential is seen, i.e. these starting potentials under irradiation Vsr are higher than the ones without irradiation Vsn:

$$(\mathrm{Vsr})\mathrm{sat} > \mathrm{Vsn}.$$

3) But in the region higher than 63°C, this effect is not seen, i.e.

$$(\mathrm{Vsr})\mathrm{sat} = \mathrm{Vsn}.$$

4) On the other hand, under the irradiation of λ2537 only, its effect of lowering the starting potential is observed in all region of wall temperature.

The abnormal temperature dependence of the starting potential Vsn without irradiation is believed to be due to a trace of impurities in the gas, because the result in Fig. 1 is derived from the measurement made soon after the exhaust of the discharge tube and, accordingly, before ageing.

In Fig. 2 which was obtained after ageing, the effect of irradiation to raise the starting potential is observed in all region of wall temperature. Besides, it is noteworthy that the saturated voltage (Vsr)sat in Fig. 2 (after ageing) is nearly equal to the abnormally high value in the region of wall temperature higher than 63°C, of Vsn in Fig. 1 (before ageing).

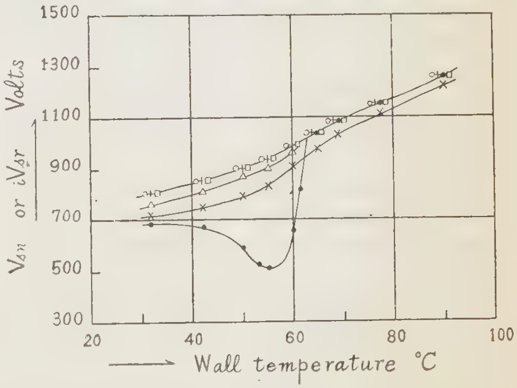

Fig. 1. Starting potential $_i$Vsr under irradiation and Vsn without irradiation respectively as a function of wall temperature.

● Vsn: not irradiated.
× $_1$Vsr: irradiated with a 15W germicidal lamp 25 cm distant.
○ $_2$Vsr: a 15W germicidal lamp 25 cm distant and interposed with a glass plate for eliminating u.v. ray.
△ $_3$Vsr: a 15W germicidal lamp 100cm distant.
☐ $_4$Vsr: a 15W germicidal lamp 100cm distant and interposed with a glass plate.
+ $_5$Vsr: a 100W incandescent lamp 100cm distant.

This result may be explained as because a trace of impurities in the gas which remained after the

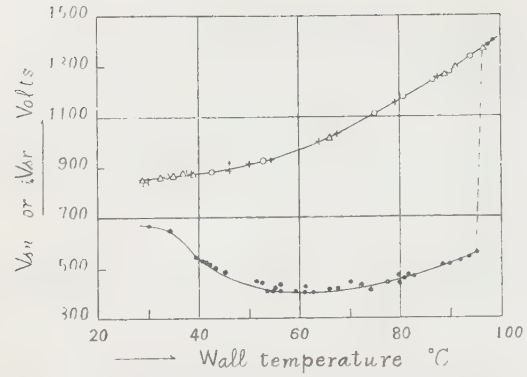

Fig. 2. Starting potential Vsn without irradiation and $_i$Vsr under irradiation respectively after ageing.
● Vsn: not irradiated.
○ $_1$Vsr: irradiated with Ne light.
△ $_2$Vsr: Ar light.
+ $_3$Vsr: a 100W incandescen lamp 30cm distant.

exhaust was purified during the discharge in mercury vapour of ageing process, and these impurities prevented the starting potential without irradiation in Fig. 1 from taking a lower value.

The sensitive part for external radiation has been found on the anode side.

One puzzling phenomenon is that the influence of irradiation persistently remains for several minutes or hours to keep the starting potential higher than the normal voltage even after the irradiation was stopped. This residual power is not so much appreciable in the case of the tube with a hot cathode and when the electrode separation distance of the tube is relatively short as compared with its diameter. However it becomes drastically increased in the case of cold cathode type tube having large electrode separation as compared with its diameter.

The remaining influence of irradiation seems to depend not only on the intensity of illumination as well as the duration of irradiation but also on the voltage of the D.C. source with which the irradiation was given to the tube.

In case the A.C. source is used, the delayed effect is not appreciable. Even an extremely faint u.v. ray such as reflection from the wall of a room with its intensity too faint to be measured, is enough to stop a intermittent visual discharge of a few μA, but the A.C. discharge starts again as soon as the radiation is cut off.

It looks that there exists a destruction of metastable mercury molecules ($6^1S_0+6^3P_{2,0}$) by external radiation and also these metastables seem to be important ion sources through the step-wise ionization for starting a discharge (i.e. from normals to mercury ions through metastables) (Hypothesis of the authors). However, further studies are required in order to discuss these experimental results.

J. Phys. Soc. Japan **10** (1955) 242~243

Gamma Rays from the Reaction ^{27}Al$(p, \gamma)^{28}$Si

By Manabu HATTORI*, Kazuo HISATAKE*,
Takasi MIKUMO**, and Teruo MOMOTA*
* *Department of Physics, Faculty of Science, University of Tokyo, Tokyo*
** *Department of Physics, Tokyo Institute of Technology, Tokyo*

(Received December 27, 1954)

The resonance character of the reaction ^{27}Al$(p, \gamma)^{28}$Si has been the subject of many experimental studies, and a number of resonance levels have been located precisely. (See, for example, review article by Ajzenberg and Lauritsen[1].) But, because little has been known about the energies of γ-rays, we have made a measurement of them, using photographic emulsion loaded with heavy water. During the course of the work, however, Gove et al[2] carried out measurements at forty-eight resonance levels in the range of proton energies from 0.65 to 2.2 Mev, and Rutherglen et al[3] at five resonance levels below 700 kev. In both of these experiments, scintillation spectrometers were used. Although the scope of our work is within that of Gove et al and the results obtained are in agreement with theirs[4], the resolution of energies of γ-rays in our work seems to be somewhat better than that in the work of Gove et al.

We used a horizontal proton beam accelerated with the electrostatic generator at the University of Tokyo to bombard a thick target of aluminum, the purity of which was 99.99%. The energy of the proton beam was kept just above 986 kev. The nuclear plates used were 100μ thick "Sakura" (Similar to Ilford C-2). Three pieces of plates. which had been soaked in heavy water untill saturated with it, and one saturated with ordinary water (control plate), were placed horizontally at a position about 3 cm downword from the target. After about ten hours irradiation, they were processed by the normal temperature development method. The integrated amount of the proton current was 124 microampere-hours. The shrinkage factor of the emulsion, measured with a screw-micrometer was between five and six.

The length of the photoproton track was calculated from its projected length in the plane of emulsion and the difference in its depths at two end points. Those tracks with length shorter than 13 microns and with dip angle greater than 45° in the wet emulsion were not counted. The range-energy relation was calibrated with 6.1 Mev and 6.9–7.1 Mev γ-rays from the ^{19}F$(p, \alpha, \gamma)^{16}$O reaction, assuming a constant factor to be multiplied to the relation given by Lattes et al[5]. In the figure, the number of tracks is plotted as a function of $(2E_p+W)$ in steps of 0.2 Mev, where E_p represents the energy of the photoproton and W the binding energy of the deuteron. The total number of tracks measured was 540.

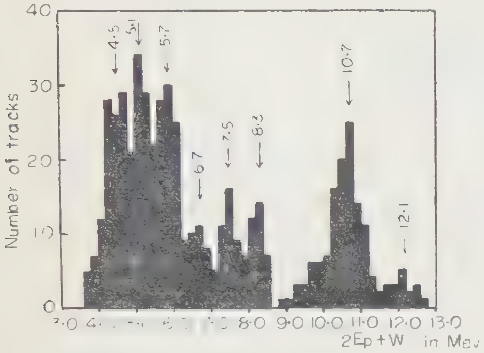

The energies of γ-rays which correspond to the peaks are as follows:

strong γ-rays: 4.5, 5.1, 5.7, 10.7 Mev.
weak γ-rays: 6.7, 7.5, 8.3, 12.1 Mev.

The relative heights of peaks are not directly proportional to the relative intensities of γ-rays, because the numbers are not corrected for the variation of photodisintegration cross section of the deuteron and the probability of termination of tracks of various lengths in the emulsion. The width of the 10.7 Mev peak is about 10% at half intensity.

The writers wish to thank the members of the Van de Graaff group at the University of Tokyo for their cooperation.

References

1) F. Ajzenberg and T. Lauritsen: Rev. Mod. Phys. **24** (1952) 321.
2) H. E. Gove, E. B. Paul, G. A. Bartholomew, and A. E. Litherland: Phys. Rev. **94** (1954) 749A.
3) J. G. Rutherglen, P. J. Grant, F. C. Flack, and W. M. Deuchars: Proc. Phys. Soc. **A66** (1954) 101.
4) H. E. Gove: private communication.
5) C. M. G. Lattes, P. H. Fowler and P. Cuer: Proc. Phys. Soc. **59** (1947) 883.

PROGRESS OF THEORETICAL PHYSICS

(Founded by H. Yukawa in 1946)

Published for the

Research Institute for Fundamental Physics

The Physical Society of Japan

Progress of Theoretical Physics Vol. 12, No. 4, 1954

Relativistic Wave Equations under the Inhomogeneous Lorentz Group .... Ken-iti GOTO....409
Theory of the Electronic Polaron and Ionization of a Trapped Electron by an Exciton .... Yutaka TOYOZAWA....421
On the Conductivity of Non-polar Crystals in the Strong Electric Field, I.... .... Jiro YAMASHITA and Mitukuni WATANABE....443
The Theory of the Dielectric Constant of Ionic Crystals, II —*Effect of Temperatures*— .... Jiro YAMASHITA....454
On the Wave Theory of Light in General Relativity, II —*Light as the Electromagnetic Wave*— .... Yoshio UENO....461
Renormalization in the Covariant Treatment of Pion-nucleon Scattering .... Shin CHIBA....481
On the Renormalization in the Tamm-Dancoff Approximation for One-nucleon Problem, I —*A Covariant Generalization of the Tamm-Dancoff Method*— .... Kiyomi ITABASHI....494
On Nuclear Force for $^3S_1+^3D_1$ State .. Masahiko MATSUMOTO and Wataro WATARI....503
Phenomenological Analysis of the Meson Theory of Nuclear Force........... .... Shoichiro OTSUKI and Saburo FUJII....521
Generalization of Feynman's Theory of Energy Levels of Liquid Helium .... Hirotsugu MATSUDA....537

Letters to the Editor:

A Remark on Tamm-Dancoff Approximation .... T. OKABAYASHI....545
On the Multiple Scattering Phase Shifts and the Nuclear Force —*Scalar Pair Theory*— .... K. HASEGAWA and S. AZUMA....546
On the Analysis of the Anomalous Magnetic Moment of the Nucleon in the Order Calculations..K. HASEGAWA, S. MATSUYAMA and T. AKIBA....548
Elastic Scattering of Alpha-particles by Heavy Nuclei........... K. IZUMO....549
On Some Notes on the so-called G. Feldman's Modified Propagator.. .... Y. MIYATAKE....551

Price $ 1.25 per copy
$ 15.00 per year (postage inclusive)
Annual dues for foreign members (individual subscribers)
$ 12.00 (postage inclusive)
〃 for foreign members of the Physical Society of Japan
$ 10.00 (postage inclusive)

Application for members, subscriptions and orders for back mumbers should be sent, directly or through book-dealers, to

The Publication Office
in
Yukawa Hall, Kyoto University, Kyoto, Japan

JOURNAL OF THE PHYSICAL SOCIETY OF JAPAN Vol. 10, No. 4, APRIL, 1955

The Lateral Distribution of Various Components in Extensive Air Showers at Sea Level

By Goro FUJIOKA

Department of Physics, Kobe University

(Received December 4, 1954)

The lateral distribution of electrons, μ-mesons, and N-components are observed at sea level up to 50 m from the core. The distribution of electrons is consistent with that calculated on the basis of cascade theory. The distribution of μ-mesons is flatter than that of electrons and is represented as $r^{-0.7}$. The distribution of N-components is similar to that of electrons. The number of μ-mesons is equal to that of N-components at several meters from the core.

§ 1. Introduction

It is well known that the extensive air showers consist mainly of electron-photon component and the number of penetrating particles contained in those showers is about 2 percent of the number of electrons. The lateral distribution of electrons at various altitudes has been observed by several authors1)2) and is fairly in good accord with the calculation3)4) based on cascade theory. The observations of the lateral distribution of the penetrating particles are meagre5)* compared with those of electrons, though the N-components in those penetrating particles play the main role, especially at the earlier stage of the development, in the air shower phenomena.

The distributions of electrons, μ-mesons, and N-components up to 50 m from the core in air showers were observed at sea level making use of a counter hodoscope. The experiment was performed on the roof of the building of the Faculty of Science, Kobe University, the altitude of which was about 40 m above sea level.

§ 2. Experimental Arrangements and Procedures

The main parts of the appartus consisted of four core selectors (abbreviated to C. S. below), four electron density detectors (E.D.D.) and a penetrating particle detector (P.P.D.). The layout of counter sets is shown in Fig. 1.

C.S. were similar to those used by Cocconi *et al.*1). Each E.D.D. contained 19 counters and the total area of one E.D.D. was 0.24 m². P.P.D. consisted of three trays, each of 23 counters and of area 0.2 m², in the lead shield as shown in Fig. 2. All counters of E.D.D. and P.P.D. were connected in a hodoscope, and the master pulse was the five-fold coincidence in any C.S. in the main part of the experiment. C.S. which gave the master pulse was also indicated by neon lamps in a hodoscope panel.

In the minor part of the experiment, the master pulse was given from the three-fold

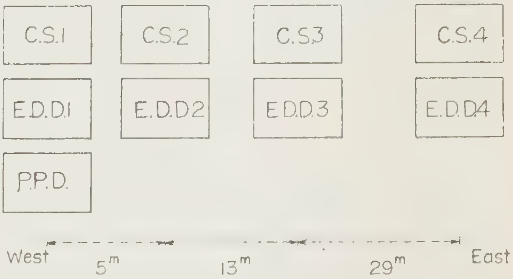

Fig. 1. Layout of counter sets.

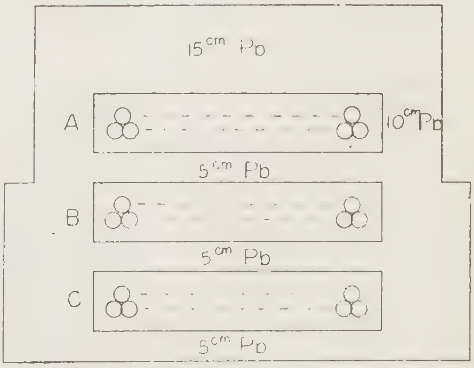

Fig. 2. Cross section of the penetrating particle detector.

---

* The results of the Russian group agree qualitatively with ours, but the data in detail are not now available to us.

coincidences of the two additional trays each of area 500 cm² and the middle seven counters of B tray of P.P.D. in parallel, the area of which was 640 cm². In this case P.P.D. counters used for the master pulse remained also connected in a hodoscope. The auxiliary experiments were divided in two parts. In the first, two trays were placed vertically above P.P.D. and the hodoscope was triggered by single penetrating particles. In the second, two trays were separated by 3 meters from P.P.D. and extensive penetrating showers were detected. Checks were made every two or three days, and at the same time the hodoscope was triggered by artificial pulses to obtain the accidental occurrence of P.P.D. records.

Table I.

	Working time (hrs)	Counts	Rate (hr⁻¹)
CS1 (with top 9 cm Pb)	784	138	0.19±0.01
CS1 (with top 7 cm Pb)	2156	607	0.28±0.01
CS2 (with top 9 cm Pb)	452	69	0.15±0.02
CS2 (with top 7 cm Pb)	2272	735	0.32±0.01
CS3	2357	804	0.34±0.01
CS4	2704	856	0.32±0.01

Table II.

Density class	1	2	3	4	5
Density (m⁻²)	0∼4	4∼8	8∼16	16∼32	32∼64
Density class	6	7	8		
Density (m⁻²)	64∼128	128∼256	256∼∞		

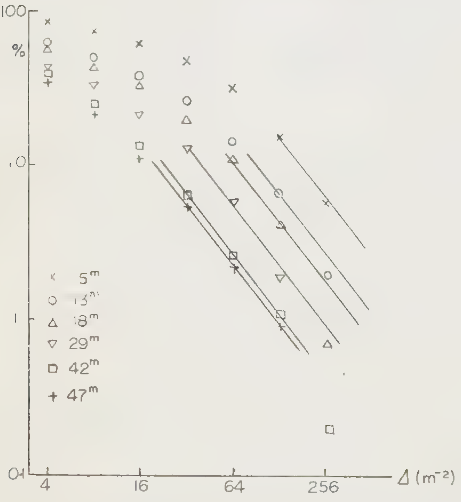

Fig. 3. Integral density distribution at various distances from the core.

The working time and the number of master pulses are collected in Table I. In the earlier part of the experiment the top lead shield of C.S. was 9 cm, and in the remainder it was 7 cm. The counting rates were fairly small in the former, but the feature of recorded showers seemed similar and the data were analysed together.

§ 3. The Distribution of Electrons

The method of analysis of E.D.D. data is similar to that devised by Cocconi *et al.*[1]. From the combination of discharged counters in every E.D.D. record, we can determine to what density class this recorded shower belongs. The density interval of each class is shown in Table II. Thus the integral distributions of electron densities at six distances (5, 13, 18, 29, 42, and 47 m) are obtained and shown in Fig. 3. If we assume that all showers have the same structure function, the horizontal distances of the parallel portion of these curves represent relative electron densities at the different distances from the core.

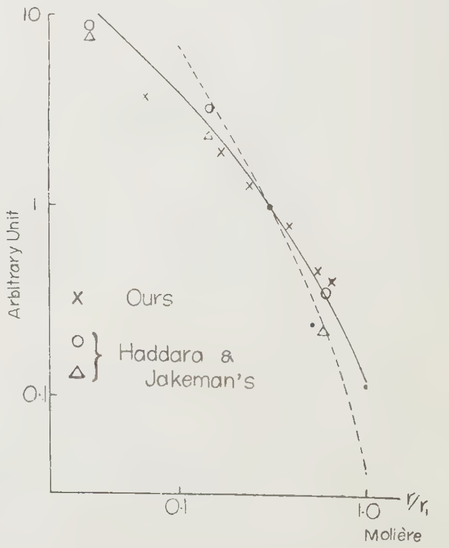

Fig. 4. Lateral distribution of electrons.

In Fig. 4, our data of lateral distribution of electrons are plotted with those obtained by Haddara and Jakeman[2]. The events in which more than two C.S. are in coincidence are discarded[6].

The solid curve is the theoretical one by Nishimura and Kamata for $s=1.4$ with energy larger than 2 MeV. and the dotted curve is Molière's. All are normalized at $r/r_1=0.3$. Both experimental data agree within experimental uncertainties, though ours may well be said to be flatter. This may be due to the ambiguity of our C.S. as pointed out by Haddara and Jakeman, or to the effect of earth's magnetic field[7]. But according to Nishimura and Kamata[6] the latter effect is not so marked, and the comparison with the existing theory is permitted. The curve of Nishimura and Kamata fits far better to the experimental data than that of Molière. This is to be expected as the shower is fairly old at sea level.

§ 4. Analysis of P.P.D. Records

P.P.D. records are divided into the following classes.

(A) Only one counter is discharged.

(O) Two or more counters are discharged but discharged counters are only in one tray.

(S) Single penetrating particle without secondaries.

(K) Single penetrating particle with one secondary seen in only one tray.

(D) Single penetrating particle with every secondary seen in two trays.

(P.T.) Parallel penetrating particles (including those with one knock-on type secondary).

(B) Single penetrating particle with two or more secondaries seen in one tray only.

(T) Secondaries observed in two trays and at least more than one secondary seen in one of these trays.

(R) A few Counters are discharged in every tray but they are scattered and difficult to interpret.

(P) Penetrating shower: more than one secondary nearby in every tray.

The numbers of pictures of every class obtained by various master pulses are collected in Table III.

The probabilities of occurrence of (A) and (O) by chance are 1% and 0.5% respectively. The values of (A) and (O) in Table III cannot be explained by chance and may be caused to some degree by inclined penetrating particles. But electron-photon components may contribute to these events, and so these are excluded in the next analysis.

The knock-on probability in air shower triggered events is somewhat larger than that in single μ-meson triggered events. The difference seems too large to be attributed to the difference of μ-meson energy. To calculate the lower limit of μ-mesons, $60/403=15\%$ of (S) are considered as μ-mesons, and for the upper limit all of (K) are considered as μ-mesons. Events (D) are very few and are considered as μ-mesons.

(B) are treated as (K).

(T) and (R) are considered as N-components to calculate the upper limit of N-components (the lower limit of μ-mesons), and half of (T) and (R) are considered as N to calculate the lower limit of N.

Thus the lower limit of μ is

Table III.

	Master Pulse.							
	only				Coincidence	Other	Aux. exp.	Aux. exp.
	CS1	CS2	CS3	CS4	(CS1, CS2)	Coincidences.	I	II
A	55	43	26	20	4	—	4	15
O	68	26	8	10	4	2	—	6
S	42	46	37	22	6	4	403	66
K	24	24	9	7	4	3	60	29
D	3	2	—	—	—	—	6	3
P.T.	4	1	3	3	5	—	—	9
B	24	13	4	5	1	—	18	10
T	48	20	9	3	13	4	—	35
R	14	9	4	2	5	—	—	6
P	25	21	5	1	24	3	1	56
Total	357	205	105	73	66	16	492	235
No. of M.P.	647	693	776	845	88	33		

Table IV.

	only				Coincidence	Aux. exp.
	CS1	CS2	CS3	CS4	(CS1, CS2)	II
Lower limit of μ	52	51	36	18	27	91
Upper limit of N	203	86	31	20	62	135
Upper limit of μ	140	100	56	35	45	147
Lower limit of N	115	37	11	3	44	76
Corrections for μ	+8	−2	−7	−8	+7	
Corrections for N	+9	+1	0	0	+9	
Total No. of electrons	1.5×10^4	8.3×10^3	4×10^3	1.6×10^3	5.3×10^3	

$$(S)+0.15(S)+(D)+0.045(S)+2(P.T.),$$

and the upper limit of μ is

$$(S)+(K)+(D)+(B)+2(P.T.)+(1/2)\{(T)+(R)\}.$$

Then the following corrections are made.

(1) Subtraction of accidental μ-meson traversals. This is 1% of the number of master pulses.

(2) Addition of lost μ-mesons coincident with N-components. This is

$$\{(S)+(K)+(D)\}\times\{(P)+(T)+(R)\}/\text{No. of M.P.}$$

(3) Addition of similar N-components as (2). This is $(P)\times(P)/\text{No. of M.P.}$

The obtained lower and upper limits of μ and N are collected in Table IV, together with corrections made and total numbers of electrons. The correction for N-components which do not interact is not made, because this is not so large, and because for N-components the effective area of P.P.D. is larger than for μ-mesons. This effect is difficult to estimate but may cancel with the correction.

§ 5. Ratios of μ-mesons and N-components to Electrons at Various Distances from the Core

To find the total numbers of electrons which fall on P.P.D., the distribution of electron densities at E.D.D. 1 above P.P.D. up to $256/\mathrm{m}^2$ and the integral distribution of $\Delta^{-1.5}$ above this density are adopted. Dividing the numbers of μ and N by the corresponding numbers of electrons, we obtain the ratios μ/e and N/e. This procedure is adopted because the running times of various C.S. are not the same.

The results are shown in Table V. In this table the data of coincidence (CS1, CS2) are included into (CS1) and (CS2) because the distance between these CS is in the region of the uncertainty of our core position determination.

Table V.

	CS1 only +(CS1, CS2)	CS2 only +(CS1, CS2)	CS3	CS4
Distance from the core	near the core	~5 m	~20 m	~50 m
μ/e (%)	0.4~0.9 (0.7)	0.6~1.1 (0.9)	0.9~1.4 (1.2)	1.1~2.2 (1.7)
N/e (%)	1.3~0.8 (1.0)	1.1~0.6 (0.8)	0.8~0.3 (0.5)	1.3~0.2 (0.7)
$\mu+N/e$ (%)	1.7	1.7	1.7	2.4
$\mu/\mu+N$ (%)	25~50 (40)	35~65 (50)	50~80 (70)	45~90 (70)

The other coincidences are excluded because they may be at a different stage in shower development, and because the number is small.

The ranges of μ/e and N/e are somewhat wide because of the difficulty in interpreting the hodoscope pictures, but the true values will be approximately the means of the lower and the upper limits, which are shown in the parentheses in Table V. As seen from the Table, it is clear that the lateral distribution of μ-mesons is significantly flatter than that of electrons. If we represent the distribution of μ in the form of r^{-n}, n is about 0.7 in the region from $r=0.07$ to $r=0.7$.

The lateral distribution of N-components seems to be similar to that of electrons.

§ 6. Note on the Auxiliary Experiment II

At first sight, when the core position is not determined $N/N+\mu$ seems to be large compared with the data of McCusker[8], but this is because in our experiment the area of shielded master pulse counters is only one third of the area of the P.P.D. counters. If we take the effective area for the N-components as the same as that of the P.P.D. counters, this ratio is 0.15~0.35 and is in good accord with his data.

The author wishes to thank Professor O. Minakawa for his kind encouragement and valuable suggestions. Thanks are also due to Messrs. J. Nishimura ant K. Kamata, who kindly communicated their unpublished results and gave helpful discussions. The assistance of Mr. T. Maeda throughout this work and of Miss T. Bansho, Messrs. C. Yokoyama, T. Okada, S. Hasegawa, and R. Tanji in part of this work, is highly appreciated. This work was partly supported by the Scientific Research Expenditure of the Ministry of Education.

References

1) G. Cocconi, V. Cocconi Tongiorgi and K. Greisen: Phys. Rev. **76** (1949) 1020.
2) S. R. Haddara and D. Jakeman: Proc. Phys. Soc. **A 66** (1953) 549.
3) G. Molière: *Cosmic Radiation*, edited by W. Heisenberg (1946).
4) J. Nishimura and K. Kamata: Progr. Theor. Phys. **6** (1951) 628.
5) G. T. Zacepin, I. L. Rozental', L. I. Saryčeva, B. G. Hristiansen, and L. H. Ejdus: reviewed by G. Wataghin: Nuovo Cimento Suppl. (1953) 497.
6) Private Communication.
7) G. Cocconi: Phys. Rev. **93** (1954) 646.
8) C. B. A. McCusker: Proc. Phys. Soc. **A 63** (1950) 1240.

JOURNAL OF THE PHYSICAL SOCIETY OF JAPAN Vol. 10, No. 4, APRIL, 1955

Virial Coefficients and Intermolecular Potential of Helium

By Taro KIHARA, Yukio MIDZUNO
and Toshio SHIZUME

Department of Physics, Faculty of Science, University of Tokyo

(Received November 19, 1954)

The intermolecular potential of helium has been determined from an analysis of the second and the third virial coefficients above the Boyle temperature, where the virial coefficients can be expanded into power series on h^2, the square of Planck's constant. The series have been calculated up to the term proportional to the third power of h^2 in case of the second virial coefficient and up to the term proportional to the first power of h^2 in case of the third virial coefficient. The following conclusion has been drawn. The two-body system of He^4 atoms has a discrete energy level while the two-body system of He^3 atoms has no discrete level.

§ 1. Introduction

Helium shows a notable quantum effect at low temperatures. Because of its shallow potential-bowl and large zero-point energy the two-body system of helium does not have many discrete energy levels corresponding to bound states. In fact it has been left undecided whether or not the system has a discrete level. The main purpose of the present article is to settle the question.

The potential energy between two helium atoms can be and has been calculated quantum mechanically; but the *a priori* calculation is not accurate enough to answer the question. We, therefore, depend upon the equation of state of the helium gas

$$pv=kT(1+Bv^{-1}+Cv^{-2}+\cdots\cdot),$$

(p is pressure, v is volume per molecule, k is Boltzmann's constant, T is temperature.) Here B and C are called the second and the third virial coefficients respectively. There exists a temperature called Boyle's temperature above which B is positive and below which B is negative.

Above the Boyle temperature the second virial coefficient can be expanded into a power series with respect to h^2, the square of Planck's constant. The series was evaluated by de Boer and Michels¹⁾ up to the term proportional to the second power of $\hbar^2$. They used the Lennard-Jones (6,12) potential and found the fact that the potential between He^4 atoms is close to the "critical" potential for which a resonance would exist at zero energy and no other discrete level would exist. In the present paper we calculate the series of the second virial coefficient up to the term proportional to the third power of $\hbar^2$ and the corresponding series of the third virial coefficient up to the term proportional to the first power of $\hbar^2$. Making use of the results of these calculations we determine the potential with sufficient accuracy and settle the problem of the existence of a discrete level.

§ 2. Depth Parameter, *s*, of the Intermolecular Potential

The notion of depth parameter introduced by Blatt and Jackson²⁾ for nuclear potential can be applied to the potential between helium atoms. Let $U(r)$ be the potential, r being the distance between the centers of the atoms. We can always choose a positive number, s, in such a way that the reduced potential $s^{-1}U(r)$ gives a resonance at zero energy and no discrete level. The number s is called the depth parameter. If one or more discrete levels exist in the two-body system s is greater than unity; if no discrete level exists s is less than unity.

By definition the Schroedinger equation

$$\frac{d^2}{dr^2}(rR)-\frac{2m^*}{\hbar^2}\frac{U(r)}{s}\,rR=0\,, \tag{2.1}$$

with the reduced potential must be satisfied by a nodeless spherically symmetric wave function $R(r)$. Here m^* is the reduced mass of the two-body system; $\hbar$ is Planck's constant divided by 2π.

In the case of the Lennard-Jones potential

$$U(r)=U_0\left[\frac{6}{n-6}\left(\frac{r_0}{r}\right)^n-\frac{n}{n-6}\left(\frac{r_0}{r}\right)^6\right],\quad n>6 \tag{2.2}$$

with the potential depth U_0 and the molecular diameter r_0 corresponding to the potential minimum, (2.1) becomes

$$\frac{d^2}{d\rho^2}R^*-6c\left(\frac{6}{n-6}\,\rho^{-n}-\frac{n}{n-6}\,\rho^{-6}\right)R^*=0\,, \tag{2.3}$$

where

$$R^*=\rho R,\quad \rho=r/r_0\,,$$

$$6c=\frac{2m^*}{\hbar^2}\frac{U_0r_0^2}{s}\,. \tag{2.4}$$

For $n=10$, the eigenvalue problem can be solved exactly with

$$c=1\,,\qquad R^*=\exp\left(-\frac{3}{4}\,\rho^{-4}\right). \tag{2.5}$$

In general, the eigenvalue c of (2.3) is determined by a variational principle i.e. by the extremum

$$6c=\mathrm{Extr}\,\frac{\displaystyle\int_0^\infty\left(\frac{dR^*}{d\rho}\right)^2 d\rho}{\displaystyle-\int_0^\infty\left(\frac{6}{n-6}\,\rho^{-n}-\frac{n}{n-6}\,\rho^{-6}\right)R^{*2}d\rho}\,. \tag{2.6}$$

For n not far from 10, we can obtain a sufficiently accurate value of c making use of the approximation

$$R^*=\exp\left(-a\rho^{-b}\right)\,, \tag{2.7}$$

where a and b are positive constants to be adjusted. This trial function enables us to integrate the numerator and denominator of (2.6) by means of the gamma-function, and gives

$c=0.905$ for $n=9$,
$c=1.174$ for $n=12$.³⁾

§ 3. High-Temperature Expansion for the Second Virial Coefficient

Above the Boyle temperature the symmetry effect is negligibly small and the Boltzmann statistics can be used. The second virial coefficient is then given by⁴⁾

$$B=2\pi\int_0^\infty[1-S(r)]r^2dr\,, \tag{3.1}$$

where $S(r)$ is the probability to find two molecules a distance r apart from each other. The quantum-mechanical expression of $S(r)$, the classical correspondence of which is the Boltzmann factor $\exp[-U(r)/kT]$, is the so-called Slater sum

$$S(r)=\sum_n\exp(-\beta E_n)\varphi_n(\boldsymbol{r})\varphi_n^*(\boldsymbol{r}),\quad \beta=1/kT, \tag{3.2}$$

normalized according to

$$S(r)\to 1\quad\text{for}\quad \beta U\to 0\,. \tag{3.3}$$

Here φ_n and E_n are eigenfunctions and corresponding energies of the relative motion of two molecules, $\boldsymbol{r}$ being the position vector of a molecule relative to the other.

Let us consider the density matrix

$$\rho(\boldsymbol{r},\boldsymbol{r}')=\sum\exp(-\beta E_n)\psi_n(\boldsymbol{r})\psi_n^*(\boldsymbol{r}')$$

or

$$\rho(\boldsymbol{r},\,\boldsymbol{r}')=\sum \exp(-\beta\mathrm{H})\psi_n(\boldsymbol{r})\psi_n{}^*(\boldsymbol{r}')\,. \tag{3.4}$$

Here H is the Hamiltonian operator

$$\mathrm{H}=-(\hbar^2/2m^*)\Delta+U(r)\,, \tag{3.5}$$

operating on the first argument $\boldsymbol{r}$; ψ_n are eigenfunctions which differs from φ_n only with regard to the normalization

$$\rho(\boldsymbol{r},\,\boldsymbol{r}')_{\beta\to 0}=\sum \psi_n(\boldsymbol{r})\psi_n{}^*(\boldsymbol{r}')=\delta(\boldsymbol{r}-\boldsymbol{r}'), \tag{3.6}$$

$\delta(\boldsymbol{r}-\boldsymbol{r}')$ being Dirac's δ-function. This density matrix can be determined as the solution of the Bloch differential equation

$$(\partial/\partial\beta)\rho(\boldsymbol{r},\,\boldsymbol{r}')=-\mathrm{H}\rho(\boldsymbol{r},\,\boldsymbol{r}')\,, \tag{3.7}$$

with the "initial" condition (3.6).

In the particular case where $U(r)=0$, the solution of Eq. (3.7) with the condition (3.6) is

$$\rho(\boldsymbol{r},\,\boldsymbol{r}')=\left(\frac{m^*}{2\pi\hbar^2\beta}\right)^{3/2}\exp\left[\frac{m^*}{2\hbar^2\beta}(\boldsymbol{r}-\boldsymbol{r}')^2\right].$$

Considering this fact we can assume the general solution to be of the form

$$\rho(\boldsymbol{r},\,\boldsymbol{r}')=\left(\frac{m^*}{2\pi\hbar^2\beta}\right)^{3/2}\exp\left[-\frac{m^*}{2\hbar^2\beta}(\boldsymbol{r}-\boldsymbol{r}')^2+W(\boldsymbol{r},\,\boldsymbol{r}')\right], \tag{3.8}$$

$$W\to 0 \quad \text{for} \quad \beta U\to 0\,, \tag{3.9}$$

in which the function W is to be determined from Eq. (3.7). By use of this function the Slater sum is given by

$$S(r)=\exp[W(\boldsymbol{r},\,\boldsymbol{r})]\,, \tag{3.10}$$

which is the diagonal element $\rho(\boldsymbol{r},\,\boldsymbol{r})$ of the density matrix renormalized according to (3.3).

Let in the following W stand for $W(\boldsymbol{r},\,\boldsymbol{r}')$ and denote its diagonal elements $W(\boldsymbol{r},\,\boldsymbol{r})$ by $\langle W\rangle$. Inserting (3.8) into (3.7) we have

$$U+\frac{\partial}{\partial\beta}W+\frac{\boldsymbol{r}-\boldsymbol{r}'}{\beta}\cdot\boldsymbol{\nabla}W=q(\boldsymbol{\nabla}W)^2+q\Delta W\,, \tag{3.11}$$

where

$$q\equiv\hbar^2/2m^*, \tag{3.12}$$

and $\boldsymbol{\nabla}$ means gradient with respect to $\boldsymbol{r}$. With this q let us expand W as

$$W=W_0+qW_1+q^2W_2+\cdots\cdot\,. \tag{3.13}$$

so that

$$S(r)=\exp[\langle W_0\rangle+q\langle W_1\rangle+q^2\langle W_2\rangle+\cdots\cdot] \tag{3.14}$$

where

$W_i\equiv W_i(\boldsymbol{r},\,\boldsymbol{r}')$, $\langle W_i\rangle\equiv W_i(\boldsymbol{r},\,\boldsymbol{r})$, $i=0,1,2,\cdots$,

Inserting the series into (3.11) we obtain as regards the coefficients of q^0, q^1, $q^2,\cdots\cdot$.

$$\begin{aligned}
&U+\frac{\partial}{\partial\beta}W_0+\frac{\boldsymbol{r}-\boldsymbol{r}'}{\beta}\cdot\boldsymbol{\nabla}W_0=0\,,\\
&\frac{\partial}{\partial\beta}W_1+\frac{\boldsymbol{r}-\boldsymbol{r}'}{\beta}\cdot\boldsymbol{\nabla}W_1=(\boldsymbol{\nabla}W_0)^2+\Delta W_0\,,\\
&\frac{\partial}{\partial\beta}W_2+\frac{\boldsymbol{r}-\boldsymbol{r}'}{\beta}\cdot\boldsymbol{\nabla}W_2=2\boldsymbol{\nabla}W_0\cdot\boldsymbol{\nabla}W_1+\Delta W_1\,,\\
&\frac{\partial}{\partial\beta}W_3+\frac{\boldsymbol{r}-\boldsymbol{r}'}{\beta}\cdot\boldsymbol{\nabla}W_3=(\boldsymbol{\nabla}W_1)^2\\
&\qquad\qquad+2\boldsymbol{\nabla}W_0\cdot\boldsymbol{\nabla}W_2+\Delta W_2\,,\\
&\qquad\qquad\cdots\cdots\cdots\cdot
\end{aligned} \tag{3.15}$$

Taking the condition (3.9) into account we have from the first equation of (3.15)

$$\langle W_0\rangle=-\beta U\,. \tag{3.16a}$$

Multiplying the first equation of (3.15) by $\boldsymbol{\nabla}$ and Δ we have

$$\boldsymbol{\nabla}U+\frac{\partial}{\partial\beta}\boldsymbol{\nabla}W_0+\frac{1}{\beta}\boldsymbol{\nabla}W_0+\frac{\boldsymbol{r}-\boldsymbol{r}'}{\beta}\cdot\boldsymbol{\nabla}\boldsymbol{\nabla}W_0=0\,,$$

$$\Delta U+\frac{\partial}{\partial\beta}\Delta W_0+\frac{2}{\beta}\Delta W_0+\frac{\boldsymbol{r}-\boldsymbol{r}'}{\beta}\cdot\boldsymbol{\nabla}\Delta W_0=0\,,$$

from which, taking the limit $\boldsymbol{r}'\to\boldsymbol{r}$, we have

$$\langle\boldsymbol{\nabla}W_0\rangle=-\frac{1}{2}\beta\boldsymbol{\nabla}U\,,\qquad \langle\Delta W_0\rangle=-\frac{1}{3}\beta\Delta U\,,$$

Inserting these into the second equation of (3.15) we obtain

$$\langle W_1\rangle=-\frac{\beta^2}{6}\Delta U+\frac{\beta^3}{12}(\boldsymbol{\nabla}U)^2. \tag{3.16b}$$

Similarly,

$$\begin{aligned}
\langle W_2\rangle=&-(1/60)\beta^5\boldsymbol{\nabla}\boldsymbol{\nabla}U:\boldsymbol{\nabla}U\boldsymbol{\nabla}U\\
&+(1/30)\beta^4\boldsymbol{\nabla}U\cdot\boldsymbol{\nabla}(\Delta U)\\
&+(1/90)\beta^4\boldsymbol{\nabla}\boldsymbol{\nabla}U:\boldsymbol{\nabla}\boldsymbol{\nabla}U\\
&-(1/60)\beta^3\Delta\Delta U\,,
\end{aligned}$$

$$\begin{aligned}
\langle W_3\rangle=&(17/5040)\beta^7\boldsymbol{\nabla}U\cdot\boldsymbol{\nabla}\boldsymbol{\nabla}U\cdot\boldsymbol{\nabla}\boldsymbol{\nabla}U\cdot\boldsymbol{\nabla}U\\
&+(1/840)\beta^7\boldsymbol{\nabla}\boldsymbol{\nabla}\boldsymbol{\nabla}U\,\vdots\,\boldsymbol{\nabla}U\boldsymbol{\nabla}U\boldsymbol{\nabla}U\\
&-(17/2520)\beta^6\boldsymbol{\nabla}\Delta U\cdot\boldsymbol{\nabla}\boldsymbol{\nabla}U\cdot\boldsymbol{\nabla}U\\
&-(1/280)\beta^6\boldsymbol{\nabla}\boldsymbol{\nabla}\Delta U:\boldsymbol{\nabla}U\boldsymbol{\nabla}U\\
&-(1/210)\beta^6\boldsymbol{\nabla}\boldsymbol{\nabla}\boldsymbol{\nabla}U\,\vdots\,\boldsymbol{\nabla}\boldsymbol{\nabla}U\boldsymbol{\nabla}U\\
&-(4/2835)\beta^6(\boldsymbol{\nabla}\boldsymbol{\nabla}U\cdot\boldsymbol{\nabla}\boldsymbol{\nabla}U):\boldsymbol{\nabla}\boldsymbol{\nabla}U\\
&+(17/5040)\beta^5\boldsymbol{\nabla}\Delta U\cdot\boldsymbol{\nabla}\Delta U\\
&+(1/280)\beta^5\boldsymbol{\nabla}\Delta\Delta U\cdot\boldsymbol{\nabla}U\\
&+(1/210)\beta^5\boldsymbol{\nabla}\boldsymbol{\nabla}\Delta U:\boldsymbol{\nabla}\boldsymbol{\nabla}U\\
&+(1/840)\beta^5\boldsymbol{\nabla}\boldsymbol{\nabla}\boldsymbol{\nabla}U\,\vdots\,\boldsymbol{\nabla}\boldsymbol{\nabla}\boldsymbol{\nabla}U\\
&-(1/840)\beta^4\Delta\Delta\Delta U\,.
\end{aligned}$$

These, according to (3.14), give $S(r)$.

Transforming $S(r)$ into

$$\begin{aligned}
e^{-\beta U}[&1+q\langle W_1\rangle+q^2(\langle W_2\rangle+(1/2)\langle W_1\rangle^2)\\
&+q^3(\langle W_3\rangle+\langle W_1\rangle\langle W_2\rangle+(1/6)\langle W_1\rangle^3)\cdots]
\end{aligned}$$

and inserting this expression into (3.1) we finally obtain the second virial coefficient in the form

$$B=B^{(0)}+qB^{(1)}+q^2B^{(2)}+\cdots. \tag{3.17}$$

Here

$$B^{(0)}=2\pi\int_0^\infty(1-e^{-\beta U})r^2dr\,,$$

$$B^{(1)}=\frac{\pi}{6}\beta^3\int_0^\infty e^{-\beta U}U'^2r^2dr\,,$$

$$B^{(2)}=-\frac{\pi}{6}\beta^4\int_0^\infty e^{-\beta U}\left[\frac{1}{10}U''^2+\frac{1}{5}\frac{U'^2}{r^2}+\frac{\beta}{9}\frac{U'^3}{r}-\frac{\beta^2}{72}U'^4\right]r^2dr\,,$$

$$B^{(3)}=\pi\beta^5\int_0^\infty e^{-\beta U}\left[\frac{1}{840}U'''^2+\frac{1}{140}\frac{U''^2}{r^2}+\frac{\beta}{756}U''^3+\frac{\beta}{180}\frac{U'U''^2}{r}+\frac{\beta}{945}\frac{U'^3}{r^3}-\frac{\beta^2}{720}U'^2U''^2-\frac{\beta^2}{6480}\frac{U'^4}{r^2}-\frac{\beta^3}{2160}\frac{U'^5}{r}+\frac{\beta^4}{25920}U'^6\right]r^2dr\,,$$

q being defined by (3.12), β being $1/kT$.

The first term, $B^{(0)}$, is the classical value; the next two terms, $qB^{(1)}$ and $q^2B^{(2)}$, were first given by Uhlenbeck and Beth[4)] and by Gropper[5)] who used Kirkwood's method[6)]. The neat method used here is essentially due to Husimi[7)].

§4. The Second Virial Coefficient for the Lennard-Jones Potential

Integration of each term in the expansion (3.17) can be performed for the Lennard-Jones potential

$$U(r)=\frac{\lambda}{r^n}-\frac{\mu}{r^6}=U_0\left[\frac{6}{n-6}\left(\frac{r_0}{r}\right)^n-\frac{n}{n-6}\left(\frac{r_0}{r}\right)^6\right], \tag{4.1}$$

in the form of the Lennard-Jones power series[8)1)] with respect to

$$y\equiv\frac{\mu}{kT}\left(\frac{kT}{\lambda}\right)^{6/n},$$

i.e.

$$B^{(0)}=-\frac{2\pi}{n}\left(\frac{\lambda}{kT}\right)^{3/n}\sum_{t=0}^{\infty}\Gamma\left(\frac{6t-3}{n}\right)\frac{y^t}{t!};$$

$$B^{(1)}=\frac{2\pi}{n}\frac{1}{kT}\left(\frac{\lambda}{kT}\right)^{1/n}\sum_{t=0}^{\infty}\Gamma\left(\frac{6t-1}{n}\right)\frac{y^t}{t!}\times J^{(1)}{}_t(6,n)$$

$$J^{(1)}{}_t(6,n)=[(n-6)6t-(n-1)]/12;$$

$$B^{(2)}=-\frac{2\pi}{n}\frac{1}{(kT)^2}\left(\frac{\lambda}{kT}\right)^{-1/n}\sum_{t=0}^{\infty}\Gamma\left(\frac{6t+1}{n}\right)\frac{y^t}{t!}\times J^{(2)}{}_t(6,n)\,,$$

$$J^{(2)}{}_t(6,n)=[21(n-6)^2(6t)^2+(6n^2+30n-42)\times(n-6)6t+(6n^3-27n^2+30n+63)]/4320;$$

$$B^{(3)}=\frac{2\pi}{n}\frac{1}{(kT)^3}\left(\frac{\lambda}{kT}\right)^{-3/n}\sum_{t=0}^{\infty}\Gamma\left(\frac{6t+3}{n}\right)\frac{y^t}{t!}\times J^{(3)}{}_t(6,n)\,,$$

$$J^{(3)}{}_t(6,n)=[93(n-6)^3(6t)^3+(82n^2+657n-741)(n-6)^2(6t)^2+(24n^4+348n^3+93n^2-810n+2241)(n-6)6t+(72n^5-126n^4-531n^3+1755n^2-405n-3645)]/362880\,.$$

Let us express the second virial coefficient in the final form

Table I.

For $n=9$

t	$\beta^{(0)}{}_t$	$\beta^{(1)}{}_t$	$\beta^{(2)}{}_t$	$\beta^{(3)}{}_t$
0	1.7061	0.3880	−0.0426	0.0287
1	−2.1263	0.1513	−0.0990	0.0956
2	−0.7500	0.2282	−0.1740	0.2055
3	−0.4259	0.2475	0.2400	0.3376
4	−0.2654	0.2350	−0.2822	0.4633
5	−0.1685	0.2039	−0.2949	0.5561
6	−0.1065	0.1652	−0.2813	0.6008
7	−0.0664	0.1265	−0.2490	0.5958
8	−0.0406	0.0924	−0.2071	0.5498
9	−0.0244	0.0648	−0.1632	0.4771
10	−0.0144	0.0438	−0.1228	0.3923
11	−0.00831	0.0286	−0.0886	0.3076
12	−0.00471	0.0182	−0.0616	0.2312
13	−0.00263	0.0112	−0.0414	0.1672
14	−0.00144	0.0067	−0.0270	0.1168
15	−0.00077	0.0040	−0.0171	0.0790
16	−0.00041	0.0023	−0.0106	0.0519
17	−0.00021	0.0013	−0.0064	0.0331
18	−0.00011	0.0007	−0.0037	0.0206
19	−0.00006	0.0004	−0.0022	0.0126
20	−0.00003	0.0002	−0.0012	0.0075

For $n=12$

t	$\beta^{(0)}{}_t$	$\beta^{(1)}{}_t$	$\beta^{(2)}{}_t$	$\beta^{(3)}{}_t$
0	1.2254	0.4838	−0.1276	0.1692
1	−1.8128	0.3694	−0.3768	0.6512
2	−0.6127	0.4471	−0.6189	1.3133
3	−0.3021	0.3981	−0.7254	1.8454
4	−0.1532	0.2979	−0.6815	2.0343
5	−0.0755	0.1965	−0.5447	1.8740
6	−0.0357	0.1173	−0.3838	1.4994
7	−0.0162	0.0645	−0.2440	1.0694
8	−0.00702	0.0330	−0.1422	0.6923
9	−0.00292	0.0159	−0.0769	0.4124
10	−0.00117	0.0072	−0.0390	0.2284
11	−0.00045	0.0031	−0.0186	0.1186
12	−0.00017	0.0013	−0.0084	0.0581
13	−0.00006	0.0005	−0.0036	0.0270

Table II.

T°K	B A^3	$C\times10^{-2}$ A^6	Reference
14.16	−25.7		a
17.30	−15.0		
20.58	− 6.0		
23.35	− 5.1		
37.4	7.6		
48.2	12.0		
20.35	− 4.6	11.3	b
65.15	15.6	7.0	
90.15	17.6	5.0	
123	18.9	5.2	
173	19.8	5.3	
223	19.8	5.0	
273	19.5	...	
273	19.7	2.1	c
323	19.2	2.0	
373	18.8	2.5	
423	18.4	3.0	

a Data are due to Nijhoff, Keesom and Iliin; the values are taken from Keesom, *Helium* (Elsevier, Amsterdam, London, New York, 1942) p. 34.

b The values are taken from J. Otto, Handbuch d. Experimentalphysik Bd. 8, Teil 2 (Akademische Verl. Leipzig, 1929) p. 144.

c A. Michels and H. Wouters, Physica 8 (1941) 923.

$$B=\frac{2\pi}{3}r_0{}^3\left[F^{(0)}(z)+\frac{F^{(1)}(z)}{cs}+\frac{F^{(2)}(z)}{(cs)^2}+\cdots\right], \tag{4.2}$$

$$z=U_0/kT\ ,$$

where (see (2,4))

$$1/cs=6q/U_0r_0{}^2, \tag{4.3}$$

$$F^{(i)}(z)=\sum\beta^{(i)}{}_t z^{[3+(n-2)i+(n-6)t]/n}, \tag{4.4}$$

$$i=0,\ 1,\ 2,\ \cdots\cdots,$$

The coefficients $\beta^{(i)}{}_t$ are given in Table I for $n=9$ and 12. The functions $F^{(i)}$ for $n=9$ are included in Table IV.

Making use of these tables and depending upon the observed values of the second virial coefficient given in Table II, we can determine s and the model parameters for helium. The result is as follows.

$s=1.15$, $r_0=3.11$A, $U_0/k=$ 7.82°K for $n=9$.

$s=1.05$, $r_0=2.88$A, $U_0/k=10.80$°K for $n=12$.

(de Boer and Michels' result is

$s=0.99$, $r_0=2.87$A, $U_0/k=10.22$°K for $n=12$.)

We shall later see that the model with $n<12$ is more adequate than the model with $n>12$.

§ 5. Quantum Correction to the Third Virial Coefficient

The expansion (3.14) of the Slater sum for a two-molecule system can be generalized to the Slater sum $S(\boldsymbol{r}_1, \boldsymbol{r}_2, \cdots, \boldsymbol{r}_N)$ for a N-molecule (single component) system, $\boldsymbol{r}_i$ being the position of the ith molecule. Thus

$$S(\boldsymbol{r}_1, \boldsymbol{r}_2,\cdots, \boldsymbol{r}_N)=\exp\left[\langle W_0\rangle+q\langle W_1\rangle+\cdots\right], \tag{5.1}$$

where q is $\hbar^2$ divided by the mass of a molecule. (See (3.12) where m^* is the reduced mass.) The first term in the argument is, as in (3.16a),

$$\langle W_0\rangle=-\beta\Phi(\boldsymbol{r}_1, \boldsymbol{r}_2,\cdots, \boldsymbol{r}_N),\quad \beta\equiv1/kT, \tag{5.2}$$

Φ being the potential energy of the system. For the second term we have, as in (3.16b),

$$\langle W_1\rangle=-\frac{1}{12}\beta^2\sum_{i=1}^{N}\frac{\partial}{\partial\boldsymbol{r}_i}\cdot\frac{\partial}{\partial\boldsymbol{r}_i}\Phi+\frac{1}{24}\beta^3\sum_{i=1}^{N}\left(\frac{\partial}{\partial\boldsymbol{r}_i}\Phi\right)^2. \tag{5.3}$$

By means of the Slater sum for $N=3$ the third virial coefficient is given by[4)]

$$C=4B^2+\frac{1}{3V}\iiint[-2+S(\boldsymbol{r}_1\ \boldsymbol{r}_2)+S(\boldsymbol{r}_1, \boldsymbol{r}_3)+S(\boldsymbol{r}_2, \boldsymbol{r}_3)-S(\boldsymbol{r}_1, \boldsymbol{r}_2, \boldsymbol{r}_3)]d\tau_1d\tau_2d\tau_3\ , \tag{5.4}$$

$$d\tau_i\equiv dx_idy_idz_i\ ,$$

V being the volume of the system.

Our object in this section is to calculate the first quantum correction $qC^{(1)}$ to

$$C=C^{(0)}+qC^{(1)}+\cdots\cdot, \tag{5.5}$$

which is similar to the expansion (3.17) of B. Let

$$C=4B^2+\bar{C}\ ,$$

and

$$C=\bar{C}^{(0)}+q\bar{C}^{(1)}+\cdots,$$

then

$$C^{(1)}=8B^{(0)}B^{(1)}+\bar{C}^{(1)} \tag{5.6}$$

$$\begin{aligned}\bar{C}^{(1)}=\frac{1}{3V}\frac{\beta^3}{24}\iiint\Big\{&-\exp[-\beta\Phi(\boldsymbol{r}_1, \boldsymbol{r}_2)]\times\sum_i\left[\frac{\partial}{\partial\boldsymbol{r}_i}\Phi(\boldsymbol{r}_1, \boldsymbol{r}_2)\right]^2\\&-\exp[-\beta\Phi(\boldsymbol{r}_1, \boldsymbol{r}_3)]\sum_i\left[\frac{\partial}{\partial\boldsymbol{r}_i}\Phi(\boldsymbol{r}_1, \boldsymbol{r}_3)\right]^2\\&-\exp[-\beta\Phi(\boldsymbol{r}_2, \boldsymbol{r}_3)]\sum_i\left[\frac{\partial}{\partial\boldsymbol{r}_i}\Phi(\boldsymbol{r}_2, \boldsymbol{r}_3)\right]^2\\&+\exp[-\beta\Phi(\boldsymbol{r}_1, \boldsymbol{r}_2, \boldsymbol{r}_3)]\sum_i\left[\frac{\partial}{\partial\boldsymbol{r}_i}\Phi(\boldsymbol{r}_1, \boldsymbol{r}_2, r_3)\right]^2\Big\}\\&\times d\tau_1d\tau_2d\tau_3\ .\end{aligned} \tag{5.7}$$

Here we have used integration by parts such as

$$\frac{1}{V}\iiint \exp(-\beta\Phi)\sum \frac{\partial}{\partial \boldsymbol{r}_i}\cdot\frac{\partial}{\partial \boldsymbol{r}_i}\Phi d\tau_1 d\tau_2 d\tau_3$$

$$=\frac{1}{V}\iiint \exp(-\beta\Phi)\sum\left(\frac{\partial}{\partial \boldsymbol{r}_i}\Phi\right)^2 d\tau_1 d\tau_2 d\tau_3 .$$

We assume as usual that the potential energy of the system is equal to the sum of the potential energies for pairs:

$$\Phi=\sum_{i<j}\Phi(\boldsymbol{r}_i,\ \boldsymbol{r}_j)=\sum_{i<j}U(r_{ij})\ ,\quad r_{ij}=|\boldsymbol{r}_i-\boldsymbol{r}_j| . \tag{5.8}$$

Hence

$$\Phi(\boldsymbol{r}_1,\ \boldsymbol{r}_2,\ \boldsymbol{r}_3)=U(r_{12})+U(r_{13})+U(r_{23}) .$$

In the last term of the integrand of (5.7),

$$\sum_i\left[\frac{\partial U(r_{12})}{\partial \boldsymbol{r}_i}+\frac{\partial U(r_{13})}{\partial \boldsymbol{r}_i}+\frac{\partial U(r_{23})}{\partial \boldsymbol{r}_i}\right]^2$$

can be replaced by

$$\sum_i\left[\left(\frac{\partial U(r_{12})}{\partial \boldsymbol{r}_i}\right)^2+\left(\frac{\partial U(r_{13})}{\partial \boldsymbol{r}_i}\right)^2+\left(\frac{\partial U(r_{23})}{\partial \boldsymbol{r}_i}\right)^2\right]$$

since the integral of cross terms vanishes. Taking into account the relations as

$$\frac{1}{2V}\iiint \exp[-\beta U(r_{12})]\sum\left(\frac{\partial U(r_{12})}{\partial \boldsymbol{r}_i}\right)^2 d\tau_1 d\tau_2 d\tau_3$$

$$=\frac{1}{V}\iiint \exp[-\beta U(r_{12})][U'(r_{12})]^2 d\tau_1 d\tau_2 d\tau_3$$

and using the transformation of integration variables

$$V^{-1}d\tau_1 d\tau_2 d\tau_3=8\pi^2 r_{12}r_{13}r_{23}dr_{12}dr_{13}dr_{23}$$

we obtain finally

$$\overline{C}^{(1)}=\frac{2\pi^2}{9}\beta^3\iiint(A_{12}+A_{13}+A_{23})$$
$$\times r_{12}r_{13}r_{23}dr_{12}dr_{13}dr_{23}\ , \tag{5.9}$$

$$A_{ij}=\{\exp[-\beta U(r_{12})-\beta U(r_{13})-\beta U(r_{23})]$$
$$-\exp[-\beta U(r_{ij})]\}[U'(r_{ij})]^2\ ,$$
$$1\leqq i<j\leqq 3 .$$

The integral is to be taken over all values of r_{12}, r_{13}, r_{23} which form three sides of a triangle.

§ 6. The Third Coefficient for the Lennard-Jones Potential

Here again we adopt the Lennard-Jones potential

$$U(r)=\frac{\lambda}{r^n}-\frac{\mu}{r^m}$$
$$=U_0\left[\frac{m}{n-m}\left(\frac{r_0}{r}\right)^n-\frac{n}{n-m}\left(\frac{r_0}{r}\right)^m\right],$$
$$n>m>3\ , \tag{6.1}$$

for which the classical $C^{(0)}$ has been obtained by Kihara and others[9]. Using

$$R=r_{12}\ ,\quad x=r_{13}/R\ ,\quad y=r_{23}/R \tag{6.2}$$

as integration variables, we can transform (5.9) into

$$\overline{C}^{(1)}=\frac{2\pi^2}{3}\beta^3\int_0^1\int_{1-x}^1\left[\int_0^\infty(A_{12}+A_{13}+A_{23})R^5 dR\right]$$
$$\times xydydx . \tag{6.3}$$

The integration with respect to R can be performed by a series expansion. The result is as follows

$$\overline{C}^{(1)}=\frac{2\pi^2}{3n}\frac{1}{kT}\left(\frac{\lambda}{kT}\right)^{4/n}\sum_{t=0}^{\infty}y^t I_t(m,\ n)\ ,$$

$$y=\frac{\mu}{kT}\left(\frac{kT}{\lambda}\right)^{m/n},$$

$$I_t(m,\ n)=\frac{1}{6n}\frac{1}{t!}\Gamma\left(\frac{mt-4}{n}\right)\int_0^1\int_{1-x}^1 F_t xydydx ,$$

$$F_t=(mt+n-4)(mt-4)[\langle 2n+2\rangle\langle m\rangle^t$$
$$\times\langle n\rangle^{(4-mt)/n-2}-\langle 6\rangle]$$
$$-2mt(mt-4)[\langle n+m+2\rangle\langle m\rangle^{t-1}$$
$$\times\langle n\rangle^{(4-mt)/n-1}-\langle 6\rangle]$$
$$+m^2t(t-1)[\langle 2m+2\rangle\langle m\rangle^{t-2}\langle n\rangle^{(4-mt)/n}$$
$$-\langle 6\rangle]\ , \tag{6.4}$$

where we have used the bracket notation in the sense

$$\langle a\rangle=1+x^{-a}+y^{-a} . \tag{6.5}$$

The values of $I_t(6, 9)$, obtained by numerical integration, are given in Table III.

By use of $\overline{C}^{(1)}$ the third virial coefficient is given by (5.5) and (5.6) up to the term proportional to the first power of q. For $m=6$ and $n=9$ Table IV gives the functions $G^{(0)}$ and $G^{(1)}$ in the expansion

Table III.

t	$I_t(6, 9)$
0	−114.5
1	+ 54.0
2	12.45
3	10.10
4	7.37
5	4.61
6	2.59
7	1.338
8	0.651
9	0.300
10	0.133
11	0.057
12	0.024

Table IV.

$-\log_{10}z$	$F^{(0)}(z)$	$F^{(1)}(z)$	$F^{(2)}(z)$	$F^{(3)}(z)$	$G^{(0)}(z)$	$G^{(1)}(z)$
0.1	−1.583	1.194	−1.007	1.684	0.369	1.0
0.2	−1.071	0.741	−0.444	0.564	0.409	0.42
0.3	−0.6995	0.4793	−0.2056	0.2024	0.357	0.222
0.4	−0.4255	0.3200	−0.0992	0.0757	0.303	0.155
0.5	−0.2218	0.2195	−0.0495	0.0295	0.264	0.121
0.6	−0.0700	0.1538	−0.0255	0.0119	0.237	0.095
0.7	0.0430	0.1095	−0.0136	0.0050	0.219	0.074
0.8	0.1265	0.0791	−0.0073	0.0021	0.206	0.059
0.9	0.1874	0.0578	−0.0040	0.0009	0.194	0.046
1.0	0.2309	0.0426	−0.0022	0.0004	0.183	0.035
1.1	0.2610	0.0316	−0.0013		0.172	0.024
1.2	0.2806	0.0236	−0.0007		0.160	0.018
1.3	0.2922	0.0177	−0.0004		0.149	0.014
1.4	0.2974	0.0134			0.137	0.011
1.5	0.2979	0.0101			0.125	0.008
1.6	0.2946	0.0077			0.114	0.006
1.7	0.2885	0.0058			0.103	0.004
1.8	0.2805	0.0044			0.093	
1.9	0.2709	0.0034			0.083	
2.0	0.2603	0.0026			0.074	

$$C=\frac{5}{18}\pi^2 r_0{}^6\left[G^{(0)}(z)+\frac{1}{cs}G^{(1)}(z)+\cdots\right].$$

$$z=U_0/kT\,,\quad 1/cs=6q/U_0r_0{}^2\,, \tag{6.6}$$

together with $F^{(i)}$ in the expansion (4.2) of the second virial coefficient.

Fig. 1 shows a comparison with experimental results given in Table II. Here curves indicate calculated values based upon the model parameters determined from the second virial coefficient. Although the experimental results do not seem to be very accurate, the comparison shows that (the negative part of) the true intermolecular potential is closer to the model with $n<12$ than the model with $n>12$.

Since the depth parameter determined from the second virial coefficient is

$$s=1.15 \text{ for } n=9,\ s=1.05 \text{ for } n=12,$$

its real value for the He^4–He^4 system is highly probably within the range $1<s<4/3$, which corresponds to $3/4<s<1$ for the He^3–He^3 system. Thus, on the assumption of the potential additivity, we draw the following conclusion. *The two-body system of* He^4 *atoms has a discrete energy level while the two-body system of* He^3 *atoms has no discrete level.*

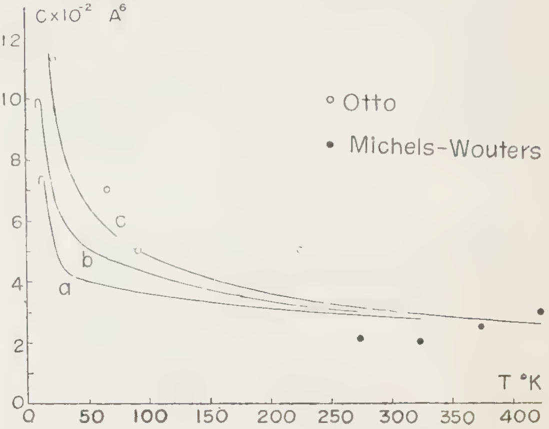

Fig. 1. The third virial coefficient of helium. The curves were calculated by use of the Lennard-Jones potential with parameters determined from the second virial coefficient. Curve "a" is for (6, 12)-potential, classical; curve "b" is for (6, 9)-potential, classical; curve "c" is for (6, 9)-potential with the first quantum correction.

References

1) J. de Boer and A. Michels: Physica **5** (1938) 945.
2) J. M. Blatt and J. D. Jackson: Phys. Rev. **26** (1949) 21.
3) This value for $n=12$ agrees with the result of J. E. and M. F. Kilpatrick: J. Chem. Phys. **19** (1951) 930.
4) G. E. Uhlenbeck and E. Beth: Physica **3** (1936) 729.
5) L. Gropper: Phys. Rev. **50** (1936) 963.
6) J. G. Kirkwood: Phys. **44** (1933) 31.
7) K. Husimi: Proc. Phys.-Math. Soc. Japan **22** (1940) 264.
8) Lennard-Jones: Proc. Roy. Soc. A **106** (1924) 463, Proc. Phys. Soc. A **43** (1931) 461.
9) T. Kihara: J. Phys. Soc. Japan **3** (1948) 265, **6** (1951) 184; Revs. Modern Phys. **25** (1953) 831; Bird, Spotz and Hirschfelder: J. Chem. Phys. **18** (1950) 1395; Epstein Hibbert, Powers and Roe: J. Chem. Phys. **22** (1954) 464.

JOURNAL OF THE PHYSICAL SOCIETY OF JAPAN Vol. 10, No. 4, APRIL, 1955

A Theory on Image Formation of Electron Microscope

By Ryozi UYEDA

Physical Institute, Nagoya University, Nagoya, Japan

(Received December 10, 1954)

This article is presented to give a consistent basis to all theories of image formation of electron microscope. The author's idea is to build up an image of a specimen from images of atoms which make up the specimen. The result obtained by developing this idea indicates that an actual image is composed of two ideal images, one of which shows phase contrast and the other constrast due to scattering absorption. By applying this result, bright and dark field images are explained. Not only images of amorphous specimens but those of crystalline specimens are treated.

§ 1. Introduction

Theories on image formation of electron microscopes were advanced by Boersch[1)], Gabor[2)], Zworykin *et al.*[3)], Scherzer[4)], Borries[5)], Ramberg[6)], and others. However, relations between these theories were not made clear. The aim of the present article* is to give a consistent underlying basis to all these theories. The author's idea is to build up an image of a specimen from images of atoms which make up the specimen.

This article begins with a survey of electron diffraction formulae for amorphous specimens. Based upon these formulae, the author's view of image formation is presented. According to this view, an actual image is composed of two ideal images, one of which shows phase contrast[6)] and the other contrast due to scattering absorption[1),5)]. Bright field and dark field images are explained accordingly. Not only images of amorphous specimens but those of crystalline specimens are treated. Finally, the author's idea is developed mathematically from Scherzer's theory[4)] which deals with the image of a free atom, extending it to specimens made up of many atoms. The result of this development proves that the view is adequate.

§ 2. Survey of Electron Diffraction Formulae for Amorphous Specimens

Let us consider the elastic scattering of electrons by a specimen which is thin enough to satisfy the condition of single scattering. The amplitude of the scattered wave at a point far from the specimen is proportional to

$$S(\boldsymbol{b})=\sum_i E_i \exp[-2\pi i\boldsymbol{b}\boldsymbol{r}_i] , \qquad (2.1)$$

$$\boldsymbol{b}=\boldsymbol{k}-\boldsymbol{k}_0 , \qquad (2.1a)$$

where $\boldsymbol{k}_0$ indicates the wave vector of the incident wave, $\boldsymbol{k}$ that of the scattered wave; i indicates the ith atom in the specimen, $\boldsymbol{r}_i$ the position of the ith atom, and the summation over all atoms in the specimen. Factor E_i is the scattering function given by

$$E_i=(2/a_0)\{(Z_i-f_i)/s^2\} , \qquad (2.1b)$$

where Z_i is the atomic number and f_i the atomic scattering factor; a_0 stands for Bohr radius $a_0=h^2/4\pi^2me^2$ and s is given by $s=2\pi|\boldsymbol{k}-\boldsymbol{k}_0|=4\pi(\sin\theta/\lambda)$, where 2θ is the scattering angle and λ the wave length of electrons. The intensity of the scattered wave is proportional to

$$I(b)=\sum_i\sum_j E_iE_j \exp[-2\pi i\boldsymbol{b}(\boldsymbol{r}_i-\boldsymbol{r}_j)] . \qquad (2.2)$$

Let us assume, for the sake of simplicity, that the specimen contains atoms of only one kind. Then (2.2) can be rewritten

$$I(b)=N\{E(s)\}^2+\{E(s)\}^2\sum_{i\neq j}\exp[-2\pi i\boldsymbol{b}(\boldsymbol{r}_i-\boldsymbol{r}_j)] , \qquad (2.3)$$

where N is the total number of atoms in the specimen. If the atomic arrangement in the specimen is assumed to be perfectly at random, the average of (2.3) becomes

$$I(\boldsymbol{b})=N\{E(s)\}^2+\{NE(s)|\Phi(\boldsymbol{b})|\}^2 , \qquad (2.4)$$

$$\Phi(\boldsymbol{b})=(1/v)\int_v \exp[-2\pi i(\boldsymbol{b}\boldsymbol{r})]d\boldsymbol{r} , \qquad (2.4a)$$

where v is the volume of the specimen and the integral is over the volume of the specimen. The two terms in (2.4) are schematically illustrated in Fig. 1.

---

* Originally presented before the Committee of High Resolution Electron Microscope at Nagoya, Japan on October 18, 1952. Also presented before the International Conference on Electron Microscopy, London, July 1954.

The second term in (2.4) is the small angle scattering familiar in X-ray optics. The function $\Phi(\boldsymbol{b})$ is considerable only for small $\boldsymbol{b}$ which satisfies the condition

$$2R\sin\theta/\lambda \approx R(2\theta)/\lambda \ll 1 \ , \qquad (2.5)$$

where R indicates the linear dimension of the specimen. Assuming $R=10$Å and $\lambda=0.05$Å, we get $2\theta < 5\times10^{-3}$ rad. Since $\Phi(\boldsymbol{b})$ is vanishingly small where $|\boldsymbol{b}|$ is large, $E(0)$ can be substituted for $E(s)$ in the second term of (2.4). Moreover, between $E(0)$ and the mean inner potential V_0 we have a relation

$$V_0=(h^2/2\pi me)(N/v)E(0)\ . \qquad (2.6)$$

Therefore the second term of (2.4) becomes the square of absolute value of

$$(2\pi me/h^2)V_0 v\Phi(\boldsymbol{b})\ . \qquad (2.7)$$

Term (2.7) expresses the wave diffracted by an imaginary specimen having a uniform potential V_0.

Although the atomic arrangement is assumed to be perfectly at random in deriving (2.4), some order is always present in actual amorphous substances. Therefore, another term appears due to interatomic correlations. However, this term is not essential to qualitative theories of image formation and is neglected in the following discussions.

§ 3. General View of Image Formation of Amorphous Specimens

Based upon the results in the previous section, a general view of image formation is here outlined. Those who do not find this outline complete, may refer to Sec. 6 wherein an exact treatment is given.

According to (2.4), the intensity of waves scattered elastically by an amorphous specimen consists of two terms. The first term is the summation of the intensity of the wave scattered by a free atom. If the elastic scattering by atoms in amorphous specimens were incoherent, only the first term would appear. Actually, however, the elastic scattering is coherent and the second term, the small angle scattering, appears as the result of interference. For convenience we call the waves corresponding to the first term the *incoherent part of the elastic scattering.*

The following discussion of the image formation takes into account the primary wave and inelastically scattered waves as well as the elastically scattered waves. We devide these into two classes: (a) Incoherent and (b) coherent waves.

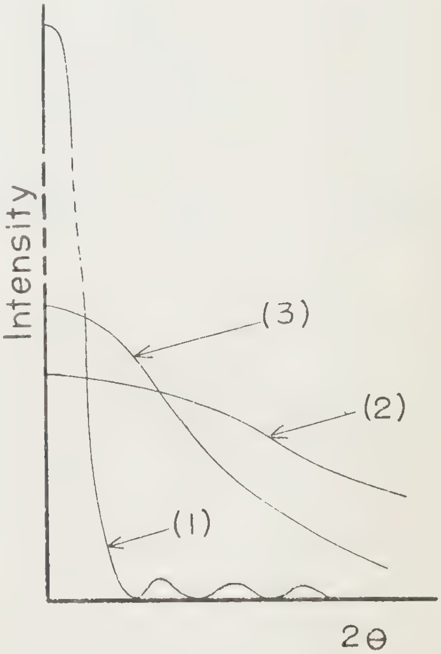

Fig. 1. Angular distribution of scattered intensity (schematical). (1) Small angle scattering, (2) incoherent part of elastic scattering, (3) inelastic scattering[7),8)].

(a) Incoherent waves consist of the *incoherent part of the elastic scattering* as well as inelastic scatterings. These waves have a similar behavior except in the defocus due to energy loss. They are incoherent to each other and also incoherent to the coherent waves. Therefore, they form images of atoms as if atoms were self-luminous. They propagate in wide solid angles as shown in Fig. 1.* If an ideal objective lens with a sufficiently large aperture and free from any aberration were available, images of atoms would be resolved by the action of these waves.

---

* It is worth mentioning that $E(s)$ calculated for free atoms cannot be applied to solid substances for small s because effects of bindings are important. The use of experimental values of mean inner potential may give better result[10)]. A survey was given by Miyake[11)] concerning experimental values of mean inner potentials and those of diamagnetic susceptibilities.

Since, however, present-day electron microscopes cannot resolve atoms, images formed by these waves are diffused in a dimension of the resolving power. Thus almost uniform brightness is produced by many atoms in a specimen.

(b) The coherent wave is composed of the primary wave and the small angle scattering. The latter is related to the external shape of the specimen as expressed in (2.4a) and propagates in a small solid angle given by (2.5). As suggested by (2.7), an image formed by the coherent waves is the same as the image of an imaginary specimen which has a uniform refractive index

$$\mu=\{1+(V_0/E)\}^{1/2} \tag{3.1}$$

where E is the kinetic energy of electrons. We can assume that the imaginary specimen absorbs waves because the incoherent waves scatter away from actual specimens. The absorption coefficient is given by

$$\kappa=(N/v)(\sigma_e+\sigma_i)=\kappa_e+\kappa_i \tag{3.2}$$

where σ_e and σ_i indicate total cross sections of the elastic and inelastic scatterings, respectively.

It should be noted that the separation of the coherent wave into the primary wave and the small angle scattering is possible only when specimens are thin as treated in Sec. 2. The coherent wave is the wave produced through diffraction by an ideal specimen with a uniform refractive index and a uniform absorption coefficient. The result mentioned above holds even for thick specimens, although the separation is impossible.

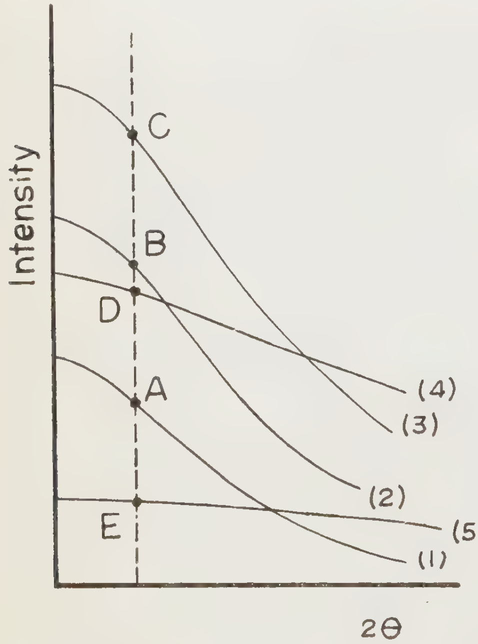

Fig. 2. Intensity distribution of incoherent waves (schematical). Specimens become thicker in the order 1,2,3,4 and 5. Concerning notations A, B,C,D and E, see Photo. 1.

The actual image is the superposition in intensity of images formed by the incoherent and the coherent waves. We find a similar circumstance when a cell filled with suspension is observed under a light microscope. For electron microscopes the fluctuation of refractive index is caused by the existence of atoms in specimens, while for light microscope it is caused by the existence of suspended particles. The appearence of the incoherent waves is due to the fluctuation of refractive index.

§ 4. Application of the General View

(a) *Bright field images.* In common practice an objective lens is provided with an aperture. The image formed by the coherent wave is little influenced by the size of the aperture because this wave is confined within a narrow solid angle. On the contrary the image formed by the incoherent waves is so influenced on that it becomes weaker as the size of the aperture is decreased because these waves extend into a large solid angle with some portion stopped by the aperture. Thus a contrast is produced by scattering absorption[12]. This contrast was studied theoretically by Boersch[1] and Borries[5] and can be estimated by the intensity distribution of the incoherent waves (Fig. 2).

It is generally known from experience that in order to get good images the illuminating beam* must be confined to a small solid angle around the optical axis. The necessity for this adjustment can be understood by considering the follows: Usually the incoherent waves are stopped by the aperture and the coherent wave plays an important part in forming images. If the adjustment is inadequate, the coherent wave may cover the whole aperture which is usually far larger than the optimum size. Thus the image is deteriorated by the spherical aberration. When the adjustment is adequate, the essential portion of the coherent wave passes through a small central area of the aperture. Since the area can be smaller than the optimum size, good images are possible even with the spherical aberration. If the incoherent waves form images, images should be deteriorated by the spherical aberration independent of the adjustment.

---

* A convergent illumination[9] can be considered a superposition of plane waves which have no mutual phase relation.

When defocused, the image formed by the incoherent waves is diffused on the edge (Fig. 3b) as was discussed in detail by Zworykin *et al.*[3] On the other hand, the image formed by the coherent waves shows maxima and minima (Fig. 3c). This phenomenon is Fresnel diffraction first observed by Boersch[13] and phase contrast later studied by Ramberg[6]. The observed image is the superposition of Figs. 3b and 3c (Fig. 3d). In most cases the part illustrated in Fig. 3c prevails over that shown in 3b because most of the incoherent waves are stopped by the aperture. When, however, the aperture is large, Fig. 3b is not negligible.

(b) *Dark field images.* Under usual conditions dark field images are formed by the incoherent waves because the esential part of the coherent wave is stopped by the aperture. Therefore, the quality of images is independent of the fine directional adjustment of an illuminating system. The brightness of dark field images increases to a maximum as the specimen thickness increases. When, however, the thickness increases beyond the thickness at the maximum, the brightness decreases. Photo. I illustrates the change in brightness with increase of thickness.

When specimens are so thick that electrons cannot penetrate them, the incoherent waves disappear. Thus the coherent wave forms images even in a dark field. Under this condition, Fresnel fringes can appear in the dark field. The author believes that Boersch[13] observed Fresnel fringes in a dark field under this condition.

§ 5. Image Formation of Crystalline Specimens

The image formation of a two-dimensional crystal was discussed by Boersch[1]. In this

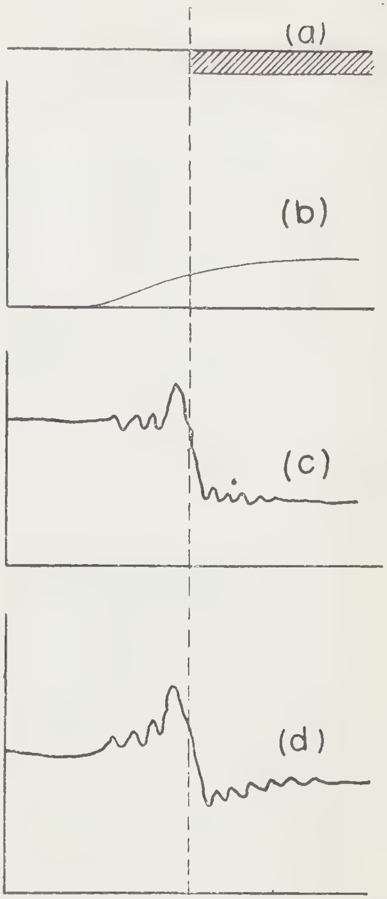

Fig. 3. Schematical drawing illustrating contour phenomena.
(a) Specimen film. (b) Image formed by incoherent waves. (c) Image formed by coherent waves. (d) Total effect.

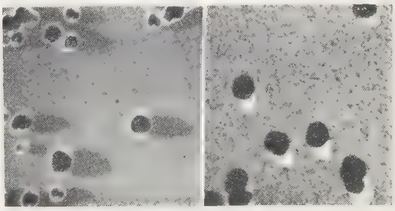
(c) (b)

Photo. 1. Dark field images of carbon black shadowed with aluminum; magnified ×10,000. (Courtesy Prof. T. Hibi)
(a) Thin supporting film,
(b) Thick supporting film.
In (a) bright rings are appearing on peripheries of particles with dark shadows, while in (b) no bright rings are appearing and shadows are bright. These contrasts are understood by the the help of Fig. 2, if we assume the thickness of specimens increases in the following order: (A) Shadows in (a), (B) background of (a), (C) peripheries of particles of (a) and shadows in (b), (D) background of (b), (E) particles of (b). Notations (A), ····, (E) correspond respectively to (A), ····, (E) in Fig. 2.

section the image formation of three-dimensional crystals is outlined.

(a) *Bright field images.* Let us consider a specimen of perfect crystal. When a primary wave falls upon a specimen, the small angle scattering appears the same as in amorphous specimens, but there is no *incoherent part of elastic scattering.* In the place of the incoherent part, Bragg reflections appear when Bragg conditions are satisfied. The disappearance of the incoherent part and the appearance of Bragg reflections are both due to the regular atomic arrangement in crystals.

When no Bragg reflection is excited, images are formed by the coherent waves and the inelastic scatterings. An image formed by the coherent waves is the same as the image of an imaginary specimen with a uniform refractive index (3.1) and an absorption coefficient κ_t. Since the absorption coefficient is less than (3.2) by κ_e, crystalline substances are more transparent than amorphous substances provided no Bragg reflection is excited.

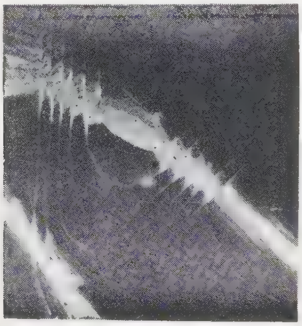

Photo. 2. Dark field image of mica; magnified ×6,000. (Courtesy Prof. T. Hibi).
The set of V-shaped sharp contours is due to imperfections in the crystal.
Diffuse contours are contours due to Bragg reflections.

When a Bragg reflection is excited, the absorption coefficient κ_t must be supplemented by a term caused by the Bragg reflection. Since this term, the extinction coefficient, is large for strong Bragg reflections, the image formed by the coherent waves becomes remarkably dark. This is the familiar phenomenon of extinction contours[15)]

(b) *Effect of imperfections.* Although the incoherent part of elastic scattering disappears perfectly in perfect crystals, it appears to a certain extent when crystals are imperfect. Since severely strained parts of crystals are remarkably imperfect, they appear dark in bright field images and appear bright in dark field images. The contours appearing in Photo. 2 are without a doubt due to imperfections. These contours remain fixed when the direction of illuminating beam is changed and this fixing cannot be observed in extinction contours.

(c) *Dark field images.* Dark field images of perfect crystalline specimens are formed mainly by inelastic scatterings provided no Bragg reflections take part in forming images. Therefore, dark field images of crystalline specimens are less bright than those of amorphous specimens, but they become anomalously bright when a Bragg reflection takes part in forming images.

According to the kinematical theory of electron diffraction, the intensity distribution of $(h_1h_2h_3)$-reflection is given by[17)]

$$|(2\pi me/h^2)V_h v\Phi(\boldsymbol{b}-\boldsymbol{h})|^2 \tag{5.1}$$

where V_h indicates $(h_1h_2h_3)$-Fourier coefficient of the periodic electric potential in the crystal, $\boldsymbol{h}$ the vector representing $(h_1h_2h_3)$-lattice point in the reciprocal lattice and Φ the function defined in (2.4a). This indicates that in forming images Bragg reflections are similar to the small angle scattering.

(d) *Images of thick crystals.* When crystals are thick, the kinematical theory of diffraction is not adequate and the dynamical theory of diffraction should be adopted. The most remarkable phenomenon explained by the dynamical theory is a set of *equal thickness striations* which are observed in images of MgO and other crystals[18),19)]. This phenomenon was explained by Kossel[19)], Heidenreich and Sturkey[20)] and later by Kato[14)].

Boersch[21)] considered a crystal to be an amplitude grating as well as a phase grating and he determined the absorption power of amplitude grating from the cross section of inelastic scatterings. Recently, however, Yoshioka[22)] treated theoretically the absorption of electrons by crystals and obtained a result which can be stated as follows: If a crystal is assumed to be a three-dimensional amplitude grating, it has a property quite different from usual gratings, because Fourier coefficients of absorption power change with the direction of the incident beam especially when Bragg reflections are excited.

(e) *Images of net planes.* Even if an ideal objective were available, no information concerning atomic arrangement could be obtained when an image is formed solely by the coherent waves or solely by a Bragg reflection. A net plane becomes visible only when an image is formed by both the coherent waves and a Bragg reflection.* An image of a set of net planes is produced by an interference between the image formed by the coherent waves and that formed by Bragg reflection. This fact is made clear by examining the wave field near the crystal (Fig. 4). It is obvious that only one net plane is visible when one Bragg reflection takes part in forming an image. The net plane which is made visible is that which excites the Bragg reflection. Therefore to get a full information on atomic arrangements many images formed by different Bragg reflections must be obtained. Crystal structures are revealed in principle by a complete set of ideal images.

§ 6. Exact Theory of Image Formation

In this section the general view described in Sec. 3 is formulated exactly. For the sake of simplicity, the illuminating beam is assumed to be parallel and only thin amorphous specimens are treated.

(a) *Image of free atoms: Survey of Scherzer's theory*[4]. According to Kirchhoff's theorem, the wave function on the image plane $\Psi(\boldsymbol{R})$ is derived from that on the back focal plane $\psi_a(\boldsymbol{r}_a)$ as follows:

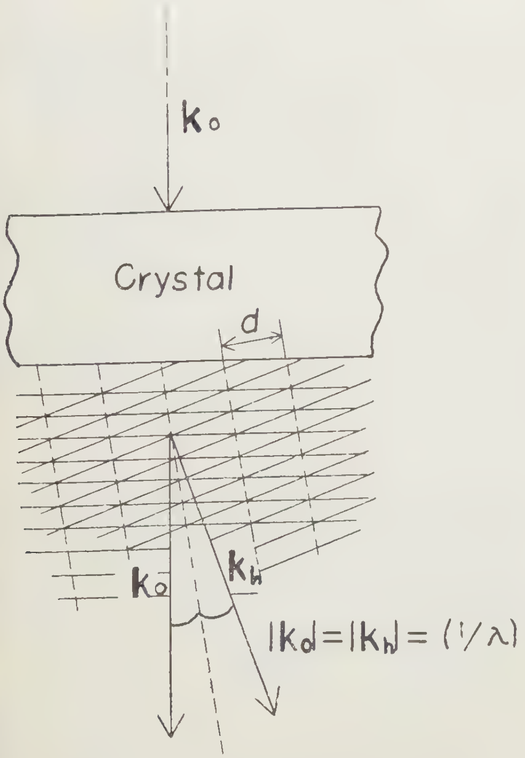

Fig. 4. Schematical drawing illustrating the interference of a transmitted wave and Bragg reflection. Distance d between fringes satisfies Bragg condition $2d\sin\theta=n\lambda$.

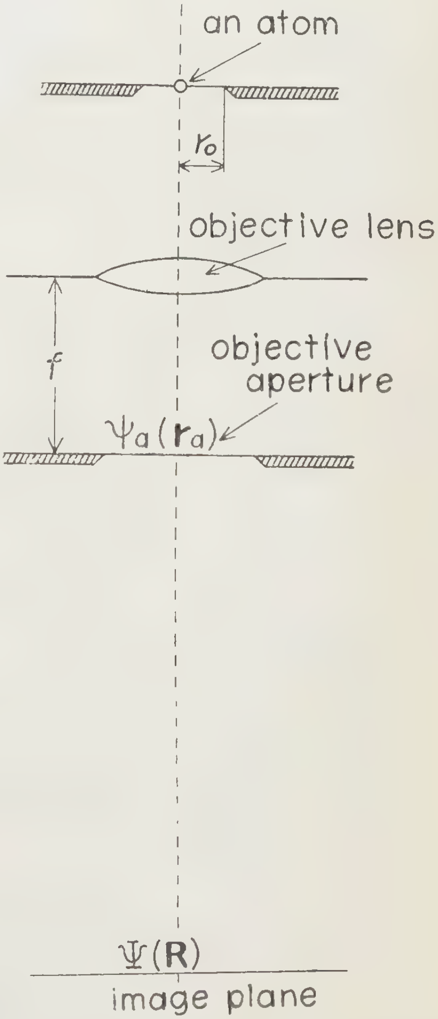

Fig. 5. Schematical drawing of imaging system.

---

* Bragg reflections are actually coherent with the primary wave. However, the word "coherent wave" is used here as mentioned in Sec. 3b, not involving Bragg reflections.

$$\Psi(\boldsymbol{R})=(1/\lambda f M)\int_A d\boldsymbol{r}_a \times\exp[2\pi i(\boldsymbol{r}_a/\lambda f)(\boldsymbol{R}/M)]\psi_a(\boldsymbol{r}_a) \quad (6.1)$$

where f is the focal length of the objective lens, M the magnification and the integral over the area of the aperture which is placed on the back focal plane.

When a single atom placed on the optical axis is illuminated by a plane wave parallel to the axis, $\psi_a(\boldsymbol{r}_a)$ turns out as

$$\psi_a(\boldsymbol{r}_a)=(1/f)\{(r_0/2\theta)J_1(sr_0)+iE(s)\}e^{i\gamma} \quad (6.2)$$

$$s=(2\pi|\boldsymbol{r}_a|/\lambda f) \quad (6.2a)$$

where θ, s and $E(s)$ are already defined in Sec. 2, $J_1(sr_0)$ is Bessel function of the first order, and γ is a phase factor determined by both the degree of defocus and coefficient of spherical aberration (see Scherzer, 1949). The first term in braces represents the primary wave diffracted by an aperture of radius r_0 (Fig. 5). The second term represents the wave elastically scattered by the atom.

Substituting (6.2) into (6.1) and assuming $|\boldsymbol{R}|$ less than Mr_0, we get

$$\Psi(\boldsymbol{R})=(1/M)+i\Psi_0(\boldsymbol{R}) \quad (6.3)$$

$$\Psi_0(\boldsymbol{R})=(1/\lambda f^2M)\int_A d\boldsymbol{r}_a \exp[2\pi i(\boldsymbol{r}_a/\lambda f)(\boldsymbol{R}/M)+i\gamma]E(s) \quad (6.3a)$$

Thus the intensity on the image plane is proportional to

$$\Psi\Psi^*=(1/M^2)+(i/M)(\Psi_0-\Psi_0^*)+\Psi_0\Psi_0^* . \quad (6.4)$$

The first term is the background formed by the primary wave, the second term is the phase contrast and the third term is the bright image of the atom. The second and the third terms are small quantities of the first and the second order, respectively. If Born's first approximation is adopted the first term contains an error of the second order, and thus the third term should be neglected. At the exact focus the second term vanishes because $E(s)$ is real under this approximation. Therefore, only defocused images can be discussed by this formula[4].

In the better approximation by Glauber and Schomaker[23], $E(s)$ has an imaginary part

$$Im\{E(\boldsymbol{b})\}=(1/2\lambda)\int E^*(\boldsymbol{b}'-\boldsymbol{b})E(\boldsymbol{b}')d\Omega_{b'} \quad (6.5)$$

where the integral is over the whole solid angle of $\boldsymbol{b}'$. Therefore, the second term does not vanish even in the exact focus. It can be proved that the third term (positive) compensates the second term (negative) at the exact focus provided the objective lens has a sufficiently large aperture with no aberration. This is evident because the incident wave is not absorbed in the atom and all the scattered rays converge on the image plane.

Although Scherzer[4] neglected the third term, the bright image of atom, we take it into account because it is important for a perfect understanding of the image formation.

(b) *Images of amorphous specimens.* When the specimen is composed of many atoms of one kind the scattering by all the atoms in the specimen must be taken into account. Provided the condition of single scattering is satisfied, the wave function on the back focal plane can be obtained by summing up the second term in (6.2)

$$\psi_a(\boldsymbol{r}_a)=(1/f)\{(r_0/2\theta)\mathrm{J}_1(sr_0) +iE(s)\sum_i \exp(-2\pi i\boldsymbol{b}\boldsymbol{r}_i)\}e^{i\gamma} . \quad (6.6)$$

Then the wave function on the image plane becomes

$$\Psi(\boldsymbol{R})=(1/M)+i\sum_i \Psi_i(\boldsymbol{R})$$

$$\Psi_i(\boldsymbol{R})=(1/\lambda f^2M)\int_A d\boldsymbol{r}_a \times\exp[2\pi i\{\boldsymbol{r}_a/\lambda f)(\boldsymbol{R}/M)-\boldsymbol{b}\boldsymbol{r}_i\}+i\gamma]E(s) \quad (6.7)$$

If the arrangement of atoms in the specimen is at random, it is convenient to write the intensity on the image plane as follows:

$$\Psi\Psi^*=(1/M^2)+\sum_i|\Psi_i|^2 +(i/M)(\sum_i\Psi_i-\sum_i\Psi_i^*)+\sum_{i\neq j}\Psi_i\Psi_j^* \quad (6.8)$$

(c) *Images formed by the incoherent part of elastic scattering.* The second term in (6.8) is the image formed by the incoherent part of elastic scattering. This term consists of the bright image of each atom in the specimen. To make this fact clear, let us write

$$\boldsymbol{b}\boldsymbol{r}_i=(\boldsymbol{r}_a/f\lambda)(\boldsymbol{R}_i/M)-\varepsilon/2\pi \quad (6.9)$$

where $\boldsymbol{R}_i$ is the coordinate of Gauss image of the ith atom and ε is a small factor determined by the axial component of $\boldsymbol{r}_i$. Substituting (6.9) into (6.7a), we get

$$\Psi_i(\boldsymbol{R})=(1/\lambda f^2M)\int_A d\boldsymbol{r}_a \times\exp[2\pi i(\boldsymbol{r}_a/\lambda f)\{(\boldsymbol{R}-\boldsymbol{R}_i)/M\}+i(\varepsilon+\gamma)]E(s) \quad (6.10)$$

Thus, if the defocus due to ε is neglected, we get

$$\Psi_i(\boldsymbol{R})=\Psi_0(\boldsymbol{R}-\boldsymbol{R}_i) . \quad (6.11)$$

This shows that the bright image of the ith atom appears at $\boldsymbol{R}_i$.

The bright images of atoms are not resolved by present-day electron microscopes and very many atoms are involved in a volume resolved by present-day electron microscopes. Therefore, the fluctuation of atomic density in the specimen can be neglected and the summation in the second term of (6.8) can be replaced by an integral

$$\sum_i |\Psi_i|^2 \rightarrow N \int_v |\Psi_i|^2 d\boldsymbol{r}_i \ . \qquad (6.12)$$

This gives the image of the specimen formed by the atomic part of elastic scattering.

(d) *Images formed by inelastic scatterings.* Let us denote the scattering function of the tth transition by $E_t(s_t)$ and let us denote the wave function on the image plane which function results from the tth transition of the the ith atom by $\Psi_{i,t}(\boldsymbol{R})$, then $\Psi_{i,t}(\boldsymbol{R})$ is calculated by (6.10) where $E(s)$ must be substituted by $E_t(s_t)$ and effect of energy loss in γ, f and λ must be taken into account. Since inelastic scatterings are incoherent to each other, the image of the ith atom can be stated as

$$\sum_t |\Psi_{i,t}|^2 \qquad (6.13)$$

where the summation is over all transitions.

(e) *Images formed by the coherent waves.* For the same reason mentioned in (c) of this section, the summations in the third and fourth terms of (6.8) can also be replaced by the integral. Then, using notations defined in (2.4a) and (2.6), the first, third and fourth terms in (6.8) become

$$\Psi'\Psi'^* = (1/M^2) + (i/M)(\Psi^s - \Psi^{s*}) + |\Psi^s|^2 \qquad (6.14)$$

$$\begin{aligned} \Psi^s = (1/\lambda f^2 M) \int_A d\boldsymbol{r}_a \\ \times \exp[2\pi i(\boldsymbol{r}_a/\lambda f)(\boldsymbol{R}/M) + i\gamma] \\ \times (2\pi me/h^2) V_0 v \Phi(\boldsymbol{b}) \ . \end{aligned} \qquad (6.14a)$$

The formula (6.14) represents the image of an imaginary specimen which has a uniform potential V_0 and is perfectly transparent. If the imaginary specimen is considered from the beginning, the summation in (6.6) is replaced by the integral and we get

$$\begin{aligned} \Psi'(\boldsymbol{r}_a) = (1/f)\{(r_0/2\theta)\mathrm{J}_1(sr_0) \\ + i(2\pi me/h^2) V_0 v \Phi(\boldsymbol{b})\} \ . \end{aligned} \qquad (6.15)$$

The equation (6.14) is readily derived from this equation.

(f) *Phase shift.* Let us consider a specimen with radius r_0 and a thickness d. Then we get

$$\begin{aligned} \Phi(\boldsymbol{b}) &= (d/v) \int_S \exp[-2\pi i(\boldsymbol{br})] ds \\ &= (d/v)(r_0/2\theta)\lambda \mathrm{J}_1(sr_0) \ . \end{aligned} \qquad (6.16)$$

Where the integral is over the area of the specimen. Then (6.15) becomes

$$\psi'(\boldsymbol{r}_a) = (1/f)(r_0/2\theta)\mathrm{J}_1(sr_0)\{1 + i(\pi d/\lambda)(V_0/E)\} \ . \qquad (6.17)$$

Where E is the kinetic energy

$$E = (h^2/2me)(1/\lambda^2) \ .$$

The term $(\pi d/\lambda)(V_0/E)$ is the phase shift φ of the wave in the specimen. It coincides with the phase shift calculated directly from the equation

$$\varphi = 2\pi d\{(\mu/\lambda) - (1/\lambda)\} = (\pi d/\lambda)(V_0/E) \ . \qquad (6.18)$$

Assuming $V_0 = 10$ *volts*, $E = 50\,kV$ and $d = 100$Å, we get $\varphi = 0.4\pi$. Since formula (6.17) is valid only for small φ, the above example shows that (6.17) cannot be applied to a collodion film of thickness 100Å. For thick specimens the term in braces of (6.17) must be replaced by

$$\exp[i(\pi d/\lambda)(V_0/E)] \ . \qquad (6.19)$$

(g) *Effect of absorptions.* In treating images formed by the coherent waves the absorption coefficient (3.2) must be assumed for the imaginary specimen, as mentioned in Sec. 3c. It is note-worthy that a formal calculation under Schomaker's approximation automatically results in κ_e. According to (6.5), we have

$$Im\{E(0)\} = (\sigma_e/2\lambda) \ , \quad \sigma_e = \int |E(b)|^2 d\Omega_b \ . \qquad (6.20)$$

Then, by (2.6) for the imaginary part of V_0 we get

$$Im\{V_0\} = (h^2/2\pi me)(N/v)(\sigma_e/2\lambda) \ . \qquad (6.21)$$

Substituting (6.21) in (6.19) and recollecting (3.2), we get

$$\exp[-(N/v)\sigma_e d] = \exp[-\tfrac{1}{2}\kappa_e d] \ . \qquad (6.22)$$

This implies that absorption coefficient is given by κ_e.

§ 7. Discussion

An actual image of electron microscope is composed of images formed by the coherent and the incoherent waves. If the coherent wave is neglected, only the contrast due to the scattering absorption appears[1),3),5)]. On the other hand, if the incoherent waves are neglected, only the phase contrast appears[3),6)]. This study explains both contrasts from a unified point of view in which an image of a specimen is built up from images of single atoms[4]. If the defocus due to energy loss in inelastic scattering is taken into account, the effect discussed by Gabor[2] can be recognized although it is not worked out here.

The separation of an actual image into two ideal images is the result of the averaging in (6.12) and (6.14). The averaging is possible because no atoms are resolved by present-day electron microscopes. The averaging in electron diffraction (2.4) is the averaging over many samples which have the same external shape. Therefore, these two averagings do not have the same physical meaning although that difference is not discussed in the text.

Recently, Glaser[24] advanced a theory on image formation of electron microscopes, but he did not take into account the fact that wave functions just behind specimens have unresolvable structures. Therefore, his theory cannot treat with that contrast due to scattering absorption.

It is the author's pleasure to express his sincere thanks to Chairman Prof. Yasumasa Tani and members of the Committee of High Resolution Electron Microscope in Japan for their encouragement and helpful discussions. Thanks also go to Prof. Tadatoshi Hibi for his generosity in giving the author many of his micrographs and to Drs. Y. Kainuma and N. Kato for their helpful criticisms.

This work is financed by the Ministry of Education in Japan for the Foundamental Scientific Research Expenditure 1953.

References

1) H. Boersch: ZS. f. Naturforschung **2a** (1947) 615.
2) D. Gabor: The Electron Microscope (Chemical Publishing Co., 1948) Chap. 6.
3) V. K. Zworykin *et al.* Electron Optics and the Electron Microscope (John Wiley and Sons, New York, 1948) Chap. 19.
4) O. Scherzer: J. Appl. Phys. **20** (1949) 20.
5) B. V. Borries: ZS. f. Naturforschung **4a** (1949) 51.
6) E. G. Ramberg: J. Appl. Phys. **20** (1949) 441.
7) W. Heisenberg: Phys. Zeit. **32** (1931) 737.
8) H. Koppe: Zeit. f. Physik **124** (1948) 658.
9) W. Kossel and G. Möllenstedt: Ann. d. Physik **36** (1939) 113.
10) F. Lenz: Naturwiss. **39** (1952) 265.
11) S. Miyake: Proc. Phys-Math. Soc. Japan **22** (1940) 666.
12) L. Marton: Physica **3** (1936) 959.
13) H. Boersch: Phys. Zeit. **44** (1943) 32
14) N. Kato: J. Phys. Soc. Japan **8** (1953) 350.
15) H. Boersch: Ann. d. Physik **26** (1936) 631.
16) J. Hillier and R. F. Baker: Phys. Rev. **61** (1942) 722.
17) M. V. Laue: Materiewellen und ihre Interferenzen (Akademische Verlagsgesellschaft, Leipzig, 1948) Chap. 3.
18) R. D. Heidenreich: Phys. Rev. **62** (1942) 291.
19) W. Kossel: Naturwiss. **31** (1943) 323.
20) R. D. Heidenreich and L. Sturkey: J. Appl. Phys. **16** (1945) 97.
21) H. Boersch: Optik **3** (1948) 24.
22) H. Yoshioka: Busseiron-kenkyu **69** (1953) 118. (in Japanese).
23) R. Glauber and V. Schomaker: Phys. Rev. **89** (1953) 667.
24) W. Glaser: Ann. d. Physik **12** (1953) 240.

JOURNAL OF THE PHYSICAL SOCIETY OF JAPAN Vol. 10, No. 4, APRIL, 1955

On the Piezoelectric Lines at Sub-microwave Frequencies

By Shoji KOJIMA, Kineo TSUKADA, Shizuko OGAWA,
Akira SHIMAUCHI and Norio MATSUMIYA
Tokyo University of Education, Otsuka, Tokyo

(Received December 11, 1954)

Piezoelectric absorption lines which had been found in the experiment of nuclear quadrupole resonance were studied in the frequency range between 3 Mc and 700 Mc. These lines were observed not only in powder, but also in single crystals. The present experiment showed that they were neither due to resonant vibrations of individual crystals in powder nor due to harmonics of the natural vibration of a single crystal. The absorption was dependent on imperfection of crystal and related to very narrow region in a crystal. The following mechanism was suggested: There are regions where the velocity of the elastic wave is smaller than the outside. Then vibrations are confined within the region because of total reflection at the boundary.

§ 1. Introduction

In the course of experiment on the nuclear quadrupole resonance of iodine nuclei, unexpected absorption lines at sub-microwave frequencies (3 Mc∼700 Mc) were found in silver iodide power. These lines were different from those of quadrupole resonances at least in the facts that they did not exhibit Zeeman effect and that their absorption was not due to magnetic component of rf field but due to electric component.

It was searched what substance produced this absorption, and zinc sulphide, quartz* and barium titanate were found out. Furthermore single crystals of Rochelle salt and quartz (rock crystal) exhibited this absorption. These results and some experiments on the nature of the absorption were reported briefly in the article "New absorption lines of crystals in sub-microwave region"[1]. A similar absorption had been discovered by Livingston at short-wave frequencies[2]**. In his paper on the nuclear quadrupole experiment of chlorine nuclei it was described that piezoelectric substances under certain conditions gave rise to absorption spectra different from quadrupole lines, though further description was not made.

Piezoelectric powders are well known to yield absorption lines due to the resonant vibrations of individual crystals and piezoelectric single crystals are also well known to yield absorption lines due to harmonics of the natural vibration.

We have attempted to study whether the absorption presented here can be interpreted by such mechanisms or not. Furthermore we have investigated nature of this absorption and gave a suggestion on the mechanism.

§ 2. Method of Detection

The apparatus used for the experiment on silver iodide was a frequency modulated superregenerative detector with a transmission line tuned circuit. The method of detection was same as the experiment of nuclear quadrupole resonance[3], but the sample was placed at the voltage loop of the transmission line. The absorption lines were viewed on an oscil-

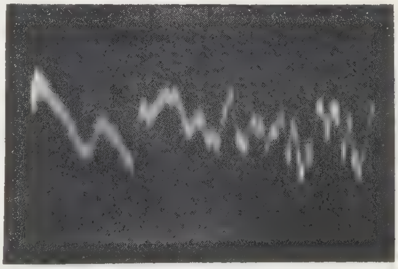

Fig. 1. Pattern for the absorption of zinc sulphide powder.

---

* At the symposium on Molecular physics at Nikko, Japan, on Sept. 12, 1953, where the results on silver iodide and zinc sulphide were reported by the authors. Dr. N. Bloembergen informed us that Dr. Schwede had observed unknown lines in quartz powder at short wave frequency.

** It was published in the Annals of New York Acad. Sci. earlier than ours. We knew it after our previous publication.

Table I.

Sample		Frequency range (Mc)	$\frac{1}{\nu}\frac{d\nu}{dT}$ (/°C)
AgI	Powder	120$\sim$270	-32×10^{-5}
ZnS	powder (fine grain)	24$\sim$500	-4.6×10^{-5}
$Ba(ClO_3)_2H_2O$*	powder	20$\sim$500	-16×10^{-5}
Rock crystal	single crystal	3$\sim$550	-0.6×10^{-5}
Rochelle salt	single crystal	3$\sim$550	-4.0×10^{-4}

* The absorption in this substance was first detected by K. Torizuka (private communication).

loscope, whose horizontal axis was swept in synchronization with the frequency modulation. Fig. 1 is a photograph of absorption lines observed in zinc sulphide. Since the spectra spreaded over very wide frequency range, four superregenerative oscillators were prepared in responce to the frequency ranges, 10 Mc$\sim$50 Mc, 45 Mc$\sim$100 Mc, 150 Mc$\sim$350 Mc and 350 Mc$\sim$700 Mc[4]. Superregenerative detectors have a high sensitivity, but they have a disadvantage that there exhibit many side lines with the spacing of the quenching frequency. In order to determine the spectra precisely two simple regenerative detectors (autodynes) with LC tuning circuit were used. One was worked in the frequency range between 3 Mc$\sim$50 Mc and the other between 50 Mc$\sim$120 Mc. The circuit diagram of the latter is shown in Fig. 2. A photograph taken with this apparatus for a single crystal of quartz is shown in Fig. 3.

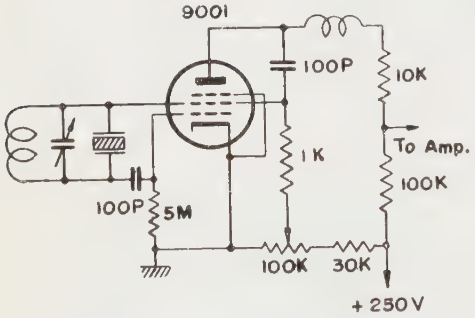

Fig. 2. Circuit diagram for the autodyne oscillator.

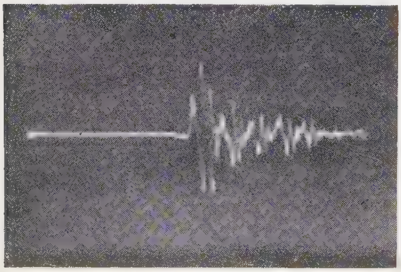

Fig. 3. Pattern for the absorption lines of a single crystal of quartz. Five lines with wiggles are shown. The frequency was swept from the left to the right between 59.94 Mc and 60.08 Mc.

§ 3. Observed Spectra

The absorption was observed in very wide frequency range. Spreading of the spectra for several substances are listed in Table I.

The spectra in powder consisted of so many lines that the individual lines were not separated as shown in Fig. 1. Single crystals, however, displayed a spectrum which was resolved into sharp lines as shown in Fig. 3. These sharp lines had the width below several kilocycles and accompanied wiggles. The frequencies of the lines were shifted by the change of temperature. The temperature coefficients defined by $(1/\nu)(d\nu/dT)$ are also listed in Table I. In addition to the substances listed in the table barium titanate, tartar emetic, CdS*, SbSI and I_2O_5 showed this absorption.

Among many quartz crystals one showed very sharp absorption lines. It was a rectangular prism with dimentions $1.305 \times 1.285 \times 4.260$ cm^3. On this crystal the lines of the spectrum was measured accurately between 10 Mc and 120 Mc. A part of the spectrum

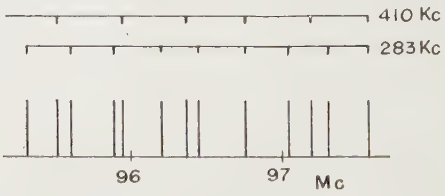

Fig. 4. Spectrum between 95 Mc and 98 Mc of a quartz crystal.

---

* This substance was first studied by K. Shimomura (private communication).

is reproduced in Fig. 4, where weak lines are omitted. This spectrum was composed of two series of equidistant lines. One has a spacing of 410 kc and the other 283 kc. Although the spacings were slightely changed, these series extended in whole range. Beside these two strong series there were some weak series. Equidistant series were also observed in the spectra of other crystals. However, the spacings were not same as the above crystal, and different crystal by crystal. Similar results were also obtained on single crystals of Rochelle salt*.

§ 4. Test on Powder Method

For qualitative indication of piezoelectricity in crystal powder Giebe and Scheibe had developed in 1925 the following method[5]. A sample of grains of crystals were placed between the electrodes of the condenser of oscillating circuit of variable frequencies. With a telephone receiver in the oscillator they heard clicks which were yielded when the frequency was tuned through natural frequencies of grains. This method is known by the name of the powder method[6]. The circuit used in the present experiment is shown in Fig. 5. This apparatus consisted of two separate parts: an oscillator and a detector. Changing the frequency by the condenser C with a constant speed, clicks were observed with the oscilloscope or the telephone receiver. By this method an envelope of the absorption lines due to the resonance vibration of individual grains were obtained.

By crushing a natural rock crystal, grains of quartz were made. The grains were arranged by classes of size with sieves. On each class an envelope of absorption spectra of grains was observed by this method. As shown in Fig. 6, the intensity maximum for the grains between 0.17 mm and 0.22 mm in diameter occurred at the frequency of 8 Mc. The frequency of intensity maximum was approximately inversely proportional to the size of grains. The frequency spectrum, as shown in Fig. 6, indicated that the intensity decreased more and more as the frequency was increased. But some absorption lines could be observed by the aid of the super-regenerative detector even at 200 Mc. This absorption in a sub-microwave frequency was almost independent on the size of grain and was rather faint for the smaller size. This experiment gave an evidence that the absorption was not interpreted by resonance vibrations of individual crystals.

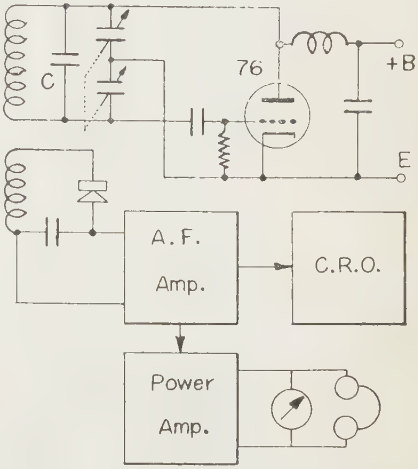

Fig. 5. Circuit diagram for the powder method. (The sample is placed between the electrodes of condenser C.)

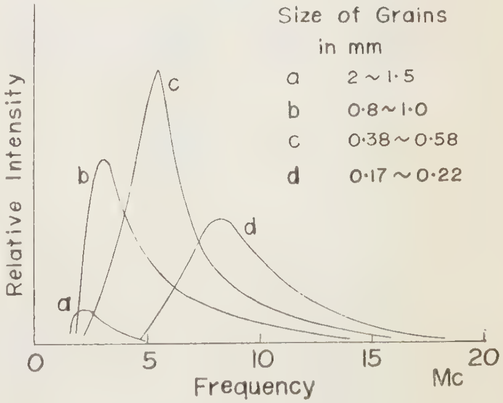

Fig. 6. Observed absorption curves by the powder method.

§ 5. Test on Harmonics of a Quartz Resonator

A quartz resonator of one megacycle, which was 1.86 mm in thickness and $3.19 \times 2.13\ \mathrm{cm}^2$ in area, was tested by the autodyne detector. It yielded the absorption lines of 1 Mc, 3 Mc, 5 Mc $\cdots\cdots$ with decending intensities as shown in Fig. 7. This quartz resonator showed weak absorption lines beside above series. The higher harmonics, as shown in Fig. 7, decreased so rapidly that the intensity of the 15th harmonic was comparable to irregular weak lines. The quartz prism described in § 3 had a natural frequency of 100 kc, which was measured by the click method. In spite of such low frequency of the fundamental vibration the spectrum described in § 3 spreaded between 3 Mc and 550 Mc with almost constant intensity. This fact could not be understood by harmonics of the natural vibration.

---

* Those results and further experiments on Rochelle salt will be published by one of the authors (S. O.) in the Natural Science Report of the Ochanomizu University.

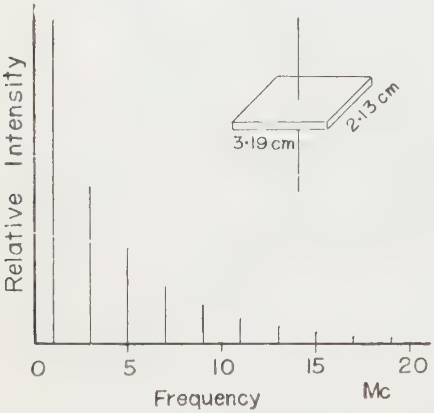

Fig. 7. Absorption spectrum of the quartz resonator of 1 Mc.

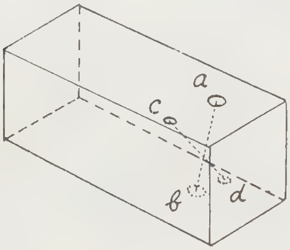

Fig. 8.

§ 6. Effect of Oil Immersion

When the samples were immersed in oil*, it was observed that almost every lines disappeared. This effect was seen in either powder or single crystal. The most interesting case was the quartz prism described in § 3. When a small drop of oil was placed at one of the spots *a* and *b* shown in Fig. 8, the series with the spacing of 410 kc was completely extinguished. On the other hand an oil drop placed on the spot *c* or *d* extinguished the series of lines of the spacing of 283 kc**. These experiments indicated that the vibrations were confirmed in very narrow region of a crystal.

§ 7. Effect of Imperfections in Crystals

The absorption was different for each specimens. Among the studied twenty natural rock crystals, some of them showed strong absorption and some of them nothing. The absorption was also affected by thermal treatments or exposures of radiations.

(i) Thermal treatment

Commercial samples of silver iodide usually observed nothing at room temperature. When they were cooled below the ice point, they exhibited absorption gradually and at the dry-ice temperature the spectrum could be observed clearly. After they were heated above the transition point of 146°C, where the colour changed from light yellow to red, some of them were cooled by natural cooling, and the others by very slow cooling taking about 100 hours. Then the absorption was tested at the room temperature. The former samples exhibited the absorption even at the room temperature whereas the latters did nothing.

The same effect of heating was also observed in rock crystals.

These results indicated that the absorption depended on inhomogeneity or imperfections in crystal.

(ii) Exposure of radiations

Since the absorption seemed to depend on the imperfection of crystals, effect of irradiation of rays were studied. It was shown that rock crystals which had no ability of the absorption gained it by receiving the irradiation of X rays of about 1 hour with 5 mA at 30 kV***. The irradiation of γ rays of cobalt-60 of 5 mc during a week gave similar effect for a rock crystal.

Phosphorescent zinc sulphide powder which was kept several days in dark seemed to be increased in the absorption by exposure of light.

Absorbing ability which was gained by the heat treatment or by the irradiation of rays decayed after several days.

---

* The oil used was a vacuum pumpoil. Carbon tetrachloride was also effective.

** The lines connecting *a* with *b* and *c* with *d* seemed to make an angle of about 60°, and to lie in the planes containing the crystal axes.

*** We are indepted Mr. S. Annaka for the exposure of X-rays.

(iii) Transient noise

When the absorption was studied on the sample of silver iodide which was changing the temperature, it was found a noise similar to the Barkhausen effect in ferromagnetic substances. This transient noise was also observed in zinc sulphide which was being exposed in light. Furthermore Rochelle salt and barium titanate yielded this noise during several second after the beginning of the observations. This noise seemed to be caused by rearrangement of internal structure of crystals.

§ 8. Discussions

In piezoelectric substances an oscillating electric field produces mechanical vibrations, which usually propagate through whole crystal as elastic waves. The experiment of the oil effect on the quartz crystal, however, indicated that the waves were confined in a small region. Furthermore the sharpness of the absorption lines required that the damping of the mechanical vibrations was very weak. In order to confine the waves within a small region the medium could not be homogenious. The effect of quenching after heating or the effect of irradiation of rays seems to be valid for the production of inhomogeneity. The transient noise mentioned in the previous section directly indicated the existense of inhomogeneity. Therefore the crystals which give rise the absorption are considered to have imperfections in their natural states. The sharpness of the lines suggests that the elastic waves produced in a small region of the crystal are confined by total reflection at the boundary. This mechanism seems to be important in this absorption.

References

1) S. Kojima, K. Tsukada, S. Ogawa and A. Shimauchi: Phys. Rev. **92** (1953) 1571. In the text "rock salt" should be read "rock crystal" (Phys. Rev. **95** (1954) 1705).
2) R. Livingston: Ann. New York Acad. Sci. **55** (1952) 800.
3) S. Kojima, K. Tsukada, A. Shimauchi and Y. Hinaga: J. Phys. Soc. Japan **9** (1954) 795.
4) S. Kojima, K. Tsukada, S. Ogawa, A. Shimauchi and Y. Abe: J. Phys. Soc. Japan **9** (1954) 805.
5) E. Giebe and A. Scheibe: Z. Physik **33** (1925) 760.
6) See W. G. Cady "*Piezoelectricity*" McGraw Hill, N. Y. (1946).

Journal of the Physical Society of Japan Vol. 10, No. 4, April, 1955

Adsorption and Surface Potential of Semi-conductors. Part 1.

Photo-enhanced Adsorption of Oxygen and Change of Contact Potential of ZnS Phosphors with Illumination

By Akio Kobayashi and Shinji Kawaji

Research Institute for Catalysis, Hokkaido University, Sapporo

(Received January 22, 1955)

When ZnS phosphor containing 10^{-2} Mol% of Cu was irradiated in oxygen gas by light with wavelengths lying within the characteristic absorption band of the host crystal, photo-enhanced adsorption and increase of the surface potential (decrease of the work function) of the crystal were observed. If we assume that the lowering of the potential energy of adsorption of oxygen is equal to the increased amount of surface potential, the photo-enhanced adsorption can be explained semi-quantitatively. The change of the surface potential of ZnS with illumination, $(\Delta\text{c.p.})_L$, increased with pressures of oxygen and decreased with temperature.

§ 1. Introduction

It is well known that there are a space charge layer at the surface of semi-conductors or insulators[1]. If we irradiate one of those crystals with photons with wavelengths lying within its characteristic absorption band, electrons and holes created by irradiation will be separated from each other by the field of this space charge layer, hence the surface potential will be changed as a result of re-distribution of surface charge[2]. This change of the surface potential will give rise to photo-enhanced adsorption or desorption of gases on the crystal.

Hedvall and his coworkers[3] were studied on the desorption and adsorption of dyes on ZnS and CdS with illumination in liquid. We have studied the correlation between the change of the surface potential of ZnS due to irradiation and the photo-enhanced adsorption of oxygen preliminarily.

§ 2. Procedure of Experiments

1) Measurements of photo-enhanced adsorption.

The phosphor used was ZnS powder of Wurtzite type containing 10^{-2} mol% Cu activator. The apparatus for adsorption is shown in Fig. 1. The inner wall of a bulb made of ultra-violet transparent glass was coated with the powder of the phosphor of 1.0 gr. in weight. The inner diameter of the bulb was 3.6 cm. The total volume of the measuring vessel cut off by a greaseless cock was 32 cc.

At the beginning of measurements, the vessel was evacuated for one hour at 400°C to 500°C, then cooled and oxygen gas was introduced into it from a gas reservoir through a liquid nitrogen trap. The pressures were measured with a Pirani gauge which had a sensitivity of 4×10^{-5} mmHg per division for oxygen. An ultra-high pressure mercury lamp of 500 watts combined with glass filters was used as a light source.

2) Measurements of contact potential and change of contact potential with illumination.

Fig. 2 shows the bulb used to measure the contact potential, c.p., and its change with illumination, $(\Delta\text{c.p.})_L$, by the method of vibrating condenser. The vibrating reed was a grid of a Fernico metal sheet goldplated, which was welded with a tungsten rod of 1 mm in dia. whose end was connected with the input of a preamplifier. The sample holder, made of a brass block of 3 mm thick and 8×10 sq.mm. in area, had four cavities into which heaters of vacuum tubes were inserted. A nickel mesh mounted on the holder was coated with ZnS powder. The holder was fixed to the stem by means of a nickel rod of 2 mm. dia. It was found easy to control temperatures of the sample over the range from −160°C upto 200°C by pouring liquid nitrogen into the stem-tube or by firing the heaters in the holder. Silicone grease was used for joint between the stem and the body of the bulb.

At the beginning of measurements the bulb

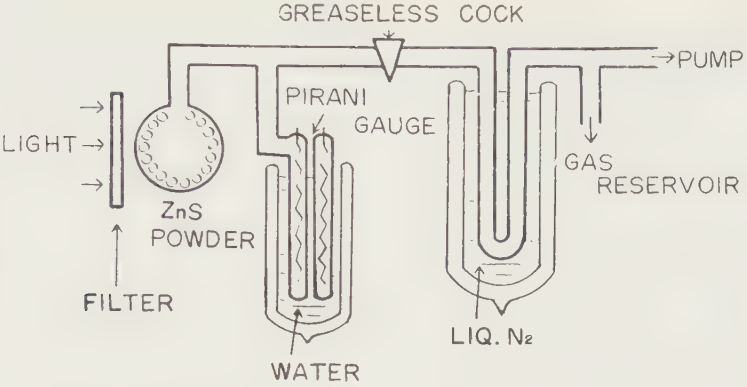

Fig. 1. Apparatus to measure photo-enhanced adsorption.

was degassed by heating in an oven at 150°C for few hours at high vacuum, and moreover the filaments in the holder of the sample were fired to rise the temperature of the sample upto 300°C. Since the grid of the reed electrode removed about one half of the light, c.p.'s observed with illumination were mean values between those of irradiated area and dark area and thus the true $(\Delta \text{c.p.})_L$'s were estimated to be twice as large as the observed. A potentiometer was used to balance the c.p.d. with a relative accuracy of 10 mV.. The frequency of the reed was 310 cps.. Gain of the amplifier was about 100 db.

In the case of recording transient change of c.p., an electromagnetic oscillograph was drived by rectified current of unbalanced signal caused by irradiation. After cession of excitation, the decay of $(\Delta \text{c.p.})_L$, which sometimes oscillated to the opposite sign in the case of ammonia ambient, could be determined by making c.p. balance during excitation. When the decay was very slow, it was easy to trace manually the balanced potential and therefore to determine the sign of the decay.

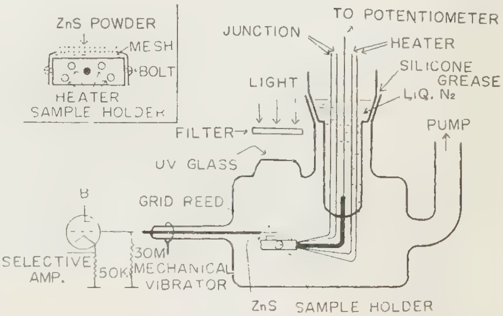

Fig. 2. Bulb used to measure the c.p.'s and $(\Delta \text{c.p.})_L$'s. The inset shows a cross section of the sample holder.

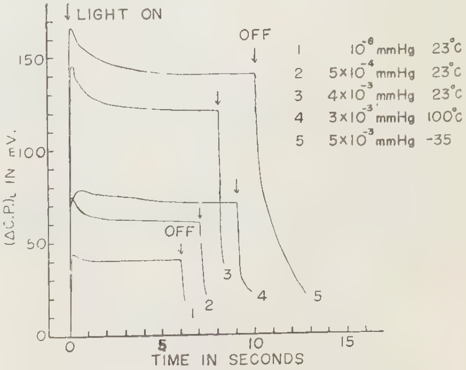

Fig. 3. Oscillogram of $(\Delta \text{c.p.})_L$.

§ 3. Results of the Experiments

The effect of irradiation on the work function and photo-enhanced adsorption were observed only with the excitation by light with wavelengths shorter than 4000 A. Both of the effects increased with the intensity of radiation as well as the energy of photon and reached a saturation, when the crystals were irradiated with photons with wavelengths lying within the characteristic absorption band of the host crystal. The radiation with wavelengths shorter than 2500 A must not be used. because this produced photoelectric emission giving rise to a confusion of the effects to be observed. We used therefore usually a glass filter transparent from 3000 A to 4000 A with a peak at 3600 A. The intensity of incident light might be enough to produce about 10^{16} pairs of electrons and holes per sec. per sq.cm..

Time dependency of $(\Delta \text{c.p.})_L$'s are shown

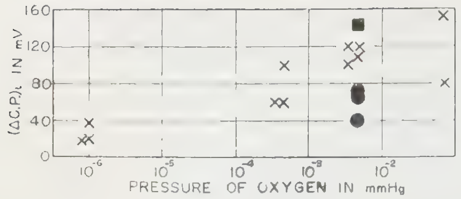

Fig. 4. $(\Delta c.p.)_L$ versus pressure of oxygen ambient. × measured at 23°C, ■ measured at −35°C and ● at 100°C.

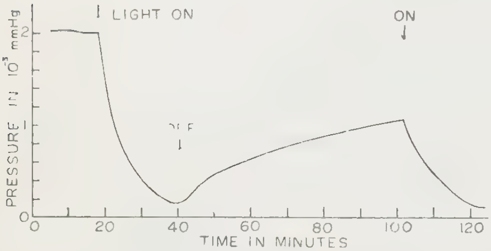

Fig. 5. The decrease of pressure with illumination and its recovery at darkening.

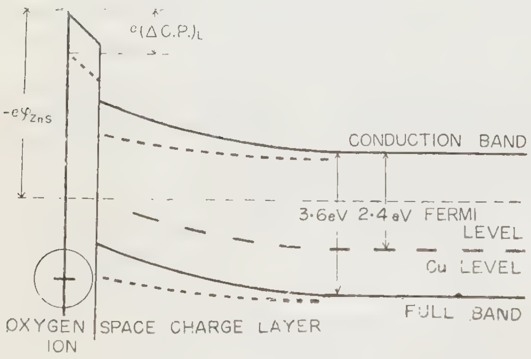

Fig. 6. Energy level diagram at ZnS surface. The dotted line shows the energy level in the case of irradiation.

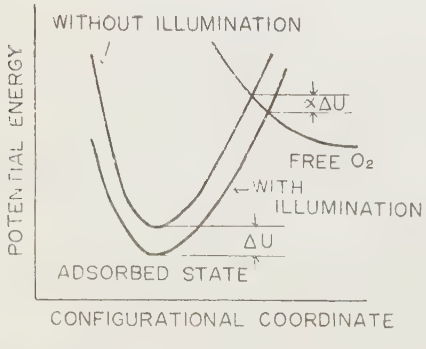

Fig. 7. Potential energy level diagram for an adsorbed ion.

in Fig. 3. The $(\Delta c.p.)_L$'s, which are twice as large as the observed for the reason mentioned above, increased with pressures of oxygen and decreased with temperature as shown in Fig. 4. Fig. 5, shows the decrease of pressure with irradiation on the phosphor and its recovery at darkening. The pressures decreased exponentially with time from 2×10^{-3} mmHg to 8×10^{-5} mmHg with irradiation. In the case of hydrogen as well as ammonia no photo-activated adsorption or desorption was observed with illumination.

§ 4. Discussion of the Results

The increase of covering factor θ by irradiation can be calculated to be about 0.07, corresponding to the decrease of pressure from 2×10^{-3} mmHg, provided that the irradiated area of the phosphor is about ten times as large as the semi-sphere of the bulb. We assumed in this case that one oxygen atom can be absorbed in ionic form on every unit cell of the cleavage surfaces of ZnS of wurtzite type.

When ZnS crystal is irradiated with the light with wavelengths lying within the characteristic absorption band, electrons in the full band will be ionized to the conduction band and thus holes and quasi-free electrons will be created. Holes and electrons will be separated from each other by the field of surface space charge. Thus the concentration of holes increases at the surface to give rise to increase of the surface potential (decrease of the work function), $(\Delta c.p.)_L$, since negative ions adsorbed on the surface produce such a field as shown in Fig. 6. Hence the potential energy of adsorbed oxygen ions decreases with the increase of surface potential by an amount of ΔU, which is equal to $(\Delta c.p.)_L$ as shown in Fig. 7. As the decrease of the activation energy of adsorption with illumination is denoted by $\alpha\Delta U$, the potential energy of adsorption decreases as much as $(1-\alpha)\Delta U$.

When an equilibrium sets up in the dark, we have the following equation,

$$\overleftarrow{k}(1-\theta)^2 p-\overrightarrow{k}\theta^2=0\,, \qquad (1)$$

where $\overleftarrow{k}$ and $\overrightarrow{k}$ are rate constants of adsorption and desorption respectively, θ is the covering factor in the dark, p the pressure in equilibrium.

When those with illumination are represented by suffix 1, the equations may be as follows,

$$\overleftarrow{k}_l=\overleftarrow{k}\exp(\alpha\Delta U/kT),$$
$$\overrightarrow{k}_l=\overrightarrow{k}\exp[(\alpha-1)\Delta U/kT]. \tag{2}$$

When a steady state sets up in the case of illumination, we have

$$\overleftarrow{k}_l(1-\theta_l)^2 p_l-\overrightarrow{k}_l\theta_l^2=0. \tag{3}$$

From Eq.'s (1), (2) and (3) it follows that

$$\left[\frac{(1-\theta_l)\theta}{(1-\theta)\theta_l}\right]^2=\frac{p}{p_l}\exp(-\Delta U/kT). \tag{4}$$

where

$$\theta_l=\theta+0.07,$$
$$p=2\times10^{-3}\ \text{mmHg},$$
$$p_l=8\times10^{-5}\ \text{mmHg},$$
$$\Delta U=0.1\ \text{eV}.$$

Solving Eq. (4) for θ, we obtain

$$\theta=0.2 \quad \text{or} \quad 0.7.$$

For the initial decay of pressure, we obtain for the decay constant τ,

$$\begin{aligned}-\frac{dp}{dt}&=\frac{s}{v}\left\{\overleftarrow{k}_l(1-\theta)^2p-\overrightarrow{k}_l\theta^2\right\}\\&=\frac{s}{v}\overleftarrow{k}(1-\theta)^2\exp\left(\frac{\alpha\Delta U}{kT}\right)\\&\quad\times\left\{1-\exp\left(-\frac{\Delta U}{kT}\right)\right\}p\\&=\frac{p}{\tau},\end{aligned} \tag{5}$$

where

s=the irradiated area 200 sq. cm.,
v=the volume of the measuring vessel 32 cc..

The observed value of τ is 540 sec.. If there is no activation energy for absorption, $\overleftarrow{k}$ can be calculated to be 0.3 cc. per sec. per sq. cm.⁴⁾. Putting the observed values of s, v and τ into Eq. (5), we obtain a value of $\overleftarrow{k}$ so small as compared with that in the case of no activation energy by the order of 100 or 1000. This shows $\overleftarrow{k}$ may have an activation energy of about 0.1 to 0.2 eV.. By similar estimation for $\overrightarrow{k}$ we obtain 2.5 eV for the heat of adsorption to be expected.

§ 5. Conclusion

The photo-enhanced adsorption of oxygen on ZnS with illumination was attributed to the increase of the energy of adsorption of oxygen in an excited state of the crystal. We showed that this effect could be explained by increase of the surface potential due to irradiation. In the case of ionic adsorption, the electrostatic self-energy of the space charge layer at the surface of the dielectrics contributes largely to the energy of adsorption⁵⁾. But even if there is no ionic adsorption, the space charge layer is always formed by surface trap levels. Therefore, in order to compare the theoretical value of the heat of adsorption to the observed one, one must first measure the physical constants of the space charge layer with the method after Brattain and Bardeen's experiments.

Further experiments will be done to measure the heat of adsorption, the activation energy of adsorption, the covering factor and the change of the surface recombination velocity due to adsorptive ions.

References

1) J. Bardeen: Phys. Rev. **71** (1947) 717.
A. H. Smith: Phys. Rev. **75** (1949) 953.
2) W. H. Brattain: Semi-conducting Materials, Butterworths Scientific Publications Ltd.: pp. 37–46 (1951).
W. H. Brattain and J. Bardeen: Bell System Tech. Journ. **32** (1953) 1.
S. Tanaka and M. Aoki: Japanese Journ. of Applied Phys. **22** (1953) 311, in Japanese.
3) J. A. Hedvall: ZS. fuer phys. Chem. (B) **32** (1936) 383, Kolloid-ZS. **94** (1941) 57.
4) S. Glasstone, K. J. Laidler and H. Eyring: Theory of Rate Processes, (1941) 349, 373.
5) H. J. Engel and K. Hauffe: ZS. fuer Elektrochem. **57** (1953) 762, **57** (1953) 773.
P. Aigrain and C. Dugas: ZS. fuer Elektrochem. **56** (1952) 363.
K. Miyahara and T. Takaishi, of this institute: unpublished report.

JOURNAL OF THE PHYSICAL SOCIETY OF JAPAN Vol. 10, No. 4, APRIL, 1955

On Extraordinary Phenomena in a Non-linear Forced Oscillation

By Akira SAKURAI

Tokyo Electrical Engineering College

(Received September 6, 1954)

The non-linear forced oscillation represented by $\ddot{x}-dF(x)/dx=p\cos\omega t$ is discussed. Transforming this equation to the variational form, the Ritz method is applied to obtain the solution in the form of Fourier series. Concerning this solution, extraordinary points of two different kinds are distinguished. This method is applied to find the jumping voltage of a circuit containing iron reactor, and result obtained is in good agreement with Katano's experiment.

§ 1. Introduction

We shall consider the non-linear oscillation of the following type,

$$\ddot{x}-dF(x)/dx=p\cos\omega t\,, \qquad (1)$$

where $F(x)$ is assumed to be a simple known function.

It is well known that there occurs a jump in the amplitude of x when, for example, p is increased gradually from zero, retaining ω constant. Moreover, it happens occasionally that x has successive jumps, if we increase p further. These jumps are considered to be caused by modes of higher harmonics. This phenomenon was already studied by Hayashi[1] considering the stability of the periodic solution of eq. (1). He obtained an equation for the extraordinary points, which correspond to the boundary of the stable and unstable regions.

In the following sections, the same problem is treated by a different method. The extraordinary position obtained is almost the same as that of Hayashi's.

§ 2. Construction of the Solution by a Variational Method

For the solution of (1) with the period $2\pi/\omega$ we have the following Fourier series expression,

$$x=\sum_{n=1}^{\infty}\{a_n\exp(in\omega t)+\bar{a}_n\exp(-in\omega t)\}\,, \qquad (2)$$

where a_n is the unknown constant to be determined and $\bar{a}_n$ its complex conjugate.

Now we transform the equation (1) into the variational form as,

$$\delta G=0,\quad G=\int_0^{2\pi/\omega}\left\{\frac{1}{2}\dot{x}^2+F(x)+px\cos\omega t\right\}dt. \qquad (3)$$

Substituting x from (2) into (3) and utilizing the relation,

$$\int_0^{2\pi/\omega}e^{in\omega t}dt=\begin{cases}2\pi/\omega\,, & n=0\\ 0\,, & n\neq 0\end{cases}\,,$$

we have

$$G=(2\pi/\omega)\{\dot{x}^2/2+F(x)+px(z+z^{-1})/2\}_c\,, \qquad (4)$$

where $\{\Psi\}_c$ signifies the constant term in the expansion of Ψ in powers of z, and

$$z=\exp(i\omega t)\,,\quad x=\sum_{n=1}^{\infty}(a_nz^n+\bar{a}_nz^{-n})\,,$$

$$\dot{x}=i\omega\sum_{n=1}^{\infty}n(a_nz^n-\bar{a}_nz^{-n})\,.$$

It is readily seen that:

$$\left.\begin{aligned}\{\dot{x}^2/2\}_c&=\sum_{n=1}^{\infty}\omega^2n^2a_n\bar{a}_n,\\ \{px(z+z^{-1})/2\}_c&=p(a_1+\bar{a}_1)/2\,.\end{aligned}\right\} \qquad (5)$$

To find $\{F(x)\}_c$, we put

$$x=a_1z+\bar{a}_1z^{-1}+\sum_{n=2}^{\infty}(a_nz^n+\bar{a}_nz^{-n})$$

and expand the function $F(x)$ in the vicinity of $a_1z+\bar{a}_1z^{-1}$ to the second order term, assuming the amplitudes of higher modes $|a_n|$ are small compared with that of the fundamental mode. Thus,

$$\begin{aligned}F(x)=&F(a_1z+\bar{a}_1z^{-1})\\ &+\left\{\sum_{n=2}^{\infty}(a_nz^n+\bar{a}_nz^{-n})\right\}F'(a_1z+\bar{a}_1z^{-1})\\ &+(1/2)\left\{\sum_{n=2}^{\infty}(a_nz^n+\bar{a}_nz^{-n})\right\}^2F''(a_1z+\bar{a}_1z^{-1}).\end{aligned} \qquad (6)$$

For convenience in calculation, we define the following quantities:

$$\left.\begin{aligned}&\{F(a_1z+\bar{a}_1z^{-1})\}_c=M\,,\\&\{z^{\pm n}F'(a_1z+\bar{a}_1z^{-1})\}_c=\alpha_{\pm n},\ (n=2,3,\cdots),\\&\{z^{\pm n}F''(a_1z+\bar{a}_1z^{-1})\}_c=\beta_{\pm n},\ (n=0,1,2,\cdots),\end{aligned}\right\}\tag{7}$$

and stipulate that the quantity $\beta_l\beta_m$, whenever it appears, should be replaced by β_{l+m}. Then, we have formally

$$\{F(x)\}_c=M+\sum_{n=2}^{\infty}(a_n\alpha_n+\bar{a}_n\alpha_{-n})+\frac{1}{2}\left\{\sum_{n=2}^{\infty}(a_n\beta_n+\bar{a}_n\beta_{-n})\right\}^2\,.\tag{8}$$

It is to be remarked here that $M, \alpha_{\pm n}, \beta_{\pm n}$ are functions of $a_1, \bar{a}_1$ and especially M is a function of $a_1\bar{a}_1$ only; and apparently

$$\alpha_{-n}=\bar{\alpha}_n\,,\quad \beta_{-n}=\bar{\beta}_n\,.\tag{9}$$

From (4), (5) and (8), G is finally expressed as,

$$G=\frac{2\pi}{\omega}\left[\sum_{n=1}^{\infty}\omega^2n^2a_n\bar{a}_n+\frac{p}{2}(a_1+\bar{a}_1)+M+\sum_{n=2}^{\infty}(a_n\alpha_n+\bar{a}_n\alpha_{-n})+\frac{1}{2}\left\{\sum_{n=2}^{\infty}(a_n\beta_n+\bar{a}_n\beta_{-n})\right\}^2\right].\tag{10}$$

Using the above expression of G, we can determine $a_n, \bar{a}_n$ $(n=1, 2, \cdots)$ by the relations

$$\partial G/\partial a_n=0,\ \partial G/\partial\bar{a}_n=0,\ (n=1,2,\cdots)\,.\tag{11}$$

§ 3. Determination of a_1, $\bar{a}_1$

To determine $a_1, \bar{a}_1$ we neglect the terms including $a_n, \bar{a}_n$; thus G is reduced to

$$G=(2\pi/\omega)\{\omega^2a_1\bar{a}_1+p(a_1+\bar{a}_1)/2+M\}\,.$$

The equations $\partial G/\partial a_1=0$, $\partial G/\partial\bar{a}_1=0$ become respectively,

$$\left.\begin{aligned}&\omega^2\bar{a}_1+p/2+\partial M/\partial a_1=0\,,\\&\omega^2a_1+p/2+\partial M/\partial\bar{a}_1=0\,.\end{aligned}\right\}\tag{12}$$

Since M is the function of $a_1\bar{a}_1$, we have

$$\partial M/\partial a_1=M'\bar{a}_1\,,\quad \partial M/\partial\bar{a}_1=M'a_1\,,$$

where $M'=d/d(a_1\bar{a}_1)\cdot M(a_1\bar{a}_1)$.

Now, subtraction of the equations (12), gives

$$(\bar{a}_1-a_1)(\omega^2+M')=0\,.$$

It is apparent from (12) that $\omega^2+M'\neq0$ if $p\neq0$. Hence, $a_1=\bar{a}_1$. This result indicates that the phase of the fundamental mode is equal to or has a difference of π from the phase of the exciting force.

Further, using the relation (9), we have

$$\alpha_{-n}=\alpha_n=\text{real},\quad \beta_{-n}=\beta_n=\text{real}.\tag{13}$$

If we put $a_1=\bar{a}_1=x_0$ (x_0 being real), (12) is reduced to

$$\omega^2x_0+p/2+M'(x_0^2)x_0=0\,,\tag{14}$$

by which we can determine x_0 as a function of the given parameters p, ω. Accordingly $\alpha_{\pm n}, \beta_{\pm n}$ can be determined as functions of p, ω.

Equation (14) corresponds to the familiar equation[1] which is obtained when the solution is represented by the equivalent harmonic motion.

§ 4. Studies on a_n, $\bar{a}_n$

Introducing (10) into (11), we have

$$\begin{aligned}&\omega^2n^2\bar{a}_n+\alpha_n+\beta_n\sum_{r=0}^{\infty}(a_r\beta_r+\bar{a}_r\beta_{-r})=0\,,\\&\omega^2n^2a_n+\alpha_{-n}+\beta_{-n}\sum_{r=0}^{\infty}(a_r\beta_r+\bar{a}_r\beta_{-r})=0\,,\\&n=2,3,\cdots\,.\end{aligned}$$

or, considering the relations (7) and (13),

$$\begin{aligned}&\omega^2n^2\bar{a}_n+\alpha_n+\sum_{r=2}^{\infty}(a_r\beta_{n+r}+\bar{a}_r\beta_{|n-r|})=0\,,\\&\omega^2n^2a_n+\alpha_n+\sum_{r=2}^{\infty}(a_r\beta_{|n-r|}+\bar{a}_r\beta_{n+r})=0\,,\\&n=2,3,\cdots\,.\end{aligned}$$

If we add and subtract the above equations and write

$$a_n=x_n+iy_n\,,$$

we have

$$x_n+(1/n^2\omega^2)\sum_{r=2}^{\infty}(\beta_{n+r}+\beta_{|n-r|})x_r=-\alpha_n/n^2\omega^2\,,\tag{15}$$

$$y_n+(1/n^2\omega^2)\sum_{r=2}^{\infty}(\beta_{|n-r|}-\beta_{n+r})y_r=0\,,\tag{16}$$

$$n=2,3,\cdots\,.$$

Equations (15) contain x_n only while (16) contain y_n. Therefore, we can find x_n and y_n separately, considering x_0 as a parameter.

Now we put

$$\varDelta_1=\begin{vmatrix} 1+(\beta_0+\beta_4)/2^2\omega^2 & (\beta_1+\beta_5)/2^2\omega^2 & (\beta_2+\beta_6)/2^2\omega^2 & \cdots\cdots \\ (\beta_1+\beta_5)/3^2\omega^2 & 1+(\beta_0+\beta_6)/3^2\omega^2 & (\beta_1+\beta_7)/3^2\omega^2 & \cdots\cdots \\ (\beta_2+\beta_6)/4^2\omega^2 & (\beta_1+\beta_7)/4^2\omega^2 & 1+(\beta_0+\beta_8)/4^2\omega^2 & \cdots\cdots \\ \text{—} & \text{—} & \text{—} & \ddots \\ \text{—} & \text{—} & \text{—} & \end{vmatrix}$$

and denote by $\varDelta_1^{(n)}$ the determinants which are obtained by replacing the $(n-1)$-th row of $\varDelta_1$ by $(\alpha_2/2^2\omega^2, \alpha_3/3^2\omega^2, \alpha_4/4^2\omega^2, \cdots)$. Then, solving (15), we have

$$x_n=-\varDelta_1^{(n)}/\varDelta_1\ , \quad n=2, 3, \cdots\ . \tag{17}$$

If we substitute the value of x_0 obtained from (14) into the right side of (17), x_n's are determined finally as functions of p, ω. However, it may happen that the value of a_n is infinite when p and ω (or x_0) take such values as to make $\varDelta_1=0$, $\varDelta_1^{(n)}\neq0$. Thus, we may see that there can take place extraordinary phenomena of the sort of resonance in the neighbourhood of these points. Accordingly,

$$\varDelta_1=0\ , \quad \varDelta_1^{(n)}\neq0\ , \tag{18}$$

give the condition for determining such extraordinary points.

On the other hand, we can see from (16) that the values of y_n's are generally zero and so the phase of the higher mode is in general equal to or has a difference of π from the phase of driving force as in the case of fundamental mode.

However, if $\varDelta_2=0$, where

$$\varDelta_2=\begin{vmatrix} 1+(\beta_0-\beta_4)/2^2\omega^2 & (\beta_1-\beta_5)/2^2\omega^2 & (\beta_2-\beta_6)/2^2\omega^2 & \cdots\cdots \\ (\beta_1-\beta_5)/3^2\omega^2 & 1+(\beta_0-\beta_6)/3^2\omega^2 & (\beta_1-\beta_7)/3^2\omega^2 & \cdots\cdots \\ (\beta_2-\beta_6)/4^2\omega^2 & (\beta_1-\beta_7)/4^2\omega^2 & 1+(\beta_0-\beta_8)/4^2\omega^2 & \cdots\cdots \\ \text{—} & \text{—} & \text{—} & \ddots \\ \text{—} & \text{—} & \text{—} & \end{vmatrix}, \tag{19}$$

it is possible that the values of y_n's do not vanish at these points. Accordingly, we may have a sudden appearance of imaginary parts and cosequently both the amplitude and phase of this mode may change there. This process seems to be somewhat different from the ordinary resonance phenomenon.

According to Hayashi[1], the periodic solution of eq. (1), now under consideration, is not always stable and there is the region of unstable state, where the above-mentioned periodic solution loses its validity. But the conditions which give the boundary of the stable and the unstable regions obtained by Hayashi using Hill's equation is found to coincide approximately with the conditions represented by (18) and (19). Namely, (18) corresponds to the boundary where the stable solution fails, while (19) corresponds to the boundary where the solution restores its stability. Moreover, Hayashi shows in the example with $F'(x)=ax+bx^3$ that the concurrence of even harmonics is a salient feature in the unstable region, on the other hand only odd harmonics appear in the stable region. This fact may be in some way related to the feature of the above-mentioned sudden appearance of imaginary parts.

Now, let us consider the convergence of the infinite determinants $\varDelta_1$, $\varDelta_1^{(n)}$, $\varDelta_2$. Generally, the infinite determinant

$$\begin{vmatrix} 1+a_{11} & a_{12} & \cdots \\ a_{21} & 1+a_{22} & \cdots \\ \cdots\cdots\cdots\cdots & & \ddots \end{vmatrix}$$

converges, provided $\sum\limits_{i,j=1}^{\infty}|a_{ij}|$ converges. Since the elements of $\varDelta_1$, $\varDelta_1^{(n)}$, $\varDelta_2$ corresponding to a_{ij} $(i>1)$ are of the order of magnitude of $(i+1)^{-2}$, if α_n and β_n are assumed to be of ordinary magnitude, $\varDelta_1$, $\varDelta_1^{(n)}$ and $\varDelta_2$ converge rapidly; and this fact is useful for the approximate determination of their values.

Thus we have the following expressions as the first approximation where a_{ij} $(i, j\geqq2)$ are neglected,

$$\varDelta_1=1+(\beta_0+\beta_4)/2^2\omega^2\ , \quad \varDelta_1^{(2)}=\alpha_2/2^2\omega^2\ ,$$

$$\Delta_1^{(n)}=0\ ,\quad n=3,4,\cdots$$

$$\Delta_2=1+(\beta_0-\beta_4)/2^2\omega^2\ .$$

Then we have

$$x_2=-\alpha_2/(2^2\omega^2+\beta_0+\beta_4)\ ,\ x_3=x_4=\cdots=0\ ,\quad (20)$$

and the extraordinary points are given by (18) and (19) as

$$\alpha_2\neq 0,\ 2^2\omega^2+\beta_0+\beta_4=0 \text{ and } 2^2\omega^2+\beta_0-\beta_4=0. \quad (21)$$

In the second approximation where a_{ij} $(i,\ j\geqq 3)$ are neglected, we have

$$\Delta_1=\begin{vmatrix} 1+(\beta_0+\beta_4)/2^2\omega^2 & (\beta_1+\beta_5)/2^2\omega^2 \\ (\beta_1+\beta_5)/3^2\omega^2 & 1+(\beta_0+\beta_6)/3^2\omega^2 \end{vmatrix},$$

$$\Delta_2=\begin{vmatrix} 1+(\beta_0-\beta_4)/2^2\omega^2 & (\beta_1-\beta_5)/2^2\omega^2 \\ (\beta_1-\beta_5)/3^2\omega^2 & 1+(\beta_0-\beta_6)/3^2\omega^2 \end{vmatrix},$$

$$\Delta_1^{(2)}=\begin{vmatrix} \alpha_2/2^2\omega^2 & (\beta_1+\beta_5)/2^2\omega^2 \\ \alpha_3/3^2\omega^2 & 1+(\beta_0+\beta_6)/3^2\omega^2 \end{vmatrix},$$

$$\Delta_1^{(3)}=\begin{vmatrix} 1+(\beta_0+\beta_4)/2^2\omega^2 & \alpha_2/2^2\omega^2 \\ (\beta_1+\beta_5)/3^2\omega^2 & \alpha_3/3^2\omega^2 \end{vmatrix},$$

$$\Delta_1^{(4)}=\Delta_1^{(5)}=\cdots=0\ . \quad (22)$$

§ 5. Application to the Circuit containing Iron Reactor

Now we consider an electric circuit containing an iron reactor which is driven by an input voltage $E\sin\omega t$ as shown in Fig. 1.

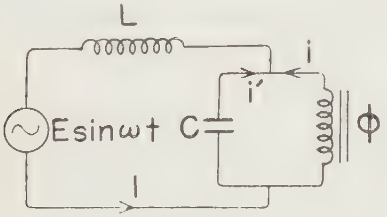

Fig. 1.

We assume that the iron reactor has the characteristics

$$i=k_1\phi+k_5\phi^5\ , \quad (23)$$

where i is the current and ϕ is the magnetic flux, k_1, k_5 being constants.

Katano[2] has designed this circuit as a stabilizer with the values $k_1=0.5$, $k_5=650$, $L=0.11H$, $c=84\,\mu F$, where the first jump was of course avoided in the range to be used. However, he found a weak jump at a comparatively large input voltage, which varied with ω. It may be considered as the phenomenon discussed in foregoing sections. Next we shall apply the formulae of § 4 to determine the jumping voltage.

First, we have from Fig. 1

$$I=i+i'\ ,\qquad i'=cd^2\phi/dt^2\ ,$$

$$E\sin\omega t=(d/dt)\cdot(\phi+LI)\ .$$

Integrating the last equation and using (23),

$$\ddot{\phi}+\{(1+Lk_1)\phi+Lk_5\phi^5\}/Lc=-(E/Lc\omega)\cos\omega t\ . \quad (24)$$

If we compare (24) with (1) and put $(1+Lk_1)/Lc=a$, $k_5/c=b$, then from (7)

$$\left.\begin{aligned} &M=-ax_0^2-10bx_0^6/3\ ,\\ &\alpha_2=0\ ,\quad \alpha_3=-5bx_0^5\ ,\quad \alpha_4=0\ ,\\ &\alpha_5=-bx_0^5\ ,\quad \alpha_6=\alpha_7=\cdots=0\ ,\\ &\beta_0=-a-30bx_0^4\ ,\quad \beta_1=0\ ,\\ &\beta_2=-20bx_0^4\ ,\quad \beta_3=0\ ,\quad \beta_4=-5bx_0^4\ ,\\ &\beta_5=\beta_6=\cdots=0\ . \end{aligned}\right\} \quad (25)$$

Then (14) becomes

$$10bx_0^5+(a-\omega^2)x_0+E/2LC\omega=0\ , \quad (26)$$

from which we can find x_0 as a function of E, ω. The condition of the first jump would be derived from the double root of (26) as usual. But, with the values given above, there is no such a jump.

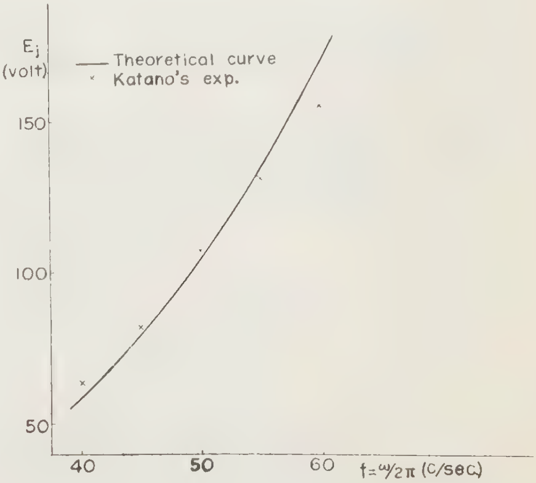

Fig. 2.

The first approximation to the higher harmonics, now under consideration is given by (20), using (25) as,

$$x_2=x_3=\cdots=0\ .$$

Then, generally, we have no higher harmonics, but an exception may happen at the point given by (21) as,

$$2^2\omega^2-a-25bx_0^4=0\ .$$

Using (26), this equation is reduced to

$$E_j=\frac{3}{5}\sqrt{\frac{2}{5}}\left(\frac{4LC\omega^2-1}{Lk_5}-Lk_1\right)^{1/4}$$
$$\times(1+k_1L+\omega^2Lc)\ , \quad (27)$$

where E_j represents the effective value of $E\sin\omega t$.

The equation (27) is exactly the same as the formula given by Katano which was derived by quite a different method. The curve of (27) together with Katano's experimental data is shown in Fig. 2.

In the second approximation, we have from (22) and (25)

$$x_2=0\ , \quad x_3=5bx_0^5/(3^2\omega^2-a-30bx_0^4)\ ,$$
$$x_4=x_5=\cdots=0\ ,$$

and

$$\Delta_2=\{1-(a+25bx_0^4)/2^2\omega^2\}\{1-(a+30bx_0^4)/3^2\omega^2\}.$$

From these equations, we have two extraordinary points as

$$2^2\omega^2-a-25bx_0^4=0\ , \quad 3^2\omega^2-a-30bx_0^4=0\ .$$

The first of them is the same as the above-mentioned first approximation. The second condition could not be verified experimentally since the circuit could not bear such a high input voltage.

Moreover, it must be mentioned that if we proceed to the third approximation, the result obtained is rather wrong. This is probably due to the fact that the order of magnitude of $a_5, a_6, \cdots$ becomes comparable with that of $a_2^2, \cdots$ which are neglected here.

The author wishes to express his thanks to Professor I. Imai, Mr. Y. Katano and Dr. K. Munakata for their helpful advice and valuable discussions.

References

1) C. Hayashi: Forced Oscillations in Non-linear Systems (Nippon Printing and Publishing Company, 1953).

2) Y. Katano: Res. Rep. of Tokyo Elec. Eng. College **1** (1951) 45.

JOURNAL OF THE PHYSICAL SOCIETY OF JAPAN Vol. 10, No. 4, APRIL, 1955

The Transformation Equations between One- and n-Dimensional Spectra in the n-Dimensional Isotropic Vector or Scalar Fluctuation Field

By Hiroshi TSUJI

Institute of Science and Technology, University of Tokyo

(Received December 1, 1954)

The transformation equations between one- and n-dimensional spectra in the n-dimensional isotropic vector or scalar fluctuation field are derived, the well-known equations for three-dimensional fluctuation field being included as a special case. It is found that the transformation equation for n-dimensional vector fluctuation is of the same form as that for $(n+2)$-dimensional scalar fluctuation except for the constant coefficient. The spectrum equations for n-dimensional isotropic turbulence and for n-dimensional isotropic temperature fluctuations in the n-dimensional isotropic turbulence are also derived. It is shown that the spectrum equations for any n-dimensional isotropic fluctuations have the same form.

§ 1. Introduction

It is well known that the fluctuation field considered in fluid dynamics is a vector field (velocity fluctuation, i.e., turbulence in incompressible fluids) or a scalar field (temperature, density, or pressure fluctuation), and these actual fluctuation fields are always three-dimensional.

Since the basic study of G. I. Taylor in 1935⁽¹⁾, who introduced the concept of isotropic turbulence and presented the first contribution toward the statistical theory of this type of flow, a considerable amount of work on isotropic turbulence has been made. Particularly, the correlation tensors between two velocity components introduced by von Kármán and Howarth[2)], and their Fourier transforms, i.e., the energy spectra, have become the basis for the further analyses of isotropic turbulence. The problem is then reduced to solving the Kármán-Howarth equation for the propagation of the velocity correlation, or the spectrum equation. A similar analysis on isotropic temperature fluctuations in an isotropic turbulent fluid motion was carried out by Corrsin[3)4)].

Although an actual fluctuation field is always three-dimensional, the two-dimensional fluctuation field, in which the third dimension is extremely small compared with the others, may be used as a simplified model in geophysical problems. With the object of applications to geophysical problems, Ogura[5)] derived the transformation equation between one- and two-dimensional spectra in the two-dimensional isotropic turbulence field. Recently, Hama[6)] gave the inverse relation of the formula obtained by Ogura and showed the similarity between the spectrum equations of three- and two-dimensional isotropic turbulence.

Similar relations can be obtained in the case of two-dimensional isotropic scalar fluctuation field, which has not yet been treated by these authors. In this paper, however, a more general treatment is made, and the transformation equations between one- and n-dimensional spectra are derived for the n-dimensional isotropic vector or scalar fluctuation field, the equations already obtained for the two- and three-dimensional fluctuation fields being included as special cases. By using these transformation equations, the spectrum equations for n-dimensional isotropic turbulence and for n-dimensional isotropic temperature fluctuations in the n-dimensional isotropic turbulence are also derived. Although it seems that the n-dimensional fluctuation field may find no application to the actual hydrodynamical problems, it is mathematically interesting to derive the general equations for n-dimensional fluctuation fields, and these equations would give the inclusive penetration on the fluctuation fields treated in fluid dynamics.

§ 2. The Transformation Equation between One- and n-Dimensional Spectra of n-Dimensional Isotropic Turbulence (Vector Fluctuation)

The velocity correlation tensor for the two points separated by the space vector $\boldsymbol{r}$ (which is the n-dimentional vector defining the configuration of the two points) is defined by

$$R_{ij}(\boldsymbol{r})=\overline{u_i(\boldsymbol{x})u_j(\boldsymbol{x}+\boldsymbol{r})}\,; \tag{2.1}$$

the dependence on time t will not be shown explicity unless different instances are under consideration. Because of isotropy, the velocity correlation $R_{ij}(\boldsymbol{r})$ is then an isotropic second-order two-point tensor and therefore has the form[7)8)]

$$R_{ij}(\boldsymbol{r})=A(r)r_ir_j+B(r)\delta_{ij}\ , \tag{2.2}$$

in which r and r_i are the magnitude and the component of $\boldsymbol{r}$, respectively, and A and B are arbitrary scalar functions of r^2. A and B are expressed in terms of the longitudinal velocity correlation coefficient $f(r)$ and the lateral velocity correlation coefficient $g(r)$ introduced by von Kármán and Howarth[2)], viz.,

$$A(r)=\frac{f(r)-g(r)}{r^2}\,\overline{u^2}\ ,\quad B(r)=g(r)\overline{u^2}\ , \tag{2.3}$$

in which $\overline{u^2}$ is the mean-square of any velocity component, i.e.,

$$\overline{u^2}=\overline{u_j{}^2}=\frac{1}{n}\overline{u_iu_i}\ . \tag{2.4}$$

From the continuity condition

$$\frac{\partial R_{ij}(\boldsymbol{r})}{\partial r_j}=\frac{\partial R_{ij}(\boldsymbol{r})}{\partial r_i}=0\ , \tag{2.5}$$

we find that

$$(n+1)A(r)+r\frac{\partial A(r)}{\partial r}+\frac{1}{r}\frac{\partial B(r)}{\partial r}=0\ , \tag{2.6A}$$

or

$$(n-1)\{f(r)-g(r)\}+r\frac{\partial f(r)}{\partial r}=0\ , \tag{2.6B}$$

which shows that only one scalar function is needed to specify the velocity correlation tensor when the turbulence is isotropic.

The general energy spectrum tensor $\Phi_{ij}(\boldsymbol{k})$ may be defined as the (n-ple) Fourier transform $R_{ij}(\boldsymbol{r})$, i.e.,

$$\Phi_{ij}(\boldsymbol{k})=\frac{1}{(2\pi)^n}\int R_{ij}(\boldsymbol{r})e^{-i\boldsymbol{k}\cdot\boldsymbol{r}}d\boldsymbol{r}\ , \tag{2.7}$$

in which $\boldsymbol{k}$ is the wave-number vector, $d\boldsymbol{r}$ is a volume element at the position $\boldsymbol{r}$, $\iota=\sqrt{-1}$, and the integration is over all space. The transformed version of (2.7) is

$$R_{ij}(\boldsymbol{r})=\int\Phi_{ij}(\boldsymbol{k})e^{\iota\boldsymbol{k}\cdot\boldsymbol{r}}d\boldsymbol{k}\,, \tag{2.8}$$

in which $d\boldsymbol{k}$ is a volume element at the position $\boldsymbol{k}$ in the wave-number space.

Results corresponding to (2.2) et seq. can be established without difficulty for the spectrum tensor. $\Phi_{ij}(\boldsymbol{k})$ is an isotropic second-order tensor which depends on a single vector argument and can be expressed in the form[7)8)]

$$\Phi_{ij}(\boldsymbol{k})=C(k)k_ik_j+D(k)\delta_{ij}\,, \tag{2.9}$$

in which k and k_i are the magnitude and the component of $\boldsymbol{k}$, respectively, and C and D are arbitrary even functions of k. The continuity condition

$$k_j\Phi_{ij}(\boldsymbol{k})=k_i\Phi_{ij}(\boldsymbol{k})=0 \tag{2.10}$$

then requires

$$D=-k^2C\,. \tag{2.11}$$

The energy density of $\overline{u_iu_i}$ in the wave-number space is

$$\Phi_{ii}(\boldsymbol{k})=k^2C+nD=-(n-1)k^2C\,,$$

and is a function of the wave-number magnitude alone.

If the contribution to the energy $\overline{u^2}$ from the part of the wave-number space between the spheres of radii k and $k+dk$ is expressed as $F(k)dk$, then

$$\begin{aligned}\overline{u^2}&=\int_0^\infty F(k)dk=\frac{1}{n}\overline{u_iu_i}=\frac{1}{n}\int\Phi_{ii}(\boldsymbol{k})d\boldsymbol{k}\\&=-\frac{1}{n}\int_0^\infty(n-1)k^2C(k)\left(\frac{2\pi^{n/2}}{\Gamma(n/2)}\right)k^{n-1}dk\\&=-\frac{n-1}{n}\cdot\frac{2\pi^{n/2}}{\Gamma(n/2)}\int_0^\infty k^{n+1}C(k)dk\,,\end{aligned}$$

in which $\Gamma(n)$ is the Gamma-function. Therefore,

$$F(k)=-\frac{n-1}{n}\cdot\frac{2\pi^{n/2}}{\Gamma(n/2)}\cdot k^{n+1}C(k),$$

or

$$C(k)=-\frac{n}{n-1}\cdot\frac{\Gamma(n/2)}{2\pi^{n/2}}\cdot\frac{F(k)}{k^{n+1}}\,. \tag{2.12}$$

The expression (2.9) for the spectrum tensor becomes

$$\Phi_{ij}(\boldsymbol{k})=\frac{n}{n-1}\cdot\frac{\Gamma(n/2)}{2\pi^{n/2}}\cdot\frac{F(k)}{k^{n+1}}[k^2\delta_{ij}-k_ik_j]\,. \tag{2.13}$$

The longitudinal one-dimensional spectrum function $F_1(k_1)$, which is defined by

$$\overline{u_1{}^2}=\overline{u^2}=\int_0^\infty F_1(k_1)dk_1\,, \tag{2.14}$$

becomes

$$\begin{aligned}F_1(k_1)&=\frac{2}{\pi}\int_0^\infty\overline{u^2}f(r)\cos k_1rdr\\&=2\int_{-\infty}^\infty\cdots\cdots\int_{-\infty}^\infty\Phi_{11}(\boldsymbol{k})dk_2\cdots\cdot dk_n\\&=2\int_0^\infty\Phi_{11}(\boldsymbol{k})\cdot\frac{2\pi^{(n-1)/2}}{\Gamma\{(n-1)/2\}}\cdot k'^{\,n-2}dk'\\&=2\int_0^\infty\frac{n}{n-1}\cdot\frac{\Gamma(n/2)}{2\pi^{n/2}}\cdot\frac{F(k)}{k^{n+1}}[k^2-k_1{}^2]\\&\quad\cdot\frac{2\pi^{(n-1)/2}}{\Gamma\{(n-1)/2\}}\cdot k'^{\,n-2}dk'\\&=\frac{n}{n-1}\cdot\frac{2\Gamma(n/2)}{\sqrt{\pi}\,\Gamma\{(n-1)/2\}}\int_{k_1}^\infty\frac{F(k)}{k^n}\\&\quad\cdot[k^2-k_1{}^2]^{\frac{n-1}{2}}dk\,.\end{aligned} \tag{2.15}$$

This is the general transformation equation between one- and n-dimensional spectra of n-dimensional isotropic turbulence. For example, for $n=2$,

$$F_1(k_1)=\frac{4}{\pi}\int_{k_1}^\infty\frac{F(k)}{k^2}[k^2-k_1{}^2]^{\frac{1}{2}}dk\,, \tag{2.16}$$

which is the formula given by Ogura[5)]. For $n=3$,

$$F_1(k_1)=\frac{3}{2}\int_{k_1}^\infty\frac{F(k)}{k^3}[k^2-k_1{}^2]dk\,, \tag{2.17}$$

which is the well-known relation derived by Heisenberg[9)].

§ 3. The Transformation Equation between One- and n-Dimensional Spectra of n-Dimensional Isotropic Scalar Fluctuation

Consider the correlation between instantaneous scalar fluctuations, θ and θ', at two points in the infinite n-dimensional isotropic scalar fluctuation field. Because of isotropy, it is obvious that this must be a scalar function of the distance r between the two points. Hence, we introduce

$$M(r)=\overline{\theta\theta'}\,. \tag{3.1}$$

This is in contrast with the general velocity double correlation function, which is a second order tensor, though depending ultimately upon just a single scalar function.

The general power spectrum function $\Psi(k)$ may be defined as the (n-ple) Fourier transform of $M(r)$, i.e.,

$$\Psi(k)=\frac{1}{(2\pi)^n}\int M(r)e^{-i\boldsymbol{k}\cdot\boldsymbol{r}}d\boldsymbol{r}\,. \tag{3.2}$$

The transformed version of (3.2) is

$$M(r)=\int\Psi(k)e^{i\boldsymbol{k}\cdot\boldsymbol{r}}d\boldsymbol{k}\,. \tag{3.3}$$

If the contribution to $\overline{\theta^2}$ from the part of the wave-number space between the spheres of radii k and $k+dk$ is expressed as $G(k)dk$, then

$$\overline{\theta^2}=\int_0^\infty G(k)dk=\int_{-\infty}^\infty\cdots\cdots\int_{-\infty}^\infty\Psi(k)dk_1\cdots\cdots dk_n$$
$$=\frac{2\pi^{n/2}}{\Gamma(n/2)}\int_0^\infty\Psi(k)k^{n-1}dk\,.$$

Therefore,

$$G(k)=\frac{2\pi^{n/2}}{\Gamma(n/2)}k^{n-1}\Psi(k)\,,$$

or

$$\Psi(k)=\frac{\Gamma(n/2)}{2\pi^{n/2}}\cdot\frac{G(k)}{k^{n-1}}\,. \tag{3.4}$$

The one-dimensional spectrum function $G_1(k_1)$, which is defined by

$$\overline{\theta^2}=\int_0^\infty G_1(k_1)dk_1\,,$$

becomes

$$G_1(k_1)=\frac{2}{\pi}\int_0^\infty M(r)\cos k_1r dr$$
$$=2\int_{-\infty}^\infty\cdots\cdots\int_{-\infty}^\infty\Psi(k)dk_2\cdots\cdots dk_n$$
$$=2\int_0^\infty\Psi(k)\cdot\frac{2\pi^{(n-1)/2}}{\Gamma\{(n-1)/2\}}\cdot k'^{n-2}dk'$$
$$=2\int_0^\infty\frac{\Gamma(n/2)}{2\pi^{n/2}}\cdot\frac{G(k)}{k^{n-1}}\cdot\frac{2\pi^{(n-1)/2}}{\Gamma\{(n-1)/2\}}$$
$$\cdot k'^{n-2}dk'$$
$$=\frac{2\Gamma(n/2)}{\sqrt{\pi}\,\Gamma\{(n-1)/2\}}\int_{k_1}^\infty\frac{G(k)}{k^{n-2}}$$
$$\cdot[k^2-k_1^2]^{\frac{n-3}{2}}dk\,. \tag{3.5}$$

This is the general transformation equation between one- and n-dimensional spectra of n-dimensional isotropic scalar fluctuation. For example, for $n=2$,

$$G_1(k_1)=\frac{2}{\pi}\int_{k_1}^\infty\frac{G(k)}{\sqrt{k^2-k_1^2}}dk\,,$$

and for $n=3$,

$$G_1(k_1)=\int_{k_1}^\infty\frac{G(k)}{k}dk\,,$$

the latter of which is the relation obtained by Kovásznay, Uberoi and Corrsin[10].

§ 4. The Inverse Transformation Equation between One- and n-Dimensional Spectra of n-Dimensional Isotropic Vector and Scalar Fluctuation

In the preceding sections we have derived the transformation equations between one- and n-dimensional spectra, i.e.,

$$F_1(k_1)=\frac{n}{n-1}\cdot\frac{2\Gamma(n/2)}{\sqrt{\pi}\,\Gamma\{(n-1)/2\}}$$
$$\cdot\int_{k_1}^\infty\frac{F(k)}{k^n}[k^2-k_1^2]^{\frac{n-1}{2}}dk\,. \tag{2.15}$$

for the n-dimensional isotropic vector fluctuations, and

$$G_1(k_1)=\frac{2\Gamma(n/2)}{\sqrt{\pi}\,\Gamma\{(n-1)/2\}}$$
$$\cdot\int_{k_1}^\infty\frac{G(k)}{k^{n-2}}[k^2-k_1^2]^{\frac{n-3}{2}}dk\,. \tag{3.5}$$

for the n-dimensional isotropic scalar fluctuations. By comparing (2.15) and (3.5), it can easily be noticed that the transformation equation for n-dimensional vector fluctuation is of the same form as that for $(n+2)$-dimensional scalar fluctuation except for the constant coefficients.

Differentiation of (2.15) with respect to k_1 gives

$$\frac{1}{k_1}\frac{dF_1}{dk_1}=\frac{2\Gamma(n/2)}{\sqrt{\pi}\,\Gamma\{(n-1)/2\}}\int_{k_1}^\infty\frac{1}{k^{n-2}}$$
$$\cdot\left\{-\frac{nF(k)}{k^2}\right\}[k^2-k_1^2]^{\frac{n-3}{2}}dk\,. \tag{4.1}$$

From equations (3.5) and (4.1), we find that the transformation equation between $G_1(k_1)$ and $G(k)$ for n-dimensional scalar fluctuations and that between $(1/k_1)(dF_1/dk_1)$ and $-nF(k)/k^2$ for n-dimensional vector fluctuations are identical with each other.

Next, let us derive the inverse relations of the above transformation equations.

I) Case when the value of n is odd.

In this case we put $n=2p+1$ $(p=1, 2,\cdots)$. Equation (3.5) becomes

$$G_1(k_1)=\frac{2\Gamma(p+\frac{1}{2})}{\sqrt{\pi}\,\Gamma(p)}\int_{k_1}^\infty\frac{G(k)}{k^{2p-1}}[k^2-k_1^2]^{p-1}dk. \tag{4.2}$$

Let us apply the operator

$$\frac{1}{k_1}\frac{d}{dk_1}\Big[\qquad\Big]$$

to both sides of (4.2) $(p-1)$ times. Then we obtain

$$\frac{1}{k_1}\frac{d}{dk_1}\left(\frac{1}{k_1}\frac{d}{dk_1}\left(\cdots\left(\frac{1}{k_1}\frac{d}{dk_1}\underbrace{\left(G_1\right)\right)\cdots\right)\right)}_{(p-1)}=(-2)^{p-1}(p-1)(p-2)\cdots2\cdot1\cdot\frac{2\Gamma(p+\frac{1}{2})}{\sqrt{\pi}\,\Gamma(p)}\int_{k_1}^{\infty}\frac{G(k)}{k^{2p-1}}dk\,. \tag{4.3}$$

Now, differentiating (4.3) with respect to k_1, we get

$$\frac{d}{dk_1}\left\{\frac{1}{k_1}\frac{d}{dk_1}\left(\frac{1}{k_1}\frac{d}{dk_1}\left(\cdots\left(\frac{1}{k_1}\frac{d}{dk_1}\underbrace{\left(G_1\right)\right)\cdots\right)\right)\right\}}_{(p-1)}=(-2)^{p}(p-1)(p-2)\cdots2\cdot1\cdot\frac{\Gamma(p+\frac{1}{2})}{\sqrt{\pi}\,\Gamma(p)}\cdot\frac{G(k_1)}{k_1^{2p-1}}\,,$$

or

$$G(k)=\frac{\sqrt{\pi}\,\Gamma(p)}{(-2)^{p}(p-1)(p-2)\cdots2\cdot1\cdot\Gamma(p+\frac{1}{2})}\left[k_1^{2p-1}\frac{d}{dk_1}\left\{\frac{1}{k_1}\frac{d}{dk_1}\left(\frac{1}{k_1}\frac{d}{dk_1}\cdot\left(\cdots\left(\frac{1}{k_1}\frac{d}{dk_1}\underbrace{\left(G_1\right)\right)\cdots\right)\right)\right\}}_{(p-1)}\right]_{k_1=k}\,. \tag{4.4}$$

This is the inverse relation of (4.2). By using the analogy between $G(k)$ and $F(k)$ mentioned above, we can readily derive the inverse relation between $F(k)$ and $F_1(k_1)$, i.e.,

$$F(k)=\frac{(-1)^{p+1}\sqrt{\pi}\,\Gamma(p)}{2^{p}(2p+1)(p-1)(p-2)\cdots2\cdot1\,\Gamma(p+\frac{1}{2})}\left[k_1^{2p+1}\frac{d}{dk_1}\left\{\frac{1}{k_1}\frac{d}{dk_1}\left(\frac{1}{k_1}\frac{d}{dk_1}\cdot\left(\cdots\left(\frac{1}{k_1}\frac{d}{dk_1}\underbrace{\left(F_1\right)\right)\cdots\right)\right)\right\}}_{(p)}\right]_{k_1=k}\,. \tag{4.5}$$

II) Case when the value of n is even.

In this case we put $n=2p$ ($p=1, 2,\cdots$). Equation (3.5) becomes

$$G_1(k_1)=\frac{2\Gamma(p)}{\sqrt{\pi}\,\Gamma(p-\frac{1}{2})}\int_{k_1}^{\infty}\frac{G(k)}{k^{2p-2}}[k^2-k_1^2]^{\frac{2p-3}{2}}dk\,. \tag{4.6}$$

Let us apply the operator

$$\frac{1}{k_1}\frac{d}{dk_1}\left[\qquad\right]$$

to both sides of (4.6) $(p-1)$ times. Then we obtain

$$\frac{1}{k_1}\frac{d}{dk_1}\left(\frac{1}{k_1}\frac{d}{dk_1}\left(\cdots\left(\frac{1}{k_1}\frac{d}{dk_1}\underbrace{\left(G_1\right)\right)\cdots\right)\right)}_{(p-1)}=(-1)^{p-1}(2p-3)(2p-5)\cdots3\cdot1\cdot\frac{2\Gamma(p)}{\sqrt{\pi}\,\Gamma(p-\frac{1}{2})}\cdot\int_{k_1}^{\infty}\frac{G(k)}{k^{2p-2}}\frac{dk}{\sqrt{k^2-k_1^2}}\,. \tag{4.7}$$

Solution of the integral equation

$$\psi(x)=\int_{x}^{\infty}\frac{\phi(\xi)}{\xi(\xi^2-x^2)^{1/2}}d\xi\,.$$

was given by Uberoi and Kovásznay[11] by reducing it to the Schlömlich equation[12], i.e.,

$$\phi(\xi)=-\frac{2}{\pi}\int_{\xi}^{\infty}\frac{d}{dx}[x\psi(x)]\cdot\frac{xdx}{(x^2-\xi^2)^{1/2}}=\frac{2}{\pi}\int_{\xi}^{\infty}\frac{d^2}{dx^2}[x\psi(x)]\cdot(x^2-\xi^2)^{1/2}dx\,. \tag{4.8}$$

Using (4.8), we can obtain the solution of (4.7) as follows:

$$G(k)=\frac{(-1)^{p-1}\Gamma(p-\frac{1}{2})}{(2p-3)(2p-5)\cdots3\cdot1\cdot\sqrt{\pi}\,\Gamma(p)}k^{2p-3}\int_{k}^{\infty}\frac{d^2}{dk_1^2}\left[k_1\left\{\frac{1}{k_1}\frac{d}{dk_1}\left(\frac{1}{k_1}\frac{d}{dk_1}\right.\right.\right.$$

$$\cdot\Big(\cdots\Big(\frac{1}{k_1}\frac{d}{dk_1}\underbrace{\Big(G_1\Big)\Big)\cdots\Big)\Big)}_{(p-1)}\Big\}\Big]\sqrt{k_1^2-k^2}\,dk_1\,, \tag{4.9A}$$

or

$$G(k)=\frac{(-1)^{p-1}\Gamma(p-\frac{1}{2})}{(2p-3)(2p-5)\cdots\cdot 3\cdot 1\cdot\sqrt{\pi}\,\Gamma(p)}k^{2p-1}\int_k^\infty\frac{d}{dk_1}\Big\{\frac{1}{k_1}\frac{d}{dk_1}\Big(\frac{1}{k_1}\frac{d}{dk_1}$$

$$\cdot\Big(\cdots\Big(\frac{1}{k_1}\frac{d}{dk_1}\underbrace{\Big(G_1\Big)\Big)\cdots\Big)\Big)}_{(p)}\Big\}\sqrt{k_1^2-k^2}\,dk_1\,. \tag{4.9B}$$

These are the inverse relations of (4.6). By using again the analogy between $G(k)$ and $F(k)$ mentioned above, we can readily derive the inverse relation $F(k)$ and $F_1(k_1)$, i.e.,

$$F(k)=\frac{(-1)^{p}\Gamma(p-\frac{1}{2})}{2p(2p-3)(2p-5)\cdots\cdot 3\cdot 1\cdot\sqrt{\pi}\,\Gamma(p)}k^{2p-1}\int_k^\infty\frac{d^2}{dk_1^2}\Big[k_1\Big\{\frac{1}{k_1}\frac{d}{dk_1}\Big(\frac{1}{k_1}\frac{d}{dk_1}$$

$$\cdot\Big(\cdots\Big(\frac{1}{k_1}\frac{d}{dk_1}\underbrace{\Big(F_1\Big)\Big)\cdots\Big)\Big)}_{(p)}\Big\}\Big]\sqrt{k_1^2-k^2}\,dk_1\,, \tag{4.10A}$$

or

$$F(k)=\frac{(-1)^{p}\Gamma(p-\frac{1}{2})}{2p(2p-3)(2p-5)\cdots\cdot 3\cdot 1\cdot\sqrt{\pi}\,\Gamma(p)}k^{2p+1}\int_k^\infty\frac{d}{dk_1}\Big\{\frac{1}{k_1}\frac{d}{dk_1}\Big(\frac{1}{k_1}\frac{d}{dk_1}$$

$$\cdot\Big(\cdots\Big(\frac{1}{k_1}\frac{d}{dk_1}\underbrace{\Big(F_1\Big)\Big)\cdots\Big)\Big)}_{(p+1)}\Big\}\sqrt{k_1^2-k^2}\,dk_1\,. \tag{4.10B}$$

These are the inverse relations of (2.15). The inverse relations for two- and three-dimentional isotropic fluctuations obtained from the above general forms are shown below.

a) Vector fluctuation:

i) For two-dimensional case,

$$F(k)=-\frac{k}{2}\int_k^\infty\frac{d^3F_1}{dk_1^3}\sqrt{k_1^2-k^2}\,dk_1\,, \tag{4.11A}$$

or

$$F(k)=-\frac{k^3}{2}\int_k^\infty\frac{d}{dk_1}\Big\{\frac{1}{k_1}\frac{d}{dk_1}\Big(\frac{1}{k_1}\frac{d}{dk_1}(F_1)\Big)\Big\}\sqrt{k_1^2-k^2}\,dk_1\,. \tag{4.11B}$$

ii) For three-dimensional case,

$$F(k)=\frac{1}{3}\Big[k_1^3\frac{d}{dk_1}\Big\{\frac{1}{k_1}\frac{d}{dk_1}(F_1)\Big\}\Big]_{k_1=k}. \tag{4.12}$$

b) Scalar fluctuation:

i) For two-dimensional case,

$$G(k)=\frac{1}{k}\int_k^\infty\frac{d^2}{dk_1^2}[k_1\,G_1]\sqrt{k_1^2-k^2}\,dk_1\,, \tag{4.13A}$$

or

$$G(k)=k\int_k^\infty\frac{d}{dk_1}\Big\{\frac{1}{k_1}\frac{d}{dk_1}(G_1)\Big\}\sqrt{k_1^2-k^2}\,dk_1\,. \tag{4.13B}$$

ii) For three-dimensional case,

$$G(k)=-\Big[k_1\frac{dG_1}{dk_1}\Big]_{k_1=k}. \tag{4.14}$$

§ 5. The Spectrum Equations in the *n*-Dimensional Isotropic Turbulence and Temperature Fluctuation Field

The Kármán-Howarth correlation equation[2] has been extended to *n*-dimensional turbulence field by Corrsin[13] as follows:

$$\frac{\partial}{\partial t}(\overline{u^2}f)+(n-1)(\overline{u^2})^{3/2}\left\{\frac{\partial h}{\partial r}+(n+1)\frac{h}{r}\right\}=2\nu\overline{u^2}\left\{\frac{\partial^2 f}{\partial r^2}+\frac{n+1}{r}\frac{\partial f}{\partial r}\right\}, \tag{5.1}$$

in which h is a typical triple velocity correlation coefficient shown in Fig. 1. A similar correlation equation for n-dimensional isotropic temperature fluctuations in the n-dimensional isotropic turbulence is easily derived by extending the correlation equation given by Corrsin[3] for three-dimensional fluctuations:

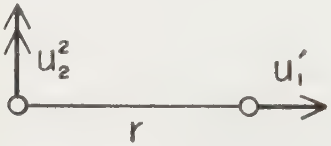

Fig. 1. $h(r)=\frac{\overline{u_2{}^2u_1{}'}}{(\overline{u^2})^{3/2}}$

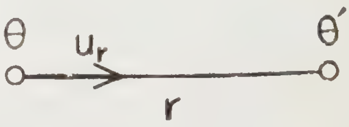

Fig. 2. $m(r)=\frac{\overline{\theta\theta'}}{\overline{\theta^2}}$ $s(r)=\frac{\overline{u_r\theta\theta'}}{\sqrt{\overline{u^2}\,\overline{\theta^2}}}$

$$\frac{\partial}{\partial t}(\overline{\theta^2}m)-2\overline{\theta^2}\sqrt{\overline{u^2}}\left\{\frac{\partial s}{\partial r}+(n-1)\frac{s}{r}\right\}=2\gamma\overline{\theta^2}\left\{\frac{\partial m^2}{\partial r^2}+\frac{n-1}{r}\frac{\partial m}{\partial r}\right\}, \tag{5.2}$$

in which m and s are the double and triple correlation coefficients (Fig. 2) defined by

$$m(r,t)=\frac{\overline{\theta\theta'}}{\overline{\theta^2}}, \qquad s(r,t)=\frac{\overline{u_r\theta\theta'}}{\sqrt{\overline{u^2}\cdot\overline{\theta^2}}},$$

and γ is the thermometric conductivity.

Multiplying (5.1) and (5.2) by $(2/\pi)\cos(k_1r)$ and integrating over r from 0 to infinity, we obtain the one-dimensional spectrum equations

$$\frac{\partial}{\partial t}\{F_1(k_1,t)\}+(n-1)\left\{k_1{}^2H_1(k_1,t)-(n+1)\int_\infty^{k_1}k_1{}'H_1(k_1{}',t)dk_1{}'\right\}$$
$$=-2\nu\left\{k_1{}^2F_1(k_1,t)-(n+1)\int_\infty^{k_1}k_1{}'F_1(k_1{}',t)dk_1{}'\right\}, \tag{5.3}$$

and

$$\frac{\partial}{\partial t}\{G_1(k_1,t)\}-2\left\{k_1{}^2S_1(k_1,t)-(n-1)\int_\infty^{k_1}k_1{}'S_1(k_1{}',t)\,dk_1{}'\right\}$$
$$=-2\gamma\left\{k_1{}^2G_1(k_1,t)-(n-1)\int_\infty^{k_1}k_1{}'G_1(k_1{}',t)dk_1{}'\right\}, \tag{5.4}$$

respectively, in which the one-dimensional transfer functions are defined by

$$\left.\begin{aligned}k_1H_1(k_1,t)&=\frac{2}{\pi}(\overline{u^2})^{3/2}\int_0^\infty h(r,t)\sin k_1r dr,\\ k_1S_1(k_1,t)&=\frac{2}{\pi}\overline{\theta^2}(\overline{u^2})^{1/2}\int_0^\infty s(r,t)\sin k_1r dr,\end{aligned}\right\} \tag{5.5}$$

respectively. If we apply the transformation (4.5) or (4.10) to (5.3), and (4.4) or (4.9) to (5.4), we finally obtain the spectrum equations

$$\frac{\partial F(k,t)}{\partial t}+(n-1)k^2H(k,t)=-2\nu k^2F(k,t), \tag{5.6}$$

and

$$\frac{\partial G(k,t)}{\partial t}-2k^2S(k,t)=-2\gamma k^2G(k,t), \tag{5.7}$$

in which the n-dimensional energy transfer functions $H(k,t)$ and $S(k,t)$ are derived respectively by applying the above transformation to the one-dimensional transfer functions.

It is found that the spectrum equations for any n-dimensional isotropic fluctuations have exactly the same form, except for the numerical factors in the second term. The similarity of the above spectrum equations suggests that the mechanism of the energy transfer and dissipation must be the same for any case of n, and therefore the n-dimensional isotropic fluctuation field can be treated in an essentially similar way as for the well-known case of three-dimensional field.

The author would like to express his sincere thanks to Dr. F. R. Hama of University of Maryland for his suggestion of this problem and his valuable discussions, and to Prof. I. Tani and Prof. I. Imai for their advice and kind inspection of the manuscript.

References

1) G. I. Taylor: Proc. Roy. Soc. London **A 151** (1935) 421.
2) T. von Kármán and L. Howarth: Proc. Roy. Soc. London. **A 164** (1938) 192.
3) S. Corrsin: Journ. Aero. Sci. **17** (1950) 417.
4) S. Corrsin: Journ. Appl. Phys. **22** (1951) 469.
5) Y. Ogura: Journ. Met. Soc. Japan **30** (1952) 59.
6) F. R. Hama: Proc. Third Midwest. Conf. Fluid Mech., Univ. Minn. (1953) 427.
7) H. P. Robertson: Proc. Camb. Phil. Soc. **36** (1940) 209.
8) S. Chandrasekhar: Phil. Trans. **A 242** (1950) 557.
9) W. Heisenberg: Z. Phys. **124** (1948) 628.
10) L. S. G. Kovásznay, M. S. Uberoi and S. Corrsin: Phys. Rev. **76** (1949) 1263.
11) M. S. Uberai and L. S. G. Kovásznay: Quart. Appl. Math. **10** (1953) 375.
12) E. T. Whittaker and G. N. Watson: Modern Analysis, 6th Ed. (1935) 229.
13) S. Corrsin: Unpublished manuscript.

JOURNAL OF THE PHYSICAL SOCIETY OF JAPAN Vol. 10, No. 4, APRIL, 1955

Diffraction of Electromagnetic Waves by Circular Plate and Circular Hole

By Yûkichi NOMURA and Shigetoshi KATSURA
Department of Applied Science Tohoku University

(Received October 8, 1954)

Rigorous solutions are presented of the problems of diffraction of plane electromagnetic waves by an infinitely thin, perfectly conducting, circular disk and by a circular hole in a plane conducting screen. The unique solution satisfying the edge condition is obtained from the two component Hertz vector, by the method of expansion in the hypergeometric polynomial. Total scattering cross section, the transmission coefficient, electric current on the disk, electric field in the hole, and electric field at the distant place are shown in the figure as a function of $ka=2\pi a/\lambda$.

§ 1. Introduction

The diffraction of electromagnetic waves by a circular hole and a circular plate are solved by Bouwkamp[1] using the power series expansion, Meixner and Andrejewski[2] using the spheroidal wave function. Levine and Schwinger[3] calculated the transmission coefficient for the perpendicular incidence by the variation method. Their results, however, are not sufficient since the variation method is dependent on the trial functions. The sphroidal wave function is not adequate to the extension to the complicated problem, for example, diffraction of spherical waves or that by two plates. Therefore we want to solve this problem by the method of expansion in the hypergeometric polynomial, which succeeded in case of acoustical waves[4].

Our theory gives the complete solution and is valid for all frequencies. The convergence, however, becomes bad when $ka=2\pi a/\lambda$ becomes large. This situation is similar to the theory of spheroidal wave function. For $ka>5$, the approximate theory of Bekefi[5] is adequate which fits well to the experiments.

The theory of circular plate and hole corresponds to each other, so the formulae for a circular plate and a circular hole are listed in the left and right side respectively.

§ 2. General Solution

We consider an infinitesimally thin circular plate or an infinitesimally thin plane screen of infinite extent with a circular aperture. A rectangular coordinate system is chosen with origin at the center of the circle, and oriented so that the screen lies in the x y-plane. We consider a plane wave incident on the circle from the negative half space, with its plane of incidence x z-plane, angle of incidence α. The electromagnetic field of the incident wave (i) and the reflected wave (r) is described by (Fig. 1)

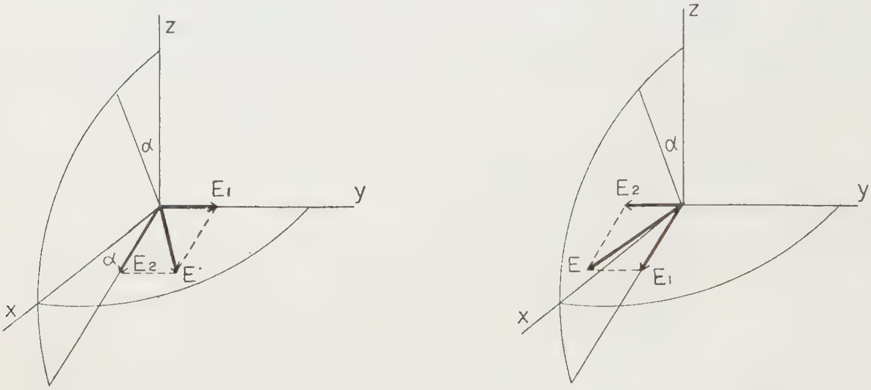

(a) Circular plate (b) Circular hale

Fig. 1.

Case of circular plate

$$E^{(i)}=(E_2\cos\alpha,\ E_1,\ -E_2\sin\alpha)\times\exp(-ikz\cos\alpha-ikx\sin\alpha)\ ,$$

$$H^{(i)}=\frac{k}{\mu\omega}(-E_1\cos\alpha,\ E_2,\ E_1\sin\alpha)\times\exp(-ikz\cos\alpha-ikx\sin\alpha)\ ,$$

for all space.

Case of circular hole

$$\begin{aligned}
E^{(i)}&=(E_1\cos\alpha,\ -E_2,\ -E_1\sin\alpha)\times\exp(-ikz\cos\alpha-ikx\sin\alpha)\ ,\\
H^{(i)}&=\frac{k}{\mu\omega}(E_2\cos\alpha,\ E_1,\ -E_2\sin\alpha)\times\exp(-ikz\cos\alpha-ikx\sin\alpha)\ ,\\
E^{(r)}&=(-E_1\cos\alpha,\ E_2,\ -E_1\sin\alpha)\times\exp(ikz\cos\alpha-ikx\sin\alpha)\ ,\\
H^{(r)}&=\frac{k}{\mu\omega}(E_2\cos\alpha,\ E_1,\ E_2\sin\alpha)\times\exp(ikz\cos\alpha-ikx\sin\alpha)\ ,
\end{aligned}\tag{1}$$

for negative half space.

Here $k=2\pi/\lambda$ is the wave number, the harmonic time dependence $\exp i\omega t$ being omitted throughout. The electromagnetic field is assumed to be derived in terms of the Hertz vector by

$$E=\operatorname{rot}\operatorname{rot}\Pi\ ,\qquad H=\frac{ik^2}{\mu\omega}\operatorname{rot}\Pi\ .$$

$$E=-ik\operatorname{rot}\Pi\ ,\qquad H=\frac{k}{\mu\omega}\operatorname{rot}\operatorname{rot}\Pi\ .\tag{2}$$

The Hertz vectors of the incident and the reflected wave are given by

$$\Pi^{(i)}=\frac{1}{k^2}\left(\frac{E_2}{\cos\alpha}, E_1, 0\right)\exp(-ikz\cos\alpha-ikx\sin\alpha)\,,$$
$$\Pi^{(r)}=\frac{1}{k^2}\left(\frac{E_2}{\cos\alpha}, E_1, 0\right)\exp(ikz\cos\alpha-ikx\sin\alpha)\,, \tag{3}$$

respectively.

The Hertz vector of the diffracted wave is assumed to be given by

$$\Pi=(\Pi_x, \Pi_y, 0)\,,$$

$$\Pi=(\mp\Pi_x, \mp\Pi_y, 0)\,, \quad \begin{pmatrix}\text{upper sign} & z>0\\ \text{lower sign} & z<0\end{pmatrix} \tag{4}$$

If we can make Π satisfy the condition on the plane $z=0$:

(i) Π_x and Π_y are continuous

(ii) for $r>a$, $$\frac{\partial\Pi_x}{\partial z}=\frac{\partial\Pi_y}{\partial z}=0\,, \tag{5}$$

(iii) for $r<a$, $$\left(\frac{\partial\Pi_x}{\partial z}\right)_{z=+0}=-\left(\frac{\partial\Pi_x}{\partial z}\right)_{z=-0}\,,\quad \left(\frac{\partial\Pi_y}{\partial z}\right)_{z=+0}=-\left(\frac{\partial\Pi_y}{\partial z}\right)_{z=-0}\,, \tag{6}$$

then it is found that

the electric and magnetic field of the diffracted wave for $r>a$ (outsides the plate) is continuous.

the tangential component of the resultant electric field and the normal component of the resultant magnetic field are zero for $r>a$, which is the condition for the perfectly conducting screen. The resultant tangential component of the electric field and the resultant normal component of the magnetic field are continuous for $r<a$.

The condition for the conducting plate, that the resultant tangential component of electric field and the resultant normal component of the magnetic field are zero for $r<a$, is expressed by

The other condition for the hole, that the resultant tangential component of the electric field and the resultant normal component of the magnetic field are continuous for $r<a$, is expressed by

$$\frac{\partial}{\partial x}\left(\frac{\partial\Pi_x}{\partial x}+\frac{\partial\Pi_y}{\partial y}\right)+\frac{\partial}{\partial x}\left(\frac{\partial\Pi_x^{(i)}}{\partial x}+\frac{\partial\Pi_y^{(i)}}{\partial y}\right)+k^2\Pi_x+k^2\Pi_x^{(i)}=0\,,$$
$$\frac{\partial}{\partial y}\left(\frac{\partial\Pi_x}{\partial x}+\frac{\partial\Pi_y}{\partial y}\right)+\frac{\partial}{\partial y}\left(\frac{\partial\Pi_x^{(i)}}{\partial x}+\frac{\partial\Pi_y^{(i)}}{\partial y}\right)+k^2\Pi_y+k^2\Pi_y^{(i)}=0\,, \tag{7}$$
$$\frac{\partial\Pi_y}{\partial x}-\frac{\partial\Pi_x}{\partial y}+\frac{\partial\Pi_y^{(i)}}{\partial x}-\frac{\partial\Pi_x^{(i)}}{\partial y}=0\,.$$

for $r<a$, $z=0$.

If we regard Π as the sum of Π_1 and Π_2, so that they satisfy

$$\Pi_x(r,\varphi,z)=\Pi_{1x}(r,\varphi,z)+\Pi_{2x}(r,\varphi,z)\,,\quad \Pi_y(r,\varphi,z)=\Pi_{1y}(r,\varphi,z)+\Pi_{2y}(r,\varphi,z)\,, \tag{8}$$

and for $r<a$, $$\Pi_{1x}(r,\varphi,0)=-\Pi_x^{(i)}(r,\varphi,0)\,,\quad \Pi_{1y}(r,\varphi,0)=-\Pi_y^{(i)}(r,\varphi,0)\,, \tag{9}$$

then (7) is transformed to

$$\frac{\partial}{\partial x}\left(\frac{\partial\Pi_{2x}}{\partial x}+\frac{\partial\Pi_{2y}}{\partial y}\right)+k^2\Pi_{2x}=0\,,\quad \frac{\partial}{\partial y}\left(\frac{\partial\Pi_{2x}}{\partial x}+\frac{\partial\Pi_{2y}}{\partial y}\right)+k^2\Pi_{2y}=0\,,\quad \frac{\partial\Pi_{2x}}{\partial y}=\frac{\partial\Pi_{2y}}{\partial x}\,. \tag{10}$$

From the third equation of (10) Π_{2x} and Π_{2y} are seen to be derived from $U(x,y)$ by

$$\Pi_{2x}(x, y, 0)=\frac{\partial U(x, y)}{\partial x}\ , \qquad \Pi_{2y}(x, y, 0)=\frac{\partial U(x, y)}{\partial y}\ .$$

From the first two equations we see that $U(x, y)$ satisfies

$$\frac{\partial^2 U}{\partial x^2}+\frac{\partial^2 U}{\partial y^2}+k^2U=0\ . \tag{11}$$

We expand the solution of (11)

$$U=\sum_{m=0}^{\infty}(U_m{}^{(1)}\sin m\varphi+U_m{}^{(2)}\cos m\varphi)J_m(kr)\ , \tag{12}$$

where $U_m{}^{(1)}$ and $U_m{}^{(2)}$ are unknown coefficients to be determined. Therefore, for $r<a$, $z=0$,

$$\begin{aligned}\Pi_{2x}&=\frac{\partial U}{\partial x}=\frac{\partial U}{\partial r}\cos\varphi-\frac{1}{r}\frac{\partial U}{\partial \varphi}\sin\varphi\\ &=\frac{k}{2}\sum_{m=0}^{\infty}\{(U^{(1)}_{m+1}-U^{(1)}_{m-1})\sin m\varphi+(U^{(2)}_{m+1}-U^{(2)}_{m-1})\cos m\varphi\}J_m(kr)\ ,\\ \Pi_{2y}&=\frac{\partial U}{\partial y}=\frac{\partial U}{\partial r}\sin m\varphi+\frac{1}{r}\frac{\partial U}{\partial \varphi}\cos\varphi\\ &=\frac{k}{2}\sum_{m=0}^{\infty}\{(U^{(1)}_{m+1}+U^{(1)}_{m-1})\cos m\varphi-(U^{(2)}_{m+1}+U^{(2)}_{m-1})\sin m\varphi\}J_m(kr)\ ,\end{aligned} \tag{13}$$

where
$$U_0{}^{(1)}=U_{-1}{}^{(1)}=0\ , \quad U_{-1}{}^{(2)}=0\ .$$

We can put the solution of the wave equation which satisfies (5) and (6) as

$$\begin{matrix}\Pi_{1x}\\ \Pi_{1y}\end{matrix}=\begin{matrix}\dfrac{E_2}{k^2\cos\alpha}\\ \dfrac{E_1}{k^2}\end{matrix}\sum_{m=0}^{\infty}\sum_{n=0}^{\infty}A_n{}^mS_n{}^m(r, z)\cos m\varphi\ , \tag{14}$$

$$\begin{matrix}\Pi_{2x}\\ \Pi_{2y}\end{matrix}=\frac{k}{2}\sum_{m=0}^{\infty}\sum_{n=0}^{\infty}\left\{\left(U^{(1)}_{m+1}\mp U^{(1)}_{m-1}\right)\begin{matrix}\sin m\varphi\\ \cos m\varphi\end{matrix}\pm\left(U^{(z)}_{m+1}\mp U^{(2)}_{m-1}\right)\begin{matrix}\cos m\varphi\\ \sin m\varphi\end{matrix}\right\}B_n{}^mS_n{}^m(r, z)\ , \tag{15}$$

where

$$S_n{}^m(r, z)=\int_0^{\infty}\frac{\sqrt{\xi}\,J_m\left(\dfrac{r}{a}\xi\right)J_{m+2n+\frac{1}{2}}(\xi)}{\sqrt{\xi^2-(ka)^2}}\exp\left(\mp\sqrt{\xi^2-(ka)^2}\,\frac{z}{a}\right)d\xi\ . \tag{16}$$

By the Weber-Schafheitlin's integral

$$\begin{aligned}\frac{\partial S_n{}^m}{\partial z}(r, 0)&=\mp\int_0^{\infty}\sqrt{\xi}\,J_m\left(\frac{r}{a}\xi\right)J_{m+2n+\frac{1}{2}}(\xi)d\xi\\ &=\mp\frac{\sqrt{2}\left(\dfrac{r}{a}\right)^m\Gamma(m+n+1)}{\Gamma\left(n+\dfrac{1}{2}\right)\Gamma(m+1)}F\left\{m+n+1,\ -n+\frac{1}{2};\ m+1;\ \left(\frac{r}{a}\right)^2\right\} && (r<a)\\ &=0\ . && (r>a)\end{aligned} \tag{17}$$

(5) is seen to be satisfied. It is evident that (6) is satisfied.

From (9) for $r<a$,

$$\begin{aligned}\sum_{m=0}^{\infty}\sum_{n=0}^{\infty}A_n{}^mS_n{}^m(r, 0)\cos m\varphi&=-\exp(-ikx\sin\alpha)\\ &=-\sum_{m=0}^{\infty}(2)(-i)^mJ_m(kr\sin\alpha)\cos m\varphi\ ,\end{aligned}$$

where

$$\begin{aligned}(2)&=1 \quad \text{for} \quad m=0\\ &=2 \quad \text{for} \quad m\geqq 1\,.\end{aligned}$$

Hence

$$\sum_{n=0}^{\infty} A_n{}^m S_n{}^m(r,0)=-(2)(-i)^m J_m(kr\sin\alpha)\,. \tag{18}$$

And from (13)

$$\sum_{n=0}^{\infty} B_n{}^m S_n{}^m(r,0)=J_m(kr)\,. \tag{19}$$

Now we expand the right hand side of (18) and (19) for $r<a$ by the hypergeometric polynomial

$$\genfrac{}{}{0pt}{}{-(2)(-i)^m J_m(kr\sin\alpha)}{J_m(kr)}=x^{m/2}\sum_{n=0}^{\infty}\genfrac{}{}{0pt}{}{a_n{}^m}{b_n{}^m}u_n{}^m(x)\,, \tag{20}$$

where

$$\begin{aligned} u_n{}^m(x)&=x^{-m/2}\int_0^{\infty}\frac{J_m(\sqrt{x}\,\xi)J_{m+2n+1/2}(\xi)}{\sqrt{\xi}}d\xi\\ &=\frac{\Gamma(m+n+1/2)}{\sqrt{2}\,n!\,\Gamma(m+1)}F(m+n+1/2,\,-n;\,m+1;\,x)\\ &=\frac{\Gamma(m+n+1/2)}{\sqrt{2}\,n!\,\Gamma(n+m+1)}x^{-m}(1-x)^{1/2}\frac{d^n}{dx^n}\{x^{m+n}(1-x)^{n-1/2}\}\,,\end{aligned} \tag{21}$$

$$x=\left(\frac{r}{a}\right)^2,$$

then

$$\begin{aligned} a_n{}^m&=-\sqrt{\frac{2}{\pi}}(2)(-i)^m(2m+4n+1)\,j_{m+2n}(ka\sin\alpha)\,,\\ b_n{}^m&=\quad\sqrt{\frac{2}{\pi}}(2m+4n+1)\,j_{m+2n}(ka)\,,\end{aligned} \tag{22)(A$_1$}$$

where

$$\sqrt{\frac{2}{\pi}}\,j_{m+2n}(x)=\frac{1}{\sqrt{x}}J_{m+2n+1/2}(x)\,.$$

Next we expand $S_n{}^m(r,0)$ in terms of $u_\nu{}^m(x)$ by

$$S_n{}^m(r,0)=\int_0^{\infty}\frac{\sqrt{\xi}\,J_m\left(\frac{r}{a}\xi\right)J_{m+2n+1/2}(\xi)}{\sqrt{\xi^2-(ka)^2}}d\xi=x^{m/2}\sum_{\nu=0}^{\infty}G_{n,\nu}{}^m u_\nu{}^m(x)\,, \tag{23}$$

then

$$G_{n,\nu}{}^m=(2m+4\nu+1)\int_0^{\infty}\frac{J_{m+2n+1/2}(\xi)J_{m+2\nu+1/2}(\xi)}{\sqrt{\xi^2-(ka)^2}}d\xi\,, \tag{24)(A$_1$}$$

Hence

$$\sum_{n=0}^{\infty}\genfrac{}{}{0pt}{}{A_n{}^m}{B_n{}^m}x^{m/2}\sum_{\nu=0}^{\infty}G_{n\nu}{}^m u_\nu{}^m(x)=\sum_{n=0}^{\infty}\genfrac{}{}{0pt}{}{a_n{}^m}{b_n{}^m}u_n{}^m(x)\,. \tag{25}$$

Using the orthogonality of $u_\nu{}^m(x)$, we have

$$\sum_{\nu=0}^{\infty}G_{\nu u}{}^m\genfrac{}{}{0pt}{}{A_\nu{}^m}{B_\nu{}^m}=\genfrac{}{}{0pt}{}{a_n{}^m}{b_n{}^m}\,. \tag{26}$$

The integral (24) will be evaluated in the next section. Denoting the inverse matrix of $[G_{n\nu}{}^m]$ by $[X_{n\nu}{}^m]$, obtained from

$$\sum_{\nu=0}^{\infty}G_{\nu n}{}^m X_{\nu s}{}^m=\delta_{sn}\,, \tag{27}$$

the unknown coefficients $A_n{}^m$ and $B_n{}^m$ are determined from

$$\genfrac{}{}{0pt}{}{A_n{}^m}{B_n{}^m}=\sum_{s=0}^{\infty}\genfrac{}{}{0pt}{}{a_s{}^m}{b_s{}^m}X_{ns}{}^m\,. \tag{28}$$

§ 3. Calculation of $G_{n\nu}{}^m$ and $X_{n\nu}{}^m$

We shall evaluate the integral $G_{n\nu}{}^m$.

Let
$$p=m+n+\nu\,,\quad q=n-\nu\,,$$
then
$$G_{n,\nu}{}^m=(2p-2q+1)\{g_1(p,q)-ig_2(p,g)\}\,, \tag{29}$$
where
$$g_1(p,q)=\int_\gamma^\infty \frac{J_{p+q+1/2}(\xi)J_{p-q+1/2}(\xi)}{\sqrt{\xi^2-\gamma^2}}d\xi\,,$$
$$g_2(p,q)=\int_0^\gamma \frac{J_{p+q+1/2}(\xi)J_{p-q+1/2}(\xi)}{\sqrt{\gamma^2-\xi^2}}d\xi\,. \tag{30}$$

Now we evaluate the real part $g_1(p,q)$. The integral representation of the product of the Bessel functions is substituted into the integrand, and the integral representation of Γ-function is used, then

$$\begin{aligned}g_1(p,q)&=\frac{2}{\pi}\int_0^{\pi/2}\cos 2q\theta\, d\theta\int_\gamma^\infty\frac{J_{2p+1}(2\xi\cos\theta)}{\sqrt{\xi^2-\gamma^2}}d\xi\\&=\frac{1}{i\pi^2}\int_0^{\pi/2}\cos(2q\theta)(\cos\theta)^{2p+1}d\theta\int_C\frac{\Gamma(-s)\cos^{2s}\theta}{\Gamma(2p+s+2)}ds\int_\gamma^\infty\frac{\xi^{2p+2s+1}}{\sqrt{\xi^2-\gamma^2}}d\xi\,.\end{aligned}$$

After the integration over ξ and θ are performed,

$$g_1(p,q)=\frac{1}{i4\sqrt{\pi}}\int_C\frac{(\gamma/2)^{2p+2s+1}\Gamma(-p-s-1/2)\Gamma(-s)\Gamma(2p+2s+2)}{\Gamma(2p+s+2)\Gamma(-p-s)\Gamma(p+q+s+3/2)\Gamma(p-q+s+3/2)}ds\,,$$

where C is an integration path along the circumference of the right half plane. The singularities of the integrand are only simple poles $\mu=0,1,2,\cdots$ $(-p-s-1/2=-\mu)$ As the residue of $\Gamma(-s)$ at $s=-\mu$ is $-(-)^\mu/\mu!$ we have

$$g_1(p,q)=\frac{\sqrt{\pi}}{2}\sum_{\mu=0}^\infty\frac{(-)^\mu\Gamma(2\mu+1)\Gamma(p+1/2-\mu)(\gamma/2)^{2\mu}}{\mu!\Gamma(1/2-\mu)\Gamma(p+\mu+3/2)\Gamma(q+\mu+1)\Gamma(\mu-q+1)}\,. \tag{31}$$

Next, we evaluate $g_2(p,q)$. Term by term integration of the series representation of the product of the Bessel functions gives

$$\begin{aligned}g_2(p,q)&=\sum_{\mu=0}^\infty\frac{(-)^\mu}{\mu!}\frac{\Gamma(2p+2\mu+2)(\gamma/2)^{2p+2\mu+1}}{\Gamma(2p+\mu+2)\Gamma(p+q+\mu+3/2)\Gamma(p-q+\mu+3/2)}\int_0^{\pi/2}(\sin\theta)^{2p+2\mu+1}d\theta\\&=\frac{\sqrt{\pi}}{2}\left(\frac{\gamma}{2}\right)^{2p+1}\sum_{\mu=0}^\infty\frac{(-)^\mu}{\mu!}\frac{\Gamma(2p+2\mu+2)\Gamma(p+\mu+1)(\gamma/2)^{2\mu}}{\Gamma(2p+\mu+2)\Gamma(p+q+\mu+3/2)\Gamma(p-q+\mu+3/2)\Gamma(p+\mu+3/2)}\,.\end{aligned} \tag{32}$$

The series expansion of $X_{n\nu}{}^m=(2m+4n+1)/(2m+4\nu+1)\cdot X_{\nu n}{}^m$ as a power series of $\beta=ka/2=\gamma/2$ is as follows.

$$\begin{aligned}X_{00}{}^0=1&+i\frac{4}{\pi}\beta-\left(\frac{16}{\pi^2}-\frac{4}{3}\right)\beta^2+i64\left(\frac{1}{9\pi}-\frac{1}{\pi^3}\right)\beta^3+0.092228\beta^4\\&-i0.015258\beta^5+0.018310\beta^6-i0.021204\beta^7+\cdots\end{aligned}$$

$$X_{10}{}^0=-\frac{2}{3}\beta^2+i\frac{8}{9\pi}\beta^3+\left(\frac{16}{21}-\frac{32}{9\pi^2}\right)\beta^4+i0.080250\beta^5+0.076337\beta^6-i0.037684\beta^7+\cdots$$

$$X_{20}{}^0=-\frac{16}{840}\beta^4+i0.014551\beta^5+0.0022519\beta^6+i0.0046310\beta^7+\cdots$$

$$X_{30}{}^0=-0.010785\beta^3-i0.012892\beta^7+\cdots$$

$$X_{01}{}^{0}=-\frac{4}{30}\beta^2+i\frac{8}{45\pi}\beta^3+0.0041396\beta^4+i0.016050\beta^5+\cdots$$

$$X_{11}{}^{0}=1-\frac{4}{21}\beta^2-\frac{16}{252}\beta^4+i0.052816\beta^5+\cdots$$

$$X_{21}{}^{0}=-\frac{4}{70}\beta^2-\frac{16}{231}\beta^4+\cdots$$

$$X_{31}{}^{0}=-0.00057720\beta^4+\cdots$$

$$X_{02}{}^{0}=-0.0021164\beta^4+i0.0016168\beta^5+\cdots$$

$$X_{12}{}^{0}=-0.031746\beta^2-0.0038480\beta^4+\cdots$$

$$X_{22}{}^{0}=\quad 1-\frac{4}{77}\beta^2+\cdots$$

$$X_{32}{}^{0}=\quad -\frac{4}{148}\beta^3+\cdots$$

$$X_{03}{}^{0}=0.010785\beta^6-i0.012892\beta^7+\cdots$$

$$X_{00}{}^{2}=1-\frac{4}{21}\beta^2-\frac{16}{105}\beta^4+i0.24144\beta^5+\cdots$$

$$X_{10}{}^{2}=-\frac{4}{70}\beta^2-\frac{16}{231}\beta^4+\cdots$$

$$X_{20}{}^{0}=-0.0005772\beta^4+\cdots \qquad \text{etc.}$$

§ 4. Edge Condition

The unknown coefficients $U_m{}^{(1)}$ and $U_m{}^{(2)}$ are determined from the edge condition, that there is no energy source at the edge and no energy radiation from the edge.

We require that the energy flow W from the surface of the torus whose center line is at the edge should tend to zero when the radius of the torus $\mathcal{E}$ tends to zero. Only the diffracted field is concerned with the energy radiation.

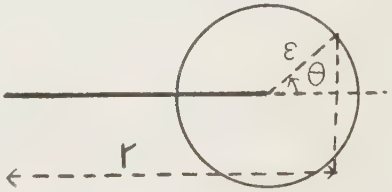

Fig. 2.

$$W=a\int_0^{2\pi}d\varphi\int_{-\pi}^{\pi}S_{\varepsilon}\mathcal{E}d\theta\ .$$

Therefore

$$S_{\varepsilon}=-\frac{1}{2}\Re(E_\theta\tilde{H}_\varphi-E_\varphi\tilde{H}_\theta)$$

$$\sim(\text{rot rot }\Pi)_\theta(\text{rot }\tilde{\Pi})_\varphi-(\text{rot rot }\Pi)_\varphi(\text{rot }\tilde{\Pi})_\theta=\mathrm{O}(\mathcal{E}^{-1+\kappa})\qquad(\kappa>0)$$

is sufficient for $W\to0$ when $\mathcal{E}\to0$. Here $\mathcal{E}$ and θ are shown in Fig. 2. It is evident that

$$\begin{aligned}(\text{rot rot }\Pi)_\theta&=-(\text{rot rot }\Pi)_r\sin\theta+(\text{rot rot }\Pi)_z\cos\theta\ ,\\(\text{rot }\Pi)_\theta&=-\quad(\text{rot }\Pi)_r\sin\theta+\quad(\text{rot }\Pi)_z\cos\theta\ ,\end{aligned}\tag{33}$$

when $\mathcal{E}\sim0$,

where

$$\begin{aligned}(\text{rot rot }\Pi)_r=&\frac{\partial^2\Pi_x}{\partial r^2}\cos\varphi+\frac{1}{r^2}\frac{\partial\Pi_x}{\partial\varphi}\sin\varphi-\frac{1}{r}\frac{\partial^2\Pi_x}{\partial r\partial\varphi}\sin\varphi+k^2\Pi_x\cos\varphi\\&+\frac{\partial^2\Pi_y}{\partial r^2}\sin\varphi-\frac{1}{r^2}\frac{\partial\Pi_y}{\partial\varphi}\cos\varphi+\frac{1}{r}\frac{\partial^2\Pi_y}{\partial r\partial\varphi}\cos\varphi+k^2\Pi_y\sin\varphi\ ,\end{aligned}$$

$$\begin{aligned}(\mathrm{rot\,rot}\,\Pi)_\varphi=&\frac{1}{r}\frac{\partial^2\Pi_x}{\partial r\partial\varphi}\cos\varphi-\frac{1}{r}\frac{\partial\Pi_x}{\partial r}\sin\varphi-\frac{1}{r^2}\frac{\partial\Pi_x}{\partial\varphi}\cos\varphi-\frac{1}{r^2}\frac{\partial^2\Pi_x}{\partial\varphi^2}\sin\varphi-k^2\Pi_x\sin\varphi\\&+\frac{1}{r}\frac{\partial^2\Pi_y}{\partial r\partial\varphi}\sin\varphi+\frac{1}{r}\frac{\partial\Pi_y}{\partial r}\cos\varphi-\frac{1}{r^2}\frac{\partial\Pi_y}{\partial\varphi}\sin\varphi+\frac{1}{r^2}\frac{\partial^2\Pi_y}{\partial\varphi^2}\cos\varphi+k^2\Pi_y\cos\varphi\ ,\end{aligned}$$

$$(\mathrm{rot\,rot}\,\Pi)_z=\frac{\partial^2\Pi_x}{\partial r\partial z}\cos\varphi-\frac{1}{r}\frac{\partial^2\Pi_x}{\partial\varphi\partial z}\sin\varphi+\frac{\partial^2\Pi_y}{\partial r\partial z}\sin\varphi+\frac{1}{r}\frac{\partial^2\Pi_y}{\partial\varphi\partial z}\cos\varphi\ , \tag{34}$$

$$\begin{aligned}(\mathrm{rot}\,\Pi)_r&=\frac{\partial\Pi_x}{\partial z}\sin\varphi-\frac{\partial\Pi_y}{\partial z}\cos\varphi\ ,\\(\mathrm{rot}\,\Pi)_\varphi&=\frac{\partial\Pi_x}{\partial z}\cos\varphi+\frac{\partial\Pi_y}{\partial z}\sin\varphi\ ,\\(\mathrm{rot}\,\Pi)_z&=-\left(\frac{\partial\Pi_x}{\partial r}\sin\varphi+\frac{1}{r}\frac{\partial\Pi_x}{\partial\varphi}\cos\varphi\right)+\left(\frac{\partial\Pi_y}{\partial r}\cos\varphi-\frac{1}{r}\frac{\partial\Pi_y}{\partial\varphi}\sin\varphi\right).\end{aligned}\tag{35}$$

In the neighbourhood of the edge

$$\begin{aligned}\frac{\partial S_n{}^m}{\partial z}(r,z)&=(-)^n\frac{1}{a\sqrt{\pi}}\varepsilon^{-1/2}\sin\frac{\theta}{2}+O(\varepsilon^0)\ ,\\\frac{\partial S_n{}^m}{\partial r}(r,z)&=(-)^n\frac{1}{a\sqrt{\pi}}\varepsilon^{-1/2}\cos\frac{\theta}{2}+O(\varepsilon^0)\ ,\\\frac{\partial^2S_n{}^m}{\partial r^2}(r,z)&=-(-)^n\frac{1}{2a^2\sqrt{\pi}}\varepsilon^{-3/2}\cos\frac{3}{2}\theta+O(\varepsilon^{-1/2})\ ,\\\frac{\partial^2S_n{}^m}{\partial r\partial z}(r,z)&=-(-)^n\frac{1}{2a^2\sqrt{\pi}}\varepsilon^{-3/2}\sin\frac{3}{2}\theta+O(\varepsilon^{-1/2})\ .\end{aligned}\tag{A.II}$$

We put

$$\begin{aligned}\begin{matrix}F_x(\varphi)\\F_y(\varphi)\end{matrix}=\frac{1}{\sqrt{\pi}}\sum_{m=0}^{\infty}\sum_{n=0}^{\infty}(-)^n\Bigg\{&\frac{k}{2}(U^{(1)}_{m+1}\mp U^{(1)}_{m-1})B_n{}^m\begin{matrix}\sin m\varphi\\\cos m\varphi\end{matrix}\pm\frac{k}{2}(U^{(2)}_{m+1}\mp U^{(2)}_{m-1})B_n{}^m\begin{matrix}\cos m\varphi\\\sin m\varphi\end{matrix}\\&+\begin{matrix}E_2\\k^2\cos\alpha\\E_1\\k^2\end{matrix}A_n{}^m\cos m\varphi\Bigg\}\ ,\end{aligned}$$

then

$$\begin{aligned}(\mathrm{rot\,rot}\,\Pi)_\theta&=-\frac{1}{2a^2}\varepsilon^{-3/2}\sin\frac{\theta}{2}(F_x\cos\varphi+F_y\sin\varphi)+O(\varepsilon^{-1/2})\ ,\\(\mathrm{rot}\,\Pi)_\theta&=-\frac{1}{a}\varepsilon^{-1/2}\cos\frac{\theta}{2}(F_x\sin\varphi-F_y\cos\varphi)+O(\varepsilon^0)\ ,\\(\mathrm{rot\,rot}\,\Pi)_\varphi&=\frac{1}{a^2}\varepsilon^{-1/2}\cos\frac{\theta}{2}\frac{\partial}{\partial\varphi}(F_x\cos\varphi+F_y\sin\varphi)+O(\varepsilon^0)\ ,\\(\mathrm{rot}\,\Pi)_\varphi&=\frac{1}{a}\varepsilon^{-1/2}\sin\frac{\theta}{2}\cdot(F_x\cos\varphi+F_y\sin\varphi)+O(\varepsilon^0)\ .\end{aligned}$$

Hence if we can make

$$F_x(\varphi)\cos\varphi+F_y(\varphi)\sin\varphi=0\ , \tag{36}$$

the term of order $\varepsilon^{-3/2}$ vanishes and this is sufficient for the edge condition. (36) is transformed to

$$\begin{aligned}&\sum_{m=0}^{\infty}\sin(m+1)\varphi\sum_{n=0}^{\infty}(-)^n\left(\frac{E_1}{2k^2}A_n{}^m+\frac{k}{2}U^{(1)}_{m+1}B_n{}^m\right)\\&\qquad-\sum_{m=0}^{\infty}\sin(m-1)\varphi\sum_{n=0}^{\infty}(-)^n\left(\frac{E_1}{2k^2}A_n{}^m+\frac{k}{2}U^{(1)}_{m-1}B_n{}^m\right)\end{aligned}$$

$$+\sum_{m=0}^{\infty}\cos(m+1)\varphi\sum_{n=0}^{\infty}(-)^n\left(\frac{E_2}{2k^2\cos\alpha}A_n{}^m+\frac{k}{2}U_{m+1}^{(2)}B_n{}^m\right)$$
$$-\sum_{m=0}^{\infty}\cos(m-1)\varphi\sum_{n=0}^{\infty}(-)^n\left(-\frac{E_2}{2k^2\cos\alpha}A_n{}^m+\frac{k}{2}U_{m-1}^{(2)}B_n{}^m\right)=0\ .$$

Moreover

$$\sum_{m=2}^{\infty}\sin m\varphi\sum_{n=0}^{\infty}(-)^n\{E_1(A_n{}^{m-1}-A_n{}^{m+1})+k^3(B_n{}^{m-1}-B_n{}^{m+1})U_m{}^{(1)}\}$$
$$+\sum_{m=2}^{\infty}\cos m\varphi\sum_{n=0}^{\infty}(-)^n\left\{\frac{E_2}{\cos\alpha}(A_n{}^{m-1}+A_n{}^{m+1})+k^3(B_n{}^{m-1}-B_n{}^{m+1})U_m{}^{(2)}\right\}$$
$$+\quad\sin\varphi\quad\sum_{n=0}^{\infty}(-)^n\{E_1(2A_n{}^0-A_n{}^2)+k^3(B_n{}^0-B_n{}^2)U_1{}^{(1)}\}$$
$$+\quad\cos\varphi\quad\sum_{n=0}^{\infty}(-)^n\left\{\frac{E_2}{\cos\alpha}(2A_n{}^0+A_n{}^2)+k^3(B_n{}^0-B_n{}^2)U_1{}^{(2)}\right\}$$
$$+\sum_{n=0}^{\infty}(-)^n\left(\frac{E_2}{\cos\alpha}A_n{}^1-k^3B_n{}^1U_0{}^{(2)}\right\}\quad=0\ .$$

Therefore

$$\begin{matrix}U_m{}^{(1)}\\U_m{}^{(2)}\end{matrix}=-\begin{matrix}\dfrac{E_1}{k^3}\\[2ex]\dfrac{E_2}{k^3\cos\alpha}\end{matrix}\ \frac{A_n{}^{m-1}\mp A_n{}^{m+1}}{B_n{}^{m-1}-B_n{}^{m+1}}\qquad(m=2,3,4,\cdots)\ ,$$
$$\begin{matrix}U_1{}^{(1)}\\U_1{}^{(2)}\end{matrix}=-\begin{matrix}\dfrac{E_1}{k^3}\\[2ex]\dfrac{E_2}{k^3\cos\alpha}\end{matrix}\ \frac{2A_n{}^0-A_n{}^2}{B_n{}^0-B_n{}^2}\ ,\qquad U_0{}^{(2)}=\frac{E_2}{k^3\cos\alpha}\,\frac{A_n{}^1}{B_n{}^1}\ . \tag{37}$$

Thus the unkown coefficients $U_m{}^{(1)}$ and $U_m{}^{(2)}$ have been determined from the edge condition.

§5. Diffracted Field at Large distances

From (14), (15), (37) the Hertz vector of the diffracted field is determined as

$$\Pi_x=\sum_{m=0}^{\infty}\sum_{n=0}^{\infty}\{{}_2C_n{}^m\cos m\varphi+{}_1C_n{}^m\sin m\varphi\}S_n{}^m(r,z)\ ,$$
$$\Pi_y=\sum_{m=0}^{\infty}\sum_{n=0}^{\infty}\{{}_1D_n{}^m\cos m\varphi+{}_2D_n{}^m\sin m\varphi\}S_n{}^m(r,z)\ , \tag{38}$$

where

$${}_2C_n{}^m=\frac{k}{2}(U_{m+1}^{(2)}-U_{m-1}^{(2)})\,B_n{}^m+\frac{E_2}{k^2\cos\alpha}A_n{}^m\ ,$$
$${}_1C_n{}^m=\frac{k}{2}(U_{m+1}^{(1)}-U_{m-1}^{(1)})B_n{}^m\ ,$$
$${}_1D_n{}^m=\frac{k}{2}(U_{m+1}^{(1)}+U_{m-1}^{(1)})\,B_n{}^m+\frac{E_1}{k^2}A_n{}^m\ , \tag{39}$$
$${}_2D_n{}^m=-\frac{k}{2}(U_{m+1}^{(2)}+U_{m-1}^{(2)})B_n{}^m\ .$$

We use the Kirchhoff solution of the wave equation

$$\Pi=\frac{1}{4\pi}\int\left\{\frac{e^{-ikR'}}{R'}\cdot\frac{\partial\Pi}{\partial n}-\Pi\frac{\partial}{\partial n}\left(\frac{e^{-ikR'}}{R'}\right)\right\}dS \tag{40}$$

to obtain the value of Π at a distant point. Here R' is the distance between the point $Q(r,\varphi_0)$ on the circle and P at the distant point. The integration is performed on the both

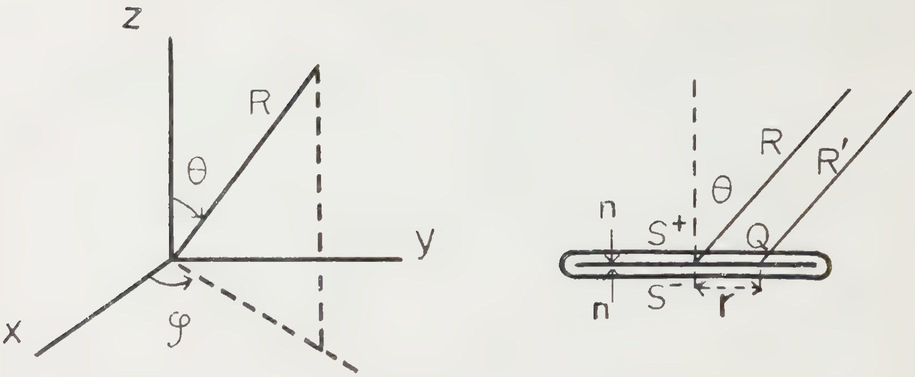

Fig. 3.

sides of S^+ and S^- enclosing S (Fig. 3).

Evidently

$$\left(\frac{\partial \Pi}{\partial n}\right)_{S^+}=-\left(\frac{\partial \Pi}{\partial z}\right)_{S^+}=\left(\frac{\partial \Pi}{\partial z}\right)_{S^-}=\left(\frac{\partial \Pi}{\partial n}\right)_{S^-}, \quad \left(\frac{\partial}{\partial n}\cdot\frac{e^{-ikR'}}{R'}\right)_{S^+}=-\left(\frac{\partial}{\partial n}\frac{e^{-ikR'}}{R'}\right)_{S^-}.$$

$$R'\doteqdot R-r\sin\theta\cos(\varphi-\varphi_0)$$

($PQ=R'$ is sufficiently large).

Therefore

$$\begin{matrix}\Pi_x\\ \Pi_y\end{matrix}=\frac{1}{2\pi a}\frac{e^{-ikR}}{R}\sum_m\sum_n\int_0^a rdr\int_0^\infty\sqrt{\xi}\, J_n\left(\frac{r}{a}\xi\right)J_{m+2n+1/2}(\xi)d\xi\int_0^{2\pi}\exp\{ikr\sin\theta\cos(\varphi-\varphi_0)\}$$
$$\times\begin{Bmatrix}{}_2C_n^m\cos m\varphi_0+{}_1C_n^m\sin m\varphi_0\\ {}_1D_n^m\cos m\varphi_0+{}_2D_n^m\sin m\varphi_9\end{Bmatrix}d\varphi_0 .$$

On the other hand

$$\int_{-\pi}^{\pi}\exp\{ikr\sin\theta\cos(\varphi-\varphi_0)\}\begin{matrix}\sin m\varphi_0\\ \cos m\varphi_0\end{matrix}d\varphi_0=2\pi(i)^m J_m(kr\sin\theta)\begin{matrix}\sin m\varphi\\ \cos m\varphi\end{matrix},$$

$$\int_0^a rdr\, J_m(kr\sin\theta)\int_0^\infty\sqrt{\xi}\, J_m\left(\frac{r}{a}\xi\right)J_{m+2n+1/2}(\xi)d\xi$$
$$=a^2\frac{J_{m+2n+1/2}(ka\sin\theta)}{(ka\sin\theta)^{1/2}}=\sqrt{\frac{2}{\pi}}a^2 j_{m+2n}(ka\sin\theta) .$$

Therefore

$$\begin{matrix}\Pi_x\\ \Pi_y\end{matrix}=\sqrt{\frac{2}{\pi}}a\frac{e^{-ikR}}{R}\sum_{m=0}^{\infty}\sum_{n=0}^{\infty}(i)^m\begin{matrix}{}_2C_n^m\cos m\varphi+{}_1C_n^m\sin m\varphi\\ {}_1D_n^m\cos m\varphi+{}_2D_n^m\sin m\varphi\end{matrix}\; j_{m+2n}(ka\sin\theta) , \tag{41}$$

If we neglect the term smaller than $1/R^2$, the electromagnetic field of the diffracted wave is given by

$$\begin{array}{l|l} E_R=0,\quad E_\theta=k^2\Pi_\theta,\quad E_\varphi=k^2\Pi_\varphi, & E_R=0,\quad E_\theta=\mp k^2\Pi_\varphi,\quad E_\varphi=\pm k^2\Pi_\theta,\\ H_R=0,\quad H_\theta=-\dfrac{k^3}{\mu\omega}\Pi_\varphi,\quad H_\varphi=\dfrac{k^3}{\mu\omega}\Pi_\theta , & H_R=0,\quad H_\theta=\mp\dfrac{k^3}{\mu\omega}\Pi_\theta,\quad H_\varphi=\mp\dfrac{k^3}{\mu\omega}\Pi_\varphi, \end{array} \tag{42}$$

$$\Pi_\theta=\Pi_x\cos\theta\cos\varphi+\Pi_y\cos\theta\sin\varphi , \qquad \Pi_\varphi=-\Pi_x\sin\varphi+\Pi_y\cos\varphi . \tag{43}$$

The energy flow from the surface of the sphere of radius R is

$$S=\Re\frac{1}{2}(E_\theta\tilde{H}_\varphi-E_\varphi\tilde{H}_\theta)$$

$$=\frac{1}{2}\frac{k^5}{\mu\omega}\{|\Pi_\theta|^2+|\Pi_\varphi|^2\}\ . \tag{44}$$

The total scattered energy is

$$W=\int_0^{2\pi}d\varphi\int_0^{\pi/2}SR^2\sin\theta d\theta=\frac{1}{2}\frac{k^5}{\mu\omega}\int_0^{2\pi}d\varphi\int_0^{\pi/2}\sin\theta d\theta R^2\{|\Pi_\theta|^2+|\Pi_\varphi|^2\}\ . \tag{45}$$

When we confine ourselves to the case of normal incidence and linear polarization, $\alpha=0$, $E_2=0$,

$$a_0^0=-\sqrt{\frac{2}{\pi}}\ ,\qquad \text{other}\quad a_n^m=0\ ,$$

$$A_n^0=a_0^0X_{n0}^0\ ,\qquad \text{other}\quad A_n^m=0\ .$$

$$U_1^{(1)}=-\frac{E_1}{k^3}\frac{2\sum\limits_{n=0}^{\infty}(-)^nA_n^0}{\sum\limits_{n=0}^{\infty}(-)^n(B_n^0-B_n^2)}\equiv\frac{2E_1}{k^3}V(k), \tag{46}$$

other $U_m^{(1)}$, $U_m^{(2)}=0$.

Using the series expansion of $X_{n\nu}^m$ in $\beta=ka/2$, $V(k)$ is expressed by

$$V=1+\frac{10}{3}\beta^2-i\frac{32}{3\pi}\beta^3+\frac{22}{5}\beta^4-i\frac{1088}{27\pi}\beta^5+\cdots \tag{47}$$

Only the next terms are not zero in (39)

$$\begin{aligned}
{}_1D_n^0&=\frac{E_1}{k^2}(VB_n^0+A_n^0)\equiv\sqrt{\frac{2}{\pi}}\frac{E_1}{k^2}A_n^0\ ,\\
{}_1D_n^2&=-{}_1C_n^2=\frac{E_1}{k^2}VB_n^2\equiv\sqrt{\frac{2}{\pi}}\frac{E_1}{k^2}A_n^2\ ,\\
{}_1C_n^0&=\frac{E_1}{k^2}VB_n^0\ .
\end{aligned} \tag{48}$$

From (28) and (47)

$$\begin{aligned}
A_0^0&=\frac{8}{3}\beta^2+\frac{256}{45}\beta^4-i\frac{512}{27\pi}\beta^5+\cdots\\
A_1^0&=\frac{4}{3}\beta^2+2.03745\beta^4-\cdots\\
A_2^0&=\frac{16}{210}\beta^4+\cdots\\
A_0^2&=\frac{4}{3}\beta^2+3.8095\beta^4+\cdots\\
A_1^2&=\frac{16}{210}\beta^4+\cdots\\
A_2^2&=0.002309\beta^4+\cdots
\end{aligned} \tag{49}$$

From (43)

$$\begin{aligned}
\Pi_\theta&=\frac{2}{\pi}\frac{E_1}{k^2}\frac{e^{-ikR}}{R}a\cos\theta\sin\varphi\sum_{n=0}^{\infty}(A_n^0j_{2n}(ka\sin\theta)+A_n^2j_{2n+2}(ka\sin\theta))\ ,\\
\Pi_\varphi&=\frac{2}{\pi}\frac{E_1}{k^2}\frac{e^{-ikR}}{R}a\cos\varphi\sum_{n=0}^{\infty}(A_n^0j_{2n}(ka\sin\theta)-A_n^2j_{2n+2}(ka\sin\theta))\ .
\end{aligned} \tag{50}$$

Substituting (49) into (50), we have

$$\Pi_\theta = \frac{2}{\pi}\frac{E_1}{k^2}\frac{e^{-ikR}}{R}\, a\cos\theta\sin\varphi\,\frac{8}{3}\beta^2\left[1+\left(\frac{32}{15}-\frac{2}{5}\sin^2\theta\right)\beta^2 - i\frac{64}{9}\beta^3+O(\beta^4)\right], \tag{51}$$
$$\Pi_\varphi = \frac{2}{\pi}\frac{E_1}{k^2}\frac{e^{-ikR}}{R}\, a\cos\varphi\,\frac{8}{3}\beta^2\left[1+\left(\frac{32}{15}-\frac{2}{3}\sin^2\theta\right)\beta^2 - i\frac{64}{9}\beta^3+O(\beta^4)\right].$$

The energy flow in (44) is expressed by

$$S = \frac{2kE_1^2}{\pi^2\mu\omega}\frac{a^2}{R^2}\{I_1(k,\theta)\sin^2\varphi + I_2(k,\theta)\cos^2\varphi\}\,, \tag{52}$$

where

$$\begin{aligned} I_1(k,\theta) &= \cos^2\theta\left|\sum_{n=0}^{\infty}(A_n^0 j_{2n}(ka\sin\theta)+A_n^2 j_{2n+2}(ka\sin\theta))\right|^2 \\ &= \cos^2\theta\cdot\frac{64}{9}\beta^4\left[1+\left(\frac{64}{15}-\frac{4}{5}\sin^2\theta\right)\beta^2+O(\beta^4)\right], \\ I_2(k,\theta) &= \left|\sum_{n=0}^{\infty}(A_n^0 j_{2n}(ka\sin\theta)-A_n^2 j_{2n+2}(ka\sin\theta)\right|^2 \\ &= \frac{64}{9}\beta^4\left[1+\left(\frac{64}{15}-\frac{4}{3}\sin^2\theta\right)\beta^2+O(\beta^4)\right]. \end{aligned} \tag{53}$$

The diffracted electric field at the distant point in the plane of incidence parallel to the incident electric vector orient to θ, irrespective of circular plate or circular hole, and its intensity distribution is given by $\sqrt{I_1(k,\theta)}$ for circular plate or $\sqrt{I_2(k,\theta)}$ for circhlar hole respectively. The diffracted field at the distant point in the plane of incidence perpendicular to the incident electric vector orient to φ, and its intensity distribution is given by $\sqrt{I_2(k,\theta)}$

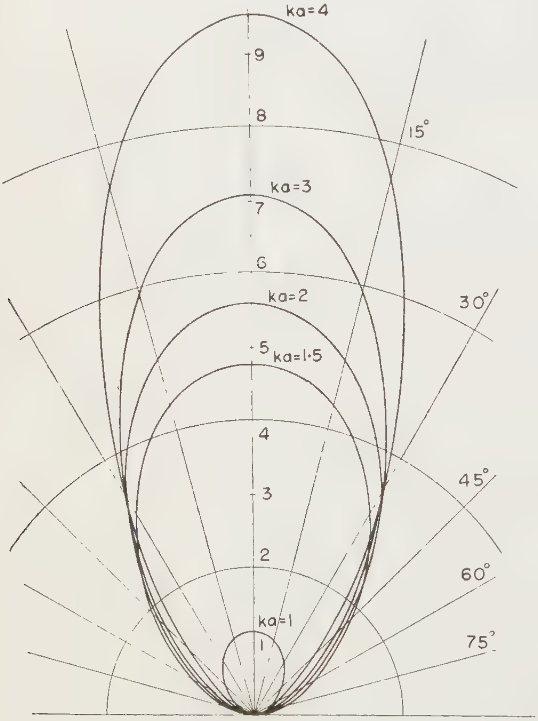

Fig. 4. $I_1(k,\theta)$.
Circular plate: Electric field in the plane parallel to E_1.
Circular hole: Electric field in the plane perpendicular to E_1.

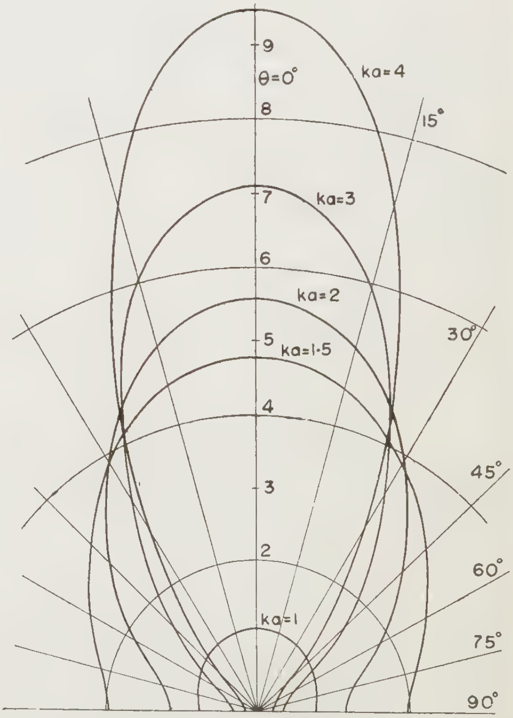

Fig. 5. $I_2(k,\theta)$
Circular plate: Electric field in the plane perpendicular to E_1.
Circular hole: Electric field in the plane parallel to E_1.

for curcular plate or $\sqrt{I_1(k,\theta)}$ for circular hole respectively. Figs. 4 and 5 show the relation of I_1 and I_2 to θ for various value of ka.

Total scattering energy in (45) is

$$W=\frac{2kE_1{}^2}{\pi\mu\omega}a^2\int_0^{\pi/2}(I_1(k,\theta)+I_2(k,\theta))\sin\theta d\theta\ .$$

Total scattering cross section of the circular plate σ, which is half of the transmission coefficient of the circular hole t, is given by

$$\begin{aligned}2\sigma=t&=\frac{W}{\dfrac{kE_1{}^2}{2\mu\omega}\pi a^2}=\frac{4}{\pi^2}\int_0^{\pi/2}(I_1(k,\theta)+I_2(k,\theta))\sin\theta d\theta\\&=\frac{1024}{27\pi^2}\beta^4\left(1+\frac{88}{25}\beta^2+\mathrm{O}(\beta^4)\right)\\&=\frac{64}{27\pi^2}(ka)^4\left[1+\frac{22}{25}(ka)^2+\mathrm{O}((ka)^4)\right].\end{aligned}\tag{54}$$

The integrand represents the differential scattering cross section. The total cross section for small ka is proportional to λ^{-4} as the Rayleigh formula of scattering by small objects.

§ 6. Electromagnetic Field on the Circular Hole and Plate

The electromagnetic field caused by the diffracted field on the circular hole and plate is given by

$$\begin{array}{l|l}
E_x=-E_2\cos\alpha\exp(-ikx\sin\alpha)\ , & E_x=ik\left(\dfrac{\partial\Pi_y}{\partial z}\right)_{z=-0}\ ,\\
E_y=-E_1\exp(-ikx\sin\alpha)\ , & E_y=-ik\left(\dfrac{\partial\Pi_x}{\partial z}\right)_{z=-0}\ ,\\
E_z=\dfrac{\rho}{\varepsilon}=\mp\left[\dfrac{\partial}{\partial z}\left(\dfrac{\partial\Pi_x}{\partial x}+\dfrac{\partial\Pi_y}{\partial y}\right)\right]_{z=-0}\ , & E_z=\mp E_1\sin\alpha\exp(-ikx\sin\alpha)\ ,\\
H_x=\pm J_y=\pm\dfrac{ik^2}{\mu\omega}\left(\dfrac{\partial\Pi_y}{\partial z}\right)_{z=-0}\ , & H_x=\mp\dfrac{kE_2}{\mu\omega}\cos\alpha\exp(-ikx\sin\alpha)\ ,\\
H_y=\mp J_x=\mp\dfrac{ik^2}{\mu\omega}\left(\dfrac{\partial\Pi_x}{\partial z}\right)_{z=-0}\ , & H_y=\pm\dfrac{kE_1}{\mu\omega}\exp(-ikx\sin\alpha)\ ,\\
H_z=-E_1\sin\alpha\exp(-ikx\sin\alpha)\ , & H_z=\dfrac{k}{\mu\omega}\left[\dfrac{\partial}{\partial z}\left(\dfrac{\partial\Pi_x}{\partial x}+\dfrac{\partial\Pi_y}{\partial y}\right)\right]_{z=-0}\ .
\end{array}\tag{55}$$

In the case of circular plate, the values of E_z, H_x, H_y are equal to those of the resultant field. ρ is the surface charge density due to the diffracted wave, and J_x, J_y are x, y-components of the surface current density caused by the diffracted field. Evidently the continuity equation

$$i\omega\rho+\mathrm{div}\,J=0$$

is satisfied. The sum of the surface current density due to the diffracted field and that of the incident wave

$$J_{0x}=\mp\frac{k}{\mu\omega}E_2\exp(-ikx\sin\alpha),\quad J_{0y}=\mp\frac{k}{\mu\omega}E_1\exp(-ikx\sin\alpha)\ ,$$

gives the total surface current density.

In the case of circular hole, the values of E_x, E_y, H_z are equal to those of the resultant field.

The surface current density of circular plate and the electric field of circular hole are determined by

$$
\begin{aligned}
\left(\frac{\partial \Pi_x}{\partial z}\right)_{z=-0} &= \sum_{m=0}^{\infty}\sum_{n=0}^{\infty} ({}_2C_n{}^m \cos m\varphi + {}_1C_n{}^m \sin m\varphi)\frac{\partial S_n{}^m}{\partial z}(r, -0) \,, \\
\left(\frac{\partial \Pi_y}{\partial z}\right)_{z=-0} &= \sum_{m=0}^{\infty}\sum_{n=0}^{\infty} ({}_1D_n{}^m \cos m\varphi + {}_2D_n{}^m \sin m\varphi)\frac{\partial S_n{}^m}{\partial z}(r, -0) \,.
\end{aligned} \tag{56}
$$

$\frac{\partial S_n{}^m}{\partial z}(r, -0)$ for $r<a$ is transformed to

$$
\begin{aligned}
\frac{\partial S_n{}^m}{\partial z}(r, -0) &= \frac{1}{a}\int_0^\infty \sqrt{\xi}\, J_m\!\left(\frac{r}{a}\xi\right) J_{m+2n+1/2}(\xi)\, d\xi \\
&= \frac{1}{a} x^{m/2} \frac{\sqrt{2}\,(m+n)!}{m!\,\Gamma(n+1/2)} F(m+n+1, 1/2-n; m+1; x) \\
&= \frac{1}{a} x^{m/2} (1-x)^{-1/2} \frac{\sqrt{2}\,(m+n)!}{m!\,\Gamma(n+1/2)} F(m+n+1/2, -n; m+1; x) \\
&= \frac{1}{a} x^{m/2} (1-x)^{-1/2} (-)^n \sqrt{\frac{2}{\pi}}\, F(m+n+1/2, -n; 1/2; 1-x) \\
&= \frac{1}{a} x^{-m/2} \frac{\sqrt{2}}{\Gamma(n+1/2)} \frac{d^n}{dx^n}\{x^{m+n}(1-x)^{n-1/2}\} \,.
\end{aligned} \tag{57}
$$

In case of normal incidence and linear polarization, the current density and the electric field are simplified to

$$
\begin{aligned}
J_x, \quad & -\frac{k}{\mu\omega} E_y = -i\sqrt{\frac{\varepsilon}{\mu}}\, E_1\{c(x)+id(x)\} \sin 2\varphi \,, \\
J_y, \quad & -\frac{k}{\mu\omega} E_x = \ \ i\sqrt{\frac{\varepsilon}{\mu}}\, E_1\{a(x)+ib(x)+(c(x)+id(x)) \cos 2\varphi\} \,,
\end{aligned} \tag{58}
$$

where

$$
\begin{aligned}
\frac{2}{\pi}\frac{1}{ka}\frac{1}{\sqrt{1-x}} \sum_{n=0}^{\infty} (-)^n A_n{}^0 F(-n, n+1/2, 1/2, 1-x) &= a(x)+ib(x) \,, \\
\frac{2}{\pi}\frac{1}{ka}\frac{x}{\sqrt{1-x}} \sum_{n=0}^{\infty} (-)^n A_n{}^2 F(-n, n+5/2, 1/2, 1-x) &= c(x)+id(x) \,.
\end{aligned} \tag{59}
$$

In this case

$$
J_{0x}=0 \,, \qquad J_{0y} = \mp\sqrt{\frac{\varepsilon}{\mu}}\, E_1 \,.
$$

Therefore

$$
\begin{aligned}
\left|\frac{J_x}{\sqrt{\frac{\varepsilon}{\mu}}E_1}\right|^2 &= (c^2+d^2)\sin^2 2\varphi \,, \\
\left|\frac{J_{0y}+J_y}{\sqrt{\frac{\varepsilon}{\mu}}E_1}\right|^2 &= (b\mp 1+d\cos 2\varphi)^2+(a+c\cos 2\varphi)^2 \,,
\end{aligned}
$$

$$
\begin{aligned}
\left|\frac{E_y}{E_1}\right|^2 &= (c^2+d^2)\sin^2 2\varphi \,, \\
\left|\frac{E_x}{E_1}\right|^2 &= (b+d\cos 2\varphi)^2+(a+c\cos 2\varphi)^2 \,.
\end{aligned} \tag{60}
$$

The resultant total current on the line $\varphi=0$ and $\varphi=\pi/2$ is parallel to the y-axis, the direction of the incident electric field, and represented by

$$
\left|\frac{J}{\sqrt{\frac{\varepsilon}{\mu}}E_1}\right|^2 = (b\mp 1+d)^2+(a+c)^2 \qquad \varphi=0
$$

and $\quad = (b\mp 1-d)^2+(a-c)^2 \qquad \varphi=\pi/2$

The resultant electric field on the line $\varphi=0$ and $\varphi=\pi/2$ is parallel to the x-axis, the direction of the incident electric field, and represented by

$$
\left|\frac{E}{E_1}\right|^2 = (b+d)^2+(a+c)^2 \qquad \varphi=0 \tag{61}
$$

and $\quad = (b-d)^2+(a-c)^2 \qquad \varphi=\pi/2$

respectively.

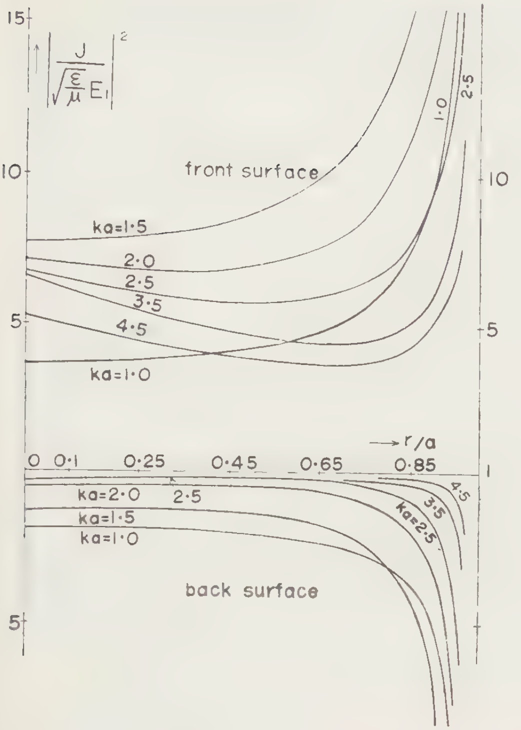

Fig. 6. Circular plate: Current distribution on the radius perpendicular to E_1.

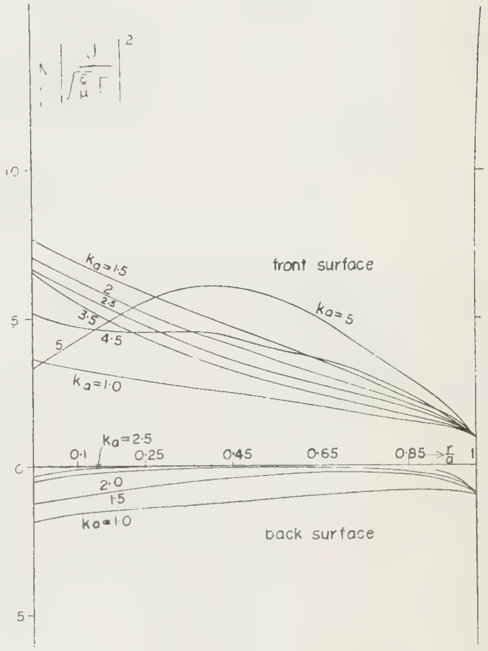

Fig. 7. Circular plate: Current distribution on the radius parallel to E_1.

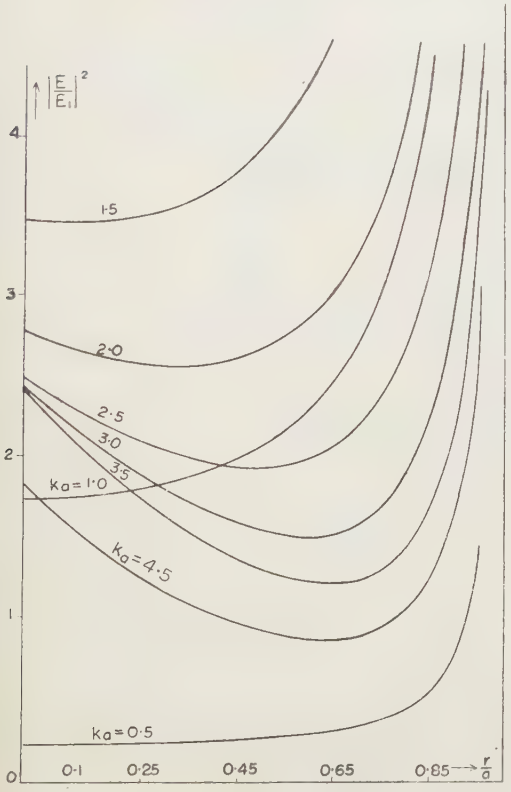

Fig. 8. Circular hole: Electric field on the radius parallel to E_1.

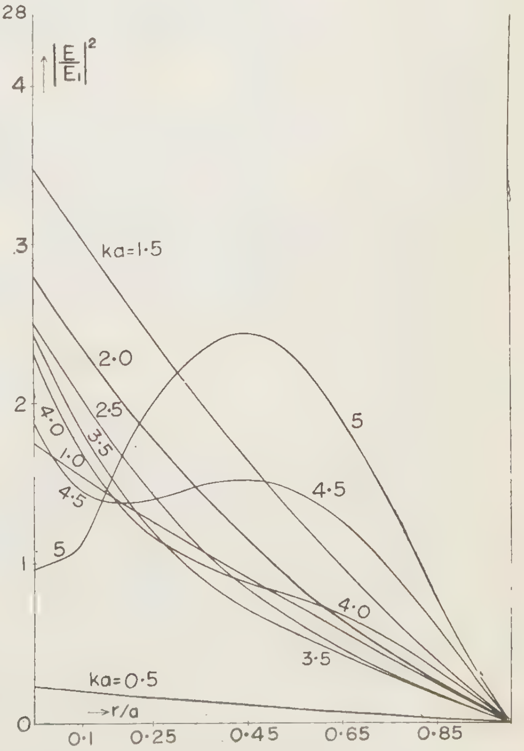

Fig. 9. Circular hole: Electric field on the radius perpendicular to E_1.

Figs. 6 and 7 show the values of J^2 on the radius perpendicular ($\varphi=0$) and parallel ($\varphi=\pi/2$) to the incident electric field for the case of the circular plate. Figs. 8 and 9 show the values of $|E|^2$ on the radius parallel ($\varphi=0$) and perpendicular ($\varphi=\pi/2$) to the incident electric field for the case of the circular hole.

The total amount of the diffracted energy flow on the upper surface of the circular plate or circular hole is equal to the scattered energy for $z>0$.

$$W=\int_0^a\int_0^{2\pi}\frac{1}{2}\Re(E_x\tilde{H}_y-E_y\tilde{H}_x)_{z=+0}rdrd\varphi$$
$$=\frac{1}{2}E_1{}^2\frac{k^2}{\mu\omega}\Re(-i)\int_0^a rdr\int_0^{2\pi}\exp(-ikx\sin\alpha)\left(\frac{\partial\Pi_y}{\partial z}\right)_{z=-0}d\varphi\ .$$

We use the Bessel series representation of $\exp(-ikx\sin\alpha)$, substitute (56) into $(\partial\Pi_y/\partial z)_{z=-0}$ and integrate over φ; then

$$W=\frac{\pi k^2}{\mu\omega}E_1{}^2\frac{1}{a}\Re(-i)\sum_{s=0}^{\infty}(-)^s\sum_{n=0}^{\infty}{}_1D_n{}^s\int_0^a J_s(kr\sin\alpha)rdr\int_0^{\infty}\sqrt{\xi}\,J_s\left(\frac{r}{a}\xi\right)J_{s+2n+1/2}(\xi)d\xi$$
$$=-\sqrt{\frac{2}{\pi}}\frac{\pi k^2}{\mu\omega}E_1{}^2a\Re i\sum_{s=0}^{\infty}(-i)^2\sum_{n=0}^{\infty}{}_1D_n{}^s j_{s+2n}(ka\sin\alpha)\ . \tag{62}$$

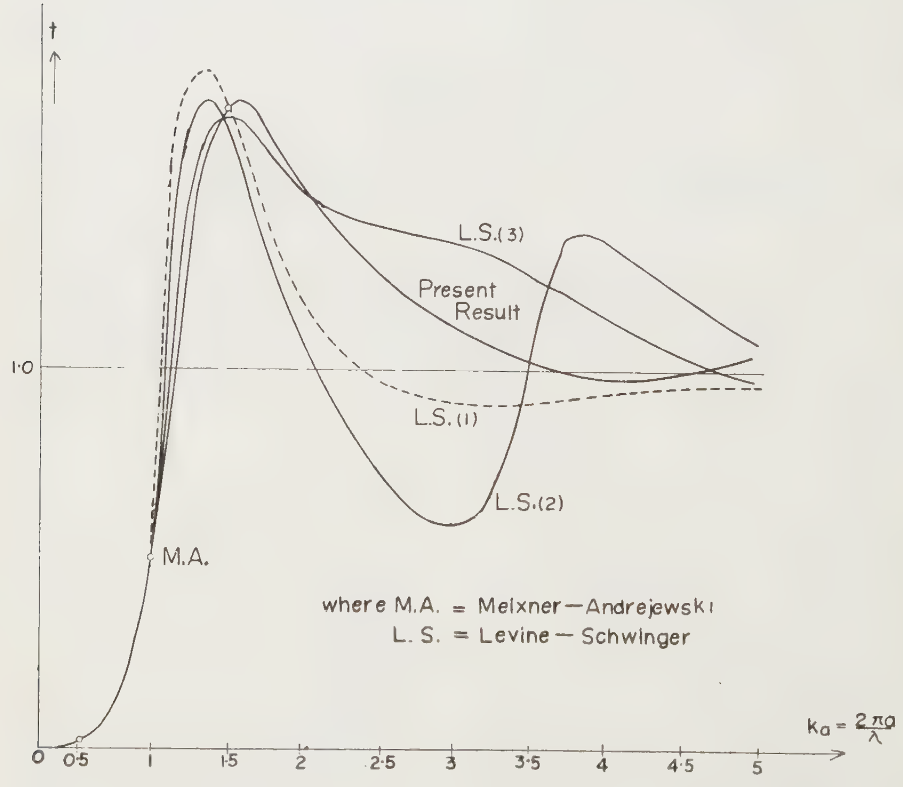

Fig. 10. Transmission coefficient of circular hole (half of the total scattering cross section of circular plate.)

The transmission coefficient t is

$$t=\frac{W}{\frac{1}{2}\frac{k}{\mu\omega}E_1{}^2\pi a^2}=-2\sqrt{\frac{2}{\pi}}\frac{k}{a}\Re(i)\sum_{s=0}^{\infty}(-i)^s\sum_{n=0}^{\infty}{}_1D_n{}^s j_{s+2n}(ka\sin\alpha) \tag{63}$$

which is the half of the total scattering cross section.

In case of vertical incidence, the only term $n=0$, $s=0$ remains and t is given by

$$t=-2\sqrt{\frac{2}{\pi}}\frac{k}{a}\Re i_1 D_0{}^0=-\frac{4}{\pi}\frac{1}{ak}\Re i\,\boldsymbol{A}_0{}^0$$

$$=\frac{1024}{27\pi^2}\beta^4[1+\mathrm{O}(\beta^2)]\;, \tag{64}$$

which is just equal to (54).

$t(k)$ obtained from the numerical calculation of $\boldsymbol{A}_0{}^0$, is shown in Fig. 10, together with the results of Levine-Schwinger and Meixner-Andrejewski.

§ 7. Summary

We put the Hertz vector of the diffracted wave as (4) and (8). They are given by (14) and (15). Unknown coefficients $A_n{}^m, B_n{}^m, U_m{}^{(1)}$ and $U_m{}^{(2)}$ are given by (28) and (37). Here $X_{n\nu}{}^m$ is the solution of the simultaneous linear equation and $G_{n\nu}{}^m$ are calculated from (29). $a_n{}^m$ and $b_n{}^m$ are given by (22). The diffracted field at large distances is given by (41) and (42). The electromagnetic field and the current distribution on the circular plate and circular hole are given by (55) with the aid of (56) and (57).

In this paper the incident wave is taken to be a plane wave; but in case of the spherical wave and of the diffracted wave from other body, the solution can be obtained as (14) and (15) with the aid of the same $X_{n\nu}{}^m$ and with suitable change of $a_n{}^m$ and $b_n{}^m$.

Appendix I

From the relation

$$n_1>n_2 \qquad \int_0^1 \frac{d^{n_1}}{dx^{n_1}}\{x^{m+n_1}(1-x)^{n_1-1/2}\}F(m+n_2+1/2,\,-n_2,\,m+1;\,x)dx=0\;,$$

$$n_1=n_2=n \qquad\qquad =\frac{n!\,\Gamma(m+1)\Gamma(n+1/2)}{(m+2n+1/2)\Gamma(m+n+1/2)}\;,$$

we have the orthogonality

$$\int_0^1 x^m(1-x)^{-1/2}u_{n_1}{}^m(x)u_{n_2}{}^m(x)dx=0 \qquad (n_1\neq n_2)\;,$$

$$\int_0^1 x^m(1-x)^{-1/2}\{u_n{}^m(x)\}^2dx=\frac{\Gamma(n+1/2)\Gamma(m+n+1/2)}{2(m+2n+1/2)n!\,\Gamma(m+n+1)}\;.$$

Hence we can expand the arbitrary function $f(x)$ in the interval $0<x<1$

$$f(x)=\sum_{n=0}^{\infty}C_n{}^m u_n{}^m(x)\;,$$

where

$$C_n{}^m=\frac{\sqrt{2}\,(m+2n+1/2)}{\Gamma(n+1/2)}\int_0^1 f(x)\frac{d^n}{dx^n}\{x^{m+n}(1-x)^{n-1/2}\}dx\;.$$

Now let

$$f(x)=x^{-m/2}J_m(p\sqrt{x})=\left(\frac{p}{2}\right)^m\sum_{s=0}^{\infty}\frac{(-)^s(p\cdot\sqrt{x}/2)^{2s}}{s!\,\Gamma(m+s+1)}\;,$$

then we have

$$C_n{}^m=\sum_{s=0}^{\infty}\frac{(-)^s(p/2)^{m+2s}}{s!\,\Gamma(m+s+1)}\frac{\sqrt{2}\,(m+2n+1/2)}{\Gamma(n+1/2)}\int_0^1 x^s\frac{d^n}{dx^n}\{x^{m+n}(1-x)^{n-1/2}\}dx$$

$$=\frac{2m+4n+1}{\sqrt{2}\,\Gamma(n+1/2)}\sum_{s=n}^{\infty}\frac{(-)^{n+s}(p/2)^{m+2s}}{\Gamma(m+s+1)(s-n)!}\int_0^1 x^{s+m}(1-x)^{n-1/2}dx$$

$$
\begin{aligned}
&=\frac{2m+4n+1}{\sqrt{2}}\sum_{s=n}^{\infty}\frac{(-)^{n+s}(p/2)^{m+2s}}{(s-n)!\,\Gamma(s+m+n+3/2)}\\
&=\frac{2m+4n+1}{\sqrt{p}}\sum_{\mu=0}^{\infty}\frac{(-)^{\mu}(p/2)^{m+2n+1/2+2\mu}}{\mu!\,\Gamma(m+2n+1/2+\mu+1)}\qquad (s=n+\mu)\\
&=(2m+4n+1)\frac{J_{m+2n+1/2}(p)}{\sqrt{p}}\ .
\end{aligned}
$$

Appendix II

$$
\begin{aligned}
I&=\int_{\gamma}^{\infty}\frac{\sqrt{\xi}\,J_m(\rho\xi)J_{m+2n+1/2}(\xi)}{\sqrt{\xi^2-\gamma^2}}\exp(-\sqrt{\xi^2-\gamma^2}\,z_1)d\xi\qquad\left(z_1=\frac{z}{a}>0,\quad \rho=\frac{r}{a}\right)\\
&=\int_0^{\infty}(\lambda^2+\gamma^2)^{-1/4}J_m(\rho\sqrt{\lambda^2+\gamma^2})J_{m+2n+1/2}(\sqrt{\lambda^2+\gamma^2})\exp(-\lambda z_1)d\lambda\qquad(\xi^2-\gamma^2=\lambda^2)\\
&=\sum_{s=0}^{\infty}\sum_{s'=0}^{\infty}(-)^{s+s'}2^{2m+2n+1/2}(m+2n+1/2+2s)(m+2s')\\
&\qquad\times\frac{\Gamma(m+2n+1/2+s)}{s!}\,\frac{\Gamma(m+s')}{s'!}\,\frac{J_{m+2n+1/2+2s}(\gamma)}{\gamma^{m+2n+1/2}}\,\frac{J_{m+2s'}(\rho\gamma)}{(\rho\gamma)^m}I_1\ ,
\end{aligned}
$$

where

$$
\begin{aligned}
I_1&=\int_0^{\infty}\frac{(\lambda^2+\gamma^2)^{m+n}J_{m+2n+1/2+2s}(\lambda)J_{m+2s'}(\rho\lambda)}{\lambda^{2m+2n+1/2}}\exp(-\lambda z_1)d\lambda\\
&=\sum_{t=0}^{m+n}\frac{(m+n)!}{t!(m+n-t)!}\gamma^{2t}I_2\ .\\
I_2&=\int_0^{\infty}\frac{J_{m+2n+1/2+2s}(\lambda)J_{m+2s'}(\rho\lambda)}{\lambda^{2t+1/2}}\exp(-\lambda z_1)d\lambda\ .
\end{aligned}
$$

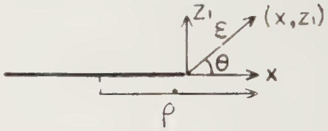

Fig. 11.

Now using

$$
J_{n+1/2}(z)=\frac{1}{\sqrt{2\pi}}\sum_{\nu=0}^{n}\frac{(n+\nu)!}{\nu!(n-\nu)!}\,\frac{i^{\nu-n-1}}{2^{\nu}}\,\frac{1}{z^{\nu+1/2}}\{\exp(iz)+(-)^{\nu-n-1}\exp(-iz)\}\ ,
$$

we have

$$
\begin{aligned}
I_2&=\frac{1}{\sqrt{2\pi}}\sum_{\nu=0}^{m+2n+2s}\frac{(m+2n+2s+\nu)!}{\nu!(m+2n+2s-\nu)!}\,\frac{i^{\nu-m-2n-2s-1}}{2^{\nu}}(-)^{2t+\nu}\left(\int^{z_1}dz_1\right)^{2t+\nu}\\
&\qquad\times\int_0^{\infty}\frac{J_{m+2s'}(\rho\lambda)}{\lambda}\{\exp(-\lambda(z_1-i))+(-)^{\nu-m-1}\exp(-\lambda(z_1+i))\}d\lambda\\
&=\frac{1}{\sqrt{2\pi}}\sum_{\nu=0}^{m+2n+2s}\frac{(m+2n+2s+\nu)!}{\nu!(m+2n+2s-\nu)!}\,\frac{i^{\nu-m-2n-2s-1}}{2^{\nu}}(-)^{2t+\nu}\left(\int^{z_1}dz_1\right)^{2t+\nu}\\
&\qquad\times\left[\frac{\{\sqrt{\rho^2+(z_1-i)^2}-(z_1-i)\}^{m+2s'}}{(m+2s')\rho^{m+2s'}}+(-)^{\nu-m-1}\frac{\{\sqrt{\rho^2+(z_1+i)^2}-(z_1+i)\}^{m+2s'}}{(m+2s')\rho^{m+2s'}}\right].
\end{aligned}
$$

Let $\rho=1+x$, then x and z are small quantities near the edge (Fig. 11).

$$
\rho+(z_1\pm i)^2=2(x\pm iz_1)+O(x^2,\ z_1{}^2)
$$

$$
\begin{aligned}
&\{\sqrt{\rho^2+(z_1-i)^2}-(z_1-i)\}^{m+2s'}+(-)^{\nu-m-1}\{\sqrt{\rho^2+(z_1+i)^2}-(z_1+i)\}^{m+2s'}\\
&\quad=(i)^{m+2s'}\left[\{1-(-1)^{\nu}\}+\frac{m+2s'}{i}(\sqrt{2(x-iz_1)}+(-)^{\nu}\sqrt{2(x+iz_1)})\right]\\
&\quad+O(x,\ z_1)\ .
\end{aligned}
$$

Since the integration over z gives higher order terms of $x+iz_1$, the lowest order term in I_1 is that for $t=0$, $\nu=0$, which is of the order of $\sqrt{x+iz_1}$. Therefore

$$
I_1=(-)^{s+s'+n}\frac{1}{\sqrt{\pi}}(\sqrt{x-iz_1}+\sqrt{x+iz_1})+O(x\pm iz_1)\ ,
$$

hence

$$I=(-)^n\frac{1}{\sqrt{\pi}}(\sqrt{x-iz_1}+\sqrt{x+iz_1})R_{m+2n+1/2}(\gamma)R_m(\rho\gamma)+\mathrm{O}(x\pm iz_1)\ .$$

Here

$$R_\nu(z)=\left(\frac{2}{z}\right)^\nu\sum_{s=0}^{\infty}\frac{(\nu+2s)\Gamma(\nu+s)}{s!}J_{\nu+2s}(z)=1\ ,$$

as shown in the end. Thus

$$I=(-)^n\frac{1}{\sqrt{\pi}}(\sqrt{x-iz_1}+\sqrt{x+iz_1})+\mathrm{O}(x\pm iz_1)\ .$$

In

$$\begin{aligned}S_n^m(r, z)&=\int_0^\infty\frac{\sqrt{\xi}J_m(\rho\xi)J_{m+2n+1/2}(\xi)}{\sqrt{\xi^2-\gamma^2}}\exp(\mp\sqrt{\xi^2-\gamma^2}z_1)\,d\xi \qquad \begin{matrix}(z\gtrless 0)\\(\gamma=ka)\end{matrix}\\&=I+K\ ,\\K&=-i\int_0^\gamma\frac{\sqrt{\xi}J_m(\rho\xi)J_{m+2n+1/2}(\xi)}{\sqrt{\gamma^2-\xi^2}}\exp(\mp\sqrt{\xi^2-\gamma^2}z_1)\,d\xi\ ,\end{aligned}$$

K and its derivative have no singularity near the edge $\rho=1$, $z_1=0$. Therefore near the edge

$$\begin{aligned}\frac{\partial S_n^m}{\partial z}&=\frac{\partial I}{\partial z}+\frac{\partial K}{\partial z}\\&=(-)^n\frac{i}{2\sqrt{\pi}a}\left(\frac{1}{\sqrt{x+iz_1}}-\frac{1}{\sqrt{x-iz_1}}\right)+\mathrm{O}((x\pm iz_1)^0)\\&=(-)^n\frac{1}{\sqrt{\pi}a}\frac{1}{\sqrt{\varepsilon}}\sin\frac{\theta}{2}+\mathrm{O}(\varepsilon^0)\ ,\\\frac{\partial S_n^m}{\partial r}&=\frac{1}{a}\frac{\partial I}{\partial x}+\frac{\partial K}{\partial r}\\&=(-)^n\frac{1}{2\sqrt{\pi}a}\left(\frac{1}{\sqrt{x+iz_1}}+\frac{1}{\sqrt{x-iz_1}}\right)+\mathrm{O}((x\pm iz_1)^0)\\&=(-)^n\frac{1}{\sqrt{\pi}a}\frac{1}{\sqrt{\varepsilon}}\cos\frac{\theta}{2}+\mathrm{O}(\varepsilon^0)\ ,\\\frac{\partial^2 S_n^m}{\partial r^2}&=-(-)^n\frac{1}{2a^2\sqrt{\pi}}\varepsilon^{-3/2}\cos\frac{3}{2}\theta+\mathrm{O}(\varepsilon^{-1/2})\ ,\\\frac{\partial^2 S_n^m}{\partial r\partial z}&=-(-)^n\frac{1}{2a^2\sqrt{\pi}}\varepsilon^{-3/2}\sin\frac{3}{2}\theta+\mathrm{O}(\varepsilon^{-1/2})\ .\end{aligned}$$

The proof for $R_\nu(z)=1$:

We consider the following expansion in the hypergeometric polynomial.

$$\frac{J_{\nu-1/2}(zr)}{(zr)^{\nu-1/2}}=\frac{1}{z^{\nu-1/2}}\sum_{s=0}^{\infty}C_s^{\nu-1/2}u_s^{\nu-1/2}(x)\qquad(x=r^2)\ ,$$

where

$$C_s^{\nu-1/2}=(2\nu+4s)\frac{J_{\nu+2s}(z)}{z^{1/2}}\ ,$$

$$u_s^{\nu-1/2}(x)=\frac{\Gamma(\nu+s)}{\sqrt{2}\,s!\,\Gamma(\nu+1/2)}F(\nu+s, -s, \nu+1/2; x)\ ,$$

Taking the lim $r\to 0$ in both sides

$$\frac{1}{2^{\nu-1/2}\Gamma(\nu+1/2)}=\frac{1}{z^{\nu-1/2}}\sum_{s=0}^{\infty}\frac{(2\nu+4s)\Gamma(\nu+s)J_{\nu+2s}(z)}{\sqrt{2}\,s!\,\Gamma(\nu+1/2)z^{1/2}}\ .$$

Therefrom we have

$$R_\nu(z)=\left(\frac{2}{z}\right)^{\nu}\sum_{s=0}^{\infty}\frac{(\nu+2s)\Gamma(\nu+s)}{s!}J_{\nu+2s}(z)=1\ .$$

References

1) C. J. Bouwkamp: Philips Research Reports, **5** (1950) 401.

2) J. Meixner and W. Andrejewski: Ann. d. Phys. (6) **7** (1950) 157.
W. Andrejewski: Naturwiss. **38** (1951) 406.

3) H. Levine and J. Schwinger: Comm. Pure. Appl. Math. **3** (1950) 355, which is republished in "The theory of electromagnetic waves, A Symposium" (Interscience Publishers, New York 1951).

4) Y. Nomura and N. Kawai: Sci. Rep. Tôhoku Univ. Series I, **33** (1949) 197; N. Kawai: Sci. Rep. Tôhoku Univ. Series I, **35** (1952) 210.

5) G. Bekefi: Jour. Appl. Phys. **24** (1953) 1123.

JOURNAL OF THE PHYSICAL SOCIETY OF JAPAN Vol. 10, No. 4, APRIL, 1955

Der Zündmechanismus im Dieselmotor (II)

Von Kunio TERAO

Technisches Laboratorium der Isuzu Motor A.G.

(Received November 17, 1954)

Following the previous report, many experimental results of the ignition in the Diesel-engine under various different conditions are obtained, and the idea of the ignition mechanism, which was proposed in the previous paper, is thoroughly discussed by the analysis of these results. The number of ignition point in the combustion-chamber is presumed by the ignition probability in unit time and an explained is given that this number is generally very few. As the special case, it is ascertained that at the Diesel-knock there is only one ignition point, from which the flame propagates very rapidly.

§ 1. Vorwort

Im vorigen Teil dieser Arbeit wurde die Wahrscheinlichkeit der Zündung in Zeiteinheit bei der Verbrennung im Dieselmotor zu den Zündverzügen gesucht und damit erörterte ich den Zündmechanismus im Dieselmotor.

Dabei dachte ich folgendmassen:

Wenn man den flüssigen Brennstoff in die Brennkammer einspritzt, wo die Luft adiabatisch gedrückt wird, verdampft der Brennstoff zuerst, sich mit der Luft durch das Diffusion-Phänomen mischend, und dann fängt die chemische Reaktion von einem oder einigen Orten an, die sich anfangs allmählich vergrössert und nachdem zündet, falls sie nicht schwindet. Deshalb ist die Wahrscheinlickeit der Zündung in Zeiteinheit hauptsächlich abhängig von der Diffusion und Verdampfung des Brennstoffes, der Dichtigkeit, der Temperatur der Luft, und der chemischen Reaktion der Mischung.

Wenn der Zündverzug nicht so gross ist, vergrössert sich diese Wahrscheinlichkeit mit der Zeit nach der Einspritzung des Brennstoffes, weil der Brennstoff sich allmählich mit der Luft durch die Diffusion und Verdampfung mischt und die Temperatur ansteigt. Wenn der Zündverzug so gross ist, muss diese Wahrscheinlichkeit beinahe konstant sein, weil der Zustand der Mischung gleichartig

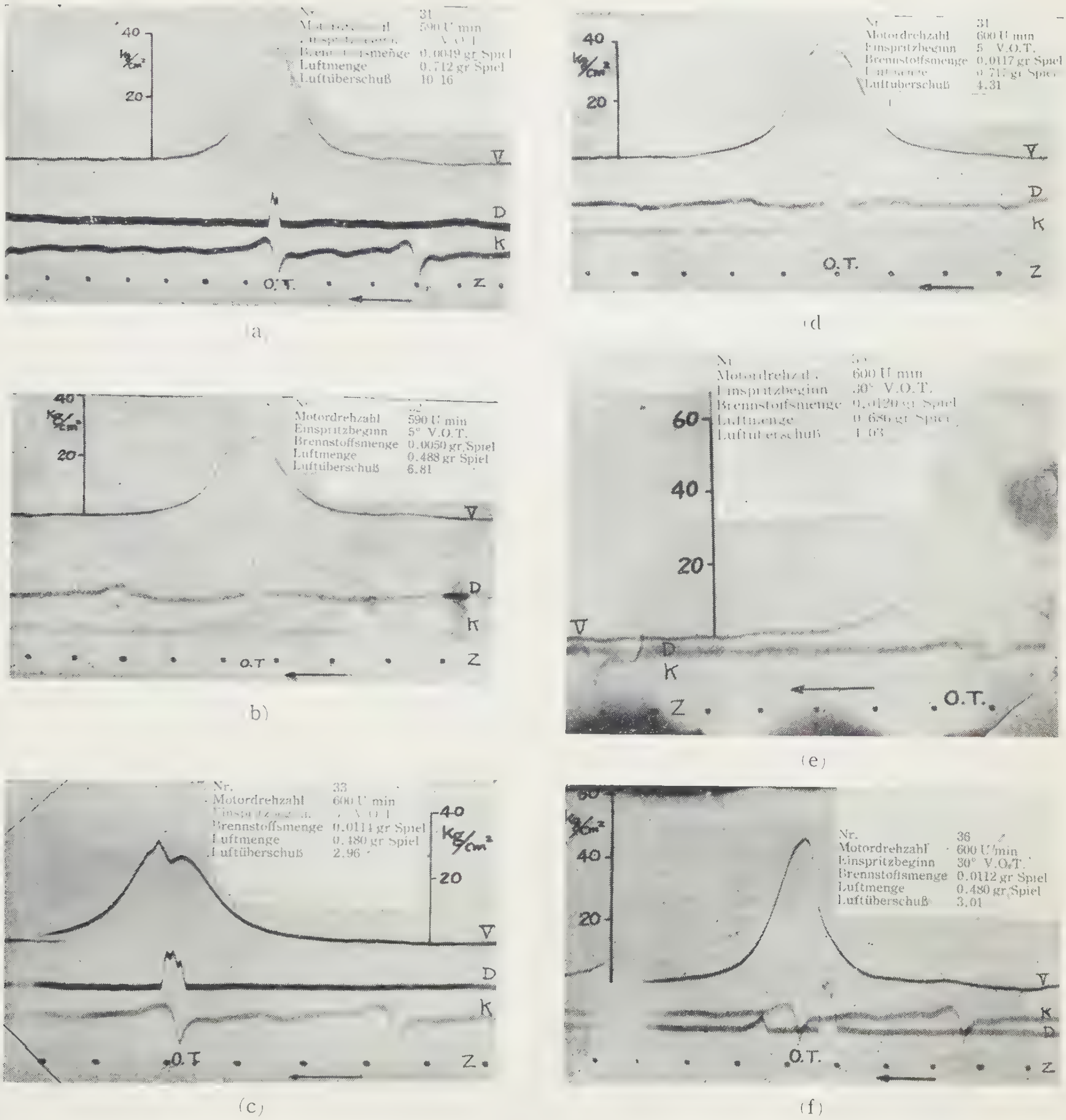

(a) (d) (b) (e) (c) (f)

Abb. 1. Indikatordiagramm.

wird.

Andererseits hat die Kurve des Zusammenhangs zwischen dieser Wahrscheinlichkeit der Zündung in Zeiteinheit und der Zeit nach der Einspritzung des Brennstoffes stets einen Teil, wo diese Wahrscheinlichkeit beinahe Null ist. Diese Ursache muss die Vergrösserung des Zündkernes sein.

Da ich jetzt noch mehre Versuchsergebnisse bekommen konnte, will ich hier noch mehr über meine Überlegung des Zündmechanismus erklären. Besonders will ich erklären, dass es sehr wenige Zündpunkte bei der Zündung im Dieselmotor gibt, besonders nur einen beim Dieselklopf.

§ 2. Versuchsergebnisse und Betrachtung

Wie schon erwähnt, besteht die Kurve des Zusammenhangs zwischen der Wahrscheinlichkeit der Zündung in Zeiteinheit und der Zeit nach der Einspritzung des Brennstoffes aus drei Teilen: Im ersten Teile vergrössert sich diese Wahrscheinlichkeit mit der Zeit, im zweiten beinahe konstant für die Zeit und im dritten beinahe Null. Deshalb erkläre ich diese drei Teile nacheinander.

(1) *Der erste Teil, wo sich die Wahrscheinlichkeit der Zündung in Zeiteinheit mit der*

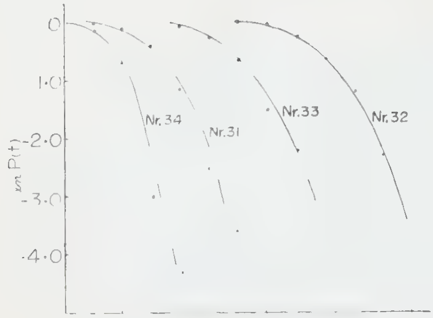

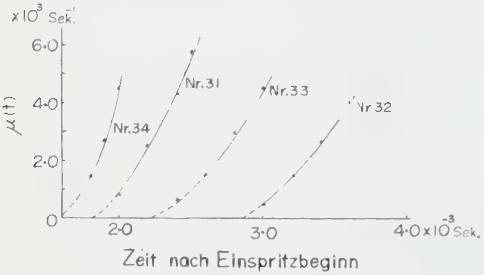

Abb. 2.

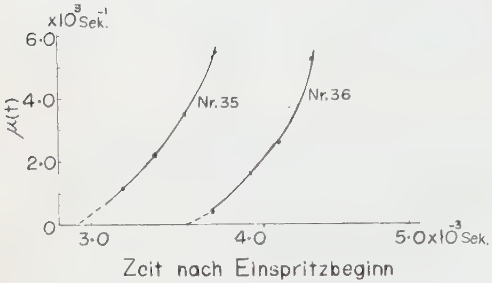

Abb. 3.

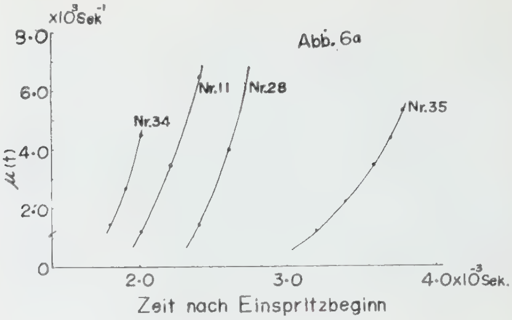

Abb. 4.

Zeit vergrössert und fast von der Diffusion und Verdampfung des Brennstoffs ausser der Temperatur und Dichtigkeit der Luft und der Eigenschaft des Brennstoffes abhängt.

Abb. 1 zeigt die Indikator-Diagramme bei verschiedenen Zuständen. In diesen Aufnahmen bedeutet **V** die Druckänderung in der Vorkammer, **D** die Erhöhungsänderung der Einspritznadeldüse, **K** den Kurbelwinkel, O.T. den Obertotpunkt und **Z** die Zeit. Abb. 2, 3, 4, zeigen die Vergleichungen der Wahrscheinlichkeiten der Zündung in Zeiteinheit bei den verschiedenen Zuständen, wo man die Indikator-Diagramme von Abb. 1 bekommen konnte.

Diese Zustände sind folgende:

Versuchsnummer	Nr. 11	28	31	32	33	34	35	36	
Motordrehzahl	620	1210	590	590	600	600	600	600	U/min.
Einspritzbeginn	10°	30°	5°	5°	5°	5°	30°	30°	V.O.T.
Brennstoffsmenge	0.0101	0.011	0.0049	0.0050	0.011	0.012	0.012	0.011	gr/Spiel
Luftmenge	0.612	0.685	0.712	0.488	0.480	0.717	0.686	0.480	,,
Luftüberschuss	4.27	4.30	10.2	6.81	2.96	4.31	4.03	3.01	
Temperatur bei der Zündung	790	830	860	970	1000	870	950	1050	°K
Druck bei der Zündung	28.0	23.0	33.0	24.0	26.0	35.0	23.0	23.0	kg/cm²

Ich denke hierbei hauptsächlich an drei Enflüsse, die die Neigung dieser Wahrscheinlichkeit beherrschen. Der erste ist das Mischungsverhältnis, der zweite die Dichtigkeit der gedrückten Luft, der dritte die Temperatur der Luft.

(*a*) *Der Einfluss des Mischungsverhältnisses:* Es ist klar in der Aufnahmen der Indikator-Diagramme des Nr. 31 und Nr. 34, dass die Zahl des Berges der Verbrennungs-druckänderung in der Vorkammer gleich derjenigen der Erhöhungsänderung der Einspritznadeldüse ist, z.B. bei Nr. 31 ist es zwei und bei Nr. 34 drei. Es bedeutet vielleicht, dass der eingespritzte Brennstoff nicht dauernd ausgeht, sondern sich unterbricht und die Verbrennung dem Einspritzzustand folgt. Nämlich die Menge des Brennstoffes in der ersten Stufe der Einspritzung wird zu der Zeit, wo die erste Steigung der Erhöhungsänderung der Einspritznadeldüse eintritt, eingespritzt und brennt in der ersten Stufe unabhängig von dem später eingespritzten Brennstoff, der sich nachher zusammen mit der Luft mischt und dem vorhergehenden folgt.

Deshalb, wenn der Zündverzug so klein ist, muss der Einfluss der eingespritzten Brennstoffsmenge klein sein, und wenn der Zündverzug so gross ist, muss dieser Einfluss gross sein, weil die mit der Luft sich mischende Brennstoffsmenge mehr wird. Abb. 2 zeigt die Vergleichungen der Kurven der Wahrscheinlichkeit der Zündung. Bei Nr. 31 und Nr. 34 waren die beiden eingesaugten Luftmengen einander fast gleich, und die Brennstoffsmenge nicht gleich und die beide Zündverzüge waren klein, wegen der vielen eingesaugten Luftmenge. Deshalb muss der Einfluss der Brennstoffsmenge bei diesem Falle klein sein. Bei Nr. 32 und Nr. 33 waren die beiden Luftmengen fast gleich aber geringer als Nr. 31 und 34, und die Brennstoffsmenge nicht gleich. Der Einfluss der Brennstoffsmenge bei Nr. 32 und 33 müsste grösser als bei Nr. 31 und 34 sein, aber meine Versuchsergebnisse zeigen es nicht so klar.

(*b*) *Der Einfluss der Dichtigkeit der gedrückten Luft*

Da die Wahrscheinlichkeit der Zündung proportional dem Quadrat der Dichtigkeit der gedrückten Luft ist, wie im ersten Teil dieser Arbeit erwähnt, ist der Einfluss der Luftdichtigkeit sehr wichtig, trotzdem der Diffusionsbeiwert umgekehrt proportional dem Druck ist.

In Abb. 2 war die Brennstoffsmenge bei Nr. 31 und bei Nr. 32 beinahe gleich und die eingesaugte Luftmenge nicht gleich, sowie bei Nr. 33 und Nr. 34.

Nr.	31	32	33	34	35	36	
Brennstoffsmenge	0.0049	0.0050	0.011	0.012	0.012	0.011	gr/Spiel
Dichtigkeit der Luft bei Zündung	0.0142	0.0098	0.0098	0.0143	0.0084	0.0059	gr/cc
Temperatur der Luft bei Zündung	860	980	1000	870	950	1050	°K

Trotzdem die Temperatur bei Nr. 32 höher als diejenige bei Nr. 31 ist, ist die Neigung der Steigung der Wahrscheinlichkeit der Zündung bei Nr. 31 als diejenige bei Nr. 32, sowie bei Nr. 33 und Nr. 34. So kann man wissen, dass der Einfluss der Luftdichtigkeit für diese Wahrscheinlichkeit sehr wichtig ist. Abb. 3 zeigt diese Sache bei früherer Einspritzzeit. Dabei sind die beiden Luftdichtigkeiten minder als diejenige bei Nr. 33 und Nr. 34 und die Neigung der Kurven dieser Wahrscheinlichkeit auch geringer.

Abb. 4 zeigt auch diese Sache bei verschiedenen Einspritzzeiten. Die Neigung der Kurve ist die grösste, wenn die Zündung und die Einspritzung bei der höchsten Dichtigkeit der Luft stattfindet. Wenn die Einspritzung zu früh vor O.T. gemacht wird, werden diese Neigung und diese Wahrscheinlichkeit klein und dabei wird es nicht zündwilling.

Warum die Neigung der Kurve der Wahrscheinlichkeit der Zündung bei Nr. 28 steiler als diejenige bei Nr. 35 ist, trotz der gleichen Einspritzzeit (in Abb. 4), ist, um Differenz der Stärke der Diffusion wegen, weil die Motordrehzahl 1200 U/min bei Nr. 28 und 600 U/min bei Nr. 35 war.

(*c*) *Der Einfluss der Temperatur*

Bei meinem Versuch war der Einfluss der Temperatur nicht klar. Die Temperatur der gedrückten Luft war immer dabei so hoch, dass man ihren Einfluss nicht finden konnte.

(2) *Der zweite Teil, wo die Wahrscheinlichkeit der Zündung in Zeiteinheit beinahe konstant ist.*

Wenn der Zündverzug nach der Einspritzung des Brennstoffes sehr gross ist, wird die Mischung der Luft und des Brennstoffes fast ganz durch das Diffusionsphänomen bewirkt und ganz gleichartig. Dann muss diese Wahrscheinlichkeit der Zündung beinahe konstant werden.

Abb. 5 zeigt die Indikator-Diagramme bei grossem Zündverzug.

Bei Nr. 37 war die Einspritzzeit auf 30° vor O.T. und die eingesaugte Luftmenge sehr wenig. Der Zündverzug ist sehr gross und die Wahrscheinlichkeit der Zündung in Zeiteinheit vergrössert sich anfangs mit der Zeit und wird nachdem konstant, wie in Abb. 6 a. Dies muss zeigen, dass der Einfluss der Diffusion für diese Wahrscheinlichkeit sehr gross und beherrschbar ist.

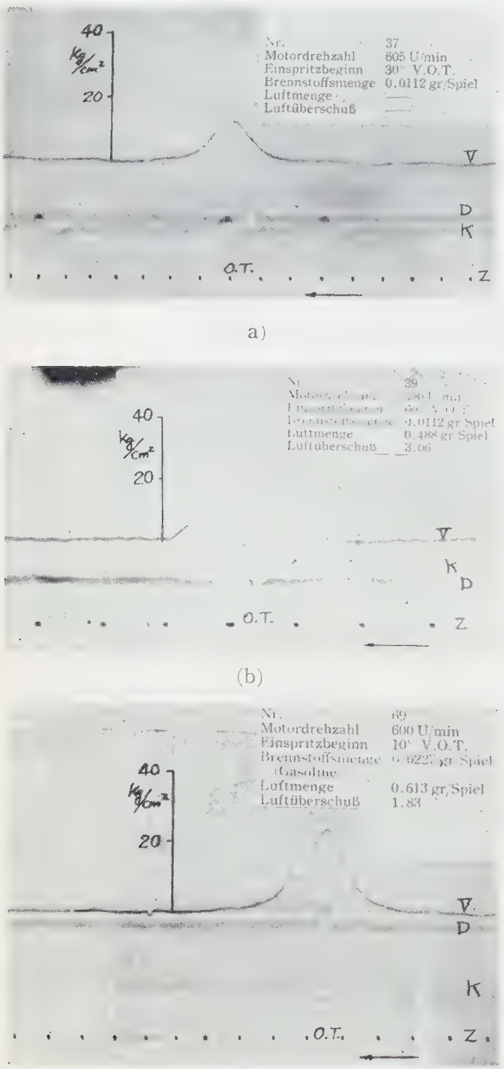

a)

(b)

(c)

Abb. 5. Indikatordiagramm.

Andere Ergebnisse der Berechnungen zeigen auch diese Sache. Bei Nr. 39 ist die Einspritz-

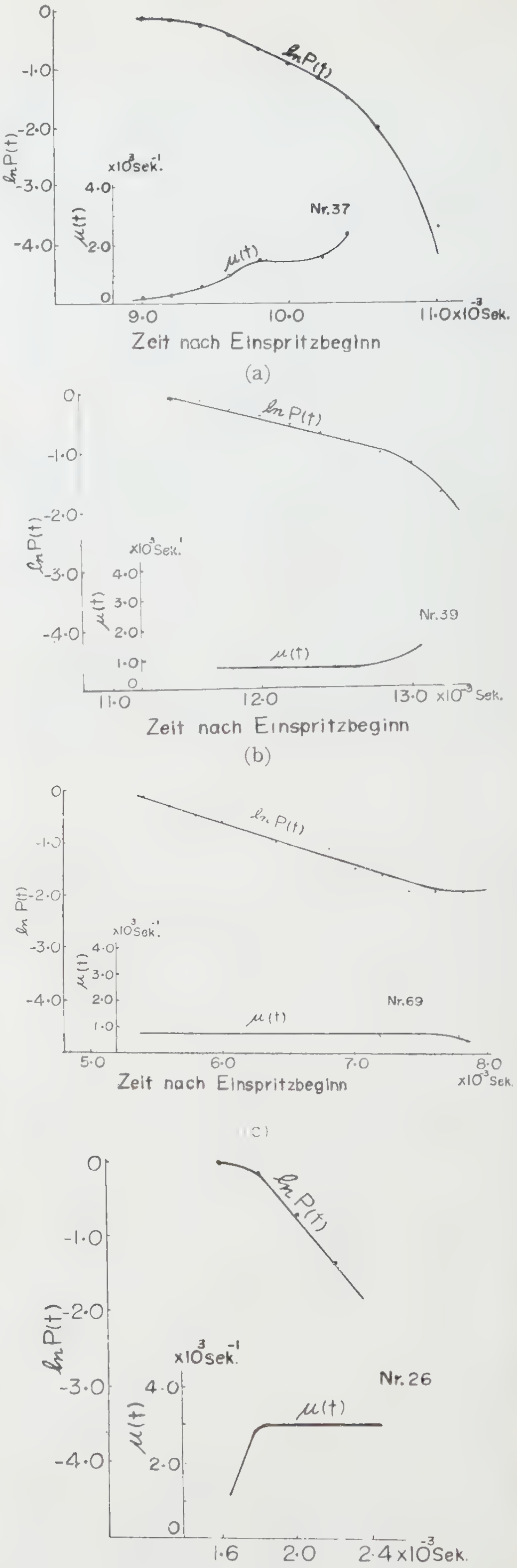

(a)

(b)

(c)

(d)

Abb. 6.

zeit auf 60° vor O.T. und die Mischung muss in der Vorkammer bei der Zündung fast ganz gleichartig werden. So ist die Wahrscheinlichkeit der Zündung in Zeiteinheit konstant. Abb. 6 b zeigt dies.

Bei Nr. 69 war der benutzte Brennstoff Gasolin, dessen Octanzahl 80 und Cetanzahl fast gleich Null ist. Wegen kleiner Cetanzahl, war der Zündverzug dabei sehr gross. Bei Abb. 6 d war die Motordrehzahl 1200 U/min und die eingespritzte Brennstoffsmenge sehr gering. Der Zündverzug ist nicht so gross, aber die Wahrscheinlichkeit der Zündung in Zeiteinheit beinahe konstant, weil die Diffusiongeschwindigkeit sehr schnell ist, wegen schneller Motordrehzahl.

(3) *Beim dritten Teil τ_0, ist die Wahrscheinlichkeit der Zündung in Zeiteinkeit beinahe Null.*

Wie in der vorigen Arbeit erwähnt, kann man denken, dass dieser Teil zwei kleinere Teile hat: Der erste Teil ist hauptsächlich abhängig von der Verdampfung einer minimalen Brennstoffsmenge, die nötig für die Zündung ist. Der zweite Teil ist hauptsächlich abhängig von der anfänglichen chemischen Reaktion, die den für die Zündung nötigen Zündkern ausmacht.

Wenn die Luft in der Umgebung des Brennstoffes niedrigere Temperatur und die grössere Dichtigkeit hat, muss die Zeit, wo die Wahrscheinlichkeit der Zündung beinahe Null und auch von der Verdampfung einer minimalen Brennstoffsmenge abhängig ist, länger sein, weil die Verdampfungsgeschwindigkeit langsamer ist. Wenn aber diese Luft höhere Temperatur und grössere Dichtigkeit hat, muss die Zeit, die abhängig von der anfänglichen chemischen Reaktion, und wo die Wahrscheinlichkeit der Zündung beinahe Null ist, kürzer sein, weil die Reaktionsgeschwindigkeit schneller ist.

Aber meine Versucnsergebnisse zeigen wie folgt:

Nr.	31	32	33	34	
Dichtigkeit der Luft	0.0142	0.0098	0.0098	0.0143	gr/cc
Temperatur der Luft	860	980	1000	870	°K
τ_0	1.8	2.8	2.2	1.6	$\times 10^{-3}$ Sek.

Als die Luftdichtigkeit grösser wurde, wurde die Zeit, in der die Wahrscheinlichkeit der Zündung beinahe Null war, trotz der niedrigerern Lufttemperatur, kürzer. Das bedeutet, dass die anfängliche chemische Reaktion dabei ganz vorherrschend ist, falls die Temperatur für $\boldsymbol{E}$ sehr hoch und ihr Einfluss sehr klein ist.

§ 3. Die Zahl des Zündpunktes und der sogenannte Dieselklopf

Es ist sehr wichtig, um den Verbrennungsmechanismus zu analysieren, wieviele Zündpunkte es bei der Verbrennung im Dieselmotor gibt. Es gibt einige Aufnahmen[1] der Verbrennung in der Brennkammer des Dieselmotors, aber ich probierte von der Wahrscheinlichkeit der Zündung ausgehend, wieviele Zündpunkte es dabei gebe.

Wenn man den Zeitabstand von der früheren Zündung zur nächsten und die Flammengeschwindigkeit messen kann, kann man die Zahl des Zündpunktes wissen.

Nun stelle ich

$$T = 1/\mu(t) ,$$

dar. Diese $\boldsymbol{T}$ bedeutet die Mittelzeit von einer Zündung zur nächsten, die ganz unabhängig von der früheren ist. Deshalb ist der Zeitabstand von einer Zündung in einem Ort der Brennkammer zur nächsten, gewöhnlich länger als diese $\boldsymbol{T}$. Also kann man den minimalen

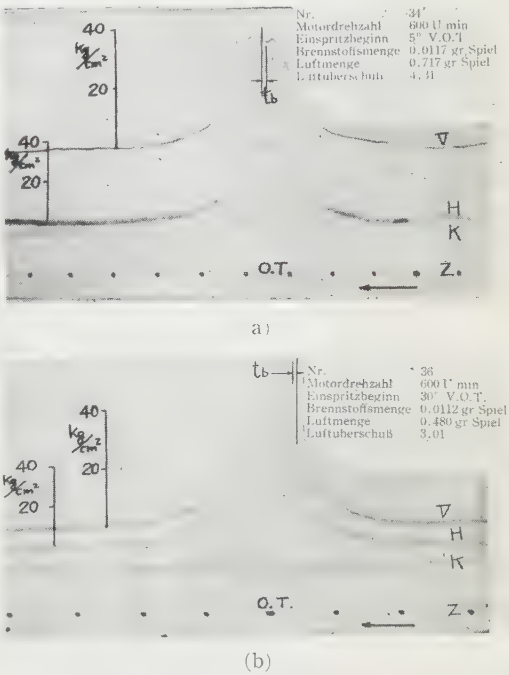

a)

(b)

Abb. 7. Indikatordiagramm.

Zeitabstand der Zündung in Zeiteinheit berechnen.

Andererseits, wenn man die Zeit, wo sich die Flamme anfangs in die ganze Brennkammer erweitert, als die Zeit von der Zündzeit zum maximalen Verbrennungsdruck in der Vorkammer ansieht, kann man diese Zeit in dem Indikator-Diagramm der Druckänderung in der Vorkammer finden.

Abb. 7 zeigt die Indikator-Diagramme, in denen die Druckänderungen in der Vor- und Hauptkammer gleichzeitig gemessen werden. ***H*** bedeutet die Druckänderung in der Hauptkammer und *V* diejenige in der Vorkammer. t_0 bedeutet die Zeit, wo sich die Flamme in der ganzen Vorkammer fortpflanzt.

Abb. 8 zeigt die Kurven des Zusammenhanges zwischen der Zeit nach der Einspritzung und dem Mittelzeitabstand der Zündung. Die Zustände bei diesem Versuche sind wie gesagt.

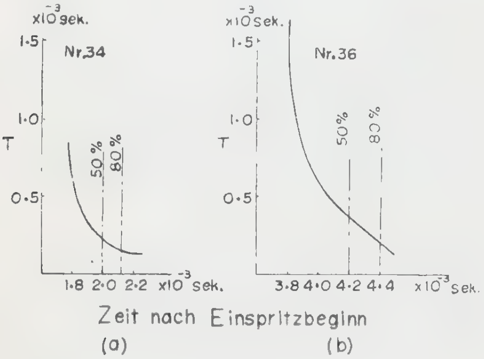

Abb. 8.

Bei Nr. 34 konnte man keinen sogenannten Dieselklopf hören. Der Dieselklopf ist ein Phänomen wie folgt: Wenn die Einspritzbeginn des Brennstoffes in die Brennkammer zu früh ist, oder die Cetanzahl des Brennstoffes sehr klein und unzündwilling ist und darum der Zündverzug sehr gross ist, brennt die viele Brennstoffsmenge in einem Augenblick und man hört ein scharfes Geräusch. Im technischen Gebiet erklärt man nicht so klar, wie die Zündung beim Dieselklopf funktioniert, und man sagt zuweilen, dass dabei die Zündung im ganzen Raum der Brennkammer in einem Augenblick geschieht.

Bei Nr. 34 sind die Zeiten, wo sich die Flamme in die ganze Vorkammer erweitert, alle etwa $1.0\sim1.4\times10^{-3}$ Sek. Dafür sind die Zeitabstände der Zündung fast alle etwa $0.5\sim0.2\times10^{-3}$ Sek., so muss die Zahl des Zündpunktes in einer Brennkammer in einem Spiel des Motors minder als $7\sim2$ sein.

Andererseit sind bei Nr. 36, wo man den Dieselklopf hören konnte, die Zeiten, wo sich die Flamme erweitert, weniger als $0.4\sim0.9\times10^{-3}$ Sek., die Zeitabstände der Zündung fast alle etwa $1.5\sim0.3\times10^{-3}$ Sek.. Also muss die Zahl des Zündpunktes minder als $3\sim1$ sein.

Diese Resultate müssen bedeuten, dass es bei der Verbrennung im Dieselmotor gewöhnlich nur einen oder einige Zündpunkte gibt. Besonders bei dem Dieselklopf gibt es weniger Zündpunkte als bei keinem Dieselklopf und vielleicht nur einen, weil die Wahrscheinlichkeit der Zündung in Zeiteinheit klein sein muss. Gewöhnlich geschieht der Dieselklopf bei dem niedrigen Druck und der niedrigen Temperatur in der Brennkammer, oder bei der kleinen Cetanzahl und grossen Aktivitätenergie, und dabei ist die Wahrscheinlichkeit der Zündung klein.

Der Druckanstieg in der Brennkammer bei dem Dieselklopf ist deshalb so steil, (darum kann man den Dieselklopf hören), weil die rasche Flammengeschwindigkeit von einem Zündpunkt gemacht ist. Da der Zündverzug bei dem Dieselklopf sehr gross ist, mischt sich der eingespritzte Brennstoff mit der Umgebungsluft genügend und wird fast ganz homogen und wird daher ein gleichmässiges brennbares Mischungsverhältnis haben. Bei meinen Versuchen muss die Flammengeschwindigkeit in der Vorkammer in Hinblick auf der Weite der Brennkammer etwa $100\sim200$ m/s sein, falls sich die Flamme von einem Punkt erweitert. Solche Flammengeschwindigkeit kann man sich bei solchen hohen Druck wie im Dieselmotor und solcher homogen gleichmässigen Mischung des Brennstoffes und der Luft denken.

Dabei kann man auch denken, dass die erste Zündung einen Einfluss auf den anderen Teil der Mischung hat, der beinahe homogen ist und noch nicht brennt, und es dort zündet. Aber dies ist die sekundäre Zündung und man kann nur denken, dass die Erweiterung der Verbrennung in der Brennkammer den Druck und die Temperatur der Mischung erhöht und darum es im anderen Teil der Mischung zündet. Also zündet es anfangs an einem oder einigen Orten und von dort pflanzt die Flamme fort und man kann nicht denken, dass es auf einmal im ganzen Gebiet der Mischung zündet. Andererseits kann die Wahrscheinlichkeit der Zündung in Zeiteinheit in Volumeneinheit des Teiles der Mischung, der noch nicht brennt, so gross werden, dass es dort zünden kann, wenn der Druck und die Temperatur der Mischung so hoch werden. Aber, um diese Wahrscheinlichkeit so sehr zu vergrössern, ist es nötig, dass die Menge der Mischung so viel brennt, in Hinblick auf dem Zusammenhang zwischen dieser Wahrscheinlichkeit der Dichtigkeit und Temperatur der Mischung. Z.B. gleich nach dem Ende der Verbrennung, ist der Druck in der Vorkammer niedriger als der zweifache Druck der gedrückten Luft bei der Zündung, wie in dem Indikatordiagramm Nr. 36, Abb. 1 f. Deshalb wird die Wahrscheinlichkeit der Zündung in Zeiteinheit in Volumeneinheit höchstens zwei- oder dreifach, weil diese Wahrscheinlichkeit beinahe proportional der Dichtigkeit der Luft ist und der Einfluss der Temperatur bei solch hoher Temperatur sehr klein ist, wie schon erwähnt. Und auch wird der Teil der Mischung, die noch nicht brennt, minder mit der Reaktion der Verbrennung. Deshalb kann die Wahrscheinlichkeit der Zündung in Zeiteinheit im ganzen Raum nicht so gross werden und es kann nicht an vielen Orten des Teiles der Mischung, der noch nicht brennt, zünden, auch wenn die erste Zündung einen Einfluss auf den anderen Teil hätte. Also beim Dieselklopf kann man denken, dass die Flamme anfangs von einigen, vielleicht nur einem ersten Zündpunkt sehr schnell fortpflanzt, wenn es auch am Ende der Verbrennung an einigen Orten des Teiles, der noch nicht brennt, zündet.

Wenn es zündet, nachdem der eingespritzte Brennstoff sich mit der Luft ganz mischt und eine gleichmässige Mischung entsteht, muss die Cetanzahl fast keine Einflüsse für den Dieselklopf haben, denn der Dieselklopf ist nur abhängig von der Flammengeschwindigkeit und unabhängig von der Zündfähigkeit. Die Cetanzahl hat den Einfluss für Dieselklopf nur in der Zeit, wo die Mischung gemacht wird. Ist die Cetanzahl des Brennstoffs sehr klein, so ist der Zündverzug so gross, dass die viele Brennstoffsmenge sich mit der Luft mischt und viele gleichmässige Mischungsmengen erzeugt werden, in der die Flammengeschwindigkeit sehr sehnell ist und der Dieselklopf entsteht.

Auch wenn der Brennstoff sich mit der Luft ganz mischte und ganz homogen würde, falls es zu dünn oder zu dick wäre, müsste die Flammengeschwindigkeit nach der Zündung langsam sein und man könnte den Dieselklopf nicht hören. Abb. 9 zeigt die Indikator-Diagramme der Druckänderungen in der Haupt-und Vorkammer, falls der Einspritzbeginn auf 340° vor O.T. (am Beginn des Saugtaktes) ist. Bei Abb. 9 a ist das Mischungsverhältnis dünn und es zündet kaum in der Nähe des O.T.. Denn die Mischung ist zu dünn und die Flammen können sich nach der Zündung kaum fortpflanzen. Bei Abb. 9 b. ist es dicker als bei Abb. 9 a und die Flamme kann sich fortpflanzen. Dabei konnte man keinen Dieselklopf hören. Und wie das Indikator-Diagramm zeigt, ist die Verbrennung in der Vorkammer anfangs langsam und steigt dann plötzlich sehr stark an. Diese Ursache ist vielleicht folgende: Da Druck und Temperatur der Luft anfangs sehr niedrig sind, ist die Flammengeschwinigkeit sehr langsam nach der Zündung auf einem Punkt. Nach dem Druckanstieg wird sie aber sehr schnell, oder eine neue Zündung an einem

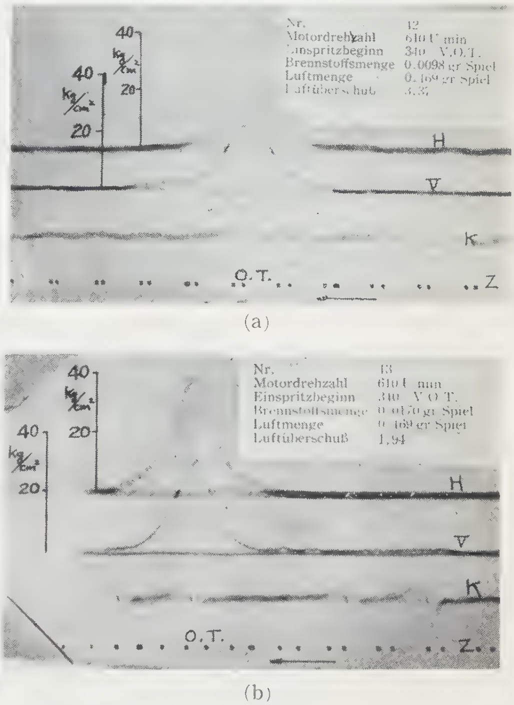

(a)

(b)

Abb. 9. Indikatordiagramm.

anderen Punkt geschieht und die Flamme pflanzt sich dadurch sehr schnell fort und der Druck steigt auch rasch.

Wenn ich das Gesagte wiederhole:

(1) Es gibt nur einen oder einigen Zündpunkte bei der Verbrennung im Dieselmotor

(2) Besonders bei dem Dieselklopf gibt es vielleicht nur einen Zündpunkt, von dem sich die Flamme sehr schnell fortpflanzt.

(3) Wenn das Mischungsverhältnis bei einem bestimmten Zustand zu dünn oder zu dick ist, falls die Mischung homogen ist, pflanzt sich die Flamme langsam fort, und, wenn es noch dünner oder dicker wird, kann es nicht brennen, weil die Flamme sich nicht fortpflanzen kann.

§ 4. Zusammenfassung

Im ersten Teil dieser Arbeit scheint der Zündmechanismus bei der Verbrennung in der Brennkammer des Dieselmotors folgendmassen zu sein:

(1) Zuerst mischt sich der eingespritzte Brennstoff mit der Umgebungsluft durch die Diffusion mit der Verdampfung.

(2) Nach dem Stoss der Moleküle des Brennstoffes und des Sauerstoffes, entstehen einige Zündkerne.

(3) Einer oder einige dieser Zündkerne vergrössern sich allmählich und sie werden mit einer grossenen Menge, deren entstandene Wärme so gross wird, dass sich davon die Flammen fortpflanzen können, gezündet.

Ich versuchte in dieser Arbeit diesem Gedanken noch weiter und genauer nachzugehen, um andere Versuche und Beweise zu erziehen. Besonders konnte ich beweisen, dass es dabei nur einen oder einige Zündpunkte gibt.

Trotzdem gibt es noch viele Unbekannten im Zündmechanismus, z.B. die Aktivitätenergie, Diffusionsgeschwindigkeit, Zündkernsgrösse, Verdampfung usw. So muss noch weiter über dieses Problem geforscht werden.

Zum Schluss möchte ich Herrn T. Okazaki, Professor der Technischen Fakulltät der Tokyo Universität, der mir während der ganzen Zeit meiner Versuche Hilfe leistete und mir viele gute Ratschläge gab, danken herzlich ebenfalls Herrn Dr. M. Hirata, Professor der Fakulltät der Naturwissenschaften der Tokyo Universität, und Herrn N. Terao, die mir auch viele gute Ratschläge gaben.

Und auch danke ich herzlich unserm Direktor, Herrn M. Ito, und meinen Mitarbeitern, Herren T. Hori und S. Miyamoto.

Schrifttum

1) P. M. Heldt: High Speed Diesel-Engines.

Short Notes

J. PHYS. SOC. JAPAN **10** (1955) 313~314

Note on the Shift of Band Edge of Germanium with Temperature

By Masao TOMURA and Eizo OTSUKA
Institute of Polytechnics,
Osaka City University, Osaka

(Received September 15, 1954)

The separation E_g between the top of the valence band and the bottom of the conduction band of germanium varies with temperature according to a linear relation of $E_g(T)=E_g(0)-\beta T$.[1] The value of β obtained from conductivity experiment is 1.1 $\times 10^{-4}$ eV/deg[2] and almost equal to the value calculated from the deformation potential theory[1]. The above value, however, is obtained on the assumption that the energy surface in the Brillouin zone of germanium is spherical and non-degenerate. Furthermore, the effective masses of electron and hole are put equal to the free electron mass.

Recent calculations of the energy bands in momentum space[3] and observations of cyclotron resonance[4][5] reveal the electronic band structure of germanium fairly well. According to these results, energy surface in the conduction band consists of six ellipsoids of revolution with the principal axes lying along the [110] type directions[3] or eight along the [111] type directions[5]. On the other hand, there are three sets of nearly spherecal energy surface centered about $k=0$ in the valence band[3]. Though no definite model of the energy band structure of germanium is available at present, recently obtained informations of germanium will give some new value of β.

In the course of obtaining β from the well-known formula

$$n_i^2=4C_cC_v\exp(-E_g/kT)\,, \tag{1}$$

the state density factors C_c and C_v should be modified in order to satisfy the requirements arising from the circumstances mentioned above. Allowing for the energy surface of the ellipsoids of revolution in the conduction band, C_c is now given as $g_c(2\pi kT/h^3)^{3/2}m_{nl}^{1/2}m_{nt}$. Here m_{nl} and m_{nt} are the effective masses of electron along the longitudinal and transversal axes of the ellipsoid of revolution, respectively, and g_c is the number of ellipsoids in the conduction band, i.e. six or eight. As for C_v, the nearly spherical energy surface in the valence band suggests the conventional form of state density. However, the valence band is triply degenerate at $k=0$ and only two values of effective mass $m_{p1}=0.04m_0$ and $m_{p2}=0.30m_0$ for holes have been observed in the cyclotron resonance experiment[5]. Hence, one of the effective masses ought to be allotted to two sets of energy surface and the other to the remaining set. Accordingly, C_v becomes either $(2\pi kT/h^3)^{3/2}(2m_{p1}^{3/2}+m_{p2}^{3/2})$ or $(2\pi kT/h^3)^{3/2}(m_{p1}^{3/2}+2m_{p2}^{3/2})$, since allocation of the effective masses is unknown. Four combinations of C_cC_v, therefore, should be considered separately.

No calculation for the temperature dependence of carrier mobility in the case of non-spherical or degenerate energy surface has been made so far. However, the recent accurate measurement of Hall mobility reports $\mu_{H_p}=1.07\times 10^8 T^{-1.82}$ for holes[6]. Then we may recalculate n_i^2 in the data of Johnson-Fan[2], using the temperature dependent mobility ratio $b=\mu_{H_n}/\mu_{H_p}$ in lieu of the constant value of 1.5 in their paper. We get a new value of 1.83$\times$ 10^{-4} eV/deg for β, as well as $E_g(0)=0.79$ eV, effective masses being put equal to the free electron mass. If we now employ $m_{nt}=0.08m_0$ and $m_{nl}=1.3m_0$ for electron, while, $m_{p1}=0.04m_0$ and $m_{p2}=0.30m_0$ for hole, allowing for the degeneracy factor, β undergoes further modification. The values of the correction term $\Delta\beta$ are listed in Table I together with the modified values of β for each case of the four combinations. If the energy minima of the ellipsoids in conduction band are situated at the zone boundaries, the degeneracy factor 6 or 8 should be replaced by 3 or 6, respectively. The values of the mentioned quantities for these cases are also listed in parentheses. The new values of β are seen to approach 4.6$\times 10^{-4}$ eV/deg, which has been obtained from the optical method[7]. As well-known, the latter corresponds to the one at $k=0$, because of the optical data analyzed in the wave length region of "direct transition". Our values derived from conductivity data may be taken to refer to the separation between the top of the valence band and the bottom of the conduction band. These two kinds of β, of course, may not be expected to coincide, although the approach of their values seems to be rather natural.

Table I. The values of correction term $\Delta\beta$ and modified β.

No. of degeneracy in C-band	Allocation of effective masses in V-band	$\Delta\beta$ (eV/deg)	β (eV/deg)
6(3)	$2m_{p1}^{3/2}+m_{p2}^{3/2}$	2.2(2.5)$\times 10^{-4}$	4.0(4.3)$\times 10^{-4}$
6(3)	$m_{p1}^{3/2}+2m_{p1}^{3/2}$	1.4(2.0)	3.2(3.8)
8(4)	$2m_{p1}^{3/2}+m_{p2}^{3/2}$	1.7(2.3)	3.5(4.1)
8(4)	$m_{p1}^{3/2}+2m_{p2}^{3/2}$	1.4(1.8)	3.2(4.6)

References

1) J. Bardeen and W. Shockley: Phys. Rev. **80** (1950) 102.

2) V. A. Johnson and F. Y. Han: Phys. Rev. **79** (1950) 899.
3) F. Herman and J. Callaway: Phys. Rev. **89** (1953) 518; F. Herman: Phys. Rev. **93** (1954) 1214.
4) G. Dresselhaus, A. F. Kip and C. Kittel: Phys. Rev. **92** (1953) 827.
5) Benjamin Lax, H. J. Zeiger, R. N. Dexter and E. S. Rosenblum: Phys. Rev. **93** (1954) 1418.
6) F. J. Morin: Phys. Rev. **93** (1954) 62. Morin gives $\mu_{Ln}=4.90\times10^7T^{-1.66}$ and $u_{Lp}=1.05\times10^9T^{-2.33}$. We have converted them to Hall mobilities, using Fig. 2 in his paper. For our purpose, usage of Hall mobility data seems to be more natural than that of drift mobility ones, since the carrier concentration in Eq. (1) is determined from the Hall effect measurement.
7) H. Y. Fan: Phys. Rev. **78** (1950) 808.

J. Phys. Soc. Japan **10** (1955) 314

On the Threshold of the Exciton Band in BaO

By Masayoshi SAKAMOTO

Department of Physics, Tokyo College of Science

(Received December 1, 1954)

It has been already known that the long wave region of the spectral sensitivity curve of photoemission or photoconductivity in BaO is enhanced remarkably by the pre-irradiation of ultra-violet ray[1][2][3]. The author studied the increase of photoconductivity at about $h\nu=2.3$ eV, when the wave length of the pre-irradiation was changed from long wave side to short one.

The behaviours are shown in Fig. 1, where $\Delta i=i-i_0$ is the increase of the photocurrent, i is the saturated photocurrent after irradiation of 30 min. and i_0 is the photocurrent just after the annealing. As seen from the figure, the current increases rapidly above the region of 3.3 eV.

On the otherhand, Sproull and Tyler[4] concluded that the absorption band in 4.0~4.2 eV was due to the excitons and that the photocurrent found in BaO single crystal above 4.0 eV was due to the thermal dissociation of these excitons.

Therefore, it is supposed that the photocurrent at 2.3 eV is due to the ionization of donors[5]. And the increase of this current may be interpreted by the temporary increase of the number of the donors, because the electrons released thermally from the excitons, which are created by the pre-irradiation of the ultra-violet light, may be trapped by the oxygen vacancies[6]. Therefore, the threshold value of 3.3 eV in Fig. 1 may be supposed as the lowest energy necessary to create these excitons in BaO powder at room temperature, which corresponds 3.9 eV measured by Sproull and his coworkers in the photoconductivity of BaO single crystal[7].

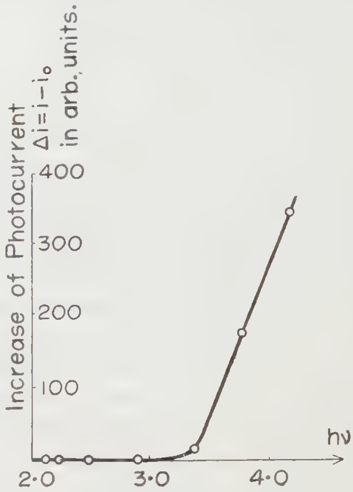

Fig. 1. The relation between the wave length of the pre-irradiation and the increase of the photocurrent.

References

1) B. D. McNary: Phys. Rev. **81** (1951) 631.
2) H. B. DeVore & J. W. Dewdney: Phys. Rev. **83** (1951) 805.
3) M. Sakamoto: J.A.P.J. **23** (1954) 171.
4) R. L. Sproull & W. W Tyler: "Semi-Conducting Materials" (1951) p. 122.
5) Kin-ichi Noga & Shoji Kawamura: J.P.S.J. **7** (1952) 287.
6) N. F. Mott & R. W. Gurney: "Electronic Processes in Ionic Crystals" Chap. IV.
7) R. L. Sproull & W. W. Tyler: ibid.

J. Phys. Soc. Japan **10** (1955) 314~315

Confirmation of the Existence of a Helium Double-Molecule

By Taro KIHARA and Shobu KANEKO

Department of Physics, University of Tokyo

(Received February 1, 1955)

One of the authors and his co-workers[1] recently analysed the second and third virial coefficients of helium above the Boyle temperature, for $T\gtrsim T_B=26.0$°K, by means of the Lennard-Jones model of the intermolecular potential. Their conclusion was that the two-body system of He^4 atoms has a discrete energy level (a bound state) while the two-body system of He^3 has no discrete level (no bound state).

The aim of the present note is to confirm the previous result by an analysis of the second virial coefficient at *low* temperatures $T \lesssim 2T_B$ by means of the square-well model of the intermolecular potential,

$$U(r)=\begin{cases} \infty & \text{for} \quad r<\sigma \\ -\varepsilon<0 & \text{for} \quad \sigma<r<g\sigma \\ 0 & \text{for} \quad g\sigma<r\,, \end{cases}$$

$$1.5 \lesssim g \lesssim 2.0\,,$$

in which r is the distance between the centers of the monatomic molecules.

The second virial coefficient B of He^4, which obeys Bose-Einstein statistics and has zero spin, can be expressed in the form$^{2)}$:

$$B=-\frac{1}{16}\left(\frac{4\pi\hbar^2}{mkT}\right)^{3/2}+2\sum\nolimits_{\text{even}\,l}(2l+1)B_l\,.$$

Here $\hbar$ is Planck's constant divided by 2π; m is the mass of a helium atom; kT is the Boltzmann constant times temperature; and the summation is to be taken over even quantum numbers $l=0,\ 2, \cdots\cdots$ of the angular momentum. The B_l is given by

$$B_l=-\frac{1}{2}\left(\frac{4\pi\hbar^2}{mkT}\right)^{3/2}\left[\sum_{\text{dicrete}}\exp\left(-\frac{E_{nl}}{kT}\right)+\frac{1}{\pi}\int_0^\infty\exp\left(-\frac{E}{kT}\right)\frac{d\eta_l}{dE}dE\right],$$

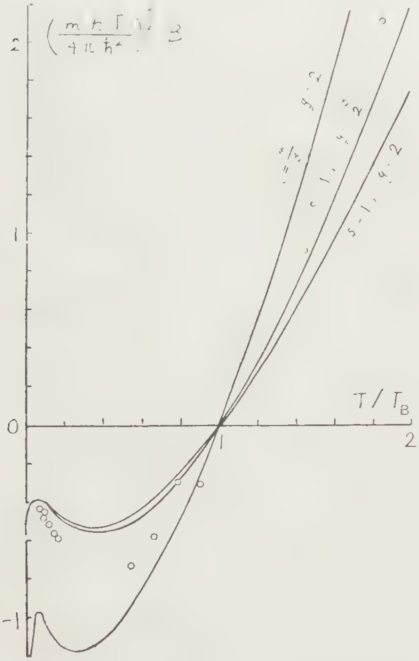

Fig. 1.

in which η_l is the phase-shift defined by the asymptotic form

$$R(r)\sim\sin(r\sqrt{mE}/\hbar-\tfrac{1}{2}l\pi+\eta_l) \quad \text{for} \quad r\to\infty\,,$$

of the regular solution of

$$\left[\frac{d^2}{dr^2}+\frac{m}{\hbar^2}(E-U(r))-\frac{l(l+1)}{r^2}\right]R(r)=0\,,$$

$E_0,\ E_1, \cdots\cdots$ (<0) being discrete energy levels or the energies of bound states of the two-body system. In reality, at most one level, E_{00}, is to be taken into account for helium.

For the square-well potential the phase-shifts η_l can be obtained by use of spherical Bessel functions, and the discrete energy levels, if any, can also be calculated easily.

Let us introduce the depth parameter$^{1)}$

$$s=\left(\frac{2(g-1)}{\pi\hbar}\sigma\right)^2 m\varepsilon\,.$$

If one or more discrete levels exist in the two-body system s is greater than unity; if no discrete level exists s is less than unity. The second virial coefficient for square-well potential then assumes, for each g and s,

$$B=\left(\frac{4\pi\hbar^2}{mkT}\right)^{3/2}f(\tau), \qquad \tau\equiv\frac{\pi^2 skT}{4(g-1)^2\varepsilon}\,,$$

the function f being given in the table.

τ	$f(\tau)$ for $s=1$ $g=3/2$	$f(\tau)$ for $s=1$ $g=2$	$f(\tau)$ for $s=4/3$ $g=2$
0.5	−0.380	−0.384	−1.017
1	−0.422	−0.453	−1.017
2	−0.522	−0.535	−1.132
4	−0.551	−0.456	−1.149
6	−0.423	−0.202	−0.983
8	−0.174	0.153	−0.701
10	0.152	0.600	−0.333
12	0.559	1.111	0.106
14	1.059	1.65	0.612
16	1.59	2.26	1.161
18	2.16	2.93	1.74
20	2.78	3.69	2.41

Calculated curves of $(mkT/4\pi\hbar^2)^{3/2}B$ are compared in the figure with experimental results obtained by Keesom et al$^{3)}$. The figure shows that the depth parameter s for the He^4–He^4 system is within the range $1<s<4/3$, which corresponds to the range $3/4<s<1$ for the He^3–He^3 system. Thus we have confirmed the previous conclusion.

References

1) T. Kihara, Y. Midzuno, T. Shizume: J. Phys. Soc. Japan **10** (1955) 249.
2) G. E. Uhlenbeck, E. Beth: Physica **4** (1937) 915; L. Gropper, Phys. Rev. **50** (1936) 963, **51** (1937) 1108.
3) W. H. Keesom: *Helium* (Elsevier, Amsterdam 1942) p. 34.

J. PHYS. SOC. JAPAN **10** (1955) 316~317

The Metabolic Turnover and the Maintenance of the Low Entropy Level

By Motoyosi SUGITA
Hitotubasi University, Tokyo

(Received December 24, 1954)

In the preceding paper[1] the metabolic turnover of F.E. (free energy) has been discussed. In the following the turnover of entropy and that of enthalpy will be considered separately.

Let G be the F.E. of a living organism and χ and S be its enthalpy and entropy respectively. Then

$$G=\chi-TS \quad \text{and} \quad \dot{G}=\dot{\chi}-T\dot{S},$$

$\dot{G}$ is written in the form

$$\dot{G}=Z_1-Z_2-D-W, \tag{1}$$

where Z_1 and Z_2 is the F.E. taken and excreted respectively, D is the chemical consumption of F.E. and W is the sum of the external work, W_L, and the internal loss, W_f, due to friction and others,

$$W=W_L+W_f.$$

In the preceding paper a special model of the organism was proposed, which is represented by Fig. 4 of that paper[1], and according to that we have

$$Z_1-Z_2=R+W+D_f, \tag{2}$$

where R is the restoration of F.E. per unit time, which is done by the feedback of energy, and D_f is the loss of F.E. during the energy transfer. Then the basal metabolism, in which $W_L=0$, may be written in the form

$$(Z_1-Z_2)_0=R+W_f+D_f,$$

and Z_1-Z_2 is measured by gas analysis.

From (1) and (2) we have

$$\dot{G}=R-D_r, \tag{3}$$

where

$$D_r=D-D_f, \tag{4}$$

is the depreciation of F.E. due to catabolism. (3) means that the depreciation is repaired by R due to anabolism. $\dot{G}>0$ means the *expanding reproduction* and $\dot{G}<0$ the *contracting reproduction* of F.E. of our body.

Now $\dot{G}<0$ or $R<D_r$ during work and $\dot{G}>0$ or $R>D_r$ during rest or sleeping. This is very important from the view print of the science of labour, for the mean value of $\dot{G}$ is never negative to maintain the life of the laborer. The metabolic turnover of the energy part of G is, however, rather simple (see Fig. 2) and its mean value may be easily repaired, but the circulation of the entropy part is complicated, which cannot be easily repaired after severe work or illness. So that let us consider the metabolic balance of our entropy.

The well known equation[2] is

$$\dot{S}=\dot{S}_e+\dot{S}_i, \tag{5}$$

where $\dot{S}_e$ is the entropy flow and $\dot{S}_i$ the entropy production per unit time. Then

$$\left.\begin{aligned}&\dot{S}_i=(D+W_f)/T\\ \text{and}\quad&\dot{S}_e=S_1-S_2-Q/T.\end{aligned}\right\} \tag{6}$$

where S_1 and S_2 is the chemical part of the entropy uptake and excretion respectively and Q is the heat flowing out of the body.

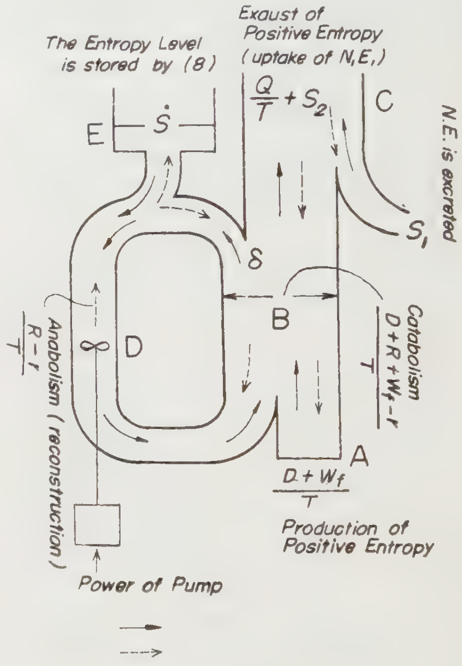

Fig. 1. Balance of Entropy.

Now let us modify our model as is shown by Fig. 1, in which r is the enthalpy part of R. Then we have

$$\left.\begin{aligned}&D+W_f=-(R-r)+D+R+W_f-r.\\ &\text{Therefore}\\ &\dot{S}_i=-\frac{R-r}{T}+\frac{D+R+W_f-r}{T},\end{aligned}\right\} \tag{7}$$

in which $(D+R+W_f-r)/T$ means the apparent production of entropy or depreciation of N.E. (negative entropy) due to destruction of the molecular order, i.e. catabolism. The behavior of N.E. is also expressed in Fig. 1 by making use of the reversed arrows (---->). $(R-r)/T$ is the reproduction of N.E. or the production of low entropy level, which is forced by anabolism, and this quantity must be subtracted as is showh in (7).

The process of anabolism is drived by the power, which is the feedback from exergonic reactions and expressed schematically by the pump at D. From (5), (6) and (7) we have

$$\dot{S} = -\frac{R-r}{T} + \delta \,, \tag{8}$$

where

$$\delta = \frac{D+R+W_f-r}{T} - \left(S_2 - S_1 + \frac{Q}{T}\right) \tag{9}$$

and it is extracted out of the apparent production of entropy (B) by the suction of the pump, if we take the model of Fig. 1. δ may be also the depreciation of the N.E. reproduced by the pump action. The remaining part of the reproduced N.E. is stored in E of Fig. 1. On the other hand E represents the entropy level of our body, which has the natural tendency to rise, if we take positive entropy into account, but is maintained at the low level by the pump action. The low entropy level or the high N.E. of our body is thus maintained.

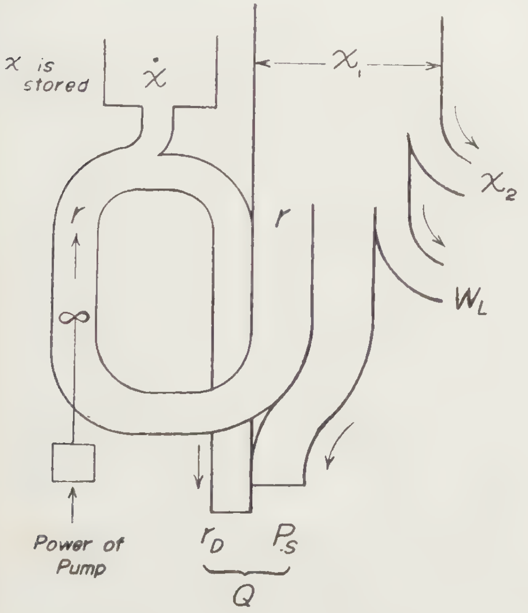

Fig. 2. Balance of Enthalpy.

S_2+Q/T is called the uptake of N.E. by Schrödinger[3]. Then S_2 might also be taken at toilet and S_1 be excreted at the dining room in the form of N.E.. There are scientists believing that the level of N.E. of our body would be maintained simply by taking N.E. from the external world. If so, the water in the tank might be also conserved by taking negative quantity of water. In reality we must take the pump action into account in both cases, N.E. and water in tank.

Fig. 2 shows the balance of enthalpy. Let χ_1 and χ_2 be its uptake and excretion respectively. Then

$$\dot{\chi} = \chi_1 - \chi_2 - W_L - Q \,, \tag{10}$$

which is the important relation in physiology.

From (5), (6) and (10) we have

$$\dot{G} = \dot{\chi} - T\dot{S} = Z_1 - Z_2 - D - W \,, \tag{11}$$

again, if we put

$$Z_1 = \chi_1 - TS_1 \qquad Z_2 = \chi_2 - TS_2 \,. \tag{12}$$

According to our model, using (2) and (12) we have

$$\begin{aligned} \chi_1 - \chi_2 &= R + W + D_f + T(S_1 - S_2) \\ &= r + W_L + P_s \,, \end{aligned} \tag{13}$$

where

$$P_s = R - r + W_f + D_f + T(S_1 - S_2) \,, \tag{14}$$

is the enthalpy consumed as power for the entropy circulation, for the internal work etc.. P_s is expelled ultimately as heat, but it is a part of Q, as is shown by Fig. 2 and also by (16).

From (10) and (13)

$$\dot{\chi} = r + P_s - Q = r - r_D \,, \tag{15}$$

where

$$r_D + P_s = Q \,. \tag{16}$$

The details of the analysis will be given in this Journal.

References

1) M. Sugita: J. Phys. Soc. Japan **8** (1953) 709, see also, Annals of the Hitotubasi Academy, Supplement 1, p. 9 (1951); Ibid. IV, No. 2, p. 103 (1954)
2) See the Works of Prigogine, de Groot and others.
3) E. Schrödinger, What is Life.

J. PHYS. SOC. JAPAN **10** (1955) 317~318

The Ionization Potentials of Some Conjugated Molecules

By I. OMURA, H. BABA and K. HIGASI

Research Institute of Applied Electricity, Hokkaido University, Sapporo

(Received November 22, 1954)

Since the method of molecular orbitals proved its usefulness in treating the problems of valence and chemical reactivities, the study of ionization potentials has increasingly gained its importance in the field of chemical physics. In the majority of conjugated molecules, where so-called π-electrons confer their characteristic properties, the energies required to remove one π-electron to infinity from these molecules are given by their first ionization potentials; and these energy values have often been employed as important parameters in the theoretical analysis of the molecular properties.1)

In the present note the writers wish to report some results of their measurements on the appearance potentials which have recently made by the use of a mass spectrometer of the Hagstrum type.2) The evaluation of these potentials was made according to Honig's critical slope method.3) And argon was employed as the reference standard.

The samples measured were carefully purified in this laboratory excepting that of cyclooctatetraene, which was kindly offered by Assist. Prof. I. Tanaka of Tokyo Institute of Technology in the purest form.

First ionization potentials of conjugated molecules, eV.

Substance	Present authors (Electron Impact)	Values in literature (Electron Impact)	(Spectroscopic)
Benzene	9.46±0.1	9.52±0.08 4)	9.24 6)
Toluene	9.15±0.1	9.23 4)	8.82 7)
Pyridine	9.70±0.05	9.8 ±0.2 5)	——
Cyclooctatetraene	8.63±0.15	——	——
Pyrrole	8.97±0.05	——	8.90 8)
Furan	9.00±0.1	9.05±0.02 4)	9.01 8)
Thiophene	9.10±0.2	——	8.91 8)

Upon the inspection of the table it will be seen that the appearance potentials reported here are in accord with the values of other investigators.4,5,6,7,8) There is no record in the literature concerning the ionization potential of cyclooctatetraene; and it may be of interest to note that the present value of 8.63 eV is close to those of other unsaturated cyclic hydrocarbons, e.g. cyclopentadiene 8.58 eV and cyclohexadiene 8.4 eV, both of them being obtained by the spectroscopic method.8) But further discussion will be postponed until afterwards when the experimental details of the method of measurement will be fully reported.

Grateful acknowledgement is made to Prof. K. Hirota, for initiating the present work. Thanks are also due to the Education Ministry for a grant-in-aid.

References

1) See for example S. Nagakura and J. Tanaka: J. Chem. Phys. **22** (1954) 236, 563.
2) H. D. Hagstrum: Rev. Mod. Phys. **23** (1951) 185; I. Omura: Bull. Res. Inst. Appl. Elec. **6** (1954) 15.
3) R. E. Honig: J. Chem. Phys. **16** (1948) 105.
4) J. D. Morrison and A.J.C. Nicholson: J. Chem. Phys. **20** (1952) 1021.
5) A. Hustrulid, P. Kusch, and J. T. Tate: Phys. Rev. **54** (1938) 1037.
6) W. C. Price and R. W. Wood: J. Chem. Phys. **3** (1935) 439; W. C. Price: Chem. Rev. **41** (1947) 257.
7) V. J. Hammond, W. C. Price, J. P. Teegan, and A. D. Walsh: Discuss. Faraday Soc. **9** (1950) 53.
8) W. C. Price and A. D. Walsh: Proc. Roy. Soc. (London) **A 179** (1941) 201.

J. Phys. Soc. Japan **10** (1955) 318～319

X-Ray Studies on Long Chain Compounds Solidified under an Alternating Electric Field

By Mitsuo Ida

Department of Physics, Faculty of Science, Kanazawa University

(Received December 2, 1954)

X-ray studies on long chain compounds solidified under an electrostatic field were performed systematically by Kakiuchi, but similar studies using an alternating electric field seem never to have been done by any author so far as the present author knows.

It was expected that in special cases, the fibre structure of long chain compounds would be formed even under an alternating electric field, which was verified by X-ray diffraction. The X-ray from a copper target was radiated in a direction perpendicular to the electric field applied to the sample. An alternating electric field was applied by the frequency of 60 c/s or about 300 kc/s. Besides, an electrostatic field was used for a comparative study. The intensity of the field was 6–8 kv/cm.

It was found that the Debye rings obtained could be classified into three types, namely, type A which has intensity maximum in the direction of the field (Fig. 1.), and type B which has intensity maximum in the direction perpendicular to it (Fig. 2.) and the third type which has a uniform ring. The results can be tabulated as follows.

The fibre structure shown by cetyl alcohol solidified under an electrostatic field can be explained by the permanent diple moment of its microcrystals as in Kakiuchi's opinion, while the fibre structures of other substances eventually be explained by the anisotropic induced polarization of their microcrystals. But the reason why there are three cases of A type, B type and uniform ring is not yet clear. Further studies are going on, and the details of the results will duly be reported.

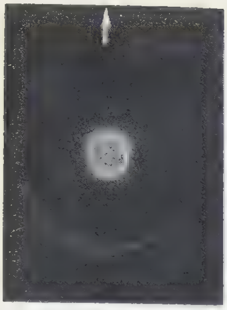

Fig. 1. White wax. (electrostatic field)

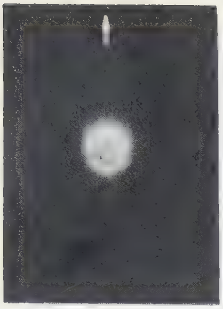

Fig. 2. White wax. (60 c/s)

Table.

	Electrostatic field	60 c/s	300 kc/s
Paraffin	A	B?	B?
Cetyl alcohol	A	No	No
Palmitic acid (added with a few percent paraffin)	A	B	B
Cetyl palmitate (added with a few percent paraffin)	A	A	A
Yellow wax	A	B	A
White wax	A	B	B
Carnauba wax	A	B?	B?
Japan wax	A	No	No

No: uniform ring.　?: ambiguous.

The author wishes to express his sincere thanks to Professor H. Shoji for his kind guidance.

Reference

Kakiuchi: Sci. Pap. I.P.C.R. **40** (1943) 189.

J. PHYS. SOC. JAPAN **10** (1955) 319~320

Isotope Shift in Cd II λ 4415

By Kiyoshi MURAKAWA

Institute of Science and Technology,
Komaba-machi, Meguro-ku, Tokyo

(Received December 24, 1954)

Using natural cadmium and a liquid-air cooled hollow-cathode tube operated by a very small discharge current, the author[1] studied the hyperfine structure (hfs) of Cd II λ4415 ($4d^{10}5p\,^2P_{3/2}-4d^95s^2\,^2D_{5/2}$) and found that the shift 114—116 is very small compared with the shift 112—114. In the mean time Hindmarsh, Kuhn and Ramsden[2] (to be referred to as HKR) and Woodward[3] and Woodward and Speck[4] (to be referred to as WS) have worked on the same subject, using separated isotopes.

The hfs of the odd isotopes would be a good material for testing the perturbation calculation, so the hfs of λ4415 has been analyzed more carefully than before. Fig. 1 shows as a summary the result of this investigation. In ref. 1, the intervals 110—112, 112—114 and 114—116 were measured separately, but now all the intervals were measured at the same time, and the position of every component is referred to the common origin 110, because 110 is best resolved.

When we plot the effective quantum number n^* of the $np\,^2P_{3/2}$ sequence (given in the article of Takahashi[5]) against the term value, we find that it is irregular at $9p\,^2P_{3/2}$. This will be probably due to the perturbation by $5d^96s6p\,^2P_{3/2}$ which lies somewhat higher than $9p\,^2P_{3/2}$, at about 9000 cm^{-1}, say. Since the multiplet analysis of the configuration $5d^96s6p$ available at present is incomplete, it is not possible to calculate the accurate mixing percentages of the wave functions. However, the wave function $5d^96s6p\,^2P_{3/2}$ (in LS coupling) with the splitting factor

$$A(d^9sp\,^2P_{3/2})=\frac{2}{9}a(s)+\frac{62}{63}a_d-\frac{7}{18}a_p$$

(for the d and p electrons the relativity corrections are neglected) will be the most remarkable one of those which affect the hfs splitting of the level $4d^{10}\,5p\,^2P_{3/2}$. A rough estimation combined with the measurement of the hfs indicates that $5p\,^2P_{3/2}$ of the odd isotopes has a splitting of around 0.05 cm^{-1} instead of 0.026–0.027 cm^{-1} of the previous calculation which neglected the perturbation. The component c should lie at about 0.152, and the observation does not contradict with this assumption. The splitting of $5d^96s^2\,^2D_{5/2}$ was also recalculated by a method to be described at another place. Assuming that the splitting of $5p\,^2P_{3/2}$ in Cd^{113} is 0.054 cm^{-1}, the diagram was constructed, and the whole hfs pattern was determined so as to fit the observed intensity distribution as accurately as possible. The determination of b and $\overline{a}$ offered the largest difficulty, and the positions of these components given in Fig. 1 will perhaps require some corrections; but the present choice lowered the interval 112—114 to 0.046 cm^{-1} from 0.054 cm^{-1} of ref. 1.

The present interpretation shows that a, b and c should lie approximately equidistant. However, WS measured by photographic photometry the intensity ratio of the components a and b (WS assumed that c is so near to b that it is masked by b) and obtained 1.35±0.05, and concluded that this is to be interpreted as 1.40 which would result if the intensity of c were superposed on that of b. This is not in agreement with the above-mentioned prediction, but the author would like to assume that the accuracy of the intensity measurement of WS is somewhat smaller and believe that the true

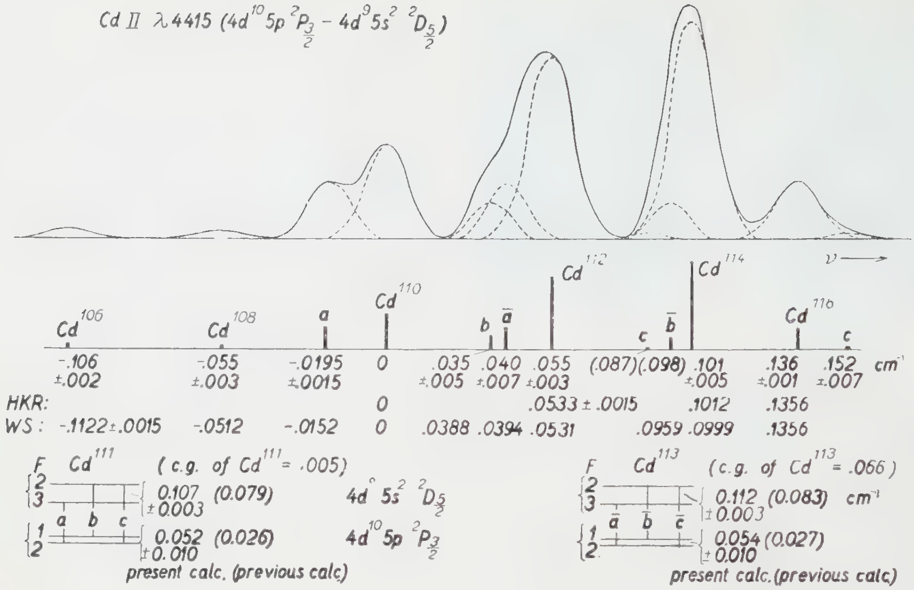

Fig. 1. Observed intensity distribution in linear scale (upper curve), hfs pattern deduced from it (calculated position is in parentheses) compared with the findings of HKR (HKR published the distances 110—112, 112—114 and 114—116 separately, so the positions of 112, 114 and 116 relative to 110 were calculated here) and WS (middle diagram) and the transition diagram of the odd isotopes (bottom diagram).

intensity ratio would turn out to be $a/b = 14/9 = 1.56$

The measurement of the positions of 110, a, 108 and 106 offered no difficulty, and essentially the same values as in the previous work[1] are given in Fig. 1. The position of 106 shows a minor disagreement with WS.

As a conclusion we might consider that the hfs of Cd II λ4415 is not yet so satisfactorily studied, and further detailed investigations are to be desired.

References

1) K. Murakawa: Phys. Rev. **93** (1954) 1232.
2) W. R. Hindmarsh: H. Kuhn and S. A. Ramsden, Proc. Phys. Soc. London **A 67** (1954) 478.
3) E. C. Woodward: Phys. Rev. **93** (1954) 948.
4) E. C. Woodward and D. R. Speck: Phys. Rev. **96** (1954) 529.
5) Y. Takahashi: Ann. d. Physik **3** (1929) 27.

J. PHYS. SOC. JAPAN **10** (1955) 320∼321

Range-Energy Relation of Triton in the Nuclear Emulsion up to 10 Mev

By Mitsuo MIWA and Katsumi KURIYAMA
Physics Department, Tokyo University of Education

(Received February 1, 1955)

Very little has so far been studied experimentally on the range-energy relation of triton in the nuclear emulsion. We have studied the relation by making use of the experimental data obtained in the course of the study of excitation function of $^{7}\text{Li}(\gamma t)^{4}\text{He}$ reaction.[1]

Table I. The range-energy relation of triton in nuclear emulsion.

E (Mev)	R (μ)	E (Mev)	R (μ)
2.0	28.0	6.5	139.8
2.5	36.8	7.0	157.2
3.0	46.2	7.5	174.9
3.5	56.4	8.0	193.1
4.0	67.3	8.5	212.8
4.5	79.2	9.0	232.7
5.0	92.5	9.5	254.0
5.5	107.0	10.0	275.0
6.0	123.0		

Lithium-loaded Ilford El nuclear emulsions were exposed to the bremsstrahlung X-rays from a betatron and the ranges of alpha and triton tracks were read separately in each alpha-triton pair. About 700 pairs observed in the study are plotted in Fig. 1, where the ordinates are the ranges of tritons and the abscissas are the ranges of alphas. An ideal curve relating the range of triton R_t and that of alpha R_α of each pair can be drawn in the figure, although the observed points are scattered along the curve because of the heterogeneous nature of the photographic emulsion and the dependence

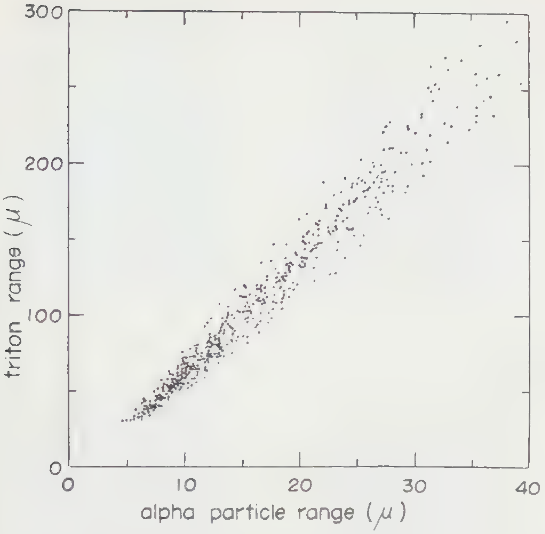

Fig. 1. The range relation of alpha-triton pair from the photodisintegration of ^{7}Li.

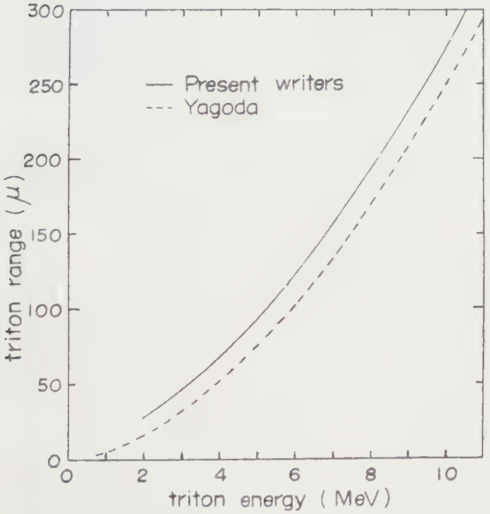

Fig. 2. The range-energy curve of triton in nuclear emulsion.

of the energies of emitted particles upon the angle of emission with respect to the incident photon beam. However, since only the particles emitted nearly normally to the incident beam were plotted in Fig. 1, the variation of their energies with angle of emission is expected to be small in the present study.

The relation between the triton E_t and that of alpha E_α of each pair, on the other hand, has been determined from the conservation of momentum and energy in the reaction. Again only the particles emitted normally have been considered. The range-energy $(R_\alpha - E_\alpha)$ relation of alpha particles in the nuclear emulsion has been studied by many workers and is quite precisely known. One can therefore easily find the missing link of the range-energy $(R_t - E_t)$ relation of triton by connecting three known links of $R_t - R_\alpha$, $R_\alpha - E_\alpha$, and $E_\alpha - E_t$.

The range-energy relation of triton thus determined on the basis of that of alpha particle given by Rotblat[2)] is shown in Table I and is also drawn in Fig. 2, together with the same obtained by Yagoda[3)] from the range-energy relation of proton by using well known conversion formula. The ranges found by us are systematically a little larger than those of Yagoda for given energies. The accuracy of the range given above of course depends on the accuracy of the range-energy relation of alpha particle used as reference. The error introduced in drawing the curve of Fig. 1, however, will be less than a few per cent.

References

1) M. Miwa: J. Phys. Soc. Japan **10** (1955) 173.
2) J. Rotblat: Nature **167** (1952) 550.
3) H. Yagoda. Radioactive Measurements with Nuclear Emulsions, John Wiley. (1949) 337.

J. Phys. Soc. Japan **10** (1955) 321~323

Energy Analysis of Electron Diffraction Patterns

By Hiroshi Watanabe
Hitachi Central Research Lab.
Kokubunji, Tokyo, Japan

(Received January 24, 1955)

Recently Leonhard[1)] reported that he succeeded in obtaining energy spectra of electron diffraction patterns by means of a velocity analyzer of Möllenstedt's type[2)]. The author also obtained similar energy spectra by making use of a three stage electron microscope attached with an analyzer lens[3)].

Figure 1a shows a schematic diagram of the electron optical system of the author's arrangement. A diffraction pattern on the back focal plane of the objective lens is imaged by an intermediate lens on a plane with a fine slit, and then the part of the projected pattern passing through the slit is analyzed by an analyzer lens. The pattern on the plane of the slit and the energy spectrum obtained in the analysis are shown schematically in (b) and (c) of Fig. 1; rings drawn by dotted lines in Fig. 1c are due to the inelastically scattered electrons losing a certain discrete energy.

Figures 2a and 3a are energy spectra of evaporated gold foil and of molybdenite, respectively. For comparison, the ordinary diffraction patterns of these specimens are shown in Figs. 2b and 3b. It

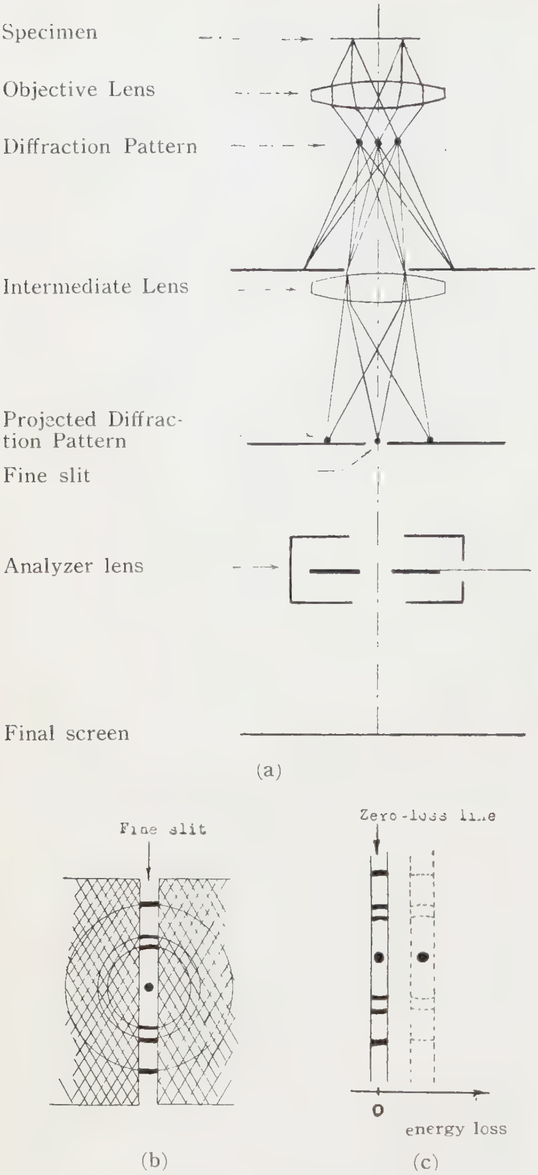

(a)

(b) (c)

Fig. 1. (a) Schematic diagram of the electron optical system. (b) Projected diffraction pattern on the plane of the slit. (c) Energy spectrum on the screen.

is revealed by these photographs that the inelastic scattering occurs mainly in the directions of diffracted beams as well as in the direction of the incident beam. The electrons scattered inelastically in the directions of diffracted beams have suffered scatterings more than twice, elastically first (reflection by net-plane) and then inelastically. These inelastically scattered electrons cause the diffusedness of spots in electron diffraction net-patterns[4].

Figure 4 shows the intensity curve of the ordinary diffraction pattern (Fig. 2b) and that of the zero-loss line in the energy spectrum of gold (Fig. 2a).

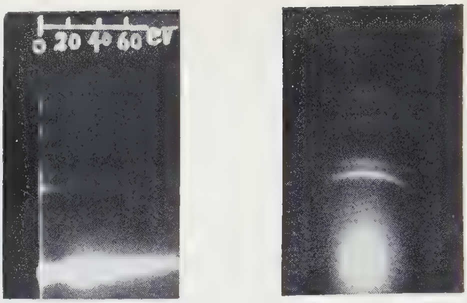

(a) (b)

Fig. 2. (a) Energy spectrum of a Debye-Scherrer ring of an evaporated gold foil. (b) Debye-Scherrer ring.

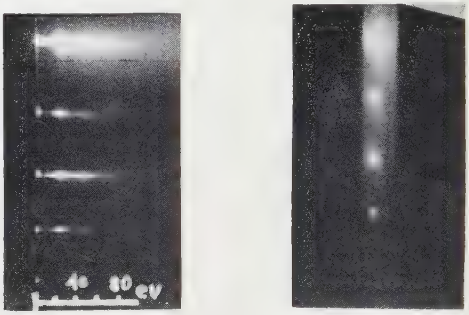

(a) (b)

Fig. 3. (a) Energy spectrum of a spot pattern of molybdenite. (b) Ordinary spot pattern.

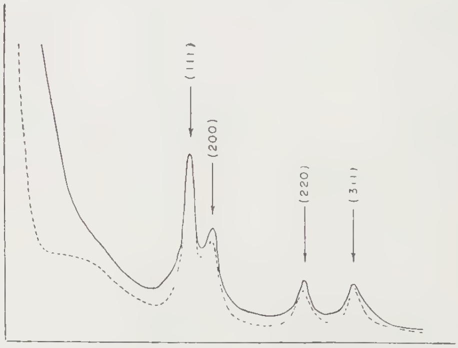

—— ordinary diffraction pattern
------ zero-loss line of the energy spectrum

Fig. 4. Intensity distribution curve of the ordinary diffraction ring (Fig. 2b) and that of the zero-loss line in the energy spectrum (Fig. 2a). The ordinate is expressed in arbitrary scale.

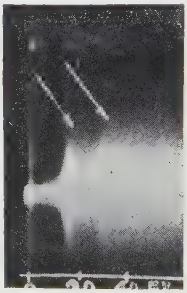

Fig. 5. Energy spectrum of a diffraction pattern of aluminium. Arrows indicate the prominences.

The latter curve represents the intensity of diffraction pattern formed solely by elastically scattered electrons. It is noteworthy that the background of the latter curve is remarkably reduced as compared with that of the former curve. However, a considerably strong background still persists in the latter. As stated by Ichinokawa and Uyeda4), this background may be attributed to either the scattering of electrons by imperfections in gold crystallites or the double scatterings of electrons in crystallites5).

Figure 5 shows energy spectrum of a diffraction pattern of aluminium foil. One can see two prominences indicated by arrows. Although their origin is not yet known*, it is worth noticing that the value of energy loss of electrons which is thought to be caused by the excitation of plasma oscillations6),3) depends on the scattering angle. Such prominences are also observed for magnesium foil.

The author is indepted to Dr. N. Kato of Kobayasi Institute of Physical Research for many helpful discussions. He is also grateful to Dr. B. Tadano and Mr. N. Morito of Hitachi Central Research Laboratory for their encouragement throughout this experiment.

References

1) F. Leonhard: Zeits. Naturforsch. **9a** (1954) 727.
2) G. Möllenstedt: Optik **5** (1949) 499.
3) H. Watanabe: J. Phys. Soc. Japan **9** (1954) 920.
4) T. Ichinokawa and R. Uyeda: Proc. Japan Acad. **30** (1954) 857.
5) J. M. Cowley, A. L. G. Rees and J. A. Spink: Proc. Phys. Soc. London **A64** (1951) 609.
6) D. Pines and D. Bohm: Phys. Rev. **85** (1952) 338.

---

* *Note added in proof*: It has been pointed out by Assist. Prof. H. Kanazawa of Tokyo University that these prominences might be caused by dispersion of the frequency of the plasma oscillation. A detailed account will be published later.

PROGRESS OF THEORETICAL PHYSICS

(Founded by H. Yukawa in 1946)

Published for the

Research Institute for Fundamental Physics

The Physical Society of Japan

Progress of Theoretical Physics Vol. 12, No. 5, 1954

On the Effects of Excited States of Nucleons upon Static Nuclear Potential in Symmetrical Pseudoscalar Meson Theory, II —*Numerical Results on Deuteron Problem*— .... Tokuji MATSUMOTO and Masao SUGAWARA....553

Beta-ray Spectra, I .... Hisao TAKEBE....561

Beta-ray Spectra, II .... Hisao TAKEBE....574

Gamma Ray Energy Spectrum from Iron Bombarded by 14-Mev Neutrons .... Satio HAYAKAWA and Ken KIKUCHI....578

On the Renormalization in Tamm-Dancoff Approximation for One-nucleon Problem, II —*Subtraction of Divergences in the Generalized Tamm-Dancoff Equations*— .... Kiyomi ITABASHI....585

Diagonalisation of Hamiltonian and Tamm-Dancoff Equation .... Susumu ÔKUBO....603

Configuration Mixing and Magnetic Moments of Odd-nuclei .... Akito ARIMA and Hisashi HORIE....623

Renormalization of Two-electron Green-function .... Sigenobu SUNAKAWA, Tsutomu IMAMURA and Ryōyū Utiyama....642

On the Binding Energy and Properties of Lower Energy Levels of Li^6 .... Masato MORITA and Tarō TAMURA....653

Letters to the Editor:

A Generalization of the Foldy Transformation in Ps-Ps Meson Theory .... P. Y. PAC, S. TANI and K. YAMAZAKI....689

Note on the Unstable Particles .... S. OGAWA, B. SAKITA and Y. TAGUCHI....691

Zero-energy Mesonic Processes and Renormalization in D.T.G.'s Formalism .... S. CHIBA and M. NAMIKI....693

Zero-energy Mesonic Processes and Renormalization in Schwinger's Formalism .... M. NAMIKI, S. CHIBA and S. HANAWA....694

Velocity-dependent Potential and Gauge Invariance of the First Kind.. .... C. H. CHANG....696

Errata 697

Price $ 1.25 per copy
$ 15.00 per year (postage inclusive)
Annual dues for foreign members (individual subscribers)
$ 12.00 (postage inclusive)
" for foreign members of the Physical Society of Japan
$ 10.00 (postage inclusive)

Application for members, subscriptions and orders for back mumbers should be sent, directly or through book-dealers, to

The Publication Office
in
Yukawa Hall, Kyoto University, Kyoto, Japan

JOURNAL OF THE PHYSICAL SOCIETY OF JAPAN Vol. 10, No. 5, MAY, 1955

A Calibration Measurement of Multiple Scattering of Slow μ-Mesons by the Constant Sagitta Method

By Shin-ichi KANEKO

Institute of Polytechnics, Osaka City University, Osaka

(Received January 17, 1955)

Multiple scattering observations have been carried out on 103 slow cosmic-ray μ-mesons coming to rest in G5 emulsions. The emulsions were coated, exposed and processed at a depth of about 17 m.w.e. underground. It is shown that the constant sagitta scheme recommended by the Göttingen group gives satisfactorily constant mean sagittae with increasing residual range at least in the region of velocity $0 \lesssim \beta \lesssim 0.46$. Observations of 81 μ-mesons are also described which were done by the scheme based upon the Williams theory of scattering and upon the range-energy relation given by Bradner *et al.* The error introduced by the use of schemes other than that of Göttingen is discussed. The results are compared with Glasser's calibration experiment on 101 artificially produced slow protons.

§1. Introduction

In recent years, the constant sagitta method has been proposed[1),2),3)] and widely been used by various workers to identify the heavy mesons and hyperons coming to rest in photographic emulsions. A committee of the Padova Conference has recommended the method as a standard for the estimation of masses of slow particles[4)]. The method has two important advantages over the constant cell length method. First, the signal-to-noise ratio is constant and then the correction for noise can be made very simply and reasonably. Second, the number of available cells is great because it is possible to use decreasing cell length with decreasing energy of the particle; in the constant cell length method, the cell length which gives the scattering signal predominating over the noise at high energy region of the track is too large at the lower energy region and so it makes a total number of available cells smaller than that obtainable by the use of the constant sagitta method.

However, the mass value estimated from the observed mean sagitta depends strongly upon the cell scheme employed and upon the standard value of mean sagitta which is adopted. The relation between the relative error of the arithmetic mean value, $\bar{D}$, of observed second differences of successive coordinates along the track and the relative error of the estimated mass, M, can be represented approximately by

$$\frac{\varDelta M}{M} \cong -2.3 \frac{\varDelta \bar{D}}{\bar{D}} . \qquad (1)$$

Therefore, a small deviation of the observed $\bar{D}$ from the genuine value may introduce an appreciable error in the mass estimate. In order to avoid this disadvantage it is necessary not only to improve a statistical accuracy of sagitta measurement by the use of a scheme which gives a value of mean sagitta as small as possible within the limits of noise level, but also to use a correct cell scheme that has been carefully calibrated.

This calibration of the cell scheme could be done by an extensive observation of the multiple Coulomb scattering of a group of particles known to have the same mass. μ-mesons seemed appropriate for this purpose, since a μ-meson track of a given length covers a wider range of velocity than a track of a heavier particle of the same length. Also, a μ-meson suffers greater scattering than heavier particles and so a larger number of cells can be measured.

In the measurement reported here, 103 μ-mesons having residual ranges greater than 2000 microns were observed making use of the cell scheme recommended by the Göttingen group[5)]. Observations were also made on 81 μ-meson tracks longer than 1500 microns by the scheme computed from the Williams theory of scattering[6),7)] and the range-energy relation given by Bradner *et al*[8)]. The results obtained here, within the experimental uncertainties, show that the Göttingen scheme is correct at least in the region of velocity $0 \lesssim \beta \lesssim 0.46$.

§ 2. The Constant Sagitta Schemes Employed

The mean angle of scattering between successive chords along the track can be expressed by the equation

$$\frac{\bar{D}}{t}\cdot\frac{180}{\pi}\cdot\frac{1}{0.96}=\frac{K}{pv}\left(\frac{t}{100}\right)^{1/2}, \qquad (2)$$

where pv is the product of momentum and velocity in Mev, t is the cell length in microns, $\bar{D}$ is the arithmetic mean value of second differences in microns, K is the scattering constant for sagitta measurement in units of deg.Mev(100 microns)$^{-1/2}$, and the numerical coefficient 0.96 is the smoothing factor which represents the correction for the fact that one observes a smoothed track taking into account the mass centers of the grains lying several microns on either side of the axis of the eyepiece scale as described in section 3. Then one has the relation

$$t=70.9\left(\bar{D}\frac{pv}{K}\right)^{2/3}, \qquad (3)$$

which gives the cell scheme for any particle. In this equation the quantity pv is obtained from an assumed range-energy relation at a given value of residual range, and K is obtained from an assumed scattering theory and is slowing varying function of residual range and cell length. Somewhat different schemes are obtained according to the use of combinations of various range-energy relations and scattering theories.

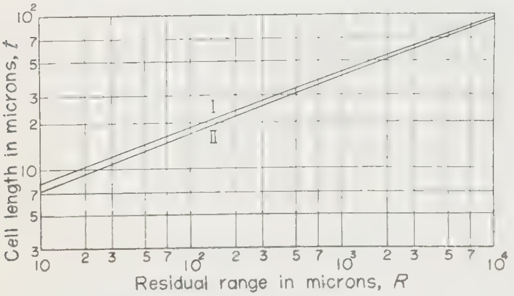

Fig. 1. The cell schemes $\bar{D}=1.0$ micron for μ-mesons. Scheme I is based upon the Molière theory of scattering and upon the range-energy relation of Göttingen. Scheme II is based upon the Williams theory of scattering and upon the range-energy relation of Bradner *et al.* It is to be noticed that only scheme I is calculated by an application of a $4\bar{D}$ cut-off.

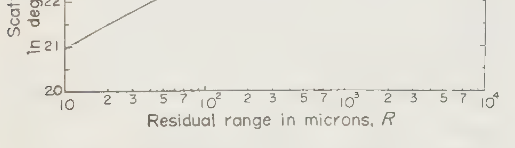

Fig. 2. The variation of the theoretical values of the scattering constants with residual range in the $\bar{D}=1.0$ micron constant sagitta schemes for μ-mesons. The curve marked a is the scattering constant predicted from the Williams theory of scattering. The curves marked b and c are predicted from the Molière theory of scattering and are without and with a $4\bar{D}$ cut-off, respectively. It is seen that the curves a and b are very nearly the same. The curves a and c were utilized for computation of schemes II and I respectively.

Scheme I employed in this experiment is based upon the Molière theory of scattering[9),10)] and the range-energy relation given by the Göttingen group[5)]. At a given value of the residual range, the quantities β and pv are obtained directly from Table I of Göttingen, and the scattering constant K with $4\bar{D}$ cut-off at given values of β and t is also determined from Figs. 1 and 2 in the article reported by the Bristol group[11)].

Scheme II is based upon the Williams theory of scattering and the range-energy relation given by Bradner *et al.* Using the Williams theory, Voyvodic and Pickup[12)] have given the following expression for the scattering constant without cut-off for sagitta measurements:

$$K=11.9\left\{1+0.837\left(\log\frac{0.94\,t}{\beta^2+0.30}\right)^{1/2}\right\}. \qquad (4)$$

Bradner *et al.*[8)] have shown that the range-energy relation for singly charged particles is represented by the simple power law formula

$$E=0.251\,M^{0.419}R^{0.581}, \qquad (5)$$

where E is the kinetic energy in Mev, R is the residual range in microns, and M is the mass of the particle expressed in proton mass units. The substitution of these relations into Eq. (3) leads to an explicit formula for cell scheme II.

Schemes I and II were computed at $\overline{D}=1.0$ micron for μ-mesons and the results are shown in the Appendix and in Fig. 1.

The values of the scattering constants predicted from the theories of Williams and of Molière are very nearly the same as shown in Fig. 2. It is then concluded that the difference between the slopes of the two cell schemes shown in Fig. 1 can be ascribed to the difference between the range-energy relations employed.

In an observation of a single track, a shorter cell scheme, for instance $\overline{D}=0.5$ microns, should be employed in order to obtain a better statistical accuracy in the mass estimate. However, the object of the present measurement is not to estimate the mass values of the individual particles, but to study a range-dependence of sagittae averaged over a number of particles. Thus, it should be suitable to use the scheme $\overline{D}=1.0$ micron which gives a quite large value of the signal-to-noise ratio.

§ 3. Experimental Method

Ilford G5 emulsions in gel form were coated, exposed and processed at a depth of about 17 m.w.e. in an underground railway tunnel in Osaka. The dimensions of the emulsions were 3 inches by 3 inches by about 500 microns. They were prepared to measure the number of slow μ-mesons and to observe the nuclear disintegrations produced by fast μ-mesons at this depth[13]. The plates were exposed vertically in a desiccator where the temperature and relative humidity were kept within 25°–30°C and 40–50 per cent respectively.

A number of 1500 microns or longer tracks of μ-mesons coming to rest were selected. A few tracks of π-mesons giving rise to π–μ decays or σ-stars at the ends of their ranges were rejected. It is then clear that the accepted tracks were almost completely composed of only μ-mesons.

Scattering and residual range were measured by means of a Cooke, Troughton, and Simms M4005 Nuclear Microscope. The plate was placed rigidly on the stage of the microscope in such a way that the track to be observed was nearly parallel with the direction of stage movement (X-axis). The inclinations of the tracks to the X-axis were kept within 20° in all the sagitta measurements. Residual ranges and cell lengths were measured by readings of the screw micrometer for stage motion. The y-coordinates of the corresponding points on the track were determined by the eyepiece graticule allowing for smoothing of grains within several microns on both sides of the scale in order to minimize the error due to random deviations of individual grains from the true trajectory of the particle.

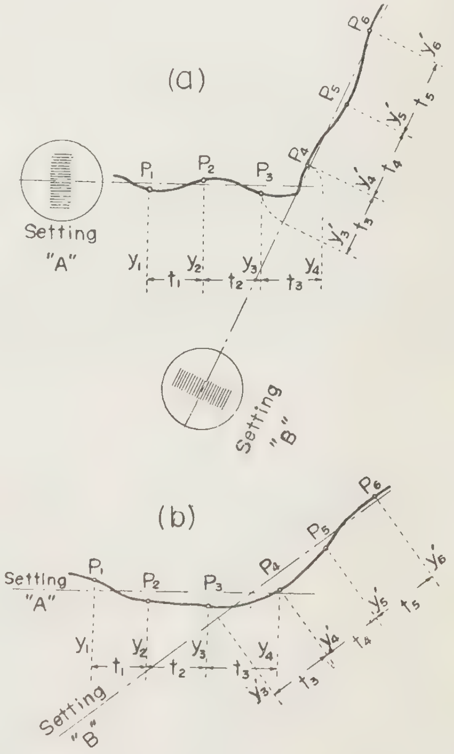

Fig. 3. Diagrams illustrating examples of successive settings along tracks showing large deviations due to (a) a single collision and (b) multiple collision. Points such as P_3 and P_4 adjacent to a point of large deviation are measured in both settings. This procedure does not exclude any large angle scatterings.

Because the tracks were very long, it was usually impossible to observe an entire track from an ending point to an entering point by only one setting of the plate. This is obviously due to the two reasons: one is the large angle single scattering (Fig. 3a) and the other is the C-shape of the track which results from the successive occurrence of a number of small angle scatterings in favour of only one direction (Fig. 3b). Thus, tracks with large deflections were divided into several sections and each section was observed separately in an appropriate setting of the plate. For example, in Fig. 3 the y-coordinates of points P_1, P_2, P_3, and P_4 were measured in setting " A " and those of P_3, P_4, P_5, $\cdots$ were measured in setting " B ". Thus, points such as P_3 and P_4 adjacent to a point of large deviation were measured twice. By this procedure the available number of second differences is just two less than the number of observed points for any track, and the large angle scattering is properly included in the scattering distribution.

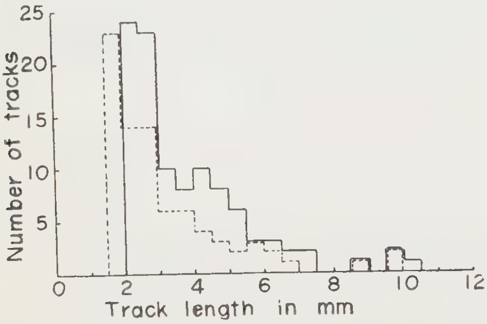

Fig. 4. The distribution of track lengths of the observed μ-mesons. Solid histogram: 103 μ-mesons observed by scheme I; Dotted histogram: 81 μ-mesons observed by scheme II.

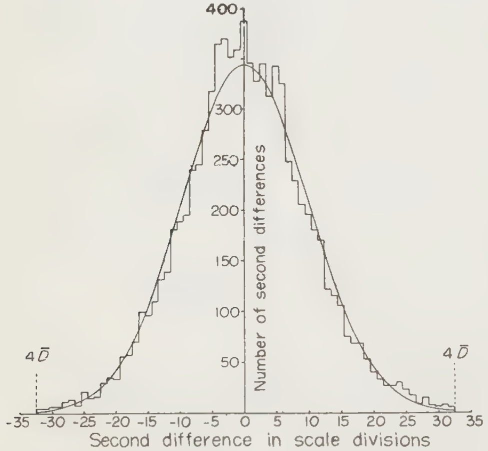

Fig. 5. The frquency distribution of 8538 second differences with $4\overline{D}$ cut-off observed by scheme I. The solid curve shows a Gaussian distribution which has the same standard deviation and the same area as the experimental histogram.

The mean value of observed second differences usually includes the so-called noise level, which is, in a measurement with short cell lengths as in this experiment, mainly composed of the reading error and the error due to the fluctuation of individual grains about the true trajectories of the particles. If one assumes that the distributions of the genuine and spurious scatterings are Gaussians and that these two quantities are independent of each other, then one has

$$\overline{D}^2_{\text{obs}}=\overline{D}^2+\overline{D}^2_n\ , \tag{6}$$

where $\overline{D}_{\text{obs}}$, $\overline{D}$ and $\overline{D}_n$ are the mean values of the observed, genuine and spurious second differences respectively. If one denotes the mean second differences observed with the cell lengths of t_1 and t_2 as $\overline{D}_1$ and $\overline{D}_2$, then the mean value of noise level $\overline{D}_n$ can be obtained by the relation

$$\overline{D}_n{}^2=\frac{t_2{}^3\,\overline{D}_1{}^2-t_1{}^3\,\overline{D}_2{}^2}{t_2{}^3-t_1{}^3}\ . \tag{7}$$

The experimental determination of $\overline{D}_n$ was made making use of observations with two cell lengths, $t_1=10$ microns and $t_2=50$ microns, at the region $R>3000$ microns of four proton tracks found in the plates. Thus, it was shown that $\overline{D}_n=0.082\pm0.004$ microns. In the observations of μ-mesons, however, the inclinations of the tracks to the X-axis were usually greater than the inclinations of the proton tracks mentioned above, so that the noise level for the μ-meson tracks could possibly be somewhat greater than that for the protons. On account of this, the upper limit of the observed noise level, $\overline{D}_n=0.086$ microns, was tentatively employed as the mean noise for the tracks of μ-meson. All the measured values of mean second differences were corrected for noise using this value and Eq. (6). It is to be noticed, however, that the arguments given in sections 4 and 5 do not depend at all sensitively upon the value of the noise level, since the signal-to-noise ratio is quite large and also since the arguments are based mainly upon the general variation of mean sagitta and are based to only a very slight extent upon the individual values of mean sagittae.

It was also shown that the spurious scattering due to emulsion distortion was exceedingly small for these low energy tracks. Thus, the effect of distortion was completely neglected.

§ 4. Experimental Results

(*1*) *Scheme I.*

Scheme I was applied to 103 μ-meson tracks whose ranges were greater than 2000 microns. The solid histogram in Fig. 4 shows the track length distribution of these particles.

A total of 8649 second differences along the tracks was obtained. The frequency distribution of 8538 second differences with a cut-off four times the resultant mean second difference is shown in Fig. 5. A Gaussian curve having the same standard deviation and the same area as the experimental histogram is shown by the solid curve. The histogram shows a somewhat more peaked distribution than the Gaussian. The measure of kurtosis, the fourth moment divided by the fourth power of the standard deviation, for the histogram is 3.25 ± 0.05, and this is somewhat greater than the value 3.00 expected for a Gaussian curve. The fact that the scattering distribution is more peaked than the Gaussian has been predicted theoretically by Molière[10)] and confirmed experimentally by several workers on high energy particles[14),15)].

The resultant mean of second differences without cut-off is 1.113 ± 0.012 microns. Applying a cut-off at four times the resultant mean, one has $\bar{D}=1.043\pm0.011$ microns, which corresponds to 94 per cent of the resultant mean. This ratio between the mean second differences with and without $4\bar{D}$ cut-off is consistent with the values predicted from the

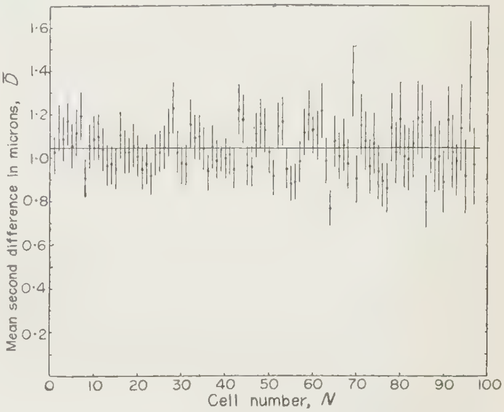

Fig. 6. The mean second differences *versus* the cell number for scheme I. The errors shown on the experimental points represent the standard deviations of the second differences. The solid straight line represents the best fitting line with the experimental points determined by the method of least squares taking into account the statistical weight of each point.

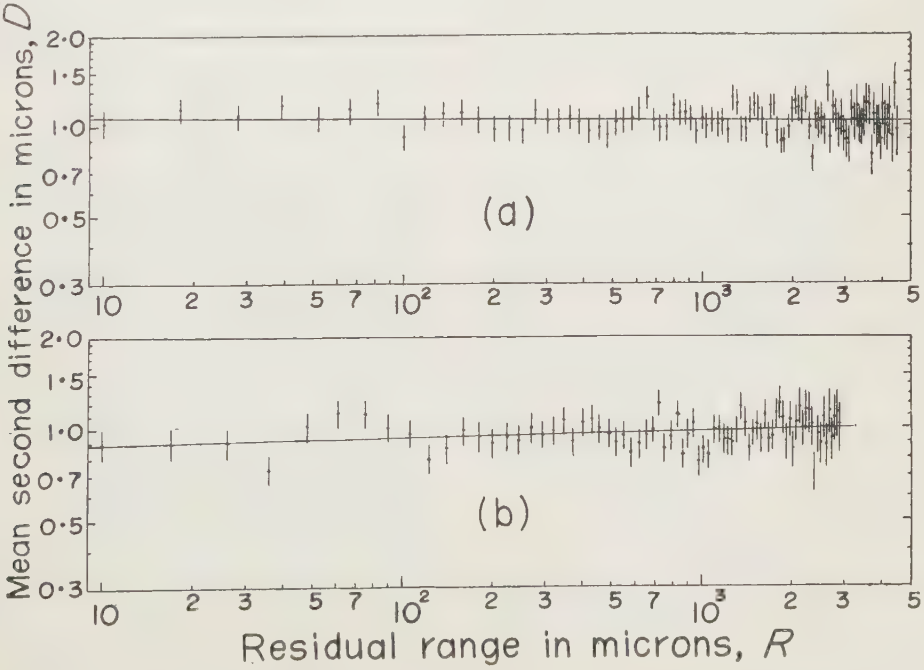

Fig. 7. The mean second differences *versus* the residual range for schemes I and II. The solid lines are those drawn by the method of least squares. (a) scheme I; (b) scheme II.

theories of multiple scattering[7),10)].

If the employed cell scheme is correct, it is of course expected that the mean values of observed second differences should fluctuate statistically about the predicted mean value. In Fig. 6 are plotted the mean values of second differences with $4\bar{D}$ cut-off along all the 103 tracks computed at each cell numbers. The best fitting line is drawn by the method of least squares taking into account the statistical weight of each point of observation. The slope of this line is $(0.14 \pm 3.84) \times 10^{-4}$, which shows a satisfactory constancy of $\bar{D}$ to the cell number N.

In order to facilitate a comparison between the results obtained by schemes I and II, the mean second differences are also plotted against the range as shown in Fig. 7(a) and the best fitting line is then drawn. Denoting the equation of this line as

$$\left.\begin{array}{ll} & \log \bar{D}_1 = \log D_{01} + m_1 \log R \\ \text{or} & \bar{D}_1 = D_{01} \cdot R^{m_1} \, , \end{array}\right\} \qquad (8)$$

one has

$$D_{01} = 1.079 \pm 0.055 \text{ microns}$$
$$m_1 = -0.0055 \pm 0.0075.$$

This value of the slope m_1 can also be regarded as zero within the statistical limits. Therefore, it seems that within the experimental uncertainties cell scheme I is correct at least in the region of $0 \lesssim R \lesssim 4500$ microns.

(2) *Scheme II.*

Previous to the publication of the paper of the Göttingen group[5)], cell scheme II has been employed to observe 81 μ-mesons some of which are the same tracks as those observed by scheme I. The track length distribution of these 81 mesons is shown by the dotted histogram in Fig. 4.

An analysis similar to the one discussed for scheme I has been carried out for scheme II. The mean second differences with $4\bar{D}$ cut-off are plotted against residual range in Fig. 7(b) for scheme II. Here,

$$D_{02} = 0.845 \pm 0.052 \text{ microns}$$
$$m_2 = 0.0196 \pm 0.0094.$$

This value of the slope m_2 suggests that the mean sagitta observed by scheme II increases with increasing residual range.

§ 5. Discussion and Conclusions

Cell schemes I and II shown in Fig. 1 can be represented approximately by the simple power formula

$$t_1 = 3.53 \, R^{0.356} \qquad \text{(scheme I)} \qquad (9)$$

$$t_2 = 2.99 \, R^{0.372} \qquad \text{(scheme II)} \, , \qquad (10)$$

in the region of $0 \lesssim R \lesssim 10^4$ microns. Since the mean sagitta at a given value of the residual range is approximately proportional to the 3/2 power of a cell length, the ratio of mean second differences to be expected by the use of schemes II and I at a same range is given by the relation

$$\bar{D}_2/\bar{D}_1 = 0.807 \, R^{0.024} \, . \qquad (11)$$

In fact, the analysis given in the preceding section results in

$$\left.\begin{array}{r} \bar{D}_2/\bar{D}_1 = (D_{02}/D_{01}) R^m \, , \\ \bar{D}_{02}/\bar{D}_{01} = 0.783 \pm 0.063 \, , \\ m = m_2 - m_1 = 0.025 \pm 0.012 \, , \end{array}\right\} \qquad (12)$$

which agree reasonably with the values in Eq. (11) expected from the direct comparison of the schemes. As stated previously, it seems that scheme I is correct within the experimental uncertainties. It is then expected from Eq. (11) that in scheme II the mean second difference should show a slight increase with the residual range. In general, if one uses a scheme given by the relation

$$t = kR^n \, , \qquad (13)$$

then one should expect the range dependence of the mean sagitta to be

$$\bar{D} = \left(\frac{k}{3.54}\right)^{1.5} R^{1.5n - 0.534} \, . \qquad (14)$$

It is to be noticed that this slight dependence on range may introduce a serious error in mass estimates. For example, in scheme II the values of $\bar{D}$ at $R = 100$ and 3000 microns are about 6 and 15 per cent greater than the value at $R = 10$ microns respectively. Remembering Eq. (1), it is clear that this trend can lead to appreciable systematic errors in mass estimates. It seems, therefore, that the use of the correct cell scheme is essential even in a study of a single track. The present calibration was done in the region of $0 \lesssim R \lesssim 4500$ microns which corresponds to the region of velocity $0 \lesssim \beta \lesssim 0.46$. Thus, the cell scheme given by the Göttingen group can be recommended at least in the region of velocity $0 \lesssim \beta \lesssim 0.46$.

Recently, Glasser[16)] has observed 101 artificially produced protons in the region of $0 \leqslant$

$R \leqq 2500$ microns making use of a constant cell length ($t=50$ microns) and has obtained a new range-scattering relation from which he has proposed the constant sagitta relation

$$t=t_0\left(\frac{R}{t_0}\right)^{0.405\pm0.011}, \qquad (15)$$

where t_0 represents the initial cell length.

It is apparent that this scheme differs considerably from scheme I given by Eq. (9). Perhaps this marked discrepancy can be explained by the difference of conditions between Glasser's experiment and the present one. Since the former was done on proton tracks, the effect of increased path length due to scattering in a given cell should be smaller than that in the case of μ-mesons, as should also be the effect due to inclinations of the tracks to the X-axis. It is evident, however, that these effects should be negligibly small except in very low energy regions. On the other hand, since Glasser used a constant cell length, the signal-to-noise ratio in his measurements should decrease with increasing residual range. This should introduce an additional uncertainty in the value of the slope of the range-scattering relation; indeed, a small variation of the value of the noise level would affect considerably the value of the slope and so also the value of the exponent in the constant sagitta relation (15). In the present study, however, since the signal-to-noise ratio remained constant, contributions from the noise level are very small and have nearly equal weights to all the mean sagittae. It is then concluded that an uncertainty of the slope due to the noise level is exceedingly small. It is also to be noticed that the present calibration covers the region of velocity $0 \lesssim \beta \lesssim 0.46$ while Glasser's covers $0 \lesssim \beta \lesssim 0.22$.

The Göttingen scheme⁵⁾ was based upon the Molière theory of scattering and upon the range-energy relation computed by the Göttingen group. Molière⁹⁾·¹⁰⁾ has carried out an exact calculation, without making use of the Born approximation, under the assumption that the distribution of the atomic electrons can be represented by the Thomas-Fermi model and has obtained a result which should be valid for all values of $\gamma=Z/137\beta$, where Z represents the atomic number of the scattering material. The scattering distribution in the low energy regions should not be affected by the finite size of nucleus which is not taken into account in the Molière theory Hanson *et al.*¹⁷⁾ have shown that the experimental scattering distribution of 15.7 Mev electrons can be well represented by the Molière theory. Therefore, it seems very improbable that the scattering constants computed from the Molière theory are very much in error.

The range-energy relation of Göttingen was computed using the experimental results of Bradner *et al.*⁸⁾, Rotblat¹⁸⁾, and Catala and Gibson¹⁹⁾ and it was found that the theoretical relations of Vigneron²⁰⁾ and Menon and O'Ceallaigh²¹⁾ were in good agreement with it. Comparisons between various theoretical and experimental range-energy relations were also made by the Rome group²²⁾ and it was shown that the relations of the Göttingen group and Vigneron agreed well with the experimental data within the experimental uncertainties in the region of proton energy less than 200 Mev. This evidence supports again the view that the Göttingen scheme is the most reliable one at present.

The arithmetic mean value, 1.043 ± 0.011 microns, of all the second differences with $4\overline{D}$ cut-off observed by scheme I is greater than the predicted value of 1.000 micron by about 4 per cent. However, taking into account the fact that the emulsions used in the experiment were prepared from G5 gel, it may be possible to ascribe this discrepancy to some difference of the stopping power from that of the ordinary G5 emulsion. Since only one μ-meson from the characteristic π–μ decay came to rest in the emulsion, a calibration of the stopping power cannot be made by observing π–μ decays. However, since it is thought that the difference, if any, of the stopping power from that of the ordinary G5 emulsion is not large, only the numerical factor in the range-energy relation would be affected as pointed out by Menon and O'Ceallaigh²¹⁾. This could lead to a slight variation of the numerical constant in the constant sagitta relation (9), but the range-exponent in the relation would remain unchanged. Hence, it seems that the arguments mentioned above on the range dependence of the mean sagitta are valid even if there exists some difference of the stopping power from that of the ordinary emulsion. The small discrepancy of the overall mean second difference may, on the other hand, also be explained by a possible error in the value of the scattering constant employed.

Fig. 8 shows the distribution of the mean second differences with $4\bar{D}$ cut-off of individual tracks of the 103 μ-mesons and a Gaussian curve with the same area and the same standard deviation as those of the experimental distribution. It is indicated from this figure that the mean second differences of the individual tracks of a known type of particle are, in fact, widely distributed about the value predicted for the particle. In the figure are also shown the five protons ($R>2000$ microns) observed by scheme I, and the mean second difference of these protons is in excellent agreement with the predicted value.*

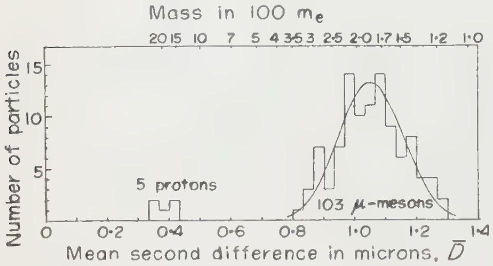

Fig. 8. The distribution of mean second differences of 103 μ-mesons and 5 protons as measured by scheme I. The solid curve represents a Gaussian fitted with the distribution of 103 μ-mesons.

Acknowledgement

The author wishes to express his gratitude to Prof. Y. Watase for interest and encouragement. Thanks are also due to Prof. M. Okazaki of the Shimane University and Messrs. O. Kusumoto and K. Watanabe for their valuable discussions, and to Dr. R. G. Glasser of the University of Chicago for permission to mention certain as yet unpublished results. It is a pleasure to acknowledge to Prof. W. L. Kraushaar of the Massachusetts Institute of Technology, who is now staying at the Osaka City University, for helpful suggestions made in the preparation of the manuscript.

The present study has been supported in part by a Grant in Aid for Fundamental Scientific Research from the Ministry of Education. The Cooke, Troughton, and Simms Nuclear Microscope used in the work was secured by a Grant in Aid for Laboratory Equipment desirable to be imported.

References

1) T. Holtebekk, N. Isachsen and S. O. Sörensen: Phil. Mag. **44** (1953) 1037.
2) S. Biswas, E. C. George and B. Peters: Proc. Ind. Acad. Sci. **38** (1953) 418.
3) C. Dilworth, S. J. Goldsack and L. Hirschberg: Nuovo Cim. **11** (1954) 113.
4) Suppl. Nuovo Cime. **11** (1954) 228.
5) H. Fay, K. Gottstein and K. Hain: Suppl. Nuovo Cim. **11** (1954) 234.
6) E. J. Williams: Proc. Roy. Soc. **A 169** (1939) 531.
7) E. J. Williams: Phys. Rev. **58** (1940) 292.
8) H. Bradner, F. H. Smith, W. H. Barkas and A. S. Bishop: Phys. Rev. **77** (1950) 462.
9) G. Molière: Z. f. Naturf. **2a** (1947) 133.
10) G. Molière: Z. f. Naturf. **3a** (1948) 78.
11) K. Gottstein, M. G. K. Menon, J. H. Mulvey, C. O'Ceallaigh and O. Rochat: Phil. Mag. **42** (1951) 708.
12) L. Voyvodic and E. Pickup: Phys. Rev. **85** (1952) 91.
13) S. Kaneko, T. Kubozoe, M. Okazaki and M. Takahata: to be published in Jour. Phys. Soc. Japan.
14) M. G. K. Menon, C. O'Ceallaigh and O. Rochat: Phil. Mag. **42** (1951) 932.
15) M. J. Berger: Phys. Rev. **88** (1952) 59.
16) R. G. Glasser: Phys. Rev. in the press.
17) A. O. Hanson, L. H. Lanzl, E. M. Lyman and M. B. Scott: Phys. Rev. **84** (1951) 634.
18) J. Rotblat: Nature **167** (1951) 550.
19) J. Catala and W. M. Gibson: Nature **167** (1951) 551.
20) L. Vigneron: Jour. Phys. et Rad. **14** (1953) 145.
21) M. G. K. Menon and C. O'Ceallaigh: Phil. Mag. **44** (1953) 1291.
22) G. Baroni, C. Castagnoli, G. Cortini, C. Franzinetti and A. Manfredini: Document circulated by CERN Secretariat for the Standardization of Measurements in Emulsions, BS 9, 1954.

---

* *Note added in Proof*: The observed 103 μ-mesons are composed of μ-e decays and ρ-mesons. The π-meson contamination in the 103 tracks can be estimated to be at most one per cent on the basis of the frequency of slow π-mesons relative to μ-mesons underground and their zenith angle distributions[13]. Of the five observed protons, only one track originated from a disintegration star in the emulsion and the other four tracks entered the emulsion.

Appendix. The Cell Schemes Employed

The following tables give the cell length t microns which has been employed at the residual range R microns in this experiment.

(*a*) *Cell scheme I.*

R	t	R	t	R	t	R	t	R	t	R	t
10	8	683	37	1947	53	3630	67	5656	78	7979	88
18	10	720	37	2000	54	3697	67	5734	78	8067	88
28	11	757	38	2054	55	3764	68	5812	79	8155	89
39	13	795	39	2109	55	3832	68	5891	79	8244	89
52	14	834	39	2164	56	3900	68	5970	80	8333	89
66	16	873	40	2220	56	3968	69	6050	80	8422	90
82	17	913	41	2276	57	4037	69	6130	80	8512	90
99	18	954	41	2333	57	4106	70	6210	81	8602	90
117	19	995	42	2390	58	4176	70	6291	81	8692	91
136	20	1037	43	2448	58	4246	71	6372	81	8783	91
156	22	1080	43	2506	59	4317	71	6453	82	8874	91
178	23	1123	44	2565	59	4388	71	6535	82	8965	92
201	24	1167	44	2624	59	4459	72	6617	82	9057	92
225	25	1211	45	2683	60	4531	72	6699	83	9149	92
250	26	1256	46	2743	60	4603	73	6782	83	9241	93
276	26	1302	46	2803	61	4676	73	6865	84	9334	93
302	27	1348	47	2864	61	4749	73	6949	84	9427	93
329	28	1395	47	2925	62	4822	74	7033	84	9520	94
357	29	1442	48	2987	62	4896	74	7117	85	9614	94
386	30	1490	49	3049	63	4970	75	7202	85	9708	94
416	31	1539	49	3112	63	5045	75	7287	85	9802	95
447	31	1588	50	3175	64	5120	75	7372	86	9897	95
478	32	1638	50	3239	64	5195	76	7458	86	9992	95
510	33	1688	51	3303	65	5271	76	7544	86		
543	34	1739	51	3368	65	5347	77	7630	87		
577	35	1790	52	3433	65	5424	77	7717	87		
612	35	1842	52	3498	66	5501	77	7804	87		
647	36	1894	53	3564	66	5578	78	7891	88		

(*b*) *Cell scheme II.*

R	t	R	t	R	t	R	t	R	t	R	t
10	7	648	34	1872	50	3514	63	5505	74	7796	84
17	9	682	35	1922	51	3577	64	5579	75	7880	84
26	10	717	35	1973	51	3641	64	5654	75	7964	85
36	12	752	36	2024	52	3705	64	5729	75	8049	85
48	13	788	37	2076	52	3769	65	5804	76	8134	85
61	14	825	37	2128	53	3834	65	5880	76	8219	86
75	15	862	38	2181	53	3899	66	5956	76	8305	86
90	16	900	38	2234	54	3965	66	6032	77	8391	86
106	17	938	39	2288	54	4031	66	6109	77	8477	87
123	18	977	40	2342	54	4097	67	6186	77	8564	87
141	19	1017	40	2396	55	4164	67	6263	78	8651	87
160	20	1057	41	2451	55	4231	68	6341	78	8738	88
180	21	1098	41	2506	56	4299	68	6419	78	8826	88
201	22	1139	42	2562	56	4367	68	6497	79	8914	88
223	23	1181	42	2618	57	4435	69	6576	79	9002	88
246	24	1223	43	2675	57	4504	69	6655	79	9090	89
270	25	1266	43	2732	58	4573	69	6734	80	9179	89
295	25	1309	44	2790	58	4642	70	6814	80	9268	89
320	26	1353	44	2848	58	4712	70	6894	80	9357	90
346	27	1397	45	2906	59	4782	71	6974	81	9447	90
373	28	1442	46	2965	59	4853	71	7055	81	9537	90
401	28	1488	46	3024	60	4924	71	7136	81	9627	91
429	29	1534	47	3084	60	4995	72	7217	82	9718	91
458	30	1581	47	3144	61	5067	72	7299	82	9809	91
488	31	1628	48	3205	61	5139	72	7381	82	9900	91
519	31	1676	48	3266	61	5211	73	7463	83	9991	92
550	32	1724	49	3327	62	5284	73	7546	83		
582	33	1773	49	3389	62	5357	74	7629	83		
615	33	1822	50	3451	63	5431	74	7712	84		

JOURNAL OF THE PHYSICAL SOCIETY OF JAPAN Vol. 10, No. 4, MAY, 1955

Directional Correlation of the Ti^{46} Gamma-Gamma Cascade

By Takeo HAYASHI, Mitsuhiro KAWAMURA
and Atsushi AOKI

Department of Physics, Saikyo University, Kyoto

(Received January 20, 1955)

The directional correlation of successive gamma-rays from Ti^{46} was measured using RCA 5819 photomultiplier tubes with NaI(Tl) scintillation crystals as the detectors. The measurements were made by counting more than 50,000 genuine coincidence counts at each angle. It was found that the successive gamma-rays were both quadrupole and the spins of the ground, 1st and 2nd excited state should be 0, 2 and 4, respectively.

§ 1. Introduction

The measurement of gamma-gamma directional correlation has been proved to be a valuable means in determining the spins of low-lying nuclear energy levels and the radiation character of transitions between states. The directional correlation of the gamma-gamma cascade in Ti^{46} was measured by Brady and Deutsch[1] in 1950, using the selected 931A photomultiplier tubes and naphthalene blocks as the detectors. However, since their first attempt no other works on Ti^{46} have been reported and the development of scintillation counting techniques has been remarkable in the past few years. Our work was undertaken to find out the correlation in the case of Ti^{46} with more improved conditions.

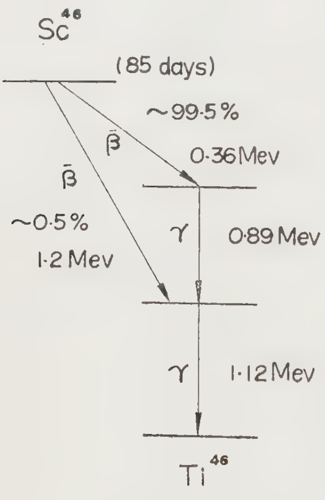

Fig. 1. Decay scheme of Ti^{46}.

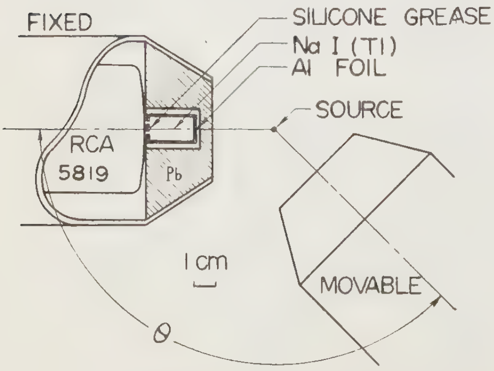

Fig. 2. Arrangement of source and detectors.

In the present experiment the gamma-rays were detected by RCA 5819 photomultiplier tubes and NaI(Tl) scintillation crystals, and an aqueous solution of $ScCl_3$ was used as the source, because the influence of electric and magnetic field on the angular correlation should be expected rather small in the liquified source material[2]. The precision of the measurement was improved by our counting more than 50,000 genuine coincidence counts at each angle.

The decay scheme of Ti^{46}, the daughter nucleus of beta-active Sc^{46}, is shown in Fig. 1.

§ 2. Experimental Procedure

The RCA 5819 photomultiplier tubes mounted with thallium activated sodium iodide crystals of $1 \times 1 \times 2$ cm were arranged as shown in Fig. 2. The crystals were protected with tapered lead shields of sufficient thickness from spurious coincidence counts caused by scattered and annihilation gamma-rays. The source material obtained from Oak Ridge National Laboratory was $ScCl_3$ in HCl solution. Its radiochemical purity was more than 99.0%. The source was prepared by dropping the solution into a 1 mm diameter hole in the glass source holder. The surface of the solution was covered with thin layer of Apiezon oil to minimize evaporation of the solvent. The distance between the source and

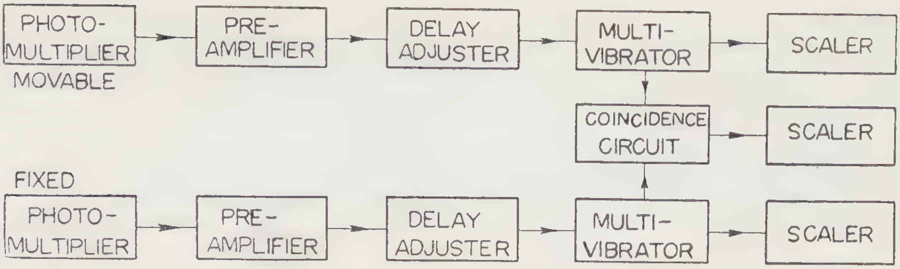

Fig. 3. Electronic block diagram.

the front face of each crystal was 3 cm. Since the slightest asymmetry in the source position affected the observed correlation, the setting of the source was performed with keen precautions.

The electronic components of the two counting channels and coincidence circuit are shown schematically in Fig. 3. The coincidence circuit used, consisted of multivibrator pulse shapers and a 6SN7 mixer tube, has the resolving time of 2.8×10^{-7} sec. The accidental coincidence rate was determined by delaying the pulses in channel from fixed counter by 1μ sec, and was found to be about 30% of the total coincidence rate. The reliability of whole apparatus was tested previously using Ni^{60} gamma-gamma cascade[3].

§ 3. Correction for Finite Angular Resolution

Since the theoretical formula of the angular correlation has been obtained for the case in which the detectors for two radiation subtend infinitely small solid angles at the source, it is neccessary to modify the theoretical correlation, in order to compare our result of finite angular resolution with the theoretical one. The original theoretical formula is

$$W(\theta)=1+0.1250\cos^2\theta+0.0417\cos^4\theta\,,\quad \text{for } 4(Q)2(Q)0, \qquad (1)$$

where 4, 2 and 0 are the spins of the 2nd, 1st excited and ground state, respectively, Q is abbreviation of quadrupole radiation and θ is the angle between the two radiations. According to the calculation of Rose[5], this formula has been corrected for the case of our geometry, taking into account the absorption of the Ti^{46} gamma-rays in such crystal, as follows:

$$\overline{W}(\theta)=1+0.1239\cos^2\theta+0.0380\cos^4\theta. \qquad (2)$$

Table I. Experimental data and corrected theoretical values for 4(Q)2(Q)0.

θ	$\overline{W}(\theta)$ experimental	$\overline{W}(\theta)$ theoretical
90.0°	1.000	1.000
112.5°	1.019±0.006	1.019
135.0°	1.077±0.006	1.071
157.5°	1.126±0.007	1.133
180.0°	1.157±0.007	1.162

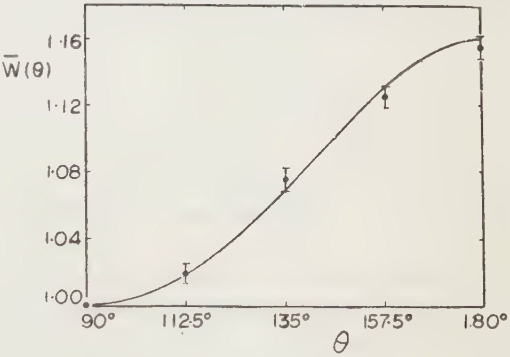

Fig. 4. Experimental values and corrected theoretical curves for 4(Q)2(Q)0.

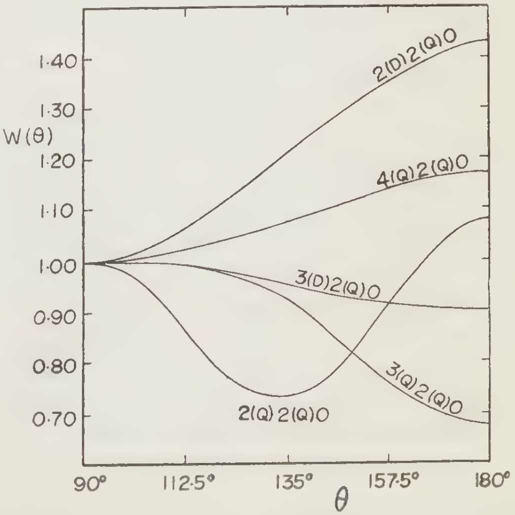

Fig. 5. Theoretical correlation curves for some spin values and multipole orders.

§ 4. Results and Discussions

The data were obtained at five angles between 90° and 180°, and more than 50,000 genuine coincidence counts were taken for each measurement. In Table I and Fig. 4 the results of these measurements and the corrected theoretical values for $4(Q)2(Q)0$ assignment are summarized. Theoretical correlation curves for some possible spin values of 2nd excited state and multipole orders of 1st gamma-rays are also shown in Fig. 5. Our results are in good agreement with the theoretical values for $4(Q)2(Q)0$. Thus, we arrive at the conclusion that the successive gamma-rays in Ti^{46} are both quadrupole and the spins of the ground, 1st and 2nd excited state should be 0, 2 and 4, respectively.

The present results are consistent with that of Brady and Deutsch1), while the existence of the isomeric state reported by Nag, Sen and Chatterjee6) seems rather doubtful.

The spurious coincidence counts due to scattered gamma-rays were roughly estimated to be less than 0.06% of the genuine coincidence counts and the one due to annihilation gamma-rays less than 0.01%.3) Therefore the effect of the spurious coincidence counts is considered within the statistical error.

We should like to thank Prof. K. Kimura and Prof. S. Shimizu of Kyoto University for their kind encouragements and suggestions.

References

1) E. L. Brady and M. Deutsch: Phys. Rev. **78** (1950) 558.
2) R. M. Steffen: Phys. Rev. **90** (1953) 1119.
3) T. Hayashi, M. Kawamura and A. Aoki: Sci. Rep. Saikyo Univ. **2** (1955) 5.
4) D. R. Hamilton: Phys. Rev. **58** (1940) 122.
5) M. E. Rose: Phys. Rev. **91** (1953) 610.
6) Nag, Sen, and Chatterjee: Nature **164** (1949) 1001.

JOURNAL OF THE PHYSICAL SOCIETY OF JAPAN Vol. 10, No. 5, MAY, 1955

Hyperfine Structure of the Spectrum of Mn I

By Kiyoshi MURAKAWA
Institute of Science and Technology, Komaba-machi, Meguro-ku, Tokyo

(Received January 14, 1955)

The hyperfine structure of the lines Mn I λ5432, λ5395 and λ4034 was measured, and the quadrupole moment of Mn^{55} was calculated to be $(0.4\pm0.2)\times10^{-24}\,cm^2$.

§ 1. Experimental Arrangement

The nucleus Mn^{55} (nuclear spin=5/2) is anomalous in that it does not follow the single particle shell model, and the investigation of its quadrupole moment (Q) would be important. The present article describes the result of the determination of Q by the optical hyperfine structure (hfs) method. An abstract of the result1) was published in 1953.

The hfs of the spectrum of Mn I has been studied by several authors2)−6) but they detected no deviation from the cosine interval rule in any level of Mn I. In the present investigation λ5432, λ5395 and λ4034 were selected as the most adequate lines for detecting the quadrupole effect.

As usual, a liquid-air cooled hollow cathode discharge tube was used as a light source, and a Fabry-Perot etalon was used in order to resolve the hfs. Some of the interference patterns are reproduced in Fig. 1.

In measuring the hfs of λ5432 it is important to keep in mind the fact that another line lies very close to the longer wave-length side.

§ 2. Result

The result of the measurement is shown in Fig. 2. All the lines studied have a common final level $3d^5\,4s^2\,{}^6S_{5/2}$ which is a ground level of the Mn I atom. Since this configuration is known to be a typical example of an LS coupling, we may expect that both the interval factor A and the quadrupole constant B of

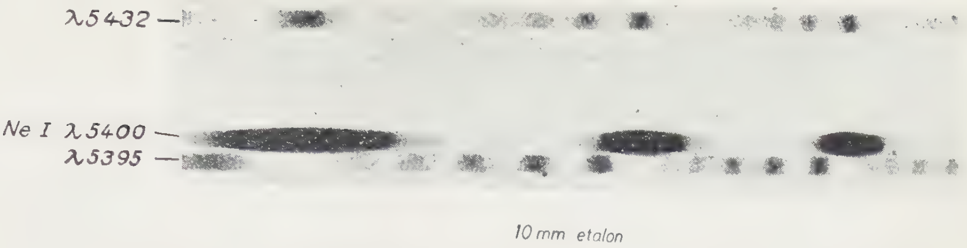

Fig. 1. Reproduction of interference patterns of Mn I. This is mainly for λ 5395. λ 5432 does not appear with sufficient intensity on this plate.

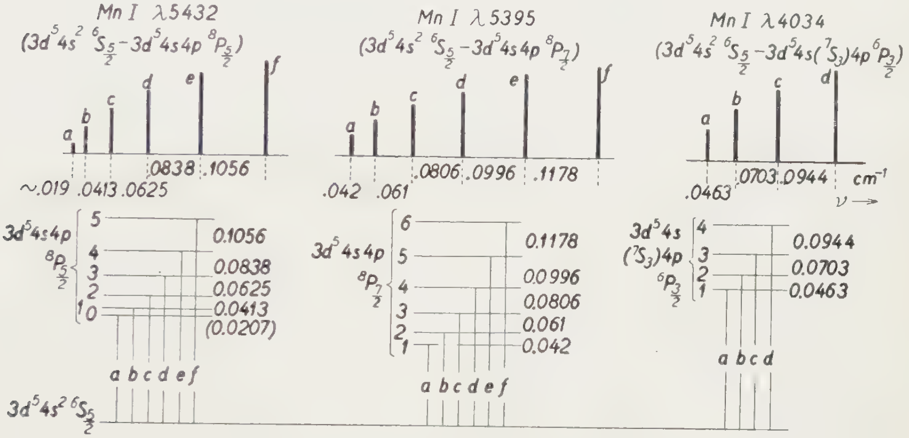

Fig. 2. Hfs and transition schemes of the three lines studied.

Table I. Hfs of Mn I levels.

Level	A (cm^{-1})	B (10^{-3}cm^{-1})	Q (10^{-24}cm^2)
$3d^5 4s^2\ {}^6S_{5/2}$	≈ 0	0	
$3d^5 4s(^7S_3)4p\ {}^8P_{7/2}$	0.01995	−0.0066	0.43
$3d^5 4s(^7S_3)4p\ {}^8P_{5/2}$	0.02097	0.0042	0.48
$3d^5 4s(^7S_3)4p\ {}^6P_{3/2}$	0.02350	0.0062	0.39

this level vanish. A slight amount of the wave function $3s\,3d^5\,4s^2\,5s\ {}^6S_{5/2}$ will probably be superposed on the wave function $3s^2\,3d^5\,4s^2\ {}^6S_{5/2}$, so that it is possible that the ground level has a small splitting factor. However, in the present experiment it was not possible to attain an accuracy to detect this splitting, so that it was assumed that $A=0$ for the ground level. With respect to the constant B, we may, with safety, assume that $B=0$ for this level. Then each of the hfs splittings of the lines listed in Fig. 2 represents directly the splitting of the respective initial level. The values of A and B for each level are listed in Table I.

We have to calculate the quadrupole moment Q from the value of B. It is known that the configuration $3d^5\,4s\,4p$ is of LS coupling, so it is convenient to start the calculation in the $m_l m_s$ representation[7]. The matrix elements of $3\cos^2\theta-1$ for the p electron are given in Table II. The notation used here is the same as that of the book of Condon and Shortley[8]. R' and S are relativity correction factors according to Casimir[9].

The wave functions in LS coupling are at first expressed in the SLM_SM_L representation and then by the antisymmetrized products of one-electron wave functions in the slm_sm_l representation. Then the matrix element of $3\cos^2\theta-1$ for each level of the configuration $d^5\,s\,(^7S_3)\,p$ can be integrated by the use of Table II, and we get:

$$({}^8P_{7/2}|3\cos^2\theta-1|{}^8P_{7/2})=(8/105)(R'+6S)$$

$$({}^8P_{5/2}|3\cos^2\theta-1|{}^8P_{5/2})=(1/147)(13R'-34S)$$

$$({}^6P_{3/2}|3\cos^2\theta-1|{}^6P_{3/2})=-(2/25)R' .$$

For Mn^{55} we have $Z=25$, $Z_p{}^*=21$ and $R'=1.02$, $S=1.03$, $H=1.01$ and $\zeta(4p)=265$. Putting these values in the above derived formulas

Table II. Matrix elements of $3\cos^2\theta-1$ for the p-electron in the $m_l m_s$ representation.

$$(1^+|3\cos^2\theta-1|1^+)=(-1^-|3\cos^2\theta-1|-1^-)=-(2/5)R'$$
$$(1^-|3\cos^2\theta-1|1^-)=(-1^+|3\cos^2\theta-1|-1^+)=(2/15)(R'-4S)$$
$$(0^+|3\cos^2\theta-1|0^+)=(\ 0^-|3\cos^2\theta-1|\ 0^-)=(4/15)(R'+2S)$$
$$(1^-|3\cos^2\theta-1|0^+)=(-1^+|3\cos^2\theta-1|\ 0^-)=(2\sqrt{2}/15)(R'-S)$$

and in the fundamental formula

$$Q=-B\frac{Z^*H(1+\delta)}{\zeta\sum(3\cos^2\theta-1)}I(2I-1)J(2J-1)$$
$$\times 1.988\times 10^{-21}$$
$$(B \text{ and } \zeta \text{ in cm}^{-1}),$$

we get the value of Q listed in Table II corresponding to the value of B of each level. In the above formula the polarisation correction factor δ (treated by Sternheimer[10)]) was assumed to be 0.04. The mean of the three values listed in Table II is

$$Q(\mathrm{Mn}^{55})=(0.4\pm 0.2)10^{-24}\ \mathrm{cm}^2.$$

While Kamei and the author were writing the manuscript of our first publication[1)] on $Q(\mathrm{Mn}^{55})$, Javan, Silvey, Townes and Grosse[11)] obtained the value of Q by the method of microwave absorption spectroscopy and Javan and Engelbrecht[12)] published the details of their method and observation. They obtained $Q=0.55\times 10^{-24}$ cm². In view of the quite different nature of the method, the agreement with our value is surprisingly good. Trees[13)] obtained $Q=1\times 10^{-24}$ cm² from the data of White and Ritschl[4)].

References

1) K. Murakawa and T. Kamei: Phys. Rev. **92** (1953) 325.
2) L. Janicki: Ann. d. Physik **29** (1909) 833.
3) Wali-Mohammad: Astrophys. Jour. **39** (1914) 185.
4) H. E. White and R. Ritschl: Phys. Rev. **35** (1930) 1146.
5) Wali-Mohammad and P. N. Sharma: Phil. Mag. **18** (1934) 1144.
6) R. A. Fisher and E. R. Peck: Phys: Rev. **55** (1939) 222.
7) T. Schmidt: Zeits. f. Physik **121** (1943) 63.
8) Condon and Shortley: *Theory of Atomic Spectra.* Cambridge (1935).
9) H. Casimir: Verhandel. Teylers Tweede Genootschap, Haarlem (1936) 11.
10) R. Sternheimer: Phys. Rev. **86** (1952) 316.
11) Javan, Silvey, Townes and Grosse: Phys. Rev. **91** (1953) 222.
12) A. Javan and A. Engelbrecht: Phys. Rev. **96** (1954) 649.
13) R. E. Trees: Phys. Rev. **92** (1953) 308.

JOURNAL OF THE PHYSICAL SOCIETY OF JAPAN Vol. 10, No. 5, MAY, 1955

Theoretical Study of Residual Resistance of Binary Alloys containing Foreign Atoms in small Concentration

By Hiroshi FUJIWARA

Department of Physics, University of Tokyo

(Received January 29, 1955)

The increase of electrical resistance due to the substitutional impurities of di- or trivalent metal for monovalent metal in dilute solid solution is calculated.

In the present paper, two steps are taken as follows:

First, a modified screened Coulomb field is exactly obtained from the Thomas-Fermi equation by numerical integration, and second, for the calculation of the cross section, the method of partial wave is used, instead of the Born approximation.

The agreement of theoretical results with experiment has been greatly improved by this method in comparison with the results obtained by the use of the Born approximation.

§ 1. Introduction

In an alloy which contains foreign atoms in the form of dilute solid solution, the dissolved atoms form impurity centers around which the charge distribution of electrons deviates from the periodic one which is characteristic of the pure solvent metal. For example, if a small quantity of divalent metal Cd is dissolved in the monovalent metal Ag, both Cd and Ag exist in the ionized states Cd^{++} and Ag^{+} respectively, and since the former ion Cd^{++} has one excess positive charge compared with the latter Ag^{+}, the conduction electrons are attracted to the impurity center so as to screen the excess charge.

It is important to find the non-periodic charge distribution around the impurity atom for the theoretical interpretation of several physical problems concerning alloys, including electrical resistance, heat of solution, etc.[1)]

The pioneer work in this field was done by Prof. Mott[2)] by using the Thomas-Fermi method, to be referred to as T. F. method hereafter, to determine the charge distribution around the impurity atom in the dilute solid solution in which the atomic valency of the impurity atom is different from that of the solvent metal. Prof. Mott applied his result to the calculation of the increase of the electrical resistance due to these dissolved foreign atoms. He treated the additional potential $V(r)$ around the foreign atom as small, and simplified the equation by linearization which yielded the solution $V(r)=\{Ze^2\exp(-qr)\}/r$ as a screened potential; here q means the screening constant and Z is the difference between the atomic valency of the solvent and that of the dissolved metal (in other words, $Z+1$ is the number of electrons outside the closed shell structure in the dissolved atom).

Further he calculated the scattering probability using the Born approximation. The calculated value of the excess resistance obtained by this method, however, was much greater than the experimental value and it was found that it was necessary to increase the theoretical value of q by a factor 2 in order to make the calculated value agree with the observed one.

In view of these circumstances, it seems to us desirable to carry out the calculation of the screened potential $V(r)$ and of the excess resistance due to the impurity atoms, based on the T. F. method as faithfully as possible without introducing the approximation mentioned above, and also to see how far the disagreement between the theory and experiment can be diminished. This paper presents the results of our study made along this line.

Recently, several authors tackled this problem without using the T. F. method; Shinohara[3)] and Friedel[4)] treated this problem by examining the modification of the wave functions of individual stationary states due to the impurity center and then evaluated the screened potential self-consistently. Shinohara took into account the exchange effect and Friedel explicity introduced the idea of bound state which exists below the lowest level of the Fermi distribution, and calculated the electronic state by the phase shift.

But in this paper, we started from the T. F. equation straight-forwardly. We treated the case in which the di- or trivalent metal is a substitutional impurity for monovalent solvent metal.

By neglecting the exchange interaction among electrons, we obtained the screened potential by carrying out numerical integration directly from the T. F. equation instead of solving the equation approximately by linearization as was done by Prof. Mott. And for the calculation of the scattering cross section, we used the phase shifts in the partial wave for the lower order, instead of the Born approximation.

A. Modified Screened Potential

§ 2. Fundamental Equation

In the dilute solid solution which consisted of two metals with different atomic valencies, the whole charge distribution is not uniform on account of the substitution of the foreign atom. For treating this problem, we can use the T. F. method at least for the first approximation, and, for the present, since the effect of exchange interaction which has some effect on the electron density around the impurity atom is neglected, the T. F. method can be used in its original form.

Let us regard the excess positive charge which represents the difference between the atomic valency of the dissolved and that of the solvent metal, as a point charge localized near the nucleus of the impurity atom and suppose that the rest positive charge is distributed with a uniform density ρ_+ in the space for the first approximation.

Then the electrostatic potential $\Phi(r)$ around the dissolved atom is now determined from the following Poisson equation:

$$\nabla^2\Phi = -4\pi\rho_+ + 4\pi e\cdot n(r)\,, \tag{1}$$

where $n(r)$ is given by the equation:

$$n(r) = (8\pi/3h^3)(2me\Phi(r))^{3/2}\,. \tag{2}$$

We assume the radial symmetry and introduce new dimensionless variables ϕ, x which are related to Φ, r in

$$a_1\phi = x\Phi\,, \tag{3a}$$

$$r = a_2 x\,, \tag{3b}$$

where a_1 and a_2 are, respectively,

$$a_1 = \frac{2^{13/3}\pi^{4/3}me^3}{3^{2/3}\cdot h^2}\,, \tag{4a}$$

and

$$a_2 = \frac{3^{2/3}\cdot h^2}{2^{13/3}\pi^{4/3}me^2} = 0.885a_H\,, \tag{4b}$$

(a_H: Bohr radius).

Then we may write the equation (1) in a simplified and dimensionless form:

$$\frac{d^2\phi}{dx^2} = \frac{\phi^{3/2}}{\sqrt{x}} - xA^{3/2}\,. \tag{5}$$

Here, A is a new constant which did not appear in the treatment of atoms. It depends only on the kind of the solvent metal and is given by:

$$A^{3/2} = \left(\frac{3\pi}{4}\right)^3\left(\frac{Z_0}{2\pi}\right)\left(\frac{a_H}{r_0}\right)^3\,, \tag{6}$$

where Z_0 and r_0 are atomic valency of solvent metal and atomic radius of the same atom respectively.

If we denote by Z the difference between the atomic valency of the dissolved and that of the solvent metal, the boundary conditions to be satisfied by the potential ϕ are given as follows: (since the solvent metal is monovalent, $Z=1$ corresponds to the case where the substitutional impurity is a divalent metal.)

$$x=0\,,\quad \phi=Z\,, \tag{7a}$$

$$x\to\infty\,,\quad \phi\to Ax\,. \tag{7b}$$

§ 3. The Solution of the Equation (5)

At first, we shall consider the form of solution ϕ in the neighbourhood of $x=0$. Since ϕ'' is infinite at the origin according to the equation (5), it is impossible to use the Taylor expansion near the origin; instead, in accordance with the treatment of Bush and Caldwell[5], we use an expansion (8) in the power series in $x^{1/2}$:

$$\phi = Z + c_2x + c_3x^{3/2} + c_4x^2 + \cdots\,. \tag{8}$$

Inserting (8) into the equation (5) and taking the boundary condition (7a) into account, we obtain the following expansion (9) which is valid for small x with one undetermined coefficient c_2:

$$\phi = Z + c_2x + (4/3)Z\sqrt{Z}x^{3/2} + (2/5)c_2\sqrt{Z}x^{5/2} + (1/6)(2Z^2 - A^{3/2})x^3 + \cdots\,. \tag{9}$$

Choosing several different numerical values for the starting slope c_2 at the origin, we obtain ϕ by performing numerical integration from the origin to large x for each value of c_2.

The behaviors of the variation of ϕ with c_2 thus obtained are shown in Fig. 1. In this figure, the solvent metal is Ag and $Z=1$. It is found that there is only one solution of the equation (5) which satisfies the boundary condition (7b) together with (7a).

Let the numerical value of c_2 corresponding to such solution be m_0. When x is large, we assume that ϕ can be written asymptotically in the form:

$$\phi=Ax+y\ , \tag{10}$$

y being small. Inserting (10) into (5) and neglecting the terms higher than the second order of y, we obtain the linear differential equation:

$$y''=\frac{3}{2}\sqrt{A}\,y\ . \tag{11}$$

The solution of (11) with two integration constants B_1 and B_2 is:

$$y=B_1\exp\left(-\sqrt{\frac{3}{2}\sqrt{A}}\cdot x\right)+B_2\exp\left(+\sqrt{\frac{3}{2}\sqrt{A}}\cdot x\right). \tag{12}$$

From the numerical values of ϕ for large x, B_1 and B_2 are determined for each assumed value of c_2. For the correct solution which satisfies the boundary condition at $x\to\infty$, B_2 becomes zero as $x\to\infty$. In this way, c_2 and B_1 which correspond to the correct solution, which are denoted by m_0 and α_1 respectively, can be determined by inter- or extrapolation.

From the above statements, ϕ can be expressed in the following form:

(a) in the region where x is small

$$\phi=Z+m_0x+(4/3)Z\sqrt{Z}\,x^{3/2}+(2/5)m_0\sqrt{Z}\,x^{5/2}+(1/6)(2Z^2-A^{3/2})x^3+\cdots. \tag{13}$$

(b) where x is considerably large

$$\phi=Ax+\alpha_1\exp\left(-\sqrt{\frac{3}{2}\sqrt{A}}\cdot x\right). \tag{14}$$

To simplify our further analytical calculation of the scattering processes, it seems to be more convenient to put these formulas (13) and (14) in one expression over the whole region of x.

After several trials, it is found that ϕ may be approximately given by appending the additional term to (14), such as:

$$\phi=Ax+\alpha_1\exp\left(-\sqrt{\frac{3}{2}\sqrt{A}}\cdot x\right)+(Z-\alpha_1)\exp(-\beta_2'x)+\alpha_2'x\exp(-\beta_3'x). \tag{15}$$

In this case, we can keep our errors which may arise from the analytical approximation of ϕ within 1%.

As is seen from (7b), when r tends to ∞, the potential $\Phi(r)=(e/r)\phi(r/a_2)$ becomes a constant value eA/a_2, but as for the potential which can be used in the scattering problem, we must take such one as tends to zero as $r\to\infty$. So our required potential $\Phi_0(r)$ can be obtained by shifting the origin of $\Phi(r)$ about eA/a_2 as follows:

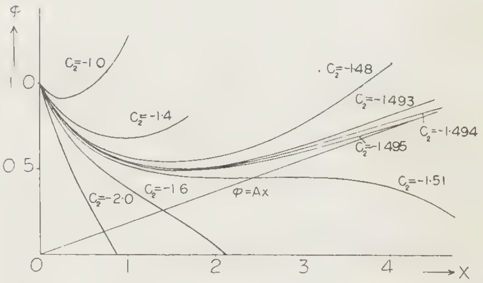

Fig. 1. The behaviors of the variation ϕ with c_2. Solvent metal is Ag and $Z=1$.

$$\Phi_0(r)=\frac{e}{r}\left[\alpha_1\exp\left(\left\{-\sqrt{\frac{3}{2}\sqrt{A}}\Big/a_2\right\}\cdot r\right)+(Z-\alpha_1)\exp(-\beta_2r)+\alpha_2r\exp(-\beta_3r)\right], \tag{16}$$

where

$$\alpha_2=\frac{\alpha_2'}{a_2}\ ,\quad \beta_2=\frac{\beta_2'}{a_2}\quad\text{and}\quad \beta_3=\frac{\beta_3'}{a_2} \tag{17}$$

From the value of A in (6) and of a_2 in (4b), the coefficient $\sqrt{\frac{3}{2}\sqrt{A}}\Big/a_2$ of the exponent of the first term in (16) agrees with the screening constant q which was obtained theoretically by Prof. Mott, so, hereafter, our screened potential $V(r)$ can be expressed as (18) by the use of this q.

$$V(r)=(e^2/r)[\alpha_1\exp(-qr)+(Z-\alpha_1)\exp(-\beta_2r)+\alpha_2r\exp(-\beta_3r)]. \tag{18}$$

To compare our modified screened potential with that of Prof. Mott's type (i.e., $\alpha_1=Z$, $\alpha_2=0$ in (18)), these two curves are shown in Fig. 2. For convenience, we plott the two curves in the dimensionless coordinates (x, ϕ).

In this figure, our curve is markedly below that of Prof. Mott's near the origin, especially in the case of $Z=2$.

This indicates the fact that the charge distribution in our case is more concentrated near the origin than in the case of Prof. Mott.

The values of A, m_0, α_1, α_2, β_2 and β_3 which we obtained are tabulated in Table I and Table II respectively. The solvent metals are Ag and Cu, and we take the case of $Z=1$ and 2.

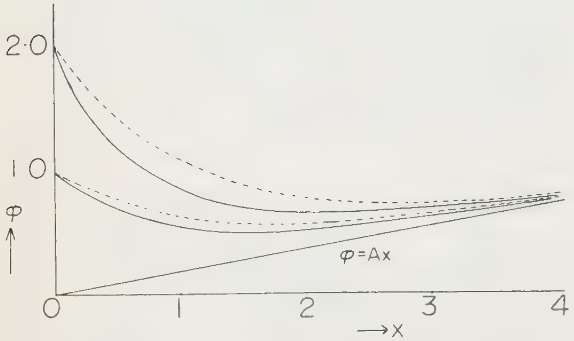

Fig. 2. Comparison ϕ with $Ax+Z\exp(-qa_2x)$ Solvent metal is Ag and $Z=1$ and 2.

—— $\phi=Ax+\alpha_1\exp\left(-\sqrt{\frac{3}{2}\sqrt{A}}\cdot x\right)+(Z-\alpha_1)\exp(-\beta_2'x)+\alpha_2'x\exp(\beta_3'x)$

.... $Ax+Z\exp(-qa_2x)$ (Mott)

B. Residual Resistance due to the Foreign Atoms

§ 4. The Calculation of the Cross Section by the Use of the Method of Partial Wave

(1) *General Formula*

Now we shall consider the elastic scattering of electrons by a foreign atom which is represented by the modified Coulomb field $V(r)$ obtained above. For the calculation of this cross section, we will use the method of partial wave.

If η_l is the phase shift of the lth order partial wave, the differential cross section $I(\theta)$ is given by

$$I(\theta)=|f(\theta)|^2\,, \tag{19}$$

where

$$f(\theta)=\frac{1}{2ik}\sum_{l=0}^{\infty}(2l+1)\{\exp(2i\eta_l)-1\}P_l(\cos\theta), \tag{20}$$

and

$$k=\frac{2\pi mv}{h}\,, \tag{21}$$

Introducing the phase shifts ζ_l given by the Born approximation, $f(\theta)$ can be written as

$$f(\theta)=\frac{1}{2ik}\left\{\sum_{l=0}^{\infty}(2l+1)(2i\zeta_l)P_l(\cos\theta)\right.$$
$$\left.+\sum_{l=0}^{\infty}(2l+1)[\{\exp(2i\eta_l)-1\}-2i\zeta_l]P_l(\cos\theta)\right\}. \tag{22}$$

The first series on the right-hand side can be summed up by substituting the formula for ζ_l and we obtain

$$f(\theta)=-\frac{2m}{\hbar^2}\int_0^{\infty}V(r)\frac{\sin Kr}{K}r\,dr$$
$$+\frac{1}{2ik}\sum_{l=0}^{\infty}(2l+1)[\{\exp(2i\eta_l)-1\}-2i\zeta_l]$$
$$\times P_l(\cos\theta)\,, \tag{23}$$

where

$$K=2k\sin\tfrac{1}{2}\theta\,.$$

In (23), the first term on the right-hand side represents the scattering amplitude by the Born approximation, and the second term is the correction term arising from the difference between the Born approximation and the exact formula.

(2) *Calculation of* ζ_l

The phase shifts of the Born approximation ζ_l can be calculated according to

$$\zeta_l=-\frac{\pi m}{\hbar^2}\int_0^{\infty}V(r)[J_{l+1/2}(kr)]^2r\,dr\,, \tag{24}$$

where $V(r)$ is given by (18).

It can be easily integrated by the use of the following formula involving the Bessel functions:

$$\int_0^{\infty}e^{-qr}[J_{l+1/2}(kr)]^2dr=\frac{1}{\pi k}Q_l\left(1+\frac{q^2}{2k^2}\right),$$
$$\int_0^{\infty}e^{-\beta_2r}[J_{l+1/2}(kr)]^2dr=\frac{1}{\pi k}Q_l\left(1+\frac{\beta_2^2}{2k^2}\right), \tag{25}$$
$$\int_0^{\infty}e^{-\beta_3r}[J_{l+1/2}(kr)]^2r\,dr=\frac{\beta_3}{\pi k^3}\frac{d}{dX}Q_l(X);$$
$$X=1+\frac{\beta_3^2}{2k^2}\,,$$

where $Q_l(X)$ denotes Legendre function of the second kind.

Thus we obtain

$$\zeta_l=-\frac{1}{a_H\cdot k}\left\{\alpha_1Q_l\left(1+\frac{q^2}{2k^2}\right)\right.$$
$$\left.+(Z-\alpha_1)Q_l\left(1+\frac{\beta_2^2}{2k^2}\right)+\frac{\alpha_2\beta_3}{k^2}\frac{d}{dX}Q_l(X)\right\}. \tag{26}$$

Table I. The values of A, m_0.

Z	Solvent	$A^{3/2}$	A	m_0	$\sqrt{\frac{3}{2}\sqrt{A}}$
1	Ag	0.0762	0.1798	−1.4939	0.7975
	Cu	0.1093	0.2286	−1.4615	0.8469
2	Ag	0.0762	0.1798	−3.9278	0.7975

Table II. The values of coefficients $\alpha_1, \alpha_2, q, \beta_2$ and β_3.

Z	Solvent	α_1	α_2	$q\left(=\sqrt{\frac{3}{2}\sqrt{A}}\Big/a_2\right)$	β_2	β_3
1	Ag	0.7476	−0.491	1.71	4.70	7.90
	Cu	0.7724	−0.448	1.81	4.80	7.47
2	Ag	1.2804	−1.408	1.71	4.70	7.90

Table III. The values of η_l and ζ_l * ($l=0, 1$ and 2).

Z	Solvent	η_0	η_1	η_2	ζ_0	ζ_1	ζ_2
1	Ag	−0.4761 (−0.5430)	−0.1021 (−0.1302)	−0.0243	−0.6995 (−0.8522)	−0.1181 (−0.1517)	−0.0250
	Cu	−0.4666	−0.1062	−0.0276	−0.6885	−0.1249	−0.0284
2	Ag	−0.6649 (−0.8180)	−0.1664 (−0.2307)	−0.0354	−1.2603 (−1.7044)	−0.2048 (−0.3034)	−0.0428

* The values in the round brackets are calculated by the use of screening potential in Prof. Mott's case.

For the purpose of calculating the residual resistance of alloys, we are interested only in the scattering of electrons at the Fermi surface, so that the energy of the electron $(1/2m)\hbar^2k^2$ is to be equated to the Fermi energy and we obtained $kr_0=(9\pi/4)^{1/3}$, where r_0 is the atomic radius of the solvent metal. Hence we have

$$k=\frac{2\pi mv}{k}=\frac{1.92}{r_0}\,. \tag{27}$$

Since ζ_l is found to become small fairly rapidly as l increases, ζ_l are given merely up to $l=2$.

(3) *Calculation of* η_l

The radial wave function χ_l for the lth partial wave is

$$\frac{d^2\chi_l}{dr^2}+\frac{2}{r}\frac{d\chi_l}{dr}+\left(k^2-U(r)-\frac{l(l+1)}{r^2}\right)\chi_l=0. \tag{28}$$

If we put

$$\chi_l=r^{-1}R_l(r)\,, \tag{29}$$

the equation (28) reduces to

$$\frac{d^2R_l}{dr^2}+\left[k^2-U(r)-\frac{l(l+1)}{r^2}\right]R_l=0\,, \tag{30}$$

where

$$k^2=(1.92/r_0)^2 \quad \text{and} \quad U(r)=(2m/\hbar^2)V(r). \tag{31}$$

In the region where r is so large that the condition

$$\left|k^2-\frac{l(l+1)}{r^2}\right|\gg|U(r)|, \tag{32}$$

is satisfied, the solution of (30) can be written in the form

$$R_l(r)=r^{1/2}(C_lJ_{l+1/2}(kr)+D_lJ_{-(l+1/2)}(kr))\,. \tag{33}$$

When we perform the numerical integration of the differential equation (30) from the origin to large r starting with the initial condition $R_l(r)\propto r^{l+1}$ at the origin, C_l and D_l are determined from the solution thus obtained, fitting it to the expression (33) for the large values of r where the condition (32) is satisfied.

Then the required phase shifts η_l are given from these values of C_l and D_l as follows:

$$\eta_l=(-1)^l\tan^{-1}(D_l/C_l)\,. \tag{34}$$

The phase shifts ζ_l and η_l calculated in the manner mentioned above are tabulated in Table III. In this table, η_l are given for $l=0$, 1 and 2 only for the same reason in ζ_l

(4) *Cross Section* $I(\theta)$

Let us represent two terms in (23) by $f_1(\theta)$ and $f_2'(\theta)$;

$$f(\theta)=f_1(\theta)+f_2'(\theta)\,, \tag{35}$$

where

$$f_1(\theta)=-\frac{2m}{\hbar^2}\int_0^\infty V(r)\frac{\sin Kr}{K}rdr\,,$$

$$f_2'(\theta)=\frac{1}{2ik}\sum_{l=0}^{\infty}(2l+1)[\{\exp(2i\eta_l)-1\}-2i\zeta_l]\times P_l(\cos\theta)\,. \tag{36}$$

In $f_2'(\theta)$, we neglect the terms for $l \geqq 2$, and moreover, since η_1 is comparatively a small quantity, $\exp(2i\eta_1)-1$ is replaced by $2i\eta_1-2\eta_1^2$ and so $f_2'(\theta)$ reduced to

$$\begin{aligned} f_2'(\theta) &= \frac{-i}{2k}\{[(e^{2i\eta_0}-1)-2i\zeta_0] \\ &\quad +3[(e^{2i\eta_1}-1)-2i\zeta_1]\cos\theta\} \\ &= \frac{1}{2k}[\sin 2\eta_0-2\zeta_0+6(\eta_1-\zeta_1)\cos\theta] \\ &\quad -\frac{i}{2k}[\cos 2\eta_0-1-6\eta_1^2\cos\theta] \\ &= f_2(\theta)-if_3(\theta)\,, \end{aligned} \tag{37}$$

where

$$f_2(\theta)=\frac{1}{2k}[\sin 2\eta_0-2\zeta_0+6(\eta_1-\zeta_1)\cos\theta], \tag{38}$$

and

$$f_3(\theta)=\frac{1}{2k}[\cos 2\eta_0-1-6\eta_1^2\cos\theta]\,. \tag{39}$$

Hence, $f(\theta)$ will be expressed in the forms:

$$f(\theta)=f_1(\theta)+f_2(\theta)-if_3(\theta)\,. \tag{40}$$

Then the cross section $I(\theta)$ is

$$\begin{aligned} I(\theta) &= |f(\theta)|^2 \\ &= f_1^2(\theta)+2f_1(\theta)\cdot f_2(\theta)+\{f_2^2(\theta)+f_3^2(\theta)\}. \end{aligned} \tag{41}$$

and the total cross section σ which is effective for our case is given by

$$\sigma=2\pi\int_0^\pi I(\theta)(1-\cos\theta)\sin\theta d\theta\,. \tag{42}$$

Substituting (41) into (42), we have

$$\sigma=2\pi\{I_1+I_2+I_3\}\,, \tag{43}$$

where I_i are

$$\begin{aligned} I_1 &= \int_0^\pi f_1^2(\theta)(1-\cos\theta)\sin\theta d\theta\,, \\ I_2 &= \int_0^\pi 2\cdot f_1(\theta)f_2(\theta)(1-\cos\theta)\sin\theta d\theta\,, \\ I_3 &= \int_0^\pi \{f_2^2(\theta)+f_3^2(\theta)\}(1-\cos\theta)\sin\theta d\theta\,. \end{aligned} \tag{44}$$

We can neglect the third term in the expression (18) of $V(r)$, because this term is small except for the very small values of r, so $f_1(\theta)$ becomes

$$\begin{aligned} f_1(\theta) &= \frac{-2me^2}{\hbar^2}\int_0^\infty [\alpha_1\exp(-qr) \\ &\quad +(Z-\alpha_1)\exp(-\beta_2 r)]\frac{\sin Kr}{K}dr \\ &= \frac{-2me^2}{\hbar^2}\left[\alpha_1\frac{1}{2k^2(1-\cos\theta)+q^2}\right. \\ &\quad \left.+(Z-\alpha_1)\frac{1}{2k^2(1-\cos\theta)+\beta_2^2}\right]. \end{aligned} \tag{45}$$

Then I_i are

$$\begin{aligned} I_1 &= \left(\frac{2me^2}{\hbar^2}\right)^2\frac{1}{4k^4}\left[\left\{\alpha_1^2\left(\log\left(1+\frac{1}{y_1}\right)-\frac{1}{1+y_1}\right)\right.\right. \\ &\quad \left.+(Z-\alpha_1)^2\left(\log\left(1+\frac{1}{y_2}\right)-\frac{1}{1+y_2}\right)\right\} \\ &\quad +\frac{2\alpha_1(Z-\alpha_1)}{(q^2-\beta_2^2)}\left\{q^2\log\left(1+\frac{1}{y_1}\right)\right. \\ &\quad \left.\left.-\beta_2^2\log\left(1+\frac{1}{y_2}\right)\right\}\right], \end{aligned} \tag{46}$$

with

$$y_1=\frac{q^2}{4k^2}\,, \qquad y_2=\frac{\beta_2^2}{4k^2}\,,$$

$$\begin{aligned} I_2 &= -\frac{2me^2}{\hbar^2 k}\int_0^2\left[\alpha_1\frac{1}{2k^2t+q^2}+(Z-\alpha_1)\frac{1}{2k^2t+\beta_2^2}\right] \\ &\quad \times(\gamma_1+\gamma_2 t)tdt\,, \end{aligned} \tag{47}$$

$$I_3=\frac{1}{4k^2}\int_0^2[(\gamma_1+\gamma_2 t)^2+(\gamma_3^2+\gamma_4 t)^2]tdt\,, \tag{48}$$

by expressing $f_2(\theta)$ and $f_3(\theta)$ as

$$\begin{aligned} f_2(\theta) &= (1/2k)(\gamma_1+\gamma_2(1-\cos\theta))\,, \\ f_3(\theta) &= (1/2k)(\gamma_3+\gamma_4(1-\cos\theta))\,, \end{aligned} \tag{49}$$

and putting $1-\cos\theta=t$. (50)

I_i which are obtained in the manner stated above and also $I_1+I_2+I_3$ and the total cross section σ are tabulated in Table IV. For the sake of comparison, we calculated the integrals I_i for the case of screened potential of Mott's type, $V(r)=Ze^2\exp(-qr)/r$ using the method of partial wave. These values are also included in the second row of this Table.

Table IV. The values of I_i and σ*
(unit of $10^{-16}\,\mathrm{cm}^2$)

Solvent	Z	I_1	I_2	I_3	$I_1+I_2+I_3$	σ
Ag	1	0.474	−0.452	0.161	0.183	1.15
		(0.714)	(−0.750)	(0.290)	(0.254)	(1.59)
		{0.714}			{0.714}	{4.49}
	2	1.529	−2.033	0.923	0.419	2.64
		(2.856)	(−4.492)	(2.094)	(0.458)	(2.88)
		{2.856}			{2.856}	{17.96}
Cu	1	0.353	−0.330	0.118	0.141	0.89

* The values in the round brackets are obtained by the use of values which are tabulated in the round brackets in Table III. And the values in the braces are those obtained in the case of Prof. Mott.

§ 5. Increase of the Electrical Resistance due to the Foreign Atom

If we denote by p the atomic ratio of dissolved metal to the solvent one, the increase $\Delta\rho$ of the electrical resistance due to the substitutional impurity is given by

$$\Delta\rho=(mv/e^2)p\cdot\sigma\ , \tag{51}$$

where v can be expressed by r_0 through the relation (27). Substituting the numerical values for the universal constants and expressing σ and r_0 in the units of $10^{-16}\,\mathrm{cm}^2$, Å respectively, we obtain

$$\Delta\rho=78\cdot p\cdot(\sigma/r_0)\ \text{microohm.cm} \tag{52}$$

As the standard concentration, we take $p=1/100$.

Hereafter, we denote $\Delta\rho$ which is calculated from the formula (52) by $(\Delta\rho)_{\mathrm{p.s}}$.

Of course, $\Delta\rho$ can be calculated entirely from the phase shifts η_l by the formula:[6]

$$\Delta\rho=\frac{2h}{e^2k}\sum_{l=0}^{\infty}[(2l+1)\sin\eta_l$$
$$-2l\sin\eta_l\cdot\sin\eta_{l-1}\cdot\cos(\eta_l-\eta_{l-1})], \tag{53}$$

if the numerical values of the phase shifts η_l are available up to sufficiently large l. We evaluated $\Delta\rho$ by this formula including $l=0$, 1 and 2, and it is denoted by $(\Delta\rho)_{\mathrm{p.p}}$, for the sake of comparison with $(\Delta\rho)_{\mathrm{p.s}}$.

Calculated values of $(\Delta\rho)_{\mathrm{p.s}}$ and $(\Delta\rho)_{\mathrm{p.p}}$ for both cases of screening potential (18) and Mott's type, are tabulated in Table V together with the experimental values[7].

Table V. Tables of $\Delta\rho$ (unit of microohm. cm) The values in the round brackets and braces have the same meaning as in Table IV.

Solvent	Z	Calculated $(\Delta\rho)$		Exp. value
		$(\Delta\rho)_{\mathrm{p.s}}$	$(\Delta\rho)_{\mathrm{p.p}}$	
Ag	1	0.56	0.63	Cd in Ag 0.38
		(0.79)	(0.82)	Zn in Ag 0.62
		{2.20}		
	2	1.29	1.15	In in Ag 1.78
		(1.41)	(1.76)	Ga in Ag 2.28
		{8.80}		
Cu	1	0.50	0.53	Cd in Cu 0.21
				Zn in Cu 0.34
				(1 atomic percent)

It is to be noted that the difference between $(\Delta\rho)_{\mathrm{p.s}}$ and $(\Delta\rho)_{\mathrm{p.p}}$ are rather small, so that the convergence of the series (53) must be fairly rapid.

§ 6. Result and Discussions

From Table IV, for example, in the case of Ag and $Z=1$, it is found that: (i) The terms I_1 and I_2 almost cancel out each other and the most effective term to σ is I_3 which is much smaller than I_1 and I_2, (ii) The values I_i in the second row are larger than the corresponding values in the first row. And also it is found from Table V that our calculated values of $\Delta\rho$, either from (52) or (53), agree fairly with the experimental ones.

As stated earlier, our processes of calculations are different from Prof. Mott's treatment in the following two points: (i) we solved the non-linear differential equation of T. F. exactly by numerical integration and obtained the modified screened potential, (ii) we did not use the Born approximation in the scattering process but employed the method of partial wave.

Putting those manners of treatment together with our results, we obtain the following conclusions:

(i) Even in the case of our simple model without considering the exchange interaction between eletrons, our calculated value $\Delta\rho$ would be in fairly good agreement with the experimental one, if we apply the method of partial wave correctly to the scattering process instead of using the Born approximation.

The effect of exchange interaction between electrons is now being studied and will be reported shortly.

(ii) In $\Delta\rho$, the difference between the values of the second and the third rows in Table V is much greater than that of the first and the second rows: i.e., the main improvement in our treatment comes from the use of the phase shift method instead of the Born approximation rather than the exactness of the potential $V(r)$.

(iii) So, the disagreement between the theoretical and observed values of $\Delta\rho$ which appeared in Prof. Mott's treatment must be mostly due to the inaccuracy of evaluating the scattering process. Therefore, if we want to take other corrective effects, i.e. the exchange interaction in the stage of a more improved approximation, it is still more necessary to discuss the reliability of the method used in resolving the scattering problem.

(iv) As is well known experimentally, $\Delta\rho$ is proportional to Z^2. Since the potential is nearly proportional to Z, this relation appear at first sight to be easily accountable by applying Born approximation to the scattering problem. However, this explanation of the proportionality of $\Delta\rho$ on Z^2 cannot be a satisfactory one, because the use of Born approximation is highly questionable in our treatment as discussed above. According to our method, $\Delta\rho$ is decidely underestimated for the case $Z=2$. The reason for this discrepancy is still to be investigated in our further studies.

(v) The method which we have used in the present paper can not be account for the difference of the values $\Delta\rho$ due to the kind of the dissolved atom of same valency. This shortcoming of our treatment is due to the fact that we have neglected the details of the charge distribution due to the core electrons of dissolved atoms and have regarded the excess positive charge due to the dissolved atom simply as a point charge.

We hope to take into account, in our further study of this problem, the fact that ρ_+ is a function of space which takes different forms depending on the kinds of the solvent and the dissolved atoms.

§ 7. Acknowledgement

The author wishes to express his sincere thanks to Prof. M. Kotani who suggested this problem and under whose kind guidance and encouragement the present work was carried out.

References

1) K. Huang: Proc. Phys. Soc. **60** (1948) 161.
K. I. Arafa: Ibid. **B62** (1949) 238.
2) N. F. Mott: Proc. Camb. Phil. Soc. **32** (1936) 281.
3) Shinohara and Toya: Butsuseiron-kenkyu No. 55 (1952).
4) J. Friedel: Phil. Mag. **43** (1952) 153.
5) V. Bush and S. H. Caldwell: Phys. Rev. **38** (1931) 1898.
6) K. Huang: loc. cit.
7) J. O. Linde: Ann. d. Physik. **14** (1932) 354.

JOURNAL OF THE PHYSICAL SOCIETY OF JAPAN Vol. 10, No. 5, MAY, 1955

Theory of the Specific Heat of Graphite II

By Kozo KOMATSU
Department of Physics, Naniwa University, Mozu-Higashi, Sakai

(Received January 8, 1955)

The previous theory by the author and Nagamiya (1951) is improved in this paper by introducing the shearing elastic constant c_{44}, which is estimated by a procedure similar to that employed by Brennan. This shearing elastic constant couples the two types of vibrations, those normal to the hexagonal layers and those parallel. The theory shows that below 10°K the deviation from T^2 law becomes appreciable and the range of transition from T^2 to T^3 laws appears at a few degrees absolute. The calculated values agree with the experimental ones over the whole temperature range below 60°K. Comments are given on recent other theories.

§ 1. Introduction

In 1951 we presented a theory of the specific heat of graphite based on a semi-continuum model.[1] Since then, two elaborate experimental works have appeared, of which one is the measurements by DeSorbo and Tyler[2] and the other quite recent ones by Bergenlid, Hill, Webb and Wilks[3]. The temperature range covered by the former is from 13° to 300°K, in which it was found that the specific heat follows a T^2 law from 13° to 54°K. The latter covered the range from 1.5° to 90°K, in which a deviation from the T^2 law was found below 15°K, increasing gradually with decreasing temperature; at the lowest temperature of the observation, the specific heat curve was found to conform to a $T^{2.4}$ law. Theories also have been presented[4)] which predicted a T^2 law at low or moderately low temperatures. However, these theories have been criticized, because they contain some unsound basic assumptions.[4),5)]

In our previous paper, we developed a semi-atomistic theory of the lattice vibrations of graphite. We considered the graphite crystal as a system of thin elastic plates spaced at a constant distance, and assumed compressional elastic couplings between adjacent plates. We calculated the elastic constants of each plate from the force constants of the benzene molecule, with certain modifications, and from the specific heat curve itself, while we estimated the coupling constant from the measured compressibility. A simplification made in our calculation was that the shearing coupling between plates was entirely neglected, which resulted in the complete separation of the lattice vibrations into two independent parts, namely the bending vibrations, in which the displacements occur normal to the plates, and the extensional and shearing vibrations of the plates, in which the displacements occur parallel to them. Each of them gave rise to a T^2 law at low temperatures. Evidently, this simplification is serious for long waves; in particular, we obtain an apparently unreasonable result in the limit of an infinitely long wave, that is, for a static shearing strain caused by a relative displacement between adjacent plates, that the crystal does not resist to this deformation. This point was criticized by Krumhansl and Brooks[4)]. We therefore take account of this shearing coupling in the present paper. Also, our previous calculation was inadequately fitted to experimental points at high temperatures, because the available data at low temperatures at that time were only those given by Nernst[6)] in 1911; this point also is improved in the present calculation. We shall estimate the constant of the coupling of the shearing mentioned above by a method similar to that employed by Brennan[7)] in his calculation of the interlayer binding of the graphite, with appropriate modifications and corrections. It will be shown that, those frequencies of the lattice vibrations which are important in the temperature range covered by DeSorbo and Tyler are little affected by the introduction of this shearing constant, while a deviation from the T^2 law becomes appreciable only below this temperature range. It will be seen that the present calculation, which was done independently of the measurments by Bergenlid, Hill, Webb and Wilks, accords reasonably well with their results at lower temperatures.

§ 2. Equations of Vibration

In I, we have started with the following equations of vibrations:

$$\frac{\partial^2 u_n}{\partial t^2}=\frac{E'}{\rho'(1-\sigma^2)}\left\{\frac{\partial^2 u_n}{\partial x^2}+\frac{1}{2}(1-\sigma)\frac{\partial^2 u_n}{\partial y^2}+\frac{1}{2}(1+\sigma)\frac{\partial^2 v_n}{\partial x\partial y}\right\}, \tag{1a}$$

$$\frac{\partial^2 v_n}{\partial t^2}=\frac{E'}{\rho'(1-\sigma^2)}\left\{\frac{1}{2}(1-\sigma)\frac{\partial^2 v_n}{\partial x^2}+\frac{\partial^2 v_n}{\partial y^2}+\frac{1}{2}(1+\sigma)\frac{\partial^2 u_n}{\partial x\partial y}\right\}, \tag{1b}$$

$$\frac{\partial^2 w_n}{\partial t^2}=-\kappa^2\left(\frac{\partial^4 w_n}{\partial x^4}+2\frac{\partial^4 w_n}{\partial x^2\partial y^2}+\frac{\partial^4 w_n}{\partial y^4}\right)+\mu^2(w_{n+1}+w_{n-1}-2w_n)\,, \tag{1c}$$

where u_n, v_n and w_n represent the displacements of a material point (x, y) in the n-th layer in the x-, y- and z-directions, respectively. (1a) and (1b) are the equations of the extensional vibrations of a thin plate[8)]; E' and ρ' are related to the Young's modulus E, the volume density ρ and the interlayer distance c of the graphite by $E'=cE$ and $\rho'=c\rho$, and σ is the Poisson's ratio. (1c) is the equation of the transverse vibration of a thin plate[9)], except for the second term on the r.h.s., which cares for the elastic interaction between neighbouring plates; κ^2 is related in a certain way to the bending modulus of the plate. In the atomistic theory of vibration, we might assume that the potential energy of a bent honey-comb net plane of the graphite is given by a constant multiple of the sum of the squares of the atomic displacements, each of these displacements being measured from the plane which passes through the three neighbours of the atom considered. The force constant in this potential energy corresponds to the bending modulus of the thin plate in our continuum model[10)].

We shall modify the above equations by taking account of the shearing stress. For

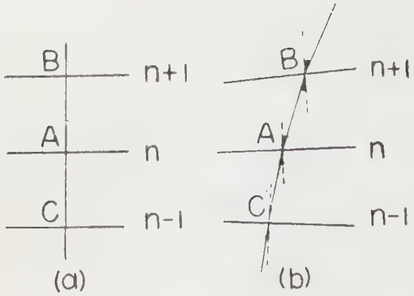

Fig. 1. (a) equilibrium state.
(b) Shearing state. The figure shows the shearing angles.

small interlayer shearing strains the strain energy φ can be considered to be independent of other strain energies. It may be assumed to be given by the following sum of the squares of shear angles produced at each layer:

$$\varphi=\frac{c\cdot c_{44}}{4}\sum_n\iint\left\{\left(\frac{u_{n+1}-u_n}{c}+\frac{\partial w_n}{\partial x}\right)^2+\left(\frac{u_n-u_{n-1}}{c}+\frac{\partial w_n}{\partial x}\right)^2+\left(\frac{v_{n+1}-v_n}{c}+\frac{\partial w_n}{\partial y}\right)^2+\left(\frac{v_n-v_{n-1}}{c}+\frac{\partial w_n}{\partial y}\right)^2\right\}dxdy\ . \qquad (2)$$

The kinetic energy T is

$$\mathrm{T}=\sum_n\iint\frac{\rho'}{2}\left\{\left(\frac{\partial u_n}{\partial t}\right)^2+\left(\frac{\partial v_n}{\partial t}\right)^2+\left(\frac{\partial w_n}{\partial t}\right)^2\right\}dxdy\ , \qquad (3)$$

so that, applying Hamilton's principle,

$$\delta\int_{t_1}^{t_2}(\mathrm{T}-\varphi)dt=0\ , \qquad (4)$$

we obtain the following equations:

$$\frac{\partial^2 u_n}{\partial t^2}=\frac{\zeta}{c^2}(u_{n+1}+u_{n-1}-2u_n)+\frac{\zeta}{2c}\left(\frac{\partial w_{n+1}}{\partial x}-\frac{\partial w_{n-1}}{\partial x}\right), \qquad (5a)$$

$$\frac{\partial^2 v_n}{\partial t^2}=\frac{\zeta}{c^2}(v_{n+1}+v_{n-1}-2v_n)+\frac{\zeta}{2c}\left(\frac{\partial w_{n+1}}{\partial y}-\frac{\partial w_{n-1}}{\partial y}\right), \qquad (5b)$$

$$\frac{\partial^2 w_n}{\partial t^2}=\zeta\left(\frac{\partial^2 w_n}{\partial x^2}+\frac{\partial^2 w_n}{\partial y^2}\right)+\frac{\zeta}{2c}\left(\frac{\partial u_{n+1}}{\partial x}-\frac{\partial u_{n-1}}{\partial x}+\frac{\partial v_{n+1}}{\partial y}-\frac{\partial v_{n-1}}{\partial y}\right), \qquad (5c)$$

where $\zeta=c_{44}\cdot c/\rho'=c_{44}/\rho$. By adding the r.h.s. of (5a), (5b) and (5c) to the r.h.s. of (1a), (1b) and (1c), respectively, we obtain the new equations of vibrations:

$$\frac{\partial^2 u_n}{\partial t^2}=\frac{E'}{\rho'(1-\sigma^2)}\left\{\frac{\partial^2 u_n}{\partial x^2}+\frac{1}{2}(1-\sigma)\frac{\partial^2 u_n}{\partial y^2}+\frac{1}{2}(1+\sigma)\frac{\partial^2 v_n}{\partial x\partial y}\right\}+\frac{\zeta}{c^2}(u_{n+1}+u_{n-1}-2u_n)+\frac{\zeta}{2c}\left(\frac{\partial w_{n+1}}{\partial x}-\frac{\partial w_{n-1}}{\partial x}\right), \qquad (6a)$$

$$\frac{\partial^2 v_n}{\partial t^2}=\frac{E'}{\rho'(1-\sigma^2)}\left\{\frac{\partial^2 v_n}{\partial y^2}+\frac{1}{2}(1-\sigma)\frac{\partial^2 v_n}{\partial x^2}+\frac{1}{2}(1+\sigma)\frac{\partial^2 u_n}{\partial x\partial y}\right\}+\frac{\zeta}{c^2}(v_{n+1}+v_{n-1}-2v_n)+\frac{\zeta}{2c}\left(\frac{\partial w_{n+1}}{\partial y}-\frac{\partial w_{n-1}}{\partial y}\right), \qquad (6b)$$

$$\frac{\partial^2 w_n}{\partial t^2}=-\kappa^2\left(\frac{\partial^4 w_n}{\partial x^4}+2\frac{\partial^4 w_n}{\partial x^2\partial y^2}+\frac{\partial^4 w_n}{\partial y^4}\right)+\mu^2(w_{n+1}+w_{n-1}-2w_n)+\zeta\left(\frac{\partial^2 w_n}{\partial x^2}+\frac{\partial^2 w_n}{\partial y^2}\right)+\frac{\zeta}{2c}\left(\frac{\partial u_{n+1}}{\partial x}-\frac{\partial u_{n-1}}{\partial x}+\frac{\partial v_{n+1}}{\partial y}-\frac{\partial v_{n-1}}{\partial y}\right). \qquad (6c)$$

In these equations, $\sqrt{\{E'/\rho'(1-\sigma^2)\}}$ is the velocity of the longitudinal wave in the plane of the layer and will be denoted as v_l. The velocity of the transverse wave, v_t, is $v_l\sqrt{\{(1-\sigma)/2\}}=\sqrt{\{E'/2\rho'(1+\sigma)\}}$.

§ 3. Solution of the Equation of Vibrations

By the usual substitution

$$\left.\begin{aligned}u_n&=U\cdot\exp\{2\pi i(\sigma_x x+\sigma_y y+\sigma_z nc-\nu t)\}\ ,\\ v_n&=V\cdot\exp\{2\pi i(\sigma_x x+\sigma_y y+\sigma_z nc-\nu t)\}\ ,\\ w_n&=W\cdot\exp\{2\pi i(\sigma_x x+\sigma_y y+\sigma_z nc-\nu t)\}\ ,\end{aligned}\right\} \qquad (7)$$

we obtain the following simultaneous equations:

$$\left.\begin{aligned}&[v_l^2\{\sigma_x^2+(1/2)(1-\sigma)\sigma_y^2\}\\ &\quad+(\zeta/c^2\pi^2)\sin^2\pi c\sigma_z-\nu^2]U\\ &\quad+[(1/2)(1+\sigma)\sigma_x\sigma_y v_l^2]V\\ &\quad+[(\zeta/2\pi c)\sigma_x\sin 2\pi c\sigma_z]W=0\ ,\\ &[(1/2)(1+\sigma)\sigma_x\sigma_y v_l^2]U+[v_l^2\{\sigma_x^2+(1/2)(1-\sigma)\sigma_y^2\}\\ &\quad+(\zeta/c^2\pi^2)\sin^2\pi c\sigma_z-\nu^2]V\\ &\quad+[(\zeta/2\pi c)\sigma_y\sin 2\pi c\sigma_z]W=0\ ,\\ &[(\zeta/2\pi c)\sigma_x\sin 2\pi c\sigma_z]U+[(\zeta/2\pi c)\sigma_y\sin 2\pi c\sigma_z]V\\ &\quad+[4\pi^2\kappa^2(\sigma_x^2+\sigma_y^2)^2+(\mu^2/\pi^2)\sin^2\pi c\sigma_z\\ &\quad+\zeta(\sigma_x^2+\sigma_y^2)-\nu^2]W=0\ .\end{aligned}\right\} \qquad (8)$$

We expect ζ to be small, so that we first neglect the non-diagonal terms such as

$$\frac{\zeta}{2\pi c}\begin{pmatrix}\sigma_x\\ \sigma_y\end{pmatrix}\cdot\sin 2\pi c\sigma_z\begin{pmatrix}U\\ V\\ W\end{pmatrix}$$

in (8). In this first approximation, the secular equation gives the following three roots:

$$\nu_{10}^2=v_t^2(\sigma_x^2+\sigma_y^2)+(\zeta/\pi^2c^2)\sin^2\pi c\sigma_z\ , \tag{9}$$

$$\nu_{20}^2=v_l^2(\sigma_x^2+\sigma_y^2)+(\zeta/\pi^2c^2)\sin^2\pi c\sigma_z\ , \tag{10}$$

$$\nu_{30}^2=4\pi^2\kappa^2(\sigma_x^2+\sigma_y^2)^2+(\mu^2/\pi^2)\sin^2\pi c\sigma_z +\zeta(\sigma_x^2+\sigma_y^2)\ . \tag{11}$$

Thus, in this approximation, the lattice vibrations separate themselves into three parts. The complete separation of (8) can be effected by the transformation matrix

$$\begin{pmatrix}\frac{\sigma_x}{\sqrt{\sigma_x^2+\sigma_y^2}} & \frac{\sigma_y}{\sqrt{\sigma_x^2+\sigma_y^2}} & 0\\ \frac{-\sigma_y}{\sqrt{\sigma_x^2+\sigma_y^2}} & \frac{\sigma_x}{\sqrt{\sigma_x^2+\sigma_y^2}} & 0\\ 0 & 0 & 1\end{pmatrix}\ . \tag{12}$$

We apply this transformation to the original matrix of (8) and have

$$\begin{pmatrix}\nu_{10}^2 & 0 & 0\\ 0 & \nu_{20}^2 & \frac{\zeta\sqrt{\sigma_x^2+\sigma_y^2}}{2\pi c}\sin 2\pi c\sigma_z\\ 0 & \frac{\zeta\sqrt{\sigma_x^2+\sigma_y^2}}{2\pi c}\sin 2\pi c\sigma_z & \nu_{30}^2\end{pmatrix}. \tag{13}$$

As the result, we obtain the exact solution

$$\left.\begin{aligned}&\nu_1^2=\nu_{10}^2\ ,\\ &\left.\begin{matrix}\nu_2^2\\ \nu_3^2\end{matrix}\right\}=\frac{1}{2}\{\nu_{20}^2+\nu_{30}^2\\ &\quad\pm\sqrt{(\nu_{20}^2-\nu_{30}^2)+(\zeta^2/\pi^2c^2)(\sigma_x^2+\sigma_y^2)\sin^2 2\pi c\sigma_z}\}.\end{aligned}\right\} \tag{14}$$

This result shows that only the longitudinal intra-layer vibrations couple with the perpendicular vibrations, i.e. the bending vibrations of the layers, but that the transverse intra-layer vibrations do not couple with them.

From (14) it is seen that the effect of the non-diagonal elements of (13) on the differences $\nu_2^2-\nu_{20}^2$ and $\nu_3^2-\nu_{30}^2$ is the greatest when $\nu_{20}=\nu_{30}$. The latter equality holds on the surface of revolution in the σ-space given by

$$4\pi^2\kappa^2(\sigma_x^2+\sigma_y^2)^2-(v_l^2-\zeta)(\sigma_x^2+\sigma_y^2) +(1/\pi^2)(\mu^2-\zeta/c^2)\sin^2\pi c\sigma_z=0\ , \tag{15}$$

which is, in another form,

$$\sigma_x^2+\sigma_y^2=\frac{1}{8\pi^2\kappa^2}[(v_l^2-\zeta) \pm\sqrt{\{(v_l^2-\zeta)^2-16\kappa^2(\mu^2-\zeta/c^2)\sin^2\pi c\sigma_z\}}]\ . \tag{16}$$

If we compare the two terms under the square root symbol of (16), whose order of magnitude can be seen from Table I, we see that the first term, $(v_l^2-\zeta)^2$, is more than one hundred times larger than the maximum value of the second term $16\kappa^2(\mu^2-\zeta/c^2)\sin^2\pi c\sigma_z$, since $v_l^2\sim 4\times10^{12}$ cm²/sec² and $4\kappa\mu\sim3\times10^{11}$ cm/sec. The upper sign of (16) thus corresponds to the wave number $(\sigma_x^2+\sigma_y^2)^{1/2}\sim v_l/2\pi\kappa\sim0.5\times10^8$ cm^{-1}, which, however, is too large to come into our consideration when we are concerned with the specific heat at low temperatures. Therefore, we take the lower sign and have approximately

$$\sigma_x^2+\sigma_y^2=\frac{\mu^2-\zeta/c^2}{\pi^2(v_l^2-\zeta)}\sin^2\pi c\sigma_z\approx\frac{\mu^2}{\pi^2v_l^2}\sin^2\pi c\sigma_z\ . \tag{17}$$

On this surface of revolution we obtain from (14) the maximum correction to ν_{20}^2 and ν_{30}^2 as

$$\begin{aligned}&\frac{\zeta}{2\pi c}\sqrt{\sigma_x^2+\sigma_y^2}\cdot\sin 2\pi c\sigma_z\\ &\qquad\approx\zeta(\sigma_x^2+\sigma_y^2)\frac{v_l}{\mu c}\cos\pi c\sigma_z\\ &\qquad\approx\frac{\zeta}{\pi^2c^2}\sin^2\pi c\sigma_z\cdot\frac{\mu c}{v_l}\cos\pi c\sigma_z\ ,\end{aligned}$$

which, apart from the factor $\cos\pi c\sigma_z$, is somewhat larger than $\zeta(\sigma_x^2+\sigma_y^2)$ of (11) and somewhat smaller than $\zeta/\pi^2c^2\cdot\sin^2\pi c\sigma_z$ of (10), since $v_l/\mu c$ is about 5 (see Table I). However, when we go out of the surface (16), the effect of the second term in the square root symbol of (14) rapidly decreases. The effect is important only within the domain of the σ-space bounded by the two surfaces,

$$\nu_{20}^2-\nu_{30}^2=\pm\frac{\zeta}{\pi c}\sqrt{\sigma_x^2+\sigma_y^2}\cdot\sin 2\pi c\sigma_z\ , \tag{18}$$

on which the two terms under the square root symbol in (14) become equal to each other. But these surfaces are close to (17) if ζ is small compared with v_l^2 and μ^2c^2. For small values of σ_x, σ_y, σ_z, for which the effect of the shearing force is most important, (18) reduce to circular cones given by

$$\begin{aligned}&\sqrt{\sigma_x^2+\sigma_y^2}\\ &\quad=\sqrt{\frac{\mu^2c^2-\zeta}{v_l^2-\zeta}}\left(1\pm\frac{\zeta}{\sqrt{v_l^2\mu^2c^2-(v_l^2+\mu^2c^2)\zeta}}\right)|\sigma_z|\\ &\quad\approx\frac{\mu c}{v_l}\left(1\pm\frac{\zeta}{v_l\mu c}\right)|\sigma_z|\ ,\end{aligned} \tag{19}$$

if ζ^2 is neglected in comparison with $v_l^2\mu^2c^2$ and further in (19) ζ neglected in comparison with v_l^2 and μ^2c^2. On the other hand, (17) reduces for small values of σ_x, σ_y, σ_z to

$$\sqrt{\sigma_x^2+\sigma_y^2}=\sqrt{\frac{\mu^2c^2-\zeta}{v_l^2-\zeta}}\,|\sigma_z|\approx\frac{\mu c}{v_l}\,|\sigma_z|\ . \tag{20}$$

Therefore, the zone in which the correction under consideration is practically important is a thin conical region bounded by the two surfaces given by (19) near the origin of the σ-space. We see therefore that the differences $\nu_2^2-\nu_{20}^2$ and $\nu_3^2-\nu_{30}^2$ are pronounced only in a negligibly small domain of the σ-space. Therefore, in computing the specific heat, we can use the approximate formulas (9), (10), (11), instead of the exact ones (14), and compute the frequency distribution functions. The coupling between the two types of the vibrations, which were separated in the treatment of our paper I, has now resulted in the ζ-dependent terms in these approximate frequency formulas. The coupled waves have directions of polarization different from those of the waves in paper I, but obviously the directions of polarization are not important for the specific heat.

§ 4. Frequency Distribution Functions

In § 3, we have obtained approximate frequency formulas (9) and (10) for the first two types of waves, whose polarization vectors lie nearly in the planes of the layers. For these waves the contours $\nu=$const. are surfaces of revolution about the σ_z-axis in the σ-space. The volume of the σ-space enclosed by one of these surfaces for $\nu\leqq\nu_z$, where $\nu_z=\sqrt{\zeta}/\pi c$, is given by

$$V(\nu)=\frac{2\pi}{v^2}\int_0^{(1/\pi c)\sin^{-1}(\nu/\nu_z)}(\nu^2-\nu_z^2\sin^2\pi c\sigma_z)d\sigma_z\ ,\quad(\nu\leqq\nu_z). \tag{21a}$$

For $\nu>\nu_z$, the contours $\nu=$const. cross the boundaries $\sigma_z=\pm1/2c$ of the Brillouin zone, so that we have to calculate the volume of the space bounded by $\nu=$const. and $\sigma_z=\pm1/2c$. This is

$$V(\nu)=\frac{2\pi}{v^2}\int_0^{1/2c}(\nu^2-\nu_z^2\sin^2\pi c\sigma_z)d\sigma_z\ ,\quad(\nu\geqq\nu_z) \tag{21b}$$

In (21a) and (21b), v stands for v_t or v_l, according as we take either (9) or (10). The frequency distribution functions are obtained directly from (21a) and (21b) as follows:

$$f(\nu)=\frac{4V}{v^2c}\,\nu\sin^{-1}\left(\frac{\nu}{\nu_z}\right),\quad(\nu\leqq\nu_z)\ , \tag{22a}$$

$$f(\nu)=\frac{4V}{v^2c}\,\nu\cdot\frac{\pi}{2}\ ,\quad(\nu\geqq\nu_z)\ , \tag{22b}$$

where V denotes the atomic volume. For very low frequencies ($\nu\ll\nu_z$), (22a) reduces to

$$f(\nu)=\frac{4V}{v^2c\nu_z}\cdot\nu^2\ , \tag{23}$$

which gives rise to a specific heat proportional to T^3 at very low temperatures. In paper I, ζ has been neglected, and hence (22b) has been used in the whole frequency range, so that the specific heat due to the intra-layer waves was proportional to T^2 at low temperatures. The introduction of ζ has an effect on $f(\nu)$ only in the range of low frequencies, $\nu<\nu_z$.

We shall distinguish the functions $f(\nu)$ for v_t and v_l by $f_1(\nu)$ and $f_2(\nu)$, respectively.

For the third type of waves, the frequency is given by (11). The volume of the σ-space enclosed by a surface $\nu=$const. alone, when $\nu\leqq\mu/\pi$, and that enclosed by this surface and the planes $\sigma_z=\pm1/2c$, when $\nu\geqq\mu/\pi$, are given respectively by

$$V(\nu)=\frac{1}{\kappa}\int_0^{(1/\pi c)\sin^{-1}(\nu/\nu_z')}[\sqrt{\{(\nu^2+\zeta^2/16\pi^2\kappa^2)-\nu_z'^2\sin^2\pi c\sigma_z\}}-\zeta/4\pi\kappa]d\sigma_z\ ,\quad(\nu\leqq\nu_z')\ , \tag{24a}$$

and

$$V(\nu)=\frac{1}{\kappa}\int_0^{1/2c}[\sqrt{\{(\nu^2+\zeta^2/16\pi^2\kappa^2)-\nu_z'^2\sin^2\pi c\sigma_z\}}-\zeta/4\pi\kappa]d\sigma_z\ ,\quad(\nu\geqq\nu_z')\ , \tag{24b}$$

where $\nu_z'=\mu/\pi$. The frequency distribution function $f_3(\nu)$ is obtained as follows:

$$f_3(\nu)=\frac{V}{\pi\kappa c}\cdot\frac{\nu}{\nu_z'}\int_0^{\sin^{-1}\{1/\sqrt{(1+\zeta^2/16\pi^2\kappa^2\nu^2)}\}}\frac{d\varphi}{\sqrt{\left\{1-\left(\frac{\nu}{\nu_z'}\right)^2\left(1+\frac{\zeta^2}{16\pi^2\kappa^2\nu^2}\right)\sin^2\varphi\right\}}}\ ,\quad(\nu\leqq\nu_z')\ , \tag{25a}$$

$$f_3(\nu)=\frac{V}{\pi\kappa c}\left(1+\frac{\zeta^2}{16\pi^2\kappa^2\nu^2}\right)^{-1/2}\int_0^{\pi/2}\frac{d\varphi}{\sqrt{\left\{1-\left(\frac{\nu_z'}{\nu}\right)^2\left(1+\frac{\zeta^2}{16\pi^2\kappa^2\nu^2}\right)^{-1}\sin^2\varphi\right\}}}\ ,\quad(\nu\geqq\nu_z')\ . \tag{25b}$$

The integrals of (25a) and (25b) are elliptic integrals of the first kind and so can be expressed by the usual notation as

$$F(\sin^{-1}\{1/\sqrt{(1+\zeta^2/16\pi^2\kappa^2\nu^2)}\}\,,\quad (\nu/\nu_z')\{1+\zeta^2/16\pi^2\kappa^2\nu^2\}^{1/2}) \qquad (26a)$$

and

$$K(\{\nu_z'/\nu\}\{1+\zeta^2/16\pi^2\kappa^2\nu^2\}^{-1/2})\,, \qquad (26b)$$

respectively. For high frequencies, for which $4\pi\kappa\nu \gg \zeta$, the above integrals reduce to $K(\nu/\nu_z')$ and $K(\nu_z'/\nu)$, respectively, and (25a) and (25b) reduce to (21) and (22) of I (see also Fig. 3 of I). The introduction of ζ affects $f_3(\nu)$ over a wide range of frequencies, as seen from (25a) and (25b), but the effect is greater for lower frequencies than for higher frequencies, and, in particular, it is practically negligible in (25b). For low frequencies, $\zeta/4\pi\kappa \ll \nu \ll \nu_z'$, (25a) reduces to $f_3(\nu)=(V/2\kappa c\nu_z')\cdot\nu$, and this gives rise to a specific heat proportional to T^2. For still lower frequencies, $4\pi\kappa\nu \ll \zeta$, (25a) reduces to

$$f_3(\nu)=\frac{4V}{c\zeta\nu_z'}\cdot\nu^2\,, \qquad (27)$$

which should give rise to a specific heat proportional to T^3 at very low temperatures.

The estimation of the temperature at which the transition from the T^2 law to the T^3 law occurs can roughly be estimated by putting $kT=h\nu$ with either $\nu=\nu_z(=\sqrt{\zeta^-/\pi c})$ or $\nu=\zeta/4\pi\kappa$. From the former one obtains $T=\Theta_z=26.7$°K and from the latter $T=2.13$°K (see Table I). We expect therfore a gradual deviation from the T^2 law below 26.7°K and a rapid deviation below 2.13°K.

§ 5. Calculation of the Specific Heat

As has been shown in I, the electronic specific heat and the C_p-C_v correction contribute a negligible amount to the specific heat of graphite in the range of temperature $T<90$°K, to which we shall confine ourselves. Therefore, we can leave them out. We derived in I the formula of the specific heat due to the vibrations parallel to the layers by the method analogous to Debye's three-dimensional theory, and obtained approximate formulas for high temperatures and for low temperatures. For the latter the formula was

$$C=2R\left\{\frac{14.42}{x^2}-\frac{2x}{e^x-1}-6x\sum_{n=1}^{\infty}e^{-nx}\left(\frac{1}{nx}+\frac{2}{n^2x^2}+\frac{2}{n^3x^3}\right)\right\}\,, \qquad (28)$$

where R is the universal gas constant, $x=\Theta/T$ and

$$\Theta=\frac{h}{k}\left\{\frac{\pi V}{2cN}\left(\frac{1}{v_t^2}+\frac{1}{v_l^2}\right)\right\}^{-1/2}=2480\text{°K}, \quad \text{(see Table I).} \qquad (29)$$

Here N denotes Avogadro's number.

The distribution functions derived in § 4 for these vibrations differ from those in I only in the low frequency range, $\nu<\nu_z$. Therefore, we shall treat the difference as a correction to the previous formula. The corrections to be added to the previous frequency distribution functions are

$$-\frac{4V}{v_t^2c}\nu\left\{\frac{\pi}{2}-\sin^{-1}\left(\frac{\nu}{\nu_z}\right)\right\}$$

and

$$-\frac{4V}{v_l^2c}\nu\left\{\frac{\pi}{2}-\sin^{-1}\left(\frac{\nu}{\nu_z}\right)\right\}$$

for the transverse and longitudinal vibrations, respectively. Accordingly, the correction $\varDelta C$ to be added to C of (28) is

$$\varDelta C=-\frac{4V}{c}\left(\frac{1}{v_l^2}+\frac{1}{v_t^2}\right)k\nu_z^2\times\int_0^1 x\left(\frac{\pi}{2}-\sin^{-1}x\right)\cdot E\left(\frac{\Theta_z x}{T}\right)dx\,, \qquad (30)$$

where E denotes the Einstein function, and $x=\nu/\nu_z$ and $\Theta_z=h\nu_z/k$.

The formula derived in I for the specific heat due to the vibrations normal to the layers was

$$C'=\frac{Vk\nu_z'}{\pi c\kappa}\left[\int_0^1 xK(x)\cdot E\left(\frac{\Theta_z'x}{T}\right)dx+\int_1^{x_1}K\left(\frac{1}{x}\right)\cdot E\left(\frac{\Theta_z'x}{T}\right)dx\right], \qquad (31)$$

where $x=\nu/\nu_z'$ and $\Theta_z'=h\nu_z'/k$. The corresponding frequency distribution function is given by (25a), so that, replacing $K(x)$ in the first integral of (31) by (26a), the correction to (31) is approximately

$$\varDelta C'=\frac{Vk\nu_z'}{\pi c\kappa}\int_0^1 x[K(x)-F(\sin^{-1}\{1/\sqrt{(1+x_0^2/x^2)}\}\,,\; x\{1+x_0^2/x^2\}^{1/2})]\cdot E\left(\frac{\Theta_z'x}{T}\right)dx\,, \qquad (32)$$

where $x_0=\zeta\nu_z'/4\pi\kappa$.

The numerical values of all the constant in the above formulas, except ζ, were determined in I, but some of them have been revised in the course of the present calculation. The estimation of ζ will be postponed to the next section. Table I shows such numerical values

Table I.

(A)	$v_t=1.23\times10^6$ cm/sec	$\Theta=\frac{h}{k}\left\{\frac{\pi V}{2cN}\left(\frac{1}{v_t^2}+\frac{1}{v_l^2}\right)\right\}^{-1/2}$
	$v_l=2.10\times10^6$ cm/sec	$=2480$°K
	$V\doteqdot5.285$ cm^3/g.atom	
	$\nu_z'=\mu/\pi=3.76\times10^{12}$/sec	$\Theta_z'=h\nu_z'/k=180.5$°K
	$c=3.35\times10^{-8}$ cm	$\mu c=3.92\times10^5$ cm/sec
(B)	$\kappa=0.611\times10^{-2}$ cm^2/sec^2	
	$\zeta=0.344\times10^{10}$ cm^2/sec^2	$h(\zeta/4\pi\kappa)/k=2.13$°K
	$\nu_z=\sqrt{\zeta}/\pi c=5.57\times10^{11}$/sec	$\Theta_z=h\nu_z/k=26.7$°K

Table II. Results of the numerical calculations of the specific heat of graphite in cal/deg. atom.

T°K	C (28)	$-\Delta C$ (30)	$C_{\mathrm{corr}}=C+\Delta C$	C' (31)	$-\Delta C'$ (32)	$C'_{\mathrm{corr}}=C'+\Delta C'$	Total sp. ht. $C_{\mathrm{corr}}+C'_{\mathrm{corr}}$	Exper. value of sp. ht.		$\frac{C_{\mathrm{corr}}+C'_{\mathrm{corr}}}{T^2}$ $\times10^5$	Calc. value of sp. ht. modified*
								(a)	(b)		
0.5			$0.0^{6}10$			$0.0^{5}366$	$0.0^{5}376$			1.50	$0.0^{5}157$
1.0			$0.0^{6}80$			$0.0^{4}212$	$0.0^{4}220$			2.12	$0.0^{4}113$
1.5			$0.0^{5}27$			$0.0^{4}553$	$0.0^{4}580$		$0.0^{4}36$	2.58	$0.0^{4}342$
2			$0.0^{5}78$			$0.0^{3}108$	$0.0^{3}116$		$0.0^{4}72$	2.90	$0.0^{4}730$
3			$0.0^{4}234$			$0.0^{3}226$	$0.0^{3}289$		$0.0^{3}20$	3.21	$0.0^{3}205$
4			$0.0^{4}580$			$0.0^{3}494$	$0.0^{3}552$		$0.0^{3}40$	3.45	$0.0^{3}416$
8			$0.0^{3}427$			$0.0^{2}214$	$0.0^{2}257$		$0.0^{2}22$	4.01	$0.0^{2}212$
10	$0.0^{3}931$	$0.0^{3}186$	$0.0^{3}745$	$0.0^{2}361$	$0.0^{3}21$	$0.0^{2}340$	$0.0^{2}415$		$0.0^{2}34$	4.16	$0.0^{2}356$
15	$0.0^{2}210$	$0.0^{3}21$	$0.0^{2}189$	$0.0^{2}862$	$0.0^{3}31$	$0.0^{2}831$	0.0102	0.0102	$0.0^{2}91$	4.53	$0.0^{2}928$
30	$0.0^{2}838$	$0.0^{3}22$	$0.0^{2}816$	0.0370	$0.0^{3}70$	0.0363	0.0445	0.0442		4.94	0.0427
45	0.0189	$0.0^{3}22$	0.0187	0.0821	$0.0^{2}11$	0.0810	0.0997	0.0998		4.93	
60	0.0335	$0.0^{3}23$	0.0333	0.136	$0.0^{2}12$	0.135	0.168	0.167		4.67	
75	0.0524	$0.0^{3}23$	0.0522	0.184	$0.0^{2}13$	0.183	0.235	0.250		4.18	
90	0.0754	$0.0^{3}23$	0.0752	0.234	$0.0^{2}14$	0.233	0.308	0.388		3.80	

(a) DeSorbo and Tyler (1953). (b) Bergenlid, Hill, Webb and Wilks (1954).

* Calculated values with the use of $c_{44}=2.34\times10^{10}$ dynes/cm^2, which is three times larger than that used in the calculation of C_{corr} and C'_{corr}. (See § 6).

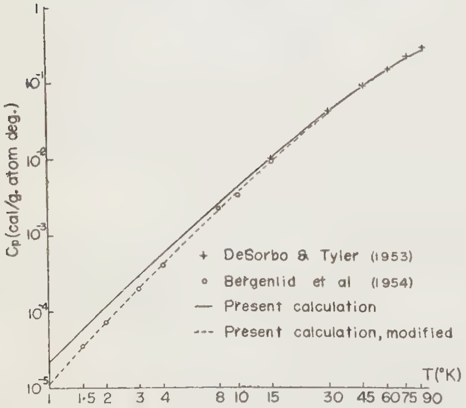

Fig. 2.

of the constants. The method of eatimating the constants of the group (A) has been described in I. We have corrected some of them with the new value of c (3.35 Å)[11]; in I we used c=3.40 Å. κ, which relates to the bending elastic constant has been determined by making the calculated specific curve fit the observed one, as in I, but this time its value was revised by making the fit at relatively low temperatures. The final results of the calculations are tabulated in Table II along with those observed by DeSorbo and Tyler and also those observed by Bergenlid, Hill, Webb and Wilks, the latter being obtained from a smooth curve which fits the measured points.

From this table and Fig. 2 we see the following interesting features:

(a) The agreement between the calculated and observed values is excellent in the temperature range from 15° to 60°K, where the T^2

law holds almost accurately.

(b) Above 60°K, the calculated values become lower than the observed ones. This is due to the failure of our continuum model, as will be discussed in the last section.

(c) Below 10°K, a deviation from the T^2 law in the calculated curve becomes gradually apparent, but the observed curve due to Bergenlid, *et al.* lies somewhat lower than that calculated for $T<15$°K. If we use a value of the shearing elastic constant, c_{44}, three times larger than that given in Table I, the calculated curve is in complete accord with the observed one. As one will see in the next section, our estimate of the value of c_{44} is a crude one, so that a factor of three can be inside the error of the calculation. But it is to be noted that the temperature at which a transition from T^2 to T^3 law occurs is in the neighbourhood of a few degrees absolute both in calculated and observed curves.

§ 6. Estimation of the Elastic Constant of Shearing

Since there is no available experimental value of c_{44}, we shall derive it theoretically.

Brennan has calculated the repulsive energy between adjacent hexagonal layers from the interaction of *LCAO* molecular orbitals in the two layers. The van der Waals attractive energy has been determined by making the energy minimum fall at the observed value of c, namely 3.37 Å. Using the effective nuclear charge $Z^*=2.03$ and the effective quantum number $n^*=1.944$ proposed by Kohlrausch, he calculated the interlayer binding energy and compressibility. The calculated value of the latter was in satisfactory agreement with the experimental value. Unfortunately, however, there are errors in his calculations, which seriously affect his numerical results. One of the errors is in his formula (18) for the interlayer binding energy per mole, U. Denoting the interaction energy between one layer and the rest of the crystal by $2E$, U can be written

$$U=(1/2)(N/n)E\,, \tag{33}$$

where n is the number of unit cells (each containing two atoms) in a layer. The numerical factor in (33) is 1/2, instead of 1/4 as in Brennan's paper. Another error is found in his formula (14) for the attractive term E_A in E. Denoting by $F(sc)$ the attractive energy between a unit cell of a hexagonal layer and a layer at a distance sc from that cell, E_A can be written

$$E_A=n\sum_{s=1}^{\infty}F(sc)\,, \tag{34}$$

instead of Brennan's formula,

$$E_A=n\sum_{s=1}^{\infty}sF(sc)\,.$$

(34) leads to

$$E_A=-\frac{n\pi\sigma A}{c^4}\sum_{s=1}^{\infty}\frac{1}{s^4}\,, \tag{35}$$

where σ is the number density of atoms in a layer and A the constant of the van der Waals energy; the sum in (35) was $\sum_{s=1}^{\infty}1/s^3$ in Brennan's paper. Using the above correct formulas and Kohlrausch's value of $\delta=Z^*/n^*$, we obtain numerical results which are quite different from those of Brennan. The first row of Table III shows our results. The calculated value of the elastic constant, c_{33}, or approximately the Young's modulus perpendicular to the layers, $E_\perp$, is seen to be more than twice larger than the experimental one, and consequently than Brennan's result. On the other hand, if we used Slater's[12)] value of δ we would have obtained too small a value of $E_\perp$ (which is not given in Table III).

Table III.

	A (atomic unit)	U_A	U_R	U	$E_\perp$ (or $1/\beta$*) (10^{12} dynes/cm^2)
			(k cal/mole)		
Kohlrausch	604.4	−21.46	13.43	−8.03	0.792
SCF	309.3	−10.98	5.75	−5.23	0.614
experimental					0.356*

The overlap integral for the Kohlrausch wave function is about twice as large as that for the *SCF* (self-consistent field) wave function at the actual interatomic distance, while the overlap integral for the Slater wave function is about half the latter. Since the repulsive energy may be supposed to be proportional

---

* Brennan's $1/\beta$ was calculated from

$$\frac{1}{\beta}=\frac{c^2}{V}\cdot\frac{\partial^2 U}{\partial z^2}\,,$$

which is to be equated to our $E_\perp$ in I, where $E_\perp$ is defined as the Young's modulus perpendicular to the layer. In I we have estimated $E_\perp$ from the compressibility data and the estimated value of the Young's modulus parallel to the layer $E_{//}$ and that of the Poisson's ratio σ. The result was $E_\perp=3.56\times10^{11}$ dynes/cm (3.60×10^{11} dynes/cm^2 in I is corrected).

to the overlap integral, it may be reasonable to choose δ so as to give the value of the overlap integral at given interatomic distances equal to those calculated by the *SCF* wave function.

With the aid of the formula and tables given by Mulliken, Rieke, Orloff and Orloff[13] we obtain in this way values of δ as shown in Table IV. Then, by use of these δ's we can calculate the repulsive energy between two atoms separated at a distance r, by changing the energy and distance scales, from the table prepared by Brennan. The results thus obtained are given in the fourth row of Table IV.

Table IV.

$p=\delta\cdot r$	7	8	10	12
δ	1.370	1.305	1.225	1.195
r (atomic unit)	5.109	6.130	8.163	10.042
$E_{\alpha\alpha}$ (a.u.)	0.02077	0.00665	0.00042	0.00002
$E'_{\alpha\alpha}$ (a.u.)	0.02077	0.00665	0.00042	0.000018

We can express the repulsive energy as a function of the distance between two atoms by an approximate formula:

$$E_{\alpha\alpha}=0.5153\exp(-0.2223r-0.07951r^2)\,. \quad (36)$$

The values calculated with this formula are given in the last row of Table IV. Summing up all the contributions from the neighbours in the adjacent layer, the total repulsive energy can be expressed as a function of the interlayer distance c, as follows:

$$E_R=2.754\exp(-0.15769c-0.08287c^2). \quad (37)$$

Putting $c=6.33$ atomic unit (3.35 Å), we obtain the value of U_R given in Table III.

The value of $E_\perp$ obtained by this calculation, given also in Table III, is about three quarters of that given by Brennan, but it is 1.72 times larger than the experimental one. The value of $E_\perp$ employed in our calculation of μ is the experimental one. However, in calculating the shearing elastic constant, c_{44}, we shall use the formula (36).

Let φ_{ij} denote the potential energy between atoms i and j at a distance r_{ij} in the crystal. According to the theory of lattice dynamics, c_{44} is given by the following formula:

$$c_{44}=\frac{N}{4V}\sum_{i=a,b}\sum_j \frac{\partial^2\varphi_{ij}}{\partial x^2}\cdot z_{ij}^2\,, \quad (38)$$

where a and b are the two atoms in a unit cell of a layer and j runs over all atoms in the crystal. On account of the equilibrium condition,

$$\sum_{i=a,b}\sum_j \frac{\partial\varphi_{ij}}{\partial z}\cdot z_{ij}=\sum_{i=a,b}\sum_j \frac{d\varphi_{ij}}{dr}\,\frac{z_{ij}^2}{r_{ij}}=0\,, \quad (39)$$

at a given distance between the layers, (38) reduces to

$$c_{44}=\frac{N}{4V}\sum_{i=a,b}\sum_j x_{ij}^2 z_{ij}^2\left(\frac{1}{r^2}\frac{d^2}{dr^2}-\frac{1}{r^3}\frac{d}{dr}\right)\varphi_{ij}\,. \quad (40)$$

In our case φ_{ij} has the following expression in atomic units:

$$\varphi_{ij}(r)=-\frac{309.3}{r^6}+0.5153\cdot\exp(-0.2223r-0.07951r^2)\,. \quad (41)$$

The van der Waals term falls slowly with increasing distance, so we evaluated the corresponding terms in (40) one by one for $r_{ij}\leqq\sqrt{(c^2+36a^2)}$ for the directly neighbouring layers, one by one for $r_{ij}\leqq\sqrt{(4c^2+36a^2)}$ for the next neighbouring layers ($a=1.42$ Å$=2.68$ a.u.), and we evaluated the contributions from further atoms by replacing the summation by integral. The final results thus obtained are

$$c_{44}=0.781\times10^{10}\text{ dynes/cm}^2\,,$$
$$=0.022\,E_\perp\,,$$

and $$\zeta=0.344\times10^{10}\text{ dynes/cm}^2.$$

The repulsive energy may also be calculated from the band theoretical standpoint, for instance by using the method of tight binding approximation. The graphite crystal may be considered to be composed of C^{4+} ions situated at the lattice points and three σ electrons per atom and one π electron per atom. The energy of the σ or π electron with a given wave vector can be expressed approximately by using the resonance energies. Adding the total energy of the electrons to the total repulsive energy between C^{4+} ions, we obtain the total repulsive energy of the crystal, which corresponds to U_R obtained above. A shearing deformation of the crystal would give rise to the deformation of the Brillouin zones and also to the change of the values of the resonance energies. If we can estimate the change of the values of the resonance energies for a given shearing deformation, we can calculate the change of the total repulsive energy of the crystal, by summing up the contributions of the change of energy of the electrons redistributed in the deformed Brillouin zones and adding to this the change of the total repulsive energy between the C^{4+} ions. The resonance energies of the π and σ electrons for the nearest neighbouring atoms in a layer can be estimated from the shape of the K_α emission band of graphite. However, the estimation of the resonance energies for two atoms separated at a farther distance, which are needed for the estimation of c_{44}, is very difficult. Therefore, this method of estimating the repulsive energy seems to be impractical.

We make here a remark about the effect of the shearing deformation on the energy band structure. If the shearing deformation of the crystal gives rise to an overlap of the energy bands, the electrons will redistribute themselves in them. Then, we must take this effect into consideration in estimating the change of the repulsive energy. However, it can be verified that the shearing deformation of the crystal does not give rise to any overlap or gap of the energy bands.

§ 7. Discussion

Our theory so far developed can interpret the specific heat of graphite in the temperature range from 60°K down to extremely low temperatures. In particular, if we use a value of the shearing elastic constant three times larger than that estimated in § 6, the agreement between theory and experiment is very satisfactory. This elastic constant has been estimated as a small difference between two large quantities which correspond to the second derivatives of the repulsive and attractive energies. Therefore, its value is sensitively affected by a slight change of the values of the constants used in the calculations, especially by that of the effective nuclear charge of the carbon atom. Thus, the value we obtained is correct only in its order of magnitude.

The discrepancy between the theoretical and observed values of the specific heat above 60°K appears to be due to the approximate nature of our continuum treatment of the layers. For small wave numbers the frequencies of the lattice vibrations are correctly given by the continuum treatment, but the situation for large wave numbers may be different. An atomistic treatment of the lattice vibrations of graphite has been done by Yoshimori and Kitano in our University (and will be published soon), which shows that the frequency distribution function for the vibrations normal to the layers is considerably different from that of the present calculation for higher frequencies. The former increases more steeply than the latter with increasing value of the frequency ; accordingly, the specific heat curve calculated atomistically is higher than that calculated in the present paper for temperatures higher than 60°K.

We shall make some remarks on the theories presented recently by several authors[4]. In these theories the elastic constants used in them have not been legitimately estimated with reference to characteristic properties of graphite, but they were merely so chosen as to make the theoretical values of the specific heat fit the observed ones. One of these theories, due to Rosenstock[4], may be regarded, in a sense, to be equivalent to Gurney's[4]. Both authors neglected the interactions among the layers and also neglected the contribution from the vibrations parallel to the layers. A more serious objection to these theories is that they tacitly assumed a 'surface tension' of the layers, because they assumed a quadratic form of the normal displacements of atoms for the potential energy.

Krumhansl and Brooks[4] have taken the interlayer interactions into consideration and derived the following frequency formula for the vibrations normal to the layers:

$$\nu^2 = A(\sigma_x^2 + \sigma_y^2) + B\sin^2 \pi c \sigma_z . \qquad (42)$$

Further they assumed that the same formula with different constants is applicable to the vibrations parallel to the layers. For these vibrations Eq. (9) or (10) of the present paper has just the same form as (42). However, the first term in our theory has been derived from the 'strong' restoring forces for the intra-layer motion and the second term from the 'weak' shearing forces acting between the layers. Moreover, we have shown that the validity of the approximate linear forms of the distribution functions $f_1(\nu)$ and $f_2(\nu)$ over a wide frequency range, which is responsible for the T^2 law of the specific heat over a wide range of temperature, are due to high values of the velocities v_t and v_l and a very low critical frequency ν_z. As ragards the normal vibrations, the circumstance is quite different. In this case our equation is (11), instead of (42). If we can omit the first term on the r.h.s. of (11), we obtain (42), but this is possible only for very long waves, since ζ is small. Thus, we see that the apparent success of Krumhansl-Brook's theory, as expressed in their numerical results, is not founded on a sound basis.

The dominant type of binding force acting between the atoms in graphite crystal is clearly the valence force between the atoms in each layer. It must act as a strong restoring force in the state of bending as well as in the state of stretching or shearing of the layers. The first term on the r.h.s. of (11) cares for this restoring force. It is only when this term is included in the frequency formula that the frequency distribution function has a linear form at moderately low frequencies. Krumhansl and Brooks criticized our paper I, stating that the strain energy should be a quadratic function of the strain components and therfore ν^2 must be a quadratic function of σ_x, σ_y, σ_z. In our theory of specific heat, terms of the fourth powers of σ_x, σ_y play a dominant role. It is true that only the strain energy quadratic in strain components is important for the specific heat of most solids, but we believe that graphite is another thing in which such a strain energy is important only for static elasticity problems or for slow vibrations.

In conclusion, the writer wishes to express his cordial thanks to Professor T. Nagamiya of Osaka University for his continual kind advices and discussions.

References

1) K. Komatsu and T. Nagamiya: J. Phys. Soc. Japan **6** (1951) 438.
This will be quoted as I in the present paper.
2) W. DeSorbo and W. W. Tyler: J. Chem. Phys. **21** (1953) 1660.
3) U. Bergenlid, R. W. Hill, E. J. Webb and J. Wilks: Phil. Mag. **45** (1954) 851.
4) R. W. Gurney: Phys. Rev. **88** (1952) 465.
J. Krumhansl and H. Brooks: J. Chem. Phys. **21** (1953) 1663.
H. B. Rosenstock: J. Chem. Phys. **21** (1953) 2064.
5) T. Nagamiya and K. Komatsu: J. Chem. Phys. **22** (1954) 1457.
6) W. Nernst: Ann. d. Phys. **36** (1911) 395.
7) R. O. Brennan: J. Chem. Phys. **20** (1952) 40.
8) A. E. H. Love: *The mathematical Theory of Elasticity* (1934) 497.
9) Load Rayleigh: *Theory of Sound I* (1937) 352.
10) Y. Kitano: Unpublished.
11) G. E. Bacon: Acta Cryst. **3** (1950) 137.
12) J. C. Slater: Phys. Rev. **36** (1930) 57.
13) R. S. Mulliken, C. A. Rieke, D. Orloff and H. Orloff: J. Chem. Phys. **17** (1949) 1248.

JOURNAL OF THE PHYSICAL SOCIETY OF JAPAN Vol. 10, No. 5, MAY, 1955

Magnetic Properties of FeTe

By Enji UCHIDA and Hisamoto KONDOH

Department of Physics, Naniwa University, Osaka

(Received November 29, 1954)

Susceptibility-temperature relation for the compound FeTe was measured over a range of temperatures between liquid air and 1150°C. Evidence was found of an antiferromagnetic character in the region of temperatures below 500°C, the molal magnetic susceptibility having been expressed by $\chi=0.92/(T+220)$. The effective number of Bohr magnetons was estimated to be 2.72. The susceptibility dependence on temperature in the region beyond 600°C showed evidences of the feeble constant paramagnetism and an anomaly at 815°C, which is the melting point of this compound. A tentative interpretation of these magnetic properties is given in terms of an electronic configuration of Fe.

§ 1. Introduction

Among the compounds in which one component is a transition metal and the other an element of the oxygen group, there are many substances which crystalize in NiAs type. FeS, FeSe, FeTe, NiTe, CoTe, etc. are such examples[1]. The magnetic properties of such substances, except FeS[2], have so far not been measured precisely. Since some of the magnetic properties of these substances may be characterized by the crystal structure and by the ionic valencies of the constituent atoms, it may be interesting to study FeSe and FeTe along with FeS. A study of FeSe has quite recently been reported by Hirone and his coworkers[3] and it was shown that its magnetic properties are, to some extent, similar to those of FeS.

Data of the magnetic properties of FeTe are yet very few. It might be due to the following reason: in this case, a slight amount of oxygen, which is inevitably contained in the compound, results in some magnetite-like substance as an impurity whose magnetization is so strong that the proper feeble magnetism of FeTe becomes wholly covered.

Therefore in order to study the thermomagnetic properties of FeTe of stoichiometric content, we intentionally added in the present work small amount of Mn as deoxydizer in the course of preparation of this compound. The work reported below was carried out, using the samples thus prepared, in order to find out the magnetic properties of FeTe.

§ 2. Experimental Arrangement

A magnetic balance of a self-recording type[4] was used for the measurements of the susceptibility. Variation was detectable to one percent of milligram, i.e., the precision of the present susceptibility measurements is usually ±2%.

For the temperature measurements, a junction of copper-constantan was used in the region below room temperature and a Pt-PtRh one in the higher temperature region. The latter was calibrated at the temperatures of the ferromagnetic Curie point of Ni (357°C), of magnetite (578°C) and of Fe (780°C), and also at the melting point of Te (452°C). The errors in the temperature measurements are estimated to be less than ±3°C.

§ 3. Preparation of Samples

The Te (99.9% pure) was distilled in vacuum (10^{-6} mmHg) three times in succession. Powder of reduced iron (99.96% pure) was heated in hydrogen stream at 650°C for two days. A mixture of the powders of these materials with the desired proportion was sealed in an evacuated silica tube, 3 mm in diameter, which was heated in a furnace for some ten hours at 1100°C and then cooled at a rate of 90°C per hour. The product was a solid material with a silvery appearance. Each sample was carefully left in the evacuated silica tube after preparation and never exposed to air throughout the experiment, as otherwise it would have suffered from the effects of oxygen.

§ 4. Results of Experiment

The results of the susceptibility measurements are given in Table I and Fig. 1. In the case of a sample which had suffered from

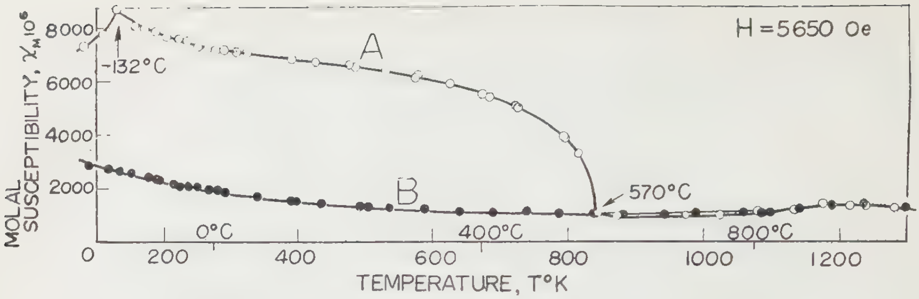

Fig. 1. Susceptibility as a function of temperature.

Curve A: a sample of stoichiometric content of FeTe, which actually contains some magnetite-like impurities owing to oxygen inevitably contained in.

Curve B: samples of stoichiometric content of FeTe to which Mn (2% of the total mass of the sample) was added as deoxydizer in the course of sampling.

Table I. Molal susceptibility and its reciprocal of FeTe.

Sample A: a sample of stoichiometric content, which actually contains some ferromagnetic impurities due to oxygen inevitably contained in the sample.

Sample B: a sample of stoichiometric content to which Mn (2% of the total mass of the sample) was added as deoxydizer in the course of sampling.

Sample A			Sample B		
T°K	$\chi_M \cdot 10^3$	$1/\chi_M \cdot 10^{-3}$	T°K	$\chi_M \cdot 10^3$	$1/\chi_M \cdot 10^{-3}$
79	7.27	0.138	80	2.81	0.356
106	7.71	0.130	114	2.64	0.378
130	8.72	0.115	132	2.57	0.389
155	8.12	0.123	149	2.49	0.398
187	7.80	0.128	186	2.28	0.438
219	7.60	0.132	211	2.15	0.465
248	7.30	0.137	235	2.00	0.500
274	7.13	0.140	265	1.87	0.535
309	7.07	0.142	278	1.83	0.546
323	7.06	0.142	287	1.78	0.562
388	6.81	0.147	337	1.62	0.617
425	6.66	0.150	387	1.50	0.666
473	6.52	0.154	437	1.37	0.730
528	6.35	0.158	492	1.27	0.787
578	6.13	0.163	537	1.22	0.820
623	5.88	0.170	587	1.16	0.861
673	5.44	0.184	637	1.11	0.909
723	4.99	0.201	687	1.07	0.934
793	3.91	0.256	737	1.03	0.971
843	1.06	0.944	787	1.01	0.990
873	0.98	1.020	837	1.03	0.975
971	0.99	1.010	882	1.04	0.962
1025	1.01	0.990	942	1.04	0.962
1078	1.13	0.885	987	1.05	0.952
1133	1.22	0.820	1057	1.04	0.962
1173	1.35	0.741	1087	1.06	0.943
1188	1.37	0.730	1097	1.08	0.930
1213	1.33	0.752	1137	1.26	0.796
1235	1.32	0.758	1187	1.38	0.724
1273	1.29	0.776	1237	1.37	0.729
1283	1.26	0.794	1295	1.30	0.769

the effects of impurity oxygen, we usually got a curve similar to Curve A, which shows, at a glance, a striking resemblance in the form to that of Fe_3O_4. It may be supposed that a slight amount of oxygen which had inevitably been contained in the materials reacted with Fe in the course of sintering to form magnetite-like substances as impurities in the compound. In spite of their slight amount, their ferromagnetic magnetizations appear to be strong enough to cover the proper magnetic properties of FeTe, which is relatively weak.

As Mn is commonly used as a deoxydizer in metallugical procedures, it is expected that an adequate amount of Mn added to the material would diminish the effects of the impurity oxygen. So we prepared two kinds of samples, those to which 2% mass of Mn was added and those whose composition is expressed as $Mn_{0.05}Fe_{0.95}Te$. The results of the susceptibility measurements for these samples almost coincided with each other. They are shown in Table I and by Curve B in Fig. 1.

As stated above, a curve similar to Curve A was usually observed in the case where the sample had suffered from effects of impurity oxygen. Sometimes, when the ferromagnetic effects were supposed to be very weak, a curve which nearly coincides with Curve B was observed. Thus Curve A is in general not reproducible, while Curve B is reproducible and must represent the real property of FeTe. The difference between Curve A and Curve B is plotted in Fig. 2 and is compared with the susceptibility curve of

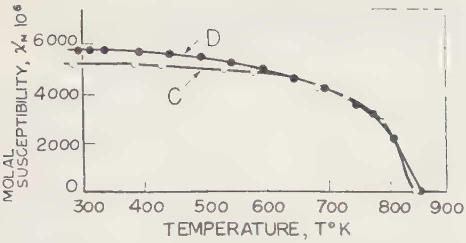

Fig. 2. Curve C: difference between the values given by Curve A and Curve B of Fig. 1 (at corresponding temperatures).
Curve D: the magnetization of magnetite as a function of temperature in arbitrary scale.

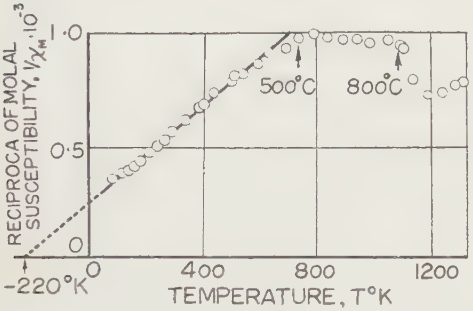

Fig. 3. Reciprocal of molal susceptibility as a function of temperature.

Fe_3O_4 (which was observed separately) reduced to about 0.1 percent in the scale of the abscissa. It can be seen that these two curves are quite similar to each other, showing the correctness of our interpretation. The slight difference probably comes from the effects of the ferromagnetic phase of FeO[5)]*.

According to the evidence mentioned above, it is clear that the added Mn has certainly acted as deoxydizer in the course of sintering, the composed impurity in this case being MnO (antiferromagnetic) instead of ferromagnetic substances. This MnO should have negligible effects on the magnetic susceptibility of the sample, because of the smallness of its mass.

Corresponding to Curve B, plots of the reciprocal of magnetic susceptibility against temperature are shown in Fig. 3. They lie on a straight line in the temperature region below 570°C, the extrapolation of this straight line crossing the temperature axis at $-220°$K. The molal magnetic susceptibility in this temperature region can be expressed as

$$\chi_M = C/(T+\theta)\ , \quad \text{where } C=0.92,\ \ \theta=220°\text{K}.$$

The effective number of Bohr magnetons, p, is computed from this value of the Curie constant to be

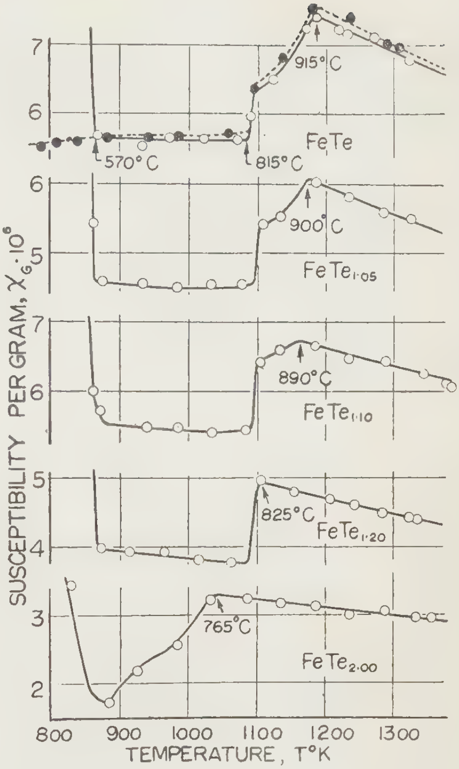

Fig. 4. The susceptibility of FeTe as a function of temperature.
Dotted line: samples of stoichiometric content to which Mn (2% of the total mass of the sample) was added as deoxydizer in the course of sampling. The kinks of the curves have been precisely checked by the self-recorded curves. (The same is done in other figures.)

$$p=\sqrt{3RC}\,/N\mu_B=2.72\ ,$$

where μ_B is the Bohr magneton, N the Avogadro number and R the gas constant. This formula suggests that the stoichiometric FeTe is antiferromagnetic. The Néel temperature, however, could not be observed in the temperature range of the present measurements, and so it may be lower than $-190°$C if it does exist.

In the region between 600°C and 800°C, the susceptibility of this compound is feeble and constant; its value is about 5×10^{-6} e.m.u./gr. However, a sudden rise of susceptibility is found at 815°C, which is followed by an anomalous hump. The temperature of the maximum of this hump is found at 915°C. These behaviors, which are shown with a magnified scale in Fig. 4, are observed with a good reproducibility. Both the samples to which Mn has been added and to which it has not been added show the similar anomaly, as seen by the upper curves in this figure. Other curves in the same figure show the anomalous behaviors of the susceptibility of FeTe$_{1+\delta}$, where δ is the excess content of Te. The features of these curves may be as follows:

---

* In our previous study on the magnetic properties of FeO, it was found that pure FeO, which is antiferromagnetic, existed only in the temperature region above 700°C, and changed into some magnetite-like substance at lower temperatures below 700°C. We called this state 'the ferromagnetic phase of FeO'. The anomalous peak at $-132°$C of Curve A in Fig. 1 is, in fact, an evidence of the ferromagnetic phase of FeO.

i) Increase in Te content lowers the temperature of the maximum of the hump, particularly for small values of δ.

ii) Also, increase in Te content lowers the height of the hump, and the hump reduces to a mere slope for $\delta\geq0.2$.

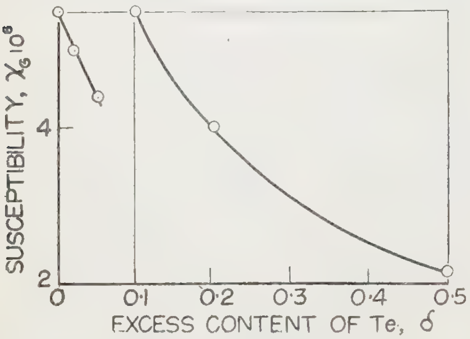

Fig. 5. Susceptibility as a function of excess content of Te measured at 620°C.

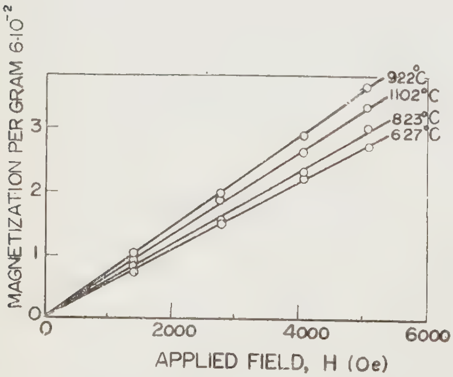

Fig. 6. Magnetization as a function of field strength.

It is not to be expected that the excess Te is uniformly solved in the material for all the values of δ investigated. In order to see the extent of the solubility of Te, the value of the feeble constant susceptibility for $\delta<0.15$ is plotted against δ in Fig. 5. It shows a jump at a value of δ smaller than 0.1. This suggests that the limit of the solubility of Te is as much as 5% (atomic) in this temperature range. Further, results on the magnetization dependence on field intensity are shown in Fig. 6 for several temperatures. The relation is quite linear. The results of susceptibility measurements on Te are shown in Fig. 7 for reference; an anomalous drop of its diamagnetic susceptibility is found at 452°C, which corresponds to the melting point of this element.

§ 5. Discussion of the Results

In several compounds of Fe the magnetic properties have been interpreted assuming that only the spin of Fe ions is effective[6)], so we assume in the following discussions that the spin of Fe^{++} alone contributes to the antiferromagnetism of FeTe and that the Fe^{++} preserves the spin magnitude in its free state, $S=2$. The effective number of Bohr magnetons should be $\sqrt{4S(S+1)}=4.91$, while the experimental value is 2.72, which corresponds to $S\approx1$. We may therefore conclude that there are two unpaired electrons or holes in

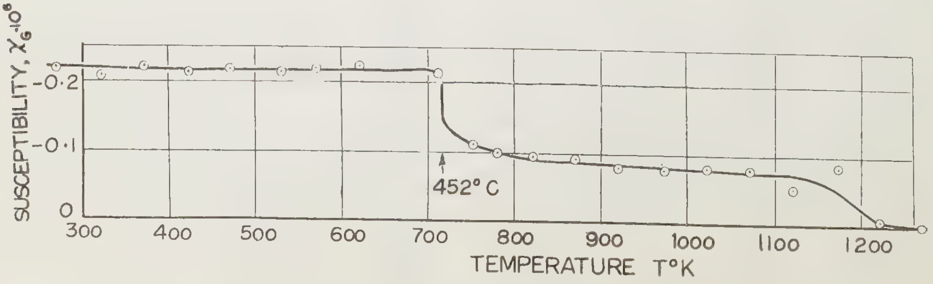

Fig. 7. The susceptibility of Te as a function of temperature.

the $3d$ shell or $3d$ band of Fe in FeTe. The atoms Fe and Te in free state possess electronic configurations $(3d)^6(4s)^2\,{}^5D_4$ and $(5p)^4\,{}^3P_2$, respectively, and in ionic state, Fe^{++} and Te^{--} possess $(3d)^6$ and $(5p)^6$, respectively; the value of S equal to 1 appears to indicate that two of the $(5p)^6$ electrons in Te^{--} are transferred to $3d$ orbits of iron, resulting in $(3d)^8$. If this is the case, the compound FeTe is an electron compound rather than an ionic compound. It is not unreasonable to consider of FeTe an alloy character, since Te is known to be more metallic than other elements of the oxygen group.

In some binary alloys in which one component is a transition element, the transition metal atoms are known to act with zero or a negative valency; for example, the magnetic properties of Ni-Cu alloy[7)] are well interpreted by the assumption that Ni atom absorbs 0.6 electrons at maximum from the $4s$ and $3d$ state of Cu atom, that is, the valency of the Ni is apparently negative. Also, in some electron compounds of transition metals with metals of higher valencies, the transition metal atoms appear to possess a negative valency, as have been recently studied experimentally by Raynor[8)] and theoretically by Jones[9)]. In other words, when alloyed with metals of relatively high valency, the transition metal atoms will absorb electrons from them. A similar circumstance might possibly be expected in the case of FeTe.

Another possible interpretation may be that Fe atoms in FeTe form a metallic antiferromagnet as in the case of metallic Cr. In the latter case, neutron diffraction experiment[10)] yielded a much smaller value of the magnetic moment per Cr atom in the metal as compared with the magnetic moment of the free Cr atom. Similar circumstance may be expected for the Fe^{++} ions in FeTe, since metallic ions in the crystal of NiAs type are known to have metallic binding with each other to some extent.

Between 600°C and 800°C, FeTe has a feeble constant susceptibility. (This is similar to the cases of $CoTe_{1.20}$[11)] and NiTe[12)].) It is known[13)] that the susceptibility of some alloys is expressible by the formula $\chi=k+C/(T-\theta)$, where k is a paramagnetic term independent of temperature and is connected with the electronic interaction between the solute and solvent atoms. The susceptibility of FeTe in the temperature range in question may correspond to the constant k, the second term $C/(T-\theta)$ being regarded as negligible.

In the specific heat measurements on a sample performed roughly by the authors, anomalies in specific heat have been found at 540°C and at 850°C. This anomalous heat at 540°C may be correlated to the evidence of a magnetic transition or a change in crystal structure which results in the dissimilarity in the magnetic character in two temperature regions, namely above 600°C and below 500°C (see Fig. 3). The anomalous heat at about 850°C as well as the appearance of the sample at temperatures higher than this temperature strongly suggests that 850°C is the melting point of this compound, so that the anomalous susceptibility in the vicinity of 850°C (see Fig. 4) should be due to the melt. Usually a substance of a strongly anisotropic character shows some anomalous susceptibility at its melting point. For example, it is known that Te is strongly anisotropic, and our observation shows a decrease in its diamagnetic susceptibility at its melting point (see Fig. 7). FeTe may be a similar case.

The authors wish to express their sincere thanks to Prof. Nagamiya of Osaka University, Prof. Hirone of Tohoku University for many valuable suggestions and discussions, Prof. Mashiyama of Naniwa University for kind advices; they would also like to express their appreciation to Miss Higashiura of Osaka Industrial Research Laboratory for her efforts in chemical analysis and Mr. Fukuoka for his assistance in the present experiment.

References

1) I. Oftendal: Z. Phys. Chem. **128** (1927) 135; R. W. G. Wycoff: *Crystal Structure* (1948) Chap. III.
2) H. Haraldsen: Z. Anorg. u. Allg. Chem. **231** (1937) 78, **246** (1941) 169; T. Hirone, S. Maeda, S. Chiba and N. Tsuya: J. Phys. Soc. Japan **9** (1954) 500; K. Yosida: Prog. Theor. Phys. **6** (1951) 356; L. Neel: Proc. Phys. Soc. **A 65** (1952) 869.
3) T. Hirone, S. Maeda and N. Tsuya: J. Phys. Soc. Japan **9** (1954) 496.
4) T. Hirone, S. Maeda and N. Tsuya: Sci. Rep. RITU. **A 6** (1954) 67·
5) E. Uchida and H. Koneoh: Busseiron-Kenkyu

(in Japanese) **71** (1954) 9, **72** (1954) 16.
6) L. F. Bates: *Modern Magnetism*, Cambridge (1951) 151.
7) R. M. Bozorth: *Ferromagnetism*, Nostrand (1951) 440.
8) G. V. Raynor: Prog. Metal Phys. **1** (1949) 1.
9) H. Jones: Phil. Mag. **44** (1953) 907.
10) C. G. Shull and M. K. Wilkinson: Rev. Mod. Phys. **25** (1953) 100.
11) E. Uchida and H. Kondoh: Busseiron-Kenkyu (in Japanese) **79** (1954) 92.
12) E. Uchida and H. Kondoh: To be published.
13) L. F. Bates: *Modern Magnetism*, Cambridge (1951) 307.

JOURNAL OF THE PHYSICAL SOCIETY OF JAPAN Vol. 10, No. 5, MAY, 1955

Emitter Efficiency of Junction Transistor

By Toshio MISAWA

Central Labs., Matsushita Elec. Ind. Co., Ltd.
Kadoma-cho, Kitakawachi-gun, Osaka-fu

(Received November 24, 1954)

After giving a brief review of the principles of the theory of the junction transistor, the emission efficiency of an efficient emitter is calculated in the electrostatic potential-imref scheme by extending the boundary conditions so as to apply to the case of the moderately high injection level. The electrostatic potential-imref diagram for this case is sketched. The obtained efficiency decrease is about one half of Webster's[2)] and is the same as Rittner's[3)] but the input characteristics are different from the latter.

§1. Introduction

Theories[1)] of a junction transistor had been concerned only with the low injection level operation. Recently some authors[2),3)] pointed out various effects of the injected carriers into the base region on the characteristics of a junction transistor. One of the effects is the deterioration of the emission efficiency of the emitter junction which decreases the current amplification factor of a transistor. Another is the buildup of the electric field in the base region which enhances the current amplification. These problems will be treated in the standpoint of Shockley's electrostatic potential-imref (or quasi-Fermi level) scheme. Only a p-n-p junction transistor of good emitter efficiency will be treated.

§2. Recapitulation of the Theory of the Junction Transistor

In this section we shall present a brief review of the theory of a junction transistor.

According to Shockley[1)], current voltage relations in an aggregate of semiconductors can be treated by solving the following equations:

$$\Delta\psi=-(4\pi q/\kappa)(N_d-N_a+p-n)\,, \qquad (1)$$

(Poisson's equation)

$$n=n_i\exp[q(\psi-\varphi_n)/kT]\,, \qquad (2)$$

(quasi-Boltzmann distribution for electrons)

$$p=n_i\exp[q(\varphi_p-\psi)/kT]\,, \qquad (3)$$

(quasi-Boltzmann distribution for holes)

$$\boldsymbol{I}_n=-q\mu_n n\,\mathrm{grad}\,\varphi_n\,, \qquad (4)$$

(definition of current density of electrons)

$$\boldsymbol{I}_p=-q\mu_p p\,\mathrm{grad}\,\varphi_p\,, \qquad (5)$$

(definition of current density of holes)

$$\boldsymbol{I}=\boldsymbol{I}_n+\boldsymbol{I}_p-(\kappa/4\pi)(\partial/\partial t)\,\mathrm{grad}\,\psi\,, \qquad (6)$$

(definition of total current density)

$$\partial n/\partial t=-(n-n_0)/\tau_n+q^{-1}\,\mathrm{div}\,\boldsymbol{I}_n\,, \qquad (7)$$

(continuity equation for electrons)

$$\partial p/\partial t=-(p-p_0)/\tau_p-q^{-1}\,\mathrm{div}\,\boldsymbol{I}_p\,, \qquad (8)$$

(continuity equation for holes)

where ψ is the electrostatic potential, φ the imref or quasi-Fermi level, $\boldsymbol{I}$ the current density, μ mobility of carriers and subscripts p, n, 0 and i refer to holes, electrons, thermal equilibrium and an intrinsic semiconductor respectively. External voltages applied through ohmic contacts are equal to φ there, toward which φ_n and φ_p approach at the contacts, corresponding to the normal carrier density there. Effects of body resistances, for example, of the base spreading resistance, in a transistor, appear as variation of imrefs in homogeneous regions. These equations are so complicated that they have been manipulated by using approximate methods.

In homogeneous regions, i.e. base, emitter and collector regions Eq. (7) or (8) is solved for the carrier density with appropriate boundary conditions under the following assumptions[3]:

(a) electrons and holes disappear by mutual recombination at identical rates:

$$(p-p_0)/\tau_p=(n-n_0)/\tau_n\ , \tag{9}$$

(b) space charge neutrality is preserved at every point:

$$p-n+N_d-N_a=0\ . \tag{10}$$

Current densities are given by Eqs. (4) and (5).

Boundary conditions for Eq. (7) or (8) are dependent on the electrostatic potential and the imref at the boundary, which, in turn, are determined from n, p, $\boldsymbol{I}_n$ and $\boldsymbol{I}_p$ by using Eqs. (2), (3), (4), and (5) and contain boundary conditions as parameters through carrier densities. Namely they are determined self-consistently. It is usual to estimate φ_n and φ_p from physical arguments. As aids to these, ratios of $d\psi/dx$, $d\varphi_n/dx$ and $d\varphi_p/dx$ to each other are calculated in the Appendix A.

Problems in homogeneous regions have been treated by many authors, whereas the boundary conditions have been left almost untouched since Schockley. The next section will concern chiefly with this.

Only those junctions are treated whose transition regions are so narrow that φ_n and φ_p have the same values respectively on the both sides of the junction[1]. Orders of magnitude of imref differences across the emitter transition region are evaluated in the Appendix B.

§ 3. Calculation of Emitter Efficiency

The electron and hole densities, n_{B1}, p_{B1}, n_{B2}, p_{B2} on the base sides of the emitter and collector junctions can be expressed by the electrostatic potentials and the imrefs there:

$$n_{B1}=n_i\exp\left[q(\psi_1-\varphi_{n1})/kT\right]\ , \tag{11}$$

$$n_{B2}=n_i\exp\left[q(\psi_2-\varphi_{n2})/kT\right]\ , \tag{12}$$

$$p_{B1}=n_i\exp\left[q(\varphi_{p1}-\psi_1)/kT\right]\ , \tag{13}$$

$$p_{B2}=n_i\exp\left[q(\varphi_{p2}-\psi_2)/kT\right]\ , \tag{14}$$

where subscript B refers to the base and *1* and *2* to the emitter and collector ends of the base region. By the electrical neutrality condition the following relation exists:

$$n=n_0+p-p_0\ . \tag{15}$$

Eqs. (11), (13), (15) and (12), (14), (15) lead to

$$n_i^2\exp\left[q(\varphi_{p1}-\varphi_{n1})/kT\right]=p_{B1}(n_{B0}+p_{B1}-p_{B0})\ , \tag{16}$$

$$n_i^2\exp\left[q(\varphi_{p2}-\varphi_{n2})/kT\right]=p_{B2}(n_{B0}+p_{B2}-p_{B0})\ . \tag{17}$$

These are the boundary conditions extended for the high injection level and, if p_B is small compared to n_{B0}, reduce to that derived by Shockley:

$$p_B=p_{B0}\exp\left[q(\varphi_p-\varphi_n)/kT\right]\ , \tag{18}$$

when use is made of the relation $n_{B0}p_{B0}=n_i^2$.

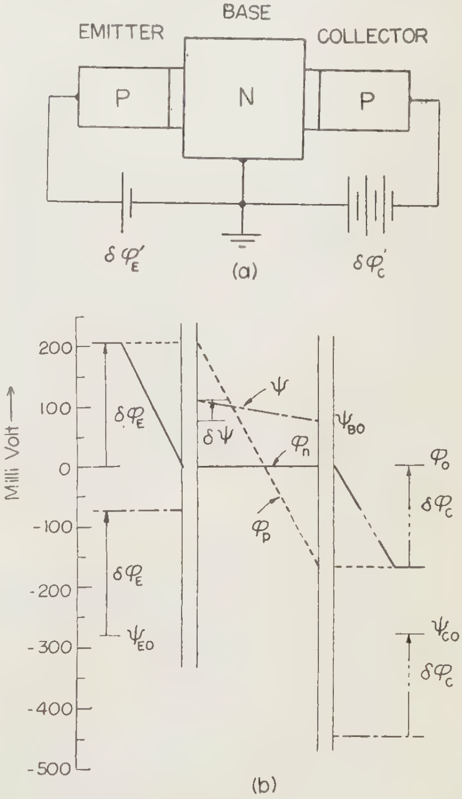

Fig. 1. Electrostatic potential-imref diagram for a properly biased *p-n-p* junction transistor. The lefthand side scale is appropriate for material parameters and temperature cited in reference 3) and for $V=10$ or $Z=4.1$. The diagram is quantitative only on the sides of the transition regions.

For a properly biased p-n-p junction transistor we get the diagram as shown in Fig. 1 (b). In the emitter and collector regions the density of the injected minority carries is small and the schema then becomes the same as Shockley's.

Since, in the base region, the electron density n is large and the electron current I_n, which is nearly equal to that across the emitter junction is small, we can regard φ_n as nearly constant throughout the base region, as seen from Eq. (4). The relative magnitude of $\partial\psi/dx$ to $d\varphi_n/dx$ and $d\varphi_p/dx$ is evaluated in the Appendix A.

The current through the base lead, which is produced by electrons, supplies, together with the saturation current through the collector junction, the recombination current in the base region and the electron current through the emitter junction. If this current can be assumed to be small and n_B large, φ_{n1} and φ_{n2} become equal to the voltage applied to the base contact by Eq. (4). This assumption is equivalent to neglecting the so-called base spreading resistance. By the way it should be noticed that "IR drop" through the base must be calculated by integrating Eq. (4) in which the effect of the conductivity modulation is taken into account through employing n instead of n_0.

For a "good junction", φ_n and φ_p have the same values on the both sides of the junctions respectively as mentioned in Sec. 2. Therefore we have $\delta\varphi_E'=\delta\varphi_E=\varphi_{p1}-\varphi_{n1}$ and $\delta\varphi_c'=\delta\varphi_c=\varphi_{p2}-\varphi_{n2}$ where $\delta\varphi_E'$ and $\delta\varphi_c'$ mean the externally applied voltages at the emitter and the collector contacts. Then from Eq. (16) we obtain

$$P^2+P=V\,, \tag{19}$$

where $P=p_{B1}/n_{B0}$, $V\equiv(p_{B0}/n_{B0})\exp(q\delta\varphi_E/kT)$ and p_{B0} was neglected compared to n_{B0}, and from Eq. (17) we can obtain

$$p_{B2}=p_{B0}\exp(q\delta\varphi_c/kT)\,, \tag{20}$$

for the highly negatively biased collector, which is the same as Eq. (18).

Eq. (20) showing that p_{B2} is small and the electrical neutrality condition lead to $n_{B2}=n_{B0}$. With $\varphi_{n2}=\varphi_0$, Eq. (12) reduces to

$$n_{B0}=n_i\exp[q(\psi_2-\varphi_0)/kT]\,, \tag{21}$$

therefore

$$\psi_2=\psi_0\,. \tag{22}$$

Eq. (11) gives

$$n_{B0}+p_{B1}-p_{B0}=n_{B0}\exp(q\delta\psi/kT)\,. \tag{23}$$

Since p_{B1} is comparable to n_{B0}, $\delta\psi$ is appreciable, namely the electric field in the base region can not be neglected and aids the hole flow with the result of the dereased recombination, therefore the increased current amplification as pointed out by Webster and Rittner. The same value of $\delta\psi$ can be obtained by using Eqs. (39) and (40) in reference 3). See the Appendix C.

φ_p can be evaluated by p which was already calculated by Webster$^{2)}$ and Rittner.$^{3)}$

In the case of the negligible recombination, negligible I_n compared to I_p in the base region and the highly negatively biased collector, the following relation between the hole current through the emitter junction J_{Ep} and p_{B1}, which is Eq. (46) of reference 3), is obtained from Eqs. (4), (5), and (20)

$$2P-\ln(1+P)=Z\,, \tag{24}$$

where $Z=wJ_{Ep}/(D_p n_{B0}qA)$, w the width of the base region and A the area of the emitter junction.

In the emitter region the conditions of low injection level prevail. As a result the electron flow into the emitter region can be expressed by Shockley's formula:

$$\begin{aligned}J_{En}&=(AqD_n/L_n)(n_E-n_{E0})\\&=(Aqn_{E0}D_n/L_n)[\exp(q\delta\varphi_E/kT)-1]\\&=(Aqn_{E0}D_n/L_n)[(n_{B0}/p_{B0})V-1]\,,\end{aligned} \tag{25}$$

where L is the diffusion length and the subscript E refers to the emitter. Note that, in the emitter region, the analogue of Eq. (19) must have $\delta\varphi_E$ which is a function of the analogue of P, because $d\psi/dx$ and $d\varphi_p/dx$ are comparable in the emitter region at high injection level. See the Appendix A.

Eqs. (19), (24) and (25) lead to the following equation

$$\begin{aligned}dJ_{En}/dJ_{Ep}&=(dJ_{En}/dP)/(dJ_{Ep}/dP)\\&=(\sigma_B w/\sigma_E L_n)(1+P)\,.\end{aligned} \tag{26}$$

Therefore we have, as a "fall-off factor",

$$f(Z)=1+P\,, \tag{27}$$

where P is a function of Z by Eq. (24). This is plotted in Fig. 2 together with Webster's approximate fall-off factor $1+Z$. Our value is about one half of Webster's.

Eq. (26) can be obtained by replacing the hole-injected base with the virtual base whose *majority* carrier density is equal to that which the real base has at that injection level on the emitter end, according to low injection level formulae. Namely

$$p_{B0}'=n_i^2/n_{B0}'=p_{B0}/(1+P)\ , \tag{28}$$

hence

$$\begin{aligned} p_{B1}'=p_{B1}&=p_{B0}'\exp(q\delta\varphi_{E}/kT)\\ &=n_{B0}V/(1+P)\ , \end{aligned}$$

i.e.,

$$P^2+P=V\ ,$$

where the prime refers to the virtual base. This method resembles that employed by Webster.

§ 4. Discussion

Injected holes into the base region have double effects on the characteristics of the junction transistor, i.e., the buildup of the electric field which increases the current amplification factor and the decrease of the emission efficiency of the emitter junction which decreases the current amplification factor. As a result the current amplification factor passes through a peak when the emitter current is increased.

Webster treated the latter problem with conception of the "conductivity modulation" by multiplying σ_B in the low level *dc* formula $J_{En}/J_{Ep}=\sigma_B w/\sigma_E L_n$ with

$$(n_{B0}+p_{B1})/n_{B0}=1+P. \tag{29}$$

This procedure seems to be an over correction, for since J_{Ep} itself is the cause of the conductivity modulation it might have taken into account the effect doubly. It seems that the modulated conductivity would be responsible for the efficiency of the incremental emitter current, therefore that the above correction would be to be made to the *ac* formula

$$\partial J_{En}/\partial J_{Ep}=\sigma_B w/\sigma_E L_n\ ,$$

which leads to Eq. (26).

According to Rittner, the hole injection into the base is not influenced by the injected holes into the base:

$$P=V\ , \tag{30}$$

and the electron injection into the emitter is increased, which was expressed quantitatively by replacing n_E in Eq. (25) with

$$\begin{aligned} &n_{E0}\exp[q\delta\varphi_E/kT](1+p_{B1}/n_{B0})\\ &\quad=(n_{E0}n_{B0}/p_{B0})(1+P)V. \end{aligned}$$

From Eqs. (24), (30) and modified (25) we get

$$dJ_{En}/dJ_{Ep}=(w\sigma_B/L_n\sigma_E)(1+P)\ . \tag{31}$$

This is the same as Eq. (26).

His boundary conditions* were obtained by subtracting the emitter-base biasing voltage from the diffusion potential at the emitter junction and making the "standard assumption of rectifier theory" that even while current flows the drop in carrier density across the junction is still given by a Boltzmann factor involving the altered potential barrier which is equivalent to constancy of imrefs in the transition region as is seen as follows: Eq. (11) and its analogue on the emitter side of the emitter junction:

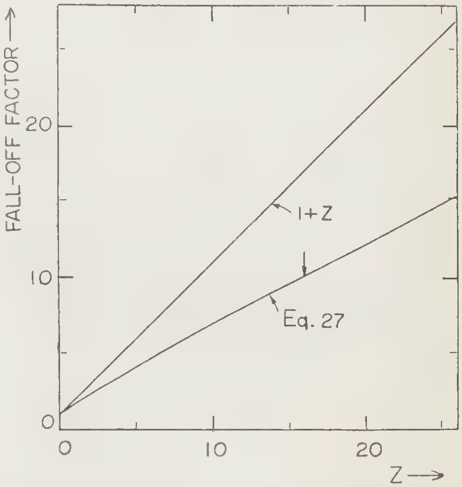

Fig. 2. Fall-off factor versus emitter current. The arrow shows the bias point where $n_E=p_{E0}10^{-4}$ for material parameters from reference 3), which is a measure of the validity range of Shockley's formulae in the emitter region. For $n_E=p_{E0}10^{-3}$, $z=60$.

$$n_E=n_i\exp[q(\psi_E-\varphi_{nE})/kT]\ ,$$

lead to

$$n_E=n_{B1}\exp[q(\psi_E-\psi_1)/kT]\ , \tag{32}$$

because of $\varphi_{nE}=\varphi_{n1}$, and the similar one for holes. The difference from ours is that he equated the voltage applied to the base contact to that on the base side of the emitter junction. He would have had the same voltage at the collector end of the base region with equal appropriateness (the reason for the former choice was not given explicitly), which leads to our boundary conditions owing to $\delta\psi$. Intuitively speaking, the change in the base region should influence the hole injection into the base region which is determined by properties of the base material at low injection level rather than the electron injection into the emitter region which is independent of these at low level.

---

* This is based on a private communication from Rittner.

Since the emitter current is mainly composed of the hole current, the current voltage relation at the emitter is different for two cases, Eqs. (19) and (24) for ours and Eqs. (24) and (30) for Rittner's, and is plotted in Fig. 3. The input impedance for the former is higher than that for the latter.

It is a pleasure for the writer to express his sincere thanks to Dr. E. S. Rittner and Dr. W. M. Webster for critical reading of the manuscript; to the former the detailed information about his method of obtaining the boundary conditions, as a result of which the above-mentioned interpretation of Shockley's conclusion has become possible; to Mr. M. Hatoyama of the Electrotechnical Laboratory for criticizing the notations in the paper and to Mr. K. Kambe for his kind pains for publishing the paper.

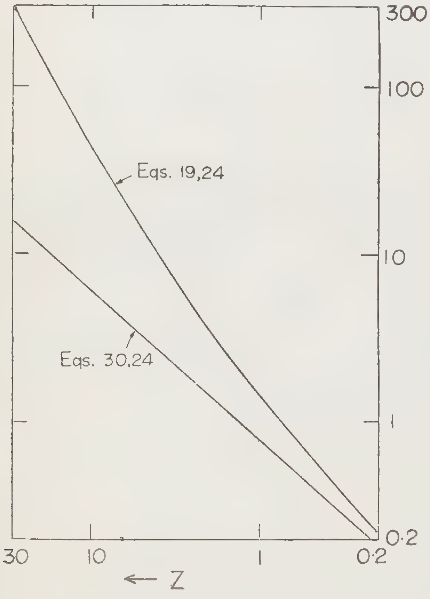

Fig. 3. Emitter characteristics of a junction transistor at high injection level with the collector highly negatively biased.

Appendix A

In this Appendix $d\psi/dx$, $d\varphi_n/dx$ and $d\varphi_p/dx$ at the same position are compared each other as an aid to sketch the electrostatic potential-imref diagram. The ratios for different regions have been already evaluated in reference 1).

Electron and hole currents, I_n, I_p, are, respectively, sums of diffusion components

$$I_{nd}=qD_n(dn/dx)\ , \tag{A1}$$

$$I_{pd}=-qD_p(dp/dx)\ , \tag{A2}$$

and of drift components

$$I_{nf}=-q\mu_n n(d\psi/dx)\ , \tag{A3}$$

$$I_{pf}=-q\mu_p p(d\psi/dx): \tag{A4}$$

$$I_n=I_{nd}+I_{nf}\ , \tag{A5}$$

$$I_p=I_{pd}+I_{pf}\ . \tag{A6}$$

In homogeneous regions we have

$$dn/dx=dp/dx\ , \tag{A7}$$

from the electrical neutrality condition, Eq. (10).

From these equations and Eqs. (4) and (5) we obtain

$$\frac{I_n}{I_p}\equiv r=b\frac{n}{p}\frac{d\varphi_n/dx}{d\varphi_p/dx}\ , \tag{A8}$$

$$\frac{I_{nd}}{I_{pd}}=-b\frac{dn/dx}{dp/dx}\ , \tag{A9}$$

$$\frac{I_{nf}}{I_{pf}}=b\frac{n}{p}\ , \tag{A10}$$

where $b=\mu_n/\mu_p$.

Therefore

$$\begin{aligned}I_n&=rI_p=r(I_{pd}+I_{pf})\\&=r\left(-\frac{1}{b}\frac{dp/dx}{dn/dx}I_{nd}+\frac{1}{b}\frac{p}{n}I_{nf}\right)\\&=r\left[-\frac{1}{b}\frac{dp/dx}{dn/dx}(I_n-I_{nf})+\frac{1}{b}\frac{p}{n}I_{nf}\right]\end{aligned}$$

namely

$$\frac{I_n}{I_{nf}}=\frac{d\varphi_n/dx}{d\psi/dx}=\frac{(dp/dx)/(dn/dx)+p/n}{(dp/dx)/(dn/dx)+b/r}\ , \tag{A11a}$$

and

$$\frac{d\varphi_n/dx}{d\psi/dx}=\frac{1+p/n}{1+b/r}\ , \tag{A11b}$$

in a homogeneous region.

The similar manipulation leads to

$$\frac{I_p}{I_{pf}}=\frac{d\varphi_p/dx}{d\psi/dx}=\frac{(dn/dx)/(dp/dx)+n/p}{(dn/dx)/(dp/dx)+r/b}\ , \tag{A12a}$$

and

$$\frac{d\psi_p/dx}{d\psi/dx}=\frac{1+n/p}{1+r/b}\ . \tag{A12b}$$

In a homogeneous region, if electron and hole currents are in the same direction, derivatives of ψ, φ_n and φ_p are of same sign. This implies the drift current flows in the same direction with the total current. If the gradient of the carrier density is favorable to the increase of the electron current, the hole current is decreased and vice versa.

As an example of use of the above relations we shall discuss the case treated in the text. The important quantity is the ratio of imref gradient for the majority carrier to the potential gradient. We regard r is nearly equal to dI_{En}/dI_{Ep}.

In the emitter region of p-type,

$$\frac{d\varphi_p/dx}{d\psi/dx} \cong 1, \tag{A14}$$

and in the base region of n-type

$$\frac{d\varphi_n/dx}{d\psi/dx} \cong \left(1+\frac{p}{n}\right)\frac{r}{b}. \tag{A15}$$

This shows that in the base region the constancy of the imref for electrons is more fairly well preserved at high injection level than that for holes in the emitter region.

Appendix B

The Appendix B compares the imref differences with the electrostatic potential difference across the junction. We shall neglect the recombination in the transition region.

In the positively biased emitter junction the electron density is increased monotonically from the emitter to the base regions. Hence the imref gradient for electrons is at maximum on the emitter boundary of the transition region. There we have

$$I_{En} \sim (qD_n/L_n)n_E, \tag{A16}$$

from Eq. (25) and

$$I_{En} = -q\mu_n n_E(d\varphi_n/dx). \tag{A17}$$

Then

$$d\varphi_n/dx \sim -(kT/q)(1/L_n), \tag{A18}$$

or

$$\Delta\varphi_n \sim -(kT)(W/L_n), \tag{A19}$$

where W is the width of the transition region and depends on material parameters, the construction of the junction and the applied voltage. For a "good junction", $\Delta\varphi_n$ must be smaller than other involved voltages. Similarly the maximum of $d\varphi_p/dx$ occurs at the base side and we obtain

$$d\varphi_p/dx \sim -(kT/q)(1/w), \tag{A20}$$

$$\Delta\varphi_p \sim -(kT/q)(W/w). \tag{A21}$$

The junction used in a usual transistor must be and is of this category. For example,

$-(kT/q)(1/w) = 5$ volt/cm,
$-(kT/q)(1/L_n) = 25$ volt/cm,
$W = 2\times10^{-4}$ cm,

are the values for the junction in reference 3) and for the potential difference of 200 mV across the junction, which show this is a fairly good one, if one takes into account $d\varphi_n/dx$ and $d\varphi_p/dx$ in average are smaller than the above values by several orders of magnitude.

Similar arguments apply to the collector junction but one must take care of the fact the currents are almost independent of the smallest carrier density across the junction.

Appendix C

The calculation of $\delta\psi$ is straight forward. From Eqs. (39) and (40) in reference 3):

$$-\frac{d\psi}{dx} = \frac{I_p - qD_p(dp/dx)}{q\mu_p p}, \tag{A22}$$

$$\frac{dp}{dx} = -\frac{qD_p}{I_p}\frac{2p+n_{B0}}{p+n_{B0}}, \tag{A23}$$

under the assumption of negligible I_n compared with I_p which is equivalent to constant φ_n in the base region, the following equation is obtained,

$$-\frac{d\psi}{dx} = -\frac{d\psi}{dp}\frac{dp}{dx} = \frac{I_p}{q\mu_p}\frac{1}{2p+n_{B0}},$$

hence

$$\frac{d\psi}{dp} = \frac{kT}{q}\frac{1}{p+n_{B0}}. \tag{A24}$$

Integrating this, we have

$$\delta\psi = \int_0^{p_{B1}} (d\psi/dp)dp = \frac{kT}{q}\ln(1+P), \tag{A25}$$

which is the same as Eq. (23) with p_{B0} negligible compared to n_{B0}.

References

1) For example, W. Shockley: B. S. T. J. **28** (1949) 435.
2) W. M. Webster: Proc. I. R. E. **42** (1954) 914.
3) Edmund S. Rittner: Phys. Rev. **94** (1954) 1161.

Journal of the Physical Society of Japan Vol. 10, No. 5, May, 1955

The Theory of Fatigue Fracture of Metals

By Takeo Yokobori*

Institute of Science and Technology, University of Tokyo

(Received January 28, 1955)

After limit of strain hardening, fatigue crack was assumed to form as a result of large tensile stress by a piled-up group of dislocations plus externally applied tensile stress component, with the aid of other stress concentration factor associated with the obstacle or inclusion itself. Nucleation theory was applied to the initiation of the crack. The theoretical S–N curve is in quantitative agreement with the data. The scatter of the number of cycles for fracture, which is an inherent characteristic of fatigue fracture, is, mostly if not wholly, explained as a stochastic phenomenon associated with nucleation process of the fatigue crack. The theoretical temperature dependence of fatigue strength is in fairly agreement with the data in literature.

§ 1. Introduction

The fatigue process is divided into three stages. The three stages are:

Stage 1. From the instant of the application of stress to the saturation or limit of work hardening.

Stage 2. From the saturation of work hardening to the initiation of micro-crack or the growth of the preexistent sub-micro-crack as a result of piling up of dislocations at obstacles in the severely cold worked regions. This stage was assumed as a stochastic process[1)2)3)] associated with nucleation process of crack. The micro-crack formed in this manner may cease to grow further by nucleation process after it has grown into size by some amount larger than the critical size, since plastic flow is then expected to occur around the crack and relieve the stress concentration at its apex.

Stage 3. During which the crack of this large size may propagate by the process other than nucleation process, possibly by OROWAN's mechanism[4)], and finally result in rupture of the whole cross section of the specimen.

§ 2. Dislocation Model of Fatigue Fracture

The dislocation theory was first applied to the problem of fatigue fracture by Machlin[5)]. His theory concerns on the growth of the preexistent sub-micro-crack in pure metals. MOTT[6)] and STROH[7)] suggested that the initiation of crack will occur as a result of piling up of dislocations at obstacles. In their theory, the initiation of crack was wholly attributed to the tensile stress near a piled-up group of dislocations caused by the externally applied shear stress only, that is, the criterion is the maximum shear stress. There, however, are many evidences[8)9)]** that the endurance limit is not determined by the maximum stress only. Hence, the applied tensile stress component was taken into account in this theory proposed.

The saturation of cold working[1)] was assumed to correspond to the state of piling-up of dislocations at an obstacle such as a grain boundary or a precipitate. Suppose that the specimen is under axially applied uniform tensile stress range $\boldsymbol{S}$. Then there exist tensile stress σ_φ $(=\boldsymbol{S}\sin^2\varphi)$ normal to and

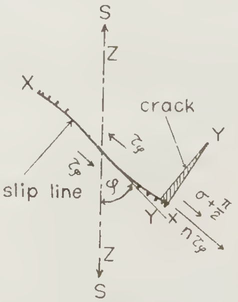

Fig. 1. Dislocation model of the initiation of fatigue crack.

---

* Now at Department of Mechanical Engineering Tohoku University, Sendai.

** The theory proposed herein concerns the fatigue stress above the endurance limit. The nature of the fatigue strength, however, does not seem to be essentially different from the endurance limit as far as the stress condition for fatigue fracture is concerned.

shearing stress τ_φ ($=S\sin\varphi\cos\varphi$) in the slip plane XX making an angle φ with the specimen axis ZZ. (Fig. 1) If n similar edge dislocations moving on this slip plane XX under shearing stress τ_φ are piled-up against at an obstacle, then large tensile stress of the order of $n\tau_\varphi$ arises[10] near a piled-up group of dislocations. Consequently, the total tensile stress on the plane YY normal to the slip plane XX at the locked dislocation is the sum of $\sigma_{\varphi+\pi/2}+n\tau_\varphi$,* which is considered as determining the fracture of metals instead of shearing stress $n\tau_\varphi$ only as assumed by MOTT[6] and STROH[7]. The value of $\sigma_{\varphi+\pi/2}+n\tau_\varphi$ has a maximum on the plane with φ_m, which satisfies the condition:

$$\partial/\partial\varphi\,|\,\sigma_{\varphi+\pi/2}+n\tau_\varphi\,|=0\,. \tag{1}$$

Hence, if the effect of thermal fluctuation is neglected, the condition of fatigue fracture will be given by

$$\sigma_{\varphi m+\pi/2}+n\tau_{\varphi m}=\text{constant}\,. \tag{2}$$

Since n is proportional to shear stress $\tau_{\varphi m}$, $n=C_0\tau_{\varphi m}$ where C_0 is constant[11]. Hence Eq. (2) is written as:

$$\sigma_{\varphi m+\pi/2}+C_0\tau_{\varphi m}{}^2=\text{constant}\,. \tag{3}$$

It is interesting to note that Eq. (2) is formally the same as the hypothetical formula[12] proposed for the criterion of endurance limit of mild steel.

The temperature dependence of fatigue strength of steel, however, is appreciable[13][14]. This seems to indicate the effect of thermal fluctuations. The effect will be taken into account by regarding the initiation of fatigue crack as a rate process. The application of the rate process theory to the fatigue fracture was previously carried out without speculating as to the detailed nature of the unit process in order to explain the observed scatter characteristic[1][2][3] of the number of cycles for fatigue fracture.** In the following section, fatigue fracture will be treated from the standpoint of nucleation theory[15].

§ 3. Nucleation Theory as Applied to Fatigue Fracture

There is other stress concentration factor q than that by piled-up dislocations described above. q may probably be that arising from the obstacle or inclusion itself against which dislocations are piled. The crack will firstly nucleate at the region where this stress concentration is largest.*** In the nucleation theory of fracture of solids, therefore, atoms which are near those weak spots with stress concentration should be preferred[17] (heterogeneous nucleation). Although the stress concentration factor must be characterized by distribution function, a single value, q, is taken as the average value as a first approximation.

The nucleation rate, I, is the net rate per volume of the following bimolecular reaction:

$$\beta_{i^*}+\alpha \rightleftarrows \beta_{i^*+1}\,,$$

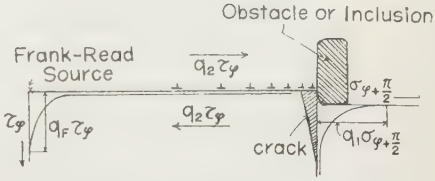

Fig. 2. Dislocation model of thc initiation of fatigue crack as affected with the stress concentration due to the obstacle or inclusion itself.

where i^* is the number of atoms in the nucleus of critical size. If I is very small compared with the equilibrium number, Zi^*, of nuclei, then the steady concentration of nuclei does not differ appreciably from the

---

* The tensile stress caused by a piled-up group of dislocations has a maximum on the plane YY making an angle $\theta(\simeq 70\frac{1}{2}°)$ with slip plane XX.[7] In the present theory, however, θ was assumed to be $\pi/2$ for convenience. For precise calculation, this maximum vale of tensile stress and $70\frac{1}{2}°$ should be used for $n\tau_\varphi$ and $\pi/2$ respectively.

** When the papers (references: (1) and (2)) were written, the author was not aware of the papers by Machlin[5], who had already applied the rate process theory to the problem. After having the opportunity of reading it recently by courtesy of Dr. Machlin, it was found that there are considerable differences in both treatments. In the author's treatment, for example, the process was regarded as stochastic.

*** In § 2 and § 3 the stress concentration factor q_1 for $\sigma_{\varphi m+\pi/2}$ and q_2 for $\tau_{\varphi m}$ are assumed to be equall in a first approximation, and are denoted by q. In general, however, q_1 may be much larger than q_2 as seen from Fig. 2, even when the stress concentration factor q_F at the place where the Frank-Read fource[16] is started to operate is the same order of magnitude as q_1 at the place where the crack is initiated in the neighbourhood of the obstacle or inclusion. Hence, Eq. (2) should be written as:

$$q_1\sigma_{\varphi m+\pi/2}+q_2n\tau_{\varphi m}=\text{constant} \tag{2$'$}$$

and therefore the number of piled-up dislocations may be much larger than n in Table I calculated by Eq. (15) as many times as q_1/q_2.

equilibrium number

$$Z_i{}^* = Z\exp(-\Delta F_i{}^*/kT)\,, \tag{4}$$

where ΔFi^* is the maximum free energy necessary for nucleus formation, Z is the number of preferred nucleation sites per volume in the system, K is Boltzmann's constant, and T is absolute temperature. If the free energy difference between the activation complex and the mean of ΔFi^* and ΔFi^*+1 will be represented by Δf^*, the rate of the forward reaction for crack nucleation may be given by

$$I^+ = LZ_i{}^*(kT/h)\exp(-\Delta f_1{}^*/kT)\,, \tag{5}$$

according to the theory of absolute reaction rates[18]. Here L is the order of unity, h is Plonck's constant. $\Delta f_1{}^*$ is expressed by the equation:

$$\Delta f_1{}^* = \Delta f^* + \tfrac{1}{2}(\Delta F_i{}^* + \Delta F_i{}^*{}_{+1}) - \Delta F_i{}^*$$
$$= \Delta f^* + \tfrac{1}{2}\mathrm{d}(\Delta F_i{}^*)/di\,.$$

Δf^* is the free energy of activation for separating a pair of atoms as the edge of the crack moves between them. When the effect of the work done by applied tensile stress T_0 upon Δf^* is taken into account, then Eq. (5) will be modified as:

$$I^+ == Z_i{}^*(kT/h)$$
$$\times\exp\left[\left(-\Delta f^* + \frac{vq^2T_0{}^2}{2E} - \frac{1}{2}\frac{\mathrm{d}(\Delta F_i{}^*)}{di}\right)\Big/kT\right], \tag{6}$$

where the elastic energy contribution by applied tensile stress T_0 is considered, and v is atomic volume, and E is Young's modulus. Assuming that

$$vq^2T_0{}^2/2EkT \gg \mathrm{d}(\Delta F_i{}^*)/kTdi\,,$$

Eq. (6) becomes

$$I^+ \simeq Z_i{}^*(kT/h)\exp\left[\left(-\Delta f^* + \frac{vq^2T_0{}^2}{2E}\right)\Big/kT\right], \tag{7}$$

The rate of reverse reaction for crack nucleation can also be written

$$I^- \simeq Z_i{}^*(kT/h)\exp\left[\left(-\Delta f^* - \frac{vq^2T_0{}^2}{2E}\right)\Big/kT\right], \tag{8}$$

by the similar treatment. From Eqs. (4), (7) and (8), the net forward rate of crack nucleation becomes approximately, therefore,

$$I = I^+ - I^- \simeq Z(kT/h)$$
$$\times\exp\left[\left(-\Delta f^* - \Delta F_i{}^* + \frac{vq^2T_0{}^2}{2E}\right)\Big/kT\right], \tag{9}$$

neglecting $\exp(-vq^2T_0{}^2/2EkT)$ compared with $\exp(+vq^2T_0{}^2/2EkT)$.

The loading cycle is assumed as sinusoidal curve: $P = S\sin(2\pi\omega t/60)$, where ω is the frequency of repeated loading cycle per minute, and t is time in second. If, under the same stress system as in Fig. 1, notations P, σ_φ' and τ_φ' are used crrresponding to S, σ_φ and τ_φ respectively, then T_0 is represented by $\sigma'_{\varphi m+\pi/2} + n\tau'_{\varphi m}$.

The net work associated with the formation of a circular crack of radius r may be written as a first approximation:

$$\Delta F = 2\pi\rho r^2 - 8(1-\nu^2)r^3[(q\sigma'_{\varphi m+\pi/2} + qn\tau'_{\varphi m})^2$$
$$+ C(qn\tau'_{\varphi m+\pi/2})^2]/3E\,, \tag{10}$$

where ρ is the solid surface tension, ν is Poisson's ratio. The second term in Eq. (10) is the decrease in strain energy for the case where the tensile stress $\sigma'_{\varphi m+\pi/2} + n\tau'_{\varphi m}$ is normal to and shearing stress $n\tau'_{\varphi m+\pi/2}$ is on the crack plane YY. C may be of the order of magnitude of unity. As the estimation of the exact value of the constant C in the case of shear seems to be more difficult than in the case of tension, the term $C(qn\tau'_{\varphi m+\pi/2})^2$ is assumed to be of the same order of magnitnde as the term $(q\sigma'_{\varphi m+\pi/2} + qn\tau'_{\varphi m})^2$ and equal to it for simplicity. ΔF has a maximum

$$\Delta F_i{}^* = \pi^3\rho^3E^2/24(1-\nu^2)^2q^4(\sigma'_{\varphi m+\pi/2} + n\tau'_{\varphi m})^4\,, \tag{11}$$

at $\quad r = r^* = \pi\rho E/4q^2(1-\nu^2)(\sigma'_{\varphi m+\pi/2} + n\tau'_{\varphi m})^2$.

Since for crystals plastic deformation will always occur during the initiation of crack, the energy associated with it must be added to the surface tension ρ. This effect is not considered here for convenience, and Eqs. (10) and (11) may be only a first application. The results, however, does not seem appreciably affected at least qualitatively.

For fatigue of metals, the nucleation rate, Ia, averaged over working half cycle will be concerned instead of I in Eq. (9) which corresponds to constant applied stress P. Ia is approximately obtained taking the average value of stress, $S_a = (2/\pi)S$, over working half cycle instead of P in Eq. (9), and using the notations σ_φ'' and τ_φ'' instead of those of σ_φ' and τ_φ' respectively[3]. The average valve, μ, over working half cycle of the nucleation rate of crack per unit cycle per specimen is re-

Table I. The numerical values used for the calculation of S—$\overline{N}_0$ curves from Eq. (15). $E=2\times10^{12}$ dyne/cm², $\nu=0.28$, $\Delta f^*=2.72\times10^{-12}$ ergs/Mol. Z is assumed as order of density of dislocations. ($=10^{12}$/cm³)

Material	Type of testing	The number of piled-up dislocations n	Stress concentration factor q	Surface tension ρ dyne/cm	Specimen volume V cm³
0.19% carbon steel	Haigh's tension compression	5 (at $S=2.3\times10^9$ dyne/cm²)	37.6	150	0.05
0.41% carbon steel	Ono's uniform rotary bending	3 (at $S=3.6\times10^9$ dyne/cm²)	48.6	300	0.144*

* The volume was calculated by assuming as the hollow cylinder with the same diameter (1 cm) as that of the specimen, and with the thickness of 0.1 mm.

lated $\boldsymbol{I}a$ by the relation*

$$\mu d\boldsymbol{N}_0=\boldsymbol{V}\boldsymbol{I}_a dt\,, \tag{12}$$

where N_0 is the number of cycles measured from the end of Stage 1, and V is the volume of specimen. The mean number of cycles for fracture, $\overline{N}_0$ is related to μ by

$$\overline{N}_0=1/\mu\,, \tag{13}$$

From Eqs. (3), (9), (12) and (13), we find

$$\frac{v}{2\boldsymbol{E}}q^2(\sigma''_{\varphi m+\pi/2}+\boldsymbol{C}_0\tau''^2_{\varphi m})^2 - \frac{\boldsymbol{A}}{4q^4(\sigma''_{\varphi m+\pi/2}+\boldsymbol{C}_0\tau''^2_{\varphi m})^4} = \Delta f^*-\boldsymbol{kT}\log\left(\frac{60\boldsymbol{VZkT}\overline{\boldsymbol{N}}_0}{h\omega}\right), \tag{14}$$

where $\boldsymbol{A}=\pi^3\rho^3\boldsymbol{E}^2/6(1-\nu^2)^2$.

In the case of reversed uniform tension-compression stress range S (mean stress zero), $\sigma''_{\varphi m+\pi/2}+C_0\tau''_{\varphi m}$ can be expressed by the term of $\boldsymbol{S}$ only. For simplicity, assuming $\sigma''_{\varphi m+\pi/2}$ equal to $\tau''_{\varphi m}(=(2/\pi)(\boldsymbol{S}/2))$, Eq. (14) is written as

$$\frac{vq^2}{2\pi^2\boldsymbol{E}}\left(1+\frac{\boldsymbol{C}_0}{\pi}\boldsymbol{S}\right)\boldsymbol{S}-\frac{\pi^4\boldsymbol{A}}{4q^4\left(1+\frac{\boldsymbol{C}_0}{\pi}\boldsymbol{S}\right)^4\boldsymbol{S}^4} = \Delta f^*-\boldsymbol{kT}\log\left(\frac{60\boldsymbol{VZkT}\overline{\boldsymbol{N}}_0}{h\omega}\right). \tag{15}$$

§ 4. The Comparison of the Theory with Experiments

(1) $\boldsymbol{S}$—$\boldsymbol{N}$ curve. The theory described above concerns on the initiation of micro-crack or the growth of the preexistent sub-micro-crack, that is, the initiation of Stage 3.** From the statistical analysis of the experiments[1)2)3)19)] the duration of Stage 2, however, is expected to be much longer than that of Stage 3. Hence, $\overline{\boldsymbol{N}}_0$, the number of cycles for the initiation of micro-crack derived from Eq. (15) may be assumed to form a considerable or probably greater part of $\boldsymbol{N}$, the number of cycles necessary for the complete fracture of the specimen. That is, the relation between $\boldsymbol{S}$ and $\boldsymbol{N}$ may be very similar to that between $\boldsymbol{S}$ and $\overline{\boldsymbol{N}}_0$, and it is justified to compare the calculated $\boldsymbol{S}$—$\overline{\boldsymbol{N}}_0$ curve from Eq. (15) with the observed $\boldsymbol{S}$—$\boldsymbol{N}$ curves. Since the experimental curves are not precisely determined due to the scatter of number of cycles for fracture, the $\boldsymbol{S}$—$\boldsymbol{N}$ curves determined by statistical experiments[1)2)19)] were taken for comparison. In these experiments, two kinds of steel were tested, one for Ono's uniform rotary bending,*** and the other for Haigh's tension-compression, and the number of speci-

---

* If μ changes with the number of cycles possibly due to the structural change or the increase of stress[1)2)], the value $\bar{\mu}$ averaged over a interval of repeated cycles concerned will be used instead of μ.

** In the theory described above the initiation of a single crack nucleus are regarded as rate-determining in fatigue fracture process. It seems more reasonable to assume that Stage 3 begins when the number of micro-cracks nucleated in a given region reaches some critical value or when this consecutive events occur at the apex of the submicroscopic crack already nucleated during fatigue process. The treatment must be suitably modified, but the result may be qualitatively uneffected. This idea is not inconsistent with SINCLAIR and DOLANS' conclusion[20)] that the formation of submicroscopic crack is initiated at a relatively early stage of the total fatigue life.

*** In the case of rotary uniform bending when the stress is not uniform through the cross section, some modification will be required in the theory. In this article, however, the theory was applied directly, since the results are believed to be essentially unaffected.

mens tested are from about seventy to hundred at each stress range. Taking numerical values as shown in Table I, the $\boldsymbol{S}-\overline{\boldsymbol{N}}_0$ curve calculated from Eq. (15) were shown as solid curves in Fig. 3. The comparison of the theory with experiments is satisfactory.

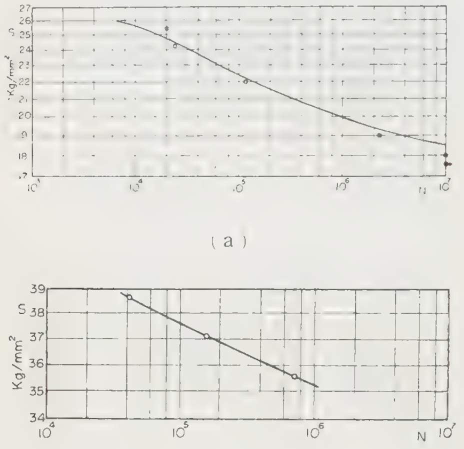

(a)

(b)

Fig. 3 (a) (b). The comparison of the theoretical and the experimental $\boldsymbol{S}-\boldsymbol{N}$ curve. The coordinates of stress range are plotted in logarithmic scale. Fig. 3. (a) 0.19% C steel[2]
Fig. 3. (b) 0.41% C steel[1]
Hollow circle denotes the mean fatigue life of about 70 to 100 specimens per stress range statistically obtained as $\boldsymbol{N}=1/\overline{\mu}$ by calculating $\overline{\mu}$ from $\log_{10}\boldsymbol{P}$ versus $\boldsymbol{N}$ curve[3], where $\boldsymbol{P}$ represents frequency of survival. Solid circle denotes the fatigue life of a single specimen.

It is interesting to note that the $\boldsymbol{S}-\boldsymbol{N}$ curve predicted by the theory has a point of inflection and bends toward the stress axis at shorter life. Although a single process does not seem to cover from the endurance limit to the static yield stress range, the $\boldsymbol{S}-\boldsymbol{N}$ curves determined by statistical experiments by EPREMIAN and MEHL[21] follow such tendency.

In a narrow range of stress level, the stress term in the left hand side of Eq. (15) is roughly approximated by $\log_{10}(C_1 S)^{1/\alpha}$. Eq. (15) simplifies then to

$$\overline{\boldsymbol{N}}_0=\left(\frac{\omega h}{60\boldsymbol{VZkT}}\right)(\boldsymbol{CS})^{-B/T}, \qquad (16)$$

where $\boldsymbol{B}=1/2\cdot 3\alpha\boldsymbol{k}$ and $\boldsymbol{C}=\boldsymbol{C}_1/\exp(2.32\alpha\Delta f^*)$. It can be seen from Figs. 3 (a) and (b) the experimental curves are approximately expressed by the linear relation between $\log \boldsymbol{S}$ and $\log \boldsymbol{N}$ predicted by Eq. (16) in a narrow range of stress level.

The value of surface tension ρ obtained by fitting the theory to the data is one order of magnitude less than the value in literature.[22] However, if the crack nucleus is assumed to form preferentially at the grain boundary, this small value seems to be interpreted from the variation of grain boundary tension with orientation[22].

The value of i^* calculated, for example, corresponding to Fig. 3 is found to be about 6 to 44 for stress range of about 25 to 19 kg/mm², and of not unreasonable order.

In the case of non-ferrous metals where large plastic flow occurs, $\boldsymbol{n}$ is assumed to be much larger and q smaller. In such case Eq. (14) approximately reduces to

$$n\tau''_{\varphi m}=\text{constant}\ , \qquad (17)$$

which is the criterion by MOTT[6] and STROH[7]. Experiments[9] shows that the fatigue strength of brass is determined by the maximum shear stress, and supports the theory.

It is also interest that there seems to be the possibility to determine the relative magnitude of the overall stress concentration in such manner as described above. In steel, the number of piling-up dislocations is found to be small, and the contribution by them to the overall stress concentration factor is smaller than the contribution by the other stress concentration factor q associated with inclusion, etc.

(2) The scatter of fatigue life. A considerable or greater, if not whole, part of the scatter of the number of cycles for fracture can be interpreted as due to the thermal fluctuations associated with nucleation process of crack similarly as other type[23][24][25][26] of failure phenomena. The nucleation rate obtained from experimental data when the process was regarded as a stochastic process associated with nucleation is found[3] to have approximately the same type of dependence upon stress range as indicated by Eqs. (13) and (16).

The fatigue is believed not due to cold work only on the basis of the observation[27] that microscopically visible crack does not form during or immediately after the termination of work hardening process, but only after an additional period of cyclic loading. The observation, however, is consistent with the theory described above, since an additional period after the termination of cold work corresponds to $\overline{N}_0$ in Eq. (15), that is, Stage 2 associated with statistical lag in nucleation process. (See, for example, ref. (1)).

Another factor contributing to the scatter may be the statistically distribution of stress concentration[28][29][30] and inhomogeneity of the applied stress system[28]. The problem remains to determine the relative magnitude of the influence of these factors upon the scatter of fatigue life.

(3) Temperature dependence of fatigue strength. Since strain aging seems to take place above room temperature, it is more reasonable to compare the theory with the experiments below room temperature. If the approximated Eq. (16) is solved for $\boldsymbol{S}$, the temperature dependence is given by

$$\log_{10}\boldsymbol{S}=-\log_{10}\boldsymbol{C}-(\boldsymbol{D}/\boldsymbol{B})\boldsymbol{T} \qquad (18)$$

where $\boldsymbol{D}=\log_{10}(60\boldsymbol{VZkT}\overline{\boldsymbol{N}}_0/\omega\boldsymbol{h})$. The values of $\boldsymbol{B}$ and $\log_{10}\boldsymbol{C}$ obtained by fitting Eq. (16) to experimental $\boldsymbol{S}-\overline{\boldsymbol{N}}$ curves (Fig. 3a) in the range of $\boldsymbol{N}$ from 10^6 to 10^7 are 1.2×10^4°K and -1.34 respectively. Taking $\boldsymbol{B}=1.2\times10^4$°K and $\log_{10}\boldsymbol{C}=-1.93$ or -2.18, the calculated $\boldsymbol{S}-\boldsymbol{T}$ curves are in fairly agreement with the experimental relation between fatigue strength at 10^7 and temperature[13][14] (Fig. 4).

(4) The influence of the frequency on the fatigue life. The dependence of the number of cycles for fracture on the frequency is qualitatively the same as that by Machlin's[5] theory, that is, $\log \boldsymbol{N}$ will be linearly related to $\log \omega$. Although the experiments in literature seem to show this tendency qualitatively, the more data are required for check.

(5) Size effect. Increasing of the length of the specimen results in increase of the total number, $\boldsymbol{ZV}$, of preferred nucleation sites, and therefore, may be expected to shorten the fatigue life as seen from Eq. (15). It is established by statistical experiments by WEIBULL[29] that the longer specimen has the shorter fatigue life than the shorter specimen.

Acknowledgments

It is a pleasure to thank Prof. M. HIRATA and Prof. F. NAKANISI for usefull discussions. This work was carried out by the finacial aids of the Ministry of Education of Japan.

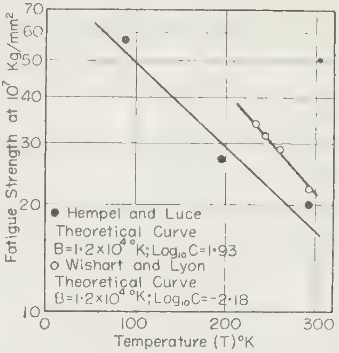

Fig. 4. The comparison of the theoretical and the experimental temperature dependence of fatigue strength.

References

1) T. Yokobori: J. Phys. Soc. Japan **6** (1951) 81.
2) T. Yokobori: Ibid. **8** (1953) 265.
3) T. Yokobori: Reports Inst. Sci. Tech., Univ. of Tokyo **8** (1954) 5.
4) E. Orowan: Proc. Roy. Soc. **A 171** (1939) 79.
5) E. S. Machlin: N.A.C.A. Tech. Note No. 1489 (1948); N.A.C.A. Tech. Report No. 929 (1949).
6) N. F. Mott: Proc. Roy. Soc. **A 220** (1953) 1.
7) A. N. Stroh: Proc. Roy. Soc. **A 223** (1954) 404.
8) H. J. Gough and H. V. Pollard: Proc. Inst. Mech. Eng., **131** (1935) 3.
9) T. Nisihara and M. Kawamoto: Trans. Soc. Mech. Eng. Japan (in Japanese) **7** (1941) 85.
10) J. S. Koehler: Phys. Rev. **85** (1952) 480.
11) J. D. Eshelby, F. C. Frank and F. R. N. Nabarro: Phil. Mag. **42** (1951) 351.
12) F. Nakanisi: Trans. Soc. Mech. Eng. Japan (in Japanese) **18** (1952) 104.
13) H. B. Wishart and S. W. Lyon: Trans. Am. Soc. Metals **25** (1937) 690.
14) M. Hempel and J. Luce: Arch. Eisenhüttenw **9** (1942) 423.
15) J. H. Hollomon and D. Turnbull: Chapter 7, Progress in Metal Physics **4** (1953) (Pergamon Press, London) p. 333.
16) F. C. Frank and W. T. Read: Phys. Rev. **79** (1950) 722.
17) T. Yokobori: J. Chem. Phys. **22** (1954) 951.
18) D. Turnbull and J. C. Fisher: Ibid. **17** (1949) 71.
19) T. Yokobori: J. Phys. Soc. Japan **8** (1953) 806.
20) G. M. Sinclair and T. J. Dolan: Proc. First Nat. Congress Appl. Mech. Am. Soc. Mech. Eng. (1951) 647.

21) E. Epremian and R. F. Mehl: Am. Soc. Test. Mat. STP No. 137 (1953) 25.
22) J. C. Fisher and G. G. Dunn: Imperfections in nearly perfect crystals (1952) (Wiley, New York) p. 317.
23) M. Hirata: Ôyô Tôkei-gaku (Applied Statistics) (1949) 11.01 (in Japanese).
24) M. Hirata and N. Terao: J. Appl. Phys. Japan (in Japanese) **20** (1951) 234.
25) T. Yokobori: J. Phys. Soc. Japan **6** (1951) 78.
26) T. Yokobori: Ibid. **7** (1952) 48.
27) H. J. Gough and W. A. Wood: J. Inst. Civil Eng. **8** (1938) 249.
28) N. N. Afanasiev: J. Tech. Phys. U.S.S.R. **10** (1940) 1553; Ibid. **11** (1941) 349.
29) W. Weibull: Trans. Roy. Inst. Tech. Stockholm, No. 27 (1949).
30) A. M. Freudenthal and E. J. Gumbel: Proc. Roy. Soc. **A 216** (1953) 309.

JOURNAL OF THE PHYSICAL SOCIETY OF JAPAN Vol. 10, No. 5, MAY, 1955

Time Lag in the Self-Nucleation

By Hiromu WAKESHIMA

The Kobe University of Mercantile Marine, Kobe Japan

(Received December 18, 1954)

An approximate but simple and general treatment of the time lag in self-nucleation is given. In this method the relation to be satisfied approximately by the rate of nucleation in non-steady state is obtained and solved without first seeking the distribution of embryos. This calculation, when applied to the problem of condensation of water vapor in a high degree of supersaturation, gives a time lag of the same order of magnitude as that obtained by Probstein who solved the problem in ordinary way. Time lag of self-nucleation in the case of transformation in a solid is also computed. Certain limitation has been set therefrom to the validity of the notion of "athermal nucleation" as proposed by Turnbull et al., which presumes a large temporary lagging in the change of embryo distribution when, e.g., metals are quenched in phase transformations.

§ 1. Introduction

The stationary Becker-Döring's theory of nucleation seems to fail in some cases to predict rightly when the condensation of water vapor occurs in a very rapid expansion in a supersonic flow of moist air[1]. In connection with the solution of this problem, the non-steady equation for the self-nucleation in a highly supersaturated vapor was solved by R. F. Probstein[2] under a special simple initial condition. But this condition, i.e., that initially no embryo exists in the gas, does not seem to correspond to the actual circumstances of the experiment. Embryos are not necessarily of smaller concentration in the initial state than in the final state where the temperature T is lower. The equilibrium number density $N(g)$, of embryos containing g vapor molecules, is larger, at least in the region of small g, in the former than in the latter[3].

On the other hand, D. Turnbull et al.[3] introduced the notion of "athermal nucleation" in connection with the problem of transformations in solids by a rapid temperature change. They imagine that the initial distribution of embryos at the new temperature does not differ much from that corresponding to the old temperature, i.e., the time available is insufficient for the embryos to shrink or grow to their stationary concentration in such cases. This situation, they presume, brings about a special transient process, the so called "athermal nucleation" which can clearly be distinguished from the stationary state of nucleation, "thermal nucleation" in their terminology. Their concept of "athermal nucleation" therefore implies that the time lag cannot be neglected, by far, as compared with the time elapsed by the temperature change. However, this presumption should be verified theoretically as well as experimentally. In view of these circumstances it is desirable to get a solution of this problem which is widely applicable, if it gives a rough estimate of the time lag.

In the following, an approximate but simpler and more general expression for the non-steady rate of nucleation than those hitherto obtained will be reported, which can be derived without first solving the complicated proble mof the non-stationary distribution of embryos.

§ 2. Derivation of the Expression for the Time Lag

The number density $f(g)$ in non-stationary state, of embryos containing g vapor molecules, satisfies the following equation[4)]

$$D(g)N(g)\frac{\partial}{\partial g}\left[\frac{f(g)}{N(g)}\right]=-I(g)\,, \qquad (1)$$

where $D(g)$ means the probability with which an embryo of size g captures a molecule in unit time and $I(g)$ the net number of droplets passing from size $g-1$ to size g per cm³ per sec. Now for the equilibrium density, $N(g)$, we have[4)]

$$N(g)\doteqdot N\cdot\exp(-\Delta\phi/kT)$$

with $$\Delta\phi=(\phi_{II}-\phi_{I})g+\mu g^{2/3}\,, \qquad (2)$$

where N denotes the number density of separate molecules, ϕ_I and ϕ_{II} the bulk free energy per molecule in phase I (metastable) and in phase II (stable) respectively; μ means the surface free energy per a surface molecule. From Eq. (1) and Eq. (2) the following equation can be obtained,

$$-I(g)=D(g)\frac{\partial f(g)}{\partial g}+\frac{1}{kT}D(g)f(g)\frac{\partial\Delta\phi}{\partial g}\,. \qquad (3)$$

Using this equation and an obvious relation

$$-\frac{\partial f(g)}{\partial t}=\frac{\partial I(g)}{\partial g}\,, \qquad (4)$$

we have

$$\frac{\partial f}{\partial t}=\frac{\partial}{\partial g}\left(D\frac{\partial f}{\partial g}\right)+\frac{1}{kT}\frac{\partial}{\partial g}\left(D\cdot f\cdot\frac{\partial\Delta\phi}{\partial g}\right). \qquad (5)$$

This is the equation which Probstein[2)] and others solved under special simple conditions to get the rate of nucleation in non-steady state, $I(g^*)\equiv I^*$, making also use of Eq. (3). g^* means here the value of g corresponding to the peak of free energy barrier, i.e., to $(\partial/\partial g)\Delta\phi=0$.

Our procedure starts from the calculation of the integral

$$\frac{f(g)}{N(g)}=\int_g^G\frac{I(g)}{D(g)N(g)}\cdot dg\,, \qquad (6)$$

which is obtained from Eq. (1). Here G is a value of g sufficiently larger than g^*; we imagine to take the droplet of size G out of the system under consideration, in exchange for separate molecules of the same total amount, just in a way similar to that given by Frenkel[4)]. This means that we assume the number density of nucleus to be zero at the size G. Now the right hand side of Eq. (2) can be expressed as $N(g^*)\exp[\chi^*(g-g^*)^2/2kT]$ in the vicinity of g^*, where χ^* denotes the value of $-[(\partial^2/\partial g^2)\Delta\phi]^*=(2/9)\mu g^{*-4/3}$; here and hereafter the notation with suffix * means quantities at $g=g^*$. The integrand of Eq. (6) have appreciable contribution to the integral only in the vicinity of g^*, because $1/N(g)=1/N(g^*)\cdot\exp[-\chi^*(g-g^*)^2/2kT]$ has a sharp maximum at g^*. Therefore $I(g)/D(g)$ can be replaced by

$$\frac{I}{D}=\frac{I^*}{D^*}+\left\{\frac{\partial}{\partial g}\left(\frac{I}{D}\right)\right\}^*(g-g^*)$$
$$+\frac{1}{2}\left\{\frac{\partial^2}{\partial g^2}\left(\frac{I}{D}\right)\right\}^*(g-g^*)^2\,. \qquad (7)$$

Furthermore it is apparent that we can approximately substitute the limit of the integral by $-\infty$ and $+\infty$. Thus we have, integrating Eq. (6), the relation

$$\frac{f(g)}{N(g)}=\frac{1}{D^*N^*}\sqrt{\frac{2\pi kT}{\chi^*}}$$
$$\times\left[I^*+D^*\left\{\frac{\partial^2}{\partial g^2}\left(\frac{I}{D}\right)\right\}^*\frac{kT}{2\chi^*}\right]. \qquad (8)$$

As $D(g)$ can be expressed as $Ag^{2/3}$, it is shown that

$$D^*\left\{\frac{\partial^2}{\partial g^2}\left(\frac{I}{D}\right)\right\}^*=\left(\frac{\partial^2 I}{\partial g^2}\right)^*-\frac{4}{3g^*}\left(\frac{\partial I}{\partial g}\right)^*$$
$$+\frac{10}{9g^{*2}}I^*\,. \qquad (9)$$

The left hand side of Eq. (8) will be nearly equal to unity for a sufficiently small value of g. Therefore if $(kT/2\chi^*)(10I^*/9g^{*2})$ can be neglected compared with I^*, which usually is the case, we have in the stationary state, where from Eq. (4), $\partial I/\partial g=0$ and $\partial^2 I/\partial g^2=0$, the rate of nucleation I_{s0}^*

$$1=\frac{1}{D^*N^*\sqrt{\dfrac{2\pi kT}{\chi^*}}}\cdot I_{s0}^*$$

$$\text{or}\qquad I_{s0}^*=D^*N^*\sqrt{\frac{\chi^*}{2\pi kT}}\,. \tag{10}$$

This is the relation first derived by Zeldovich[5]. But actually the term mentioned above may not be neglected in some cases and then we have to use, instead of Eq. (10), the relation

$$I_s^*=\frac{D^*N^*(\chi^*/2\pi kT)^{1/2}}{1+(kT/2\chi^*)(10/9g^{*2})}=\frac{I_{s0}^*}{B}\,. \tag{11}$$

Now for any continuous function $\varphi(g,t)$, we have generally

$$\frac{d\varphi^*}{dt}=\left(\frac{\partial\varphi}{\partial t}\right)^*+\left(\frac{\partial\varphi}{\partial g}\right)^*\frac{dg^*}{dt}\,, \tag{12}$$

where $\varphi^*(t)$ means the function $\varphi(g^*(t),\ t)$. Using this relation and Eq. (4) as well as Eq. (3), we have, for the second term of Eq. (9),

$$-\left(\frac{\partial I}{\partial g}\right)^*=\left(\frac{\partial f}{\partial t}\right)^*=\frac{df^*}{dt}-\left(\frac{\partial f}{\partial g}\right)^*\frac{dg^*}{dt}$$
$$=\frac{df^*}{dt}+\frac{I^*}{D^*}\frac{dg^*}{dt}\,.$$

When we take the integral of Eq. (6) between g^* and G, it is obviously equal to half the value of Eq. (8), i.e., $f^*=N^*/2$. From this relation and the equation

$N^*=N\cdot\exp(-\mu g^{*2/3}/3kT)$ we get

$$\frac{df^*}{dt}=\frac{1}{2}\frac{dN^*}{dt}\sim\frac{\chi^*}{2kT}g^*N^*\frac{dg^*}{dt}\,.$$ [*]

So far as we consider down to a limit, say

$$I^*\sim I_s^*\times10^{-2}\fallingdotseq N^*D^*(\chi^*/2\pi kT)^{1/2}\times10^{-2}$$
$$\sim N^*D^*\times10^{-2},\quad\text{then we have}$$
$$df^*/dt\sim(\chi^*/2kT)g^*\times10^2(I^*/D^*)(dg^*/dt).$$

Thus the term $(kT/2\chi^*)(4/3g^*)(\partial I/\partial g)$ contained in Eq. (8) is neglegible compared with I^* if dg^*/dt is to a certain degree smaller than D^*. This degree depends upon the magnitude of kT/χ^* as well as that of g^*. The first term in the bracket on the right hand side of Eq. (9) can be transformed, using Eq. (4), Eq. (3) and Eq. (12), as follows

$$\left(\frac{\partial^2 I}{\partial g^2}\right)^*=\left\{\frac{\partial}{\partial g}\left(-\frac{\partial f}{\partial t}\right)\right\}^*=-\left\{\frac{\partial}{\partial t}\left(\frac{\partial f}{\partial g}\right)\right\}^*$$
$$=-\frac{d}{dt}\left(\frac{\partial f}{\partial g}\right)^*+\left(\frac{\partial^2 f}{\partial g^2}\right)^*\frac{dg^*}{dt}$$
$$=\frac{d}{dt}\left(\frac{I^*}{D^*}\right)+\left(\frac{\partial^2 f}{\partial g^2}\right)^*\frac{dg^*}{dt}\,. \tag{13}$$

Now we have from Eq. (5)

$$\left(\frac{\partial^2 f}{\partial g^2}\right)^*\frac{dg^*}{dt}=\left[\left(\frac{\partial f}{\partial t}\right)^*-\left(\frac{\partial D}{\partial g}\right)^*\left(\frac{\partial f}{\partial g}\right)^*\right.$$
$$\left.+\frac{D^*\chi^*}{kT}f^*\right]\frac{1}{D^*}\frac{dg^*}{dt}\sim$$
$$\left[\frac{\chi^*}{2kT}g^*\times10^2\cdot\frac{1}{D^*}\frac{dg^*}{dt}+\frac{1}{D^*}\frac{dg^*}{dt}+\frac{2}{3}\frac{1}{g^*}\right.$$
$$\left.+\frac{\chi^*}{2kT}\times10^2\right]\frac{I^*}{D^*}\cdot\frac{dg^*}{dt}\,. \tag{14}$$

Estimation of the order of magnitude of all the quantities in this equation as done above, shows that the last term of Eq. (13) can be neglected also if dg^*/dt is sufficiently smaller than D^*. When such a condition is satisfied, we have, instead of Eq. (10), as the non-steady equation

$$1=\frac{B}{D^*N^*\sqrt{\dfrac{2\pi kT}{\chi^*}}}\left[I^*+\frac{kT}{2B\chi^*}\cdot\frac{d}{dt}\left(\frac{I^*}{D^*}\right)\right],$$

which we can put, using Eq. (11), into the form

$$\frac{I^*}{D^*}-\frac{I_s^*}{D^*}=-\frac{kT}{2B\chi^*D^*}\cdot\frac{d}{dt}\left(\frac{I^*}{D^*}\right). \tag{15}$$

If we denote $I^*/D^*\equiv F(t)$, $I_s^*/D^*\equiv F_s(t)$ and $\phi_*\equiv 2B\chi^*D^*/kT$, then we obtain

$$dF/dt+\phi_*F=\phi_*F_s\,, \tag{16}$$

which gives a general solution

$$F=e^{\Phi}\left(\int_{t_0}^{t}\phi_*F_se^{\Phi}\,dt+F_0\right)$$

$$\text{with}\qquad \Phi=\int_{t_0}^{t}\phi_*dt\,. \tag{17}$$

Computing Eq. (17) with given $\phi_*(t)$, $F_s(t)$ and F_0, we can obtain I^*, the rate of self-nucleation in non-stationary state. If we define an "effective time lag" τ_e which satisfies

$$F_s(t)\equiv F(t+\tau_e)\fallingdotseq F(t)+(dF/dt)_t\cdot\tau_e\,,$$

we have

$$\phi_*\tau_e=1\quad\text{or}\quad\tau_e=kT/2D^*\chi^*\,. \tag{18}$$

This quantity will serve as an approximate measure of the magnitude of time lag in the self-nucleation.

§ 3. Some Properties of the Solution

When the rate of nucleation is 0 at $t=0$ and a constant value of I_s^* and ϕ_* is given, then Eq. (17) becomes very simple, namely

$$F=F_s(1-\exp(-\phi_*t))\,. \tag{19}$$

It is interesting to note that this expression is similar to that obtained by the author previously[6] with another assumption (we will call this the previous assumption in the following). In that case ϕ_* in Eq. (19) is just half the above value. In Fig. 1 both curves computed with Eq. (19), each corresponding to the case considered by Probstein, i.e., the case of nucleation in a supersaturated water vapor, are given together with his curve[2]. We see from this figure that the time lag is of the same order of magnitude, but somewhat smaller in our cases, especially in this calculation. Moreover the tendency of change in the rate is very different in the initial stage of the process. This difference is not unexpected. Because Probstein assumes in his calculation that there exist no embryos at the beginning; therefore embryos must grow step by step from size $g=1$ to $g=g^*$ before the nucleation begins, while in our case only the condition

---

[*] Here μ/T was approximately treated as a constant, for simplicity.

$-I^*=D^*(\partial f/\partial g)^*=0$ at $t=0$, but $f(g)=N(g)$ for small g, is assumed. In the previous assumption most of the process under consideration is looked upon to lie in a region where circumstances come near to that of stationary state and therefore part of the change $\partial f/\partial t$ in the vicinity of g^*, due to the gradient of $D\cdot\partial f/\partial g$, can be replaced by that in thestationary state; that is the condition,

$$\frac{\partial}{\partial g}\left(D\frac{\partial f}{\partial g}\right)\doteq\frac{\partial}{\partial g}\left(D\frac{\partial f_s}{\partial g}\right)=-\frac{Df_s}{kT}\chi^*$$

holds, f_s being the stationary distribution of embryos. There, stress was laid upon the change in the magnitude of $f(g)$ in the vicinity of g^* and not in the slop of $f(g)$, while here the change in the slop is emphatically considered. Which of these stand points fits better to the actual circumstances will not be discussed here. The important result is that whatever the initial condition may be, the stationary state will be established within the time interval of the order of magnitude of $\sim 10\tau_e$, when ambient condition is kept constant.

This conclusion is valid, as stated above, when g^* is a function of the time also, so far the change in g^* is not too rapid. $kT/2\chi^*$, β^* and g^* for the case taken up by Probstein[2] are 6.40, 7.28×10^6/sec and 15 respectively and the argument stated in § 2 shows that $dg^*/dt \lesssim 2.15\times10^4$ when the neglected terms are less than 10 percent of those not neglected. But this does not necessarily mean that the time lag becomes far more prominent when the rate of change of the ambient condition exceeds beyond this limit.

On the contrary it seems natural to suppose that the time lag remains to be of the same order of magnitude as that given by Eq. (17), even in the region where an appreciable change of conditions takes place in a time interval of, e.g., τ_e. In fact, if it is assumed that the actual continuous change of g^* can approximately be replaced by a stepwise change with infinitesimal jumps, then the solution is shown to be that of Eq. (17). Let the actual continuous change of g^* between, e.g., $t=0$ to $t=t$ be replaced by a series of steps corresponding to g_1^*, $g_2^*\cdots\cdots$ respectively, each with equal duration Δt, as shown in Fig. 2. F_s and ϕ_* corresponding to each step will be denoted by F_{s1}, ϕ_{*1}; F_{s2}, ϕ_{*2}; $\cdots\cdots$.

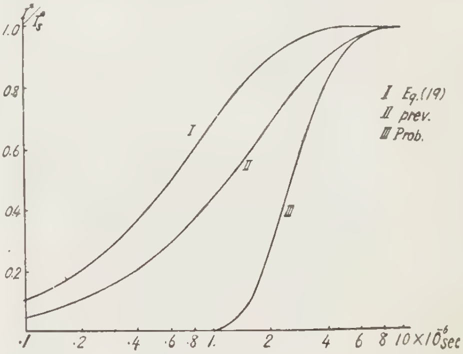

Fig. 1.

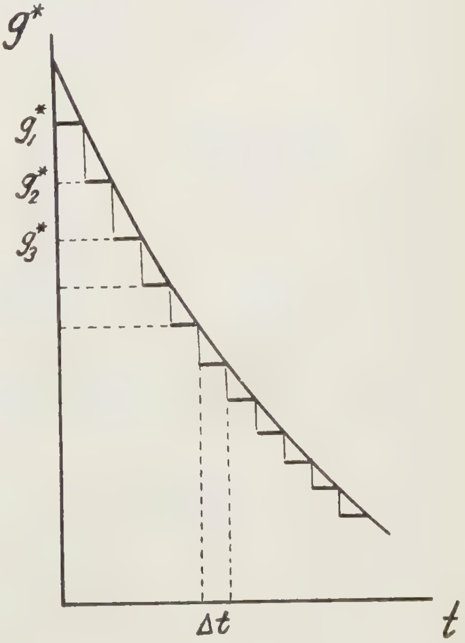

Fig. 2.

Then for the first step we have, from Eq. (19), the final value F_1 satisfying

$$F_1=F_{s1}\{1-\exp(-\phi_{*1}\Delta t)\}+F_0\exp(-\phi_{*1}\Delta t).$$

If we take as the initial value of F in the second step the final value in the first, we will get

$$\begin{aligned}F_2&=F_{s2}\{1-\exp(-\phi_{*2}\Delta t)\}+F_1\exp(-\phi_{*2}\Delta t)\\&=\exp\{-(\phi_{*1}+\phi_{*2})\Delta t\}\\&\quad\times[F_{s2}\{1-\exp(-\phi_{*2}\Delta t)\}\\&\quad\times\exp\{(\phi_{*1}+\phi_{*2})\Delta t\}\\&\quad+F_{s1}\{1-\exp(-\phi_{*1}\Delta t)\}\exp(\phi_{*1}\Delta t)+F_0]\\&\quad\cdots\cdots\cdots.\end{aligned}$$

The general expression is

$$F_n=\exp\left(-\sum_{i=1}^{n}\phi_{*i}\Delta t\right)\left[\sum_{i=1}^{n}F_{si}\{1-\exp(-\phi_{*i}\Delta t)\right.\\\left.\times\exp\left(\sum_{j=1}^{i}\phi_{*j}\Delta t\right)+F_0\right],$$

or for sufficiently small Δt satisfying

$$\exp(-\phi_{*i}\Delta t)\doteqdot 1-\phi_{*i}\Delta t,$$

$$F_n=\exp\left(-\sum_{i=1}^{n}\phi_{*i}\Delta t\right)\left[\sum_{i=1}^{n}\phi_{*i}F_{si}\right.\\\left.\times\exp\left(\sum_{j=1}^{i}\phi_{*j}\Delta t\right)\cdot\Delta t+F_0\right].$$

Consider the limit $\Delta t\to 0$, then we have

$$F=\exp\left(-\int\phi_*dt\right)\left[\int\phi_*F_s\exp\left(\int\phi_*dt\right)\cdot dt\right.\\\left.+F_0\right],$$

namely the solution given by Eq. (17). By this argument is not meant, of course, the proof that Eq. (17) be valid however rapidly the surrounding condition varies; it simply suggests that the order of magnitude of the time lag given by Eq. (17) is not erroneous, so far as the actual continuous change in ambient condition can approximately be replaced by the stepwise one, which assumption does not seem to be unnatural from physical point of view.

§ 4. Result of the Theory for a Case of Nucleation in Solids

Next we will proceed to the application of our theory to the problem of nucleation in solids and take up the simplest case we can consider; the transformation in a binary metallic system with a complete solid solubility at higher temperatures and a miscibility gap at lower temperatures. The stationary nucleation in such a transformation was first discussed by Becker[7]. Using Bragg-William's approximation in the treatment of interaction between atoms, he derived the free energy of the solid solution per atom as a function of the composition, the result being

$$\phi(c)=VZc(1-c)+kT[c\ln c+(1-c)\ln(1-c)]\,, \tag{20}$$

where c is the relative concentration of one component atoms A (the other will be denoted as B), Z the number of nearest neighbors and $V=V_{AB}-(1/2)(V_{AA}+V_{BB})$, V_{AB}, V_{AA} and V_{BB} being the respective energies of pairs of atoms. From the condition $(\partial/\partial c)\phi(c)=0$, the equation

$$\frac{1-2c}{\ln(1-c)/c}=\frac{kT}{ZV} \tag{21}$$

is obtained which gives the phase diagram and its solution c_1 and c_2 satisfy the following relation

$$1-c_1=c_2 \quad\text{or}\quad 1-c_2=c_1\,. \tag{22}$$

Furthermore Becker assumed embryos t constitute a simple cubic lattice with equa edge length and calculated the free energ for the formation of such an embryo of edg length a in atomic unit and of concentratio c_2 of A-atom, in the mother phase of concentration c, the result being

$$\Delta\phi=-a^3[\phi(c)-\phi(c_2)+\phi'(c)(c_2-c)]+6a^2V(c-c_2) \tag{23}$$

Considering the relation $g=a^3$, it is easy t obtain, from the comparison of this equatio with that in Eq. (2), such quantities as μ, g or χ^* that are necessary for the computatio of the time lag. But Becker gave only th relative rate of nucleation and, to calculat D^*, we have to use the theory of absolut rate of reactions as was done previously[8] Now before we apply this treatment to th case mentioned above, i.e., nucleation in binar systems, we have to make some preparation

Suppose our meta-stable binary alloy (phase consists of two metallic components A and with an average relative concentration c_1 A-atom and there appears in the alloy embry of a stable phase (phase II) with concentr tion c_2. Consider a cluster which includes atoms of phase II and let the probabilit with which A-atom of phase I on the inte face between two phases penetrate throug the boundary in unit time, be β_A and t probability for reversed transition α_{gA}. Co responding probabilities for the jump of the B-atoms will be denoted by β_B and α_{gB} respectively (see Fig. 3). Then in order that the growing cluster remains to be of the same composition on the average, the following relation must hold for any value of g.

$$\frac{c_1\beta_A-c_2\alpha_{gA}}{(1-c_1)\beta_B-(1-c_2)\alpha_{gB}}=\frac{c_2}{1-c_2}\,. \tag{24}$$

From this condition and that of equilibrium in A and in B for the embryo distribution $N(g)$, namely

$$\left.\begin{aligned} N(g-1)s(g-1)c_1\beta_A&=N(g)s(g)c_2\alpha_{gA}\,, \\ N(g-1)s(g-1)(1-c_1)\beta_B&=N(g)s(g)(1-c_2)\alpha_{gB}\,, \end{aligned}\right\} \tag{25}$$

we have

$$\alpha_{gA}=\alpha_{gB}\equiv\alpha_g$$

and
$$\frac{c_1}{c_2}\,\beta_A=\frac{1-c_1}{1-c_2}\,\beta_B\,, \tag{26}$$

$s(g)$ means here the number of atoms on the surface of a cluster containing g atoms. In a non-steady state there will be the net number of embryos $I_A(g)$ passing from size $g-1$ to size g per cm^3 per sec, through addition of one A-atom, and also $I_B(g)$, through the increase of one B-atom. And it is easy to show that these satisfy the relation

$$\left.\begin{aligned} -I_A(g)&=N(g)s(g)c_1\beta_A\,\frac{\partial}{\partial g}\left\{\frac{f(g)}{N(g)}\right\}\,, \\ -I_B(g)&=N(g)s(g)(1-c_1)\beta_B\,\frac{\partial}{\partial g}\left\{\frac{f(g)}{N(g)}\right\}\,, \end{aligned}\right\} \tag{27}$$

respectively. The total flow $I(g)=I_A(g)+I_B(g)$ satisfies therefore Eq. (1) in which $D(g)$ should be replaced by $D(g)=s(g)\{c_1\beta_A+(1-c_1)\beta_B\}$, which becomes from Eq. (26)

$$D(g)=s(g)\frac{c_1}{c_2}\beta_A \quad \text{or} \quad D(g)=s(g)\frac{1-c_1}{1-c_2}\,\beta_B\,. \tag{28}$$

According to Eq. (26) the last two equations are identical. From Eq. (22), we have furthermore,

$$\frac{c_1}{c_2}\,\beta_A=\frac{1-c_1}{1-c_2}\beta_B=\frac{c_2}{c_1}\,\beta_B\,. \tag{29}$$

We assume therefore, in accordance with the theory of the absolute rate of reaction

$$\frac{c_1}{c_2}\,\beta_A=\frac{c_2}{c_1}\,\beta_B=\frac{kT}{h}\exp\left(-\Delta f^*/kT\right)\,. \tag{30}$$

Here Δf^*, the average free energy of activation for the capture of one atom by an embryo, can approximately be evaluated from the diffusion measurements for the atoms in the alloy. As for $s(g)$, we have $s(g)=6a^2$. Thus we are prepared to the computation of $D(g^*)$ and consequently, of τ_e, the time lag of nucleation, from known experimental data.

Actual calculation was carried out for the case of nucleation taken up by Becker, i.e., the nucleation in a solid solution in which the miscibility gap closes at 1500°K. Particulary the case of concentration of 15 atomic percent which is unstable below 1200°K was considered for computation. Becker tried to compare the results of his theory of nucleation with the experimental data for Au-Pt alloy obtained by Johanssen and Hagsten[9], and for this alloy, diffusion data give an activation energy of 39,000 cal/mole. We assumed, with Becker, this value for the calculation. In Fig. 4 the

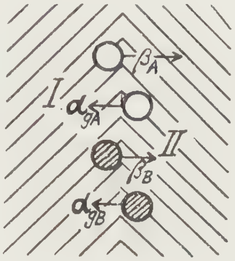

Fig. 3.

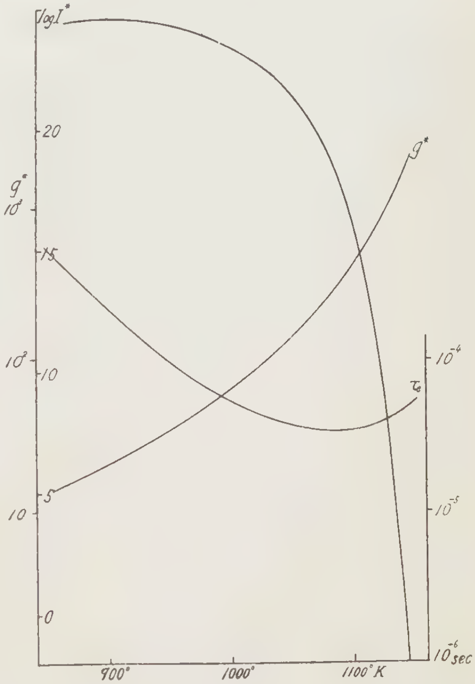

Fig. 4.

value of τ_e as computed with Eq. (18) is given together with the absolute rate of nucleation I^* as well as g^*, as a function of the temperature. We see from this figure that τ_e is of the order of magnitude $3\sim5\times10^{-5}$ sec in the region where I^* has a reasonable value. Therefore, at least in such a transformation, it is unlikely that the time elapsed by the temperature change during an usual quenching, is insufficient for embryos to shrink or grow to their stationary concentration. This conclusion will not be essentially altered even when we examine the limit of the validity of our formula (17). The discussion mentioned in § 2, when applied to this case, gives, e.g., at higher temperatures than 1000°K (in the region mentioned above), the result $dg^*/dt \lesssim 10^{4-5}$; this means that nearly to the limit of $\sim10^3$ deg/sec, Eq. (17) would approximately be valid. Thus some doubt is cast upon the applicability, at least in such cases as considered here, of the concept of "athermal nucleation" as proposed by Turnbull et al.[3], on the ground that the magnitude of time lag is not compatible with their presumption. On the other hand, this concept will retain its value when the time lag is far more prominent, namely in the situation which is expected in the case where Δf^* is much larger or nucleation attains a considerable amount at temperatures much lower, than in the case taken up here.

In conclusion the author wishes to express his gratitude to Dr. I. Syozi and other colleagues in our institute for fruitful discussions. He is indebted also to Prof. T. Nagamiya of Osaka University for advices and criticism.

References

1) R. Head, "Investigation of spontaneous condensation phenomena" Guggenheim Aero. Lob. Calif. Inst. of Tech. Ph D. Dissertaion 1949.
2) R. F. Probstein: J. Chem. Phys. **19** (1951) 619.
3) J. C. Fisher, J. H. Hollomon and D. Turnbull: J. Appl. Phys. **19** (1948) 775.
4) J. Frenkel: Kinetic Theory of Liquids (Oxford Univ. Press, London (1946) p. 394.
5) J. Zeldovich: J. Exptl. Theoret. Phys. (USSR) **12** (1942) 525.
6) H. Wakeshima: J. Phys. Soc. Japan **10** (1955 65.
7) R. Becker: Ann. Physik **32** (1938) 128.
8) See ref. (6): Also, D. Turnbull and J. C Fisher: J. Chem. Phys. **17** (1949) 71.
9) C. K. Johanssen and G. Hagsten: Ann. Physik **28** (1937) 520.

JOURNAL OF THE PHYSICAL SOCIETY OF JAPAN Vol. 10, No. 5, MAY, 1955

A Statistical-Mechanical Theory of Surface Tension of Curved Surface Layer I*

By Sohei KONDO

Kyusyu-Zyogakuin High School, Simizu-mati, Kumamoto

(Received January 26, 1955)

Combining with a thermodynamical definition, an extension of Harasima's statistical-mechanical method to calculate the plane surface tension leads to general expressions for the surface tension of cylindrical and spherical interface. A new definition of "surface of tension" is introduced and the familiar Kelvin relation is derived more strictly by using this definition than by the traditional method. From the point of view of this definition Tolman's conclusion on the curvature dependency of surface tension turns out to be questionable and necessary to be re-examined.

§ 1. Introduction

The general statistical-mechanical theory of surface tension of plane interface has been developed by making use of two different methods: one, the mechanical method, was used by J. G. Kirkwood and F. P. Buff1) and H. S. Green2); and the other, the thermodynamical method, by A. G. MacLellan3) and A. Harasima4). In the case of plane interface the two methods lead to the same result.

The case of curved interface, however, presents many special difficulties to be overcome, and the crux of the special difficulty lies in the ambiguity of the definition of surface tension. For example, the word "surface" thought of in the concept of "surface tension" implies a geometrical surface, but any actual interface consists of a heterogeneous transition zone with at least several atomic layers. So there always exists an essential ambiguity of the position of interface, which causes an ambiguity of the value of surface tension in the case of curved interface. Furthermore, there can be as many kinds of surface tension as there are methods to define it; and there is no reason that they would lead to the same result, insofar as the definitions are mutually independent.

The case of cylindrical interface has recently been examined by T. Segawa and E. Teramoto5) under certain assumptions, with the application of the two methods mentioned above. Without such assumptions, in this article we will apply the two methods to the cases of spherical interface as well as cylindrical interface. The details of the methods are different from those developed by T. Segawa and E. Teramoto5).

In this paper an extention of Harasima's method4) is made and applied to the cases of cylindrical interface and spherical interface. First, the thermodynamical definition of surface tension referred to an arbitrary Gibbs dividing surface6) is given by the Gibbs fundamental equation, which is restricted by the special condition that the *curvature* of the interface must be kept *constant* in performing the virtual variations in the conditions of the given system. Second, statistical-mechanical expression is obtained by applying the Born-Green method7) for the change in the Helmholtz free energy of the system. Combining these two results we obtain the desired statistical-mechanical expression for the surface tension of curved interface referred to an arbitrary dividing surface. Then if we choose the location of the dividing surface so as to give the minimum value of the surface tension, we reach the Kelvin relation. So this dividing surface is what Gibbs intended to call "surface of tension"; thus Gibbs and Tolman *et al.*1)6)8)9) seem to have made a mistake, at least, in the concept of "surface of tension".

The above-mentioned treatment is carried out in parallel in both cases of cylindrical interface and spherical interface. The mechanical method and the curvature dependency of surface tension will be reserved for treatment in the following series.

---

* The main content of the present paper was published in the Japanese publication: Busseiron Kenkyu, No. 74 (1954) 60; ibid., No. 77 (1954) 75.

§ 2. Thermodynamical Considerations

We consider a system of particles, which consists of two effectively homogeneous phases designated as α- and β-phase respectively in contact, and consists of the inhomogeneous layer (to be called "surface layer") formed by this contact. Corresponding to an arbitrary infinitesimal virtual variation in the state of our system, the change in the total Helmholtz free energy, F, is according to Gibbs fundamental equation[6], given by

$$\delta F = -S\delta T + \mu\delta N - p_\alpha \delta V_\alpha - p_\beta \delta V_\beta + \gamma \delta A + C_1 \delta c_1 + C_2 \delta c_2 \,, \qquad (1)$$

in which S, T, μ, p_α and p_β denote respectively the total entropy, the absolute temperature, the chemical potential, the hydrostatic pressure of the homogeneous α-phase and of the homogeneous β-phase; and V_α, V_β, A, c_1 and c_2 denote respectively the volume of α- and β-phase separated by an arbitrary Gibbs dividing surface, the area of the dividing surface, and its two principal curvatures.

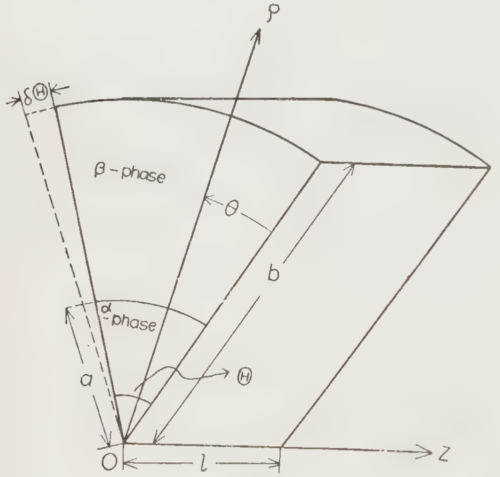

Fig. 1.

Here we shall specify the particular variation in the state of the system to be treated by the requirement that we start from a state of equilibrium and make infinitesimal arbitrary variations in V_α, V_β and A, keeping the temperature T of the system, the total number of the particles of the system, N, and particularly *the curvatures of the surface layer unaltered.* Then Equation (1) is reduced to

$$\delta F = -p_\alpha \delta V_\alpha - p_\beta \delta V_\beta + \gamma \delta A \,. \qquad (2)$$

Now we define a "surface tension" of the system, with respect to the corresponding dividing surface, by the coefficient γ in Eq. (2). We should note that such a surface tension depends not only on the variation in the Helmholtz free energy of the surface layer but also on *the choice of the location of our imaginary dividing surface.*

§ 3. Geometry of Surface Layers and Thermodynamical Expressions for Variations

A. *the Case of Cylindrical Surface Layer*

Here we shall limit the treatment to a "surface layer" having cylindrical form, with the effectively homogeneous phases located on its opposite sides, the so-called interior phase being referred to as α-phase and the exterior phase as β-phase. To apply Eq. (2) to our system, it seems to be a necessary condition that we should further limit the treatment to a sectoral portion of the above-mentioned system. So we shall imagine a vessel with a sectoral cross-section and axial length, l, which contains the sectoral portion of the system. Now let us consider an arbitrary Gibbs dividing surface with radius a within the cylindrical surface layer of physical inhomogeneity. Hence we can get the following relations:

$$V_\alpha = la^2\Theta/2 \,, \qquad (3)$$

$$V_\beta = l(b^2 - a^2)\Theta/2 \,, \qquad (4)$$

$$A = la\Theta \,, \qquad (5)$$

where b and Θ denote respectively the radius of the vessel and the angle spanned by the sectoral cross-section of the vessel. (Fig. 1)

Then the infinitesimal virtual variations considered in Eq. (2) will be reduced to the infinitesimal variation in Θ alone, for we should keep the curvatures constant. Thus Eq. (2) will be reduced to

$$(\partial F/\partial \Theta)\delta\Theta = l[-(p_\alpha - p_\beta)a^2/2 - p_\beta b^2/2 + \gamma a]\delta\Theta. \qquad (6)$$

Hence we obtain the desired thermodynamical expression for the surface tension of cylindrical surface layer:

$$\gamma = a^{-1}[(p_\alpha - p_\beta)a^2/2 + p_\beta b^2/2 + l^{-1}(\partial F/\partial \Theta)]. \qquad (7)$$

B. *the Case of Spherical Surface Layer*

The above treatment of the cylindrical surface layer can be readily extended to the case of a spherical layer. In this case the surface layer has spherical form, so we restrict ourselves to a special portion of the spherical system to apply Eq. (2) to this case. We imagine that the portion is contained in a vessel, which is expressed by the following:

$$0 \leq r \leq b ; \quad \Theta_1 \leq \theta \leq \Theta_2 ; \quad 0 \leq \varphi \leq \Omega , \tag{8}$$

where r, θ and φ are polar coordinates, the origin of which is located at the center of the curvature of our surface layer, and $r=b$, $\theta=\Theta_1$, $\theta=\Theta_2$, $\varphi=0$ and $\varphi=\Omega$ denote respectively the surrounding inner walls of the vessel. (Fig. 2.)

Corresponding to Eqs. (3), (4) and (5) we at once get the following equations:

$$V_\alpha=(a^3/3)(\cos\Theta_1-\cos\Theta_2)\Omega , \tag{9}$$

$$V_\beta=\{(b^3-a^3)/3\}(\cos\Theta_1-\cos\Theta_2)\Omega , \tag{10}$$

$$A=a^2(\cos\Theta_1-\cos\Theta_2)\Omega . \tag{11}$$

Here again $r=a$ denotes an arbitrary Gibbs dividing surface. Corresponding to the infinitesimal variations considered in Eq. (2), we take the infinitesimal variation in Ω alone. Then we get the following equation:

$$(\partial F/\partial\Omega)\delta\Omega=(\cos\Theta_1-\cos\Theta_2)[-(p_\alpha-p_\beta)a^3/3 \\ -p_\beta b^3/3+\gamma a^2]\delta\Omega , \tag{12}$$

which corresponds to Eq. (6).

Hence: for the surface tension of spherical surface layer we get the following thermodynamical equation:

$$\gamma=a^{-2}[(p_\alpha-p_\beta)a^3/3+p_\beta b^3/3 \\ +(\partial F/\partial\Omega)/(\cos\Theta_1-\cos\Theta_2)] . \tag{13}$$

§ 4. Statistical-Mechanical Expressions for $\partial F/\partial\Theta$ and $\partial F/\partial\Omega$

The Helmholtz free energy F of our system is given by

$$e^{-F/kT}=\left(\frac{2\pi mkT}{h^2}\right)^{3N/2} Q ,$$

where

$$Q=\frac{1}{N!}\int\cdots\cdots\int_V \exp(-\Phi/kT)\prod_{i=1}^{N} dx^{(i)}, \tag{14}$$

in which V and $x^{(i)}$ denote respectively the total volume of the system and the position vector of the i-th particle, and Φ is the potential energy of the system which we assume to be of the form $\Phi=\sum_{i<j}^{N}\phi_{ij}$. To calculate $\partial F/\partial\Theta$ and $\partial F/\partial\Omega$, we are going to make use of the Born-Green method as used by MacLellan[3] and Harasima[4] in their treatments of plane surface layer.

A. *$\partial F/\partial\Theta$: the Case of Cylindrical Surface Layer*

In this case we use cylindrical coordinates: (Fig. 1.)

$$dx^{(i)}=\rho_i d\rho_i d\theta_i dz_i \quad (i=1,\ 2,\cdots,\ N). \tag{15}$$

Let us introduce a new variable ξ_i:

$$\theta_i=\Theta\xi_i \qquad (0\leq\xi_i\leq 1) . \tag{16}$$

Then

$$Q=\frac{\Theta^N}{N!}\int\cdots\int\prod_{i=1}^{N}\rho_i d\rho_i dz_i\int_0^1\cdots \\ \cdots\int_0^1\exp(-\Phi/kT)\prod_{i=1}^{N}d\xi_i . \tag{17}$$

Here we note that the distance R_{ij} between i-th and j-th particle can be written in the form

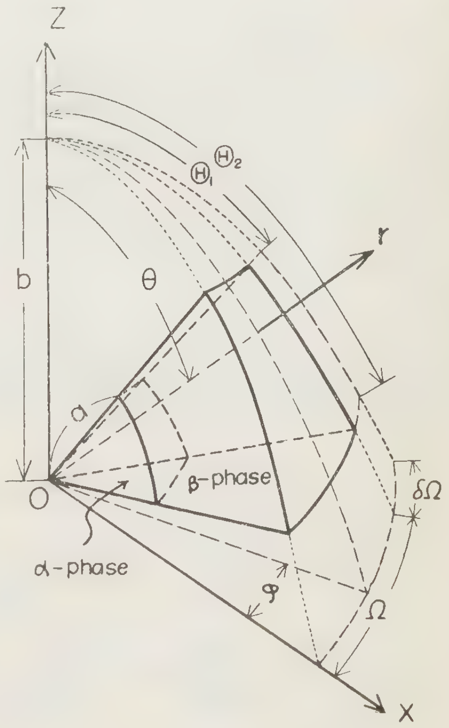

Fig. 2.

$$R_{ij}=\sqrt{\rho_i^2+\rho_j^2-2\rho_i\rho_j\cos[\Theta(\xi_i-\xi_j)]+(z_i-z_j)^2} . \tag{18}$$

Then we obtain, with the use of the definition of the pair distribution function $n_2(x^{(1)}, x^{(2)})$,

$$\frac{\partial F}{\partial\Theta}=-\frac{NkT}{\Theta}+\frac{1}{2\Theta}\iint_V n_2(x^{(1)},\ x^{(2)}) \\ \times\frac{d\phi_{12}}{dR_{12}}\frac{\rho_1\rho_2(\theta_1-\theta_2)\sin(\theta_1-\theta_2)}{R_{12}}dx^{(1)}dx^{(2)} . \tag{19}$$

Assuming that the edge effect of our system is negligible, we may write:

$$n_1(\boldsymbol{x}^{(1)})=n_1(\rho_1);\quad n_2(\boldsymbol{x}^{(1)},\boldsymbol{x}^{(2)})=n_2(\rho_1,\boldsymbol{R}_{12}), \tag{20}$$

$$\boldsymbol{R}_{12}=\boldsymbol{x}^{(2)}-\boldsymbol{x}^{(1)}, \tag{21}$$

where n_1 denotes the number density of the system.

Then introducing relative coordinates and considering symmetry, Eq. (19) can be expressed as follows:

$$\frac{\partial F}{\partial \Theta}=-l\int_0^b \rho_1 d\rho_1\Big[n_1(\rho_1)kT-\frac{1}{2}\iiint n_2(\rho_1,\boldsymbol{R}_{12})\frac{d\phi_{12}}{d\boldsymbol{R}_{12}}\frac{\rho_1\rho_2\theta_{12}\sin\theta_{12}}{R_{12}}d\boldsymbol{R}_{12}\Big], \tag{22}$$

where

$$\theta_{12}=\theta_2-\theta_1\,. \tag{23}$$

Here we may define the effective tangential component of the point function pressure tensor $p_T(\rho_1)$ by the following equation:

$$p_T(\rho_1)=n_1(\rho_1)kT-\frac{1}{2}\iiint n_2(\rho_1,\boldsymbol{R}_{12})\frac{d\phi_{12}}{d\boldsymbol{R}_{12}}\frac{\lambda_{12}x_{12}}{R_{12}}d\boldsymbol{R}_{12}\,, \tag{24}$$

where

$$\lambda_{12}=\rho_1\theta_{12};\quad x_{12}=\rho_2\sin\theta_{12}. \tag{25}$$

If we can assume that the radius of the surface layer is large enough compared with the range of the intermolecular forces, we may put

$$\lambda_{12}=x_{12}\,, \tag{25a}$$

where x_{12} means one component of relative coordinates with lateral direction. Then

$$p_T(\rho_1)=n_1(\rho_1)kT-\frac{1}{2}\iiint n_2(\rho_1,\boldsymbol{R}_{12})\frac{d\phi_{12}}{d\boldsymbol{R}_{12}}\frac{x_{12}^2}{R_{12}}d\boldsymbol{R}_{12}. \tag{24a}$$

Here we note that Eq. (24a) for p_T is identical in form with that given by J. G. Kirkwood and F. P. Buff[1] for plane surface layer. Therefore we understand that the difference between the plane p_T and the cylindrical p_T is solely hidden in the number density and the pair distribution function so far as Eq. (25a) is valid.

B. $\partial F/\partial\Omega$: *the Case of Spherical Surface Layer*

In this case we use polar coordinates as mentioned in §3. A., so (Fig. 2.)

$$d\boldsymbol{x}^{(i)}=r_i^2\sin\theta_i dr_i d\theta_i d\varphi_i\quad (i=1,2,\cdots,N). \tag{26}$$

Again introducing a new variable η_i:

$$\varphi_i=\Omega\eta_i\qquad (0\leq\eta_i\leq 1). \tag{27}$$

Eq. (17) becomes

$$Q=\frac{\Omega^N}{N!}\int\cdots\int\prod_{i=1}^N r_i^2\sin\theta_i dr_i d\theta_i\int_0^1\cdots\int_0^1\exp(-\Phi/kT)\prod_{i=1}^N d\eta_i\,. \tag{28}$$

Considering the following expression for the distance R_{ij} between i-th and j-th particle

$$R_{ij}=\sqrt{r_i^2+r_j^2-2r_ir_j[\sin\theta_i\sin\theta_j\cos\{\Omega(\eta_i-\eta_j)\}+\cos\theta_i\cos\theta_j]}\,, \tag{29}$$

we get

$$\frac{\partial F}{\partial\Omega}=-\frac{NkT}{\Omega}+\frac{1}{2\Omega}\iint_V n_2(\boldsymbol{x}^{(1)},\boldsymbol{x}^{(2)})\frac{d\phi_{12}}{dR_{12}}\frac{r_1r_2(\varphi_2-\varphi_1)\sin\theta_1\sin\theta_2\sin(\varphi_2-\varphi_1)}{R_{12}}d\boldsymbol{x}^{(1)}d\boldsymbol{x}^{(2)}, \tag{30}$$

which corresponds to Eq. (19) in the cylindrical case.

Again we may assume

$$n_1(\boldsymbol{x}^{(1)})=n_1(r_1);\quad n_2(\boldsymbol{x}^{(1)},\boldsymbol{x}^{(2)})=n_2(r_1,\boldsymbol{R}_{12})\,. \tag{31}$$

Here we should remark that Eq. (30) is not reducible to the one corresponding to Eq. (22) by making use of relative coordinates.

In fact, if we put

$$\varphi_{12}=\varphi_2-\varphi_1;\quad \theta_{12}=\theta_2-\theta_1\,, \tag{32}$$

$$\nu_{12}=r_1(\varphi_2-\varphi_1)\sin\theta_1\,, \tag{33}$$

$$x_{12}=r_2\sin\theta_2\sin(\varphi_2-\varphi_1), \tag{34}$$

we find ν_{12} is dependent on θ_1. But, here again if the radius of the surface layer can be assumed large enough compared with the range of the intermolecular forces, we may put

$$\nu_{12}=x_{12}\,. \tag{35}$$

Then

$$\frac{\partial F}{\partial\Omega}=-(\cos\Theta_1-\cos\Theta_2)\int_0^b r_1^2dr_1\Big[n_1(r_1)kT-\frac{1}{2}\iiint n_2(r_1,\boldsymbol{R}_{12})\frac{d\phi_{12}}{dR_{12}}\frac{x_{12}^2}{R_{12}}d\boldsymbol{R}_{12}\Big]. \tag{36}$$

In this case we may define the tangential component of the pressure tensor p_T by the following equation:

$$p_T(r_1)=n_1(r_1)kT-\frac{1}{2}\iiint n_2(r_1,\, \boldsymbol{R}_{12})\frac{d\phi_{12}}{dR_{12}}\frac{x_{12}{}^2}{R_{12}}d\boldsymbol{R}_{12}\,. \tag{37}$$

So again we find that p_T in the case of spherical surface layer is identical in form with that of plane surface layer, provided that Eq. (35) is valid.

§ 5. Statistical-Mechanical Expression for Surface Tension Referred to an Arbitrary Dividing Surface

A. the Case of Cylindrical Surface Layer

Substitution of Eqs. (22) and (24a) into Eq. (7) gives the desired expression for the surface tension of the cylindrical surface layer:

$$\gamma=a^{-1}\int_0^b(p_\beta-p_T(\rho_1))\rho_1 d\rho_1+(p_\alpha-p_\beta)a/2\,, \tag{38}$$

or

$$\left.\begin{aligned}&\gamma=\int(p_{\alpha\beta}-p_T(a+z))(1+cz)dz\,,\\&p_{\alpha\beta}=p_\alpha[1-A(z)]+p_\beta A(z)\,,\\&c=1/a;\ A(z)=0,\ z<0;\ A(z)=1,\ z\geqslant 0,\end{aligned}\right\} \tag{38a}$$

where z is a coordinate directed outward from the arbitrary dividing surface of curvature c, and $A(z)$ is the unit step function.

B. the Case of Spherical Surface Layer

Substitution of Eqs. (36) and (37) into (13) gives the desired expression for the surface tension of the spherical surface layer:

$$\gamma=a^{-2}\int_0^b(p_\beta-p_T(r_1))r_1^2 dr_1+(p_\alpha-p_\beta)a/3\,, \tag{39}$$

or

$$\left.\begin{aligned}&\gamma=\int(p_{\alpha\beta}-p_T(a+z))(1+cz)^2 dz\,,\\&p_{\alpha\beta}=p_\alpha[1-A(z)]+p_\beta A(z)\,,\\&c=1/a;\ A(z)=0,\ z<0;\ A(z)=1,\ z\geqslant 0\,.\end{aligned}\right\} \tag{39a}$$

Putting aside the undermined value of curvature, c, of the dividing surface, Eq. (39a) is identical in form with the formula suggested by R. C. Tolman[6] and F. P. Buff[9] in their thermodynamical treatment of the spherical surface layer, and in this paper we have the statistical-mechanical expression for p_T in Eq. (37).

§ 6. Surface of Tension and Final Results

Eqs. (38) and (39) show that the surface tension of curved surface depends on the choice of the location of the dividing surface even if all the physical quantities of the system are fixed.

Now we define the radius of " surface of tension " by such a value as to give the minimum value of surface tension when *the whole physical state of the system* is kept *unaltered*. This definition of " surface of tension " is different from that given by Gibbs and Tolman. It should be noted that our definition always guarantees both the existence of " surface of tension " and the familiar Kelvin relation.

A. the Case of Cylindrical Surface Layer

From Eq. (38) we get

$$\frac{\partial\gamma}{\partial a}=-a^{-2}\int_0^b(p_\beta-p_T(\rho_1))\rho_1 d\rho_1+(p_\alpha-p_\beta)/2\,. \tag{40}$$

Putting $\partial\gamma/\partial a=0$, the radius, a_S, of " surface of tension " is given by

$$a_S=\left[\,2\int_0^b(p_\beta-p_T(\rho_1))\rho_1 d\rho_1/(p_\alpha-p_\beta)\right]^{1/2}, \tag{41}$$

Substituting Eq. (41) into Eq. (38), the desired expression for the surface tension referred to our " surface of tension " will be reduced to

$$\gamma=2a_S{}^{-1}\int_0^b(p_\beta-p_T(\rho_1))\rho_1 d\rho_1\,, \tag{42}$$

or to the familiar Kelvin relation:

$$\gamma=a_S(p_\alpha-p_\beta)\,, \tag{43}$$

or to

$$\gamma=\int(p_{\alpha\beta}-p_T(a_S+z))(1+c_S z)dz\,, \tag{38b}$$

where

$$c_S=1/a_S\,.$$

B. the Case of Spherical Surface Layer

From Eq. (39) we get

$$\frac{\partial\gamma}{\partial a}=-2a^{-3}\int_0^b(p_\beta-p_T(r_1))r_1^2 dr_1+(p_\alpha-p_\beta)/3. \tag{44}$$

Putting $\partial\gamma/\partial a=0$, the radius, a_S, of " surface of tension " will be given

$$a_S=\left[\,6\int_0^b(p_\beta-p_T(r_1))r_1^2 dr_1/(p_\alpha-p_\beta)\right]^{1/3}. \tag{45}$$

Substituting Eq. (45) into Eq. (39), the desired expression for the surface tension referred to our " surface of tension " will be reduced to

$$\gamma=3a_S{}^{-2}\int_0^b(p_\beta-p_T(r_1))r_1{}^2dr_1\ , \tag{46}$$

or to the familiar Kelvin relation:

$$\gamma=a_S(p_\alpha-p_\beta)/2\ , \tag{47}$$

or to

$$\gamma=\int(p_{\alpha\beta}-p_T(a_S+z))(1+c_Sz)^2dz\ , \tag{39b}$$

where

$$c_S=1/a_S\ .$$

§ 7. Conclusions

It will have been appreciated that the derivation given for the familiar Kelvin relation (43) or (47) involve the assumption that the radius of the corresponding surface layer, compared with the range of the intermolecular forces, is large enough that first, the thermodynamical definition, Eq. (2), of surface tension is applicable and second, Eq. (25a) or (35) is accurate; and that the radius of " surface of tension " should be defined by Eq. (41) or (45). Under such assumptions, we have obtained the general expression in § 5. and § 6. for surface tension of both cylindrical and spherical surface layer. From Eqs. (41), (38b), (45), and (39b), it should be noted that the surface tension depends partly on the radius, a_S, of the " surface of tension " and partly on the tangential component, p_T, of the pressure tensor.

The conclusion given by R. C. Tolman[6)10)11)] that the surface tension of small drops decreases with increasing curvature was based on an assumption which ignores the curvature dependency $p_{\alpha\beta}$ and p_T, and especially on the fact of ill-defining the " surface of tension ". From the stand-point of the molecular theory, $p_{\alpha\beta}$, p_T and a_S could be calculated only if the number density and pair distribution function were exactly obtained, but this is the real crux of the problem. At the present stage of statistical mechanics we cannot but make use of the mathematical surface of discontinuity as the approximation for the actual distribution functions as done by J. G. Kirkwood and F. P. Buff[1)] in the case of plane surface layer. Re-examination of the curvature dependency of surface tension by such an approximation will be presented in the following series.

Putting it briefly, the essential key to solve the surface tension is solely hidden in the distribution functions; and this paper has presented the general expressions for the surface tensions of cylindrical and spherical surface layer in terms of these unsolved distribution functions.

Acknowledgements

It is a pleasure for me to thank Dr. Syu Ono, Assistant Professor of the University of Tokyo, for his invaluable suggestions and constant encouragement from the start of this work and Dr. Akira Harasima, Professor of Tokyo Institute of Technology, for his warm-hearted guidance especially during the two-week seminar in Research Institute for Fundamental Physics in Kyoto held last fall, which is responsible for much of the work on the new concept of " surface of tension ". The author is very grateful to my colleagues, Mr. T. Tikazawa, Mr. T. Nagata and Mr. K. Kaminisi for generous assistance. I am especially indebted to Mr. K. Kaminisi for reading the entire manuscript and to the professors of the Department of Physics in Kumamoto University for their kind guidance and for a generous grant to make possible my study there.

References

1) J. G. Kirkwood and F. P. Buff: J. Chem. Phys. **17** (1949) 338.
2) H. S. Green: Molecular Theory of Fluids (North-Holland Publishing Co.) P. 37 and P. 190 (1952).
3) A. G. MacLellan: Proc. Roy. Soc. A. **213** (1952) 274.
4) A. Harasima: J. Phys. Soc. Japan **8** (1953) 343.
5) T. Segawa and E. Teramoto: Prog. Theor. Phys. **11** (1954) 528.
6) R. C. Tolman: J. Chem. Phys. **16** (1948) 758.
7) H. S. Green: ibid., P. 51.
8) F. O. Koenig: J. Chem. Phys. **18** (1950) 449.
9) F. P. Buff: J. Chem. Phys. **19** (1951) 1591.
10) R. C. Tolman: J. Chem. Phys. **17** (1949) 118.
11) R. C. Tolman: J. Chem. Phys. **17** (1949) 333.

Journal of the Physical Society of Japan Vol. 10, No. 5, May, 1955

Receiving Tubes with Very Small Grid Current

By Hisao Takayama and Koichi Shimoda
Department of Physics, Faculty of Science, University of Tokyo, Tokyo, Japan

(Received January 28, 1955)

The use of miniature receiving tubes as electrometer tubes with large voltage gain and low grid current has been investigated. 6AK5 and 3S4 have been found to be appropriate. The grid current of a 3S4 has been reduced to 1×10^{-15}A by proper treatments. Under the condition, the voltage gain of 20∼40 has been measured.

§ 1. Introduction

The presence of grid current gives a limit of sensitivity in any type of vacuum tube electrometer. This is true even for the dynamic condenser electrometer, because it is impossible to discriminate the low frequency component of the fluctuating grid current from the signal. As the noise in a high input-resistance circuit mostly comes from the shot noise due to grid current, the reduction of noise requires the reduction of grid current. Various types of electrometer tubes are known with low grid current of $10^{-13}\sim10^{-15}$ A.[1] Although these tubes are favorably used in current amplification, they do not give good performance in voltage amplification.

It was noticed* by one of the authors that one can measure smaller current by a kind of dynamic condenser electrometer than an usual d.c. current amplifier. It was suggested to use a miniature pentode such as 6AK5, because the tube is small and it can hold a better vacuum, and has better insulation between electrodes and high transconductance at lower anode voltage. Later, 3S4 was recommended by Hay[2], who selected this type of tube because of its smaller power consumption and larger power dissipation. The grid current of the order of 10^{-14} A with an amplification factor of 150 was given by Hay, however no information about the grid current characteristics has been reported.

In this paper some precautions in measuring the small grid current and methods to reduce grid current are discribed with experimental verifications.

§ 2. Experimental Procedures

The grid current as small as $10^{-12}\sim10^{-16}$ A can be measured from the rate of drift in the floating grid potential. The circuit diagram of this method is shown in Fig. 1. Though the preliminary experiment was done in an unshielded room, the later observations have been carried out in a well-shielded room.** All the necessary d.c. powers are supplied by well-charged batteries. A suspension type microammeter is used to avoid irregular movement of the needle in measuring the anode current. The tube is suspended in a light-tight shield chamber by thin wires directly soldered to the pins in its base. The grid circuit is switched inside the chamber by a cross contact of a thin wire with another short one soldered on the grid pin of the tube. This switch has negligible capacitance between its electrodes.

All the d.c. supplies must be turned on at

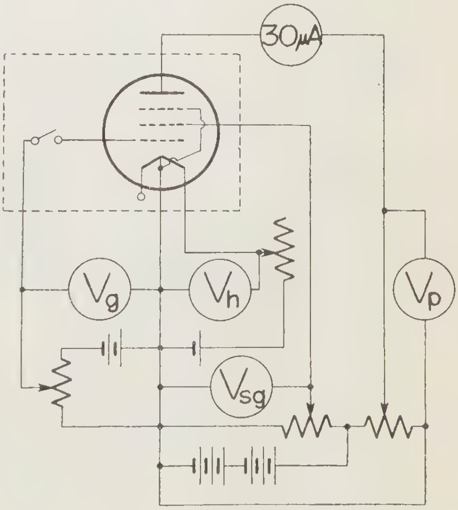

Fig. 1. Circuit diagram.

---

* Koichi Shimoda: Tokyo meeting of Phys. Soc. Japan: April 1949.

** A small room shielded perfectly by copper plates soldered together on walls and floor.

least one hour before starting the measurement. After giving proper negative charge on the grid, the floating grid potential drifts towards the equilibrium potential at a rate determined by the grid current. Anode current is measured with time and plotted as shown in Fig. 2. Since one can know the grid characteristics, I_p-V_g, of the tube at the same operating voltages, grid voltage, V_g, as a function of time is obtained. Thus one can find the grid current, I_g, from the equation

$$I_g=C_{\rm in}\frac{dV_g}{dt}$$

where $C_{\rm in}$ is the total input capacitance. The total input capacitance of the tube under the operating condition is obtained by double measurements with and without a small standard condenser connected between the grid and cathode.

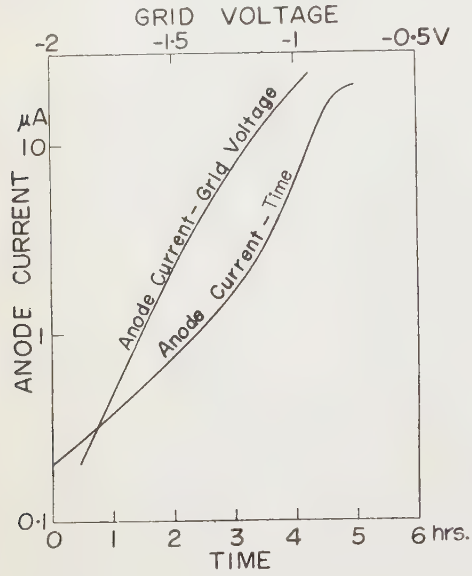

Fig. 2. An example of plotting.

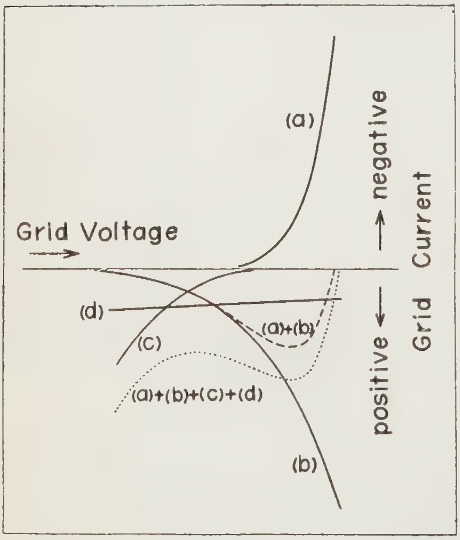

Fig. 3. Types of grid current components.

Tubes have been coated by silicone SC-87 of General Electric Co. Ltd. according to the techniques described in ref. 2.

Grid current consists of various components. They may be classified into four types (a), (b), (c), and (d) as shown in Fig. 3.

The component (a) is the only "negative" component among these four, which is attributed to the flow of electrons from cathode by their thermal energies.

The component (b) is the positive current changing in proportion to the anode current when the other electrode voltages are maintained constant. The lower the anode voltage or screen voltage the smaller this component. This is due to positive ions produced from the residual gas by collisions of electrons and soft X-rays from the anode. Photo-electrons emitted from the grid by soft X-rays also contribute to positive grid current which may be included in (b).

The component (c) is characterized by a rapid increase with negative grid voltage and is proved to be due to positive ions emitted from the cathode.

The component (d) is nearly independent of grid voltage and can be attributed to photo-electrons ejected from the grid as a result of incident light coming from the cathode and outside of the tube. Also leakage current along the surfaces of insulators inside and outside the tube causes such current.

The actual grid current is a resultant of these components, which is illustrated typically by the dotted curve in Fig. 3. Fortunately, positive ions and light emissions from the cathode (the components of type (c) and (d)) are reduced more rapidly than electron emissions by decreasing filament temperature. The other components in type (d) are not inherent in the operation of the tube, and can be eliminated by proper treatments without causing any effect on the operation of the tube. After all, if one get a curve consisting of two components (a) and (b) as shown by the broken curve in Fig. 3, one can not expect the reduction of grid current without considerable loss of gain. Therefore one must look for the optimum anode and screen grid voltage in order to get a compromise between an appreciable voltage gain and the smallest possible grid current.

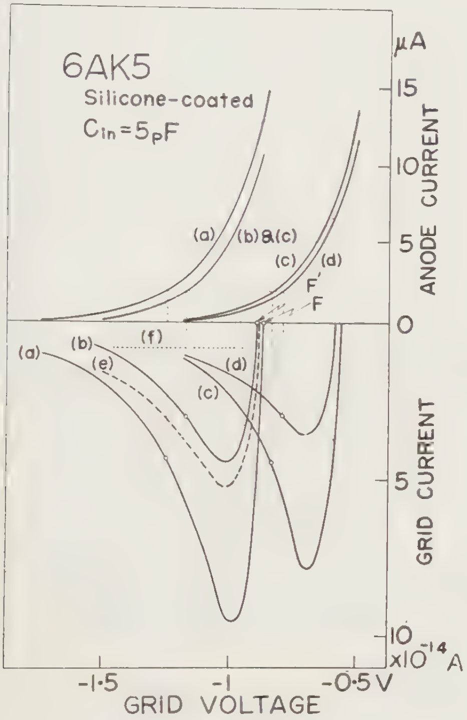

Fig. 4. Grid current and grid characteristics of 6AK5.

(a): $V_h=4\text{V}$, $V_{sg}=42\text{V}=V_p$; $\mu=4000$, $r_p=70\text{M}\Omega$ at F.
(b): $V_h=4\text{V}$, $V_{sg}=42\text{V}$, $V_p=10\text{V}$; $\mu=250$, $r_p=5\text{M}\Omega$ at F′.
(c): $V_h=3\text{V}$, $V_{sg}=43\text{V}=V_p$.
(d): $V_h=3\text{V}$, $V_{sg}=43\text{V}$, $V_p=10\text{V}$·
(e): At the same operating conditions as (b) except in a hunid air (July 13, 1954).
(f): (e)−(b); Leakage current due to humidity.

§ 3. Results of Measurements

Fig. 4 shows the grid current characteristics of a single specimen selected from ten RCA 6AK5's, together with corresponding anode currents. The tube is operated at the filament voltage of one-half or more of the rated value and at the screen grid voltages of about 40 V. The effects of filament voltage and anode voltage upon grid current and anode current are also shown. Comparing points at equal values of anode current, it can be seen that a small change of filament voltage does not cause any appreciable variation of the grid current. However, a decrease in anode voltage results in a sensible reduction of grid current. In order to take precaution against leakage, silica-gel was put in the chamber during all the measurements except in the case (e). The leakage current on the glass surface was found to be less than 10^{-14}A even at high humidity (about 90%), corresponding to a resistance of more than $4\times10^{15}\Omega$ between the grid pin and the anode pin.

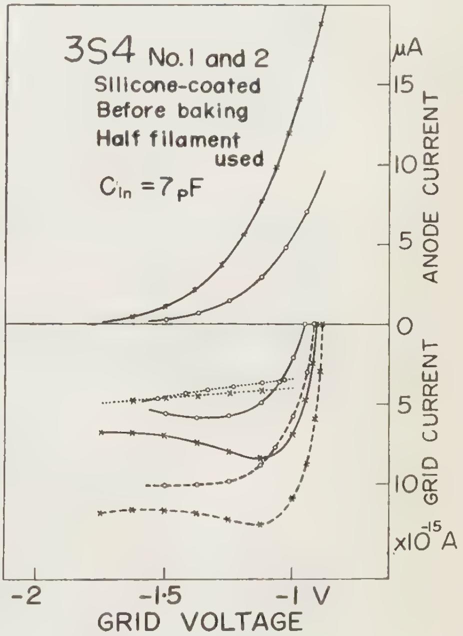

Fig. 5. Grid current and grid characteristics of silicone-coated 3S4 (before baking).

No. 1.

—×—×—×—	$V_h=0.7\text{V}$, $V_{sg}=9.5\text{V}$, $V_p=6\text{V}$.
--×-×-×-	At the same operating conditions. as above except in a humid air (July 23, 1954).
··×··×···×··	Leakage current due to humidity.

No. 2.

—○—○—○—	$V_h=0.7\text{V}$, $V_{sg}=7.5\text{V}$, $V_p=6\text{V}$.
-○-○--○-	At the same operating conditions as above except in a humid air (July 31, 1954).
··○···○···○··	Leakage current due to humidity.

Two 3S4's, No. 1 and No. 2, were silicone-coated and their grid currents were measured in the chamber dried with silica-gel. Not a little component of type (d) appeared in their grid current curves as shown in Fig. 5. The grid current of another specimen (No. 3) which had not been coated, was measured after washing with alcohol and ether, enclosed in the chamber with silica-gel, left for a day and heated with rated filament voltage for

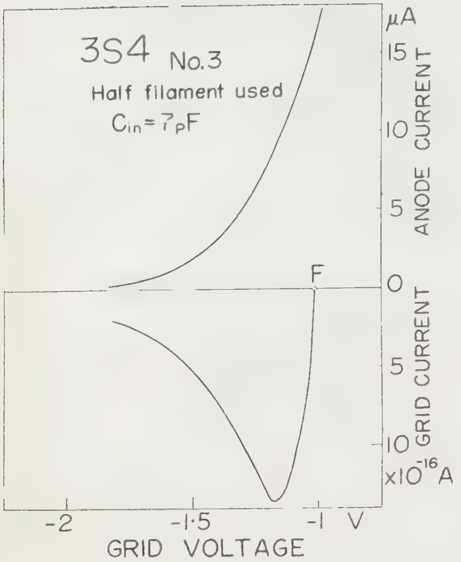

Fig. 6. Grid current and grid characteristics of 3S4 (without coating).
$V_h=0.7$V, $V_{sg}=10.5$V, $V_p=6$V;
$\mu=150$, $r_p=2.5$MΩ at F.

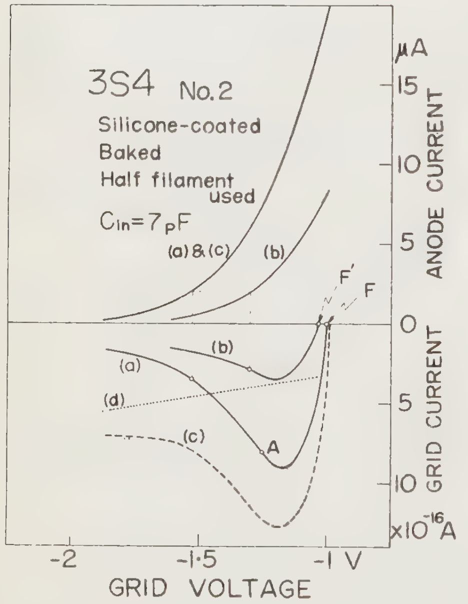

Fig. 7. Grid current and grid characteristics of silicone-coated 3S4 (baked).

(a): $V_h=0.7$V, $V_{sg}=9.5$V, $V_p=6$V;
$\mu=160$, $r_p=2$MΩ at F.

(b): $V_h=0.7$V, $V_{sg}=8.5$V, $V_p=6$V;
$\mu=150$, $r_p=5$MΩ at F'.

(c): At the same conditions as (a) except in a humid air (Oct. 4, 1954).

(d): (c)−(a); Leakage current due to humidity.

several hours. The result is shown in Fig. 6. The grid current of the order of 10^{-15}A has been attained. The curve seems to be an almost typical one, showing that there is no appreciable leakage current. Then the first two 3S4's, No. 1 and No. 2, were baked at 200°C and 170°C respectively, for several hours. No. 1 was damaged, showing evaporation of getter and extinction of thermionic emission. The result for No. 2 is shown in Fig. 7. The grid current of about 1×10^{-15}A or less has been obtained, together with the voltage gain of 20∼40. For example, at point A, grid current is less than 8×10^{-16}A, and the amplification factor of 150 and the plate resistance of 5MΩ give the voltage gain of 35, provided load resistance is taken as 1.5MΩ. It takes several hours for measuring a full curve of grid current of this order, but no effect of variations of supply voltages was experienced. Comparing Fig. 5 and Fig. 7, one can see the change of leakage current by humidity. The resistances between the adjacent pins of 3S4 were measured to be 2×10^{15}Ω in July (humidity=90∼100%) and 2×10^{16}Ω in October (humidity≈50%).

§ Discussions

One may conclude from these examples that it is necessary to bake the tube in the process of silicone-coating as usually recommended. Naturally, silicone-coating does not improve substantially the final result, but it can serve to simplify procedures for avoiding leakage current. Since we have reduced the grid current to as small as 1×10^{-15}A it is necessary to keep leakage current less than the grid current by any means. It is not unreasonable that 3S4's have so small grid currents comparable with those of excellent electrometer tubes, if one takes into account large maximum power dissipation and low filamentary power consumption of the tubes. The tube, 3S4, operates satisfactorily as a voltage amplifier with the anode and screen grid voltage less than 10 volts. It should be particularly noted that the small grid current is obtained without space-charge grid, thus enabling us to get a considerable voltage gain. Perhaps the only defect of this tube is its larger input capacitance of about 7pF. However, the loss of sensitivity by larger capacitance is overcompensated by larger voltage gain. Some residual constant components of grid current are found at the foots of the curves in Figs. 6 and 7. It might be caused by leakage across residual water film, leakage across inner surface or natural leakage. However, little reduction in grid current could be expected by endeavouring to remove these leakages. Further improvements in the effective use of 3S4 or its equivalents as an electrometer might be expected along the following lines.

1. Higher degree of vacuum.
2. Top-cap grid connection.
3. Larger mutual conductance if larger input capacitance is tolerable.

We are now planning to use 3S4 tubes for an electrometer with high sensitivity.

§ 5. Aknowledgement

The authors appreciate the valuable discussions by all members in their laboratory.

References

1) J. Yarwood and D. H. Le Croissette: Electronic Eng. **26** (1954) 14.
2) G. A. Hay: Electronic Eng. **23** (1951) 258.

JOURNAL OF THE PHYSICAL SOCIETY OF JAPAN Vol. 10, No. 5, MAY, 1955

The Direct Current associated with Microwave Gas Discharge between Coaxial Cylinders, IV

By Kenji MITANI

Yoshida College, University of Kyoto

(Received December 1, 1954)

The author has devised a new double probe method to investigate the microwave gas discharge. In this method, the electrodes of the cavity themselves can be used as probes, as he has practiced in the previous papers1)2)3). Brown's theory of the microwave discharge has applied to this method and a good agreement between theory and experiment has been found.

§ 1. Introduction

In the present paper, the author treats the case when a d.c. voltage of several volts is applied to the central wire against the outer cylinder of the coaxial type cavity resonator in which a microwave gas discharge continues. In the previous paper, Part III3), the author has shown that the direct current flowing in the outer circuit should be interpreted as a probe current of the double probe method4), and has been able to determine the electron temperature and the electron density in the discharging space on the basis of the idea originated by Langmuir5)6).

However, being not contented with the treatment of this current on the basis of the said idea, the author has applied Brown's theory7)8), because the direct current in the author's case1)2) is produced by zero applied d.c. voltage in the probe current circuit. Thus, with the intention of deriving the form of the probe current in question from Brown's idea, the author has tried to obtain the electron density from the fundamental equation of the microwave gas discharge when a small d.c. voltage is applied and then the probe current as the difference between the gradients of this electron density at both electrodes. However, in the case of coaxial cavity resonator, to carry out calculation has been found to be very difficult, so the author has performed the calculation for the case of a parallel plate cavity resonator and moreover, as we now have the case of the weak discharge on the grounds as will be discussed later, the space charge effect can be neglected. A good agreement between theory and experimental results has been found.

§ 2. Theory

As shown in Fig. 1, a microwave steady-state weak gas discharge is held between the parallel electrodes G and G' which are mutually electrostatically isolated. To simplify the problem, we assume the gap length L between these electrodes is very small in comparison with side dimensions. In this way, we can treat this problem as one-dimensional. Now we fix the coordinate origine at one electrode G and take z-axis perpendicular to the electrodes. Between these electrodes, a d.c. voltage V, which can be varied in magnitude, is applied independently of the microwave gas discharge and this d.c. potential produces the d.c. electric field $\boldsymbol{E}_{dc}$ in the direction of the z-axis.

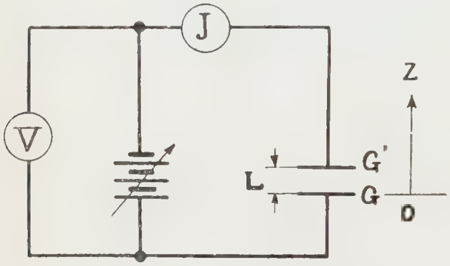

Fig. 1. The basic diagram of the experiment.

The current densities Γ_+ and Γ_-, when a small d.c. field is applied, respectively are to be given as follows,

$$\Gamma_+ = -D_+\frac{dn_+}{dz} + \mu_+ E_{dc} n_+ \,, \tag{1}$$

$$\Gamma_- = -D_-\frac{dn_-}{dz} - \mu_- E_{dc} n_- \,, \tag{2}$$

where D's are the diffusion coefficients, μ's the mobilities and the subscripts $+$ and $-$ refer to the positive ions and the electrons. Combining these equations with the steady-state continuity equation div $\boldsymbol{\Gamma} = \nu n$, we obtain,

$$D_+\frac{d^2n_+}{dz^2} - \mu_+ E_{dc}\frac{dn_+}{dz} + \nu n_- = 0\,, \tag{3}$$

$$D_-\frac{d^2n_-}{dz^2} - \mu_- E_{dc}\frac{dn_-}{dz} + \nu n_- = 0\,, \tag{4}$$

or

$$\frac{d^2n_+}{dz^2} - \frac{\mu^+}{D_+}E_{dc}\frac{dn_+}{dz} + \frac{\nu}{D_+}n_- = 0\,, \tag{5}$$

$$\frac{d^2n_-}{dz^2} + \frac{\mu_-}{D_-}E_{dc}\frac{dn_-}{dz} + \frac{\nu}{D_-}n_- = 0\,, \tag{6}$$

where ν is the volume rate of production of new positive ions and of electrons per an existing electron. (5) and (6) are the desired fundamental equations.

The boundary conditions require the concentrations of positive ions and of electrons to be approximately zero at the surfaces of electrodes. Subject to these conditions, the solution of Eq. (6) becomes:

$$n_- = C\sin\pi\frac{z}{L}\cdot\exp\left(-\frac{\mu_- V}{2D_-}\frac{z}{L}\right), \tag{7}$$

where C is a certain constant and also we have used the relation $V = E_{dc}L$. Furthermore, Eq. (6) gives the following relation:

$$\frac{\nu}{D_-} = \left(\frac{\pi}{L}\right)^2 + \left(\frac{\mu_- E_{dc}}{2D_-}\right)^2. \tag{8}$$

By using (7), Eq. (5) gives the following solution,

$$n_+ = \frac{\nu CL^2}{D_+(\pi^2+a^2)\{\pi^2+(a+b)^2\}}\cdot$$
$$\Big[\{\pi^2 - a(a+b)\}\cdot\sin\pi Z\cdot\exp(-aZ) - \pi(a+b)\cdot$$
$$\Big\{\cos\pi Z\cdot\exp(-aZ) - \frac{1+\exp(-a)}{1-\exp(b)}\exp(bZ)$$
$$+\frac{\exp(-a)+\exp(b)}{1-\exp(b)}\Big\}\Big], \tag{9}$$

where

$$a = \frac{\mu_- V}{2D_-}, \qquad b = \frac{\mu_+ V}{D_+} \tag{10}$$

and

$$Z = \frac{z}{L}\,. \tag{11}$$

The constant C contained in (7) and (9) can be determined as follows. We can consider the total number of electrons between the electrodes G and G′ is approximately constant even if a d.c. potential is applied to them, provided that it is small. Now we denote the number of electrons between the unit areas of both electrodes with N, then N/L gives the mean concentration n_0 of electrons.

Using (7), this number N is given as follows,

$$N = \int_0^L n_- dz = \pi CL\{1+\exp(-a)\}/(\pi^2+a^2). \tag{12}$$

So we get,

$$C = n_0(\pi^2+a^2)/\pi\{1+\exp(-a)\}\,. \tag{13}$$

This relation leads to the following results from (7) and (9):

$$n_- = n_0(\pi^2+a^2)\sin\pi Z\cdot\exp(-aZ)/\pi\{1+\exp(-a)\}\,, \tag{14}$$

and

$$n_+=rn_0\frac{\pi^2+a^2}{\{\pi^2+(a+b)^2\}\{1+\exp(-a)\}}$$
$$\Big[\Big\{\pi-\frac{1}{\pi}a(a+b)\Big\}\cdot\sin\pi Z\cdot\exp(-aZ)-(2a+b)\cdot$$
$$\Big\{\cos\pi Z\cdot\exp(-aZ)-\frac{1+\exp(-a)}{1-\exp(b)}\cdot\exp(bZ)$$
$$+\frac{\exp(-a)+\exp(b)}{1-\exp(b)}\Big\}\Big], \qquad (15)$$

where

$$r\equiv D_-/D_+ \ . \qquad (16)$$

In Eq. (15) we have used the following relation, (see Eq. (8))

$$\frac{\nu L^2}{D_+}=\frac{D_-}{D_+}L^2\frac{\nu}{D_-}=\frac{D_-}{D_+}\Big\{\pi^2+\Big(\frac{\mu_-V}{2D_-}\Big)^2\Big\} \ . \qquad (17)$$

Now, the current J flowing in the outer circuit is related to the current densities Γ_+ and Γ_- as follows,

$$J=Ae[\{(\Gamma_+)_{z=0}+(\Gamma_+)_{z=L}\}$$
$$-\{(\Gamma_-)_{z=0}+(\Gamma_-)_{z=L}\}] \ , \qquad (18)$$

where A is the discharging area and e is the charge of an electron. Also $(\Gamma)_{z=0}$ and $(\Gamma)_{z=L}$ denote respectively the values of Γ at $z=0$ and $z=L$ (i.e. the surfaces of the electrodes G and G′.)

When we calculate respectively the current J_+ by positive ions and the current J_- by electrons from (1) (2) (14) (15) and (18), they have the same form as follows,

$$J_+=J_-=\frac{n_0eAD_-}{L}(\pi^2+a^2)\tanh a \ . \qquad (19)$$

So the total current J becomes

$$J=J_0(\pi^2+a^2)\tanh a \ , \qquad (20)$$

where

$$J_0\equiv 2n_0eAD_-/L \ . \qquad (21)$$

This is the desired theoretical form of the current J in the outer circuit. When the gas pressure and the microwave power are constant, J is to be function of the d.c. voltage V alone. From Eq. (20), we get the following relation:

$$\phi\equiv\frac{dJ}{J}\Big/\frac{dV}{V}$$
$$=x\{8x\tanh x+(\pi^2+4x^2)\,\mathrm{sech}^2x\}/$$
$$(\pi^2+4x^2)\tanh x \ , \qquad (22)$$

where

$$x\equiv\mu_-V/4D_-=a/2 \ . \qquad (23)$$

The curve ϕ in Fig. 2 shows that the current J is linearly proportional to V at first and then gradually to the square of V. Fig. 3 shows the curve of the following equation acquired from (20),

$$y=J/J_0=(\pi^2+4x^2)\tanh x \ . \qquad (24)$$

In this way it is found that the current J corresponds to the probe current in the double probe method but has no saturation as the ordinary probe current[4)6)].

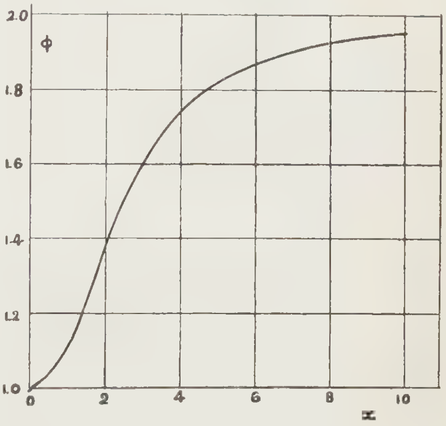

Fig. 2. The curve ϕ as the function of x.

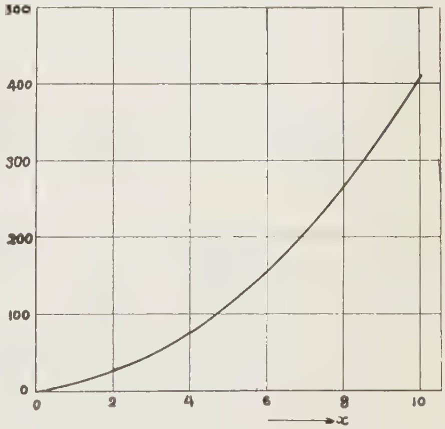

Fig. 3. Characteristic curve of the probe current (24).

§ 3. Experimental Procedure and its Results

As shown in Fig. 4, the discharge tube has two plane electrodes G and G′, whose areas are respectively about 3×10^{-1} cm² and whose gap length L is about 0.1 cm. The used gas was Ar labeled 97% and so it was not purified any further. The wavelength of the microwave power was about 11.5 cm. The discharge tube was connected to the Lecher line coupled to the magnetron of the maximum output power about 200 watts, and it constituted a resonant circuit with the

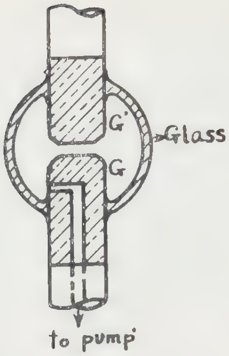

Fig. 4. The cross section of the discharge tube used in this experiment.

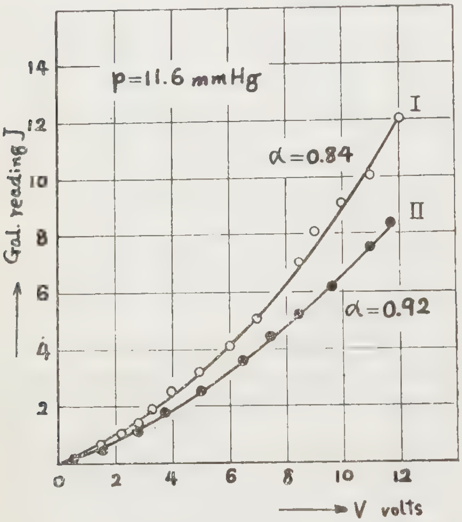

Fig. 5_1. The probe current J for p=11.6 mmHg.
——: Theoretical curves.

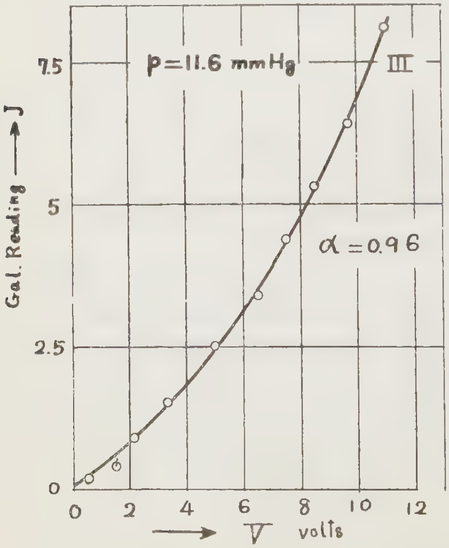

Fig. 5_2. The probe current J for p=11.6 mmHg.
——: Theoretical curves.

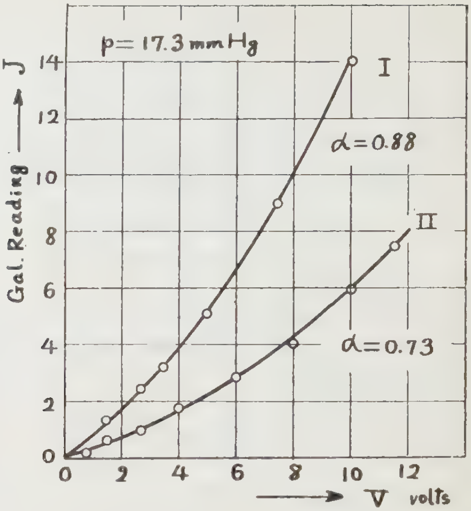

Fig. 6. The probe current J for p=17.3 mmHg.
——: Theoretical curves.

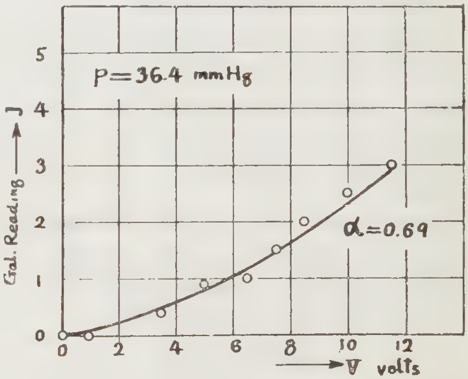

Fig. 7. The probe current J for p=36.4 mmHg.
——: Theoretical curve.

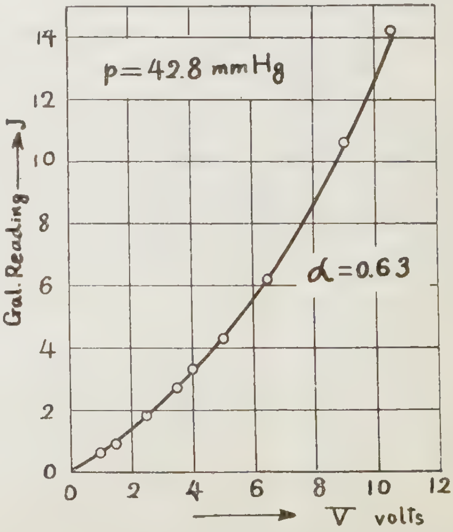

Fig. 8. The probe current J for p=42.6 mmHg.
——; Theoretical curve.

Table I. The values D_-/μ_- and the electron temperatures T_e for the various gas pressures.

p(mmHg)	11.6		17.3		36.4		42.8	
	D_-/μ_-	T°K	D_-/μ_-	T°K	D_-/μ_-	T°K	D_-/μ_-	T°K
D_-/μ_- and T_e	(I) 0.84 (II) 0.92 (III) 0.96	9,800 11,000 11,000	(I) 0.88 (II) 0.73	10,000 8,500	0.69	8,100	0.63	7,400

Table II. The values of J_0 corresponding to the experimental conditions shown in Table I.

p (mmHg)	11.6		17.3		36.4		42.8	
	No.	J_0	No.	J_0	No.	J_0	No.	J_0
	I	0.20	I	0.14	I	0.38	I	0.18
	II	0.17	II	0.24				
	III	0.20						

Lecher wires. In order to apply a d.c. voltage, one electrode G′ of the discharge tube was condenser-coupled to the Lecher lines.

We have measured the current J for the various voltages of the d.c. potential while keeping the discharge state constant. In Figs. 5_1, 5_2, 6, 7 and 8, the signs ○ and ● denote the experimental values obtained in this way and the solid lines the theoretical values; Figs. 5_1 and 5_2 correspond to $p=11.6$ mmHg, Fig. 6 to $p=17.3$ mmHg, Fig. 7 to $p=36.4$ mmHg and Fig. 8 to $p=42.8$ mmHg. These experimental values have very different curves from what may be expected in the case of ordinary glow discharge.

§ 4. Discussions

We name the adjoining values of d.c. voltage in these experiments by V_i and V_{i+1} and the corresponding d.c. currents by J_i and J_{i+1}, and also we set $\Delta V=V_{i+1}-V_i$, and $\Delta J=J_{i+1}-J_i$. Then the values of the function ϕ corresponding to each d.c. potential can be obtained from the experimental data according to the following equation:

$$\phi=\frac{\Delta J}{J_i+\Delta J/2}\bigg/\frac{\Delta V}{V_i+\Delta V/2}\,. \tag{25}$$

From Eqs. (22) and (25), we obtain the values of x and V corresponding to the same values of the function by use of Fig. 2. Then we can get D_-/μ_- from Eq. (23) independently on J_0 or n_0.

Table I shows the values D_-/μ_- obtained in this way. Accordingly, by suitable selection J_0, we can get the semitheoretical values of J from Eq. (20). The solid curves in Figs. 5_1, 5_2, 6, 7, and 8 are obtained in this way and show the very good agreement with experimental values. In these curves α denotes D_-/μ_-.

The values of J_0 are shown in Table II; wherein, their units are arbitrary but their order is about $10^{-6}\sim10^{-7}$A, as the current J has been measured by suitably adjusting the sensibility of the galvanometer whose maximum sensibility is 28×10^{-8}A. Moreover, the values of J_0 are somewhat scattered and it seems to be because the microwave powers are different in each case.

When we assume that the electron possess the Maxwellian energy distribution, D_-/μ_- relates to the electron temperature T_e in the following form:[10)]

$$D_-/\mu_-=kT_e/e\,, \tag{26}$$

where k is Boltzmann's constant. From this equation and the experimental data D_-/μ_- listed in Table I, the electron temperature can be determined. These values are also given in Table I and plotted in Fig. 9. In this figure the value on Ar at $p=1$ mmHg and $\lambda=1.7$ m obtained by Kojima and Takayama[11)] is also plotted for reference. The dependency of the electron temperature on the pressure shown in this figure is almost the same as the curves given by Engel[12)] and others[13)], but as a whole the electron temperatures obtained by us are small. This is thought to be originated from the fact that this discharge is weak.

Here we consider the mean electron concentration n_0. This is to be obtained from Eq. (21). The values of J_0 which are necessary to calculate n_0 are given in Table II. As stated above, the order of these values is about $10^{-6}\sim10^{-7}$A. The discharging area A in (21) may be different in each case and further we could not measure these areas so accurately in our experiments. But we could observe that these areas extended almost over the whole area of the electrode, so we now use the electrode area (3×10^{-1} cm^2) itself as A. The gap length L is about 10^{-1} cm and D_- is about 3×10^5 cm^{2}sec^{-1}. Then we can get $n_0 \doteqdot 10^7$cm^{-3}. This is considered a reasonable value for a weak discharge.

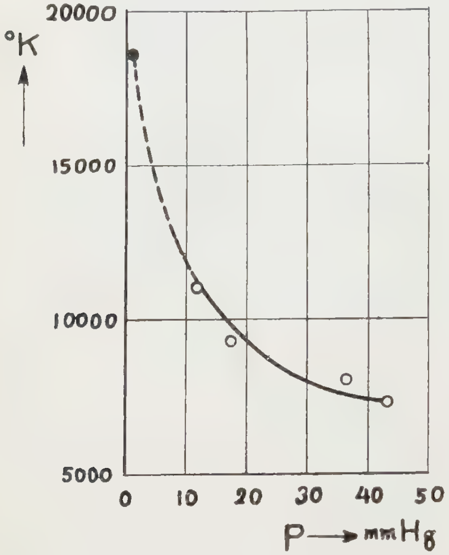

Fig. 9. The electron temperature T_e versus pressure p on Ar.
●: Kojima's value.

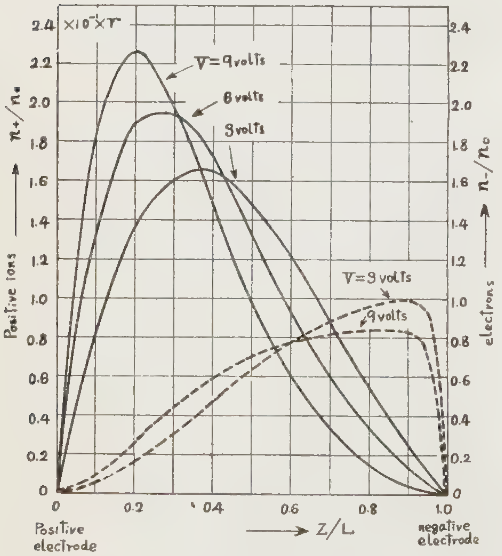

Fig. 10. The spatial distributions of positive ions and of electrons.
---- positive ions, —— electrons.

As mentioned before, the J–V curves obtained in our experiments have had the forms very different from what may be expected in the normal glow discharge. On the other hand, Honda, Takeda, Tamagawa and Kihara[14] have reported in their paper that the weak discharge can occur easily in the high frequency discharge. Following their theory, it can be expected that in the microwave region the discharge of this type can occur more easily.

By developing a theory on these grounds, the author has been able to obtain such J–V curve that fits very good to our experiments and at the same get reasonable values of electron temperature and mean electron concentration.

Finally we consider the spatial distribution of positive ions and electrons. Here we consider the following points: For the Maxwellian energy distribution, D_+/μ_+ has also the following relation

$$D_+/\mu_+ = kT_+/e$$

where T_+ is the positive ion temperature and can be approximately regarded as the room temperature, so we assume $\mu_+/D_+ \doteqdot 40$. And also for convenience we take $\mu_-/D_- \doteqdot 1$ (this corresponds to $T_e = 1.17\times10^4$ °k) which value falls very near the experimental value above mentioned. In this way Eqs. (15) and (14) give the spatial distributions of positive ions and of electrons as shown in Fig. 10. This figure and Eq. (15) show that the positive ion concentration is nearly $r = D_-/D_+$ times as large as the electron concentration.

§ 5. Conclusions

The author has developed the theory of the d.c. current associated with the d.c. potential which is applied between the electrodes of the resonator, one of which is electrostatically isolated when between the electrodes a microwave steady-state gas discharge is held. And we have found that the observed values are in very good agreement with the author's theory and we have been able to determine the electron temperature.

In conclusion, the author gratefully acknowledges his indebtedness to Professor K. Honda of Tokyo University and Professor S. Kojima of Tokyo University of Education for their encouragement and helpful discussions. The author's thanks are also due to Professor I.

Takahashi for his kind suggestion and encouragement.

References

1) K. Mitani: J. Phys. Soc. Japan **7** (1952) 634.
2) K. Mitani: J. Phys. Soc. Japan **7** (1952) 637.
3) K. Mitani: J. Phys. Soc. Japan **8** (1953) 642.
4) E. O. Johnson and L. Malter: Phys. Rev. **80** (1950) 58.
5) Langmuir and Mott-Smith: Phys. Rev. **28** (1928) 727.
6) L. B. Loeb: Fundamental Process of Electrical Discharge in Gases (John Wiley and Sohns, Inc., New York, (1939). first edition,) p. 238.
7) M. A. Herlin and S. C. Brown: Phys. Rev. **74** (1948) 291.
8) M. A. Herlin and S. C. Brown: Phys. Rev. **74** (1948) 910.
9) L. J. Vernelin and S. C. Brown: Phys. Rev. **79** (1950) 946.
10) L. B. Loeb: loc. cit., p. 167.
11) S. Kojima and K. Takayama: Read at the annual meeting of Electrical Soc. Japan on May, 1951.
12) A. V. Engel und M. Steenbeck: Elektrische Gasentladungen. (Julius Springer 1934) II, p. 85.
13) S. Kojima and K. Takayama: J. Phys. Soc. Japan **8** (1953) 55.
14) K. Honda, S. Takeda, H. Tamagawa and T. Kihara: Proc. Phys. Soc. Japan **5** (1950) 75.

JOURNAL OF THE PHYSICAL SOCIETY OF JAPAN Vol. 10, No. 5, MAY, 1955

Rayleigh's Problem for a Cylinder of Arbitrary Shape, II

By Hidenori HASIMOTO

Department of Physics, Faculty of Science, University of Tokyo

(Received December 24, 1954)

Continuing the previous work I (J. Phys. Soc. Japan **9** (1954) 611), the author discusses the frictional force on an arbitrary cylinder which is started to move suddenly from rest with uniform velocity W in the direction of its length. By using the WKB method, a new asymptotic expansion formula in powers of $\sqrt{\nu t}/R$ is derived for the frictional drag τ on the cylinder with no corners;

$$\frac{\tau}{\mu W}=\frac{1}{\sqrt{\pi\nu t}}+\frac{1}{2R}-\frac{\sqrt{\nu t}}{4\sqrt{\pi}R^2}+\frac{\nu t}{8}\left[\frac{1}{R^3}+\frac{\partial^2}{\partial s^2}\left(\frac{1}{R}\right)\right]+O((\nu t)^{3/2})$$

where ν is the kinematic viscosity, t is the time measured from the start, R is the local radius of curvature of the surface measured inwards, and ds is the line element along the surface. The first approximation gives the naturally expected value $\mu W/\sqrt{\pi\nu t}$ for the frictional drag per unit area, which is the same as that for a flat plate of infinite breadth. As far as the second approximation the total frictional drag on the cylinder is the same as that on a circular cylinder with the same perimeter, and is in accord with the results recently obtained by Batchelor. The effect of the variation of the curvature along the surface on the local friction first appears in the fourth order of approximation. The correction due to the presence of corners is made in the second approximation, and some errors in Batchelor's paper are corrected. For the intermediate value of νt the drag calculated by these formulae shows a good agreement with that calculated by the formulae in powers of $(\nu t)^{-1}$ as given in I.

§ 1. Introduction

In a previous paper (J. Phys. Soc. Japan **9** (1954) 611), the author studied the motion of an incompressible viscous fluid generated by a cylinder of arbitrary cross-sectional form which is started to move suddenly from rest with uniform velocity W in the direction of its length, assuming $a^2/(\nu t)$ to be small, where

a is the characteristic length of the cross-section, ν is the kinematic viscosity, and t is the time measured from the instant of start.

Thus, the asymptotic solution in powers of $a^2/(\nu t)$ was obtained correct to the order of $a^2/(\nu t)$ (the second approximation).

Now, it will be natural to expect that the solution will give a smooth matching with the solution valid when $a^2/\nu t \gg 1$. Indeed this was verified clearly in the case of a flat plate of finite breadth[4], and to some extent in the other cases[5]. In view of the importance of the effect of the curvature as well as of the edges and corners of the surface of the cylinder, the author has studied a new asymptotic expansion formula in powers of $\sqrt{\nu t}/R$, correct to the order of νt (the fourth approximation), assuming $\sqrt{\nu t}/R$ to be small and using the WKB method, where R is the local radius of curvature of the surface.

After the completion of the work, the author became aware that the same problem had been treated by Batchelor[1]. Although his results are in accord with the author's, his methods of derivation, which depend greatly on the physical intuition, are different from the author's. Moreover he gives only the first approximation correct to the order $\mathbf{O}(1)$ for the case when $a^2/(\nu t)$ is small, and the second approximation correct to the order $\mathbf{O}(1)$ for the case when $\sqrt{\nu t}$ is small. Thus the matching of these two separated regions does not seem to be very good.

In the same paper, Batchelor discussed the effect of the existence of corners in the cylinder cross-section when $\sqrt{\nu t}$ is small, on the basis of the corner correction formula for a corner of exterior angle $\pi+\alpha$, namely:

$$\mu W\overline{K}(\alpha)=E(\pi+\alpha), \tag{1.1}$$

which had been calculated by the author[3] and Sowerby[9][10] and Cooke[10]. He pointed out a peculiar result that the total friction for a regular polygon with N corners does not give the drag appropriate to a circular cylinder as $N\to\infty$, which contradicts our common view.

Further, his result for the skin friction on a flat plate of finite breadth, (Eq. (21) and Fig. 2) does not agree with the result obtained by the author[4] a few years ago, which gives a smooth matching with the values for $a^2 \ll \nu t$ even in the intermediate region.

The origin of this discrepancy seems to lie in his erroneous treatment of the corner correction. From the derivation, it is obvious that E represents the excess of the skin friction for one side of an angle. When the total friction is discussed, it must be multiplied by 2 taking into account the presence of two sides for one corner. In Batchelor's paper this is not taken into account.

In this paper the author derives the general formula for the frictional drag on the cylinder of arbitrary cross-sectional shape with no corners, correct to the fourth approximation, assuming $\sqrt{\nu t}$ to be small. The WKB method is used for its derivation. The author believes that the present problem is an interesting example of the application of this powerful method. The correction due to the presence of corners is made in the second approximation, by use of the values of corner correction previously obtained by the author[3]. The drag calculated by these formulae shows a good agreement with that calculated by the formulae in powers of $a^2/(\nu t)$ in I, for the intermediate values of $a^2/(\nu t)$. It is confirmed that the total friction for a regular polygon with N corners tends to the value for a circular cylinder as $N\to\infty$.

§ 2. Fundamental Equations

The equations of motion and continuity possess a solution for which the velocity components parallel to the x- and y-axes vanish everywhere, provided that w, the velocity component parallel to the z-axis, can be found as a function of x and y satisfying the equation:

$$w_t=\nu \Delta w=\nu(w_{xx}+w_{yy}) , \tag{2.1}$$

subject to the initial condition:

$$\psi=w/W=0 \quad \text{when} \quad t=0 , \tag{2.2}$$

and the boundary condition (when $t>0$):

$$\psi=w/W \begin{cases} =1 \text{ at the surface of the cylinder: S,} & (2.3) \\ \to 0 \text{ as } x^2+y^2\to\infty. & (2.4) \end{cases}$$

Multiplying (2.1) by e^{-pt}, integrating with respect to t from 0 to ∞, and using (2.2) we obtain

$$(\Delta-k^2)\psi^*=0 , \tag{2.5}$$

where ψ^* is the Laplace transform of ψ, so that

$$\psi^*(x, y, p)=\int_0^\infty \psi(x, y, t)e^{-pt}dt , \tag{2.6}$$

and

$$k^2 = p/\nu \quad (\mathbf{Re}\ p > 0). \tag{2.7}$$

From (2.3) and (2.4) it follows that the boundary conditions on the function ψ^* are

$$\psi^* = 1/p \text{ on S}, \tag{2.8}$$

$$\psi^* \to 0 \quad \text{as } x^2+y^2 \to \infty. \tag{2.9}$$

On account of the relation (2.7), the solution of (2.5) when $|k| \to \infty$ $(0 < |\arg k| < \pi/2)$ will be investigated. For this purpose, since it is not permitted to neglect $\Delta\psi^*$, we shall adopt the WKB technique[8]. Thus, putting

$$\psi^* = (1/p) \exp\{k\phi(x, y)\} \tag{2.10}$$

in (2.5) we obtain

$$k^2(\operatorname{grad}\phi)^2 + k\Delta\phi - k^2 = 0. \tag{2.11}$$

As will be seen later the second term may be neglected compared with the first term, if $|k|R$ is large and if there is no corner on S, where R is the local radius of curvature of S. Thus, (2.11) reduces to

$$(\operatorname{grad}\phi)^2 = 1, \tag{2.12}$$

while the boundary conditions (2.8) and (2.9) become respectively

$$\phi = 0 \quad \text{on S}, \tag{2.13}$$

and

$$\partial\phi/\partial n = \phi_n < 0 \quad \text{on S}, \tag{2.14}$$

where n denotes the outward normal to S. The condition (2.14) exactly reflects the boundary layer nature of the problem. For when $\sqrt{\nu t}$ is small, the thickness of the region in which ψ is not small, compared with unity is so small that in the vicinity of the surface ψ rapidly tends to zero, and hence ϕ shall be negative there. This immediately gives (2.14).

From (2.12)—(2.14) we obtain

$$\bar{\phi}_n = \left(\frac{\partial\phi}{\partial n}\right)_{\text{surface}} = -1, \tag{2.15}$$

and

$$\phi = -n, \tag{2.16}$$

in the vicinity of the cylinder, where $\bar{\phi}_n$ denotes the value of ϕ_n on the surface.

The quantity of the greatest practical interest is the frictional force per unit area on the surface, τ. Its Laplace transform is given by

$$\tau = -\mu\bar{w}_n^* = (\mu W/p)k \exp(k\bar{\phi}) = \mu W/\sqrt{\nu p}\,. \tag{2.17}$$

Hence, by use of the formula for the inverse Laplace transform

$$L^{-1}[p^{-1/2}] = 1/\sqrt{\pi t}\,, \tag{2.18}$$

we have

$$\tau = \mu W/\sqrt{\pi\nu t}\,. \tag{2.19}$$

This is the value given by Rayleigh for a plate of infinite breadth, which is what we should have expected when the thickness of the boundary layer is small compared with the radius of curvature R of S.

Further, the velocity distribution near the cylinder is obtained as

$$\begin{aligned} w/W = \psi = L^{-1}[\psi^*] &= L^{-1}[(1/p)\,e^{-kn}] \\ &= 1 - \operatorname{erf}(n/2\sqrt{\nu t})\,, \end{aligned} \tag{2.20}$$

which is also appropriate to a flat plate of infinite breadth; and the normal derivative of (2.20) at S again gives (2.19).

Higher approximations may be obtained by expanding ϕ in the form:

$$\phi = \sum_{m=0}^{\infty} k^{-m}\phi_m\,. \tag{2.21}$$

Introducing this into (2.11) and equating the same powers of k it is found that

$$(\operatorname{grad}\phi_0)^2 = 1, \tag{2.22}$$

$$(\operatorname{grad}\phi_0\cdot\operatorname{grad}\phi_1) = -\tfrac{1}{2}\Delta\phi_0, \tag{2.23}$$

$$(\operatorname{grad}\phi_0\cdot\operatorname{grad}\phi_2) = -\tfrac{1}{2}[\Delta\phi_1 + (\operatorname{grad}\phi_1)^2], \tag{2.24}$$

$$\cdots\cdots$$

$$\begin{aligned} (\operatorname{grad}\phi_0\cdot\operatorname{grad}\phi_m) = -\tfrac{1}{2}[&\Delta\phi_{m-1} \\ &+ \sum_{j=1}^{m}(\operatorname{grad}\phi_j\cdot\operatorname{grad}\phi_{m-j})], \end{aligned} \tag{2.25}$$

$$\cdots\cdots$$

§ 3. Orthogonal Curvilinear Coordinates and the Solution at the Surface of the Cylinder

To solve (2.22) etc., it will be convenient to introduce an orthogonal curvilinear coordinate system (ξ, η), where the line element of length dl is given, as shown in Fig. 1, by

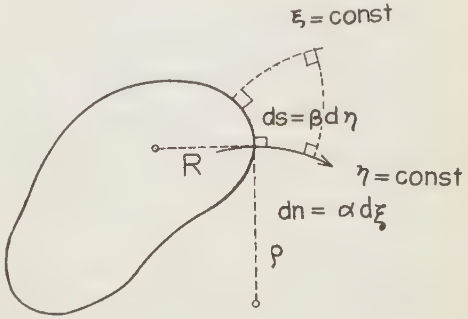

Fig. 1.

$$dl^2=\alpha^2 d\xi^2+\beta^2 d\eta^2=dn^2+ds^2 \quad (\alpha,\beta>0). \tag{3.1}$$

Let the line elements on the n-curves ($\eta=$const) and the s-curves ($\xi=$const) be denoted by $dn=\alpha d\xi$ and $ds=\beta d\eta$, respectively. For this coordinate system, all the n-curves are normal to the boundary of the cylinder cross-section, which corresponds to a particular s-curve $\xi=\xi_0$.

Now we have

$$\partial/\partial n=\partial/(\alpha\partial\xi)\,, \quad \partial/\partial s=\partial/(\beta\partial\eta)\,, \tag{3.2}$$

$$(\text{grad}\,\phi_i\cdot\text{grad}\,\phi_j)=(1/\alpha\beta)(\phi_{i\xi}\phi_{j\xi}+\phi_{i\eta}\phi_{j\eta})$$
$$=\phi_{in}\phi_{jn}+\phi_{is}\phi_{js}\,, \tag{3.3}$$

$$\Delta\phi=\frac{1}{\alpha\beta}\left\{\frac{\partial}{\partial\xi}\left(\frac{\beta}{\alpha}\frac{\partial\phi}{\partial\xi}\right)+\frac{\partial}{\partial\eta}\left(\frac{\alpha}{\beta}\frac{\partial\phi}{\partial\eta}\right)\right\}$$
$$=\phi_{nn}+\kappa\phi_n+\phi_{ss}+\lambda\phi_s\,, \tag{3.4}$$

where κ and λ are respectively the curvatures of the curves $\xi=$const, and $\eta=$const. κ, λ and the corresponding radii of curvatures R, ρ are given by[7)]

$$\kappa=1/R=(1/\alpha\beta)\beta_\xi, \quad \lambda=1/\rho=(1/\alpha\beta)\alpha_\eta\,, \tag{3.5}$$

and we have the relation:

$$\kappa_n+\lambda_s=-\kappa^2-\lambda^2\,. \tag{3.6}$$

Here it should be noted that the operations $\partial_n=\partial/\partial n$ and $\partial_s=\partial/\partial s$ are not commutative and satisfy the following commutation rule derived from (3.2) and (3.5):

$$\phi_{sn}-\phi_{ns}=\partial_n\phi_s-\partial_s\phi_n=-\kappa\phi_s+\lambda\phi_n\,, \tag{3.7}$$

or

$$[\partial_n,\,\partial_s]=-\kappa\partial_s+\lambda\partial_n\,. \tag{3.7$'$}$$

Now we have

$$\tau^*=-\mu\overline{w}_n{}^*=-\mu W(k/p)\overline{\phi}_n{}^*$$
$$=-\mu W\sum_{j=0}^{\infty}\nu^{(j-1)/2}p^{-(j+1)/2}\overline{\phi}_{jn}{}^*. \tag{3.8}$$

Hence

$$\tau=-\mu W\sum_{j=0}^{\infty}\frac{(\nu t)^{(j-1)/2}}{\Gamma\{(j+1)/2\}}\left(\frac{\partial\phi_j}{\partial n}\right), \tag{3.9}$$

where use has been made of the formula:

$$L^{-1}[p^{-q}]=t^{q-1}/\Gamma(q) \qquad (q>0)\,. \tag{3.10}$$

$\overline{\phi}_{jn}$ can be easily obtained by noting the relation:

$$\overline{\phi}_j=0 \quad \text{or} \quad \overline{\phi}_{js}=0\,, \tag{3.11}$$

as derived from (2.13).

Thus for the first approximation we have from (2.22)

$$\phi_{0n}{}^2+\phi_{js}{}^2=1\,. \tag{3.12}$$

On account of (3.11) and (2.14), $\overline{\phi}_{0n}$ is given by

$$\overline{\phi}_{0n}=(\partial\phi_0/\partial n)_{\text{surface}}=-1\,. \tag{3.13}$$

This is the result already obtained in § 2.

Differentiating (3.12) with respect to n we obtain

$$\phi_{0n}\phi_{0nn}+\phi_{0s}\phi_{0sn}=0\,, \tag{3.14}$$

which gives, on introducing (3.11) and (3.13) into (3.14),

$$\overline{\phi}_{0nn}=0\,. \tag{3.15}$$

By (3.7) and (3.13), we have

$$\overline{\phi}_{0sn}=\overline{\phi}_{0ns}-\kappa\overline{\phi}_{0s}+\lambda\overline{\phi}_{0n}=-\lambda\,. \tag{3.16}$$

Successive applications of commutation rule (3.17), as well as (3.13), (3.15) and (3.16) give

$$\overline{\phi}_{0nsn}=0\,, \tag{3.17}$$

$$\overline{\phi}_{0snn}=\kappa\lambda-\lambda_n\,, \tag{3.18}$$

$$\overline{\phi}_{0ssn}=-\lambda^2-\lambda_s\,, \tag{3.19}$$

$$\phi_{0snsn}=\kappa\lambda^2+\kappa\lambda_s+\kappa_s\lambda-\lambda_{sn}\,, \tag{3.20}$$

$$\phi_{0ssnn}=3\kappa\lambda^2+2\kappa\lambda_s+\kappa_s\lambda-2\lambda\lambda_n-\lambda_{sn}\,. \tag{3.21}$$

Differentiating (3.14) with respect to n once or twice, and using (3.13)—(3.19) we obtain

$$\phi_{0nnn}=\lambda^2\,, \tag{3.22}$$

$$\phi_{0nnnn}=-3\kappa\lambda^2+3\lambda\lambda_n\,. \tag{3.23}$$

These formulae are useful in the derivation of the higher approximations.

§ 4. The Second Approximation

From (2.23), (3.3) and (3.4) the equation for ϕ_1 is expressed as follows:

$$\phi_{0n}\phi_{1n}+\phi_{0s}\phi_{1s}=-\tfrac{1}{2}[\phi_{0nn}+\kappa\phi_{0n}+\phi_{0ss}+\lambda\phi_{0s}]\,, \tag{4.1}$$

which gives, on account of (3.11), (3.13) and (3.15),

$$\overline{\phi}_{1n}=-\frac{1}{2}\kappa=-\frac{1}{2}\frac{1}{R}\,. \tag{4.2}$$

Introducing (4.2) and (3.13) into (3.9) we obtain the second approximation to τ:

$$\tau/\mu W=1/\sqrt{\pi\nu t}=1/2R\,. \tag{4.3}$$

This is the same as the friction on the circular cylinder of radius R as far as the second approximation and is in accord with Batchelor's result.

The total friction D on unit length of an arbitrary cylinder without sharp corners is obtained by integrating (4.3) over the boundary S

$$D=\oint\tau ds=\mu W\left[\frac{L}{\sqrt{\pi\nu t}}+\frac{1}{2}\oint\frac{d\theta}{ds}ds\right]$$
$$=\mu W\left[\frac{L}{\sqrt{\pi\nu t}}+\pi\right], \tag{4.4}$$

where L is the perimeter, and $d\theta$ is the angle between the adjacent tangents of S. This is the same as the drag on a circular cylinder of radius $L/(2\pi)$, and consequently the frictional drag on any arbitrary cylinder is the same irrespective of the cross-sectional form, if the perimeter is the same and $R/\sqrt{\nu t}$ is uniformly large. This too is in accord with Batchelor's result.

Next, using (4.2) and (3.7′) we obtain

$$\overline{\phi}_{1sn}=-\tfrac{1}{2}\kappa_s-\tfrac{1}{2}\kappa\lambda\ , \tag{4.5}$$

$$\overline{\phi}_{1ssn}=-\tfrac{1}{2}\kappa_{ss}-\kappa_s\lambda-\tfrac{1}{2}\kappa\lambda_s-\tfrac{1}{2}\kappa\lambda^2. \tag{4.6}$$

Also, differentiation of (4.1) with respect to n gives easily

$$\overline{\phi}_{1nn}=\tfrac{1}{2}\kappa^2, \tag{4.7}$$

$$\overline{\phi}_{1nnn}=-\kappa^3+\tfrac{1}{2}\kappa\lambda^2+\tfrac{3}{2}\kappa_s\lambda\ , \tag{4.8}$$

where use has been made of the relation (3.6) and its normal derivative:

$$\kappa_{nn}+\lambda_{sn}=-2\kappa\kappa_n-2\lambda\lambda_n\ . \tag{4.9}$$

§ 5. The Third Approximation

From (2.24), (3.3) and (3.4) the equation for ϕ_2 is expressed as:

$$\phi_{0n}\phi_{2n}+\phi_{0s}\phi_{2s}=-\tfrac{1}{2}[\phi_{1nn}+\kappa\phi_{1n}+\phi_{1ss}+\lambda\phi_{1s}+\phi_{1n}{}^2+\phi_{1s}{}^2]\ , \tag{5.1}$$

which gives

$$\overline{\phi}_{2n}=\tfrac{1}{2}[\overline{\phi}_{1nn}+\kappa\overline{\phi}_{1n}+\overline{\phi}_{1n}{}^2]\ . \tag{5.2}$$

Substituting for $\overline{\phi}_{1n}$ and $\overline{\phi}_{1nn}$ the values given by (4.2) and (4.7) respectively, we obtain

$$\overline{\phi}_{2n}=\frac{1}{8}\kappa^2=\frac{1}{8}\frac{1}{R^2}\ . \tag{5.3}$$

Thus, (3.9) becomes

$$\frac{\tau}{\mu W}=\frac{1}{\sqrt{\pi\nu t}}+\frac{1}{2R}-\frac{\sqrt{\nu t}}{4\sqrt{\pi}}\frac{1}{R^2}\ . \tag{5.4}$$

As far as the third approximation $\tau/(\mu W)$ is determined by the local radius of curvature R, and is the same as the friction on a circular cylinder of radius R. This result seems to be rather surprising.

§ 6. The Fourth Approximation

Let us proceed to the fourth approximation. From (2.25), (3.3) and (3.4) the equation for ϕ_3 is given by

$$\phi_{0n}\phi_{3n}+\phi_{0s}\phi_{3s}=-\tfrac{1}{2}[\phi_{2nn}+\kappa\phi_{2n}+\phi_{2ss}+\lambda\phi_{2s}+2\phi_{1n}\phi_{2n}+2\phi_{1s}\phi_{2s}]\ . \tag{6.1}$$

Taking account of (3.11), (3.13) and (5.3), we obtain from (6.1)

$$\overline{\phi}_{3n}=\tfrac{1}{2}\overline{\phi}_{2nn}\ . \tag{6.2}$$

Differentiating (5.1) with respect to n we obtain easily

$$\overline{\phi}_{2nn}=-\tfrac{1}{4}(\kappa^3+\kappa_{ss})\ , \tag{6.3}$$

where we have used (4.2)—(4.8) and (3.6).

Introducing (6.3) into (6.2) we have

$$\overline{\phi}_{3n}=-\frac{1}{8}(\kappa^3+\kappa_{ss})=-\frac{1}{8}\left[\frac{1}{R^3}+\frac{\partial^2}{\partial s^2}\left(\frac{1}{R}\right)\right]. \tag{6.4}$$

Substituting (6.4) in (3.9) and remembering (5.4) we find

$$\frac{\tau}{\mu W}=\frac{1}{\sqrt{\pi\nu t}}+\frac{1}{2R}-\frac{\sqrt{\nu t}}{4\sqrt{\pi}}\frac{1}{R^2}+\frac{\nu t}{8}\left[\frac{1}{R^3}+\frac{\partial^2}{\partial s^2}\left(\frac{1}{R}\right)\right]+O((\nu t)^{3/2})\ . \tag{6.5}$$

This shows a very interesting result that the total frictional force is perfectly determined by the value of the local radius of curvature as far as the order of $O(\sqrt{\nu t})$, and that the effect of the variation of the curvature along the surface first appears in the fourth approximation. When there is no corner or abrupt change of curvature along the cylinder cross-section so that $R/\sqrt{\nu t}$ is uniformly large, (6.5) will provide a good approximation to the truth. Thus, in order that (6.5) may be uniformly valid throughout the whole surface, it will be necessary that R should be of the same order of magnitude throughout the whole surface. We may also note that the last term of (6.5) contributes nothing to the total frictional force;

$$\oint\frac{\partial^2}{\partial s^2}\frac{1}{R}\,ds=0\ . \tag{6.6}$$

Thus, the total frictional drag on unit length of the cylinder is given by

$$\frac{D}{\mu W}=\frac{L}{\sqrt{\pi\nu t}}+\pi-\frac{\sqrt{\nu t}}{4\sqrt{\pi}}\oint\frac{ds}{R^2}+\frac{\nu t}{8}\oint\frac{ds}{R^3}+\cdots, \tag{6.7}$$

where we have used (4.4), (6.5) and (6.6).

§ 7. Correction due to the Presence of Corners

In the vicinity of the corner where R is zero or small compared with $\sqrt{\nu t}$ (6.5) ceases to be a valid approximation to the truth. If $\sqrt{\nu t}$ is so small that the influence of the corner is limited to a region over a distance of order $\sqrt{\nu t}$, the above analysis will apply to the region not near the corner, and the region near the corner may be treated as if it were one of a bent flat plate. In particular the excess of the total friction per unit length of the cylinder, due to a corner of exterior angle $\pi+\alpha$, over that for one side of a plate treated as though there were no corner, is given by

$$\mu W\overline{K}(\alpha)=E(\pi+\alpha)=\int_0^\infty\left(\tau-\frac{\mu W}{\sqrt{\pi\nu t}}\right)ds\,, \tag{7.1}$$

for one side of an angle. The values of $\overline{K}$ or E have been calculated by the author[3], and Sowerby[9)10)] and Cooke[10)], and are shown in Fig. 2. If the boundary of the cross-section is constituted only of N straight line segments of length $L_j \gg \sqrt{\nu t}$, we can write down the total frictional drag per unit length of the cylinder as

$$\frac{D}{\mu W}=\frac{1}{\sqrt{\pi\nu t}}\sum_{j=1}^{N}L_j+2\sum_{j=1}^{N}\overline{K}(\alpha_{j,j+1})$$

$$(\alpha_{N,N+1}=\alpha_{N,1})\,, \tag{7.2}$$

to the order of $(\sqrt{\nu t}/L_j)^0$. The first term corresponds to the uniform drag for a flat plate of infinite breadth, and the second term is the excess due to the presence of the corners, the factor 2 being due to the presence of two sides for each corner. In Batchelor's paper this point seems to be overlooked.

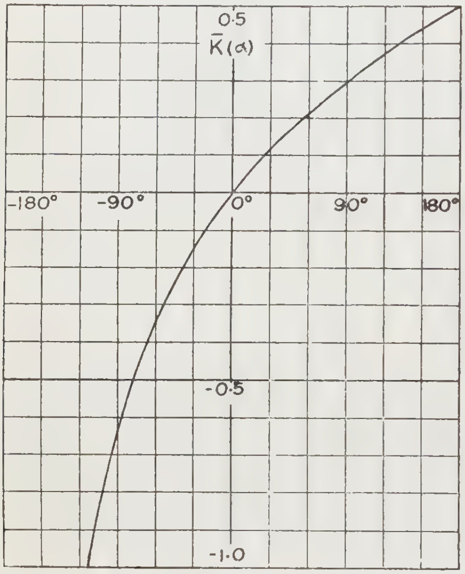

Fig. 2.

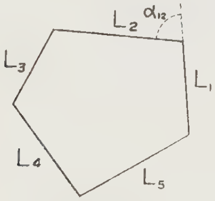

Fig. 3.

For a regular polygon with N corners, we have $\alpha_{j,j+1}=2\pi/N$, so that

$$2\sum_{j=1}^{N}\overline{K}(\alpha_{j,j+1})=2N\overline{K}(2\pi/N)\,. \tag{7.3}$$

This takes a minimum value 2 for $N=2$ (a flat plate) and the total frictional drag for a flat plate of width $2\pi l$ to the order of $(l/\sqrt{\nu t})^0$ is

$$\frac{D}{2\pi l}=\frac{\mu W}{l}\left[\frac{l}{\sqrt{\pi\nu t}}+\frac{1}{\pi}\right]. \tag{7.4}$$

This is in accord with the result of the previous paper[4)] for a plate of finite breadth.

The value of (7.4) increases with N and the limiting value for $N\to\infty$ is obtained as follows. According to the author's paper[3)]

$$\overline{K}(\alpha)=-\frac{2}{\pi}+\frac{8\beta K}{\pi^2}\sin\frac{\beta\pi}{2}$$

when $\qquad \pi+\alpha>\pi/2\,, \qquad (7.5)$

where

$$\beta=\frac{\pi}{\pi+\alpha}\,,\qquad K=\int_0^\infty\frac{u\,\mathrm{tgh}\,u\cosh\beta u}{\cosh 2\beta u-\cos\beta\pi}\,du\,,$$

and

$$K_{\beta=1}=\pi/4,\qquad \overline{K}(0)=0\,.$$

From (7.5) we have for $\alpha\sim 0$

$$\overline{K}(\alpha)\sim\alpha\left(\frac{d\overline{K}}{d\alpha}\right)_{\alpha=0}=\alpha\left(\frac{d\beta}{d\alpha}\right)_{\alpha=0}\left(\frac{d\overline{K}}{d\beta}\right)_{\beta=1}$$
$$=-\frac{8\alpha}{\pi^3}\left[K_{\beta=1}-\frac{1}{2}\int\frac{u^2\sinh^2 u}{\cosh^3 u}\,du\right]. \tag{7.6}$$

The infinite integral in the bracket is easily evaluated by taking the integration path $-\infty\to+\infty$ and $\pi i-\infty\to\pi i+\infty$, as

$$4\int_0^\infty\frac{u^2\sinh^2 u}{\cosh^3 u}\,du=2\pi i\,\mathbf{Res.}\left[\frac{u^2\sinh^2 u}{\cosh^3 u}+\frac{\pi^2}{2}\frac{\sinh^2 u}{\cosh^3 u}\right]_{u=(\pi/2)i}$$
$$=2\pi i\left[-\frac{\pi^2}{4i}\left(\frac{1}{2}-\frac{4}{\pi^2}\right)+\frac{\pi^2}{2}\cdot\frac{1}{2i}\right]=\frac{\pi^3}{4}+2\pi\,. \tag{7.7}$$

Substituting (7.7) into (7.6) we obtain

$$\overline{K}(\alpha)=\alpha/4+O(\alpha^2). \tag{7.8}$$

Hence (7.3) becomes as $N=2\pi/\alpha\to\infty$

$$\lim_{\alpha\to 0} 2\times\frac{2\pi}{\alpha}\left[\frac{\alpha}{4}+\mathrm{O}(\alpha^2)\right]=\pi\,, \tag{7.9}$$

which is the value appropriate to a circular cylinder, as should be expected. It might be thought that when N tends to ∞, adjacent corners would be within a distance of order $\sqrt{\nu t}$ from each other. This indeed was Batchelor's opinion. However, it can be shown that this distance must be multiplied by a factor which tends to 0 when $\alpha\to 0$ and tends to ∞ when $\alpha\to -\pi$.

The case when corners are separated by smooth curves with length of $\sqrt{\nu t}$ or more and curvature of order $1/R\sim 1/\sqrt{\nu t}$ or less can be treated by the same reasoning as Batchelor's. The curvature correction must be added to (7.2), which is found from (4.3) and (4.4) as:

$$\mu W\sum_{j=1}^{\infty}\int_j^{j+1}\frac{1}{2}\frac{d\theta}{ds}ds=\frac{\mu W}{2}\left(2\pi-\sum_{j=1}^{N}\alpha_{j,j+1}\right). \tag{7.10}$$

The total frictional drag D per unit length of the cylinder to the order of $(\sqrt{\nu t}/L_j)^0$ is then

$$\frac{D}{\mu W}=\frac{L}{\sqrt{\pi\nu t}}+\pi+2\sum_{j=1}^{N}\left[K(\alpha_{j,j+1})-\tfrac{1}{4}\alpha_{j,j+1}\right], \tag{7.11}$$

where L is the perimeter.

§ 8. Numerical Example. Elliptic Cylinder

As an illustrative example, let us consider the case of an elliptic cylinder treated in I:

$$x=a(1+\sigma^2)\cos\theta,\quad y=a(1-\sigma^2)\sin\theta, \tag{8.1}$$

whose major and minor axes are respectively $2a(1+\sigma^2)$ and $2a(1-\sigma^2)$. Its perimeter L and radius of curvature R are given by

$$L=4a\int_0^{\pi/2}\Theta^{1/2}d\theta=4a(1+\sigma^2)\boldsymbol{E}\left(\frac{2\sigma}{1+\sigma^2}\right), \tag{8.2}$$

and

$$R=a\Theta^{3/2}/(1-\sigma^4)\,, \tag{8.3}$$

where

$$\Theta=1-2\sigma^2\cos 2\theta+\sigma^4\,, \tag{8.4}$$

and $\boldsymbol{E}$ is the complete elliptic integral of the second kind.

Introducing these expression into (6.5) and (6.7) we obtain

$$\frac{a\tau}{\mu W}=\frac{a}{\sqrt{\pi\nu t}}+\frac{(1-\sigma^4)}{2\Theta^{3/2}}-\frac{(1-\sigma^4)^2}{4\sqrt{\pi}\,\Theta^3}\frac{\sqrt{\nu t}}{a}$$
$$+\frac{(1-\sigma^4)^3}{8\Theta^{9/2}}\frac{\nu t}{a^2}[1+12\sigma^2(1-\sigma^4)$$
$$\times\{4\sigma^2-(1+\sigma^4)\cos 2\theta-2\sigma^2\cos 4\theta\}]$$
$$+\mathrm{O}\left(\frac{\sqrt{\nu t}}{a}\right)^3, \tag{8.5}$$

and

$$\frac{D}{2\pi\mu W}=\frac{\overline{L}}{\sqrt{\pi\nu t}}+\frac{1}{2}-\frac{\overline{G}_2}{4\sqrt{\pi}}\frac{\sqrt{\nu t}}{a}$$
$$+\frac{\overline{G}_3}{8}\frac{\nu t}{a^2}+\mathrm{O}\left(\frac{\sqrt{\nu t}}{a}\right)^3, \tag{8.6}$$

where

$$\overline{L}=L/(2\pi)\,,$$

$$2\pi\overline{G}_2=4(1-\sigma^4)^2\int_0^{\pi/2}\Theta^{-5/2}d\theta$$
$$=\frac{4}{3}\frac{1}{(1+\sigma^2)(1-\sigma^2)^2}\left[4(1+\sigma^4)\boldsymbol{E}\left(\frac{2\sigma}{1+\sigma^2}\right)\right.$$
$$\left.-(1-\sigma^2)^2\boldsymbol{K}\left(\frac{2\sigma}{1+\sigma^2}\right)\right],$$

$$2\pi\overline{G}_3=4(1-\sigma^4)^3\int_0^{\pi/2}\Theta^{-4}d\theta$$
$$=2\pi\frac{1+\sigma^4}{(1-\sigma^4)^4}[1+8\sigma^4+\sigma^8]\,, \tag{8.7}$$

and $\boldsymbol{K}$ is the complete elliptic integral of the first kind.

For an elliptic cylinder of thickness ratio 1/2, we have $\sigma^2=1/3$, and hence $\overline{L}=1.028$, $\overline{G}_2=1.584$, $\overline{G}_3=3.384$. Table I and Fig. 4 show the numerical value of (8.5) in this case, where we take $a/\sqrt{\nu t}=1$ (beyond the region of convergence) and $a/\sqrt{\nu t}=5$ (a little beyond the region of convergence at the end of the minor axis where $R/\sqrt{\nu t}=0.6$) in order to test the validity and usefulness of the asymptotic formulae (8.5) and (8.6). In the former case divergence of (8.6) is evident near the end of the major axis. We see, however, that the convergence is good near the end of the minor axis and a good agreement is obtained with the values calculated in I, by assuming $a/\sqrt{\nu t}\ll 1$. In the latter case the convergence is good except in the region near the end of the major axis. The effect of the last term of (8.6) corresponding to $\partial^2(1/R)/\partial s^2$ is considerably great, so that the non-uniform and asymptotic character of the convergence of our expansion will be evident. For practical purposes it may be convenient to take only the first two terms or to use the exact value of τ for a circular cylinder of radius a taking account of this asymptotic character of our expansion; here the formulae given in I will be conveniently employed as a check.

Table I. Frictional drag on an elliptic cylinder of thickness ratio 1/2.

$a/\sqrt{\nu t}=1$

$\theta°$	1st approx. (1)	2nd approx. (2)	3rd approx. (3)	4th approx. (4)	without $\partial^2(1/R)/\partial s^2$ (4′)	$a/\sqrt{t\nu}<1$ (1)
0		2.064	0.795	−3.42	4.170	1.406
9		1.913	0.887	−0.08	3.340	1.359
18		1.592	0.996	3.338	2.082	1.247
27		1.293	0·993	3.116	1.380	1.120
36		1.080	0.930	2.132	1.068	1.007
45	0.564	0.944	0.862	1.470	0.917	0.917
54		0.858	0.809	1.120	0.835	0.850
63		0.805	0.773	0.942	0.787	0.803
72		0.774	0.749	0.853	0.758	0.771
81		0.757	0.736	0.810	0.743	0.753
90		0.752	0.732	0.798	0.738	0.747

$a/\sqrt{\nu t}=5$

$\theta°$	1st approx. (1)	2nd approx. (2)	3rd approx. (3)	4th approx. (4)	without $\partial^2(1/R)/\partial s^2$ (4′)	$a/\sqrt{t\nu}<1$ (1)
0		4.321	4.067	3.898	4.202	
9		4.170	3.964	3.932	4.063	
18		3.849	3.730	3.823	3.773	
27		3.550	3.490	3.575	3.505	
36		3.337	3.307	3.355	3.313	
45	2.821	3.200	3.184	3.208	3.186	
54		3.115	3.105	3.118	3.106	
63		3.062	3.056	3.062	3.056	
72		3.031	3.026	3.030	3.026	
81		3.014	3.010	3.013	3.010	
90		3.008	3.005	3.007	3.005	

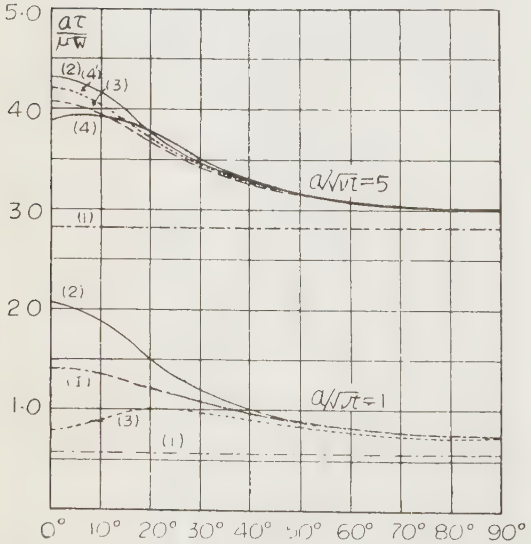

Fig. 4. Frictional drag on an elliptic cylinder of thickness ratio 1/2.

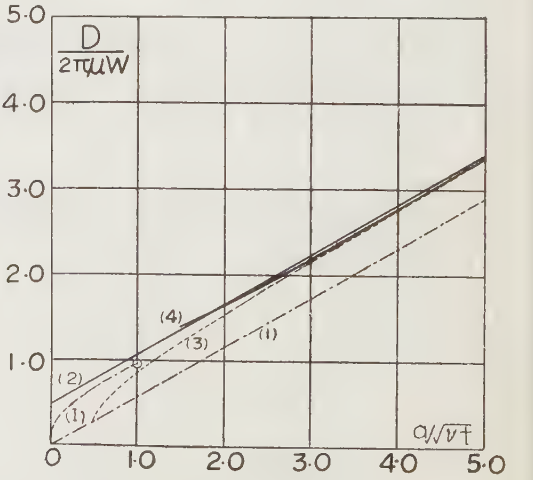

Fig. 5. Total frictional drag for an elliptic cylinder of thickness ratio 1/2.

Fig. 5 and Fig. 6 show the values of (8.6) for an elliptic cylinder of thickness ratio 1/2 ($\sigma^2=1/3$) and for a circular cylinder ($\sigma^2=0$), together with the values obtained by using the formula (7.7) in I. The values when $a/\sqrt{\nu t}\to 0$ are nearly the same for the two cylinders.

Fig. 7 and Fig. 8 reproduce Fig. 2 and Fig. 1 of the previous paper[4], which give the values of $a\tau/(\mu W)$ and $D/(2\pi\mu W)$ for a plate of width $2a$; these values were calculated by using the formulae which are the same as

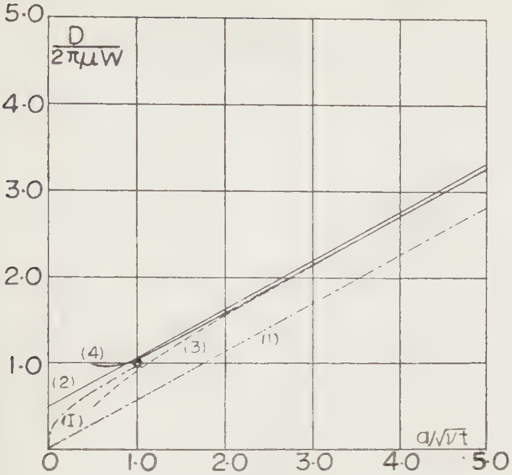

Fig. 6. Total frictional drag for a circular cylinder of radius a. ° ...Exact value.

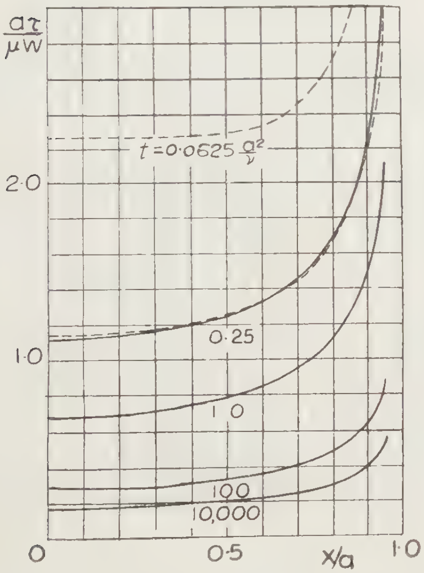

Fig. 7. $a\tau/(\mu W)$ for a plate of width $2a$. —— $a/\sqrt{\nu t}\ll 1$, ---- $a/\sqrt{\nu t}\gg 1$.

(7.9) and (7.10) in I and (7.4) in the present paper together with Table I in Howarth's paper[6]. The agreement is very good for the intermediate values of $a/\sqrt{\nu t}$.

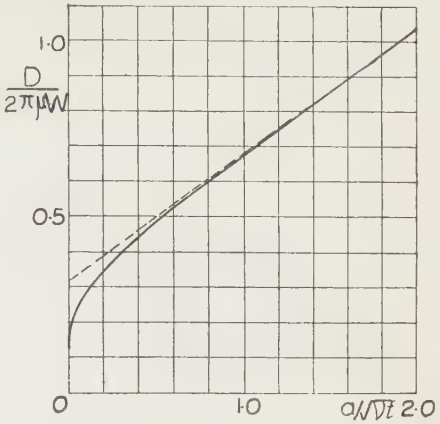

Fig. 8. $D/(2\pi\mu W)$ for a plate of width $2a$. —— $a/\sqrt{\nu t}\ll 1$, ---- $a/\sqrt{\nu t}\gg 1$.

From these examples it will be seen that our formulae are useful when $R/\sqrt{\nu t}$ is uniformly large; here it should be stressed that even the presence of corner is allowed for if the appropriate correction is made.

In conclusion the author expresses his cordial thanks to Professor Isao Imai for his continual guidance.

References

1) G. K. Batchelor: Quart. J. Mech. and Appl. Math. **7** (1954) 179.
2) H. S. C. Carslaw and J. C. Jaeger: Conduction of Heat in Solids (1947) 280.
3) H. Hasimoto: J. Phys. Soc. Japan **6** (1951) 400.
4) H. Hasimoto: Proc. 1st Japan Nat. Congr. Appl. Mech. (1951) 447.
5) H. Hasimoto: J. Phys. Soc. Japan **9** (1954) 611.
6) L. Howarth: Proc. Cambr. Phil. Soc. **46** (1950) 127.
7) L. Howarth: Modern Developements in Fluid Dynamics (1953): High Speed Flow Vol. I (1953) 72.
8) W. Pauli: Handbuch der Physik, XXIV 166.
9) L. Sowerby: Phil. Mag. (7) **42** (1951) 176.
10) L. Sowerby and J. C. Cooke: Quart. J. Mech. and Appl. Math. **6** (1953) 50.

Errata to 3), 4) and 5)

	page	line			should be read
3)	400	-10		$\cos k2\beta u$	$\cosh 2\beta u$
		-2		$(\cosh 2\beta z-\cos\beta)^{-1}\sin kz$	$(\cosh 2\beta z-\cos\beta\pi)^{-1}\sinh z$
	401	5		$\sum\limits_{n=2}$	$\sum\limits_{n=1}$
		9	(8)	$\int_8^\infty$	$\int_0^\infty$
		11		k	K
4)	447	-10 right,	(2.3)	$\int_0^t$	$\int_0^\infty$
	448		(3.1)	$\int_\delta^\pi$	$\int_0^\pi$
	449	12	(3.13)	$-\frac{5}{128s}$	$+\frac{5}{128s}$
	450	19, 22 right		$\frac{\nu t}{a^2}$	$\left(\frac{\nu t}{a^2}\right)^{-1}$
	451	-14 right		$\frac{9}{256}$	$\frac{9s}{256}$
		-13		$\frac{7}{256}$	$\frac{7}{256s}$
5)	614	19	(4.9)	$(1+c_1z^{-2}+\cdots)$	$(1+c_1z^{-2}+\cdots)^{-n}$
		20		$-c_1z^{-n-2}$	$-nc_1z^{-n-2}$
			(5.10)	$E_n^m\left(\frac{a}{\sqrt{\nu t}}\right)\ \int$	$E_n^m\left(\frac{a}{\sqrt{\nu t}}\right)=\int$
	615	(6.3)—(6.5)		dz	$d\zeta$
	617	Fig. 4		$\frac{\omega}{\mu W}$	$\frac{a\omega}{W}$
		Fig. 5 ordinate		1.0	1.1
	618	12		express	expresses
		-1 right	(I.11)	$\sum\limits_{n=1}^{\infty}$	$\sum\limits_{n=1}^{N}$
	619	-1	(I.15)	$[(\beta+\log x)^2+\pi^2]$	$[(\beta+\log x)^2+\pi^2]^2$

JOURNAL OF THE PHYSICAL SOCIETY OF JAPAN Vol. 10, No. 5, MAY, 1955

The Forces on a Circular Cylinder moving with Low Speeds in a Semi-infinite Viscous Liquid bounded by a Plane Wall

By Yorisaburo TAKAISI

Department of Physics, Faculty of Education,
Ehime University, Matsuyama

(Received February 14, 1955)

The steady slow motion of a circular cylinder in a semi-infinite viscous liquid bounded by a plane wall is discussed on the basis of Oseen's linearized equations of motion, assuming that the cylinder is moving parallel to the bounding wall. The forces acting on the cylinder are calculated to Lamb's approximation. By carrying out detailed numerical calculations, it is shown that at sufficiently small Reynolds numbers the drag on the cylinder is of the Stokes type, as in the case of White's experiments on metal wires moving with low speeds in a viscous liquid bounded by two parallel plane walls.

It is also shown that the cylinder experiences a repulsive force from the bounding wall.

§ 1. Introduction and Summary

The steady slow motion of a sphere in a semi-infinite viscous liquid bounded by a plane wall was discussed by H. A. Lorentz[1], J. Stock[2] and H. Faxén[3]. As far as the present writer is aware, however, no detailed discussion has yet been carried out on a similar problem for a circular cylinder. The object of the present paper lies in the discussion of the latter problem.

Thus, the steady motion with low speed U of a circular cylinder in a semi-infinite viscous liquid parallel to its bounding wall is discussed on the basis of Oseen's linearized equations of motion, by developing an analysis similar to that in Faxén's treatment of the sphere problem.

The formulae for the components of the force, parallel and perpendicular to the bounding wall respectively, acting on the circular cylinder are obtained to Lamb's approximation. By carrying out detailed numerical calculations, it is thus shown that the drag on the cylinder is of the so-called Stokes type, as in the case of White's experiments[4] on metal wires falling with low speeds in a viscous liquid bounded by two parallel plane walls; namely, the drag is independent of either of the two Reynolds numbers $R(=Ud/\nu)$ and $R^*(=Ub/\nu)$, where d is the diameter of the cylinder, b is the distance between its centre and the wall and ν is the kinematic viscosity of the liquid concerned.

It is also shown that as in the case of a sphere, the cylinder experiences a repulsive force from the bounding wall.

The writer wishes to express his cordial thanks to Professor S. Tomotika for his guidance and encouragement throughout the present work. The writer's thanks are also due to Professor K. Tamada, Osaka City University, for his invaluable discussions.

§ 2. Method of Solution

Suppose that a circular cylinder of radius a is moving, with constant slow velocity U, from right to left in a semi-infinite viscous liquid at rest parallel to its bounding plane wall. Referring to rectangular coordinates $0x$, $0y$ with its origin at the centre of the cylinder, where the x- and y-axes are taken parallel and perpendicular to the wall respectively, the fluid at infinity flows, with constant velocity U, past the cylinder at rest in the positive direction of the x-axis (Fig. 1). In this case the bounding wall should also move, with the same velocity U, from left to right in its own plane, so as to satisfy the boundary conditions.

The stream function Ψ may be written as:

$$\Psi = Uy + \psi , \tag{2.1}$$

where ψ is the stream function for the perturbation and is connected with the components of the perturbation velocity as:

$$u = \partial\psi/\partial y , \quad v = -\partial\psi/\partial x . \tag{2.2}$$

Oseen's linearized equations of motion for the two-dimensional steady motion of an incompressible viscous fluid reduce, in this case, to

$$\Delta(\Delta-2k\partial/\partial x)\psi=0\ , \tag{2.3}$$

where

$$2k=U/\nu\ , \tag{2.4}$$

and Δ stands for $\partial^2/\partial x^2+\partial^2/\partial y^2$.

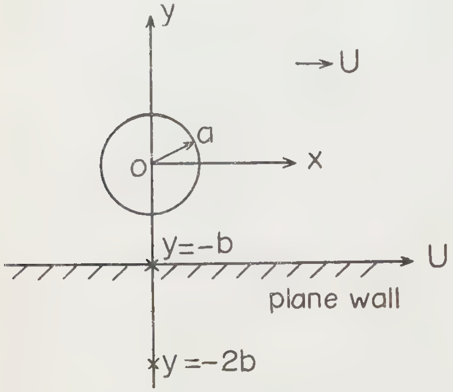

Fig. 1.

The solution of (2.3) can be written in the form:

$$\psi=\psi_1+\psi_2\ , \tag{2.5}$$

where

$$\Delta\psi_1=0\ , \tag{2.6}$$

$$(\Delta-k^2)(e^{-kx}\psi_2)=0\ . \tag{2.7}$$

According to L. N. G. Filon[5], the appropriate solutions of (2.6) and (2.7) which satisfy the boundary conditions at infinity are given respectively by

$$\psi_1=A_0\ln r+B_0\theta + \sum_{n=1}^{\infty} r^{-n}(A_n\cos n\theta+B_n\sin n\theta)\ , \tag{2.8}$$

and

$$\begin{aligned}\psi_2=&a_0 e^{kx}K_0(kr)\\ &+b_0\int_0^\theta kr\{K_1(kr)+K_0(kr)\cos\theta\}e^{kr\cos\theta}d\theta\\ &+e^{kx}\sum_{n=1}^{\infty}K_n(kr)(a_n\cos n\theta+b_n\sin n\theta)\ ,\end{aligned} \tag{2.9}$$

where $x=r\cos\theta$, $y=r\sin\theta$, and

$$b_0=-B_0\ . \tag{2.10}$$

$K_n(x)$ is the modified Bessel function of the second kind. The condition (2.10) ensures that the stream function Ψ is one-valued and continuous throughout the whole field of flow.

If we confine ourselves to Lamb's approximation, it suffices to take only the first two terms in (2.8) and (2.9) respectively. We then have

$$\left.\begin{aligned}u=&A_0r^{-1}\sin\theta+B_0r^{-1}\cos\theta\\ &-ka_0e^{kx}K_1(kr)\sin\theta\\ &+kb_0e^{kx}\{K_1(kr)\cos\theta+K_0(kr)\}\ ,\\ v=&-A_0r^{-1}\cos\theta+B_0r^{-1}\sin\theta\\ &+ka_0e^{kx}\{K_1(kr)\cos\theta-K_0(kr)\}\\ &+kb_0e^{kx}K_1(kr)\sin\theta\ .\end{aligned}\right\} \tag{2.11}$$

Now, $\ln r$ and $e^{kx}K_0(kr)$ can be expressed respectively in integral forms as:

$$\left.\begin{aligned}\ln r&=-\frac{1}{2}\int_{-\infty}^{\infty}\frac{1}{|\alpha|}\exp(i\alpha x-|\alpha||y|)d\alpha+C_1\ ,\\ e^{kx}K_0(kr)&=\frac{1}{2}\int_{-\infty}^{\infty}\frac{1}{\lambda_0}\exp(i\alpha x-\lambda_0|y|)d\alpha\ ,\end{aligned}\right\} \tag{2.12}$$

where C_1 is an appropriate constant so chosen as to make the integral convergent, and

$$\lambda_0=\sqrt{\alpha^2+2ik\alpha}\ , \qquad (i=\sqrt{-1})\ .$$

It is readily found that $\boldsymbol{Re}(\lambda_0)>0$.

Differentiating (2.12) with respect to x or y, we obtain

$$\left.\begin{aligned}\frac{1}{r}\cos\theta&=-\frac{1}{2}\int_{-\infty}^{\infty}\frac{i\alpha}{|\alpha|}\exp(i\alpha x-|\alpha||y|)d\alpha\ ,\\ \frac{1}{r}\sin\theta&=\frac{1}{2}\frac{|y|}{y}\int_{-\infty}^{\infty}\exp(i\alpha x-|\alpha||y|)d\alpha\ ,\\ e^{kr}K_1(kr)\cos\theta&=-\frac{1}{2k}\int_{-\infty}^{\infty}\frac{i\alpha-k}{\lambda_0}\\ &\qquad\times\exp(i\alpha x-\lambda_0|y|)d\alpha\ ,\\ e^{kx}K_1(kr)\sin\theta&=\frac{1}{2k}\frac{|y|}{y}\\ &\qquad\times\int_{-\infty}^{\infty}\exp(i\alpha x-\lambda_0|y|)d\alpha\ .\end{aligned}\right\} \tag{2.13}$$

If we substitute from (2.12) and (2.13) into (2.11), we obtain integral expressions for the components of perturbation velocity in the forms:

$$\left.\begin{aligned}u=&\frac{1}{2}\int_{-\infty}^{\infty}\left(\frac{|y|}{y}A_0-\frac{i\alpha}{|\alpha|}B_0\right)\\ &\qquad\times\exp(i\alpha x-|\alpha||y|)d\alpha\\ &-\frac{1}{2}\int_{-\infty}^{\infty}\left(\frac{|y|}{y}a_0+\frac{i\lambda_0}{\alpha}b_0\right)\\ &\qquad\times\exp(i\alpha x-\lambda_0|y|)d\alpha\ ,\\ v=&\frac{1}{2}\int_{-\infty}^{\infty}\left(\frac{i\alpha}{|\alpha|}A_0+\frac{|y|}{y}B_0\right)\\ &\qquad\times\exp(i\alpha x-|\alpha||y|)d\alpha\end{aligned}\right.$$

$$+\frac{1}{2}\int_{-\infty}^{\infty}\left(-\frac{i\alpha}{\lambda_0}a_0+\frac{|y|}{y}b_0\right)\times\exp(i\alpha x-\lambda_0|y|)d\alpha\,. \qquad (2.14)$$

Further, making use of the relations:

$$e^{kx}=I_0(kr)+2I_1(kr)\cos\theta+\cdots\,,$$

$$e^{kx}\cos\theta=I_1(kr)+\{I_0(kr)+I_2(kr)\}\cos\theta+\cdots\,,$$

$$e^{kx}\sin\theta=\{I_0(kr)-I_2(kr)\}\sin\theta+\cdots\,,$$

where $I_n(x)$ is the modified Bessel function of the first kind, and introducing the conjugate complex velocity $w=u-iv$, we obtain from (2.11), on neglecting all terms higher than k^2r^2,

$$\begin{aligned}\frac{w}{k}&=\left(\frac{1}{2}-\gamma-\ln\frac{kr}{2}\right)b_0-i\left(\frac{1}{2}+\gamma+\ln\frac{kr}{2}\right)a_0\\&\quad+e^{-i\theta}\left[i\frac{A_0}{kr}+\frac{B_0}{kr}+\frac{b_0}{kr}\right.\\&\qquad\left.-i\left\{\frac{1}{kr}+kr\left(\gamma+\ln\frac{kr}{2}\right)\right\}a_0\right]\\&\quad+\cdots\,,\end{aligned} \qquad (2.15)$$

where $\gamma=0.57721\cdots$ is Euler's constant.

In order to satisfy the boundary conditions on the bounding plane wall, we now superpose, as done by Faxén in the case of sphere problem, a flow due to images, which is defined as:

$$\left.\begin{aligned}u^*&=-\frac{1}{2}\int_{-\infty}^{\infty}|\alpha|f_1(\alpha)\times\exp\{i\alpha x-|\alpha|(y+2b)\}d\alpha\\&\quad-\frac{1}{2}\int_{-\infty}^{\infty}\lambda_0 f_2(\alpha)\exp\{i\alpha x-\lambda_0(y+2b)\}d\alpha\,,\\v^*&=-\frac{1}{2}\int_{-\infty}^{\infty}i\alpha f_1(\alpha)\exp\{i\alpha x-|\alpha|(y+2b)\}d\alpha\\&\quad-\frac{1}{2}\int_{-\infty}^{\infty}i\alpha f_2(\alpha)\exp\{i\alpha x-\lambda_0(y+2b)\}d\alpha\,,\end{aligned}\right\} \qquad (2.16)$$

where b denotes the distance of the centre of the cylinder from the wall (see Fig. 1), and $f_1(\alpha)$ and $f_2(\alpha)$ are unknown functions to be determined by the under-mentioned boundary conditions.

The conjugate complex velocity $w^*=u^*-iv^*$ for the superposed flow due to images can be written as:

$$\begin{aligned}w^*&=-\frac{1}{2}\int_{-\infty}^{\infty}(|\alpha|+\alpha)f_1(\alpha)\times\exp\{i\alpha x-|\alpha|(y+2b)\}d\alpha\\&\quad-\frac{1}{2}\int_{-\infty}^{\infty}(\lambda_0+\alpha)f_2(\alpha)\times\exp\{i\alpha x-|\alpha|(y+2b)\}d\alpha\,.\end{aligned} \qquad (2.17)$$

Since the conditions at infinity are already satisfied automatically by w and w^* as given respectively by (2.15) and (2.17), we have only to consider the boundary conditions on the bounding plane wall $y=-b$ as well as at the surface of the cylinder. They are

(i) $$(w+w^*)_{y=-b}=0\,, \qquad (2.18)$$

or $$(u+u^*)_{y=-b}=0\,,\quad (v+v^*)_{y=-b}=0\,, \qquad (2.18a)$$

and

(ii) $$(w+w^*)_{r=a}=-U\,. \qquad (2.19)$$

§ 3. Determination of the Functions $f_1(\alpha)$ and $f_2(\alpha)$

Inserting the values of u, v and u^*, v^* as given respectively by (2.14) and (2.16) into (2.18a), we get

$$\begin{aligned}\int_{-\infty}^{\infty}e^{i\alpha x}&\left[\left\{-A_0-i\frac{\alpha}{|\alpha|}B_0-|\alpha|f_1(\alpha)\right\}\right.\\&\times\exp(-b|\alpha|)+\left\{a_0-i\frac{\lambda_0}{\alpha}b_0-\lambda_0 f_2(\alpha)\right\}\\&\left.\times\exp(-b\lambda_0)\right]d\alpha=0\,,\end{aligned} \qquad (3.1)$$

$$\begin{aligned}\int_{-\infty}^{\infty}e^{i\alpha x}&\left[\left\{i\frac{\alpha}{|\alpha|}A_0-B_0-i\alpha f_1(\alpha)\right\}\right.\\&\times\exp(-b|\alpha|)+\left\{-i\frac{\alpha}{\lambda_0}a_0-b_0-i\alpha f_2(\alpha)\right\}\\&\left.\times\exp(-b\lambda_0)\right]d\alpha=0\,.\end{aligned} \qquad (3.2)$$

In order that these relations are satisfied for all values of x, the quantities in the square brackets must be identically zero. Thus, the functions $f_1(\alpha)$ and $f_2(\alpha)$ so far undetermined can be expressed in terms of the unknown constants A_0, B_0, a_0 and b_0 as:

$$\left.\begin{aligned}f_1(\alpha)&=\frac{1}{2k}\left\{-i\frac{(\lambda_0+|\alpha|)^2}{\alpha|\alpha|}A_0+\frac{(\lambda_0+|\alpha|)^2}{\alpha^2}B_0\right\}\\&\quad+\frac{1}{k}\left\{i\frac{\lambda_0+|\alpha|}{\alpha}a_0+\frac{\lambda_0(\lambda_0+|\alpha|)}{\alpha^2}b_0\right\}\\&\quad\times\exp\{-b(\lambda_0-|\alpha|)\}\,,\\f_2(\alpha)&=\frac{1}{k}\left\{i\frac{\lambda_0+|\alpha|}{\alpha}A_0-\frac{\lambda_0+|\alpha|}{|\alpha|}B_0\right\}\\&\quad\times\exp\{b(\lambda_0-|\alpha|)\}\\&\quad+\frac{1}{2k}\left\{-i\frac{(\lambda_0+|\alpha|)^2}{\lambda_0\alpha}a_0-\frac{(\lambda_0+|\alpha|)^2}{\alpha^2}b_0\right\}\,.\end{aligned}\right\} \qquad (3.3)$$

Inserting these expressions into (2.17) we have

$$
\begin{aligned}
w^* = {} & \frac{iA_0}{2k}\int_0^\infty \frac{(\lambda_0+\alpha)^2}{\alpha}\exp(-2b\alpha+i\alpha x-\alpha y)d\alpha \\
& -\frac{B_0}{2k}\int_0^\infty \frac{(\lambda_0+\alpha)^2}{\alpha}\exp(-2b\alpha+i\alpha x-\alpha y)d\alpha \\
& -\frac{ia_0}{k}\int_0^\infty (\lambda_0+\alpha) \\
& \qquad \times\exp\{-b(\lambda_0+\alpha)+i\alpha x-\alpha y\}d\alpha \\
& -\frac{b_0}{k}\int_0^\infty \frac{\lambda_0(\lambda_0+\alpha)}{\alpha} \\
& \qquad \times\exp\{-b(\lambda_0+\alpha)+i\alpha x-\alpha y\}d\alpha \\
& +\frac{iA_0}{2k}\Bigg[-\int_0^\infty \frac{(\lambda_0+\alpha)^2}{\alpha} \\
& \qquad \times\exp\{-b(\lambda_0+\alpha)+i\alpha x-\lambda_0 y\}d\alpha \\
& \qquad +\int_0^\infty \frac{\lambda_0'^2-\alpha^2}{\alpha} \\
& \qquad \times\exp\{-b(\lambda_0'+\alpha)-i\alpha x-\lambda_0' y\}d\alpha\Bigg] \\
& +\frac{B_0}{2k}\Bigg[\int_0^\infty \frac{(\lambda_0+\alpha)^2}{\alpha} \\
& \qquad \times\exp\{-b(\lambda_0+\alpha)+i\alpha x-\lambda_0 y\}d\alpha \\
& \qquad +\int_0^\infty \frac{\lambda_0'^2-\alpha^2}{\alpha} \\
& \qquad \times\exp\{-b(\lambda_0'+\alpha)-i\alpha x-\lambda_0' y\}d\alpha\Bigg] \\
& +\frac{ia_0}{4k}\Bigg[\int_0^\infty \frac{(\lambda_0+\alpha)^3}{\lambda_0\alpha} \\
& \qquad \times\exp(-2b\lambda_0+i\alpha x-\lambda_0 y)d\alpha \\
& \qquad -\int_0^\infty \frac{(\lambda_0'+\alpha)^2(\lambda_0'-\alpha)}{\lambda_0'\alpha} \\
& \qquad \times\exp(-2b\lambda_0'-i\alpha x-\lambda_0' y)d\alpha\Bigg] \\
& +\frac{b_0}{4k}\Bigg[\int_0^\infty \frac{(\lambda_0+\alpha)^3}{\alpha^2} \\
& \qquad \times\exp(-2b\lambda_0+i\alpha x-\lambda_0 y)d\alpha \\
& \qquad +\int_0^\infty \frac{(\lambda_0'+\alpha)^2(\lambda_0'-\alpha)}{\alpha^2} \\
& \qquad \times\exp(-2b\lambda_0'-i\alpha x-\lambda_0' y)d\alpha\Bigg],
\end{aligned}
\tag{3.4}
$$

where $\lambda_0'=\sqrt{\alpha^2-2ik\alpha}$.

Putting $\alpha=k\beta$, $\lambda=\sqrt{\beta^2+2i\beta}$ and $\lambda'=\sqrt{\beta^2-2i\beta}$, this expression for w^* can also be rewritten as:

$$
\begin{aligned}
\frac{w^*}{k} = {} & \frac{iA_0}{2}\int_0^\infty \frac{(\lambda+\beta)^2}{\beta}\exp(-2kb\beta+ik\beta x-k\beta y)d\beta \\
& -\frac{B_0}{2}\int_0^\infty \frac{(\lambda+\beta)^2}{\beta}\exp(-2kb\beta+ik\beta x-k\beta y)d\beta \\
& -ia_0\int_0^\infty (\lambda+\beta)\exp\{-kb(\lambda+\beta)+ik\beta x-k\beta y\}d\beta \\
& -b_0\int_0^\infty \frac{\lambda(\lambda+\beta)}{\beta}\exp\{-kb(\lambda+\beta)+ik\beta x-k\beta y\}d\beta \\
& +\frac{iA_0}{2}\Bigg[-\int_0^\infty \frac{(\lambda+\beta)^2}{\beta}\exp\{-kb(\lambda+\beta)+ik\beta x-k\lambda y\}d\beta \\
& \qquad +\int_0^\infty \frac{\lambda'^2-\beta^2}{\beta}\exp\{-kb(\lambda'+\beta)-ik\beta x-k\lambda' y\}d\beta\Bigg] \\
& +\frac{B_0}{2}\Bigg[\int_0^\infty \frac{(\lambda+\beta)^2}{\beta}\exp\{-kb(\lambda+\beta)+ik\beta x-k\lambda y\}d\beta \\
& \qquad +\int_0^\infty \frac{\lambda'^2-\beta^2}{\beta}\exp\{-kb(\lambda'+\beta)-ik\beta x-k\lambda' y\}d\beta\Bigg] \\
& +\frac{ia_0}{4}\Bigg[\int_0^\infty \frac{(\lambda+\beta)^3}{\lambda\beta}\exp(-2kb\lambda+ik\beta x-k\lambda y)d\beta \\
& \qquad -\int_0^\infty \frac{(\lambda'+\beta)^2(\lambda'-\beta)}{\lambda'\beta}\exp(-2kb\lambda'-ik\beta x-k\lambda' y)d\beta\Bigg] \\
& +\frac{b_0}{4}\Bigg[\int_0^\infty \frac{(\lambda+\beta)^3}{\beta^2}\exp(-2kb\lambda+ik\beta x-k\lambda y)d\beta \\
& \qquad +\int_0^\infty \frac{(\lambda'+\beta)^2(\lambda'-\beta)}{\beta^2}\exp(-2kb\lambda'-ik\beta x-k\lambda' y)d\beta\Bigg].
\end{aligned}
\tag{3.5}
$$

Using the obvious relations:

$$x=r\cos\theta=\frac{1}{2}r(\mathrm{e}^{i\theta}+\mathrm{e}^{-i\theta})\,,\qquad y=r\sin\theta=-\frac{1}{2}ir(\mathrm{e}^{i\theta}-\mathrm{e}^{-i\theta})\,,$$

we have

$$\left.\begin{aligned}
\exp(ik\beta x-k\beta y)&=1+ik\beta r\mathrm{e}^{i\theta}+\cdots\,,\\
\exp(ik\beta x-k\lambda y)&=1-\frac{1}{2}ikr(\lambda-\beta)\mathrm{e}^{-i\theta}+\frac{1}{2}ikr(\lambda+\beta)\mathrm{e}^{i\theta}+\cdots\,,\\
\exp(-ik\beta x-k\lambda' y)&=1-\frac{1}{2}ikr(\lambda'+\beta)\mathrm{e}^{-i\theta}+\frac{1}{2}ikr(\lambda'-\beta)\mathrm{e}^{i\theta}+\cdots\,.
\end{aligned}\right\}\tag{3.6}$$

Thus, inserting these expressions into (3.5) and retaining only constant terms as well as terms involving $\mathrm{e}^{-i\theta}$, we obtain, on neglecting all terms higher than k^2r^2,

$$\begin{aligned}
\frac{w^*}{k}=&\left(\frac{iA_0}{2}-\frac{B_0}{2}\right)\int_0^\infty\frac{(\lambda+\beta)^2}{\beta}\exp(-2kb\beta)d\beta\\
&-ia_0\int_0^\infty(\lambda+\beta)\exp\{-kb(\lambda+\beta)\}d\beta\\
&-b_0\int_0^\infty\frac{\lambda(\lambda+\beta)}{\beta}\exp\{-kb(\lambda+\beta)\}d\beta\\
&-\frac{iA_0}{2}\left[\int_0^\infty\frac{(\lambda+\beta)^2}{\beta}\exp\{-kb(\lambda+\beta)\}d\beta-\int_0^\infty\frac{\lambda'^2-\beta^2}{\beta}\exp\{-kb(\lambda'+\beta)\}d\beta\right]\\
&+\frac{B_0}{2}\left[\int_0^\infty\frac{(\lambda+\beta)^2}{\beta}\exp\{-kb(\lambda+\beta)\}d\beta+\int_0^\infty\frac{\lambda'^2-\beta^2}{\beta}\exp\{-kb(\lambda'+\beta)\}d\beta\right]\\
&+\frac{ia_0}{4}\left[\int_0^\infty\frac{(\lambda+\beta)^3}{\lambda\beta}\exp(-2kb\lambda)d\beta-\int_0^\infty\frac{(\lambda'+\beta)^2(\lambda'-\beta)}{\lambda'\beta}\exp(-2kb\lambda')d\beta\right]\\
&+\frac{b_0}{4}\left[\int_0^\infty\frac{(\lambda+\beta)^3}{\beta^2}\exp(-2kb\lambda)d\beta+\int_0^\infty\frac{(\lambda'+\beta)^2(\lambda'-\beta)}{\beta^2}\exp(-2kb\lambda')d\beta\right]\\
&+kr\mathrm{e}^{-i\theta}\left\{-\frac{A_0}{4}\left[\int_0^\infty\frac{(\lambda+\beta)^2(\lambda-\beta)}{\beta}\exp\{-kb(\lambda+\beta)d\beta\right.\right.\\
&\qquad\left.-\int_0^\infty\frac{(\lambda'+\beta)^2(\lambda'-\beta)}{\beta}\exp\{-kb(\lambda'+\beta)\}d\beta\right]\\
&\quad-\frac{iB_0}{4}\left[\int_0^\infty\frac{(\lambda+\beta)^2(\lambda-\beta)}{\beta}\exp\{-kb(\lambda+\beta)\}d\beta\right.\\
&\qquad\left.+\int_0^\infty\frac{(\lambda'+\beta)^2(\lambda'-\beta)}{\beta}\exp\{-kb(\lambda'+\beta)\}d\beta\right]\\
&\quad+\frac{a_0}{8}\left[\int_0^\infty\frac{(\lambda+\beta)^3(\lambda-\beta)}{\lambda\beta}\exp(-2kb\lambda)d\beta\right.\\
&\qquad\left.-\int_0^\infty\frac{(\lambda'+\beta)^3(\lambda'-\beta)}{\lambda'\beta}\exp(-2kb\lambda')d\beta\right]\\
&\quad-\frac{ib_0}{8}\left[\int_0^\infty\frac{(\lambda+\beta)^3(\lambda-\beta)}{\beta^2}\exp(-2kb\lambda)d\beta\right.\\
&\qquad\left.\left.+\int_0^\infty\frac{(\lambda'+\beta)^3(\lambda'-\beta)}{\beta^2}\exp(-2kb\lambda')d\beta\right]\right\}.
\end{aligned}\tag{3.7}$$

Various definite integrals in the above expression can be evaluated by use of the following integrals, which can be obtained by appropriate transformations, and their derivatives with respect to x,

$$\int_0^\infty\frac{1}{\lambda}\,\mathrm{e}^{-x\beta}d\beta=-i\frac{\pi}{2}\,\mathrm{e}^{ix}\{J_0(x)-iY_0(x)\}\,,\qquad\int_0^\infty\frac{1}{\lambda'}\,\mathrm{e}^{-x\beta}d\beta=i\frac{\pi}{2}\,\mathrm{e}^{-ix}\{J_0(x)+iY_0(x)\}\,,$$

$$\int_0^\infty \frac{1}{\lambda}\,\mathrm{e}^{-x\lambda}\,d\beta+\int_0^\infty \frac{1}{\lambda'}\,\mathrm{e}^{-x\lambda'}\,d\beta=2K_0(x)\,,\qquad \int_0^\infty \frac{1}{\lambda}\,\mathrm{e}^{-x\lambda}\,d\beta-\int_0^\infty \frac{1}{\lambda'}\,\mathrm{e}^{-x\lambda'}\,d\beta=-i\pi\{I_0(x)-\mathbf{L}_0(x)\}\,,$$

$$\int_0^\infty \frac{1}{u^2+1}\,\mathrm{e}^{-xu}\,du=g_1(x)\,,\qquad \int_0^\infty \frac{u}{u^2+1}\,\mathrm{e}^{-xu}\,du=h_1(x)\,.$$

Thus, we have finally the expression for w^* in the form:

$$\begin{aligned}
\frac{w^*}{k}=A_0\Big[&\frac{1}{2kb}-g_2(kb)+\frac{\pi}{4}\{J_0(2kb)+J_2(2kb)\}\cos 2kb+\frac{\pi}{4}\{Y_0(2kb)+Y_2(2kb)\}\sin 2kb\\
&+i\Big[-\frac{1}{4k^2b^2}-\frac{1}{2}h_1(kb)+h_2(kb)+\frac{\pi}{4}\{J_0(2kb)+J_2(2kb)\}\sin 2kb\\
&\qquad-\frac{\pi}{4}\{Y_0(2kb)+Y_2(2kb)\}\cos 2kb\Big]\Big]\\
+B_0\Big[&\frac{1}{4k^2b^2}+\frac{1}{2}h_1(kb)+h_2(kb)-\frac{\pi}{4}\{J_0(2kb)+J_2(2kb)\}\sin 2kb+\frac{\pi}{4}\{Y_0(2kb)+Y_2(2kb)\}\cos 2kb\\
&+i\Big[-\frac{1}{2kb}-g_1(kb)+g_2(kb)+\frac{\pi}{4}\{J_0(2kb)+J_2(2kb)\}\cos 2kb\\
&\qquad+\frac{\pi}{4}\{Y_0(2kb)+Y_2(2kb)\}\sin 2kb\Big]\Big]\\
+a_0\Big[&-g_1(kb)+g_2(kb)+\frac{\pi}{4}\Big\{I_0(2kb)-\mathbf{L}_0(2kb)+I_2(2kb)-\mathbf{L}_2(2kb)-\frac{4kb}{3\pi}\Big\}\\
&+i\Big[-\frac{1}{4k^2b^2}-\frac{1}{2}h_1(kb)+h_2(kb)-\frac{1}{2}K_0(2kb)+\frac{1}{2}K_2(2kb)+\frac{\pi}{2}\Big\{I_1(2kb)-\mathbf{L}_1(2kb)-\frac{2}{\pi}\Big\}\Big]\Big]\\
+b_0\Big[&-\frac{1}{4k^2b^2}-\frac{1}{2}K_0(2kb)+\frac{1}{2}K_2(2kb)-\frac{1}{2}h_1(kb)-h_2(kb)-\frac{\pi}{2}\Big\{I_1(2kb)-\mathbf{L}_1(2kb)-\frac{2}{\pi}\Big\}\\
&+i\Big[-\frac{1}{kb}+g_2(kb)-\frac{\pi}{4}\Big\{I_0(2kb)-\mathbf{L}_0(2kb)+I_2(2kb)-\mathbf{L}_2(2kb)-\frac{4kb}{3\pi}\Big\}\Big]\Big]\\
+ikr\,\mathrm{e}^{-i\theta}\Big\{&\frac{1}{2}A_0\Big[-\frac{1}{k^2b^2}-h_1(kb)+2h_2(kb)\Big]+B_0[-g_1(kb)+g_2(kb)]\\
&+\frac{1}{2}a_0\Big[-K_0(2kb)+K_2(2kb)+\frac{1}{2k^2b^2}+\pi\Big\{I_1(2kb)-\mathbf{L}_1(2kb)-\frac{2}{\pi}\Big\}\Big]\\
&+\frac{1}{2}b_0\Big[-\frac{\pi}{2}\Big\{I_0(2kb)-\mathbf{L}_0(2kb)+I_2(2kb)-\mathbf{L}_2(2kb)-\frac{4kb}{3\pi}\Big\}\Big]\Big\}\,,
\end{aligned}\tag{3.8}$$

where $J_n(x)$ is the Bessel function of the first kind, $Y_n(x)$ is Neumann's Bessel function of the second kind and $\mathbf{L}_n(x)$ is Struve's function[6] of imaginary argument defined as:

$$\mathbf{L}_n(x)=\sum_{m=0}^{\infty}\frac{(x/2)^{n+2m+1}}{\Gamma(m+3/2)\Gamma(n+m+3/2)}\,.\tag{3.9}$$

Also, the functions $g_n(x)$ and $h_n(x)$ $(n=1, 2)$ are given by

$$\begin{aligned}g_1(x)&=\int_0^\infty\frac{1}{u^2+1}\,\mathrm{e}^{-xu}\,du\\&=\mathrm{Ci}(x)\sin x-\mathrm{Si}(x)\cos x+\frac{\pi}{2}\cos x\,,\end{aligned}\tag{3.10a}$$

$$\begin{aligned}g_2(x)&=\int_0^\infty\frac{1}{(u^2+1)^2}\,\mathrm{e}^{-xu}\,du\\&=\frac{1}{2}\Big\{\mathrm{Ci}(x)\sin x-\mathrm{Si}(x)\cos x+\frac{\pi}{2}\cos x\Big\}\\&\quad-\frac{x}{2}\Big\{\mathrm{Ci}(x)\cos x+\mathrm{Si}(x)\sin x-\frac{\pi}{2}\sin x\Big\}\,,\end{aligned}\tag{3.10b}$$

$$\begin{aligned}h_1(x)&=\int_0^\infty\frac{u}{u^2+1}\,\mathrm{e}^{-xu}\,du\\&=-\mathrm{Ci}(x)\cos x-\mathrm{Si}(x)\sin x+\frac{\pi}{2}\sin x\,,\end{aligned}\tag{3.10c}$$

$$\begin{aligned}h_2(x)&=\int_0^\infty\frac{u}{(u^2+1)^2}\,\mathrm{e}^{-xu}\,du\\&=\frac{1}{2}-\frac{x}{2}\Big\{\mathrm{Ci}(x)\sin x-\mathrm{Si}(x)\cos x\\&\qquad+\frac{\pi}{2}\cos x\Big\}\,,\end{aligned}\tag{3.10d}$$

with

$$\mathrm{Si}(x)=\int_0^x \sin u/u du\ ,\quad \mathrm{Ci}(x)=-\int_x^\infty \cos u/u du\,. \tag{3.11}$$

§ 4. Determination of the Constants A_0, B_0, a_0 and b_0

The constants A_0, B_0, a_0 and b_0 can be determined by inserting from (2.15) and (3.7) into (2.19). Thus, writing, for the sake of brevity,

$$\begin{aligned} F_1(kb)=&\frac{1}{2kb}-g_1(kb)\\ &+\frac{\pi}{4}\{J_0(2kb)+J_2(2kb)\}\cos 2kb\\ &+\frac{\pi}{4}\{Y_0(2kb)+Y_2(2kb)\}\sin 2kb\\ &+\frac{\pi}{4}\Big\{I_0(2kb)-\mathbf{L}_0(2kb)+I_2(2kb)\\ &\quad-\mathbf{L}_2(2kb)-\frac{4kb}{3\pi}\Big\}\ , \end{aligned} \tag{4.1}$$

$$\begin{aligned} F_2(kb)=&\frac{1}{2k^2b^2}+h_1(kb)+\frac{1}{2}K_0(2kb)-\frac{1}{2}K_2(2kb)\\ &-\frac{\pi}{4}\{J_0(2kb)+J_2(2kb)\}\sin 2kb\\ &+\frac{\pi}{4}\{Y_0(2kb)+Y_2(2kb)\}\cos 2kb\,, \end{aligned} \tag{4.2}$$

$$F_3(kb)=2h_2(kb)+\frac{\pi}{2}\Big\{I_1(2kb)-\mathbf{L}_1(2kb)-\frac{2}{\pi}\Big\}\ , \tag{4.3}$$

and

$$S=\gamma+\ln(ka/2)\ ,$$

we have, after some calculations,

$$a_0=A_0\ , \tag{4.4}$$

$$b_0=-B_0\ , \tag{4.5}$$

$$A_0=\frac{F_1(kb)}{\{1/2-F_3(kb)\}^2-\{F_1(kb)\}^2-\{S+F_2(kb)\}^2}\frac{U}{k}\ , \tag{4.6}$$

$$B_0=\frac{1/2-F_3(kb)+S+F_2(kb)}{\{1/2-F_3(kb)\}^2-\{F_1(kb)\}^2-\{S+F_2(kb)\}^2}\frac{U}{k}\ , \tag{4.7}$$

The relation (4.5) has been obtained again independently of (2.9).

§ 5. The Lift and Drag Experienced by the Cylinder

Now, it is easily shown that, as in the case of a cylinder immersed in an unlimited stream of viscous liquid as treated by Filon[5], the lift L and the drag D experienced by the circular cylinder under discussion per its unit length can be expressed as:

$$L=2\pi\rho UA_0\ , \tag{5.1}$$

$$D=2\pi\rho UB_0\ , \tag{5.2}$$

where ρ is the density of the fluid concerned.

Hence, if use is made of (4.6) and (4.7), we have

$$\frac{L}{\mu U}=\frac{4\pi F_1(kb)}{\{1/2-F_3(kb)\}^2-\{F_1(kb)\}^2-\{S+F_2(kb)\}^2}\ , \tag{5.3}$$

$$\frac{D}{\mu U}=\frac{4\pi\{1/2-F_3(kb)+S+F_2(kb)\}}{\{1/2-F_3(kb)\}^2-\{F_1(kb)\{^2-\{S+F_2(kb)\}^2}\ , \tag{5.4}$$

μ being the viscosity of the fluid.

When the bounding plane wall recedes away to infinity from the centre of the cylinder, the value of kb tends to infinity and our case is reduced to Lamb's case of a circular cylinder in an unbounded stream of viscous liquid. The value of ka is, however, kept to be small.

Making use of the asymptotic expressions for the Bessel functions $J_n(x)$, $Y_n(x)$ and $K_n(x)$, together with

$$I_n(x)-\mathbf{L}_n(x)=\frac{1}{\pi}\sum_{m=0}^{p-1}(-1)^m \times\frac{\Gamma(m+1/2)}{\Gamma(n+1/2-m)(x/2)^{2m-n+1}}+O(x^{n-2p-1})\ , \tag{5.5}$$

and

$$\mathrm{Si}(x)\sim\frac{\pi}{2}-\frac{\cos x}{x}\ ,\qquad \mathrm{Ci}(x)\sim\frac{\sin x}{x}\ ,$$

we easily find that

$$\lim_{kb\to\infty}F_1(kb)\to 0,\quad \lim_{kb\to\infty}F_2(kb)\to 0,\quad \lim_{kb\to\infty}F_3(kb)\to 0.$$

Thus, we have ultimately

$$\left.\begin{aligned} &\lim_{kb\to\infty}\frac{L}{\mu U}\to 0\ ,\\ &\lim_{kb\to\infty}\frac{D}{\mu U}\to\frac{4\pi}{1/2-\gamma-\ln(ka/2)}\,. \end{aligned}\right\} \tag{5.6}$$

As should be expected, the latter result is in perfect agreement with Lamb's formula for the drag experienced by a circular cylinder moving steadily at low speeds in an unlimited viscous liquid.

On the other hand, in case when the value of kb becomes small subject to the restriction

Table I. Values of $D/\mu U$

b/a \ R	By (5.8) ~ 0	By (5.4) 0.002	0.004	0.02	0.04	0.2	0.4	1
2	9.06	9.07	9.07	9.07	9.08	9.26	9.59	10.57
4	6.04	6.04	—	6.05	—	6.32	—	8.21
5	5.46	—	5.46	—	5.49	—	6.23	—
10	4.19	4.20	4.20	4.21	4.24	4.65	5.22	—
20	3.41	—	—	—	3.50	4.06	—	6.47
40	2.87	2.87	—	2.93	—	—	4.41	6.33
50	2.73	—	2.47	—	2.92	—	—	—
80	2.48	—	—	—	—	—	—	6.29
100	2.37	2.38	2.39	2.52	2.68	3.55	4.33	—
By (5.6)		1.52	1.67	2.12	2.41	3.48	4.31	6.28

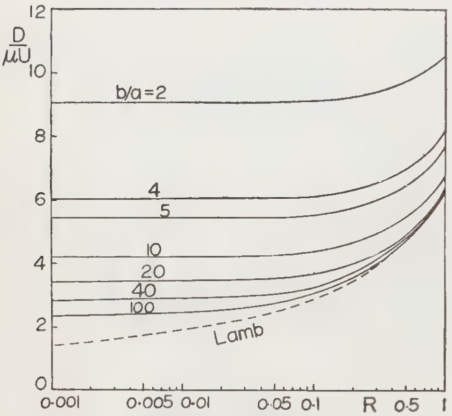

Fig. 2. Drag coefficient $D/\mu U$ plotted against Reynolds number R.
—— calculated by (5.4)
---- calculated by (5.6) (Lamb's formula)

$b>a$ so that all terms higher than k^2b^2 can be neglected, we can make use of the following approximate formulae:

$$\mathrm{Si}(kb)=kb+\mathrm{O}(k^3b^3)\,,$$
$$\mathrm{Ci}(kb)=\gamma+\ln kb+\mathrm{O}(k^2b^2)\,.$$

Then we get

$$g_1(kb)=kb(\gamma+\ln kb)-kb+\frac{\pi}{2}+\mathrm{O}(k^2b^2)\,,$$
$$h_1(kb)=-(\gamma+\ln kb)+\frac{\pi}{2}kb\quad+\mathrm{O}(k^2b^2)\,,$$
$$h_2(kb)=\frac{1}{2}-\frac{\pi}{4}kb\qquad\qquad+\mathrm{O}(k^2b^2)\,.$$

Further, making use of these expansions together with the well-known expansion formulae for the Bessel functions as well as for the circular functions, we have

$$F_1(kb)=-\frac{1}{2}kb+\mathrm{O}(k^3b^3)\,,$$
$$F_2(kb)=\frac{1}{2}-\gamma-\ln kb+\mathrm{O}(k^2b^2)\,,$$
$$F_3(kb)=\mathrm{O}(k^2b^2)\,.$$

Thus, we get ultimately approximate formula for $L/\mu U$ and $D/\mu U$, which are valid for sufficiently small kb and ka, in the forms:

$$\frac{L}{\mu U}\sim\frac{2\pi ka(b/a)}{\{1/2-\ln(2b/a)\}^2-1/4}\,, \tag{5.7}$$

$$\frac{D}{\mu U}\sim\frac{4\pi}{\ln(2b/a)}\,. \tag{5.8}$$

§ 6. Numerical Discussions

The values of the drag coefficient $D/\mu U$ have been calculated by using the three formulae (5.4), (5.6) and (5.8) respectively for various values up to unity of the Reynolds number $R(=Ud/\nu=4ka)$ as well as for various values ranging from 2 to 100 of the ratio b/a. They are given in Table I and are also plotted in Fig. 2 against R.

As far as the writer is aware, there seem unfortunately no available experimental data which may be directly comparable with our theoretical results. In the paper already cited[4)], C. M. White has given the results of his experiments with metal wires falling sideways in viscous liquids between two vertical parallel walls. According to his results, the drag coefficient $D/\mu U$ of wires falling, at very low speeds, midway between the walls is, when properly corrected for end-effects, independent of the Reynolds number R, while, at higher speeds, the drag coefficient becomes independent of the distance b of the centre of the

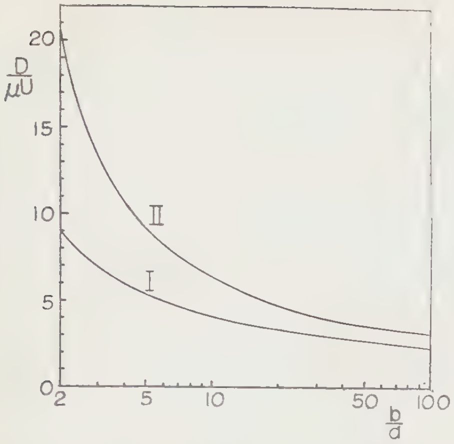

Fig. 3. Drag coefficient $D/\mu U$ at very low speeds ($R\sim0$) plotted against b/a.
I: case of single wall; calculated by (5.8)
II: White's case; calculated by (6.1)

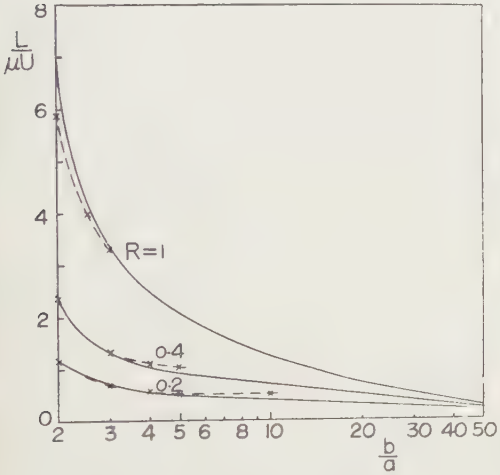

Fig. 4. Lift coefficient $L/\mu U$ plotted against b/a.
—— calculated by (5.3)
-- calculated by (5.7)

cylinder from the walls, thus agreeing with the well-known Lamb's formula for the drag coefficient of a circular cylinder moving in an unlimited mass of viscous liquid. For the case of very low speeds, White has deduced an empirical formula for $D/\mu U$, which, in our notations, may be written as:

$$\frac{D}{\mu U}=\frac{6.4}{\log(b/a)}\ . \tag{6.1}$$

It is worth noticing that, as can be seen from Fig. 2, the drag coefficient $D/\mu U$ in our case is, at very low speeds, independent of the Reynolds number R, the formula (5.8) corresponding to the above White's empirical formula (6.1).

The values of the drag coefficient $D/\mu U$ as calculated by the formula (5.8) are plotted against the ratio b/a in Fig. 3, where those calculated by the formula (6.1) are also shown for comparison.

As an addendum, the values of the lift coefficient $L/\mu U$ as calculated respectively by the formulae (5.3) and (5.7) for three values of the Reynolds number R are shown in Fig. 4 against the ratio b/a.

It will readily be seen that the cylinder experiences a repulsive force from the bounding plane wall, as in the case of a sphere moving in a semi-infinite viscous liquid along its bounding plane wall.

References

1) H. A. Lorentz: Abhandlungen über theoretische Physik. Teubner (Leipzig) (1907) 23.
2) J. Stock: Krak. Anz. (1911) 18.
3) H. Faxén: Diss. Uppsala (1921).
4) C. M. White: Proc. Roy. Soc. **A 186** (1946) 472.
5) L. N. G. Filon: Proc. Roy. Soc. **A 113** (1926) 7.
6) G. N. Watson: Theory of Bessel Functions. 2nd Ed. Cambridge Univ. Press (1948) 329.

Short Note

J. Phys. Soc. Japan **10** (1955) 416

Intensity Variations of Electron Diffraction Patterns from Metal Films of Various Thicknesses

By Shigeya Kuwabara
Faculty of Science, Hiroshima University, Hiroshima, Japan

(Received March 2, 1955)

It is well known that there are many of electron diffraction phenomena which should be interpreted according to the dynamical theory of diffraction. However, the kinematical theory may be applied for samples made up of very small crystallites. The critical limit of applicability of the two theories, which is important for the application of electron diffraction to the crystal structure determination, has been studied theoretically and experimentally by many workers1). Pinsker2), for instance, stated that the kinematical theory can safely be applied for films composed of crystallites smaller than ~ 10^{-6} cm.

In the present work an intensity measurement was carried out on Debye rings from metal films of various thicknesses. Films investigated were aluminium, silver and gold obtained by vacuum evaporation on collodion substrates. Random orientations of crystallites in the films were proved experimentally with special precautions. The experimental procedures in the present work were almost the same to those of Kimoto3).

The results were as follows:

(1) When the crystalline films were very thin the kinematical theory was applicable; however, the theory was also applicable for thicker films when the evaporation speed was smaller and the temperture of the substrate was lower.

(2) The intensity anomaly of (200)-reflexion was observed in the case of silver and gold when the films were very thin, in accordance with the other investigators.3),4)

(3) When the thickness of the films was increased gradually, at first the reflexions of lower indices showed the dynamical intensity, and fillany all the reflexions showed the dynamical one.

(4) When the films were very thick, the background of the patterns became strong and the diffraction rings became broad as the result of incoherent scattering.

(5) A close relation was found between the grain size estimated by Scherrer's formula and the limit of applicability of the two theories: i.e. the kinematical theory was applicable for the crystallites smaller than the size shown in Table 1 within the errors of few Angstroms.

Table 1. The range of application of the kinematical theory (accelerating potentials, 40 KV).

Substance	Al	Ag	Au
Grain size	<68A	<29A	<27A

The range of appicability of the kinematical theory seems to be determined not by the thickness of the films but by the grain size of crystallites.

Finally, the author wishes to express his hearty thanks to Prof. H. Tazaki of this University for his encouragement and also to Prof. S. Miyake of Tokyo Institute of Technology and Prof. R. Uyeda of Nagoya University for their fruitful suggestions and advice given in the course of the study.

References

1) G. P. Thomson: Proc. Roy. Soc. **A 125** (1929) 352.
H. Mark and R. Wierl: Zeits. f. Physik **60** (1930) 741.
S. Shirai: Proc. Phys.-Math. Soc. Jap. **15** (1933) 420.
M. Blackman: Proc. Roy. Soc. **173** (1939) 68.
2) Z. G. Pinsker: Electron Diffraction (Butterworths Scientific Publications, London, 1953) p. 167.
3) K. Kimoto: Jour. Phys. Soc. Japan **8** (1953) 762.
4) L. H. Germer: Phys. Rev. **56** (1939) 58.

JOURNAL OF THE PHYSICAL SOCIETY OF JAPAN Vol. 10, No. 6, JUNE 1955

The Zeeman Effect in Ammonia Microwave Spectra

By Yosiharu TORIZUKA, Yuzo KOJIMA and Tosihiko OKAMURA
Research Institute for Scientific Measurements, Tohoku University, Sendai
and Kozo KAMIRYO
Uda Laboratory, Research Institute of Electrical Communication, Tohoku University, Sendai

(Received December 17, 1954)

The microwave Zeeman effect of $N^{14}H_3$ inversion spctra was investigated at strong magnetic field to observe molecular g-factor in the decoupled state of spin-rotation interaction. The result on $J, K=1, 1$ line shows the transition from Zeeman effect to Paschen-Back effect near 10,000 oersteds. The obtained molecular g-factors for several different JK value give some information on g-factor of $N^{14}H_3$ both parallel and perpendicular to the molecular axis.

§1. Introduction and Experimental Procedure

The microwave Zeeman effect in the inversion spectra of $N^{14}H_3$ has been investigated by several workers[1,2,3,4,5] at relatively low magnetic fields of several thousand oersteds. But at such fields the decoupling of the spin-rotation interaction is unsatisfactory, as suggested by C.K. Jen[3].

We attempted to study the Paschen-Back effect of $N^{14}H_3$ at a strong magnetic field in the complete decoupling state, in which the molecular g-factor of $N^{14}H_3$ should be observed, unaffected by nuclear g-factor of N^{14}.

In order to investigate the Zeeman effect of microwave spectrum at a strong magnetic field, a 10-ton electromagnet having ring-shaped pole pieces was constructed. And for the absorption cell, a K-band waveguide of about 2 meter length was circularly bended at a diameter of 70 cm and placed between pole pieces described above in such a way that the narrow side of waveguide wall would be perpendicular to the static magnetic field. Thus the magnetic field up to 15,000 oe, perpendicular to the r-f electric field, was easily applied to the full length of 2-meter absorption cell when the width of pole face was 4 cm and the gap between two pole pieces was 1.55 cm. The uniformity of magnetic field was within 0.4% along the longitudinal axis of the absorption cell.

The common sweep method was employed to observe the spectral line of $N^{14}H_3$; the third harmonics from the output of a type 723 A/B klystron was generated by a crystal multiplier as the source of radiation.

In order to measure the frequency differences between separated Zeeman components, two methods were employed. The frequency modulation of the klystron source by a 5 Mc/sec quartz crystal oscillator produced images of the spectral lines spaced by the modulating frequency, namely, at the intervals of 5 Mc/sec, so the frequency differences between the separated Zeeman components could be measured from these 5 Mc/sec scales in oscilloscope photograph.

A variable frequency oscillator was used for another method, in which one could vary the modulating frequency so as to make images from adjacent lines coincide with one another, and could read the frequency differences directly from the frequency of oscillator calibrated by means of the standard frequency of 4 Mc/sec of JJY. The results by both methods were in agreement within experimental errors. Whole setups of experimental apparatus are shown in Photo. 1.

The pressure of $N^{14}H_3$ gas in the absorption cell was kept at about 10^{-2} mm Hg during the experiment in order to make observations under suitable conditions.

§2. Theoretical Background and Experimental Results

The molecule in the $^1\Sigma$ ground state has very small magnetic moment due to molecular rotation. It is possible to detect small frequency splitting with microwave Zeeman effect as follows:

$$\Delta\nu = g(\mu_0/h)H\,, \tag{1}$$

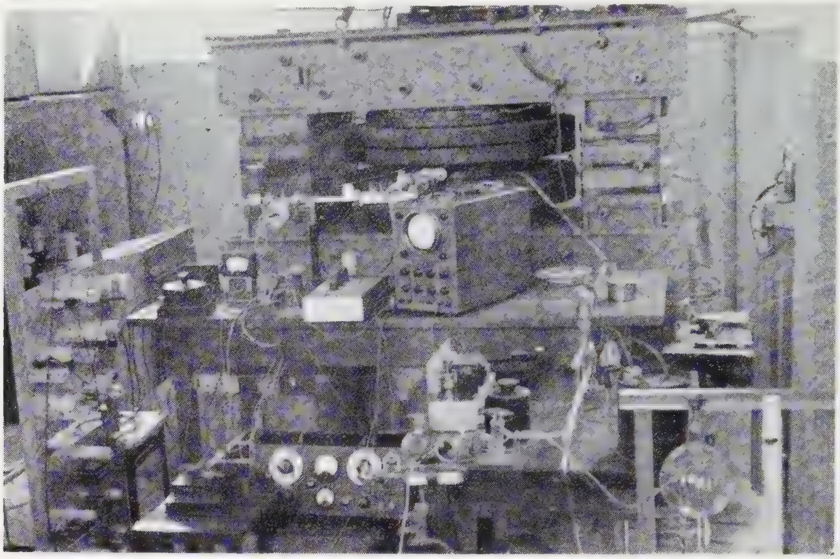

Photo. 1. The microwave spectroscope for measuring Zeeman and Paschen Back effects.

where $\Delta\nu$ = difference between the frequency of a Zeeman component and that of the undisplaced line, μ_0 = nuclear magneton, g = gyromagnetic ratio.

On the other hand, magnetic moment of nuclei is often strongly coupled with molecular axis.

In $N^{14}H_3$ there exists an interaction between nucleus and molecular axis. In the absence of an external field spin-rotation coupling is still in effect.

The Zeeman effect on the resulting hyperfine pattern has been treated theoretically by Jen[2)]. When the Zeeman energy is smaller than the spin rotation coupling, the unperturbed state is labeled by J, I, F, M, where J = angular momentum quantum number, $F = J+I, J+I-1, \cdots, J-I+1, J-I$ and $M = F, F-1, \cdots, -F+1, -F$. The total hamiltonian $\mathscr{H}$, including the interaction with an external magnetic field, of a molecule having a molecular g-factor and single nucleus coupled with the molecular axis, is

$$\mathscr{H} = \mathscr{H}_0 - g_{\text{mole}}\,\mu_0\,\boldsymbol{J}\cdot\boldsymbol{H} - g_{\text{nuc}}\,\mu_0\,\boldsymbol{I}\cdot\boldsymbol{H}, \qquad (2)$$

where g_{mole} = g-factor of the molecule along J, g_{nuc} = g-factor of the nucleus coupled with molecule, $\boldsymbol{J}$, $\boldsymbol{I}$ = vector operators of J, I.

The interaction energy stated by Jen is

$$\Delta W = -M\mu_0 H(\alpha_J\, g_{\text{mole}} + \alpha_I\, g_{\text{nuc}}), \qquad (3)$$

where

$$\alpha_J = [F(F+1) + J(J+1) - I(I+1)]/2F(F+1),$$

$$\alpha_I = [F(F+1) + I(I+1) - J(J+1)]/2F(F+1).$$

For the Zeeman splitting of $N^{14}H_3$ inversion spectrum, splitting of Zeeman component takes the following form for the central line.

$$\Delta\nu_0 = \pm\frac{\mu_0 H}{h}\left\{\frac{g_{\text{mole}}+g_{\text{nuc}}}{2} + \frac{J(J+1)-I(I+1)}{F(F+1)}\,\frac{(g_{\text{mole}}-g_{\text{nuc}})}{2}\right\}, \qquad (4)$$

where selection rules for σ transition of $N^{14}H_3$ inversion spectrum are

$$\Delta J = 0, \qquad \Delta M = \pm 1, \qquad \Delta F = 0.$$

When the magnetic field is so strong that spin-rotation coupling breaks down, the splitting of the Zeeman effect changes to Paschen-Back effect.

Paschen-Back effect is observed by Jen[3)] in $N^{14}N^{14}O$ but his result in $N^{14}H_3$ is not complete.

Fig. 1 shows the Zeeman effect of $N^{14}H_3$ with assigned rotational quantum number $J = 1$, $K = 1$. It is seen that a linear relation is maintained up to 8,000 oersteds which corresponds to g-factor being equal to 0.475. For still higher magnetic field, there is a slight non-linearity and gradual approach to a new straight line, of which the slope corresponds to g-factor of 0.550. The experimental errors are limited to the range of 1% which arise mainly from magnetic field measurement. The change in g-factor shows the transition from the Zeeman effect in which molecular g-factor was combined with nuclear g-factor, to Paschen-Back effect in the decoupled state.

The splitting of Paschen-Back effect in $N^{14}H_3$ is given as follows.

$$\Delta\nu=\pm\frac{2\mu_0 H}{h}g_{\text{mole}}. \tag{5}$$

That is, splitting is proportional to molecular g-factor. We obtained from the present results using equations (4) and (5),

$$g_{\text{mole}}=0.550\pm0.005,$$
$$g_{\text{nuc}}=0.400\pm0.004.$$

The value of nuclear g-ractor of N^{14} determined from present study coincides with published nuclear resonance data of 0.403 within the range of experimental errors.

Fig. 2 gives experimental results of 3–3 line in $N^{14}H_3$. The separation of the Zeeman component is linearly proportional to the applied magnetic field up to 14,000 oersteds. In 3–3 line we could not observe Paschen-Back effect explicitly, but from the separation at 14,000 oe, we could estimate $g_{\text{mole}}=0.510$ in 3–3 line. In the range of weak field, if we substitute $g_{\text{mole}}=0.510$ and $g_{\text{nuc}}=0.403$ in equation (4), g-factors at weak field is shown to consist of three factors as follows:

$g=0.483$ for $F=4$,
$g=0.501$ for $F=3$,
$g=0.546$ for $F=2$.

The observed g-factor should be some intermediate value of the above three, according to the transition probability of each component of fine structure. Therefore, the coincidence of the observed g-factor in 3–3 line at low and high field seems to be reasonable.

In 2–2 and 6–6 line of $N^{14}H_3$, the similar field dependence, having a slope slight different from that observed in 3–3 line was observed.

Table I shows rotational g-factor of $N^{14}H_3$ determined at 14,000 oe for different JK value.

In the nonlinear molecule, molecular g-factor is a fuction of J and K. For the symmetric molecule, T.R. Eshbach and M.W.P. Strandberg[5] have found the following equation:

$$g(J,K)=g_N+(g_K-g_N)\frac{K^2}{J(J+1)}, \tag{6}$$

g_K, g_N defines the component of magnetic moment $g_K\mu_0 K$ along the symmetry axis and the component of $g_N\mu_0 N$ (where $N=\sqrt{J(J+1)-K^2}$) perpendicular to this axis respectively.

Table 1. Molecular g-factors of $N^{14}H_3$ deduced from σ component Zeeman effect measurements at 14,000 oersteds.

J,K	1,1	2,2	3,3	6,6
g(J,K)	0.55	0.53	0.51	0.50

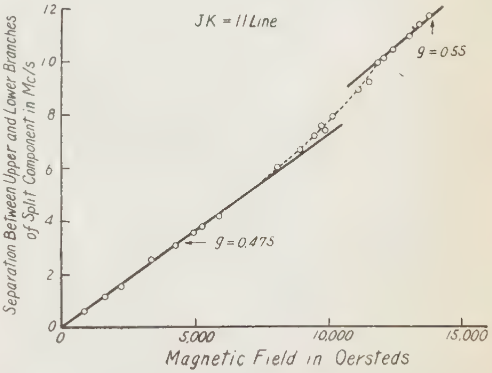

Fig. 1. Zeeman and Paschen-Back splitting for JK = 11 line of $N^{14}H_3$ as a function of the magnetic field.

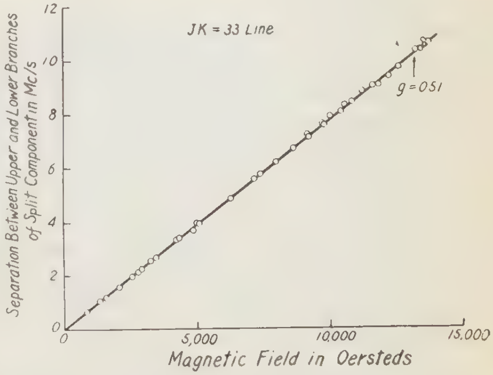

Fig. 2. Zeeman splitting for JK = 33 line of $N^{14}H_3$ as a function of the magnetic field.

From our data, the extrapolated g_N and g_K are

$$g_N=0.62\pm0.02\,,$$
$$g_K=0.48\pm0.01\,.$$

These results can be compared with Eshbach and Strandberg's in $N^{15}H_3$.

Acknowledgement

We wish to thank Mr. K. Sinozuka and Mr. K. Inagaki for their technical assistance in construction of the apparatus.

References

1) D. K. Coles and W. E. Good: Phys. Rev. **70** (1946) 979.
2) C. K. Jen: Phys. Rev. **74** (1948) 1396.
3) C. K. Jen: Phys. Rev. **76** (1949) 1494.
4) C. K. Jen: Phys. Rev. **81** (1951) 197.
5) J. R. Eshbach and M. W. P. Strandberg: Phys. Rev. **85** (1952) 24.

JOURNAL OF THE PHYSICAL SOCIETY OF JAPAN Vol. 10, No. 6, JUNE 1955

Variation in the Lattice Constant of Evaporated Potassium Chloride

By Yasushige FUKANO*

Faculty of Engineering, Nagoya University, Nagoya, Japan

(Received February 3, 1955)

The lattice constant of evaporated KCl-crystals was measured with an accuracy of 0.01% using gold foil as a standard. The lattice constant of gold foil was calibrated in terms of TlCl and was found in agreement with the X-ray value. Spacings of KCl measured just after evaporation are larger than the X-ray value by about 0.15%, provided the size of KCl-crystals are larger than 150Å. Spacings decrease when evaporated specimens are exposed to the air or are heated in vacuum. The lowest value of lattice constant obtained in this experiment is in agreement with the X-ray value within the experimental error.

§ 1. Introduction

Finch and Fordham[1] measured lattice constants of twelve alkali halides using gold foil as a standard. They found that the measured values of most specimens were higher than the corresponding X-ray values by about 0.5%. Then, Finch and Wilman[2] measured the lattice constant of the gold foil in terms of a colloidal graphite standard, and found the mean value of the measured spacing to be in agreement with the X-ray value within the experimental error.

Boochs[3] measured the lattice constants of evaporated alkali halides in terms of evaporated gold. He found that the measured values were about 0.1% less than the corresponding X-ray values when the halides were composed of small (less than 100Å) crystallites. After the crystallites were recrystallized by exposing them to air, the measured value were in agreement with the X-ray value. Boswell[4] measured the lattice constants of alkali halides in terms of TlCl standard, and obtained almost the same results as those of Boochs. The probable error of his experiment was 0.05%. He interpreted the change in lattice constants of very small crystallites as Lennard-Jones' effect.

Garrod[5] reported that the lattice constant of NaCl measured in terms of a graphite standard was in agreement with the X-ray value to within the probable error of ±0.05 %, provided the crystal size was larger than 100Å. Moreover, he measured the lattice constant of gold foil in terms of the graphite standard and obtained a value which was 0.12% less than the X-ray value. Therefore, he concluded in his thesis that gold foil was not suitable as a standard substance. Rymer and Butler[6] accurately measured the lattice constant of gold foil, and they concluded that the influence of surface tension is considerable in measured values of the constant. Rymer and Wright7) also obtained the same result and they concluded that gold foil is unreliable as a standard substance. Riedmiller8), Chia-Si Lu and Malmberg9) and Boswell4) suggested that gold foil was unreliable as a standard substance.

---

* Now at Research Institute for Iron, Steel and Other Metals, Tōhoku University.

Rymer and Wright7) carried out the absolute measurement of wave-length of electrons and pointed out that the lattice constant of KCl is in agreement with the X-ray value to within the probable error of ±0.011%. Hambling10) suggested that KCl is suitable as a standard substance because the X-ray value he accurately measured is in agreement with Rymer and Wright's result.

Garrod11), citing the results of Boochs, Boswell and Garrod concluded that a lattice constant of alkali halide measured by means of X-rays and one measured by electrons are in good agreement provided the crystal size is larger than 100Å.

On the other hand, Katō12) found that the lattice constant of evaporated KCl measured by electrons in terms of gold foil was larger than the X-ray value provided the crystal size was larger than 150Å. The lattice constant decreased gradually when specimens were exposed to the air and finally reached a stationary value. The stationary value was 0.13% larger than the X-ray value. Although the deviations he observed were not as large as those observed by Finch and Fordham, Katō's results were not in agreement with those obtained by Boochs, Boswell, Garrod and Rymer and Wright.

The present work was undertaken to confirm Katō's results with greater accuracy using a high resolution electron diffraction camera.

§2. Experimental Method

In the present work, KCl was evaporated on gold foil in vacuum. Gold foil was commercial beaten foil which was of the same origin as that used by Katō. The sample of KCl was produced by Merk (German). The evaporation was carried out in a vacuum evaporation unit. Specimens were exposed to the air for at least one minute when they were transferred from the evaporation unit to a diffraction camera.

Specimens examined were prepared under the following five conditions:

(1) Pressure of vacuum was changed from 10^{-2} to 10^{-5} mmHg.

(2) Evaporation was carried out by tungsten or platinum filaments.

(3) Distance between a filament and a substrate gold foil was 5 or 15 cm.

(4) Mean thickness of evaporated KCl was 200 or 400Å (calculated from evaporaed mass).

(5) A few specimens were annealed for about two minutes in the evaporation unit by heating a tungsten filament to red-white, which filament was placed at a distance of 2 cm from the specimen.

Superimposed patterns (Finch1)) of KCl and Au were obtained by a high resolution electron diffraction camera. The diameters of superimposed patterns were measured by means of an optical comparator. To calculate

Table I. An example of calculation.

Au (a=4.070 kX)				KCl			
$h\ k\ l$	D (mm)	Probable error (%)	$2\lambda L$ (mmkX)	$h\ k\ l$	D (mm)	Probable error (%)	a (kX)
1 1 1	19.171	0.004	45.0383	2 0 0	14.329	0.008	6.2870
2 0 0	22.138	0.003	45.0379	2 2 0	20.267	0.006	6.2868
2 2 0	31.316	0.009	45.0378	4 0 0	28.680	0.002	6.2844
3 1 1	36.731	0.009	45.0370	4 2 0	32.051	0.004	6.2879
				4 4 0	40.553	0.002	6.2884
				6 0 0	43.049	0.008	6.2840
				6 2 0	45.358	0.001	6.2875
	Average		45.0378		Average		6.2866
	Probable error		±0.001%		Probable error		±0.004%

lattice spacings from measured ring diameters we adopted an approximate Bragg formula expressed in the following form (Boswell[4]):

$$\frac{dD}{1+\frac{3}{32}\left(\frac{D}{L}\right)^2}=2\lambda L \qquad (1)$$

where λ is the wave-length, D a ring diameter, d a lattice spacing and L the camera length. The camera length was about 40 cms. The value of $2\lambda L$ was determined from diffraction rings of gold by assuming its lattice constant to be 4.070 kX, (Wyckoff[13]).

All the systematic errors in the determination of lattice constant (Katō[12]) were either eliminated or proved to be negligible. Since a high resolution electron diffraction camera was used in the present experiment, effects of unfavorable geometrical arrangements were easily excluded. After excluding all the effects of systematic errors, the lattice constant of KCl was determined from each photograph to within the probable error ±0.01%. An example of data is given in Table I.

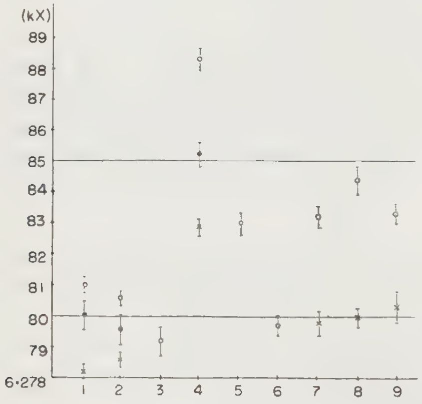

Specimen nos.	1	2	3	4	5	6	7	8	9
Vacuum (mmHg)	10^{-5}	10^{-5}	10^{-5}	10^{-5}	10^{-5}	10^{-5}	10^{-3}	10^{-3}	10^{-2}
Filament	Pt	W	W	W	W	W	W	W	W
Distances between a filament and a substrate (cm)	5	5	5	15	15	15	5	5	5
Annealing	no	no	yes	no	yes	yes	no	no	no
Thickness (Å)	200	200	400	400	400	200	200	400	200

Fig. 1. Variations in the lattice constant of evaporated KCl.

§ 3. Lattice Constant of Gold Foil

Since several authors mentioned that gold foil is inadequate as a standard substance, the following experiments were carried out: Superimposed diffraction patterns of Au and TlCl were taken, and $2\lambda L$ was calculated for both Au and TlCl, assuming X-ray value of lattice constant for TlCl to be $a=3.8340$ kX. It was found that both values of $2\lambda L$ were in agreement within a probable error of 0.007%. To examine fluctuations of λL's obtained from rings of gold, deviations

$$\delta_{(hkl)}=\frac{\lambda L_{(hkl)}-\lambda L_{(111)}}{\lambda L_{(111)}} \qquad (2)$$

were calculated. The result is given in Table II. The mean deviation for many specimens is less than 0.01%. After the foil was annealed at about 400°C* the deviation decreases to 0.002%.

Table II. Fluctuations of λL calculated from each ring of gold.
$\delta_{(hkl)}=[\lambda L_{(hkl)}-\lambda L_{(111)}]/\lambda L_{(111)}$

Sample Nos.	$\delta_{(200)}$	$\delta_{(220)}$	$\delta_{(311)}$
1	0.001	0.001	0.003
2	0.002	−0.001	0.002
3	0.007	−0.012	0.004
4	0.013	−0.012	−0.003
5	0.009	0.006	−0.009
6	0.002	0.001	−0.000
7	0.003	0.002	−0.000
8	0.011	0.005	0.004
9	0.008	0.003	0.001
10	0.014	−0.017	−0.009
Mean	0.007	0.000	−0.001

Form these results, gold foil used in the present experiment was reliable as a standard with an error less than 0.01%. The influence of surface tension as observed by Rymer and Butler was of a negligible order.

§ 4. Experimental Results and Discussions

Rings of KCl are broad (a half width is about 200 μ), intense and continuous just after evaporation. The rings become sharper, weaker and often spotty after specimens are exposed to the air. Finally, they become invisible; the period after which rings become invisible depends on the temperature and the humidity. Crystal sizes determined from breadth of rings and electron-micrographs are about 150Å just after the evaporation and are about 500Å after exposure to the air. We observed under an electron microscope the variation of crystal sizes through recrystallization under the influence of water vapor existing in the air.

---

* The intensity of rings changed remarkably after the annealing.

Spacings of KCl obtained in the present work are illustrated in Fig. 1, in the legend of which the five conditions mentioned in the previous section are indicated. Each column corresponds to one specimen; specimen numbers are given on the first line. The X-ray value 6.278 kX is indicated in the figure by a horizontal line. Plots indicated by open circles are spacings measured just after evaporation, crosses are spacings measured after long exposure,* and solid circles are those measured after medium exposure. Vertical lines attached to each plot show probable error.

The following tendencies are found in Fig. 1.

(a) For all the specimens measured lattice constants are larger than the X-ray value and they decrease as the period of exposure increases. Lattice constants also decrease after annealing (see, Nos. 3, 5 and 6 in Fig. 1). Relatively low values in Nos. 1 and 2 may also be due to annealing effect because in these cases filaments are near the substrate. Because it is most unlikely that the lattice constant of gold changes during an experiment it is natural to conclude that evaporated KCl has a larger lattice constant than that of bulk crystals. The larger constant decreases by the process of recrystallization and finally become the same as in bulk crystals. The present author believes that the large deviation observed by Finch & Fordham is in part attributable to an actual change of lattice constants of alkali halides, although Garrod attributed all the deviation to the change of the constant of gold.

(b) In the present experiment, the stationary value of lattice constant as stated by Katō was not observed and the observed lowest value was in agreement with the X-ray value. The present author interprets Katō's result as follows: Since diffraction rings become weaker and weaker as the recrystallization proceeds, Katō was unable to measure rings from sufficiently recrystallized specimens which should have given spacings smaller than the stationary value. The same circumstance is also experienced in our specimens Nos. 3–9. Although Katō confirmed the existence of the stationary value by using specimens prepared by drying the solution, it may not be reasonable to put any great weight on his experiment because such specimens are difficult to handle and Katō carried out a few measurements only.

Garrod[5] and Rymer and Wright[7] stated that the spacing of evaporated KCl is in agreement with that of bulk crystals within an experimental error of 0.05%. Their result is in accordance with the present results of Nos. 1, 2 and 3 (Fig. 1). It must be noted that the agreement does not usually occur as shown by Nos. 4–9 (Fig. 1).

(c) The question as to why the lattice constant of KCl is increased after evaporation has not yet been answered. The cause of this phenomenon is supposed to be impurities or imperfections in evaporated crystals. The most probable impurity is WO_3 which is evaporated from tungsten filaments. Since the deviation becomes larger as the vacuum becomes lower, WO_3 may be one of the causes (compare Nos. 2 and 9 in Fig. 1). However, because the deviation is observable also when KCl is evaporated from a platinum filament, it is sure that there is a cause other than WO_3.

The present author supposes that imperfections in crystals may be that other cause. According to Miller & Russell[14], the lattice constant should be increased about 0.001% when there is one vacancy per 10^5 atoms. In order to explain the present experimental results, KCl crystals just after evaporation should have one vacancy per 10^3 atoms. This density of vacancies is one hundred times greater than the previously observed largest value, one per 10^5 atoms.

§ 5. Conclusion

From the results of the present experiment the author concludes as follows:

(1) Just after evaporation the lattice constant of KCl is larger than the X-ray value by about 0.15%.

(2) The larger lattice constant decreases when KCl-crystals recrystallize by the influence of humidity or by annealing.

(3) After sufficient recrystallization the lattice constant of KCl coincides with X-ray value.

(4) The cause of the increasing of lattice

---

* If the exposure is extended, rings become too weak to be measured with sufficient accuracy.

constant is not yet clear. Impurities and imperfections in crystallites are suggested to be the cause.

Acknowledgement

It is a pleasure for the author to express his appreciation to Professor R. Uyeda for his kind guidance and encouragement throughout this work. He is also indebted to Mr. T. Ichinokawa for his collaboration at some stages of this work.

References

1) G. I. Finch and S. Fordham: Proc. Phys. Soc. London **48** (1936) 85.
2) G. I. Finch and H. Wilman: Ergebn. exakt. Naturw. **16** (1937) 353.
3) H. Boochs: Ann. Phys., Lpz. **35** (1939) 333.
4) F. W. C. Boswell: Proc. Phys. Soc. **A64** (1951) 465.
5) R. I. Garrod: Thesis (University of London) (1947).
6) T. B. Rymer and C. C. Butler: Proc. Phys. Soc. **59** (1947) 541.
7) T. B. Rymer and K. H. R. Wright: Proc. Phys. Soc. London **A215** (1952) 550.
8) R. Riedmiller: Z. Phys. **102** (1936) 408.
9) Chia-Si Lu and E. W. Malmberg: Rev. Sci. Instrum. **14** (1943) 271.
10) P. G. Hambling: Acta Cryst. **6** (1953) 98.
11) R. I. Garrod: Proc. Phys. Soc. **A65** (1952) 292.
12) N. Katō: J. Phys. Soc. Japan **6** (1951) 502.
13) R. W. G. Wyckoff: The Structure of Crystals, 3rd Edition Supplement.
14) P. H. Miller and B. R. Russell: J. App. Phys. **24** (1952) 1163.

JOURNAL OF THE PHYSICAL SOCIETY OF JAPAN Vol. 10, No. 6, JUNE 1955

Elastic Properties of Lead Zirconate

By Masakazu MARUTAKE and Takuro IKEDA

Kobayasi Institute of Physical Research, Kokubunji, Tokyo

(Received February 18, 1955)

Elastic properties of $PbZrO_3$ and its solid solutions with $PbTiO_3$, $BaZrO_3$ and $SrZrO_3$ were studied by measuring resonant frequencies of bars by the composite-bar method. In the antiferroelectric range, they show elastic behaviors similar to barium titanate; and to explain these anomalies, interactions between strains and anti-parallel oriented dipoles —micro-piezoelectric effects—were introduced in a phenomenological theory. It was also pointed out that the elastic compliance coefficient for constant polarization (s^P) of $BaTiO_3$ changes discontinuously at the Curie point and that the Devonshire's theory is insufficient.

In addition, it was revealed from elastic and dielectric measurements that $(Pb_{0.85}-Sr_{0.15})ZrO_3$ has another new phase, the nature of which, however, could not be determined.

§ 1. Introduction

It is well known that the ferroelectric materials (rochelle salt, KDP and barium titanate) show anomalous behaviors in the dielectric, piezoelectric and elastic properties, and the relations between these properties have been studied both experimentally and theoretically by many authors. The antiferroelectric materials, however, show no piezoelectric effects due to antiparallel dipole orientations, so it is to be expected at first that the relationship between the dielectric and elastic properties of these materials is different from that of ferroelectric ones. In this study, elastic properties of lead zirconate[1] and its families[2][3] are measured and are compared with those of barium titanate for the purpose of elucidating these points.

Usually, elastic constants of piezoelectric materials are measured by the self-resonance method. This method, however, is not applicable for lead zirconate, because it is non-piezoelectric. Accordingly, we adopt the so-called "composite-bar method"[4], which was previously used by S.L. Quimby, J. Zacharias, L. Balamuth and others[5] in measuring the elastic constants and losses of non-piezoelectric materials.

As the specimens here employed are polycrystalline ceramics, the measured values are averaged constants of those of the single crystals. Although this is not favorable to quantitative discussions, yet it is sufficient to make qualitative discussion on the anomalous properties of lead zirconate, by introducing the "micro-piezoelectric" interactions. In this connection, elastic properties of barium titanate are also discussed.

§ 2. Experimental Procedure

An X-cut quartz bar, with its length along Y-axis, and with silver electrodes on its X-faces, is cemented endwise to a sample with equal cross-section (Fig. 1 (a)). When the constant alternating voltage is applied and its frequency is varied, a resonance curve is obtained by measuring the electric current through the electrodes (Fig. 1 (b)). We shall denote maximum and minimum current by I_m and I_n, and the corresponding frequencies by f_m and f_n, respectively, then the resonant frequency f_0 of the composite bar is given as follows[5]:

$$f_0 = f_m + (f_n - f_m) \cdot I_n / (I_m + I_n) . \qquad (1)$$

If the resonant frequency of the quartz bar alone is f_q and $f_0 - f_q$ is small, the resonant frequency of the sample is given by

$$f_s = f_0 - (f_q - f_0)(m_q / m_s) , \qquad (2)$$

where m_q and m_s are masses of the quartz and the sample. When the density ρ and the length l of the sample are known, the elastic compliance coefficient is calculated by

$$s = 1/(4 \rho l^2 f_s^2) . \qquad (3)$$

The logarithmic decrement is given by

$$\begin{aligned} \delta &= 2\pi (1 + m_q/m_s) \{ (f_n - f_0)(f_0 - f_m) \}^{1/2} / f_0 \\ &= 2\pi (1 + m_q/m_s)(f_n - f_m)/f_0 \\ &\quad \times (I_m I_n)^{1/2} / (I_m + I_n) . \qquad (4) \end{aligned}$$

In this experiment, several quartz bars were employed with resonant frequencies (f_q) of *ca.* 90 kc, and with cross-sections of 3×3 mm². The resonant frequencies of samples (f_s) were chosen within 90±10 kc, and so the lengths of samples were about 20 mm.

The composite bar is supported at the nodal lines of the quartz bar with knife edges, which serve also as leads, and is suspended in an electric furnace (Fig. 2). The temperature is measured with a mercury thermometer which is placed near the sample. The bar and a small resistance (R) in series are connected to a variable-frequency oscillator with a low output impedance. The electric current is measured by measuring the voltage through the resistance R with a valve voltmeter. The frequency is measured by the use of a mixer and beat-counter apparatus (a double-heterodyne method), and as this measurement is very accurate, the accuracy of the experiment is mainly determined by that of measuring the dimensions of the samples.

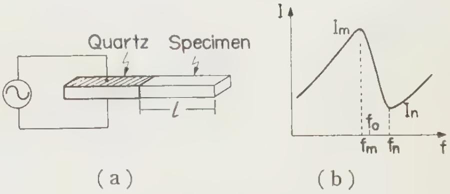

(a) (b)

Fig. 1. The composite bar method.

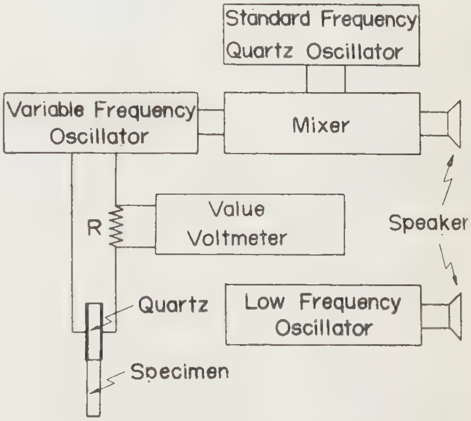

Fig. 2. Measuring apparatus.

§ 3. Preparation of Samples and Experimental Results

All samples are ceramics, and are sintered at 1300~1400°C, the porosity p (the ratio of the volume of the holes to the whole volume) of each sample being between 10~20% as determined from density measurements.

Fig. 3 shows the elastic compliance coefficient of PbZrO₃ at various temperatures. At the Curie point, a large change is seen. For comparison, the compliance coefficient of barium titanate is measured by the same method, and is shown in the same figure.

In Fig. 4, the elastic properties of $Pb(Zr_{0.95}-Ti_{0.05})O_3$ and $Pb(Zr_{0.90}-Ba_{0.10})O_3$ are shown, which are known to have three phases (antiferro-, ferro- and paraelectric)[2)3)]. Corresponding to the variation of dielectric constants with temperature, two transition points are seen in their elastic properties.

Finally, in Fig. 5 the properties of (Pb–Sr)ZrO_3 system are shown, which have three phases (antiferro-, antiferro- and paraelectric)[3)].

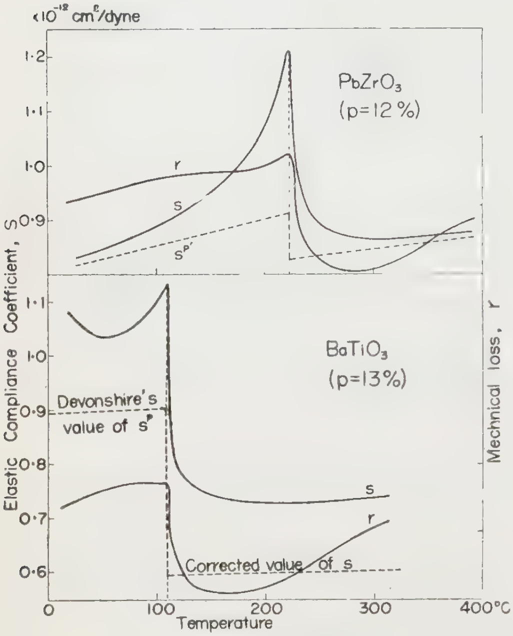

Fig. 3. The elastic compliance coefficient and the mechacinal loss of $PbZrO_3$ and $BaTiO_3$.

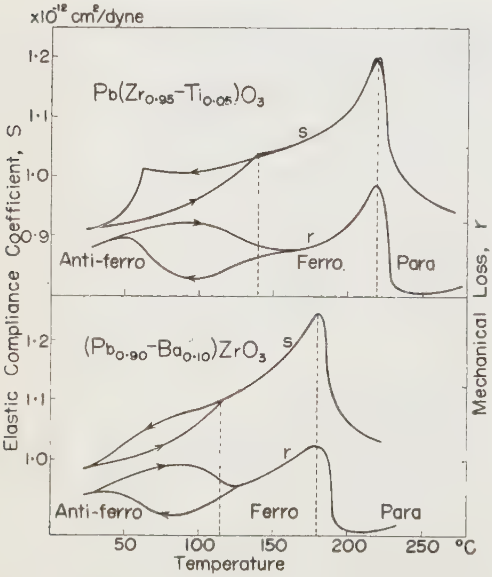

Fig. 4. The elastic compliance coefficient and the mechanical loss of $Pb(Zr_{0.95}-Ti_{0.05})O_3$ and $(Pb_{0.90}-Ba_{0.10})ZrO_3$.

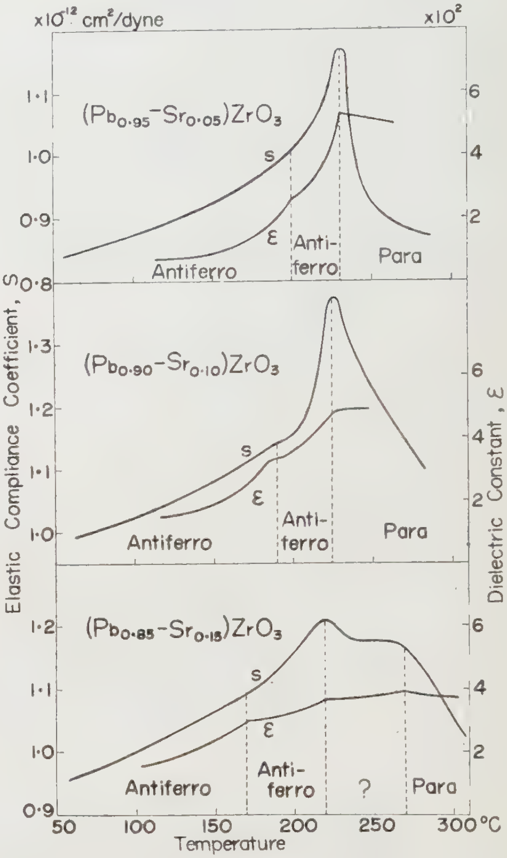

Fig. 5. The elastic compliance coefficient and the dielectric constant of (Pb–Sr)ZrO_3 system.

With regard to mechanical losses, exact values are not evaluated, but the ratios of the minimum of the current to the maximum ($I_n/I_m=r$) are shown in Figs. 3 and 4, which give approximate measures of losses (*cf.* Eq. (4)).

§ 4. Discussion

(a) Lead Zirconate and Barium Titanate

In Fig. 3, a large peak is seen in the elastic compliance coefficient of lead zirconate as in the case of barium titanate. Let us consider, first, on the elastic properties of ferroelectric substances.

In rochelle salt, H. Mueller[6)] previously found that all anomalies should be attributed to the dielectric anomaly by taking account of the piezoelectric interactions, and his method is considered to be valid generally for ferroelectric substances. Especially, A.F. Devonshire[7] discussed the elastic and piezoelectric properties of barium titanate. He assumed that the elastic compliance coefficient for constant polarization s^P is nearly independent of temperature and is unaffected by phase transition. And he calculated that $s_{11}{}^P=0.90\times10^{-12}$ cm^2/dyne etc., by using the data of W.P. Mason and others[8], who measured the elastic constants of the single crystal at room temperature by the pulse method. The present result, however, gives $s\approx0.6\times10^{-12}$ cm^2/dyne above the Curie point, after taking account of the porosity correction.[9] (In the paraelectric region, we need not distinguish s^P from s^E.) Accordingly, s^P, the "proper" compliance coefficient, is considered to jump from 0.6 to 0.9×10^{-12} cm^2/dyne at the transition point, and the remainder of the elastic anomaly is to be attributed to the piezoelectric interaction (*cf.* Fig. 3). In the case of rochelle salt and KDP, such jumps of s^P are small and can be neglected.[10] A large change of s^P in barium titanate is considered to be due to the greater deformation at the transition.

Next, we shall consider on lead zirconate. The crystal deformation is large at the transition point, and a jump of the elastic constant is expected. It has, however, no piezoelectric interaction; therefore, in order to explain the remaining anomalies, we shall have to take into account the microscopic interactions. That is, an external stress deforms the crystal and changes the magnitude of the individual dipole. Accordingly, the measured elastic constant may be different from the proper elastic constant without dipole change.

Namely, after Devonshire's method,[11] we shall denote by P_a and P_b the polarizations of the two equivalent lattices, each of which can be polarized, and put

$$\left.\begin{aligned} P&=P_a+P_b\,,\\ p&=P_a-P_b\,, \end{aligned}\right\} \tag{5}$$

then the free energy can be expressed in the following form by omitting unnecessary terms. (Devonshire's notations are used.)

$$A=\tfrac{1}{2}c^p x^2+g'xp^2+\tfrac{1}{2}\chi'^x p^2+\tfrac{1}{4}\xi'^x p^4\,, \tag{6}$$

where x represents strain components and a cross term $g'xp^2$ is newly introduced. Here the terms in powers of P are also omitted, because they do not affect the following discussions.

In the antiferroelectric range, there exist a spontaneous antiparallel polarization p_s and a spontaneous deformation x_s, and we shall replace p and x by $p+p_s$ and $x+x_s$. Then by differentiating A and after simple calculations, we obtain the following formulae.

$$\left.\begin{aligned} X&=-(\partial A/\partial x)=-c^p x-(2g'p_s)p\\ E'&=(\partial A/\partial p)=(2g'p_s)x+(\chi'^x+2p'x_s+3\xi'^x p_s{}^2)p. \end{aligned}\right\} \tag{7}$$

Here, X is a stress, and E' may be considered to be a microscopic field, though it is not an observable quantity; also, cross terms $(2g'p_s)$ may represent microscopic piezoelectric effects.

As usual c^p, the proper elastic constant for constant polarization, is considered to be nearly independent of temperature, except a jump at the transition point, but it cannot be measured under ordinary conditions; and if we assume that measurements are under constant-E' conditions, measured values $s^{E'}$ are easily shown to have anomalies in the antiferroelectric range. Although we used ceramic samples, and are unable to discuss quantitatively, we may conclude that elastic anomalies are due partly to an abrupt change of s^p, which is tentatively shown by a dotted line in Fig. 3, and partly to a micro-piezoelectric interaction.

(b) Solid Solutions of $PbZrO_3$ with $PbTiO_3$, $BaZrO_3$ and $SrZrO_3$

Elastic properties of $Pb(Zr-Ti)O_3$ and $(Pb-Ba)ZrO_3$ systems correspond with dielectric behaviors. Origins of small losses in the ferroelectric range are not clear.

The dielectric properties of $(Pb-Sr)ZrO_3$ system were studied in detail by G. Shirane[3], and were reported to have three phases: antiferro-, antiferro- and paraelectric. In this study, elastic properties of $(Pb-Sr)ZrO_3$ with 5 and 10% Sr correspond with Shirane's results. In the elastic properties of $(Pb_{0.85}-Sr_{0.15})ZrO_3$, however, another peak was found at *ca.* 270°C, and this was found to correspond to the peak of the dielectric constant which we measured till higher temperature (Fig. 5). Nevertheless, as X-ray measurements[12] detect no anomaly at this temperature, it is not clear whether a phase transition occurs or not. (The solid solution of $Pb(Zr-Sn)O_3$ has similar properties to this[12].)

§ 5. Summary

In this study, following results were obtained:

(a) Elastic compliance coefficients for constant polarization s^P's of barium titanate have discontinuous changes at the Curie point, and Devonshire's theory is insufficient. Amount of such a change will be related to the magnitude of the spontaneous deformation of the crystal and is known to be very small in rochelle salt and KDP.

(b) Lead zirconate shows similar behaviors in the elastic properties to those of barium titanate, and this is explained qualitatively.

(c) $(Pb_{0.85}-Sr_{0.15})ZrO_3$ seems to have another new phase.

Finally, we wish to express our sincere thanks to Dr. H. Kawai and to Dr. O. Nomoto for their kind encouragement and criticism, to Mr. A. Takeda for his helpful discussions and to Mr. K. Uchino for the preparation of specimens. This work was financially supported by the Scientific Research Fund of the Ministry of Education.

References

1) G. Shirane, E. Sawaguchi and Y. Takagi: Phys. Rev. **84** (1951) 476.
2) G. Shirane and A. Takeda: J. Phys. Soc. Japan **7** (1952) 5; E. Sawaguchi: J. Phys. Soc. Japan **8** (1953) 615.
3) G. Shirane: Phys. Rev. **86** (1952) 219.
4) *cf.* O. Nomoto and T. Ikeda: J. Acous. Soc. Japan **9** (1953) 83 (in Japanese).
5) S. L. Quimby: Phys. Rev. **25** (1925) 558; J. Zacharias: Phys. Rev. **44** (1933) 116; L. Balamuth: Phys. Rev. **45** (1934) 715.
6) H. Mueller: Phys. Rev. **57** (1940) 829, **58** (1940) 565, **58** (1940) 805.
7) A. F. Devonshire: Phil. Mag. **40** (1949) 1040, **42** (1951) 1065.
8) W. L. Bond, W. P. Mason and H. J. McSkimin: Phys. Rev. **82** (1951) 442.
9) M. Marutake and T. Ikeda: To be published in this Journ.
10) W. P. Mason: *Piezoelectric Crystals and their Application to Ultrasonics* (1950) p. 127 and p. 147.
11) A. F. Devonshire: Phil. Mag. Supplement. **3** (1954) 85.
12) A. Takeda, T. Ikeda and M. Marutake: Bull. Kobayasi Inst. Phys. Res. **5** (1955) (in Japanese).

JOURNAL OF THE PHYSICAL SOCIETY OF JAPAN Vol. 10, No. 6, JUNE 1955

On the Structure of Evaporated Thin Films of Metals

By Shiro OGAWA, Denjiro WATANABE and F. Eiichi FUJITA
The Research Institute for Iron, Steel and Other Metals,
Tohoku University, Sendai, Japan

(Received January 12, 1955)

It has been confirmed by many electron diffraction works that the singlecrystal-like films of silver, gold, copper, and nickel which are formed on heated cleavage surfaces of rocksalt by evaporation *in vacuo* have the repeated twinning structures. However, the thickness, the area, and the repeat frequency of the twinned layer have not yet been studied. The present work was undertaken to study these points by means of electron microscope. Parallel, linear stripes are observed in electron micrographs of the films. These stripes are attributed to the twinned lattice, the thickness of which is of the order of one hundred Å. Parallel, linear stripes are not observed for aluminium. This agrees with the fact that no twinning occurs in this metal.

§ 1. Introduction

The electron diffraction patterns from thin films of silver (less than about 500 Å thick), which are formed by evaporation on cleavage surface of rocksalt heated above 150°C *in vacuo*, generally show, besides the normal diffraction spots, certain abnormal streaks and spots. The latter are often called "irrational" spots, and become strong, especially when the positions situated in 1/3 of the distance between the neighbouring lattice points along the body diagonal in the reciprocal lattice are intersected by the sphere of reflection. Since Lassen's1) first observation, such irrational spots have been confirmed by many workers2),3),4),5) in silver and also in other face-centred cubic metals such as gold, nickel3), etc. A similar phenomenon was observed by Cochrane6) in nickel films electrodeposited on copper single crystal, and he explained the 1/3 spots from these films as due to the twin formation. A half of the 1/3 spots in evaporated films can also be attributed to the twinning as explained by Cochrane, but to explain the other half a periodic error in the [111] direction must be assumed7), with the period three times as large as (111) spacing. This error is caused by the junction between twinned layers.

Thus the twin formation in evaporated films was confirmed by electron diffraction. However, the thickness, the area and the repeat frequency of the twinned layer have not yet been studied. The present work was undertaken to study these points by means of electron microscope. The present paper gives the results of the work with a discussion concerning the initial growth of evaporated films.

§ 2. Experimental Results

Both an electron microscope and an electron diffraction camera made by Hitachi company were used. The former was equipped with magnetic lenses and had the resolving power of about 30 Å. The camera length of the latter was 309 mm. The high voltage (~50 KV) circuit was common to both apparatus, and the focussing lens current of the diffraction camera was supplied from the source of the condenser lens of the microscope.

a) *Observations on silver*

Fig. 1 shows one of transmission electron

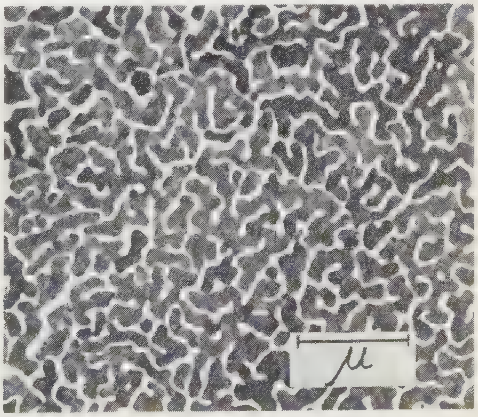

Fig. 1. Electron micrograph of silver film of 300Å in thickness, formed by vacuum-evaporation on cleavage surface of rocksalt heated at 200°C.

micrographs of evaporated silver films, having well-developed patch-like structures. The film had a singlecrystal-like structure as shown in the diffraction patterns (reflection pattern in Fig. 2*a* and transmission pattern in Fig. 3*a*) in which the twin spots appear besides the normal spots. In Fig. 1 are seen a number of dark parallel stripes along the two directions, perpendicular to each other and almost coherent over the whole film, although a slight misorientation occurs from patch to patch. The width as well as the interval of the stripes ranges from one to several hundred Å. The directions of the stripes was determined from comparison between Fig. 1 and an optical micrograph of the film to be parallel to [110] and [1$\bar{1}$0] in the substrate crystal.

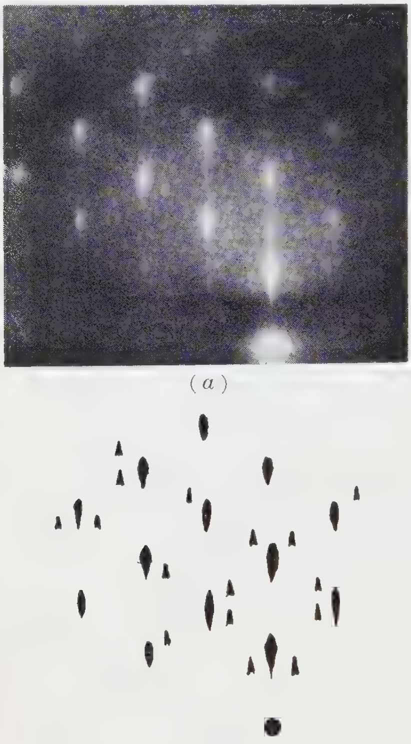
(*a*)

(*b*)

Fig. 2. *a*. Electron diffraction (reflection) pattern of nickel film formed by vacuum-evaporation on cleavage surface of rocksalt heated at 430°C. The incident beam is parallel to [$\bar{1}$10] direction. This photograph was adopted instead of that of silver film, because the twin spots in the former are more clearly visible than in the latter.
b. Illustration of the elongation of the normal spots and the twin spots.

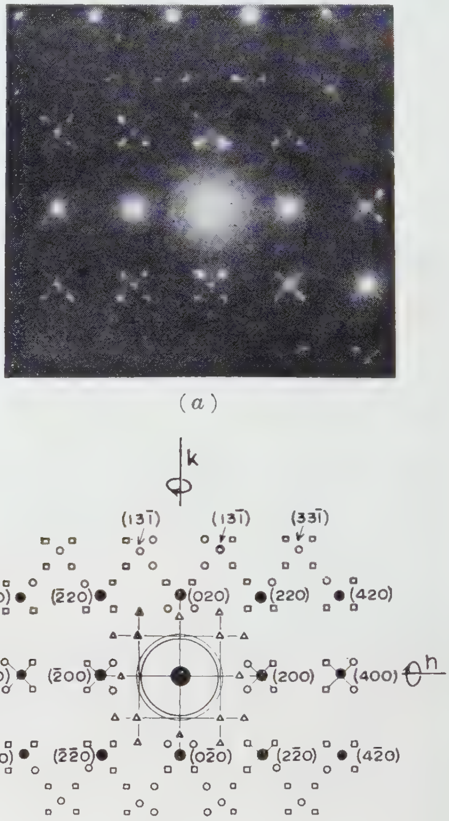
(*a*)

(*b*)

Fig. 3. *a*. Electron diffraction (transmission) pattern of silver film such as shown in Fig. 1. The incident beam is nearly perpendicular to the film plane.
b. Schematic representation of Fig. 3*a*. The normal {*hk*0} spots are represented by the full circles, other normal {*hkl*} spots and twin spots by the open circles, and junction spots by the small squares. The spots except the normal {*hk*0} spots appear as a result of the crystal rotation about [100] or [010] axis in the film. Both the cross grating pattern including the spots represented by the small triangles and the two sharp rings surrounding the incident spot are not identified.

In order to examine the change of the aspect of the stripes with the grade of orientation, several silver films were formed on rocksalt, the temperature of the substrate and the thickness of films being changed. The structure of a film of 150 Å thick formed at room temperature appeared to be comparatively continuous, and the stripes were seen in small regions of about 1000 Å in extent, their directions being varied at random from region to region. This film yielded Debye rings in its diffraction pattern. A film of 100 Å thick formed at 200°C gave Debye rings, showing that the orientation was not yet set on due to the small thickness. The large part of the film is occupied by interstices, and fine stripes can also be seen in patches. A film of 200Å thick formed at 200°C has a better orientation due to the increase of thickness, and the directions of the stripes became more uniform. Fig. 4 shows the structure of a film in which the stripes are sharp and distinct and their directions are varied from patch to patch. This film showed spots and rings in its diffraction pattern. Thus, the peculiar striped pattern is observable in each crystalline patch in all cases mentioned above, and the direction of the stripes is apt to become uniform as the diffraction pattern transforms from rings to spots.

The crystallographic directions of the stripes suggest that they are related to the (111) twinning in face-centred cubic metals. Such a well orientated silver film as shown in Fig. 1 was mounted on a collodion film and heated up to high temperatures *in vacuo*. The behaviour of the stripes with heating temperature was examined at room temperature by electron microscope, for Goche and Wilman[4] found that the twin spots and junction spots in the diffraction pattern vanished after heating between 500 and 600°C for a short period. In Fig. 5*a* dark stripes are clearly visible, but not in Fig. 5*b* and *c*. However, the absence of the stripes does not necessarily mean that the cause giving rise to the stripes has vanished, because the vaporization and diffusion violently take place at higher temperatures, resulting in very thin and very thick parts in the film and hence the striped pattern is masked, even if its cause exists. In fact the twin spots remained in the diffraction patterns up to 650°C, against the results

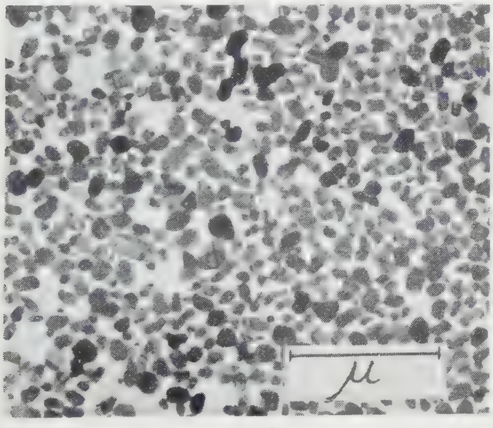

Fig. 4. Silver film of 300Å in thickness, formed on rocksalt heated at 300°C.

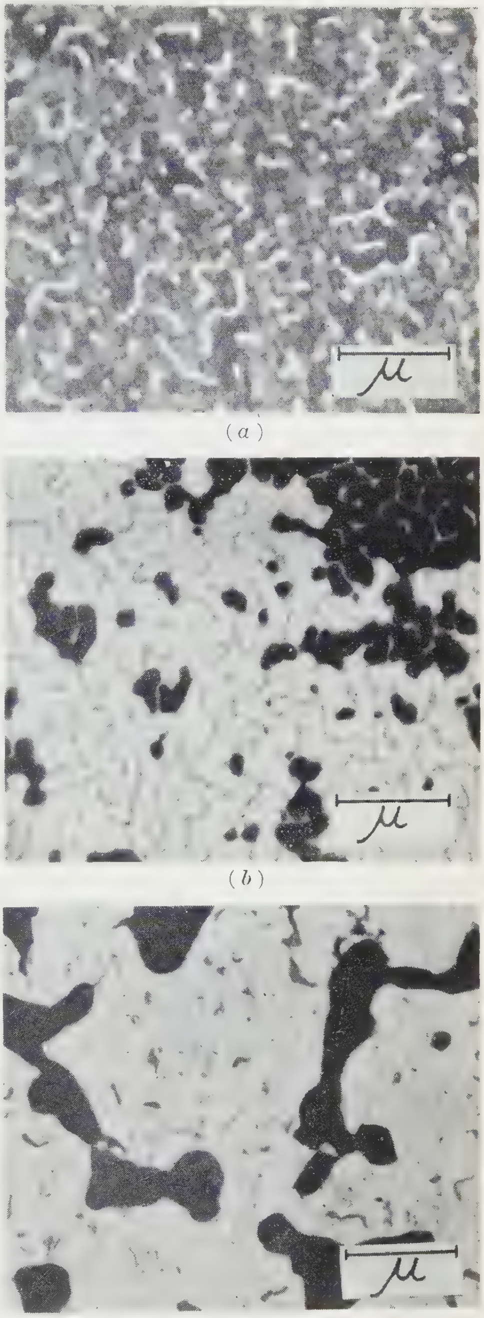

Fig. 5. Silver films subjected to various heat-treatments.
a: heated at 500°C, *b*: heated at 650°C,
c: heated at 700°C.

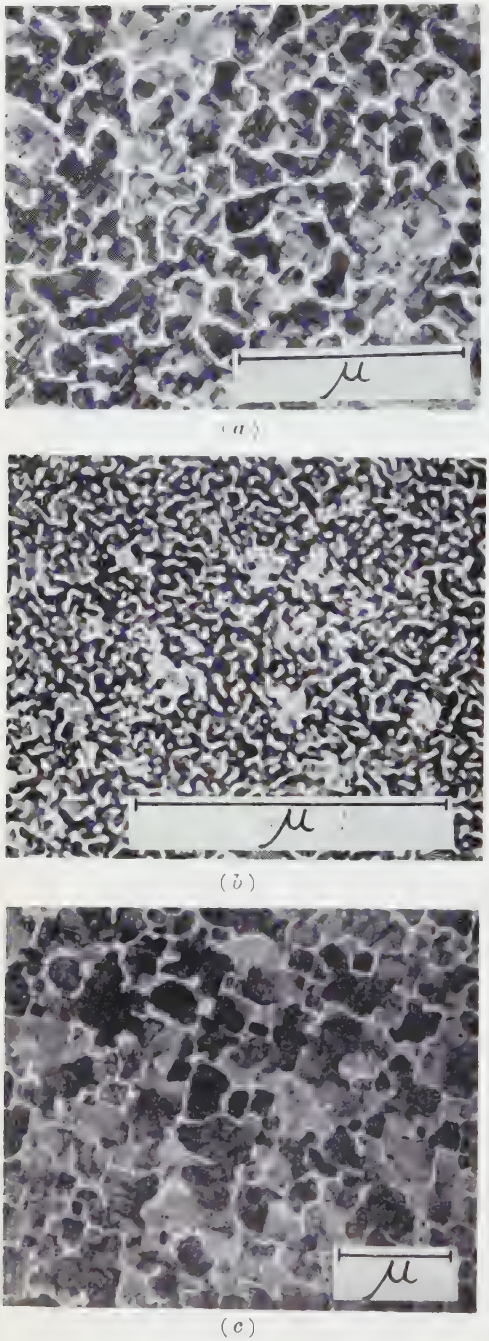

Fig. 6. Films of f.c.c. metals.
a: nickel, 250Å, formed at 430°C,
b: palladium, 250Å, formed at 350°C,
c: aluminium, 500Å, formed at 450°C.

obtained by Goche and Wilman, but the detection of them was impossible at 700°C, due to the appearance of Debye rings.

b) *Observations on other metals*

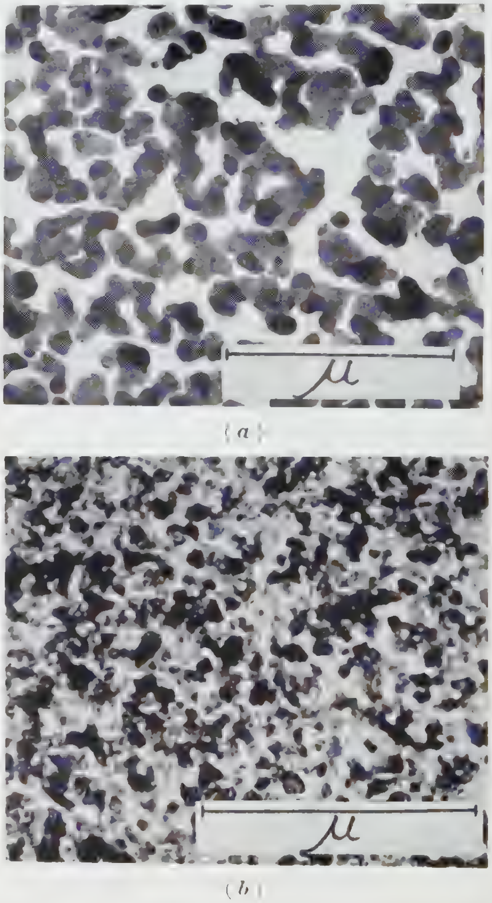

Fig. 7. Films of b.c.c. metals.
a: iron, 300Å, formed at 540°C,
b: chromium, 300Å, formed at 540°C.

Stripes similar to those for silver were also visible for gold, copper, nickel and palladium, but not for aluminium. Gold and copper resemble silver in the aspect of the striped pattern as well as of the patches, the stripes for nickel appear to be sharper (Fig. 6*a*), and the patches and stripes for palladium are the most minute (Fig. 6*b*). For aluminium, on the other hand, the stripes due to the twinning do not exist (Fig. 6*c*). Although diffuse and curved stripes are seen for aluminium (Fig. 6*c*), these may be due to bendings of crystallites as pointed out by Heidenreich.[8] At any rate, one glance is enough to distinguish the difference between this metal and the other face-centred cubic metals. It should be noted that the twin structure is seldom for aluminium after annealing or cold-woking. Observations on iron and chromium which are both body-centred cubic were also carried out (Fig. 7*a* and *b*). The diffraction patterns corresponding to them exhibited Debye rings. Parallel, linear stripes such as observed for silver are not observable in Fig. 7*a* and *b*.

c) *Observations on replica*

In order to study the surface structure of films, surface replicas of silver films were examined under electron microscope. Silica replicas were prepared under the following conditions: The direction of evaporation was in the plane perpendicular to the surface and passing through one of the cube edges of rocksalt lying on the surface and made an angle of 45° with this. After silica film was formed, silver was dissolved away by acid. Fig. 8 shows one of electron micrographs of such replicas and corresponds to a silver film of 400 Å in thickness. We can see many stripes in this figure, though in the less contrast than in Fig. 1. There are two sets of the stripes perpendicular to each other. The width of these stripes is about 100 Å, while that for metal films ranges from one to several hundred Å.

The stripes were observed also for the replica of a silver film of 800 Å in thickness, and the reflection pattern of this film yielded the twin spots. The surface structure of evaporated films known from the micrographs of the replica seems to have some connection with the inner structure known from the transmission micrographs of evaporated films themselves, due to the resemblance in both striped patterns.

§ 3. Interpretations and Discussions for the Experimental Results

When a crystal in a thin film has the varying thickness, *e.g.*, it is wedge-shaped, or when it is distorted by bending, contour lines appear in the transmission electron micrographs. They are called stripes of "equal-thickness" in the former case and those of "equal-inclination" in the latter case. The stripes in question, observed in the micrographs of silver, gold, copper, nickel and palladium do not seem, however, to have the above origins, due to the following reasons: First, the remarkable elongation of the normal diffraction spots towards the shadow edge (Fig. 2) indicates that the most part of the film surface is smooth and parallel to the substrate surface. On the other hand, if the stripes would be due to wedge-shaped crystals, the most part of the film should steeply incline towards the surface. This consideration contradict the above result, and hence the existence of wedge-shaped crystals is improbable. Secondly, if the bending of crystals would be responsible for the stripes in question, it should be cylindrical because of the straightness of the stripes, and two types of such bending should occur simultaneously in places where two sets of the stripes perpendicular to each other coexist. The crossing of the stripes inevitable in such places is, however, scarcely found actually. Therefore, the existence of the bending of crystals is also difficult to consider as the origin of the stripes in question.

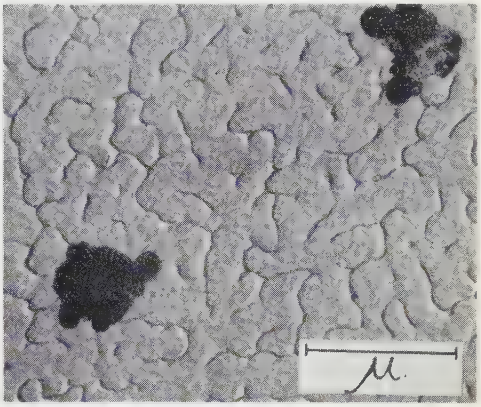

Fig. 8. Silica replica of well-orientated silver films such as shown in Fig. 1. The thickness of replica was about 100Å. Dark lumps are residua after solution of silver substrate.

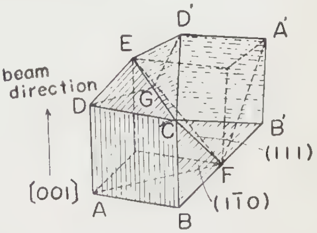

Fig. 9. Two f.c.c. crystals twinned on (111) plane.

Fig. 7 shows two cubic crystals twinned on the (111) plane (CEF in the figure). We suppose that the crystal on the left side is parallel to rocksalt crystal and we shall hereafter call the lattice of this crystal "parallel lattice" and that of the crystal on the right side "twin lattice." Bragg reflections (200), (020), (220), (2$\bar{2}$0) etc. will occur in the paral-

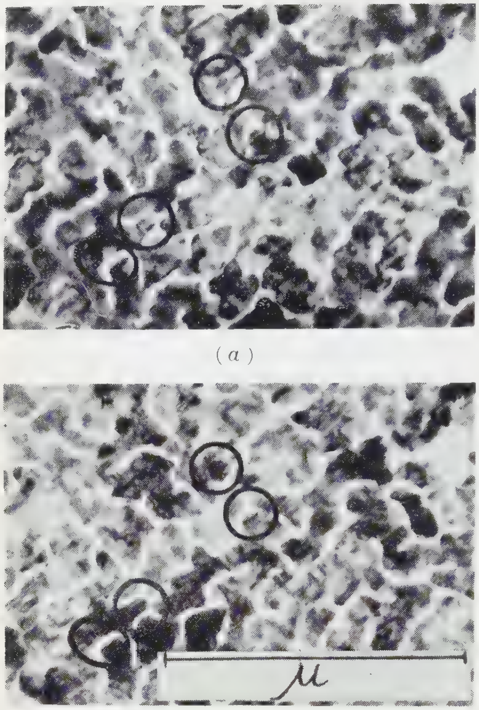

Fig. 10 *a* and *b*. Micrographs of a nickel film. The incident angles of the electron beam are slightly different from each other. The marked regions should be compared.

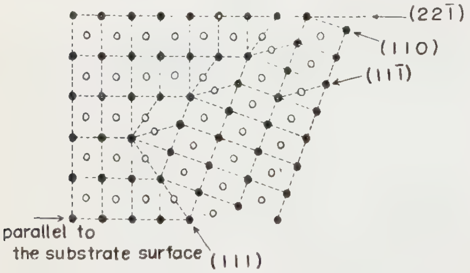

Fig. 11. F.c.c. lattices twinned on (111) plane, viewed from $[1\bar{1}0]$ direction, and the disturbed regions between them.

lel lattice, if the electron beam is parallel to [001]. Possible reflections in the twin lattice are $(2\bar{2}0)$, (204) etc., as the beam direction is parallel to $[22\bar{1}]$. Both lattices can reflect the electron beam simultaneously only when the reflection due to the common $(2\bar{2}0)$ plane (ADGD′A′F) takes place. Except this case, the two lattices behave themselves differently in Bragg reflections, and therefore two sets of parallel, dark and white stripes should be observed in the transmission electron micrographs, if the twinning develops along the ⟨110⟩ directions in the film plane. There occur usually considerable rotations of crystallites in the films, after they have been detatched from substrates[4], and therefore, the twin lattice has more chances for Bragg reflection in the [001] incidence than stated above, that is, the 1/3 points along the bodydiagonals in the reciprocal lattice are frequently intersected by the sphere of reflection in the [001] incidence (Fig. 3*a* and *b*). Hence, it can not immediately be determined which of both crystals corresponds to dark stripes. The following consideration, however, may be possible: The total volume of the twin lattice is far smaller than that of the parallel lattice, as easily seen from the intensities of the twin and normal spots in the diffraction photographs, and therefore the breadth of individual twin lattice should be considerably smaller than that of individual parallel lattice, as the twinnings frequently occur. If the parallel lattice in a patch reflects the electron beam, a greater part of the region should appear dark and narrow stripes due to the twin lattice should appear bright. Of cource, the whole patch becomes dark, if Bragg reflections simultaneously occur in both lattices. On the other hand, if only the twin lattice in a patch reflects the electron beam, narrow dark stripes should be seen in bright region due to the parallel lattice. This consideration explains, at least, qualitatively the observed facts.

If the observed stripes originate from the Bragg reflections, as stated above, their aspect should be sensitive to the direction of the incident beam. Fig. 10*a* and *b* show electron micrographs of a nickel film in which the incident angle is slightly changed. We can easily find the distinct difference between both micrographs. The similar micrographs were taken also for a silver film, and the sensitivity to the incident angle was confirmed.

For the stripes in the micrographs of replica, on the other hand, the above interpretation is useless because only the surface structure is visible in this case. Fig. 11 shows both lattices twinned on the (111) plane. The paper plane is parallel to $(1\bar{1}0)$. In Fig. 2*a* the normal diffraction spots are elongated towards the shadow edge, and those with smaller diffraction angles are slightly displaced as a whole towards the same direction. These aspects of the normal diffraction spots, together with that of the electron micrograph of replica, indicate that the parallel lattice is upwards bounded with (001) parallel to the substrate surface, though some waviness might occur, but none has been known about upper boundary surfaces of the twin lattice. Watching the figure, possible surfaces may probably be $(11\bar{1})$ and (110) of this lattice. (The Miller's indices of the twin lattice are so indexed that the twinning plane is (111)). These surfaces incline towards the boundary surface of the parallel lattice, which corresponds to $(22\bar{1})$ of the twin lattice, by 15°48′ and 19°28′ respectively. When we carefully examine the twin spots in such a reflection pattern as Fig. 2*a* in which the direction of the incident beam is parallel to $[1\bar{1}0]$, we can find that each twin spot elongates downwards along two directions both of which make about 20° with the normal to the shadow edge. These elongations are so faint and diffuse that they can not be reproduced in Fig. 2*a*. They are roughly illustrated in Fig. 2*b*. If these elongations are attributable to the refraction effect due to upper boundary surfaces of the twin lattice, it is concluded that these surfaces are probably both $(11\bar{1})$ and (110), taking considerable errors in measuring the directions of faint and diffuse elongations into account. The narrow stripes in the micrograph of the replica, therefore, correspond to the actual breadth of the twin lattice. The breadth of the stripes in the micrographs of evaporated films themselves, on the other hand, is in general larger than the actual one, because the twinning plane considerably inclines to the incident beam. Thus, the structure of thin evaporated films of several hundred Å in thickness which have the {111} twinning can roughly be illustrated as in Fig. 12. The twin lattice penetrates up to the surface in such thickness of films. This figure is considered to reproduce the structure of the most part of a film, but does not give any information to the structure of its bottom.

§ 4. Discussion on Initial Growth of Evaporated Films

According to Menzer's view[7], four types of {111} twin lattice of silver or nickel grow up immediately on the cleavage surface of rocksalt, due to a better fitness between the spacings of deposit and substrate, and as the thickness increases, the "buffer lattice" between twin layers is formed, and this is nothing but the lattice parallel to the substrate. This consideration seemed adequate from the viewpoint of the lattice fitness, but has become doubtful since Uyeda's experiment[9]. He observed directly in the diffraction camera the growing process of silver on molybdenite, rocksalt and zincblende. According to him, the normal spots initially appeared superposed on the pattern of the substrate, and as the thickness increased, 1/3 spots began to appear. That is, the twin lattice did not grow immediately on the cleavage surfaces. Raether's experiment[10] also did not support Menzer's view, i.e., he examined the backside of a silver film after detachment from rocksalt and found that the pattern consisted of the normal spots only, whereas the twin spots should appear according to Menzer.

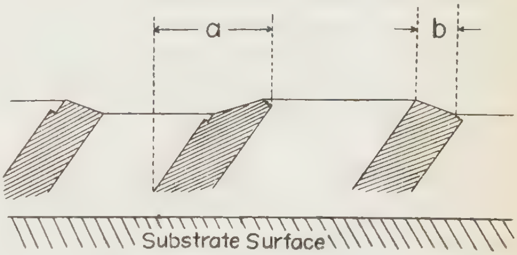

Fig. 12. A rough picture of (110) cross section of evaporated films of f.c.c. metals of some hundred Å in thickness, in which the {111} twinnings frequently occur.
a: breadth of stripes observed in electron micrographs of films themselves, several hundred Å.
b: breadth of stripes observed in electron micrographs of replicas, about one hundred Å.

We repeated this experiment and confirmed his result. This result might reasonably be interpreted by Menzer's idea, if the twin lattices which had initially grown up would have vanished as a result of recrystallization at room temperature after detachment from the substrate. Uyeda's direct observation, however, denies this interpretation. Recently Lüdemann[11] has observed in the diffraction camera the growing manner of alkalihalides formed on alkalihalide crystals by evaporation, several kinds of deposit being combined with several kinds of substrate. He obtained the results similar to those by Uyeda, i.e., the initial deposit was orientated parallel to the substrate in every case. Among Lüdemann's results it was especially noticeable that the {111} twinning occurred also in such a case that deposit and substrate were of the same kind, *e.g.*, rocksalt on rocksalt. This means that the difference of lattice constants is not the cause of twin formation, and a similar circumstance may probably holds for the case of metal-on-rocksalt. Thus, the cause of the twinning in evaporated films of face-centred cubic metals remains unexplained at the present stage.

§ 5. Conclusion

(1) Parallel, linear stripes are observed in electron micrographs of evaporated films of face-centred cubic metals such as silver, gold, copper, nickel and palladium.

(2) These stripes are attributed to the twinned lattice which is revealed by twin spots in the electron diffraction patterns of these films.

(3) The thickness of twin layers is estimated to be of the order of one hundred Å.

(4) From refraction effect in diffraction patterns and from micrographs of replica of the films, it is concluded that the surface of parallel lattice is (001) parallel to the substrat surface while that of twin lattice is incline to the substrate surface.

(5) Parallel, linear stripes are not observe for aluminium. This agrees with the fac that no twinning occurs in this metal.

The present authors wish to express thei sincere thanks to Professor R. Uyeda for hi kind discussions.

The present investigation has been supporte partly by the fund of the Ministry of Education in Aid of Scientific Researches.

References

1) H. Lassen: Phys. Z. **35** (1934) 179.
2) F. Kirchner und H. Lassen: Ann. Phys. **22** (1935) 65.
3) L. Brück: Ann. Phys. **26** (1936) 233.
4) O. Goche and H. Wilman: Proc. Phys. Soc. **51** (1939) 625.
5) R. Uyeda: Proc. Phys.-Math. Soc. Japan **22** (1940) 1023.
6) W. Cochrane: Proc. Phys. Soc. **48** (1936) 723.
7) G. Menzer: Z. Kristallogr. **99** (1938) 378, 410.
8) R. D. Heidenreich: J. Appl. Phys. **20** (1949) 993.
9) R. Uyeda: Proc. Phys.-Math. Soc. Japan **24** (1942) 809.
10) H. Raether: Ergebn. Exakt. Naturw. **24** (1951) 54.
11) H. Lüdemann: Z. f. Naturf. **9a** (1954) 252.

JOURNAL OF THE PHYSICAL SOCIETY OF JAPAN Vol. 10, No. 6, JUNE, 1955

On the Relations between Electron Emission, Conduction and Noise of Oxide-coated Cathodes

By Junkichi NAKAI, Yoshio INUISHI
and Yang TSUNG-CHE

Faculty of Engineering, Osaka University, Miyakojima, Osaka, Japan.

(Received May 17, 1954)

The relations between the electron emission, the electrical conduction and the noise of the oxide coated cathode have been studied. The Richardson plot of the conduction current showed two straight line regions. The temperature dependence of the conduction current was found to be the same as that of the emission current, and the density of the former was a few times larger than that of the latter. The noise current accompanying with the conduction current showed sharp increase when the conduction current saturated. This is owing to the disappearance of the space charge in the pore. From these experimental results the pore conduction mechanism of the oxide-coated cathode was ascertained.

§ 1. Introduction

In the electric conduction of oxide cathode, it has been observed that there are many experimental facts hard to explain by means of the simple one impurity model. In an effort to clarify it, Loosjes and Vink[1] have advanced a new theory. They considered two types of electric conduction mechanism. One of them is the crystal conduction which is carried by the electrons passing through crystals, and the other is the pore conduction which is carried by the electron gas existing in the pore among the oxide grains. At a comparatively low temperature the conduction due to the former mechanism is predominant. However, at higher temperatures than the temperature where the electron emission from the oxide cathode can be observed, the pore conduction becomes predominant because the electron gas in the pore becomes denser. The pore conduction was treated theoretically by Hensley[2] followed by the experiment carried out by Young[3]. We performed the conduction measurement by the similar method as Young. However, in our case, the measurements of the emission and the noise are carried out at the same time, whereby the relations among these three factors shall be known. Thus the validity of the pore conduction mechanism was ascertained.

§ 2. Method of Experiment

Fig. 1 shows the outline of electrode construction of the test tube. The oxide (Ba·Sr)O is held between two rectangular nickel-sleeves being pressed by tungsten-springs from the both sides. Applying pulse voltage between two sleeves, the voltage-current characteristics of conduction were observed with a oscilloscope. And, applying pulse voltage between the sleeves and the anode which is faced to the one side of the oxide coating, the emission characteristics was measured. Also, we made the noise measurements with a circuit as shown in Fig. 2. The cathode temperature was measured by W-Ni thermo-junction welded on the middle of the sleeve.

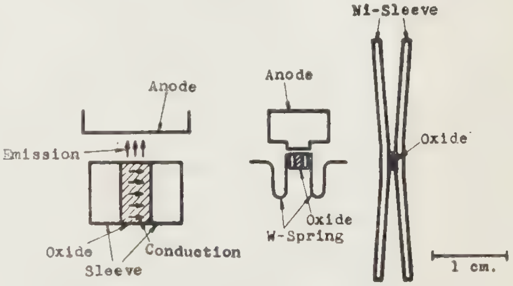

Fig. 1. Construction of Electrode.

The carbonate (Ba·Sr)CO_3 was plastered between two sleeves and converted into the oxide.

§ 3. Measurements of Emission and Conduction Current

Fig. 3 indicates one example obtained by

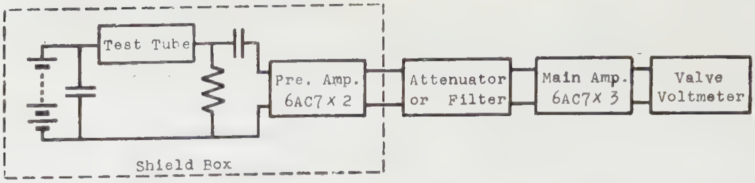

Fig 2. Circuit for Noise Measurement.

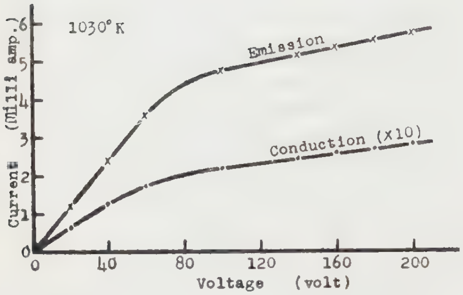

Fig. 3. Voltage-Current Characteristics of Emission and Conduction Current.

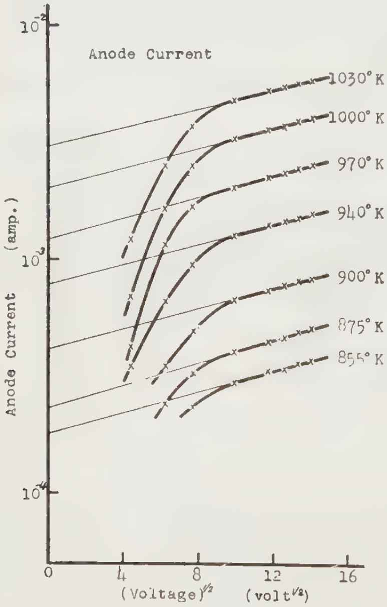

Fig. 4. Schottky Plot of Anode Current.

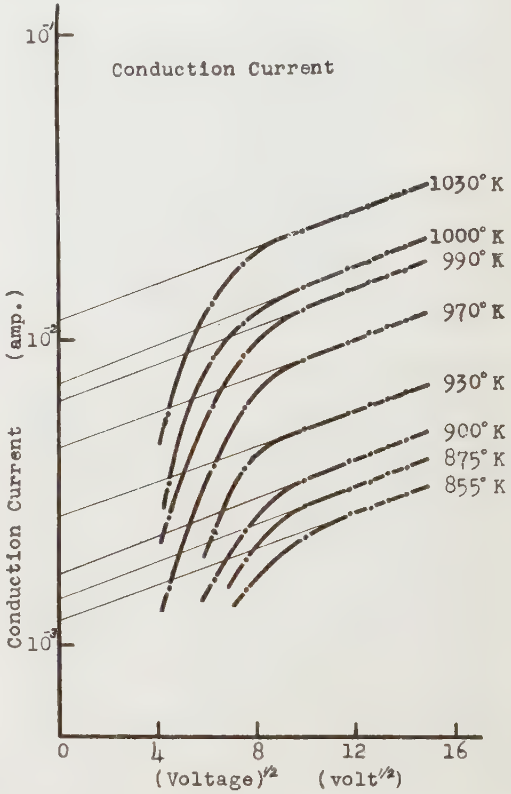

Fig. 5. Schottky Plot of Conduction Current.

the voltage-current characteristics measurements of the anode currents and the conduction current by using a rectangular wave form pulse voltage of 6 μ sec. in width and 200 cycles/sec. in recurrence frequency (duty$=1.2\times10^{-3}$). Both curves have a saturation tendency at high voltage. By plotting the voltage-current characteristics in Schottky plot, Figs. 4 and 5 were obtained. It is observed that the measured points are located on nearly straight lines at high voltage range. The field free currents for each temperature were obtained from the intersections of ordinate by the extents of the straight lines, and those were converted into current densities J_0 per unit area. By plotting $J_0/T^{5/4}$ against reciprocal temperature, we obtained the result as shown in Fig. 6. In this figure it is obvious that the conduction has an activation energy of 1.1 e.v., a value in agreement with that of the emission, at higher temperatures approximately above 900°K, neverthless, at lower temperatures it shows a low activation energy. But no break like this is seen in the emission over the whole temperature range used for measurements.

The above mentioned tendencies have so far been ascertained by Young[3] and others[1][4].

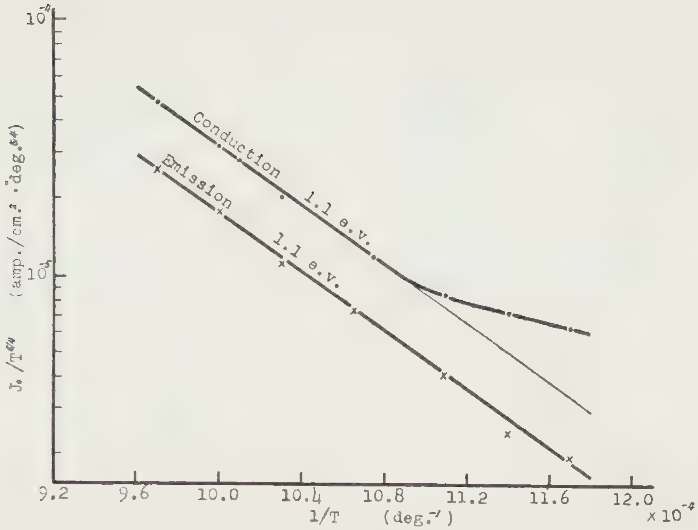

Fig. 6. Reciprocal Temperature Plot of $J_0/T^{5/4}$.

They asserted that the conduction of oxide cathode is represented by the parallel mechanism of pore conduction and crystal conduction. And, they reached the conclusion that the former is predominant at high temperature while the latter is predominant at low temperature. Namely, at high temperature the electric conduction is mainly governed by the flow of electron gas emitted from the oxide grains and filling the pore. Hence, under the condition that the considerable electric field is applied through the oxide layer, whereby the electron gas in the pore becomes extremely rare, the activation energy of the saturated pore conduction will be expected to accord with the activation energy of emission. The crystal conduction has a lower activation energy than the pore conduction so it becomes predominant at low temperature. In the reciprocal temperature plot, the fact that the inclination of conduction line was steep at higher temperatures but flat at lower temperatures indicates that the both conduction mechanisms exist in parallel. However, when the electric field in the oxide layer is weak and the pore is filled by dense electron gas, the electric current may flow from one electrode to the other only by the flow of electron gas. But, when the electric field becomes strong enough to maintain the condition of saturated pore conduction, this conduction mechanism which depends merely on the flow of electron gas will be impossible. Consequently, we wish to advocate the parallel-series mechanism in which the pore-grain series conduction mechanism and the crystal conduction mechanism exist in parallel. If the fine structure of the oxide layer is considered, the equivalent circuit of conduction under the condition of the saturated pore conduction becomes as shown in Fig. 7. Here, R_c, r_g and r_p represent the resistance of crystal contact, grain and pore, respectively. It is assumed that r_g's are much smaller than r_p's. An electron appeared in a pore after passing through an oxide grain enters the neighbouring grain, then it is emitted into the next pore. By repeating these movements the electron would proceed from the negative electrode to the positive. By this assumption the following questions can be interpreted.

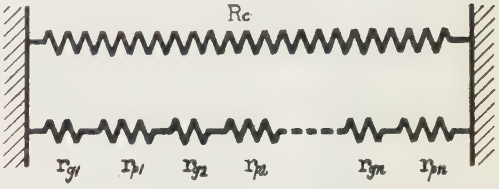

Fig. 7. Parallel-Series Mechanism of Conduction.

Current Dencity:

When the current densities of emission is compared with those of conduction, the latter is several times larger than the former as seen in Fig. 6. The causes may be attributed to the following reasons.

(1) Due to the fact that excess Ba evaporates from the oxide surface, the excess Ba den-

sity inside the layer is larger, so the activity is also larger than the surface.

(2) The inside temperature of the layer is higher than the surface temperature because the heat is lost by thermal radiation from the surface.

Schottky Slope:

If the high electric field is applied to the cathode surface, the emission current increases at the following equation by the Schottky theory:

$$i=i_0 \exp\left(e^{3/2}F^{1/2}/kT\right),$$

where

i_0= field free emission current,
F= intensity of electric field,
e= charge of electron,
k= Boltzmann constant.

Then, putting

V= anode voltage,
d= distance between cathode and anode,

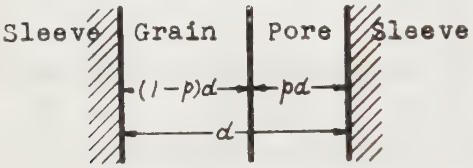

Fig. 8.

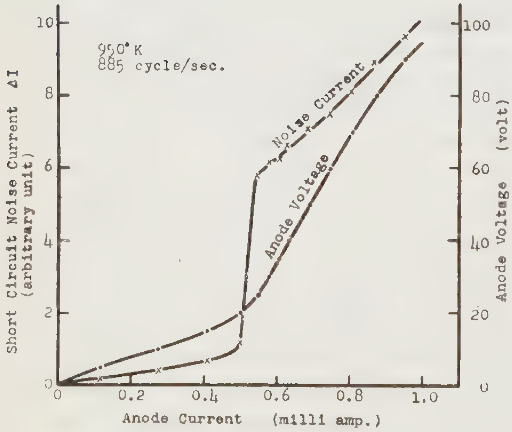

Fig. 9. Emission Noise.

the apparent surface field intensity is represented by V/d. However, if we suppose the actual field intensity acting on the surface is β times as large as V/d, the emission current becomes

$$i=i_0 \exp\left\{\left(\frac{e^{3/2}}{kT}\right)\left(\frac{\beta V}{d}\right)^{1/2}\right\}.$$

From the above,

$$\log_{10} i=\log_{10} i_0+1.92(\beta^{1/2}/T d^{1/2})V^{1/2}.$$

Where i in amp., V in volt and d in cm. Then the Schottky slope becomes

$$1.92(\beta^{1/2}/T d^{1/2}).$$

Where β is named " Grobfeinfaktor ". β_e's were obtained from the slopes of Schottky lines of emission current. And also, in the case of the conduction current, putting the oxide layer thickness as d, β_c's were computed. These values of β_e's and β_c's are summarized in the following table. Tube No. 1 indicates an example when the oxide layer is pressed with comparatively strong pressure. Tube No. 2 indicates an example when the oxide layer is pressed loosely. β_e's for the emission are 5∼6 in both tubes, but β_c's for the conduction current are several times larger than β_e's. For the series mechanism, if the portion $p\cdot d$ of the whole path d of current is the pore conduction and the rest $(1-p)\cdot d$ is the grain conduction as shown in Fig. 8, β_c/β_e is estimated as

Tube No.	T (°K)	„ Grobfeinfaktor "	
		Emission β_e	Conduction β_c
1	1030	5.3	23
	1000	5.8	25
	990	—	23
	970	6.2	21
	940	5.3	—
	930	—	19
	900	4.9	20
	875	5.8	19
	855	4.9	16
2	1175	6.2	13
	1130	5.7	12
	1080	5.8	11
	1020	6.5	11
	960	6.1	11

$$\beta_c/\beta_e \approx 1/p\ .$$

That is to say, β_c/β_e represents the extent to which the oxide grains are packed if they are of equal size. In the table, the difference in β_c's between two tubes are regarded as the influence arising from the spring pressure.

Moreover, in Richardson plot for the conduction current as shown in Fig. 6, the temperature at which the straight line begins to break is about 900°K in Tube No. 1. But in Tube No. 2 it was approximately 750°K. This difference is regarded to be attributable to the fact that the stronger is the spring pressure, the tighter is the mutual contact between the oxide grains, so the increase of the crystal conduction occurs and it leads to upward displacement of the straight line possessing the low activation energy.

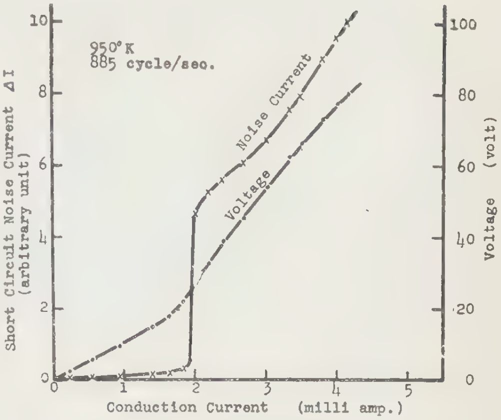

Fig. 10. Conduction Noise.

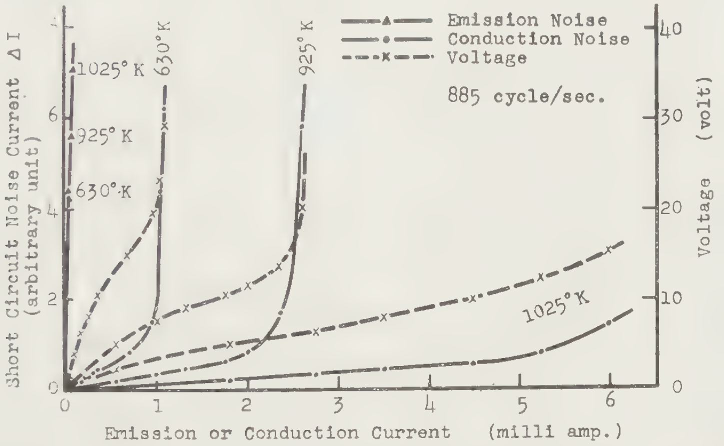

Fig. 11. Noise accompanying with Emission and Conduction Current.

§ 4. Measurements of Flicker Noise

Figs. 9 and 10 represent the results of measurements of the short circuit noise currents accompanying with the anode current and the conduction current respectively, at cathode temperature of 950°K, in regard to Tube No. 1. The abscissa represents the anode or conduction current, and the ordinates represent the root of mean square of short circuit noise current and the anode voltage. In accordance with the gradual rise of the anode voltage, the anode currents increase gradually, but it is limited under the space charge condition at the beginning, so the noise current accompanying with the anode current suffers the reducing action by the space charge. When the anode voltage rises enough and the space charge disappears, the anode current becomes to show a saturation tendency and the subsequent increase of anode current owes to the Schottky effect. Then, the reducing action by the space charge for noise disappears and the sharp rise of the noise current is seen at this point. This fact is seen from Fig. 9. So is the case with the conduction current as shown in Fig. 10, in which the sharp rise of the short circuit noise current ΔI appears at a point where the saturation of the conduction current takes place, and afterwards ΔI increases nearly in proportion to the conduction current. This endorses the existence of space charge even in the case of the conduction current provided the current is unsaturated. The flow of considerable current causes the disappearance of the space charge and its reducing action for noise. This means the fact that the conduction current is governed by the factor similar to the electron emission.

Fig. 11 shows a representative result of the noise measurement at various cathode temperature with Tube No. 2. In this case, alike in Tube No. 1, the short circuit noise current increases sharply at the point where the conduction current saturates. Beside, by applying 100 volts on the anode so as to draw out the saturation current from the cathode, the emission noise current is measured. It is seen that the emission noise current is much larger than the conduction noise current. In comparison with the saturation tendencies between the conduction currents of Tube No. 1 and that of Tube No. 2, the latter is much sharper. It is perhaps due to the fact that the strong spring in Tube No. 1 causes close packing of the oxide grains whereby the strong Schottky effect results.

Fig. 12 indicates the result of the measurement on the frequency distribution of the emission noise current at $T=947°\mathrm{K}$ with Tube No. 2. In the range of center frequency f from 700 to 10,000 cycles/sec., it is observed that the short circuit noise current ΔI is proportional to $1/f^{1/2}$. Consequently, in the case of Figs. 9~11, in which the center frequency is 885 cycles/sec., we may consider that almost all the noise current is composed of Flicker noise.

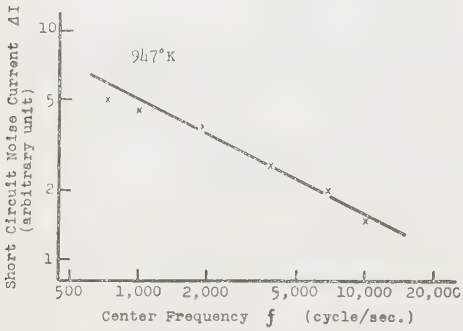

Fig. 12. Frequency Distribution of Noise Current.

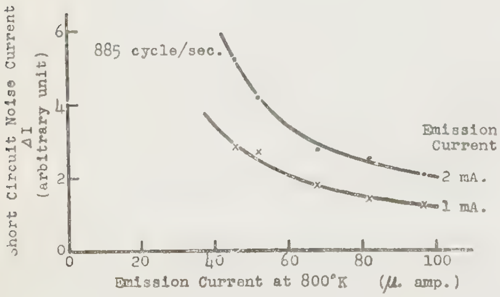

Fig. 13. Activity Dependency of Emission Noise.

According to the interpretation of "Generalized Treatment of Noise"⁵⁾ developed by one of the writers, the noise is believed to be caused by that the current is modulated by the fluctuation of the fluctuation-agent. A part of the results of the research having applied this theory to the noise of Th-W and oxide cathode were made public.⁵⁾⁶⁾⁷⁾⁸⁾ In the case of oxide cathode, it is concluded as follows:

If we suppose n represents the number of excess Ba, the emission current i of the oxide cathode is proportional to $n^{1/2}$. Therefore, it is generally represented by

$$i=n^{1/2}F(T,\ V)\ , \tag{1}$$

where

$F(T,\ V)$ = function concerning cathode temperature and anode voltage V.

Taking the assumption that the noise is generated by the fluctuation of n, the current fluctuation Δi becomes as follows:

$$\Delta i=\tfrac{1}{2}F(T,\ V)(\Delta n/n^{1/2})\ .$$

Δi shows short circuit noise current. Then, the mean square value of Δi is

$$\langle(\Delta i)^2\rangle=\tfrac{1}{4}\{F(T,\ V)\}^2\{\langle(\Delta n)^2\rangle/n\}\ .$$

If n is the number of particle subjecting to the canonical ensemble, it has the following relation,

$$\langle(\Delta n)^2\rangle=n.$$

Hence,

$$\langle(\Delta i)^2\rangle=\tfrac{1}{4}\{F(T,\ V)\}^2=\tfrac{1}{4}(i^2/n)\ .$$

The root of mean square fluctuation of current, ΔI, is

$$\Delta I=\{\langle(\Delta i)^2\rangle\}^{1/2}=\tfrac{1}{2}(i/n^{1/2})\ . \tag{2}$$

Therefore, ΔI is proportional to the current i and inversely proportional to $n^{1/2}$. Fig. 13 shows the result of the measurement on the variation of ΔI when the activity of the cathode is modified by aging or other methods. If we suppose i_0 as the emission current at a certain temperature T_0 and a certain anode voltage V_0,

$$i_0=n^{1/2}F(T_0,\ V_0)\ .$$

Hence,

$$\Delta I=\tfrac{1}{2}F(T_0,\ V_0)(i/i_0)\ .$$

When $i=\mathrm{const.}$, ΔI is in inverse proportion to i_0. This characteristics is roughly seen in Fig. 13 in which the abscissa indicates the emission current at $T_0=800°\mathrm{K}$, $V_0=100$ volts, and the parameter is the emission current at the time of measurement.

We have so far advanced our discussion concerning the short circuit noise current accompanying with the emission current of oxide cathode. On the other hand, the conduction current through oxide layer may also be represented by a similar equation as Eq. (1), so Eq. (2) becomes applicable to the short circuit noise current for conduction. In either event, the short circuit noise current is inversely proportional to $n^{1/2}$. It is accepted that the excess Ba density at the grain surface inside the oxide cathode is larger than that on the outside surface. Therefore, when the emission current is drawn out from oxide cathode, the noise is believed to be generated mostly at the cathode surface.

§ 5. Summary

(1) The measurements have been made on the voltage-current characteristics of the anode current and the conduction current of the oxide cathode. And, by means of the Schottky plot and the reciprocal temperature plot of the field free current, the validity of the pore conduction mechanism was recognized.

(2) The values of "Grobfeinfaktor" obtained from the Schottky slopes for the emission are 5∼6, but the values for the conduction are several times larger than the former.

(3) If we suppose the parallel-series conduction mechanism, the apparent "Grobfeinfaktor" β_c for the conduction may become larger than β_e for the emission.

(4) As same as the case of the emission current, the sharp increase of the short circuit noise current accompanying with the conduction current is seen when the conduction current begins to saturate. It is because of the disappearance of the reducing action by space charge at this state. It is also to ascertain the existence of the pore conduction.

The authors wish to express their appreciation to Prof. E. Sugata and Prof. T. Suita for their continuous encouragements, and thank to Mr. S. Nakamura, Mr. M. Uchihashi, Mr. Y. Hosoma and Mr. S. Takimoto for their co-operation. And also, we express our deep gratitude to the engineers of the vacuum tube manufacturing companies and the members of the laboratories in our country for their instructive discussions and their favourable supports. A part of this research was supported with the Scientific Research Fund by the Ministry of Education of Japan.

References

1) R. Loosjes and J. J. Vink: Philips Research Rept. **4** (1949) 449.
2) E. B. Hensley: J. App. Phys. **23** (1952) 1122.
3) J. R. Young: J. App. Phys. **23** (1952) 1129.
4) R. C. Hughes and P. P. Coppola: Phys. Rev. **88** (1952) 364.
5) Y. Inuishi: Technology Report of the Osaka University. **3** (1953) 41.
6) T. Yang, Y. Inuishi and T. Suitc: Proceeding for the Lecture at the 7th Annual Meeting of the Phys. Soc. of Japan, No. 1952. (in Japanese).
7) Y. Inuishi, J. Nakai and Q. Yang: Proceeding for the Lecture at the Professional Meeting of the Phys. Soc. of JapaL, May 1953. (in Japanese).
8) Y. Inuishi and T. Yang: J. Phys. Soc. of Japan **8** (1953) 565.

JOURNAL OF THE PHYSICAL SOCIETY OF JAPAN Vol. 10, No. 6, JUNE 1955

The Temperature Dependence of the Capacity of the Copper Oxide Rectifier

By Tatsuya NIIMI

The electrical Communication Laboratory, Musashino-shi, Tokyo

(Received August 21, 1954)

The temperature dependence of the capacity of the space charge layer at a metal semiconductor contact is investigated. The variation in the capacity with temperature has been calculated on the assumption that it should be caused by the temperature variation of the density of free charge carriers in the semiconductor. The results are compared, for an example, with the experimental data of the capacity of copper oxide rectifiers, which are measured by superimposing a small alternating voltage on the d.c. bias voltages, at the several temperatures between −160°C and +60°C, and are analysed on the assumption that there exist some donor impurities in the bulk cuprous oxide layer in addition to the usual acceptor type. The comparison makes it clear that the equation derived theoretically can successfully explain the following facts: (1). At lower temperatures, the magnitude of capacity increases with increasing temperature, and reaches a maximum at a certain temperature and then begins to decrease at higher temperatures. (2). But, the temperature at which the magnitude of capacity reaches a maximum experimentally is slightly higher than that which the theoretical equation predicts. (3). The measurements at −110°C and −160°C show that the values of the capacity at these temperatures may be regarded as those affected by the temperature variation in the electrical resistivity of the bulk Cu_2O layer rather than the values of the pure barrier capacity. (4). The absolute value in the temperature variation of a barrier capacity expected from the derived equation is about 250 $\mu\mu$ farads/cm² for copper oxide rectifiers, with −0.5 volt d.c. bias voltage applied between 0°K and 300°K, and this value agrees comparatively well with the experimental results. (5). The variations in capacity are dependent upon the d.c. bias voltage applied and will be smaller when the bias voltage becomes larger.

List of Symbols

a_0	$\hbar^2/m_e\cdot e^2$.
C	Capacity per unit area introduced in this paper.
C_{Bulk}	Capacity of a capacitor composed of the bulk cuprous oxide layer and two electrodes.
C_M	Capacity given by the Mott's theory.
C_S	Capacity given by the Schottky's theory.
D_a	Density of acceptor impurities in the p-type semiconductor, $D_a > D_d$.
D_d	Density of donor impurities in the p-type semiconductor.
d	Width of the blocking layer of the Mott's theory.
E_a	Energy level for acceptor impurities.
E_c	Energy level for the bottom of the conduction band.
E_d	Energy level for donor impurities.
E_f	Fermi level.
E_v	Energy level for the top of the valence bond band.
ΔE	Energy difference between the bottom of the conduction band and donor level or between the top of the valence bond band and acceptor level.
e	Absolute value of an electronic charge.
F	Electric field at the metal semiconductor interface.
$\hbar$	$h/2\pi$, h Planck's constant.
m	Mass of an electron.
m_e	Effective mass for an electron in the the conduction band.
m_h	Effective mass for a hole in the valence bond band.
N_a	Density of acceptor impurities in the n-type semiconductor.
N_d	Density of donor impurities in the n-

	type semiconductor, $N_d > N_a$.
n	Density of electrons in the conduction band in the interior of the semiconductor, considered infinitely distant from the metal semiconductor interface.
p	Density of holes in the valence bond band in the interior of the semiconductor, considered infinitely distant from the metal semiconductor interface.
T	Absolute temperature.
V	D.C. bias voltage applied to a rectifier, taken positive when operated in the forward direction.
V_D	Diffusion potential in the Schottky's theory.
V_s	Height of the potential barrier measured on the basis of the bottom of the conduction band in the interior of the semiconductor, considered infinitely distant from the metal semiconductor interface.
W	Width of the bulk cuprous oxide layer.
ε	Dielectric constant of the semiconductor for a static field.
ε_0	Dielectric constant of the semiconductor for high frequency fields.
η	$E_a - E_f$.
Θ	$h\nu/k$, Characteristic temperature.
μ	Mobility.
ν	Frequency of the longitudinal vibrations.
ξ	$E_f - E_d$.
φ	Electron potential energy.
χ	Electron affinity of the semiconductor.
ψ	Work function for a metal.

§ 1. Introduction

The capacity per unit area of the copper oxide rectifier is given by Mott[1)]

$$C_M = \varepsilon/4\pi d\,, \tag{1}$$

and by Schottky[2)]

$$C_S = [\varepsilon e N_d / 8\pi(V_D - V)]^{1/2}\,. \tag{2}$$

The experimental relations of the capacity of a rectifier to the applied d.c. bias voltage show that Eq. (2) is prefarable to Eq. (1). However, both of these equations do not refer to the temperature dependence of the capacity. Kubo[3)] has introduced the equation which expresses the temperature dependence,

$$C_K = (\varepsilon/4\pi) \cdot \frac{1}{\sqrt{d^2 + \dfrac{\varepsilon(V_s' - V)}{2\pi e N_d} + \dfrac{2\varepsilon k T n}{\pi e^2 N_d^2} \sinh^2 \dfrac{\Delta E}{4kT}}}\,, \tag{3}$$

where

$$V_s' = V_s - \Delta E/2\,.$$

This equation is introduced on the assumption that there is an insulating layer of the width d in the semiconductor, immediately adjancent to the metal, which is succeeded by the space charge layer of uniform density N_d of ionized impurity atoms. But Eq. (3) fails to express the experimental results usually observed, showing that the magnitude of capacity will become smaller when the temperature is raised. Moreover, generally speaking, Eq. (3) cannot explain that the capacity has a maximum at a certain temperature. It is reported in this paper that the equation which explains fairly well the behaviour of the capacity with temperature could be introduced, showing the comparison with the experimental results.

§ 2. Derivation of the Equation That Expresses the Temperature Dependence of Capacity

The energy level diagram of the space charge layer which arises when a metal is brought into contact with an n-type semiconductor is shown in Fig. 1, with energy of electrons increasing upward. The diagram is drawn for the equilibrium condition with no applied voltage. The positive x axis extends into the semiconductor from the metal surface. When the equilibrium is established after the contact, the Fermi level E_f in the semiconductor comes to coinside with that in the metal. The origin of electron potential energy φ is taken at the bottom of the conduction band in the interior of the semiconductor, infinitely distant from the metal surface. Put there

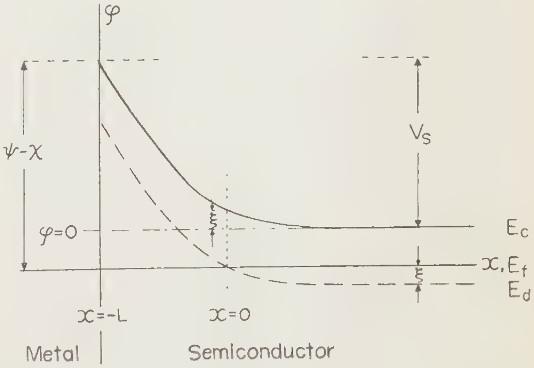

Fig. 1. Schematic energy diagram at a metal semiconductor contact.

$$E_f-E_a=\xi\,. \tag{4}$$

The height of the barrier above the Fermi level is $\psi-\chi$. The origin of the abcissa is taken at $\varphi=\xi$. The interface of the metal semiconductor contact is at $x=-L$. Then φ satisfies the Poisson equation,

$$\frac{d^2\varphi}{dx^2}=\frac{4\pi N_a e^2}{\varepsilon}-\frac{4\pi ne^2}{\varepsilon}\exp\left(-\frac{\varphi}{kT}\right),$$
$$-L<x<0\,. \tag{5}$$

The first term in the right side can be obtained when all the impurity atoms in the layer $-L<x<0$ are ionized, assuming that $N_a-N_a\simeq N_a$, and the second term concerns with electrons in the conduction band.

The density of the ionized impurity atoms in the place where x is considerably large is given by

$$N_a\{\exp[\{E_f-(E_a+\varphi)\}/kT]+1\}^{-1}\,. \tag{6}$$

As the relation

$$\exp[(E_f-E_a)/kT]\gg 1 \tag{7}$$

holds in general at such temperatures as discussed later and in the place fairly distant from the origin where x is large and φ is small, the relation

$$\exp[\{E_f-(E_a+\varphi)\}/kT]\gg 1 \tag{8}$$

holds, therefore the density of holes bound to impurity atoms is given by

$$N_a\exp[(-\xi+\varphi)/kT]\,. \tag{9}$$

Then, the Poisson equation which φ satisfies at $0<x$ is written down

$$\frac{d^2\varphi}{dx^2}=\frac{4\pi e^2}{\varepsilon}N_a\exp\left(\frac{-\xi+\varphi}{kT}\right)$$
$$-\frac{4\pi e^2}{\varepsilon}n\exp\left(-\frac{\varphi}{kT}\right),\quad 0<x. \tag{10}$$

The boundary conditions are assumed as follows,

(B I) $\varphi=\xi$ at $x=0$, for Eqs. (5) and (10).

(B II) Derivatives of φ at $x=0$ are equal and continuous for Eqs. (5) and (10).

(B III) $\varphi=eV_s$ at $x=-L$, for Eq. (5).

(B IV) $\varphi=0$ and $d\varphi/dx=0$ at $x=\infty$, for Eq. (10).

Integrating Eq. (10) under (B IV), we have

$$\left(\frac{d\varphi}{dx}\right)^2=\frac{8\pi e^2}{\varepsilon}kTN_a\exp\left(-\frac{\xi-\varphi}{kT}\right)$$
$$+\frac{8\pi e^2}{\varepsilon}kTn\exp\left(-\frac{\varphi}{kT}\right)$$
$$-\frac{8\pi e^2}{\varepsilon}kTN_a\exp\left(-\frac{\xi}{kT}\right)$$
$$-\frac{8\pi e^2}{\varepsilon}kTn\,. \tag{11}$$

When Eq. (11) is extraporated to the origin, combining with (B I), we have

$$\left(\frac{d\varphi}{dx}\right)^2_{x=0}=\frac{8\pi e^2}{\varepsilon}kTN_a+\frac{8\pi e^2}{\varepsilon}kTn\exp\left(-\frac{\xi}{kT}\right)$$
$$-\frac{8\pi e^2}{\varepsilon}kTN_a\exp\left(-\frac{\xi}{kT}\right)-\frac{8\pi e^2}{\varepsilon}kTn\,. \tag{12}$$

Integrating Eq. (5) under the conditions (B I) and (B II), we have the equation which φ satisfies at $-L<x<0$,

$$\left(\frac{d\varphi}{dx}\right)^2=\frac{8\pi e^2}{\varepsilon}N_a\varphi+\frac{8\pi e^2}{\varepsilon}kTn\exp\left(-\frac{\varphi}{kT}\right)$$
$$-\frac{8\pi e^2}{\varepsilon}N_a(\xi-kT)$$
$$-\frac{8\pi e^2}{\varepsilon}kT\left[N_a\exp\left(-\frac{\xi}{kT}\right)+n\right]. \tag{13}$$

At the metal semiconductor interface, the relations $x=-L$ and $\varphi=eV_s$ hold, then we have,

$$\left(\frac{d\varphi}{dx}\right)^2_{x=-L}=\frac{8\pi e^2}{\varepsilon}N_a[eV_s+kT-\xi]$$
$$-\frac{8\pi e^2}{\varepsilon}kT\left[n+N_a\exp\left(-\frac{\xi}{kT}\right)\right.$$
$$\left.-n\exp\left(-\frac{eV_s}{kT}\right)\right]. \tag{14}$$

When an external voltage is applied to the junction, we have

$$\left(\frac{d\varphi}{dx}\right)^2_{x=-L}=\frac{8\pi e^2}{\varepsilon}N_a[e(V_s-V)+kT-\xi]$$
$$-\frac{8\pi e^2}{\varepsilon}kT\left[n+N_a\exp\left(-\frac{\xi}{kT}\right)\right.$$
$$\left.-n\exp\left(-\frac{e}{kT}(V_s-V)\right)\right]. \tag{15}$$

As $d\varphi/dx$ is negative and $n\gg n\exp[-e(V_s-V)/kT]$ holds at $-L<x<0$,

$$\left(\frac{d\varphi}{dx}\right)_{x=-L}=-\left\{\frac{8\pi e^2}{\varepsilon}N_a[e(V_s-V)+kT-\xi]\right.$$
$$\left.-\frac{8\pi e^2}{\varepsilon}kT\left[n+N_a\exp\left(-\frac{\xi}{kT}\right)\right]\right\}^{1/2}. \tag{16}$$

The capacity per unit area is defined as follows,

$$C=\frac{\varepsilon}{4\pi}\left(\frac{dF}{dV}\right)_{x=-L}=\frac{\varepsilon}{4\pi e}\cdot\frac{d}{dV}\left(\frac{d\varphi}{dx}\right)_{x=-L}, \tag{17}$$

so we have,

$$C=\sqrt{\frac{\varepsilon e N_d}{8\pi(V_s-V)}}\cdot\frac{1}{\left[1-\frac{\xi-kT}{e(V_s-V)}-\frac{kT}{e(V_s-V)}\cdot\left(\frac{n}{N_a}+\exp\left(-\frac{\xi}{kT}\right)\right)\right]^{1/2}}\,. \qquad (18)$$

The terms in the bracket of the denominator represent the temperature dependence of the capacity. Eq. (18) will agree with the Schottky's expression when $T=0$, and enables us to calculate the temperature dependence of the capacity if the the temperature dependence of ξ is known.

§ 3. Temperature Dependence of ξ.

The equilibrium condition for temperatures below the intrinsic range may be regarded as resulting from the "pseudo chemical" reaction[4], excess electron + ionized donor ⇄ neutral donor. If the equilibrium condition is combined with the condition for electrical neutrality, we can have next equations.

$$\frac{n(n+N_a)}{N_d-N_a-n}=K\,, \qquad (19)$$

$$K=N_c\exp[(E_d-E_c)/kT]\,, \qquad (20)$$

$$N_c=2(2\pi m_e kT/h^2)^{3/2}\,, \qquad (21)$$

and the density of electrons in the conduction band is given by

$$n=N_c\exp[-(E_c-E_f)/kT]\,. \qquad (22)$$

(3.1) The case of low temperatures, where $N_d-N_a\gg n$ and $N_a\gg n$.
From Eq. (19),

$$n=\frac{N_d-N_a}{N_a}K\,. \qquad (23)$$

From Eqs. (20), (23) and (22),

$$\xi=E_f-E_d=kT\log\left[\frac{N_d-N_a}{N_a}\right]. \qquad (24)$$

(3.2) the case of low temperatures, where $N_d-N_a\gg n$ and $n\gg N_a$.
From Eq. (19),

$$n=(N_d-N_a)^{1/2}K^{1/2}\,. \qquad (25)$$

From Eqs. (20), (25) and (22),

$$\xi=\frac{E_c-E_d}{2}+kT\log\left[\frac{N_d-N_a}{N_c}\right]^{1/2}. \qquad (26)$$

(3.3) the case of high temperatures, where K is very large.

$$n\simeq N_d-N_a\,. \qquad (27)$$

(3.4) General case. By solving Eq. (19) for n, we have

$$n=\tfrac{1}{2}\left[-(N_a+K)+\sqrt{(N_a+K)^2+4K(N_d-N_a)}\right]. \qquad (28)$$

On the other hand, from Eqs. (20) and (22), we have

$$n=K\exp[(E_f-E_d)/kT]\,. \qquad (29)$$

Combining Eqs. (28) and (29), we have

$$\exp(\xi/kT)=(1/2K)\cdot\left[-(N_a+K)+\sqrt{(N_a+K)^2+4K(N_d-N_a)}\right]. \qquad (30)$$

From this equation, we can obtain ξ as the function of temperature. We can reasonably assume that the above mentioned equations would hold in the deep interior of such a semiconductor as has a contact with a metal at one end.

When we apply the above equations to the copper oxide rectifier which is composed of a p-type semiconductor, we obtain next equations, because of the symmetrical properties of electrons and holes.

$$[p(p+D_d)/(D_a-D_d-p)]=J,\quad D_a\gg D_d\,, \qquad (31)$$

$$J=N_v\exp[(E_v-E_a)/kT]\,, \qquad (32)$$

$$N_v=(2\pi m_h kT/h^2)^{3/2}\,, \qquad (33)$$

$$p=N_v\exp[-(E_f-E_v)/kT]\,. \qquad (34)$$

(3.5) the case of low temperatures, where $D_a-D_d\gg p$ and $D_d\gg p$.

$$p=[(D_a-D_d)/D_d]N_v\exp[(E_v-E_a)/kT]\,, \qquad (35)$$

$$\eta=E_a-E_f=kT\log[(D_a-D_d)/D_d]\,. \qquad (36)$$

(3.6) the case of low temperatures, where $D_a-D_d\gg p$ and $p\gg D_d$.

$$p=(D_a-D_d)^{1/2}N_v^{1/2}[(E_v-E_a)/2kT]\,, \qquad (37)$$

$$\eta=\Delta E/2+kT\log[(D_a-D_d)/N_v]^{1/2}\,. \qquad (38)$$

(3.7) the case of high temperatures,

$$p\simeq D_a-D_d\,. \qquad (39)$$

(3.8) General case,

$$p=\tfrac{1}{2}\left[-(D_d+J)+\sqrt{(D_d+J)^2+4J(D_a-D_d)}\right] \qquad (40)$$

$$\exp(\eta/kT)=p/J\,. \qquad (41)$$

From these equations, we can obtain η as the function of T. The capacity per unit area is given by the equation

$$C=\sqrt{\frac{\varepsilon e D_a}{8\pi(V_s-V)}}\cdot\frac{1}{\left[1-\frac{\eta-kT}{e(V_s-V)}-\frac{kT}{e(V_s-V)}\left(\frac{p}{D_a}+e^{-\eta/kT}\right)\right]^{1/2}}\,. \tag{42}$$

If we take the value of C at $T=0°\mathrm{K}$ and $V_s-V=1.0$ volt equal to C_0, Eq. (42) can be rewritten as follows,

$$C=\frac{C_0}{\sqrt{V_s-V}}\cdot\frac{1}{\left[1-\frac{\eta-kT}{e(V_s-V)}-\frac{kT}{e(V_s-V)}\left(\frac{p}{D_a}+e^{-\eta/kT}\right)\right]^{1/2}}\,. \tag{43}$$

Using the values of D_a, D_d and ΔE, determined by the measurements of usual copper oxide rectifiers, we can plot the value of η *versus* T as shown in Fig. 2, according to Eqs. (40) and (41). The value of η has a maximum at a certain temperature and consequently the capacity will have such a maximum as expected from Eq. (42). In the calculation of N_v, m_h is taken equal to the mass of a free electron.

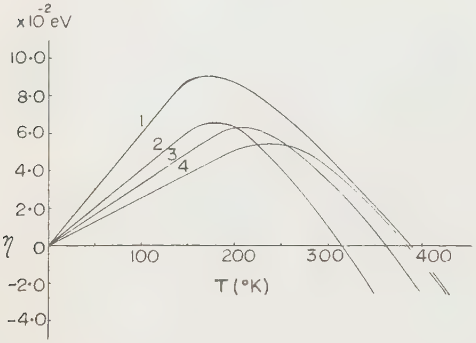

Fig. 2. Temperature dependence of η.

Curve 1.
$D_a=10^{16}\mathrm{cm}^{-3}$, $D_d=10^{13}\mathrm{cm}^{-3}$, $\Delta E=0.3\,\mathrm{eV}$.
Curve 2.
$D_a=10^{15}\mathrm{cm}^{-3}$, $D_d=10^{13}\mathrm{cm}^{-3}$, $\Delta E=0.3\,\mathrm{eV}$.
Curve 3.
$D_a=5\times10^{15}\mathrm{cm}^{-3}$, $D_d=10^{14}\mathrm{cm}^{-3}$, $\Delta E=0.3\,\mathrm{eV}$.
Curve 4.
$D_a=10^{16}\mathrm{cm}^{-3}$, $D_d=5\times10^{14}\mathrm{cm}_{-3}$, $\Delta E=0.3\,\mathrm{eV}$.

§ 4. Experiments

The capacity and static characteristics of a number of copper oxide rectifiers have been measured at temperatures between −160°C and +80°C. The diameter of the rectifiers used is 5×10^{-1} cm and the width of bulk $\mathrm{Cu_2O}$ layer is approximately 7×10^{-3} cm and almost the same for all specimens. The temperature data of the static characteristics have been used to estimate the densities of acceptors D_a, donors D_d and the activation energy ΔE.

(4.1) *Analysis of temperature dependence of static characteristics.*

In order to analysis the temperature dependence of static characteristics, the mobility of holes in $\mathrm{Cu_2O}$ layer has been assumed as stated below and the conductivity of the layer has been obtained from the limiting ohmic resistance in the forward direction. By combining these two values, the variation of concentration of holes with temperature has been deduced.

The mobility of free electrons in polar crystals was given by Frölich[5].

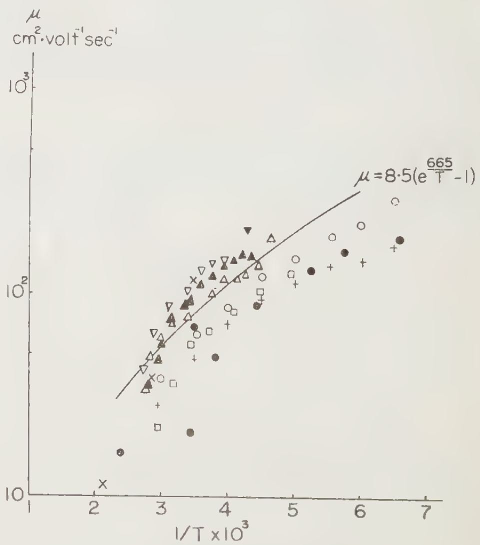

Fig. 3. μ *vs.* 1/T.
● Schottky and Waibel, □ Vogt,
+, ○ Engelhard, △ ▲ ▽ Angello,
× Feldmann.

$$\mu=2\sqrt{\frac{3}{\pi mk\Theta}}\cdot\frac{\varepsilon-\varepsilon_0+1}{\varepsilon-\varepsilon_0}ea_0(e^{\Theta/T}-1)\,. \tag{44}$$

We can apply this equation to holes in $\mathrm{Cu_2O}$ layer and can simply rewrite down as follows:

$$\mu=A(e^{\Theta/T}-1)\,.$$

In order to fit the experimental results, $A=$

10.5 cm^2/volt.sec. and $\Theta=665°$K were adopted by Brattain$^{6)}$. But in this paper $A=8.5$ cm^2/volt.sec. and $\Theta=665°$K are adopted.

$$\mu=8.5(e^{665/T}-1)\ \text{cm}^2/\text{volt.sec.} \tag{45}$$

The comparison of Eq. (45) with the experimental data of mobility obtained by W. Schottky$^{7)}$, V.W. Vogt$^{8)}$, E. Engelhard$^{9)}$, S.J. Angello$^{10)}$ and W. Feldmann$^{11)}$ is given in Fig. 3. Some of the points plotted in Fig. 3 have been calculated from their experimental data of Hall coefficient and conductivity. The Brattain's function gives more weight to Angello's values than to the others. By using the values of mobility μ determined by Eq. (45) and the conductivity σ deduced by the limiting ohmic resistance in the forward direction of rectifiers, the density of holes can be estimated by

$$\sigma=ep\mu\,. \tag{46}$$

The two typical samples of density of holes thus determined are shown in Fig. 4. If it is assumed that donor impurities$^{6)}$ in addition to usual acceptor impurities are present in the Cu_2O layer, the slope at low temperatures corresponds to the activation energy $\varDelta E=E_a-E_n$, according to Eqs. (35), (37) and (39) and the values of D_a and D_d can be obtained by solving the two Eqs. (35) and (39). The results are shown in Table I.

Table I.

Specimen No.	D_a (cm^{-3})	D_d (cm^{-3})	ΔE (eV)
I·C–1	162×10^{14}	12×10^{14}	0.25
I·D–1	67×10^{14}	5×10^{14}	0.27

(4.2) Measurements of Capacity.

The circuit diagram of measurements of capacity is shown in Fig. 5. The frequency used is 1 KC/s and an a.c. voltage applied to a specimen is about 7 millivolts, which are kept constant during the measurements. The measurements have been performed by a substitution method. The key K is at first switched on the specimen S and the circuit is balanced by the resistance R_1 and capacity C_1, and then the key K is in turn switched on the parallel circuit of R_2 and C_2 and the whole circuit is balanced again by adjusting the values of R_2 and C_2. The values of R_2 and C_2 thus obtained can be regarded as the resistance and capacity of the specimen.

The d.c. bias voltage on the specimen is applied by a battery B. In Figs. 6 and 7 the results of measurements at temperatures between $-50°$C and $+60°$C are shown; i.e. $1/C^2$ is plotted as a function of an applied bias voltage V. As the d.c. bias voltage is applied in the reverse direction of rectifiers, it may be considered resonably that the whole applied voltage will be dropped across the space charge layer. As Schottky has showed already, the plots obtained at a constant temperature have proved to be a straight line.

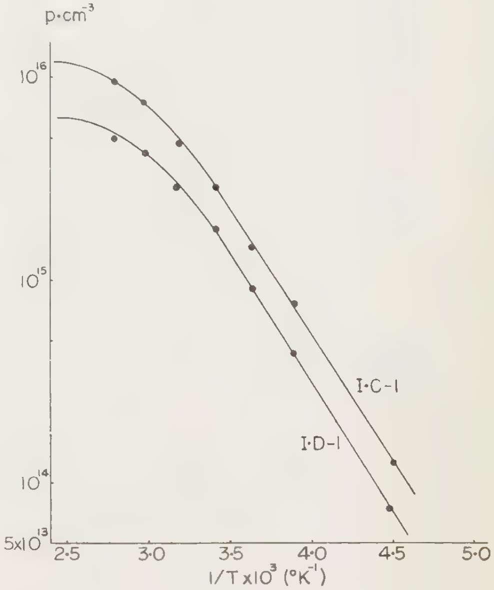

Fig. 4. p *vs.* 1/T.

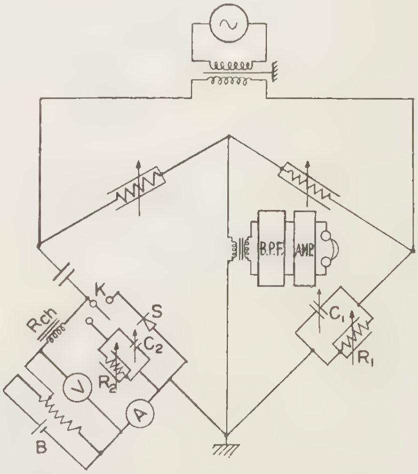

Fig. 5. Circuit diagram for capacity measurements.

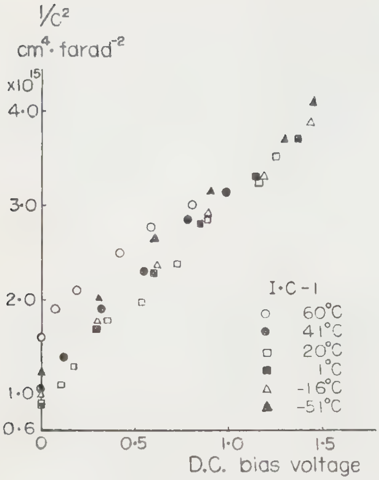

Fig. 6. 1/C² *vs.* V.

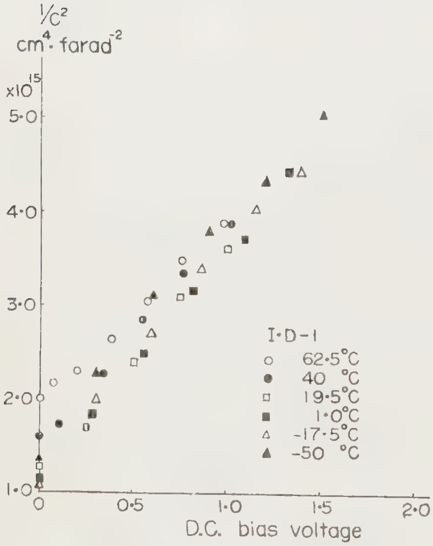

Fig. 7.

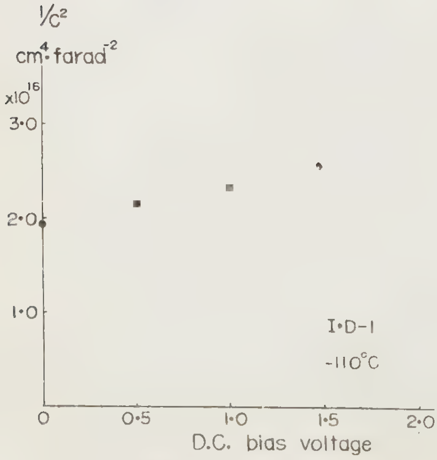

Fig. 8. 1/C² *vs.* V.

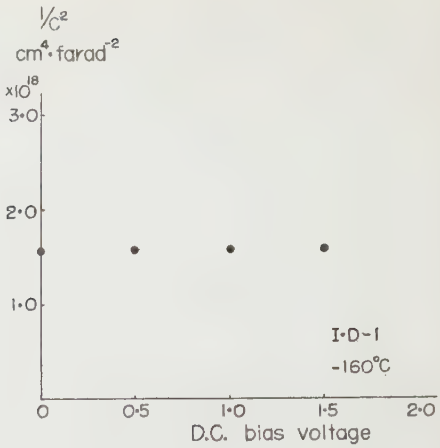

Fig. 9. 1/C² *vs.* V.

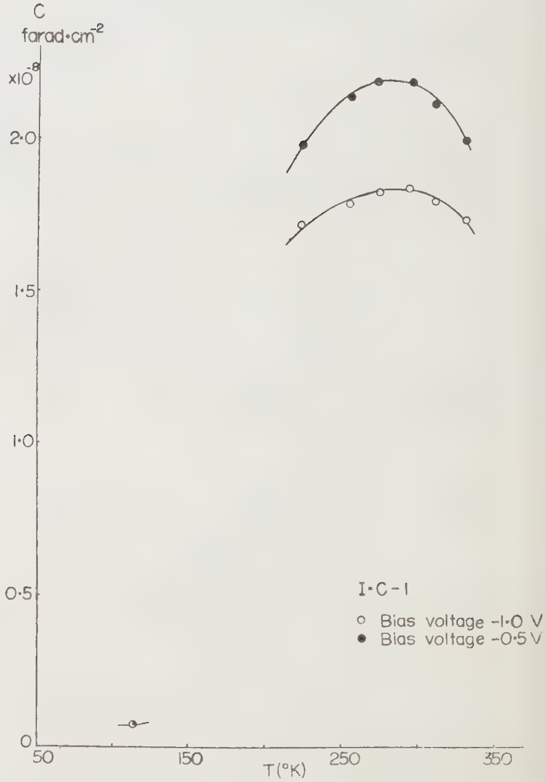

Fig. 10. Capacity *vs.* Temperature.

In Figs. 8 and 9, the results at −110°C and −160°C are shown respectively. The remarkable differences between the values observed at −160°C and those at room temperatures are the fact that the decreasing of temperature will make both the values of capacity and the slope of a straight line $1/C^2$ *vs.* V extremely smaller. The measurements at −160°C have shown that the capacity is quite independent of a d.c. applied voltage. The measurements at $-110°C$ have shown that the linear relation of $1/C^2$ *vs* V still holds approximately at this temperature. These facts will be discussed later.

From the data of above mentioned experiments, the plots of capacity *vs* temperature at a constant bias voltage can be given in Figs. 10 and 11.

§ 5. Comparison of the Experimental Results with the Equation Derived

Schottky indicated that the plots of $1/C^2$ as a function of V should be a straight line with an intercept equal to V_s (Figs. 6 and 7.). From this intercept, V_s has been determined to be 0.5 volt approximately. By substituting into Eq. (43) the numerical values of D_a, D_d and ΔE shown in Table I and V_s, the capacity of sample I. C—1 and I. D—1 with a d.c. bias voltage applied can be calculated. The results are shown in Figs. 12–15, where C_0 should take a different value for sample I. C—1 and I. D—1 respectively.

The comparison with the experimental results are summarized as follows,

(5.1) Eq. (43) shows a general agreement with experimental results, indicating that it has a maximum at a certain temperature and that below the temperature the capacity increases with increasing temperature and decreases above it.

(5.2) The temperature at which Eq. (43) reaches a maximum is lower as much as about 60°K for sample I. C—1 and I. D—1 than the experimental results.

(5.3) Capacity measured at $-110°C$ and $-160°C$.

When the temperature is lowered below $-50°C$, the capacity begins to decrease rapidly and reaches the value 0.08×10^{-8} farad/cm^2 at $-160°C$, independent of the applied d.c. bias voltage. All of the specimens have had nearly the same value. At $-110°C$, the value of capacity is different a little for each specimen, and is about 0.68×10^{-8} farad/cm^2 for I. D—1, dependent on the d.c. bias voltage. The slope of a plot, $1/C^2$ *vs* V, becomes slightly larger than that observed at room temperatures. These experimental facts can be interpretated as follows:

When the temperature is lowered and the resistance of Cu_2O layer becomes so high that it can be comparable with the barrier resist-

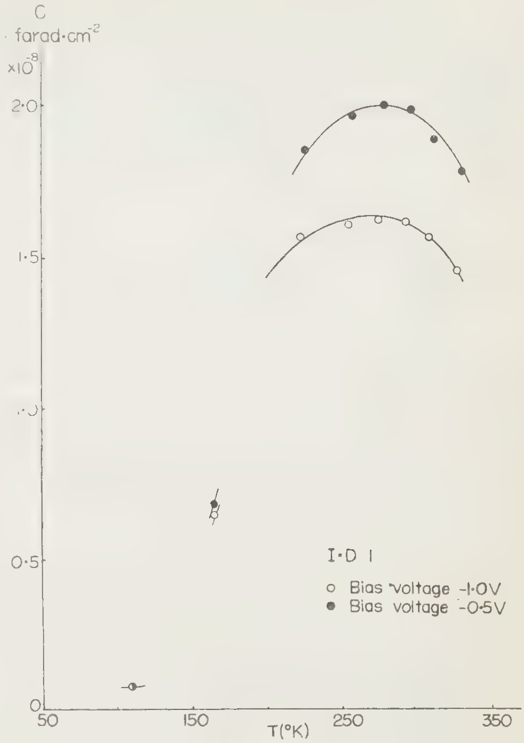

Fig. 11. Capacity *vs.* Temperature.

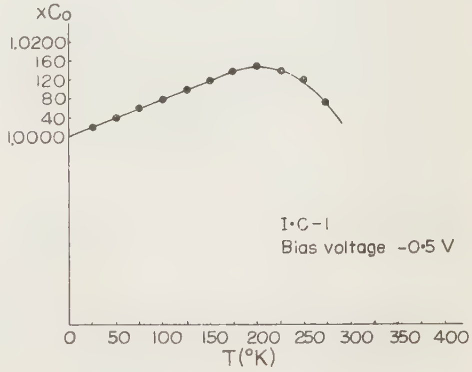

Fig. 12. C *vs.* T.

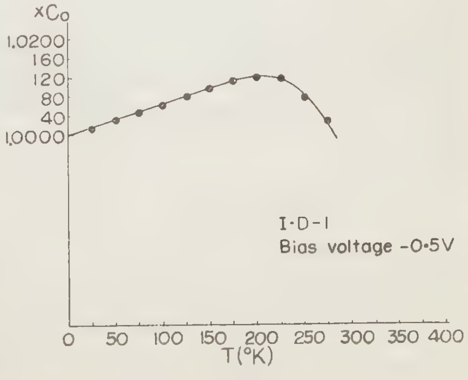

Fig. 13. C *vs.* T.

ance at room temperatures, the bias voltage applied to a rectifier may not be considered to be dropped across the barrier layer only, but across the Cu_2O layer itself between the copper and the counterelectrode (Fig. 16).

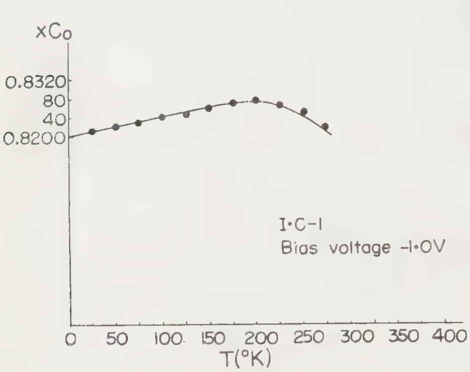

Fig. 14. C *vs.* T.

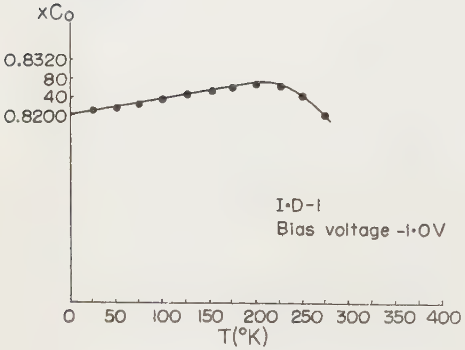

Fig. 15. C *vs.* T.

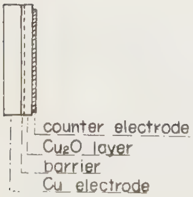

Fig. 16. A section of a Cu_2O rectifier.

And the capacity, measured in this case, may not be a barrier capacity, but a capacity of the parallel plate condenser composed of the Cu_2O layer and the two electrodes attached to it. Therefore, the capacity is expected to be given by

$$C_{\mathrm{Bulk}}=\mathcal{E}/4\pi W\,. \tag{47}$$

By substituting into Eq. (47) $\mathcal{E}=10$ and $W=7\times10^{-3}$ cm, we have

$$C_{\mathrm{Bulk}}=0.013\times10^{-8}\ \text{farad/cm}^2\,,$$

which may be considered to agree comparatively well with the observed value 0.08×10^{-8} farad/cm². The above considerations wi
enable one to understand that the capacit
measured at −160°C is rather not a capacit
of the barrier, but that of the Cu_2O laye
itself and consequently that it may be independent of the bias voltage applied.

The magnitude of capacities measured a
−110°C lies between the values of the barrie
capacity at room temperature and those c
bulk capacity C_{Bulk} at −160°C. These fact
may be considered as follows: when the am
bient temperature becomes as low as −110°C
the hole density at the valence band of th
bulk cuprous oxide layer will become smaller
and the hole depleted layer will be extende
from the metal surface into the interior o
the bulk cuprous oxide, thus the capacit
measurement will give the capacity of thi
hole depleted layer. The d.c. bias dependenc
of the capacity at these temperatures show
that the width of the hole depleted layer wil
be dependent on the bias voltage which i
applied to the rectifier.

(5.4) If the capacity data measured at to
low temperatures were adopted in order t
calculate the absolute value of the temperature variation of the barrier capacity C, the
would be proved quite inadequate accordin
to the above discussions, because they woul
contain not only a barrier capacity but a
capacity of the bulk Cu_2O layer. For an example, we shall discuss about the specime
I. D−1. Suppose that the lowest temperature at which the capacity of the bulk Cu_2
layer can be neglected compared with th
barrier capacity with a bias voltage −0.
volt applied would be −30°C (the hole densit
at this temperature is approximately on
tenth of that at room temperature). The absolute value of temperature variation of th
barrier capacity C from −30°C to 40°C i
obtained approximately 0.05×10^{-8} farad/cm
from the experiments and the theoretical calculations according to Eq. (43) gives 0.025×10^{-8} farad/cm² to the absolute value of th
temperature variation from 0°K to 290°K
when C_0 is taken 2×10^{-8} farad/cm². Th
theoretical value is about one half of the experimental and the coincidence seems to b
good.

(5.5) It can be expected from Eq. (43) tha
the absolute value of the temperature varia
tion in the barrier capacity should depend o

an applied bias voltage and this expectation is also proved to be true by the experimental observations.

Finally, it should be added to the above discussions that the variation in V_s with temperature is completely disregarded.

According to such a simple model as shown in Fig. 1, the change in the Fermi level with temperature means readily a change in the diffusion potential $V_s=\psi-\chi-\Delta E+\xi$. However, as Okazaki *et al*[13)13)] reported already, the experimental measurements of temperature dependence of V_s showed that V_s decreased with increasing temperature and that the results were quite in disagreement with their theory. In this paper we have assumed that the change in V_s with temperature will be negligibly small or that V_s will increase only a little even if the Fermi level did change so much. Owing to the various simplifications for calculations adopted when Eqs. (5)–(10) were introduced, especially the ignoring of the existence of the reserve layer near the origin, it may happen that the capacity C decreases as V_s increases. Also it must be added that the differences of the capacities in the two equivalent circuits—one is a parallel circuit of C and R used at the measurements and the other is a circuit with a bulk resistance in series to it—are very small over the measured temperature ranges and the experimental results are not changed by the measuring equivalent circuit.

In conclusion, the author expresses his sincere thanks to Prof. R. Kubo of the Tokyo University for his valuable discussions, Mr. Nijo for his encouragements and Mr. H. Baba for his helps during the work.

References

1) N. F. Mott: Proc. Roy. Soc. **171** (1939) 27.
2) W. Schottky: ZS. f. Phys. **113** (1939) 367, **118** (1942) 539.
3) R. Kubo: Denshi Hosha to Handotai (in Japanese) (1950).
4) W. Schockley: Electrons and Holes in Semiconductors (D Van Nostrand Company Inc.) p.p. 248.
5) H. Fröhlich: Proc. Roy. Soc. (A) **160** (1937) 230.
6) W. H. Brattain: Rev. Mod. Phys. **23** (1951) 203.
7) W. Schottky and F. Waibel: Phys. Z. **34** (1933) 858.
8) V. W. Vogt: Ann. Phys. **7** (1930) 183.
9) E. Engelhard: Ann. Phys. **17** (1933) 501.
10) S. J. Angello: Phys. Rev. **62** (1942) 371.
11) W. Feldmann: Phys. Rev. **64** (1943) 113.
12) A. Okazaki *et al*: Kyusyu Univ. Kenkyu Hokoku Vol. 1, No. 5 (1952) (in Japanese).
13) H. Tubota, Y. Matsukura and A. Okazaki: Memo. of the Faculty of Sci. Kyusyu Univ. Ser. B. Vol. 1, No. 4 (1954) 127.

JOURNAL OF THE PHYSICAL SOCIETY OF JAPAN Vol. 10, No. 6, JUNE 1955

On the Mechanism of Aging in Aluminium-Silver Alloys, III. Variation of the Young's Modulus

By (Miss.) Kayako TANAKA, Hidetaro ABE
Department of Physics, Ochanomizu University, Otsuka, Bunkyo-ku, Tokyo
and Ken-ichi HIRANO
Department of Physics, Tokyo Institute of Technology, Oh-okayama, Meguro-ku, Tokyo

(Read July 11, 1954; Received January 27, 1955)

Variations of the Young's modulus and the internal friction during the aging of the supersaturated solid solution of 20 weight percent silver in aluminium has been examined on polycrystalline specimens by the high frequency method at about 13 kilocycles per second; both isothermal aging curves and heating curves have been obtained.

It has been found that the formation of the Guinier-Preston zone results in decrease of the Young's modulus, whereas precipitation of the new phase results in increase of it. The results have been discussed based on the point of view that the formation of the Guinier-Preston zone is not a preliminary stage of the precipitation process.

The effect of the aging on the internal friction measured at the room temperature has been found negligible.

Further, temperature variations of the Young's modulus and the internal friction have been examined on the pure aluminium specimen in comparison with those of the present alloy.

§ 1. Introduction

It seems that the Young's modulus is suitable as a measure for the study of the aging process in alloys, because of its sensitivity to changes in the atomic configuration and concentration of the solute atoms in the matrix solid solution.

Some experimental results were reported on the composition dependence of the Young's modulus at the equilibrium state in various aluminium base alloys[1)-4)], but few on its change accompanied by the aging reaction, so the present investigation was planned to obtain the isothermal aging curves and the heating curves of the Young's modulus on various age-hardening alloys, such as Al–Ag, Al–Cu, Al–Zn, Al–Mg–Zn and so on, as well as some copper base alloys.

The objects of the work described in the present paper are to examine the aging characteristics of Al–Ag alloy, and, as one of a series conducted by one of the authors (K.H.)[5)6)], to add another information on the mechanism of the aging especially on the relation between the formation of the Guinier-Preston zone and the precipitation of the $AlAg_2$ phase.

§ 2. Specimens and Experimental Procedure

Polycrystalline rods of the alloy, containing 20.18 weight percent silver, and pure aluminium, were prepared by using super-pure aluminium (99.99%) and assay silver (99.99%).

The metals were melted in a graphite crucible, well stirred by a graphite rod, and cast into a chill mould. The specimens have the dimension, 1.3 cm in diameter and about 17 cm in length. They were annealed in a electrical furnace at about 550°C for 200 hours after some cold working in order to disperse the casting structure.

The alloy was solution-heat-treated by annealing at 540°C for 2 hours. Supersaturated solid solution was obtained by quenching the specimen into the quenching oil of the room temperature, about 19°∼22°C. Then it was aged at various temperatures in a electrical furnace.

Measurements for the isothermal aging curves were made at about 20°C after quenching the specimen from the aging temperature to the room temperature at every measuring procedures. Heating curves were obtained during heating the specimen at a rate of 0.5°∼1°C per minute. The temperature of the specimen was measured by the Copper-Constantan thermocouple, which is set closely by the specimen.

The Young's modulus and the internal friction were determined from the resonance frequency curve of the forced longitudinal vibration given to the specimen7)-10). Details of the measuring apparatus were illustrated in the previous paper11).

Fig. 1 shows the block diagram of the measuring system. The center of the specimen, that is, a node of the longitudinal vibration is mounted on the knife edge supporter which has the earth potential. The specimen is free at its both ends, each of which is faced to fixed plate, "excitor" and "detector" respectively. By alternating the potential difference fed by an oscillator between the exciting plate and one of the end faces of the specimen, the longitudinal vibration is excited in the specimen. The oscillator consists of three parts; master oscillator, one stage of buffer and one stage of power amplifier. The master oscillator is the usual Hartley circuit and supplied by an electronically stabilized power source. The oscillator was calibrated by comparison with the standard crystal oscillator before each measurement.

A condencer is formed between the other end face of the specimen and the detecting plate, the capacity of which changes when the specimen vibrates. The capacity change is translated to the current change in the detecting circuit (Inoue-Kanda Circuit12)), then it is amplified with a broad band-pass amplifier and examined by a cathod ray oscillograph or the vacuum tube voltmeter.

From the maximum amplitue of the vibration, the resonance frequency (f) can be determined, from which the Young's modulus (E) is calculated, using the equation13)

$$E=(2/n)^2(\rho_{20})(L_{20}{}^2)(L_{20}/L_T)\cdot f^2\left(1+\frac{1}{2}An^2\frac{\Sigma^2}{L_{20}{}^2}\right),$$

in which ρ_{20} and L_{20} are the density and length, respectively, of the specimen at 20°C, L_T the length at the temperature of the measurement, n the number of half-waves in the rod, Σ the average Poisson's ratio and A its cross-sectional area. In the present case, $n=1$ since the fundamental frequency is used.

At the same time, from the half width of the resonance curve, the internal friction at that frequency can be determined.

For the study of the isothermal aging, it is necessary to know merely the relative values of the Young's modulus of aged specimen to that of as-quenched one. Since it has been recognized14) that the change in length due to the aging process in the present alloy is so small that it affects the value of the Young's modulus negligibly, and L_{20} may be regarded as constant. Since all measurements were carried out at the same temperature, about 20°C, the relative value of square resonance frequency, $f^2/f_0{}^2$ may be taken as a measure of the change of the Young's modulus, where f and f_0 are the resonance frequency of aged and as-quenched specimens respectively.

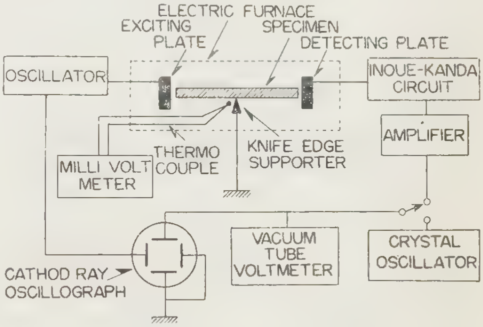

Fig. 1. Block Diagram of the Measuring System.

On the other hand, in the case of the heating measurements, effect of thermal expansion can not be neglected, but it does not affect the general feature of the Young's modulus versus temperature curves, so we have taken the value of f^2 as a measure of the Young's modulus.

At the measurements of the internal friction we have no regard for the effect of air viscosity at the gaps between the end faces of the specimen and the exciting and the detecting plates, and the plotted value must be somewhat larger than the true value.

The measurements have been carried out under the condition that the applied strain is not larger than the limited range to obtain the amplitude independent internal friction.

The effect of small change of the mounting condition of the specimen on the knife edge supporter to the Young's modulus and

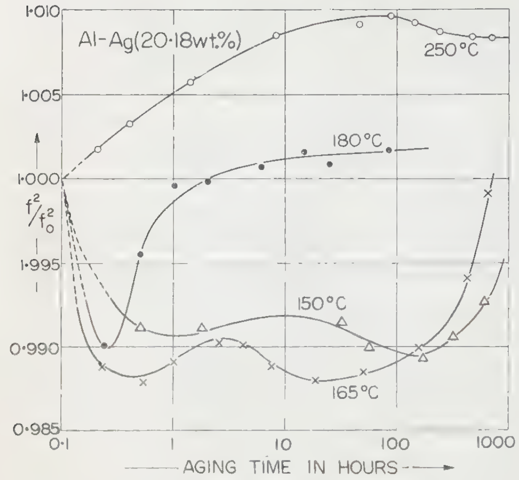

Fig. 2. Variation of the Young's Modulus during Aging. (Isothermal Aging Curves).

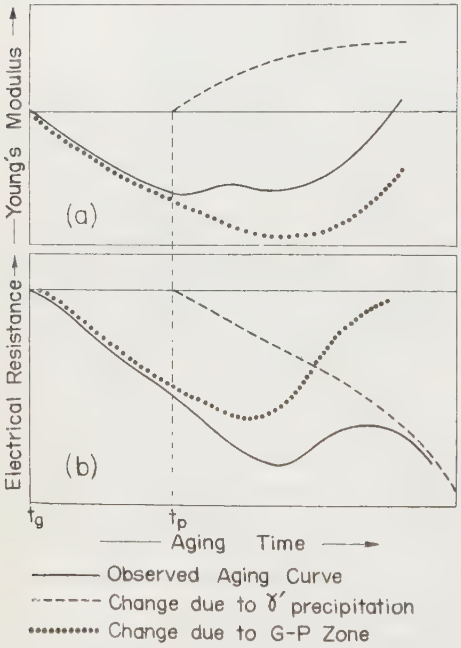

Fig. 3 (a) and (b). Integration of Two Reactions Contributing to Changes in the Young's Modulus and the Electrical Resistance during Aging.
t_p: Incubation time for γ′ precipitation.
t_g: Incubation time for G–P zone.

the internal friction have been found negligible for the required accuracy in this work.

§ 3. Experimental Results and Discussions

Fig. 2 represents the isothermal aging curves of the Young's modulus, which were obtained with Al–Ag (20.18 wt.%) alloy. It will be noted that at the early stage of the aging at 150°, 165° and 180°C, the values decrease from the initial point, but at the later stage they turn into increase, on the other hand the value of 250°C–aging increases from the begining without the initial decrease.

Comparing above results with the age-hardening curves[15)–17)], it may be recognized that the initial decrease and subsequent increase of the Young's modulus during aging at lower than about 200°C, correspond respectively to the first and the second stage of hardening at the low temperature aging (*cold-aging*), whilst the smooth increase at 250°C–aging corresponds to the single stage hardening curve at the high temperature aging (*hot-aging*).

Based on the X-ray analysis[18)–20)], calorimetric analysis[5)] and electrical resistivity measurements[6)], it has been shown that the first stage of the low temperature aging is the formation of the Guinier-Preston zone and the second stage is the precipitation of the new phase, therefore the initial decrease of the Young's modulus observed in the present investigation may be attributable to the formation of the Guinier-Preston zone and the subsequent increase to the precipitation of the γ′ phase (coherent to the matrix), $AlAg_2$. Appearance of the intermediate small maximum in the 150°– and 165°C–aging curves, may be interpreted as a result of superposition of the decrease and the increase as shown schematically in Fig. 3 (a), as inferred from the knowledge of the electrical resistance curve shown in Fig. 3 (b). Detailed examination of Fig. 3 (b) has been carried out previously by one of the authors (K.H.)[6)].

On the other hand, it has been shown by many workers that the Guinier-Preston zone can not be formed at above 210°C which is the limiting temperature of the formation of it. In the case of 250°C–aging, therefore, the Young's modulus increases monotonously from the starting and any decrease can not be recognized. The slight decrease at the later stage of 250°C–aging must be due to the transformation of the γ′ phase to the incoherent γ phase accompanied by the recrystallization[21)].

The effect of above aging treatments on the internal friction measured at the room temperature has been found negligible, which shows that the changes of the Young's modulus in Fig. 2 are not in relation to the annelastic phenomena.

The fact that the change of the Young's modulus due to the formation of the Guinier-Preston zone is in opposite direction to that due to the precipitation, may be regarded as a powerful evidence for the standpoint that the former is not a preparative stage of the latter and that there is a discontinuity between them.

Fig. 4 represents the results of the heating measurements. The curve denoted by *A* was obtained by slow cooled alloy, where the Young's modulus decreases monotonously with increasing temperature up to about 300°C, where it begins to deviate downward slightly. The curve denoted by *B* was obtained by the as-quenched alloy, where two inflexion points (*R* and *T*) were observed. The downward deviation (*PQ*) in the region between 50° and 180°C may be attributed to the formation of the Guinier-Preston zone during the measurement, the phenomena relating to which were already been observed in the specific heat versus temperature curves⁵⁾ and the electrical resistance versus temperature curves⁶⁾. Subsequent rise (*QR*) between 170° and 200°C may be attributed to the dispersion of the Guinier-Preston zone. From the fact that the point *R* of the curve *B* just lies on the dashed line *BS* of the quenched state, it will be deduced that the alloy returns to the quenched state just after the dispersion of the Guinier-Preston zone. After the upward deviation (*ST*) between 250° and 310°C, the curve *B* coincides with the curve *A* completely. The upward deviation (*ST*) is obviously due to the precipitation of the γ' phase during the measurement.

The curve denoted by *C* was obtained by the specimen which was aged at 100°C for 40 hours (low temperature aging). In this case the Young's modulus had decreased before the measurement due to the Guinier-Preston zone which was formed during the aging. At the range between 170° and 200°C, the curve *C* deviates upward owing to the dispersion of the Guinier-Preston zone, and at higher temperatures it coincides with the curve *B* completely.

The temperature limit of the existence of

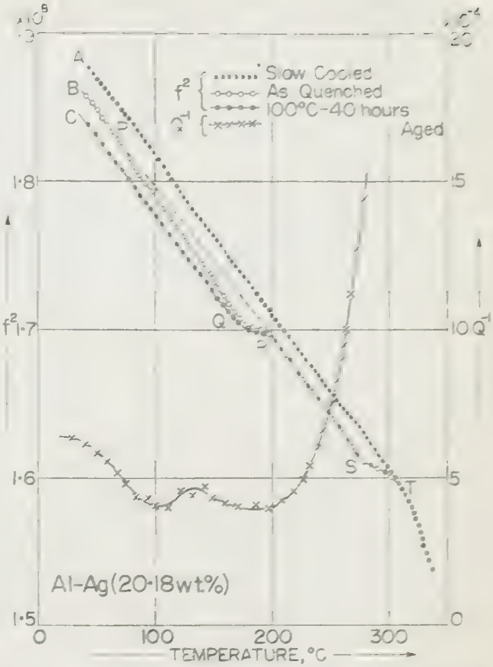

Fig. 4. Young's Modulus *versus* Temperature Curves and Internal Friction *versus* Temperature Curve of Al–Ag (20.18 wt.%) alloy. Unit of f^2 is cycle^2/sec^2.

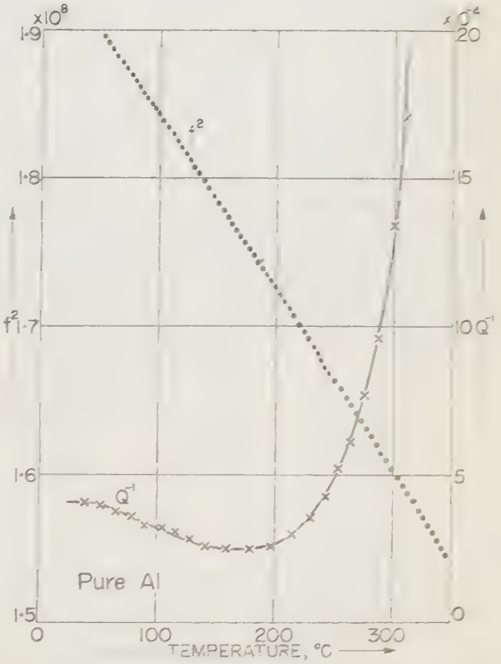

Fig. 5. Young's Modulus *versus* Temperature Curve and Internal Friction *versus* Temperature Curve of Pure Aluminium. Unit of f^2 is cycle^2/sec^2.

the stable Guinier-Preston zone determined from Fig. 4, which is about 200°C, is in good agreement with those determined from the results of the calorimetric[5] and the electrical resistance measurements[6].

The internal friction versus temperature curve is also shown in Fig. 3, where we can not detect any difference among as-quenched, low temperature aged and slow cooled alloys. However Damask and Nowick have recently reported that they could detect the effects of the aging treatment on the low frequency internal friction[22].

Steep increase of the internal friction was observed at above 250°C, but any peak can not be observed in the temperture range of the present experiment. The steep increase of similar form was observed also with the polycrystalline specimen of pure aluminium, as shown in Fig. 5. Origins of this steep increase and the slight maximum of the internal friction at about 130°C in Fig. 4, are yet not obvious, although it was confirmed that they are independent of the aging process.

§ 4. Acknowledgements

The authors wish to express their appreciation to members in the laboratory of Professor Hasiguti (University of Tokyo) for their helpful discussions, particularly on the measuring procedure. They also grateful to Professor Yutaka Takagi and Mr. Hideyo Maniwa (Tokyo Institute of Technology) for encouragement throughout the research. The present work was supported by the Grant in Aid for Fundamental Scientific Research from the Ministry of Education.

References

1) L. Guillet: Rev. Met.. **36** (1937) 497.
2) W. Köster and W. Rauscher: Z. Metallkunde **39** (1948) 111.
3) N. Dudzinski: J. Inst. Met. **81** (1952–3) 49.
4) T. Fukuroi and Y. Shibuya: Sci. Rep. RITU. **A5** (1953) 405.
5) K. Hirano: J. Phys. Soc. Japan **8** (1953) 603.
6) K. Hirano and H. Sakai: J. Phys. Soc. Japan **10** (1955) 23.
7) R. H. Randall, F. C. Rose and C. Zener: Phys. Rev. **56** (1939) 343.
8) D. Bancroft and R. B. Jacobs: Rev. Sci. Instrument, **8–9** (1937–8) 279.
9) C. Zener: Elasticity and Anelaticity of Metals, (Univ. of Chicago Press) 1948.
10) A. S. Nowick: Progress in Metal Physics **4** (Butterworths Scientific Publication) 1953.
11) K. Tanaka, H. Abe and K. Hirano: Ochanomizu Sci. Rep., in press.
12) J. Ito: Proc. Phys. Soc. Japan **6** (1952) 32, (in Japanese.).
13) R. A. Artman and D. O. Thompson: J. Appl. Phys. **23** (1953) 470.
14) K. Hirano: unpublished work.
15) R. Watanabe and S. Koda: J. Inst. Met. Japan **16** (1952) 208 (in Japanese).
16) A. H. Geisler, C. S. Barrett and R. F. Mehl: Trans. AIME. **152** (1943) 182.
17) W. Köster and F. Braumann: Z. Metallkunde, **43** (1952) 193.
18) C. B. Walker and A. Guinier: Acta Metallurgica, **1** (1953) 568.
19) B. Belbeoch and A. Guinier: Compt. rend. **238** (1954) 1003.
20) R. Glocker, W. Köster, J. Scherb and G. Ziegler: Z. Metallkunde, **43** (1952) 208.
21) A. H. Geisler: Phase Transformation in Solids, (John Wiley and Sons) 1951.
22) A. C. Damask and A. S. Nowick: Phys. Rev. **94** (1954) 1421.

JOURNAL OF THE PHYSICAL SOCIETY OF JAPAN Vol. 10, No. 6, JUNE 1955

On the Amorphous State of the Binary System of Nickel-Sulfur

By Masao SAWADA, Kenjiro TSUTSUMI, Toshio SHIRAIWA
and Masayoshi OBASHI

Department of Physics, Faculty of Science, Osaka University

(Received February 4, 1955)

We prepared the simultaneously electro-deposited Ni-S containing 0, 9, 13, 17 and 25 *wt.%* sulfur and studied their crystalline forms by X-ray diffraction patterns. The diffraction patterns of Ni-S containing 13 and 17% S show a uniform fog, and 7% S shows a halo, and 0 and 25% S are the same as those of Ni and Ni_3S_2 respectively. All amorphous samples crystallized after they had been heated to 180°C, and their diffraction patterns show the crystalline states of the two phase region of Ni and Ni_3S_2. The electrical resistances of these samples were measured in a vacuum furnace and in an oil bath. The resistances of these samples containing 9, 13 and 17% S gradually decrease as the temperature increases and suddenly drop at 180°C, then follow the usual behavior of the common metals for both increasing and decreasing temperatures. In the case of 0% S it does not differ from that of the pure nickel. We conclude that the amorphous state has the structure of a certain regularity, and that 180°C is the transition point of the amorphous Ni-S to the perfect crystal.

§1. Introduction

It has been reported by a few authors that the Ni-S system prepared by the simultaneous electrolysis is not crystalline over a range of its composition. According to R. Brill's[1] experiment on the range of the sulfur content from 0 *wt.%* to 12 *wt.%*, the size of the crystals decreases as the sulfur content increases, and the X-ray diffraction lines due to the nickel structure become broad and grow to a halo at the position of the Ni (111) diffraction line. He calculated the crystalline size by the Laue's theory from the widths of the halos. W. T. Young and H. Kersten[2] carried out the experiment over a wider range. According to them the X-ray diffraction pattern from samples with the sulfur content from 10% to 17% shows a halo indicating an amorphous structure. The composition ratio of the electrodeposited Ni-S depended on the electrolytic current density.

The amorphous state of these substances is not stable and crystallizes by heating to 180° C. H. Kersten and W. T. Young[3] measured the electrical resistance on the sample of 13% S and found that it was larger than that of the usual metals and decreased suddenly at 180°C, the modification temperature from an amorphous state into a crystalline state. This change was not reversible.

In order to investigate the nature of the amorphous state, we studied on these materials the electrical conductivity, the crystal structure, and the fine structure of the X-ray absorption spectrum.

In this paper we report the results of the measurements of the electrical resistances and the crystal structures. The results of the other properties will be published in the forthcoming issue as the Report II.

§2. Preparation of the Sample

Following Young and Kersten's method, the electrolyte was of the following composition:

Table I. Compositions and structures of electrodeposits for various electrolytic current densities.

Per cent of Sulfur	Current Density Amp./dm^2	Structure	
0	0.55	Ni	
9.3	1.20	Amorphous	halo Ni (111)
13.2	0.55	Amorphous	uniform fog
17.4	0.20	Amorphous	uniform fog
25.6	0.15	Ni_3S_2 [4]	

nickel-ammonium sulfate $NiSO_4(NH_4)_2SO_4 : 6H_2O$, 50 g, sodium thiosulfate (hypo) $Na_2S_2O_3 : 7H_2O$, 5 g, sodium citrate $Na_3C_6H_5O_7 : 5H_2O$, 7.5 g as a buffer, and water H_2O, 500 cc..

The pH of this solution was 6.4 at the beginning and more acid as the electrodeposition progressed.

The electrodeposition was carried out in a 500 cc. beaker, kept in the water bath held at 30°C±0.5°C. We used a stainless steel cathode 4.5 cm wide immersed to a depth of 7 cm placed 4 cm apart from a lead anode having the same dimensions. The composition of a deposit depends on the current density; the relation between the current densities and the compositions of deposits is shown in Table I. The sample containing 0% S corresponds to the pure nickel and 25% S corresponds nearly to the composition of Ni_3S_2. The pure nickel can be deposited when the electrolyte does not contain sodium thiosulfate, and in this case the current density has no influence on the structure.

The electrolytic voltage was controlled so that the current density was constant. This voltage decreased as electrodeposition progressed. The time of electrolysis was 2 hours for all the samples but in the case of the sample containing 9% S the deposit became too thick to obtain the X-ray absorption photographs, therefore we reduced the time to 45 minutes. The results obtained by the latter sample however were the same as the former with respect to the electrical conductivity and the powder diffraction pattern. Deposits were $10\mu-20\mu$ in thickness and could be easily stripped off from the cathode plate together with the cigarette paper pasted on it. This paper was used to protect the brittle samples without loss of X-ray transmission. Deposits had the semi-metallic luster on the outside surface and metallic luster on the surface which had been in contact with the cathode plate. All samples used for experiment were chosen from the central part of the cathode where the current density was considerably uniform.

§ 3. Experimental Procedure

Diffraction pattern: For the diffraction study the electrodeposit stripped from the cathode with the paper pasted on it was cut into 0.2—0.5 mm width and 10 mm length sheets, and the several sheets were pasted one over the other to prevent the crystallization by the frictional heat when grinding into the fine powder. The amorphous samples crystallized by heating and these treatment were done in a vacuum furnace or an oil bath in which we measured the electrical resistance at the same time. Each sample was photographed at the room temperature immediately after the electrolysis (non-heated state) and then photographed when they had been cooled to the room temperature after heating to 180°C at which we were able to ascertain the crystallization by the change of electrical resistance. A sample containing 13% S among others, was photographed at the room temperature after heating to 80°C, 120°C, 160°C and 180°C.

The radius of the camera used for the diffraction pattern was 3.5 cm and the dimensions of the slit was $1\times0.03\,mm^2$. X-ray examinations were carried out under the conditions of 30 kV, 5 mA, 20 hours exposure and with Cu $K\alpha$ radiation. In order to ascertain that there is no crystalline constituent in an amorphous sample, longer time of exposure than proper was applied. Some non-heated samples were rotated and others were fixed in order to investigate the prefered orientations, but no trace of crystals was found. Photo. I, II and Table I show the diffraction patterns and crystallographic data of each sample.

The diffraction patterns of non-heated samples containing 0% S and 24% S are the same as those due to Ni and Ni_3S_2[4] respectively. The sample containing 9% S shows a halo which corresponds to reflection (111) of Ni, and sample containing 13% S and 17% S show only a uniform fog. It is supposed that the halo is not discerniable because its width is too broad. The photographs of these amorphous samples after heating to 180°C show the crystalline state of the two phase region of Ni and Ni_3S_2. In the case of the sample containing 13% S when heated to the temperature below the crystallization point, a halo appears faintly at 80°C, and distinctly at 120°C, then at 160°C distinct lines corresponding only to the strong reflection of Ni and Ni_3S_2 appear.

Measurement of Electrical Resistance: As samples were thin and brittle, measurements were very difficult. After many trials, we used the following method. The dimension of the sample was limited to about 1—2 mm width and 1 cm length because the smaller the sample the less crack appeared by fastening or heating, and moreover by this dimen-

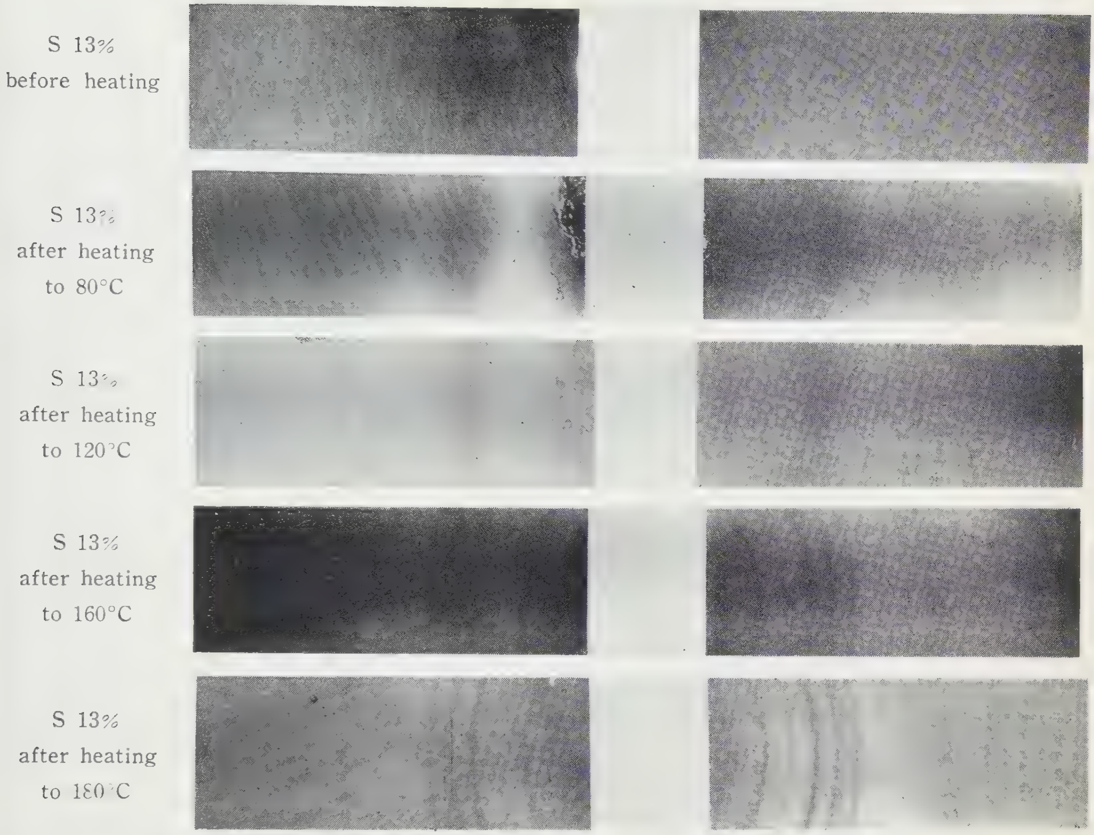

Photo. I. Diffraction patterns of electrodeposited Ni–S in various conditions.

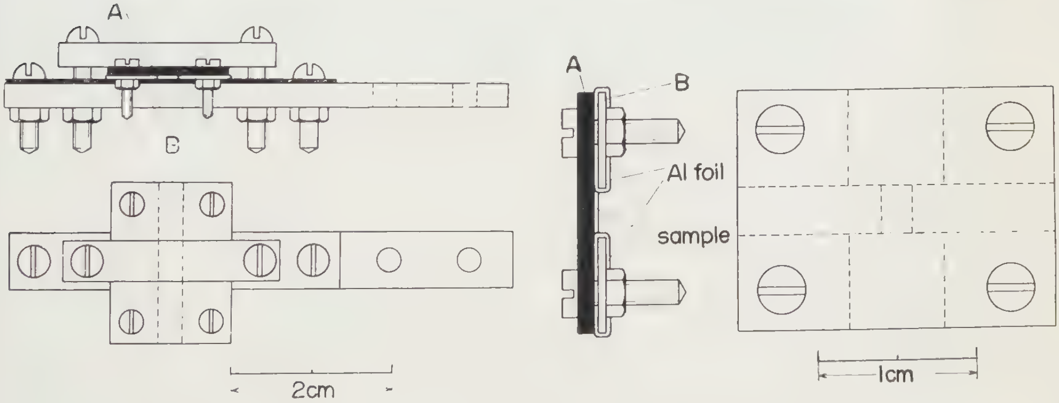

Fig. 1. Holder of a sample for measurement of electrical resistance.

sion we could avoid the crack when the sample was stripped off from the cathode. The holder of the sample is shown in Fig. 1. The sample was held on the mica plate (A) 2 cm × 1.5 cm by two copper electrodes (B) and fastened by screws. The electrode was covered by about 10 sheets of 10μ thick aluminium foils. These foils protected the sample from breaking at coming into contact with the copper electrode and also assured in making a close electrical contact of the sample to the electrode. It is necessary that a sample is fastened to the electrode as tightly as possible. The above mentioned holder was put in a vacuum tube made of fused quartz, and heated by an electric furnace. Also we meas-

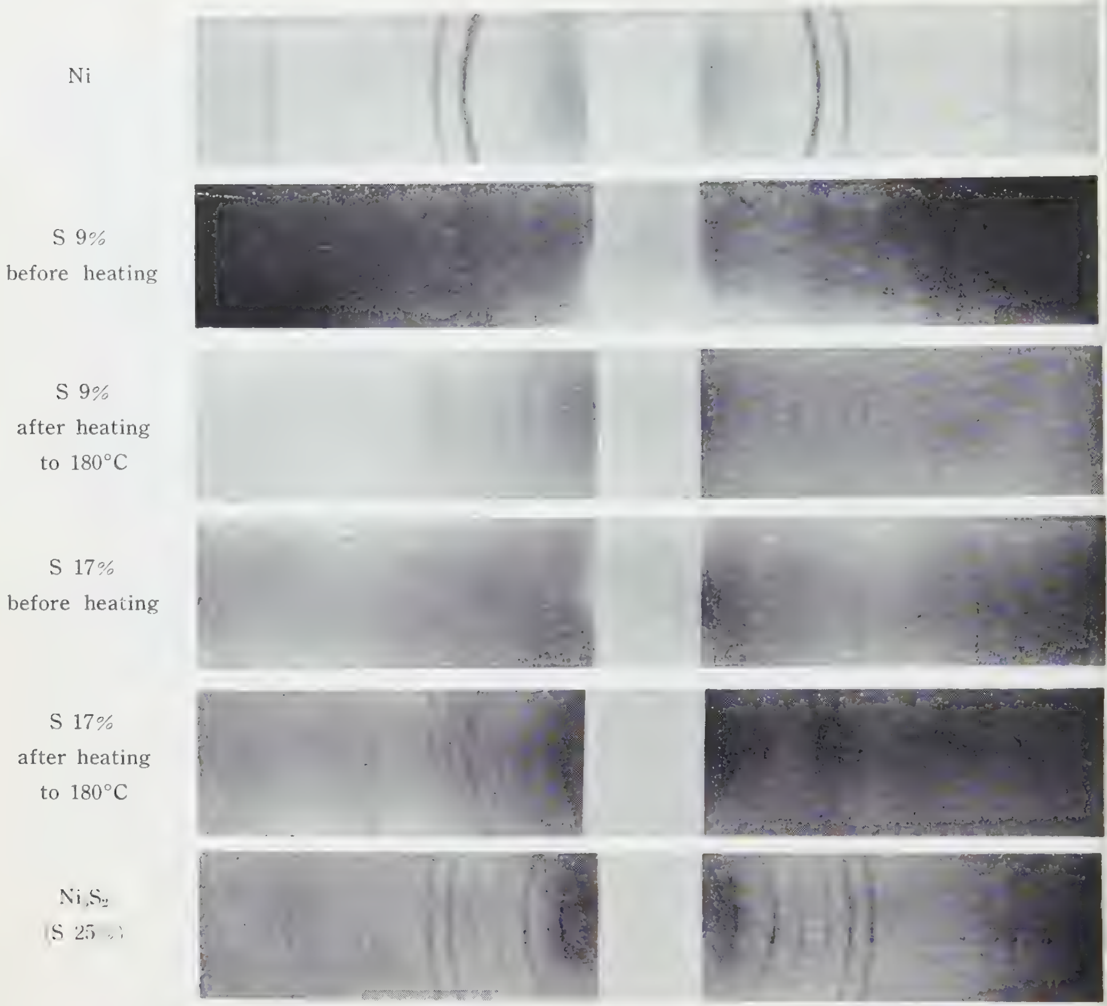

Photo. II. Diffraction patterns of electrodeposited Ni–S in various conditions.

ured in an oil bath to avoid the evaporation of sulfur that might occur in vacuum, but we could find no difference between the two cases. Resistance was measured by the Wheatstone Bridge. The current which flowed in the sample was always limited to 10 mA in order to avoid the heat damage. The rate of temperature increase was 1°C per minute, and we measured at nearly equal intervals of 5°C. Results are shown in Fig. 2. The value of the resistance of the above mentioned sample is about 100 ohms in the amorphous state and 20—30 ohms in the crystalline state. The values of the ordinate in the graph are arbitrarily chosen.

The sample containing 0% S (Ni) shows no difference from the pure nickel. In the case of 9%, 13% and 17% S the resistance decreases gradually to 180°C and drops suddenly at that temperature. After crystallization it follows the curve B, then it shows the usual behavior of the common metals for both increasing and decreasing temperatures. When an amorphous sample is cooled from any point below 180°C, the resistance follows the curve C. The resistance of the same sample follows the curve C on increasing the temperature. The inclination of the curve A is minimum in the case of 13% S and becomes larger for any other sulfur contents.

§ 4. Results

It has been inferred from R. Brill's experiment that the amorphous Ni-S is made of very fine crystals. As expected from Laue's theory and R. Brill's experiment, the width of the diffraction pattern depends intimately on the size of the crystal. We conclude that

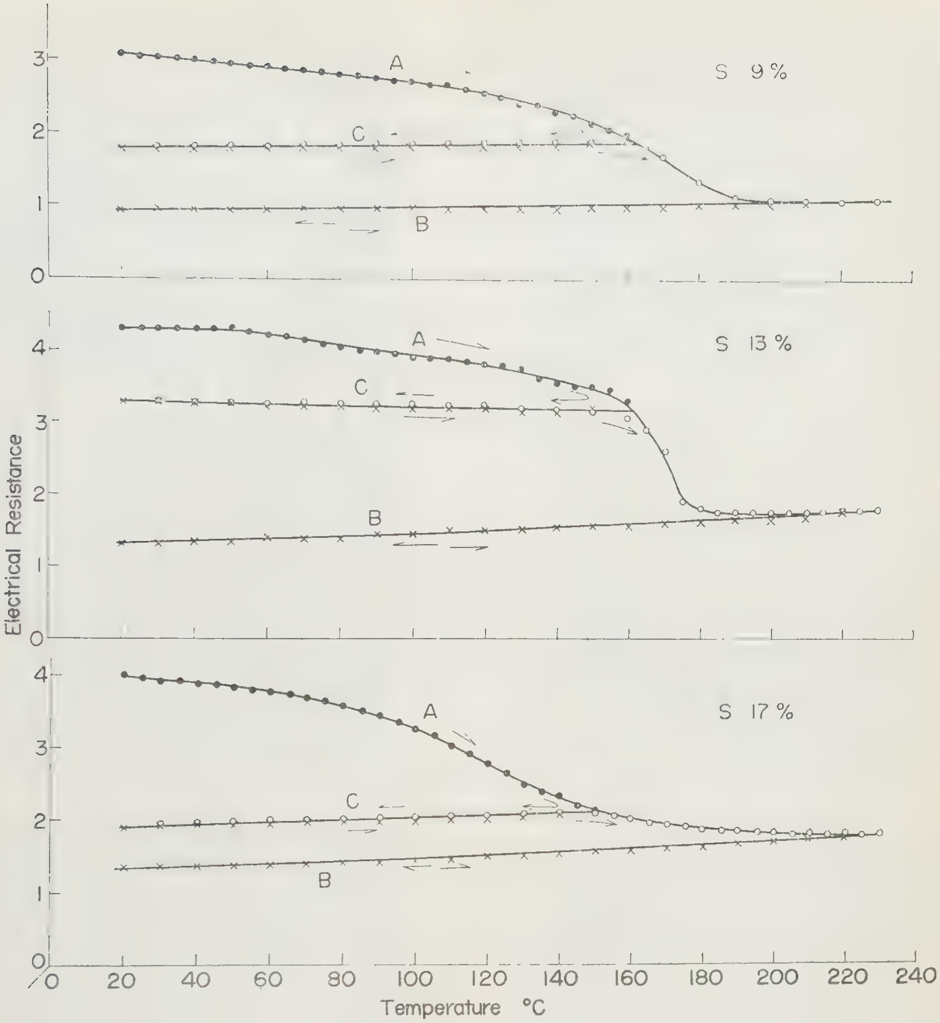

Fig. 2. Change of the electrical resistance of the electrodeposited Ni–S with temperature.
A: The amorphous sample is heated from the room temperature. It is not reversible.
C: The temperature decreased from a point below the crystallization point. This is reversible.
B: After crystallization. It is the same behavior as a common metal.

the size of the crystal becomes progressively larger with temperature since the width of diffraction pattern of these amorphous Ni-S becomes narrower with temperature rise as shown in our experiment and also in Kersten and Young's[3] experiment. We also assure the same conclusion from the fact that the electrical resistance decreases gradually to 180°C and this change is not reversible. All the foregoing facts show that the amorphous state has the structure having a certain regularity, and this domain of the regularity grows larger with temperature. As shown in Kramer's[5] experiment for the amorphous metals, the sudden decrease of the electrical resistance at 180°C shows that the amorphous samples perfectly crystallize. This conclusion will be also assured by our another experiment of the fine structure of X-ray absorption spectra.

We are indebted to the members of Tagaya Laboratory in the Faculty of Engineering of Osaka University, where the chemical analysis of our samples was undertaken.

References

1) R. Brill: ZS. f. Krist. **75** (1930) 217.
2) W. T. Young and H. Kersten: Trans. Electrochem. Soc. **121** (1937) 225.
3) H. Kersten and W. T. Young: J. A. P. **8** (1937) 133.
4) A. Westgren: ZS. f. anorg. allg. Chem. **239** (1938) 82.
5) J. Kramer: ZS. f. Phys. **106** (1937) 675.

JOURNAL OF THE PHYSICAL SOCIETY OF JAPAN Vol. 10, No. 6, JUNE 1955

On the Fine Structures of X-ray Absorption Spectra of Amorphous Substances

The Amorphous State of the Binary System of Nickel-Sulfur. II.

By Masao SAWADA, Kenjiro TSUTSUMI, Toshio SHIRAIWA
and Masayoshi OBASHI

Department of Physics, Faculty of Science, Osaka University

(Received February 4, 1955)

We prepared the simultaneously electrodeposited Ni-S containing 0, 9, 13, 17 and 25 *wt.* % sulfur and studied their crystalline forms and electrical resistances. Of these samples, those containing 9, 13 and 17% sulfur are amorphous and crystallize when heated to 180°C. The above results were reported in paper I.[1]

We photographed the fine structures of Ni *K* X-ray absorption spectra in the amorphous and crystalline states of the same samples. We measured the wave-lengths of the fine structures of the Ni *K* absorption edge and intensities of their non-absorption maxima. We find the fine structures in the amorphous states; their shapes and wave-lengths show a similarity to those shown by the substances which have undergone crystallization. But generally, in the amorphous state, the fine structure is less pronounced at the shorter wave-length side than in the crystalline state.

We conclude from the above results and previous results in paper I that the amorphous Ni-S is the aggregate state of fine crystals, and that the crystal size influences the region of the extended fine structure.

§ 1. Introduction

According to Kroning[2] the origin of the extended fine structure observed in the *K* X-ray absorption spectrum of crystal is as follows; the X-rays are absorbed by the electrons which make transitions from the X-ray *K* levels to empty levels lying above the Fermi distribution. These empty levels are grouped into zones and exist as forbidden and allowed bands caused by the periodic field in a crystal. As the absorption coefficient is proportional to the product of the transition probability and the state density, a fine structure occurs. Also, in the absorption spectra of gaseous molecules there are less extended fine structures corresponding to their molecular structures[3].

The structure of an amorphous substance, whose diffraction pattern shows no diffraction line but only a halo, can not deeply be investigated by X-ray analysis. But if this substance has some structure (the aggregate state of very fine crystals or of morecules), one expects the exsistence of the corresponding fine structure in the X-ray absorption spectrum and, inversely, one would be able to infer the structure of the amorphous substance from it.

In order to study the relation between the structure of an amorphous substance and the fine structure of the X-ray absorption spectrum, we take up the amorphous Ni–S system as the samples to which we have already related the diffraction patterns and the electrical resistances in paper I[1], and we take the photograms of *K* X-ray absorption spectra of nickel.

§ 2. Experiment

The method of the preparation of the samples was given in paper I. Samples used as the screens for the X-ray absorption spectrum contained 0% and 25% S (pure Ni and Ni_3S_2, both in crystalline states) and 9, 13 and 17% S (each in an amorphous and a crystalline state). As the amorphous Ni–S crystallizes at 180°C, we can take the absorption spectrum in the crystalline state for the same sample which has been already photographed in the amorphous state. There is, therefore, an advantage that we can compare the spectra in the amorphous and

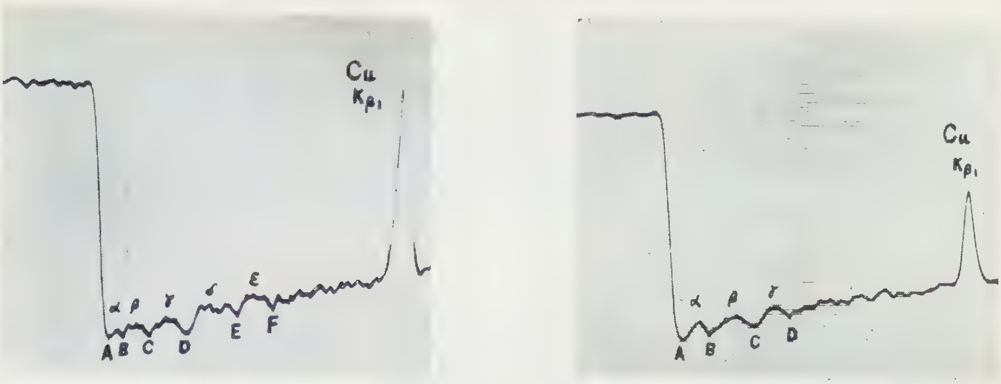

Ni

Ni_3S_2 (S 25%)

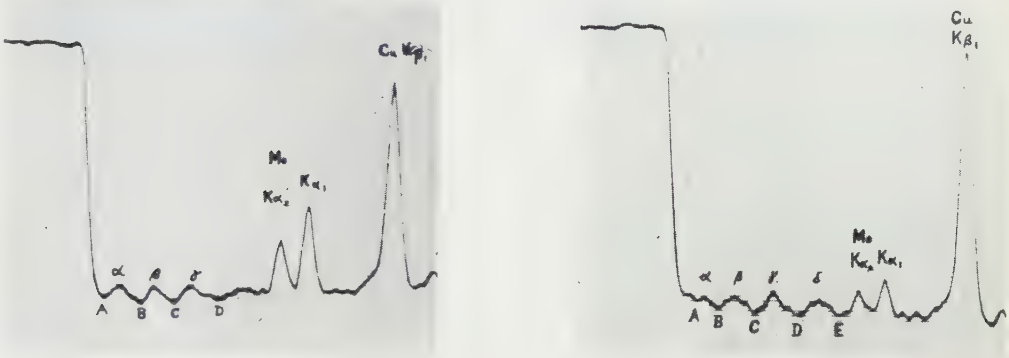

S 9% before heating

S 9% after heating to 180°C

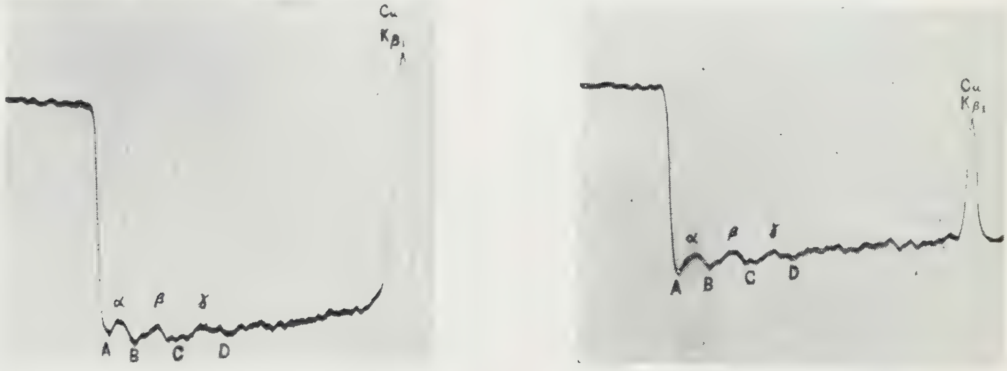

S 13% before heating

S 13% after heating to 180°C

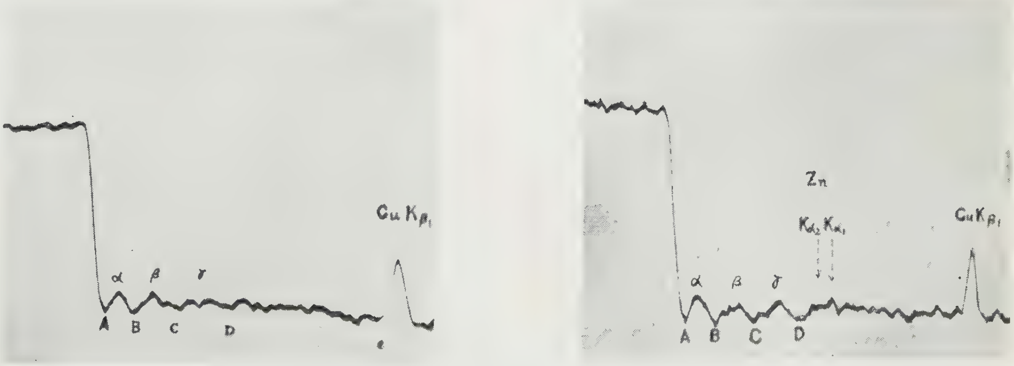

S 17% before heating

S 17% after heating to 180°C

Photo. I. Micro-photograms of absorption spectrograms at Ni *K* edge of electrodeposited Ni–S in various conditions.

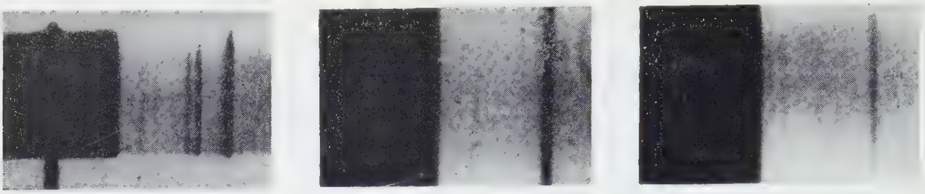

S 9% before heating
S 13% before heating
S 17% before heating

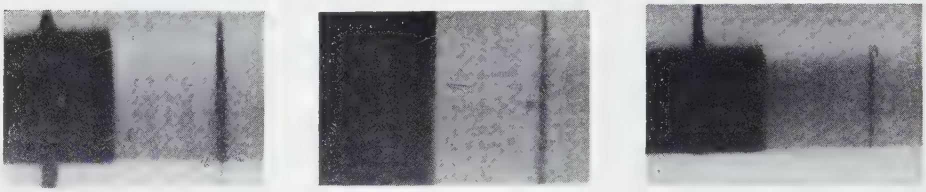

S 9% after heating to 180°C
S 13% after heating to 180°C
S 17% after heating to 180°C

Photo. II. Several spectro-photograms of Ni K absorption spectra of Ni–S.

crystalline states of the same sample, without careing for the change of thickness. The diffraction patterns of amorphous samples show a halo at 9% S and a uniform fog at both 13% S and 17% S, and those of the crystalline state show the structure of the two phase region of Ni and Ni_3S_2.

The electrodeposited samples were about 10 μ in thickness and a few sheets of them were superimposed as absorbers. A gas-ion type X-ray tube was chosen to avoid the W $L\alpha_{1,2}$ lines. The Mo target was used and the tube voltage was limited to 10 kV to eliminate the Mo $K\alpha_{1,2}{}^{II}$ lines. These lines appear in the neighbourhood of Ni K edge. All spectrograms were taken on an X-ray spectrograph of the transmission-focusing type with a quartz crystal bended to a radius of 20 cm, and we used the second order reflection of the (100) plane. All absorption edges were photographed on Fuji A–I plates. The tube current was 10 mA and the time of exposure was 10–15 hours. For the measurement of the intensity of the fine structure, aluminium absorbers of various thicknesses were set in front of the photo-plate and thus we took photograms of the three kinds of 1, 1/5 and 1/25 relative intensities on the same plate in a single exposure.

The micro-photograms and several spectro-photograms of absorption spectra are reproduced in Pohto. I and Photo. II. The results obtained are collected in Table I. The wave-length values of the edge and the fine structure in nickel coincide with those data alraedy published. In Ni_3S_2 (25% S) the form of the fine structure differs from that of nickel itself. In the case of the amorphous states (9%, 13% and 17% S) the wave-lengths of the absorption maxima and minima of the fine structures are not different from those in the crystalline states. The absorption edge slightly moves to the shorter wave-length in the caystalline state. There is a similar phenomenon in the case that the element is combined in a compound. In the neighbourhood of edges the shapes of the fine structures of the amorphous substance are similar to those of the crystalline substances which have been crystallized by heating from the amorphous states. The fine structures of these crystalline substances are the same as the superpositions of those of Ni and Ni_3S_2. At the high energy region relative to the Fermi suface the third non-absorption maximum γ is low in the amorphous state compared to that of in the crystalline state as is clearly seen in Photo. I. This phenomenon is pronounced in the case of the samples 13% S and 17% S. In order to estimate the quantitative change of the feature in the fine structures between the amorphous and crystalline states, we calculated the following quantities R from the three microphotograms of the spectrograms which had been taken at the same time as mentioned above.

Table I. Wave-length values of fine structures at Ni K absorption edge of the electrodeposited Ni–S. (*in X.U.*)

Sub-stance	Ni	Ni–S S 9%		Ni–S S 13%		Ni–S S 17%		Ni_3S_2 S 25%	
Treat-ment		Before Heating	After Heating	Before Heating	After Heating	Before Heating	After Heating		(ΔeV)
Ni K_{abs}	1483.8	1483.8	1483.8	1484.5	1483.5	1484.2	1482.8	1483.7	(0)
A	1479.8	1478.6	1476.6	1480.2	1479.5	1480.3	1479.9	1479.4	(24)
α	1477.7	1472.9	1473.2	1475.5	1474.4	1475.6	1476.4	1474.8	(50)
B	1475.8	1467.1	1468.7	1470.1	1469.7	1470.8	1470.9	1470.5	(75)
β	1471.6	1462.6	1463.4	1464.5	1462.7	1465.1	1464.8	1463.8	(113)
C	1466.9	1456.9	1456.6	1459.3	1456.4	1459.9	1458.5	1457.0	(153)
γ	1460.4	1450.7	1451.6	1450.6	1450.4	1450.7	1451.6	1450.6	(191)
D	1455.2	1443.2	1445.3	1440.9	1445.4	1444.4	1444.9	1445.7	(219)

Table II. Values of $R=(I_{\max}-I_{\min})/I_0$.

	Ni–S (S 9%)		Ni–S (S 13%)		Ni–S (S 17%)	
	Before Heating	After Heating	Before Heating	After Heating	Before Heating	After Heating
Ni K_{abs}	1/1	1/1	1/1	1/1	1/1	1/1
α	1/25	1/36	1/27	1/24	1/22	1/18
β	1/23	1/29	1/28	1/24	1/22	1/18
γ	1/28	1/16	1/44	1/29	1/44	1/18

$$R=\frac{I_{\max}-I_{\min}}{I_0},$$

where $I_{\max}$ is the intensity of the non-absorption maximum (α,β,γ) and $I_{\min}$ is the average intensity of the non-absorption minimum at both sides, (for example A and B for α). I_0 is the intensity of the jump at the principal edge. They are listed in Table II. For the fourth non-absorption maximum no reference was made in this table because this coincide with the Zn $K\alpha_{1,2}$ lines. But generally, in the amorphous states, the fine structures were less pronounced at the shorter wave-length side than those in the crystalline states.

§ 3. Discussion

The fact that the X-ray diffraction pattern of an amorphous substance is a halo means that the domain in which the atomic arrangement is regular is very small, or the atomic arrangement is the same as in the liquid state. In either cases we can not know its real structure in detail by the X-ray diffraction analysis. In the case of the samples 13% and 17% S their diffractisn photographs show only a uniform fog and we cannot therefore confirm any existence of the structure in them.

We can infer that these amorphous samples are the aggregate states of very fine crystals from the change of the diffraction pattern with the temperature and the relation of electrical resistance to temperature. These results were reported in paper I. In the present research we find the fine structures in the absorption spectra in the amorphous states, and their shapes and wave-lengths show a similarity to those shown by the substances which have undergone crystallization. This means that the amorphous Ni-S is not an irregular assembly of the atoms as suggested by Kramer[4)] for amorphous metals, but has a definite structure, and it may exist as a crystalline state. This coincides with our result shown in our paper I. The variation of the intensity in the high energy region may be due to the effect of the crystal size. From the fact that the non-absorption band γ scarecely appears in the samples containing 13% and 17% S whose crystal sizes are smaller (giving a fog pattern) than those containing 9% S (giving a halo), one expects that the fine structure becomes less apparent at the shorter wave-length side as the crystal size becomes smaller.

§ 4. Conclusion

We confirm that the fine structure of X-ray absorption spectrum exists even for an amorphous substance and that this fine structure is useful as a tool to study the structure of the amorphous substance. From the results of the absorption spectra together with the diffraction photograms and the electrical resistances we expect that the amorphous Ni-S consists of very fine crystals whose structure does not profoundly differ from that of the crystalline state. The change of the crystal size influences the region of the extended fine structure.

References

1) M. Sawada, K. Tsutsumi, T. Shiraiwa and M. Obashi: J. Phys. Soc. Japan **10** (1955) 459.
2) R. de L. Kronig: ZS. f. Phys. **70** (1931) 317, **75** (1932) 191.
3) R. de L. Kronig: ZS. f. Phys. **75** (1932) 468. H. Petersen: ZS. f. Phys. **76** (1932) 768.
4) J. Kramer: ZS. f. Phys. **106** (1937) 675.

JOURNAL OF THE PHYSICAL SOCIETY OF JAPAN Vol. 10, No. 6, JUNE 1955

On Producing Thin Single Crystal Foils of Aluminium which have any Desired Crystallographic Orientations

By Hiroshi FUJIWARA
Department of Physics, University of Tokyo
and Takao ICHIKI
Department of Physics, Hiroshima University

(Received January 25, 1955)

By using Prof. T. Fujiwara's method, we have succeeded in producing the aluminium single crystal foils ($0.06\times5\times100$ mm^3, 99.53% in purity) having their definite crystallographic orientations; for example, they are orientated in [110]—(110) or [110]—(100) or D_s or D_d, etc.

It was found that the easiness with which a single crystal foil was produced was remarkably different according to its crystallographic orientation. For the specimens D_s and D_d, it was also found that the bending behaviors caused by some mechanical shock were different from each other.

§ 1. Introduction

Up to the present, Prof. T. Fujiwara and his co-workers produced the metallic single crystal wires or plates having definite crystallographic orientations exactly[1)], and we have produced such single crystals according to the previous method and by the use of the improved one[2)]. In these cases, the thickness of produced plates was about 0.5 mm∼5 mm.

Some complexity due to the thickness of a single crystal plate, however, comes to have large effect in the course of research into the physical properties of the single crystal plate, such as cracks in metals, anisotropic behaviors of plastic deformation and the behaviors of crystal-growth in the surface plane, etc.

So, it is more desirable to produce the thin single crystal foils, especially the single crystal foils having any special crystallographic orientations exactly.

We made the experiment along this line and succeeded in producing the aluminium single crystal foils ($0.06\times5\times100$ mm^3) having the special crystallographic orientations exactly, for example, they are orientated in [110]-(110) or [110]-(100) or D_s or D_d, etc., the definitions of these notations being explained in Appendix.

By the use of the specimens thus obtained, we made some investigations on some of the anisotropic properties of the specimens D_s and D_d, and others.

§ 2. Experimental Procedures and Results

At first, many slender pieces ($1 \times 5 \times 100$ mm^3) of aluminium were cut out from the commercial plate (1 mm in thickness, 99.53% in purity) in the same manner as in the former process[3]. Then each of them was reduced in its thickness in the following three steps: first, each of them was reduced to the suitable amount by successive cold rolling in the same direction; second, these specimens thus rolled were annealed at suitable temperature. And then, these annealed specimens were again reduced finally to the required amount (0.06 mm) by rolling in such a manner as in the first step. These rolled foils were cut in length of 200 mm and after suitable annealing in the same furnace, each of them was stretched in its lengthwise direction about 2.5%.

The special specimen-holder was prepared from aluminium plate (0.25 mm in thickness and of the same nature as the specimen to be converted into single crystal), such as shown in Fig. 1-b. This holder has several semi-circular holes c_1, c_2, etc, for the X-ray radiographs to be taken of the specimen which is to be sandwiched, as shown in the same figure.

A foil which was treated in the manner mentioned above, was sandwiched between two holders H_1 and H_2, and was fastened by fine wires in both edges, such as shown in Fig. 2. Then the whole body was coated on with paraffin and the portions indicated by the thick full line about 1 mm in width, in Fig. 3, were stripped off very carefully on both sides, so that the body surface of the sandwiched foil was exposed. The exposed portions thus made were etched off by hydrochloric acid and then the coated paraffin was cleaned up by xyrol.

So, the form of the sandwiched foil became the same as the holder, and, hereafter, these three, i.e. one foil and two holders thus piled-up, were treated as one specimen and we call these three as a specimen.

Secondly, the extremity of the narrow part of the specimen including the first hole c_1, was converted into one crystal-seed in such a manner as in the processes of the former cases.

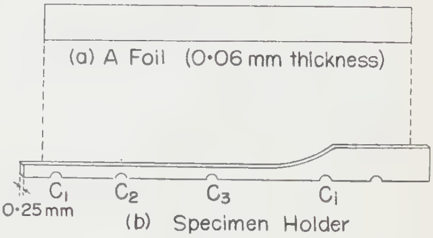

Fig. 1.

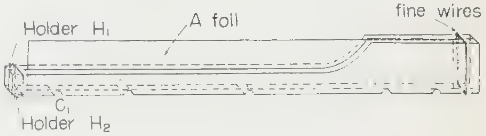

Fig. 2. A foil which is sandwiched between two holders H_1 and H_2.

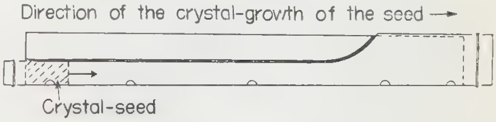

Fig. 3.

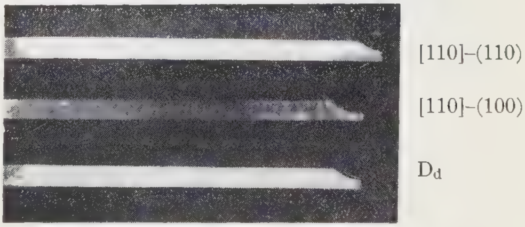

Fig. 4. Photographs of etched surface of the produced single crystal foil.

The crystallographic orientation of the crystal-seed was determined by taking Laue photograph by X-ray which incident through the hole c_1. In the subsequent processes of production of required single crystal, we have followed our improved method.

The single crystal foils, such as [110]-(110), [110]-(100), D_s and D_d, were thus produced. And some of the photographs of the etched ones are shown in Fig. 4, where on the right side of each specimen, its crystallographic orientations such as [110]-(110) etc. are indicated.

Through the whole treatment, we could scarcely find any difference as to the existence of oxide film covered on the plate surfaces of our specimen foil as compared with the previous cases.

In the present experiment, it was found that, the easiness of producing single crystal foils [110]-(100) is much greater than in the case of [110]-(110), and also the production of D_d is easier than that of D_s.

The anisotropic property of growth-temperature, growth-speed and the form of growth-edge of thick aluminium single crystal plates having the special exact crystallographic orientations have already been studied by Yamashita[4] and later by Irie[5]. By Yamashita, it was found that the crystal-growth of the specimen [110]-(100) is greater than that of the specimen [110]-(110) at the same temperature and also it was found by Irie that the crystal-growth in the direction of [110] axis is much greater than that of [100] axis.

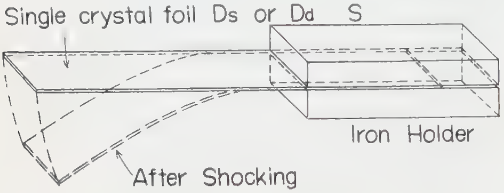

Fig. 5.

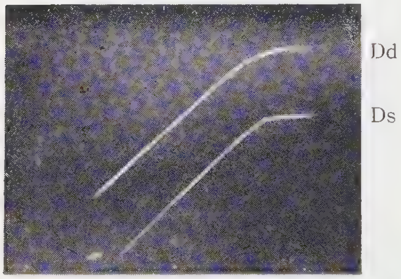

Fig. 6-a. Photograph of bending behaviors of D_d and D_s.

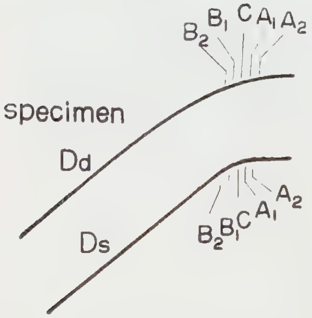

Fig. 6-b. Explanation to Fig. 6-a.

As for the process of crystal-growth of a single crystal plate even when it is in the lengthwise direction, we can not treat it without considering the crystal-growth in the breadthwise and depthwise direction. In the single crystal plates [110]-(100) and [110]-(110), the crystallographic axes [110] and [100] are orientated in the breadthwise direction respectively. So, the ability of the crystal-growth for the direction [110] or [100], i.e. in the breadthwise direction, of course, should give the influence on the crystal-growth of single crystal plate in the lengthwise direction. According to Irie's results, the crystal-growth of [110] in the breadthwise direction is greater than that of [100], thus, on the whole, the crystal-growth of single crystal plate [110]-(100) in the lengthwise direction becomes greater than that of [110]-(110). This consideration coincides with Yamashita's results.

In our case, it is only the thickness of specimen-foil that is much thinner than that of specimen which was used previously. Then the crystal growth in the depthwise direction will proceed more rapidly, and so the ability of the crystal-growth in the breadthwise direction has more remarkable influence on the crystal-growth in the lengthwise direction than in the previous cases.

In view of these circumstances, the remarkable easiness, which we found in this experiment, of producing single crystal foils [110]-(100) may be reasonable from the considerations stated above.

Moreover by using the specimens D_s and D_d thus obtained, we carried out the following experiment. A specimen was sandwiched between the holders such as sketched in Fig. 5, and then some mechanical shock was given perpendicularly to the plate surface at the place S. By this shock, each single crystal foil bent down in such a manner as shown in Fig. 5, with dotted line. However, the bending behaviors were different according to the crystallographic orientations of the foils as photographically shown in Fig. 6-a; i.e. in the case of D_s, the specimen bent downwards sharply at the place C, while in the case of D_d, the specimen bent down gently. By taking X-ray radiographs of the places, as indicated in Fig. 6-b, A_1, A_2, C, B_1 and B_2 of each specimen, it was found qualitatively that, in the case of D_s, the deformation of the specimen appeared mainly in the part C and rapidly decreased in the parts A_1 and B_1, while in the case of D_d, the deformation appeared rather uniformly than in D_s in the whole region A_2-C-B_2.

§ 3. Acknowledgements

The authors wish to express their sincere thanks to Prof. Takeo Fujiwara of Hiroshima University, under whose kind guidance and encouragement this experiment has been carried out, and also to Prof. Moriso Hirata of University of Tokyo, under whose kind suggestions this experiment has been started, and especially, one of the authors, H. Fujiwara expresses his sincere thanks to Prof. Masao Kotani of University of Tokyo, who kindly permitted the author to carry out his experiment.

Appendix

(1) Notation [110]-(110) or [110]-(100)

[110]-(110) designates such a single crystal plate that its crystallographic axis [110] coincides with the lengthwise direction of the plate, and its crystallographic plane (110) is parallel to the surface plane of the plate.

(2) Notation D_s and D_d

D_s or D_d is a single crystal plate in which one of the active slip planes (111) is inclined at an angle 45° to the surface plane or the side of the plate and at the same time, in each case, (111) is perpendicular to the side or the surface plane as schematically shown in the annexed figure, Fig. 7.

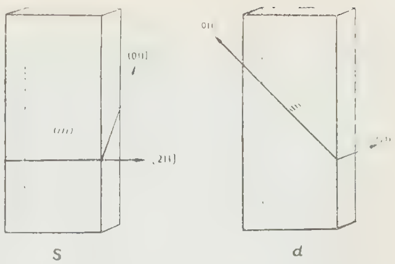

Fig. 7. Schematic explanation to D_s and D_d.

The single crystal plates, 0.5 mm in thickness, having such crystallographic orientations were firstly produced by T. Mukai⁶⁾.

References

1) T. Fujiwara: J. Sci. of Hiroshima Univ. **9** (1939) 227.
T. Fujiwara and K. Yamasaki: Ibid. **11** (1941) 89.
T. Fujiwara and E. Tatsumoto: Ibid **12** (1942) 169.
T. Fujiwara and E. Tatsumoto: Ibid. **13** (1944) 235.
T. Mukai: Ibid. **15** (1951) 147.
T. Fujiwara and K. Koizumi: Ibid. **16** (1952) 81.
2) H. Fujiwara: Ibid. **16** (1952) 111.
3) H. Fujiwara: loc. cit.
4) T. Fujiwara and T. Yamashita: Ibid. **12** (1942) 163, in Japanese.
T. Yamashita: Ibid. **13** (1944) 229, in Japanese.
5) T. Irie: Ibid. **15** (1951) 45.
T. Irie: Ibid. **15** (1951) 47.
6) T. Mukai: Ibid. **19** (1955) in press.

Journal of the Physical Society of Japan Vol. 10, No. 6, June 1955

Statistical Theory of Turbulence, I
Hypothesis of Vortex Chaos Motion

By Yutaka Shigemitsu

Transportation Technical Research Institute, Tokyo

(Received June 24, 1954)

In this paper fundamental aspects of our statistical theory of turbulence are described. At first, some experimental observations are made on the production and transition to turbulent flow, and in view of those observations the turbulent flow is defined as an irregular motion of many large and small vortices. Next, kinematical expressions of intensity and scale of turbulence are given in the form of area integrals of product of mean velocities $\overline{V_*}^2$ and $\overline{V_*}'^2$ in many vortices and a probabity density function P, where the latter means physically the character of an irregularity in the relative arrangement of many vortices. With these expressions and the Reynolds equations introduced, fundamental equations of motion of turbulence are set up. Then, the statistical principle to determine the functional form of P is mentioned by referring to the physical meaning of the ergodic hypothesis in the statistical mechanics. At last, hydrodynamical discussions on $\overline{V_*}^2$ and $\overline{V_*}'^2$ are made with reference to the known solution of the Navier-Stokes equations for a certain vortex motion.

§ 1. Introduction

Statistical studies of turbulance opened by O. Reynolds have been developed by G.I. Taylor and many other investigators. Their theoretical ground can be divided into two groups of different aspects. One is based on the Reynolds equations which are the hydrodynamical equations of motion concerning time means. But, as well known, the states of turbulent flow cannot be determined in principle by these equations only. To derive definite results on mean values of velocity fluctuations, some other hypothesis must be introduced concerning the statistical property of turbulence. Hypotheses of isotropy in velocity fluctuations, preservation of similarity in Euler correlation, distribution of mixture length, and so forth, are all included in the second group. Of these two grounds, the Reynolds equations hold in the general case of turbulence, but as to the second group as yet no theoretical unification of the various hypotheses can be found. Moreover, owing to recent developments of hot-wire technique, many experimental facts have been presented which are beyond the scope of these statistical theories. Thus, in the study of turbulence it is essentially important to study more fundamental aspects of these statistical hypotheses.

It seems to the author that the weak point of the above-mentioned statistical studies lies in the fact that these hypotheses have been introduced without being necessarily based upon sufficient consideration of the mechanism of velocity fluctuations themselves. First it is necessary to give a physical interpretation to the question why the velocity fluctuates about its mean value in turbulent flow. As easily supposed we interpret that turbulent fluctuations are caused by an irregular motion of large and small vortices. When such a physical conception is taken, it becomes important at the next stage how to express this conception mathematically.

We believe that the most essential point of the statistical theory in physics is to introduce the physical conception of irregularity or randomness of the chaotic state into the foundations of theory. For instance, the statistical mechanics has two aspects of its foundations – Hamilton equations of motion and so-called ergodic hypothesis. The fact that the statistical mechanics is not merely the Newton dynamics concerning time means, as the Reynolds equations in hydrodynamics, is very instructive. In the study of turbulence, H.L. Dryden has emphasized that the ir-

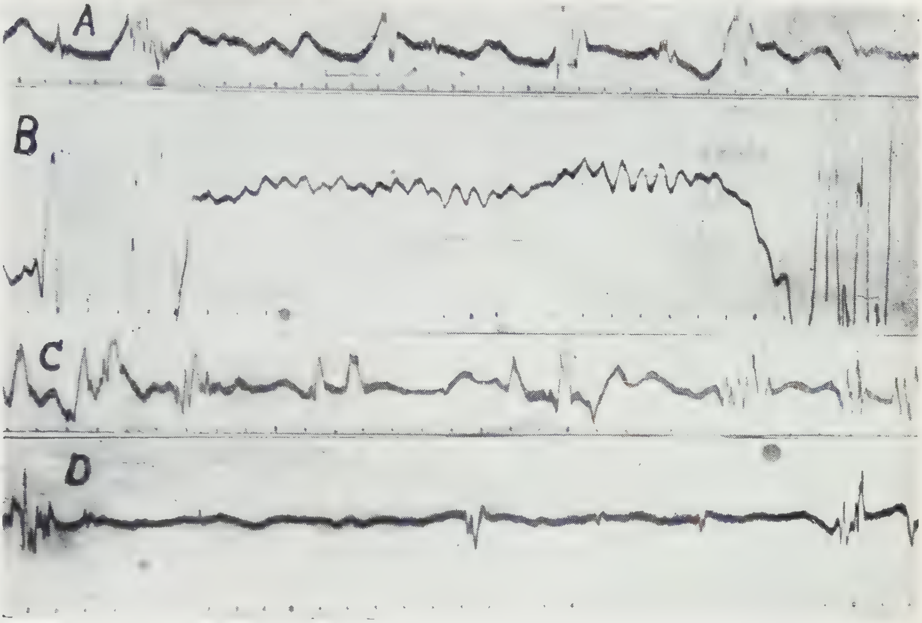

Fig. 1. Comparison of u-fluctuations in transition flow and others. Timing mark is 1/100 s.

(A) Transition region in a boundary layer along a flat plate. $\overline{U}_0=14.3\,\mathrm{m/s}$ with u-intensity of 0.45 per cent. $x=49.0\,\mathrm{cm}$ and $y=0.3\,\mathrm{mm}$.

(B) Transition region in a boundary layer along another flat plate. $\overline{U}_0=7.4\,\mathrm{m/s}$ with u-intensity of 0.03 per cent. $x=78.7\,\mathrm{cm}$ and $y=0.4\,\mathrm{mm}$.

(C) Separation region in a laminar boundary layer with a positive pressure gradient. $\overline{U}_0=14.3\,\mathrm{m/s}$ with u-intensity of 0.45 per cent. $x=35.0\,\mathrm{cm}$ and $y=1.1\,\mathrm{mm}$.

(D) Intermittent flow in a turbulent wake. $\overline{U}_0=3.74\,\mathrm{m/s}$ with u-intensity of 0.02 per cent. $x=47.8\,\mathrm{cm}$ and $y=8.0\,\mathrm{cm}$ from the center of wake.

regularity in velocity fluctuations is essentially important character of turbulence. We consider that his opinion touches the key point to solve the turbulence problem, which cannot be found in the previous statistical theories of turbulence. But, unfortunately his interpretation does not surpass the scope of a qualitative discussion. In this paper, we try to develop his physical conception into mathematical expressions based upon the above-mentioned hypothesis of vortex chaos motion and to lay the theory on a more fundamental statistical foundation than before. Then, in the subsequent seriese of papers, we will study how to describe the general case of turbulent phenomena and how to derive the results of previous successful theories as our special cases.

In completion of this series of papers the author wishes to acknowledge his indebtedness to Prof. I. Tani and Prof. I. Imai for their valuable advice. To Prof. T. Maekawa he is indebted as well for his advice and encouragement during the work.

§ 2. Transition to Turbulent Flow

To clarify the physical mechanism of turbulent flow, it is first necessary to consider the cause of production of trubulence. Concerning this problem, such an interpretation will be taken that the transition is generally a steady or unsteady (local) laminar separation[1]. It is now difficult to verify this assumption quantitatively, but the experimental fact that in the transition region the frequency of velocity fluctuation changes always discontinuously into higher one, is an important support to this supposition. In Fig. 1, (A) and (B) are u-oscillograms of transition flow in the laminar boundary layer. It is shown that when the degree of turbulence in the main flow decreases, the laminar-bound-

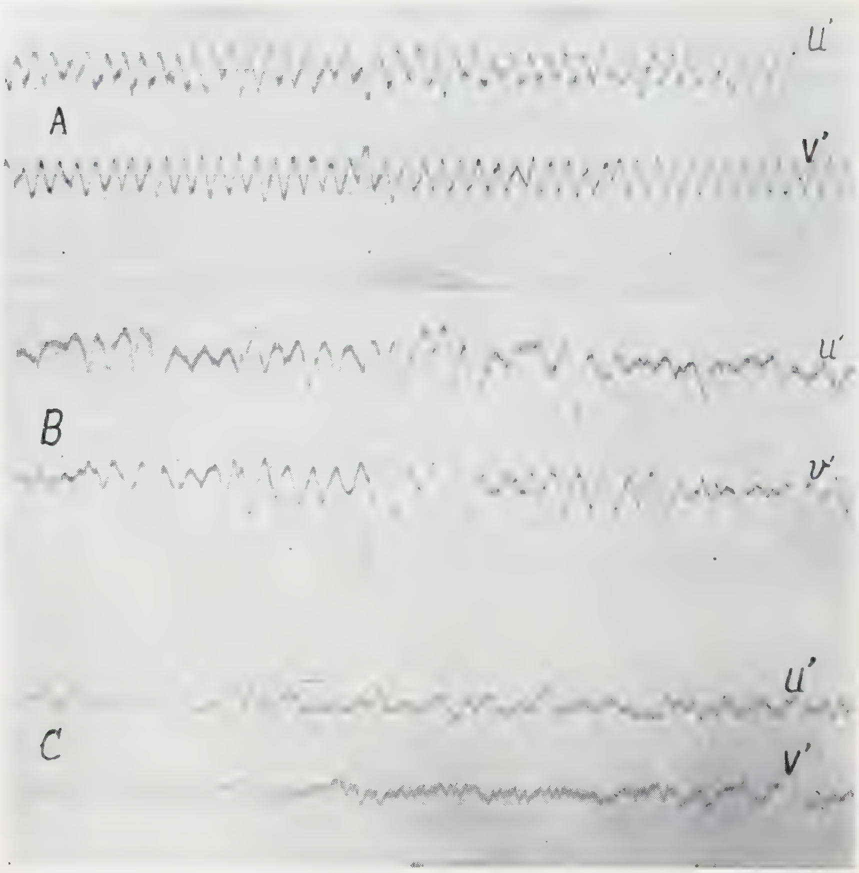

Fig. 2. u- and v-oscillograms behind a circular cylinder. $\overline{U}_0=14.3$ m/s with u-intensity of 0.45 per cent. $d=2$ cm.
(A) is 9 cm behind the cylinder, (B) is 14 cm, and (C) is the undisturbed main flow.

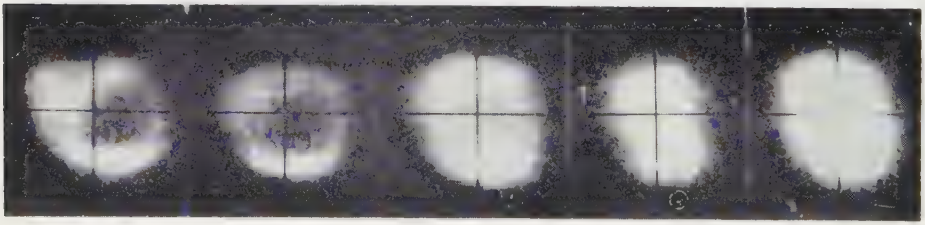

$x=9$ cm $x=11$ cm $x=14$ cm $x=18$ cm $x=25$ cm

Fig. 3. Change of forms of frequency distribution function $F(u/\boldsymbol{u}, v/\boldsymbol{v})$. The states of flow is the same as in Fig. 2. These photographs were taken on the surface of a braun-tube oscillograph with an exposure time of 15 seconds. The origin of the coordinates is the position of mean velocity, with the ordinates as v-fluctuation and the abscissae as u-fluctuation.

ary-layer oscillation comes to take the form of Tollmien's wave, but the aspects of production of turbulence are the same as each other. For comparision, the oscillograms in separation region of laminar boundary layer and in intermittent region of turbulent wake are shown. It is obvious that (C) and (D) show the states of mixing flow of laminar motion and vortex motion. These figures suggest that the transition flow has also the same mechanism of flow.

Then, some experimental measurements will be given which show the transition phonomena from laminar separation to turbulent flow. At first, as a typical case the flow behind a circular cylinder was taken. Fig. 2 shows u- and v-oscillograms along the center line of the wake[2]. Each case in these figures has a definite mean value of velocity fluctuation, and so the Reynolds equations hold equally true of each case. But, as pointed out by H.L. Dryden[3], it is clear that these flows have entirely different statistical characters. To ascertain this point further, forms of the frequency distribution function $F(u, v)$ were observed at several points behind the cylinder. They are shown in Fig. 3. The most significant character is that a simple functional relation between u and v changes gradually into a complicated one with increasing distance from the cylinder. Namely, F tends to a constant functional form F_0;

$$\lim_{x\to\infty} F(u/\boldsymbol{u},\ v/\boldsymbol{v})=F_0(u/\boldsymbol{u},\ v/\boldsymbol{v})\,. \tag{2.1}$$

Further, measurements of u-spectrum were made at several points behind another circular cylinder. Viewed from these observations in Fig. 4, it can be said that the line spectrum just behind a body tends to a continuous one as the distance increases from the body. These transition phenomena ought appear in the change of velocity distributions across the wake. Figs. 5 and 6 show the change of the distributions of fluctuational and mean velocities in the transition region. The above character that a regular velocity fluctuation becomes always irregular, can also be found in the boundary-layer flow. It is suggested in Fig. 1 (B).

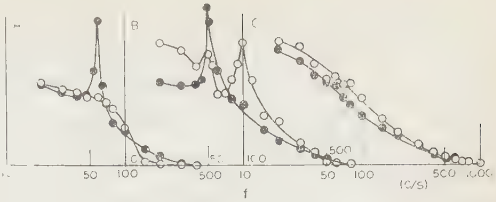

Fig. 4. Distributions of u-spectrum in transition region behind a circular cylinder. $\overline{U}_0=3.74$ m/s with u-intensity of 0.02 per cent. $d=1.5$ cm. (A), (B) and (C) were obtained respectively at 3.0 cm, 15.7 cm and 84.6 cm behind the cylinder. The ordinates are their different relative intensities. ○ are observed values at the center line and ● are at the positions where u-intensity is maximum across the wake.

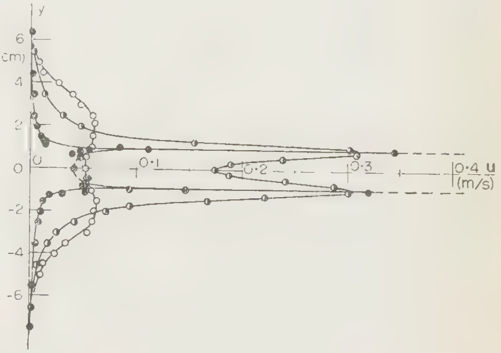

Fig. 5. Distributions of u-intensity across the wake in its transition region. The states of flow is the same as in Fig. 4. ●, ◑ and ○ are observed values respectively at 0.8 cm, 3.0 cm and 84.6 cm behind the cylinder. The ordinates mean the distance from the center line of the wake.

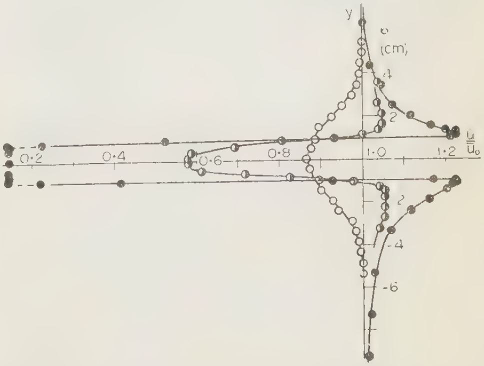

Fig. 6. Distributions of the mean velocity across the wake corresponding to the measuring points in Fig. 5.

§ 3. Hypothesis of Vortex Chaos Motion

By referring to the above experimental results, the following significant character can be pointed out; with the increases of distance behind the place of production of vortices, a regular simple relation between u- and v-fluctuation changes into an irregular complicated one. From the statistical point of view, however, it can be said that a complicated statistical relation of u and v becomes a simple statistical relation.

To the above experimental fact the following physical interpretation will be given. The vortex motion is generally caused by steady or unsteady laminar separation, and these vortices are carried in a regular arrangement just behind the separation point, for instance in the flow pattern of Kármán vortex street. But this stable regular flow pattern is transformed by many random unknown causes into an irregular chaotic state of vortices. It is important that many experimental observations show always that a regular flow pattern of vortices changes eventually into an irregular one. Such an experimental evidence has never been found that an irregular vortex chaos motion returns to the flow of Kármán vortex street, even if the latter flow pattern is very stable hydrodynamically. Hence, it becomes clear by this character of irreversibility that there exits a wide range of statistically stable chaotic state of vortices behind the transition region. This chaotic motion of vortices is defined as turbulent flow. This is the fundamental conception of our hypothesis of a vortex chaos motion. In many characters of turbulence, that of the statistical simplicity is the most essentially important. Because of this character, it becomes possible to introduce a statistical method of evaluation of mean values, apart from the mathematical treatment of functional relation which has been used widely in the study of hydrodynamics.

§ 4. Probability Density Function

In the vortex chaos motion, the vortices have generally their different characters; for instance their intensities of circulations or scales may be different. But the change of relative positions of vortices is the most important to be considered statistically in detail. In this section, a probability density function will be defined by which the conception of randomness in the relative positions of vortices is expressed mathematically.

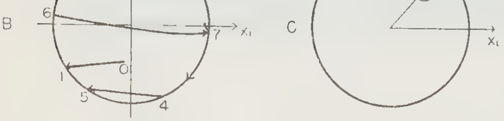

Fig. 7. Conceptional diagrams illustrating a vortex chaos motion.

At first, the flow is taken to be two-dimensional, and the state of running of vortex centers near a fixed point in the field (denoted by A-point) is considered. The change of relation between the position of A-point and those of vortex centers which run near A-point irregularily one after another, can be considered relatively as the movement of A-point through an incessantly changing arrangement of positions of these vortex centers. Namely, when the flow of vortex chaos motion is observed at A-point continuously in time, it can be supposed that A-point moves always in this observed relative arrangement of vortex centers. Such a relative pattern is shown in Fig. 7 (A), where · are vortex centers, × is the position of A-point at $t=0$, and the line is the trajectory of movement of A-point. In Fig. 7 (A), the change of relative position of vortex centers is shown by a single figure, but exactly speaking, they must be considered to be varying in time.

Then, let this figure be covered, without a gap, with many domains of the same form which have their centers at the positions of ·. Here the arrows show the direction of circulation of vortices. The trajectories in the area overlapped by two or three domains in (A) are counted twice or thrice. The time interval which takes account of these repetitions in t in the movement of A-point, is written as $T(=t+\Delta t)$. Next let these domains be taken out from the figure and piled up, with their centers and directions of arrows coinciding respectively. Namely, many domains in (A) are changed into a single domain with their same form and direction of circulation. Then the trajectory of A-point in (A) appears in a single domain as shown in (B). Let it be denoted as the D-domain where x_1- and y_1-axis are chosen to be parallel with x- and y-axis in the field of flow. When the polar coordinates of A-point in the D-domain are written as

$$r(t) \qquad \theta(t)\,, \tag{4.1}$$

the change of arrangement of vortex centers passing near A-point in the field of flow can be represented by the motion of (4.1) in D-domain. In (B) the trajectories are not necessarily shown with parallel lines so that it may mean the time change of positions of vortex centers in (A).

Then, the motion of the coordinates (4.1) is observed in the infinitesimal domain about a fixed point $(r,\ \theta)$ in the D-domain, whose area is denoted by dS (cf. (C)). Let $T_{r,\,\theta}$ be taken as the sum of time intervals in which this motion appears in this infinitesimal domain in a time interval T. Then the following function $P(r,\ \theta)$ can be defined

$$P(r,\ \theta)dS=\lim_{t\to\infty}(T_{r,\,\theta}/T)\,, \qquad (4.2)$$

where we have clearly

$$\iint_D P(r,\ \theta)dS=1\,. \qquad (4.3)$$

$P(r,\ \theta)$ is the probability density function which expresses the probability of existence of (4.1) in D-domain.

§ 5. Transformation of Time Means into Area Means

If u, v are x-, y-component of the velocity fluctuation at a point (A-point) in the field of turbulent flow, and $\boldsymbol{u}^2$, $\boldsymbol{v}^2$, $\overline{\boldsymbol{uv}}$ are their mean square values, then by definition

$$\begin{aligned} \boldsymbol{u}^2&=\lim_{t\to\infty}(1/t)\int_0^t u^2(t)dt\\ \boldsymbol{v}^2&=\lim_{t\to\infty}(1/t)\int_0^t v^2(t)dt \qquad (5.1)\\ \overline{\boldsymbol{uv}}&=\lim_{t\to\infty}(1/t)\int_0^t u(t)v(t)dt\,, \end{aligned}$$

where $u(t)$ and $v(t)$ are complicated functions of t as shown in Fig. 2 (C). By the hypothesis of a vortex chaos motion, the state of flow can be represented by a relative flow pattern as shown in Fig. 7 (A). In this figure, the time integral in (5.1) is taken along the trajectory of A-point. Let $T(=t+\Delta t)$ be taken as the time interval as defined in § 4, and let the following functions $u_1^2(t)$ etc. be defined as

$$\begin{aligned} u_1^2(t)&=\begin{cases} u^2(t) & \text{in} \quad t\\ (1/t)\int_0^t u^2(t)dt & \text{in} \quad \Delta t \end{cases}\\ v_1^2(t)&=\begin{cases} v^2(t) & \text{in} \quad t\\ (1/t)\int_0^t v^2(t)dt & \text{in} \quad \Delta t \end{cases} \qquad (5.2)\\ uv_1(t)&=\begin{cases} u(t)v(t) & \text{in} \quad t\\ (1/t)\int_0^t u(t)v(t)dt & \text{in} \quad \Delta t. \end{cases} \end{aligned}$$

Then, it can be easily proved that

$$(1/T)\int_0^T u_1^2(t)dt=(1/t)\int_0^t u^2(t)dt\,, \quad \text{etc.}$$

Hence, by use of the functions defined in (5.2), (5.1) can be transmitted into the D-domain so that the time integral is taken along the whole trajectories in it; (5.1) becomes

$$\begin{aligned} \boldsymbol{u}^2&=\lim_{t\to\infty}(1/T)\int_0^T u_1^2(r(t),\ \theta(t),\ t)dt,\\ \boldsymbol{v}^2&=\lim_{t\to\infty}(1/T)\int_0^T v_1^2(r(t),\ \theta(t),\ t)dt, \qquad (5.3)\\ \boldsymbol{uv}&=\lim_{t\to\infty}(1/T)\int_0^T uv_1(r(t),\ \theta(t),\ t)dt, \end{aligned}$$

where the values of u_1^2 etc., change along the trajectories but even at the same point on the trajectories they do not necessarily take the same value at different times.

From the integration of $\boldsymbol{u}^2$ in (5.3), the part of $\boldsymbol{u}_{r,\,\theta}$ will be evaluated which appears in the infinitesimal domain about a point $(r,\ \theta)$. When $T_{r,\,\theta}$ and dS are defined as in § 4, we have

$$\boldsymbol{u}^2_{r,\theta}=\lim_{t\to\infty}(1/T)\int_{T_{r,\,\theta}} u_1^2(r,\ \theta,\ t)dt\,. \qquad (5.4)$$

Let the mean and fluctuational parts of $u_1(r,\ \theta,\ t)$ in $T_{r,\,\theta}$ be written respectively as

$$\bar{u}_1(r,\ \theta,\ T_{r,\,\theta}) \quad \text{and} \quad u_1'(r,\ \theta,\ t),$$

and let the mean square value of u_1' in $T_{r,\theta}$ be

$$u_1'^2(r,\ \theta,\ T_{r,\,\theta})\,,$$

then we have

$$\int_{T_{r,\,\theta}} u_1'(r,\ \theta,\ t)dt=0$$

and

$$\bar{u}_1'^2(r,\ \theta,\ T_{r,\,\theta})=(1/T_{r,\,\theta})\int_{T_{r,\,\theta}} u_1'^2(r,\ \theta,\ t)dt\,.$$

Thus (5.4) becomes

$$\begin{aligned} \boldsymbol{u}^2_{r,\,\theta}&=\lim_{t\to\infty}(1/T)\int_{T_{r,\theta}}\{\bar{u}_1(r,\ \theta,\ T_{r,\,\theta})\\ &\qquad +u_1'(r,\ \theta,\ t)\}^2dt\\ &=\lim_{t\to\infty}(T_{r,\,\theta}/T)\{u_1^2(r,\ \theta,\ T_{r,\,\theta})\\ &\qquad +u_1'^2(r,\ \theta,\ T_{r,\,\theta})\}\,, \end{aligned}$$

The limiting value of $T_{r,\,\theta}/T$ has been defined by (4.2), and so when

$$u_1^2(r,\ \theta) \quad \text{and} \quad u_1'^2(r,\ \theta)$$

are taken as the limiting values at $t\to\infty$ of

$$\bar{u}_1^2(r,\ \theta,\ T_{r,\,\theta}) \quad \text{and} \quad \bar{u}_1'^2(r,\ \theta,\ T_{r,\,\theta}),$$

we have

$$\boldsymbol{u}^2_{r,\,\theta}=P(r,\ \theta)\{\bar{u}_1^2(r,\ \theta)+\bar{u}_1'^2(r,\ \theta)\}dS\,. \qquad (5.5)$$

Then the total value of $\boldsymbol{u}^2$ is written as

$$\boldsymbol{u}^2=\iint_D P(r,\ \theta)\{\bar{u}_1^2(r,\ \theta)+\bar{u}_1'^2(r,\ \theta)\}dS\,.$$

In the same manner the time integrals in (5.1) are transformed into the following area integrals

$$\boldsymbol{u}^2=\iint_D P(r,\ \theta)\{\bar{u}_1^2(r,\ \theta)+\bar{u}_1'^2(r,\ \theta)\}\,dS$$

$$\boldsymbol{v}^2=\iint_D P(r,\ \theta)\{\bar{v}_1^2(r,\ \theta)+\bar{v}_1'^2(r,\ \theta)\}\,dS \qquad (5.6)$$

$$\overline{\boldsymbol{uv}}=\iint_D P(r,\ \theta)\{\overline{uv}_1(r,\ \theta)+\overline{uv}_1'(r,\theta)\}dS\,.$$

§ 6. Expressions for Intensity and Scale of Turbulence

The above transformation from (5.1) to (5.6) is purely mathematical without any neglect; (5.6) holds independently of the form of the D–domain. Here, the physical hypothesis of a vortex chaos motion will be introduced into the transformed expressions in (5.6). D–domain means the relative mean scale of vortices in their chaotic state and P means the randomness of the arrangement of these vortices running in the field of flow. Moreover it is assumed that

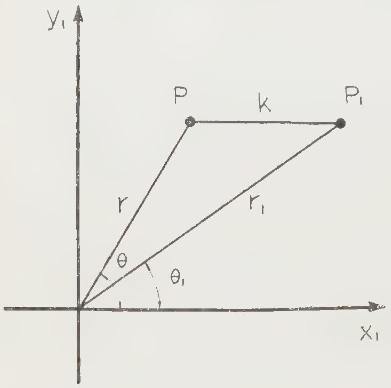

Fig. 8.

$$\bar{u}_1^2(r,\ \theta)+\bar{u}_1'^2(r,\ \theta) \quad \text{etc.}$$

are caused by velocity distributions in these vortices. Namely we assume

$$\begin{aligned}&\bar{u}_1^2(r,\ \theta)+\bar{u}_1'^2(r,\ \theta)\\&\quad=\{\overline{V}_*^2(r,\ \theta)+\overline{V}_*'^2(r,\ \theta)\}\sin^2\theta\\&\bar{v}_1^2(r,\ \theta)+\bar{v}_1'^2(r,\ \theta)\\&\quad=\{\overline{V}_*^2(r,\ \theta)+\overline{V}_*'^2(r,\ \theta)\}\cos^2\theta \qquad (6.1)\\&uv_1(r,\ \theta)+uv_1'(r,\ \theta)\\&\quad=-\{\overline{V}_*^2(r,\ \theta)+\overline{V}_*'^2(r,\ \theta)\}\sin\theta\cos\theta\ ,\end{aligned}$$

where $\overline{V}_*(r,\ \theta)$ and $\overline{V}_*'^2(r,\ \theta)$ are respectively mean velocity distribution in vortices and mean square value of its fluctuation, and θ is chosen so that it may be equal to the angle between the mean velocity vector $\overline{V}_*(r,\ \theta)$ and the y_1–axis in the D–domain. Then (5.6) becomes

$$\begin{aligned}\boldsymbol{u}^2&=\iint_D P(r,\ \theta)\{\overline{V}_*^2(r,\ \theta)+\overline{V}_*'^2(r,\ \theta)\}\\&\qquad\sin^2\theta\,dS\\\boldsymbol{v}^2&=\iint_D P(r,\ \theta)\{\overline{V}_*^2(r,\ \theta)+\overline{V}_*'^2(r,\ \theta)\}\\&\qquad\cos^2\theta\,dS \qquad (6.2)\\-\overline{\boldsymbol{uv}}&=\iint_D P(r,\ \theta)\{\overline{V}_*^2(r,\ \theta)+\overline{V}_*'^2(r,\ \theta)\}\\&\qquad\sin\theta\cos\theta\,dS\,.\end{aligned}$$

(6.2) is the expression of intensity of turbulence based upon the hypothesis of vortex chaos motion.

As for the magnitude of scale of turbulence, the scale of D–domain can be taken to correspond to it. But as the mathematical expression Euler correlation or its spectrum function is preferable. For instance, the correlation function for two points lying along the mean stream direction with a distance k will be considered. When the D–domain is chosen wide enough to include these points in it, they can be translated parallel with x_1–axis in D–domain as shown in Fig. 8. In the same manner as the derivation of (6.2), mean value of $\overline{\boldsymbol{uu}}_1$ can be evaluated by

$$\begin{aligned}\overline{\boldsymbol{uu}}_1=\iint_D P(r,\ \theta)\{&\overline{V}_*(r,\ \theta)\overline{V}_*(r_1,\ \theta_1)\\&+\overline{V_*'(r,\ \theta)V_*'(r_1,\ \theta_1)}\}\sin\theta\sin\theta_1\,dS,\end{aligned} \qquad (6.3)$$

where r_1 and θ_1 are functions of $(r,\ \theta;\ k)$ (cf. Fig. 8). Thus the correlation function f or g can easily be expressed also in area integrals by (6.3) and (6.2).

The assumption of two-dimensional flow has been made because of the brevity of expression, and the derivation of $\boldsymbol{u}^2$ etc. can be made also in three-dimensional flow. In this case D–domain becomes three dimensional. When the coordinates in it are taken in the same manner as two-dimensional case (cf. Fig. 9), $\boldsymbol{u}^2$ etc. can be transformed as follows:

$$\begin{aligned}\boldsymbol{u}^2=\iiint_D P(r,\ \phi,\ \theta)\{&\overline{V}_*^2(r,\ \phi,\ \theta)\\&+\overline{V}_*'^2(r,\ \phi,\ \theta)\}\sin^2\phi\sin^2\theta\,dS\end{aligned}$$

$$\boldsymbol{v}^2=\iiint_D P(r,\ \phi,\ \theta)\{\overline{V}_*^2(r,\ \phi,\ \theta)+\overline{V}_*'^2(r,\ \phi,\ \theta)\}\sin^2\phi\cos^2\theta\,dS$$

$$\boldsymbol{w}^2=\iiint_D P(r,\ \phi,\ \theta)\{\overline{V}_*^2(r,\ \phi,\ \theta)+\overline{V}_*'^2(r,\ \phi,\ \theta)\}\cos^2\phi\sin^2\theta\,dS \qquad (6.2')$$

$$\boldsymbol{vw}=-\iiint_D P(r,\ \phi,\ \theta)\{\overline{V}_*^2(r,\ \phi,\ \theta)+\overline{V}_*'^2(r,\ \phi,\ \theta)\}\sin\phi\cos\phi\sin\theta\cos\theta\,dS$$

$$\overline{\boldsymbol{wu}}=\iiint_D P(r,\ \phi,\ \theta)\{\overline{V}_*^2(r,\ \phi,\ \theta)+\overline{V}_*'^2(r,\ \phi,\ \theta)\}\sin\phi\cos\phi\sin^2\theta\,dS$$

$$\boldsymbol{uv}=-\iiint_D P(r,\ \phi,\ \theta)\{\overline{V}_*^2(r,\ \phi,\ \theta)+\overline{V}_*'^2(r,\ \phi,\ \theta)\}\sin^2\phi\sin\theta\cos\theta\,dS\,.$$

§ 7. Equations of Motion of Turbulence

The above-mentioned expressions of intensity and scale hold at an arbitrary point in the field of flow, and so, strictly speaking, (6.2) becomes

$$\boldsymbol{u}^2=\iint_{D(x,\ y)} P(r,\ \theta;\ x,\ y)\{\overline{V}_*^2(r,\ \theta;\ x,\ y)+\overline{V}_*'^2(r,\ \theta;\ x,\ y)\}\sin^2\theta\,dS$$

$$\boldsymbol{v}^2=\iint_{D(x,\ y)} P(r,\ \theta;\ x,\ y)\{\overline{V}_*^2(r,\ \theta;\ x,\ y)+\overline{V}_*'^2(r,\ \theta;\ x,\ y)\}\cos^2\theta\,dS \qquad (7.1)$$

$$-\overline{\boldsymbol{uv}}=\iint_{D(x,\ y)} P(r,\ \theta;\ x,\ y)\{\overline{V}_*^2(r,\ \theta;\ x,\ y)+\overline{V}_*'^2(r,\ \theta;\ x,\ y)\}\sin\theta\cos\theta\,dS\,.$$

Hence, $\boldsymbol{u}^2$ etc. can be determined as functions of x and y. It is the Reynolds equations that determine the mean velocity distribution when the values of $\boldsymbol{u}^2$ etc. are given. They are

$$\overline{U}\frac{\partial\overline{U}}{\partial x}+\overline{V}\frac{\partial\overline{U}}{\partial y}=\frac{-1}{\rho}\frac{\partial P}{\partial y}+\nu\nabla^2\overline{U}-\left(\frac{\partial u^2}{\partial x}+\frac{\partial\overline{uv}}{\partial y}\right)$$

$$\overline{U}\frac{\partial\overline{V}}{\partial x}+\overline{V}\frac{\partial\overline{V}}{\partial y}=\frac{-1}{\rho}\frac{\partial P}{\partial y}+\nu\nabla^2\overline{V}-\left(\frac{\partial\overline{uv}}{\partial x}+\frac{\partial v^2}{\partial y}\right)$$

$$\frac{\partial\overline{U}}{\partial x}+\frac{\partial\overline{V}}{\partial y}=0\,. \qquad (7.2)$$

(7.2) and (7.1) are the fundamental equations of motion in turbulent flow which determine the mean velocity distribution including that of intensity of its fiuctuation. The Reynolds equations are made complete here by the introduction of the expressions (7.1). Concerning the correlation functions, (6.3) can be taken as a function of x and y in the same manner.

(7.1) have been derived by taking a single D-domain, which corresponds to the relative mean scale of all the vortices passing near A-point. The transformation from (5.1) to (7.1) can be made also by taking several different domains of D. When there are different kinds of vortices in the flow, for instance, vortices are produced under different conditions, it becomes more appropriate to take area integrals separately on these different kinds of vortices. When there are N kinds of vortices passing near A-point, $\boldsymbol{u}^2$ etc. can also be expressed as follow instead of (7.1);

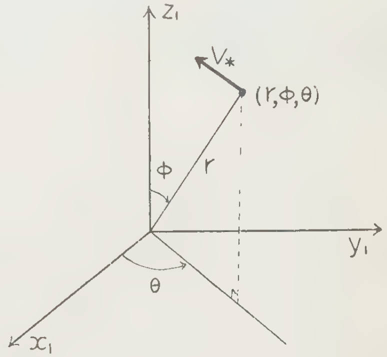

Fig. 9.

$$\boldsymbol{u}^2=\sum_{i=1}^{N}\Bigg[\iint_{D_i(x,y)} P_i(r,\ \theta;\ x,\ y)\{\overline{V}_{*i}^2(r,\ \theta;\ x,\ y)+\overline{V}_{*i}'^2(r,\ \theta;\ x,\ y)\}\sin^2\theta\,dS\Bigg]$$

$$\boldsymbol{v}^2=\sum_{i=1}^{N}\Bigg[\iint_{D_i(x,y)} P_i(r,\ \theta;\ x,\ y)\{\overline{V}_*^2(r,\ \theta;\ x,\ y)+\overline{V}_{*i}'^2(r,\ \theta;\ x,\ y)\}\cos^2\theta\,dS\Bigg] \qquad (7.3)$$

$$-\overline{\boldsymbol{uv}}=\sum_{i=1}^{N}\iint\Bigg[_{D_i(x,y)} P_i(r,\ \theta;\ x,\ y)\{\overline{V}_{*i}^2(r,\ \theta;\ x,\ y)+\overline{V}_{*i}'^2(r,\ \theta;\ x,\ y)\}\sin\theta\cos\theta\,dS\Bigg],$$

where in this case we have

$$\sum_{i=1}^{N}\iint_{D_i} P_i(r,\ \theta)\,dS=1\,. \qquad (7.4)$$

(7.1) or (7.3) is the complete expression of intensity of turbulence derived on the hypothesis of vortex chaos motion. It is considered that $\overline{V_*'^2}$ is the fluctuational part of velocity distributions of many vortices and is caused by the difference of their characters and their interactions etc. If these effects are neglected, a simplified vortex chaos motion can be defined as an ideal state of turbulence. As it were, the ideal turbulence corresponds to the ideal gas in the statistical mechanics. In this case, (7.1) becomes.

$$\begin{aligned} u^2 &= \iint_{D(x,\,y)} P(r,\ \theta;\ x,\ y) \\ &\quad \overline{V}_*^2(r,\ \theta;\ x,\ y)\sin^2\theta\, dS \\ v^2 &= \iint_{D(x,\,y)} P(r,\ \theta;\ x,\ y) \\ &\quad \overline{V}_*^2(r,\ \theta;\ x,\ y)\cos^2\theta\, dS \qquad (7.5) \\ -uv &= \iint_{D(x,\,y)} P(r,\ \theta;\ x,\ y) \\ &\quad \overline{V}_*^2(r,\ \theta;\ x,\ y)\sin\theta\cos\theta\, dS\,. \end{aligned}$$

In the ideal state, the determination of the form of D-domain becomes very important so that (7.5) may give a good approximative value.

§ 8. Statistical Principle for the Vortex Chaos Motion

It is well known that a supposition called the ergidic hypothesis is introduced into the statistical mechanics as one of its bases, besides the equation of motion. Let us consider the physical meaning of this hypothesis. In the statistical mechanics, gas is considered as a molecular chaos motion, and this molecular motion is supposed to be dependent upon the dynamics of a system of particles. So, in principles, the state of this chaotic motion can be determined completely under any initial and boundary conditions. As a matter of fact, this determination cannot be made because of the difficulty of the mathematical method of evaluatian. But in molecular motions in a gas state, an important character of the statistical simplicity can be found. It is usually expressed in the word of "chaos" or "at random". The ergodic hypothesis is a quantitative expression in the phase space of the character of the most irregular state of molecules. It was a great merit of L. Boltzmann that he introduced this hypothesis into the study of gas, without encountering the difficulty of correctly solving the equations of motion. The name of ergodic hypothesis is peculiar to the statistical mechanics in which the Newton dynamics is taken as the basis of mechanics. But the fundamental physical idea of this hypothesis is an expression of of the character of statistical simplicity, and it is not necessarily peculiar to the dynamics of discrete particles. This is an important fact for us who are studying random phenomena such as turbulent flow.

Returning to the discussion of the vortex motion, we shall consider the concept of regularity or irregularity in the flow pattern of many vortices. It has been mentioned in § 2, that a regular flow pattern of Kármán vortex street changes always into an irregular state of chaotic motion. As an example of idealized most regular state of many vortices, that of a stationary Kármán vortex street can be taken. In this case it is supposed that P-function is expressed as

$$P(r,\ \theta)=\delta\,, \qquad (8.1)$$

where δ is the Dirac delta-function. Namely, when a moving point in D-domain coincides with a fixed point $(r,\ \theta)$, P tends to the infinity of the second order but in other points it vanishes. Even if a stationary Kármán vortex street is moved by the mean flow retaining its regular flow pattern, (8.1) is also fulfilled. But in this case, P tends to the infinity of the first order when a moving point is on a fixed line $r(\theta)=0$ in the D-domain. It can be considered that when such a moving Kármán vortex street loses its regularity in the arrangement of each vortex center, P comes to take a simpler form than δ-function. In our hypothesis of a vortex chaos motion, turbulence is defined as a statistical simple chaotic motion of vortices. Thus, in a turbulent flow P has a simple form of continuous function. When it is written as

$$P(r,\ \theta)=P_1(r,\ \theta)/S\,, \qquad (8.2)$$

it holds in every vortex chaos motion in a turbulent state.

When a vortex chaos motion comes to be in the most irregular state, P can be supposed to become constant in the D-domain. Namely, by the condition of (4.3),

$$P_1(r,\ \theta)=1 \qquad (8.3)$$

holds everywhere in the field of flow. Vortex chaos motion represented by (8.2) and (8.3) will be called respectively shear and shearless turbulence. These discussions are illustrated by the conceptional diagrams in Fig. 10.

As for the derivation of (8.3) or (8.2), the Navier-Stokes equations must be solved exactly under a given boundary and a complicated initial condition. At present, however, such a derivation of complicated nonstationary solution cannot be expected owing to mathematical difficulties. Thus, in our statistical study (8.3) or (8.2) must be introduced *a priori*. This is the statistical principle of our theory having two aspects of foundations, statistical and hydrodynamical. It means physically the conception of irregularity, whose importance in the study of turbulence has been emphasized by H.L. Dryden, and also it has the same physical meaning as the ergodic hypothesis in the statistical mechanics. At any rate, our statistical theory can be reduced to the hydrodynamics, when P-function is made to be δ-function of the second or the first order.

§ 9. Determination of Mean Vortex Motion in the Chaotic State

As for the determination of $\overline{V_*^2}$ and $\overline{V_*'^2}$, hydrodynamical considerations are necessary. We assume that in the completely irregular vortex chaos motion in shearless turbulence $\overline{V_*}$ is the same as the velocity distribution of a single vortex motion which is carried in the same flow not being affected by other vortices. In the not-completely irregular state in shear turbulence, it is also supposed that $\overline{V_*}$ depends chiefly upon the single vortex motion under the same condition. As the theoretical ground to determine the above single vortex motion, the Navier-Stokes equations are taken where effects of dissipation by molecular viscosity are taken into account. If the Euler equations for the perfect fluid are taken, this statistical theory will give such a result that decay or diffusion does not occur. Concerning $\overline{V_*'^2}$ some other physical principle on the interations of vortices and so forth must be introduced, but such a consideration can be neglected in the ideal state of turbulence.

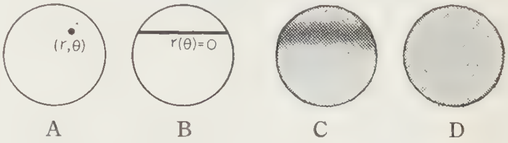

Fig. 10. Conceptional diagrams which illustrate the character of regularity or irregularity in vortex motions by assuming the form of P-function. (A) is a stationary state, (B) simple nonstationary state, (C) shear turbulence, and (D) shearless turbulence. Figs. 2, 3 and 4 show transition states from (B) to (C) or (D). In the state of (A) there is no spectrum in velocity fluctuation, (B) produces a line spectrum and (C), (D) produce continuous ones. Even in chaotic state, (C) shows a little the character of regularity, while (D) is in the completely irregular state. To study vortex motions in (A) and (B) hydrodynamics is convenient, but as for the states of (C) and (D) statistical theory becomes essentially important.

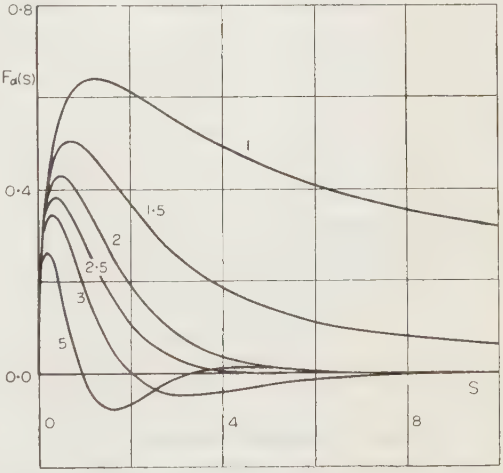

Fig. 11. Curves of $F_\alpha(s)$. Numbers on curves are the value of α.

In the study of viscous fluid, a vortex motion can be taken as the phenomenon of diffusion of vorticity which is concentrated at first on one point of a fluid. Also it can be admitted that the flow pattern of a vortex is symmetrical about its center in a uniform flow. If ω is taken as vorticity, the circulatory velocity V_* is expressed in the form

$$V_*(r,\ t)=(2/r)\int r\,\omega(r,\ t)dr\,. \qquad (9.1)$$

The vorticity distribution $\omega(r,\ t)$ has been known as an exact solution of the Navier Stokes equations[4]. Using this solution V_* can easily be evaluated. When expressed in elementary functions it becomes

$$V_*(s,\ t)=F_\alpha(s)G_\alpha(t) \tag{9.2}$$

$$F_\alpha(s)=\left\{1+\sum_{i=0}^{\infty}\frac{(2-\alpha)(3-\alpha)\cdots(i+1-\alpha)}{(i+1)!}\cdot\frac{s^i}{i!}\right\}\sqrt{s}\,e^{-s} \qquad (\alpha>1)$$

$$F_\alpha(s)=(1-e^{-s})/\sqrt{s} \qquad (\alpha=1)$$

$$G_\alpha(t)=2c\sqrt{\nu t}^{\,\frac{1}{2}-\alpha}, \qquad (\alpha\geqq 1)$$

where

$$s=r^2/(4\nu t)\,. \tag{9.3}$$

The solutions (9.2) correspond to the boundary conditions of $V_*=0$ at $r=0$ and $V_*\rightarrow 0$ as $r\rightarrow\infty$, and the suffix α and the integration constants depend upon the initial condition. Namely, there exist many types of vortex motions which have their respective different initial conditions. In Fig. 11 several examples of $F_\alpha(s)$ are shown.

References

1) Y. Shigemitsu: J. Phys. Soc. Japan **5** (1950) 298.
2) Y. Shigemitsu: J. Phys. Soc. Japan **5** (1950) 207.
3) H. L. Dryden: N A C A Tech. Rep. 562 (1936).
4) K. Terazawa: Rep. Aero. Res. Inst. No. 4 (1922).

JOURNAL OF THE PHYSICAL SOCIETY OF JAPAN Vol. 10, No. 6, JUNE 1955

Application of the Thin-Wing-Expansion Method to the Flow of a Compressible Fluid past a Symmetrical Circular Arc Aerofoil

By Saburô ASAKA

Department of Physics, Faculty of Science, Ochanomizu University

(Received February 19, 1955)

Imai's thin-wing-expansion method is presented in somewhat modified and extended form. Then the method is applied to the flow of a compressible fluid past a symmetrical circular arc aerofoil. Analytical expressions for the velocity potential and the velocity distribution over its surface are obtained. For the profile of thickness ratio $t=0.1$, numerical computations have been carried out at $M=0.7$ and 0.8. The present method has been proved very useful, because its procedures are simple and clear, and because its convergency and accuracy are very good up to considerably high Mach numbers. Comparisons with the theoretical results for related profiles as well as experimental data have been made.

§ 1. Introduction and Summary

It has been shown that the small perturbation theory is the most effective one for investigations of the flow of a compressible fluid past an obstacle of given shape. The higher the speeds of flow which we are concerned with have become, the more the importance of thin aerofoils and slender bodies has been recognized. Accordingly the merits of this theory have become more and more conspicuous. As is well known, the first approximation of the small perturbation method is Prandtl and Glauert's formula. On the basis of this idea, Kaplan has calculated the flow past a cusped symmetrical aerofoil, now called the Kaplan bump[1], and a circular arc aerofoil[2] as well as an elliptic cylinder[3], taking account of the effects of their thickness or camber up to the third order. Later he has formulated the general procedures of the method as "the particular integrals of the Prandtl-Busemann iteration equations."[4]

On the other hand, more than ten years ago Imai established independently his thin-wing-expansion method, by which the influences of an obstacle on the flow can be de termined accurately in principle up to the order of approximations as high as required. First he gave the analytical expressions for velocity and pressure distributions, lift and moment of an aerofoil placed in the flow of a compressible fluid up to the second approximation5), and investigated in detail the characteristics of generalized Joukowski profiles6). Further Imai and Ôyama have given the formulae for the third approximation7) and applied them to the study of the flow along a sinusoidal wall8). Imai's thin-wing-expansion method has the great advantages, that its procedures are more systematic and less laborious than any other similar methods, and that it enables us to take into account the boundary conditions very easily. In fact, Hasimoto applied this method to the compressible flow past an elliptic cylinder9) and Matunobu recalculated the velocity distribution over the surface of a Kaplan bump10), and they proved that the analysis could be much simplified by this method. Naruse computed numerically the velocities on the surface of specific aerofoils, for which the existence of the mixed transonic flow has been demonstrated by Tomotika and Tamada. The convergency of this method was found satisfactory even in this case11).

The present author has contributed to this method some modifications and extensions and utilized it for the study of the flow past a symmetrical circular arc aerofoil12). Since this aerofoil is interesting from both theoretical and practical points of view, the analysis for it will be developed here in a somewhat different form.

In the first part of this paper the outline of Imai's thin-wing-expansion method is summarized for the sake of convenience (§ **2** and **3**). Then the analysis for a symmetrical circular arc aerofoil is described in detail (§ **4** and **5**). The velocity distributions for an aerofoil of thickness ratio $t=0.1$ have been calculated numerically at various Mach numbers of the oncoming flow, and the validity of the iteration method was examined. Comparing these results with those for related profiles and with experimental data, some discussions were made (§ **6**).

Outline of the Thin-Wing-Expansion Method

§ 2. The Basic Formulae of the Thin-Wing-Expansion Method

We shall consider the two-dimensional steady flow of a compressible fluid past a cylindrical body. If the effects of viscosity and heat transfer can be ignored, the flow is homentropic and can be decribed by a velocity potential Φ or a stream function Ψ, such that

$$u=\frac{\partial\Phi}{\partial x}=\frac{\rho_\infty}{\rho}\frac{\partial\Psi}{\partial y}\,,\qquad v=\frac{\partial\Phi}{\partial y}=-\frac{\rho_\infty}{\rho}\frac{\partial\Psi}{\partial x}\,. \tag{2.1}$$

Here u, v are velocity components, ρ is the density of the fluid and the suffix ∞ denotes the corresponding value at a great distance from the body. Combining Bernoulli's equation and the adiabatic law for the changes of state of fluid, we get the following relation:

$$\frac{\rho}{\rho_\infty}=\left[1-\frac{\gamma-1}{2}M^2\left(\frac{q^2}{q_\infty{}^2}-1\right)\right]^{1/(\gamma-1)}, \tag{2.2}$$

where q is the magnitude of the velocity, M is the Mach number for the undisturbed flow and γ is the ratio of specific heats.

Without loss of generality, we can assume that the undisturbed flow is parallel to the x-axis and the magnitude of its velocity is unity. Accordingly we may put $\Phi=x$ and $\Psi=y$ when a body is absent. The fundamental assumption for the thin-wing-expansion method is that the velocity, pressure and density differ from those in the undisturbed flow by small amounts when the cylinder is sufficiently thin. So long as this statement is valid, Φ and Ψ can be expanded as follows:

$$\begin{aligned}\Phi&=x+\phi_1+\phi_2+\phi_3+\cdots\,,\\ \Psi&=y+\psi_1+\psi_2+\psi_3+\cdots\,,\end{aligned} \tag{2.3}$$

where $\phi_1,\psi_1;\phi_2,\psi_2;\phi_3,\psi_3;\cdots$ are the quantities of the order of magnitude of $\varepsilon,\varepsilon^2,\varepsilon^3$, $\cdots$ respectively, ε being a small parameter representing the thickness ratio of the cylinder. Substituting from (2.2) and (2.3) into (2.1) and comparing terms of same powers of ε, we obtain a set of differential equations for ϕ_m and ψ_m $(m=1, 2, 3,\cdots)$ suitable for the iterative method.

As for the first approximation, we can reduce the equations for the flow of a compressible fluid to those for an incompressible fluid by the well known Prandtl-Glauert transformation:

$$x=\xi\,,\qquad y=\eta/\mu\,;\qquad \mu=\sqrt{1-M^2}\,. \tag{2.4}$$

In order to solve these equations, Imai has introduced a set of conjugate complex variables ζ and $\overline{\zeta}$ as independent variables instead of ξ and η, that is

$$\zeta=\xi+i\eta\,,\qquad \overline{\zeta}=\xi-i\eta\,. \tag{2.5}$$

Putting further

$$\left.\begin{aligned} &G_m=\phi_m+i\psi_m/\mu \quad (m=1,2,3,\cdots)\,,\\ &G=G_1+G_2+G_3+\cdots\,, \end{aligned}\right\} \tag{2.6}$$

he has given the following integrals as the solutions of iterative equations[5),7)].

$$G_1=f(\zeta)\,, \tag{2.7}$$

$$\begin{aligned} G_2=\frac{M^2}{4}\Big[\nu\left(\frac{df}{d\zeta}\right)^2\overline{\zeta}+(1+\nu)\Big\{2\left(\frac{df}{d\zeta}\right)\overline{f}\\ +\int\left(\frac{d\overline{f}}{d\overline{\zeta}}\right)^2 d\overline{\zeta}\Big\}\Big]+f_2(\zeta)\,, \end{aligned} \tag{2.8}$$

$$\begin{aligned} G_3=A\left(\frac{df}{d\zeta}\right)^3\overline{\zeta}+B\int\left(\frac{d\overline{f}}{d\overline{\zeta}}\right)^3 d\overline{\zeta}+3B\left(\frac{df}{d\zeta}\right)^2\overline{f}\\ +C\frac{df}{d\zeta}\int\left(\frac{d\overline{f}}{d\overline{\zeta}}\right)^2 d\overline{\zeta}+D\int\left(\frac{df}{d\zeta}+\frac{d\overline{f}}{d\overline{\zeta}}\right)\\ \times\left(\frac{\partial G_2}{\partial\zeta}+\frac{\partial G_2}{d\overline{\zeta}}+\frac{\partial\overline{G}_2}{\partial\zeta}+\frac{\partial\overline{G}_2}{\partial\overline{\zeta}}\right)d\overline{\zeta}\\ -\frac{M^2}{2}\frac{df}{d\zeta}\int\left(\frac{\partial G_2}{\partial\zeta}+\frac{\partial\overline{G}_2}{d\zeta}\right)d\overline{\zeta}+f_3(\zeta)\,. \end{aligned} \tag{2.9}$$

Here

$$\begin{aligned} \nu&=(\gamma+1)M^2/4\mu^2\,,\\ A&=-(1+\gamma)(3-2\gamma)M^6/96\mu^2\,,\\ B&=-M^4\{6(1-\gamma)-(1-2\gamma)(3-\gamma)M^2\}/96\mu^2\,,\\ C&=\ M^2\{8-8(3-\gamma)M^2\\ &\qquad+(13-9\gamma+2\gamma^2)M^4\}/32\mu^2\,,\\ D&=\ M^2\{4-(3-\gamma)M^2\}/8\mu^2\,. \end{aligned}$$

$f(\zeta)$, $f_2(\zeta)$ and $f_3(\zeta)$ are analytic functions of ζ, which must be determined by the following conditions:

(i) $\partial G_m/\partial\zeta$ is one-valued and continuous throughout the flow field,

(ii) as $\zeta\to\infty$, $\partial G_m/\partial\zeta\to 0$, and

(iii) on the surface of the cylinder,

$$\Im(\zeta/\mu^2+G)=0\,.$$

§ 3. Boundary Conditions

We denote the profile in the x, y-plane and the distorted profile in the ξ, η-plane as P and P' respectively and take their chord length as 2, that is $-1\leq x,\ \xi\leq 1$. In order to determine the functions $f(\zeta)$, $f_2(\zeta)$ and $f_3(\zeta)$, it is convenient to transform the region outside P' onto the region outside the unit circle C in the Z-plane. It is known that such a mapping function can be expanded as follows:

$$\begin{aligned} \zeta(Z)=\frac{1}{2}\left(Z+\frac{1}{Z}\right)+\zeta_1(Z)\\ +\zeta_2(Z)+\zeta_3(Z)+\cdots\,, \end{aligned} \tag{3.1}$$

where $\zeta_m(Z)$ is the analytic function of the order of magnitude of ε^m. Each of them as well as $\zeta(Z)$ must have the expansion outside C such that,

$$\begin{aligned} \zeta_m(Z)=c_{-1}{}^m Z+c_0{}^m+\frac{c_1{}^m}{Z}+\frac{c_2{}^m}{Z}+\cdots\\ (m=1,\,2,\,3,\cdots)\,, \end{aligned} \tag{3.2}$$

By virtue of this transformation, the boundary conditions for G_m can be stated alternatively:

(i) $\dfrac{\partial G_m}{dZ}\Big/\dfrac{\partial\zeta}{\partial Z}$ is one-valued and continuous throughout the flow field,

(ii) as $Z\to\infty$, $\dfrac{\partial G_m}{\partial Z}\to 0$, and

(iii) on C $(Z\overline{Z}=1)$, $\quad\Im(\zeta_m/\mu^2+G_m)=0$.

As for the first approximation, we can easily verify that the function

$$f(Z)=-\frac{1}{\mu^2}\left\{\zeta_1(Z)-c_{-1}{}^1 Z-c_0{}^1-\frac{\overline{c_{-1}{}^1}}{Z}\right\}\,, \tag{3.3}$$

satisfies the above conditions.

By means of this function, we can determine the second approximation G_2 as follows:

$$G_2=f_2{}^0(Z)+\sum_{j=1}^{3}A^j\{g_2{}^j(Z,\overline{Z})+f_2{}^j(Z)\}\,, \tag{3.4}$$

where

$$f_2{}^0(Z)=-\frac{1}{\mu^2}\left\{\zeta_2(Z)-c_{-1}{}^2 Z-c_0{}^2-\frac{\overline{c_{-1}{}^2}}{Z}\right\}\,, \tag{3.5}$$

$$\left.\begin{aligned} A^1&=\frac{M^2}{4}\nu\,, & g_2{}^1&=\left(\frac{df}{d\zeta}\right)^2\overline{\zeta}\,,\\ A^2&=\frac{M^2}{2}(1+\nu)\,, & g_2{}^2&=\left(\frac{df}{d\zeta}\right)\overline{f}\,,\\ A^3&=\frac{M^2}{4}(1+\nu)\,, & g_2{}^3&=\int\left(\frac{d\overline{f}}{d\overline{\zeta}}\right)^2 d\overline{\zeta}\,, \end{aligned}\right\} \tag{3.6}$$

and $f_2{}^j(Z)$ are analytic functions of Z such that $g_2{}^j+f_2{}^j$ obey the boundary conditions (i), (ii) and

(iii) on the boundary, $\Im(g_2{}^j+f_2{}^j)=0$.

It follows readily from these conditions that

$$f_2^{1}=-\left(\frac{df}{d\zeta}\right)^2\zeta \quad \text{and} \quad f_2^{3}=\int\left(\frac{df}{d\zeta}\right)^2 d\zeta\,. \tag{3.7}$$

The expressions for G_3 and higher order terms can be obtained in a similar manner[12].

The mapping function $\zeta(Z)$ may be determined by means of the appropriate one of various methods proposed by several authors. When the mapping function $z(Z)$ for the original profile is known, $\zeta(Z)$ can be easily derived from it by taking advantage of the slenderness of the profile. This idea has been developed and pursued up to the second approximation by Imai, and extended to the third approximation by the present author.

Let a point A on P be translated to a point B on P' by the transformation (2.4), and the images of these points on the unit circle C be $e^{i\omega}$ and $e^{i\theta}$ respectively (see Fig. 1). If we put for the points on the boundary

$$z(e^{i\omega})=x_P(\omega)+iy_P(\omega)$$

and

$$\zeta(e^{i\theta})=\xi_P(\theta)+i\eta_P(\theta)\,,$$

the following relations hold:

$$x_P(\omega)=\xi_P(\theta)\,, \qquad \mu y_P(\omega)=\eta_P(\theta)\,. \tag{3.8}$$

Since ω differs only slightly from θ, we may assume

$$\omega=\theta+\omega_1(\theta)+\omega_2(\theta)+\cdots\,, \tag{3.9}$$

where $\omega_1(\theta)$, $\omega_2(\theta)$, $\cdots$ are functions of θ of the order of magnitude of $\varepsilon, \varepsilon^2, \cdots$ respectively. Substituting from (3.9) into (3.8) and taking account of the nature of singularity as shown in (3.1) and (3.2), we can determine $\omega_1(\theta)$, $\omega_2(\theta)$, $\cdots$ and $\xi_P(\theta)$ and $\eta_P(\theta)$ in terms of x_P and y_P.

For practical purpose it is often rather convenient to give the shape of the profile in a form $y=y(x)$. In this case, we map the chord line onto the contour of C. If D is the projection on the chord line of a point A on P and the image of D on the unit circle C is $e^{i\vartheta}$ (see Fig. 1),

$$x_P=\cos\vartheta\,, \qquad y_P=y_P(x_P)=g(\vartheta)\,. \tag{3.10}$$

Quite similarly to the case for ω, a relation exists between θ and ϑ:

$$\vartheta=\theta+\vartheta_1(\theta)+\vartheta_1(\theta)+\cdots\,, \tag{3.11}$$

by means of which $\xi_P(\theta)$ and $\eta_P(\theta)$ can be expressed in terms of $g(\theta)$[12].

The Flow past a Symmetrical Circular Arc Aerofoil

§ 4. Mapping Functions and Velocity Potentials

We shall now apply the thin-wing-expansion method in order to investigate the flow of a compressible fluid past a lenticular aerofoil. The profile is composed of two equal circular arcs, which subtend an angle 4β at the leading and the trailing edges (Fig. 2). As is well known, the region outside this profile in the z-plane is mapped onto the region outside the unit circle in the Z-plane by the following transformation due to von Kármán and Trefftz:

$$\frac{z-1}{z+1}=\left(\frac{Z-1}{Z+1}\right)^{\kappa}\,, \qquad \kappa=2-\frac{4\beta}{\pi}\,. \tag{4.1}$$

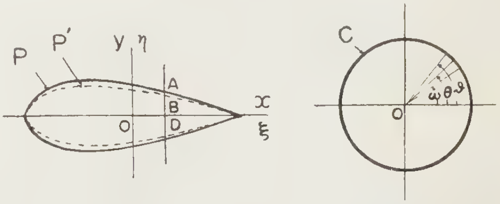

the z, ζ-plane the Z-plane

Fig. 1.

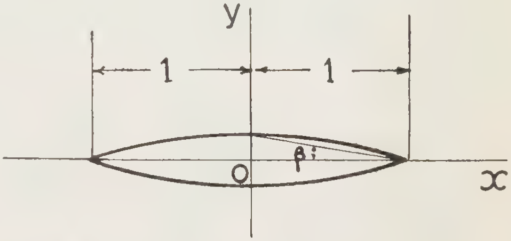

Fig. 2. Symmetrical circular arc aerofoil.

When the thickness ratio $t=\tan\beta$ is small, z can be expanded as follows:

$$\left.\begin{aligned} &z(Z)=C+z_1(Z)+z_2(Z)+z_3(Z)+\cdots\,,\\ &\text{where}\\ &z_1(Z)=\beta(2/\pi)S^2L\,,\\ &z_2(Z)=-\beta^2(4/\pi^2)S^2CL^2\,,\\ &z_3(Z)=-\beta^3(8/3\pi^3)S^2(1-3C^2)L^3\,. \end{aligned}\right\} \tag{4.2}$$

In these formulae as well as in later ones, we put for brevity

$$\left.\begin{aligned} C=\frac{1}{2}\left(Z+\frac{1}{Z}\right), \quad S=\frac{1}{2i}\left(Z-\frac{1}{Z}\right), \\ L=\log\frac{Z-1}{Z+1}. \end{aligned}\right\} \tag{4.3}$$

According to the procedures described above, the mapping function $\zeta(Z)$ can be derived in the following form:

$$\left.\begin{aligned} &\zeta(Z)=C+\zeta_1(Z)+\zeta_2(Z)+\zeta_3(Z)+\cdots, \\ &\text{where} \\ &\zeta_1(Z)=\beta\mu(2/\pi)S^2L, \\ &\zeta_2(Z)=-\beta^2\mu^2(4/\pi^2)SCL^2, \\ &\zeta_3(Z)=-\beta^3\mu^3(8/3\pi^3)S^2(1-3C^2)L^3 \\ &\qquad +\beta^3\mu M^2(2/3\pi)S^2\{3C+(1+3C^2)L\}. \end{aligned}\right\} \tag{4.4}$$

We can now obtain velocity potentials by straightforward calculations using the formuae in § **2** and § **3**. From (3.3) and (4.4), the first approximation is given as

$$G_1=f(Z)=(\beta/\mu)(2/\pi)(C-S^2L). \tag{4.5}$$

Using the formulae (3.4), (3.5) and (3.6), the second approximation can be determined as follows:

$$\left.\begin{aligned} &G_2=f_2{}^0(Z)+\sum_{j=1}^{3}A^j\{g_2{}^j(Z,\bar{Z})+f_2{}^j(Z)\}, \\ &f_2{}^0=\beta^2(4/\pi^2)(1+S^2L^2)C, \\ &g_2{}^1=(\beta^2/\mu^2)(16/\pi^2)(1+CL)^2\bar{C}, \\ &f_2{}^1=(\beta^2/\mu^2)(16/\pi^2)(1+CL)^2C, \\ &g_2{}^2=(\beta^2/\mu^2)(8/\pi^2)(1+CL)(\bar{C}-\bar{S}^2\bar{L}), \\ &f_2{}^2=-(\beta^2/\mu^2)(8/\pi^2)L, \\ &g_2{}^3=\overline{f_2{}^3}, \\ &f_2{}^3=(\beta^2/\mu^2)(16/3\pi^2) \\ &\qquad \times(C-2S^2L-S^2CL+S_2). \end{aligned}\right\} \tag{4.6}$$

In the last expression, we have defined

$$S_2=\frac{1}{2}\int_\infty^Z L^2\left(1-\frac{1}{Z^2}\right)dZ. \tag{4.7}$$

This function is regular everywhere in the region outside the unit circle of the Z-plane.

We can proceed to the third approximation G_3 in quite a similar but somewhat lengthy manner. Final results are summarized in Appendix.

In the expressions for G_3 appear newly a function and two constants, that is

$$S_3=\frac{1}{2}\int_\infty^Z L^3\left(1-\frac{1}{Z^2}\right)dZ, \tag{4.8}$$

$$\left.\begin{aligned} \sigma_2=\frac{1}{2}\int_1^\infty L^2\left(1-\frac{1}{Z^2}\right)dZ=\frac{\pi^2}{6}=1.6449, \\ \sigma_3=\frac{1}{2}\int_1^\infty L^3\left(1-\frac{1}{Z^2}\right)dZ=-\frac{3}{2}\zeta(3)=-1.8031. \end{aligned}\right\} \tag{4.9}$$

$\zeta(n)$ denotes the Riemann ζ-function.

Real parts of G_1, G_2 and G_2 give ϕ_1, ϕ_2, and ϕ_3 respectively, and thus the velocity potential $\varPhi$ (2.3) has been determined up to the third approximation.

§ 5. Velocity Distribution

We can now calculate the fluid velocity at any point in the flow field, but we are mainly interested in the velocity distribution over the surface of the profile. The trailing and the leading edges correspond to $\theta=0$ and π (or $-\pi$) respectively, hence the upper and the lower surfaces of the profile onto the semicircles $0<\theta<\pi$ and $0>\theta>-\pi$ respectively. Further we note that the functions C, S, L, S_2 and S_3 are evaluated on the unit circle ($Z=e^{i\theta}$) as follows:

$$C=\cos\theta, \qquad S=\sin\theta, \tag{5.1}$$

$$L=l(\theta)\pm i\pi/2, \quad l(\theta)=\log|\tan(\theta/2)|, \tag{5.2}$$

$$\left.\begin{aligned} &S_2=-[\{(s_2(\theta)+\sigma_2)-(\pi^2/4)(1-\cos\theta)\}\pm i\pi s_1(\theta)], \\ &S_3=-[\{(s_3(\theta)+\sigma_3)-(3\pi/4)s_1(\theta)\} \\ &\qquad \pm i(\pi/2)\{3s_2(\theta)-(\pi^2/4)(1-\cos\theta)\}], \\ &\text{where} \\ &\qquad s_1(\theta)=\int_0^\theta \sin\theta\, l(\theta)d\theta, \qquad {}^{*} \\ &\qquad s_2(\theta)=\int_0^\theta \sin\theta\, l^2(\theta)d\theta, \\ &\text{and} \quad s_3(\theta)=\int_0^\theta \sin\theta\, l^3(\theta)d\theta, \end{aligned}\right\} \tag{5.3}$$

and the sign ± indicates that we shall take + for the upper surface and − for the lower one.

By making use of these values, we can get the values of $\varPhi$ on the surface in terms of θ. Their expressions are omitted here for brevity.

The magnitude of the velocity may be calculated by the formulae.

$$\left.\begin{aligned} q(\theta)=\frac{d\varPhi}{d\theta}\Big/\frac{ds}{d\theta}, \\ \frac{ds}{d\theta}=\mp\left\{\left(\frac{d\xi_P}{d\theta}\right)^2+\left(\frac{d\eta_P}{d\theta}\right)^2\right\}^{1/2}. \end{aligned}\right\} \tag{5.4}$$

---

* $s_1(\theta)=(1-\cos\theta)\log|\sin(\theta/2)| +(1+\cos\theta)\log|\cos(\theta/2)|$.

Here s is the distance measured from the leading edge along the surface of the profile.

In our previous analysis, however, $\xi_P(\theta)$ and $\eta_P(\theta)$ were determined only up to the third order with respect to β. Hence the formula (5.4) fails at the leading and the trailing edges, where $ds/d\theta$ vanishes. To avoid this inconvenience, we must take into account exactly the singularity of the transformation at the edges, having recourse to the relation (4.1). For a point on the surface of the profile,

$$\left.\begin{aligned} z_P&=\{1+(i\tan(\omega/2))^\kappa\}/\{1-(i\tan(\omega/2))^\kappa\}\ ,\\ \frac{d\omega}{ds}&=\mp\left|\frac{d\omega}{dz}\right|=\mp\frac{\sin\omega}{2\kappa}\left\{\left(\tan\frac{\omega}{2}\right)^\kappa\right.\\ &\qquad\left.+\left(\tan\frac{\omega}{2}\right)^{-\kappa}-2\cos\frac{\kappa\pi}{2}\right\}\ . \end{aligned}\right\}\quad(5.5)$$

The relation (3.9) between ω and θ can be solved for θ. Thus, for the profile under consideration,

$$\left.\begin{aligned} \theta&=\omega+\theta_1(\omega)+\theta_2(\omega)+\cdots\ ,\\ \text{where}&\\ \theta_1(\omega)&=-(2\beta/\pi)(1-\mu)\sin\omega\, l(\omega)\ ,\\ \theta_2(\omega)&=-(\beta^2/\pi^2)\{\pi^2(1-\mu^2)\sin\omega\cos\omega\\ &\quad+4\mu(1-\mu)\sin\omega\, l(\omega)\\ &\quad-2(1-\mu)^2\sin\omega\cos\omega\, l^2(\omega)\}\ . \end{aligned}\right\}\quad(5.6)$$

By the use of this relation, we can easily obtain alternative expressions for Φ and consequently for q in terms of ω, which are omitted here for saving space.

In the application of the thin-wing-expansion method, however, the flow pattern near the stagnation points is not a matter of main concern. Outside these regions, it seems most convenient for practical computations to convert the argument from θ into ϑ as suggested at the end of § **3**. Then q is given by

$$q(\vartheta)=\frac{d\Phi(\vartheta)}{d\vartheta}\Big/\frac{ds}{d\vartheta}\ .$$

On expanding this expression into a series in the thickness ratio $t(=\tan\beta)$ and substituting x for $\cos\vartheta$, we arrive at the following simple formula for the velocity distribution:

$$q(x)=1+q_{\mathrm{I}}(x)+q_{\mathrm{II}}(x)+q_{\mathrm{III}}(x)+O(t^4)\ ,\quad(5.7)$$

where

$$q_{\mathrm{I}}\ (x)=(t/\mu)(4/\pi)(1+x\lambda(x)),\qquad(5.8)$$

$$\begin{aligned} q_{\mathrm{II}}\ (x)=&\ t^2[-(1-x^2)+(4/\pi^2)\{3(1+2x\lambda(x))-(1-3x^2)\lambda^2(x)\}]\\ &+t^2(M^2/\mu^2)(1+\nu)[-(1-x^2)+(4/\pi^2)\{5(1+2x\lambda(x))-(1-5x^2)\lambda^2(x)\}]\ ,\end{aligned}\qquad(5.9)$$

$$\begin{aligned} q_{\mathrm{III}}(x)=&\ t^3(1/\mu)[(4/3\pi)\{-2(2-3x^2)-(7x-6x^3)\lambda(x)\}\\ &\qquad+(32/\pi^3)\{(1+3x\lambda(x))-(1-3x^2)\lambda^2(x)-(\tfrac{2}{3}x-x^3)\lambda^3(x)\}]\\ &+t^3(M^2/\mu)[(8/3\pi)\{(\tfrac{2}{3}-x^2)+(x-x^3)\lambda(x)\}\\ &\qquad+(16/3\pi^3)\{-2(1+3x\lambda(x))+3(1-2x^2)\lambda^2(x)+2(x-x^3)\lambda^3(x)\}]\\ &+t^3(M^2/\mu)(1+\nu)[(4/3\pi)\{-(22/3)+5x^2-(9x-5x^3)\lambda(x)\}\\ &\qquad+(16/3\pi^3)\{17(1+3x\lambda(x))-3(4-17x^2)\lambda^2(x)-(9x-17x^3)\lambda^3(x)\}]\\ &+t^3(M^4/\mu^3)\{(5+3\gamma)+2(7+2\gamma)\nu+12\nu^2\}[(2/3\pi)\{-(5/6)+2x^2-(x-2x^3)\lambda(x)\}\\ &\qquad+(4/3\pi^3)\{2(1+3x\lambda(x))-3(1-4x^2)\lambda^2(x)-2(x-2x^3)\lambda^3(x)\}]\\ &+t^3(M^2/\mu^3)[1+\tfrac{1}{2}M^2\{2(1+\gamma)+(9+2\gamma)\nu+7\nu^2\}][(8/9\pi)\{-(10/3)+8x^2+1(1+x)\\ &\qquad+(1-3x+8x^3)\lambda(x)-3\sigma_1(x)\}+(32/9\pi^3)\{8(1+3x\lambda(x))-3(1-8x^2)\lambda^2(x)\\ &\qquad-2(x-4x^3)\lambda^3(x)+3x\sigma_2(x)/(1-x^2)-3\lambda(x)\sigma_2(x)+(\sigma_3(x)+\sigma_3)\}]\\ &+t^3(M^4/\mu^3)\{3(3+\gamma)+2(11+2\gamma)\nu+6\nu^2\}[(2/\pi)\{-x^2-x^3\lambda(x)\}\\ &\qquad+(8/3\pi^3)\{(1+3x\lambda(x))+(3x^2\lambda^2(x)+x^3\lambda^3(x)\}]\\ &+t^3(M^4/\mu^3)(1+\nu)^2[(8/3\pi)\{-(31/12)+5x^2-(3x-5x^3)\lambda(x)\}\\ &\qquad+(8/3\pi^3)\{20(1+3x\lambda(x))-15(1-4x^2)\lambda^2(x)-4(3x-5x^3)\lambda^3(x)\}]\ .\end{aligned}\qquad(5.10)$$

In these formulae, following notations are adopted for shortness:

$$\left.\begin{aligned} \lambda(x)&=\frac{1}{2}\log\frac{1-x}{1+x}\ , &\qquad \sigma_1(x)&=-\int_1^x\lambda(x)dx\ ,\\ \sigma_2(x)&=-\int_1^x\lambda^2(x)dx\ , &\qquad \sigma_3(x)&=-\int_1^x\lambda^3(x)dx\ . \end{aligned}\right\}\qquad(5.11)$$

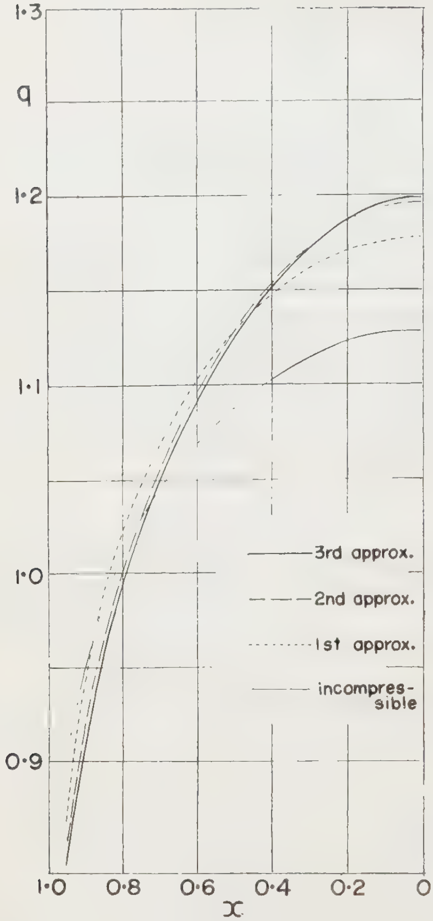

Fig. 3. Velocity distribution over the surface of a symmetrical circular arc aerofoil, $t=0.1$, $M=0.7$.

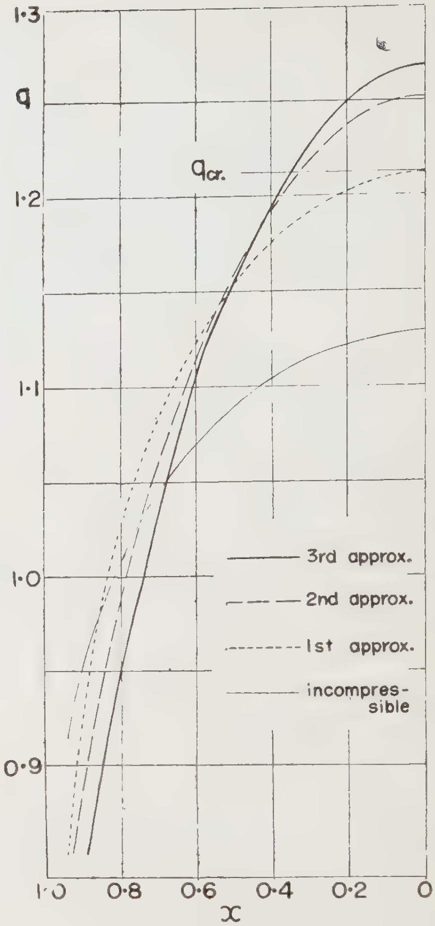

Fig. 4. Velocity distribution over the surface of a symmetrical arc aerofoil, $t=0.1$, $M=0.8$.

When we have calculated the parts depending on x, the velocity distributions for any value of the thickness ratio of the profile and of the Mach number of the main stream can be obtained quite easily according to the above formulae.

§ 6. Numerical Results and Discussions

The velocity distributions over the surface of a symmetrical circular arc aerofoil of thickness ratio $t=0.1$ have been computed for the Mach number of the main stream $M=0.7$ and 0.8, by use of the simplified formulae (5.7)~(5.11). The calculated results are shown in Figs. 3 and 4. The velocity distribution curves do not indicate any peculiarity even at $M=0.8$ such as seen in the case of an elliptic cylinder[9]. This result seems to prove the validity of the thin-wing-expansion method for a profile with sharp edges.

We may notice that there is no supersonic region on the surface when $M=0.7$, while the fluid velocities in some region near the mid-chord point exceed the local speed of sound at $M=0.8$. On the other hand, these curves suggest that the convergency of the process of iterations would be confirmed at $M=0.7$, but that it would be open to question at $M=0.8$. Fig. 5 will make the situations clearer. In this figure the maximum velocities $q_{\max}$ are plotted against Mach numbers for each step of approximation. There is also contained the curve of the so-called critical speed versus Mach number.

Our iterative method would surely fail to converge at a certain Mach number of the main stream. The labours necessary for proceeding to the higher approximations are so much that it seems generally impossible to determine more accurately the Mach num-

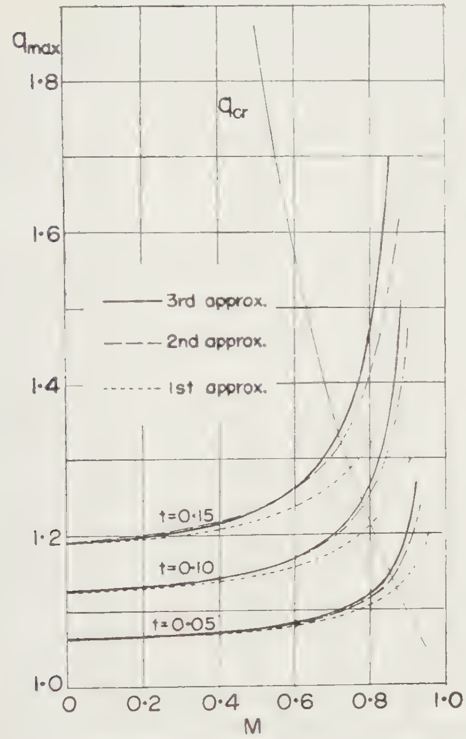

Fig. 5. Maximum velocity at the surface of symmetrical circular arc aerofoils.

ber at which the continuous flow first breaks down. But Kaplan has shown with the aid of his method of iteration together with the theory of transonic similarity that "smooth, steady flow along the infinite sinusoidal wall would certainly cease to continue, when the maximum velocity on the wall attains to the local speed of sound there"[13]. On the contrary, by means of the elaborate analysis using the hodograph transformation, Cherry and Tomotika and Tamada have proved theoretically that there exist some examples of continuous, steady flow past obstacles, about which the fluid velocities become supersonic in a limited region and are subsonic elsewhere. These examples seem to contradict Kaplan's prediction mentioned above. One of the possible explanations to reconcile them will be the following conjecture: "The smooth transonic flow calculated by the hodograph transformation may be exceptional cases pertaining to particular, ideal boundary shapes, and they have no neighbouring solutions for slightly different boundaries····"[14]. To clarify this would surely be one of the most important problems in the high speed aerodynamics and calling for further investigations.

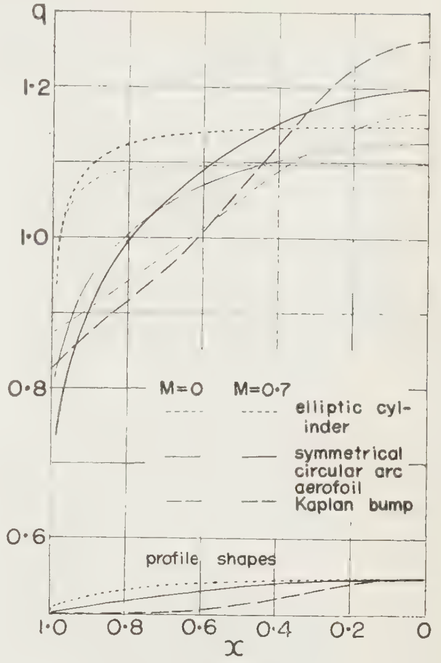

Fig. 6. Velocity distributions over the surfaces of three symmetrical profiles, $t=0.1$.

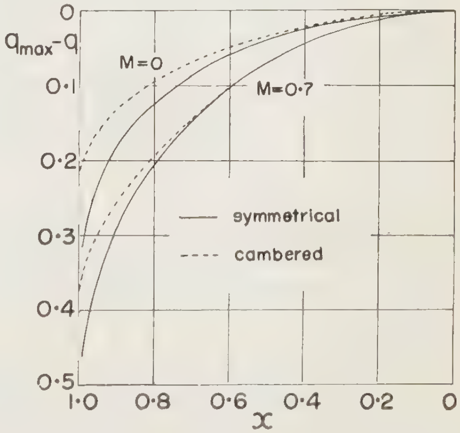

Fig. 7. Velocity distributions over the surface of a symmetrical circular arc aerofoil ($t=0.10$) and over the upper surface of a cambered circular arc aerofoil ($f=0.05$).

When M is lower than 0.7, the convergence of the iteration process seems to have been established for any profile of thickness ratio about or smaller than 0.1. For three representative types of symmetrical profiles, namely, an elliptic cylinder[9], a symmetrical circular arc aerofoil and a Kaplan bump[10], the velocity distributions over their surfaces at $M=0.7$ are compared in Fig. 6. It may be noted that the shape of the velocity distribution curve closely resembles the shape

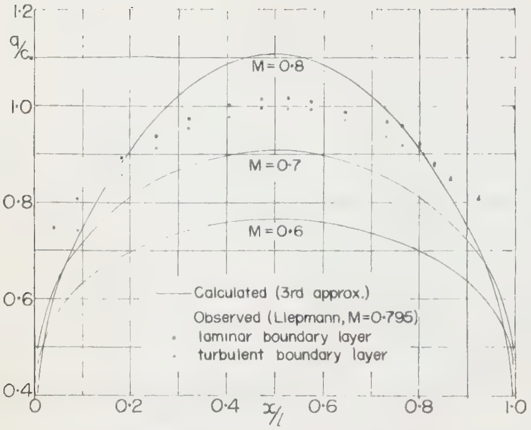

Fig. 8. Calculated and observed velocity distributions over the surface of a symmetrical circular arc aerofoil, $t=0.12$, c_*: critical speed of sound.

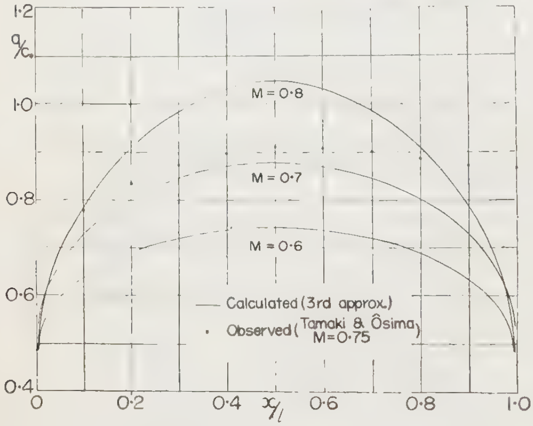

Fig. 9. Calculated and observed velocity distributions over the surface of a symmetrical circular arc aerofoil, $t=0.1$, c_*: critical speed of sound.

of profile itself.

Kaplan has calculated the velocities on the surface of a cambered circular arc aerofoil of infinitesimal thickness[2)]. Its upper surface is of the same form as that of our profile. The rates of change in velocity on their surface are shown in Fig. 7 and represent almost complete agreement with each other. This offers an example, that confirms even in the case of compressible flow the late Professor Fukatsu's statement: The velocity distribution over the upper (lower) surface of an aerofoil is determined by its own shape and almost independent of the shape of the lower (upper) surface.

As for the experiments on our profile, the pressure distributions over its surface were measured in a high speed wind tunnel by Liepmann[15)] and in a shock tube by Tamaki and Ôsima[16)]. But the main purpose of these authors were to investigate how shock waves would be formed on the surface of an aerofoil and related phenomena, hence there are few data suitable for testing validity of the present analysis. Some of their results are reproduced in Figs. 8 and 9, and compared with the calculated values. The agreement between the calculated and observed values is not satisfactory. The reasons for this discrepancy are probably due to the limited dimensions of the test section and to the existence of the boundary layer and wake, and possibly to the appearance of weak shock waves.

Acknowledgement

The author wishes to express his sincere and unbounded gratitude to Prof. I. Imai, who suggested the present problem and helped him always with warmest advice and encouragement through this work. His cordial thanks are due to Prof. I. Tani for his continual and kindly support. The author is also indebted to the Minstry of Education and the Staff of Ochanomizu University for affording facilities to study. His acknowledgement is tendered to Prof. H. Tamaki and Mr. K. Ôsima for kind information of their unpublished data.

Appendix. Expressions for G_3

$$G_3=f_3{}^0(Z)+\sum_{j=1}^{21}B^j\{g_3{}^j(Z,\overline{Z})+f_3{}^j(Z)\}$$

$$f_3{}^0=\beta^3\mu(8/3\pi^3)\{3C+S^2(1-3C^2)L^3\}+(\beta^3M^2/\mu)(2/3\pi)\{2C-3S^2C-S^2(1+3C^2)L\}$$

$$B^1=M^2\nu/4\,,\qquad g_3{}^1=(\beta^3/\mu)(32/\pi^3)(1+CL)^2\overline{S}{}^2\overline{L}$$

$$f_3{}^1=-(\beta_3/\mu)(32/\pi^3)\{\tfrac{1}{3}(2-\tfrac{1}{3}\pi^2)C+\tfrac{1}{3}\pi^2S^2C-S^2L+\tfrac{1}{3}S^2C^2(L^3+\pi^2L)\}$$

$$B^2=M^2\nu/4\,,\qquad g_3{}^2=(\beta^3/\mu)(64/\pi^3)(1+CL)^2(1+2CL)\overline{C}$$

$$f_3{}^2=-(\beta^3/\mu)(64/\pi^3)(1+CL)^2(1+2CL)C$$

$$\begin{aligned}
&B^3=M^2(1+\nu)/2\,, && g_3{}^3=(\beta^3/\mu)(16/\pi^3)(1+3CL+2C^2L^2)(\overline{C}-\overline{S}^2\overline{L})\\
& && f_3{}^3=-(\beta^3/\mu)(16/\pi^3)\{\tfrac{2}{3}(1+\tfrac{1}{3}\pi^2)C-\tfrac{2}{3}\pi^2SC+(1+2C^2)L+C^3L^2-\tfrac{2}{3}S^2C^2(L^3+\pi^2L)\}\\
&B^4=M^2(1+\nu)/4\,, && g_3{}^4=\overline{f_3{}^4}\\
& && f_3{}^4=(\beta^3/\mu)(16/3\pi^3)\{C-5S^2L-7S^2CL^2-3S^2(1+C^2)L^3-2S_2\}\\
&B^5=M^2\nu/2\,, && g_3{}^5=(\beta^3/\mu)(8/\pi^3)\{1-CL+(1-5C^2)L^2+C(1-3C^2)L^3\}\overline{C}\\
& && f_3{}^5=-(\beta^3/\mu)(8/\pi^3)\{1-CL+(1-5C^2)L^2+C(1-3C^2)L^3\}C\\
&B^6=M^2(1+\nu)/2\,, && g_3{}^6=(\beta^3/\mu)(16/\pi^3)(1+CL)(1+\overline{S}^2\overline{L}^2)\overline{C}\\
& && f_3{}^6=-(\beta^3/\mu)(16/\pi^3)\{\tfrac{1}{3}(1+\tfrac{1}{3}\pi^2)C-\tfrac{1}{3}\pi^2S^2C+C^2L-S^2CL^2-\tfrac{1}{3}S^2C^2(L^3+\pi^2L)\}\\
&B^7=M^2(1+\nu)/2\,, && g_3{}^7=\overline{f_3{}^7}\\
& && f_3{}^7=(\beta^3/\mu)(4/3\pi^3)\{7C-5S^2L+11S^2CL^2+3S^2(1+3C^2)L^3+10S_2\}\\
&B^8=M^2(1+\nu)/2\,, && g_3{}^8=(\beta^3/\mu)(8/\pi^3)\{1-2CL+(1-3C^2)L^2\}(\overline{C}-\overline{S}^2\overline{L})\\
& && f_3{}^8=(\beta^3/\mu)(8/\pi^3)[C-\pi^2S^2C-(1-3C^2)\{L+CL^2-\tfrac{1}{3}S^2(L^3+\pi^2L)\}]
\end{aligned}$$

$$\begin{aligned}
&B^9=M^4\nu(3+\gamma+3\nu)/12\,, && g_3{}^9=(\beta^3/\mu^3)(64/\pi^3)(1+CL)^3\overline{C}\\
& && f_3{}^9=-(\beta^3/\mu^3)(64/\pi^3)(1+CL)^3C
\end{aligned}$$

$$\begin{aligned}
&B^{10}=M^4\{(5+3\gamma)+2(7+2\gamma)\nu+12\nu^2\}/16\,, \quad g_3{}^{10}=(\beta^3/\mu^3)(32/\pi^3)(1+CL)^2(\overline{C}-\overline{S}^2\overline{L})\\
&\qquad f_3{}^{10}=-(\beta^3/\mu^3)(32/\pi^3)\{\tfrac{1}{3}(1+\tfrac{1}{3}\pi^2)C-\tfrac{1}{3}\pi^2S^2C+(1+C^2)L+C^3L^2-\tfrac{1}{3}S^2C^2(L^3+\pi^2L)\}\\
&B^{11}=M^2[1+\tfrac{1}{2}M^2\{2(1+\gamma)+(9+2\gamma)\nu+7\nu^2\}]/8\,, \quad g_3{}^{11}=(\beta^3/\mu^3)(64/3\pi^3)(1+CL)(\overline{C}-2\overline{S}^2\overline{L}-\overline{S}^2\overline{C}\overline{L}^2+\overline{S}_2)\\
&\qquad f_3{}^{11}=-(\beta^3/\mu^3)(64/3\pi^3)\{\tfrac{1}{3}\pi^2-\tfrac{1}{3}(1+\tfrac{4}{3}\pi^2)C+\tfrac{1}{3}\pi^2S^2C+(2-C^2)L+\tfrac{1}{3}\pi^2C(1-C^3)L\\
&\qquad\qquad +S^2CL^2+\tfrac{1}{3}S^2C^2L^3-(1+CL)(S_2+2\sigma_2)+\tfrac{2}{3}CS_3\}\\
&B^{12}=M^4\{3(3+\gamma)+2(11+2\gamma)\nu+16\nu^2\}/48\,, \quad g_3{}^{12}=\overline{f_3{}^{12}}\\
&\qquad f_3{}^{12}=(\beta^3/\mu^3)(16/\pi^3)\{C-3S^2L-3S^2CL-(1-C^4)L^3\}
\end{aligned}$$

$$\begin{aligned}
&B^{13}=-M^4\nu/8\,, && g_3{}^{13}=(\beta^3/\mu^3)(64/\pi^3)(1+CL)^2\{L-(C/S^2)\}(C-\overline{C})\overline{C}\\
& && f_3{}^{13}=0\\
&B^{14}=-M^4\nu^2/8\,, && g_3{}^{14}=(\beta^3/\mu^3)(64/\pi^3)(1+CL)^2\{L-(C/S^2)\}C\overline{C}\\
& && f_3{}^{14}=-(\beta^3/\mu^3)(64/\pi^3)(1+CL)^2\{L-(C/S^2)\}C^2\\
&B^{15}=-M^4\nu(1+\nu)/4\,, && g_3{}^{15}=(\beta^3/\mu^3)(32/\pi^3)(1+CL)\{L-(C/S^2)\}(\overline{C}-\overline{S}^2\overline{L})(C-\overline{C})\\
& && f_3{}^{15}=0\\
&B^{16}=M^4\nu(1+\nu)/8, && g_3{}^{16}=(\beta^3/\mu^3)(64/\pi^3)(1+CL)(1+\overline{C}\overline{L})^2(C-\overline{C})\\
& && f_3{}^{16}=0\\
&B^{17}=M^4\nu(1+\nu)/12, && g_3{}^{17}=(\beta^3/\mu^3)(64/\pi^3)(1+\overline{C}\overline{L})^3(C-\overline{C})\\
& && f_3{}^{17}=0\\
&B^{18}=M^4\nu(1+\nu)/4, && g_3{}^{18}=(\beta^3/\mu^3)(32/\pi^3)(1+CL)\overline{C}/S^2\\
& && f_3{}^{18}=-(\beta^3/\mu^3)(32/\pi^3)(1+CL)C/S^2\\
&B^{19}=M^4(1+\nu)^2/4, && g_3{}^{19}=(\beta^3/\mu^3)(32/\pi^3)[\{C-(1-2C^2)L-S^2CL^2\}(1+\overline{C}\overline{L})-(1+CL)\overline{L}]\\
& && f_3{}^{19}=-(\beta^3/\mu^3)(32/\mu^3)\{\tfrac{1}{3}(1+\tfrac{1}{3}\pi^2)C-\tfrac{1}{3}\pi^2S^2C+C^2L-S^2CL^2-\tfrac{1}{3}S^2C^2(L^3+\pi^2L)\}\\
&B^{20}=M^4(1+\nu)^2/8, && g_2{}^{20}=(\beta^3/\mu^3)(32/\pi^3)\{(C-S^2L)(1+\overline{C}\overline{L})^2-(2\overline{L}+\overline{C}\overline{L}^2-\overline{S}_2)\}\\
& && f_3{}^{20}=(\beta^3/\mu^3)(32/\pi^3)\{\tfrac{1}{3}(1+\tfrac{1}{3}\pi^2)C-\tfrac{1}{3}\pi^2S^2C-S^2L-S^2CL^2-\tfrac{1}{3}S^2C^2(L^3+\pi^2L)+S^2\}\\
&B^{21}=M^4(1+\nu)^2/8, && g_3{}^{21}=(\beta^3/\mu^3)(16/\pi^3)\{2-(C-S^2L)(\overline{C}-\overline{S}^2\overline{L})\}(\overline{C}-\overline{S}^2\overline{L})/S^2\\
& && f_2{}^{21}=-(\beta^3/\mu^3)(16/\pi^3)\{(C/S^2)-\tfrac{1}{3}(1-\tfrac{2}{3}\pi^2)C+\tfrac{1}{3}\pi^2S^2C+(2-C^2)L+S^2CL^2\\
& && \qquad -\tfrac{1}{3}S^4(L^3+\pi^2L)\}\,.
\end{aligned}$$

References

1) C. Kaplan: N. A. C. A. Tech. Rep. No. 768 (1943).
2) C. Kaplan: ibid. No. 794 (1944).
3) C. Kaplan: ibid. No. 834 (1946).
4) C. Kaplan: ibid. No. 1039 (1951).
5) I. Imai: Rep. Aero. Res. Inst., Tokyo Imp. Univ. No. 294 (1944).
6) I. Imai: Kagaku (Science) **14** (1944) 44 (in Japanese).
7) I. Imai and S. Ôyama: Rep. Inst. Sci. Tech., Univ. Tokyo **2** (1948) 37.
8) I. Imai and S. Ôyama: ibid. **2** (1948) 39.
9) H. Hasimoto: J. Phys. Soc. Japan **7** (1952) 322.
10) Y. Matunobu: read at the 7th annual meeting of the Phys. Soc. Japan, Kyoto (1952).
11) H. Naruse: read at the 8th annual meeting of the Phys. Soc. Japan, Tokyo (1953).
12) S. Asaka: Natural Science Report, Ochanomizu Univ. **4** (1953) 213, and **5** (1954) 59.
13) C. Kaplan: N. A. C. A. Tech. Note No. 2383 (1951) and No. 2748 (1952).
14) W. R. Sears and Y. H. Kuo: *Plane Subsonic and Transonic Potential Flows*, General Theory of High Speed Aerodynamics ed. by Sears, Sec. F. Princeton Univ. Press, N. J. (1954).
15) H. W. Liepmann: J. Aero. Sci. **13** (1946) 423.
16) K. Ôsima: to be published in this Journal.

Short Notes

J. PHYS. SOC. JAPAN **10** (1955) 493

Influence of Infrared Rays on the Photoconductivity of the Polycrystalline CdS

By Seiichi YOSHIMATSU, Chikashi KANZAKI,
Sumiaki IBUKI and Naomichi MURAI

Eng'g Laboratory, Mitsubishi Elec. Mfg. Co., Ltd., Amagasaki, Hyogo

(Received March 30, 1955)

We reported about the photoconductivity of polycrystalline CdS at the Semiconductor Meeting held by the Physical Society of Japan, in April, 1954. We report here again about a part of it including some results obtained thereafter.

We used those samples treated as follows: CdS was precipitated from aqueous solution of $Cd(NO_3)_2$ and Na_2S recrystallized many times, and then press-molded and sintered at 450°C for about ten hours in air.

The dark resistivity of these samples is about 10^8 ohm-cm and lower than that of the single crystals which were made by Frölichs' method[1], whereas the photocurrent is comparable with that of the single crystals.

However, the spectral sensitivity of the photoconductivity of these samples is quite different from that of the single crystals; i.e. the peak at 5200Å (2.40 ev) is lower and there is another peak whose maximum lies at 6100Å (2.03 ev). Moreover, the shape of curve varies according to the rise of the temperature of the sample; i.e. the red peak shifts to the shorter and the green peak to the longer wavelengths side. The rate of the shift is about 9×10^{-4} ev/°C for the red peak and -7×10^{-4} ev/°C for the green peak. The height of the green peak increases a little, while that of the red peak decreases. Consequently, the relative height of the red peak becomes considerably lower. This is shown in Fig. 1.

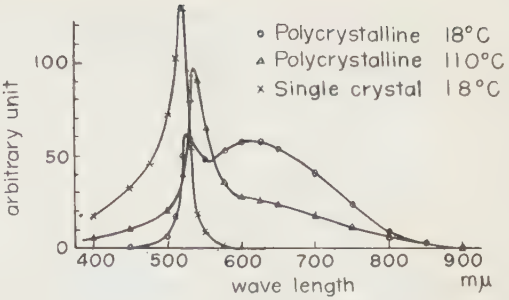

Fig. 1. Spectral sensitivity of the photoconductivity and its temperature dependence.

The photocurrent which is produced by irradiation of visible rays is diminished by superposing irradiation of infrared rays. The spectral sensitivity of this photocurrent reduction for superposed infrared rays is shown in Fig. 2. The peak in longer wavelengths side is at 1.45μ (0.85 ev) (the same position as the single crystals), but the peak in the shorter wavelengths side is at 0.97μ (1.28 ev) in contrast with that of the single crystals which is at 0.85μ (1.43 ev). Also this varies exceedingly with the temperature of the sample; i.e. the peak at 0.97μ diminishes in its height and shifts to the longer wavelengths side with the rate of about -14×10^{-4} ev/°C according to the rise of temperature, while the peak at 1.45μ does not change its position and its sensitivity is nearly same up to about 100°C, but decreases gradually over 100°C. These appearances are shown in Fig. 3.

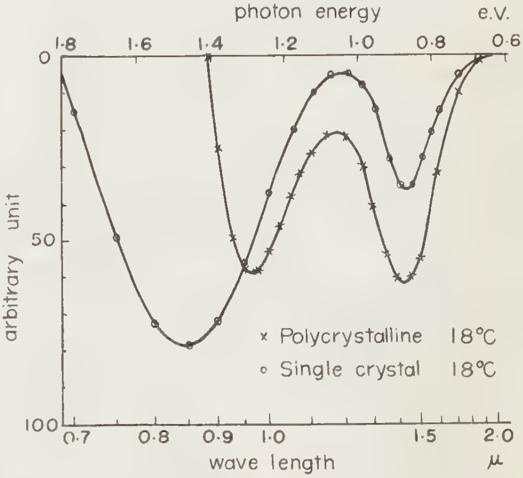

Fig. 2. Infrared reduction.

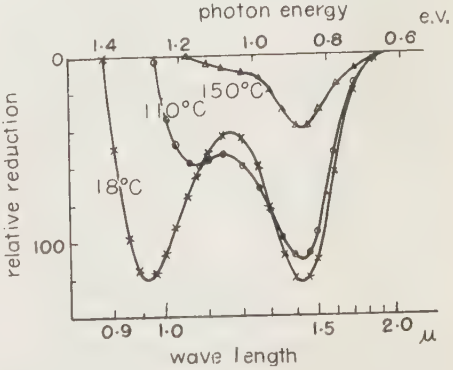

Fig. 3. Temperature dependence of the infrared reduction.

Considering above mentioned phenomena, it seems that there is a correlation between the red center of the photoconductivity and the center of the infrared reduction at 0.97μ. Moreover, if we investigate the luminescence and photo-voltaic effect[2] combined with these facts, the mechanism of the conductivity of CdS will be almost clear. In this case, the study by the irradiation of infrared rays will become a key point for the solution of the problem combined with the study about the mobility of holes.

References

1) R. Frölichs: Phys. Rev. **72** (1947) 595.
2) D. C. Reynolds et al: Phys. Rev. **96** (1954) 533.

J. PHYS. SOC. JAPAN **10** (1955) 494

An Interesting Phenomenon Observed on Some Dielectrics

By Inosuke SUMOTO
Scientific Research Institute, Tokyo

(Received April 16, 1955)

In the course of an investigation on dielectric behaviors of electrets, a new phenomenon was observed. It was found that a glass tube placed between two metall electrodes, which are immersed in melted carnauba wax about 10 cm apart, begins to rotate with high angular velocity under the application of about 10 kV. D.C. The apparatus used is shown in Fig. 1. Following experimental results are obtained in preliminary experiments. a). Liquid dielectrics, which are polar substances having small conductivities, such as melted carnauba wax, higher alcohol, stearic acid, palmitic acid and xylol, gives rise to rotation. Non polar substances such as melted paraffin seems to resist the rotation. b). The glass tube rotates better when it is filled with polar liquid substance such as H_2O or CH_3OH. A metal rotor can not rotate, but it does when it is sealed in a glass tube. c). Shapes and arrangements of electrodes that make the electric field more inhomogeneous allow the rotor to rotate more easily. An example is given by electrodes formed by a combination of a plate and a wire (Fig. 1. b.). d). Static field causes rotation but alternating field of 50 cps does not. e). There is a lower limit of the applied voltage above which it rotates.

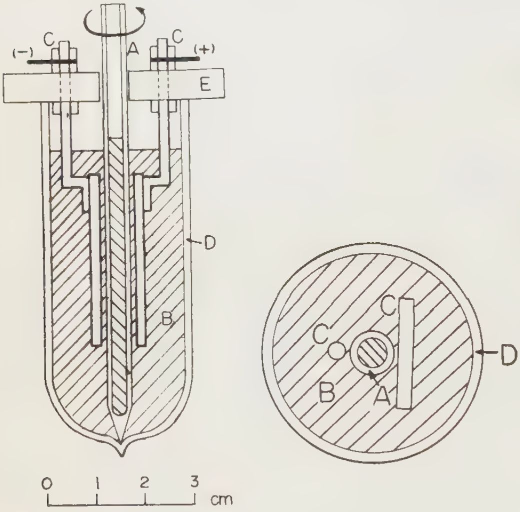

(a) (b)

Fig. 1. Experimental Apparatus.
A. Rotor, B. Liquid dielectrics, C. Electrode, D. Glass vessel, E. Ebonite insulator.

When the above conditions are satisfied, the rotor begins to rotate spontaneously or at a slight shock. The direction of rotation, however, is not predetermined. It speeds up and continues to rotate in the direction in which it first started.

Table I. Electrode: Fig. 1. b.
Rotor: water sealed in a thin walled glass tube.

Liquid dielectrics	The rate of increase of the current. $(I_R-I_0)/I_0\times 100$	Starting Voltage of rotation in V.
carnauba wax	36.0	4,000
higher alcohol	31.0	1,000
stearic acid	58.0	1,500
palmitic acid	60.0	700
xylol	31.0	300

The rotor continues to rotate as long as the electric field is on. The conduction current is of the order of a few μA and increases when the rotor begins to rotate. The rate of increase of the current may be expressed by $(I_R-I_0)/I_0$, where I_0 and I_R are respectively the values of the conduction current when the rotation is prevented by some external force and when it is rotating freely. It depends on the kind of the rotor, the liquid dielectrics and the field strength. It increases with the applied voltage and the angular velocity of rotation. Most probably, the increased expenditure of electric energy is consumed by the rotation.

Some examples of experimental results are given in Table I.

Futher expriment is in progress to make the mechanism of the rotation clear.

JOURNAL OF THE PHYSICAL SOCIETY OF JAPAN Vol. 10, No. 7, JULY, 1955

Scintillation Spectrometer Studies on the Beta-activity of K^{40}

By Soji KONO

Tokyo University of Education, Otsuka, Tokyo

(Received March 7, 1955)

The beta-ray spectrum of potassium-40 has been studied using the scintillations from the crystal of potassium iodide activated with thallium iodide. The Kurie plot of the spectrum gave the forbidden shape, which was straightened from the end-point 1320±20 kev down to well below 300 kev by the third forbidden tensor (or axial vector) correction factor. Measurement on the specific activity has also been carried out and resulted in the value $\lambda(\beta)=5.0\pm0.2\times10^{-10}$ per year. This value is in good agreement with recent determinations.

§1. Introduction

The radioactive decay of potassium-40 has been studied by many investigators. The long half life of the decay and the low concentration of K^{40} in the natural potassium combine to make accurate measurement of the decay constant extremely difficult.

In recent years electromagnetical enrichment of potassium in K^{40} has been achieved which enabled to determined the beta-ray spectrum by the usual magnetic lens spectrometer[1),2),3)], without excessive distortion due to source thickness. Feldman and Wu used the average thickness of 2.5 mg/cm² of KCl which was enriched to 7.13 percent in K^{40} as the source on Nylon backing of 0.6 mg/cm² thickness, and obtained the result which showed definitly forbidden shape. The third forbidden tensor and axial vector correction factor provides a good fit to the data from the endpoint, 1325±15 kev, down to 500 kev. Bell, Weaner, and Cassidy using a scintillation counter and source of 2.5 mg/cm² KCl enriched to 1.3 percent in K^{40}, found the simillar results but their corrected Kurie plot begin to deviate at about 700 kev. John H. Marshall[4)] used a liquid argon ionization chamber to measur the shape of beta-ray spectrum of K^{40}.

The upper half of the spectra obtained so far nearly coincide with each other, but that of energy below 500 kev are ambiguous due to the distortion by source thickness and other origins. Further information about the lower energy part of the spectrum is necessary to provide a test for the possible theories of beta-decay.

We have investigated the spectrum of K^{40} using crystal of KI as the scintillation phosphor which contains a source of K^{40} in natural abundance. This method was first developed by B. Smaller et al[5)]. They used the crystal of KI as the source, the scintillations within which was viewed by a 931A photomultiplier. They measured the relative pulse heights by using a constant discriminator level and by varying the photomultiplier voltage, hence the gain. The resulting integral curve for the counting rate *vs.* pulse height was differentiated graphically to obtain the energy spectrum. However, their result was not accurate enough to discuss the spectrum shape.

The advantage of the method is that it has a 4π solid angle geometry, a source thickness which is practically equivalent to zero, no need of window and backing correction. Hence this method is suitable for the measurement of low activity and it will permit direct determination of the scheme with greater accuracy than the other methods by removing ambiguous correction.

§2. Experimental Procedure

Several crystals ranging from 10 to 40 grams of potassium iodide activated with 0.5 to 2 percent of thallium iodide were prepared by the pointed-bottom crucible method.

Such a crystal was mounted on an RCA 5819 photomultiplier tube. MgO refrector was used as in a usual way. The system was enclosed by a 5 cm thickness of lead to minimize the background counts. The output of the photomultiplier was amplified by a linear amplifier and led into a single channel pulse height analyzer.

Energy calibrations were effected by impressing the radiation of external sources, such as 661-kev gamma-ray of Cs^{137}, 1.38 and 2.76 Mev gamma-rays of Na^{24}, upon the crystal and measuring the position of the photoelectron peaks. The results show that potassium iodide gives a linear response of pulse height *vs.* energy for electrons up to 2.76 Mev.

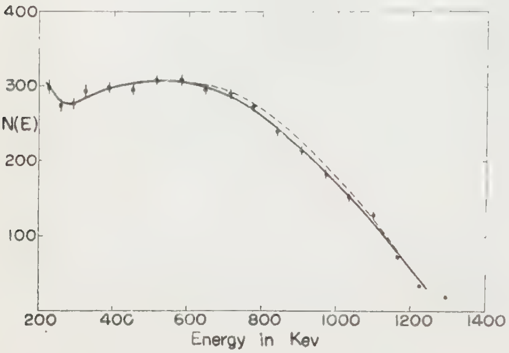

Fig. 1. Spectrum of K^{40} obtained using an activated crystal of KI. The dotted line: Spectrum corrected for the escape of electrons from the crystal and the resolution of the instrument.

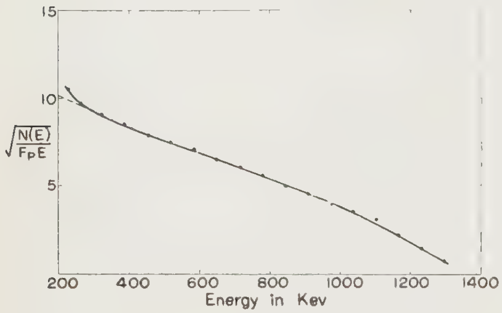

Fig. 2. Allowed Kurie plot of K^{40} spectrum constructed from the corrected data.

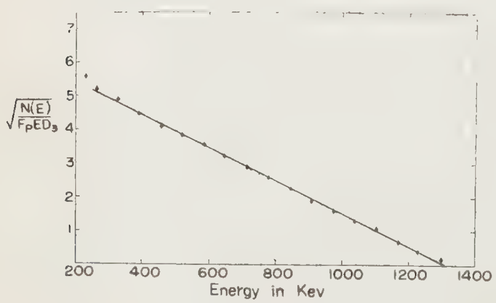

Fig. 3. Kurie plot of the K^{40} spectrum corrected for the factor $D_3=p^6+7p^4q^2+7p^2q^4+q^6$.

§ 3. Result

The pulse height distribution using a crystal of about 30 gram was shown in Fig. 1. The vertical line on the observed points represent a statistical error. The full curve represent the uncorrected experimental results. Owing to the finite size of the crystal, some electrons originated in the surface layer will escape from the crystal before they give up all their energy and they are observed as electrons of smaller energy than they really are. Correction must be made for the escape of electrons from the surface of the crystal[6]. The dotted curve represent the data corrected for the escape of electrons from the surface of the crystal and the resolution of the instrument[7]. The Kurie plot shown in Fig. 2 were then constructed from the corrected data. It concaves downward and show apparently forbidden shape. When the third forbidden correction factor[8]

$$D_3=p^6+7p^4q^2+7p^2q^4+q^6 ,$$

where

$$q=W_0-W ,$$

$$p=(W^2-1)^{1/2} ,$$

W is the energy in unit of mc^2, and W_0 is the end-point energy, is applied, the Kurie plot become linear to well below 300 kev at which point it begins to deviate from the straight line. It is shown in Fig. 3. The deviation is attributable to the spurious pulses due to the delayed phosphorescence of the crystal. When the Kurie plot is extended to the energy axis, endpoint energy of 1320±20 kev is obtained.

The total counts above 250 kev has been determined and the crystal of weight 30.22 gram gave a total counts of 10,521/min. To estimate the counts below 250 kev, the Kurie plot is extended along the dotted line to zero energy, which involved an addition of 1915 counts/min. The specific activity of 29.2±1.0 counts/sec./gram of ordinary potassium was obtained. This value is greater than that of Smaller et al[5] (318±10 betas/min./gram of KI), but in good agreement with the value obtained by Sawyer and Wiedenbeck[9] (28.3±1.0 betas/sec./gram of potassium) and the recent determination by Delaney[10] of 32.0±3 betas/sec./gram of potassium. When an isotopic concentration[11] of 1.19×10^{-4} for K^{40} was assumed, this corresponds to a decay constants of $\lambda(\beta)=5.0\pm0.2\times10^{-10}$/year.

§4. Discussion

The spin of K^{40} has been found to be four[12], while that of Ca^{40}, the product nucleus, is assumed to be zero because it is an even-even nucleus. Accordingly the spin change in the transition K^{40}—Ca^{40} is $\Delta J=4$. On the other hand according to the shell model, K^{40} consists of 19 protons and 21 neutrons, has a configurations $(3d)^{-1}(4f)^1$ and the parity is odd, while that of Ca^{40} is even. Parity should, therefore, change in the transition. Marshak showed that the transition in this case should be third forbidden and the possible interaction should be either tensor or axial vector types.

It may be said that the observed spectrum, whose Kurie plot is linearized from the end-point, 1320±20 kev, down to 300 kev by the correction factor D_3, gives a stronger support to the present calculation for the third forbidden transition than the results obtained so far.

The writer wishes to express his scincere thanks to Prof. S. Kojima for the guidance in all phases of this work. He also wishes to thank Mr. E. Kawasaki of The Scientific Research Institute for giving him a sample of Na^{24}, and Mr. M. Okamoto for the preparation of scintillation crystals. This work was partly supported by the research grant from the Ministry of Education.

References

1) P. R. Bell and J. M. Cassidy: Phys. Rev. **77** (1950) 399.
2) D. E. Alburger: Phys. Rev. **78** (1950) 629.
3) L. Feldman and C. S. Wu: Phys. Rev. **87** (1952) 1091.
4) John H. Marshall: Phys. Rev. **91** (1953) 905.
5) B. Smaller, J. May, and M. Freedman: Phys. Rev. **79** (1950) 490.
6) A method was suggested by F. der Mateosian and A. Smith: Phys. Rev. **88** (1952) 1182.
7) An approximation method was first used by D. J. Hughes, and D. E. Alburger: Phys. Rev. **77** (1950) 726.
8) R. E. Marshak: Phys. Rev. **75** (1940) 513.
9) G. A. Sawyer and M. L. Wiedenbeck: Phys. Rev. **79** (1950) 490.
10) C. F. G. Delaney: Phys. Rev. **81** (1951) 1581.
11) A. O. Nier: Phys. Rev. **77** (1950) 789.
12) J. E. Zacharias: Phys. Rev. **60** (1949) 168.

JOURNAL OF THE PHYSICAL SOCIETY OF JAPAN Vol. 10, No. 7, JULY, 1955

Zeeman Splitting of Nuclear Quadrupole Resonance in Paradibromobenzene

By Shoji KOJIMA, Kineo TSUKADA and Yasushi HINAGA

Department of Physics, Tokyo University of Education
Otsuka, Tokyo

(Received April 8, 1955)

Zeeman patterns of the nuclear quadrupole resonance line of Br^{79} were studied with a single crystal of paradibromobenzene. The crystal contains two classes of molecules with equal positive and negative inclinations against the crystallographic *b*-axis. Changing the orientation of magnetic field in the plane perpendicular to the *b*-axis, the Zeeman patterns were measured. The asymmetry parameter of the coupling, η, was determined from the pattern at the magnetic field perpendicular to all carbon-bromine bonds. The result was $\eta=0.12\pm0.01$. The coupling constant, eQq, was measured as 535.19 Mc at 14°C. If the asymmetry parameter is completely due to the resonance of a double bond structure in the carbon-bromine bond, the observed value gives 4.5 per cent double bond character.

§ 1. Introduction

Previously we studied the Zeeman patterns of the nuclear quadrupole resonance line of bromine nuclei with a single crystal of bromine and determined the asymmetry parameter of the coupling[1]. Now we have carried out similar experiments on *p*-dibromobenzene. Dean[2] studied already *p*-dichlorobenzene and determined the asymmetry parameter as 8 percent. Dean[2] and Bersohn[3] pointed out that the asymmetry parameter gave a measure of the partial double bond character of the carbon-chlorine bond. Manring, Brown and Williams[4] measured the resonance frequency of Br^{79} in *p*-dibromobenzene at room temperature and obtained $\nu_0=267.6\pm0.5$ Mc. Recently Bray and Barnes[5] $\nu_0=270.97$ Mc at 77°K. But the asymmetry parameter has not yet been obtained.

§ 2. Calculations of Zeeman Patterns

Paradibromobenzene forms a monoclinic crystal of a layer-like structure. The lattice constants are as follows[6]: $a_0=15.36$ A, $b_0=5.75$ A, $c_0=4.10$ A and $\beta_0=112°30'$. The positions of atoms are shown in Fig. 1 as a projection on the *ab*-plane, where the figures are expressing vertical distances in Angstrom unit. There are two classes of molecules with equal positive and negative inclinations against the *b*-axis.

By the Zeeman effect on the nuclei of spin 3/2, a single resonance line splits into four lines, which correspond to the transitions:

$$\text{(I)}\ \frac{3}{2}-\longrightarrow\frac{1}{2}+,\qquad \text{(II)}\ \frac{3}{2}+\longrightarrow\frac{1}{2}-,$$

$$\text{(III)}\ \frac{3}{2}-\longrightarrow\frac{1}{2}-\ \text{ and }\ \text{(IV)}\ \frac{3}{2}+\longrightarrow\frac{1}{2}+.$$

The frequencies of these lines are expressed by

$$\nu_{\mathrm{I,II}}=\nu_0\pm\tfrac{1}{2}S\,,\quad \nu_{\mathrm{III,IV}}=\nu_0\pm\tfrac{1}{2}s\,, \qquad (1)$$

where

$$\nu_0=\frac{eQq_{zz}}{2h}\sqrt{1+\tfrac{1}{3}\eta^2}\,. \qquad (2)$$

The theory of the first-order Zeeman effect[7][1] gives

$$\left.\begin{matrix}S\\ s\end{matrix}\right\}=\frac{2\mu}{3h}\Big\{\sqrt{9H_z^2+\eta^2(H_x^2+H_y^2-\tfrac{1}{2}H_z^2)}$$
$$\pm\sqrt{4(H_x^2+H_y^2)+H_z^2-4\eta(H_x^2-H_y^2)+\eta^2(H_x^2+H_y^2-\tfrac{1}{2}H_z^2)}\Big\}\,, \qquad (3)$$

where H_x, H_y and H_z are the components of the magnetic field refered to the principal axis system of the field gradient tensor and μ is the magnetic moment of the nucleus.

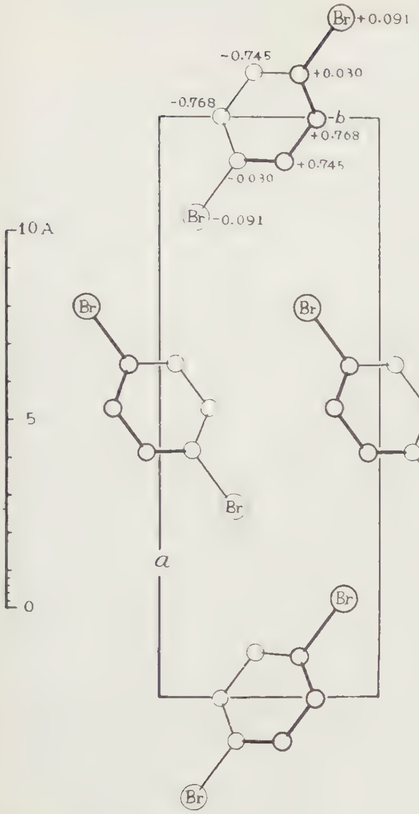

Fig. 1. Vertical projection of atoms in *p*-dibromobenzene crystal.

The principal axis system for a free molecule is usually so chosen that the x-axis is perpendicular to the plane of benzene ring, the z-axis lies along to the carbon-bromine bonds and the y-axis is perpendicular to the x- and z-axes. Corresponding to the two classes of molecules two sets of coordinate axes x_1, y_1, z_1 and x_2, y_2, z_2 must be taken into account. In order to calculate the Zeeman patterns it is convenient to use the following X-, Y- and Z-axes: The X-axis lies along the crystallographic b-axis, the Y-axis is perpendicular to all carbon-bromine bonds and the Z-axis is perpendicular to the X- and Y-axes. In this axis system, the carbon-bromine bond axes of the two classes of molecules, i.e. the z_1- and z_2-axes, incline to the Z-axis with the equal angle Θ, and the normals of the planes of benzene rings, i.e. the x_1- and $_2x$-axes, incline to the Y-axis with equal angle Φ, where Θ and Φ are 35°46′ and 37°52′ respectively. (Fig. 2).

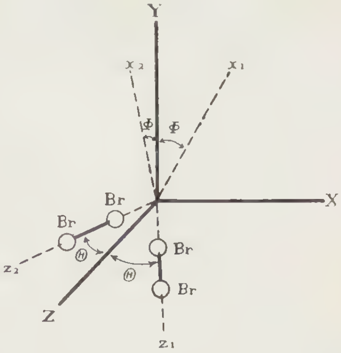

Fig. 2.

Generally the Zeeman patterns consist of eight lines, four of which are due to the molecules of one class and the other four to those of the other class. When the applied magnetic field is parallel to the YZ-plane, the molecules of the two classes give rise same patterns. Therefore only four lines will appear. In this case, the components of the applied magnetic field are expressed by

$$\left.\begin{aligned} H_x &= H(\cos\Phi\cos\theta - \sin\Theta\sin\Phi\sin\theta)\,, \\ H_y &= \pm H(\sin\Phi\cos\theta + \sin\Theta\cos\Phi\sin\theta)\,, \\ H_z &= H\cos\Theta\sin\theta\,, \end{aligned}\right\} \tag{4}$$

where θ is the angle between the direction of the magnetic field and the Y-axis, and the double signs, $\pm$, correspond to the two classes. Putting Eq. (4) to Eq. (3), we can calculate the separations of lines.

When the magnetic field is parallel to the Y-axis, the resonance frequencies are expressed by

$$\left.\begin{aligned} \nu_{\mathrm{I,II}} &= \nu_0 \pm \frac{2}{3}\frac{\mu H}{h}\left\{1 + \frac{1}{2}(|\eta| - \eta\cos 2\Phi)\right\}, \\ \nu_{\mathrm{III,IV}} &= \nu_0 \mp \frac{2}{3}\frac{\mu H}{h}\left\{1 - \frac{1}{2}(|\eta| + \eta\cos 2\Phi)\right\}. \end{aligned}\right\} \tag{5}$$

These equations give

$$\frac{\nu_{\mathrm{I}} - \nu_{\mathrm{IV}}}{2} = \frac{2}{3}\frac{\mu H}{h}|\eta|\,, \tag{6}$$

$$\frac{\nu_{\mathrm{I}} + \nu_{\mathrm{IV}}}{2} = \frac{2}{3}\frac{\mu H}{h}\left(1 - \tfrac{1}{2}\eta\cos 2\Phi\right). \tag{7}$$

If the magnetic field is measured, Eq. (6) yields the absolute value of η. The ratio of Eqs. (6) and (7) is expressed by

$$\frac{\nu_{\mathrm{I}} - \nu_{\mathrm{IV}}}{\nu_{\mathrm{I}} + \nu_{\mathrm{IV}}} = \frac{|\eta|}{1 - \frac{1}{2}\eta\cos 2\Phi}\,. \tag{8}$$

If the sign of η is assumed, Eq. (8) determines η without the measurement of the intensity of the magnetic field. When the magnetic field lies on the YZ-plane but not parallel to the Y-axis, the separations of th frequencies are approximately expressed by

$$\left.\begin{matrix} S \\ s \end{matrix}\right\} = \frac{2}{3}\frac{\mu H}{h}\left[3\cos\Theta|\sin\theta| \pm \sqrt{4-3\cos^2\Theta\sin^2\theta}\right.$$
$$\left.\times\left\{1-2\eta\frac{\cos 2\Phi-(1+\sin^2\Theta)\cos 2\Phi\sin^2\theta-\sin\Theta\sin 2\Phi\sin 2\theta}{4-3\cos^2\Theta\sin^2\theta}\right\}\right]. \tag{9}$$

When Θ and Φ do not vanish, the separations become slightly asymmetric for positive and negative values of θ.

When the direction of the magnetic field is so chosen that

$$2H_z^2=H_x^2+H_y^2-\eta(H_x^2-H_y^2)\ , \tag{10}$$

two resonance frequencies, $\nu_{\rm III}$ and $\nu_{\rm IV}$, coincide with each other and the Zeeman pattern becomes a triplet. The angle giving the triplet spectrum, θ_t, is expressed by

$$1-3\cos^2\Theta\sin^2\theta_t=\eta\{\cos 2\Phi$$
$$-(1+\sin^2\Theta)\cos 2\Phi\sin^2\theta_t$$
$$-\sin\Theta\sin 2\Phi\sin 2\theta_t\}\ . \tag{11}$$

If η vanishes, θ_t becomes ±45°21′. For non-vanishing η the positive and negative values of θ_t are unequal.

When the magnetic field lies on the XY-plane, generally the Zeeman patterns of the molecules of the two classes are slightly different. At the magnetic field parallel to the X-axis, however, they are reduced to four lines. In this case the separations can be calculated by putting

$$H_x=\pm H\cos\Theta\sin\Phi,\quad H_y=-H\cos\Theta\cos\Phi,$$
$$H_z=\pm H\sin\Theta\ .$$

The obtained expression is

$$\left.\begin{matrix} S \\ s \end{matrix}\right\} = \frac{2}{3}\frac{\mu H}{h}\left[3\sin\Theta\pm\sqrt{4-3\sin^2\Theta}\right.$$
$$\left.\times\left\{1+2\eta\frac{\cos^2\Theta\cos 2\Phi}{4-3\sin^2\Theta}\right\}\right]. \tag{12}$$

§ 3. Experimental Procedure

Paradibromobenzene is a solid at room temperature, whose melting and boiling points are 86.9°C and 217°C respectively. Single crystals of about 25 gr. were made by the method of "pointed bottom crucible". The cylindrical glass crucible, diameter of 2 cm, was dropped slowly from upper hot place to lower cold place. The temperature gradient was about 10° per cm, and the falling spee was about 1.1 cm per hour. The sample use was purified by the way of recrystalization.

For the detection the frequency modulate super-regenerative spectrometer which wa previously described[1] was used. The presen experiment, however, carried out at roo temperature. Therefore the orientations o applied magnetic field and of the crystal wer determined more acculately than the previou case. The orientation of the crystal wa determined by the following way. The orientation, at which only four lines appeared an the separation between outer two lines, $\nu_{\rm I}$ an $\nu_{\rm IV}$, became minimum, was searched. Thi direction was considered to be parallel to th Y-axis. Next the orientation giving triple pattern was searched. The plane, whic contained this direction and the Y-axis, fixe the YZ-plane. And then the X-axis wa determined to be perpendicular to this plane

§ 4. Experimental Results

In order to study the general aspect of th Zeeman patterns we have set the magneti field to be parallel to the YZ-plane, wher the molecules of the two classes incline sam angle against the magnetic field. The inclination of the magnetic field against the Y-axis θ, was changed from −100° to +50°. Th field used was of 66 gauss for almost a measurements. Since the separations at th vicinity of the Y-axis were small, the fiel intensity was increased up to 200 gauss. Th separations of lines, $|\nu_{\rm I}-\nu_{\rm II}|/2$ or $|\nu_{\rm III}-\nu_{\rm IV}|/2$ were plotted against angle θ. The result i reproduced in Fig. 3 where the separation are reduced to values for 100 gauss. Th theoretical curves with $\eta=0$ and $\eta=0.12$ ar also shown in the figure. The general tendency of distribution of the observed points ar in accordance with the theory. This fac

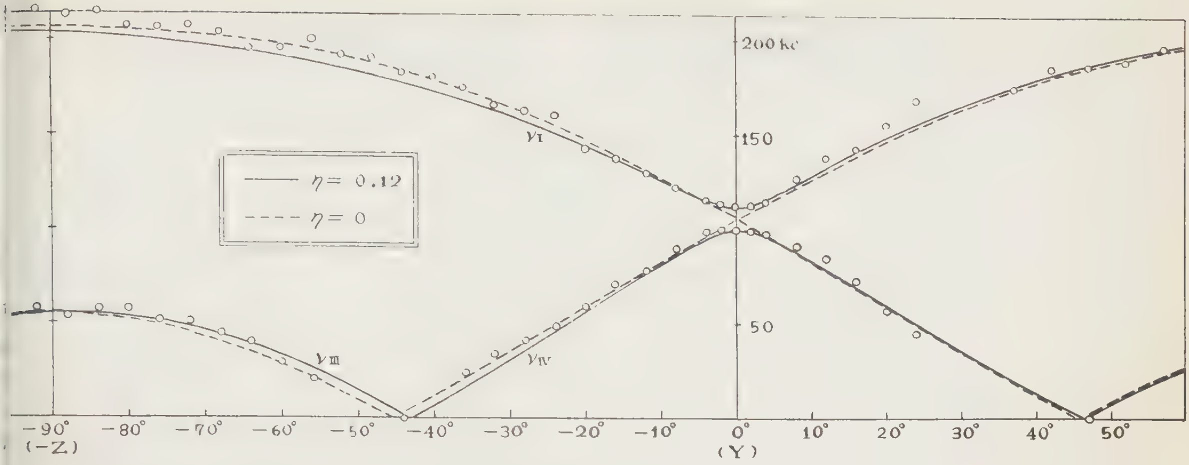

Fig. 3. The Zeeman splittings when the magnetic field lies on the YZ-plane. The values are reduced to those of 100 gauss.

indicates that the crystal structure mentioned in § 1 is supported by the present results.

The asymmetry parameter was determined from the measurement at the magnetic field parallel to the Y-axis. The results at 200 gauss were $\nu_{\mathrm{I}}-\nu_{\mathrm{IV}}=(49.6\pm4)$ kc, and $\nu_{\mathrm{I}}+\nu_{\mathrm{IV}}-2\nu_0=(400\pm20)$ kc. Assuming positive η, we obtained η by the aid of Eq. (7), to be 0.122 ± 0.01. Using the well known value of $(\mu)_{\mathrm{Br}^{79}}=2.10576$ nuclear magneton, and Eq. (6) we obtained, $|\eta|=0.116\pm0.01$.

The determination of sign of η is very difficult because of smallness of $\cos 2\Phi$, such as 0.12. The positive and negative angles giving triplet pattern expressed by Eq. (11) are sensitive to sign of η. The calculated values are, $\theta_t=+47°1'$ and $-43°7'$ with $\eta=+0.12$, and $\theta_t=+43°43'$ and $-47°31'$ with $\eta=-0.12$. The observed values of θ_t, however $|47°\pm2°|$ and $|44°\pm1°|$. Since we have determined the direction of the axis system by the Zeeman patterns, we could not find out the sign of the axes. Therefore the measured values of the angle had to be interpreted as absolute values. The difference of the absolute values, $47°31'-47°1'$ and $43°43'-43°7'$, are too small to determine the sign of η.

When the magnetic field is parallel to the X-axis, the separation between ν_{I} and ν_{II} depends on η comparatively strong, as the coefficient of η in Eq. (12) is larger than the other cases. The calculated values at 73.2 gauss are 273 kc and 269 kc with $\eta=+0.12$ and $\eta=-0.12$ respectively. The observed value at this field intensity was 273 ± 2 kc. This result favours the positive η. Finally we determined that

$$\eta=0.12\pm0.01\ .$$

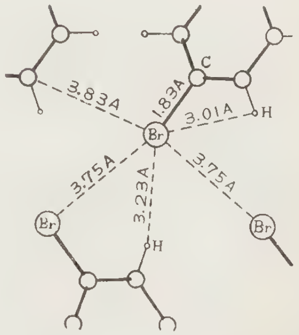

Fig. 4. Distances between atoms in p-dibromobenzene.

The resonance frequency at zero field was measured as 268.13 ± 0.02 Mc at 14°C. The quadrupole coupling coefficient was determined by Eq. (2). The result was

$$(eQq_{zz})_{\mathrm{Br}^{79}}=535.19\ \mathrm{Mc}.$$

§ 5. Discussion

The large asymmetry parameters of iodine and bromine crystals were interpreted well by intermolecular couplings[8)1)]. The distances of a bromine atom to neighbouring atoms in p-dibromobenzene crystal were calculated from the structure shown in Fig. 1. The calculated distances were given in Fig. 4. All the distances are approximately equal to the sum of the Van der Waal's radii, which are $(3.90\ \mathrm{A})_{\mathrm{Br-Br}}$, $(3.80\ \mathrm{A})_{\mathrm{Br-C}}$ and $(3.15\ \mathrm{A})_{\mathrm{Br-H}}$. Therefore the intermolecular couplings are small compared to the intramolecular coupling. The carbon-bromine bond consists principally of a covalent bond. However, in addition to the covalent bond, C–Br, the resonance of a small amount of ionic character of the bond, C^+Br^-, and of partial double bond character, $C^-=Br^+$. are also possible. For these three types of bonds, the number of electrons in the p_x, p_y and p_z orbitals, N_x, N_y and N_z respectively, are as given in Table I, where α

Table I.

	C–Br	C^+Br^-	$C^-=Br^+$
N_x	2	2	$1(1+c)$
N_y	2	2	$2(1+c)$
N_z	$1+\alpha$	2	$1(1+c)$

represents the s character of the bonding orbitals and c is a correction for the change in screening. c was estimated by Townes and Dailey as 0.25[10]. The number of unbalanced p-electrons contributing to q_{zz} is given by[9]

$$U_z=\tfrac{1}{2}(N_x+N_y)-N_z\,. \qquad (13)$$

If β represents the per cent ionic character of the bond and ρ represents the per cent double bond character, the weighted value of the unbalanced p-electrons is

$$U_z=(1-\beta-\rho)(1-\alpha)+\tfrac{1}{2}\rho(1+c). \qquad (14)$$

This quantity, U_z, is determined from the observed quadrupole coupling constant, $[eQq]_{\text{obs.}}$, by the equation,

$$U_z=[eQq]_{\text{obs.}}/[eQq]_{\text{c}}\,. \qquad (15)$$

Where $[eQq]_{\text{c.}}$ is the coupling constant for the pure covalent bond. This value is usually given by doubling the value for the atom which was obtained from the atomic beam method.

Using the present result $[eQq]_{\text{obs.}}=535.19$ Mc and the usually accepted value $[eQq]_{\text{c}}=769.62$ Mc [9], we obtain $[U_z]_{\text{obs.}}=0.70$.

The asymmetry parameter is expressed by[9]

$$\eta=\frac{U_x-U_y}{U_z}=\frac{3}{2}\,\frac{N_y-N_x}{U_z}=\frac{3}{2}\,\frac{\rho(1+c)}{U_z}\,. \qquad (15$$

Putting $\eta=0.12$, $U_z=0.70$ and $c=0.25$, we obtain the partial double bond character of about 4.5%. On p-dichlorobenzene Dean obtained the results that $\eta=0.08$ and $(eQq)_{Cl^{35}}=69.6$ Mc If we use Eq. (15), we obtain the partial double bond character of about 3%. The double bond character in the C–Br bond of p-dibromozenzene is larger than that of p-dichlorobenzene about 50%.

The partial double bond character contributes directly to the asymmetry parameter, η, but little to the coupling constant, eQq. Eq. (14) shows that the decrease of the coupling constant from the pure covalent bond, about 30%, is mainly due to ionic character and sp-hybridization of the bond.

This work was partially supported by the Scientific Research Expenditure of the Ministry of Education.

References

1) S. Kojima, K. Tsukada, S. Shimauchi and Y. Hinaga: J. Phys. Soc. Japan **9** (1954) 795.
2) C. Dean: Phys. Rev. **86** (1952) 607.
3) R. Bersohn: J. Chem. Phys. **22** (1954) 2078.
4) E. Manring: C. Brown and D. Williams: Phys. Rev. **90** (1953) 348.
5) P. J. Bray and R. G. Barnes: J. Chem. Phys. **22** (1954) 2023.
6) R. W. G. Wyckoff: "Crystal Structures" Int. Sci. Pub. Inc., New York, (1948).
7) R. Bersohn: J. Chem. Phys. **20** (1952) 1505.
8) C. H. Townes and B. P. Dailey: J. Chem. Phys. **20** (1952) 35.
9) U. Gordy, W. V. Smith and R. F. Trambarulo; "Microwave Spectroscopy" John Wiley and Sons. Inc., New York (1953).
10) C. H. Townes and B. P. Dailey: J. Chem. Phys. **17** (1949) 782.

JOURNAL OF THE PHYSICAL SOCIETY OF JAPAN Vol. 10, No. 7, JULY, 1955

Calculated Energy of A-O-A Type Molecules by Mulliken's Magic Formula

By Yoshimasa AOKI

The Institute of Polytechnics, Osaka City University

(Received October 18, 1954)

Mulliken's Magic Formula is applied to the calculation of the dissociation energies of molecules of the type A–O–A. $s\,p$ hybrid atomic orbitals are used as wave functions of oxygen orbitals, and dissociation energies are derived for various values of the bond angle and the interatomic distance. In the case of H_2O, dissociation energy was obtained to be 9.39 eV., bond angle, 100°, and interatomic distance, 2.0 a_H. In the case of F_2O, these were 5.62 eV., 92°, and 2.8 a_H. These values are close to the experimental values, as expected. It might be concluded, therefore, that Mulliken's Magic Formula is useful in the calculation of properties of molecules of such type as A–O–A with the help of Pauling's electro-negativity scale.

In the Appendix, the numerical values of some overlap integrals between $2s\,2p$ hybrid atomic orbitals and other atomic orbitals are taublated.

§1. Introduction

Theories on physical and chemical behaviour and properties of molecules are being developed more actively than ever. Theoretical computation yields results which agree more and more closely with the experimentally observed values. However, because of the increasing complexity of calculation, it is desirable and worthwhile to establish a semi-empirical approximation formula with the simplest possible expression which will lead to the desired degree of approximation, even though it may not be very rigorous. Mulliken's Magic Formula[1)], hereafter referred to as M.M.F., is based on the assumption that the bond strength is a function of overlap integrals of valence electrons. Some of the values calculated by M.M.F. are very close to the experimental values while others show quite a large discrepancy[1)]. Such shortcoming of the M.M.F. is emphasized by R.S. Mulliken himself. However, the author expects that M.M.F. can be improved so that it will satisfy the above stated requirements.

The original M.M.F. is expressed as

$$D=\sum X_{ij}-\tfrac{1}{2}\sum Y_{kl}+\tfrac{1}{2}\sum K_{mn}-P+R.E., \qquad (1)$$

where X_{ij} expresses the bonding energy of the valence electrons and is given by

$$X_{ij}=A_jS_{ij}\overline{I}_{ij}/(1+S_{ij}) . \qquad (2)$$

Here, A_j is a coefficient to be adjusted empirically. $\overline{I}_{ij}$ is the mean ionization energy, and S_{ij} is the overlap integral. Y_{kl} designates the repulsion energy between homogeneous non-bonded pairs which may be express as

$$Y_{kl}=\nu A_kS_{kl}{}^2\overline{I}_{kl} . \qquad (3)$$

Here, ν is a constant to be determined emperically. K_{mn} denotes the exchange energy between heterogeneous non-bonded pairs, which can be obtained theoretically. However, this will be determined by an approximate method as will be shown in the present paper*. The letter P which appears in (1) denotes the promosion energy, and $R.E.$ refers to the resonance energy.

The following section of the paper is devoted to the discussion of the comparison of calculation according to M.M.F. and the experimental result.

§2. Atomic Orbits of Oxygen

As shown in Fig. 1, the origin 0 is chosen at the position of oxygen nucleus. The direction of an O-H bond is denoted by i, while the other O-H bond is designated by j. In accordance with the symmetrical property of an A-O-A molecule, the orbital of the lone pair in the molecule plane will be in the x direction. Each orbital function is expressed in terms of s, p_{σ_i} and p_{π_i}. Here, s and p_{σ_i}

---

* See $K_{\pi h}$ of §3.

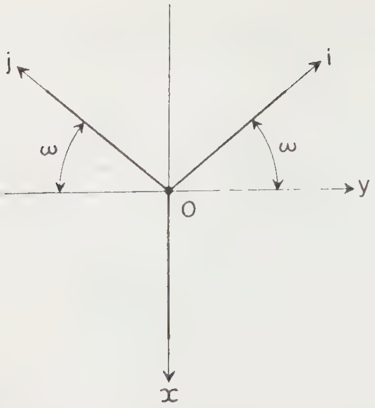

Fig. 1. Atomic Orbits of Oxygen. O represents the position of the oxygen nucious. Directions i and j are taken along the two O–H bonds. X is in the direction of the lone pair bonds.

Table I. The values of α, β, α' and β'.

Bond Angle	ω	α	β	α'	β'
180°	0°	0.7071	0.7071	1.0000	0.0000
170°	5°	0.7044	0.7098	0.9924	0.1233
163°58′	8°01′	0.7000	0.7141	0.9802	0.1980
160°	10°	0.6961	0.7180	0.9694	0.2455
150°	15°	0.6812	0.7321	0.9305	0.3660
140°	20°	0.6586	0.7525	0.8752	0.4837
137°02′	21°29′	0.6500	0.7599	0.8553	0.5181
130°	25°	0.6255	0.7802	0.8017	0.5976
125°12′	27°54′	0.6000	0.8000	0.7500	0.6614
120°	30°	0.5773	0.8165	0.7071	0.7071
110°	35°	0.5049	0.8632	0.5849	0.8112
109°32′	35°14′	0.5000	0.8660	0.5774	0.8165
103°34′	38°13′	0.4359	0.9000	0.4843	0.8748
100°56′	39°32′	0.4000	0.9165	0.4364	0.8992
100°	40°	0.3846	0.9231	0.4166	0.9091
95°40′	42°10′	0.3000	0.9539	0.3145	0.9493
92°28′	43°46′	0.2000	0.9798	0.2041	0.9789
90°38′	44°41′	0.1000	0.9950	0.1005	0.9949
90°	45°	0.0000	1.0000	0.0000	1.0000

denote the atomic orbits of oxygen $2s$ and $2p_\sigma$ whose maximum densities are in the i direction, while p_{π_i} denotes $2p_\pi$ atomic orbit whose maximum density is in the direction in the molecular plane and perpendicular to i. Expressing the i, j and the lone pair orbital functions by ψ_i, ψ_j and ψ_n,

$$\psi_i=h_\beta=\alpha s+\beta p_{\sigma_i}\,, \qquad (4)$$

$$\psi_j=\alpha' h_{0\beta}+\beta' p_{\pi_i}\,, \qquad (5)$$

$$\psi_n=\beta' h_{0\beta}-\alpha' p_{\pi_i}\,, \qquad (6)$$

where

$$h_{0\alpha}=\beta s-\alpha p_{\sigma_i}\,, \qquad (7)$$

$$\alpha=(1/\sqrt{2})\sqrt{\cos 2\omega}/\cos\omega\,,$$

$$\beta=(1/\sqrt{2})1/\cos\omega\,, \qquad (8)$$

$$\alpha'=\alpha/\beta, \quad \beta'=\sqrt{\beta^2-\alpha^2}/\beta\,, \qquad (9$$

These expressions are easily obtained from the consideration of orthogonality and symmetrical property. The values of α, β, α' and β' are tabulated in Table I.

§ 3. Dissociation Energies of H_2O*

In the first place, the H-O-H molecule is calculated using Slater's type atomic orbitals. ψ's in equations (4), (5), (6), and k, the 1s atomic orbital of oxygen, are used as atomic orbitals of oxygen. h's are used to denote two hydrogen orbits in H_2O molecule. Considering the forces between hydrogen and oxygen, Eq. (1) will transformed into

$$D=2X_{\beta h}-2Y_{kh}-(1-\beta'^2)Y_{0h}-\tfrac{1}{2}Y_{hh}$$
$$+(3+\alpha'^2)K_{h\pi}+P_0+2\alpha^2\Delta P+R.E. \qquad (10)$$

each term of which will be described in the following paragraphs:

Referring to Eq. (2), $X_{\beta h}$ denotes the force between h_β (Eq. (4)) and h. $\bar{I}_{\beta h}$ is equal to $\frac{1}{2}$(21,22+13,60) e.V.=17,41 e.V.[1] See appendix on $S_{\beta h}$.

Referring to Eq. (3), Y_{kh}, Y_{0h}, Y_{hh} denote the repulsions between k and h, $h_{0\beta}$ and h, and h and h, respectively. $\bar{I}_{kh}=\frac{1}{2}$(542+13,60)=277,8 e.V., $\bar{I}_{0h}$=17,41 e.V. and I_{hh}=13,60 e.v. The values of S_{kh} and S_{hh} are interpolated from the tables of reference (2). See appendix on S_{0h}.

$K_{\pi h}$ denotes the force between p_π and h. The values of this have been calculated theoretically by M. Kotani and A. Amemiya.[3] However, approximations due to R. S. Mulliken[1] were used in the present paper. In these approximations, it is assumed that $K_{\pi h}$ is proportional to S_{sh}^2. To determine this proportional constant, R. S. Mulliken used

Table II. Some values of $K_{\pi h}$.

R/a_H	From C=0	From C–H	From K.A[3]
1.0	1.21	1.83	
1.2	1.02	1.54	
1.4	0.84	1.28	1.35
1.6	0.68	1.03	
1.8	0.54	0.81	
2.0	0.41	0.63	0.58
2.2	0.32	0.48	
2.4	0.24	0.36	
2.6	0.18	0.28	
2.8	0.13	0.20	
3.0	0.10	0.15	

---

* It is assumed that the bonds are non-bending bonds in this and the next calculations.

Table III. The values of dissociation energies for H_2O.

a. ($\nu=0.55$, $A_\sigma=1.07$)

R/a_H \ ω	0°	10°	20°	30°	35°	40°	45°
1.0	3.02	3.18	3.76	4.71			
1.2	3.83	4.05	4.85	6.18			
1.4	3.97	4.25	5.21	6.92	8.06	8.91	4.92
1.6	3.48	3.83	4.87	6.96	8.65	9.62	6.20
1.8	2.57	2.95	4.17	6.48	8.05	9.70	8.02
2.0					7.38	9.46	8.68
2.2					6.63	8.90	8.94
2.4					5.70	8.16	8.95
2.6							
2.8							
3.0							

b. ($\nu=0.7$, $A_\sigma=1.16$)

R/a_H \ ω	0°	10°	20°	30°	35°	40°	45°
1.0	1.49	1.58	1.92	2.28	2.08	0.91	−8.00
1.2	3.17	3.34	3.95	4.80	5.22	4.66	−2.85
1.4	3.94	4.17	4.98	6.31	6.98	7.22	+1.05
1.6	3.85	4.16	5.20	6.89	7.92	8.67	4.03
1.8	3.19	3.53	4.67	6.76	8.09	9.28	6.07
2.0	2.15	2.53	3.88	6.15	7.65	9.38	7.35
2.2	0.97	1.41	2.76	5.30	7.07	9.05	8.05
2.4	−0.35	0.11	1.57	4.26	6.22	8.45	8.41
2.6	−1.57	−1.12	0.38	3.23	5.32	7.76	8.49
2.8	−2.81	−2.36	−0.81	2.16	4.34	7.04	8.51
3.0	−4.00	−3.51	−1.94	1.06	3.32	6.21	8.13

c. ($\nu=0.85$, $A_\sigma=1.25$)

R/a_H \ ω	0°	10°	20°	30°	35°	40°	45°
1.0							
1.2	2.27	2.37	2.77	3.09			
1.4	3.75	3.93	4.57	5.48	5.73	5.20	
1.6	4.13	4.39	5.31	6.68	7.37	7.48	
1.8	3.73	4.04	5.08	6.93	7.99	8.67	
2.0	2.83	3.18	4.47	6.55	7.82	9.17	5.76
2.2	1.71	2.14	3.44	5.84	7.45	9.10	6.97
2.4					6.69	8.67	7.73
2.6							8.09
2.8							8.36
3.0							8.08

Mulligan's value of $K_{\pi s}$ for C=0 (0,37 e.V.), but the present paper adopts $K_{\pi s}$ for C-H (0,80 e.V.)[1], because the values determined from the latter is closer to the values interpolated from M. Koiami and A. Amemiya's Table[3] than those from the former as shown in Table II.

P_0, ΔP: Promotional energy P is equal to $P_0+2\alpha^2\Delta P$, where P_0 expresses the promotional energy from the ground state to ($s^2\sigma^2\cdot\pi\pi'^2$), and ΔP expresses the energy from ($s^2\sigma\pi\pi'^2$) to ($s\sigma^2\pi\pi'^2$) whose values are P_0=0,67 e.V., ΔP=16,49 e.V.[1]

R.E.: Resonance energy of H_2O will be mainly the ionic resonance energy. Pauling's electro-negativity scale[5] was used as values of resonance energy. *R.E.*=1,4²×2=3,92 e.V. It may certainly be said that resonance

Table IV. Components of D of H_2O at $\nu=0.7$, $A_\sigma=1.16$ and $\omega=40°$ with R/a_H as variable.

R/a_H	$2X_{\beta h}$	$(1+\beta'^2)Y_{0h}$	$2Y_{kh}$	$\frac{1}{2}Y_{hh}$	$(3+\alpha'^2)K_{\sigma h}$	P	RE	D
1.0	15.64	8.43	7.64	2.84	5.81	5.55	3.92	0.91
1.2	15.52	6.63	5.30	2.19	4.89	5.55	3.92	4.66
1.4	15.14	5.13	3.58	1.64	4.06	5.55	3.92	7.22
1.6	14.54	3.91	2.38	1.22	3.27	5.55	3.92	8.67
1.8	13.78	2.98	1.58	0.88	2.57	5.55	3.92	9.28
2.0	12.94	2.20	1.10	0.63	2.00	5.55	3.92	9.38
2.2	12.00	1.64	0.76	0.44	1.52	5.55	3.92	9.05
2.4	10.99	1.19	0.56	0.30	1.14	5.55	3.92	8.45
2.6	10.00	0.89	0.40	0.21	0.89	5.55	3.92	7.76
2.8	9.04	0.62	0.24	0.14	0.63	5.55	3.92	7.04
3.0	8.10	0.45	0.20	0.09	0.48	5.55	3.92	6.21

Table V. Components of D of H_2O at $\nu=0.7$. $A_\sigma=1.16$ with ω as variable. Here, maximum values of D with respect to R/a_H for each steps of ω in Table 3 b are chosen.

ω	$2X_{\beta h}$	$(1+\beta'^2)Y_{0h}$	$2Y_{kh}$	$\frac{1}{2}Y_{hh}$	$(3+\alpha'^2)K_{\pi h}$	P	RE	D
0°	16.96	0.48	3.58	0.84	5.12	17.16	3.92	3.94
10°	16.90	0.58	3.58	0.88	5.04	16.65	3.92	4.17
20°	16.04	0.62	2.38	0.87	3.88	14.97	3.92	5.20
30°	15.68	1.41	2.38	0.87	3.61	11.66	3.92	6.89
35°	14.50	1.67	1.58	0.71	2.71	9.08	3.92	8.09
40°	12.94	2.20	1.10	0.63	2.00	5.55	3.92	9.38
45°	6.90	1.81	0.24	0.19	0.60	0.67	3.92	8.51

energy will be a function of the bond angle. Subsequenly, the author calculated the resonance energy by using Mulliken's absolute electro-negativity,[4)] but the results did not comply with our expectation.

The dissociation energy was calculated under each of the following conditions, namely, $\omega=0°$, $10°$, $20°$, $30°$, $35°$, $40°$, $45°$ and $R/a_H=1.0$, 1.2, $1.4, \cdots\cdots$, 3.0 where a_H is the Bohr radius. Here, calculations were carried out for three pairs of ν and A_σ, $\nu=0{,}55$ and $A_\sigma=1{,}07$, $\nu=0{,}7$ and $A_\sigma=1{,}16$ and $\nu=0{,}85$ and $A_\sigma=1{,}25$. These values are tabulated in Table III. The maximum values of D are 9,70 e.V. at $\nu=0{,}55$ and $A_\sigma=1{,}07$, 9,38 e.V. at $\nu=0{,}7$ and $A_\sigma=1{,}16$, and 9,17 e.V. at $\nu=0{,}85$ and $A_\sigma=1{,}25$. Since the true maximum values could be expected somewhat larger than these values owing to the discrete values of ω and R/a_H chosen for the calculation, the most probable constants lie somewhere around $\nu=0{,}7$ and $A_\sigma=1{,}16$ in view of the experimental value 9,54 e.V. as D. This result agree with that of Mulliken. This condition corresponds to $\omega=40°$ or bond angle of 100°, and $R/a_H=2{,}0$. These are very close to the experimental values 104,5° and 1,81 under the approximation used. Tables IV and V show the values of the components of D. Table IV is composed by varing R/a_H for $\nu=0{,}7$, $A_\sigma=1.16$, and $\omega=40°$. Values of terms in Eq. (10) which give maximum D's for given values of ω are tabulated in Table V, whereby the two constants ν and A_σ are chosen equal to those of Table IV. These values are in accord with the expected ones.

§ 4. Dissociation Energies of F_2O

Dissociation energies of F_2O are calculated using Slater type atomic orbitals, wherein the configuration of electrons of F is assumed to be $1s)^2\ 2s)^2\ p_\sigma)^1\ p_\pi)^2\ p_{\pi'})^2$ or $k_F)^2\ s_F)^2\ \sigma_F)^1\ \pi_F)^2\ \pi'_F)^2$. These energies are formulated by the 30 terms which are tabulated in the Table VI. The subscripts of terms appearing in Table VI are the same as those in Eq. (10) for oxygen, and those of fluorine denote the same state as mentioned above.

The mean ionization energies of each term are as follows:

Table VI. The terms and their coefficients for D of F_2O.

Term	Coefficient	Term	Coefficient	Term	Coefficient
$X_{\beta o_F}$	$+2$	$Y_{k_F k_F}$	-2	$K_{\pi s_F}$	$+2(3+\alpha'^2)$
$Y_{\beta s_F}$	-2	$Y_{k_F s_F}$	-4	$K_{\pi\pi'_F}$	$+2(3+\alpha'^2)$
$Y_{\beta k_F}$	-2	$Y_{k_F \sigma_F}$	$-2(1+\sin^2\omega)$	$K_{\pi\sigma_F}$	$+\ (3+\alpha'^2)$
$Y_{0\sigma_F}$	$-(1+\beta'^2)$	$Y_{s_F s_F}$	-2	$K_{\beta\pi_F}$	$+4$
$Y_{0 s_F}$	$-2(1+\beta'^2)$	$Y_{s_F \sigma_F}$	$-2(1+\sin^2\omega)$	$K_{k_F \pi_F}$	$+2(1+\cos^2\omega)+4$
Y_{0k_F}	$-2(1+\beta'^2)$	$Y_{\sigma_F \sigma_F}$	$-\frac{1}{2}(1+\sin^2\omega)^2$	$K_{s_F \pi_F}$	$+2(1+\cos^2\omega)+4$
$Y_{k\sigma_F}$	-2	$Y_{\pi_F \pi_F}$	$-\{\frac{1}{2}(1+\cos^2\omega)^2+2\}$	$K_{\sigma_F \pi_F}$	$+(1+\sin^2\omega)(3+\cos^2\omega)$
Y_{ks_F}	-4	$K_{k\pi_F}$	$+8$	$K_{\pi_F \pi'_F}$	$+2(1+\cos^2\omega)$
Y_{kk_F}	-4	$K_{0\pi_F}$	$+4(1+\beta'^2)$	P	$+1$
$Y_{\pi\pi_F}$	$-2(3+\alpha'^2)$	$K_{\pi k_F}$	$+2(3+\alpha'^2)$	$R.E.$	$+1$

$X_{\beta\sigma_F}$. $Y_{\beta s_F}$, $Y_{0\sigma_F}$, Y_{0s_F}, $Y_{\pi\pi_F}$; $\bar{I}=23.05$ e.V.

$Y_{\beta k_F}$, Y_{0k_F}; $\bar{I}=358.6$ e.V.

$Y_{k\sigma_F}$, Y_{ks_F}; $\bar{I}=283.4$ e.V.

Y_{kk_F} ; $\bar{I}=619$ e.V.

$Y_{k_F k_F}$; $\bar{I}=696$ e.V.

$Y_{k_F s_F}$; $\bar{I}=360$ e.V.

$Y_{s_F s_F}$, $Y_{s_F \sigma_F}$, $Y_{\sigma_F \sigma_F}$, $Y_{\pi_F \pi_F}$: $\bar{I}=24.88$ e.V.

The proportional constants of K's are derived from $K_{\pi h}$ of C-H for $K_{k\pi_F}$, $K_{\pi k_F}$, $K_{k_F \pi_F}$; and from Mulligan's $K_{\pi s}$ of C=O for others. The values of R.E. are equal to $0.5^2 \times 2 = 0.50$ e.V. by Pauling's electro-negativity scales[5].

The results are tabulated in Table VII in which the empirical constants ν, A_σ and A_π are put epual to 0.7, 1.16 and 1.53 which were expected to be the most probable values in § **3**. The maximum dissociation energy (5.62), its bond angle ($\omega=43°$), and R/a_H (=2.8) are close to the experimental values $D=5.08$, which is derived by doubling the value of Pauling's F-O bond energy, and $\omega=40°$ and $R/a_H=2.66$. And at last, the components of D are tabulated in Table VIII, whose values correspond to the case of $\omega=43°46'$.

§ 5. Conclusion

Although it may not be complete to derive a comclusion with not more than two examples, H_2O and F_2O, the dissociation energy of a polar molecule of the type A-O-A may be computed at least to a fair approximation by applying M.M.F. with the aid of Pauling's electro-negativity scale. This is justified by the fact that the values of components of each D's obtained by the above mentioned process agree well with the expected tendency, which implies various interesting aspects.

Acknowledgement

I wish to express my indebtedness to Professor R. S. Mulliken for many useful suggestions, and also to Professor S. Mito for his helpful discussion. I would like to express my thanks to Miss M. Mito, Miss E. Mito and Mrs. Aoki who helped in numerical calculations.

Table VII. The dissociation energies of F_2O.

α	0.5	0.4	0.2	0.0
ω	35°14′	39°32′	43°46′	45°
R/a_H \ Bond Angle	109°32′	100°56′	93°28′	90°
2.0	−6.71	−5.36	−5.64	−9.36
2.2	−1.88	+0.15	+0.99	+1.59
2.4	+0.18	2.42	4.32	2.80
2.6	0.41	3.12	5.47	4.73
2.8	0.07	2.68	5.62	5.30
3.0	−0.87	1.82	5.04	5.17
3.2	−3.67	−0.70	4.23	4.59

Table VIII. The components of D for F_2O.

R/a_H	2.0	2.2	2.4	2.6	2.8	3.0	3.2
$2X_{\beta\sigma_F}$	14.54	13.58	12.30	10.74	9.30	7.76	6.36
$2Y_{\beta s_F}$	6.96	4.88	3.28	2.10	1.32	0.80	0.48
$2Y_{\beta k_F}$	1.90	0.94	0.46	0.24	0.12	0.06	0.02
$(1+\beta'^2)Y_{0\sigma_F}$	2.27	1.57	1.04	0.65	0.41	0.25	0.14
$2(1+\beta'^2)Y_{0s_F}$	4.23	2.66	1.61	0.98	0.55	0.31	0.20
$2(1+\beta'^2)Y_{0k_F}$	0.47	0.23	0.12	0.04	0.04	0.00	0.00
$2Y_{k\sigma_F}$	0.98	0.44	0.20	0.10	0.04	0.02	0.00
$4Y_{ks_F}$	0.68	0.32	0.16	0.04	0.04	0.00	0.00
$4Y_{kk_F}$	0.00	0.00	0.00	0.00	0.00	0.00	0.00
$2(3+\alpha'^2)Y_{\pi\pi_F}$	4.62	2.68	1.46	0.79	0.43	0.24	0.12
$2Y_{k_F k_F}$	0.00	0.00	0.00	0.00	0.00	0.00	0.00
$4Y_{k_F s_F}$	0.00	0.00	0.00	0.00	0.00	0.00	0.00
$2(1+\sin^2\omega)Y_{k_F\sigma_F}$	0.03	0.00	0.00	0.00	0.00	0.00	0.00
$2Y_{s_F s_F}$	0.28	0.12	0.04	0.02	0.00	0.00	0.00
$2(1+\sin^2\omega)Y_{s_F\sigma_F}$	0.71	0.33	0.12	0.06	0.03	0.00	0.00
$\frac{1}{2}(1+\sin^2\omega)^2 Y_{\sigma_F\sigma_F}$	0.40	0.20	0.09	0.03	0.01	0.00	0.00
$\{\frac{1}{2}(1+\cos^2\omega)^2+2\} Y_{\pi_F\pi_F}$	0.03	0.00	0.00	0.00	0.00	0.00	0.00
$8K_{k\pi_F}$	0.00	0.00	0.00	0.00	0.00	0.00	0.00
$4(1+\beta'^2)K_{0\pi_F}$	0.94	0.55	0.31	0.23	0.16	0.08	0.08
$2(3+\alpha'^2)K_{\pi k_F}$	0.00	0.00	0.00	0.00	0.00	0.00	0.00
$2(3+\alpha'^2)K_{\pi s_F}$	1.28	0.85	0.55	0.30	0.18	0.12	0.06
$2(3+\alpha'^2)K_{\pi\pi'_F}$	0.37	0.24	0.12	0.06	0.06	0.00	0.00
$(3+\alpha'^2)K_{\pi\sigma_F}$	0.61	0.46	0.30	0.24	0.12	0.09	0.06
$4K_{\beta\pi_F}$	1.52	1.08	0.72	0.44	0.28	0.16	0.12
$\{2(1+\cos^2\omega)+4\} K_{k_F\pi_F}$	0.00	0.00	0.00	0.00	0.00	0.00	0.00
$\{2(1+\cos^2\omega)+4\} K_{s_F\pi_F}$	0.07	0.07	0.00	0.00	0.00	0.00	0.00
$(1+\sin^2\omega)(3+\cos^2\omega)K_{\sigma_F\pi_F}$	0.10	0.05	0.00	0.00	0.00	0.00	0.00
$2(1+\cos^2\omega)K_{\pi_F\pi'_F}$	0.00	0.00	0.00	0.00	0.00	0.00	0.00
P	1.99	1.99	1.99	1.99	1.99	1.99	1.99
$R.E.$	0.50	0.50	0.50	0.50	0.50	0.50	0.50
$D.$	−5.64	0.99	4.32	5.47	5.62	5.04	4.23

Appendix. Overlap Integrals

The method of calculations of overlap integrals used in this paper is the same as the one published in the previous paper[6] and R. S. Mulliken's paper[7] The values of overlap integrals between $2s\,2p$ hybrid atomic orbital and others are tabulated. For overlap integral between orbits a and b, which is denoted by $S(ab)$ are as follow.

$$t=(\mu_a-\mu_b)/(\mu_a+\mu_b)\ ,$$

$$\rho=\tfrac{1}{2}(\mu_a+\mu_b)R/a_H\ ,$$

where

$$\mu_a=Z_{an}/n\ .^{2)}$$

For $S_{h\beta}$ and S_{h0}, $t=-0.39$.

For $S_{k_F\beta}$ and S_{k_F0}, $t=0.59$.

For $S_{\sigma_F\beta}$, S_{σ_F0}, $S_{s_F\beta}$ and S_{s_F0}, $t=0.07$.

Table IX. $S(1s, \beta)$ $t=-0.39$.

ω	0°	5°	10°	15°	20°	25°	30°	35°	40°	45°
α	0.7071	0.7044	0.6961	0.6812	0.6586	0.6255	0.5773	0.5049	0.3846	0.0000
ρ \ β	0.7071	0.7098	0.7180	0.7321	0.7525	0.7802	0.8165	0.8632	0.9231	1.0000
0.0	0.665	0.662	0.654	0.640	0.619	0.588	0.543	0.475	0.362	0.000
0.5	765	763	757	745	728	701	663	603	502	159
1.0	816	814	809	800	786	765	733	683	595	282
1.5	814	813	809	803	792	775	750	708	635	356
2.0	767	766	763	758	750	737	718	685	624	383
2.2	738	737	734	730	723	712	694	664	608	383
2.4	706	706	704	699	693	684	667	640	588	379
2.6	672	672	670	667	661	652	638	613	565	371
2.8	637	636	635	632	626	618	605	583	539	359
3.0	600	599	598	596	591	584	572	552	511	345
3.2	562	562	560	558	554	548	537	519	483	329
3.4	524	523	523	520	518	511	503	486	453	312
3.6	488	488	487	485	482	477	469	454	423	294
4.0	417	417	417	415	412	409	402	390	365	257
4.5	338	337	337	336	334	331	326	317	299	213
5.0	269	270	269	269	267	265	261	254	240	173
6.0	166	166	166	166	165	164	162	158	149	109
7.0	099	099	099	098	099	097	097	094	089	066
8.0	058	058	058	058	057	057	057	056	053	039

Table X. $S(1s, O)$ $t=-0.39$.

ω	0°	5°	10°	15°	20°	25°	30°	35°	40°	45°
β	0.7071	0.7098	0.7180	0.7321	0.7525	0.7802	0.8165	0.8632	0.9231	1.0000
ρ −α	−0.7071	−0.7044	−0.6961	−0.6812	−0.6586	−0.6255	−0.5773	−0.5049	−0.3846	0.0000
0.0	0.665	0.667	0.675	0.688	0.707	0.733	0.768	0.811	0.868	0.940
0.5	541	543	552	568	590	621	662	717	791	923
1.0	418	420	430	446	470	504	549	611	697	872
1.5	310	313	323	339	364	397	443	506	597	795
2.0	225	228	236	252	276	307	351	412	500	701
2.2	196	198	207	222	245	275	318	377	462	660
2.4	170	173	181	196	217	247	287	344	426	620
2.6	148	151	158	172	192	221	260	314	392	580
2.8	129	131	138	151	171	197	235	286	361	541
3.0	112	114	121	133	152	176	212	260	331	503
3.2	096	098	105	116	133	157	190	235	302	465
3.4	082	085	091	101	118	140	170	212	276	429
3.6	072	074	079	090	104	125	153	194	253	396
4.0	053	055	060	069	082	099	124	157	208	333
4.5	036	037	042	048	059	073	093	120	162	264
5.0	025	026	029	034	043	054	070	093	125	208
6.0	012	012	014	018	023	030	040	054	074	126
7.0	005	007	007	009	013	017	022	031	043	074
8.0	002	004	004	004	006	010	012	017	025	043

Table XI. $S(1s, \beta)$ $t=0.59$.

α	0.5	0.43589	0.4	0.3	0.2	0.1	0.0
ρ \ β	0.86603	0.9	0.91652	0.95394	0.97980	0.99499	1.0
10	0.082	0.084	0.082	0.081	0.078	0.075	0.071
12	0.044	0.044	0.044	0.043	0.041	0.040	0.038
15	0.016	0.016	0.016	0.015	0.016	0.015	0.014
20	0.004	0.004	0.004	0.004	0.003	0.003	0.003

Table XII. $S(1s, O)$ $t=0.59$.

β	0.86603	0.9	0.91652	0.95394	0.97980	0.99499	1.0
ρ $-\alpha$	−0.5	−0.43589	−0.4	−0.3	−0.2	−0.1	0.0
10	0.000	0.007	0.010	0.019	0.027	0.035	0.042
12	0.001	0.003	0.005	0.010	0.014	0.018	0.022
15	0.000	0.001	0.001	0.004	0.005	0.007	0.008
20	0.000	0.001	0.001	0.001	0.001	0.002	0.002

Table XIII. $S(2s, \beta)$ $t=0.07$.

α	0.5	0.43589	0.4	0.3	0.2	0.1	0.0
ρ β	0.86603	0.9	0.91652	0.95394	0.97980	0.99499	1.0
4.6	0.534	0.524	0.519	0.498	0.473	0.443	0.409
5.0	0.464	0.456	0.451	0.434	0.413	0.388	0.359
5.5	0.380	0.374	0.370	0.357	0.341	0.322	0.299
6.0	0.305	0.301	0.299	0.289	0.276	0.261	0.243
6.5	0.242	0.239	0.237	0.229	0.219	0.208	0.194
7.0	0.188	0.182	0.184	0.179	0.171	0.162	0.152
7.5	0.145	0.143	0.142	0.139	0.133	0.126	0.118
8.0	0.110	0.108	0.107	0.105	0.101	0.096	0.090

Table XIV. $S(2s, O)$ $t=0.07$.

β	0.86603	0.9	0.91652	0.95394	0.97980	0.99499	1.0
ρ $-\alpha$	−0.5	−0.43589	−0.4	−0.3	−0.2	−0.1	0.0
4.6	0.106	0.145	0.165	0.219	0.270	0.316	0.359
5.0	0.084	0.119	0.136	0.183	0.227	0.267	0.305
5.5	0.059	0.087	0.101	0.140	0.176	0.210	0.241
6.0	0.042	0.064	0.076	0.107	0.136	0.164	0.189
6.5	0.030	0.047	0.057	0.082	0.105	0.127	0.147
7.0	0.021	0.035	0.042	0.061	0.079	0.096	0.112
7.5	0.015	0.026	0.031	0.046	0.059	0.073	0.085
8.0	0.010	0.018	0.022	0.033	0.044	0.054	0.063

Table XV. $S(2p_\sigma, \beta)$ $t=0.07$.

α	0.5	0.43589	0.4	0.3	0.2	0.1	0.0
ρ \ β	0.86603	0.9	0.91652	0.95394	0.97980	0.99499	1.0
3.6	0.451	0.432	0.420	0.388	0.352	0.313	0.271
4.0	0.471	0.456	0.446	0.418	0.386	0.349	0.311
4.4	0.464	0.453	0.444	0.420	0.391	0.360	0.325
4.6	0.455	0.444	0.437	0.414	0.387	0.358	0.325
5.0	0.425	0.416	0.410	0.391	0.368	0.342	0.313
5.5	0.375	0.368	0.363	0.348	0.329	0.309	0.284
6.0	0.320	0.315	0.311	0.300	0.285	0.268	0.248
6.5	0.265	0.261	0.259	0.249	0.239	0.225	0.209
7.0	0.215	0.212	0.210	0.203	0.195	0.183	0.171
7.5	0.171	0.168	0.167	0.162	0.155	0.146	0.137
8.0	0.134	0.131	0.131	0.127	0.122	0.115	0.108
8.5	0.103	0.102	0.101	0.098	0.094	0.090	0.084
9.0	0.078	0.078	0.077	0.078	0.072	0.069	0.064

Table XVI. $S(2p_\sigma, O)$ $t=0.07$.

β	0.86603	0.9	0.91652	0.95394	0.97980	0.99499	1.0
ρ \ $-\alpha$	−0.5	−0.43589	−0.4	−0.3	−0.2	−0.1	0.0
3.6	0.237	0.270	0.287	0.330	0.368	0.402	0.431
4.0	0.193	0.227	0.245	0.291	0.333	0.370	0.403
4.4	0.154	0.187	0.205	0.251	0.294	0.331	0.366
4.6	0.138	0.170	0.188	0.234	0.275	0.312	0.347
5.0	0.109	0.140	0.156	0.199	0.238	0.274	0.307
5.5	0.081	0.107	0.122	0.160	0.195	0.228	0.257
6.0	0.058	0.081	0.093	0.126	0.156	0.184	0.210
6.5	0.040	0.060	0.070	0.097	0.123	0.146	0.168
7.0	0.029	0.045	0.054	0.076	0.096	0.115	0.133
7.5	0.020	0.033	0.039	0.057	0.074	0.088	0.103
8.0	0.014	0.024	0.029	0.043	0.055	0.068	0.079
8.5	0.010	0.017	0.021	0.032	0.042	0.052	0.060
9.0	0.007	0.013	0.019	0.024	0.031	0.039	0.045

References

1) R. S. Mulliken: J. Phys. Chem. **56** (1952) 295.
2) R. S. Mulliken, C. A. Rike, D. Orloff and H. Orloff: J. Chem. Phys. **17** (1949) 1248.
3) M. Kotani and A. Amemiya: Proc. Phys. Math. Soc. Japan **22** (1940) Extra.
4) R. S. Mulliken: J. Chem. Phys. **2** (1934) 782.
5) L. Pauling: "The nature of the chemical bond". Cornell University Press. Ithaca, N.Y., 1940.
6) Y. Aoki: J. Phys. Soc. Japan **7** (1952) 451.
7) R. S. Mulliken: J. Chem. Phys. **19** (1951) 900.

JOURNAL OF THE PHYSICAL SOCIETY OF JAPAN Vol. 10, No. 7, JULY, 1955

On the Theory of Quantum Liquids.
I. Surface Tension and Stress

By Morikazu TODA

Department of Physics, Faculty of Science, Tokyo University of Education

(Received April 15, 1955)

Pressure and stress of monatomic liquid is calculated by a modification of perturbation method in which the boundary of the system is subject to change. If we use the phase space distribution function of Wigner the expression becomes identical to classical stress tensor. The same method applies to the calculation of surface tension. The result is

$$\gamma=\frac{1}{A}\left[\frac{2\,\mathrm{Tr}\left\{-\frac{\hbar^2}{2m}\sum_{j=1}^{N}\left(\frac{\partial^2}{\partial z_j{}^2}-\frac{\partial^2}{\partial x_j{}^2}\right)\right\}\rho(\boldsymbol{x},\boldsymbol{x}')}{\mathrm{Tr}\,\rho(\boldsymbol{x},\boldsymbol{x}')}+\iint\frac{x_{12}{}^2-z_{12}{}^2}{2r_{12}}\frac{d\phi(r_{12})}{dr_{12}}n(z_1)n(z_2)g(\boldsymbol{x}_1,\boldsymbol{r}_{12})\mathrm{d}\boldsymbol{x}_1\,\mathrm{d}\boldsymbol{x}_2\right]$$

in which $\rho(\boldsymbol{x},\boldsymbol{x}')$ is the density matrix for the states with a definite liquid film with area A perpendicular to the z-axis. The first term represents quantum effect. And the second term is identical in form to the expression obtained by Harasima for classical liquids. It is shown that the relation

$$\gamma=\int(P-P_T)dz$$

holds also for quantum liquid. Here P and P_T are respectively the pressure in the liquid and the pressure component tangential to the surface $z=$const. Surface effect on ideal gases and comparison with experiments are also discussed.

§ 1. Introduction

Since the days of Laplace or more recently of van der Waals surface tension of liquids has been one of the main subjects of the theory of liquids. Born and Courant[1] applied Debye's model of specific heat including surface vibration and obtained a quantum mechanical expression for surface tension which could explain its temperature coefficient. Brillouin[2] considered the temperature variation of surface tension as caused by the pressure exerted by the surface waves, and taking the dispersion of wave velocity, the relation between energy-density and pressure and the equipartition law into consideration he could explain the temperature variation of surface tension of classical liquids. Their ingeneous treatments successfully aimed the explanation of experimental laws such as Eötvös and Ramsey-Shields', but could hardly be considered rigorous.

Passing through the thermodynamical treatment of Gibbs, approach from orthodox ways of statistical mechanics has been done by Fowler[3], Kirkwood[4] and most recently by Harasima[5]. Compact expression obtained by Harasima for classical liquids is of the form

$$\gamma=\frac{1}{A}\iint\frac{x_{12}{}^2-z_{12}{}^2}{2r_{12}}\frac{d\phi(r_{12})}{dr_{12}}n(z_1)n(z_2)\times g(\boldsymbol{x}_1,\boldsymbol{r}_{12})d\boldsymbol{x}_1d\boldsymbol{x}_2\,, \tag{1}$$

where γ is the surface tension, ϕ the intermolecular potential, g the correlation function between two molecules; $n(z_1)$, $n(z_2)$ are the number-density at $\boldsymbol{x}_1$, $\boldsymbol{x}_2$, and the vapor-liquid boundary is selected perpendicular to the z-axis, and A is its area.

We are now going over to derive the quantum mechanical expression of surface tension, which will be of some value for the theory of liquid helium and for certain other problems. Since the line of thoughout is quite analogors to that the author[6] took up to formulate the quantum mechanical expression of the virial theorem, we shall review briefly the latter treatment, and then we shall calculate surface tension in § 3. Comparison with experiments will be found in §§ 4 and 5.

where the effect of boundary surface on ideal gases is also considered.

§2. Stress Tensor

Consider a system of N particles contained in a box. For simplicity we shall assume a cubic box of dimension l. The Schroedinger equation for an eigen-value E is

$$\left\{-\frac{\hbar^2}{2m}\sum_{i=1}^{N}\nabla_i^2+\sum_{i>j=1}^{N}\phi(r_{ij})\right\}\psi=E\psi(x,\,y,\,z)$$
$$(0\leq x,\,y,\,z\leq l)\,. \tag{2}$$

We impose on ψ the boundary condition $\psi=0$ at the wall. Rewriting the variables as

$$x\to x/(1+\delta\lambda),\quad z\to z/(1+\delta\lambda),\quad z\to z/(1+\delta\lambda)\,, \tag{3}$$

and neglecting the higher powers of $\delta\lambda$ we get the wave equation

$$\left\{-\frac{\hbar^2}{2m}\sum\nabla_i^2+\sum\phi(r_{ij})\right\}\varphi$$
$$+\delta\lambda\left\{-\frac{\hbar^2}{m}\sum\nabla^2-\sum r_{ij}\frac{d\phi}{dr_{ij}}\right\}\varphi=E\varphi(x,\,y,\,z)\,. \tag{4}$$

with

$$\varphi(x,\,y,\,z)=\psi\left(\frac{x}{1+\delta\lambda},\,\frac{y}{1+\delta\lambda},\,\frac{z}{1+\delta\lambda}\right)$$
$$(0\leq x,\,y,\,z\leq l(1+\delta\lambda))\,.$$

The boundary condition is $\varphi=0$ at the wall of the enlarged box of dimension $l(1+\delta\lambda)$. Treating negative of the second term on the left hand side of the above equation as an excess hamiltonian we can apply perturbation method. We get thus the energy shift caused by the enlargement of the volume, which can be written with normalized ψ as

$$\frac{\partial E}{\partial V}=-\frac{1}{3V}\int\psi^*(\boldsymbol{x})\left\{-\frac{\hbar^2}{m}\sum\nabla_i^2-\sum r_{ij}\frac{d\phi}{dr_{ij}}\right\}$$
$$\times\psi(\boldsymbol{x})d\boldsymbol{x}\,. \tag{5}$$

If we take the average of $-\partial E/\partial V$ we achieve the virial theorem

$$P=-\frac{\sum\frac{\partial E}{\partial V}e^{-E/kT}}{\sum e^{-E/kT}}$$
$$=\frac{2}{3V}\frac{\mathrm{Tr}\left\{-\frac{\hbar^2}{2m}\sum\nabla_i^2-\frac{1}{2}\sum r_{ij}\frac{d\phi}{dr_{ij}}\right\}\rho(\boldsymbol{x},\,\boldsymbol{x}')}{\mathrm{Tr}\,\rho(\boldsymbol{x},\,\boldsymbol{x}')}\,, \tag{6}$$

where $\rho(\boldsymbol{x},\,\boldsymbol{x}')$ is the density matrix of the system.

It must be noticed that the above treatment is irrespective of the symmetric character of the system, i.e. it holds for Einstein as well as Fermi system, and that it avoids some of the unnecessary complexity in the discussion of the virial theorem.

We can obtain the pressure tensor in a similar way, but instead of uniform deformation we have to perform elongation and shearing deformation in this case. The result is

$$\boldsymbol{P}=-\frac{1}{V}\mathrm{Tr}\left\{\frac{\hbar^2}{m}\sum_j\frac{\partial^2}{\partial\boldsymbol{x}_k\partial\boldsymbol{x}_j}+\sum_{i>j}\frac{\boldsymbol{r}_{ij}\boldsymbol{r}_{ij}}{r_{ij}}\frac{\partial\phi}{\partial r_{ij}}\right\}$$
$$\times\rho(\boldsymbol{x},\,\boldsymbol{x}')\Big/\mathrm{Tr}\,\rho(\boldsymbol{x},\,\boldsymbol{x}')\,, \tag{7}$$

and the hydrostatic pressure is given by

$$P=\tfrac{1}{3}(P_{xx}+P_{yy}+P_{zz})\,. \tag{8}$$

We must note that the pressure obtained above does not express the stress in the system, but it does express the force exerted on each side of the container.

To get the stress in the system we shall calculate the equation of motion. The current density at $\boldsymbol{r}$ is, with normalized ρ,

$$\boldsymbol{j}(\boldsymbol{r})=\frac{\hbar}{2i}\mathrm{Tr}\sum_{j=1}^{N}\left(\frac{\partial}{\partial\boldsymbol{x}_j}\delta(\boldsymbol{x}-\boldsymbol{r})+\delta(\boldsymbol{x}_j-\boldsymbol{r})\frac{\partial}{\partial\boldsymbol{x}_j}\right)$$
$$\times\rho(\boldsymbol{x},\,\boldsymbol{x}')\,. \tag{9}$$

The rate of change of this quantity is easily obtained using the Schroedinger equation. The result can be written in the form

$$\frac{\partial}{\partial t}\boldsymbol{j}+\nabla\cdot\rho\boldsymbol{u}\boldsymbol{u}=\nabla\cdot\sigma,\quad\sigma=\sigma_k+\sigma_\phi\,, \tag{10}$$

where σ_k stands for the kinetic part of the stress tensor in the system and is given by

$$\sigma_k(\boldsymbol{r})=\mathrm{Tr}\sum\left\{-\left(\frac{\hbar}{im}\frac{\partial}{\partial\boldsymbol{x}_j}-\boldsymbol{u}\right)m\delta(\boldsymbol{x}_j-\boldsymbol{r})\right.$$
$$\left.\times\left(\frac{\hbar}{im}\frac{\partial}{\partial\boldsymbol{x}_j}-\boldsymbol{u}\right)+\left(\frac{\hbar}{2m}\right)^2m\delta''(\boldsymbol{x}_j-\boldsymbol{r})\right\}\rho(\boldsymbol{x},\,\boldsymbol{x}')\,, \tag{11}$$

with the density ρ and the drift velocity $\boldsymbol{u}$ given by $\boldsymbol{j}=\rho\boldsymbol{u}$. And

$$\sigma_\phi=\frac{1}{2}\iint\frac{\boldsymbol{r}\boldsymbol{r}}{r}\frac{d\phi}{dr}n(\boldsymbol{x}_1)n(\boldsymbol{x}_2)g(\boldsymbol{x}_1,\,\boldsymbol{r})d\boldsymbol{x}_1d\boldsymbol{r}\,. \tag{11'}$$

In the last expression we have made use of the expansion

$$\delta(\boldsymbol{x}_k-\boldsymbol{r})-\delta(\boldsymbol{x}_j-\boldsymbol{r})=-\nabla_r\cdot[\boldsymbol{r}_{jk}\{1-\tfrac{1}{2}\boldsymbol{r}_{jk}\cdot\nabla+\cdots\}$$
$$\times\delta(\boldsymbol{x}_j-\boldsymbol{r})]\,,$$

which was used by Kirkwood et al.7) in the theory of classical fluids.

To establish the parallelism to classical stress tensor we make use of the phase distribution function of Wigner definen by

$$f(\boldsymbol{r}, \boldsymbol{p}, t)=\left(\frac{1}{\pi\hbar}\right)^{3N}\int_{-\infty}^{\infty}\cdots$$

$$\times\int \exp\left(\frac{2i}{\hbar}\boldsymbol{p}\cdot\boldsymbol{Y}\right)\rho(\boldsymbol{r}-\boldsymbol{Y}, \boldsymbol{r}+\boldsymbol{Y}, t)d\boldsymbol{Y}. \tag{12}$$

then Eq. (11) takes the form (hereafter we shall assume the case $\boldsymbol{u}\cong 0$)

$$\sigma_k=-\frac{1}{m}\iint \boldsymbol{pp}\delta(\boldsymbol{x}-\boldsymbol{r})f(\boldsymbol{r}, \boldsymbol{p})d\boldsymbol{r}d\boldsymbol{p}\ , \tag{13}$$

which is same in form to the classical formula for stress tensor and was derived by Irving and Zwanzig[7].

We see by comparison that the average value of σ coincides with $-\boldsymbol{P}$ defined by Eq. (7). We may also define an alternative stress tensor

$$\sigma'(\boldsymbol{x})=\left[\left.\frac{\hbar^2}{m}\sum\frac{\partial^2}{\partial \boldsymbol{x}\partial \boldsymbol{x}}+\sum\frac{\boldsymbol{rr}}{r}\frac{d\phi}{dr}\right\}\rho(\boldsymbol{xx}')\right]_{\boldsymbol{x}=\boldsymbol{x}'}. \tag{14}$$

This is the coarse-grained average of σ and represents macroscopic value of the stress tensor at $\boldsymbol{x}$.

§ 3. Surface Tension

The free energy of the system of liquid and its vapor in thermal equilibrium can be written in the form

$$F=F_l+F_v+F_{vw}+F_{lw}+F_{lv}\ , \tag{15}$$

where F_l and F_v denote the free energies of the liquid and vapor in bulk, and F_{vw}, F_{lw} and F_{lv} are the free energies of vapor-wall, liquidwall and liquid-vapor interfaces respectively. Surface tension is given by

$$\gamma=\frac{dF_{vl}}{dA}=\frac{\partial F}{\partial A}\ , \tag{16}$$

where A denotes the area of the liquid-vapor surface and the partial derivative means that the valumes of the liquid and the vapor as well as the areas of liquid-wall and vapor-wall interfaces are to be maintained fixe during the variation in the surface area o the liquid-vapor boundary.

The mode of deformation which fulfils th above requirements is that adopted by Harasima. We shall use it for our calculation We stretch a macroscopic film of liquid at th middle of a cubic box of dimension l. W assume the coordinates along the sides of th cube and the liquid film with area l^2 at $z=\frac{1}{2}l$ The width of the fiim d is small compared t the cube side l, but is large compared to th range of interaction between molecules. Th remaining part of the box is filled wit satulated vapor.

In order to perform the required variatio we rewrite the variables as

$$x\to x/(1+\delta\lambda),\quad y\to y,\quad z\to(1+\delta\lambda)z\ . \tag{17}$$

This corresponds to elongation in the x-direction and at the same time contraction in th z-direction in the same amount $\delta\lambda$. Accordingly the liquid film is expanded in the x direction, but the volume of the system an are areas of the vapor-wall and the liquid wall contact are not changed if we neglec the terms higher than the second power wit respect to the deformation $\delta\lambda$ and the rati d/l.

We know physically and as a general rul that any macroscopic restriction imposed o a quantum mechanical system does not violat the thermodynamic nature of the system Therefore we select the set of eigen-state which correspond to the system of liquid an its saturaged vapor mentioned above. Let ψ be one of these eigen-states; then from th wave equation

$$\left\{-\frac{\hbar^2}{2m}\sum\nabla_i^2+\sum\phi(r_{ij})\right\}\psi=E\psi\ ,$$

we can easily calculate the energy shift, whic is

$$\frac{dE}{d\lambda}=-\int\psi^*\left[\frac{\hbar^2}{m}\sum_{j=1}^{N}\left(\frac{\partial^2}{\partial z_j^2}-\frac{\partial^2}{\partial x_j^2}\right)+\sum_{i>j}\frac{z_{ij}^2-x_{ij}^2}{r_{ij}}\frac{d\phi}{dr_{ij}}\right]\psi(\boldsymbol{x})d\boldsymbol{x}\ . \tag{18}$$

The free energy of the total system is given by

$$F=-kT\log\sum_E e^{-E/kT}\ , \tag{19}$$

and its partial derivative with respective to the area of the liquid surface tension of th liquid. During the deformation there occurs no vaporization nor condensation. The surfac tension of the liquid under saturated vapor is given accordingly by

$$\gamma=\frac{1}{2l^2}\frac{\sum e^{-E/kT}\int\psi_E^*\left\{-\frac{h^2}{m}\sum\left(\frac{\partial^2}{\partial z_i^{\,2}}-\frac{\partial^2}{\partial x_i^{\,2}}\right)+\sum\frac{x_{ij}^{\,2}-z_{ij}^{\,2}}{r_{ij}}\frac{d\phi}{dr_{ij}}\right\}\psi_E dx}{\sum e^{-E/kT}}\,. \tag{20}$$

Here we have taken into consideration the fact that there are two surfaces, the upper and the lower sides of the film, each enlarged by the amount $l^2\partial\lambda$.

If we denote the density matrix of the film-vapor system by

$$\rho(\boldsymbol{x}\boldsymbol{x}')=\sum_{E}e^{-E/kT}\psi_E^*(\boldsymbol{x}')\psi_E(\boldsymbol{x})\,, \tag{21}$$

the expression for surface tension becomes

$$\gamma=\frac{1}{2l^2}\left[\frac{-2\mathrm{Tr}\left\{-\frac{h^2}{2m}\sum\left(\frac{\partial^2}{\partial z^2}-\frac{\partial^2}{\partial x^2}\right)\rho\right\}}{\mathrm{Tr}\,\rho}+\iint\frac{x_{12}^{\,2}-z_{12}^{\,2}}{2r_{12}}\frac{d\phi}{dr_{12}}n_1n_2g(\boldsymbol{x}_1,\,\boldsymbol{r}_{12})d\boldsymbol{x}_1d\boldsymbol{x}_2\right]. \tag{22}$$

It is well known that surface tension may be attributed to the stress distribution near the surface. In fact for classical liquids one has the relation[4)]

$$\gamma=\int(P-P_T)dz\,, \tag{23}$$

where P and P_T denote the pressure in the liquid and the pressure parallel to the surface.

It is quite easy to see that an anologous relation holds in the case of quantum liquids. As a matter of fact from Eq. (11) we get, after integrating by part,

$$\gamma=-\frac{1}{A}\iiint(\sigma-\sigma_T)dxdydz\,, \tag{24}$$

where

$$\sigma=\tfrac{1}{3}(\sigma_{xx}+\sigma_{yy}+\sigma_{zz})\,. \tag{25}$$

We may write it in the form

$$\gamma=\int(P'-P_T')dz\,, \tag{26}$$

where P' is the macroscopic pressure in the liquid defided by Eq. (14) or

$$P'=-\tfrac{1}{3}(\sigma_{xx}'+\sigma_{yy}'+\sigma_{zz}')\,, \tag{27}$$

and

$$P_T'=-\sigma_{xx}'=-\sigma_{yy}'\,. \tag{27'}$$

§4. Discussion

Experimentally we can except the quantum effect on surface tension only in liquid helium and hydrogen if we are concerned with molecular liquids, because other liquids solidify before the effect becomes appreciable at lowest temperatures. It was remarked that the calculated value of surface tension turned out to be too high in the case of liquid helium. This was clearly due to the quantum effect. In Fig. 1 we have the plot

$$\gamma^*\equiv\frac{\sigma^2}{\phi_0}\gamma\ \text{vs.}\ \frac{T}{T_c}\,,$$

with molecular diameter σ, depth of interaction potential ϕ_0 and critical temperature T_c. We see the law of corresponding states of de Boer[8)] exhibits the marked departure of liquid helium from classical liquids.

Theoretical estimation of the quantum effect is rather difficult. We shall return to this problem in the next section, but here we shall be content with its order of magnitude. Since the main contribution will come from a few layers of molecules near the surface, we may assume that only the molecules on the first layer of the surface are different in vibration from other molecules. We may use Einstein's model to descrive the vibration. The frequency of vibration tangential to the surface will not differ appreciably from that in the liquid, which we shall denote by ν. The frequency of vibration ν_n normal to the surface will be smaller than ν. Therefore at lowest temperatures

$$-\frac{h^2}{2m}\left(\frac{\partial^2}{\partial z^2}-\frac{\partial^2}{\partial x^2}\right)\sim\frac{1}{2}h(\nu_n-\nu)\,.$$

Thus we may except the effect to be of the order

$$\Delta\gamma^*=\frac{\sigma^2}{\phi_0}(\gamma-\gamma_{\text{class}})\sim-k\Theta/2\phi_0\,.$$

For liquid helium the characteristic temperature $\Theta=h\nu/k$ is about 15.5°K, and $(1/k)\phi_0\sim$ 10°K: the quantum effect will be $\Delta\gamma^*\sim0.78$, which is of the right order of magnitude as is seen in Fig. 1.

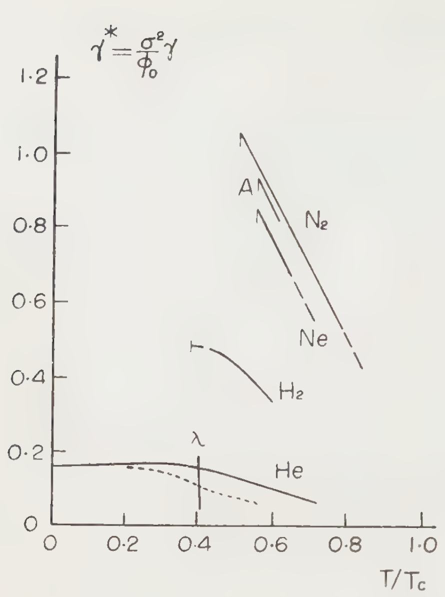

Fig. 1. Corresponding states for surface tension.
Dotted curve: calculated by Eq. (35).

As we approach the absolute zero of temperature the curve, suaface tension vs. temperature, becomes parallel to the temperature axis. This is in accordance with the third law of thermodynamics, because the derivative of surface tension or free energy is entropy itself.

§ 5. Surface Effect on Ideal Gases

Consider an ideal gas contained in a finite volume. If the shape of the container is changed keeping the volume constant, we have the energy shift given by the kinetic term in Eq. (18). The boundary condition has much to do with the actual value. For instance, for the boundary condition $\psi=0$ the surface tension of a Boltzmann gas is

$$\gamma = \frac{1}{2l^2}\left[-\frac{\hbar^2}{2m}\,\mathrm{Tr}\,\Sigma\left(\frac{\partial^2}{\partial z^2}-\frac{\partial^2}{\partial x^2}\right)\rho\right]\Big|\,\mathrm{Tr}\,\rho$$
$$=\frac{NkT}{2l^2}\left[2\Sigma\frac{h^2n_z^2}{8mkTl_z^2}\exp\left(-\frac{h^2n_z^2}{8mkTl_z^2}\right)\Big/\Sigma\exp\left(-\frac{h^2n_z^2}{8mkTl_z^2}\right)-1\right]$$
$$=\frac{h}{4\sqrt{\pi}}\sqrt{\frac{kT}{2m}}\frac{N}{V}+\mathrm{o}\left(\frac{h^2}{8mkTl_z^2}\right). \tag{28}$$

We know that the level density of an ideal gas consists of two part, i.e.

$$g(E)=Vs\sqrt{E}+At\,, \tag{29}$$

where the first term is proportional to the volume V, and the second to the surface area A. s and t are constants;

$$s=2\pi(2m)^{3/2}/h^3\,. \tag{29'}$$

The constant t can be determined using the expression for surface tension we have just obtained. In fact from Eq. (29) the partition function for one particle is seen to be

$$Z=\int e^{-E/kT}g(E)dE$$
$$=V\frac{\sqrt{\pi}}{2}s(kT)^{3/2}\left(1+\frac{2}{\sqrt{\pi}}\frac{A}{V}\frac{t}{s}\frac{1}{\sqrt{kT}}\right). \tag{30}$$

Surface tension is the derivative of the free energy $F=-NkT\log Z$, and is given by

$$\gamma=-\frac{2}{\sqrt{\pi}}\frac{t}{s}\sqrt{kT}\frac{N}{V}\,. \tag{31}$$

Comparing the equation with Eq. (28) the constant t is obtained; namely, for the boundary condition $\psi=0$

$$t=-\frac{\pi}{4}\frac{2m}{h^2}\,. \tag{32}$$

For the boundary condition $\partial\psi/\partial n=0$ ($n=$ normal) we can proceed analogously, and obtain

$$t=\frac{\pi}{4}\frac{2m}{h^2}\,. \tag{32'}$$

We may combine these results in the form

$$g(E)=V\frac{2\pi(2m)^{3/2}}{h^2}\sqrt{E}+\theta A\frac{\pi}{4}\frac{2m}{h^2}$$
$$(-1\leq\theta\leq1)\,, \tag{33}$$

which is identical to Husimi's result.[9]

We can calculate surface tension of Bose-Einstein gas and Fermi-Dirac gas using the level density given above. We get

$$\gamma=-\theta\frac{\pi}{4}\frac{2m}{h^2}\int_0^\infty\frac{EdE}{e^{\alpha+E/kT}\mp1}\,, \tag{34}$$

with

$$N=Vs\int_0^\infty \frac{\sqrt{E}\,dE}{e^{\alpha+E/kT}\mp 1}. \tag{34'}$$

For Bose-Einstein gas α is zero below the condensation temperature T_0. Surface tension is continuous, but it has a kink at T_0. To compare the result with liquid helium cohesion term is added and

$$\gamma=\gamma_0-C(kT)^2\int_0^\infty \frac{x\,dx}{e^{\alpha+x}-1}, \tag{35}$$

is shown in Fig. 1 in reduced units adjusting the value of surface tension at 0°K and T_c.

It will be of some interest to point out a possible surface effect on Fermi-Dirac gas, i.e. an analogue of de Haas-van Alphen effect. That is to say the pressure of an Fermi-Dirac gas oscillates in principle as the box is elongated in one direction keeping the volume constant. Unfortunately the period of oscillation is too small to detect. Only if the mass of the particle were quite small and the temperature low enongh we may anticipate this effect.

References

1) Born and Courant: Phys. Zeits. **14** (1916) 731.
2) Brillouin: Compt. Rend. **180** (1925) 1248.
3) Fowler and Guggenheim: "Statistical Thermodynamics", 1939. R. H. Fowler: Proc. Roy. Soc. A **159** (1937) 229.
4) J. G. Kirkwood and F. P. Buff: J. Chem. Phys. **17** (1949).
5) A. Harasima: J. Phys. Soc. Japan **8** (1953) 343.
6) "Recent Problems in Physics," Iwanami press, 1948.
7) Kirkwood et al: The Statistical Mechanical Theory of Transport Processes: J. Chem. Phys. **14** (1946), 180; **15** (1947) 72; **17** (1949) 988; **18** (1950) 817; **19** (1951) 1173; **21** (1953) 2050; **22** (1954) 783; **22** (1954) 1094.
H. S. Green: "The Molecular Theory of Fluids," 1952.
8) J. de Boer et al: Physica **14** (1948) 139, 149, 510; D. Ter Haar: Physica **19** (1953) 375.
9) K. Husimi: Proc. Phys. Math. Soc. Japan **21** (1939) 759, cf. H. Koppe: J. Chem. Phys. **18** (1950) 638.

JOURNAL OF THE PHYSICAL SOCIETY OF JAPAN Vol. 10, No. 7, JULY, 1955

Magnetic Properties of Cobalt Telluride

By Enji UCHIDA

Department of Physics, Naniwa University, Osaka

(Received April 11, 1955)

Experimental results are reported of the magnetic properties of telluride of cobalt, $CoTe_x$, where x is the molal content of tellurium. Measurements of the magnetization have been made over a range of temperatures between liquid air and 1150°C. The results of these measurements show that this compound, when stoichiometric, possesses a ferromagnetic character. The value of the saturation magnetization is 7.52 gauss per gram ($0.25\,\mu_B$). Evidence was found of a magnetic transition with a sudden disappearance of ferromagnetism at about 1000°C. These characteristic magnetic properties are similar to those of MnAs studied by Guillaud. Increase in tellurium content decreases the saturation moment of this compound, and when x is equal to 1.20 the compound is no longer ferromagnetic but shows a feeble constant paramagnetism which is independent of temperature.

§ 1. Introduction

According to Tengner's study[1], CoTe has a crystal structure of the NiAs type, all the octahedral voids in the closed packed hexagonal tellurium lattice being filled by cobalt atoms. He has also found that there is a wide homogeneity range which includes the equiatomic composition. If only half these voids are filled, CdI_2 type of the lattice results. This accounts for the formation $CoTe_2$, which, according to him, is formed continuously from CoTe by a partial loss of cobalt atoms from the structure. Some changes of magnetic properties are expected with this change of crystalline structure. However, reports on the magnetic properties of CoTe are yet very few. We can find only one which has been studied by Galperin and Perkalina[2] who made measurements on CoTe in the lower region of temperature below room temperature. The experiment described below were made with the object of investigating the magnetization as a function of composition in the interval $1.00<x<2.00$, and of temperature in the range between liquid air and 1150°C.

§ 2. Experimental

The compound $CoTe_x$ was obtained by heating in vacuum (10^{-6} mmHg) the mixed power of cobalt and tellurium, both 99.9% pure, with a desired proportion during 12 hours at 1200°C. The product is a solid material with a silvery appearance. By x-ray diffraction measurements of the samples of various tellurium contents, we obtained i) a Debye-Scherrer pattern which is compatible with the NiAs crystal structure and the lattice spacings $a=3.88$ A and $c=5.37$ A, in the case of stoichiometric composition, ii) for the composition in the interval $1.00<x\leq 1.20$, a pattern in which nothing different from the former is observable, iii) for the composition in the interval $1.30\leq x<2.00$, a pattern with several split lines besides that which is compatible with the NiAs structure.

The apparatus used for the magnetization measurements was a magnetic balance of a self-recording type.[3] Variation was detectable to the extent of one percent of milligram, i.e., the precision of the magnetization measurements was usually ±2%. A specimen of mass m, when placed in an inhomogeneous magnetic field of strength H, experiences a force F, given by $F=\sigma m dH/dz$, where σ is the intensity of magnetization and dH/dz is the gradient of magnetic field in the direction perpendicular to the field. The quantity dH/dz was determined by measuring a standard substance, nickel in the ferromagnetic case and the solution of the salt $NiCl_2$ or $CuCl_2$ in the paramagnetic case. The field gradient is estimated to be constant over the working volume of the specimen because of the smallness of the mass of the specimen which is usually less than fifty milligrams. Since the high fields used in our experiments appreciably surpass the possible demagnetizing field, the correction due to the demagnetization is considered to be unimportant[4]. Measurements of temperature were made with a copper-constantan thermocouple in the region below room temperature and with a Pt-PtRh one in the higher temperature region, the junction being located close to the specimen. Errors in the observed values of temperature are estimated to be less than ±3°C.

§ 3. Results

Table I and curves in Fig. 1 represent, as a function of temperature, the magnetization of the compound CoTe of stoichiometric content. They have essentially ferromagnetic behaviours though a sudden disappearance of ferromagnetism is observed at about 1000°C.

Table I. Specific magnetization of CoTe.

T (°K)	σ (gauss/gram)	H (oe)
81	7.50	8400
285	7.52	〃
340	7.50	〃
434	7.44	〃
605	7.25	〃
733	7.21	〃
855	6.84	〃
954	6.25	〃
1062	5.75	〃
1173	4.74	〃
1231	4.29	〃
1270	2.49	〃
1276	Magnetic transition	
1280	9.55×10^{-3}	5650
1286	9.80×10^{-3}	〃
1270	9.92×10^{-3}	〃
1295	10.98×10^{-3}	〃
1325	10.94×10^{-3}	〃
1375	10.94×10^{-3}	〃
1425	10.91×10^{-3}	〃
1449	10.91×10^{-3}	〃

Fig. 2 shows the results of magnetization versus field intensity at various temperatures. As shown in this figure, the higher the temperature, the more easily the saturation is attained. However, the magnetization at room

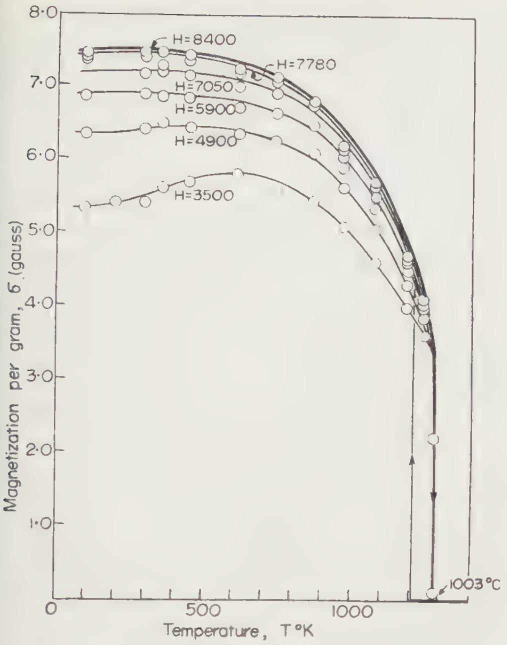

Fig. 1. Dependence of the magnetization of CoTe on temperature, measured at various fields.

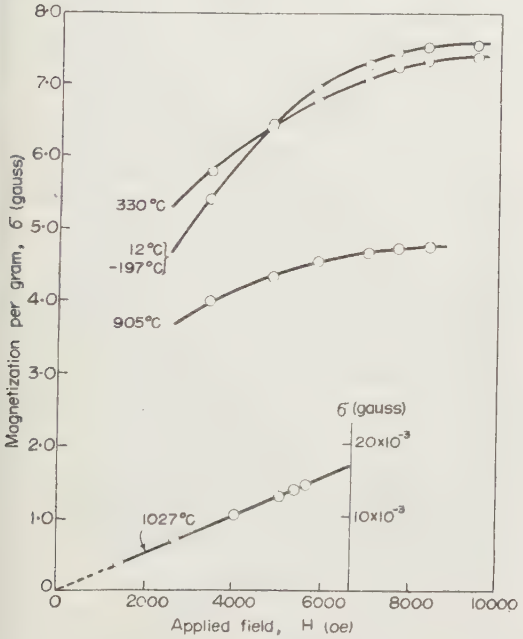

Fig. 2. Dependence of the magnetization of CoTe on field intensity, measured at various temperatures.

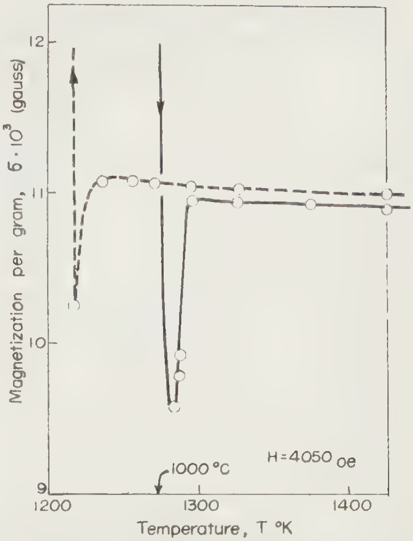

Fig. 3. Dependence of the magnetization of CoTe on temperature in the region above the magnetic transition temperature. Solid line indicates the warming curve and broken line the cooling curve.

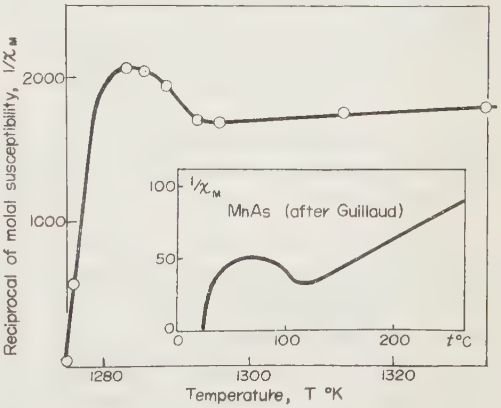

Fig. 4. Reciprocal of the molal susceptibility of CoTe as a function of temperature, in the region above the magnetic transition temperature.

temperature increases so little for fields higher than 7000 oe that the magnetization at about 10000 oe can reasonably be considered to be the saturation magnetization. From the data of Fig. 2 the saturation magnetization of the stoichiometric compound is estimated as 7.52 gauss per gram, which corresponds to 0.25 Bohr magnetons. Such a small value might suggest that the compound CoTe is either a ferrimagnetic substance or an alloy in which the magnetic moment of cobalt atoms is diluted by tellurium atoms. We shall later give some discussions on this matter.

The magnetization-temperature curves, in the heating run, show an almost vertical drop which finishes at 1003°C; the residual magnetization after this transition is of the order of 0.1 percent. On the other hand, in

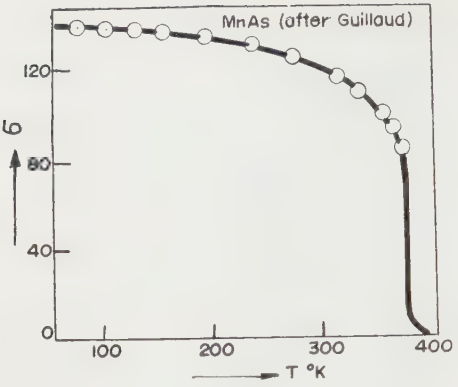

Fig. 5. Dependence of the magnetization of MnAs on temperature (after Guillaud).

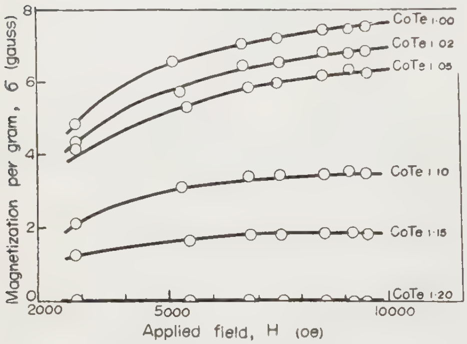

Fig. 6. Dependence of the magnetization of CoTe$_x$ on field intensity, measured at room temperature.

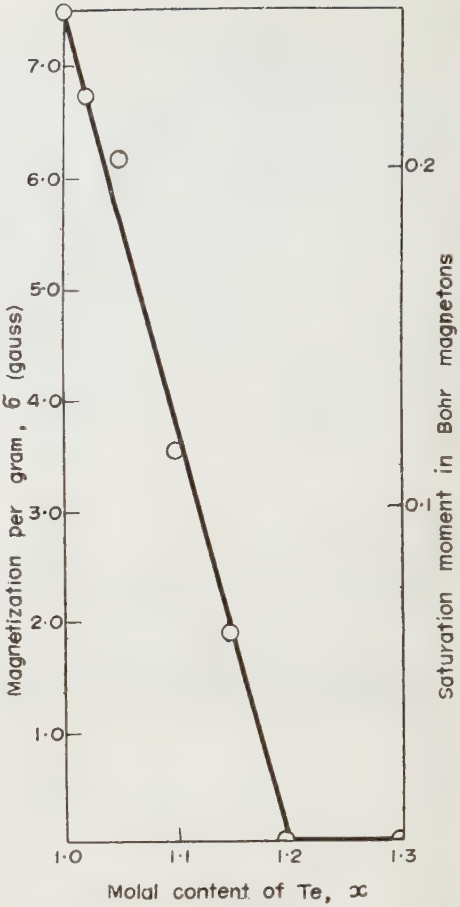

Fig. 7. The magnetization of CoTe$_x$ as a function of molal content of tellurium.

the cooling run, the transition in the reverse direction, i.e., the recovery of ferromagnetism, occurs at a temperature lower than 1003°C which varies according to the cooling rate. It finishes in an instant with some rise of temperature of the specimen. All magnetization-temperature curves in Fig. 1 are found to be reproducible except for a narrow region around the transition temperature in the cooling run.

In the region above the temperature of magnetic transition, the dependence of magnetization on field strength is linear (see Fig. 2). Fig. 3 shows the magnetization-temperature relation and Fig. 4 the characteristic feature of the reciprocal susceptibility-temperature relation, both in the temperature region in question. We note that the curve $1/\chi=f(T)$ in Fig. 4 shows a feature which appears to be somewhat similar to that characteristic of

Table II. Dependence of the specific magnetization of CoTe$_x$ on field intensity, measured at room temperature.

$x=1.00$		$x=1.02$		$x=1.05$		$x=1.10$		$x=1.15$		$x=1.20$	
H (oe)	σ (e.m.u.)	H (oe)	σ (e.m.u.)	H (oe)	σ (e.m.u.)	H (oe)	σ (e.m.u.)	H (oe)	σ (e.m.u.)	H (oe)	σ (e.m.u.)
9500	7.52	9450	6.83	9540	6.25	9450	3.56	9500	1.92	5650	7.45×10^{-3}
9090	7.48	9120	6.82	9100	6.40	9050	3.58	9120	1.92	4950	6.55×10^{-3}
8450	7.50	8430	6.88	8400	6.22	8450	3.49	8450	1.90_5	4050	4.93×10^{-3}
7460	7.28	7530	6.62	7410	6.02	7450	3.48	7530	1.85	2750	3.84×10^{-3}
6680	7.06	6720	6.51	6780	5.92	6720	3.45	6750	1.84	1400	2.00×10^{-3}
5100	6.64	5270	5.85	5370	5.38	5180	3.14	5270	1.76		
2870	4.89	2870	4.41	3200	4.22	3200	2.20	2870	1.40		

ferrimagnetics.

The manganese compound MnAs has been shown, by Guillaud[5], to have a magnetic transition and a charactiristic feature of the reciprocal susceptibilfty-temperature relation similar to those found in the present case. The curves for MnAs are shown in Fig. 4 and Fig. 5 for reference. Guillaud has suggested that the compound MnAs is a ferromagnet and transforms into an antiferromagnetic state at 45°C and then transforms into a paramagnetic state at 130°C. Results of the x-ray study on this compound, recently reported by Willis and Rooksby[6], have supported this suggestion. The transition in CoTe seems to be similar to this interesting thermal change of magnetic structure; however, further studies of x-ray and thermal analyses may be necessary for its definite evidences. We note here only the following facts:

a) When we give a constant thermal input in the warming run, the temperature rise of the sample becomes remarkably slower near the magnetic transition point, a fact which suggests the existence of an anomalous specific heat associated with the transition.

b) A Debye-Scherrer pattern compatible with the NiAs structure is also obtained with a sample which has been quenched from a temperature above the transition temperature.

The behaviour of the magnetization curves for excess tellurium contents remains, as long as $x<1.20$, the same as that of the stoichiometric compound. However, the magnitude of the magnetization decreases with increasing tellurium content. Table II and Fig. 6 show the dependence of the magnetization on field intensity for various compositions and Fig. 7 the magnetization-composition relation, or the saturation moment-composition relation, obtained from the data in Fig. 6. When $x=0.95$ (a cobalt rich composition), the magnetization-temperature curve presents a Curie point at about 1115°C, which coincides with that of pure cobalt. This evidence shows that the sample of this composition consists of two phases, CoTe and pure cobalt.

Fig. 8 shows the magnetization-temperature curves of the compound $CoTe_{1.20}$ at various fields, and Fig. 9 the linearity of the field dependence of magnetization at various temperatures. Similar results are usually obtained for compounds of any composition in the interval $1.20 \leq x < 2.00$. In this case, as shown by these figures, the compound is no longer ferromagnetic but shows a feeble paramagnetism which is independent of temperature. Similar magnetic character has been found by the author in the cases of FeTe and NiTe. As we have noted in a previous paper[7], it seems that this magnetic property is attributable to an alloyic character which certainly is present in this substance.

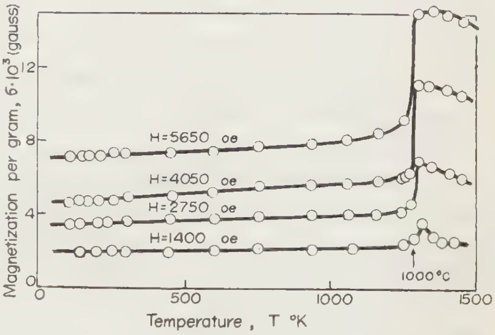

Fig. 8. Dependence of the magnetization of $CoTe_{1.20}$ on temperature, measured at various fields.

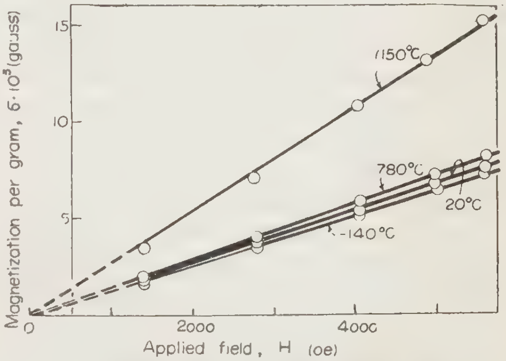

Fig. 9. Dependence of the magnetization of $CoTe_{1.20}$ on field intensity, measured at various temperature.

According to Tengner[1], the lattice of the composition $CoTe_x$, with $x>1.00$, contains holes or vacancies in every other plane of cobalt atoms and the lattice expands in the direction of the c-axis with increasing tellurium content but the homogeneous phase is retained. While we have obtained somewhat different results from Tengner's, we have observed no change in the diffraction pattern at any composition in the interval $1.00 \leq x \leq 1.20$. A distinct change with composition, accompanied by several split lines, was observed for $x>1.30$. These results may suggest a sudden change in the lattice spacing or in the structure at a composition in $1.20<x<1.30$.

It is possible to correlate these results with those obtained by the magnetic measurement. In the magnetization-composition relation (Fig. 7) a sharp break is found at a composition approximately equal to that mentioned above. We regard the decrease of magnetization with increasing content of tellurium to be intimately related to the increase of holes in the crystalline lattice.

§ 4. Interpretation of the Mechanism of the Magnetism of CoTe

In order to explain the saturation moment of CoTe, we consider two different states of cobalt atoms, $(3d)^7\ (4s)^2$ and $(3d)^9$, according to their positions in the structure. We suppose that the positions of these two kinds of cobalt atoms of different moment, of which one possesses three Bohr magnetons and the other one Bohr magneton, are analogous to the positions of holes and atoms in the NiAs lattice of pyrrhotite, Fe_7S_8, determined by Bertaut[8]. The holes in pyrrhotite are replaced by the cobalt atoms of three Bohr magnetons and iron atoms by the cobalt atoms of one Bohr magneton. This supposition may be supported by the similarity between the crystal structures of $CoTe_x$ and FeS_x[9]; they retain the NiAs type both in the range $1.00<x\leq 1.20$, containing holes in the crystal lattice. We also suppose, as in pyrrhotite, an antiparallel alignment of the spins of cobalt atoms in successive plane layers perpendicular to the hexagonal axis. This supposition is supported by the striking smallness of the experimental value of the saturation moment. In the configuration proposed here, we then readily obtain a saturation moment equal to a quater of one Bohr magneton per cobalt atom, in agreement with the experimental result.

It is also possible to correlate this picture of the spin configuration with the variation in saturation moment with composition. Assuming that holes appear in the lattice of CoTe for an excess tellurium content by a partial loss of the cobalt atoms in the $(3d)^7$ $(4s)^2$ state, we can expect a linear decrease of the resultant moment. The zero resultant moment must then be attained at the com position $CoTe_{1.08}$, while the present exper ment gives a larger excess compositio $CoTe_{1.20}$ for vanishing resultant moment.

§ 5. Conclusion

The marked feature of the results of th present experiment on the compound CoT is its close similarity in magnetic propertie to that of the manganese compound MnAs studied by Guillaud.

A more thorough understanding of the magnetic structure of the compound CoTe would, however, require further experiments such as the measurements of the thermal and electrical properties and more detailed studies with x-ray.

The author wishes to express his sincere thanks to Professor T. Nagamiya of Osaka University for many valuable suggestions and discussions, Professor T. Hirone of Tohoku University and Professor Y. Mashiyama of Naniwa University for their kind interest and encouragement during the course of this work and to Professor Y. Shimomura for kind permission to work with his x-ray equipments. The author also would like to thank his colleague Mr. Kondoh for his eager assistance in this work and to Mr. Fukuoka for his helpful assistance in the measurements. This work has been supported in part by the research expenditure of the group 'Research on Ferromagnetic Oxides' organized by Professor S. Kaya.

References

1) S. Tengner: Z. Anorg. u. Allgem. Chem. **239** (1938) 126; Naturwissenschaften, **26** (1938) 429.
2) F. M. Gal'perin and T. M. Perkalina: Doklady Akad. Nauk. S. S. S. R. **69** (1949) 19. [Chem. Abstr. **41** (1950) 1251.]
3) T. Hirone, S. Maeda and N. Tsuya: Sci. Rep. RITU. **A6** (1954) 67.
4) W. Sucksmith: Proc. Roy. Soc. **170** (1939) 551.
5) C. Guillaud: Colloque de Ferromagnetisme et D'antiferromagnetisme, Grenoble, (1951) 77.
6) T. M. Willis and H. P. Rooksby: Proc. Phys. Soc. **67** (B) (1954) 290.
7) E. Uchida and H. Kondoh: J. Phys. Soc. Japan **10** (1955)
8) F. Bertaut: Compt. Rend. **234** (1952) 1295.
9) V. H. Haraldsen: Z. Anorg. u. Allgem. Chem. **231** (1937) 78.

JOURNAL OF THE PHYSICAL SOCIETY OF JAPAN Vol. 10, No. 7, JULY, 1955

On the Maze Domain of Silicon-Iron Crystal (I)

By Sōshin CHIKAZUMI and Kenzō SUZUKI

Department of Physics and Chemistry, Gakushuin University,
Mejiro, Tokyo, Japan

(Received March 12, 1955)

By using powder pattern technique, the maze-like domain which appears on the mechanically polished surface of Si-Fe crystal was examined. The maze domain was found to be a sort of the closure domain, which transports the magnetic flux of the underlying domains. It was also found that the boundaries between these domains are zigzag-shaped. This is interpreted as a general character of 90° wall. The agreement between theory and experiment is good. The degree of zigzag depends also upon the magnitude of the internal stress. From this relation the internal stresses up to 360 kg/mm^2 was found in the vicinity of the scratch.

§ 1. Introduction

It is well known that the domain pattern of the ferromagnetic caystal, which has been polished by mechanical means, is a very fine and maze-like one. A number of investigators[1),3)] had studied on this pattern, regarding it as a typical domain structure until it was found to be different from the inner domain structure. The domain patterns which correspond to the inner domain structure were obtained by Williams, Bozorth and Shockley[2)] by removing the effect of mechanical polishing by electrolytic means.

Although it is known that the maze domain is caused by influence of the mechanical polishing, detailed structure has not yet been known. In this connection the present investigation has been made.

§ 2. Specimens and Experimental Technique

Specimens used in this experiment are the single crystals of 4% Si-Fe alloy with (100) surface, which were prepared by solidifying from the melt. The preparation of the colloidal suspension of magnetic powder and the method of electrolytic polishing were the same one as described by Williams, Bozorth and Shockley. The mechanical polishing was made with emery papers of 0/1, 0/2 and 0/3 and then with the colloidal powder of chromium oxide, and were sometimes followed by a light electrolytic polishing.

In order to make a large maze domain, a strong scratch was drawn on the electrolytically polished surface. This was made by using a ruling engine with a ball point pen, the diameter of which was 0.7 mm. The pen was weightened by 1 kg. The pressure given by the ball was estimated to be about 100 kg/mm^2.

§ 3. General Feature of Maze Domain

The typical types of the maze domain are shown in Figs. 1a, 1b and 1c for various grinding conditions. They depend upon the direction of grinding[3)]. Their boundaries tend to run parallel to the ⟨100⟩ direction which is nearest to the normal of the grinding direction.

Since these boundaries are vague and broad as compared with that of the inner domain, we thought it doubtful whether they are true domain boundaries or nothing but the free poles which appeared on account of the unevenness of the surface. When, however, the specimen was annealed 2 hours at 850°C in hydrogen atomsphere, the maze domain as shown in Fig. 2a disappeared and instead of this the inner domain appeared on the same surface (Fig. 2b). It was verified by this that a maze pattern is caused not by the uneveness but by the internal stress of the surface.

In order to measure the depth of the strained layer, the surface layer was removed by means of the electrolytic polishing and the variation of the patterns was observed (Fig. 3). The depth of the removed layer was estimated by measuring the reduction of weight. No substantial change was observed until the depth of removed layer amounts to about 6 microns (Fig. 3a). Further polishing

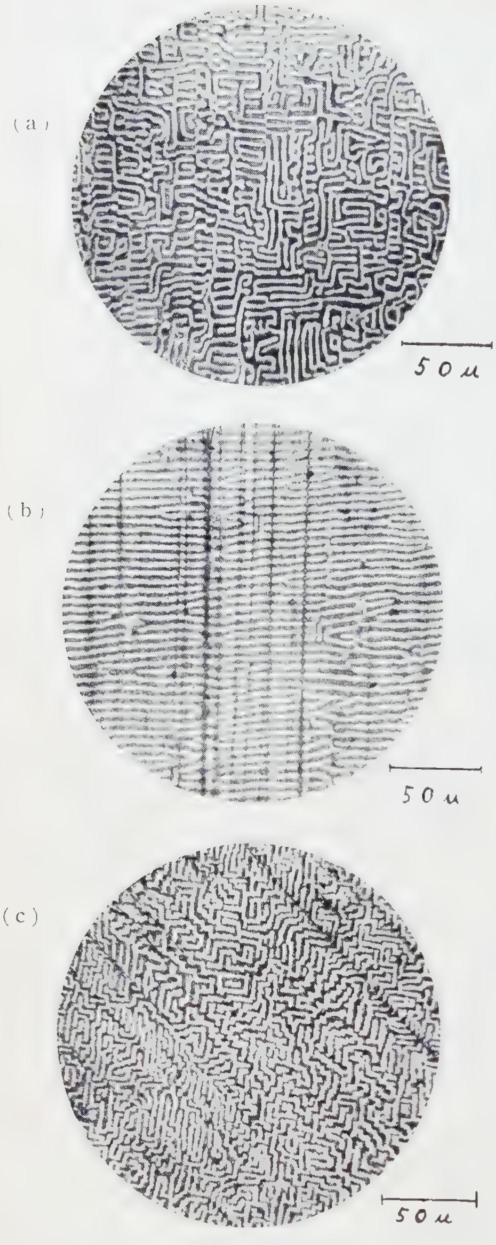

Fig. 1. Maze patterns for various grinding conditions: a. grinding at random; b. grinding along ↕ ; c. grinding along ↖.

destroyed the greater part of the maze patterns leaving those along the traces of strong scratches (Figs. 3b and 3c), and finally the regular patterns of the inner domains appeared (Figs. 3e and 3f). Some irregular boundaries, small spikes or tree domains remained along the traces of strong scratches. The depth of the strained layer was estimated to be from 5 to 15 microns, depending upon the degree of grinding.

In order to investigate more details of the structure, the authors stadied on the large maze domain which appeared along the strong scratch made by ball point pen. The method was described in § 2. Figs. 4a, 4b, 4c and 4d show such patterns for two kinds of the scratching directions. One of the important knowledges obtained from these patterns is that the boundaries are zigzag-shaped. It was also found by a careful observation that the usual maze patterns have also the zigzag boundaries (Fig. 5a). This is the reason why they appear as undefined lines when they collect too much colloid (Fig. 5b).

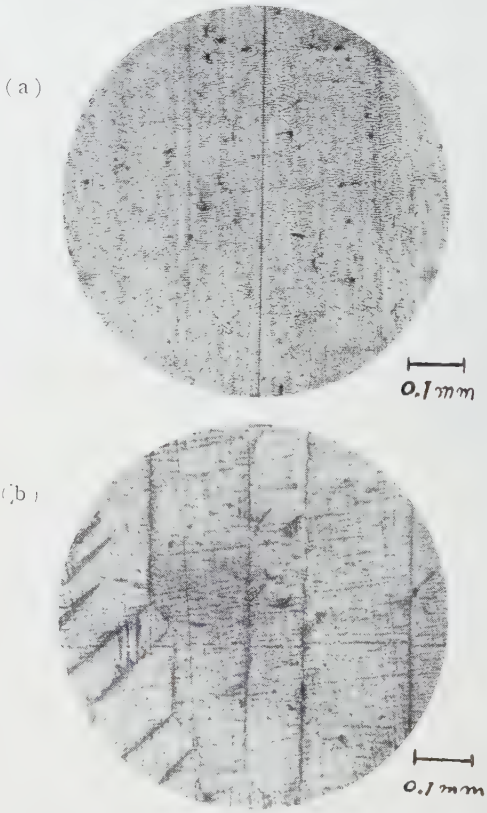

Fig. 2. Maze pattern (a) disappeared by the annealing for 2 hours at 850°C and inner domain appeared on the same surface (b).

The neighboring boundaries of the maze domain have the magnetic free poles of different signs. This was known from the fact that the colloidal particles diffuse out of every other boundaries when the magnetic field was applied vertically to the surface. These behaviors are reproduced in Figs. 6a and 6b.

By using the scratch technique described by Williams, Bozorth and Shockley²⁾, the direc-

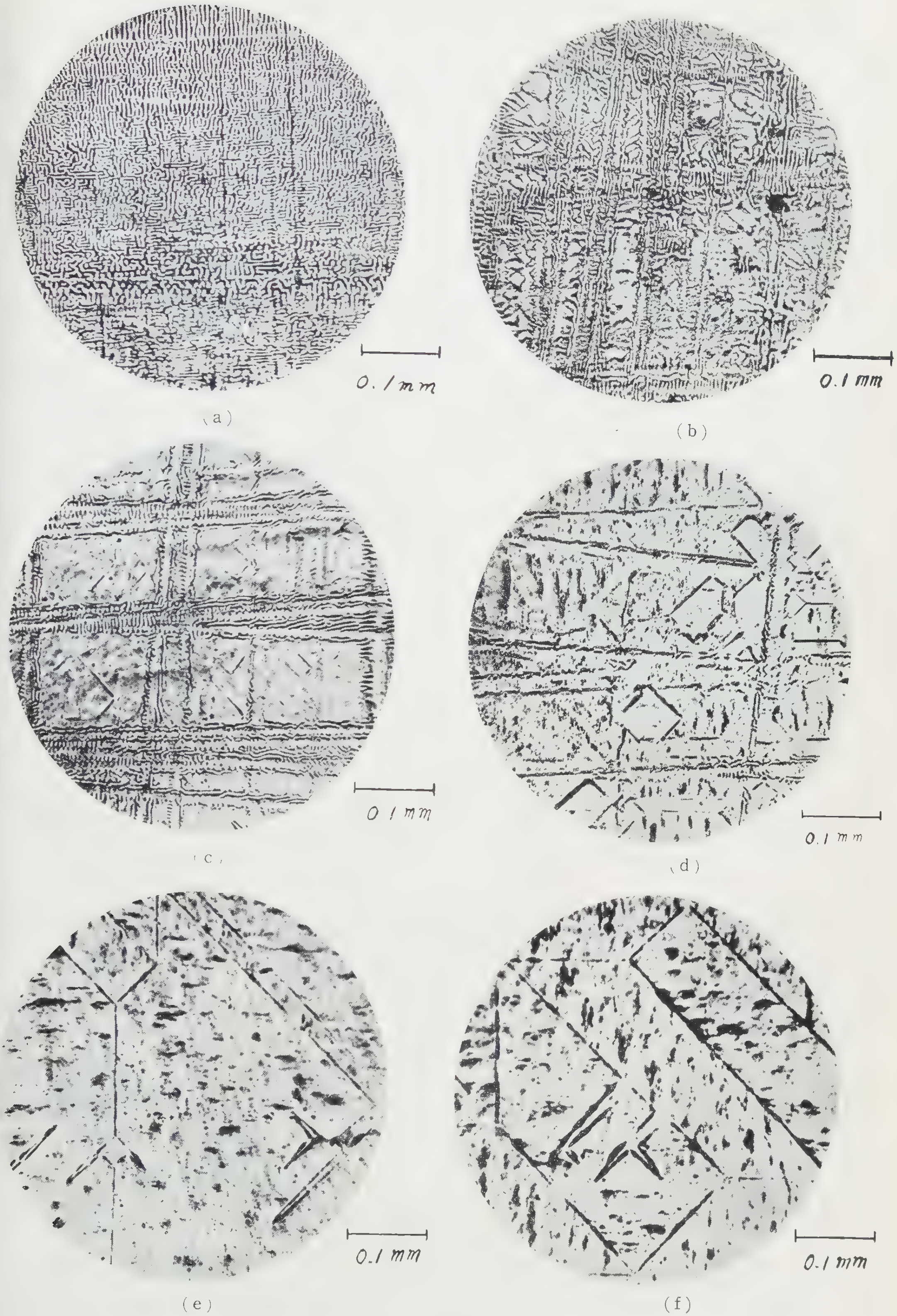

Fig. 3. Variation of maze pattern due to electropolishing. Thickness of the removed layer is: a, 6; b, 8; c, 10; d, 13; e, 19; f, 28 microns respectively.

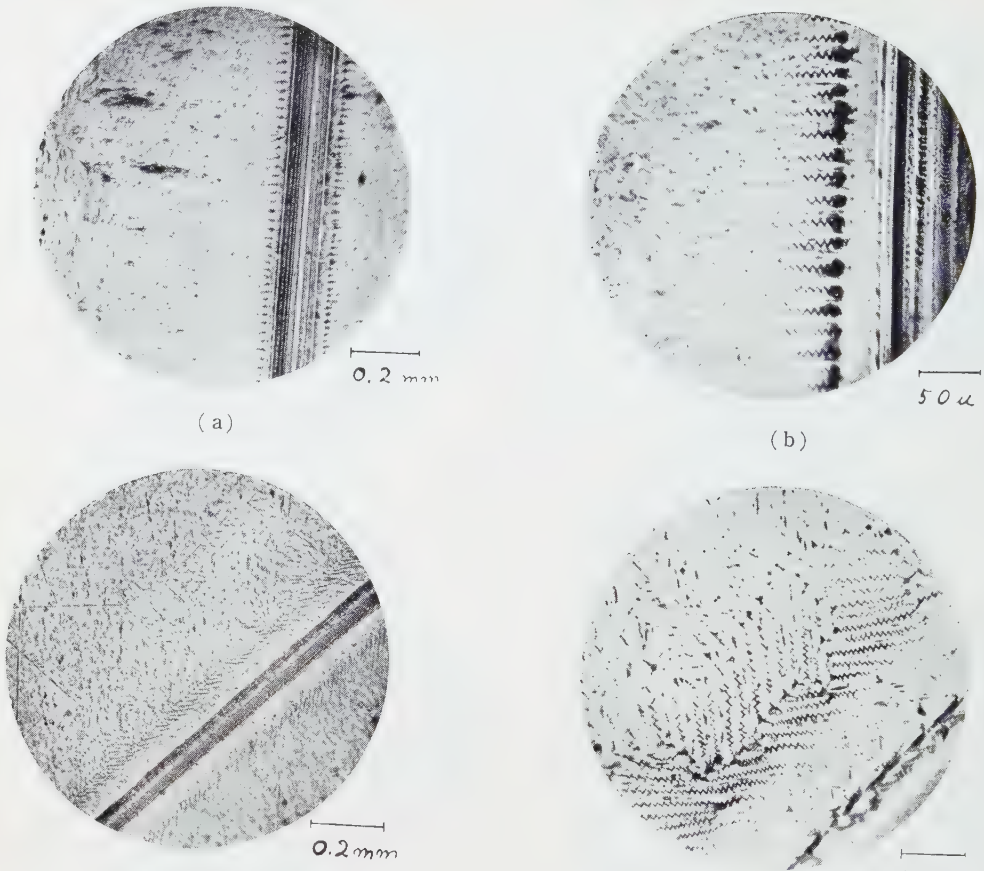

(a) (b) (c) (d)

Fig. 4. The large maze domains appearing along the strong scratches made by the ball point pen: a and b, scratch is in ⟨100⟩; c and d, a scratch is in ⟨110⟩.

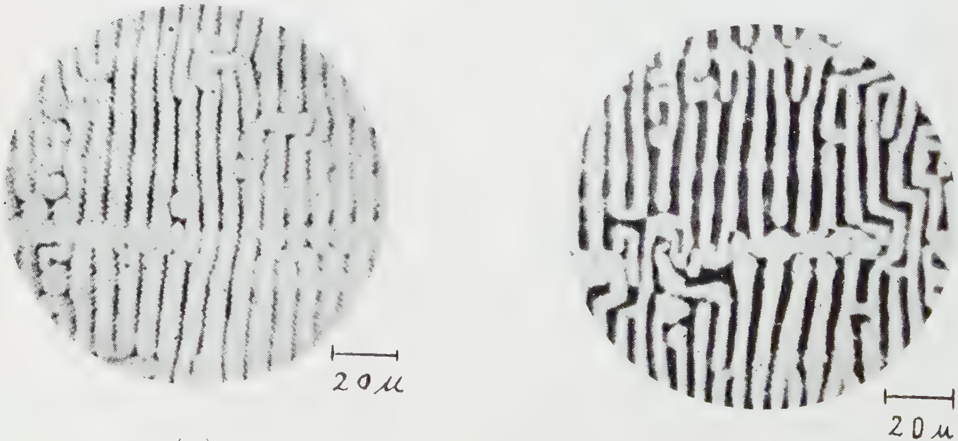

(a) (b)

Fig. 5. Fine structure of usual maze pattern: a, with diluted colloidal suspension; b, with dense one.

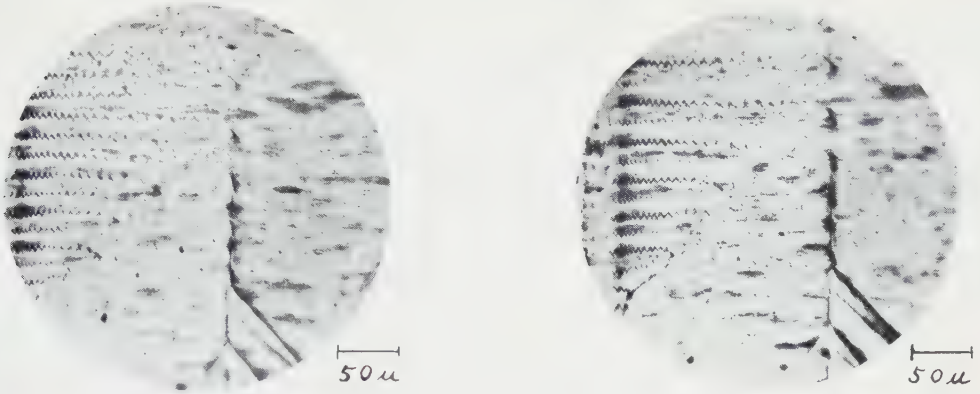

(a) (b)

Fig. 6. Effect of the vertical field on the large maze pattern: a, without field; b, with vertical field.

tion of magnetization was determined. Fig. 7 is a picture of the large maze domains containing many fine scratches made by fine glass fibres. It is known that the scratches are visible as black lines at the places where they are parallel to the magnetization and are invisible where they are perpendicular. It is concluded, therefore, from Fig. 7 that the direction of magnetization is normal to the zigzag boundary. Furthermore it was observed that the neighboring pairs of the zigzag boundaries are connected by the 180° boundaries at their ends near to the scratch (Fig. 8). This means that the sense of the magnetization differs by 180° across the zigzag boundary as indicates by the arrows in Fig. 8.

T. Soller[4] have observed that the maze boundaries rotate to the normal of applying tension, and concluded the same distribution of magnetization. We could not, however, accept this conclusion without any doubt, because his conclusion was made without any consideration about the presence of the underlying domain, which may have some influence on the surface domain.

§4. The Structure of Maze Domain

The domain structure described above seems, at first sight, to have a large magnetostatic energy. We can, however, understand the stability of this structure by assuming the presence of the underlying domains which have magnetization vectors normal to the crystal surface (Fig. 11) The magnetic flux of these domains can be transported by the surface domain so as to reduce the surface free poles.

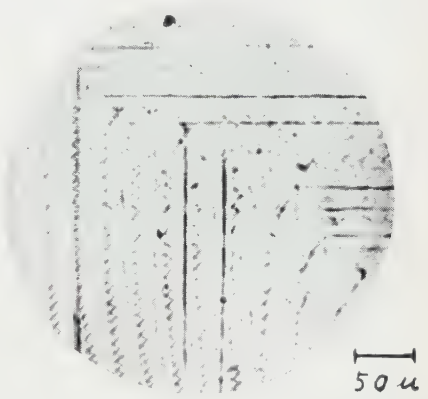

Fig. 7. Large maze pattern containing the fine scratches made by glass fibres. Colloidal particles are attracted when the scratch is normal to the magnetization.

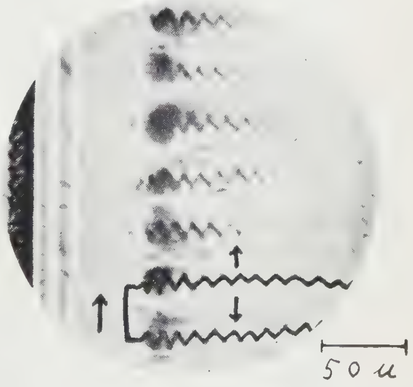

Fig. 8. The zigzag walls are connected by 180° wall at their ends. The arrows indicate the directions of magnetization. Partially retouched.

There is a direct evidence in believing the presence of such underlying domains. Fig. 9

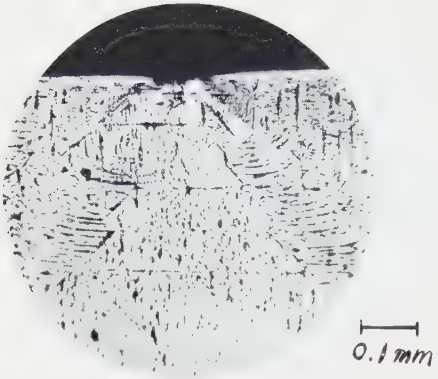

Fig. 9. Domain pattern at the side surface of the crystal. The groove in the upper edge was made by pressing a knife edge onto the surface.

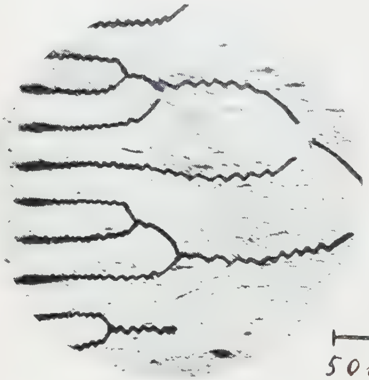

Fig. 10. Variation of the width of the large maze domain. Vertical field was applied. (Retouched).

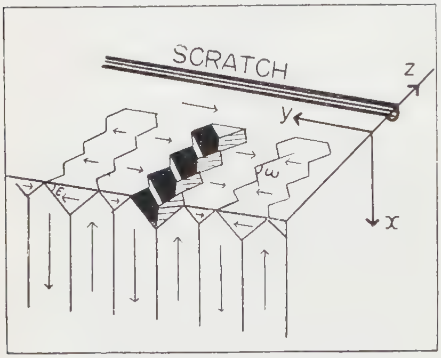

Fig. 11. Illustration of the structure of large maze domain caused by a strong scratch.

shows a domain pattern on a side surface of the crystal. The groove at the upper edge was made by pressing a knife edge onto the upper surface. There appear many domains surrounding a pressed position, some of them being vertical to the upper edge.

These underlying domains may be caused by the internal stress made by the scratches. We can estimate the magnitude of the internal stress by calculating the domain width. Since the component T_{xx} of the stress tensor favors the underlying x-domain and disfavors the closure y-domain (Fig. 11), it makes the width of these domains smaller. On the other hands, the reduction of the domain width is necessarily followed by an increase of the wall area. By minimizing the sum of the magnetoelastic and the wall energies, we obtain the width of the maze domain

$$D=\left(\frac{8\sigma_w L}{3\lambda_{100}T_{xx}}\right)^{1/2}, \qquad (1)$$

where σ_w : surface energy of wall,
L : depth of the underlying domain,
λ_{100}: coefficient of magnetostriction,
$\overline{T}_{xx}$: the mean value of stress in the closure domain.

The derivation of Eq. (1) is given in Appendix A.

Now we shall estimate the value of T_{xx} for 4% Si–Fe, in which $\lambda_{100}=25\times10^{-6}$ and $\sigma_w=1.4\,\text{erg/cm}^2$. For mechanically polished surface D is 1.5~2.5 microns as is known from Fig. 1 and $L=10$ microns as is proved by the experiment of Fig. 3. Putting these values into Eq. (1) we have $\overline{T}_{xx}=70\sim25\,\text{kg/mm}^2$. In the case of strong scratches $D=10$ microns and $L=0.2$ mm as is estimated in Fig. 9, so we have $\overline{T}_{xx}=32\,\text{kg/mm}^2$. Discussion about these values will be given in § 6.

Eq. (1) also predicts that the domain size D may increase with an increase of the distance from a scratch because of a decrease of T_{xx} and of an increase of L. In fact such variation of domain size takes place as shown in Fig. 10.

§ 5. Zigzag Boundaries

The zigzag character of the maze boundary may have the following two origins. The first is the general character of 90° wall that its wall energy depends upon its orientation. The other is related with the magnetostatic energy of the free pole which appears on the wall.

It would be important to point out that the 90° wall can change its orientation even under the restriction that the normal component of magnetization should be constant across the wall (Cf. Fig. 12). No free pole, therefore, appears on the wall even after the wall is deformed zigzagwise. It turns out, however, that the wall energy does change its value when the orientation of the wall is changed. The energy of 90° wall per unit area is given by

$$\sigma_w = 2\sqrt{A}\,\sin\theta\int_{\varphi_1}^{\varphi_2} g(\theta,\varphi)^{1/2}d\varphi\ , \qquad (2)$$

where $g(\theta, \varphi)$ is an anisotropy energy, θ being the angle between the normal of the wall and the magnetization and φ being the azimuth of spin in the wall plane (Fig. 13). The calculation is given in Appendix B.

The energy σ_w is plotted in Fig. 14 as a function of the orientation of the wall Ψ, where 2Ψ means the angle between the neighboring strips of the zigzag surface. This variation of the wall energy is mainly caused by the variation of the azimuthal range of the spin rotation in a wall plane, $\varphi_2-\varphi_1$.

The energy per unit area of the average plane of the zigzag wall is then given by

$$U_w = \frac{\sigma_w}{\sin\Psi}\ . \qquad (3)$$

It would be interesting to note that the function $U_w(\Psi)$ has a minimum at a finite value of Ψ (Fig. 14). It is, therefore, concluded that the stable configuration of 90° wall is not a plane but a zigzag surface, even without any other cause. The stable configuration corresponds to $\Psi=62°$. In order to compare with the experiment, we had better translate it to the angle ω i.e. the angle between the adjoining segments of the zigzag line which we observe on the crystal surface (Cf. Fig. 11). We shall call it the zigzag angle. The relation between ω and Ψ is given by

$$\tan\frac{\omega}{2} = \frac{\tan\Psi}{\sqrt{2}} \qquad (4)$$

or approximately

$$\omega = 2.09\Psi - 25.1 \qquad (4a)$$

Putting $\Psi=62°$ into Eq. (4), we have $\omega=106°$, which gives a stable zigzag angle.

This result was confirmed by the experiment. One may find in Figs. 4, 6 or 8 the zigzag angles from 103° to 109° distributed at the regions far from the scratch. The variation of ω along one of these zigzag lines are shown in Fig. 15 as a function of distance from a scratch.

It would be interesting to remark here that the value 106° is a general constant for the cubic ferromagnets with ⟨100⟩ easy direction, being independent of the magnitude or the functional form of the cubic anisotropy. This is because the variation of the wall energy is caused mainly by the variation of the azimuthal range of spin rotation.

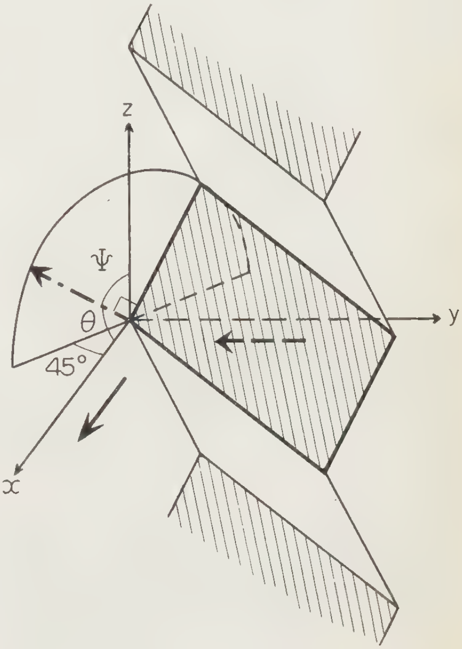

Fig. 12. Configuration of 90° wall between x and y domains. Normal component of magnetization is constant across the wall as far as a normal of the wall is in (110) plane.

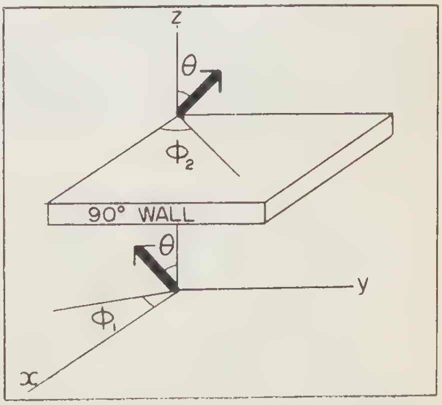

Fig. 13. Directions of spins on both side of the 90° wall.

The variation of the zigzag angle may be caused by the free pole which appears on the wall. Firstly we shall estimate the magnitude of the free pole. The internal stress T_{xx} may favor the underlying domain and disfavor the closure domain, thus it makes the depth o the latter smaller. Then the normal component of magnetization of both domains are not continuous across the wall and accordingly the free pole appears on the wall. The surface density of this free pole, m, can be solved by determining the shape of the closure domain. By minimizing the sum of the magnetoelastic and the magnetostatic energies (Appendix C), we have

$$m=0.18\frac{\lambda_{100}T_{xx}}{I_s}. \qquad (5)$$

The relation between m and T_{xx} given here is directly verified by observation. Namely it is observed that the colloidal particles are attracted more densely at the wall near to the scratch, showing the presence of the strong free poles there (Figs. 4, 6 and 8).

The free pole calculated here is not changed when the wall is deformed zigzagwise. This is easily proved by Gauss's divergence theorem. The magnetostatic energy of this free pole, however, may be reduced by this deformation of the wall, for in that case the free pole is diluted in the larger area. The magnetostatic energy is calculated as a function of angle Ψ in Appendix D, which gives

$$U_{\mathrm{mag}}=-\frac{\pi m^2 c}{8\tan\Psi}\left(1-\frac{\pi^2}{12\tan^2\Psi}\right) \quad \text{for } \Psi>57.5^\circ$$
$$=-m^2c \quad \text{for } \Psi\leqslant 57.5^\circ, \qquad (6)$$

where c is the amplitude of zigzag (Cf. Fig. 16). The function of Eq. (6) is also shown graphically in Fig. 17.

When the internal stress is present, the zigzag angle decreases from 106° so as to decrease the magnetostatic energy. The angle realized in this case is given by minimizing

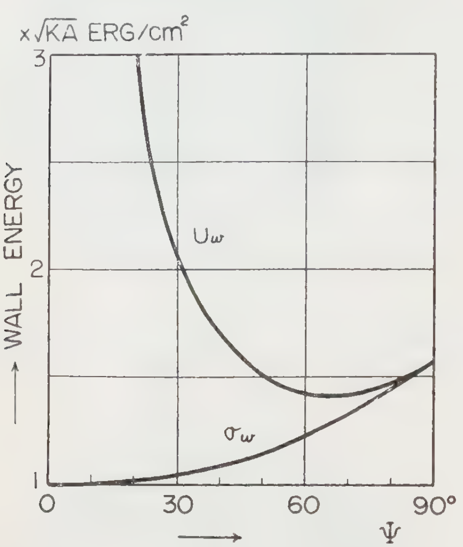

Fig. 14. Energy of 90° wall as function of wall orientation Ψ. σ_w is an energy per unit area of the 90° wall, whereas U_w is an energy per unit area of the average plane of the zigzag surface.

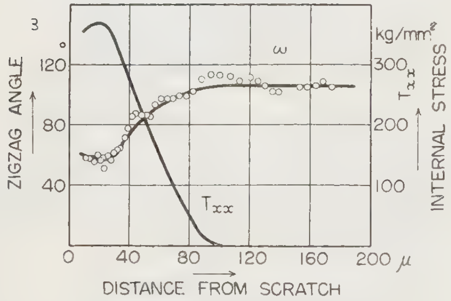

Fig. 15. Zigzag angles ω observed along a zigzag boundary. An approach to 106° is in good agreement with the theory. T_{xx} is a theoretical value of the internal stress derived from the deviation from 106°.

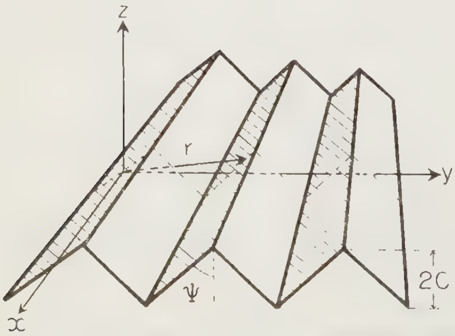

Fig. 16. Zigzag wall in x-y plane.

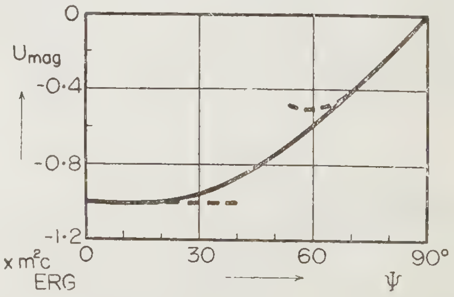

Fig. 17. Variation of magnetostatic energy as a function of zigzagness of the wall. Dotted lines are approximations.

the total energy

$$U=U_w+U_{\text{mag}} \tag{7}$$

where U_w and U_{mag} are given by Eqs. (5) and (6) respectively. For $\Psi\simeq\Psi_0=62°$, they are expressed approximately by

$$U_w=\text{const.}+6.73\times10^{-4}\sqrt{K_1A}\,(\Psi-\Psi_0)^2 \tag{8}$$

$$U_{\text{mag}}=\text{const.}-1.23\times10^{-4}m^2c\Psi^2. \tag{9}$$

Then we have

$$\Psi=\frac{6.73\sqrt{K_1A}}{6.73\sqrt{K_1A}+1.23m^2c}\Psi_0\,. \tag{10}$$

By using Eqs. (4), (5) and (10), we can solve the zigzag angle ω as a function of internal stress T_{xx}, thus for 4% Si–Fe

$$T_{xx}=492\sqrt{\frac{\Psi_0-\Psi}{\Psi}}$$

$$=492\sqrt{\frac{\omega_0-\omega}{\omega+25.1}}\quad(\text{kg/mm}^2) \tag{11}$$

The function of Eq. (11) is also shown graphically in Fig. 18.

Using this relation we can estimate the magnitude of the internal stress from the observed zigzag angle ω. An example is given in the curve in Fig. 15 which shows the variation of the internal stress as a function of the distance from the scratch. The decaying character of this curve is quite reasonable. Discussion about the magnitude of the stress will be given in § 6.

§ 6. Conclusions and Discussion

Experimentally the following points were concluded:

(1) The boundaries of the maze domain are perpendicular to the grinding direction.

(2) The internal stress is prerequisite to the presence of the maze domain.

(3) The depth of the strained layer is 5～15 microns, depending upon the degree of grinding.

(4) The shape of boundary is zigzag, its way being emphasized at the place where the strong internal stress prevails.

(5) The magnetic free pole at the boundaries changes its sign from boundary to boundary.

(6) The direction of magnetization in the maze domain is perpendicular to the boundary and differs by 180° with that of the neighboring domains.

Theoretically the following conclusions were obtained:

(i) The model as shown in Fig. 11 is consistent with the facts (1), (2), (5) and (6). Using this model the size of domain was calculated. In order to explain the observed size, the internal stress 25～70 kg/mm² is necessary.

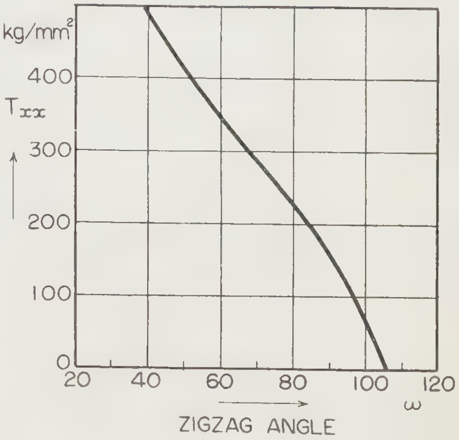

Fig. 18. Relation between internal stress T_{xx} and zigzag angle ω.

(ii) The surface energy of 90° wall depends upon the orientation of the wall. The stable configuration of 90° wall, therefore, is zigzag, whose neighboring segments forms the angle $\omega=106°$. This is in good agreement with the observed value 103°～109°.

(iii) The prism-shaped domain becomes flatter at the place where the strong stress prevails. This results in an appearance of the free pole on the wall. The relation between the intensity of the free pole and the magnitude of the internal stress was qualitatively verified by experiment.

(iv) The zigzag angle is influenced by the presence of the free pole on the wall. The variation was calculated as a function of internal stress. By using this relation magnitude of the internal stress was estimated. It was found that the stress amounts to 370 kg/mm² at the region about 0.02 mm distant from a scratch.

It should be noticed here that the stress obtained from zigzag angle is not inconsistent with the value obtained from the domain width, for the latter is a mean value over the whole range of unit maze domain. When the stresses obtained from the zigzag angle are averaged along one domain (Cf. Fig. 15), one obtains the value 93 kg/mm², which is consistent with that obtained from the domain width.

Although the residual stresses are usually compared with the yield strength, it must be recalled here that the yield strength may correspond not to the upper but rather to the lower limit of the internal stress. It may not be strange, therefore, that the stress larger than the yield strength are concentrated at some regions in the material. Since a direct calculation of the residual stress is very difficult, we cannot compare the result with theoretical one. Further we do not know any other experiment which furnishes any informations about the magnitude of the residual stress (not the residual deformation) in such a small region as in this case.

Although the stress obtained here may not be very accurate because of the approximation used in the calculation, it may be not far from the truth, because the results of the several calculations are consistent with each other. Anyhow it may furnish a useful method for the study of the magnitude or microscopic distributions of the residual stress.

Further investigation has been made on the special type of maze domain and its response to the application of field or tension. These results will be published in the near future.

Acknowledgement

The authors are indebted to Prof. A. Ookawa, Dr. M. Nishida, Mr. Y. Yamada and Mr. H. Kanzaki for their full discussions about the problem of the residual stress. They also wish to thank Prof. S. Kaya for his kind interest throughout the work. This research was supported by the research grant of the Ministry of Education.

Appendix A

Calculation of the Size of Maze Domain

The difference of energy between x- and y-domain in Fig. 11 is given by

$$f_{el}=(3/2)\lambda_{100}T_{xx}\,, \qquad (A.1)$$

where T_{xx} is the component of the stress tensor. This energy does not depend upon T_{zz}, although it is necessary that the sign of latter is negative (compression) in order to make the zigzag boundary run vertically to a scratch. The magnetostrictive energy per unit area of a crystal surface is

$$W_{el}=(3/8)\lambda_{100}\overline{T}_{xx}D\,, \qquad (A.$$

where D is the width of y-domain and $\overline{T}$
is the mean value of T_{xx} over the surface
90° wall. On the other hand the wall energ
per unit area of crystal is

$$W_{wall}=\sigma_w L/D\,, \qquad (A.$$

where L is the depth of x-domain. The tota
energy

$$W=W_{el}+W_{wall} \qquad (A.4$$

is minimized by the condition

$$\partial W/\partial D=0\,, \qquad (A.5$$

which gives the stable width

$$D=(8\sigma_w L/3\lambda_{100}\overline{T}_{xx})^{1/2}\,. \qquad (A.6$$

Appendix B

Dependence of the Surface Energy of 90° Wall upon its Orientation

Exchange energy stored per unit volume i
expressed by

$$f_{ex}=A[(\nabla\alpha_1)^2+(\nabla\alpha_2)^2+(\nabla\alpha_3)^2]\,, \qquad (B.1$$

where $(\alpha_1, \alpha_2, \alpha_3)$ is the set of directio
cosines of spin and

$$A=2JS^2/a \qquad (B.2$$

for body-centered cubic crystal (Cf. Kittel
p. 526).

Now we put the wall into x-y plane and ex
press the direction cosines of spin by the pola
coordinate (Cf. Fig. 13)

$$\begin{cases}\alpha_1=\sin\theta\cos\varphi\\ \alpha_2=\sin\theta\sin\varphi\\ \alpha_3=\cos\theta\end{cases} \qquad (B.3$$

Assuming that the normal component o
spin is continuous across the wall i.e.

$$\alpha_3=\text{const.}\,, \qquad (B.4$$

so that Eq. (B.1) becomes

$$f_{ex}=A\sin^2\theta(\partial\varphi/\partial z)^2\,. \qquad (B.5$$

The wall energy per unit area is then

$$\sigma_w=\int_{-\infty}^{+\infty}\left(g(\theta,\varphi)+A\sin^2\theta\left(\frac{\partial\varphi}{\partial z}\right)^2\right)dz\,, \qquad (B.6$$

where $g(\theta,\varphi)$ is the anisotropy energy. $\varphi($
is to be determined by solving the variationa
problem, which leads to the Euler equatio
and finally to

$$g(\theta,\varphi)=A\sin^2\theta(\partial\varphi/\partial z)^2\,. \qquad (B.7$$

Then Eq. (B.6) becomes

$$\sigma_w=2\sqrt{A}\,\sin^2\theta\int_{\varphi_1}^{\varphi_2} g(\theta,\varphi)^{1/2}d\varphi\,. \tag{B.8}$$

For 180° wall $\theta=\pi/2$, $\varphi_1=0$ and $\varphi_2=\pi$ independently of the wall orientation, so the wall energy does not depend upon its orientation. On the contrary, for 90° wall θ, φ_1 and φ_2 depend upon the wall orientation, so its energy varies with its orientation.

Now we consider 90° wall between x- and y-domain (Fig. 12). Normal of the wall must lie in (110) plane in order to maintain the normal component of magnetization constant across the wall. We shall denote the angle between the normal of wall and the z axis Ψ, which is related with θ, φ_1 and φ_2 by

$$\sin\Psi=\sqrt{2}\cos\theta$$

$$\sin\theta=\frac{1}{\sqrt{2}\sin\varphi_1}=\frac{1}{\sqrt{2}\sin\varphi_2}\,. \tag{B.9}$$

Furthermore, $g(\theta,\varphi)$ can be expressed by Fourier series

$$g(\theta,\varphi)=g_0+g_1\cos\left(\pi\frac{\varphi}{\varphi_1}\right)+g_2\cos\left(2\pi\frac{\varphi}{\varphi_1}\right)+\dots, \tag{B.10}$$

which is approximately equal to

$$g(\theta,\varphi)=2g_0\cos^2(\pi\varphi/2\varphi_1)\,, \tag{B.11}$$

where

$$\begin{aligned} g&=g(\theta,0)\\ &=(K_1/8)\sin^2(\theta+\Psi)(3\cos^2(\theta+\Psi)+1). \end{aligned} \tag{B.12}$$

On putting Eq. (B.11) into Eq. (B.8), we have

$$\sigma_w=\frac{8}{\pi}\sqrt{g_0A}\left(\frac{\varphi_1}{\sin\varphi_1}\right). \tag{B.13}$$

This is plotted as a function of Ψ in Fig. 14.

Appendix C

Calculation of the Free Pole Density on Zigzag Wall

Firstly we shall estimate the depth of the closure domain. The magnetoelastic energy per unit area of the crystal surface is given by

$$\begin{aligned} W_{el}&=(1/4)f_{el}D\tan\mathcal{E}\\ &=(3/8)\lambda_{100}T_{xx}D\tan\mathcal{E} \end{aligned} \tag{C.1}$$

where $\mathcal{E}$ is the angle between 90° wall and the crystal surface (Fig. 11). When $\mathcal{E}<(\pi/4)$, there appears the free pole on 90° wall, the surface density of which is given by

$$m=I_s(\cos\mathcal{E}-\sin\mathcal{E}) \tag{C.2}$$

The magnetostatic energy in this case can be estimated as follows: When the free poles are projected to the crystal surface, the magnetostatic energy is then given by $2\times0.85\times m^2D$ (Cf. Kittel[5], p. 559), where the factor 2 comes from the fact that the pole density is $\sqrt{2}\,m$. Nextly we shall estimate the work necessary to bring the free pole from the crystal surface to the original position. Since the mean distance between each strips is not altered by this process, the main contribution comes from the dilution of free pole in each strips. Considering that the potential is logarithmic, we can easily estimate that the change of magnetic potential is $-\log\sqrt{2}\cdot mD$ which contributes $0.25\,m^2D$ to the magnetostatic energy. Thus the magnetostatic energy becomes

$$\begin{aligned} W_{mag}&=(2\times0.85-0.25)m^2D\\ &=1.45\,m^2D\\ &=1.45\,I_s^2D(\cos\mathcal{E}-\sin\mathcal{E})^2\,. \end{aligned} \tag{C.3}$$

The total energy

$$W=W_{el}+W_{mag} \tag{C.4}$$

is minimized by the condition

$$\partial W/\partial\mathcal{E}=0\,, \tag{C.5}$$

which gives the stable angle

$$\cos\mathcal{E}=(1+k)/\sqrt{2}\,, \tag{C.6}$$

where

$$k=f_{el}/11.6I_s^2=0.13(\lambda_{100}T_{xx}/I_s^2)\,. \tag{C.7}$$

Then the free pole density becomes

$$\begin{aligned} m&=I_s(\cos\mathcal{E}-\sin\mathcal{E})\\ &=\sqrt{2}\,I_sk\\ &=0.18(\lambda_{100}T_{xx}/I_s)\,. \end{aligned} \tag{C.8}$$

Appendix D

Calculation of Magnetostatic Energy of Free Pole Distribution on the Zigzag Wall

We shall calculate here the magnetostatic energy of the free poles distributed uniformly on the zigzag plane as shown in Fig. 16. By neglecting the effect of edges, we can treat the problem as two dimensional one, where the magnetic potential φ_m is expressed by logarithmic function. In order to avoid the appearance of infinity, φ_m is taken to be zero when the free poles are in x-y plane. Then we have the magnetic potential at the origin

$$\varphi_m=-m\int_0^\infty\log\frac{r^2}{y^2}dy\,, \tag{D.1}$$

where m is the intensity of free pole per unit area of x-y plane and r is the distance measured in the y-z plane. For brevity we shall replace the zigzag by sinusoidal function:

$$r^2 = y^2 + c^2 \sin^2 qy \,, \tag{D.2}$$

where

$$q = \pi / 2c \tan \Psi \tag{D.3}$$

and 2Ψ is the angle between the adjoining strips of the zigzag surface.

When $\Psi \geqslant 57.5°$, we find that $(c^2 \sin^2 qy)/y^2 \ll 1$ for any value of y, so we can expand the logarithm by series and finally we have

$$\varphi_m = -mc\left(\frac{\pi^2}{4 \tan \Psi} - \frac{\pi^4}{48 \tan^3 \Psi} + \cdots\right). \tag{D.4}$$

When Ψ is small enough, we can rewrite φ_m as

$$\varphi_m = = m \sum_{n=0}^{\infty} \int_{y_n}^{y_{n+1}} \log\left(1 + \frac{c^2}{{y_n}^2} \sin^2 qy\right) dy \,, \tag{D.5}$$

where

$$y_n = nc \tan \Psi \tag{D.6}$$

or

$$\varphi_m = -\frac{m\pi}{q} \sum_{n=0}^{\infty} \log \frac{1}{2}\left(1 + \sqrt{1 + (1/n \tan \Psi)^2}\right). \tag{D.7}$$

By replacing the summation by integratio we have finally

$$\varphi_m = -2mc \tan \Psi \int_0^{\infty} \log \frac{1 + \sqrt{1 + (1/n \tan \Psi)^2}}{2} \, d$$
$$= -2mc \,. \qquad \text{(D.}$$

Thus we have the magnetostatic energy pe unit area of x-y plane

$$U_{mag} = \frac{1}{2} m \varphi_m$$
$$= -\frac{m^2 c \pi}{8 \tan \Psi}\left(1 - \frac{\pi^2}{12 \tan^2 \Psi}\right) \qquad \text{for} \quad \Psi \geqslant 57.5°$$
$$= -m^2 c \qquad \text{for} \quad \Psi \leqslant 57.5°. \quad \text{(D.}$$

This function is shown as a graph in Fig. 1

References

1) W. C. Elmore: Phys. Rev. **53** (1938) 757.
2) Williams, Bozorth and Shockley: Phys. Rev **75** (1949) 155.
3) S. Kaya: ZS. f. Phys. **89** (1934) 796.
4) T. Soller: ZS. f. Phys. **106** (1937) 485.
5) C. Kittel: Rev. Mod. Phys. **21** (1949) 541.

JOURNAL OF THE PHYSICAL SOCIETY OF JAPAN Vol. 10, No. 7, JULY, 1955

Optical Observation of the First-Order Transition of Barium Titanate Single Crystal at the Curie Point

By Atsuo NISHIOKA

Electrical Communication Laboratory, Musashino, Tokyo, Japan

(Received November 16, 1954)

This first-order transition of Barium Titanate single crystal was observed optically at the Curie point of about 120°C by polarizing microscope, and the domain boundary movement was recorded by 16 mm motion picture. The crystal was so called c-plate, and the area and the thickness were about 0.1 mm^2 and 0.03 mm respectively. With increasing temperature, no change was observed up to the Curie point, but at about 120°C the domains begin to move rapidly and discontinuously and the heterogeneous transformation of c-plate to a-plate occurs. Then discontinuous and rapid changes of a-plate to cubic phase occur, and the transition is finished. During this transition, we observed some interesting domain patterns, caused by the penetration of two perpendicular domains.

§ 1. Introduction

The ferroelectric properties of Barium Titanate have been studied recently by many workers, and the transition at the Curie point about 120°C was found to be a first-order one. But in some impure crystals, the transition is not so sharp and sometimes appears as if it were a second-order one[1]. Perfect single domain c-plate crystals are not easily grown, so that the transition often seems not to be an ideal first-order one. But optical observation by polarizing microscope enables us to confirm the first-order transition even in slightly impure crystals by the occurrence of discontinuous and heterogeneous rapid changes of domain boundary movement. The transition temperature range which shows the discontinuous changes of domain boundaries, is ranged over about 1°C around 120°C. As the coercive field will become very small at this transition region, the domain boundaries seems to be very easy to move, and some interesting domain patterns were observed. These patterns are formed by the penetration of two domains, which are polarized perpendicularly to each other. They separate two parallel or perpendicular domains and look apparently like the 90° and 180° walls. 90° domain wall was already shown by Matthias[2] and Forsbergh[3], and 180° wall was also confirmed recently by Merz[4]. But the patterns which we have observed, are slightly different from their results. The triangular and crossed patterns were observed. The rate of change of domain boundary movement is dependent upon the heating and cooling rate of temperature.

§ 2. Method of Experiments

The single crystals of Barium Titanate were grown from the ternary melts of $BaCO_3$, TiO_2 and $BaCl_2$ in molar ratio of 1:1:3 by the use of corundum or graphite crucibles. The method is found elsewhere.[5][6] The crystals grown from corundum crucible are light yellow and $3\times3\times0.5$ mm^3 in size, but the domain structure is not simple. On the other hand, in the case of graphite crucible, we had light blue or almost colourless small thin plate about $0.5\times0.5\times0.03$ mm^3 in size. These crystals were found to be simpler in the do-

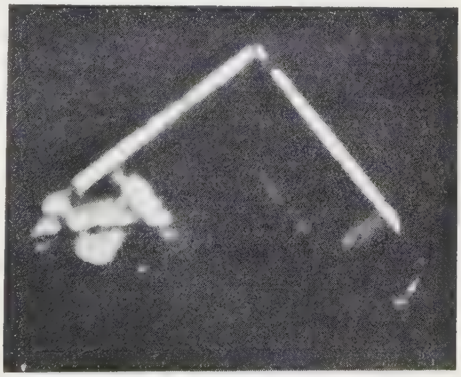

Fig. 1. Under crossed nicols at room temperature (×100).

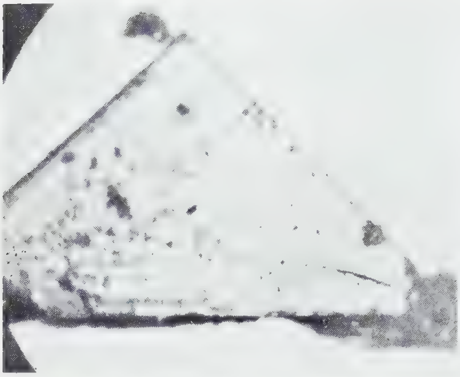

Fig. 2. Under parallel nicols at room temperature.

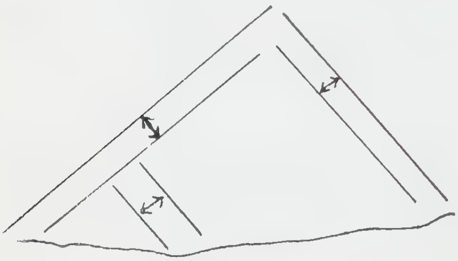

Fig. 3.

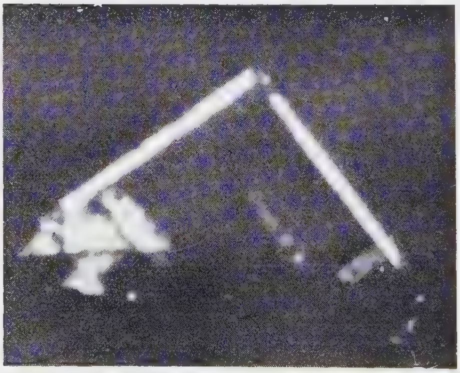

Fig. 4.

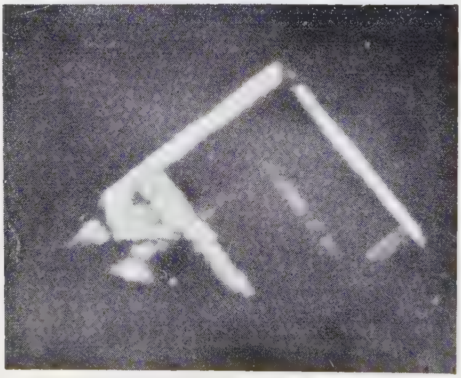

Fig. 5.

main structure, and considered as fairly good c-plate as shown in Fig. 1.

In order to heat the crystal we prepared the apparatus such as used by Kay[7] on the stage of the polarizing microscope, having the magnification of ×100. The 16 mm Cine Kodak movie camera was attached to the eyepiece of the microscope, and the film speed was 8 sections per second. The heating rate was varied from 1°C per minute to 5°C per minute, and the corresponding time interval of the transition ranged from 20 seconds to 4 minutes. To observe the domain boundary movement, the stage of the microscope was rotated 45° from the straight extinction position under the crossed nicols, and so we could observe the domain patterns in the brightest condition.

§ 3. Observation of the Domain Boundary Movement

The domain structures of the crystals are different depending on samples and the behavior of their domain boundary movement is not so simple, but there seems to be some tendencies as follows. In general, up to the temperature about 1°C below the Curie point, almost no change was observed in the domain pattern, but as the temperature reached the transition range, the discontinuous changes of domain structures were observed. The domain boundary movement begins from a corner position and in a short time the c-plate crystal is transformed to a-plate, i.e., we observed the crystal very bright in the whole area, but after some pause in this state, very rapid discontinuous changes of comparatively large area of a-plate to cubic phase occurs and the transition finishes into the cubic phase over the whole crystal. The direction of the domain boundary movement in the former stage seems to be perpendicular to the latter. When the crystal is cooled down from the temperature above the Curie point, similar change is observed, and the final domain pattern is almost the same as the initial one at the room temperature before heating. We may confirm the first-order transition by the occurrence of these heterogeneous and discontinuous changes of domain patterns.

In the course of the transition, we observed some interesting domain patterns which seems to be formed due to the penetration of two perpendicular domains. They look apparently like the boundaries of 90° domains and parallel or antiparallel domains. But these boundaries would not be the so called domain boundary layers in the usual sense, but transient interstitial layers. The thickness is seen to be very large compared with the expected domain boundary thickness of molecular dimensions, and that of the 90° domain interstitial layer is roughly estimated about the order of one micron, but that of the parallel one is slightly less.

Now let us explain the domain patterns in detail by the following figures picked up from one run of the heating cycle of the motion picture. The whole interval of the transition is about 30 seconds.

In Fig. 1 the crystal is shown at room temperature at the 45° position under crossed nicols, and the direction of c-axis in the bright stripe domain is verified as the arrows in Fig. 3 by the use of gypsum plate. The width of the stripe is about 0.03 mm. Fig. 4 shows the state just before the beginning of transition at about 120°C, which is almost the same as Fig. 1. 2.5 seconds after Fig. 4, new triangular pattern appears as shown in Fig. 5 and Fig. 6 due to the penetration of two 90° domains. Schematic pictures are given in Fig. 7(a). Besides the triangular pattern A, we can observe two patterns B and C.

In general, the interstitial layer may be observed as dark lines under the crossed nicols, at 45° from the straight extinction position in any of the following three cases: firstly, the interstitial layer belongs to tetragonal phase and its c-axis is perpendicular to the plane of the crystal plate; secondly the c-axis lies in the plane of the plate and parallel to one of the polarized plane of the crossed nicols; and thirdly the layer is in cubic phase.

Firstly let us consider the A pattern. Due to the penetration of the two domains, there would be large stresses near the interstitial layer, and as the crystal is very thin plate, the stress would be two-dimensional rather than three-dimensional. Whereas the hydrostatic pressure tends to drop the Curie point linearly[8)], the two-dimensional pressure will raise it as Forsbergh recently found.[9)] So the interstitial layer would have slightly higher Curie point than the outside domains and c-axis perpendicular to the plate. Therefore the A-pattern may belong to the first case. The second case seems to be unreasonable because the stress tends to change the c-axis lying in the plane of the crystal to become perpendicular to the plane. The third case is perhaps also possible. Because of the large stresses near the interstitial layer, originally elongated two c-axis ab and cd in Fig. 7(b) would be slightly shortened and become nearly equal, and so the interstitial layer would be considered as nearly cubic phase and appear as dark lines. Therefore, both the first

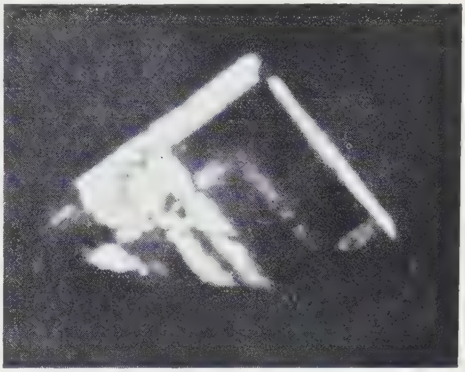
Fig. 6.

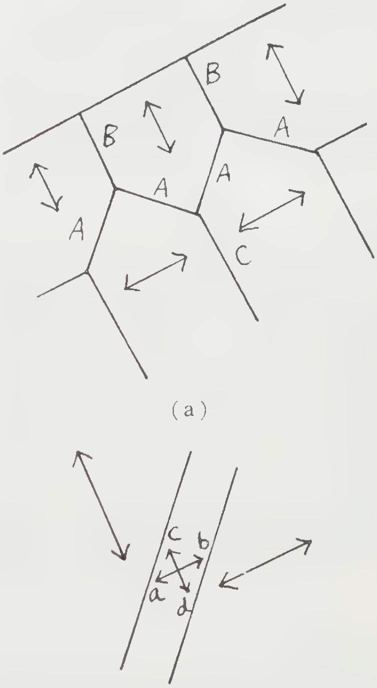

(a)

(b)

Fig. 7.

and the third cases would be possible, but we cannot decide whether the A-pattern belongs to c-domain or to cubic phase.

Next we consider the B-pattern in Fig. 8. Before the formation of this triangular pattern, I and II domains were same ones, bu after the penetration of III into I–II domains these domains are separated by the layer B Whether I and II are in parallel or antiparalle direction, we cannot distinguish optically except by applying electric field perpendicula to the direction of polarization like the metho by Merz.[4] As in the case of A-pattern, th stress near the interstitial layer between I an II domains would cause the polarization of th interstitial layer to become perpendicular t the plane of the crystal, but it would b smaller near the top of the triangular A pattern than at the base of it. So the dark lin would be diffused as is really observed in Figs. 5 and 6. The cubic phase may be also possible, for the stress near the B layer tends to elongate the ab direction and shorten the cd direction as shown in Fig. 8(b). So the layer would have nearly cubic phase as in Fig. 8(a).

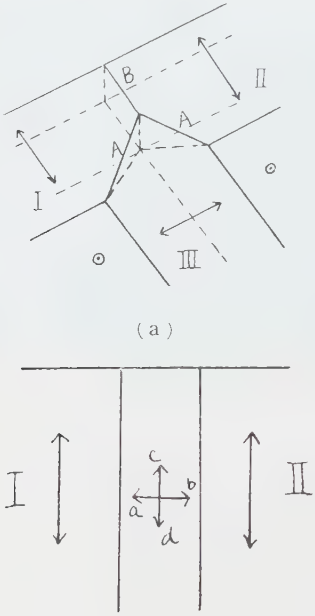

(a)

(b)

Fig. 8.

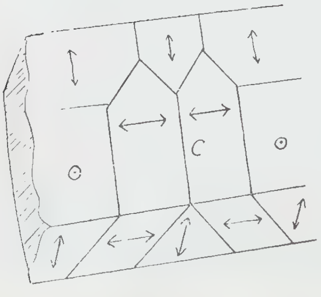

Fig. 9.

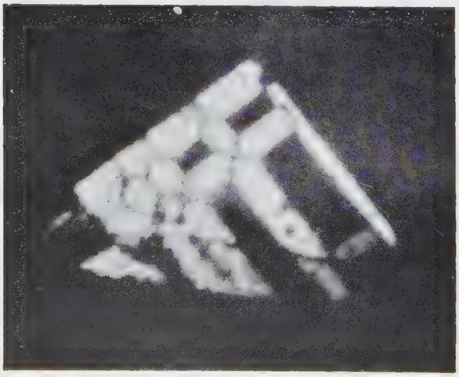

Fig. 10.

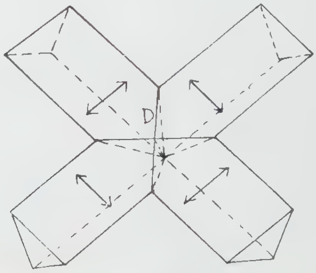

Fig. 11.

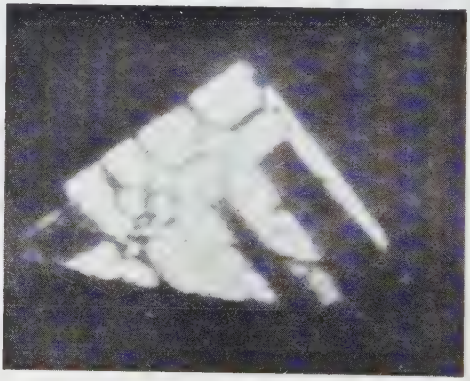

Fig. 12.

C-pattern is apparently curious because the line is perpendicular to the polarized direction of the adjacent domains. But, if we suppose the section of this plate as in Fig. 9, it may be explained reasonably as c-domain. Due to the head-to-tail arrangement this line must be the edge of the triangular prism polarized in c-direction.

Lastly we explain the D-pattern of crossed layer shown in Fig. 10 which appears 1/8 second Fig. 6 has been taken. This pattern is a bit similar to that found by Forsbergh[3], but differs in its simple domain structure. These two crossed stripes may contain 180° domains but not 90° ones. When two prism domains cross as shown in Fig. 11, the interstitial layers are formed at right angle to the plane of the crystal, but this layer seems to be the combination of four A-patterns. Like the A type, this layer will also consist of either cubic or c-domain. Since the width of each domain is about 0.03 mm, the width of the dark line is roughly estimated as the order of one micron.

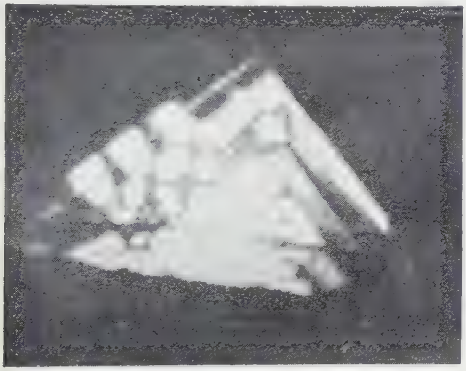

Fig. 13.

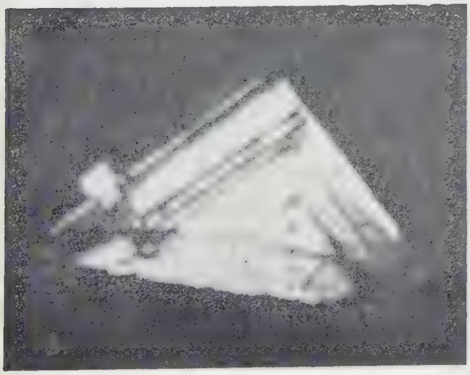

Fig. 14.

These four types of interstitial layers, which arise from the penetration of two perpendicular domains near the transition temperature, seem to be different from the domain wall at room temperature. They are formed temporarily by the strong stress due to the penetration of two perpendicular domains and would be considered as c-domain or cubic phase.

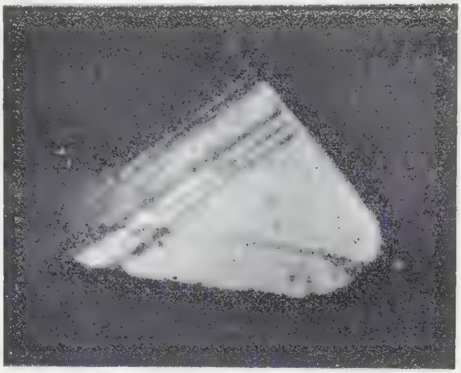

Fig. 15.

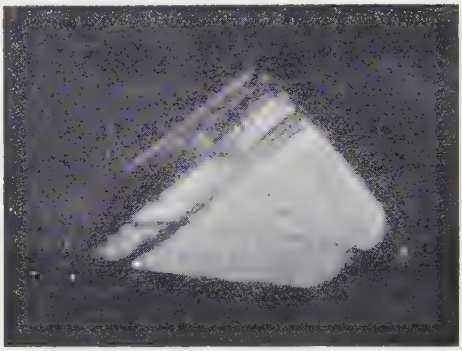

Fig. 16.

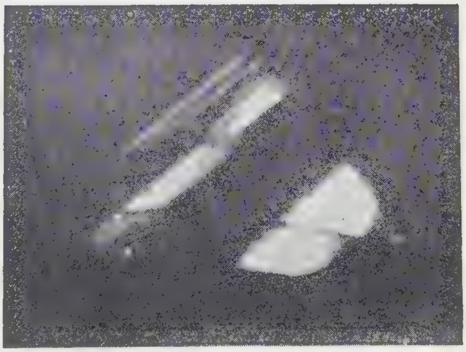

Fig. 17.

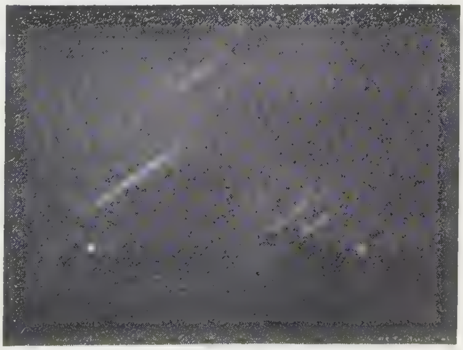

Fig. 18.

The thickness of the layers is too large to be a simple domain wall. After the appearance of these patterns, the c-domain is transformed into a-plate as shown in Figs. 12∼15. Compared with the relatively short period of the primary stage, the formation of a-domain is much slower. But as shown in Figs. 16 and 17, the discontinuous change of a-domain to cubic phase occurs in a relatively short time with in 1/8 seconds. After this change the residual a-domains are slowly changed into cubic phase and the transition finishes as shown in Fig. 18. The relation of time interval to the corresponding figures is shown in Table I.

Table I.

No. of Figure	Time (sec.)	Time interval (sec.)
4	0	
		2.5
5	2.5	
		0.6
6	3.1	
		0.7
10	3.8	
		1.2
12	5.0	
		1.25
13	6.25	
		2.5
14	8.75	
		3.75
15	12.5	
		5.65
16	18.15	
		0.25
17	18.4	
		3.0
18	21.4	

§ 4. Conclusion

By the direct observotion of the discontinuous and heterogeneous changes of the domain boundary movement at the Curie point, the first-order transition of this substance is confirmed. During the transition, four types of interstitial layers are formed, which are not observed at the room temperature. They would be considered as either cubic phase o c-domain caused by the strong stresses du to the penetration of two perpendicular domains. The discontinuous changes of domai patterns occur within 1/8 seconds, so that w must study in further detail by means of hig speed camera. Though the above discussion are very qualitative, the transition of fairl good crystal is found to be not simple, followed by complicated changes of domain structures. Furthermore, since the coercive fiel will be almost negligibly small near the Curi point, the movement of domain boundar would be very easy and would be affecte sensitively by thermal fluctuations, impuritie and localized stresses. To clarify the movement of domain wall in detail, we must stud the frequency dependence of the hysteresi effect, field dependence of displacement velocity and the relaxation time.

The author wishes to thank Dr. H. Takahashi and Mr. W. Kinase for their helpfu discussions, and to Mr. Kamijo and Mr. Sekikawa for their valuable help on this work.

References

1) L. E. Cross: Phil. Mag. **44** (1953) 1161.
2) B. T. Matthias and A. von Hippel: Phys. Rev. **73** (1948) 1378.
3) P. W. Forsbergh: Phys. Rev. **76** (1949) 1187.
4) W. J. Merz: Phys. Rev. **88** (1952) 421, **91** (1953) 513, **95** (1954) 690.
5) H. Blattner et al: Helv. Phys. Acta **22** (1948) 35.
6) H. F. Kay: Acta Cryst. **1** (1948) 229.
7) H. F. Kay and P. Vousden: Phil. Mag. **40** (1949) 1019.
8) W. J. Merz: Phys. Rev. **78** (1950) 52.
9) P. W. Forsbergh: Phys. Rev. **93** (1954) 686.

Journal of the Physical Society of Japan Vol. 10, No. 7, July, 1955

Thermal Transition of Transparency in Ferroelectric Single Crystal of Barium Titanate

By Tadao HORIE, Kazuo KAWABE, Masashi TACHIKI,
Faculty of Science, Osaka University
and Shozo SAWADA
Institute of Science and Technology, Tokyo University

(Read November 2, 1954, Received April 2, 1955)

The ferroelectric single crystal of barium titanate exhibits a strong absorption in the ultra-violet region at any temperature including the three transition points. The threshold for the ultra-violet absorption shifts gradually towards longer wave-lengths as the temperature rises, and the temperature coefficient of it is about one Angstrom per degree centigrade. In addition to this ultra-violet absorption, the crystal exhibits another absorption in the visible region. The intensity of natural light with wave-lengths in the neighbourhood of 5000 A transmitted through the crystal is measured by means of a multiplier phototube. It shows quite steep and sudden changes near the transition temperatures, especially in thin crystals. Let $I(\mathrm{T})$, $I(\mathrm{O})$ and $I(\mathrm{R})$ be the intensity of transmitted light in the tetragonal, orthorhombic and rhombohedral phases respectively. Then the following relations can be drawn out of the various curves for the thermal transition of transparency. They are $I(\mathrm{O}) \gtrsim \frac{1}{2} I(\mathrm{T})$ and $I(\mathrm{R}) \lesssim \frac{1}{4} I(\mathrm{T})$. From calculations on optical paths through the adjacent domains in the orthorhombic phase, the former relation is derived. The same considerations in the rhombohedral phase lead to the latter. Furthermore for polarized light, the behaviours are partially different from those for natural light. In the present paper experimental results for the thermal transition of transparency for both natural and polarized light are interpreted from the standpoints of the theories of ferroelectric domains and crystal optics.

§ 1. Introduction

The threshold for the optical absorption in single crystal of $BaTiO_3$ has recently been measured by the authors in dependence on temperature ranging from −100°C to 150°C and the result has been reported in the previous paper [1]. The crystal exhibits a quite strong absorption in the ultra-violet region with wave-lengths shorter than 3900 A at room temperature. Recently J. A. Noland[2] found that $SrTiO_3$ single crystals exhibit a quite similar absorption in the ultra-violet region with wave-lengths shorter than 3850 A. The latter has the same crystal structure of perovskite type as the former. These ultra-violet absorptions may be due to electronic transitions from the valence band to the conduction band.

As is well known, $BaTiO_3$ exhibits a striking ferroelectricity and has not only a Curie point near 120°C but also the other two transition points near 0°C and −80°C. On the contrary, $SrTiO_3$ is not ferroelectric and has no transition point down to 1.3°K[3]. The threshold for the ultra-violet absorption in $BaTiO_3$ shifts gradually towards longer wave-lengths as the temperature rises and its temperature coefficient is about one Angstrom per degree centigrade. This temperature shift has already been reported in some details in the reference 1). The present paper will be devoted to a study of the optical behaviours in the visible region.

According to J. A. Noland, $SrTiO_3$ single crystals are quite transparent in the region ranging from the threshold for the ultra-violet absorption to near infra-red. The coefficient of transmission exceeds 70%, even when the crystal is as thick as 1 mm. On the contrary, the circumstances are quite different in $BaTiO_3$ single crystals. According to precise measurements in dependence on temperature, the coefficient of transmission changes abruptly near the transition points and shows quite steep hysteresis loops, especially in thin crystals. Below −80°C, the crystal becomes rather opaque even when it is as thin as 20 μ. The authors will call this phenomenon *thermal transition of transparency* and discuss it in some details from the standpoints of the theories of ferroelectric domains and crystal optics in the present paper.

§ 2. Thermal Transition of Transparency

Quite a number of $BaTiO_3$ single crystals have been prepared by means of Na_2CO_3 flux[4]. The specimens picked out of them are all thin enough to ensure measurements of the optical transmission. Most of them are so-called *ac*-crystals but a few *c*-crystals are also found among them. Fig. 1 shows samples of these crystals.

Under constant illumination (about 5000 A), the intensity of light, which has passed through the central part of the crystal, is measured with a combination of a multiplier phototube, a D.C. amplifier and a microammeter. The temperature is varied gradually up and down between −100°C and 150°C. The results obtained for natural light are shown in Fig. 2. Near 120°C, there is no loop good enough to be detected. Near 0°C and −80°C, however, quite striking loops can be found. The thicker the crystal is, the more the loop is round; the thinner, the more angular.

Let $I(\mathrm{T})$, $I(\mathrm{O})$ and $I(\mathrm{R})$ be the intensity of the transmitted light in the tetragonal, orthorhombic and rhombohedral phases respectively. Then for every crystal we have

$$I(\mathrm{R}) < I(\mathrm{O}) < I(\mathrm{T}) \,,$$

and besides the following relations may be deduced readily from these experimental curves. In the first place, between 0°C and −80°C, $I(\mathrm{O})$ is always more or less weaker than $I(\mathrm{T})$. Although the ratio $\{I(\mathrm{T})-I(\mathrm{O})\}/I(\mathrm{T})$ somewhat varies for different crystals, it does not exceed 1/2 and we have

$$\frac{I(\mathrm{T})-I(\mathrm{O})}{I(\mathrm{T})} \lesssim \frac{1}{2} \,. \qquad (1)$$

This ratio is about 1/4 in the crystal No. 1, and about 1/2 in No. 4. In the second place,

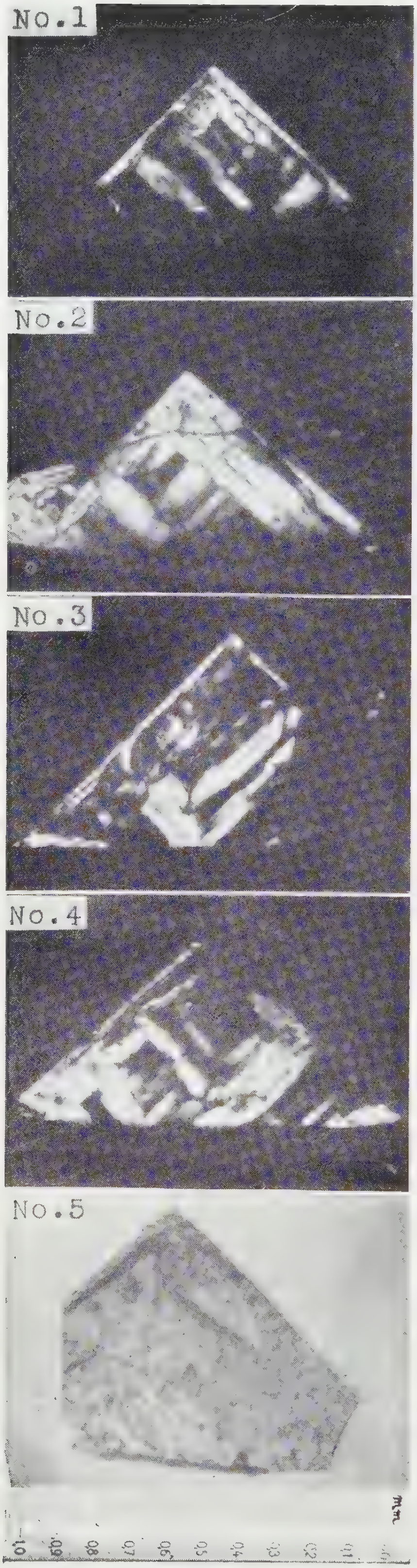

Fig. 1. Photographs of specimens placed between crossed Polaroids at room temperature, except No. 5.

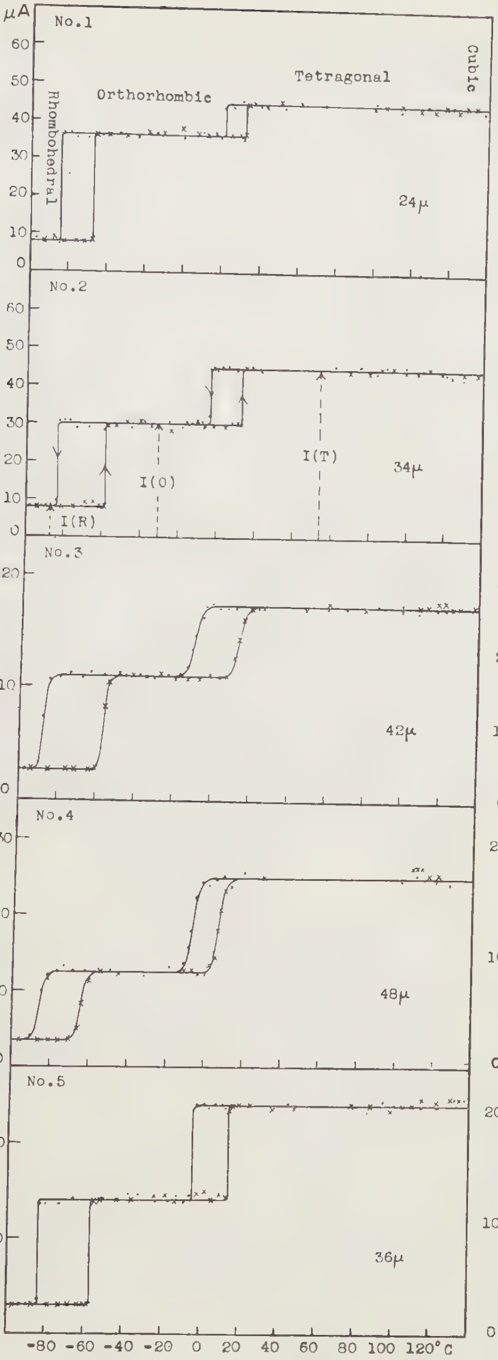

Fig. 2. Thermal transition of transparency, natural.

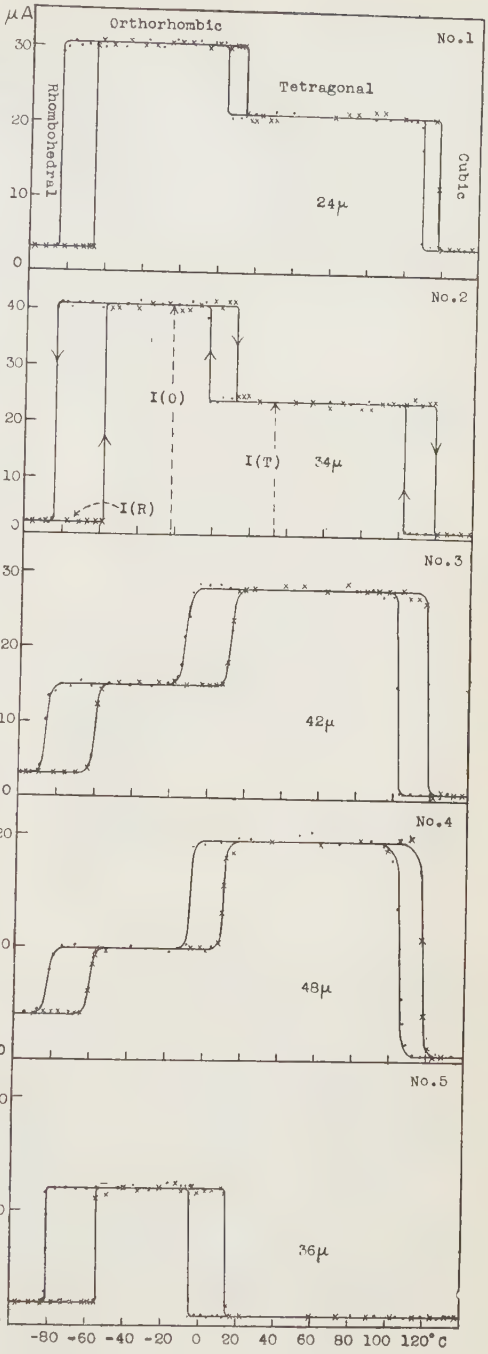

Fig. 3. Thermal transition of transparency, polarized.

below $-80°C$, $I(R)$ is always much weaker than $I(T)$. Although the opacity in the rhombohedral phase sowewhat varies for different crystals, the ratio $I(R)/I(T)$ is alway about 1/4 or less and we have

$$I(R) \lesssim \tfrac{1}{4} I(T) . \qquad (2)$$

Thermal transition of transparency for polarized light is shown in Fig. 3. In this case a crystal is placed between crossed Polaroids and the intensity of light transmitted through it is measured in the same way as above. It is different from the case of natural light that these curves have distinguished loops near 120°C, with the only one exception of the curve in the *c*-crystal No. 5. It is quite similar to the case of natural light that *I*(R) is always much weaker than *I*(T) and *I*(O). Near 0°C, however, the circumstances are quite different and *I*(O) is sometimes weaker and sometimes stronger than *I*(T).

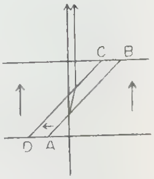

Fig. 4. Optical paths in tetragonal phase.

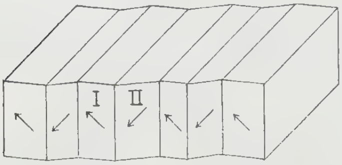

Fig. 5. Twinning in orthorhombic phase.

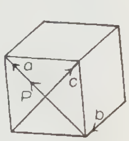

Fig. 6. Unit cell in orthorhombic phase.

§ 3. Interpretation, Natural Light

The light employed is of much longer wavelengths than the threshold for the intrinsic absorption of the crystal. The experimental curves obtained may be considered to be connected directly with the appearance and disappearance of polydomains in phase transitions. The single crystal of $BaTiO_3$ has usually polydomains below its Curie point and its crystal structure is tetragonal between 120°C and 0°C, orthorhombic between 0°C and −80°C and rhombohedral below −80°C[5)6)].

In the tetragonal phase, there are several striations of *a*-domains in which spontaneous polarization is parallel to the crystal surface. When viewed from one side of the crystal, a striation is a lamina as shown in Fig. 4[5)]. The incident light is propagated into the crystal as the ordinary and extraordinary rays. The extraordinary one is refracted at the boundary AB. After passing through the boundary CD, both rays have the same direction again. Hence it appears likely that the double refraction in this phase makes only a minor contribution to the decrement in the intensity of the transmitted light.

Below 0°C, all of the boundaries are at right angles to the crystal surface and the polar axis alternates its direction as shown in Fig. 5[6)]. In order to obtain the optical paths the optically biaxial property of this crystal phase should be taken into account. On entering the crystal the incident beam is decomposed into two waves; both waves are extraordinary. The polar axis and crystal axes of a unit cell in the domain I are shown in Fig. 6. In an orthorhombic crystal, every one of the crystal axes ***a***, ***b*** and ***c*** is parallel to one of the optic elasticity axes. Accordingly the intersections of the two extraordinary wave surfaces with the *ac*-plane consist of a circle and an ellipse as shown in Fig. 7.

The wave with circular section may be transmitted without deviation through the crystal*. On the other hand, the wave with elliptic section may be refracted by an angle of θ_0 towards the boundary surface. Since the birefringence in the *b*-direction is 0.075[6)] and the optical index of refraction is smaller parallel to the polar axis (α) than perpendicular to it (γ)[7)], we have

$$\gamma-\alpha=0.075. \tag{3}$$

As is shown in text-books on optics, the equation of the elliptic section is

$$\gamma^2a^2+\alpha^2c^2-1=0\,. \tag{4}$$

Let R(a, c) be the point of contact of the plane wave-front with the ellipse. Then from (4) we have

$$\frac{da}{dc}=-\frac{\alpha^2}{\gamma^2}\frac{c}{a}=-1\,, \tag{5}$$

and the line $\overline{\mathrm{OR}}$ gives the direction of refraction for the extraordinary ray considered. Since the index of refraction is 2.4[8)], from (3) and (5) we have

$$\tan\angle c\mathrm{OR}=\frac{a}{c}=\frac{\alpha^2}{\gamma^2}=\left(1-\frac{0.075}{\gamma}\right)^2, \tag{6}$$

and $\angle c\mathrm{OR}=43°10'$.

Hence this extraordinary ray is deflected from the direction of incidence $\overline{Ox}$ to the side by the angle of $\theta_0=1°50'$. When this refracted ray happens to pass through a domain boundary, it may be refracted and reflected again as shown in Fig. 8. According to the calculations in § 5,

---

* Owing to the twin angle of 8.4′, the angle of incidence is not zero in the strict sense of the word. As will be discussed later in § 6, it is no matter whether the incident beam is normal or slightly inclined to the crystal surface, particularly in the orthorhombic phase.

$$\theta_1=\theta_1'\approx\theta_0\ ,$$

and $$\theta_2=\theta_2'\approx 8°40'\ .$$

The apparatus is insensitive to the beams deflected from the direction of incidence to the side by angles larger than 1°30′. Let D and $\varDelta$ be the thickness and the width of the domain I respectively. Then the beam of light entering the region, $\mathrm{TW}=D\tan\theta_0$, which is close to the boundary WW′, may be decreased in intensity by about one half in comparison with the beam entering the region distant from the same boundary. In the specimens used, both D and $\varDelta$ may probably be not uniform all over the crystal. The more the domains in which $D\tan\theta_0$ covers $\varDelta$ are abundant, the more the intensity of transmitted light may be weakened. Now let $\overline{D}$ and $\overline{\varDelta}$ be the average values over the area observed in the crystal, and we have readily

$$\frac{I(\mathrm{T})-I(\mathrm{O})}{I(\mathrm{T})}\approx\frac{1}{2}\ \frac{\overline{D}\tan\theta_0}{\overline{\varDelta}}\ . \tag{7}$$

It may then be concluded that the ratio $\{I(\mathrm{T})-I(\mathrm{O})\}/I(\mathrm{T})$ does not become larger than 1/2 in any case. Consequently the relation (7) is in good agreement with the empirical one (1) in § 2.

Let us now make an estimate of the value of $\overline{\varDelta}$ for the specimens used, by making use of (7). For example, in the specimen No. 1, from Fig. 2 the ratio $\{I(\mathrm{T})-I(\mathrm{O})\}/I(\mathrm{T})$ is about one quarter and hence from (7) we have $\overline{\varDelta}\approx 1.5\mu$. Similarly we have the values of 1.6μ, 1.8μ, 1.5μ and 1.4μ in the specimens No. 2, No. 3, No. 4 and No. 5 respectively. In spite of the expectation that the boundary separation $\varDelta$ can not only fluctuate widely but also depend on the thickness and other conditions of the crystal, the average values derived above are fairly comparable with the value estimated as $\sim 5\mu$ by H. F. Kay and P. Vousden[6].

Below −80°C, the crystal is rhombohedral and becomes again optically uniaxial. The optic axis coincides with the polar axis and alternates its direction as shown in Fig. 9[5]. On entering the crystal the beam of light is decomposed into an ordinary wave, *o*, and an extraordinary wave, *e*. It is the same as above that the wave, *e*, is deflected sideways by refractions at crystal surfaces and domain boundaries. Furthermore the ordinary ray, *o*, is also now deflected away by total reflection at the boundary wall in the course of passage through a narrow domain as will be discussed in § 6. Consequently in the rhombohedral phase, not only the extraordinary ray but also the ordinary one can not be transmitted without deviation. Hence the intensity becomes much weaker in this phase than in the orthorhombic phase and we can expect the relation (2).

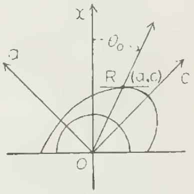

Fig. 7. Wave surfaces in orthorhombic phase.

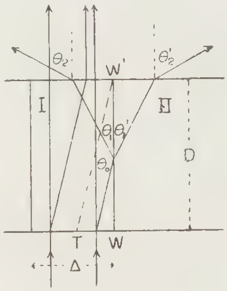

Fig. 8. Optical paths in orthorhombic phase.

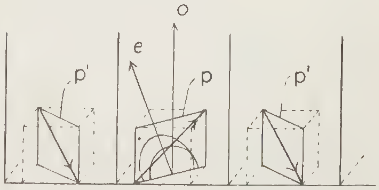

Fig. 9. Double refraction in rhombohedral phase.

§ 4. Interpretation, Polarized Light

When the crystal is mounted between crossed Polaroids, the effect of interference occurs in addition to the scattering effect discussed above, because the optic axes are inclined to the direction of incidence. After emerging from the polarizer, the plane polarized ray is decomposed into two rays inside the crystal. The latter are an ordinary ray and an extraordinary ray in the tetragonal or rhombohedral phase and two extraordinary rays in the orthorhombic phase. After having been transmitted through the crystal, they are compounded again by the analyzer into a single ray with the intensity determined by interference.

In the tetragonal phase, the interference may take place only in the domain with the polar axis parallel to the crystal surface. As mentioned in the last section, there is scarcely any loss due to the scattering effect. Consequently the transmitted light may be suddenly increased in intensity as the cubic crystal cools down through the Curie temperature.

Similarly in the orthorhombic phase, the transmitted light would be increased in intensity by the interference effect. At the same time, however, the scattering becomes also remarkable, because there appear quite fine polydomains. As a consequence, there will be two different cases as seen in Fig. 3, depending on which one of these two effects is stronger than the other.

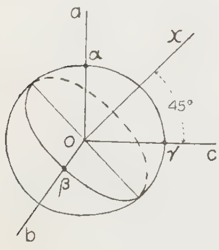

Fig. 10. Indicatrix in orthorhombic phase.

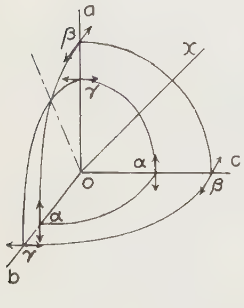

Fig. 11. Index surface in orthorhombic phase.

In the rhombohedral phase, although the interference may be expected, the scattering is much more prevailing as mentioned above. Hence the intensity is always weakened remarkably. We may conclude that the experimental curves for polarized light can be interpreted as a superposition of the scattering and the interference effects.

§ 5. Optical Paths in Orthorhombic Phase

Let α, β and γ be the three principal indices of refraction. Then the indices of refraction of the two extraordinary waves in the direction $\overline{OX}$ in Fig. 10 are given by the two semi-axes of the ellipse, that is the intersection of the indicatrix, $a^2/\alpha^2+b^2/\beta^2+c^2/\gamma^2=1$, with the plane through the centre of the ellipsoid at right angles to OX. They are β and $\sqrt{2}\,\alpha\gamma/\sqrt{\alpha^2+\gamma^2}$ respectively. The former corresponds to the extraordinary wave vibrating at right angles to the *ac*-plane and the latter to the extraordinary wave vibrating in the same plane. Hence the birefringence in the direction OX is as follows:

$$\beta-\frac{\sqrt{2}\,\alpha\gamma}{\sqrt{\alpha^2+\gamma^2}}=R_1\,. \tag{8}$$

Similarly the birefringence in the *b*-direction is given by the difference between the two semi-axes (α and γ) of the ellipse, that is the intersection of the indicatrix with the *ac*-plane. Then as is in the equation (3) in § 3,

$$\gamma-\alpha=R_x\,. \tag{9}$$

From (8) and (9) we have

$$\beta-(\alpha+R_x)\left(1+\frac{R_x}{\alpha}+\frac{R_x{}^2}{2\alpha^2}\right)^{-1/2}=R_1\,.$$

Consequently $\beta-\alpha=R_1+R_x/2\,.$ (10)

From (9) and (10)

$$\beta-\alpha=R_1-R_x/2\,, \tag{11}$$

and from (9), (10) and (11) we have

$$\beta>\gamma>\alpha\,,$$

where the observed values of R_1 and R_x are 0.045 and 0.075 respectively6). As the consequence, the optic axes lie in the *ab*-plane as shown in the index surface in Fig. 11.

As far as the *ac*-plane is concerned, one of the extraordinary wave has a constant value of the index of refraction, β, and so a constant velocity independent of direction of propagation, while the other has varied values between α and γ. Consequently the intersections of their wave surfaces with the *ac*-plane result in what we have already seen in Fig. 7, and only the wave with elliptic section suffers a refraction by the angle of $\theta_0=1°50'$. When the refracted wave encounters the domain boundary, it may be refracted again into the adjacent domain. Let us now trace its optical path throughout the crystal as follows.

The adjacent domains I and II in Fig. 8 are enlarged in Fig. 12. The ellipse around the centre A, a point on the wave-front AB, contacts tangentially to the wave-front EF at the point E on the boundary surface WW′. The inverted heart shaped figure around the centre B consists of two ellipses inside the domains I and II. Through the point E two tangents can be drawn to the latter. Let S and S′ be the points of contact, then $\overline{\mathrm{BS}}$ and $\overline{\mathrm{BS'}}$ give the reflected and refracted rays respectively. The optic elasticity axes in the adjacent domains are symmetric with respect to the boundary surface. It is for this reason why the reflected and refracted rays are symmetric with respect to the wall.

Let c_0 be the velocity of light in vacuo and t be the time required for the wave to travel from A to E. Then the semi-major and minor axes of these ellipses are c_0t/α and c_0t/γ respectively, and we have the following equation of the ellipse which emanates from the point B into the domain I:

$$\alpha^2c^2+\gamma^2a^2=K^2\ , \tag{12}$$

where K is c_0t. Let (a_1, c_1) be the coordinates of the point S. Then the tangent at S is given by

$$\alpha^2c_1c+\gamma^2a_1a=K^2\ .$$

If it passes through the point E (l, l), we have

$$\alpha^2lc_1+\gamma^2la_1=K^2\ . \tag{13}$$

From (12) we have

$$\alpha^2c_1{}^2+\gamma^2a_1{}^2=K^2\ . \tag{14}$$

From (13) and (14) we have

$$\left.\begin{aligned} a_1&=\frac{\gamma K^2+\alpha KQ}{\gamma l(\gamma^2+\alpha^2)}\ ,\\ \text{and}\qquad c_1&=\frac{\alpha K^2-\gamma KQ}{\alpha l(\gamma^2+\alpha^2)}\ ,\end{aligned}\right\} \tag{15}$$

where $\qquad Q=\sqrt{\gamma^2l^2+\alpha^2l^2-K^2}\ .$

From (15) we have

$$\tan\theta_1=\frac{(\alpha^2+\gamma^2)Q}{2(\alpha\gamma K+\alpha^2Q)}\ . \tag{16}$$

If we take the distance AB as $\sqrt{2}\,d$ and displace the origin from B to A, the ellipse around the point A is given by the same equation (12) and the coordinates of the point E by $(l-d,\ l+d)$. Then we have

$$K^2=(\alpha^2+\gamma^2)l^2+(\alpha^2+\gamma^2)l^2\tan^2\theta_0 \\ -2(\alpha+\gamma)l^2R_{\mathrm{x}}\tan\theta_0\ , \tag{17}$$

since $\qquad d/l=\tan\theta_0\ .$

From (16) and (17) we have

$$\tan\theta_1=\sqrt{\frac{2R_{\mathrm{x}}\tan\theta_0-\alpha\tan^2\theta_0}{\alpha}}\ , \tag{18}$$

since $\quad \alpha,\ \gamma\gg R_{\mathrm{x}}\ $ and $\ \tan\theta_0\ll 1\ .$

From (6) in § 3 and (9) we have

$$\tan\theta_0=R_{\mathrm{x}}/\alpha\ . \tag{19}$$

From (18) and (19) we have

$$\theta_1=\theta_1{}'\approx\theta_0\ .$$

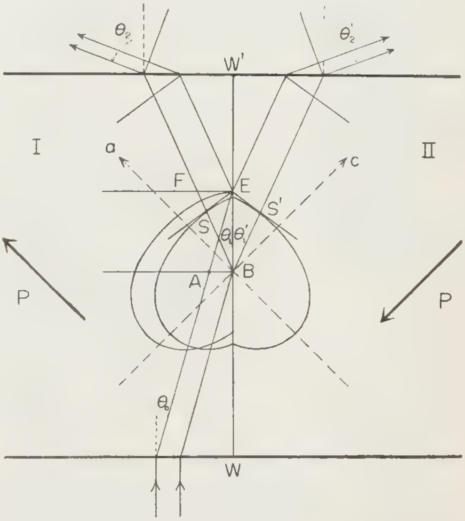

Fig. 12. Deflections at boundary in orthorhombic phase. The *a* and *c* axes refer to the domain I.

On the other hand, the angle between the incident wave-front AB and the refracted one ES′ can be calculated to be about 3°30′. Consequently it appears likely that the refraction at the boundary wall makes only a minor contribution to the change in the direction of propagation, but a major contribution to the change in the orientation of the wave-front.

Similar considerations at the upper crystal surface lead to the following relation

$$\sin\theta_2=\alpha\tan\theta_1+R_{\mathrm{x}}\ ,$$

and we have

$$\theta_2=\theta_2{}'\approx 8°40'\ .$$

Thus, one of the two extraordinary waves is deflected from the direction of incidence to the side by the angle of 8°40′, owing to the successive refractions.

§ 6. Optical Paths in Rhombohedral Phase

The empirical relation (2) requires that almost all the incident light must be scattered away in this phase. The extraordinary wave, e, is vibrating in the principal plane, p, as shown in Fig. 9. On entering the adjacent domain, it is decomposed again into an ordinary wave, o', and an extraordinary one, e', as shown in Fig. 13. Both of them are refracted again at the upper crystal surface and then scattered away in the same manner as that we saw in the last section.

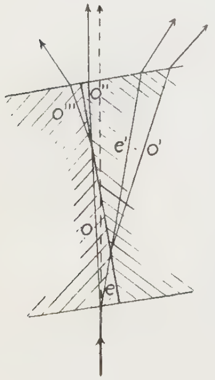

Fig. 13. Deflections at boundary in rhombohedral phase.

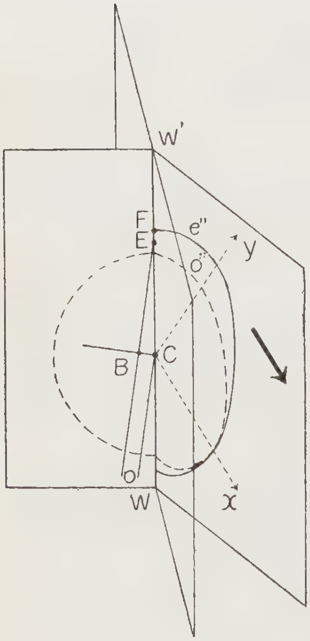

Fig. 14. Total reflection in rhombohedral phase.

On the other hand, the ordinary wave, o, is vibrating at right angles to the principal plane, p. Notwithstanding that it is considered to be transmitted without deviation through the crystal, it is expected practically to encounter the boundary for the reasons as follow. Owing to strains existing in the crystal the domain boundary may be slightly varying in orientation from place to place all over the crystal. Moreover the crystal surfaces are uneven, and it is, in strict terms, impossible to set them at right angles to the incident beam. Furthermore the incident rays are actually somewhat converging. Under these circumstances, the incident rays are not always exactly parallel to the domain walls. Such being the case, the ordinary wave, o, also may probably encounter the boundary.

For brevity, only the ordinary ray, the plane of incidence of which is at right angles to the boundary wall, is taken into consideration. In Fig. 14, let CB be the incident wave-front and let WW′ be the intersection of the plane of incidence with the boundary wall. Furthermore let n_e and n_o be the indices of refraction parallel and perpendicular to the polar axis and let t be the time required for the wave to travel from B to E. Regard C as a secondary source; with it as centre describe a sphere with radius BE and also an ellipsoid of revolution, the semi-axes of which are given by c_0t/n_e and c_0t/n_o and which touches the sphere at its intersections with the polar axis and has the x-axis as axis of revolution. As far as the extraordinary wave, e'', is concerned, we see at the instant when the disturbance from B has reached E that the disturbance from C has reached the surface of the ellipsoid. If, therefore, we can draw a tangent plane through E to the ellipsoid, this plane is the refracted wave-front. In our case, however, the ellipsoidal wave has higher velocity of propagation than the spherical. When CF is longer than CE, we can not do so and the total reflection should occur. Since the equation of the elliptic section is

$$n_o^2x^2+n_e^2y^2=(c_0t)^2\ ,$$

we have

$$\mathrm{CF}=\frac{\sqrt{3}\,c_0t}{\sqrt{2n_e^2+n_o^2}}\ .$$

Let $\pi/2-\theta$ be the critical angle of total reflection, then we have

$$\overline{\mathrm{CE}}=\frac{c_0t}{n_o\cos\theta}=\overline{\mathrm{CF}}\ ,$$

and

$$\cos\theta=1-\frac{2\delta}{3n_o}\ ,$$

where $\delta=n_o-n_e$.

If n_o and δ are taken to be 2.4 [8] and 0.07 [6], θ is nearly equal to 11°. Thus in the rhombohedral phase, the ordinary wave, o, may partly be deflected sidewards by total reflection and partly be transmitted without deviation through the boundary as an ordinary wave, o''. The only one, o'', of the four, o', e', o'' and o''', is transmitted through the crystal to the direction of observation.

On the contrary in the orthorhombic phase, the principal *ac*-planes in the adjacent domains are all co-planar as mentioned in the last section. Therefore, even when the extraordinary wave with circular section happens to pass through the domain wall, it is totally transmitted without deviation through the crystal, because no transformation takes place from the circular to the elliptic section.

References

1) T. Horie, K. Kawabe and S. Sawada: J. Phys. Soc. Japan, **9** (1954) 823.
2) J. A. Noland: Phys. Rev. **94** (1954) 724.
3) H. D. Megaw: Acta Cryst. **5** (1952) 739.
4) S. Sawada, S. Nomura and S. Fujii: Rep. Inst. Sci. Tech., Univ. Tokyo **5** (1951) 7.
5) P. W. Forsbergh: Jr., Phys. Rev. **76** (1949) 1187.
6) H. F. Kay and P. Vousden: Phil. Mag. **40** (1949) 1019.
7) A. v. Hippel: Rev. Mod. Phys. **22** (1950) 230.
8) W. J. Merz: Phys. Rev. **75** (1949) 687; **76** (1949) 1221.

JOURNAL OF THE PHYSICAL SOCIETY OF JAPAN Vol. 10, No. 7, JULY, 1955

Photoconductivity of Stibnite (Sb_2S_3)

By Sumiaki IBUKI and Seiichi YOSHIMATSU

Engineering Laboratory, Mitsubishi Elec. Mfg. Co., Ltd.
Amagasaki, Hyogo

(Received February 1, 1955)

We have investigated experimentally the photoconductivity of stibnite, a natural single crystal of Sb_2S_3. The results obtained up to the present are as follows:

1. The maximum spectral sensitivity at room temperature is found at the wavelength of 770 mμ and with the rise of temperature it shifts to the longer wavelength side.
2. The photo-current when illuminated by illuminant A varies with half power of the light intensity between 1 and 100 feetcandles.
3. The thermal activation energy for the dark current is 0.48 e.v. between room temperature and 200°C, and temperature dependence of the photo-current is also investigated.
4. The time lag of response is about 3 m sec. for the base photo-current of 10 μA.
5. Moss's constant, n^4/λ, is calculated to be 82 from our measurements on dielectric constant and refractive index.
6. The crystal is found to be an n-type semiconductor from its rectifying characteristics.
7. The response for X-rays is considerably high, while that for ultra-violet rays, β-rays or γ-rays, is low.

§ 1. Introduction

In recent years, antimony-trisulphide has been again attended as one of the photoconductive material sensitive to the visible rays.[1],[2] Large pieces of pure stibnite, the natural antimony-trisulphide crystal, have been fortunately produced in our country, so we were hit upon by an idea to use this stibnite for the study of the photoconductivity of Sb_2S_3. There are some papers[3] on the photoconductivity of stibnite, but their conclusions are not consistent with each other, and therefore it seems worthwhile to report the results of our fundamental experiments.

§ 2. Properties of Stibnite and Our Samples

The already known physical properties of stibnite are as follows:

1. It has the grey rhombic crystal form with metallic lustre and has the lines and grooves in the longitudinal direction on the surface.
2. Its crystal form belongs to the orthorhombic system, the axial ratio $a:b:c$ being 0.993:1:0.339,[4] and the space group belongs to V_h^{16}.[5]
3. It can be cleavaged perfectly along the surface of (010).
4. The unit cell includes four molecules and they make stacking layers with infinite chains of Sb_2S_3 as shown in Fig. 1.

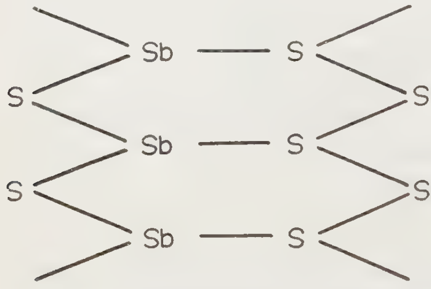

Fig. 1. Chain structure of stibnite.

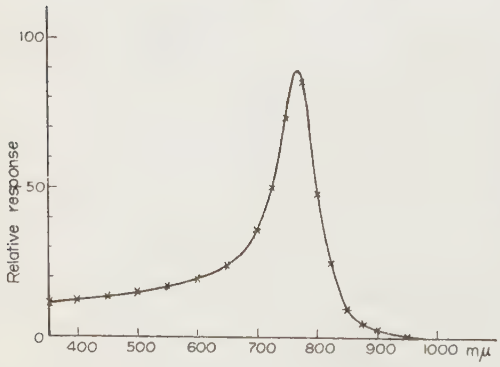

Fig. 2. Spectral sensitivity for equal energy of illumination.

5. The melting point is 548°C and the specific gravity is about 4.6.
6. When heated in air, surface oxidation is slow at about 200°C and rapid above 270°C.

The samples used in the present experiment were cut down along the plane of cleavage of the famous Ichinokawa stibnite* to the siz of about $3 \times 1.5 \times 0.2\,mm^3$. One of such piece was held between two nickel electrodes which were insulated by steatite or glass and fixed to the electrodes with aquadag. The ligh beam was projected perpendicularly to the cleavage surface under the applied electric field parallel to the surface.

According to the results of spectrochemical analysis, the sample was so pure that only extremely weak lines of Si, Cu, Fe and Mg could be observed and under irradiation of the ultraviolet rays no luminescence could be observed at the absorption edge. Applying the electric field of about 500 V/cm to the sample, the photoelectric current of several μA was obtained by indoor brightness. But no photovoltaic effect was recognized.

From the results of X-ray analysis, the lattice plane distances seem to be a little smaller than the values in Hanawalt's table.

§ 3. Experimental Results

In the following, if not specified, the samples were those described in § 2 and a balanced circuit consisting of two 954 tubes was used in these measurements.

(a) *Spectral sensitivity*

The experimental results for the spectral sensivity of photoconductivity is shown in Fig. 2. The measurement was carried out with the Beckmann DU spectrophotometer and the plotted values are those corrected for the spectral energy distribution of the light source. At room temperature the maximum spectral sensitivity lies at 770 mμ (1.62 e.v.) and the wavelength at half maximum in the longer wavelength side is 800 mμ (1.55 e.v.). This maximum did not shift even though we increased the applied field strength from 100 V/cm to 1000 V/cm. On raising the temperature of the sample, however, it shifted towards the longer wavelength side, for example, to 795 mμ (1.56 e.v.) at 90°C and to 810 mμ (1.53 e.v.) at 130°C. These values at room temperature agree with J. W. Meller's[7] and T. Moss's data[8], but not with D. S. Elliott's.[3] The curve of absorption coefficient of the film evaporated by using this sample is shown in Fig. 3. According to these results it seems reasonable to assume that the maximum spectral sensitivity lies near the absorption edge.

---

* This material is presented by courtesy of the Mining and Metallurgical Research Laboratory of Mitsubishi Metal Mining Co., Ltd.

Infra-red rays longer than 1μ gave no appreciable effect on the photoconductivity and the photoconductivity for the visible rays also was not affected by the superposed infra-red rays in contrast with the case of CdS.9)

(b) *Dark current*

Stibnite is so stable in air that it is not necessary to protect the crystal against the moisture as in the case of CdS.

As shown in Fig. 4, the dark current increases proportionally to the applied voltage below the field strength of 100 V/cm, but above this it is proportional to 1.5 powers of the applied voltage.

Temperature dependence of dark current between room temperature and 200°C was investigated and the results are shown in Fig. 5, from which the thermal activation energy for dark current is calculated to be about 0.48 e.v. From the results in Fig. 4, we can calculate the specific resistance. This is about $3\times10^7\,\Omega$cm below the field strength of 10 V/cm and a little smaller than F. M. Jager's value.3) While, under the applied field perpendicular to the cleavage surface, the specific resistance is about $5\times10^8\,\Omega$cm.

(c) *Photo-current*

The results for the voltage dependence of photo-current are shown in Fig. 6. For this measurement we used the illuminant A as the light source, because from the data of spectral sensitivity it was considered unnecessary to use the monochromatic light. The voltage dependence is greater than linear at lower voltages, while it is linear in the region between 200 V/cm and 500 V/cm. In this measurement, greater sensitivity was observed by illuminating the negative electrode than in the case of illuminating the positive electrode.

The photo-current increases slowly with the rise of the temperature of the sample, but begins to decrease from about 140°C and is scarcely recognized at about 180°C as shown in Fig. 5. Thermal activation energy for the photo-current is 0.07 e.v. between room temperature and 130°C.

The variation of the photo-current for the light intensity of illuminant A is shown in

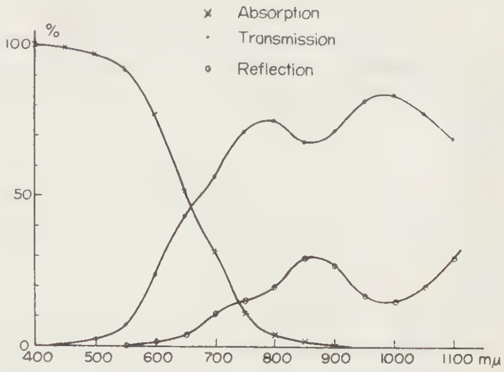

Fig. 3. Optical properties of evaporated film.

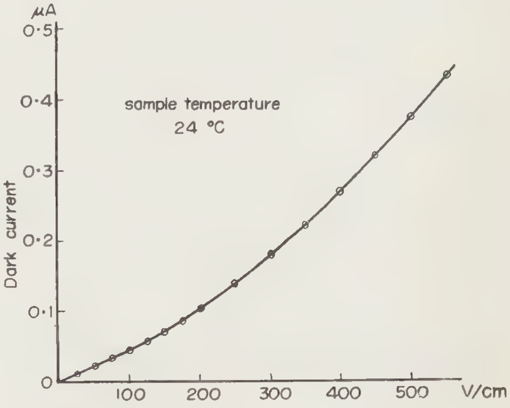

Fig. 4. Voltage dependence of dark current.

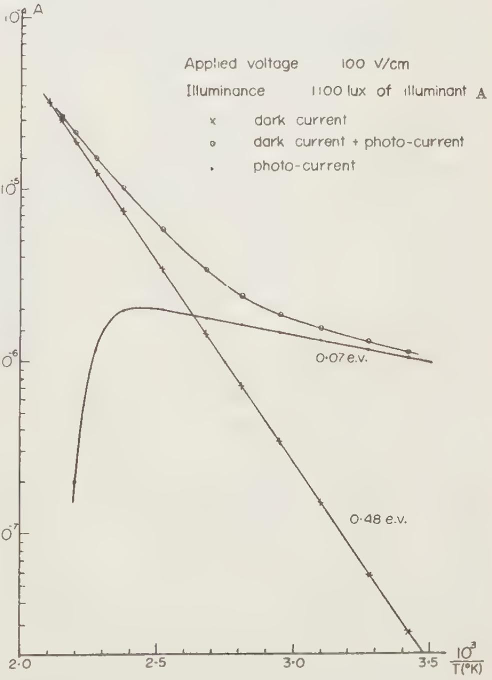

Fig. 5. Temperature dependence of the dark current and the photo-current.

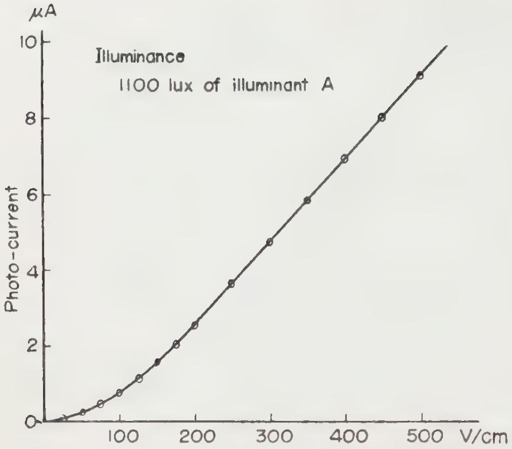

Fig. 6. Voltage dependence of photo-current.

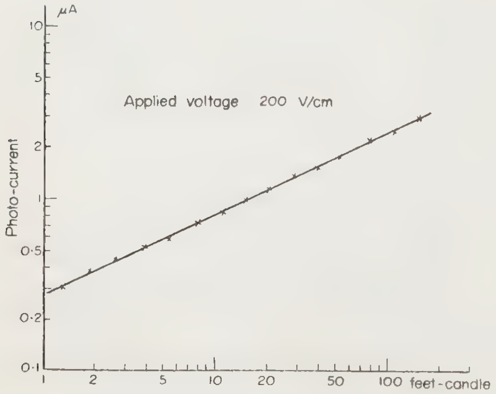

Fig. 7. Photo-current *versus* irradiation characteristics.

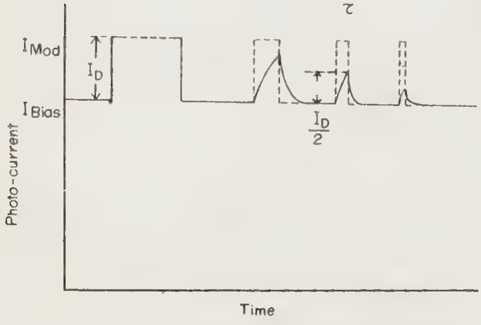

Fig. 8. Time constant measurement.

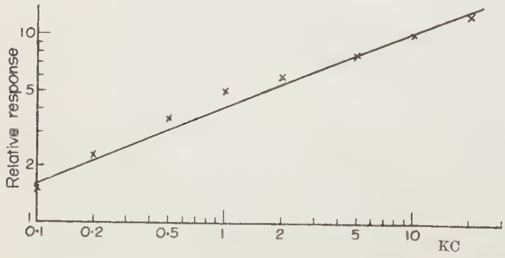

Fig. 9. Frequency response of the dark current.

Fig. 7. That is, the photo-current increase proportionally to half power of light intensit and this relation holds for lower intensit than in the case of CdS. From this experimental fact, we can also conclude that these samples are very pure.[8]

(d) *Time lag*

The time lag was measured by Rose's method.[10] As shown in Fig. 8, the base photo-current was previously raised to a certain level I_{bias}, on which small photo-current caused by another lightsource was superposed. Then, the secondary irradiation was formed into square pulses through a rotating disc and varying the angular-velocity of the disc, the pulse duration τ was measured at the time when the pulse height of the superposed photo-current became half of the initial value. The results of this measurement are as follows; for the base photo-current of 20, 10, and 5μA, the obtained time lag is 1.7, 2.5 and 4 m sec. respectively. These values are fairly consistent with S. V. Forgue's value.[2]

Instead of applying the pulse form irradiation, rectangular publses of voltage were superposed on the constant base voltage and then the wave form of the modulated photo-current was observed on the oscilloscope. In this case the time lag was found to be 50μsec. or so for the base photo-current of 10μA.

(e) *Dielectric constant and refractive index*

The frequency dependence of dark current was investigated by applying a constant A.C. voltage to the sample. The dark current increases with frequency as shown in Fig. 9, but the photo-current itself for the irradiation of illuminant A is constant up to 10 K.C.. Consequently it seems to be reasonable to assume that the time lag is shorter than 100 μ sec.

The above-mentioned fact that the dark current under the applied A.C. voltage increases with frequency seems to be due to the capacitance of the cell. We therefore measured the dielectric constant of samples by three methods.

In the first method, the sample size was about 10×10×1 mm³ and tin foils were stuck onto the both 10×10 mm² surfaces with shellac and the capacitance was measured by Q-meter applying the field perpendicularly to the cleavage surface. The capacitance at 500 KC was 10 PF and therefore dielectric constant $\mathcal{E}$ is 9.6.

Next, the optical dielectric constant $\mathcal{E}_0$ was measured. This value $\mathcal{E}_0$ is obtained from the following equations;

$$\mathcal{E}_0 = n^2 \quad \text{and} \quad 2nd(1/\lambda_1 - 1/\lambda_2) = 1$$

where n is the refractive index, d the thickness of the film and λ_1, λ_2 the wavelengths at the transmission maxima. As shown in Fig. 3, the maxima of transmission lie at 785 mμ and 990 mμ, and the thickness of the film was measured by means of interferometory and was found to be 650 mμ. Substituting these values in the above equations, we find that $n=2.90$ and $\mathcal{E}_0 = n^2 = 8.46$.

The reflectivity of the cleavage surface of stibnite was also measured with the Hardy type spectrophotometer. A very good cleavage surface was obtained after every available effort, and the result for such surface is shown in Fig. 10. From this curve, its specular reflectivity at 800 mμ is estimated to be 23% by extrapolation. Using the following equation:

$$R = (n-1)^2/(n+1)^2 ,$$

where R is the specular reflectivity for faint absorption, we find that n is 2.85. Calculating from this value, Moss's constant[8] $n^4/\lambda_c = 82$, where λ_c is the critical wavelength, i.e. the wavelength (800 mμ in this case) at half maximum in the longer wavelength side. The value seems to be reasonable.

(f) *Rectifying characteristics*

We measured the rectifying characteristics of stibnite in the dark for the perpendicular direction to its cleavage surface. The result is shown in Fig. 11. A tungsten probe was used in this measurement.

Illuminating the probe side of the sample with the incandescent light perpendicularly to its cleavage surface, the photo-current when the probe was negative was four to five times greater than that when the probe was positive.

According to these results, it may be concluded that stibnite is an n-type semiconductor.

(g) *Sensitivity to the radiation other than visible rays*

We now describe the sensitivity to several radiations when the electric field of 800 V/cm is applied to the sample of $2 \times 1 \times 0.2$ mm^3.

As mentioned above, infra-red rays gave no appreciable effect. The sensitivity to ultraviolet rays was faint. For example, photocurrent of about 0.03 μA could be observed for the radiation of wavelength 2537 A of 0.8 mW/cm^2. This value is only about one-tenth of the dark current.

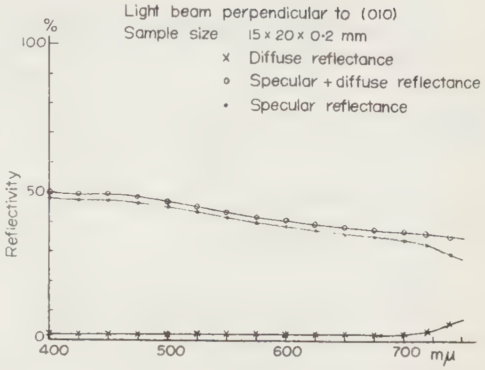

Fig. 10. Reflectivity of freshly cleavaged surface.

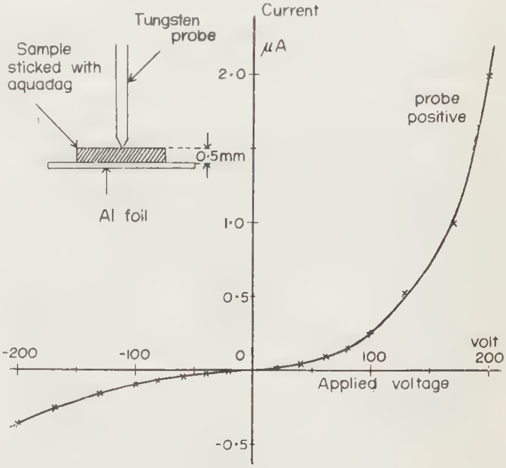

Fig. 11. Rectifying property in the dark.

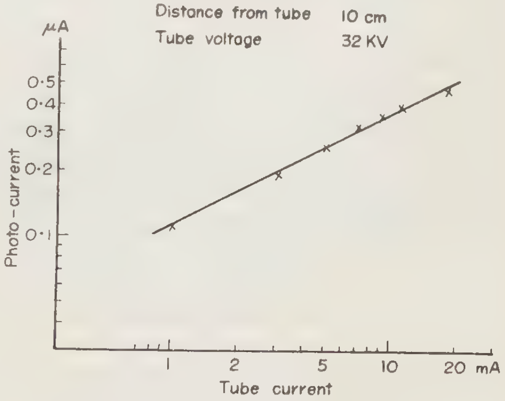

Fig. 12. Photo-current by X-rays. (varying tube current)

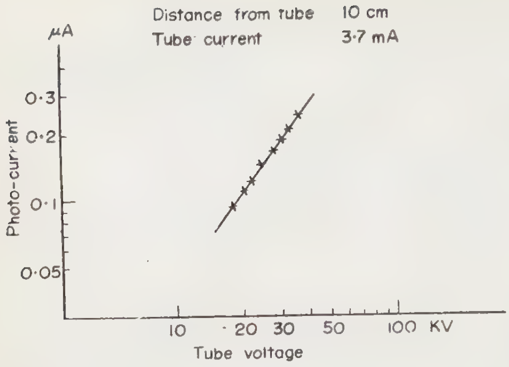

Fig. 13. Photo-current by X-rays.
(varying tube voltage)

For X-rays from Cu-target, however, considerable response could be observed. The relation between the photo-current and the X-ray intensity is shown in Figs. 12 and 13, and the relation varies with the voltage and the current of X-ray tube. The photo-current by the X-rays increases proportionally to about half power of the X-ray intensity, and this relation seems to be similar to that obtained for visible rays. In addition, the time lag for X-rays was observed to be several seconds.

The same sample was also exposed to the γ-rays from C_0^{60} of 13 mC. and the β-rays from Sr^{90} of 20 mC. at the distance af 5 cm. In this case the response which exceeded the order of fluctuations of the dark current, i.e. 10^{-9} A, was not observed.

§ 4. Conclusion and Acknowledgement

In the present paper we described the photoconductive properties of stibnite. Briefly, stibnite is a typical n-type photoconductive material which has the sharp peak of sensitivity at 770 mμ and the very small time lag. But it has some faults, that is, its dark current is considerably high and its sensitivity is n so excellent as that of CdS.

We wish to express our sincere thanks Mr. S. Ōno, director of the laboratory, f his constant guidance in the course of tl work and to Prof. Y. Uchida of Kyo University for his valuable discussions. W are also indebted to Mr. T. Tomiki of Kyo University for his measurements of th specular reflectance and to Mr. G. Imamur and Mr. M. Nakamura of our laboratory fo their works in the X-ray analysis.

References

1) P. K. Weimer et al: RCA Rev. **12** (195 306.
2) S. V. Forgue et al: RCA Rev. **12** (1951) 33
3) F. M. Jager: Proc. Roy. Acad. Sci. Amste dam **9** (1907) 808.
C. Ries: Ann. d. Phys. **36** (1911) 1055.
J. Olie and H. R. Krugt: Proc. Roy. Aca Sci. Amsterdam **14** (1912) 740.
F. M. Jager: Zeit. anorg. Chem. **78** (191 246.
D. S. Elliot: Phys. Rev. **5** (1915) 53.
C. Tubandt and M. Haidicke: Zeit. anorg Chem. **160** (1927) 297.
4) Z. Ooe: J. Geol. Soc. Tokyo **33** (1926) 186.
5) C. Gottfried and E. Lubberger: Z. Krist. **7** (1929) 257.
6) S. Miyake: Sci. Pap. Inst. Phys. Chem. Res Tokyo **34** (1938) 565.
7) J. W. Meller: A Comprehensive Treatise o Inorganic and Theoretical Chemistry, Longmans, Vol. IX, (1947).
8) T. S. Moss: Photoconductivity in th elements, Academic Press, New York, (1952
9) R. Frerichs: Phys. Rev. **72** (1947) 595.
E. A. Taft and M. H. Hebb: J. O. S. A. **4** (1952) 249.
10) A. Rose: RCA Rev. **12** (1951) 362.

JOURNAL OF THE PHYSICAL SOCIETY OF JAPAN Vol. 10, No. 7, JULY, 1955

An X-Ray Study of Barium-Strontium-Calcium Triple Oxide

By Jitsuo TERADA

Matsuda Research Laboratory, Tokyo Shibaura Electric Co.,
Kawasaki, Kanagawa, Japan

Received February 11, 1955)

Triple oxide coatings were studied by means of x-ray powder patterns using a protective film coating technique. Uniform solid solution of the three constituents was not found. Three phases of oxide solid solution were usually found with the heat treatment at a temperature where the preferential evaporation loss of the BaO component does not yet take place. When treated with the temperature above 1000°C, the evaporation loss of BaO became appreciable, causing a remarkable deformation of the shape, and also broadening, of the x-ray diffraction lines. In some cases this line broadening is explained by so-called microstress theory. A possible explanation for the reason of the good emission of the triple oxide cathode is given.

§ 1. Introduction

The thermionic emission properties of barium-strontium oxide cathodes related to their chemical and physical structures have been studied by several authors[1)~7)]. In these studies it was made clear that when a mechanical mixture or solid solution of barium carbonate and strontium carbonate was decomposed in vacuum during the formation of an oxide cathode, a simple conversion to the mixed oxides, BaO and SrO, took place. Further heating caused the formation of a uniform solid solution, (BaSr)O. The lattice constant of such a solid solution was found to vary linearly with composition from 100 percent BaO to 100 percent SrO. They also showed that higher emission was obtainable when the oxide was homogeneous throughout than when it consisted of two or more phases. The optium emission was observed from an oxide solid solution which was approximately of equal molar composition.

Recent progress in electronic vacuum tubes has made it necessary to review the virtues of triple oxide coating as an electron emitter. In spite of its usefulness, we have little knowledge of the crystal structures of triple oxide, and it is believed that an analogy would persist between the barium-strontium double oxide and the triple oxide. Grey[8)] studied the emission contours from the BaO-SrO-CaO system and showed that a large central area appeared in the triple diagram in which the emission is greater than the maximum obtained from any barium-strontium double oxides. In the BaO-SrO system, the emission current of a mechanical mixture of BaO and SrO is equal to the sum of the emission currents of the two components of the mixture. An oxide coating of the corresponding solid solution, however, gives a larger emission current than is obtained by adding the shares of BaO and SrO. Thus it was natural to suppose that a larger emission value of a triple oxide would be associated with an oxide solid solution of the three constituents.

In the previous paper[9)], we examined the crystal structures of the co-precipitated triple carbonates and showed that a uniform solid solution of carbonate was found in a wide area in the triple diagram. However, it is undoubtedly of importance to study directly the crystal structures of triple oxide. The present work was directed toward finding some of the crystal structures of triple oxide.

§ 2. Experimental Method

All of the carbonate specimens which we used in the present study were carbonate solid solutions made by co-precipitation[9)]. These carbonate powders were coated with a proper binder on a rectangular flat nickel sleeve which had an outside dimension of 15 mm × 6.5 mm. Each cathode was mounted in a glass bulb which was evacuated by an oil diffusion pump. After a bulb-baking at 300°C, cathode was heated in order to convert the carbonate to oxide. The heater current was gradually increased in regular steps, and the decomposition was finished in about 15 minutes. Finally, the getter was flashed and the bulb was tipped off from the exhausting system. Heat treatment of the oxide was made in a quiescent state, for all of the test tubes were consuructed as monodes.

Since the oxides of barium, strontium and calcium are chemically unstable in an atmosphere containing carbon dioxide or water vapour, a technique of protective film coating[5)6)] was employed to prepare the oxide specimen for x-ray examination. After breaking the tube in an air-tight glass-windowed manipulation box, in which the atomosphere was maintained chemically inert by an adequate flow of carefully dried nitrogen, the cathode was coated with protective film. Rubber gloves attached to the box by wrist bands, permitted this operation. Polystyrene in a benzene solvent was used as a protective material in this work. The cathode was then mounted in a special sample holder for x-ray examination. X-ray patterns were taken by an automatic recording Geiger-counter x-ray spectrometer employing filtered copper K-radiation. Fig. 1 shows the setting of an oxide specimen on the spectrometer for x-ray examination. Although deformations of the shape of diffraction lines from the oxide specimen were often encountered in this study, the lattice constant of an oxide solid solution was usually determined from the lines of relatively small diffraction angles, 111, 200 and 220. Favourably in some cases, in addition to the oxide pattern, known diffraction lines from the base metal appeared and correct measurements of x-ray diffraction angles were made. The results obtained in this work were ordinarily tested at least two times to avoid accidental errors. Unless otherwise stated, all temperatures of heat treatmen were uncorrected pyrometered temperatures.

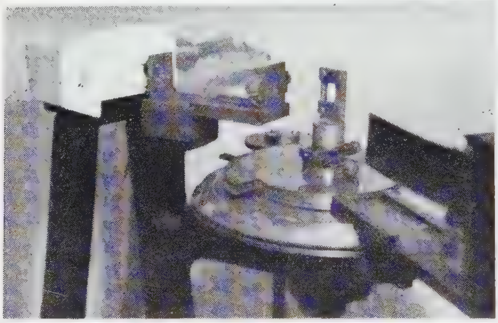
Fig. 1. Setting of an oxide specimen for x-ray examination.

§ 3. Results

All of the alkaline earth oxides in questio have a crystal structure of the NaCl type and the lattice constants are 5.523A for BaO 5.144 A for SrO and 4.797 A for CaO[10)]. We shall first describe the behaviours of the thre kinds of double oxide. The observations o the decomposition of carbonate solid solutio are also given.

BaO-SrO System

A barium-strontium oxide solid solution has been used extensively in commercial vacuum tubes. As mentioned before, its crystal structures had been cleared and we can see a uniform solid solution of oxide over the entire composition range from 100 percent BaO to 100 percent SrO. The lattice constant of such a solid solution obeys linear law. The only problem in this system was that: Whether a carbonate solid solution $(BaSr)CO_3$ decomposes separately to BaO and to SrO and then converts to an oxide solid solution $(BaSr)O$ (as Eisenstein first pointed out[6)]), or it converts directly to an oxide solid solution.

An oxide specimen which was decomposed from an equal molar carbonate solid solution in the usual manner always showed two oxide phases immediately after the decomposition. One of them was almost pure SrO or it contained at most 5 mole percent BaO, and the other was an oxide solid solution of composition near 70 mole percent BaO. As the temperature of decomposition of $(BaSr)CO_3$ in our study was slightly higher than that quoted in Eisenstein's paper, we may conclude that a carbonate solid solution of barium and strontium decomposes separately to BaO and to SrO.

BaO-CaO System

Huber and Wagener[5)] showed that no barium-calcium oxide solid solutions were present even after heating the mixture of BaO and CaO for two hours at a high temperature of 1400°K. Grey[11)] also found the same result. In the case of a carbonate crystal, an aragonite-type solid solution of barium and calcium was found in the range from 100 percent $BaCO_3$ to 80 mole percent $BaCO_2$-20 mole percent $CaCO_3$[9)]. The difference between the lattice constants of the two carbonates is nearly the same to that between BaO and CaO.

We examined the series of BaO-CaO, especially on the composition range near 100 per cent BaO. We could not find, however, any traces of oxide solid solution over the entire composition range after heating the oxide specimens to 1000°C or more for a sufficiently long time. As is predicted from the rates of evaporation of the oxides12), the preferential evaporation loss of the BaO component becomes appreciable above 1000°C. Consequently the temperature of heat treatment on such an oxide mixture was limited, and no barium-calcium oxide solid solutions were formed in vacuum. A carbonate solid solution of barium and calcium (BaCa)CO$_3$ decomposes, of course, separately to BaO and to CaO.

SrO-CrO System

We decomposed the series of carbonate solid solution of strontium and calcium (SrCa)CO$_3$ at an appropriate true temperature of 1300°K. Such an oxide specimen showed usually two oxide phases when examined immediately after the completion of decomposition. Heat treatment was carried out at 900°C and 1000°C for two hours. This caused the formation of uniform oxide solid solution of strontium and calcium. Fig. 2 shows the observed oxide lattice constant after heating at 900°C and 1000°C *vs.* molar composition of the coating. In this figure the straight line represents the linear variation in lattice constant of the solid solution with the conposition. A diviation from the straight line is apparent even after heating at 1000°C. Moreover, even at this high temperature there still remained two phases in the range where the CaO percentage is more than 50. The observed lattice constants in the oxide specimens which were heated at 1100°C for three hours on a platinum base metal are also plotted in Fig. 2. A deviation from the straight line is obvious, as before, after such a severe heat treatment. There is, however, a tendency that the higher the temperature of heat treatment, the closer the observed lattice constant to the linear law. Thus we may conclude that strontium and calcium oxide form a uniform solid solu- over the entire composition range, and the lattice constant of the solid solution varies linearly with molar composition after an appropriate heat treatment above 1100°C. It is likely that the observed lattice constant depends mainly upon the temperature and not on the duration of the heating. For, in our case, the lattice constant of an oxide solid solution was practically unchanged for the heating duration from about thirty minutes to two hours at 900°C.

An oxide solid solution, whose lattice constant is found above the straight line in Fig. 2, contains more SrO component than the composition determined by the linear law. On the other hand, an oxide crystal of the lattice canstant below the straight line contains a richer CaO component. From the observed lattice constants in Fig. 2, the mole composi-

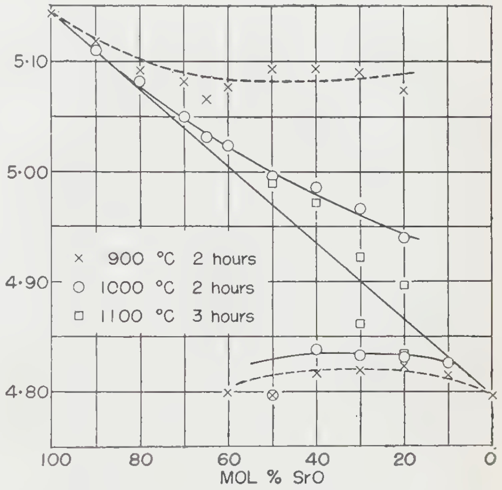

Fig. 2. Composition *vs.* observed lattice constant after heating the cathode of SrO-CaO.

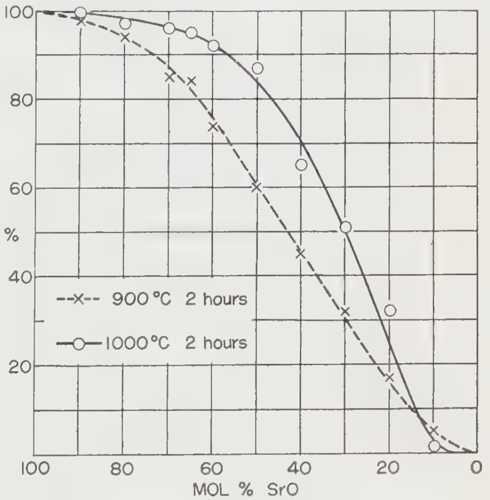

Fig. 3. Composition *vs.* resulted amount of the SrO richer crystal after heating the cathode of SrO-CaO.

tions of the oxide solid solutions precipitated in the coating are determined by the linear law. Then the molecular amounts of the respective oxides are easily calculated using the molecular ratio in the coating, as shown in Fig. 3. As the sum of the percentages of the precipitated SrO richer crystal and the CaO richer one always amounts to 100, the curves of the CaO richer crystal are symmetrical about the line of 50 percent. At 900°C, equal amounts of the two oxide solid solutions precipitate in the vicinity of the system composition of 40 mole percent SrO-60 mole percent CaO. The equal precipitation point shifts towards the CaO side as the temperature of heating is increased. According to Huber and Wagener[5], SrO and CaO also form a continuous series of solid solution with a linear variation of the lattice constant immediately after the decomposition from a carbonate solid solution at 1300°K. In our case, the plots of heating temperature of 1000°C in Fig. 2 would become more closer to the linear law if an average x-ray diffraction angle of double-peaked line is adopted. One of the examples of double-peaked diffraction lines is shown in Fig. 4. Apparently two phases of oxide solid solution coexist even after heating at 1100°C for three hours. Thus the SrO is hard to solve in the CaO crystal and the formation of a uniform solid solution in this system does not seem to occur so easily as reported by Huber and Wagener.

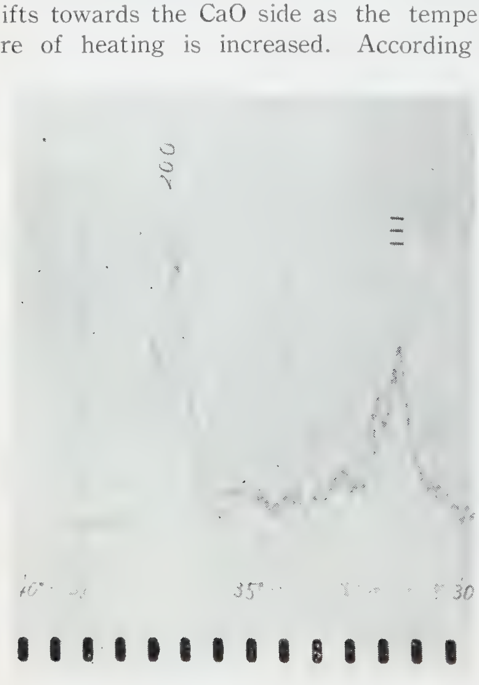

Fig. 4. Double-peaked x-ray diffraction lines observed after heating the 20 mole percent SrO--80 mole percent CaO cathode at 1100°C for three hours.

The conversion of an equal molar carbonate solid solution $(SrCa)CO_3$ was studied by means of a series of x-ray diffraction patterns. As is predicted from the behavious of oxides in Fig. 2, such a carbonate solid solution is likely to decompose separately to SrO and to CaO. Each of a series of identical cathodes was converted. They were all stopped at different steps in the conversion process. X-ray patterns were taken using the protective film technique previously described. Table I gives an example of the qualitative variations of cathode temperature and pressure value in the conversion. The temperature of the cathode was measured by a thermo-couple attached to the center of the cathode surface, so that the values of cathode temperature in Table I are true temperatures. There were clearly two stages of degassing from the cathode when the cathode heater voltage was raised stepwise from a low temperature. The first degassing became appreciable at about 850°K, then it ceased once and a high vacuum recovered. Further heating at a higher temperature caused the remarkable second degassing at about 1100°K. Fig. 5 shows the x-ray

Table I. Example of the conversion of an equal molar $(SrCa)CO_3$ cathode.

Time duration at each stage	Cathode temperature	Pressure change
1/2 min.	715°K	End vacuum of the exhausting system
1/2	770	No change
1	810	Degassing due to the decomposition of the first stage occurred
2	865	Appreciable degassing
1/2	925	High vacuum recovered
2	985～1000	Degassing of the second stage began
2	1065～1175	Degassing finished at the end of this stage
1	1205	High vacuum restored
1/2	1240	End vacuum
1/2	1305	No change

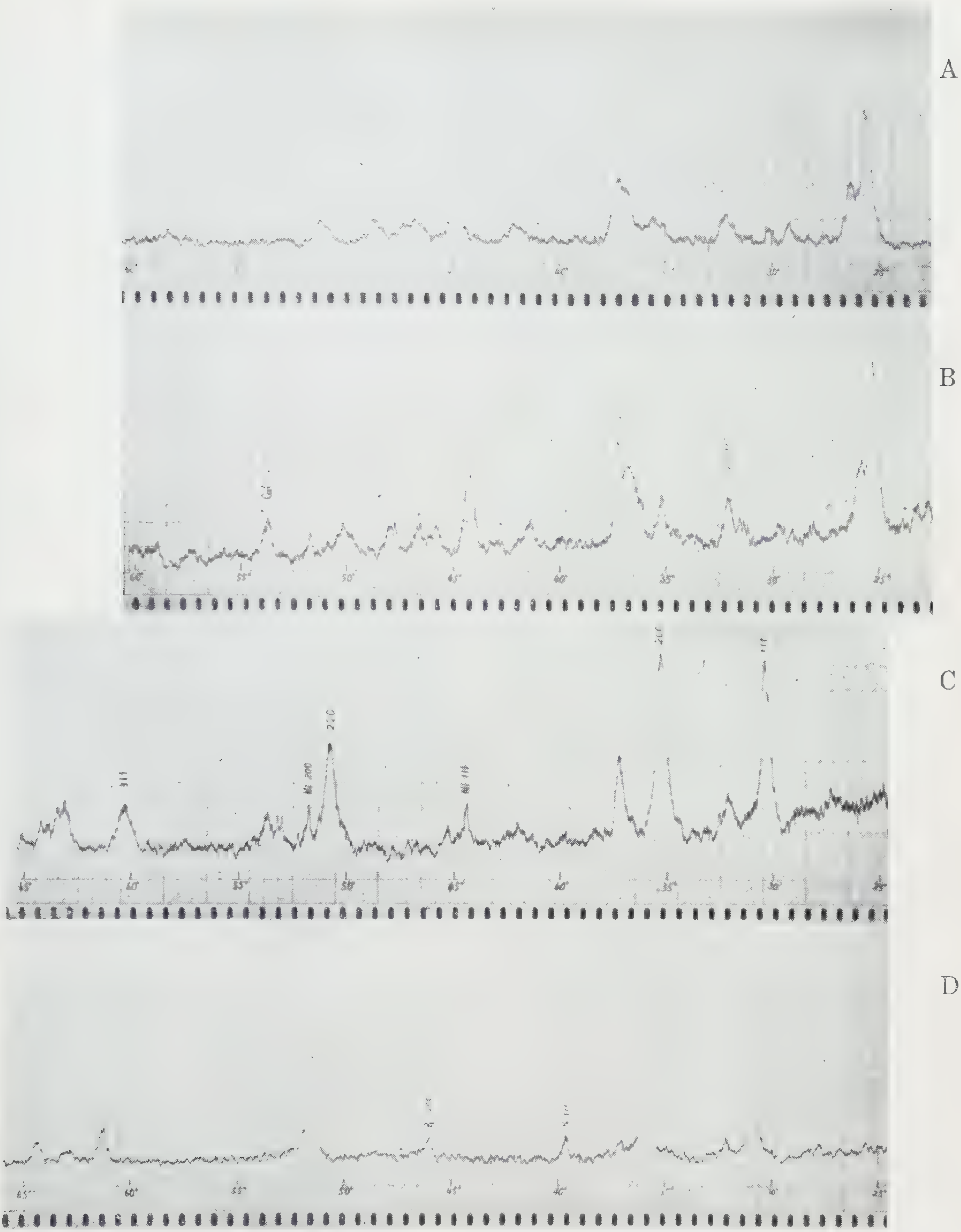

Fig. 5. X-ray diffraction patterns of SrO-CaO cathode samples. See text.

patterns at various stages of heating. Pattern 5 A shows the original aragonite-type carbonate solid solution of strontium and calcium. At the end of the first degassing, see pattern 5B, diffraction lines of CaO appear in the carbonate pattern, and at the same time the diffraction lines of remaining carbonate crystal shift towards the smaller diffraction angles untill they coincide with those corresponding to $SrCO_3$. Pattern 5C shows two oxides coexisting immediately after the completion of decomposition. One of the oxides is almost pure CaO and the other is an oxide solid solution, the composition of which is 90 mole percent SrO-10 mole percent CaO. Inhomogeneities of the formation of oxide solid solution frequently appeared during this stage. Because of the extreme temperature sensitivity of the initial rate of formation of oxide solid solution, composition variations were often encountered.

Subsequent heat treatment caused a formation of a uniform solid solution as described before. Pattern 5D, taken after three hours heat treatment at 1100°C, shows a typical x-ray pattern of oxide solid solution in this series. It is noticeable that the CaO-like diffraction peaks are still visible in pattern 5D. In conclusion, the carbonate solid solution $(SrCa)CO_3$ decomposes separately to SrO and to CaO. A larger difference of decomposition pressure between the two constituent carbonates in $(SrCa)CO_3$ compared to that in $(BaSr)CO_3$ makes it ersier to observe and control each stage in the conversion of a $(SrCa)CO_3$ cathode.

Triple Oxide

Cathodes of triple carbonate solid solution $(BaSrCa)CO_3$ were converted in vacuum and measured, varying the triple composition, to find out an oxide solid solution of single phase. All of the attempts, however, were unsuccessful, and there were usually three kinds of oxide solid solution when examined immediately after the completion of decomposition. These three oxide solid solutions were still present after heat treatment at 900°C for two hours. X-ray patterns similar to those of single oxide phases were obtained when the triple composition approached the apices of the triple diagram, or while the percentage of CaO was small. Patterns similar to those of single oxide phases were also obtained when a cathode was heated at a higher temperature above 1000°C for a sufficiently long time. In this case, as we shall discuss later, a remarkable shift of composition was observed. Heat treatment above 1000°C caused an appreciable loss of the BaO component from a (BaSr)O cathode due to the preferential evaporation of BaO, while the loss was negligibly small at 900°C. These circumstances will hold even in a cathode of triple oxide coating. Therefore the experiments of triple oxide were carried out, in this study, under a constant heat treatment at 900°C for two hours. As the triple composition range, in which a uniform triple oxide solid solution will easily be formed, was unlikely to exist, and as a triple oxide coating which is composed of equal molar barium and strontium oxides and a fraction of calcium oxide is used most extensively in vacuum tubes, we focussed our attension to those cothodes; BaO:SrO:CaO= a:a:x (mole percent).

Fig. 6 shows an idealized representation of the 200 diffraction lines of the three oxide solid solutions which were usually observed over a wide triple composition range. The first peak appears at an intermediate position between BaO and SrO, of (BaSr)O type, and we may call it as type-I oxide solid solution. The second peak appears between the diffraction angles of SrO and CaO (type-II solid solution). The third one is found near the diffraction angle of CaO with a slight deviation towards the smaller angle (type-III solid solution). Type-II and type-III solid solutions

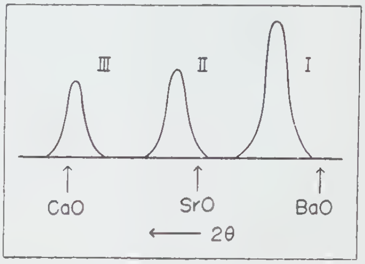

Fig. 6. Idealized 200 diffraction lines from a triple oxide coating after heat treatment at 900°C for two hours.

Fig. 7. The humps accompanied with the diffraction lines observed from a triple oxide specimen containing 1 mole percent CaO. The cathode was heated at 900°C for two hours.

are of the type (SrCa)O. For further analysis, we may reasonably assume from the behaviours of the three kinds of double oxide that: (1) type-I oxide contains all of the barium oxide and most of the strontium oxide, *i.e.* it is a (BaSr)O crystal, (2) type-II oxide contains most of the remaining strontium oxide and a small fraction of calcium oxide: a (SrCa)O crystal, (3) type-III oxide contains most of the calcium oxide and a small fraction of the remaining strontium oxide; a (CaSr)O crystal. The results of triple oxide coating of the type BaO:SrO:CaO=a:a:x mole ratio are shown in Table II. Though not all of the three diffraction peaks were distinguishable in a triple oxide coating such that the CaO fraction was below 5 mole percent, the diffraction lines from such a triple oxide specimen were always accompanied with humps on the larger diffraction angles. Moreover, the positions of the diffraction lines were apparently at smaller diffraction angles (larger spacings) than those expected from an equal molar barium-strontium oxide solid solution. One of the examples is shown in Fig. 7 which was observed from a triple oxide coating containing 1 mole percent CaO. The larger spacing of the oxide crystal and the hump, observed in such a triple oxide specimen, seem to indicate a distribution of lattice parameters even when the x-ray pattern of the specimen seems to be of a single phase oxide solid solution. As a reference, the result of an equal molar barium-strontium double oxide is also shown in Table II. A uniform solid solution (BaSr)O was formed in 10 or 20 minutes by heating at 900°C and the observed lattice constant agreed well to that expected from the composition. The insertion of a small amount of CaO in a barium-strontium double oxide will greatly hinder the formation of a uniform (BaSr)O solid solution. In spite of a wide variation in molar fraction of CaO, the mole composition of type-I crystal (BaSr)O observed in a series of such triple oxide coatings stays at almost constant value, 65 mole percent BaO-35 mole percent SrO. The molecular compositions of type-II and type-III oxide crystal also remain at nearly constant values. Type-II crystal (SrCa)O contains from 80 to 85 mole percent SrO, and type-III crystal (CaSr)O contains at most 5 mole percent CaO. The molecular ratios of the three oxide solid solutions precipitated after heating at 900°C for two hours are obtained by simple calculation using their respective mole compositions, and the calculated values are also tabulated in Table II. It is seen that the most abundant oxide crystal among the three oxides formed in the coating is the type-I oxide (BaSr)O regardless of a wide variation in molar fraction of CaO. The (BaSr)O crystal in a triple oxide coating will be responsible for the emission characteristics of a triple oxide cathode as is the case with a barium-strontium oxide. It is also remarkable that the CaO component in a triple oxide coating hardly reacts on the other components in the coating. This is seen from the fact that the molecular amount of type-III crystal remains almost at the same value of the inserted molar fraction of CaO even after heating at 900°C for two hours.

Next, the temperature effect of the heat treatment on a triple oxide coating was tested using a series of equal molar triple oxide cathodes. Each of a series of identical triple oxide cathodes was heated under different conditions. Fig. 8 shows the x-ray patterns of the equal molar triple oxide coatings after different heat treatment. The analytical results of the patterns are listed in Table III. The x-ray intensities of diffraction lines from such a triple oxide coating were generally weakened because of the coexistence of different kinds of oxide or of a distribution of lattice parameters in the coating, and just the 111, 200 and 220 groups of diffraction lines were present in our study. The three kinds of oxide solid solution,

Table II. Results of triple oxide coatings of mole ratio:
BaO : SrO : CaO = a : a : x (%).

Mole percent of CaO. (x)	Time of heating at 900°C.	Mole percent of BaO in type-I crystal, (BaSr)O.	Molecular ratio of the resultant three oxide crystals. I : II : III (%)
0	10 min.	52	
1	2 hours	64	
2	〃	63	
5	〃	63	75 : 22 : 3
10	〃	64	70 : 23 : 7
20	〃	62	65 : 17 : 18
33	〃	66	50 : 19 : 31
50	〃	68	37 : 9 : 54

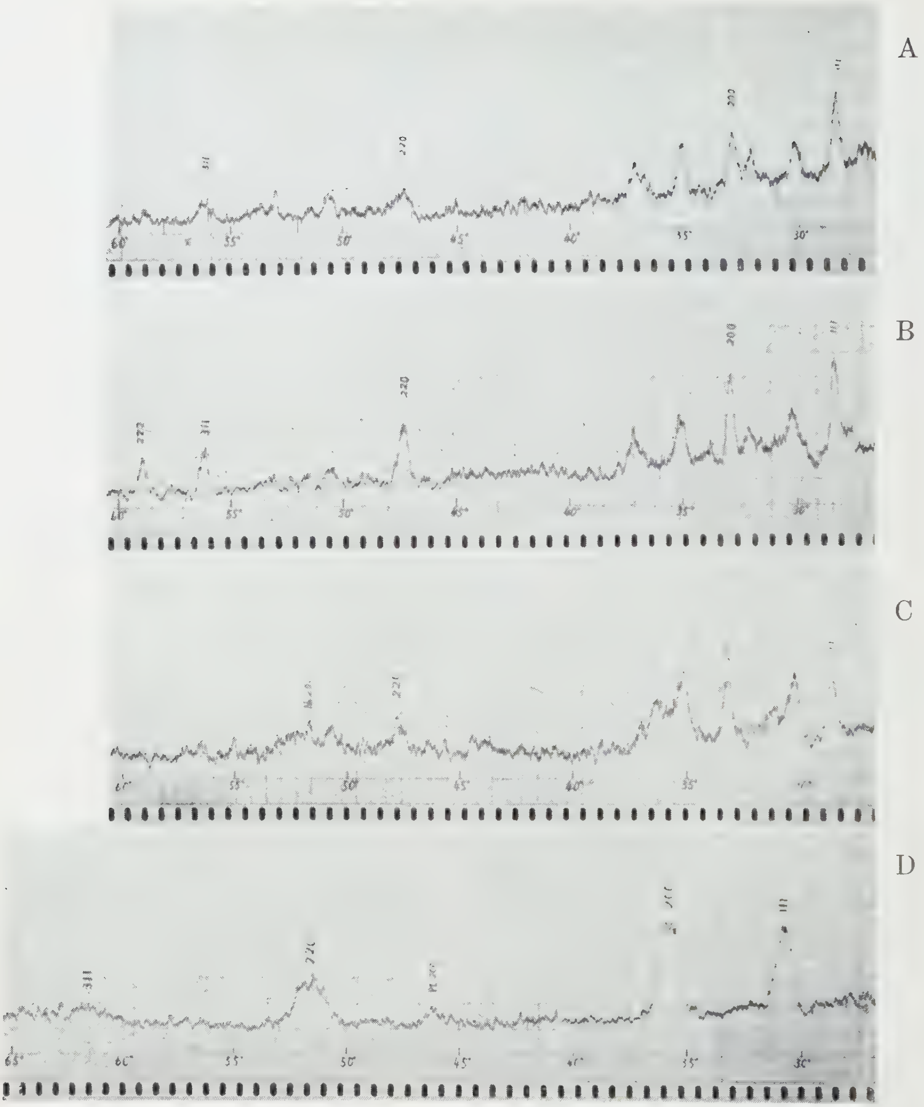

Fig. 8. X-ray diffraction patterns of triple oxide specimens. See text.

Table III. Effect of heat treatment on the equal molar triple oxide coatings.

Pattern	Heat treatment	Mole percent of BaO in type-I crystal, (BaSr)O.	Mole persent of SrO in type-II crystal, (SrCa)O.	Mole percent of CaO in type-III crystal, (CaSr)O.	Molecular ratio of the resultant three oxide crystals. I : II : III (%)	Evaporation of the BaO component from the coating.
8A	After decomposition	73	86	95	45 : 23 : 32	Negligible
8B	900°C 2 hours	66	81	95	50 : 19 : 31	Negligible
8C	1000°C 2 hours	60	83	60		Appreciable
8D	1100°C 3 hours	—	60	—		Complete

I, II and III, are appeared in pattern 8A which was taken immediately after the decomposition of the carbonate solid solution. The three oxide crystals are still distinct after heating the cathode at 900°C for two hours, see pattern 8B. It is evident from the somewhat sharper lines in pattern 8B, especially those of type-I oxide, that crystal growth has begun during this stage. At the same time a slight variation in mole compositions of the three crystals has occurred by this heating. The shift of peak positions towards the smaller diffraction angles and the shape deformation of the diffraction lines of type-III crystal in pattern 8C, taken after heating at 1000°C for two hours, show that the reaction of the CaO component has become appreciable at this temperature. The lattice constant of type-III crystal in pattern 8C is hardly determined because of the asymmetric form of the diffraction lines. At any rate, the lattice constant determined from the difiraction angles at the maximum intensities of the deformed lines is used for the analysis. It is interesting that the ratio of the molecular amounts of the three crystals can not be determined from the mole compositions of the respective oxides in pattern 8C. This will imply that there occurred an appreciable evaporation loss of the BaO component from the coating at such a high temperature. A complete preferential evaporation loss of the BaO has occurred when the cathode is heated at 1100°C for three hours on a platinum sleeve, pattern 8D. The type-I crystal has disappeared completely and a unification between type-II and type-III crystals has occurred. Furthermore, a remarkable line broadening is observed at this stage. The composition of the resulted oxide is 60 mole percent SrO-40 mole percent CaO. The diffraction lines from an oxide solid solution of the same mole composition in the SrO-CaO system was always sharp enough even after heating at such a high temperature, therefore the line broadening observed in pattern 8D may show a temperature effect characteristic to a triple oxide coating. There will be three causes which produce a broadening of the x-ray powder pattern lines in the case of a solid solution: microcrystal, microstress and a distribution of mole compositions. The former two are usually discussed in the x-ray studies of the cold-work of metals. In the microstress theory it is assumed that residual strains are left in the material, the strains in every grain are varying in magnitude. Therefore different grains have slightly different spacings of net planes d, and the reflected beams from the grains merge into one broadened reflection. It is possible to distinguish between the broadening of microcrystal and that of the microstress by considering the dependence of line breadth B on λ and θ;[13)]

$$\text{microcrystal:}\quad B=K\lambda/L\cos\theta\ ,$$

$$\text{microstress}:\quad B=f(\Delta d/d)\tan\theta\ ,$$

where L means the crystal size, $f(\Delta d/d)$ is a functional coefficient of the root-mean-square strain $\Delta d/d$, and λ, θ have the usual meanings. Though it is difficult to analize, the third broadening effect due to the distribution of mole compositions in the solid solution will be characterized by an asymmetric form of the diffraction line or by an irregular deformation of the line shape. The observed extraordinarily broad widths of the 111, 200, 220 and 311 diffraction lines in pattern 8D were reduced by an appropriate correction of the apparatus broadening and were plotted against $\tan\theta$. The plots were well on a straight line drawn through the origin. This indicates that the microstress broadening is better fit than the broadening due to the microcrystal in pattern 8D. Thus in a triple oxide coating, we must consider all of the microcrystal broadening, microstress broadening and the broadening due to the distribution of mole compositions in the solid solutions as the origin of the observed line broadenings of x-ray powder patterns. The microstress broadening will be of major importance in a triple oxide coating especially after the forced evaporation loss of the BaO component from the coating.

§ 4. Discussion

As was mentioned in the previous section, so far as we have measured we have not been able to find any uniform single phase triple oxide solid solutions. Where the composition was in the neighbourhood of the apices of the triple diagram, x-ray patterns were often obtained which may be interpreted as a single phase solid solution. Some of these cases, however, were found to be of two or more phases on reexamination. Some of the triple oxide coatings showed always single lines characteristics of a single phase solid solution in the x-ray powder patterns. For example, the triple oxide coating of the composition; BaO:SrO:CaO=5:10:85 mole percent, showed this characteristics with the observed lattice constant of 4.83_6 A. On the other hand, assuming the linear law, which would be a fairly good approximation in the case of a uniform triple oxide solid solution, the lattice constant of this solid solution is calculated to be 4.867 A. The calculated value is somewhat larger than the observed. This discrepancy was seen for every other example in the vicinities of the pure CaO and SrO. The observed lattice constant smaller than the calculated one indicates an incomplete dissolution of the BaO component into the major crystal. There is another possibility as to why we could not succeed in finding any true triple oxide solid solution, *e.g.* if a uniform solid solution of the three constituents can exist only in narrow composition regions near the BaO-SrO side or the SrO-CaO side, we would hardly be able to verify such solution by the x-ray diffraction method. At least at 900°C, there are no uniform oxide solid solutions over the entire triple composition range. The higher the temperature of heat treatment, the more excess evaporation loss of the BaO component from the coating occurs. The preferential evaporation of the BaO cannot be suppressed in the vacuum, and this causes the shift of the triple composition coordinate towards the BaO deficient side in the triple diagram and makes it impossible to study the triple diagram. As it is impossible, at present, to estimate the evaporated molecular amount of the BaO component from a triple oxide coating and as the single line characteristic of the x-ray pattern cannot be the whole evidence of a uniform solid solution, so we can hardly recognize the existence of a uniform triple oxide solid solution even at a higher temperature than 900°C. It is likely that, for any temperatures of heat treatment, there are no single phase triple oxides over the entire composition range so far as the study is carried out in the vacuum.

As the next problem, we consider the role of the added CaO component in a triple oxide coating. The added CaO causes two or more phases of oxide solid solution in the coating unless an extreme reduction in the BaO component has occurred by a severe heat treatment. Particularly in the case of the coatings used extensively in vacuum tubes, their compositions lie around the points of the equal molar barium and strontium oxides and an appropriate fraction of the calcium oxide. In these coatings there appear three kinds of oxide solid solution as described in the previous section. At thermal equilibrium or quasi-equilibrium the mole compositions of eac oxide crystals and the abundance ratio amon them have definite values corresponding the composition coordinate in the triple diagram. Futhermore, the mole compositions each oxide crystals will not be so differen from those values listed in Table II regardles of a little variation in the triple compositio coordinate. That is to say, type-I oxide wi contain about 65 mole percent BaO, type- oxide will contain about 80 mole percent SrO and type-III oxide will contain at most 5 mol percent SrO. If the temperature is raise above 1000°C, as is the case with flashing aging for the activation of cathode, the preferential evaporation of the BaO become appreciable causing a shift of the triple composition coordinate of the coating towards th BaO deficient side. The evaporation loss the BaO from the coating causes a SrO riche state in type-I crystal. This must initiate forced transition of the SrO component fro type-I oxide to the other, because the equilibrium mole composition of type-I oxide cannot stay at such a SrO richer state even afte the shift of the triple composition coordinate The transition of the SrO from type-I oxid would mainly occur to type-II oxide, and simultaneous transition of the CaO componen from type-III oxide to type-II oxide shoul occur to keep the equilibrium mole compositions of the respective oxides. Thus the evaporation loss of the BaO requires a rearrangement of the whole system, and a larg amount of components must be transporte across the crystal boundaries. Fig. 9 illustrate schematically the net flows of the three constituent components among the oxide crystals The SrO and CaO components may be transported from one crystal to the other b surface migration and diffusion through th crystal boundaries or by the evaporation acros the crystal boundaries (or pores). As one the cases, consider the transitions of SrO an CaO by the evaporation across the boundaries The rates of evaporation of both the SrO an CaO in a triple oxide coating may be considered definitely smaller than the value the BaO even at a hige temperature whe the evaporation loss of the BaO becomes appreciable. Although we cannot estimate th velocities of surface migration and diffusio of the SrO and CaO components in a triple oxide coating, it may be supposed from Woods and Wright's experiment on multilayered oxide films[14] that the diffusion of the SrO is more difficult than the BaO. Moreover, the CaO component hardly reacts on the other components even at a high temperature. Thereby it is likely that the transitions of the SrO and CaO will not be able to follow the variation in the triple composition coordinate of the system caused by the preferential loss of the BaO. Thus the whole system will be left in a distorted state which will produce the observed line broadening of the x-ray powder patterns. The situation will be understood more clearly when we compare the triple oxide with the barium-strontium double oxide. In the double oxide a uniform single phase oxide solid solution is easily formed over the entire composition range by a comparatively brief heat treatment. Then the variation in oxide composition due to the preferential evaporation loss of the BaO component does not require any loss of the SrO from the oxide crystals, and the equilibrium will be readily established after a temporary mutual diffusion of ions within the crystal. The mutual ion diffusion within an oxide crystal will be easily performed and will not be a rate determining factor for the establishment of the equilibrium. The distorted oxide crystal is in a higher energy state than the undistorted. It is likely that the higher the energy of the oxide, the more easily is the oxide activated by a given heat treatment causing a greater increase in emission as is he case with a small crystalline state of an oxide[15]. The triple oxide is superior to the double oxide because the former has more possibilities of attaining the crystal distortion han the latter by a given heat treatment. The distortion in oxide crystal is probably the reason for the improved emission of the triple oxide coating. This in turn will indicate the superiority of the double to the single. The role of the CaO component in the triple oxide coating is entirely to produce the complexity n crystalline state of oxides, and complexity facilitates the occurrence of distorted oxide crystals in the coating.

Finally, each of the double carbonate solid solutions, $(BaSr)CO_3$, $(SrCa)CO_3$ and $(BaCa)CO_3$, decomposes separately to the constituent oxides. Presumably the triple carbonate solid solution $(BaSrCa)CO_3$ will also decompose separately to the constituent oxides. The exact mechanism of the processes cannot be studied at present because of the sensitive dependence of the mechanism on the cathode temperature and the pressure of conversion gases.

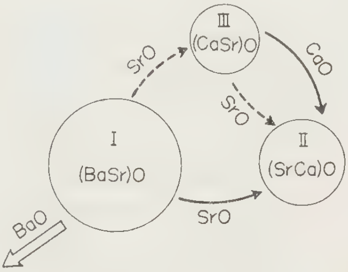

Fig. 9. Schematic illustration of the transitions of the constituent oxides in a triple coating associated with the preferential evaporation loss of the BaO.

The author is indebted to Mr. K. Noga for his valuable discussions during the course of this investigation.

References

1) W. G. Burgers: Zeits. f. Physik **80** (1933) 352.
2) M. Benjamin and H. P. Rooksby: Phil. Mag. **15** (1933) 810.
3) M. Benjamin and H. P. Rooksby: Phil. Mag. **16** (1933) 519.
4) M. Benjamin, R. J. Huck and R. O. Jenkins: Proc. Phys. Soc. **50** (1938) 345.
5) H. Huber and S. Wagener: Zeits. f. tech, Physik **23** (1942) 1.
6) A. Eisenstein: J. App. Phys. **17** (1946) 434.
7) A. Eisenstein: J. App. Phys. **17** (1946) 654.
8) L. E. Grey: Nature **167** (1951) 522.
9) J. Terada: J. Phys. Soc. Japan **8** (1953) 158, Nature **171** (1953) 517.
10) R. W. G. Wyckoff: "Crystal Structures" Interscience Publishers, New York, (1948).
11) L. E. Grey: Nature **165** (1950) 773.
12) A. Claassen and C. F. Veenemans: Zeits. f. Physik. **80** (1933) 342.
13) C. S. Smith and E. E. Stickley: Phys. Rev. **64** (1943) 191.
14) J. Woods and D. A. Wright: Brit. J. App. Phys. **5** (1954) 74.
15) H. Kawamura, A. Shinohara and K. Takahashi: J. Phys. Soc. Japan **3** (1948) 301.

JOURNAL OF THE PHYSICAL SOCIETY OF JAPAN Vol. 10, No. 7, JULY, 1955

Surface Treatment of Core Metal used for Oxide-coated Cathode

By Junkichi NAKAI and Shōgo NAKAMURA

Faculty of Engineering, Osaka University, Higashinoda, Miyakojima, Osaka, Japan

(Received November 5, 1954)

In the oxide cathode coated with alkaline earth metal oxide on a nickel sleeve, it is generally known that the active material contained in the core significantly influences the thermionic electron emission. That is, the active material produces excess Ba through the reduction of oxide. The produced excess Ba diffuses in the oxide and appears on the cathode surface so as to enhance its thermionic activity. On the other hand, however, nickel sleeve is generally made by drawing method. Because of severe mechanical processings and heat treatments, the surface of the sleeve is subject more or less to contamination. As long as this surface contamination exists, the diffusion of the active material to the sleeve surface is impeded, whereby causing an inferior activity.

The following is the result of research showing the existence of these contaminated layers which exert some evil influences.

§1. Method of Experiment

The nickel sleeves mainly used in this research were 1.6 mm in diameter, 32 mm in length, containing Mg:0.10% and Si:0.17% as the active materials. After the firing with hydrogen (1000°C, 15 minutes), it was treated with electrolytic etching as shown by Fig. 1. The electrolyte was sulphuric acid (specific gravity 1.84) diluted by nine times water (by volume). To observe the influence arising from the electrolytic etching on the electron emission under the same condition, each half of the sleeve was subjected to different ele trolytic treatments, or only one half wa treated. After coating with carbonate ((Ba·S CO_3) to a thickness of 5∼8 mg/cm^2 by ele trophoresis as shown in Fig. 2, the test tub was composed as shown in Fig. 3. Afte degassing, conversion and activation processe the emission current from each half of th cathode was measured by the application o triangular pulse voltage of 500 volts (peak In this way we investigated the difference du to the treatments.

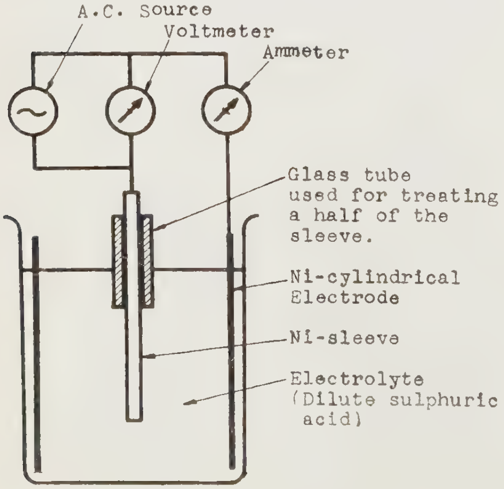
A.C. Source
Voltmeter
Ammeter
Glass tube used for treating a half of the sleeve.
Ni-cylindrical Electrode
Ni-sleeve
Electrolyte (Dilute sulphuric acid)

Fig. 1. Electrolytic treatment method of Ni-sleeve.

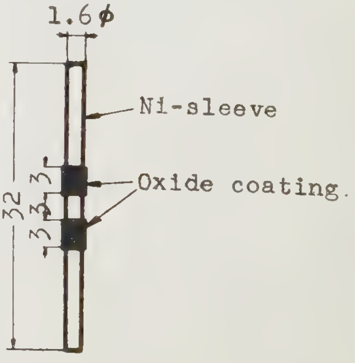

Fig. 2. Oxide coated cathode.

§2. Influence of Electrolytic Treatment c Activation Velocity and Emission Current

Fig. 4 indicates the result of our experime on the cathode with a sleeve whose one ha was treated by an electrolytic current of A. C. 1.5 A/cm², a thickness of 6μ having been removed by this treatment, and the other half was left untreated. After degassing and conversion in the usual manner, the cathode was kept at a temperature of 1230°K on the evacuation system. Occasionally the temperature was lowered to 1050°K, and the emission current was measured. As shown in Fig. 4, the activation velocity is larger for the electrolytically treated part compared with the untreated part.

Table I. Effect of A. C. electrolytic treatment to the emission current.

	I_3/I_0	I_6/I_0		I_9/I_3	I_{12}/I_6
Mean ratio of five tubes	1.60	2.12	2.23	1.41	1.10

I_t: Emission current from the part which the sleeve surface of a thickness of t microns has been removed by electrolytic treatment.

In addition to the difference in activation velocity, an increase in emission current by electrolytic treatment was also observed. Table I indicates this difference by comparing the emission currents from both parts at 1050°K after the activation has been done for 30 minutes under the above-stated condition (cathode temperature 1230°K, on the evacuation system). Here, I_t is the emission current from the treated half where the sleeve surface of a thickness of t microns has been removed by electrolytic treatment. t was estimated from the amount of nickel reduced. We see that, for the sleeves used in the present experiment, the emission current increases with the electrolytic treatment until the removed thickness reaches 6μ, but any further advances of the electrolytic treatment have little effect on the emission current.

3. Measurement of the Diffusion Energy of Active Material

As seen from the above results, the electrolytic treatment can increase the emission current. This is ascribable to a removal of he surface contaminated layer established in the manufacturing process of sleeve. During he severe mechanical processings and heat reatments, the impurities of various kinds are involved in the surface, and a part of the active materials near the surface may be

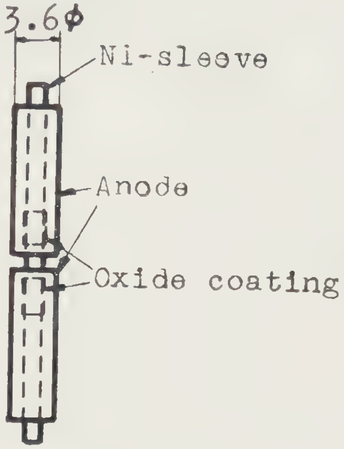

Fig. 3. Construction of electrode.

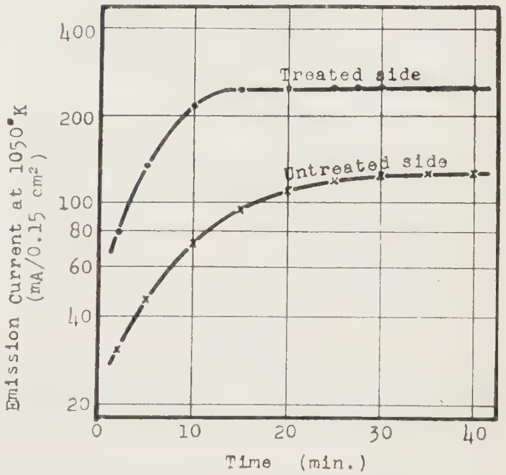

Electrolyte: Sulphuric acid (s.g. = 1.84): water = 1:9 (by volume).
Electrolytic current density: A.C. 1.5 A/cm².
Treated time: 30 sec.

Fig. 4. Effect of electrolytic treatment to activation velocity.

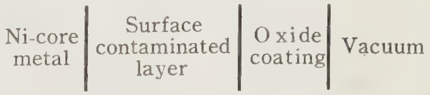

(a) Untreated case.

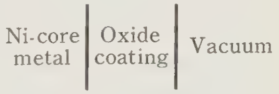

(b) By electrolytic treatment the contaminated layer is removed so as to let the clean core surface contact directly with the oxide coating.

Fig. 5. Sections of oxide coated cathode.

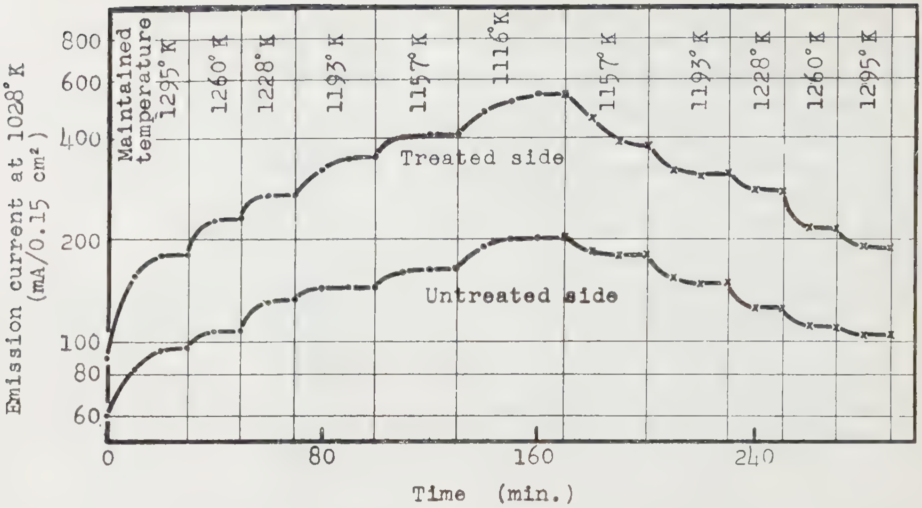

Fig. 6. Measurement of diffusion energy.

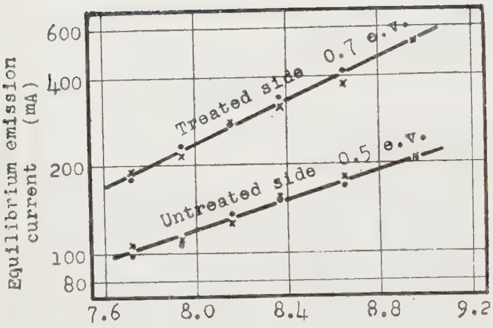

Fig. 7. Logarismic plot of the equilibrium emission current as the function of the temperature of the heat treatment of the cathode.

combined with oxygen. These compounds remain unaffected by the hydrogen firing. Therefore, the active materials must diffuse through this contaminated layer in order to reduce the oxide and to produce excess Ba. But, when the contaminated layer is removed, the clean sleeve surface can directly contact with the oxide as shown in Fig. 5, and this facilitates the reducing action of the active materials and improves the activity.

Next we composed a test tube of Fig. 3 in which half part of the sleeve underwent the electrolytic treatment by A. C. 1.5 A/cm², a thickness of 8μ having been removed by this treatment. The difference in diffusion energy of the active material in both parts was measured. After a conversion process, the cathode was kept at various temperatures, T, evacuating the test tube by a vacuum pump. Occasionally, the cathode temperature wa lowered to 1028°K in order to check th emission current. The result obtained is show in Fig. 6. Fig. 7 shows the logarismic plo of the equilibrium emission current as th function of the temperature of the heat treat ment of the cathode.

Under the equilibrium condition the forma tion velocity of the excess Ba is equal to th evaporation velocity from the oxide surface The active material contained in the cor produces excess Ba through the reduction o oxide. The produced excess Ba diffuses i the oxide and appears on the oxide surface So, it may be thought that the rate of suppl of excess Ba is determined by the diffusio velocity of the active material in the sleeve.

Let n : represent "the density of the ex cess Ba at the oxide surface,"
E_d: "the diffusion energy of th active material in the core," an
E_e: "the evaporation energy of th excess Ba from the oxide sur face."

The diffusion velocity of the activ material in the core $\propto \exp(-E_d/kT$

The evaporation velocity of the exces Ba from the oxide surface $\propto n \exp(-E_e/kT)$.

Therefore, if A and B are constant,

$$A \exp(-E_d/kT) = Bn \exp(-E_e/kT) ,$$

so

$$n = \frac{A}{B} \exp((E_e - E_d)/kT) .$$

In the above experiment, the emission curren i at a specified temperature is proportional t the excess Ba density n, since the activity is insufficient and the relation $i \propto n$ rather than $i \propto n^{1/2}$ holds. Hence the slope of the lines in Fig. 7 gives $(E_e - E_d)/k$. The values of E_d obtained by assuming $E_e = 2.3$ e.v. listed in Table II. The value of $E_d = 1.6$ e.v. agrees with that measured by Kawamura[1] for the diffusion energy of Mg in Ni. For the sleeves used in the present experiment, it may be supposed that the diffusion energy of the active material has increased by 0.2 e.v. owing to the existence of a contaminated layer in the untreated case.

Table II. Diffusion energy of active material in the core metal.

	$E_e - E_d$	E_d
Electrolytically treated side	0.7 e.v.	1.6 e.v.
Untreated side	0.5 e.v.	1.8 e.v.

Assuming $E_e = 2.3$ e.v.

§4. Gas-evolution from Sleeve by Electron-bombardment

After a hydrogen firing, a sleeve was cut into two pieces of equal lengths. One of these was subject to electrolytic treatment so that a thickness of 8μ was removed from the surface. As illustrated in Fig. 8, they are used as the anodes which face to the Th-W cathode. After getter-flashing the test tube was tipped off. And, after activating the Th-W cathode, an emission current was taken out (cathode temperature=1600°K). The emission current from the Th-W cathode when the electrolytically treated sleeve A was used as the anode and that when the untreated sleeve B was used, respectively, are shown in Fig. 9. The temperatures of A and B measured by Ni-W thermocouple were maintained constantly at 800°K by their own heating filaments during the experiment. The decay of emission current as shown in Fig. 9 is ascribed to the gas-evolution from the anode which affects to the adsorbed Th on the Th-W surface. It has been recognized that the decay velocity was faster in the case of untreated sleeve B than in the another case. However, when, instead of taking out the emission current continuously from the Th-W cathode, occasional short period measurements of the emission current using the treated sleeve A were made, the result was as shown by C in Fig. 9; no decay of the emission current was observed unless the sleeve was continuously bombarded by electrons. The reason why A and B were kept at a constant temperature of 800°K during the experiment is that the gas-evolution velocity increases sharply with rising anode temperature, even if the electron bombardment is carried out under the same condition. From this phenomenon it may be supposed that there exists on the sleeve surface a layer of a different nature from that of the interior, which yields a large quantity of gas evolution when bombarded by electrons. In other words, this can be regarded as an evidence of the existence of the surface con-

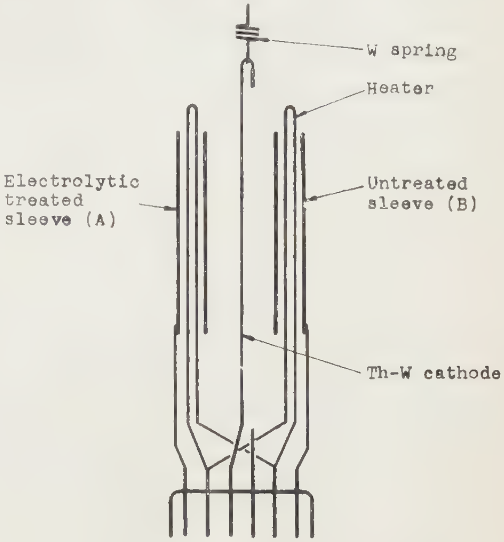

Fig. 8. Construction of test tube.

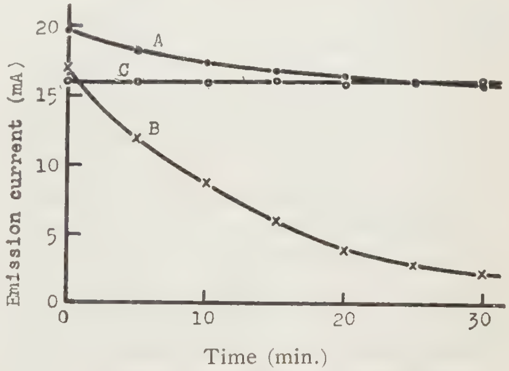

A: By using the electrolytic treated sleeve for the anode.
B: By using the untreated sleeve for the anode.
C: By using the electrolytic treated sleeve for the anode, but non continuous electron bombardment to the anode was held.

Fig. 9. Emission decay of Th-W cathode.

taminated layer.

§ 5. Effect of D. C. Electrolytic Treatment

The above-stated experiment is exclusively the case of A. C. electrolytic treatment. Table III illustrates the effect in another case, namely, of D. C. electrolytic treatment. Like the A. C. electrolytic treatment, diluted sulphuric acid was used as the electrolyte, and the same electrolytic current density of 1.5 A/cm² was used. The thickness removed was always 8μ. The method of experiment was the same as that in § 2. In Table III I_a and I_b are both the emission current from the oxide cathode of the treated part of the sleeve, but I_a means that which we have when the sleeve was used as anode in the electrolytic treatment, while I_b that which we have when first a thickness of 8μ of the sleeve surface was removed using the sleeve as anode, and then a reverse direct current of 1.5 A/cm² was passed for 30 sec. using now the sleeve as cathode. Nickel is electrolytically insoluble when the sleeve is used as the cathode, so the latter method was adopted. I_0 is the emission current from the part of untreated sleeve surface. As indicated in Table III, an increase in emission current by these D. C. electrolytic treatments is observed. But little difference in the emission current was recognized for the two directions of the current in the electrolytic treatment. Moreover, there was no remarkable difference between A. C. and D. C. electrolytic treatments as shown in Table IV.

Table III. Effect of D.C. electrolytic treatment to the emission current.

	I_a/I_0	I_a/I_b
Ratio	2.22	1.20
	2.10	1.12
	1.96	1.04
	1.96	0.90
	1.78	0.85
Mean value	2.00	1.02

Table IV. Comparison between A.C. and D.C. electrolytic treatment.

	$I_{A.C.}/I_{D.C.}$
Ratio	1.22
	1.16
	1.08
	0.90
	0.88
Mean value	1.05

Consequently, the increase in emission curren by electrolytic treatment must be ascribable the removal of the surface contaminated laye but not to some chemical or electrolytic reactions on the surface of nickel. Therefor the same effect is to be expected in the cas of acid treatment, and we actually confirme this experimentally.

§ 6. Conclusion

From the above results it may be conclude as follows. If the nickel-sleeve was produce by an inferior management in the workin processes, it has a surface contaminated laye This layer impeades the diffusion of the activ material in the core, so the activation actio by the active material is reduced. This bring a poor activity and a large dispersion in th emission currents. In such a case, if th contaminated layer is removed by means electrolytic or acid treatment, the pure co substance contacts directly with the oxide The activation by the active materials co tained in the core goes on vivaciously, thu increasing the emission current. With a certai improved control of the working process however, such an electrolytic treatment woul not be effective because there is no surfac contaminated layer.

The above is the results obtained from e periments using a certain type of sleeve mentioned in § 1. In experiments wit other types of sleeves, we met some case where no effect of the electrolytic treatmen was observed. However, it was generall observed that the emission current was mor or less enhanced.

In conclusion, we wish to express our dee appreciations to Prof. E. Sugata for his co tinual encouragement and to Mr. T. Hiros Mr. S. Takai, Mr. R. Fujita, Mr. K. Echikaw and Mr. K. Tabei for their co-operation. Als we are grateful to the research people an engineers of numerous electron tube man facturing companies and laboratories for the valuable discussions and helps.

This work has been partly supported by th Scientific Research Expenditure from th Ministry of Education.

Reference

1) H. Kawamura: J. Phys. Math. Soc. Japan, **1** (1943) 159.

JOURNAL OF THE PHYSICAL SOCIETY OF JAPAN Vol. 10, No. 7, JULY, 1955

Shock Tube Study of the Flow past Circular-Arc Airfoils Using a Mach-Zehnder Interferometer

By Kôichi ÔSHIMA

Institute of Industrial Science, University of Tokyo

(Received March 22, 1954)

Interferometer measurements are given of pressure distributions of circular-arc airfoils with thickness ratios

10%, 15%, 20%

at angles of attack

0°, 1.6°, 3.2°, 4.8°, 6.4°

in the flow of Mach numbers

0.75, 0.85, 0.95, 1.03, 1.1, 1.2, 1.3, 1.4, 1.55, 1.7, 1.9

with Reynolds numbers based on chord length

$2.2 \sim 1.9 \times 10^5$.

From these data, drag coefficients, lift coefficients and pitching moment coefficients were calculated for each case.

These coefficients and lift-angle of attack curves are in good agreement with transonic similarity law. Results are also compared with other wind tunnel experiments.

§ 1. Introduction

On the flow past a thin two-dimensional airfoil, there have been many researches in the case of low subsonic and high supersonic speeds. Hence our knowledge concerning the flow in these speed ranges is almost complete. However, it seems that, in the case when the flow speed is nearly sonic, the research is yet in early stage of its development. Th. von Kármán made a great contribution to this research by presenting the transonic small perturbation equation. Although due to its mathematical difficulty, this equation has been solved only for a few special cases, a similarity law concerning the body shape, free stream Mach number and specific heat ratio can be deduced from this equation. Based on this law, characteristics of an airfoil can be calculated from the characteristics of an airfoil with similar shape but different thickness.

At the GALCIT, A. E. Bryson¹⁾ measured the drag coefficients of half wedges with semi-wedge angles 4.5°, 7.5°, 10° at zero angle of attack and checked this similarity law. J. D. Cole²⁾ measured the lift coefficients and center of pressure coefficients of a 5% double wedge airfoil at small angle of attack. But these data lack the values at near sonic speed owing to the wind tunnel choking.

D. K. Weimer³⁾ pointed out the possibility of transonic experiments using the quasi-stable state of shock tube flow. At the Princeton 4×18 in. shock tube, W. Griffith⁴⁾ obtained the drag curve in the transonic range of a half wedge with semi-wedge angle 7.5° at zero angle of attack. His data agree with Bryson's results at subsonic and supersonic speeds.

A few experiments are reported for circular-arc airfoils, but these data do not seem to be sufficient for the examination of the transonic similarity law. So in order to criticize this law, systematic experiments of these airfoils with various thickness ratios at various angles of attack in the wide range of Mach numbers, including the neighborhood of Mach number of 1, are carried out.

This work was conducted at the Institute of Industrial Science, University of Tokyo. Grateful acknowledgement is made to Prof. F. Tamaki for his continued encouragement and useful advice. Thanks are also due to Mr. Y. Sakurai for his helpful assistance in carrying out the experimental work.

§ 2. Notations

c : airfoil chord length
C_D: pressure drag coefficient
C_L: lift coefficient
C_M: pitching moment coefficient about 1/2 chord point
C_P: pressure coefficient

Photo. I. Test window and Interferometer.

Photo. II. Models.

M : Mach number of undisturbed flow
t : maximum thickness of airfoil
x : distance from leading edge along center line of airfoil
α : angle of attack
γ : specific heat ratio
ξ : transonic similarity parameter
$\tilde{C}_D$: reduced pressure drag coefficient
$\tilde{C}_L$: reduced lift coefficient
$\tilde{C}_M$: reduced pitching moment coefficient about 1/2 chord point.

§ 3. Shock Tube and Models

Measurements were made in the Institute of Industrial Science 6×15 cm shock tube. For the description of the shock tube, calibration equipments and optical systems employed see references 5 and 6. Experiments were carried out in the so-called "cold-air" of shock tube flow. Detailed examination of this flow and full data of this investigation will be published by the present author in the Report of the Institute of Industrial Science, University of Tokyo.

Three circular-arc airfoils with different thickness ratios were used in the experiments. All airfoils have the chord length of 2 cm and the span of 6 cm, and the maximum thickness are 2 mm, 3 mm and 4 mm, respectively. They are made of mild steel and supported in the flow by two thin stings attached to the wing tips. These stings are in close contact with side walls, and so the disturbance due to them are quite small.

Photos. I and II show the Mach-Zehnder interferometer used and the three models with supports, respectively.

§ 4. Flow Patterns

Some typical interferograms of flow about 15% airfoil are shown in Photos. III and IV. The error of measurement of fringe shift of interferogram is smaller than 1/10 of one fringe, and the maximum fringe deviations from undisturbed flow are 3∼5 fringes; consequently the error of pressure coefficient is smaller than 2∼4% of their maximum value. Pressure coefficients corresponding to these

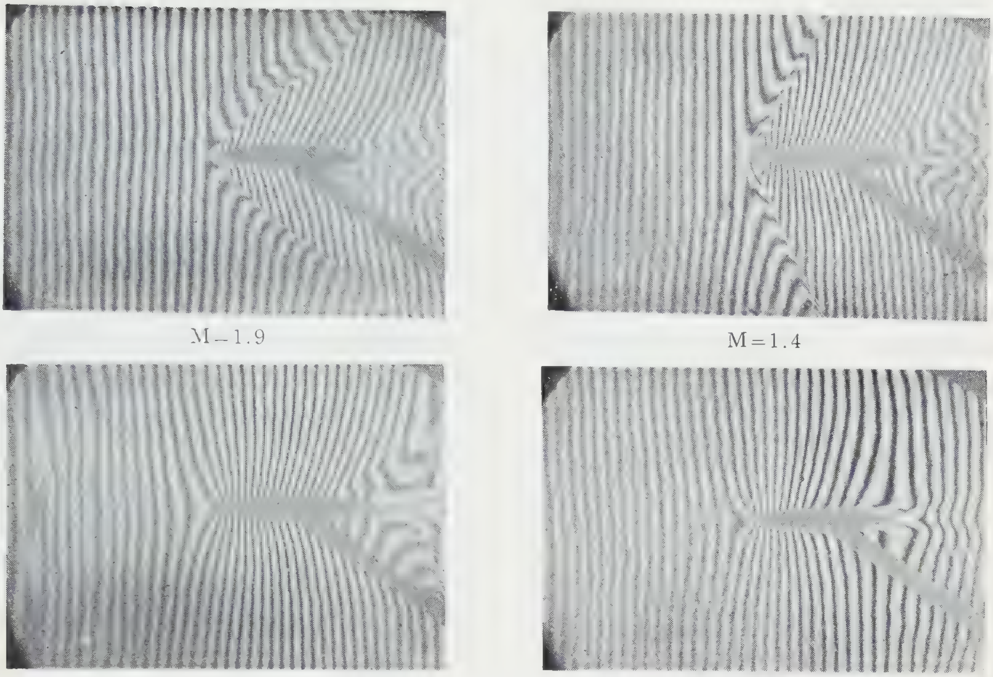

M=1.9 M=1.4

M=1.1 M=0.75

Photo. III. 15% airfoil $\alpha=0°$.

photographs are shown in Figs. 1 and 2. The figure corresponding to M=1.9 shows purely supersonic pressure distribution on the airfoil, and the one corresponding to M=0.75 shows purely subsonic distribution. The distributions at Mach numbers between these values change gradually from supersonic to subsonic type distribution.

Reynolds numbers based on chord length are $1.9\sim2.2\times10^5$. So laminar boundary layer separation occurs in every case, and shock wave, which appears when the flow speed on the surface exceeds local sound speed, takes the so-called λ-configuration. Both the shock wave position and the separation point move downstream as the free stream Mach number is raised.

Fig. 2 corresponding to Photo. IV shows C_P at $\alpha=4.8°$. Distributions on the lower surface are similar to those at $\alpha=0°$, but those on the upper surface take very complicated feature owing to the leading edge separation and the reattachment of the flow to the wing surface.

All other experiments carried out for different thickness ratios, angles of attack and free stream Mach numbers show similar

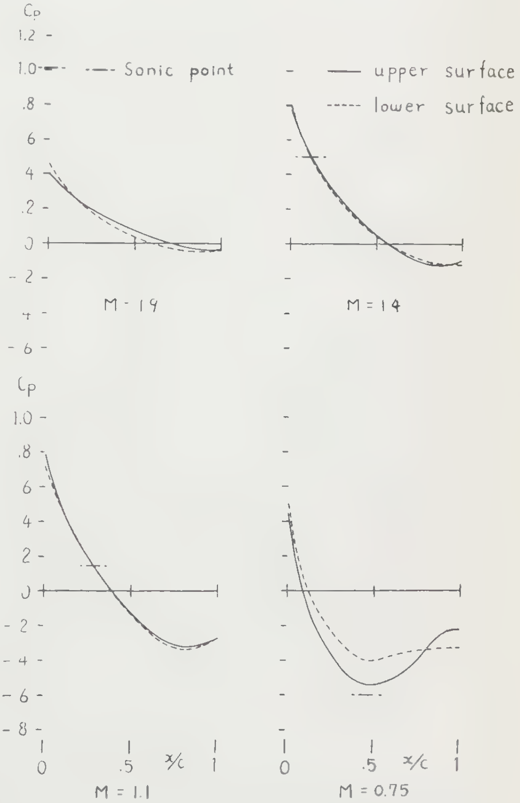

Fig. 1. Pressure distribution of 15% circular-arc airfoil at zero angle of attack.

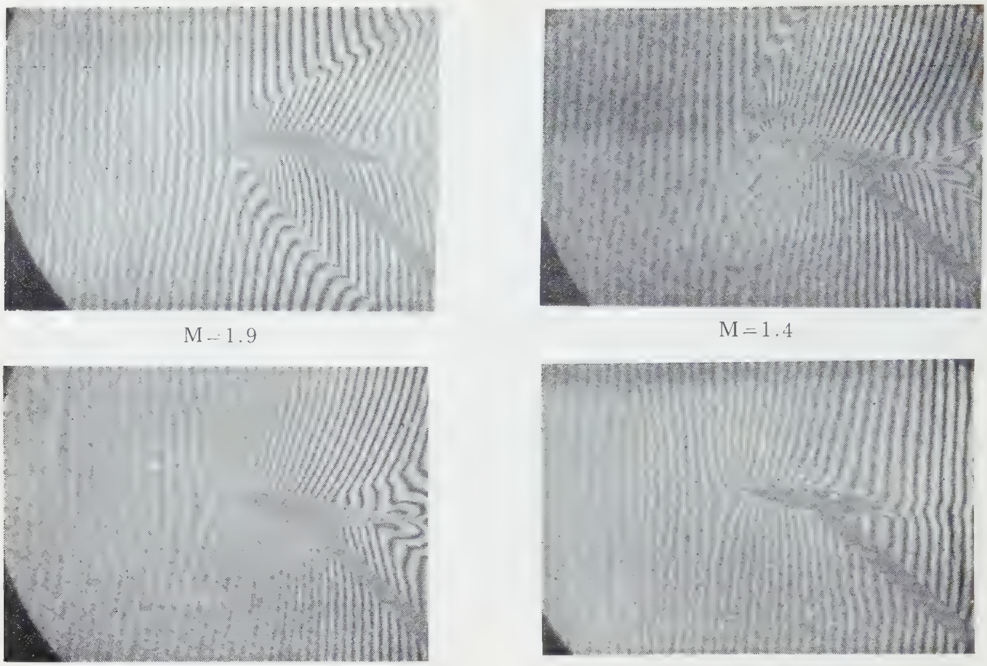

M=1.9 M=1.4

M=1.1 M=0.75

Photo. IV. 15% airfoil $\alpha=4.8°$.

characters of the flow as mentioned above, and so the figures and photographs are omitted here.

§ 5. Results

Pressure force components of normal and tangential direction to chord are calculated by numerical integration of the corresponding components of C_P. These are transformed to pressure drag coefficients and lift coefficients. Pitching moment coefficients are also calculated by numerical integration of moment components.

These coefficients are transformed to reduced coefficients by the following formulas to present the experimental results in terms of the transonic parameter:

$$\xi=\frac{M^2-1}{[(\gamma+1)t/c]^{2/3}}\,, \qquad \tilde{C}_D=\frac{(\gamma+1)^{1/3}C_D}{(t/c)^{5/3}}\,,$$

$$\tilde{C}_L=\frac{(\gamma+1)^{1/3}C_L}{(t/c)^{2/3}}\,, \qquad \tilde{C}_M=\frac{(\gamma+1)^{1/3}C_M}{(t/c)^{2/3}}\,.$$

Fig. 3 (a) and (b) show $\tilde{C}_D$ of the front half and rear half of airfoils, respectively, at zero incidence. Calculations based on Busemann's approximation about 10% and 15% airfoils are also included. Even at the highest Mach number tested (M=1.9), 20% airfoil has not attached shock wave, and so the calculation

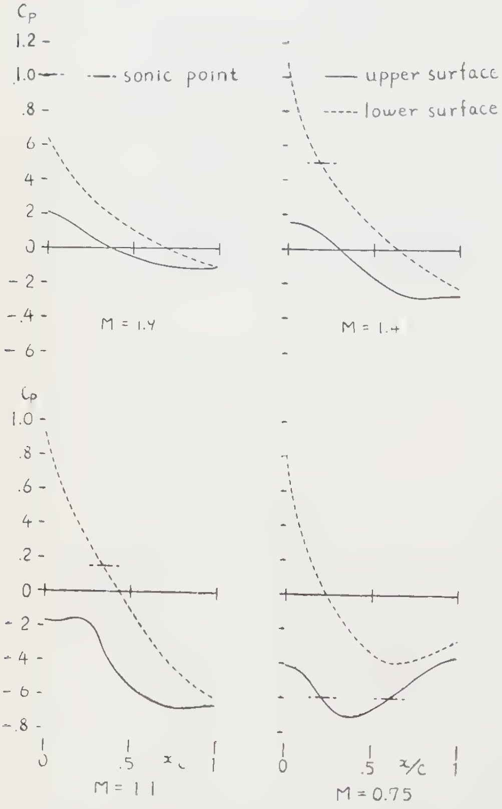

Fig. 2. Pressure distribution of 15% circular-arc airfoil at angle of attack 4.8°.

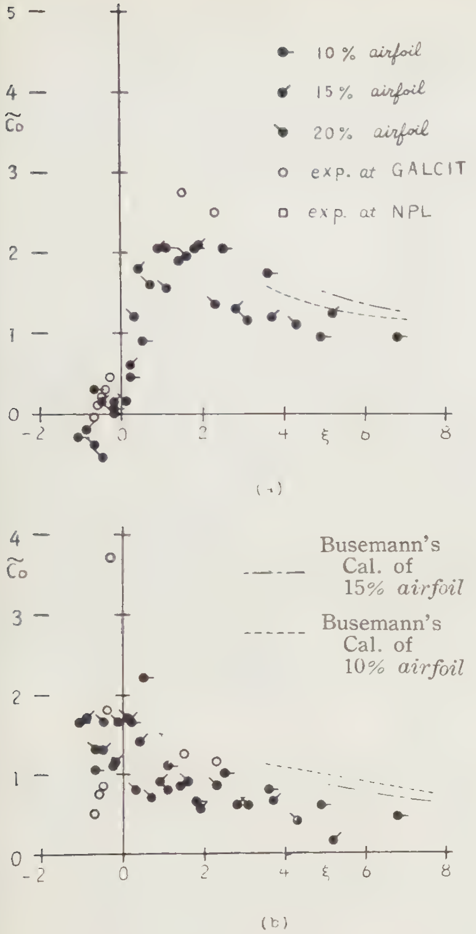

Fig. 3. Reduced drag coefficient at zero angle of attack of front half-(a) and rear half-(b).

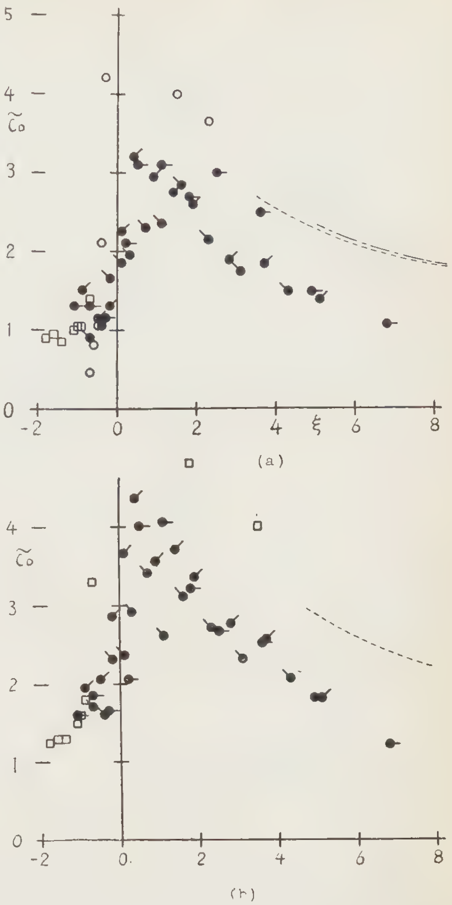

Fig. 4. Reduced drag coefficient at zero angle fo attack-(a) and at $\alpha/(t/c)=0.56$-(b).

for this case is not presented. Fig. 4 (a) shows $\tilde{C}_D$ of the total profile at zero incidence. It is the sum of Fig. 3 (a) and (b).

10% airfoil at $\alpha=3.2°$, 15% airfoil at $\alpha=$ 4.8° and 20% airfoil at $\alpha=6.4°$ have the same value of $\alpha/(t/c)$, so they are similar profiles. Fig. 4 (b) shows $\tilde{C}_D$ for these cases. Fig. 5 (a) and (b) show $\tilde{C}_L$ and $\tilde{C}_M$ for the same cases, respectively.

Fig. 6 shows the reduced lift curve at nearly equal values of ξ. This indicates that $\tilde{C}_L$ at the same ξ are proportional to $\alpha/(t/c)$. The relation between $\tilde{C}_L/[\alpha/(t/c)]$ and ξ is shown in Fig. 7.

§ 6. Comparison with Wind Tunnel Data

Pressure distributions of a half 8.8% circular-arc profile followed by straight section at zero angle of attack at high subsonic and low supersonic speeds were measured by A. E. Bryson at the GALCIT 10×4 in. wind tunnel using a Mach-Zehnder interferometer. In the two cases of Mach numbers, at which the airfoil has detached shock wave and the shape of the rear half does not affect the pressure distribution of the front half, the pressure distribution of the rear half of a circular-arc airfoil instead of the straight section was calculated from the front half data on the assumption of Prandtl-Meyer flow. A 12% circular-arc airfoil at zero incidence with artificially developed turbulent boundary layer was experimented by H. W. Liepmann, H. I. Ashkenas and J. D. Cole in the subsonic range. Reduced drag coefficients from these data are plotted in Figs. 3 and 4 (a).

Drag coefficients, lift coefficients, moment coefficients and center of pressure coefficients of a 7.5% circular-arc airfoil at angles of

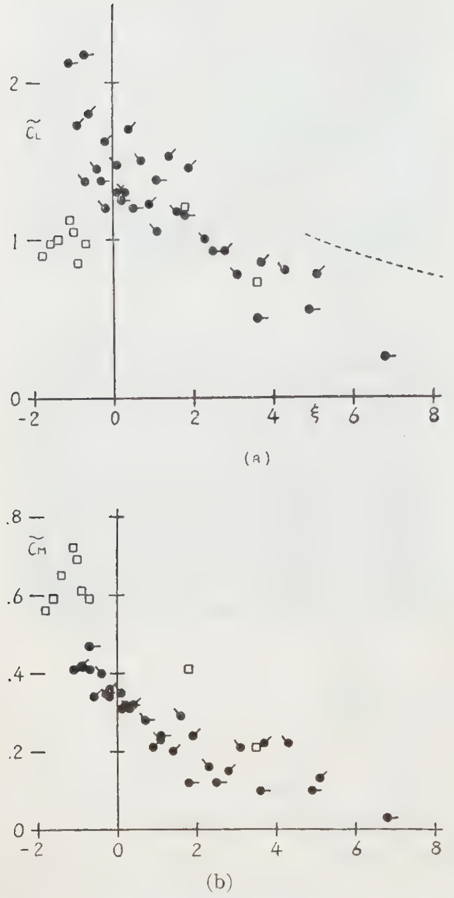

Fig. 5. Reduced lift coefficient-(a) and moment coefficient-(b) at $\alpha/(t/c)=0.56$.

attack 0°, 1°, 2°, 3° and 4° were measured at the NPL 1 ft wind tunnel by W. F. Hilton. These data are plotted in Figs. 4, 5 and 6. In his experiments, forces are measured directly by a balance, and Reynolds numbers are $0.4\sim0.88\times10^6$, which are slightly higher than the present experiments.

The above-mentioned data are either the results with calculated rear half airfoil or with turbulent boundary layer or with large Reynolds number. Hence so the flow patterns are different from the present experiments, that is, they have no λ-shock and laminar separation. Accordingly it is natural that some systematic deviations from our data are found, and they are especially remarkable at low Mach numbers at which λ-shock wave appears on the airfoil surface. Drag coefficients of front half profiles and lift coefficients are in good agreement with our data, but drag coefficients of rear half profiles and momen coefficients do not agree because thes coefficients are strongly influenced by th pressure distributions near the trailing edge Drag coefficients of Hilton's data include frictional drag, so that they are larger than othe data.

As is well known, the detached bow wav moves very far ahead of the profile as th flight Mach number decreases toward 1 an the radius of curvature of detached shoc wave at the point directly ahead of the profil becomes extremely large; and the local Mac number distribution of the airfoil surface ha a stationary value at flight Mach number and varies only slowly in the neighborhood o it. On consideration of these facts it is concluded that the drag curve of rear half o circular arc airfoil has negative gradient a $\xi=0$ and has the maximum value at the poin just below $\xi=0$. This fact gives a possibilit of predicting the drag coefficient at nearl sonic speed which cannot be obtained by win tunnel test.

Our experiments show: the local Mac number at a surface point upstream of th separation point has a stationary value in th neighborhood of $\xi=0$, but the separation poin moves monotonically upstream as free strea Mach number decreases, so that the local Mac number at a surface point downstream o the separation point has not a stationar value but decreases monotonically in th neighborhood of $\xi=0$. Accordingly the dra coefficient of the rear half profile has a positiv gradient at $\xi=0$ and has the maximum valu at a certain point above $\xi=0$.

§ 7. Conclusions

Experimental investigation of transonic flo past circular-arc airfoils was made by shoc tube using a Mach-Zehnder interferometer The conclusions may be stated as follows:

1. Experimental values of force coefficient verified the transonic similarity theory.

2. Because of the shift of separation point local Mach numbers at the surface point downstream of the separation point hav not a stationary value at M=1 and maximum of the drag curve of rear hal airfoil appears above M=1.

3. In the transonic range, the ratio o reduced lift coefficient to angle of attac

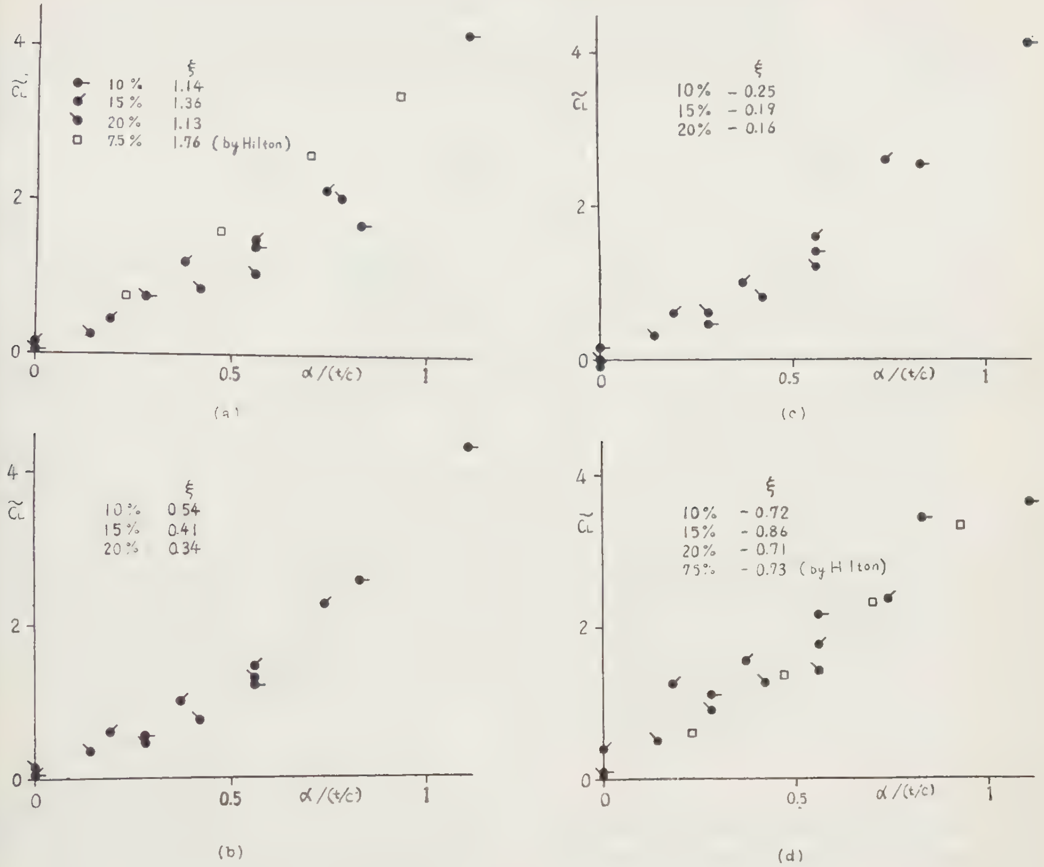

Fig. 6. Relation between reduced lift coefficient and $\alpha/(t/c)$ for various groups of ξ.

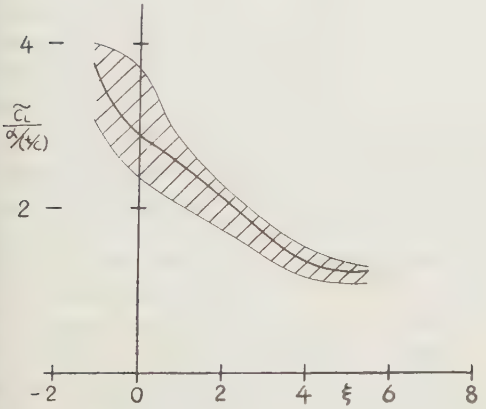

Fig. 7. Reduced lift curve slope.

divided by maximum thickness ratio is constant.

References

1) A. E. Bryson: NACA Report 1094.
2) J. D. Cole, G. E. Solomon and W. W. Willmarth: J. Aero. Sci. **17** (1950) 723.
3) D. K. Weimer, C. H. Fletcher and W. Bleakney: J. App. Phy. **20** (1949) 418.
4) W. C. Griffith: J. Aero. Sci. **19** (1952) 249.
5) F. Tamaki: Seisankenkyu **4** (1952) 75.
6) F. Tamaki and K. Ôshima: Seisankenkyu **5** (1953), 87.
7) W. F. Hilton: R and M 2196.

JOURNAL OF THE PHYSICAL SOCIETY OF JAPAN Vol. 10, No. 7, JULY, 1955

Experimental Studies on the Characteristics of Isotropic Turbulence behind Two Grids

By Hiroshi TSUJI

Institute of Science and Technology, University of Tokyo, Tokyo

(Received February 28, 1955)

In order to study the characteristics of isotropic turbulence produced under various initial conditions and at high Reynolds numbers, hot-wire measurements were made to determine the decay and the g-correlation of turbulence behind two grids, the upstream grid having a larger mesh length than the downstream one, in the 1.5-meter wind tunnel at the Institute of Science and Technology.

The linear decay law, $\overline{u^2}\sim x^{-1}$, does not hold in the presence of a large-scale, slowly-decaying turbulence produced by the first grid ahead of the second grid. On the other hand, Lin's decay law, $\overline{u^2}\sim[x^{-1}+const.]$, which is supposed to be valid for the turbulence either behind a single grid or with a superposed disturbances of low frequencies, is confirmed unless the large-scale turbulence produced by the first grid is overwhelmingly predominant, though the deviation from the self-preservation of correlation at large value of r is marked. The constant term in Lin's decay law, which expresses the deviation from the complete similarity, is negative for the single grid, but is positive in the presence of a superposed, large-scale turbulence.

§1. Introduction

Many works have been done theoretically or experimentally in the study of isotropic turbulence, and have made clear much of the mechanism of turbulence in the process of decay. However, the Kármán-Howarth equation for the propagation of correlation function, or its Fourier transformation—i.e. the spectrum equation--which governs the motion of turbulence during decay, cannot be solved, in general, because of itsnon-linear nature. Only when the Reynolds number of turbulence is small, i.e., the decay is in the final period, the non-linear term, which expresses the transfer of energy between frequency components, can be neglected so that the solution can be obtained in an explicit form as confirmed by experiments[1]. On the other hand, when the Reynolds number of turbulence is large and the energy transfer between frequency components plays an important role, the problem has been treated by many authors by making plausible assumptions, such as the self-preservation of correlation function or the similarity of spectrum during the process of decay. The similarity spectrum, however, is expected to be only asymptotically correct for the range of large wave numbers, its limit depending on the initial conditions and decreasing as the decay proceeds; therefore the law of decay might also depend o the initial conditions.

The effect of the upstream turbulence o the decay of turbulence behind the grid wa first mentioned by Taylor[2]. Some experiment on the decay of turbulence behind two grid were carried out by Atsumi[3] and Hama[4], bu the results were not entirely satisfactory t test the effect of the upstream turbulence Recently, the importance of an experiment t test the dependence of the law of decay o the initial conditions has been reemphasize by Lin[5][6], and Goldstein[7], in connection wit the validity of the existing decay laws.

In order to study the nature of isotropi turbulence produced under various initial conditions, measurements were made on turbulence produced by two grids, the upstrea grid having a larger mesh length than th downstream one. In order to investigate th characteristics of turbulence in more detail, is necessary to measure the spectrum or co relation. As well known, the correlation an the spectrum have the Fourier transform r lation to each other, and one of thes quantities can be evaluated from the othe

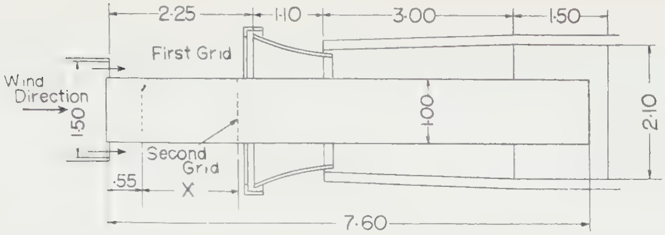

Fig. 1. Schematic diagram of duct installed in the wind tunnel (All dimensions in meters).

However, the correlation is useful for understanding the lage-scale physical process of turbulence during decay while the spectrum for the small-scale process, so that it was planned to measure both correlation and spectrum in our continuing research project. In this paper the results of decay and g-correlation measurements are presented. The spectrum measurement is undertaken and will be reported shortly.

§ 2. Experimental Equipment and Procedure

a) *Wind Tunnel*

Measurements were carried out in the 1.5-meter closed-circuit wind tunnel at the Institute of Science and Technology. A wooden duct, 7.6 m long and 1×1 m^2 square section, was installed to eliminate the free boundary contamination from the original open-jet[8] and to have a longer test section (Fig. 1). The mean wind-velocity distribution along the axis of the duct was sufficiently uniform, as shown in Fig. 2, except near the grid. There was a tendency that the velocity became larger in the region approximately 60 to 80 mesh lengths behind the second grid[4]. The mean turbulence level of the wind tunnel was approximately 0.2 per cent for the mean wind velocity of 5 to 20 m/sec.

b) *Grids*

The first grid (half-morticed square wooden rods) had a mesh length, M_1, of 5 cm, and rod size, d_1, of 1 cm. The second grid (interfaced circular steel rods) had those, M_2 and d_2, of 1 and 0.2 cm, respectively. The geometrical solidity factor of both grids was 0.36. The first grid was fixed at the position of 55 cm from the entrance of the duct in the course of all measurements, and the second grid was located at several positions to have different distances between the two grids for each experimental run.

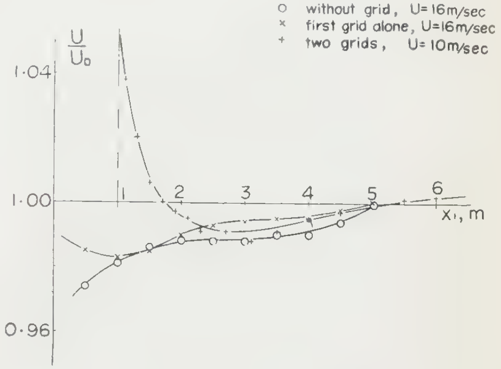

Fig. 2. Mean wind-velocity distribution along the axis of duct.

c) *Hot-Wire Anemometer*

A 0.0003-inch Wollaston wire was soft soldered to the tips of the two needles, spaced 5 mm apart, so as to form an arc, and the silver cover of the central part of the arc was etched off by the method described in detail in reference 8. The etched part of the wire was approximately 1 mm long. Working temperature was about 300°C at heating current of 100 mA and the resistance of the wire was about 6 ohms. The time constant was then about 1.4 milli-seconds.

d) *Traversing Mechanism*

In order to traverse one hot-wire anemometer relative to the other fixed one in a vertical plane normal to the mean wind direction for the measurements of g-correlation, the unit shown in Fig. 3 was used. A micrometer screw with 1 mm pitch, on which the hot-wire support was fastened, was driven through a set of worm-gears and a shaft by a Selsyn motor controlled from outside the tunnel. This hot-wire holder unit, on which the total-head and static tubes were also mounted, was moved fore and aft along the guide rails on the floor of the duct by means of a piano-wire and pulleys manually operated from outside the wind tunnel. The minimum distance (0.4 mm) between the two hot-wires was adjusted by an ocular micrometer at the beginning of each run.

e) *Amplifier*

The compensating amplifier used for this experiment was that of conventional resistance-capacitance compensating, push-pull, balanced type[9)][10)] (Fig. 4). All the vacuum tubes were heated with direct current drawn from the battery, and the plate power source was a

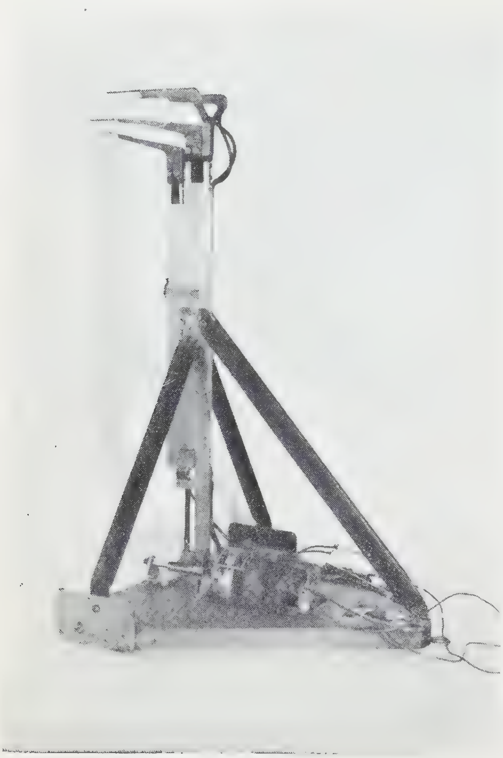

Fig. 3. Traversing mechanism of the hot-wire holder unit.

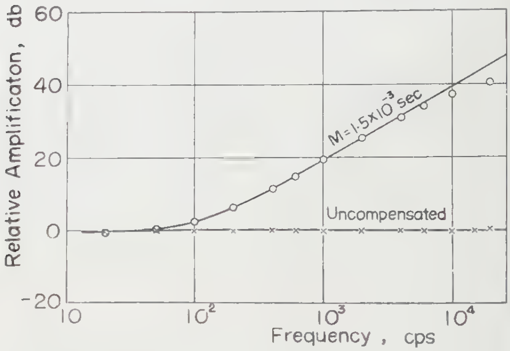

Fig. 5. Frequency characteristics of compensating amplifier.

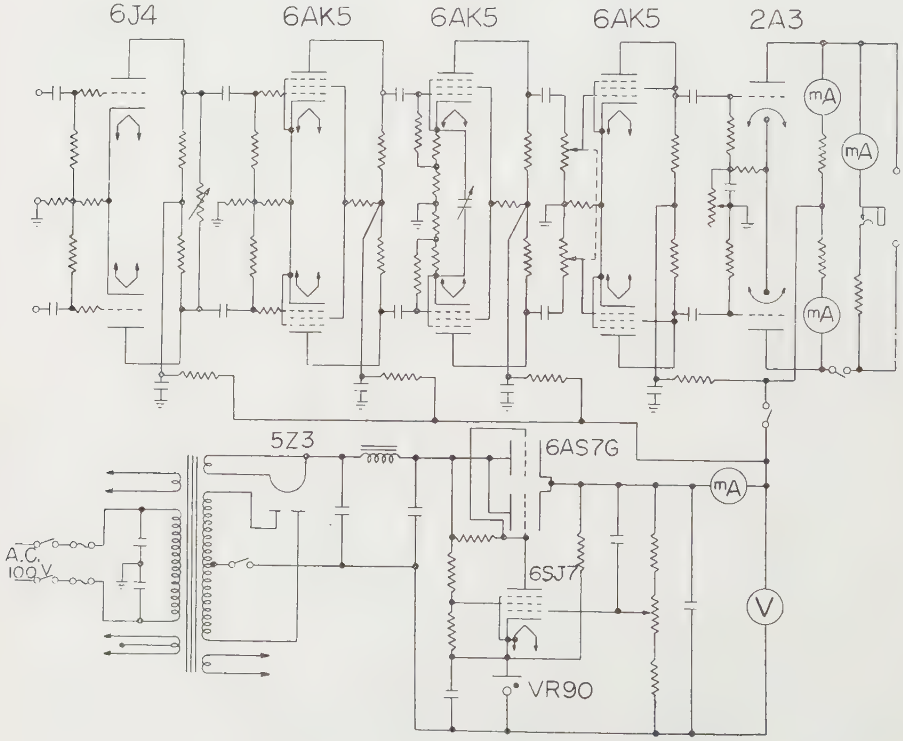

Fig. 4. Circuit diagram of compensating amplifier and stabilized power supply.

conventional regulated power supply (300 V, 120 mA) with additional filtering incorporated with the compensating amplifier unit. Since 6J4-tubes in the first stage, which had a high transconductance, were rather microphonic, the entire amplifier was hung by the damping spring in a special anti-microphonic case. The amplifier had good compensation characteristics up to approximately 6 kilo-cycles for the wire used in this experiment (Fig. 5). Mean-square out-put was read on a thermocouple milliammeter.

f) *Measurement of Decay of Turbulence*

Measurements of the decay of the energy of turbulence were made for mean wind velocities of 5, 10, and 15 m/sec behind two grids or a single grid alone. The distance, X, between the two grids was 50, 100, 150, 200, 250, 350, or 450 cm. Measurements were repeated several times for each setting.

g) *Measurement of g-correlation*

The longitudinal velocity-correlation coefficient $f(r)$ and the lateral velocity-correlation coefficient $g(r)$ introduced by von Kármán and Howarth[11] are related to each other by the continuity condition,

$$g(r)=f(r)+\frac{r}{2}\frac{\partial f(r)}{\partial r},$$

and thus the measurement of either one of the coefficients is sufficient. Measurement of the lateral correlation coefficient $g(r)$ being more convenient technically, $g(r)$-curve was determined at a number of sections downstream from the second grid or a single grid for the mean velocities of 5, 10, and 15 m/sec. The usual "sum-and-difference method" described in reference 12 was used to determine $g(r)$. The distance between the two grids was 50, 200, 250, 350, or 450 cm.

h) *Determination of Microscale*

The microscale, or the dissipation length, λ, defined by the relation

$$\frac{1}{\lambda^2}=-\left[\frac{\partial^2 g(r)}{\partial r^2}\right]_{r=0},$$

can be measured by various methods: e.g., the differentiation circuit[9][13], or by zero counting[14][15]. In this paper, however, values of λ were evaluated from the $g(r)$-curves plotted against r^2, in view of investigating the self-preservation of the measured correlation curves.

§ 3. Experimental Results and Discussion

a) *Decay of Turbulence*

Results of the measurement of the decay of turbulence for $X=250$ cm is shown in Fig. 6 as an example, in which x_2 is the distance downstream of the second grid, U the mean velocity, and $\overline{u^2}$ the mean-square turbulent velocity.

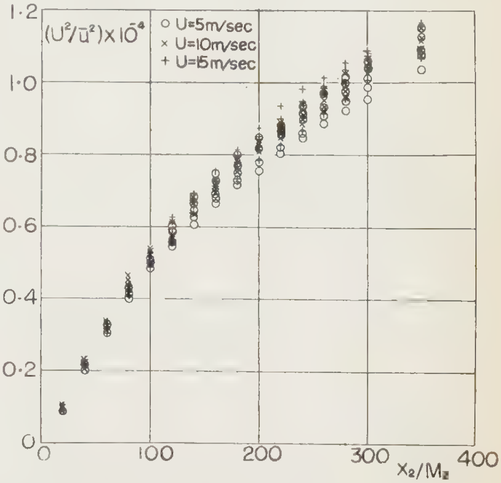

Fig. 6. Decay of turbulence: $X=250$ cm, $U=5$, 10, and 15 m/sec.

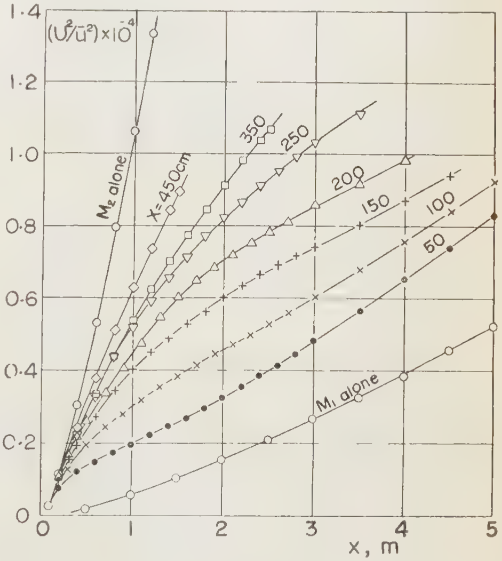

Fig. 7. Summary of decay of turbulence: $U=10$ m/sec.

A summary of the experimental results for the mean velocity of 10 m/sec is shown in Fig. 7. Each point plotted is an arithmetic mean of at least four measurements from

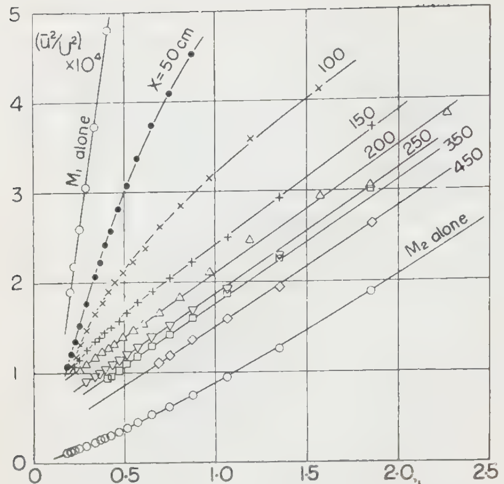

Fig. 8. Decay of turbulence: $U=10$ m/sec.

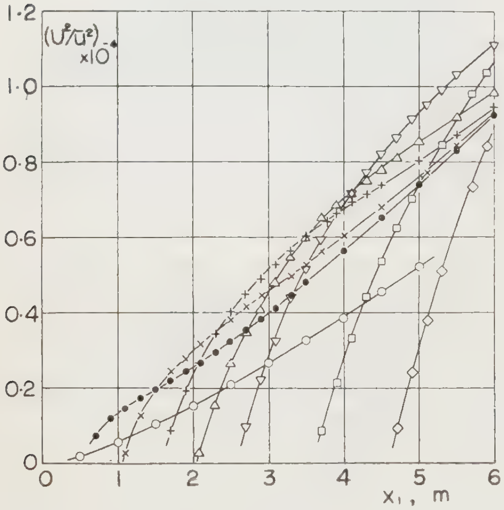

Fig. 9. Decay of turbulence: $U=10$ m/sec.

different runs. It seems that turbulence produced by the second grid with finer mesh decays rapidly at the early stage of decay. However, the effect of the first grid is marked if the distance between the two grids is small. In this case the effect of turbulence produced by the first grid is so strong that, as the decay proceeds, the fine-scale turbulence produced by the second grid decays out rapidly and the decay curve resembles that for the first grid alone. From these experimental results, it is easily found that the decay law of turbulence in the early stage of decay depends on the initial conditions, especially on the low-frequency components. The value of n in the power law, $(U^2/\overline{u^2})\sim(x/M)^n$, depends on the initial conditions and has no universal value. n is generally larger than 1 for turbulence produced by a single grid, while it is smaller than 1 for turbulence which contains superposed low-frequency components. As suggested by Lin and Goldstein, the linear decay law, $\overline{u^2}\sim x^{-1}$, does not hold in the presence of a large-scale turbulence ahead of the grid.

In order to check the decay law

$$\overline{u^2}\sim[(x-x_0)^{-1}+const.]\ ,$$

which has been originally put forward by Lin5) and later endowed with firmer reasoning by Goldstein7), the same data as in Fig. 7 are replotted in Fig. 8 in a different manner16). From Fig. 7, the origin x_0 is chosen as 0.06 m. Lin's formula, which is supposed to be valid for the turbulence either behind a single grid or with a superposed disturbances of low frequencies, seems to be confirmed unless the large-scale turbulence produced by the first grid is overwhelmingly predominant.

The discrepancy between two decay curves for a single grid plotted in a reduced scale (x_2/M_2 or x_1/M_1) may have resulted from the inequality of the effective solidity factor of the two grids, the square-rod grid having an effective opening less than that of the circular-rod grid of the same d/M ratio.

In case of $X=100\sim200$ cm, it is found that the decay curves show a slight dependence on the mean velocity, while in other cases the decay curves scarcely depend on the mean velocity.

In Fig. 9, values of $U^2/\overline{u^2}$ for $U=10$ m/sec are plotted, the distance x_1 from the first grid being taken as the abscissa. In this figure, it is possible to draw an envelope to the curves, which gives the minimum value of $\overline{u^2}/U^2$ at each point behind grids. It may be clearer if $U^2/\overline{u^2}$ is plotted against X, the distance between two grids, x_1 being a parameter (Fig. 10). There exists a maximum point on each curve and a smooth curve can be drawn connecting these extreme points. The curve corresponds to the envelope which may be presented in Fig. 9. It is seen therefore that, in view of reducing the intensity of large-scale turbulence at a section by means of the so-called damping screen of fine mesh, there should exist the most efficient location for the

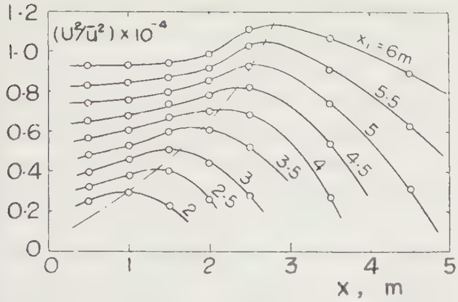

Fig. 10. Decay of turbulence: $U=10$ m/sec.

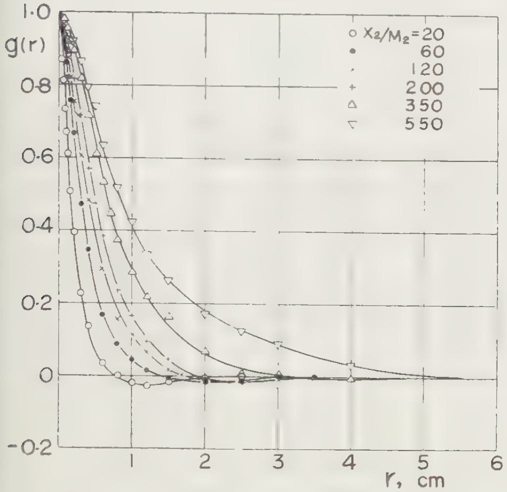

Fig. 11. Correlation coefficient $g(r)$: Second grid alone, $U=10$ m/sec.

damping screen.

b) *g-correlation*

Fig. 11 shows the correlation coefficient $g(r)$ behind the second grid alone for $U=10$ m/sec. The measured correlation agrees with the results obtained by Batchelor and Townsend[17]. As is well known, $g(r)$ is negative at large values of r and then tends to zero from negative side. The results of correlation measurement made at various distances downstream of the first grid alone for $U=10$ m/sec are presented in Fig. 12, and it is seen that the scale of turbulence is very large because of the large mesh length of the first grid.

Fig. 13 shows the correlation coefficient $g(r)$ at various distances downstream of the two grids placed 350 cm apart for $U=10$ m/sec. X being large in this case, the high-frequency components of turbulence produced by the first grid have already decayed out and the low-frequency components are superposed to the turbulence produced by the second grid. Comparison between these results and those of Fig. 11 shows that the effect of the large-scale turbulence produced by the first grid

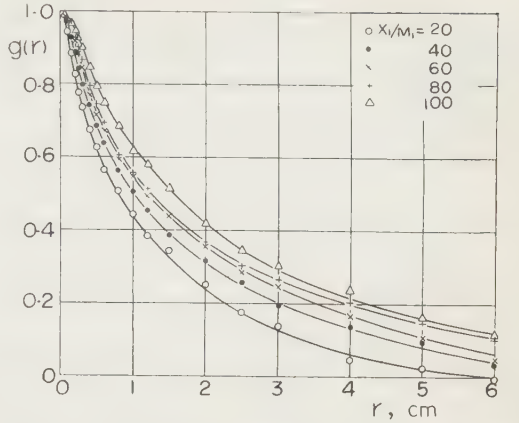

Fig. 12. Correlation coefficient $g(r)$: First grid alone, $U=10$ m/sec.

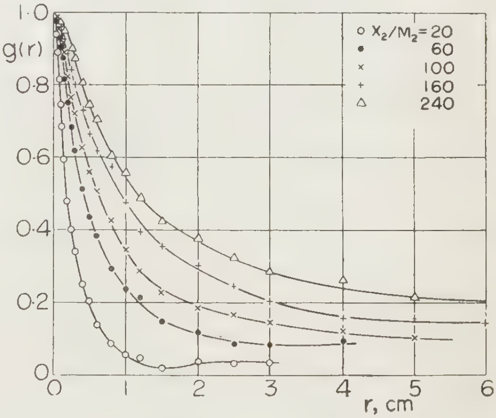

Fig. 13. Correlation coefficient $g(r)$: $X=350$ cm, $U=10$ m/sec.

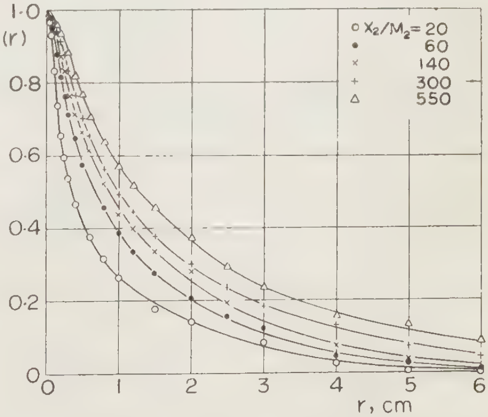

Fig. 14. Correlation coefficient $g(r)$: $X=50$ cm, $U=10$ m/sec.

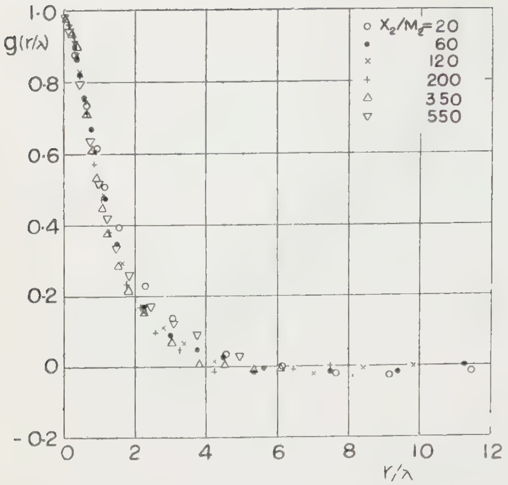

Fig. 15. Correlation coefficient $g(r/\lambda)$: Second grid alone, $U=10$ m/sec.

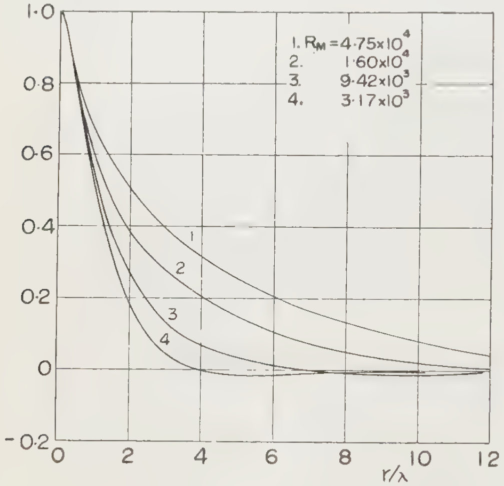

Fig. 16. Mean curve of $g(r/\lambda)$ behind a single grid for various mesh Reynolds numbers.

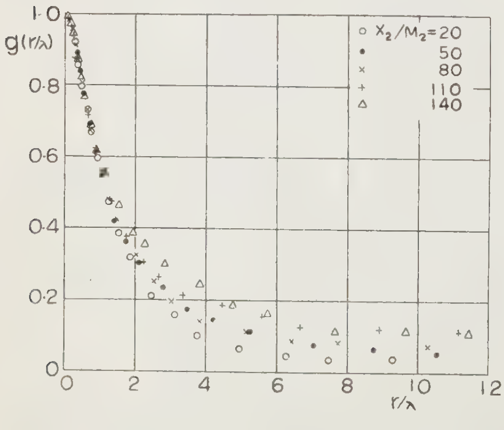

Fig. 17. Correlation coefficient $g(r/\lambda)$: $X=450$ cm, $U=10$ m/sec.

predominates and the correlation exists up t much larger values of r than expected fro the second grid alone. The correlation coefficient $g(r)$ for $X=200$, 250, and 450 cm ar found to be similar to those in Fig. 13.

Fig. 14 shows the correlation coefficient $g(r$ for $X=50$ cm and $U=10$ m/sec. In this case X is very small and the shape of $g(r)$ quite resembles those for the first grid alone except at small values of x_2/M_2. This is due to the fact that the fine-scale turbulence produced by the second grid decays out rapidly and the large-scale turbulence produced by the first grid remains almost untouched.

c) *Self-preservation of Correlation*

By using λ obtained from the $g(r)$-curves, the measured g-correlation is replotted against r/λ. Fig. 15 shows $g(r/\lambda)$ for the second grid alone. As is well known from Batchelor and Townsend's measurement[17], the chief feature of $g(r)$-curve is that, outside the self-preserving region for which r/λ is less than approximately 1, the values of r/λ corresponding to a given value of g decrease with increasing x_2/M_2. In other words, outside the self-preserving region $g(r)$-curves maintain roughly the same shape but contract as x_2/M_2 increases. The same tendency is observed in the results of measurement at $U=5$, and 15 m/sec, and also for the first grid alone. It is seen, moreover, that outside the self-preserving region the mean curve of $g(r/\lambda)$ in any family during the process of decay, e.g., the mean curve which may be drawn in Fig. 15, contracts laterally as the mesh Reynolds number $R_M=UM/\nu$ decreases (Fig. 16).

Fig. 17 shows $g(r/\lambda)$ for $X=450$ cm and $U=$ 10 m/sec. Precise self-preservation of g seems to hold for r/λ less than 1, and the effect of non-self-preserving large-scale turbulence is relevant. It is to be noted that, outside the self-preserving region, values of r/λ corresponding to a given value of g increase x_2/M_2, contrary to the tendency observed for a single grid. In other words, outside the self-preserving region the $g(r/\lambda)$-curves of any family expand laterally as x_2/M_2 increases. The correlation coefficient $g(r/\lambda)$ for $X=200$, 250, and 350 cm are similar to those in Fig. 17.

Fig. 18 shows $g(r/\lambda)$ in the presence of two grids placed 50 cm apart for $U=10$ m/sec. In this case the shape of $g(r/\lambda)$ resembles those with the first grid alone except at small values of x_2/M_2, and the deviation from self-preservation at large values of r/λ is not so marked as in Fig. 17. For small X, the turbulence produced by the first grid is predominant, and the small-scale turbulence produced by the second grid is merely superposed to the high-frequency range of turbulence produced by the first grid for the latter of which the similarity of spectrum holds. The fact that the superposed small-scale turbulence decays rapidly and the correlation curve tends to resemble the original one indicates the stability of spectrum. The experimental evidence thus supports Lin's theoretical discussion on the stability of spectrum[6].

d) Decay of $\overline{u^2}g(r)$

Fig. 19 shows $(\overline{u^2}/U^2)g(r)$ plotted against r in the case of $X=250$ cm and the mean wind velocity of 10 m/sec. In this case, $(\overline{u^2}/U^2)g(r)$ at small values of r decays rapidly as x_2/M_2 increases, but those at large values of r scarcely decay and retain positive values. This is due to the existence of the slowly-decaying, large-scale turbulence.

e) Variation of R_λ *during Decay*

The turbulence Reynolds number

$$R_\lambda=\sqrt{\overline{u^2}}\,\lambda/\nu$$

obtained from the experiment is plotted against x in Fig. 20, for the mean wind velocity of 10 m/sec. R_λ decreases gradually in the case of a single grid; it increases in the case of large X, while it increases at first and then decreases in the case of small X.

The theoretical relation

$$R_\lambda=\sqrt{\frac{10\alpha U}{\nu}}\left[1+\frac{\beta}{\alpha}(x-x_0)\right],$$

which is deduced from the decay law

$$\frac{\overline{u^2}}{U^2}=\alpha(x-x_0)^{-1}+\beta\ ,$$

is also presented in this figure. It is interesting that R_λ increases as the decay proceeds in the presence of slowly-decaying, large-scale turbulence ahead of the grid.

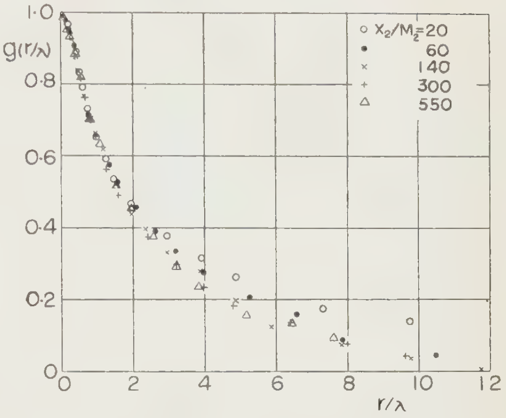

Fig. 18. Correlation coefficient $g(r/\lambda)$: $X=50$ cm, $U=10$ m/sec.

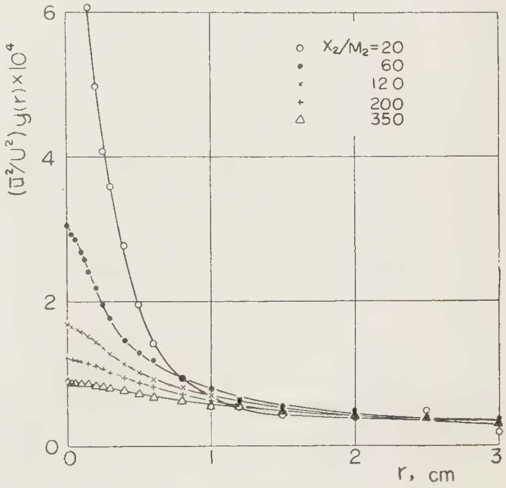

Fig. 19. Decay of $\overline{u^2}g(r)$: $X=250$ cm, $U=10$ m/sec.

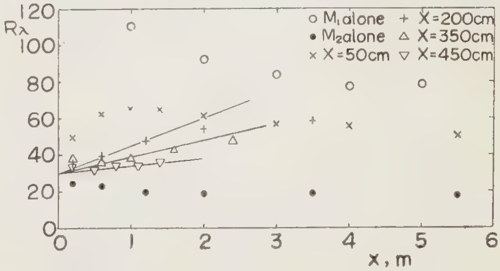

Fig. 20. Variation of R_λ during decay: $U=10$ m/sec.

4. Conclusion

The experinental investigation of turbulence behind two grids has led to the following conclusions:

a) The decay law of turbulence in the early stage of decay at high Reynolds numbers depends on the initial conditions, especially low-frequency components. The value of n in the power law, $(U^2/\overline{u^2})\sim(x/M)^n$, depends on the initial condition and has no universal value. n is generally larger than 1 for the turbulence produced by a single grid, while it is smaller than 1 for the turbulence which contains superposed low-frequency components.

The linear decay law, which may be deduced from the assumption of the complete similarity, is not observed in general.

b) The low-frequency characteristics of turbulence depend on the initial conditions and exhibit no similarity during decay, while the high-frequency components are independent of the initial conditions and retain the similarity. Therefore, Lin's decay law, $\overline{u^2}=\alpha x^{-1}+\beta$, which is derived by the assumption that the actual deviation from the similarity will be limited only for small values of wave number and hence the effect of the deviation will enter only in the calculation of energy but be negligible in the computation of the rate of energy dissipation, is expected to be valid for the turbulence either behind a single grid or with a superposed disturbances of low frequencies. The additive constant β in this law depends on the initial condition, i.e., on the spectrum of low-frequency components.

c) A superposed disturbance of high frequencies destroys the similarity of spectrum, so that Lin's decay law cannot be realized. The disturbance, however, decays out rapidly and the similarity spectrum is stable.

The author would like to express his sincere thanks to Dr. F. R. Hama for his suggestion of this problem and his continual guidance and encouragement in the course of the investigation, to Prof. I. Tani and Prof. I. Imai for their advice and kind inspection of the manuscript, and to Mr. Y. Onda for his active assistance in conducting the experiments. This work is supported partly by the fund of the Ministry of Education in Aid of Scientific Research.

References

1) G. K. Batchelor and A. A. Townsend: Proc Roy. Soc. London A **194** (1948) 527.
2) G. I. Taylor: Proc. Roy. Soc. London A **151** (1935) 421; **156** (1936) 307.
3) S. Atsumi: Journ. Aero. Soc. Japan **9** (1942 1.
4) R. Hama, S. Mitsuishi and Y. Onda: Journ Aero. Res. Inst., Tokyo Imp. Univ. **245** (1945 25.
5) C. C. Lin: Proc. Nat. Acad. Sci., U.S.A. **34** (1948) 540.
6) C. C. Lin: Proc. 4th Symp. Appl. Math (1953) 19.
7) S. Goldstein: Proc. Camb. Phil. Soc. **47** (1951) 554.
8) R. Hama: Rep. Inst. Sci. Tech., Univ. Tokyo **7** (1953) 145.
9) A. A. Townsend: Proc. Camb. Phil. Soc. **43** (1947) 560.
10) L. S. G. Kovásznay: NACA TN **2839** (1953),
11) T. von Kármán and L. Howarth: Proc. Roy. Soc. London A **164** (1938) 192.
12) H. L. Dryden, G. B. Schubauer, W. C. Mock and H. K. Skramstad: NACA Rep. **581** (1937).
13) G. K. Batchelor and A. A. Townsend: Proc. Roy. Soc. London A **190** (1947) 534.
14) H. W. Liepmann, J. Laufer and K. Liepmann: NACA TN **2473** (1951).
15) H. W. Liepmann and M. S. Robinson: NACA TN **3037** (1953).
16) H. Tsuji and F. R. Hama: Journ. Aero. Sci. **20** (1953) 848.
17) G. K. Batchelor and A. A. Townsend: Proc. Roy. Soc. London A **193** (1948) 539.

Short Notes

J. Phys. Soc. Japan **10** (1955) 587~588

Origin of Guinier-Preston Zones in Alloys

By Ken-ichi Hirano, Yutaka Takagi
and Hideyo Maniwa
Department of Physics,
Tokyo Institute of Technology,
Oh-okayama, Meguro-ku, Tokyo

(Received April 15, 1955)

In previous publications[1] the author (K.H.) has mentioned based on experimental results on Al-Ag[2]-[4], Al-Cu[5], Al-Mg-Zn[6][7], Al-Zn[8] and Mg-Pb[9] alloys that the aging characteristics of quench-annealed alloys are interpreted satisfactorily from the unified standpoint that the formation of Guinier-Preston zones, which are flat aggregations of the solute atoms on some crystallographic planes of the matrix lattice, is not a preparative process of precipitation of the new phase. Further it has been shown that if the concentration of the solute atoms in the matrix solid solution is suitable, supersaturation of alloy in the sense of the equilibrium phase diagram is not always required for the formation of G-P zones.

Taking into account the interaction of solute atom with lattice defects, two possible mechanisms of G-P zones are considerable and are now under tests.

As has been shown by quenching experiments[10][11], it is likely that if the alloy is quenched from a high temperature, excess vacancies may be frozen-in. They have enough mobility at or near the room temperature, so on annealing they may form aggregates in the form of planar sheets (disc-shaped aggregate) on some simple atomic plane.

If disc-shaped one-layer aggregate of vacancies on (111) plane of a F.C.C. crystal is sufficiently large it can collapse to give a stacking fault surrounded by a sessile dislocation[12].

Two-layer condensation on (100) or (110) may become the dislocation ring if it is sufficiently large[13]. Fujita[13] suggested that disc of vacancies on (110) plane is the most favourable to become the dislocation ring. It is likely that one-layer disc on (100) plane remains in the crystal.

If there is enough difference in size between solute atom and solvent atom, the solute atoms will aggregate on the disc-shaped vacancy plane, so the elastic energy can be reduced. This seems to be the first type of G-P zone which have been found in Al-Cu[14] and Cu-Be[15][16] alloys, in both alloys size of the solute atom is about 10% smaller than that of the solvent and it is observed by X-ray examination that one-layer aggregation of solute atoms on the (100) plane is formed during annealing after quenching.

The second type of G-P zone may be possible if the chemical interaction of solute atoms with a stacking fault, which was first suggested by Suzuki[17], can serve to form a solute atom rich hexagonal layer on (111) plane. Results of X-ray examinations on quench-annealed Al-Ag[18][19] and Al-Zn[20] alloys seem to suggest that this type of G-P zone is formed. In this case defference in atom-size can not be important. (In both alloys difference in atomic diameter is less than 0.5%). The solute atom concentration at the G-P zone must satisfy the Hume-Rothery law, 7/4 electron atom ratio for hexagonal close packed intermetallic compound.

The fact[21][22] that small amount of additional element can suppress the formation of G-P zones may be interpreted by the possibility that impurities widely dispersed in alloys might act as traps for vacancies and prevent them from coagulating.

Recently Hasiguti[23] gave a proposed theory on the anneal-hardening of cold-worked α-brass and stated that various phenomena accompanying it are well explained by possible mechanism of G-P zone. He put forward the theory based on the α-phase solid solubility curve of Shinoda and Amano[24], regarding the formation of G-P zone as a preliminary stage of β′-phase precipitation. But it may be noted that recent experiments by Tanaka and one of the authors (K.H.)[25] on annealing of quenched α-brass show usefulness of above model of the second type of G-P zone, which is independent of β′-phase precipitation.

Detailed account on the stability of above two types of G-P zones, on the energy of dispersion of them, on the effect of cold-working, on the extension of above model to alloys of H.C.P. lattice, and so on, will be treated in the next paper in relation with our experimental results.

References

1) K. Hirano: J. Japan Inst. Metals, **19** (1955) 136.
2) K. Hirano: J. Phys. Soc. Japan **8** (1953) 603.
3) K. Hirano and H. Sakai: ibid. **10** (1955) 23.
4) K. Tanaka, H. Abe and K. Hirano: ibid. **10** (1955) 454.
5) K. Hirano: read at the meeting of Japan Phys. Soc. at Univ. of Osaka, Oct. 31, 1954.
6) K. Hirano and Y. Takagi: J. Phys. Soc. Japan **10** (1955) 187.
7) K. Hirano and Y. Takagi: read at the meeting of Japan Inst. Metals at Ehime Univ., Oct. 24, 1954.
8) K. Hirano: read at the meeting of Japan Inst. Metals at Univ. of Tokyo, April 7, 1955.
9) K. Hirano, H. Maniwa and Y. Takagi: J.

Phys. Soc. Japan **10** (1955) 193.
10) F. Seitz: Advances in Physics **1** (1952) 43.
11) T. Broom: ibid. **3** (1954) 26.
12) W. T. Read: Dislocations in Crystals, McGraw Hill, 1953, p. 95.
13) F. E. Fujita: Sci. Rep. RITU. **A6** (1954) 125.
14) V. Gerold: Z. Metallkunde **45** (1954) 593, 599.
15) A. Guinier and P. Jacquet: Compt. Rend. **217** (1943) 22.
16) A. Guinier and P. Jacquet: Rev. Metallurgie **41** (1944) 1.
17) H. Suzuki: Sci. Rep. RITU. **A4** (1952) 455.
18) C. B. Walker and A. Guinier: Acta Metallurgica **1** (1953) 568.
19) R. Glocker, W. Köster, J. Scherb and G. Ziegler: Z. Metallkunde, **43** (1952) 208.
20) A. Guinier: Metaux et Corrosion **18** (1943) 209.
21) H. K. Hardy: J. Inst. Metals **80** (1952) 483, **78** (1950) 169.
22) K. Hirano: Unpublished work on Al–Ag–Sn and Al–Ag–In alloys.
23) R. R. Hasiguti: J. Japan Inst. Metals **19** (1955) 103.
24) G. Shinoda and Y. Amano: J. Phys. Soc. Japan **6** (1951) 508.
25) K. Hirano and K. Tanaka: to be published.

J. PHYS. SOC. JAPAN **10** (1955) 588~589

Effect of Mechanical Stress on Dielectric Breakdown of Alkali-Halide Single Crystals

By Yoshio INUISHI and Tokuo SUITA
Faculty of Engineering, Osaka University

(Received May 13, 1955)

Artificial large crystals of KCl were grown by Kyropoulus method. In first annealing cycle these crystals were heated to 600°C and kept for 1~2 days at this temperature, then cooled slowly to room temperature at the rate of 10°C per hour. These crystals were then cleaved to flat plate and recessed at one side carefully by rubbing softly with paint brush wetted by alchohol-water mixture until required thickness 0.3 mm at its center like Fig. 1. Then samples were subjected to the second annealing cycle which was quite similar to the first cycle. After coating aquadug as electrode, samples were dried at 200°C and cooled to room temperature at the rate of 10°C/hour. Thus prepared samples gave no stress pattern in crossed polarizer, and can be thought to be "comparatively stress free". D.C. and impulse breakdow voltage were obtained under simultaneous applic tion3) of mechanical stress by the apparatus show in Fig. 1. Weight W added on the crystal may

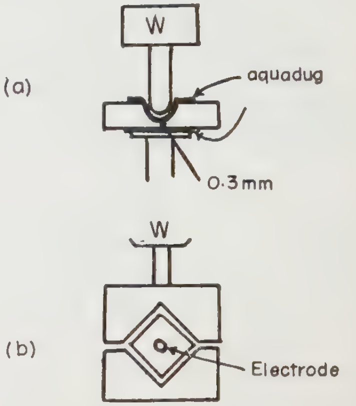

Fig. 1. (a) Field (100), Stress (100)
(b) Field (100), Stress (110).

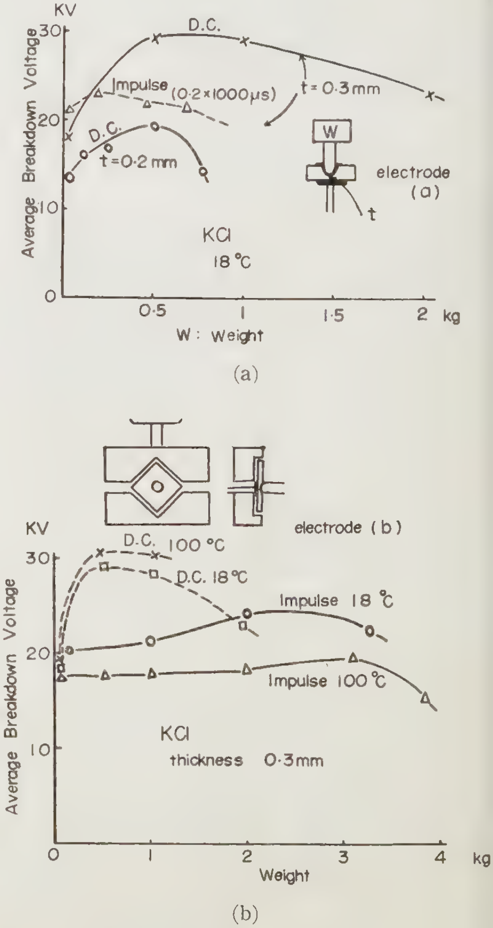

(a)

(b)

Fig. 2.

taken as a measure of mechanical stress. In Fig. 2 average breakdown strength is shown as a function of applied weight, and the histograms of breakdown strength are shown in Fig. 3. As is seen there, the breakdown strength shows wide scattering even in well annealed crystals, and consists of two groups: low strength group 0.4∼0.6 MV/cm and high strength group 0.7∼1.0 MV/cm.

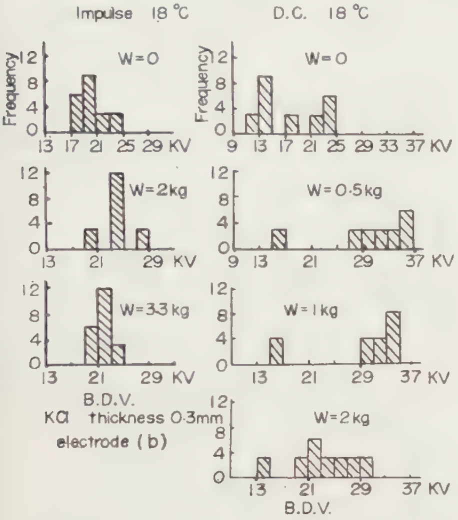

Fig. 3. Histogram of B.D.V.

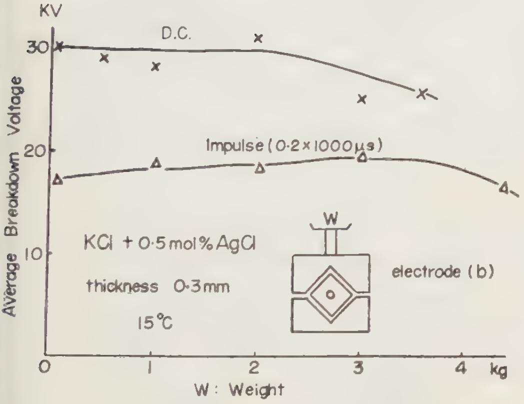

Fig. 4.

In well annealed samples of KCl, the low voltage group predominates. With increasing mechanical stress the high voltage group become to be predominant and average breakdown strength increases. But at larger mechanical stresses, the breakdown voltage decreases again. Finally mechanical cracks set in and breakdown voltage drop sharply. These changes are more remarkable in case of D.C., than in impulse. Impulse value has comparatively smaller spread and lower than D.C. value at various values of the mechanical stress. These situations are similar at 100°C as is seen in Fig. 2. Fig. 4 shows the breakdown stress *vs.* mechanical stress in KCl–0.5 mol% AgCl mixed crystals. In this case D.C. breakdown strength is high even in stress free crystals, but impulse breakdown strength is much similar to pure KCl.

Quenching, mechanical work (drilling), D.C. prestressing all work to raise D.C. and impulse breakdown strength in thinner KCl samples as was stated in the previous report[3]. In stressed samples breakdown voltage is higher when recessed electrode is negative. Change in the manner of mechanical stress application does not alter the situation remarkably as is seen in Fig. 5, the tendency mentioned above is in good agreement with Cooper's reports[1][2] except that (i) at larger stress, breakdown voltage decreases again (ii) low stress group is more predominant in our experiment. (iii) D.C. strength is always slightly higher than impulse at lower temperatures. These situations are much similar to Saito's experiment[4].

We shall try some speculation on above phenomena. Dislocations due to mechanical stress produce various vacancies as was stated by Seitz. Some of these vacancies can trap conduction electrons and form a sort of space charge. Trapping of avalanche electrons and recombination at these vacancies can act to raise breakdown both in D.C. and impulse by decreasing net multiplication[3]. Moreover, dislocated crystal might have heterogeneous structure which produces a sort of space charge in its interface[3]. So that D.C. breakdown which includes space charge effect may be affected much deeply than in impulse, as was stated above.

Decrease of breakdown stress at very large mechanical stress can not be explained by these idea. Enhancement of ionic conduction due to mechanical stress might have some connection to these phenomena[4].

References

1) J. H. Calderwood, R. Cooper and A. Wallace: Proc. I.E.E. **100** (1953) 104.
2) R. Cooper and A. Wallace: Proc. Phys. Soc. **B LXVI** (1953) 1113.
3) Y. Inuishi and T. Suita: Tech. Rep. Osaka Univ. **4** (1954) 203.
4) S. Saito: I.E.E. Japan **56** (1936) 1036.

J. Phys. Soc. Japan **10** (1955) 590~591

Effects of Mechanical Stress on Dielectric Breakdown of Alkali-Halides II (Time Effect)

By Yoshio Inuishi and Tokuo Suita
Faculty of Engineering, Osaka University

(Received May 18, 1955)

In our previous reports[1)2)3)] we have mentioned that the D.C. breakdown strength of KCl single crystal increases, in general with increasing simultaneouly applied mechanical stress and finally it decreases at larger stresses where minute cracks set in. Impulse breakdown strength is much more insensitive to the mechanical stress.

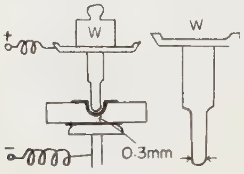

Fig. 1.

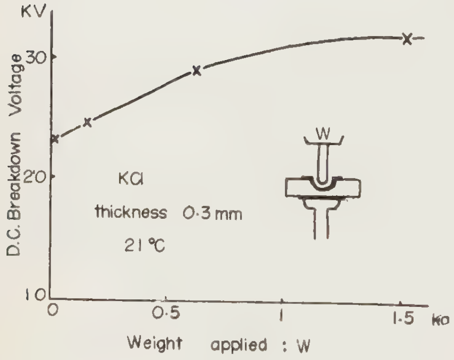

Fig. 2.

These phenomena are speculated to be the results of space charge effect of trapped electrons and holes at vacancies created by dislocations.

There is also the possibility that the created vacancies and interstitial ions may act as additional scattering centers for the conduction electrons.

To clarify these situations we have worked on the time effect of the breakdown strength under the mechanical stress.

The samples were prepared from well annealed KCl crystals made by Kyropoulus method. After shaping the samples were subjected to second annealing cycle which started from 600°C to room temperature at the rate of 10°C/hr as was specified in the previous[1)2)3)] reports. After coating aquadug as the electrodes, these well annealed samples were immersed in Xylol and breakdown voltages were obtained under mechanical stress in the apparatu shown in Fig. 1.

We found that the breakdown voltage in this cas is a function of time τ after mechanical weigh application.

Fig. 2 shows the D.C. breakdown voltage (mea of 12 samples) 5 seconds after mechanical weigh application as a function of the mechanical weigh W.

In Fig. 3 the D.C. breakdown voltages (mean about 20 samples) are shown as a function of th time τ after mechanical stress application for tw values of applied weight. As is seen there th breakdown voltage increases at the instant mechanical stress application and decreases wit the elapse of time.

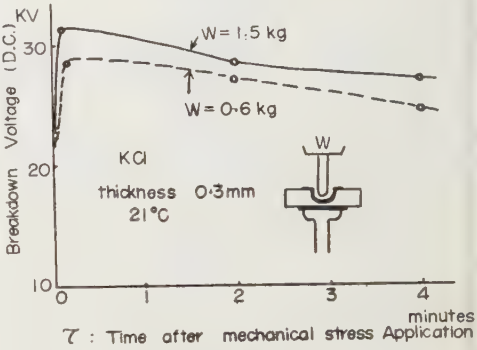

Fig. 3.

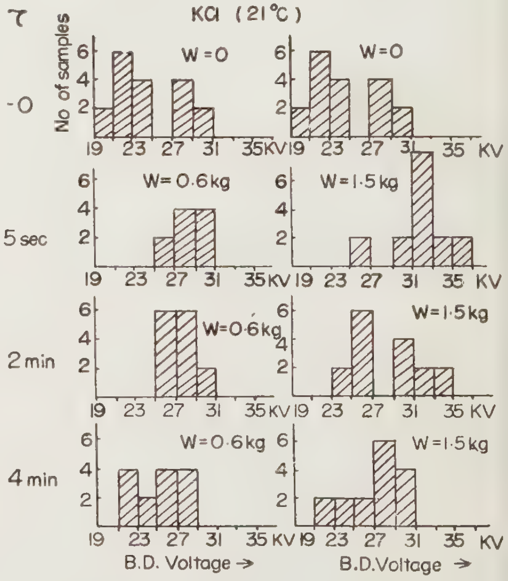

Fig. 4.

" Relaxation time " of these effects seems to ca. 3~5 minutes. To investigate these situatio further, histograms of the breakdown voltage a shown for various time τ in Fig. 4.

As was stated in previous reports2)3), distributions of breakdown voltages are divided into two groups: low voltage group and high voltage group.

At the instant of mechanical stress application the low voltage group disappears and the high voltage group predominates, but after ca. 4 minutes the low voltage group recovers again.

These time effects are much similar to the effect of mechanical stress on electrical conductivity published by Gyulai and Hartly4). Accordingly it s reasonable to expect that also in our case vacancies evaporated or produced by moving dislocations may be responsible for increasing D.C. voltage as was suggested by Seitz5) for Gyulai and Hartly experiments.

The vacancies created may trap avalanche electrons and form space charge layers which suppress avalance growth and continuation. But as time elapses after stress application, vacancy creation decreases and they may begin to recombine to form clusters5) or diffuse to the boundaries, and thus the trapping effect may decreases. The speculation above mentioned seems to explain our results o some extent.

References

) Y. Inuishi and T. Suita: Tech. Rep. Osaka Univ. **4** (1954) 203.
) Y. Inuishi and T. Suita: Tech. Rep. Osaka Univ. (in press).
) Y. Inuishi and T. Suita: J. Phys. Soc. Japan (to be published).
) Z. Gyulai and D. Hartly: Z. Physik **51** (1928) 378.
) F. Seitz: Phys. Rev. **80** (1950) 239.

J. PHYS. SOC. JAPAN **10** (1955) 591~592

Fine Structure of Pure Quadrupole Spectrum in Iodine Crystal

By Shoji KOJIMA and Kineo TSUKADA
Tokyo University of Education

(Received April 12, 1955)

Nuclear quadrupole resonance of I^{127} in solid odine has been investigated by many authors1)2)3). orresponding to the transitions, $m_z=|\frac{1}{2}|\rightarrow|\frac{3}{2}|$ and $m_z=|\frac{3}{2}|\rightarrow|\frac{5}{2}|$, two resonance frequencies of $\nu_1=332$ Mc and $\nu_2=644$ Mc, at room temperature are known. The width of the lower frequency line was reported y Dehmelt1) as 40 kc.

In order to study the Zeeman effect we produced ingle crystals of about 30 gr. With these single rystals we observed a fine structure in the lower requency line at zero magnetic field. The apparatus used was a frequency modulated super-regenerative detector and an oscilloscope. Fig. 1 shows a display of the oscilloscope with about 100 kc sweep width. In Fig. 2 the sweep width was decreased so that the second and third lines were well separated. The fine structure of the spectrum consisted of five lines spreading in the range of 50 kc. The frequency differences of those lines from the strongest line were −24 kc, −8 kc, 0, 12 kc and 26 kc respectively. The intensity ratios of the lines seemed to be approximately 2:2:5:1:1. On the two strong lines, *A* and *C*, their intensity was measured as a function of the orientation of radio-frequency field. The measured changes of the intensity for the both lines were expressed by a same sinusoidal curve. This fact indicates that the principal axis system of the quadrupole couplings were the same.

When a weak magnetic field was applied, each lines shifted differently. When the magnetic field increased above 50 gauss, the usual Zeeman pattern which was predicted by the theory on a single line was observed with the line width of about 25 kc. So that we could determine the asymmetry parameter and the orientation of the principal axes by the Zeeman effect. The results were that the asymmetry parameter was $16\pm1\%$ and that the angle between the principal axes of the two classes of molecules was $63°54'\pm2.0°$.

The fine structure at zero field was observed in powder, though it was very faint. The high frequency line, ν_2, having the line width of about 45 kc, showed no fine structure. Such fine structures were observed in crystals of ICl and of Br_2 at the dry ice temperature.

The separations of the lines in the fine structure are too great to be interpreted by the direct nuclear magnetic dipole-dipole interaction. The electron coupled nuclear spin-spin interaction4) may improve the interpretation.

We wish to thank Dr. T. Itoh of Tokyo University for helpful discussion on the interpretation of the fine structure.

References

1) H. G. Dehmelt: Z. Physik **130** (1951) 346.
2) R. V. Pound: Phys. Rev. **82** (1951) 343.
3) T. Kamei: J. Phys. Soc. Japan **7** (1952) 649.
4) N. F. Ramsey: Phys. Rev. **91** (1953) 303.

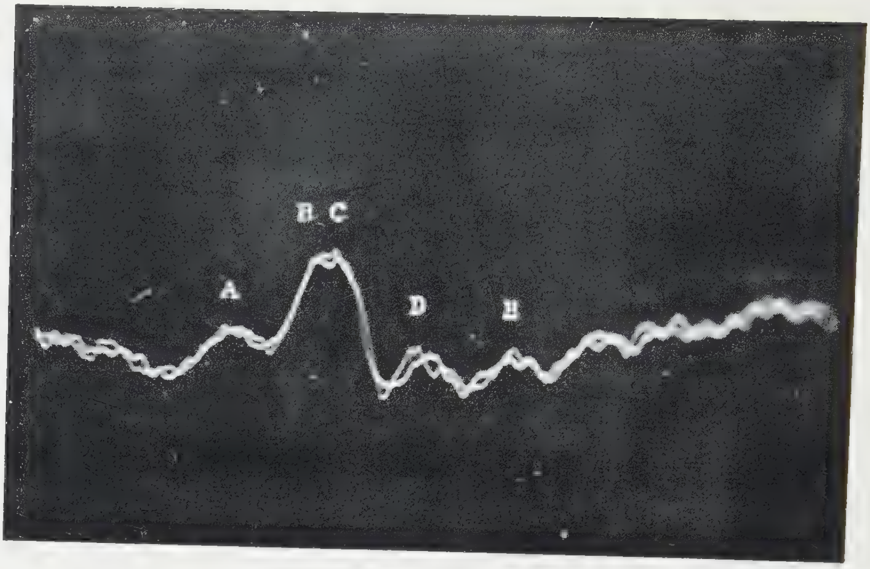

Fig. 1.

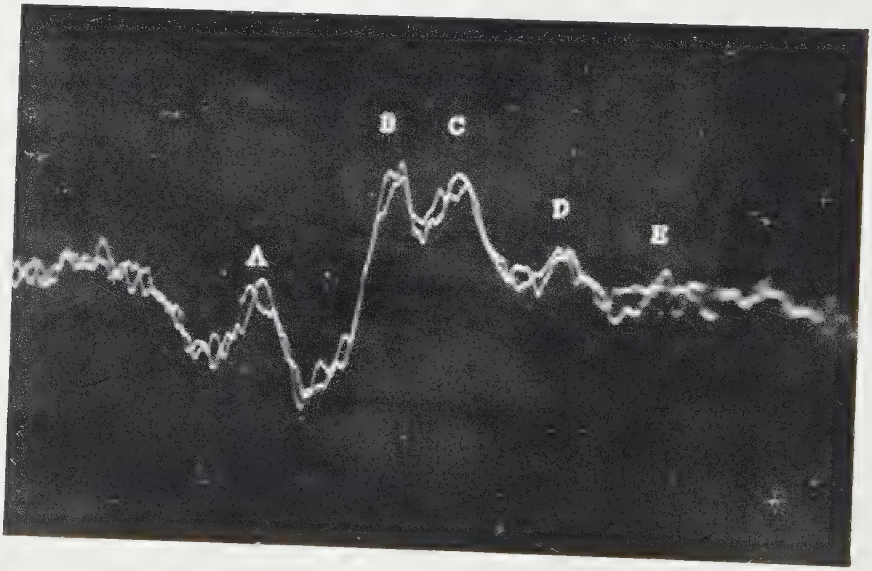

Fig. 2.

Errata

Application of the Thin-Wing-Expansion Method to the Flow of a Compressible Fluid past a Symmetrical Circular Arc Aerofoil

By Saburô ASAKA

J. PHYS. SOC. JAPAN, Vol. 10, No. 6, pp. 482~492

(page)	(column)	(line)			(should be read)
483, 485, 487, 489, and 491; Heading				*Aeroloil*	*Aerofoil*
484	left	-1		$-1\leq x,\ \xi\leq 1.$	$-1\leq x\leq 1$, and $-1\leq\xi\leq 1.$
〃	right	22	Eq. (3.3)	, (comma)	(should be omitted)
485	left	-3	Eq. (3.11)	$\cdots+\vartheta_1(\theta)+\vartheta_1(\theta)+\cdots$	$\cdots+\vartheta_1(\theta)+\vartheta_2(\theta)+\cdots$
486	left	-17	Eq. (4.6)	$f_2{}^1=(\beta^2/\mu^2)(\cdots$	$f_2{}^1=-(\beta^2/\mu^2)(\cdots$
〃	right	5		G_2 and G_2	G_2 and G_3
〃	〃	-20	Eq. (5.3)	$S_3=\cdots-(3\pi/4)s_1(\theta)$	$S_3=\cdots-(3\pi^2/4)s_1(\theta)$
487		-10	Eq. (5.10)	$1\ (1+x)$	$1/(1+x)$
		-6	〃	$+(3x^2\lambda^2(x)+\cdots$	$+3x^2\lambda^2(x)+\cdots$
488	right		Fig. 4	symmetrical arc	symmetrical circular arc
490		-3	$f_3{}^1$	$-(\beta_3/\mu)(\cdots$	$-(\beta^3/\mu)(\cdots$
491		2	$f_3{}^3$	$-\frac{2}{3}\pi^2SC$	$-\frac{2}{3}\pi^2S^2C$
〃		21	$f_3{}^{12}$	$-3S^2CL$	$-3S^2CL^2$
〃		22	B^{13}	$-M^4\nu/8$	$-M^4\nu^2/8$
〃		-4		$g_2{}^{20}$	$g_3{}^{20}$
〃		-1		$f_2{}^{21}$	$f_3{}^{21}$
492	right	6	Ref. 13)	(should be added)	or N.A.C.A. Tech. Rep. Nos. 1069 (1952) and 1149 (1953).
〃	〃	-1	Ref. 16)	K. Ôsima: to be published in this Journal.	K. Ôshima: J. Phys. Soc. Japan **10** (1955) 571.

PROGRESS OF THEORETICAL PHYSICS

(Founded by H. Yukawa in 1946)

Published for the

Research Institute for Fundamental Physics

The Physical Society of Japan

Progress of Theoretical Physics Vol. 12, No. 6, 1954

The Cut-Off Method in Meson Theory .... Shigeo GOTO....699

Note on the Angular Distribution of Photo-Reaction .... Masato MORITA, Atsushi SUGIE and Shiro YOSHIDA....713

On the Meaning of the Solution to the One-Body Dirac Equation .... Sumio TANI and Kazuo YAMAZAKI....723

Beta-Ray Spectra, III.. Hisao TAKEBE....747

Kinematical Investigation of the S–Matrix .... Masaaki KAWAGUCHI....758

Pion-Nucleon Scattering in Tamm-Dancoff Approximation .... Shin CHIBA, Miwae YAMAZAKI and Nobuyuki FUKUDA....767

On the Relation between Meson-Nucleon Scattering and Photomeson Production........................ Masaaki KAWAGUCHI and Shigeo MINAMI....789

Letters to the Editor:

The Relaxation Process in Ferromagnetic Resonance Absorption...... .... T. KASUYA....802

The Relaxation Process in Ferromagnetic Resonance Absorption...... —*The Effect of the Conduction Electron*— .... T. KASUYA....803

The Method of Generating Function applied to Radiative and Non-Radiative Transition of a Trapped Electron in a Crystal........ .... R. KUBO and Y. TOYOZAWA....805

Meson Theoretical Potentials in Triplet Odd State................. .... S. OTSUKI and R. TAMAGAKI....806

A Note on Superexchange Interaction .... J. YAMASHITA....808

A Remark on Convergence Factor .... N. ITO....809

On the Hydrodynamical Representation of Non-Relativistic Spinor Equation.. T. TAKABAYASI....810

A Classical Treatment of the Scattering of Electromagnetic Waves by Nucleons.............................. I. SATO and Y. ICHIKAWA....812

Errata 814

Contents and Index to Volume 12..i—viii

Price $ 1.25 per copy
$ 15.00 per year (postage inclusive)
Annual dues for foreign members (individual subscribers)
$ 12.00 (postage inclusive)
〃 for foreign members of the Physical Society of Japan
$ 10.00 (postage inclusive)

Application for members, subscriptions and orders for back mumbers should be sent, directly or through book-dealers, to

The Publication Office
in
Yukawa Hall, Kyoto University, Kyoto, Japan

JOURNAL OF THE PHYSICAL SOCIETY OF JAPAN Vol. 10, No. 8, AUGUST, 1955

On the Extensive Air Showers Penetrating 10 cm of Lead Observed at 2,760 Meters above Sea Level

By Isao MIURA, Tsuneo MATANO, Yoshio TOYODA
and Takashi MURAYAMA
Physical Institute, Nagoya University, Nagoya, Japan

(Received January 29, 1955)

The density distribution and the zenith angle distribution of extensive air showers were measured at 2,760 meters elevation, geomagnetic latitude 25°N, by a cloud chamber in connection with a hodoscope consisted of Geiger counter trays shielded by lead absorbers.

Results obtained were as follows: (1) The integral density spectrum of the extensive air showers followed the power law distribution and its exponent was 1.70 ± 0.13, (2) The projected angle distribution of the extensive air showers followed the empirical law of $\cos^n\theta$, where $n = 6.9 \pm 1.3$.

§ 1. Introduction

The fact that penetrating ionizing particles exist in the extensive air showers has already been shown by cloud chamber photographs[1] and by Geiger counter experiments[2,3]. During the experiments for the study of the penetrating showers produced in graphite and paraffin, many photographs were obtained which showed some parallel tracks passing the cloud chamber. Most of such events are regarded as parts of the extensive air showers originated in the upper atmosphere being detected by the penetrating components included in the air showers. So, in this paper, comparison of the density distribution and the zenith angle distribution of the extensive air showers triggered by the penetrating component with those of the extensive air showers observed by ordinary detecting methods is performed. Also the frequency of occurrence of the extensive air showers is compared with other experiments by different detecting method.

The experiment was carried out at Mt. Norikura (geomagnetic latitude 25°N), elevation 2,760 meters, mean pressure about 760 g/cm², during the summer of 1952.

§ 2. Experimental Arrangement

The experimental arrangement is shown in Fig. 1.

The cloud chamber is in cylindrical shape, 30 cm in diameter, and 14 cm in illuminated depth, containing a few gram/cm² of carbon and paraffin plates. The hodoscope is arranged in three Geiger counter trays (A, B and C in Fig. 1) underneath the cloud chamber. Above the second and third counter trays 5 cm of lead absobers are interposed. Trays are also shielded by side with 10-cm Pb. The cloud chamber is operated by master pulses A(≥2), B(≥2), C(≥1): Two or more counters in the tray A, two or more counters in B and one or more counters in C are activated simultaneously. Although most of showers photographed originate in the sourrounding materials above the counter trays (chamber body and frames etc.), showers originated in the air far from the apparatus are also recorded, which show usually some parallel tracks

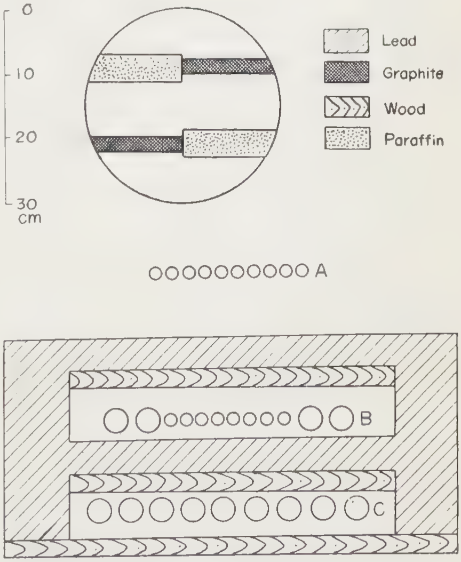

Fig. 1. Arrangement of experimental apparatus.

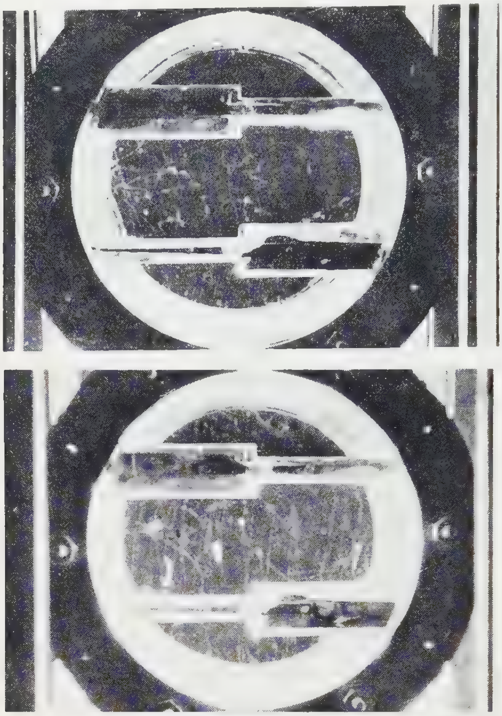

Fig. 2. Cloud chamber photographs of the typical examples of the extensive air showers.

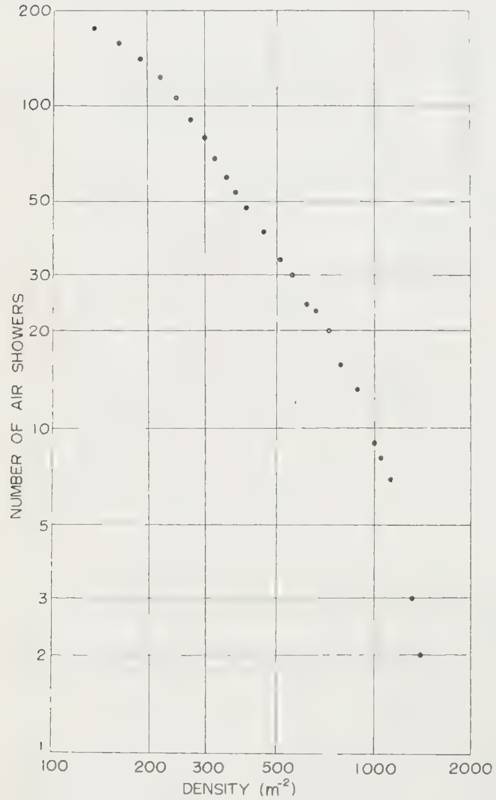

Fig. 3. The integral distribution of number of events as a function of the particle density.

in the cloud chamber. From the parallelism and the number of shower particles we can distinguish the extensive air showers from the locally originated penetrating showers. In the present experiment, the extensive air showers are selected by the criterion that at least five parallel tracks are seen in the cloud chamber photographs.

§ 3. Results

From about 5,000 photographs obtained in 106 hours, 172 air showers were selected by the criterion described above. Two examples among them are shown in Fig. 2.

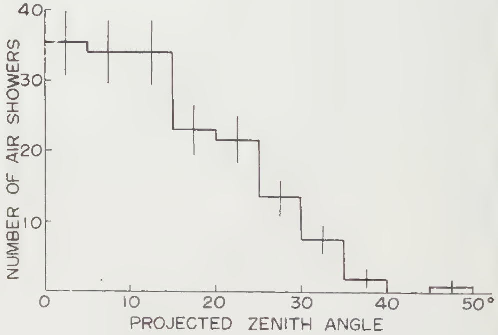

Fig. 4. The distribution in projected zenith angle of air showers.

The integral density distribution and the projected zenith angle distribution of these extensive air showers are shown in Fig. 3 and Fig. 4, respectively. Since the illuminated area of the cloud chamber is about 370 g/cm², N particles in the chamber correspond to 27N particles in a square meter. So the minimum density of the showers in our data is 135/m². It is well known that the frequency of occurrence of the extensive air showers of density greater than Δ follows the empirical law

$$f(\Delta)=K\Delta^{-\gamma}\,. \tag{1}$$

From Fig. 3, it is apparently seen that the density distribution curve consists of three parts:

a) $950/\text{m}^2>\Delta>270/\text{m}^2$. The distribution curve in this region is approximately straight line. This fact means that the frequency of occurrence of the extensive air showers follows the equation (1).

b) $\Delta>950/\text{m}^2$. The distribution curve is diverted downward from the line defined in the region of (a).

c) $270/\mathrm{m}^2 > \Delta$. The distribution curve is also diverted downward.

Such tendency of the density distribution curve is explained by the following reasons. Owing to lack of resolving power of the photographs for each tracks of the extensive air showers with large density, the distribution curve is bent down in the region (b). Showers with low density sometimes fail to reach the third tray particularly when they come from an inclined direction because of 10 cm of lead absorber. That is main reason why the density distribution curve is bent down in the region (c).

§ 4. Discussion

(A) Correction for the triggering bias

In this section the correction concerning to the effect of the lead absorber between the counter trays which deformed the shapes of experimental curves shown in the preceding section was applied.

a) *Density Distribution*

The frequency of occurrence of the extensive air showers in a solid angle $d\Omega$ is represented in the form of the following equation:

$$dN = I_0 \cos^n \theta d\Omega \,, \qquad (2)$$

where θ means the zenith angle of $d\Omega$. Although n in this formula is not determined exactly, we put tentatively $n=6$ in the following discussion, but the result is insensitive to the value of n. With the equation (2), the total number of the extensive air showers of density Δ/m^2 is represented as follows

$$I_1(\Delta) = 2\pi I_0(\Delta) \int_0^{\pi/2} \cos^6\theta \sin\theta \, d\theta \,. \qquad (3)$$

Now we define the function $R(t)$, the fractional number of shower particles capable of penetrating the lead absorber of thickness t. As an absorber thickness above the third tray is 10 cm Pb, showers with zenith angle θ must penetrate $10 \cdot \sec\theta$ cm Pb in order to be detected. Hence we can translate the function $R(t)$ to the function of the zenith angle: $r(\theta)$. Using $r(\theta)$, we can write the probability of detecting the extensive air showers with the density Δ and with the zenith angle θ followingly:

$$P(\Delta, \theta) = \Delta S r(\theta) \cos\theta \,, \qquad (4)$$

where S means the area of the third tray (C tray in Fig. 1). Accordingly the detectable numbers of the extensive air showers are represented as follows:

$$I_2(\Delta) = 2\pi I_0(\Delta) \left[\int_0^{\theta_0} \cos^6\theta \sin\theta \, d\theta + \int_{\theta_0}^{\pi/2} \cos^6\theta \sin\theta \, P(\Delta, \theta) d\theta \right] , \qquad (5)$$

where θ_0 is such a value that $P(\Delta, \theta)$ equals to unity, namely all of the extensive air showers having zenith angle less than θ_0 are recorded. Consequently the value I_2/I_1 means the probability for the detection of showers. This value varies with Δ, and almost equals to unity for the large value of Δ.

In the equation (5), the actual form of $r(\theta)$ is not well known. Cocconi et al[2] measured the function $R(t)$ with the extensive air showers of about $8/\mathrm{m}^2$ in density, which are reproduced in Fig. 5 in the form of $r(\theta)$. Particles capable of penetrating 10–20 cm Pb are classified into two kinds: Penetrating particles (nucleons, mesons etc.) which are absorbed gradually with increasing absorber thickness and electronic components which are absorbed rapidly. Cocconi et al. showed that the fractional number of penetrating particles to the number of total particles in the case of the extensive air showers of about $100/\mathrm{m}^2$ is smaller than that in the case of $8/\mathrm{m}^2$. Assuming that the energy spectrum of the electronic component of the extensive air showers does not vary with density, $r(\theta)$ for the showers with density $100/\mathrm{m}^2$ is deduced from $R(t)$ for

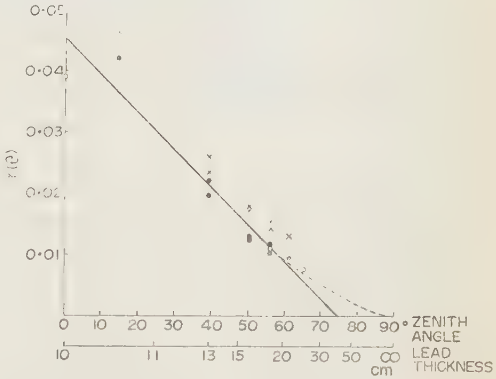

Fig. 5. $R(t)$ versus absorber thickness represented in the form of $r(\theta)$. A solid line represents $(4.5-3.5\theta)\times 10^{-2}$ which is discrepant with the true curve (dashed line) in the region of large value of θ. This, however, is not important in the calculation that $r(\theta)$ coexists with $\cos^6\theta$ in Eq. (5) which is nearly zero in this region.

those of $8/\mathrm{m}^2$, which exhibits approximately straight line in Fig. 5. This line corresponds to the empirical formula

$$r(\theta)=(4.5-3.5\,\theta)\times10^{-2}\,. \qquad (6)$$

Substituting (6) to (5), we can obtain the value of I_2 and I_1/I_2 which means the correction factor.

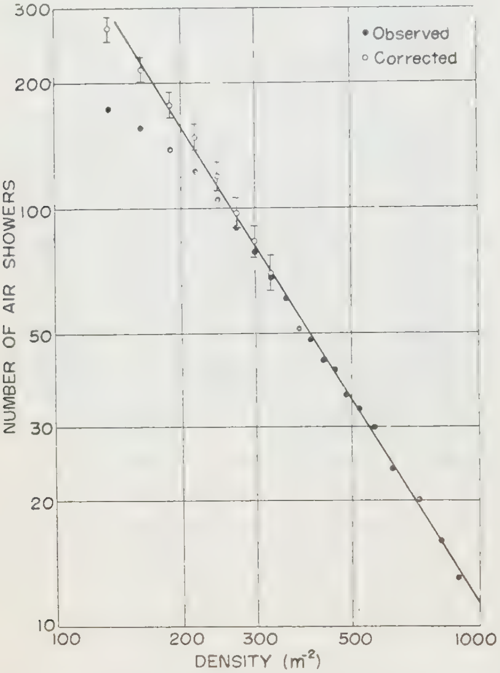

Fig. 6. Corrected curve for the integral density distribution of air showers. The solid line is of the form $\Delta^{-1.7}$.

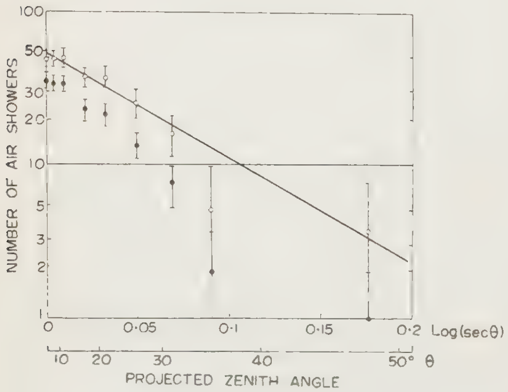

Fig. 7. Corrected curve for the projected zenith angle distribution of air showers. The solid line is of the form $\cos^{6.9}\theta$.

Fig. 6 shows the corrected density distribution of the extensive air showers which shows the straight line compared with that uncorrected. This fact means that the absorption of the particles in the extensive air showers in the lead block is in such a manner shown in Fig. 5. γ in the equation (1) is determined by the least square method. As a consequency, $\gamma=1.70\pm0.13$. The error introduced from the uncertainty of $r(\theta)$ in (4) is not taken in account. This value is in good agreement with the value obtained by Brown and McKay[1] in similar method by using the cloud chamber.

b) *Zenith Angle Distribution*

Similar correction above mentioned should be applied to the result of the projected zenith angle distribution. Extensive air showers coming from the direction of α in projected zenith angle, have the true zenith angle in the region α to $\pi/2$. As the solid angle for the direction which has the true zenith angle in the interval θ to $\theta+d\theta$ and the projected zenith angle α to $\alpha+d\alpha$ is

$$d\Omega=\frac{\sin\theta\cdot d\theta\,d\alpha}{\cos^2\alpha\sqrt{\tan^2\theta-\tan^2\alpha}}\,,$$

the intensity of the extensive air showers from the direction of α to $\alpha+d\alpha$ in the projected zenith angle is represented by the equation

$$J_1=J_0\int_\alpha^{\pi/2}\int_{135}^{\infty}\Delta^{-(\gamma-1)}\cos^6\theta \times\frac{\sin\theta}{\cos^2\alpha\sqrt{\tan^2\theta-\tan^2\alpha}}\,d\theta d\Delta d\alpha\,, \qquad (7)$$

while the intensity of the showers detectable under 10 cm of lead is represented as follows:

$$J_2=J_0\Bigg[\int_\alpha^{\pi/2}\int_{135}^{\Delta_0}\Delta^{-(\gamma-1)}r(\theta)\cos^6\theta\,\Delta S\cos\theta \times\frac{\sin\theta\cdot d\theta\cdot d\Delta\cdot d\alpha}{\cos^2\alpha\sqrt{\tan^2\theta-\tan^2\alpha}} +\int_\alpha^{\pi/2}\int_{\Delta_0}^{\infty}\Delta^{-(\gamma-1)}\cos^6\theta \times\frac{\sin\theta\,d\theta\,d\Delta\,d\alpha}{\cos^2\alpha\sqrt{\tan^2\theta-\tan^2\alpha}}\Bigg], \qquad (8)$$

where Δ_0 is such a value that the following equation is satisfied

$$\Delta_0 S\cos\theta\,r(\theta)=1\,. \qquad (9)$$

From the equations (7) and (8), the correction factor J_1/J_2 is obtained for the projected zenith angle distribution. The corrected curve is shown in Fig. 7, where the straight line determined by the least square method corresponds to the equation

$$N=N_0\cos^n\alpha\,d\alpha\,, \qquad (10)$$

in which $n=6.9\pm1.3$.

The determination of the value n in the equation (10) was tried in several experiments. Brown and McKay[1] obtained that $n=5$ at 3260 m elevation, while the result of Deutschman[4] at sea level is $n=6$–8, both of which are not contradict with ours.

(B) Frequency of Occurrence of the Extensive Air Showers

Chief difference between many experiments previously performed and ours exists in the selection of the extensive air showers. Owing to the small horizontal extension of our aparatus the locally produced showers may be included in our data.

At first, estimation of the probability that the penetrating showers produced in the roof of the laboratory (wood and thin metal plate) are containing in the data should be done. As the distance between the cloud chamber and the roof is about three meters, the penetrating showers must have at least 5 particles in 0.1 radian in order to be adopted in the data. Although estimation of the energy of the particles capable of producing such events is somewhat difficult, if we assume this energy about 100 BeV, the numbers of the penetrating showers included in the data are only 2 or 3. Furthermore the angles between two extreme particles in the cloud chamber of such events are about 5 degree, which are almost omitted by the parallelism criterion.

Next, the so called narrow showers are probable to be included, which originate in the air comparatively near the apparatus, and have such extent that the ordinary extensive air shower detectors miss them. But unfortunately quantitative treatment of the frequency of occurrence of these events are not able to be performed.

Williams[5] detected about one shower per hour employing two pairs of ionization chambers separated by about 50 cm, which can record the events with the density larger than 460/m^2 at 3,050 meters elevation. Assuming that the value of the absorption mean free path of the extensive air showers equals to 130 g/cm^2, this frequency corresponds to 0.79/hour at our altitude, which is larger than ours (0.53/hour). This discrepancy seems to be a little larger than that due to the statistical fluctuation. Cocconi et al[6] found at 2,200 m by using a triangular arrangement of counter trays separated by 4 meters one another, that the frequency of occurrence of the extensive airshowers was

$$f(\varDelta)=3600\varDelta^{-1.55} \quad (\text{hour}^{-1}). \qquad (11)$$

The rate of occurrence of the extensive air showers with the density larger than 135/m^2 deduced from this equation is 2.9/hour, which is in fair agreement with ours (3.5/hour). As their apparatus has a larger area than ours, this fact means that the frequency of occurrence of the showers observed by us seems somewhat smaller than theirs. These differences are probably due to the difference of the detecting methods.

It is a pleasure to acknowledge the useful discussion of Professor Y. Sekido. The authors also wish to express their thanks to Professor Y. Watase and Mr. Y. Miyazaki who offered many facilities for the performance of the present experiment. This work was financially supported by the Scientific Research Expenditure of the Department of Education.

References

1) W. W. Brown and A. S. McKay: Phys. Rev. **76** (1949) 1034.
2) G. Cocconi, V. Cocconi Tongiorgi and K. Greisen: Phys. Rev. **75** (1949) 1063.
3) D. Broadbent and L. Janossy: Proc. Roy. Soc. **A191** (1947) 517; **A192** (1948) 364.
B. Chaudhuri: Nature **161** (1948) 680.
J. Ise, Jr. and W. B. Fretter: Phys. Rev. **76** (1949) 933.
4) M. Deutschman: Zeits. f. Naturforsch. **A2** (1947) 61.
5) R. W. Williams: Phys. Rev. **74** (1948) 1689.
6) G. Cocconi, A. Loverdo and V. Tongiorgi: Phys. Rev. **70** (1946) 846.

JOURNAL OF THE PHYSICAL SOCIETY OF JAPAN Vol. 10, No. 8, AUGUST, 1955

Observations of Slow Particles and Stars in Nuclear Emulsions Exposed at 17 m.w.e. Underground

By Shin-ichi KANEKO, Tadayoshi KUBOZOE*, Moroe OKAZAKI**
and Masaomi TAKAHATA

Institute of Polytechnics, Osaka City University, Osaka

(Received April 20, 1955)

Observations were carried out at a depth of 17 m.w.e. underground by nuclear plates made from Ilford G5 emulsions in gel form. The frequencies of μ-mesons and protons coming to rest in the emulsions were found to be $0.262\pm0.008\,\mathrm{cm}^{-3}\mathrm{day}^{-1}$ and $0.049\pm0.004\,\mathrm{cm}^{-3}\mathrm{day}^{-1}$, respectively. The angular distribution of these slow protons was found to be isotropic and so they are regarded as being of secondary origin from fast μ-mesons underground. In addition to the stars of the types of N_h+1_p with $N_h\geqslant 3$, several stars of the types of $1+1_p$ and $2+1_p$ were found with a cross section for production of a few times $10^{-30}\,\mathrm{cm}^2$ per nucleon. Some of the stars of the type of $1+1_p$ may possibly be explained by photoproton production through the giant resonance absorption by emulsion nuclei of virtual photons associated with high energy μ-mesons.

§1. Introduction

The nuclear interactions of high energy μ-mesons underground have been investigated by various workers. George and Evans[1] have explained the nuclear disintegrations and penetrating showers produced by fast μ-mesons in terms of the photomesonic process of virtual photons associated with the μ-mesons. However, recent experimental results on the anomalous scattering and associated penetrating particles may imply some possibility of the existence of a short range non-electromagnetic interaction of μ-mesons with nucleons. It seems necessary, therefore, to accumulate more experimental data on μ-mesons underground from various standpoints.

In this laboratory, an experiment using a counter hodoscope has been carried out in order to measure the absorption of μ-mesons and to examine the energy dependence of the cross section for hard shower production by high energy μ-mesons[2]. The present investigation, using nuclear emulsions, is a part of a general continuation of the above study.

In a previous paper[3], it was reported that the corrected frequency of μ-mesons coming to rest in emulsions at 23 m.w.e. underground was found to be $0.22\pm0.03\,\mathrm{cm}^{-3}\mathrm{day}^{-1}$.*** This value is considerably greater than the value published by George and Evans[1].**** We describe in this paper results obtained by a further investigation at a depth of about 1
m.w.e. The absolute frequencies of slow μ-mesons and protons coming to rest in th emulsions have been measured. The slow protons are thought to have arisen from fas μ-mesons underground.

We have paid special attention to an examination of the previously uninvestigatin low energy nuclear interactions of fast μ mesons. The subject is interesting in connection with the recent experiments on th photonuclear effect and the anomalous scattering of μ-mesons. Our results, although th statistical precision is poor, seem to b explained satisfactorily in terms of the gian resonance absorption of the virtual photon associated with fast μ-mesons. This effec can be expected to play only a minor role i the interpretation of the experimental data o the anomalous scattering of μ-mesons.

---

* Now at the National Defence Academy, Yoko suka.

** On leave from the Department of Physics Shimane University, Matsue.

*** The shrinkage factor of G5 emulsion wa assumed to be 2.5 in the previous paper. If th factor is 2.7 as pointed out by Voyvodic[4], th above value of the frequency reduces to $0.20\pm$ $0.03\,\mathrm{cm}^{-3}\mathrm{day}^{-1}$. In the present study we make us of the value of 2.7.

**** In a recent article[5], George and Evans hav presented results obtained with thick emulsions A satisfactory agreement between their value an ours can be seen.

§ 2. Experimental Method

Nuclear plates were made from Ilford G5 emulsions in gel form at an underground cosmic-ray observatory, north of the Yodoyabashi Station of the Osaka Municipal Subway (24°N geomagnetic latitude). The dimensions of the plates were three inches by three inches by about 500 microns. In order to prevent fading of the latent image, the plates were put vertically in a desiccator where the temperature and relative humidity were kept within 25°—35°C and 40—50 per cent, respectively. They were exposed at a depth of 17 m.w.e. during periods of 78 to 121 days. The emulsions were processed by the usual temperature cycle method at the same depth.

The general scanning was made under a total magnification of ×225. The volume of emulsions searched was about 45 cm^3. Single tracks ending in the emulsions were carefully examined with oil immersion objectives and only those with projected residual ranges greater than 100 microns were recorded. By inspecting the characteristics of the tracks, the accepted events were classified as μ-mesons, π-mesons, protons and heavier particles, or stars.

§ 3. Results

The observed numbers of various events are shown in Table I. Unfortunately, tracks in layers near the emulsion surfaces suffered from the so-called "corrosion effect". The stars found in the corroded layers were discarded, since it could not be determined whether or not they were accompanied with minimum ionization tracks. Tracks which stopped in the corroded regions were included in the data, however, since their heavy ionization permitted easy recognition. The depths of the ending points of all the particles were distributed uniformly within the statistical uncertainty throughout all layers of the emulsions.

(1) μ-Mesons

A total of 1125 μ-meson tracks was observed to come to rest. Since the tracks whose projected ranges were less than 100 microns have not been included, this value for the total number of stopped μ-mesons must be corrected. Using the correction factor given in the previous paper[3]), we obtain $0.262 \pm 0.008\ \mathrm{cm}^{-3}\mathrm{day}^{-1}$ for the frequency of μ-mesons stopped at 17 m.w.e. This value is greater than that published by George and Evans[1]) by a factor of about 2.5, but seems to agree with their recent data[5]). The frequency we have observed at 23 m.w.e.[3]) is consistent with the present value taking into account the difference in depth between the two exposure locations.

The projected zenith angle distribution of the observed μ-mesons is shown in Fig. 1. At angles less than 70°, the distribution can be represented by $N(\theta)=N(0)\cos^n\theta$ with $n=$

Table I. The observed numbers and frequencies of various events.

Event	Observed number	Observed frequency ($\mathrm{cm}^{-3}\mathrm{day}^{-1}$)	Corrected frequency ($\mathrm{cm}^{-3}\mathrm{day}^{-1}$)
μ-mesons stopped	1125	0.233 ± 0.007	0.262 ± 0.008
π-mesons stopped	11	$(2.3 \pm 0.7) \times 10^{-3}$	$(5.7 \pm 1.7) \times 10^{-3}$
π^+	6		
π^-	5		
Protons stopped	202	0.042 ± 0.003	0.049 ± 0.004
(1) entered	87	0.018 ± 0.002	0.022 ± 0.002
(2) produced sigly	45	0.009 ± 0.001	0.012 ± 0.002
(3) ejected from stars	70	0.015 ± 0.002	0.015 ± 0.002
Stars initiated by neutral particles ($N_h \geqslant 3$)	24	0.0071 ± 0.0014	
Stars initiated by charged particles	15	0.0044 ± 0.0011	
$1+1_p$	4		
$2+1_p$	2		
$\geqslant 3+1_p$	5		
showers	4		

2.2±0.2, which agrees with the value given by Creamer[6]. About four per cent of the μ-mesons have entered the emulsions from below the horizontal, and these tracks may by explained, as pointed out by George and Evans, by μ-mesons from the π–μ decays of π-mesons produced underground, and in part by the large angle Coulomb scattering of μ-mesons near the end of their ranges but coming initially from directions above the horizontal.

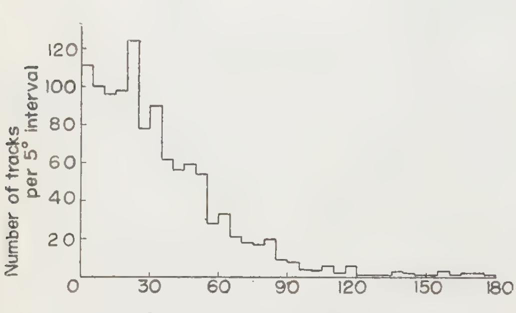

Fig. 1. The distribution of the projected zenith angles of 1125 tracks of slow μ-mesons incident upon the emulsions. At angles less than 70°, the distribution can be represented by $N(\theta) = N(0)\cos^n\theta$ with $n = 2.2 \pm 0.2$.

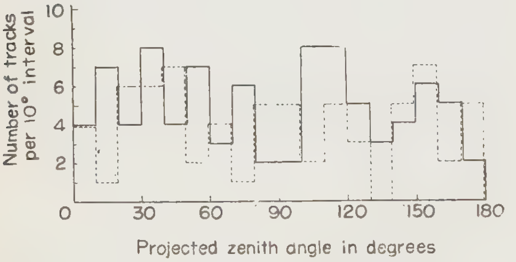

Fig. 2. The projected zenith angle distributions of the tracks of the stopped protons. The solid histogram represents the first group of protons which have entered the emulsions and stopped. The dotted histogram represents the second group of protons which have been produced singly and have stopped in the emulsions.

(2) π-Mesons

Six positive π-mesons showing π-μ decays were found. Out of 32 σ-stars observed, five stars could be ascribed to negative π-mesons. Some π-mesons that would have stopped in the emulsions decayed in flight in passing from the walls of the room (about two meters from the emulsions) to the emulsions. If our deta are corrected for this effect, we obtain $(5.7 \pm 1.7) \times 10^{-3}$cm^{-3}day^{-1} for the frequency of slow π-mesons. However, the uncertainty i (perhaps about two times) larger than tha indicated, because the classification of observed events into the π-μ decays and th capture stars of negative π- and μ-mesons i not certain especially when the secondar particles of these events leave the emulsion before the end of their ranges.

Our value of the frequency of stopped π mesons is about twice as large as that give by George and Evans[1], but the frequenc relative to that of stopped μ-mesons agree well with theirs. The discrepancy betwee the absolute values could possibly be attributed to the difference between the thicknesses c the emulsions employed[3].

(3) Protons

Tracks showing multiple scattering les than that characteristic of π- and μ-meson are chiefly due to protons and perhaps som heavier particles. Hereafter we shall ca these collectively protons.

The number of protons that were observe to come to rest in the emulsions was 20 These have been divided into three group as shown in Table I. The first group is composed of tracks which entered the emulsion and stopped. The second group is those produced singly and stopped in the emulsions and the third is those ejected from stars an stopped in the emulsions.

The angular distributions of the protons c the first and second groups can be regarde as isotropic as shown in Fig. 2. Thus, th geometrical correction factor given by Latte *et al.*[7] can be applied to the observed numbers of these protons. The corrected frequencies are shown in Table I. It is the found that the corrected frequency of a protons stopped at 17 m.w.e. is 0.049±0.00 cm^{-3}day^{-1}. This gives the absolute intensit of protons of energy less than about 30 Mev but the relative numbers in each group show in Table I depend sensibly upon the thicknes of emulsion.

The third group of protons is composed, c course, of the evaporation products of th emulsion nuclei. The second group is probabl protons resulting from the scattering or absorption of low energy neutrons or protons fron one-prong stars initiated by neutrons c photons. Garski[8] has observed similar proton at a mountain altitude and has shown that the frequency of these protons depends strongly upon the neutron excess of the nuclei of the surrounding material. It is possible that the second group of protons we have observed is similar in character as the ones observed by him.

The isotropic angular distribution observed for the first group of protons suggests that these protons are secondary particles from nuclear interactions that occurred in the matter surrounding the emulsions. The frequency of stars in the surrounding materials is assumed to be 0.003 star g^{-1}day^{-1} as taken from the present data. If we assume further that the mean number of visible prongs from the star is 5 and that the mean energy of protons ejected from the stars is about 10 Mev, then we can expect about 110 prongs to end in our emulsions. The experimental number of the first group protons is $87\times1.23=107$, the factor 1.23 being the geometrical correction. The agreement is seen to be satisfactory. In addition, we have observed 111 protons which left the emulsions but were produced in the emulsions as star prongs or single protons. The fact that the number (107) of protons incident upon but stopping in the emulsions is about equal to the number (111) of protons produced within but leaving the emulsions supports well the above view.

One of us[9] has measured the multiple Coulomb scattering of 108 tracks whose ranges were greater than 2000 microns in the emulsions in order to calibrate a constant sagitta scheme. The mass spectrum obtained (Fig. 8 in reference 9) showed that the observed tracks were well explained as a mixture of μ-mesons and a few protons.

(4) Stars with Three or More Heavily Ionizing Prongs

The stars having three or more heavily ionizing prongs that we have observed are quite similar in frequency and in character to those observed by George[10]. The cross section for the production of such stars by fast μ-mesons is found to be $(3\pm1)\times10^{-30}$ cm^2 per nucleon, which agrees with that of George within the statistical uncertainties.

(5) Stars with One or Two Heavily Ionizing Prongs Initiated by μ-Mesons

In the course of observation of single slow protons starting from points within the emulsions, we found that some of these protons were accompanied with two minimum ionization tracks as shown in Fig. 3. The stars of this type are expressed as N_h+1_p with $N_h=1$ according to the Bristol notation, where N_h is the number of black and grey tracks ejected from the star and 1_p means that the star is produced by a relativistic charged particle and emits a single relativistic charged secondary. We have observed also two stars of the type $2+1_p$ as shown in Fig. 4.

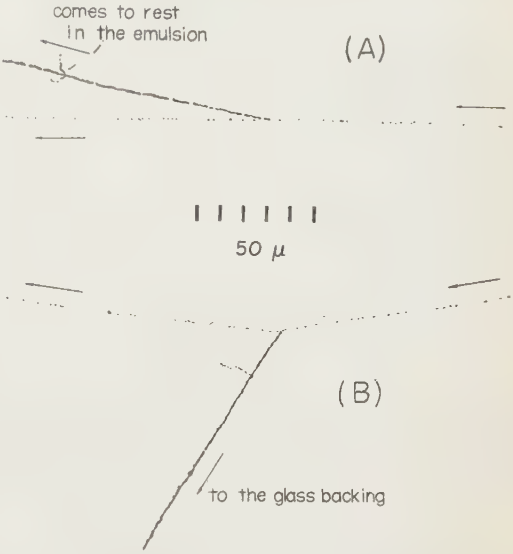

Fig. 3. Projected views of two stars of the type $1+1_p$. (A) event 1 and (B) event 4 from Table II.

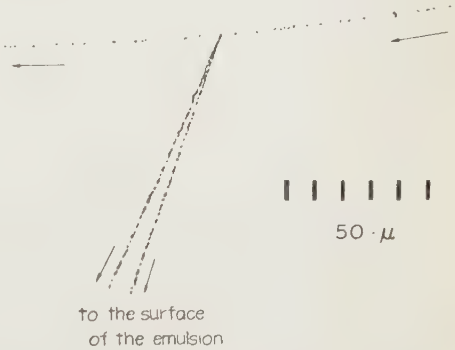

Fig. 4. A projected view of a star of the type $2+1_p$.

Since all the starting and stopping points of slow protons have been carefully observed, the number of $1+1_p$ stars shown in Table I should be fairly reliable. But the number of $2+1_p$ stars is really only a lower limit for the number of events of this type. This is, be-

Table II. Summary of the data of the four $1+1_p$ stars. θ and ϕ represent the angles projected into the plane of the emulsion of the secondary thin and black tracks, respectively, measured from the extended and projected direction of the primary. Θ and Ψ represent the spatial angles of the secondary thin and black tracks, respectively, measured from the extended direction of the primary. The errors in the projected and spatial angle measurements are estimated to be about ±15′ and ±30′, respectively.

Event number	1	2	3	4
Projected zenith angle of the primary, (deg.)	3	34	35	20
Projected angle				
thin track, θ	45′	1°15′	1°00′	14°30′
black track, ϕ	8°30′	31°30′	−39°45′	51°30′
Spatial angle				
thin track, Θ	3°45′	1°15′	1°00′	15°15′
black track, Ψ	36°45′	62°45′	64°45′	68°15′
pv or energy E (Mev)				
primary track, pv	>100			400±60
secondary thin track, pv				190±25
secondary black track, E	5.8	4.6	>8.8	>8.9

cause in the general scanning under low magnification, these events are liable to be overlooked as large angle single scatterings of slow protons.

The data for the four events of the type of $1+1_p$ are summarized in Table II. Thin tracks found in the upper hemisphere were assumed to be due to incident charged particles. Spatial angles of two secondary tracks to the direction of the primary were determined by measurements of the dip angles and projected angles of the tracks taking into account the emulsion contraction. The values of the product of momentum and velocity of some of the primary and secondary thin tracks were estimated by multiple scattering measurements. However, the lengths of the measured tracks were less than 3000 microns and so the errors in the results are seen to be quite large. The energies of the secondary slow particles stopping in the emulsions were determined from their ranges assuming that they were slow protons. Observations of the ionization and multiple scattering of all of these tracks were consistent with the assumption that they were due to the slow protons. The negative sign of the value of ϕ for event 3 in Table II means that both the secondary thin and black tracks were emitted on the same side with respect to the primary direction in the plane of projection. An enormous contamination of slow electrons has been accumulated during the long time of exposure and so it has not been possible to determine definitely whether or not slow electrons due to β-disintegration or internal conversion have been emitted from the residual nuclei. But it is likely that slow electron tracks do not accompany the stars. Nor were any visible nuclear recoil tracks observed.

§ 4. Discussion of $1+1_p$ Stars

(1) General

These events were probably initiated by fast μ-mesons. The primary particles of events 1 and 4 could not be protons from a consideration of their ionization and multiple scattering, but the possibility that they are fast π-mesons or electrons can not be excluded. However, it has been shown by several workers[1),11)] that high energy π-mesons and electrons are very few as compared with fast μ-mesons at this depth underground. In addition, the results obtained by Lock and Yekutieli[12)] concerning stars produced by relativistic π-mesons imply a very large energy loss of the π-meson at the interaction and a large angle of emergence of the secondary π-meson with respect to the primary direction. As shown later, this does not agree with the general features of the present $1+1_p$ stars. It seems probable, therefore, that the events we have observed were produced by relativistic μ-mesons.

It is possible that some of the $1+1_p$ stars are really just recoil protons resulting from elastic Coulomb interactions of μ-mesons with hydrogen nuclei in the emulsion. A crude estimate shows, in fact, that about one event of this type with an energy transfer of 5 Mev or more can be expected. Event 3 can not be regarded as being such a two-body collision from an examination of the emission angles of the secondary tracks shown in Table II. An appreciable deviation from coplanarity is apparent for event 4. For event 1 and 2, definite conclusions on coplanarity can not be drawn, because the angular deviations of the secondary thin tracks from the primary directions are too small for reliable measurements. However, the following consideration of the angles of μ-meson scattering and proton recoil excludes the interpretation in terms of two-body collisions. In an elastic collision, the angle of recoil, Ψ, of the proton can be represented[13] approximately by the following equation provided the energy transferred in the collision is small as compared with the rest energy of the proton:

$$\cos\Psi=\frac{E_\mu+mc^2+Mc^2}{p_\mu c}\left(\frac{E_p}{2Mc^2}\right)^{1/2},$$

where E_μ and p_μ are the kinetic energy and the momentum of the μ-meson before the collision, respectively, E_p is the kinetic energy of the proton after the collision, and m and M are the rest masses of the μ-meson and proton, respectively. If we insert values of E_p and Ψ appropriate to our events 1 and 2 (5 Mev and $\lesssim 70°$, respectively) in the above equation, E_μ turns out to be less than 100 Mev. The ionization and multiple scattering of the incident μ-mesons are not consistent with this small energy. Further, even if the μ-meson energies were near 100 Mev, the scattering angles would be large ($\sim 30°$) if the collisions were simply of the μ-meson-proton type, and the observed scattering angles were both less than 4°. It seems, therefore, that these four events are due to interactions of μ-mesons with emulsion nuclei other than hydrogen.

It should be noted that the present events are dissimilar to the $\geqslant 3+1_p$ stars observed by George. Out of the four events, three μ-mesons suffer angular deflections of less than 4°. In contrast, the deflected angles of μ-mesons producing $\geqslant 3+1_p$ stars distribute widely up to about 90° according to George's analysis[10]. Furthermore, the four slow particles from the $1+1_p$ stars are emitted in the forward direction as shown in Table II. Of the four heavy particles ejected from the two $2+1_p$ stars we have observed, three were in the forward direction. In the evaporation process, all the heavy particles should be emitted isotropically. Of course we have only a very small number of events, and it is possible that the observed anisotropy is due simply to a statistical fluctuation.

(2) The Heavy Prongs

George has interpreted $\geqslant 3+1_p$ stars as events in which a π-meson is produced by one of the virtual photons associated with the μ-mesons. The π-meson is then absorbed in the parent nucleus, and the nucleus subsequently evaporates. The excitation energy of the nucleus should not then be less than the rest energy of a π-meson. Also, the number of charged particles evaporated from a nucleus is known to fluctuate very widely even with a given excitation energy. On this view, then, the number of heavy prongs from the 1_p stars produced by μ-mesons should differ very widely from event to event. Then, the $1+1_p$ or $2+1_p$ stars might be considered as events in which one or two charged particles are evaporated from a nucleus having relatively high excitation energy (greater than 140 Mev). In fact, event 4 in Table II and the two $2+1_p$ stars are in accordance with this view. It is believed, however, that the non-mesonic process discussed in section (4) is more likely interpretation for most of the $1+1_p$ stars.

A quantitative knowledge of the fluctuation of the number of heavy prongs can be obtained from the experimental results of nuclear disintegrations by high energy photons. Kikuchi[14], using Ilford G5 and C2 emulsions, has observed stars produced by high energy synchrotron γ-rays. Since the energy spectrum of the virtual photons associated with fast μ-mesons is nearly the same in shape as that of the bremsstrahlung γ-rays of maximum energy 300 Mev*, it is justified to compare directly the prong distribution of the 1_p stars we have observed with those studied by Kikuchi. In Kikuchi's work, 170±20 single protons of energy less than 20 Mev were produced as compared with 100 stars with three or more heavy prongs. Most of the single protons and about one-third of the observed stars could be attributed to photons of energy less than 150 Mev. On the other hand, we have observed four $1+1_p$ stars and five $\geqslant 3+1_p$ stars. It is likely, therefore, that the $1+1_p$ stars were those initiated by virtual photons of energy less than 150 Mev; i.e., it is suggested that the photomesonic process is not necessarily responsible for all of the four $1+1_p$ stars and that some other process or processes may be involved.

---

* The energy spectrum of the virtual photons associated with μ-mesons can be represented approximately by an inverse power of the photon energy neglecting a slight (logarithmic) dependence on the energy of the parent μ-mesons. The bremsstrahlung spectrum is also well approximated by an inverse power law below the maximum energy. Of course, the virtual photon spectrum has a long tail above 300 Mev resulting from extremely high energy μ-mesons underground. But the higher energy virtual photons should produce, to a lesser extent, only the nuclear disintegrations with greater energy transfers or π-meson showers and should not play any important role in the low energy nuclear reactions.

(3) The Deflections of the Thin Tracks

Despite the above, we assume for the moment that all the $1+1_p$ and $\geqslant 3+1_p$ stars are due to the photomesonic process*; i.e., we assume that a π-meson is produced by a virtual photon associated with the parent μ-meson and is absorbed by a nucleon in the same nucleus. We can then estimate, according to George[10)], the kinetic energy of the primary μ-meson from its angle of deflection and an assumed nuclear excitation energy by an application of the conservation laws. It is reasonable to assume the excitation energy for the $1+1_p$ stars to be 150 Mev (i.e., a π-meson produced with very little kinetic energy). The results are shown in Fig. 5, in which is also shown the theoretical energy spectrum of μ-mesons causing 1_p stars by the photomesonic procoss given by George. He ha shown that the spectrum agrees well with a experimental histogram obtained from hi analysis of some thirty $\geqslant 3+1_p$ stars. If th $1+1_p$ stars are due to the photomesonic process, their primary energies thus estimated would fit with George's theoretical spectrum However, a considerable discrepancy can be seen from Fig. 5. The primary energies of events 2 and 3 seem to be too large for this interpretation. Events 1 and 4 may be ascribed to the photomesonic process, but the multiple scattering observations of the primary particles of these events shown in Table I give the energies much smaller than those shown in Fig. 5. It seems likely, therefore that the photomesonic process is not responsible at least for event 1. This also suggests that some of the events (say, events 1, 2, and 3) should be ascribed to some other process giving rise to a lower energy transfer than the photomesonic process.

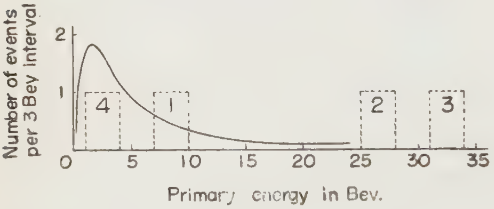

Fig. 5. Primary energies of four μ-mesons causing the $1+1_p$ stars (dotted rectangles). The energies have been estimated from the angles of deflection of the μ-mesons assuming that the energy transfer to the nuclei was 150 Mev. The solid curve has been calculated by George[10)] assuming the photoproduction of π-mesons by the virtual photons accompanying the μ-mesons. The curve has been normalized to four paticles. The figures given in the dotted rectangles denote the event numbers shown in Table II.

(4) The Non-Mesonic Photonuclear Process

As a result of numerous recent investigations of the photonuclear effect, it has been established that the absorption of photons by nuclei exhibits a "giant resonance" around 20 Mev. The compound nuclei formed by the photon absorption emits preferentially an evaporation neutron but sometimes a proton according to the binding energy and selection rules.

The virtual photons associated with a high energy μ-meson could induce the low energy photonuclear effect. Recently, Annis, Wilkins and Miller[16)] have measured the slow neutrons resulting from nuclear interactions of high energy μ-mesons. They have attributed these neutrons to high energy stars induced through the photomesonic process and to the low energy photonuclear process. The non-mesonic photonuclear process can result in the emission of protons as well as neutrons, and i turns out that the $1+1_p$ stars we have observed can be explained at least in part by this process, utilizing, of course, the virtual photons of the high energy μ-mesons. This view is supported by the quantitative considerations of the cross section as follows.

---

* Although the non-mesonic photonuclear process is expected to occur even at photon energy above the π-meson threshold, its contribution to the total integrated cross section for photon absorption seems to be small according to Levinger[15)]. In the present paper, we assume tentatively that all the reactions taking place at above 150 Mev are the mesonic process and those at below 150 Mev are the non-mesonic.

Halpern and Mann[17)] have measured the photoproton excitation functions for carbon, aluminium, nickel, cobalt, and columbium up to 24 Mev photon energy. The energies at maximum cross section are nearly the same (about 20 Mev) for these elements and the integrated cross sections amount to $(1-2)\times 10^{-25}$ Mev cm^2 per nucleus. We shall assume then that the integrated cross section for the emulsion nuclei is about 1.2×10^{-25} Mev cm^2 per nucleus (the mean mass number of the emulsion nuclei is taken to be 70). According to the Williams-Weizsäcker formula, the number of photons at a given energy associated with a μ-meson depends only insensitively upon the energy of the parent μ-meson. Thus, it is sufficient to consider a μ-meson of 10 Bev which is about the mean energy at 17 m.w.e, underground. The number of photons at 20 Mev associated with a μ-meson of 10 Bev is about 1.4×10^{-3} per Mev. Therefore, the cross section for photoproton production by high energy μ-mesons is

$$\sigma \cong 1.4\times 10^{-3}\times 1.2\times 10^{-25}/70$$
$$\cong 2.4\times 10^{-30}\ \text{cm}^2 \text{ per nucleon.}$$

This is, of course, a very crude estimate, but is thought to be sufficient to give an order of magnitude. The observed frequency of $1+1_p$ stars corresponds to a cross section of about 1×10^{-30} cm^2 per nucleon. Hence, the agreement between the predicted and observed values is satisfactory.

An another estimate of the cross section can be obtained from the sum-rule calculation of electric dipole transitions in the photonuclear effect. Levinger[18)] has recently calculated the cross sections for photon absorption by nuclei using a simple harmonic oscillator independent particle model. The bremsstrahlung weighted cross section is given by

$$\int \sigma(E)\,\frac{dE}{E} = 0.36A^{4/3} \qquad \text{(mb)},$$

where $\sigma(E)$ is the photon absorption cross section at a photon energy E and A is the mass number of the nucleus. Although the branching ratio between neutron and proton emissions is not well known, we can roughly estimate the contribution of the photoproton production cross section to the photon absorption cross section by light and medium weight nuclei making use of the results calculated by Heidmann and Bethe[19)] and Schiff[20)]. Taking into account the chemical composition of our emulsions, therefore, we obtain about 2×10^{-30} cm^2 per nucleon for the photoproton production cross section of emulsion nuclei by high energy μ-mesons*. This theoretical value is also consistent with the observed value.

The energy and angular distributions of photoprotons from various nuclei have been found by several authors to be considerably different from nucleus to nucleus. Sometimes, a large fraction of direct photoeffect such as proposed by Courant[21)] seems to be necessary to account for the observed anomaly of the energy and angular dependences[22)]. The complex composition of elements in the emulsion makes it impossible at present to predict the nature of photoprotons from the nuclei of the emulsion. We assume tentatively that the energy and anguler distributions are represented by the evaporation theory. The observed energies of the slow protons ejected from the present $1+1_p$ stars are consistent with the evaporation model. Thus, if we assume the observed forward asymmetry of the angles of emission to be fortuitous as already mentioned, then we can explain the slow protons by an evaporation process which occurs subsequently to the giant photon absorption by the emulsion nuclei.

(5) Concluding Remarks

The present experiment then gives some evidence for a non-mesonic photonuclear process by high energy charged particles, although any final conclusions should be reserved because of the very poor statistical precision. Such a process is expected to occur, of course, and the closely analogous mesonic process is presumably resonsible for the production of penetrating showers and high energy nuclear disintegrations by μ-mesons. The cross section for production of the $\geqslant 3+1_p$ stars by μ-mesons is about 3×10^{-30} cm^2 per nucleon according to George[10)]. The cross section for photoproton production by μ-mesons is thus of the same order of magnitude as that for photomesonic process presumably responsible for the $\geqslant 3+1_p$ stars observed by George. It is possible that future investigation will decide quantitatively the contributions to stars induced by μ-mesons through the non-mesonic and mesonic photonuclear processes.

---

* According to this estimate, the bremsstrahlung weighted cross section per nucleus for photoproton production by the nuclei of Ag and Br is about the same as that by the nuclei of C, N and O.

Hewever, it must be noted that there is an another possible interpretation of the $1+1_p$ stars. The giant resonance absorption of virtual photons described above is regarded as the interaction of the photon with the nucleus as a whole. The photons could also be scattered by the individual protons consisting of the nucleus and so result in the formation of a compound nucleus or the direct emission of protons. The cross section for the scattering process is perhaps very small[23]. However, the observed angular anisotropy of the emitted protons may be an indication of the existence of such a direct interaction process.

In the present experiment, recoil protons resulting from the elastic Coulomb interaction of μ-mesons with hydrogen nuclei have not been detected. Experiments of this subject using high energy μ-mesons or electrons would be interesting because some knowledge of the charge distribution of the proton can be obtained from the results.

(6) The Anomalous Scattering of μ-Mesons

In conclusion, let us consider the effect of the low energy photonuclear process on the large angle scattering of μ-mesons. When a giant resonance absorption has taken place, capturing a photon associated with a few hundred Mev μ-meson, there would result a considerable deflection of the μ-meson and, most frequently, neutron emission. This would be observed as a large angle scattering of the μ-meson. Kannangara and Shrikantia[24] have observed 120 meters path length of high energy μ-meson tracks in emulsions and have found seven events of anomalous scattering greater than 7°. The seven events they observed involved μ-mesons of energies less than 600 Mev. In particular, four events showed momentum transfers of 10 to 30 Mev/c. Therefore, from the standpoint of kinematics, these events may well be ascribed to photoneutron production involving the giant resonance phenomena. However, the cross section for this process is estimated by Davidson[25] to be about 10^{-29} cm^2 per nucleon for the emulsion nuclei, and so seems to be too small to explain the cross section of about 3×10^{-27} cm^2 per nucleon observed by Kannangara and Shrikantia. Other observations making use of cloud chambers have given much smaller cross sections of the order of 10^{-28} cm^2 per nucleon for the anomalous scatering[26]. The anomalously high scattering cross section of μ-mesons at energies above 1 Bev has recently been reported by McDiarmid[27]. The giant photon absorption can not be responsible for these events. Even if we take into account the long tail of the non-mesonic effect extending from the giant resonance to above the π-meson threshold[28], it would be difficult to explain all of the observed scattering cross section by the low energy photonuclear process alone.

Acknowledgement

We wish to express our hearty thanks to Prof. Y. Watase for continuous interest and encouragement, and to Prof. W. L. Kraushaar* and Prof. S. Hayakawa of the Research Institute for Fundamental Physics for their numerous discussions and comments. Thanks are also due to Prof. K. Morikawa of the Tokushima University for able collaboration in the early course of the work, and to Prof. S. Kikuchi of the Osaka University for helpful discussion.

We would like to take this opportunity of thanking Mr. S. Shimomura, Director of the Osaka Municipal Transportation Bureau, and the staff of the Yodoyabashi Station of the Osaka Municipal Rapid Transit System for making facilities available for carrying out the experiment.

This study has been supported in part by a Grant in Aid for Fundamental Scientific Research from the Ministry of Education, and in part by a grant from Mr. T. Shiota, to whom we wish to acknowledge gratefully. One of us (M.O.) is also indebted to the Ministry of Education for a Grant in Aid for Developmental Scientific Research.

---

* Fulbright research professor from the Massachusetts Institute of Technology, Cambridge, Mass., U.S.A.

References

1) E. P. George and J. Evans: Proc. Phys. Soc. **A63** (1950) 1248.
2) T. Oshio: *Proceedings of the International Conference of Theoretical Physics*, Kyoto and Tokyo, September 1953, p. 117. A full account of the results will be published by S. Higashi, I. Higashino, T. Kubozoe, M. Oda, T. Oshio, H. Shibata. K. Watanabe and Y. Watase.
3) S. Kaneko, T. Kubozoe and M. Takahata: J. Phys. Soc. Japan **9** (1954) 147.
4) L. Voyvodic: *Progress in Cosmic Ray Physics*, Vol. II, edited by J. G. Wilson, North-Holland Publishing Co., Amsterdam, 1954, p. 228.
5) E. P. George and J. Evans: to be published.
6) R. Creamer: M. Sci. Thesis, London, 1951 cited in p. 433 of ref. 10.
7) C. M. G. Lattes, G. P. S. Occhialini and C. F. Powell: Nature **160** (1947) 453.
8) H. Garski: Z. f. Naturf. **7a** (1952 565.
9) S. Kaneko: J. Phys. Soc. Japan **10** (1955) 325.
10) E. P. George: *Progress in Cosmic Ray Physics*, edited by J. G. Wilson, North-Holland Publishing Co., Amsterdam, 1952, p. 395 ff.
11) S. J. Goldsack and M. L. T. Kannangara: Phil. Mag. **44** (1953) 811.
12) W. O. Lock and G. Yekutieli: Phil. Mag. **43** (1952) 231. See also M. Blau and M. Caulton: Phys. Rev. **96** (1954) 150.
13) L. Jánossy: *Cosmic Rays*, second edition, Oxford, 1950, p. 83.
14) S. Kikuchi: Phys. Rev. **86** (1952) 41.
15) J. S. Levinger: Phys. Rev. **85** (1952) 43.
16) M. Annis, H. C. Wilkins and J. D. Miller: Phys. Rev. **94** (1954) 1038.
17) J. Halpern and A. K. Mann: Phys. Rev. **83** (1951) 370.
18) J. S. Levinger: Phys. Rev. **97** (1955) 122.
19) J. Heidmann and H. A. Bethe: Phys. Rev. **84** (1951) 274.
20) L. I. Schiff: Phys. Rev. **73** (1948) 1311.
21) E. D. Courant: Phys. Rev. **82** (1951) 703.
22) For instance, M. E. Toms and W. E. Stephens: Phys. Rev. **92** (1953) 362.
23) M. Gell-Mann, M. L. Goldberger and W. E. Thirring: Phys. Rev. **95** (1954) 1612.
24) M. L. T. Kannangara and G. S. Shrikantia: Phil. Mag. **44** (1953) 1091. A further account of this work has been given by G. D. Rochester and A. W. Wolfendale: Phil. Mag. **45** (1954) 980.
25) J. P. Davidson: Nuovo Cim. **11** (1954) 205.
26) See, B. Leontic and A. W. Wolfendale: Phil. Mag. **44** (1953) 1101.
27) I. B. McDiarmid: Phil. Mag. **45** (1954) 933.
28) L. W. Jones and K. M. Terwillinger: Phys. Rev. **91** (1953) 699.

JOURNAL OF THE PHYSICAL SOCIETY OF JAPAN Vol, 10, No. 8, AUGUST, 1955

The Theory of the Dielectric Constant of Ionic Crystals III

By Jiro YAMASHITA and Tatumi KUROSAWA

Institute of Science and Technology, University of Tokyo

(Received April 15, 1955)

A general theory of the dielectric constant of simple ionic crystals is proposed. The energy change due to the electric field is expressed by a quadratic form of quantities p_x, p_1 and p_2, which represent the dipole moments due to the displacement of ions, the deformation of the negative ion and the deformation of the positive ion in the electric field respectively. Using this formalism it is possible to derive several important relations concerning the dielectric properties of ionic crystals. When the polarizability of the positive ion is much smaller than that of the negative ion, we may be allowed to put $p_2=0$. In this case our quadratic formalism has only three unknown constants, which are determined by using three observed quantities. For NaCl we determine them by using κ_0, κ and β (the optical dielectric constant, the static dielectric constant and the compressibility). Then we discuss the pressure effect of dielectric constants from our standpoints, and then we have computed the Reststrahlenfrequenz of NaCl considering the ionic polarization. The result agrees well with observation. Finally we propose a method of determining the phenomenological repulsive potential between ions of ionic crystals, which may be more accurate than the previous one.

§ 1. Introduction

The dielectric properties of non-conducting substances are usually discussed on the basis of the Lorentz formula. Surely it holds very well for gases, but with liquids or ionic crystals there are noticeable deviations from it.[1)] In the case of liquids the origin of the deviation is mainly ascribed to the fluctuation in the arrangement of molecular dipoles in it. Using the statistical mechanics Kirkwood[2)] and others[3)] have succeeded in deriving the formulas which give a good agreement with experiments. In the case of ionic crystals the fluctuation effect is supposed to be negligible. In solids, however, each constituent ion overlaps appreciablly with its nearest neighbouring ions, which is not consistent with the assumption of point dipoles in the Lorentz formula. Thus we find it necessary to treat quantum-theoretically the electronic structure of constituent atoms, ions or molecules in dielectrics in order to take into account the effect of charge overlapping.

Such a quantum theory of dielectrics was proposed by one of us[4)] and was applied to LiF crystals. In that theory the perturbed wave function of 2p-electrons of a negative ion was assumed to be[5)]

$$\psi(\boldsymbol{r})=\psi_0(\boldsymbol{r})(1+\lambda r\cos\theta)\,, \qquad (1)$$

where $\psi_0(\boldsymbol{r})$ is the unperturbed wave function, λ is the variational constant and θ is measured from the field direction. The deformation of a positive ion was neglected, because the polarizability of Li ions is much smaller than that of F ions. Under these assumptions the energy change per ion pair was expressed approximately as follows:

$$\begin{aligned}\Delta E=&-p_eF-\frac{1}{2}\frac{4\pi N}{3}p_e^2+A_0\lambda^2+A\lambda^2\\&-p_xF-\frac{1}{2}\frac{4\pi N}{3}p_x^2+Cx^2\\&-\frac{4\pi N}{3}p_ep_x+Bx\lambda\,. \qquad (2)\end{aligned}$$

where is N is the number of ion pairs in the unit volume, F is the external electric field, $2x$ is the relative displacement of ions, p_x is the electric dipole due to the ion-displacement, being equal to $2ex$ and p_e is the electric dipole due to the charge deformation of a negative ion, which is equal to $4\bar{r}^2e\lambda$, with $\bar{r}^2$ defined by

$$\bar{r}^2=\int r^2\psi_0(\boldsymbol{r})d\tau\,.$$

$A_0\lambda^2$ is the change of the intra-energy of a negative ion (if we use the Kirkwood approximation, it becomes $3\lambda^2$ in atomic units) $-\frac{1}{2}4\pi Np_x^2/3$ the mutual interaction energy of dipoles p_x, $-\frac{1}{2}4\pi N p_e^2/3$ that between dipoles p_e, and $-4\pi N p_x p_e/3$ is that between dipoles p_x, p_e. The so-called Lorentz field is derived from the last three terms. Besides these it further contains three terms Cx^2, $Bx\lambda$ and $A\lambda^2$, which are caused by the change of the degree of charge-overlap due to the displacement or deformation of ions.

In general we may expand the change of the internal energy (interaction energy between ions) as the power series of x and λ:

$$\Delta U = a_0\lambda + C_0 x + A\lambda^2 + Bx\lambda + Cx^2 + \cdots .$$

The term Cx^2 is the usual repulsive potential in ionic crystals, and when the repulsive force is assumed to be effective only between the nearest neighbouring ions, C is given by

$$C = 12r_0/\beta \tag{3}$$

where β is the compressibility and r_0 is the interionic distance. The term $A\lambda^2$ is caused by the mutual interaction of the deformed parts of the wave function $\lambda\psi_0(\boldsymbol{r})r\cos\theta$. The linear term of x vanishes because of the equillibrium condition. The linear term of λ consists of several integrals containing $(\cos\theta)^1$, and if we express the interaction between a pair of ions of opposite signs as $\lambda S\exp(-pr_0)$, there is another term of the type

$$-\lambda S\exp(-pr_0),$$

when all ions are in equilibrium positions. Thus the linear term of λ is also canceled out because of the symmetry. However, when positive ions are displaced by $2x$ relative to negative ions, the above two terms become $\lambda S\exp[-p(r_0+2x)]$ and $-\lambda S\exp[-p(r_0-2x)]$ respectively. Thus in that case the term $Bx\lambda$ remains, since the crystal symmetry is destroyed by the external field. The parameters x and λ are to be determined so as to minimize the energy change of the total system. In the case of high frequency field x is to be assumed as zero.

In the previous paper we have computed the values of A and B of *LiF* quantum mechanically and obtained theoretical values of the static dielectric constant κ and the optical dielectric constant κ_0. From the results we have found that the energy change due to the electric field is well expressed by a quadratic form of two quantities p_x and p_e with three constants A, B and C. However, it is a rather laborious task to compute these constants for each substances quantum theoretically as we have done for LiF, and the accuracy of the computation is not very good. Thus, in this paper we shall follow the inverse process, that is, we shall determine three constants phenomenologically with three experimental values. Then we shall have a energy formula for each dielectrics containing no arbitrary constant, which is very useful for analysing observed data or for deriving relations between observable quantities.

§ 2. Polarization in high frequency field

We shall begin with the dielectric constant at the high frequency field. Neglecting the polarization of the positive ion, ΔE is:

$$\Delta E = -4\bar{r}^2\lambda F - \frac{1}{2}\frac{4\pi}{3}\frac{(4\bar{r}^2\lambda)^2}{2r_0^3} + A_0\lambda^2 + A\lambda^2 . \tag{4}$$

From the condition $\partial\Delta E/\partial\lambda = 0$, λ is determined as:

$$\lambda = 4\bar{r}^2 F \Big/ \left[2(A_0+A) - \frac{4\pi}{3}\frac{(4\bar{r}^2)^2}{2r_0^3}\right], \tag{5}$$

and accordingly ΔE is:

$$\Delta E = -\frac{1}{2}(4\bar{r}^2)^2 F^2 \Big/ \left[2(A_0+A) - \frac{4\pi}{3}\frac{(4\bar{r}^2)^2}{2r_0^3}\right], \tag{6}$$

and

$$p_e = (4\bar{r}^2)^2 F \Big/ \left[2(A_0+A) - \frac{4\pi}{3}\frac{(4\bar{r}^2)^2}{2r_0^3}\right]. \tag{6'}$$

On the other hand, the relation between the energy change and the dielectric constant κ_0 is expressed by

$$\Delta E = -\left(\frac{1}{N}\right)\frac{1}{8\pi}(\kappa_0 - 1)F^2 , \tag{7}$$

where $N = 1/2r_0^3$ is the number of ion-pairs in the unit volume. From (6) and (7) κ_0 is given by

$$\kappa_0 = 1 + \frac{2\pi}{r_0^3}(4\bar{r}^2)^2 \Big/ \left[2(A_0+A) - \frac{4\pi}{3}\frac{(4\bar{r}^2)^2}{2r_0^3}\right]. \tag{8}$$

Or we can obtain the same result from relations $\kappa_0 - 1 = 4\pi P/F$ and $P = Np$, and (6′).

Introducing the quantity a defined by

$$a = (A_0+A)/(4\bar{r}^2)^2 , \tag{9}$$

κ_0 and p_e become:

$$\kappa_0 = 1 + \frac{\pi}{r_0^3}\Big/(a - \pi/3r_0^3) , \tag{10}$$

$$p_e = F \Big/ \left(2a - \frac{4\pi}{3}\frac{1}{2r_0^3}\right) . \tag{11}$$

Using the experimental value of κ_0 we are able to determine the value of a for each crystal. The results are shown in Table I. In the Lorentz theory we use quantities such as the effective field F_{eff} and the polarizability of ions. Although these quanitities do not appear explicitly in our theory, it is sometimes convenient to make clear the mutual relation. If we define the quantity α_n by

$$\alpha_n = 1/2a\ , \tag{12}$$

then we find easily that α_n satisfies the following relation

$$p_e = \alpha_n\left(F + \frac{4\pi}{3}\frac{p_e}{2r_0^3}\right). \tag{13}$$

Thus we see that the quantity $(1/2a)$ corresponds to the apparent polarizability of ions in the crystal. However, the quantity a depends not only on the nature of the corresponding atom, but also depends on the nature of the crystal through the interionic interaction A. Thus we find that the apparent polarizability of ions should not be constant in the strict sense. On the other hand, we see from Table I that the polarizability of each negative ion is nearly constant (here we must remember that we neglect the small contribution from the positive ion). In fact, it is only an example of the constancy of the apparent polarizability of one kind of ion in various crystals, which has been well established in all alkali-halide crystals by the detailed investigation of Shockley and others⁶⁾. We shall later on mention the reason why such an additivity rule of the polarizability is approximately valid for alkali-halide crystals.

Table I.

	κ_0	a	α_n
LiF	1.92	0.550×10^{24}	0.90×10^{-24}
NaF	1.74	0.429	1.16
LiCl	2.75	0.168	2.97
NaCl	2.25	0.161	3.10
LiBr	3.16	0.120	4.17
NaBr	2.62	0.113	4.42
LiI	3.80	0.0803	6.23
NaI	2.91	0.0799	6.25

Now, we want to know the role of the interaction for the polarizability. In the previous paper⁴⁾ we computed A_0 by the Kirkwood's approximation and A of *LiF* by the Löwdin's approximation. The results were $A_0=3.0$ and $A=0.8$ respectively in atomi units. Thus the theoretical value $A/(A_0+A$ of *LiF* is about 0.2. On the other hand, i order to have the experimental value o $A/(A_0+A)$ we must separate A from a. Sinc the dielectric constant is related only to a, i is useless for our purpose. However, th pressure effect of the dielectric constant i just what we wish. In Table II we show th rate of change of the refractive index n ($\kappa_0=$ n^2) due to the pressure change according t the experiments of Burstein and Smith⁷⁾. A first, they assumed that this change of n wa caused only by the decrease of the volume due to the hydrostatic pressure and they neglected the change of the polarizability Using the Lorentz formula they obtained the following formula of the pressure effect.

$$\rho\left(\frac{dn}{d\rho}\right) = -\frac{V}{2}\frac{1}{\sqrt{\kappa_0}}\frac{d\kappa_0}{dV} = \frac{(\kappa_0-1)(\kappa_0+2)}{6\sqrt{\kappa_0}} \quad (14$$

where V is the volume and ρ is the density However, they found that this equation gave much larger values of the pressure effect (the second column of Table II), and they concluded that the polarizability of ions must change under the effect of high pressure. In our theory there exists the interionic interaction term $A\lambda^2$, which will be the sensitive function of the interionic distance. When the lattice constant decreases under the hydrostatic pressure, $A\lambda^2$ will increase rapidly so as to reduce the polarizability of ions. Assuming the simple functional form of A

Table II.

	$\rho(dn/d\rho)_{obs.}$	(14)
LiF	~0.1	0.43
NaCl	0.24	0.59
KCl	0.23	0.53
KBr	0.35	0.63
KI	0.43	0.81
MgO	~−0.4	0.94

$$A(r) = \mathfrak{A}\exp(-pr) \tag{15}$$

we have obtained the formula of the pressure effect of κ_0 as follows:

$$\rho\left(\frac{dn}{d\rho}\right) = \frac{(\kappa_0-1)(\kappa_0+2)}{6\sqrt{\kappa_0}} - \frac{1}{2r_0^3}\frac{A(r_0)}{(4\bar{r}^2)^2}\frac{r_0 p}{6\sqrt{\kappa_0}} \times\frac{2}{\{2a-(4\pi/3)(1/2r_0^3)\}^2}\ , \tag{16}$$

where $2r_0$ is the lattice constant under zero pressure and $2(r_0-\delta r_0)$ is that under the high pressure. Accordingly $A(r_0-\delta r)$ is given by:

$$A(r_0-\delta r)=A(r_0)(1+p\delta r)\ .$$

The derivation of Eq. (16) is given in Appendix I. If we assume the difference

$$(\Delta n)=\left(\rho\frac{dn}{d\rho}\right)_{o\cdot s}-\frac{(\kappa_0-1)(\kappa_0+2)}{6\sqrt{\kappa_0}} \tag{17}$$

is caused solely by the increase of $A\lambda^2$, we have the following equation for $A/(4\bar{r}^2)^2$:

$$A/(4\bar{r}^2)^2=(\Delta n/r_0 p)(3\sqrt{\kappa_0}/2\pi)r_0^3 \times\{2a-(4\pi/3)(1/2r_0^3)\}^2. \tag{18}$$

From Eqs. (11) and (17) we see that all quantities on the right hand of Eq. (18) are observed values except for p. Now, the repulsive potential of the type $C\exp(-r/\rho)$ has been widely used for analysing the cohesive energy of alkali-halide crystals. The results of such analysis show that values of (r_0/ρ) lie between 7 and 10 in many cases. Thus we suppose that values of (pr_0) in Eq. (18) will lie also near 10. The results of computation are shown in Table III. We find that the interaction A amounts to about 30 or 20% of the total energy change $(4\bar{r}^2)^2a$. If we decide the value $\bar{r}^2$ so as to fit the diamagnetic susceptibility, we obtain the absolute value of A. The estimated value of A of *LiF* is 1.5~1.0 in atomic units ($\bar{r}^2=1.9$), while our computed value was 0.8. Now, the interaction energy A is different in each crystal, but we suppose that the difference is not large for the same negative ion by the analogy of the behaviours of the repulsive potential energy computed by Born and others (see Table IV). The difference of the repulsive potential energy is about 30 or 20%.

Table III.

	$[A/(4\bar{r}^2)^2]/a$	
	$pr_0=7$	$pr_0=10$
LiF	0.31	0.21
NaCl	0.28	0.19

Table IV.

	Repulsive energy (Kcal/Mol)
LiF	44.1
NaF	35.3
LiCl	26.8
NaCl	23.5
KCl	21.5

Hence the values of a of crystals with the same negative ion and different positive ions are expected to be not widely different, because the variable part of a is small quantity in itself and the variation of it is also small. ($\delta A/A$ may be 0.2 or so, and $A/(A_0+A)$ may be 0.3 or 0.2, and then $\delta a/a$ may be the order of 0.05.)

§ 3. Static Dielectric Constant

When the static field is applied, ions are not only deformed, but also are displaced as a whole. If we neglect the deformation of the positive ion, the energy change per ion-pair is expressed as:

$$\begin{aligned}\Delta E=&-2exF-\frac{1}{2}\frac{4\pi}{3}\frac{(2ex)^2}{2r_0^3}-\frac{4\pi}{3}\frac{(2ex)(4\bar{r}^2\lambda)}{2r_0^3}\\&-4\bar{r}^2\lambda F-\frac{1}{2}\frac{4\pi}{3}\frac{(4\bar{r}^2\lambda)^2}{2r_0^3}+(A_0+A)\lambda^2\\&+Bx\lambda+Cx^2.\end{aligned} \tag{19}$$

Introducing

$$b=B/(2e)(4\bar{r}^2) \tag{20·1}$$

and

$$c=C/4e^2\ , \tag{20·2}$$

ΔE becomes:

$$\begin{aligned}\Delta E=&-p_xF-\frac{1}{2}\frac{4\pi}{3}\frac{p_x^2}{2r_0^3}-\frac{4\pi}{3}\frac{p_xp_e}{2r_0^3}-p_eF\\&-\frac{1}{2}\frac{4\pi}{3}\frac{p_e^2}{2r_0^3}+ap_e^2+bp_xp_e+cp_x^2\ ,\end{aligned} \tag{21}$$

where p_x and p_e are determined by the conditions

$$\partial\Delta E/\partial p_x=0 \quad\text{and}\quad \partial\Delta E/\partial p_e=0\ .$$

They are:

$$\begin{aligned}p_x=(2a-b)F\Big/\Big[&\left(2c-\frac{4\pi}{3}\frac{1}{2r_0^3}\right)\left(2a-\frac{4\pi}{3}\frac{1}{2r_0^3}\right)\\&-\left(b-\frac{4\pi}{3}\frac{1}{2r_0^3}\right)^2\Big]\end{aligned} \tag{22·1}$$

and

$$\begin{aligned}p_e=(2c-b)F\Big/\Big[&\left(2c-\frac{4\pi}{3}\frac{1}{2r_0^3}\right)\left(2a-\frac{4\pi}{3}\frac{1}{2r_0^3}\right)\\&-\left(b-\frac{4\pi}{3}\frac{1}{2r_0^3}\right)^2\Big].\end{aligned} \tag{22·2}$$

The polarization per unit volume is:

$$\begin{aligned}P&=(p_x+p_e)/2r_0^3\\&=(a+c-b)F\Big/r_0^3\Big[\left(2c-\frac{4\pi}{3}\frac{1}{2r_0^3}\right)\end{aligned}$$

Table V.

	κ	β	C	b	$(4\pi/3)/2r_0^3$
LiF	9.27	1.4×10^{-12}	17.2×10^4	0.220×10^{24}	0.2578×10^{24}
NaF	6.0	2.07	13.4	0.170	0.1698
NaCl	5.62	4.18	8.07	0.099	0.0944
NaBr	6.0	4.98	7.18	0.072	0.0791
NaI	6.6	6.94	5.58	0.055	0.0621

$$\times\left(2a-\frac{4\pi}{3}\frac{1}{2r_0^3}\right)-\left(b-\frac{4\pi}{3}\frac{1}{2r_0^3}\right)^2\Bigg]. \quad (23)$$

The dielectric constant in the static field is determined by the energy relation (7) or the following relation as:

$$\kappa=1+4\pi P/F$$
$$=1+\frac{\pi}{r_0^3}(a+c-b)\Bigg/\left[\left(a-\frac{\pi}{3r_0^3}\right)\left(c-\frac{\pi}{3r_0^3}\right)\right.$$
$$\left.-\left(\frac{b}{2}-\frac{\pi}{3r_0^3}\right)^2\right]. \quad (24)$$

This equation contains three material constant a, b and c, in which a was already determined in the previous section.

If we assume that the interaction potential has central character, and the short range repulsive potential is effective only between the nearest neighbouring ions, then the constant C is connected with the compressibility β by the relation:

$$C=12r_0/\beta\,. \quad (25)$$

The validity of those assumptions will be examined later on. Using Eq. (24) with the observed value of κ we can easily determine b. The results are shown in Table *V*. Putting $\bar{r}^2$ of *LiF* as 1.9, B becomes 0.50 in atomic units, while our computed value of B of *LiF* was 0.5. Considering the approximate nature of our computation such good agreement seems to be accidental.

Now, the term bp_xp_e is very important for dielectric properties of alkali-halide crystals. We shall discuss this in detail. We find at first that the large part of the Lorentz energy $-(4\pi/3)(p_xp_e/2r_0^3)$ is canceled out by the con tribution from bp_xp_e. This fact was firs pointed out by Mott[8]. Thus we can no have any good quantitative results withou bp_xp_e. If we neglect b entirely, Eq. (24) be comes:

$$\kappa=1+\frac{\pi}{r_0^3}(a+c)\Bigg/\left\{ac-\frac{\pi}{3r_0^3}(a+c)\right\}. \quad (26$$

Then we get the values of κ as listed at Tabl VI. They are much larger than the observe values.

If we interprete this effect as apparen decrease of the polarizability of ions in th static field and define the effective polarizabi lity α^* by the relation

$$p_e=\alpha^*\left(F+\frac{4\pi}{3}P\right)=\alpha^*\frac{1}{3}(\kappa+2)F\,,$$

we obtain the values of α^* as shown in Tabl VI. We see that the values α^*/α are abou 2/3∼1/2. The apparent decrease of th polarizability in the static field was alread noticed by Seitz[9], who pointed out that th assumption $\alpha=\alpha^*$ led to the paradoxica result:

$$\kappa/\kappa_0=(\kappa+2)/(\kappa_0+2)\,.$$

Next, we shall discuss the pressure effect c the static dielectric constant[10]. Since th interaction a, b and c depend on the interioni distance, they will contribute to the pressur effect. The pressure effect of the stati dielectric constant is expressed as:

Table VI.

	p_e/F	p_x/F	$\kappa(b=0)$	α^*
LiF	1.60×10^{-24}	9.20×10^{-24}	56	0.43×10^{-24}
NaF	1.45	8.36	11.9	0.54
NaCl	4.14	12.17	15.8	1.62
NaBr	7.58	12.90	18.8	2.84
NaI	11.6	18.4	28.6	4.04

Table VII. difference = *obs.* − {(I)+(II)}

	$(1/\kappa\cdot\delta\kappa/\delta P_r)_{obs.}$	$1/\rho$	(I)	(II)	difference	qr_0
LiF	-0.45×10^{-5}	$3.46\ \times10^{8}$	0.469×10^{-5}	-0.800×10^{-5}	-0.12×10^{-5}	4.8
NaCl	-0.98×10^{-5}	3.067×10^{8}	0.873×10^{-5}	-1.485×10^{-5}	-0.37×10^{-5}	5.3

$$\frac{1}{\kappa}\frac{\delta\kappa}{\delta P_r}=\frac{1}{\kappa}\left(\frac{\delta\kappa}{\delta r_0}\right)\left(\frac{\delta r_0}{\delta P_r}\right)$$

$$=-\frac{1}{\kappa}\left(\frac{\beta}{3}\times10^{6}r_0\right)\frac{\delta\kappa}{\delta r_0} \qquad (27\cdot1)$$

and

$$\frac{\delta\kappa}{\delta r_0}=-\frac{(\kappa-1)(\kappa+2)}{r_0}-\frac{8\pi}{F^2}\left[\frac{da}{dr_0}p_e^2+\frac{db}{dr_0}p_ep_x\right.$$

$$\left.+\frac{dc}{dr_0}p_x^2\right]\frac{1}{2r_0^3}\,. \qquad (27\cdot2)$$

The derivation of Eq. (27) is given in Appendix II. In Eq. (27) da/dr_0 was already computed, that is, $-pA(r_0)/(4\bar{r}^2)$; and if we express the repulsive potential between the nearest neighbouring ions by constant $\times\exp(-r/\rho)$ as usual, dc/dr_0 is given by

$$\frac{dc}{dr_0}p_x^3=\frac{dC}{dr_0}x^2=-\frac{2e^2\alpha_M}{3r_0^3}\left(\frac{r_0}{\rho^2}-\frac{2}{\rho}-\frac{2}{r_0}\right)x^2\,.$$

Finally, if we assume the functional form of B as constant $\times\exp(-qr)$, db/dr becomes: $db/dr_0=-qb(r_0)$. Thus we have the final expression of $(1/\kappa)(\delta\kappa/\delta P_r)$:

$$\frac{1}{\kappa}\frac{\delta\kappa}{\delta P_r}=\frac{1}{\kappa}\left(\frac{1}{r_0}\frac{\delta r_0}{\delta P_r}\right)\Bigg[\{-(\kappa-1)(\kappa+2)\}$$

$$+\frac{8\pi}{2r_0^3F^2}\left\{\frac{2e^2\alpha_M}{3r_0^2}\left(\frac{r_0}{\rho^2}-\frac{2}{\rho}-\frac{2}{r_0}\right)\left(\frac{p_x}{2e}\right)^2\right\}$$

$$+\frac{8\pi}{2r_0^3F^2}\{r_0pap_e^2\}+\frac{8\pi}{2r_0^3F^2}\{r_0qbp_xp_e\}\Bigg]$$

$$\equiv(\mathrm{I})+(\mathrm{II})+(\mathrm{III})+(\mathrm{IV})\,. \qquad (28)$$

Here we shall discuss the physical meaning of each term of Eq. (28). When the volume of the crystal decreases under the hydrostatic pressure, the density of dipoles increases. The term (I) expresses this density effect. On the other hand, when the interionic distance decreases, the interionic interaction energy increases. This effect works to hinder the deformation of ions or displacement of ions. The term (II) expresses the effect caused by the increase of the usual repulsive potential energy, the term (III) expresses the effect caused by the increase of the interaction $A\lambda^2$, which is found to be much smaller than the others, and the last term (IV) expresses the effect caused by the increase of the interaction $Bx\lambda$. The term (I) is positive and others are negative. Using the values p_x, p_e determined before and the value of ρ determined by Born and Mayer[11]) we obtain the results as shown in Table VII. From Table we see that the effects of (I) and (II) are not sufficient to explain the pressure effect. If we assume that this difference is caused only by the effect (IV), we can determine the parameter q so as to fit the theoretical value to the observed value. The values of (qr_0) are also tabulated. Since the difference

$$[\{(1/\kappa)(\delta\kappa/\delta P_r)\}_{obs}-(\mathrm{I})-(\mathrm{II})]$$

lies well outside the region of the experimental error, the pressure effect may also suggest the existence of the B term.

§ 4. Frequency of Lattice Vibration

We have determined the three constant a, b and c by using the three observed quantities κ, κ_0, and β. Then the fundamental equation (2) contains no arbitrary constant any more. Now, using these constants we are able to compute other observable quantities without arbitrary assumptions. In this section we compute the frequency of the lattice vibration. The frequency of the lattice vibration of NaCl was computed in detail by Lyddane and Herzfeld[12]) However, there remain some ambiguous points in their computation, because they had not any precise knowledge about the relation between the lattice vibration and the lattice polarization.

According to L–H. the frequency of the transverse long wave in the optical mode is given by:

$$\omega_t^2=\left(\frac{4\pi e^2}{\mu r_0^3}\right)\left\{C_1+2C_2-\frac{1}{6-k}\right\} \qquad (29)$$

and that of the longitudinal long wave is also given by:

$$\omega_l^2=\left(\frac{4\pi e^2}{\mu r_0^3}\right)\left\{C_1+2C_2+\frac{1}{3+k}\right\}, \qquad (30)$$

where μ is the reduced mass of two ions and $k=(4\pi\alpha_n/r_0^3)$. The force constant (C_1+2C_2) in their notation is to be related to our force constant C by:

$$(4\pi e^2/r_0^3)(C_1+2C_2)=C/2\,. \qquad (31)$$

Taking $C_1=0.4220$ and $C_2=-0.0427$, they found that the computed value of ω_t was $2.40\times10^{13}\,\text{sec}^{-1}$ with the assumption of $\alpha_n=2.90\times10^{-24}$ and $3.08\times10^{13}\,\text{sec}^{-1}$ with the assumption of $\alpha_n=0$. Observed value of ω_t of NaCl is about $3.0\times10^{13}\text{sec}^{-1}$. Thus they found that the assumption of $\alpha_n=0$ gave the good result, but they did not know the reason. On the other hand, their computed value of the frequency of the longitudinal wave ω_l was $5.54\times10^{13}\text{sec}^{-1}$ with the assumption of $\alpha_n=2.90\times10^{-24}$ and $6.12\times10^{13}\text{scc}^{-1}$ with the assumption of $\alpha_n=0$. In the former case $(\omega_l/\omega_t)^2$ becomes 5.33, and in the latter case it becomes 3.95. However, it is well known that there exists the relation $(\omega_l/\omega_t)^2=(\kappa/\kappa_0)$, which tells us that $(\omega_l/\omega_t)^2$ is 2.49. Thus it is obvious that the relation between the lattice vibration and the polarization must be investigated more carefully. In the following we shall complement their computation by taking account of the electronic polarization. We shall let $\vec{r}(l,k)$ be the vector which represents the equilibrium position of the k-th ion in the l-th lattice cell and $\vec{u}(l,k)$ be the variable that measures the displacement of the (l,k) ion from its equilibrium position. Here $k=1$ refers to the positive ion and $k=2$ refers to the negative ion. Let us further denote the force acting on (l,k) ion by $K(l,k)$. Then the equation of the motion is

$$m_K\frac{d^2\vec{u}(l,k)}{dt^2}=\vec{K}(l,k)\,, \qquad (32)$$

whose solution must satisfy the usual periodic boundary conditions. This equation has the solution of the type:

$$\vec{u}(l,k)=\vec{U}(k)\exp\{-i\omega t+i(\vec{S}\cdot\vec{r}(l,k)\} \qquad (33)$$

where $\vec{S}$ is the wave-number vector of the lattice vibration and ω is the frequency. The force $\vec{K}(l,k)$ consists of three parts:

$$\vec{K}(l,k)=(e_K\vec{F}(k)+\vec{R}(k)+\vec{T}(k))$$
$$\times\exp\{-i\omega t+i(\vec{S}\cdot\vec{r})\}\,. \qquad (34)$$

Here $e_k\vec{F}(k)$ is ths electrostatic force, $\vec{R}(k)$ is the usual repulsive force and $\vec{T}(k)$ is a sort of the repulsive force accompanying the electronic polarization of ions. In the H–L theory $\vec{F}(k)$ and $\vec{R}(k)$ were taken into account but $\vec{T}(k)$ was not.

(I) *transverse long wave*

At first we investigate the transverse wave. Disregarding the polarization due to the ion-deformation $F(k)$ was obtained by H–L. as follows:

$$F(1)=F(2)=\frac{1}{6}\left(\frac{4\pi e}{r_0^3}\right)\Big(U(1)-U(2)\Big)$$
$$=\frac{4\pi}{3}\frac{p_d}{2r_0^3}\,, \qquad (35)$$

where e is the absolute value of the electron charge and

$$p_d=e(U(1)-U(2)) \qquad (36$$

is the polarization per ion pair due to the ion-displacement. Next, we shall consider the polarization p_e due to the deformation of the negative ion. Since the direction of the force is the same as the direction of the displacement in the case of the transverse wave, the Lorentz force caused by the displacement acts to polarize the charge cloud of the negative ion to the same direction. Thus the electrostatic force $\vec{F}(k)$ becomes:

$$eF(1)=\frac{1}{6}\left(\frac{4\pi e^2}{r_0^3}\right)\Big(U(1)-U(2)\Big)+\frac{4\pi e}{3}\frac{1}{2r_0^3}p_e \qquad (37\cdot1$$

and

$$(-e)F(2)=\frac{-1}{6}\left(\frac{4\pi e^2}{r_0^3}\right)\Big(U(1)-U(2)\Big)$$
$$-\frac{4\pi e}{3}\frac{1}{2r_0^3}p_e\,. \qquad (37\cdot2)$$

The repulsive force $\vec{R}(k)$ was given by L–H.:

$$R(1)=-R(2)$$
$$=-\left(\frac{4\pi e^2}{r_0^3}\right)(C_1+2C_2)(U(1)-U(2))\,. \qquad (38)$$

In the preceeding section we saw that the energy change due to the interaction of ion-displacement and ion-deformation was $Bx\lambda$ or bp_xp_e, when the relative displacement of ions was $2x$. Thus we find the force $\vec{T}(k)$ is given by:

$$T(k)=\left(\frac{B}{2}\right)\lambda=bp_e\,. \qquad (39$$

Since the motion of ions is slow enough as compared with the electron motion, the parameter λ or p_e should be determined by the minimum condition of the deformation energy

$$\partial\Delta E/\partial p_e=0\,, \qquad (40$$

where ΔE is:

$$\Delta E = -\frac{4\pi}{3}\frac{1}{2r_0^3}p_a p_e + b p_a p_e + a p_e^2$$

$$-\frac{1}{2}\frac{4\pi}{3}\frac{1}{2r_0^3}p_e^2 . \qquad (41)$$

The result is:

$$p_e = \left(\frac{b}{2} - \frac{\pi}{3r_0^3}\right)p_a \Big/ \left(a - \frac{\pi}{3r_0^3}\right) . \qquad (42)$$

Inserting Eqs. (37), (38) and (39) into Eq. (32) we obtain the following simultaneous equations concerning $U(1)$ and $U(2)$.

$$-m_1\omega_t^2 U(1) = -\left(\frac{4\pi e^2}{r_0^3}\right)$$

$$\times\left\{C_1 + 2C_2 - \frac{1}{6} - \frac{r_0^3}{4\pi}D\right\}\Big(U(1) - U(2)\Big) , \qquad (43\cdot 1)$$

$$-m_2\omega_t^2 U(2) = \left(\frac{4\pi e^2}{r_0^3}\right)$$

$$\times\left\{C_1 + 2C_2 - \frac{1}{6} - \frac{r_0^3}{4\pi}D\right\}\Big(U(1) - U(2)\Big) , \qquad (43\cdot 2)$$

where D is defined by:

$$D = 2\left(\frac{b}{2} - \frac{\pi}{3r_0^3}\right)^2 \Big/ \left(a - \frac{\pi}{3r_0^3}\right) . \qquad (44)$$

Solving these equations the frequency of the transverse long wave is found to be

$$\omega_t^2 = \left(\frac{4\pi e^2}{\mu r_0^3}\right)\left(C_1 + 2C_2 - \frac{1}{6} - \frac{r_0^3}{4\pi}D\right) . \qquad (45)$$

After simple calculation it becomes:

$$\omega_t^2 = \left(\frac{4\pi e^2}{\mu r_0^3}\right)\left\{C_1 + 2C_2 - \frac{1}{6-k}\right.$$

$$\left. + \left(\frac{r_0^3}{4\pi e^3}\right)\frac{b}{a}\left(\frac{2\pi}{3r_0^3} - \frac{b}{2}\right)\right\} , \qquad (46)$$

where k is defined by:

$$k = \frac{4\pi}{r_0^3}\frac{1}{2a} = \frac{4\pi\alpha_n}{r_0^3} . \qquad (47)$$

Except for the last term Eq. (46) coinsides with Eq. (29). Since the last term is positive, it contribute to increase the frequency. In NaCl we found that D was nearly equal to zero. Then Eq. (45) becomes:

$$\omega_t^2 = \left(\frac{4\pi e^2}{\mu r_0^3}\right)\left(C_1 + 2C_2 - \frac{1}{6}\right) . \qquad (48)$$

Thus, we understand why L–H. 's computation led to the good agreement with the observation. Here we notice that the numerical value of the force constant $(4\pi e^2/r_0^3)(C_1 + C_2)$ of L–H. is somewhat different from our force constant $C/2$. Using the value of $C = 8.07 \times 10^4$ (see Table V), ω_t becomes 2.90×10^{13} sec^{-1} instead of $3{,}08 \times 10^{13}$, and if we omit b, ω_t becomes 2.10×10^{13} sec^{-1}. However, the very accurate comparison between the theoretical and the experimental value is not possible, because the experimental values which we use, were observed at the room temperature, while the theory should be concerned with the absolute zero temperature. Considering these circumstances the agreement between the theory and the experiment seems to be satisfactory.

We have determined three constants ***a***, ***b*** and c by using three experimental values κ_0, κ and β and with these constants the fourth observed quantity ω_t has been computed. Since the result is found to be good, we may conclude that our assumptions concerning the force-law, that is, (1) the interionic force has the central character and (2) the short range repulsive force is effective only between the nearest neighbouring ions, are approximately valid in NaCl. Later on we shall see that these assumptions are valid in many alkali-halide crystals. Concerning the assumption (1) one may argue that the Cauchy-Poisson relations are not valid even in alkali-halide crystals. However, if the deviation from the Cauchy-Poisson relations may be interpreted by the Lowdin's mechanism, our conclusions need not be altered as we showed in the previous paper[13]. At any rate, the amount of the deviation is rather small in alkali-halide crystals and moreover the deviation itself seems to be explained fairly well by the Lowdin's many-body forces without introducing any homopolar binding forces. Thus we may say that the assumption of the central force seems to be appropriate in alkali-halides. Concerning the assumption (2) we shall discuss in a later section.

(II) *longitudinal long wave*

Next, we discuss the longitudinal long wave. Disregarding the deformation of ions $\vec{F}(k)$ was given by L–H. as follows:

$$F(1) = F(2) = \frac{1}{3}\left(\frac{4\pi e}{r_0^3}\right)\Big(U(1) - U(2)\Big)$$

$$= -\left(\frac{8\pi}{8}\right)p_a/2r_0^3 . \qquad (49)$$

In the case of the longitudinal wave the direction of the force is opposite to the direction of the displacement of ions. The Lorentz force caused by the displacement of ions acts to polarize the charge cloud of the negative ions to the opposite direction. Thus the electrostatic force $F(k)$ becomes:

$$\begin{aligned} eF(1) &= -\frac{1}{3}\left(\frac{4\pi e^2}{r_0^3}\right)\Big(U(1)-U(2)\Big) \\ &\qquad +\frac{8\pi e}{3}\frac{1}{2r_0^3}p_e\,, \\ (-e)F(2) &= \frac{1}{3}\left(\frac{4\pi e^2}{r_0^3}\right)\Big(U(1)-U(2)\Big) \\ &\qquad -\frac{8\pi e}{3}\frac{1}{2r_0^3}p_e\,. \end{aligned} \qquad (50)$$

The repulsive force $\vec{R}(k)$ is the same as the transverse wave and $\dot{T}(k)$ is the same in magnitude but with the opposite sign.

Thus the equation of the motion is expressed as:

$$\begin{aligned} -m_1\omega_l^2U(1) &= -\frac{1}{3}\left(\frac{4\pi e^2}{r_0^3}\right)\Big(U(1)-U(2)\Big) \\ &\quad -\left(\frac{4\pi e^2}{r_0^3}\right)(C_1+2C_2)\Big(U(1)-U(2)\Big) \\ &\quad +\frac{8\pi}{3}\frac{1}{2r_0^3}p_e+bp_e \end{aligned} \qquad (51\cdot1)$$

$$\begin{aligned} -m_2\omega_l^2U(2) &= \frac{1}{3}\left(\frac{4\pi e^2}{r_0^3}\right)\Big(U(1)-U(2)\Big) \\ &\quad +\left(\frac{4\pi e^2}{r_0^3}\right)(C_1+2C_2)\Big(U(1)-U(2)\Big) \\ &\quad -\frac{8\pi}{3}\frac{1}{2r_0^3}p_e-bp_e\,. \end{aligned} \qquad (51\cdot2)$$

As is in the case of the transverse wave p_e is determined by the minimum condition of ΔE:

$$\theta\Delta E/\partial p_e=0 \qquad (52)$$

where

$$\begin{aligned} \Delta E &= -\frac{8\pi}{3}\frac{1}{2r_0^3}p_e p_a-bp_ep_a+ap_e^2 \\ &\qquad +\frac{1}{2}\frac{8\pi}{3}\frac{1}{2r_0^3}p_e^2\,. \end{aligned} \qquad (53)$$

The result is:

$$p_e=\left(\frac{b}{2}+\frac{2\pi}{3r_0^3}\right)p_a\Big/\left(a+\frac{2\pi}{3r_0^3}\right). \qquad (54)$$

Inserting Eq. (54) into Eq. (51) we obtain the following simultanious equations:

$$\left.\begin{aligned} -m_1\omega_l^2U(1) &= -\left(\frac{4\pi e^2}{r_0^3}\right)\Big(C_1+2C_2+\frac{1}{3} \\ &\qquad -\frac{r_0^3}{4\pi}D'\Big)\Big(U(1)-U(2)\Big) \\ -m_2\omega_l^2U(2) &= \left(\frac{4\pi e^3}{r_0^3}\right)\Big(C_1+2C_2+\frac{1}{3} \\ &\qquad -\frac{r_0^3}{4\pi}D'\Big)\Big(U(1)-U(2)\Big) \end{aligned}\right\} \qquad (55)$$

where D' is defined by:

$$D'=2\left(\frac{b}{2}+\frac{2\pi}{3r_0^3}\right)\Big/\left(a+\frac{2\pi}{3r_0^3}\right). \qquad (56$$

Solving these equations we obtain the frequency of the longitudinal long wave,

$$\begin{aligned} \omega_l^2 &= \left(\frac{4\pi e^2}{\mu r_0^3}\right)\Big\{C_1+2C_2+\frac{1}{3+k} \\ &\qquad -\frac{r_0^3}{4\pi e^2}\frac{b}{a}\left(\frac{b}{2}+\frac{4\pi}{2r_0^3}\right)\Big\}\,. \end{aligned} \qquad (57$$

Except for the last term Eq. (57) coinside with Eq. (30). Since the last term is negative it contributes to decrease the frequency Inserting the numerical value of C_1+2C_2 o L–H. the value ot ω_l is found to be 4.80×10^{1} $\sec^{-1}$, while it becomes $4.60\times10^{13}\sec^{-1}$, whe we use our C-value ($C=8.07\times10^4$). In both cases the relation $(\omega_l/\omega_t)^2=(\kappa/\kappa_0)$ is wel satisfied. Thus we find that the introductio of the term bp_xp_e enables us to understan the behavious of the lattice vibration.

The transverse wave of ionic crystals is very important, since it interacts with the conduction electron in ionic crystals. As is well known, the interaction between conduction electrons and lattice vibrations in ionic crystals was first investigated by Frohlich and Mott[14], and then was complemented by Callen[15], Frohlich and others[16]. According to Callen the interaction potential is given by

$$-\frac{4\pi e^*}{2r_0^3}(U^++U^-) \qquad (58$$

where U^+ and U^- are the absolute value of the displacement of the positive and negative ion respectively and e^* is defined by

$$e^*=(r_0/2\pi)(\kappa-\kappa_0/\kappa_0^2)\mu\omega_t^2. \qquad (59$$

Later on we shall also derive this equation from our formalism. Frohlich has derived another expression of the interaction[16]. The equivalence of these two expressions was proved by Fan[17] The physical meaning of e^* is clear in our theory. The polarization of the medium consists of two parts, one is the polarization due to the displacement of ions and the other is that due to the deformation of ions. In the longitudinal wave the effect of the former is partly canceled by the latter since the direction of two polarizations is opposite with each other. Thus, if we want to treat the lattice vibration as the vibration of the rigid ions, we must include the effect of the polarization of ion-cores in the form of the apparent reduction of the ionic charge. That is the meaning of the effective charge. Now, we shall compute the effective charge of NaCl. From Eq. (54) we know that p_e is equal to $1.10ex$. Thus the real polarization per ion pair is

$$p_a - p_e = 2ex - 1.10ex = 0.90ex \ ,$$

and the effective charge is found ts be

$$2e^*x = 0.90ex \quad \text{and} \quad e^*/e = 0.45 \ .$$

(III) *short waves*

The frequency of short waves of NaCl was computed by L–H. for three cases:

(1) $S = (\pi/2r_0,\ \pi/2r_0,\ \pi/2r_0)$
(2) $S = (\pi/r_0,\ 0,\ 0)$ and
(3) $S = (\pi/r_0,\ \pi/2r_0,\ 0)$.

However, they computed them disregarding the deformation of ions. The assumption of rigid-sphere ions is found to be not good in long waves. Now we want to know whether this approximation is good or not in the case of short waves. Taking the deformation of ions into account we have recalculated the frequency of short waves for above three cases. The procedures of computation are given in Appendix III. Here we show only the results. (See Table VIII). In case (1) the motion of positive ions and that of negative ions are independent. In short waves optical modes and acoustical modes are mixed. In Table VIII the second row shows the results which are obtained by using the previously determined constants. The third row shows the results obtained without b. The last row shows the results obtained by L–H. from the rigid sphere approximation ($b=0$ and $\alpha=0$). Comparing the second row with the fourth row we see that the rigid sphere approximation is rather good, but not very good even in short waves.

§ 5. Extension to More General Cases

Hitherto we discussed the dielectric properties of the materials, in which the polarizability of the positive ion is much smaller than that of the negative ion. Although the general aspects of the dielectric properties of ionic crystals are comprehensible by those special examples, it is still desirable to extend the theory to more general cases.

In general, we assume that the energy change of the system due to the electric field is given by:

$$\begin{aligned} N\varDelta E = N\Big[& -F(p_1+p_2+p_x) - \frac{1}{2}\frac{4\pi}{3}N(p_1+p_2 \\ & +p_x)^2 + a_1p_1^2 + a_2p_2^2 + a_{12}p_1p_2 \\ & + b_1p_1p_x + b_2p_2p_x + cp_x^2 \Big] , \end{aligned} \tag{60}$$

where p_x is the dipole due to the displacement of ions and p_1 is the dipole due to the deformation of the positive ion and p_2 is the dipole due to the deformation of the negative ion, and a_1, a_2, a_{12}, b_1, b_2 and c are material constants, and the physical meaning of these constants may be comprehensible by the analogy of the previous sections. In the previous sections we started from the wave function of the type

$$\psi(\vec{r}) = \psi_0(\vec{r})\{1+\lambda f(r)\cos\theta\} \ ,$$

but the following discussions do not depend on the form of the variational functions. Here we only assume that the energy change in the electric field is expressed by the form like Eq. (60). The appropriateness of this approximation is to be justified only by the comparison with experiment.

Now, since Eq. (60) contains six material constants, we can not determine them by experimental values, unless we introduce some arbitrary assumptions. However, we shall show that from Eq. (60) we can derive useful relations between the observed quantities.

(a) *dielectric constant*

In the high frequency field $\varDelta E$ becomes:

$$\begin{aligned} \varDelta E = -F(p_1+p_2) - \frac{1}{2}\frac{4\pi}{3}N(p_1+p_2)^2 & \\ + a_1p_1^2 + a_2p_2^2 + a_{12}p_1p_2 \ . & \end{aligned} \tag{61}$$

The condition $\partial\varDelta E/\partial p_1 = 0$ and $\partial\varDelta E/\partial p_2 = 0$ lead to

$$\left.\begin{aligned} 2a_1p_1 + a_{12}p_1 - \frac{4\pi}{3}N(p_1+p_2) = F \ , \\ 2a_2p_2 + a_{12}p_1 - \frac{4\pi}{3}N(p_1+p_2) = F \ . \end{aligned}\right\} \tag{62}$$

Using the solution of these equations κ_0 is given by

$$(\kappa_0 - 1)F = 4\pi N(p_1+p_2) \ . \tag{63}$$

Next, in the static field $\varDelta E$ is given by (60), and p_1 p_2 and p_x are determined by the following equations:

$$\left.\begin{aligned} &2a_1p_1+a_{12}p_2+b_1p_x-\frac{4\pi}{3}N(p_1+p_2+p_x)=F \\ &a_{12}p_1+2a_2p_2+b_2p_x-\frac{4\pi}{3}N(p_1+p_2+p_x)=F \\ &b_1p_1+b_2p_2+2cp_x-\frac{4\pi}{3}N(p_1+p_2+p_x)=F \end{aligned}\right| \tag{64}$$

and κ is given by:

$$(\kappa-1)F=4\pi N(p_1+p_2+p_x)\,. \tag{65}$$

Here we introduce the following functions

$$\left.\begin{aligned} &[K_1{}^0(q;p_1,p_2)]\equiv 2a_1p_1+a_{12}p_2+\frac{4\pi N}{3}q(p_1+p_2) \\ &[K_2{}^0(q;p_1,p_2)]\equiv a_{12}p_1+2a_2p_2+\frac{4\pi N}{3}q(p_1+p_2) \end{aligned}\right\} \tag{66}$$

and

$$[B_0(q)]\equiv(1/3)\{(\kappa_0+2)+q(\kappa_0-1)\}\,, \tag{67}$$

where q is a certain parameter. Using these functions Eqs. (62) are expressed as:

$$\left.\begin{aligned} &[K_1{}^0(-1;p_1,p_2)]=[B_0(-1)]F \\ &[K_2{}^0(-1;p_1,p_2)]=[B_0(-1)]F \end{aligned}\right\} \tag{68}$$

Since

$$\frac{\partial}{\partial q}\{[K_1{}^0(q;p_1,p_2)]-[B_0(q)]F\} =-\frac{1}{3}\{(\kappa_0-1)F-4\pi P\},$$

for p_1 and p_2, which satisfy the condition $(\kappa_0-1)F=4\pi P$, the following equations are always satisfied.

$$\left.\begin{aligned} &[K_1{}^0(q;p_1,p_2)]=[B_0(q)]F \\ &[K_2{}^0(q;p_1,p_2)]=[B_0(q)]F \end{aligned}\right\} \tag{69}$$

Corresponding to Eq. (66) let us define the functions:

$$\left.\begin{aligned} [K_1(q;p_1,p_2,p_x)]&\equiv 2a_1p_1+a_{12}p^2+b_1p_x \\ &\quad+\frac{4\pi N}{3}q(p_1+p_2+p_x) \\ [K_2(q;p_1,p_2,p_x)]&\equiv a_{12}p_1+2a_2p_2+b_2p_x \\ &\quad+\frac{4\pi N}{3}q(p_1+p_2+p_x) \\ [K_3(q;p_1,p_2,p_x)]&\equiv b_1p_1+b_2p_2+2cp_x \\ &\quad+\frac{4\pi N}{3}q(p_1+p_2+p_x) \end{aligned}\right| \tag{70}$$

and

$$[B(q)]=(1/3)\{(\kappa+2)+q(\kappa-1)\}\,. \tag{71}$$

Then for p_1, p_2 and p_x, which satisfy the condition

$$(\kappa-1)F=4\pi N(p_1+p_2+p_x)\,,$$

the following equations are always satisfie without regard to the value of q.

$$\begin{aligned} [K_1(q;p_1,p_2,p_x)]&=[K_2(q;p_1,p_2,p_x)] \\ &=[K_3(q;p_1,p_2,p_x)]=[B(q)]F\,. \end{aligned} \tag{72}$$

(b) *lattice vibration*

When long waves propagate in the lattice the lattice is polarized. Denoting the polarization by p_1, p_2 and p_x the energy change i given by:

$$\begin{aligned} \varDelta E(q)=a_1p_1{}^2+a_2p_2{}^2+cp_x{}^2+a_{12}p_1p_2+b_1p_1p_x \\ +b_2p_2p_x+\frac{1}{2}\frac{4\pi}{3}Nq(p_1+p_2+p_x)^2, \end{aligned} \tag{73}$$

where q is a certain parameter. The values $q\equiv-1$, 2 and 0 correspond to the transverse wave, the longitudinal wave and the homogeneous vibration of a sphere respectively.

Since the motion of ions is slow enough as compared with the motion of electrons, the state of electronic polarization follows instantaneously with the motion of ions. Thus, the electronic polarization is determined by the conditions:

$$\partial\varDelta E(q)/\partial p_1=0 \quad\text{and}\quad \partial\varDelta E(q)/\partial p_2=0\,, \tag{74}$$

$$\text{or}\quad [K_1(q;p_1,p_2,p_x)]=0 \quad\text{and}\quad [K_2(q)]=0\,. \tag{74'}$$

Solving these equations p_1 and p_2 are expressed by certain functions of p_x:

$$p_1=g_1(q)p_x \quad\text{and}\quad p_2=g_2(q)p_x\,. \tag{75}$$

Inserting these functions into

$$[K_3(q;p_1,p_2,p_x)]\equiv\partial\varDelta E(q)/\partial p_x\,, \tag{76}$$

$[K_3(q)]$ is expressed by a certain linear function of p_x,

$$(K_3(q)]_{p_1=g_1(q)p_x,\ p_2=g_2(q)p_x}=f(q)p_x\,. \tag{76'}$$

$[K_3(q)]$ is the restoring force, which acts to draw back the ion to the equilibrium point. Thus the frequency of the vibration is determined by:

$$\omega^2(q)=e^2f(q)/\mu\,. \tag{77}$$

After some computations, which are written in Appendix IV (a), we obtained the following relation.

$$\frac{\omega^2(q)}{\omega^2(0)}=\frac{f(q)}{f(0)}=\frac{(\kappa+2)+q(\kappa-1)}{(\kappa_0+2)+q(\kappa_0-1)}\cdot\frac{\kappa_0+2}{\kappa+2}\,. \tag{78}$$

From (78) the following relations are derived,

$$\omega_t{}^2=\{\kappa_0+2)/(\kappa+2)\}\omega(0)^2\,, \tag{79}$$

and

$$\omega_l{}^2=(\kappa/\kappa_0)\{(\kappa_0+2)/(\kappa+2)\}\omega(0)^2\,, \tag{80}$$

and from these we have the well-known relation:

$$\omega_l^2/\omega_t^2=\kappa/\kappa_0\ . \tag{81}$$

As is mentioned in the previous section, if ions were presumed as the rigid sphere, the polarization accompanying the lattice vibration would be given by Zex, where x is the relative displacement of ions of opposite signs. In actual cases, however, ions are deformable, and both ions polarize when the displacement of ions produces an electric field. Moreover, even when the polarization does not bring forth any polarizing field, ($q=0$), the electronic polarization of both ions by no means vanishes, because there is the connection between the displacement of ions and the deformation of ions, which is expressed by the terms $b_1p_1p_x$ and $b_2p_2p_x$. Thus the total polarization is not Zex, but $Zex+p_1+p_2=p_x+p_1+p_2$. In order to describe the motion of the system as if rigid-sphere ions were vibrating, we must introduce the so-called effective charge $e^*(q)$, which is defined by $Ze^*(q)x=p_1+p_2+p_x$. As is seen from the definition, $e^*(q)$ is the function of q, that is, $e^*(q)$ has the different value in each different mode. The fact that (e^*/e) is smaller than one even in the case $q=0$ indicates that an electronic polarization in the opposite direction is induced by the short range interactions $b_1p_1p_x$ and $b_2p_2p_x$.

In Appendix IV (b) we have derived the following relation:

$$\omega(q)^2=\frac{Z^3e^*(q)^2}{\mu}\frac{4\pi N}{9(\kappa-\kappa_0)}\times\{(k+2)+q(\kappa-1)\}\{(\kappa_0+2)+q(\kappa_0-1)\}\ . \tag{82}$$

From (82) we find:

$$\omega(0)^2=\frac{Z^2e^*(0)^2}{\mu}\frac{2\pi}{r_0^3}\frac{(\kappa+2)(\kappa_0+2)}{9(\kappa-\kappa_0)}\ . \tag{83}$$

Using the relation (79) we obtain:

$$\omega_t^2=\frac{2\pi Z^2e(0)^2}{\mu r_0^3}\frac{(\kappa_0+2)^2}{9(\kappa-\kappa_0)}\ . \tag{84}$$

This important relation was first derived by Szigeti[18] by a different method. If we take $q=2$ in (82), we have:

$$\omega_l^2=\frac{Z^2e^*(2)^2}{\mu}\frac{4\pi N}{\kappa-\kappa_0}\kappa\kappa_0\ . \tag{85}$$

Using the relation (81) we obtain the relation:

$$\omega_t^2=\frac{2\pi Z^2e^*(2)}{\mu r_0^3}\frac{\kappa_0^2}{\kappa-\kappa_0}\ . \tag{86}$$

This relation was first derived by Callen, when he discussed the interaction between the lattice vibration and conduction electrons. Using (82), (84) and (86) we find:

$$e^*(2)=\{(\kappa_0+2)/3\kappa_0\}e^*(0) \tag{87}$$

and

$$e^*(-1)=\kappa_0e^*(2)=\{(\kappa_0+2)/3\}e^*(0)\ . \tag{88}$$

Finally, we introduce the following important relations, which will be used afterwards. The derivation of these is written in Appendix IV (c).

$$\frac{(2a_2-a_{12})b_1+(2a_1-a_{12})b_2}{2(a_1+a_2-a_{12})}=\frac{\kappa_0+2}{\kappa_0+1}\left\{1-\frac{e^*(0)}{e}\right\}\frac{4\pi}{3}N\ , \tag{89}$$

and

$$c=\frac{\mu}{2Z^2e^2}\frac{\kappa+2}{\kappa_0+2}\omega_t^2+\frac{1}{2}\frac{4\pi}{3}N\frac{\kappa_0+2}{\kappa_0-1}\times\left\{1-\frac{e^*(0)}{e}\right\}^2+\frac{(b_1-b_2)^2}{4(a_1+a_2-a_{12})}\ . \tag{90}$$

§ 6. Estimation of the Magnitude of Constants

Eq. (60) contains too many constants to be determined from available experimental data. In this section, however, we shall attempt to find some general tendencies about the magnitude of constants from the experimental facts. We begin with the optical dielectric constant. If we neglect the term $a_{12}p_1p_2$, Eqs. (62) become

$$\left.\begin{aligned}2a_1p_1&=F+\frac{4\pi}{3}N(p_1+p_2)\\2a_2p_2&=F+\frac{4\pi}{3}N(p_1+p_2)\ ,\end{aligned}\right\}$$

where the right hand side of these equations is the Lorentz field. Thus, using Eqs. (12) and (13) p_1 and p_2 become

$$\left.\begin{aligned}p_1&=F_{eff}/2a_1=\alpha_pF_{eff}\\p_2&=F_{eff}/2a_2\equiv\alpha_nF_{eff}\end{aligned}\right\} \tag{91}$$

The constants a_1 and a_2 consist of two parts A_0 and A (cf. Eq. (9)). A_0 does not depend on the mutual interaction of ions, while A does. As we have seen that A_0 is much larger than A in some alkali-halide crystals, we expect that it is the general character of the alkali-halides. The constant a_{12} depends only on the mutual interaction of ions. It then follows that a_{12} is much smaller than a_1 or a_2. Further, we expect also that A takes a nearly constant value for each ion and is not very sensitive to the partner ions, because we know that the interaction constant C satisfies this condition approximately. Then we are led to the additivity-rule of the optical polarizability, which is widely recognized by Shockley and others in alkali-halides. Thus we assume here that $a_1(=1/2\alpha_p)$ and $a_2(=1/2\alpha_n)$ have the values which were determined by Shockley[6].

Since we know from Table V that $b^2/4a$ is much smaller than $(4\pi N/6)(\kappa_0+2)/(\kappa_0-1)$ in light alkali-halides, we may suppose that the last term of (90) is in general much smaller than other terms and may be neglected. Then we obtain the following relation

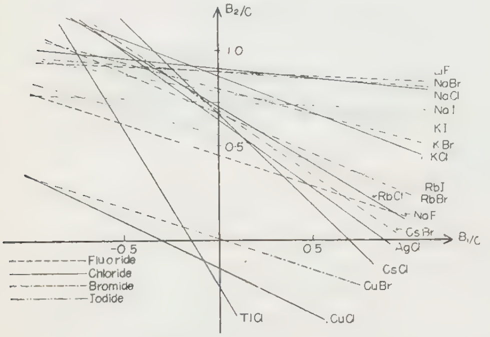

Fig. 1.

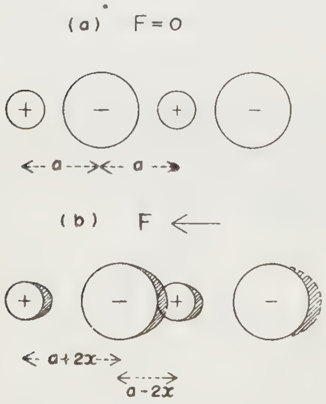

Fig. 2. Polarization of positive and negative ions.

$$c=\frac{\mu}{2Z^2e^2}\frac{\kappa+2}{\kappa_0+2}\omega_t^2+\frac{1}{2}\frac{4\pi N}{3}\frac{\kappa_0+2}{\kappa_0-1}\times\left\{1-\frac{e^*(0)}{e}\right\}^2 . \qquad (92)$$

The right side of this equation contains only observable quantities, because $e^*(0)$ is also expressed by observable quantities. Szigeti[19] also computed c by another method and obtained the very similar relation

$$c=\frac{\mu}{2Z^2e^2}\frac{\kappa+2}{\kappa_0+2}\omega_t^2 . \qquad (93$$

The difference between (92) and (93) is no remarkable, because the second term of (92 is much smaller than the first. In Table I we show both values of c for many ioni crystals.

Next, if we neglect a_{12}, then Eq. (89) be comes:

Table VIII. s: single mode, d: double mode, unit: 10^{13}sec^{-1}. The upper is the results of ours, the lower is those of L–H. and the middle is those obtained by the assumption of $b=0$. (+) shows the frequency of the positive ion and (−) shows that of the negative ion.

	Case 1.	Case 2.	Case 3.
(+)	4.59 (s) 2.56 (d)	3.51 (s) 2.72 (s)	2.38 (s) 3.05 (s)
(−)	2.97 (s) 2.06 (d)	3.24 (d) 1.62 (d)	3.37 (d) 2.33 (d)
(+)	4.59 2.56	3.24 1.02	2.42 3.05
(−)	3.41 1.79	2.49 1.18	2.89 1.29
(+)	4.59 2.56	4.26 3.21	2.46 3.05
(−)	3.71 2.06	3.27 1.83	3.55 2.82

Table IX.

	c	c (Szigeti)
LiF	1.82×10^{23}	1.76×10^{23}
NaF	1.75	1.73
NaCl	0.96	0.86
NaBr	0.81	0.71
NaI	0.66	0.60
KCl	0.82	0.77
KBr	0.73	0.67
KI	0.61	0.55
RbCl	0.77	0.74
RbBr	0.69	0.66
RbI	0.63	0.59
AgCl	1.11	1.07
CsCl	0.71	0.69
CsBr	0.66	0.63
TlCl	1.35	1.35
CuCl	2.25	2.23
CuBr	2.29	2.29

$$a_2b_1+a_1b_2=(a_1+a_2)\frac{\kappa_0+2}{\kappa_0+1}\left\{1-\frac{e^*(0)}{e}\right\}\frac{4\pi N}{3}\ . \tag{94}$$

Since we know values of a_1, and a_2 and $e^*(0)$, we can regard Eq. (94) as a linear relation between b_1 and b_2. Fig. 1 shows the relation between b_1/c and b_2/c. The remarkable characteristic of this figure is that many straight lines (95) concentrate in the region

$$b_1/c=-0.2\sim-0.4 \quad \text{and} \quad b_2/c=0.8\sim1.0.$$

Although it is not convincing, we suppose that values of b_1/c and b_2/c of many alkali-halides lie in the above mentioned region.

From this point of view, CuCl and CuBr are rather exceptional substances, while TlCl is the ordinary one, although these substances have large dielectric constants. The reason why TlCl has the large dielectric constant may be attributed to the large polarizability of Tl ion.

We have already mentioned that the ionic displacement in the static field acts to hinder the polarization of the charge cloud of a negative ion, because a negative ion must polarize in the region where the overlap becomes larger. On the other hand, we expect that the polarization of a positive ion becomes easier in a static field, because an ion polarizes in the region where the ionic distance becomes wider. (cf. Fig. 2) From the above mentioned reason we may expect that the sign of b_1 is negative and the sign of b_2 is positive. Moreover, since b_1 and b_2, and c are caused by the overlap of ions, they must not be utterly independent of each other. Thus, we may have some reason to expect that b_1/c and b_2/c of many alkali-halides have nearly constant values.

Next, if we draw a line which passes a point in the region ($b_1/c=-0.2\sim-0.4$; $b_2/c=0.8\sim1.0$) and has the derivative $-a_2/a_1$, the distance from the origin to the line is related to $\{1-e^*(0)/e\}$. We see from Fig. 1 that, when we proceed from Li to Cs for a fixed halogen ion, or from *I* to *F* for a fixed alkali ion, the distance becomes smaller and $e^*(0)$ becomes larger.

We have already mentioned that the additivity rule is well established experimentally about the optical polarizability of ions. Moreover, Roberts found the similar additivity rule about the static dielectric constant. If α_s is defined by

$$\frac{\kappa-1}{\kappa+2}=\frac{4\pi}{3}N\alpha_s \tag{95}$$

the values of α_s in many alkali-halides can be approximately separated into two parts

$$\alpha_s=\alpha_{sp}+\alpha_{sn}\ ,$$

where the static polarizability of each positive ion α_{sp}, or each negative ion α_{sn} has its own characteristic value. Of course, we can not explain this additivity rule from the purely theoretical standpoint. But it is very interesting to make clear the inter-relation between Roberts' rule and our theory. In the following we shall investigate this problem. From (64) and (65) α_s is given by:

$$\alpha_s=\frac{\begin{vmatrix} 2(a_1+c-b_1), & 2c+a_{12}-b_1-b_2 \\ 2c+a_{12}-b_1-b_2, & 2(a_2+c-b_2) \end{vmatrix}}{\begin{vmatrix} 2a_1 & a_{12} & b_1 \\ a_{12} & 2a_2 & b_2 \\ b_1 & b_2 & 2c \end{vmatrix}}\ . \tag{96}$$

If we neglect a_{12} and $(b_1-b_2)^2/4a_1a_2$, it becomes:

$$\alpha_s=\frac{\frac{1}{2}\left\{\frac{1}{c}+\frac{1}{a_1}+\frac{1}{a_2}-\frac{b_1}{a_1c}-\frac{b_2}{a_2c}\right\}}{\left\{1-\frac{b_1{}^2}{4a_1c}-\frac{b_2{}^2}{4a_2c}\right\}}\ . \tag{97}$$

Since $b_i{}^2\ll 4a_ic$, it becomes approximately:

$$\alpha_s=\frac{1}{2c}+\frac{1}{2a_1}\left(1-\frac{b_1}{2c}\right)^2+\frac{1}{2a_2}\left(1-\frac{b_2}{2c}\right)^2 . \tag{98}$$

We have already assumed that b_1/c and b_2/c are nearly constant for the most of alkali-halides, and a_1 and a_2 are also nearly constant. And the additivity concerning c may be easily verified by the properties of the repulsive potential of Born and Mayer. According to them the repulsive potential is given by

$$R(r)=b\exp\{-(r-r_1-r_2)/\rho\}\ , \tag{99}$$

where r_1 or r_2 is a characteristic constant of each ion, ρ is a constant which has a common value 0.345×10^{-8}cm. for all alkali-halides and b has also a common value 4×10^{-12}erg. Thus $1/2c$ becomes:

$$1/2c=\exp\{(r_0-r_1-r_2)/\rho\}\Big/2b\left(\frac{1}{\rho^2}-\frac{2}{\rho r_0}\right). \tag{100}$$

As is well known the distance r_0 is given approximately by the sum of the ionic radius of two ions r_{01} and r_{02},

$$r_0=r_{01}+r_{02}\ .$$

Table X.

	$1/2c$	$\frac{1}{2a_1}\left(1-\frac{b_1}{2c}\right)$	$\frac{1}{2a_2}\left(1-\frac{b^2}{2c}\right)$	Sum	α_s from (95)
LiF	2.7×10^{-24}	0.0×10^{-24}	0.3×10^{-24}	3.0×10^{-24}	2.8×10^{-24}
NaF	2.9	0.4	0.3	3.6	3.7
NaCl	5.2	0.4	1.1	6.7	6.5
NaBr	6.2	0.4	1.5	8.1	7.9
NaI	7.6	0.4	2.3	10.3	10.5
KCl	6.1	1.5	1.1	8.7	8.1
KBr	6.8	1.5	1.5	9.8	9.6
KI	8.2	1.5	2.3	12.0	11.9
RbCl	6.5	2.4	1.1	10.0	9.5
RbBr	7.3	2.4	1.5	11.2	11.0
RbI	7.9	2.4	2.3	13.4	13.4
AgCl	4.5	2.9	1.1	8.5	8.1
CsCl	7.0	3.9	1.1	12.0	11.2
CsBr	7.6	3.9	1.5	13.0	12.2
TlCl	3.7	6.6	1.1	11.4	12.3
CuCl	2.2	1.9	1.1	5.2	7.1
CuBr	2.2	1.9	1.5	5.6	7.7

If we denote the average values of $r_{01}-r_1$ and $r_{02}-r_2$ for all alkali and halogen ions by $\overline{(r_{01}-r_1)}$ and $\overline{(r_{02}-r_2)}$ respectively and put

$$r_{01}-r_1=\overline{r_{01}-r_1}+\delta r_1$$
$$r_{02}-r_2=\overline{r_{02}-r_2}+\delta r_2 \ ,$$

then δr_1 and δr_2 are rather small and do not much depend on partner ions. Thus it becomes:

$$\exp\{(r_0-r_1-r_2)/\rho\}=\exp\{(\overline{r_{01}-r_1}+\overline{r_{02}-r_2})/\rho\}$$
$$\times\{e^{\delta r_1/\rho}+e^{\delta r_2/\rho}-1+(e^{\delta r_1/\rho}-1)(e^{\delta r_2/\rho}-1)\} \ .$$

Since the last term is expected to be very small, we obtain an interpretation of the Roberts' additivity rule.

Putting $(1-b_1/2c)=1.3$ and $(1-b_2/c)=0.3$ and using Shockley's values for a_1 and a_2, and determinig c from (25) we have obtained the computed value of α_s from (98). The values are shown in Table X, where the values of α_s computed from (95) with observed values of κ are also tabulated.

§ 7. Determination of the Interionic Potential

In the preceeding section we mentioned that Szigeti and we determined the force constant between the nearest neighbouring ions ; where the procedures do not depend on the existence of the repulsive force between the next nearest neighbours. Now, if one adds one more assumption that the short range repulsive for is effective only between the nearest neig bouring ions, then the relation (25) is easi derived. From (25) and (93) Szigeti[19] h derived the following equation

$$\frac{1}{\beta}=\frac{\kappa+2}{6(\kappa_0+2)}\frac{\mu\omega_t^2}{r_0} \ , \qquad (10$$

and compared the computed values of co pressibility β with the observation. Since t agreement is good for many alkali-halide we may conclude that the assumption of t nearest neighbour interaction is approximate valid for many alkali-halides.

If we express the potential between t nearest neighbouring ions and the next neare neighbours as

$$U=-z^2e^2/r+p\exp(-r/\rho) \ ,$$
$$V=z^2e^2/r+q\exp(-r/\sigma\sqrt{2}) \qquad (10$$

respectively, (the so-called Van der Wa energy is included approximately in the sh range part of the potential), then four co stants in (102) are determined by the follo ing four relations.

lattice energy ; $-z^2e^2\alpha_M/r_0+x+y=-E$

lattice constant ; $-z^2e^2\alpha_M/r_0^2+x/\rho+y/\sigma=0$

compressibility ; $-2z^2e^2\alpha_M/r_0^3+x/\rho^2$
$+y/\sigma^2=18r_0/\beta \quad (1$

Szigeti-relation ;

$$\left\{\begin{aligned} C&=(2ze)^2c=\frac{2}{3}\left(\frac{x}{\rho}\right)\left(\frac{1}{\rho}-\frac{2}{r_0}\right)\\ c&=\frac{\mu}{2e^2z^2}\frac{\kappa+2}{\kappa_0+2}\omega_t^2\end{aligned}\right.$$

$$+\frac{1}{2}\frac{4\pi}{3}\frac{1}{2r_0^3}\frac{\kappa_0+2}{\kappa_0-1}\left(1-\frac{e^*(0)}{e}\right)^2$$

where E is the lattice energy, and x and y are efined by:

$$x=6p\exp(-r_0/\rho)\,,\quad y=6q\exp(-r_0/\sigma)\,.$$

Thus we have a new method of determining he interaction constants. In the following ve shall show a few examples.

a) NaCl

We have already shown that we can fit the above equations (103) with the assumption of $q=0$.

b) MgO

As to the static dielectric constant of MgO, our procedure mentioned in § 3 has not succeeded in obtaining reasonable value of B. If we assume that $Bx\lambda$ is equal to $4\pi Np_xp_c/3$ and C is determined by (25), then κ becomes 52.6, which is much larger than the observed value 9.8. Therefore, we used another method, that is, we determined these constants from the three observed values κ_0, κ and ω_t instead of β. We found that the so-determined C-value is about two times larger than that determined from compressibility. In this case our two fundamental assumptions about the force, which was mentioned in 4(I), seem to be not valid. Which one of the two assumptions may be inadequate for MgO? At present we can not answer the question. However, if we assume that the origin of the discrepancy lies in the next nearest neighbour interaction, we may determine the force constants from (102). Such a treatment was given by us in another paper[20)].

c) AgCl

Since the Van der Waals force is very important in this case, we assume the following potentials:

(1) (Ag···Ag) $\quad -\dfrac{c_1}{r^6}-\dfrac{d_1}{r^8}$

(2) (Ag···Cl) $\quad A\exp\{-r/\rho\}-\dfrac{c_2}{r^6}-\dfrac{d_2}{r^8}$

(3) (Cl···Cl) $\quad B\exp\{-r/\sigma\}-\dfrac{c_3}{r^6}-\dfrac{d_3}{r^8}\,.$

Here we suppose that the interaction between the nearest neighbours is much more important than that of the next nearest neighbours. Under these assumptions we may take Mayer's[21)] value for the constants between the second neighbouring ions and d_2

$$\left\{\begin{aligned} d_1&=150\times10^{-76}\ \text{erg cm}^8\\ d_2&=268\times10^{-76}\quad ''\\ d_3&=\ \ 91\times10^{-76}\quad ''\end{aligned}\right.$$

$$\left\{\begin{aligned} c_1&=\ \ 67\times10^{-60}\ \text{erg cm}^6\\ c_3&=133\times10^{-60}\quad ''\\ B&=0.449\times10^{-8}\ \text{erg}\\ \sigma&=0.345\times10^{-8}\ \text{cm}\end{aligned}\right.$$

Also Mayer has determined the value of c_2 as 91×10^{-60} erg cm^6; we think, however, that some caution is necessary before determining the value c_2, because Jost-and Nehlep's result[22)] shows us that the van der Waals energy plays an important role in silver halide crystals. Now, if we once assume the value of c_2, then we have only two unknown constants, A and ρ. On the other hand, there are four experimental quantities which serve to determine them; those are lattice energy, lattice constant, compressibility and the Szigeti's relation.

$$\left(\frac{1}{\rho^2}-\frac{2}{r_0\rho}\right)Ae^{-r_0/\rho}-\frac{30.7c_2}{r_0^8}=\frac{\mu}{2}\frac{\kappa+2}{\kappa_0+2}\omega_t^2.$$

Then we tentatively chose three values for c_2, and have determined A and ρ by the least square method using all four quantities.

The results are as follows:

$$\text{(I)}\quad\left\{\begin{aligned} &c_2=91\times10^{-60}\ \text{erg cm}^6\\ &A\exp(-r_0/\rho)=0.344\times10^{-12}\ \text{erg}\\ &r^0/\rho=10.47\end{aligned}\right.$$

$$\text{(II)}\quad\left\{\begin{aligned} &c_2=136\times10^{-60}\ \text{erg cm}^6\\ &A\exp(-r_0/\rho)=0.455\times10^{-12}\ \text{erg}\\ &r_0/\rho=9.73\end{aligned}\right.$$

$$\text{(III)}\quad\left\{\begin{aligned} &c_2-64\times10^{-60}\ \text{erg cm}^6\\ &A\exp(-r_0/\rho)=0.284\times10^{-12}\ \text{erg},\\ &r_0/\rho=11.11\,.\end{aligned}\right.$$

Although each value of the repulsive energy and the van der Waals energy is different in the above three sets, the potential energy (sum of two terms) is almost the same (within 5%) in three cases from $r=0.8$ to $1.1\,r_0$.

Now, let us compute the formation energy of both the Frenkel and Schottky defects in silver chloride crystals and compare them with the observed values. For that purpose we shall use the method of Mott-Littelton[23)], which has been applied to alkali-halide crystals with success. As the interaction potentials we shall adopt the set I. After the formal computation we have obtained the following results. We also refer to Mott-Littleton's results of NaCl, KCl and KBr for the purpose of the comparison. In the last column the contribution from the van der Waals energy is shown (ev. unit).

As we have determined the constants based on the experimental data near the equilibrium point, we suppose that the computed value of the formation energy of the Schottky defects may be reliable. But in the case of the Frenkel defects we must not expect our potential to be entirely reliable for such small distances.

Table XI.

(I) the energy necessary for removing a positive ion to infinity.
(II) the energy necessary for removing a negative ion to infinity.
(III) the energy necessary for removing a pair of ions.
(IV) the energy necessary for removing a positive ion from infinity to $(\frac{1}{2}, \frac{1}{2}, \frac{1}{2})$.
W_L: the lattice energy per ion pair.
W_S: $W_S = W_L + \text{(III)}$; the formation energy of a Schottky defect.
W_F: $W_F = \text{(I)} + \text{(IV)}$; the formation energy of a Frenkel defect.

	NaCl	KCl	KBr	AgCl	V
(I)	4.62	4.47	4.23	5.50	1.03
(II)	5.18	4.47	4.60	5.35	1.19
(III)	9.80	9.26	8.83	10.85	2.22
W_L	−7.94	−7.19	−6.91	−8.89	−1.24
W_S	1.86	2.08	1.92	1.96	−0.98
(IV)	−1.71			−3.36	−2.37
W_F	2.91			1.83	−1.35

On the other hand, the observed value of the formation energy of the lattice defects in silver chloride crystals may be estimated as 1.5 ev. It is about 0.4 ev. smaller than the computed values of the Schottky type. Thus we may conclude that the lattice defect in silver chloride crystals at low temperature should be predominantly the Frenkel type. Also the above computation shows that the contribution from the van der Waals energy is very large, if we use Mayer's value for c_2, but as mentioned above the division of the potential energy into the repulsive energy and the van der Waals energy can not be performed uniquely from the phenomenologica standpoint; therefore it is safe to discuss th important role of the van der Waals energ with some reservation.

Finally we wish to express our sincer thanks to Prof. T. Muto for his helpful discussions.

Appendix I

Pressure effect of the high-frequency dielectri constant

Let us denote the lattice constant with zer pressure by $2r_0$ and that under the hig pressure by $2(r_0-\delta r)$. The energy change o the system due to the high frequency fiel under the hydrostatic pressure is given by:

$$(N\Delta E)=\frac{1}{2(r_0-\delta r)^3}\Big[-4\bar{r}^2\lambda F-\frac{1}{2}\frac{4\pi}{3}\frac{(4\bar{r}^2\lambda)^2}{2(r_0-\delta r)}$$
$$+\{A_0+A(r_0-\delta r)\}\lambda^2-\frac{4\pi}{3}\frac{(4\bar{r}^2\lambda)(\alpha_P F)}{2(r_0-\delta r)^3}$$
$$-\frac{1}{2}\alpha_P\left(1+\frac{4\pi}{3}\frac{\alpha_P}{2(r_0-\delta r)^3}\right)F^2\Big]. \qquad (A\cdot 1$$

The quantity A depends on the interionic distance, and we assume the simple functiona form of A as: $A(r)=\mathfrak{A}\exp(-pr)$.

Then (A·1) becomes:

$$(N\Delta E)=\frac{1}{2r_0^3}\Big[-4\bar{r}^2\lambda F-\frac{1}{2}\frac{4\pi}{3}\frac{(4\bar{r}^2\lambda)^2}{2r_0^3}$$
$$-\frac{4\pi}{3}\frac{(4\bar{r}^2\lambda)(\alpha_P F)}{2r_0^3}+\{A_0+A(r_0)\}\lambda^2$$
$$-\frac{1}{2}\alpha_P\left(1+\frac{4\pi}{3}\frac{\alpha_P}{2r_0^3}\right)F^2\Big]$$
$$+\frac{1}{2r_0^3}\Big[-4\bar{r}^2\lambda F-\frac{1}{2}\frac{4\pi}{3}\frac{(4\bar{r}^2\lambda)^2}{2r_0^3}$$
$$-\frac{4\pi}{3}\frac{(4\bar{r}^2\lambda)(\alpha_P F)}{2r_0^3}+\{A_0+A(r_0)\}\lambda^2$$
$$-\frac{1}{2}\alpha_P\left(1+\frac{4\pi}{3}\frac{\alpha_P}{2r_0^3}\right)F^2\Big]\left(\frac{3\delta r}{r_0}\right)$$
$$+\frac{1}{2r_0^3}\Big[-\frac{1}{2}\frac{4\pi}{3}\frac{(4\bar{r}^2\lambda)^2}{2r_0^3}-\frac{4\pi}{3}\frac{(4\bar{r}^2\lambda)(\alpha_P F)}{2r_0^3}$$
$$-\frac{1}{2}\frac{4\pi}{3}\frac{\alpha_P F^2}{2r_0^3}\Big]\left(\frac{3\delta r}{r_0}\right)+A(r_0)(p\delta r)\lambda^2\,. \qquad (A\cdot 2$$

We see that Eq. (A·2) separates into tw parts:

$$(N\Delta E)=(N\Delta E)_0+\delta(N\Delta E)\,. \qquad (A\cdot 3$$

Since $\delta(N\Delta E)$ is very small as compared wit

$(N\Delta E)_0$, we may allowed to use the value of λ to be determined by the condition

$$\partial(N\Delta E)_0/\partial\lambda=0\ . \qquad (\mathrm{A}\cdot 4)$$

Then λ is given by Eq. (5) and $(\Delta E)_0$ is also given by Eq. (6). Using Eqs. (5), (6) and (9) and the definitions $p_{en}=4\bar{r}^2\lambda$ and $p_{ep}=\alpha_P F$ we find:

$$\begin{aligned}\delta(N\Delta E)=&-\left(\frac{1}{8\pi}\right)(\kappa_0-1)F^2\left(\frac{3\delta r}{r_0}\right)\\&+\frac{1}{2r_0^3}\left[-\frac{1}{2}\frac{4\pi}{3}\frac{1}{2r_0^3}(p_{en}^2+2p_{ep}p_{en}+p_{ep}^2)\right]\left(\frac{3\delta r}{r_0}\right)\\&+A(r_0)(p\delta r)F^2\Big/(4\bar{r}^2)^2\left(2a-\frac{4\pi}{3}\frac{1}{2r_0^3}\right)^2 .\end{aligned} \qquad (\mathrm{A}\cdot 5)$$

The second term is easily transformed to

$$\begin{aligned}(\text{second term})&=-\frac{1}{8\pi}\frac{1}{3}\left(\frac{4\pi}{2r_0^3}\right)^2(p_{en}+p_{ep})^2\\&=-\left(\frac{1}{8\pi}\right)\frac{1}{3}(4\pi P)^2\\&=-\left(\frac{1}{8\pi}\right)\frac{1}{3}(\kappa_0-1)^2F^2 .\end{aligned}$$

Then $\delta(N\Delta E)$ becomes:

$$\begin{aligned}\delta(N\Delta E)=&-\left(\frac{1}{8\pi}\right)\frac{(\kappa_0-1)(\kappa_0+2)}{3}\left(\frac{3\delta r}{r_0}\right)F^2\\&+\frac{1}{2r_0^3}\frac{A(r_0)}{(4\bar{r}^2)^2}\frac{pr_0}{3(2a-2\pi/3r_0^3)^2}\left(\frac{3\delta r}{r_0}\right)F^2 .\end{aligned} \qquad (\mathrm{A}\cdot 6)$$

On the other hand, $\rho(dn/d\rho)$ is expressed as:

$$\begin{aligned}\rho\left(\frac{dn}{d\rho}\right)&=-\frac{1}{2\sqrt{\kappa_0}}\left(V\frac{d\kappa_0}{dV}\right)=\frac{1}{2\sqrt{\kappa_0}}\frac{8\pi}{F^2}V\frac{\delta(N\Delta E)}{\delta V}\\&=\frac{1}{2\sqrt{\kappa_0}}\frac{8\pi}{F^2}\frac{r_0}{3}\frac{\delta(N\Delta E)}{\delta r} .\end{aligned} \qquad (\mathrm{A}\cdot 7)$$

Thus we obtain the final expression for $\rho(dn/d\rho)$ as follows:

$$\begin{aligned}\rho\left(\frac{dn}{d\rho}\right)=&\frac{(\kappa_0-1)(\kappa_0+2)}{\sqrt{\kappa_0}}\\&-\frac{8\pi}{2r_0^3}\frac{A(r_0)}{(4\bar{r}^2)^2}\frac{pr_0}{6\sqrt{\kappa_0}}\Big/\left(2a-\frac{4\pi}{3}\frac{1}{2r_0^3}\right)^2 .\end{aligned} \qquad (\mathrm{A}\cdot 8)$$

A simpler derivation of Eq. (16) is as follows: Differentiating Eq. (10) we obtain

$$\begin{aligned}\frac{d\kappa_0}{dr}&=-\frac{\pi}{r_0^3}\frac{1}{a-\pi/3r_0^3}\left(\frac{3}{r_0}+\frac{\pi}{r_0^3}\frac{1}{r_0}\frac{1}{a-\pi/3r_0^3}\right)-\frac{\pi}{r_0^3}\frac{(da/dr)}{(a-\pi/3r_0^3)^2}\\&=-(\kappa_0-1)(\kappa_0+2)/r_0-\left(\frac{\pi}{r_0^3}\right)\left(\frac{da}{dr}\right)\Big/(a-\pi/3r_0^3)^2 .\end{aligned}$$

From Eqs. (9) and (15)

$$(da/dr)_{r_0}=\{1/(4\bar{r}^2)^2\}(dA/dr)_{r_0}=-pA(r_0)/(4\bar{r}^2)^2 .$$

Thus we find

$$\left(\frac{d\kappa_0}{dr}\right)_{r_0}=-\frac{(\kappa_0-1)(\kappa_0+2)}{r_0}+\left(\frac{\pi}{r_0^3}\right)\frac{A(r_0)}{(4\bar{r}^2)^2}\frac{p}{r_0^3}\Big/(a-\pi/3r_0^3)^2$$

and

$$\rho\frac{dn}{d\rho}=-\frac{r_0}{6\sqrt{\kappa_0}}\frac{d\kappa_0}{dr}=\frac{(\kappa_0-1)(\kappa_0+2)}{6\sqrt{\kappa_0}}-\frac{1}{2r_0^3}\frac{A(r_0)}{(4\bar{r}^2)^2}\frac{pr_0}{6\sqrt{\kappa_0}}\frac{2\pi}{(a-\pi/3r_0^2)^2} .$$

Appendix II

Pressure effect of the static dielectric constant

The energy change of the system due to the static field under the hydrostatic pressure is given by:

$$\begin{aligned}(N\Delta E)=&\frac{1}{2(r_0-\delta r)^3}\left[-2exF-\frac{1}{2}\frac{4\pi}{3}\frac{(2ex)^2}{2(r_0-\delta r)^3}-\frac{4\pi}{3}\frac{(4\bar{r}^2\lambda)(2ex)}{2(r_0-\delta r)^3}\right.\\&\left.-4\bar{r}^2\lambda-\frac{1}{2}\frac{4\pi}{3}\frac{(4\bar{r}^2\lambda)^2}{2(r_0-\delta r)^3}+(A_0+A)\lambda^2+Bx\lambda+Cx^2\right]\\=&\frac{1}{2r_0^3}[\cdots\cdot]+\frac{3\delta r}{r_0}\frac{1}{2r_0^3}[\cdots\cdot]\\&+\frac{3\delta r}{r_0}\frac{1}{2r_0^3}\left\{-\frac{1}{2}\frac{4\pi}{3}\frac{(2ex)^2}{2r_0^3}-\frac{4\pi}{3}\frac{(4\bar{r}^2\lambda)(2ex)}{2r_0^3}-\frac{1}{2}\frac{4\pi}{3}\frac{(4\bar{r}^2\lambda)^2}{2r_0^3}\right\}\end{aligned}$$

$$+\frac{1}{2r_0^3}\{\delta A\cdot\lambda^2+\delta B\cdot x\lambda+\delta C\cdot x^2\}\,. \qquad (\mathrm{A}\cdot 9$$

Here we separate Eq. (A·9) into two parts:

$$(N\varDelta E)=(N\varDelta E)_0+\delta(N\varDelta E) \qquad (\mathrm{A}\cdot 10$$

where

$$\delta(N\varDelta E)=\left(\frac{3\delta r}{r_0}\right)\left\{\frac{1}{2r_0^3}[\cdots\cdot]-\frac{1}{2r_0^3}\frac{1}{2}\frac{4\pi}{3}\frac{1}{2r_0^3}(p_x+p_z)^2\right\}+\frac{1}{2r_0^3}\{\delta A\cdot\lambda^2+\delta B\cdot x\lambda+\delta C\cdot x^2\}\,. \qquad (\mathrm{A}\cdot 11$$

Since $\delta(N\varDelta E)$ is very small as compared with $(N\varDelta E)_0$, we may be allowed to use the values of x and λ to be determined by the conditions:

$$\partial(N\varDelta E)_0/\partial x=0 \quad\text{and}\quad \partial(N\varDelta E)_0/\partial\lambda=0\,.$$

Thus $\delta(N\varDelta E)$ becomes:

$$\delta(N\varDelta E)=\left(\frac{3\delta r}{r_0}\right)\left\{-\frac{1}{8\pi}(\kappa-1)F^2\right\}+\left(\frac{3\delta r}{r_0}\right)\left\{-\frac{1}{8\pi}\frac{(4\pi P)^2}{3}\right\}+\frac{1}{2r_0^3}\{\delta A\cdot\lambda^2+\delta B\cdot x\lambda+\delta C\cdot x^2\}. \qquad (\mathrm{A}\cdot 12$$

Using the relation $(\kappa-1)F=4\pi P$ it becomes

$$\delta(N\varDelta E)=\frac{F^2}{8\pi}(\kappa-1)(\kappa+2)\left(\frac{\delta r}{r_0}\right)+\frac{1}{2r_0^3}\{\delta A\cdot\lambda^2+\delta B\cdot x\lambda+\delta C\cdot x^2\}\,.$$

Again using the relation $\delta(N\varDelta E)=-(F^2/8\pi)\delta\kappa$ we find:

$$\frac{\delta\kappa}{\delta r_0}=-\frac{(\kappa-1)(\kappa+2)}{r_0}-\frac{8\pi}{F^2}\left\{\frac{\delta A}{\delta r_0}\lambda^2+\frac{\delta B}{\delta r_0}x\lambda+\frac{\delta C}{\delta r_0}x^2\right\}\frac{1}{2r_0^3}\,. \qquad (\mathrm{A}\cdot 13$$

If we change the variables from λ and x to p_x and p_z, we obtain the equation (27):

$$\frac{\delta\kappa}{\delta r_0}=-\frac{(\kappa-1)(\kappa+2)}{r_0}-\frac{8\pi}{F^2}\frac{1}{2r_0^3}\left\{\frac{\delta a}{\delta r_0}p_z^2+\frac{\delta b}{\delta r_0}p_xp_z+\frac{\delta c}{\delta r_0}p_x^2\right\}\,. \qquad (\mathrm{A}\cdot 14$$

Appendix III. Lattice vibration

If we do not take account of the ionic polarization, the relation between $\vec{F}(k)$ and the displacement is given by:

$$\vec{F}(1)=A_{11}\vec{U}(1)+A_{12}\vec{U}(2)\,, \qquad \vec{F}(2)=A_{21}\vec{U}(1)+A_{22}\vec{U}(2)\,, \qquad (\mathrm{A}\cdot 15)$$

A_{11}, A_{12}, A_{21} and A_{22} are the certain 3–3 matrices. For special cases they were computed by Lydane and Hertzfeld. In fact, we must consider the Coulomb force due to the polarization of negative ions $p(2;1)$.

If we put,

$$\vec{p}(2;l)=\vec{P}\exp\{-i\omega t+i\vec{S}\cdot r(2;l)\}=4\bar{r}^2\vec{\lambda}(l)$$

$$=4\bar{r}^2\vec{\varLambda}\exp\{-i\omega t+i\vec{S}\cdot\vec{r}\}\,, \qquad (\mathrm{A}\cdot 16$$

then $F(1)$ and $F(2)$ become:

$$\vec{F}(1)=A_{11}\vec{U}(1)+A_{12}\{\vec{U}(2)-4\bar{r}^2\vec{\varLambda}\}\,, \qquad \vec{F}(2)=A_{21}\vec{U}(1)+A_{22}\{\vec{U}(2)-4\bar{r}^2\vec{\varLambda}\}\,. \qquad (\mathrm{A}\cdot 17$$

And $R(1)$ and $R(2)$ is given by:

$$\vec{R}(1)=-G\vec{U}(1)+\boldsymbol{H}\vec{U}(2)\,, \qquad \vec{R}(2)=\boldsymbol{H}\vec{U}(1)-(C/2)\vec{U}(2)\,, \qquad (\mathrm{A}\cdot 18$$

where

$$C/2=\frac{4\pi e^2}{r_0^3}(C_1+2C_2)\,, \qquad (\mathrm{A}\cdot 19$$

$$\boldsymbol{H}=\begin{pmatrix} H_x & 0 & 0\\ 0 & H_y & 0\\ 0 & 0 & H_z\end{pmatrix} \tag{A·20}$$

and

$$\left.\begin{aligned} H_x&=\frac{4\pi e^2}{r_0^3}\,[C_1\cos r_0S_x+C_2\{\cos r_0S_y+\cos r_0S_z\}]\\ H_y&=\frac{4\pi e^2}{r_0^3}\,[C_1\cos r_0S_y+C_2\{\cos r_0S_z+\cos r_0S_x\}]\\ H_z&=\frac{4\pi e^2}{r_0^3}\,[C_1\cos r_0S_z+C_2\{\cos r_0S_x+\cos r_0S_y\}]\ .\end{aligned}\right\} \tag{A·21}$$

Now, let us consider the non-electrostatic interaction energy ΔE_1 between a negative ion $\vec{r}(2;l)$ with the polarization λ and the six nearest neighbour positive ions, when the ionic displacement is given by

$$\vec{u}(k,l)=\vec{U}(k)\exp\{i\omega t+i\vec{S}\cdot\vec{r}\}\ . \tag{A·22}$$

We assume that ΔE_1 is given by

$$\Delta E_1=\lambda\sum q_1(r)\cos\theta\ , \tag{A·23}$$

where summation is taken over the six nearest neighbour positive ions and (r,θ) are the coordinates specifying the six positive ions relative to the central negative ion.

Performing the summation we obtain

$$\Delta E_1=\{-\vec{\lambda}\cdot g\vec{U}(2)+\vec{\lambda}\boldsymbol{h}\vec{U}(1)\}\exp\{-i\omega t+i\vec{S}\cdot\vec{r}\}\ , \tag{A·24}$$

where

$$g=2q_1'(r_0)+4q_1(r_0)/r_0\ , \tag{A·25}$$

and

$$\boldsymbol{h}=\begin{pmatrix} h_x, & 0, & 0\\ 0, & h_x, & 0\\ 0, & 0, & h_x\end{pmatrix} \tag{A·26}$$

$$\left.\begin{aligned} h_x&=2q_1'(r_0)\cos r_0S_x+(2q_1(r_0)/r_0)(\cos r_0S_y+\cos r_0S_z)\\ h_y&=2q_1'(r_0)\cos r_0S_y+(2q_1(r_0)/r_0)(\cos r_0S_z+\cos r_0S_x)\\ h_z&=2q_1'(r_0)\cos r_0S_z+(2q_1(r_0)/r_0)(\cos r_0S_x+\cos r_0S_y)\end{aligned}\right\} \tag{A·27}$$

In the case of long waves it becomes

$$h_x=h_y=h_z=g \tag{A·28}$$

and

$$\{\vec{U}(1)-\vec{U}(2)\}\exp(-i\omega t)=2x\ . \tag{A·29}$$

Thus ΔE_1 becomes $\Delta E_1=2gx\lambda$, and we find

$$2g=B\ . \tag{A·30}$$

For the purpose of the practical computation we assume the functional form of $q_1(r)$ as constant × $\exp(-r/\rho)$, so that it becomes:

$$q_1'(r_0)/q_1(r_0)=-1/\rho\ . \tag{A·31}$$

From (A·30) and (A·31) we have determined $q_1(r_0)$ and $q_1'(r_0)$, and we take the value of r_0/ρ as 9.

The energy change due to the ionic deformation is given by

$$\partial\Delta E/\partial\vec{\lambda}(l)=0\ ,$$

and

$$\Delta E=(A_0+A)\vec{\lambda}^2(l)-4\bar{r}^2\vec{\lambda}(l)\vec{F}(2)\exp\{-i\omega t+i\vec{S}\cdot\vec{r}(2;l)\}$$
$$+\{-\vec{\lambda}(l)g\vec{U}(2)+\vec{\lambda}(l)\boldsymbol{h}\vec{U}(1)\}\exp\{-i\omega t+i\vec{S}\cdot\vec{r}(2;l)\}\,. \qquad \text{(A·32)}$$

From these Λ is determined as:

$$\vec{\Lambda}=\{4\bar{r}^2\vec{F}(2)+g\vec{U}(2)-\boldsymbol{h}\vec{U}(1)\}/2(A_0+A)\,. \qquad \text{(A·33)}$$

Inserting $F(2)$ of (A·17) we obtain the final expression for Λ as follows:

$$\Lambda=\boldsymbol{K}\cdot\frac{1}{2(A_0+A)}\{(4\bar{r}^2A_{21}-\boldsymbol{h})\vec{U}(1)+(4\bar{r}^2A_{22}+g)\vec{U}(2)\} \qquad \text{(A·34}$$

where

$$\boldsymbol{K}=\left\{1+\frac{A_{22}}{2a}\right\}^{-1}=\{1+\alpha_nA_{22}\}^{-1}\,. \qquad \text{(A·35}$$

Eliminating $\vec{\Lambda}$ from (A·17) and (A·34) we obtain the Lorentz field as follows:

$$\left.\begin{aligned}
e_1\vec{F}(1)&=\left\{e_1A_{11}-\frac{1}{2a}A_{12}\boldsymbol{K}\left(A_{21}-\frac{\boldsymbol{h}}{4\bar{r}^2}\right)\right\}\vec{U}(1)+\left\{e_1A_{12}-\frac{1}{2a}A_{12}\boldsymbol{K}\left(A_{22}+\frac{g}{4\bar{r}^2}\right)\right\}\vec{U}(2)\,,\\
e_2\vec{F}(2)&=\left\{e_2A_{21}+\frac{1}{2a}A_{22}\boldsymbol{K}\left(A_{21}-\frac{\boldsymbol{h}}{4\bar{r}^2}\right)\right\}\vec{U}(1)+\left\{e_2A_{22}+\frac{1}{2a}A_{22}\boldsymbol{K}\left(A_{22}+\frac{g}{4\bar{r}^2}\right)\right\}\vec{U}(2)\,.
\end{aligned}\right\} \qquad \text{(A·36}$$

Finally $T(k)$ is determined as follows:

$$\vec{T}(1)=-\boldsymbol{h}\vec{\Lambda}\,, \qquad \vec{T}(2)=g\vec{\Lambda}\,. \qquad \text{(A·36′}$$

Thus, from (A·36), (A·18), (A·37) and (A·33) $\vec{F}(k)$, $\vec{R}(k)$ and $\vec{T}(k)$ are expressed as the function of $\vec{U}(1)$ and $\vec{U}(2)$. Then we need only to solve the following equations in order to get the frequency ω.

$$-m_1\omega^2\vec{U}(1)=e_1\vec{F}(1)+\vec{R}(1)+\vec{T}(1)\,, \qquad -m_2\omega^2\vec{U}(2)=e_2\vec{F}(2)+\vec{R}(2)+\vec{T}(2)\,. \qquad \text{(A·37)}$$

(1) *long waves*

In this case:

$$A_{11}=A_{21}=\frac{4\pi e}{r_0^3}\begin{pmatrix}-1/3, & 0, & 0\\ 0, & 1/6, & 0\\ 0, & 0, & 1/6\end{pmatrix}, \qquad A_{22}=A_{12}=-A_{11}\,, \qquad \boldsymbol{h}=g\begin{pmatrix}1, & 0, & 0\\ 0, & 1, & 0\\ 0, & 0, & 1\end{pmatrix},$$

$$\boldsymbol{H}=\frac{C}{2}\begin{pmatrix}1, & 0, & 0\\ 0, & 1, & 0\\ 0, & 0, & 1\end{pmatrix}, \qquad \boldsymbol{K}=\begin{pmatrix}1/(1+k/3), & 0, & 0\\ 0, & 1/(1-k/6), & 0\\ 0, & 0, & 1/(1-k/6)\end{pmatrix}, \qquad k=4\pi\alpha_n/r_0^3.$$

Solving equations (A·37) we obtain the same value of ω as given by (45) and (57).

(2) $\vec{S}=(\pi/2r_0,\ \pi/2r_0,\ \pi/2r_0)$

$$\cos S_xr_0=\cos S_yr_0=\cos S_zr_0=0\,. \qquad A_{11}=-A_{22}=-0.1438\,\frac{4\pi e}{r_0}\begin{pmatrix}0 & 1 & 1\\ 1 & 0 & 1\\ 1 & 1 & 0\end{pmatrix},$$

$$A_{12}=A_{21}=0\,, \qquad \boldsymbol{h}=\boldsymbol{H}=0\,, \qquad \boldsymbol{K}=\frac{1}{1+K_1-2K_1^2}\begin{pmatrix}1+K_1 & -K_1 & -K_1\\ -K_1 & 1+K_1 & -K_1\\ -K_1 & -K_1 & 1+K_1\end{pmatrix}, \qquad K_1=0.1438\,k\,.$$

(3) $\vec{S}=(\pi/r_0,\ 0,\ 0)$

$$\cos S_xr_0=-1\,, \qquad \cos S_yr_0=\cos S_zr_0=1\,, \qquad A_{11}=-A_{22}=0{\cdot}0862\times\frac{4\pi e}{r_0^3}\begin{pmatrix}-2 & 0 & 0\\ 0 & 1 & 0\\ 0 & 0 & 1\end{pmatrix},$$

$$A_{12}=-A_{21}=0.2992\times\frac{4\pi e}{r_0^3}\begin{pmatrix}2&0&0\\0&-1&0\\0&0&-1\end{pmatrix},\qquad K=\begin{pmatrix}1/(1+2K_2)&0&0\\0&1/(1-K_2)&0\\0&0&1/(1-K_2)\end{pmatrix},$$

$$K_2=0.0862k\ .$$

(4) $\vec{S}=(\pi/r_0,\ \pi/2r_0,\ 0)$

$$\cos S_x r_0=-1\ ,\qquad \cos S_y r_0=0\ ,\qquad \cos S_z r_0=1\ .$$

$$A_{11}=-A_{22}=0.03135\times\frac{4\pi e}{r_0^3}\begin{pmatrix}-1&0&0\\0&2&0\\0&0&-1\end{pmatrix},\qquad A_{12}=-A_{21}=0.4371\times\frac{4\pi e}{r_0^3}\begin{pmatrix}1&0&0\\0&0&0\\0&0&-1\end{pmatrix},$$

$$K=\begin{pmatrix}1/(1+K_3)&0&0\\0&1/(1+K_3)&0\\0&0&1/(1+K_3)\end{pmatrix},\qquad K_3=0.03135k\ .$$

Appendix IV

(a) Solving p_1 and p_2 from Eqs. (74′) we obtain

$$p_1=g_1(q)p_x \quad\text{and}\quad p_2=g_2(q)p_x\ . \tag{A·38}$$

$g_1(q)$ and $g_2(q)$ are some functions of a and b, for example,

$$g_1(0)=(a_{12}b_2-2a_2b_1)/(4a_1a_2-a_{12}^2)\ ,\qquad g_2(0)=(a_{12}b_1-2a_1b_2)/(4a_1a_2-a_{12}^2)\ . \tag{A·38′}$$

Similarly from Eqs. (72) p_1 and p_2 are expressed as

$$p_1=g_1(q)p_x+h_1(q)F\ ,\qquad p_2=g_2(q)p_x+h_2(q)F\ . \tag{A·39}$$

Substituting these into Eq. (76′) we obtain

$$[K_3(q;\,g_1(q)p_x+h_1(q)F,\ \cdots,\ p_x)]=f(q)p_x+\left\{h_1(q)\left(b_1+\frac{4\pi}{3}Nq\right)+h_2(q)\left(b_2+\frac{4\pi N}{3}q\right)\right\}F. \tag{A·40}$$

If we substitute p_x, which satisfies (64), into (A·40), $[K_3(q)]$ must be equal to $[B(q)]F$ because of (72). Thus we have:

$$f(q)p_x=\left\{[B(q)]-h_1(q)\left(b_1+\frac{4\pi N}{3}q\right)-h_2(q)\left(b_2+\frac{4\pi N}{3}q\right)\right\}F. \tag{A·41}$$

Since p_x/F is independent of q, we find:

$$\frac{\omega^2(q)}{\omega^2(0)}=\frac{f(q)}{f(0)}=\frac{[B(q)]-h_1(q)\left(b_1+\frac{4\pi N}{3}q\right)-h_2(q)\left(b_2+\frac{4\pi N}{3}q\right)}{[B(0)]-h_1(0)b_1-h_2(0)b_2}, \tag{A·42}$$

Next, let us consider the equations

$$[K_1^0(q;p_1,p_2)]=[K_1(q;p_1,p_2,0)]=[B(q)]F\ ,\ \ [K_2^0(q;p_1,p_2)]=[K_2(p;p_1,p_2,0)]=[B(q)]F\ . \tag{A·43}$$

In this case, from (72) and (A·39) we see that p_1 and p_2 is given by

$$p_1=h_1(q)F \quad\text{and}\quad p_2=h_2(q)F\ , \tag{A·44}$$

and from (63) and (69) we have:

$$p_1+p_2=(K_0-1)F/4\pi N\cdot[B(q)]/[B_0(q)]\ , \tag{A·45}$$

and from (A·43) and (70) we also find:

$$p_1/p_2=(2a_2-a_{12})/(2a_1-a_{12})\ . \tag{A·46}$$

From these equations $h_1(q)$ and $h_2(q)$ are solved explicitly as follows:

$$h_1(q)=\frac{\kappa_0-1}{4\pi N}\frac{[B(q)]}{[B_0(q)]}r_1, \quad \text{and} \quad h_2(q)=\frac{\kappa_0-1}{4\pi N}\frac{[B(q)]}{[B_0(q)]}r_2\,,$$ (A·47

where

$$r_1=\frac{2a_2-a_{12}}{2(a_1+a_2-a_{12})}\,, \qquad r_2=\frac{2a_1-a_{12}}{2(a_1+a_2-a_{12})}\,.$$ (A·48

Substituting (A·47) into (A·47) into (A·42) we obtain the relation which is to be proved,

$$\frac{\omega(q)^2}{\omega(0)^2}=\frac{(\kappa+2)+q(\kappa-1)}{(\kappa_0+2)+q(\kappa_0-1)}\frac{\kappa_0+2}{\kappa+2}\,.$$ (78

(b) By the definition of $e^*(q)$ and (75) it becomes

$$e^*(q)/e=(p_x+p_1+p_2)/p_x=1+g_1(q)+g_2(q)\,.$$ (A·49

Now, let us transform Eqs. (74′) into

$$[K_1^0(q;p_1,p_2)]=-\left(b_1+\frac{4\pi N}{3}q\right)p_x\,, \qquad [K_2^0(q;p_1,p_2)]=-\left(b_2+\frac{4\pi N}{3}q\right)p_x$$

and compare them with (A·43). From the facts that (A·38) is a solution of the above equations and (A·44) is a solution of (A·43) we obtain after some calculations the following relation:

$$g_1(q)+g_2(q)=-\frac{1}{[B(q)]}\left\{\left(b_1+\frac{4\pi N}{3}q\right)h_1(q)+\left(b_2+\frac{4\pi N}{3}q\right)h_2(q)\right\}\,.$$ (A·50

Inserting (A·50) into (A·41) and using (A·49) we find

$$f(q)p_x=[B(q)](1+g_1(q)+g_2(q))F=\frac{e^*(q)}{e}[B(q)]F\,.$$ (A·51

Now, we notice that the solution of (72) satisfies the relation

$$p_1+p_2+p_x=(\kappa-1)F/4\pi N\,.$$ (A·52

On the other hand, from Eqs. (39) we find:

$$p_1+p_2+p_x=\{1+g_1(q)+g_2(q)\}p_x+\{h_1(q)+h_2(q)\}F\,.$$

Using (A·49) and (A·47) we have:

$$p_1+p_2+p_x=\frac{e^*(q)}{e}p_x+\frac{(\kappa_0-1)F}{4\pi N}[B(q)]/[B_0(q)]\,.$$ (A·53

Eliminating p_1 and p_2 from Eqs. (A·52) and (A·53) we obtain:

$$\frac{e^*(q)}{e}\frac{4\pi N[B_0(q)]}{\kappa-\kappa_0}p_x=F\,.$$ (A·54

Comparing (A·54) with (A·51) and using (77) we find

$$f(q)=\left[\frac{e^*(q)}{e}\right]^2\frac{4\pi N}{\kappa-\kappa_0}[B_0(q)][B(q)]\,,$$ (A·55

and

$$\omega^2(q)=\frac{z^2e^*(q)^2}{\mu}\frac{4\pi N}{\kappa-\kappa_0}[B_0(q)][B(q)]\,,$$ (A·56

which is identical with (82).

(c) Inserting (A·50) into (A·49) and using (A·48) and (67) we obtain:

$$\frac{e^*(q)}{e}=\frac{(\kappa_0+2)\frac{4\pi N}{3}-(\kappa_0-1)(b_1r_1+b_3r_2)}{4\pi N[B_0(q)]}\,.$$ (A·57

If we put $q=0$, we find:

$$r_1b_1+r_2b_2=\frac{\kappa_0+2}{\kappa_0-1}\left\{1-\frac{e^*(0)}{e}\right\}\frac{4\pi N}{3}\,. \tag{A$\cdot$58}$$

Putting $q=0$ in (70) we find

$$[K_3(0;p_1,p_2,p_x)]=\{2c+b_1g_1(0)+b_2g_2(0)\}p_x\,.$$

Thus the restoring force $f(0)$ is given by

$$f(0)=\mu\omega(0)^2/z^2e^2=(\mu/z^2e^2)(\kappa+2/\kappa_0+2)\omega_t^2=2c+b_1g_1(0)+b_2g_2(0)\,. \tag{A$\cdot$59}$$

Now, from (A·58) we find:

$$b_1=\frac{\kappa_0+2}{\kappa_0-1}\left\{1-\frac{e^*(0)}{e}\right\}\frac{4\pi N}{3}+r_2(b_1-b_2)\,,\qquad b_2=\frac{\kappa_0+2}{\kappa_0-1}\left\{1-\frac{e^*(0)}{e}\right\}\frac{4\pi N}{3}-r_1(b_1-b_2)\,.$$

Using these equations and also (A·38′) we easily find the following relation,

$$\begin{aligned}c&=\frac{\mu}{2z^2e^2}\frac{\kappa+2}{\kappa_0+2}\omega_t^2-\frac{1}{2}\frac{\kappa_0+2}{\kappa_0-1}\left\{1-\frac{e^*(0)}{e}\right\}\frac{4\pi N}{3}\{g_1(0)+g_2(0)\}+\frac{1}{2}(b_1-b_2)(r_1g_2(0)-r_2g_1(0)\\&=\frac{\mu}{2z^2e^2}\frac{\kappa+2}{\kappa_0+2}\omega_t^2-\frac{1}{2}\frac{\kappa_0+2}{\kappa_0-1}\left\{1-\frac{e^*(0)}{e}\right\}^2\frac{4\pi N}{3}+\frac{(b_1-b_2)^2}{4(a_1+a_2-a_{12})}\,.\end{aligned} \tag{60}$$

References

1) C. G. F. Bottcher: Theory of Electric Polarization.
H. Frohlich: Theory of Dielectrics.
Mott and Gurney: Electronic Processes in Ionic Crystals.
2) J. G. Kirkwood: Jour. Chem. Phys. **4** (1936) 592.
3) W. F. Brown: Jour. Chem. Phys. **18** (1950) 1193.
4) J. Yamashita: Prog. Theor. Phys. **8** (1952) 280; **12** (1954) 454; Proceedings of the International Conference of Theoretical Physics (1953) 813.
5) J. C. Slater and J. G. Kirkwood: Phys. Rev. **37** (1931) 682.
J. G. Kirkwood: Phys. ZS. **33** (1932) 57.
6) J. R. Tessman, A. H. Kahn and W. Shockley: Phys. Rev. **92** (1953) 890.
7) Burstein and Smith: Phys. Rev. **74** (1948) 229.
8) Mott and Gurney: loc cit.
9) F. Seitz: Phys. Rev. **74** (1948) 1014.
10) S. Mayburg: Phys. Rev. **79** (1950) 375.
11) Born and Mayer: Handb. d. Physik **24:2** (1933) 623.
12) Lydane and Herzfeld: Phys. Rev. **54** (1938) 846.
13) J. Yamashita and T. Kurosawa: Jour. Phys. Soc. Japan **9** (1954) 944.
14) H. Frohlich and N. F. Mott: Proc. Roy. Soc. London **171** (1939) 496.
15) H. Callen: Phys. Rev. **76** (1949) 1394.
16) H. Frohlich, H. Pelzer and S. Zienau: Phil. Mag. **41** (1950) 221.
17) H. Y. Fan: Phys. Rev. **82** (1951) 900.
18) B. Szigeti: Trans. Faraday Soc. **45** (1949) 155.
19) B. Szigeti: Proc. Roy. Soc. London **204** (1950) 1076.
20) Yamashita and Kurosawa: loc cit.
21) J. E. Mayer: Jour. Chem. Phys. **1** (1933) 270, 327.
22) W. Jost and G. Nehlep: Zeits. Phys. Chem. **32** (1936) 1.
23) N. F. Mott and M. J. Littleton: Trans. Faraday Soc. **34** (1938) 485.

JOURNAL OF THE PHYSICAL SOCIETY OF JAPAN Vol. 10, No. 8, AUGUST, 1955

On the Anomaly of the Dielectric Properties of *n*-Higher Alcohols

By Kenjiro ASAI, Eiji YODA and Sueo YAMANAKA

Department of Physics, University of Kyoto

(Received March 22, 1955)

The cause of the abnormally high value of the dielectric constant of *n*-higher alcohols was investigated on the basis of some experimental results. To begin with, the discrepancies between D.C. conductivity and A.C. conductivity were examined in order to clarify the behaviour of the net conduction-current and the absorption-current due to dipole rotation.

Next, the frequency dependency of the dielectric constant in the low frequency region (30 c/sec∼5 kc/sec) was observed and the results were discussed in connexion with Maxwell-Wagner's formula on the composite dielectric and with Cole's theory on the conductive dielectric.

Thus, it seems to be reasonable to think that the high value of the dielectric constant of *n*-higher alcohols is an apparent value due to the higher electrical conductivity of its molecular rotating phase. An idea on the mechanism of the proton transfer in the solid alcohol is presented.

§1. Introduction

The dielectric properties of the *n*-higher alcohols have been investigated by Kubo[1)], Smyth[2),3)], Kakiuchi[4),5)] and others, and the discussion from the standpoint of "molecular rotation" was made by Smyth and Hoffman[3)]. The structure analysis of *n*-alcohols was done by Ott[6)] and others. The three types, i.e. α, β_1, β_2, of the crystal structure have been found by them.

The first phase which crystallizes initially from the melt on freezing is the α phase. It is an "opaque state" and takes the hexagonal structure, and is molecular rotating phase, but on further cooling this phase transforms into β_1 at a "transition point", In this latter phase the molecular rotation ceases to occur and the crystal structure changes to orthorhombic. On the other hand, the β_2 phase is the most stable one throughout the whole solid phase range, and it is obtained by the crystallization from the solution or by very slow transformation from the α phase. Its crystal structure is monoclinic and the molecular rotation does not occur in this phase too.

In the α phase the high electrical conductivity and the large dielectric constant are observed which are attributed to the molecular rotation in this phase. On the other hand, both the electrical conductivity and the dielectric constant take low values in the β_1 and β_2 phases owing to the lack of the molecular rotation. Especially the large dielectric constant of the α phase has been noticed by several investigators, the value of which often reaches to 10 or more and far exceeds the value (about 3.4) in the liquid state. However, this is by no means a definite value, but varies according to different investigators and different experimental conditions. This character was investigated systematically by Smyth for the *n*-higher alcohols containing more than 14 carbon atoms. Smyth[3)] explained that the fact is due to the composite dielectric which is composed of the α phase and the β_2 phase, the former being the molecular rotating phase and conductive, while the latter being non-rotating phase and far less conductive.

On the other hand, Kakiuchi and Suzuki[5)] explained this fact as being an abnormal value due to ionic polarization and concluded that the "true" dielectric constant might be about 3.

In the present paper an attempt is made to explain the origin of the "abnormal value" of the dielectric constant of higher alcohols.

§2. Experimental Results

(*a*) *Electrical conductivity*

At first the electrical conductivities of cetyl

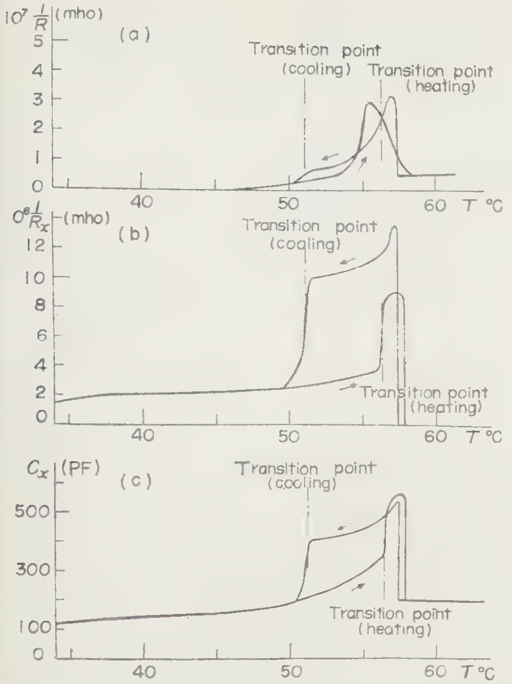

Fig. 1. Temperature dependency of the conductivity and the dielectric constant of the octadecyl alcohol.
(a): D. C. measurements; $1/R$ is plotted against temperature. (b) and (c): A. C. measurements (5 kc); $1/R_x$ and C_x are plotted against temperature respectively.

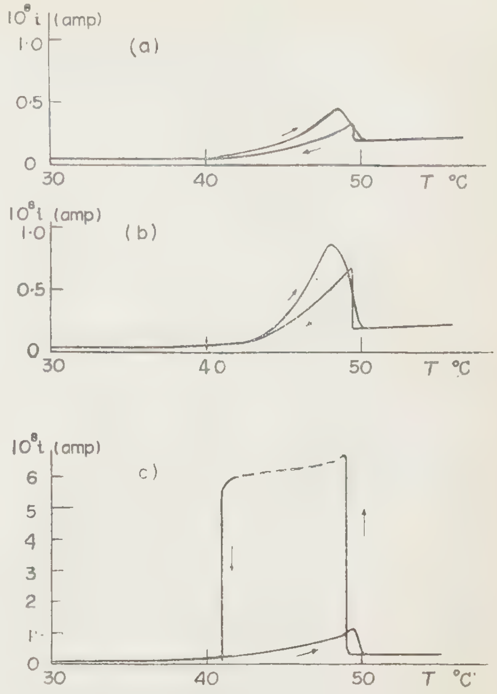

Fig. 2. Effect of the rate of temperature change upon the D. C. conductivity of cetyl alcohol. The conduction-currents are plotted against temperature under various conditions.
(a): $dT/dt=0.2$°C/min., (b): $dT/dt=0.5$°C/min. (c): $dT/dt=5$°C/min.

alcohol ($C_{16}H_{33}OH$) and octadecyl alcohol ($C_{18}H_{37}OH$) were measured under various conditions. D.C. conductivity was measured by a galvanometer inserted in series with the sample. For the A.C. measurements the ordinary capacity bridge was used in the low frequency range of 30 c/sec∼5 kc/sec, and the equivalent resistance was taken, on assuming the parallel model of C_x and R_x for the dielectrics.

The temperature dependency of the conductivities are given in Figs. 1a and 1b. The experimental results are very different for D.C. and A.C. measurements, especially in cooling stage. Namely, in D.C. measurements, a distinct lowering of the resistance takes place only just below the melting point (or the freezing point in the case of cooling). On the other hand, the curve in A.C. case is very similar to the ε versus temperature curve (Fig. 1c). In a word, the transition point is clearly observed in the cooling curve in A.C. case, but not so in D.C. case. Moreover, the melting point is also indistinct in D.C. measurements. Speaking in more detail, the D.C. conduction current begins to increase near the transition temperature as the temperature rises and reaches to a maximum value, and then decreases rather gradually to that of the liquid state. But, in A.C. measurements the equivalent conductance drops suddenly at the melting point. This discrepancy will be discussed later, but in brief it may be ascribed to the fact that the D.C. conduction current is due to the real transfer of the charges, while the A.C. conductance means only certain freedom of polar groups. Also, it is to be noted that the D.C. conductivity of the β_1 phase at room temperature is lower than that of the liquid state, but the A.C. conductance of the β_1 phase is higher than that of the liquid state. The conductivity is very much affected by a small amount of impurities (for example, by foreign ions), but the characteristic feature of the $\sigma-T$ curve is unchanged.

The effect of the cooling speed dT/dt is very remarkable in D.C. case (Fig. 2). Thus, when the temperature is decreased at the rate of 0.2°C/min (Fig. 2a), the current becomes

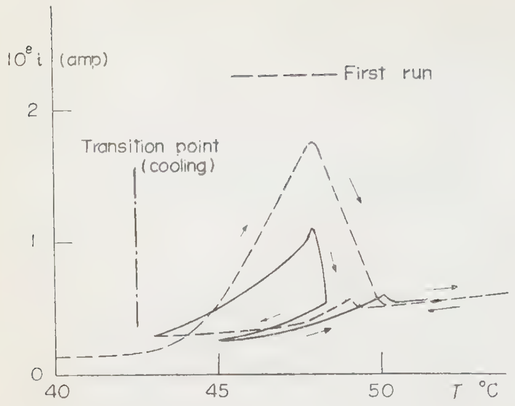

Fig. 3. Damping of the D. C. conduction-current of the alcohol which was held in the α phase temperature region.

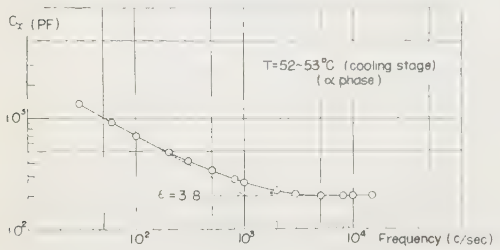

Fig. 4. Frequency dependency of the dielectric constant of the octadecyl alcohol (α phase). The capacity of the sample condenser is plotted directly against temperature.

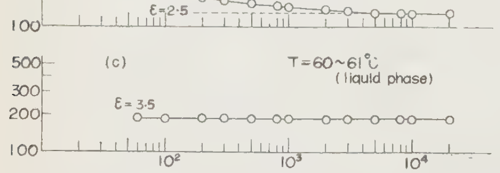

Fig. 5. Frequency dependency of the dielectric constant of the octadecyl alcohol (β_1 and liquid phases).

less than half of that in the ordinary case (0.5°C/min) (Fig. 2b). On the other hand, when a sample is cooled rapidly from the liquid state by putting the condenser on the copper plate which has been cooled at 0°C previously, the current becomes very large but fluctuates and then drops suddenly near the transition point ($\alpha\rightarrow\beta_1$) and settles ultimately at the value for the β_1 phase (Fig. 2c). But, in A.C. case the R_x is not affected so markedly by the cooling speed.

When the temperature of a sample is raised and lowered repeatedly in the narrow temperature range between the freezing point and the transition point (i.e., in the range of the α phase) (Fig. 3), the D.C. current decreases gradually, and by keeping the sample within this temperature range for about an hour, the peak in the α phase becomes non-detectable.

When a sample is cooled from the liquid state down to the room temperature on applying the D.C. field of about 5000 volt/cm, and then the sample condenser is shortcircuited through a galvanometer and thereafter warmed again, a very small discharge current flows just below the melting point. The maximum point of the curve of this discharge current versus temperature coincides with that of the ordinary curve of conduction current.

(*b*) *Measurements of the dielectric constant*

The freqcency characteristics of the dielectric constants of *n*-higher alcohols were measured in low frequency range of 30 c/sec ~5 kc/sec for each phase, namely for the α phase, the β_1 phase and the liquid phase respectively. The measurements for 4~5 mc/sec were also carried out by the tuning method. In the latter case, however, the experiments were aimed at examining the behaviour of the phase transformation under various conditions as well as observation of the effect of foreign ions rather than the measurement of the dielectric properties themselves.

The ε-f curves for the low frequency measurements are given in Figs. 4 and 5. The frequency dependency is most remarkable for the α phase and less for the β_1 phase. For the liquid phase the dielectric constant is almost independent of the frequency. It is to be noted that the linear relationship between log ε and log (frequency) is obtained in low frequency side, i.e. 30 c/sec~1 kc/sec, and almost frequency-independent part is seen in rather high frequency side, i.e. 2~5 kc/sec. This diagram suggests a relation of the following form:

$$\varepsilon_{o\ s}=\varepsilon_0+A\omega^{-n}\ ,$$

where $\varepsilon_{\mathrm{obs}}$ is the observed value of the di-

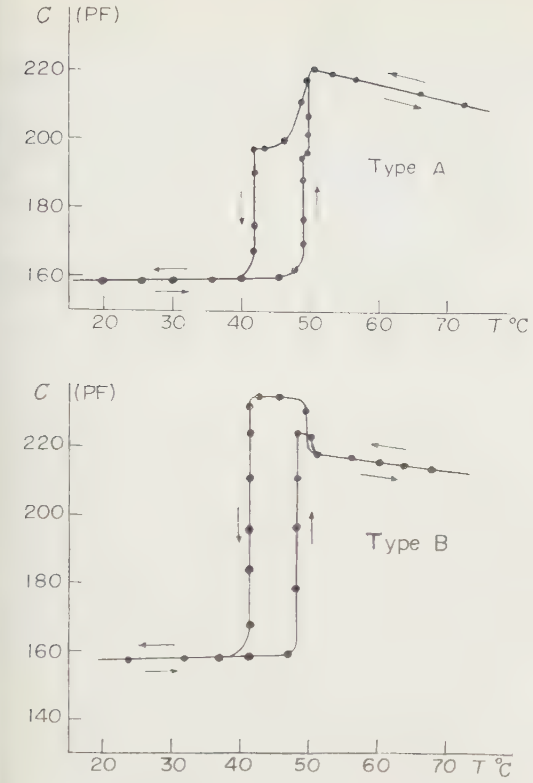

Fig. 6. Temperature dependency of the dielectric constant of the cetyl alcohol in the high frequency measurements (4 mc). The variation of the capacity is plotted against temperature. (a): Normal case, (b) Case when a sample was exposed to HCl vapour.

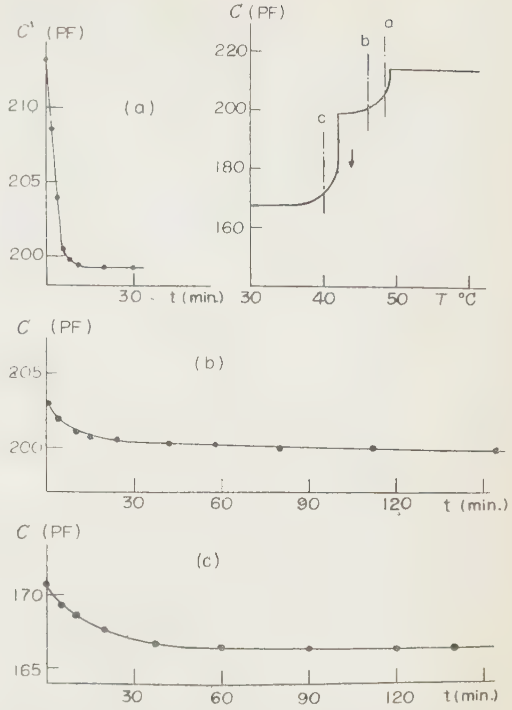

Fig. 7. Time dependency of the variation of ε in high frequency measurements (4 mc). The variation of the sample condenser is plotted against the time.

electric constant, ω is the angular frequency and $\mathcal{E}_0$, A, n are certain constants. The standard C–T curve for high frequency is shown in Fig. 6a. The most striking difference as compared with the low frequency character is the fact that $\mathcal{E}$ of the α phase takes a lower value than that of the liquid state, and therefore the dielectric constant increases or decreases on melting or freezing respectively. However, when a sample is likely to contain some foreign ions, its dielectric behaviour resembles to that in the case of low frequency. Fig. 6b shows the result for a sample which has been exposed to HCl vapour for a moment. When a sample is exposed to the atmosphere for some months, especially in the rainy season, its characteristic approaches to the type as shown in Fig. 6b, but it recovers to the original state by holding the sample in vacuum for about 30 minutes at a temperature by 5$\sim$10°C above the melting point.

In order to check the process of the phase transformation from α to β_2, the time dependency of the dielectric constant was investigated for 4 mc/sec and at different temperatures (Fig. 7). Inferring from these experimental result it is unlikely that the growth of the β_2 phase in the α phase is actually taking place to a considerable extent. Because, if small crystallites of β_2 grow in the α phase, the dielectric constant of a sample must change as the time elapses, and when the dielectric constant has reached to the steady-state value the phase transformation would be almost complete. However, when a sample has been held in the temperature region of the α phase for about 4 hours, it exhibits the normal C–T curves as shown in Fig. 6a, giving the sharp $\alpha \rightarrow \beta_1$ transition point, and when it is heated again, the distinct $\beta_1 \rightarrow \alpha$ transition is observed. If the phase change from α to β_2 would have partly taken place in the cooling process by keeping the temperature of a sample in the α phase region, the $\alpha \rightarrow \beta_1$ transition would be observed less markedly in the subsequent heating process contrary to the observation, because the β_2 phase is the most stable phase and does not transform to other solid phases giving any transition point. The more is a part which has been transformed to the β_2 phase, the less a remaining part becomes, in which the $\alpha\to\beta_1$ transformation will be able to happen. But such a process is not suggested from our experimental results. Experiments of the same kind were also carried out at low frequency (0.5 kc/sec), especially concerning with the relation between R_x and C_x (Fig. 8), but this method isnot so convenient for speedy measurement that only the rough tendency was noticed. A discussion on these results will be given later.

(*c*) *Other experiments*

In order to check the growth of the β_2 phase in the α phase, an X-ray investigation and a microscopic observation have also been carried out. However, it may be concluded that the $\alpha\to\beta_2$ transformation in the temperature range below the freezing point is so sluggish that it is hardly observable in 4 hours or so. Therefore, the composite dielectric of a binary system of α and β_2 phases will not be formed so easily.

§ 3. Discussion

In the α phase the alcohol molecules are conjugated to each other by hydrogen bonds and rotate co-operatively about their own long axis. It is said that in this state the O–H net plane is formed and proton transfer occurs under the action of an electric field, and therefore this phase gives the very high conductivity[11]. But, the β_1 and β_2 phases are not the molecular rotating phases and hence the conductivity is much smaller. For the purpose of explaining the high dielectric constant of such higher alcohols, Smyth[3] adopted Maxwell-Wagner's formula for the composite dielectric. According to his model, the small particles of the β_2 phase are dispersed in the α phase and forms a binary system in the temperature range between the freezing point and the transition point.

According to Wagner[7] the admittance of the composite dielectric such as described above is given by

$$\Lambda_0=\Lambda_2\left(1-3p\,\frac{\Lambda_2-\Lambda_1}{2\Lambda_2+\Lambda_1}\right), \tag{1}$$

where

$$\left.\begin{aligned}\Lambda_1&=\lambda_1+j\omega\varepsilon_1/4\pi\,,\\ \Lambda_2&=\lambda_2+j\omega\varepsilon_2/4\pi\,,\end{aligned}\quad (j=\sqrt{-1})\ \right\} \tag{2}$$

and λ_1, λ_2, ε_1 and ε_2 are the specific conductivities and the dielectric constants of the dispersed small particles and the surrounding medium respectively, and p is a fraction of the dispersed substance and is assumed to be $p\ll 1$ in the present case.

If use is made of (2), the formula (1) is transformed into

$$\begin{aligned}\Lambda_0=&\left(\lambda_2+j\frac{\omega\varepsilon_2}{4\pi}\right)\\ &\times\left\{1-3p\,\frac{\lambda_2-\lambda_1+j\omega(\varepsilon_2-\varepsilon_1)/4\pi}{2\lambda_2+\lambda_1+j\omega(2\varepsilon_2+\varepsilon_1)/4\pi}\right\}.\end{aligned} \tag{3}$$

If, for simplicity, we assume with Smyth that $\varepsilon_1=\varepsilon_2\equiv\varepsilon$ and $\lambda_2=n\lambda_1\equiv n\lambda$, we have

$$\Lambda_0=\left(n\lambda+j\frac{\omega\varepsilon}{4\pi}\right)\left\{1-3p\,\frac{\lambda(n-1)}{\lambda(2n+1)+j\omega 3\varepsilon/4\pi}\right\}.$$

Since the α phase is conductive and the β_2 phase is not, $n>1$. Separating the real and imaginary parts of Λ_0 we have

$$\text{R.P.}=\lambda\left[n-p\,\frac{(n-1)\{3n(2n+1)+(K\omega)^2\}}{(2n+1)^2+(K\omega)^2}\right], \tag{5}$$

$$\text{I.P.}=\frac{\omega\varepsilon}{4\pi}\left[1+3p\frac{(n-1)^2}{(2n+1)^2+(K\omega)^2}\right], \tag{6}$$

with

$$K=3\varepsilon/4\pi\lambda\,.$$

The real part represents the specific conductivity, and in the special case when $\omega=0$, i.e. in D.C. case, this becomes

$$\text{R.P.}_{(\omega=0)}=\lambda\left[n-p\,\frac{3n(n-1)}{2n+1}\right], \tag{7}$$

and the dielectric constant of this system will be expressed as follows:

$$\varepsilon^*=\varepsilon\left[1+3p\,\frac{(n-1)^2}{(2n+1)^2+(K\omega)^2}\right]. \tag{8}$$

It will readily be seen from (6) and (7) that as p increases, the conductance decreases and the capacitance increases. Namely, ε^* *must* increase when the β_2 phase grows in the α phase. In reality, however, the value of ε of a sample decreases with time when the temperature is kept constant in the α phase region (Fig. 8). Smyth[3] explained this decrease of dielectric constant by taking account of the growth of the β_2 phase in the α phase, but it contradicts to (8). From this point of view it seems that Smyth's explanation is insufficient. In our experiments both the dielectric constant and the conductivity decreased with time when the temperature of a sample was held in the region of the α phase (Fig. 8). On investigating by X-ray diffraction, it was found however that such a sample contained no detectable amount of the β_2 phase. Moreover, in the process of further cooling and then heating the sample still showed the $\alpha\rightarrow\beta_1$ transition both in the dielectric observation and in X-ray diffraction investigation. In other words, the β_2 phase did not grow at least by such a heat treatment. If the β_2 phase had grown, the $\alpha\rightarrow\beta_1$ transition would not be observed as mentioned above. In spite of these evidences, the dielectric constant of the α phase is higher than that of the liquid state. Therefore, it is unlikely that the abnormal value of ε of n-alcohols is due to the coexistence of the α and β_2 phases.

Surely the existence of the supercooled liquid phase in the α phase might be suspected, but it is difficult to explain the heating curve from this reason because in this case the supercooled liquid phase must exist for a day or more in the β_1 phase at room temperature which is about 40°～50°C below the melting point. According to our experimental results as revealed, for example, from Figs. 7 and 8, supercooled liquid phase, if any, seems to transform rather quickly, so that even if the supercooled liquid phase coexists with the α phase, it will be restricted in a very narrow temperature range just below the freezing point.

Another discussion was made by Kakiuchi and Suzuki⁵⁾ from the standpoint of the ionic polarization. In our experiments the dielectric constant of the α phase increased markedly by blending a small amount of foreign ions (Fig. 6b). Taking such evidences into account it is certain that the existence of ions increases the apparent dielectric constant of the α phase on account of the high mobility of ions in this phase. In our experiments the ionic polarization plays an important role in the high frequency measurements such as 4 mc/sec or so, and changes the form of ε–T curve into the low frequency type. In reality, however, the frequency dependency of ε of the α phase in the low frequency region is such as shown in Fig. 4. In this figure the dielectric constant decreases rapidly as the frequency increases, but soon settles itself to a certain constant value. Inferring from these results it does not seem to be adequate to explain the origin of the abnormal value of alcohols in the low frequency region by the simple ionic polarization, because the abnormal high value of the dielectric constant of the α phase is conspicuous in the low frequency region. Thus, the frequency dependency of ε and equivalent parallel resistance R_x were examined in detail (Figs. 4 and 5). If this is Maxwell-Wagner dispersion, the ε–f curve should take a more different shape. Namely, the apparent dielectric constant ε^* of the composite dielectric is expressed by the following formula which has been obtained from (8) by a simple transformation.

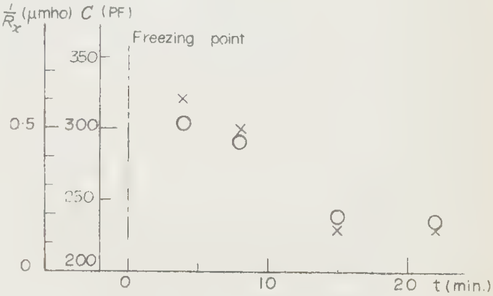

Fig. 8. Time dependency of C_x and R_x in low frequency measurements (0.5 kc).
○: C_x ×: $1/R_x$.

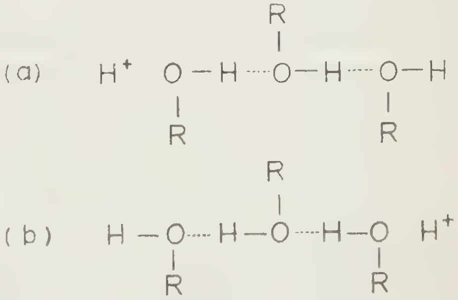

Fig. 9. A model of the proton transfer and the dipole rotation.

$$\varepsilon^*=\varepsilon[1+k/(1+\omega^2\tau^2)]\,, \qquad (9)$$

with

$$k=3p(n-1)^2/(2n+1)^2, \quad \tau=3\varepsilon/[4\pi\lambda(2n+1)]\,.$$

Therefore ε^* must approach a certain steady value when $\omega\tau\ll 1$. If we assume that $\varepsilon=\varepsilon_{\beta_1}\fallingdotseq 3$, $n\fallingdotseq 6$, $\lambda=\lambda_{\beta_1}\fallingdotseq 20\times10^{-10}$ mho/cm, then the value of k becomes approximately of the order of 0.02 and τ is nearly equal to 0.036×10^{-3}. Thus, $f_m=1/(2\pi\tau)=5.2$ kc/sec. Our experiments were carried out at 30 c/sec, but there is no sign that the curve becomes convex on the low frequency side in the diagram (Fig. 4). This result, too, does not support the "composite dielectric theory".

The frequency dependency of ε was also examined for the β_1 and the liquid phases (Fig. 5). The said dependency was slightly observed in the β_1 phase, but not in the liquid phase. It seems therefore that such ε–f characteristics is closely related to the conductivity of a sample. Cole noticed that it is necessary to take account of the "electrode impedance" which results in the increase of the apparent dielectric constant in the measurements of the conductive substances, and he applied this idea to the measurements of the formic acid. According to his result, the observed value of ε^* decreases with increasing frequency in log–log diagram on the frequency side, but it approaches by and by to a certain finite value, i.e. the 'true' dielectric constant. For example, under some experimental conditions allowing for some simplification, the apparent dielectric constant $\varepsilon_{\mathrm{app}}$ is expressed as:

$$\varepsilon_{\mathrm{app}}=\varepsilon_0+f(n)\omega^{-n},$$

where n is a certain constant independent of the frequency. This relation will be expressed in a linear relation plotted in the log–log diagram. Our results for higher alcohols well satisfy this relationship except for some details, i.e. in our case the susceptance $\omega c_0\varepsilon$ is of the comparable order of magnitude with the conductance $4\pi c_0\lambda$, so that Cole's simplification condition does not hold as in the case of the formic acid, but qualitatively the frequency dependency is of the same nature.

Therefore it seems likely that the abnormal value of the dielectric constant of higher alcohols is due to the electrode impedance which originates from the charge distribution close to the electrode on account of the appreciable conductivity of the molecular rotating phase of the normal higher alcohols. This problem has already been discussed by Johnes and Christian[9] and Ferry[10] and others. Thus, if this idea be correct in our case, the steady value, being about 3.8, in 1∼5 kc/sec region of the ε–f curve will be the 'true' dielectric constant of the α phase of higher alcohols in the low frequency region.

In spite of taking such effect into account a marked difference in the ε–T curve still exists between the results for low frequency regions, which are now under investigation.

§ 4. Proton Transfer

It is difficult to decide whether the proton originates from alcohol itself by decomposition or from some inevitable impurities, and whether decomposition occurs thermally or electrically, but anyhow it is certain that the main part of the conduction current is carried by proton transfer[11]. But its mechanism should be discussed in detail in connection with the dipole rotation.

When a sample was held at the α phase under the field, the conduction current was damped gradually but attained again a high value at the α phase in cooling after it was once brought to the liquid state, or in warming stage from the room temperature after it was cooled once to the β_1 phase where the current had been damped down to a low value. If the ion (proton) be supplied by dissociation of the alcohol, the only reason for the damping of the conduction current would be the formation of the space charge adjacent to the electrode. This space charge will be disappeared at the β_1 phase and then liquid phase, because the further supply of the charge by proton transfer will be interrupted on account of the vanishing of the proton conducting O-H net plane. So a part of the space charge will be fade out at the electrode and another part will be diverged by the thermal agitation (in the liquid state) or by rearrangement of the molecules (in the β_1 phase). The latter mechanism will be discussed later in detail.

The transfer of protons will be performed by the cooperative action of the molecular rotation and the jump of the proton in the hydrogen bond from one potential minimum to another. Therefore, the velocity of the proton transfer will be limited by the frequency of the less frequent process of the above two. Moreover, the conduction current will be damped by and by owing to the formation of the space charge and the establishment of the equilibrium in the dipole orientation. On the other hand, the rotation of the dipole becomes possible by any one of the above two processes. So the frequency of the rotation will be determined by the easier process of the two. The rotation of dipoles is accompanied by the displacement current, and its damping factor is determined by the relaxation time. Usually this displacement current will not be observed in the D.C. measurements except some particular cases, and plays a role mainly in the A.C. measurements. The reason why the conductance of a sample takes a larger value in the A.C. measurements than in the D.C. case will partly be related to displacement current and partly due to space charge formation.

When the equilibrium in the charge distribution of the ions and the dipole orientation has been once established, the D.C. conduction current will not flow any more, even if the molecular rotation exists. Because the net flow of charge to the field direction is disappeared according to the mechanism mentioned above. But the A.C. current flows as long as the freedom for the displacement of ions and dipoles exists as discussed above. Consequently, the transition point, which is the limit of the molecular rotating phase, is observed clearly in the A.C. measurements (Fig. 1).

The effect of the cooling speed upon the D.C. conductivity cannot be well explained, but it seems to be unreasonable to suppose as follows. The free ions will be distributed more broadly in the liquid phase than in the α phase as the result of the thermal motion of molecules and ions themselves, and owing to the lack of the O-H net plane carrying the ions, the disturbed charge distribution cannot return to the initial equilibrium state under the action of an external field, so that the charge distribution becomes broad more and more. However, when the solidification occurs and the α phase begins to grow, the proton transfer becomes possible and the charge distribution begins to be established, giving rise to the flow of the D.C. current. This current will be small, however, when the crystallization advances gradually and the stable charge distribution will be almost established with the formation of the solid α phase. This idea seems to be supported by the experimental facts that the maximum of D.C. current exists at higher temperature side in the case of cooling than in the case of heating in spite of supercooling of some degree.

In the case of rapid cooling the ions are still distributed widely in the solid phase and the formation of the space charge is not developed, so a large current due to the proton transfer will be observed. Moreover, the displacement current due to the orientation of dipoles under the influence of external field might be taken into account in such cases. However, no experimental data confirming this phenomenon have yet been obtained.

Nevertheless it may be possible to suppose as follows. In the case of slow cooling the dipoles take some equilibrium positions "on solidification", and on the other hand in the case of rapid cooling randomly orientated dipoles take preferred orientations "in the solid phase" under the action of external field. Consequently the displacement current will be larger in the latter case. Of course, this is not the case in the A.C. measurements, where the effect of cooling speed is not so important and the equivalent conductance is not damped with the decreasing temperature in the α phase but remains to be almost constant as long as the dipole rotation is possible.

In Fig. 9 it is to be noticed that the proton may be transferred by the dipole rotation, which is important in the $\alpha \rightleftarrows \beta_1$ transformation. In the β_1 phase the molecular rotation ceases to occur and the molecules are fixed at lattice points by certain intermolecular forces which overcome the external electrical field of ordinary intensity. In this state nearly equal numbers of dipoles have opposite directions and no spontaneous polarization occurs, and consequently the proton distribution is smoothed out to some extent. This state is determined by the intensity of an external field and the effect of the previous thermal history is dimished. Therefore, similar R–T curves would be obtained in every case under the same field intensity irrespective of the variation of the previous cooling speed.

Sure in fact, the free migration of ions will be considered to take place which does not depend upon the proton transfer. Thus, the real conduction current will be the sum of these two kinds of current.

Acknowledgement

In conclusion the authors wish to express their thanks to Prof. K. Tanaka for his helpful discussions and to Prof. R. Goto who offered them pure samples. This work has been carried out by a grant-in-aid of the Ministry of Education.

References

1) K. Higashi and M. Kubo: Sci. Pap. I. P. C. R. **36** (1938) 286.
2) W. O. Baker and C. P. Smyth: J. A. C. S. **60** (1938) 122.
3) J. D. Hoffman and C. P. Smyth: J. A. C. S. **71** (1949) 431.
4) Y. Kakiuchi, T. Sakurai and T. Suzuki: J. Phys. Soc. Japan **5** (1950) 369.
5) Y. Kakiuchi and T. Suzuki: Lectured at the meeting of the Physical Society of Japan, April 1951.
6) H. Ott: Z. f. Phys. Chem. **193** (1944) 218.
7) K. W. Wagner: Ark. f. Elektrotech. **2** (1941) 371.
8) J. F. Johnson and R. H. Cole: J. A. C. S. **73** (1951) 4536.
9) G. Jones and S. M. Christian: J. A. C. S. **57** (1935) 272.
10) J. D. Ferry: J. C. P. **16** (1948) 737.
11) Y. Kakiuchi, H. Komatsu and S. Kyoya: J. Phys. Soc. Japan **6** (1951) 321.

JOURNAL OF THE PHYSICAL SOCIETY OF JAPAN Vol. 10, No. 8, AUGUST, 1955

Anomalous Lattice Spacings Caused by Stacking Disorder

By Hiroshi NIMURA*

Physical Institute, Nagoya University, Nagoya, Japan

(Received May, 10, 1955)

Evaporated metal crystallites (gold, silver and aluminium) were studied by means of electron diffraction. As was previously reported by E. C. Williams (Research, **5**, 1952, 392), measured spacings deviated from the cubic formula by the order of 0.1 percent for gold and silver while no deviation was detected for aluminium. We attributed the deviation to stacking faults in crystallites while Williams attributed it to a dislocation line penetrating through a crystallite.

§ 1. Introduction

Williams[1] studied evaporated metal crystallites (gold, silver, copper and aluminium) by means of electron diffraction and found that except for aluminium measured spacing d_{hkl} are not in accordance with well-known cubic formula $d_{hkl}=a_0/\sqrt{h^2+k^2+l^2}$. He interpreted this phenomenon as due to a tension which arose from a single dislocation in a metal crystallite. In the present work, Williams' experiment was repeated and a similar result was obtained. On interpreting the result, however, we adopted Kimoto's[2] idea that stacking faults exist in evaporated metal crystallites. The purpose of the present paper is to describe our experiment and to give an interpretation of it.

§ 2. Experimental

Specimens and their electron diffraction patterns. Metals studied were gold, silver and aluminium. These metals were evaporated in vacua and deposited on Formvar film of a thickness of about 100 Å. The evaporation was carried out in vacua higher than 1×10^{-4} mmHg. The mean thickness of evaporated film was from 100 Å to 500 Å; almost all of the specimens were 200 Å thick.

Specimens were studied by a high resolution electron diffraction camera, with a camera length of 40 cm. Diffraction patterns showed the orientation of crystallites in specimens at random. The rings of gold and silver were broader than those of aluminium; especially the (200) rings of gold and silver were remarkably broad and, moreover, were unusually faint[2)].

---

* Now at Tokyo Metropolitan University, Tokyo.

Measurement of ring diameters. Diameters D_{hkl} of six rings given in the heading of Table I were measured on original photographic plates by a comparator. Measurements were carried out in four directions making angles of $\pi/4$ and in each of the four directions readings were taken four times. The result of the measurements indicated that rings were slightly elliptic. This was due to the deviation of the incident beam from the normal to the photographic plate. This effect was corrected after measurements were made. An example of a set of corrected values is given in Table I. The mean values $\bar{D}_{hkl}$ of diameters and their probable errors ${}_{\Delta}\bar{D}_{hkl}$ are also given.

Table I. Corrected values of diameters D_{hkl}, their mean values $\bar{D}_{hkl}$ and probable errors ${}_{\Delta}\bar{D}_{hkl}$. Gold film of mean-thickness 200 Å.

	(111)	(200)	(220)	(311)	(331)	(420)
	cm	cm	cm	cm	cm	cm
D_{hkl} 0	1.9461	2.2452	3.1809	3.7284	4.9031	5.0311
$\pi/4$	1.9462	2.2455	3.1811	3.7285	4.9035	5.0295
$2\pi/4$	1.9462	2.2463	3.1798	3.7267	4.9051	5.0300
$3\pi/4$	1.9465	2.2464	3.1785	3.7271	4.9068	5.0292
$\bar{D}_{hkl}$	1.9463	2.2459	3.1801	3.7277	4.9046	5.0300
${}_{\Delta}\bar{D}_{hkl}$	0.0001	0.0002	0.0004	0.0003	0.0006	0.0003

Result of the experiment. In the present work Bragg relation is rewritten[3)] as

$$\lambda L = \frac{1}{2} D_{hkl}\, d_{hkl}\{1-(3/32)(D_{hkl}/L)^2\} \qquad (1)$$

where L is the camera length, λ the wave length, D_{hkl} the ring diameter and d_{hkl} the spacing. We inserted in the right-hand side the mean diameter $\bar{D}_{hkl}$ and X-ray value of spacing d_{hkl} calculated by the cubic formula. We put an approximate value 40 cm. for the camera length L. If the spacing obeys the cubic formula, the left-hand side should come out constant independent of (*hkl*). In the present experiment, however, the left-hand side calculated as above depends on (*hkl*) indicating a deviation from the cubic formula. We denote the value of (λL) thus calculated by $(\lambda L)_{hkl}$.

To study the deviation we calculated

$$\Delta_{hkl} = \frac{(\lambda L)_{111} - (\lambda L)_{hkl}}{(\lambda L)_{111}} \qquad (2)$$

Table II gives the values of $(\lambda L)_{hkl}$ and Δ_{hkl} for the example cited in Table I.

Table II. Values of $(\lambda L)_{hkl}$, Δ_{hkl} and probable errors ${}_{\Delta}\Delta_{hkl}$ calculated from the data in Table I.

	(111)	(200)	(220)	(311)	(331)	(420)
	cm·Å	cm·Å	cm·Å	cm·Å	cm·Å	cm·Å
$(\lambda L)_{hkl}$	2.2862	2.2845	2.2868	2.2853	2.2867	2.2858
$\Delta_{hkl}\times 10^4$	0	7.4	−2.6	3.9	−2.2	1.7
${}_{\Delta}\Delta_{hkl}\times 10^4$	0	1.4	1.8	1.3	1.7	1.1

Figs. 1a, b, c and d show examples of Δ_{hkl} for gold and silver. The values of Δ_{hkl} are different in Figs. 1a and b although they are both obtained from gold film of 200 Å. This indicates that the values of Δ_{hkl} vary remarkably through a slight difference in the conditions of evaporation. Fig. 1d shows values of Δ_{hkl} for gold films of thicknesses of 100 Å and 500 Å simultaneously prepared. Fig. 1d suggests that there is a general tendency for the deviation Δ_{hkl} to decrease as the thickness increases. Fig. 1e shows the result for aluminium. It is noteworthy that for aluminium the deviation is less than 10^{-4}.

Effect of annealing. By annealing gold specimens for 15 minutes at 200°C in a vacuum, the rings became sharp and the deviation was reduced. Fig. 2 gives the results of the sample obtained by annealing the sample in Fig. 1a.

§ 3. Theoretical Calculation of Δ_{hkl}.

The intensity of X-ray diffraction by crystals with stacking faults was calculated by Wilson[4)] and Paterson[5)]. According to Paterson, the intensity distribution I by face-centred cubic crystal is generally expressed as

$$I = \sum_j \sum_m F_j F^*_{j+m} \exp 2\pi i\left(h_1 m_1 + h_2 m_2 + \frac{h_3 m_3}{3}\right) \qquad (3)$$

where h_1, h_2 and h_3 are indices of hexagonal axes (Fig. 3), and F_j the structure factors of the atoms at the points $\mathbf{r}_j = j_1\mathbf{a}_1 + j_2\mathbf{a}_2 + j_3\mathbf{a}_3/3$. The factor 1/3 of the third term in the exponentiol is introduced because the period $\mathbf{a}_3$ corresponds to three layers of cubic (111). The factor F_j is independent of j_1 and

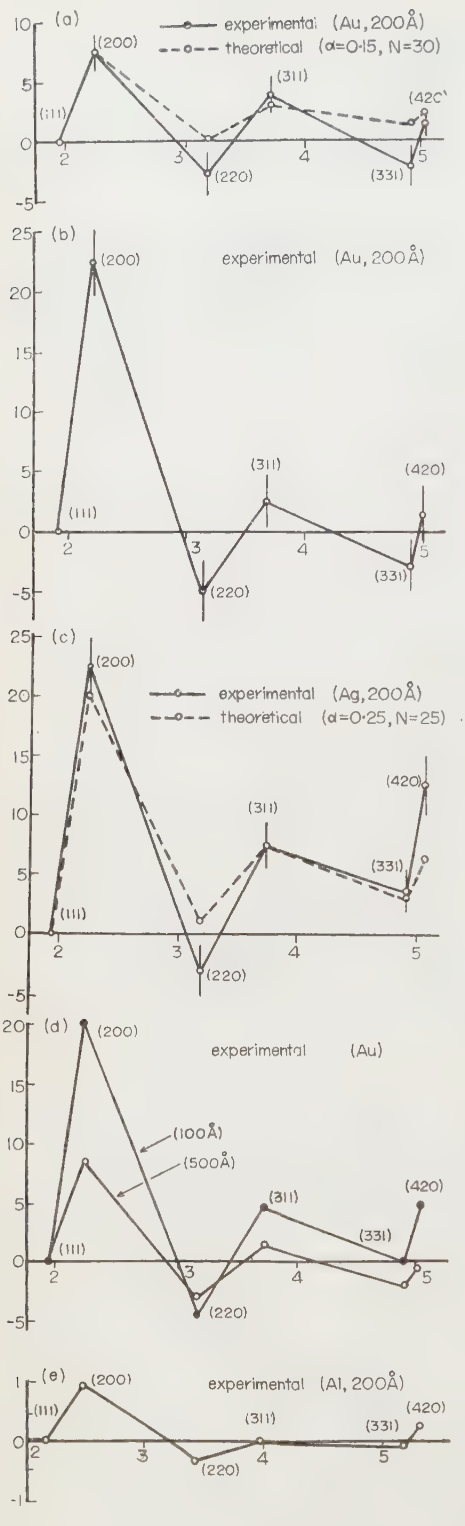

Fig. 1. Values of Δ_{hkl}. Ordinate, $\Delta_{hkl}\times 10^4$; abscissa, diameter (cm). Bars indicate probable errors.

j_2, but depends on j_3. The mean value J_m of $F_jF^*_{j+m}$ in the crystal depends on m_3, even when there are stacking faults on layers of cubic (111). Thus we get

$$\sum_j F_jF^*_{j+m} = (N_1-|m_1|)(N_2-|m_2|)(N_3-|m_3|)J_n \tag{4}$$

where N_1 and N_2 are numbers of unit cells in the directions of $\mathbf{a}_1$ and $\mathbf{a}_2$ respectively and N_3 is the number of layers.

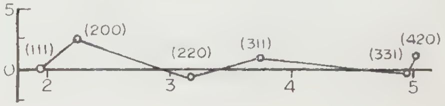

Fig. 2. Gold specimen after annealing for 15 minutes at 200°C in vacua of 10^{-2} mmHg. The data before annealing are shown in Fig. 1a.

When there are growth faults, ···ABCAB(A)CBA···, in the crystal, J_m turns out to be

$$J_m=(-1)^m\sqrt{1-2\alpha}^{\,m}\sqrt{\frac{3-6\alpha}{3-6\alpha-\alpha^2}}\times\cos\left(m\tan^{-1}\frac{\sqrt{3-6\alpha-\alpha^2}}{1-\alpha}-\tan^{-1}\frac{\alpha}{\sqrt{3-6\alpha-\alpha^2}}\right) \tag{5a}$$

for both $h_1-h_2=3n+1$ and $3n-1$, while for $h_1-h_2=3n$

$$J_m=1 \tag{5b}$$

where, for simplicity, m_3 is written as m, n indicates an integer and α is the probability of the occurence of stacking faults. Eq. (5a) holds, provided $\alpha<2\sqrt{3}-3=0.46$. From Eqs. (3), (4) and (5), the intensity turns out to be

$$I=C\Bigg[N+\sum_{m=1}^{N-1}(N-m)\sqrt{1-2\alpha}^{\,m}\times\Bigg\{\cos 2\pi m\left(\frac{h_3}{3}+\frac{1}{2}+\frac{\Theta}{2\pi}\right)+\cos 2\pi m\left(\frac{h_3}{3}+\frac{1}{2}-\frac{\Theta}{2\pi}\right)+\frac{\alpha}{\sqrt{3-6\alpha-\alpha^2}}\left(\sin 2\pi m\left(\frac{h_3}{3}+\frac{1}{2}+\frac{\Theta}{2\pi}\right)-\sin 2\pi m\left(\frac{h_3}{3}+\frac{1}{2}-\frac{\Theta}{2\pi}\right)\right)\Bigg\}\Bigg] \tag{6a}$$

for $h_1-h_2=3n\pm1$, while, or $h_1-h_2=3n$

$$I=C\sin^2\pi N\frac{h_3}{3}\Big/\sin^2\frac{h_3}{3} \tag{6b}$$

where $N=N_3$,

$$C=\sin^2\pi N_1h_1/\sin^2\pi h_1\cdot\sin^2\pi N_2h_2/\sin^2\pi h_2,$$

and

$$\theta=\tan^{-1}\frac{\sqrt{3-6\alpha-\alpha^2}}{1-\alpha}.$$

Provided α is very small, Eq. (5a) is written approximately as

$$I=C\Big[N+\sum_{m=1}^{N-1}(N-m)\sqrt{1-2\alpha^m}$$
$$\times\Big\{\cos 2\pi m\Big(\frac{h_3}{3}+\frac{2}{3}-\frac{\alpha^2}{4\sqrt{3}\,\pi}\Big)$$
$$+\cos 2\pi m\Big(\frac{h_3}{3}+\frac{1}{3}+\frac{\alpha^2}{4\sqrt{3}\,\pi}\Big)\Big\}\Big] \qquad (7)$$

Because of the two cosine terms in Eq. (7), the intensity is symmetric across the plane $h_3=0$. This indicates that a growth fault results in a twin and thus an intensity region splits symmetrically into two regions. Thus for powder samples, the intensity I turns out to be

$$I=C\Big[N+2\sum_{m=1}^{N-1}(N-m)\sqrt{1-2\alpha^m}$$
$$\times\cos 2\pi m\Big(\frac{h_3}{3}+\frac{1}{2}\pm\Big(\frac{1}{6}-\frac{\alpha^2}{4\sqrt{3}\,\pi}\Big)\Big)\Big] \qquad (8)$$

for $h_1-h_2=3n\pm1$.

Eq. (7) indicates that each of the splitted peaks shifts as much as

$$\Delta h_3=\pm\sqrt{3}\;\alpha^2/4\pi$$

from the reciprocal lattice point concerned, where +sign corresponds to the first cosine and the −sign to the second. The shift $\delta D'(h_1h_2h_3)$ of ring diameters with hexagonal index $(h_1h_2h_3)$ is given by

$$\delta D'(h_1h_2h_3)=\frac{2L\lambda^2h_3|\boldsymbol{b}_3|^2}{\sin 2\theta(1-\sin^2 2\theta)}\;\Delta h_3$$

where 2θ is the scattering angle and $\boldsymbol{b}_3$ the reciprocal lattice vector in c-direction of hexagonal lattice. Because a cubic index corresponds to several hexagonal indices and because for different hexagonal indices the value of $\delta D'(h_1h_2h_3)$ are different, the shift δD_{hkl} of a ring of cubic index (hkl) is obtained by a weighted mean

$$\delta D_{hkl}=\frac{\sum_i \nu_i A_i\delta D'_i}{\sum_i \nu_i A_i}$$

where ν_i is the multiplicity, A_i the integrated intensity of the i-th peak and suffix i refers to the hexagonal indices $(h_1h_2h_3)$ which belong to a cubic index (hkl). In order to calculate the integrated intensity, Eq. (8) is written approximately as

$$I=C\frac{\sin^2\pi N'\Big(\frac{h_3}{3}+\frac{1}{2}\pm\Big(\frac{1}{6}-\frac{\alpha^2}{4\sqrt{3}\,\pi}\Big)\Big)}{\sin^2\pi\Big(\frac{h_3}{3}+\frac{1}{2}\pm\Big(\frac{1}{6}-\frac{\alpha^2}{4\sqrt{3}\,\pi}\Big)\Big)} \qquad (8')$$

where N' is decided so that maximum values of Eqs. (8) and (8′) become equal. Thus δD_{hkl} can be calculated when α and N are given. From Eq. (1) theoretical $(\lambda L)_{hkl}$ are written as

$$(\lambda L)_{hkl}=(\lambda L)_0+\frac{1}{2}\,\delta D_{hkl}\,d_{hkl}$$

where $(\lambda L)_0$ is the value for a crystal which is free from growth faults. Then the theoretical Δ_{hkl} are given by

$$\Delta_{hkl}=\frac{1}{2}\,\frac{\delta D_{111}\,d_{111}-\delta D_{hkl}\,d_{hkl}}{(\lambda L)_0+\frac{1}{2}\delta D_{111}d_{111}} \qquad (9)$$

Since the denominator of Eq. (9) is almost equal to the experimental $(\lambda L)_{111}$, Eq. (9) is rewritten as

$$\Delta_{hkl}=\frac{1}{2}\,\frac{\delta D_{111}\,d_{111}-\delta D_{hkl}\,d_{hkl}}{(\lambda L)_{111}} \qquad (9')$$

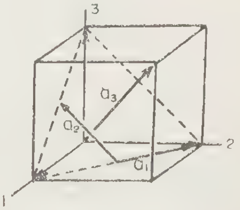

Fig. 3. The relation between cubic and hexagonal axes.

Table III. Theoretical values of Δ_{hkl} calculated to agree with the data of Fig. 1a.

α	N	(111)	(200)	(220)	(311)	(331)	(420)
0.18	30	0	10.5	0.4	3.9	2.2	3.5
0.15	30	0	7.4	0.3	3.1	1.7	2.6
0.13	30	0	5.1	0.2	1.9	1.0	1.6

In the present work the parameters α and N are estimated from experimental values of Δ_{hkl} and the breadth of rings. Inserting these parameters in equation (9′) the theoretical values of Δ_{hkl} are calculated. Then the parameters are corrected by trial method so that the theoretical values are in better agreement with the experimental values. In

Figs. 1a and 1c the theoretical values thus calculated are shown by dotted lines. In Table III theoretical values for three different α are given: the second line of this table is the values shown in Fig. 1a.

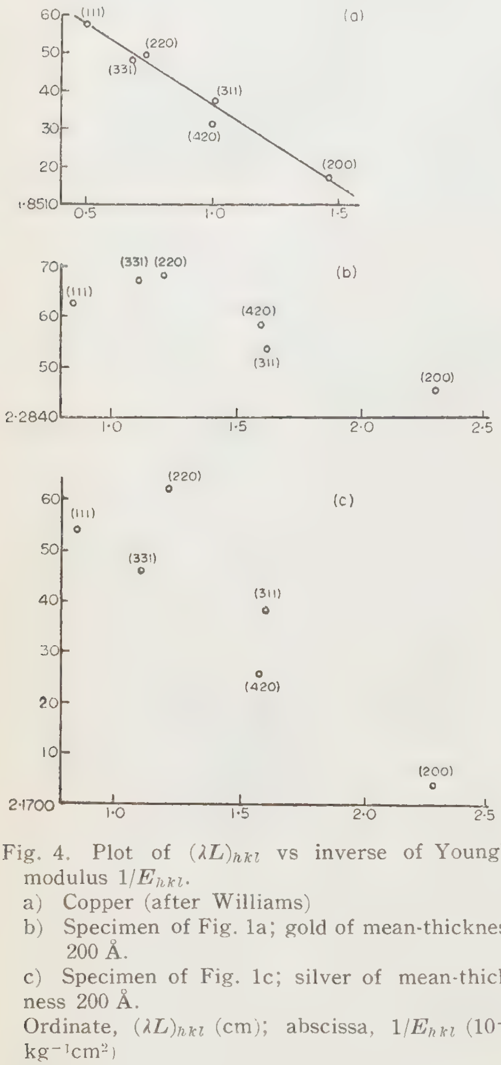

Fig. 4. Plot of $(\lambda L)_{hkl}$ vs inverse of Young's modulus $1/E_{hkl}$.
a) Copper (after Williams)
b) Specimen of Fig. 1a; gold of mean-thickness 200 Å.
c) Specimen of Fig. 1c; silver of mean-thickness 200 Å.
Ordinate, $(\lambda L)_{hkl}$ (cm); abscissa, $1/E_{hkl}$ (10^{-6} kg^{-1}cm^{2})

§ 4. Discussions

Williams¹⁾ plotted experimental $(\lambda L)_{hkl}$ against $1/E_{hkl}$ where E_{hkl} is Young's modulus in $\langle hkl \rangle$ direction. He found the linear relation as reproduced in Fig. 4a and interpreted it as follows: A single dislocation exists in a crystallite and it results in a uniform tension. Under this tension the spacings d_{hkl} are enlarged by $d_{hkl}\,\sigma/E_{hkl}$, and $(\lambda L)_{hkl}$ become

$$(\lambda L)_{hkl} = (\lambda L)_0 - \left(\frac{1}{2}\, D_{hkl}\, d_{hkl}\, \sigma/E_{hkl}\right)$$

where σ is the tension. Since $D_{hkl}\, d_{hkl}\, \sigma$ is almost constant, the left-hand side changes linearly with $1/E_{hkl}$. In our experiment, however, the linear relation is difficult to recognize as shown in Figs. 4b and 4c.

On the other hand, by adopting our idea that stacking faults result in the deviation from the cubic formula, calculated values of Δ_{hkl} agree qualitatively with experimental values. The agreement, however, is not exact, especially at (220). Even if an exact agreement were obtained, we could not conclude that our idea is absolutely correct because our calculation is approximate and the basic assumption for the calculation is too simple for quantative treatment.

The deviation from the cubic formula is negligible for aluminium. Williams ascribed this phenomenon to be due to the negligible anisotropy of aluminium. Our view point is that this phenomenon is due to the large twin energy of aluminium.

Thus it is difficult to decide which one of us has the right idea. However, we stand on our idea because Kimoto²⁾ explained the intensity anomaly of election diffraction patterns of evaporated silver by assuming stacking faults and, moreover, Kimoto and Morimoto⁶⁾ confirmed the stacking faults by radial distribution analysis of the diffraction patterns.

In conclusion, the author expresses his sincere thanks to Prof. Ryozi Uyeda for his guidance throughout this work.

The expense of this experiment is partly defrayed by Scientific Research Grant of the Educational Ministry of Japan.

References

1) E. C. Williams: Research **5** (1952) 392.
2) K. Kimoto: J. Phys. Soc. Japan **8** (1953) 762.
3) T. B. Rymer and C. C. Butler: Proc. Phys. Soc. **LIX** (1947) 541.
4) A. J. C. Wilson: Proc. Roy. Soc. **A 180** (1942) 277.
5) M. S. Paterson: J. Appl. Phys. **23** (1952) 805.
6) K. Kimoto and H. Morimoto: Read before the Annual Meeting of the Physical Society of Japan, Tokyo, Oct. 1953.

JOURNAL OF THE PHYSICAL SOCIETY OF JAPAN Vol. 10, No. 8, AUGUST, 1955

On the Structure of the X-Ray Non-diagram Lines $K\beta_\eta$ for Elements from Cr(24) to Zn(30)

By Masao SAWADA, Kenjiro TSUTSUMI, Toshio SHIRAIWA
and Masayoshi OBASHI

Department of Physics, Faculty of Science, University of Osaka

(Received May 17, 1955)

With a bent crystal X-ray spectrograph of the Cauchois type, the non-diagram line $K\beta_\eta$ was resolved into two components and the longer wave-length one was designated as $K\beta_l$ line. The intensity ratios of the $K\beta_\eta$ and $K\beta_l$ to the $K\alpha_1$ line were both estimated approximately to be the order of 10^{-4} or less.

On the basis of the wave-length positions, we could ascribe the origin of these lines to the two-electron jump between the double-hole levels ($1s2p$) and ($2s3s$). The hypothesis of such a two-electron jump which obeys the Heisenberg selection rule was first proposed by one of the present authors.[3]

The $K\beta_\eta$ originates from the transition $KL_{\text{II}}-L_{\text{I}}M_{\text{I}}$, and $K\beta_l$ from $KL_{\text{III}}-L_{\text{I}}M_{\text{I}}$.

§1. Introduction

Numerous faint lines are observed in X-ray spectra whose frequencies cannot be accounted for by transitions between the ionized states in which one electron is missing from one of the levels. These weak lines are known as non-diagram lines since they cannot be directly derived from the well known system of the energy-level diagram usually adopted. They are also called as satellites, since they appear close by the more prominent diagram lines or parent lines. Usually they appear on the shortwave-length side of the latter, and are explained as the results of single-electron jumps in atoms having two or more inner electrons removed. On the other hand, satellites on the long wave-length side are also known. In the $K\beta$ series there are the non-diagram lines $K\beta_\eta$ detected and named by Beuthe[1] in many elements between Ge(32) and V(23).

Also these very faint diffuse lines were detected in six elements from Cr(24) to K(19) by Ford[2]. These non-diagram lines are situated on the long wave-length side of $K\beta_1$, and their separations from the $K\beta_1$ are comparatively large, and it seems to be inadequate to call them the $K\beta$ satellites. We resolved these very faint diffuse lines into two components and designated the longer wave-length one as $K\beta_l$ lines, in association with the explanation of the origin of these non-diagram lines proposed formerly by one of the present authors[3]. In this paper the results of our measurements of these $K\beta_\eta$ and $K\beta_l$ lines over the range of elements from Zn(30) to Cr(24) are reported and the origin of their lines is discussed.

§2. Experimental Procedure

All spectrograms were taken with a bent crystal focussing spectrograph of the Cauchois type. The diameter of the focal circle was 20 cm, and the second order reflection by the (100) plane of a quartz crystal was used. Generally a current 10 mA at 15 to 20 kV was passed through an ion-type X-ray tube. The time of exposure was varied from 10 to 20 hours. All spectrograms were photographed on Fuji A-I plates and measured by means of a comparator with low magnification approximately five, and some of them were measured also by microphotometer records. For the measurements of the relative intensities aluminium absorbers of various thickness were set in front of the photographic plate and thus we took photograms of five kinds of the photograms of five kinds of relative intensities 1, 1/10, 1/100, 1/1000 and 1/10000 in the same plate in a single exposure.

The microphotometer curves of the $K\beta$ spectral region of iron and of nickel are shown in Photo I. Table I gives the results on the $K\beta_\eta$ and $K\beta_l$ lines over the range of

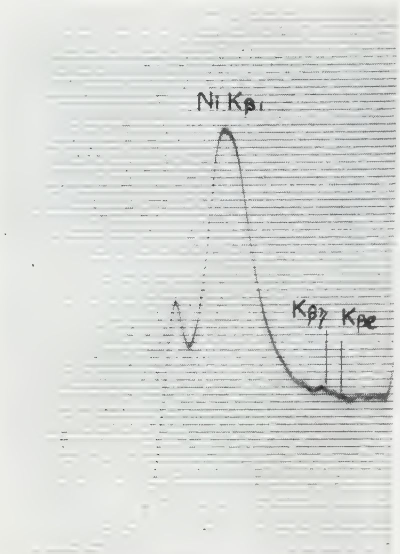

Ni

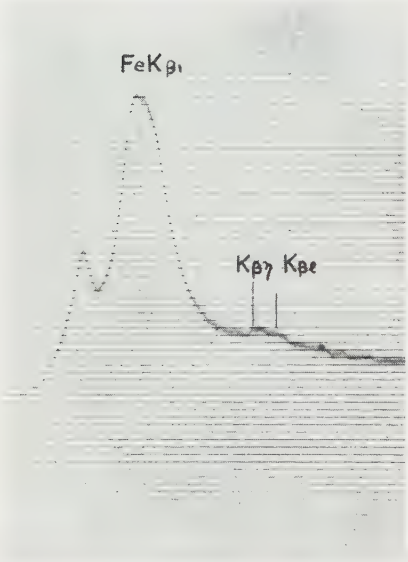

Fe

Photo. I. Microphotometer curves of the $K\beta$ spectral region of Ge and Ni.

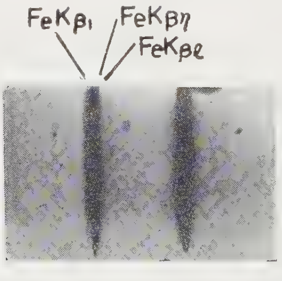

Photo. II. A spectrogram of Fe $K\beta_\eta$ and $K\beta_l$.

elements from Zn(30) to Cr(24). Column on gives the elements in which the non-diagram line was measured. Column three gives th wave-length values of the references line taken from the table in Siegbahn's "*Spektro skopie der Röntgenstrahlan*" *Zweite Anflage* The separation of the non-diagram line from the main reference line, measured on th photographic plate is recorded in column six Column seven contains the calculated wave length values of the non-diagram lines whil in the last column the values of ν/R are given The accuracy with which its wave-length ca be determined reaches an error of abou ± 0.5 xu. The values of relative intensity o the $K\beta_\eta$ and $K\beta_l$ to the $K\alpha_1$ are both estimat ed approximately to be the order of 10^{-4} o less.

§ 3. Discussion and Conclusion

To establish a scheme for the non-diagram lines in the $K\beta$ series, one of the presen authors3) assumed a two-electron jump in doubly-ionized atom which obeys the Heisen berg selection rule4) and arrived at a resul which seems to account for the origin of th present $K\beta_\eta$ lines. On the basis of wave length positions, we can ascribe the origin o the $K\beta_\eta$ and $K\beta_l$ to the following doubl transitions:

$$(1s2p)\,{}^1P,\ {}^3P \text{ --- } (2s3s)\,{}^1S,\ {}^3S$$

where the electron configurations represen electrons missing from the complete shells Now let $KL(Z)$ be the energy (in ν/R unit) o an initial state $(1s2p)$ of a doubly ionized atom of atomic number Z, from which a K and a L electron have been removed, then in th first approximation

$$KL(Z)=K(Z)+L(Z+1)\,, \qquad (1$$

since, owing to the vacancy in the inner shell, the outer L electron is moving in th field approximately equivalent to the field o an atom of atomic number $Z+1$. In equation (1), $K(Z)$ is the value of ν/R for the K ab sorption edge of the atom concerned, and $L(Z+1)$ is the value of ν/R for the L absorp tion edge of an atom of atomic number $Z+1$ Next let $L_{\mathrm{I}}M_{\mathrm{I}}(Z)$ be that of a final state 2s3 of a doubly ionized atom of atomic numbe Z,

$$L_{\mathrm{I}}M_{\mathrm{I}}(Z)=L_{\mathrm{I}}(Z)+M_{\mathrm{I}}(Z+1)\,. \qquad (2$$

Table I.

Element		Line	Reference lines main	in xu	Reference lines aux	in xu	Distance between reference lines in mm	Dispersion in xu/mm	Distance from the main reference line in mm	Wave-length in xu	Mean wave-length in xu	Mean values of $\frac{\nu}{R}$
Cr	1	$K\beta_\eta$	Cr$K\beta_1$	2080.6	Cr$K\alpha_1$	2285.0	9.15	22.34	1.4	2111.9	2111.7	431.5
	2		Cr$K\beta_5$	2066.7	Cr$K\alpha_3$	2273.3	9.45	21.86	2.05	2111.5		
	1	$K\beta_l$	Cr$K\beta_1$	2080.6	Cr$K\alpha_1$	2285.0	9.15	22.34	1.55	2115.2	2116.1	430.6
	2		Cr$K\beta_5$	2066.7	Cr$K\alpha_3$	2273.3	9.45	21.86	2.30	2117.0		
Fe	3	$K\beta_\eta$	Fe$K\beta_5$	1740.8	Fe$K\alpha_3$	1923.3	9.50	19.21	2.05	1780.2	1779.9	512.0
	4		〃	〃	〃	〃	9.37	19.48	2.00	1779.8		
	5		〃	〃	〃	〃	9.35	19.52	2.00	1779.8		
	3	$K\beta_l$	〃	〃	〃	〃	9.50	19.21	2.35	1785.9	1785.7	510.3
	4		〃	〃	〃	〃	9.37	19.48	2.30	1785.6		
	5		〃	〃	〃	〃	9.35	19.52	2.30	1785.7		
Co	6	$K\beta_\eta$	Co$K\beta_5$	1605.7	Co$K\alpha_3$	1777.4	8.95	19.18	1.82	1640.6	1640.6	555.5
	6	$K\beta_l$	〃	〃	〃	〃	〃	〃	1.98	1643.7	1643.7	554.4
Ni	7	$K\beta_\eta$	Ni$K\beta_2$	1485.6	Ni$K\alpha_3$	1647.6	8.33	19.45	1.78	1520.2	1520.1	599.5
	8		〃	〃	〃	〃	8.25	19.64	1.75	1520.0		
	7	$K\beta_l$	〃	〃	〃	〃	8.33	19.45	1.91	1522.7	1522.8	598.4
	8		〃	〃	〃	〃	8.25	19.64	1.90	1522.9		
Cu	9	$K\beta_\eta$	Cu$K\beta_2$	1378.2	Cu$K\alpha_1$	1537.4	7.90	20.15	1.45	1407.4	1407.3	647.5
	10		〃	〃	Cu$K\alpha_3$	1530.9	8.02	19.04	1.52	1407.1		
	9	$K\beta_l$	〃	〃	Cu$K\alpha_1$	1537.4	7.90	20.15	1.70	1412.5	1412.5	645.2
	10		〃	〃	Cu$K\alpha_3$	1530.9	8.02	19.04	1.80	1412.5		
Zn	11	$K\beta_\eta$	Zn$K\beta_2$	1281.1	Zn$K\alpha_3$	1428.8	6.54	22.58	1.20	1308.2	1308.5	696.4
	12		〃	〃	〃	〃	6.68	22.11	1.25	1308.7		
	11	$K\beta_l$	〃	〃	〃	〃	6.54	22.58	1.45	1313.8	1314.1	693.4
	12		〃	〃	〃	〃	6.68	22.11	1.50	1314.3		

Thus the energy change of the atom by the two-electron jump in these double-hole levels is given by

$$KL(Z)-L_{\mathrm{I}}M_{\mathrm{I}}(Z)=K(Z)-L(Z+1)-M_{\mathrm{I}}(Z+1)\,. \qquad (3)$$

When the energy L (in ν/R unit) is taken as the L_{II} or L_{III} value, the value of ν/R for the emitted quantum is respectively expressed as follows:

$$K(Z)-L(Z)+L_{\mathrm{II}}(Z+1)-M_{\mathrm{I}}(Z+1) \qquad (4)$$

or

$$K(Z)-L_{\mathrm{I}}(Z)+L_{\mathrm{III}}(Z+1)-M_{\mathrm{I}}(Z+1)\,. \qquad (5)$$

Then we write (4) or (5) in the form

$$K(Z)-L_{\mathrm{I}}(Z)+L\eta(Z+1) \qquad (6)$$

Table II. Computed ((6) and (7)) and observed values ν/R of $K\beta_\eta$ and $K\beta_l$.

Element	Observed ν/R $K\beta_\eta$	Observed ν/R $K\beta_l$	Computed ν/R $K\beta_\eta$	Computed ν/R $K\beta_l$
Cr	431.5	430.6	431.9	431.0
Fe	512.0	510.3	521.4	511.1
Co	555.5	554.4	555.2	553.9
Ni	599.5	598.4	600.4	599.0
Cu	647.5	645.2	647.2	645.5
Zn	696.4	693.4	695.7	693.7

or

$$K(Z)-L_{\mathrm{I}}(Z)+L_l(Z+1)\,, \qquad (7)$$

where $L\eta(Z+1)$ and $Ll(Z+1)$ are the values of ν/R for the $L\eta$ and Ll emission lines.

The values of $K(Z)$, $L_1(Z)$, $L\eta(Z+1)$ and $Ll(Z+1)$ in (6) and (7) are taken from experimental[5][6] and calculated [7] values. The values of (6) then computed are given in column four of Table II, and those of (7) column five.

This Table II shows the comparison of these computed values with the observed values by the present authors.

The computed values for the $K\beta_\eta$ and $K\beta_l$ agree well with those observed. Naturally the extremelly weak intensity of these lines follows from the fact that their origin is the two-electron jump between the double-hole levels.

References

1) H. Beuthe: ZS. f. Phys. **60** (1930) 603.
2) O. R. Ford: Phys. Rev. **41** (1932) 577.
3) M. Sawada: Kyoto Coll. Sci. Mem. **A 15** (1932) 43.
4) W. Heisenberg: ZS. f. Phys. **32** (1925) 841.
5) Y. Cauchois and H. Hulubei: Longueurs d'Onde des Émissions X et des Discontinuites d'Absorption X. Hermann, Paris (1947).
6) M. Siegbahn: Spektroskopie der Röntgenstrahlen, Zweite Auflage. Julius Springer, Berlin (1931).
7) B. C. Mukerjee and B. B. Ray: ZS. f. Phys. **57** (1929) 345.

Journal of the Physical Society of Japan Vol. 10, No. 8, August, 1955

A Theory of Fracture and Fatigue*

By N. F. Mott

H. H. Wills Physical Laboratory, University of Bristol,
Now at Cavendish Laboratory, University of Cambridge,
England

The concept of a piled-up group of dislocations is discussed, and its relation to ductile fracture, to brittle fracture and to fatigue. It is suggested that a large enough stress induces fracture at a piled-up group, and a large number of such small cracks can join together to produce a ductile or fatigue fracture.

§ 1. Introduction

In two previous papers (Mott 1952, 1953) the present author has discussed theories of work-hardening, recovery and creep. The aim of this paper is to attempt, in terms of the same dislocation model, a theoretical description of ductile fracture and of fatigue.

We shall first, however, give some further discussion of the theory of work-hardening. In the author's second paper the distinction was emphasized between coarse and fine slip.

The distinction is shown in Fig. 1. It is supposed that the specimen is subjected to a gradually increasing stress. In coarse slip, n, the number of dislocations, and so the slip distance on a given active slip phase, increases suddenly and thereafter slowly, if at all (Chen and Pond 1952). In fine slip n increases gradually. It was suggested that fine slip was mainly responsible for the cell formation that occurs without annealing, coarse slip for the increase of flow stress that occurs in straining (work-hardening). Fine slip is probably predominent at the beginning of deformation, and in creep.

If the dislocations generated by a source are trapped in a material, one would expect at first sight the behaviour illustrated in Fig. 1, (b), fine slip. The difficulty is to account for coarse slip, while allowing fine slip under certain circumstances. Fisher, Hart and Pry (1952) and the present author (paper I) gave an explanation of coarse slip based on the hypothesis that dislocations could move with nearly the speed of sound (the dynamic hypothesis). The present author (paper II) suggested that fine slip occurred under conditions such that a frictional force within the lattice prevented this rapid motion. The dynamic hypothesis is, however, by no means established. If it should turn out to be wrong, another mechanism must be found to explain coarse slip. A possible one is as follows. We suppose that there exist in metals dislocation networks of the kind observed in silver bromide by Hedges and Mitchell (1953), and as illustrated in Fig. 2. Suppose that a dislocation line AB serves as a Frank-Read source. When the line passes through the form shown by the dotted line, the forces due to the line-energy at the points A, B will be reversed. Certainly the points A, B will shift. It is possible that some *irreversible* re-arrangement of the surrounding network may occur, by the collapse of a hexagon or the formation of a sessible dislocation. This would leave AB permanently longer or shorter. In the former case, since if AB is denoted by l, Gb/l is the stress required to operate the source, we shall expect coarse slip; in the latter case the operation of the source will be choked after the formation of a single dislocation. If there is no change we expect to observe fine slip.

---

* This paper was read at the Symposium on Crystal Plasticity and Dislocation held at Nikko on September 12th and 13th, 1953, on the occasion of International Conference of Theoretical Physics. No alteration of the text was made since then.

In this paper we shall suppose that there is some mechanism which sometimes allows a source to produce a large number of dislocations all at once, up to a thousand, but our considerations do not depend on what this mechanism is. We need not ask, either, how long it takes a given source to generate 1000 dislocations, as long as this time is small compared with the highest period used in fatigue tests (c.10^{-3} sec.).

Turning now to the mechanism of work-hardening, two mechanisms have been proposed. There is first of all the mechanism of Taylor (1934), according to which the elastic interaction between stored dislocations hinders the motion of any mobile dislocation. This has been generalized by the present author (1952), who suggests that work-hardening is mainly due to the elastic stresses round piled-up groups of dislocations at the ends of slip lines. Then there is the suggestion of Cottrell (1953) that the stress required to force dislocations past screw dislocations which cut the slip plane will contribute to work-hardening, and his experimental demonstration that the introduction of screw dislocations, by twisting a single crystal, does, in fact, increase the flow stress (reported at Bristol Conference, July 1953). This mechanism has also been used by the present author (paper II) in a discussion of logarithmic creep.

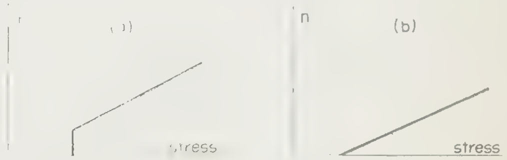

Fig. 1. Showing n, the number of dislocations produced by a source, as a function of the applied stress, (a) for coarse slip and (b) for fine slip.

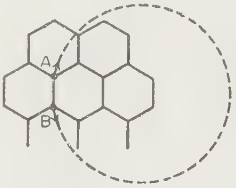

Fig. 2. Action of a Frank-Read source.

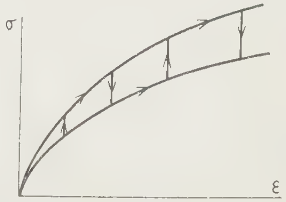

Fig. 3. Reversible change with temperature in the flow stress of a metal.

In our view both mechanisms contribute to the work-hardening, but under normal conditions, for face-centred metals at any rate, the first is the more important. The elastic forces between piled-up groups will give a slowly varying internal stress, of wave-length say 10^{-3} cm, and the resulting flow stress will be almost independent of temperature so long as no recovery occurs. The crossing screw dislocations will be spaced say at 10^{-4} cm. apart in an annealed material and much less in a cold-worked material. They may therefore be treated as introducing a frictional force impeding the movement of dislocations, and, moreover, a frictional force which is strongly dependent on temperature. (Mott Paper II).

Orowan (1947) has published some curves

showing the reversible change of the flow stress of a metal when the temperature is varied between 0°C and −180°C. These results are reproduced in Fig. 3. It is suggested that the temperature-dependent part is due to this frictional term.

In this paper we shall make use both of the long-range stress, which impedes flow because the Frank-Read sources tend to be found in minima of the potential energy curve, and short-range stresses which act like a frictional force. We may add that sessile dislocations distributed at random may produce a frictional force in the lattice by the Taylor mechanism (elastic interaction between the dislocations), and that this frictional force will not be temperature-dependent. It will exist, however, only if the movement of dislocation is sufficiently damped through interaction with lattice waves, so that the energy gained from the internal stress where the sign is favourable cannot help the dislocation to surmount the next potential hill.

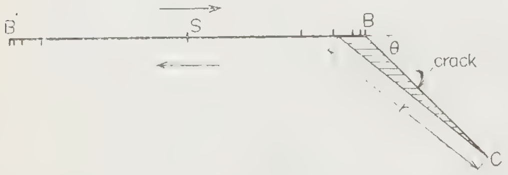

Fig. 4. Showing a crack BC at the end of a slip line BB′.

We may, at this stage, suggest that further experiments on the temperature-dependence of the flow stress of work-hardened metal would be of interest, especially in the range where there is no recovery, e.g., Cu or Ni at and below room temperature. If, as we believe, thermal recovery is due to the dispersal of piled-up groups, the flow stress of a material after recovery, but before recrystallization, should show a much greater relative temperature-dependence than before recovery.

§ 2. A Model for Fracture in Metals

Any fracture process involves the existence somewhere of a stress-concentration, so that the stress can approach locally the true fracture stress (∼0.2 G). For amorphous brittle materials the hypothesis of Griffith (1921) is generally accepted, namely that the stress concentration exists at pre-existing surface cracks. In ductile or fatigue fractures in metals, however, it is most unlikely that any such pre-existing cracks play an essential role.

It has sometimes been suggested that the vacant lattice sites formed by cold-work may coagulate and initiate fracture. While this process may possibly play a part in creep, e.g., in intercrystalline fracture, it cannot be essential in ductile fracture or fatigue, which can occur at very low temperatures.

In our view the required stress concentration exists in the piled-up groups of dislocations at the ends of slip lines. Similar stress concentrations can be produced by kinking (Frank 1952) and mechanical twinning, but as these do not occur in face-centred cubic metals, we confine our discussion to slip.

The stress concentration due to a piled-up group of dislocations and the effect on crack formation has been considered in detail by Stroh (to be published). Here we outline some of the results. Suppose that a material contains a Frank-Read source S (Fig. 4) which can generate dislocations which move freely along the slip plane BB' until they come up against the barriers B, B' which may be grain boundaries or sessile dislocations. Suppose that a *shear* stress σ is applied to the material, so that the source generates dislocations which pile up against B, B'. Then in the neighbourhood of B, B' strong *tensile* stresses will exist. These are very similar to those at the ends of a Griffiths crack, falling off at a point distant r from B as

$$\sigma A\sqrt{(L/r)}\,, \qquad (1)$$

where A is a numerical factor depending on θ and having its maximum for $\theta=45°$, and L is the length BB' of the slip line. This formula is valid at all distances r from B, provided that r is small compared with L and large compared with the distance between the leading dislocations in the piled-up group. Under practical conditions at the ends of slip lines in piled-up groups, this is likely to be three or four atomic distances at most.

We may next ask, what is the conditions that, if a crack extends from B to C, the application of a shear stress will cause it to extend further. The stress required, according to the analysis used by Griffiths, to extend a crack of length r, is of order

$$\sigma=A'G\sqrt{(b/r)}\,, \qquad (2$$

where A' is a numerical constant. It is as sumed that the surface energy, which occurs in Griffith's analysis, is of the form const. Gb per unit area. Comparing (1) and (2), we see that the crack will open if

$$\sigma A\sqrt{(L/r)} > A'G\sqrt{(b/r)}\ .$$

This gives

$$\sigma/G > C\sqrt{(b/L)}\ , \qquad (3)$$

where C is a numerical constant of order unity.

The important point about (3) is that it is independent of r, for all r above a few atomic spacings. It is reasonable to suppose, then, that it represents the condition that the shear stress σ will *initiate* a crack, of the type shown in Fig. 4.

It is interesting to compare (3) with the stress at which a Frank-Read source in an annealed material will generate dislocations, namely Gb/L. With $l\sim10^{-4}$ cms, $L\sim$ say 10^{-2} cm, it is clear that (3) may be perhaps ten times larger than the initial flow stress. Thus cracks will not form at the ends of the first slip lines formed in an annealed metal, but may form as the work-hardening proceeds. We consider that they will form at stresses of the order $100\,Gb/l$, not 10 times this factor, as would appear at first sight from the above argument. The reason is that formula (3) is misleading for a cold-worked material, because something stops the source acting after about 1000 dislocations are formed, so that the dislocations pile up at the end of the slip line, the middle part being free of them. A description of how this might occur is given in the author's previous paper (paper I). As a consequence L in formula (3) must be replaced by $L\sigma_0/\sigma$, where σ_0 is Gb/l. The conditions for the formation of a crack becomes

$$\sigma/G > l/L\ , \qquad (4)$$

which, with $l\sim10^{-4}$ cm. and $L\sim10^{-2}$ cm, gives stresses of the order of those for which actual polycrystalline cubic metals break.

Stroh's analysis shows that under the influence of the shear stress σ acting on the source S, the crack once formed will spread a distance of order L in the annealed material or $L\sigma_0/\sigma$ in the cold-worked material. It will not spread further unless a tensile stress is applied across the crack obeying the Griffith criterion for spread of a crack. The value of this stress will be given by the formulae (3), (4) though the numerical factors may be different.

We now apply these formulae to different types of fractures. Formulae (3) might be applicable to the recent experiment at Sheffield (Greenwood e.a.) on the fracture of polycrystalline zinc at low temperatures, which occurs after little or no plastic deformation. Greenwood finds that the fracture stress is inversely proportional to the square root of the grain size. If the slip line length is identified with the grain size, this result should follow from (3). An objection is that no slip lines have been observed for these small deformations, and that, in any case, fine slip is to be expected for zinc. We feel, therefore, that the applicability of the formula to this case is doubtful. Similar considerations for fractures in iron have been advanced by Petch 1953.

We turn now to ductile fracture. In this case it is known that an irregular fissure forms within the neck of the tensile specimen, and extends to the surface only with further plastic deformations (Orowan 1948). It seems fairly clear that a number of the cracks of the type that we have described must form and the material between them tear apart, some time before a visible crack appears. The evidence for this comes from Bridgman's work (1945). He shows that if a tensile specimen is pulled out under high hydrostatic pressure, it has considerably greater ductibility when the pressure is removed than it would have had if the pressure had never been applied. The suggestion is that the pressure prevents the cracks from forming or, at any rate, from reaching their maximum length.

We have now to ask why a crack, once formed, does not normally extend across the specimen under the influence of the applied tensile stress; and why, especially in ferrous materials, it sometimes does, giving the phenomenon of notch brittleness. The answer must be that in a face-centred metal such as copper, the generation of dislocations by other sources, i.e., ordinary plastic flow, relieves the stress at the apex C of the crack of Fig. 4. This may well occur before the crack reaches its maximum allowed length ($L\sigma_0/\sigma$, say 10^{-3} cm) at which it becomes dangerous, and may spread under the tensile stress. If, on the other hand, the surrounding sources are locked by carbon or dissolved gases in the sense described by Cottrell for iron, time and the effect of temperature are required to release them. The whole process of slip line formation taking place rather suddenly, brittle fracture may occur if the temperature is low enough.

Finally, we give a short discussion of the effect of temperature on ductile fracture. Fig. 3 shows the type of effect expected on the stress strain curve; the curve rises more steeply at low temperature owing to the increased effect of Cottrell's hardening mechanism, the "forest" of screw dislocations which cut the active slip planes. Curves of this type would mean that the onset of necking would be delayed at low temperatures. The tables published by Teed (1950) show that, in fact, for copper and nickel the elongation at fracture is considerably *increased* at liquid air temperature compared with room temperature, but there seems to be little, if any, change in the reduction of area at fracture. This seems to suggest that the temperature-dependent part of the applied stress is without effect in producing fracture. This is to be expected if it has its origin in a frictional force on the movement of dislocations, as suggested above.

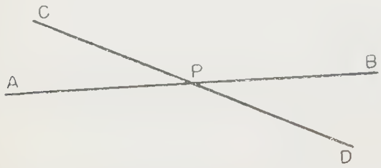

Fig. 5. Showing two octahedral planes on which dislocations move.

§ 3. The Fatigue Loop

Before the turning to fatigue fracture, we give a discussion of the energy loop in fatigue tests. We base our work first on the investigations of N. Thompson and his colleagues on single crystals of aluminium submitted to slow cycles of tensile and compressive stresses for about 1000 cycles. Thompson has given a discussion of these results, and for any given cycle the form of the hysteresis loop, and also the creep if the stress is held constant, fits well with the assumption that there are a number of free dislocations in the material which move backwards and forwards through a *large* distance (large compared with, say, 10^{-4} cm, the distance between the dislocations of the mosaic network), there being a frictional force (short range fluctuations in internal stress, energy in cutting crossing dislocations ?) which is responsible for the dissipation of energy, and also a non-reversible hardening process. This is thought to be due to the existence of barriers (sessile dislocations) in the active slip planes, so that when the moving dislocations approach their barriers, fixed groups of two or more are formed. As already emphasized, any grouping together of the dislocations already in a material increases the mean value of the internal stress and so the hardness.

Of particular interest to us, however, is the slow decrease in the area of the hysteresis loop which occurs during the first 1000 cycles. A similar initial drop is observed for pure copper in the first few thousand cycles with the high speed fatigue machine. This must mean either that the number of mobile dislocations decreases or that more sessile dislocations form on the slip planes, thus decreasing the slip distance. In any case, what we have to explain is the following:

Dislocations are moving backwards and forwards along octahedral planes such as *AB* and *CD* in Fig. 5. Usually they do so without meeting, but perhaps once in 1000 cycles they do meet, and form a sessile dislocation at *P*.

A slow hardening, presumably by the formation of sessile dislocations, seems typical of the whole fatigue process (compare Head 1953). Obviously such a thing could not occur if the internal movement of dislocations were periodic with the same period as the applied stress. We do not believe that this can be so. Part of the frictional force impeding the movement of free dislocations is, as we have seen, due to the screw dislocations which cut the active slip plane. These themselves will move about all the time. The density of jogs on the moving dislocations will get steadily greater, at any rate for the first few thousand cycles, after which perhaps jogs will be destroyed as fast as they are made. There is no reason to suppose that the motion will repeat itself, and we may well have to wait several thousand cycles before a particularly fortunate event enables the two dislocations of Fig. 5 to join up.

§ 4. Fatigue Fracture

The slow hardening described in the last section will not produce fracture; this, in our view, depends, essentially on the formation of slip lines.

With regard to fatigue, we must emphasize that the process can take place at the lowest temperatures. It is, therefore, unlikely to depend essentially on the formation of vacancies by moving dislocations and their subsequent coagulation to form cracks.* It seems to us much more probable that it is due to the stresses round the piled-up groups of dislocations at the ends of slip lines.

Confining ourselves to face-centred cubic metals of reasonable purity, the relevent facts seem to be:

(1) There is little, if any, dependence of the fatigue life on speed in the range 50–1000 cycles a second.

(2) Early in the fatigue life slip lines appear, and some observers (e.g. Thompson) note an increase in the number throughout the test. Some of the lines gradually broaden by forming a large cluster of lines very close together; it is here that the crack eventually starts. According to Duce (1952) these lines are oriented close to the plane of maximum shear stress.

(3) According to Thompson, in copper in push-pull a single grain first breaks across a cleavage plane, and a jagged fracture spread from there (Fig. 6). Using Head's analysis of the spread of a fatigue crack, one would guess that the fracture of the initial grain occupies more than half the total fatigue life.

(4) Repeated annealing up to the softening temperature does not increase the fatigue life, so the early "damage" must be of the form that is not easily removed by annealing, and thus a crack rather than a piled-up group of dislocations.

With regard to the slow formation of slip lines, the arguments of the previous part of this paper suggest that, if a Frank-Read source is subjected to a stress above a certain level σ_1 for a short time (less than 10^{-3} sec. should suffice), a slip line will be formed. The stress σ_1 can be identified with the sum of Gb/l and the local internal stress σ_i. The latter will increase as work-hardening increases. We have already seen that the material will contain loose or mobile dislocations which move backwards and forwards on each cycle, but that the motion is not periodic. Thus the local stress at any point fluctuates in a random way. Occasionally it reaches a particularly high value, so that a slip band is formed.

As work-hardening proceeds, we should expect more mobile dislocations and hence a higher hysteresis loop (which Thompson finds) and a larger fluctuating internal stress. On the other hand, σ_i increases. It is not clear, therefore, whether the rate of formation of slip lines should increase or decrease.

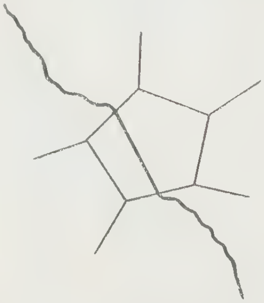

Fig. 6. Showing type of fracture in fatigue.

For an understanding of fatigue, however, we need to consider the broadening of the slip lines which are formed early on. We suggest that those on which the shear stress is a maximum may produce, at their limits, high enough local stresses to produce the kind of local crack, a few mutiples of a micron long and, say, 1000 atoms wide, which is illustrated in Fig. 3. During subsequent cycles this will enhance the stress in the neighbourhood of this particular slip line. Thus, after waiting again for a favourable fluctuation of stress, a new slip line will form in the immediate neighbourhood, producing another crack. The cumulative effect of 10 or 20 of such events cracks the whole grain; producing the effect illustrated in Fig. 6. The fatigue crack then spreads by the mechanism outlined by Head.

References

1) P. W. Bridgman: Rev. Mod. Phys. **17** (1947) 3.

2) Chen and N. K. Pond: Trans. AIME **194** (1952) 1085 (in J. of Metals 4).

3) A. H. Cottrell: J. Mech. Phys. Solids **1** (1953) 53.

4) A. G. Duce: Thesis, Cambridge (1952).

---

* Note added July 1955. Some evidence now exists that this may occur.

5) J. C. Fisher, E. W. Hart, R. H. Pry and Frank: Phys. Rev. **87** (1953) 958 (in Press).
6) A. A. Griffith: Phil. Trans. Roy. Soc. **A221** (1920) 163.
7) Greenwood (to be published)
8) A. K. Head: Phil. Mag. (1953) (in press).
9) J. M. Hedges and J. W. Mitchell: Phil. Mag. **44** (1953) 223.
10) N. F. Mott: Phil. Mag. **43** (1952) 1151 (Paper I); **44** (1953) 742 (Paper II).
11) E. Orowan: J. West. Scotland Iron Steel Inst. **54** (1947) 45; Rep. Prog. Phys. **12** (1948) 185.
12) N. J. Petch: J. Iron and Steel Inst. May (1953) 25.
13) P. L. Teed: The Properties of Metallic Materials at Low Temberatures; Royal Aeronautical Society (1950).
14) N. Thompson: (1953) (to be published).

JOURNAL OF THE PHYSICAL SOCIETY OF JAPAN Vol. 10, No. 8, AUGUST, 1955

The Interpretation of Etch Patterns on Aluminium*

By A. J. FORTY and F. C. FRANK

H. H. Wills Physical Laboratory, University of Bristol, England

An examination of etch patterns obtained with Lacombe's etchant on polycrystals of "super-purity" aluminium suggests that an etch pit is produced only where there is a precipitate of impurity present in the surface, and that these are located on dislocations which can therefore be regarded as an indirect cause of etching. It is tentatively estimated that, at best, only about 60 or 70 per cent of the dislocations in super purity Al produce etch pits.

§ 1. Introduction

The localised solution or etching of a crystal often develops pits in the surface. The cause of the formation of an etch pit at one particular point on a surface and not at other places has aroused considerable speculation but it has been generally agreed that it can only be due to a surface singularity of either a physical or chemical nature.

The recent work of Horn (1952) who observed the solution of growth surfaces of crystals of silicon carbide has shown very convincingly that, since etch pits are always developed at the centres of spiral growth hills, the crystal dissolves much faster at those places where screw dislocations meet the surface. Similar observations have been made with crystals of cadmium iodide (Forty; unpublished). It is certain, therefore, that an etch pit can be formed, possibly by a mechanism similar to that responsible for crystal growth, wherever dislocations meet habit surfaces.

The further possibility that dislocations might be responsible for the formation of etch pits on surfaces other than habit faces has been suggested by the studies of micro-etch patterns on pure aluminium crystals made by Lacombe (1944–1948). The alignments of pits often found after the polished surface (of an arbitrary orientation) of a well-annealed crystal had been etched could be identified with the traces of sub-boundaries. The small change of orientation of the lattice detected by X-ray measurements across an alignment predicted a wall of dislocations whose spacing approximately equalled that of a etch pits. Shockley (1949) among others, suggested that each pit should therefore be developed where a dislocation in the boundary meets the free surface. This idea has been emphasized by Cahn's studies of the polygonisation of ben and annealed crystals where he used the preferential etching along their traces in the surface to detect polygonisation boundarie (1949).

---

* This paper was read at the Symposium o Crystal Plasticity and Dislocation held at Nikko o September 12th and 13th, 1953, on the occasion o International Conference of Theoretical Physics No alteration of the text was made since then.

Fig. 1. ×150

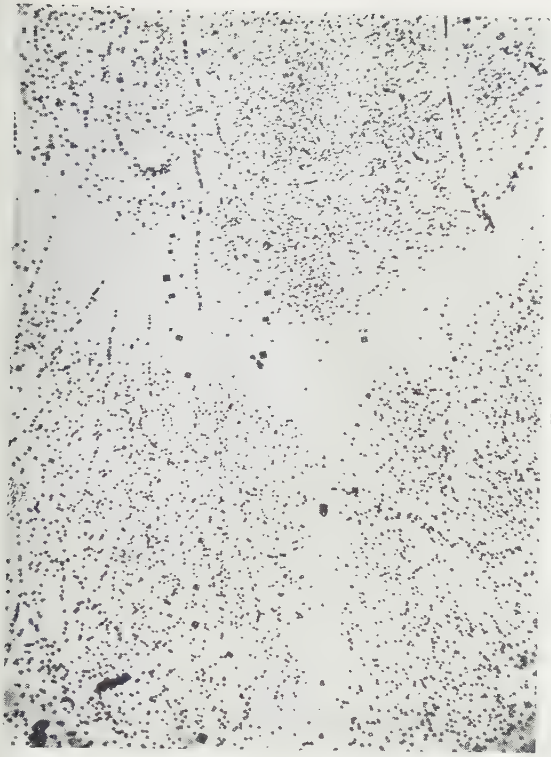

Fig. 2. ×150

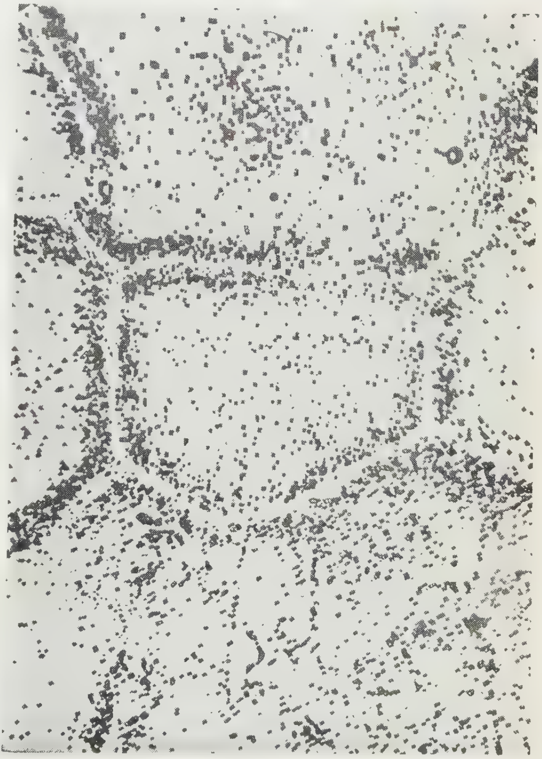

Fig. 3. ×150

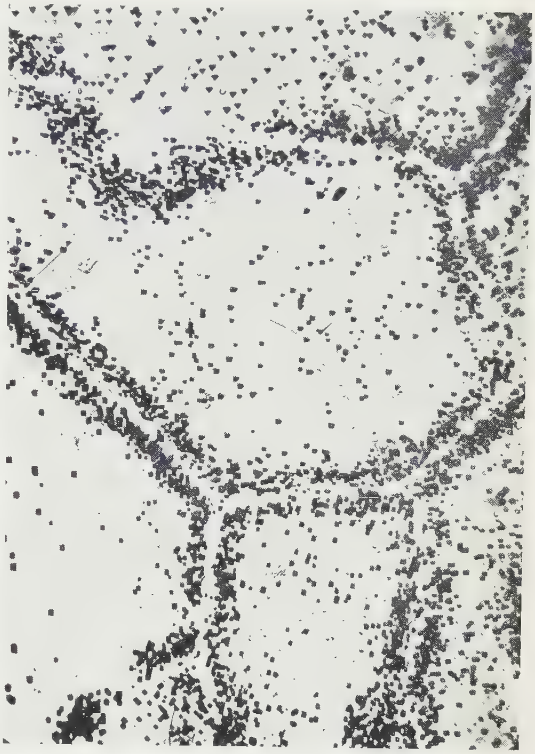

Fig. 4. ×150

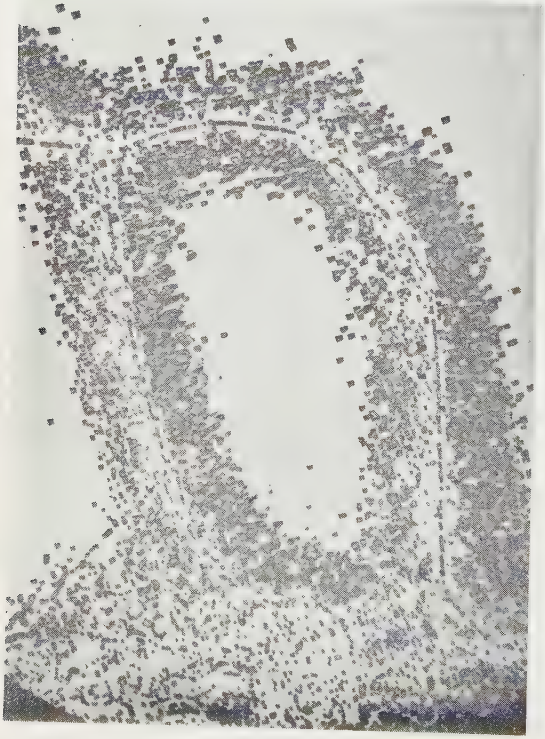

Fig. 5. ×150

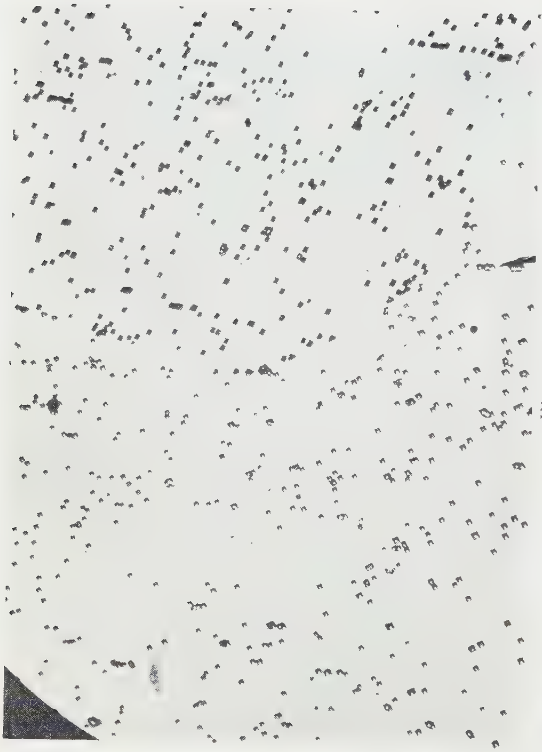

Fig. 6. ×150

Fig. 7. Section perpendicular to plane of grain boundary. ×150

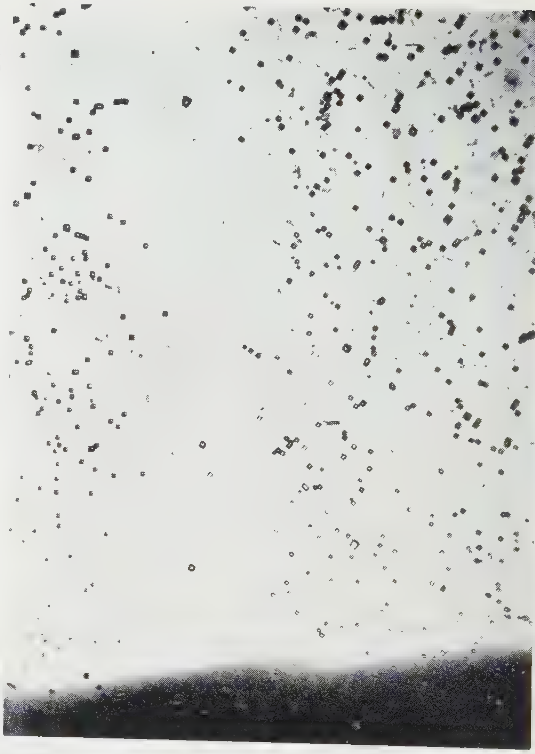

Fig. 8. Section making oblique angle of 30° with plane of grain

However, although we know that dislocations can stimulate etching, there remain the the questions of how many of the etch pits are due to dislocations and how many of the dislocations in a crystal produce etch pits. The number of dislocations in a simple tilt boundary can be determined from a measurement of the change of lattice orientation $\theta = 2\sin^{-1}(b/2h)$ where b is the length of the Burgers vector of each dislocation and h is their spacing in the wall. This relation has been investigated very carefully by Vogel et al. (1953) for (110) boundaries which meet (100) surfaces in Germanium crystals. The value of h calculated from X-ray measurements agrees so well with the spacing of etch pits along the boundaries that at least 90 per cent of the dislocations in Germanium must produce pits. On the other hand, as a result of our observations on the etching of super purity aluminium by a technique similar to that of Lacombe, we have concluded that only a fraction of the dislocations in sub-boundaries produce etch pits and that these can only do so because they hold suitable amounts of chemical impurity. This work is still in progress, and the X-ray determinations of orientation difference have yet to be made. In the meantime any quantitative estimates made below are only tentative.

§ 2. Description of Etch Patterns on Aluminium

The observations to be discussed here have arisen from a re-investigation of the etching of aluminium described earlier by Lacombe (1948). We have prepared large grain-size polycrystalline specimens from super purity aluminium (99.999%, supplied by the British Aluminium Company) in four different ways. The surfaces of these have been carefully prepared by a 'polish etch' technique,* followed by a lengthy 'electropolish' in a bath of perchloric acid, alcohol and ether, and then etched by immersion in a concentrated mixture of nitric acid, hydrochloric acid and hydrofluoric acid (Lacombe's etchant). All of the micrographs described here are of surfaces which have been etched for one or two seconds only.

§ 3. The Growth of Etch Pits

From a succession of polishes followed by etching for successively longer periods from 1 second to 32 seconds we have concluded that, whereas the density of pits does not increase, the pit size is very dependent on the length of etching. Successive immersions in the etchant with an intermediate polishing of the surface which does not completely remove the old pattern produce new distributions of etch pits; that is, pits already established in the surface cannot usually be further developed after one removal from the etchant.

§ 4. The Formation of Pit-lines

The alignments of pits already described by Lacombe represent the traces of small angle sub-boundaries which lie approximately perpendicular to the free surface. Fig. 1 shows part of the surface of a crystal which has been grown slowly from the melt by a travelling furnace technique; the alignments here tend to follow the growth direction. The pits in the alignments are by no means regularly spaced and we suggest that, since the dislocation array in a sub-boundary can be expected to have a fairly regular structure, only a fraction of the dislocations actually produce pits. Although the general form of the alignments can be reproduced by polishing and etching the surface again there is no pit for pit correspondence between the patterns even when only a few microns of aluminium are removed. The selection of dislocations which form etch pits appears to be more or less random.

A 'clear lane' or strip of surface about 10 microns on either side of the alignments which is almost free from etch pits will also be noticed in Fig. 1. A clear lane might be explained by the condensation of dislocations from the surrounding crystal into the more stable arrays which we call sub-boundaries but there are alternative explanations which we shall discuss later.

§ 5. Grain Boundaries in Crystals which have been Grown Slowly from the Melt

Large grained polycrystals have been prepared 'in vacuo' by a moving furnace technique. A polished and etched surface shows a fairly uniform distribution of pits inside each grain which is broken only by pit-lines along the traces of sub-boundaries. There is nevertheless a recognizable "texture" in the grouping of the pits over the surface of each grain, when seen at low magnification. It is remarkable that when grain boundary migration occurs, after growth or in a subsequent anneal, this "texture" still corresponds to the original grain pattern. The density of pits in a typical grain in about 10^6 per sq. cm., which is considerably lower than that of 10^8 per sq. cm. usually quoted for the number of dislocations crossing each sq. cm. inside a well annealed metal crystal. This must mean that either only about 1 per cent of the dislocations in aluminium can produce etch pits or that present ideas of dislocation content must be modified.

---

* 'Brasso' metal polish on a rotating Selvyt Cloth pad.

Fig. 2 is a typical micrograph showing the junction of three large graing in one of these specimens. Rather surprisingly we find that, although the individual grains are fairly uniformly etched, there are very few etch pits lying on the grain boundary itself and in the surrounding surface for about 20 microns on either side. This lack of pits on large-angle grain boundaries and in the surrounding 'clear lanes' is not a surface phenomenon only since it has been reproduced after the removal of a large thickness of aluminium by electropolishing. Therefore we conclude that in these specimens the grain boundaries are enclosed in a slab of metal, 40 microns in thickness, which will not etch because it is free from dislocations, or contains only dislocations which do not meet the free surface, or is chemically different from the greater part of the metal. These possibilities will be reviewed later in the light of further observations. Our observations differ notably from those of Lacombe in that, whereas he found a few exceptional grain boundaries which were not attacked, we very rarely observe any attack on the grain boundary itself.

§ 6. Grain Boundaries in Crystals Grown by the Rapid Cooling of Melts

A fairly coarsely grained polycrystal is grown when an aluminium melt in a graphite boat placed inside a quartz tube with an atmosphere of argon is cooled rapidly by the removal of the furnace. Fig. 3 shows the kind of etch pattern produced on the polished surface of such a specimen. The density of pits inside individual grains is about the same as that found for slowly grown grains and is fairly uniformly random apart from occasional pit-lines which must locate the traces of sub-boundaries. Again, there are very few pits lying on the grain boundaries and in the surrounding clear lanes. The important distinction between this kind of etch pattern and that described in the previous section, however, is that the clear lanes are separated from the uniform distribution inside each grain by dense clusters of pits. The pits in the clusters are some three or four times closer together than in the centres of the grains.

It is this clustering of pits around the grain boundaries which has suggested to us that the formation of an etch pit in the surface of an aluminium crystal is dependent on the accumulation of impurities as well as on the presence of a dislocation. We can expect most kinds of solute to remain preferentially in solution in the melt during growth until a certain concentration is reached. Therefore, when a large number of different grains nucleated at about the same time are growing from a rapidly cooled melt, the impurities will largely separate from the melt only during the final stages of growth to be accumulated around the boundaries where neighbouring grains meet. It is possible that these impurities are precipitated on dislocation lines from solid solution during the cooling down process, and that preferential etching at a dislocation is due simply to the presence of the precipitate. The precipitate need not be uniformly distributed along a dislocation line, indeed, the micrographs showing the segregation of photolytic silver on dislocation lines in crystals of silver bromide prepared by Hedges and Mitchell (1953) shows clearly that the silver separates in discrete particles. This means that a surface prepared by taking a section through a crystal containing a uniform array or network of dislocations each with a randomly distributed precipitate will not show a uniform etch pattern but will contain etch pits only where it cuts through precipitate. The precipitates on the dislocation lines can be expected to be more closely spaced and therefore more likely to be intersected by the surface where impurities are initially concentrated in solid solution. In the example under discussion here (Fig. 3) this occurs around the grain boundaries where we observe the dense clusters of etch pits. Further support for this idea that the clusters of pits coincide with accumulations of impurity might be derived from Fig. 4 which shows how a grain boundary has straightened out from its 'cast' position (indicated by the clusters of pits in the upper right hand corner) to its new position where it is no longer surrounded by clusters.

It is unlikely that the 40 micron wide slab of metal beneath the clear lanes around grain boundaries in these and the slowly grown specimens is completely free from dislocations and we might have to infer that it consists of very pure aluminium where none of the dislocations hold impurities and therefore cannot stimulate etching.

§ 7. Boundaries in a Dendritically Grown Crystal

When a melt of aluminium in a graphite boat inside an evacuated quartz tube is cooled rapidly by removing the furnace quickly, it undergoes a certain degree of super-cooling and solidifies dendritically. A dendritic skeleton of solid aluminium, essentially good single crystal, grows rapidly through the melt. The solidification in layers near the surface is completed by a thickening of the dendrite arms and where portions of solid growing on neighbouring arms meet a 'dendrite boundary' is formed. Should the arms become slightly misoriented during growth, by mechanical shock or by the action of convection currents in the melt, we can expect a small change of lattice orientation here; that is dendrite boundaries are likely to be sub-boundaries, consisting of grids of dislocations. As expected a dendrite boundary is often delineated by a line of etch pits (Fig. 5).

Again the appearance of dense clusters of pits around the boundaries, where we expect impurities to be accumulated during the final stages of solidification, is consistent with the hypothesis that precipitates of impurity are primarily responsible for the etching. The surface beyond the clusters contains only very few etch pits. This is understandable if the impurities in the melt fail to separate until the final stage of solidification under the conditions of cooling responsible for dendritic growth.

§ 8. Boundaries in a Polycrystal where Grain Growth has taken Place After Straining and Annealing

Large grains have been prepared by initially straining and then annealing fine grain polycrystals cut from a stock of super purity aluminium. The pattern of etch pits on these can be completely described as a random one (see Fig. 6 for example). There are no pit lines in the individual grains, which agrees with the results of the investigation of substructures in aluminium by Lacombe (1948) and by Guinier and Tennevin (1950) who found that polygonisation did not occur if the conditions of straining and annealing supported ordinary recrystallisation. The random distribution of pits is unaffected by the presence of a grain boundary; there is no outstanding lack or concentration of pits on or around it. There is thus a remarkable difference between boundaries in specimens which have been melted 'in vacuo' or in argon and those in specimens which have never been heated above about 600°C since manufacture. This suggests to us that some impurities in the metal as received are present in the form of particularly stable precipitates which cannot be totally dispersed without heating to a higher temperature than this, or melting, and that these remain as nuclei determining the sites of solute precipitation on cooling, and the location of etch pits, irrespective of solute concentration and dislocation structure.

§ 9. A Mechanism for the Etching of Aluminium

The alignment of pits along the traces of sub-boundaries in the crystals is a clear indication that solution can occur where dislocations meet the surface. However, the lack of regularity in the spacing of pits in the alignments suggests that every dislocation cannot stimulate etching. The clustering of etch pits around grain and dendrite boundaries in specimens solidified from a rapidly cooled melt can be explained by the accumulation of impurities here if we visualise an increased case of attack of the aluminium around dislocations where the impurities have been precipitated during cooling. Solution of aluminium in the etchant used should proceed easily once the protective oxide film on the surface has been pierced and it is likely that this penetration would be assisted by small amounts of precipitate in the surface. Therefore, we consider that etch pits in aluminium are formed at dislocations only where these function as precipitation centres for impurities. There cannot, on the other hand, be any large proportion of pits due to precipitate particles not associated with dislocations (except in the strain-anneal specimens), or the alignments of pits at subboundaries would not be so clearly recognizable.

The precipitate need not be continuously distributed along the dislocation lines but might be expected to be more concentrated on those dislocations where impurities have been accumulated during solidification. Therefore, etch pits, formed only where the surface cuts through the precipitates, tend to cluster around grain and dendrite boundaries, but are more widely spaced over the remainder of the surface.

A discontinuous precipitate is necessary to explain why the etch patterns cannot be reproduced pit for pit after intermediate polishing. It will also account for the non-regularity in the spacing of pits in the alignments. It is here that we can estimate the fraction of dislocations which produce pits. If this fraction is p, elementary statistical theory shows that if p is 0.1 or less, 13.5% of the intervals in a pit-line will exceed twice the mean interval, whereas if p exceeds 0.5 this fraction is less than 8.7%. By this sort of test we judge that in Lacombe's specimens p is fairly large, exceeding 0.5, whereas in our specimens p is only as large as this where there is reason to believe impurities are locally concentrated. The probable reason for the difference is the higher purity of our Aluminium (99.999% against Lacombe's 99.99%).

§ 10. The Origin of the 'Clear Lanes' Around Grain Boundaries

Clear lanes where the surface is free from attack by the etchant are apparent around grain boundaries in both rapidly and slowly cooled melts, around dendrite boundaries and around sub-boundaries. The original sites of grain boundaries from slowly cooled melts, where impurities presumably originally accumulated are marked by bands where the attack, although not so markedly absent as around the present positions of the boundaries, is very limited.

In some cases it can be seen that considerable grain boundary migration must have taken place during cooling. If the boundaries are moved further by successive anneals at 600°C the etch patterns always cantain clear lanes around their new positions but show no trace of the previous intermediate positions of the boundaries or of their passage through the material.

We consider here only two of the possible explanations for the occurrence of clear lanes. Neither of these is completely satisfactory.

The first explanation considers that the clear lane lies above a slab of material which is chemically different from the remainder of the metal. If a boundary, whether a small angle sub-boundary or a large angle grain boundary, presents a better site for the precipitation of impurities than a single dislocation, solute will tend to diffuse with it from the surrounding grains during cooling. Less solute will be precipitated on the dislocations surrounding the boundary so that the probability of an etch pit being formed here will be considerably lowered. Such a diffusion process taking place during only a few minutes cooling would demand a diffusivity of about 10^{-8} cms.^{2} per sec. which is improbable unless the impurities are dissolved interstitially in the aluminium.

The second explanation considers that the dislocation lines surrounding the boundaries, having a considerable line tension, will tend to orient themselves normal to the boundaries. Since grain boundaries likewise tend to orient themselves perpendicular to the free surface, a surface of polish parallel to the free surface will likewise be parallel to the dislocation lines in the neighbourhood of the grain boundary, while making a fair random section of them elsewhere, provided that it is at a depth of a few tens of microns. Such an effect must logically be expected, but it has been shown not to be the principal cause of the clear lanes, by comparing the width of the clear lane on a surface which cuts a grain boundary perpendicularly with that on a surface which cuts the boundary obliquely at an angle of 30 degrees. Figs. 7, 8 show that the clear lane appears to be considerably wider on the oblique surface which is what we might except only if it lies above a slab of chemically different material. We therefore conclude that the absence of etch pits near a grain boundary is to be attributed to an absorption of solute into it. The high diffusivity at a boundary would allow this solute to be precipitated as a small number of large precipitate particles, giving only a small number of etch-pits. The difficulty regarding the high diffusivity is removed if we suppose the diffusivity to be high along the dislocalion lines. This would suffice to reduce the solute concentration along these lines, in the neighbourhood of a boundary, and so suppress the nucleation of precipitates, while still leaving the concentration in the remainder of the surrounding crystal high.

References

1) F. H. Horn: Phil. Mag. **43** (1952) 1210.
2) P. Lacombe: "Strength of Solids" (Report on Bristol Conference) (Physical Soc. London).
3) P. Lacombe and L. Beaujard: C. R. Acad. Sci. Paris **218** (1944) 878.
4) R. W. Cahn: J. Inst. Metals **76** (1949) 121.
5) F. L. Vogel, W. G. Pfann, H. E. Carey and E. E. Thomas: Phys. Rev. **90** (1953) 489.
6) J. M. Hedges and J. W. Mitchell: Phil. Mag. **44** (1953) 223.
7) W. Shoekley and W. T. Read: Phys. Rev. **75** (1949) 692.

JOURNAL OF THE PHYSICAL SOCIETY OF JAPAN Vol. 10, No. 8, AUGUST, 1955

On the Plasticity of Silver Bromide*

H. KANZAKI

Institute of Industrial Science, University of Tokyo, Chiba City, Japan

Experimental study on the plastic deformation and the recovery process from strain hardening is described on the single crystals of silver bromide.

The various sorts of defects created during deformation are separated in each stage of recovery process, because of the difference of mobility energies. The difference of the mobility energies is also revealed in the change of the temperature dependence of excess ionic conductivity during the recovery process.

From the measurements of the change of excess ionic conductivity and the release of energy in the recovery process, the number of defects produced by deformation at room temperature was determined to be 10^{-7} per atom of anti-Schottky defects and 10^{-4} per atom of Schottky defects.

Some discussions are given on the mechanism of recovery from hardening and on the life time of defects in the recovery from strain hardening and in that from thermal quenching.

§ 1. Introduction

There are close connections between lattice defects and dislocations. In the case of silver halides, we have already several experimental results which indicate the intimate connections between defects and dislocations[1].

Some experimental investigations on the nature of defects introduced by the plastic deformation of silver bromide single crystals will be described in this article.

The reasons for our selection of silver bromide as an example of inoic crystals are as follows.

---

* This paper was read at the Symposium on Crystal Plasticity and Dislocation held at Nikko on September 12th and 13th, 1953, on the occasion of International Conference of Theoretical Physics. No alteration of the text was made since then.

(1) The nature of the ionic conduction has been studied in detail by Teltow[2] and Kurnick[3].

(2) The direct experimental evidence has been obtained by Hedges and Mitchell[4] on the polygonized structure in the recovery process, and by Goddard and Urbach[5] on the preferential ionic conduction through grain boundaries.

§ 2. Experimental Results Obtained

§ 2–1. Specimens

Sample used in this experiment was prepared from the powder of silver bromide specially made by the Research Laboratory Fuji Photo Film Co., Ltd.. Single crystals (5 cm in diameter and 2 cm in height) were obtained by slow cooling method from the melt. The purification by "zone melting" method was adopted in the solidification process. The virgin specimens were cut from these crystals, annealed at about 400°C and then slowly cooled to the room temperature.

§ 2–2. Strain hardening

Plastic deformation was given by compression at the room temperature of about 25°C. Fig. 1 shows the stress-strain curve of our crystals. The magnitude of strain-hardening is nearly equal to that of aluminium crystals.

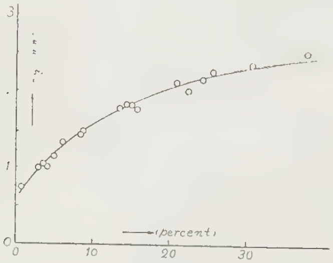

Fig. 1. Stress-strain curve for AgBr crystals (after compression test).

§ 2–3. Enhancement of ionic conductivity and its recovery

Conductivity of the specimen, in this experiment, was measured by the method of voltage pulse and galvanometer, similar to that used by Etzel and Maurer[6]. The charge passed through in the single measurement was about 10^{-8} coulomb for specimens of 1 cm × 1 cm and 0.5 cm in thickness. The direction of the current was reversed in each measurement and the validity of the Ohm law was checked in every experiment by varying the height of voltage pulses. All measurements at and below room temperature were carried out in the vacuum of about 10^{-2} mmHg.

The knee point in the log (conductivity) vs. $1/T$ curves was about 50°C for annealed specimens. The activation energy for conduction below the knee point was about 7,800∼8,200 cal/mol (from the measurements between 28°C and 0°C). This value of activation energy corresponds to the value of Ag^+ vacancy mobility energy of 8,300 cal/mol obtained by Kurnick[3].

The specific conductivity at 28°C increased from $2\sim3\times10^{-8}$ $(\Omega.\,\mathrm{cm})^{-1}$ to $13\sim16\times10^{-8}$ $(\Omega.\,\mathrm{cm})^{-1}$, by the deformation of about 35 percent (decrease in height). All recovery experiments described below were carried out on the specimens subjected to almost the same degree of cold-work of 35 percent compression.

Preliminary experiments on the temperature dependence of excess conductivity due to cold work have shown that conductivity of deformed crystal is given by the following formula.

$$\sigma = A\exp(-U/kT) + B\exp\left(-\left(\frac{W_0}{2}+U_0\right)\Big/kT\right) \qquad \cdots (1)$$

where,

σ, ionic conductivity of deformed crystal,

U, mobility energy of defects introduced by cold work.

U_0, mobility energy of defects existed in thermal equilibrium.

W_0, formation energy of defects existed in thermal equilibrium,

and values of A and U are the function of degree of cold-work and of time of annealing.

Fig. 2(a) shows the change of excess conductivity in the course of annealing, obtained for two different samples with almost the same degree of cold working. These curves were obtained under strictly uniform heating rate of 1.5 minute per 2°C (the same heating rate as the specific heat measurement described later). All measurements were carried out at 28°C, after corresponding annealing. It is seen that the recovery, the decrease of excess conductivity, is composed of three succeeding processes.

Fig. 2(b) shows the change of mobility energy U of excess conductivity obtained from the measurements of conductivity below room temperature.

Fig. 2(c) shows the change of hardness (indentation depth of steel ball of 3.18 mm in diameter).

§ 2–4. Anomalous specific heat due to recovery

Specific heat of deformed crystals was measured from room temperature to about 300°C under constant heating velocity of 1.5 min. per 2°C. The apparatus for specific heat measurement was that used in the measurement of specific heat anomaly of cold worked Cu single crystals⁷⁾. But the measurements in this case were carried out in the atmospheric pressure. The accuracy and reproducibility of the measured value of the specific heat was within one percent in the case of annealed crystals. The values of Cp of cold worked crystals and annealed crystals have shown good coincidence within 0.5 percent at the temperature where no anomaly was observed.

Fig. 2(d) shows the existence of three groups of anomalous specific heat. It is seen that each group of anomaly is composed of two stages; two valleys of specific heat are observed in each recovery process. This corresponds to the existence of two stages in the recovery of cold worked copper⁷⁾.

In the measurements of three samples subjected to the same degree of cold work, the temperature of anomaly was reproducible within 10°C under the standard heating rate and was almost the same for a sample which was heated under one and a half as large heating rate.

Energy released in each of these six stages was found to be as follows,

first recovery process,
first stage ·····2.6∼2.8 cal/mol,
second stage···1.4∼1.9 cal/mol,
second recovery process,
first stage ·····1.8∼2.1 cal/mol,
second stage···2.3∼2.6 cal/mol,
third recovery process,
first stage ·····1.9∼2.5 cal/mol,
second stage···1.3∼1.9 cal/mol.

These values were obtained from the measurements for three samples subjected to almost the same degree of deformation. Total energy released, 12 cal per mol, corresponds to 30 percent of the external work of 40 cal per mol.

§ 2–5. Activation energy of recovery process

Activation energy of recovery process was obtained for three recovery processes from

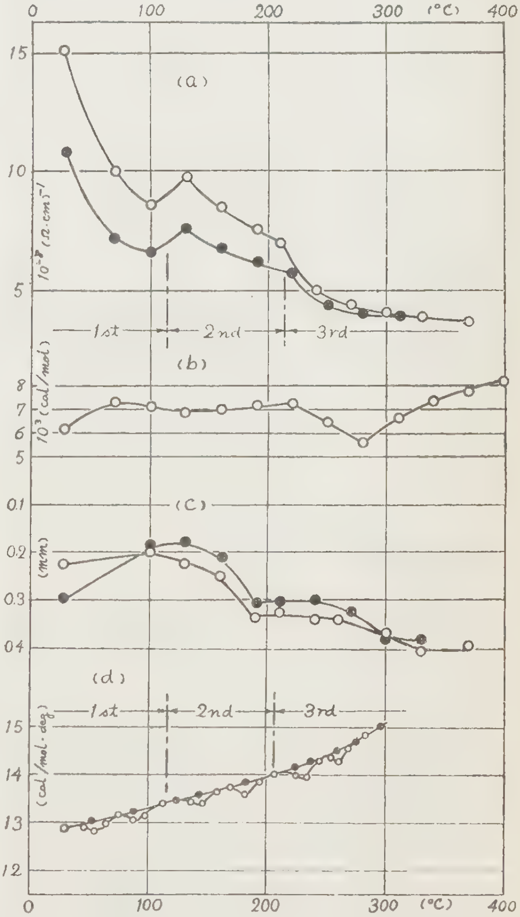

Fig. 2. Recovery of cold worked single crystals of AgBr (subjected to 35 percent compression) under constant heating velocity of 1.5 min. per 2°C.

(a) Specific conductivity at 28°C against annealing temperature (for two samples).
(b) Mobility energy U of ionic conduction (from the value of conductivity between 0°C and 28°C).
(c) Hardness at room temperature; indentation depth of steel ball of 3.18 mm in diameter (for two samples).
(d) Specific heat C_p vs. temperature. White circles are obtained for deformed sample and black circles for annealed sample.

the decrease of excess conductivity at constant temperature. In the usual expression.

$$\tau=\tau_0 \exp(E/kT) \qquad \cdots(2)$$

the value of relaxation time τ was obtained from the inflection point in a plot of conductivity against log (annealing time). This method of obtaining τ is convenient, because it does not require a knowledge of the final value after complete recovery.

Fig. 3 shows the temperature dependence of the value of τ obtained from the measurements of conductivity and hardness. The values of τ_0 and E in equation (2) were calculated from these data.

For the first recovery process

$$\tau_0=4\sim8\times10^{-1}\text{ sec},\ E=3{,}900\sim4{,}600\text{ cal/mol}.$$

This value of E may agree with the mobility energy of Ag^+ interstitial ions 3,400 cal/mol by Kurnick[3].

For the second recovery process,

$$\tau_0=1\sim3\times10^{-2}\text{ sec},\ E=8{,}500\sim9{,}300\text{ cal/mol}.$$

For the third recovery process,

$$\tau_0=1\sim2\times10^{-1}\text{ sec},\ E=8{,}500\sim9{,}300\text{ cal/mol}.$$

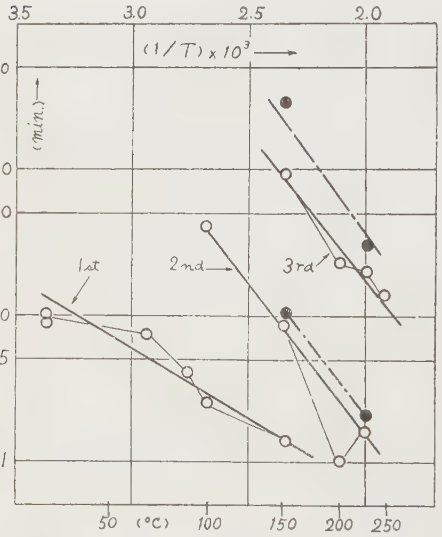

Fig. 3. Relaxation time τ for the three recovery processes from strain hardening vs. $1/T$. White circles from conductivity measurements and black circles from hardness measurements.

This value of E in the second and the third recovery processes may agree with the mobility energy of Ag^+ vacancies 8,300 cal/mol by Kurnick[3].

§ 3. Discussions

§ 3-1. Classification of defects generated by the motion of dislocations

The mechanisms of production of defects from moving dislocation may be divided into two following categories[8];

(1) thermal creation, and (2) geometrical creation of defects.

Thermal creation of defects may be thought as similar to the thermal quenching of defects near slip bands. Defects thermally created in our case may be,

> Ag^+ interstitials and Ag^+ vacancies (Frenkel type), and Ag^+ vacancies and Br^- vacancies (Schottky type).

Geometrical creation of defects may be the production of defects in the "wake" of jogs in the screw dislocations. Defects geometrically created in our case may be,

> the row of Ag^+ interstitials and Br^- interstitials (anti-Schottky defects), and the row of Ag^+ vacancies and Br^- vacancies (Schottky defects).

§ 3-2. Existence of two stages in each of three recovery processes

(1) In the first stage of each recovery process, experimental results obtained show;

> large decrease of conductivity,
> decrease of mobility energy U (second and third recovery processes), no change of hardness (second and third recovery processes), and anomalous specific heat.

It may be concluded that this stage may be thought as the process of diffusion of defects to the "jogs" of edge dislocations. This stage may bring the decrease of number of free defects and the decrease of the projected area of dislocations in the plane normal to the Burgers vector.

(2) In the second stage of each recovery process, obtained results show;

> small decrease of conductivity,
> increase of mobility energy U (second and third recovery processes), decrease of hardness (second and third recovery processes), and anomalous specific heat.

It may be concluded that the decrease of dislocation density, or the annihilation of dislocation rings occur in this stage. In the next paragraph, we may treat these three processes rather quantitatively.

§ 3–3. Three recovery processes

(1) First recovery process.

The faster moving component in this recovery process is thought to be Ag^+ interstitial ions from the value of activation energy of the recovery process obtained in § 2–5.

Decrease of conductivity of 5×10^{-8} $(\Omega.\mathrm{cm})^{-1}$ at 28°C corresponds to the vanishing of 10^{-7} Ag^+ interstitial ions per atom. If the vanishing pair is that of Ag^+ interstitials and Ag^+ vacancies, the released energy is expected to be only 0.003 cal/mol, because the formation energy of Frenkel defects is 28,000 cal/mol after Kurnick[3]. In order to satisfy the value of 2.5 cal/mol released in the first stage, we presumably must adopt the vanishing pair of Ag^+ intersitials and Br^- interstitials.

Vanishing of Ag^+ interstitials results the increase of mobility energy U, because the components govering the ionic conductivity change from the mixed state of Ag^+ interstitials and Ag^+ vacancies to the state of Ag^+ vacancies only.

In the second stage, we expect the annihilation of dislocations. But, on the other hand, two following possibilities might be expected in order to explain the increase of conductivity and hardness as observed in Fig. 2. These are;

1. formation of jogs or replenishment of jogs and creation of defects during shrinkage of dislocation rings by the intersection of dislocations with each other.

2. Collision of dislocations with clusters of defects during passage of dislocations. This may result the dissociation of cluster on the one hand and the formation of new jogs on the other hand.

We may favour the second mechanism considering the energy consumed in the process.

(2) Second and third recovery processes.

The faster moving component in these two processes may be the Ag^+ vacancy from the value of activation energy of recovery obtained in § 2–5. These two processes are satisfactorily explained by the vanishing of Schottky type defects, Ag^+ vacancies and Br^- vacancies. From the decrease of conductivity, 10^{-4} Ag^+ vacancies per atom vanish in these processes. If we adopt the value 34,000 cal/mol for the formation energy of Schottky defects[3)9)], the released energy is 3.4 cal/mol, which shows good agreement with the measured value of $2.0+2.0=4.0$ cal/mol released in the first stages of these processes.

The difference between these two processes, that is, the difference of τ_0 between them may be explained as follows. In the second recovery process defects may condense to the jogs replenished in the later stage of the first recovery process, that is, jogs in the rather small dislocation rings. In the third recovery process, on the other hand, defects may condense to jogs in the rather large dislocation rings. The rather large decrease of U in the third process shows that the defects spend their time and wander to and fro in the neighborhood of dislocations. The calculation on the change of U was done by using the results obtained by Kurnick[3] on the change of mobility energy due to hydrostatic pressure. The result shows that the decrease of U observed here may well occur near dislocation centers.

The results obtained above may agree with results by Hedges and Mitchell[4] who observed polygonized structure in deformed specimens which was annealed at about 350°C.

The sum of the energy released in the second stages in three recovery processes may be thought as the total energy of dislocations produced in the course of deformation. If we assume the energy of dislocations as 2 eV per atomic plane, we obtain the dislocation density of 10^{11} lines per cm^2 from the value of released energy 5.5 cal/mol.

§ 3–4. Life time of defects

We shall briefly discuss the problem of life time of defects from our experimental results.

Nowick[10] has made experiments on the recovery from thermal quenching of silver-zinc alloys and obtained the value of $10^4\sim10^6$ jumps for the life time of thermally quenched defects. The life time of Schottky defects of thermally quenched AgBr crystals was found to be about $10^7\sim10^8$ jumps[11], and, from the value of τ_0 obtained in § 2–5, the life time of defects produced by cold working is calculated to be $10^{10}\sim10^{11}$ jumps. The life time of defects produced by plastic deformation is, in our case, larger than that of defects quenched thermally.

It may be concluded that number of jumps of defects is determined by the density of jogs in dislocations rather than the density of dislocations as postulated by Nowick. Details of the quenching experiments and discussions will be reported elsewhere[11].

§ 3-5. Cluster of defects

Considering the rather small binding energy of defect pairs in AgBr compared with NaCl[12], pairs of opposite sign may have only transient existence in our case. But, of course, diffusion of Br^- ions may require the assistance of clusters. Measurements on the dielectric loss of deformed crystals will be reported by Sumita.

Acknowledgements

The writer wishes to express his gratitude to Professor Y. Tani for his valuable suggestions and encouragement, and to Messrs. Y. Koseki and E. Mizuki of Fuji Photo Film Co., Ltd. for their kindness of preparing the samples and many constructive suggestions.

References

1) F. Seitz: Revs. Modern Phys. **23** (1951) 328.
2) J. Teltow: Ann. Physik **5** (1950) 63.
3) S. W. Kurnick: J. Chem. Phys. **20** (1952) 218.
4) J. M. Hedges and J. W. Mitchell: Phil. Mag. **44** (1953) 223.
5) P. E. Goddard and F. Urbach: J. Chem. Phys. **20** (1952) 1975.
6) H. W. Etzel and R. J. Maurer: J. Chem. Phys. **18** (1950) 1003.
7) H. Kanzaki: J. Phys. Soc. Japan **6** (1951) 90 (for polycrystalline copper) **6** (1951) 456 (for copper single crystals). The results for polycrystalline copper show qualitative agreement with those by T. Suzuki (Sci. Rep. RITU **A 1** (1949) 193). The conclusion obtained in this article strongly supports the view that the first recovery process observed in copper in above articles is due to the disappearance of defects produced by deformation.
8) F. Seitz: Advances in Physics **1** (1952) 43.
9) H. Kanzaki: Phys. Rev. **81** (1951) 884. see also ref. (11).
10) A. S. Nowick and R. J. Sladek: Acta Metal. **1** (1953) 131.
11) H. Kanzaki: Proc. of the Syposium on the Photographic Sensitivity (to be published). Professor Seitz has kindly informed the writer that Professor Koehler of University of Illinois has obtained almost the same number of jumps for the recovery of thermal quenching of gold.
12) From experimental results on the dissociation of divalent impurity∼vacancy complex in doped AgBr, the binding energy of the complex was found to be 0.2 eV and this value is smaller than that of 0.3 eV in the case of NaCl[6]. See also ref. (11).

JOURNAL OF THE PHYSICAL SOCIETY OF JAPAN Vol. 10, No. 8, AUGUST, 1955

The Velocity of Dislocations[*][†]

By J. S. KOEHLER

University of Illinois Urbana, Illinois, U.S.A.

The theory of Mott and of Fisher, Hart, and Pry for the production of slip bands is considered. This theory suggests that the kinetic energy of dislocations is what keeps glide on a slip band going; it also asserts that the process is stopped by the back stress resulting from dislocation loops previously generated at the Frank-Read source. Experimental observations giving the damping experienced by a dislocation and giving the velocity of glide are used to show that the potential energy of a dislocation is in general more than a hundred times the kinetic energy. Present evidence indicates that the rate of glide decreases by a factor of about fifty during the production of a single slip band in aluminum. Present data also indicates that twinning requires rapid dislocations whereas slip seems to demand slow dislocations. A way of reconciling these observations is suggested.

Experimentally it is found that during deformation of a crystalline material a shearing displacement of several thousand angstroms will often occur on what appears to be a single atomic plane. In aluminum the amount of shear per plane is about 2000 Å and is nearly independent of temperature and rate of deformation. Mott1) and Fisher, Hart and Pry2) suggest that this result can be understood by supposing that damping is unimportant so that energy is conserved in the formation of such a glide lamella. It is the purpose of this note to present evidence which indicates that damping is important, and that the generation of Frank-Read dislocation loops3) is not materially aided by kinetic energy. Differences in the rate of slip and twinning are noted.

Mott and Fisher, Hart and Pry suggest that the development of a glide lamella using a single Frank-Read sourca of dislocations occurs in the following way. The first dislocation loop is generated from an initially static dislocation. The applied resolved shearing stress necessary to reach the critical state (i.e., stage 2 in Fig. 1) is:

$$\sigma = Gb/L \qquad (1)$$

where L is the free length of the dislocation, G is the shear modulus, and b is the Burger's vector giving the strength of the dislocation. According to the above authors the additional length of the central portion of the dislocation in stage 4 (see Fig. 1, portion AAA) represents additional potential energy which is converted into kinetic energy as the source snaps through the initial position BBB of Fig. 1. They suggest that this kinetic energy is the reason why many loops rather than one loop are generated at a single source. They also propose that the loops already emitted exert a back stress which increases as the number of completed loops increases and that this eventually stops generation.

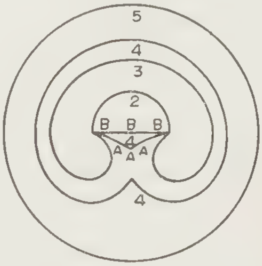

Fig. 1. Various stages in Frank Read loop generation.

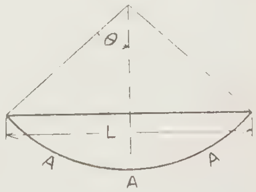

Fig. 2. Configuration adopted for K.E. calculation.

---

[*] This research supported in part by the U.S. Office of Ordnance Research.

[†] This paper was presented to the Symposium on Crystal Plasticity and Dislocation held at Nikko on September 12th and 13th, 1953, on the occasion of International Conference of Theoretical Physics. No alteration of the text was made since then.

They suppose that the kinetic energy available can be calculated approximately if the portion AAA of the dislocation which will again become the source is taken to be a circular arc as in Fig. 2. The kinetic energy available is then:

$$\text{K.E.}=r\left(\frac{L\theta}{\sin\theta}-L\right)\quad \text{no damping} \qquad (2)$$

where $r=Gb^2/2$ is the potential energy per unit length of dislocation line, and θ is half the angle subtended by the arc. It should be emphasized that equation 2 is only valid if the energy dissipated during the straightening of the arc is negligible.

Consider the straightening of the arc when damping is present. The equation of motion of the pinned down dislocation loop is[4]:

$$\pi\rho b^2\frac{\partial^2 y}{\partial t^2}-\frac{Gb^2}{2}\frac{\partial^2 y}{\partial x^2}+B\frac{\partial y}{\partial t}+(\sigma-\sigma_b)b=0 \qquad (3)$$

where the coordinates are shown in Fig. 3.

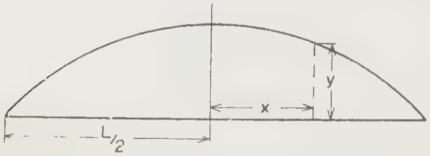

Fig. 3. Coordinates used for damped loop motion.

In equation 3 the first term on the left is the inertial force; the second term is the force on an element of the dislocation which results from its line tension; the third term is the damping force, which is assumed proportional to the velocity of the element. The fourth term represents the force resulting from the applied stress σ and the back stress σ_b. In the above equation ρ is the density of the material and B is the damping constant. The boundary conditions are:

$$\begin{aligned}&\frac{\partial y}{\partial t}=0 && \text{at all } x && t=0\\ &y=f(x) && \text{at} \quad t=0 && \\ &y=0 && \text{at} \quad x=\pm L/2 && \text{all } t\end{aligned} \qquad (4)$$

where $f(x)$ is a given even function of x which should describe initial displacements resembling the arc of Fig. 2. A suitable trial solution is:

$$y=\{R_1e^{-\beta_1 t}+R_2e^{-\beta_2 t}\}\cos\frac{\pi x}{L}-A\left(1-\frac{yx^2}{L^2}\right). \qquad (5)$$

This satisfies the differential equation if:

$$\begin{aligned}\beta_1&=\frac{1}{2\pi\rho b^2}\left\{B+\sqrt{B^2-\frac{2\pi^3\rho Gb^4}{L^2}}\right\}\\ \beta_2&=\frac{1}{2\pi\rho b^2}\left\{B-\sqrt{B^2-\frac{2\pi^3\rho Gb^4}{L^2}}\right\}\end{aligned} \qquad (6)$$

and

$$A=\frac{(\sigma-\sigma_b)L^2}{4Gb}.$$

This trial solution satisfies the last two boundary conditions (4). It satisfies the first boundary condition if:

$$R_1\beta_1+R_2\beta_2=0. \qquad (7)$$

In order to decide whether dynamical effects are important it will be necessary to insert numerical values for the quantities which appear in equations (6). The particular trial solution used is appropriate only if the motion is overdamped so that β_1 and β_2 are real quantities. This will be true if:

$$B^2>\frac{2\pi^3\rho Gb^4}{L^2}. \qquad (8)$$

Measurements of the high frequency damping of elastic vibrations in very pure metal crystals can be interpreted by treating the damped oscillations of the pinned down dislocations present[5]. Two methods of treatment both lead to a value of B for copper which is 5×10^{-3} gm sec^{-1}cm^{-1}. This, as will be seen shortly, is a rather large damping constant. At present there is no adequate theoretical proposal giving a value of B as large as necessary. Eshelby[6] and Leibfried[7] have devised theories which lead to values of B which are about one hundred times smaller than that given above. The assumptions made in evaluating B from the experimental data were:

(1) The damping force increases linearly with the velocity (as in equation 3).

(2) A reasonable value of the density of dislocations in an annealed crystal was assumed (i.e. 10^7 to 10^8 dislocation lines per cm^2). If smaller values for the dislocation densities are assumed then a larger value of B will be required to fit experiment. In addition the value of the yield stress which results from this dislocation density assumption agrees reasonably well with experiment.

If we suppose that this large value of the damping constant is appropriate then the inequality (8) becomes for copper:

$$2.5\times10^{-5}>0.972\times10^{-8}\ .$$

Hence our supposition that the motion is overdamped is correct. From equation (6) it can be seen that with the values of the constants used here $\beta_1 \gg \beta_2$ and $R_1 \ll R_2$. In fact for copper:

$$\begin{aligned} \beta_1 &= 2.86\times10^{11}\text{sec}^{-1} \\ \beta_2 &= 2.78\times10^{7}\text{sec}^{-1} \\ R_1 &= -0.445\times10^{-8}\text{cm} \\ R_2 &= 0.457\times10^{-4}\text{cm} \\ A &= 0.250\times10^{-4}\text{cm} \end{aligned}$$

where we have assumed that the displacement at the center of the loop initially is $0.207\,L=0.207\times10^{-4}$cm. We have also taken $\sigma-\sigma_b=1.12\times10^{8}$ dyne cm^{-2} which is the yield stress for $L=10^{-4}$ cm. The time for the displacement to drop to zero is 2.18×10^{-8} sec. Since the distance traveled is 2.07×10^{-5} cm, the average velocity is 950 cm sec^{-1}. The velocity when the displacement at the center of the loop is zero is 695 cm sec^{-1}. This is much less than the speed of sound in copper. When the displacement is zero the ratio of the kinetic energy of the loop to the potential energy is:

$$\frac{\text{K. E.}}{\text{P. E.}}=\frac{\pi\rho v^2}{G}=3.0\times10^{-5}\ .$$

Hence there is only sufficient kinetic energy available to generate about one tenth of an atomic length of dislocation.

There is other experimental evidence that the dislocations responsible for slip travel slowly. Leibfried[8] has used a very sensitive mechanical strain gauge to observe the deformation in pure aluminum single crystals when small increments of load are added. The great majority of the strain occurred gradually without sudden increments in strain. There were, however, occasionally increases in the strain rate which died out after times ranging from one second to one minute. The total change in length which occurred during such a transient was about 1000 Å. This length increase is just that expected for a process producing glide of 2000 Å. Since the diameter of the specimen was 1.8 mm we can estimate the velocity of the dislocations by assumming that the fastest transients occur in the case where the dislocation loops move freely to the surface without being held up at obstacles. There are two ways to calculate the time required for one dislocation to travel to the surface. Either one can suppose that the source will not emit a second dislocation loop while the first loop is in the solid because of the back stress. Or we can suppose that the spacing is πL as Fisher, Hart and Pry did. Since the first assumption results in a larger velocity and since we wish to show that no matter how one interprets the data one is still led to slow dislocations we shall use the first assumption. Thus the time required for one dislocation to travel to the surface is 1 sec/no. of dislocs. per lamella=1/800 sec. The distance traversed is $0.09\times1.414=0.127$ cm thus the velocity is about 100 cm sec^{-1} which is not in serious disagreement with the figures resulting from the damping experiments.

Becker and Haasen[9] have also made optical observations on the rate at which the glide steps appear on aluminum single crystals. The maximum rate of shearing displacement found by them at a glide step was 10^{-3} cm sec^{-1}. If each dislocation must travel about 0.5 cm to reach the surface and upon doing so produces an offset of 2.5×10^{-8} cm, then if we make our previous assumption that only one dislocation at a time travels from source to surface one obtains a maximum velocity for dislocations of 2×10^{4} cm sec^{-1}, i.e. about a tenth the speed of sound. This is of the order of the speed predicted by Leibfried[7] and Eshelby[6]. If one supposes that many dislocations are emitted during the time one travels to the surface then slower velocities are obtained. It should be pointed out that Becker and Haasen found that the rate of shear is a maximum in the early stages of the formation of a glide band. This may indicate that in the early stages of formation the damping is small and that it increases as glide occurs. Such an interpretation is consistent with the damping measurements which are made after a large number of oscillations of the dislocation loops have occurred.

If this large initial value of the dislocation velocity is used then the ratio of the kinetic to the potential energy of the dislocation becomes:

$$\frac{\text{K. E.}}{\text{P. E.}}=\frac{\pi\rho v^2}{G}=1.4\times10^{-2}\ .$$

Since this is about a tenth of the value used by Fisher, Hart and Pry it seems unlikely that dynamic effects can be of importance in the generation of slip bands.

There is however a phenomena in which dislocations may play a role which occurs rapidly. It has long been known that twinning is accompanied by audible clicks. Mason, McSkimin and Shockley[10] and Marx and Koehler[11] have observed transient stress pulses resulting from twinning in tin and zinc respectively. Both groups of observers detected the pulses by using piezoelectric crystals. Both groups looked for transients resulting from slip in aluminum and did not find pulses. Cottrell and Bilby[12] and Millard and Thompson[13] have suggested that twinning can result from the motion of a suitable dislocation. Mason, McSkimin and Shockley claimed that a fine structure in their stress pulse resulted from the motion of dislocations with the speed of sound.

Further experimental work aimed at measurements of the velocities of dislocations in the slip process and in twinning would be extremely valuable. It may be that the distinction between slip and twinning arises because in slip the dislocations which follow the initial dislocation on the glide plane must travel through material which has in some way been altered by the initial dislocation. In twinning if Cottrell and Bilby's mechanism is correct a large twin can be produced by moving a single twin dislocation through undisturbed material.

References

1) N. F. Mott: Phil. Mag. **43** (1952) 1151.
2) J. C. Fisher, E. W. Hart and R. H. Pry: Phys. Rev. **87** (1952) 538.
3) F. C. Frank and W. T. Read: Phys. Rev. **79** (1950) 722.
4) J. S. Koehler: Imperfections in Almost Perfect Crystals, (1952) 197 (John Wiley).
5) See Reference 4; See also J. Weertman and J. S. Koehler: J. Appl. Phys. April, 1953.
6) J. D. Eshelby: Proc. Roy. Soc. **A197** (1949) 396.
7) G. Leibfried: Z. f. Phys. **127** (1950) 344.
8) G. Leibfried: Z. f. Phys. **127** (1950) 580.
9) R. Becker and P. Haasen: Acta Metallurgica **1** (1953) 325.
10) W. P. Mason, H. J. McSkimin and W. Shockley: Phys. Rev. **73** (1948) 1213. See also W. P. Mason Piezoelectric Crystals and Their Uses, (1950) 433 (Van Nostrand).
11) J. Marx and J. S. Koehler: unpublished.
12) A. H. Cottrell and B. A. Bilby: Phil. Mag. **42** (1951) 573.
13) N. Thompson and D. J. Millard: Phil. Mag. **43** (1952) 422.

JOURNAL OF THE PHYSICAL SOCIETY OF JAPAN Vol. 10, No. 8, AUGUST, 1955

The Migration of Solute Atoms to Dislocation Arrays*

By B. A. BILBY

Royal Society Sorby Research Fellow, Metallurgy Department,
University, Sheffield, England

The dislocation theory of strain ageing, as previously given for an isolated dislocation, is applied to the ageing of the dislocation array representing a small angle tilt boundary, and a change in the time law of ageing is predicted. The ageing of the array, and of isolated dislocations, is also considered using a model which allows for diffusion, and for competition for the solute atoms between arrays, or between isolated dislocations. The results are compared with available data for the initial stages of ageing and further experiments are suggested.

§ 1. Introduction

In a recent theory of strain ageing (Cottrell and Bilby, 1949†) the number of solute atoms $N(t)$ which have arrived after time t per unit length of a stationary edge dislocation initially in a matrix of uniform concentration n_0 cm^{-3}. was shown to be:

$$N(t)=3\,n_0(\pi/2)^{1/3}(A/k)^{2/3}(Dt/T)^{2/3} \qquad (1)$$

k, D, and T are Boltzmann's constant, the diffusion co-efficient of the solute, and the absolute temperature respectively. A is a constant depending on the maximum binding energy V_m of a solute atom in a dislocation, and for $V_m=0.5$ eV, has the value $A=1.5\times10^{-20}$ dyne cm^2. The theory predicts the initial ageing rates surprisingly well (Harper, 1951).

In the analysis an isolated dislocation was considered, and it was assumed that the solute atoms were attracted to the dislocation only because of the dilatation they produced˙ The effect of Fick's Law and of "saturation" were ignored, so that the treatment applies only to the initial stages of ageing and when $V_m \gg kT$. The role of diffusion caused by concentration gradients is quite different when $V_m \gg kT$ and when $V_m \ll kT$. In the latter situation, the final concentration everywhere is of the form

$$n=n_0\exp\{-V/kT\}$$

and diffusion hinders the ageing process. This is the "unsaturated atmosphere", and we do not discuss ageing under these conditions in the present paper. When $V_m \gg kT$, there is a region near the dislocation where the final concentration is limited by saturation (C.B.). The dislocation then acts as a kind of sink, lowering the concentration in its immediate neighbourhood. As ageing proceeds solute atoms will diffuse towards the dislocation to restore the concentration. Diffusion thus increases the rate of ageing.

In this paper we consider how the rate of ageing is modified when the dislocations are not isolated but in arrays. This problem is of interest in connection with the well known phenomenon of preferential precipitation of impurities in grain boundaries and intragranular networks, and in the stabilisation of martensite and mechanical twin boundaries. Bend planes (Washburn, Parker et alia, 1952, 1953) should also exhibit ageing phenomena. In § 2 we apply the "initial stages" treatment of C.B. to the ageing of a small angle tilt boundary. This is not satisfactory for large angles of tilt, and we therefore treat also a different model allowing for diffusion. For comparison a single dislocation is treated in § 3 using a similar model. Finally in § 4 we allow for competition for solute atoms between collections of isolated dislocations. The results are discussed in § 5.

§ 2. The Ageing of a Small Angle Tilt Boundary

The hydrostatic pressure P at a point (x, y) due to an infinite array of positive edge dislocations of strength b' at the points $x=0$, $y=nh$ is readily calculated from the formulae of Burgers (1939). An atom producing local dilatation at any point has there an interaction energy V in the stress field of the array which is proportional to P. Thus:

---

* This paper was presented to the Symposium on Crystal Plasticity and Dislocation held at Nikko on September 12th and 13th, 1953, on the occasion of International Conference of Theoretical Physics. No alteration of the text was made since then.

† Referred to as C.B. in the sequel.

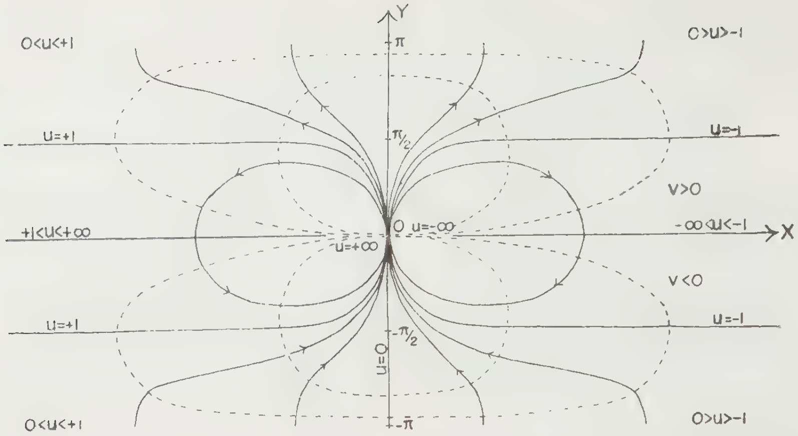

Fig. 1. The Co-ordinate Lines u and v. The continuous lines are the lines of constant u, and the dotted lines are those of constant v. There is a positive dislocation at the origin, and the arrows indicate the direction of motion of an atom causing local dilatation.

$$V=\frac{C\sin Y}{\cosh X-\cos Y} \qquad (2)$$

where C is a constant and $X=2\pi x/h$, $Y=2\pi y/h$. The interaction due to the relief of shear stresses is neglected. For small X, Y:

$$V\sim\frac{2CY}{X^2+Y^2}=\frac{Ch}{\pi}\frac{\sin\theta}{r} \qquad (3)$$

where $x=r\cos\theta$, $y=r\sin\theta$. Thus $C=A\pi/h$, where A is the parameter occurring in the single dislocation theory (C.B.).

Consider now the migration of solute atoms towards a stationary array of this type, the initial solute concentration being everywhere n_0 cm^{-3}. A solute atom moving in the stress field acquires a drift velocity relative to the array of $\boldsymbol{s}=-(D/kT)\nabla V$. This velocity is modified as the ageing proceeds by the effects of saturation and concentration differences, but these are ignored in the "initial stages" treatment. As with the single dislocation, ∇^2V 0, and the equation of continuity:

$$\nabla\cdot\{(nD/kT)\nabla V\}=\frac{\partial n}{\partial t}$$

shows that the concentration (except at the singularities of V) remains constant and equal to n_0 for all times t. This result is of general validity in problems of dilatation interaction in this approximation, provided that the body forces F_i in the elastic problem are such that;

$$\partial F_i/\partial x_i=0\ .$$

It is convenient to introduce an orthogonal curvilinear co-ordinate system (u, v) by the transformation:

$$W=u+iv=-\coth(\pi z/h) \qquad (4)$$

where $z=x+iy$. The loci u=constant, which are the flow lines, and v=constant, which are the lines of constant V, are shown in Fig. 1; this drawing indicates only the general nature of the u and v lines, and not their exact shape. The drift velocity becomes:

$$\boldsymbol{s}=-(DC/kTH)\boldsymbol{i}$$

where $\boldsymbol{i}$ is a unit vector perpendicular to the line v=constant and:

$$H(u,v)=\frac{dz}{dw}$$

$$=\frac{h}{\pi}\frac{1}{[\{(u+1)^2+v^2\}\{(u-1)^2+v^2\}]^{1/2}}\ . \qquad (5)$$

The dislocation at the origin is typical. It collects solute atoms from a strip bounded by two successive lines $|u|=1$, $v>0$; where $|X|$ is large this is approximately the strip $-3\pi/2\leqslant Y\leqslant\pi/2$. All the atoms in this strip enter the line sink at the origin, and the number which cross the boundary $v=-v_0$, $v_0>0$ between t and $t+dt$ in a filament of unit length along the dislocation line is;

$$dN(t)=(n_0DC/kT)du\,dt$$

which is independent of v_0. As the ageing proceeds the regions near the dislocation are drained of solute atoms and the limits of the integration required to find $N(t)$ are functions of t. These limits are found by calculating the time

$$t(u)=(kTh^2/DC\pi^2)\int_{-\infty}^{+\infty}H^2dv$$

for complete transit of a flow line from $v=+\infty$ to $v=-\infty$, and solving the resulting equation for u. This gives a qradratic equation for $u_1(t)$, $|u|<1$ and a cubic for $u_2(t)$, $|u|>1$. Thus

$$N(t)=(2n_0DC/kT)\int_0^t\left\{\int_{u_1}^{+1}du+\int_{+1}^{u_2}du\right\}dt$$
$$=(2n_0DC/kT)\int_0^t(u_2-u_1)dt\ . \qquad (6)$$

We introduce a characteristic time $t_0=(kTh^2/2DC\pi)$, the time for an atom to move by the shortest path from the $v=+\infty$ region of one dislocation to the $v=-\infty$ region of the next. $N(t)$ is a complicated function, but approximations for the regions $t\ll t_0$ and $t\gg t_0$ may be obtained as follows. All flow lines in the region $|u|<1$ contribute until $t=t_0$ so $u_1(t)=0$ for $t<t_0$. When $t\ll t_0$, u is large and $u^3\gg u$, so $u_2(t)\sim(t_0/t)^{1/3}$. Thus for $t\ll t_0$, $N(t)$ tends to the expression (1) for the single dislocation. On the other hand, if $t\gg t_0$, $u_1(t)=(1-t_0/t)^{1/2}\sim 1-\frac{1}{2}(t_0/t)$, while a simple iteration method gives $u_2(t)\sim 1+\frac{1}{2}(t_0/t)$, thus;

$$N(t)\sim\frac{n_0h^2}{\pi}\ln(t/t_0) \qquad (7)$$

where t_0 replaces zero in the lower limit of the integral. It is not easy to make a reliable estimate of the range of h values for which the approximations (1) and (7) are valid. For iron we may take $A=1.5\times10^{-20}$ dyne cm.^{2}; then for $T=288°$K we find for $Dt>10^{-14}$cm.^{2} that $t>10\ t_0$ when $\psi=b'/h>9.5°$, and for $Dt<10^{-12}$cm.^{2}, $t<t_0/10$ when $\psi<0.43°$. It does not seem worthwhile to evaluate (6) numerically for intermediate t/t_0 values until the appropriate experimental data are available.

The form of equation (7) suggests however that it is not legitimate to ignore the effect of diffusion. The array rapidly absorbs the solute atoms in its immediate neighbourhood, and thereafter the rate of accumulation is very slow. In fact, solute atoms will diffuse towards the array to restore the concentration in its neighbourhood, and $N(t)$ will increase more quickly than (7) indicates. This process may be simply discussed by treating the dislocation wall as a plane sink so that the problem is one-dimensional, each dislocation collecting solute atoms from a strip of width h. Let the concentration of solute atoms in the immediate neighbourhood of each dislocation be maintained at $n(t)$ by the diffusion process. Then in (6) $u_1=0$ and $u_2=u_0$, where u_0 is some large constant value, and

$$\frac{dN}{dt}=\frac{2DCu_0}{kT}n(t)=gn(t)\ . \qquad (8)$$

Thus the equation of diffusion,

$$\frac{\partial n}{\partial t}=D\frac{\partial^2 n}{\partial x^2} \qquad (9)$$

must be solved with the boundary conditions;

$$n(x,0)=n_0 \qquad 0<x<+\infty \qquad (10)$$

$$hD\frac{\partial n}{\partial x}=\frac{1}{2}gn \qquad x=0 \qquad (11)$$

These equations, and also those treated in §3 and §4 below, are identical with equations occurring in standard problems of heat conduction. The solutions, which are readily obtained by using the LaPlace Transformation, are discussed by Carslaw and Jaeger (1947). We find;

$$n/n_0=\operatorname{erf}(\bar{x})+\exp(\lambda x+\lambda^2Dt)\operatorname{erfc}(\bar{x}+\lambda\sqrt{Dt}) \qquad (12)$$

where $\bar{x}=x/2\sqrt{Dt}$ and $\lambda=g/2hD$. $N(t)$, the number of solute atoms which have arrived per unit length of each dislocation line after time t, is given by;

$$N(t)=2hD\int_0^t\left(\frac{\partial n}{\partial x}\right)_{x=0}dt$$
$$=\frac{2hn_0}{\lambda}F(m) \qquad (13)$$

where

$$F(m)=\frac{2}{\sqrt{\pi}}m^{1/2}+e^m\operatorname{erfc}m^{1/2}-1$$

and $m=\lambda^2Dt$. We have $\lambda^2=(\pi Au_0/h^2kT)^2$, and since for large u, $u\sim-h/\pi\xi$ where $\xi=r/\cos\theta$ is the parameter of the single dislocation theory (C.B.), we set $u_0=h/\pi\xi$, $\xi_0=3\times10^{-8}$cm. When $m\gtrsim50$, $F(m)\sim(2/\sqrt{\pi})m^{1/2}-1$; an asymptotic expansion can be obtained by expanding the LaPlace transform of (12), applying the inversion theorem and integrating term by term. Thus we find:

$$F(m)\sim\frac{2}{\sqrt{\pi}}m^{1/2}+\frac{\sqrt{\pi}}{m^{1/2}}-\frac{\sqrt{\pi}}{2}\frac{1}{m^{3/2}}+O\left(\frac{1}{m^{5/2}}\right) \qquad (14)$$

§ 3. The Single Dislocation

We now treat the migration of solute atoms to a single dislocation using the model which for the array, leads to (13). We assume that there is a cylindrical surface of radius a about the dislocation line at which the concentration is maintained at $n(t)$ by diffusion. This leads to the equations:

$$\frac{\partial n}{\partial t}=D\left(\frac{1}{r}\frac{\partial n}{\partial r}+\frac{\partial^2 n}{\partial r^2}\right) \qquad (15)$$

$$\frac{\partial n}{\partial r}=\mu n \qquad r=a \qquad (16)$$

$$n=n_0 \qquad \text{for all } r \text{ at } t=0 \qquad (17)$$

where $\mu=(g/2\pi aD)$. For the rate of arrival of solute atoms per unit length we find:

$$\frac{dN}{dt}=\frac{8D\mu^2a^2n_0}{\pi}I(1, a\mu, M) \qquad (18)$$

with

$$I(1, a\mu, M)=\int_0^\infty \frac{\exp(-Mz^2)dz}{z(Q^2+R^2)}$$

where $M=(Dt/a^2)$ and

$$Q=zY_1(z)+a\mu Y_0(z)$$

$$R=zJ_1(z)+a\mu J_0(z)$$

$Y_n(z)$ and $J_n(z)$ are Bessel functions. We expect $a\sim10^{-7}$ cm. so that (Dt/a^2) varies from 1 to 100 as Dt varies from 10^{-14} cm.^{2} to 10^{-12} cm.^{2} The notation $I(1, a\mu, M)$ is due to Jaeger (1942) who gives an asymptotic expansion of I for large M. Integrating this we find:

$$\frac{N(t)}{4\pi a^2n_0}\sim\left(\frac{Dt}{a^2}\right)\left\{\frac{1}{y}+\frac{1-\gamma}{y^2}+\frac{2(1-\gamma)+\gamma^2-\pi^2/6}{y^3}+O\left(\frac{1}{y^4}\right)\right\} \qquad (20)$$

where $y=2/a\mu-2\gamma+\log_e 4(Dt/a^2)$ and γ is Euler's constant. For small M, Jaeger (1942) gives a series for I which when integrated becomes;

$$N(t)\sim gn_0t-\frac{2}{3\sqrt{\pi}}\left(\frac{g}{D}\right)^2\frac{n_0}{a}(Dt)^{3/2}+O(Dt)^2\,. \qquad (21)$$

The first term agrees with (8). It is clear from (20) and (21) that for large and small values of (Dt/a^2), $N(t)$ does not change in form rapidly with a. For intermediate values,

$$\int_0^t Idt$$

must be evaluated numerically.

§ 4. The Effect of Competition between Dislocations for Solute Atoms

Consider a collection of parallel straight dislocations and let ρ be the dislocation density. Then we can make some allowance for their competition for solute atoms by requiring that the concentration gradient be zero on a cylindrical surface of radius $b=1/\rho^{1/2}$ about each dislocation line. The diffusion problem is now defined by the equations (15) and (16) together with the additional boundary conditions:

$$n=n_0 \quad a\leqslant r\leqslant b \qquad \text{for } t=0 \qquad (22)$$

$$\frac{\partial n}{\partial r}=0 \qquad r=b \qquad (23)$$

The expression for $N(t)$ is;

$$N(t)=4\pi\mu^2n_0\sum_{m=1}^{\infty}(1-\exp(-\alpha_m{}^2Dt))\Psi(\alpha_m) \qquad (24)$$

with;

$$\alpha_m{}^2\Psi(\alpha_m)=\frac{J_1{}^2(\alpha_m b)}{[\alpha_m J_1(\alpha_m a)+\mu J_0(\alpha_m a)]^2-(\alpha_m{}^2+\mu^2)J_1{}^2(\alpha_m b)} \qquad (25)$$

where α_m, $m=1, 2, 3, \cdots$ are the roots of;

$$\frac{\alpha J_1(\alpha a)+\mu J_0(\alpha a)}{J_1(\alpha b)}=\frac{\alpha Y_1(\alpha a)+\mu Y_0(\alpha a)}{Y_1(\alpha b)}\,. \qquad (26)$$

If we take $a\sim10^{-7}$ cm. and $b\sim10^{-4}$cm., then for $10^{-14}<Dt<10^{-12}$cm.^{2}, corresponding to the early stages of ageing in iron, we have $1<(Dt/a^2)<100$ and $10^{-6}<(Dt/b^2)<10^{-4}$. Thus we require an approximation to (24) for large (Dt/a^2) and small (Dt/b^2). It is readily shown in the following way that this is given by (20). The LaPlace transform of (24) involves the Bessel functions $K_n(qb)$, $K_n(qa)$, and $I_n(qb)$, $I_n(qa)$, where $n=0$ and 1, and $q=(p/D)^{1/2}$, p being the argument of the transform $\overline{N}(p)$. Since (Dt/a^2) is large and (Dt/b^2) is small we may expand the Bessel functions using asymptotic expansions for those of argument qb and ascending series for those of argument qa (Goldstein, 1942). In this way we obtain:

$$p\overline{N}(p)\sim\frac{2\pi aD\mu n_0}{p}\left[\frac{qK_1(qa)}{qK_1(qa)+\mu K_0(qa)}\right] \qquad (27)$$

from which (18) follows by the inversion theorem. It is of course clear on physical grounds that the boundary conditions remote from the dislocation do not affect the initial ageing rate. In the later stages of ageing after heavy cold work the solution (24) would probably be required.

The array problem can be treated similarly.

If we take a sequence of parallel arrays distant $2l$ apart, then we have the equations (9) and (11) together with:

$$\frac{\partial n}{\partial x}=0 \qquad x=l \tag{28}$$

$$n=n_0 \qquad 0<x<l \text{ at } t=0 \tag{29}$$

The exact solution leads to:

$$\frac{N(t)}{2hDl^3\lambda^2 n_0}=\sum_{m=1}^{\infty}\frac{1-\exp(-z_m{}^2\tau)}{z_m{}^2(z_m{}^2+\lambda l+\lambda^2 l^2)} \tag{30}$$

where $\tau=Dt/l^2$ and z_m, $m=1, 2, 3, \cdots$ are the roots of;

$$z\tan z=\lambda l\ . \tag{31}$$

These are tabulated by Carslaw and Jaeger (1947). For $l\sim 10^{-4}$cm. we require an approximation for small values of Dt/l^2. This can be obtained by expanding the LaPlace transform $\bar{N}(p)$ of $N(t)$ in powers of $1/p$. On inversion, the leading term is the expression (13).

§ 5. Discussion

In order to test (6) and (13) directly, observations on the strain ageing of small angle tilt boundaries are required. The experiments on the motion of bend planes (Washburn and Parker at alia, 1952, 1953), suggest that such observations might be possible using nitrogen loaded zinc single crystals. Experiments of this kind should provide a valuable test of the dislocation theory, since there is a specific model for the bend plane, and the above simple calculation could probably be refined, perhaps to the extent of enabling a quantitative test to be made. Further experiments on initial ageing rates in polycrystals of various grain sizes, and in single crystals with and without a pronounced mosaic structure would also be of interest.

Meanwhile it is desirable to compare the available strain ageing data with the theory to see if this indicates whether the dislocations involved are isolated or in arrays. The most accurate published data are those of Harper (1951) who studied the decrease in internal friction after cold work of iron specimens containing carbon and nitrogen. From the quantity $N(t)$ calculated in the previous sections either the degree of formation of the atmosphere, $d=N(t)/N_s=b'N(t)$, or the fraction of the original solute atoms removed from the matrix, $f=\rho N(t)/n_0$, can be obtained. The quantity d is appropriate for analysing hardness or yield point data (C.B.), and f, which is used by Harper, for measurements of internal friction or electrical resistance. Harper modifies (1) by assuming that the rate of "precipitation" is proportional to the fraction of solute remaining in solution to obtain:†

$$f=1-\exp[-3\rho(\pi/2)^{1/3}(ADt/kT)^{2/3}] \tag{32}$$

By plotting $\log(1-f)$ against t Harper shows that this relation holds up to about 90% of the total ageing. This modification, like that of the treatments given in § 4 above, leads to a slowing down of the ageing process, and so allows indirectly for the effect of saturation (C.B.). It does not do so, however, by making the attractive force causing the ageing a decreasing function of the time. Nevertheless, since to first approximation the dislocation stresses are relieved by ageing, but not the strains, it seems likely that the progressive alteration of V at large distances will be a second order effect, so that modifications of this kind may represent the ageing well at large times. We shall not attempt here to analyse the results for long ageing times, but shall confine our attention to the formulae (1), (13) and (20) appropriate to the early stages of ageing. It is worth nothing however that since $d/b'=fn_0/\rho$ we can define an $f_s=\rho/b'n_0$ corresponding to $d=1$. Then if in long time ageing experiments $f>f_s$, the removal of the solute atoms can no longer be due simply to their elastic interaction with dislocations. For Harper's results (Fig. 1 of his paper) we find $f<f_s$, so that they are consistent with the removal of solute atoms by the dislocation mechanism.

For the initial stages of ageing, say, $f<0.25$, Harper's treatment of the results is not a very sensitive test of the variation of f with Dt, although for large f his law (32) is clearly obeyed very closely. We have therefore calculated Dt for Harper's results (Figs. 2 and 3 of his paper) using his estimates of the activation energies, and the values of D_0 given by Wert and Zener (1949).*

We first compare (1) and (13). The latter is clearly a bad approximation when $Dt<Dt_0$.

---

† The exponent in Harper's formula differs by a factor 2/3 from that of (32).

* The author is indebted to Dr. Harper for kindly furnishing details of his experimental data.

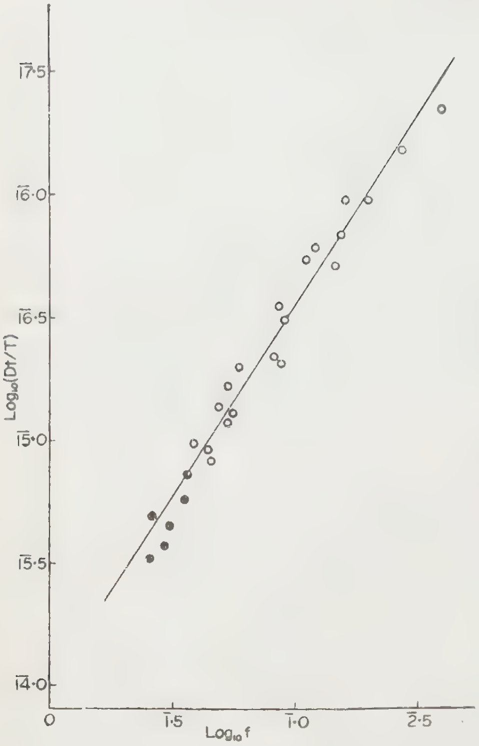

Fig. 2. Regression line of $\log f$ on $\log (Dt/T)$ for ageing of specimens containing carbon.

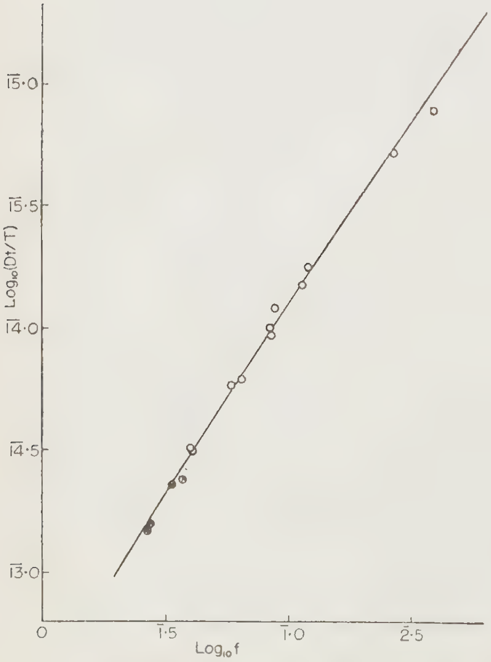

Fig. 3. Regression line of $\log f$ on $\log (Dt/T)$ for ageing of specimens containing nitrogen.

This limits our choice of h to $h<4\times10^{-7}$cm. ($\psi>4.3°$) for the carbon results, and $h<10^{-6}$ cm. ($\psi>1.7°$) for the nitrogen results. If we take $h=1.5\times10^{-7}$cm. ($\psi=11.4°$) then, for the resulting m values, we can use the first term only of (14), except perhaps for the early Dt values for carbon. (1) and (13) are thus of the form $f=B_1(Dt/T)^{\delta_1}$ and $f=B_2(Dt)^{\delta_2}$ respectively. Regression lines, fitted by least squares, of $\log f$ on $\log (Dt/T)$ are shown in Figs. 2 and 3 for the carbon and nitrogen results. In calculating these lines only the values of f less than 0.25 have been used, although for each temperature the first experimental point with $f>0.25$ is shown as a full circle in the Figures. The values of δ_1 are 0.618 for nitrogen and 0.654 for carbon. Regression lines of $\log f$ on $\log Dt$, which are more appropriate for testing (14), have also been calculated, and give δ_2 values of 0.643 for nitrogen and 0.654 for carbon. It is thus clear that the initial stages of ageing are represented much more closely by (1) than by (13), and we infer that the important dislocations are probably not in boundary arrays of large angle.

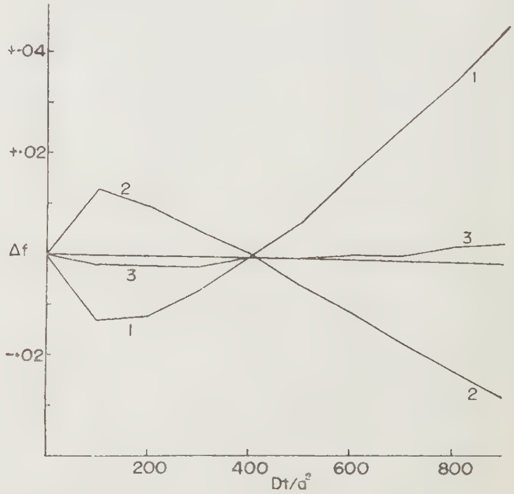

Fig. 4. Graph of differences Δf between the f values obtained from fitted curves, and those obtained from the regression line of $\log f$ on $\log Dt$ for the nitrogen loaded specimens.

We have compared (1), (14) and (20) in Fig. 4, where the differences Δf between the f values obtained from fitted curves corresponding to these equations and the f values obtained from the regression line on $\log f$ on $\log Dt$ for nitrogen, are plotted against Dt/a^2. The lines 1, 2 and 3 correspond to the first two terms of (20), the first term of (14), and to (1) respectively. The results for nitrogen are used, since for $Dt > 10^{-13}$ cm.^{2}, these simple approximations to (14) and (20) are permissible; (20) is in fact very nearly linear in this range of Dt/a^2 values. The value of a is 10^{-7}cm. Clearly 3 gives the best fit, but 1 and 2 both fit badly. We infer that the initial stages treatment leading to (1) is a better approximation than (20). However, the additional parameter a gives a certain flexibility to (20), and to examine this fully (18) must be integrated numerically. It is clear, however, that more definite conclusions could be drawn from experiments in which the arrangement of dislocations is known, such as those suggested with bend planes.

§6. Acknowledgments

The author is indebted to Professor Cottrell and Dr. Nabarro for a discussion of §2, and to Mr. R. Bullough for a discussion of (20) and for assistance with the numerical work. His interest in the ageing of dislocation arrays was first aroused by Dr. P. Samuel.

References

1) J. M. Burgers: Proc. Acad. Sci. Amst. **42** (1939) 293.
2) H. S. Carslaw and J. C. Jaeger: Conduction of Heat in Solids, Oxford, 1947.
3) A. H. Cottrell and B. A. Bilby: Proc. Phys. Soc. **A62** (1949) 49.
4) S. Goldstein: Proc. Lond. Math. Soc. **34** (1932) 51.
5) S. Harper: Phys. Rev. **83** (1951) 709.
6) J. C. Jaeger: Proc. Roy. Soc. Edin. **A61** (1942) 223.
7) J. Washburn and E. R. Parker: Journ. Met. **4** (1952) 1076 and C. H. Li, E. H. Edwards, J. Washburn and E. R. Parker: Acta Met. **1** (1953) 223.
8) C. Wert and C. Zener: Phys. Rev. **76** (1949) 1169.

JOURNAL OF THE PHYSICAL SOCIETY OF JAPAN Vol. 10, No. 8, AUGUST, 1955

On the Theory of the Kirkendall Effect*

By Frederick SEITZ

University of Illinois, Urbana, Illinois, U.S.A.

The problem of determining the nature of the lattice defects which are responsible for transport of atoms in metals is discussed. The value of the Kirkendall effect in deciding that most of the transport is associated with migrating vacancies or interstitial atoms is restated. It is emphasized that we do not yet possess a satisfactory experimental method for deciding which of the two types of imperfection most important in typical metals.

§1. Introduction

The marker shift first observed by Kirkendall⁽¹⁾ in the interdiffusion of copper and brass has now been established beyond any reasonable doubt in a number of couples of face-centered cubic metals. Several independent groups of investigators, in particular Correa da Silva and Mehl⁽²⁾, Alexander, Kuczynski and Balluffi⁽³⁾, Barnes⁽⁴⁾, Bückle and Blin⁽⁵⁾ and Seith and Kottman⁽⁶⁾, have studied the effect and have demonstrated that it depends primarily upon the existence of a gradient in chemical composition. Couples of CuZn-Cu, Ni-Cu and Ag-Au have received particular attention; however, several other systems show the effect to a comparable extent. To use the macroscopic concepts first introduced by Darken⁽⁷⁾, there is little doubt that the intrinsic diffusion coefficients of the constituent atoms, D_a and D_b, differ appreciable. In fact, the ratio of the larger to the smaller diffusion

---

* This paper was received January 20, 1954 by the organizing commitee of the Symposium on Crystal Plasticity and Dislocation held at Nikko on September 12th and 13th, 1953, on the occasion of International Conference of Theoretical Physics. No alteration of the text was made since then.

coefficient may be as large as five, as is the case in the copper-brass system. Only one body-centered cubic system has been studied[3] to date, namely that of beta brass in which case the ratio $D_{Zn}/D_{Cu}=3.4$.

Thus far two factors have not been clarified to the extent for which one might hope. First, it is not known to what degree the diffusion coefficients depend upon the overall difference in composition which appears in the specimen being studied and hence are influenced by the chemical gradient; second, it is not known with certainty whether the imperfections responsible for transport in the cases studied are interstitial atoms or vacancies. It is assumed fairly generally that they are vacancies, and this course will be adopted in the present account of the topic. Nevertheless, a convincing experimental proof of this matter would be highly desirable. Proposed methods of proof will be discussed further below.

The primary equation[8] governing the vacancy current I_v in a cubic material is

$$I_v = -D_v \operatorname{grad} n_v + K n_v \operatorname{grad} N_a . \qquad (1)$$

Here D_v is the diffusion coefficient for vacancies, which is a function of composition, n_v is the concentration of vacancies, grad n_v is a gradient of vacancy concentration, grad N_a is the gradient of A atoms, and K is the Kirkendall coefficient which provides a measure of the pumping action of the concentration gradient. The first term on the right hand side is the normal Fick current, whereas the second term represents the current responsible for the Kirkendall effect. The two terms have opposite sign in the cases studied to date, if we assume that diffusion occurs by means of vacancies; in fact we must conclude that the second term overwhelms the first since the vacancies diffuse from the member of the couple in which their density is presumably smallest (i.e., Cu in the Cu-CuZn system) to that in which the density is highest. The flow of vacancies evidently is a typical 'irreversible' effect associated with the presence of a non-equilibrium distribution of the chemical constituents.

§2. Void Formation

A number of couples which have been studied, particularly those mentioned above, display porosity near the diffusion boundary on a scale of about 0.1 mm. Such porosity suggests that not all the vacancies formed on one side of the diffusion boundary and pumped across this boundary condense at dislocations and thereby permit the specimen to retain its normal density. Instead, it appears that an appreciable fraction of the vacancies may condense to form voids. Barnes, who has devoted particular attention to this phenomenon, has shown that the fraction may constitute half the vacancy current in typical specimens of Cu-Ni.

The observation of porosity implies that the vacancy concentration becomes supersaturated on the side of the boundary where pores form. The existence of such a superconcentration is not surprising in view of the pumping action of the chemical gradient. A fundamental problem arises, however, concerning the magnitude of the excess concentration at various stages during the diffusion process. An elementary analysis[8] based on a study of solutions of equation (1) shows that one might expect excess concentrations of the order of unity relative to the equilibrium concentration in a zone of thickness $a\sqrt{\omega}$ where a is the lattice spacing and ω is the number of jumps a vacancy makes from birth to death. Thus, one might expect superconcentrations of the order of twice the equilibrium value when the width of the diffusion zone is 1μ if ω is 10^8; whereas such superconcentrations could persist until the width of the diffusion zone is 100μ if ω is as large as 10^{12}. A basic question which arises is the following: Does the existence of porosity for a range of width of the order 0.1 mm (100μ) imply that superconcentrations of this magnitude are retained until the width of the diffusing zone is 0.1 mm? This would imply in turn that ω is of the order of 10^{12}. The answer to this question revolves about the magnitude of the relative superconcentration needed to form pores.

§3. Magnitude of Superconcentration

It is doubtful if the superconcentration of vacancies become sufficiently large to nucleate pores in the perfect crystal at any stage of the diffusion process. This would require relative superconcentrations of the order of 100 or greater which do not seem probable, although the possibility cannot be excluded at this time. Instead, it seems much more likely that the pores are nucleated at specks of foreign matter, perhaps analogous to the nuclei for solidification which enter in the experiments of Turnbull[9] and which were avoided by using small droplets. According to the Thomson-Gibbs equation, the concentration of vacancies n_v required to condense at a spherical particle of radius r is

$$\log (n_v/n_{v_0})=2s/kTNr\ , \qquad (2)$$

where s is the energy per unit area of the void, k is Boltzmann's constant, T is the absolute temperature and N is the atomic density. Excess relative concentrations of the order of two are needed if the radius of the nucleating particles is of the order of 10 atomic distances; whereas values of the order of 0.1% excess relative concentration are sufficient if r is as large as 1,000 atomic distances. At the present time we do not know which of these two limits corresponds most nearly with the situation in actual metals. In the first case, which we shall designate as case *I*, the observation of porosity over distances of the order of 0.1 mm implies that ω is as large as 10^{12}, whereas the second possibility which we should designate as case II, implies that the pores may form for very low superconcentrations and implies that ω need not be larger than 10^8 or 10^9.

§4. Experimental Evidence for Two Cases

The experimental evidence available for making a decision between the two alternatives is not very satisfactory at the present time. In fact, there is evidence favoring both sides of the issue. A summary of this evidence is as follows:

Case I: *Small Nuclei*

Perhaps the outstanding evidence in support of the postulate of small nuclei, corresponding to values of ω of the order of 10^{12}, is the observation of Buffington and Cohen[10] that the self diffusion coefficient in specimens of alpha iron increases if the specimen is strained during the diffusion experiment. The investigators found that the diffusion rate could be increased by a factor of 15 at 890°C by inducing sufficiently rapid creep; moreover, the diffusion rate was found to be proportional to the strain rate. This experiment implies that vacancies produced by plastic flow increase the rate of diffusion and that excess vacancy concentrations of the order of 15 can be attained during plastic flow.

Cottrell[11] has proposed a theory of the Portevin-LeChatelier effect based on the hypothesis that vacancies produced during plastic flow increase the rate of diffusion of foreign substitutional impurities and that the latter lock the moving dislocations when the diffusion rate becomes sufficiently high. The strain needed to produce discontinuities in plastic flow at a given rate of strain decreases with increasing temperature because fewer excess vacancies are needed to produce the required diffusion rate. Cottrell has shown that the critical strain is given by the relation

$$\varepsilon=5\times10^{-9}\times\exp(7500/RT)\ , \qquad (3)$$

when the strain rate $\dot{\varepsilon}$ is $10^{-5}\,\mathrm{sec}^{-1}$, in the case of a series of aluminium alloys studied by McReynolds. The experiments imply that the vacancies produced endure for the entire time $\varepsilon/\dot{\varepsilon}$. Since the jump frequency of vacancy should be of magnitude

$$10^{13}\exp(-7500/RT)\ ,$$

it follows the number of jumps during a lifetime should be at least 5×10^9. This result obviously provides only nominal support for Case I.

Case II: *Large Condensation Nuclei*

Koehler and Kauffman[12] have carried out quenching experiments on wires of gold which indicate that vacancies may be retained from temperature above about 700°C. The extra residual resistance associated with quenched vacancies is observed only if the quenching time for wires of the order of 0.4 mm in diameter is 10^{-2} sec or less. Apparently the vacancies disappear at dislocations or other sinks if the quenching rate is slower. A simple analysis, based on the assumption that the activation energy for migration of the vacancies is about 1.0 ev, indicates that the vacancies cannot have made appreciably more than 10^7 jumps in the specimens before disappearing. This experiment would furnish strong support for Case II if it were not for the fact that the specimens probably have appreciable quenching strains, which imply that the density of dislocations is abnormally high. Thus the lifetime of vacancies may be abnormally short.

If the lifetime of vacancies in appropriately chosen specimens of some metals actually corresponds to values of ω as large as 10^{12} it might prove possible to cool such specimens very slowly and still retain the density of vacancies corresponding to high temperature equilibrium. In the case of a metal having the general properties of gold, for example, it might then be possible to cool wires in times of the order of 10^3 sec instead of 10^{-2} sec. Rates of this type are sufficiently slow that one might expect to avoid serious quenching strains. It would be interesting to repeat quenching experiments of the Kauffman-Koehler type using well-annealed single crystals and cooling slowly instead of rapidly.

Balluffi and Seigle[3)] have observed the Kirkendall effect in specimens of brass-zinc and copper-nickel without any evidence for porosity. They suggest that it is possible, with moderate care, to eliminate the nuclei for pores. This would indicate that such nuclei may be large, although the result is not strongly conclusive. They also found that the marker shift varies as $\sqrt{t}$ for shifts in the range from 60μ to 210μ in the silver-gold system, and for shifts in the range from 50μ to 120μ in the zinc-brass system. These results show that ω is probably less than 10^{12} in these cases, and may actually by considerably less.

Ellwood and Bagley[13)] have found visible porosity in many alloy specimens when annealed for long periods of time. For example, porosity sufficient to decrease the density of 80Cu20Ni specimen by 4.5% was obtained by annealing it for 4,125 hours at 900°C. The result suggests that pores can be produced by relatively slight concentration gradients and hence do not require large excess concentrations of vacancies.

§ 5. Proposed Experiments

The writer would like to propose two avenues of study:

First, it would be interesting to add sols of varying size to the alloys used in diffusion couples to see if there is a critical size at which porosity becomes prevalent. At the present time it is possible to obtain carbon blacks and silica sols in a range of size extending to well under 100 Å. Experiments with alloys containing contamination of this kind might disclose the extent to which the development of pores is sensitive to foreign particles.

Second, it would be exceedingly valuable to carry out diffusion experiments which provide a test of the basic principles underlying the Matano[14)] method during the very early stages of diffusion. The two key assumptions are that the chemical diffusion coefficient is purely a function of the local concentration and that the diffusion equation can be reduced to an ordinary differential equation by introduction of the variable $\eta=x/\sqrt{t}$, where x is the distance along the gradient and t is the time. When these conditions are satisfied the chemical diffusion coefficient may be computed from the relation

$$D_c(c_a)=-\frac{1}{2}\frac{\int dc_a}{dc_a/d\eta}, \tag{4}$$

where c_a is the density of A atoms, which should be a function of η. The limits of integration and the origin of coordinates must be selected in accordance with the Matano stipulations. We should not expect the Matano method to be applicable when the width d of the diffusion zone is less than or comparable to $a\sqrt{\omega}$ because the density of imperfections is far from equilibrium in the zone. Under these conditions it should not be possible to reduce the concentration versus distance curves $c_a(x, t)$ for different values of t into coincidence by introducing the variable η. Moreover, diffusion coefficients computed by arbitrary application of (4) from measured values of $c_a(x, t)$ for fixed t should give abnormally high values in the region where the density of imperfections is abnormally high and abnormally low ones in the region, on the opposite side of the boundary, where the density of perfections is abnormally low, the 'normal' values being determined from couples in which diffusion has progress to a point where $d \gg a\sqrt{\omega}$ so that the condition required for application of the Matano method presumably are satisfied. A test of (4) of the type described here would be particularly valuable if the slices could be reduced to the order of 1μ so that the width of the diffusion zone could be made appreciably smaller than 100μ. For a given thickness of diffusion zone the deviations should be more marked the larger the difference in composition in the two halves of the original specimen, that is the larger the concentration gradient.

As always, the use of ingenuity may make it unnecessary to carry out slicing. For example, the extension of the techniques employed by Balluffi and Seigle to a scale of dimensions ten or more times smaller, plus the introduction of a sequence of radial markers might make it possible to test the $\sqrt{t}$ law without the need for slicing.

It may be observed that the second type of experiment offers a means of determining whether the imperfections responsible for diffusion are vacancies or interstitial atoms, provided the diffusion coefficient at a given composition is found to be a function of the overall change in composition through the diffusion zone for sufficiently small values of the width of this zone. If the marker shifts from A to B, in a couple A-B, vacancies would be pumped through the diffusion zone in the direction A to B, provided they are the dominant carrier; whereas interstitial atoms would be pumped in the opposite direction in the alternative case. Thus the superconcentration of imperfections occurs on opposite sides of the diffusion zone in the two cases.

In other words, an experiment, based on the Matano analysis, which succeeds in detecting a dependence of diffusion coefficient on concentration gradient for sufficiently small values of the width of the diffusion zone offers the hope of determining both the magnitude of ω and the nature of the imperfections responsible for diffusion.

§ 6. Shockley's Proposal for Determining Imperfections

Recently, Shockley[15] has proposed that one study the Kirkendall shift produced in a pure monatomic substance by a temperature gradient in order to determine whether the imperfections responsible for transport are vacancies or interstitial atoms. His proposal is based on the assumption that a current of the dominant imperfection will inevitably flow in the direction of decreasing temperature because the density of imperfections is higher in the high temperature portion of the specimen than in the low temperature portion. This is equivalent to the assumption that the main driving force for the current of imperfections is the term in the chemical potential which originates in the mixing entropy of the imperfections. The writer is inclined to regard this assumption with very great reservation. The mixing entropy of imperfections does not seem to play a preponderant role in the ordinary Kirkendall effect, as we have seen above. It is quite possible that other contributions to the chemical potential arising from lattice vibrational entropy terms may exert a force inducing the current to flow in opposite direction. Still further, the flow of imperfections in a temperature gradient cannot be regarded as a purely equilibrium process so that quantities other than the chemical potential will be important. In the case of vacancy migration, for example consideration shows that an atom on the hot side of the vacancy will jump into the vacancy more rapidly than an identical atom on the cold side of the vacancy. This effect is in such a direction as to induce a current to flow in the direction of increasing temperature. Moreover, its influence probably is of the same order of magnitude as the effect arising from mixing entropy which would induce a current of vacancies to flow down the temperature gradient.

To consider the process more quantitatively, we may recognize two types of force which drive the imperfections in the specimen. The first is related to thermodynamic factors and is potentially reversible, whereas the second is related to the dependence of the rate-determining factors upon the temperature gradient. Only the first type of force appears in an isothermal system, in which case the current I of imperfections is given by the equation

$$I=-\frac{Dn}{kT}\operatorname{grad}\mu\,. \tag{5}$$

Here n is the density of imperfections, D is the isothermal diffusion coefficient, k is Boltzmann's constant, T is the absolute temperature and μ is the chemical potential of the imperfections which may be expressed in the form

$$\mu=kT\log\frac{n}{N}+\mu_f\,. \tag{6}$$

The first term is associated with the mixing entropy, whereas the second is the intrinsic chemical potential, which would describe the driving force if only a single imperfection were present. N is the number of potential imperfection sites per unit volume. μ_f is a constant in a homogeneous isothermal system, so that only the first term in (6) determines the current in this case. The equilibrium density of imperfections is given by the equation

$$n=N\exp(-\mu_f/kT)\,. \qquad (7)$$

We may expect a current of imperfections when a temperature gradient is present. From a kinetic viewpoint, this current may be determined by examining the behavior of the expression for the jump frequency of an imperfection in the presence of a thermal gradient. We shall assume for simplicity that the imperfection is surrounded symmetrically by sites into which it can jump and shall designate the various sites by an index α. The distance the imperfection moves when it jumps to αth site, projected on the direction of the thermal gradient, an algebraic quantity, will be designated by δ_α. The jumping frequency for any one of the equivalent sites may be expressed in the form

$$\nu=\nu_0\exp(-\mu_m/kT) \qquad (8)$$

in the isothermal case. Here ν_0 is presumed to be a slowly varying function of temperature. μ_m is the change in free energy of the imperfection in passing from the normal position to the saddle point for the transition. μ_m may be expected to be a function of temperature.

The net current of imperfections in the presence of a thermal gradient is given by the expression

$$I=-D\,\mathrm{grad}\,n+nD\frac{d}{dT}\left(\frac{-\mu_m}{kT}\right)\mathrm{grad}\,T \qquad (9)$$

in which

$$D=\frac{1}{2}\sum_\alpha \nu\delta_\alpha^2 \qquad (10)$$

Terms arising from the temperature dependence of ν_0 are neglected. The second term in (9) evidently arises from the fact that the atoms in the surrounding sites are not equivalent in the presence of the termal gradient. Generally speaking, atoms on the 'hot side' of the imperfection will move at a different rate from those on the colder side. If μ_m varies sufficiently slowly with temperature, this effect will exert a force tending to cause the imperfections to drift in the direction of the temperature gradient.

The first term in (9) has a simple form if n retains the equilibrium value locally. In this case the two terms of (9) may be combined to

$$I=nD\frac{d}{dT}\frac{(\mu_f-\mu_m)}{kT}\,\mathrm{grad}\,T\,. \qquad (11)$$

In the simplest conceivable case μ_f and μ_m may be regarded as constants equal to the activation energies $\mathcal{E}_m$ and $\mathcal{E}_f$ for migration and formation of the imperfections, respectively. The considerations valid for this case are also valid if $\mu_m-\mu_f$ contains no terms which vary more rapidly than the first power of T, for linear terms in these quantities will not contribute to the derivative in (11). Since the activation energy for formation is generally supposed to be larger than that for migration, one would expect the current of imperfections to be in the direction of $-\mathrm{grad}\,T$ in this case. It appears, however, that $\mathcal{E}_f-\mathcal{E}_m$ may be substantially smaller than $\mathcal{E}_f$. For example, it is generally supposed, in the case of metals such as copper, silver and gold, that $\mathcal{E}_m$ is not smaller than one half of $\mathcal{E}_f$. Hence the counter current term should be far from negligible in such cases. On the whole, it appears risky to assume that additional terms arising from the temperature dependence of $\mu_m-\mu_f$, as well as from terms not explicitly considered here, cannot combine with those considered above in such a way as to cause the imperfections to flow from low temperatures to high. It seems very desirable to have an independent method of determining the nature of the carriers which is not subject to an assumption of this type. The second type of experiment discussed in the previous section, based on a test of the Matano method, does not appear to suffer from this shortcoming.

It is a pleasure for the writer to thank his Japanese colleagues for the stimulating privilege of attending the Nikko Conference on dislocations and for their warm hospitality throughout the meetings in Japan. It is also a pleasure to thank the Office of Scientific Research of ARDC for the privileges which made it possible to attend the conference. Still further, he would like to acknowledge the opportunity for discussing this topic with Dr. L. S. Darken provided by a meeting of the New York section of A.I.M.E.

References

1) E. O. Kirkendall: Trans. Amer. Inst. Min. Met. Eng. **147** (1942) 104; A. D. Smigelskas and E. O. Kirkendall: *ibid* **171** (1947) 130.
2) A. C. Correa da Silva and R. F. Mehl, Trans. Amer. Inst. Min. Met. Eng. **191** (1951) 155.
3) R. Balluffi and B. H. Alexander: J. App. Phys. **23** (1952) 953, 1237; Jour. Metals **4** (1952) 1315; G. C. Kuczynski and B. H. Alexander: J. App. Phys. **22** (1951) 1344; G. C. Kuczynski: *ibid* **21** (1950) 632; R. W. Balluffi: Acta Met. (to be published); R. W. Balluffi and L. I. Seigle: Jour. App. Phys. (to be published).
4) R. S. Barnes: Proc. Roy. Soc. **B65** (1952) 512.
5) H. Bückle and J. Blin: Jour. Inst. Metals **78** (1952) 385.
6) W. Seith and A. Kottman: Naturwiss. **39** (1952) 40, 41.
7) L. S. Darken: Trans. Amer. Inst. Min. Met. Eng. **175** (1948) 184.
8) A summary of theoretical and experimental work appears in the paper, F. Seitz, Acta Met. **1** (1953) 355.
9) J. H. Hollomon and D. Turnbull: *The Solidification of Metals and Alloys* (Amer. Inst. of Min. Met. Eng., New York, 1951) p. 1; D. Turnbull, Principles of Solidification (ASM Symposium on Thermodynamics in Physical Metallurgy, Cleveland, 1949); D. Turnbull: Jour. Chem. Phys. **18** (1950) 768; *ibid* **20** (1952) 411.
10) F. S. Buffington and M. Cohen: J. Metals **4** (1952) 859.
11) A. H. Cottrell: Phil. Mag. **44** (1953) 829.
12) J. W. Kauffman and J. S. Koehler: Phys. Rev. **88** (1952) 149.
13) E. C. Ellwood: Nature **163** (1949) 722; **170** (1952) 580; Jour. Inst. Metals **80** (1952) 217; E. C. Ellwood and K. Q. Bagley: *ibid* **80** (1952) 617.
14) C. Matano: Japan. Jour. Phys. **8** (1930–33) 109.
15) W. Shockley: Phys. Rev. **91** (1953) 1563.

JOURNAL OF THE PHYSICAL SOCIETY OF JAPAN Vol. 10, N0. 8, AUGUST, 1955

The Drag on a Circular Cylinder moving with Low Speeds in a Viscous Liquid between Two Parallel Walls

By Yorisaburo TAKAISI

Department of Physics, Faculty of Education,
Ehime University, Matuyama

(Received April 27, 1955)

The steady slow motion of a circular cylinder in a viscous liquid bounded by two parallel plane walls is discussed on the basis of Oseen's linearized equations of motion, confining ourselves to the case when the cylinder is moving midway between the bounding walls. The drag experienced by the cylinder is then calculated to Lamb's approximation. It is shown that at sufficiently small Reynolds numbers, the drag on the cylinder is independent of the Reynolds number, namely, it is of the so-called Stokes type, as was shown by White's experiments on wires falling in viscous liquids between two vertical plates. When the ratio of the distance between the walls to the diameter of the cylinder is greater than 20, our theoretical results coincide fairly well with White's experiments, allowing for some experimental errors.

§1. Introduction

The steady slow motion of a sphere in a viscous liquid bounded by two parallel plane walls was discussed by H. A. Lorentz[1)], R. Ladenburg[2)] and H. Faxén[3)4)]. Faxèn seems to have studied a similar problem for a circular cylinder, but as far as the present writer is aware, no paper on the problem has been published by him, and moreover, no detailed theoretical discussion has yet been carried out by any one.

C. M. White[5)] studied the problem by carrying out experiments on wires or ebonite rods falling midway between two vertical plane walls in viscous liquids, and obtained an empirical formula for the drag coefficient. At sufficiently slow velocity, there is a very marked difference between White's empirical formula and the well-known Lamb's formula for unbounded fluid; the former is independent of the Reynolds number, while the latter depends on it.

The object of the present paper lies in theoretical treatment of the problem. Thus, the steady motion with low speed U of a circular cylinder in a viscous liquid bounded by two parallel plane walls is discussed on the basis of Oseen's linearized equations of motion, by developing an analysis similar to that in Faxén's treatment of the sphere problem.

The formula for the drag coefficient is obtained and is compared with White's empirical formula.

§ 2. Method of Solution

Suppose that a circular cylinder of radius a is moving, with constant slow velocity U, from right to left in a viscous liquid at rest, which is bounded by parallel plane walls. Referring to rectangular coordinate-system $0x$, $0y$ with origin at the centre of the cylinder, where the x- and y-axes are taken parallel and perpendicular to the walls respectively, the liquid at infinity flows, with constant velocity U, past the cylinder at rest in the positive direction of the x-axis (Fig. 1). In this case the bounding plane walls should also move with the same velocity U from left to right in their own planes, so as to satisfy the boundary conditions.

In the case of no bounding walls, the stream function Ψ may be written as:

$$\Psi = Uy + \psi \,, \qquad (2.1$$

where ψ is the stream function for the perturbation and is connected with the components of perturbation velocity as:

$$u = \frac{\partial \psi}{\partial y}\,, \qquad v = -\frac{\partial \psi}{\partial x}\,. \qquad (2.2$$

If we confine ourselves to Lamb's approximation, the components of perturbation velocit which satisfy Oseen's linearized equations o motion and the boundary conditions at infinit can be expressed as:

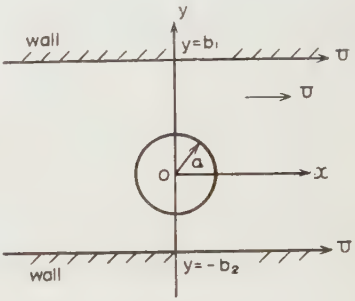

Fig. 1.

$$\left.\begin{aligned} u &= A_0 r^{-1}\sin\theta + B_0 r^{-1}\cos\theta - k a_0 \mathrm{e}^{kx} K_1(kr)\sin\theta + k b_0 \mathrm{e}^{kx}\{K_1(kr)\cos\theta + K_0(kr)\}\,, \\ v &= -A_0 r^{-1}\cos\theta + B_0 r^{-1}\sin\theta + k a_0 \mathrm{e}^{kx}\{K_1(kr)\cos\theta - K_0(kr)\} + k b_0 \mathrm{e}^{kx} K_1(kr)\sin\theta\,, \end{aligned}\right\} \qquad (2.3$$

where $x = r\cos\theta$, $y = r\sin\theta$, and

$$2k = U/\nu\,, \qquad (2.4$$

$$b_0 = -B_0\,. \qquad (2.5$$

$K_n(x)$ is the modified Bessel function of the second kind and ν is the kinematic viscosity o the liquid concerned. The condition (2.5) ensures that the stream function Ψ is one-value and continuous throughout the whole field of flow.

Introducing the conjugate complex velocity $w = u - iv$ $(i = \sqrt{-1})$, we obtain from (2.3) neglecting all terms higher than $k^2 r^2$,

$$\begin{aligned} \frac{w}{k} &= \left(\frac{1}{2} - \gamma - \ln\frac{kr}{2}\right) b_0 - i\left(\frac{1}{2} + \gamma + \ln\frac{kr}{2}\right) a_0 \\ &\quad + \mathrm{e}^{-i\theta}\left[\, i\frac{A_0}{kr} + \frac{B_0}{kr} + \frac{b_0}{kr} - i\left\{\frac{1}{kr} + kr\left(\gamma + \ln\frac{kr}{2}\right)\right\} a_0\right] \\ &\quad + \cdots, \end{aligned} \qquad (2.6$$

where $\gamma = 0.57721\cdots$ is Euler's constant.

We can express (2.3) in integral forms as shown in our previous paper[6], namely:

$$\begin{aligned} u = &\ \frac{1}{2}\int_{-\infty}^{\infty}\left(\frac{|y|}{y}A_0 - \frac{i\alpha}{|\alpha|}B_0\right)\exp(i\alpha x - |\alpha||y|)\,d\alpha \\ &- \frac{1}{2}\int_{-\infty}^{\infty}\left(\frac{|y|}{y}a_0 + \frac{i\lambda_0}{\alpha}b_0\right)\exp(i\alpha x - \lambda_0|y|)\,d\alpha\,, \end{aligned}$$

$$\left.\begin{aligned} v= & \frac{1}{2}\int_{-\infty}^{\infty}\left(\frac{i\alpha}{|\alpha|}A_0+\frac{|y|}{y}B_0\right)\exp(i\alpha x-|\alpha||y|)d\alpha \\ & +\frac{1}{2}\int_{-\infty}^{\infty}\left(-\frac{i\alpha}{\lambda_0}a_0+\frac{|y|}{y}b_0\right)\exp(i\alpha x-\lambda_0|y|)d\alpha\,, \end{aligned}\right\} \tag{2.7}$$

where $\lambda_0=\sqrt{\alpha^2+2ik\alpha}$.

In order to satisfy the boundary conditions on the bounding plane walls, we now superpose, as done by Faxén in the case of the sphere problem, flows due to images, which are defined as:

$$\left.\begin{aligned} u^*= & -\frac{1}{2}\int_{-\infty}^{\infty}|\alpha|f_1(\alpha)\exp(i\alpha x-|\alpha|y)\,d\alpha-\frac{1}{2}\int_{-\infty}^{\infty}\lambda_0 f_2(\alpha)\exp(i\alpha x-\lambda_0 y)d\alpha\,, \\ v^*= & -\frac{1}{2}\int_{-\infty}^{\infty}i\alpha f_1(\alpha)\exp(i\alpha x-|\alpha|y)d\alpha-\frac{1}{2}\int_{-\infty}^{\infty}i\alpha f_2(\alpha)\exp(i\alpha x-\lambda_0 y)d\alpha\,, \end{aligned}\right\} \tag{2.8}$$

$$\left.\begin{aligned} u^{**}= & \ \frac{1}{2}\int_{-\infty}^{\infty}|\alpha|f_3(\alpha)\exp(i\alpha x+|\alpha|y)\,d\alpha+\frac{1}{2}\int_{-\infty}^{\infty}\lambda_0 f_4(\alpha)\exp(i\alpha x+\lambda_0 y)d\alpha\,, \\ v^{**}= & -\frac{1}{2}\int_{-\infty}^{\infty}i\alpha f_3(\alpha)\exp(i\alpha x+|\alpha|y)d\alpha-\frac{1}{2}\int_{-\infty}^{\infty}i\alpha f_4(\alpha)\exp(i\alpha x+\lambda_0 y)d\alpha\,, \end{aligned}\right\} \tag{2.9}$$

where $f_n(\alpha)$'s are unknown functions to be determined by undermentioned boundary conditions.

The conjugate complex velocities $w^*=u^*-iv^*$ and $w^{**}=u^{**}-iv^{**}$ for the superposed flows due to images can be written as:

$$w^*=-\frac{1}{2}\int_{-\infty}^{\infty}(|\alpha|+\alpha)f_1(\alpha)\exp(i\alpha x-|\alpha|y)\,d\alpha-\frac{1}{2}\int_{-\infty}^{\infty}(\lambda_0+\alpha)f_2(\alpha)\exp(i\alpha x-\lambda_0 y)d\alpha\,, \tag{2.10}$$

$$w^{**}=\ \frac{1}{2}\int_{-\infty}^{\infty}(|\alpha|-\alpha)f_3(\alpha)\exp(i\alpha x+|\alpha|y)\,d\alpha+\frac{1}{2}\int_{-\infty}^{\infty}(\lambda_0-\alpha)f_4(\alpha)\exp(i\alpha x+\lambda_0 y)d\alpha\,. \tag{2.11}$$

Since the conditions at infinity are already satisfied automatically by (u, v), w^* and w^{**} as given respectively by (2.3), (2.10) and (2.11), we have only to consider the boundary conditions on the bounding plane walls $y=b_1$ and $y=-b_2$ as well as at the surface of the cylinder. They are

(i) $$(w+w^*+w^{**})_{y=b_1}=0\,, \tag{2.12}$$

or $$(u+u^*+u^{**})_{y=b_1}=0\,, \qquad (v+v^*+v^{**})_{y=b_1}=0\,, \tag{2.12a}$$

(ii) $$(w+w^*+w^{**})_{y=-b_2}=0\,, \tag{2.13}$$

or $$(u+u^*+u^{**})_{y=-b_2}=0\,, \qquad (v+v^*+v^{**})_{y=-b_2}=0\,, \tag{2.13a}$$

and

(iii) $$(w+w^*+w^{**})_{r=a}=-U\,. \tag{2.14}$$

§ 3. Determination of the Functions $f_n(\alpha)$'s

Inserting the values of (u, v), (u^*, v^*) and (u^{**}, v^{**}) as given respectively by (2.7), (2.8) (2.9) into (2.12a) and (2.13a), we get

$$\begin{aligned} \int_{-\infty}^{\infty}\exp(i\alpha x)\Big[& A_0\exp(-b_1|\alpha|)-B_0\frac{i\alpha}{|\alpha|}\exp(-b_1|\alpha|) \\ & -a_0\exp(-b_1\lambda_0)-b_0\frac{i\lambda_0}{\alpha}\exp(-b_1\lambda_0)-|\alpha|f_1(\alpha)\exp(-b_1|\alpha|)-\lambda_0 f_2(\alpha)\exp(-b_1\lambda_0) \\ & +|\alpha|f_3(\alpha)\exp(b_1|\alpha|)+\lambda_0 f_4(\alpha)\exp(b_1\lambda_0)\Big]d\alpha=0\,, \end{aligned} \tag{3.1}$$

$$\int_{-\infty}^{\infty}\exp(i\alpha x)\Big[A_0\frac{i\alpha}{|\alpha|}\exp(-b_1|\alpha|)+B_0\exp(-b_1|\alpha|)$$
$$-a_0\frac{i\alpha}{\lambda_0}\exp(-b_1\lambda_0)+b_0\exp(-b_1\lambda_0)-i\alpha f_1(\alpha)\exp(-b_1|\alpha|)-i\alpha f_2(\alpha)\exp(-b_1\lambda_0)$$
$$-i\alpha f_3(\alpha)\exp(b_1|\alpha|)-i\alpha f_4(\alpha)\exp(b_1\lambda_0)\Big]d\alpha=0\,, \tag{3.2}$$

$$\int_{-\infty}^{\infty}\exp(i\alpha x)\Big[-A_0\exp(-b_2|\alpha|)-B_0\frac{i\alpha}{|\alpha|}\exp(-b_2|\alpha|)$$
$$+a_0\exp(-b_2\lambda_0)-b_0\frac{i\lambda_0}{\alpha}\exp(-b_2\lambda_0)-|\alpha|f_1(\alpha)\exp(b_2|\alpha|)-\lambda_0 f_2(\alpha)\exp(b_2\lambda_0)$$
$$+|\alpha|f_3(\alpha)\exp(-b_2|\alpha|)+\lambda_0 f_4(\alpha)\exp(-b_2\lambda_0)\Big]d\alpha=0\,, \tag{3.3}$$

$$\int_{-\infty}^{\infty}\exp(i\alpha x)\Big[A_0\frac{i\alpha}{|\alpha|}\exp(-b_2|\alpha|)-B_0\exp(-b_2|\alpha|)$$
$$-a_0\frac{i\alpha}{\lambda_0}\exp(-b_2\lambda_0)-b_0\exp(-b_2\lambda_0)-i\alpha f_1(\alpha)\exp(b_2|\alpha|)-i\alpha f_2(\alpha)\exp(b_2\lambda_0)$$
$$-i\alpha f_3(\alpha)\exp(-b_2|\alpha|)-i\alpha f_4(\alpha)\exp(-b_2\lambda_0)\Big]d\alpha=0\,. \tag{3.4}$$

In order that these relations are satisfied for all values of x, the quantities in the square brackets must be identically zero. Thus, the functions $f_n(\alpha)$'s so far undetermined can be expressed in terms of four unknown constants A_0, B_0, a_0 and b_0.

In the special case when the cylinder is moving midway between two bounding plane walls, we may put, due to the symmetry of the flow,

$$A_0=a_0=0. \tag{3.5}$$

Making use of the relations (2.5) and (3.5), and putting $b_1=b_2=b$, we have finally from (3.1), (3.2), (3.3) and (3.4)

$$\left.\begin{aligned}
&f_1(\alpha)=-f_3(\alpha)\\
&=\frac{(\lambda_0+|\alpha|)\exp\{b(\lambda_0-|\alpha|)\}+(\lambda_0-|\alpha|)\exp\{-b(\lambda_0+|\alpha|)\}-2\lambda_0}{(\lambda_0-|\alpha|)[\exp\{b(\lambda_0+|\alpha|)\}-\exp\{-b(\lambda_0+|\alpha|)\}]-(\lambda_0+|\alpha|)[\exp\{b(\lambda_0-|\alpha|)\}-\exp\{-b(\lambda_0-|\alpha|)\}]}\\
&\quad\times\frac{iB_0}{\alpha}\,,\\
&f_2(\alpha)=-f_4(\alpha)\\
&=\frac{(\lambda_0+|\alpha|)\exp\{-b(\lambda_0-|\alpha|)\}-(\lambda_0-|\alpha|)\exp\{-b(\lambda_0+|\alpha|)\}-2|\alpha|}{(\lambda_0-|\alpha|)[\exp\{b(\lambda_0+|\alpha|)\}-\exp\{-b(\lambda_0+|\alpha|)\}]-(\lambda_0+|\alpha|)[\exp\{b(\lambda_0-|\alpha|)\}-\exp\{-b(\lambda_0-|\alpha|)\}]}\\
&\quad\times\frac{iB_0}{\alpha}\,.
\end{aligned}\right\} \tag{3.6}$$

Inserting these expressions into (2.10) and (2.11), and putting $\alpha=k\beta$, $\lambda=\sqrt{\beta^2+2i\beta}$ and $\lambda'=\sqrt{\beta^2-2i\beta}$, we have

$$\frac{w^*}{k}=iB_0\Big\{-\int_0^{\infty}\exp(ik\beta x-k\beta y)d\beta$$
$$\times\frac{(\lambda+\beta)\exp\{kb(\lambda-\beta)\}+(\lambda-\beta)\exp\{-kb(\lambda+\beta)\}-2\lambda}{(\lambda-\beta)[\exp\{kb(\lambda+\beta)\}-\exp\{-kb(\lambda+\beta)\}]-(\lambda+\beta)[\exp\{kb(\lambda-\beta)\}-\exp\{-kb(\lambda-\beta)\}]}$$
$$-\frac{1}{2}\int_0^{\infty}\frac{\lambda+\beta}{\beta}\exp(ik\beta x-k\lambda y)d\beta$$

$$\begin{aligned}
&\times\frac{(\lambda+\beta)\exp\{-kb(\lambda-\beta)\}-(\lambda-\beta)\exp\{-kb(\lambda+\beta)\}-2\beta}{(\lambda-\beta)[\exp\{kb(\lambda+\beta)\}-\exp\{-kb(\lambda+\beta)\}]-(\lambda+\beta)[\exp\{kb(\lambda-\beta)\}-\exp\{-kb(\lambda-\beta\}]}\\
&\quad+\frac{1}{2}\int_0^\infty\frac{\lambda'-\beta}{\beta}\exp(-ik\beta x-k\lambda' y)d\beta\\
&\times\left.\frac{(\lambda'+\beta)\exp\{-kb(\lambda'-\beta)\}-(\lambda'-\beta)\exp\{-kb(\lambda'+\beta)\}-2\beta}{(\lambda'-\beta)[\exp\{kb(\lambda'+\beta)\}-\exp\{-kb(\lambda'+\beta)\}]-(\lambda'+\beta)[\exp\{kb(\lambda'-\beta)\}-\exp\{-kb(\lambda'-\beta)\}]}\right\},
\end{aligned}\tag{3.7}$$

$$\begin{aligned}
\frac{w^{**}}{k}=iB_0&\left\{\int_0^\infty\exp(-ik\beta x+k\beta y)d\beta\right.\\
&\times\frac{(\lambda'+\beta)\exp\{kb(\lambda'-\beta)\}+(\lambda'-\beta)\exp\{-kb(\lambda'+\beta)\}-2\lambda'}{(\lambda'-\beta)[\exp\{kb(\lambda'+\beta)\}-\exp\{-kb(\lambda'+\beta)\}]-(\lambda'+\beta)[\exp\{kb(\lambda'-\beta)\}-\exp\{-kb(\lambda'-\beta)\}]}\\
&\quad-\frac{1}{2}\int\frac{\lambda-\beta}{\beta}\exp(ik\beta x+k\lambda y)d\beta\\
&\times\frac{(\lambda+\beta)\exp\{-kb(\lambda-\beta)\}-(\lambda-\beta)\exp\{-kb(\lambda+\beta)\}-2\beta}{(\lambda-\beta)[\exp\{kb(\lambda+\beta)\}-\exp\{-kb(\lambda+\beta)\}]-(\lambda+\beta)[\exp\{kb(\lambda-\beta)\}-\exp\{-kb(\lambda-\beta)\}]}\\
&\quad+\frac{1}{2}\int_0^\infty\frac{\lambda'+\beta}{\beta}\exp(-ik\beta x+k\lambda' y)d\beta\\
&\times\left.\frac{(\lambda'+\beta)\exp\{-kb(\lambda'-\beta)\}-(\lambda'-\beta)\exp\{-kb(\lambda'+\beta)\}-2\beta}{(\lambda'-\beta)[\exp\{kb(\lambda'+\beta)\}-\exp\{-kb(\lambda'+\beta)\}]-(\lambda'+\beta)[\exp\{kb(\lambda'-\beta)\}-\exp\{-kb(\lambda'-\beta)\}]}\right\}.
\end{aligned}\tag{3.8}$$

In this case (2.6) reduces simply to

$$\frac{w}{k}=-\left(\frac{1}{2}-\gamma-\ln\frac{kr}{2}\right)\beta_0\,.\tag{3.9}$$

§ 4. Determination of the Constant B_0

Using the obvious relations:

$$x=r\cos\theta=\tfrac{1}{2}r(e^{i\theta}+e^{-i\theta})\,,$$
$$y=r\sin\theta=-\tfrac{1}{2}ir(e^{i\theta}-e^{-i\theta})\,,$$

we have

$$\left.\begin{aligned}
\exp(ik\beta x-k\beta y)&=1+ik\beta re^{i\theta}+\cdots\,,\\
\exp(ik\beta x-k\lambda y)&=1+\tfrac{1}{2}ikr(\lambda+\beta)e^{i\theta}-\tfrac{1}{2}ikr(\lambda-\beta)e^{-i\theta}+\cdots\,,\\
\exp(-ik\beta x-k\lambda' y)&=1+\tfrac{1}{2}ikr(\lambda'-\beta)e^{i\theta}-\tfrac{1}{2}ikr(\lambda'+\beta)e^{-i\theta}+\cdots\,,
\end{aligned}\right\}\tag{4.1}$$

and

$$\left.\begin{aligned}
\exp(-ik\beta x+k\beta y)&=1-ik\beta re^{i\theta}+\cdots\,,\\
\exp(ik\beta x+k\lambda y)&=1-\tfrac{1}{2}ikr(\lambda-\beta)e^{i\theta}+\tfrac{1}{2}ikr(\lambda+\beta)e^{-i\theta}+\cdots\,,\\
\exp(-ik\beta x+k\lambda' y)&=1-\tfrac{1}{2}ikr(\lambda'+\beta)e^{i\theta}+\tfrac{1}{2}ikr(\lambda'-\beta)e^{-i\theta}+\cdots\,.
\end{aligned}\right\}\tag{4.2}$$

Thus, inserting these expressions into (3.7) and (3.8) respectively and retaining only constant terms as well as terms involving $e^{-i\theta}$, we obtain, on neglecting all terms higher than k^2r^2,

$$\begin{aligned}
\frac{w^*}{k}&=iB_0\\
&\times\left\{-\int_0^\infty\frac{(\lambda+\beta)\exp\{kb(\lambda-\beta)\}+(\lambda-\beta)\exp\{-kb(\lambda+\beta)\}-2\lambda}{(\lambda-\beta)[\exp\{kb(\lambda+\beta)\}-\exp\{-kb(\lambda+\beta)\}]-(\lambda+\beta)[\exp\{kb(\lambda-\beta)\}-\exp\{-kb(\lambda-\beta)\}]}d\beta\right.\\
&\quad-\frac{1}{2}\int_0^\infty\frac{\lambda+\beta}{\beta}
\end{aligned}$$

$$\times\frac{(\lambda+\beta)\exp\{-kb(\lambda-\beta)\}-(\lambda-\beta)\exp\{-kb(\lambda+b)\}-2\beta}{(\lambda-\beta)[\exp\{kb(\lambda+\beta)\}-\exp\{-kb(\lambda+\beta)\}]-(\lambda+\beta)[\exp\{kb(\lambda-\beta)\}-\exp\{-kb(\lambda-\beta)\}]}d\beta$$

$$+\frac{1}{2}\int_0^\infty\frac{\lambda'-\beta}{\beta}$$

$$\times\frac{(\lambda'+\beta)\exp\{-kb(\lambda'-\beta)\}-(\lambda'-\beta)\exp\{-kb(\lambda'+\beta)\}-2\beta}{(\lambda'-\beta)[\exp\{kb(\lambda'+\beta)\}-\exp\{-kb(\lambda'+\beta)\}]-(\lambda'+\beta)[\exp\{kb(\lambda'-\beta)\}-\exp\{-kb(\lambda'-\beta)\}]}d\beta\Bigg\}$$

$$+\frac{1}{4}krB_0\mathrm{e}^{-i\theta}\Bigg\{-\int_0^\infty\frac{\lambda^2-\beta^2}{\beta}$$

$$\times\frac{(\lambda+\beta)\exp\{-kb(\lambda-\beta)\}-(\lambda-\beta)\exp\{-kb(\lambda+\beta)\}-2\beta}{(\lambda-\beta)[\exp\{kb(\lambda+\beta)\}-\exp\{-kb(\lambda+\beta)\}]-(\lambda+\beta)[\exp\{kb(\lambda-\beta)\}-\exp\{-kb(\lambda-\beta)\}]}d\beta$$

$$+\int_0^\infty\frac{\lambda'^2-\beta^2}{\beta}$$

$$\times\frac{(\lambda'+\beta)\exp\{-kb(\lambda'-\beta)\}-(\lambda'-\beta)\exp\{-kb(\lambda'+\beta)\}-2\beta}{(\lambda'-\beta)[\exp\{kb(\lambda'+\beta)\}-\exp\{-kb(\lambda'+\beta)\}]-(\lambda'+\beta)[\exp\{kb(\lambda'-\beta)\}-\exp\{-kb(\lambda'-\beta)\}]}d\beta\Bigg\}, \tag{4.3}$$

$$\frac{w^{**}}{k}=iB_0$$

$$\times\Bigg\{\int_0^\infty\frac{(\lambda'+\beta)\exp\{kb(\lambda'-\beta)\}+(\lambda'-\beta)\exp\{-kb(\lambda'+\beta)\}-2\lambda'}{(\lambda'-\beta)[\exp\{kb(\lambda'+\beta)\}-\exp\{-kb(\lambda'+\beta)\}]-(\lambda'+\beta)[\exp\{kb(\lambda'-\beta)\}-\exp\{-kb(\lambda'-\beta)\}]}d\beta$$

$$-\frac{1}{2}\int_0^\infty\frac{\lambda-\beta}{\beta}$$

$$\times\frac{(\lambda+\beta)\exp\{-kb(\lambda-\beta)\}-(\lambda-\beta)\exp\{-k\beta(\lambda+\beta)\}-2\beta}{(\lambda-\beta)[\exp\{kb(\lambda+\beta)\}-\exp\{-kb(\lambda+\beta)\}]-(\lambda+\beta)[\exp\{kb(\lambda-\beta)\}-\exp\{-kb(\lambda-\beta)\}]}d\beta$$

$$+\frac{1}{2}\int_0^\infty\frac{\lambda'+\beta}{\beta}$$

$$\times\frac{(\lambda'+\beta)\exp\{-kb(\lambda'-\beta)\}-(\lambda'-\beta)\exp\{-kb(\lambda'+\beta)\}-2\beta}{(\lambda'-\beta)[\exp\{kb(\lambda'+\beta)\}]-\exp\{-kb(\lambda'+\beta)\}]-(\lambda'+\beta)[\exp\{kb(\lambda'-\beta)\}-\exp\{-kb(\lambda'-\beta)\}]}d\beta\Bigg\}$$

$$+\frac{1}{4}krB_0\mathrm{e}^{-i\theta}\Bigg\{\int_0^\infty\frac{\lambda^2-\beta^2}{\beta}$$

$$\times\frac{(\lambda+\beta)\exp\{-kb(\lambda-\beta)\}-(\lambda-\beta)\exp\{-kb(\lambda+\beta)\}-2\beta}{(\lambda-\beta)[\exp\{kb(\lambda+\beta)\}-\exp\{-kb(\lambda+\beta)\}]-(\lambda+\beta)[\exp\{kb(\lambda-\beta)\}-\exp\{-kb(\lambda-\beta)\}]}d\beta$$

$$-\int_0^\infty\frac{\lambda'^2-\beta^2}{\beta}$$

$$\times\frac{(\lambda'+\beta)\exp\{-kb(\lambda'-\beta)\}-(\lambda'-\beta)\exp\{-kb(\lambda'+\beta)\}-2\beta}{(\lambda'-\beta)[\exp\{kb(\lambda'+\beta)\}-\exp\{-kb(\lambda'+\beta)\}]-(\lambda'+\beta)[\exp\{kb(\lambda'-\beta)\}-\exp\{-kb(\lambda'-\beta)\}]}d\beta\Bigg\}. \tag{4.4}$$

The constant B_0 in this case can be determined by inserting (3.9), (4.3) and (4.4) into (2.14). Writing for brevity

$$F(kb)$$

$$=\int_0^\infty\frac{4\lambda\exp\{-kb(\lambda+\beta)\}-2(\lambda-\beta-i)\exp\{-2kb(\lambda+\beta)\}-(\lambda+\beta)\exp(-2kb\beta)-(\lambda+\beta+2i)\exp(-2kb\lambda)}{\lambda\{1+\exp(-2kb\lambda)\}\{1-\exp(-2kb\beta)\}-\beta\{1-\exp(-2kb\lambda)\}\{1+\exp(-2kb\beta)\}}$$

$$\times d\beta-\mathrm{C.C.}\,, \tag{4.5}$$

we have

$$B_0=\frac{1}{1/2-\gamma-\ln(ka/2)-iF(kb)}\frac{U}{k}. \tag{4.6}$$

In (4.5) the notation C.C. stands for "the conjugate complex of the foregoing integral".

§ 5. Evaluation of the Function $F(kb)$

Since it seems very difficult to evaluate exactly the integral in (4.5), we confine ourselves to the evaluation of $F(kb)$ for sufficiently small values of kb such that all terms higher than $(kb)^{1/2}$ can be neglected.

In the first place, we put

$$F_1(l)$$

$$=\int_0^{1/l^{1/2}}\frac{4\lambda\exp\{-l(\lambda+\beta)\}-2(\lambda-\beta-i)\exp\{-2l(\lambda+\beta)\}-(\lambda+\beta)\exp(-2l\beta)-(\lambda+\beta+2i)\exp(-2l\lambda)}{\lambda\{1+\exp(-2l\lambda)\}\{1-\exp(-2l\beta)\}-\beta\{1-\exp(-2l\lambda)\}\{1+\exp(-2l\beta)\}}$$

$$\times d\beta-\text{C.C.}\,, \tag{5.1}$$

where $l=kb$.

If we expand all the expotential functions in (5.1) into Taylor's series with respect to l, we have, after some calculations,

$$F_1(l)=-\frac{1}{2}\left\{\int_0^{1/l^{1/2}}\frac{\lambda}{\beta}\,d\beta-\text{C.C.}\right\}+O(l^{1/2})=i\left(\frac{1}{2}\ln l-\ln 2-1\right)+O(l^{1/2})\,. \tag{5.2}$$

In the second place, we put

$$G(l)$$

$$=\int_{1/l^{1/2}}^{\infty}\frac{4\lambda\exp\{-l(\lambda+\beta)\}-2(\lambda-\beta-i)\exp\{-2l(\lambda+\beta)\}-(\lambda+\beta)\exp(-2l\beta)-(\lambda+\beta+2i)\exp(-2l\lambda)}{\lambda\{1+\exp(-2l\lambda)\}\{1-\exp(-2l\beta)\}-\beta(1-\exp(-2l\lambda)\}\{1+\exp(-2l\beta)\}}$$

$$\times d\beta-\text{C.C.}\,. \tag{5.3}$$

The functions $\lambda(=\sqrt{\beta^2+2i\beta})$ and $\exp(-l\lambda)$ can be expanded into Taylor's series with respect to $1/\beta$ aβ:

$$\lambda=\beta+i+\frac{1}{2\beta}-\frac{i}{2\beta^2}-\frac{5}{8\beta^3}+\frac{7i}{8\beta^4}+\frac{21}{16\beta^5}-\frac{231i}{112\beta^6}+\cdots\,,$$

$$\exp(-l\lambda)=\left(1-il-\frac{1}{2}l^2+\frac{1}{6}il^3-\frac{l}{2\beta}+\frac{il^2}{2\beta}+\frac{5l^2}{8\beta^2}+\frac{il}{2\beta^2}+\frac{5l}{8\beta^3}-\frac{7il}{8\beta^4}+\cdots\right)\exp(-l\beta)\,,$$

and if we insert these into (5.3) and neglect higher order terms, we have

$$G(l)\sim-2i\int_{1/l^{1/2}}^{\infty}\frac{(1-2l\beta+2l^2\beta^2)\exp(-2l\beta)-\exp(-4l\beta)}{\beta\{1-4l\beta\exp(-2l\beta)-\exp(-4l\beta)\}}\,d\beta\,,$$

which, by putting $l\beta=v$, can also be written as:

$$G(l)\sim-2i\int_{l^{1/2}}^{\infty}\frac{(1-2v+2v^2)\exp(-2v)-\exp(-4v)}{v\{1-4v\exp(-2v)-\exp(-4v)}\,dv\,. \tag{5.4}$$

For the sake of convenience in evaluating the integral on the right-hand side, we divide the range of integration from $\sqrt{l}$ to ∞ into three parts and we write

$$G(l)=F_2(l)+F_3(l)+F_4(l)\,,$$

where

$$F_2(l)=-2i\int_{l^{1/2}}^{1}\frac{(1-2v+2v^2)\exp(-2v)-\exp(-4v)}{v\{1-4v\exp(-2v)-\exp(-4v)\}}\,dv\,, \tag{5.6}$$

$$F_3(l)=-2i\int_{1}^{2}\frac{(1-2v+2v^2)\exp(-2v)-\exp(-4v)}{v\{1-4v\exp(-2v)-\exp(-4v)\}}\,dv\,, \tag{5.7}$$

$$F_4(l)=-2i\int_{2}^{\infty}\frac{(1-2v+2v^2)\exp(-2v)-\exp(-4v)}{v\{1-4v\exp(-2v)-\exp(-4v)\}}\,dv\,, \tag{5.8}$$

In order to evaluate $F_2(l)$, we expand the integrand in (5.6) into Taylor's series with respect to v. We thus have

$$F_2(l) \sim -i\int_{l^{1/2}}^{1} \frac{1}{v}\left(1-\frac{1}{2}v+\frac{1}{30}v^3-\frac{1}{525}v^5+\frac{1}{15750}v^7-\cdots\right)dv = i\left(\frac{1}{2}\ln l+0.4893\right). \tag{5.9}$$

Next, the integral in (5.7) has been evaluated numerically by making use of Simpson's rule, and we have found that

$$F_3(l) = -0.2603i\,. \tag{5.10}$$

Finally, the function $F_4(l)$ can be calculated as follows:

$$F_4(l) \sim -2i\int_2^{\infty}\frac{1}{v}\{(1-2v+2v^2)\exp(-2v)-(1-4v+8v^2-8v^3)\exp(-4v)$$
$$+(1-6v+18v^2-32v^3+32v^4)\exp(-6v)+\cdots\}dv = -0.0674i\,. \tag{5.11}$$

Thus, by (5.2), (5.9), (5.10) and (5.11), we have

$$F(l) = \sum_{n=1}^{4} F_n(l) = i\left(\ln\frac{l}{2}-0.8384\right),$$

or

$$F(kb) = i\left(\ln\frac{kb}{2}-0.8384\right), \tag{5.12}$$

and inserting this into (4.6), we have finally

$$B_0 = \frac{1}{\ln(b/a)-0.9156}\,\frac{U}{k}\,. \tag{5.13}$$

As in the case of a cylinder immersed in an unlimited stream of viscous liquid, the drag D experienced by the circular cylinder under discussion per its unit length can be expressed as:

$$D = 2\pi\rho U B_0\,,$$

where ρ is the density of the fluid concerned.

Hence, making use of (5.13), we have

$$\frac{D}{\mu U} = \frac{4\pi}{\ln(b/a)-0.9156} = \frac{5.457}{\log(0.4003\,b/a)}, \tag{5.14}$$

μ being the viscosity of the fluid.

§ 6. Discussion of the Result

Lamb has shown analytically that the drag experienced by a circular cylinder moving laterally in an infinite viscous fluid with constant slow velocity U is given by

$$\frac{D}{\mu U} = \frac{4\pi}{1/2-\gamma-\ln(ka/2)} = \frac{5.46}{\log(1.85/ka)}\,. \tag{6.1}$$

By carrying out experiments with wires falling sideways in viscous liquids in a circular jar or between two vertical parallel plates, White has found however that Lamb's formula can be applied only in an infinite or nearly infinite fluid, and that in any practical case when the fluid is limited by outer boundaries there is a very marked deviation from (6.1).

At sufficiently slow speeds, experimental results conformed closely with a formula:

$$D/\mu U = \text{const}\,, \tag{6.2}$$

where the value of the constant depends only on the shape of outer boundaries and on their distance from the cylinder, but not on Reynolds numbers.

In the previous paper[6], the present writer has shown analytically that the drag experienced by a circular cylinder moving in a semi-infinite viscous liquid parallel to its bounding wall is of the type (6.2).

It is seen that our present result (5.14) is also of the same type: namely, the drag coefficient $D/\mu U$ is independent of either of the two Reynolds numbers R $(=Ud/\nu)$ and R^* $(=UH/\nu)$, where d is the diameter of the cylinder and H is the distance between the walls. In other words, the drag on a circular cylinder moving in a viscous liquid midway between two parallel walls is also of the so-called Stokes type, as in the case of a circular cylinder moving in a semi-infinite viscous liquid parallel to its bounding wall.

The values of the drag coefficient $D/\mu U$ have been calculated by our formula (5.14) and they are shown by curve I in Fig. 2 plotted against the ratio b/a.

By the above-mentioned experiments on wires falling in a viscous liquid midway between two vertical plates, White obtained the

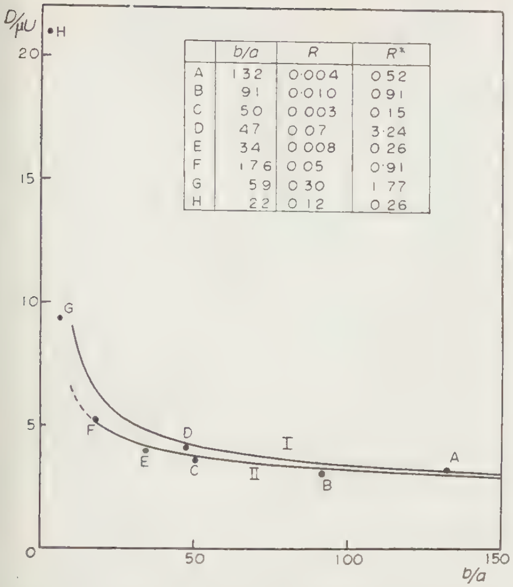

	b/a	R	R*
A	132	0·004	0·52
B	91	0·010	0·91
C	50	0·003	0·15
D	47	0·07	3·24
E	34	0·008	0·26
F	176	0·05	0·91
G	59	0·30	1·77
H	22	0·12	0·26

Fig. 2. Curve I. Drag coefficient calculated by (5.14).
Curve II. Drag coefficient calculated by (6.3).
● A, B...H. Data obtained by White's experiment.

data, corrected properly for end-effects, which are shown in Fig. 2 by points A, B, $\cdots$, G and H. Excluding, due mainly to experimental uncertainties—perhaps 20% in error—, the two data shown by G and H, White obtained an empirical formula for the drag in the form:

$$\frac{D}{\mu U}=\frac{6.4}{\log (b/a)}. \tag{6.3}$$

The values of $D/\mu U$ have also been calculated by this empirical formula and they are shown for comparison by curve II in Fig. 2. Allowing for some experimental errors, it is seen that the coincidence of our theoretical results with White's experimental ones is fairly well, provided the values of the ratio b/a are greater than 20.

However, when the ratio b/a is smaller than 20, we should perhaps proceed with approximation one step or more, and the analysis would then become more and more lengthy and difficult.

In conclusion, the writer wishes to express his cordial thanks to Professor S. Tomotika for his guidance and encouragement throughout the present work. The writer's thanks are also due to Professor I. Imai, University of Tokyo, and to Professor K. Tamada, Osaka City University, for their invaluable discussions.

References

1) H. A. Lorentz: Abhandlungen über theoretische Physik. Teubner (Leipzig) (1907) 23.
2) R. Ladenburg: Ann. d. Phys. **23** (1907) 453.
3) H. Faxén: Diss. Uppsala (1921).
4) H. Faxén: Ann. d. Phys. **68** (1922) 89.
5) C. M. White: Proc. Roy. Soc. **A 186** (1946) 472.
6) Y. Takaisi: J. Phys. Soc. Japan, **10** (1955) 407.

JOURNAL OF THE PHYSICAL SOCIETY OF JAPAN Vol. 10, No. 8, AUGUST, 1955

The Critical Reynolds Number for the Flow past a Sphere

By Mitutosi KAWAGUTI

Institute of Science and Technology, University of Tokyo

(Received April 18, 1955)

The stability of the flow past a sphere which has been calculated previously by use of the Galerkin method was investigated by the method of small perturbation and the Galerkin method. Thus, the ciritical Reynolds number for the flow past a sphere was determined as 51 which should be compared with the experimental value of about 100.

§ 1. Introduction

It is well known that the flow around an obstacle submerged in a viscous fluid can be treated successfully with the Stokes or the Oseen approximation to the Navier-Stokes equations, when the Reynolds number of the flow is sufficiently low. On the other hand, it has been shown experimentally that above certain critical Reynolds number the flow becomes unstable and periodic and transforms into flow with von Kármán's vortex-street (two-dimensional), or with distorted loops of vorticity arranged with some measure of symmetry [1] (axi-symmetrical). But unfortunately, Stokes' and Oseen's approximations become worse as the Reynolds number is increased, so that we must grapple with the exact Navier-Stokes equations in order to investigate the phenomena, such as the existence of the critical Reynolds number, which correlate with the flow with Reynolds number close to the critical Reynolds number.

For such an intermediate régime, the author investigated the flow past a circular cylinder and a sphere by use of Gelerkin's method and Liebmann's method [2], [3], [4], [5], [6]. Also he investigated the limiting form of the flow past a circular cylinder when the Reynolds number is increased indefinitely [7]. From these studies, he concluded that the Navier-Stokes equations have a steady solution even when the Reynolds number of the flow is so high that the steady flow cannot be found experimentally. Further he suggested that the origin of the non-existence of the steady flow at higher Reynolds numbers may be found in the instability of the steady flow which is expected to exist theoretically.

In this paper, the stability of the flow past a sphere, which has been calculated by use of the Galerkin method [3], will be investigated by the method of small perturbation and the Galerkin method.

§ 2. The Steady Flow past a Sphere

The equation of motion for the axi-symmetrical flow of viscous fluid can be given in the non-dimensional form as:

$$\frac{\partial(D^2\Psi)}{\partial t}-\frac{1}{r^2\sin\theta}\frac{\partial(\Psi,\, D^2\Psi)}{\partial(r,\,\theta)}+\frac{2}{r^2}\frac{D^2\Psi}{\sin^2\theta}\left(\frac{\partial\Psi}{\partial r}\cos\theta-\frac{1}{r}\frac{\partial\Psi}{\partial\theta}\sin\theta\right)-\frac{2}{R}D^4\Psi=0\,, \tag{2.1}$$

with

$$D^2=\frac{\partial^2}{\partial r^2}+\frac{\sin\theta}{r^2}\frac{\partial}{\partial\theta}\left(\frac{1}{\sin\theta}\frac{\partial}{\partial\theta}\right), \tag{2.2}$$

where $(r,\,\theta,\,\omega)$ are the polar coordinates, $R(=Ud/\nu)$ is the Reynolds number, U is the undisturbed velocity, d is the characteristic length, ν is the kinematic viscosity, and Ψ is Stokes' stream function. If $(u,\,v,\,w)$ and $(\xi,\,\eta,\,\zeta)$ are the r-, θ-, ω-components of the non-dimensional velocity and vorticity respectively, they are given by

$$u=\frac{1}{r^2\sin\theta}\frac{\partial\Psi}{\partial\theta},\quad v=-\frac{1}{r\sin\theta}\frac{\partial\Psi}{\partial r}\,,$$

$$w=0;\quad \xi=\eta=0,\quad \zeta=-\frac{1}{r\sin\theta}D^2\Psi\,. \tag{2.3}$$

In this section, we deal only with the steady flow case, so that (2.1) becomes

$$-\frac{1}{r^2\sin\theta}\frac{\partial(\Psi,\, D^2\Psi)}{\partial(r,\,\theta)}+\frac{2}{r^2}\frac{D^2\Psi}{\sin^2\theta}\left(\frac{\partial\Psi}{\partial r}\cos\theta-\frac{1}{r}\frac{\partial\Psi}{\partial\theta}\sin\theta\right)-\frac{2}{R}D^4\Psi=0\,. \tag{2.4}$$

Table I.

R	A_1	B_1	C_D	$[\zeta]_{r=1}$
10	-4.4785	-0.9237	4.4855	$-3.0177\sin\theta+0.4105\sin 2\theta$
20	-4.4145	-1.8498	2.4557	$-3.0707\sin\theta+0.8221\sin 2\theta$
40	-4.1621	-3.7605	1.6513	$-3.2796\sin\theta+1.6713\sin 2\theta$
60	-3.7564	-5.7848	1.5628	$-3.6153\sin\theta+2.5710\sin 2\theta$
80	-3.2241	-7.9509	1.6406	$-4.0558\sin\theta+3.5337\sin 2\theta$

Table II.

R	A_1	B_1	C_D	$[\zeta]_{r=1}$
0	-0.7500	0	$24/R$	$-1.5000\sin\theta$
1	-0.7491	-0.0477	24.0301	$-1.5014\sin\theta+0.0477\sin 2\theta$
2	-0.7463	-0.0941	12.0594	$-1.5056\sin\theta+0.0941\sin 2\theta$
5	-0.7264	-0.2399	4.9511	$-1.5354\sin\theta+0.2399\sin 2\theta$
10	-0.6491	-0.5171	2.7230	$-1.6514\sin\theta+0.5171\sin 2\theta$
20	-0.1810	-1.5323	2.1104	$-2.3535\sin\theta+1.5323\sin 2\theta$
21.75	0	-1.8953	2.2728	$-2.6250\sin\theta+1.8953\sin 2\theta$

The boundary conditions for the viscous flow past a sphere can be given as

$$\text{(i)}\quad \Psi\rightarrow\frac{1}{2}r^2\sin^2\theta\,,\quad \text{as } r\rightarrow\infty, \tag{2.5}$$

$$\text{(ii)}\quad \Psi=\partial\Psi/\partial r=0\,,\quad \text{on the surface } (r=1). \tag{2.6}$$

Owing to the mathematical difficulty, the exact solution of equation (2.4) with the boundary conditions (2.5) and (2.6) has not yet been obtained. In a previous paper [3], however, the author has obtained approximate solutions for the case of a sphere by use of the Galerkin method, which will be reproduced here for the sake of convenience.

According to the Galerkin method, we assume an appropriate functional form involving some undetermined parameters for the stream function Ψ, and determine such parameters by the boundary condition and some approximate conditions which replace the exact Navier-Stokes equation.

We have adopted two forms for the solution:

$$\text{(a)}\quad \Psi=\left(\frac{1}{2}r^2+\frac{A_1}{r}+\frac{A_2}{r^2}+\frac{A_3}{r^3}+\frac{A_4}{r^4}\right)\sin^2\theta+\left(\frac{B_1}{r}+\frac{B_2}{r^2}+\frac{B_3}{r^3}+\frac{B_4}{r^4}\right)\sin^2\theta\cos\theta\,, \tag{2.7}$$

$$\text{(b)}\quad \Psi=\left(\frac{1}{2}\,r^2+A_1r+A_2+\frac{A_3}{r}+\frac{A_4}{r^2}\right)\sin^2\theta+\left(B_1r+B_2+\frac{B_3}{r}+\frac{B_4}{r^2}\right)\sin^2\theta\cos\theta\,, \tag{2.8}$$

where A_i, and B_i are the undetermined parameters. The form (2.8) is appropriate for small Reynolds number, and reduces to the Stokes approximation as the Reynolds number tends to zero. The form (2.7) is chosen for higher Reynolds number régime. These two forms satisfy the condition at infinity. For the approximate conditions replacing the Navier-Stokes equation we take following two conditions:

$$(NS)\equiv 0,\ \text{on the surface } (r=1), \tag{2.9}$$

$$\left\{\begin{aligned}&\int_1^\infty\!\int_{-1}^1 r^{-1}\{P_0-P_2(z)\}(NS)\,dz\,dr=0\,, &(2.10)\\ &\int_1^\infty\!\int_{-1}^1 r^{-2}\{P_1(z)-P_3(z)\}(NS)\,dz\,dr=0\,, &(2.11)\end{aligned}\right.$$

where (NS) is the left-hand side of equation (2.4), $P_n(z)$ is the Legendre function of order n, and $z=\cos\theta$. The conditions (2.10) and (2.11) have been derived by the consideration that if we expand (NS) in the orthogonal function system

$$r^{-(n+2)}(1-\cos^2\theta)P_n'(\cos\theta)$$

each term must be zero. (2.10) and (2.11) correspond respectively to $n=1,\ 2$.

The conditions (2.6), (2.9), (2.10), (2.11) give respectively 4, 2, 1, 1 relations between the eight coefficients A_i, B_i. Thus we can determine the parameters completely. The values

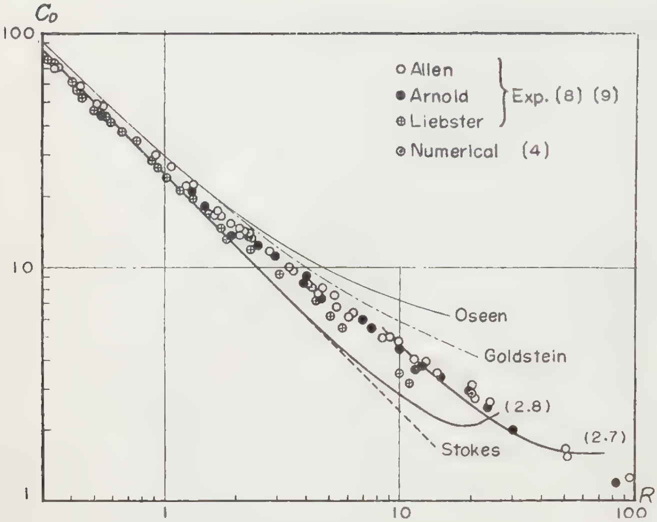

Fig. 1. Drag coefficiento f a sphere.

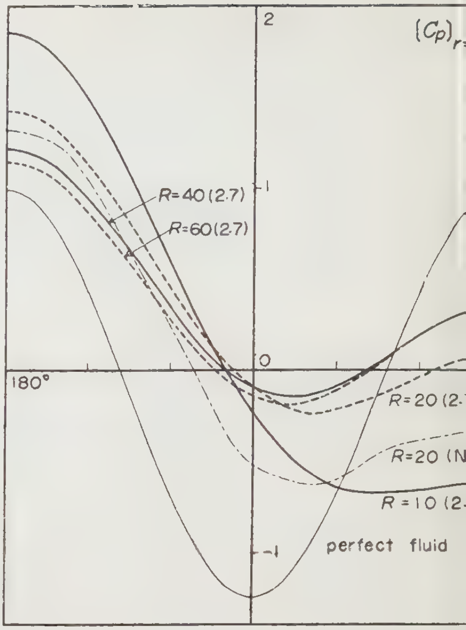

Fig. 2. Pressure distribution over the surface.

of A_1, and B_1, the calculated drag coefficient, and the vorticity distribution over the surface are given in Tables I and II for the case (a) and (b) respectively. $A_2, \cdots, B_2, \cdots$ can be found by the following relations:

For the form (a)—

$$\left\{\begin{aligned} A_2&=-\left(\frac{120}{29}+\frac{75}{29}A_1\right), \\ A_3&=\left(\frac{153}{29}+\frac{63}{29}A_1\right), \\ A_4&=-\left(\frac{95}{58}+\frac{17}{29}A_1\right), \end{aligned}\right. \qquad \left\{\begin{aligned} B_2&=-\frac{23}{9}B_1, \\ B_3&=\frac{19}{9}B_1, \\ B_4&=-\frac{5}{9}B_1, \end{aligned}\right. \tag{2.12}$$

and for the form (b)—

$$\left\{\begin{aligned} A_2&=-\left(\frac{27}{16}+\frac{9}{4}A_1\right), \\ A_3&=\left(\frac{11}{8}+\frac{3}{2}A_1\right), \\ A_4&=-\left(\frac{3}{16}+\frac{1}{4}A_1\right), \end{aligned}\right. \qquad \left\{\begin{aligned} B_2&=-2B_1, \\ B_3&=B_1, \\ B_4&=0. \end{aligned}\right. \tag{2.13}$$

The calculated drag coefficient and the pressure and vorticity distributions over the surface are given in Figs. 1, 2, 3 respectively.

The author has also treated the same problem numerically for the Reynolds number of 20 [4], and the results are also shown in Figs. 1, 2, 3, for the sake of of comparison.

Comparing our results obtained by the Galerkin method with the numerical and experimental ones, we can conclude that the Galerkin method gives satisfactory results if an appropriate functional form is used; the form (a) is appropriate for the régime $10<R<80$, and the form (b) for the régime $R<2Q$.

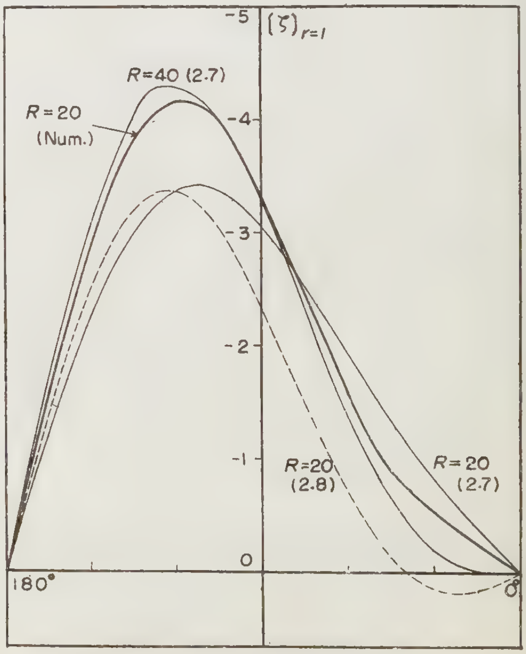

Fig. 3. Vorticity distribution over the surface.

§ 3. Discussion of the Stability of the Steady Solution

The Navier-Stokes equation has always steady solution, which is very similar to the actual flow when the Reynolds number is below the critical Reynolds number (about 100 in the case of the flow past a sphere). But we cannot produce steady flow whose Reynolds number is much higher than the critical one. The author suggested that the origin of the non-existence of the steady flow at higher Reynolds numbers may be found in the instability of the steady flow which must exist theoretically.

In this section, the stability of the steady solution which is obtained in § 2 by means of the Galerkin method will be investigated by adding a certain type of small perturbation to the steady solution and considering whether this perturbation will die out or grow up.

The basic equation for this problem is

$$\begin{aligned}\frac{\partial(D^2\Psi)}{\partial t}&-\frac{1}{r^2\sin\theta}\frac{\partial(\Psi, D^2\Psi)}{\partial(r,\ \theta)}\\&+\frac{2}{r^2}\frac{D^2\Psi}{\sin^2\theta}\left(\frac{\partial\Psi}{\partial r}\cos\theta-\frac{1}{r}\frac{\partial\Psi}{\partial\theta}\sin\theta\right)\\&-\frac{2}{R}D^4\Psi=0\,.\end{aligned}\tag{2.1}$$

where Ψ is the function of r, θ, and t. Here we put

$$\Psi(r,\ \theta,\ t)=\Psi_0(r,\ \theta)+\psi(r,\ \theta,\ t),\tag{3.1}$$

where Ψ_0 is the steady solution, of which approximation has been given in § 2, and ψ is the perturbation term which depends on the time t.

Substituting Ψ from (3.1) to (2.1) and neglecting the second order terms in ψ and its derivatives, we have

$$\begin{aligned}\frac{\partial(D^2\psi)}{\partial t}&-\frac{1}{r^2\sin\theta}\left\{\frac{\partial(\Psi_0, D^2\psi)}{\partial(r,\ \theta)}+\frac{\partial(\psi,\ D^2\Psi_0)}{\partial(r,\ \theta)}\right\}\\&+\frac{2}{r^2}\frac{D^2\Psi_0}{\sin^2\theta}\left(\frac{\partial\psi}{\partial r}\cos\theta-\frac{1}{r}\frac{\partial\psi}{\partial\theta}\sin\theta\right)\\&+\frac{2}{r^2}\frac{D^2\psi}{\sin^2\theta}\left(\frac{\partial\Psi_0}{\partial r}\cos\theta-\frac{1}{r}\frac{\partial\Psi_0}{\partial\theta}\sin\theta\right)\\&-\frac{2}{R}D^4\psi=0\,.\end{aligned}\tag{3.2}$$

If we put

$$\psi=e^{kt}F(r,\ \theta)\,,\tag{3.3}$$

(3.2) becomes

$$\begin{aligned}kD^2F&-\frac{1}{r^2\sin\theta}\left\{\frac{\partial(\Psi_0,\ D^2F)}{\partial(r,\ \theta)}+\frac{\partial(F,\ D^2\Psi_0)}{\partial(r,\ \theta)}\right\}\\&+\frac{2}{r^2}\frac{D^2\Psi_0}{\sin^2\theta}\left(\frac{\partial F}{\partial r}\cos\theta-\frac{1}{r}\frac{\partial F}{\partial\theta}\sin\theta\right)\\&+\frac{2}{r^2}\frac{D^2F}{\sin^2\theta}\left(\frac{\partial\Psi_0}{\partial r}\cos\theta-\frac{1}{r}\frac{\partial\Psi_0}{\partial\theta}\sin\theta\right)\\&-\frac{2}{R}D^4F=0\,.\end{aligned}\tag{3.4}$$

For $F(r,\ \theta)$, we assume a functional form

$$\begin{aligned}F=&(C_1r+C_2+C_3/r+C_4/r^2)\sin^2\theta\\&+(D_1r+D_2+D_3/r+D_4/r^2)\sin^2\theta\cos\theta,\end{aligned}\tag{3.5}$$

which is analogous to (2.8) for $\Psi(r,\ \theta)$.

The boundary conditions are

i) $F=\partial F/\partial r=0$, at $r=1$, (3.6)

and

ii) *The perturbed velocity* tends to 0 as $r\to\infty$. (3.7)

The condition (3.7) is automatically satisfied by the form (3.5), and from the conditions (3.6) we have

$$\begin{cases}C_3=-(3C_1+2C_2),\\C_4=(2C_1+C_2)\,,\end{cases}\qquad\begin{cases}D_3=-(3D_1+2D_2),\\D_4=(2D_1+D_2)\,.\end{cases}\tag{3.8}$$

On the other hand, we use the approximate conditions for equation (3.4) which are analogous to the conditions (2.9)—(2.11), i.e.

$$(ns)=0,\ \text{on the surface}\ (r=1),\tag{3.9}$$

$$\begin{cases}\displaystyle\int_1^\infty\int_{-1}^1 r^{-1}\{P_0-P_2(z)\}(ns)dz\,dr=0\,, & (3.10)\\ \displaystyle\int_1^\infty\int_{-1}^1 r^{-2}\{P_1(z)-P_3(z)\}(ns)dz\,dr=0, & (3.11)\end{cases}$$

where (ns) stands for the left-hand side of (3.4).

If we use (3.6), (3.8) and the form (2.8) for the steady solution, the conditions (3.9)—(3.11) give

$$(144R^{-1}-3k)C_1+(64R^{-1}-k)C_2=0\,,\tag{3.12}$$

$$(96R^{-1}-3k)D_1+(48R^{-1}-k)D_2=0\,,\tag{3.13}$$

$$\begin{aligned}(-288B_1&+282240R^{-1})C_1\\&+(-112B_1+117700R^{-1})C_2\\&+(723+4A_1)D_1+(201+20A_1)D_2=0,\end{aligned}\tag{3.14}$$

$$\begin{aligned}(2763&+1404A_1)C_1+(666+360A_1)C_2\\&+(-208B_1+136080R^{-1})D_1\\&+(-56B_1+60480R^{-1})D_2=0\,.\end{aligned}\tag{3.15}$$

If, in place of (2.8), we use (2.7) for the steady solution, we have four relations analogous to (3.12)–(3.15). The equations (3.12)–(3.15) are a system of homogeneous, simultaneous, algebraic equations for the four undetermined parameters C_1, C_2, D_1, D_2. Therefore we can determine the eigenvalue k (as the function of Reynolds number R) from the condition that the system has non-trivial solutions. The eigenvalue k may be complex, and the sign of its real part gives the criterion for determining whether the perturbed flow may die out or grow up; i.e. the positive sign means the growing up of the perturbed flow and hence the instability of the steady flow, and the negative sign means the dying out of the perturbed flow and the stability of the steady flow. Actually we have two real eigenvalues from the system (3.12)–(3.15) for each Reynolds number considered.

We have calculated the eigenvalues k for the Reynolds numbers 1, 5, 10, 20, and 30 using the form (2.8) as the steady solution Ψ_0, and for the Reynolds numbers 10, 20, 40, 60, and 80 using the form (2.7) as Ψ_0. These eigenvalues are tabulated in Table III, and are shown in Fig. 4. By interpolation, we can determine the critical Reynolds number for which one of eigenvalues vanishes and the other is negative. Thus, we have 51 as the critical Reynolds number for the flow past a sphere, above which the steady flow may be unstable.

Table III. Eigenvalue k.

R	(I)		(II)	
1	−15.452	−16.562		
5	− 2.6217	− 3.8429		
10	− 1.0416	− 2.2950	−1.4976	−9.8137
20	− 0.2688	− 1.6992	−0.6111	−5.2077
30	− 0.1418	− 2.1094		
40			−0.1054	−3.0974
60			0.0648	−2.4468
80			0.1307	−2.0620

(I) with (2.8) as Ψ_0, (II) with (2.7) as Ψ_0.

§ 4. Discussions

In § 3, we have succeeded in the theoretical determination of the critical Reynolds number for the flow past a sphere, but several points are left to be discussed.

First of all, since we have used a specia type for the perturbation, the calculate critical Reynolds number should be highe than the "*lower critical Reynolds number*" below which the steady flow is stable fo any type of perturbation. Experimentally the lower critical Reynolds number for th flow past a sphere is known to be abou 100, but our critical Reynolds number whic should be larger than 100 is 51. This discrepancy between the theory and experimen is rather large, but considering that we hav used an approximate solution for the stead solution, and the Galerkin approximation i place of solving the exact Navier-Stoke equation, our result may be regarded to b fairly satisfactory.

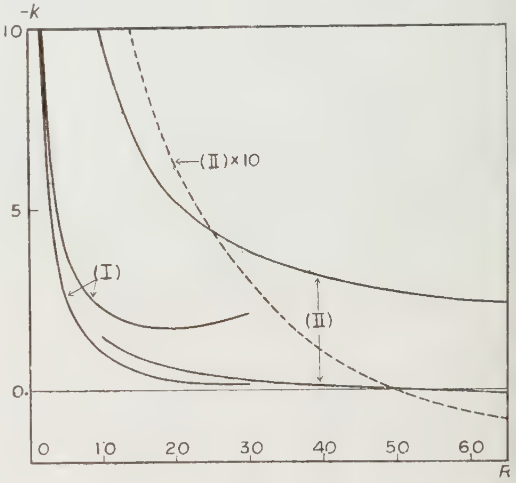

Fig. 4. Eigenvalue k.

The origin of the discrepancy between th theory and experiment may be found in that

i) We have used an approximation for th steady solution. The result due to th Galerkin method seems fairly good in th case of the steady flow past a sphere, if w compare the calculated drag with the experimental one, but the vorticity and pressur distributions over the surface may be fairl different from the reality, as we can se from Figs. 2 and 3 where the results of th numerical method which are expected to b more accurate are also given for the case o Reynolds number 20.

ii) We have used the Galerkin metho without solving exactly the Navier-Stoke equation (3.4). It seems very plausible tha this procedure may produce fairly larg quantitative discrepancy in such a delicate problem as the determination of the critical Reynolds number.

We have used the same form (3.5) for both forms of the steady solution (2.7) and (2.8). We have also tried to use a functional form analogous to (2.7) for the perturbation in the case of the steady solution (2.7). But this procedure gave the critical Reynolds number less than 20, and therefore this form seems inappropriate for the perturbation function. The two upper branches of curves in Fig. 4 are nearly coincident in the adjoining régime of both types of steady solution, and it may suggest that the use of the same form for the perturbation was appropriate.

It seems to the author that the success (at least qualitatively) of the theoretical determination of the critical Reynolds number for the flow past a sphere suggests the possibility of explanation of the critical phenomena related to the transition from laminar to turbulent flow past obstacle, by means of the Navier-Stokes equation and the perturbation method. In relation to this problem, further study of the steady flow, both theoretical and experimental, seems to be important.

§ 5. Summary

The author studied the stability of the steady solution for the flow past a sphere which has been obtained previously by use of the Galerkin method, and determined the critical Reynolds number for the flow past a sphere as 51 which should be compared with the experimental value of about 100.

In conclusion the author wishes to express his hearty gratitude to Professor Isao Imai for his kind suggestion and discussion in the course of this work.

References

1) L. Rosenhead: *Advances in Applied Mechanics, Vol. 3* (1953) p. 185.
2) M. Kawaguti: Rep. Inst. Sci. Technol. Tokyo **2** (1948) 33 (in Japanese).
3) M. Kawaguti: Rep. Inst. Sci. Technol. Tokyo **2** (1948) 66 (in Japanese).
4) M. Kawaguti: Rep. Inst. Sci. Technol. Tokyo **4** (1950) 154 (in Japanese).
5) M. Kawaguti: J. Phys. Soc. Japan **8** (1953) 747.
6) M. Kawaguti: Rep. Inst. Sci. Technol. Tokyo **8** (1954) 1 (in Japanese).
7) M. Kawaguti: J. Phys. Soc. Japan **8** (1953) 403.
8) S. Goldstein: *Modern Developments in Fluid Dynamics, Vol. 1,* (1938) p. 16.
9) H. D. Arnold: Phil. Mag. **22** (1911) 755.

JOURNAL OF THE PHYSICAL SOCIETY OF JAPAN Vol. 10, No. 8, AUGUST, 1955

On the Propagation of the Electromagnetic Waves in an Inhomogeneous Atmosphere

By Yûkichi NOMURA
Department of Applied Science, Faculty of Engineering Tohoku University
and Kôshun TAKAKU
Department of Physics, Faculty of Arts and Science Fukushima University

(Received April 2. 1955)

We obtained the rigorous solutions of Maxwell's equations in an inhomogeneous medium, which led to descriptions of the electromagnetic waves from a dipole source in the medium, where the inductive capacity is an arbitrary function of the distance from the center of the earth sphere. The first approximation of these descriptions give more abundant and complete results than those which have as yet been obtained by Fermat's principle of geometrical optics and lead to a satisfactory theory for the so-called superrefracted propagation in a layer called the duct.[1][2][3]

§ 1. Introduction

The geometric optical descriptions[4] of the electromagnetic waves, derived from Fermat's principle, are usually used for practical purposes. It is interesting as well as practically important to deduce these descriptions directly from Maxwell's equations and establish the method of calculation of the field strength.

Theories on the propagation of the electromagnetic waves in an inhomogeneous atmosphere have been put forward by many writers,[5],[6],[7],[8] among whom only Bremmer[8] is concerned with the above geometric optical solutions. He has obtained approximate solutions of Maxwell's equations in an inhomogeneous medium by means of the W.K.B. method, and connected them with usual solutions in a homogeneous medium by the help of the coeficients of reflection. He resorts, however, to too much artifice in treating this subject, so the physical meaning of his calculation is not clear. We have found an easier and clearer method of calculation which starts from the rigorous solutions of Maxwell's equations in an inhomogeneous medium.

The atmosphere is assumed to be composed of many concentric spherical layers, in each of which the inductive capacity ε is proportional to r^{2m}, where r is the distance from the center of the eath, and the constant m_μ gives the measure of inhomogeneity of the μ-th layer.* As seen in the following, $kr^m=(\omega/c)\sqrt{\mu\varepsilon}$ which characterizes the propagation of electromagnetic waves, varies continuously from layer to layer, i.e. kr^m is continuous a each boundary between the layers.

We shall find the rigorous solutions of Maxwell's equations in such an inhomogeneou medium, which lead to the diverging elementary wave and converging one, the forme propagating in the direction of the radia vector $\vec{r}$, and the latter conversely. Thes waves propagate from layer to layer with n reflections, so long as the radius r is large compared with the wave length. The diverging elementary wave reflects at the sphere which is assumed to be at infinity, into converging elementary wave. The latter wav reflects at the infinitesimal sphere at the center as well as at the discontinuous surfaces, int the diverging elementary wave.

These waves will be summed up to describ the electromagnetic waves transmitted from dipole source. This summation will be transformed into a contour integral, which is form convenient for the calculation by th method of the saddle point. This approximat calculation will give the formulas, which hav a simple form and a clear physical meaning The geometrical ray curves will also be give in the same form as obtained by the Fermat' principle, except their additional factors. Ou theory gives such waves as will propagat through the atmosphere and reach at infinit and return back to us. These waves, however, have an infinitely large phase, so tha the time needed for them to travel along these rays become infinitely long. Such waves need not be considered for practical purposes. Neglecting them and putting $m=0$, our theory can be reduced to the usual one in a homogeneous medium.[9]

---

* Suffix μ is used without being confused with the permeability μ.

§2. Solutions of Maxwell's Equations

If we adopt the Gauss system and omit the time factor $\exp(i\omega t)$, Maxwell's equations are reduced into

$$\operatorname{rot}\boldsymbol{H}=\frac{i\omega\varepsilon}{c}\boldsymbol{E}\,,\qquad \operatorname{rot}\boldsymbol{E}=-\frac{i\omega\mu}{c}\boldsymbol{H}\,,$$

$$\operatorname{div}\varepsilon\boldsymbol{E}=\rho\,,\qquad \operatorname{div}\mu\boldsymbol{H}=0\,,\tag{1}$$

where $\boldsymbol{E}$ is the electric field, $\boldsymbol{H}$ the magnetic field, and ε the inductive capacity, μ the permeability of medium. Owing to the fact that μ is a constant while ε is a function of r, $\boldsymbol{E}$ and $\boldsymbol{H}$ lose the symmetric property as seen in the case where the medium is homogeneous, and the differential equations deduced from the Maxwell's equations are different from each other according to the type of the source, and the field of each type can be described in terms of the series of the solutions of each type respectively.

1. Magnetic type

On the assumption of no space charge,* we can put

$$\boldsymbol{E}=\operatorname{rot}\boldsymbol{r}\phi_1\,,\tag{2}$$

where $\phi_1(r,\theta,\varphi)$ is a scalar function of polar coordinates, and from the second of the equations (1), we get

$$\boldsymbol{H}=-\frac{c}{i\omega\mu}\operatorname{rot}\boldsymbol{E}=-\frac{c}{i\omega\mu}\operatorname{rot}\operatorname{rot}\boldsymbol{r}\phi_1\,.\tag{3}$$

When ϕ_1 is determined, the field $\boldsymbol{E}$ and $\boldsymbol{H}$ can be determined by ϕ_1 by means of these two equations (2), and (3). For simplicity ϕ_1 is assumed to be a function of r and θ, and not to depend upon φ. Operating "rot" on the both sides of (3), and using the first equation of (1) and (2), we have

$$-\frac{\omega^2}{c^2}\mu\varepsilon\frac{\partial\phi_1}{\partial\theta}=\frac{1}{r}\left[\frac{\partial^2}{\partial r^2}\left(r\frac{\partial\phi_1}{\partial\theta}\right)+\frac{\partial}{\partial\theta}\left\{\frac{1}{r\sin\theta}\frac{\partial}{\partial\theta}\left(\sin\theta\frac{\partial\phi_1}{\partial\theta}\right)\right\}\right].\tag{4}$$

If we write

$$\frac{\omega^2}{c^2}\mu\varepsilon=f(r)\,,$$

and
$$\phi_1=g(r)P_n(\cos\theta)\,,\tag{5}$$

the equation (4) splits into two equations for $g(r)$ and $P_n(\cos\theta)$:

$$\frac{d^2}{dr^2}(rg)+\left(f-\frac{n(n+1)}{r^2}\right)rg=0\,,\tag{6}$$

and

$$\frac{1}{\sin\theta}\frac{d}{d\theta}\left(\sin\theta\frac{dP_n}{d\theta}\right)+n(n+1)P_n=0\,.$$

If $\varepsilon(r)$ and thus $f(r)$ are proportional to $r^{2m}(m\neq-1)$, (6) becomes

$$\frac{d^2g}{dr^2}+\frac{2}{r}\frac{dg}{dr}+\left(k^2r^{2m}-\frac{n(n+1)}{r^2}\right)g=0\,.$$

This equation has particular solutions expressed by using the Hankel function H,

$$g=Y_{nm}^{(1),(2)}(k,r)\equiv\sqrt{\frac{\pi}{2r}}H_\nu{}^{(1),(2)}\left(\frac{kr^{m+1}}{m+1}\right)\,,\tag{7}$$

where

$$\nu=\frac{n+\frac{1}{2}}{m+1}\,.$$

Connecting this Y-function with the Legendre function $P_n(\cos\theta)$, a particular solution of the equation (4) is

$$Y_{nm}^{(1),(2)}(k,r)P_n(\cos\theta)\,.\tag{8}$$

The fields due to this solution are

$$\boldsymbol{E}=\operatorname{rot}\boldsymbol{r}\,Y_{nm}^{(1),(2)}(k,r)P_n(\cos\theta)\,,\tag{9}$$

$$\boldsymbol{H}=-\frac{c}{i\omega\mu}\operatorname{rot}\operatorname{rot}\boldsymbol{r}Y_{nm}^{(1),(2)}(k,r)P_n(\cos\theta)\,,\tag{9}$$

the components of which are

$$E_r=0\,,\qquad H_r=\frac{c}{i\omega\mu}\frac{n(n+1)}{r}Y_{nm}^{(1),(2)}P_n\,,$$

$$E_\theta=0\,,\qquad H_\theta=\frac{c}{i\omega\mu}\frac{1}{r}\frac{d}{dr}(rY_{nm}^{(1),(2)})\frac{dP_n}{d\theta}\,,$$

$$E_\varphi=-Y_{nm}^{(1),(2)}\frac{dP_n}{d\theta}\,,\quad H_\varphi=0\,.$$

When the field vector $\boldsymbol{E}$ has no radial component near the source, Maxwell's equations lead to the equation (6), and the field can be developed in the series of $Y_{nm}^{(1),(2)}$. In a particular case where the sourse is an infinitesimal loop, the series of the functions (8) is sufficient to describe the field.

2. Electric Type

In the case of electric type, too, let us make a start on the same assumption of no charge distribution,

$$\operatorname{div}\varepsilon\boldsymbol{E}=0\,,\tag{10}$$

---

* $\operatorname{div}\varepsilon\boldsymbol{E}=\operatorname{div}(\varepsilon\operatorname{rot}\boldsymbol{r}\phi_1)=\operatorname{grad}\varepsilon\cdot\operatorname{rot}\boldsymbol{r}\phi_1=0$.

or

$$\operatorname{div} f\boldsymbol{E}=0 \ .$$

Where f has been given in (5). In order that this condition may be satisfied, it is sufficient to put

$$f\boldsymbol{E}\equiv\frac{\omega^2}{c^2}\mu\varepsilon\boldsymbol{E}=\operatorname{rot}\operatorname{rot}\boldsymbol{r}\phi_2 \ , \qquad (11)$$

Taking into consideration that all coefficients are constant except the inductive capacity ε in the Maxwell's equations (2), we get

$$\operatorname{rot}\operatorname{rot}\boldsymbol{E}=f\boldsymbol{E} \ , \qquad (12)$$

after cancelling the field vector $\boldsymbol{H}$ out of them. In order to obtain the solution ϕ_2 in (11), which satisfies the equation (12), we put

$$\phi_2=g(r)P_n(\cos\theta) \ . \qquad (13)$$

Substituting (13) and (11) into the equation (12), we get

$$-\frac{n(n+1)}{r^2}\left[\frac{d}{dr}\left\{\frac{1}{f}\frac{d}{dr}(rg)\right\}-\frac{n(n+1)}{fr}g\right]$$
$$=\frac{n(n+1)}{r}g$$

for the r-component, and

$$-\frac{1}{r}\frac{d^2}{dr^2}\left\{\frac{1}{f}\frac{d}{dr}(rg)\right\}$$
$$+\frac{1}{r}\frac{d}{dr}\left\{\frac{n(n+1)}{fr}g\right\}=\frac{1}{r}\frac{d}{dr}(rg)$$

for the θ-component. Putting

$$\varphi=rg(r) \ , \qquad (14)$$

we satisfy the above two equations by the solution of the equation

$$\frac{d}{dr}\left\{\frac{1}{f}\frac{d}{dr}\varphi\right\}+\left\{1-\frac{n(n+1)}{fr^2}\right\}\varphi=0 \ . \qquad (15)$$

Now we put

$$z=\int_0^r f\,dr=\int_0^r k^2r^{2m}dr=\frac{k^2r^{2m+1}}{2m+1} \ .$$

The equation (15) leads to

$$\frac{d^2\varphi}{dz^2}+\left\{\xi^2 z^{2s}-\frac{p(p+1)}{z^2}\right\}\varphi=0 \ , \qquad (16)$$

where

$$\xi=\frac{1}{k}\left(\frac{k}{2m+1}\right)^{m/(2m+1)} , \qquad s=-\frac{m}{2m+1} ,$$

and

$$p=\left\{\frac{n(n+1)}{(2m+1)^2}+\frac{1}{4}\right\}^{1/2}-\frac{1}{2} \ .$$

The equation (16) is the same differential equation as seen in the previous paragraph, and a particular solution of (16) is

$$\varphi(z)=zY_{nm}^{(1),(2)}(\xi,z)$$

in terms of the above Y-function. Therefor

$$g(r)=kr^m\sqrt{\frac{\pi}{2(2m+1)r}}H_\nu{}^{(1).(2)}\left(\frac{kr^{m+1}}{m+1}\right)$$
$$\equiv Z_{nm}^{(1),(2)}(k,r) \ , \qquad (17$$

where

$$\nu=\{n(n+1)+m^2+m+\tfrac{1}{4}\}^{1/2}/(m+1) \ .$$

The fact that the function (17) satisfies th equations

$$\operatorname{rot}\operatorname{rot}\boldsymbol{E}=f\boldsymbol{E} \ , \qquad f\boldsymbol{E}=\operatorname{rot}\operatorname{rot}\boldsymbol{r}\phi_2 \ ,$$
$$\text{and} \quad \phi_2=gP_n \ ,$$

and the relation

$$\boldsymbol{H}=-\frac{c}{i\omega\mu}\operatorname{rot}\boldsymbol{r}\phi_2 \qquad (18$$

lead to relation

$$\operatorname{rot}\boldsymbol{E}=\operatorname{rot}\boldsymbol{r}\phi_2=-\frac{i\omega\mu}{c}\boldsymbol{H} \ ,$$

and

$$\operatorname{rot}\boldsymbol{H}=-\frac{c}{i\omega\mu}\operatorname{rot}\operatorname{rot}\boldsymbol{r}\phi_2=-\frac{c}{i\omega\mu}f\boldsymbol{E}=i\frac{\omega\varepsilon}{c}\boldsymbol{E}$$

These equations are the Maxwell's equation themselves, and the fields derived from thi particular solution ϕ_2 are

$$\left.\begin{aligned}
&E_r=\frac{n(n+1)}{k^2r^{2m+1}}gP_n \ , && H_r=0 \ , \\
&E_\theta=\frac{1}{k^2r^{2m+1}}\frac{d}{dr}(rg)\frac{dP_n}{d\theta} \ , && H_\theta=0 \ , \\
&E_\varphi=0 \ , && H_\varphi=\frac{c}{i\omega\mu}g\frac{dP_n}{d\theta} \ ,
\end{aligned}\right\} \qquad (19$$

When the electric field vector $\boldsymbol{E}$ has th radial component in the vicinity of the source and the field is symmetric around the axi $\theta=0$, it can be described by superposing suc particular solutions as ϕ_2. Based on whethe the field vector $\boldsymbol{E}$ has the r-component o not, differential equations different from eac other have been derived from the Maxwell' equation. These two equations have th particular solution ϕ_1 and ϕ_2 respectively.

§ 3. General Description of the Field

The radius of the earth is r_0, and its propagating constant is $k_0=k$. The atmospher is composed of N layers, which are concentri spherical shells. In each layer the quantity

$$\frac{\omega}{c}\sqrt{\mu\varepsilon}$$

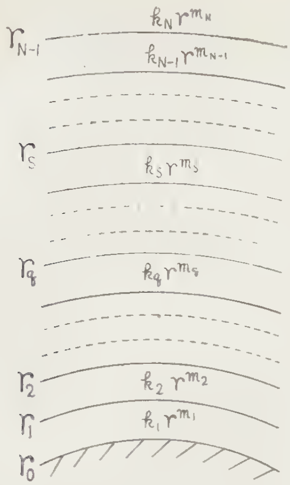

Fig. 1. The multilyered atmosphere.
r_0: The earth's surface.
$r_1, r_2, \cdots, r_{N-1}$: Surfaces where the medium is continuous, but k_μ and m_μ may be discontinuous.

varies as

$$k_\mu r^{m_\mu} \equiv k(\mu, r)\ , \qquad \mu = 1, 2, \cdots, N$$

and is continuous at the boundaries

$$r = r_\mu \qquad \mu = 1, 2, \cdots, N-1\ ,$$

$$\text{i.e.}\quad k(\mu, r_\mu) = k(\mu+1, r_\mu)\ .$$

The constants $m_\mu (\mu = 1, 2, \cdots, N)$ give the measure of inhomogeneity of the μ-th layer, where the Maxwell's equations have particular solutions

$$Y^{(1),(2)}_{nm_\mu}(k_\mu, r) \quad (7) \qquad \text{for magnetic type,}$$

$$\text{and} \quad Z^{(1),(2)}_{nm_\mu}(k_\mu, r) \quad (17) \qquad \text{for electric type.}$$

In the following we shall write these two kinds of solutions together as

$$H_n{}^{(1),(2)}(k_\mu, r) \equiv \begin{cases} \sqrt{\dfrac{\pi}{2r}}\, H^{(1),(2)}_{\nu(m)}\left(\dfrac{k(\mu, r) r}{m_\mu + 1}\right) & \text{for magnetic type,} \\ k(\mu, r) \sqrt{\dfrac{\pi}{2(2m_\mu+1) r}}\, H^{(1),(2)}_{\nu(e)}\left(\dfrac{k(\mu, r) r}{m_\mu + 1}\right) & \text{for electric type.} \end{cases} \tag{20}$$

and

$$J_n(k_\mu, r) = \tfrac{1}{2}\{H_n{}^{(1)}(k_\mu, r) + H_n{}^{(2)}(k_\mu, r)\}\ , \tag{21}$$

where

$$\nu(m) = \frac{n + (1/2)}{m_\mu + 1}\ , \qquad \text{and} \qquad \nu(e) = \frac{\{n(n+1) + m_\mu{}^2 + m_\mu + (1/4)\}^{1/2}}{m_\mu + 1}\ . \tag{22}$$

and H_ν on the right side denotes the Hankel function. The source $Q(\bar{r}, 0, 0)$ and the observing point $P(r, \theta, 0)$ are assumed to be in the q-th and the s-th layer respectively.

The primary wave from the source Q is written as follows:

$$u = A \sum_{n=0}^{\infty} (2n+1) P_n(\cos\theta) \begin{matrix} J_n(k_q, \bar{r}) H_n{}^{(2)}(k_q, r) & \bar{r} \leq r \leqq r_q \\ H_n{}^{(2)}(k_q, \bar{r}) J_n(k_q, r) & r_{q-1} \leqq r \leqq \bar{r} \end{matrix} \tag{23*}$$

where

$$A = \begin{cases} -\dfrac{i}{4\pi(m_q+1)} & \text{for magnetic} \\ -\dfrac{i}{4\pi\{k(q, \bar{r})\}^2} \dfrac{2m_q+1}{m_q+1} & \text{for electric.} \end{cases} \tag{24}$$

The expression (23) is split into

---

* It is proved that (23) is the solution of the equation

$$\left\{\frac{1}{r} \frac{\partial^2}{\partial r^2}(ru) \text{ or } \frac{f}{r} \frac{\partial}{\partial r}\left(\frac{1}{f} \frac{\partial ru}{\partial r}\right)\right\} + fu + \frac{1}{r^2 \sin\theta} \frac{\partial}{\partial\theta} \sin\theta \frac{\partial u}{\partial\theta} + \frac{1}{r^2 \sin^2\theta} \frac{\partial^2 u}{\partial\varphi^2}$$

$$= -\frac{\delta(r-\bar{r})\delta(\theta)\delta(\varphi)}{r^2}\ , \quad f(r) = k^2 r^{2m}\ ,$$

and therefore it takes the form

$$u = \exp(-ikr^m R)/4\pi R, \ (R = PQ)$$

in the vicinity of the source Q.

$$\left.\begin{aligned} C_0&=\frac{A}{2}\sum_{n=0}^{\infty}(2n+1)P_n(\cos\theta)H_n^{(2)}(k_q,\bar{r})H_n^{(1)}(k_q,r)\,, && \bar{r}\geqq r\geqq r_{q-1}\,,\\ D_0&=\frac{A}{2}\sum_{n=0}^{\infty}(2n+1)P_n(\cos\theta)H_n^{(1)}(k_q,\bar{r})H_n^{(2)}(k_q,r)\,, && r_q\geqq r\geqq \bar{r}\,. \end{aligned}\right\} \tag{25}$$

For brevity's sake we shall write

$$C_0=\sum_{n=0}^{\infty}C_{0n}=\sum_{n=0}^{\infty}\alpha_n H_n^{(1)}(k_q,r)\,,\qquad\text{and}\qquad D_0=\sum_{n=0}^{\infty}D_{0n}=\sum_{n=0}^{\infty}\beta_n H_n^{(2)}(k_q,r)\,, \tag{26}$$

where

$$\alpha_n=\frac{A}{2}(2n+1)P_n(\cos\theta)H_n^{(2)}(k_q,\bar{r})\,,\qquad\text{and}\qquad \beta_n=\frac{A}{2}(2n+1)P_n(\cos\theta)H_n^{(1)}(k_q,\bar{r})\,, \tag{27}$$

Besides the converging wave C_0 and the diverging wave D_0, the expression (23) contains

$$\sum_{n=0}^{\infty}\alpha_n H_n^{(2)}(k_q,r)\,,$$

which can be regarded as a part of the secondary wave, reflected on the earth's surface. and it need not be considered as a primary wave. On the other hand the coefficients of reflection of the diverging wave $H_n^{(2)}(k_s, r)$ and the converging wave $H_n^{(1)}(k_{\mu+1}, r)$ at the boundaries $r=r_s$ and r_μ are

$$\frac{\{\log r_sH_n^{(2)}(k_{s+1},r_s)\}'-\{\log r_sH_n^{(2)}(k_s,r_s)\}'}{\{\log r_sH_n^{(1)}(k_s,r_s)\}'-\{\log r_sH_n^{(2)}(k_{s+1},r_s)\}'}\,,$$

$$\text{and}\qquad \frac{\{\log r_\mu H_n^{(1)}(k_{\mu+1},r_\mu)\}'-\{\log r_\mu H_n^{(1)}(k_\mu,r_\mu)\}'}{\{\log r_\mu H_n^{(1)}(k_\mu,r_\mu)\}'-\{\log r_\mu H_n^{(2)}(k_{\mu+1},r_\mu)\}'}\,,\qquad s,\mu=1,2,\cdots,M-1\,,$$

respectively for both magnetic and electric types.

As the medium varies continuously from layer and r_μ and r_s are very large, these coefficients are all negligibly small of the order $1/r_\mu$ or $1/r_s$. Thus C_{0n} and D_{0n} may propagate from layer to layer, without reflection and they can be expressed as

$$\begin{aligned} C_{0n}&=\alpha_nH_n^{(1)}(k_q,r) && r_q>r>\bar{r}\\ &=\alpha_nC_n(s,\,q-1)H_n^{(1)}(k_s,r) && r_s>r>r_{s-1}\qquad s=1,2,\cdots,q-1\,, \end{aligned} \tag{28}$$

where

$$C_n(p,q)=\prod_{\mu=p}^{q}\frac{H_n^{(1)}(k_{\mu+1},r_\mu)}{H_n^{(1)}(k_\mu,r_\mu)}=C_n(q,p)\,. \tag{29}$$

This converging wave C_{0n} reflects on the earth's surface into the diverging wave D_{1n},

$$D_{1n}^{(0)}=\alpha_nC_n(1,q-1)\frac{H_n^{(1)}(k_1,r_0)}{H_n^{(2)}(k_1,r_0)}R_n\cdot D_n(1,s-1)H_n^{(2)}(k_s,r)\,,\qquad r_s>r>r_{s-1}\,,\qquad s=1,2,\cdots,N\,,$$

$$\tag{30}$$

$$D_n(p,q)=\prod_{\mu=p}^{q}\frac{H_n^{(2)}(k_\mu,r_\mu)}{H_n^{(2)}(k_{\mu+1},r_\mu)}\,,\qquad D_n(1,0)=1\,,$$

and

$$\begin{aligned} R_n&=\frac{\{\log r_0H_n^{(1)}(k_1,r_0)\}'-\{\log r_0H_n^{(1)}(k_0,r_0)\}'}{\{\log r_0H_n^{(1)}(k_0,r_0)\}'-\{\log r_0H_n^{(2)}(k_1,r_0)\}'}\,, && \text{for magnetic type,}\\ &=\frac{\dfrac{1}{\{k(1,r_0)\}^2}\{\log r_0H_n^{(1)}(k_1,r_0)\}'-\dfrac{1}{\{k(0,r_0)\}^2}\{\log r_0H_n^{(1)}(k_0,r_0)\}'}{\dfrac{1}{\{k(0,r_0)\}^2}\{\log r_0H_n^{(1)}(k_0,r_0)\}'-\dfrac{1}{\{k(1,r_0)\}^2}\{\log r_0H_n^{(2)}(k_1,r_0)\}'} && \text{for electric type ,} \end{aligned}$$

$$\tag{32}$$

where the earth is assumed to be homogeneous, and its propagation constant is k, therefore $H_n^{(1),(2)}(k_0, r_0)$ and $k(0, r)$ are reduced into

$$H_n^{(1),(2)} = \zeta_n^{(1),(2)}(k_0, r) \equiv \sqrt{\frac{\pi}{2r}}\, H^{(1),(2)}_{n+1/2}(k_0 r)\ ,$$

and

$$k(0, r) = k_0 = k\ .$$

The converging wave C_{0n} goes into the earth partly, and transmits to and fro between the center and the surface of the earth κ-times ($\kappa = 1, 2, \cdots$) and goes out of the earth as a diverging wave $D_{1n}^{(\kappa)}$,

$$D_{1n}^{(\kappa)} = \alpha_n C_n(1, q-1) T_n^{(\kappa)} D_n(1, s-1) H_n^{(2)}(k_s, r) \qquad r_s > r > r_{s-1}\ , \qquad s = 1, 2, \cdots, N \tag{33}$$

where

$$T_n^{(\kappa)} = \frac{H_n^{(1)}(k_1, r_0)}{\zeta_n^{(1)}(k_0, r_0)} \frac{\zeta_n^{(2)}(k_0, r_0)}{H_n^{(2)}(k_1, r_0)} (1+R_n)(1+R_n') \cdot \left\{ \frac{\zeta_n^{(2)}(k_0, r_0)}{\zeta_n^{(1)}(k_0, r_0)} R_n' \right\}^{\kappa-1}\ , \tag{34}$$

$$T_n^{(0)} = 1\ ,$$

and

$$R_n' = \frac{\{\log r_0 H^{(2)}{}_n(k_1, r_0)\}' - \{\log r_0 \zeta^{(2)}{}_n(k_0, r_0)\}'}{\{\log r_0 \zeta^{(1)}{}_n(k_0, r_0)\}' - \{\log r_0 H^{(2)}{}_n(k_1, r_0)\}'}\ . \qquad \text{for magnetic type}\ ,$$

$$= \frac{\dfrac{1}{\{k(1, r_0)\}^2}\{\log r_0 H^{(2)}{}_n(k_1, r_0)\}' - \dfrac{1}{k_0^2}\{\log r_0\, \zeta^{(2)}{}_n(k_0, r_0)\}'}{\dfrac{1}{k_0^2}\{\log r_0 \zeta_n^{(1)}(k_0, r_0)\}' - \dfrac{1}{\{k(1, r_0)\}^2}\{\log r_0 H^{(2)}{}_n(k_1, r_0)\}'} \qquad \text{for electric type.} \tag{35}$$

Thus the total diverging wave coming out of the earth caused by the primary converging wave C_{0n} is

$$D_{1n} = \sum_{\kappa=0}^{\infty} D_{1n}^{(\kappa)}\ . \tag{36}$$

Next we shall pay our attention to the primary diverging wave D_{0n}. In the same way as above, we get the following expression:

$$\begin{aligned} D_{0n} &= \beta_n H_n^{(2)}(k_q, r) \qquad r_q > r > \bar{r} \\ &= \beta_n D_n(q, s-1) H_n^{(2)}(k_s, r) \qquad r_s > r > r_{s-1}, \qquad s = q+1,\ q+2, \cdots, N \end{aligned} \tag{37}$$

This diverging wave reflects into a converging wave C_{1n} at the sphere which is assumed to be at infinity, so

$$C_{1n} = \beta_n D_n(q, N-1) C_n(s, N-1) H_n^{(1)}(k_s, r), \qquad r_s > r > r_{s-1}, \qquad s = 1,\ 2, \cdots, N \tag{38}$$

This converging wave C_{1n} reflects on the earth's surface into the diverging wave D_{2n},

$$D_{1n} = \sum_{\kappa=0}^{\infty} D_{2n}^{(\kappa)}, \tag{39}$$

on the same way as the primary converging wave C_{0n} reflects into the diverging wave D_{1n}. The diverging waves D_{1n} and D_{2n} reflect into converging waves C_{2n} and C_{3n} respectively at $r = \infty$. Such transmissions and reflections are repeated without limitation between $r = 0$ and $r = \infty$, and the final expression of the field produced by the primary wave (25) is

$$u = \sum_{t=0}^{\infty} (D_t + C_t)\ , \tag{40}$$

where

$$\mathrm{C}_0 = \sum_n C_{0n}\ , \quad D_0 = \sum_n D_{0n}\ , \quad C_t = \sum_n C_{tn}\ , \quad D_t = \sum_\kappa D_t^{(\kappa)} = \sum_{n,\,\kappa} D_{tn}^{(\kappa)}\ . \tag{41}$$

§4. Geometrical Expression

Transforming the summation formula of D and C, obtained in the previous section, into the contour integral in the complex n-place, we get

$$\left.\begin{matrix} C_0 \\ \\ D_1^{(0)} \\ \\ D_1^{(\kappa)} \end{matrix}\right\} = \frac{A}{2}\int_{\Gamma_1+\Gamma_2} \frac{ndn}{\cos n\pi} P_\nu\{\cos(\pi-\theta)\} H_\nu^{(2)}(k_q, \bar{r}) \cdot$$

$$\cdot \begin{cases} C_\nu(s, q-1) H_\nu^{(1)}(k_s, r) \\ C_\nu(1, q-1) R_\nu \dfrac{H_\nu^{(1)}(k_1, r_0)}{H_\nu^{(2)}(k_1, r_0)} D_\nu(1, s-1) H_\nu^{(2)}(k_s, r) \\ C_\nu(1, q-1) T_\nu^{(\kappa)} D_\nu(1, s-1) H_\nu^{(2)}(k_s, r), \end{cases} \tag{42}$$

$$\left.\begin{matrix} D_0 \\ C_1 \end{matrix}\right\} = \frac{A}{2}\int_{\Gamma_1+\Gamma_2} \frac{ndn}{\cos n\pi} P_\nu\{\cos(\pi-\theta)\} H_\nu^{(1)}(k_q, \bar{r}) \cdot$$

$$\cdot \begin{cases} D_\nu(q, s-1) H_\nu^{(2)}(k_s, r) \\ D_\nu(q, N-1) C_\nu(s, N-1) H_\nu^{(1)}(k_s, r), \end{cases}$$

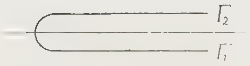

Fig. 2.

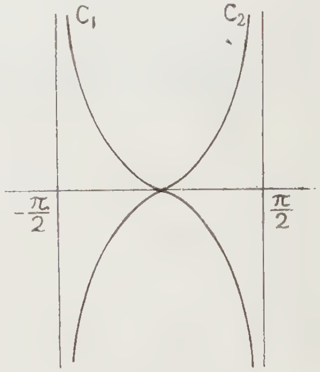

Fig. 3.

where $\nu = n - 1/2$, and $r_s > r > r_{s-1}$.

If we neglect all waves which propagate round more than once along the great circle of the earth, $1/\cos n\pi$ takes the value $2\exp(-in\pi)$ on the contour Γ_1 and $2\exp(in\pi)$ on the contour Γ_2. The integral on the latter can be neglected as compared with the former, as will be clear after calculating the integral along the contour Γ_1 and Γ_2 seperately by the method of saddle point.

We shall introduce the following integral representation of the Hankel and the Legendre functions in order to make use of the saddle point method.

$$H_\nu^{(1),(2)}(k, r) = \begin{cases} \dfrac{1}{\sqrt{2\pi r}} \displaystyle\int_{c_1, c_2} \exp\left\{\pm i \frac{kr^{m+1}}{m+1} \cos\tau \pm i \frac{n}{m+1}\left(\tau - \frac{\pi}{2}\right)\right\} d\tau \\ \qquad\qquad \text{for magnetic type,} \\ \dfrac{kr^m}{\sqrt{2\pi(2m+1)r}} \displaystyle\int_{c_1, c_2} \exp\left\{\pm i \frac{kr^{m+1}}{m+1} \cos\tau \pm i \frac{\sqrt{n^2 + m(m+1)}}{m+1}\left(\tau - \frac{\pi}{2}\right)\right\} d\tau \\ \qquad\qquad \text{for electric type,} \end{cases} \tag{44}$$

and

$$P_\nu(\cos\theta) = \frac{1}{2\pi}\int_{-\pi}^{\pi} \frac{\exp\{n\log(\cos\theta + i\sin\theta\cos\varphi)\}}{\sqrt{\cos\theta + i\sin\theta\cos\varphi}} d\varphi. \tag{45}$$

We multiply both the numerator and the denominator of the expression (42) and (43) by $H^{(1)}$ and $H^{(2)}$ in order to make each $H^{(1)}$ and $H^{(2)}$ in the denominator become such non exponential functions as $H_\nu^{(1)}(k, r) H_\nu^{(2)}(k, r)$. Next we substitute the above expression for H and P function into the numerator as follows. At first we shall write

$$H_\nu(k_q,\ \bar{r})=\int\cdots d\tau_Q, \qquad H_\nu(k_s,\ r_t)=\int\cdots d\tau_{st}, \qquad H_\nu(k_s,\ r)=\int\cdots d\tau_P,$$

for the various H-functions in the expression, and we get

$$C_0=\frac{A'}{(2\pi)^2(m_q+1)\sqrt{r\bar{r}}}\int_{\tau_1} ndn\, K_\nu^{-1}\int d\tau_Q \int d\tau_P \prod_{\mu=s}^{q-1}\int d\tau_{\mu+1,\ \mu}\int d\tau_{\mu\mu}$$
$$\cdot\int_{-\pi}^{\pi}\{\cos(\pi-\theta)+i\sin(\pi-\theta)\cos\varphi\}^{-1/2}\, e^{F(\tau)}\, d\varphi\ , \tag{46}$$

where

$$A'=\begin{cases} -\dfrac{1}{4\pi} \\[2ex] -\dfrac{k(s,\ r)}{4\pi k(q,\ \bar{r})}\left(\dfrac{2m_q+1}{2m_s+1}\right)^{1/2} \end{cases}$$

$$K_\nu=\prod_{\mu=s}^{q-1} H_\nu^{(1)}(k_\mu,\ r_\mu)\, H_\nu^{(2)}(k_\mu,\ r_\mu)\cdot\begin{cases} (2\pi)^{q-s}\cdot\displaystyle\prod_{\mu=s}^{q-1} r_\mu \\[2ex] (2\pi)^{q-s}\displaystyle\prod_{\mu=s}^{q-1}\frac{(2m_\mu+1)r_\mu}{\{k(\mu,,\ r_\mu)\}^2}\ . \end{cases} \tag{47}$$

Upper part of these double expressions is taken for the magnetic type, and the other for the electric type, and

$$\begin{aligned} F(\tau)=&-i\frac{k(q,\ \bar{r})\bar{r}}{m_q+1}\cos\tau_Q+i\frac{k(s,\ r)r}{m_s+1}\cos\tau_P \\ &+i\sum_{\mu=s}^{q-1}\left\{\frac{k(\mu+1,\ r_\mu)r_\mu}{m_{\mu+1}+1}\cos\tau_{\mu+1,\ \mu}-\frac{k(\mu,\ r_\mu)r_\mu}{m_\mu+1}\cos\tau_{\mu\mu}\right\} \\ &-in_q\frac{\tau_Q-\pi/2}{m_q+1}+in_s\frac{\tau_P-\pi/2}{m_s+1}+i\sum_{\mu=s}^{q-1}\left\{n_{\mu+1}\frac{\tau_{\mu+1,\ \mu}-\pi/2}{m_{\mu+1}+1}-n_\mu\frac{\tau_{\mu\mu}-\pi/2}{m_\mu+1}\right\} \\ &-in\pi+n\log\{\cos(\pi-\theta)+i\sin(\pi-\theta)\cos\varphi\}, \end{aligned}$$

where

$$n_\mu=\begin{cases} n & \textit{mag} \\ \sqrt{n^2+m_\mu(m_\mu+1)} & \textit{electr.} \end{cases}$$

The approximate value of (46) is given by the values at the saddle point, where

$$\frac{\partial F}{\partial\tau}=0\ , \qquad \frac{\partial F}{\partial\varphi}=0 \qquad \text{and} \qquad \frac{\partial F}{\partial n}=0\ .$$

If τ_s, φ and n denote their values at the saddle point, from the first of these equations. We get

$$n_q=k(q,\ \bar{r})\bar{r}\sin\tau_Q=k(q,\ r_{q-1})r_{q-1}\sin\tau_{q,\ q-1}\ ,$$
$$n_s=k(s,\ r)r\sin\tau_P=k(s,\ r_s)r_s\sin\tau_{ss}\ ,$$
$$n_\mu=k(\mu,\ r_{\mu-1})r_{\mu-1}\sin\tau_{\mu,\ \mu-1}=k(\mu,\ r_\mu)r_\mu\sin\tau_{\mu\mu},\ \mu=s+1,\ s+2,\ \cdots,q-1\ ,$$

where all ns on the left hand are very large except the case in which τ_Q is very small, and we may put

$$n_q=n_\mu=n_s=n$$

for both the magnetic and the electric type. Thus it follows that

$$n=k(q,\ \bar{r})\bar{r}\sin\tau_Q=k(\mu+1,\ \mu)r_\mu\sin\tau_{\mu+1,\ \mu}=k(\mu,\ r_\mu)r_\mu\sin\tau_{\mu\mu}=k(s,\ r)r\sin\tau_P\ , \tag{48}$$

where

$$\mu=s,\ s+1,\ \cdots,\ q-1\ .$$

Under the condition that the medium is continuous at the boundaries $r=r_\mu$

$$k(\mu+1,\ r_\mu)=k(\mu,\ r_\mu)\,, \qquad \mu=1,\ 2,\ \cdots,\ N\,.$$

we get

$$\tau_{\mu+1,\ \mu}=\tau_{\mu,\ \mu}\equiv\tau_\mu\,,$$

which shows that the incident angle is equal to the refracted angle at the boundary where the medium is continuous.

Next we get

$$\varphi=0 \quad \text{from} \quad \partial F/\partial\varphi=0\,. \tag{49}$$

Substituting (49) into $\partial F/\partial n=0$, we get

$$\theta=-\frac{\tau_Q-\pi/2}{m_q+1}+\frac{\tau_P-\pi/2}{m_s+1}+\theta(s,\ q-1)\,, \tag{50}$$

where

$$\theta(\alpha,\ \beta)=\sum_{\mu=\alpha}^{\beta}\left\{\frac{1}{m_{\mu+1}+1}-\frac{1}{m_\mu+1}\right\}(\tau_\mu-\pi/2) \tag{51}$$

If we let F be the value of $F(\tau)$ at the saddle point, we may write

$$F=-i\frac{k(q,\ \bar{r})\bar{r}}{m_q+1}\cos\tau_Q+i\frac{k(s,\ r)r}{m_s+1}\cos\tau_P+iF(s,\ q-1)\,, \tag{52}$$

where

$$F(\alpha,\ \beta)=\sum_{\mu=\alpha}^{\beta}\left\{\frac{1}{m_{\mu+1}+1}-\frac{1}{m_\mu+1}\right\}k(\mu,\ r_\mu)r_\mu\cos\tau_\mu\,. \tag{53}$$

When

$$k(\mu,\ r_\mu)r_\mu>k(q,\ \bar{r})\bar{r}\sin\tau_Q=n\,, \qquad \mu=s,\ s+1,\ \cdots,\ q-1\,,$$

and

$$k(s,\ r)r>n$$

are all satisfied for a real angle τ_Q, the saddle point gives a geometric optical ray S from Q to P, which satisfies the Fermat's principle, as shown in Fig. 4, and a brief calculation gives F (52) an integral form

$$\frac{\omega}{c}\int_Q^P\sqrt{\mu\varepsilon}\,ds\,,$$

where the contour of the integral should be taken along the ray S.

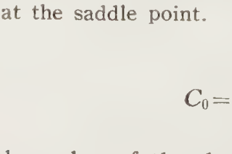

Fig. 4. The geometric optical ray of the primary converging wave C_0. The angles $\tau_Q,\ \cdots,\ \tau_P$ are the values at the saddle point.

Substituting the values at the saddle point into K_ν, and denoting it by K, we get

$$C_0=\frac{A'n(2\pi)^{q-s}}{(m_q+1)\sqrt{r\bar{r}}\,K\sqrt{\varDelta}}\cdot e^{F-i(\pi-\theta)/2}\,,$$

where $\varDelta$ is the value of the determinant of the order $2(s-q)+4$:

$$|\partial^2F/\partial x_i\,\partial x_j| \qquad x_i=\tau_Q,\ \cdots,\ n,\ \varphi,$$

at the saddle point, and

$$\varDelta=n\sin\theta\cdot\exp\{-(\pi-\theta)\}\frac{k(q,\ \bar{r})\bar{r}}{m_q+1}\cos\tau_Q\cdot\frac{k(s,\ r)r}{m_s+1}\cos\tau_P\prod_{\mu=s}^{q-1}\frac{\{k(\mu,\ r_\mu)r_\mu\cos\tau_\mu\}^2}{(m_{\mu+1}+1)(m_\mu+1)}\cdot\Theta\,,$$

and

$$\Theta=\frac{\partial\theta}{\partial n}=\frac{-1}{(m_q+1)k(q,\ \bar{r})\bar{r}\cos\tau_Q}+\frac{1}{(m_s+1)k(s,\ r)r\cos\tau_P}+\Theta(s,\ q-1)\,, \tag{54}$$

where

$$\Theta(\alpha,\beta)=\sum_{\mu=\alpha}^{\beta}\left\{\frac{1}{m_{\mu+1}+1}-\frac{1}{m_{\mu}+1}\right\}\frac{1}{k(\mu,r_{\mu})\,r_{\mu}\cos\tau_{\mu}}\,. \tag{55}$$

Furthermore, substituting the approximate relations

$$\begin{aligned} H_{\nu}^{(1)}(k_{\mu},r_t)H_{\nu}^{(2)}(k_{\mu},r_t)&\sim\frac{m_{\mu}+1}{k(\mu,r_t)r_t\cos\tau_t} && \text{Mag.}\\ &\sim\frac{m_{\mu}+1}{2m_{\mu}+1}\frac{k(\mu,r_t)}{r_t^2\cos\tau_t} && \text{Elect.}\end{aligned}$$

into K, we may write

$$K=(2\pi)^{q-s}\sum_{\mu=s}^{q-1}\frac{m_{\mu}+1}{k(\mu,r_{\mu})r_{\mu}\cos\tau_{\mu}}$$

for both types. On the other hand n can be written as

$$n=[k(q,\bar{r})\bar{r}\sin\tau_Q\quad k(s,r)r\sin\tau_P]^{1/2}$$

by the help of the values at the saddle point, we get as a final formula for C_0,

$$C_0=A'\left[\frac{\tan\tau_Q\tan\tau_P}{nr\bar{r}\sin\theta\,\Theta}\right]^{1/2}e^F\,. \tag{56}$$

Integral formula for $D_1^{(0)}$ is written in the form

$$\begin{aligned} D_1^{(0)}=&\frac{A'}{(2\pi)^2(m_q+1)\sqrt{r\bar{r}}}\int_{\Gamma_1}ndnK_{\nu}^{-1}R_{\nu}\int d\tau_Q\cdot\int d\tau_P\\ &\cdot\int d\tau_{10}\int d\tau_{20}\prod_{\mu=1}^{q-1}\int k\tau_{\mu+1,\mu}\int d\tau_{\mu\mu}\prod_{\sigma=1}^{s-1}\int d\tau_{\sigma+1;\sigma}\int d\tau_{\sigma\sigma}\cdot\\ &\cdot\int\{\cos(\pi-\theta)+i\sin(\pi-\theta)\cos\varphi\}^{-1/2}\exp\{F(\tau)\}d\varphi\,,\end{aligned}$$

where

$$\nu=n-\tfrac{1}{2}\,,$$

$$\begin{aligned} K_{\nu}=&\prod_{\mu=1}^{q-1}H_{\nu}^{(1)}(k_{\mu},r_{\mu})H_{\nu}^{(2)}(k_{\mu},r_{\mu})\prod_{\sigma=0}^{s-1}H_{\nu}^{(2)}(k_{\sigma+1},r_{\sigma})H_{\nu}^{(1)}(k_{\sigma+1},r_{\sigma})\cdot\\ &\cdot\begin{cases}(2\pi)^{q+s-1}\prod\limits_{\mu=1}^{q-1}r_{\mu}\prod\limits_{\sigma=0}^{s-1}r_{\sigma} & \text{Mag.}\\[2ex] (2\pi)^{q+s-1}\prod\limits_{\mu=1}^{q-1}\dfrac{(2m_{\mu}+1)r_{\mu}}{\{k(\mu,r_{\mu})\}^2}\prod\limits_{\sigma=0}^{s-1}\dfrac{(2m_{\sigma+1}+1)r_{\sigma}}{\{k(\sigma+1,r_{\sigma}\}^2}\,, & \text{Elect.}\end{cases}\end{aligned}$$

$$\begin{aligned} F(\tau)=&-i\frac{k(q,\bar{r})\bar{r}}{m_q+1}\cos\tau_Q+i\frac{k(s,r)r}{m_s+1}\cos\tau_P\\ &+i\frac{(k(1,r_0)r_0}{m_1+1}\cos\tau_{10}+i\frac{k(1,r_0)r_0}{m_1+1}\cos\tau_{20}\\ &+i\sum_{\mu=1}^{q-1}\left\{\frac{k(\mu+1,r_{\mu})r_{\mu}}{m_{\mu+1}+1}\cos\tau_{\mu+1,\mu}-\frac{k(\mu,r_{\mu})r_{\mu}}{m_{\mu}+1}\cos\tau_{\mu\mu}\right\}\\ &+i\sum_{\sigma=1}^{s-1}\left\{\frac{k(\sigma+1,r_{\sigma})r_{\sigma}}{m_{\sigma+1}+1}\cos\tau_{\sigma+1,\sigma}-\frac{k(\sigma,r_{\sigma})r_{\sigma}}{m_{\sigma}+1}\cos\tau_{\sigma\sigma}\right\}\\ &-in_q\frac{\tau_Q-\pi/2}{m_q+1}-in_s\frac{\tau_P-\pi/2}{m_s+1}+in_1\frac{\tau_{10}-\pi/2}{m_1+1}+in_1\frac{\tau_{20}-\pi/2}{m_1+1}\\ &+i\sum_{\mu=1}^{q-1}\left\{n_{\mu+1}\frac{\tau_{\mu+1,\mu}-\pi/2}{m_{\mu+1}+1}-n_{\mu}\frac{\tau_{\mu\mu}-\pi/2}{m_{\mu}+1}\right\}\\ &+i\sum_{\sigma=1}^{s-1}\left\{n_{\sigma+1}\frac{\tau_{\sigma+1,\sigma}-\pi/2}{m_{\sigma+1}+1}-n_{\sigma}\frac{\tau_{\sigma\sigma}-\pi/2}{m_{\sigma}+1}\right\}\,.\end{aligned}$$

In the same way as above we get the following equations at the saddle point.

$$n=k(q,\bar{r})\bar{r}\sin\tau_Q=k(s,r)r\sin\tau_P=k(1,r_0)r_0\sin\tau_{10}=k(1,r_0)r_0\sin\tau_{20}$$

$$=k(t+1,r_t)r_t\sin\tau_{t+1,t}=k(t,r_t)r_t\sin\tau_{tt}\ ,$$

$$t=\begin{cases}\mu & \mu=1,2,\cdots,q-1\\ \sigma & \sigma=1,2,\cdots,s-1\ ,\end{cases}$$

$$\varphi=0\ ,$$

and

$$\theta=-\frac{\tau_Q-\pi/2}{m_q+1}-\frac{\tau_P-\pi/2}{m_s+1}+\frac{2\tau_0}{m_1+1}+\theta(1,q-1)+\theta(1,s-1)\ , \tag{57}$$

where, from the condition that the medium is continuous at the boundaries $r=r_\mu$, it follows that first relation above leads to

$$\tau_{\mu+1,\mu}=\tau_{\mu\mu}\equiv\tau_\mu\ ,\qquad \tau_{10}=\tau_{20}\equiv\tau_0$$

$$\text{and}\quad \tau_\mu=\tau_\sigma\quad\text{for}\quad \mu=\sigma\ .$$

In case all the τs are real, the above saddle point determines such a geometrical ray S as shown in Fig. 5, and the geometrical expression of $D_1^{(0)}$ is

$$D_1^{(0)}=A'\left[\frac{\tan\tau_Q\tan\tau_P}{n r\bar{r}\sin\theta\,\Theta}\right]^{1/2}Re^F\ , \tag{58}$$

where

$$\begin{aligned}F=&-i\frac{k(q,\bar{r})\bar{r}}{m_q+1}\cos\tau_Q-i\frac{k(s,\bar{r})\bar{r}}{m_s+1}\cos\tau_P\\ &+2i\frac{k(1,r_0)r_0}{m_1+1}\cos\tau_0\\ &+iF(1,q-1)+iF(1,s-1)\ ,\end{aligned} \tag{59}$$

and

$$\begin{aligned}\Theta=&\frac{-1}{(m_q+1)k(q,\bar{r})\bar{r}\cos\tau_Q}-\frac{1}{(m_s+1)k(s,r)r\cos\tau_P}\\ &+\frac{2}{(m_1+1)k(1,r_0)r_0\cos\tau_0}\\ &+\Theta(1,q-1)+\Theta(1,s-1)\ .\end{aligned} \tag{60}$$

R is the value of R_ν at the saddle point, and making use of the approximate relation, we have

$$\{\log r_0\zeta_\nu^{(1),(2)}(k_0,r_0)\}'\sim\pm ik_0\cos\tau_0'\ ,$$

$$\text{and}\quad \{\log r_0H_\nu^{(1),(2)}(k_1,r_0)\}'\sim\pm ik(1,r_0)\cos\tau_0\ , \tag{61}$$

where $k_0\sin\tau_0'=k(1,r_0)\sin\tau_0$. R_ν is reduced to

$$R=\begin{cases}\dfrac{k_0\cos\tau_0'-k(1,r_0)\cos\tau_0}{k_0\cos\tau_0'+k(1,r_0)\cos\tau_0}\ , & \text{Mag.}\\[2ex] \dfrac{(1/k_0)\cos\tau_0'-(1/k(1,r_0))\cos\tau_0}{(1/k_0)\cos\tau_0'+(1/k(1,r_0))\cos\tau_0}\ , & \text{Elect.}\end{cases} \tag{62}$$

In case $k(\mu,r_\mu)r_\mu>n$ for $\mu=q-1,q-2,\cdots,j$, and

$$k(j,r_{j-1})r_{j-1}<n\ ,$$

there exists such a radius r_b as

$$k(j,r_b)r_b=n\ ,\qquad r_{j-1}<r<r_j\ .$$

Upon putting

$$\begin{aligned}\tau_\mu&=\tau_\mu & \mu&>j\ ,\\ &=\pi-\tau_\mu & \mu&<j\ ,\end{aligned}$$

which satisfies the conditions at the saddle point, we get geometrical ray curves as shown in Fig. 6.

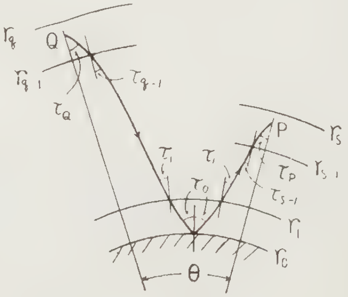

Fig. 5. The geometric optical ray of $D_1^{(0)}$.

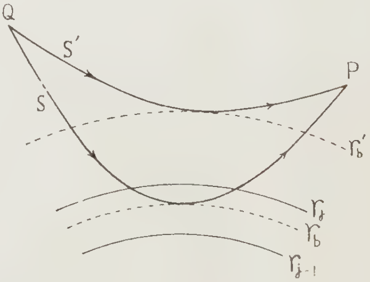

Fig. 6. The geometric optical ray of D_1.
r_b, r_b': Boundary surfaces where the angle τ can be real, which have the physical meaning of total reflection.

The geometrical expression of $D_0^{(0)}$ for this case is the same as that of C_0 except the value of f and Θ, which are now as follows:

$$F=-i\frac{k(q,\bar r)\bar r}{m_q+1}\cos\tau_Q-i\frac{k(s,\bar r)\bar r}{m_s+1}\cos\tau_P$$
$$+iF(j,q-1)+iF(j,s-1)\,, \qquad (63)$$

and

$$\Theta=-\frac{1}{(m_q+1)k(q,\bar r)\bar r\cos\tau_Q}$$
$$-\frac{1}{(m_s+1)k(s,r)r\cos\tau_P}$$
$$+\Theta(j,q-1)+\Theta(j,s-1)\,. \qquad (64)$$

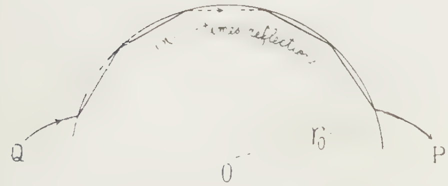

Fig. 7. The geometric optical ray of $D_1^{(\kappa)}$. The ray is the straight line in the earth $r<r_0$, since the earth is assumed to be homogeneous.

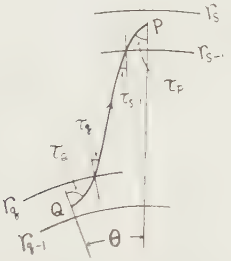

Fig. 8a. The geometric optical ray of D_0.

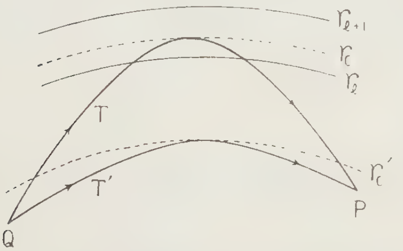

Fig. 8b. The geometric optical ray of C_1.
r_c, r_c': The distances from the center, where the total reflection occurs.

To the wave along S not only $D_1^{(0)}$ but also $D_1^{(\kappa)}$ makes a contribution. Now let us examine the latter wave in the following. When at first

$$k(\mu,r_\mu)r_\mu>n\,,\qquad \mu=q-1,q-2,\cdots,1,0,$$

the geometrical expression of $D_1^{(\kappa)}$ shows as that it is a wave which, after having transmitted into the earth, reflected $(\kappa-1)$-times on the inner side of the earth's surface, and again refracted out into the atmosphere. (Fig. 7)

As the conductivity of the earth is considerably large, such a wave fades out in the earth. Thus we need not consider such waves. Next in case

$$k(\mu,r_\mu)r_\mu>n\,,\quad \mu=q-1,q-2,\cdots,j\,,$$

and

$$k(j,r_j)r_j<n\,,$$

we obtain such a ray **S** as in Fig. 6, and along this ray $D_1^{(\kappa)}$ is expressed as

$$D_1^{(\kappa)}=A'\left[\frac{\tan\tau_Q\tan\tau_P}{n r\bar r\sin\theta\,\Theta}\right]^{1/2}T^{(\kappa)}e^F\,,$$

where F and Θ are the same as given in (63) and (64) respectively, on the other hand $T^{(\kappa)}$ is

$$(1+R_\nu)(1+R_\nu')R_\nu'^{\kappa-1}\,,$$

into which the values at the saddle point should be substituted.

As $R'=-R$, which is obtained by the help of the approximate relations (61), we get

$$T^{(\kappa)}=(1+R)(1-R)(-R)^{\kappa-1}\,.$$

Thus we get

$$D_1=D_1^{(0)}+\sum_{\kappa=1}^{\infty}D_1^{(\kappa)}$$
$$=A'\left[\frac{\tan\tau_Q\tan\tau_P}{n r\bar r\sin\theta\,\Theta}\right]^{1/2}\cdot\left\{R+\sum_{\kappa=1}^{\infty}T^{(\kappa)}\right\}e\,.$$

By

$$\sum_{\kappa=1}^{\infty}T^{(\kappa)}=(1+R)(1-R)\sum_{\kappa=1}^{\infty}(-R)^{\kappa-1}$$
$$=1-R\,,$$

therefore

$$D_1=A'\left[\frac{\tan\tau_Q\tan\tau_P}{n r\bar r\sin\theta\Theta}\right]^{1/2}e^F,$$

which is the same expression as that of C_0.

The geometrical expression of the primary diverging wave D_0 is the same in form as that of C_0, except the value of F and Θ, which are now given as follows. When $k(\mu,r_\mu)r_\mu>n$ for $s>\mu>q$, we get

$$F=i\frac{k(q,\bar r)\bar r}{m_q+1}\cos\tau_Q-i\frac{k(s,\bar r)r}{m_s+1}\cos\tau_P$$
$$+iF(q,s-1)\,, \qquad (65)$$

$$\Theta=\frac{1}{(m_q+1)k(q,\bar r)\bar r\cos\tau_Q}$$
$$-\frac{1}{(m_s+1)k(s,r)r\cos\tau_P}+\Theta(q,s-1)\,, \qquad (66)$$

and

$$\theta=\frac{\tau_Q-\pi/2}{m_s+1}-\frac{\tau_P-\pi/2}{m_s+1}+\theta(q,\, s-1)\,, \qquad (67)$$

when

$$k(\mu,\, r_\mu)r_\mu>n\,,\quad \mu=q,\, q+1,\, \cdots,\, l-1,$$

and

$$k(l,\, r_l)r_l<n\,,$$

there exists such a radius r_c as given by

$$k(l,\, r_c)r_c=n\,,\quad r_{l-1}<r_c<r_l\,.$$

In such a case the rays $\boldsymbol{S}$, $\boldsymbol{S}'$, $\cdots$ which make a total reflection at $r=r_c$, r_c' $\cdots$ are presented as Fig. 8, and the expressions of these waves C_1 are the same in forms as those of C_0 (56), except F and Θ, which are now given as follows,

$$F=i\frac{k(q,\, \bar{r})\bar{r}}{m_q+1}\cos\tau_Q+i\frac{k(s,\, \bar{r})\bar{r}}{m_s+1}\cos\tau_P\,.$$
$$+iF(q,\, l-1)+iF(s,\, l-1)\,, \qquad (68)$$

$$\Theta=\frac{1}{(m_q+1)k(q,\, \bar{r})\bar{r}\cos\tau_Q}$$
$$+\frac{1}{(m_s+1)k(s,\, r)r\cos\tau_P}$$
$$+\Theta(q,\, l-1)+\Theta(s,\, l-1), \qquad (69)$$

and

$$\theta=\frac{\tau_Q-\pi/2}{m_q+1}+\frac{\tau_P-\pi/2}{m_s+1}+\theta(q,l-1)+\theta(s,l-1)\,, \qquad (70)$$

§ 6. Geometrical Expressions of the Waves which reflect Many Times

We shall consider at first the waves which reflect on the earth's surface. When

$$k(\mu,\, r_\mu)r_\mu>k(q,\, \bar{r})\bar{r}\sin\tau_Q=n$$

for $\qquad 0\leqq\mu\leqq l-1\,,$

and

$$k(l,\, r_l)r_l<n\,,$$

there exists such a radius r_c that satisfies

$$k(l,\, r_c)r_c=n\,,\qquad r_{l-1}<r<r_l\,,$$

where r_c is the height which the ray waves can reach. In such a case we get the geometrical expressions of the waves which reflect on the earth's surface, say Z-times, as shown in Figs. 9 and 10, where we shall write $u(P_i)$ which makes the above Z-times reflections and arrives at the point P_i ($i=1$, 2, 3, 4)

$$u(P_i)=A'\sqrt{\frac{\tan\tau_Q\tan\tau_P}{nr\bar{r}\sin\theta_i\Theta_i}}R^Z\exp F_i\,,$$
$$i=1,\, 2,\, 3,\, 4, \qquad (71)$$

where

$$\left.\begin{matrix}F_1\\F_2\end{matrix}\right\}=-i\frac{k(q,\, \bar{r})\bar{r}}{m_q+1}\cos\tau_Q\mp i\frac{k(s,\, r)r}{m_s+1}\cos\tau_P$$
$$+iF(1,\, q-1)+i(2Z-1)F(1,\, l-1)\mp iF(s,\, l-$$
(7

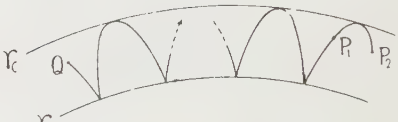

Fig. 9. The geometrical optical ray of $u(P_1)$ o $u(P_2)$, which arrived at P_1 or P_2 after makin Z times reflection against earth's surface $r=r_0$

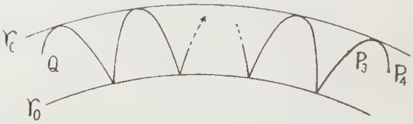

Fig. 10. The geometric optical ray of $u(P_3)$ and $u(P_4)$.

$$\left.\begin{matrix}F_3\\F_4\end{matrix}\right\}=i\frac{k(q,\, \bar{r})\bar{r}}{m_q+1}\cos\tau_Q\mp i\frac{k(s,\, \bar{r})\bar{r}}{m_s+1}\cos\tau_P$$
$$-iF(1,\, q-1)+i(2Z-1)F(1,\, l-1)\mp iF(s,\, l-1$$
(72

and

$$\left.\begin{matrix}\Theta_1\\\Theta_2\end{matrix}\right\}=\frac{-1}{(m_q+1)k(q,\, \bar{r})\bar{r}\cos\tau_Q}$$
$$\mp\frac{1}{(m_s+1)k(s,\, r)r\cos\tau_P}$$
$$+\Theta(1,\, q-1)+(2Z-1)\Theta(1,\, l-1)\mp\Theta(s,\, l-1)\,,$$
(73

$$\left.\begin{matrix}\Theta_3\\\Theta_4\end{matrix}\right\}=\frac{1}{(m_q+1)k(q,\, \bar{r})\bar{r}\cos\tau_Q}$$
$$\mp\frac{1}{(m_s+1)k(s,\, r)r\cos\tau_p}$$
$$-\Theta(1,\, q-1)+(2Z-1)\Theta(1,\, l-1)\pm\Theta(s,\, l-1)\,,$$
(73

$$\left.\begin{matrix}\theta_1\\\theta_2\end{matrix}\right\}=-\frac{\tau_Q-\pi/2}{m_q+1}\mp\frac{\tau_P-\pi/2}{m_s+1}+\theta(1,\, q-1)$$
$$+(2Z-1)\theta(1,\, l-1)\mp\theta(s,\, l-1)\,; \qquad (74$$

$$\left.\begin{matrix}\theta_3\\\theta_4\end{matrix}\right\}=\frac{\tau_Q-\pi/2}{m_q+1}\mp\frac{\tau_P-\pi/2}{m_s+1}-\theta(1,\, q-1)$$
$$+(2Z-1)\theta(1,\, l-1)\mp\theta(s,\, l-1)\,. \qquad (74$$

The waves, whose rays make total reflec tions at $r=r_b$ in the j-th layer ($q>j$) and a $r=r_c$ in the l-th layer ($l>q$), propagate to an fro between these two surfaces $r=r_b$ an

$r=r_c$. The waves which reflect Z times at $r=r_b$, are written in the form of $u(P_i)$, whose meaning is obviously seen from Fig. 11 and 12.

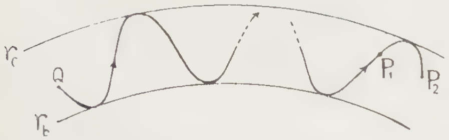

Fig. 11. The geometric optical ray which does'nt meet earth's surface.

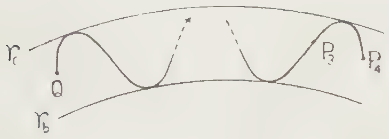

Fig. 12. The geometric optical ray which does'nt meet earth's surface.

Then we may write

$$u(P_i)=A'\left[\frac{\tan\tau_Q\tan\tau_P}{nr\bar{r}\sin\theta_i\Theta_i}\right]^{1/2}\exp\{F_i\}\,, \tag{75}$$

where

$$\left.\begin{matrix}F_1\\F_2\end{matrix}\right\}=-i\frac{k(q,\bar{r})\bar{r}}{m_q+1}\cos\tau_Q\mp i\frac{k(s,r)r}{m_s+1}\cos\tau_P$$
$$+iF(j,q-1)+i(2Z-1)F(j,l-1)\mp iF(s,l-1), \tag{76}$$

$$\left.\begin{matrix}F_3\\F_4\end{matrix}\right\}=i\frac{k(q,\bar{r})\bar{r}}{m_q+1}\cos\tau_Q\mp i\frac{k(s,r)r}{m_s+1}\cos\tau_P$$
$$-iF(j,q-1)+i(2Z-1)F(j,l-1)\mp iF(s,l-1). \tag{76'}$$

and

$$\left.\begin{matrix}\Theta_1\\\Theta_2\end{matrix}\right\}=\frac{-1}{(m_q+1)k(q,\bar{r})\bar{r}\cos\tau_Q}$$
$$\mp\frac{1}{(m_s+1)k(s,r)r\cos\tau_P}$$
$$+\Theta(j,q-1)+(2Z-1)\Theta(j,l-1)\mp\Theta(s,l-1)\,, \tag{77}$$

$$\left.\begin{matrix}\Theta_3\\\Theta_4\end{matrix}\right\}=\frac{1}{(m_q+1)k(q,\bar{r})\bar{r}\cos\tau_Q}$$
$$\mp\frac{1}{(m_s+1)k(s,r)r\cos\tau_P}$$
$$-\Theta(j,q-1)+(2Z-1)\Theta(j,l-1)\mp\Theta(s,l-1)\,, \tag{77'}$$

$$\left.\begin{matrix}\theta_1\\\theta_2\end{matrix}\right\}=-\frac{\tau_Q-\pi/2}{m_q+1}\mp\frac{\tau_P-\pi/2}{m_s+1}$$
$$+\theta(j,q-1)+(2Z-1)\theta(j,l-1)\mp\theta(s,l-1)\,, \tag{78}$$

$$\left.\begin{matrix}\theta_3\\\theta_4\end{matrix}\right\}=\frac{\tau_Q-\pi/2}{m_q+1}\mp\frac{\tau_P-\pi/2}{m_s+1}$$
$$-\theta(j,q-1)+(2Z-1)\theta(j,l-2)\mp\theta(s,l-1)\,. \tag{78'}$$

§ 7. Conclusions

In this paper we started from the rigorous solutions of Maxwell's equations in an inhomogeneous medium, whose inductive capacity is proportial to r^{2m} and generalized the expression of the dipole field in such a medium for the expression in a medium whose inductive capacity is an arbitrary function of r by deviding it into many laminar spherical shells.

The geometrical expressions of the first approximation have a clear physical meaning, and the derived geometrical ray satisfies Fermat's principle. So long as the first approximation is concerned, the above geometrical expressions suggest the possibility of being generalized for the case of an arbitrary inhomogeneous medium. As the saddle point coincides with Fermat's principle, the former can be generalized as

$$f\sin\tau=n\,,\qquad f=(\omega/c)\sqrt{\mu\varepsilon(r)}\,r\,, \tag{79}$$

for an arbitrary medium, and this relation determines the ray S, along which

$$d\theta=\pm\frac{n}{\sqrt{f^2-n^2}}\frac{dr}{r}\,,\qquad ds=\frac{n}{\sqrt{f^2-n^2}}dr\,.$$

On the other hand we get

$$\frac{\partial\tau}{\partial n}=\frac{1}{\sqrt{f^2-n^2}}\,,$$

by differentiating the above relation partially. Therefore we get

$$\frac{\partial\theta}{\partial n}=\int_Q^P\frac{f^2}{\sqrt{f^2-n^2}^3}\frac{dr}{r}\,,$$

which appeared in the denominator of all the geometrical expressions in the previous section. As is easily seen, in the limiting case when the thickness of all layers tends to zero, the expressions of $\partial\theta/\partial n$ in the previous section coincide with the above one. But the above expression is very difficult to integrate, when ε is an arbitrary function. The exponential part F in the previous expression is written in the form:

$$F=-i\frac{\omega}{c}\int_s\sqrt{\mu\varepsilon}\,ds\,,$$

which is integrated along the ray S. Using these generalized expressions we may rewrite the previous expression, say (56), as

$$c_0=A'\left[\frac{\tan\tau_Q\tan\tau_P}{n r\bar{r}\sin\theta\int_Q^P f^2(f^2-n^2)^{-3/2}\frac{dr}{r}}\right]^{1/2}$$

$$\cdot\exp\left\{-i\frac{\omega}{c}\int_s\sqrt{\mu\varepsilon}\,ds\right\}.$$

with the boundary conditions

$$n=\frac{\omega}{c}\sqrt{\mu\varepsilon}\,\bar{r}\sin\tau_Q=\frac{\omega}{c}\sqrt{\mu\bar{\varepsilon}}\,r\sin\tau_P\ .$$

Returning again to the discussion of the previous sections we have calculated numerically the propagation of the electromagnetic waves in N.A.C.A. standard atmosphere.

The measure m of the inhomogeneity of the N.A.C.A. standard atmosphere is

$$m=\begin{cases}-0.1677 & \text{for dry standard atmosphere,}\\ -0.2715 & \text{for 60\% moist standard atmosphere}\end{cases}$$

which is calculated from the table of the standard atmosphere between the earth's surface and the height of 1500 meters.

For the numerical calculation we take the following values

$$\varepsilon=\begin{cases}4\ \text{(e.s.u)}\\ 80\ \text{(e.s.u)}\end{cases}$$

$$\sigma=\begin{cases}10^{-15}\ \text{(e.m.u.)} & \text{for the earth,}\\ 10^{-11}\ \text{(e.m.u')} & \text{for the sea water,}\end{cases}$$

where σ denotes the conductivity. Both the dipole source and the observing point are at the height of 100 m, and the strength of the source is 1 K.W. The strength of the direct wave at a distant point from the source is larger in the moist standard atmosphere than in the dry. Conversely the once reflected wave is stronger in the dry atmosphere. The vertical broken line in the Fig. 13 denotes the distance of sight. If the atmosphere were homogeneous, there would be only diffracted waves on the right side of this line. In the case of the standard atmosphere, the longest distance D on the ground, which the direct wave can reach is larger than that in the case of the homogeneous atmosphere. Taking the central angle θ in place of D, we get θ

$$=\begin{cases}\sqrt{2h/a}\ , & \text{for homogeneous atmosphere,}\\ \sqrt{2h/(m+1)a}\ , & \text{for standard atmosphere,}\end{cases}$$

where a is the earth's radius and h is the height of the source ($h<a$). When we take into account the results in the previous section, the field strengths as well as the central angle in the homogeneous atmosphere coincide roughly with those in the standard atmosphere, if we use $a/(m+1)$ in place of the actual earth's radius a. But

$$\frac{a}{m+1}=\begin{cases}a/0.7285\ , & \text{for 60\% moist standard atmosphere,}\\ a/0.8323\ , & \text{for dry atmosphere.}\end{cases}$$

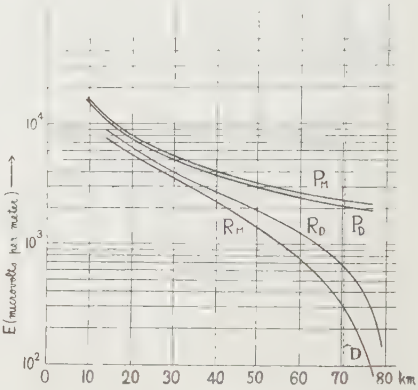

Fig. 13. The intensity of the electric field E in N.A.C.A. standard atmosphere. (microvolts per metre.)

The absissa: The distance of the observing point from the source.

The ordinate: The intensity of the electric field E.

P: The primary waves.

R: The waves reflected once at the earth's surface.

The suffixes D and M denote that the atmosphere is dry and 60% moist respectively. The vertical broken line denotes the distance of sight, i.e. the distance that the source can just be seen from the observing point if the atmosphere were homogeneous.

Therefore we can safely affirm that the well-known (4/3)a law is reasonable in the moderate atmosphere. We shall give further discussions about the propagation of the electromagnetic waves in the ionized layer and in the duct and etc. in the following papers.

References

1) H. G. Booker: Quart. Jour. Roy. Met. Soc. **74** No. 321–322 (1948).
2) D. E. Kerr: Propagation of Short Radio Waves (1951).
3) K. Hirao, K. Tao: Kagaku **12** (1954) 590.
4) C. Eckart, H. Plendl: Z. techn. Physik **18** (1937) 441.
Hochfrequenz teck. u. Elektroak. **52** (1938) 44.
Ergebn. exakt. Naturwiss. **17** (1938) 334.
5) M. Goto: Reports of Researches of Elec. Comm. Laboratory No. 2 (1951).
6) K. Tao: J. Jour. Geophys. Vol. 1, No. 1 (1954).
7) R. Yamada: J. Phys. Soc. Japan **10** (1955) 71.
8) H. Bremmer: Terrestial Radio Waves, (1949) Part II.
9) B. van der Pol, H. Bremmer: Phil. Mag. **24** (1937) 825.
H. Bremmer: ditto. Part I.

Short Notes

J. PHYS. SOC. JAPAN **10** (1955) 715~716

Effects of Infrared on Emission of ZnS:Cu Phosphors

By Ken-ichi NAKAMURA

Shizuoka University, Oiwa-machi, Shizuoka-city

(Read, April 8, 1955, Received June 9, 1955)

ZnS:Cu phosphors have the maximum sensitivities of a stimulation band approximately at 0.85μ and 1.3μ[1]. Bube[2] reported that a stimulation band at 1.3μ corresponded to the difference between the conduction band and the excited state of the green emitting center as a result of his experiment using a broad band of infrared from 0.8μ to 3.0μ.

The present paper reports the interesting results obtained when hex-ZnS:Cu phosphors with 0.009% silver[3] are irradiated at various temperature with infrared, transmitted through a Matzuda 1R-DI filter (ir) or combination (red) of a V–RI filter with a V–VI filter in addition to the steady radiation of 3650 A ultraviolet. Effective wavelength through the former is approximately from 0.95μ to 4μ Results obtained, when above three filters are combined are the same as when a IR–DI is used alone. As the latter combinated filter transmits the light of wavelength above 0.7μ, the difference between ir and red filter corresponds to the range in wavelength approximately from 0.7μ to 0.95μ. Eight samples of hex-ZnS phosphors (NaCl, 2.5%) with copper contents from 0 to 0.03% in weight percent are prepared, being heated for thirty minutes at 1200°C. These phosphors have the blue emission band of the peak approximately at 4400 A and the green emission band at 5200 A. When they are irradiated with ir or red under the steady ultraviolet excitation, the brightness increases instantaneously and decreases later, and when ir or red is interrupted it decreases instantaneously and recovers slowly. However, the feature of blue emission is not the same as that of green emission and also the feature under ir irradiation is not the same as that under red radiation. Fig. 1 and Fig. 2 show the features. A Matzuda V–G1(B) filter and a V-O3 filter are used to isolate the green emission band and a

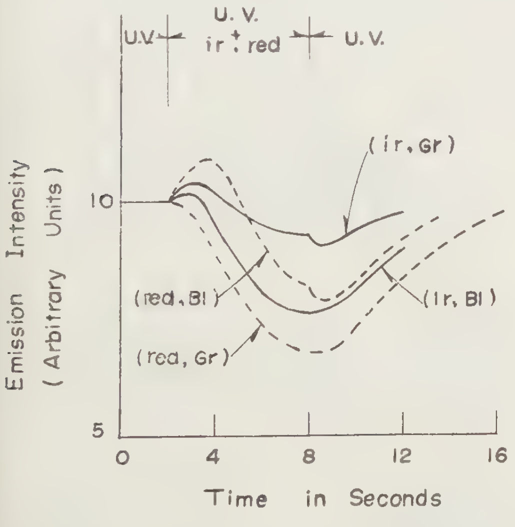

Fig. 1. Effects of ir and red irradiation added to ultraviolet excitation on emission in ZnS:Cu (0.0001%) at 15°C. Other samples show similar feature.

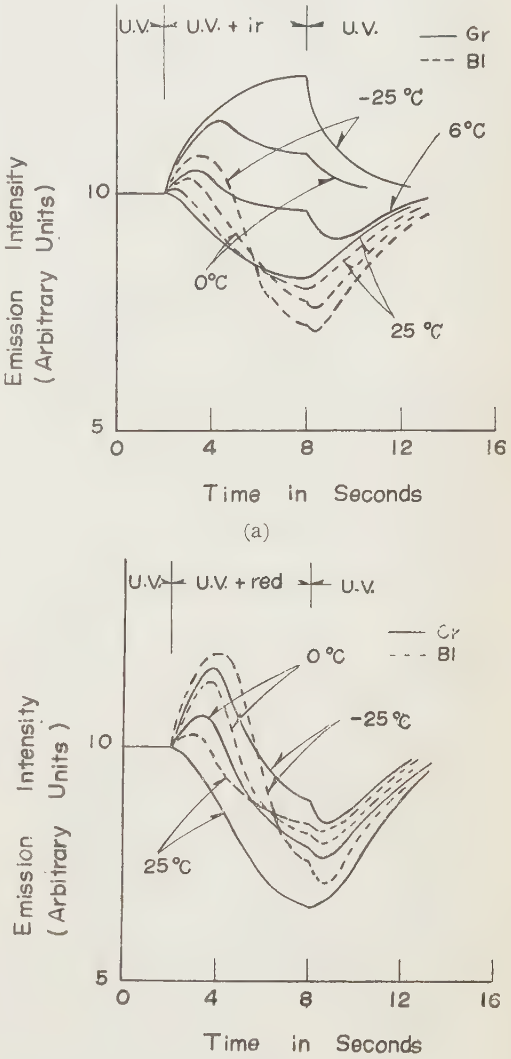

(a)

(b)

Fig. 2. Effects of ir and red irradiation added to ultraviolet excitation on emission in ZnS:Cu (0.0001%) at various temperature.
(a): ir, (b): red.

Matzuda V–B2(A) filter and a V–V1 filter to isolate the blue emission band. At low temperature, the brightness of the green emission increases during ir irradiation (stimulation), whereas the brightness of the blue emission decreases (quenching). Above a certain temperature, the initial increase is not observed. In wide range of temperature the blue emission is much quenched than the green emission when ir is irradiated. In case of red radiation, however, the feature is different, although both intensities are not the same. In this case the quenching effect on the green emission is more remarkable. In other words, the present investigation shows a spectral shift to the green under ir irradiation and to the blue under red radiation. The results are not consistent with Bube's conclusion[2]. Our results may lead to the following assumption. Deep traps[4] caused by activators may be associated with the blue emitting center or green emitting center. Ir irradiation perhaps makes the strong coupling of the trap with the green emitting center situated near and free electrons are removed from conduction band through this process, and consequently the decrease of the blue emission is observed. Red radiation perhaps makes the coupling of the trap with the blue emitting center near the trap stronger. Moreover, as to quenching effect, it is observed that this effect is remarkable under red radiation. In any case, however, it depends upon temperature and the green emission is more sensitive than the blue emission. Above all, the green emission under ir irradiation is remarkably affected by temperature, and yet the blue emission is not so. Therefore it can be concluded that infrared irradiation, particularly red radiation, may cause trapped electron recombine directly with the free positive holes in valence band without emission[5], but the effect of temperature on this process is predominant in the green emitting center, and at low temperature this quenching effect is not observed under ir irradiation. It seems that these results give a clue to obtain the information of quenching mechanism.

We wish to express our hearty thanks to Prof. K. Takagi for his encouragement and his discussion. This research is carried out by the Scientific Research Grant of the Ministry of Education.

References

1) S. Asano: Journ. of Appl. Phys. **22** (1953) 273 (in Japanese).
2) R. H. Bube: Phys. Rev. **80** (1950) 764.
3) G. F. J. Garlick and A. F. Gibson: J.O.S.A. **39** (1947) 937.
4) R. H. Bube: Phys. Rev. **80** (1950) 655.
5) H. Kallmann and B. Kramer: Phys. Rev. **87** (1952) 91.

J. Phys. Soc. Japan **10** (1955) 716~718

On Chemical Change of n-Higher Alcohol Caused by the Influence of Strong Electric Field

By Kenjiro Asai

Department of Physics, University of Kyoto

(Received May 6, 1955)

It is found that the electric breakdown occurs in n-higher alcohol at a certain field strength of several thousands volts per mm, the value of which fluctuates depending on the purity of a sample. In this case the breakdown occurs locally, so that almost the whole part of the substance is not damaged. However, if we apply a strong electric field by such a method as shown in Fig. 1, chemical change in the whole part of a sample becomes possible to occur. The degree of chemical change was detected by measuring the temperature dependency of the capacity of the sample condenser as is described below, where a mica plate was used to prevent the electric breakdown of the condenser, so that only a small fraction of the total applied voltage V acted on the sample. The ratio V_1/V_2 will be proportional to the ratio of the impedance of the mica plate to that of the sample, and in our experiment it was nearly of the order of 10, but V_2 did not exceed the breakdown voltage of a sample. The measuring frequency of the capacity was 5 mc and the field applied to the sample was an alternating field of 60 c.

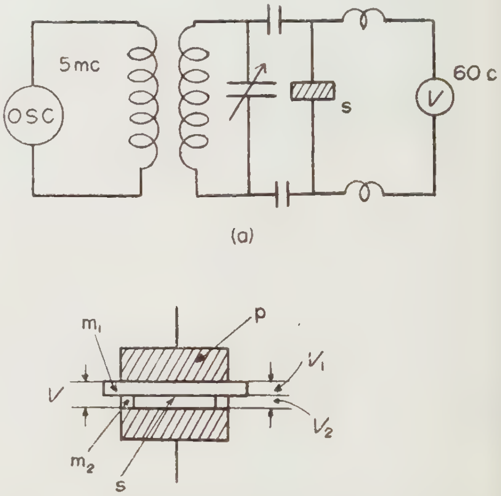

Fig. 1. (a) Measuring circuit. s: sample condenser.
(b) Sample condenser. p: condenser plate, m_1: mica plate (2/100 mm), m_2: mica speck (2/100 mm) s: sample.

The normal capacity *versus* temperature curve for the sample, which suffered no treatment, is given in Fig. 2 (a). But, once the strong field of about 20,000 volts per mm (average value) was applied for several hours to the condenser containing the sample in molten state. The feature of capacity *versus* temperature curve in this case changed into the type given in Fig. 2 (b), showing the lower transition point and the indistinct freezing point which are characteristic to the sample of less purity. It is known that the transition point of n-higher alcohol is sensitive to its purity and shifts to the lower temperature side by adding a small amount of impurities such as other alcohols, paraffins, esters, etc. In this case V_2 is considered to be nearly equal to thebre akdown voltage.

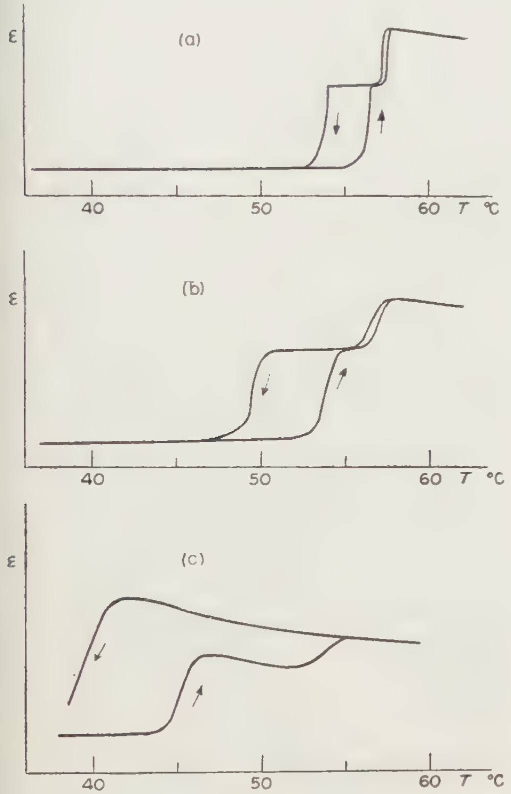

Fig. 2. Temperature dependency of the dielectric constant of octadecyl alcohol suffered various treatments. Each measurement was done under no external field.
(a) Curve for the sample which has been suffered no previous treatment (standard curve).
(b) 800 v of 60 c was applied to the sample condenser for about 3 hours at 60∼62°C.
(c) 800 v was applied again for about 5 hours under the same conditions.

After repeating the treatment mentioned above, the form of the capacity *versus* temperature curve became finally as that given in Fig. 2 (c). The similar strong field was applied to the sample in solid states of α and β_1 phases[1], but no detectable change was observed for the treatment of the same interval of time. Thus, it seems certain that the degree of chemical change of a sample is determined by the time duration during which the sample is exposed to the electric field at the liquid state. This point of view is supported by the following experiment. The dependency of the capacity of a sample upon the applied voltage was measured at each phase of α, β_1 as well as at the liquid phase under the existence of the applied field. It was found that the influence of the external field was not so remarkable in α and β_1 phases (Fig. 3), but in the liquid phase the capacity increased initially with voltage and began to decrease for the voltage exceeding a certain value ($V \approx 15{,}000$ volts per mm). In this last stage the change in the capacity was irreversible and proceeded under the constant applied voltage. The change of the capacity *versus* temperature curve from a type shown in Fig. 2 (a) to those shown in Fig. 2 (b) and (c) occurred only in a sample which had been suffered an irreversible chemical change in the liquid state. In other words, the occurrence of the irreversible chemical change is revealed by the evidence that the dielectric constant of a sample decreases with increasing voltage or time. As a result of this process a part of the original pure alcohol changes into some other substances, and thus the formation of a mixture gives rise to the lowering of the transition point of the sample. By the test in which the fuchsin solution decolourized by SO_2 gas was again coloured by such a damaged

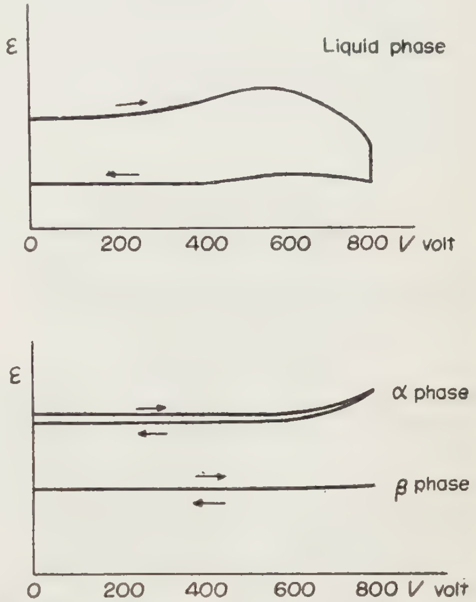

Fig. 3. Voltage dependency of the dielectric constant at each phase (α, β_1 and liquid).

sample, it was found that the main part of new substances produced was probably aldehyde.

The damaged sample was also examined by the electron diffraction investigation at different temperatures, and it was confirmed that the structure change of hexagonal (α) $\rightleftarrows$ orthorhombic (β_1) occurred at the transition point, which was observed in the dielectric investigation. But, the observed Debye-Scherrer rings of the α phase were very diffuse in this case, suggesting the increment of the amorphous part in this phase as a result of the chemical change of the sample. This part of the experiment was carried out by Mr. K. Harada, to whom the author wishes to express his cordial thanks.

Reference

1) J. D. Hoffman and C. P. Smyth: J.A.C.S. **71** (1941) 431.

J. PHYS. SOC. JAPAN **10** (1955) 718~719

On the Galvanomagnetic Effects in n-type Indium Antimonide

By Yasuo KANAI

The Electrical Communication Laboratory,
Nippon Telegraph and Telephone Corps. Tokyo

(Read March 29, 1955; Received May 18, 1955)

In the usual theory of the galvanomagnetic effects in conductors it is assumed that the influences of the magnetic field on the energy states of electrons are small compared to those of scattering processes by the lattice vibrations and/or impurities, and so they can be treated as small perturbations. This condition is expressed by the following relation[1];

$$e\tau H/m^*c \ll \sim 1\ ,$$

where

e; the absolute value of electronic charge.
τ; the collision time of the carrier.
m^*; the effective mass of the carrier.
c; light velocity in vacuum.
H; the magnetic field strength.

and the above relation is expressed also in a more convenient formula;

$$\mu H\times 10^{-8} \ll \sim 1\ ,$$

where

μ; the mobility of the carrier in the unit of cm²/volt.sec.
H; the magnetic field strength in the unit of Gauss.

On the other hand, due to the recent pregresses in the techniques of the preparations of pure homopolar semiconductors, the mobility of the carrier in some of these semiconductors become so high, especially at low temperatures, that the above relation ceases to be valid in the usual experimental conditions. For instance, in pure germanium, the electron mobility is higher than 10^5 cm²/volt.sec. in the temperature ranges below 40°K[2], so the condition, $\mu H\times 10^{-8} > 1$, holds even in such weak magnetic field as 1 kilo Gauss. In such cases, the validity of the usual theory of galvanomagnetic effects may become doubtful.

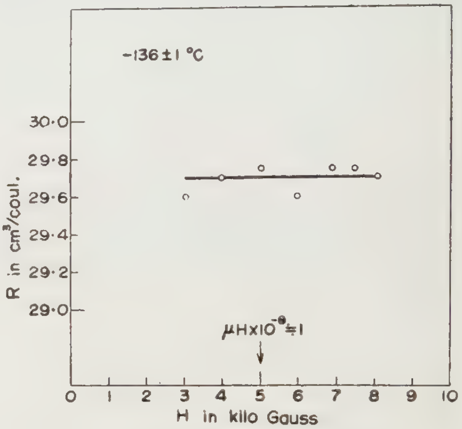

Fig. 1. The magnetic field dependency of the Hall coefficient in n-type InSb.

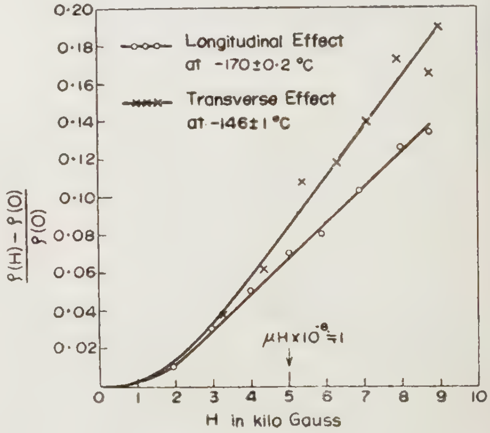

Fig. 2. The magnetoresistance effect of n-type InSb.

To investigate the galvanomagnetic effects in the case of $\mu H\times 10^{-8} \ll \sim 1$, the magnetoresistance and Hall effect of n-type InSb were measured. In this material, the electron mobility was so large[3] that the strong magnetic field was not necessary to realize the above condition, $\mu H\times 10^{-8} \ll \sim 1$, and furthermore as this material was isotropic[4], the analysis of the experimental data may be simple. The samples used here were the polycrystals of n-type InSb prepared by fusion of In and Sb in stoichiometric quantities in vacuum crucibles. The resistivity and Hall coefficient of these samples were measured from room temperature to liquid air temperature, and it was found that these quantities and the electron mobility, which value was about 2×10^4 cm^2/volt.sec. in our samples, had constant values independent of temperatures. The electron density, which was given approximately by the following equation;

$$n=1/ecR\ ,$$

where

R; the Hall coefficient.

was about 2.9×10^{17}/c.c.. As the effective mass of electrons in InSb was as small as 0.03 m⁵⁾, the state density of conduction band was about 1.6×10^{17}/c.c.⁶⁾, so in this sample the electrons were almost degenerated. Therefore, the constancy of resistivity and Hall coefficient would be explained by the scattering process of degenerated electrons by the impurity ions⁷⁾.

The magnetic field dependency of Hall coefficient measured at −136°C was shown in Fig. 1, and it shown that the Hall coefficient had a constant value independent of magnetic field strength. At this temperature the electron was almost completely degenerated, the constancy of Hall coefficient might be reasonable. The transverse and longitudinal magnetoresistance of this sample were measured at low temperatures and these were shown in Fig. 2. It seemed to us that the magnetoresistance data would be unexplainable by the usual theory; for when the electrons are completely degenerated and the sample is isotropic, the magnetoresistance effects would not be expected. So if we consider the existence of magnetoresistance effect in our experiment, and especially if we notice the fact that the magnitude of the longitudinal effect was the same order as that of the transverse one⁸⁾, the magnetoresistance of n-type InSb would be caused by the unusual mechanism, probably the quantization of the electron orbit as was discussed already by Titeica⁹⁾.

Further investigations are now in progress.

References

1) For instance, Wilson: "The Theory of Metals", 2nd edition (1953) 52, 210.
2) Debye and Conwell: Phys. Rev. **93** (1954) 693.
3) Welker: Z. Naturforsch, **7a** (1952) 744; **8a** (1953) 248.
4) Tanenbaum, Pearson and Feldman: Phys. Rev. **93** (1954) 912.
5) Tanenbaum and Maita: Phys. Rev. **91** (1953) 1009.
6) Burstein: Phys. Rev. **93** (1954) 632.
7) Pearson and Bardeen: Phys. Rev. **75** (1949) 865.
8) McDonald and Sarginson: Reports on Progress in Physics, **XV** (1952) 259.
9) Titeica: Ann. Phys. Lpz. **22** (1935) 129.

J. Phys. Soc. Japan **10** (1955) 718~720

On the Inductive Part in the a.c. Characteristics of the Semiconductor Diodes

By Yasuo Kanai

The Electrical Communication Laboratory, Nippon Telegraph and Telephone Corps., Tokyo

(Received May 18, 1955)

The small signal a.c. characteristics of p-n junction diodes of silicon and germanium were measured by the bridge method in the frequency range from 3.k.c.p.s. to 5m.c.p.s., at various temperatures and various bias voltages. The a.c. characteristics measured at zero and negative bias voltages were well explained by the Shockley's theory¹⁾. But in the measurements at forward bias voltages, it was found that the susceptance began to decrease at high frequency, and thus experimental results deviated from the Shockley's theory. These decrement of susceptance at high frequency range

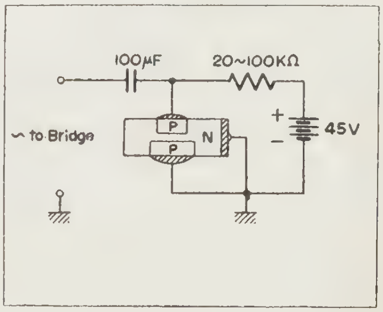

Fig. 1. Schematic diagram of the circuit by which the small signal a.c. characteristic of the hole flow in the n-region was measured.

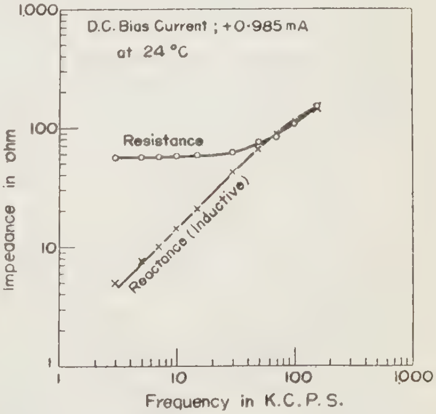

Fig. 2. The impedance curve of a junction transistor which was connected as shown in Fig. 1. Notice that the reactance was completely inductive.

would be explained by introducing an inductive part which were in series with the impedance of the barrier of the p-n junction. Independent of our experimental results, H. Shimura in our Laboratory found the similar inductive part in the measurement of the small signal a.c. characteristics of the point contact germanium diodes at forward bias in the frequency range of the several m.c.p.s.. Considering these experimental results, it would be sure that such inductive part in the a.c. characteristics of the semiconductor diodes arise only when they were biased positively, namely this phenomenon occurs in accompany with the hole injection.

On the other hand, it was well known already that the forward resistance of point contact and p-n junction diodes of germanium was higher in the high frequency than in the low frequency. It was investigated in detail by Bray and Gossick²⁾ and this phenomenon could be explained as follows; it was caused by the decrement of the bulk resistance by the hole injection, namely by the conductivity modulation. As this phenomenon, the higher resistance at higher frequency, is equivalent with the inductive part, it may be reasonable to assume that the origin of the inductive part is the conductivity modulation caused by the hole injection. Following this assumption, the large conductivity modulation is necessary in order to obtain the large inductive part. When the p-n-p junction transistor is connected and biased as shown in Fig. 1 the a.c. characteristic is determined chiefly by the current flow through the thin n-region. Then the large conductivity modulation in this region will occur, and hence large inductive part will be expected. The experimental result, which is shown in Fig. 2, indicate that this is the case.

Now the existence of the inductive part can be calculated by the following very simple assumptions; The a.c. current i, which is to be considered here, will be given approximately by the next formula;

$$i=\Delta p\cdot q\cdot(\mu_p+\mu_n)\cdot E\ ,$$

where

Δp; the total number of injected holes in the n-region.

q; the absolute value of the electronic charge.

u_p, μ_n; the mobilities of holes and electrons.

E; the electric field strength in the n-region.

For simplicity, the field strength E is assumed to have a constant value indesendent of the position in the n-region. When sinusoidal small a.c. voltage $ve^{i\omega t}$ is applied, the hole density which is injected from p-region is given1) by;

$$pe^{i\omega t}=(qp_n/kT)\cdot e^{qV/kT}ve^{i\omega t}\ ,$$

where

p_n; the hole density in the n-region.

V; the d.c. bias voltage.

On the other hand, Δp is given approximately by the following formula;

$$\Delta p(i\omega t)=C\int_0^{bT}pe^{i\omega(t-t')}e^{-t'/\tau}b\,dt'$$

$$=Cpe^{i\omega t}\frac{b\tau}{1+i\omega\tau}[1-\exp(-T/\tau-i\omega T)]\ ,$$

where

C; the cross section of the n-region.

τ; the lifetime of the injected holes.

b; the velocity at which the injected holes travel in the n-region.

T; the time which is required the injected holes to travel across the n-region.

Using the equations calculated above, the a.c. impedance (z) is given approximately as follows;

Case (1). When the n-region is wide enough, and the condition, $T\gg\tau$, is valid, then

$$\Delta p(i\omega t)\fallingdotseq C\cdot pe^{i\omega t}\frac{b\tau}{1+i\omega\tau}\ ,$$

so,

$$z=\frac{ve^{i\omega t}}{i}\fallingdotseq A\times(1+i\omega\tau)\ ,$$

where A is a real quantity in which $i\omega$ is not included. Thus in this case there is inductive part, and this is the case of the usual p-n junction or the point contact diodes.

Case (2). When the n-region is so narrow that the condition, $T\ll\tau$, is valid, and furthermore the frequency of applied a.c. voltage is so low that the condition, $\omega T\ll 1$, is valid, then

$$\Delta p(i\omega t)\fallingdotseq C\cdot pe^{i\omega t}\cdot bT\{1-(T/2\tau)(1+i\omega\tau)\}\ ,$$

so,

$$z=\frac{ve^{i\omega t}}{i}\fallingdotseq B\times\{1+i\omega(T/2)\}\ ,$$

where B is the same quantity as A. In this case, there is also inductive part, and this is the case of our experiments on the p-n-p junction transistor as it was shown in Figs. 1 and 2.

To explain the a.c. characteristics of the semiconductor diode completely, it is necessary to obtain an exact solution of the equation of the hole flow in n-region, but it is very difficult3). However, considering the above calculations, which was based on the very simple assumptions and concerned with the effects of condtctivity modulation only, it might be reasonable to suppose that the inductive part, at least a part of it, will be due to the conductivity modulation caused by the hole injection.

References

1) Shockley: B.S.T.J. **28** (1949) 435.
2) Bray and Gossick: Phys. Rev. **91** (1953) 1011.
3) van Roosbroeck: Phys. Rev. **91** (1953) 282.

J. Phys. Soc. Japan **10** (1955) 000~000

Specific-Heat versus Temperature Curves of Aged Cu-Be Alloys

By Ken-ichi Hirano

Department of Physics,
Tokyo Institute of Technology
Oh-okayama, Meguro-ku, Tokyo

(Received May 20, 1955)

Supersaturated solid solution of beryllium in copper is obtained when it is quenched from the temperature at which only one phase is stable. The breakdown of the supersaturated solid solution during aging at various temperatures has been investigated using a 1.8 weight percent beryllium alloy by means of Nagasaki-Takagi's high temperature calorimeter.

Before quenching, the specimens were held at 800°C for more than 4 hours for the solution heat treatment.

Specific-heat versus temperature curves have been obtained on the alloys aged at 130°, 190°, 300° and 400°C respectively after quenching. The heating rate employed was about 2°C per minute which seems to be suitable to detect the changes in the apparent specific-heat with sufficient accuracy for the present investigation.

Figs. 1 and 2 show the specific-heat versus temperature curves obtained on 130°C- and 300°C-aged specimens respectively. The period of aging is described in the figures. If the specimen is reheated immediately after quenching, the dashed curve is obtained. From the known values of the specific-heat of pure copper and pure beryllium, the specific-heat of the alloy is calculated and shown in the figures as denoted by XY. XY should be the specific-heat versus temperature curve of the alloy when no change in atomic configuration takes place.

The specific-heat versus temperature curves obtained show marked deviations from XY at higher than 160°C. The heat evolution (diminution of the apparent specific-heat) between 160° and 450°C may be attributed to the precipitation of the new phase during heating. Above 450°C an absorption of heat is observed, which seems to be due to re-solution of the precipitate.

It will be noted, as seen in Fig. 1, with 130°C-aged alloy, another heat absorption is observed at about 200°C which represents the energy to redissolve a product formed at 130°C. This effect has not been reported by the previous workers[4]. Very similar phenomena have been observed in low temperature aged Al-Cu alloys[1)-3)].

As in the case of the Al-Cu alloy, above fact may be taken as one suggestion of the formation of Guinier-Preston zone which is an aggregation of solute atoms on some crystallographic planes of the matrix lattice. Other evidence for Guinier-

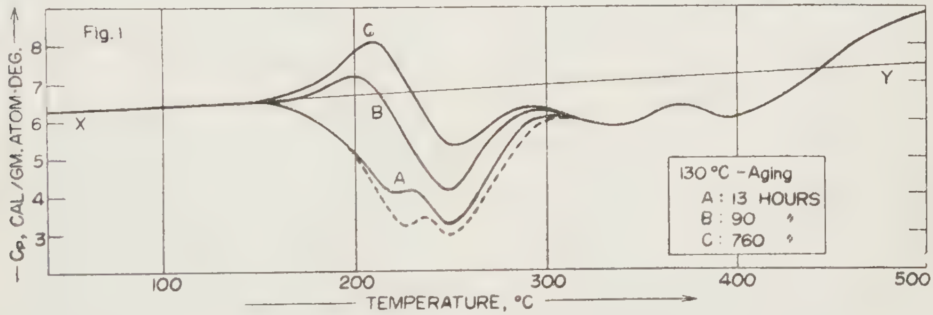

Fig. 1. Specific-Heat *versus* Temperature Curves of 130°C-Aged Alloy.

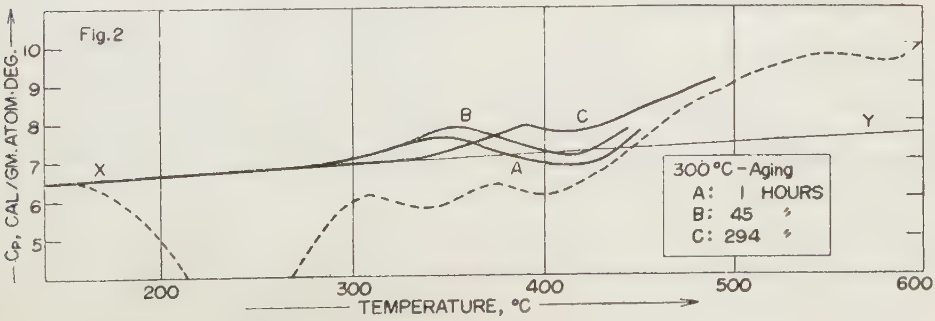

Fig. 2. Specific-Heat *versus* Temperature Curves of 300°C-Aged Alloy.

Preston zone in Cu-Be alloy has been put forward by Guinier and Jacquet on 2.3 weight percent alloy(5),(6). Their x-ray small angle scatter films indicated the presence of beryllium-rich platelets on {100} planes in the early stage of aging.

Fig. 2 shows that some metastable state occurs during aging at 300°C before completion of final γ-precipitation, this result is in agreement with that of Jones and Leech[4] on the 2.5 weight percent alloys and further with the results of X-ray examination carried out by Geisler, Mallery and Steigert[7], who reported the work on the 1.73 weight percent alloy aged at 300°C and suggested the occurrence of γ'' and γ' intermediate structures. Similar process has been also reported on high temperature aged Al-Cu alloys[8].

With 190°C- and 400°C-aged specimens, qualitatively the same curves as in Fig. 2 have been obtained.

Thus it is suggested that the aging characteristics of this system are similar in many ways to Al-Cu age-hardening alloys.

In conjunction with the results of other measurements such as the Young's modulus, hardness and X-ray measurements carried out in co-operation with Tanaka and Mishima, full report will be published later.

References

1) N. Swindells and C. Sykes: Proc. Roy. Soc. **A168** (1938) 237.
2) T. Suzuki: Sci. Rep. Res. Inst. Tohoku Univ. **A1** (1949) 183.
3) K. Hirano: Read at the Meeting of Japan Physical Society at Osaka Univ., Oct. 31. 1954; will be published.
4) F. W. Jones and P. Leech: J. Inst. Metails, **67** (1941) 9.
5) A. Guinier and P. Jacquet: Compt. Rend. **217** (1943) 22.
6) A. Guinier and P. Jacquet: Rev. Metallurgie, **41** (1944) 1.
7) A. H. Geisler, J. H. Mallery and F. E. Steigert: J. Metals, **4** (1952) 307.
8) J. M. Silcock, T. J. Heal and H. K. Hardy: J. Inst. Metals, **82** (1953–54) 239.

J. Phys. Soc. Japan **10** (1955) 722~723

"Step" and "Oscillation" Phenomena in the Collector of A-type Transistors

By M. Kikuchi and Y. Tarui
Electrotechnical Laboratory, Tokyo, Japan

(Received May 20, 1955)

We have already reported about the "step" phenomenon which was found in the backwar direction of Ge point contact rectifiers[1]. That i a sudden decrease of resistance which occurs afte the application of high reverse voltage (>150 V When certain voltage is applied to the rectifie instantaneously in the backward direction, th current remains almost constant for first severa microseconds and it suddenly increases. It ha also been found out that the time τ_s, i.e., the tim spent until the "step" occurs after the applicatio of the voltage, was quite dependent on the produc of the values of the voltage and the current befor the "step."

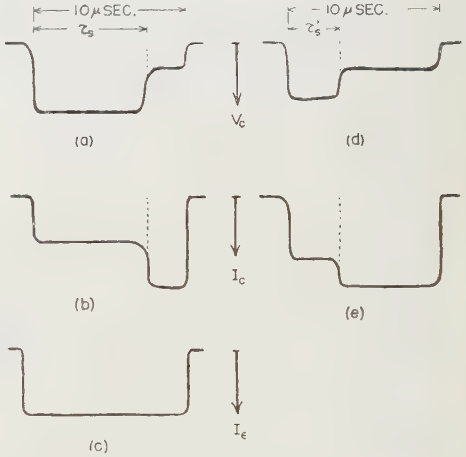

Fig. 1. Shape of V_c, I_c and I.
(a) (b) show the "step" for the case of no emitter current, (d) (e) for the case of I_ϵ pulse like (c) is being applied.

We have proposed a possible explanation assuming that the "step" occurs when the contact temperature reaches to a certain characteristic temperature Θ, and that the contact temperature is raised by the self-heating. Experimental results seemed to support this physical picture, and Θ was estimated to be about 90°C for our samples[2].

Recently, we have observed new effects about this phenomenon with point contact transistors using the collector as a diode, and the emitter a a subsidiary electrode.

It has been found out that under the presence of hole current from the emitter, the "step" occurred far sooner than in the case of no emitte current. Typical results are shown in Fig. 1.

When the emitter circuit is being opened, the collector voltage V_c and the collector current I show "step" as in Fig. 1 (a), (b). If an emitte current pulse (Fig. 1 (c)) is applied to the abov situation, the shape of V_c and I_c varies like Fig 1 (d), (e). As is shown, the time τ_s is far reduce by the emitter current.

We next measured the values of V_c and I_c be fore the "step" as a function of the emitter current, always adjusting V_c so as the "step" to occur just certain value of τ_s after the application of V_c. The product of V_c and I_c decreased almost linearly with the emitter current as shown in Fig. 2. It must be noticed that almost the same results were obtained by the emitter current pulse of 1 μ-sec. length applied just before the step.

One possible explanation may be as follows. Sudden decrease of the collector reverse resistance occurs when the hole concentration n_h just beneath the collector contact reaches to a certain critical amount $n_h{}^c$. The hole concentration n_h can be increased by the self-heating of the contact and/or by the hole injection from the emitter. From this model, it is expected that the power dissipation ($\propto V_c \cdot I_c$) before the "step" for a fixed τ_s will decrease linearly with the emitter current just as shown in Fig. 2.

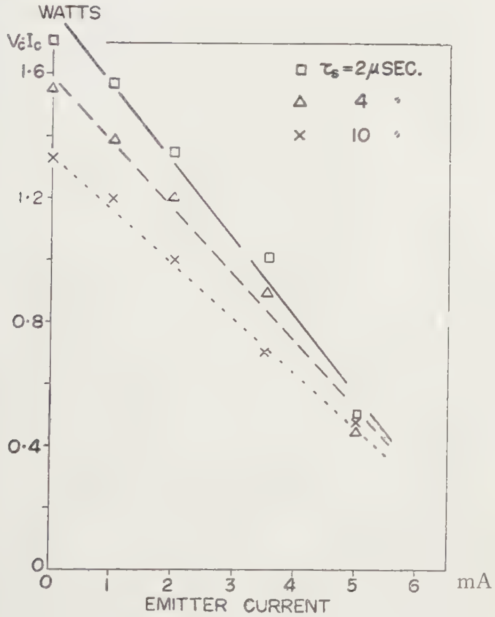

Fig. 2. Power *versus* emitter current relation.

"Oscillation" has been sometimes observed in these transistors even if the emitter circuit was kept opened, but it was stabilized by connecting the emitter to the base directly (or by an a. c. means). The shape of such an oscillation is shown in Fig. 3. This photograph shows the oscillation in the collector voltage when the emitter is directly grounded. The oscillation seemed to follow just after the "step." A possible explanation is as follows.

When the "step" occurs, the potential just below the emitter contact abruptly falls to a large negative value, which in turn enforces large hole injection from the emitter. The collector current, therefore, increases but it will become to a situation soon that the power dissipation at the collector contact begins to decrease, since the collector voltage decreases very fast. Hence, the contact temperature goes down. This cycle repeats again and again in the mood of relaxation oscillation oscillator. The frequency of the oscillation increased when the transistor was heated externally, which is consistent with the model mentioned above.

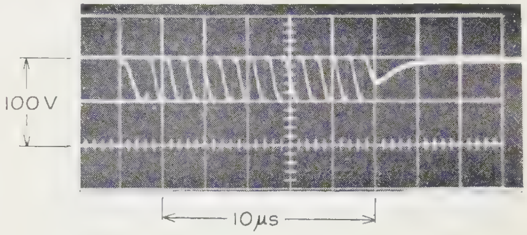

Fig. 3. Shape of the oscillation in V_c when the emitter current is flowing.

Strictly speaking, some other factors, such as multicontact structure of the contact, must be taken into account for more detailed and general explanation. More detailed investigations are now being undertaken.

References

1) M. Kikuchi and Y. Tarui: J. Phys. Soc. Japan **9** (1954) 642.
2) Lempicki and Wood: Proc. Phys. Soc. **67** (1954) 328.
They reported similar investigation independently.

J. PHYS. SOC. JAPAN **10** (1955) 723~724

Multipolarization in the Hexagonal Barium Iron Oxide Magnets

By Buichi KUBOTA and Chisato OKAZAKI
Research Section, Matsushita Electric Industrial Co., Ltd., Kadoma-cho, Kitagawachi-Gun, Osaka, Japan

(Received June 13, 1955)

In this paper some experimental results are reported on the unusual phenomena of multipolarization found in the magnetization process of barium iron oxide magnet: $BaO \cdot 6Fe_2O_3$. In the present experiment, we used rod-shaped polycrystalline specimens of this material (length: 50 mm, diameter: 3.5 mm and 1.5 mm). At first the specimen was magnetized to its saturation in the longitudinal field, then the field was removed. When it was heated up to about 350–400°C, a suitable strength of magnetic field was applied in opposite direction; and it was cooled to room temperature without applying the magnetic field. Then it was found that the specimen was divided into several regions, each of which was magnetized in the direction parallel or antiparallel to the axis of the rod. These regions could be observed by sprinkling the iron powder on the specimen (Fig. 1 and 2). The volume of the reversed regions increased with an increase of the strength of applied magnetic field of opposite direction. Several important points concerning this phenomenon are as follows:

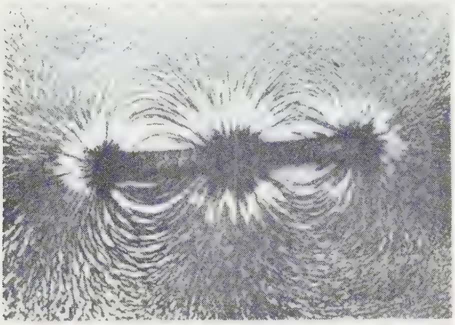

Fig. 1.

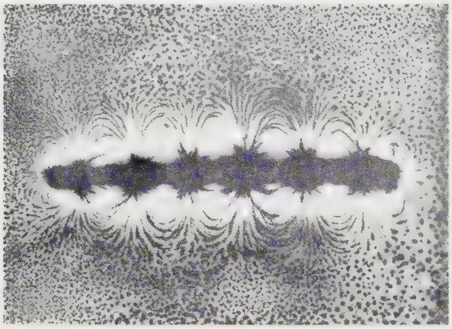

Fig. 2.

Iron powder indicates the direction of magnetization of alteanately alined poles.

The magnetic field 3000 *Oe* was applied, when the temperature of the specimens was 350°C at their centre and temperature gradient in the longitudinal direction were as follows:

Fig. 1. 12°C/cm at the centre, and

Fig. 2. About 40°C/cm at the six boundary points, where the direction of the magnetization were reversed and the sign of the temperature gradient at each points changes alternately. The length of the specimen in Fig. 2 was 70 mm.

1. Effects of the temperature at which the reverse magnetic field was applied.

When the reverse magnetic field was applied above 300°C and when the temperature gradient along the longitudinal axis of the specimen was considerably large the specimen began to reverse its magnetization at the part of higher temperature. When the temperature gradient was large, the boundary between two regions was clear. As the temperature gradient decreased, the boundary become broad and obscure. When the reverse magnetic field was applied below 300°C, the specimen began to reverse its magnetization at the part of lower temperature and the boundary was broad and not so distinct as that above 300°C. These phenomena may be explained by the fact that the coercive force-temperature curve has a maximum about 300°C and its slope is steeper at the high temperature side than at the low temperature side.

2. Effects of grain size.

The finer the grain size was, the clearer the boundary was. The specimen which had the grains of various size began to reverse its magnetization at the part where the large grains were included and showed the multipolarization even where there was no temperature gradient. These phenomena hardly occurred in the specimens composed of coarse grains (larger than about 2–3 μ) even under larger temperature gradient.

3. Effects of internal field.

These phenomena were not observed in the specimen with no temperature gradient and with uniform grain size distribution. But when the reversely magnetized chip of the specimen was attached to one end of such a specimen, the specimen began to reverse its magnetization at the part where the chip was attached. This may be explained by the local field which the oppositely magnetized chip or region produces. Besides this, there is a demagnetizing field acting on the whole unreversed region. When the resultant of these internal fields and the external field, which act on the grain near the boundary, exceeds the value of the turn over field strength of the grain, the magnetization of the grains near the boundary reverses its direction and accordingly the boundary displaces.

In many cases the nucleus of the formation of reversed regions would be the large grains included in the specimen. And the internal fields produced by the reversely magnetized large grains would play a rôle in reversing the magnetization of the neighbouring grains.

The authors express their thanks to Dr. K. Yosida for his helpful discussions. Acknowledgment is made to Dr. T. Suita, Mr. S. Kisaka and the other members in this laboratory for their assistance.

Reference

1) G. W. Rathenau: Rev. Mod. Phys. **25** (1953) 297.

J. PHYS. SOC. JAPAN **10** (1955) 725~726

On an Empirical Formula for the Ferromagnetic Anisotropy Constant in Cubic Crystals

By Mikio YAMAMOTO

Research Institute for Iron, Steel and Other Metals, Tōhoku University, Sendai

(Received June 17, 1955)

Previously the present author[1-3] indicated experimentally that the absolute value of the first ferromagnetic anisotropy constant, K, in cubic crystals was given by a quater of the product of the saturation magnetization, I_s, and the saturation field, H_s, of quasi-isotropic polycrystal, namely

$$|K|=I_sH_s/4\,. \tag{1}$$

For nickel-cobalt and nickel-copper alloys values calculated from this formula and those measured directly with single crystal specimens[4,5] are compared in Figs. 1 and 2. The theoretical ground for this empirical formula will be given in this note.

Theoretically, for quasi-isotropic polycrystal of cubic ferromagnetics the magnetization, I, as a function of the magnetic field, H, in moderately high fields may be expressed, to a first approximation, as[6]

$$I=I_s\left(1-a\cdot\frac{I_s}{H}-b\cdot\frac{8}{105}\cdot\frac{K^2}{I_s^2H^2}\right) \tag{2}$$

The term aI_s/H in parenthesis may be considered, according to Néel[7], as due to the inevitable existence of cavities or non-magnetic inclusions in the specimen. The term $b(8/105)(K^2/I_s^2H^2)$ originates from the reversible rotation of magnetization vectors toward the field direction[8] and the factor b representing the effect of magnetic interaction among crystal grains in the specimen is approximately 1/2, according to Néel[8]. When $|K|$ is very large so that the former term may be negligible as compared to the latter one in moderately high fields, as in iron and nickel[6], Eq. (2) becomes, taking b as 1/2,

$$I=I_s\left(1-\frac{4}{105}\cdot\frac{K^2}{I_s^2H^2}\right). \tag{3}$$

Now, since Eq. (2) shows that I attains I_s when H increases to infinity, the saturation field, H_s, for polycrystal has no meaning theoretically. Practically, however, for most cubic metals and alloys the magnetization attains a saturation at a moderately high field, which may be defined experimentally as the saturation field. Thus, it may be seen that the saturation field depends on the accuracy in the magnetization measurement. Then, denoting this accuracy $(I_s-I)/I_s$ as x, we have, from Eq. (3),

$$|K|=\sqrt{(105/4)x}\cdot I_sH_s \tag{4}$$

As mentioned above, the present author found experimentally that $\sqrt{(105/4)x}=1/4$, which yields $x=1/420$. This value of accuracy is that of an usually adopted ballistic method of the magnetization measurement. Thus, the empirical formula (1) has been interpreted theoretically.

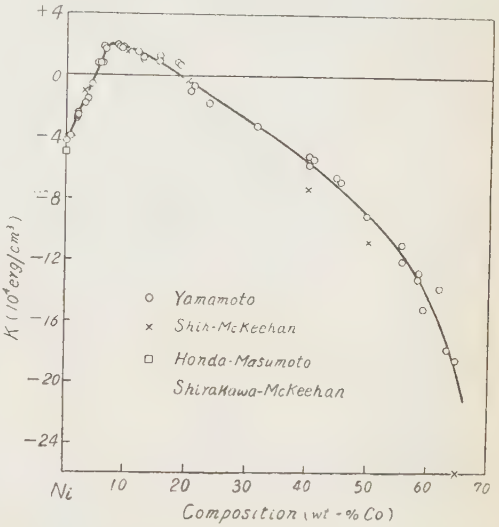

Fig. 1. Ferromagnetic anisotropy constant, K, in face-centered nickel-cobalt alloys, as calculated from Eq. (1) (○) and as measured with single crystal specimens (□ and ×).

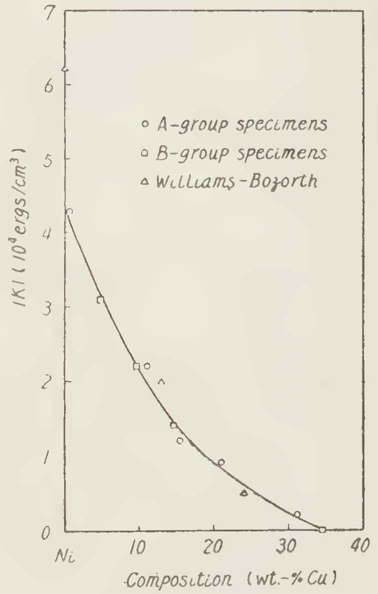

Fig. 2. Absolute values of the ferromagnetic anisotropy constant, $|K|$, of nickel-copper alloys, as calculated from Eq. (1) (○ and □) and as measured with single crystal specimens (△).

The above consideration incidates that if the saturation magnetization of quasi-isotropic polycrystalline specimen of cubic ferromagnetics is measured with an accuracy of approximately 1/400 and the corresponding lowest field or saturation field is determined, then the absolute value of the first anisotropy constant is given approximately by Eq. (1). It is to be noted, however, that when $|K|$ is so small that the term aI_s/H in Eq. (2) may be not negligible, Eq. (1) offers an overestimated value for $|K|$ unless I_s is also small as in nickel-copper alloys3).

In closing, the present author thanks to Mr. S. Taniguchi for helpful discussions.

References

1) M. Yamamoto: Nippon Kinzoku Gakkai-shi (J. Japan Inst. Metals) **11** (1947) No. 11–12; **1** (1949), No. 6 (in Japanese) (Ni-Co alloys).

2) M. Yamamoto and S. Taniguchi: Nippon Kin zoku Gakkai-shi: **17** (1953) 532 (in Japanese (Fe).

3) M. Yamamoto: Sci. Rep. Res. Inst. Tôhok Univ. **A6** (1954) 446 (Ni-Cu alloys).

4) J.W. Shih: Phys. Rev. **50** (1936) 376; L.W McKeehan, Phys. Rev. **51** (1937) 136 (Ni-C alloys).

5) H.J. Williams and R.M. Bozorth: Phys. Rev **55** (1939) 67 (Ni-Cu alloys).

6) See for instance R. Becker and W. Döring *Ferromagnetismus* (1939) p. 167.

7) L. Néel: J. de phys. **9** (1948) 184.

8) L. Néel: J. de phys. **9** (1948) 193.

Errata

Theoretical Study of Residual Resistance of Binary Alloys Containing Foreign Atoms in small Concentration

By Hiroshi FUJIWARA

J. Phys. Soc. Japan Vol. 10 (1955) 339～346

Unfortunately there was an oversight of minus sign in the screened Coulomb potential, formula (18) page 341. Accordingly, the values η_l, ζ_l in Table III in page 343, I_l in Table IV in page 344 and $\Delta\rho$ in Table V in page 345 should be read as follows.

Table III.

Z	Solvent	η_0	η_1	η_2	ζ_0	ζ_1	ζ_2
1	Ag	1.1374 (1.4187)	0.1349 (0.1847)	0.0262	All other minus signs should be read plus		
	Cu	1.0705 *(1.3041)	0.1420 (0.1862)	0.0276	(0.8217)	(0.1585)	
2	Ag	2.0803 (2.6911)	0.2138 (0.4919)	0.0356			

* This case is added in this report.

Table IV.

Z	Solvent	I_1	I_2	I_3	$I_1+I_2+I_3$	σ
1	Ag	0.474 (0.714)	−0.521 (−0.642)	1.052 (1.192)	1.005 (1.264)	6.31 (7.94)
	Cu	0.353 (0.535)	−0.332 (−0.494)	0.690 (0.751)	0.711 (0.792)	4.47 (4.97)
2	Ag	1.529	−4.797	4.285	1.017	6.39

Table V.

Z	Solvent	Calculated $\Delta\rho$	
		$(\Delta\rho)_{p\cdot s}$	$(\Delta\rho)_{p\cdot p}$
1	Ag	3.09 (3.89)	3.15 (4.10)
	Cu	2.50 (3.28)	2.55 (3.33)
2	Ag	3.12	3.35

From these corrected values, we find that the calculated values $\Delta\rho$ which are obtained by using the method of partial waves, are greater than the ones which are calculated with the Born approximation, thus the discrepancy between the theory and experiment is enlarged by the use of partial waves. But, in the case of $Z=2$, this circumstance is inverse. Some parts of the discussions in the previous paper should be modified and will be reported shortly together with the results of the study in which the exchange effects are taken into account.

P. 342 formula (26) first minus sign should be read plus

P. 344 formulas (45) and (47) 〃

P. 344 line −21 right $V(r)=Ze^2\cdots$ should be read $V(r)=-Ze^2\cdots$

P. 345 formulas (53) $\Delta\rho=\frac{2h}{e^2k}\sum_{l=0}^{\infty}[(2l+1)\sin\eta_l-\cdots]$

should be read $\Delta\rho=\frac{2h}{e^2k}p\cdot\sum_{l=0}^{\infty}[(2l+1)\sin^2\eta_l-\cdots]$

P. 343 formula (27) $k=\frac{2\pi mv}{k}$ should be read $k=\frac{2\pi mv}{h}$

PROGRESS OF THEORETICAL PHYSICS

(Founded by H. Yukawa in 1946)

Published for the

Research Institute for Fundamental Physics

The Physical Society of Japan

Progress of Theoretical Physics Vol. 13, No. 1, 1955

On the Plural-Multiple Model of High Energy Meson Showers.............. .... Yoshinosuke TERASHIMA.... 1

Spin-Orbit Coupling in the Pseudoscalar Meson Theory of Nuclear Forces.... .... Gentaro ARAKI.... 13

On the Universality of the Weak Boson-Fermion Interaction................. Kenzo IWATA, Shuzo OGAWA, Hisaichiro OKONOGI, Bunji SAKITA and Sadao ÔNEDA.... 19

The Combinational Method and the Two-Dimensional Ising Model .... R. B. POTTS and J. C. WARD.... 38

Intermediate Coupling Meson Theory of Nuclear Forces, I —*General Formulation*— ....Hiroichi HASEGAWA.... 47

Derivation of the Value of the Coupling Constant g from the Rest Energy of the Nucleon..Ferdinand CAP.... 62

Statistical Models of Ferrimagnetism.............Itiro SYOZI and Huzio NAKANO.... 69

The Properties of the Meson Theoretical Potential in Li^6.................. ....Shoichiro OTSUKI, Tatsuro SAWADA and Syota SUEKANE.... 79

Fluctuations in the Number of Photons in an Electron-Photon Cascade .... Alladi RAMAKRISHNAN and S. K. SRINIVASAN.... 93

Letters to the Editor:

- Effect of Radiation on the Self-Energy of an Electron............... ....D. S. KOTHARI and F. C. AULUCK....100
- On Fermi's Theory of Multiple Production ....K. ONO and K. YOKOI....101
- A Note on the Damping of Pair Formation in Pseudoscalar Meson Theory.................................. T. HAMADA and Y. SHÔNO....102
- Recoil Correction to the Adiabatic Nuclear Potential ....M. SHINDO and K. NISHIJIMA....103
- On the Equivalence Theorem ....Y. TAKAHASHI....105
- On the Structure of Dirac Wave Function ....T. TAKABAYASI....106
- A Tentative Analysis of π-2π Process ....D. ITO and S. MINAMI....108
- Wave Equations in Conformal Space —*Wave Equation for Nucleon*—.. ....Y. MURAI....109
- On the Multiple Scattering of an Electron in Lattice................ ....N. FUKUDA and S. OTAKE....110
- On the Interaction of V-Particles.................................S. IWAO....111
- On Products of Quantities as Distributions........................K. GOTÔ....112
- Beta-Alpha Angular Correlation of Li_8 ....M. MORITA and M. YAMADA....114
- On the Penetrating Showers Produced in Paraffin and Graphite ....I. MIURA, T. MATANO, Y. TOYODA and T. MURAYAMA....115
- Matrix Elements of β-Decay for a Spheroidal Core Model ....M. NOMOTO....117
- On the Thermal Conductivity of Ferromagnetics ....H. SATO....119
- Some Comments on the Specific Heat of Liquid He^3..........Z. MIKURA....120
- On the Specific Heat of a Solution of He^3 in Liquid He^4 ......Z. MIURA....122
- On Double Pion Production in Nucleon-Nucleon Collision............D. ITO....123
- On the Electron-Neutron Interaction ....M. YAMADA....124

Errata 127

Price $ 1.25 per copy
$ 15.00 per year (postage inclusive)
Annual dues for foreign members (individual subscribers)
$ 12.00 (postage inclusive)
〃 for foreign members of the Physical Society of Japan
$ 10.00 (postage inclusive)

Application for members, subscriptions and orders for back mumbers should be sent, directly or through book-dealers, to

The Publication Office
in
Yukawa Hall, Kyoto University, Kyoto, Japan

JOURNAL OF THE PHYSICAL SOCIETY OF JAPAN Vol. 10, No. 9, SEPTEMBER 1955

Angular Correlation of Gamma Rays from Fe^{*56}

By Mitsuo SAKAI*

Department of Physics and Astronomy, the Ohio State University,
Columbus, Ohio

(Received June 7, 1955)

The gamma rays emitted in the decay of Co^{56} were studied by gamma-gamma angular correlation measurements. The results of these experiments permitted the discussion of the energy levels of the daughter nucleus, Fe^{56}. The gamma-gamma coincidence experiment showed the presence of 2.03-Mev. gamma ray decaying to the second excited level. One part of the decay scheme was confirmed by positron-gamma coincidence experiment. The first and the second excited levels were assigned to be 2+ and 4+ respectively from the special consideration on the angular correlation data. The spins of the other levels were discussed also.

§ 1. Introduction

The radiations from Co^{56} were already studied by several groups[1,2]. But, so far, the decay scheme was not quite established. Moreover the spin assignment to the second excited state seems very interesting since the 1.24-Mev. gamma ray associated with this level has not been detected in the decay of Mn^{56} and the main positron component of Co^{56} decaying to this level has a high ft value. Unfortunately the insufficient knowledge of the decay scheme and the Compton tail from higher energy gamma rays have made it impossible to determine the spin value of this level.

The determination of the decay scheme by the improved coincidence apparatus was described in the following section. The angular correlation measurement for the assingnment of the spin of this level and the others was treated in the next section. A method was devised for this purpose in order to avoid the contribution from other higher energy gamma rays to the genuine correlation.

§ 2. Decay Scheme

A. Gamma Ray Measurement by Scintillation Crystals

The gamma ray spectra were measured by two NaI(Tl) crystals, of 1½-in. in diameter by 1½-in. thick and 2-in. in diameter by 2-in. thick, taking advantage of the fact that the ratio of photo peak, pair peak and Compton bump varies with the crystal size. This method is very useful in the case of the presence of many high energy gamma rays such as the present case. The results are presented in Fig. 1. It is very obvious that the 2.03-Mev. peak appeared and was more eminent in the case of larger crystal. This means that the previously reported 2.30-Mev. gamma ray[2] could be attributed to the pair peak of the 3.25-Mev. most energetic gamma ray but its presence is not completely excluded by this measurement.

B. Beta-Gamma Coincidence Experiment

An RCA 5819 photomultiplier tube coupled with a 1-in. in diameter by 1-in. thick crystal of stilbene served as the beta counter and an RCA 5819 photomultiplier tube coupled with a 1½-in. in diameter by 1½-in. thick crystal of NaI(Tl) was used as the gamma counter for the other channel. The coincidence time constant was 5×10^{-7} sec. The curve A in Fig. 2 is the pulse-height spectrum of the beta counter. The curves B and C are the coincidence curves taken with the gamma gate fixed at the peak of 0.845-Mev. and 1.24-Mev. gamma rays respectively. Remarking the end point of each coincidence curve is same, one can confirm clearly the cascade relation of positron component, 1.24-Mev. and 0.845-Mev. gamma rays as proposed by former reports[1,2].

C. Gamma-Gamma Coincidence Experiment.

The same coincidence apparatus as the preceding section was used. The counter of the first channel consisted of a 1½-in. in diameter by 1½-in. thick crystal of NaI(Tl)

---

* Now at Tokyo University, Tokyo, Japan.

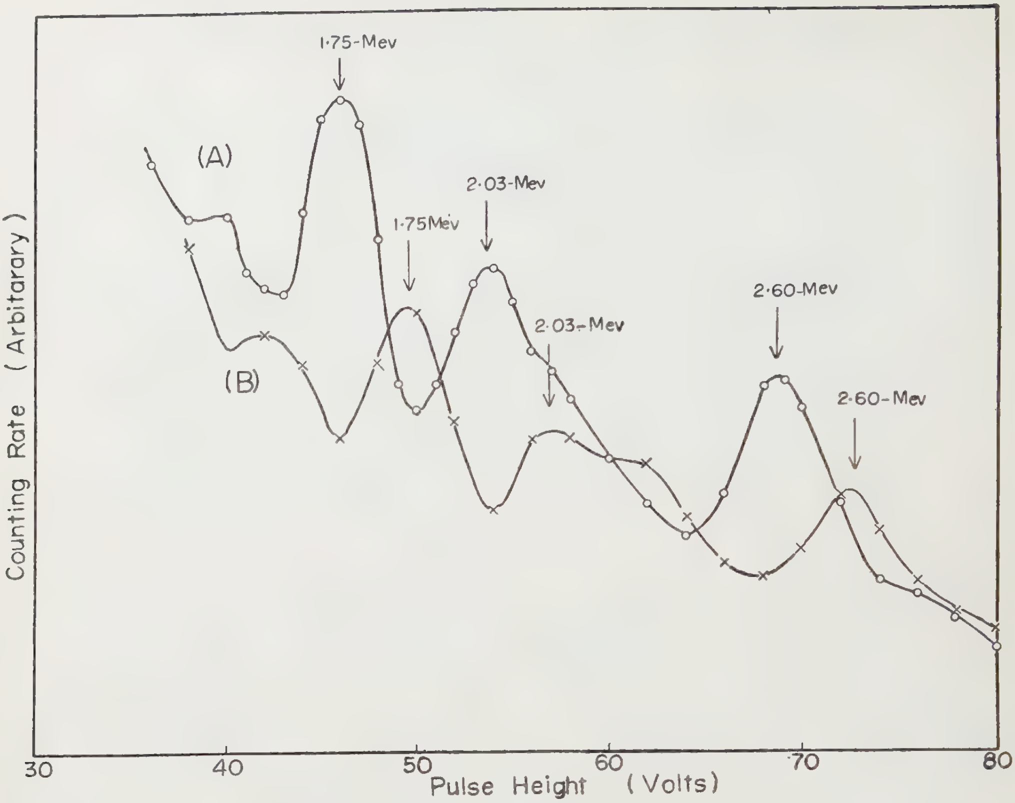

Fig. 1. Gamma ray pulse-height distribution. The curve A was taken with an RCA 6342 photomultiplier tube coupled with a 2-in. in diameter by 2-in. thick NaI(Tl) crystal. The curve B was taken with a DuMont 6292 photomultiplier tube coupled with a $1\frac{1}{2}$-in. in diameter by $1\frac{1}{2}$-in. thick NaI(Tl) crystal.

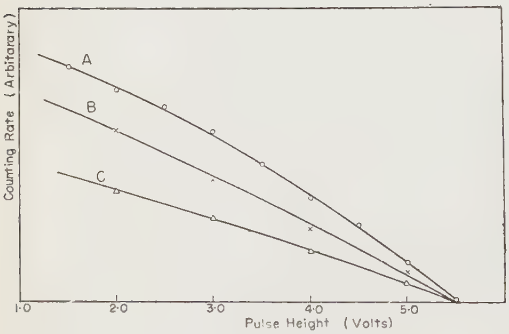

Fig. 2. Positron pulse-height spectrum. The curve A is the single channel spectrum. The curves B and C are the coincidence spectra taken with the gamma ray gate fixed to the peak of 0.845-Mev gamma rays and 1.24-Mev gramma ray respectively.

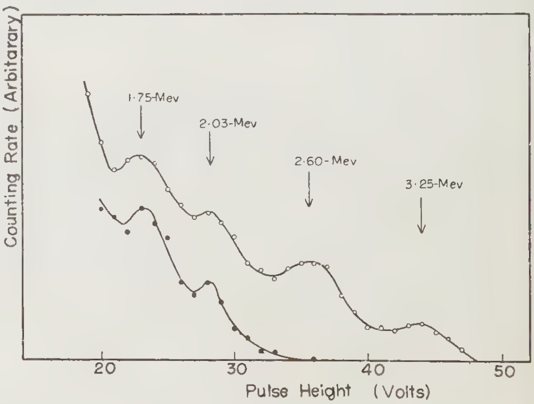

Fig. 3. Pulse-height distribution of high energy radiation from Fe^{56}. The open points are obtained with the channel II. The closed points are the coincidence counts taken with the gate of channel I fixed to the 1.24-Mev peak.

mounted on a DuMont 6292 photomultiplier tube and that of the second channel of a 2-in. in diameter by 2-in. thick crystal of NaI(Tl) mounted on an RCA 6342 photomultiplier tube. A special attention was payed to the genetic relation of 2.03-Mev. gamma ray which was masked by 2.30-Mev. peak in the previous work[2]. The coincidence spectrum was taken by fixing the gate of the first channel at 1.24-Mev. gamma ray. This spectrum is presented in Fig. 3, indicating the cascade relation between 2.03-Mev. and 1.24 Mev. gamma rays. It must be borne in mind that this experiment can not exclude the possibility for the very weak 2.09-Mev. cross-over transition between the second excited state and the ground state.

D. Proposed Decay Scheme.

Based on the above experimental facts, a decay scheme is proposed as is shown in Fig. 4. The 3.25-Mev. and 2.03-Mev. gamma rays are tentatively assumed to have originated from the same excited state. But this point remains to be verified.

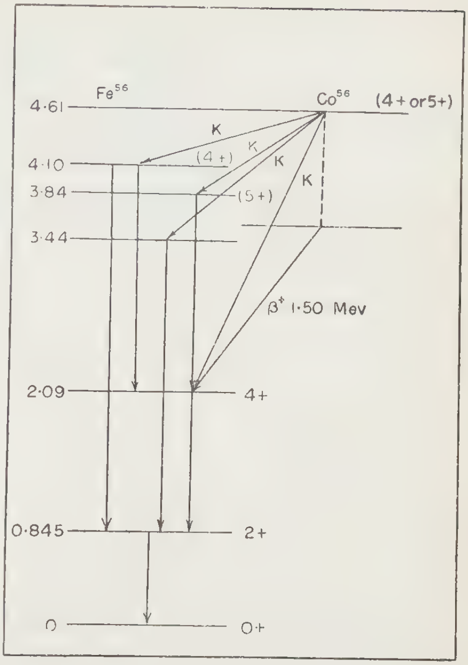

Fig. 4. Proposed nuclear energy levels of Fe^{56}.

§ 3. Angular Correlation Measurement

A. Experimental Procedure

The apparatus used for the angular correlation work was the same as that of the gamma-gamma coincidence experiment. The angular resolution curve was measured by using the annihilation gamma ray. The full width at the half maximum was 30.0°. The geometrical attenuation coefficients were calculated from this curve according to the Church and Kraushaar's method[3] and were found to be 0.866 and 0.607 for G_2 and G_4 respectively (See § 3. B). The experimental results were discussed, in taking account of this effect.

The angular correlation measurement of the 0.845-Mev. and 1.24-Mev. gamma rays was first attempted. As mentioned above, the analysis of this angular correlation data was very complicated because of the contributions from many gamma rays other than the ones in question. In order to avoid this effect, the following method was devised. The counting rate, N_i, at each peak point on the pulse height spectrum were decomposed into the contributions of each gamma ray, n_i' or n_i'' as follows,

$$N_1(p_1')=n_1(p_1')+n_2(p_1')+n_3(p_1')+n_4(p_1')+n_5(p_1')$$

$$N_3(p_3')=n_3(p_3')+n_4(p_3')+n_5(p_3')$$

$$N_2(p_2'')=n_2(p_2'')+n_3(p_2'')+n_4(p_2'')+n_5(p_2'')$$

$$N_3(p_3'')=n_3(p_3'')+n_4(p_3'')+n_5(p_3'')\ ,$$

where each peak point is designated by p_i' or p_i'' and the single prime refers to the first channel and the double prime to the second channel and the subscript numbers 1, 2, 3, 4 and 5 indicate 0.845-Mev., 1.24-Mev., 1.75-Mev., 2.03-Mev. and other higher energy gamma rays, respectively, in the order of their energies. The angular correlations of the following points were measured; $\langle N_1(p_1'), N_2(p_2'')\rangle$, $\langle N_1(p_1'), N_3(p_3'')\rangle$ and $\langle N_3(p_3'), N_2(p_2'')\rangle$. From the decay scheme these angular correlations can be decomposed by the following ways.

$$\begin{aligned}\langle N_1(p_1'), N_2(p_2'')\rangle &= n_1\langle(p_1'), n_2(p_2'')\rangle\\ &+\langle n_1(p_1'), n_3(p_2'')\rangle+\langle n_1(p_1'), n_4(p_2'')\rangle\\ &+\langle n_1(p_1'), n_5(p_2'')\rangle+\langle n_2(p_1'), n_3(p_2'')\rangle\\ &+\langle n_2(p_1'), n_4(p_2'')\rangle+\langle n_3(p_1'), n_2(p_2'')\rangle\\ &+\langle n_4(p_1'), n_2(p_2'')\rangle\ ,\end{aligned}$$

$$\begin{aligned}\langle N_1(p_1'), N_3(p_3'')\rangle &= \langle n_1(p_1'), n_3(p_3'')\rangle\\ &+\langle n_1(p_1'), n_4(p_3'')\rangle+\langle n_1(p_1'), n_5(p_3'')\rangle\\ &+\langle n_2(p_1'), n_3(p_3'')\rangle+\langle n_2(p_1'), n_4(p_3'')\rangle\end{aligned}$$

$$\begin{aligned}\langle N_3(p_3'), N_2(p_2'')\rangle &= \langle n_3(p_3'), n_2(p_2'')\rangle\\ &+\langle n_4(p_3'), n_2(p_2'')\rangle\ .\end{aligned}$$

The angular correlation between 0.845-Mev. and 1.24-Mev. gamma rays is deduced from these equations.

$$\begin{aligned}\langle n_1(p_1'), n_2(p_2'')\rangle &= \langle N_1(p_1'), N_2(p_2'')\rangle\\ &-\langle N_1(p_1'), N_3(p_3'')\rangle-\langle N_3(p_3'), N_2(p_2'')\rangle\\ &+\langle n_1(p_1'), n_3(p_2'')\rangle\left\{1-\frac{n_3(p_2'')}{n_3(p_3'')}\right\}\\ &+\langle n_2(p_1'), n_3(p_3'')\rangle\left\{1-\frac{n_3(p_2'')}{n_3(p_3'')}\right\}\end{aligned}$$

Table I.

θ \ $n_c(\theta)$/min	$\langle N_1(p_1'), N_2(p_2'')\rangle$	$\langle N_1(p_1'), N_3(p_3'')\rangle$	$\langle N_3(p_3'), N_2(p_2'')\rangle$	$\langle a\rangle$
180°	73.89±0.95	17.10±0.46	4.91±0.18	51.88±1.07
157.5°	72.90±0.95	17.29±0.47	4.82±0.20	50.79±1.08
135°	69.53±0.93	18.54±0.48	5.11±0.22	45.88±1.07
112.5°	69.08±0.86	19.25±0.49	5.34±0.23	44.49±1.02
90°	68.42±0.85	19.78±0.49	5.57±0.19	43.07±1.00

$$+\langle n_3(p_3'), n_2(p_2'')\rangle\left\{1-\frac{n_3(p_1')}{n_3(p_3')}\right\}$$
$$+\langle n_1(p_1'), n_4(p_3'')\rangle\left\{1-\frac{n_4(p_2'')}{n_4(p_3'')}\right\}$$
$$+\langle n_2(p_1'), n_4(p_3'')\rangle\left\{1-\frac{n_4(p_2'')}{n_4(p_3'')}\right\}$$
$$+\langle n_4(p_3'), n_2(p_2'')\rangle\left\{1-\frac{n_4(p_1')}{n_4(p_3')}\right\}$$
$$+\langle n_1(p_1'), n_5(p_3'')\rangle\left\{1-\frac{n_5(p_2'')}{n_5(p_3'')}\right\}.$$

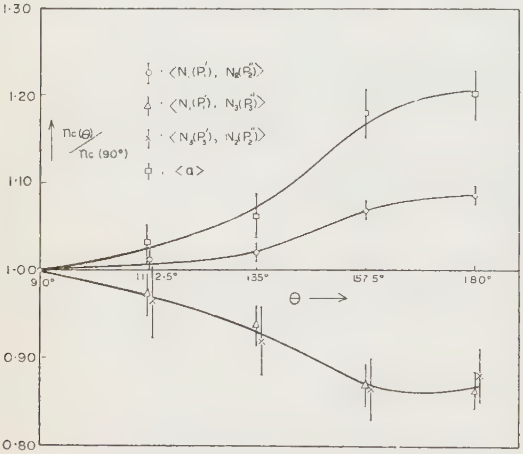

Fig. 5. Angular correlations of $\langle N_1(p_1'), N_2(p_2'')\rangle$, $\langle N_1(p_1'), N_3(p_3'')\rangle$, $\langle N_3(p_3'), N_2(p_2'')\rangle$ and $\langle a\rangle$. The data are presented as a function of $n_c(\theta)/n_c(90°)$.

It is easy to obtain the pulse height distribution of $n_3(p_1')$ being equal to $n_3(p_3')$ and of $n_3(p_2'')$ being equal to $n_3(p_3'')$ by the appropriate choice of the crystal size and the gate width*. Then the following formula is obtained.

$$\langle n_1(p_1'), n_2(p_2'')\rangle=\langle N_1(p_1'), N_2(p_2'')\rangle$$
$$-\langle N_1(p_1'), N_3(p_3'')\rangle-\langle N_3(p_3'), N_2(p_2'')\rangle$$
$$+\langle n_1(p_1'), n_4(p_3'')\rangle\left\{1-\frac{n_4(p_2'')}{n_4(p_3'')}\right\}$$
$$+\langle n_2(p_1'), n_4(p_3'')\rangle\left\{1-\frac{n_4(p_2'')}{n_4(p_3'')}\right\}$$
$$+\langle n_4(p_3'), n_2(p_2'')\rangle\left\{1-\frac{n_4(p_1')}{n_4(p_3')}\right\}$$
$$+\langle n_1(p_1'), n_5(p_3'')\rangle\left\{1-\frac{n_5(p_2'')}{n_5(p_3'')}\right\}.$$

From the pulse height distribution of 2.19-Mev. gamma ray of Pr^{144}, we have a good reason to believe of $n_5(p_2'')\approx n_4(p_3'')$ and of $n_4(p_1')\approx n_4(p_3')$. And $n_4(p_2'')$ should be nearly equal to $n_5(p_3'')$ because the points p_2'' and P_3'' lay on the Compton plateau of pulse height spectrum of the high energy gamma rays. Since $\langle n_1(p_1'), n_4(p_3'')\rangle$, $\langle n_2(p_1'), n_4(p_3'')\rangle$, $\langle n_4(p_3'), n_2(p_2'')\rangle$ and $\langle n_1(p_1'), n_5(p_3'')\rangle$ are all small quantity, the last four terms are the product of two small quantities. Therefore the formula

$$\langle n_1(p_1'), n_2(p_2'')\rangle=\langle N_1(p_1'), N_2(p_2'')\rangle$$
$$-\langle N_1(p_1'), N_3(p_3'')\rangle-\langle N_3(p_3'), N_2(p_2'')\rangle$$
$$\cdots\cdots\ \langle a\rangle\,,$$

can be considered as a good approximation. The results of these three angular correlation data and the value of $\langle a\rangle$ are tabulated in Table I. Each angular correlation curve was presented as a function of $n_c(\theta)/n_c(90°)$ in Fig. 5 where $n_c(\theta)$ is the coincidence counting rate at the angle θ.

B. Discussion of the Results

The correlation function is generally described as $W(\theta)=1+G_2A_2P_2(\cos\theta)+G_4A_4P_4\cdot(\cos\theta)$, where G_2 and G_4 are the attenuation coefficients and A_2 and A_4 are the angular correlation coefficients. For the following discussion G_2 and G_4 are regarded as the geometrical attenuation coefficients. From the experimental results the most probable values of G_2A_2 and G_4A_4 can be deduced by the least square method and A_2 and A_4 are found to be 0.126±0.014 and 0.045±0.033 respectively. Since the spin and parity of the first excited state was assigned to be 2+, the experimental values A_2 and A_4 were compared with the theoretical correlation coefficients calculated for the possible decay sequence such as $j_2(Q+D)2(Q)0$, assuming the intensity ratio δ^2 and 0° or 180° relative nuclear phase[4]. Two sequences were found to be passable for the comparison with the experimental values. The one is the sequence $4(Q)2(Q)0$ of which A_2 and A_4 are 0.102 and 0.0091 respectively and the other is the sequence $2(2.56\%Q-D)2(Q)0$ of which A_2 and A_4 are 0.126 and 0.0082 respectively. The angular correlation coefficients as a function of $|-\delta|$ for the decay sequence $2(Q-D)2(Q)0$ are presented in Fig. 6. Those for the decay sequence $4(Q)2(Q)0$ and of the experimental values are also put on the same figure.

---

* The required pulse-height distribution was obtained experimentaly, by making use of the spectra of 1.12-Mev gamma ray of Zn^{65}, 1.51-Mev gamma ray of K^{42} and 2.19-Mev gamma ray of Pr^{144} and by interporating to the case of 1.75-Mev gamma ray.

For the further comparison the results were examined in taking account of two effects. The first is that of the resolution curve. The resolution curve was assumed to be same for all correlation experiments. But this is not the case as pointed out by Lawson and Frauenfelder[5]. The resolution curves of the correlations $\langle N_1(p_1'), N_3(p_3')\rangle$ and $\langle N_3(p_3'), N_2(p_2'')\rangle$ are narrower than that of $\langle N_1(p_1'), N_2(p_2'')\rangle$ because the former correlations contain the gamma rays of which the energies are higher than that of the latter one. If the attenuation coefficients G_2 and G_4 of $\langle N_1(p_1'), N_3(p_3'')\rangle$ and $\langle N_3(p_3'), N_2(p_2'')\rangle$ are assumed to be 10% larger than those of $\langle N_1(p_1'), N_2(p_2'')\rangle$, 0.33 counts per min. should be subtracted from the counting rate of $\langle a\rangle$ at 180° in order to reduce all resolution curves to that of $\langle N_1(p_1'), N_2(p_2'')\rangle$.

The next effect is the annihilation gamma rays from the positron component. Since the positron component has a cascade relation to the 0.845-Mev. and 1.24-Mev. gamma rays, there is a possibility that these gamma rays impinge on the counter in coincidence with the annihilation gamma rays.

This case can take place in the counting of $\langle N_1(p_1'), N_2(p_2'')\rangle$ at 180°. The positron may annihilate at the inside of the source, the source holder and both of counter windows. This probability was estimated taking account of the geometrical configuration of the apparatus and the branching ratio of positron component. The contribution was found to be 0.7% of the coincidence counting rate of $\langle a\rangle$ at 180° which corresponds to 0.36 counts per min.

In taking account of these two effects the angular correlation coefficients A_2 and A_4 were recalculated and were found to be 0.112 and 0.038 respectively. Since these values were deduced by using G_2 and G_4 calculated by the resolution curve for the annihilation radiation, the true values should be lower than these values. Any way, the situation is so delicate* that it seems almost impossible to decide from the above experimental data which one of these two alternatives is correct.

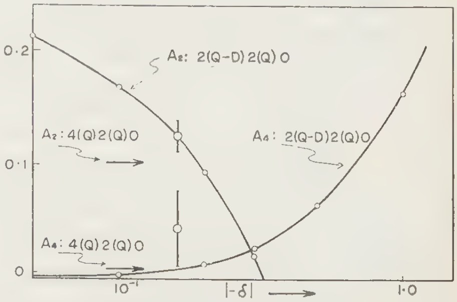

Fig. 6. Angular correlation coefficients A_2 and A_4 as a function of $|-\delta|$ for the decay sequence $2(Q-D)2(Q)0$. The angular correlation coefficients for the decay sequence $4(Q)2(Q)0$ are indicated by arrows. The experimental values are also presented with the probable error.

However the following discussion leads to the favorable conclusion for the decay sequence $4(Q)2(Q)0$. It is easy to see from Fig. 5 that the angular correlation functions of $\langle N_1(p_1'), N_3(p_3'')\rangle$ and $\langle N_3(p_3'), N_2(p_2'')\rangle$ are same within the experimental error. This fact can be satisfied if any gamma ray decaying to the second excited state have always the same angular correlation for both of the 1.24-Mev. and 0.845-Mev. gamma rays**. One can deduce easily from the theory[4] that this condition can be fulfilled only in the case of the decay sequence $j_3(L_2)j_2(Q)2(Q)0$. This reasoning might exclude the altanative sequence $2(2.56\% Q-D)2(Q)O$[*].

---

* For instance if the value of δ is taken as -0.195, A_2 and A_4 for the decay sequence $2(Q+D)2(Q)0$ become 0.102 and 0.012 respectively, while those for the decay sequence of $4(Q)2(Q)0$ are 0.102 and 0.0091.

** In this discussion a very small term of $\langle n_1(p_1'), n_5(p_3'')\rangle$ was neglected.

The angular correlation $\langle N_4(p_4'), N_2(p_2'')\rangle$ was also measured. Then the $\langle n_3(p_3'), n_2(p_2'')\rangle$ and $\langle n_4(p_4'), n_2(p_2'')\rangle$ are deduced from the following formulae.

$$\langle n_3(p_3'), n_2(p_2'')\rangle = \langle N_3(p_3'), N_2(p_2')\rangle - \frac{n_4(p_3')}{n_4(p_4')}\langle N_4(p_4'), N_2(p_2'')\rangle ,$$

$$\langle n_4(p_4'), n_2(p_2'')\rangle = \langle N_4(p_4'), N_2(p_2'')\rangle .$$

These correlation functions are presented in Fig. 7. In this case, $\langle n_3(p_3'), n_2(p_2'')\rangle$ was obtained by putting $n_4(p_3')$ equal to $n_4(p_4')$ as an approximation. The results were compared with the theoretical correlation function for the case of the sequence $j_3(Q \text{ or } D)4(Q)2$. It appeared that the $\langle n_3(p_3'), n_2(p_2'')\rangle$ was consistent with the sequence $3(D)4(Q)2$ or $5(Q)$-$4(Q)2$. But the latter sequence could be adopted, because if the 3.84-Mev. excited level was assigned to be 3+, the cross-over transition gamma ray between this level and the 0.845-Mev. excited level should be expected and there was no evidence for its presence. The $\langle n_4(p_4'), n_2(p_2'')\rangle$ seemed to be comparable with that of $4(Q)4(Q)2$ with a small mixture of D. These theoretical correlation functions are presented also in Fig. 7. But the accuracy of the measurement did not permit to decide the definite decay sequence. These tentative spin assignments were put on the decay scheme in parenthesis. (See Fig. 4)

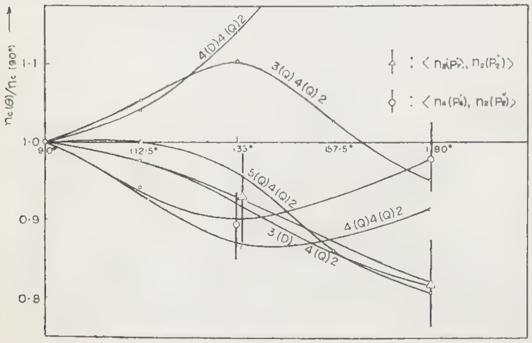

Fig. 7. Angular correlations of 2.03–1.24–Mev cascade and 1.75–1.24–Mev cascade as function of $n_c(\theta)/n_c(90°)$. The theoritical correlation functions for the sequences $5(Q)4(Q)2$, $4(Q)4(Q)2$, $4(D)4(Q)2$, $3(Q)4(Q)2$ and $3(D)4(Q)2$ are presented for the comparison.

§ 4. Conclusion and Acknowledgement

The experiment was intended for the determination of the spin value of the second excited state of Fe^{56} by the angular correlation measurement. But the experimental accuracy did not permit to discriminate clearly the either one of two alternative values 4+ and 2+. In this case it should be stressed that the correlation coefficients for the decay sequences $4(Q)2(Q)O$ and $2(Q+D)2(Q)O$ are too similar to distinguish one from the other by the angular correlation measurement if the quadrupole and dipole mixing ratio of the latter sequence is appropriate. But from the behaviors of the angular correlation functions of $\langle N_1(p_1'), N_3(p_3'')\rangle$ and $\langle N_3(p_3'), N_2(p_2'')\rangle$ the spin of the second excited state was concluded to be favorable for 4+.

This assignment may explain why this level did not appear in the decay of Mn^{56} of which the spin and parity could be 2+[6]. As the configuration of Co^{56} is $(f_{7/2})^{-1}(p_{3/2})^1$ from the shell model, its spin may be 4+ or 5+ according to the Nordheim's rule[7]. Therefore the characteristic of the positron component decaying to this level is the allowed type. The abnormally high log ft value 8.64[2] then might be explained by the very slightly mixed configuration[8] of $(f_{7/2})^{-2}(f_{5/2})^1(p_{3/2})^1$ in this level.

The author would like to express his sincere thanks to Professor J. D. Kurbatov for his constant encouragement of this work. He is indebted to Mr. M. Morita for his valuable theoretical discussion and to Mr. H. J. Sathoff for help with the chemical separation of Co^{56}. This work was supported in part from funds granted to the Ohio State University by the Research Foundation for aid in fundamental research. The author express his deep gratitude to the Ohio State University Development Fund for the grant which made this work possible.

---

[*] Mr. M. Morita kindly checked this reasoning more carefully, making use of his formula for the correlation with intermidiate mixed radiation unobserved. He showed that even if the experimental errors were taken account for, the sequence $j_3(Q+D)2(2.56\% Q-D)2(Q)0$ could not explain the behaviours of $\langle N_1(p_1'), N_3(p_3'')\rangle$ and $\langle N_3(p_3'), N_2(p_2'')\rangle$. He also proved that in the decay sequence $j_3(\gamma_3)j_2(\gamma_2)j_1(\gamma_1)0$ the correlation function $\langle\gamma_3, \gamma_1\rangle$ was in general more isotropic than that of $\langle\gamma_3 \gamma_2\rangle$ if the γ_2 had a mixed characteristic.

References

1) L. G. Elliot and M. Deutsch: Phys. Rev. **64** (1943) 321.
2) Sakai, Dick and Kurbatov: Phys. Rev. **95** (1954) 101.
3) E. L. Church and J. J. Kraushaar: Phys. Rev. **88** (1952) 419.
4) L. C. Biedenharn and M. E. Rose: Revs. Modern Phys. **25** (1953) 729.
5) J. S. Lawson and H. Frauenfelder: Phys. Rev. **91** (1953) 649.
6) F. R. Metzger and W. B. Todd.: Phys. Rev. **92** (1953) 904.
7) L. W. Nordheim: Revs. Modern Phys. **23** (1951) 322.
8) A. De-shalit and M. Goldhaber: Phys. Rev. **92** (1953) 1211.

JOURNAL OF THE PHYSICAL SOCIETY OF JAPAN Vol. 10, No. 9, SEPTEMBER 1955

On the Momentum Spectrum of μ-Mesons near Sea-Level at 24°N

By Shūji FUKUI,
Department of Physics, Osaka University, Osaka
Takashi KITAMURA and Yōjirō MURATA
Institute of Polytechnics, Osaka City University, Osaka

(Received May 24, 1955)

The momentum spectrum of μ-mesons near sea-level and at geomagnetic latitude 24°N has been obtained by means of a magnet cloud chamber. Above 700 Mev/c the results are in agreement with the momentum spectrum derived from Olbert's production spectrum at 24°N. At lower momenta, our spectrum is found to decrease more rapidly than the corresponding spectra derived from differential range measurements. This discrepancy, which is not understood, may be due to some systematic error in either the magnetic deflection or differential range method.

§ 1. Introduction

Study of the geomagnetic latitude effect of the μ-meson spectrum has a important bearing on the analysis of the development of cosmic rays through the atmosphere. Except for the differential range measurements of del Rosario and Dávila-Aponte[1] at 29°N little data has, hitherto, been available at low latitude.

In the present paper we discuss our measurements of the differential momentum spectrum, taken at this latitude, 24°N. In § 4 our results are compared with a differential momentum spectrum derived from Olbert's production spectrum[2]. Our results are also compared with the differential range spectrum found by del Rosario and Dávila-Aponte and various other differential range[3] and momentum spectra[4),5),6)], which have been obtained at high latitude, including the curve given by Rossi[7].

The present investigation, using a magnet cloud chamber, is a part of a general continuation of the study of μ-meson underground in this laboratory.

§ 2. Apparatus and Procedure

The arrangement of the apparatus is shown in Fig. 1. The cloud chamber was of the cylindrical type, 30 cm in diameter and had an illuminated depth of about 9 cm. The thickness of the glass wall was 1 cm. The chamber was filled with argon gas at about one atmosphere pressure. The vapor source was a mixture of equal parts of isopropyl and ethyl alcohol. The chamber and two of the counter trays (A and B) were enclosed in a thermally insulated box where the temperature was held constant to about ±0.2°C.

Three fold coincidences, A–B–C, served to trigger the cloud chamber. Trays A and B

defined the solid angle and trays *C*, *D* and *E* were connected to a hodoscope. These latter three trays were appreciably larger than the area subtended by this telescope solid angle, and were used to set limits on the particles ranges. All of the counters were made of 1 mm wall aluminium tubing with 0.1 mm center-wires made of tungsten. The size and number of counters in each tray is listed in Table I.

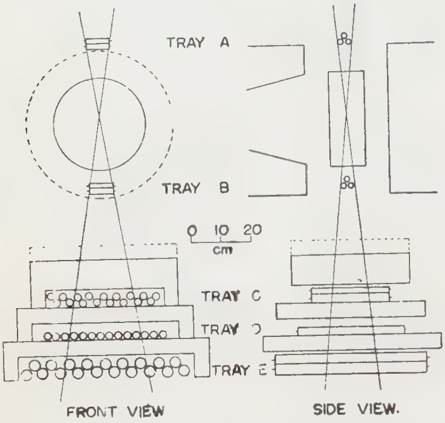

Fig. 1. Arrangement of apparatus for observation of momentum spectrum of μ-mesons.

Table I. The dimensions and the number of the counters.

Tray	Inner Diameter	Effective Length	Number of Counters
A	2.0 cm	6.6 cm	3
B	2.0	6.7	3
C	3.0	24.0	17
D	3.0	35.0	16
E	4.0	54.0	19

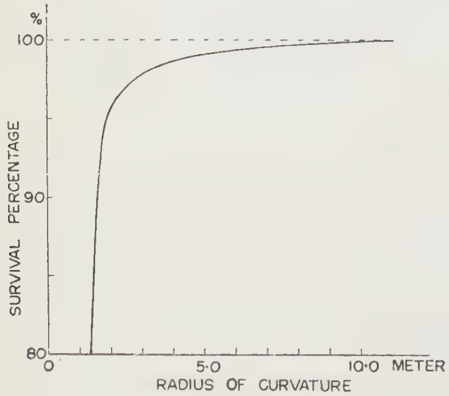

Fig. 2. The correction for the magnet cut-off.

The photographs of the cloud chamber were taken stereoscopically by two "Robot" cameras which were placed in a hole bored in one of the magnet pole pieces. One of the cameras was placed right in front of the chamber and the other made an angle of 6 degrees with the axis of the chamber. The magnification of the image was 1/23. Coordinate plots of the tracks were obtained with a comparator. The plots were fitted to a parobola by means of the method of least square[8]. The curvature and hence also the momentum of each particle was found from the parobola parameters. The maximum detectable momentum in the present work was 22 Bev/c when the field intensity was 7000 gauss.

The total thickness of material (concrete and wood) covering the apparatus was evaluated to be 110 g/cm² air equivalent. Consequently the data obtained in the present observation correspond to 1140 g/cm² atmospheric depth.

§ 3. Measurement of the Momentum Spectrum

We were able to make a very rough measurement of mass for low momentum particles, since the hodoscope data set wide limits on the particles' ranges. Six particles in the momentum range 650–1400 Mev/c had ranges too small for mesons of their measured momenta, and five particles in the momentum range 200–600 Mev/c had ranges too great for mesons of their measured momenta.

Presumably the particles in the first group were protons, and those in the second group electrons, although the cascade process of electrons in lead make the identification, particularly of the latter group of particles, uncertain, if deduced from our data above. The total numbers of particles in each of the above groups were about 300 and 100, respectively, so that the fraction of particles rejected was small, and the final results was influenced hardly at all.

A detailed summary of the data is shown in Table II. The columns headed "Measurement error at middle point" are the errors for the momentum measurements in each of momentum groups, and are those implied from measurements of the curvature of no-field track. The data for positive and negative particles have been examined separately

Table II. Crude and corrected number of particles.

A) Magnetic Field 3000 Gauss.

Momentum Regions	Mid. Pt.	Measurement Errors at Mid. Pt.	Number of Particle	Corrected Number	Abs. Int.
Mev/c	Mev/c	Mev/c			$\mathrm{cm^{-2}\,sec^{-1}\,st^{-1}(Mev/c)^{-1}\times 10^{-6}}$
240–309	275	+9 −7	5	5.88	0.73±0.33
310–449	380	+15 −14	18	20.2	1.25±0.29
450–549	550	+36 −24	41	44.5	1.93±0.30
650–939	795	+68 −57	70	73.3	2.19±0.27
Bev/c	Bev/c	Bev/c			
0.94–1.39	1.17	+0.15 −0.12	114	119	2.22±0.21
1.4 –1.99	1.7	+0.33 −0.24	106	108	1.56 ±0.15
2.0 –2.79	2.4	+0.72 −0.45	88	89.4	0.97±0.11
2.8 –4.09	3.45	+1.72 −0.87	77	77.9	0.52±0.06
4.1 –5.99	5.05	+4.82 −1.66	67	67.4	0.31±0.04
6.0 –10.69	8.35	+7.55 −3.53	68	68	0.13±0.02
>10.7			90	90	
			Total 743	Total 763.6	
		>300 Mev/c	739		
		>2 Bev/c	390		

B) Magnetic Field 6000 Gauss

Momentum Regions	Mid. Pt.	Measurement Errors at Mid. Pt.	Number of Particle	Corrected Number	Abs. Int.
Mev/c	Mev/c	Mev/c			$\mathrm{cm^{-2}\,sec^{-1}\,st^{-1}(Mev/c)^{-1}\times 10^{-6}}$
300–429	365	+8 −5	13	15.2	1.15±0.31
430–619	525	+15 −12	28	30.9	1.60±0.31
620–899	760	+29 −27	60	63.6	2.22±0.31
Bev/c	Bev/c	Bev/c			
0.9–1.29	1.10	+0.06 −0.06	67	69.1	1.69±0.21
1.3–1.89	1.60	+0.12 −0.12	94	95.9	1.57±0.15
1.9–2.79	2.35	+0.31 −0.24	90	91.3	0.99±0.10
2.8–3.89	3.35	+0.67 −0.45	79	79.1	0.71±0.08
3.9–5.69	4.7	+1.37 −0.88	65	65.1	0.40±0.05
5.7–8.29	7.0	+3.6 −1.77	40	40.0	0.15±0.02
8.3–11.79	10.05	+9.55 −3.28	22	22.0	0.062±0.01
11.8–20.69	16.25	+58.75 − 7.15	28	28.0	0.031±0.006
>20.7			32	32.0	
			Total 618	Total 632.3	
		>2 Bev/c	346		

and compared. The momentum distributions for the two groups were the same within the statistical uncertainty. Two different values of the magnetic field were used, 3000 and 6000 gauss, and after the corrections discussed below were applied, the data for the two groups were in agreement. (See Fig. 3).

The amount, by which the measured intensities should be increased owing to the effect of the magnetic field has been computed as a function of the radius of curvature of the tracks. The result of this computation, given in Fig. 2, indicates that the effect of the magnetic field is not a slowly varying function of curvature but something like a step function. In fact, no particle with momentum less than a definite value, which depends on the intensity of the magnetic field, should be, nor was, observed.

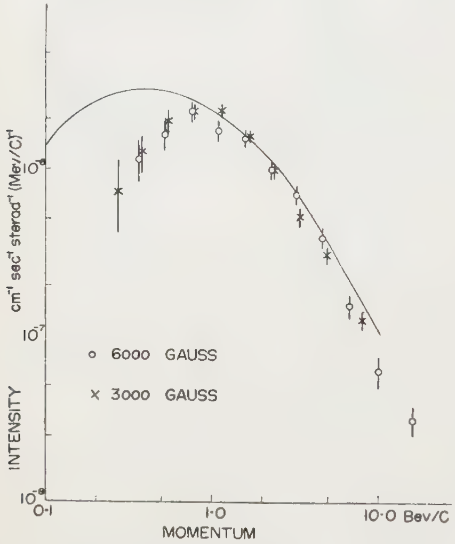

Fig. 3. Corrected momentum spectrum of μ-mesons at 1140 g/cm^2 atmospheric depth obtained in the field of 3000 and 6000 gauss.

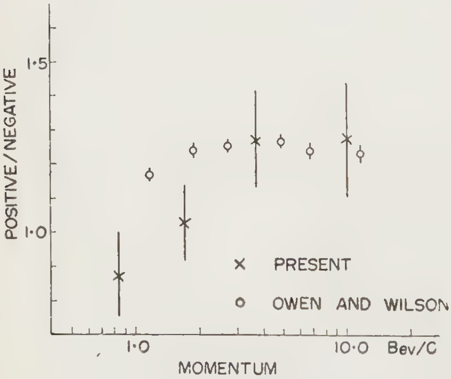

Fig. 4. Ratio of numbers of positive to negative mesons at 24°N geomagnetic latitude.

In addition, a correction for scattering in the material between trays A and B was applied. Particles traversing the 10 cm lead absorber above tray C were scattered in the lead, and so traversed more than the 10 cm of material. Some mesons having momenta in our nominally accepted range, therefore, were excluded because they failed to penetrate as far as tray C. We have made an approximate computation of this effect, and find it to be small. At 250 Mev/c it is an 8% effect, and at 280 Mev/c is only 2%. The corrected numbers of particles for these combined effects are given in the fifth column of Table II.

Our normalization procedure was direct in the sense that we have used the solid angle and effective area of the telescope AB to determine intensities. The aperature of the telescope was 0.57 sterad cm^2. For technical reasons it was not possible to measure the counting rate of the telescope during the cloud chamber operation. Rather, we measured the counting rate (with the field of 3000 gauss on) in an auxiliary experiment. From this measured rate and total number of measured tracks (with 3000 gauss) we deduced an effective operating time, t. We were then able to express the observed number of tracks in a given momentum interval in terms of absolute differential intensity by using this effective time, t, and the known telescope aperture. The 6000 gauss data were normalized to 3000 gauss data by relating the number of tracks with momentum greater than 2 Bev/c.

The intensities, including all corrections, are given in the sixth column of Table II.

§ 4. Discussion and Results

A. Positive Excess

It has been found by many workers that at sea-level positively charged particles predominate over negatively charged ones[9]. This positive excess has been interpreted theoretically considering the developement of the nucleonic component and the production of mesons in the atmosphere. Relative to the behavior of protons, neutrons favor the production of negative mesons. Since at low energies there are more neutrons than protons, one expects the positive excess to diminish as the meson energy decreases. At low geomagnetic latitudes, the number of low energy neutrons, relative to protons of that same energy is less, the above tendency should be enhanced[10]. The positive to negative ratio, r, from the present experiments is shown in Fig. 4. While the statistical precision is poor, there does seem to be a more pronounced falling-off of the ratio, r, at low momenta at this latitude than at 50°N where the data of Owen and Wilson[11] were taken.

B. Anomaly found by Glaser

We find no evidence for or against the anomaly in the momentum spectrum reported by Glaser et al[12]. (See Fig. 5.)

C. The Integral Vertical Intensity at 24°N

From the observed counting rate and measured telescope aperture, we have found a value of $(6.6\pm0.2)\times10^{-3}\text{cm}^{-2}\text{sec}^{-1}\text{sterad}^{-1}$ for the vertical intensity of particles able to penetrate 15 cm Pb* plus the 110 g/cm² of air equivalent material comprising the structure over our apparatus. This intensity has been corrected slightly to allow for the effect of the magnetic field and scattering. The measured intensity has been decreased by 6.4%, since that was the measured proportion of showers found during the cloud chamber observations. The corresponding intensity at sea-level for particles with momentum greater than 300 Mev/c (obtained by extrapolating our spectrum) is $(6.7\pm0.2)\times10^{-3}\text{cm}^{-2}\text{sec}^{-1}\text{sterad}^{-1}$.

D. Momentum Spectrum at 24°N

The empirical μ-meson spectrum at production which was introduced originally by Sands[13] has proven to be very useful in dealing with the phenomenological analysis of the mesonic component of cosmic rays in the atmosphere. Olbert[2] has recently improved this production spectrum and also studied the dependence on geomagnetic latitude. Olbert's production spectrum makes it possible to compute the differential range spectrum of μ-mesons at any desired altitude and latitude. It seems interesting, therefore, to compare our differential momentum spectrum with the one expected from Olbert's production spectrum. Olbert expressed the production spectrum of μ-mesons having range R at geomagnetic latitude λ by the following formula.

$$G(R:\lambda)=(7.3\times10^{4})/(a(\lambda)+R)^{3.68}. \qquad (\text{g}^{-2}\text{cm}^{2}\text{sec}^{-1}\text{sterad}^{-1})$$

where $a(\lambda)$ is the latitude parameter.

The differential momentum spectra of μ-mesons at sea-level at 50°N($a(\lambda)=520$) and 24°N($a(\lambda)=613$) were derived from this production spectrum using the μ-meson survival probabilities and the absorption length of the N-component given by Olbert. These are shown in Fig. 6 with the observed momentum spectrum converted at sea-level. For comparison, Rossi's momentum spectrum[7] at geomagnetic latitude larger than 45°N is shown, too.

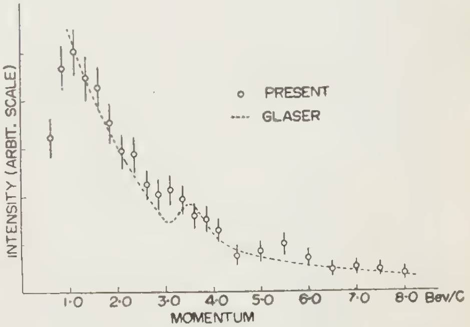

Fig. 5. The differential momentum distribution at 6000 gauss in linear scale. The dashed curve represents Glaser's distribution showing an anomaly.

At momenta higher than about 5 Bev/c, our spectrum is in agreement with the momentum spectrum given by Caro et al.[4] which was chosen by Olbert as the basis of his production spectrum. Our observations and those of Caro et al. both indicate that the slope of the momentum spectrum at these higher momenta is steeper than the slope shown by Rossi. Between 1 Bev/c and 4 Bev/c, our spectrum agrees reasonably well with the spectrum computed from Olbert's production spectrum. It is expected of course, that the intensities at low momenta (500 Mev/c—1.0 Bev/c) at our latitude, 24°N, should be lower than those at 50°N because of the difference of the geomagnetic energy cut-off of the primary component. However, the fact that our intensities are lower than those calculated from Olbert's spectrum at 24°N is interesting. It should be noted that other normalization procedures have little effect on this tendency of the spectrum.

---

* Five cm of Pb were added to the absorber for this part of experiment to conform with the usual phenomenological definition of hard component.

Olbert's production spectrum has been based on the results of altitude and latitude dependence of slow mesons using the delayed and anti-coincidence methods of detection. Olbert's spectrum at low momenta is in agreement with the experimental results at 29°N obtained by del Rosario and Dávila-Aponte[1] using the delayed coincidence and anti-coincidence methods. Most of the measurements on the differential range spectrum of low energy μ-mesons (10–250 g/cm^2 air equivalent) near 50°N are in agreement with the spectrum given by Rossi[7] and Olbert[2]. On the other hand, the magnetic deflection method[5],[14] has given results somewhat lower than those obtained by the differential range method in spite of careful corrections for magnetic deflection and scattering. A similar tendency has been noted at mountain altitude[5],[6],[15].

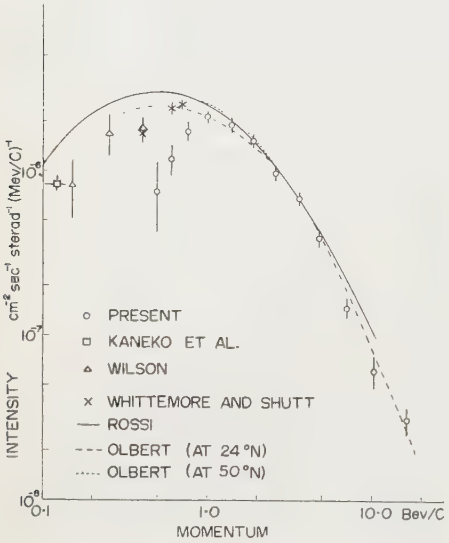

Fig. 6. The differential momentum spectra at sea level. Figure shows that points obtained by the magnet cloud chamber fall somewhat lower than obtained by differential range method.

The intensity of μ-mesons stopped in nuclear-emulsions at sea-level has been measured by another group in this laboratory. The differential intensity was found to be $(2.6\pm0.2)\times10^{-6}$ g^{-1}sec^{-1}sterad^{-1} at (15 ± 5) g/cm^2 air equivalent[16]. This value appears to be inconsistent with our momentum measurements as shown in Fig. 6. The emulsion method is essentially the same as the delayed coincidence and anti-coincidence methods, since the quantity actually measured is the differential range intensity. The inconsistency is in the same direction as the inconsistencies which has been reported many times before between differential range and differential momentum measurements. Among the possible causes of the difficulty we may mention the possibility of meson production in the absorbers which are normally over a differential range apparatus. Since absorbers are characteristic only of differential range measurements, locally produced mesons tend to increase the intensities measured by these methods but not the intensities measured by magnetic deflection. Olbert's production spectrum predicts that only about 3% of the mesons stopping under 125 g/cm^2 air equivalent of absorber are produced locally. On the other hand, Olbert's spectrum was derived from differential range measurements, including measurements at high altitude where local production should be more pronounced.

Our momentum spectrum (24°N) and those of Wilson[14] and Whittemore and Shutt[5] (50°N) are compared in Fig. 6. The difference between the two at low momenta is larger than the difference predicted from Olbert's spectra at these two latitudes, and as pointed out before, the actual predicted intensities are appreciably greater than the measured ones.

§ 5. Summary

We have measured the differential momentum spectrum of mesons at 24°N geomagnetic latitude. The spectrum falls off rather sharply at low momenta, and our differential momentum measurements indicate appreciably smaller intensities at low momenta than differential range measurements made at this latitude. If our momentum spectrum is compared with momentum spectra obtained at high latitude, the decrease in the intensity at low momentum is larger than the decrease predicted by Olbert's production spectrum. The positive to negative ratio falls off more rapidly at this latitude than at higher latitude.

Acknowledgement

We wish to express our thanks to Prof. Y. Watase for his invaluable advice and encouragement. It is a pleasure to acknowledge to Prof. W. L. Kraushaar of the Massachusetts Institute of Technology, who is now staying at the Osaka City University, for his criticism and suggestions made in the preparations of the manuscript. Thanks are also due to Messers. S. Ozaki and S. Kaneko for their discussion and Mr. T. Shiota for his financial support during this work.

References

1) L. del Rosario and J. Dávila-Aponte: Phys. Rev. **88** (1952) 998.
2) S. Olbert: Phys. Rev. **96** (1954) 1400.
3) L. Germain: Phys. Rev. **80** (1950) 616.
J. L. Zar: Phys. Rev. **83** (1951) 761.
C. M. York: Phys. Rev. **85** (1952) 998.
D. Brimi, O. Rimondi and I. Filosofo: Nuo. Cim. **9** (1952) 505.
G. R. Heyland and W. E. Duncanson: Proc. Phys. Soc. (London) **A66** (1953) 40.
P. G. Lichtenstein: Phys. Rev. **93** (1954) 858.
A. Fafarman and M. H. Shamos: Phys. Rev. **96** (1954) 1096.
4) D. E. Caro, J. K. Parry and H. D. Rathgeber: Aust. J. Sci. Res. **A4** (1951) 16.
5) W. L. Whittemore and R. P. Shutt: Phys. Rev. **86** (1952) 940.
6) A. Z. Rosen: Phys. Rev. **93** (1954) 211.
7) B. Rossi: Rev. Modern Phys. **20** (1948) 537.
8) S. Fukui, T. Kitamura and S. Ozaki: Jour. Inst. Polytechnics, Osaka City University **5** (1954) 11.
9) G. Puppi and N. Dallaporta: *Progress in Cosmic Ray Physics* edited by J. G. Wilson (North Holland Publishing Company, Amsterdam), p. 315 ff.
10) P. C. Caldirola, R. Fieschi and P. Gulmanelli: Nuo. Cim. **9** (1952) 5.
11) B. G. Owen and J. G. Wilson: Proc. Phys. Soc. (London) **A64** (1951) 417.
12) P. A. Glaser, B. Hamermesh and G. Safonov: Phys. Rev. **80** (1950) 625.
13) M. Sands: Phys. Rev. **77** (1950) 180.
14) J. G. Wilson: Nature **158** (1946) 415.
15) C. E. Miller, J. E. Henderson, D. S. Potter and J. Todd, Jr.: Phys. Rev. **84** (1951) 981.
16) S. Kaneko, T. Kubozoe and M. Takahata: unpublished.

JOURNAL OF THE PHYSICAL SOCIETY OF JAPAN Vol. 10, No. 9, SEPTEMBER 1955

On the Penetrating Showers Produced in Paraffin and Graphite*

By Isao MIURA

Physical Institute, Nagoya University, Nagoya, Japan

(Received January 29, 1955)

The production of the penetrating showers in paraffin and graphite was studied by a cloud chamber connected with a hodoscope at an elevation 2760 meters, geomagnetic latitude 25°N. Results indicate:

(1) There is an evidence of multiple production of mesons in the collision of an incident nucleon with a hydrogen nucleus. (2) There is no appreciable difference between paraffin and graphite in the projected angle distribution of lightly ionizing shower particles with respect to the primary particles. (3) The flux of ionizing particles which produce the local penetrating showers is $(3.0\pm 0.4)\times 10^{-5}/\text{cm}^2$. sec. sterad.

§ 1. Introduction

Hitherto, most experiments[1)-7)] for the study of the penetrating showers have been performed by the use of dense materials such as lead or iron as producer. From those experiments, it was difficult to know directly the elementary process of meson production in the nucleon nucleon collision. In order to obtain more precise information about the elementary process, many experiments[8)-20)] of the penetrating showers with light materials such as graphite, paraffin, lithium, beryllium and hydrogen, have been performed. But there was a large discrepancy among their conclusions. Some of them12)13)15)18) reported an evidence of the production of penetrating showers in the nucleon-nucleon collision, but others14)17) denied this fact. Such discrepancy will be considered to be arisen from different conditions of their measurements: for instance, differences of altitude and of the detecting efficiency of the penetrating showers. A recent investigation by Cosmotron21) has shown directly the production of two π mesons in the nucleon-nucleon collision in the region of a few Bev of incident energies.

---

* Presented at the annual meeting of the physical Society of Japan, April, 1953.

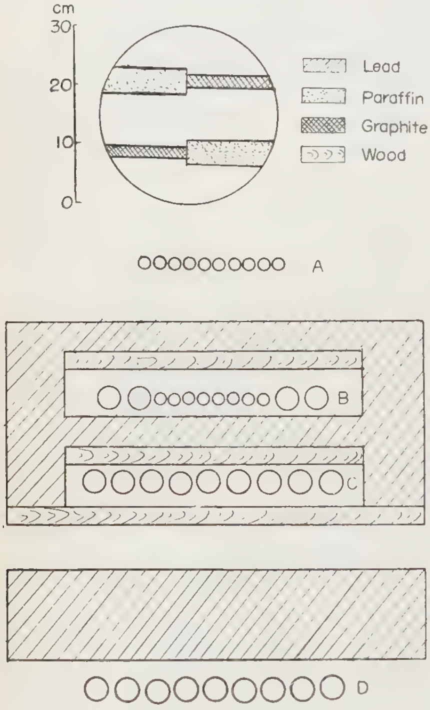

Fig. 1. Arrangement of experimental apparatus.

The present experiment was undertaken to obtain the information about the meson production in hydrogen nuclei, comparing the penetrating showers produced in a graphite plate with those in a paraffin plate containing the same quantities of carbon. Because the present experiment was performed with a cloud chamber in which two paraffin and graphite plates were interposed, combined with a hodoscope, we could obtain not only the information about the elementary process, but also some informations about multiplicity, angular divergence and the penetrating power of shower particles.

The experiment was performed at an elevation 2760 meters above sea level (Laboratory at Mt. Norikura, Japan), during the summer of 1952.

§ 2. Apparatus

The entire apparatus was set up inside a house with a roof of about 2 cm of wood and 0.3 cm of iron. The cloud chamber (see Fig. 1) had a diameter of 30 cm and an illuminated depth of 14 cm. The chamber was filled with 85cm Hg of air and was saturated with vapour of a mixture of 60% of ethyl alcohol and 40% of water.

Two pairs of a graphite plate of 14 cm × 14 cm × 2.0 cm and a paraffin plate of 14 cm × 14 cm × 4.35 cm were arranged in the illumination region keeping each pair in the same level. Each pair corresponds to 3.3 g/cm^2 of graphite or 0.063 radiation length and 3.9 g/cm^2 of paraffin, the latter consisting of 3.3 g/cm^2 of carbon and 0.6 g/cm^2 of hydrogen. This arrangement was suitable for the comparison of the penetrating showers produced in two different materials, because the detection probability was kept constant against possible variation of the flux of the incident nucleons and the other experimental conditions.

Underneath the cloud chamber, four G.M. counter trays (A, B, C and D) were arranged as shown in Fig. 1. All counters in A and eight counters in B trays were 2 cm in diameter and 20 cm in length and all the other counters were 4 cm in diameter and 28 cm in length. Two lead plates (each 5 cm thick) were placed between A and B trays and B and C trays. Lead plates between C and D trays were varied from 0 to 20 cm to measure the penetrability of shower particles. Sides of G.M. counter trays were surrounded by 10 cm of lead to reduce the number of unnessary expansions caused by the electronic component of the extensive air showers and the local showers generated in surrounding materials.

Pulses of the coincidences A $(\geqslant 2)$ B$(\geqslant 2)$ C $(\geqslant 1)$ which had a resolving time of 10 microsecond, expanded the cloud chamber and operated the hodoscope. The hodscope was constructed by the method designed by

Table I.

1	2	3	4	5
Position of shower producing materials	Number of shower particles	Number of showers produced in paraffin	Number of shower produced in graphite	ratio of (3) to (4)
upper	$\geqslant 4$	64	43	1.49 ±0.19*
lower	$\geqslant 4$	26	17	1.53±0.36*
upper and lower	$\geqslant 4$	90	60	1.50±0.17*

* the errors are only the statistical one.

Regener[22]. The cloud chamber was photographed stereoscopically. Simultaneous photographs of the hodoscope were taken automatically by another camera.

Although various events are observed in the cloud chamber photographs, care must be taken to pick up the penetrating showers. Usually the penetrating showers are defined as such showers whose particles satisfy one of the following conditions: (a) Two or more particles penetrate at least one or two thin lead plates without any cascade multiplication, (b) one or more penetrating particles and one or more heavily ionizing particles. In the present experiments, the penetrating showers could not be distinguished solely by the cloud chamber photographs, because no lead plate was interposed in the cloud chamber. However, examination of the ionization of tracks and the correspondency between cloud chamber tracks and hodoscope tracks were sufficient for the selection of the penetrating showers.

In fact, the penetrating showers were adopted by the following condition: Two or more counters in B tray and one or more in C tray lying on the direction of tracks of shower particles, discharged simultaneously. In order to ascertain the correspondency, cloud chamber tracks were projected in 2/5 scale of actual dimension on a paper where counter disposition were drawn in the same scale. We took care especially when any accompanied particles with shower were detected in the photograph, for there was a possiblility that the cloud chamber and the hodoscope were worked by those accompanied particles while no penetrating shower particles were contained in the observed showers.

Thus 204 event were obtained from about 4400 photographs taken in the experiment. Two examples among them are shown in Fig. 2 (a) and (b).

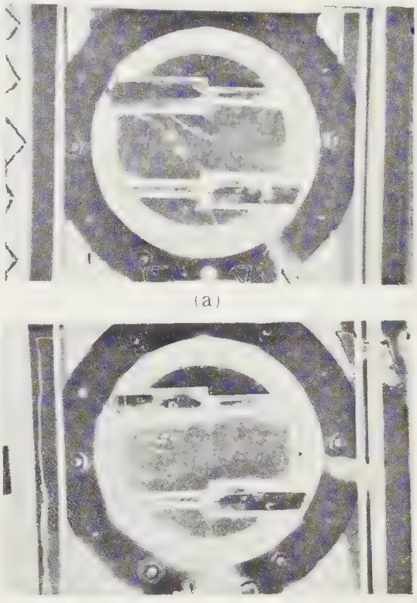

Fig. 2. Cloud chamber photographs of the typical examples of the penetrating showers. In Fig. (a), six shower particles are emitted from the penetrating shower produced in a paraffin plate. In Fig. (b), the penetrating shower with five shower particlcs is originated in a graphite plate by the charged particle.

§ 3. Results

(1) The Ratio of Numbers of the Penetrating Showers in Paraffin to Those Generated in Graphite

Numbers of the penetrating showers generated in paraffin and graphite and their ratios are shown in Table I.

In Table I, numbers of shower particles (3rd column) do not include heavily ionizing particles, numbers of showers (4th or 5th column) are normalized to the equivalent area of source materials. Numbers of the penetrating showers generated in the lower producer in the cloud chamber are comparatively less than those in the upper producer. This is caused by the fact that the space available for detecting the penetrating shower under the second plate is smaller than that under the first plate (see Fig. 1).

As is easily seen from Table I, the ratios of numbers of the penetrating showers in paraffin to those generated in graphite obtained in various positions of shower initiating layers are nearly equal to 1.5 within the statistical accuracy. Large fraction of these penetrating showers contain the penetrating particles which can penetrate 5 and 10 cm of lead and generate master pulses for triggering. But a small fraction may be attributable to spurious events, such as, (a) high energy cascade showers originated in graphite or paraffin layer and capable of triggering, (b) low energy cascade showers coming into the cloud chamber accidentally during the sensitive time interval of the cloud chamber and (c) stars accompanied with penetrating particles. Number of cascade showers in cases (a) and (b) which contain four or more particles under thin graphite plates (0.063 radiation length) was calculated and was found to be only about a few-tenth percent of the obtained total showers. In the case (c), only small fraction of star particles can appear in the space under the graphite or paraffin plates, because of their small energy and large angular divergence. Moreover they can be excluded simply by observing their hodoscope correspondence and their heavy ionization. Thus the effect of such spurious events will be negligible in the present experiments. Although a small fraction of them must be contained in the data, the number of them may be identical in both materals because almost all spurious events are produced in carbon. Therefore the ratio of the numbers of the penetrating showers corrected for them will be a little larger than the observed one.

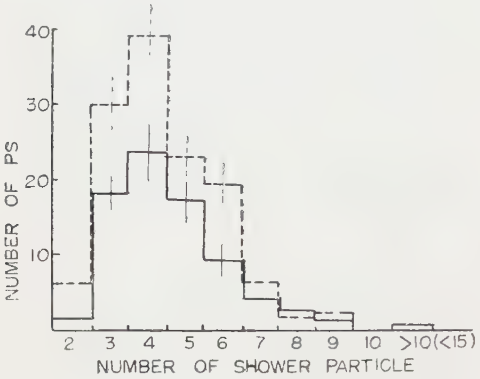

Fig. 3a. The multiplicity distributions of all lightly ionizing shower particles produced in paraffin (dotted line) and in graphite (solid line).

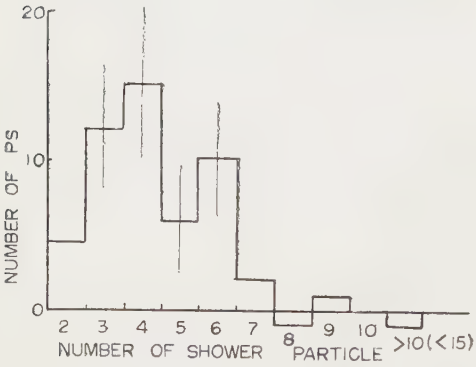

Fig. 3b. The multiplicity distribution of difference between the penetrating showers produced in paraffin and in graphite.

From the data and the above consideration, we conclude that more penetrating showers are produced in paraffin than in graphite, namely, the penetrating showers are generated in hydrogen nuclei contained in paraffin plates.

(2) Multiplicities of Shower Particles.

The multiplicity distribution of all lightly ionizing shower particles produced in paraffin, graphite and paraffin minus graphite (hydrogen), are shown in Fig. 3a and Fig. 3b respectively.

These Figs. show that the number of showers with low multiplicities are remarkably small. This will be explained as follows: Because the solid angle sustained by counter tray A, B, and C is very small (0.23 steradian), the detection probability of the penetrating showers with low multiplicities must be considerably smaller than those with high multiplicities and because at least two shower particles coming into small solid angle have to penetrate more than 5 cm and 10 cm of lead, only a small part of the penetrating showers with low multiplicities can be detected. Therefore the shape of low multiplicity parts of the distribution curve will be considerably different from no-biased one[23]. The detection probabilities of the penetrating showers in paraffin and graphite are equal to each other. Thus it is possible to compare the distribution curves of graphite, paraffin minus graphite. Remarkable difference among them cannot be proved because of their poor statistics.

From the charge conservation, the multiplicities of shower particles produced in hydrogen must be even or odd number, if the penetrating showers are generated in proton-proton or neutron-proton collision, respectively. Multiplicity distributions of difference between the numbers of the penetrating showers produced in paraffin and in graphite were taken in the case of the charged or neutral primaries. From them, the tendency was recognized that the number of showers with even multiplicity (4 and 6) seemed to predominate in the case of charged primary particles and that with odd multiplicity (3 and 5) seemed to predominate in the case of the neutral primary particles.

(3) Angular Distribution of Shower Particles with Respect to the Direction of the Primary Particles.

The histogram in Fig. 4 represents the relative number of all lightly ionizing shower particles of the penetrating showers produced in graphite, observed per degree as a function of the projected angle between the primary particles and shower particles. Dotted histogram represents the Green's result[8)] obtained for graphite. Both distributions are nearly equal to each other if the statistical errors and the difference in geometry of counter trays are taken into account.

By comparison of the angular distribution of shower particles from paraffin with those from graphite, some informations of that from hydrogen will be obtained. In Fig. 5 solid and dotted line show the distributions obtained with paraffin and graphite, respectively. From general shapes of both distributions, no remarkable difference more thanstatistical errors can be noticed between them. This fact may be interpreted as either that shower particles from hydrogen have no contribution to the angular distribution from paraffin, or that the shape of the angular distribution from hydrogen is similar to that from graphite. The former may be less probable because hydrogen nuclei contribute considerably to the penetrating showers from paraffin as shown in § **3**, (1). Therefore the latter will be favourable. In that case, it will be tentatively concluded that shower particles produced in a carbon nucleus will not be suffered large deflection when they pass through the same nucleus.

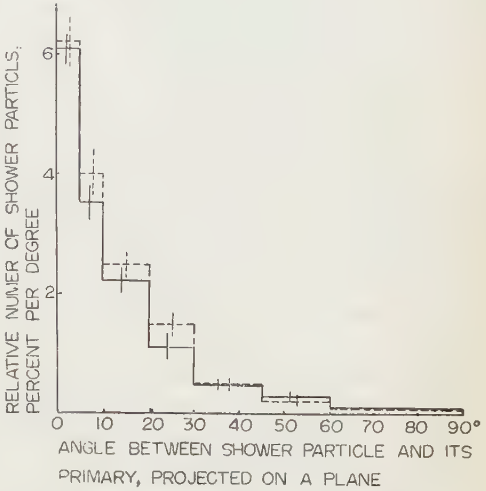

Fig. 4. The projected angular ditributions of ionizing shower particles of the penetrating showers produced in graphlte, with respect to the direction of the primary particles. The dotted and the solid histograms represent the Green's result and ours, respectively.

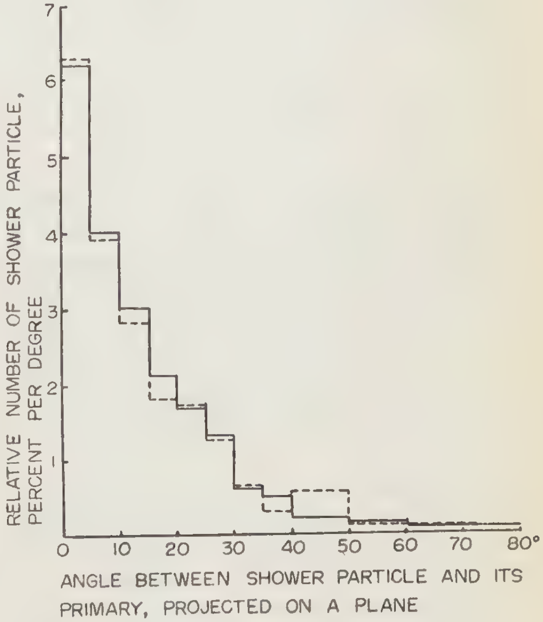

Fig. 5. The projected angular distributions of shower particles from paraffin (dotted histogram) and from graphite (solid one).

(4) The Flux at 2760 Meters of Ionizing Particles that produce the Local Penetrating Showers.

The flux of ionizing particles that produce the local penetrating showers at 2760 meters, geomagnetic lattitude 25°N, was obtained from the experiments. The flux is

$$N_0=\frac{N}{\Omega\cdot t\cdot S\{1-\exp(-x/\lambda)\}},$$

where N is observed number of the local penetrating showers generated in the plate of x g/cm^2 thick, with an active area S cm^2, in a net observation time t sec. Ω is the solid angle sustained by counter trays and λ is the collision mean free path of ionizing primary particles in the layer.

For instance, in the upper position of shower producing layer $\Omega=0.23$ steradian, $S=196$ cm^2, $t=2\times10^5$ sec and $x=3.3$ g/cm^2 of graphite. Using the theoretical value for λ,

$$N_0=(3.0\pm0.6)\times10^{-5}/\text{cm}^2.\ \text{sec. steradian.}$$

This value is equal to the one obtained from the data in the lower position within the statistical errors. From these values it is concluded that the flux of ionizing particles that produce the local penetrating showers is $(3.0\pm0.4)\times10^{-5}$/cm^2. sec. steradian at 2760 meters.

The value is several times larger than the value obtained by Hazen et al.[23] if the altitude difference is taken into account. But such discrepancy is not so serious, if we consider the following facts: We selected the local penetrating showers containing at least two penetrating particles which penetrated a 55 g/cm^2 and a 110 g/cm^2 of lead, While Hazen et al. selected such penetrating showers as containing three penetrating particles which penetrated 115 g/cm^2 of lead. Thus energy region of the events observed by us is considerably lower than those observed by Hazen et al.

If the lower limits of energy regions in two experiments were determined, energy spectrum between two limits could be obtained. This is an interesting problem, but the esitimation of the lower limit is difficult owing to different loss of the penetrating showers due to different geometry or angular spread and penetrability of shower particles.

(5) Absorption of Shower Particles in Lead.

From combination of track in the cloud chamber photographs and the array of lighting neon bulbs, the behavior of absorption in lead of shower particles produced in paraffin and graphite was investigated by varying the thickness of Lead absorber from 0 to 20 cm with interval of 5 cm between C and D trays.

Before the study of the absorption in the variable lead, penetrating shower particles were selected by the following condition, they could penetrate three counter trays A, B and C and had such direction as possible to hit the D tray from the front view. Although we excluded particles which passed through gaps between neighbouring counters of A, B and C trays or the outside of the effective region, there remained the ambiguity whether selected penetrating shower particles were contained certainly in the solid angle sustained by A, B, C and D trays or not, because those passed the front or the near of the D tray could not be excluded from the front view only. So the ratio of such particles to the selected penetrating particles was measured in the case of no absorber. This value was consistent with the value expected from geometrical consideration of counter arrangement. Of course, the ratio will depend on the thickness of the absorber, for there must be nuclear interactions in the absorber. But correction for such events could not be done, as the measurement was done with simple counter trays (not crossed trays).

From data obtained from the front views, events suffering a large angle scattering above 50° respect to the selected penetrating particles at the central point of lead absorber are classified as absorption. Thus the absorption mean free paths of shower particles generated in paraffin and graphite were about 340 g/cm^2 and about 250 g/cm^2 of lead with probable errors of order of 100 cm^2 of lead, respectively. Unfortunately, because of large errors, we failed to determine whether two value were different or not.

§ 4. Discussion

As seen in chapter 3-1, it is evident that the penetrating showers with four or more shower particles are produced in hydrogen nuclei contained in the paraffin layer. However, the following consideration is necessary to conclude the multiple production of mesons in a single nucleon nucleon collision.

In the first place, we have to consider the effect of secondary collision in materials. In graphite, the number of the penetrating showers with 4 or more particles generated by a single collision in the thickness of graphite between x and $x+dx$ g/cm², is

$$dn_1=n_0\exp(-x/\lambda_c)\cdot\frac{dx}{\lambda_c}\cdot\exp[-(x_0-x)/\lambda_c]$$

and the number of the penetrating showers which have low multiplicity in the first collision occured in the thickness between x and $x+dx$ g/cm² and then developed into 4 or more particles by secondary collision through x_0-x g/cm² of graphite is

$$dn_2=n_0'\exp\left(-\frac{x}{\lambda_c}\right)\cdot\frac{dx}{\lambda_c}\cdot m\{1-\exp[-(x_0-x)/\lambda_c]\}\,,$$

where n_0 and n_0' are numbers of incident nucleons which can generate the penetrating showers with multiplicity of 4 or more, and those with 3 or 2, respectively. λ_c is the collision mean free path of nucleons in graphite, x_0 is total thickness of graphite and m means average number of shower particles which can produce successive high energy nuclear collision. Taking $x_0\ll\lambda_c$ and neglecting higher terms, total number of the penetrating showers produced in the total absorber is

$$n_c=\int_0^{x_0}dn_1+\int_0^{x_0}dn_2 \sim n_0\left\{\frac{x}{\lambda_c}+\left(\frac{m}{2}\cdot\frac{n_0'}{n_0}-1\right)\left(\frac{x_0}{\lambda_c}\right)^2\right\}.$$

For paraffin, the number of secondary events occuring in hydrogen are added to n_c: (a) The first collision of incident nucleon N with carbon nucleus C and the secondary collision of m shower particles with hydrogen nucleus H, and (b) the first collision of N with H and the second collision of m' shower particles with C or H.

The number of the penetrating showers generated by (a) or (b) at the depth of fx' g/cm² of carbon or $(1-f)x'$ g/cm² of hydrogen are, respectively.

$$dn_a=n_0'\exp\left(-\frac{fx'}{\lambda_c}\right)\cdot\frac{f\,dx'}{\lambda_c}\cdot m\left\{1-\exp\left[\frac{-(1-f)(x_0'-x')}{\lambda_H}\right]\right\},$$

$$dn_b=n_0'\exp\left[\frac{-(1-f)x'}{\lambda_H}\right]\cdot\frac{(1-f)dx'}{\lambda_H}\cdot m'\left\{1-\exp\left[\frac{-f(x_0'-x')}{\lambda_c}\right]+1-\exp\left[\frac{-(1-f)(x_0'-x')}{\lambda_H}\right]\right\}.$$

where f is the fraction of carbon quantity in unit g/cm² of paraffin ($f\doteqdot 0.85$), λ_H is the collision mean free path of nucleons in hydrogen and x_0' is thickness of the paraffin layer.

Taking $fx_0'\ll\lambda_c$ and $(1-f)x_0'\ll\lambda_H$, total number of the penetrating showers produced in the total absorber is

$$\begin{aligned}n_{CH_2}&=n_c+\int_0^{x_0'}dn_a+\int_0^{x_0'}dn_b\\&=n_c+n_0'\left\{\left[(m+m')\frac{f\cdot(1-f)}{\lambda_c\cdot\lambda_H}+m'\frac{(1-f)^2}{\lambda_H^2}\right]\frac{x_0'^2}{2}\right.\\&\qquad\left.-\left[m\cdot\frac{f^2(1-f)}{\lambda_c^2\lambda_H}+m'\frac{f\cdot(1-f)^2}{\lambda_c\cdot\lambda_H^2}+m'\frac{(1-f)^3}{\lambda_H^3}\right]\frac{x_0'^3}{6}\right\}.\end{aligned}$$

Thus the ratio of the numbers of the penetrating showers produced in both materials expected from single production of mesons is n_{CH_2}/n_c. Taking $x_0=3.3$ g/cm², $x_0'=3.9$ g/cm² and assuming λ_c and λ_H have values expected from geometrical cross section,

$$n_{CH_2}/n_c=1+\varphi(m,m')\,.$$

The value of n_{CH_2}/n_c is depend on the function of m and m', $\varphi(m,m')$, but the dependence is not remarkable. For instance, the values of n_{CH_2}/n_c are 1.06 or 1.04 respectively for $m=m'=3$ or $m=m'=2$.

As shown in Table I, the observed value 1.50±0.17 is obviously larger than the value expected from single production of mesons, even though errors are taken into account. Therefore, the surplus penetrating showers produced in paraffin must be interpreted as those produced by a single collision of an incident nucleon with a hydrogen nucleus. Thus we can conclude that the multiple production of mesons occurs in collisions of nucleons with protons. This conclusion is furthermore supported by the fact that the shape of the multiplicity distribution of difference between the penetrating showers generated in paraffin and in graphite seems to fit the shape expected from the charge conservation [in § **3** (2)].

In the second place, in the collision of the nucleon with the carbon nucleus, there is a possibility that some or all of shower particles are fast nucleons (knock on proton). Such events would not be distinguished from the penetrating showers containing mesons in the present measurement, but a rough estimation of the number of such events is possible from the combination of the following data obtained by several authors[24)25)]: (a) Integral spectrum of the shower initiating particles, (b) distribution of the number penetrating particles produced by the primary particle of definite energy, (c) the frequencies of π mesons and protons contained in penetrating particles which are able to penetrate 5 cm or 10 cm of lead and (d) the angular distribution of shower particles with respect to the direction of the primary particles in the no-biased measurement for shower selection. As a result of estimation, about 12% of the penetrating showers produced in graphite is attributted to the penetrating showers which contain less than two mesons. Taking this correction into account, the ratio of the numbers of the penetrating showers containing 2 or more mesons turns out to be 1.63±0.20 which is larger than the value 1.06 expected from the single production of meson.

From the present experiments, the threshold energy of multiple production of mesons was not determined, because the determination of energies of the penetrating showers was difficult. To determine the energy spectra of shower particles, further experiment by a cloud chamber connected with an electromagnet is now in preparation.

§ 5. Conclusion

From the experiments, the following conclusions were obtained:

(a) The observed excess of production of the penetrating showers in paraffin as compared with those in carbon must be interpreted as an evidence of multiple production of mesons in the collision of incident nucleons with protons.

(b) The projected angular distributions of lightly ionizing shower particles with respect to primary particles, produced in paraffin and in graphite, are similar as shown in Fig. 4.

(c) The flux of ionizing particles which produce the local penetrating shower is $(3.0\pm0.4)\times10^{-5}/\mathrm{cm}^2$. sec. steradian at an elevation of 2760 meters, geomagnetic lattitude 25°N.

The author wishes to express his gratitude to Professor Y. Sekido for his valuable discussions and encouragement. He is also very grateful to Mr. T. Matano, Y. Toyoda and T. Murayama for their cooperation and valuable help in carring out this experiments, and to Professor Y. Watase who gave him facilities to achieve the work. This work was financially supported by the Scientific Reasearch Expenditure of the Department of Education.

References

1) W. B. Fretter: Phys. Rev. **73** (1948) 41; **76** (1949) 511.
2) W. W. Brown and A. S. McKay: Phys. Rev. **77** (1950) 342.
3) A. Lovati, A. Mura, G. Salvini and G. Tagliaferri: Nuovo Cimento **7** (1950) 943.
4) B. Gregory and J. Tinlot: Phys. Rev. **81** (1950) 667.
5) W. A. Walker, S. P. Walker and K. Greisen: Phys. Rev. **80** (1950) 546.
6) M. Gottlieb: Phys. Rev. **82** (1951) 349.
7) Froelich, Harth and Sitte: Phys. Rev. **87** (1952) 504.
8) I. Kita and O. Minakawa: J. Phys. Soc. Japan **8** (1953) 139; **9** (1954) 6.
9) Higashi, Kitamura, Kubozoe, Oda, Ozaki and Watase: J. Phys. Soc. Japan **8** (1953) 584.
10) J. R. Green: Phys. Rev. **80** (1950) 832.
11) W. B. Fretter: Phys. Rev. **80** (1950) 921.
12) Walker, Duller and Sorrels: Phys. Rev. **86** (1952) 865.
13) Chang, del Castillo and Grodzins: Phys. Rev. **84** (1952) 865; **89** (1953) 408.
14) Bertolino, Cini, Colombino and Wataghin: Nuovo Cimento **9** (1952) 407.
15) Colombino, Ferroni and Wataghin: Nuovo Cimento **11** (1954) 572.
16) MacCusker, Poter and Wilson: Phys. Rev. **91** (1953) 384.
17) O. Haxel and R. P. Scultz: Zeits. f. Naturforsch. **9**a (1954) 178.
18) M. L. Vidale and M. Schein: Phys. Rev. **84** (1951) 593.
19) A. B. Weaver: Phys. Rev. **90** (1953) 86.
20) Kusumoto, Miyake, Suga and Watase: Phys. Rev. **90** (1953) 998.
21) Fowler, Shutt, Thorndike and Whittemore: Phys. Rev. **95** (1954) 1026.
22) L. Janossy: *Cosmic Rays*, Oxford, 1950.
23) Hazen, Randall and Tiffany: Phys. Rev. **75** (1949) 694.
24) J. G. Wilson: *Progress in Cosmic Ray Physics* Vol. 1, 1952.
25) M. G. Mylroi and J. G. Wilson: Proc. Phys. Soc. A **64** (1951) 404.

JOURNAL OF THE PHYSICAL SOCIETY OF JAPAN Vol. 10, No. 9, SEPTEMBER 1955

Systematization of the Approximate Solutions of the Thomas-Fermi Equation

By Kwai UMEDA

Department of Physics, Okayama University, Okayama

and Shigehiro KOBAYASHI

Department of Physics, Kagawa University, Takamatsu

(Received May 21, 1955)

Based on the generalized Brinkman's remark that $x^\sigma\phi$ can be treated as a constant over the whole range of x, three homologues of the approximate TF solutions, i.e. 1. Brinkman, 2. Kerner-Tietz-Umeda and 3. Sommerfeld-March, are systematically established under either of two different guiding principles, the linearization of the TF equation in regard to ϕ and the elimination of the explicit x in the TF equation.

§ 1. Scope of the Present Investigation

Since the exact solution of the Thomas-Fermi (abbreviated as TF) equation ,$\phi''=\phi^{3/2}/x^{1/2}$, is given only numerically, its approximate expression in a closed analytical form is strongly desired for the practical purpose. Hitherto several different forms are known, as follows.

1. *Sommerfeld*[1] *asymptotic form*

$$\phi(x)=1/[1+(x/12^{2/3})^\lambda]^{3/\lambda}\ , \tag{1}$$

$\lambda=0.7722$ being determined by the asymptotic behavior of ϕ.

1a. *March*[2] *modification*

March treated in this formula Eq. (1) λ as an adjustable parameter and determined the value $\lambda=0.8034$ by the mean value method

$$\int_0^\infty\left(\phi''-\frac{\phi^{3/2}}{x^{1/2}}\right)x\,dx=0\ . \tag{2}$$

1b. *Umeda*[3] *modification*

Umeda determined in the March modification the value of $\lambda=0.8371$ by the minimization of the "approximation degree" of ϕ

$$I[\phi]=\int_0^\infty\left\{(\phi')^2+\frac{4}{5}\frac{\phi^{5/2}}{x^{1/2}}\right\}dx \tag{3}$$

proposed by him.

2. *Kerner*[4] *form*

$$\phi(x)=1/(1+Bx) \tag{4}$$

with $B=1.3501$.

2a. *Umeda*[3] *modification*

Umeda adjusted the value of $B=1.3679$ by means of the approximation degree.

3. *Rozental*[5] *form*

$$\phi(x)=0.7345\,e^{-0\cdot562x}+0.2655\,e^{-3\cdot392x} \tag{5}$$

and

$$\phi(x)=0.255\,e^{-0\cdot246x}+0.581\,e^{-0\cdot947x}+0.164\,e^{-4\cdot356x}. \tag{5a}$$

Recently there have been added two new kinds of those, i.e.

4. *Brinkman*[6] *form*

$$\phi(x)=\text{const}\ x^{1/2}K_1(2ax^{1/2})\ , \tag{6}$$

K_1 being a modified Bessel function of the second kind, derived by the transformation

$$\phi''=\frac{\phi^{3/2}}{x^{1/2}}=(x\phi)^{1/2}\frac{\phi}{x}\approx a^2\frac{\phi}{x}\ , \tag{7}$$

and 5. *Tietz*[7] *form*

$$\phi(x)=1/[1+(b/6^{1/2})x]^2 \tag{8}$$

derived by an alternative transformation

$$\phi''=\frac{\phi^{3/2}}{x^{1/2}}=\frac{1}{(x\phi)^{1/2}}\phi^2\approx b^2\phi^2\ . \tag{9}$$

In these both cases the common basic idea is the Brinkman's remark that $x\phi$ is so slowly varying that it can be treated as if it were a constant over the whole range of x while the guiding principle is found for the former in the linearization of the TF equation with regard to ϕ by rearranging $x^{1/2}$ and for the latter in the elimination of the explicit x from the TF equation by rearranging $\phi^{1/2}$.

In this paper the systematization of these approximate TF solutions is carried out theoretically by generalizing the Brinkman's remark and obeying these guiding principles, except that the Rozental forms are laid aside since they are nothing but the Prony expressions of the exact values of ϕ.

§ 2. Generalization of the Brinkman's Remark

Now, it may be expected that the better transformations than those mentioned above could be obtained by rearranging the optimum power of x or ϕ instead of their square roots respectively, as follows.

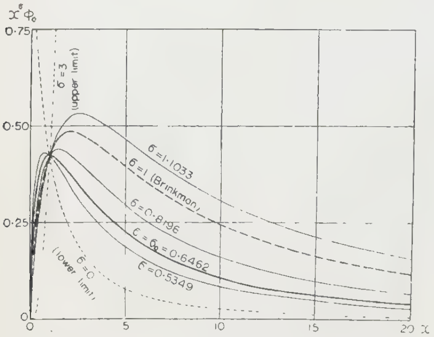

Fig. 1. Generalized Brinkman's remark. $x^\sigma\phi_0$-curves for a number of the values of σ.

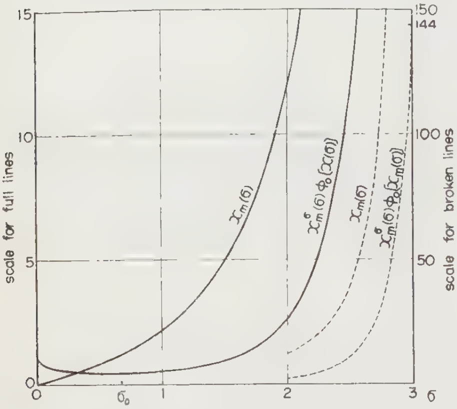

Fig. 2. Height $x_m{}^\sigma(\sigma)\phi_0[x_m(\sigma)]$ and place $x_m(\sigma)$ of the top of the $x^\sigma\phi$-curve for given value of σ in the allowed range 0 to 3, cf. Eqs. (12) and (14).

$$\phi''=\frac{\phi^{3/2}}{x^{1/2}}=(x^{2\alpha-1}\phi)^{1/2}\frac{\phi}{x^\alpha}\approx(x^{2\alpha-1}\phi_0)^{1/2}\frac{\phi}{x^\alpha} \tag{10}$$

$$\phi''=\frac{\phi^{3/2}}{x^{1/2}}=(x^{1/(2\beta-3)}\phi)^{-(2\beta-3)/2}\phi^\beta$$
$$\approx(x^{1/(2\beta-3)}\phi_0)^{-(2\beta-3)/2}\phi^\beta \tag{11}$$

ϕ_0 being the exact TF function, because then the Brinkman's remark can be more effectively generalized by determining the value of the exponent σ which makes the expression $x^\sigma\phi_0$ as slowly varying as possible over the whole range of x. In other words the maximum value of $x^\sigma\phi_0$ should be made as low as possible or the radius of curvature at the maximum point of the $x^\sigma\phi_0$-curve should be made as large as possible.

Since $x^\sigma\phi_0$ should vanish at the both limits $x=0$ and ∞, the allowable value of σ is restricted in the range

$$3>\sigma>0\,. \tag{12}$$

The optimum value of σ denoted by σ_0 is found by the condition of the lowest height of the $x^\sigma\phi$-curve

$$\frac{d}{d\sigma}[x_m{}^\sigma(\sigma)\phi_0\{x_m(\sigma)\}]=0 \tag{13}$$

where $x_m(\sigma)$ is the root of the equation which determines the maximum of $x^\sigma\phi_0$.

$$\frac{d}{dx}[x^\sigma\phi_0(x)]=0 \quad \text{or} \quad \phi_0'+\sigma\frac{\phi_0}{x}=0\,. \tag{14}$$

Eq. (13) is reduced due to Eq. (14) simply to

$$x_m(\sigma)=1 \tag{15}$$

which enables us to evaluate the value of σ_0 from Eq. (14), that is

$$\sigma_0=(-x\phi_0'/\phi_0)_{x=1}=0.6462, \tag{16}$$

the Miranda[7] value of the exact TF function being herein substituted. This value of σ_0 lies in the above allowed range, Eq. (12), as it must be, and determines the corresponding optimum values of α and β in Eqs. (10) and (11) respectively

$$\alpha_0=0.8231 \quad \text{and} \quad \beta_0=2.274\,, \tag{17}$$

while $\sigma_{\text{Brinkman-Tietz}}=1$, $\alpha_{\text{Brinkman}}=1$ and $\beta_{\text{Tietz}}=2$. It is noteworthy that the values of Brinkman and Tietz are very near to the optimum values.

According to the alternative method of the maximum curvature the optimum value of σ is 0.8196.

In Fig. 1 the $x^\sigma\phi_0$-curves for a number of the value of σ are given. Fig. 2 shows the dependence of $x_m(\sigma)$ and $x_m{}^\sigma(\sigma)\phi_0[x_m(\sigma)]$ upon σ. Since $x_m{}^\sigma(\sigma)\phi_0[x_m(\sigma)]$ remains nearly constant over wide range of the value of σ in the neighborhood of σ_0, we find there the freedom of adjusting the value of σ in such a way that it may satisfy any further condition in addition to the condition of lower height.

§ 3. Brinkman Homologue

By putting in Eq. (10) according to the generalized Brinkman's remark

$$x^{2\alpha-1}\phi_0=\text{const}\equiv a^4\ , \tag{18}$$

we obtain a generalized form of Eq. (7)

$$\phi''=a^2\phi/x^\alpha \tag{19}$$

which can be solved in general in terms of the Bessel function with purely imaginary argument, as well known[8]. The boundary condition $\phi(\infty)=0$ determines the form of the approximate TF solution

$$\phi(x)=\text{const}\ x^{1/2}\ K_{1/(2-\alpha)}\left(\frac{2}{2-\alpha}ax^{(2-\alpha)/2}\right), \tag{20}$$

a homologue, of which the special case of $\alpha=1$ is just the Brinkman form, Eq. (6). The only drawback of this solution is that it does not satisfy the other boundary condition $\phi(0)=1$.

The value of α is restricted according to Eq. (12) in the range

$$2>\alpha>1/2\ , \tag{21}$$

so that $\alpha=1$, Brinkman value, is the only one possible integer. Correspondingly the order of the Bessel function lies in the range

$$\infty>1/2(2-\alpha)>2/3 \tag{22}$$

so that $1/(2-\alpha)=1$, Brinkman value, is the smallest possible integer, which gives K_1. This circumstance characterizes the Brinkman form, Eq. (6).

The values of the adjustable parameters α and a can be determined conveniently by the mean value method, Eq. (2).

§ 4. Kerner-Tietz-Umeda Homologue

Next, by putting in Eq. (11) according to the generalized Brinkman's remark

$$x^{1/(2\beta-3)}\phi_0=\text{const}=b^{-4/(2\beta-3)} \tag{23}$$

we obtain a generalized form of Eq. (9)

$$\phi''=b^2\phi^\beta \tag{24}$$

which gives, in virtue of the boundary condition $\phi(\infty)=\phi'(\infty)=0$ and the subsidiary condition $\phi'(x)<0$, the first integral

$$-\phi'\left(\frac{\beta+1}{2}\right)^{1/2}\phi^{-(\beta+1)/2}=b\ , \tag{25}$$

and further, on account of the boundary condition $\phi(0)=1$, the approximate TF solution

$$\phi(x)=1/(1+Bx)^n \tag{26}$$

with

$$B\equiv\frac{\beta-1}{2}\left(\frac{2}{\beta+1}\right)^{1/2}b\quad\text{and}\quad n\equiv\frac{2}{\beta-1}\ , \tag{26a}$$

a homologue proposed ever by Umeda[9], of which the special cases of $n=1$ and 2 are just the forms given by Kerner, Eq. (4), and Tietz, Eq. (8), respectively.

The value of β is restricted due to Eq. (12) in the range

$$\infty>\beta>5/3\approx1.7\ , \tag{27}$$

so that $\beta=2$, Tietz value, and $\beta=3$, Kerner value, are the smallest and the next smallest possible integers respectively. Correspondingly, the value of n lies in the range

$$3>n>0\ , \tag{28}$$

so that $n=1$, Kerner value, and $n=2$, Tietz value, are the only two possible integers. These circumstances characterize both forms, Kerner and Tietz, Eqs. (4) and (8):

The most suitable values of the adjustable parameters B and n follow from the approximation degree of the above solution Eq. (26); thus

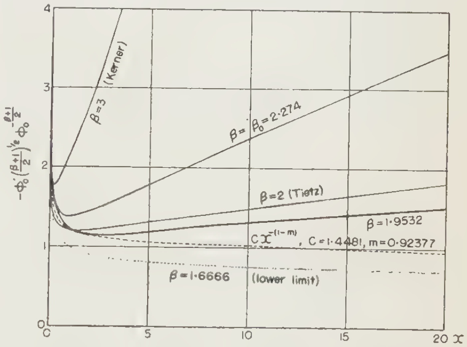

Fig. 3. Dependence of the lefthand side of the first integral of the generalized Tietz equation, $-\phi_0'[(\beta+1)/2]^{1/2}\phi_0^{-(\beta+1)/2}$, upon x and its approximation by a power function $cx^{-(1-m)}$ with $c=1.4481$ and $m=0.92377$, cf. Eq. (25).

$$B=0.8861\quad\text{and}\quad n=1.394 \tag{29}$$

and correspondingly

$$b=1.864,\ \beta=2.435\ \text{ and }\ \sigma=0.5349 \tag{29a}$$

The detailed discussion on this homologue has been recently carried out by Tietz[10] in close connection with us.

§ 5. Sommerfeld-March Homologue

Meanwhile we have evaluated the lefthand side of the above first integral, Eq. (25), for a number of values of β by substituting the exact TF function ϕ_0, as shown in Fig. 3. The weak upward concavities of these curves could be taken into consideration if the constant b in the righthand side of the first integral, Eq. (25), would be replaced by a slowly varying power function $cx^{-(1-m)}(m<1)$ with likewise weak upward concavity. Then, we obtain an approximate TF solution with three adjustable parameters, more generalized than Eq. (26) with two of these,

$$\phi(x)=1/(1+Cx^m)^n \tag{30}$$

with

$$C\equiv\frac{\beta-1}{2}\left(\frac{2}{\beta+1}\right)^{1/2}c \quad\text{and}\quad n\equiv\frac{2}{\beta-1}\ , \tag{30a}$$

a homologue, of which the Sommerfeld-March-Umeda asymptotic solutions, Eqs. (1) to (3), are the special cases satisfying in addition the asymptotic condition $\phi(x\gg1)\sim144/x^3$.

The values of the adjustable parameters C, m and n should be determined on the basis of the approximation degree of the above solution Eq. (30)

$$I\left[\frac{1}{(1+Cx^m)^n}\right]=mn^2C^{1/m}B\left(2n+\frac{1}{m}\ ,\ 2-\frac{1}{m}\right)+\frac{4}{5m}\frac{1}{C^{1/(2m)}}B\left(\frac{5n}{2}-\frac{1}{2m}\ ,\ \frac{1}{2m}\right), \tag{31}$$

$B(p, q)$ being beta-function, by three simultaneous equations

$$C^{(3/2m)}=\frac{2}{5m^2n^2}\left[\Gamma\left(\frac{5n}{2}-\frac{1}{2m}\right)\Gamma\left(\frac{1}{2m}\right)\Gamma(2n+2)\right]\Big/\left[\Gamma\left(\frac{5n}{2}\right)\Gamma\left(2-\frac{1}{m}\right)\Gamma\left(2n+\frac{1}{m}\right)\right],$$

$$m=\psi\left(2-\frac{1}{m}\right)+\psi\left(\frac{5n}{2}-\frac{1}{2m}\right)-\psi\left(\frac{1}{2m}\right)-\psi\left(2n+\frac{1}{m}\right),$$

and

$$n=1\Big/\left[\psi(2n+2)-\psi\left(2n+\frac{1}{m}\right)+\frac{5}{2}\psi\left(\frac{5n}{2}\right)-\frac{5}{2}\psi\left(\frac{5n}{2}-\frac{1}{2m}\right)\right], \tag{32}$$

ψ being psi-function. These equations give in turn the following suitable values of parameters

$$C=0.51092,\quad m=0.92377 \text{ and } n=2.0982 \tag{33}$$

and correspondingly

$$c=1.4481,\quad \beta=1.9532 \quad\text{and}\quad \sigma=1.1033\ . \tag{33a}$$

The corresponding value of the degree of approximation is

$$I[1/(1+Cx^m)^n]=1.3614, \tag{34}$$

a value surprisingly near to its limiting value

$$I_{\text{limit}}=I[\phi_0]=1.36124 \tag{35}$$

which has been evaluated anew by us using the most accurate values of the standard TF function recalculated recently by Matsukuma, Nagai and us[11]. Thus, the above approximate solution, Eq. (30), has the highest approximation degree among the hitherto known approximate solutions.

Since the above values of m, n and β Eqs. (33) and (33a) can be rounded into $m=1$, $n=2$ and $\beta=2$, Tietz values, it can be said that the Tietz form, Eq. (8), is quite a good approximation.

§ 6. Remark

This work was supported by a Grant in Aid for Fundamental Scientific Research from the Ministry of Education of Japan as a program of Research Group for the Study of Atomic and Molecular Structure.

References

1) A. Sommerfeld: Z. Phys. **78** (1932) 283.
2) N. H. March: Proc. Camb. Phil. Soc. **46** (1950) 356.
3) K. Umeda: J. Phys. Soc. Japan **9** (1954) 290.
4) E. H. Kerner: Phys. Rev. **83** (1951) 71.
5) H. C. Brinkman: Physica **20** (1954) 44.
6) T. Tietz: J. Chem. Phys. **22** (1954) 2094; Ann. d. Phys. VI **15** (1955) 186.
7) C. Miranda: Mem. Acc. Italia **5** (1934) 283.
8) For instance, G. N. Watson: *Theory of Bessel Functions*, Cambridge, 1922, p. 96.
9) K. Umeda: Private Communication to Dr. Tietz.
10) T. Tietz: Private Communication, scheduled to be published shortly in Phys. Rev.
11) S. Kobayashi, T. Matsukuma, S, Nagai and K. Umeda: J. Phys. Soc. Japan **10** (1955) 759.

JOURNAL OF THE PHYSICAL SOCIETY OF JAPAN Vol. 10, No. 9, SEPTEMBER, 1955

On the Influence of the Packing on the Atomic Scattering Factor Based on the Thomas-Fermi Theory*

By Kwai UMEDA and Yasuo TOMISHIMA

Department of Physics, Faculty of Science, Okayama University

(Received May 6, 1955)

The influence of the juxtaposition in the crystal on the atomic scattering factor has been investigated on the basis of the Thomas-Fermi (abbreviated as TF) theory, using the TF functions appropriate to the packed neutral atoms. It is pronounced especially for the smaller values of $\sin\theta/\lambda\cdot Z^{-1/3}$. The values of the atomic scattering factor for free neutral atom have been recalculated anew, using the most accurate Miranda values of the free neutral TF function.

§ 1. Previous Calculations of the Atomic Scattering Factor

The atomic scattering factor (the atomformfactor) of a spherically symmetrical atom or ion at rest, i.e. without thermal agitation and zero point vibration, denoted according to James by f_0, is defined by a general expression

$$f_0=\int_0^{r_0}\frac{\sin kr}{kr}\rho\,4\pi r^2dr \qquad (1)$$

with r_0=radius of the atomic sphere or half the lattice spacing, ρ=electron number density, $k=4\pi\sin\theta/\lambda$ and θ=half the angle of of scattering or glancing angle of reflexion. The values of f_0 have been extensively calculated and tabulated, ρ being expressed in terms of

1. hydrogenlike wave function (Pauling and Sherman[1]),
2. Hartree selfconsistent field (James and Brindley[2]),
3. TF function for free neutral atom or ion (Bragg and West[3]),
4. approximate TF function for free neutral atom (Nagy[4], Kerner[5] and Umeda[6])

or the like. It is necessary to emphasize the fact that these f_0-curves refer all to the free atoms or the free ions.

§ 2. Scope of the Present Calculation

As many investigators[2),3)] remarked, the f_0-curve appropriate to an atom in the crystal will be somewhat different from that calculated for the atom in the free space. In determining the shape of the f_0-curve, the inner electrons which are not influenced by the exterior are in general of prime importance, while the outer electrons can play a role only for small values of k, since their effects cancel so rapidly by interference as k increases. The juxtaposition of the atom in the crystal must disturb mainly the outer electrons, so that its influence on the shape of the f_0-curve should be noticeable only for small values of k. This expected influence of the packing on the atomic scattering factor has been investigated in this paper on the basis of the TF theory, using the TF functions appropriate to the packed neutral atoms, since for atoms with $Z>25$ the TF method may be quite accurate enough.

§ 3. Process of the Calculation

In the case of an atom with atomic number Z, substituting the TF density

$$\rho=\frac{Z}{4\pi\mu^3}\left(\frac{\phi}{x}\right)^{3/2}, \qquad (2)$$

$$=\frac{Z}{4\pi\mu^3}\frac{\phi''}{x}, \qquad (2a)$$

with ϕ=TF function, $x=r/\mu$ and μ=TF unit in Eq. (1), we have the basic expression of the atomic scattering factor per electron** for a packed TF atom

$$\mathfrak{f}_0=\frac{f_0}{Z}=\frac{1}{k\mu}\int_0^{x_0}\sin(k\mu)x\cdot\frac{\phi^{3/2}}{x^{1/2}}dx\,, \qquad (3)$$

$$=1-(k\mu)\int_0^{x_0}\sin(k\mu)x\cdot\phi dx+\left(\frac{\sin(k\mu)x_0}{(k\mu)x_0}-\cos(k\mu)x_0\right)\phi(x_0)\,, \qquad (3a)$$

---

* Published partly in the form of a Letter to the Editor in the J. Chem. Phys. **21** (1953) 2085.

** The concept of the atomic scattering factor per electron and its notation $\mathfrak{F}$ are due to Bethe. In regard to the notation we adopt, however, rather $\mathfrak{f}_0$ instead of $\mathfrak{F}_0$, since for the atomic scattering factor itself we take with James. f_0, while Bethe uses F.

with $x_0 = r_0/\mu$, provided that Eq. (3a) is valid for a neutral atom only, since the boundary condition for neutrality

$$\phi'(x_0) = \phi(x_0)/x_0 \tag{4}$$

determining the value of x_0, is contained in it.

It is noteworthy that for the packed TF atom, $\mathfrak{f}_0$ is likely an universal function of the arguement

$$k\mu = \frac{\sin\theta}{\lambda}\frac{1}{Z^{1/3}}\pi\left(\frac{9\pi^2}{2}\right)^{1/3} a_0\,,$$
$$= \xi\cdot 5.88706\,, \tag{5}$$

this numerical coefficient being due to the currently most accurate value given by Du Mond and Cohen[7] $a_0 = 0.529151\cdot 10^{-8}$ cm, or the arguement introduced by Bethe[8]

$$\xi = \frac{\sin\theta}{\lambda}\frac{1}{Z^{1/3}}\cdot 10^{-8} \tag{6}$$

alone, and not dependent upon $\sin\theta/\lambda$ and Z individually, as it has been previously pointed out by Bethe to be the case for the free TF atom. Thus, we will consider in the followings rather $\mathfrak{f}_0$ than f_0 itself.

For the direct numerical evaluation of $\mathfrak{f}_0$, Eq. (3) is more suitable than Eq. (3a), since Eq. (3) is less sensible than Eq. (3a) to the boundary values which can be determined in general only with comparatively poor precision. The values of the TF functions for a number of the value of x_0 were tabulated previously by Slater and Krutter[9], then by Feynman, Metropolis and Teller[10], and recently with higher accuracy by March[11]. By means of the Slater-Krutter values of ϕ for x_0=0.825, 1.194, 1.69 and 2.205, ignoring their lower accuracy, as well as the March ones for x_0=2.800, 3.043, 3.285, 3.704, 4.330, 5.229, 6.206 and 7.790, we have numerically calculated the values of $\mathfrak{f}_0$ for sixteen different values of $k\mu$,, from 0° to 200° in step of 12.5°, by the Filon[12] method for evaluating the Fourier integrals. The values of $\mathfrak{f}_0$ thus obtained are columned in Table I.

Table I. Values of $\mathfrak{f}_0$ in function of ξ and x_0, cf. Eqs. (3), (5) and (6).

$k\mu$	$\frac{\xi}{0.03706}$	ξ	$\mathfrak{f}_0(\xi, x_0)$													
			$x_0=0$	0.825	1.194	1.69	2.205	2.800	3.043	3.285	3.704	4.330	5.229	6.206	7.790	∞(free)
0°	0	0	1.0000	1.0000	1.0000	1.0000	1.0000	1.0000	1.0000	1.0000	1.0000	1.0000	1.0000	1.0000	1.0000	1.0000
12.5°	1	0.0371	1.0000	0.9983	0.9975	0.9938	0.9861	0.9768	0.9729	0.9700	0.9644	0.9562	0.9449	0.9333	0.9167	0.8641
25.0°	2	0.0741	1.0000	0.9898	0.9807	0.9635	0.9384	0.9100	0.8984	0.8872	0.8682	0.8406	0.8051	0.7727	0.7343	0.7035
37.5°	3	0.1112	1.0000	0.9758	0.9536	0.9146	0.8653	0.8095	0.7876	0.7665	0.7321	0.6865	0.6354	0.5990	0.5739	0.5834
50.0°	4	0.1482	1.0000	0.9564	0.9164	0.8498	0.7723	0.6884	0.6572	0.6286	0.5848	0.5341	0.4911	0.4750	0.4823	0.4904
62.5°	5	0.1853	1.0000	0.9319	0.8704	0.7723	0.6668	0.5617	0.5259	0.4951	0.4528	0.4143	0.3996	0.4080	0.4242	0.4192
75.0°	6	0.2224	1.0000	0.9026	0.8168	0.6868	0.5572	0.4432	0.4093	0.3829	0.3533	0.3390	0.3509	0.3675	0.3666	0.3631
87.5°	7	0.2594	1.0000	0.8689	0.7568	0.5964	0.4523	0.3437	0.3178	0.3014	0.2908	0.3001	0.3222	0.3260	0.3152	0.3181
100.0°	8	0.2965	1.0000	0.8313	0.6925	0.5060	0.3575	0.2691	0.2554	0.2514	0.2586	0.2801	0.2927	0.2824	0.2805	0.2819
112.5°	9	0.3335	1.0000	0.7901	0.6250	0.4190	0.2781	0.2202	0.2196	0.2262	0.2441	0.2624	0.2569	0.2471	0.2539	0.2515
125.0°	10	0.3706	1.0000	0.7460	0.5561	0.3390	0.2169	0.1934	0.2032	0.2159	0.2340	0.2388	0.2235	0.2246	0.2269	0.2265
137.5°	11	0.4077	1.0000	0.6997	0.4873	0.2684	0.1739	0.1821	0.1975	0.2102	0.2199	0.2105	0.1998	0.2076	0.2035	0.2050
150.0°	12	0.4447	1.0000	0.6498	0.4203	0.2093	0.1473	0.1796	0.1941	0.2018	0.1997	0.1840	0.1853	0.1893	0.1869	0.1869
162.5°	13	0.4818	1.0000	0.6028	0.3563	0.1622	0.1351	0.1784	0.1873	0.1876	0.1762	0.1647	0.1738	0.1704	0.1723	0.1711
175.0°	14	0.5188	1.0000	0.5516	0.2961	0.1273	0.1317	0.1741	0.1751	0.1686	0.1545	0.1534	0.1610	0.1555	0.1573	0.1576
187.5°	15	0.5559	1.0000	0.5014	0.2422	0.1039	0.1341	0.1646	0.1582	0.1483	0.1384	0.1464	0.1460	0.1455	0.1448	0.1456
200.0°	16	0.5929	1.0000	0.4519	0.1953	0.0904	0.1366	0.1505	0.1396	0.1305	0.1290	0.1394	0.1328	0.1366	0.1355	0.1350

§4. The Packed $\mathfrak{f}_0(\xi)$-Curve with x_0 as Parameter

For the sake of simplicity only two packed $\mathfrak{f}_0(\xi)$-curves of x_0=2.800 and 4.330 respectively are shown in Fig. 1 in comparison with the free one ($x_0=\infty$) in function of ξ. From the figure we see the expected influence of the packing on the atomic scattering factor in such a way that the deviation of the packed $\mathfrak{f}_0$-curve from the free one is of course more noticeable with the increasing packing and pronounced especially for the smaller values of ξ. It seems to be of interest that the packed $\mathfrak{f}^0$-curves ($x_0=$finite) converge into the free one, fluctuating about this more frequently with weakened packing, i.e. with increasing value of x_0. The systematic fluctuating course of the value of

$$\delta f_0=f_{0\ \mathrm{exp}}-f_{0\ \mathrm{Hartree\ (free)}}$$

in function of $\sin\theta/\lambda$, in particular the positive values of δf_0 for the very small values of $\sin\theta/\lambda$, observed by Wasastjerna[13] (cf. his Fig. 1), seems to be in favor to our theoretical results.

§ 5. The Packed $\mathfrak{f}_0(\xi)$-Curve in the Neighborhood of $\xi=0$

For the packed atom the sufficiently small values of k simplify the definition formula Eq. (1) in such a way as

$$\mathfrak{f}_0(k\ll 1,\ r_0=\text{finite})$$
$$=\int_0^{r_0}\left[1-\frac{1}{6}(kr)^2\right]\frac{\rho}{Z}4\pi r^2 dr\ ,$$
$$=1-\frac{k^2}{6}\overline{r^2}\ , \tag{7}$$

where $\overline{r^2}$ means the mean value of r^2 taken over the volume of the atomic sphere. It should be remembered that this expansion is not allowable for free atom ($r_0=\infty$).

The value of $\overline{r^2}$ can be evaluated for any neutral atom, packed as well as free, by means of Eqs. (2a) and (4) in such a way as

$$\overline{r^2}(x_0)=6\mu^2\left(\int_0^{x_0}x\phi dx-\frac{1}{3}x_0^2\phi(x_0)\right) \tag{8}$$

which becomes in the limiting case of the extremely high compression, i.e. $x_0\rightarrow 0$,

$$\overline{r^2}(x_0)=6\mu^2\frac{x_0^2}{8} \tag{9}$$

by the use of the TF function appropriate to this case

$$\phi(x)=1+\frac{1}{2}\left(\frac{x}{x_0}\right)^3-\frac{3}{2}\frac{x}{x_0}+3^{2/3}\frac{x}{x_0^2} \tag{10}$$

given by Gilvarry[14] recently, and in the other limiting case of the free state, i.e. $x_0\rightarrow\infty$,

$$\overline{r^2}(\text{free})=6\mu^2\int_0^\infty x\phi_{\text{free}}\,dx \tag{11}$$

since $x_0^2\phi(x_0)\approx x_0^2\phi_{\text{free}}(x_0)\approx 144/x_0\rightarrow 0$. Thus, the normalized value of $\overline{r^2}$ or the ratio of $\overline{r^2}$ (packed) to $\overline{r^2}$ (free)

$$\omega(x_0)\equiv\frac{\overline{r^2}(x_0)}{\overline{r^2}(\text{free})}=\left[\int_0^{x_0}x\phi dx-\frac{1}{3}x_0^2\phi(x_0)\right]\Big/\int_0^\infty x\phi_{\text{free}}\,dx \tag{12}$$

is an universal, monotonously increasing function of x_0 independent upon Z, and its values

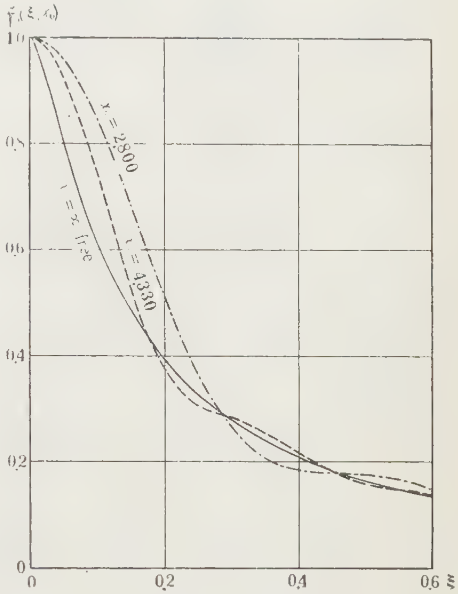

Fig. 1. Two packed $\mathfrak{f}_0(\xi, x_0=\text{const})$-curves of $x_0=2.800$ and 4.330 in comparison with the free one ($x_0=\infty$).

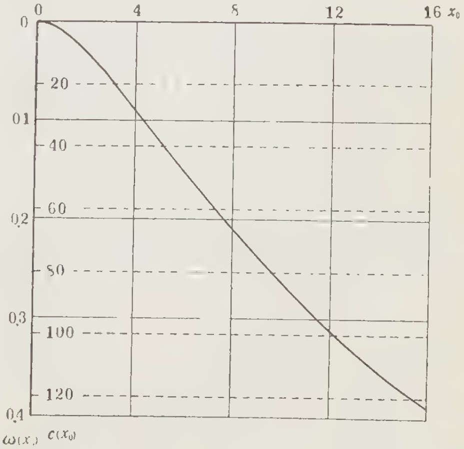

Fig. 2. $\omega(x_0)$- or $c(x_0)$-curve, ω- or c-axis being taken downwards for the sake of convenience to determine the initial slopes of $\mathfrak{f}_0(\xi, x_0=\text{finite})$-curves in Fig. 1 as well as $\mathfrak{f}_0(x_0, \xi=\text{finite})$-curve in Fig. 4, cf. Eqs. (12), (14), (14a) and (18).

Table II. Values of $\omega(x_0)$ and $c(x_0)$, cf. Eqs. (12), (14) and (14a).

x_0	$\omega(x_0)$	$c(x_0)$
0.000	0.00000	0.00
0.825	0.00652	2.07
1.194	0.01288	4.09
1.69	0.02362	7.50
2.205	0.03687	11.71
2.800	0.05392	17.12
3.043	0.06120	19.43
3.285	0.06861	21.79
3.704	0.08163	25.92
4.330	0.10140	32.20
5.229	0.12971	41.19
6.206	0.15984	50.76
7.385	0.19473	61.84
7.790	0.20610	65.45
8.588	0.22782	72.34
9.565	0.25355	80.51
10.804	0.28367	90.08
11.963	0.31017	98.49
15.870	0.38711	122.92
16.000	0.38858	123.39
∞(free)	1.00000	315.81

are given numerically in Table II and graphically in function of x_0 in Fig. 2. Due to the x_0^2-dependence given by Eq. (9), the $\omega(x_0)$-curve commences at the origin tangentially to the x_0-axis and approaches asymptotically to the limiting value unity.

The dependence of $\overline{r^2}$ upon x_0 embodies mutatis mutandis the dependence of the diamagnetic susceptibility of the spherically symmetrical atom upon its radius

$$\chi_{at}\,(\text{packed}) = -\frac{Le^2}{6mc^2}\sum\overline{r^2}(x_0)$$
$$=\chi_{at}\,(\text{free})\;\omega(x_0) \qquad (13)$$

At any rate, so long as the packing is finite, i.e. $x_0<\infty$, Eq. (7) may be written due to Eqs. (5) and (8) in such a simple function of ξ as

$$\mathfrak{f}_0(k\mu\ll 1,\ x_0=\text{finite}) = 1-c(x_0)\xi^2 \qquad (14)$$

where

$$c(x_0) = 34.657\left[\int_0^{x_0} x\phi dx - \frac{1}{3}x_0^2\,\phi(x_0)\right] \qquad (14\text{a})$$
$$=3.1581\cdot 10^2\omega(x_0)$$

the numerical coefficient

$$34.657=(5.88706)^2=\pi^2(9\pi^2/2)^{2/3}a_0^2$$

following from that in Eq. (5). Eq. (14) is also equally derivable from Eq. (3a) on putting $k\mu\ll 1$. The numerical values of $c(x_0)$ are given in Table II, too. Due to the ξ^2-dependence given by Eq. (14) the packed $\mathfrak{f}_0(\xi)$-curves with definite values of x_0 commence all at the value unity with the initial tangent parallel to the ξ-axis, whatever x_0 is, and decrease with increasing value of ξ the more steeply, the weaker the compression is, i.e. the greater x_0 is, as shown in Fig. 1.

In the contrary, for the free atom it is needed rather to proceed from the rigorous formula following from Fq. (3a)

$$\mathfrak{f}_0(k\mu=\text{finite},\ x_0=\infty)$$
$$=1-(k\mu)\int_0^\infty \sin\,(k\mu)x\cdot\phi_{\text{free}}\,dx \qquad (15)$$

The dependence of $\int_0^\infty \sin\,(k\mu)x\cdot\phi_{\text{free}}\,dx$ upon $k\mu$ in the limit $k\mu\to 0$ demands the careful investigation. Since ϕ_{free} behaves asymptotically like $144/x^3$, the approximation

$$\int_0^\infty \sin\,(k\mu)x\cdot\phi_{\text{free}}\,dx \approx k\mu\int_0^\infty x\phi_{\text{free}}\,dx \qquad (16)$$

may be allowable, while the approximate analytical formulas for ϕ_{free} do not give straightforwards the linear dependence of the integral upon $k\mu$, for instance the Rozental[15] three exponential terms formula gives $(k\mu)$ 4.8704 and the Kerner formula a diverging value. Thus, Bethe has rounded Eq. (15) into the following form similar to Eq. (14)

$$\mathfrak{f}_0(\xi\ll 1,\ \text{free})$$
$$=1-(5.85\,\xi)^2\int_0^\infty x\phi_{\text{free}}\,dx \approx 1-160\,\xi^2\,. \qquad (17)$$

This numerical coefficient 160 seems to be less reliable, as it resultates $\int_0^\infty x\phi_{\text{free}}\,dx\approx 4.62$, while the Sommerfeld[16] asymptotic formula and the most accurate Miranda[17] values for ϕ_{free} give $\int_0^\infty x\phi_{\text{free}}\,dx=8.8065$ and 9.1124 respectively and followingly the numerical coefficient corresponding to 160 in Eq. (17) such as 305.21 and 315.81 respectively.

§ 6. The Free $\mathfrak{f}_0(\xi)$-Curve as the Convergence Limit of the Sequence of the Packed Ones

As mentioned above, the packed $\mathfrak{f}_0(\xi)$-curves converge with vanishing compression, i.e. $x_0\to\infty$, naturally into the free $\mathfrak{f}_0(\xi)$-curve, in particular more closely in the region of larger larger values of ξ. The free TF $\mathfrak{f}_0(\xi)$-curve accepted usually as the standard is that calculated by Bragg and West from the charge distribution given by Thomas[18] initially. That has, however, in the region of larger values of ξ, somewhat too small values for the convergence limit of the sequence of the packed $\mathfrak{f}_0(\xi)$-curves. Therefore, we have recalculated the values of the free $\mathfrak{f}_0$ anew using in Eq. (3) the most accurate Miranda values of ϕ_{free}. Our numerical values are given in Table III in comparison with the Bragg-West values. Our free $\mathfrak{f}_0(\xi)$-curve runs just in the position expected from the sequence of the packed ones, as shown in Fig. 3.

Table III. Values of staadard $\mathfrak{f}_0$(free) recalculated by Umeda and Tomishima anew in comparison with those given by Bragg and West in function of $(\sin\theta/\lambda)_{\text{Cs}}$ or ξ, cf. Eqs. (3) and (6).

$\left(\frac{\sin\theta}{\lambda}\right)_{\text{Cs}}\cdot 10^{-8}$	ξ	$\mathfrak{f}_0$(free)	
		U–T	B–W
0.0	0.00000	1.0000	1.000
0.1	0.02630	0.9130	0.922
0.2	0.05259	0.7983	0.796
0.3	0.07889	0.6857	0.684
0.4	0.10518	0.6002	0.589
0.5	0.13148	0.5295	0.522
0.6	0.15777	0.4702	0.469
0.7	0.18407	0.4212	0.422
0.8	0.21036	0.3799	0.378
0.9	0.23666	0.3446	0.342
1.0	0.26295	0.3143	0.309
1.1	0.28925	0.2884	0.284
1.2	0.31554	0.2656	0.264
1.3	0.34184	0.2455	0.240
1.4	0.36814	0.2280	0.224
1.5	0.39443	0.2123	0.205
1.6	0.42073	0.1983	0.189
1.7	0.44702	0.1859	0.175
1.8	0.47332	0.1745	0.167
1.9	0.49961	0.1644	0.156
2.0	0.52591	0.1551	0.147

§ 7. The Packed $\mathfrak{f}_0(x_0)$-Curves with ξ as Parameter

Now, on interchanging the roles of ξ and x_0 in Fig. 1, all values of $\mathfrak{f}_0$ are plotted in Fig. 4 in function of x_0 with ξ as parameter, which embodies the expected influence of the packing on the atomic scattering factor more directly in the following way. That is, as the packing proceeds on from the free state, i.e. as the value of x_0 decreases from ∞, the $\mathfrak{f}_0(x_0)$-curves with smaller scattering angles (smaller values of ξ) increase immediately and further monotonously, while those with larger scattering angles (larger values of ξ) remain nearly unaffected up to the very high packing, except of small fluctuations.

For sufficiently high packing ($x_0 \ll 1$) we obtain from Eq. (3a) just the same equation as Eq. (14)

$$\mathfrak{f}_0(x_0 \ll 1,\ k/\mu = \text{finite}) = 1-(k/\mu)^2\left[\int_0^{x_0} x\phi\, dx - \frac{1}{3}\, x_0^2\,\phi(x_0)\right]. \quad (18)$$

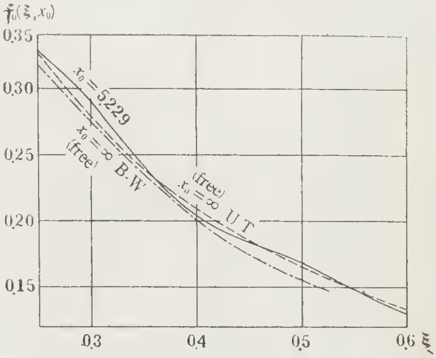

Fig. 3. Comparison of $\mathfrak{f}_0$(free)-curve recalculated by Umeda and Tomishima (U–T) anew with that given by Bragg and West (B–W) previously for the convergence limit of the sequence of the $\mathfrak{f}_0$(packed)-curves in function of ξ.

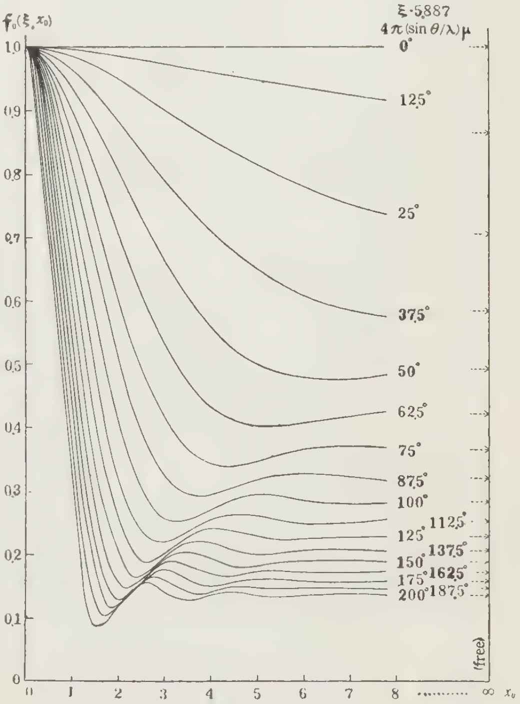

Fig. 4. $\mathfrak{f}_0(x_0, \xi = \text{const})$-curves.

which means that the shapes of all the $\mathfrak{f}_0(x_0)$-curves are similar to the $\omega(x_0)$-curve given in Fig. 3 in scale of $(k\mu)^2$.

Finally, in the limit of $x_0 \approx 0$, Eq. (18) reduces by taking account of Eqs. (8) and (9) to

$$\mathfrak{f}_0(x_0\approx 0,\ k\mu=\text{finite}) = 1-(k\mu)^2\frac{x_0^2}{8}\ . \qquad (19)$$

Due to this x_0^2-dependence all the $\mathfrak{f}_0(x_0)$-curves meet together with the same tangent parallel to the x_0-axis at the limiting value unity, i.e. the value of $\mathfrak{f}_0$ for a point charge, whatever the value of $k\mu$ is.

§ 8. Remarks

The expected influence of the packing on the atomic scattering factor is hereby theoretically ascertained. But, by taking it into account that the packings in the existing crystals are of such order of magnitude as $x_0=8$ to 20 for atoms with $Z > ca.$ 10, as seen from the table given by Mott and Jones[19], it may be said that the values of the atomic scattering factors for the free atoms can be simply sufficient for practical use without regard to the packing, whereas for lighter atoms with $Z < ca.$ 10 the influence of the packing should be taken into consideration, since for instance $x_0=5.3$ (Li), 4.2 (Be) etc.

A supplement to this paper containing the figures for Cs-atom taken usually as the standard atom for the calculation of the TF atomic scattering factor will be shortly published in the Research Notes of the Department of Physics, Faculty of Science, Okayama University, Okayama, Japan.

In conclusion, the authors wish to express their best thanks to Professors James at University of Cape Town and MacGillavry at University of Amsterdam for their kind interests in this work after the publication of their letter to the editor referred to above.

This work was supported by a Grant in Aid for Fundamental Scientific Research from the Ministry of Education of Japan, which was given to one of the authors (U) a member of the Research Group for the Study of Atomic and Molecular Structure as well as of that of Mathematical Physics.

References

1) L. Pauling and J. Sherman: Z. Kritst. **81** (1932) 1.
2) W. L. Bragg and J. West: Z. Krist. **69** (1928) 118.
3) R. W. James and G. W. Brindley: Phil. Mag. **12** (1931) 81.

Appendix

Table IV. Radii of atomic spheres of metals, r_0 in 10^{-8} cm and x_0 in TF unit.

Z	Metal	r_0	x_0	Z	Metal	r_0	x_0
3	Li	1.72	5.30	42	Mo	1.55	11.5
4	Be	1.24	4.20	44	Ru	1.48	11.2
11	Na	2.10	9.97	45	Rh	1.49	11.3
12	Mg	1.76	8.60	46	Pd	1.54	11.8
13	Al	1.58	7.93	47	Ag	1.59	12.3
19	K	2.61	14.9	48	Cd	1.73	13.3
20	Ca	2.16	12.5	49	In	1.84	14.4
22	Ti	1.62	9.69	50	Sn	1.86	14.6
23	V	1.52	9.23	51	Sb	1.93	15.3
24	Cr	1.42	8.74	55	Cs	3.04	24.7
25	Mn	1.43	8.93	56	Ba	2.47	20.2
26	Fe	1.40	8.85	57	La	2.07	17.0
27	Co	1.38	8.84	72	Hf	1.76	15.6
28	Ni	1.38	8.95	73	Ta	1.64	14.6
29	Cu	2.41	15.8	74	W	1.56	14.0
30	Zn	1.53	10.15	75	Re	1.51	13.6
31	Ga	1.67	11.2	76	Os	1.49	13.5
32	Ge	1.74	11.8	77	Ir	1.50	13.6
33	As	1.73	11.8	78	Pt	1.53	14.0
37	Rb	2.81	20.0	79	Au	1.59	14.6
38	Sr	2.36	16.9	80	Hg	1.76	16.2
39	Y	1.97	14.3	81	Tl	1.89	17.5
40	Zr	1.71	12.5	82	Pb	1.93	17.9
41	Nb	1.63	12.0	83	Bi	2.03	18.9

The values of r_0 are reproduced from N. F. Mott and H. Jones: *The Theory of the Properties of Metals and Allops*, Oxford, 1936, p. 318.

4) B. v. Sz. Nagy: Z. Phys. **91** (1934) 105.
5) E. H. Kerner: Phys. Rev. **83** (1951) 71.
6) K. Umeda: J. Fac. Sci., Hokkaido Univ., Japan, Ser. II, **4** (1951) 57.
7) J. V. W. Du Mond and E. R. Cohen: Phys. Rev. **82** (1951) 555.
8) H. A. Bethe: Ann. d. Phys. V **5** (1930) 325.
9) J. C. Slater and H. M. Krutter: Phys. Rev. **47** (1935) 559; P. Gombás: *Die statistische Theorie des Atoms und ihre Anwendungen*, Springer-Verlag, Vienna (1949), p. 357.
10) R. P. Feynman, N. Metropolis and E. Teller: Phys. Rev. **75** (1949) 1561.
This was not used in our calculation, since the arguement is $(2x)^{1/2}$ and the values of the initial slope are inconsistent with the Slater-Krutter as well as March ones.
11) N. H. March: Proc. Camb. Phil. Soc. **48** (1952) 665.
12) I. N. G. Filon: Proc. Roy. Soc. Edinburgh A**49** (1929) 38.
13) J. A. Wasastjerna: Soc. Sci. Fennica, Comm. Phys.-Math. **13** (1946) 1.
14) J. J. Gilvarry: Phys. Rev. **96** (1954) 934.
15) S. Rozental: Z. Phys. **98** (1935) 742.
16) A. Sommerfeld: Z. Phys. **78** (1932) 283.
17) C. Miranda: Mem. Acc. Italia **5** (1934) 283.
18) L. H. Thomas: Proc. Camb. Phil. Soc. **23** (1927) 542.
19) N. F. Mott and H. Jones: *The Theory of the Properties of Metals and Alloys*, Oxford, 1936, Appendix II, p. 318.

JOURNAL OF THE PHYSICAL SOCIETY OF JAPAN Vol. 10, No. 9, SEPTEMBER, 1955

Accurate Value of the Initial Slope of the Ordinary TF Function

By Shigehiro KOBAYASHI
Department of Physics, Kagawa University, Takamatsu,
late Takehiko MATSUKUMA
Department of Astronomy, Tohoku University, Sendai,
Sokichi NAGAI
Department of Mathematics, Iwate University, Morioka,
and Kwai UMEDA
Department of Physics, Okayama University, Okayama

(Received June 17, 1955)

By the inward numerical integration of the TF equation the accurate values of the initial slope as well as the asymptotic parameter of the ordinary TF function have been ultimately determined as

$$B_0=1.5880710$$

and

$$F_0=13.270934,$$

and the exact values of the function itself have been tabulated.

§ 1. Scope of the Present Calculation

The ordinary Thomas-Fermi (abbreviated as TF) function, i.e. the solution of the TF equation

$$\phi''=\phi^{3/2}/x^{1/2} \tag{1}$$

subject to the boundary conditions for an isolated neutral atom

$$\phi(0)=1 \tag{2}$$

and

$$\phi(\infty)=\phi'(\infty)=0 \tag{2a}$$

has been computed hitherto by a number of investigators referred to in Table I. They have carried out the outward numerical integration ($x=0\rightarrow\infty$) for a sequence of values of initial slope converging step-by-step to that of the final curve which should approach the x-axis asymptotically. However, the integral curve is very sensitive to small change in the initial slope and its tangency to the x-axis at infinity is very difficult to ascertain so that the final values of the initial slope obtained by them are different from each other as seen in Table I, even though the calculation has been carried out in particular by Miranda so extensively and so precisely.

One of us (M) noted that these difficulties could be avoided by using the inward numerical integration ($x=\infty\rightarrow 0$), and a similar procedure was employed by another of us (U)[7] successfully to overcome the similar difficulties occuring in the case ot the TFD function subject to the Brillouin boundary condition. In regard to the former, only the final value of the initial slope obtained preliminarily by him, $B_0=1.5880706$, was cited by the latter[6]. Recently, quite independently from us, March[7] has extensively discussed about the inward integration in order to obtain the TF function of the type needed in the investigation of the TF field for molecules with tetrahedral and octahedral symmetry.

Table I. Values of the initial slope of the ordinary TF function given by several investigators.

Investigator	$B_0=-\phi_0'(0)$
Baker (1930)[1]	1.588558
Bush-Caldwell (1931)[2]	1.589
Miranda (1934)[3]	1.5880464
Slater-Krutter (1935)[4]	1.58808
Feynman-Metropolis-Teller (1949)[5]	1.58875

In this paper we have evaluated again along the line of calculation mentioned above the value of the initial slope of the ordinary TF function ultimately as accurate as possible and also the values of the function itself.

§ 2. Process of Calculation

For the first range $\infty\geqslant x\geqslant 1$ it is convenient to introduce the change of variables $y\equiv 1/x$ as taken usually about infinity, and $\psi\equiv -x^2\phi'$.

1. We start from $y=0$ ($x=\infty$) and calculate first the values of ϕ, $d\phi/dy$, $d^2\phi/dy^2$ for six small values of y, $y=0.0200$ to 0.0225 in step

0.0005, the starting values for the numerical integration routine of $y=0\to1$, with accuracy of ten effective digits for ϕ, for instance $\phi=0.00063\ 94955\ 298$, $d\phi/dy=0.08241\ 97762\ 3$ and $d^2\phi/dy^2=6.05194\ 032$ for $x=0.0200$, using the Coulson-March[8] aymptotic expansion

$$\phi(x\gg1)\sim144y^3[1-c_1y^\lambda+c_2y^{2\lambda}-c_3y^{3\lambda}+\cdots] \tag{3}$$

$$\sim144y^3[1-Fy^\lambda+c_2'(Fy^\lambda)^2-c_3'(Fy^\lambda)^3+\cdots] \tag{3a}$$

with $\lambda=0.77200\ 18726\ 58766$,

$$c_1=F \quad\text{and}\quad c_n=c_n'F^n\ . \tag{3b}$$

The numerical coefficients up to c_{17}' have been calculated anew with accuracy of fifteen decimal places as seen in Table II, while the ones up to c_{10}' were previously given by March[7] with accuracy of five decimal places.

Table II. Numerical coefficients of the asymptotic expansion of the TF function, cf. Eq. (3a).

$c_2'=0.62569\ 74977\ 82349$	$c_{10}'=0.00027\ 83738\ 39349$
$c_3'=0.31338\ 61150\ 73309$	$c_{11}'=0.00008\ 88230\ 01411$
$c_4'=0.13739\ 12767\ 19371$	$c_{12}'=0.00002\ 78360\ 15974$
$c_5'=0.05508\ 34346\ 64149$	$c_{13}'=0.00000\ 85895\ 00194$
$c_6'=0.02070\ 72584\ 99192$	$c_{14}'=0.00000\ 26150\ 62632$
$c_7'=0.00741\ 45294\ 78496$	$c_{15}'=0.00000\ 07867\ 99377$
$c_8'=0.00255\ 55311\ 67949$	$c_{16}'=0.00000\ 02342\ 63579$
$c_9'=0.00085\ 41653\ 77807$	$c_{17}'=0.00000\ 00691\ 03239$

A particular value of the asymptotic parameter F affords a particular solution ϕ_F which satisfies of course the boundary condition Eq. (2a) but not the other one Eq. (2) in general. We have adopted rather an approximate value $F=13$, while March[7] calculated the case $F=\pm1$ referred to as Master Solutions.

2. We integrate numerically Eq. (1) in the form of simultaneous equations of the first order written in terms of y, ϕ and ψ,

$$\frac{d\phi}{dy}=\psi$$
$$\frac{d\psi}{dy}=\frac{1}{y^2}\left[\left(\frac{\phi}{y}\right)^{3/2}-2y\psi\right], \tag{4}$$

where the interval for each step of the numerical integration is taken such as

$$\begin{array}{llll} \Delta y=0.0005 & \text{for}\ \ y=0.023 & \text{to} & 0.0280 \\ 0.001 & \phantom{\text{for}\ \ y=}0.027 & \text{to} & 0.080 \\ 0.005 & \phantom{\text{for}\ \ y=}0.080 & \text{to} & 0.200 \\ 0.01 & \phantom{\text{for}\ \ y=}0.20 & \text{to} & 1.06 \end{array}$$

and occasionally up to $\Delta^6\phi$ and $\Delta^6\psi$ are taken into account. The error in each step is $<0.0^{12}2$ in ϕ.

For the second range $1\geqslant x\geqslant0$ it is covenient to introduce change of variables $z\equiv x^{1/2}$* capable of removing the difficulties at origin, and $\chi\equiv2\phi'$.

3. In the neighborhood of the continuation point $x=y=z=1$ we continue the (y, ϕ, ψ)-system adequate for the range $\infty\geqslant x\geqslant1$ to the (z, ϕ, χ)-system adequate for the range $1\geqslant x\geqslant0$ by the connecting relations

$$z=1/y^{1/2}$$
$$\phi(z)=\phi(y) \tag{5}$$
$$\chi(z)=-y^2\psi(y)\ .$$

Actually, calculating the values of ϕ and ψ for $y=(1.06)^{-2}$, $(1.04)^{-2}$, $(1.02)^{-2}$ and 1.00 by means of Bessel as well as Stirling interpolations we provide the values of ϕ and χ for $z=1.06$, 1.04, 1.02 and 1.00, the starting values for the numerical integration routine of $z=1\to0$.

4. We integrate numerically Eq. (1) in the form of simultaneous equations of the first order written in terms of z, ϕ and χ

$$\frac{d\phi}{dz}=z\chi$$
$$\frac{d\chi}{dz}=4\phi^{3/2} \tag{6}$$

where the interval for each step of the numerical integration is taken such as

$$\Delta z=0.02 \quad \text{for} \quad z=1.00 \text{ to } 0.00\ .$$

The error in each step is $<0.0^{12}2$ in ϕ.

5. The integral curve does cut the ϕ-axis in a finite nonvanishing angle so that it determines the point of intersection as well as the slope there very accurately as follows:

$$\phi_{F=13}(0)=1.0834\ 68762$$
$$\chi_{F=13}(0)=-3.5344\ 49460$$
$$\phi'_{F=13}(0)=-1.7672\ 24730\ .$$

Evidently, this integral curve does not satisfy the boundary condition Eq. (2).

6. Based on the Sommerfeld[9] invariance property of the TF equation we apply such scale factors as

---

* Instead of $w\equiv(2x)^{1/2}$ taken by Feynman-Metropolis-Teller as well as March, we have rather preferred $z\equiv x^{1/2}$ since it makes the arguments in both regions take the same value unity at the cantinuation point ($x=1$).

$$\begin{aligned} [\phi_F(0)]^{1/3}\cdot x_F &\to x\,, \\ [\phi_F(0)]^{-1}\cdot \phi_F &\to \phi_0\,, \\ [\phi_F(0)]^{-4/3}\cdot \phi_F' &\to \phi_0'\,, \\ [\phi_F(0)]^{\lambda}\cdot F &\to F_0\,, \end{aligned} \tag{7}$$

in order to make the above obtained solution satisfy additionally the boundary condition Eq. (2), too. This normalization by the scale factors gives the correct value of the initial slope

$$B_0 = -\phi_0'(0) = 1.5880\ 70972 \tag{8}$$

in contrast to the values collected in Table I, as well as the correct value of the asymptotic parameter

$$F_0 = 13.270\ 97391 \tag{9}$$

while the value given by one of us (M) preliminarily combined with his value of B_0 is 13.2684 and the value given by Coulson-March[8] is 13.21.

§ 3. Tabulation of the Exact Values of the Ordinary TF Function

Now, it is inconvenient that the values of the TF function normalized thus by the scale factors are given only for irregular values of x. Therefore, we have recalculated the values of the TF function for regular values of x using the usual outward numerical integration initiated with the accurate value of the initial slope obtained above, Eq. (8), which

Table III. Some coefficients in the series expansion of the TF function for smaller values of x.

$$a_{12} = \frac{4}{405} + \frac{4}{1575}a_2^{\,3}$$

$$a_{13} = \frac{557}{100100}a_2^{\,2} - \frac{3}{9152}a_2^{\,5}$$

$$a_{14} = \frac{4}{693}a_2 - \frac{29}{24255}a_2^{\,4}$$

$$a_{15} = \frac{101}{52650} - \frac{623}{351000}a_2^{\,3} + \frac{7}{49920}a_2^{\,6}$$

$$a_{16} = -\frac{46}{45045}a_2^{\,2} + \frac{68}{105105}a_2^{\,5}$$

$$a_{17} = -\frac{113}{1178100}a_2 + \frac{153173}{116424000}a_2^{\,4} - \frac{3}{43520}a_2^{\,7}$$

Table IV. Exact values of the ordinary TF function and its derivative.

x	$\phi_0(x)$	$-\phi_0'(x)$	x	$\phi_0(x)$	$-\phi_0'(x)$	x	$\phi_0(x)$	$-\phi_0'(x)$
0.00	1.00000	1.588071	1.20	0.37424	0.22591	8.0	0.036587	$0.0^{2}80886$
1	0.98545	1.38956	1.25	36320	21579	8.5	32833	69642
2	97198	1.30930	1.30	35265	20631	9.0	29591	60331
3	95920	1.24897	1.4	33290	18904	9.5	26774	52559
4	94696	1.19910	1.5	31478	17374	10.0	24314	46029
0.05	0.93519	1.15600	1.6	0.29810	0.16011	11	0.020250	$0.0^{2}35798$
6	92383	1.11774	1.7	28271	14793	12	17064	28305
7	91282	1.08319	1.8	26847	13700	13	14526	22705
8	90215	1.05161	1.9	25527	12715	14	12478	18445
9	89178	1.02246	2.0	24301	11824	15	10805	15153
0.10	0.88170	0.99535	2.1	0.23159	0.11017	16	$0.0^{2}94241$	$0.0^{2}12574$
12	86229	94619	2.2	22095	10283	17	82728	10529
14	84381	90245	2.3	21101	096140	18	73048	$0.0^{3}88883$
16	82616	86303	2.4	20170	090026	19	64847	75592
18	80927	82714	2.5	19298	084426	20	57849	64725
0.20	0.79306	0.79423	2.6	0.18480	0.079286	25	$0.0^{2}34738$	$0.0^{3}32404$
25	75520	72231	2.7	17711	74558	30	22558	18067
30	72064	66180	2.8	16988	70200	35	15509	10891
35	68888	60987	2.9	16306	66178	40	11136	$0.0^{4}69668$
40	65954	56464	3.0	15663	62457	50	$0.0^{3}63226$	32499
0.45	0.63233	0.52481	3.2	0.14482	0.055813	60	$0.0^{3}39391$	$0.0^{4}17198$
50	60699	48941	3.4	13425	50077	70	26227	$0.0^{5}99566$
55	58332	45772	3.6	12474	45098	80	18355	61662
60	56116	42917	3.8	11617	40753	90	13355	40245
65	54036	40332	4.0	10840	36944	100	10024	27393
0.70	0.52079	0.37979	4.2	0.10136	0.033590	200	$0.0^{4}14502$	$0.0^{6}20575$
75	50235	35831	4.4	094942	30625	300	$0.0^{5}45486$	$0.0^{7}43660$
80	48493	33861	4.6	089085	27995	400	19797	14367
85	46847	32049	4.8	083725	25653	500	10341	$0.0^{8}60344$
90	45286	30378	5.0	078808	23560	600	$0.0^{6}60687$	29618
0.95	0.43806	0.28832	5.5	0.068160	0.019221	700	$0.0^{6}38618$	$0.0^{8}16198$
1.00	42401	27399	6.0	59423	15858	800	26081	$0.0^{9}95924$
1.05	41065	26067	6.5	52173	13236	900	18437	60377
1.10	39793	24828	7.0	46098	11143	1000	13513	39880
1.15	38580	23671	7.5	40962	$0.0^{2}94583$	∞	0	0

has enabled us on the other hand to check our computation by the inward numerical integration carried through above. In this case it was needed first to calculate anew the coefficients a_{12} to a_{17}* of the Baker[1] series expansion of the TF function for smaller values of x,

$$\phi(x \ll 1) = 1 + a_2 x + a_3 x^{3/2} + a_4 x^2 + \cdots \tag{10}$$

with $a_2 = \phi'(0) \equiv -B$.

as given in Table III, since the ones up to a_{11} were previously tabulated by Metropolis-Reitz[10].

The exact values of the ordinary TF function thus obtained are columned in Table IV against to the regular values of argument x. It is practically convenient that the values of ϕ for larger values of x are being given in as many effective digits as the ones for smaller values of x.

§ 4. Acknowledgement

This work is indebted to the Scientific Research Fund of the Japanese Ministry of Education granted to the Research Group for the Study of Atomic and Molecular Structure as well as to that of Mathematical Physics. Further thanks are due the Matsudaira Fund at Takamatsu which donated an electric calculator to help us in this calculation.

References

1) E. B. Baker: Phys. Rev. **36** (1930) 630.
2) V. Bush and S. H. Caldwell: Phys. Rev. **38** (1931) 1898.
3) C. Miranda: Mem. Acc. Italia **5** (1934) 283.
4) J. C. Slater and H. M. Krutter: Phys. Rev. **47** (1935) 559.
5) R. P. Feynman, N. Metropolis and E. Teller: Phys. Rev. **75** (1949) 1561.
6) K. Umeda: Phys. Rev. **58** (1940) 92; J. Fac. Sci., Hokkaido Univ., Japan III **5** (1942) 171.
7) N. H. March: Proc. Camb. Phil. Soc. **48** (1952) 665.
8) C. A. Coulson and N. H. March: Proc. Phys. Soc. A **63** (1950) 367.
9) A. Sommerfeld: Z. Phys. **78** (1932) 283.
10) N. Metropolis and J. R. Reitz: J. Chem. Phys. **19** (1951) 555.
11) S. Kobayashi: J. Phys. Soc. Japan **10** (1955) 824.

---

* These expressions of a_{12} to a_{17} have been checked as the special cases of the coefficients in the series expansion of the TFD function for smaller values of x which were recently calculated by one of us (K)[11].

JOURNAL OF THE PHYSICAL SOCIETY OF JAPAN Vol. 10, No. 9, SEPTEMBER 1955

A Note on the Paramagnetic Relaxation

By Mario YOKOTA

Department of Physics, Faculty of Science, University of Tokyo

(Received June 6, 1955)

Introducing the spin-spin relaxation time and the spin-lattice relaxation time in Bloch's equation simultaneously, we have calculated the relaxation equation of paramagnetic substances. As the contribution from the spin-spin relaxation to the imaginary part of the complex susceptibility, a term proportional to $(1-F)^2$ instead of $(1-F)$ given by Broer has been obtained. Our theory explains the experimental results obtained by Gorter *et al* for the depedence of the spin-spin relaxation time on the static field strength.

§ 1. Introduction

An exhaustive study has been made during the war on the paramagnetic relaxation by Gorter and his collaborators. The experimental results and the theories are discussed by Gorter in his famous book "Paramagnetic Relaxation."[1]

Although the theories developed by Casimir and DuPre[2], Broer[3], Van Vleck[4], and Wright[5] have been successful in interpreting most of the important features of the phenomena, some discrepancies still remain unexplained. Especially, as many authors pointed out, the dependence of the spin-spin relaxation time on the strength of the longitudinal static magnetic field requires a further examination from the theoretical side[1)5)].

The first thing to be done to discuss these phenomena in detail seems to us to reconstruct a more precise phenomenological theory treating the spin-spin relaxation and the spin-lattice relaxation simultaneously. This is the main purpose of the present paper and is done in § 3 with the use of Bloch's equation for the longitudinal relaxation. It seems appropriate to start with the discussion of the previous theories, so we make a survey of them in § 2. The dependence of the spin-spin relaxation time on the intensity of the static magnetic field is discussed in § 4 for the case of weak exchange coupling, and in § 5 strong exchange.

§ 2. The Previous Theories

In the presence of a static magnetic field H, a paramagnetic substance has the magnetization M, following the equation,

$$M=\chi_0 H\,, \tag{1}$$

where χ_0 is the magnetic susceptibility generally being a tensor. For simplicity, however, we take it as a scalar.

When we abruptly reduce the magnetic field strength by H_1 at a time t_0, the magnetization relax in course of time to M_0 which satisfies the relation

$$M_0=\chi_0(H-H_1)\,. \tag{2}$$

The relaxation function $\phi(\tau)$ is defined by

$$M(t)-M_0=\phi(t-t_0)H_1\,, \tag{3}$$

where $M(t)$ is the magnetization at t.

If the relaxation function is known, the complex susceptibility is obtained by the equation

$$\chi^*=\chi'-i\chi''=-\frac{1}{V}\int_0^\infty\frac{d\phi(\tau)}{d\tau}e^{-i\omega\tau}d\tau\,, \tag{4}$$

where V is the volume of the sample and ω the frequency of the oscillating magnetic field.

Casimir and Du Pre assumed that the spin-spin relaxation time is so short that it can be regarded as infinitesimally small compared with the spin-lattice relaxation time. This means to assume $\phi(\tau)$ to be of the form shown in Fig. 1, so that $d\phi/d\tau$ in Eq. (4) is assumed to be

$$\frac{1}{V}\frac{d\phi}{d\tau}=-\chi_0(1-F)\delta(0)-\frac{\chi_0 F}{\rho}e^{-\tau/\rho}\,. \tag{5}$$

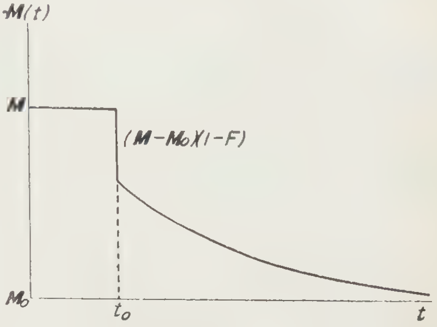

Fig. 1. Relaxation function of Casimir and Du Pre.

In Eq. (5), ρ is the spin-lattice relaxation time and F is defined by

$$F=\frac{C_H}{C_H+C_I}\,, \tag{6}$$

where C_H and C_I denote the specific heat of the interaction with the static external field and that of the magnetic interaction including the exchange coupling, respectively.

The derivation of Eq. (6) is given in Appendix.

Using Eqs. (4) and (5) we get the susceptibility as

$$\chi^*=\chi_0(1-F)+\frac{\chi_0 F}{1+\omega^2\rho}-i\frac{\chi_0 F\omega\rho}{1+\omega^2\rho^2}\,. \tag{7}$$

Broer has considered the finiteness of the spin-spin relaxation time. In this case the relaxation function may be written in the form such as

$$\frac{1}{V}\phi(\tau)=\chi_0\{(1-F)e^{-\tau/t_1}+F\}e^{-\tau/\rho}\,, \tag{8}$$

where t_1 is the spin-spin relaxation time.

There are, however, certain ambiguities in this expression about the meaning of ρ, because here we have two processes of the energy transfer to the lattice from the spin system. The first is the energy transfer from the Zeeman coupling and the second from the magnetic interaction to the lattice.

Van Vleck considered these two processes and showed that the apparent spin-lattice relaxation time ρ is given by

$$\rho=\frac{C_I+C_H}{C_I+PC_H}t_{SL}\,. \tag{9}$$

Here P represents the ratio of the two relaxation times t_{SL} from the magnetic interaction energy to the lattice and t_{FL} from the Zeeman energy to the lattice. Even when we take account of these facts, still the meaning of F is not very clear.

§ 3. Relaxation Equation

To treat the paramagnetic substance placed in a static magnetic field, we assume that the whole system can be separated into three parts and define the temperature for each part. The energy transfer between these systems can be characterized by the relaxation times. Taking account of these relaxation times simultaneously, we can obtain Eq. (9) phenomenologically and can clarify the meaning of F in the relaxation function (8).

The first system is the coupling energy of the magnetic moment with the magnetic field and may be called the "field system," having its own temperature T_F defined by

$$M_z = \frac{N\mu^2}{3kT_F} H_z\,, \tag{10}$$

where N is the total number of atoms, μ the atomic magnetic moment, and k the Boltzmann constant.

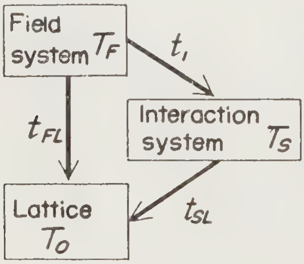

Fig. 2.

The second system is the magnetic interaction which contains the dipole energy and exchange energy and will be called the "interaction system." The temperature of this denoted by T_S.

The third system is the energy of the lattice and is assumed to be at a constant lattice temperature T_0. This is justified because the specific heat of the lattice is large compared with the other two systems provided that T_0 is high enough. These situations are shown in Fig. 2.

In order to carry out our programm, we start from Bloch's equation. Similar procedure has been employed by Anderson⁶⁾ and Bloembergen⁷⁾ in their treatments of the paramagnetic resonance. Bloch's equation for the longitudinal magnetic moment can be written as

$$\dot{M}_z = -\frac{1}{t_1}(M_z - M_{0z}{}^S) - \frac{1}{t_{FL}}(M_z - M_{0z})\,, \tag{11}$$

where

$$M_{0z}{}^S = \frac{N\mu^2}{3kT_S} H_z(t) \quad \text{and} \quad M_{0z} = \frac{N\mu^2}{3kT_0} H_z(t)\,. \tag{12}$$

Since the oscillating field is now parallel to the static field, its direct effects are not included in Eq. (11). Our assumption expressed by (11) and (12) is a good approximation when temperature is so high that Curie's law is valid and the frequency ω of the oscillating field is fairly small compared with $1/t_1$ because the temperature of the interaction system T_S may be defined when $\omega\, t_1 \ll 1$. We further assume that the amplitude of the oscillating magnetic field is very small in comparison with the static field, to eliminate the possibility of the appearance of a negative temperature.

The change of the magnetic moment is caused by the variations in the magnetic field and in the temperature of the field system. So we have

$$\dot{M}_z = \frac{N\mu^2}{3k}\left(H_z \frac{d}{dt}\left(\frac{1}{T_F}\right) + \frac{1}{T_F}\frac{dH_z}{dt}\right). \tag{13}$$

Using Eqs. (10) and (11) we get equation for the temperature variation as follows:

$$\frac{d}{dt}\frac{1}{T_F} = \frac{1}{t_1}\left(\frac{1}{T_S} - \frac{1}{T_F}\right) + \frac{1}{t_{FL}}\left(\frac{1}{T_0} - \frac{1}{T_F}\right) - \frac{1}{T_F H_z}\frac{dH_z}{dt}\,. \tag{14}$$

In order to consider the time dependence of the temperature of the interaction system, it is now necessary to get the power-balance equation of the interaction system. This equation was already obtained by Anderson⁶⁾, so we repeat his procedure briefly here.

The energy of the interaction system U_I can be written as

$$U_I = \int^{T_S} C_I dT_S\,. \tag{15}$$

At high temperatures C_I can be approximated as $C_I = D/T^2$. Thus one has

$$U_I = -\frac{D}{T_S} + \text{constant} \tag{16}$$

and

$$\frac{dU_I}{dt} = -C_I T_S^2 \frac{d}{dt}\frac{1}{T_S}. \tag{17}$$

The power input to the interaction system is the same as the rate of energy transfer from the field system to the interaction system, which is given by

$$\frac{1}{t_1}\frac{N\mu^2 H_z^2}{3k}\left(\frac{1}{T_S} - \frac{1}{T_F}\right) = \frac{1}{t_1} C_H T_S^2 \left(\frac{1}{T_F} - \frac{1}{T_S}\right). \tag{18}$$

Thus, taking account of the energy transfer to the lattice, the relaxation equation of the interaction system becomes

$$\frac{d}{dt}\left(\frac{1}{T_S}\right) = \frac{1}{t_1}\frac{C_H}{C_I}\left(\frac{1}{T_F} - \frac{1}{T_S}\right) - \frac{1}{t_{SL}}\left(\frac{1}{T_S} - \frac{1}{T_0}\right). \tag{19}$$

The magnetic field is now written as

$$H_z = H_{z0} + H_z' e^{i\omega t}, \tag{20}$$

where we assume $H_z' \ll H_{z0}$.

In the steady state the temperatures of the systems are expressed as

$$\frac{1}{T_F} = \frac{1}{T_0}\left(1 - \frac{T_F'}{T_0} e^{i\omega t}\right) \tag{21}$$

and

$$\frac{1}{T_S} = \frac{1}{T_0}\left(1 - \frac{T_S'}{T_0} e^{i\omega t}\right), \tag{22}$$

where T_F' and T_S' are complex and $|T_F'| \ll T_0, |T_S'| \ll T_0$.

The fundamental equations of our problems, Eq. (14) and Eq. (19), are written with Eqs. (20), (21) and (22) as

$$T_S' = T_F'\left(\frac{t_1}{t_{FL}} + 1 + i\omega t_1\right) - i\omega T_0 t_1 \frac{H_z'}{H_{z0}} \tag{23}$$

and

$$T_F' = T_S'\left(1 + i\omega K t_1 + K\frac{t_1}{t_{SL}}\right), \tag{24}$$

where

$$K = C_I/C_H. \tag{25}$$

From Eq. (10) we also have

$$-\frac{T_F'}{T_0} = \frac{M_z'}{M_{z0}} - \frac{H_z'}{H_{z0}} \tag{26}$$

and

$$M_z'/H_z' = \chi^* \text{ and } M_{z0}/H_{z0} = \chi_0. \tag{27}$$

Using Eqs. (23), (24), (26) and (27) we express the complex susceptibility as

$$\chi^* = \chi_0 - \frac{i\omega t_1 \chi_0}{\left(1 + i\omega t_1 + \frac{t_1}{t_{FL}}\right) - \left(1 + i\omega K t_1 + K\frac{t_1}{t_{SL}}\right)^{-1}} \tag{28}$$

If the condition $\omega t_1 \ll 1 \ll \omega\rho$ is satisfied, ρ being given by (9), we easily get the expression for χ'' as

$$\chi'' = \left\{(1-F)^2 t_1 + \frac{F\rho}{1+\omega^2\rho^2}\right\}\chi_0\omega. \tag{29}$$

However, Broer's equation corresponding to this, under the condition $\omega t_1 \ll 1$, is

$$\chi'' = \left\{(1-F)t_1 + \frac{F\rho}{1+\omega^2\rho^2}\right\}\chi_0\omega. \tag{30}$$

When the condition $1 \ll \omega\rho$ is not satisfied, the expression of χ'' is not so simple as Eq. (29), and it is difficult to separate the spin-spin relaxation time from experimentally obtained χ''.

We reproduce here the definition of ρ:

$$\rho = \frac{C_I + C_H}{C_I + PC_H} t_{SL} \text{ with } P = t_{SL}/t_{FL}. \tag{31}$$

This Van Vleck's equation, Eq. (31), means that when the strength of the static magnetic field is raised, the energy of the field system is increased, and that the energy transfer to the lattice takes place mainly through the direct way from the field system to the lattice, so that ρ approaches t_{FL}.

Van Vleck assumed that the energy transfer from the field system to the lattice is always accompanied by that from the interaction system to the lattice and got a result $P=1/2$. However, the relaxation corresponding to t_{SL} is not always attended by the flipping of spins. The relaxation mechanism without flipping of spins is especially important in the case of large exchange coupling, because the energy of exchange coupling is transferable to the lattice keeping the magnetization constant. Hence t_{SL} is generally smaller than $t_{FL}/2$, i.e. $P<1/2$.

§4. Spin-Spin Relaxation without Exchange

The essential difference between Eqs. (29) and (30) lies in the coefficient of the spin-

Table I. Comparison with experiments.

Substance	$FeNH_4(SO_4)_2\cdot 12H_2O$	$Mn(NH_4)_2(SO_4)\cdot 6H_2O$	$Gd_2(SO_4)_3\cdot 8H_2O$
$\gamma(H_z)_{\min}$	0.52	0.87	0.75
H_z for min.	800	400	1600~2400
$H_i/\sqrt{2}$	320	420	976

spin relaxation time. In our theory it is $(1-F)^2$, while Broer's is proportional to $1-F$. Following Gorter, we give the expression for the first term of χ'' as

$$\chi_{SS}''=(1-F)\gamma(H_z)t_1(0)\ , \tag{32}$$

and considering Eq. (29) we have

$$\gamma(H_z)=(1-F)t_1(H_z)/t_1(0)\ , \tag{33}$$

where $t_1(H_z)$ is the spin-spin relaxation time when H_z is applied.

The amount of energy transfer due to the flipping of a spin increases with increasing H_z, and the energy density of the interaction system decreases at the corresponding energy values. This results in the prolongation of the relaxation time. This fact was already pointed out by Kronig and Bouwkamp[8] for paramagnetic substances without exchange coupling, and by Kubo and Tomita[9] for substances with strong exchange coupling. Kronig and Bouwkamp expressed this situation by

$$t_1(H_z)/t_1(0)=\exp(H_z^2/H_i^2)\ , \tag{34}$$

where H_i is the internal field produced by the surrounding spin dipole moments, and $t_1(0)$ is the limiting value of $t_1(H_z)$ when H_z tends to zero. Then we have

$$\gamma(H_z)=(1-F)\exp(H_z^2/H_i^2)\ . \tag{35}$$

Waller[10] and Van Vleck[11] showed that $C_I=CH_i^2/2T^2$ (C is the Curie's constant) and F is expressed as

$$F=\frac{H_z^2}{\frac{1}{2}H_i^2+H_z^2}\ . \tag{36}$$

This gives the minimum value $\frac{1}{2}e^{1/2}=0.824$ to $\gamma(H_z)$ at $H_z=H_i/\sqrt{2}$. Comparison of our results with the experimental data obtained by Gorter *et al*[12] is made in Table I. Their experiments satisfy the condition $1\ll\omega\rho$, since they used an oscillating field with a frequency of 78×10^6 H_z and the spin-lattice relaxation times observed are about 10^{-6} sec. for most of the salts.

Remembering that the spin-spin relaxation function has the form $\exp(-t^2/2t_1^2)$ rather than $\exp(-t/t_1)$, we cannot define t_1 by Eq. (11). This fact, however, may not change the feature of the theories qualitatively.

§5. Spin-spin Relaxation in the Existence of Exchange

Kubo and Tomita[9] have shown that the spin-spin relaxation time of the paramagnetic substance with exchange coupling is expressed as

$$\frac{1}{t_1(H_z)}=\frac{1}{2\hbar^2}\sum_{\gamma\neq 0}\int_{-\infty}^{\infty}\exp(i\gamma\omega_z)dt \times\frac{\langle[S_z\mathscr{H}_\gamma'(t)][\mathscr{H}_{-\gamma}'(0),S_z]\rangle}{\langle S_z^2\rangle}\ , \tag{37}$$

where ω_z is the Larmor frequency and $\mathscr{H}_\gamma'$ are the components of the dipolar interaction defined by

$$\mathscr{H}_\gamma'=\sum_{jk}\Phi_{jk}^{-\gamma}\{jk\}_\gamma \tag{38}$$

The abbreviations used are the same as those in the paper of Kubo and Tomita[9]. Using the approximations which are used in calculating the 10/3 effect of the paramagnetic resonance for the case of a strong exchange interaction, Eq. (37) can be transcribed as

$$\begin{aligned}\frac{1}{t_1(H_z)}&=\frac{1}{2\hbar^2}\sum_{\gamma\neq 0}\int_{-\infty}^{\infty}\exp(i\gamma\omega_z t)dt\times\frac{\langle[S_z,\mathscr{H}_\gamma'(0)][\mathscr{H}_{-\gamma}(0),S_z]\rangle}{\langle S_z^2\rangle}\\&\qquad\times\exp\left[-\frac{t^2}{2\hbar^2}\frac{\langle[\mathscr{H}_{ex},[S_z,\mathscr{H}_\gamma'(0)]][\mathscr{H}_{-\gamma}'(0),S_z],\mathscr{H}_{ex}]\rangle}{\langle[S_z,\mathscr{H}_\gamma'(0)][\mathscr{H}_{-\gamma}'(0),S_z]\rangle}\right]\\&=\omega_{p1}^2\int_{-\infty}^{\infty}\exp(i\omega_z t)dt\exp-\frac{t^2}{2}\omega_{e1}^2+\omega_{p2}^2\int_{-\infty}^{\infty}\exp(i2\omega_z t)\,dt\ \exp-\frac{t^2}{2}\omega_{e2}^2\\&=\sqrt{2\pi}\frac{\omega_{p1}^2}{\omega_{e1}}\exp-\frac{\omega_z^2}{2\omega_{e1}^2}+\sqrt{2\pi}\frac{\omega_{p2}^2}{\omega_{e2}}\exp-\frac{2\omega_z^2}{\omega_{e2}^2}\ .\end{aligned} \tag{39}$$

Here

$$\omega_{p\gamma}^2 = \frac{1}{\hbar^2}\frac{\langle [S_z, \mathscr{H}_\gamma'(0)][\mathscr{H}_{-\gamma}'(0), S_z]\rangle}{\langle S_z^2\rangle} \tag{40}$$

and

$$\omega_{e\gamma}^2 = \frac{1}{\hbar^2}\frac{\langle \mathscr{H}_{ex}, [S_z, \mathscr{H}_\gamma'(0)]][[\mathscr{H}_{-\gamma}'(0), S_z], \mathscr{H}_{ex}]\rangle}{\langle [S_z, \mathscr{H}_\gamma'(0)][\mathscr{H}_{-\gamma}'(0), S_z]\rangle} . \tag{41}$$

The quantity (41) has been calculated by Negishi and Obata for crystals with a good symmetry[13]. Using their results we obtain for $S=1/2$

$$\frac{\omega_{e1}^2}{\omega_{e2}^2} \simeq 1 , \qquad \frac{\omega_{p1}^2}{\omega_{p2}^2} \simeq 2/5 \tag{42}$$

and

$$C_I \simeq (N/3kT^2)(9\hbar^2\omega_{e1}^2/8) . \tag{43}$$

Defining the exchange field H_E by $\mu H_E = \hbar\omega_{e1} = \hbar\omega_{e2}$, we have

$$\gamma(H_z) = \frac{H_z^2 + 9H_E^2/8}{9H_E^2/8} \times\left(\frac{2}{7}\exp(-H_z^2/2H_E^2) + \frac{5}{7}\exp(-2H_z^2/H_E^2)\right) . \tag{44}$$

Assuming $\gamma(H_z)=1.5$ at the field strength of $H_z=3000$ oe, we apply (44) to $CuSO_4 \cdot 5H_2O$ and get $9H_E^2/8 = 2.0\times10^7$ oe^2, which agrees fairly well with the value of 2.0×10^7 oe^2 obtained by Gorter *et al* from the spin-lattice relaxation.

For a substance with strong exchange coupling the function $\gamma(H_z)$ should be constant, because $(1-F)$ and $t_1(H_z)/t_1(0)$ remain unity for a considerably wide range of the static field strength.

This is also confirmed experimentally by Gorter *et al*[12] for $CuCl_2 \cdot 2H_2O$ and $Cu(BrO_3) \cdot 6H_2O$. The above explanation is not applicable to $MnSO_4 \cdot 4H_2O$ because of its weak exchange coupling.

In spite of the existence of a strong exchange coupling, $\gamma(H_z)$ in $FeNH_4(SO_4)_2$ and $MnSO_4$ depends upon H_z[12]. This cannot be explained by the present theory.

The approximation used in the derivation of Eq. (39) may be good for weak field case, but the dependence of $\gamma(H_z)$ on H_z is somewhat exaggerated in this equation. This discrepancy seems to be found in the 10/3 effect of the paramagnetic resonance in $K_2CuCl_4 \cdot 2H_2O$[14][15].

When the paramagnetic crystal contains two kinds of inequivalent ions with different anisotropic g-factors, the following term should be added to Eq. (39)[16]

$$\frac{2\beta^2}{J}\sqrt{\frac{3\pi}{2S(S+1)z}}(g'H)_x \exp\left(-\frac{3\hbar^2\omega_z^2}{8S(S+1)zJ^2}\right) , \tag{45}$$

where β is the Bohr magneton and $(g'H)_x$ is the x-component of the effective field when we take z-axis in the direction of $(\boldsymbol{g}'+\boldsymbol{g}'')\cdot H$ and x-axis to lie in the plane containing the direction of $\boldsymbol{g}'H$ and $\boldsymbol{g}''H$. The contribution of this effect to $t_1(H)$ is most efficient when $\hbar\omega_z \lesssim J$, so if the exchange coupling is strong, this effect should play some role in the relaxation phenomena.

§6. Conclusions

The spin-spin relaxation phenomena can be explained by a thermodynamical treatment under the conditions that ωt_1 is much smaller than unity and that the temperature is not very low.

Apparent decrease of the spin-spin relaxation time accompanied with an increase in static field is due to the factor $(1-F)$ in Eq. (33).

The function $\gamma(H_z)$ can be written in the form of $(H_z^2)(H_z^2+\alpha H_i^2)^{-1}\exp(-H_z^2/H_i^2)$, and the value of this function is quite sensitive to the parameter α, which depends upon the exchange coupling, the hyperfine interaction, the initial splitting and dipolar interaction in a complicated way. This explains the fact that $\gamma(H_z)$ varies for different substances.

Finally we should like to express our indebtedness to Dr. P.W. Anderson. The problem of this paper was inspired by his lecture at the University of Tokyo. Our thanks are also due to Professor R. Kubo for his valuable discussions, and to Messrs T. Negishi and Y. Obata for supplying the results of their calculations before publication.

Appendix

When the magnetic field is suddenly reduced from H to $H-H_1$, the temperature of the field system drops down from T_F to $T_F-\delta T_F$. Then the spin-spin relaxation reduces δT_F to δT_I given by

$$\delta T_I=\frac{C_H}{C_H+C_I}\delta T_F=F\delta T_F\ . \tag{A-1}$$

The change of static field and of temperature by H_1 and δT_I induces a change of magnetization, i.e. the magnetization is reduced to

$$M_z'=C\frac{(H-H_1)}{T_O-\delta T_I}\ . \tag{A-2}$$

The difference from the initial value $M_z=CH/T_O$ is therefore

$$M_z-M_z'=C\frac{H}{T_O}\left(\frac{H_1}{H}-\frac{\delta T_I}{T_O}\right). \tag{A-3}$$

Since the change of field strength corresponds to the change of temperature of the field system, we can express

$$C\frac{H}{T_O}=C\frac{H-H_1}{T_O-\delta T_F}\ . \tag{A-4}$$

Then

$$H_1/H=\delta T_F/T_O\ . \tag{A-5}$$

Using Eqs. (A-3) (A-5) and (A-1) we have

$$M_z-M_z'=C\frac{H}{T_O^2}(\delta T_F-\delta T_I)=C\frac{H\delta T_F}{T_O^2}(1-F)$$
$$=C\frac{H_1}{T_O}(1-F)=(M_z-M_{zO})(1-F)\ . \tag{A-6}$$

References

1) C. J. Gorter: Paramagnetic Relaxation (1947).
2) H. B. G. Casimir and F. K. Du Pre: Physica **5** (1938) 507.
3) L. J. F. Broer: Physica **10** (1943) 801.
4) J. H. Van Vleck: Phys. Rev. **57** (1940) 426.
5) A. Wright: Phys. Rev. **76** (1949) 1826.
6) P. W. Anderson: unpublished.
7) N. Bloembergen and S. Wang: Phys. Rev. **93** (1954) 72.
8) R. Kronig and C. J. Bouwkamp: Physica **5** (1938) 521.
9) R. Kubo and K. Tomita: J. Phys. Soc. Japan **9** (1954) 888.
10) I. Waller: Z. Phys. **104** (1937) 132.
11) J.H. Van Vleck: J. Chem. Phys. **5** (1937) 320.
12) Vorger, De Vrijer and Gorter: Physica **13** (1947) 621.
13) T. Negishi and Y. Obata: to be published.
14) K. Tomita: Proc. International Conference on Theoretical Physcis, 1953.
15) K. Ono, H. Abe and J. Shimada: Phys. Rev. **92** (1953) 551; J. Phys. Soc. Japan **9** (1954) 814.
16) M. Yokota and S. Koide: J. Phys. Soc. Japan **9** (1954) 953.

JOURNAL OF THE PHYSICAL SOCIETY OF JAPAN Vol. 10, No. 9, SEPTEMBER 1955

Formation Energy of Superlattice in Ni_3Fe
Part (IV)

A Theoretical Treatment of Vacancy Migration and Disorder-order Transformation in Alloys

By Shūichi IIDA

Faculty of Science, University of Tokyo

(Received March 3, 1955)

The paper consists of two parts. In part I, the disorder-order transformation of AB type superlattice was studied by postulating an elementary mechanism of atomic diffusion through vacancy, that is, the exchange of a vacancy and its neighbouring atom. The height of potential for the atomic migration was assumed to be a constant plus nearest neighbour energies of the atom. The kinetics of the ordering was treated in an approximation which is equivalent to the well known. Bethe Peierls' approximation. This is described by five differential equations to determine five time dependent variables, three of which are concerned with vacancies. By solving these equations, it was shown that if an AB type alloy is quenched from a high temperature disordered state to a temperature somewhat below the critical temperature, and then annealed at that tempertature, the following disorder-order transformation will exhibit a multiple-step character. In part II, this prediction was compared with the experimental results of Ni_3Fe. It was found that the theory can describe at least qualitatively, each of the observed four stages of the disorder-order transformation at 490°C of this alloy. Namely, the first stage is the abrupt change in the state of imperfections, the second, the development of short range order without long range order, the third, the cooperative formation of long range order, and the fourth, the process to complete its long range order against the retarding effect of antiphase and imperfections.

Part I. A Theoretical Treatment of Vacancy Migration and Disorder-order Transformation in Alloys

§ 1. Introduction

Since 1949, we reached to several general conclusions of the mechanism of disorder-order transformation in the superlattice. They were obtained through a series of calorimetric studies of Ni_3Fe superlattice[1),2),3)]. One of them is concerned with the development of long range order below critical temperature. It states that the development of long range order on constant temperature anneal starts very slowly at first, and the rate increases gradually, reaches its maximum, and then decreases gradually to zero. We called this the cooperative development of long range order. The experiment showed also a multiple-step character of disorder-order transformation of Ni_3Fe at 490°C. The transformation was supposed to consist of four processes with different mechanisms, which will be discussed in detail in the last section of this paper. The kinetic theory of superlattice formation has been worked out, for example, by Y. Takagi and others[4)]. It seems however, worth while to examine the theory again from a view point of the vacancy theory of atomic diffusion, because the former theories did not take account of the migration mechanism.

Our theory deals only with *AB* type superlattice, so that the essential characteristic of A_3B type superlattice, that is, the first order transition, is left out of the scope of our theory. Moreover, there is much doubt as to the question, which process is dominant in b.c.c. lattices among ring diffusion, vacancy diffusion and interstitialcy diffusion etc., though it is generally accepted that vacancy migration is dominant in f.c.c. lattices. Our study may be regarded as a first attack to the problem of order-disorder transformation and atomic migration mechanisms. Our purpose is to obtain a qualitative interpretation of the experimental facts.

§ 2. Derivation of Basic Equations

We treat vacancies as the third component atoms. Whole lattice points are occupied by A-atoms, B-atoms and vacancies. The lattice is composed of two sublattices I and II, the nearest neighhour lattice points of a lattice point on sublattice I being always on the other sublattice II. Each of the states of atomic arrangement is specified by the numbers of A, B, and D (vacancies) on I, and II sites and the numbers of pairs

$$\left[\frac{A}{I}\frac{A}{II}\right],\ \left[\frac{A}{I}\frac{B}{II}\right],\ \left[\frac{A}{I}\frac{D}{II}\right],\ \left[\frac{B}{I}\frac{A}{II}\right]\cdots$$

expressed by suitable parameters. We consider only the changes in state at constant temperature.

We define the concentration parameter of vacancy $p_{\mathrm{I}}, p_{\mathrm{II}}$ and the long range order parameter s as follows;

$$\begin{aligned}
&\left[\frac{D}{I}\right]=Mp_{\mathrm{I}}\,, && \left[\frac{D}{II}\right]=Mp_{\mathrm{II}} \\
&\left[\frac{A}{I}\right]=M\frac{1+s}{2}+\frac{M}{4}(p_{\mathrm{II}}-p_{\mathrm{I}})\,, && \left[\frac{A}{II}\right]=M\frac{1-s}{2}+\frac{M}{4}(p_{\mathrm{I}}-p_{\mathrm{II}}) \\
&\left[\frac{B}{I}\right]=M\frac{1-s}{2}+\frac{M}{4}(p_{\mathrm{II}}-p_{\mathrm{I}})\,, && \left[\frac{B}{II}\right]=M\frac{1+s}{2}+\frac{M}{4}(p_{\mathrm{I}}-p_{\mathrm{II}}) \\
&N=2M+M(p_{\mathrm{I}}+p_{\mathrm{II}})\,.
\end{aligned} \tag{1}$$

where D means the vacant site, $[A/I]$ the number of A-atoms on sublattice I, M the total number of A or B atoms and N the total number of lattice sites.

Next, we define the short range order parameters σ_A, σ_B and the quasi-long range order parameter r as follows;

$$\begin{aligned}
&\left[\frac{A}{I}\frac{A}{II}\right]=zM\frac{1-\sigma_A}{4}\,, \quad \left[\frac{B}{I}\frac{B}{II}\right]=zM\frac{1-\sigma_B}{4}\,, \\
&\left[\frac{A}{I}\frac{B}{II}\right]=zM\left\{\left(\frac{1}{2}-\frac{p_{\mathrm{I}}+p_{\mathrm{II}}}{2}+\frac{\sigma_A+\sigma_B}{4}\right)\frac{1}{2}+\frac{r}{2}\right\}, \\
&\left[\frac{B}{I}\frac{A}{II}\right]=zM\left\{\left(\frac{1}{2}-\frac{p_{\mathrm{I}}+p_{\mathrm{II}}}{2}+\frac{\sigma_A+\sigma_B}{4}\right)\frac{1}{2}-\frac{r}{2}\right\}, \\
&\left[\frac{A}{I}\frac{D}{II}\right]=zM\left\{+\frac{s}{2}+\frac{p_{\mathrm{II}}}{2}+\frac{1}{2}\left(\frac{\sigma_A-\sigma_B}{4}\right)-\frac{r}{2}\right\}, \\
&\left[\frac{B}{I}\frac{D}{II}\right]=zM\left\{-\frac{s}{2}+\frac{p_{\mathrm{II}}}{2}+\frac{1}{2}\left(\frac{\sigma_B-\sigma_A}{4}\right)+\frac{r}{2}\right\}, \\
&\left[\frac{D}{I}\frac{A}{II}\right]=zM\left\{-\frac{s}{2}+\frac{p_{\mathrm{I}}}{2}+\frac{1}{2}\left(\frac{\sigma_A-\sigma_B}{4}\right)+\frac{r}{2}\right\}, \\
&\left[\frac{D}{I}\frac{B}{II}\right]=zM\left\{+\frac{s}{2}+\frac{p_{\mathrm{I}}}{2}+\frac{1}{2}\left(\frac{\sigma_B-\sigma_A}{4}\right)-\frac{r}{2}\right\},
\end{aligned} \tag{2}$$

where $\left[\frac{A}{I}\frac{A}{II}\right]$ means the number of nearest neighbour pairs which are constructed by an A-atom on I site and an A-atom on II site, and z the coordination number of the lattice. Here, we neglected the possibility of nearest neighbour pairs consist of two vacancies.

The elementary process of atomic diffusion is assumed to be an exchange of an atom and a vacancy. That is

$$\genfrac{}{}{0pt}{}{A}{I}\rightarrow\genfrac{}{}{0pt}{}{D}{II}, \quad \genfrac{}{}{0pt}{}{B}{I}\rightarrow\genfrac{}{}{0pt}{}{D}{II}, \quad \genfrac{}{}{0pt}{}{A}{II}\rightarrow\genfrac{}{}{0pt}{}{D}{I}, \quad \genfrac{}{}{0pt}{}{B}{II}\rightarrow\genfrac{}{}{0pt}{}{D}{I},$$

where $A/I\rightarrow D/II$ means an elementary process in which an A-atom on I site jumps into a nearest neighbour vacant site on II site.

For convenience, we divide each elementary process into two processes such as

$$\left(\genfrac{}{}{0pt}{}{A}{I}\rightarrow\right), \quad \left(\rightarrow\genfrac{}{}{0pt}{}{A}{II}\right), \quad \left(\genfrac{}{}{0pt}{}{A}{II}\rightarrow\right), \quad \left(\rightarrow\genfrac{}{}{0pt}{}{A}{I}\right),$$

$$\left(\genfrac{}{}{0pt}{}{B}{I}\rightarrow\right), \quad \left(\rightarrow\genfrac{}{}{0pt}{}{B}{II}\right), \quad \left(\genfrac{}{}{0pt}{}{B}{II}\rightarrow\right), \quad \left(\rightarrow\genfrac{}{}{0pt}{}{B}{I}\right),$$

where $(A/I\rightarrow)$ means the number of elementary process occurring in unit time in which an A-atom on I site jumps out into II site leaving a vacancy on I site, and $(\rightarrow A/II)$ means the number of another elementary process per unit time in which a vacant site on II site is filled by an A-atom migrated from a nearest neighbour I site. Evidently,

$$\left(\genfrac{}{}{0pt}{}{A}{I}\rightarrow\right)=\left(\rightarrow\genfrac{}{}{0pt}{}{A}{II}\right), \quad \left(\genfrac{}{}{0pt}{}{B}{I}\rightarrow\right)=\left(\rightarrow\genfrac{}{}{0pt}{}{B}{II}\right), \quad \left(\genfrac{}{}{0pt}{}{A}{II}\rightarrow\right)=\left(\rightarrow\genfrac{}{}{0pt}{}{A}{I}\right), \quad \left(\genfrac{}{}{0pt}{}{B}{II}\rightarrow\right)=\left(\rightarrow\genfrac{}{}{0pt}{}{B}{I}\right).$$

Then, the change of the system per unit time will be expressed by

$$\frac{d}{dt}\left|\begin{matrix} \left[\genfrac{}{}{0pt}{}{D}{I}\right] \\ \left[\genfrac{}{}{0pt}{}{D}{II}\right] \\ \left[\genfrac{}{}{0pt}{}{A}{I}\right] \\ \left[\genfrac{}{}{0pt}{}{B}{I}\right] \\ \left[\genfrac{}{}{0pt}{}{A}{II}\right] \\ \left[\genfrac{}{}{0pt}{}{B}{II}\right] \end{matrix}\right| = \begin{pmatrix} +1 & +1 & 0 & 0 & 0 & 0 & -1 & -1 \\ 0 & 0 & +1 & +1 & -1 & -1 & 0 & 0 \\ -1 & 0 & 0 & 0 & 0 & 0 & +1 & 0 \\ 0 & 1 & 0 & 0 & 0 & 0 & 0 & +1 \\ 0 & 0 & -1 & 0 & +1 & 0 & 0 & 0 \\ 0 & 0 & 0 & -1 & 0 & +1 & 0 & 0 \end{pmatrix} \cdot \left|\begin{matrix} \left(\genfrac{}{}{0pt}{}{A}{I}\rightarrow\right) \\ \left(\genfrac{}{}{0pt}{}{B}{I}\rightarrow\right) \\ \left(\genfrac{}{}{0pt}{}{A}{II}\rightarrow\right) \\ \left(\genfrac{}{}{0pt}{}{B}{II}\rightarrow\right) \\ \left(\rightarrow\genfrac{}{}{0pt}{}{A}{II}\right) \\ \left(\rightarrow\genfrac{}{}{0pt}{}{B}{II}\right) \\ \left(\rightarrow\genfrac{}{}{0pt}{}{A}{I}\right) \\ \left(\rightarrow\genfrac{}{}{0pt}{}{B}{I}\right) \end{matrix}\right| . \tag{3}$$

But here only two equations $d[A/I]/dt$ and $d[B/I]dt$ are independent. It should be remembered that we are dealing with constant temperature, and the total number of vacancies, being assumed to be dependent only on temperature, does not change during the annealing.

Next,

$$\frac{d}{dt}\begin{pmatrix}\begin{bmatrix}A&A\\I&II\end{bmatrix}\\\begin{bmatrix}B&B\\I&II\end{bmatrix}\\\begin{bmatrix}B&A\\I&II\end{bmatrix}\\\begin{bmatrix}A&B\\I&II\end{bmatrix}\\\begin{bmatrix}A&D\\I&II\end{bmatrix}\\\begin{bmatrix}B&D\\I&II\end{bmatrix}\\\begin{bmatrix}D&A\\I&II\end{bmatrix}\\\begin{bmatrix}D&B\\I&II\end{bmatrix}\end{pmatrix}=\begin{pmatrix}-\bar{i}&0&-\bar{i}&0&+(i-1)&0&+(\overline{i-1})&0\\0&-\bar{i}&0&-\bar{i}&0&+(i-1)&0&+(i-1)\\0&-(z-1-i)&-(z-1-\bar{i})&0&+(\overline{z-i})&0&0&+(\overline{z-i})\\-(z-1-i)&0&0&-(z-1-i)&0&+(z-i)&+(z-i)&0\\-1&0&+\bar{i}&+(z-1-i)&-(i-1)&-(z-i)&+1&0\\0&-1&+(z-1-i)&+i&-(z-i)&-(i-1)&0&+1\\+\bar{i}&+(z-1-i)&-1&0&+1&0&-(i-1)&-(z-i)\\+(z-1-i)&+\bar{i}&0&-1&0&+1&-(z-i)&-(i-1)\end{pmatrix}\cdot\begin{pmatrix}\left(\begin{matrix}A\\I\end{matrix}\rightarrow\right)\\\left(\begin{matrix}B\\I\end{matrix}\rightarrow\right)\\\left(\begin{matrix}A\\II\end{matrix}\rightarrow\right)\\\left(\begin{matrix}B\\II\end{matrix}\rightarrow\right)\\\left(\rightarrow\begin{matrix}A\\II\end{matrix}\right)\\\left(\rightarrow\begin{matrix}B\\II\end{matrix}\right)\\\left(\rightarrow\begin{matrix}A\\I\end{matrix}\right)\\\left(\rightarrow\begin{matrix}B\\I\end{matrix}\right)\end{pmatrix}\tag{4}$$

---

where $\bar{i}$, $(z-i)$, $\cdots$ are used symbolically. That is $\bar{i}(\rightarrow A/I)$ indicates the total number increased per unit time by elementary processes $(\rightarrow A/I)$ in the kind of pairs considered. Meaning of this will be given more in detail in the following.

As can be seen easily, only three of the eight equations are independent and we can obtain the final basic equations

$$\frac{d}{dt}\begin{pmatrix}\begin{bmatrix}A\\I\end{bmatrix}\\\begin{bmatrix}B\\II\end{bmatrix}\\\begin{bmatrix}A&A\\I&II\end{bmatrix}\\\begin{bmatrix}B&B\\I&II\end{bmatrix}\\\begin{bmatrix}A&B\\I&II\end{bmatrix}\end{pmatrix}=\begin{pmatrix}-1&0&0&0&0&0&+1&0\\0&0&0&-1&0&+1&0&0\\-\bar{i}&0&-\bar{i}&0&+(i-1)&0&+(\overline{i-1})&0\\0&-\bar{i}&0&-\bar{i}&0&+(i-1)&0&+(i-1)\\-(z-1-i)&0&0&-(z-1-i)&0&+(\overline{z-i})&+(z-i)&0\end{pmatrix}\cdot\begin{pmatrix}\left(\begin{matrix}A\\I\end{matrix}\rightarrow\right)\\\left(\begin{matrix}B\\I\end{matrix}\rightarrow\right)\\\left(\begin{matrix}A\\II\end{matrix}\rightarrow\right)\\\left(\begin{matrix}B\\II\end{matrix}\rightarrow\right)\\\left(\rightarrow\begin{matrix}A\\II\end{matrix}\right)\\\left(\rightarrow\begin{matrix}B\\II\end{matrix}\right)\\\left(\rightarrow\begin{matrix}A\\I\end{matrix}\right)\\\left(\rightarrow\begin{matrix}B\\I\end{matrix}\right)\end{pmatrix}\tag{5}$$

Next problem is to set up the mechanism of elementary process. The elementary process of state change is an exchange of a vacancy and its nearest neighbour atom. The probabilities of finding, for instance, an A-atom on I site which has i-A-atom, $z-1-i$ B-atom and a vacancy on its nearest neighbour II sites are calculated in the same degree of approximation as the Bethe-Peierls' method. Next, the mechanism for an A-atom which has i A-atom, $z-1-i$ B-atom and a vacancy as nearest neighbours to exchange its position with its nearest neighbour vacancy is assumed to be a simple thermal activation process, in which the activation energy varies with the kinds of surrounding atoms by the change of the total amount of nearest neighbour pair energies.

First we consider an A-atom on I site. If there is a vacancy on a nearest neighbour II site, there will be some probability for the A-atom to exchange its position with the vacancy. Now we assume that the A-atom have i like atoms, $z-1-i$ unlike atoms and a vacancy on its nearest neighbour II sites. Then the probability for the A-atom to exchange its position with the neighbouring vacancy per unit time is assumed to be

$$\kappa_A \exp\left\{\frac{-(v_{AA}-v_{AD})i-(v_{AB}-v_{BD})(z-1-i)}{kT}\right\}$$
$$=\kappa_A \exp\left\{-\frac{(z-1)(v_{AB}-v_{BD})}{kT}+\frac{i(v_{AB}-v_{BD}-v_{AA}+v_{AD})}{kT}\right\} \quad (6)$$

where, v_{AA}, v_{AB}, v_{AD} and v_{BD} are the nearest neighbour energies of $A-A$, $A-B$, A-Vacancy and B-Vacancy pairs, and κ_A is a temperature dependent function. In the derivation of the above expression, we assumed that the potential energy of an A atom on I site varies with the kind of nearest neighbour atoms, while that at the top of the potential barrier is not very much changed as shown in Fig. 1. If the vacancy present initially on II site has $j+1$ A-atoms and $z-j-1$ B-atoms on its nearest neighbours, the total energy difference between before and after the atomic migration will be expressed by

$$\delta E=-[(v_{AA}-v_{AD})i+(v_{AB}-v_{BD})(z-1-i)]$$
$$+[(v_{AA}-v_{AD})j+(v_{AB}-v_{BD})(z-1-j)]. \quad (7)$$

Therefore it will be reasonable to assume as a first approximation that the activation energy $\mathcal{E}_A$ of atomic migration through a vacancy is expressed by

$$\mathcal{E}_A=q_A+(v_{AA}-v_{AD})i+(v_{AB}-v_{BD})(z-1-i) \quad (8)$$

where q_A is a constant. Thus the expression of equation (6) is obtained. Adding to a part coming from q_A, κ_A contains temperature dependent parts which come from the entropy consideration. However, it is assumed that κ_A contains no part which would be influenced by the kind of nearest neighbours. A similar expression will be given to a B-atom.

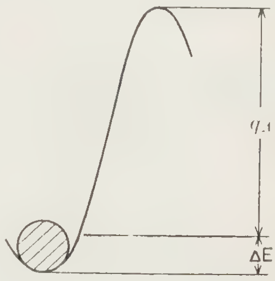

Fig. 1. $\Delta E=(v_{AA}-v_{AD})i+(v_{AB}-v_{BD})(z-1-i)$

Then

$$\left(\begin{matrix}A\\I\end{matrix}\rightarrow\right)=\sum_i K_A\left[\frac{AIIDiA}{I}\right]\exp\left(+i\frac{w_A}{kT}\right) \quad (9)$$

$$K_A=\kappa_A \exp-\frac{(z-1)(v_{AB}-v_{BD})}{kT},$$

$$w_A=v_{AB}-v_{AA}+v_{AD}-v_{BD} \quad (10)$$

where, $[AIIDiA/I]$ indicates the number of A-atoms on I site which have one vacancy, i A-atoms and $(z-i-1)$ B-atoms on its nearest neghbour II sites. $[AIIDiA/I]$ will be expressed approximately,

$$\left[\begin{matrix}AIIDiA\\I\end{matrix}\right]=\left[\begin{matrix}A\\I\end{matrix}\right]\left(\frac{[A\ A/I\ II]}{[A/I]\cdot z}\right)^i\cdot\left(\frac{[A\ B/I\ II]}{[A/I]\cdot z}\right)^{z-1-i}\cdot\left(\frac{[A\ D/I\ II]}{[A/I]\cdot z}\right)^1\cdot{}_zC_1\cdot{}_{z-1}C_i\cdots \quad (11)$$

Therefore,

$$\therefore\ \left(\begin{matrix}A\\I\end{matrix}\rightarrow\right)=\sum_i K_A\left[\begin{matrix}A\ D\\I\ II\end{matrix}\right]{}_{z-1}C_i\left(\frac{[A\ A/I\ II]}{[A/I]z}\right)^i\left(\frac{[A\ B/I\ II]}{[A/I]\ z}\right)^{z-1-i}\cdot\exp\left(i\frac{w_A}{kT}\right)$$

$$=K_A\begin{bmatrix} A & D \\ I & II \end{bmatrix}\cdot\left(\frac{[A\ A/I\ II]}{[A/I]z}\exp\left(\frac{w_A}{kT}\right)+\frac{[A\ B/I\ II]}{[A/I]z}\right)^{z-1}$$

$$=K_A Mz\left(\frac{s-r}{2}+\frac{p_{\mathrm{II}}}{2}+\frac{\sigma_A-\sigma_B}{8}\right)$$

$$\times\left\{\frac{\{(1-\sigma_A)/2\}\exp(w_A/kT)+[(1/2)+\{\sigma_A+\sigma_B\}/4]+r-(p_{\mathrm{I}}+p_{\mathrm{II}})/2}{1+s+1/2(p_{\mathrm{II}}-p_{\mathrm{I}})}\right\}^{z-1} \tag{12}$$

By taking the first power of p we obtain

$$\begin{pmatrix} A \\ I \end{pmatrix}\!\!\rightarrow\ \doteq K_A Mz\left(\frac{s-r}{2}+\frac{p_{\mathrm{II}}}{2}+\frac{\sigma_A-\sigma_B}{8}\right)\left\{\frac{\{(1-\sigma_A)/2\}\exp(w_A/kT)+[(1/2)+\{\sigma_A+\sigma_B\}/4]+r}{1+s}\right\}^{z-1} \tag{13}$$

The other terms will be obtained by permutation.

Next, we define $\left\{\begin{bmatrix} A & A \\ I & II \end{bmatrix}-\Big/\begin{matrix} A \\ I \end{matrix}\rightarrow\right\}$ as the number of $\begin{bmatrix} A & A \\ I & II \end{bmatrix}$ pairs decreased by $(A/I\rightarrow)$ processes.

$$\left\{\frac{[A\ A/I\ II]-}{A/I\rightarrow}\right\}=\sum_i K_A i\begin{bmatrix} AIIDiA \\ I \end{bmatrix}\exp\left(i\frac{w_A}{kT}\right)$$

$$=K_A\begin{bmatrix} A & D \\ I & II \end{bmatrix}(z-1)\left(\frac{[A\ A/I\ II]}{[A/I]\cdot z}\exp\left(\frac{w_A}{kT}\right)+\frac{[A\ B/I\ II]}{[A/I]\cdot z}\right)^{z-2}\cdot\frac{[A\ A/I\ II]}{[A/I]\cdot z}\cdot\exp\left(\frac{w_A}{kT}\right)$$

$$\doteq K_A\cdot M\cdot z\cdot(z-1)\left(\frac{s-r}{2}+\frac{\sigma_A-\sigma_B}{8}+\frac{p_{\mathrm{II}}}{2}\right)$$

$$\times\frac{\{\{(1-\sigma_A)/2\}\exp(w_A/kT)+[(1/2)+\{\sigma_A+\sigma_B\}/4]+r\}^{z-2}\cdot\{1-\sigma_A\}/2\exp(w_A/kT)}{(1+s)^{z-1}} \tag{14}$$

The other representations are obtained in similar ways.

Next, we assume

$$\left\{\frac{[A\ A/I\ II]+}{\rightarrow A/II}\right\}=\begin{pmatrix} A \\ I \end{pmatrix}\!\!\rightarrow\ \cdot\frac{\sum(i-1)i[(DIiA)/II]}{\sum i[DIiA/II]} \tag{15}$$

where $\left\{\begin{bmatrix} A & A \\ I & II \end{bmatrix}+\Big/\rightarrow\begin{matrix} A \\ II \end{matrix}\right\}$ means the number of $\begin{bmatrix} A & A \\ I & II \end{bmatrix}$ pairs increased by $(\rightarrow A/II)$ processes and $\begin{bmatrix} DIiA \\ II \end{bmatrix}$ means the number of vacancies on II site which have i A-atoms and $z-i$ B-atoms on its nearest neighbour I sites. This procedure involves an approximation equivalent to that in the Bethe-Peierls' treatment and does not take account of the influence of second nearest neighbours. Then,

$$\begin{bmatrix} DIiA \\ II \end{bmatrix}=\begin{bmatrix} D \\ II \end{bmatrix}\cdot\left(\frac{[A\ D/I\ II]}{[D/II]\cdot z}\right)^{1}\cdot\left(\frac{[B\ D/I\ II]}{[D/II]\cdot z}\right)^{z-1}\cdot{}_zC_i \tag{16}$$

$$\therefore\quad\left\{\frac{[A\ A/I\ II]+}{\rightarrow A/II}\right\}\doteq\begin{pmatrix} A \\ I \end{pmatrix}\!\!\rightarrow\ \cdot(z-1)\cdot\left(\frac{s-r}{2}+\frac{\sigma_A-\sigma_B}{8}+\frac{p_{\mathrm{II}}}{2}\right)\Big/p_{\mathrm{II}} \tag{17}$$

And

$$\left\{\frac{[A\ B/I\ II]+}{\rightarrow B/II}\right\}=\begin{pmatrix} B \\ I \end{pmatrix}\!\!\rightarrow\ \cdot\frac{\sum_i i(z-i)[DIiB/II]}{\sum i[DIiB/II]} \tag{18}$$

$$\therefore\quad\left\{\frac{[A\ B/I\ II]+}{\rightarrow B/II}\right\}\doteq\begin{pmatrix} B \\ I \end{pmatrix}\!\!\rightarrow\ \cdot(z-1)\cdot\left(\frac{s-r}{2}+\frac{\sigma_A-\sigma_B}{8}+\frac{p_{\mathrm{II}}}{2}\right)\Big/p_{\mathrm{II}} \tag{19}$$

The other terms will be obtained by permutation.

By these notations equations (5) become

$$
\begin{array}{lcccc}
\dfrac{d}{dt}\begin{bmatrix}A\\I\end{bmatrix} = & -\left(\substack{A\\I}\rightarrow\right) & & & +\left(\rightarrow\substack{A\\I}\right) \\
\dfrac{d}{dt}\begin{bmatrix}B\\II\end{bmatrix} = & & -\left(\dfrac{B}{II}\rightarrow\right) & +\left(\rightarrow\dfrac{B}{II}\right) & \\
\dfrac{d}{dt}\begin{bmatrix}A & A\\I & II\end{bmatrix} = & -\left(\begin{matrix}\begin{bmatrix}A & A\\I & II\end{bmatrix}-\\ \substack{A\\I}\rightarrow\end{matrix}\right) & -\left(\begin{matrix}\begin{bmatrix}A & A\\I & II\end{bmatrix}-\\ \substack{A\\II}\rightarrow\end{matrix}\right) & +\left(\begin{matrix}\begin{bmatrix}A & A\\I & II\end{bmatrix}-\\ \rightarrow\substack{A\\II}\end{matrix}\right) & +\left(\begin{matrix}\begin{bmatrix}A & A\\I & II\end{bmatrix}+\\ \rightarrow\substack{A\\I}\end{matrix}\right) \\
\dfrac{d}{dt}\begin{bmatrix}B & B\\I & II\end{bmatrix} = & -\left(\begin{matrix}\begin{bmatrix}B & B\\I & II\end{bmatrix}-\\ \substack{B\\I}\rightarrow\end{matrix}\right) & -\left(\begin{matrix}\begin{bmatrix}B & B\\I & II\end{bmatrix}-\\ \dfrac{B}{II}\rightarrow\end{matrix}\right) & +\left(\begin{matrix}\begin{bmatrix}B & B\\I & II\end{bmatrix}+\\ \rightarrow\substack{B\\II}\end{matrix}\right) & +\left(\begin{matrix}\begin{bmatrix}B & B\\I & II\end{bmatrix}+\\ \rightarrow\substack{B\\I}\end{matrix}\right) \\
\dfrac{d}{dt}\begin{bmatrix}A & B\\I & II\end{bmatrix} = & -\left(\begin{matrix}\begin{bmatrix}A & B\\I & II\end{bmatrix}-\\ \substack{A\\I}\rightarrow\end{matrix}\right) & -\left(\begin{matrix}\begin{bmatrix}A & B\\I & II\end{bmatrix}-\\ \substack{B\\II}\rightarrow\end{matrix}\right) & +\left(\begin{matrix}\begin{bmatrix}A & B\\I & II\end{bmatrix}+\\ \rightarrow\substack{B\\II}\end{matrix}\right) & +\left(\begin{matrix}\begin{bmatrix}A & B\\I & II\end{bmatrix}+\\ \rightarrow\substack{A\\I}\end{matrix}\right)
\end{array}
\quad , \qquad (20)
$$

which can be expressed by our parameters defined by Eqs. (1) and (2). We put further

$$
\left.\begin{array}{ll}
p_{\mathrm{I}}+p_{\mathrm{II}}=p\,, & p_{\mathrm{II}}-p_{\mathrm{I}}=p\cdot\rho\,, \\
s-r=pk\,, & \sigma_A-\sigma_B=4p\kappa
\end{array}\right\} \qquad (21)
$$

and expand all the terms in powers of p. It is quite reasonable to retain the first power of p in these expressions. The equation obtained by this simplification is

$$
\begin{pmatrix}
p\dfrac{d\rho}{dt} \\[2ex]
p\dfrac{d\alpha}{dt} \\[2ex]
p\dfrac{d\beta}{dt} \\[2ex]
\dfrac{ds}{dt} \\[2ex]
\dfrac{d\sigma}{dt}
\end{pmatrix}
=
\left(\begin{array}{cc}
-2 & +2 \\[1ex]
+\dfrac{2}{1-\rho}\left[(1-\beta)-\dfrac{2(z-1)}{z}\left(\dfrac{1+\sigma}{2}+s\right)\Big/R_A{}^{+}\right] & +\dfrac{2}{1-\rho}\left(\dfrac{1+\beta}{z}\right) \\[2ex]
-\dfrac{2}{1+\rho}\left(\dfrac{1-\alpha}{z}\right) & +\dfrac{2}{1+\rho}\left[-(1+\alpha)+\dfrac{2(z-1)}{z}\left(\dfrac{1+\sigma}{2}+s\right)\Big/R_B{}^{+}\right] \\[2ex]
-1 & -1 \\[1ex]
+\dfrac{2(z-1)}{z}\left[\dfrac{1-\alpha}{2}-\left(\dfrac{1+\sigma}{2}+s\right)\Big/R_A{}^{+}\right] & +\dfrac{2(z-1)}{z}\left[\dfrac{1+\beta}{2}-\left(\dfrac{1+\sigma}{2}+s\right)\Big/R_B{}^{+}\right]
\end{array}\right.
$$

$$
\left.\begin{array}{cc}
+2 & -2 \\[1ex]
-\dfrac{2}{1-\rho}\left(\dfrac{1-\beta}{z}\right) & +\dfrac{2}{1-\rho}\left[-(1+\beta)+\dfrac{2(z-1)}{z}\left(\dfrac{1+\sigma}{2}-s\right)\Big/R_B{}^{-}\right] \\[2ex]
+\dfrac{2}{1+\rho}\left[+(1-\alpha)-\dfrac{2(z-1)}{z}\left(\dfrac{1+\sigma}{2}+s\right)\Big/R_A{}^{-}\right] & +\dfrac{2}{1+\rho}\left(\dfrac{1+\alpha}{z}\right) \\[2ex]
+1 & +1 \\[1ex]
+\dfrac{2(z-1)}{z}\left[\dfrac{1-\beta}{2}-\left(\dfrac{1+\sigma}{2}-s\right)\Big/R_A{}^{-}\right] & +\dfrac{2(z-1)}{z}\left[\dfrac{1+\alpha}{2}-\left(\dfrac{1+\sigma}{2}-s\right)\Big/R_A{}^{-}\right]
\end{array}\right|
$$

$$\times\left|\begin{array}{l} pK_Az\left(\frac{1+\alpha}{2}\right)\left(\frac{1+\rho}{2}\right)(R_A{}^+)^{z-1}/(1+s)^{z-1} \\ pK_Bz\left(\frac{1-\beta}{2}\right)\left(\frac{1-\rho}{2}\right)(R_B{}^+)^{z-1}/(1+s)^{z-1} \\ pK_Az\left(\frac{1+\beta}{2}\right)\left(\frac{1-\rho}{2}\right)(R_A{}^-)^{z-1}/(1-s)^{z-1} \\ pK_Bz\left(\frac{1-\alpha}{2}\right)\left(\frac{1+\rho}{2}\right)(R_B{}^-)^{z-1}/(1-s)^{z-1} \end{array}\right| \qquad \begin{array}{c} \text{(i)} \\ \text{(ii)} \\ \text{(iii)} \\ \text{(iv)} \\ \text{(v)} \end{array} \tag{22}$$

where we have used the notations,

$$\left.\begin{array}{l} \sigma_A=\sigma_B=\sigma\ , \qquad \gamma=s\ , \\ \exp(w_A/kT)=e^A\ , \quad \exp(w_B/kT)=e^B\ , \\ \kappa+k=\frac{1+\rho}{2}\alpha\ , \\ \kappa-k=\frac{1-\rho}{2}\beta\ , \\ R_A{}^{\pm}=\frac{1+\sigma}{2}\pm s+\frac{1-\sigma}{2}e^A\ , \\ R_B{}^{\pm}=\frac{1+\sigma}{2}\pm s+\frac{1-\sigma}{2}e^B\ . \end{array}\right\} \tag{23}$$

Thus we could obtain five basic equations to determine the change of the system with time in terms of five variables ρ, α, β, s, and σ, of which s and σ are the usual long range order and the short range order parameters respectively. The physical meaning of other variables is seen from the relations

$$\begin{array}{l} \rho=\frac{[D/II]-[D/I]}{[D/II]+[D/I]}\ , \\ \alpha=\frac{[A\ D/I\ II]-[B\ D/I\ II]}{z[D/II]}\ , \\ \beta=\frac{[D\ A/I\ II]-[D\ B/I\ II]}{z[D/I]}\ . \end{array} \tag{24}$$

Namely, ρ is concerned with the difference of vacancy concentrations of the two sites, α with the unbalance of atomic distribution on I site neighbouring to a vacancy on II site, and β, with that on I site. In a perfectly ordered state

$$\rho=0\ , \quad \alpha=1\ , \quad \beta=-1 \tag{25}$$

They are the characteristic parameters of this theory, in which vacancy migration mechanism for atomic diffusion is considered.

It will be noticed that the time derivatives of these three parameters are multiplied by p in equations (22). It shows that the rates of variation of these parameters with time are larger than those of s and σ by a facter of $1/p$. In the approximation used, it indicates that the parameters ρ, α and β have always their equilibrium values determined by s and σ. That is, if we assume initially arbitrarily ρ_0, α_0, β_0, s_0, and σ_0 at a given temperature T, the variation of ρ, α, and β will occur very rapidly to attain equilibrium values $\rho_e(T, s_0, \sigma_0)$, $\alpha_e(T, s_0, \sigma_0)$ and $\beta(T, s_0, \sigma_0)$ without resulting in any change of s and σ. The equilibrium values are obtained by putting $d\rho/dt=0$, $d\alpha/dt=0$, and $d\beta/dt=0$ in equations (22). Therefore we have actually two differential equations of motion for the system and equations (i), (ii) and (iii) may be regarded as auxiliary relations to determine the functional relation of ρ, α and β to s and σ.

Besides the five variables, the equations contain vacancy concentration p, nearest neighbour energy $w_A=v_{AB}-v_{AA}+v_{AD}-v_{BD}$, $w_B=v_{AB}-v_{BB}+v_{BD}-v_{AD}$ and two atomic migration coefficients K_A and K_B independently. Thus the difference in properties of A- and B-atoms can be considered in our treatment.

p, K_A and K_B will change exponentially with temperature. But in this paper, we shall not discuss the temperature variation characteristics of these.

§ 3. The Equilibrium State

Using the basic equations (22), we shall study first the equilibrium state of the system, for which we put all time derivatives equal to zero. Let us consider first the case where no long range order exists. This state is stable above the critical temperature. Then $T>Tc$, $\rho=0$, $\alpha=\beta$, $s=0$ and we can obtain easily

$$\left.\begin{aligned}\alpha&=\frac{\exp\{(A-B)/2\}-1}{\exp\{(A-B)/2\}+1},\\ \sigma&=\frac{\exp\{(A+B)/2\}-1}{\exp\{(A+B)/2\}+1},\end{aligned}\right\}\qquad(26)$$

where

$$\exp\left(\frac{A\pm B}{2}\right)=\exp\frac{w_A\pm w_B}{2kT}.\qquad(27)$$

The expression of σ accords perfectly with the Bethe's solution of short range order,

$$(w_A+w_B=-v_{AA}-v_{BB}+2v_{AB})$$

but we have another parameter α, when $w_A\neq w_B$. The non-zero value of α indicates that the vacancy associates some atomic cluster on its nearest neighbours and the characteristic energy of this cluster is determined by

$$w_A-w_B=(-v_{AA}+v_{BB})+2(v_{AD}-v_{BD})\qquad(28)$$

It will be noticed that in our treatment the first term of the expression, which comes from an indirect coupling between vacancies and atoms, has the same order of contribution to the characteristic energy as that from direct coupling.

Next the general case having long range order will be studied. It is realized below the critical temperature. After some calculations we obtain the following equations;

$$\left.\begin{aligned}
\frac{\alpha+\beta}{2}&=\frac{e^A-e^B}{e^A+e^B+2\{(1+\sigma)/(1-\sigma)\}} &&\text{(A)}\\
\frac{\alpha-\beta}{2}&=\frac{2s}{(1-\sigma)/2(e^A+e^B)+(1+\sigma)} &&\text{(B)}\\
\frac{1+\rho}{1-\rho}&=\left[\frac{[\{(1-\sigma)/2\}e^A+(1+\sigma)/2-s][\{(1-\sigma)/2\}e^B+(1+\sigma)/2+s]}{[\{(1-\sigma)/2\}e^A+(1+\sigma)/2+s][\{(1-\sigma)/2\}e^B+(1+\sigma)/2-s]}\right]^{z/2} &&\text{(C)}\\
1&=\left(\frac{1+s}{1-s}\right)^{z}\left[\frac{[\{(1-\sigma)/2\}e^A+(1+\sigma)/2-s][\{(1-\sigma)/2\}e^B+(1+\sigma)/2-s]}{[\{(1-\sigma)/2\}e^A+(1+\sigma)/2+s][\{(1-\sigma)/2\}e^B+(1+\sigma)/2+s]}\right]^{z/z-1} &&\text{(D)}\\
s^2&=\left(\frac{1+\sigma}{2}\right)^2-\left(\frac{1-\sigma}{2}\right)^2e^{A+B} &&\text{(E)}
\end{aligned}\right\}\qquad(29)$$

By the above equations it is possible, in principle, to obtain the solution. For a given temperature we can determine s and σ by equations (D) and (E), and using these s and σ we can obtain α, β and ρ by (A), (B) and (C). There is a significant feature that these equations are not containing the atomic diffusion coefficients K_A and K_B. Hence, the solution is not influenced by the variation on the atomic diffusion coefficients K_A and K_B. Moreover a careful examination proves that the long range order s and the short range order σ are dependent only on the sum of w_A and w_B as was the case in the usual treatments, and the solution obtained accords exactly with Bethe's result as far as the behaviour of s and σ is concerned. Thus the critical temperature and the values of specific heat just above and below the critical temperature are

$$\left.\begin{aligned}
T_C&=\frac{w}{k}\Big/\log\frac{z}{z-2},\\
C_+&=\frac{zM}{4}\cdot\frac{z(z-2)}{(z-1)^2}\cdot\frac{w^2}{kT_C{}^2},\\
C_-&=\frac{zM}{4}\cdot\frac{z(z-2)(3z-2)}{(z-1)^2}\cdot\frac{w^2}{kT_C{}^2}
\end{aligned}\right\}\qquad(30)$$

where

$$w=\frac{w_A+w_B}{2}$$

The vacancy parameters ρ, α and β show also second order changes at the critical temperature. Hence, there is no abrupt change in these parameters. With development of long range order, α increases and β decreases. But here, the behaviour of α and β at low temperature is worth noting. As can be seen easily in (A) and (B) of (29), α and β have a singular point at $T=0$. Namely, when $T\to0$, then $s\to1$, $\sigma\to1$, $e^A\to\infty$, $e^B\to\infty$ and we can obtain arbitrary values of α and σ apparently. This kind of anomalous behaviour of the vacancy parameters seems to correspond to the phenomenon of frozen imperfections at low temperatures. The problem will be discussed later.

§ 4. Development of Short Range Order without Long Range Order

Although s and σ in the equilibrium state were described only by w_A+w_B, the vacancy parameters ρ, α and σ are affected by the variation of w_A-w_B, as shown in (26) and (29). In general nonequilibrium cases, however, all of the parameters are strongly dependent on K_A, K_B and w_A-w_B. For instance, in a nonequilibrium state of $s=0$, the vacancy parameters $\alpha=\beta$ is expressed by

$$\alpha=\beta=\frac{\sqrt{\left(\frac{D_A}{E_A}+\frac{D_B}{E_B}\right)^2+(D_A-D_B)^2-2(D_A-D_B)\left(\frac{D_A}{E_A}-\frac{D_B}{E_B}\right)}-\left(\frac{D_A}{E_A}+\frac{D_B}{E_B}\right)}{D_A-D_B} \tag{31}$$

where

$$\begin{aligned} D_A&=K_A\left(\frac{1+\sigma}{2}+\frac{1-\sigma}{2}e^A\right)^{z-1},\\ D_B&=K_B\left(\frac{1+\sigma}{2}+\frac{1-\sigma}{2}e^B\right)^{z-1},\\ E_A&=\left(1+\frac{1-\sigma}{1+\sigma}e^A\right),\\ E_B&=\left(1+\frac{1-\sigma}{1+\sigma}e^B\right), \end{aligned} \tag{32}$$

Hence, the different characteristics of development process of actual superlattices will be ascribed to the difference of K_A, K_B and w_A, w_B. To avoid too much complications, we assume hereafter $K_A=K_B=K$ and $w_A=w_B=w$. By this assumption, ρ vanishes automatically, $\alpha=\beta=0$ when $s=0$, and $\beta=-\alpha$ when $s\neq 0$. Thus we have two differential equations ds/dt and $d\sigma/dt$ and one equation to determine α. They are

$$\left.\begin{aligned} \frac{1}{pK}\frac{ds}{dt}&=-2z.\left(\frac{R_+}{1+s}\right)^{z-1}+2z.\left(\frac{R^-}{1-s}\right)^{z-1}\\ \frac{1}{pK}\frac{d\sigma}{dt}&=4(z-1)\left[\left(\frac{1-\sigma}{2}e/R^+\right)-\frac{1+\alpha}{2}\right]\frac{1+\alpha}{4}\cdot\left(\frac{R^+}{1+s}\right)^{z-1}\\ &\quad+4(z-1)\left[\left(\frac{1-\sigma}{2}e/R^-\right)-\frac{1-\alpha}{2}\right]\cdot\frac{1-\alpha}{4}\cdot\left(\frac{R^-}{1-s}\right)^{z-1}\\ 0&=-\left[\left\{(z-1)\frac{1-\alpha}{2}-z\right\}+(z-1)\left(\frac{1+\sigma}{2}+s\right)\Big/R^+\right]\frac{1+\alpha}{4}\left(\frac{R^+}{1+s}\right)^{z-1}\\ &\quad+\left[\left\{(z-1)\frac{1+\alpha}{2}-z\right\}+(z-1)\left(\frac{1+\sigma}{2}-s\right)\Big/R^-\right]\frac{1-\alpha}{4}\left(\frac{R^-}{1-s}\right)^{z-1}\\ R^{\pm}&=\frac{1+\sigma}{2}+\frac{1-\sigma}{2}e\pm s \end{aligned}\right\} \tag{33}$$

where, e means $\exp\cdot(w/kT)$.

In Fig. 2 the internal energy-temperature diagrams for the equilibrium state are shown for a case of $z=8$. Below the Curie temperature, there are two lines σ_0 and σ_s. σ_s gives the real equilibrium state which has long range order s. σ_0 means the hypothetical equilibrium state having no long range order. In equation (33), if we put $s_0=0$ as the initial state then $\alpha=0$ and $ds/dt=0$. Hence, there is no possibility for the long range order to grow at any temperature. In the actual case there may be a certain probability for the generation of long range ordered nuclei when temperature is lower than the critical temperature. In the present theory, this situation is described partly by the stability of the disordred state. The Taylor's expansion of equation (33) for the parameter s is

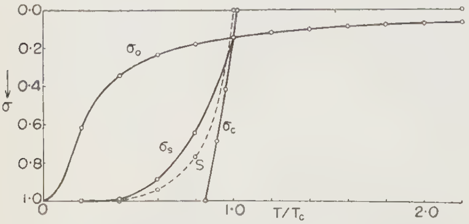

Fig. 2. Equilibrium diagram of short range order with temperature.

$$\frac{1}{pK}\frac{ds}{dt}=z(z-1)\left(\frac{1+\sigma}{2}+\frac{1-\sigma}{2}e\right)^{z-2}\cdot\left(\frac{1-\sigma}{2}\right)\left\{\frac{(e-1)\frac{z-1}{2}\left(\frac{1+\sigma}{2}+\frac{1-\sigma}{2}e\right)-e}{\frac{1+\sigma}{2}+z\cdot\frac{1-\sigma}{2}\cdot e}\right\}s+\cdots \tag{34}$$

Then, the stability of the state $s=0$ is determined by the sign of

$$(e-1)\cdot\frac{z-1}{2}\cdot\left(\frac{1+\sigma}{2}+\frac{1-\sigma}{2}e\right)-e$$

$$= -\frac{z-1}{z}\frac{(e-1)^2}{2}(\sigma-\sigma_c) \tag{35}$$

where

$$\sigma_c = \frac{(z-1)(e^2-1)-4e}{(z-1)(e-1)^2}$$

The dotted line in the figure illustrates σ_c against temperature.

Below the critical temperature, the equilibrium state with $s=0$ becomes unstable. The situation is clearly shown in the figure. But if we fix the temperature the results indicate that the stability of the state $s=0$ increases with the increase of σ. This expectation is contrary to our experiments of Ni_3Fe[3], and it will be due to the neglect of nucleation mechanism.

Hereafter, we shall make some attempts to solve equations (33) by using numerical integrations. At first, we calculated the rate of formations of short range order σ without long range order namely $s=0$. The initial state is a perfectly disordered state. In the case, $s=0$ and $\alpha=0$, equations (33) become

$$\frac{1}{pK}\cdot\frac{d\sigma}{dt}=7\left(\frac{1+\sigma}{2}+\frac{1-\sigma}{2}e\right)^6\left(\frac{1-\sigma}{2}e-\frac{1+\sigma}{2}\right). \tag{36}$$

In Fig. 3 $d\sigma/dt$ is plotted against σ where the initial values are adjusted. In Fig. 4 $d\sigma/pKe^7dt$ are plotted against pKe^7t, where θ denotes T/T_c. Of course the curves for $\theta<1$ are hypothetical but the curves will have some physical meaning, which will be discussed later. As shown in the figure, the processes are represented quite well by a relaxation of the simplest type above the critical temperature, but at lower temperatures, some deviation appears.

§ 5. Development of Long Range Order

As can bee seen in Fig. 2, there is a development of long range order below the critical temperature. If we cool the actual alloy from a higher temperature to a temperature below the critical temperature, the initial state will be a perfectly disordered state and developments of short range order and long range order will occur simultaniously. But in our treatment, if we start from an initial state $s=0$ and $\sigma=0$, then σ will develop independently until it reaches the final value $\sigma=\sigma_0$ in Fig. 2, and there is no possibility of growth for s. Of course if we give small deviation of s; $\delta s\neq 0$, at the initial state, then a cooperative formation of s and σ will occur until they reach their final equilibrium values s_e and σ_e. But in this case the whole character will be strongly dependent on the magnitude of the initial value δs. Therefore we attempt first to calculate the cooperative development of long range order, starting from the states of short range order equilibrium $\alpha=0$, $s=0$, $\sigma=\sigma_0$, which correspond to the upper curve of Fig. 2. In this case the initial states are in equilibrium, but they are not stable as to the variation of s. Hence, if we take $\delta s=0.01$ for example, the whole mechanism begins to work consistently towards the final equilibrium state having long range order.

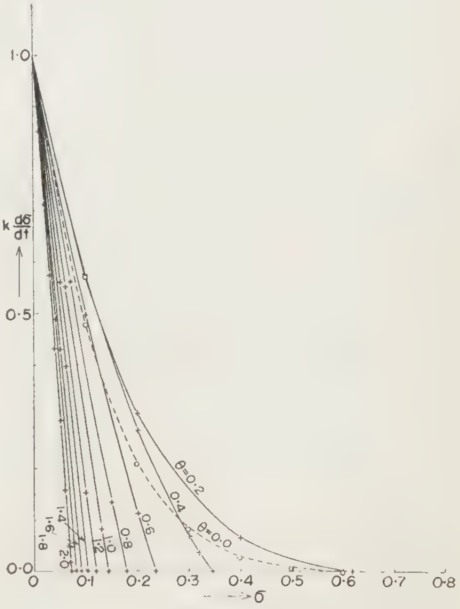

Fig. 3. $d\sigma/dt-\sigma$ for annealings at various temperatures, with $s=0$.

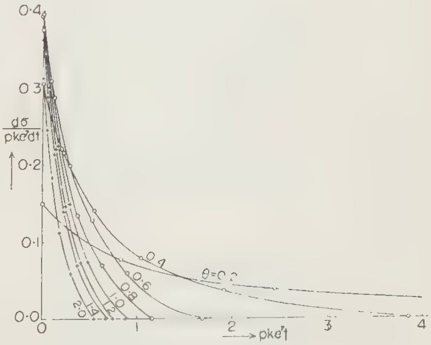

Fig. 4. $d\sigma/dt-\sigma$ for annealings at various temperatures, with $s=0$.

The method of numerical calculations is

Table I.

$pkt_0=0$	$pkt_1=pkt_0+(\Delta pkt)_0$	$pkt_2=pkt_1+(\Delta pkt)_1$	..
$s_0=0.01$	$s_1=0.1$	$s_2=0.2$	..
$\sigma_0=\sigma_0$			..
$\frac{1}{pk}\frac{ds}{dt}(s_0,\sigma_0)$	$\frac{1}{pk}\frac{ds}{dt}(s_1,\sigma_1)$	$\frac{1}{pk}\frac{ds}{dt}(s_2,\sigma_2)$	..
$\frac{1}{pk}\frac{d\sigma}{dt}(s_0,\sigma_0)$	$\frac{1}{pk}\frac{d\sigma}{dt}(s_1,\sigma_1)$	$\frac{1}{pk}\frac{d\sigma}{dt}(s_2,\sigma_2)$	..
$(\Delta pkt)_0=\frac{0.09}{(ds/pkdt)_0}$	$(\Delta pkt)_1=\frac{0.10}{(ds/pkdt)_1}$	$(\Delta pkt)_2=\frac{0.20}{(ds/pkdt)_2}$	..

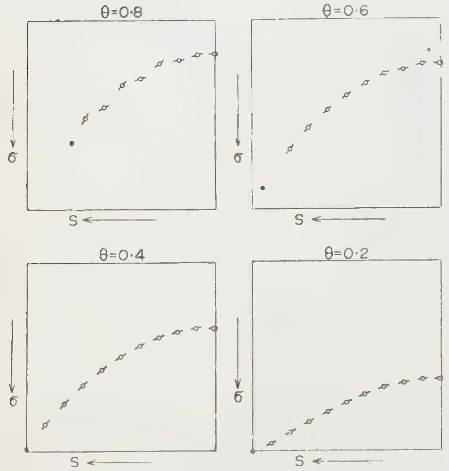

Fig. 5. The variation behaviours of σ against s on the annealings.

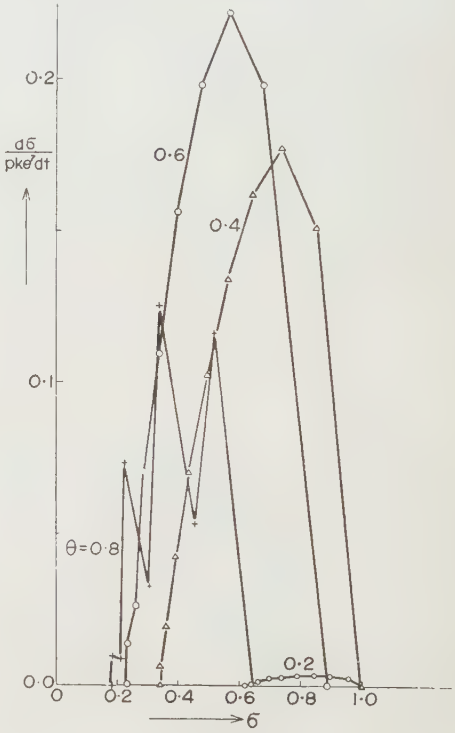

Fig. 6.

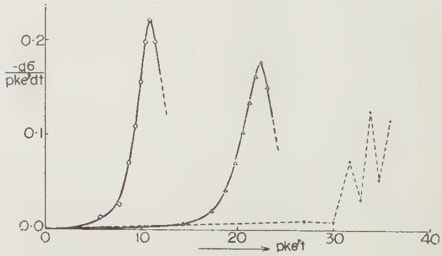

Fig. 7.

shown in Table 1. We give $s_0=\delta s=0.01$ at $t=0$ and calculate the corresponding values of $(ds/dt)_0$, $(d\sigma/dt)_0$. Using this $(ds/\mathrm{dt})_0$, the time for s to develop to the value 0.1 is calculated as $\Delta t_0=0.09/ds/dt$ (s_0, σ_0). Then $t_1=t_0+\Delta t_0$, $\sigma_1=\sigma_0+(d\sigma/dt)_0\cdot\Delta t_0$, $ds/dt(s_1, \sigma_1)$, $d\sigma/dt(s_1, \sigma_1)$ are calculated. These procedures are repeated with $\Delta s=0.1$, until the final state is attained.

The results are illustrated in Fig. 5. in $s-\sigma$ plane. Here we plotted the point (s_i, σ_i) and $(d\sigma/ds)_i=ds/dt(s_i, \sigma_i)/ds/dt(s_i, \sigma_i)$. The last values are illustrated by the inclinations of short lines. In Fig. 6, $d\sigma/pKe^7dt$ plotted against σ and in Fig. 7 $d\sigma/pke^7dt$ are plotted against pKe^7t.

The cooperative characteristics of long range order development can be seen quite clearly; The rate is sufficiently small in the beginning and increases gradually to its maximum and then decreases to zero. Near the critical temperature, the transformation course of the internal state is decisively determined to one route on $s-\sigma$ plane. Namely the route from disordered to ordered state is a very stable one. But at lower temperatures, the route seems to be not so stable. Small deviation in the initial state will cause a much different route. The conclusions are obtained from the fluctuation behaviour of $d\sigma/ds$ and $d\sigma/pKe^{\tau}dt$ in the figures. By lowering the temperature of anneal, the development of long range order s is retarded gradually and becomes slower than the development of short range order σ. Namely, $d\sigma/ds$ near the final state decreases. The last statement is important because it is related at least partly to the antiphase problem in superlattice[3]. Next, in Fig. 8 we showed variation behaviours of α in these processes as functions of σ. Here ,α is the vacancy cluster parameter as was expressed in equation (24). The variation characteristics of α in $\theta=0,2$ are very much interesting. In the case, the value of α in equilibrium is 1,000 at $\sigma=0.9999$. Regardless of this value, the final value of α in the process seems to reach 0.4 at $\sigma=0.9999$. This phenomenon will be due to the fact that α has a singularity at $T=0$ as was already mentioned. It will not be due to the systematic error of the calculation but due to the essential characteristics of the theory. This is presumably connected to the effect of frozen imperfections[3]. The effect will be discussed later.

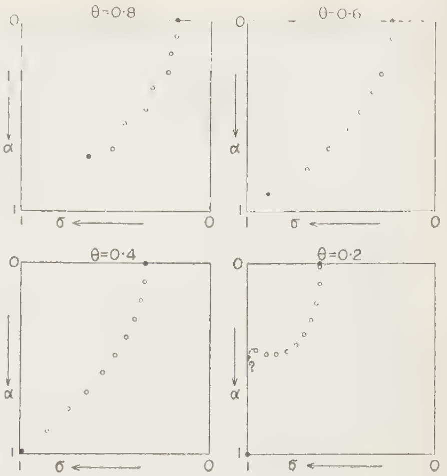

Fig. 8. The variation behaviour of vacancy cluster parameter α against short range order σ.

§ 6. Jumping Frequency of Atom and the Development of Order

Here we add one more interesting feature of the theory. According to our theory we can calculate the number of atomic migration per unit time. The general expression is

$$\frac{dn}{dt}=pKMz\cdot\left[\left(\frac{R^{+}}{1+s}\right)^{z-1}\cdot\frac{1+\alpha}{2}+\left(\frac{R^{-}}{1-s}\right)^{z-1}\cdot\frac{1-\alpha}{2}\right]=pKM\cdot F \tag{37}$$

In Fig. 9, F is plotted against σ for the development of short range order without and with long range order.

For the case without long range order, the variation of F are small at the temperatures about and above the critical temperature. But the variation increases greatly by decreasing the temperature of anneal. It will represent the effect of frozen atoms by the ordering energy at low temperature. For the case with long range order, we must notice that the derivatives $dF/d\sigma$ at $s=0$ are almost zero.

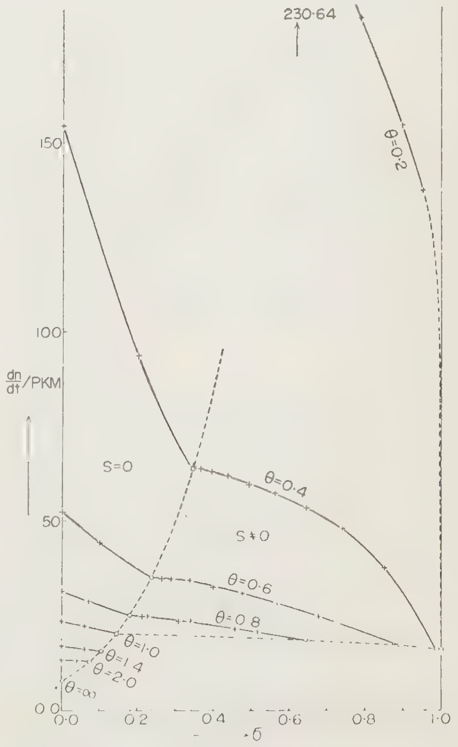

Fig. 9. The variations of atomic diffusion frequency against the development of short range order at constant temperatures.

Before the calculation we expected that F might show some maximum in the process. Namely, we expected that the requirement for ordering overcomes that for the stability of vacancies when the rate of ordering is maximum. The stability will be proportional to F in our theory. Though the results obtained is not so clear, the characteristic mentioned

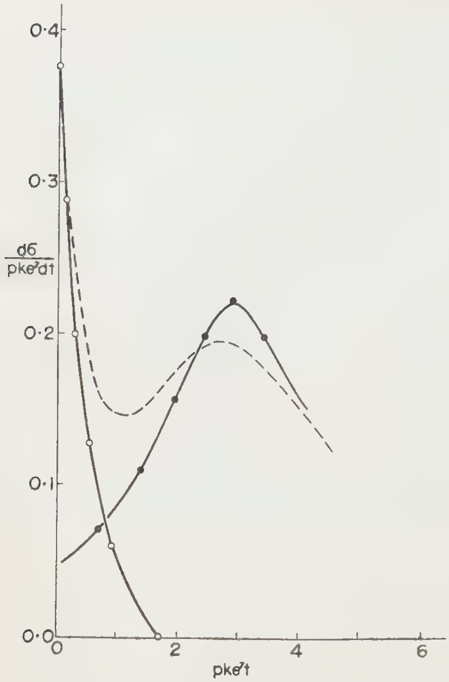

Fig. 10. Multiple-step characteristic of disorder-order transformation as superposition of the development of short range order without and with long range order.

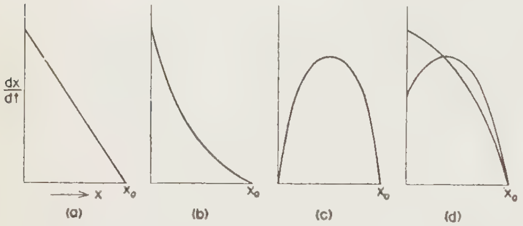

Fig. 11. Various characteristics of relaxation processes illustrated in $dX/dt-X$ plane.

above will show the existence of the expected tendency. It must be noticed that the variation of F for $\theta=0.8$ is small in spite of the large fluctuations of $d\sigma/dt$ as shown in Fig. 6.

The next schedule for calculations will be the investigation of the cooperative development of both long and short range order below the critical temperature, starting from a disordered state $s=0$, $\sigma=0$. But there is complications as mentioned before, and here we only show the two previous results for $\theta=0{,}6$ in Fig. 10 with the same scales.

As shown in Fig. 10, the rate of the two processes are almost equal, and then if we calculate strictly starting from $s=\delta s$, $\sigma=0$, we would obtain a curve like the one shown by a dotted line in the figure. This is similar to a curve observed experimentally for Ni_3Fe[3].

§ 7. Cooperative Characteristics of the Process

In a simplest relaxation process, the equation is

$$\frac{dX}{dt}=\frac{X_0-X}{\tau}$$

and it will be illustrated in a $dX/dt-X$ plane with a straight line as shown by (a) in Fig. 11. We can see that the same illustration for the development of short range order without long range order in Fig. 3 shows some deviation from straight lines as (b) in Fig. 11. It will be expressed by

$$\frac{dX}{dt}=\frac{X_0-X}{\tau(X)}=(X_0-X)(A+BX) \qquad (39)$$

where

$$B<0$$

Thus the relaxation time τ is a function of X in this case and becomes larger with the increase of X. Therefore we can say that the process is anticooperative. The development of short range order without long range order has the characteristic of an anticooperative rate process and the degree of anticooperation increases with the decrease of temperature. In the writer's first paper[1] we defined the cooperative rate process as

$$\frac{dX}{dt}=(X_0-X)\cdot BX \qquad B>0 \qquad (40)$$

which is shown by (c) in Fig, 11. It was postulated that the formation of superlattice with long range order has a cooperative character.

Now we shall extend the definition. In the expression of (39), the process will be called a cooperative rate process if $B>0$. The characteristics are shown by (d) in Fig. 11. We see that the development of short range order with long range order below the critical temperature has a character of the cooperative rate process. Therefore, there is an essential difference of cooperation characters between the development of order with and without long range order. This concept has an important physical meaning. Standing on this point of view, we can understand much better the experimental results of Fig. 14 or Fig. 15 in the writer's third paper[3].

Part II. The Disorder-order Transformation in Ni_3Fe Superlattice

§ 1. The Four Stages of Disorder-order Transformation in Ni_3Fe

In 1938, Prof. S. Kaya found a multiple-step character of disorder-order transformation in Ni_3Fe superlattice at its critical temperature annealing[5]. He investigated the transformation by measuring the change of electric resistivity with time and concluded that a completely ordered state would be attained by two week's annealing from 490°C to 400°C, especially one week annealing at 490°C. The critical temperature of the alloy is just above 490°C, and the alloy shows a first kind disorder-order transformation at that temperature. In this annealing at 490°C, the total change in resistivity of about 9 $\mu\Omega$ cm was attained not by a single process but by two processes apparently. Since then a number of experiments were carried out in our laboratory directed by Professor S. Kaya, seeking after the transitional behaviour of ferromagnetic alloy Ni_3Fe in this disorder-order transformation at its critical temperature annealing[6],[7],[8],[9].

The procedures most frequently used in this study was as follows; firstly the specimen alloy was quenched from 600°C, and measurements of various physical quantities were carried out at the room temperature. They indicate the values correponding to the disordered state. Then the specimen was inserted in a furnace kept at 490°C. After a certain time interval, the specimen was quenched to room temperature and measurements were again carried out to obtain the values of the quantities corresponding to partially ordered state. After that the specimen was again inserted in the furnace to anneal more at 490°C. The procedures were repeated until further variation of the quantities ceased.

All these data concerning variations of various physical quantities of Ni_3Fe with times of annealing at 490°C indicated the interesting multiple-step character of this transformation. (electric resistivity, internal energy, hardness, internal friction constant, magnetic properties, dilatation, thermoelectric power etc.).

Since 1947, we have also engaged in the study of this transformation by measuring thermal effect of the transformation. And the whole annealing was devided into four stages as follows[1];

1st stage 0∼20 minutes of annealing,

2nd stage 20 minutes ∼ 10 hours of annealing,

3rd stage 10∼60 hours of annealing,

4th stage 60∼150 hours of annealing.

In the first stage, structure sensitive quantities are largely influenced. At the end of the second stage, the variation of all physical quantities seem to attain their apparent saturations. After that the variation of all physical quantities begins again and they show their maximum rate of variation at about 30 hours of annealing and then gradually reach their equilibrium values at about 60 hours of annealing. This stage is named the third stage and the main variations of all physical quantities occur at this stage. Further annealing shows no large effect for many physical quantities, but there are certain evidences for the existence of the fourth stage (electric resistance, rigidity, hardness).

From our studies we concluded the existence of following four kinds of processes in this disordes-order transformation. Each corresponds to one of the above four stages respectively.

(A process.)

In an alloy having a superlattice, the stability of the imperfections such as vacancies impurities and dislocations will be influenced by the ordering tendency of atoms. Hence, the atomic configuration arround the imperfections will be a suitable one which minimize the ordering free energy at that temperature. We shall call it the cluster of atoms. If the specimen has been quenched from 600°C, the cluster will have the equilibrium configuration at 600°C. When this is inserted in a furnace at 490°C, the configuration will become unstable at that temperature, and a change will occur abruptly to establish the stable cluster at that temperature. In the neighbourhood of imperfections the activation energy for atoms to migrate will be so low that the change will proceed sufficiently fast without resulting in appreciable change in the degree of order in the bulk lattice, finishing by only several jumps of neighbouring atoms. The process will make the first stage of the transformation.

(B process.)

Development of local order without long range order. This type of ordering has a characteristic of simple type relaxation process. Therefore, the process starts with a maximum rate at the beginning of the anneal and the ordering rate decreases monotonously to zero at about, 10 hours of annealing.

(C process.)

Development of order with long range order. We concluded in the first paper[1)] that, as the equilibrium state having no long range order is stable at above the critical temperature, the state should still be fairly stable just below the critical temperature and the rate of the development of long range order at 490°C will be very small at first, but it increases gradually up to its maximum at about 30 hours of annealing and then gradually decreases to zero at about 60 hours of annealing. The process has a cooperative characteristic and will make a main process of the transformation corresponding to the third stage.

(D process)

In the end of the third process, there exists several reasons to prevent the completion of long range order. One reason is the existence of antiphase boundaries which can be as stable as the twin boundary in Ni_3Fe superlattice[3)]. The other is the existence of frozen imperfections. These two may interact each other. For instance, the imperfections will associate atomic clusters arround them, the antiphase boundary combining with dislocation lines. Hence, the completing process of long range order will require much time to result in the existence of the fourth process of the transformation.

§ 2. The Comparison of Each Stage Between the Theory and the Experiment

In the mathematical treatment of this paper we first proposed to describe only *B* and *C* processes. However, the results contain the whole processes at least qualitatively. It must be remembered that our theory treats *AB* type only, although the Ni_3Fe superlattice is a typical A_3B type. Therefore we assume that the problem disorder-order transformation of Ni_3Fe at the critical ordering temperature is similar to the associated change occurring when the *AB* type alloy is abruptly cooled to the temperature $T=T_t$ sufficiently below the critical temperature from a higher temperature T_∞ at disorded state and annealed at that temperature. The description by equations (22) is as follows;

(The first process)

At high temperature $T=T_\infty$,

$\rho_\infty=0$, $\alpha_\infty\doteqdot0$, $\beta_\infty\doteqdot0$, $s_\infty=0$ and $\sigma_\infty\doteqdot0$,

and the equation will be satisfied with zero time derivatives. Then the temperature is changed abruptly to $T=T_t$. The equilibrium conditions are destroyed and the induced relaxation prosess will occur according to the equations derived from the initial values $\rho_0=0$, $\alpha_0=\beta_0\doteqdot0$, $s_0=0$ and $\sigma_0\doteqdot0$. However we must remember the fact that the change of ρ, α and β is much faster than that of s and σ. Namely, the vacancies will take their stable clusters sufficiently faster than the development of order in bulk. It will make the first process and thereafter equations (i), (ii) and (iii) must be regarded as auxiliary relations to determine ρ, α and β for given s and σ in any time of annealing.

(The second process)

At the same time, as calculated before, the development of σ begins with a pretty large rate from the first and then decreases monotonously without associating any change of s. The process has an anticooperative tendency.

(The third process)

Though this theory does not take account of the nucleation mechanism, small fluctuations of s will cause a cooperative rate formation of long range order. As calculated before it starts with a zero rate at first, but the rate increases gradually to its maximum and decreases to zero. It is the main process of the transformation.

(The fourth process)

Our theory can not contain the antiphase and the dislocation mechanism. Hence there is no possibility for the existence of the fourth process if T_t is near the critical temperature, as will be seen in Fig. 5. But if it is sufficiently lower than T_c, there are interesting features as to the existence of the fourth process. As has been noticed already in the curves of $\theta=0.2$ in Fig. 5 and Fig. 7, $d\sigma/ds$ at the end of the process is fairly small for this case and α seems to reach an apparent saturation value different from the equilibrium value. The phenomena must be regarded as the effect of frozen vacancies. Namely, if we anneal the alloy sufficiently below the critical temperature the vacancies construct some clusters arround them and stabilize themselves. The existence of the clusters will make the completion of long range order very much difficult. In the calculation we treat the only one case $K_A=K_B$ and $w_A=w_B$. In this case, there is no special preference for vacancies between A- and B-atoms. Therefore, though the equilibrium value of α is almost equal to one, the clusters have a tendency to take their statistical configuration of $\alpha=0$, before the completion of long range order. The tendency would make the apparent final value of α to about 0.4, and as the result the development of long range order is retarded compared with that of short range order. We consider that the phenomena represent one feature of the interaction between imperfections and atomic ordering.

Concerning the first process, the description of our theory is only for vacancies and it does not take account of the generation and annihilation mechanism of these. The expected relaxation time is too short compared with the experimental results. In the actual case the behaviour of imperfections which have more longer relaxation times will play a main rôle in the process.

Concerning the second process, the description of the theory will be fairly good.

Concerning the third process, the omission of nucleation mechanism and antiphase problem will be essential and we cannot say the degree of approximation of the theory. It must be borne in mind that the internal friction constant shows an anomalous peak at about 30 hours of annealing, when the ordering rate of the alloy Ni_3Fe reaches its maximum. Such an experiment was carried out by T. Tomizuka[10] and our theory could only show the presence of the expected tendency as described before. It should also be necessary here to introduce the mechanism of generation of imperfections.

Concerning the fourth stage also the neglect of antiphase, dislocation and impurity will be essential. The introduction of these mechanism will undoubtedly result in an elongation of the fourth process and which will appear already just below the critical temperature. But the theory showed that even the vacancy itself still has such an effect at low temperature.

As a whole, our theoretical treatment accords well with the experimental results of Ni_3Fe superlattice and our explanation about them. We hope a further study will be done by introducing the effect of dislocation and nucleation mechanism and the difference of AB and A_3B type superstructure.

The writer expresses his sincere thanks to Professor Seiji Kaya for his constant encouragement and guidance. He also wishes to express his thanks to Professor Yutaka Takagi and Professor Ryogo Kubo for their valuable discussions.

References

1) S. Iida: J. Phys. Soc. Japan **7** (1952) 373.
2) S. Iida: J. Phys. Soc. Japan **9** (1954) 946.
3) S. Iida: J. Phys. Soc. Jayan **10** (1955) 9.
4) Y. Takagi, T. Oguchi and G. Shirane: Bull Tokyo Inst. Tech. **B 3** (1950) 225.
5) S. Kaya: J. Hokkaido Univ. **2** (1938) 29.
6) S. Kaya, M. Nakayama and H. Sato: Proc. Phys. Math. Soc. Japan **25** (1943) 179.
7) T. Nagasima: J. Appl. Phys. Japan **19** (1950) 53.
8) S. Chikazumi: J. Phys. Soc. Japan **5** (1950) 332.
9) S. Kaya, H. Sato and K. Kumasaka: J. Metal Soc. Japan **6** (1942) 188.
10) T. Tomizuka: unpublished.

JOURNAL OF THE PHYSICAL SOCIETY OF JAPAN Vol. 10, No. 9, SEPTEMBER 1955

On the Polarization of Silver Sulfide

By Shin-ya MIYATANI

Department of Physics, Faculty of Science, Niigata University

(Received May 9, 1955)

The variation of the chemical potential of electrons in Ag_2S with the variation of the Ag/S ratio was measured with the help of the e.m.f. measurements of the galvanic cell Ag|AgI|Ag_2S|Pt. The relation between the chemical potential of electrons and the density of conduction electrons was found to be in accordance with the theory, and it was found that the conduction electrons in β-Ag_2S obey the classical statistics while those in α-Ag_2S are degenerate. Polarization phenomena when weak direct current of constant intensity is sent through Ag_2S specimen were also studied. The potential distributions along the specimen and the time rate of building up or decay of polarization show good agreement with the theory in both α- and β-phases. The conductivities were measured and discussed.

§ 1. Introduction

Silver sulfide is an n-type semiconductor and silver ions are mobile in both α (stable above 178°C) and β (stable below 176°C) phases. Its conductivities and the transport numbers of both charge carriers, electrons and silver ions, have been measured by Tubandt and others[1]. M. H. Hebb[2] has deduced its electronic component as a function of the chemical potential of silver from his probe measurements on polarized samples. C. Wagner[3] has studied the variability of the Ag/S ratio with the use of the galvanic cell Ag|AgI|Ag_2S|Pt.

The present author, with the collaboration by Y. Suzuki[4] has carried out probe measurements on polarization and its decay processes of β-cuprous sulfide, a p-type semiconductor with mobile copper ions. His experimental results have been analyzed theoretically by I. Yokota[5].

The present study on the polarization of silver sulfide has been carried out with the help of the galvanic cell Ag|AgI|Ag_2S|Pt following C. Wagner, and with the use of the theory developed by I. Yokota with some adaptations.

§ 2. General Principles

(*a*) *Electromotive force of the galvanic cell* Ag|AgI|Ag_2S|Pt[3]

In the galvanic cell Ag|AgI|Ag_2S|Pt, AgI is essentially an ionic conductor. The chemical potential of a silver atom in Ag_2S, μ_{Ag}, is, therefore, related to the electromotive force, E, of the cell by

$$\mu_{Ag}-\mu_{Ag}{}^0=-eE\,, \tag{1}$$

where $\mu_{Ag}{}^0$ is the chemical potential of a silver atom in the pure metallic silver, i.e. that in Ag_2S which is in equilibrium with the metallic silver. The chemical potential of a silver atom is equal to the sum of the chemical potential of a silver ion, μ_i, and that of an electron, μ_e. μ_i is, however, independent of the deviation from the ideal stoichiometric ratio of Ag to S, since Ag_2S is an " average crystal ", i.e. its sublattice for Ag is so disturbed that the small deviation does not contribute anything to the chemical potential. Hence, it follows from Eq. (1) that

$$\mu_e-\mu_e{}^0=-eE\,. \tag{2}$$

On the other hand, the density of conduction electrons, n_e, is related to μ_e, as well known, by

$$n_e=\frac{2N_c}{\sqrt{\pi}}\int_0^\infty\frac{\sqrt{\eta}\,d\eta}{1+\exp(\eta-\eta_e)}\,, \tag{3}$$

where $N_c=2(2\pi m^*kTh^{-2})^{3/2}$, $\eta\equiv\mathcal{E}/kT$, and $\eta_e\equiv\mu_e/kT$. In these notations m^* is the effective mass of conduction electron and $\mathcal{E}$ its kinetic energy. When the density, n_e, is sufficiently small, Eq. (3) is reduced to

$$\mu_e=kT\log\frac{n_e}{N_c} \tag{4}$$

(classical case). In this case E is related to n_e by

$$eE=kT\log\frac{n_e{}^0}{n_e}\,. \tag{5}$$

When the density is not so small, the exact formula Eq. (3) must be used (degenerate case). For a narrow range of n_e values, however, the following approximation may be available;

$$\mu_e = ckT \log \frac{n_e}{N'}, \tag{6}$$

where c and N' are constant parameters depending upon the mean value of n_e within the range considered.

A well-defined amount of silver can be added to, or removed from, a Ag_2S specimen by sending a current across the cell for a definite period. In this way the Ag/S ratio of the specimen can be varied easily.

(***b***) *Polarization and its decay*[2,5]

When a direct current of a constant intensity is sent through a Ag_2S specimen with platinum electrodes, silver ions in it move toward the cathode and when the current intensity is so small that the silver ions do not deposit at the cathode, a stationary state where the current is carried only by electrons is attained (*polarization process*). When the current is switched off, the residual potential is left and decays according as the previous homogeneous state is recovered (*decay process*).

In general, the current intensity, I, is related to the potential, V, according to Ohm's law, by $I = \mp \sigma dV/dx$, using the minus and plus signs for positive and negative charge carriers respectively. V is given by $\mu_e/e - \Phi$ for electrons, and by $\mu_i/e + \Phi$ for positive ions, where Φ is the electrostatic potential. Then the electronic and ionic components of the current intensity are given respectively by

$$I_e = \sigma_e \frac{d}{dx}\left(\frac{\mu_e}{e} - \Phi\right), \quad I_i = -\sigma_i \frac{d}{dx}\left(\frac{\mu_i}{e} + \Phi\right), \tag{7}$$

where σ_e and σ_i are electronic and ionic conductivities respectively. The first terms of the right-hand side of Eqs. (7) represent the diffusion current and the second terms represent the conduction current. Since μ_i is independent of the composition in our case, the second equation of (7) becomes $I_i = -\sigma_i d\Phi/dx$.

In the polarization process, the ionic conduction current causes the gradient of the chemical potential for electrons along the specimen, resulting in the electronic diffusion current which causes the electric field with the opposite direction to the original field. According as the polarization builds up, the total electric field and hence also the ionic current decrease and a stationary state is attained. In the decay process, the electric field left with the gradient of the composition leads the ions to move back to the previous homogeneous distribution. On this subject, we can obtain the following formulae by simple calculations.

At the instant of switching on, when the specimen is homogeneous, the current intensity, I, is given by

$$I = I_e + I_i; \quad I_e = -\bar{\sigma}_e \frac{d\Phi}{dx}, \quad I_i = -\bar{\sigma}_i \frac{d\Phi}{dx}, \tag{8}$$

where the bars above σ's denote their respective initial values. σ_i is independent of the composition as seen later and so the bar is unnecessary for σ_i. Then the ions move toward cathode and the gradient of composition takes place gradually. Eqs. (7) may be applied to this process. From these equations and the total current intensity, I, which is maintained constant in this process, we have

$$\frac{I_e}{\sigma_e} = \frac{\sigma_i}{\sigma_t}\frac{d}{dx}\left(\frac{\mu_e}{e}\right) + \frac{I}{\sigma_t}, \quad \frac{d\Phi}{dx} = \frac{\sigma_e}{\sigma_t}\frac{d}{dx}\left(\frac{\mu_e}{e}\right) - \frac{I}{\sigma_t}, \tag{9}$$

where σ_t is the total conductivity, i.e. $\sigma_e + \sigma_i$. As seen in these equations, I_e increases and $d\Phi/dx$ and hence also I_i decrease according as the gradient of μ_e builds up. In the stationary state I_i is zero and hence also $d\Phi/dx$ becomes zero and I is given by

$$I = I_e = \sigma_e \frac{d}{dx}\left(\frac{\mu_e}{e}\right). \tag{10}$$

In the classical case, we have, using Eq. (4),

$$I = p_e kT \frac{dn_e}{dx}, \tag{11}$$

where p_e is the mobility of electrons. From Eq. (11) we see that the distribution of n_e in the stationary state is linear along the specimen. In the degenerate case, too, as far as the current intensity is not too large, we have, using Eq. (6),

$$I = cp_e kT \frac{dn_e}{dx}. \tag{12}$$

Integrating this equation, we have

$$n_e = \bar{n}_e + \frac{I}{cp_e kT}(x-a), \tag{13}$$

where a is the integration constant which will be $L/2$ (L being the total length of the specimen) if the total number of conduction electrons is conserved in the specimen. Then the potential difference between two probes is given by

$$\begin{aligned} eV_s(x)&=\mu(x_2)-\mu(x)\\ &=-ckT\log\left(1-\frac{\boldsymbol{i}(x_2-x)}{1+\boldsymbol{i}(x_2-a)}\right), \end{aligned} \tag{14}$$

where $\boldsymbol{i}$ is defined by $eI/c\bar{\sigma}_e kT$.

After the current has been switched off, the equations corresponding to Eqs. (9) become

$$\frac{I_e}{\sigma_e}=\frac{\sigma_i}{\sigma_t}\frac{d}{dx}\left(\frac{\mu_e}{e}\right), \qquad \frac{d\Phi}{dx}=\frac{\sigma_e}{\sigma_t}\frac{d}{dx}\left(\frac{\mu_e}{e}\right). \tag{15}$$

At the instant of switching off, the ratios V_r/V_s and Φ_r/V_s are given by

$$\frac{V_r}{V_s}=\frac{\sigma_i}{\bar{\sigma}_t}, \qquad \frac{\Phi_r}{V_s}=\frac{\bar{\sigma}_e}{\bar{\sigma}_t}, \tag{16}$$

where V_r is the residual potential and Φ_r is the residual electrostatic potential.

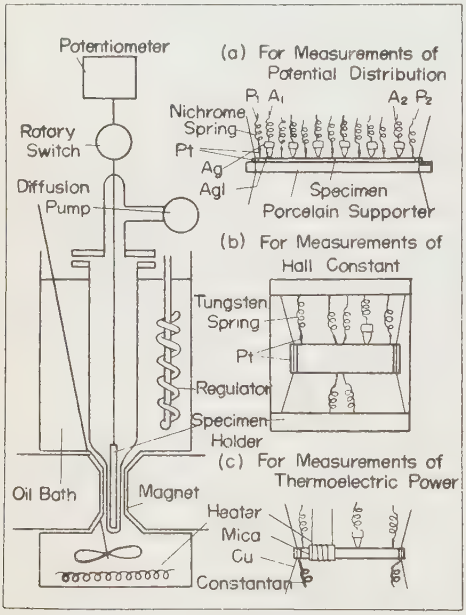

Fig. 1. Schematic diagram of apparatus.

Now, the rate of the change of n_e in the processes mentioned above may be given by

$$\frac{\partial n_e}{\partial t}=\frac{\partial}{\partial x}\left(\frac{I_e}{e}\right)+G, \tag{17}$$

where the first term comes from drift motion of electrons and the second, G, from capture or donation of them. If the current intensity is not too large, Eq. (17) may be reduced, using Eqs. (6) and (8) or (15), to

$$\frac{\partial n_e}{\partial t}=\frac{p_e kTc}{e}\frac{\sigma_i}{\bar{\sigma}_t}\frac{\partial^2 n_e}{\partial x^2}+G. \tag{18}$$

When G is given by $-g(\partial n_e/\partial t)$ (see later), then n_e and hence the potential differences between probes will change approximately with the time constant, τ, given by

$$\frac{1}{\tau}=\frac{\pi^2}{L^2}\frac{p_e kT}{e}\frac{c}{1+g}\frac{\sigma_i}{\bar{\sigma}_t}. \tag{19}$$

§ 3. Experimental Arrangements

Silver has been reduced from $AgNO_3$ and melted into a block in the stream of hydrogen. Ag_2S samples are prepared by direct reaction of a silver block and sulfur powder both sealed together in a vacuum hard glass tube. The dimensions of the specimens are various, e.g. 50×1×0.5 *mm* for the measurements at the α phase temperatures, 30×2×2 *mm* for β and 35×8×0.5 *mm* for the Hall constant measurements etc.. Fig. 1 shows a schematic diagram of the apparatus. A specimen holder (porcelain) is inserted in a glass tube immersed in an auto-controlling oil bath and evacuated by a diffusion pump. Platinum foils coated with carbon powder are used as electrodes, and copper or nichrome wires are wound tightly on Pt foils. When a thin specimen is used, it is laid on a porcelain supporter in order to protect the specimen from bending. Tungsten or nichrome springs with Pt heads are used as potential probes, and nichrome springs with Ag–AgI heads are used as chemical potential probes and as the cells to supply or remove Ag ions. The volumes or cross sections of specimens are calculated from their weight with the use of the value of the density (7.3 $gr\ cm^{-3}$).

§ 4. Experimental Results

(*a*) *Measurements on* Ag|AgI|Ag_2S|Pt

When a current is sent across the cell, Ag ions are added to or removed from Ag_2S, as described above. In this procedure, the situation is simple in the α phase. That is, when the current is switched off, an equilibrium state is attained very soon. Moreover, the ratio of the total amount of electricity, Q, to the increase (or decrease) of the electronic conductivity, $\Delta\sigma_e$, is almost independent of the Ag/S ratio, at least at the lower temperature range of the α phase. It follows that every electron accompanied by the introduction of a silver ion into α-Ag_2S specimen is introduced into the conduction band of Ag_2S. Accordingly, we have $Q/\Delta\sigma_e=v/p_e$, where v is the volume of the specimen. Using this relation, p_e is estimated as 160 ± 5 $cm^2\ sec^{-1}\ volt^{-1}$ at 180°C. In the β phase, however, the situation is not so much simple: The equilibrium state is not attained so soon as in the α phase, and, moreover, the ratio $Q/\Delta\sigma_e$ depends upon the compositions. Fig. 2 shows an example of a series of such measurements. The e.m.f. of the cell, E, does not depend on whether the Ag_2S sample is in true equilibrium state or not, but depends only on the momentary value of n_e. Hence, the change of e.m.f., E, reveals that of n_e. The rate of change of n_e may approximately be expressible as

$$\frac{dn_e}{dt}=\frac{I}{ve}+G-\frac{n_e-n_{et}}{\tau_1}\,, \qquad (20)$$

where the first terms comes from the current, the second from capture or donation of electrons, and the last from unknown mechanism with a large relaxation time, τ_1 (one hour or more), n_{et} being the equilibrium value of n_e at each moment. If the second term, G, is assumed to be reducible to $-g dn_e/dt$ (see later discussions), then Eq. (20) is reduced to

$$\Delta\sigma_e=\frac{p_eQ}{v(1+g)}-\frac{\sigma_e-\sigma_{et}}{\tau_1(1+g)}\,. \qquad (21)$$

In practice, the change of σ_e between just before and after sending a current is taken as $\Delta\sigma_e$ in such cases as represented by the curves 1 and 2 in Fig. 2, whereas the change of σ_e during initial two or three minutes is picked up in such cases as represented by the curves 3 and 4 in the same figure, in order to avoid the influence of the second term of Eq. (21), for we are interested only in fast changes in our present work. The $(1+g)$ values corresponding to Fig. 2 will be shown in Fig. 6, where p_e will be assumed to be 50 $cm^2\ sec^{-1}\ volt^{-1}$.

Now, although the relation between σ_e and the Ag/S ratio is difficult to determine, one can measure the relation between σ_e and E with ease. Fig. 3 shows $\log\sigma_e$ vs eE/kT plots at several temperatures. Eq. (5) holds good for the β phase, whereas theoretical values deduced from Eqs. (2) and (3) fit to experimental values quite well for the α phase. In the latter case, moreover, using $p_e=160$, N_c can be estimated as $5.5\times10^{18}\ cm^{-3}$ and μ_e^0 as $4.2\,kT$ above the bottom of the conduction band. It follows from the N_c-value that the effective mass of conduction electrons, m^*, is equal to 0.24 m. By the way, the experimental values of the thermoelectric power, Θ, of α-Ag_2S at 180°C can be expressed as

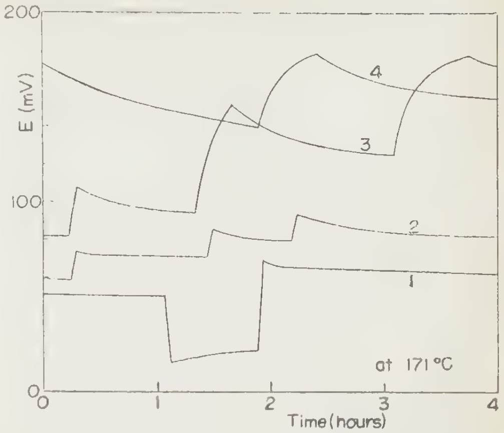

Fig. 2. E vs time in removing Ag from βAg_2S.

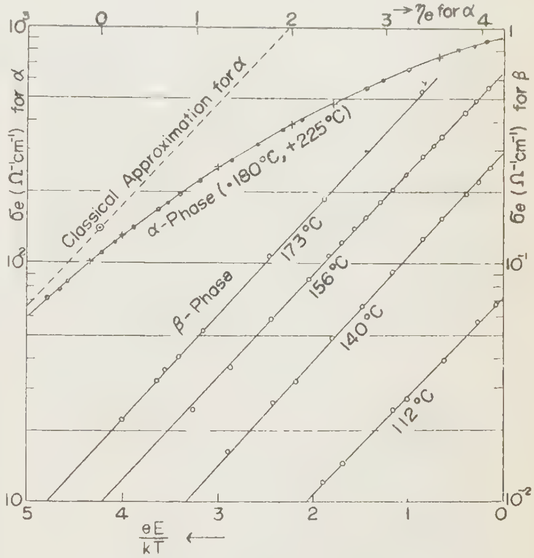

Fig. 3. $\log\sigma_e$ vs eE/kT.

$$\Theta=\frac{k}{e}\log\frac{n_{const}}{n_e}\,, \qquad (22)$$

for nearly classical regions ($eE/kT>1.5$), where $n_{const}=6.7\times10^{19}$, while for more highly degenerate regions, Θ becomes to deviate from Eq. (22) appreciably. Using the classical formula $\Theta=(k/e)(2+r+\log N_c/n_e)$, and $r=1/2$, N_c may be estimated as 5.5×10^{18}. The coincidence of these two N_c-values deduced from quite different experimental bases is interesting, although it may be rather fortuitous.

(*b*) *Polarization and its decay*

Fig. 4 shows two examples of the potential changes during polarization and decay processes, *A* for the α phase and *B* for the β phase. The potential difference between two Pt probes (P_1 and P_2 in Fig. 1 (a)), V_1, and that between two Ag-AgI probe (A_1 and A_2 in the same figure), V_2, are shown with full lines. If the current intensity is not too large, the potential difference, V_1, is given, integrating the first equation of Eqs. (9), by

$$V_1=\frac{\sigma_i}{\bar{\sigma}_t}\frac{\mu_e(x_2)-\mu_e(x_1)}{e}+V_i, \tag{23}$$

for the polarization process, where V_i is the initial potential difference given by Eqs. (8), whereas by the first term only of Eq. (23) for the decay process. The potential difference between two Ag-AgI probes, V_2, is the sum of the difference of the e.m.f. of two cells, each of which consists of the Ag-AgI probe and Ag_2S specimen and a imaginary Pt probe at the same position of the specimen, E_2-E_1, and the potential difference between such two imaginary Pt probes, $(\mu_e/e-\Phi)_2-(\mu_e/e-\Phi)_1$, but the former is equal to the difference of $-\mu_e/e$ according to Eq. (2) and V_2 is, therefore, equal to the difference of the electrostatic potential, Φ. Hence, V_2 is given, integrating the second equation of Eqs. (9), by

$$V_2=V_i'-\frac{\bar{\sigma}_e}{\bar{\sigma}_t}\frac{\mu_e(x_2')-\mu_e(x_1')}{e}, \tag{24}$$

for the polarization process and by the second term only of this equation for the decay process, where the prime indicates the small difference of the positions between P_1 and A_1, or P_2 and A_2. The difference, V_1-V_2, with a proper correction for the difference of the positions of the probes, is equal to the difference of the chemical potential divided by e, $(\mu_e(x_2)-\mu_e(x_1))/e$, which is also shown as broken lines in Fig. 4.

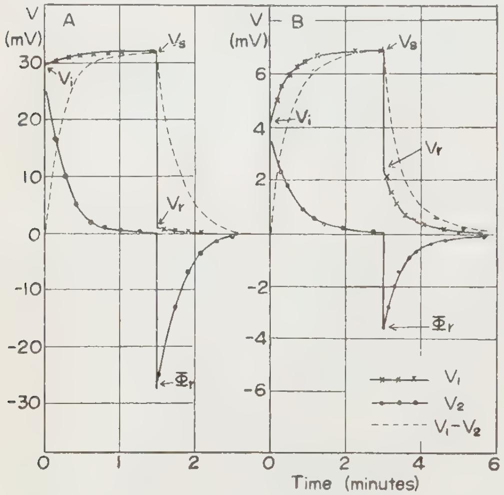

Fig. 4. Potential vs time.

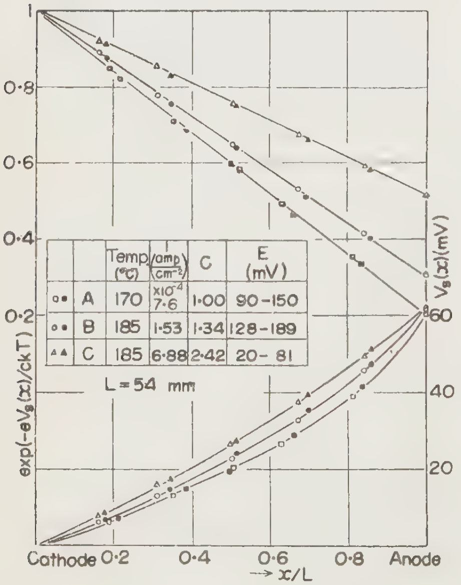

		Temp (°C)	I (amp/cm⁻²)	C	E (mV)
○●	A	170	×10⁻⁴ 7·6	1·00	90-150
○●	B	185	1·53	1·34	128-189
△▲	C	185	6·88	2·42	20- 81

Fig. 5. Stationary potential distribution.

All features seen in the figure are just as expected from the theory described in § **2** (***b***). The experimental data for those two examples are as follows, where the first value in each parentheses is referred to *A* of those two, and the second is to *B*: Temperature (185; 170)°C the e.m.f., *E*, (152; 149)*mV*; the current intensity, *I*, (0.84; 4.0×10^{-5}) *amp*/*cm*^{2}; the stationary potential, V_s, (31.7; 6.8)*mV*; the residual potential, V_r, (0.7; 2.4)*mV*; the electronic conductivity, σ_e, (140; 3.1×10^{-2}) Ω^{-1} *cm*$^{-1}$; the ionic conductivity, σ_i, (3.1; 1.7×10^{-2}) Ω^{-1} *cm*$^{-1}$; the time constant, τ, (17.4; 35) *sec*; *c* (1.5; 1.0); *g* (0;9); the mobility of electrons obtained with the use of Eq. (19), p_e, (142; 70) *cm*^{2} *sec*$^{-1}$ *volt*$^{-1}$: the total length of the specimen, *L*, 5.7 *cm*; and the distance between P_1, and P_2 is 5.2 *cm* for both *A* and *B*.

In the stationary state, the potential distribution is given by Eq. (14). Fig. 5 shows three examples, *A* for the β phase, and *B* and C for the α phase. $V_s(x)$ vs x/L plots are shown in the lower part of the figure and $\exp(-eV_s(x)/kT)$ vs x/L plots are in the upper part of the figure, where x is the distance from the cathode. The e.m.f. of the end cells (A_1-P_1 and A_2-P_2 in Fig. 1 (a)) are also shown in the figure. The difference between them is equal to V_s and potentials of six Ag-AgI probes are equal to each other.

In regard to the rate of change of potentials one cannot expect so high accuracy, but, nevertheless, the experimental results are proved to be in accordance with the theory within their accuracies. The time constant, τ, is expected to be given by Eq. (19) with $g=0$ and proper c-values for the α phase, whereas with $c=1$ and proper g-values for the β phase. The c-values can be evaluated easily from Fig. 3 as a function of σ_e or eE/kT, and the g-values may be obtained from measurements described in (*a*) of this section. Rigorously speaking, the third term of Eq. (20) should be taken into consideration for the β phase. In fact, such slow changes are observed, but may be left out of consideration for our present purposes, since the amount of the slow change is not so large and its time constant, τ_1, is far larger than τ for the polarization process. Fig. 6 shows the results of two series of measurements with the same specimen, one for the α phase (183°C) and the other for the β phase (170°C). In the figure are plotted the ionic conductivity σ_i ($\Omega^{-1}\ cm^{-1}$), the mobility of electrons obtained from τ with the use of Eq. (19), p_e ($cm^2\ sec^{-1}\ volt^{-1}$), for both cases, c-values for α, and $(1+g)$-values obtained from measurements shown in Fig. 2 for β, against eE/kT. σ_i and p_e are independent of the compositions and the p_e-values are always in accordance with the values obtained from the Hall constant (170±10 for α and 60±10 for β) and with those obtained from the ratio $Q/\Delta\sigma_e$ (160±5 for α) within the accuracy of measurements. The similar consistency has been observed at other temperatures.

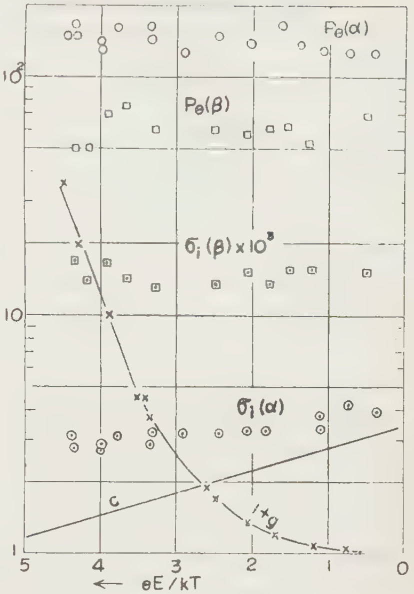

Fig. 6. σ_i and p_e vs eE/kT.

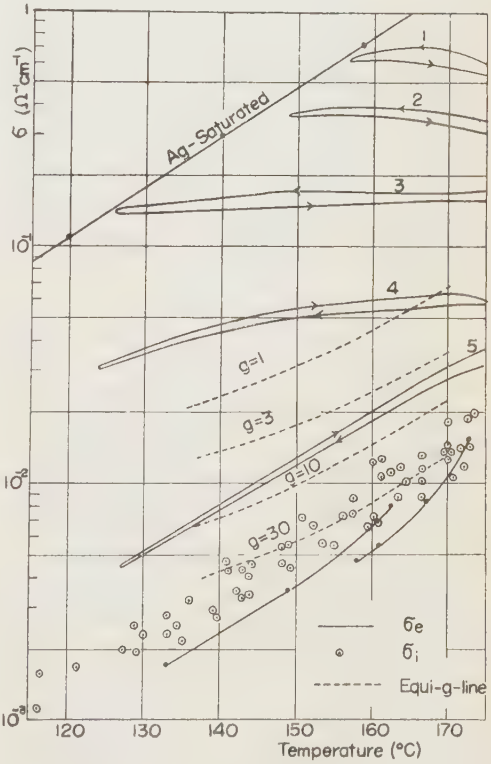

Fig. 7. σ_e and σ_i vs Temperature.

(*c*) *Electronic and ionic conductivities*

In the α phase, the electronic conductivity, σ_e, is almost independent of the temperature as seen in Fig. 3. The situation is similar to that of the β–Cu_2S[4)] except the current is carried by electron-holes in the latter case. In the β-phase, however, the situation is rather complicated. Fig. 7 shows σ_e and σ_i vs temperature plots in the β phase. σ_i is almost independent of the compositions and increases with rising temperature, whereas σ_e is varied by about 100 times according as the Ag/S ratio is varied. The upper limit of σ_e

is that of a sample which is in equilibrium with metallic silver, while the lower limit is that of a sample which is treated at about 450°C in a glass tube sealed together with sulfur. In these two limiting cases, σ_e increases exponentially with increasing temperature with the similar activation energy (0.8 eV). The temperature dependency of σ_e of a sample with a fixed Ag/S ratio is, however, not always similar to these limiting cases. The loop-like curves from 1 to 5 in Fig. 7 represent σ_e at varying temperatures when the temperature of the specimen (measured with Cu-Constantan thermocouples attached to the both electrodes as shown in Fig. 1 (c)) is lowered, starting from 174°C, and then immediately raised back to 174°C at the rate of about 2°C/*min*.. The hysteresis effect is not remarkable. Although these plots do not represent σ_e vs T relation in the true equilibrium state at each moment since it takes several hours for the specimen to attain equilibrium state at each temperature, they may be useful as far as only the fast changes are concerned. They will be discussed later. In the same figure, σ_e with the same g-values vs temperature plots (equi-g-lines) are shown as dotted lines, where the g-values are estimated from Fig. 8 in which the g-values obtained from experimental τ-values and Eq. (19), assuming $p_e=50$, are plotted against σ_e in log-log-scale. g may be related to σ_e and the absolute temperature, T, approximately by

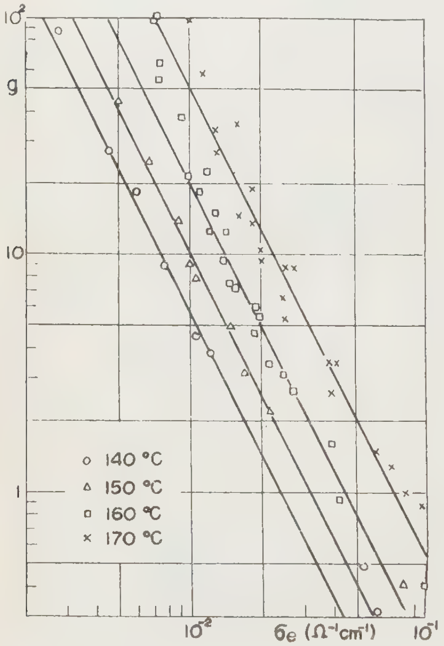

Fig. 8. g vs σ_e.

$$g=g_0\exp(-U/kT)/\sigma_e^2\ , \qquad (25)$$

where U is about 1.1 eV.

§ 5. Discussions

The experimental results on polarization and its decay processes have been proved to be in good accordance with the phenomenological theory. Upon the atomic view-point, however, some problems remain still unsolved, particularly for the β phase. We should like to discuss those circumstances for a while. The situation seems to be simple for the α phase. As has been deduced from x-ray investigations by Rahlfs[6)], silver ions are distributed among a large number of nearly equivalent lattice sites. The excess Ag atoms over the stoichiometric ratio may be situated among these available sites and may be in ionized state, delivering the same number of electrons into conduction band. It is therefore very plausible that the same number of conduction electrons as Ag ions are introduced when a current is sent across the cell, and that the density of conduction electrons does not increase with increasing temperature. In the β phase, however, the situation is not so simple.

As seen in Fig. 7, the circumstances for the higher conductivity range are rather similar to those of the α phase. That is, g is almost zero and σ_e is almost independent of the temperatures. It may be supposed, therefore, that atomic features are also similar to those of the α phase described above. In the lower conductivity range, however, g is far larger than unity and σ_e increases as the temperature rises. In the case shown in Fig. 2, for example, 3.8×10^{17} of Ag atoms must be removed from the specimen per 1 cm^3 in order to change σ_e from 0.7 $\Omega^{-1}\,cm^{-1}$ ($E=22\,mV$, $n_e=9\times10^{16}$) to 0.03 $\Omega^{-1}\,cm^{-1}$ ($E=140\,mV$, $n_e=4\times10^{15}$) at 171°C. If we suppose that the density of excess Ag atoms is nearly equal to that of conduction electrons in high conductivity specimens, then we must conclude that Ag atoms are deficient to a remarkable extent in low conductivity specimens. In spite of this deficit, Ag_2S is still n-type. It follows then that a large number of Ag ion vacancies exists and plays a particular role in the lower-σ_e range. Let us propose a possible model which has the required properties: Suppose a Ag ion vacancy forms a neutral "complex" cooperating with its neighboring sulfur ions, so that it may act as a sink for a silver atom. M. H. Hebb[2)] has suggested that a certain fraction of sulfur may exist in the form of S_2 in Ag_2S. Our complex might be a combination of Ag ion vacancy and S_2. In any way, such complexes will be in equilibrium with the Ag ions at the interstitial or available sites if there are several equivalent lattice sites as in the α phase. Let the density of the former be n_c, and the latter, n_i. Then

$$n_i n_c = f(T); \quad n_i = n_e . \tag{26}$$

Hence, g may be expressed as

$$g = -\frac{dn_c}{dn_e} = \frac{f(T)}{n_e^2} . \tag{27}$$

This expression is in accordance with Eq. (25). Moreover, in a sample with a fixed Ag/S ratio, $n_i - n_c$ $(\equiv n)$ will remain constant for varing temperatures. Then n_e may be related to the temperature by

$$n_e(n_i - n) = f(T) . \tag{28}$$

It follows from Eqs. (27) and (28) that $n \approx n_e$ if $g \ll 1$, whereas $n_e = f(T)/-n$ $(n<0)$ if $g \gg 1$. These two extreme cases can be seen in Fig. 7; the curve No.1 or 2 in it represents the former case and the curve No. 5 is an example of the latter. Thus the general features are consistent with our model at least qualitatively. Alternative models may be of course possible.

Finally, we have not payed much attention to the slow change which might be attributed to the diffusion of sulfur ions or vacancies. The more detailed discussions on this subject should be left to the investigation in future.

The author wishes to express his sincere thanks to Mr. Y. Suzuki who kindly prepared the samples and to Mr. I. Yokota for his kind discussions and advices. This work was supported by the research grant of the Ministry of Education.

References

1) C. Tubandt: Z. anorg. u. allgem. Chem. **115** (1921) 105.
2) M. H. Hebb: J. Chem. Phys. **20** (1952) 185.
3) C. Wagner: J. Chem. Phys. **21** (1953) 1819.
4) S. Miyatani and Y. Suzuki: J. Phys. Soc. Japan **8** (1953) 680; J. Fac. Sci. Niigata Univ. Ser. I, **1** (1953) 1.
5) I. Yokota: J. Phys. Soc. Japan **8** (1953) 595.
6) P. Rahlfs: Z. physik. Chem. **B 31** (1935) 157.

JOURNAL OF THE PHYSICAL SOCIETY OF JAPAN Vol. 10, No. 9, SEPTEMBER 1955

X-ray Studies on the Structures of Solid Solutions NaCl-CaCl$_2$

II. Structures of {111} and {310} Plate-Zones

By Kazuo SUZUKI

Tokyo Institute of Technology, Oh-Okayama, Meguro, Tokyo

(Received June 18, 1955)

Structures of {111} and {310} plate-zones explaining the rod distributions of intensity weight in reciprocal space revealed in X-ray patterns from solid solutions of NaCl containing a few per cent of CaCl$_2$ (reported in Part I) is proposed. The plate-zones are considered to be composed of a number of smaller units, called platelets, which are disposed in anti-phase relation among themselves in a plate-zone. We proposed probable models of the structures of the two kinds of platelets making up the {111} plate-zone and the {310} plate-zone respectively by assuming that each platelet has crystal structure resembling that of CaCl$_2$, retaining, however, coherency with the matrix. The qualitative agreement was found between observed and calculated intensities of rod distributions in reciprocal space.

The proposed CaCl$_2$-like structure of the {111} platelet seems to be plausible one, since it was found that its orientation was followed by that of CaCl$_2$ particle which precipitated by a certain heat treatment. In the case of the <310> rods, the proposed structure of the {310} plate-zones is rather tentative. Absolute intensity of the <111> rods was roughly estimated by comparing it with that of thermal diffuse scattering from pure NaCl crystal. It was found that we could expect the intensity of the diffuse spots due to the rods to be of the same order as that of thermal diffuse scattering even when only a few per cent of the dissolved Ca^{++} ions are participating in the {111} plate-zones.

§ 1. Introduction

In previous papers[1),2)], Miyake and the present author have studied the diffuse scattering of X-rays from single crystals of the solid solutions NaCl–CaCl$_2$, and have revealed that there are rod-like distributions of intensity weight in reciprocal space, running along $\langle 111\rangle_r$ and $\langle 310\rangle_r$ through some of reciprocal-lattice points corresponding to the matrix. These rods were interpreted as being due to small plate-like precipitates formed in the solid solution. These thin plate-like regions, called the *plate-zones*, which are perpendicular to the rod concerned, were considered to be the places where the dissolved Ca^{++} ions and accompanying positive ion vacancies are concentrated by the process of the motivated precipitation.

As was fully discussed in Part I, the structure of the plate-zone explaining the observed distribution of rods in reciprocal lattice (which are reproduced again in Figs. 1a and b for $[11\bar{1}]_r$ rods and $[031]_r$ rods respectively) can not be a simple inclusion having a coherent crystalline pattern, but should be a dense aggregate of a number of smaller units. It was supposed that these units, called the *platelets*, have certain crystalline structures with superlattice periods, composed of Ca^{++} ion, positive ion vacancy as well as Na$^+$ and Cl$^-$ ions. The platelets contained in a plate-zone were assumed to be disposed in anti-phase relations among themselves. The positions of ions in a platelet were regarded to be generally displaced from the lattice sites of the original matrix.

The further step of our study is to propose suitable models of the structures of platelets. This can naturally be not easy, because besides the observed distribution of rods in reciprocal space only few knowledges are available for this purpose. The following conditions, however, may be presumed: (i) the packing of ions in a platelet should be reasonable with respect to their ionic radii, and also compatible with the structure of matrix surrounding the platelet; (ii) the arrangement of ions in a platelet should be electrostatically reasonable.

The presumption as follows may also be permissible: (iii) the arrangement of ions around a Ca^{++} ion in a platelet and that in the crystal structure of CaCl$_2$ are similar to each other.

Guided by the above principles, we propose in the present paper probable models of the structures of the two kinds of platelets making up the {111} plate-zone and the {310} plate-zone respectively. The qualitative agreement was found between observed and calculated intensities of rod distributions in reciprocal space. Concerning the structure of {111} platelet, there is an evidence favouring the proposed model (§ 4). The model for {310} platelet is of much more tentative nature.

The theoretical basis for interpreting the diffraction patterns are to be referred to Part I.

§ 2. Model for Structure of {111} Platelet

a) *Characteristic feature of distribution of $\langle 111\rangle_r$ rods in reciprocal space.*

As mentioned in Part I, many of reciprocal-lattice points other than the reciprocal-space origin are accompanied by $\langle 111\rangle_r$ rods, but their intensities are uneven. For instance, $[11\bar{1}]_r$ rods are absent at the reciprocal-lattice points (000), $(11\bar{1})$, $(22\bar{2})$ etc., and very faint at some of the {220} reciprocal-lattice points (Fig. 1a). These features may be summarized as follows:

The intensities of the $[11\bar{1}]_r$ rods are missing or very weak at the reciprocal-lattice points with the indicies having the relation

$$h+k+2l=0 \quad (mod\ 3). \qquad (1)$$

The $[11\bar{1}]_r$ rods other than above mentioned, so far as observed, show appreciable and all comparable intensities. As has already been explained in Part I, the missing of rod at the reciprocal-space origin is in accordance with the assumption that the number of dissolved Ca^{++} ions and that of positive ion vacancies resultingly produced are equal to each other.

b) *Analogous features in crystal structures of* NaCl *and* CaCl$_2$

The crystal structure of CaCl$_2$ possesses a rhombic lattice with parameters $a=6.24$ Å, $b=6.43$ Å and $c=4.20$ Å$^{3)}$. Fig. 2 shows its (001)

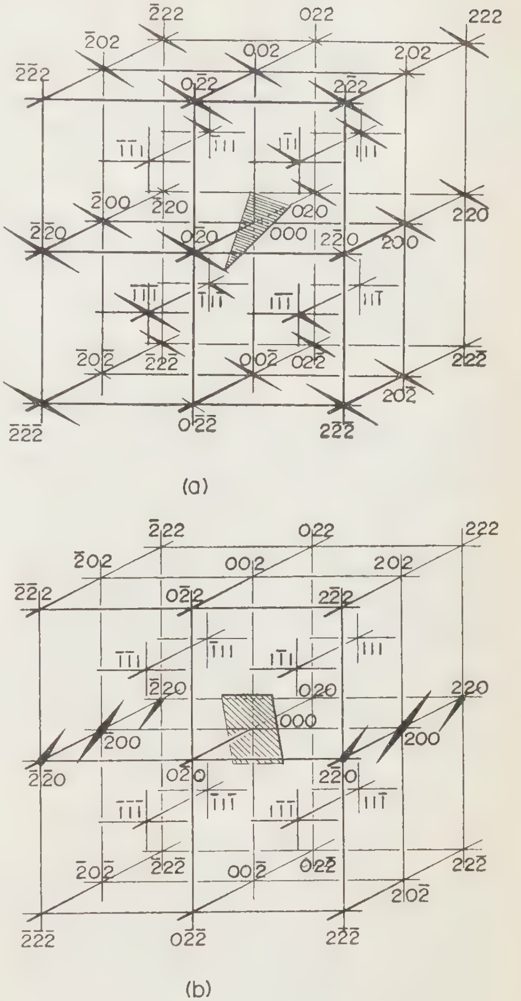

Fig. 1. Distribution of rods for a single plate orientation.

(a) for the $(11\bar{1})$ plate; (b) for the (031) plate.

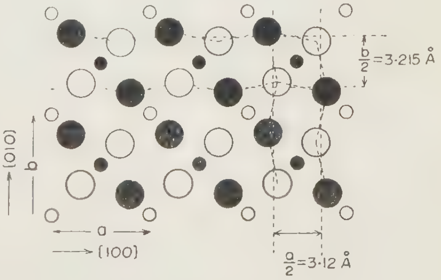

Fig. 2. (001) projection of CaCl$_2$ structure. Small circles are Ca^{++} ions, and large circles are Cl$^-$ ions. Open circles are on O-th layer; solid circles are on 1/2-th layer. Dotted lines connecting the Cl$^-$ ions in [100] and [010] directions respectively are drawn so as to indicate the wavy structure of Cl$^-$ layers.

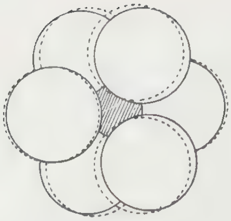

Fig. 3. Mode of packing of six Cl^- ions around a cation (shaded circle) for NaCl and $CaCl_2$. Solid circles correspond to NaCl structure and dotted circles to $CaCl_2$ structure. Direction of projection for NaCl is [111].

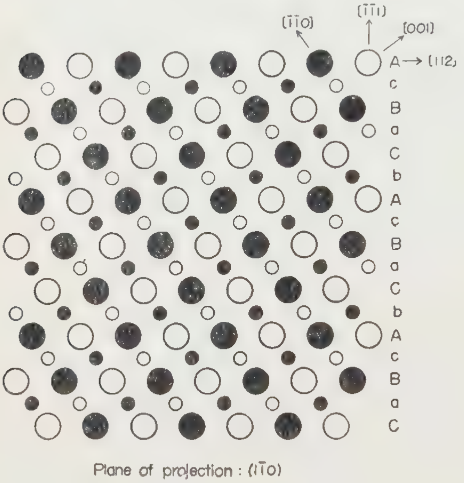

Fig. 4. $(1\bar{1}0)$ projection of NaCl structure. Small circles are Na^+ ions, and large circles are Cl^- ions. Open circles are on the plane of the paper; solid circles are on a plane at the 1/2 height from the plane of the paper.

projection. It is noticed that the crystal structures of NaCl and of $CaCl_2$ have analogous features as follows:

(i) In the both of structures each cation is surrounded by six anions and the configurations of these seven ions are quite similar (Fig. 3).

(ii) The NaCl structure contains close-packed planes of anions parallel to {111} according to the layer order ⋯*ABCABC*⋯, planes of cations being alternately inserted between them. Similarly, the $CaCl_2$ structure also contains nearly close-packed planes of anions parallel to both (100) and (010) planes, according to the hexagonal order ⋯*ABABAB* ⋯, though these planes are not planar but wavy. The layers of cations, which are not wavy, are packed alternately between the anion-layers (Fig. 2).

(iii) The value of Cl^- layer distance in the NaCl structure, 3.25 Å, is near that of the Cl^- layer distance in the $CaCl_2$ structure, 3.12 Å in the [100] direction and 3.215 Å in the [010] direction.

(iv) The value of Na^+–Na^+ (or Cl^-–Cl^-) distance in the ⟨110⟩ direction of NaCl, 3.98 Å, is near (within 10%) that of the Ca^{++}–Ca^{++} (or Cl^-–Cl^-) distance in the [001] direction of $CaCl_2$, 4.20 Å.

On the basis of the above mentioned similarities, we can show that the $CaCl_2$ structure can result by a simple procedure from the NaCl structure, by replacing Na^+ ions at certain lattice sites by Ca^{++} ions and correspondingly removing Na^+ ions from certain other lattice sites, and, finally, suitably distorting the resultant structure. Then the following assumption becomes plausible: The platelet is a transient product preluding to the precipitation of the full structure of $CaCl_2$, having a structure which resembles closely the $CaCl_2$ structure and at the same time maintains the coherency with the original NaCl matrix.

c) *Proposed model of structure of* {111} *platelet*

We propose in this paragraph a model for the structure of {111} platelet in accordance with the above anticipation. In order to make clear the essential features of the proposed structure, we explain below how this structure follows from the structure of original matrix, although the explained procedure does not necessarily imply the actual process of the formation of platelets.

Fig. 4 is the projection of NaCl structure along $[\bar{1}10]$ on $(1\bar{1}0)$ plane, where the species of Cl^- and Na^+ layers parallel to $(11\bar{1})$, which is perpendicular to the figure, are discriminated by symbols ⋯*ABCABC*⋯ and ⋯*abcabc* ⋯ respectively. Let us replace a few adjacent Na^+ layers in certain region of the NaCl matrix by layers composed of Ca^{++} ions and positive ion vacancies (the Ca^{++} layers). The Ca^{++} ions and vacancies, replacing Na^+ ions in the previous layers, are assumed respectively to align in chains in the $[\bar{1}10]$ direction, the two kinds of chains in one layer being arranged in an alternating sequence (cf. Fig. 7). Let us denote the new layers as ⋯$a'b'c'$ etc.⋯ according to the

Table I. Examples of stacking order of ionic planes in {111} platelet. α corresponds to the region of CaCl$_2$-like structure, and β corresponds to the region of stacking fault.

$$A\ c\ B\ a\ C\ b\ A\ c\ B\ a\ C\ b\ A\ c\ B\ a\ C\ b\ A\ c\ B\ a\ C$$

$$A\ c\ B\ a\ C\ b\ \underbrace{A\ c'}_{\alpha}\ B\ a\ C\ b\ A\ c\ B\ a\ C\ b\ A\ c\ B\ a\ C$$

$$A\ c\ B\ a\ C\ b\ \underbrace{A\ c'\ B\ c'}_{\alpha}\ \underbrace{A\ b\ C}_{\beta}\ a\ B\ a\ C\ b\ A\ c\ B\ a\ C$$

$$A\ c\ B\ a\ C\ b\ \underbrace{A\ c'\ B\ c'\ A\ c'\ B}_{\alpha}\ \underbrace{c\ A}_{\beta}\ b\ C\ b\ A\ c\ B\ a\ C$$

$$A\ c\ B\ a\ C\ b\ \underbrace{A\ c'\ B\ c'\ A\ c'\ B\ c'}_{\alpha}\ \underbrace{A\ b}_{\beta}\ C\ b\ A\ c\ B\ a\ C$$

sequence $\cdots abc$ etc.$\cdots$ of the previous layers. Let us next consider a process such that the cubic close-packed layers of Cl$^-$ ions in the replaced regions are transformed into hexagonal order, i.e., into $\cdots ABABAB \cdots$, and, at the same time, the Ca^{++} layers between them are displaced so as to fit these hexagonal Cl$^-$ layers. Then we obtain a CaCl$_2$-like structure locally imbeded within the original NaCl matrix.

There may be a lot of varieties in both the number of Ca^{++} layers replacing Na$^+$ layers and the mode of their distributions. In Table I some of the most simple types are shown, where the first row corresponds to the original NaCl matrix. The type shown in the 2nd row, in which only one Na$^+$ layer is replaced by a Ca^{++} layer without any change in ionic sites, can contribute only little to the intensity of rods (see Part I, § 5). However, we can expect appreciable rod intensities, when more than one adjoining Na$^+$ layers are replaced by Ca^{++} layers as indicated in the 3rd, 4th and 5th rows in Table I and then a CaCl$_2$–like structure is formed there in a way as mentioned above. The arrangement of ions for the case of the 4th row is drawn in Fig. 5.

In these examples we have assumed that the original NaCl matrix is subjected to no change except for the part of the CaCl$_2$-like structure, although we should permit stacking faults to occur for a few atomic layers adjacent to the CaCl$_2$-like structure. The fault of this kind contributes to the intensities of rods as well.

The {111} platelet is, then, regarded as the region having the CaCl$_2$-like structure, accompanied by an additional part containing a few stacking faults.

§ 3. Intensity Comparison for $\langle 111 \rangle_r$ Rods

In this section relative intensities of rods expected from the plate-zone composed of the platelets having structures proposed in the previous section are compared with those experimentally obtained.

The structures of platelets mentioned above are two-dimensionally periodic along directions parallel to the plane of platelet. Let us now consider a $(11\bar{1})$ platelet composed of N_3 atomic planes (counting Ca^{++}, Cl$^-$ and Na$^+$ layers together), in which Ca^{++} ions and vacancies aligning in chains along the $[\bar{1}10]$

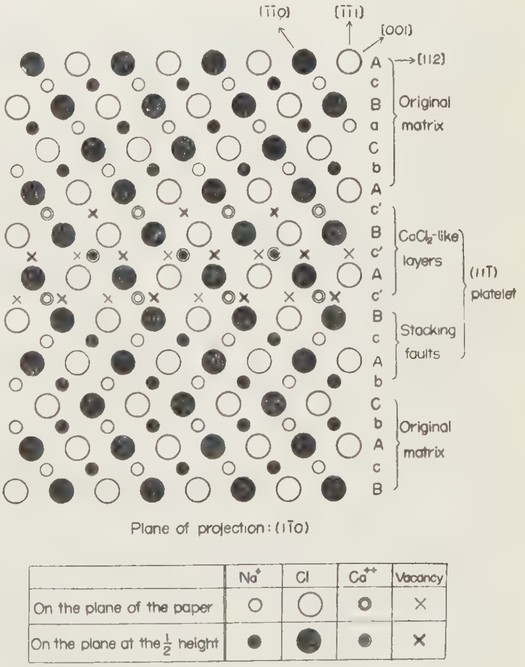

Fig. 5. Structure of $(11\bar{1})$ platelet corresponding to the stacking of the type as shown in the 4-th row of Table I. Plane of projection is $(1\bar{1}0)$ of the matrix.

direction. Then the structure amplitude F' (corresponding to the expression (3) of Part I, contributing to the diffuse scattering) is given by

$$F' = F(\boldsymbol{h}) \sum_{n_1} \exp 2\pi i n_1 \boldsymbol{h}(-\tfrac{1}{2}\boldsymbol{a}_1 + \tfrac{1}{2}\boldsymbol{a}_2) \times \sum_{n_2} \exp 2\pi i n_2 \boldsymbol{h}(\boldsymbol{a}_2 + \boldsymbol{a}_3)\,, \tag{2}$$

where $\boldsymbol{a}_1$, $\boldsymbol{a}_2$ and $\boldsymbol{a}_3$ are the vectors of the cubic unit cell for NaCl, $-\frac{1}{2}\boldsymbol{a}_1 + \frac{1}{2}\boldsymbol{a}_2$ and $\boldsymbol{a}_2 + \boldsymbol{a}_3$ are the vectors parallel to $(11\bar{1})$ and are respectively the lattice period along the lattice rows $[\bar{1}10]$ (parallel to the chains) and $[011]$ (across the chains) (cf. Fig. 7); $\sum_{n_1}$ and $\sum_{n_2}$ mean the sums over the lattice points on these rows.

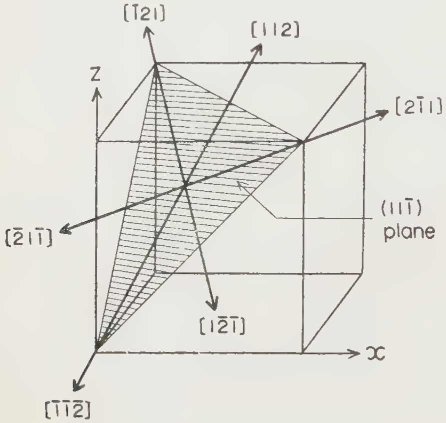

Fig. 6. Possible directions of lateral displacements of layers in the $(11\bar{1})$ platelet.

The structure amplitude $F(\boldsymbol{h})$ which depends on the arrangement of layers in the platelet is expressed by

$$\begin{aligned} F(\boldsymbol{h}) = \sum_{n_3} \{ & -f_{\mathrm{Na}^+}(1 + \exp 2\pi i \boldsymbol{h}(\tfrac{1}{2}\boldsymbol{a}_2 + \tfrac{1}{2}\boldsymbol{a}_3)) \\ & + f_{\mathrm{Ca}^{++}} \exp 2\pi i \boldsymbol{h}\boldsymbol{\delta}_{n_3} \} \exp 2\pi i n_3 \boldsymbol{h}\boldsymbol{a}_3 \\ & + \sum_{n_3}{}' (-f_{\mathrm{Cl}^-} + f_{\mathrm{Cl}^-} \exp 2\pi i \boldsymbol{h}\boldsymbol{\delta}_{n_3}) \\ & \times (1 + \exp 2\pi i \boldsymbol{h}(\tfrac{1}{2}\boldsymbol{a}_2 + \tfrac{1}{2}\boldsymbol{a}_3)) \exp 2\pi i (n_3 + \tfrac{1}{2}) \boldsymbol{h}\boldsymbol{a}_3 \\ & + \sum_{n_3}{}'' (-f_{\mathrm{Na}^+} + f_{\mathrm{Na}^+} \exp 2\pi i \boldsymbol{h}\boldsymbol{\delta}_{n_3}) \\ & \times (1 + \exp 2\pi i \boldsymbol{h}(\tfrac{1}{2}\boldsymbol{a}_2 + \tfrac{1}{2}\boldsymbol{a}_3)) \exp 2\pi i n_3 \boldsymbol{h}\boldsymbol{a}_3\,, \end{aligned} \tag{3}$$

where co-ordinate origin is taken at a Na^+ site of the original matrix and n_3 the index specifying each atomic layer in the platelet, ranging from 0 to $N_3 - 1$ irrespective of the species of the layer, and $\boldsymbol{\delta}_{n_3}$ the vector of the lateral displacement of the layer concerned. The sum $\sum_{n_3}$ corresponds to the layers composed of Ca^{++} ions and vacancies, the sums $\sum_{n_3}{}'$ and $\sum_{n_3}{}''$ correspond respectively to Cl^- layers and Na^+ layers that are subjected to lateral displacements.

a) *Extinction rule of rods*

The equation (2) gives a rod distribution in reciprocal space. The relative intensities of rods are proportional to $|F(\boldsymbol{H})|^2$, where $\boldsymbol{H}$ represents the vector of reciprocal-lattice points corresponding to the matrix.

There are six possible directions for lateral displacements of layers in the $(11\bar{1})$ platelet, i.e., $\pm[112]$, $\pm[2\bar{1}1]$ and $\pm[\bar{1}21]$ (Fig. 6). When we assume the displacement to be parallel to $\pm[112]$, $\boldsymbol{\delta}_{n_3}$ for each mode of displacement is given as follows:

$$\left.\begin{aligned} \boldsymbol{\delta}_{n_3} &= \frac{1}{6}\boldsymbol{a}_1 + \frac{1}{6}\boldsymbol{a}_2 + \frac{1}{3}\boldsymbol{a}_3 \\ & \qquad \text{for e.g. } A \to B,\ b \to c'\,, \\ \boldsymbol{\delta}_{n_3} &= -\frac{1}{6}\boldsymbol{a}_1 - \frac{1}{6}\boldsymbol{a}_2 - \frac{1}{3}\boldsymbol{a}_3 \\ & \qquad \text{for e.g. } B \to A,\ a \to c'\,. \end{aligned}\right\} \tag{4}$$

Then it follows from (3) that $F(\boldsymbol{H}) \approx 0$ for the reciprocal-lattice points with indices satisfying (1) when the relation $2f_{\mathrm{Na}^+} \approx f_{\mathrm{Ca}^{++}}$ is taken into account. The same result also follows for the displacements parallel to $\pm[2\bar{1}1]$ or $\pm[\bar{1}21]$. The experimental features of the $[11\bar{1}]_r$ rods mentioned in § 2 a) is thus explained by the proposed model.

b) *Formation of platelets in anti-phase relation*

Though the $\langle 111 \rangle_r$ rods are not observed at the reciprocal-lattice points corresponding to the super-lattice indices, e.g., (100), (110) etc., F' given by (2) does not necessarily vanish at these points because the summation corresponding to $\sum_{n_2}$ in (2) has maxima when $\boldsymbol{h}(\boldsymbol{a}_2 + \boldsymbol{a}_3) = m_2$ (m_2: integer). ($\sum_{n_1}$ in (2) has maxima when $\boldsymbol{h}(-\boldsymbol{a}_1 + \boldsymbol{a}_2) = 2m_1$ (m_1: integer), so that this summation gives no super-structure maxima.) As discussed in Part I, this discrepancy is removed by assuming the formation of platelets in anti-phase relations among themselves.

Doubled circles and crosses in Fig. 7 show the positive ion sites in a $(11\bar{1})$ layer of the matrix. Let us consider a platelet such that the Ca^{++} chains assume the $[\bar{1}10]$ rows corresponding to double circles and the chain of vacancies the $[\bar{1}10]$ rows corresponding to crosses. We can conceive another platelet having a structure which is different from the former only by the fact that the Ca^{++} chains assume the position of crosses and the chains of vacancies assume the position of double circles.

Between the structure amplitudes $F(\boldsymbol{h})$ for these two kinds of platelets, $F_1(\boldsymbol{h})$ and $F_2(\boldsymbol{h})$, we have a relation

$$F_2(\boldsymbol{h})=F_1(\boldsymbol{h})\exp 2\pi i\boldsymbol{h}(\tfrac{1}{2}\boldsymbol{a}_2+\tfrac{1}{2}\boldsymbol{a}_3)\,. \qquad (5)$$

When the $(11\bar{1})$ plate-like region is made up of an aggregate of such anti-phase platelets disposed laterally from each other (Fig. 8), we can readily see, according to the consideration in Part I, that the rods appear only at the normal reciprocal-lattice points but not at the super-reciprocal-lattice points.

(c) *Relative intensities of* $\langle 111\rangle_r$ *rods*

The relative intensities of rods at the normal reciprocal-lattice points are not influenced by the formation of anti-phase structure, and are proportional to $|F(\boldsymbol{H})|^2$ as before; the extension of rods depends on the thickness of the plate-zone.

The 4th column in Table II shows experimental relative intensities of the $[11\bar{1}]_r$ rods according to visual estimation. The 3rd column corresponds to the relative values of $|F(\boldsymbol{H})|^2$ calculated from the model shown in Fig. 5. In the calculation we have neglected the effect due to absorption, polarization and temperature factors etc. We can readily verify that other types listed in Table I give almost the same results.

Table II. Relative intensities of $[11\bar{1}]_r$ rods.

$(h\,k\,l)$	$h+k+2l$	Cal.	Obs.
(000)	0	0	—
(111)	4	0.4	s
$(11\bar{1})$	0	0	—
(200)	2	10	vs
(020)	2	10	vs
(002)	4	10	vs
$(00\bar{2})$	−4	10	vs
(220)	4	8	s
(202)	6	0	vw
(022)	6	0	vw
$(20\bar{2})$	−2	8	s
$(02\bar{2})$	−2	8	s
(222)	8	6	m
$(22\bar{2})$	0	0	—

The agreement between observed and calculated intensities is generally good except for the rod at the (111) point for which the observed intensity of the rod is stronger than the result of calculation. This discrepancy seems to arise from the idealization in our model that the ions in the platelet are assumed to occupy precisely the sites, say as given in Fig. 5. If such is the case, the contributions to the (111) reciprocal-lattice point from the positive ion layers and the Cl^- layers have always the phase difference π with each other. Consequently, the intensities of the rods at (111) points can never become appreciable. However, we can conceive that shifts of Cl^- ions as well as of Ca^{++} ions adjacent to vacancies from the assumed positions are actually quite possible. When we take into account this possibility the phase relation between Ca^{++} layers and Cl^- layers are altered, and we can expect stronger intensities of rods at the (111) points of the matrix. From the similar ground, stronger

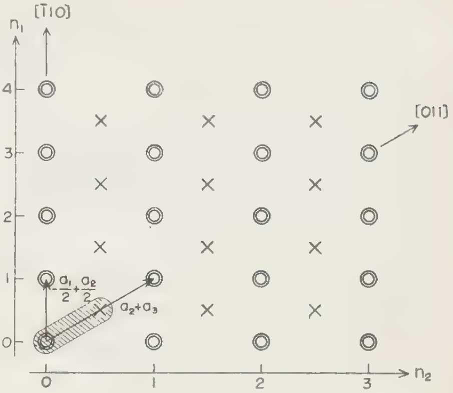

Fig. 7. Ca^{++} layer parallel to $(11\bar{1})$. Double circles are Ca^{++} ions; crosses are vacancies. n_1 and n_2 are indexes corresponding to $\sum\limits_{n_1}$ and $\sum\limits_{n_2}$ in Eq. (2) respectively. Pair of Ca^{++} and vacancy enclosed by a hatched area corresponds to a supper structure unit of Ca^{++} layer.

Fig. 8. A plate-like precipitate as an assembly of super-structure domains in anti-phase relation.

intensities can be expected also for the $\langle 111\rangle_r$ rods through some of the $\{220\}$ points, for which the intensites calculated from our model are approximately zero.

§ 4. Orientational Relationship between {111} Platelets and Precipitated Particles of CaCl₂

The $CaCl_2$-like structure assumed in the above discussions is described by an orthorhombic lattice. The orientational relation between this (P) and the matrix lattice (M) is as follows.

$$\left.\begin{aligned}&(11\bar{1})_M//(010)_P\,,\\&[1\bar{1}0]_M//[001]_P\,.\end{aligned}\right| \qquad (6)$$

Though the $CaCl_2$-like structure is by no means the perfect $CaCl_2$ structure (C), the similarity between the both structure is obvious when we note that $(010)_P$ corresponds to $(100)_C$ or $(010)_C$ and $[001]_P$ to $[001]_C$.

In view of the close similarity of both structures, one may suppose that if there took place the precipitation of $CaCl_2$ particle in the matrix by a certain heat treatment, its orientation would be similar to that of $CaCl_2$-like structure of platelet indicated by (6). This anticipation is proved to be actually the case. When the specimen was heated at 300°C for 1 hour, the diffraction photograph taken by the rotating-crystal method showed a sharp spotty pattern superposed on the diffraction pattern of the NaCl matrix. It was found that these spots are due to $CaCl_2$ crystals having the orientational relation with the lattice of matrix as follows:

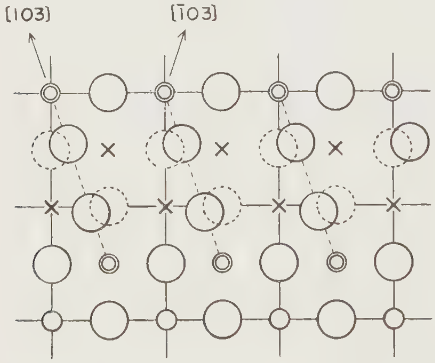

Fig. 9. (010) projectian of NaCl matrix lattice containing Ca^{++}–Cl^{-}–Cl^{-}–Ca^{++} chains in [103] direction. Double circles are Ca^{++} ions; crosses are vacancies. (Chains in $[\bar{1}03]$ direction are also equally possible.)

$$\left.\begin{aligned}&\{111\}_M//(100)_C \text{ or } (010)_C\,,\\&\langle 110\rangle_M//[001]_C\,.\end{aligned}\right\} \qquad (7)$$

This relation is in accordance with that anticipated from (6) and the similarity between the $CaCl_2$ and the $CaCl_2$-like structure.

The above result not only favours the proposed model of the structure of $\{111\}$ platelet, but also suggests the fact that the precipitated particles of $CaCl_2$ have grown up from the $\{111\}$ plate-zones by succeeding the orientation of the platelets. We can conceive that, when the crystal is heated at higher temperatures, some of the platelets in plate-zones have greater opportunity to grow by consuming the rest of the platelets, and the ions in the plate-zones may rearrange themselves so as to result in the normal structure of $CaCl_2$ which is incoherent with the matrix.

§ 5. Structure of {310} Platelet

Let us now discuss the structure of the $\{310\}$ plate-zone. As in the case of the $\{111\}$ plate-zone, the $\{310\}$ plate-zone is assumed to be composed of a number of platelets. We propose below a tentative model for the (031) platelet which is qualitatively in accordance with the main characteristics of Fig. 1 as follows:

(i) There are no rods through the reciprocal-lattice points (000), (020) $(0\bar{2}0)$, (002), $(00\bar{2})$, (022), $(02\bar{2})$, $(0\bar{2}2)$ and $(0\bar{2}\bar{2})$, for all of which we have $h=0$.

(ii) There appear no rods around the reciprocal-lattice points (202), $(20\bar{2})$, $(\bar{2}02)$, $(\bar{2}0\bar{2})$ and all of $\{222\}$ (for which $l=\pm 2$).

(iii) There appear no rods through all of the $\{111\}$ points.

On proceeding to our consideration we presume firstly that in the (031) plate-zone the displacements of ions from the original sites of matrix occur nearly in the directions [100] or $[\bar{1}00]$. This presumption renders the relation (i), for, if an ion at an original site is displaced along [100] by the distance x/a (a: the lattice constant of the NaCl matrix), it may contribute to the structure amplitude (corresponding to the diffuse pattern) the factor proportional to $-1+\exp(2\pi i h x/a)$, which is zero when $h=0$.

Next, we consider that the following relation is important:

(iv) In Fig. 9 showing the (010) projection of NaCl structure, we see that the Na^+–Na^+ distance along [103] direction, 8.90 Å, is approximately equal to the length of Ca^{++}–Cl^-–Cl^-–Ca^{++}, 8.96 Å, in the [110] direction of the $CaCl_2$ structure.

Interpreting this numerical coincidence as not accidental, we assume that platelets making up the (031) plate-zone contain Ca^{++}–Cl^-–Cl^-–Ca^{++} chains in the direction [103] of the matrix. The formation of this kind of chain is compatible with the framework of matrix lattice. In Fig. 9, it is shown that the Ca^{++}–Cl^-–Cl^-–Ca^{++} chain results when two Na^+ ions of the original matrix are replaced by Ca^{++} ions (indicated by double circles), and then the two Cl^- ions (indicated by broken circles) are displaced to the positions between the two Ca^{++} ions. Two Na^+ ion vacancies are simultaneously produced at positions indicated by crosses. By taking account of the relation of ionic radii, the components of Cl^- displacements are assumed to be approximately $\pm x/a=1/6$ and $\pm z/a=1/18$. Though these displacements are not exactly parallel to [100], the relation (i) is scarcely detracted as the z-component is quite small.

We further presume that the structure of {310} platelet is again a $CaCl_2$-like structure. Noticing the fact that the $CaCl_2$ structure is built of the two kinds of atomic layers parallel to (001), one composed of the Ca^{++}–Cl^-–Cl^-–Ca^{++} chain in the direction [110], and the other the similar chains in the direction [$\bar{1}10$] (cf. Fig. 2), we assume that also the (031) platelet is composed of two species of layers, one containing the Ca^{++}–Cl^-–Cl^-–Ca^{++} chains in the direction [103] and the other the short chains of new kind as indicated in Fig. 10.

The new chains, being the short chains Cl^-–Ca^{++}–Cl^- nearly parallel to [$\bar{4}03$], can be reasonably introduced into the NaCl frame work by locating Ca^{++} ions at the positions midway between two adjacent Cl^- (or Na^+) sites of the original matrix, and displacing these Cl^- ions by the amount $\pm x/a=1/6$, $\pm z/a=1/18$ (in the direction which is again nearly parallel to [100]). This displacement as well as the position of the Ca^{++} ion is spatially allowable since the neighbouring two Na^+ ions (indicated by crosses) are regarded to be removed according to the condition of neutrality of charge.

Fig. 11 shows the structure of thus proposed model for (031) platelet. This structure, composed of the two kinds of chains as assumed above, being a sheet of about 4.45 Å thick perpendicular to (031), is compatible with the frame work of NaCl lattice, and is $CaCl_2$-like although the angle between the two kinds of chains is not equal to 90° and the spacing between two successive (010) layers containing either of the two kinds of chains (2.81 Å) is much larger than the corresponding spacing 2.10 Å in the $CaCl_2$ structure.

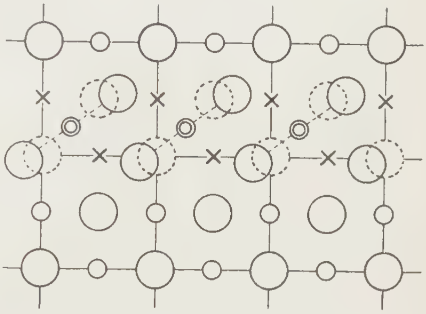

Fig. 10. (010) projection of NaCl matrix lattice containing Cl^-–Ca^{++}–Cl^- chains.

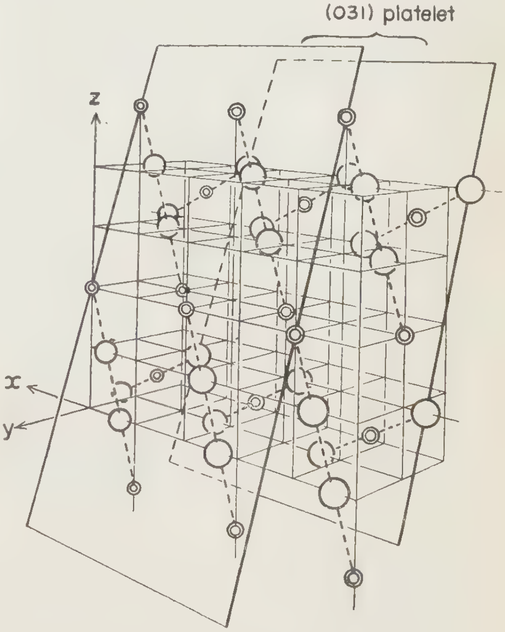

Fig. 11. (031) platelet composed of two kinds of chains shown in Figs. 9 and 10.

We can consider as well another possible (031) platelet which is built of the Ca^{++}–Cl^-–Cl^-–Ca^{++} chain in the [$\bar{1}03$] direction and the

Cl^-–Ca^{++}–Cl^- chain in nearly parallel to [403].

The formation of these platelets in antiphase relation is also possible.

By taking account of the above circumstances, the intensities of $[031]_r$ rods due to the (031) plate-zone composed of the proposed platelets are calculated as shown in Table III.

Table III. Relative intensities of $[031]_r$ rods.

$(h\,k\,l)$	Cal.	Obs.
(000)	0	—
(111)	0	—
(200)	10	vs
(020)	0	—
(002)	2	—
(220)	7	s
(202)	3	—
(022)	1.5	—
(222)	3	—

The result is in accordance with the experimental relation (i), and also qualitatively with (ii) and (iii).

The above model for {310} plate-zone, however, is by no means free from objections. Especially, the assumption concerning the presence of the ionic chains (Ca^{++}–Cl^-–Cl^-–Ca^{++} and Cl^-–Ca^{++}–Cl^-) is only weakly founded. Furthermore, experimental evidences favouring this model, such that described in § 4 with respect to the model of {111} plate-zone, is wanting. As the number of rods observable is very scanty for $\langle 310\rangle_r$ rods as seen in Fig. 1, it seems to be difficult to arrive at the conclusive model of {310} plate-zone. The consideration presented in this section is, therefore, to give a probable model of the {310} plate-zone among other possibilities.

§ 6. Discussions

a) *Absolute intensities of diffuse spots due to plate-zone*

In the above sections we estimated the relative intensities of rods on the basis of the proposed models for the structures of plate-zones. The result was especially successful for the case of $\langle 111\rangle_r$ rods.

There remain, however, questions concerning their absolute intensities, since the intensity of diffuse spot corresponding to rods is seemingly too strong in spite of small proportions, only a few per cent, of dissolved component.

To estimate experimentally the absolute intensity of diffuse spot due to plate-zones, the intensity of thermal diffuse spot from a pure NaCl crystal can be conveniently utilized as comparison, since the theoretical formula is available for the thermal diffuse spot, and moreover, the intensities of both kinds of spot are comparable with each other in many cases as revealed by the following observation.

We took series of stationary crystal X-ray photographs for two samples having the same external dimension, one the solid solution of NaCl–$CaCl_2$ containing 2% $CaCl_2$ and the other a pure NaCl crystal, by varying the angle around [001], with incident beam (filtered Cu radiation) in the direction perpendicular to [001] (cf. § 2, Part I). Each photograph was taken under similar conditions of X-ray source and exposure. We compared specifically the intensity of diffuse spot from the solid solution due to the $\langle 111\rangle_r$ rod passing through the (200) reciprocal-lattice point and that of thermal diffuse spot from the pure crystal accompanying the same reciprocal-lattice point. It was confirmed, for example, that the intensity of the diffuse spot from the solid solution for the angle φ (the angle between incident X-ray beam and $[0\bar{1}0]$)$=23°$, and that of the thermal spot from the pure crystal for $\varphi=21°$, agree to each other in order of magnitude.

The intensity of thermal diffuse spot from the pure crystal is approximately given by[4)]

$$J=I_eA(kT/m_0)(h/\tau)^2(1/C)(F/8)^2e^{-2M}(\delta V/v_0)\ , \quad (8)$$

where I_e is the X-ray intensity scattered from a single electron, δV the whole volume of the crystal, v_0 the one eighth of the unit cell volume, F the structure factor of NaCl crystal, C the average velocity of the elastic waves in the crystal, m_0 the average mass of a Na^+ ion and a Cl^- ion, h the distance of the reciprocal-lattice point concerned from the origin, τ the distance from the point concerned in the reciprocal space to the relevant reciprocal-lattice point, and e^{-2M} the Debye temperature factor. Corresponding to the thermal spot accompanying (200) (for which $F/8=\frac{1}{2}(f_{Na^+}+f_{Cl^-})\sim 10$, $e^{-2M}\sim 1$ and $h=5\,cm^{-1}$) for $\varphi=21°$ (which corresponds to $\tau=0.5\,cm^{-1}$), J becomes

$$J\sim 100\cdot I_e\cdot A\delta V/v_0\,. \qquad (9)^*$$

A formula giving the absolute intensities of the diffuse spots due to plate-zones can be derived by simplifying the structure of matrix crystal (NaCl) and that of plate-zones as follows:

i) The matrix crystal is composed of one species of ions having the average scattering amplitude $f_0=\frac{1}{2}(f_{Na^+}+f_{Cl^-})$ occupying sites of a simple cubic lattice.

ii) The plate-zones concerned are all identical among themselves, and are again composed of one species of ions occupying the original sites of matrix but with an averaged structure amplitude f_0+f. Moreover, each of plate-zones are assumed to be composed of only one atomic sheet so that the intensity of rods in reciprocal space is homogeneous along their elongation.

The total number of ions in the crystal with the volume δV is given by $\delta V/v_0$. Let $p\delta V/v_0$ be the total number of ions contained in all of the plate-zones concerned. Then the number of the plate-zones contained in the crystal is given by $(p/N)(\delta V/v_0)$, where N is the number of ions contained in a single plate-zone.

When each plate-zone scatters X-rays independently, the intensity of diffuse spot at its maximum, which corresponds to the centre of the cross section of rod concerned, is given by

$$I=I_eA(Nf)^2(p/N)(\delta V/v_0)\,. \qquad (10)$$

The (200) thermal diffuse spot from the pure crystal appearing for $\varphi=21°$ (as specifically exemplified above) is fairly distinct (althouth its intensity is very weak in comparison with the Bragg spot). If the diffuse spot due to plate-zones shows a comparable intensity with it, we have by equating (9) and (10) the relation

$$pNf^2\sim 100\,, \qquad (11)$$

where the factor A and δV in (9) and (10) are assumed as common.

The lateral dimension of plate-zones found in the $NaCl$–$CaCl_2$ solid solution is thought, as was estimated in Part I, § 7 from the observed thickness of rods concerned in reciprocal space, to be about 100 Å in order of magnitude. Then we obtain N by assuming the mean inter-ionic distance in the layer of the plate-zone to be about 4 Å. The value f corresponding to the model for (111) plate-zone given in § 3 is $\sim$13. Substituting these values to (11) we have

$$p\sim 0.1\%\,.$$

Since the contribution from the plate-zone to the diffuse spot comes not only from the dissolved Ca^{++} ions but also from the displacement of Na^+ and Cl^- from its original matrix lattice sites, the ratio of Ca^{++} ions contained in the plate-zones to the total number of ions in the sample should be a certain fraction of the above value of p.

Summarizing the above consideration, we can say that even when only a few percent of the total of the dissolved Ca^{++} ions (which is already only a few percent of the total number of ions contained in the sample) are used to form plate-zones concerned, the appreciable intensity of diffuse spot due to rods is possible to appear, provided, that the value of N is sufficiently large, i.e. the lateral dimension of plate-zone is as large as 100 Å. When N increases, the intensity of diffuse spot increases though the total number of plate-zones decreases by a fixed p.

The above consideration assumed the plate-zone of one atomic sheet. When the plate-zone contains more than one atomic layers, intensity of rod becomes not homogeneous along its elongation, but its intensity becomes more remarkable than in the above consideration in the vicinity of the reciprocal-lattice point concerned.

b) *Asymmetric rods*

It is observed that both $\langle 111\rangle_r$ and $\langle 310\rangle_r$ rods are asymmetric across some of the reciprocal-lattice points. For example $[11\bar{1}]_r$ rods at the $(1\bar{1}1)$, $(1\bar{1}\bar{1})$, $(\bar{1}11)$ and $(\bar{1}1\bar{1})$ points of the matrix are asymmetric, and $[031]_r$ rods at the (220), $(2\bar{2}0)$, $(\bar{2}20)$ and $(\bar{2}\bar{2}0)$ points of the matrix are also asymmetric (Fig. 1). Concerning the $[031]_r$ rods, the asymmetry is easily explained when we assume an expansion of the (031) plate-zone in the direction perpendicular to the lateral extension. This expansion is conceivable in view of the relation of ion packing when the (031) platelet possesses the structure as depicted in Fig. 11.

On the other hand, the asymmetry of the

---

* $m_0=\frac{1}{2}(m_{Na^+}+m_{Cl^-})\sim 5\times 10^{-23}g$, $C\sim 3\times 10^5$ cm sec^{-1}, $T\sim 300°$K.

$\langle 111\rangle_r$ rods seems to be hard to explain, because the feature of the asymmetry is complicated as seen in Fig. 1. The expansion of plate-zone is improbable, because the space of the presumed model is quite reasonable with respect to ion sizes of Ca^{++}, Cl^- and Na^+ (Fig. 5).

The author wishes to express his sincere thanks to Professor S. Miyake for his kind guidance and encouragement in the course of the research.

References

1) S. Miyake and K. Suzuki: Acta Cryst. **7** (1954) 514.
2) S. Miyake and K. Suzuki: J. Phys. Soc. Japan, **9** (1954) 702.
3) R. W. G. Wyckoff: *Crystal Structures*, Section I (1948, Interscience Publishers, Inc., New York).
4) R. W. James: *The Optical Principles of the Diffraction of X-rays*, Chapter V (1950, Bell and Sons, London).

JOURNAL OF THE PHYSICAL SOCIETY OF JAPAN Vol. 10, No. 9, SEPTEMBER, 1955

Theory of Viscoelasticity of Amorphous Polymers

By Osamu NAKADA

Kobayasi Institute of Physical Research, Kokubunji, Tokyo

(Received May 31, 1955)

A statistical mechanical theory of the intra-chain relaxation (or relaxation of the micro-Brownian motion) in amorphous polymers is presented. The generalized diffusion equation of configurational changes of a chain imbedded in polymer environment is solved for a dynamical case under suitable potentials assumed. In order to avoid the complication of the chain space geometry, an artifice is adopted such that we replace each chain bond with a fictitious spring. The derived spectrum of relaxation times just coincides with the experimental formula of the wedge type spectrum found by Tobolsky for polyisobutylene, manifesting a characteristic slope of $-1/2$ in the log-log plot of the relaxation spectrum. The theoretical expression also satisfies the condition of the thermo-rheological simplicity.

§ 1. Introduction

In these ten years viscoelastic properties of various solid polymers have been examined by many investigators over such a wide range of frequency and of temperature enough to enable one to deduce the essential feature of the phenomena and to clarify the underlying mechanism from the molecular structural view-point. Among many experimental data on viscoelasticity of amorphous polymers those of polyisobutylene will be the most complete and reliable ones ever investigated owing to an excellent cooperation of so many workers and laboratories in several countries[1].

According to the investigation of Tobolsky and coworkers[2] in this cooperation project the spectrum of relaxation times (or relaxation spectrum) of polyisobutylene for stress relaxation or for dynamic modulus consists of two distinct parts: a " wedge " type spectrum ranging from 10^{-9} sec. to 10^{-2} sec., and a " box " type spectrum ranging from 10^{-1} to 10^5 sec. (for unfractionated sample, at 25°C.) Such a " wedge-box " spectrum seems to be found commonly in most amorphous polymers or plastics, though polymers with a permanent network structure seems to lack the box spectrum[3]. Inspection of various experimental facts about these two relaxation spectra will naturally lead us to imagine that the wedge spectrum will be due primarilly to relaxation of the configurational change of a single chain between junctions and the box spectrum will originate from relaxation of the relative displacement of many chains accompanying therewith breakdowns and reformations of junctions and thus relating closely to the viscous flow of polymers. Accordingly the former may be called the *intra-chain* relaxation and the latter the *inter-chain* relaxation.

Phenomenological theories of linear viscoelasticity have been developed by Alfrey, Gross, Leaderman, Schwarzl, Staverman and others$^{4)}$. The molecular theoretical treatments of these relaxation phenomena have also been made by several authors as well. For example the inter-chain relaxation have been treated by Tobolsky, Eyring$^{5)}$, Green$^{6)}$ and others and recently Yamamoto$^{7)}$ developed a general theory of it, while the intra-chain relaxation have been investigated theoretically by Alfrey$^{8)}$, Kirkwood$^{9)}$, Blizard$^{10)}$, Bueche$^{11)}$ and others. Especially Kirkwood$^{12)}$ developed an elegant general formulation of irreversible processes in polymers involving treatments of dielectric and dynamic relaxation phenomena. On the other hand, suggestive approximation methods are deviced by Rouse$^{13)}$ in viscoelasticity of dilute polymer solutions and also by Bueche$^{11)}$ in the treatment of viscoelasticity of plastics. But through the works referred in the above the wedge-box spectrum of amorphous polymers has not been explained on the molecular theoretical basis. The present author proposed recently a semi-quantitative theory of the intra-chain relaxation phenomena which involves the possibility to give the wedge spectrum$^{14)}$.

In this article we resume the same problem, the intra-chain relaxation. In constrast to the previous treatment we here develope a theory along the line of Kirkwood's general formulation, introducing the "random spring model" (see § 2) which leads to analogous equation used by Rouse.

§ 2. A molecular model of the intra-chain relaxation

Here we consider a network structure of high polymer chains containing virtually no crystalline region. Network junctions may be composed either of permanent chemical cross-links such as sulpher bridges in vulcanized rubber or of temporary ones caused by chain entanglements as in linear polymers. The latter kind of links may not usually be called junctions. But whenever fulfilled the condition that the period of the applied force is so small compared with the mean life time of temporary links that practically no breaking of them could ocurr during one period, there will be no need to distinguish between permanent junctions and temporary ones according to their ultimate nature. Such an assumption is supporte by the fact that the spectral shapes of linear polymers and of nonlinear polymers with permanent network structure are found to be quite similar as far as shorter relaxation times are concerned.

Now we shall confine our attention to a single representative network chain imbedded in a matrix of polymer segments which we smear out as a viscous fluid. Let q denote symbolically the variables which describe the configuration of a chain and t the time, and we introduce the probability distribution function $f(q, t)$ such that $f(q, t)dq$ equals the probability that the chain would take configurations within the range q to $q+dq$ at time t. The function $f(q, t)$ is governed by a generalized diffusion equation of many dimensions, and thus once we could have determined the function $f(q, t)$ by solving the diffusion equation provided the equation could have been set up explicitly, we should be able to predict the time dependent behaviour of the given network structure.

Now suppose the representative chain to be made up of n segments, numbered from 1 to n. We will express the configuration of the representative chain as a point in $3n$ dimensional configuration space formed by all the orthogonal coordinates of n segments. Such a representative point is not allowed to locate in any position in the space except on a certain supersurface, i.e. in the *chain space* of Kirkwood$^{12)}$, which is determined by the geometrical restraints such as fixation of each bond length and of each bond angle. But if we bring these geometrical restraints straightforward into the diffusion equation, the resulting equation will become considerably complicated and intractable one, the solution of which may not be hoped in general.

In order to avoid the complication we adopt in place of the literal geometrical restraints a fictitious potential field V_f which will attract the representative point to the neighborhood of the supersurface *in a statistical average*. For convenience of later calculations we assume here

$$V_f=\alpha\sum_{i=1}^{n-1}r_i^2=\alpha\sum_{i=1}^{n-1}(\xi_i^2+\eta_i^2+\zeta_i^2)\,, \qquad (1)$$

where r_i denotes the distance between the i-th segment and the $i+1$-th segment, ξ_i, η_i, ζ_i being its x-, y-, z-component respectively, and α is the force constant. In other words, neighboring segments are connected by a fictitious spring instead of a chemical bond with a fixed distance. Thus the model might be called the "random spring model." The constant α is determined by the condition that the mean square root of the distance between neighboring segments equals the bond length a:

$$\sqrt{\langle r_i^2\rangle}=\left[\int_0^\infty r_i^2\exp(-\alpha r_i^2/kT)r_i^2dr_i \Big/ \int_0^\infty \exp(-\alpha r_i^2/kT)r_i^2dr_i\right]^{1/2}=a\,. \qquad (2)$$

The above condition leads immediately to

$$\alpha=3kT/2a^2\,. \qquad (3)$$

Though the random spring model does not express satisfactorily the short range relation between neighboring segments it will nevertheless describe sufficiently well the chain connection as a whole. The model will operate likely in good approximation as far as the frequency of the applied force is not so high that direct interaction of neighboring segments becomes important.

Besides the geometrical restraint mentioned above, motion of the segments forming a chain suffers also a certain force caused by the internal pressure and by network junctions at both ends. Such a force will be of an intricated nature which has not been elucidated completely. Hence we shall express it simply as an internal tension which gives to the average chain length a fixed finite value. The corresponding potential V_i will be

$$V_i=\beta(e_1X+e_2Y+e_3Z)\,,$$

$$X=\sum_{i=1}^{n-1}\xi_i, \qquad Y=\sum_{i=1}^{n-1}\eta_i, \qquad Z=\sum_{i=1}^{n-1}\zeta_i, \quad (4)$$

where e_i's are direction cosines of the vector directing from one end of a chain to the other end, and β is a constant.

Finally the external potential V_e of the oscillating applied field acts on the chain. Provided the field is in x-direction the potential V_e may be expressed as

$$V_e=\gamma e^{i\omega t}X\,, \qquad (5)$$

The molecular qauntity which we seek for in order to get the dynamic compliance is the expectation value of X, the x-component of the end-to-end vector of the representative chain. It is given by the weighted mean of X with a weight function $f(q, t)$. Having specified the potential acting on a chain, we now turn in the following section to construct the diffusion equation for $f(q, t)$ into which we substitute the potential V_f, V_i and V_e.

§ 3. The diffusion equation

The generalized diffusion equation for the distribution function $f(q, t)$ of n particles in viscous fluid under the influence of potential field V can be written symbolically as

$$\frac{\partial f_q}{\partial t}=\frac{kT}{\zeta}\operatorname{div}\left(\operatorname{grad} f_q+f_q\operatorname{grad}\frac{V}{kT}\right), \qquad (6)$$

where ζ denotes the friction constant of a particle and the suffix of f is added in order to specify the variable for convenience of following transformations. In Cartesian coordinates of each particle, x_i, y_i and z_i, it will be expressed explicitly as

$$\begin{aligned}\frac{\partial f_x}{\partial t}=\frac{kT}{\zeta}\sum_{i=1}^{n}\left(\frac{\partial^2 f_x}{\partial x_i^2}+\frac{\partial^2 f_x}{\partial y_i^2}+\frac{\partial^2 f_x}{\partial z_i^2}\right)\\ +\frac{1}{\zeta}\sum_{i=1}^{n}\left\{\frac{\partial}{\partial x_i}\left(f_x\frac{\partial V}{\partial x_i}\right)\right.\\ \left.+\frac{\partial}{\partial y_i}\left(f_x\frac{\partial V}{\partial y_i}\right)+\frac{\partial}{\partial z_i}\left(f_x\frac{\partial V}{\partial z_i}\right)\right\}\,. \qquad (7)\end{aligned}$$

If we use the coordinate system, ξ_i, η_i and ξ_i which correspons to each bond length and defined by

$$\xi_i=x_{i+1}-x_i,\ \eta_i=y_{i+1}-y_i,\ \xi_i=z_{i+1}-z_i, \qquad (i=1, 2, \cdots, n-1)$$

$$\zeta_n=\frac{1}{n}\sum_{i=1}^{n}x_i, \quad \eta_n=\frac{1}{n}\sum_{i=1}^{n}y_i\,, \quad \zeta_n=\frac{1}{n}\sum_{i=1}^{n}z_i\,. \qquad (8)$$

Eq. (7) is transformed into

$$\begin{aligned}\frac{\partial f_\xi}{\partial t}=\frac{kT}{\zeta}\sum_{i=1}^{n-1}g^{ik}\left(\frac{\partial^2 f_\xi}{\partial\xi_i\partial\xi_k}+\frac{\partial^2 f_\xi}{\partial\eta_i\partial\eta_k}+\frac{\partial^2 f_\xi}{\partial\zeta_i\partial\zeta_k}\right)\\ +\frac{1}{\zeta}\sum_{i=1}^{n-1}g^{ik}\left\{\frac{\partial}{\partial\xi_i}\left(f_\xi\frac{\partial V}{\partial\xi_k}\right)\right.\\ \left.+\frac{\partial}{\partial\eta_i}\left(f_\xi\frac{\partial V}{\partial\eta_k}\right)+\frac{\partial}{\partial\zeta_i}\left(f_\xi\frac{\partial V}{\partial\zeta_k}\right)\right\}\,. \qquad (9)\end{aligned}$$

Here we omitted the degree of freedom of mass centre, ξ_n, η_n and ζ_n, assuming that the translational motion of a molecule as a whole does not occur. The metric tensor g^{ik} appearing in Eq. (9) has the form

$$G=(g^{ik})=\begin{array}{c} n-1 \text{ columns} \\ \left[\begin{array}{cccccc} 2 & -1 & & & & \\ -1 & 2 & -1 & & 0 & \\ & -1 & 2 & & & \\ & & & \ddots & & \\ & & & & 2 & -1 \\ & 0 & & & -1 & 2 \end{array}\right] \end{array} \begin{array}{c} n-1 \\ \text{rows} \end{array} \tag{10}$$

The explicit form of the potential V is given by

$$\begin{aligned} V&=V_f+V_i+V_e \\ &=\alpha\sum_{i=1}^{n-1}\xi_i^2+\eta_i^2+\zeta_i^2)-\beta\{e_1\sum_{i=1}^{n-1}\xi_i \\ &\quad+e_2\sum_{i=1}^{n-1}\eta_i+e_3\sum_{i=1}^{n-1}\zeta_i\}-\gamma e^{i\omega t}\sum_{i=1}^{n-1}\xi_i\,. \end{aligned} \tag{11}$$

We remark here that the form of Eq. (9) is analogous to the equation used by Rouse in his theory of viscoelasticity of the dilute solution[13].

§4. Solution by linearization

It can be shown that Eq. (9) is transformed into the following form[12]:

$$\begin{aligned} &\frac{\partial}{\partial t}\left[\exp\left\{\frac{V_f+V_i}{2kT}\right\}f_\xi\right] \\ &\qquad=L\left[\exp\left\{\frac{V_f+V_i}{2kT}\right\}f_\xi\right]+Q\,, \\ L&\equiv\frac{kT}{\zeta}\left[\sum_{i=1}^{n-1}g^{ik}\left(\frac{\partial^2}{\partial\xi_i\partial\xi_k}+\frac{\partial^2}{\partial\eta_i\partial\eta_k}+\frac{\partial^2}{\partial\zeta_i\partial\zeta_k}\right)\right. \\ &\quad+\frac{1}{2kT}\sum_{i=1}^{n-1}g^{ik} \\ &\quad\times\left(\frac{\partial^2}{\partial\xi_i\partial\xi_k}+\frac{\partial^2}{\partial\eta_i\partial\eta_k}+\frac{\partial^2}{\partial\zeta_i\partial\zeta_k}\right)(V_f+V_i) \end{aligned} \tag{12}$$

$$\begin{aligned} &-\left(\frac{1}{2kT}\right)^2\sum_{i=1}^{n-1}g^{ik}\left\{\frac{\partial^2(V_f+V_i)}{\partial\xi_i\partial\xi_k}\right. \\ &\qquad\left.+\frac{\partial^2(V_f+V_i)}{\partial\eta_i\partial\eta_k}+\frac{\partial^2(V_f+V_i)}{\partial\zeta_i\partial\zeta_k}\right\}, \\ Q&\equiv\frac{\gamma}{\zeta}\exp\left\{i\omega t+\frac{V_f+V_i}{2kT}\right\}\sum_{i=1}^{n-1}g^{ik}\frac{\partial}{\partial\xi_i}\left(f_\xi\frac{\partial X}{\partial\xi_k}\right). \end{aligned}$$

Now we shall expand the function f_ξ in power series of γ, provided the applied force is sufficiently small, in the following form

$$f_\xi=f_0+\gamma\exp(i\omega t)\exp\{-(V_f+V_i)/2kT\}f_1+O(\gamma^2). \tag{13}$$

By substitution of Eq. (13) into Eq. (12) it is easily shown that

$$\begin{aligned} &Lf_1-i\omega f_1=K\,, \\ &K\equiv-\frac{1}{\zeta}\exp\{(V_f+V_i)/2kT\} \\ &\qquad\qquad\times\sum g^{ik}\frac{\partial}{\partial\xi_i}\left(\frac{\partial X}{\partial\xi_k}f_0\right). \end{aligned} \tag{14}$$

The equilibrium distribution function f_0 is, of course, given by

$$\begin{aligned} f_0=&\exp\{-(V_f+V_i)/kT\} \\ &\Big/\int_{-\infty}^{\infty}\cdots\int_{-\infty}^{\infty}\exp\{-(V_f+V_i)/kT\}\prod_{i=1}^{n-1}d\xi_i d\eta_i d\zeta_i\,. \end{aligned} \tag{15}$$

The solution of Eq. (14) is expressed by eigenfunctions and eigenvalues of the operator L as follows,

$$f_1=-\sum_\lambda\frac{K_\lambda\psi_\lambda}{\lambda+i\omega}\,, \tag{16}$$

where λ, ψ_λ and K_λ are defined by

$$L\psi_\lambda+\lambda\psi_\lambda=0\,, \tag{17}$$

$$K_\lambda=\int\cdots\int\psi_\lambda{}^*K\prod_{i=1}^{n-1}d\xi_i d\eta_i d\zeta_i\,. \tag{18}$$

Hence the expectation value of $X, \overline{X}$ is given by

$$\begin{aligned} \overline{X}(t)&=\int\cdots\int Xf_\xi\Pi d\xi_i d\eta_i d\zeta_i \\ &=X_0-\gamma\exp(i\omega t)\sum_\lambda\frac{K_\lambda X_\lambda}{\lambda+i\omega}\,, \end{aligned} \tag{19}$$

$$\begin{aligned} X_\lambda\equiv&\int\cdots\int X\exp\{-(V_f+V_i)/2kT\} \\ &\times\psi_\lambda\prod_{i=1}^{n-1}d\xi_i d\eta_i d\zeta_i\,. \end{aligned} \tag{20}$$

The eigenvalue problem of many variables expressed by Eq. (17) can be separated into those of a single variable by an orthogonal transformation and each of them is reduced to an Hermitian differential equation. Thus we have Hermitian polynomials as eigenfunctions. Details of calculation are described in Appendix. I. The normalized eigenfunctions aer given by

$$\begin{aligned} \psi_\lambda=&\prod_{i=1}^{n-1}\frac{(-1)^{k_i+l_i+m_i}}{\sqrt{2^{k_i+l_i+m_i}k_i!\,l_i!\,m_i!\sqrt{\pi^3}}} \\ &\times\exp\{1/2(s_i^2+t_i^2+v_i^2)\}\frac{d^{k_i}e^{-s_i^2}}{ds_i^{k_i}}\frac{d^{l_i}e^{-t_i^2}}{dt_i^{l_i}}\frac{d^{m_i}e^{-v_i^2}}{dv_i^{m_i}}\,, \end{aligned}$$

$$s_i=\sqrt{\frac{\alpha}{kT}}\left[\sum_k u_{ik}\xi_k-\frac{\beta e_1}{2\alpha}\sum_k u_{ik}\right]$$

$$t_i=\sqrt{\frac{\alpha}{kT}}\left[\sum_k u_{ik}\eta_k-\frac{\beta e_2}{2\alpha}\sum_k u_{ik}\right]$$

$$v_i=\sqrt{\frac{\alpha}{kT}}\left[\sum_k u_{ik}\zeta_k-\frac{\beta e_3}{2\alpha}\sum_k u_{ik}\right], \quad (21)$$

where each of k_i, l_i and m_i can take any positive integer, $1, 2, 3, \cdots$, and u_{ik}'s are elements of the transformation matrix U which diagonalizes the metric tensor G of Eq. (10):

$$\mathrm{U}\cdot\mathrm{G}\cdot\mathrm{U}^*=\begin{pmatrix} \mu_1 & & & \\ & \mu_2 & & 0 \\ & & \ddots & \\ 0 & & & \mu_{n-1} \end{pmatrix}. \quad (22)$$

Here μ_k is given by (see Appendix II)

$$\mu_k=4\sin^2\frac{k\pi}{2n}. \quad (23)$$

The eigenvalue λ corresponding to the eigenfuction (21) is

$$\lambda=2\left(\frac{\alpha}{\zeta}\right)\sum_{i=1}^{n-1}(k_i+l_i+m_i)\mu_i. \quad (24)$$

Using these eigenfunctions and eigenvalues given above, K_λ and X_λ can be calculated by Eq. (18) and Eq. (20). And finally we get the required expectation value $\overline{X}$ in the following form (Appendix III):

$$\overline{X}=X_0+\gamma\exp(i\omega t)\sum\frac{\phi_k}{1+i\omega\tau_k}$$

$$\tau_k=\frac{\zeta}{2\alpha\mu_k}=\frac{\zeta}{8\alpha}\operatorname{cosec}^2\frac{k\pi}{2n}$$

$$\phi_k=\frac{1}{\alpha n}\cot^2\frac{k\pi}{2n}. \quad (25)$$

The summation in Eq. (25) may be approximated by an integral as follows

$$\overline{X}=X_0+\gamma\exp(i\omega t)\int_{\tau_\alpha}^{\tau_\beta}\frac{\phi(\tau)d\tau}{1+i\omega\tau}$$

$$\phi(\tau)=\frac{1}{\pi}\sqrt{\frac{2}{\alpha\zeta}}\sqrt{\frac{\tau-\tau_\alpha}{\tau}}$$

$$\tau_\alpha\equiv\tau_{n-1}\simeq\frac{\zeta}{8\alpha}$$

$$\tau_\beta\equiv\tau_1\simeq\frac{\zeta n^2}{2\alpha\pi^2}. \quad (26)$$

§5. Dynamic compliance and its transformation into dynamic modulus

Now in order to arrive at the bulk properties of the network structure from the molecular quantity obtained in the preceding section the structure of the network should be specifield in detail. For simplicity we shall assume here, as often done in the theory of rubber elasticity, that the network is composed of equal number of three kinds of chains each of which is directed along x-, y-, and z-axis. The more detailed specification of the chain orientation would not affect the essential feature of the phenomena. Then according to Eq. (26) the strain in x-direction $\mathcal{E}_x$ is given by

$$\mathcal{E}_x=\frac{\overline{X}-X_0}{X_0}=\frac{\gamma\exp(i\omega t)}{X_0}\int_{\tau_\alpha}^{\tau_\beta}\frac{\phi(\tau)d\tau}{1+i\omega\tau}.$$

If we denote the density of chains per unit cross section by M, the applied stress in x-direction per unit initial cross section σ is given by

$$\sigma=M\gamma\exp(i\omega t).$$

Hence the complex compliance J^* is expressed as

$$J^*=J_\infty+\frac{\mathcal{E}_x}{\sigma}=J_\infty+\int_0^\infty\frac{\phi_J(\tau)d\tau}{1+i\omega\tau}$$

$$\phi_J(\tau)\begin{cases}=C\sqrt{\dfrac{\tau-\tau_\alpha}{\tau}}, & \tau_\alpha\leqq\tau\leqq\tau_\beta\\ =0, & \text{otherwise}\end{cases}$$

$$C=\frac{1}{\pi MX_0}\sqrt{\frac{2}{\alpha\zeta}}. \quad (27)$$

Here J_∞ is inserted to express the instantaneous elastic compliance. $\phi_J(\tau)$ is usually called the retardation time spectrum, and τ the retardation time.

Now that the experimental data to be compared with the theory is given in the form of relaxation spectrum, it is necessary to transform the retaradtion spectrum $\phi_J(\tau)$ into the relaxation spectrum $\phi_E(\tau)$. A convenient formula for such a transformation has been given by Gross as follows:

$$\phi_E(\tau)=\frac{1}{\pi\tau^2}\frac{\pi\phi_J(\tau)}{[\Omega(\tau)]^2+[\pi\phi_J(\tau)]^2}$$

$$\Omega(\pi)=J_\infty/\tau+\int_0^\infty\frac{\phi_J(u)}{\tau-u}du. \quad (28)$$

Further we shall change the variable τ to $\log\tau$, introducing the function $\Phi_E(\log\tau)$ which relates to $\phi_E(\tau)$ as

$$\Phi_E(\log\tau)d(\log\tau)=\phi_E(\tau)d\tau \qquad \text{or} \qquad \Phi_E(\log\tau)=\tau\phi_E(\tau)\,. \tag{29}$$

Substituting $\phi_J(\tau)$ obtained above to Eq. (28) and using the relation (29) we get

$$\Phi_E(\log\tau)\begin{cases}=\dfrac{C\sqrt{\tau-\tau_\alpha}}{\left(J_\infty+C\sqrt{\tau-\tau_\alpha}\,\log\dfrac{\sqrt{\tau_\beta-\tau_\alpha}+\sqrt{\tau+\tau_\alpha}}{\sqrt{\tau_\beta-\tau_\alpha}-\sqrt{\tau-\tau_\alpha}}+2C\sqrt{\tau\alpha}\tan^{-1}\sqrt{\dfrac{\tau_\beta-\tau_\alpha}{\tau_\alpha}}\right)^2+\pi^2C^2(\tau-\tau_\alpha)}\,, & \text{for } \tau_\alpha\le\tau\le\tau_\beta \\ =0\,, & \text{otherwise}\end{cases}$$

$$C=\frac{1}{\pi MX_0}\sqrt{\frac{2}{\alpha\zeta}}\,. \tag{30}$$

If $\tau_\alpha \ll \tau \ll \tau_\beta$ and J_∞ is sufficiently small compared with the static compliance J_0 as it is usually the case, Eq. (30) is approximated by

$$\Phi_E(\log\tau)\simeq A\tau^{-1/2}, \qquad \tau_\alpha\ll\tau\ll\tau_\beta$$

$$A=\frac{MX_0}{\pi}\sqrt{\frac{\alpha\zeta}{2}}\,. \tag{31}$$

If we assume that each chain segment is a sphere of radius b immersed in a viscous fluid of viscosity η, the friction constant ζ of a segment is given with the use of Stokes' approximation by

$$\zeta=6\pi b\eta \tag{32}$$

Substitution of Eqs. (3) and (32) into expressions for A, τ_α and τ_β given in Eqs. (26) and (31) leads to

$$A=\frac{3}{\sqrt{2\pi}}\frac{\sqrt{bkT\eta}}{a}MX_0$$

$$\tau_\alpha=\frac{\pi a^2 b\eta}{2kT}\,, \qquad \tau_\beta=\frac{2a^2b\eta n^2}{\pi kT}\,. \tag{33}$$

Accordingly dynamic modulus E is expressed as

$$E=E_0+\omega^2\tau^2\int_{-\infty}^{\infty}\frac{\Phi_E(\log\tau)}{1+\omega^2\tau^2}d(\log\tau)\,. \tag{34}$$

Here E_0 represents the static modulus. In Fig. 1 $\log\Phi_E$ calculated by Eqs. (30) and by (31) are plotted against $\log\tau$, where values of parameters are chosen appropriately. (see § 6). Behaviors of the curve when temperature or chain length is altered is also shown in the figure. It is seen from the figure that Eq. (31) is a fairly good approximation to Eq. (30). So we shall hereafter handle with $\Phi_E(\log\tau)$ mainly in the form (30).

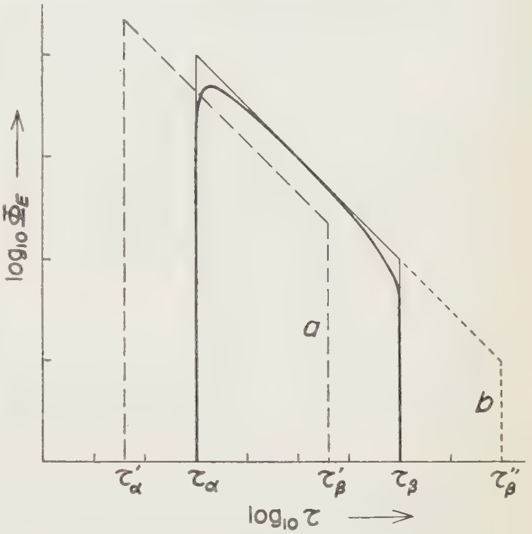

Fig. 1. The theoretical curve of the intra-chain relaxation spectrum.
The thick solid line: calculated from Eq. (30).
The thin solid line: calculated from Eq. (31).
The dashed line (a) shows shift of the spectrum when tempercture is increased.
The dotted line (b) shows shift of τ_β when chain length n is increased by ten times.

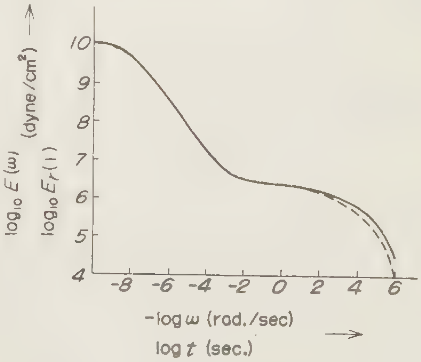

Fig. 2. The experimental curve of dynamic midulus $E(\omega)$ (the solid line) and stress relaxation modulus $E_r(t)$ (the dashed line) for polyisobutylene at 25°C (Marvin[1]).

§ 6. Comparison with experiment and discussions

The experimental curve of dynamic modulus $E(\omega)$ and stress relaxation modulus $E_r(t)$ for

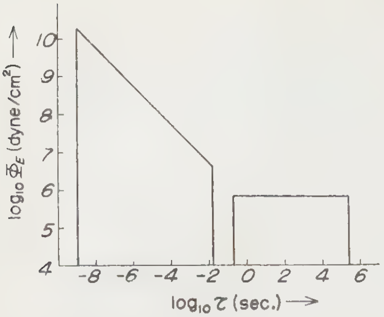

Fig. 3. The "wedge-box" spectrum for polyisobutylene at 25°C (Tobolsky[2]).

polyisobutylene and the coresponding wedge-box spectrum of relaxation times obtained by Tobolsky are shown in Fig. 2 and Fig. 3[1),2)]. The analytical formula of wedge spectrum (at 25°C) is given by[2)]

$$\Phi_E(\log\tau)\begin{cases}=0\,, & \tau<\tau_\alpha\\ =A\tau^{-1/2}\,, & \tau_\alpha\leq\tau<\tau_\beta\\ =0\,, & \tau_\beta<\tau\end{cases}$$

$$\tau_\alpha=1.1\times10^{-9}$$

$$\tau_\beta=1.4\times10^{-2}$$

$$A=3.4\times10^5\times(T/298). \qquad (35)$$

On the other hand, it is found in the preceding section that the theory also predicts a wedge type relaxation spectrum, (30). And it is remarkable that an approximated form (31) of the relaxation spectrum just coincides with the idealized experimental formula (35).

In order to evaluate τ_α, τ_β and A theoretically, it is necessary to know the magnitude of a, b, n, η, X_0 and M. First we shall assign for a, b and n the following values,

$$a\sim b\sim10^{-7},\ n\sim10^2,$$

and hence

$$X_0\sim\sqrt{na^2}\sim10^{-6}\ .$$

The density of chains per unit cross section M can be written as

$$M=\frac{X_0\rho N_L}{3mn}\,, \qquad (36)$$

where ρ and m represent respectively the density of the polymer and the molecular weight of chain segment, and N_L is Avogadro's number. Taking account of the molecular structure of the polyisobutylene monomer, we may take

$$m\sim50\,,\qquad \rho\sim1\ .$$

Hence

$$M\sim4\times10^{13}\,,$$

which results in a correct order of the static modulus at room temperature:

$$E_0=\frac{9kTMX_0}{na^2}\sim10^7\ .$$

Now η means in our theory effective viscosity of the circumstance acting on a segment, and it is obviously not the same as macroscopic viscosity of the bulk system. It will probably take an intermediate value between the viscosity of the monmeor liquid and that of the polymer itself. But so far as a priori estimation of its magnitude is not known, we shall determine the value of η so that the theoretical value of A agrees with the experimental one, and then proceed to calculate the values of τ_α and τ_β. This procedure gives

$$\eta\sim10^2\,,$$

and $\qquad \tau_\alpha\sim10^{-6}\,,\qquad \tau_\beta\sim10^{-2}\ .$

It is seen that the theory gives the correct magnitude of τ_β. On the other hand the culculated τ_α deviates considerably from the experimental value. But such a deviation, especially towards longer time scale, is naturally anticipated in this treatment, because tight chain bonds are replaced artificially by loose springs and accordingly the short range motion among proximate segments along a chain may considerably be affected, or, in other words, the shorter end of the relaxation times may be shifed towords longer by such a treatment. It should be noted that the assigned value of η just lies in an expected region, i.e. between the values $\sim10^{-3}$ for isobutylene and $\sim10^{10}$ for polyisobutylene.

Next we shall examine the temperature dependence of the spectrum. It is clear from Eq. (31) that temperature does not affect the form of $\Phi_E(\log\tau)$. Temperature comes in the spectrum only implicity through τ_α, τ_β and A. In other words, when temperature is changed the whole spectrum will shift as a whole along both axes without any change of the spectral shape. Such a behavior is just the essence of the well-known working hypothesis of "*thermorheological simplicity*" introduced by Ferry and others[15)16)]. Thus the present treatment establishes the theoretical foundation of the thermorheological simplicity. According to Eq. (33) the temperature dependence of τ_α, τ_β and A is primarily governed by η, so that they decreases as temperature increases. Thus, whereas the temperature dependence of τ is the same with experiment, that of A is opposite to the experiment. But the factor $T/298$ in the experimental formula (35) was introduced rather arbitrarily by an analogy with the equilibrium rubber elasticity, so it is open to question. Thus in the present state the details of the temperature dependence of A has not been uniquely elucidated even on the experimental side.

Finally we consider the effect of the chain length on the shape of the spectrum. It will be seen from Eqs. (33) and (36),

$$\tau_\alpha \sim n^2 \ ,$$

and τ_α and A are independent of n, assuming

$$X_0 \sim \sqrt{n}\, a \ ,$$

Thus if the chain length between juctions is increased, i.e. if the density of cross-links is decreased, only the longer time end of the spectrum will shift towards still longer side without any change in the height and the shorter time end of the spectrum. The dotted line in Fig. 1 shows the spectrum when n is ten times larger than that of the original curve. Unfortunately the experimental data to ascertain the effect have not been available. In this connection it should be remarked that in linear polymers the initial molecular weight of the chains constituting the sample does not correspond to the chain length n in our case. It is known experimentally that in polyisobutylene the initial molecular weight does not affect the wedge spectrum so far as the molecular weight is sufficiently high[2]. This fact may be considered rather natural, because there should be no direct correlation between the initial molecular weight of the polymer and the chain length between junctions.

In conclusion the statistical theory of the intra-chain relaxation based on the random spring model has been found to explain satisfactorily the primary feature of the wedge type spectrum of amorphous polymers in the higher frequency region. Especially we may conclude that the slope of $-1/2$ in the $\log \Phi_E$ vs. $\log \tau$ plot is characteristic of the intra-chain relaxation. Recently Tobolsky and coworkers[17] proposed a more accurate experimental formula of the relaxation spectrum to replace the idealized wedge type spectrum. It may be considered as an higher approximation when we regard the wedge spectrum as a first approximation. Accordingly it will be necessary on the theoretical side to refine the model in order to adapt the experiment in such a higher approximation.

Acknowledgement

The author would express his sincere thanks to Prof. S. Oka, Prof. N. Seito, Mr. Y. Ikeda and others in the Kobayashi Institute of Physical Research and Mr. M. Yamamoto in Kyoto University for their encouragement and valuable discussions. The present investigation has been supported partly by the Scientific Research Funds of the Ministry of Education.

Appendix I

Solution of the eigenvalue problem of Eq. (17).

As one sees from Eq. (17), the operator L is given as a sum of three identical operators,

$$L = L_\xi + L_\eta + L_\zeta \ , \qquad \text{(AI-1)}$$

where L_ξ, L_η and L_ζ mean operators which involve respectively only one kind of variables denoted by suffix. So it is sufficient to solve the one of seprated equations,

$$L_\xi \psi_\xi + \lambda_\xi \psi_\xi = 0 \ . \qquad \text{(AI-2)}$$

The eigenfunction ψ and the eigenvalue λ of the original problem are given by

$$\psi = \psi_\xi \psi_\eta \psi_\zeta$$

$$\lambda = \lambda_\xi + \lambda_\eta + \lambda_\zeta \ . \qquad \text{(AI-3)}$$

We denote a orthogonal transformation matrix of the metric tensor G by U, i.e.

$$\mathrm{U}\cdot\mathrm{G}\cdot\mathrm{U}^* = \begin{pmatrix} \mu_1 & & & \\ & \mu_2 & & 0 \\ & & \ddots & \\ & 0 & & \ddots \\ & & & & \mu_{n-1} \end{pmatrix} , \qquad \text{(AI-4)}$$

where G means the matrix of g^{ik} and we shall express each element of U by u_{ik}. Then the change of variables defined by

$$w_i = \sum_{k=1}^{n-1} u_{ik}\xi_k - \frac{\beta e_1}{2\alpha}\sum_{k=1}^{n-1} u_{ik} \ , \qquad \text{(AI-5)}$$

leads L_ξ into a separable form,

$$L_\xi = \sum_{i=1}^{n-1} L_i$$

$$L_i \equiv \frac{kT\mu_i}{\zeta}\left[\frac{\partial^2}{\partial w_i^2} - \left(\frac{\alpha}{kT}\right)^2 w_i^2 + \frac{\alpha}{kT}\right] . \qquad \text{(AL-6)}$$

Each of separated eigenvalue problems,

$$L_i\psi_i+\lambda_i\psi_i=0 \qquad \text{(AI-7)}$$

is reduced to a Hermitian differential equation,

$$\frac{\partial^2\chi_i(s_i)}{\partial s_i^2}-2s_i\frac{\partial\chi_i(s_i)}{\partial s_i}+\frac{\zeta\lambda_i}{\alpha\mu_i}\chi_i(s_i)=0 \qquad \text{(AI-8)}$$

by a transformation,

$$s_i=\sqrt{\frac{\alpha}{kT}}w_i\ , \qquad \psi_i=\exp(-s_i^2/2)\,\chi_i(s_i)\ . \qquad \text{(AI-9)}$$

Hence ψ_i and λ_i are given by

$$\psi_i=\frac{(-1)^{k_i}}{\sqrt{2^{k_i}k_i!}\sqrt{\pi}}\exp(s_i^2/2)\frac{d^{k_i}\exp(-s_i^2)}{ds_i^{k_i}}$$

$$\lambda_i=2\left(\frac{\alpha}{\zeta}\right)\sum_{i=1}^{n-1}k_i\mu_i\ . \qquad \text{(AI-10)}$$

Eigenfunctions and eigenvalues of the operator L are easily constructed from (AI-10) resulting in the form Eqs. (21) and (24).

Appendix II

Diagonalization of the metric tensor G

Eq. (22) can be written as

$$\left\{\begin{array}{l} 2u_{j1}-u_{j2}=\mu_j u_{j1} \\ -u_{j1}+2u_{j2}-u_{j3}=\mu_j u_{j2} \\ \quad\cdots\cdots \\ -u_{j,i-1}+2u_{j,i}-u_{j,i+1}=\mu_j u_{j,i} \\ \quad\cdots\cdots \\ -u_{j,n-3}+2u_{j,n-2}u_{j,n-1}=\mu_j u_{j,n-2} \\ -u_{j,n-2}+2u_{j,n-1}=\mu_j u_{j,n-1} \end{array}\right.$$

$$(j=1, 2, \cdots, n-1)\ . \qquad \text{(AII-1)}$$

This is just the secular equation to determine the j-th vibration mode for vibration of particles connected by identical springs when both ends, the 1st and the n-th paticale, are fixed. μ_i means square of the i-th characteristic frequency and u_{ji} expresses the amplitude of vibration of the i-th particle for the j-th mode. Taking account of the boundery condition, we may put

$$u_{jk}=A_j\sin\frac{kj\pi}{n}\ , \quad k, j=1, 2, \cdots. n-1\ , \qquad \text{(AII-2)}$$

where A_j can be determined by normalization $\sum_{k=1}^{n-1}u_{jk}^2=1$. Thus we get

$$u_{jk}=\sqrt{\frac{2}{n}}\sin\frac{kj\pi}{n}\ . \qquad \text{(AII-3)}$$

Insertion of the u_{jk} into the first equation of (AII-1) gives

$$\mu_i=4\sin^2\frac{j\pi}{2n}\ . \qquad \text{(AII-4)}$$

Also from Eq. (AII-2) we get

$$u_j=\sum_{k=1}^{n-1}u_{jk}=\sqrt{\frac{2}{n}}\cot\frac{j\pi}{2n}\ , \qquad \text{(AII-5)}$$

$$j:\ \text{odd}\geq n$$

Appendix III

Calculation of ϕ_k in Eq. (25)

From Eqs. (14), (1), (2) and (15)

$$\begin{aligned} K&=-\frac{1}{\zeta}\exp\left\{\frac{V_f+V_i}{2kT}\right\}\cdot\left\{\sum g^{ik}\frac{\partial}{\partial\xi_i}\left(\frac{\partial X}{\partial\xi_k}f_0\right)\right\} \\ &=-\frac{\pi^{-3(n-1)/2}}{\zeta}\exp\left\{-\frac{3(n-1)\beta^2}{8\alpha kT}\right\} \\ &\quad\times\exp\left[\frac{1}{2kT}\{\alpha(\sum\xi_i^2+\sum\eta_i^2+\sum\zeta_i^2)\right. \\ &\qquad\left.-\beta\{e_1\sum\xi_i+e_2\sum\eta_i+e_3\sum\zeta_i\}\right] \\ &\quad\times\left\{\sum g^{ik}\frac{\partial}{\partial\xi_i}\exp\left[\frac{-1}{kT}\left\{\alpha(\sum\xi_i^2+\sum\eta_i^2+\sum\zeta_i^2)\right.\right.\right. \\ &\qquad\left.\left.\left.-\beta(e_1\sum\xi_i+e_2\sum\eta_i+e_i\sum\zeta_i)\right\}\right]\right\} \\ &=-\frac{2\pi^{-3(n-1)/2}}{\zeta}\sqrt{\frac{\alpha}{kT}}\exp\left\{-\frac{3(n-1)\beta^2}{8\alpha kT}\right\}\{\sum\mu_i u_i s_i\} \\ &\quad\times\exp\left\{-\frac{1}{2}(\sum s_i^2+\sum t_i^2+\sum v_i^2)\right\}\ , \end{aligned} \qquad \text{(AIII-1)}$$

where $u_i=\sum_{k=1}^{n-1}u_{ik}$, and μ_i, s_i t_i and v_i are defined by Eqs. (22) and (21).

Hence

$$\begin{aligned} K_\lambda&\equiv\int\psi_\lambda{}^*K\Pi d\xi_i d\eta_i d\zeta_i \\ &=-\frac{2\pi^{-3(n-1)/2}}{\zeta}\sqrt{\frac{\alpha}{kT}}\exp\left\{-\frac{3(n-1)\beta^2}{8\alpha kT}\right\} \\ &\quad\times\int\cdots\int(\sum\mu_i u_i s_i)\exp\left\{-\frac{1}{2}(\sum s_i^2+\sum t_i^2\right. \\ &\quad\left.+\sum v_i^2)\right\}H_{k_i}(s_i)H_{l_i}(t_i)H_{m_i}(v_i)\Pi ds_i dt_i dv_i\ , \end{aligned} \qquad \text{(AIII-2)}$$

where $H_n(x)$ means an orthogonalized Hermitian polynomial. Now using the relation

$$\int_{-\infty}^{\infty}x\frac{d^l}{dx^l}\exp(-x^2)dx\ \left\{\begin{array}{l}=-\sqrt{\pi}\ ,\ \ l=0 \\ =0,\ \ l=0, 2, 3, \cdots\end{array}\right. \qquad \text{(AIII-3)}$$

we get

$$K_\lambda \begin{cases} = \dfrac{\pi^{-3(n-1)/4}}{\zeta} \sqrt{\dfrac{2\pi}{kT}} \exp\left\{-\dfrac{3(n-1)\beta^2}{8\alpha kT}\right\} \mu_j u_j, \\ \qquad \text{if } k_j=1, \text{ and all other } k_i's, \\ \qquad l_i's \text{ and } m_i's = 0 \\ = 0, \qquad \text{otherwise.} \end{cases} \tag{AIII-4}$$

Similarly

$$X_\lambda = \int \Sigma \xi_i \exp\left\{-\frac{V_j+V_i}{2kT}\right\} \psi_\lambda \Pi d\xi_i d\eta_i d\zeta_i$$

$$\begin{cases} = \sqrt{\dfrac{kT}{2\alpha}} \exp\left\{\dfrac{3(n-1)\beta^2}{8\alpha kT}\right\} \pi^{3(n-1)/4} u_j, \\ \qquad \text{if } k_j=1, \text{ and all other } k_i's, \\ \qquad l_i's \text{ and } m_i's = 0. \\ = 0, \qquad \text{otherwise}. \end{cases} \tag{AIII-5}$$

Hence

$$K_\lambda X_\lambda \begin{cases} = \dfrac{1}{\zeta} \mu_j u_j^2, & \text{if } \lambda = \dfrac{2\alpha}{\zeta} \mu_j \\ = 0, & \text{otherwise.} \end{cases} \tag{AIII-6}$$

Substituting Eq. (AIII-6) as well as Eqs. (24), (AII-3) and (AIII-4) for λ_i, μ_i and u_i we get immediately Eq. (25).

References

1) R. S. Marvin: "Proceedings of the Second International Congress on Rheology" (1954) 156.

2) A. V. Tobolsky and J. R. McLonghlin: J. Polymer Sci. **8** (1952) 543.
A. V. Tobolsky: J. Amer. Chem. Soc. **74** (1952) 3786.

3) D. G. Ivey, B. A. Mrowca and E. Guth: J. Appl. Phys. **20** (1949) 486.
J. D. Ferry and E. R. Fitzgerald: "Proc. of the 2nd Intn. Congr. on Rheology" (1954) 140.

4) For phenomenological theories see B. Gross: "Mathematical Structure of the Theories of Viscoelasticity" (1953).

5) A. V. Tobolsky and H. Eyring: J. Chem. Phys. **11** (1943) 125.

6) M. S. Green and A. V. Tobolsky: J. Chem. Phys. **14** (1946) 80.

7) M. Yamamoto: Busseiron-Kenkyu No. **55** (1952) 25, No. **59** (1953) 1, No. **60** (1953) 38, No. **67** (1953) 17.

8) T. Alfrey: J. Chem. Phys. **12** (1944) 374.

9) J. G. Kirkwsod: J. Chem. Phys. **14** (1946) 51.

10) R. B. Blizard: J. Appl. Phys. **19** (1951) 730.

11) F. Bueche: J. Chem. Phys. **22** (1954) 603.

12) J. G. Kirkwood: Rec. des travaux chim. des Pays-Bas. **68** (1949) 649.

13) P. E. Rouse, Jr: J. Chem. Phys. **21** (1953) 1272.

14) O. Nakada: Busseiron-Kenkyu No. **81** (1955) 84.

15) R. S. Marvin, E. R. Fitzgerald and J. D. Ferry: J. Appl. Phys. **21** (1950) 197.

16) F. Schwarzl and A. J. Staverman: J. Appl. Phys. **23** (1952) 838.

17) E. Catsiff and A. V. Tobolsky: J. Appl. Phys. **25** (1954) 145.

Journal of the Physical Society of Japan Vol. 10, No. 9, September 1955

Application of the Thin-Wing-Expansion Method to the Compressible Flow past a Kaplan Bump

By Yaso'o Matunobu

Department of Physics, Faculty of Science, University of Tokyo

(Received June 14, 1955)

About ten years ago Kaplan calculated the velocity distribution over a certain cusped aerofoil set in a compressible flow as far as $O(t^3)$, t being the thickness ratio. Here the same problem is reinvestigated by use of the thin-wing-expansion method due to Imai, which is believed to be more convenient than the usual perturbation method. Both results completely agree with each other in the analytical expressions, although the labour is considerably less in the present analysis than Kaplan's.

§ 1. Introduction and Summary

It is well known that the compressible flow past a two-dimensional thin aerofoil can be treated successfully by the so-called thin-wing-expansion method which is originally due to Prandtl and Glauert. About ten years ago the method was elegantly developed up to the second order of approximation by Imai[1], and later the third aproximation was formulated by Imai and Ôyama[2]. The examples, thus far calculated as far as the third approximation on the basis of these formulations, are as follows: the flow along a sinusoidal wall by Imai and Ôyama[3], the flow past an elliptic cylinder by Hasimoto[4], and the flow past a biconvex circular arc aerofoil by Asaka[5],[6],[7].

As another example of the calculation of the third approximation, we shall consider in this paper the flow around a kind of cusped aerofoil which is usually called Kaplan bump. It is true that Kaplan himself has already obtained the analytical expression for the velocity distribution over the Kaplan bump[8], correct to the third approximation, and that the method to which he resorted is essentially equivalent to ours. But it is worth while to reattack this problem, since much simplification is expected with Imai's analysis. In Kaplan's procedure the whole region of flow was taken into account and moreover manipulation of some infinite series was needed. On the other hand, in Imai's procedure, we have only to deal with the quantities on the surface of the obstacle, as a result of employing the stream function and the conception of conjugate Fourier series.

It will be shown that the final expression for the velocity distribution agrees completely with Kaplan's result within the third approximation and can be brought into a more refined form than Kaplan's.

§ 2. Outline of Imai's Method

It will be convenient to start with a brief account of the thin-wing-expansion method due to Imai.

The two-dimensional irrotational flow of a compressible fluid is governed by the equations:

$$u=\frac{\partial\Phi}{\partial x}=\frac{\rho_\infty}{\rho}\frac{\partial\Psi}{\partial y}\,,\qquad v=\frac{\partial\Phi}{\partial y}=-\frac{\rho_\infty}{\rho}\frac{\partial\Psi}{\partial x}\,,\tag{2.1}$$

and

$$\frac{\rho}{\rho_\infty}=\left\{1-\frac{\gamma-1}{2}M^2\left(\frac{q^2}{U^2}-1\right)\right\}^{1/\gamma-1},\tag{2.2}$$

where (u, v) are the component velocities in the x- and y-directions, Φ is the velocity potential, Ψ is the stream function, ρ is the density, ρ_∞ is the density of the undisturbed fluid, U and M are respectively the velocity and the Mach number of the undisturbed flow, q is the magnitude of velocity, i.e. $q^2=u^2+v^2$ and, γ is the ratio of specific heats.

On the assumption that the disturbance caused by an obstacle would be small, Φ and Ψ may be expressed as

$$\Phi=x+\phi=x+\phi_1+\phi_2+\phi_3+\cdots\,,\tag{2.3}$$

$$\Psi=y+\psi=y+\psi_1+\psi_2+\psi_3+\cdots\,,\tag{2.4}$$

where ϕ_1, ψ_1; ϕ_2, ψ_2; $\cdots$ are respectively of the order of magnitude $\varepsilon, \varepsilon^2, \cdots$; ε being a small parameter. We now write

$$\xi=x\,,\qquad \eta=\mu y\,,\tag{2.5}$$

$$\chi=\psi/\mu\,,\quad \chi_n=\psi_n/\mu\ (n=1, 2, 3, \cdots),\tag{2.6}$$

$$\mu=\sqrt{1-M^2}\ , \tag{2.7}$$

and introduce the complex quentities

$$\zeta=\xi+i\eta\ ,\quad \bar{\zeta}=\xi-i\eta\ , \tag{2.8}$$

$$G(\zeta,\bar{\zeta})=\phi+i\chi\ ,\quad G_n(\zeta,\bar{\zeta})=\phi_n+i\chi_n\ . \tag{2.9}$$

Substituting the relations (2,3) to (2.9) into (2.1) and (2.2), then considering the order of magnitude of each term, and performing integration after successive iterations, one obtains

$$G_1=f(\zeta)\ , \tag{2.10}$$

$$G_2=\frac{M^2}{4}\left[\nu\left(\frac{df}{d\zeta}\right)^2\bar{\zeta}+(1+\nu)\left\{2\frac{df}{d\zeta}\bar{f}+\int\left(\frac{d\bar{f}}{d\bar{\zeta}}\right)^2 d\bar{\zeta}\right\}\right]+f_2(\zeta)\ , \tag{2.11}$$

$$\begin{aligned}G_3=&A\left(\frac{df}{d\zeta}\right)^3\bar{\zeta}+B\int\left(\frac{d\bar{f}}{d\zeta}\right)^3 d\bar{\zeta}\\&+3B\left(\frac{df}{d\zeta}\right)^2\bar{f}+C\frac{df}{d\zeta}\int\left(\frac{d\bar{f}}{d\zeta}\right)^2 d\bar{\zeta}\\&+\frac{M^2}{2}(1+\nu)\int J\left(\frac{df}{d\zeta}+\frac{d\bar{f}}{d\bar{\zeta}}\right)d\bar{\zeta}\\&-\frac{M^2}{2}\frac{df}{d\zeta}\int\frac{\partial}{\partial\zeta}(G_2+\bar{G}_2)d\bar{\zeta}+f_3(\zeta)\ ,\end{aligned} \tag{2.12}$$

where

$$J=\partial G_2/\partial\zeta+\partial G_2/\partial\bar{\zeta}+\partial\bar{G}_2/\partial\zeta+\partial\bar{G}_2/\partial\bar{\zeta}\ , \tag{2.13}$$

$$\nu=(\gamma+1)M^2/4\mu^2\ , \tag{2.14}$$

$$A=-(\gamma+1)(3-2\gamma)M^6/96\mu^2\ , \tag{2.15}$$

$$B=\{6(\gamma-1)-(2\gamma-1)(3-\gamma)M^2\}M^4/96\mu^2, \tag{2.16}$$

$$C=\{8-8(3-\gamma)M^2+(13-9\gamma+2\gamma^2)M^4\}M^2/32\mu^2\ . \tag{2.17}$$

$f(\zeta)$, $f_2(\zeta)$, and $f_3(\zeta)$ are analytic functions of ζ to be determined from the following boundary conditions: (i) $\partial G/\partial\zeta$ is one-valued and continuous in the field of flow, (ii) $\partial G/\partial\zeta$ vanishes at infinity, (iii) $\Psi=$const $(=0$, say), on the profile P; accordingly

$$\mathrm{Im}\{\mu^2 G(\zeta_P,\bar{\zeta}_P)+\zeta_P\}=0\ , \tag{2.18}$$

where ζ_P is the value of ζ on the profile.

§ 3. Kaplan Bump and its Mapping Function

Suppose a Kaplan bump of thickness ratio t is set in a uniform flow with its chord parallel to the x-axis. Then, according to Ref. 8), the profile can be given parametrically by

$$\left\{\begin{aligned}x_P&=\cos\varphi-\frac{t}{4}(\cos\varphi-\cos 3\varphi)\ ,\\ y_P&=\frac{t}{4}(3\sin\varphi-\sin 3\varphi)\ ,\end{aligned}\right.$$

or

$$\left\{\begin{aligned}\xi_P&=\cos\vartheta\ , && (3.1)\\ \eta_P&=\mu\sin^3\vartheta\Big\{t-3t^2\cos^2\vartheta\\ &\quad+\frac{3}{2}t^3\cos^2\vartheta(8\cos^2\vartheta-3)+O(\varepsilon^4)\Big\}\ . && (3.2)\end{aligned}\right.$$

The latter expansion has been made on the assumption that $t=O(\varepsilon)$.

It must be noted that the profile given by (3.1) and (3.2) in the ζ-plane does not represent a Kaplan bump in the correct sense. So that it is rather troublesome to determine an analytic function which maps the region outside the surface in the ζ-plane onto the region outside the unit circle $Z=e^{i\theta}$ in the Z-plane. The practical procedure has been reported in detail in Ref. 1). Here we follow its prescription with some appropriate modification.

In general the mapping function $\zeta(Z)$ is assumed in the form

$$\zeta(Z)=\frac{1}{2}\left(Z+\frac{1}{Z}\right)+C(Z)\ , \tag{3.3}$$

with

$$C(Z)=C^{(-1)}Z+C^{(0)}+C^{(1)}Z^{-1}+\cdots, \tag{3.4}$$

where

$$C^{(n)}=A^{(n)}+iB^{(n)}\quad(n=-1,0,1,\cdots)\ . \tag{3.5}$$

When the obstacle in the ζ-plane is sufficiently thin, the function $C(Z)$, and hence the coefficients $C^{(n)}$, $A^{(n)}$ and $B^{(n)}$ are all small quantities, say, of $O(\varepsilon)$. Then writing

$$C(e^{i\theta})=A(\theta)+iB(\theta)\ , \tag{3.6}$$

and using (3.1) and (3.3), we separate the real and imaginary parts of $\zeta_P=\zeta(\theta)$:

$$\xi_P=\cos\vartheta=\cos\theta+A(\theta)\ , \tag{3.7}$$

$$\eta_P=B(\theta)\ , \tag{3.8}$$

whence we see that $\vartheta-\theta$ as well as $A(\theta)$ and $B(\theta)$ is of $O(\varepsilon)$. So that we put

$$A(\theta)=a_1(\theta)+a_2(\theta)+a_3(\theta)+O(\varepsilon^4)\ , \tag{3.9}$$

$$B(\theta)=b_1(\theta)+b_2(\theta)+b_3(\theta)+O(\varepsilon^4)\ , \tag{3.10}$$

$$\vartheta-\theta=\delta_1(\theta)+\delta_2(\theta)+\delta_3(\theta)+O(\varepsilon^4)\ , \tag{3.11}$$

where the subscripts 1, 2, 3 denote the order of magnitude. The relations between $a(\theta)$ and $\delta(\theta)$ are given from (3.7) and (3.9) by

$$a_1(\theta)=-\delta_1(\theta)\sin\theta\ , \tag{3.12}$$

$$a_2(\theta)=-\frac{1}{2}\delta_1^2(\theta)\cos\theta-\delta_2(\theta)\sin\theta\ , \tag{3.13}$$

$$a_3(\theta)=\frac{1}{6}\delta_1^3(\theta)\sin\theta-\delta_1(\theta)\,\delta_2(\theta)\cos\theta$$
$$-\delta_3(\theta)\sin\theta\ . \tag{3.14}$$

On the other hand, comparison of (3.2) and (3.10) yields

$$b_1(\theta)=\mu h_1(\theta)\ , \tag{3.15}$$

$$b_2(\theta)=\mu\{\delta_1(\theta)h_1'(\theta)+h_2(\theta)\}\ , \tag{3.16}$$

$$b_3(\theta)=\mu\Big\{\delta_2(\theta)h_1'(\theta)+\frac{1}{2}\delta_1^2(\theta)h_1''(\theta)$$
$$+\delta_1(\theta)h_2'(\theta)+h_3(\theta)\Big\}\ , \tag{3.17}$$

where the functions $h_n(\theta)$, in the case of Kaplan bump, have the form

$$h_1(\theta)=t\sin^3\theta\ , \tag{3.18}$$

$$h_2(\theta)=-3t^2\sin^3\theta\cos^2\theta\ , \tag{3.19}$$

$$h_3(\theta)=\frac{3}{2}t^3\sin^3\theta\cos^2\theta\,(8\cos^2\theta-3)\ . \tag{3.20}$$

Now the function $C(Z)-C^{(-1)}Z-C^{(0)}$, according to (3.4), must be one-valued and regular in the region $|Z|>1$, and its value on the circle $Z=e^{i\theta}$ is

$$C(e^{i\theta})-C^{(-1)}e^{i\theta}-C^{(0)}=A(\theta)-A^{(-1)}\cos\theta$$
$$+B^{(-1)}\sin\theta-A^{(0)}+i\{B(\theta)-A^{(-1)}\sin\theta$$
$$-B^{(-1)}\cos\theta-B^{(0)}\}\ .$$

Therefore the real part should be equal to the conjugate Fourier series of the imaginary part:

$$A(\theta)-A^{(-1)}\cos\theta+B^{(-1)}\sin\theta-A^{(0)}$$
$$=\{B(\theta)-A^{(-1)}\sin\theta-B^{(-1)}\cos\theta-B^{(0)}\}^*\ ,$$

or

$$A(\theta)=B^*(\theta)+2A^{(-1)}\cos\theta-2B^{(-1)}\sin\theta+A^{(0)}\ , \tag{3.21}$$

where $F^*(\theta)$ denotes in general the conjugate Fourier series associated with $F(\theta)$, and use has been made of the relations: $(\text{const})^*=0$, $(\sin n\theta)^*=-\cos n\theta$ and $(\cos n\theta)^*=\sin n\theta$.

Putting

$$2A^{(-1)}=\alpha_1+\alpha_2+\alpha_3+O(\varepsilon^4)\ ,$$
$$-2B^{(-1)}=\beta_1+\beta_2+\beta_3+O(\varepsilon^4)\ ,$$
$$A^{(0)}=\gamma_1+\gamma_2+\gamma_3+O(\varepsilon^4)\ ,$$

and then splitting (3.21) in accordance with the order of magnitude, one obtains

$$\left.\begin{aligned}a_1(\theta)&=b_1^*(\theta)+\alpha_1\cos\theta+\beta_1\sin\theta+\gamma_1\ ,\\ a_2(\theta)&=b_2^*(\theta)+\alpha_2\cos\theta+\beta_2\sin\theta+\gamma_2\ ,\\ a_3(\theta)&=b_3^*(\theta)+\alpha_3\cos\theta+\beta_3\sin\theta+\gamma_3\ .\end{aligned}\right\} \tag{3.22}$$

For a Kaplan bump, we have, from (3.15) and (3.18),

$$b_1(\theta)=\mu t\sin^3\theta=\frac{1}{4}\mu t(3\sin\theta-\sin 3\theta)\ .$$

Further we assume that the trailing edge at $\zeta=1$ corresponds to the point $Z=1$, i.e., $\delta_1(0)=\delta_2(0)=\delta_3(0)=0$. Hence from (3.12), (3.13) and (3.14) we get $a_1(0)=a_2(0)=a_3(0)=0$ and $a_1'(0)=a_2'(0)=a_3'(0)=0$. In addition the symmetry of the body yields $a_1(\pi)=a_2(\pi)=a_3(\pi)=0$. With the aid of these three conditions the constants α_1, β_1 and γ_1 are fixed, whence $a_1(\theta)$ is determined. Then we also obtain $\delta_1(\theta)$ from (3.12).

Thus repeating the similar procedure successively, we can obtain the expressions for $b_2(\theta)$, $a_2(\theta)$, $\delta_2(\theta)$; $b_3(\theta)$, $a_3(\theta)$, $\delta_3(\theta)$; $\cdots$, and hence we can ultimately build up the mapping function $\zeta(Z)$. Here only the results up to the third approximation will be given:

$$a_1(\theta)=-\frac{\mu t}{4}(\cos\theta-\cos 3\theta)\ , \tag{3.23}$$

$$a_2(\theta)=\frac{3}{16}\mu(1-\mu)t^2(\cos 3\theta-\cos 5\theta)\ , \tag{3.24}$$

$$a_3(\theta)=\frac{3}{32}\mu(1-\mu)t^3\{2(1-\mu)\cos\theta$$
$$-(3-2\mu)\cos 3\theta-(1-2\mu)\cos 5\theta$$
$$+2(1-\mu)\cos 7\theta\}\ , \tag{3.25}$$

$$b_1(\theta)=\frac{\mu t}{4}(3\sin\theta-\sin 3\theta)\ , \tag{3.26}$$

$$b_2(\theta)=-\frac{3}{16}\mu(1-\mu)t^2(2\sin\theta+\sin 3\theta-\sin 5\theta)\ , \tag{3.27}$$

$$b_3(\theta)=\frac{3}{32}\mu(1-\mu)t^3\{2\mu\sin\theta+(3-2\mu)\sin 3\theta$$
$$+(1-2\mu)\sin 5\theta-2(1-\mu)\sin 7\theta\}\ , \tag{3.28}$$

$$\delta_1(\theta)=\frac{1}{2}\mu t\sin 2\theta\ , \tag{3.29}$$

$$\delta_2(\theta)=-\frac{1}{16}\mu t^2\{2\mu\sin 2\theta+(6-5\mu)\sin 4\theta\}\ , \tag{3.30}$$

$$\delta_3(\theta)=\frac{1}{96}\mu t^3\{-9(4-9\mu+4\mu^2)\sin 2\theta$$
$$+6(3-2\mu^2)\sin 4\theta$$
$$+(36-63\mu+28\mu^2)\sin 6\theta\}\ , \tag{3.31}$$

$$\zeta(Z)=\frac{1}{2}\left(Z+\frac{1}{Z}\right)+\frac{\mu t}{4}Z\left(1-\frac{1}{Z^2}\right)^2$$
$$-\frac{3t^2}{16}\mu(1-\mu)\left(Z+\frac{1}{Z}\right)\left(1-\frac{1}{Z^2}\right)^2$$
$$+\frac{3t^3}{32}\mu(1-\mu)\left(Z+\frac{1}{Z}\right)\left(1-\frac{1}{Z^2}\right)^2$$
$$\times\left\{1+\frac{2(1-\mu)}{Z^2}\right\}. \tag{3.32}$$

§ 4. First Approximation

To begin with, we shall determine the first-order perturbation velocity potential $\phi_1(\theta)$. Since $\mathrm{Im}\left(Z+\frac{1}{Z}\right)=0$ on the circle $Z=e^{i\theta}$, we have from (3.32)

$$\mathrm{Im}\,\zeta_{\mathrm{P}}=-\,\mathrm{Im}\left[\frac{\mu t}{4}\left(\frac{3}{Z}-\frac{1}{Z^3}\right)\right]+O(t^2)\,.$$

So far as the terms of $O(\mathcal{E})$ are concerned, the boundary condition (2.18) is rewritten as

$$\mathrm{Im}\left[\mu^2 f(\zeta_{\mathrm{P}})-\frac{\mu t}{4}\left(\frac{3}{Z}-\frac{1}{Z^3}\right)\right]=0\,.$$

Therefore if we assume that

$$f(\zeta)=\frac{t}{4\mu}\left(\frac{3}{Z}-\frac{1}{Z^3}\right), \tag{4.1}$$

all the boundary conditions are satisfied for the first order of approximation. Taking the real part of (4.1), we obtain

$$\phi_1(\theta)=\frac{t}{4\mu}(3\cos\theta-\cos 3\theta)\,. \tag{4.2}$$

§ 5. Second Approximation

Now the unknown function $f_2(\zeta)$ must be chosen so as to satisfy the boundary conditions. To do this we define a function $H_2(Z,\bar{Z})$ such that

$$H_2(Z,\bar{Z})$$
$$=\frac{M^2}{4}\left[\nu f'^2\bar{\zeta}+(1+\nu)\left(2f'\bar{f}+\int\bar{f}'^2d\bar{\zeta}\right)\right], \tag{5.1}$$

and put

$$G_2(\zeta_{\mathrm{P}},\bar{\zeta}_{\mathrm{P}})=\phi_2(\theta)+i\chi_2(\theta)\,, \tag{5.2}$$
$$H_2(e^{i\theta},e^{-i\theta})=P_2(\theta)+iQ_2(\theta)\,, \tag{5.3}$$
$$f_2(\zeta_{\mathrm{P}})=R_2(\theta)+iI_2(\theta)\,. \tag{5.4}$$

Then

$$G_2(\zeta,\bar{\zeta})=H_2(Z,\bar{Z})+f_2(\zeta)\,, \tag{5.5}$$
$$\phi_2(\theta)=P_2(\theta)+R_2(\theta)\,,\quad \chi_2(\theta)=Q_2(\theta)+I_2(\theta)\,. \tag{5.6}$$

Since $f(\zeta)$ as defined by (4.1) has already satisfied the conditions (i) and (ii) in § **2**, the same conditions are obviously valid with $H_2(Z,\bar{Z})$, and consequently with $f_2(\zeta)$: $df_2/d\zeta$ is one-valued and continuous in the field of flow and vanishes at infinity. It may be expected in the present case that $f_2(\zeta)$ will contain no logarithmic terms related to circulation. Thus $f_2(\zeta)$ will be a one-valued regular function for $|Z|>1$. Therefore (5.4) yields the relation $R_2(\theta)=I_2{}^*(\theta)$ for the same reason as mentioned in § **2**. Hence

$$\phi_2(\theta)=P_2(\theta)-Q_2{}^*(\theta)+\chi_2{}^*(\theta)\,, \tag{5.7}$$
$$f_2(\zeta_{\mathrm{P}})=\chi_2{}^*(\theta)+i\chi_2(\theta)-[Q_2{}^*(\theta)+iQ_2(\theta)]\,. \tag{5.8}$$

The boundary condition (2.18) takes the form $\mu^2\chi_2(\theta)+b_2(\theta)=O(\mathcal{E}^3)$ for the second approximation, so that

$$\chi_2(\theta)=\frac{3}{16}t^2(2\sin\theta+\sin 3\theta-\sin 5\theta)\,. \tag{5.9}$$

On the other hand, substituting (4.1) into (5.1), we have

$$P_2(\theta)+iQ_2(\theta)=\frac{9t^2}{16}\nu\frac{M^2}{\mu^2}e^{-4i\theta}\cos\theta$$
$$-\frac{3t^2}{32}(1+\nu)\frac{M^2}{\mu^2}\left(6e^{-i\theta}-2e^{i\theta}\right.$$
$$\left.+e^{3i\theta}-\frac{3}{5}e^{5i\theta}\right)+O(\mathcal{E}^3)\,. \tag{5.10}$$

Thus, substitution of (5.9) and (5.10) into (5.7) and (5.8) gives respectively

$$\phi_2(\theta)=\frac{3t^2}{16}(1+\nu)\frac{M^2}{\mu^2}\left(2\cos\theta-\cos 3\theta+\frac{3}{5}\cos 5\theta\right)$$
$$-\frac{3t^2}{16}\left(\frac{1}{\mu}-1\right)(2\cos\theta+\cos 3\theta-\cos 5\theta)\,, \tag{5.11}$$

$$\left.\begin{aligned}
&f_2(\zeta_{\mathrm{P}})=t^2(F_1e^{-i\theta}+F_3e^{-3i\theta}+F_5e^{-5i\theta})\,,\\
&\text{where}\\
&F_1=\frac{3}{4}\nu\frac{M^2}{\mu^2}+\frac{3}{8\mu^2}(1-\mu)(2+\mu)\,,\\
&F_3=-\frac{3}{8}\nu\frac{M^2}{\mu^2}-\frac{3}{32\mu^2}(1-\mu)(1+3\mu)\,,\\
&F_5=-\frac{9\nu}{40}\frac{M^2}{\mu^2}+\frac{3}{160\mu^2}(1-\mu)(3+13\mu)\,.
\end{aligned}\right\} \tag{5.12}$$

§ 6. Third Approximation

Before calculating the velocity potential for the third approximation, it should be noted that in the previous sections stream functions have been chosen from the boundary condition (2.18) in such a manner that χ should be expanded in a power series of the small parameter t, and that consequently G_1 an G_2 have been evaluated as the terms of the first and the second order in t respectively. Therefore if we wish to expand the velocity potential ϕ in powers of t, we must make a slight alteration in (2.12) just as

$$G_3(\zeta, \bar{\zeta}) = H_{2,1}(Z, \bar{Z}) + H_3(Z, \bar{Z}) + f_3(\zeta) \,, \qquad (6.1)$$

where $H_{2,1}$ denotes the terms of $O(\mathcal{E}^3)$ involved in H_2, which have been omitted in deriving (5.10), and

$$H_3(Z, \bar{Z}) = Af'^3\bar{\zeta} + B\int \bar{f}'^3 d\bar{\zeta} + 3Bf'^2\bar{f} + C\bar{f}'\int \bar{f}'^2 d\bar{\zeta} \\ + \frac{M^2}{2}(1+\nu)\int J(f'+\bar{f}')d\bar{\zeta} - \frac{M^2}{2} f'\int \frac{\partial}{\partial\zeta}(G_2+\bar{G}_2)d\bar{\zeta} \,. \qquad (6.2)$$

Further, inserting (2.11) in (6.2), and considering that it is permissible to add arbitrary functions of ζ to H_3, we write H_3 in the form

$$H_3(Z, \bar{Z}) = A'f'^3(\bar{\zeta}-\zeta) + B'\int \bar{f}'^3 d\bar{\zeta} + 3B'f'^2\bar{f} + C'f'\int \bar{f}'^2 d\bar{\zeta} \\ + \frac{M^4}{24}\nu(1+\nu)\{2\bar{f}'^3\zeta + 3f'\bar{f}'^2\zeta + 6f'f''(\bar{f}\bar{\zeta} - f\zeta)\} \\ + \frac{M^4}{8}(1+\nu)^2\{f\bar{f}'^2 + 2ff'\bar{f}' + f''(\bar{f}^2 - f^2)\} + \frac{M^4}{8}\nu^2 f'^2 f''(\bar{\zeta}^2 - \zeta^2) \\ + \frac{M^2}{2}\nu f' f_2'(\bar{\zeta}-\zeta) + \frac{M^2}{2}(1+\nu)\{f_2'(\bar{f}-f) + f'\bar{f}_2 + \int \bar{f}'\bar{f}_2' d\bar{\zeta}\} \,, \qquad (6.3)$$

where

$$A' = A + \frac{M^4}{4}\nu(1+\nu), \qquad B' = B + \frac{M^4}{8}(1+\nu)(1+2\nu) \,,$$

$$C' = C + \frac{M^4}{8}(5+10\nu+6\nu^2) \,. \qquad (6.4)$$

(Of course, $f_3(\zeta)$ in (6.1) then undergoes some modification.)
Thus we can avoid the singularities at $Z=\pm 1$, which are caused by differentiation of $df/d\zeta$ and f_2 with respect to ζ.

Put

$$G_3(\zeta_P, \bar{\zeta}_P) = \phi_3(\theta) + i\chi_3(\theta) \,,$$

$$H_{2,1}(e^{i\theta}, e^{-i\theta}) = P_{2,1}(\theta) + iQ_{2,1}(\theta) \,,$$

$$H_3(e^{i\theta}, e^{-i\theta}) = P_3(\theta) + iQ_3(\theta) \,. \qquad (6.5)$$

Then we obtain a relation similar to that for the case of ϕ_2;

$$\phi_3(\theta) = [P_{2,1}(\theta) - Q_{2,1}{}^*(\theta)] + [P_3(\theta) - Q_3{}^*(\theta)] + \chi_3{}^*(\theta) \,. \qquad (6.6)$$

In deriving (6.6) the same discussion as asserted in § **5** has been made with $f_3(\zeta)$. From the the boundary condition (2.18)

$$\chi_3(\theta) = -\frac{1}{\mu^2} b_3(\theta) = -\frac{3}{32}\left(\frac{1}{\mu} - 1\right)t^3\{2\mu\sin\theta + (3-2\mu)\sin 3\theta \\ + (1-2\mu)\sin 5\theta - 2(1-\mu)\sin 7\theta\} \,, \qquad (6.7)$$

and from (5.1)

$$P_{2,1}(\theta) - Q_{2,1}{}^*(\theta) = \frac{3M^2}{32\mu}(1+\nu)t^3\left(-2\cos\theta + \cos 3\theta + \frac{6}{5}\cos 5\theta - \frac{9}{7}\cos 7\theta\right) . \qquad (6.8)$$

In order to calculate $P_3(\theta) - Q_3{}^*(\theta)$, it is convenient to tabulate $H_3(e^{i\theta}, e^{-i\theta})$ term by term in the following way:

Constant factor	Value on the surface
i) A'	$f'^3(\bar{\zeta}-\zeta)=O(\varepsilon^4)$
ii) B'	$\int \bar{f}'^3 d\bar{\zeta}=3\beta\left(\frac{1}{5}e^{3i\theta}-\frac{1}{7}e^{7i\theta}\right)$
iii) $3B'$	$f'^2\bar{f}=\cdots$
iv) C'	$f'\int \bar{f}'^2 d\bar{\zeta}=3\beta\left(\frac{1}{3}e^{i\theta}-\frac{1}{5}e^{3i\theta}\right)$
v) $M^4\nu(1+\nu)/12$	$\bar{f}'^3\zeta=-3\beta(e^{5i\theta}+e^{7i\theta})$
vi) $M^4\nu(1+\nu)/8$	$f'\bar{f}'^2\zeta=-3\beta(e^{i\theta}+e^{3i\theta})$
vii) $M^4\nu(1+\nu)/4$	$f'f''(\bar{f}\bar{\zeta}-f\zeta)=\cdots$
viii) $M^4(1+\nu)^2/8$	$f\bar{f}'^2=-\beta(e^{i\theta}-3e^{3i\theta})$
ix) $M^4(1+\nu)^2/4$	$ff'\bar{f}'=\cdots$
x) $M^4(1+\nu)^2/8$	$f''(\bar{f}^2-f^2)=\frac{2}{3}\beta(-5e^{i\theta}+e^{3i\theta}+\cdots)$
xi) $M^4\nu^2/8$	$f'^2f''(\bar{\zeta}^2-\zeta^2)=O(\varepsilon^4)$
xii) $M^2\nu/2$	$f'f_2'(\bar{\zeta}-\zeta)=O(\varepsilon^4)$
xiii) $M^2(1+\nu)/2$	$f_2'(\bar{f}-f)=(t^3/2\mu)(F_1e^{i\theta}+\cdots)$
xiv) $M^2(1+\nu)/2$	$f'\bar{f}_2=(-3t^3/2\mu)(F_3e^{i\theta}+F_5e^{3i\theta}+\cdots)$
xv) $M^2(1+\nu)/2$	$\int \bar{f}'\bar{f}_2' d\bar{\zeta}=(-3t^3/2\mu)\left(\frac{1}{3}F_1e^{3i\theta}+\frac{3}{5}F_3e^{5i\theta}+\frac{5}{7}F_5e^{7i\theta}\right)$,

where $\beta=9t^3/16\mu^3$, and dots denote the terms which involve negative powers of $e^{i\theta}$; for, when $P_3(\theta)-Q_3^*(\theta)$ is sought, we require only the terms involving positive powers of $e^{i\theta}$. In general let a function $g(Z)$ be a Laurent series

$$g(Z)=\sum_{n=-\infty}^{\infty} c_nZ^n\ ,\quad c_n=a_n+ib_n\ ,$$

and assume the form $g(e^{i\theta})=h(\theta)+ik(\theta)$ on the unit circle. Then we can easily verify that

$$h(\theta)-k^*(\theta)=a_0+2\sum_{n=1}^{\infty}(a_n\cos n\theta-b_n\sin n\theta)\ . \tag{6.9}$$

Since $b_n=0$ and $a_{2n}=0$ in the present case, the formula (6.9) enables us to obtain

$$\left.\begin{aligned} P_3(\theta)-Q_3^*(\theta)&=2\sum_{n=0}^{3} a_{2n+1}\cos(2n+1)\theta\\ &=t^3(S_1\cos\theta+S_3\cos 3\theta+S_5\cos 5\theta+S_7\cos 7\theta)\ ,\\ \text{where}\qquad&\\ S_1&=\frac{M^2}{2\mu}(1+\nu)(F_1-3F_3)-\frac{27M^4}{64\mu^3}\nu(1+\nu)-\frac{39M^4}{64\mu^3}(1+\nu)^2+\frac{9}{8\mu^3}C'\ ,\\ S_3&=-\frac{M^2}{2\mu}(1+\nu)(F_1+3F_5)-\frac{27M^4}{64\mu^3}z(1+\nu)+\frac{33M^4}{64\mu^3}(1+\nu)^2-\frac{27}{40\mu^3}C'\ ,\\ S_5&=-\frac{9M^2}{10\mu}(1+\nu)F_3-\frac{9M^4}{32\mu^3}\nu(1+\nu)+\frac{27}{40\mu^3}B'\ ,\\ S_7&=-\frac{15M^2}{14\mu}(1+\nu)F_5-\frac{9M^4}{32\mu^3}\nu(1+\nu)-\frac{27}{56\mu^3}B'\ . \end{aligned}\right\} \tag{6.10}$$

Substitution of (6.7), (6.8) and (6.10) into (6.6) yields

$$\phi_3(\theta)=t^3(T_1\cos\theta+T_3\cos 3\theta+T_5\cos 5\theta+T_7\cos 7\theta)\,,$$

with

$$\left.\begin{aligned}
T_1&=\frac{3}{16}\frac{M^2}{\mu}+\frac{3}{64}(1+18\kappa)\frac{M^4}{\mu^3}+\frac{3\kappa}{64}(11+24\kappa)\frac{M^6}{\mu^5}+\frac{3}{4}\kappa^2\frac{M^8}{\mu^7}+\frac{3}{32}N-\frac{3}{16}\left(\frac{1}{\mu}-1\right),\\
T_3&=-\frac{27}{160}\frac{M^2}{\mu}-\frac{3}{320}(3+52\kappa)\frac{M^4}{\mu^3}-\frac{9\kappa}{320}(11+24\kappa)\frac{M^6}{\mu^5}\\
&\qquad\qquad-\frac{9\kappa^2}{20}\frac{M^8}{\mu^7}-\frac{3}{32}N+\frac{15}{32}\left(\frac{1}{\mu}-1\right),\\
T_5&=-\frac{39}{160}\frac{M^2}{\mu}+\frac{9}{320}(3+4\kappa)\frac{M^4}{\mu^3}+\frac{9\kappa}{320}(9+8\kappa)\frac{M^6}{\mu^5}\\
&\qquad\qquad+\frac{9\kappa^2}{40}\frac{M^8}{\mu^7}+\frac{27}{160}N+\frac{9}{32}\left(\frac{1}{\mu}-1\right),\\
T_7&=\frac{15}{56}\frac{M^2}{\mu}-\frac{9}{448}(3+2\kappa)\frac{M^4}{\mu^3}-\frac{9\kappa}{448}(9+8\kappa)\frac{M^6}{\mu^5}-\frac{9\kappa^2}{56}\frac{M^8}{\mu^7}-\frac{45}{224}N-\frac{3}{8}\left(\frac{1}{\mu}-1\right),
\end{aligned}\right\}\tag{6.11}$$

where

$$\kappa=\frac{1}{4}(\gamma+1)\,,\tag{6.12}$$

$$N=\frac{M^2}{\mu^2}+\kappa\frac{M^4}{\mu^4}\,.\tag{6.13}$$

§ 7. Velocity Distribution

If the line element ds is taken along the surface in the positive sense, the velocity $q(\vartheta)$ can be calculated by means of the relation

$$\frac{1}{U}q(\vartheta)=-\frac{1}{U}\frac{d\Phi}{ds}=-\frac{d}{ds}\{\cos\vartheta+\phi_1(\theta)+\phi_2(\theta)+\phi_3(\theta)\}\,.\tag{7.1}$$

To this end it is necessary to know ϕ_1, ϕ_2 and ϕ_3 as functions of ϑ. Using the expressions for δ in § **3**, we have

$$\left.\begin{aligned}
\cos\theta&=\cos\vartheta+\frac{\mu t}{4}(\cos\vartheta-\cos 3\vartheta)-\frac{\mu t^2}{16}\{2\mu\cos\vartheta+(3-2\mu)\cos 3\vartheta+3\cos 5\vartheta\}+O(\varepsilon^3)\,,\\
\cos 3\theta&=\cos 3\vartheta+\frac{3}{4}\mu t(\cos\vartheta-\cos 5\vartheta)-\frac{3}{16}\mu t^2\{(3-\mu)\cos\vartheta+3\mu\cos 3\vartheta\\
&\qquad\qquad-\mu\cos 5\vartheta-(3+\mu)\cos 7\vartheta\}+O(\varepsilon^3)\,,\\
\cos 5\theta&=\cos 5\vartheta+\frac{5}{4}\mu t(\cos 3\vartheta-\cos 7\vartheta)+O(\varepsilon^2)\,,\\
\cos 7\theta&=\cos 7\vartheta+O(\varepsilon)\,.
\end{aligned}\right\}\tag{7.2}$$

Hence one is led to

$$\begin{aligned}\frac{1}{U}\Phi=\cos\vartheta+\frac{t}{4\mu}(3\cos\vartheta-\cos 3\vartheta)+t^2(D_1\cos\vartheta+D_3\cos 3\vartheta+D_5\cos 5\vartheta)\\
+t^3(E_1\cos\vartheta+E_3\cos 3\vartheta+E_5\cos 5\vartheta+E_7\cos 7\vartheta)\,,\end{aligned}\tag{7.3}$$

where

$$D_1=\frac{3}{8}\left(N-\frac{1}{\mu}+1\right),\qquad D_3=-\frac{3}{16}\left(N+\frac{1}{\mu}\right),\qquad D_5=\frac{9}{80}N+\frac{3}{16}\frac{1}{\mu}\,,\tag{7.4}$$

$$\left.\begin{aligned}
E_1&=\frac{3}{64}\frac{M^2}{\mu}+\frac{3}{64}(1+17\kappa)\frac{M^4}{\mu^3}+\frac{3\kappa}{64}(11+24\kappa)\frac{M^6}{\mu^5}+\frac{3}{4}\kappa^2\frac{M^8}{\mu^7}+\frac{3}{32}N-\frac{3}{32}\left(\frac{1}{\mu}-1\right),\\
E_3&=-\frac{9}{320}\frac{M^2}{\mu}-\frac{3}{320}(3+47\kappa)\frac{M^4}{\mu^3}-\frac{9\kappa}{320}(11+24\kappa)\frac{M^6}{\mu^5}-\frac{9\kappa^2}{20}\frac{M^8}{\mu^7}-\frac{3}{32}N+\frac{3}{8\mu}-\frac{9}{32},\\
E_5&=\frac{27}{320}\frac{M^2}{\mu}+\frac{27}{320}(1+3\kappa)\frac{M^4}{\mu^3}+\frac{9\kappa}{320}(9+8\kappa)\frac{M^6}{\mu^5}+\frac{9\kappa^2}{40}\frac{M^8}{\mu^7}+\frac{27}{160}N+\frac{3}{32\mu},\\
E_7&=-\frac{27}{448}\frac{M^2}{\mu}-\frac{27}{448}(1+3\kappa)\frac{M^4}{\mu^3}-\frac{9\kappa}{448}(9+8\kappa)\frac{M^6}{\mu^5}-\frac{9\kappa^2}{56}\frac{M^8}{\mu^7}-\frac{45}{224}N-\frac{3}{16\mu}.
\end{aligned}\right\}\qquad(7.5)$$

Now differentiation of (3.1) and (3.2) with respect to ϑ gives

$$\frac{d\vartheta}{ds}=\left[\left(\frac{d\xi_{\mathrm{P}}}{d\vartheta}\right)^2+\frac{1}{\mu^2}\left(\frac{d\eta_{\mathrm{P}}}{d\vartheta}\right)^2\right]^{-1/2}=\frac{1}{\sin\vartheta}\left[1-\frac{9t^2}{16}(1-\cos 4\vartheta)+\frac{9t^3}{32}(2+5\cos 2\vartheta-2\cos 4\vartheta-5\cos 6\vartheta)\right],\qquad(7.6)$$

while differentiating (7.3) with respect to $\cos\vartheta$, we get

$$\begin{aligned}
-\frac{1}{\sin\vartheta}\cdot\frac{1}{U}\frac{d\Phi}{d\vartheta}&=1-\frac{3t}{2\mu}\cos 2\vartheta+t^2\{(D_1+3D_3+5D_5)+2(3D_3+5D_5)\cos 2\vartheta+10D_5\cos 4\vartheta\}\\
&\quad+t^3\{(E_1+3E_3+5E_5+7E_7)+2(3E_3+5E_5+7E_7)\cos 2\vartheta+2(5E_5+7E_7)\cos 4\vartheta+14E_7\cos 6\vartheta\}.\qquad(7.7)
\end{aligned}$$

Thus using (7.1), (7.6) and (7.7), we finally arrive at the expression for the velocity distribution

$$\frac{1}{U}q(\vartheta)=1-\frac{3t}{2\mu}\cos 2\vartheta+\frac{1}{U}q_2(\vartheta)+\frac{1}{U}q_3(\vartheta),\qquad(7.8)$$

with

$$\frac{1}{U}q_2(\vartheta)=t^2\left[\left(\frac{3}{8}N-\frac{3}{16}\right)+\frac{3}{4\mu}\cos 2\vartheta+\left(\frac{9}{8}N+\frac{15}{8}\frac{1}{\mu}+\frac{9}{16}\right)\cos 4\vartheta\right],\qquad(7.9)$$

$$\begin{aligned}
\frac{1}{U}q_3(\vartheta)=-t^3\Bigg[&\left\{\frac{3}{80}\frac{M^2}{\mu}+\frac{3}{80}(1+14\kappa)\frac{M^4}{\mu^3}+\frac{3\kappa}{80}(11+24\kappa)\frac{M^6}{\mu^5}+\frac{3}{5}\kappa^2\frac{M^8}{\mu^7}+\frac{3}{4}N-\frac{3}{16}\left(\frac{1}{\mu}-1\right)\right\}\\
&+\left\{\frac{27}{160}\frac{M^2}{\mu}+\frac{9}{160}(3+47\kappa)\frac{M^4}{\mu^3}+\frac{27\kappa}{160}(11+24\kappa)\frac{M^6}{\mu^5}+\frac{27}{10}\kappa^2\frac{M^8}{\mu^7}+\frac{27}{16}N-\frac{63}{64}\frac{1}{\mu}+\frac{9}{32}\right\}\cos 2\vartheta\\
&+\left\{\frac{9}{8}N+\frac{27}{16}\frac{1}{\mu}+\frac{9}{16}\right\}\cos 4\vartheta\\
&+\left\{\frac{27}{32}\frac{M^2}{\mu}+\frac{27}{32}(1+3\kappa)\frac{M^4}{\mu^3}+\frac{9\kappa}{32}(9+8\kappa)\frac{M^6}{\mu^5}+\frac{9}{4}\kappa^2\frac{M^8}{\mu^7}+\frac{45}{16}N+\frac{195}{64}\frac{1}{\mu}+\frac{45}{32}\right\}\cos 6\vartheta\Bigg].
\end{aligned}\qquad(7.10)$$

The maximum velocity q_{max} is obtained by putting $\vartheta=\pi/2$ in the above expressions. Thus

$$\begin{aligned}
\frac{1}{U}q_{max}=1+\frac{3t}{2\mu}+t^2\left(\frac{3}{2}N+\frac{9}{8}\frac{1}{\mu}+\frac{3}{8}\right)+t^3\Bigg\{&\frac{39}{40}\frac{M^2}{\mu}+\frac{3}{40}(13+62\kappa)\frac{M^4}{\mu^3}\\
&+\frac{3\kappa}{40}(53+72\kappa)\frac{M^6}{\mu^5}+\frac{87}{20}\kappa^2\frac{M^8}{\mu^7}+\frac{21}{8}N+\frac{9}{16}\frac{1}{\mu}+\frac{15}{16}\Bigg\}.
\end{aligned}\qquad(7.11)$$

These expressions for the velocity distribution around a Kaplan bump and the maximum value of the velocity can be verified to coincide with those reported in Ref. 8).

The author wishes to express his sincere thanks to Prof. Isao Imai for his continual guidance throughout this work. He is also indebted to Dr. H. Hasimoto for his advice in the course of calculation.

References

1) I. Imai: Rep. Aeron. Res. Inst., Tokyo Imp. Univ. No. 294 (1944).
2) I. Imai and S. Ôyama: Rep. Inst. Sci. Tech., Univ. Tokyo **2** (1948) 37.
3) I. Imai and S. Ôyama: ibid **2** (1948) 39.
4) H. Hasimoto: Journ. Phys. Soc. Japan **7** (1952) 322.
5) S. Asaka: Natural Sci. Rep., Ochanomizu Univ. **4** (1953) 213.
6) S. Asaka: ibid **5** (1954) 59.
7) S. Asaka: Journ. Phys. Soc. Japan **10** (1955) 482.
8) C. Kaplan: N. A. C. A. Tech. Rep. No. 768 (1943).

Short Notes

J. PHYS. SOC. JAPAN **10** (1955) 822~823

Interaction Between Slip Bands and Particles of Precipitate in an Aluminium Alloy

By Shigeyasu KODA and Taro TAKEYAMA
Faculty of Engineering, Hokkaido University

(Received May 9, 1955)

The cause of hardening in age-hardenable alloys is considered that the movement of dislocations is interfered by local segregation of solute atoms (Guinier-Preston aggregates) or precipitation of the intermeadiate phase which is coherent to the parent lattice.[1] From this point of view, we tried to observe by the electron microscope how slip bands are affected by particles of precipitate. The specimen is a polycrystalline aluminium alloy of 4% copper, and its shape is a sheet of 0.5 mm in thickness. It was age-hardened at 250°C for 2.5 hrs after water quenching from 530°C, stretched about 1% in length, and then prepared the replica for the electron microscope by the ordinary anodic oxiding process. By this heat-treatment the alloy may be at a little over-aged state.[2]

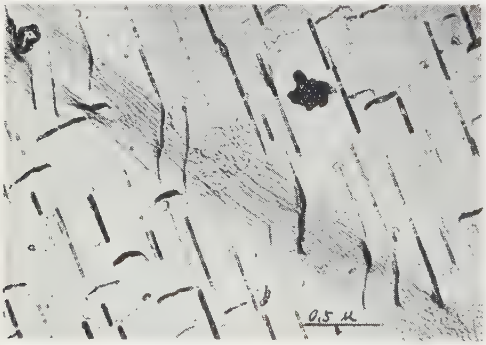

Fig. 1.

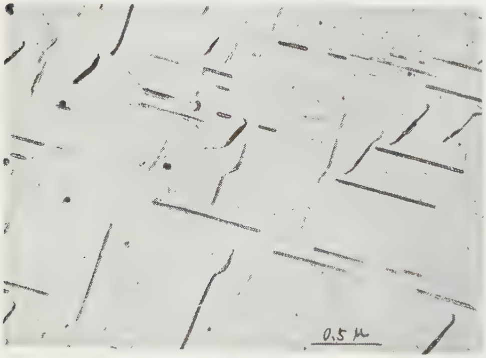

Fig. 2.

From the electron micrographs obtained, we may conclude the following characteristics. (Figs. 1, 2)

(1) Slip bands are not a sharp and distinct line, but are composed of many elementary slip lines, i.e. the slip bands have a fine structure of Heidenreich-Shockley type.[3]

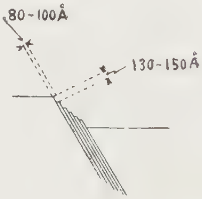

Fig. 3.

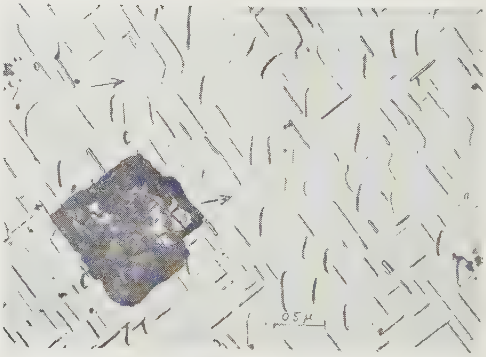

Fig. 4.

Table I.

Total Slip Distance of a Band (Å)	2640	2680	2580	1165	1110	815	890	1515	1465
Total Slip Interval of a Band (Å)	1390	1490	1440	745	750	415	555	1040	1440
Number of Elementary Slip Lines	18 or 17	18 or 17	18 or 17	9 or 8	9 or 8	6	7 or 6	13 or 12	13
Mean Slip Distance of each Elementary Slip (Å)	~150	~160	~150	~140	~130	~135	~140	~120	~110
Mean Interval between Elementary Slips (Å)	~85	~90	~90	~100	~100	~80	~100	~85	~120

(2) The length of each slip band is short. Appearently they are broken into about 2–3 microns in length.

(3) The plate-like particles of precipitate are bent by slip bands. This indicates the dislocations can pass through the particles.

Moreover in our case we know the fact that the plate-like precipitates are the intermeadiate phase and are formed on the {100} planes of the parent lattice.[4] So we can determine the orientation of the surface of the specimen by means of stereographic analysis.[5] And we know also the slip planes are {111} planes and slip directions <110>, so we can determine the active slip plane and the active slip direction from the change of shape of plate-like particles. Thus we can draw the true three-dimentional shape of slip bands which are composed of many elementary slips, and can determine the mean slip distances and intervals of them. The results are shown in Table I and Fig. 3.

Finally, as shown in Fig. 4, these bent particles of precipitate were observed on the specimen which was dissolved by electropolishing over 0.1 mm in thickness (of course we cannot see any slip band), so in our case the slip bands in the interior of the alloy have the same structure as on the surface.

References

1) N. F. Mott and F. R. N. Nabarro: Report of a Conference of Strength of Solids (Phys. Soc., London) 1948, p. 1.
J. C. Fisher, E. W. Hart and R. H. Pry: Acta Metall. **1** (1953) 336.
Recently one of the authors proposed a theory of age-hardening; Bulletin of the Fac. of Eng. Hokkaido Univ. No. 11 (1954) 157.
2) M. L. V. Gayler and R. Parkhouse: J. Inst. Metals **66** (1940) 67.
J. Calvet, P. Jacquet and A. Guinier: J. Inst. Metals **65** (1939) 121.
H. K. Hardy: J. Inst. Metals **79** (1951) 321.
3) R. D. Heidenreich and W. Shockley: J. Appl. Phys. **18** (1947) 1029; Report of a Conference on the Strength of Solids, 1948, p. 57.
4) D. Preston: Phil. Mag. **26** (1938) 855.
5) C. S. Barrett: Structure of Metals, 1952, p. 39.

J. Phys. Soc. Japan **10** (1955) 823~824

On Upper and Lower Bounds of the Eigenvalues of a Free Plate

By Yoshimoto Nakata and Hiroshi Fujita

Department of Physics, Faculty of Science, University of Tokyo

(Received June 9, 1955)

The present note is concerned with the vibration of a thin elastic plate in the xy-plane bounded by a sufficiently regular contour C. In case of free edges, the vertical deformation satisfies the differential equation (1) in D, the interior of C, and is subjected to the boundary conditions (2) on C:[1]

$$\Delta\Delta w=\lambda_0{}^2 w \qquad \text{in } D\,, \tag{1}$$

$$\left.\begin{aligned} &\frac{\partial}{\partial n}\left[\Delta w+(1-\mu)\frac{\partial^2 w}{\partial s^2}\right]=0 \quad \text{on } C\,,\\ &\mu\Delta w+(1-\mu)\frac{\partial^2 w}{\partial n^2}=0 \quad \text{on } C\,,\end{aligned}\right\} \tag{2}$$

where $\mu(0\leqq\mu<1)$ denotes Poisson's ratio and $\partial/\partial n$ and $\partial/\partial s$ have their usual meanings. We intend to calculate the upper and lower bounds of λ_0, the positive square root of an eigenvalue $\lambda_0{}^2$.

Once the above differential system (1) (2) is reduced to the form $T^*Tw=\lambda_0{}^2 w$ by a suitable choice of the operator T between Hilbert spaces and, T^* being the adjoint of T, then the following approximating theorem[2] is applicable.

Kato's Theorem. Let an open interval $0\leqq\alpha<\lambda<\beta$ contain no square roots of any eigenvalues but λ_0. Let u and v be trial vectors belonging to the domains of T and T^* respectively and normalized as $\|u\|=\|v\|=1$, $\eta=(Tu,v)\geqq0$. Then we have the following estimate of λ_0.

$$\eta-\frac{\varepsilon^2}{\beta-\eta}\leqq\lambda_0\leqq\eta+\frac{\varepsilon^2}{\eta-\alpha} \tag{3}$$

where $\qquad \varepsilon^2=(\|Tu\|^2+\|T^*v\|^2)/2-\eta^2\,.$

It is remarked that as for the smallest eigenvalue the estimation $\lambda_0\leqq\|Tu\|$ by the Rayleigh's principle is more convenient than the right inequality of (3) in most cases. We perform the decomposition of the operator[3] as follows. Denoting by $L^2(D:\rho)$ the Hilbert space consisting of functions in $L^2(D)$ with the inner product defined by the integral with the density ρ, we construct two Hilbert spaces $\mathfrak{H}$

and $\mathfrak{H}'$ as

$$\mathfrak{H}=L^2(D:1)$$

$$\mathfrak{H}'=L^2(D:\mu)\times L^2(D:1-\mu)\times L^2(D:1-\mu)\times L^2(D:2-2\mu)\,.$$

Let T be the operator from $\mathfrak{H}$ to $\mathfrak{H}'$ such that

$$Tu=\left(\Delta u\,,\ \frac{\partial^2 u}{\partial x^2}\,,\ \frac{\partial^2 u}{\partial y^2}\,,\ \frac{\partial^2 u}{\partial x\partial y}\right).$$

A function u belonging to the domain of T must satisfy certain conditions of regularity but is free from any boundary conditions. Then it is seen that the domain of T^* is the set of 4-component vector functions $v=(v_1, v_2, v_3, v_4)$ which obey, besides some conditions of regularity, the boundary conditions

$$P(v)+\frac{\partial}{\partial s}R(v)=0\,,\quad Q(v)=0\quad\text{on } C \tag{4}$$

where

$$P(v)=\mu\frac{\partial v_1}{\partial n}+(1-\mu)\left\{\frac{\partial v_2}{\partial x}n_x+\frac{\partial v_3}{\partial y}n_y+\frac{\partial v_4}{\partial x}n_y+\frac{\partial v_4}{\partial y}n_x\right\}\,,$$

$$Q(v)=\mu v_1+(1-\mu)\{v_2 n_x{}^2+v_3 n_y{}^2+2v_4 n_x n_y\}\,,$$

$$R(v)=(1-\mu)\{v_2 s_x n_x+v_3 s_y n_y+v_4(s_x n_y+s_y n_x)\}\,,$$

(n_x, n_y)=unit normal vector,
(s_x, s_y)=unit tangential vector.

Furthermore, we have

$$T^*v=\mu\Delta v_1+(1-\mu)\left(\frac{\partial^2 v_2}{\partial x^2}+\frac{\partial^2 v_3}{\partial y^2}+2\frac{\partial^2 v_4}{\partial x\partial y}\right).$$

The equivalence between the differential system (1) (2) and the equation $T^*Tw=\lambda_0{}^2 w$ can be easily verified.

As a numerical example we treat the case where C is the square with vertices at (1, 1), (−1, 1), (−1, −1), (1, −1), and calculate the bounds of the eigenvalue corresponding to the vibration with its nodal line coincident with two coordinate axes. In consideration of the symmetry and physical analogy we put $u=\|u'\|^{-1}\cdot u'$,

$$u'=\frac{3}{2}xy+a\{xf(y)+yf(x)\}$$

where a is a constant to be determined later and $f(x)$ is the corresponding approximate eigenfunction of a vibrating bar[4], i.e.,

$$f(x)=\sin\frac{5\pi}{4}x-\left(\sqrt{2}\sinh\frac{5\pi}{4}\right)^{-1}\cdot\sinh\frac{5\pi}{4}x\,.$$

In this case v must satisfy, besides (4), a subsidiary condition ($v=0$) at vertices of C owing to the lack of smoothness.[1][4] In accordance with these conditions we set $v=\|v'\|^{-1}\cdot v'$,

$$v_1'=\frac{\mu-1}{\mu}(1-b)xy\,,\qquad v_2'=y(x^3-bx)\,,$$

$$v_3'=x(y^3-by)\,,\qquad v_4'=1-\frac{x^2+y^2}{2}\,,$$

where b is a constant to be determined later. Poisson's ratio μ is taken to be 0.225 for the convenience of comparison with the results of Ritz[4]. We calculate the upper bound by the Rayleigh's principle. In obtaining the lower bound by the left inequality of (3), we adopt $\beta=18.5$ which seems to be sufficiently smaller than the approximate value of the square root of the next eigenvalue according to Ritz[4]. Making use of these quantities and choosing a and b to get good approximation, we arrive, finally, at

$$3.418<\lambda_0<3.554\,.$$

All detailed discussions and calculations will be published later.

References

1) K. O. Friedrichs: Math. Ann. **98** (1927) 205.
2) T. Kato: Math. Ann. **126** (1953) 253.
3) H. Fujita: J. Phys. Soc. Japan **10** (1955) 1.
4) W. Ritz: Ann. Phys. **28** (1909) 737.

J. PHYS. SOC. JAPAN **10** (1955) 824~825

Some Coefficients of the Series Expansion of the TFD Function

By Shigehiro KOBAYASHI
Department of Physics, Kagawa University, Takamatsu

(Received June 17, 1955)

The TFD (Thomas-Fermi-Dirac) function, i.e. the solution of the TFD equation $\psi''=x[\varepsilon+(\psi/x)^{1/2}]^3$ subject to the boundary condition $\psi(0)=1$, can be expanded about the origin in a semi-convergent power series such as $\psi=\sum_{n=0}^{\infty}a_n x^{n/2}$, where the coefficients up to a_{11} were previously tabulated by Metropolis and Reitz[1]. Now, the present author has calculated further the coefficients a_{12} to a_{17} with the intention that one can check the corresponding coefficients of the series expansion of the TF function as their special cases, which were recently needed by the present author *et al*[2] in the most accurate evaluation of the TF function. The expressions of a_{12} to a_{17} are as follows.

$$a_{12}=\frac{4}{405}+\frac{4}{1575}a_2{}^3+\left(\frac{1}{21}a_2\varepsilon+\frac{8}{525}a_2{}^2\varepsilon^2+\frac{509}{5040}\varepsilon^3-\frac{2}{175}a_2\varepsilon^4\right),$$

$$a_{13}=-\frac{557}{100100}a_2{}^2-\frac{3}{9152}a_2{}^5+\left(\frac{272}{9009}\varepsilon+\frac{47}{48048}a_2{}^3\varepsilon+\frac{21457}{400400}a_2\varepsilon^2-\frac{15}{4576}a_2{}^4\varepsilon^2+\frac{41}{4004}a_2{}^2\varepsilon^3+\frac{149}{6600}\varepsilon^4-\frac{1}{286}a_2\varepsilon^5\right),$$

$$a_{14}=\frac{4}{693}a_2-\frac{29}{24255}a_2{}^4+\Big(\frac{211}{26950}a_2{}^2\varepsilon+\frac{1711}{38808}\varepsilon^2$$
$$-\frac{232}{24255}a_2{}^3\varepsilon^2+\frac{74363}{1940400}a_2\varepsilon^3$$
$$+\frac{1}{147}a_2{}^2\varepsilon^4-\frac{1517}{277200}\varepsilon^5\Big),$$

$$a_{15}=\frac{101}{52650}-\frac{623}{351000}a_2{}^3+\frac{7}{49920}a_2{}^6+\Big(\frac{1916}{135135}a_2\varepsilon$$
$$-\frac{43}{54912}a_2{}^4\varepsilon-\frac{557911}{72072000}a_2{}^2\varepsilon^2+\frac{7}{4160}a_2{}^5\varepsilon^2$$
$$+\frac{896903}{21621600}\varepsilon^3-\frac{9}{1144}a_2{}^3\varepsilon^3+\frac{438893}{18018000}a_2\varepsilon^4$$
$$+\frac{1}{520}a_2{}^2\varepsilon^5-\frac{1369}{257400}\varepsilon^6\Big),$$

$$a_{16}=-\frac{46}{45045}a_2{}^2+\frac{68}{105105}a_2{}^5+\Big(\frac{3481}{540540}\varepsilon$$
$$-\frac{104413}{38012975}a_2{}^3\varepsilon+\frac{225137}{27747720}a_2\varepsilon^2+\frac{136}{21021}a_2{}^4\varepsilon^2$$
$$-\frac{78089}{3853850}a_2{}^2\varepsilon^3+\frac{69047}{2217600}\varepsilon^4-\frac{12}{2695}a_2{}^3\varepsilon^4$$
$$+\frac{15323}{1101100}a_2\varepsilon^5-\frac{1}{660}\varepsilon^7\Big).$$

$$a_{17}=-\frac{113}{1178100}a_2+\frac{153173}{116424000}a_2{}^4-\frac{3}{43520}a_2{}^7$$
$$+\Big(\frac{81773}{71471400}a_2{}^2\varepsilon+\frac{305}{622366}a_2{}^5\varepsilon$$
$$+\frac{39993240031}{3199488692400}\varepsilon^2+\frac{310983079}{33297264000}a_2{}^3\varepsilon^2$$
$$-\frac{63}{65280}a_2{}^6\varepsilon^2-\frac{55975069}{5145940800}a_2\varepsilon^3$$
$$+\frac{13225}{2333760}a_2{}^4\varepsilon^3-\frac{183913487}{8576568000}a_2{}^2\varepsilon^4$$
$$+\frac{302233}{14137200}\varepsilon^5-\frac{1}{816}a_2{}^3\varepsilon^5+\frac{1822471}{306306000}a_2\varepsilon^6$$
$$-\frac{1}{6120}\varepsilon^8\Big).$$

The bracketed parts in these expressions are proper to the TFD function.

The author wishes to express his sincere thanks to Professor Umeda for his kind guidance. This work was supported by the Scientific Research Expenditure administered by the Ministry of Education.

References

1) N. Metropolis and J. R. Reitz: J. Chem. Phys. **19** (1951) 555.
2) S. Kobayashi, T. Matsukuma, S. Nagai and K. Umeda: J. Phys. Soc. Japan **10** (1955) 759.

J. Phys. Soc. Japan **10** (1955) 825~826

Ultraviolet Absorption Spectra of Uranium Glasses

By Kikusaburo OSADA

Faculty of Engineering, Nagoya University

(Received July 4, 1955)

It has been known that an absorption band appears near 250 mμ in glasses containing one of heavy metals[1)2)]. But an absorption spectrum of uranium glass has not yet been measured at the shorter wave-length than 400 mμ[3)4)].

Therefore, absorption spectra of thin films of commercial and experimental uranium glass (c.u.g. and e.u.g.) were measured to 180 mμ with a quartz spectrograph. The e.u.g. was prepared by melting a mixture of SiO_2, $NaHCO_3$, and $UO_2(CH_3CO_2)_2$ in proportion corresponding to the formula $3Na_2O \cdot 7SiO_2 \cdot 0.2UO_3$. The results obtained are shown in Fig. 1.

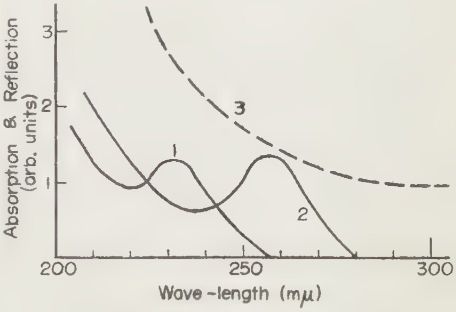

Fig. 1. Absorption (solid line) and reflection (broken line) of uranium glasses. (1), (3) commercial; (2) experimental.

The spectrum of the c.u.g. shows a band with a maximum at 230 mμ and the e.u.g. at 257 mμ.

The relative reflectivity of a plate of the c.u.g. was also measured to 220 mμ under an angle of about 45°. The relative intensity of light source was determined by the reflectivity of aluminium. As shown in Fig. 1, it was found that the reflectivity of the glass increases gradually below 280 mμ. This result is expected from the absorption spectrum of the glass.

When illuminated with ultraviolet radiations, these glasses fluoresce emitting a green light or a yellowish one. So their out see copy spectrograph. Then, as the exciting radiation we used the mercury line 254 mμ[5)] or 366 mμ[6)] isolated by means of a filter.

By the irradiation of the former line, the e.u.g. emits a yellowish light which distributes in the region between 490~650 mμ, while by the latter no emission can be observed. By any radiation the c.u.g. emits a green light which distributes in the region between 490~620 mμ and has a maximum at 520 mμ.

Variation of their fluorescent efficiency with the wave-length was also measured *continuously* in this region by the same method as in the author's previous paper[1], although the efficiency had been known at several discrete points[7]. In the c.u.g. its maxima appear near 390,320, and 235 mμ, and in the e.u.g. near 260 mμ. The maximum at 235 or 260 mμ appears near the maximum of the absorption spectrum respectively.

It has been considered that uranium in glass is present in two kinds of state; *i.e.* the one is uranyl groups, and the other uranate groups. When excited with a mercury line at 365 mμ, the former emits a green light and the latter a yellowish one only at low temperatures[3].

On the other hand, the uranyl acetate emits a yellowish light by the excitation of the radiation at 254 mμ. This is composed of some bands with maxima near 620, 510, 495, 470 and 455 mμ. This spectrum differs from that of the e.u.g. So the fluorescence of the e.u.g. does not originate from the uranyl acetate.

From these results of the fluorescent phenomena, it may be considered that uranium in the e.u.g. forms uranate groups and in the c.u.g. uranyl groups. So it may be concluded that in uranium glass an absorption band with maximum at 230 mμ originates from uranyl groups and at 257 mμ from uranate groups. And glass containing uranate groups fluoresces emitting a yellowish light at room temperature only when illuminated with a radiation of the shorter wave-length than 300 mμ.

References

1) K. Osada: J. Phys. Soc. Japan **6** (1951) 191; **8** (1953) 226.
2) V. A. Florinskay, A. V. Yakovleva, R. S. Pechenkina and M. K. Ivanova: Izvest. Akad. Nauk. S.S.S.R. Ser. Fiz. **17** (1953) 736.
3) F. A. Kröger, J. M. Stevels and Th. P. J. Botden: Philips Res. Rep. **3** (1948) 46.
4) W. Colbert and N. J. Kreidl: J.O.S.A. **35** (1945) 731.
5) K. Osada: J. Phys. Soc. Japan **9** (1954) 136.
6) Matsuda UV-D1.
7) G. R. Harrison and P. A. Leighton: Phys. Rev. **38** (1931) 899.

J. Phys. Soc. Japan **10** (1955) 826~827

The Thermoluminescence of Glasses

By Takeo Kikuchi

The Institute of Polytechnics,
Osaka City University

(Received July 5, 1955)

With regard to his theory of the electric breakdown of amorphous substances, Fröhlich has suggested that in the glass state there are various shallow traps of electrons, characteristic of its random network structure, under the conduction band[1]. According to the analysis of our previous research in the electric breakdown of glasses, we have guessed the existence of these shallow traps[2]. Recently Yokota has found that the glow curve of fused quartz colored by X-ray irradiation is more complicated than that of the crystal, and he has emphasized that this is related to the properties characteristic of glass structure[3].

In this experiment, we observed the thermoluminescence of glasses at the temperature range from −150°C to 300°C. The specimen whose composition is $0.6Na_20\cdot 2SiO_2$, prepared from pure quartz powder[4], was irradiated with X-ray (40KV, 12 mA, W-target) for 4 hours, at −150°C. After irradiation, the temrerature was raised at the rate of 5°C per minute and the intensity of the thermoluminescence was detected by a photomultiplier and recorded.

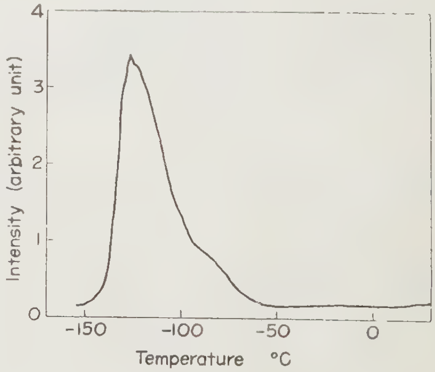

Fig. 1. The glow curve of glass irradiated at −150°C.

Fig. 1 shows the glow curve thus obtained. The same specimen irradiated at room temperature showed the glow curve as Fig. 2. It is found that these curves consist of two groups, each of which has several peaks, centered at about −120°C and 150°C. Corresponding to these peaks, we can consider that this specimen has two groups of traps, shallow and deep, apart each other.

The depth of the trap E may be obtained by[5]

$$E=kT^*\ln S\{1+\ln(kT^{*2}/\beta E)/\ln S\}\ ,$$

where k is Boltzmann constant, T^* the temperature of maximum glow and β the rate of temperature raise. Assuming S, the jumping factor to be 10^9 per second, we find the depths of shallow traps lie between about 0.32～0.43 eV. and the deep ones between about 0.82～1.16 eV. These agree approximately with the values estimated from our experiments of the electric breakdown. As described above, we expect that these traps are related to the network structure of glass.

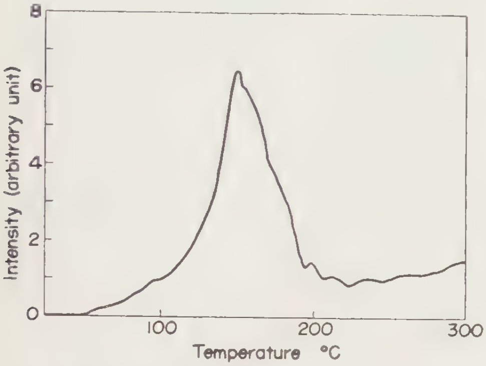

Fig. 2. The glow curve of glass irradiated at room temperature.

The absorption bands are all completely bleached after heated to 350°C.

We also studied the other glasses of more complicated compositions, and found that they exhibit no or at most very weak thermoluminescence. This fact shows that the radiationless transitions are enhanced by the more complicated structure.

The author is indebted to Mr. R. Yokota for his valuable specimen and he also wishes to thank professor H. Kawamura for guidance and counsel through the course of this work.

References

1) H. Fröhlich: Proc. Roy. Soc. **188** (1947) 521.
2) M. Tomura and T. Kikuchi: J. Phys. Soc. Japan **7** (1952) 538.
3) R. Yokota: Phys. Rev. **91** (1953) 1013.
4) This specimen was kindly offered by R. Yokota.
5) J. T. Randall and M. H. F. Wilkins: Proc. Roy. Soc. **A184** (1945) 366.

J. PHYS. SOC. JAPAN **10** (1955) 827～828

On Exact Solution of the Blast Wave Problem

By Akira SAKURAI
Tokyo Electrical Engineering College

(Received July 9, 1955)

Recently J. L. Taylor1) has presented an exact solution of the equations determining the initial stage of a spherical blast wave which was assumed to start at a point. The object of this note is to show that his idea is also useful for the corresponding problems of cylindrical and plane waves and that the same kind of solutions can be obtained for both cases.

The problem under consideration is reduced to finding the solutions $f^{(0)}(x)$, $g^{(0)}(x)$, $h^{(0)}(x)$, $(0 \leqq x \leqq 1)$ satisfying the equations2):

$$\left.\begin{aligned} (f^{(0)}-x)f_x{}^{(0)}+\frac{g_x{}^{(0)}}{\gamma h^{(0)}} &= \frac{\alpha+1}{2}f^{(0)}\,, \\ (x-f^{(0)})\frac{g_x{}^{(0)}}{g^{(0)}} &= \gamma f_x{}^{(0)}+\frac{\alpha\gamma}{x}f^{(0)}-\alpha-1\,, \\ (x-f^{(0)})\frac{h_x{}^{(0)}}{h^{(0)}} &= f_x{}^{(0)}+\frac{\alpha}{x}f^{(0)}\,, \end{aligned}\right\} \qquad (1)$$

supplemented by the boundary conditions:

$$f^{(0)}(1)=\frac{2}{\gamma+1}\,,\quad g^{(0)}(1)=\frac{2\gamma}{\gamma+1}\,,\quad h^{(0)}(1)=\frac{\gamma+1}{\gamma-1}\,, \qquad (2)$$

where α takes on the values 0, 1 and 2 for plane, cylindrical and spherical wave respectively and γ is the ratio of specific heats. These equations were found by G. I. Taylor3) at first for the case of $\alpha=2$ and were solved by a numerical step-by-step method. The solution for $\alpha=0$ was obtained also numerically by the author2) and that for $\alpha=1$ by the author2) and S. C. Lin4).

By combining the above equations (1) and (2), we get the following two intermediate integrals, namely:

$$f^{(0)}=x\left(\frac{f^{(0)2}}{2}+\frac{1}{\gamma}\frac{1}{\gamma-1}\frac{g^{(0)}}{h^{(0)}}\right)\left(\frac{f^{(0)2}}{2}+\frac{1}{\gamma-1}\frac{g^{(0)}}{h^{(0)}}\right)^{-1},$$

or

$$\frac{g^{(0)}}{h^{(0)}}=\frac{\gamma(\gamma-1)}{2}f^{(0)2}\frac{x-f^{(0)}}{\gamma f^{(0)}-x}\,, \qquad (3)$$

and

$$\frac{g^{(0)}}{h^{(0)\gamma-1}}=\frac{2\gamma}{\gamma+1}\left(\frac{\gamma-1}{\gamma+1}\right)^{\gamma}(x-f^{(0)})^{-1}x^{-\alpha}\,, \qquad (4)$$

the first of which was found by Kynch5) and the second by the author2).

J. L. Taylor1) has found that for the case of $\alpha=2$ first order differential equation for $f^{(0)}$ as obtained from the elimination of $g^{(0)}$, $h^{(0)}$ from the above equations (1), (3) and (4) can be solved exactly. Now we shall show that this result can be extended to the general case of any α.

Eliminating $g^{(0)}$ from (3) and (4), we get

$$h^{(0)}=\{4(\gamma+1)^{\gamma+1}(\gamma-1)^{-(\gamma-1)} \times x^{\alpha}f^{(0)2}(x-f^{(0)})^{-2}(\gamma f^{(0)}-x)\}^{1/(2-\gamma)}\,.$$

Taking the logarithmic derivative of this equation and inserting it into the third of equations (1), we have the differential equation for $f^{(0)}$ as

$$\frac{x-f^{(0)}}{2-\gamma}\left\{\frac{\alpha}{x}+\frac{2f_x^{(0)}}{f^{(0)}}-2\frac{1-f_x^{(0)}}{x-f^{(0)}}+\frac{\gamma f_x^{(0)}-1}{\gamma f^{(0)}-x}\right\} =f_x^{(0)}+\frac{\alpha}{x}f^{(0)}\,,$$

which can be easily integrated if we put $f^{(0)}/x=F$ (say) and the result obtained is

$$\begin{aligned}2\log f^{(0)}=&-\frac{\alpha(\alpha+3)(\gamma-1)}{(\alpha+1)\gamma-(\alpha-1)}\log x\\ &+\frac{(\alpha+3)(\gamma-1)}{2\gamma+\alpha-1}\log(\gamma f^{(0)}-x)\\ &-\frac{(\alpha^2+2\alpha+5)\gamma^2+(-3\alpha^2+2\alpha+1)\gamma+4(\alpha^2-1)}{(2\gamma+\alpha-1)\{(\alpha+1)\gamma-(\alpha-1)\}}\\ &\times\log\left|x-\frac{(\alpha+1)\gamma-(\alpha-1)}{\alpha+3}\right|+\log C\,,\end{aligned}$$

where C is a constant to be determined by the condition (2). It is easily verified that this solution is reduced to that of J. L. Taylor for the case of $\alpha=2$.

References

1) J. L. Taylor: Phil. Mag. **46** (1955) 317.
2) A. Sakurai: J. Phys. Soc. Japan, **8** (1953) 662; **9** (1954) 256.
3) G. I. Taylor: Proc. Roy. Soc. London **A201** (1950) 159.
4) S. C. Lin: J. Appl. Phys. **25** (1954) 54.
5) G. J. Kynch: In L. Howarth (editor), *Modern Developments in Fluid Dynamics, High-Speed Flow*, Vol. I (1953).

Errata

Zeeman Splitting of Nuclear Quadrupole Resonance in Paradibromo Benzene

By Shoji KOJIMA, Kineo TSUKADA and Yasushi HINAGA

J. Phys. Soc. Japan **10** (1955) 498~502

The term $\nu_{\rm I}-\nu_{\rm IV}$ in Eqs. (6) and (8) should be multiplied by two. The term $\nu_{\rm I}+\nu_{\rm IV}$ in Eqs. (7) and (8) should be replaced by $\nu_{\rm I}+\nu_{\rm IV}-2\nu_0$. The equation $\nu_{\rm I}-\nu_{\rm IV}=(49.6\pm2)$ kc, which appeared at 6th line of the left column in page 501, must be ammended as $\nu_{\rm I}-\nu_{\rm IV}=(24.8\pm2)$ kc. This establishes agreement with the Fig. 3. The correct equations were used in deriving the results.

JOURNAL OF THE PHYSICAL SOCIETY OF JAPAN Vol. 10, No. 10, OCTOBER, 1955

Rotational Analysis of the CrO Bands

By Masayoshi NINOMIYA

Department of Phisics, Faculty of Sience, University of Tokyo

(Received June 20, 1955)

The (0, 1), (0, 0) and (1, 0) bands of the CrO, which appear in the red and yellow region, are analysed rotationally, and we have been able to show that these bands owe to the transition $^5\Pi - {}^5\Pi$. We have shown the theoretical formulae for the quintet state, which can be applied in the case of nearly (a), and obtained the molecular constants as follows,

$$\begin{aligned} B_e'' &= 0.5286 \pm 0.0002\ \mathrm{cm}^{-1} \\ B_e' &= 0.4750 \pm 0.0002\ \mathrm{cm}^{-1} \\ \alpha'' &= 0.0050\ \mathrm{cm}^{-1} \\ \alpha' &= 0.0057\ \mathrm{cm}^{-1} \\ r_e'' &= 1.627 \times 10^{-8}\ \mathrm{cm} \\ r_e' &= 1.716 \times 10^{-8}\ \mathrm{cm} \\ A'' &= 110\ \mathrm{cm}^{-1} \\ A' &= 100\ \mathrm{cm}^{-1} \end{aligned}$$

§ 1. Introduction

The band spectrum of CrO, which appears in the region between 5500A and 6500A, has been analysed vibrationally by C. Ghosh[1], and he has predicted it as the triplet transition involving Q branches. But as far as we know, no other report on this subject has been published. The present paper is to give a rotational analysis of the (0, I) at λ 6395A, (0, 0) at λ605IA and (I, 0) at λ5794A bands and to present an example of the quintet band for the first time.

§ 2. Experimental Procedure

The source of the spectrum was obtained as usually from the arc between two carbon poles, one of which was of a diameter of 30 mm and had a bored hole of 15 mm charged with chemically pure chromic oxide powder and the other a usual rod of a diameter of 8 mm and between them a direct current of about I5 Amps. was discharged. It was necessary to fill up several times the hole with powder in 2∼4 hours, which were suitable to take a good spectrogram.

Figure Spectrogram of CrO

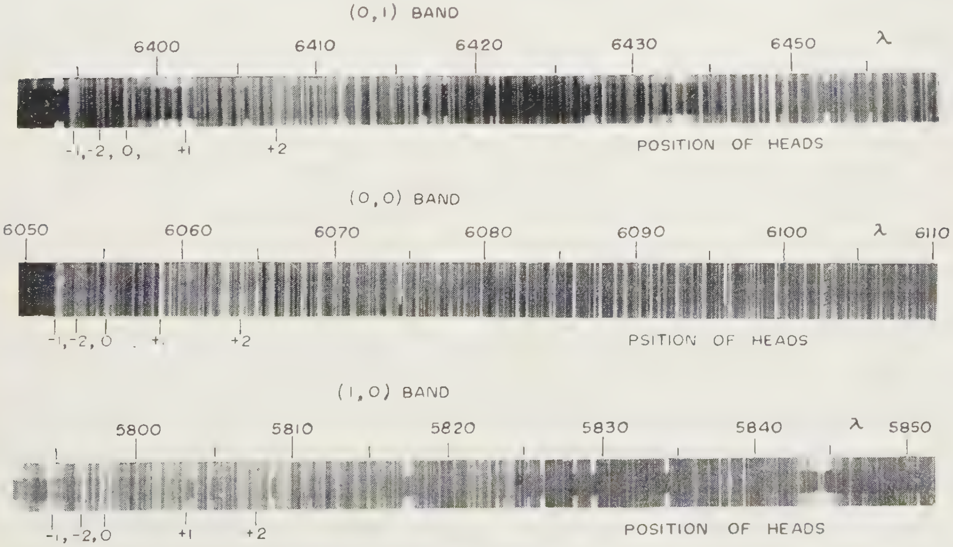

Fig. 1.

Spectrograms were taken in the third order of the 2I-foot concave grating in Eagle's mounting and their dispersion was about 0.73 Å/mm. Iron arc lines and sometimes neon red lines were used as comparison. The parts of the spectrum are shown in the accompanying figure.

§ 3. Quintet States Intermediate Between Cases (a) and (b)

The general equations for the intermediate multiplet states between cases (a) and (b) have been given by Hill and Van Vleck[2)], and for the doublet, triplet and quarted states have been solved[3,4)]. For the quintet states the following equation to is be solved,

$$\begin{aligned}
&w^5+w^3[5\Lambda^2A^2-20\Lambda^2AB+20B^2J(J+1)+12B^2]\\
&\quad+w^2[-28\Lambda^2A^2B\\
&\qquad+28\Lambda^2AB^2+56B^3J(J+1)+16B^3]\\
&\quad+w[-4\Lambda^4A^4+32\Lambda^4A^3B-32\Lambda^2A^2B^2J(J+1)\\
&\qquad+32\Lambda^2A^2B^2-64\Lambda^4A^2B^2\\
&\qquad+128\Lambda^2AB^3J(J+1)^2+48\Lambda^2AB^3\\
&\qquad-64B^4J^2(J+1)^2+32B^4J(J+1)]\\
&\quad+16\Lambda^4A^4B-80\Lambda^4A^3B^2+32\Lambda^2A^2B^3J(J+1)\\
&\qquad+64\Lambda^4A^2B^3+64\Lambda^2AB^4J(J+1)\\
&\qquad-128B^5J^2(J+1)^2=0 \qquad (1)
\end{aligned}$$

where

$$w=W+2\Lambda^2B-B[J(J+1)+2] \qquad (2)$$

Since the eq. (I) can not be solved in analytical formula, we must solve this approximately. In the case of nearly (a), we can obtain the series solution in B/A by means of the expansion of w as follows,

$$\left.\begin{aligned}
w_{-2}&=-2A\Lambda+4B(\Lambda-1)-\frac{4B^2}{A\Lambda}[J(J+1)+(1-\Lambda)(3-4\Lambda)]+\left(\frac{B}{A}\right)^2[\cdots]+\cdots\\
w_{-1}&=-A\Lambda+2B(\Lambda+1)-\frac{2B^2}{A\Lambda}[J(J+1)+(1-\Lambda)(4+\Lambda)]+\left(\frac{B}{A}\right)^2[\cdots]+\cdots\\
w_0&=4B+\frac{12B^2}{A}+\left(\frac{B}{A}\right)^2[\cdots]+\cdots\\
w_1&=A\Lambda-2B(\Lambda-1)+\frac{2B^2}{A\Lambda}[J(J+1)+(1+\Lambda)(4-\Lambda)]+\left(\frac{B}{A}\right)^2[\cdots]+\cdots\\
w_2&=2A\Lambda-4B(\Lambda+1)+\frac{4B^2}{A\Lambda}[J(J+1)+(1+\Lambda)(3+4\Lambda)]+\left(\frac{B}{A}\right)^2[\cdots]+\cdots
\end{aligned}\right\} \qquad (3)$$

where the suffix of w is the value of Σ.

In consequence we can express the energy of the state neglecting the higher order terms than $(B/A)^2$ as

$$\left.\begin{aligned}
W_{-2}&=-2A\Lambda-2B(\Lambda-1)^2-4B^2/A\Lambda\cdot(1-\Lambda)(3-4\Lambda)+BJ(J+1)\left[1-\frac{4B}{A\Lambda}\right]+\cdots\\
W_{-1}&=-A\Lambda-2B(\Lambda+1)(\Lambda-2)-2B^2/A\Lambda\cdot(1-\Lambda)(4+\Lambda)+BJ(J+1)\left[1-\frac{2B}{A\Lambda}\right]+\cdots\\
W_0&=-2B(\Lambda^2-3)+12B^2/A+BJ(J+1)+\cdots\\
W_1&=A\Lambda-2B(\Lambda-1)(\Lambda+2)+2B^2/A\Lambda\cdot(1+\Lambda)(4-\Lambda)+BJ(J+1)\left[1+\frac{2B}{A\Lambda}\right]+\cdots\\
W_2&=2A\Lambda-2B(\Lambda+1)^2+4B^2/A\Lambda\cdot(1+\Lambda)(3+4\Lambda)+BJ(J+1)\left[1+\frac{4B}{A\Lambda}\right]+\cdots
\end{aligned}\right\} \qquad (4)$$

Therefore in the same way as in the doublet and triplet cases we may express the rotational energy omitting the terms independent of J,

$$W_{rot}=B_{eff}J(J+1) \qquad (5)$$

where

$$\left.\begin{aligned}
&B_{eff}=B\left(1+\frac{2B}{A\Lambda}\Sigma\right)\\
&\Sigma=-2,\,-1,\,0,\,1,\,2
\end{aligned}\right\} \qquad (6)$$

§ 4. Rotational Analysis

Considering the combination principle we

Table I. Wave-number of the lines of the (0, 1) (0, 0) and (1, 0) bands and Δ_2F for the $\sum=-2$ states.

J	(0, 1)				(0, 0)				(1, 0)			
	Δ_2F''	$R(J)$	$P(J)$	Δ_2F'	Δ_2F'	$R(J)$	$P(J)$	Δ_2F''	Δ_2F''	$R(J)$	$P(J)$	Δ_2F'
9						1651636				1724767		
10		1563012	1561057	1955	1967	1617	1649650	2191	2178	4738	1722823	1915
11	2355	3004	0862	2142	2142	1587	9445	2398	2366	4666	2607	2089
12	2559	2992	0657	2355	2327	1546	9219	2609	2579	4642	2372	2270
13	2768	2958	0445	2513	2516	1494	8978	2800	2780	4577	2117	2460
14	2965	2921	0224	2697	2685	1431	8746	3009	3000	4501	1862	2639
15	3174	2872	1559993	2879	2876	1361	8485	3212	3196	4404	1577	2827
16	3379	2816	9747	3069	3060	1279	8219	3424	3404	4309	1305	3004
17	3583	2748	9493	3255	3255	1191	7937	3636	3627	4196	1000	3196
18	3786	2670	9233	3437	3437	1080	7643	3856	3847	4071	0682	3389
19	3991	2584	8962	3622	3613	0949	7336	4056	4043	3929	0349	3580
20	4197	2487	8679	3808	3804	0826	7024	4245	4239	3780	0028	3752
21	4401	2382	8387	3995	3997	0701	6704	4455	4452	3634	1719690	3944
22	4607	2264	8086	4178	4185	0556	6371	4681	4683	3462	9328	4134
23	4809	2140	7775	4365	4378	0398	6020	4885	4880	3278	8951	4327
24	5015	2005	7455	4550	4556	0227	5671	5109	5091	3088	8582	4506
25	5225	1859	7125	4734	4744	0033	5289	5317	5303	2877	8187	4690
26	5427	1708	6783	4925	4924	1649834	4910	5507	5505	2657	7785	4872
27	5634	1542	6432	5110	5115	9641	4526	5719	5710	2426	7372	5054
28	5835	1366	6074	5292	5297	9412	4115	5929	5915	2183	6947	5236
29	6041	1176	5707	5469	5475	9187	3712	6119	6120	1927	6511	5416
30	6238	0986	5325	5661	5651	8944	3293	6323	6323	1660	6063	5597
31	6447	0779	4938	5841	5831	8695	2864	6525	6524	1382	5604	5778
32	6648	0562	4539	6023	6017	8436	2419	6728	6729	1091	5136	5955
33	6847	0338	4131	6207	6202	8159	1957	6950	6932	0786	4653	6133
34	7050	0107	3715	6392	6391	7877	1486	7147	7131	0481	4159	6322
35	7256	1559858	3288	6570	6569	7581	1012	7353	7341	0150	3655	6495
36	7453	9603	2851	6752	6750	7274	0524	7539	7539	1719815	3140	6675
37	7651	9340	2405	6935	6927	6961	0034	7741	7742	9469	2611	6858
38	7853	9066	1952	7114	7111	6644	1639533	7943	7948	9123	2073	7050
39	8048	8781	1487	7294	7292	6310	9018	8147	8162	8742	1521	7221
40	8249	8489	1018	7471	7475	5972	8497	8354	8354	8352	0961	7391
41	8453	8188	0532	7656	7655	5614	7959	8559	8540	7962	0388	7574
42	8653	7875	0032	7836	7838	5251	7413	8769	8750	7561	1709812	7749
43	8851	7552	1549535	8017	8023	4878	6855	8964	8970	7145	9212	7933
44	9052	7222	9024	8198	8200	4487	6287	9169	9150	6718	8591	8127
45	9254	6883	8500	8383	8380	4089	5709	9369	9365	6281	7995	8386
46	9454	6584	7968	8566	8559	3677	5118	9570	9566	5822	7353	8469
47	9653	6178	7429	8749	8737	3256	4519	9773	9760	5360	6715	8645
48	9857	5809	6881	8928	8928	2832	3904	9955	9958	4892	6062	8821
49	10057	5429	6321	9108	9091	2392	3301	10176	10166	4392	5402	8990
50	10253	5040	5772	9288	9288	1939	2656	10376	10374	3889	4726	9163
51		4641	5176	9465	9464	1480	2016			3381	4018	9363
52												

could assign the band lines as shown in the Tables I～V for each subband respectively, in which we have had the each branches from the band head at about $J=9$ to about $J=50$, since the R branches under $J=9$ were weak and blended with the other lines and the P branches over $J=50$ were so apart from the band head that could not be put in one plate. In the order from left to right $\Delta_2F''(J)$, $R(J)$, $P(J)$ and $\Delta_2F'(J)$ of the (0, I) band; $\Delta_2F'(J)$, $R(J)$, $P(J)$, and $\Delta_2F''(J)$ of the (0, 0) band; $\Delta_2F''(J)$, $R(J)$, $P(J)$ and $\Delta_2F'(J)$ of the (I, 0) band are shown in each Table, where Δ_2F'' and Δ_2F' are calculated by the relations

$$\Delta_2F''(J)=R(J-1)-P(J+1)$$

and

$$\Delta_2F'(J)=R(J)-P(J)$$

respectively and all values are expressed in I/100 cm^{-1}.

We may prove the rightness of the analysis from the satisfactory agreements between Δ_2F' of (0, I) and (0, 0) bands, and between Δ_2F'' of (0, 0) and (I, 0) bands within the

Table II. Wave-number of the lines of the (0, 1), (0, 0) and (1, 0) and Δ_2F for the $\Sigma=-1$ states.

J	(0, 1)				(0, 0)				(1, 0)			
	Δ_2F''	$R(J)$	$P(J)$	Δ_2F'	Δ_2F'	$R(J)$	$P(J)$	Δ_2F''	Δ_2F''	$R(J)$	$P(J)$	Δ_2F'
9		1563413	1561625	1788	1767	1651994	1650227			1725288	1723510	1778
10	2178	3408	1435	1973	1957	1985	0028	2179	2191	5255	3311	1944
11	2378	3393	1235	2158	2151	1966	1649815	2388	2384	5196	3097	2099
12	2587	3369	1030	2339	2339	1936	9597	2605	2589	5148	2871	2277
13	2797	3339	0806	2533	2534	1895	9361	2808	2785	5086	2607	2479
14	3006	3290	0572	2718	2718	1846	9128	3005	3009	5009	2361	2648
15	3208	3237	0333	2904	2899	1789	8890	3216	3211	4916	2077	2839
16	3413	3173	0082	3091	3091	1721	8630	3437	3414	4815	1798	3017
17	3619	3100	1559824	3276	3292	1644	8352	3625	3626	4705	1502	3203
18	3823	3017	9554	3463	3464	1560	8096	3841	3839	4595	1189	3406
19	4027	2926	9277	3649	3658	1461	7803	4045	4041	4467	0866	3601
20	4233	2826	8990	3836	3837	1352	7515	4263	4262	4327	0554	3873
21	4437	2716	8693	4023	4032	1230	7198	4475	4461	4178	0205	3973
22	4649	2599	8387	4212	4219	1096	6877	4683	4680	4012	1719866	4146
23	4853	2472	8567	4405	4405	0952	6547	4891	4891	3839	9498	4341
24	5061	2330	7746	4584	4583	0788	6205	5099	5099	3649	9121	4528
25	5263	2189	7411	4778	4780	0633	5853	5298	5305	3453	8740	4713
26	5476	2032	7067	4965	4968	0458	5490	5517	5511	3239	8344	4895
27	5682	1867	6713	5154	5155	0271	5116	5726	5726	3017	7942	5075
28	5884	1691	6350	5341	5340	0072	4732	5934	5936	2779	7513	5266
29	6104	1506	5983	5523	5526	1649863	4337	6138	6140	2539	7081	5458
30	6304	1310	5587	5723	5721	9655	3934	6343	6343	2281	6642	5639
31	6510	1105	5202	5903	5907	9427	3520	6559	6547	2002	6196	5806
32	6715	0891	4800	6091	6091	9187	3096	6760	6760	1717	5734	5983
33	6922	0667	4390	6277	6281	8948	3667	6971	6955	1432	5242	6190
34	7128	0433	3969	6464	6466	8682	2216	7177	7158	1136	4762	6374
35	7333	0190	3539	6651	6651	8422	1771	7393	7381	0807	4274	6533
36	7539	1559939	3100	6839	6840	8129	1289	7594	7590	0476	3755	6721
37	7748	9678	2651	7027	7027	7855	0828	7794	7788	0132	3217	6915
38	7952	9404	2193	7211	7218	7553	2335	8015	8015	1719771	2688	7083
39	8155	9124	1726	7398	7396	7236	1639840	8223	8220	9407	2117	7290
40	8358	8832	1249	7583	7588	6918	9330	8420	8426	9035	1551	7484
41	8559	8531	0766	7765	7766	6582	8816	8634	8634	8647	0981	7666
42	8758	8220	0273	7947	7950	6237	8287	8826	8829	8252	0401	7851
43	8970	7899	1549773	8126	8129	5885	7756	9023	9023	7836	1709818	8018
44	9169	7564	9250	8314	8313	5527	7214	9237	9234	7410	9229	8181
45	9354	7230	8730	8500	8505	5153	6648	9444	9453	6980	8602	8378
46	9574	6880	8208	8672	8678	4761	6083	9676	9674	6526	7957	8569
47	9777	6522	7656	8866	8878	4355	5477	9873	9867	6069	7306	8763
48	9993	6153	7103	9050	9062	3950	4888	10069	10062	5600	6659	8941
49	10201	5776	6529	9247	9247	3533	4286	10276	10265	5121	6007	9114
50	10392	5386	5952	9434	9422	3096	3674	10471	10466	4642	5335	9307
51	10581	4987	5384	9603	9592	2654	3062	10675	10677	4139	4655	9484
52	10785	4578	4805	9773	9773	2192	2421	10870	10875	3625	3965	9660
53		4157	4202	9952	9957	1741	1784			3092	3264	9828

experimental error.

§ 5. Molecular Constants

If the states are nearly of the case (a) and we can neglect the higher terms than $(B/A)^2$, we can obtain the following expression according to § 3,

$$\left.\begin{aligned}\Delta_2F''_v(J)&=F''(J+1)-F''(J-1)\\&=(4B''_{v.eff}-6D_v'')(J+\tfrac{1}{2})\\&\quad-8D_v''(J+\tfrac{1}{2})^3\end{aligned}\right\}$$

and

$$\left.\begin{aligned}\Delta_2F_v'(J)&=F'(J+1)-F'(J-1)\\&=(4B'_{v.eff}-6D_v')(J+\tfrac{1}{2})\\&\quad-8D_v'(J+\tfrac{1}{2})^3\end{aligned}\right\} \quad (7)$$

Therefore from these eqs. and the values of Δ_2F'' and Δ_2F' in Tables I∼V we can evaluate $B'_{v.eff}$, $B''_{v.eff}$, D_v' and D_v''. But the number of the lines are not sufficient to obtain D_v accurately, we have calculated D_v from the theoretical formula,

Table III. Wave-number of the lines of the (0, 1), (0, 0) and (1, 0) and Δ_3F for the $\sum=0$ states.

J	(0, 1)				(0, 0)				(1, 0)			
	Δ_2F''	$R(J)$	$P(J)$	Δ_2F'	Δ_2F'	$R(J)$	$P(J)$	Δ_2F''	Δ_2F''	$R(J)$	$P(J)$	Δ_2F'
9		1562619	1560845	1774	1773	1651077	1649304			1724333	1722574	1759
10	2159	2619	0659	1960	1961	1066	9105	2184	2198	4302	2364	1938
11	2369	2616	0460	2156	2157	1050	8893	2404	2410	4268	2135	2133
12	2590	2610	0250	2360	2360	1022	8662	2624	2627	4211	1892	2319
13	2812	2570	0026	2544	2556	0982	8426	2841	2841	4140	1641	2499
14	3011	2525	1559798	2727	2746	0927	8181	3045	3045	4068	1370	2698
15	3214	2484	9559	2925	2927	0864	7937	3257	3257	3976	1095	2881
16	3431	2437	9311	3127	3118	0788	7670	3471	3459	3878	0811	3067
17	3651	2347	9053	3294	3305	0698	7393	3683	3674	3783	0517	3266
18	3838	2269	8786	3483	3486	0591	7105	3886	3888	3656	0204	3452
19	4047	2191	8509	3682	3673	0485	6812	4088	4100	3530	1719895	3635
20	4268	2096	8222	3874	3865	0368	6503	4302	4302	3382	9556	3826
21	4476	1983	7923	4060	4057	0240	6193	4515	4516	3232	9228	4004
22	4683	1869	7620	4249	4243	0096	5853	4727	4729	3064	8866	4198
23	4893	1723	7300	4423	4421	1649938	5517	4931	4930	2889	8503	4386
24	5083	1581	6977	4603	4609	9774	5165	5136	5142	2702	8134	4568
25	5280	1435	6640	4795	4798	9600	4802	5348	5360	2503	7747	4756
26	5499	1288	6301	4987	4994	9420	4426	5559	5574	2283	7342	4941
27	6706	1123	5936	5187	5181	9222	4041	5778	5784	2052	6929	5123
28	5923	0962	5582	5380	5376	9018	3642	5778	5989	1812	6499	5313
29	6154	0757	5200	5557	5550	8792	3242	6189	6196	1554	6063	5491
30	6359	0548	4808	5740	5740	8569	2829	6395	6398	1287	5616	5671
31	6550	0338	4398	5940	5941	8338	2397	6609	6619	1008	5156	5852
32	6748	0130	3998	6132	6128	8088	1960	6829	6816	0715	4668	6047
33	6961	1559894	3590	6304	6311	7820	1509	7033	7031	0413	4192	6221
34	7163	9663	3169	6494	6504	7559	1055	7240	7240	0095	3684	6412
35	7376	9404	2731	6673	6688	7268	0580	7447	7447	1719771	3173	6598
36	7572	9152	2287	6865	6868	6980	0112	7646	7638	9431	2649	6782
37	7782	8900	1832	7068	7055	6677	1639622	7855	9846	9079	2133	6946
38	8002	8611	1370	7241	7243	6368	9125	8062	8056	8713	1585	7128
39	8197	8325	0898	7427	7427	6042	8615	8282	8264	8340	1023	7317
40	8403	8031	0414	7617	7626	5712	8086	8482	8475	7959	0449	7510
41	8611	7745	1549922	7823	7816	5376	7560	8696	8696	7555	1709865	7690
42	8837	7428	9420	8008	8000	5018	7018	8904	8898	7145	9263	7882
43	9052	7099	8908	8191	8184	4656	6472	9108	9105	6723	8657	8066
44	9236	6755	8376	8379	8373	4283	5910	9314	9314	6287	8040	8247
45	9436	6427	7863	8564	8556	3891	5342	9528	9528	5851	7409	8442
46	9656	6073	7319	8754	8746	3501	4755	9733	9733	5374	6759	8615
47	9860	5707	6771	8936	8936	3094	4158	9944	9931	4906	6118	8788
48	10060	5325	6213	9112	9110	2667	3557	10148	10144	4421	5443	8978
49	10254	4941	5647	9294	9284	2230	2946	10345	10350	3924	4762	9162
50	10472	4546	5071	9475	9471	1793	2322	10542	10553	3422	4071	9351
51		4142	4469	9673	9657	1345	1688		10762	2899	3371	9528
52										2371	2660	9711

$$D_v=\frac{4B_e^3}{\omega_e^2}\left[1+\left(\frac{8\omega_e x_e}{\omega_e}-\frac{5\alpha_e}{B_e}-\frac{\alpha_e\omega_e}{24B_e^3}\right)\left(v+\frac{1}{2}\right)\right]$$

using the values of ω_e and $\omega_e x_e$ given by C. Ghosh[1] and 0.528, 0.475 for B_e'' and B_e' respectively and 0.005 for α'' and α', and then determined $B_{v\cdot eff}$ from the relation

$$4B_{v\cdot eff}\ (J+\tfrac{1}{2})=\Delta_2F(J)+8D_v(J+\tfrac{1}{2})^3$$

where we have neglected $6D_v$ against $4B_{v\cdot eff}$. Since in $J<20$ many lines are blended and in $J>40$ the effect of D_v term becomes large, whose calculated value is not so certain especially for $\sum\neq0$, we have obtained $B_{v\cdot eff}$ from Δ_2F between $J=21$ and 40, as shown in Table VI. The probable error of $B_{v\cdot eff}$. varies from each other but is below 0.0002 cm^{-1}. In spite of the inverse order of the heads of $\sum=-2$ and $\sum=-1$ their $B_{v\cdot eff}$ are in right order, as the similar phenomenon has been shown in the case of the triplet bands of TiO by A. Christy[5].

Table IV. Wave-number of the lines of the (0, 1), (0, 0) and (1, 0) bands and $\Delta_2 F$ for the $\sum=1$ states.

J	(0, 1)				(0, 0)				(1, 0)			
	Δ_2F''	$R(J)$	$P(J)$	Δ_2F'	Δ_2F'	$R(J)$	$P(J)$	Δ_2F''	Δ_2F''	$R(J)$	$P(J)$	Δ_2F'
9		1561710	1559895	1815	1808	1650109	1648301			1723222		
10	2219	1705	9700	2005	2002	0096	8094	2235	2250	3192	1721215	1977
11	2435	1688	9491	2197	2197	0071	7874	2451	2468	3147	0972	2175
12	2644	1661	9270	2391	2391	0036	7645	2662	2677	3094	0724	2370
13	2851	1620	9044	2576	2581	1649990	7409	2882	2891	3023	0470	2553
14	3062	1577	8810	2767	2778	9932	7154	3094	3103	2942	0203	2739
15	3277	1522	8558	2964	2969	9865	6896	3307	3307	2850	1719920	2930
16	3490	1452	8300	3152	3152	9777	6625	3524	3526	2746	9635	3111
17	3696	1376	8032	3344	3344	9685	6341	3730	3736	2634	9324	3310
18	3906	1291	7756	3535	3548	9595	6047	3936	3957	2506	9011	3495
19	4122	1196	7470	3726	3732	9481	5749	4160	4163	2366	8677	3689
20	4338	1084	7169	3915	3915	9350	5435	4368	4366	2224	8343	3881
21	4539	0967	6858	4109	4106	9219	5113	4570	4581	2056	8000	4056
22	4751	0840	6545	4295	4292	9072	4780	4790	4790	1892	7643	4249
23	4961	0698	6216	4482	4488	8917	4429	4995	5004	1708	7266	4442
24	5167	0547	5879	4668	4675	8752	4077	5208	5215	1515	6888	4627
25	5372	0387	5531	4856	4863	8572	3709	5426	5430	1310	6493	4817
26	5579	0224	5175	5049	5058	8384	3326	5638	5642	1092	6085	5007
27	5794	0046	4808	5249	5249	8183	2934	5842	5847	0860	5668	5192
28	6000	1559857	4430	5427	5427	7969	2542	6056	6062	0615	5245	5370
29	6209	9666	4046	5620	5625	7752	2127	6263	6276	0360	4798	5562
30	6424	9460	3648	5812	5812	7518	1706	6482	6479	0097	4339	5758
31	6633	9238	3242	5996	6009	7279	1270	6690	6690	1719815	3881	5934
32	6833	9019	2827	6192	6196	7024	0828	6898	6895	9526	3407	6119
33	7048	8782	2405	6377	6380	6761	0381	7097	7105	9224	2920	6304
34	7254	8530	1971	6559	6555	6482	1639927	7316	7316	8910	2421	6489
35	7454	8278	1528	6750	6757	6202	9445	7523	7536	8585	1908	6677
36	7664	8013	1076	6937	6948	5907	8959	7743	7738	8252	1374	6878
37	7871	7745	0614	7131	7136	5595	8459	7951	7955	7906	0847	7059
38	8083	7459	0142	7317	7322	5278	7956	8156	8165	7543	0297	7246
39	8284	7169	1549662	7507	7509	4948	7439	8367	8371	7168	1709741	7427
40	8491	6871	9175	7696	7696	4607	6911	8584	8581	6794	9172	7622
41	8699	6568	8678	7890	7894	4258	6364	8795	8793	6393	8587	7806
42	8911	6244	8172	8072	8087	3899	5812	9006	9002	5678	8001	7977
43	9114	5914	7657	8257	8257	3515	5258	9217	9208	5551	7391	8160
44	9318	5579	7130	8449	8444	3125	4681	9419	9410	5118	6770	8348
45	9526	5226	6588	8638	8630	2726	4096	9627	9620	4671	6141	8530
46	9728	4865	6045	8820	8821	2319	3498	9831	9829	4216	5498	8718
47	9930	4498	5490	9008	9006	1901	2895	10037	10035	3751	4842	8909
48	10133	4118	4927	9191	9188	1470	2282	10245	10244	3269	4181	9088
49		3732	4357	9375	9381	1037	1656		10446	2769	3507	9262
50										2274	2823	9451
51											2127	

We shall be able to calculate the value of $A\Lambda$ from the difference of $B_{v\cdot eff}$ for the different $\sum$ and the eq. (6), but, because each head does not stand in regular arrangement as shown in the Fig. and actually the calculated values were widely disperse, we have only estimated it as

$$(A\Lambda)''=110\ \mathrm{cm}^{-1} \text{ and}$$

$$(A\Lambda)'=100\ \mathrm{cm}^{-1}\ .$$

The α_e can be obtained from the difference between $B_{0\ eff}$ and $B_{1\ eff}$ for $\sum=0$ and so

$$\alpha''=0.0050\ \mathrm{cm}^{-1} \text{ and } \alpha'=0.0057\ \mathrm{cm}^{-1}.$$

On the other hand we have obtained from the Pekeris's relation,

$$\alpha_e=\frac{6\sqrt{\omega_e x_e B_e{}^3}}{\omega_e}-\frac{6B_e{}^2}{\omega_e}\ ,$$

$$\alpha''=0.0049\ \mathrm{cm}^{-1} \text{ and } \alpha'=0.0051\ \mathrm{cm}^{-1}$$

and the agreement between the observed and calculated values of them is satisfactory.

Consequently it can be obtained

$$B_e''=0.5286\pm0.0002\ \mathrm{cm}^{-1}$$

$$B_e'=0.4750\pm0.0002\ \mathrm{cm}^{-1}$$

and then

$$r_e''=1.627\times10^{-8}\ \mathrm{cm}$$

Table V. Wave-number of the lines of the (0, 1), (0, 0) and (1, 0) bands and Δ_2F for the $\sum=+2$ states.

J	(0, 1)				(0, 0)				(1, 0)			
	Δ_2F''	$R(J)$	$P(J)$	Δ_2F'	Δ_2F'	$R(J)$	$P(J)$	Δ_2F''	Δ_2F''	$R(J)$	$P(J)$	Δ_2F'
9		1560294	1558465	1829	1834	1648665	1646831			1722280	1720474	1806
10	2232	0294	8266	2028	2028	8658	6630	2233	2243	2260	0253	2007
11	2429	0289	8062	2227	2211	8643	6432	2456	2460	2227	0037	2190
12	2652	0275	7865	2410	2419	8621	6202	2674	2681	2183	1719800	2383
13	2866	0250	7637	2613	2598	8567	5969	2916	2903	2126	9546	2580
14	3083	0216	7409	2807	2812	8517	5705	3129	3127	2058	9280	2778
15	3313	0168	7167	3001	3020	8458	5438	3351	3345	1978	8999	2979
16	3528	0111	6903	3208	3215	8381	5166	3570	3558	1879	8713	3166
17	3737	0046	6640	3406	3412	8300	4888	3773	3769	1791	8420	3371
18	3954	9975	6374	3601	3601	8208	4607	3990	3994	1675	8110	3565
19	4173	1559880	6092	3788	3786	8096	4310	4211	4209	1548	7797	3751
20	4378	9782	5802	3980	3974	7971	3997	4419	4408	1412	7466	3946
21	4590	9675	5502	4173	4178	7855	3677	4623	4630	1259	7140	4119
22	4802	9559	5192	4367	4374	7722	3348	4846	4845	1100	6782	4318
23	5015	9435	4873	4562	4571	7580	3009	5060	5063	0928	6414	4514
24	5229	9295	4544	4751	4753	7415	2662	5273	5266	0745	6037	4708
25	5437	9151	4206	4945	4933	7236	2303	5482	5477	0549	5662	4887
26	5650	8990	3858	5132	5132	7065	1933	5691	5699	0339	5262	5071
27	5856	8822	3501	5321	5324	6869	1545	5913	5918	0117	4850	5267
28	6065	8649	3134	5515	5519	6671	1152	6121	6122	1719883	4421	5462
29	6280	8465	2757	5708	5708	6456	0748	6341	6343	9641	3995	5646
30	6494	8266	2369	5897	5905	6235	0330	6551	6551	9383	3540	5843
31	6704	8062	1971	6091	6094	5999	1639905	6767	6771	9120	3090	6030
32	6919	7846	1562	6284	6284	5752	9468	6983	6977	8822	2612	6210
33	7134	7621	1143	6478	6479	5492	9016	7194	7186	8547	2143	6404
34	7338	7380	0712	6668	6672	5230	8558	7409	7409	8255	1636	6619
35	7554	7130	1273	6857	6862	4948	8086	7624	7624	7945	1138	6807
36	7763	6870	1549826	7044	7053	4659	7606	7833	7832	7623	0631	6992
37	7972	6602	9367	7235	7241	4356	7115	8048	8045	7301	0113	7188
38	8178	6223	8898	7425	7433	4044	6611	8257	8262	6956	1709578	7378
39	8386	6034	8424	7610	7616	3715	6099	8469	8474	6588	9039	7549
40	8598	5739	7937	7802	7799	3374	5575	8678	8681	6210	8482	7728
41	8811	5429	7436	7993	7994	3031	5037	8885	8893	5836	7907	7929
42	9017	5106	6928	8178	8183	2672	4489	9100	9089	5447	7317	8130
43	9220	4776	6412	8364	8372	2303	3931	9307	9307	5038	6747	8301
44	9428	4438	5886	8552	8568	1933	3365	9517	9526	4632	6140	8492
45	9627	4094	5348	8746	8754	1540	2786	9736	9748	4210	5512	8698
46	9836	3737	4811	8926	8933	1130	2197	9943	9953	3781	4884	8897
47		3363	4255	9108	9118	0715	1597		10175	3322	4257	9065
48									10378	2865	3606	9259
49											2944	
50												

$$r_e'=1.716\times10^{-8}\text{ cm}.$$

It sees that these values are reasonable as compared with the ones of TiO, VO and the other diatomic oxides.

Although we have calculated the values of D from the theoretical relation as mentioned above, we have been able to evaluate them also from the observed Δ_2F. It seems that D of the states of $\sum=-1, 0$ and 1 are nearly equal to the theoretical value but D of the states of $\sum=-2$ and 2 are larger than the theoretical one. However it is uncertain because J is not large enough to obtain D accurately.

§ 6. Classfication of Levels

As described in the previous sections we have been able to obtain 5 R-branches and 5 P-branches in each band and to show that no Q-branch exists except near the band origin, where it is impossible to denominate the lines certainly since the blending of all lines. Consequently the type of the transition for the CrO bands seems to be the one of $\varDelta\varLambda=0$. Futhermore the multiplet separations are so large that the lower and upper states must not be $\sum$ state. Therefore the possible transitions are ${}^5\Pi-{}^5\Pi$, ${}^5\varDelta-{}^5\varDelta$, etc. In order to distinguish between these possible transi-

Table VI. $B_{v \cdot eff}$.

State Σ	F_0''	F_1''	F_0'	F_1'
2	0.5386	0.5337	0.4852	0.4808
1	0.5324	0.5275	0.4777	0.4729
0	0.5259	0.5209	0.4723	0.4666
−1	0.5215	0.5179	0.4700	0.4630
−2	0.5196	0.5126	0.4650	0.4600

tions it is necessary to determine just what lines are missing in vicinity of the origin, but in the present case, as well as in the case of the Swan, N_2 and TiO bands already investigated, it is quite impossible to do this due to the blending of lines near the origin.

However, if we assume that the lower level is the normal state of CrO, we can determine Λ. For the reason, the normal state of the Cr and O atoms are ^7S and ^3P respectively and then the quintet states within the possible normal states of CrO may be only $^5\Sigma$ and $^5\Pi$. This assumption seems to be true because the intensity of the bands is considerably strong and the other band system has not been found.

In previous section, the values of the product of $A\Lambda$ have been found and due to the description just above we have A as follows;

$$A''=110\,\mathrm{cm}^{-1} \text{ for lower } {}^5\Pi\ ,$$

$$A=100\,\mathrm{cm}^{-1} \text{ for upper } {}^5\Pi\ .$$

Therefore we may be able to consider the transition of the CrO bands as the one between two normal $^5\Pi$.

We could not find the Λ-doubling, but this is not strange because only the difference between the Λ-doublings of the lower and upper states is observable.

§ 7. Acknowledgement

In conclusion, the author wishes to express his sincere thanks to Prof. T. Tanaka and Prof. Z. Koana, under whose kind guidance and encouragement this work has been carried out, and also to Dr. K. Ikenoue for his helpful discussions.

References

1) C. Ghosh: Z. Physik **78** (1932) 521.
2) E. L. Hill and J. H. Van Vleck: Phys. Rev. **32** (1928) 250.
3) A. Budo: J. Physik **96** (1935) 219; **98** (1936) 437; **105** (1937) 73.
4) W. H. Brandt: Phys. Rev. **50** (1936) 778.
5) A. Chirsty: Phys. Rev. **33** (1929) 701.
6) G. Herzberg: *Spectra of Diatomic Molecules* (D. Van Nostrand Co. Inc.) 1950, pp. 108.

JOURNAL OF THE PHYSICAL SOCIFTY OF JAPAN Vol. 10, No. 10, OCTOBER, 1955

The Magnetic Properties and Phase Diagram of Iron Tellurium System*

By Shoko CHIBA

The Research Institute for Iron, Steel and Other Metals, Tôhoku University, Sendai

(Received June 20, 1955)

In the present paper, studies on the phase diagram and magnetic properties of *Fe–Te* system are reported. It was found by X-ray and thermal analysis that a number of intermetallic compounds are formed from melt through peritectic reactions, and an eutectoid reaction was seen to occur between two compounds α (ca *FeTe*) and β (ca $FeTe_2$) at 520°C, the reactions product having the *NiAs* structure. The α phase shows an antiferromagnetic behavior with asymptotic Curie temperature $\theta=130°K$, Curie-Weiss constant $C=0.57$, but the crystal lattice type of this compound is obscure at present. The β phase has a crystal lattice of the *markasite* type and is antiferromagnetic, with $\theta=67°K$ and $C=1.31$. The γ phase which has a crystal lattice of the *NiAs* type shows an antiferromagnetic behavior, with $\theta=800°K$ and $C=1.15$. A short discussion on the antiferromagnetism of these compounds is given.

§ 1. Introduction

Many researchers have hitherto investigated the magnetic properties of various kinds of calcogenides of transition elements which crystallize in the structure of the *NiAs* type. It was known that the substance *CrTe*1) shows ferromagnetism, whereas *MnTe*2) and *CoTe*3) are antiferromagnetic and ferrimagnetic, respectively. This suggests the idea that the sign of exchange interaction between a pair of magnetic cations separated by an anion with a completely filled shall depends on whether the 3d shell of these cations are less than or more than half filled. From this point of view it is interesting to examine the orientation of spins in the compound *Fe–Te* with a *NiAs* structure, in which the cation is located between *Mn* and *Co* in the periodic table. It is expected that, for the same reason as in the case of *MnTe* and *CoTe*, the nature of exchange interaction in the iron telluride with a *NiAs* structure is also antiferromagnetic. Unfortunately, however, the crystal structure and phase diagram of this system is not well known. It was once reported by Oftedal that Fe_xTe_y has the crystal structure of *NiAs* type, but it seems to us that Oftedal's results are incomplete in some respects. And recently an interesting investigation of *FeTe* was reported by Uchida and Kondoh4). But it was difficult for us to elucidate an answer to the above mentioned problem therefrom since their result does not concern to the single phase region of this system. Hence, the investigation of the phase diagram of the *FeTe* system together with crystal analysis were undertaken using the specimens with a wide range of concentration of tellurium including *FeTe* and $FeTe_2$. The specimen $FeTe_x$ ($x=0.5\sim2.00$) were prepared, and thermal and X-ray analyses together with the determination of thermomagnetic behaviors were undertaken. In the following pages, the results of the present investigation are shown.

§ 2. Specimens and Measuring Apparatus

The specimens used were prepared by heating proper quantities of iron and tellurium in evacuated silica tubes. Tellurium used was obtained by purifying crude tellurium (99.7%) by double vacuum distillation. Electrolytic iron of purity 99.98% was crushed by a stamp mill and then reduced in hydrogen stream for 48 hrs. at 800°C. The reaction between tellurium and iron took place at 1100°C for 24 hrs in an electric furnace; the reaction product was then cooled down slowly. The

---

* The investigation was supported in part by the Grant-in-Aid of Fundamental Scientific Research of Ministry of Education and was carried out at Hirone's Laboratory of the institute above cited.

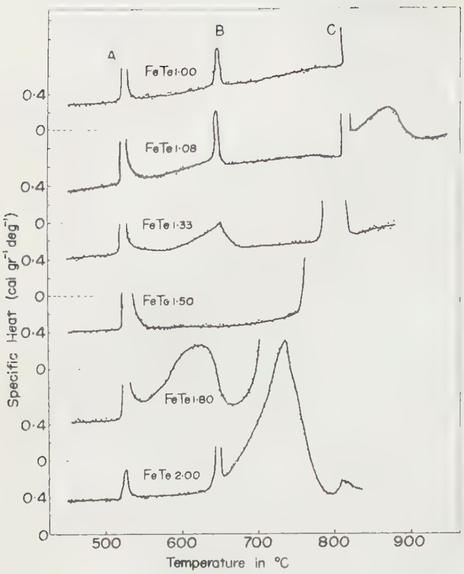

Fig. 1. The curves of specific heat vs. temperature for various tellurium contents x in $FeTe_x$.

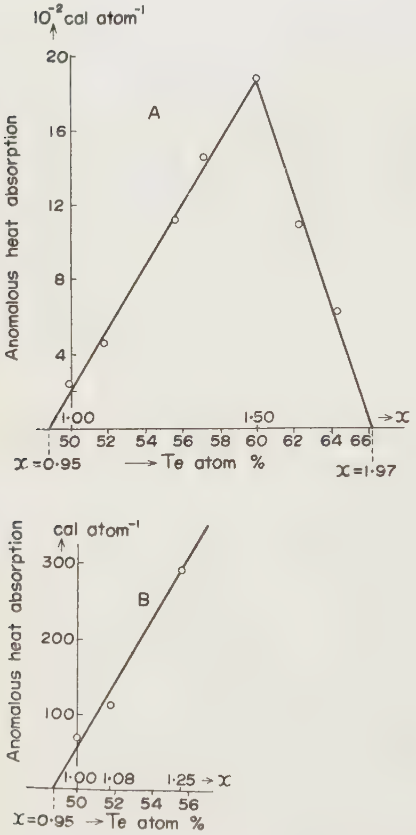

Fig. 2. The curves of anomalous heat absorption.
Curve A; absorption at 520°C.
Curve B; absorption at about 640°C.

oxygen absorbed in iron and tellurium is supposed to form a very small quantity of magnetite, the ferromagnetic behaviors of which may give rise to spurious effects in the measurement of magnetic susceptibility. In order to eliminate this effect, manganese of 0.5 atomic percent of *Fe* was added to the mixed powder of iron and tellurium as a deoxidizer. Spurious effects in the measurement of thermomagnetic properties due to the formation of ferromagnetic oxides was considered to be completely eliminated by this process.

The method of thermal analysis used here was due to Nagasaki and Takagi. A detailed description[5] will be omitted here. The automatic type magnetic balance used for measuring the susceptibility was the same as already reported[6].

§ 3. Experimental Results and Discussions

a) *Thermal analysis*

The specific heat of the compound $FeTe_x$, the value of x ranging from 1.00 to 2.00, was measured from room temperature to ca 1000°C. Some results of the measurement are shown in Fig. 1. As seen in the figure some anomalous heat absorptions were found in the range between 500° and 900°C. These anomalies can be classified into three types A, B and C by the order of temperature at which the anomaly takes place.

(A) A lambda shaped heat absorption A was found in all specimens at a definite temperature $T_A=520$°C. The temperature range of the anomalous heat absorption was about ten degrees. In Fig. 2 the total heat absorption Q at T_A is plotted against the atomic concentration c of tellurium. The amount of heat absorption Q_A reaches its maximum at $c=60$ at. % ($x=1.50$) and decreases linearly on both sides, disappearing at $C=48.2$ ($x=0.95$) and $c=66.3$ ($x=1.97$). It is to be noticed here that only a small difference (less than 10%) in the amount of Q_A was found between both specimens annealed at 590°C (just above T_A) and 490°C (just below T_A) for five hours, so that the measured value of Q_A can be seen to correspond approximately to the quasi-static change. This fact can be well understood by assuming an eutectoid reaction occuring at the temperature T_A. The compositions corresponding to the values $x=0.95$ and $x=1.97$ are supposed to be the phase boundaries, and hereafter these two phases will be denoted by α and β respectively. In the composition range between $x=0.95$ and $x=1.97$, α and β phase coexist at temperatures lower than the eutectoid temperature $T_A=520$°C. The proposed phase diagram based on the above result of thermal analysis is shown in Fig. 3. The third phase γ is interpreted as a result of the proposed eutectoid reaction. The existence of this phase can be attributed to the anomaly B mentioned below. Furthermore, the boundary of iron side of the α-phase was confirmed by X ray and magnetic analyses, that is, the samples in the α-phase region have no X ray pattern and ferromagnetic Curie point of iron.

(B) Next, in the specimens of composition $x<1.50$ (iron side of the eutectoid point) a small hump B appeared above the anomalous temperature T_A in the specific heat vs temperature curve. This hump becomes gradually larger as x decreases from $x=1.50$, and in the sample with $x=1.25$ its width becomes suddenly narrow. With further decrease in x, the anomalous heat absorption decreases linearly, then disappears at $x=0.95$. (Fig. 2, B) This fact may be attributed to the peculiar feature of the solubility curve of the γ phase on the α phase side. As shown in Fig. 3, the solubility curve has a steep slope just above T_A and then a gradual bending at 640°C. In the composition range $x>1.50$ there appears a broad hump with a width extending over 100°C above T_A. This hump is supposed to be caused by the gradual change of the solubility curve of γ on the β phase side. Therefore the solubility curve in Fig. 3 was plotted by the terminal temperature of the right hand side of this hump along the specific heat vs temperature curve.

(C) Anomaly *C* consists of a very narrow heat absorption at 805°C accompanied by a large heat absorption which extends rather broadly over into the high temperature range. In the samples, where the concentration x is greater than 1.25, the onset temperature of the heat absorption, T_c, becomes lower with the increase of x. Also the peak of the heat absorption curve becomes less sharp, and at $x=$ 1.80 its onset temperature approaches the final temperature of hump B. The locus of T_c is shown in Fig. 3. The temperature T_c, at which the above mentioned absorption occurs, is considered to be the peritectic temperature of γ and liquid phase. The terminal temperature of T_c gives the liquidus curve. According to the phase diagram based on thermal analysis, the composition $x=0.95$ corrsponds to the α monophase alone in temperature range up to 800°C and the composition $x=1.97$ to the β phase up to 660°C.

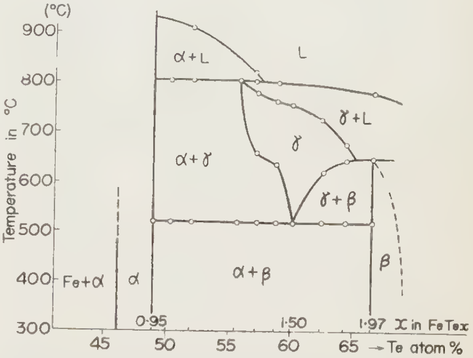

Fig. 3. The phase diagram of the systems of iron tellurium.

b) *X-ray analysis*

Next, we shall describe the results of X-ray analysis. Firstly, we took the Debye-Scherrer photograph at room temperature for the samples having compositions between $x=1.00$ and 2.00 and measured the angles of the diffraction lines. With the exception of a few

Table I. The results of X-ray analysis on the α, β and γ phases.

α phase $FeTe_{0.95}$?	β phase $FeTe_{2.00}$ markasite-type		γ phase $FeTe_{1.50}$ (at 600°C) *NiAs*-type	
$\sin^2\theta$	*hkl*	$\sin^2\theta$	*hkl*	$\sin^2\theta$
vs 0.089	111	vs 0.120	101	s 0.112
w 0.095	012	vs 0.128	102	s 0.196
s 0.128	121	vs 0.218	110	s 0.251
s 0.212	200	s 0.252	103	w 0.334
vs 0.221	103	s 0.277	201	w 0.361
w 0.256	113	w 0.310	202	w 0.448
s 0.278	212	s 0.380	203	w 0.584
s 0.344	032	w 0.390	211	s 0.608
s 0.379	123	w 0.408	114	s 0.696
s 0.442	024	w 0.512	300	s 0.746
s 0.533	232	s 0.642	105	w 0.786
s 0.634			213	w 0.831
s 0.698				
s 0.719				
s 0.735				

notation of intensity; vs=very strong, s=strong, w=weak.

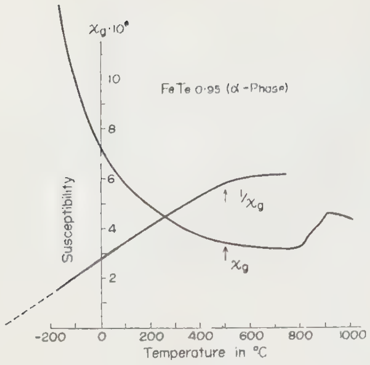

(a)

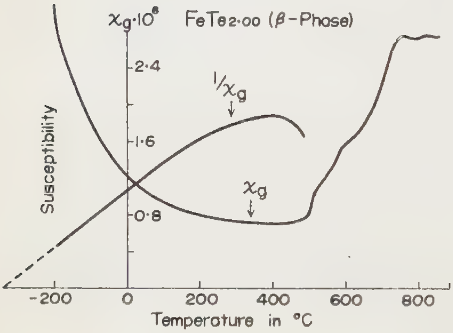

(b)

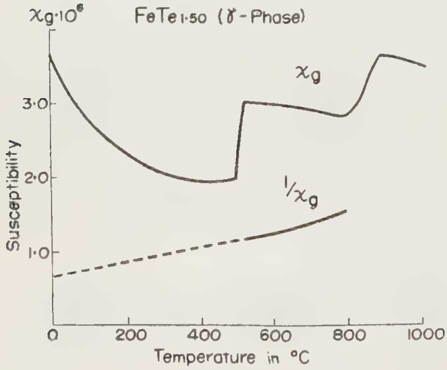

(c)

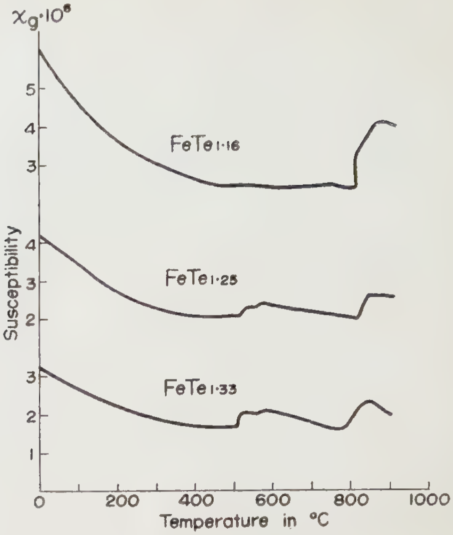

(d)

Fig. 4. The curves of suscedtibility vs. temperature for various concentrations x in $FeTe_x$.

special lines, each line can be classified into two kinds of group. As x becomes larger than 1.00, the intensity of lines belonging to the 1st group decreases and finally disappears near $x=2.00$. The intensity of lines belonging to the other group decreases as x becomes smaller than $x=2.00$ and disappears near $x=1.00$. The former is regarded as the characteristic lines of the α phase and the latter as that of β. Therefore we can be sure that the composition range $0.95<x<1.97$ is the coexistence region of the α and β phase. The intensity and $\sin^2\theta$ of the lines in each phase which we observed are shown in Table 1. It was once reported by Oftedal that iron telluride near the composition $x=1.00$ crystallizes in a *NiAs* structure[7) and its axial ratio c/a was shown to be about 1.51. However according to the present result, the characteristic diffraction lines due to the *NiAs* type lattice was completely unrecognized in all specimens at room temperature. However the Debye Scherrer photograph taken at about 650°C shows that the crystal structure of γ phase, which exists at the temperature range above 520°C in the sample of $x=1.50$, is surely the *NiAs* type with almost the same axial ratio as reported by Oftedal. All the diffraction lines corresponding to the β phase can be identified with those due to Tengner[8), and it is concluded that the lattice type belongs to the markasite structure. This results agrees satisfactorily with that of Tengner's report. The lines corresponding to α phase cannot be identified with any simple type of crystal lattice, but they contain a few lines common with markasite.

c) *Thermomagnetic measurements*

The changes of magnetic susceptibility χ_g with temperature were measured for samples with various concentrations x of *Te*. The results were sufficient to confirm the phase diagrams mentioned in the former section. They are shown in Fig. 4. The values of χ_g at room temperature against the tellurium content x is shown in Fig. 5. The measured point show a linear change of χ_g with atomic concentration as is expected by the coexistence of two phases of α and β in the range $x=1.00 \sim 2.00$. Susceptibilities of samples of pure α ($x=0.95$) and β ($x=1.97$) phases were measured at the temperature range from the boiling point of nitrogen to 1000°C. The curves of χ_g-T together with its reciprocals are shown in Fig. 4. The $1/\chi_g-T$ curve of $\alpha-FeTe_{0.95}$ is sufficiently linear with respect to temperature below 500°C and follows the Curie-Weiss law $x=\frac{C}{T+\theta}$. The shape of the χ_g-T curve at temperatures above 500°C becomes rather flat. Extrapolating the linear part of the χ_g-T curve, it is found that the asymptotic Curie temperature θ is 130°K, the Curie constant $C=0.57$ and the effective magneton number $\mu_{eff}=2.05$. From the positive value of θ, it seems that the α phase has an antiferromagnetic behavior. The behaviors of the curves of χ_g-T above 500°C may be explained by the existence of a small quantity of the β phase, which changes into γ phase at temperatures above 520°C due to eutectoid reaction. This tendency of the curve χ_g-T in the case of $x=0.95$ is consistent with the behavior of χ_g-T curves in the case of compositions $x=1.16$, $x=1.25$, which contain the small quantity of β phase.

The curve of susceptibility vs. temperature of the β phase ($x=2.00$) bellow 300°C shows an antiferromagnetic behavior (as well as the α phase). The Curie temperature θ and Curie constant C are 67°K and 1.31 respectively, and the effective magneton number calculated from the value of Curie constant is 3.25. The magnetic proporties of the γ phase with the *NiAs* type structure are as follows. The sample with $x=1.50$ shows the typical γ phase characteristics at the temperature range between 520°C and 790°C. Therefore, by measuring the susceptibility of $FeTe_{1.50}$ in this temperature range, it is possible to obtain the magnetic proporties of the γ phase alone. The values of Curie temprature, Curie constant and effective magneton number for this case can also be obtained from the $1/\chi_g-T$ curves and the values were $C=1.15$, $\theta=800$°K and $\mu_{eff}=3.00$, respectively. It should be concluded from the experimental results mentioned above that the superexchange interaction between the irons in the *NiAs* type crystal lattice of *FeTe* system has the same sign as the cations in *MnTe*, and hence a different sign with that of *CrTe*. From the fact that a large value of Curie temperature $\theta=800$°C was obtained, the magnetic nature of the γ phase of iron telluride may be considered as antiferromagnetic. Furthermore the resultant spin moment S of *Fe* ion in this substance, which is caluculated from the Curie-Weiss constant, is nearly one, that is, the iron atom is in the triplet state. This corresponds to the neutral state of an iron atom. Furthermore, for the cases of $\alpha-FeTe$ and $\beta-FeTe$ the spin moments based on the results in the present experiment are nearly 1/2 and 1, respectively. These values are somewhat smaller than that for cations in other compounds with oxygen or sulfur. The reason for small S may attributable to the fact that the tellurium has a smaller electronegativity than sulfur and oxygen.

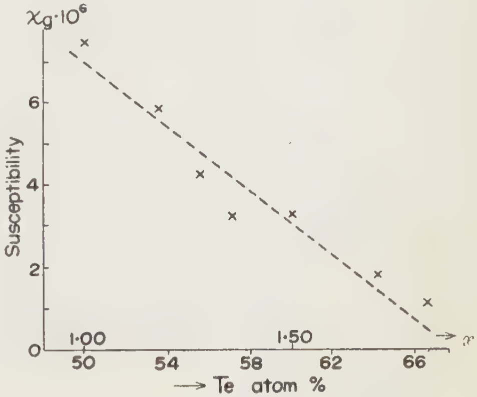

Fig. 5. The curve of χ_g at room temperature as a function of tellurium content.

Acknowledgements

The author wishes to experess her thanks to Profs. T. Hirone, S. Maeda, N. Tsuya and S. Nagasaki for their encouragement and valuable discussion. Also she wishes to express her hearty thanks to Dr. E. Uchida, Assistant Prof. of Naniwa Univ., who gave her especially valuable suggestions on the preparation of samples.

References

1) H. Haraldsen and E. Kowalski: Z. anorg. allgem. Chem., **224** (1935) 329.

2) A. Serre: J. de Phys., **28** (1947) 146.
C. F. Squire: Phys. Rev., **56** (1939) 922.
3) E. Uchida: private communication
4) E. Uchida and Kondoh: J. Phys. Soc. Japan **10** (1955) 357.
5) S. Nagasaki and Y. Takagi: J. Appl. Phys. Japan **17** (1948) 104. (in Japanese)
6) T. Hirone, S. Maeda and N. Tsuya: Rev. Sci. Instr. **25** (1954) 516.
7) I. Oftedal: Z. physik. Chem. **132** (1928) 208.
8) S. Tengner: Z. anorg. allgem. Chem. **239** (1938) 126.

JOURNAL OF THE PHYSICAL SOCIETY OF JAPAN Vol. 10, No. 10, OCTOBER, 1955

On the Origin of Magnetic Anisotropy Induced by Magnetic Annealing

By Sōshin CHIKAZUMI and Tatsurō OOMURA*

Department of Physics and Chemistry, Gakushuin University, Mejiro, Tokyo, Japan

(Received July 15, 1955)

The magnitude of magnetic anisotropy induced by the magnetic annealing was measured as a function of composition for iron-nickel alloys. It is concluded that the magnitude of the anisotropy is proportional neither to the magnetostriction nor to the saturation magnetization. The origin of this anisotropy, therefore, can be explained neither by the theory of "strain of directional order" nor by the theory of "elongated order phase". The result can be consistently explained by the dipole-dipole interaction in directionally ordered arrangement of atoms. The result is compared with Néel's formulas.

§ 1. Introduction

It has been found that the magnetic properties of some alloys, for instance Permalloy, Perminver, Alnico etc., are very sensitive to the magnetic annealing. When these alloys are annealed or cooled in a magnetic field, the intrinsic magnetization in them becomes stable in the direction of the annealing field. When, therefore, the magnetization curve is measured by applying the magnetic field in the same direction as that of annealing-field, magnetization takes place easily by the displacement of 180° walls and accordingly the magnetization curve in this case has a high maximum permeabilty. On the contrary, when the field is applied in the direction perpendicular to the annealing-field, magnetization takes place by the rotation, and accordingly the magnetization curve in this case is an inclined straight line.

This phenomenon was found first by G.A. Kelsall[1] for iron-nickel alloys and was investigated in details by Dillinger and Bozorth[2]. The latter investigators proposed the mechanism of this effect in terms of "plastic deformation." Lately one of the present authors[3] suggested that the mechanism in terms of "plastic deformation" is incompatible with experiments and proposed a new mechanism in terms of "directional order."

On the other hand, the effect of magnetic annealing was found[4] in some permanent magnet alloys, foy instance Mishima alloy, Alnico 2, Alnico 5 etc. Several investigators[5] proposed a mechanism for these alloys in terms of the "elongated precipitate phase."

Suggested by this idea, S. Kaya and S. Iida[6] proposed another possible interpretation of the effect for permalloy in terms of "elongated order phase." This theory, as well as the theory of "strain in directional order," explain almost all the features of this effect: for instance the functional form of the anisotropy, its order of magnitude for the alloys nearby Ni_3Fe, and the disappearance of the effect at perfect order[3].

Although both theories are related with the order formation, they are quite different with respect to the cause of the anisotropy. The anisotropy in the former theory is related to the magnetostriction, while that in the latter is related to the difference of saturation magnetization between order and disorder phase. In order to find out a true mechanism, therefore, it is necessary to measure an anisotropy as a function of composition and to compare it with a variation of the magnetostriction or that of the difference of the saturation magnetization. Several investigators[2),7)] studied the effect of magnetic annealing for various compositions of this alloy, but they dealed only with the permeability in longitudinal direction, from which the magnitude of the anisotropy energy cannot be estimated. Here we shall report the measurement of the anisotropy energy for various compositions of iron-nickel alloy and discuss the mechanism of this effect, on the basis of the experimental results.

---

* Now at Technical Research Laboratory, Ishikawajima Heavy Industrial Company, Tsukudajima, Tokyo, Japan.

§ 2. Specimens and Heat Treatment

Specimens used were the rods of the iron-nickel alloys, whose composition ranges from 60% to 100% Ni. These alloys were prepared by melting the electrolytic nickel and iron in a vacuum induction furnace. Each contained a small amount of manganese (ca. 0.5~0.8%). The rods were about 30 cm in length and 1.0 ~1.3 mm in diameter.

Heat treatment were carried out in a non-inductively wound electric furnace in an atomosphere of pure hydrogen. Several specimen rods were set in parallel in a furnace at intervals of about 1 cm. After annealed for about 1 hour at 1000°C, they were cooled in a longitudinal or in a circular magnetic field. The magnitude of the longitudinal field was about 30 *Oe*, which is large enough to magnetize the specimens to their saturation. The circular field was made by passing a d.c. current of 2 amperes through each specimen. The magnitude of the circular field is given by

$$H=\frac{0\cdot 2i}{r^2}x \qquad (\text{in } Oe) \qquad \text{for } x\leqq r\,, \tag{1}$$

where r is the radius of the rod, x is the distance from the central axis and i is the current in amperes. For $i=2$ amp, H amounts to about 8 *Oe* at the surface of the rod, which is large enough to magnetize the specimen in circular direction. The region in which the field is less then the coercive force (about 0.3 *Oe*), is confined in the small region around the central axis, whose volume is less than about 1% of the total volume.

The process of cooling from 600°C was controlled at a constant rate between 150°C /hour and 10°C/hour. The lower limit of temperature to which the field was applied and the cooling rate was controlled was given in the Table I.

§ 3. Experimental Results

The magnetization curves measured for various compositions are given in Figs 1, 2, 3, 4, 5, 6, and 7. The curve having high maximum permeability in each figure is that of the specimen which was treated with longitudinal field. Since the magnetization curve for such treatment is insensitive to the cooling rate, only one for 82°/hour was given in each figure. The curves with figures are that of the specimen which were treated in a circular field. The linear shape of these curves is a characteristic of the material having the uniaxial anisotropy, which is expressed by

$$E=-K_u\cos^2\theta\,, \tag{2}$$

where θ is an angle between intrinsic magnetization and its stable direction. The coefficient K_u is obtained from the triangular area which is surrounded by the magnetization curve for longitudinal field and that for the circular field, where the latter curve is linearly extrapolated to its saturation.

The anisotropy energy, K_u, thus obtained are given in Table I and shown graphically in Fig. 8 as a function of the alloy composition. For comparatively rapid cooling the anisotropy seems to have a trace of hump at the vicinity of Ni_3Fe, where the superlattice formation is most effective. For slow cooling, however, this hump disappears and instead of this a small mimimum appears at Ni_3Fe. This may be interpreted as a result of the general character that the effect disappears at perfect order.

It is to be noted that a considerable increase of the anisotropy takes place when the magnetic cooling continued to below 200°C (Cf. Tab. I). The effect is remarkable for the alloy of large iron content. This may be partly

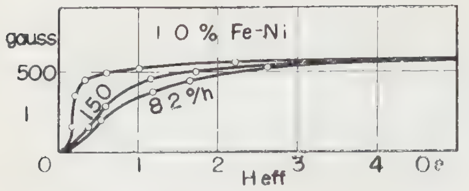

Fig. 1.

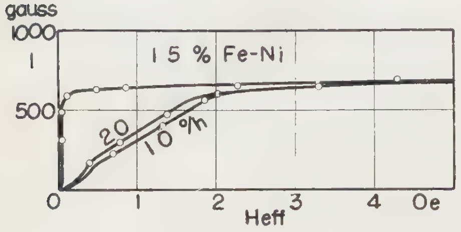

Fig. 2.

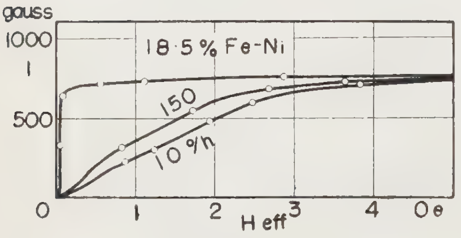

Fig. 3.

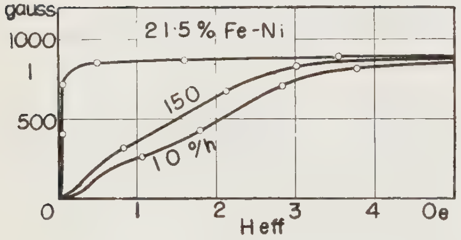

Fig. 4.

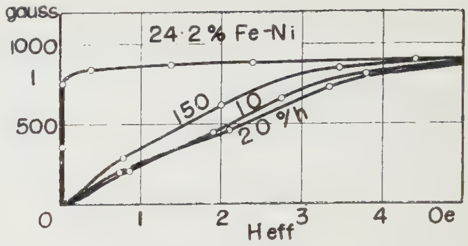

Fig. 5.

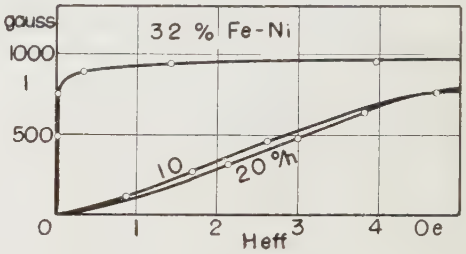

Fig. 6.

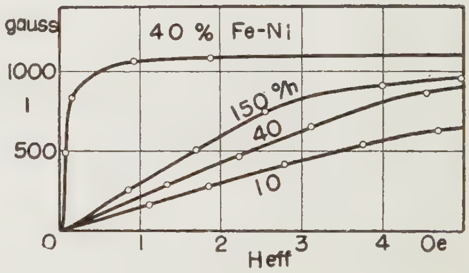

Fig. 7.

Figs. 1–7. Magnetization curves for various compositions of iron-nickel alloy. The curve without figures is obtained after cooling in a longitudinal magnetic field (82°/h). The curves with figures are obtained after cooling from 600°C in a circular magnetic field. The figures mean the cooling rate.

Table I. The coefficient of magnetic anisotropy induced by the magnetic annealing. (K_u in Eq. (2) in erg/cc)

Cooling rate	150°/h	82°/h	40°/h	20°/h	20°/h	10°/h	
temp. range	600–160°	600–190°	600–285°	600–285°	600–80°	600–80°	max. value
10% Fe	136	236	148		124	148	180
15% Fe					550	605	600
18.5%Fe	760	846	883	1010	990	1090	1090
21.5%Fe	1090	1300	1390	1510	1510	1510	1520
24.2%Fe	1230	1440	1540	1780	1540	1540	1860
32% Fe					2710	2400	2700
40% Fe	1680	2230	2570	2950	3460	3830	3830

because the Curie point of order-disorder transformation is lowered with a departure of the composition from Ni_3Fe.

In Fig. 9, the anisotropy energy are plotted as a function of the cooling duration. The abscissa in this graph means the total duration of cooling during which the field was applied. It is seen in this figure that the duration of the slowest cooling (10°C/hour from 600° to 80°C) is long enough for every composition to attain the limiting value of the anisotropy. We can, therefore, regards the envelope of the curves in Fig. 9 as the maximum values of the anisotropy which can be attained by the magnetic annealing.

Specific resistance was also measured for a rapid and the slowest cooling. The result is shown in Fig. 10 as a function of composition. It is seen that the specific resistance decreases by a considerable amount when the specimens are cooled slowly. This may be due to the atomic ordering. It is to be noted that the atomic ordering takes place over a wide range of the composition.

§ 4. Interpretation of the Experimental Results

According to the theory in terms of "strain in directional order[3),8)]," the energy of uniaxial anisotropy is given by

$$K_u = \frac{3}{2} \lambda E \varepsilon , \qquad (3)$$

where λ is a coefficient of magnetostriction, E is the Young's modulus and ε is the strain of directional order. If we assume that the directionally ordered state is attained by the magnetostrictive force, the strain ε would be proportional to the magnetostriction λ_0 at this temperature. If we assume that λ_0 is proportional to λ, i.e. the magnetostriction at room temperature, the strain ε is proportional to λ and accordingly K_u is proportional to λ^2. On the other hand, it is also possible that the strain ε is initiated by the magnetostrictive force but its increase is limited by natural consequence (for instance by decrease of entropy). In such a case the magnitude of the strain ε is not particularly concerned with the magnitude of λ, and then K_u is proportional to λ.

For the purpose of comparison with the above theory, the limiting values of K_u (the envelope in Fig. 8) are devided by λ or λ^2,

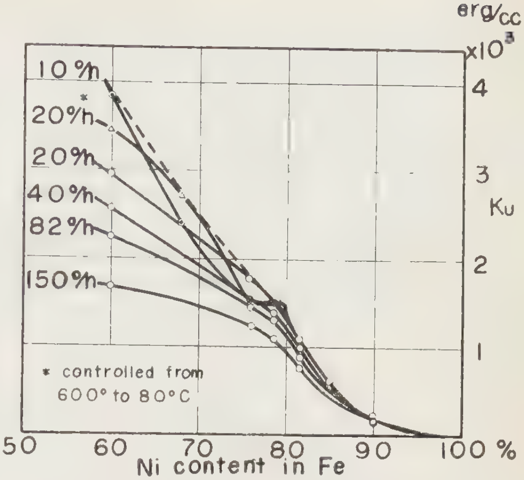

Fig. 8. Coefficient of magnetic anisotropy induced by magnetic cooling for various cooling rate. Ni content is in weight per cent.

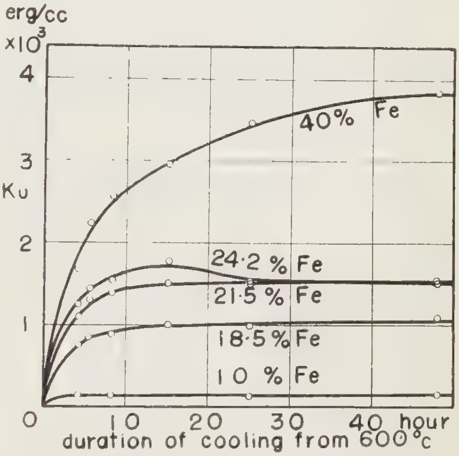

Fig. 9. Coefficient of magnetic anisotropy as a function of duration of cooling for various composition of iron-nickel alloy.

and the ratios are plotted as a function of the alloy composition (Fig. 11). The values of the magnetostriction used here are calculated by the equation

$$\lambda = \sqrt{\frac{2\lambda_{100}^2 + 3\lambda_{111}^2}{5}} \qquad (4)$$

using the numerical values of λ_{100} and λ_{111} measured by F. Lichtenberger[9)]. The Eq. (4) can be derived by averaging the anisotropy of the individual crystallites which is assumed to have an anisotropic magnetostriction.

It was expected that these ratios should be nearly constant or have a maximum value at Ni_3Fe, where ordering is most effective. The maximum in Fig. 11, however, are not at

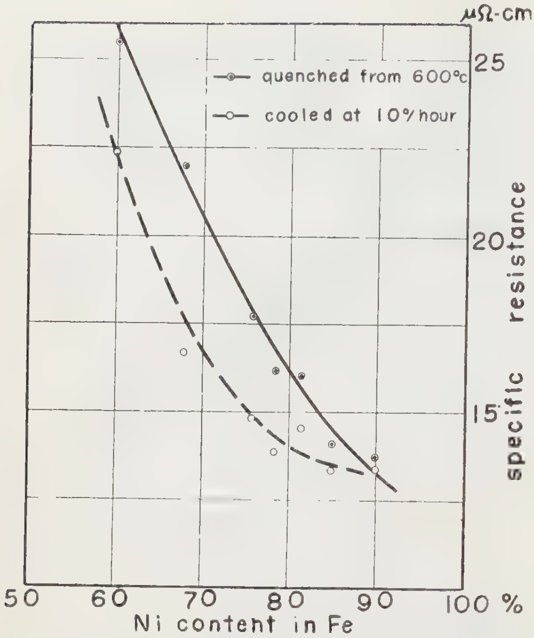

Fig. 10. Specific resistance of iron-nickel alloy after quenched or slowly cooled from 600°C.

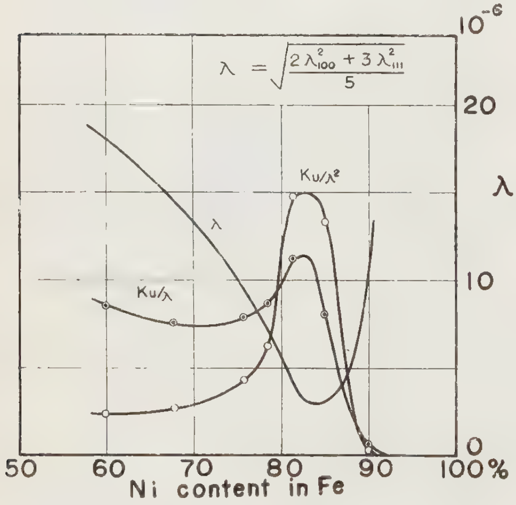

Fig. 11. Comparison of variation of magnetic anisotropy due to magnetic cooling and the variation of the magnetostriction.

Ni_3Fe but at about 82~83%Ni, which corresponds to the composition having the least magnetostriction. This means that the effect is not so small as the magnitude of the magnetostriction at this composition. This cannot be explained by any reasonable modification of the present theory.

According to the theory of "elongated order phase"[6] the coefficient of the uniaxial anisotropy energy is expressed by

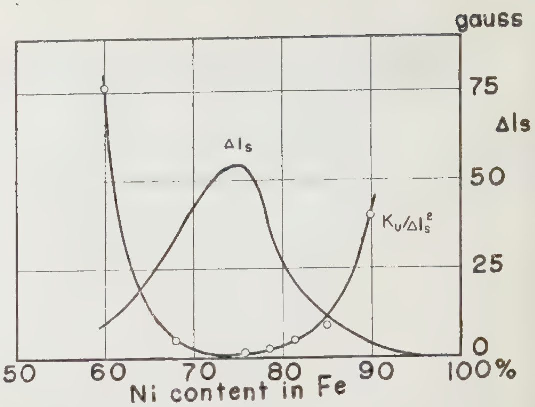

Fig. 12. Comparison of variation of magnetic anisotropy due to magnetic cooling and the variation of the difference of saturation magnetization of between order and disorder phase.

$$K_u = \tfrac{1}{2} N (\Delta J_s)^2 V(1-V) , \qquad (5)$$

where ΔJ_s is the difference of saturation magnetization between order and disorder phase, N is the demagnetizing factor and V is the fractional volume of the order phase. For the purpose of comparison with this theory, the limiting values of K_u (the envelope of the curves in Fig. 8) are devided by $(\Delta J_s)^2$ and the ratios are plotted in Fig. 12. The values of ΔJ_s used here are of E.M. Grabbe[10]. It is to be expected that the ratio $K_u/(\Delta J_s)^2$ is nearly constant or takes a maximum value at Ni_3Fe where the ordering is most effective. The curve in Fig. 12, however, has a deep minimum at about Ni_3Fe, where ΔJ_s takes the maximum value. This means that the effect of magnetic annealing is not so large as the magnitude of $(\Delta J_s)^2$ at this composition. The experimental fact is thus also unfavorable for the theory of "elongated order phase."

Since the anisotropy energy K_u varies in a simple way with the composition as shown in Fig. 8, it is supposed that the origin of the anisotropy is not directly related to any property which varies in a complicated way with composition. It is suggested that the true origin should be described not in terms of the macroscopic property, for instance magnetostriction, saturation magnetization etc., but in terms of the microscopic property, for instance the property of constituent atoms, that of atomic pairs etc..

Thus the authors arrived at a conclusion that the dipole-dipole interaction between adjacent magnetic moments must be taken into consideration. When two dipoles are arranged always in parallel, dipole-dipole interaction gives rise to the anisotropy which have the same functional form as Eq. (2). When, however, the directions of dipole-dipole pairs are distributed with cubic symmetry, as is the case for usual cubic ferromagnets, the uniaxial anisotropies of individual dipole-dipole pairs are compensated with each other. If, we assume, however, that the energy of the dipole-dipole interaction are different between different sorts of atomic pairs, namely between A–A, A–B and B–B pairs and that the atoms are arranged in the directionally ordered manner (i.e. anisotropic distribution of B–B pairs), we can expect that the total dipole-dipole pairs should result in a finite anisotropy. The resultant anisotropy, then, should be related only to the properties of the several sorts of atomic pairs and their distribution. When the system of solid solution is given, the anisotropy should depends merely upon the concentration of the unbalancing pairs. When the concentration of B atoms, C_b, is small, the probability of finding B–B pairs are proportional to C_b^2. This is in good agreement with the fact that the curve in Fig. 8 is approximately parabolic for low concentration of Fe. The comparison with parabolic curve are given in Fig. 13. The agreement is fairly good.

The same interpretation of this effect was proposed by L. Néel[11] and independently by S. Taniguchi and M. Yamamoto[12] at almost the same time as the authors arrived at this conclusions. They carried out the detailed calculations. According to Néel, K_u is given by

$$K_u = nSl_0l_1/15vkT_1 , \tag{6}$$

where n is the number of the nearest neighboring atoms, v is the volume of one atom, k is the Boltzmann factor and T_1 is the temperature at which the field is applied. l_0 and l_1 are the values of l gived by following equation at T_0 (the temperature at which the measurement was made) and T_1 respectively. l is given by

$$l = l_{aa} + l_{bb} - 2l_{ab} , \tag{7}$$

where l_{aa}, l_{bb} and l_{ab} are the coefficients of the dipole-dipole interaction for A–A, B–B and A–B pairs respectively.

S in Eq. (6) is a function of the composition and in the case of ideal solid solution (i.e. having no ordinary superlattice) it is given by

$$S = C_a^2 C_b^2 . \tag{8}$$

This function was plotted in Fig. 13. The agreement with experiment seems to be rather better than C_b^2.

Furthermore Néel carried out the calculation by considering the influence of the ordinary superlattice and showed that in such a case S is given by

$$S = 4C_a^2 C_b^2 \exp(-v/kT)/\sqrt{1+x}\,(1+\sqrt{1+x})^2 , \tag{9}$$

where

$$x = 4C_aC_b[\exp(-v/kT)-1] . \tag{10}$$

v in this equation is an energy unit concering the interchange of the different sorts of atoms and is given by

$$v = v_{aa} + v_{bb} - 2v_{ab} , \tag{11}$$

and it is related to the energy of superlattice formation, Q, by the equation

$$Q = 0.36 \times (3/4) N_v , \tag{12}$$

where N is the Avogadro's number.

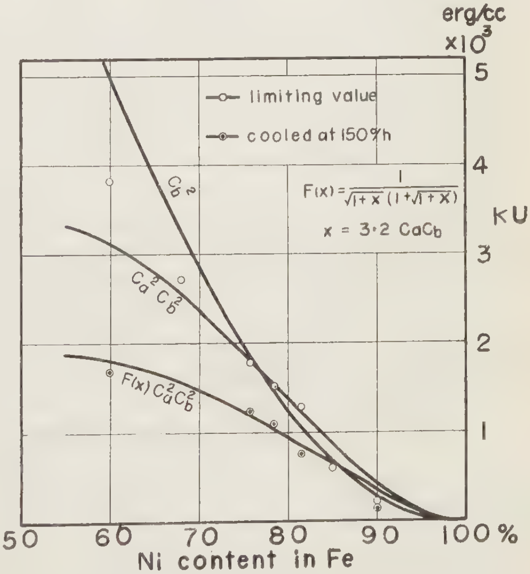

Fig. 13. Dependence of magnetic anisotropy due to magnetic cooling on composition. Comparison between experiment and various functional form.

According to the measurement by S. Iida[13] $Q = 650$ cal/g-atom and hence we have $v = 1.67 \times 10^{-13}$ erg. Assuming that $T_1 = 273° + 500° = 773°$, Eq. (10) becomes $x = 3.2\, C_a C_b$. Putting it into Eq. (9) we have the function S for non-ideal solid solution (i.e. with ordinary ordering). The agreement with experiment is, however, found to be rather worse than Eq. (8), because the expression (9) becomes smaller than (8) with an increase of C_b, the deflection of which is opposite to the experiment. It is to be noted, however, that when it is compared with K_u for relatively rapid cooling, the agreement is considerably improved as shown in Fig. 13. This is probably due to the following reason: The development of ordinary order means an increase of A-B pairs. In the derivation of Eq. (9), the influence of the ordinary order was taken into consideration only through such variation of the total number of A-B pairs. The ordinary order, however, may also have such influence as to oppose the formation of directional order when it approaches to perfect order. This could be taken into consideration, if the entropy at the state of the coexistense of ordinary and directional order were calcurated acculately. Such calculation, however, is rather difficult. The calculation of Eq. (6) was made by treating the problem as a dilute solution of B-B pairs. This may be the reason why Eq. (9) is compatible with experiment only when the degree of ordinary order is small.

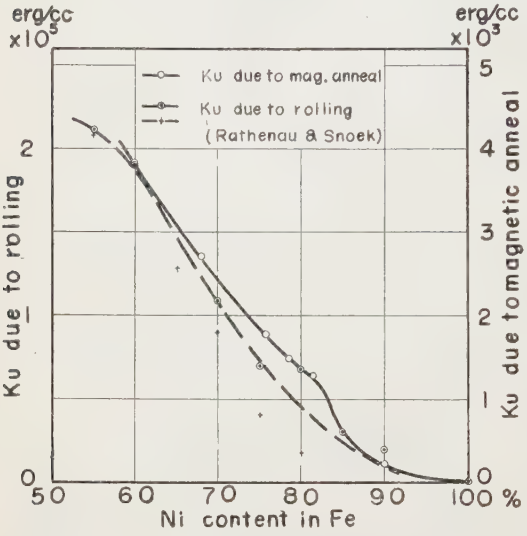

Fig. 14. Comparison of magnetic anisotropy due to magnetic annealing and that induced by mechanical rolling. Roll was made on the specimen which was previously in unicrystalline state [100] (001). Reduction was 2.2 times (after Rathenau and Snoek).

Anyhow, if we consider the accuracy of the experiment and the approximations used in the calculations, we must be satisfied with such degree of the agreement.

In conclusion, we wish to point out that the dependence of K_u obtained here is closely analogous to that of the magnetic anisotropy which is induced by the mechanical rolling. The comparison is shown in Fig. 14. The data for rolling is of G.W. Rathenau and J.L. Snoek[14]. It is induced by the rolling (reduction 2.2 times) of the pseudounicrystalline state (i.e. [100], (001)), which was obtained by recrystalization after severe cold-rolling. It is interesting that K_u in both cases are closely similar in the dependence upon the composition, although they are quite different in the order of magnitude. It is supposed that the anisotropy due to rolling may also have the same origin as that of the magnetic annealing.

§ 5. Summary

The magnetic anisotropy induced by the magnetic annealing was measured as a function of composition for various cooling rate. The limiting values of the anisotropy for each composition were compared with the theory of "strain in directional order" and with that of "elongated order phase." It was concluded that neither theory is compatible with experiment. It was found that the directionally ordered arrangement would result in an anisotropy if the dipole-dipole interaction differs with different sorts of atomic pairs. According to this consideration the magnitude of the anisotropy should be proportional to C_b^2, or according to the Néel's formula to $C_a^2C_b^2$. These functional forms are in good agreement with experiment. It was also found that Néel's formula for the alloy which has the ordinary order is compatible with experiment only when the cooling rate is comparatively rapid, but the agreement is rather worse when the cooling rate is sufficiently slow. The reason may be attributed to the approximation used in the calculation. Comparison was also made with the anisotropy which is induced by the mechanical rolling.

The authors wish to postpone more precise disscussions about this problem to a forthcoming paper, in which the precise measurement of the anisotropy taken for the single crystal of Ni_3Fe shall be reported.

This research was supported by the research grant of the Ministry of Education.

References

1) G. A. Kelsall: Physics **5** (1934) 169.
2) J. F. Dillinger and R. M. Bozorth: Physics **6** (1935) 279.
R. M. Bozorth and J. F. Dillinger: Physics **6** (1935) 285.
3) S. Chikazumi: J. Phys. Soc. Japan **5** (1950) 327, 333.
4) D. A. Oliver and J. W. Shedden: Nature **142** (1938) 209.
5) L. Néel: Compt. Rend. **225** (1947) 109.
L. A. Shubina and J. S. Shur: J. Tech. Phys. USSR **19** (1949) 88.
Kittel, Nesbitt and Shockley: Phys. Rev. **77** (1950) 739.
6) S. Kaya: Rev. Mod. Phys. **25** (1953) 49.
7) S. Kaya: J. Fac. Sci. Hokkaido Imp. Univ. II (1938) 29.
8) S. Chikazumi: Phys. Rev. **85** (1952) 918.
9) F. Lichtenberger: Ann. Phys. **10** (1932) 45.
10) E. M. Grabbe: Phys. Rev. **57** (1940) 728.
11) L. Néel: Compt. Rend. **237** (1953) 1953; J. Phys. et Rad. **15** (1954) 225.
12) S. Taniguchi and M. Yamamoto: Sci. Rep. Res. Inst. Tohoku Univ. **A 6** (1954) 330; S. Taniguchi: Sci. Rep. Res. Inst. Tohoku Univ. **A 7** (1955) 269.
13) S. Iida: J. Phys. Soc. Japan **7** (1952) 373.
14) G. W. Rathenau and J. L. Snoek: Physica **VIII** (1941) 555.

JOURNAL OF THE PHYSICAL SOCIETY OF JAPAN Vol. 10, No. 10, OCTOBER, 1955

Proton Transfer in Hydrogen Bond and Its Participation in π-Electron Systems

By Isao OSHIDA, Yuzuru OOSHIKA and Reikiti MIYASAKA

Kobayasi Institute of Physical Research, Kokubunzi, Tokyo

(Received June 30, 1955)

The infrared spectra of OH or NH groups in hydrogen bonds in 3μ region are divided into two (or three) types according to their wavelengths and intensities. The first group is of the alcoholic type, and the second group is observed when conjugated π-electron systems combine the hydrogen bonds and when the effect of the proton transfer across the hydrogen bond and the "Antenna Effect" are important. Qualitative discussions on the proton transfer are developed and numerical calculations are carried out with simple symmetrical double minimum potentials. The linear combination method solving such problems is shown to be numerically incorrect, though it is convenient for a qualitative consideration. Further evidence and biological importance of the hydrogen transfer participating π-electron systems are discussed.

§ 1. Introduction

In recent years correlations between the infrared absorption spectra of OH or NH streething vibrations and their hydrogen bond forming property have become more and more obvious. The infrared absorption spectra of hydrogen-bonded OH or NH in 3μ region show general trends, *i.e.*, the shift of the absorption maximum towards the longer wave-length, the broadening of the band and the change in the absorption intensity. The problem of the origin and the nature of the hydrogen bond is, in principle, to be solved on the basis of the electronic structure of associated molecules. Theoretical studies along this line have recently been carried out by several investigators. Lennard-Jones and Pople[1] reached the conclusion that the lone-pair electrons in the proton-accepting molecule play important role and that the origin of the hydrogen bond is primarily ascribed to the electrostatic interaction between the donor and the acceptor

Table I. Infrared absorption in 3μ region.

In carbontetrachloride solution

Compound	Monomer	Dimer	Polymer	Literature
Methanol	3640 cm^{-1}	3520 cm^{-1}	3340 cm^{-1}	a
Ethanol	3640		3350	a
n-Propanol	3640		3340	a
t-Butanol	3640	3510	3340	a
Phenol	3610	3470	3390	a
N-methylacetamide	3470	3370	3300, 3090	b
δ-Valerolactam	3430	3230, 3090		b
Acetic acid	3520	3060 2700 2920 2570		c
Benzoic acid	3550	3060 2700 2920 2570		c
Pyrrole	3490	3420——3395		d
Indole	3490	3430——3400		d
Enolized acetylacetone	(intramolecular)		2700	e
In crystal				
Maleic acid (O–H–O=2.47A)			2000	f
Urea oxalate (O–H–O=2.50A)			2100	f
Oxalic acid (O–H–O=2.50A)			1900	f
KH_2PO_4 (O–H–O=2.54A)			2370	f
$NaHCO_3$ (O–H–O=2.55A)			2680	f
Adipic acid (O–H–O=2.68A)			2775	f
Ni-dimethylglyoxime (O–H–O=2.44A)			1775	g

a) Fox and Martin: Proc. Roy. Soc. **A 162** (1937) 419.
b) Tsuboi: Bull. Chem. Soc. Japan **22** (1949) 215.
c) Buswell, Rodebush and Roy: J. Am. Chem. Soc. **60** (1938) 2239.
d) Fuson, Josien. Powell and Utterback: J. Chem. Phys. **20** (1952) 145.
e) Tsuboi: Bull. Chem. Soc. Japan **25** (1952) 385.
f) Lord and Merrifield: J. Chem. Phys. **21** (1953) 166.
g) Rundle and Parasol: J. Chem. Phys. **20** (1952) 1487.

molecule, from their study on the electronic structure of the water molecule[2]. Though their model has been applied to other molecules successfully[3] and though its essential correctness is now considered to be of no doubt, the dynamical aspects of the hydrogen bond, such as the infrared absorption, the proton transfer across the bond towards the acceptor molecule, and the mutual action with conjugated π-electron systems, which are now drawing much attention of investigators, especially from the view of the acid-base problem[4] and from the biological interests, cannot be considered to be treated with by such a simple electrostatic model, and their complete understanding would require the more detailed information about the electronic structure, if we wished to solve the problem straightforward in the orthodox manner. In this paper, we do not attempt such a straightforward treatment, but we shall carry out a qualitative discussion based on the published works and shall bring to light the various interesting properties of the proton in the hydrogen bond.

§ 2. Infrared Absorption of the Hydrogen Bond

It is now well known that the infrared absorption of the OH or NH groups in 3μ region is primarily due to the motion of the proton along the bond direction. If we could obtain the adiabatic potential for the proton in the hydrogen bond by calculating the electronic states for all positions of the proton, we might predict both the position and intensity of the infrared absorption spectra of the hydrogen bond. Unfortunately, a limited number of compounds has been treated on this basis theoretically[5], and the results obtained cannot be considered quite satisfactory. Giving up such a purely theoretical calculation, it is very fruitful to understand various anomalous phenomena which the hydrogen bond exhibits qualitatively on the basis of a simple and unified model.

Coggeshall[6] placed an assumption that the proton in the hydrogen bond beween alcohol molecules moves in an uniform electrostatic field superposed on the proper OH valence force field, and showed a shift of the absorption maximum in the 3μ region towards the longer wave-length and an increase in the absorption intensity. His results seemed to agree with experiments quantitatively, but Francis[7] pointed out that, even though the observed increase in intensity at the absorption maximum is not so large, the broadness of the absorption curve is greatly enhanced and that the integrated intensity does not agree well with Coggeshall's calculation.

In Table I, we listed experimental data on the infrared absorption caused by OH and NH stretching vibration in hydrogen bonds. In general, the absorption maxima shift towards the longer wave-lengths, but the total integrated intensity changes have not neccessarily such a general tendency, though they are not listed in the above table, since they have not always been measured accurately. It is noted that there exist two types of absorption spectra.

i. The total absorption intensity of the valence vibration is more or less increase when the hydrogen bond is formed, but the diffuseness of the band does not become so large, and only one absorption maximum by the bonded group is clearly recognized. These are observed in the case of alcohols and pyrroles.

ii. The total absorption intensity is greatly increased and the diffuseness of the band is much larger than in the case i, and more than two absorption maxima are often recognized. These are observed in the case of *N*-methylacetamide, lactams, and carboxyls.

The above phenomena can be explained as follows on the basis of the relative ease of the proton transfer across the hydrogen bond and its combination with the conjugated π-electron systems.

Case i. Saturated alcohol molecules are considered to be associated into a chain or ring by the hydrogen bond, such as

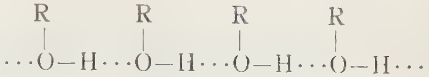

$$\cdots\overset{\overset{R}{|}}{O}-H\cdots\overset{\overset{R}{|}}{O}-H\cdots\overset{\overset{R}{|}}{O}-H\cdots\overset{\overset{R}{|}}{O}-H\cdots \qquad \text{I}$$

Then, if a proton transfer takes place in a chain, a structure

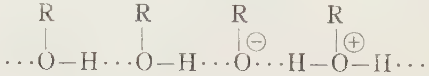

$$\cdots\overset{\overset{R}{|}}{O}-H\cdots\overset{\overset{R}{|}}{O}-H\cdots\overset{\overset{R}{|\ominus}}{O}\cdots H-\overset{\overset{R}{|\oplus}}{O}-H\cdots \qquad \text{II}$$

with a charge separation must be constructed. The energy difference between the structures I and II is chiefly originated from the charge separation and no other contributions seem to be large. In this case, the potential minimum at the acceptor molecule affects the infrared absorption of the hydrogen-bonded OH, but the fraction of the transferred protons in the the chain is not large enough to exhibit another absorption band.

Phenol molecules are also considered to be associated into a chain, such as

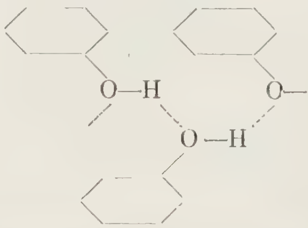

III

If a proton transfer occurs, the structure

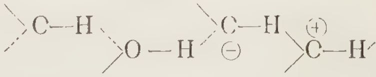

IV

is to be formed. In this case, the difference between the resonance energy of two phenol molecules and the sum of those of a phenolate and a phenolinium ion, as well as the energy of the charge separation, contributes to the difference between the energies of the structure III and IV. The resonance energy of a phenolate ion is larger and that of a phenolinium ion is smaller than that of a neutral phenol molecule itself, both by about 7～8 kcal/mole[8]. Thus the contributions from the resonance energies may compensate each other and may be relatively small compared with the contribution due to the charge separation, and the circumstances are similar with those in alcohol molecules, even though a conjugated system affects the proton transfer. (But, in this case, the absorption intensity is slightly decreased by the hydrogen bond formation[9] which may indicate that the intensity depends on the precise form of the adiabatic potential curve and that a small difference in the force field causes a large difference in intensity.)

Case ii. *N*-methylacetamide molecule is of trans-configuration, and aggregates into a chain, such as

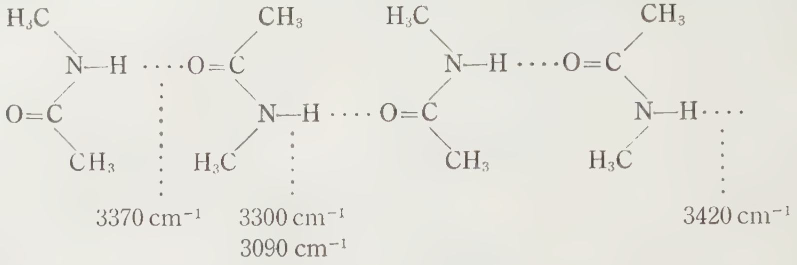

V

Tsuboi[10] observed four infrared bands in 3μ region in addition to the 3470 cm^{-1}. band ascribed to the perfect free NH group. He ascribed these bands as follows: 3420 cm^{-1}. to the free NH at the neighbour of the bonded CO, 3370 cm^{-1}. to the bonded NH at the neighbour of the free CO, 3300 and 3090 cm^{-1}. to the bonded NH at the neighbour of the bonded CO. (These are illustrated above in the structure V.) Now it is the 3300 and 3090 cm^{-1}. bands that we are interested in. If a proton transfer occurs in a chain, the structure

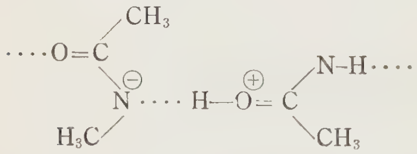

VI

must be formed. As contrasted to the case i, the contribution to the energy required to the proton transfer is not simply that due to the charge separation, but a factor exists that stabilizes the structure of the ionic form VI. In the acceptor cations, the resonance

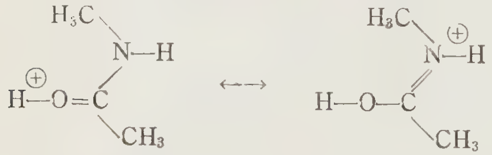

VIIa VIIb

is much larger than in the parent molecule, because the resonance between VIIa and VIIb accompanies no charge separation. In the donor anions, similarly, the resonance

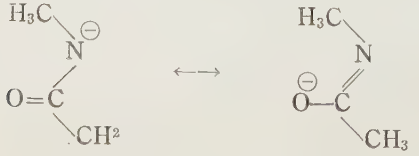

VIIIa VIIIb

is also much larger than in the parent molecule. The sum of the energy of the σ-bonds in the anion and cation is almost the same as that of the two neutral parent molecules. Then the probability of the proton transfer may be much larger than in the case i, if the cooperative effect of hydrogen bonds in a chain is not taken into account. Further, even when the proton in the hydrogen bond remains in its original molecule, the change of the dipole moment accompaying the motion of the proton is greatly enhanced by the induced polarization of the conjugated systems in the neighbouring molecules in the chain. This effect does not exist in the phenol system, because, in this case, the conjugated systems do not form the principal skeleton of the chain and connect with the latter as side groups. This amplification of the motion of the proton means the increase in the effective charge for the light absorption, which was pointed out by one of the authors[11] for the first time in 1951 and named " Antenna Effect." According to his calculation, the change of the dipole moment induced by the NH stretching vibration in the chain, which increases with increasing chain length, is several times larger than that in an isolated molecule. In addition, this effect increases the probability of the proton transfer with increasing chain length, because the interaction between the proton in the chain is much larger than that where no conjugated systems exist in the chain skeleton and thus the cooperative feature is much enhanced. Thus the proton tranfer and the Antenna Effect, together with their mutual action, enhance the perturbation upon the potential of the hydrogen-bonded proton and the infrared absorption spectrum becomes more complex than in the case i. In the following section, we shall discuss these points in more detail. In the dimer band, the cooperative feature is not expected to be large, and we observe only one absorption band.

The carboxylic acid molecules associate into ring dimers,

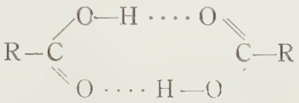

and the circumstances are similar but more convenient to treat quantitatively, though the interaction of two bonds in a ring is stronger than in a chain, and the two band maxima observed in *N*-methylacetamide split into two groups of doublets, of which the lower frequency group is less intense than the higher frequency group as in the case of *N*-methylacetamide. These effects are qualitatively expected from the theoretical point of view, as shown in the next section.

The proton transfer mechanism described above is especially interesting in connection with the acid-base problem[4] and with energy transfer mechanisms in biological systems[12]. Recently, very short and possibly symmetrical hydrogen bonds have been reported in several papers for crystals, *e.g.*, maleic acid, urea oxalate[13], Ni-dimethylglyoxime[14], and enolized acetylacetone in solution[15]. These may be called the case iii. The very short hydrogen bonds ($<$2.50 A) show very long wave-length band ($<$20000 cm.$^{-1}$), and the central potential hill between the two maxima is almost perfectly flattened out and the bonded proton moves freely between the donor and the acceptor groups. Nordman and Lipscomb[16], and Baker[17] tried to calculate their infrared absorption frequency, assuming that the potential for the proton can be represented by the superposition of two symmetrical Morse potential curves. The result of Nordman and Lipscomb is inconvenient for the numerical calculation, and Baker's method for solving the Schrödinger equation is the linear combination of the solutions for the single Morse potential. We solved the Schrödinger equation for the symmetrical Morse potential both by the linear combination method and the numerical integration. It will be shown in § 4 that, although the former method is usually used in the calculation of electronic energy levels of molecules, it is numerically inaccurate in the case under consideration. On the contrary, the linear combination method is very convenient to deduce the general feature of various effects in the hydrogen bonds, and, hence, we shall develop a qualitative discussion by use of that method in the next section, before showing the results of a calculation for a conventional symmetrical model.

§ 3. Qualitative Discussions on the Proton Transfer

In order to illustrate the effect of a proton transfer upon the infrared absorption spectrum, we adopt a typical symmetrical double minimum potential, for which the effect of the proton transfer is expected to be the largest.

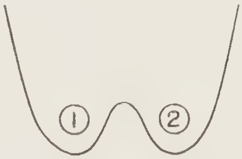

Fig. 1.

Let $\psi_1{}^g, \psi_2{}^g; \psi_1{}^e, \psi_2{}^e$ are the wave functions of the ground and first excited states for the single minimum, 1 and 2 in Fig. 1, respectively. Then the wave functions of the potential under consideration are given by

$$\varphi_1 \approx a(\psi_1{}^g+\psi_2{}^g)+b(\psi_1{}^e+\psi_2{}^e)$$
$$\varphi_2 \approx a'(\psi_1{}^g-\psi_2{}^g)+b'(\psi_1{}^e-\psi_2{}^e)$$
$$\varphi_3 \approx b(\psi_1{}^g+\psi_2{}^g)-a(\psi_1{}^e+\psi_2{}^e)$$
$$\varphi_4 \approx b'(\psi_1{}^g-\psi_2{}^g)-a'(\psi_1{}^e-\psi_2{}^e)$$
$$a^2+b^2 \approx a'^2+b'^2 \approx 1$$

neglecting the contribution from the higher energy states. The dipole moment matrix elements for the transitions causing the infrared absorption in 3μ region, are

$$M_{13}=M_{24}=0$$
$$M_{14}=(a'b-ab')le^*-2(aa'-bb')M_0$$
$$M_{23}=-(a'b-ab')le^*-2(aa'-bb')M_0$$

where $M_{ij}=\int\varphi_i M\varphi_j d\tau\equiv(\varphi_i|M|\varphi_j)$. M is the dipole moment operator of the system, including all electrons and nuclei; $M_0=(\psi_1{}^g|M|\psi_1{}^e)=-(\psi_2{}^g|M|\psi_2{}^e)$; e^*, the effective charge; l, the distance between the two minima; terms such as $(\psi_1{}^k|M|\psi_2{}^{k'})(k, k'=g, e)$ are assumed to be neglected, which does not affect the essential point appreciably. As shown by these equations, the transitions between φ_1 and φ_4 and between φ_2 and φ_3 are allowed and we are to observe two infrared absorption bands due to the proton vibration in a hydrogen bond. (In an unsymmetrical case, mixings of φ's can occur, but only two transitions are expected to be strong.) There appears a term $(a'b-ab')le^*$ in the transition moment expression, and, since it is proportional to le^*, it is possible that the term becomes considerably large, if $a'b$ and ab' are of appropriate values. l is itself large compared with the length involved in the ordinary bond transition moment and further e^* may become much larger than the true protonic charge because of the Antenna Effect. Under the actual circumstances, neither the potential would be symmetrical, nor the proton transfer might be not so easy as described above, except for special cases, but the effect of the proton transfer and the Antenna Effect do still exist, and the term containing le^* appears in the transition moment matrix, though the coefficient is relatively small and though all four transitions are allowed, of which only two are expected to be strong.

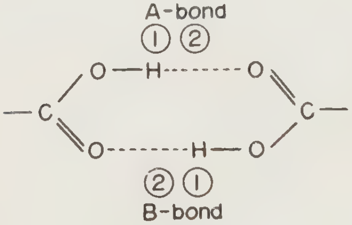

Fig. 2.

Thus it is quite understandable that the variation of the infrared spectra caused by the formation of the hydrogen bonds, when the resonance effect favors the pronton transfer and amplifies the protonic motion, show a considerable different feature from that when such an effect does not exist or rather prevents the proton transfer.

In a ring dimer of two carboxylic acid molecules, the interaction between two hydrogen bonds is larger than that in a chain, and we observe two groups of doublets. In this case, two protons exist either in the potential minimum 1 or 2 in the bonds A and B, in Fig. 2. Let the wave functions for a single minimum ψ_{ki}^{p} $(k=A, B, \mathrm{i}=1, 2; p=e, g.)$ Then the ground state of the dimer splits into four states by the mutual action; we can obtain the corresponding wave functions from their symmetry properties easily,

$$\left.\begin{array}{lll} \mathrm{A}_1 & \Psi_{\mathrm{I}}^{g} & =\psi_{A1}^{g}\psi_{B1}^{g}+\psi_{A2}^{g}\psi_{B2}^{g} \\ \mathrm{A}_2 & \Psi_{\mathrm{II}}^{g} & =\psi_{A1}^{g}\psi_{B1}^{g}-\psi_{A2}^{g}\psi_{B2}^{g} \end{array}\right\}\text{(covalent)}$$

$$\left.\begin{array}{lll} \mathrm{A}_1 & \Psi_{\mathrm{III}}^{g} & =\psi_{A1}^{g}\psi_{B2}^{g}+\psi_{A2}^{g}\psi_{B1}^{g} \\ \mathrm{A}_2 & \Psi_{\mathrm{IV}}^{g} & =\psi_{A1}^{g}\psi_{B2}^{g}-\psi_{A2}^{g}\psi_{B1}^{g} \end{array}\right\}\text{(ionic)}$$

Of course, mixing of Ψ_{I} and Ψ_{III}, and Ψ_{II} and Ψ_{IV} can always occur, respectively, and the expression above is only of approximative one. Similarly, we obtain the following eight wave functions for the configurations where one proton is excited to the higher level,

$$\begin{array}{lll} \mathrm{A}_1 & \Psi_{\mathrm{I}}^{e} & =\psi_{A1}^{e}\psi_{B1}^{g}+\psi_{A1}^{g}\psi_{B1}^{e}+\psi_{A2}^{e}\psi_{B2}^{g} \\ & & \quad +\psi_{A2}^{g}\psi_{B2}^{e} \\ \mathrm{B}_1 & \Psi_{\mathrm{II}}^{e} & =\psi_{A1}^{e}\psi_{B1}^{g}-\psi_{A1}^{g}\psi_{B1}^{e}+\psi_{A2}^{e}\psi_{B2}^{g} \\ & & \quad -\psi_{A2}^{g}\psi_{B2}^{e} \\ \mathrm{B}_2 & \Psi_{\mathrm{III}}^{e} & =\psi_{A1}^{e}\psi_{B1}^{g}-\psi_{A1}^{g}\psi_{B1}^{e}-\psi_{A2}^{e}\psi_{B2}^{g} \\ & & \quad +\psi_{A2}^{g}\psi_{B2}^{e} \\ \mathrm{A}_2 & \Psi_{\mathrm{IV}}^{e} & =\psi_{A1}^{e}\psi_{B1}^{g}+\psi 1_{1}^{g}\psi_{B1}^{e}-\psi_{A2}^{e}\psi_{B2}^{g} \\ & & \quad -\psi_{A2}^{g}\psi_{B2}^{e} \end{array}$$

These are of nonionic structure.

$$\begin{array}{lll} \mathrm{A}_1 & \Psi_{\mathrm{V}}^{e} & =\psi_{A1}^{e}\psi_{B2}^{g}+\psi_{A1}^{g}\psi_{B2}^{e}+\psi_{A2}^{e}\psi_{B1}^{g} \\ & & \quad +\psi_{A2}^{g}\psi_{B1}^{e} \\ \mathrm{B}_1 & \Psi_{\mathrm{VI}}^{e} & =\psi_{A1}^{e}\psi_{B2}^{g}-\psi_{A1}^{g}\psi_{B2}^{e}+\psi_{A2}^{e}\psi_{B1}^{g} \\ & & \quad -\psi_{A2}^{g}\psi_{B1}^{e} \\ \mathrm{B}_2 & \Psi_{\mathrm{VII}}^{e} & =\psi_{A1}^{e}\psi_{B2}^{g}+\psi_{A1}^{g}\psi_{B2}^{e}-\psi_{A2}^{e}\psi_{B1}^{g} \\ & & \quad -\psi_{A2}^{g}\psi_{B1}^{e} \\ \mathrm{A}_2 & \Psi_{\mathrm{VIII}}^{e} & =\psi_{A1}^{e}\psi_{B2}^{g}-\psi_{A1}^{g}\psi_{B2}^{e}-\psi_{A2}^{e}\psi_{B1}^{g} \\ & & \quad +\psi_{A2}^{g}\psi_{B1}^{e} \end{array}$$

These are of ionic structure.

The selection rule shows that, among many transitions from Ψ^{g} to Ψ^{e}, only four transitions

$$\begin{array}{l} \Psi_{\mathrm{I}}^{g} \rightarrow \Psi_{\mathrm{III}}^{e} \\ \Psi_{\mathrm{II}}^{g} \rightarrow \Psi_{\mathrm{II}}^{e} \\ \Psi_{\mathrm{III}}^{g} \rightarrow \Psi^{e}_{\mathrm{VII}} \\ \Psi_{\mathrm{IV}}^{g} \rightarrow \Psi_{\mathrm{V}}^{e} \end{array}$$

are allowed, if we neglect such terms as $\int\psi_i M\psi_j d\tau (i \neq j)$. Thus we can expect to observe four transitions in agreement to experiments. Further, wave functions with the same symmetry property can be mixed with each other, and better wave functions are to be given by the linear combinations of the above wave functions. For example, we can form linear combinations of symmetry A_1, Ψ_{I}^{g}, Ψ_{III}^{g}, Ψ_{I}^{e}, and Ψ_{V}^{e}, or of symmetry B_2, Ψ_{III}^{e}, and Ψ_{VII}^{e}. Then the transitions $\Psi_{\mathrm{I}}^{g} \rightarrow \Psi_{\mathrm{III}}^{e}$ and $\Psi_{\mathrm{III}}^{g} \rightarrow \Psi_{\mathrm{VII}}^{e}$ are slightly modified and split into more than two transitions and a term involving *le** appears in the expressions of the transition moments. Thus, as in the case of *N*-methylacetamide, we can expect that the contribution from *le** term is important for infrared absorption, but, now, four transitions instead of two are considered to be strong and the experimental facts are understandable.

In the above consideration, it is necessary in order that we observe the expected band structure, that some fraction of protons in hydrogen bonds have transferred across the bond towards the acceptor molecule by gaining the thermal energy. In most of carboxylic acids, *pK* for the dissociation of the acidic proton in aqueous solution is 3∼4.5, this corresponds to the free energy required for removing a proton from an acid molecule and attaching it to an water molecule far from the parent acid molecule. We can expect that the energy for transferring a proton across a hydrygen bond is smaller than the energy of dissociation in an aqueous solution, because of the smaller charge separation, and the decrease can be estimated to be about 2 kcal. and the energy for the proton transfer is expected to be in the range of 2∼3 kcal. In chain polymers such as *N*-methylacetamide, this figure may become much smaller due to the cooperative effect, and thus the fraction of transferring protons may be large enough to give the observed band maxima, though the observed fine structure[18] of the infrared spectra is too complex to be predicted satisfactorily by means of the present model.

§ 4. Numerical Calculation for the Symmetrical Potential

The validity of the linear combination method, which we used in a qualitative discussion in the last section and also Baker did, should be examined carefully, since it has not been established that that method would give a satisfactorily good result when we would apply it to obtain numerical results concerning the states involving the excited base wave functions as well as the ground ones. Actually, a comparison with the results of the numerical integrations shows that the linear combination method is only a poor approximation.

In tables and figures below are shown the numerical results of calculations by both linear combination method and numerical integration for the symmetrical potential.

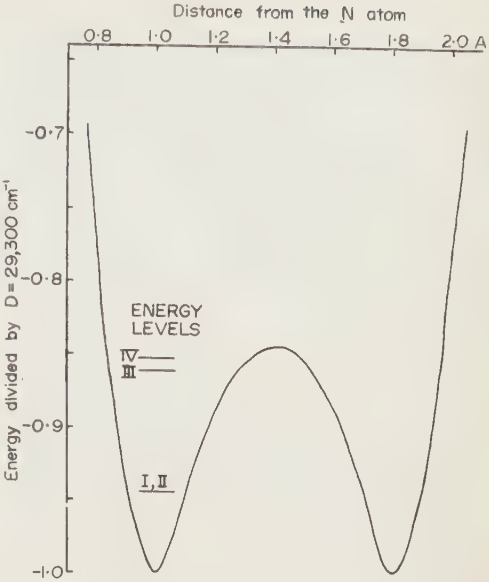

Fig. 3.

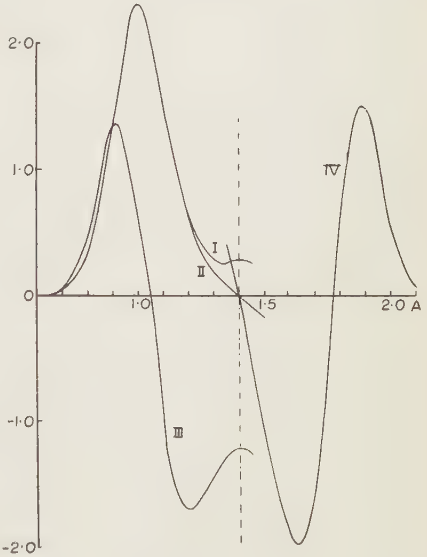

Fig. 4.

With the superposition of the two symmetrical Morse potentials, we carried out calculations both by the linear combination method and the numerical method. We take in the Morse potential

$$V=D(e^{-2a(x-x_e)}-2e^{-a(x-x_e)})$$

where x_e is the position of the potential minium,

$$D=84\,\text{kcal./mole}$$

$$a=2.395\cdot 10^{8}\,\mathrm{cm}^{-1}$$

i.e., the first excitation wave number $=3470\ \mathrm{cm}^{-1}$ for the reduced mass $=1.56\cdot 10^{-24}$gr

For convenience, we adopted these values so as to give the actual N-H dissociation energy and N-H streching frequency, but the calculation below must not be considered to correspond the hydrogen bond including the the N-H group accurately. It is only a model calculation.

Table II. Result by L.C. method for Morse potential.

x_0(A)	0.8	0.85	0.9	1.1	1.47
D (kcal)	4.5	6.3	14.6	27.2	——
ν_{14} (cm^{-1})	3484	3475	3416	3070	3470
ν_{23} (cm^{-1})	3279	3393	3387	3070	3470

Table III. Result by N.I. method at $x_0=0.8$ A.

ΔD (kcal)	4.5 (Morse)	8.5	13.0	20.4
ν_{14}	2380	2230	2700	3150
ν_{23}	1230	1710	2400	3120
ν_{12}	155	18	10	6

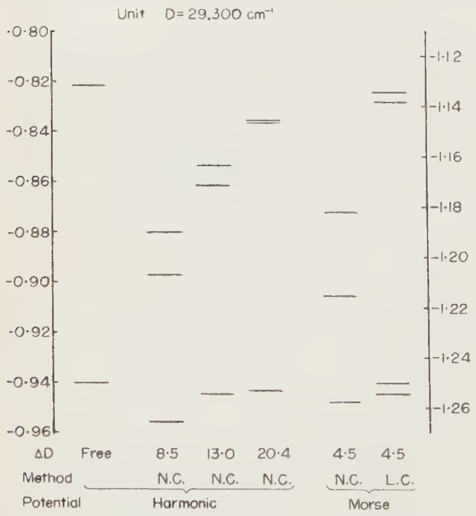

Fig. 5.

N.C. : Numerical calculation.
L.C. : Linear combinetion method.

For the given distance x_0 between the two potential minima formed by the superposition of two Morse potentials, the height of the central potential hill ΔD and the position of the energy levels in unit of D are given in Table II. For $x_0=0.8$A ($\Delta D=4.5$ kcal/mole), the result of our numerical integration shows that the discrepancy between the two method is quite serious and that the linear combination method is no longer useful for quantitative calculations. We also carried out numerical integrations at $x_0=0.8$ A for the potentials formed by the connection of parabolic curves. In this case, we can take arbitrary ΔD by the suitable choice of the central part of the potential curve keeping x_0 constant.

The resutls are shown in Table III and in Fig. 5. For $\Delta D=13$ kcal, the potential curve and the wave functions are also shown. From the result with the superposition of the Morse curve at $x_0=0.8$ A, it is evident that, also for the parabolic types of potentials, the shifts of the energy levels calculated by the linear combination method may be too small, and we cannot use the latter even for larger ΔD at $x_0=0.8$ A. In this respect, Baker's calculation cannot be considered to be numerically correct.

Our calculation using parabolic types of potentials is expected to be applied to short and symmetrical hydrogen bonds as Lord and Merrifiled[13] have reported. Although our numerical calculation was performed for only a fixed value of $x_0(=0.8$ A), the calculated transition wave numbers are in good agreements with the observed wave numbers for 0 ···0 distance between 2.50 A and 2.70 A, when varying ΔD (See Table I). The fixed x_0 does not appear to affect the general trends of the obtained results, if we choice ΔD suitably.

Table IV. Transition moment data $(M/M_0)^2$.

D (kcal)	4.5 (Morse)	8.5	13.0
1—4	0.5	1.1	3.3
2—3	3.8	1.6	3.9
1—2	12.2	24.8	117

Further, we calculated the transition moments of the allowed transitions, neglecting the change in the effective charge, and in Table IV are shown the square of the ratio M/M_0. But the results were not so satisfactory, possibly because of the neglect of the change in the effective charge by the Antenna Effect. The correct theoretical prediction of the absorption intensity or the fine structure of the spectra is, in general, considered to be very difficult. However, it is not unreasonable from the above results to mention that the diffuseness or fine structure of the spectra is predominantly controlled by the proton transfer and that the intensification is due to the Antenna Effect as well as the proton transfer.

In addition, we listed in the tables the transition $\varphi_1\rightarrow\varphi_2$, which will be referred in the next section.

§ 5. Further Remarks on the Proton Transfer

According to the foregoing discussions, it is of no doubt that the proton transfer plays an important role in the infrared absorption due to the longitudinal motion of a proton in the hydrogen bonds. If so, the hydrogen bonds are to show various interesting features which are ascribed to the effects of the proton transfer.

In crystals, it is well established that some of the ferroelectric phenomena and other second order phase transitions, e.g., in Rochelle salt and ammonium chloride, are caused by the cooperative proton transfer, and it may be unecessary to refer these interesting topics[19]. Further, also on the residual entropy in ice crystals[8] and the anomalous proton mobility in water[20], we shall give no comment here. But there is a fact interesting from our point of view in crystals. The replacement of hydrogen-bonded H by D causes usually the expansion of the crystal lattice, if the length of A-H-B is not larger than 2·75 A[4,16], which means that a kind of forces originated in overlapping of the hydrogen wave functions at the two potential minima contributes to the hydrogen bond formation, for, otherwise, the replacement of H by D would be accompanied by the contraction of the wave functions, hence decreasing of the repulsion between the two molecules and the resulting contraction of the lattice. Then it is evident that the simple electrostatic model of the hydrogen bond does not fit this observed fact.

Existence of long wave-length transition, possibly in the far infrared region—In § 3, we gave a qualitative discussion on the energy states of the proton in a double minimum potential, and explained the change of the absorption curves in 3μ region. It is worth while noting that, in addition to the usual absorption in the near infrared region, new long wave-length transitions are to be found in the far infrared region. The transitions $\varphi_1\rightarrow\varphi_2$ in the one-bond system, and $\Psi_{\mathrm{III}}{}^{g}\rightarrow\Psi_{\mathrm{IV}}{}^{g}$ in the ring system, both have transition dipole moments proportional to le^*. Since the wave functions described in § 3 are not exact and their mixing always takes place, several transitions may be actually observed and there may exist also Raman active transitions. Because these transitions prove to be solely due to the proton transfer, we call them "proton transfer transitions." Though, as far as we know, these long wave-length transitions have not yet been clearly identified in the literature published in the "Free World," there exist several phenomena which are explained successfully by the above mechanism. Among these, Saxton and Lane[21] found an anomalous absorption, when measuring the dielectric dispersion of water and alcohol, near 10^{-2} and 1 cm, respectively. These absorptions are successfully explainable by Fröhlich's resonance absorption mechanism[22], but, concerning what resonance they are, Saxton did not give any reference. We propose that these dielectric absorptions may be due to the proton transfer in hydrogen bonds. The wave-lengths of the transitions are in the expected region. But possibilities that they are due to the molecular rotations or intermolecular vibrations cannot be eliminated. In the last few years Russian investigators have studied the fine structure of the infrared absorption curve in 3μ region and the Raman spectrum in the low frequency region[23]. They found several lines near 200 cm^{-1}. in the Raman spectra of ice and organic acids, and also found in the near infrared spectra frequency distances of about the same order of magnitude as the Raman lines. They seem to attempt to ascribe these low frequency transitions to the translational motion of the proton in the hydrogen bonds, which corresponds just to our proton transfer mechanism, though we cannot know the details of their investigations.

Proton and electron transfer in amide chains — After the War II, the molecular mechanism of the biological oxidation and reduction, and that of the energy transfer have attracted much interest of investigators in the related field. In proteins, the polypeptide chain forms cooperative hydrogen bond systems intermediated by conjugated π-electron systems $-\overset{|}{\mathrm{N}}-\overset{|}{\mathrm{C}}=0$, just as in N-methylacetamide discussed previously. Wirtz[24] proposed a hypothesis that the cooperative hydrogen transfer in protein system plays an important role in the energy transfer and estimated that the energy difference between the peptide and peptenol structures was decreased by the resonance in the conjugated systems by about 1 kcal. Schmidt[25], and Geissman[26], who developed Schmidt's view point further, postulate that π-electrons transfer across the hydrogen bonds in proteins by the cooperation with the proton transfers, and that this is just responsible for the enzymatic oxide-reduction. In this respect, it is interesting that Evans and Gergely[27] estimated the energy gap between the filled and unoccupied conduction bands in proteins may be $\sim$2 eV. Eley *et. al*[28]. measured the semiconductivity of a protein film and showed that the estimated energy band separation agreed well with the above figure, but, since the conductivity values measured by them is too high, it is doubtful whether the measured conductivity would be wholly due to the electrons in polypeptide chains. Thus all the hypothesis described above are, at present, neither based on any experimental foundation, nor derived from any established molecular structure.

Tomita and Nakajima[29] studied the photoconductivity of a gelatin film in detail. They found anomalies in various properties at about 75°C; the dark current increases and the photocurrent decreases sharply, and the specific heat shows a λ-type anormally characteristic to the second order phase transition. The carrier of the dark current was the hydrogen only. They ascribed these phenomena to the cooperative proton transfer in the hydrogen bond system in the amide chain. If we accept the phase transition at 75°C, the energy required for the cooperative proton transfer is expected to be about three times kT, *i.e.*, 2 kcal.

Yamamoto[30] also studied the phosporescence of the gelatin-dye systems and found that the formation of hydrogen bonds between the protein and the dye molecules was necessary for phosphorescence and that the experimental results could be excellently interpreted on the basis of the opinion that electrons moved from the dye molecules towards the protein.

Kratky and Schauenstein[31] found that all proteins they had studied showed a characteristic ultraviolet absorption near 25000 cm^{-1}, which they ascribed to the formation of the peptenol structure $H{-}O{-}\overset{|}{C}{=}\overset{|}{N}$ by the proton transfer. Further, the fact that proteins and polypeptides have two NH stretching frequencies near 3300 and 3060 cm^{-1}. has been usually interpreted as due to a frequency interaction between two NH groups, but it is also quite possible that the splitting is caused by the proton transfer, just as in *N*-methylacetamide. Thus various facts found in protein systems can be quite resonably explained by the cooperative proton transfer and their interaction with conjugated systems, though no direct evidence has yet been established.

Hitherto we have discussed the possibility of the proton transfer and its role in various dynamic phenomena. Although it cannot be helped that the discussion stays at largely qualitative steps at present, its importance in biological transfer phenomena and in other chemical aspects is of no doubt. The proton transfer is closely connected with the electron transfer through the participation in conjugated systems and should be treated with as an acid-base problem from the broader point of view. It is most desirable to proceed the theory along this line and to make it as quantitative as possible, though it might be unable to work out completely the problem by the methods established up to the present, for example, we might be forced to abandon the adiabatic approximation.

Acknowledgement

In conclusion, the authors express their sincere thanks to the following; Professors Yamanouchi, Kotani, and Watanabe, Messrs. Miita, Kayama, Sugimoto, and Ariyama for their kindness in providing facilities for using the differential analyzer at the Institute of Industrial Science, Chiba; the members of Prof. Mizushima's Laboratory in University of Tokyo, especially Prof. Shimanouchi and Mr. Tsuboi who kindly gave the experimental data to the authors; Mr. Tsubomura and Mr. Yamaguchi who informed them of the important literatures; Mr. Tomita who showed the details of his unpublished investigation; and Miss Nameki for her help in carrying out the numerical calculation. This work was financially supported by the Scientific Research Fund of the Ministry of Education.

References

1) J. Lennard-Jones and J. A. Pople: Proc. Roy. Soc. **A 206** (1951) 155.
2) J. A. Pople: *ibid.* **A 202** (1950) 323.
3) W. S. Fyfe: J. Chem. Phys. **21** (1954) 2.
W. G. Schneider: *ibid.* **22** (1955) 26.
4) A. R. Ubbelohde and K. J. Gallagher: Acta Cryst. **8** (1955) 71.
5) S. Nagahara: Prog. Rep. (Research Group for the Study of Molecular Structure) No. 3 (1954) 17.
I. Fischer: Arkiv. Fysik **1** (1949) 495.
6) N. D. Coggeshall: J. Chem. Phys. **18** (1950) 978.
7) S. A. Francis: *ibid.* **18** (1951) 505.
8) L. Pauling: "*Nature of the Chemical Bond.*" (Cornell University Press, Ithaca, New York).
9) R. Mecke: Discussions of Faraday Soc. **9** (1950) 161.
10) M. Tsuboi: J. Chem. Soc. Japan **76** (1955) 376.
11) I. Oshida: Lecture at Symposium on π-Electron (1951); Res. Rep. of the Faculty of Engineering, Nagoya University **4** (1951) 69.
12) T. Bücher: Advances in Enzymology **14** (1953) 1.
13) R. C. Lord and R. E. Merrifield: J. Chem. Phys. **21** (1953) 166.
14) R. E. Rundle and M. Parasol: *ibid.* **20** (1952) 1487.
15) M. Tsuboi: Bull. Chem. Soc. Japan **25** (1952) 385.
16) C. E. Nordman and W. N. Lipscomb: J. Chem. Phys. **19** (1951) 1422; **21** (1953) 2077.
17) A. N. Baker: *ibid.* **22** (1954) 1625.
18) For example, V. N. Nikitin and N. G. Yazoslavskĭ: Doklady Nauk. S.S.S.R. **77** (1951) 1015.
I. D. Polyakova, Sh. Sh. Raskin and A. V. Sechkarev: Izvest. Akad. Nauk. S.S.S.R. ser. Fiz. **14** (1950) 419.
19) For example, H. D. Megaw: Acta Cryst. **7** (1954) 187.
20) J. D. Bernal and R. H. Fowler: J. Chem. Phys. **1** (1933) 515.
A. Gierer and K. Wirtz: Ann. Phys. **6** (1949) 257.
21) J. A. Lane and J. A. Saxton: Proc. Roy. Soc. **A 213** (1952) 400.
J. A. Saxton: *ibid.* 473.
22) H. Fröhlich: "*Theory of Dielectrics.*" (Oxford).
23) E. F. Gross and V. I. Vavilov: Doklady Akad. S.S.S.R. **67** (1949) 619; **68** (1949) 473; **74** (1950) 453.
P. D. Simova: *ibid.* **69** (1949) 27.
M. I. Batuev: Zhur. Fiz. Khim. **23** (1949) 1399, 1405.
M. A. Kovner and V. A. Chuenkov: Izvest. Akad. Nauk. S.S.S.R. ser. Fiz. **14** (1950) 435.
N. D. Sokolov: Doklady Akad. Nauk. S.S.S.R. **82** (1952) 369. See also reference 18.
24) K. Wirtz: ZS. f. Naturforsch. **2b** (1947) 94; **2a** (1947) 267; **3b** (1948) 131.
25) W. Schmidt: ZS. f. Naturforsch. **2b** (1947) 98.
W. Schmidt and R. Purrman: *ibid.* **3b** (1948) 411.
26) T. A. Geissmann: Quart. Rev. in Biol. **24** (1949) 309.
27) M. G. Evans and J. Gergely: Biochim. et Biophys. Acta **3** (1949) 188.
28) D. D. Eley, G. D. Parfitt, M. J. Perry and D. H. Taysum: Trans. Faraday Soc. **49** (1953) 79.
29) G. Tomita and T. Nakajima: Reps. Res. Inst. Sci. Ind., Kyushu University, No. 16 (1955).
30) D. Yamamoto: J. Chem. Soc. Japan **73** (1952) 739; **74** (1953), 173.
31) O. Kratky and E. Schauenstein: ZS. f. Naturforsch **5 b** (1950) 281; E. Schauenstein and E. Treiber: J. Polymer Sci. **5** (1950) 145.
O. Kratky and E. Schauenstein: Discussions of Faraday Soc. **11** (1951) 173.

JOURNAL OF THE PHYSICAL SOCIETY OF JAPAN Vol. 10, No. 10, OCTOBER, 1955

Equation of State for Vapor-Liquid-Solid System

By Ikuro SHIMOSE

Faculty of Literature and Science, Yamaguchi University

(Received February 14, 1955)

Generalizing the idea of order-disorder in the alloy theory, we can calculate the unified equation of state for a lattice gas with many interstitial sublattices in the degree of approximation similar to that developed by Bragg-Williams. For $n=9$ (n is the number of sublattices), the concrete equation of state is estimated and the ratio of the number of molecules belonging to each sublattice to their total number is given as a function of molecular density. Then the critical temperature and density for vapor-liquid transition are estimated for $n=4$, 9, 16. Furthermore, it is shown that the density region in the stable liquid phase is very narrow for $n=4$, but that it becomes wider for $n=9$, 16.

§ 1. Introduction

We shall mention some principal methods by which the equation of state for the cooperative system consisting of many molecules can be statistically caluculated. Kirkwood and his co-workers$^{1)}$ numerically calculated the equation of state for the vapor and liquid phases by using the molecular distribution function. Kirkwood and Monroe$^{2)}$ applied this method to the phenomenon of fusion. However, since this method is complicated in its treatment, it may be difficult to calculate the concreate equation of state through the vapor, liquid and solid phases by the above method. Then, Lennard-Jones and Devonshire$^{3)}$, Cernuschi and Eyring$^{4)}$, Ono$^{5)}$, Peek and Hill$^{6)}$, Rowlinson and Curtiss$^{7)}$, and others obtained the equation of state for the vapor and liquid phases by using the cell method. But, since the (solidlike) structure of crystal is used in this method, we may not be able to extend the equation of state to the solid phase by the above method. Furthermore, Frenkel$^{8)}$, Lennard-Jones and Devonshire$^{9)}$, and others statistically interpreted the phenomenon of melting by applying the idea of order-disorder in the alloy theory. Nevertheless, they did not try to extend it to calculation of the unified equation of state through the vapor, liquid and solid phases.

Recently, Kikuchi$^{10)}$ proposed the statistical theory in a general form, by which the unified equation of state through the vapor, liquid and solid phases is given for a lattice gas with interstitial sublattices. It is, however, difficult to calculate it numerically by this theory. Particularly, in his preliminary illustration for a lattice gas (triangular lattice type) with 3 sublattices, he has been obliged to assume a very unnatural potential between molecules in order to obtain the stable liquid phase. Then he has inferred that this may be due to the small number of sublattices, and that such unnaturalness will disappear by increasing this number.

In this paper, by extending the idea of order-disorder in the alloy theory to the case with many ordered parameters, we calculate the concrete equation of state for a lattice gas with many sublattices in the degree of approximation similar to that developed by Bragg-Williams$^{11)}$. Thus we wish to show that the stable liquid phase results from the natural potential between molecules, and to make still clearer the relation between the vapor-liquid and liquid-solid trasitions.

§ 2. Free Energy

We shall deal with a lattice gas having many interstitial sublattices, and confine ourselves to one of the square lattice type (two dimensional) for simplicity. However, the theory of this paper will be applied also to three dimensional systems of any lattice type as well as to two dimensional systems of other types than the square lattice type.

In this section, we shall take up a lattice gas with 4 sublattices (cf. Fig. 1) in order to simplify the description. In the first place, we shall consider the system composed of N molecules and $4M$ lattice points, 4 sublattices each containing M points. Then we shall assume the potential energy $\varphi(r)$ between any two molecules as follows.

$$\begin{aligned} &\varphi(r)=+\infty \quad \text{for} \quad 0\leq r<a\ , \\ &\varphi(r)=-\varepsilon \quad (\varepsilon>0) \quad \text{for} \quad a\leq r<\sqrt{2}\,a\ , \qquad (1) \\ &\varphi(r)=0 \qquad \text{for} \quad r\geq\sqrt{2}\,a\ , \end{aligned}$$

where r is the distance between two molecules and a is the lattice constant for each sublattice. Next we distribute N molecules among $4M$ lattice points in such a way that distance between any two molecules will be equal to or greater than a. In the following method we estimate the number of the above configurations, in which the number of molecules belonging to the sublattices (1), (2), (3), (4) are given by x_1M, x_2M, x_3M, x_4M respectively, where molecular density $\rho=\sum_{i=1}^{4}x_i(=N/M)$. If x_2M, x_3M and x_4M molecules are fixed on the definite lattice points belonging to (2), (3) and (4) sublattices respectively, the number of configurations, in which x_1M molecules are distributed among the lattice points of (1) sublattice under the above condition of the distance between two molecules, is given by

$$\frac{M(1-f_2x_2-f_3x_3-f_4x_4)!}{Mx_1!\cdot M(1-f_2x_2-f_3x_3-f_4x_4-x_1)!}\ ,$$

where $2\geq f_2$, $f_3\gtrsim 1$, $4\geq f_4\gtrsim 1$. We are, however, able to infer from the molecular configurations that all f_i's ($i=2, 3, 4$) may be almost equal to unity in the whole density region except that satisfying a relation

$$\sum_{i=2}^{4}x_i(=\rho-x_1)\lessdot 1\ .$$

Thereupon, we shall assume in order to simplify the estimation that all f_i's are equal to unity in the whole density region. Accordingly, we have

$$\frac{M(1-\rho+x_1)!}{Mx_1!\cdot M(1-\rho)!}$$

for the number of the above cofigurations. Similarly, if x_1M, x_3M and x_4M molecules are fixed, the number of configurations for the distribution of x_2M molecules is given by

$$\frac{M(1-\rho+x_2)!}{Mx_2!\cdot M(1-\rho)!}\ ,$$

and so on. Consequently, the total number of the above configurations is expressed by

$$\prod_{i=1}^{4}\frac{M(1-\rho+x_i)!}{Mx_i!\cdot M(1-\rho)!}\ . \qquad (2)$$

From Eq. (2) the entropy S of the system is given as follows,

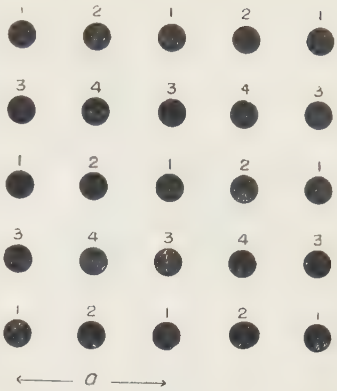

Fig. 1. Square lattice with 4 interstitial sublattices. The figure affixed to each lattice point shows the number of sublattice to which that lattice point belongs.

$$S=k\log\prod_{i=1}^{4}\frac{M(1-\rho+x_i)!}{Mx_i!\cdot M(1-\rho)!}\ ,$$

where k is Boltzmann constant. Applying the Stirling formula, we have

$$S=kM\sum_{i=1}^{4}\{(1-\rho+x_i)\log(1-\rho+x_i) \\ -x_i\log x_i-(1-\rho)\log(1-\rho)\}\ . \qquad (3)$$

Then we shall estimate the internal energy E of the system. Developing Bragg-Williams' approximation, we suppose that each lattice point belonging to (i) sublattice ($i=1, 2, 3, 4$) is occupied by any molecule at the rate of x_i. Thereupon, if we take no account of the pairs of two molecules existing at the smaller distance than a, E is given by

$$E=-\varepsilon M\left\{2\sum_{i=1}^{4}x_i^2+4(x_1x_2+x_1x_3+x_2x_4+x_3x_4)\right\}\ . \qquad (4)$$

As already noticed by Lennard-Jones and Devonshire[9)], Kikuchi[10)], and others, the solid state is ordered and the liquid and vapor states are disordered. Accordingly, it is expected that molecules exist chiefly on one of the four sublattices in the solid state. Without loss of generality, we may choose this sublattice to be (1). Then we introduce the ordered parameters s_i ($i=1, 2, 3, 4$) as follows,

$$x_1=\frac{\rho}{4}(1+s_1)\ , \quad x_j=\frac{\rho}{4}(1-s_j)\ ,$$

$$s_1=\sum_{j=2}^{4}s_j\ , \qquad j=2, 3, 4\ .$$

Now the Helmholtz free energy A is given by the equation $A=E-TS$, where T is the temperature of the system. The values $s_i^{(0)}$ (or $x_i^{(0)}$) of s_i (or x_i, $i=1, 2, 3, 4$) that make A a minimum under the condition $\rho=$constant are given by

(i) for $\rho<\rho_1$, $s_1^{(0)}=s_2^{(0)}=s_3^{(0)}=s_4^{(0)}=0$ (or $x_1^{(0)}=x_2^{(0)}=x_3^{(0)}=x_4^{(0)}=\rho/4$) ,

(ii) for $\rho>\rho_1$, all of $s_1^{(0)}$, $s_2^{(0)}$, and $s_4^{(0)}$ do not equal zero (or all of $x_1^{(0)}$, $x_2^{(0)}$, and $x_4^{(0)}$ do not equal each other), where $s_2^{(0)}=s_3^{(0)}$ (or $x_2^{(0)}=x_3^{(0)}$.

ρ_1 is the definite value of ρ and is obtained in the following method. We choose x_i's ($i=1$, 2, 3) independent variables and x_4 a dependent one, where $x_4=\rho-(x_1+x_2+x_3)$. Then we substitute $x_1=q+2\delta$, $x_2=x_3=q+\delta$, $x_4=q$ into the equations $(\partial A/\partial x_i)_T=0$ ($i=1, 2, 3$), where δ is infinitesimal (of course, $\delta \ll q$).

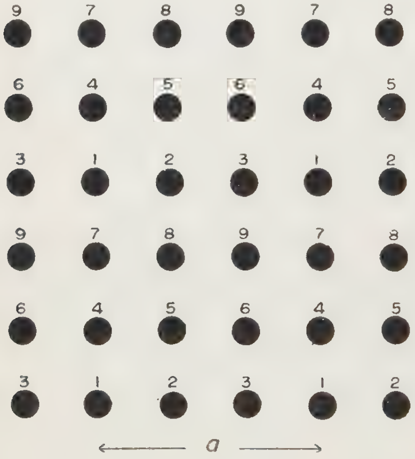

Fig. 2. Square lattice with 9 interstitial sublattices. The figure affixed to each lattice point shows the number of sublattice to which that lattice point belongs.

Further, we expand the terms of the above three equations as the power series in δ and neglect the infinitesimal terms of the higher order than δ. Thus, when $\delta \neq 0$ and $q\approx\rho/4$, the above three equations are all reduced to a relation

$$\frac{1-\rho_1}{\frac{\rho_1}{4}\left(1-\frac{3}{4}\rho_1\right)}=4\frac{\varepsilon}{kT}, \tag{6}$$

which determines the value of ρ_1. Furthermore, the thermal equilibrium state of the system is characterized by the nimimum value of A. Hence, the state of the system for $\rho\leq\rho_1$ corresponds to the disordered state or the vapor and liquid phases. That for $\rho\geq\rho_1$ corresponds to the ordered state or the solid state.

§ 3. Equation of State

If we express the volume V (the area in two dimensional case) of the system by $V=M\tau$, its equation of state is given by

$$p=-\left(\frac{\partial A_{\min}}{\partial V}\right)_T=-\frac{1}{\tau}\left(\frac{\partial A_{\min}}{\partial M}\right)_T, \tag{7}$$

where p is the pressure of the system, and $A_{\min}$ is the minimum value of A under the condition $\rho=$constant.

Now let us deal with the case for $n=9$ (cf. Fig. 2), where n is the number of sublattices. By the same consideration as in the case for $n=4$, we have the following expression for the free energy A.

$$\begin{aligned}A=-M\Big[&2\varepsilon\sum_{i=1}^{9}x_i^2+5\varepsilon\{x_1(x_2+x_3+x_4+x_7)\\&+x_2(x_3+x_5+x_8)+x_3(x_6+x_9)+x_4(x_5+x_6+x_7)\\&+x_5(x_6+x_8)+x_6x_9+x_7(x_8+x_9)+x_8x_9\}\\&+2\varepsilon\{x_1(x_5+x_6+x_8+x_9)+x_2(x_4+x_6+x_7+x_9)\\&+x_3(x_4+x_5+x_7+x_8)+x_4(x_8+x_9)+x_5(x_7+x_9)\\&+x_6(x_7+x_8)\}-kT\sum_{i=1}^{9}\{(1-\rho+x_i)\log(1-\rho+x_i)\\&-x_i\log x_i-(1-\rho)\log(1-\rho)\}\Big],\end{aligned} \tag{8}$$

where the potential energy $\varphi(r)$ between any two molecules is given by Eq. (1), and x_i ($i=1$, 2, 3, $\cdots$, 9) are defined in the same way as in § 2. The ordered parameters s_i ($i=1$, 2, 3, $\cdots$, 9) are introduced as follows,

$$x_1=\frac{\rho}{9}(1+s_1), \quad x_j=\frac{\rho}{9}(1-s_j)$$

$$s_1=\sum_{j=2}^{9}s_j, \quad j=2, 3, \cdots, 9. \tag{9}$$

Then the values $s_i^{(0)}$ (or $x_i^{(0)}$) of s_i (or x_i, $i=1, 2, 3, \cdots, 9$), which make the Helmholtz free energy A a minimum, are given as follows,

(i) for $\rho<\rho_1$, all $s_i^{(0)}$'s ($i=1,2,3,\cdots,9$) equal zero (or all $x_i^{(0)}$'s equal $\rho/9$),

(ii) for $\rho>\rho_1$, all of $s_1^{(0)}$, $s_2^{(0)}$, and $s_5^{(0)}$ do not equal zero (or all of $x_1^{(0)}$, $x_2^{(0)}$, and $x_5^{(0)}$ do not equal each other), where

$$s_2^{(0)}=s_3^{(0)}=s_4^{(0)}=s_7^{(0)},$$
$$s_5^{(0)}=s_6^{(0)}=s_8^{(0)}=s_9^{(0)},$$

that is

$$x_2^{(0)}=x_3^{(0)}=x_4^{(0)}=x_7^{(0)}\,,$$
$$x_5^{(0)}=x_6^{(0)}=x_8^{(0)}=x_9^{(0)}\,. \qquad (10)$$

ρ_1 is determined from the relation

$$\frac{1-\rho_1}{\frac{\rho_1}{9}\left(1-\frac{8}{9}\rho_1\right)}=5\frac{\varepsilon}{kT}\,, \qquad (11)$$

which is obtained by the same consideration as the case for $n=4$.

From Eqs. (7), (8), and (10), the equation of state is given by

$$\begin{aligned}\frac{p\tau}{kT}=&\log(1-\rho+x_1^{(0)})\\&+(x_1^{(0)}-\rho(x_1^{(0)})')\log\frac{1-\rho+x_1^{(0)}}{x_1^{(0)}}\\&+4\sum_{i=2,5}\Big\{\log(1-\rho+x_i^{(0)})\\&+(x_i^{(0)}-\rho(x_i^{(0)})')\log\frac{1-\rho+x_i^{(0)}}{x_i^{(0)}}\\&-9\log(1-\rho)\\&+\frac{2\varepsilon}{kT}\Big[((x_1^{(0)})^2+13(x_2^{(0)})^2+16(x_5^{(0)})^2\\&+10x_1^{(0)}x_2^{(0)}+4x_1^{(0)}x_5^{(0)}+28x_2^{(0)}x_5^{(0)})\\&-2\rho\{x_1^{(0)}(x_1^{(0)})'+13x_2^{(0)}(x_2^{(0)})'\\&+16x_5^{(0)}(x_5^{(0)})'+5(x_1^{(0)}(x_2^{(0)})'+(x_1^{(0)})'x_2^{(0)})\\&+2(x_1^{(0)}(x_5^{(0)})'+(x_1^{(0)})'x_5^{(0)})\\&+14(x_2^{(0)}(x_5^{(0)})'+(x^{(0)})'x_5^{(0)})\}\Big]\,,\end{aligned} \qquad (12)$$

where $(x_i^{(0)})'=(\partial x_i^{(0)}/\partial\rho)_T$, $i=1, 2, 5$. From Eq. (12) we can estimate the value of ε/kT_c $(=1.794)$, where T_c is the critical temperature for the vapor-liquid transition. Next, at the temperature T $(=0.95T_c)$, the values of $x_i^{(0)}$ $(i=1, 2, 5)$ estimated from Eq. (8) are shown in Fig. 3, where ρ_1 $(=0.732)$ is obtained from Eq. (11). Furthermore, the isotherm at the temperature T $(=0.95T_c)$ in $p-1/\rho$ diagram is shown in Fig. 4 and Fig. 5 . In Fig. 4 it corresponds to the vapor and liquid phases (the case for $\rho\leq\rho_1$) and in Fig. 5 the solid phase (the case for $\rho\geq\rho_1$), where ρ_c $(=0.352)$ is the molecular density at the critical point for the vapor-liquid transition.

§ 4. Values of ρ_1 and ρ_c

we can infer the width of the density region in the stable liquid phase from the difference between the values of ρ_1 (at the temperature T_c) and ρ_c, though not with complete accuracy. The values of ρ_1 (at the temperature T_c), ρ_c and ε/kT_c for $n=4, 9, 16$ are given in Table I.

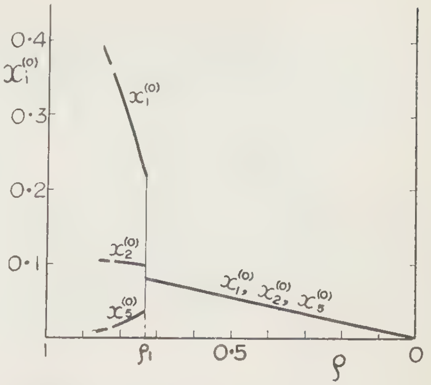

Fig. 3. $x_i^{(0)}-\rho$ curves $(i=1, 2, 5)$. $x_2^{(2)}=x_3^{(0)}=x_4^{(0)}=x_7^{(0)}$, $x_5^{(0)}=x_6^{(0)}=x_8^{(0)}=x_9^{(0)}$.

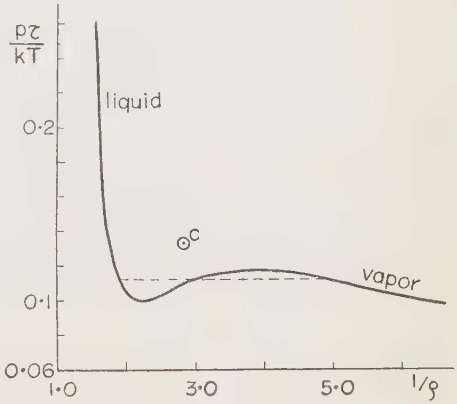

Fig. 4. Isotherm at $T=0.95\ T_c$ for $\rho\leq\rho_1$. C: critical point for vapor-liquid transition, $\rho_c=0.352$.

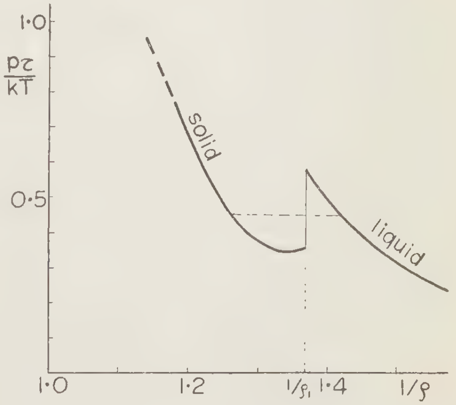

Fig. 5. Isotherm at $T=0.95\,T_c$ for $\rho\geq\rho_1$. $\rho_1=0.732$.

Table I.

n	ρ_1	ρ_c	ε/kT_c
4	0.426	0.377	1.979
9	0.751	0.352	1.794
16	0.696	0.344	2.013

The methods estimating the above values for $n=16$ are obtained by developing those for $n=4$, 9, and the value of ρ_1 for $n=16$ is, particularly, determined from a relation

$$\frac{1-\rho_1}{\frac{\rho_1}{16}\left(1-\frac{15}{16}\rho_1\right)}=10\frac{\varepsilon}{kT}\,. \tag{13}$$

We shall see from Table I that the density region in the stable liquid phase is very narrow for $n=4$, but that it becomes wider for $n=9$, 16.

§ 5. Conclusion

Though the degree of approximation was not completely accurate, we have numerically calculated the unified equation of state through the vapor, liquid and solid phases for a lattice gas with many interstitial sublattices. It is, however, possible that even the qualitative correctness of the above form of the equation of state may not be wholly reliable in the regions of two phase transitions, that is the vapor-liquid and liquid-solid transitions. Recently, by applying the idea of molecular clusters, the author[12)] proposed the statistical theory of the phase transition for a lattice gas with no sublattice, which theory is expected to be qualitatively correct, though only approximate from the quantitative point of view. It is hoped that the above problem may be solved by extending this theory to a lattice gas with many sublattices.

References

1) J. G. Kirkwood, V. A. Lewinson and B. J. Alder: J. Chem. Phys. **20** (1952) 929.
2) J. G. Kirkwood and E. Monroe: J. Chem. Phys. **9** (1941) 514.
3) J. E. Lennard-Jones and A. F. Devonshire: Proc. Roy. Soc. **A 163** (1937) 53; **165** (1938) 1.
4) F. Cernuschi and H. Eyring: J. Chem. Phys. **7** (1939) 547.
5) S. Ono: Memois Fac. Eng. Kyushu Univ. **10** (1947) 195.
6) H. M. Peek and T. L. Hill: J. Chem. Phys. **18** (1950) 1252.
7) J. S. Rowlinson and C. F. Curtiss: J. Chem. Phys. **19** (1951) 1519.
8) J. Frenkel: Trans. Farad. Soc. **33** (1937) 58.
9) J. E. Lennard-Jones and A. F. Devonshire: Proc. Roy. Soc. **A 169** (1939) 317; **170** (1939) 464.
10) R. Kikuchi: J. Chem. Phys. **19** (1951) 1230.
11) W. L. Bragg ane E. J. Williams: Proc. Roy. Soc. **A 145** (1934) 699.
12) I. Shimose: J. Phys. Soc. Japan **9** (1954) 451, 457.

JOURNAL OF THE PHYSICAL SOCIETY OF JAPAN Vol. 10, No. 10, OCTOBER, 1955

An Equivalent Circuit of a Bolometer

By Yoshio URANO
Osaka Industrial Research Institute, Osaka

(Received July 9, 1955)

Regarding a bolometer as an active four-terminal network which connects the heat-flow circuit to the electrical circuit, the equivalent circuit of a bolometer is obtained. By means of this equivalent circuit a physical meaning of the dynamic impedance of a bolometer is made clear. Also, the stability considerations of a bolometer circuit is given.

§ 1. Introduction

Recently R.C. Jones[1)] reported an extensive theory of bolometer performances. Using the dynamic impedance of a bolometer, he discussed the responsivity and the stability of a bolometer circuit. In his theory, however, nothing was mentioned about the relations between this important quantity of the dynamic impedance and the structure of bolometer or the material of the bolometer element. If such points are made clear the theory will give a more useful guide in the design and the application of a bolometer.

For a radiation thermocouple, on the other hand, P.B. Fellgett[2)] introduced a notion of a dynamic impedance. He showed that in terms of an equivalent circuit which is derived from the concept of dynamic impedance the theory of radiation thermocouples can be developed in a compact and unified way.

Since a bolometer is an active element, one cannot apply to it Fellgett's procedure which connects the heat-flow circuit to the electrical circuit by means of an ideal transformer representing the thermoelectric conversion mechanism. But an equivalent circuit theory for an active four-terminal network which is proposed by T. Okabe will give a partinent concept of the dynamic impedance of a bolometer. In the following discussions it is assumed that the all parts of the bolometer element have the same temperature at any given instant, so that the end-effect of the element and the difference between Joulean heating and the heating by incident radiation are both neglected. This assumption may be permitted in almost every cases. And we confine our considerations in the region in which the variations of such quantities as temperature, resistance, current etc. of a bolometer are very small and in linear relations with one anothers. In general, each of these variations is severally a function of the frequency of the variation. It will be easily seen that the formula derived in § 2 and 3 are valid for any frequency, though the frequency-dependence of the various quantities are not explicitly noted.

§ 2. Heat-flow Impedance for Radiation

Since a bolometer as a circuit element is a sort of non-linear resistance, its static properties are given from its voltage-current characteristics. For representing this characteristics it is convenient to take the logarithms of the values of voltage and current as the coordinates. In this representation the diagonal axes correspond to the resistance and the power dissipation of the bolometer.

We denote the biasing current and the resistance of a given bolometer in its operating point with I and R respectively. The bolometer is supposed to be in a radiation field and the radiant power incident upon the bolometer element is denoted as W. Then the total power dissipation P of the bolometer is given by

$$P = I^2R + W\,.$$

If, leaving the radiation field unchanged, we increase the biasing current to $I+dI$, the power dissipation will be increased by an amount

$$dP = I^2 dR + 2IR dI\,. \qquad (1)$$

On the other hand, we suppose that the biasing current is supplied from a constant current generator and the incident radiant power is changed by an amount dW. If the change of the total dissipation equal to it in Eq. (1) is obtained, then

$$dP = I^2 dR' + dW\,. \qquad (2)$$

Now, when the temperature of the environment is held constant, the temperature θ of a given bolometer element is uniquely determined by its total power dissipation. And the resistance of a bolometer is a one-valued function of its temperature. Since equal increase of the power dissipation is given to the same bolometer in its same operating point, the changes of the resistance in Eq. (1) and (2) must be the same: $dR = dR'$. Hence

$$dW = 2IR dI\,,$$

or

$$\frac{dW}{d\theta} = 2IR\frac{dI}{d\theta}\,. \qquad (3)$$

The left hand side of this equation represents the power of the incident radiation which produces unit increase of temperature of the element which is biased from a constant current source or connected to an infinite load impedance. The reciprocal of this quantity may reasonably be called the heat-flow impedance Z_θ of the bolometer for radiation. The right hand side of Eq. (2) is the quantity which can be given from the load curve. Eq. (2) indicates that the heat-flow impedance for radiation is obtained from the load curve.

Now from Eq. (2) and (3)

$$\frac{1}{Z_\theta} = \frac{dW}{d\theta} = \frac{dP}{d\theta} - I^2\frac{dR}{d\theta}\,.$$

The first term of the right hand side is clearly the coefficient of heat loss K from the element to its surroundings. The second term is equal to αP, where α is the temperature coefficient of specific resistance of the element material. Hence

$$\frac{1}{Z_\theta} = K - \alpha P = K\left(1 - \alpha\frac{P}{K}\right)\,. \qquad (4)$$

In this equation P/K gives the working temperature of the bolometer. Therefore, if we use the same element at the same operating temperature, the heat-flow impedance for incident radiation is inversely proportional to the coefficient of heat loss from the element to its surroundings.

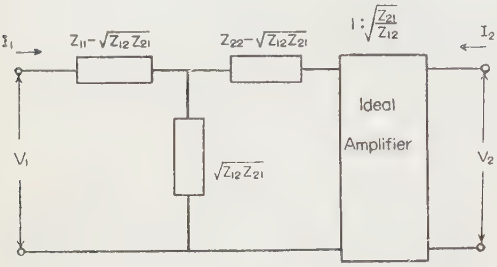

Fig. 1. An equivalent circuit of an active four-terminal network after T. Okabe.

It is to be noted that for a negative type bolometer i.e. a bolometer with negative coefficient of resistance Z_θ is always positive, for K and P must be positive. But for a positive type bolometer Z_θ may become negative when $K<\alpha P$.

Now Eq. (4) may be modified as

$$\begin{aligned}\frac{1}{Z_\theta}&=I^2\frac{dR}{d\theta}\left(\frac{1}{I^2}\frac{dP}{dR}-1\right)\\&=I^2\frac{dR}{d\theta}\left\{\frac{1}{I^2}\frac{d(EI)}{d(E/I)}-1\right\}\\&=I^2\frac{dR}{d\theta}\cdot\frac{2IR}{Z-R}\,,\end{aligned}\tag{5}$$

where E is the voltage drop between the terminals of the bolometer and

$$Z=\frac{dE}{dI}$$

is the dynamic impedance of the bolometer at its operating point.

§ 3. Equivalent Circuits of a Bolometer

According to T. Okabe[3], any linear active four-terminal network can be represented by an equivalent circuit having an ideal amplifier. Let the equations of the network be

$$\begin{aligned}V_1&=z_{11}I_1+z_{12}I_2\,,\\V_2&=z_{21}I_1+z_{22}I_2\,,\end{aligned}\tag{6}$$

where z_{11} and z_{22} are the open-circuit driving point impedances and z_{12} and z_{21} are the open-circuit transfer impedances. Introducing an ideal amplifier of which only function is to multiply the voltage and current by a factor

$$a=\sqrt{\frac{z_{21}}{z_{12}}}\,,\tag{7}$$

one can obtain the equivalent circuit shown in Fig. 1.

Now it is well known that the flow of heat in a conductor and the storage of it in a thermal capacity are represented by the same form of differential equations as that of corresponding electrical phenomena. According to M.J.E. Golay[4] and P.B. Fellgett[2] the thermal quantities corresponding to an electrical current and a resistance in this analogy are respectively a heat flow divided by its absolute temperature and the reciprocal of heat conductivity multiplied by its temperature.

If we consider only the relations between the variations of the various parameters from their values at the given biasing point, we can regard the bolometer as a four-terminal network whose input circuit is the heat-flow circuit and the output circuit is the electrical circuit. Then V_1 and I_1 in Eq. (6) correspond respectively to the temperature rise of the element $d\theta$ and the radiant power dW incident upon the element divided by the absolute temperature θ of the element. V_2 and I_2 correspond respectively to the increase of the voltage dE and that of the current dI of the bolometer.

As has been mentioned in the last section, Z_θ is the heat-flow impedance for radiant power of the bolometer with an infinite load impedance, hence it is easily seen that θZ_θ corresponds to z_{11} in Eq. (6). It is easily seen that the temperature rise of the element by the incident radiation increases the electrical potential drop between the bolometer terminals by an amount

$$dE=I\frac{dR}{d\theta}(\theta Z_\theta)\frac{dW}{\theta}\,.$$

Hence $I(dR/d\theta)\theta Z_\theta$ corresponds to z_{21} of Eq. (6). Next, we consider the case when we increased the biasing current by dI, keeping the incident radiation constant. Owing to the increase of the electrical power dissipation the temperature of the element will be increased by $(d\theta/dI)dI$, while the voltage increase is given as ZdI from the definition of the dynamic impedance Z. Hence $d\theta/dI$ and Z correspond respectively to z_{12} and z_{22} of Eq. (6). Therefore we get as the four-terminal equations for the bolometer

$$d\theta = \theta Z_\theta \frac{dW}{\theta} + \frac{d\theta}{dI} dI ,$$

$$dE = I \frac{dR}{d\theta} \theta Z_\theta \frac{dW}{\theta} + Z dI . \qquad (8)$$

According to the definition

$$\frac{d\theta}{dI} = \frac{d\theta}{dR} \frac{dR}{dI} = \frac{Z-R}{I(dR/d\theta)} .$$

Putting this relation in Eq. (8) and comparing with Eq. (6), we obtain the equivalent circuit of the bolometer shown in Fig. 2.

From the diagram the responsivity of the bolometer with a load impedance Z_L is easily given by

$$S = \frac{Z_L}{Z_L + Z} I \frac{dR}{d\theta} Z_\theta ,$$

or using the relation (5)

$$S = \frac{Z_L}{Z_L + Z} \frac{Z-R}{2IR}$$

which is the formula given by Jones.

For a positive type bolometer the circuit of Fig. 2 can be transformed into its equivalent shown in Fig. 3 in terms of an ideal transformer. In the figure the turns ratio N of the transformer is

$$N^2 = \frac{Z-R}{\theta Z_\theta} = \frac{2IR}{\theta} I \frac{dR}{d\theta}$$

$$= E^2 \frac{2\alpha}{\theta} . \qquad (9)$$

From this diagram the dynamic impedance Z of a bolometer in its given operating point is seen to be

$$Z = R + N^2 \theta Z_\theta ,$$

or

$$Z = R(1 + 2\alpha P Z_\theta) . \qquad (10)$$

Thus the dynamic impedance of a bolometer is composed of the electrical resistance R and the equivalent impedance of the heat-flow circuit $N^2 \theta Z_\theta$. For a negative type bolometer the above transformation gives a transformer with an imaginary turns ratio. This situation can be avoided if one uses the amplification factor of the ideal amplifier

$$a' = \sqrt{-\frac{Z_{21}}{Z_{12}}}$$

instead of a given in Eq. (7). In this case the impedance of the parallel branch of the T-circuit of Fig. 1 is $\sqrt{-z_{12} z_{21}}$, and the turns ratio of the ideal transformer of Fig. 3 is

$$N' = \sqrt{\frac{R-Z}{\theta Z_\theta}} .$$

In this case, however, the ideal amplifier does not only affect the voltage and current but also changes the sign of impedance. And we obtain the corresponding expression for the dynamic impedance of a negative type bolometer which is the same form with Eq. (10).

§ 4. Stability of a Bolometer Circuit

In using a bolometer as a radiation detector it is common to bias the bolometer through a series resistance from a battery or an appropriate source of emf. In this case, however, depending on the values of this resistance it is possible that the operating point of the bolometer be changed irreversibly by a slight disturbance, since the bolometer can have a negative resistance. R.C. Jones discussed this problem in graphical means and gave criterions for unstability. However, his discussions were confined to the steady components or values when the frequency was zoro. It is well known that connecting an appropriate reactance to a negative resistance element the system will oscillate with a certain frequency. Even if a given operating point of a bolometer was stable according to the criterion given by Jones, it is possible that the system oscillates with a non-zero frequency. In this case, of course, the bolometer cannot be regarded as a stable detector. A general answer to this problem will be given from the network theory and especially Nyquist's criterion[5],

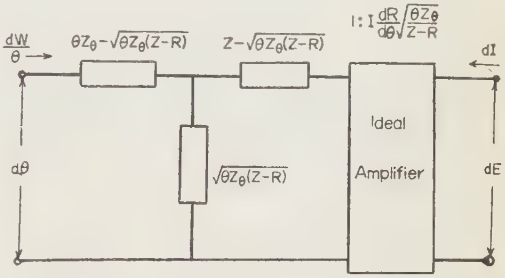

Fig. 2. An equivalent circuit of a bolometer.

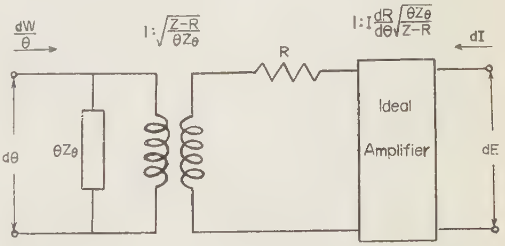

Fig. 3. An alternate form of the circuit of Fig. 2.

As has been mentioned in the last section, a heat-flow circuit is represented as an equivalent RC circuit. Therefore, letting p be a complex frequency, the coefficient of heat loss $K(p)$ from the bolometer element to its environment is a positive real function. Since the dynamic impedance of a bolometer is from Eq. (4) and (10)

$$Z(p)=R\left\{1+\frac{2\alpha P}{K(p)-\alpha P}\right\},$$

$Z(p)$—this is the driving point impedance looked at the electrical terminals— may have poles but cannot have any zeros on the region in which the real part of p is positive, and so a positive type bolometer is a so-called short-circuit stable element. Similarly, a negative type is concluded to be open-circuit stable.

According to Nyquist's theorem a series combination of such an impedance $Z(p)$ and a given load impedance $Z_L(p)$ cannot be stable when it is driven from a voltage source with zero internal impedance, if at all real frequeny

$$|Z_L|>|Z|$$

for a positive type and

$$|Z_L|<|Z|$$

for a negative type.

Without further knowledge of $Z_L(p)$ one cannot generally obtain closer conditions. But if Z_L is, for example, a resistance independent of frequency, we obtain Jones's conditions. For, since $K(p)$ is an RC admittance it may be developed as

$$K(p)=a_\infty p+a_0+\sum_i \frac{a_i p}{p+C_i},$$

where a's and c's are positive real constants. Therefore the dynamic impedance takes the form

$$Z(p)=\frac{a_\infty j\omega+(a_0+\alpha P)+\sum_i \dfrac{a_i j\omega}{j\omega+C_i}}{a_\infty j\omega+(a_0-\alpha P)+\sum_i \dfrac{a_i j\omega}{j\omega+C_i}}$$

on the imginary axis of p i.e. the real frequency axis. Therefore the imaginary part of $Z(j\omega)$ vanishes only at $\omega=0$ and infinity, and there the values of the impedance are respectively R and Z_0, the latter is the slope of the static load curve at the operating point. Hence if

$$-\frac{1}{R}<\frac{1}{Z_L}<-\frac{1}{Z_0},$$

then the real part of the impedance of the series combination has the opposite sign of that of Z at $\omega=0$ and infinity, hence the system is short circuit unstable. For a negative type bolometer we obtain in a similar fashion the corresponding conditions.

§ 5. Conclusion

In the above discussions it is shown that a bolometer can be regarded as an active four-terminal network and is given the equivalent circuit representations for it. In terms of the equivalent circuit one can give a concrete interpretation to the dynamic impedance of a bolometer which is an important quantity in the consideration of bolometer performance. It may easily be shown that other performance characteristics such as a minimum detectable power can be derived in a compact way by means of the equivalent circuit.

Also it is pointed out that Jones's conditions for unstability of a bolometer circuit are adequate only for special cases.

It is a pleasure to acknowledge the constant encouragement of Professor Y. Uchida of Kyoto University. The writer gratefully acknowledge the valuable suggestions from the referees. He also wishes to thank Dr. M. Iwata of this Institute for his discussions during this work and to Miss K. Kosasa for her help in preparing the manuscript.

References

1) R. C. Jones: J.O.S.A. **43** (1953) 1.
2) P. B. Fellgett: Proc. Phys. Soc. **B 62** (1949) 351.
3) T. Okabe: Journ. Jnst. El. Comm. of Japan **36** (1953) 685.
4) M. J. E. Golay: Rev. Sci. Instr. **18** (1947) 347.
5) H. W. Bode: *Network Analysis and Feedback Amplifier Design* (D. van Nostrand Co., 1952), Chapt. IX.

JOURNAL OF THE PHYSICAL SOCIETY OF JAPAN Vol. 10, No. 10, OCTOBER, 1955

On Some Singular Solutions of the Tricomi Equation relating to Transonic Flow

By Kinzo HIDA

Department of Applied Physics, Faculty of Engineering, Naniwa University

(Received June 13, 1955)

Among many investigations hitherto made by making use of the Tricomi equation of mixed type, a series of investigations by Guderley and his collaborators on the flow at Mach number one have given the most reliable informations.

In the present paper are presented two singular solutions of the Tricomi equation relating to transonic flow, both of which have a singularity corresponding to a uniform flow at infinity upstream—either subsonic or supersonic— and tend to Guderley's solution when the Mach number at infinity approaches unity.

First, the solutions are given formally in integral forms, and then their analytic continuations, which are valid within various portions in the hodograph plane, are studied. Special references are also made to the behaviour of the solution in the vicinity of their singular point.

§ 1. Introduction

As is well known, the Tricomi equation of mixed type is suitable for theoretical studies of a two-dimensional transonic flow in the hodograph plane.

Among many investigations hitherto made on the basis of this equation, Guderley's pioneering work[1] and a series of his subsequent works in collaboration with Yoshihara and Barish on the flow at Mach number one[2,3,4] have given the most reliable informations, because the sonic flow can be rigorously formulated as a boundary-value problem as will be seen in the famous Tricomi's original paper[5].

Besides these writers we have found the names such as Cole[6], Trilling and Walker[7] and Trilling[8] with their contributions to studies on the drag of a finite wedge placed in a high-subsonic flow. But the singular solutions adopted by these writers, which correspond to a free-stream at infinity upstream, are of a doublet type, either of the usual form or of order 1/2. According to the analogy to the incompressible flow, the singularity, at least of the latter type, may be considered as a proper one, nevertheless both of them do not coincide with Guderley's one when the Mach number at infinity approaches unity. Quite recently, Mackie and Pack[9] attacked also the same problem by making use of the exact equation for an isentropic inviscid flow, but their solution is merely a generalization of the corresponding one for the incompressible flow by standard method.

In the present paper are presented two singular solutions of the Tricomi equation, both of which tend to Guderley's one in a limiting case of Mach number one. They are considered to correspond with a high-subsonic flow and a low-supersonic flow respectively. (In what follows, we shall refer to these two as "Type I" and "Type II" respectively.)

At first the solutions are given formally in integral forms, and then their series representations, which are valid within various portions in the hodograph plane, as well as the analytic continuation between them, are studied. Special references are made to the behaviour of the solutions in the neighbourhood of their singular point.

Applications of these singular solutions to some physical problems will be reported in separate papers.

§ 2. The Tricomi Equation and its Several Existing Solutions

In this section, we shall give a brief summary of Guderley's limiting solution for a sonic flow as well as Cole's and Trilling's singular solutions for a high-subsonic flow. Special references will be made to the limiting behaviour of the singularity of the latter two when a free-stream speed tends to the sonic speed.

As is well known, the equations of motion for a two-dimensional steady isentropic flow of an inviscid flow can be reduced to simplified forms by making use of the similarity law for transonic flow.

First, we define the non-dimensional components of disturbed velocity u (or w), v in place of the velocity components q_x, q_y by the formulae:

$$u=\frac{\gamma+1}{a_*}(q_x-a_*)=-w\ ,\quad v=\frac{\gamma+1}{a_*}q_y\ ,\qquad (2.1)$$

where a_* is the critical speed at which a local speed of flow becomes equal to the sonic speed and γ denotes the adiabatic constant of the fluid concerned. If we retain only the first order terms of disturbance, the fundamental equations of motion in the hodograph plane for both the transformed Legendre's potential Φ and the stream function ψ can be reduced to the Tricomi equations:

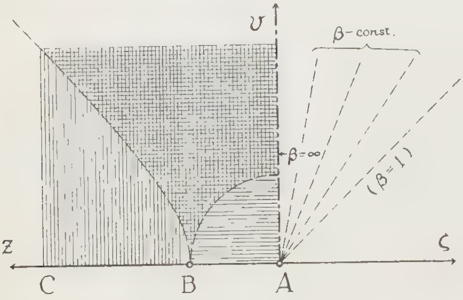

Fig. 1. Reduced hodograph plane.
A: sonic point, B: singular point,
AD: characteristics corresponding to the limiting Mach wave.

$$\left.\begin{aligned}\Phi_{ww}+w\Phi_{vv}=0\ ,\\ \psi_{ww}+w\psi_{vv}=0\ .\end{aligned}\right\}\qquad (2.2)$$

To the same order of approximation, the Cartesian coordinates x and y in the physical plane are connected with the two functions Φ and ψ by the relations:

$$\psi=\rho_*(\gamma+1)\Phi_v\ ,\qquad (2.3)$$

and

$$\left.\begin{aligned}x(w,v)=-\frac{\gamma+1}{a_*}\Phi_w\ ,\\ y(w,v)=\frac{\gamma+1}{a_*}\Phi_v\ ,\end{aligned}\right\}\qquad (2.4)$$

where ρ_* is the density of the fluid at the critical state.

It is evident from Eqs. (2.2) and (2.4) that the differential equation for $y(w, v)$ is also reduced to the Tricomi equation.

Since Eqs. (2.2) are of mixed type, there are two real characteristics through any point in the hyperbolic region where $w<0$ ($u>0$), which are given by

$$v\pm\frac{2}{3}u^{3/2}=\text{const.}\qquad (2.5)$$

For future work a new variable ζ defined by

$$\frac{2}{3}u^{3/2}=\zeta\qquad (2.6)$$

is conveniently used, so that Eq. (2.5) is rewritten in the form:

$$v\pm\zeta=\text{const.}\qquad (2.7)$$

(A) *Cuderley's singular solution*

When the Mach number of a free stream is exactly equal to unity, the solution of the Tricomi equation, having a singularity at the sonic point (*A* in Fig. 1), which corresponds to the infinity upstream in the physical plane, can be determined uniquely up to a scale factor under the following three conditions:

(i) The limiting Mach wave *AD* should not be completely mapped to the point at infinity;

(ii) $\Phi_v=0$ and $\psi=0$ along the w-axis (*ABC*), which are required to show the symmetric flow pattern; and

(iii) Φ_v, ψ must be single-valued functions throughout the region ranging from the infinity upstream to the limiting Mach wave and their values should become infinite at the point *A* as shown in Fig. 1.

The important fact that the solution of the Tricomi equation can be determined uniquely subject to the above three conditions has been first discovered by Guderley[1)], who constructed an appropriate solution for Legendre's transformed potential Φ in the form:

$$\Phi=|u|^{-1}f(\beta,-1)\ ,\quad \beta=v^2/\zeta^2\ .\qquad (2.8)$$

Here, the function $f(\beta, -1)$ should satisfy the ordinary differential equation:

$$\beta(\beta-1)f''+\left(2\beta-\frac{1}{2}\right)f'+\frac{2}{9}f=0\qquad (2.9)$$

and can be expressed in terms of the hypergeometric series $F(a, b;\ c;\ z)$ as follows:

$$f=\beta^{-1/3}F\left(\frac{1}{3},\ \frac{5}{6};\ \frac{3}{2};\ 1-\beta^{-1}\right).\qquad (2.10)$$

As is easily confirmed, this solution is subject to the above three conditions, but is valid only in the hyperbolic (supersonic) region:

$$1<\beta<\infty\,.$$

(B) *Cole's singular solution*

In order to express the high-subsonic flow in the region far from the body, Cole has given a singular solution of the Tricomi equation which is subject to the conditions:

(i) The solution must be regular in the upper-half plane of subsonic region ($z>0$, $v>0$);

(ii) $\psi=0$ and $y=0$ along the z-axis ($v=0$) except at the point B as shown in Fig. 1; and

(iii) ψ should have a singularity of doublet type at the point B.

By using the Fourier-Bessel expansion formula, he obtained two singular solutions in integral forms:

$$\left.\begin{aligned}&\Gamma_-(z, v;\, z_1)\\&\quad=\frac{1}{4}\left(\frac{2}{3}zz_1\right)^{1/3}\int^{\infty}e^{-\alpha v}J_{-1/3}(\alpha z)J_{-1/3}(\alpha z_1)d\alpha\,,\\&\Gamma_+(z, v;\, z_1)\\&\quad=\frac{1}{4}\left(\frac{2}{3}zz_1\right)^{1/3}\int_0^{\infty}e^{-\alpha v}J_{1/3}(\alpha z)J_{1/3}(\alpha z_1)d\alpha\,.\end{aligned}\right\}\tag{2.11}$$

where z is a new variable standing for w, z_1 is the value of z in the undisturbed flow with Mach number M_∞, and $J_\nu(z)$ denotes the Bessel function of the first kind of order ν. The relations between z, w and z_1, w_1 are given by

$$\left.\begin{aligned}z&=\frac{2}{3}w^{3/2}\,,\\z_1&=\frac{2}{3}w_1^{3/2}=\frac{2}{3}(1-M_\infty^2)^{3/2}\,.\end{aligned}\right\}\tag{2.12}$$

Now, tending z_1 in Eq. (2.11) to zero, we have

$$\begin{aligned}&\Gamma_-(z, v;\, 0)\\&\quad=\frac{1}{4\Gamma(2/3)}\left(\frac{4z}{3}\right)^{1/3}\int_0^{\infty}e^{-\alpha v}\alpha^{-1/3}J_{-1/3}(\alpha z)d\alpha\,,\\&\Gamma_+(z, v;\, 0)=0\,.\end{aligned}$$

Further, making use of the relations

$$w=ue^{\pi i}\,,\quad z=\zeta e^{3\pi i/2}\tag{2.13}$$

we obtain an alternative form of the solution, which is valid in the supersonic region, in the form:

$$\Gamma_-(\zeta, v;\, 0)=\frac{3^{2/3}[\Gamma(1/3)]^3}{4\pi^2}\frac{1}{(v^2-\zeta^2)^{1/6}}\,,\quad(v>\zeta)\,.$$

Evidently, this solution has a singularity of order 1/6 on the characteristics $v=\zeta$ ($\beta=1$), and consequently does not satisfy the condition (i) for Guderley's solution.

Later, Cole[10)] investigated the fundamental solution of the Tricomi equation by using the Fourier transforms and found that the solution regular up to the characteristics $v=\zeta$ is given by adding some regular term to the previous one in the form:

$$\left.\begin{aligned}&\Phi=\Gamma_-+\Gamma_++\Gamma_r\,,\\&\text{with}\\&\Gamma_r=-\frac{1}{2\pi^2}\left(\frac{2zz_1}{3}\right)^{1/3}\\&\qquad\times\int_0^{\infty}K_{1/3}(\beta z)K_{1/3}(\beta z_1)\sin\beta v d\beta\,.\end{aligned}\right\}\tag{2.14}$$

But, as z_1 tends to zero, Eq. (2.14) reduces to the form:

$$\frac{3^{1/6}}{2^{2/3}\pi}\frac{\zeta^{2/3}}{v}F\left(1,\ \frac{1}{2};\ \frac{7}{6};\ 1-\beta^{-1}\right)$$

in the supersonic region, so that this solution is still of a different type from Eq. (2.8).

(C) *Trilling's solution*

Trilling's solution is subject to the conditions:

$$\lim_{\substack{w\to w_1\\v\to 0}}x,\,y\sim\frac{C}{\sqrt{w_1-w}}\,,$$

which are imposed to keep the similarity to the analogous incompressible flow at infinity, and is written as follows:

$$\left.\begin{aligned}\Phi=z^{1/3}\int_0^{\infty}e^{-\lambda v}\Big\{&-\frac{\sin\lambda z_1}{\sqrt{3}}[J_{1/3}(\lambda z)+J_{-1/3}(\lambda z)]\\&+\cos\lambda z_1[J_{1/3}(\lambda z)-J_{-1/3}(\lambda z)]\Big\}\frac{d\lambda}{\lambda}\,.\end{aligned}\right\}\tag{2.15}$$

Letting z_1 tend to zero, we have

$$\Phi=z^{1/3}\int_0^{\infty}e^{-\lambda v}[J_{1/3}(\lambda z)-J_{-1/3}(\lambda z)]\frac{d\lambda}{\lambda}\,,$$

which in the supersonic region degenerates to a simple algebraic function as:

$$\Phi=3\left\{[v+(v^2-\zeta^2)^{1/2}]^{1/3}-\frac{\zeta^{2/3}}{[v+(v^2-\zeta^2)^{1/2}]^{1/3}}\right\}\,,\quad(v>\zeta)\,.\tag{2.16}$$

Eq. (2.16) is identically zero at $v=\zeta$ and so has no singularity even at the sonic point A. Obviously, this contradicts to the condition (iii) for Guderley's solutions.

§ 3. Proposal of New Singular Solutions of Type I

Now we proceed to give new singular solutions which have the same singularity as Guderley's one when the Mach number at infinity tends to unity (i.e. $z_1 \to 0$).

At first we consider a solution of Type I, the singular point of which is located on the positive z-axis and which may be considered to correspond with a high-subsonic flow.

We notice first that if we have a certain solution of the Tricomi equation, Eq. (2.2), then we can get another solutions immediately by differentiating it any times with respect to v. Cole pointed out that the singular solutions of doublet type of the higher order could be obtained by applying this procedure to Eq. (2.11), that is, the singular solutions

$$\frac{1}{4}\left(\frac{2}{3}zz_1\right)^{1/3}\int_0^\infty (-\alpha)^n e^{-\alpha v} J_{-1/3}(\alpha z) J_{-1/3}(\alpha z_1)\, d\alpha$$

$$(n\text{: positive integer})$$

are derived from Γ_-.

Generalizing this procedure to the case where n is not necessarily a positive integer, we can find the proper value of n so as to make a solution to have the required property.

Let us consider for the Legendre potential Φ a function defined by

$$T_-(z,\, v;\, z_1) = \left(\frac{2zz_1}{3}\right)^{1/3}\int_0^\infty \alpha^{1/3} e^{-\alpha v} J_{-1/3}(\alpha z_1) \times [J_{-1/3}(\alpha z) + J_{1/3}(\alpha z)]\, d\alpha\,. \quad (3.1)$$

Taking z_1 to be zero, we have

$$T_-(z,\, v;\, 0) \equiv T_-^*(z,\, v) = \frac{2^{1/3}}{\Gamma(2/3)}\left(\frac{2z}{3}\right)^{1/3}\int_0^\infty e^{-\alpha v}[J_{-1/3}(\alpha z) + J_{1/3}(\alpha z)]\, d\alpha\,.$$

Replacing z by ζ as defined in Eq. (2.13) and evaluating the resulting integral, we have the expression valid in the supersonic region as

$$T_-^*(z,\, v) = \frac{1}{\Gamma(2/3)}\left(\frac{2}{3v^2}\right)^{1/3}\left[2^{2/3} F\left(\frac{1}{3},\, \frac{5}{6};\, \frac{2}{3};\, \frac{\zeta^2}{v^2}\right) - \left(\frac{\zeta}{v}\right)^{2/3} F\left(\frac{2}{3},\, \frac{7}{6};\, \frac{4}{3};\, \frac{\zeta^2}{v^2}\right)\right].$$

By making use of the formula for the analytic continuation between hypergeometric function of z and of $1-z$, it reduces finally, with the notations in Eqs. (2.6) and (2.8), to

$$T_-^*(z,\, v) = \frac{2^{1/3}}{\Gamma(2/3)}\left(\frac{2}{3}\right)^{2/3} u^{-1}\beta^{-1/3} F\left(\frac{1}{3},\, \frac{5}{6};\, \frac{3}{2};\, 1-\beta^{-1}\right),$$

which is coincident, except a numerical factor, with Guderley's solution, that is, Eq. (2.8) with the substitution of Eq. (2.10) for the function f.

Next, we shall consider the asymptotic behaviour near the singular point at $z=z_1$, $v=0$. Since the stream function is more interesting than the Legendre potential from the point of view of the applications to physical problems, the new function ψ_{T-} is introduced as

$$\psi_{T-}(z,\, v;\, z_1) = \left(\frac{2zz_1}{3}\right)^{1/3}\int_0^\infty \alpha^{4/3} e^{-\alpha v} J_{-1/3}(\alpha z_1) \times [J_{-1/3}(\alpha z) + J_{1/3}(\alpha z)]\, d\alpha\,, \quad (3.2)$$

which can be obtained with a slight change of numerical factor by the substitution of Eq. (3.1) in Eq. (2.3).

Expanding the Bessel function $J_{-1/3}(\alpha z_1)$ in Eq. (3.2) into a power series and integrating term by term, we have

$$\psi_{T-} = \frac{2^{8/3}3^{1/6}}{\pi} vz^{-8/3} \sum_{m=0}^\infty \frac{\Gamma\{m+(4/3)\}\Gamma\{m+(5/3)\}}{\Gamma\{m+(2/3)\}\Gamma(m+1)} \times \left(\frac{{z_1}^2}{z^2}\right)^m F\left(m+\frac{4}{3},\, m+\frac{5}{3};\, \frac{3}{2};\, -\frac{v^2}{z^2}\right). \quad (3.3)$$

In this derivation, use has been made of the formula for the generalized Lipschitz integral due to Hankel*

$$\int_0^\infty e^{-at} J_\nu(bt) t^{\mu-1}\, dt = \frac{1}{2}\frac{\Gamma\{(\mu+\nu)/2\}}{\Gamma[\{(\nu-\mu)/2\}+1]}\left(\frac{2}{b}\right)^\mu F\left(\frac{\mu+\nu}{2},\, \frac{\mu-\nu}{2};\, \frac{1}{2};\, -\frac{a^2}{b^2}\right)$$
$$- \frac{1}{2}\frac{\Gamma\{(\mu+\nu+1)/2\}}{\Gamma\{(\nu-\mu+1)/2\}}\left(\frac{2}{b}\right)^{\mu+1} aF\left(\frac{\mu+\nu+1}{2},\, \frac{\mu-\nu+1}{2};\, \frac{3}{2};\, -\frac{a^2}{b^2}\right), \quad (3.4)$$
$$(\Re(\mu+\nu)>0\,,\quad \Re(a\pm ib)>0\,,\quad |a|<|b|)\,.$$

Eq. (3.3) can be rewritten by means of the Kummer transformation of hypergeometric function. It follows that

---

* See G. N. Watson, *Theory of Bessel Functions*, Cambridge, (1922), p. 385. This formula is derived from Eq. (2) in the text by making an analytic continuation of a hypergeometric function.

$$\psi_{T-}=\frac{2^{8/3}3^{1/6}}{\pi}\frac{v}{(v^2+z^2)^{4/3}}\sum_{m=0}^{\infty}\frac{\Gamma\{m+(4/3)\}\Gamma\{m+(5/3)\}}{\Gamma\{m+(2/3)\}\Gamma(m+1)}\left(\frac{z_1^2}{v^2+z^2}\right)^m$$
$$\times F\left(m+\frac{4}{3},\ -m-\frac{1}{6};\ \frac{3}{2};\ \frac{v^2}{v^2+z^2}\right). \tag{3.5}$$

With the interpretation of $F(a, b; c; z)$ as a hypergeometric series, this expression may be considered as a double infinite series as long as it has non-zero region of convergence.

We notice first that the asymptotic expansion of a hypergeometric function for large m is given in the form:*

$$F(m+a,\ -m+b;\ c;\ \sin^2\phi)\sim\frac{\Gamma(m+1-b)\Gamma(c)}{\sqrt{\pi}\,\Gamma(m+c-b)}m^{-1/2}(\sin\phi)^{(1/2)-c}(\cos\phi)^{c-a-b-(1/2)}$$
$$\times\cos\left[(2m+a-b)\phi+\frac{\pi}{4}(1-2c)\right]\times\left[1+O\left(\frac{1}{m}\right)\right]. \tag{3.6}$$

It follows from this formula that

$$\left|F\left(m+\frac{4}{3},\ -m-\frac{1}{6};\ \frac{3}{2};\ \frac{v^2}{v^2+z^2}\right)\right|\sim\frac{1}{2}\frac{\Gamma\{m+(7/6)\}}{\Gamma\{m+(5/3)\}}\frac{1}{\sqrt{m}}\frac{(v^2+z^2)^{7/12}}{vz^{1/6}}\left|\sin\left(2m+\frac{3}{2}\right)\phi\right|$$
$$<\frac{\Gamma\{m+(7/6)\}}{\Gamma\{m+(5/3)\}}\frac{(v^2+z^2)^{7/12}}{vz^{1/6}},$$

with

$$\sin^2\phi=\frac{v^2}{v^2+z^2}.$$

Bearing in mind that only the terms of large m are responsible for the convergence of series and substituting this value in Eq. (3.5), then we have

$$\frac{2^{8/3}3^{1/6}}{\pi}\frac{z^{-1/6}}{(v^2+z^2)^{3/4}}\sum_{m=0}^{\infty}\frac{\Gamma\{m+(4/3)\}\Gamma\{m+(7/6)\}}{\Gamma\{m+(2/3)\}\Gamma(m+1)}\left(\frac{z_1^2}{v^2+z^2}\right)^m$$
$$=\frac{2^{8/3}3^{1/6}}{\pi}\frac{z^{-1/6}}{(v^2+z^2)^{3/4}}\frac{\Gamma(4/3)\Gamma(7/6)}{\Gamma(2/3)}F\left(\frac{4}{3},\ \frac{7}{6};\ \frac{2}{3};\ \frac{z_1^2}{v^2+z^2}\right).$$

Hence, it can be confirmed that Eq. (3.5) in absolutely convergent in the region:

$$z_1^2<v^2+z^2,\qquad z\neq 0. \tag{3.7}$$

For convenience's sake, we show this region in Fig. 1 by shading with vertical lines.

In particular, when $v\sim 0$, Eq. (3.5) becomes

$$\psi_{T-}=\frac{2^{8/3}3^{1/6}}{\pi}\frac{v}{z^{8/3}}\left[\frac{\Gamma(4/3)\Gamma(5/3)}{\Gamma(2/3)}F\left(\frac{4}{3},\ \frac{5}{3};\ \frac{2}{3};\ \frac{z_1^2}{z^2}\right)+O(v^2)\right].$$

Taking into account the well-known relation**

$$F(2a,\ a+1;\ a;\ z)=(1-z)^{-2a-1}(1+z),$$

we have finally

$$\psi_{T-}=\frac{2^{11/3}\Gamma(1/3)}{3^{11/6}\pi}v\frac{z^2+z_1^2}{(z^2-z_1^2)^{7/3}}+(Ov^3),\quad (z>z_1). \tag{3.8}$$

Since this expression may exihibit the same feature as

$$\psi=v/(z-z_1)^{7/3} \tag{3.9}$$

as far as the singularity near the point $z=z_1$, $v=0$ is concerned, a few typical streamlines for Eq. (3.9) are drawn in Fig. 2.

---

* A. Erdélyi, *Higher Transcendental Functions*, Vol. 1, McGraw-Hill, (1953), p. 77. The above Eq. (3.6) has been derived from Eq. (17) in the text after some algebraic reductions.

** A. Erdélyi, *loc. cit.* p. 101, Eq. (7).

As is evidently seen from Eq. (3.7), Eq. (3.5) is not valid near the sonic point A and therefore we shall seek for an alternative expression valid within other region.

Now, after expanding the Bessel functions $J_{\pm 1/3}(\alpha z)$ instead of $J_{-1/3}(\alpha z_1)$, the term by term integration of Eq. (3.9) gives

$$\psi_{T-}=\frac{2^{5/3}}{3^{1/3}\sqrt{\pi}}\frac{v^{-5/3}}{\Gamma(2/3)}\left\{\sum_{m=0}^{\infty}\frac{\Gamma\{m+(5/6)\}\Gamma\{m+(4/3)\}}{\Gamma\{m+(2/3)\}\Gamma(m+1)}\left(-\frac{z^2}{v^2}\right)^m F\left(m+\frac{5}{6},\ m+\frac{4}{3};\ \frac{2}{3};\ -\frac{z_1^2}{v^2}\right)\right.$$
$$\left.+\left(\frac{z}{v}\right)^{2/3}\sum_{m=0}^{\infty}\frac{\Gamma\{m+(7/6)\}\Gamma\{m+(5/3)\}}{\Gamma(m+1)\Gamma\{m+(4/3)\}}\left(-\frac{z^2}{v^2}\right)^m F\left(m+\frac{7}{6},\ m+\frac{5}{3};\ \frac{2}{3};\ -\frac{z_1^2}{v^2}\right)\right\}, \tag{3.10}$$

where use has been made of the generalized Lipschitz integral in the form:*

$$\int_0^\infty e^{-at}J_\nu(bt)t^{\mu-1}dt=\frac{b^\nu}{2^\nu a^{\mu+\nu}}\frac{\Gamma(\mu+\nu)}{\Gamma(\nu+1)}F\left(\frac{\mu+\nu}{2},\ \frac{\mu+\nu+1}{2};\ \nu+1;\ -\frac{b^2}{a^2}\right),$$
$$(\Re(\mu+\nu)>0\ ,\quad \Re(a\pm ib)>0\ ,\quad |b|<|a|)\ .$$

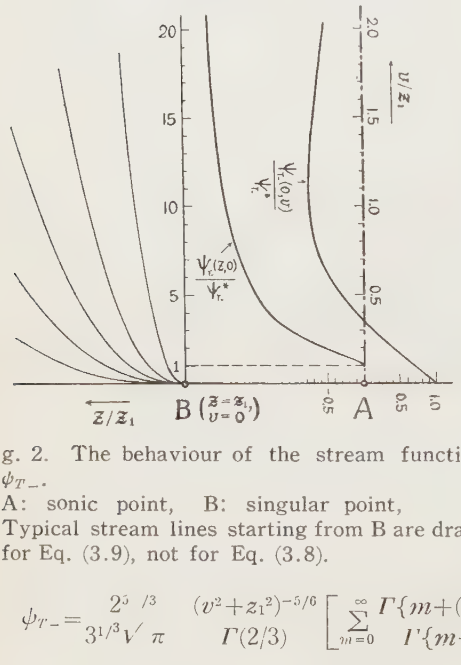

Fig. 2. The behaviour of the stream function: ψ_{T-}.
A: sonic point, B: singular point,
Typical stream lines starting from B are drawn for Eq. (3.9), not for Eq. (3.8).

Rewriting Eq. (3.3) by the analytic continuation between the hypergeometric functions with z and with z^{-1}, and interchanging the order of summation of the double infinite series which results after the hypergeometric series is explicitly written down, then we can easily find that Eq. (3.3) is transformed into Eq. (3.10).

It may be interesting to note that this relation is the case only for the particular combination like in Eq. (3.2) and not for each integral contained in it.

To supplement the above proof of the analytic continuation, we must further show that the two series have at least a portion of their converging region in common. For this purpose, Eq. (3.10) is written by using the Kummer transformation in an alternative form:

$$\psi_{T-}=\frac{2^{5/3}}{3^{1/3}\sqrt{\pi}}\frac{(v^2+z_1^2)^{-5/6}}{\Gamma(2/3)}\left[\sum_{m=0}^{\infty}\frac{\Gamma\{m+(5/6)\}\Gamma\{m+(4/3)\}}{\Gamma\{m+(2/3)\}\Gamma(m+1)}\left(-\frac{z^2}{v^2+z_1^2}\right)^m\right.$$
$$\times F\left(m+\frac{5}{6},\ -m-\frac{2}{3};\ \frac{2}{3};\ \frac{z_1^2}{v^2+z_1^2}\right)+\left(\frac{z^2}{v^2+z_1^2}\right)^{1/3}$$
$$\left.\times\sum_{m=0}^{\infty}\frac{\Gamma\{m+(7/6)\}\Gamma\{m+(5/3)\}}{\Gamma(m+1)\Gamma\{m+(4/3)\}}\left(-\frac{z^2}{v^2+z_1^2}\right)^m F\left(m+\frac{7}{6},\ -m-1;\ \frac{2}{3};\ \frac{z_1^2}{v^2+z_1^2}\right)\right] \tag{3.11}$$

For sufficiently large m, we have from Eq. (3.6)

$$F\left(m+\frac{5}{6},\ -m-\frac{2}{3};\ \frac{2}{3};\ \frac{z_1^2}{v^2+z_1^2}\right)\sim\frac{\Gamma(2/3)}{\sqrt{\pi}}\frac{\Gamma\{m+(5/3)\}}{\Gamma\{m+(4/3)\}}\frac{1}{\sqrt{m}}\frac{(v^2+z_1^2)^{1/12}}{z_1^{1/6}}$$
$$\times\cos\left[\left(2m+\frac{3}{2}\right)\phi-\frac{\pi}{12}\right]\times\left[1+O\left(\frac{1}{m}\right)\right],$$

$$F\left(m+\frac{7}{6},\ -m-1;\ \frac{2}{3};\ \frac{z_1^2}{v^2+z_1^2}\right)\sim\frac{\Gamma(2/3)}{\sqrt{\pi}}\frac{\Gamma(m+2)}{\Gamma\{m+(5/3)\}}\frac{1}{\sqrt{m}}\frac{(v^2+z_1^2)^{1/12}}{z_1^{1/6}}$$
$$\times\cos\left[\left(2m+\frac{13}{6}\right)\phi-\frac{\pi}{12}\right]\times\left[1+O\left(\frac{1}{m}\right)\right],$$

---

* G. N. Watson, *loc. cit.* p. 385, Eq. (2).

with

$$\sin^2\phi = z_1^2/(v^2+z_1^2)\ .$$

By the same deduction as before, Eq. (3.11) is surely an absolutely convergent series in the region:

$$z^2 < v^2+z_1^2\ , \qquad z_1 \neq 0\ . \tag{3.12}$$

In Fig. 1, this region is shown by hatching it with horizontal lines.

In the region $0<z<z_1$ on the z-axis, we have from Eq. (3.11)

$$\psi_{T-}(z,0;z_1) = -\frac{2^{2/3}}{3^{4/3}}\frac{z_1^{-5/3}}{\Gamma(2/3)}\left\{F\left(\frac{5}{6},\ \frac{7}{6};\ \frac{2}{3};\ \frac{z^2}{z_1^2}\right) + \frac{3}{2^{1/3}}\left(\frac{z}{z_1}\right)^{2/3} F\left(\frac{7}{6},\ \frac{3}{2};\ \frac{4}{3};\ \frac{z^2}{z_1^2}\right)\right\}\ ,$$

while Cole's solution, Eq. (2.11), has a corresponding value to be zero.

Further, we put $z=0$ in this formula, then the value of ψ_{T-} at the sonic point A is given by

$$\psi_{T-}(0,0;z_1) \equiv \psi_{T-}^* = -\frac{\Gamma(1/3)}{2^{1/3}3^{5/6}\pi}\, z_1^{-5/3}\ .$$

To study the behaviour near $z=z_1$, it is preferable to take the expression

$$\psi_{T-}(z,0;z_1) = \psi_{T-}^*\, 2\sqrt{3}\left(1-\frac{z^2}{z_1^2}\right)^{-4/3} F\left\{-\frac{1}{6},\ -\frac{1}{2};\ -\frac{1}{3};\ \left(1-\frac{z^2}{z_1^2}\right)\right\}\ ,$$

which is easily obtained from the above formula by the analytic continuation of hypergeometric function.

Finally, for the values on the sonic line, we have, from Eq. (3.11) with $z=0$,

$$\psi_{T-}(0,v;z_1) = \frac{2^2}{3^{4/3}}\frac{(v^2+z_1^2)^{-5/6}}{\Gamma(2/3)} F\left(\frac{5}{6},\ -\frac{2}{3};\ \frac{2}{3};\ \frac{z_1^2}{v^2+z_1^2}\right)\ .$$

In Fig. 2 are also shown the values of ψ_{T-} referred to ψ_{T-}^* on both z- and v-axis.

To this place, we have considered exclusively the solution corresponding to the first of Cole's solution, i.e. Γ_- in Eq. (2.11), but the second solution, which corresponds to Γ_+, can be given as well in the form:

$$T_+(z,v;z_1) = \left(\frac{2zz_1}{3}\right)^{1/3}\int_0^\infty \alpha^{1/3}e^{-\alpha v}J_{1/3}(\alpha z_1)[J_{-1/3}(\alpha z) - 2J_{1/3}(\alpha z)]d\alpha\ . \tag{3.13}$$

Since this expression tends to zero together with z_1, it is quite different from Guderley's solution, but it remains still to be the singularity at the point $z=z_1$, $v=0$.

Defining the stream function ψ_{T+} instead of the Legendre potential T_+, as

$$\psi_{T+}(z,v;z_1) = \left(\frac{2zz_1}{3}\right)^{1/3}\int_0^\infty \alpha^{4/3}e^{-\alpha v}J_{1/3}(\alpha z_1)[J_{-1/3}(\alpha z) - 2J_{1/3}(\alpha z)]d\alpha\ , \tag{3.14}$$

then we have the formulae, which correspond with Eqs. (3.5) and (3.11) respectively, in the form:

$$\left.\begin{aligned}
\psi_{T+} &= -\frac{2^{8/3}3^{1/6}}{\pi}\frac{vz_1^{2/3}}{(v^2+z^2)^{5/3}} \\
&\quad\times\sum_{m=0}^{\infty}\frac{\Gamma\{m+(5/3)\}\Gamma(m+2)}{\Gamma(m+1)\Gamma\{m+(4/3)\}}\left(\frac{z_1^2}{v^2+z^2}\right)^m F\left(m+\frac{5}{3},\ -m-\frac{1}{2};\ \frac{3}{2};\ \frac{v^2}{v^2+z^2}\right)\ , \\
&\text{and} \\
\psi_{T+} &= \frac{2^{5/3}3^{2/3}}{\sqrt{\pi}\,\Gamma(1/3)}\frac{z_1^{2/3}}{(v^2+z_1^2)^{7/6}} \\
&\quad\times\left[\sum_{m=0}^{\infty}\frac{\Gamma\{m+(7/6)\}\Gamma\{m+(5/3)\}}{\Gamma\{m+(2/3)\}\Gamma(m+1)}\left(-\frac{z^2}{v^2+z_1^2}\right)^m F\left(m+\frac{7}{6},\ -m-\frac{1}{3};\ \frac{4}{3};\ \frac{z_1^2}{v^2+z_1^2}\right)\right.
\end{aligned}\right\}$$

$$-2\left(\frac{z^2}{v^2+z_1^2}\right)^{1/3}\sum_{m=0}^{\infty}\frac{\Gamma\{m+(3/2)\}\Gamma(m+2)}{\Gamma(m+1)\Gamma\{m+(4/3)\}}\left(-\frac{z^2}{v^2+z_1^2}\right)^m \times F\left(m+\frac{3}{2}, -m-\frac{2}{3}; \frac{4}{3}; \frac{z_1^2}{v^2+z_1^2}\right)\Bigg]. \tag{3.15}$$

It is easily shown as before that these series are absolutely convergent in the regions

$$z^2+v^2>z_1^2 \quad \text{and} \quad z^2-v^2<z_1^2 \tag{3.16}$$

respectively.

In the close vicinity of the point $z=z_1$, $v=0$, we have, after some reductions, the following representations from Eq. (3.15)

$$\psi_{T+}=-\frac{2^{11/3}\Gamma(1/3)}{3^{11/6}\pi}v\frac{(z^2+z_1^2)}{(z^2-z_1^2)^{7/3}}+\frac{2^{11/3}}{7\cdot 3^{1/3}}\frac{vz^{-8/3}}{[\Gamma(1/3)]^2}F\left(\frac{4}{3}, \frac{5}{3}; \frac{10}{3}; 1-\frac{z_1^2}{z^2}\right)+O(v^3) \quad (\text{for} \quad z_1<z),$$

$$\psi_{T+}=\frac{2^{5/3}}{3^{5/6}\Gamma(2/3)}\frac{z_1}{(z_1^2-z^2)^{4/3}}F\left(-\frac{1}{6}, -\frac{1}{2}; -\frac{1}{3}; 1-\frac{z^2}{z_1^2}\right)+O(v^2) \quad (\text{for} \quad z_1>z).$$

By comparing these formulae with the corresponding ones for ψ_{T-}, it can be found that the combined stream function from ψ_{T-} and ψ_{T+} in the form:

$$\psi_T=\psi_{T+}+\psi_{T-} \tag{3.17}$$

becomes less singular at $z=z_1$, $v=0$. (It may be, at best, of the type $\mathfrak{J}[Z\log Z]$, Z being $(z-z_1)+iv$.) Nevertheless, Eq. (3.17) has still the property that the singularity of Guderley's type will appear as z_1 tends to zero.

The values of ψ_{T+} on the sonic line and especially on the sonic point are easily evaluated from Eq. (3.15), namely,

$$\psi_{T+}(0, v; z_1)=\frac{2^{7/3}}{3^{4/3}\pi}\frac{1}{\Gamma(2/3)}\frac{z_1^{2/3}}{(v^2+z_1^2)^{7/6}}F\left(-\frac{1}{3}, \frac{7}{6}; \frac{4}{3}; \frac{z_1^2}{v^2+z_1^2}\right),$$

and

$$\psi_{T+}(0, 0; z_1)\equiv\psi_{T+}^* = \frac{2^{2/3}z_1^{-5/3}}{3^{4/3}\Gamma(2/3)}=-\psi_{T-}^*.$$

§ 4. Proposal of New Singular Solutions of Type II

While the solutions mentioned in the previous section have a singularity at a point in the subsonic region, solutions with their singularity in the supersonic region will now be given.

Considering that the variables ζ, z, which are real in supersonic and subsonic regions respectively, are connected with Eq. (2.13), we define ζ_1 as a real parameter by

$$\zeta_1=z_1e^{-3\pi i/2} \tag{4.1}$$

and then the following relations hold identically

$$z_1^{1/3}J_{\pm 1/3}(\alpha z_1)=\mp\zeta_1^{1/3}I_{\pm 1/3}(\alpha\zeta_1).$$

Now, we shall consider new solutions corresponding to Eqs. (3.1), (3.13), respectively, as follows:

$$\left.\begin{aligned} S_-(z, v; \zeta_1)&=\left(\frac{2z\zeta_1}{3}\right)^{1/3}\int_0^\infty \alpha^{1/3}e^{-\alpha v}I_{-1/3}(\alpha\zeta_1)[J_{-1/3}(\alpha z)+J_{1/3}(\alpha z)]d\alpha, \\ S_+(z, v; \zeta_1)&=\left(\frac{2z\zeta_1}{3}\right)^{1/3}\int_0^\infty \alpha^{1/3}e^{-\alpha v}I_{1/3}(\alpha\zeta_1)[2J_{1/3}(\alpha z)-J_{-1/3}(\alpha z)]d\alpha. \end{aligned}\right\} \tag{4.2}$$

In the limiting case when $\zeta_1 \to 0$, these equations tend, respectively, to the forms:

$$S_-(z, v; 0) \equiv S_-^*(z, v) = \frac{2^{1/3}}{\Gamma(2/3)} \left(\frac{2z}{3}\right)^{1/3} \int_0^\infty e^{-\alpha v} [J_{-1/3}(\alpha z) + J_{1/3}(\alpha z)] d\alpha ,$$

$$S_+(z, v; 0) = 0 .$$

It is obviously seen that $S_-^*(z, v)$ is identical with $T_-^*(z, v)$ as defined before.

Although Eqs. (4.1) are derived formally, these integrals are certainly convergent under the condition:

$$v > \zeta_1 , \qquad z > 0 ,$$

which is easily found by substituting, in the integrand, the asymptotic forms for both the Bessel functions $J_{\pm 1/3}(\alpha z)$ and the modified Bessel functions $I_{\pm 1/3}(\alpha \zeta_1)$.

From the mathematical theory of partial differential equations, it is clear that the singularity in the hyperbolic region will extend, in general, along its characteristics passing through the point, but in the elliptic region there are no real characteristics and so the above condition for v should become unnecessary.

Then, we shall consider the various expressions of Eq. (4.2), together with their domains of convergence. As in the previous section, we begin with the stream functions defined by

$$\left.\begin{aligned} \psi_{S-} &= \left(\frac{2z\zeta_1}{3}\right)^{1/3} \int_0^\infty \alpha^{4/3} e^{-\alpha v} I_{-1/3}(\alpha \zeta_1) [J_{-1/3}(\alpha z) + J_{1/3}(\alpha z)] d\alpha , \\ \psi_{S+} &= \left(\frac{2z\zeta_1}{3}\right)^{1/3} \int_0^\infty \alpha^{4/3} e^{-\alpha v} I_{1/3}(\alpha \zeta_1) [2J_{1/3}(\alpha z) - J_{-1/3}(\alpha z)] d\alpha . \end{aligned}\right\} \tag{4.3}$$

In the first place, we expand the modified Bessel functions in power series and perform the integrations term by term. Then, after some calculations, the following formulae are obtained:

$$\left.\begin{aligned} \psi_{S-} &= \frac{2^{8/3}3^{1/6}}{\pi} \frac{v}{(v^2+z^2)^{4/3}} \sum_{m=0}^\infty \frac{\Gamma\{m+(4/3)\}\Gamma\{m+(5/3)\}}{\Gamma\{m+(2/3)\}\Gamma(m+1)} \left(-\frac{\zeta_1^2}{v^2+z^2}\right)^m \\ &\qquad \times F\left(m+\frac{4}{3}, -m-\frac{1}{6}; \frac{3}{2}; \frac{v^2}{z^2+v^2}\right) , \\ \psi_{S+} &= \frac{2^{8/3}3^{1/6}}{\pi} \frac{v\zeta_1^{2/3}}{(v^2+z^2)^{5/3}} \sum_{m=0}^\infty \frac{\Gamma\{m+(5/3)\}\Gamma(m+2)}{\Gamma(m+1)\Gamma\{m+(4/3)\}} \left(-\frac{\zeta_1^2}{v^2+z^2}\right)^m \\ &\qquad \times F\left(m+\frac{5}{3}, -m-\frac{1}{2}; \frac{3}{2}; \frac{v^2}{z^2+v^2}\right) , \end{aligned}\right\} \tag{4.4}$$

which correspond to Eq. (3.5) and the first of Eq. (3.15) respectively and which also are obtained by using the substitution (4.1) in these equations. Both series are absolutely convergent in the region:

$$z^2 + v^2 > \zeta_1^2 .$$

The expression valid in the region near the sonic point can be obtained from Eq. (4.4) by transforming the hypergeometric functions in it into the alternative expressions with the variable $-v^2/z^2$ by the Kummer transformation, then interchanging the order of summation of the resulting double series and finally making use of the Kummer transformation again. Thus, we have

$$\begin{aligned} \psi_{S-} &= \frac{2^{5/3}3^{1/6}}{\sqrt{\pi}\,\Gamma(1/3)} \frac{v}{(z^2+\zeta_1^2)^{4/3}} \sum_{m=0}^\infty \frac{\Gamma\{m+(4/3)\}\Gamma\{m+(5/3)\}}{\Gamma(m+1)\Gamma\{m+(3/2)\}} \left(-\frac{v^2}{z^2+\zeta_1^2}\right)^m \\ &\qquad \times F\left(m+\frac{4}{3}, -m-1; \frac{2}{3}; \frac{\zeta_1^2}{\zeta_1^2+z^2}\right) , \end{aligned}$$

$$\left.\begin{aligned}\psi_{S+}=&\frac{2^{5/3}3^{1/6}}{\sqrt{\pi}\,\Gamma(4/3)}\frac{v\zeta_1^{2/3}}{(z^2+\zeta_1^2)^{5/3}}\sum_{m=0}^{\infty}\frac{\Gamma\{m+(5/3)\}\Gamma(m+2)}{\Gamma(m+1)\Gamma\{m+(3/2)\}}\left(-\frac{v^2}{z^2+\zeta_1^2}\right)^m\\&\times F\left(m+\frac{5}{3},\,-m-\frac{2}{3};\,\frac{4}{3};\,\frac{\zeta_1^2}{\zeta_1^2+z^2}\right).\end{aligned}\right\}\tag{4.5}$$

For sufficiently large m, the hypergeometric functions appeared in this equation have asymptotic expansions in the form:

$$\left.\begin{aligned}F\left(m+\frac{4}{3},\,-m-1;\,\frac{2}{3};\,\frac{\zeta_1^2}{\zeta_1^2+z^2}\right)\sim&\frac{\Gamma(2/3)}{\sqrt{\pi}}\frac{\Gamma(m+2)}{\Gamma\{m+(5/3)\}}\frac{1}{\sqrt{m}}\frac{(\zeta_1^2+z^2)^{1/6}}{\zeta_1^{1/6}z^{1/6}}\\&\times\cos\left[\left(2m+\frac{7}{3}\right)\phi-\frac{\pi}{12}\right],\\F\left(m+\frac{5}{3},\,-m-\frac{2}{3};\,\frac{4}{3};\,\frac{\zeta_1^2}{\zeta_1^2+z^2}\right)\sim&\frac{\Gamma(4/3)}{\sqrt{\pi}}\frac{\Gamma\{m+(5/3)\}}{\Gamma(m+2)}\frac{1}{\sqrt{m}}\frac{(\zeta_1^2+z^2)^{1/2}}{\zeta_1^{5/6}z^{1/6}}\\&\times\cos\left[\left(2m+\frac{7}{3}\right)\phi-\frac{5}{12}\pi\right],\end{aligned}\right\}\tag{4.6}$$

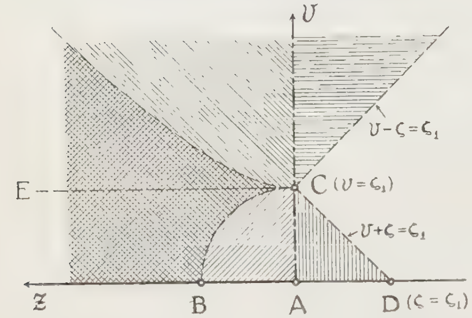

Fig. 3. The region in which various formulae are valid.

▧ for Eq. (4.4), ▨ for Eq. (4.5),
▤ for Eq. (4.8), ▥ for Eq. (4.9).

with $\sin^2\phi=\zeta_1^2/(\zeta_1^2+z^2)$.

Then, it is easily proved as before that Eqs. (4.5) are the absolutely convergent series in the domain:

$$v^2<z^2+\zeta_1^2\,,\qquad z,\,\zeta_1\neq 0\,.$$

In Fig. 3 are shown the regions for which various representations are of use.

While the singularity at B disappears in these solutions as is evident from Eq. (4.5), a new singularity appears at C.

To see this more clearly, we take $z=0$ in Eqs. (4.4), (4.5), and then these equations turn out, on the sonic line, to the form:

$$\begin{aligned}\psi_{S-}(0,v;\zeta_1)=&-\frac{2^{11/3}\Gamma(1/3)}{3^{11/6}\pi}\frac{v\zeta_1^{1/3}}{(\zeta_1^2-v^2)^{3/2}}F\left(\frac{1}{6},\,-\frac{1}{6};\,\frac{3}{2};\,\frac{v^2}{\zeta_1^2}\right)&&(\text{for}\quad 0<v<\zeta_1)\,,\\=&\ \frac{2\Gamma(1/3)}{3^{5/6}\pi}\frac{v^{4/3}}{(v^2-\zeta_1^2)^{3/2}}F\left(-\frac{2}{3},\,-\frac{1}{6};\,\frac{2}{3};\,\frac{\zeta_1^2}{v^2}\right)&&(\text{for}\quad v>\zeta_1)\,,\\\psi_{S+}(0,v;\zeta_1)=&\ \psi_{S-}(0,v;\zeta_1)&&(\text{for}\quad 0<v<\zeta_1)\,,\\=&-\frac{2^{4/3}\Gamma(1/3)}{3^{5/6}\pi}\frac{v^{2/3}\zeta_1^{2/3}}{(v^2-\zeta_1^2)^{3/2}}F\left(-\frac{1}{3},\,\frac{1}{6};\,\frac{4}{3};\,\frac{\zeta_1^2}{v^2}\right)&&(\text{for}\quad v>\zeta_1)\,.\end{aligned}$$

Retaining only the singular terms near C, we have

$$\begin{aligned}\psi_{S-}(0,v;\zeta_1)=&-\frac{3^{2/3}\Gamma(1/3)}{2^{1/3}\pi}\zeta_1^{-5/3}\left\{\left(1-\frac{v^2}{\zeta_1^2}\right)^{-3/2}-\frac{4}{9}\left(1-\frac{v^2}{\zeta_1^2}\right)^{-1/2}\right\}&&(\text{for}\quad 0<v<\zeta_1)\,,\\=&\ \frac{3^{1/6}\Gamma(1/3)}{2^{1/3}\pi}v^{-5/3}\left\{\left(1-\frac{\zeta_1^2}{v^2}\right)^{-3/2}-\frac{2}{9}\left(1-\frac{\zeta_1^2}{v^2}\right)^{-1/2}\right\}&&(\text{for}\quad v>\zeta_1)\,,\\\psi_{S+}(0,v;\zeta_1)=&\ \psi_{S-}(0,v;\zeta_1)&&(\text{for}\quad 0<v<\zeta_1)\,,\\=&-\psi_{S-}(0,v;\zeta_1)&&(\text{for}\quad v>\zeta_1)\,.\end{aligned}$$

Unlike the previous case, the singularity at C cannot be weakened by any combination of these two functions, ψ_{S-} and ψ_{S+}.

Since there are no singularity in the region $z>0$ even at $v=\zeta_1$, we can expect to have the expression valid along the line *CE* in Fig. 3, which is, in fact, obtained by the following procedures.

At first expanding $z^{1/3}J_{\pm 1/3}(\alpha z)$ in a power series of z, performing the integrations term by term provided that $\zeta_1 < v$, and then continuing analytically the hypergeometric functions, we arrive at another hypergeometric function with the variable $-4z^2v^2/(v^2-\zeta_1^2)^2$ on the neglect of higher order terms of $1-(\zeta_1^2/v^2)$.

Furthermore, if the Kummer transformation is applied to change the variable into

$$u = 1/\{1+(v^2-\zeta_1^2)^2/4z^2v^2\} ,$$

it follows that

$$\begin{aligned}\psi_{s-} \sim \frac{3^{1/6}\Gamma(1/3)}{2^{1/3}\pi}\Bigg[&\frac{v^{1/3}}{\{(v^2-\zeta_1^2)^2+4v^2z^2\}^{3/4}}F\left(\frac{3}{4},\, -\frac{7}{12};\, \frac{2}{3};\, u\right)\\ &+\frac{7}{3\cdot 2^{1/3}}\,\frac{v^2z^{2/3}}{\{(v^2-\zeta_1^2)^2+4v^2z^2\}^{13/12}}F\left(\frac{13}{12},\, -\frac{1}{4};\, \frac{4}{3};\, u\right)\Bigg],\\ \psi_{s+} \sim -\frac{3^{1/6}\Gamma(1/3)}{2^{1/3}\pi}\left(\frac{\zeta_1}{v}\right)^{2/3}\Bigg[&\frac{v^{4/3}}{\{(v^2-\zeta_1^2)^2+4v^2z^2\}^{3/4}}F\left(\frac{3}{4},\, -\frac{7}{12};\, \frac{2}{3};\, u\right)\\ &-\frac{7\cdot 2^{2/3}}{3}\,\frac{v^2z^{2/3}}{\{(v^2-\zeta_1^2)^2+4v^2z^2\}^{13/12}}F\left(\frac{13}{12},\, -\frac{1}{4};\, \frac{4}{3};\, u\right)\Bigg].\end{aligned}$$

Although these equations are not rigorous as they submit to some approximation, they may be useful to see the singular character in the neighbourhood of the point *C*.

Finally we shall seek for the expression valid in the supersonic region.

Two functions corresponding to Eq. (4.3) are defined formally by means of the transformation of the variable from z to ζ by Eq. (2.13), namely

$$\left.\begin{aligned}\psi_{s-}(\zeta, v;\, \zeta_1) &= \left(\frac{2\zeta\zeta_1}{3}\right)^{1/3}\int_0^\infty \alpha^{4/3}e^{-\alpha v}I_{-1/3}(\alpha\zeta_1)[I_{-1/3}(\alpha\zeta)-I_{1/3}(\alpha\zeta)]d\alpha ,\\ \psi_{s+}(\zeta, v;\, \zeta_1) &= \left(\frac{2\zeta\zeta_1}{3}\right)^{1/3}\int_0^\infty \alpha^{4/3}e^{-\alpha v}I_{1/3}(\alpha\zeta_1)[-I_{-1/3}(\alpha\zeta)-2I_{1/3}(\alpha\zeta)]d\alpha .\end{aligned}\right\} \tag{4.7}$$

Taking account of the asymptotic form of the modified Bessel functions, we can easily find that Eqs. (4.7) are convergent only for the region:

$$v+\zeta > \zeta_1 \quad \text{and} \quad v-\zeta > \zeta_1$$

respectively. (See Fig. 3.)

Expansion of $\zeta_1^{1/3}I_{\pm 1/3}(\alpha\zeta_1)$ and term by term integration of the resulting series give the following formulae:

$$\left.\begin{aligned}\psi_{s-} = \frac{2^{5/3}}{3^{1/3}}\frac{v^{-5/3}}{\sqrt{\pi}\,\Gamma(2/3)}\Bigg[&\sum_{m=0}^{\infty}\frac{\Gamma\{m+(5/6)\}\Gamma\{m+(4/3)\}}{\Gamma\{m+2/3)\}\Gamma(m+1)}\left(\frac{\zeta^2}{v^2}\right)^m F\left(m+\frac{5}{6},\, m+\frac{4}{3};\, \frac{2}{3};\, \frac{\zeta_1^2}{v^2}\right)\\ &-\left(\frac{\zeta}{v}\right)^{2/3}\sum_{m=0}^{\infty}\frac{\Gamma\{m+(7/6)\}\Gamma\{m+(5/3)\}}{\Gamma(m+1)\Gamma\{m+(4/3)\}}\left(\frac{\zeta^2}{v^2}\right)^m F\left(m+\frac{7}{6},\, m+\frac{5}{3};\, \frac{2}{3};\, \frac{\zeta_1^2}{v^2}\right)\Bigg],\\ \psi_{s+} = -\frac{2^{5/3}}{3^{1/3}}\frac{v^{-5/3}}{\sqrt{\pi}\,\Gamma(4/3)}\left(\frac{\zeta_1}{v}\right)^{2/3}\Bigg[&\sum_{m=0}^{\infty}\frac{\Gamma\{m+(7/6)\}\Gamma\{m+(5/3)\}}{\Gamma\{m+(2/3)\}\Gamma(m+1)}\left(\frac{\zeta^2}{v^2}\right)^m\\ &\times F\left(m+\frac{7}{6},\, m+\frac{5}{3};\, \frac{4}{3};\, \frac{\zeta_1^2}{v^2}\right)+\left(\frac{\zeta}{v}\right)^{2/3}\sum_{m=0}^{\infty}\frac{\Gamma\{m+(3/2)\}\Gamma(m+2)}{\Gamma(m+1)\Gamma\{m+(4/3)\}}\\ &\times\left(\frac{\zeta^2}{v^2}\right)^m F\left(m+\frac{3}{2},\, m+2;\, \frac{4}{3};\, \frac{\zeta_1^2}{v^2}\right)\Bigg].\end{aligned}\right\} \tag{4.8}$$

The values on the sonic line, as evaluated from these equations with $\zeta=0$, are, of course, equal to those obtained from the subsonic side.

As Eqs. (4.8) are formally derived, we shall investigate the convergency of them. To this end, it may be sufficient to consider only for one infinite series in Eq. (4.8). The first infinite series in Eqs. (4.8) is taken up as an example and is written down in a full expression of double series as follows:

$$\frac{1}{\Gamma(2/3)}\sum_{m=0}^{\infty}\frac{\Gamma\{m+(5/6)\}\Gamma\{m+(4/3)\}}{\Gamma\{m+(2/3)\}\Gamma(m+1)}\left(\frac{\zeta^2}{v^2}\right)^m F\left(m+\frac{5}{6},\ m+\frac{4}{3};\ \frac{2}{3};\ \frac{\zeta_1^2}{v^2}\right)$$

$$=\sum_{m=0}^{\infty}\sum_{n=0}^{\infty}\frac{\Gamma\{m+n+(4/3)\}\Gamma\{m+n+(5/6)\}}{\Gamma(m+1)\Gamma\{m+(2/3)\}\Gamma(n+1)\Gamma\{n+(2/3)\}}\frac{\zeta_1^{2n}\zeta^{2m}}{v^{2(m+n)}}\ .$$

Putting $m+n=k$, we have

$$\sum_{k=0}^{\infty}\sum_{n=0}^{k}\frac{\Gamma\{k+(4/3)\}\Gamma\{k+(5/6)\}}{\Gamma(n+1)\Gamma\{n+(2/3)\}\Gamma(k-n+1)\Gamma\{k-n+(2/3)\}}\frac{\zeta_1^{2n}\zeta^{2(k-n)}}{v^{2k}}\ .$$

For sufficiently large k, an inequality:

$$\frac{\Gamma\{n+(2/3)\}\Gamma\{k-n+(2/3)\}}{\Gamma\{n+(1/2)\}\Gamma\{k-n+(1/2)\}}>1$$

is easily proved by use of Stirling's formula concerning the Gamma function, therefore irrespective of n there holds the relation:

$$\Gamma(n+1)\Gamma\left(n+\frac{2}{3}\right)\Gamma(k-n+1)\Gamma\left(k-n+\frac{2}{3}\right)>\Gamma(n+1)\Gamma\left(n+\frac{1}{2}\right)\Gamma(k-n+1)\Gamma\left(k-n+\frac{1}{2}\right)$$

$$=2^{-2k}\pi\Gamma(2n+1)\Gamma(2k-2n+1)\ .$$

Thus, we have

$$\sum_{k=0}^{\infty}\sum_{n=0}^{k}<\frac{1}{\pi}\sum_{k=0}^{\infty}\frac{\Gamma\{k+(4/3)\}\Gamma\{k+(5/6)\}}{\Gamma(2k+1)}\frac{2^{2k}}{v^{2k}}\sum_{n=0}^{k}\frac{(2k)!}{(2n)!(2k-2n)!}\zeta_1^{2n}\zeta^{2(k-n)}$$

$$<\frac{1}{\sqrt{\pi}}\sum_{k=0}^{\infty}\frac{\Gamma\{k+(4/3)\}\Gamma\{k+(5/6)\}}{\Gamma\{k+(1/2)\}\Gamma(k+1)}\left(\frac{\zeta_1+\zeta}{v}\right)^{2k}$$

$$=\frac{\Gamma(4/3)\Gamma(5/6)}{\pi}F\left\{\frac{4}{3},\ \frac{5}{6};\ \frac{1}{2};\ \left(\frac{\zeta_1+\zeta}{v}\right)^2\right\}.$$

Consequently, it is said with confidence that this series is absolutely convergent in the region:

$$\zeta_1+\zeta<v.$$

The triangular region bounded by the sonic line and the characteristics passing through the point, $\zeta=\zeta_1$, $v=0$, is left to study. But the analytic continuation in this region is easily performed by Riemann's method of integration for a partial differential equation of hyperbolic type.

A convenient formula* to our case is given by

$$\psi(\zeta,\ v;\ \zeta_1)=\frac{2^{2/3}\pi}{3[\Gamma(1/3)]^3}\int_0^1\tau[v+\zeta(2t-1)]t^{-5/6}(1-t)^{-5/6}dt$$

$$+\frac{[\Gamma(1/3)]^3}{3^{1/2}2^{2/3}\pi^2}(-u)\int_0^1\nu[v+\zeta(2t-1)]t^{-1/6}(1-t)^{-1/6}dt\ ,$$

where $\tau(v)=\psi(0,\ v;\ \zeta_1)$,

$$\nu(v)=\frac{\partial\psi(0,\ v;\ \zeta_1)}{\partial w}\ .$$

---

* See Ref. **5**. Formulae (2.05) and (2.06).

Evaluation of the integrals needs only the values of ψ and ψ_z on the segment of the sonic line, cut from two characteristics passing through the point in consideration. To know the values for $v<0$, the expression for $v>0$ is used without any change, which is justifiable by the reason that $\psi(z, v; \zeta_1)$ has no singularity on the z-axis. As is easily seen, the normal derivative of ψ vanishes on the sonic line, and on slight change of the integration variable we have

$$\psi_{S-}(\zeta, v; \zeta_1)=\psi_{S+}(\zeta, v; \zeta_1) - \frac{2^5\zeta_1^{1/3}\zeta^{2/3}}{3^{17/6}[\Gamma(1/3)]^2}\int_{v-\zeta}^{v+\zeta}\frac{\alpha F(1/6, -1/6; 3/2; \alpha^2/\zeta_1^2)}{(\zeta-v+\alpha)^{5/6}(\zeta+v-\alpha)^{5/6}(\zeta_1^2-\alpha^2)^{3/2}}d\alpha\,. \tag{4.9}$$

This integral clarifies the property that the singularity extends along the two characteristics in the supersonic region.

§ 5. Summary

In this paper, two singular solutions of the Tricomi equation are discussed, both of which tend to Guderley's singularity at Mach number one when the singular point approaches the sonic one.

At first, these solutions are given in integral forms and then by making use of the analytic continuation of a hypergeometric function, the expressions in terms of double infinite series are deduced for various portions in the hodograph plane. The convergence of each series, as well as the region in which they are safely used, are also studied.

Further, special attention is given to the asymptotic behaviour near the singular point. One of the solution has its singularity isolated in the elliptic region of the fundamental differential equation, while the other has that extended along the characteristics in the hyperbolic region. From the physical point of view, they may be cosidered to correspond with the subsonic and the supersonic flow respectively, but the applications of these singular solutions to some transonic problems are left to future works.

In conclusion, the writer wishes to express his cordial thanks to Professor S. Tomotika for his continual guidance and encouragement during this work and especially for his kind inspection of the manuscript. The writer is also indebted to Dr. K. Tamada and Dr. Z. Hasimoto for their valuable suggestions and discussions.

References

1) G. Guderley: USAF Tech. Rep. No. F–TR–1171–ND, June, 1948.
2) G. Guderley and H. Yoshihara: J. Aero. Sci. **17** (1950) 723.
3) G. Guderley and D. T. Barish: J. Aero. Sci. **20** (1953) 491.
4) G. Guderley and H. Yoshihara: J. Aero. Sci. **20** (1953) 757.
5) F. Tricomi: Atti Accad. Naz. Lincei, Ser. 5, **14** (1923) 134.
6) J. D. Cole: J. Math. Phys. **30** (1951) 79.
7) L. Trilling and K. Walker, Jr.: J. Math. Phys. **32** (1953) 72.
8) L. Trilling: Z. a. Math. Phys. **4** (1953) 358.
9) A. G. Mackie and D. C. Pack: J. Rat. Mech. Analys. **4** (1955) 177.
10) J. D. Cole: Z. a. Math. Phys. **3** (1952) 286.

JOURNAL OF THE PHYSICAL SOCIETY OF JAPAN Vol. 10, No. 10, OCTOBER, 1955

Asymptotic Behaviour of the Location of a Detached Shock Wave in a Nearly Sonic Flow

By Kinzo HIDA

Department of Applied Physics, Faculty of Engineering,
Naniwa University

(Received July 4, 1955)

This paper gives an example of physical applications of our results on some singular solutions of the Tricomi equation.

Making use of the solution subject to appropriate boundary conditions in the hodograph plane, we have some informations about the asymptotic behaviour of a detached shock wave in a nearly sonic flow, as follows.

The distance, b, of a detached shock wave from an obstacle and the curvature of a shock at its nose, $1/R$, vary, respectively, with such powers of $(M_\infty-1)$ as

$$1/b \propto (M_\infty-1)^2\,, \quad 1/R \propto (M_\infty-1)^3\,,$$

M_∞ being the Mach number at infinity.

In axisymmetrical cases, we can obtain similar results by assuming that the flow behind a detached shock wave may be expressed by the asymptotic solution of the sonic flow due to Guderley and Barish. With the same notations as before, the results are

$$1/b \propto (M_\infty-1)^{2/3}, \quad 1/R \propto (M_\infty-1)^{5/3}.$$

§ 1. Introduction and summary

In a recent paper[1], the writer has obtained some singular solutions of the Tricomi equation of mixed type, and this paper gives an example of their applications to some transonic problems.

So far, the flow with a detached shock wave has been attacked by many writers, but owing to rather artificial or over-simplified assumptions we have had few decisive informations about this problem.

The difficulty of this problem is partly due to the indeterminancy of boundaries, on which the prescribed conditions should be satisfied, and is partly due to the comlexity of the fundamental equations governing this flow field, which is necessarily non-isentropic and transonic.

K. Tamada[2] and T. Kawamura[3] studied, independently, this problem in the physical plane by some ingenious devices. They have been secured from the first difficulty by assuming the shape of a shock wave with some parameters, which are determined later so as to satisfy the shock conditions in the close vicinity of the nose of a shock, and from the second by taking the corresponding flow pattern of an incompressible irrotational flow in place of a true (compressible, non-isentropic) field behind the shock.

The present writer[4,5,6] has also attacked along these lines the detached shock wave in front of a circular cylinder and a sphere. Provided that the flow behind the detached shock wave may be expressed by either incompressible rotational flow or compressible irrotational flow, we have found that the agreement between the theoretical predictions on the location of a detached shock wave and some experimental data is very good for a sphere, but is rather poor for a circular cylinder though a little improvement has been always brought in.

On the other hand, if all affairs are considered in the hodograph plane, then the shock wave is fixed as a shock polar, while the wall of an obstacle becomes open. However, if we confine ourselves to a nearly sonic flow, in which the Mach number at infinity upstream is a little larger than unity, we are favoured with some fortunate circumstances.

In this case, the shock polar is decreasing in size with decreasing Mach number and consequently the relative position of a streamline corresponding to the wall of an obstacle recedes so farther that its influence on the flow near the nose of a shock may safely be neglected (See Fig. 1.). Furthermore, we can assume without any serious error an isentropic flow in the region near the point N as shown in Fig. 1, because the shape of a shock wave is almost straight there.

These assumptions make us possible to use the similarity law for a transonic flow, which reduces not only the fundamental equations of motion to the Tricomi equation but also the shock polar with spines to the so-called "baby-hedgehog."

As is well known, each streamline in the hodograph plane should start from the points on the shock polar in the direction prescribed by the shock-spines and further the flow behind the shock is almost uniform near the axis of symmetry, which requires the singular solution in the hodograph plane.

Now, if we use the shock conditions only in the region near the nose of a shock as in the previous papers, it may be sufficient to consider only the singular solutions of the Tricomi equation, whose singularity is located near the point N in Fig. 1 (b). (Of course, many other solutions—singular or regular—must be added to satisfy all the boundary conditions.) The writer's solutions obtained in the previous paper[1] have their singularities in either subsonic or supersonic regions and both of them tend to Guderley's solution at the Mach number one when the singular point approaches the sonic point.

As we are concerned only with the region outside the shock polar, the point of singularity may be adjusted inside the shock polar so as to satisfy the boundary condition prescribed by the shock-spines. The solution with its singularity in the supersonic region is able to accommodate itself to this requirement, while the solution with a subsonic singularity cannot do so, except for the limiting case when the singularity locates on the shock polar.

Hitherto, it has been believed that a low-supersonic flow with the Mach number greater than unity by a small quantity corresponds to a high-subsonic flow with the Mach number smaller than unity by the same quantity, but it may be more probable that the former case will occur, namely a low-supersonic flow will correspond to another supersonic flow even if they pass through a shock wave.

Combining this solution with the boundary conditions in the physical plane, we can deduce some interesting results about the detached shock wave appeared in a nearly sonic flow.

Let b, R and $M_\infty(=1+m)$ be the distance of the nose of a detached shock from an obstacle, the radius of curvature of the shock at its nose and the Mach number at infinity upstream respectively. Then, we have

$$\frac{1}{b}\propto m^2\,, \qquad \frac{1}{R}\propto m^3\,.$$

Of course, the validity of these results is confined to two-dimensional cases, but we can obtain similar results in axisymmetrical cases, provided that the flow behind a shock wave may be expressed by the asymptotic solution of the sonic flow, which is obtained by Guderley and Barish[7] and is valid far from the body in the physical plane.

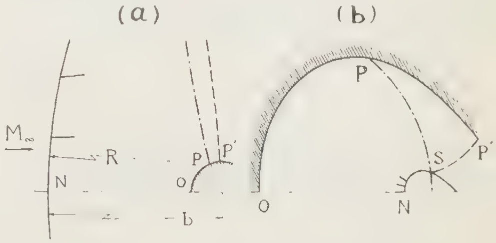

Fig. 1. (a) Physical plane. (b) Hodograph plane.

////////// wall on an obstacle,
— — — — limiting Mach wave,
—·—·— sonic line,
N : nose of a shock wave,
S : sonic point on a detached shock wave,
P : sonic point on an obstacle.

Proceeding in the same way as before, we have, in axisymmetrical cases,

$$\frac{1}{b}\propto m^{2/3}\,, \qquad \frac{1}{R}\propto m^{5/3}\,.$$

It may be of some interest to note that the previous results obtained in the above-cited papers[2,3,4,5] had the common properties as

$$\frac{1}{b}\propto m \text{ for two-demensional cases,}$$

$$\frac{1}{b}\propto m^{2/3} \text{ for axisymmetrical cases.}$$

Although the latter coincides with our results, the former is quite different from us, and this fact may be responsible for rather large discrepancies between the theoretical predictions and some experimental data for the case of a circular cylinder.

In conclusion, the writer wishes to express his cordial thanks to Professor S. Tomotika for his continual guidance and encouragement throughout this work and especially for his kind inspection of the manuscript. Thanks are also due to Dr. K. Tamada for his useful suggestions and discussions.

§ 2. Singular Solutions subject to the Boundary Conditions

As in a previous paper[1] we take the Cartesian coordinates x and y in the directions parallel and perpendicular to a uniform flow respectively and define the components of the disturbed velocity from the sonic free stream, w (or u) and v, in place of the rectangular velocity components q_x and q_y, by the formulae

$$-w=u=(\gamma+1)\left(\frac{q_x}{a_*}-1\right), \qquad v=(\gamma+1)\frac{q_y}{a_*}, \tag{2.1}$$

where γ and a_* denote respectively the adiabatic index of the gas concerned and the critical sonic speed.

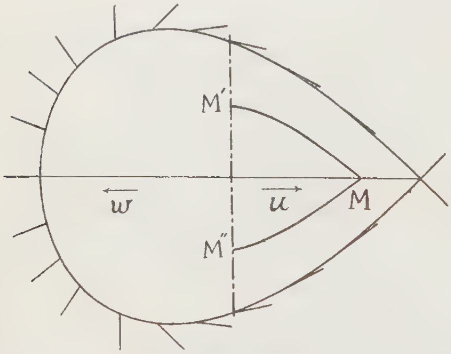

Fig. 2. "Baby-hedgehog".

If we confine ourselves to the region in which the similarity law for a transonic flow is valid, the shock polar reduces to the "baby-shock" defined by

$$v=(w-w_\infty)\sqrt{-\frac{(w+w_\infty)}{2}}, \tag{2.2}$$

and the direction of the shock-spines, with which the initial direction of streamlines should be coincident, is given by

$$\frac{dv}{dw}=\sqrt{-\frac{(w+w_\infty)}{2}}\;\frac{7w+w_\infty}{5w+3w_\infty}, \tag{2.3}$$

where w_∞ is the corresponding value of w to a free-stream at infinity upstream and is connected with the Mach number there, M_∞, by the relation:

$$w_\infty=-(M_\infty^2-1)<0\,. \tag{2.4}$$

Fig. 2 shows the so-called "baby-hedgehog" in the reduced hodograph plane.

To the same order of our approximation, the flow behind a detached shock wave is isentropic and the fundamental equations for the stream function ψ, Legendre's transformed potential Φ and the y-coordinate in the physical plane, are reduced to the Tricomi equation. Hence, we need to find the singular solution of that equation for which the streamlines may start in the direction prescribed by Eq. (2.3) from the points on the shock polar given in Eq. (2.2). Provided that the boundary conditions are considered only in the region close to the nose of a shock, we may neglect safely the effect of the wall on the solution, and consequently we can expect to have the general results of the asymptotic behaviour of a detached shock wave independently of the individual shape of an obstacle.

Retaining only the lowest order terms, we have from Eq. (2.2)

$$w\sim-w_\infty, \qquad v\sim0 \tag{2.5}$$

and Eq. (2.3) is simplified into the form:

$$\frac{dv}{dw}=-\frac{3}{2}\,\frac{v}{w_\infty}\,. \tag{2.6}$$

Now, the closer the Mach number at infinity approaches unity, the farther the shock wave recedes away and in the limiting case when the Mach number becomes just unity, the flow is wholly isentropic and should be transferred to Guderley's solution for the sonic flow. A few singular solutions having these properties can be written down immediately from the previous paper in the form:

ψ_{T-}+regular solutions,

$\psi_{T-}+\psi_{T+}$+regular solutions,

ψ_{S-}+regular solutions,

$\psi_{S-}+\psi_{S+}$+regular solutions.

The first two have the isolated singularity in the subsonic region while the other two have the continuous singularity extended along the characteristics in the supersonic region.

In the first place, we take the stream function defined as

$$\psi_S(z,v;\zeta_1)=\psi_{S-}+\psi_{S+}\,, \tag{2.7}$$

where ζ_1 is the parameter corresponding to the location of a singularity and is determined so as to satisfy the condition (2.6).

In the close vicinity to the z-axis ($i.e$ $v\sim0$), the two functions ψ_{S-}, ψ_{S+} are given respectively in the form:

$$\psi_{S-}=\frac{2^{8/3}3^{1/6}}{\pi}vz^{-8/3}$$

$$\times\sum_{m=0}^{\infty}\frac{\Gamma\{m+(4/3)\}\Gamma\{m+(5/3)\}}{\Gamma\{m+(2/3)\}\Gamma(m+1)}\left(-\frac{\zeta_1^2}{z^2}\right)^m+O(v^3),$$

$$\psi_{S+}=\frac{2^{8/3}3^{1/6}}{\pi}vz^{-8/3}\left(\frac{\zeta_1}{z}\right)^{2/3}$$

$$\times\sum_{m=0}^{\infty}\frac{\Gamma\{m+(5/3)\}\Gamma(m+2)}{\Gamma(m+1)\Gamma\{m+(4/3)\}}\left(-\frac{\zeta_1^2}{z^2}\right)^m+O(v^3),$$

which have been obtained by using Eq. (4.4) in Ref. **1.**

Substituting these expressions in Eq. (2.7), we have, after some reductions,

$$\psi_S=\frac{2^{11/3}\Gamma(1/3)}{3^{11/6}\pi}\Bigg[\frac{z^2-\zeta_1^2}{(z^2+\zeta_1^2)^{7/3}}+\frac{2\cdot3^{3/2}\pi}{[\Gamma(1/3)]^3}F\left(2,\frac{5}{3};\frac{4}{3};-\left(\frac{\zeta_1^2}{z^2}\right)\right)\Bigg]\times v+O(v^3). \qquad (2.8)$$

Here, the new variable z stands for the variable w by the relation:

$$z=(2/3)w^{3/2} \qquad (2.9)$$

and $F(a, b; c; Z)$ denotes the hypergeometric function.

The inclination of a streamline is easily found by the simple differentiation of Eq. (2.8) in the form:

$$\frac{dv}{dw}=\frac{v}{w}\times\frac{2\left\{\frac{2-5a}{(1+a)^{10/3}}+\frac{15\sqrt{3}\,\pi}{[\Gamma(1/3)]^3}F\left(2,\frac{8}{3};\frac{4}{3};-a\right)\right\}}{\left\{\frac{1-a}{(1+a)^{7/3}}+\frac{6\sqrt{3}\,\pi}{[\Gamma(1/3)]^3}F\left(2,\frac{5}{3};\frac{4}{3};-a\right)a^{1/3}\right\}}, \qquad (2.10)$$

with

$$a=\zeta_1^2/z^2. \qquad (2.11)$$

Comparing this foumula with Eq. (2.6), and taking into account the well-known identity for the hypergeometric function:*

$$F(a, b; c; z)+(a/c)zF(a+1, b+1; c+1; z)=F(a, b+1; c; z),$$

then we have finally the transcendental equation for determining the parameter A as

$$\frac{3A^2-20A+5}{(A+1)^{10/3}}=\frac{2\cdot3^{3/2}\pi A^{1/3}}{[\Gamma(1/3)]^3}\Bigg[3F\left(2,\frac{5}{3};\frac{4}{3};-A\right)-10F\left(2,\frac{8}{3};\frac{4}{3};-A\right)\Bigg], \qquad (2.12)$$

where A corresponds to the location of a singularity referred to z_N and is given by

$$A=\zeta_1^2/z_N^2 \qquad (2.13)$$

and z_N is the coordinate of the point N as shown in Fig. 2, which is obtained from Eqs. (2.4), (2.5), (2.9) in the form:

$$z_N^2=(4/9)(M_\infty^2-1)^3.$$

For the numerical computation, it is preferable to take an alternative expression for Eq. (2.12) as follows:

$$3A^2-20A+5=\frac{2\sqrt{3}\,\pi}{[\Gamma(1/3)]^3}\frac{(A+1)^{7/3}}{A^{2/3}}(3F_1-13F_2+10F_3),$$

where

$$F_1=F(1, -1/3; 1/3; U),$$
$$F_2=F(1, -4/3; 1/3; U),$$
$$F_3=F(1, -7/3; 1/3; U),$$

and U is a new parameter connected with A by the relation:

$$U=A/(A+1).$$

As long as the region $(0<A<1)$ is concerned, the above series with U are rapidly convergent. For example, even in the case $U=1/2$ (or $A=1$), which is the slowest converging case, it is sufficient to take the first 15 or 25 terms of series expansion of F_1 in order to have the 4 or 7 significant figures respectively.

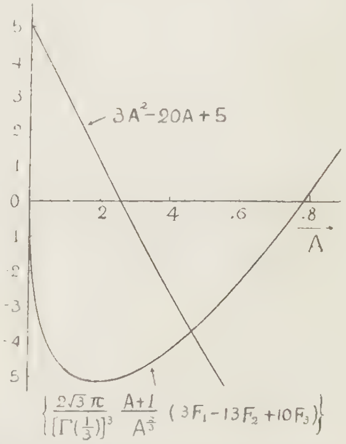

Fig. 3. The root of Eq. (2.12).

Performing numerical calculations, we get

$$U=0.46650 \quad \text{and} \quad \zeta_1/z_N=0.68301.$$

(See Fig. 3.)

---

* E. T. Whittaker and G. N. Watson, *Modern Analysis*, Cambridge, (1950), p. 296.

In Fig. 2 are also shown the singular point M as well as the two characteristics passing through it, MM' and MM'', along which the singularities extend.

Next, we shall consider the stream function with its singularity in the subsonic region:

$$\psi_T(z, v;\, z_1) = \psi_{T-} + \psi_{T+}\ . \tag{2.14}$$

For satisfying the condition due to the spines, Eq. (2.6), we should have the relation:

$$\begin{aligned} &3B^2+20B+5 \\ &\quad = \frac{2\cdot 3^{3/2}\pi B^{1/3}}{[\Gamma(1/3)]^3}\left\{10F\left(-\frac{2}{3}, -\frac{4}{3}; \frac{4}{3}; B\right)\right. \\ &\quad \left. -3(1-B)F\left(-\frac{1}{3}, -\frac{2}{3}; \frac{4}{3}; B\right)\right\}, \end{aligned} \tag{2.15}$$

with

$$B = z_1{}^2/z_N{}^2\ .$$

It is to be noted that Eq. (2.15) is derived formally from Eq. (2.12) by changing merely the sign of A. But we shall show that this equation has no positive root in the region (0,1). By making use of the analytic continuation between the hypergeometric functions with the variable B and $C(=1-B)$, we can ultimately reduce Eq. (2.15) into an alternative form as:

$$\begin{aligned} &B^{1/3}C^{10/3}[4F(2, 8/3;\, 13/3;\, C) \\ &\quad -3F(2, 5/3;\, 10/3;\, C)] = 0\ . \end{aligned}$$

Since each term of the first hypergeometric series is always larger than the corresponding term of the second, it follows that the expression in the square bracket does not vanish for any positive value of C. Further, it is easily seen from Eq. (2.15) that $B=0$ cannot be a root. Thus, the above equation is satisfied when and only when $C=0$, that is $B=1$. Obviously this means that the singular point is coincident with the point N on the shock polar and the condition due to the spines can no longer be satisfied except at the point N itself. As is already noted in the introduction, this case corresponds with the belief hitherto prevailed that a low-supersonic flow with the Mach number $1+m$, when it passes through a shock, may be considered as a high-subsonic flow with the Mach number $1-m$.

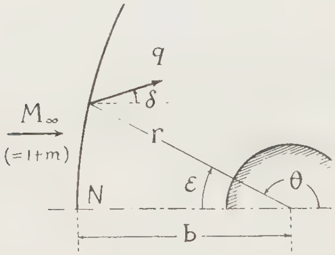

Fig. 4.

§ 3. Asymptotic Behaviour of the Detached Shock Wave in Two-Dimensional Cases

In this section, we shall study the shock conditions in more detail.

At first, we assume that the shock wave is expressed by the formula:

$$r = b(1+\lambda\varepsilon^2+O(\varepsilon^4))\ , \quad \varepsilon = \pi - \theta\ , \tag{3.1}$$

where r and θ are the polar coordinates with its origin at the centre of an obstacle and with its initial line parallel to a free-stream direction. As is shown in Fig. 4, b denotes the distance of the nose of a detached shock wave from the centre of a body (if it exists) and λ a parameter related to the curvature of the shock at its nose, $1/R$, by the formula:

$$\frac{1}{R} = \frac{1-2\lambda}{b}\ . \tag{3.2}$$

Let q_2 and δ be the magnitude and the direction of the velocity vector just behind a detached shock wave respectively, and if we neglect all terms higher than ε^3, we have the following two shock conditions:

$$\left.\begin{aligned} \tan\delta &= \frac{(1-2\lambda)(M_\infty{}^2-1)^2}{1+\{(\gamma-1)M_\infty{}^2/2\}}\ , \\ \left(\frac{q_2}{a_*}\right)^2 &= \frac{2}{(\gamma+1)M_\infty{}^2}\left\{\left(1+\frac{\gamma-1}{2}M_\infty{}^2\right)\right. \\ &\quad \left. + \frac{(1-2\lambda)^2(1+\gamma M_\infty{}^4)}{1+\{(\gamma-1)M_\infty{}^2/2\}}\varepsilon^2\right\}\ . \end{aligned}\right\} \tag{3.3}$$

(See Eqs. (7), (8) in Ref. 4.)

Bearing in mind that we are concerned only with a nearly sonic flow, we put $M_\infty = 1+m$ and retain only the first order terms of m. Then, the above conditions are reduced to the forms:

$$\tan\delta = \frac{4mA}{(\gamma+1)}\varepsilon\ ,$$

$$\frac{q_2}{a_*} = 1 - \frac{2}{\gamma+1}m + \frac{2A^2}{\gamma+1}\varepsilon^2\ ,$$

with

$$A = 1-2\lambda\ . \tag{3.4}$$

Further, to the same order of approximation the reduced velocity components as defined in Eq. (2.1) are also simplified into the form:

$$\left.\begin{aligned} w_2&=2m-2A^2\varepsilon^2\,,\\ v_2&=4m\varepsilon A\,. \end{aligned}\right\}\qquad(3.5)$$

As is well known, the coordinates x, y in the physical plane are derived conveniently from Legendre's potential Φ instead of the stream function ψ, by the formulae:

$$\left.\begin{aligned} x(w,v)&=-\frac{\gamma+1}{a_*}\Phi_w\,,\\ y(w,v)&=\frac{\gamma+1}{a_*}\Phi_v\,, \end{aligned}\right|$$

but the two functions Φ and ψ are related each other by the relation:

$$\psi=\rho_*(\gamma+1)\Phi_v\,.$$

Thus, the x-, y-values corresponding to the stream function given in Eq. (2.7) are found, except for a common numerical factor, as follows:

$$\begin{aligned} x=\xi_0 z^{-1/3}&\Big[-a^{1/3}F\Big(1,\frac{5}{3};\frac{4}{3};-a\Big)\\ &-\eta_0(1+a)^{-4/3}\Big]-\frac{10}{3}\xi_0 v^2 z^{-10/3}\Big[-a^{1/3}\\ &\times F\Big(2,\frac{8}{3};\frac{4}{3};-a\Big)-\frac{8}{15}\eta_0(1+a)^{-10/3}\\ &\times\Big(1-\frac{5}{2}a\Big)\Big]+O(v^4)\,,\\ y=-\xi_0\frac{2^{4/3}}{3^{1/3}}vz^{-8/3}&\Big[-a^{1/3}F\Big(2,\frac{5}{3};\frac{4}{3};-a\Big)\\ &-\frac{2}{3}\eta_0(1+a)^{-7/3}(1-a)\Big]+O(v^3)\,, \end{aligned}$$

with

$$\xi_0=\frac{2^{10/3}}{3^{4/3}}\,,\qquad \eta_0=\frac{[\Gamma(1/3)]^3}{4\sqrt{3}\,\pi}\qquad(3.6)$$

Since we can put, from Eqs. (2.9), (2.11), (2.13) and (3.5),

$$\begin{aligned} v&=4mA\varepsilon\,,\\ z&=\frac{2}{3}(2m)^{3/2}\Big(1-\frac{3}{2}\frac{A^2}{m}\varepsilon^2\Big)\,,\\ a&=A\frac{z_N{}^2}{z^2}=A\Big(1+3\frac{A^2}{m}\varepsilon^2\Big)\,, \end{aligned}$$

we have finally the following results:

$$\left.\begin{aligned} x&=-x_0(1/m^2)+x_2(A^2/m^3)\varepsilon^2+O(\varepsilon^4)\,,\\ y&=y_1(A/m^3)\varepsilon+O(\varepsilon^3)\,. \end{aligned}\right\}\qquad(3.7)$$

Here, x_0, x_2 and y_1 are the constants defined by

$$\left.\begin{aligned} x_0&=A^{1/3}F\Big(1,\frac{5}{3};\frac{4}{3};-A\Big)+\eta_0(1+A)^{-4/3}\,,\\ x_2&=3A^{1/3}\Big[5F\Big(2,\frac{8}{3};\frac{4}{3};-A\Big)\\ &\quad-F\Big(2,\frac{5}{3};\frac{4}{3};-A\Big)\Big]\\ &\quad+2\eta_0(1+A)^{-10/3}(3-10A+A^2)\,,\\ y_1&=3A^{1/3}F\Big(2,\frac{5}{3};\frac{4}{3};-A\Big)\\ &\quad+2\eta_0(1+A)^{-7/3}(1-A) \end{aligned}\right\}\qquad(3.8)$$

respectively. In the derivation of this second equation, use has been made of the following identities for the hypergeometric function:*

$$\begin{aligned} &(c-a-b)F(a,b;c;z)+a(1-z)F(a+1,b;c;z)\\ &\qquad-(c-b)F(a,b-1;c;z)=0\,,\\ &c(1-z)F(a,b;c;z)-cF(a-1,b;c;z)\\ &\qquad+(c-b)zF(a,b;c+1;z)=0\,. \end{aligned}$$

Remembering that the constant A should satisfy Eq. (2.12), we can easily confirm the relation:

$$2x_2=y_1\,.\qquad(3.9)$$

On the other hand, we have from Eq. (3.1)

$$\left.\begin{aligned} x&=r\cos\theta=-b+(bA/2)\varepsilon^2+O(\varepsilon^4)\,,\\ y&=r\sin\theta=b\varepsilon+O(\varepsilon^3)\,, \end{aligned}\right\}(3.10)$$

which hold on the shock wave in the close vicinity of its nose.

Comparing these expressions with Eq. (3.7), we can obtain the following relations:

$$\left.\begin{aligned} b&=K\frac{x_0}{m^2}\,,\\ \frac{bA}{2}&=Kx_2\frac{A^2}{m^3}\,,\\ b&=Ky_1\frac{A}{m^3}\,, \end{aligned}\right\}\qquad(3.11)$$

K being a constant depending on the form of an obstacle. It should be noted that only the two relations of these three are independent but they are compatible on account of Eq. (3.9).

Together with Eqs. (3.2), (3.4), we have finally the results

$$1/b\propto m^2\,,\qquad 1/R\propto m^3\,,\qquad(3.12)$$

and in particular

$$\frac{A}{m}=\frac{b}{Rm}=\frac{x_0}{y_1}\,,$$

---

* A. Erdélyi, *Higher Transcendental Functions, Vol. 1*, McGraw-Hill, (1953), p. 103.

which is found by numerical calculations to be

$$x_0/y_1=0.80002\ .$$

As was pointed out in § **1**, the previous papers[2,3,4,5] on the detached shock wave due to a circular cylinder show the common property that

$$1/b\propto m\ ,$$

which contradicts with Eq. (3.12).

Here, we shall suggest a semi-empirical formula for predicting the location of a detached shock wave, which is in accordance with the requirement of Eq. (3.12).

Let b_i be the distance of the shock wave as obtained by assuming an incompressible flow pattern behind the shock, and then the corrected value, b_c, will be found by the formula:

$$\frac{1}{b_c}=\frac{1}{b_i}(M_2{}^2-1)\ , \tag{3.13}$$

where M_2 is the Mach number immediately behind the shock wave at its nose.

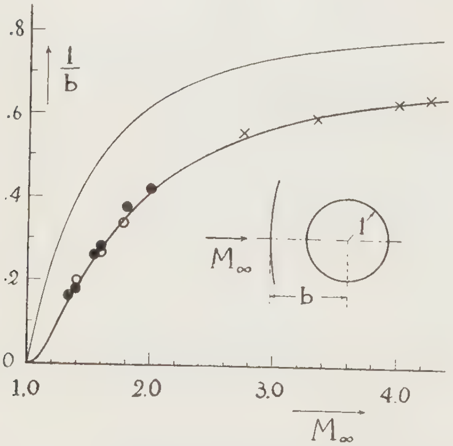

Fig. 5. Location of the detached shock wave due to a circular cylinder.

Incompressible irrotational case (Tamada[2])

—— Corrected value (Eq. (3.13))

● (Alperin[8])

○ (Holder and Chinneck[9]) Experimental values

× (Kim[10])

Although this formula stands on the insufficient and unsound basis, the agreement between the corrected values and some experimental data[8,9,10] are excellently good in a wider region of Mach number, as will readily be seen in Fig. 5.

§ 4. Asymptotic Behaviour of the Detached Shock Wave in Axisymmetrical Cases

It may be difficult to extend the previous method to axisymmetrical cases, because in this case the fundamental equation is not linear even in the hodograph plane and furthermore the shock-spines are not independent of the individual flow.

But, due to Guderley and Barish[7] we know the asymptotic solution of the Tricomi equation for the sonic flow, which is valid far from the body in the physical plane.

Then, we shall study the asymptotic behaviour of the shock by assuming that the flow behind a detached shock may be expressed by this solution.

Guderley and Barish's solution is given for the disturbed potential φ, which is connected with the velocity components w, v by the relations:

$$(\gamma+1)\varphi_x=-w\ , \qquad (\gamma+1)\varphi_y=v\ , \tag{4.1}$$

and it is written in the form:

$$\left.\begin{aligned}&\varphi=y^{3n-2}f(\chi)\\ \text{with}\quad&\\ &\chi=(\gamma+1)^{-1/3}xy^{-n}\ ,\end{aligned}\right\} \tag{4.2}$$

where n is a constant to be taken 4/5 for two-dimensional cases and 4/7 for axisymmetrical cases.

For larger positive value of χ, they had given the asymptotic solution of $f(\chi)$ with proper constants B_λ in the form:

$$f(\chi)=\chi^\alpha\sum_{\lambda=0}^{\infty}B_\lambda\chi^{(\alpha-3)\lambda}\ , \tag{4.3}$$

where

$$\left.\begin{aligned}\alpha&=\ \ 1/2 \text{ for two-dimensional cases,}\\ \alpha&=-1/2 \text{ for axisymmetrical cases,}\end{aligned}\right\} \tag{4.4}$$

and they further pointed out that if $f(\chi)$ is replaced by $c^{-3}f(c\chi)$ with an arbitrary constant c, Eq. (4.2) remains still to be the solution.

Since χ takes the negative large value in the region far upstream from the body, we shall take, with slight change of notations, the function $f(\chi)$ in the form:

$$f(\chi)=c^{\alpha-3}|\chi|^\alpha\{b_0+b_1(c|\chi|)^{\alpha-3}+\cdots\}\ , \tag{4.5}$$

where $b_0, b_1, \cdots$ are certain constants and c is an arbitrary constant.

Substituting Eq. (4.2) together with this expression for $f(\chi)$ in Eq. (4.1), we have

$$w=(\gamma+1)^{2/3}y^{2n-2}f'(\chi)\,,$$

$$v=(\gamma+1)y^{3n-3}\{(3n-2)f(\chi)-n\chi f'(\chi)\}\,,$$

which, on account of Eq. (3.10), are reduced further to the forms:

$$\left.\begin{aligned} w&=-b_0\alpha c^{\alpha-2}(\gamma+1)^{1-(\alpha/3)}b^{\alpha-1}+O(\varepsilon^2)\,,\\ v&=2b_1c^{2(\alpha-1)}(\gamma+1)^{2-(2\alpha/3)}b^{2(\alpha-1)}\varepsilon+O(\varepsilon^3)\,. \end{aligned}\right\} \tag{4.6}$$

These equations should be compared with Eq. (3.5), and we are able to have the following relations:

$$\left.\begin{aligned} m&=-b_0\alpha b^{\alpha-1}L\,,\\ m\Lambda&=2b_1b^{2(\alpha-1)}L\,, \end{aligned}\right\} \tag{4.7}$$

where for brevity's sake we have put

$$L=1/2c^{\alpha-3}(\gamma+1)^{1-(\alpha/3)}\,.$$

Eq. (4.7) gives immediately the results on the asymptotic behaviour of the detached shock wave as

$$1/b\propto m^{1/(1-\alpha)}\,,\quad 1/R=\Lambda/b\propto m^{(2-\alpha)/(1-\alpha)}\,. \tag{4.8}$$

Putting $\alpha=1/2$, we can arrive at the same results as in Eq. (3.12) and this fact gives some confidence to justify the assumption made in this section.

In axisymmetrical cases, we need only to take $\alpha=-1/2$ in Eq. (4.8) and obtain the similar results as before

$$1/b\propto m^{2/3}\,,\qquad 1/R\propto m^{5/3}\,. \tag{4.9}$$

Finally, we shall note some error caused by assuming the sonic flow. In the first equation of (4.6) the terms of the order ε^2 are neglected. At first sight, this may be considered to contradict with the previous assumptions but in truth it corresponds with the neglect of $O(\varepsilon^3)$ from the second equation of (3.10). If we retain the terms of $O(\varepsilon^3)$ in Eq. (3.10), then w is given to the order of ε^2, but the condition derived from its comparison with Eq. (3.5) is not compatible with the two conditions of Eq. (4.7).

Moreover, it follows from Eq. (4.7) that

$$\frac{\Lambda}{m}=\frac{2b_1}{\alpha^2b_0^{\,2}}=8\,\frac{b_1}{b_0^{\,2}}\,.$$

Since the numerical value of $b_1/b_0^{\,2}$ has been found to be 1/16 for two-dimensional cases, the above formula differs from that in the previous section, but there remains the property that Λ is proportional to m and all the results in this paper may still continue to hold.

References

1) K. Hida: Journ. Phys. Soc. Japan **10** (1955) 869.
2) K. Tamada: Unpublished.
3) T. Kawamura: Mem. Coll. Sci. Kyoto Univ. **26** (1950) 207.
4) K. Hida: Journ. Phys. Soc. Japan **8** (1953) 740.
5) K. Hida: Journ. Phys. Soc. Japan **10** (1955) 79.
6) K. Hida: Bull. Naniwa Univ. Ser. A, **3** (1955) 31.
7) G. Guderley and D. T. Barish: Journ. Aeron. Sci. **20** (1953) 757.
8) M. Alperin: Progress Rep. No. 4–44 Jet Propul. Lab. C. I. T. (1950).
9) D. W. Holder and A. Chinneck: Aeron. Quart. **4** (1954) 317.
10) C. S. Kim: Unpublished.

JOURNAL OF THE PHYSICAL SOCIETY OF JAPAN Vol. 10, No. 10, OCTOBER, 1955

Statistical Theory of Turbulence, II
Foundation of Similarity Theory of Turbulence

By Yutaka SHIGEMITSU

Transportation Technical Research Institute, Tokyo

(Received June 20, 1955)

As the first stage of developments of our statistical theory of turbulence, fundamental aspects of the similarity laws are investigated through the three cases of isotropic turbulence (A), turbulent wake (B) and turbulent boundary layer (C). In (A), it is first interpreted as the essential character of shearless turbulence that the distribution function $F_0(u, v, w)$ takes the form of Gauss function without correlation. Next, the hypothesis of isotropic turbulence due to G. I. Taylor is proved to hold in the case of shearless turbulence with a uniform mean velocity distribution. Then, the hypothesis of similarity preservation introduced first by Kármán-Howarth is derived as one of our theoretical result under the supposition of ideal state. Under this supposition we get the diffusion law $L^2 \backsim t$. The decay law in the initial period $\boldsymbol{u}^2 \backsim t^{-1}$ is derived by taking the vortex chaos motion of $\alpha=1$. Further, some interpretations are made on the problem of energy transmission from large vortices to small ones. In (B), at first the existence of turbulent shearing stress is interpreted attributed to the form of P-function. Next, the initial-period similarity-law in (A) is extended into this case of shear turbulence. Such theoretical results as $\boldsymbol{u}^2$, $\boldsymbol{v}^2$, $-\overline{\boldsymbol{uv}}$, $U_1{}^2 \backsim t^{-1}$ and $L^2 \backsim t$ are derived and compared with experimental measurements. The fundamental hypotheses in transfer theory in this case are derived from this exfended similarity law. Then, the transition phenomenon of similarity law from the initial period to the final period is surveyed experimentally. In (C), the existence of laminar sublayer is first interpreted physically attributed to the stability theory of laminar viscous flow. By introducing such an interpretation, it can be proved that Reynolds stress at a point are not determined as functions of only this point, and the previously derived similarity law in the initial period is developed into the non-decaying type. Theth eoretical result under a constant pressure distribution is compared with experiments. As for the distribution of Prandtl's mixture length, the relation $l(\eta) \backsim (\eta-\eta_0)^{1/2}$ is derived where η_0 corresponds to the boundary of laminar sub-layer.

§1. Introduction

At present, we have no theory which has a common theoretical basis through all the types of turbulence. It can be said, however, that in the previously presented successful theories such as that of isotropic turbulence or of mixture length, hypotheses introduced besides the Reynolds equations are all appropriate. They have been developed chiefly from a practical point of view, and sufficient considerations have not been given to their theoretical foundations. In Part I, general bases of our statistical theory of turbulence are established, and in this paper we will first lay these phenomenological theories on our theoretical bases.

Viewing all the cases of turbulence, they can be divided most essentially into the two groups, the one with a decaying character and the other without it. As the former case isotropic turbulence, turbulent wake or turbulent free jet can be taken, and turbulent boundary layer or tube turbulence is included in the latter. In our theory, (7.1) and (7.3) (I) give respectively their different descriptions of velocity fluctuations. The decaying turbulence is divided further into the two cases, the one with a finite shearing stress and the other without it, being attributed to the statistical characters of (8.2) and (8.3) (I). Then, discussions in this paper will be proceeded through the three cases of shearless turbulence (A), decaying shear turbulence (B) and non-decaying turbulence (C).

It is noteworthy that in many phenomenological hypotheses, assumptions due to the conception of similarity preservation are often found out. Those due to Kármán-Howarth in isotropic turbulence, to Kolmogoroff in locally isotropic turbulence, to Prandtl in transfer theory and so forth, are widely supported by experimental verifications. The common point of this paper is to derive these hypotheses from our one similarity character expressed in P-function, and to get decay or diffusion laws through the above three cases.

As different aspects of disussions, in (A) we derive the fundamental hypotheses in the theory of isotropic turbulence initiated by G. I. Taylor, as the results in the simplest case of our statistical study of shearless turbulence. Particularly, definite interpretations are given to the vortex chaos motion in the initial period of decay. In (B), an extension of our similarity law in (A) will be made into a turbulent wake as a simple shear turbulence. Discussions are made chiefly on the initial period because shear turbulent state is caused by the vortex chaos motion in it, and it is also important to prove the hypotheses in Prandtl's transfer theory as the results of our initial-period similarity-law. The character in (C) is the derivation of a non-decaying feature. The existence of laminar sub-layer becomes essentially important from this point of view, which is interpreted in our study by the character of lower limit of stability in laminar viscous flow. Founded on this interpretation, the decaying similarity law in (B) or (A) is extended into the non-decaying one in (C).

A. Fundamental Character of Shearless Turbulence

§ 2. Distribution Law

The shearless turbulence is defined by the condition $P_1=1$, and such a completely irregular vortex chaos motion can be realized by putting a grid in a potential flow. In this case the disturbing effects of each vortex are independent on the direction in D-domain, even if the mean states of vortices may be deformed by the main flow. Then, when an idealized two-dimensional case is taken, $\overline{V}_*^2$ and $\overline{V}_*'^2$ are supposed to be symmetrical about x_1-axis in D-domain and $-\overline{uv}$ in (6.2) (I) is evaluated to be zero. In a three-dimensional case Reynolds shearing stress in (6.2′) (I) can also be proved to vanish for the same reason;

$$\overline{v\boldsymbol{w}}=\overline{\boldsymbol{wu}}=\overline{\boldsymbol{uv}}=0\ . \tag{2.1}$$

The other intensities remain with their not necessarily equal values. But they are usually so small compared with the mean normal pressure, that the mean velocity distribution can be regarded as that of the perfect fluid.

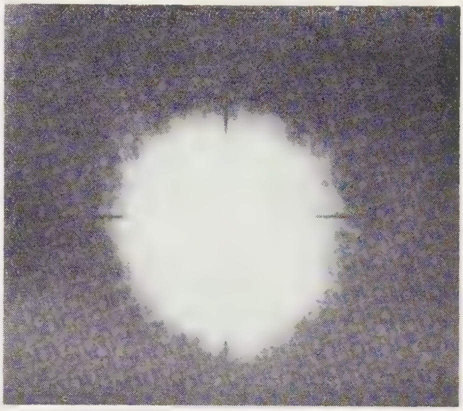

Fig. 1. A photograph showing the Gauss distribution in u-, v-fluctuation. It was taken on the surface of a braun-tube oscillograph with an exposure time of 20 seconds. The ordinate is v-fluctuation and the abscissa u-fluctuation. The observation was made in a shearless turbulence in the test section of a wind tunnel. $\overline{U}=14.3$ m/s with u-intensity of 0.45 per cent.

In the shearless turbulence, the causes by which $\boldsymbol{u}(t)$ etc. are produced, are completely at random in a long time, but $\boldsymbol{u}(\boldsymbol{t})$ etc. have their definite mean square values. So the condition of central limit theorem can be adapted in their distributions (cf. (2.1) (I));

$$F_0(u,v,w)=\{1/(\sqrt{\pi^3}\,\boldsymbol{uvw})\}\times\{\exp-(u^2/\boldsymbol{u}^2+v^2/\boldsymbol{v}^2+w^2/\boldsymbol{w}^2)\}\ . \tag{2.2}$$

Fig. 1 is an example of our measurements of two-dimensional charactor of F_0. By quantitative measurements on u-distribution the Gauss distribution has been well verified[1),2)]. The time in which (2.2) appears clearly is different according to the kind of turbulent flow. In a wind-tunnel flow, for instance, it appears in a few seconds. Fig. 2 shows such an example.

§ 3. Condition of Isotoropic Turbulence

Hereafter, the shearless turbulence with a

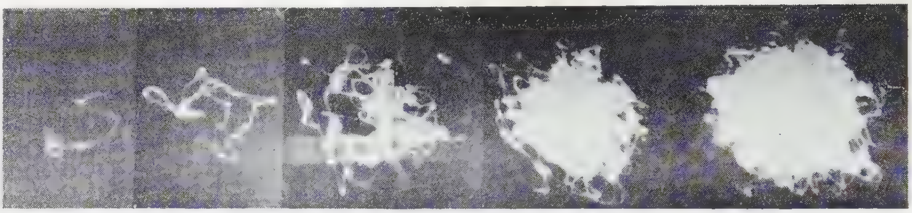

$t=0.008$ s, $t=0.02$ s, $t=0.1$ s, $t=0.5$ s, $t=3.0$ s

Fig. 2. Photographs showing formation of Gauss distribution function. They were obtained in another small wind tunnel. The flow was made to be a shearless turbulence by putting a two-dimensional grid before the two-dimensional contracting section of tunnel. $\overline{U}=2.30$ m/s with u-intensity of 1.26 per cent and v-intensity of 4.21. t is the exposure time.

uniform mean velocity distribution will be considered. In this case deformation of vortex motion caused by the main flow does not exist, and so $\overline{V}_*^2$ and $\overline{V}_*^{2\prime}$ are considered to be functions of only r in D-domain. Then, by (6.2′) (I) we have

$$\boldsymbol{u}=\boldsymbol{v}=\boldsymbol{w}\ . \tag{3.1}$$

This character of spherical symmetry in D-domain means the assumption of isotropy in velocity fluctuation.

In the theory of isotropic turbulence, it is assumed by Taylor's hypothesis that velocity fluctuations are not affected by the mean velocity distribution. With this hypothesis and the assumption of isotropy introduced, the Reynolds equations can be simplified into so-called equation of motion of isotropic turbulence. The interrelation between them can be predicted as the above explanation. In our study the assumption of isotropy can be derived if only P-function has the character of spherical symmetry as $\overline{V}_*^2$ and $\overline{V}_*^{\prime 2}$, but our condition of isotropic turbulence requires $P_1=1$ instead of spherical symmetry. Namely, our isotropic turbulence has irregular velocity fluctuations, while Taylor's one has not necessarily this important character. At any rate, it can be said that the vortex chaos motion which has the statistically and hydrodynamically simplest conditions

$$P=\text{constant} \quad \overline{U}=\text{constant}\ , \tag{3.2}$$

represents the isotropic turbulence as seen from the Eulerian point of view.

§ 4. Distribution of Intensity and Scale

For brevity, two-dimensional uniform shearless turbulence is taken under the supposition of ideal state. In this case, it is sufficient to survey only the effect of $\overline{V}_*$ which corresponds to the state of a single vortex motion. We take the flow whose vortex chaos motion is consisted of one type.

As D-domain a circle of radius R is taken where the similar velocity distribution is preserved; by (9.2) and (9.3) (I) we have

$$R^2=(4\nu s_0)t \tag{4.1}$$

where s_0 is a constant. The form of $\overline{V}_*$ is the same as (9.2) (I), and so by (7.5) (I) we get

$$\boldsymbol{u}^2=\{1/(\pi R^2)\}\int_0^{2\pi}\int_0^R F_\alpha{}^2(s)G_\alpha{}^2(t)\sin^2\theta\, r\,d\theta\, dr\ .$$

It leads to

$$\boldsymbol{u}^2=\left[\{(2c^2\nu)/s_0\}\int_0^{s_0}F_\alpha{}^2(s)ds\right]t^{1-2\alpha}\ ,\quad (\alpha\geqq 1) \tag{4.2}$$

where the first term does not depend upon t. (4.2) and (4.1) are the expressions of the distributions of intensity and scale for the ideal state of turbulence where one type of vortices is produced at one position in the field of flow.

For the ideal state, Euler correlation functions f and g can be evaluated in the same manner (cf. (6.3) and Fig. 8 (I)). They become

$$f=\frac{\displaystyle\int_0^{2\pi}\int_0^{s_0}F_\alpha(s)F_\alpha(s_1)\sin\theta\sin\theta_1\,d\theta\, ds}{\displaystyle\int_0^{2\pi}\int_0^{s_0}F_\alpha{}^2(s)\sin^2\theta\, d\theta\, ds}$$

$$g=\frac{\displaystyle\int_0^{2\pi}\int_0^{s_0}F_\alpha(s)F_\alpha(s_1)\cos\theta\cos\theta_1\,d\theta\, ds}{\displaystyle\int_0^{2\pi}\int_0^{s_0}F_\alpha{}^2(s)\cos^2\theta\, d\theta\, ds} \tag{4.3}$$

$$s_1=r_1{}^2/(4\nu t)\ .$$

When we write $\zeta = k/(2\sqrt{\nu t})$, s_1 and θ_1 are expressed respectively in the functions of $(s, \theta; \zeta)$, and (4.3) takes the forms $f = f(\zeta)$ and $g = g(\zeta)$. When L_f and L_g are the scales defined by $\int_{-\infty}^{\infty} f(\zeta) dx$ etc., they become $L_f = 2\sqrt{\nu t} \int_{-\infty}^{\infty} f(\zeta) d\zeta$ etc. Namely, it is seen that for the ideal state, the correlations for two points preserve their similar forms, and the linear dimensional scale L_f or L_g corresponds to that of D-domain.

As seen from Fig. 11 (I), $F_\alpha(s)$ has a character of rapidly tending to zero at a large value of s, and so the form of f or g can be written approximately in the expression where s_0 is made to be infinity. In this case, (4.3) can be evaluated definitely. In the case of $\alpha = 2, 3, \cdots$, they are expressed in elementary functions;

$$f = \exp\left(-\frac{1}{2}\zeta^2\right) \qquad g = (1-\zeta^2)\exp\left(-\frac{1}{2}\zeta^2\right)$$

$$\alpha = 2;$$

$$f = \left(1 - \frac{1}{2}\zeta^2 + \frac{1}{24}\zeta^4\right)\exp\left(-\frac{1}{2}\zeta^2\right)$$

$$g = \left(1 - \frac{5}{2}\zeta^2 + \frac{17}{24}\zeta^4 - \frac{1}{24}\zeta^6\right)\exp\left(-\frac{1}{2}\zeta^2\right)$$

$$(\alpha = 3)$$

$$\cdots . \tag{4.4}$$

The forms of f and g in the cases of $\alpha = 1$, 2, 3 are shown in Figs. 3 and 4. In (4.4) it can be found that in each case of α, such a relation $g = f + r(\partial f/\partial r)$ exists between f and g. It is the same form as the two-dimensional equation of continuity expressed in correlation functions, which has been derived by Kármán-Howarth in the theory of isotropic turbulence.

In the three-dimensional case, if two-dimensional character of vortices is preserved, i.e. if effects of elongation and curvature of vortex filaments are neglected, the same functional relations in this section can also be derived by taking a spherical D-domain with the same radius R.

§ 5. Conception of Similarity Preservation

Considerations will be given to the general case apart from shearless turbulence. When the ideal state is taken in a given turbulent flow where vortices are produced at one point in the field, the second moments of velocity fluctuations are expressed as (7.5) (I). It may be seen that if function of t is separated in $\overline{V}_*^2(r, \theta; x, y)$ and $P(r, \theta; x, y)$ by some variable transformations, Euler correlation functions become similar independently upon t. The similarity law of turbulence consists of the two parts - hydrodynamical similarity in the mean vortex motion and statistical similarity in the probability function expressing the chaotic state of vortices.

In the shearless turbulence, the condition of statistical similarity is clearly fulfilled by $P_1 = 1$. When a uniform flow is taken, the condition of hydrodynamical similarity is also fulfilled when elongation of vortex filament is neglected. The similarity law in this case belongs to the most fundamental case. In the theory of isotoropic or locally isotropic turbulence, the similarity hypothesis has been supposed to touch some fundamental point of the mechanism of turbulent flow. In our study this is proved to be one result of the expressions of mean values of velocity fluctuations under the supposition of the ideal state of turbulence.

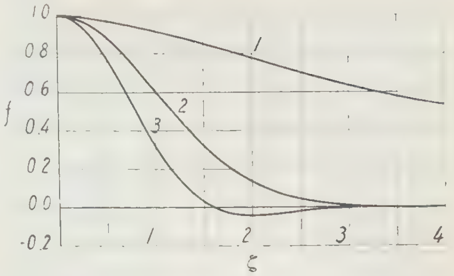

Fig. 3. Theoretical curves of f. Numbers on curves are values of α.

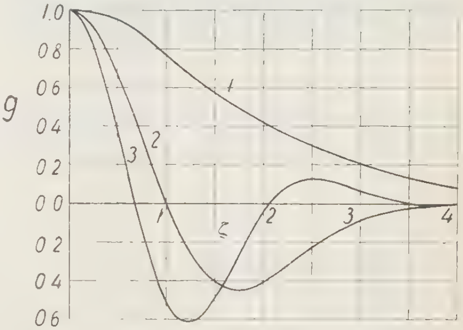

Fig. 4. Theoretical curves of g.

§ 6. Dissipation of Turbulent Energy

Similarity laws derived in the previous sections, holds for respective initial conditions of the outbreak of vortices. It depends upon these conditions which similarity law will hold for the real turbulent flow. But, having no exact knowledge about them, these theoretical results must be considered through experimental studies.

By many experimental studies on decay of turbulence, the following results can be fully confirmed; for a fairly wide range of time

$$u^2 \backsim t^{-1}\,, \tag{6.1}$$

and then a tendency

$$u^2 \backsim t^{-n} \quad (n>1) \tag{6.2}$$

comes to be found3)4)5). Experimental data on the distribution of scale show clearly the character2)3)6)

$$L_g{}^2 \backsim t\,. \tag{6.3}$$

As for the distribution of scale, (4.1) indicates (6.3). For the intensity (4.2) can explain the experimental results favourably. By comparing with (6.1), it may be deduced that each vortex produced by laminar separation from rods of a grid corresponds to that of the theoretical form of $\alpha=1$, and in a fairly wide range behind the grid its two-dimensional character is predominant in every vortex motion even if directions of these vortex filaments are three-dimensionally at random. This is our interpretation on the experimental fact of (6.1). In the theory of isotropic turbulence, the range where (6.1) holds experimentally has been defined as the initial period of decay5). In our study, the vortex chaos motion where the vortices of $\alpha=1$ play a predominant role can be generally called as the turbulent flow in the initial period.

It is important that the tendency (6.2) has been found. This character can be found more clearly in the measurements of decay by spectrum analysis7). To this experimental fact the three-dimensional effects of vortices (elongation of vortex filaments etc.) will make some contributions, but the essential point is considered as follows. When the vortices of α_1 $(=1)$ grow in scale and come to be mixed irregularily in the flow, there occur discontinuous flows between adjacent vortices, where new small vortices are produced by taking their energy. It may be also considered that the initial condition is different from that of α_1 and corresponds to some theoretical form of α_2 (>1). In the same manner, outbreak of a new group of α_3 is supposed in a vortex chaos motion of α_2, being attributed to a different initial condition. If $\overline{E}$ is taken as the mean kinetic energy of vortices contained in the extent difined by (4.1), it is evaluated as

$$\overline{E}=\left\{8\pi c^2\nu^2\int_0^{s_0}F_\alpha{}^2(s)\,ds\right\}t^{2(1-\alpha)}\,. \tag{6.4}$$

Hence, the mean kinetic energy of vortices is conserved for $\alpha=1$, but in others the rate of dissipation becomes larger with increase of the value of α, until the total energy is changed into heat. From the Eulerian point of view, the turbulent field of flow represents the combined result of the similarity laws of $\alpha_1, \alpha_2, \cdots$ one after another with increasing distance from the grid. This is our physical interpretation of the problem of energy transmission in turbulent flow.

The above-mentioned problem can be described exactly by taking area integrals separately according to the number of α as expressed in (7.3) (I). Under the supposition of ideal state it becomes

$$\begin{gathered} \boldsymbol{u}^2=\sum_{\alpha=1}^{N}\left\{(P_{1\alpha}/S_\alpha)\iint_{D_\alpha}\overline{V}{}^2_{*\alpha}(r)\sin^2\theta\,ds\right\} \\ \sum_{\alpha=1}^{N}(P_{1\alpha}/S_\alpha)=1\,, \end{gathered} \tag{6.5}$$

where N is the total number of types of vortices and $P_{1\alpha}/S_\alpha$ means the probability weight to express the rate of their mixture. If some theoretical ground is given to determine $P_{1\alpha}$, the problem of energy transmission can be investigated more precisely. At any rate, it can be concluded that the Reynolds stress is chiefly caused by the vortices of $\alpha=1$ in the initial period. It becomes important as well in the study of non-isotropic turbulence.

§ 7. Existence of Locally Isotropic Turbulence

The condition of isotropic turbulence is given with the expression (3.2), and the discussions from § 3 to § 6 have been made under these two conditions for all the types of vortices. We can easily suppose the case where they hold only for the new small vortices and do not hold for the large vortices of $\alpha=1$. This is our physical interpretation of the assumption of locally isotropic turbulence.

In a turbulent flow such as wake behind a single body or free jet, turbulent energy is considered to be dissipated in the same manner as mentioned in § 6. Such a type of turbulence will be called generally as the decaying turbulence. In this case, vortex chaos motion in the initial period comes easily to deviate from isotropic state under a different condition from (3.2). As will be mentioned in § 14, P_α tends to be constant as the number of α is increased. Hence, the similarity law in the final period[8)] is supposed to hold widely in decaying turbulent flows.

B. Shear Turbulence with Decaying Character

§ 8. Fundamental Characters of Shear Turbulence

The shear turbulence is defined by the condition of a simple continuous fuction of P_1 as shown in Fig. 10 C (I). Such a not completely irregular vortex chaos motion can be found, for instance, in a turbulent wake behind a single body or free jet. Behind the transition region near a body, vortices run irregularly but in this case the most probable path of these runnings can be pointed out unlike turbulence behind a grid.

The disturbing effects of each vortex have the character of some regularity, and the mean scale of vortices may be deformed. It is difficult to give generally the condition of axial symmetry to the forms of $\overline{V_*^2}$, $\overline{V_*^{2\prime}}$ and P_1 as the shearless turbulence, and it cannot be proved that all the Reynolds shearing stress are zero. It causes a deformation to the mean velocity distribution. Fig. 5 shows an example of our measurements of two-dimensional character of the distribution function F_0. It has a statistically stable form like the Gauss function with a correlation, and measurements of u-distribution indicate this character clearly[1)9)].

By the functional form of P_1 as shown in Fig. 10 (C) (I), it is easily considered that when a velocity fluctuation is observed near the boundary of wake, its record is mixed irregularly by the parts which are effected remarkably by vortices and the parts effected little. This is our qualitative interpretation of intermittency phenomena of shear turbulence. If P is a constant or the δ-function, it becomes difficult to explain them.

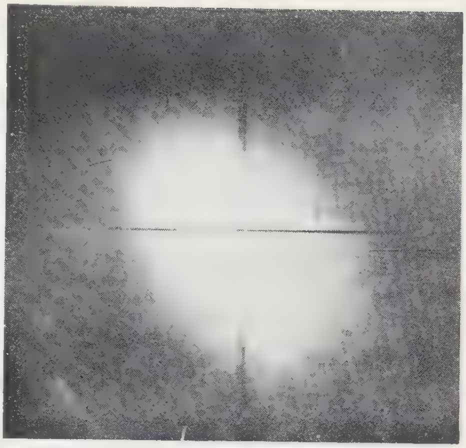

Fig. 5. A photograph showing the distribution of u- and v-fluctuation in shear turbulence. It was obtained in a turbulent boundary layer along a flat plate. $\overline{U}=9.41$ m/s. The character of this picture is the same as that in Fig. 1.

§ 9. Extension of Similarity Hypothesis in the Initial Period

We consider two-dimensional shear turbulence where vortices are produced at one point in the field of flow. By the discussions on the irreversibility given in Part I, it is considered that behind the transition region there is a wide range along the flow where the chaotic state of vortices is invariable statistically, even if each vortex may be growing in time. By the character of some regularity, mean states of the chaotic motion may be changed from those of shearless turbulence. But, in a uniform undisturbed velocity distribution the interaction of vortices is not affected by the mean flow, and its effect is also similar along the flow.

Then, in the initial period where the vortex chaos motion of $\alpha=1$ is predominant $\overline{V}_*$ can be written as

$$\overline{V}_*=F_1'(s,\theta)G_1(t) \quad s=r^2/(4\nu t)\ , \tag{9.1}$$

where $G_1(t)=2c\sqrt{\nu}\ t^{-1/2}$. As the boundary of D-domain we take

$$s_0(\theta)=R^2(\theta)/(4\nu t)\ . \tag{9.2}$$

In the shearless turbulence, $R_0(\theta)$, $s_0(\theta)$ and $F_1'(s,\theta)$ become respectively R, s_0 and $F_1(s)$. As for P_1-function, by the above consideration it does not depend on x; we have

$$P_1(r, \theta; x, y) = P_1(s, \theta; \eta) \quad \eta = y/R_y , \tag{9.3}$$

where R_y is a relative length of D-domain along y_1-axis given by (9.2). When the ideal state is taken, (9.3) and (9.1) give respectively the statistical and hydrodynamical conditions of similarity preservation. Namely, the conception of initial-period-similarity in the isotropic turbulence can be extended to the shear turbulence retaining the same physical meaning.

§ 10. Decay and Diffusion

The intensity of turbulence in the ideal state evaluated by (7.5) (I) leads to the following expressions

$$\begin{aligned}
&\boldsymbol{u}^2 = C_{u^2}(\eta)t^{-1} \qquad \boldsymbol{v}^2 = C_{v^2}(\eta)t^{-1} \qquad -\overline{\boldsymbol{uv}} = C_{\overline{vu}}(\eta)t^{-1} , \\
&C_{u^2}(\eta) = \left\{4c^2\nu \int_0^{2\pi}\int_0^{s_0} P_1(s, \theta;\, \eta) F_1'^2(s, \theta) \sin^2\theta \, ds\, d\theta\right\} \Big/ \int_0^{2\pi} s_0(\theta) d\theta \\
&C_{v^2}(\eta) = \left\{4c^2\nu \int_0^{2\pi}\int_0^{s_0} P_1(s, \theta;\, \eta) F_1'^2(s, \theta) \cos^2\theta \, ds\, d\theta\right\} \Big/ \int_0^{2\pi} s_0(\theta) d\vartheta \\
&C_{\overline{uv}}(\eta) = \left\{4c^2\nu \int_0^{2\pi}\int_0^{s_0} P_1(s, \theta;\, \eta) F_1'^2(s, \theta) \sin\theta \cos\theta \, ds\, d\theta\right\} \Big/ \int_0^{2\pi} s_0(\theta) d\theta .
\end{aligned} \tag{10.1}$$

$C_{u^2}(\eta)$ etc. are functions of η which indicate the distributions of $\boldsymbol{u}^2$ etc. to y-direction. In a uniform shearless turbulence $C_{u^2}(\eta)$ etc. become constant with the relations $C_{u^2} = C_{v^2}$ and $C_{\overline{uv}} = 0$, and (10.1) becomes (4.2) in the case of $\alpha = 1$. (10.1) is the generalized decay law of a uniform decaying tubulence in the initial period.

In (9.2) the value of $s_0(\theta)$ is invariable along the flow and so we have

$$R^2(\theta) = C_{R^2}(\theta)t \qquad (R_y^2 = C_{Ry}t) , \tag{10.2}$$

which expresses the state of distribution of scale. When g_η is taken as the correlation coefficient of $\boldsymbol{u}$-fluctuations at a point η and other point with a distance $\boldsymbol{k}$ across the wake, it can be written in the ideal state as

$$g_\eta = \frac{\iint_D P_1(s, \theta; \eta) F_1'(s, \theta) \sin\theta F_1'(s_1, \theta_1) \sin\theta_1 \, dS}{\left\{\iint_D P_1(s, \theta; \eta) F_1'^2(s, \theta) \sin^2\theta \, dS\right\}^{1/2} \left\{\iint_D P_1(s_1, \theta_1; \eta) F_1'^2(s_1, \theta_1) \sin^2\theta_1 dS\right\}^{1/2}} . \tag{10.3}$$

when $k/(2\sqrt{\nu t})$ is written as ζ, s_1 and θ_1 are expressed respectively in the functions of $(s, \theta; \zeta)$, and (10.3) takes the form $g_\eta = g_\eta(\zeta)$. It is easily proved that a form of every correlation coefficient is also preserved, and the scale length $L_{g_\eta} \left(= \int_{-\infty}^{\infty} g_\eta(\zeta) dy\right)$ corresponds to R_y. (10.2) is the general expression of diffusion law in decaying turbulence.

§ 11. Decay of Mean Velocity

To determine the mean velocity distribution based upon the values of $\boldsymbol{u}^2$ etc., the Reynolds equations are required. In this case of turbulent wake they can be simplified into

$$\overline{U}_0 \frac{\partial \overline{U}_1}{\partial x} = \frac{\partial \overline{uv}}{\partial y} , \tag{11.1}$$

where $\overline{U}_0$ and U_1 are undisturbed and defected mean velocities. Substituting (10.1) and (10.2) in (11.1), the form of $\overline{U}_1$ is determined as

$$\begin{gathered} \overline{U}_1 = C_{\overline{U}_1}(\eta) t^{-1/2} \\ C_{\overline{U}_1}(\eta)\eta = (2/C_{R_y}) C_{\overline{uv}}(\eta) + c_1 , \end{gathered} \tag{11.2}$$

where c_1 is an integration constant. Therefore, if the forms of P_1 and F_1' are given exactly in (10.1) the form of $\overline{U}_1$ can also be determined as fuction of η.

It is known by the consideration of mean momentum, that the drag affected on a body is written as

$$D_y = \rho \overline{U}_0 \int_{-\infty}^{\infty} \overline{U}_1 dy . \tag{11.3}$$

Apparently the expression (11.3) holds approximately, and strictly speaking its value should vary along the flow because effects of turbulent dissipation and so forth are all neglected in it. Taking the relation (11.2), (11.3) can be proved to be constant independently upon t. It has been proved by (6.4) that the mean energy of vortex chaos motion of $\alpha=1$ is conserved, and in the ideal state of initial period, effects of dissipation caused by other vortices $\alpha_2, \alpha_3, \cdots$ are neglected. It is clarified here that the supposition of ideal state of $\alpha=1$ gives to the drag such a result that (11.3) becomes constant. If some other vortex chaos motion ($\alpha>1$) were taken in the initial period, the value of (11.3) would decrease along the flow.

§ 12. Experimental Verifications of the Similarity Law

By experimental studies on turbulent wake behind a circular cylinder it is known that a similarity is well preserved in the distribution of $\overline{U}_1$ along the flow, except a narrow transition region just behind the body (cf. Fig. 6 (I)). It is also recognized that the expression (11.2) is well supported by them[10]. As for the drag, (11.3) is known to be constant by the experience that the pitot-traverse method gives an exact value to the measurement of drag independently on the position of traverse.

By experimental measurements on velocity fluctuations, it has been clarified that the distributions of $\boldsymbol{u}$ etc. have their similar forms along the flow[11]. Fig. 6 shows our measurement of $\boldsymbol{u}$-distribution in turbulent wake behind an ansymmetric airfoil. It shows that the similarity is well preserved excepting just behing the body. Concerning Euler correlation Fig. 7 shows an example of measurements of its preservative character. As for the spreading of wake, it is well known that (10.2) has been supported by many experiments. At present, however, an experimental verification has not been presented to the generalized decay law. In the measurements in Fig. 6 the values at $\eta=0$ and 0.4 are plotted against x in Fig. 8. By the above experimental studies, it may be deduced that our similarity law mentioned in the previous sections can describe the essentiality of the mechanism of this case of turbulent flow.

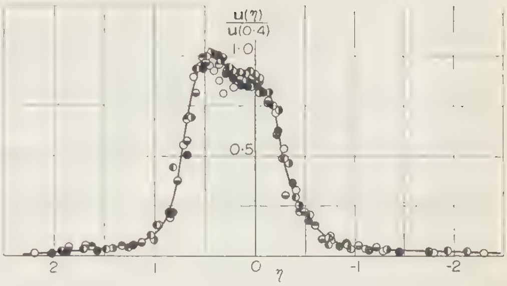

Fig. 6. Similarity preservation in $\boldsymbol{u}$-distribution behind an airfoil of NACA-2412. c (chord)=17 cm, $\overline{U}_0=7.28$ m/s with $\boldsymbol{u}$-intensity of 0.03 per cent and the attack angle=5°. ○, ●, ◐, ◑, ◒ and ◓ are observed values at $x/c=0.37$, 1.38, 2.32, 3.23, 4.41 and 5.13. η is taken using the half width in $\boldsymbol{u}$-distribution, and the center line $\eta=0$ is taken parallel to the main flow from the trailing edge.

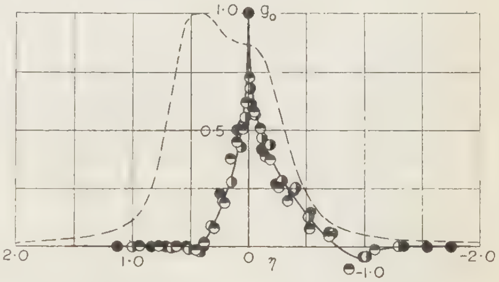

Fig. 7. Similarity preservation in the Euler correlation function g_0. The state of flow is the same as in Fig. 6. ●, ◑ and ◓ are observed values at the positions as in Fig. 6, and the broken line represents the $\boldsymbol{u}$-distribution.

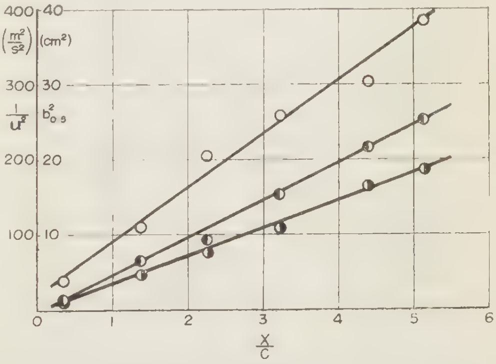

Fig. 8. Experimental measurements of the generalized decay and diffusion laws. The state of flow is the same as in Fig. 6. ◐ and ◑ are observed values of u-intensities at $\eta=0$ and 0.4. ○ is that of half width in $\boldsymbol{u}$-distribution.

§ 13. Transfer Hypotheses in the Initial Period

The essential point of the transfer theory is as follows; when the Reynolds shearing stress is written as $-\rho\overline{uv}=\rho l^2(d\overline{U}_1/dy)^2$, the quantity l can be taken as a length that is

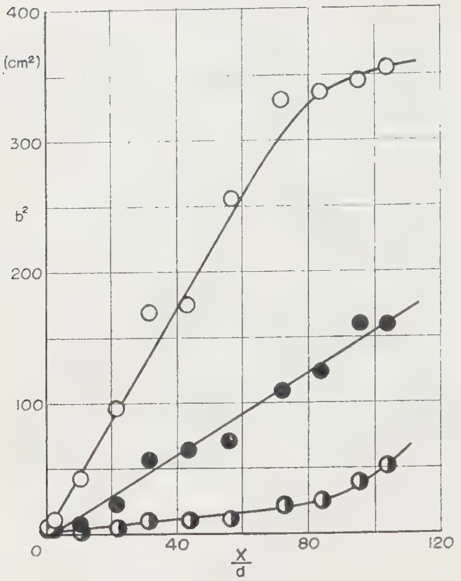

Fig. 9. Distribution of the width of wake behind a circular cylinder. d (diameter)$=1.5$ cm and $\overline{U}_0=3.74$ m/s with u-intensity of 0.02 per cent. ◑, ○ and ○ are observed values at the sections where $\overline{U}_1(\eta)/\overline{U}_1(0)=0.95$, 0.50 and 0.10.

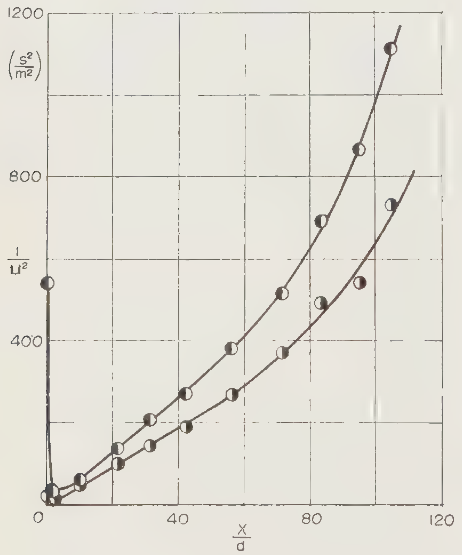

Fig. 10. The decaying process behind the cylinder. ◐ and ◑ are observed values at $\eta=0$ and 0.4 (maximum across the wake). The state of flow is the same as in Fig. 9.

proportional to the mean free path to y-direction of a part of fluid. In our study of vortex chaos motion, it is natural to suppose that the mixture length at a point in the field of flow corresponds to a mean length to y-direction of all the vortices passing near this point.

To apply momentum-transfer theory to turbulent wake, the following three independent hypotheses must be introduced[12]: (i) there is a similarity character in $\overline{U}_1$-distribution along the flow, (ii) the approximate value of drag (11.3) is constant, (iii) l is proportional to the width and is constant over any section. The first two hypotheses have been proved in § 11 from the conception of an ideal state of the vortex chaos motion of $\alpha=1$. In such a simplified vortex chaos motion, the mean scale of vortices can be taken as that of only $\alpha=1$ vortices which are produced at at one point in the field; we have

$$l \backsim R_y , \qquad (13.1)$$

and so l is constant to y-direction. Moreover, the relation (13.1) is favourable to the experimental fact that the value of l is comparable with that of half width of the wake[13]. Namely, it can be proved that our similarity law in the initial period supports the fundamental hypotheses of transfer theory by L. Prandtl.

§ 14. Deviation from the Initial-Period-Similarity

As in the isotropic turbulence, it is important to survey the limit of the initial-period similarity-law in the case of shear turbulence. We surveyed the state of turbulent wake behind a circular cylinder far downstream. Such a tendency was found that the rate of spreading of wake decreased and the forms of $\overline{U}_1$- and $\boldsymbol{u}$-distribution became flat near the center. Fig. 9 shows the distributions of width of wake at three sections, which indicates the above character clearly. As for turbulent intensity, it was found that the decaying became faster than (10.1). Fig. 10 shows the whole decaying process. It is significant that this deviation occurs at the same position where the similarity in $\overline{U}_1$-distribution begins to break down.

The above deviation phenomenon is an important character of decaying turbulence. The same physical intepretation can be given as the case of isotropic turbulence. In a turbulent wake the disturbing effects of each vortex of $\alpha=1$ occur easily near the center wake, and new vortex chaos motion of α_2, α_3, $\cdots$ are produced as well one after another. The scales of new vortices are small so that

P-function tends to be constant in D-domain, and these vortex chaos motions come easily to be in the isotropic states. The experimentally found tendency of flatness near the center is an appearance of this character. In the isotoropic turbulence, the above deviation can be found only by surveying decaying process or the forms of correlation function (distribution of spectrum). While, in the shear turbulence, it appears also in the distributions of $\overline{U}_1$ and $\boldsymbol{u}$ etc. to y-direction. If the decaying is proceeded further, the character of local isotropy become more predominant until the whole flow represents the state in the final-period similarity-law8).

When the effects of vortices of α_2 etc. appear in the initial period the mean scale of vortices comes to vary across the wake, and by the similarity law of α_2 etc. (11.3) is not constant. Hence, it can be proved that Prandtl's three hypotheses in the transfer theory does not hold except initial period. It is seen by Fig. 9 that $\overline{U}_1$-distribution across the wake comes to differ from that derived by this theory far downstream.

C. Mechanism of Non-Decaying Turbulence

§ 15. Existence of Laminar Sub-Layer

As the case of turbulence which has no decaying character, turbulent boundary layer or tube flow can be taken. The essential feature of turbulent boundary layer is the existence of a wall. Under an ordinary Reynolds number laminar boundary layer exists from the forward stagnation point, and usually it separates from the wall unsteadly or steadly at some distance from this point. Turbulent boundary layer is formed in the case where the vortices caused by such a laminar separation are carried along the wall further.

In the turbulent boundary layer the direction of mean velocity is parallel with the wall in spite of the existence of vortices, and the molecular viscosity is affected near the wall remarkably. There is one type of laminar boundary layer near the wall, which is generally called as laminar sub-layer. According to Prandtl's theory the thickness of laminar boundary layer can grow to any extent under the stationary main flow, but thickness of laminar sub-layer cannot become large because of large veloicty fluctuation above it. When the Reynolds number formed by this thickness and mean velocity at its boundary reaches that of the lower limit of stability of laminar flow, transition occurs to turbulence and vortices are produced at the boundary. Namely, the vortex flow by laminar separation at upstream causes production of many vortices at the boundary of laminar sub-layer one after another along the wall. On the other hand, above the sub-layer these vortices form a very complicated vortex chaos motion which cannot be considered in the previous decaying turbulence.

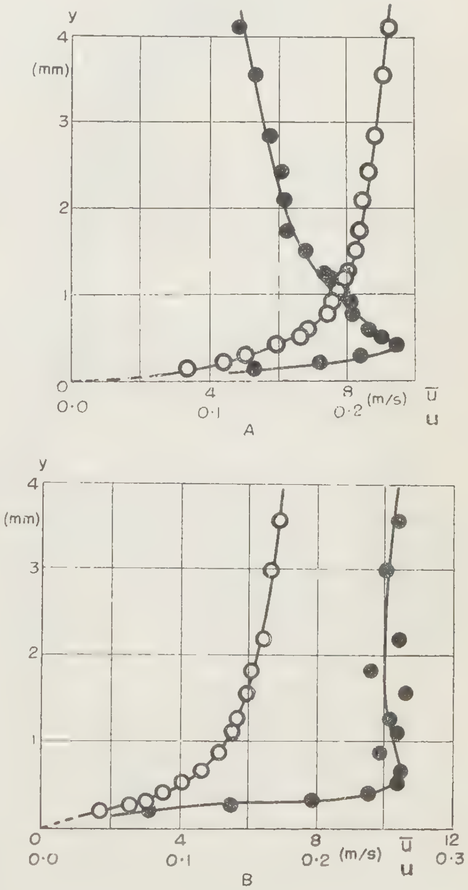

Fig. 11. Distributions of mean velocity (○) and u-intensity (●) near the wall in a turbulent boundary layer. (A) has a negative and (B) has a positive pressure gradient along the wall.

The above interpretations are well suggested by recent experimental investigations. Conspicuous viscous effect in the vicinity of wall and the production of strong Reynold stress outside it, are significant experimental facts[14]. For example, some of our measurements are shown in Fig. 11. The part between the wall and the sharp edge of $\boldsymbol{u}$-distribution curve is considered to correspond to the laminar sub-layer.

§ 16. Character of Non-Local Expression

In the turbulent boundary layer, vortices have their different positions of production and many types of vortices are carried near a fixed point (A-point). They have respective large contributions to the turbulent intensity at A-point. Then, even under the ideal state, the expressions of $\boldsymbol{u}$ etc. must be given by separating their area integrals into every group of vortices with the same initial condition. When two-dimensional description is taken they are

$$\left.\begin{aligned} \boldsymbol{u}^2 &= \sum_i \left\{(1/S_i)\iint_{D_i} P_{1i}(r,\theta\,;x_1,y_1)\overline{V}^2_{*i}(r,\theta\,;x_1,y_1)\sin^2\theta\,dS\right\} \\ \boldsymbol{v}^2 &= \sum_i \left\{(1/S_i)\iint_{D_i} P_{1i}(r,\theta\,;x_1,y_1)\overline{V}^2_{*i}(r,\theta\,;x_1,y_1)\cos^2\theta\,dS\right\} \\ -\overline{\boldsymbol{uv}} &= \sum_i \left\{(1/S_i)\iint_{D_i} P_{1i}(r,\theta\,;x_1,y_1)\overline{V}^2_{*i}(r,\theta\,;x_1,y_1)\sin\theta\cos\theta\,dS\right\}\,, \\ &\sum_i \left\{1/S_i)\iint_{D_i} P_{1i}(r,\theta\,;x_1,y_1)dS\right\}=1\,. \end{aligned}\right. \tag{16.1}$$

(x_1, y_1) is the position of A-point and the suffix i means the position of production of vortices whose summination is made along the upstream before A-point.

It is very difficult to give exact functional forms of $P_{1\alpha}$ and $\overline{V}_{*i}$ etc. in every D_i-domain. But it is considered that every P_{1i}-function has a simple continuous form and many of them have the condition of shear turbulence. The value of $-\overline{uv}$ is not vanish through the summination of these area integrals. This may be seen in the form of u-, v-distribution function shown in Fig. 5. Also the existence of intermittency phenomena found in recent experimental observations[15] is a powerful support to suppose that at least near the main flow P_{1i}-function may have the condition of shear turbulence.

The most important character of non-decaying turbulence is that the value of $\boldsymbol{u}$ etc. in (16.1) are depending not noly on the coordinates of A-point but also on all the values of i which correspond to the states of production of every type of vortices upstream. It is the same in the expressions of Euler correlations. We can say that the intensity and scale in the non-decaying turbulence have the character of non-local expression. It is also the reason why turbulent boundary layer is said to forget his history. It is proved by the simplified Reynolds equations that mean velocity distribution has also the same character. This is the reason why it is difficult in turbulent boundary layer to search for an appropriate parameter which describes the effects of pressure gradient favourably in the mean velocity distribution.

§ 17. Non-Decaying Similarity Law

In this section some idealized treatments will be made. First we take the ideal state of $\alpha=1$ vortices and neglect the effects of transition point far upstream from A-point. Under a constant pressure distribution, the effects of main flow to the vortex chaos motion are unifom along the wall, and the supposition of similarity preservation discussed in § 9 can be introduced to each vortex chaos motion with the same condition of production. We have

$$P_{1\xi}(r,\theta\,;x_1,y_1)=P_{1\xi}(s,\theta\,;\eta) \quad \eta_1=y_1/\delta\,, \tag{17.1}$$

where ξ $(=x/L)$ means a non-dimensional abscissa indicating the position of production of vortices, (s, θ) are transformed coordinates in a similar form of D_ξ-domain, and δ is the depth of boundary layer. For the vortex chaos motion of $\alpha=1$

$$\overline{V}_{*1}=F_1'(s,\theta)G_1(t_\xi)\,. \tag{17.2}$$

Substituting these statistical and hydrodynamical conditions of similarity in (16.1), it leads to

$$\boldsymbol{u}^2=\int_{-\infty}^{\xi_1}\left\{(1/S_\xi)\iint_{D_\xi}P_{1\xi}(s,\theta;\eta_1)F_1'^2(s,\theta)G_1^2(t_\xi)\sin^2\theta dS\right\}d\xi$$

$$\boldsymbol{v}^2=\int_{-\infty}^{\xi_1}\left\{(1/S_\xi)\iint_{D_\xi}P_{1\xi}(s,\theta;\eta_1)F_1'^2(s,\theta)G_1^2(t_\xi)\cos^2\theta dS\right\}d\xi \tag{17.3}$$

$$-\overline{\boldsymbol{uv}}=\int_{-\infty}^{\xi_1}\left\{(1/S_\xi)\iint_{D_\xi}P_{1\xi}(s,\theta;\eta_1)F_1'^2(s,\theta)G_1^2(t_\xi)\sin\theta\cos\theta dS\right\}d\xi\,.$$

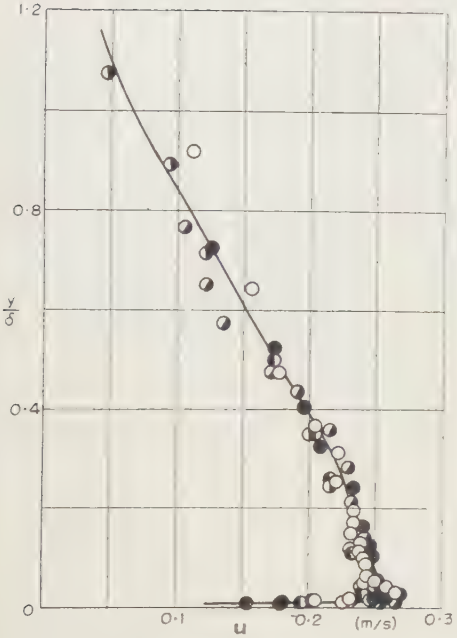

Fig. 12. Experimental result on the distributions of u-intensity in a turbulent boundary layer under a constant pressure distribution. Turbulence was produced by spreading a wire on a flat plate across the flow. $\overline{U_0}=10.13$ m/s with u-intensity of 0.04 per cent. ○, ●, ◑, ◐ and ◒ are the observed values at x 149.3, 76.5, 102.5, 121.2 and 141.5 cm from the wire.

In (17.3) $G_1^2(t_\xi)\backsim t_\xi^{-1}$ and approximately $t_\xi\backsim(\xi_1-\xi)$, but by the previous considerations in § 6 or § 14, it is supposed that vortices of $\alpha=1$ produced far upstream affect at A-point as another vortices of $\alpha>1$. Then, the term including t_ξ comes to be constant by definite integral from the negative infinity. As the expression of $\boldsymbol{u}$ etc. we get

$$\boldsymbol{u}^2=C_{u^2}(\eta)\quad \boldsymbol{v}^2=C_{v^2}(\eta)\quad -\overline{\boldsymbol{uv}}=C_{\overline{uv}}(\eta)\,. \tag{17.4}$$

It is important that the previously mentioned assumpsion of the initial-period similarity gives the similarity law with a non-decaying character in the case of turbulent boundary layer. For an experimental verification, results of our measurements are shown in Fig. 12.

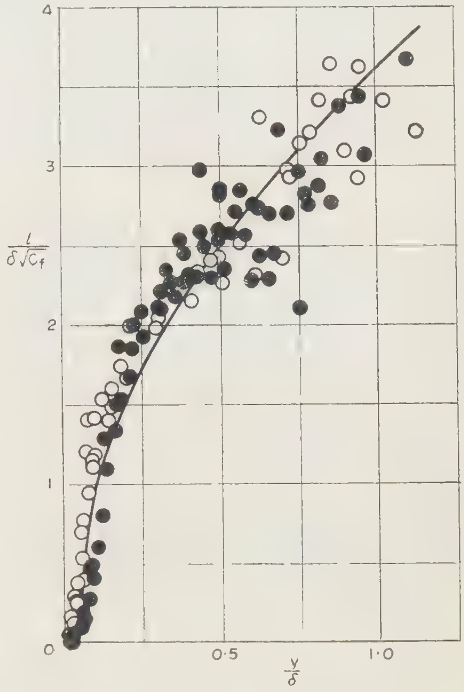

Fig. 13. Non-dimensional distribution of l in the turbulent boundary layer along a flat plate. The data were evaluated by I. Tani and R. Hama from their experimental measurements of mean velocity distributions. The curve shows (18.3), where it is drawn from 0.04 which is considered to be the boundary of laminar sub-layer.

§ 18. Distribution of Mixure Length

Our interpretations on the mixture length in transfer theory are given in § 13. Under the assumption of an ideal state of fully developed turbulent boundary layer along a flat plate, the distribution of $l(\eta_1)$ at a point ξ_1 is written as

$$l(\eta_1)\backsim\int_{-\infty}^{\xi_1}R_\xi\bar{P}_\xi(\eta_1)d\xi\,. \tag{18.1}$$

$\bar{P}_\xi(\eta_1)\left(=(1/S_\xi)\iint_{D_\xi}P_{1\xi}(s,\theta;\eta_1)dS\right)$ means a probability with which a group of vortices produced at ξ-point is carried near A-point (ξ_1,η_1), and R_ξ is the mean length to y-direction of these vortices.

It is difficult to determine the functional form of $\bar{P}$ exactly, and as an approximative estimation it is written as

$$P_\xi(\eta_1)=\delta(\xi) \quad \xi_1-\xi=c(\eta_1-\eta_0)\,, \tag{18.2}$$

where δ is the delta-function, c is a constant and η_0 corresponds to the boundary of laminar sub-layer. Namely, we suppose that in the types of vortices passing at A-point vortices produced at ξ $(=\xi_1-c(\eta_1-\eta_0))$ is predominant. On the other hand $R_\xi{}^2\backsim t$ and $t_\xi\backsim(\xi_1-\xi)$. Then, in the whole section of boundary layer we have

$$l(\eta_1)\backsim(\eta_1-\eta_0)^{1/2}\,. \tag{18.3}$$

The above relation will hold approximately in general case of non-decaying turbulence. Prandtl's hypothesis $1\backsim\eta$ is a simplified expression of (18.3) near the wall with the effect of laminar sub-layer neglected. For comparin with experimental data, measurements by I. Tani and R. Hama[16] are shown in Fig. 13. It shows the existence of laminar sub-layer clearly. Many other observations in turbulent boundary layer or tube flow indicate also the parabolic distribution of l in the whole section.

References

1) L. F. G. Simmons and C. Salter: Proc. Roy. Soc. **A 145** (1934) 212.
2) R. Hama: Rep. Inst. Sci. Tech., University of Tokyo **7** (1953) 145.
3) H. L. Dryden, G. B. Schubauer, W. C. Mock and H. K. Scramstad: NACA Tech. Rep. **581** (1937).
4) Th. v. Kármán: Proc. 5th Intern. Cong. Appl. Mech. (1938) 347.
5) G. K. Batchelor and A. A. Townsend: Proc. Roy. Soc. **A 193** (1948) 539.
6) G. I. Taylor: Proc. 5th Intern. Cong. Appl. Mech. (1938) 294.
7) H. Sato: J. Phys. Soc. Japan **7** (1952) 392.
8) G. K. Batchelor: Quart. Appl. Math. **6** (1948) 97.
9) G. I. Taylor: Proc. Roy. Soc. **A 156** (1936) 307.
10) H. Schlichting: Ing-Arch **1** (1930) 533.
11) A. A. Townsend: Proc. Roy. Soc. **A 190** (1947) 551.
12) S. Goldstein: Modern Developments in Fluid Dynamics § **252** (1938).
13) G. K. Batchelor: Journ. Aero. Sci. **17** (1950) 441.
14) P. S. Klevanoff: NACA Tech. Note 3178 (1954).
15) S. Corrsin and A. L. Kistler: NACA Tech. Note 3133 (1954).
16) I. Tani and R. Hama: Senken-Hokoku **1–4** (1945).

Short Notes

J. Phys. Soc. Japan **10** (1955) 903

On the Specific Heat of Normal Solid Alcohol of Probable Carbon Number 32

By Ren Shishikura

Institute of Science and Technology,
University of Tokyo

(Received July 15, 1955)

A preliminary specific heat measurement of a normal solid alcohol was accomplished in the temperature range from 35°C to 105°C.

The sample was offered from Mr. T. Takamatsu in Scientific Research Institute. It was extracted from commercially pure carnauba wax, refined, and then recrystallized repeatedly from benzol and ligroin solutions until it showed no further variation of its melting point. Carbon number of the sample was estimated by Takamatsu1) to be about 32, from elementary analysis and x-ray measurement of the longest spacing of the crystal.

The method and apparatus of specific heat measurement are similar to the ones described previously.2)

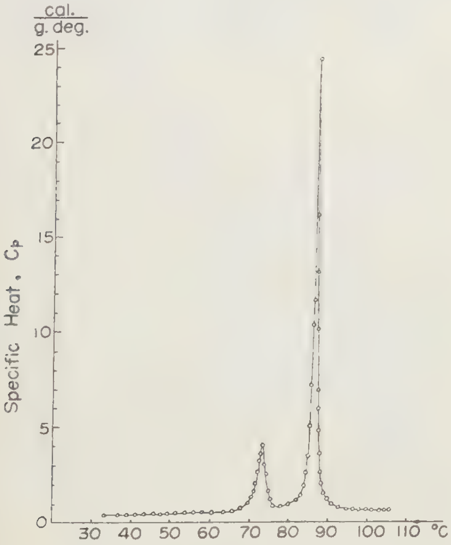

Fig. 1.

As shown in the figure, our sample melts at 86.4°C, and a sharp peak of specific heat appears at 73°C. It is supposed that this peak is of the same nature with that which has been found in pure hexadecyl alcohol, and proved to be the rotational transformation which accompanies the change of lattice symmetry and the rise of dielectric constant at the very temperature2).

The author believes the present data to be the first one which indicates the existence of rotational transition in long chain alcohol with carbon number higher than 30.

The heats of transition and fusion are 11.5 cal./g. and 40.3 cal./g. respectively.

Recently, Takamatsu1) found a new dielectric dispersion of Debye type between 0°C and 60°C in the same substance. The specific heat curve does not seem to indicate any remarkable feature at the corresponding temperature range. The gradual rise of the specific heat, however, is suspected in this region, which might have some relation to dielectric dispersion above mentioned.

The author wishes to thank Mr. Takamatsu for offering sample and valuable discussions.

References

1) T. Takamatsu: KAGAKU-KENKYŪ-JO HŌKOKU (Reports of the Scientific Research Institute) **31** (1955) 241 (in Japanese); J. Phys. Soc. Jap. (to be published).
2) Y. Kakiuchi, T. Sakurai and T. Suzuki: J. Phys. Soc. Japan **5** (1950) 369.

J. Phys. Soc. Japan **10** (1955) 903～905

On the Spectral Distribntion of Infrared-Stimulated Phosphorescence of Pb-activated ZnS-Type Phosphors* **

By Sumitada Asano

Department of Physics, Faculty of Science,
Okayama University

(Received July 19, 1955)

The influences of the addition of ZnSe, CdS or CdSe upon the IR-responsive behaviors of various ZnS phosphors are already reported in previous papers.1-4) In these investigations it was found that the color of IR-stimulated phosphorescence of a Pb-activated ZnS phosphor and its spectral IR-responsivity (stimulation spectra) are scarcely affected by the addition of any one of these foreign ingredients, whereas the peak wave-length of UV-excited luminescence and that of IR-quenchable natural phosphorescence gradually shift towards longer wave-lengths with increasing proportion of the added foreign ingredient. In the present experiment the spectral-distribution curves of IR-quenchable natural phosphorescences and IR-stimulated phosphorescences of some selected near-ZnS members*** in these three phosphor families have been measured at room temperature.

---

* The results published in this paper were partialy reported at the regular meeting, held at Tottori in July, 1955, of the Chugoku-Sikoku-Branch of the Physical Society of Japan.

** The term "ZnS-type phosphors" is used here in the broad sense that it covers not only ZnS phosphors but also Zn(S:Se), (Zn:Cd)S and (Zn:Cd)(S:Se) phosphors.

To all the phosphors investigated were added 2 mole % of KCl as flux and 1 weight % of Pb as an activator in the form of chloride and then these phosphors were crystallized at 850°C for 20 min. in N_2-atomosphere.1-4)

The apparatus used for the measurements is schematically snown in Fig. 1. The time-dependence of the photo-current from the receptor was measured directly with a galvanometer (YEW. D3–A. 2.43×10^{-10} amp/mm) in the case of a slowly decaying phosphorescence, and in the case of a quickly decaying one, it was recorded by an electro-magnetic type oscillograph (YEW. N–3) with a sensitive vibrator (YEW. D-type. 1.5 μA/mm). In the latter case the photo-current could be linearly amplified by a DC amplifier.5) The details of the measuring apparatus have been stated in the cited reference.3) All the measurements were made under the same exciting conditions at various phosphorescent wave-lengths. In every particular measurement the response to a standard lamp was read at a constant wavelength so that the decay-curves obtained in different measurements might be correlated with each other by these readings. The spectral-distribution curve of phosphorescence was derived both from the relative values on a set of these correlated decay-curves which correspond to various phosphorescent wave-lengths, and from the spectral sensitivity of the receptor fixed to the monochromator.

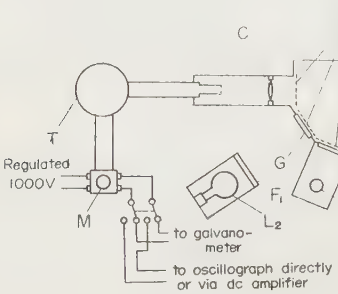

Fig. 1. Schematic diagram of measuring apparatus.

C: Glass lens F$_1$: Mazda IRD–1 Filter F$_2$: Mazda UVD–2 Filter G: Opal glass-plate M: Mazda Multiplier MS–9S L$_1$: Mazda Hg-lamp HL–300 L$_2$: Mazda Heating Lamp (100 V. 250 W. S-type) P: Sample S: Shutter T: Glass monochiomator (Shimadzu GW–30).

The results obtained are shown in Fig. 2 a–c. Besides, in Fig. 3 are shown the spectral-distribution curves of IR-stimulated phosphorescences of the doubly activated ZnS:Pb:Cu and ZnS:Pb:Mn phosphors which were crystallized at 1100°C.6) The heights of distribution curves, in Figs. 2 and 3, of IR-stimulated phosphorescences belonging to different members or different irradiating conditions are plotted relatively to their own radiances. The IR-stimulated phosphorescences were measured after the natural phosphorescence had dropped to a neglegible value. With regard to members which contain larger proportions of foreign ingredient than those are shown in Fig. 2, accurate curves could not be obtained, because the radiances of their stimulated phosphorescences were too small

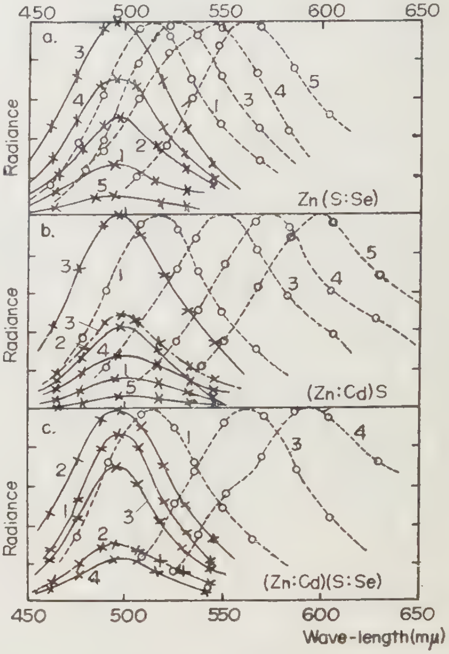

Fig. 2. Spectral-distribution cuives of phosporescences.

UV excitation: Mazda HL–300+Mazda UVD–2, distance at 25 cm for 3 min.

IR irradiation: Mazda Heating Lamp+Mazda IRD–1. IR irradiance: 0.6 mW/cm^2.

t: time after the cessation of UV excitation.

t_i: time after the beginning of IR irradiation.

t_n: natural-decay duration between the cessation of UV excitation and the beginning of IR irradiafion.

Dotted curves: IR-quenchable natural phosphorescence ($t=2$ sec.)

Real curves: IR-stimulated phosphorescence ($t_n=3$ min. $t_i=3$ sec.)

Chain curves: IR-stimulated phosphoresce ($t_n=3$ min. $t_i=7$ sec.)

Curve no.	1	2	3	4	5
Foreign Ingredient Proportion (mole %)	0	2	5	10	20

*** Near-ZnS member means a member which contains a comparatively small proportion of foreign ingredient.

to be measured spectro-photometrically.

From the results obtained the following facts may be pointed out:

(1) The peak wave-length of IR-stimulated phosphorescence of a Pb-activated ZnS phosphor shows no definite displacement by the addition of the forein ingredient ZnSe, CdS or CdSe, whereas that of IR-quenchable natural phosphorescence gradually shifts towards longer wave-lengths with the increase of the foreign ingredient added.

(2) The radiance and duration of IR-stimulated phosphorescence rise markedly in members which contain foreign ingredient up to several mole %; beyond which, they fall more rapidly than those of IR-quenchable natural phosphorescence.

(3) Since the decay-curves of IR-stimulated phosphorescences obtained at various wave-lengths under the same irradiating conditions are quite similar to each other in one particular phosphor, the shape of its spectral-distribution curve is independent of the time-duration t_i after the beginning of IR irradiation, as exemplified in Fig. 2 b and c.

(4) In the Pb:Mn-activated ZnS phosphor the characteristic stimulation band (5900 Å) ascribable to Mn-centers is observed simultaneously with that of Pb-centers (4950 Å). The latter is not affected by the existence of the former.

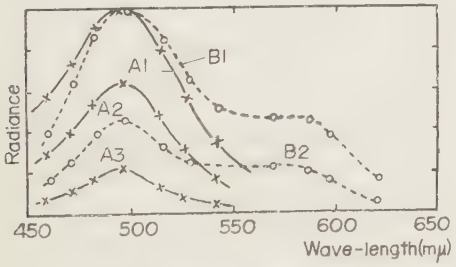

Fig. 3. Spectral-distribution curves of IR-stimulated phosphorescences.

A. ZnS:Pb[SO$_4$](5) Cu[SO$_4$](0.005) 1100°C.
B. ZnS:Pb[SO$_4$](5) Mn[SO$_4$](1) 1100°C.
Curve No. 1. $t_n=3$ min. $t_i=5$ sec. } IR irradiance:
2. $t_n=10$ min. $t_i=2$ sec. } 0.8 mW/cm^2
3. $t_n=5$ min. $t_i=5$ sec. IR irradiance: 0.2 mW/cm^2

Measured under the same exciting conditions as in Fig. 2. The numerals in round brackets show the weight % of the added activator-atoms.

(5) Although the form of the decay-curve of IR-stimulated phosphorescence of one particular phosphor considerably varies with irradiating conditions³⁾ (IR irradiance and duration t_n of natural decay), the spectral-distribution curves obtained under various conditions are nearly similar to each other even in the case of the Pb:Mn-activated phosphor, as shown in Fig. 3. On the other hand, in a hex-ZnS:Mn:Cu phosphor the stored quanta decrease more rapidly with the increase of t_n value than in the corresponding Pb:Cu-activated ZnS phosphor.⁶⁾

These results suggest that among Pb emission-centers in a near-ZnS member only those which are hardly affected by foreign ingredient atoms which are located substitutionally can be operative as stimulation centers. Some of the remainder are concerned in IR-quenchable natural phosphorescence as phosphorescence centers and the others which are not associated with electron traps quickly recombine with electrons after the cessation of UV excitation. Hence, they can operate only as fluorescence centers. The numbers of these stimulation centers and phosphorescence centers decrease with the increase of foreign ingredient and finally the phosphor becomes non-phosphorescent.

According to the item (5), the electrons released from deep traps by IR irradiation may be considered capable of recombining freely, to some extent, with ionized emission-centers in a phosphor crystal. The electron transfer processes mainly contributing to IR-stimulated phosphorescence will be, therefore, a second-order process, at least in the tail-part after several seconds from the beginning of IR irradiation.

References

1) S. Asano: Jour. Appl. Phys. Japan **64** (1954) 527.
2) S. Asano: Science of Light **4** (1955) 16.
3) S. Asano: ibid. **4** (1955) 32.
4) S. Asano: ibid. **4** (1955) 48.
5) K. L. McDonald et al: Jour. Opt. Soc. Am. **46** (1952) 321.
6) S. Asano: Jour. Phys. Soc. Japan **9** (1954) 580.

J. PHYS. SOC. JAPAN **10** (1955) 905~906

Effect of Directional Precipitation on Hardness in an Age-hardened Alloy

By Tadayasu MITUI

Department of Physics, Faculty of Science, University of Hokkaido, Sapporo, Japan

(Received July 14, 1955)

A detailed study of Alnico V was carried out by R. D. Heidenreich and E. A. Nesbitt[1][2] by means of the electron microscope. The purpose of this study was to examine the mechanism of precipiation which is supposed to be responsible for the unusual permanent magnet properties of the alloy. They showed that the alloy is divided into plates of precipitates and rod-like units of matrix, and their nuclei grow preferentially parallel to the direction of magnetic field applied during heat treatments. They found out the fact that the magnetic field suppressed completely the nucleation of precipitate of right angles to the field.

The similar effect[3)4)5)] was found by the present author in Cu–Co alloy. The author showed there that the precipitates tend to grow in the direction of the applied magnetic field during heat treatments.

The specimen we used are the alloy of copper including ca. 2 weight per cent of cobalt. We select it as the most appropriate precipitate-hardened alloy because it is metallographically simple and its precipitate has a high curie point.

If the clusters of ferromagnetic precipitate in the alloy which is annealed in a magnetic field have a directional distribution, it is to be expected that the uniaxial anisotropy is also found in the Vickers' hardness.

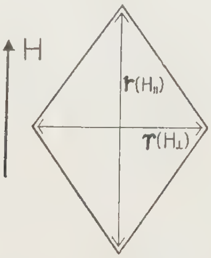

Fig. 1. A pair of diagonal lengths $r(H_{//})$ and $r(H_{\perp})$ of a mark on the specimen.

Micro-Vickers' hardness with weight of 500 gr. have been measured on the surface of the disk-shaped polycrystal specimen after various heat treatments in a magnetic field. Great care was taken in the polishing of the specimen so as to avoid the deformation. The method of the measurement is as follows: a pair of diagonal lengths $r(H_{//})$ and $r(H_{\perp})$ of a mark was measured, where one of the diagonals is parallel and the other is perpendicular to the direction of the magnetic field. (see Fig. 1)

The mean of $\bar{X}$, that is $\bar{X}=[\sum_{i=1}^{N} X_i]/N$, and the dispersion $\sigma^2=[\sum_{i=1}^{N}(X_i-\bar{X})^2]/N$ of the X_i was calculated, where $X_i=[r_i(H_{//})-r_i(H_{\perp})]/r_i(H_{//})$, N, total number of the measurement is ca. 100 and $r_i(H_{//})$ and $r_i(H_{\perp})$ are i-th measured values.

Since we knew that the magnetic heat treatment was most effective in the vicinity of 750°C, the isothermal magnetic heat treatments were made exclusively at this temperature. The results are shown in Table 1.

The results show that the specimen exhibits the anisotropy on micro-Vickers, which depends upon the direction of applied field. However, in our case, the effect is likely to be detectable only at an initial stage of the precipitation process. This coincides with the disappearence of the uniaxial anisotropy at the tempering time of ca. 15.0 hr. as shown in the previous work.[4)]

Table I.

Tempering time in isothermal heat treatment	Strength of magnetic field at heat treatment	$\bar{X}$	σ^2
5.0 hr.	1000 Oe.	0.0072	0.0002
5.0 hr.	without field	0.0008	0.0001
15.0 hr.	1000 Oe.	0.0006	0.0002
15.0 hr.	without field	0.0005	0.0002
5.0 hr.	7000 Oe.	0.0306	0.0019

Moreover, heat treatments under a strong magnetic field control the orientation and the shape of precipitates effectively, and this will be useful for the examination of the models[6)7)8)] proposed for the explanation of precipitation hardening. The author will study the stress-strain relation and other mechanical properties for the specimens which were treated in a magnetic field.

In conclusion the author wishes to express his cordial thanks to Prof. S. Miyahara and Prof. S. Koda for many valuable suggestions and discussions. The author is also indebted to Mr. M. Maki, who helped him through this work.

References

1) R. D. Heidenreich and E. A. Nesbitt: J. Appl. Phys. **23** (1952) 352.
2) E. A. Nesbitt and R. D. Heidenreich: J. Appl. Phys. **23** (1952) 366.
3) S. Miyahara and T. Mitui: J. Phys. Soc. Japan **7** (1952) 536.
4) S. Miyahara and T. Mitui: J. Fac. Sci. Hokkaido Univ. **4** (1953) 275.
5) T. Mitui and S. Miyahara: Read at the Meeting of Phys. Soc. Japan at Tôhoku Univ., July 1954.
6) Fisher, Hart and Pry: Acta Met. **1** (1953) 336.
7) S. Koda and Y. Hamaguchi: J. Fac. Tec. Hokkaido Univ. **11** (1954) 157 (in Japanese).
8) N. F. Mott and F. R. N. Nabarro: Report of a Conference of Strength of Solids, Phys. Soc. London (1948) 1.

J. Phys. Soc. Japan **10** (1955) 907

Origin of the Uniaxial Anisotropy in Iron-Cobalt Ferrites

By Shūichi Iida, Hisashi Sekizawa
and Yoshimichi Aiyama
Faculty of Science, Tokyo University, Tokyo, Japan

(Received August 1, 1955)

It is well known that the solid solution of magnetite and cobalt ferrite acquires a large uniaxial anisotropy when it is cooled in a magnetic field from the temperature above 300°C.[1][2][3] So far, no plausible explanation of the origin of this uniaxial anisotropy has been given. Two years since, we reached to a conclusion that the anisotropy is induced by the directional order between Co^{++} ions and cation vacancies. It was found experimentally that the magnitude of the uniaxial anisotropy depends essentially on the degree of oxidation of the specimens.

Fig. 1 indicates the dependence of the anisotropy constants of the same specimens on the degree of oxidation. In the figure the composition of each specimen is expressed in atomic ratio of iron to cobalt. Six disc-shaped specimens, with various atomic ratios of iron to cobalt, were heated to 1400°C in an alumina tube, and then cooled slowly to room temperature, with careful controlling of the pressure of oxygen atmosphere so as to keep it just below the upper boundary of a domain in the pressure-temperature phase diagram in which the spinel phase is stable for all specimens. Then they were put in a silica tube which was inserted in a furnace mounted between pole pieces of an electromagnet. In high vacuum they were thus heated up to 1000°C, kept five hours and cooled naturally in a magnetic field of about 4000 Oe. The anisotropy constants measured after this treatment are shown by the curve (1) in the figure. The magnitude of the constants is very small in this case, though the structure of spinel has not been destroyed by this treatment. The specimens were again put in the silica tube, the pressure of oxygen atmosphere was maintained at 0.7 mm Hg, and were heated up to 400°C, and then cooled in a magnetic field of the same magnitude. The results were shown by the curve (2) in the figure. The procedure of the same kind was repeated, increasing the pressure of oxygen atmosphere. They were shown by the curves (3), (4), (5), (6) and (7). Here the attached numbers indicate the pressures of oxygen atmosphere during the treatments. These experiments have shown that the magnitude of the uniaxial anisotropy of iron-cobalt ferrites depends essentially on the degree of oxidation of the specimens.

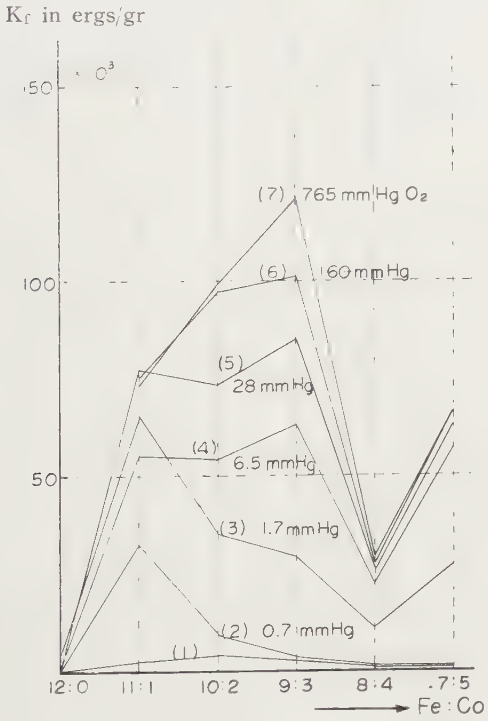

Fig. 1.

Together with the magnetic study mentioned, above thermal, electrical and X-ray studies have been carried out. From these results, we conclude that the diffusion rate of cations in these ferrites decreases rapidly under about 300°C in the course of cooling, and the uniaxial anisotropy of these ferrites is induced by the directional short range order between Co^{++} ions and cation vacancies. The spin-orbit coupling of Co^{++} ions and the anisotropic crystalline field originating from the presence of cation vacancies would interact mutually to produce the directional order below the Curie temperature, and this order would be fixed by the decrease of diffusion rate on the course of cooling under 300°C. The details will be published later.

Finally, the authors wish to express their hearty thanks to Professor S. Kaya for his constant encouragement.

References

1) I. Sugiura: J. Appl. Phys. (Japan) **20** (1951) 98.
2) C. Guillaud: Rev. Mod. Phys. **25** (1953) 64.
3) L. Néel: J. Phys. Rad. **15** (1954) 225.

J. PHYS. SOC. JAPAN **10** (1955) 908~909

Energy Analysis of Kikuchi Lines

By Hiroshi WATANABE

Hitachi Central Research Lab. Kokubunji, Tokyo

(Received July 29, 1955)

Kikuchi lines in electron diffraction pattern are produced when divergent secondary waves which produce the background of the pattern are reflected by net-planes in a crystal. Several authors[1] assumed that the divergent waves were produced by the inelastic scattering. Boersch[2] proved this assumption by using his electron filter and stated that the energy loss at the inelastic scattering was more than several electron volts. There is a possibility[3],[4], however, that the divergent waves are produced partly by the temperature scattering and partly by the elastic scattering at imperfections in the crystal.

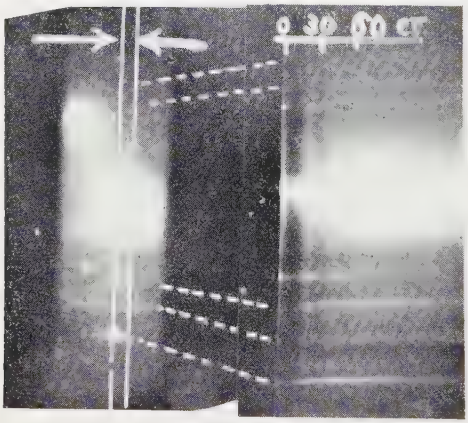

(a) (b)

Fig. 1. Electron diffraction pattern from molybdenite (a), and the corresponding energy spectrum (b).
Arrows indicate the part to be limited by a fine slit.

To make clear the nature of the divergent waves, the present author studied Kikuchi lines by an electron velocity analyzer of Möllenstedt type[5],[6]. Fig. 1a shows an electron diffraction pattern from molybdenite of thickness ca. 250 Å, the accelerating voltage being 25 kv. The pattern limited by a fine slit as indicated in the figure was analyzed into an energy spectrum (Fig. 1b). The extreme left vertical line in Fig. 1b corresponds to the electrons with no energy loss. Microphotometer traces along the line of no energy loss and the lines of energy losses of 23 ev and 46 ev are reproduced in Figs. 3a, b and c.

In Fig. 3 Kikuchi lines and an ordinary diffraction spot are indicated. As the energy loss increases the peak due to the diffraction spot becomes gradually weak while the peaks due to Kikuchi lines do not become so weak. It is worth noticing that peaks due to Kikuchi lines are clearly appearing on the line of no energy loss. Since the least energy loss detectable by the analyzer is ca. 1ev, this proves that *the divergent waves are partly due to the thermal or elastic scattering*. It is not correct to assume that the divergent waves are solely produced by inelastic scattering.

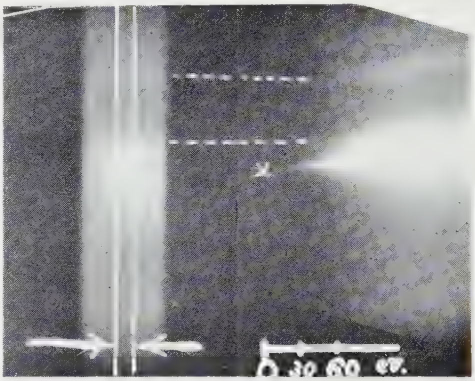

(a) (b)

Fig. 2. Electron diffraction pattern from thicker crystal of molybdenite (a), and the corresponding energy spectrum (b).
"x" shows the position of central spot.

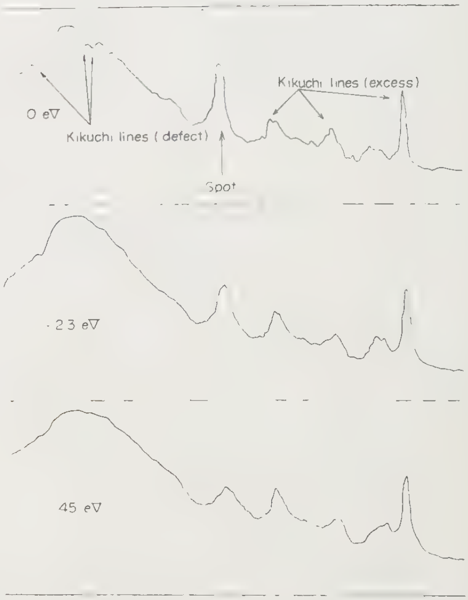

Fig. 3. Microphotometer traces in Fig. 1b along the line of no energy loss (a), along the line of 23 ev loss (b) and along the line of 46 ev loss (c).
The horizontal line above each trace is the dark line.

When thicker crystals are used, the line corresponding to no energy loss does not appear (Fig. 2) and Kikuchi lines are solely due to the inelastic scattering. In this case, since the multiple scattering prevails, it is reasonable that most of the electrons suffer inelastic scatterings in their course through the crystal.

The author is indepted to Prof. R. Uyeda of Nagoya University and Dr. N. Kato of Kobayashi Institute of Physical Research for their critisisms and helpful discussions. He is also grateful to Dr. B. Tadano and Mr. N. Morito of Hitachi Central Research Lab. for their encouragements throughout this experiment.

References

1) M. v. Laue: *Materiewellen und ihre Interferenzen.* 2 te Aufl. Leipzig, Akademische Verlagsgesellschaft.
Z. G. Pinsker: *Electron Diffraction* (1953) London, Butterworths Scientific Publications.
2) H. Boersch: Zeits. f. Physik **134** (1953) 156.
3) Y. Kainuma: private communication, to be published in Acta Cryst.
4) T. Ichinokawa and R. Uyeda: Proc. Japan Acad. **30** (1954) 857.
5) G. Möllenstedt: Optik **5** (1949) 499.
6) H. Watanabe: Journ. Phys. Soc. Japan **10** (1955) 321.

J. PHYS. SOC. JAPAN **10** (1955) 909~910

Specific-Heat Measurements on Quench-Annealed Al, Cu and α-phase Alloys of Cu

By Ken-ichi HIRANO, Hideyo MANIWA and Yutaka TAKAGI

Department of Physics, Tokyo Institute of Technology, Oh-okayama, Meguroku, Tokyo

(Received July 16, 1955)

Recently we have proposed a theory of the formation of G–P zone in quench-annealed alloys.[1] If the alloys are quenched from a high temperature, they have excess frozen-in vacancies, which on subsequent annealing may form disc-shaped vacancy planes or planes of stacking fault. The solute atoms may aggregate on these vacancy planes, thus yielding G–P zones.

The former half of the above reaction, i.e. the formation of vacancy planeor stacking fault, if it is true at all, must be present in alloys without any solvus line or even in pure metals.

Now measurements of the instantaneous specific-heat on heating have been carried out on quench-annealed Al and Cu of high purity and Cu-Ni alloy as well as others, to examine whether existence of vacancy plane and stacking fault could be detected by thermal measurements. The rate of heating for the measurement was 2.5°~3°C per minute.

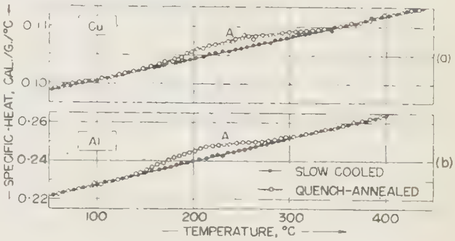

Fig. 1. Specific-Heat versus Temperature Curves of superpure Al and Cu.

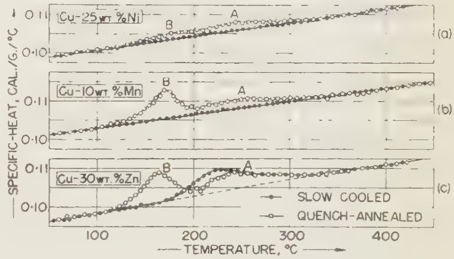

Fig. 2. Specific-Heat versus Temperature Curves of Cu–25 wt.% Ni, Cu–10 wt.% Mn, and Cu–30 wt.% Zn Alloys.

Curves given by open circles in Fig. 1 show the specific-heat versus temperature curves (S–T curves) obtained on super-pure Al (99.996%) and Cu (99.998%), which were quenched from 600°C in water of room temperature and annealed at 130°C for about 100 hours. Curves given by solid circles show the S–T curves of the metals measured after slowly-cooling them from 600°C to room temperature at a rate of 5°C per minute. The S–T curves of quench-annealed metals lie definitely above those of slowly cooled metals at a region between 150° and 350°C. Since this anomalous heat absorption does not appear in slow-cooled state, it can neither be attributed to re-solution of precipitate of unknown impurities whatsoever, nor to any reaction in equilibrium state of the metals. The most probable origin of this heat absorption may be dispersion of the disc-shaped vacancy plane or the stacking fault.

Curves given by open circles in Fig. 2 show the S–T curves obtained on three copper rich α-phase alloys, namely, Cu–25 wt.% Ni, Cu–10 wt.% Mn, and Cu–30 wt.% Zn (α-brass) alloys, which were quenched from 800°C (Cu–Ni and Cu–Mn) and 600°C (Cu–Zn) respectively, and annealed at 130°C for 2000 hours (Cu–Ni and Cu–Mn) and at 70°C for 860 hours (Cu–Zn). Curves given by solid circles were obtained after slowly cooling the alloys from 600°C at a rate of 3°C per minute. The S–T curves of quench-annealed alloys show two heat absorption peaks denoted by A and B. The heat absorption A's at higher temperature range seem to correspond with those observed in quench-annealed pure metals and may be attributed to the same origin.

Annealing-temperature and -time dependence of position of the peak B and amount of absorbed energy at B have been examined and it has been revealed that the nature of this heat absorption is very similar to that observed in the S–T curves of low temperature aged Al-alloys, such as Al–Cu,[2] Al–Ag[3] and Al–Zn[4]. So, the heat absorption B may be attributed to dispersion of solute atoms which are going away from vacancy planes or stacking fault.

The fact that the peak B is not so conspicuous in Cu–Ni alloys as in the other two alloys may imply poor aggregation of solute atoms on vacancy planes or stacking fault.

The S–T curve of slow-cooled Cu–Zn alloy show a heat absorption at the region between 170° and 330°C, which is absent in Cu–Ni and Cu–Mn alloys. It seems that some quantities of stacking fault and G–P zone may form even during the process of slow-cooling in Cu–Zn alloys, full account on this will be published elsewhere.[5]

Hasiguti[6] attributed the anneal-hardening of α-brass to the formation of G–P zone at stacking fault in the cold-worked matrix lattice, but it is to be emphasized that our results show possibility of G–P zone in quench-annealed specimen, *not cold-worked*.

We are carrying out same experiments on pure Ag as well as a number of α-phase alloys of it, such as Ag–Cd and Ag–Zn, the results will be reported soon.

References

1) K. Hirano, Y. Takagi and H. Maniwa: J. Phys. Soc. Japan **10** (1955) 587.
2) K. Hirano: read at the meeting of Japan Phys. Soc. at Univ. of Osaka, Oct. 31, 1954.
3) K. Hirano: J. Phys. Soc. Japan **8** (1953) 603.
4) K. Hirano: J. Phys. Soc. Japan **10** (1955) in press.
5) K. Hirano, K. Tanaka and Y. Takagi: Metal Physics **1** (1955) in press.
6) R. R. Hasiguti: J. Japan Inst. Metals **19** (1955) 103. (in Japanese).

J. PHYS. SOC. JAPAN **10** (1955) 910~912

Noise in Germanium

By Susumu OKAZAKI and Hiroshi OKI

Department of Physics, Faculty of Science, Okayama University

(Received July 6, 1955)

The current noise of germanium have been first carried out by Montgomery[1] using the germanium single crystal filaments for the frequency range of from 20 to 1,000 kilocycles. Van der Ziel[2][3][4] has reported on the deviations from the $1/f$ spectrum. We have studied the noise in bulk semiconductors such as germanium single crystals for the frequency range of from 100 kilocycles to 10 megacycles. The measuring apparatus was a superheterodyne amplifier, whose output was connected to the square-law detector and cathode-ray oscilloscope. The input circuit of the preamplifier is shown in Fig. 1.

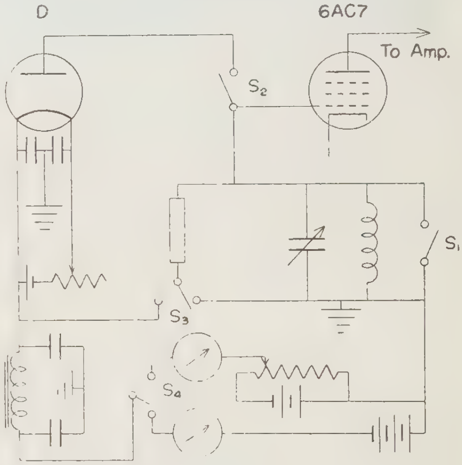

Fig. 1. Diagram of the input circuit. D: The diode for the shot noise. The variation of the diode current is made by changing the heater current of the filament.

Table I.

No. of samples	Resistivity Ω·cm	α	β
I 1	5.9	2.9	1.5
II 1	24	2.0	1.8
II 2	18	2.0	1.7
II 4	21	2.9	2.6
II 5	18	4.3	2.2

Samples have been cut from the thin slabs of the materials whose resistivity is from 10 to 20 Ω-cm. Typical dimensions are 1×0.1×0.02 cm. After these are etched in the solution consisting of

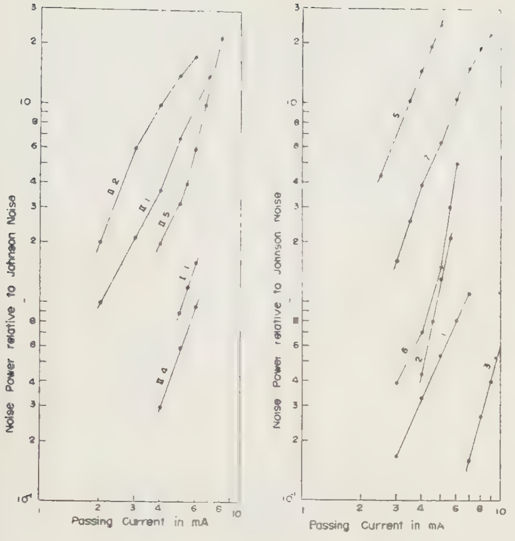

A B

Fig. 2. Variation of noise in germanium with dc current at 1 megacycles.

hydrogen fluoride and nitric acid, copper is evaporated as terminals. The current versus voltage characteristic is strictly linear. At 1 megacycles the current dependence of the noise is shown in Fig. 2 for a number of samples which are n-type. The outstanding feature is that the

Table II.

No. of samples	Resistivity Ω-cm	α	β
E 1	9.8	2.3	2.0
E 2	12	4.9	1.3
E 3	9.8	3.4	2.0
E 5	7.8	2.5	1.4
E 6	10	3.7	1.5
E 7	9.0	2.5	1.1

current noise power always increases with the passing current. In many cases at some current the noise power abruptly comes out, increasing according to I^α law in which α is 2 or above 2. The frequency spectrum of the excess current noise power, when the passing current is fixed at 5 mA, are shown in Fig. 3. The frequency dependence is described by the $1/f^\beta$ law, where β is always larger than 1, mostly approximately 2. If the current noise is represented by the following formula,5)

$$\Delta I^2=\gamma I^\alpha f^{-\beta}\Delta f$$

then α and β are computed, as is shown in Table I and II, using these figures. The samples in Table I are different from those in Table II according to manufacturing company. The noise figure at 100

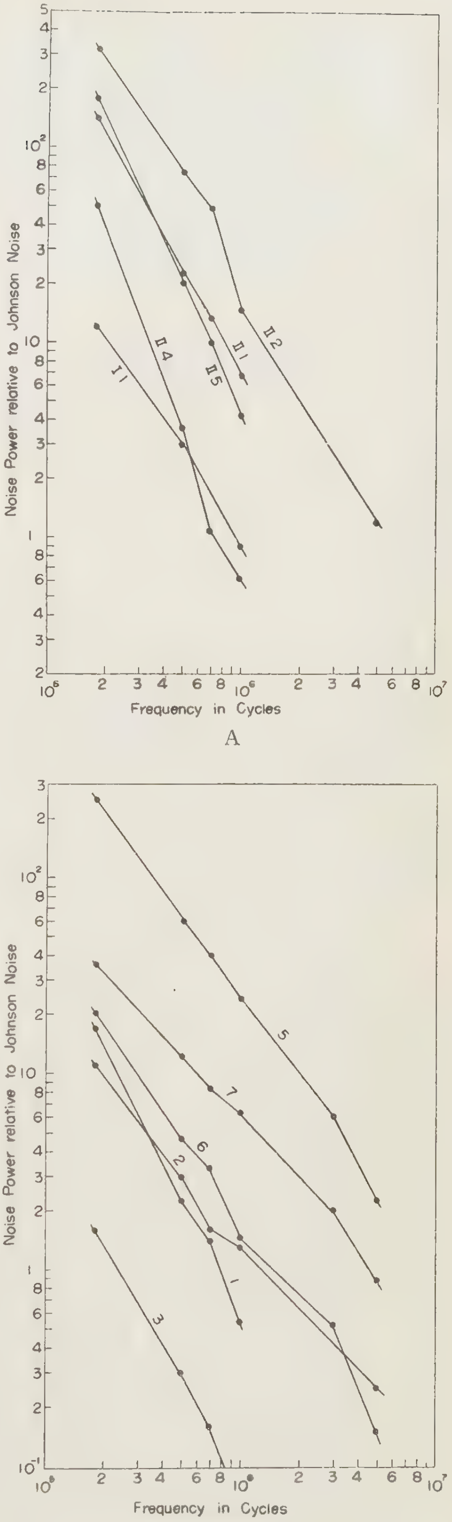

A

B

Fig. 3. The spectra of noise in germanium filaments carrying 5 mA dc current.

kilocycles is about from 10 to 20 db when the passing current is 5 mA.

In conclusion the authors wish to express their sincere acknowledgements to Prof. K. Yamashita of Okayama University for his kind encouragement. This work has been made possible partly thanks to the Ministry of Education Grant in Aid of Scientific Researches.

References

1) H. C. Montgomery: B. S. T. J. **31** (1952) 950.
2) R. H. Mattson and A. Van der Ziel: J. Appl. Phys. **24** (1953) 222.
3) A. Van der Ziel: J. Appl. Phys. **24** (1953) 222.
4) C. B. Herzog and A. Van der Ziel: Phys. Rev. **84** (1951) 1249.
5) S. Kojima and others: Zatsuon (E. C. F. Japan Press. 1951) p. 71.

J. PHYS. SOC. JAPAN **10** (1955) 912~913

Effect of Electron Bombardment on Secondary and Photoelectric Emission of Cesium-antimonide

By Kiyoshi MIYAKE

Electrical Communication Laboratory, Nippon Telegraph and Telephon Cooperation, Tokyo, Japan

(Received March 8, 1955)

The changes in secondary and photoelectric emission properties of Cs–Sb layer caused by electron bombardment have been studied, and a few results were reported[1]. In the previous experiment, an initial increase of secondary yield during continued electron bombardment was observed, though it was not mentioned in the paper. The experiment to be reported here was mainly tried concerning such a phenomenon. Cs–Sb samples used were prepared on a movable basket-shaped target made from thin nickel plate after usual processes. Secondary and photoelectric emission were measured at separate positions in an experimental tube. Secondary yield curve was obtained in the range of primary voltage (V_p) from 50 V to 1000 V, and relative spectral photo-response was measured between 400 mμ and 750 mμ.

The maximum yield $\delta_{\max}$ of samples having high photoelectric response, amounts to 4~6 at $(V_p)_{\max} = 500\ V \sim 800\ V$. The photo-electric threshould of these samples was about 680 mμ. On the other hand, $\delta_{\max}$ of a few samples having low photoelectric response was less than 4 and their photoelectric threshold was less than 620 mμ. In Fig. 1, the curve (a) shows a typical change of secondary yield of high photo-emissive samples caused by electron bombardment. At the beginning their yield increased gradually with the duration of bombardment, then reached a maximum value higher than initial one by 0.3~0.6. Later these values decreased slowly to an almost steady value. Fig. 2 shows the relation between the maximum secondary yield (solid line) and photo-response on the same sample shown in Fig. 1 (a). Chain and broken lines show the relative photo-response for blue-green and red light filtered by Corning No. 4784 (transmission approximately below 600 mμ) and

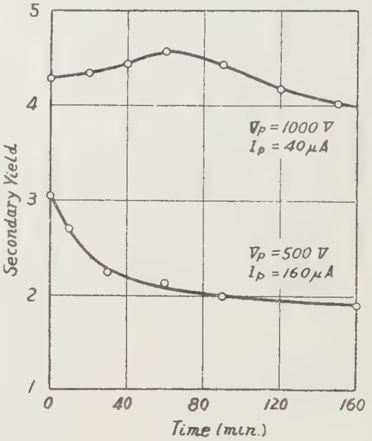

Fig. 1. Changes of secondary yield by electron bombardment. Bombarding voltage (V_p) and current (I_p) are shown for each curve.

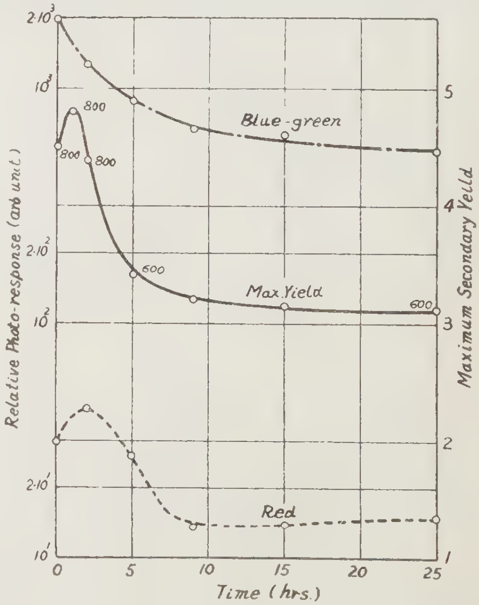

Fig. 2. Relation between maximum secondary yield and photo-response for blue-green and red light. Numbers on solid curve show $(V_p)_{\max}$ at each bombarded state.

No. 2412 (transmission approximately above 600 mμ) respectively. As shown in the figure, the photo-response for blue-green light decreased gradually with the duration of electron bombardment. While, the photo-response for red light rised to a maximum value after the maximum for secondary emission had been passed, then fell rapidly to a steady value. Fig. 3 shows the change of spectral photo-response caused by electron bombardment. Comparing to the photo-response at the initial state, the response obtained after two hour bombardment decreased in the range below 600 mμ and increased in the range above this wavelength. The long wave limit of photo-emission shifted towards longer wavelength by about 30 mμ. The spectral response obtained after more than 9 hour bombardment, decreased all over the measured range and thereafter the response did not change substantially.

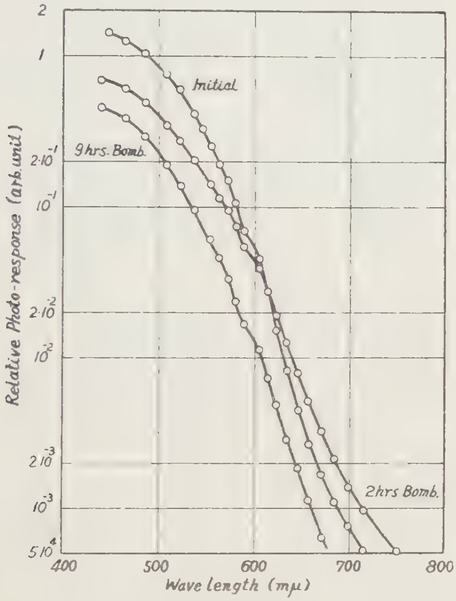

Fig. 3. Change in spectral photo-response.

The yield of a few samples of low secondary emission, which were obtained accidentally owing to insufficient amount of cesium to fully react with antimony, decreased within very short time as shown in Fig. 1 curve (b). Their maximum yield decreased nearly to that of antimony itself²⁾ and their photoelectric threshold varied from about 620 mμ at initial state to about 550 mμ at severely bombarded state, as well as decreasing in photo-response. Moreover, the activation of both emissions was not entirely observed. It is likely, therefore, that the changes in emission properties of above mentioned samples are merely due to the dissociation of cesium from Cs–Sb film. On the other hand, the yield of samples having high emissive properties was maintained at fairly high value even after 25 hour bombardment. The photoelectric threshold of such samples was not remarkably affected, though the gradual decresae of photo-response was observed. It is then supposed that in this case the dissociation of cesium also occurs to some extent and results in producing the defects in the lattice. A transient activation of photoelectric and secondary emission induced by the bombardment may be related to the formation of such defects. The author would like to continue some experiments with respect to these activation phenomena.

The author wishes to express his hearty thanks to Dr. S. Yoshida and Dr. T. Sakata for their advices and interests to this experiment, and Mr. S. Munesue for his help in the measurement of spectral photo-response.

References

1) K. Miyake: J. Phys. Soc. Japan **10** (1955) 164.
2) K. McKay: Advances in Electronics Vol. 1, p. 69, (Academic Press, New York, 1948.).

J. PHYS. SOC. JAPAN **10** (1955) 913~915

Fatigue of Photoelectric Emission of Cesium antimonide

By Kiyoshi MIYAKE

Electricrl Communication Laboratory, Nippon Telegraph and Telephon Cooperation, Tokyo, Japan

(Received June 18, 1955)

It is a well known fact that the photoelectric response of the cesium-antimonide or silver-oxygen-cesium photocathode decreases when it is used under intense light. The fatigue of these photocathodes has been studied by many investigators and supposed to be caused by ion-bombardment, thermal effect, or the diffusion of cesium atoms.¹⁾²⁾³⁾⁴⁾ The author has studied the fatigue occuring while the cesium-antimonide photocathode is exposed to intense illumination with blue-green and red light. The former light was used for the purpose of studying the effect by light itself, and the latter light mainly for the thermal effect. For these experiments an incandescent lamp was used in connection with a blue-green filter (Corning No. 4784; trasmission approximately below 6000 Å) or a red filter (Corning No. 2412; transmission approximately above 6000 Å).

Six experimental tubes having the same structure of electrodes as that used in the previous experiment⁵⁾ were used. The film of cesium-antimonide was prepared on the nickel plate. The photoelectric response of samples was 17~38 μA/lumen for a color temperature of c.a. 2900°K, and their maximum seconary yields $\delta_{\max}$ were 3.7～5.3 at primary voltage $(V_p)_{\max}=500\sim600$ V. An incandescent lamp was used as the source of intense illumination, and arranged with concave and plain mirror so as to focus the light flux about 1.3 lumen (16000 lux) on the photocathode.

Fig. 1 shows a typical change of photoelectric response and maximum yield produced by the intense illumination with blue-green or red light. The initial photoelectric response and $\delta_{\max}$ of the sample were c.a. 26 μA/lumen and 4.34 respectively. The illumination with blue-green light was carried for 10 hours, and with red light followed 15 hours. The photoelectric response for blue-green and red light was measured after the every illumination of a definite time. As shown in the figure, the radiation of blue-green light caused an increase of $\delta_{\max}$ and response for red light. The radiation of red light produced an abrupt decrease of secondary and photoelectric emission. Fig. 2 and Fig. 3 show the secondary yield curve and spectral photoelectric response at each illuminated state about the same sample shown in Fig. 1 respectively. Fig. 2 curve (1) shows the secondary yield curve at the initial state. By intense illumination with blue-green light for 10 hours the yield curve shifted to the curve (2), and $\delta_{\max}$ increased by 0.3. Corresponding to this change, the photoelectric threshold shifted the longer wavelength side as shown in Fig. 3 curve (2). The intense illumination with red light for 15 hours produced the change in the shape of yield curve as well as the decrease of $\delta_{\max}$. Curve (3) in Fig. 3 shows the response after 15 hour illumination and fairly differs in the characteristics comparing to other curves.

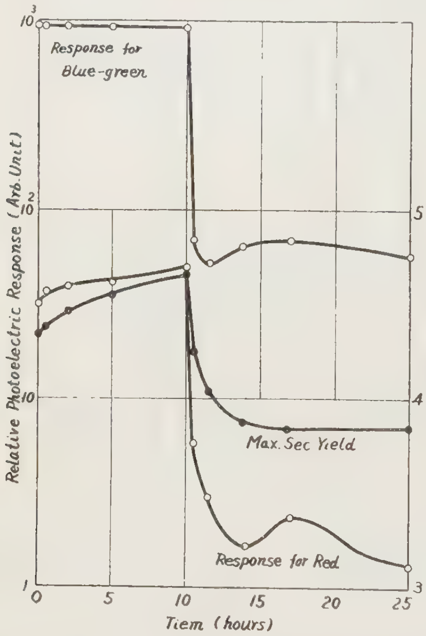

Fig. 1. Change in maximum secondary yield and photoelectric response caused by intense illumination.

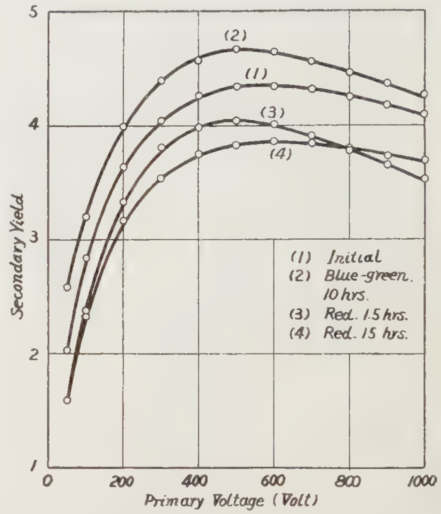

Fig. 2. Secondary yield curves at initial and illuminated states.

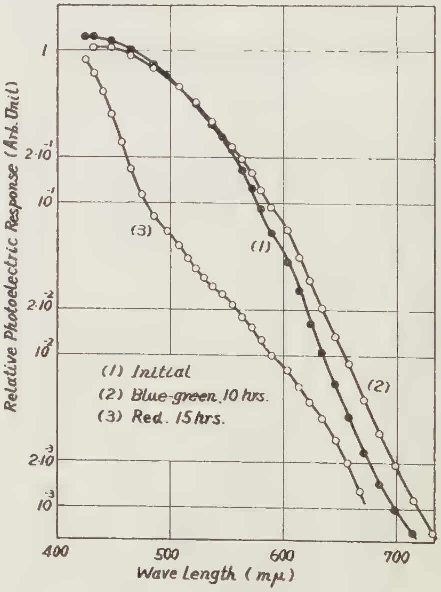

Fig. 3. Change in spectral photoelectric response.

From these results it is clear that the radiation of red light has a very remarkable effect and gives rise to large decrease in both emission. These decreases may be due to the change in the composition of cesium-antimonide resulted from the vaporization of a small number of cesium atoms. For, the film in this experiment was prepared on the nickel plate instead of glass wall, in which case the thermal effect of light will become large. On the other hand, the radiation of blue-green light has a comparatively small effect. The photoelectric current during the illumination is the order of 20 μA, beside the specific resistance of cesium-antimonide is extremely lower than that of cesium oxide. Therefore, the electric field across the film used is estimated less than 10^{-2} V/cm, so that the diffusion of cesium atoms will not occur[6]. Now it is reasonable to assume that during the intense illumination with blue-green light an extremely small deviation from the stoichiometric composition, presumably the lattice defects, in cesium-antimonide is produced either by ion-bombardment or by light-illumination. Taking these results into consideration, the author would like to continue some experiments on the fatigue of photoelectric emission of the sample prepared on glass plate.

The author wishes to express his hearty thanks to Dr. T. Sakata and Dr. S. Yoshida for their suggestions and interests to this experiment, and Mr. S. Munesue for his help in the measurement of spectral photoelectric response.

References

1) V. Zworykin and E. Ramberg: "Photoelectricity and its Application" p. 53 (John Wiley and Sons, Inc., New York 1949).
2) A. Sommer: "Photoelectric Cells" p. 77 (Chemical Publishing Co., Inc., New York 1951).
3) Technical Phys. U.S.S.R. **5** (1938) 245: A conference on the photoelectric effect and secondary emission.
4) I. Kwanzchewa: Phy. Zeit. d. Sowjetunion **10** (1936) 809.
5) K. Miyake: J. Phys. Soc. Japan **10** (1955) 164.
6) T. Sakata: private communication; to be published.

J. PHYS. SOC. JAPAN **10** (1955) 915~916

Intensities of Low Energy μ-Mesons and N-Component near Sea Level at 24°N

By Shin-ichi KANEKO, Tadayoshi KUBOZOE,* and Masaomi TAKAHATA

Institute of Polytechnics, Osaka City University, Osaka

* *Now at National Defence Academy, Yokosuka*

(Received July 27, 1955)

Many workers have measured the momentum or range distribution of μ-mesons near sea level at the geomagnetic latitude around 50°. At the lower latitude, so far as we know, only a measurement of the range spectrum (29°) by del Rosario and Dávila-Aponte[1] has been reported. Recently, a measurement of the momentum spectrum at 24°N has been carried out by Fukui *et al.*[2] in this laboratory making use of a magnet cloud chamber.

The absolute intensity of μ-mesons at residual ranges of a few tens g·cm^{-2} can also be determined measuring the frequency ot slow μ-mesons coming to rest in emulsions which have been exposed under a thin absorber. The frequency N(cm^{-3}day^{-1}) can be written

$$N=\frac{\rho}{1.5}(60\times60\times24)\cdot2\pi\int_0^{\pi/2} i_v \cos^n\theta \sin\theta d\theta\ , \qquad (1)$$

where i_v is the differential vertical intensity of μ-mesons in g^{-1}sec^{-1}sterad^{-1}, $\cos^n\theta$ represents the zenith anlge dependence of slow μ-mesons, ρ is the density of the emulsion in g·cm^{-3}, and the numerical coefficient 1.5 represents the stopping power of the air relative to the emulsion. Assuming the exponent n to be 3.2 according to Creamer[3], we obtain

$$i_v=3.0\times10^{-6}N\,. \qquad (2)$$

We have observed slow particles and stars in thick (600 and 1000 microns) nuclear plates which were made from G5 emulsions in gel form at the Isohama Railway Tunnel[4] and at a tunnel of the Osaka Municipal Subway[5] and were exposed under 15±5 g·cm^{-2} of air equivalent at sea level during two or three months. The geometrical correction factor of the frequency of μ-mesons can be represented by the following equation assuming $n=3$:

$$\frac{N_0}{N_T}=1\Big/\left[1-\frac{2}{\pi}\left\{\tan^{-1}\frac{T}{d}-\frac{Td}{3(T^2+d^2)}\right\}\right], \qquad (3)$$

where N_0 is the total number of the stopped particles, N_T is the observed number of the stopped particles having the projected ranges greater than T microns, and d is the thickness of the emulsion in microns. The corrected frequency of μ-mesons was found to be 1.29 ± 0.08 cm^{-3}day^{-1}, assuming that the shrinkage factor was 2.7. It should be noted that this frequency includes the μ-mesons arising from the decay of π-mesons produced in the ground. The contribution of these backward μ-mesons amounts to about thirty per cent. Thus, the differential vertical intensity of μ-mesons at the range 15±5 g·cm^{-2} becomes

$$i_v=(2.6\pm0.2)\times10^{-6}\text{g}^{-1}\text{sec}^{-1}\text{sterad}^{-1}\,.$$

The value of i_v thus estimated depends sensitively upon the assumed value of n, as can be seen from Eq. (1). Since the observed number of μ-mesons was not sufficient to determine experimentally the value of n at 24°, we have assumed that the value of n at 24° is the same as the one[3] at 54°.

As shown in Fig. 1, the vertical intensity we have obtained at 24° is somewhat smaller than

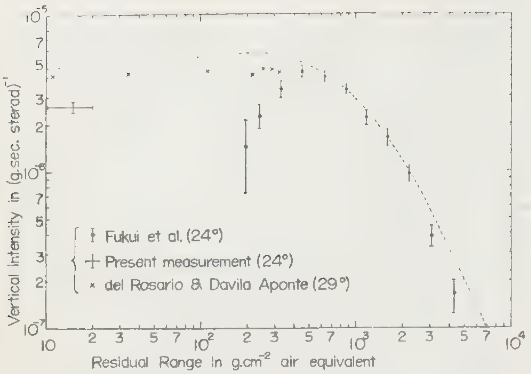

Fig. 1. The differential range spectrum of μ-mesons near sea level at low geomagnetic latitude. For comparison, the spectrum at ~50° given by Rossi has been shown by the dotted curve.

those given by del Rosario and Dávila-Aponte at 29°. On the other hand, since the lowest momentum measured by Fukui *et al.* corresponds to the range of $\sim 200\,\mathrm{g\cdot cm^{-2}}$, a direct comparison between their values and ours cannot be made. It seems, however, that a rapid fall of their spectrum at low momentum regions is inconsistent with our measurement. (In this respect, a detailed discussion has been given in reference 2.) At a high latitude, George and Evans[6] have measured the frequency of slow μ-mesons coming to rest in emulsions at London (54°N) and have found that the vertical intensity of slow mesons computed from this frequency agrees well with the range spectrum given by Rossi[7].

The frequency of stars with three or more heavy prongs, $0.23 \pm 0.04\,\mathrm{cm^{-3}day^{-1}}$, is quite small as compared with those observed at high latitudes. According to George and Evans, the frequency of stars at London is $1.46 \pm 0.07\,\mathrm{cm^{-3}day^{-1}}$. The ratio between the frequencies at 54° and 24°, 6.3 ± 1.3, is consistent with the value~6 observed by Yagoda and Kaplan[8] between 50° and 1°, and should be ascribed to the latitude effect of the N-component at energies of several hundred Mev.

We wish to express our gratitude to Prof. Y. Watase for suggesting this study as well as for continual encouragement. Thanks are also due to Messrs. S. Fukui, T. Kitamura and Y. Murata for helpful discussions.

References

1) L. del Rosario and J. Dávila-Aponte: Phys. Rev. **88** (1952) 998.
2) S. Fukui, T. Kitamura and Y. Murata: J. Phys. Soc. Japan **10** (1955) 735.
3) R. Creamer: M. Sci. Thesis, London, 1951 cited in E. P. George: *Progress in Cosmic Ray Physics*, edited by J. G. Wilson, North-Holland Publishing Co., Amsterdam, 1952, p. 433.
4) S. Kaneko, T. Kubozoe and M. Takahata: J. Phys. Soc. Japan **9** (1954) 147.
5) S. Kaneko, T. Kubozoe, M. Okazaki and M. Takahata: J. Phys. Soc. Japan **10** (1955) 600.
6) E. P. George and J. Evans: Proc. Phys. Soc. **A 63** (1950) 1248.
7) B. Rossi: Rev. Mod. Phys. **20** (1948) 537.
8) H. Yagoda and N. Kaplan: Phys. Rev. **75** (1959) 339.

Errata

The Drag on a Circular Cylinder moving with Dow Speeds in a Viecous Eiquid between Two Parallel Walls

By Yorisaburo TAKAISI

J. Phys. Soc. Japan, Vol. 10, No. 8, pp. 685~693

(page)	(column)	(line)		(should be read)
686		37	$\frac{w}{k}=\left(\frac{1}{2}-\gamma-\mathrm{In}\frac{kr}{2}\right)b_0-\cdots$	$\frac{w}{k}=\left(\frac{1}{2}-\gamma-\ln\frac{kr}{2}\right)b_0-\cdots$
689		11	$\frac{w}{k}=-\left(\frac{1}{2}-\gamma-\ln\frac{kr}{2}\right)\beta_0$	$\frac{w}{k}=-\left(\frac{1}{2}-\gamma-\ln\frac{kr}{2}\right)B_0$
691		18	aβ:	as:

Ultraviolet Absorption Spectra of Uranium Glasses

By Kikusaburo OSADA

J. Phys. Soc. Japan **10** (1955) 825~826

P. 825, right column, line 8 from the bottom should be read as follows:
······· So their spectra were measured with a small glass spectrograph.

PROGRESS OF THEORETICAL PHYSICS

(Founded by H. Yukawa in 1946)

Published for the

Research Institute for Fundamental Physics
The Physical Society of Japan

Progress of Theoretical Physics Vol. 13, No. 2, February 1955

On the Para- and Antiferromagnetic States of Cobalt Fluoride..Tuto NAKAMURA and Hiroshi TAKETA....129
A Theory of Antiferromagnetism, II ....Takehiko OGUCHI....148
Application of the Method of Generating Function to Radiative and Non-Radiative Transitions of a Trapped Electron in a Crystal ....Ryogo KUBO and Yutaka TOYOZAWA....160
Potential in Quantum Field Theory ....Tsutomu IMAMURA....183
Nonadiabatic Treatment of Nuclear Forces, I —*Static Limit*—....Junji IWADARE....189
The D-Wave Contribution to Pion-Nucleon Scattering ....Taiji YAMANOUCHI and Nobuyuki FUKUDA....200
The Energy Balance of Cosmic Rays..............................Hiroo Komori....205
Letters to the Editor:
  An Example of Five-Dimensional Field......................T. YAMAMOTO....217
  Non-Static Corrections to the Fourth Order Nuclear Forces....J. IWADARE....218
  Ward's Identity in Neutral Scalar Mesoo-Nucleon System ....K. HIIDA and S. MACHIDA....219
  On the Consistency of the Quantum Field Theory Based on the Renormalization Hypothesis ....T. YOSHIMURA....220
  Relativistic Hydrodynamics Equivalent to the Dirac Equation .... T. TAKABAYASI....222
Errata 224

Progress of Theoretical Physics Vol. 13, No. 3, March 1955

On the Theory of Plasma Oscillations in Metals ....Hideo KANAZAWA....227
Collisions between Non-Spherical Molecules, I —*Molecular Collisions in Hydrogen Gas at Lower Temperatures*—.. Kazuo TAKAYANAGI and Kimio OHNO....243
Nuclear Matrix Element for β-Decay and the Ratio of Coupling Constants... Jun-ichi FUJITA....260
On Statid Solutions of Einstein's Generalized Theory of Gravitation, II ....Mineo IKEDA....265
On the β–γ Angular Correlations of Tm^{170} and Sb^{124}—*VT Interaction*— .... Yusuke KATO and Masato MORITA....276
Charge Independence Theory of V Particles ....Kazuhiko NISHIJIMA....285
Many-Body Problem in Quantum Field Theory, III ....Kazuhiko NISHIJIMA....305

Letters to the Editor:
Formula for Differential Cross Section in Nucleon-Nucleon Scattering .... M. MATSUMOTO....329
On the Jauch Field .... S. KAMEFUCHI and S. TANAKA....334
A Remark on the Interaction of the Second Kind .... T. YOSHIMURA....336
Note on the Bound State Problem .... T. OKABAYASHI....338

Progress of Theoretical Physics Vol. 13, No. 4, April 1955

Electromagnetic Properties of Deuteron .... Iwao SATO and Kiyomi ITABASHI....341
Multiple Scattering Phase Shifts and Nuclear Potential .... Kazu HASEGAWA and Jhuko AZUMA....360
Oh the Competition between Decay and Capture of the Unstable Particles due to the Weak Interactiohs .... Shuzo OGAWA....367
Point Transformation and its Application .... Shinzo NAKAI....380
On Higher Order Corrections in the Meson Theory of Nuclear Forces .... Shigeru MACHIDA and Kei SENBA....389
General Formula of the Racah Coefficient .... Masachiyo SATO....405
Nuclear Reactions at Moderate Energies and Fermi Gas Model .... Satio HAYAKAWA, Mitsuji KAWAI and Ken KIKUCHI....415
On the Foundation of the Unified Nuclear Model, I .... Toshio MARUMORI, Jiro YUKAWA and Ryokichi TANAKA....442
Letters to the Editor:
Some Remarks on Lee's Model in Renormalizable Field Theory .... Y. MUNAKATA....45
Recoil Effect and Spin-Orbit Coupling .... S. SATO....457
The Relation between Jordan's Non-Localized Theory and Pais.Uhlenbeck's Theory .... Y. MIYATAKE....458
Elastic Production of Neutral Photo-Pions in Helium .... Y. YAMAGUCHI....459
The Non-Mesonic Photonuclear Reactions Initiated by High Energy μ-Mesons....S. KANEKO, T. KUBOZOE, M. OKAZAKI and K. TAKAHATA....461
A Possible Effect of Cosmic Rays on Celestial Chemical Composition .... S. HAYAKAWA....464

Price	\$ 1.25 per copy
	\$ 15.00 per year (postage inclusive)
Annual dues for foreign members (individual subscribers)	
	\$ 12.00 (postage inclusive)
〃 for foreign members of the Physical Society of Japan	
	\$ 10.00 (postage inclusive)

Application for members, subscriptions and orders for back mumbers should be sent, directly or through book-dealers, to

The Publication Office
in
Yukawa Hall, Kyoto University, Kyoto, Japan

JOURNAL OF THE PHYSICAL SOCIETY OF JAPAN Vol. 10, No. 11, NOVEMBER 1955

Hyperfine Structure of the Spectrum of Ruthenium
Part III

By Kiyoshi MURAKAWA

Institute of Science and Technology, Komaba-machi, Meguro-ku, Tokyo

(Received July 29, 1955)

The hyperfine structure of the spectrum of Ru I was studied, and it was found that the ratio of the distances of the components due to the even isotopes is given by $\Delta(104-102):\Delta(102-100):\Delta(100-96)/2=1:1.05\pm0.10:0.75\pm0.15$. There is reason to suppose that the shift $\Delta(98-96)$ is anomalously small compared with the shift $\Delta(104-102)$ or $\Delta(102-100)$. The magnetic moments of the odd isotopes were calculated to be $\mu(\mathrm{Ru}^{101})=-0.69\pm0.15$ nm. and $\mu(\mathrm{Ru}^{99})=-0.63\pm0.15$ nm.

§ 1. Introduction

In two preliminary papers[1)2)], which will be referred to as Part I and Part II respectively, the general aspect of the hyperfine structure (hfs) of the spectrum of Ru I was described. In Part I the sample of Ru that was used contained some impurities, only λ4554 being free from neighboring impurity line. In Part II the sample was greatly improved, the only impurity that was practically detected being osmium. Shift of even isotopes was detected in many lines, and the magnetic moments of the odd isotopes (Ru^{101} and Ru^{99}) were determined to be -0.6 ± 0.2 nm. The present paper describes somewhat more fully the experimental material obtained in Part II.

The liquid-air-cooled hollow cathode that was used as a light source was described in detail previously[3)]. The hfs was resolved by a Fabry-Pérot étalon; the thickness of the spacer ranged from 6 to 70 mm. Some of the interference patterns of the spectrum of Ru I were reproduced in Part I and Part II, so they will not be repeated here. In order to make the discussion clear, some of the hfs schemes published in Part II are included in the present paper. Measurement of the hfs of the line λ3799.3 was made extremely difficult by the neighboring line λ3798.9, so a very rough estimate was given in Part II, denoting it by the symbol $\sim$. In the present work we will consider only the fact $0.009\ \mathrm{cm}^{-1}\geqq\Delta(104-102)\geqq0$ as definite and leave the detailed structure of this line undetermined.

The isotopic composition[4)] of natural ruthenium which is given in Table I will be frequently needed.

The spectrum of Ru I was classified by Sommer[5)], Meggers and Laporte[6)], and Harrison and McNally[7)]. The work of the last named authors is the most complete, and their notation for the level will be employed here.

§ 2. Shift of the Even Isotopes

The hfs of the spectrum of Ru I can be classified into the following four groups.

(**i**) No hfs. This means that practically

Table I. Isotopic constitution of natural ruthenium.

A	104	102	101	100	99	98	96
N	60	58	57	56	55	54	52
Abundance (%)	18.27	31.34	16.98	12.70	12.81	2.22	5.68

Table II. List of lines having unresolvable isotope shift.

Line (A)	Classification	Line (A)	Classification	Line (A)	Classification
4397.8	$d^8\ {}^3F_4-z\,{}^3G_3^0$	4293.3	$d^6s^2\,{}^5D_2-z\,{}^7P_2^0$	3964.9	$d^7s\,{}^5F_5-z\,{}^7D_5^0$
4361.2	$d^7s\,{}^3F_4-y\,{}^5F_5^0$	4217.3	$d^7s\ {}^3F_4-z\,{}^7P_4^0$	3925.9	$d^7s\,{}^5F_5-z\,{}^7D_4^0$
4295.9	$d^8\ {}^3F_3-z\,{}^3D_3^0$	4023.8	$d^7s\ {}^5F_4-z\,{}^7D_3^0$		

no shift of the even isotopes is detected and the splittings of the odd isotopes are small. Some of the lines belonging to this category and to (iv) are listed in Table II.

(**ii**) Lines in which the shift of the even isotopes is detected and the odd isotopes have finite splittings. In this case it is difficult to measure accurately the hfs of the odd isotopes; the apparent positions of the even isotope components are more or less affected by the odd isotope components. Fig. 1 represents qualitatively the scheme of the hfs of this category, and Table III represents the result of measurement for the even isotopes only.

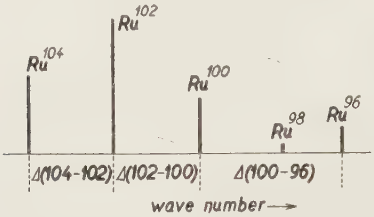

Fig. 1. Explanation of Table III. (The components of the odd isotopes 101 and 99 are distributed, in such a way that the measurement of their positions is difficult, so they are not shown in this figure).

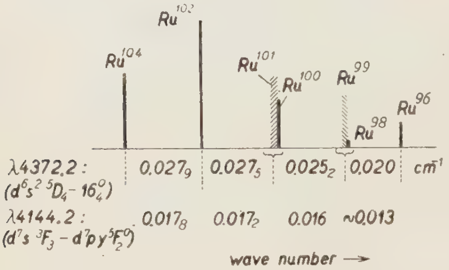

Fig. 2. Hfs of Ru I λ4372.2 and λ4144.2.

(**iii**) Lines in which the shift of the even isotopes is detected and each of the splittings of the odd isotopes is negligibly small. In this case the complex 101+100 is approximately of the same intensity as 102, (Fig. 2). The intensity ratio 99+98 : 104 should be 15.0 : 18.3, and this is in agreement with the observation, so that 98 is approximately coincident with 99 and not with 96.

From the measurement given in Table III and Fig. 2 we get the ratio

$$\Delta(104-102):\Delta(102-100):\Delta(100-96)/2 \\ =1\,;\,1.05\pm0.10:0.75\pm0.15.$$

Table III. Shift of the even isotopes in the spectrum of Ru I*.

Line (A)	Classification	Δ(104 −102) cm⁻¹	Δ(102 −100) cm⁻¹	Δ(100 −96) cm⁻¹
4554.5	$d^7s\ ^3F_4-z\,^3G_5^0$	0.016	0.018	0.027
4449.3	$d^6s^2\ ^5D_3-y\,^5F_3^0$	0.029	0.029	0.049
4297.7	$d^7s\ ^3F_3-z\,^3G_4^0$	0.015	0.016	0.020
4294.8	$d^6s^2\ ^5D_3-z\,^3G_3^0$	0.029	0.029	0.048
4284.3	$d^6s^2\ ^5D_2-z\,^3D_3^0$	0.024	0.026	0.037
4206.0	$d^7s\ ^3F_3-z\,^3G_3^0$	0.021	0.024	0.037
4199.9	$d^7s\ ^3F_4-16_4^0$	0.015	0.016	0.025
4167.5	$d^7s\ ^3F_2-z\,^3D_2^0$	0.023	0.025	0.038
4145.7	$d^6s^2\ ^5D_2-z\,^3D_2^0$	0.020	0.020	0.029
4080.6	$d^7s\ ^3F_4-y\,^5F_3^0$	0.018	0.017	0.029
3984.9	$d^7s\ ^3F_3-z\,^3D_2^0$	0.018	0.018	0.031

* The initial levels of the lines listed here belong to the configuration $4d^75p$.

Table IV. Relative shift Δ(104−102) in various levels of Ru I.

Term	Term value cm⁻¹	Isotope shift Δ(104−102) cm⁻¹
$4d^7\,5s\ ^5F_4$	1190.67	0.016
$4d^7\,5s\ ^3F_4$	6545.05	0.018
$4d^7\,5s\ ^3F_3$	8084.13	0.021
$4d^7\,5s\ ^3F_2$	9183.69	0,028
$4d^6\,5s^2\ ^5D_4$	7483.14	0.031
$4d^6\,5s^2\ ^5D_3$	8575.45	0.029
$4d^6\,5s^2\ ^5D_2$	9057.64	0.026
$4d^7\,5p\ z\,^3G_5^0$	28495.26	0.001
$4d^7\,5p\ 16_4^0$	30348.49	0.003
$4d^7\,5p\ y\,^5F_3^0$	31044.36	0.000
$4d^7\,5p\ y\,^3G_4^0$	31345.86	0.006
$4d^7\,5p\ z\,^3G_3^0$	31852.94	0.000
$4d^7\,5p\ y\,^5F_2^0$	32207.68	0·004
$4d^7\,5p\ z\,^3D_3^0$	32392.00	0.002
$4d^7\,5p\ z\,^3D_2^0$	33172.07	0.004

The general regularity concerning the isotope shift teaches us that the center of gravity of the 99-hfs must be between 98 and 100. On the other hand 98 and 99 are approximately coincident. It is therefore probable that the distance Δ(98−96) is anomalously small compared with the shift Δ(104−102) or Δ(102−100).

Assuming that the shift of even isotopes in the level $4d^75pz\,^3G_3^0$ vanishes, we can calculate on the basis of the observed hfs the shift of even isotopes in various levels. This is shown in Table IV*.

(**iv**) Lines in which the shift of the even isotopes is negligibly small and the odd isotopes have large splittings. This case is met in λ4361 and λ4284 as was shown in Part I and Part II.

§ 3. The Magnetic Moments of the Odd Isotopes

The nuclear spins and magnetic moments of the odd isotopes (99 and 101) can be found from the hfs of the lines belonging to the category (iv) of § 2. In Part II it was found that each of the odd isotopes possesses nuclear spin 5/2. This had been found in a somewhat earlier work by Griffiths and Owen⁹⁾ by the method of paramagnetic resonance absorption. These authors found the ratio of the magnetic moments to be $\mu^{101}/\mu^{99}=1.09\pm0.03$.

The values of the magnetic moments can be calculated from the same lines as those mentioned above (Fig. 3). In each case the final level is $d^7s\,^3F_4$. In order to see the nature of this level, nearly all the even levels given by Harrison and McNally⁷⁾ are shown schematically in Fig. 4. These authors showed that $d^7s\,^3F_2$ and $d^6s^2\,^5D_2$ are close together and share their properties, so it is difficult to distinguish to which electron configurations they belong. With respect to the level $d^7s\,^3F_4$ the matter is not so confusing. In order to show this, the energy matrix must be solved. The elements of electrostatic interaction are given in several literatures, so they will not be repeated here. The matrix of spin-orbit interaction is given in the Appendix of the present paper. It was soon felt thal solving the energy matrix exactly is a hard task for the author, and it was decided to do this after a computor would be available in this Institute, and to be satisfied with a very rough solution at present. The positions of the levels** shown in Fig. 4 can be qualitatively (roughly) explained by choosing the parameters

$$\zeta_d=890,\ F_2=950,\ F_4=75,\ G_2=1520,$$

$$H_2=R^2(dd,\ ds)/35\approx400.$$

It is assumed that the values of the parameters are common to all the configurations considered. These values were put into the

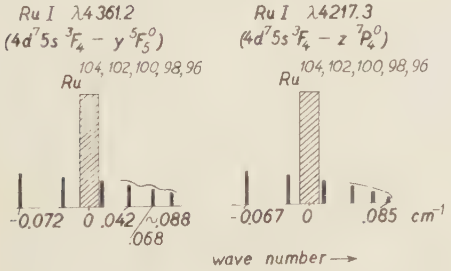

Fig. 3. Hfs of Ru I λ4361.2 and λ4217.3.

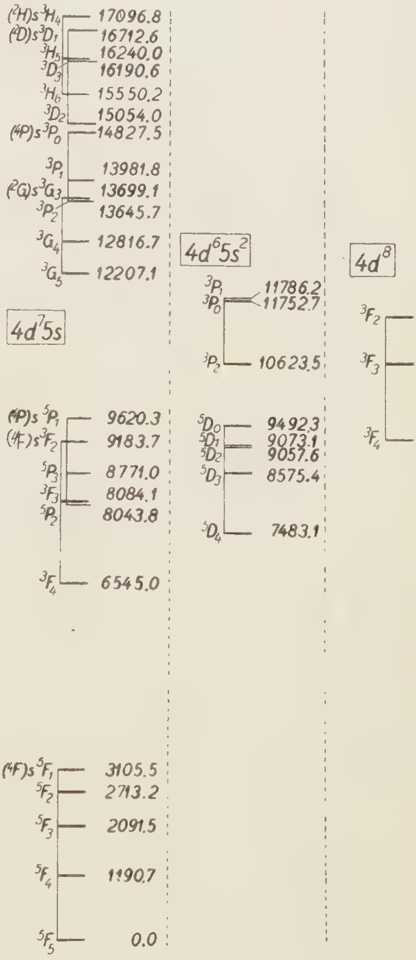

Fig. 4. Schematic representation of the low even configurations of the spectrum of Ru I.

---

* Recently Kopfermann et al⁸⁾ have worked on the same subject. Kopfermann could not resolve the shift of the even isotopes in any line, and estimated the shift by a photometric method, under the assumption that each of the odd isotopes does not split in each line that he studied. Since this assumption is incorrect, the results obtained by Kopfermann are invalid.

** In the determination of these parameters, no consideration was given to the configuration $4d^8$, owing to the small number of levels that are detected in this configuration.

energy matrix, and the secular equations solved. Then by the usual procedure the composition of the level $d^7s\,{}^3F_4$ can be computed. In addition to this, the condition that the wave functions must satisfy the g-value published by Harrison and McNally was taken into consideration. Since we have to be satisfied with an accuracy of about 10%, all the terms that contribute an amount smaller than this (namely $K^2<0.09$) were neglected, and finally the composition of $d^7s\,{}^3F_4$ as a linear combination of LS-coupling wave functions was obtained:

$$d^7s\,{}^3F_4{}' = K_1\,{}^3F_4(d^7s) + K_2\,{}^5D_4(d^6s^2)\ .$$

$$K_1=0.909\ ,\quad K_2=0.417\ .$$

The hfs of λ4361 was better resolved than that of λ4217, so the former will be considered first. It was impossible to separate the hfs of Ru^{99} and Ru^{101}, so the present calculation is concerned with a weighted mean of μ^{99} and μ^{101}.

The initial level $d^6sp\,y\,{}^5F_5{}^0$ of λ4361 was found to be located approximately at the position where the level $d^6sp\,{}^7F_5{}^0$ is expected. The other pair, namely $d^6sp\,{}^7F_6{}^0$ would be probably the level at 28571.8 that was detected by Meggers and Laporte⁶⁾. The level $d^7p\,{}^3G_5$ is near the level $y\,{}^5F_5{}^0$, so it is possible that the latter contains some percent of $d^7p\,{}^3G_5$.

For the moment we will assume that the wave function of $y\,{}^5F_5{}^0$ is pure (namely $d^6sp\,{}^7F_5{}^0$). In order to calculate the magnetic moment from the hfs of λ4361, we need the following LS-coupling formulas, in addition to those given in Part II.

$$A(d^6\,{}^5D_4)=\frac{1}{20}(19a_d{}'+a_d{}''+32a_d{}''')\ ,$$

$$A(d^6sp\,{}^7F_5)=\frac{1}{12}a(s)+\frac{1}{150}(107a_d{}'-7a_d{}''+136a_d{}''')+\frac{1}{180}(a_p{}'+4a_p{}''+8a_p{}''')\ .$$

$$a_d{}'=a(d_{5/2}),\quad a_d{}''=a(d_{3/2}),\quad a_d{}'''=a(d_{5/2},\ d_{3/2})$$

$$a_p{}'=a(p_{3/2}),\quad a_p{}''=a(p_{1/2}),\quad a_p{}'''=a(p_{3/2},\ p_{1/2}).$$

Putting $\zeta(4d)=890$, $Z_d{}^*=44-19=25$, $\zeta(5p)=560$, $Z_p{}^*=44-4=40$, and $Z=44$, $1-\delta=0.975$ (finite nuclear volume correction factor), $F=1.23$, $(dn^*dn)/n^{*3}=0.478$ (to be described in the Appendix) into these formulas and comparing them with the observed hfs of λ4361, we get $\mu=-0.64$ nm.

If we assume that $y\,{}^5F_5{}^0=K_1\,{}^7F_5(d^6sp)+K_2\,{}^3G_5(d^7p)$, $K_1{}^2=0.9$, $K_2{}^2=0.1$, then we get $\mu=-0.68$ nm.

The true value would lie between -0.64 nm and -0.68 nm. Remembering that this is a weighted mean of μ^{101} and μ^{99}, we might consider

$$\mu(\mathrm{Ru}^{101})=-0.69\pm0.15\ \mathrm{nm}\ ,$$

$$\mu(\mathrm{Ru}^{99})\ =-0.63\pm0.15\ \mathrm{nm}$$

the best values available at present.

With respect to the hfs of λ4284, it may be remarked that the initial level $z\,{}^7P_4{}^0$ is partly $4d^65s5p\,{}^7P_4$ and partly $4d^75p\,{}^5G_4$. The magnetic moments deduced from the hfs of this line are in agreement with the above-mentioned values, but in this case the accuracy is somewhat smaller.

Appendix

§ 4. The Matrix of Spin-orbit Interaction

The matrices of spin-orbit interaction of the configurations d^7s and d^6s^2 are identical with those of d^3s and d^4 respectively, if the spin-orbit interaction parameter ζ_d is considered as negative. They can be calculated readily by the use of Racah coefficients¹⁰⁾. Tables of the Racah coefficients have been prepared by Biedenharn and his co-workers¹¹⁾ and by Obi, Ishidzu, Horie and their co-workers¹²⁾. The result of calculation is given in Tables V and VI.

§ 5. Table of $(dn^*/dn)/n^{*3}$ for Optical s-Electrons

The interval factor $a(s)$ of an s-electron is given by Goudsmit-Fermi-Segre formula:

$$a(s)=\frac{ZZ_0{}^2(1-\delta)F}{117.8}\,\frac{dn^*/dn}{n^{*3}}\,\frac{\mu}{I}\ ,$$

where the finite nuclear volume correction δ is given by the usual formula

$$\delta=\frac{2(j'-\rho)\rho(2\rho+1)y_1{}^{2\rho-1}}{(2j'-1)\Gamma^2(2\rho+1)}\ ,$$

in which $j'=-1$ for s-electrons, and

$$y_1\doteqdot y_0=2Zr_0/a_H\ ,$$

and

$$\rho=\sqrt{1-Z^2\alpha^2}\ .$$

The above-mentioned Goudsmit-Fermi-Segre formula was derived so as to represent the hfs of alkali-atoms exactly, but it is generally assumed that the formula holds for other atoms also. The calculation of $(dn^*/dn)/n^{*3}$

Table V. Matrix of spin-orbit interaction of the configuration d^3s (the unit of the element is ζ_d).

$J=6$	$(^2H)\,^3H$
$(^2H)\,^3H$	$\frac{1}{2}$

$J=5$	$(^4F)\,^5F$	$(^2H)\,^3H$	$(^2H)\,^1H$	$(^2G)\,^3G$		
	$\frac{3}{2}$	0	0	$\frac{\sqrt{5}}{\sqrt{2}}$		
$J=4$		$-\frac{1}{10}$	$\frac{\sqrt{30}}{10}$	$-\frac{6}{5}$		
$(^4F)\,^5F$	$\frac{1}{4}$		0	$\frac{\sqrt{6}}{\sqrt{5}}$		
$(^4F)\,^3F$	$\frac{\sqrt{5}}{4}$	$\frac{5}{4}$		$\frac{3}{5}$		
$(^2H)\,^3H$	0	0	$-\frac{3}{5}$			
$(^2G)\,^3G$	$\frac{\sqrt{15}}{4}$	$\frac{5}{4\sqrt{3}}$	$-\frac{4\sqrt{11}}{5\sqrt{6}}$	$-\frac{3}{20}$		
$(^2G)\,^1G$	0	$\frac{\sqrt{5}}{\sqrt{3}}$	$-\frac{2\sqrt{55}}{5\sqrt{6}}$	$\frac{3\sqrt{5}}{10}$	0	
$(^2F)\,^3F$	$-\frac{\sqrt{5}}{4}$	$\frac{1}{4}$	0	$\frac{5}{4\sqrt{3}}$	$-\frac{\sqrt{5}}{2\sqrt{3}}$	$-\frac{1}{4}$

$J=3$	$(^4F)\,^5F$	$(^4F)\,^3F$	$(^4P)\,^5P$	$(^2G)\,^3G$	$(_1{}^2D)\,^3D$	$(_3{}^2D)\,^3D$	$(^2F)\,^3F$	$(^2F)\,^1F$		
	$-\frac{3}{4}$	$\frac{\sqrt{5}}{4}$	0	$\frac{5}{4\sqrt{7}}$	$\frac{\sqrt{15}}{5}$	$-\frac{\sqrt{5}}{\sqrt{7}}$	$-\frac{\sqrt{5}}{4}$	0		
$J=2$		$-\frac{5}{12}$	0	$\frac{3\sqrt{5}}{4\sqrt{7}}$	$-\frac{1}{\sqrt{3}}$	$\frac{5}{3\sqrt{7}}$	$-\frac{1}{12}$	$-\frac{1}{\sqrt{3}}$		
$(^4F)\,^5F$	$-\frac{3}{2}$		$\frac{1}{2}$	0	$\frac{2\sqrt{3}}{\sqrt{5}}$	0	0	0		
$(^4F)\,^3F$	$\frac{1}{\sqrt{6}}$	$-\frac{5}{3}$		$-\frac{3}{4}$	0	0	$\frac{3\sqrt{5}}{4\sqrt{7}}$	$\frac{3\sqrt{5}}{2\sqrt{21}}$		
$(^4P)\,^5P$	0	0	$-\frac{1}{4}$		$\frac{1}{2}$	$-\frac{\sqrt{21}}{6}$	$-\frac{2}{\sqrt{3}}$	1		
$(^4P)\,^3P$	0	0	$\frac{1}{4}$	$\frac{5}{12}$		$-\frac{1}{6}$	$-\frac{2}{3\sqrt{7}}$	$\frac{1}{\sqrt{21}}$		
$(^2P)\,^3P$	0	0	$-\frac{\sqrt{14}}{2}$	$\frac{\sqrt{14}}{6}$	$\frac{1}{3}$		$\frac{1}{12}$	$-\frac{\sqrt{3}}{6}$		
$(_1{}^2D)\,^3D$	$\frac{\sqrt{35}}{5}$	$-\frac{\sqrt{42}}{6\sqrt{5}}$	$\frac{\sqrt{3}}{\sqrt{5}}$	$\frac{\sqrt{3}}{\sqrt{5}}$	$\frac{\sqrt{42}}{4\sqrt{5}}$	$-\frac{1}{4}$		0		
$(_1{}^2D)\,^1D$	0	$\frac{\sqrt{7}}{\sqrt{5}}$	0	$\frac{4}{\sqrt{10}}$	$-\frac{\sqrt{7}}{2\sqrt{5}}$	$\frac{\sqrt{3}}{2\sqrt{2}}$	0			
$(_3{}^2D)\,^3D$	$-\frac{\sqrt{15}}{3}$	$\frac{\sqrt{10}}{6}$	0	0	$-\frac{9\sqrt{2}}{4\sqrt{5}}$	$\frac{\sqrt{21}}{12}$	$-\frac{\sqrt{7}}{2\sqrt{2}}$	$\frac{1}{12}$		
$(_3{}^2D)\,^1D$	0	$-\frac{\sqrt{5}}{\sqrt{3}}$	0	0	$\frac{3\sqrt{3}}{2\sqrt{5}}$	$-\frac{\sqrt{7}}{2\sqrt{2}}$	0	$-\frac{\sqrt{3}}{6\sqrt{2}}$	0	
$(^2F)\,^3F$	$-\frac{1}{\sqrt{6}}$	$-\frac{1}{3}$	0	0	0	$-\frac{\sqrt{42}}{3\sqrt{5}}$	$-\frac{\sqrt{7}}{\sqrt{5}}$	$-\frac{\sqrt{2}}{3\sqrt{5}}$	$-\frac{1}{\sqrt{15}}$	$\frac{1}{3}$

from the spectroscopic data (gross structure only) is easy in the case of alkali-atoms, but not in other atoms. However, when the value of the magnetic moment (μ) is known by the nuclear induction method, it is possible to calculate $(dn^*/dn)/n^{*3}$, using the spectroscopic

Table V. continued.

$J=1$

$(^4F)\,^5F$	$(^4P)\,^5P$	$(^4P)\,^3P$	$(^2P)\,^3P$	$(^2P)\,^1P$	$(_1{}^2D)\,^3D$	$(_3{}^2D)\,^3D$
-2	0	0	0	0	$\frac{\sqrt{210}}{10}$	$-\frac{\sqrt{10}}{2}$
	$-\frac{3}{4}$	$\frac{\sqrt{5}}{12}$	$-\frac{\sqrt{70}}{6}$	0	$\frac{1}{\sqrt{15}}$	0
		$-\frac{5}{12}$	$-\frac{\sqrt{14}}{6}$	$-\frac{2\sqrt{7}}{3}$	$\frac{1}{\sqrt{3}}$	0
			$-\frac{1}{3}$	$\frac{\sqrt{2}}{3}$	$\frac{\sqrt{42}}{12}$	$-\frac{3\sqrt{2}}{4}$
				0	$\frac{\sqrt{21}}{6}$	$-\frac{3}{2}$
					$-\frac{3}{4}$	$\frac{\sqrt{21}}{4}$
						$\frac{1}{4}$

$J=0$

$(^4P)\,^3P$	$-\frac{5}{6}$	
$(^2P)\,^3P$	$-\frac{\sqrt{14}}{3}$	$-\frac{2}{3}$

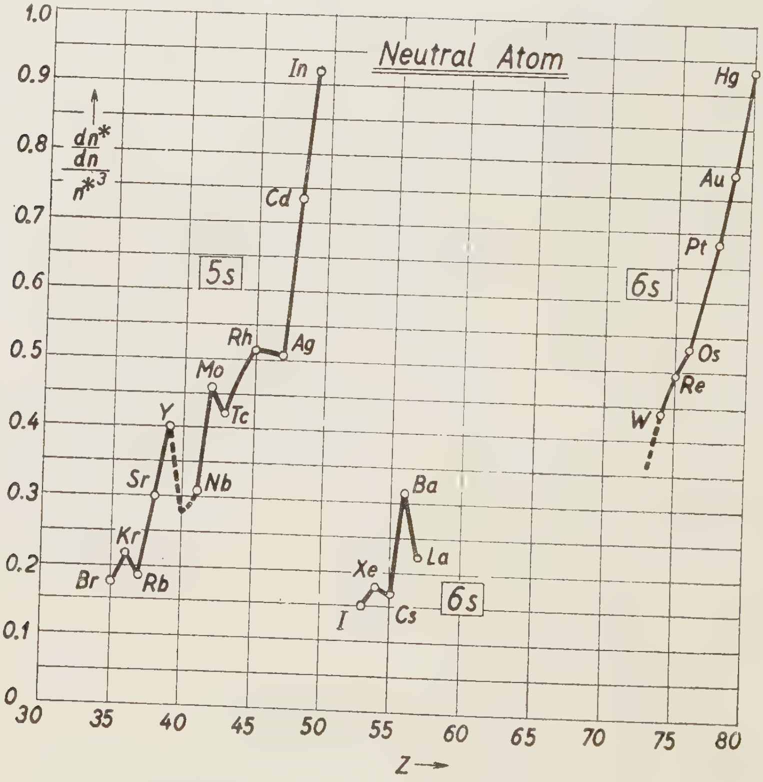

Fig. 5. Plot of $(dn^*/dn)/n^{*3}$ versus Z in neutral atoms.

value of $a(s)$. The values of $(dn^*/dn)/n^{*3}$ for optical s-electrons in neutral atoms calculated in this way are plotted versus Z in Fig. 5*.

From this graph the value of $(dn^*/dn)/n^{*3}$ for the $5s$-electron in Ru I can be determined by interpolation and was found to be 0.478.

In Fig. 5 the small value of $(dn^*/dn)/n^{*3}$ $(5s)$ for Nb I is worthy of note. In a recent work the author[14] has shown that $a(5s)=0.169$

---

* In the construction of Fig. 5, the nuclear induction values of $\mu(\mathrm{Rh}^{103})$ and $\mu(\mathrm{W}^{183})$ were of valuable help[13]. The kindness of Dr. Jeffries in showing me the manuscript prior to publication is greatly appreciated.

Table VI. Matrix of spin-orbit interaction of the configuration d^4 (the unit of the element is ζ_d).

$J=6$

	^3H	^1I
^3H	$\frac{1}{2}$	$\frac{\sqrt{6}}{2}$
^1I	$\frac{\sqrt{6}}{2}$	0

$J=5$

	^3G	^3H
^3G	$\frac{3}{5}$	$-\frac{6}{5}$
^3H	$-\frac{6}{5}$	$-\frac{1}{10}$

$J=4$

^5D	$_2{}^3F$	$_4{}^3F$	^3G	$_2{}^1G$	$_4{}^1G$	^3H
1	$\sqrt{2}$	$-\sqrt{2}$	0	0	0	0
	$\frac{1}{2}$	$-\frac{1}{2}$	$-\frac{5}{2\sqrt{3}}$	$\frac{1}{3}$	$-\frac{\sqrt{11}}{3}$	0
		$-\frac{1}{4}$	$\frac{5}{4\sqrt{3}}$	$-\frac{5}{3}$	$\frac{\sqrt{11}}{6}$	0
			$-\frac{3}{20}$	$\frac{1}{\sqrt{3}}$	$\frac{\sqrt{11}}{2\sqrt{3}}$	$-\frac{2\sqrt{22}}{5\sqrt{3}}$
				0	0	$-\frac{\sqrt{22}}{3}$
					0	$\frac{2\sqrt{2}}{3}$
						$-\frac{3}{5}$

$J=3$

^5D	0					
^3D	$\frac{\sqrt{42}}{6}$	$-\frac{1}{6}$				
$_2{}^3F$	$\frac{\sqrt{6}}{3}$	$-\frac{10}{3\sqrt{7}}$	$-\frac{1}{6}$			
$_4{}^3F$	$-\frac{\sqrt{6}}{3}$	$-\frac{2}{3\sqrt{7}}$	$\frac{1}{6}$	$\frac{1}{12}$		
^1F	0	$\frac{2\sqrt{5}}{\sqrt{21}}$	$\frac{\sqrt{15}}{3}$	$\frac{\sqrt{15}}{6}$	0	
^3G	0	0	$-\frac{3\sqrt{5}}{2\sqrt{7}}$	$\frac{3\sqrt{5}}{4\sqrt{7}}$	$\frac{9}{2\sqrt{21}}$	$-\frac{3}{4}$

$J=2$

^5D	$_2{}^3P$	$_4{}^3P$	^3D	$_2{}^1D$	$_4{}^1D$	$_2{}^3F$	$_4{}^3F$
$-\frac{3}{4}$	$\frac{2\sqrt{105}}{15}$	$-\frac{7\sqrt{30}}{60}$	$\frac{7\sqrt{3}}{12}$	0	0	$\frac{\sqrt{30}}{15}$	$-\frac{\sqrt{30}}{15}$
	$\frac{1}{6}$	$-\frac{\sqrt{14}}{3}$	0	$\frac{\sqrt{14}}{2\sqrt{15}}$	$-\frac{2\sqrt{7}}{\sqrt{15}}$	0	0
		$\frac{1}{3}$	$-\frac{9\sqrt{2}}{4\sqrt{5}}$	$-\frac{2}{\sqrt{15}}$	$-\frac{1}{\sqrt{30}}$	0	0
			$\frac{1}{12}$	$\frac{2\sqrt{2}}{\sqrt{3}}$	$-\frac{1}{\sqrt{3}}$	$-\frac{\sqrt{10}}{3}$	$-\frac{\sqrt{2}}{3\sqrt{5}}$
				0	0	$\frac{2}{\sqrt{15}}$	$\frac{4}{\sqrt{15}}$
					0	$\frac{\sqrt{2}}{\sqrt{15}}$	$-\frac{4\sqrt{2}}{\sqrt{15}}$
						$-\frac{2}{3}$	$\frac{2}{3}$
							$\frac{1}{3}$

$J=1$

^5D	$-\frac{5}{4}$			
$_2{}^3P$	2	$-\frac{1}{6}$		
$_4{}^3P$	$-\frac{\sqrt{14}}{4}$	$\frac{\sqrt{14}}{3}$	$-\frac{1}{3}$	
^3D	$\frac{\sqrt{7}}{4}$	0	$-\frac{3\sqrt{2}}{4}$	$\frac{1}{4}$

cm^{-1} for Nb I, which leads to $(dn^*/dn)/n^{*3}(5s)=0.305$. For the neighboring element Zr I, we might predict $(dn^*/dn)/n^{*3}(5s)=0.26_5-0.28_0$.

It is also worthy of note that the trend of Fig. 5 is different at Mo I and W I.

§ 6. Table of $\zeta(5p)$

Since the spectra of neutral atoms in the neighborhood of Ru I are well known, it is

Table VI. continued.

$J=0$

	^5D	$_2{}^3P$	$_4{}^3P$	$_0{}^1S$	$_4{}^1S$
	$-\frac{3}{2}$	$\frac{4}{\sqrt{3}}$	$-\frac{\sqrt{42}}{6}$	0	0
		$-\frac{1}{3}$	$\frac{2\sqrt{14}}{3}$	-3	$\frac{\sqrt{7}}{\sqrt{3}}$
			$-\frac{2}{3}$	0	$-\frac{2\sqrt{2}}{\sqrt{3}}$
				0	0
					0

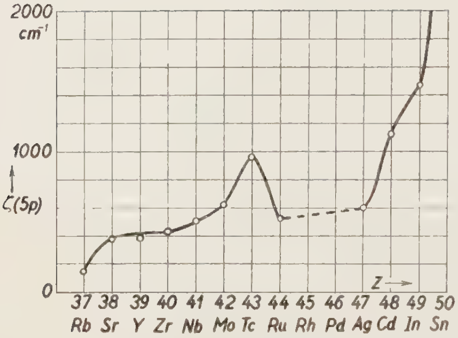

Fig. 6. Plot of $\zeta(5p)$ versus Z in neutral atoms.

possible to calculate the spin-orbit interaction parameters $\zeta(5p)$ for neutral atoms[15]. They are plotted in Fig. 6. Of particular interest is $\zeta(5p)$ for Tc I. It attains a maximum; the same trend was found in the graphs for $\zeta(4p)$ and $\zeta(6p)$ at Mn I and Re I respectively. Dr. Trees kindly checked some of the $\zeta(5p)$ around Tc I, so the fact is now well established. The interpretation is still difficult at present.

In the calculation of $\zeta(p)$ it is important to choose a term free from perturbation. For example, in the spectrum of Y I, the term $5s^2 5p\,^2P$ (possibly perturbed) has a separation 830.5 cm^{-1} and therefore leads to $\zeta(5p)=554$, whereas the term $4d^2 5p\,^4G$ has separations 456.2, 375.3 and 294.9, so that $\zeta(^4G)=83.4$ and therefore $\zeta(5p)=365$. The latter value must be given a larger weight.

References

1) K. Murakawa: J. Phys. Soc. Japan **8** (1953) 535.

2) K. Murakawa: J. Phys. Soc. Japan **9** (1954) 427, corrected in J. Phys. Soc. Japan **9** (1954) 651.

3) K. Murakawa: J. Phys. Soc. Japan **9** (1954) 391.

4) H. Ewald, quoted by G. T. Seaborg and I. Perlman: Rev. Mod. Phys. **20** (1948) 585.

5) L. A. Sommer: Zeits. f. Phys. **37** (1926) 1.

6) W. F. Meggers and O. Laporte: J. Washington Acad. Sci. **16** (1926) 143.

7) G. R. Harrison and J. R. McNally: Phys. Rev. **58** (1940) 703.

8) H. Kopfermann et al: Zeits. f. Phys. **138** (1954) 309.

9) Griffiths and J. Owen: Proc. Phys. Soc. London **65** (1952) 951.

10) G. Racah: Phys. Rev. **62** (1942) 438; **63** (1943) 367.

11) L. C. Biedenharn, J. M. Platt and M. E. Rose: Rev. Mod. Phys. **24** (1952) 249.
A. Simon, J. H. van der Sluis and L. C. Biedenharn: Tables of the Racah Coefficients. ORNL-1679 (1954).

12) S. Obi, T. Ishidzu, H. Horie, S. Yanagawa, Y. Tanabe and M. Sato: Ann. Tokyo Astron. Observatory **3** (1953) 89; **4** (1954) 3.

13) P. B. Sogo and C. D. Jeffries: Phys. Rev. (1955) in press.

14) K. Murakawa: Phys. Rev. (1955) in press.

15) $\zeta(5p)$ of Zr I and Tc I were taken from the calculations of S. Suwa [J. Phys. Soc. Japan **8** (1953) 734] and K. G. Kessler and R. E. Trees [Phys. Rev. **92** (1953) 303] respectively. The other values were newly calculated in the present work.

16) W. F. Meggers and H. N. Russell: J. Res. Bur. Standards **2** (1929) 733.

JOURNAL OF THE PHYSICAL SOCIETY OF JAPAN Vol. 10, No. 11, NOVEMBER, 1955

The Quadrupole Moment of La^{139}

By Kiyoshi MURAKAWA

Institute of Science and Technology, Komaba-machi, Meguro-ku, Tokyo

(Received August 11, 1955)

The hyperfine structure of the spectra of La I and La II was studied, and data that are more accurate than the previous investigation were obtained. These data, together with an improved value of the screening correction of the d-electron, yielded the result that the quadrupole moment of La^{139} is $(0.6\pm0.2)\times10^{-24}\,cm^2$, in which the polarization correction due to Sternheimer is taken into account.

§ 1. Introduction

In a previous work1),2) the hyperfine structure (hfs) of the spectra of La I and La II was studied, and the quadrupole moment of La^{139} was deduced to be $0.9\times10^{-24}\,cm^2$. Somewhat later the screening correction of the d-electron was studied, and this gave the author an opportunity of studying the hfs of the La spectrum more fully than before, and to revise the value of $Q(La^{139})$. The abstract has just appeared3).

The light source that was used was described previously2) and need not be mentioned in detail here. The hfs was resolved by a Fabry-Pérot etaon. The classification of the spectra of La I and La II was published by Russell and Meggers4); their level notations will be employed here.

§ 2. Hfs of the Spectrum of La I

In the present work in addition to the line $\lambda\,5106$ $(5d^26s\,{}^4F_{3/2}-5d^26p\,{}^4D_{1/2})$ that was studied previously some other arc lines were studied. With respect to the level $5d^26s\,{}^4F_{3/2}$ the splitting $F5$–$F4$ given previously was again well confirmed, but the splitting $F3$–$F2$ showed a slight scatter among the data. The hfs of $\lambda5106$ was therefore studied more carefully, and it was found that a very faint neighboring line was slightly disturbing the measurement. The lanthanum sample was replaced by a new purer one, and the foreign line disappeared. The result of the new measurement is shown schematically in Fig. 1. The splitting $F3$–$F2$ is now $0.0492\,cm^{-1}$ instead of the previous $0.0501\,cm^{-1}$. We now get

$$A=-0.01615\,cm^{-1},\quad B=0.0062\times10^{-3}cm^{-1}$$

for the level $5d^24s\,{}^4F_{3/2}$. The formula that is necessary for the evaluation of the quadrupole moment Q was given in a previous paper2). We will, however, take the polarization correction Δ due to Sternheimer5) into account:

$$Q=-B\frac{Z^*H(1+\Delta)}{\zeta\langle\sum3\cos^2\theta-1\rangle_{Av}}\quad I(2I-1)J(2J-1)$$
$$\times1.988\times10^{-21}$$

(B and ζ in cm^{-1}).

The notations for the relativity corrections are the same as those of Casimir6). As was shown in the author's article3), the effective Z for the d-electron in La I is 39.7 instead of the previous 57–10=47. As usual we may put $H_2=1.01$, and $\Delta_d=0.164$. The term $5d^26s$ ${}^4F$ is of intermediate coupling. Crawford7) obtained $\zeta(5d)=400$, $G_2=1377$, $F_2=370$, $F_4=56$ for the same configuration. Kamei and the author put these values in the energy matrices and solved the secular equations and, without taking the coufiguration interaction into account, obtained the coupling coefficients (K)

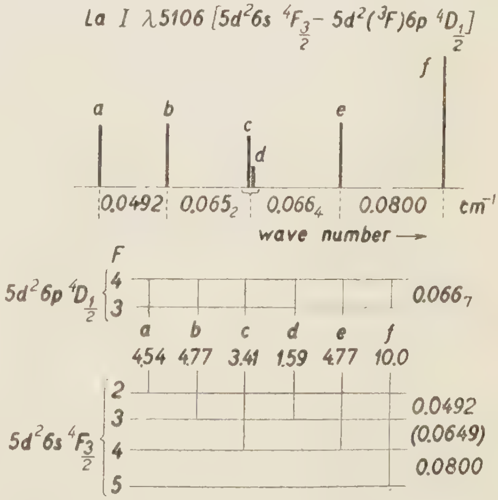

Fig. 1. Hfs of La I λ5106.

that are somewhat different from those of Crawford. Since, however, it seems that Crawford took the configuration interaction into account and since he successfully accounted for the hfs interval factors[8] of the ^4F levels, we will adopt his coupling coefficients at present. Then the value of $\langle \sum \omega \rangle_{\mathrm{Av}}$ (we will put $\omega = 3\cos^2\theta - 1$ for brevity) for the level $5d^26s\,^4F_{3/2}$ is -0.1352, as shown in the previous work[2]. Of particular importance (for the evaluation of Q) is the value of $\zeta(5d)$. It seems to us that Crawford's $\zeta(5d)=400$ is too low, and we tentatively put $\zeta(5d)=450$ in the previous works[1],[2]. In the present work, however, we will assume that $\zeta(5d)=4.2_5 \times 10^2$, which seems to be more reasonable. Putting these values in the aforementioned formula, we get

$$Q(\mathrm{La}^{139}) = 0.6 \times 10^{-24}\,\mathrm{cm}^2.$$

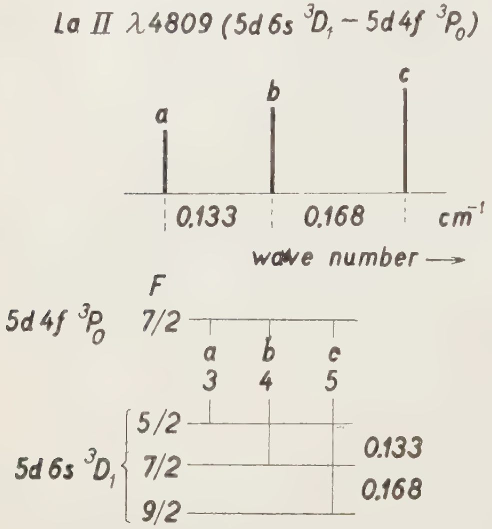

Fig. 2. Hfs of La II λ4809.

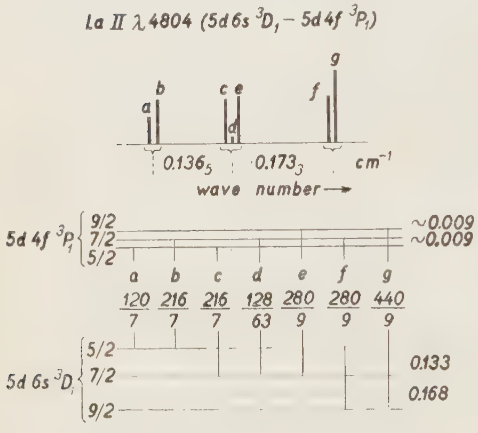

Fig. 3. Hfs of La II λ4804.

§ 3. Hfs of the Spectrum of La II

In the previous work it was mentioned that the measurement of the hfs of La II λ4809 ($5d6s\,^3D_1 - 5d4f\,^3P_0$) is disturbed by a very close lying line. In the present work various methods of excitation of the spectrum was tried, and it was found that the data for the splitting $F(5/2)-F(7/2)$ of $5d6s^3D_1$ showed a considerable scatter. This situation was not improved at all when the lanthanum sample was replaced by a new purer one. It seems that the disturbing line belongs to lanthanum. It was therefore decided to measure the hfs on plates that were taken under the condition in which the disturbance was the least; the result of measurement is shown schematically in Fig. 2. From this we get

$$A = -0.0376\,\mathrm{cm}^{-1}, \quad B = 0.0209 \times 10^{-3}\,\mathrm{cm}^{-1}$$

for the level $5d6s\,^3D_1$. Putting

$$(ds\,^3D^1{}_1 | \omega | ds\,^3D^1{}_1) = -(1/5)R_2''$$

and $\zeta(5d) = 542$, $R_2'' = 1.15$, $\varDelta_d = 0.164$ in the fundamental formula, we get

$$Q(\mathrm{La}^{139}) = 0.4 \times 10^{-24}\,\mathrm{cm}^2.$$

Since the hfs of λ4809 was not so accurately measured, the hfs of λ4804($5d6s\,^3D_1 - 5d4f\,^3P_1$) was analyzed independent of the hfs of λ4809. The hfs of λ4804 is shown in Fig. 3. This, being not disturbed by a neighboring line, is essentially the same as reported in the previous work[2]. The group of components *c*, *d* and *e* was found to show a broadening, when examined by a thick spacer. However in the present work they were measured, assuming that they are not resolved. Denoting the interval factor and the quadrupole coupling constant of the final and the initial level of λ 4804 by A, B and A', B' respectively, we get from the observed hfs:

$$A - (A'/2) = -0.03869\,\mathrm{cm}^{-1}\,,$$
$$B + (B'/2) = 0.0153 \times 10^{-3}\,\mathrm{cm}^{-1}\,.$$

Since B and B' cannot be found separately, we have to find a relation between B and B'. The configuration $5d4f$ was discussed by Condon and Shortley[9], and the term $5d4f\,^3P$ does not seem to be appreciably perturbed. As a first approximation we will assume that the configuration $5d4f$ is of *LS*-coupling, and that $\zeta(4f)=443$, $\zeta(5d)=542$. Under this assumption the matrix elements of ω are given in Table I.

Table I. Diagonal matrix elements of $\omega=3\cos^2\theta-1$ of $df\,{}^3P$ (*LS*-coupling).

$$\langle {}^3P_2{}^2|\omega/r^3|{}^3P_2{}^2\rangle$$
$$=(1/875)(88\,R_2'-42\,R_2''-96\,S_2)\langle 1/r_d{}^3\rangle_{\rm Av}$$
$$+(1/1225)(-300\,R_3'+8\,R_3''+96\,S_3)\langle 1/r_f{}^3\rangle_{\rm Av}$$
$$\langle {}^3P_1{}^1|\omega/r^3|{}^3P_1{}^1\rangle$$
$$=(1/875)(68\,R_2'-7\,R_2''-36\,S_2)\langle 1/r_d{}^3\rangle_{\rm Av}$$
$$+(1/1225)(-50\,R_3'+76\,R_3''+72\,S_3)\langle 1/r_f{}^3\rangle_{\rm Av}$$

Treatment of the quadrupole coupling constant for a configuration in which at least two non-*s* electrons are involved was published by the author[3)]. Assuming that $\Delta_d=0.164$, $\Delta_f=0.230$, $Z_d^*=39.7$, $Z_f^*=24$ for La II, we get[10)]

$$B'=-0.654B\,,$$

which leads to

$B(5d6s\,{}^3D_1)=0.0227\times10^{-3}\,\text{cm}^{-1}$, $B'(5d4f\,{}^3P_1)=-0.0148\times10^{-3}\,\text{cm}^{-1}$. From this B we get

$$Q=0.4\times10^{-24}\,\text{cm}^2.$$

Thus the value of $B(5d6s\,{}^3D_1)$ obtained from λ 4809 has been confirmed to be in reasonable agreement with that obtained from λ4804.

The difference between the Q values obtained from $B(5d^26s\,{}^4F_{3/2})$ and $B(5d6s\,{}^3D_1)$ is difficult to explain at present. However, since we have not yet examined the configuration interaction among $5d6s$, $6p4f$ and $4f^2$, we will assume that the value of Q obtained from $5d^26s\,{}^4F_{3/2}$ is somewhat more reliable than that from $5d6s\,{}^3D_1$, and we might therefore consider

$$Q(\text{La}^{139})=(0.6\pm0.2)\times10^{-24}\,\text{cm}^2$$

the best value available at present.

It is interesting to note that the value of Q (La^{139}) that has been calculated by Horie and Arima[11)] theoretically is $0.44\times10^{-24}\,\text{cm}^2$, and is reasonably close to the value empirically deduced here.

Finally it may be noted that in ref. 2 the hfs of the level $5d6s\,{}^1D_2$ of La II was given a consideration, but in the present work this was abandoned owing to the configuration interaction with $5d^2\,{}^1D_2$.

References

1) K. Murakawa and T. Kamei: Phys. Rev. **92** (1953) 325.
2) K. Murakawa: Jour. Phys. Soc. Japan **9** (1954) 391.
3) K. Murakawa: Phys. Rev. **98** (1955) 1285.
4) H. N. Russell and W. F. Meggers: Jour. Res. Natl. Bur. Standard **9** (1932) 625.
5) R. Sternheimer: Phys. Bev. **86** (1952) 316.
6) H. Casimir: Verh. Teylers Tweede Genootschap, Haarlem **11** (1936).
7) M. F. Crawford: Phys. Rev. **47** (1935) 768.
8) O. E. Anderson: Phys. Rev. **46** (1934) 473.
9) E. U. Condon and G. H. Shortley: *The Theory of Atomic Spectra*. Cambridge (1935).
10) The screening correction for *f*-electrons was studied by K. Murakawa and S. Suwa, Jour. Phys. Soc. Japan **9** (1954) 93.
11) H. Horie and A. Arima: Phys. Rev. **99** (1955) 778.

Journal of the Physical Society of Japan Vol. 10, No. 11, November, 1955

Observation of Nuclear Quadrupole Resonances with a Coaxial-cavity Spectrometer

By Shoji Kojima, Akira Shimauchi, Shigeo Hagiwara
and Yoshihito Abe

Tokyo University of Education, Otsuka, Tokyo

(Received August 13, 1955)

A super-regenerative spectrometer with two cavity grid-separation oscillator of a lighthouse tube was constructed and operated in the frequency region between 700 Mc and 1000 Mc. With this spectrometer, nuclear quadrupole resonances of I^{127} in solid NH_4I_3 and ICl were observed. The coupling constants for NH_4I_3 and ICl were 2440 Mc and 3008 Mc at room temperature and the asymmetry parameters were 1.8 percent and 2.0 percent respectively.

§ 1. Introduction

Nuclear quadrupole resonances in solid have been studied by many authors in the frequency range between radio frequencies and several hundreds megacycles. Among them the highest frequency was observed in solid iodine. The iodine nuclei, which have a spin of 5/2, show two resonances, corresponding to the transitions: $m_z=\pm\frac{1}{2}\longleftrightarrow\pm\frac{3}{2}$ and $\pm\frac{3}{2}\longleftrightarrow\pm\frac{5}{2}$. The frequency of the first resonace, ν_1, is approximately a half of the frequency of the second resonance ν_2. The observed highest frequency of iodine, 645 Mc, was the second resonance of I^{127}, whereas the first resonance was 332 Mc. The frequencies of the doublet of the first resonance of I^{127} in solid ICl were measured by Dehmelt as 455.6 Mc and 458.2 Mc at 83°K[1]. This suggested the frequency of the second resonance to be about 900 Mc. But any study in this frequency region has not yet been carried out.

Since Dehmelt's experiment the super-regenerative oscillator with parallel wire tuning circuit has been employed by many authors. The parallel wire resonator, however, is not adequate for the frequency region beyond 700 Mc, since the spacing between the sample and the oscillator tubes becoms small because of the shortness of the wave length. For this reason a coaxial cavity spectrometer was designed, and operated in the frequency region between 700 Mc and 1000 Mc. By this spectrometer the frequencies of the second resonances of iodine monochloride and ammonium tri-iodide were measured in the temperature range between −40°C and room temperature*.

§ 2. Spectrometer

The spectrometer is the super-regenerative type as usual, but uses a two-cavity grid-separation oscillator with a light-house tube. The drawing of this spectrometer and the circut diagram are shown in Figs. 1 and 2. The two coaxial cavities are tuned with plungers. The feed back coupling between both cavities is achieved by a slot in the grid-disk. The frequency of the oscillator is mainly determined by the positions of the plate plunger, whereas the position of the cathode plunger affects the feed back. The relation between the frequency and the lengths of the cavities are listed in Table I.

Table I. Frequency *v.s.* cavity lengths.

Length of cathode cavity (mm)	Length of plate cavity (mm)	Frequency of oscillation (Mc)
116	98	700.8
〃	84	752.4
100	86	798.0
〃	72	874.8
88	75	911.4
〃	66	952.8
〃	63	1035

The maximum of the magnetic flux of the oscillating field occurs before the plate plunger. Therefore a sample shaped like a doughnut is set in front of the plunger. The amounts of the samples were about 35 gr and 20 gr for iodine monochloride and ammonium tri-iodide

---

* Some of the results were cited in reference 2).

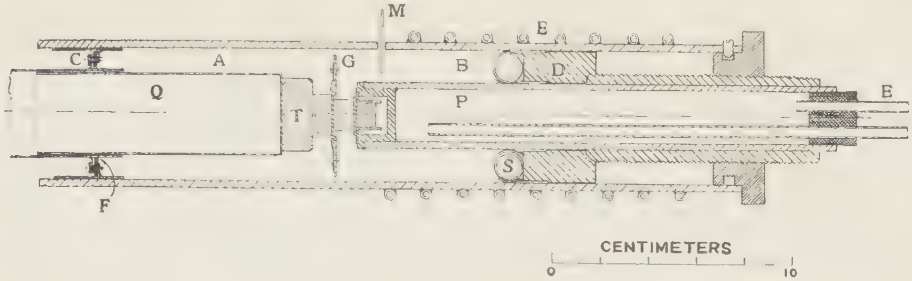

Fig. 1. Coaxial-cavity Spectrometer.

A: Cathode cavity
B: Plate cavity
C: Cathode plunger
D: Plate plunger
E: Cooling pipe
F: Mica insulator
G: Grid disk
M: Modulation stub
P: Plate cylinder
Q: Cathode cylinder
S: Sample
T: Lighthouse tube 2C43

respectively.

The frequency modulation is establised by a stub which is inserted into the plate cavity as indicated in Fig. 1. One end of the stub was attached to the membrane of a dynamic speaker and the vertical vibration of the stub yielded the frequency modulation of about 2 Mc.

In order to prevent the temperature rise of the sample, the outer cylinder is cooled by a water jacket and the inner cylinder is filled with flowing water. Also this equipment is useful for experiments at decreased temperature. By means of alcohol, which was cooled by dry ice, we could easily maintain the sample at −40°C.

The cavity spectrometer is almost completely shielded. Therefore it has no ghost which is usually experienced with the parallel-wire spectrometer. Small leakage of the oscillation through lead wires was utilized for the measurement of the frequencies.

The frequency was measured by compairing it with the third harmonics of a UHF signal generator of the frequency range between 200 Mc and 350 Mc, which was simultaneously measured by a precision frequency meter of the range from 30 Mc to 500 Mc.

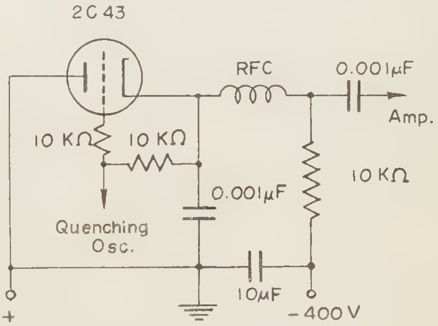

Fig. 2. Circuit diagram of oscillator unit.

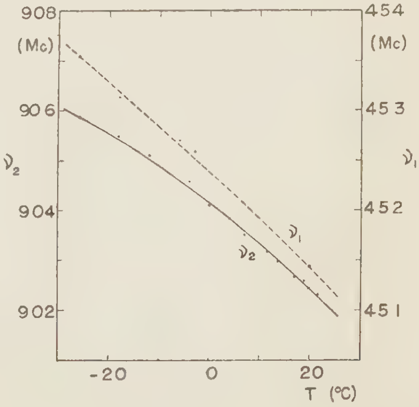

Fig. 3. Resonance frequencies of I^{127} in ICl.

§ 3. Results of Measurement

Measured iodine monochloride was in α state which was achieved by slow crystallization at about 20°C. The measurement for the second resonance was carried out in the temperature region between −30°C and +25°C. The observed frequencies ranged from 902 Mc to 906 Mc. The first resonance, which was reported by Dehmelt to be a doublet, was also measured with a usual parallel-wire spectrometer by our colaborators[2]. One component of the doublet was several times stronger than the other. The stronger line, whose frequency was 2.8 kc lower than the weaker line at the liquid nitrogen temperature, has smaller negative temperature coefficient than the weaker line and the frequency of the former became 10.6 kc higher than the latter at room temperature. For the second resonance, however,

Table II. Observed results for I^{127}.

Compounds	T (°C)	ν_1 (Mc)	ν_2 (Mc)	$\frac{1}{\nu_1}\frac{d\nu_1}{dT}(10^{-4})$	$\frac{1}{\nu_2}\frac{d\nu_2}{dT}(10^{-4})$
ICl	20	451.46±0.01*	902.46±0.02	−1.11	−1.08
	−26	453.56±0.01	905.84±0.02	−0.96	−0.62
NH_4I_3	25	366.23±0.01	732.13±0.02	−0.46	−0.46
	−40	367.06±0.02	733.81±0.02	−0.28	−0.29

* The weaker line of the doublet is omitted. For this line, see reference 2).

Table III. Nuclear quadrupole couplings of I^{127}.

Compounds	T (°C)	eQq (Mc)	η (%)	$\frac{1}{eQq}\frac{d(eQq)}{dT}(10^{-4})$	$\frac{d\eta^2}{dT}(10^{-4})$
ICl	20	3008.3	2.0	−1.08	−0.023
	−26	3020.1	3.3	−0.67	−0.262
NH_4I_3	25	2440.6	1.8	−0.46	0.000
	−40	2446.2	1.8	−0.29	0.008

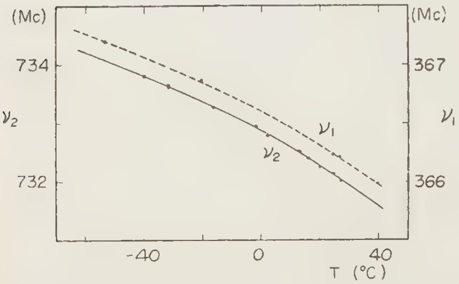

Fig. 4. Resonance frequencies of I^{127} in NH_4I_3.

only a single line was observed, which probably corresponded to the stronger line of the doublet of the first resonance. The frequencies of the second resonance and of the stronger line of the doublet are plotted in Fig. 3. The error of the measurement of the frequency was less than 10 kc. The irregular deviations from the curve, which amounted to 50 kc, presumably arised from the error in the determination of temperature of the sample and from the shape of the absorption curve.

Ammonium tri-iodide was prepared from iodine and ammonium iodide by the following procedure³⁾. Iodine was dissolved in a strong aqueous solution of ammonium iodide. The solution was then evaporated to dryness in a desiccator. After several days ammonium tri-iodide crystal grew in the mother liquid.

The first and second resonances were observed in the temperature range between −40°C and +30°C with the parallel-wire spectrometer and the coaxial cavity spectrometer respectively. The results are shown in Fig. 4.

The summary of the observed frequencies and the temperature coefficients are listed in Table II.

§ 4. Discussion of Results

The observation of the frequencies of the first and second resonances allows to determine the coupling constant, **eQq**, and the asymmetry parameter of the field gradient tensor, η, simultaneously. When η is small enouugh, the following equations are applied⁴⁾,

$$\eta^2 = 0.77\,\frac{2\nu_1 - \nu_2}{\nu_2}\,, \qquad (1)$$

$$eQq = \frac{10}{3}\nu_2(1 + 0.204\,\eta^2)\,. \qquad (2)$$

The temperature coefficients of these quantities are derived from the Eqs. (1) and (2). They yield.

$$\frac{d\eta^2}{dT} = 0.77\left(\frac{1}{\nu_1}\frac{d\nu_1}{dT} - \frac{1}{\nu_2}\frac{d\nu_2}{dT}\right), \qquad (3)$$

$$\frac{1}{eQq}\frac{d(eQq)}{dT} = \frac{1}{\nu_2}\frac{d\nu_2}{dT} + 0.204\frac{d\eta^2}{dT}\,. \qquad (4)$$

The coupling constant, the asymmetry parameter and their temperature coefficients determined from the data given in Table II are listed in Table III.

The obtained coupling constant of iodine monochloride in solid state, 3008.3 Mc at 20°C, was only two percent larger than the value in gaseous state, which was explained with the twenty-three percent ionic character of the bond⁵⁾. At decreased temperatures the coupling constant and the asymmetry parameter differed from the values at gaseous state more.

The atomic configuration of ammonium tri-iodide crystal was studied by Mooney⁶⁾. According to his analysis the tri-iodine group was a nearly linear configuration, the calculated angle between the bonds differing from 180° by three degrees, and the iodine atoms at both ends are unequally spaced with the distances of 3.10 Å and 2.82 Å respectively. This small unequality, however, might be due to small inaccuracies in the position.

The observed resonance line seemed to have no multiplet. The coupling constant of this line, 2441 Mc, was only six percent larger than the pure covalent bond. The spacing of 2.82 Å indicates covalent bonding, whereas the spacing of 3.10 Å is slightly larger than the sum of the covalent radii. Therefore the observed resonance seems to arise from the iodine atoms with the smaller spacing. If it is so and if broadning of the line does not occur, the iodine atoms with the larger spacing will also give rise resonance of almost same intensity. But the observed resonance was a single line. This may suggest that the configuration is symmetric and the resonances are due to the iodine atoms at both ends.

This study was supported by the Scientific Research Expenditure of the Ministry of Education.

References

1) H. G. Dehmelt: Z. Physik **130** (1951) 356.
2) S. Kojima, K. Tsukada, S. Ogawa and A. Shimauchi: J. Chem. Phys. **23** (1955) Oct. in press.
3) G. S. Johnson: J. Chem. Soc. **33** (1938) 397.
4) W. Gordy, W. V. Smith and R. F. Trambarulo: "*Microwave Spectroscopy*" John Wiley and Sons, Inc. New York (1953).
5) B. P. Dailey and C. H. Townes: J. Chem. Phys. **23** (1955) 118.
6) R. C. L. Mooney: Z. Krist. **90 A** (1935) 143.

JOURNAL OF THE PHYSICAL SOCIETY OF JAPAN Vol. 10, No. 11, NOVEMBER, 1955

Absorption of Ultrasonic Waves in Organic Liquids (III) Liquids with Negative Temperature Coefficient of Sound Absorption (b) o-Chlorophenol and Aniline

By Tadashi KISHIMOTO and Otohiko NOMOTO

Kobayasi Institute of Physical Research, Kokubunzi, Tokyo

(Received June 21, 1955)

Ultrasonic absorption coefficient (at 15–20 Mc/sec) in o-chlorophenol and aniline decreases with temperature rise. The excess absorption obtained by subtracting the classical absorption from the observed one is nearly independent of temperature for both liquids and is ascribed to the molecular absorption. The absorption due to bulk viscosity, if present, is small, and estimated to be less than 1/2 the classical absorption due to shear viscosity.

§ 1. Introduction

There are various mechanisms of ultrasonic absorption in liquids, such as the shear viscosity, bulk viscosity and the molecular absorption, and these take place in various combinations in practical cases. The knowledge of the temperature dependence of ultrasonic absorption coefficient gives an important clue for elucidating the mechanism of absorption in a given liquid. We have seen that in some organic liquids, benzene, carbon tetrachloride, *et. al.*, the ultrasonic absorption increases with temperature rise and that the chief absorption mechanism in these liquids is the molecular absorption¹⁾. On the other hand, the sound absorption decreases with temperature rise in glycols, cyclohexanol and m-crosol[2], the rate of decrease being nearly the same as for the classical viscosity absorption. In these latter liquids the mechanisms of sound absorption are the shear viscosity and the bulk viscosity, as in the cases of alcohols and water.

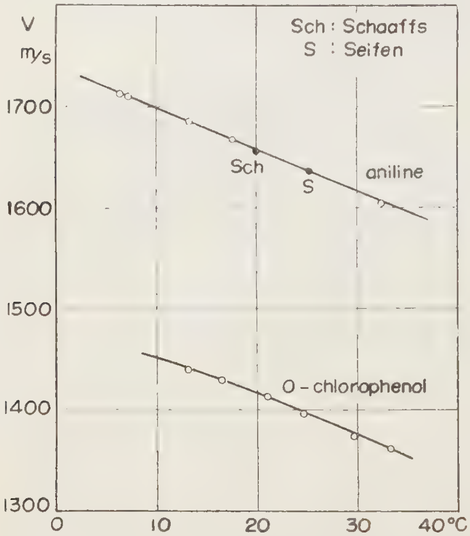

Fig. 1. Temperrture dependence of ultrasonic velocity in o-chlorophenol and aniline (1.43 Mc/sec).

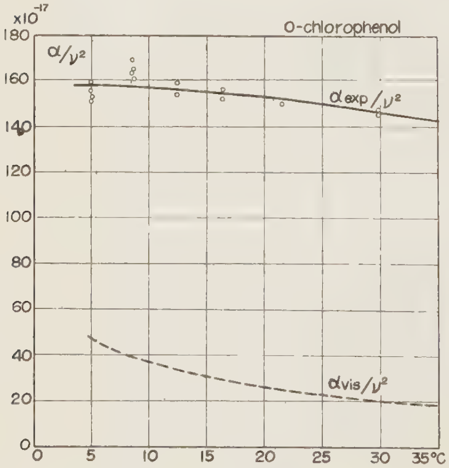

Fig. 2. Temperature dependence of ultrasonic absorption in o-chlorophenol (15 Mc/sec)

The ultrasonic absorption in o-chlorophenol and aniline, to be described in this paper, is somewhat different from the above two groups of liquids. Although the absorption coefficient decreases with temperature rise also in this case, the rate of decrease is smaller than in the case of shear viscosity absorption and the excess absorption is nearly independent of the temperature. The thermal relaxation of the molecular vibrations, therefore, makes a contribution of the same order of magnitude as the shear viscosity to the ultrasonic absorption in these liquids.

The method of experiment is the same as in the previous two papers[1)2)], the absorption coefficient being obtained by the pulse technique at frequencies of 15–20 Mc/sec, and the velocity by the ultrasonic interferometry (at 1.43 Mc/sec). The viscosity-density ratio (η/ρ) was obtained by employing Ostwald's viscosimeters.

§ 2. Experimental result and discussions

The temperature dependence of the sound velocity is reproduced in Fig. 1. The accuracy of the curves is of the order of ±2 m/sec. Existing results on aniline (Schaaffs[3]) and Seifen[4]) are in good agreement with the present measurement.

(1) *o*-chlorophenol ($C_6H_4Cl \cdot OH$)

Fig. 2 shows the temperature dependence of ultrasonic absorption (at 15 Mc/sec) in this liquid and Table 1 shows the values of the viscosity-density ratio (η/ρ), sound velocity (V) and absorption coefficients (α/ν^2; where $\nu=$ frequency). The dotted line in the figure indicates the classical absorption ($\alpha_{\text{vis}}/\nu^2$) computed by the Stokes' formula. The activation energy was obtained from the temperature dependence of viscosity as in the previous paper[2]) and was found to be $E_{\text{vis}}=6.58$ kcal/mole.

The excess absorption $(\alpha_{\text{exp}}-\alpha_{\text{vis}})/\nu^2$ is nearly independent of the temperature, slightly increasing with temperature rise. Therefore, it is natural to ascribe this to the molecular absorption due to the thermal relaxation of molecular vibrational energy and write

$$\alpha_{\text{exp}}=\alpha_{\text{vis}}+\alpha_{\text{mol}} \,. \qquad (1)$$

The values of α_{mol} tabulated in Table 1 are computed under this assumption. If we assume this, the temperature coefficient of α_{mol} becomes as

$$\frac{1}{\alpha_{\text{mol}}}\left(\frac{d\alpha_{\text{mol}}}{dT}\right)=0.31\ \%/\text{deg} \,. \qquad (2)$$

If we assume, on the other hand, also a small bulk viscosity and write

Table I. Temperature dependence of ultrasonic velocity and absorption in o-chlorophenol (15 Mc/sec).

t°C	η/ρ centipoise gr^{-1}cm^3	V (1.43 Mc) m/sec	$\frac{\alpha_{exp}}{\nu^2}\times10^{17}$	$\frac{\alpha_{vis}}{\nu^2}\times10^{17}$	$\frac{\alpha_{mol}}{\nu^2}\times10^{17}$
5	5.30		157	45.5	111.5
10	4.23	(1450)	156	36.4	119.6
15	3.45	1435	154	30.6	123.4
20	2.90	1417	151	26.8	124.2
25	2.45	1395	149	23.7	125.3
30	2.10	1372	148	21.3	127.3
35	1.85	1350		19.8	
40	1·65				

$$\alpha_{exp}=\alpha_{vis}+\alpha_{bulk}+\alpha_{mol}\ , \qquad (3)$$

and assume a common temperature coefficient —i.e., common activation energy—, for both the shear and the bulk viscosity, we obtain as the temperature coefficient of the molecular absorption a slightly higher value. For example, the assumption $\alpha_{bulk}=0.4\times\alpha_{vis}$ gives $(1/\alpha_{mol})\ (d\alpha_{mol}/dT)=0.61$ %/deg in place of (2).

We have seen in a previous paper[1)] that the temperature coefficient of sound absorption is included in the range 0.25–1.1%/deg for 12 organic liquids in which the molecular absorption is far greater than the viscosity absorption. And this coefficient was between 0.5–0.6%/deg for most of the liquids investigated. It is natural to suppose that the temperature coefficient of the molecular absorption is also of the same order of magnitude for those liquids in which the molecular absorption is small. So we may conclude that the temperature coefficients here obtained, 0.31–0.61%/deg, are reasonable values, and therefore, also that the estimation of bulk viscosity absorption $\alpha_{bulk}=(0\sim0.4)\times\alpha_{vis}$ is reasonable.

It is interesting that *o*-chlorophenol does not show bulk viscosity in spite of the fact that there is an OH-group in the molecule of this substance. This corresponds, presumably, to the fact that this substance is known to exhibit intramolecular association, but not the intermolecular association (cf. Kellner[5)]). The lack of intermolecular association results in a weak interaction between the molecules and therefore gives rise to the molecular absorption, i.e., the slowing down of the establishment of equilibrium between the vibrational energy and the translational energy of the molecules.

(2) Aniline ($C_6H_5NH_2$)

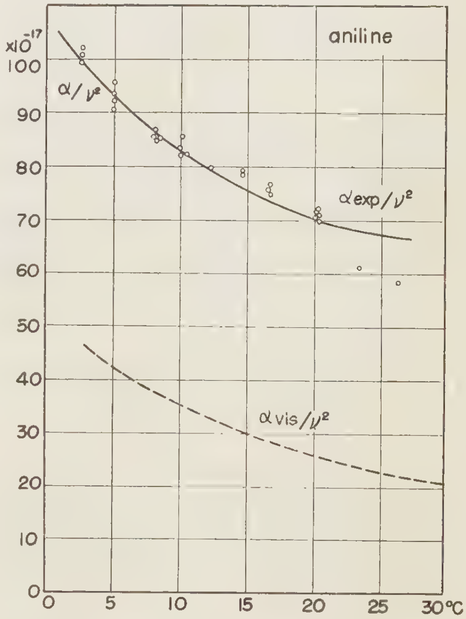

Fig. 3. Temperature dependence of ultrasonic absorption in aniline (20 Mc/sec).

Fig. 3. shows the temperature dependence of ultrasonic absorption (at 20 Mc/sec) in this liquid and Table 2 shows the values of the viscosity-density ratio (η/ρ), sound velocity (V) and absorption coefficients. The observed absorption is higher than the classical viscosity absorption shown in dotted line, but the difference is nearly independent of the temperature. Although the excess absorption ($\alpha_{exp}-\alpha_{vis}$) is mostly attributed to the molecular absorption also in this case, there may exist also a small absorption due to bulk viscosity, for the excess absorption slightly decreases with temperature rise.

If we assume (3) and $\alpha_{bulk}=0.5\times\alpha_{vis}$, and a common temperature coefficient for both viscosities, then we obtain the values of α_{bulk}

Table II. Temperature dependence of ultrasonic velocity and absorption in aniline (20 Mc/sec).

t°C	V (1.43 Mc) m/sec	$\frac{\alpha_{\text{exp}}}{\nu^2}\times 10^{17}$	$\frac{\alpha_{\text{vis}}}{\nu^2}\times 10^{17}$	$\frac{\alpha_{\text{bulk}}}{\nu^2}\times 10^{17}$	$\frac{\alpha_{\text{mol}}}{\nu^2}\times 10^{17}$
0		110			
5	1717	93.5	42.1	21.1	30.3
10	1698	82.5	34.2	17.1	31.2
15	1678	75.0	29.1	14.6	31.3
20	1658	70.0	25.2	12.6	32.2
25	1637	67.0	22.8	11.4	32.8

and α_{mol} indicated in Table 2, and the temperature coefficient of α_{mol} becomes 0.4%/deg, while we have temperature coefficients of 0 and 0.75%/deg respectively from assumptions $(\mu_{\text{bulk}}/\alpha_{\text{vis}})=0.4$ and 0.6. The estimation of the magnitude of bulk viscosity absorption, therefore, is not so greatly influenced by the uncertainty in the knowledge of the temperature coefficient of the molecular absorption.

Considering of the experimental errors, however, it cannot be excluded to think that there is not bulk viscosity at all and to attributed all the excess absorption to the molecular absorption.
At any rate, the bulk viscosity, if present, is small and of the order of half the shear viscosity at most.

Conclusion

The chief mechanisms of ultrasonic absorption in *o*-chlorophenol and aniline are the molecular absorption and the shear viscosity. These two mechanism make contributions of the same order of magnitude in these liquids. The effect of the decrease of viscosity with temperature rise covers the effect of increase of molecular absorption and makes the total temperature coefficient of absorption negative. The bulk viscosity, if present, is small and of the order of half the shear viscosity at most.

References

1) T. Kishimoto and O. Nomoto: J. Phys. Soc. Japan **9** (1954) 620.
2) T. Kishimoto and O. Nomoto: J. Phys. Soc. Japan **9** (1954) 1021.
3) W. Schaaffs: Zeits. Phys. Chem. **194** (1944) 28.
4) N. Seifen: Zeits. Phys. **108** (1938) 681.
5) L. Kellner: The hydrogen bond. Report on Progress in Physics **15** (1952) 1.

JOURNAL OF THE PHYSICAL SOCIETY OF JAPAN Vol. 10, No. 11, NOVEMBER, 1955

Residual Magnetization and Magnetostriction of Nickel Single Crystals

By Yoji NAKAMURA
Faculty of Science, University of Kyoto

(Received July 7, 1955)

By use of long cylindrical single crystals of pure nickel with various crystallographic orientations, magnetization and magnetostriction were measured at room temperature. It was found that the remanent magnetization I_r is given approximately by the following relation: $I_r/I_s=1/\sqrt{3}\beta_1$, where I_s is the saturation magnetization and β_1 is the direction cosine of the rod axis with respect to the nearest [100] direction. On the basis of this relation the magnetostriction constants and also the crystal anisotropy constants were determined. Magnetostriction curves constructed theoretically from the obtained values of magnetostriction constants agree with the experimental curves.

§ 1. Introduction

Magnetic properties of single crystals of pure nickel were studied by many workers. Kaya[1] measured the magnetization of pure nickel on single crystals for each principal direction at room temperature and Mashiyama[2] studied the magnetostriction on the same samples used by Kaya. Williams[3] measured the permeabilities of nickel at low field and showed that there is no anisotropy of μ_0 for nickel. Magneto-thermoelectric powers of nickel single crystals were measured by Miyata and Funatogawa[4]. On the other hand, the domain patterns of pure nickel have been observed by many workers[5],[6],[7] and our knowledge about the domain structures and the mechanism of magnetization in pure nickel has become concrete and clear. Recently Bozorth and Hamming[8] published data of magnetostriction on single crystals of nickel by means of the strain gauges and determined the magnetostriction constants by the five-constant expression. However, so far as we know, many experiments have been done on the samples in the form of a disk or of a block so that the precise behaviour of magnetic properties dependent on the field strength would not have been sufficiently studied, up to present. We could produce long single crystals with various crystallographic orientations, therefore magnetic properties were measured on these samples to study the precise mechanism of magnetization, especially the remanence and the behaviour of magnetostriction of single crystals of nickel.

§ 2. Preparation of Specimens and Imperfections of Single Crystal

By means of a modified form of the Bridgman method we have succeeded in obtaining long cylindrical single crystals with various crystallographic orientations. Material to produce single crystals is vacuum-melted pure nickel whose chemical analyses are tabulated in Table I. The details of the experimental procedures to produce single crystals have been reported in this *Journal*[9]. However, it must be emphasized that the crucible, in which the polycrystalline specimens are inserted, must be lowered through the Tammann furnace smoothly and at a slow velocity which is smaller than the maximum velocity for growing a crystal. We can produce single crystals with any desired orientation by certain very slow velocities, but when the velocity is rather fast we can not obtain single crystals with certain orientations. Thus

Table I.

Ni (%)	C (%)	Cu (%)	Mg (%)	Fe (%)	Si (%)	Mn (%)
99.36	0.02	0.01	0.18	0.21	trace	0.22

All elements were analyzed before annealing.

Table II.

No.	Length in mm.	Demag. Factor	Direction Cosine			$\left(\frac{I_r}{I_s}\right)_{Obs.}$	H_c in Oersteds	μ_0	Growth Velocity in mm/min	$\left(\frac{\delta l}{l}\right)_{Sat.-Rem.Obs.} \times 10^6$
			β_1	β_2	β_3					
14	244.0	0.00610	0.999	0.026	0.003	0.539	1.02	130	3.4	−46.2
15	211.4	0.00930	0.747	0.657	0.099	0.729	0.50	370	1.5	−17.7
16	229.2	0.00805	0.599	0.585	0.547	0.914	1.40	90	0.6	− 3.7
28	237.0	0.00755	0.921	0.288	0.261	0.596	0.62	300	1.4	−27.9
29	231.5	0.00876	0.970	0.240	0.047	0.567	0.61	300	2.4	−36.2
30	236.3	0.01769	0.867	0.417	0.274	0.647	0.42	470	1.3	−20.0
44	202.0	0.01016	0.820	0.558	0.124	0.686	0.43	430	1.2	−18.5
52	185.6	0.01150	0.683	0.567	0.462	0.820	0.55	220	1.1	− 9.8
58	253.7	0.00580	0.644	0.554	0.528	0.851	0.53	190	1.1	− 4.1

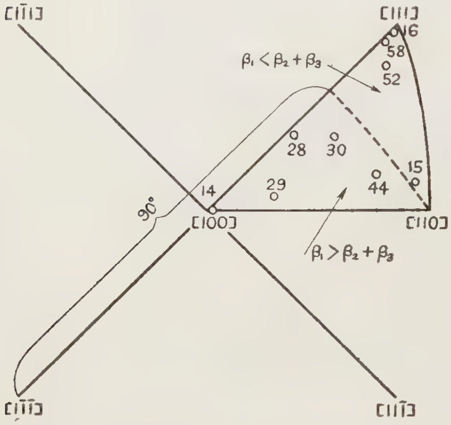

Fig. 1. Stereographic projection of the orientations of the specimens and the easy directions of magnetization. Dotted line divides the stereographic triangle into two regions, namely $\beta_1>\beta_2+\beta_3$ and $\beta_1<\beta_2+\beta_3$.

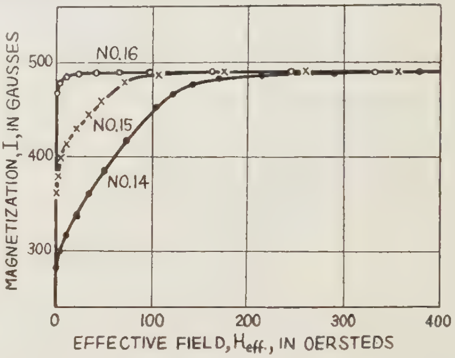

Fig. 2. Magnetization curves for three principal directions.

the single crystal has the maximum velocity for growing large in each crystallographic orientation. The anisotropy of the maximum velocity is very large and the maximum velocity is largest in [100] and is smallest in [111], namely in near [100] 8.8 mm/min, in near [110] 1.8 mm/min and in near [111] 1.4 mm/min. The growth velocities for each single crystal, which are of course smaller than the maximum velocities, are shown in Table II.

The single crystals thus obtained are not perfect crystals but have some imperfections. It was found from the back reflection Laue patterns that the single crystals thus obtained are made of small and long rod crystals with the deviation of the orientation of the order of one degree each other. Corresponding to these Laue patterns, on the side surface of the crystal the so-called *lineage structures* are observed and on the sectional plane perpendicular to the rod axis *cellular structures* can be detected. These macromosaic imperfections in the single crystal differ with the velocity for growing crystal. The precise description about these problems will be given soon in this *Journal*.

The orientations of the single crystals, shown in Table II, which are long cylindrical, about 3 mm in diameter, were determined by the back reflection Laue patterns and the stereographic projection of the orientations of the specimens are shown in Fig. 1.

§ 3. Experimental Results and Discussion

Before measuring the magnetic properties the specimens were annealed in a vacuum electric furnace at 1000°C for 2 hrs in order to remove internal stress. After being annealed, they were slowly cooled in the furnace down to about 200°C, and then rapidly cooled to room temperature by taking them out of the furnace. Some magnetic properties are tabulated in Table II.

Magnetization curves were measured by the conventional ballistic method and those for three principal directions are shown in Fig. 2. The crystal anisotropy energy can be expressed by the following relation:

$$E_k=K_0+K_1(\beta_2^2\beta_3^2+\beta_3^2\beta_1^2+\beta_1^2\beta_2^2)+K_2\beta_1^2\beta_2^2\beta_3^2\ . \quad (1)$$

where K_0, K_1 and K_2 are the crystal anisotropy constants and β_1, β_2 and β_3 are the direction cosines of the rod axis with respect to the three cubic axes. Fortunately we have single crystals with various crystallographic orientations, so by measuring the areas enclosed between the ordinate and magnetization curves of each direction these constants can be determined as follows:

$$K_1=-(42.6\pm0.1)\times10^3\ \text{ergs/cm}^3\ ,$$
$$K_2=\ (10.9\pm1.1)\times10^3\ \text{ergs/cm}^3\ ,$$
$$\text{at room temperature.}$$

The value of K_0 can be estimated from No. 14 as 14×10^3 ergs/cm^3, but it is not reliable.

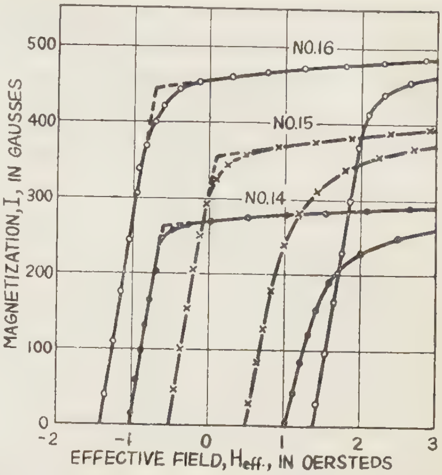

Fig. 3. Hysteresis curves of magnetization for three principal directions.

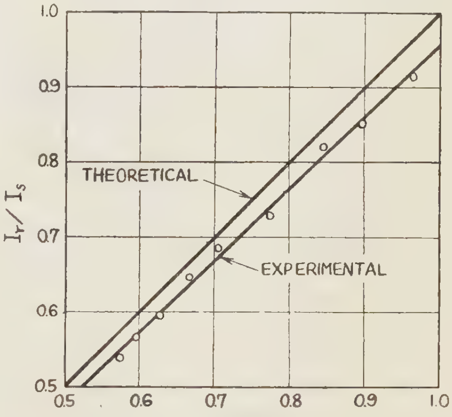

Fig. 4. I_r/I_s vs. $1/\sqrt{3}\beta_1$.

As shown in Fig. 3, the descending hysteresis curves of magnetization show fairly sharp corners near the point where the effective magnetic field equals to zero. Now it may be considered that the measured magnetization is the average value of magnetization of some range near the middle point of the specimen and owing to the difference of the domain structures and the demagnetization foctors according to the positions of the specimen, the magnetization at just the middle point of the specimen is higher than that at the neighbours of the middle point. Therefore if we use a sufficiently long specimen, the magnetization at the middle point will be large as compared with our experiment, so we can assume the intersection point of the extention of two straight lines on the magnetization curves, one of which is due to pure rotation of the direction of magnetization and the other is pure wall displacement, shown by the dotted lines in the Fig. 3, as the remanent magnetization I_r. Furthermore, if we assume that the normal component of magnetization at remanence is zero and magnetic domains distribute in the easy directions near the direction of the magnetic field and the remanence has the maximum value among those determined by above two assumptions, the stereographic triangle is divided into two regions, as shown in Fig. 1. One is the regions where $\beta_1>\beta_2+\beta_3$ and the domains distribute in four easy directions, [111], [11$\bar{1}$], [1$\bar{1}$1] and [1$\bar{1}\bar{1}$] at remanence, and the other is the region where $\beta_1<\beta_2+\beta_3$ and domains distribute in three easy directions, [111], [11$\bar{1}$] and [1$\bar{1}$1] at remanence and even in this region the domains do not distribute to [1$\bar{1}\bar{1}$]. In both regions one can easily derive the following relation:

$$I_r/I_s=1/\sqrt{3}\,\beta_1\ . \quad (2)$$

where I_s is the saturation magnetization and β_1 is the direction cosine of the rod axis with respect to the nearest [100] direction. One can easily determine the domain distribution at remanence in the region $\beta_1<\beta_2+\beta_3$. That is to say, if a, b and c are the fractional amounts of domains distributed in [111], [11$\bar{1}$] and [1$\bar{1}$1], respectively, they are given as follows:

$$a=\frac{\beta_2+\beta_3}{2\beta_1}\,,\quad b=\frac{\beta_1-\beta_3}{2\beta_1}\,,\quad c=\frac{\beta_1-\beta_2}{2\beta_1}\,,\qquad (3)$$

However, we can not determine the distribution of magnetic domains uniquely at remanence in the region $\beta_1>\beta_2+\beta_3$. As seen in Fig. 4, the relation (2) holds fairly well. Therefore at remanence the normal component of magnetization nearly equals to zero and domains distribute in the easy directions near the direction of the magnetic field, as in iron[10] and silicon steel[11],[12]. However, the theoretical values are higher than those of experimental about 5% on an average. This difference would be mainly ascribed to the residual internal stress in the crystal, because the magnetic properties of nickel are more sensitive to stress than those of iron and silicon steel because of its larger magnetostriction and the lower anisotropy. This conclusion is consistent with the domain pattern observation by Williams and Walker[6] in which some of the domain boundaries are not straight but have some curves.

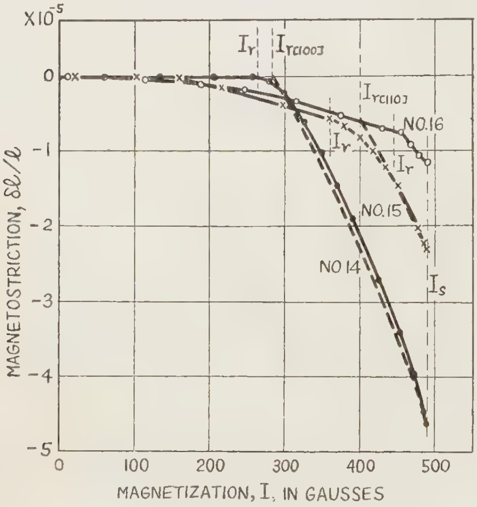

Fig. 5. The descending hysteresis curves of magnetostriction for three principal directions. Dotted lines show the calculated curves for [100] and [110].

Initial permeabilities for each crystallographic orientation, represented in Table II, show the anisotropy of μ_0 and among three principal directions μ_0 for [111], the direction of easy magnetization, is smallest and for [110] is largest. This result is contrary to Williams' result[3] which showed an absence of anisotropy of μ_0. Furthermore, coercive force are largest for [111] and smallest for [110] among three principal directions, as seen also in Table II. The dependencies of initial permeabilities and coercive forces on the crystal orientations are consistent with each other. The origin of anisotropy of these two properties can not be explained at present. However, as previously mentioned, these single crystals are not perfect but are made of small and long rod crystals with axes almost parallel to the specimen axis, so it may be considered that the boundaries of these lineage structures hinder the motion of domain wall and this effect is strong for [111] specimen. This may be an origin of the anisotropy of these two magnetic properties.

Magnetostriction was measured at room temperature by the usual mechano-optical method. To avoid the end effect the measurements were made on the middle part of 4 cm. Fig. 5 shows the change of length along the descending hysteresis for three principal directions. As previously mentioned, in the region $\beta_1<\beta_2+\beta_3$ we can determine the domain distribution at remanence uniquely as given by relation (3), so we can adopt this point as one of the standard point. On the other hand, at saturation the domain distribution is of course uniquely determined. If the two-constant expression is adopted, using the relation (3) at remanence, the change of length between at saturation and at remanence is expressed as follows:

$$\left(\frac{\delta l}{l}\right)_{\text{Sat.-Rem.}}=\frac{3}{2}\lambda_{100}\left(\beta_1^4+\beta_2^4+\beta_3^4-\frac{1}{3}\right)$$
$$+\lambda_{111}\Big\{3(\beta_2^2\beta_3^2+\beta_3^2\beta_1^2+\beta_1^2\beta_2^2)$$
$$-\beta_2^2-\beta_3^2+\beta_2\beta_3-\frac{\beta_2\beta_3(\beta_2+\beta_3)}{\beta_1}\Big\}\,,\qquad (4)$$
$$\text{for}\quad \beta_1<\beta_2+\beta_3\,.$$

where λ_{100} and λ_{111} are the magnetostriction constants. On the other hand, in the region $\beta_1>\beta_2+\beta_3$ the domain distribution at remanence can not be determined uniquely, so that we fail to obtain the general expression of the change of magnetostriction between at saturation and at remanence for each direction. Then, as seen in Fig. 1, for the specimen which is on the straght line between [100] and [110] in the stereographic triangle, namely

$\beta_3=0$, domains may distribute equally in amount for [111] and [11$\bar{1}$], and equally for [1$\bar{1}$1] and [1$\bar{1}\bar{1}$] at remanence. So we can obtain

$$\left(\frac{\delta l}{l}\right)_{\text{Sat.-Rem.}}=\frac{3}{2}\lambda_{100}\left(\beta_1^4+\beta_2^4-\frac{1}{3}\right)+\lambda_{111}(3\beta_1^2\beta_2^2-\beta_2^2)\,, \quad (5)$$

$$\text{for}\quad \beta_3=0\,.$$

No. 14 is available for equation (5). Using the relation (4) and (5) and the observed values, $\left(\frac{\delta l}{l}\right)_{\text{Sat.-Rem. Obs.}}$, tabulated in Table II, one can determine the magnetostriction constants as follows:

$$\lambda_{100}=-(46.1\pm1.0)\times10^{-6}\,,$$
$$\lambda_{111}=-(22.7\pm2.2)\times10^{-6}\,,$$

at room temperature.

These values and those obtained by Bozorth and Hamming[8] agree fairly well. Furthermore, by use of the five-constant expression, we can obtain five constants of magnetostriction. But owing to the slight difference between the theoretical remanence and the observed one, we failed to obtain the reasonable values. By use of these constants, one can easily obtain the domain distribution at remanence for any crystallographic orientation. However, to verify the results obtained with regard to the residual magnetization, it is necessary to observe the domain pattern of our samples at remanence. Now we will try to construct the magnetostriction curves during rotation process theoretically by means of these two constants. For [100] direction, the domain distribute equally in amount for [111], [11$\bar{1}$], [1$\bar{1}$1] and [1$\bar{1}\bar{1}$] at remanence and $\beta_1=1$ and $\beta_2=\beta_3=0$, so that if the direction cosines of the spontaneous magnetization are α_1, α_2 and α_3, the magnetostriction at the region between saturation and remanence is given as follws:

$$\left(\frac{\delta l}{l}\right)_{\alpha,\,[100]}=\frac{3}{2}\lambda_{100}\left(\alpha_1^2-\frac{1}{3}\right).$$

On the other hand, in this case $\alpha_1=I/I_s$ where I is the magnetization. So the change of length between at saturation and at magnetization I is given by

$$\left(\frac{\delta l}{l}\right)_{\text{Sat.-I},\,[100]}=\frac{3}{2}\lambda_{100}\left\{1-\left(\frac{I}{I_s}\right)^2\right\}. \quad (6)$$
$$(1/\sqrt{3}<I/I_s<1)$$

In case of [110] direction, the domains distribute equally in amount for [111] and [11$\bar{1}$] at remanence, and $\beta_1=\beta_2=1/\sqrt{2}$ and $\beta_3=0$. If we assume that when the magnetic field is increased, the directions of magnetization turn to [110] direction in the plane which contains [111] and [110] directions, one can obtain

$$\left(\frac{\delta l}{l}\right)_{\alpha,\,[110]}=\frac{3}{2}\lambda_{100}\left(\frac{\alpha_1^2+\alpha_2^2}{2}-\frac{1}{3}\right)+\frac{3}{2}\lambda_{111}\alpha_1\alpha_2\,,$$

and $\alpha_1=\alpha_2=(1/\sqrt{2})(I/I_s)$. So the magnetostriction between at saturation and at magnetization I is given as follows:

$$\left(\frac{\delta l}{l}\right)_{\text{Sat.-I},\,[110]}=\frac{3}{4}(\lambda_{100}+\lambda_{111})\left\{1-\left(\frac{I}{I_s}\right)^2\right\}. \quad (7)$$
$$(\sqrt{2/3}<I/I_s<1)$$

The theoretical magnetostriction curves for [100] and [110] which are given (6) and (7), are represented in Fig. 5 as dotted lines. As seen, they agree fairly well with the experimental curves.

In conclusion the author wishes to express his hearty thanks to professor H. Takaki of the University of Kyoto for his kind guidance and encouragement throughout the work and also thanks to Messrs. F. J. Hayashi, S. Nakamura and Y. Deguchi for their helpful assistances in preparation of specimens and for their discussion. The expense of this research has been partly defrayed by the Scientific Research Expenditure of the Ministry of Education.

References

1) S. Kaya: Sci. Rep. Tohoku Imp. Univ. **17** (1928) 639.
2) Y. Mashiyama: Sci. Rep. Tohoku Imp. Univ. **17** (1928) 945.
3) W. J. Williams: R. M. Bozorth, *Ferromagnetism* 1951.
4) N. Miyata and Z. Funatogawa: J. Phys. Soc. Japan **9** (1954) 967.
5) M. Yamamoto and T. Iwata: Phys. Rev. **81** (1951) 887, Sci. Rep. RITU **A 5** (1953) 433.
6) H. J. Williams and J. G. Walker: Phys. Rev. **83** (1951) 634.
7) L. F. Bates and G. W. Wilson: Proc. Phys. Soc. **A 64** (1951) 691, **A 66** (1953) 819.
8) R. M. Bozorth and R. W. Hamming: Phys. Rev. **89** (1953) 865.
9) H. Takaki, S. Nakamura, Y. Nakamura, J. Hayashi, K. Furukawa and M. Aso: J. Phys. Soc. Japan **9** (1954) 204.
10) S. Kaya: ZS. f. Phys. **84** (1933) 705.
11) H. Takaki and Y. Nakamura: J. Phys. Soc. Japan **9** (1954) 507.
12) H. Takaki and Y. Nakamura: J. Phys. Soc. Japan **9** (1954) 748.

JOURNAL OF THE PHYSICAL SOCIETY OF JAPAN Vol. 10, No. 11, NOVEMBER, 1955

Theory of Spontaneous Deformation of Barium Titanate

By Wataru KINASE and Hidetoshi TAKAHASHI

Department of Physics, Faculty of Science, University of Tokyo, Tokyo

(Read November 2, 1954 and April 10, 1955; Received August 8, 1955)

The spontaneous ferroelectric deformation of the $BaTiO_3$ crystal to tetragonal form is calculated, taking account of the electrostatic energy and the short-range interaction of the type $\lambda r^{-9}-\mu r^{-6}$, but neglecting the effect of thermal motion. It can be deduced that ionic shift causes the lattice spacing to extend a few percent to the same direction (i.e. the direction of spontaneous polarization). The result is sensitive to the choice of the "effective charge" of the Ti ion. However, for a certain range of this parameter, the dependence of the lattice constant on it shows a striking resemblance to the observed dependence of the lattice constant on temperature. Contraction perpendicular to the direction of polarization is also calculated here considering the interaction among ions. We can show that the extension and contraction suddenly occur when the dipole interaction becomes stronger than some critical value. By taking a proper value for the dipole interaction energy the result can be made to agree with the experimental data.

§ 1. Introduction

The lattice of ferroelectric crystal such as $BaTiO_3$ is said to be pseudocubic in the temperature region of its ferroelectric phases, that is, its atomic arrangement is the same as in a cubic crystal (the form of the same crystal above Curie temperature), but the lattice constants are a little different in the three directions of coordinates and/or the coordinate angle is a little different from 90°. This is usually interpreted as electrostriction caused be spontaneous polarization. Although various works have appeared that deal with the spotaneous polarization of $BaTiO_3$, there seems to be no attempt to deal with the spontaneous deformation by a molecular theory. In this paper, the spontaneous deformation of $BaTiO_3$ in tetragonal form will be treated theoretically using known interaction energies between the ions.

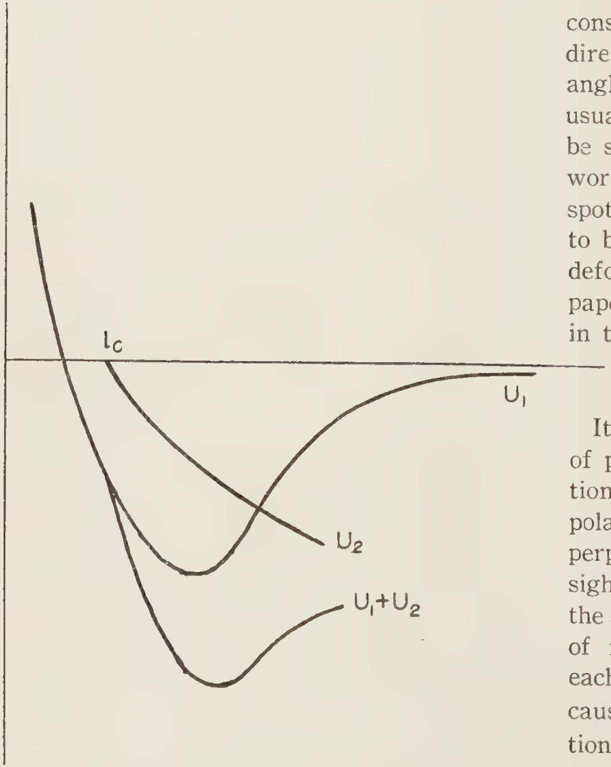

Fig. 1. Lattice energy U_1, dipole interaction energy U_2 and their sum U_1+U_2 respectively vs. lattice spacing in arbitrary unit. The minimum point of U_1+U_2 corresponds to larger lattice spacing than that of U_1.

It is known that every forroelectric crystal of perovskite type has a positive electrostriction, that is, elongates in the direction of its polarization, while it contracts in the direction perpendicular to it 1)2)3). This seems at first sight paradoxical, because if we assume that the spontaneously polarized crystal is composed of rigid electric dipoles aligned parallel to each other, the attraction of dipoles would cause *contraction* in the direction of polarization, and elongation perpendicular to it. This paradox may be cleared just by noting the fact that the actual polarization in $BaTiO_3$ is caused by shift of ions from their symmetrical positions, and that these shifts depend on the lattice spacing.

The dipole interaction energy is defined by the strength of the internal field and the magnitude of the shift of the ions. If the lattice had somewhat extended spacing in the direction of spontaneous polarization, repulsion between the ions would become weaker and the shift would become greater than in the case of shorter spacing. This mechanism explains qualitatively the electrostriction of $BaTiO_3$ crystal. Fig. 1 shows schematically the relation between the lattice spacing and the energy. Here U_1 is the energy when we assume that the crystal is non-polar, and U_2 is the additional energy caused by the dipole interaction. The dipole interaction energy is equal to zero as long as the lattice spacing is less than a critical value l_c. When the lattice spacing exceeds l_c, there occurs a spontaneous shift of ions due to the dipole interaction, which gives the additional negative energy U_2. Comparing the curves for U_1 and U_1+U_2, it will be readily found that the minimum point is shifted rightwards by the addition of the term U_2 in accordance with the fact that $BaTiO_3$ crystal extends its lattice spacing in the direction of spontaneous polarization.

The aim of this article is to obtain a quantitative theory of the spontaneous electrostriction of $BaTiO_3$ crystal in the tetragonal phase. As a first step we shall neglect the effect of temperature altogether in this paper for the sake of simplicity. This would seem rather inadequate, because the real lattice is deformed in rhombohedral form at the lowest temperature region[3]. However, it will be seen later that even such a simplified theory is adequate to explain certain aspects of the ferroelectric transition.

§ 2. The Energy Expression for the Spontaneously polarized Crystal

The energy of $BaTiO_3$ crystal will be written simply as

$$U=U_1+U_2\ , \tag{1}$$

Where U is total energy, and U_1 is that of a virtual unpolarized crystal (which, however, has the same lattice spacing as the real, polarized crystal), and U_2 is the additional energy term caused by the dipole interaction.

Now, U_1 may be supposed to consist of three types of interatomic interaction, that is, overlap energy, van der Waals' energy and Coulomb energy, namely,

$$U_1=U_{\text{overlap}}+U_{\text{Waals}}+U_{\text{Coulomb}}\ . \tag{2}$$

The term U_2 is caused by the shift of the ions. For the sake of simplicity, we shall consider hereafter the shift of only one sort of the ions, namely, the titanium ions. If we denote the magnitude of the shift of a Ti ion from the centre of the tetragonal unit lattice by x, the additional term caused by the shift (in other words, the potential for the Ti ion in the lattice composed of other ions) will be written as

$$U_2=(ax^2+bx^4)+a'x^2\ , \tag{3}$$

where the terms in the bracket mean the potential for a Ti ion owing to overlap and van der Waals' interaction, and $a'x^2$ is the term produced by the (electrostatic) Coulomb interaction. We have neglected here the higher power terms than x^4. It will be shown later by numerical calculation that both a and b take positive values, while a' is generally negative.

From the three equations (1), (2) and (3) we can write the energy as

$$U=U_{\text{overlap}}+U_{\text{Waals}}+U_{\text{Coulomb}}+U_2\ . \tag{4}$$

In the expression (4) the first three terms do not contain x, so we can readily get the value of x by minimizing U with respect to x. Namely

$$0=\frac{\partial U}{\partial x}=(2ax+4bx^3)+2a'x\ . \tag{5}$$

Solving (5), we get

$$x=0 \quad \text{or} \quad \pm\sqrt{\frac{-a'-a}{2b}}\ . \tag{6}$$

If the absolute value of a' is greater than a, that is $a'+a<0$, $x=0$ and $x=\pm\sqrt{\frac{-a'-a}{2b}}$ correspond respectively to a maximum and double minimum of U. The minimum value of U with respect to x is thus obtained if we put $x=\pm\sqrt{\frac{-a'-a}{2b}}$ into equ. (4), namely

$$U=U_{\text{overlap}}+U_{\text{Waals}}+U_{\text{Coulomb}}-\frac{(a'+a)^2}{4b}\ . \tag{7}$$

We shall be concerned from now on with the energy expression (7) that does not contain x explicitly.

If the absolute value of a' is not greater than a, that is, $a+a'\geqq 0$, equ. (5) has only one real solution $x=0$ corresponding to a single minimum of U. Apparently this corresponds to the paraelectric state. In this case the energy expression is simply

$$U=U_{\text{overlap}}+U_{\text{Waals}}+U_{\text{Coulomb}}\,. \qquad (7)'$$

§ 3. Overlap and Van der Walls' energies of the Tetragonal Lattice

The overlap and Van der Waals' energies[4] of BaTiO$_3$ crystal has been worked out in detail by A.F. Devonshire[5], and explicit formulas for them have heen given for the case of cubic crystal. We shall follow his method and apply it to the case of tetragonal lattice.

The dimension of a unit call of BaTiO$_3$ crystal lattice is nearly equal to a cube of which edges are 4Å. So it is convenient to express the three edges of a unit cell in the tetragonal phase as $2l(1+\varDelta_a)$, $2l(1+\varDelta_{b1})$ and $2l(1+\varDelta_{b2})$, where $l=2$Å. $\varDelta_a$, $\varDelta_{b1}$ and $\varDelta_{b2}$ show the ratios of the magnitude of extension of the cube edges to those of the standard cube 4Å in the direction parallel to the polarization and to the two directions perpendicular to it respectively. These three directions correspond to the lines connecting a titanium and three neighbouring oxygens. If we consider only the interaction among the nearest neighbour ions, the overlap and Van der Waals' energies will be expressed as follows:

$$\begin{aligned}U_{\text{overlap}}=&\,2\lambda_{OT}l^{-s}\{(1+\varDelta_a)^{-s}+(1+\varDelta_{b1})^{-s}+(1+\varDelta_{b2})^{-s}\}\\&+(4\lambda_{OO}+4\lambda_{BO})l^{-s}[\{(1+\varDelta_{b1})^2+(1+\varDelta_{b2})^2\}^{-s/2}+\{(1+\varDelta_{b2})^2+(1+\varDelta_a)^2\}^{-s/2}\\&\qquad+\{(1+\varDelta_a)^2+(1+\varDelta_{b1})^2\}^{-s/2}]\\&+8\lambda_{BT}l^{-s}\{(1+\varDelta_a)^2+(1+\varDelta_{b1})^2+(1+\varDelta_{b2})^2\}^{-s/2}\\&+(3\lambda_{OO}+\lambda_{BB}+\lambda_{TT})(2l)^{-s}\{(1+\varDelta_a)^{-s}+(1+\varDelta_{b1})^{-s}+(1+\varDelta_{b2})^{-s}\}\,, \qquad (8)\end{aligned}$$

$$\begin{aligned}U_{\text{Waals}}=&-2\mu_{OT}l^{-t}\{(1+\varDelta_a)^{-t}+(1+\varDelta_{b1})^{-t}+(1+\varDelta_{b2})^{-t}\}\\&-(4\mu_{OO}+4\mu_{BO})l^{-t}[\{(1+\varDelta_{b1})^2+(1+\varDelta_{b2})^2\}^{-t/2}+\{(1+\varDelta_{b2})^2+(1+\varDelta_a)^2\}^{-t/2}\\&\qquad+\{(1+\varDelta_a)^2+(1+\varDelta_{b1})^2\}^{-t/2}]\\&-8\mu_{BT}l^{-t}\{(1+\varDelta_a)^2+(1+\varDelta_{b1})^2+(1+\varDelta_{b2})^2\}^{-t/2}\\&-(3\mu_{OO}+\mu_{BB}+\mu_{TT})(2l)^{-t}\{(1+\varDelta_a)^{-t}+(1+\varDelta_{b1})^{-t}+(1+\varDelta_{b2})^{-t}\}\,. \qquad (9)\end{aligned}$$

Here λ_{OT} and μ_{OT} mean the overlap and van der Waals' energy coefficients between oxygen and titanium ions respectively. Similarly λ_{OO} and μ_{OO} mean those between two oxygen ions, λ_{BO} and μ_{BO} those between barium and oxygen ions etc. Eqs. (8) and (9) have been obtained by using the current expression $\lambda_{AB}r^{-s}-\mu_{AB}r^{-t}$ for the interaction between A and B atoms distant by r to each other.

The numerical values of λ's and μ's for $s=9$ and $t=6$ respectively have been taken from Fowler's book[6] as were done by A.F. Devonshire[4] and E. Sawaguchi[7]. They are given as follows (in c.g.s. unit)

$$\begin{aligned}\lambda_{OT}&=\ \ 15.6\times10^{-82}\,, & \mu_{OT}&=\ \ 31.3\times10^{-60}\,,\\ \lambda_{OO}&=113.5\times10^{-82}\,, & \mu_{OO}&=135.0\times10^{-60}\,,\\ \lambda_{BO}&=\ \ 99.0\times10^{-82}\,, & \mu_{BO}&=162.0\times10^{-60}\,,\\ \lambda_{BB}&=\ \ 82.7\times10^{-82}\,, & \mu_{BB}&=239.0\times10^{-60}\,,\\ \lambda_{BT}&=\ \ 12\ \ \ \ \times10^{-82}\,, & \mu_{BT}&=\ \ 43\ \ \ \ \times10^{-60}\,,\\ \lambda_{TT}&=\ \ \ \ 1.1\times10^{-82}\,, & \mu_{TT}&=\ \ 10\ \ \ \ \times10^{-60}\,.\end{aligned} \qquad (10)$$

Now, by differentiating and expanding Eqs. (8) and (9) with regard to $\varDelta_a$, $\varDelta_{b1}$ and $\varDelta_{b2}$ we obtain

$$\begin{aligned}&\frac{\partial}{\partial\varDelta_a}(U_{\text{overlap}}+U_{\text{Waals}})\\&=-2s\lambda_{OT}l^{-s}\{1-(s+1)\varDelta_a\}+2t\mu_{OT}l^{-t}\{1-(t+1)\varDelta_a\}\\&\quad-s(4\lambda_{OO}+4\lambda_{BO})l^{-s}\cdot2^{-s/2}\{1-s/2\cdot\varDelta_a-(s+2)/4\cdot(\varDelta_{b1}+\varDelta_{b2})\}\\&\quad+t(4\mu_{OO}+4\mu_{BO})l^{-t}\cdot2^{-t/2}\{1-t/2\cdot\varDelta_a-(t+2)/4\cdot(\varDelta_{b1}+\varDelta_{b2})\}\\&\quad-8s\lambda_{BT}l^{-s}\cdot3^{-(s+2)/2}\{1-(s-1)/3\cdot\varDelta_a-(s+2)/3\cdot(\varDelta_{b1}+\varDelta_{b2})\}\end{aligned}$$

$$+8t\mu_{BT}l^{-t}\cdot 3^{-(t+2)/2}\{1-(t-1)/3\cdot\Delta_a-(t+2)/3\cdot(\Delta_{b1}+\Delta_{b2})\}$$
$$-s(3\lambda_{OO}+\lambda_{BB}+\lambda_{TT})(2l)^{-s}\{1-(s+1)\Delta_a\}$$
$$+t(3\mu_{OO}+\mu_{BB}+\mu_{TT})(2l)^{-t}\{1-(t+1)\Delta_a\}\ , \tag{11A}$$

$$\frac{\partial}{\partial\Delta_{bi}}(U_{\text{overlap}}+U_{\text{Waals}})$$
$$=-2s\lambda_{OT}l^{-s}\{1-(s+1)\Delta_{bi}\}+2t\mu_{OT}l^{-t}\{1-(t+1)\Delta_{bi}\}$$
$$-s(4\lambda_{OO}+4\lambda_{BO})l^{-s}\cdot 2^{-s/2}\{1-s/2\cdot\Delta_{bi}-(s+2)/4\cdot(\Delta_{bj}+\Delta_a)\}$$
$$+t(4\mu_{OO}+4\mu_{BO})l^{-t}\cdot 2^{-t/2}\{1-t/2\cdot\Delta_{bi}-(t+2)/4\cdot(\Delta_{bj}+\Delta_a)\}$$
$$-8s\lambda_{BT}l^{-s}\cdot 3^{-(s+2)/2}\{1-(s-1)/3\cdot\Delta_{bi}-(s+2)/3\cdot(\Delta_{bj}+\Delta_a)\}$$
$$+8t\mu_{BT}l^{-t}\cdot 3^{-(t+2)/2}\{1-(t-1)/3\cdot\Delta_{bi}-(t+2)/3\cdot(\Delta_{bj}+\Delta_a)\}$$
$$-s(3\lambda_{OO}+\lambda_{BB}+\lambda_{TT})(2l)^{-s}\{1-(s+1)\Delta_{bi}\}$$
$$+t(3\mu_{OO}+\mu_{BB}+\mu_{TT})(2l)^{-t}\{1-(t+1)\Delta_{bi}\}\ , \tag{11B, C}$$
$$\begin{cases} i=1 \\ j=2 \end{cases} \quad \text{or} \quad \begin{cases} i=2 \\ j=1 \end{cases}$$

where we have neglected the higher power terms Δ^2_a, Δ^2_{b1}, Δ^2_{b2}, $\Delta_a\Delta_{b1}$, $\Delta_a\Delta_{b2}$, $\Delta_{b1}\Delta_{b2}$; Δ^3_a etc.

§ 4. Coulomb energy for the Tetragonal Lattice

Here we shall again use the expression for the Coulomb energy for BaTiO$_3$ calculated by A.F. Devonshire[5)], namely $-49.1e^2/R$ c.g.s. unit, where e is the electron charge and R is the lattice constant. To obtain the Coulomb energy for the tetragonal lattice we adopt the following approximation. Namely, we take the arithmetic mean of Coulomb energies for three cubic lattices whose edge lengths are respectively equal to those of the three edges of the tetragonal unit cell. Thus, the Coulomb energy will be expressed approximately as

$$U_{\text{Coulomb}}=-49.1e^2$$
$$\times\frac{1}{3}\left\{\frac{1}{2l(1+\Delta_a)}+\frac{1}{2l(1+\Delta_{b1})}+\frac{1}{2l(1+\Delta_{b2})}\right\}\ . \tag{12}$$

If we differentiate U_{Coulomb}, we readily obtain

$$\frac{\partial}{\partial\Delta_a}U_{\text{Coulomb}}=\frac{49.1e^2}{6l}(1-2\Delta_a)\ ,$$
$$\frac{\partial}{\partial\Delta_{b1}}U_{\text{Coulomb}}=\frac{49.1e^2}{6l}(1-2\Delta_{b1})\ ,$$
$$\frac{\partial}{\partial\Delta_{b2}}U_{\text{Coulomb}}=\frac{49.1e^2}{6l}(1-2\Delta_{b2})\ , \tag{13A, B, C}$$

where we have neglected the higher power terms Δ^2, Δ^3 etc. in the expansion.

Using (11) and (13) we can determine the lattice constants of the unpolarized crystal by solving the equations

$$0=\frac{\partial}{\partial\Delta_a}(U_{\text{overlap}}+U_{\text{Waals}}+U_{\text{Coulomb}})\ ,$$
$$0=\frac{\partial}{\partial\Delta_{b1}}(U_{\text{overlap}}+U_{\text{Waals}}+U_{\text{Coulomb}})\ ,$$
$$0=\frac{\partial}{\partial\Delta_{b2}}(U_{\text{overlap}}+U_{\text{Waals}}+U_{\text{Coulomb}})\ , \tag{14A, B, C}$$

with the result

$$\Delta_a=\Delta_{b1}=\Delta_{b2}=0.00811\ . \tag{15}$$

Thus the lattice shape of the unpolarized crystal is cubic with lattice constant

$$4(1+0.00811)\text{Å}\fallingdotseq 4.0324\text{Å}\ . \tag{16}$$

Here we have neglected the long range contribution of the overlap and van der Waals' energy. The result is in good agreement with Devonshire's calculation[5)] and also with the experimental data[1)2)].

§ 5. Dipole Interaction Energy in the Tetragonal System

Since it seemed to be too laborious to evaluate precisely the dipole energies for the tetragonal lattice of perovskite type, an approximate method has been adopted to obtain them by using the known values for the cubic lattices as starting values and modifying them for the tatragonal distortion, taking into account the nearest lattice points only. If we admit this approximation, the field of an array of unit dipoles directed to z-axis will be given by $S_z(\mathrm{l, m, n})$ in the following equations (17), (l, m, n) being the coordinates of the points in question with respect to the unit lattice.

$$
\begin{aligned}
S_z(0, 0, 0;\ \varDelta_a) &= -12\varDelta_a\,, \\
S_z(1/2, 1/2, 1/2;\ \varDelta_a) &= (512/9\sqrt{3})\varDelta_a\,, \\
S_z(1/2, 1/2, 0;\ \varDelta_a) &= -p\,, \\
S_z(1/2, 0, 1/2;\ \varDelta_a) &= p/2+12\sqrt{2}\,\varDelta_a\,, \\
S_z(0, 1/2, 1/2;\ \varDelta_a) &= p/2+12\sqrt{2}\,\varDelta_a\,, \\
S_z(0, 0, 1/2;\ \varDelta_a) &= q-96\varDelta_a\,, \qquad (17) \\
S_z(0, 1/2, 0;\ \varDelta_a) &= -q/2\,, \\
S_z(1/2, 0, 0;\ \varDelta_a) &= -q/2\,,
\end{aligned}
$$

where $\varDelta_a$ corresponds to the relative elongation z-axis of the lattice, where $p=8.668$[8], $q=30.081$[9]. We assume here that $S_z(1/2, 1/2, 0)$, $S_z(0, 1/2, 0)$ and $S_z(1/2, 0, 0)$ are unaltered because the nearest lattice points are not shifted by the extension of the z-axis of the lattice.

In the same manner we can modify S_z's for the relative extension $\varDelta_{b1}$ and $\varDelta_{b2}$, but the crystalline field at Ti ion may be little affected by $\varDelta_{b1}$ and $\varDelta_{b2}$ because the dipole interaction between Ti and Oa ions would be considerably greater than that between Ti and Ob$_1$ or Ob$_2$ ions[10][11]. For this reason we calculate here the dipole interaction only for the extension ratio $\varDelta_a$, neglecting $\varDelta_{b1}$ and $\varDelta_{b2}$ altogether.

By using the modified S_z's in (17), we can evaluate the change of the dipole interaction caused by the extension of the lattice in z-direction. To do this, however, we have to know the local field acting on Ti ions caused by the shift of the Ti ions themselves[10][11][12]. Thus, we have to solve a system of simultaneous equations as was done by J.C. Slater[12]: (Dipole moment of one ion)=(Polarizability of the ion) multiplied by (Local field at its location).

By expressing the local field as a function of dipole moments of all ions, we can write down the simultaneous equations. Here we must pay attention to the fact that coefficient for the local field also needs to be modified in tetragonal lattice. By taking account of only the nearest neighbours, the local field acting on Ti ion directly produced by the shift of Ti itself will be shown to be expressed approximately as

$$\left\{\frac{4\pi}{3}+\left(\frac{-256}{9\sqrt{3}}-48\right)\varDelta_a\right\}u_0 \qquad (18)$$

instead of simply $4\pi/3\cdot u_0$ as in the cubic lattice, where u_0 means the product of the shift of Ti ion and its charge.

Thus we obtain the simultaneous equations:

$$
\begin{aligned}
u=\alpha_{Ti}\frac{1}{(2l)^3}\Bigg[&\left\{\frac{4\pi}{3}+\left(\frac{-256}{9\sqrt{3}}-48\right)\varDelta_a\right\}u_0+\left(\frac{4\pi}{3}-12\varDelta_a\right)u \\
&+\left(\frac{4\pi}{3}+\frac{512}{9\sqrt{3}}\varDelta_a\right)v+\left(\frac{4\pi}{3}+q-96\varDelta_a\right)w \\
&+\left(\frac{4\pi}{3}-\frac{q}{2}\right)(x_1+x_2)\Bigg],
\end{aligned}
$$

$$
\begin{aligned}
u=\alpha_{Ba}\frac{1}{(2l)^3}\Bigg\{&\left(\frac{4\pi}{3}+\frac{512}{9\sqrt{3}}\varDelta_a\right)(u_0+u)+\left(\frac{4\pi}{3}-12\varDelta_a\right)v \\
&+\left(\frac{4\pi}{3}-p\right)w+\left(\frac{4\pi}{3}+\frac{p}{2}+12\sqrt{2}\,\varDelta_a\right)(x_1+x_2)\Bigg\},
\end{aligned}
$$

$$
\begin{aligned}
w=\alpha_0\frac{1}{(2l)^3}\Bigg\{&\left(\frac{4\pi}{3}+q-96\varDelta_a\right)(u_0+u)+\left(\frac{4\pi}{3}-p\right)v \\
&+\left(\frac{4\pi}{3}-12\varDelta_a\right)w+\left(\frac{4\pi}{3}+\frac{p}{2}+12\sqrt{2}\,\varDelta_a\right)(x_1+x_2)\Bigg\},
\end{aligned}
$$

$$
\begin{aligned}
x_1=\alpha_0\frac{1}{(2l)^3}\Bigg\{&\left(\frac{4\pi}{3}-\frac{q}{2}\right)(u_0+u)+\left(\frac{4\pi}{3}+\frac{p}{2}+12\sqrt{2}\,\varDelta_a\right)(v+w) \\
&+\left(\frac{4\pi}{3}-12\varDelta_a\right)x_1+\left(\frac{4\pi}{3}-p\right)x_2\Bigg\},
\end{aligned}
$$

$$x_2=\alpha_0\frac{1}{(2l)^3}\left\{\left(\frac{4\pi}{3}-\frac{q}{2}\right)(u_0+u)+\left(\frac{4\pi}{3}+\frac{p}{2}+12\sqrt{2}\,\Delta_a\right)(v+w)+\left(\frac{4\pi}{3}-p\right)x_1+\left(\frac{4\pi}{3}-12\Delta_a\right)x_2\right\}, \qquad (19\text{A, B, C, D, E})$$

where u, v, w, x_1 and x_2 are induced dipole moments caused by electron clouds of Ti, Ba, Oa, Ob$_1$ and Ob$_2$ respectively; α_{Ti}, α_{Ba} and α_0 are polarizabilities of Ti, Ba and O ions respectively; l represents 2Å; p, q and Δ_a are the symbols already mentioned in Eq. (17).

Using the values by P.W. Anderson and W. Shockley[13]:

$$4\pi\alpha_{Ti}=0.0365(2l)^3,\quad 4\pi\alpha_{Ba}=0.382(2l)^3$$
$$\text{and}\quad 4\pi\alpha_0=0.470(2l)^3,$$

we can solve the simultaneous equations numerically, the result being

$$\begin{aligned}u&=0.1974\ (1-\ 7.30\Delta_a)u_0\ ,\\ v&=-0.0630\ (1-40.8\ \Delta_a)u_0\ ,\\ w&=1.9090\ (1-\ 3.71\Delta_a)u_0\ ,\\ x_1&=0.1014\ (1+\ 2.65\Delta_a)u_0\ ,\\ x_2&=0.1014\ (1+\ 2.65\Delta_a)u_0\ .\end{aligned} \qquad (20\text{A, B, C, D, E})$$

When we consider only the shift of Ti ion and deal with the potential acting on Ti, the first equation in (20) proves to be useful. Denoting the charge and the shift of Ti ion as ne and x respectively the energy of the dipole interaction will be expressed as

$$a'x^2=a_0'(1-7.30\Delta_a)x^2\ , \qquad (21)$$

where

$$a_0'=\frac{0.1974(ne)^2}{2\alpha_{Ti}}$$

Here we notice the fact that the numerical factor 7.30 in (21) is somewhat greater than the factor 3 which we would obtain when we assume that the ions have a rigid dipole in z-direction regarding Ti-Oa chain interaction. (The factor 3 is given by expanding $(1+\Delta_a)^{-3}$ which is proportional to the dipole-dipole interaction). In a later section we shall discuss the spontaneous deformation for the various values of a_0', the factor 7.30 remaining constant.

§ 6. The potential acting on Ti Ion

The potential of Ti ion due to overlap repulsion and van der Waals' attraction will be represented as ax^2+bx^4, where the coefficients a and b may be explicitly given by expanding the expressions (8) and (9) for the interatomic forces between Ti and other ions in power series in x*. Taking account of the nearest ions we can write them as

$$\begin{aligned}a=&\lambda_{OT}s(s+1)\{l(1+\Delta_a)\}^{-s-2}-\mu_{OT}t(t+1)\{l(1+\Delta_a)\}^{-t-2}\\ &-\lambda_{OT}s\{l(1+\Delta_{b1})\}^{-s-2}+\mu_{OT}t\{l(1+\Delta_{b1})\}^{-t-2}\\ &-\lambda_{OT}s\{l(1+\Delta_{b2})\}^{-s-2}+\mu_{OT}t\{l(1+\Delta_{b2})\}^{-t-2}\\ &+\lambda_{BT}\frac{4s(s-1)}{3}(\sqrt{3}\,l)^{-s-2}-\mu_{BT}\frac{4t(t-1)}{3}(\sqrt{3}\,l)^{-t-2}\\ &+f_{BT}(\Delta_a,\Delta_{b1},\Delta_{b2})\end{aligned} \qquad (22)$$

and

$$\begin{aligned}b=&\lambda_{OT}\frac{s(s+1)(s+2)(s+3)}{12}\{l(1+\Delta_a)\}^{-s-4}\\ &-\mu_{OT}\frac{t(t+1)(t+2)(t+3)}{12}\{l(1+\Delta_a)\}^{-t-4}\\ &+\lambda_{OT}\frac{s(s+2)}{4}\{l(1+\Delta_{b1})\}^{-s-4}-\mu_{OT}\frac{t(t+2)}{4}\{l(1+\Delta_{b1})\}^{-t-4}\\ &+\lambda_{OT}\frac{s(s+2)}{4}\{l(1+\Delta_{b2})\}^{-s-4}-\mu_{OT}\frac{t(t+2)}{4}\{l(1+\Delta_{b2})\}^{-t-4}\end{aligned}$$

---

* x corresponds to the shift in the z (or a)-direction, that is, the shift of Ti in the direction of Oa location.

$$+\lambda_{BT}\left\{s(s+2)-\frac{2s(s+2)(s+4)}{3}+\frac{s(s+2)(s+4)(s+6)}{27}\right\}(\sqrt{3}\,l)^{-s-4}$$

$$-\mu_{BT}\left\{t(t+2)-\frac{2t(t+2)(t+4)}{3}+\frac{t(t+2)(t+4)(t+6)}{27}\right\}(\sqrt{3}\,l)^{-t-4}$$

$$+g_{BT}(\Delta_a, \Delta_{b1}, \Delta_{b2})\,, \tag{23}$$

where λ's, μ's and Δ's are the symbols already mentioned, and $s=9$ and $t=6$; f_{BT} and g_{BT} are terms in these coefficients that originate from the interaction between Ti and Ba ions. We shall neglect f_{BT} and g_{BT} in later treatment because of their smallness. The numerical calculation shows that the potential acting on Ti ion is mainly determined by the interaction with the nearest neighbour oxygen ions

Numerical values for a and b is obtained, if we put $l=2$Å, as

$$a=5.123\times10^5-7.130\times10^6\Delta_a+6{,}954\times10^5\Delta_{b1}+6.954\times10^5\Delta_{b2}$$
$$+4.340\times10^7\Delta^2{}_b-4.2605\times10^6\Delta^2{}_{b1}-4.2605\times10^6\Delta^2{}_{b2} \tag{24}$$

and

$$b=1.895\times10^{22}-2.374\times10^{23}\Delta_a-5.760\times10^{21}\Delta_{b1}-5.760\times10^{21}\Delta_{b2}$$
$$+1.673\times10^{24}\Delta^2{}_a+4.087\times10^{22}\Delta^2{}_{b1}+4.087\times10^{22}\Delta^2{}_{b2}\,, \tag{25}$$

where we adopt the c.g.s. unit. The two equations show that a and b are both diminished by the extension in the a-direction; on the other hand, a will be increased and b will be diminished by the extension in the b_1- or b_2- direction.

§7. Calculation of the Spontaneous Deformation

To determine the equilibium state of the spontaneous deformation we have to solve the equations

$$\frac{\partial U}{\partial \Delta_a}=0\,,\quad \frac{\partial U}{\partial \Delta_{b1}}=0\,,\quad \frac{\partial U}{\partial \Delta_{b2}}=0 \tag{26A, B, C}$$

with the usual method, paying attention to the fact that the last two equations are quite equivalent because the energy expression described before contains Δ_{b1} and Δ_{b2} in an equivalent manner. So we put $\Delta_{b1}=\Delta_{b2}=\Delta_b$ for simplification.

Now we can write down Eq. (26) explicitly, by differentiating Eq. (7), as

Table I.

dipole interaction (c.g.s.)	lattice deformation ratio //**P**	lattice deformation ratio ⊥**P**	tetragonality	volume excess	Ti shift (Å)
$a_0'\times10^{-5}$	Δ_a	Δ_b	$\Delta_a-\Delta_b$	$\Delta_a+2\Delta_b$	$\sqrt{\frac{-a'-a}{2b}}$
−4.941	0.00811	0.00811	0	0.02433	0
−5	0.01224	0.00674	0.00550	0.02573	0.07085
−5.1	0.01802	0.00474	0.01328	0.02749	0.1172
−6	0.04196	−0.00530	0.04725	0.03137	0.2600
−7	0.04677	−0.00998	0.05675	0.02681	0.3269
−8	0.04564	−0.01270	0.05834	0.02024	0.3727
−10	0.03951	−0.01642	0.05593	0.00667	0.4421
−14	0.02761	−0.02212	0.04973	−0.00166	0.5457
−19.557	0.01648	−0.02783	0.04432	−0.03918	0.6574

Δ_a and Δ_b represent the relative deviation from the standard value 4 Å. //**P** and ⊥**P** mean "parallel and perpendicular to the polarization" respectively.

Table II.

dipole interaction (c.g.s.)	lattice deformation ratio //**P**	lattice deformatien ratio ⊥**P**	tetragonality	volume excess	polarization (μ coulomb)
$a_0' \times 10^{-5}$	Δ_a'	Δ_b'	$\Delta_a' - \Delta_b'$	$\Delta_a' + 2\Delta_b'$	**P**
− 4.941	0	0	0	0	0
− 5	0.00410	−0.001359	0.00546	0.001379	7.611
− 5.1	0.00983	−0.00334	0.01317	0.00314	12.50
− 6	0.03358	−0.01330	0.04687	0 00698	28.18
− 7	0.03835	−0.01794	0.05629	0.00246	37.94
− 8	0.03723	−0.02064	0.05787	−0.00406	46.69
−10	0.03115	−0.02433	0.05548	−0.01752	63.79
−14	0.01934	−0.02999	0.04933	−0.04063	98.39
−19.557	0.00830	−0.03565	0.04395	−0.06300	147.52

Δ_a' and Δ_b' represent the relative deviation from the standard value 4.03244 Å. The values of Δ_a' and Δ_b' in Table II are easily calculated from those of Δ_a and Δ_b in Table I, whereas those of polarization are deduced from the dipole moments of the ions in Eqs. (20) corresponding to those of Ti shift in Table I.

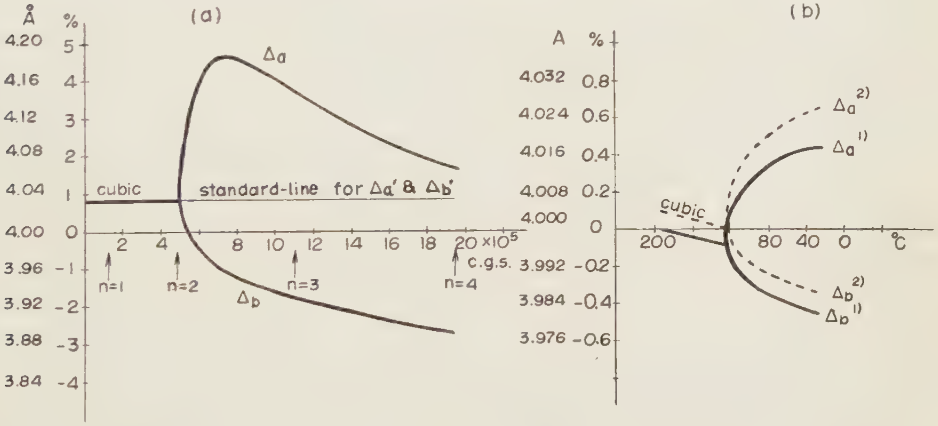

Fig. 2 (a). Calculated values of Δ_a and Δ_b vs. dipole interaction.

(b). Observed values of Δ_a and Δ_b vs. temperature by S. Miyake, R. Ueda[1)] and H. D. Megaw[2)].

The standard cubic lattice is 4.03244 Å. n's denote the various effective charges of Ti ion for the dipole interaction.

$$0=\frac{\partial U}{\partial \varDelta_a}=\frac{\partial}{\partial \varDelta_a}(U_{\text{overlap}}+U_{\text{Waals}}+U_{\text{Coulomb}})$$

$$-\frac{a'+a}{2b}\left(\frac{\partial a'}{\partial \varDelta_a}+\frac{\partial a}{\partial \varDelta_a}\right)+\frac{(a'+a)^2}{4b^2}\frac{\partial b}{\partial \varDelta_a},$$

$$0=\frac{\partial U}{\partial \varDelta_b}=\frac{\partial}{\partial \varDelta_b}(U_{\text{overlap}}+U_{\text{Waals}}+U_{\text{Coulomb}})$$

$$-\frac{a'+a}{2b}\left(\frac{\partial a'}{\partial \varDelta_b}+\frac{\partial a}{\partial \varDelta_b}\right)+\frac{(a'+a)^2}{4b^2}\frac{\partial b}{\partial \varDelta_b}. \tag{27A, B}$$

By putting (11), (13), (21), (24) and (25) in the above equations, we obtain the explicit equations for $\varDelta_a$ and $\varDelta_b$. The numerical results are given in Table 1 and Table 2. The result is also shown in Figs. 2, 3, 4, 5, 6 and 7.

§ 8. Discussion

A glance at Fig. 2(a), however, suggests its striking resemblance with the observed dependence of lattice constants on temperature (Fig. 2(b)) by S. Miyake, R. Ueda[1)] and by H.D. Megaw[2)]. Further data[1)2)] are shown with corresponding "theoretical" values in

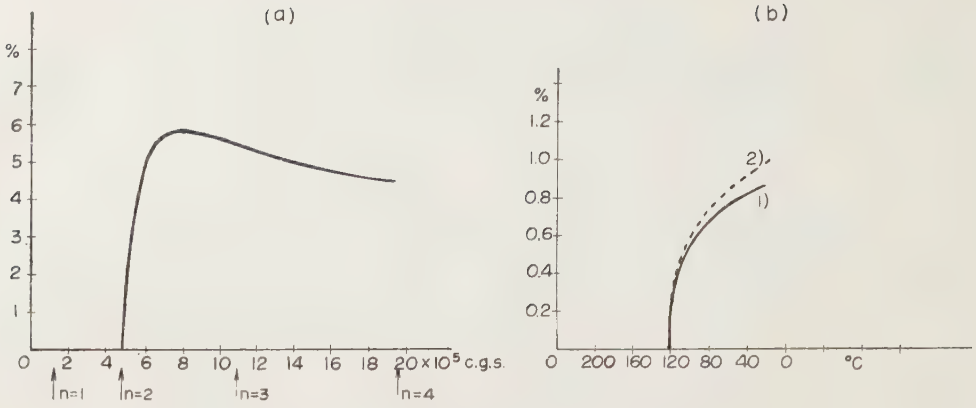

Fig. 3 (a). Calculated value of tetragonality $\Delta_{\alpha}-\Delta_b$ vs. dipole interaction.
(b). Observed values of tetragonality $\Delta_{\alpha}-\Delta_b$ vs. temperature by S. Miyake, R. Ueda[1] and H. D. Megaw[2].

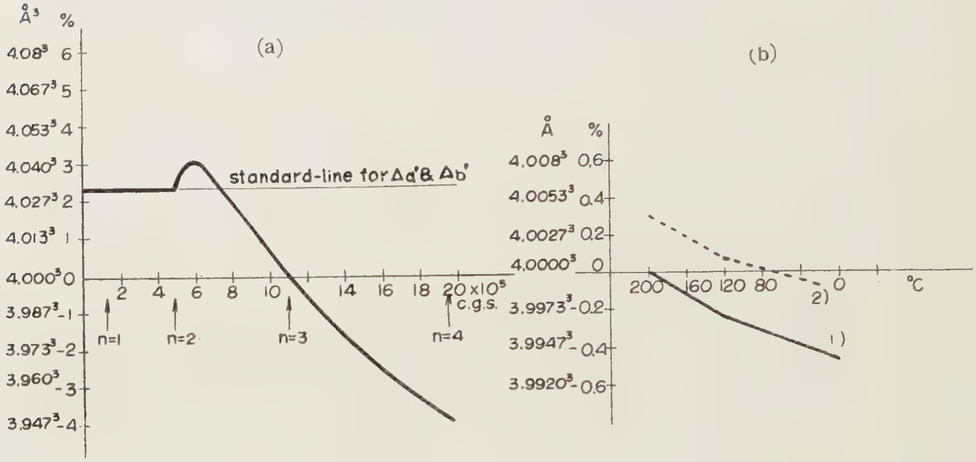

Fig. 4 (a). Calculated value of volume excess $\Delta_{\alpha}+2\Delta_b$ vs. dipole interaction.
(b). Observed values of volume excess $\Delta_{\alpha}+2\Delta_b$ vs. temperature by S. Miyake, R. Ueda[1] and H. D. Megaw[2].
The standard cubic lattice is 4.03244 Å.

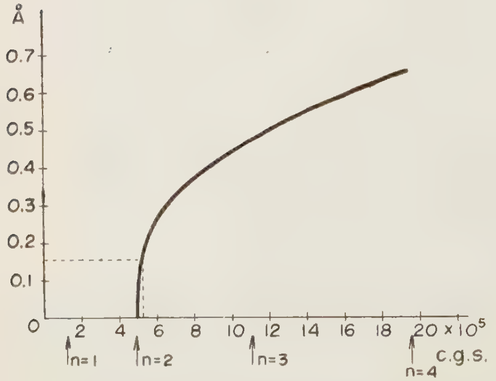

Fig. 5. Calculated value of the shift of Ti ion vs. dipole interaction. The dotted line corresponds to the shift 0.156 Å of Ti relative to Oa observed by H. T. Evans.[14]

Figs. 3 and 4, where the abscissas are temperature for observed values and a_0' (dipole interaction coefficient) for calculated values. From this one may conclude that the effect of temperature is something that is equivalent to the variation of the dipole interaction coefficient a_0'. This conclusion must not be made too hastily, because it may be argued that the form of the curve in Figs. 2 (a and b) is characteristic to any phase change of the second order, whatever the underlying process may be. Nevertheless, we consider it of some value to use our result in a semi-empirical way, by attributing to a_0' values that is a suitable function of temperature.

The last value of -19.557×10^5 for a_0' in

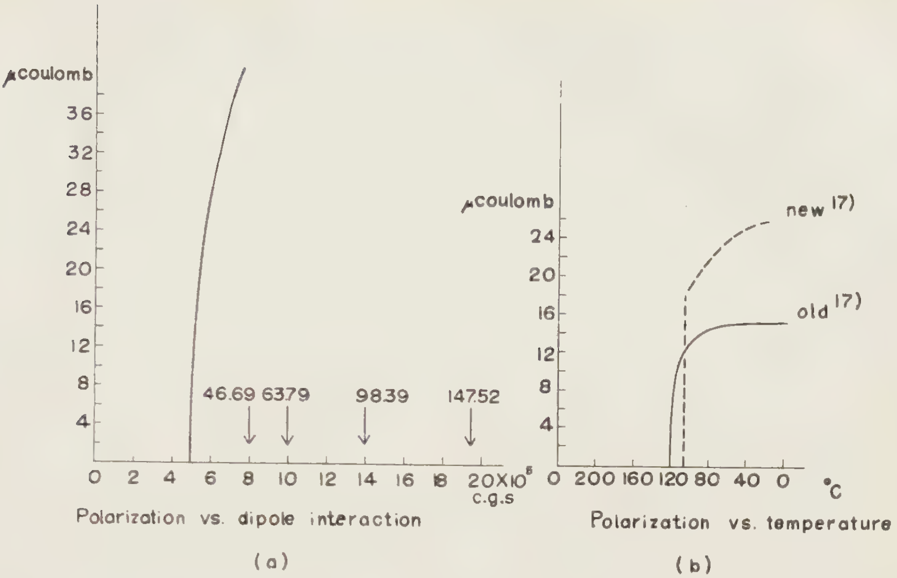

Fig. 6.

Table 1 corresponds to the value calculated from the simple dipole model with a charge $+4e$ of the Ti ion. The ionic shift for this value 0.6574Å is, however, much too large compared with H.T. Evans' 0.156Å for the shift of Ti ion relative to Oa ion at room temperature14)*. In order to reproduce the observed value 0.156Å one must assume the effective charge of Ti ion to be 2.06**, which corresponds to $a_0'=-5.2\times10^5$. The corresponding tetragonality $\Delta_a-\Delta_b$ will be found to be about 2% from Fig. 3 (a), which may be compared with the observed value of about 1%1)2)3)***

From the fifth column of the Table 1 we obtain the volume change 0.37% for $a_0'=-5.2\times10^5$ as the difference between the tabulated volume and that for $a_0'=-4.941\times10^5$. This can be compared with the experimental values 0.225%, which is obtained as the difference between the real volume at room temperature and that extrapolated from the values for the cubic phase (above 120°C)1)2)3). If, on the other hand, we take the effective charge so as to give the observed tetragonality 1%1,2,3), the volume difference is obtained as 0.268%, in better agreement with the experimental data.

Looking at Fig. 2(a), 3(a) and 4(a) you will notice the existence of the maxima in the lattice deformation Δ_a, tetragonality $\Delta_a-\Delta_b$ and volume $\Delta_a+2\Delta_b$ so that these quantities begin to decrease for very strong dipole interaction. This is perfectly understandable since the direct effect of dipole interaction is to make the lattice contract and less deformable. However, it is doubtful whether these parts of the curves have any real significance.

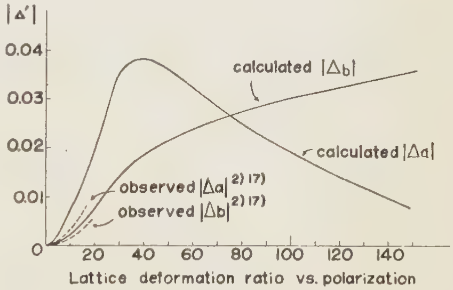

Fig. 7. The nnit of palarization is μ coulomb. See also Table II.

We can also evaluate the spontaneous polarization as tabulated in Table 2 using the ionic shift of Ti in Table 1. Fig 6(a) shows the polarization vs. the dipole interaction, which gives the result that the polarization is about 17μ coulomb/cm^2 corresponding to the dipole interaction -5.2×10^6. This may be compared with the observed data Fig. 6(b), that is, 15μ coulomb/cm^2 (old) or 26μ coulomb/cm^2 (new) at room temperature by W.J. Merz[17]. Fig. 7 shows the magnitude of the deformation ratio vs. polarization, in which the theoretical values may be compared with the observed data[2][16] near the origin of the coordinates*.

---

* Recent measurement of Ti shift relative to Oa with neutron diffraction by Frazer, Danner and Pepinsky15) is in agreement with 14). The data have been communicated by G. Shirane to the authors.

** This effective charge has been used, in somewhat inconsistent way, for the dipole interaction, whereas we have regarded the charge always as 4 (constant) for calculating the Madelung lattice energy.

*** The data using the electron diffraction by M. Anliker, H. R. Brugger, and W. Känzig show the anomalous behavior at the surface of extremely small particle, the tetragonality being 1.5% these16). The authors are indebted to W. Känzig for his suggestion.

Logically our calculation is valid only at the absolute zero, since we have entirely neglected the thermal motion. Since, however, the real crystal is polarized in (111) direction at 0°K, we should have to consider the spontaneous polarization in that direction with the accompanying deformation into rhombohedral lattice. The calculation in this direction is now in progress.

The work was supported by the Grant for Scientific Researches from Education Ministry.

References

1) S. Miyake and R. Ueda: Jour. Phys. Soc. Japan **2** (1947) 93.
2) H. D. Megaw: Proc. Royal Soc. London **A 189** (1947) 261.
3) H. F. Kay and P. Vousden; Phil. Mag. (7) **40** (1949) 1019.
4) M. Born: Ann. d. Phys. **61** (1919) 87.
5) A. F. Devonshire: Phil. Mag. **40** (1949) 1040.
6) R. H. Fowler: "*Statistical Mechanics.*"
7) E. Sawaguchi: Lecture in the annual meeting of the Phys. Soc. of Japan Apr. 1954 in Tokyo.
8) L. W. McKeehan: Phys. Rev. **43** (1933) 913.
9) H. Takahashi: unpublished.
10) Y. Takagi: Proceedings of the International Confecence of Theoretical Physics Sep. 1953, in Kyoto.
11) W. Kinase: ibid. and Prog. Theor. Phys. **13** (1955) 529.
12) J. C. Slater: Phys. Rev. **78** (1950) 748.
13) P. W. Anderson and W. Shockley: unpublished. This value was also used in 12).
14) H. T. Evans: Acta Cryst. **4** (1951) 377.
15) Frazer, Danner and Pepinsky: unpublished.
16) M. Anliker, H. R. Brugger and W. Känzig: Helv. Phys. Acta, **27** (1954) 99.
17) W. J. Merz: Phys. Rev. **76** (1949) 1221; **91** (1953) 513.

---

* The authors are indebted to S. Sawada for his suggestion about the polarization.

JOURNAL OF THE PHYSICAL SOCIETY OF JAPAN Vol. 10, No. 11, NOVEMBER. 1955

Statistical Properties of Lattice Chains*

By E. TERAMOTO, M. KURATA**, R. CHÛJÔ, C. SUZUKI,
K. TANI*** and T. KAJIKAWA***
Department of Physics, Kyoto University, Kyoto

(Received July 25, 1955)

The statistical problems of chains are divided into three classes i.e. ideal type, real type and production type, and these three types of the chain problems are investigated by the use of relatively short lattice chains. We performed the complete enumeration of the dimensions of two-dimensional square lattice chains up to the bond number $N=20$ and three dimensional simple cubic lattice chains up to $N=8$. As for the mean square end-to-end distance $\langle R_N{}^2\rangle$, we obtained the results that the chains of real type have always larger values of $\langle R_N{}^2\rangle/N$ than that of the chain of production type and its value seems to diverge as $N\to\infty$. The distribution of the end-to-end distances has a form which appreciably deviates from that of Gaussian distribution. A study also is made on the total number of configurations of lattice chains.

§1. Introduction

Previously one of the present authors and M. Yamamoto[1] developed the statistical mechanical theory of a long chain molecule in two ways, using the pearl necklace model and obtained the same expression of the mean square end-to-end distance

$$\langle R^2{}_N\rangle=Na^2\left[1+\frac{4}{3}\sqrt{\frac{6}{\pi}}\left(\frac{b}{a}\right)^3\sqrt{N}+\cdots\right] \tag{1}$$

where N is the number of bonds, b is the diameter of bead and a is the bond length. Similar results which show that the value of the ratio $\langle R^2{}_N\rangle/N$ does not converge as $N\to\infty$, were also obtained by many authors[2]. While J.J. Hermans, M.S. Klamkin and R. Ullman[3] obtained the expression of the mean square end-to-end distance which is proportional to N even when the volume effects are taken into consideration. In order to clarify the discrepancy of these results on one hand and on the other hand to examine the statistical properties of the chains in which the volume effects are taken into account, we classify the statistical problems of chains into three classes and perform the complete enumeration of the dimensions of the lattice chains. The lattice chain used in this calculation are as follows;

(a) Two-dimensional square lattice chains in which the bond angles are restricted only to 90°,

(b) Two-dimensional square lattice chains in which the bond angles 0°, 90° and 180° are taken with equal probability,

(c) Three-dimensional simple cubic lattice chains in which the bond angles are 90°.

Chains (a) and (b) are examined by writing down all configurations on cards up to the bond number $N=20$ in (a) and $N=8$ in (b). For chains (c), the coordinates of each bond in all configurations are noted down in tables up to the bond number $N=8$. Using these cards and tables we can evaluate the statistical quantities of these lattice chains. In our calculations, we adopted three classes of the chain problems which will be presented in the next section and it will be shown that the results obtained here are also mutually distinguished.

Recently the similar investigations have been done by several authors[4] using the high speed digital computers and similar results have been obtained. Though they could treat relatively longer chains than ours, inevitably they could not give the exact informations because of the statistical method of computation adopted in their investigations. So that it seems worth while to present here our results in spite of its restriction to the relatively short lattice chains.

---

* A part of the contents of this paper was previously read by one of the present authors at the International Conference of Theoretical Physics held at Kyoto in 1953; *Proceedings of the International Conference of Theoretikal Physics*, (1953), 410.

** Department of Industrial Chemistry, Kyoto University.

*** Department of Chemistry, Kyoto University.

§ 2. Classification of the Chain Problems

In the first place we shall make a remark about the classification of the chain problems. It seems that various chain-like problems can be classified into three types and these three types of the problems must be distinguished one another from the physical and mathematical points of view. The three types are defined as follows;

(I) *Ideal Type* (Markoff Chain) This class involves such problems as random walk problem, diffusion problem and statistical mechanical problems of a chain molecule with zero volume or with the interactions of finite order. A common characteristic of this type of problems is that mathematically they can be exactly reduced to the simple Markoff chain problem.

(II) *Production Type* We shall consider a chain molecule and assume that this chain is produced by attaching one bond after another consecutively in such a way that these bonds do not overlap one another, then we are concerned only with the probability distribution of their configurations which appear just after all attachments of bonds have finished and a complete chain has been formed. The chain which was used in Hermans' paper seems to belong to this class, and he treated this type of chain approximately as a Markoff chain and obtained the mean square end-to-end distance which is again proportional to N just as in the case of ideal type. Mathematically this type of chain is not exactly Markoffian but it may be reduced approximately to it.

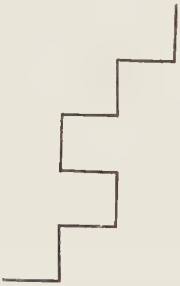
Fig. 1.

(III) *Real Type* In this case the complete chains really exist in advance and they have complete interactions or complete volume interferences. So that this is just the case of real chain molecules. This kind of chains have no longer the properties of Markoff chain.

We shall present an example which will visualize this classification a little more clearly. In Fig. 1 a configuration of the two-dimensional square lattice chain with ten bonds and bond angle 90°, is shown. If the configuration given by Fig. 1 is one of the configurations of ideal random flight chain with ten bonds (or steps) in which the overlaps of bonds are being allowed, then the probability of the occurrence of this configuration is $1/2 \cdot 2^{10} = 1/2048$, because each bond can be located in two ways that is right or left side of foregoing one except the first bond which has four possible directions. Clearly the total number of possible configurations is also 2048 in this case. On the other hand, our complete enumeration shows that if the overlaps between the bonds are completely excluded, only 440 configurations are allowable. If we take the configuration in Fig. 1 as one of the configurations of the chains of production type, then its probability is given by $(1/4)\cdot(1/2)^4\cdot 1\cdot(1/2)\cdot 1\cdot(1/2)^2=(1/2)^9=1/512$, since the first step goes to the right with probability one-fourth and next step goes upwards with the probability one-half and after three steps with same probability sixth step goes certainly upwards, that is, with probability unity, and so on. On the contrary, in real chain problem this probability is 1/440, because all allowable configurations are apriori equal probable.

Consequently the mean square end-to-end distance and other statistical properties calculated using these probabilities are led inevitably to different results.

§ 3. Total Number of Configurations

The total number of configurations of ideal lattice chains with N bonds Ω^0_N is obviously given by (a) 2^{N+1} for the two-dimentional square lattice chain with a bond angle 90°, (b) 4^N for the two-dimensional square lattice chain with bond angles 0°, 90°, 180° and (c) $6\cdot 4^{N-1}$ for the three-dimensional simple cubic lattice chain with a bond angle 90°. If the overlaps are completely excluded, the number of possible configurations is reduced by large amount. Table I gives the values of Ω_N in these three cases (a), (b) and (c), and in Fig. 3 log Ω_N *versus* N are plotted. From these data it is seen that Ω_N can be expressed ap-

Table I. Total Number of Configurations.
$\Omega_N{}^0$: ideal case, Ω_N: exact number, $\Omega_N{}'$: empirical formula i.e. $=3.93(1.60)^N$ in the case (a), $=1.69(2.78)^N$ in the case (b) and $=1.98(3.69)^N$ in the case (c), $\Omega_N{}^{(1)}$: first order overlaps are excluded, $\Omega_N{}^{(2)}$: first and second order overlaps are excluded.

(a) two-dimensional square lattice chain (bond angle 90°).

N	$\Omega_N{}^0$	Ω_N	$\Omega_N{}'$	$\Omega_N{}^{(1)}$	$\Omega_N{}^{(2)}$
1	4	4	(6)	—	
2	8	8	(10)	—	
3	16	16	16	—	
4	32	24	26	24	
5	64	40	42	40	
6	128	64	66	64	
7	256	104	108	104	
8	512	168	172	168	
9	1024	272	274	272	
10	2048	440	438	440	
11	4096	712	702	712	
12	8192	1128	1122	1152	
13	16384	1808	1796	1864	
14	32768	2896	2872	3016	
15	65536	4600	4592	4886	
16	131072	7352	7346	7896	
17	262144	11712	11750	12776	
18	524288	18656	18800	20672	
19	1048576	29752	30072	33448	
20	2097152	47128	48096	54120	

(b) two-dimensional square lattice chain (bond angles 0°, 90° and 180°).

1	4	4	(5)	—	—
2	16	12	(13)	12	—
3	64	36	36	36	—
4	256	100	101	108	100
5	1024	284	281	324	284
6	4096	780	780	972	804
7	16384	2188	2170	2916	2228
8	65536	5964	8201	8748	6220

(c) three-dimensional cubic lattice chain (bond angle 90°).

1	6	6	(7)	—	
2	24	24	(27)	—	
3	96	96	97	—	
4	384	360	363	360	
5	1536	1368	1336	1368	
6	6144	4992	4915	5184	
7	24576	18504	18087	19656	
8	98304	64770	66561	74520	

proximately in the form $\Omega_N=3.93(1.60)^N$ in the case (a), $\Omega_N=1.69(2.78)^N$ in case (b) and $\Omega_N=1.98(3.69)^N$ in case (c). However this linearity of log Ω_N *versus* N for large value of N perhaps is not ensured.

Furthermore in Table I (a) we can find the relation

$$\Omega_N=\Omega_{N-1}+\Omega_{N-2} \tag{2}$$

which holds for $4\leqslant N\leqslant 11$. For these numbers of bonds, the possible overlaps in their configurations are only that of first order in which four bonds form an enclosure and second order overlaps in which twelve bonds form an enclosure appear only beyond $N=12$. Actually it is not difficult to show that the relation (2) holds for the two-dimentional square lattice chains with bond angle 90°, in which only first order overlaps are excluded. We shall consider the configurations of this chain with N–1 bonds, then its end has always either of two forms (i) or (ii) in Fig. 2. Let

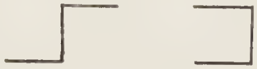

Fig. 2. (i) (ii)

Ω'_{N-1} and Ω''_{N-1} be the number of configurations in which the ends have respectively the form (i) and (ii). By adding another bond to each end of these chains one obtains the configurations of the chain with N bonds, and it is apparent that from Ω'_{N-1} configurations of N–1 bonds either type of configurations can be formed but from Ω''_{N-1} configurations only that of type (i) are derived, namely the relations $\Omega'_N=\Omega'_{N-1}+\Omega''_{N-1}=\Omega_{N-1}$ and $\Omega''_N=\Omega'_{N-1}$ hold. Then we can write these relations in a form $\Omega_N=\Omega'_N+\Omega''_N=\Omega_{N-1}+\Omega'_{N-1}=\Omega_{N-1}+\Omega_{N-2}$.

In just the same manner we can derive a similar recurrence formula in the case of three dimensional simple cubic lattice chain with a bond angle 90° in the form

$$\Omega_N=3\Omega_{N-1}+3\Omega_{N-2}\,, \tag{3}$$

which is valid only when the first order overlaps (4-bonds enclosures) are excluded. As for the two dimensional square lattice chains with bond angles 0°, 90° and 180°, the first order overlap is to be taken as the turning back of bond and the 4-bonds enclosure corresponds to the second order overlap in this case. The reccurrence formula of this type of chains which holds when the overlaps are excluded up to the second order, is given by

$$\Omega_N=2\Omega_{N-1}+2\Omega_{N-2}+\Omega_{N-3}\,. \tag{4}$$

These difference equations (2), (3) and (4)

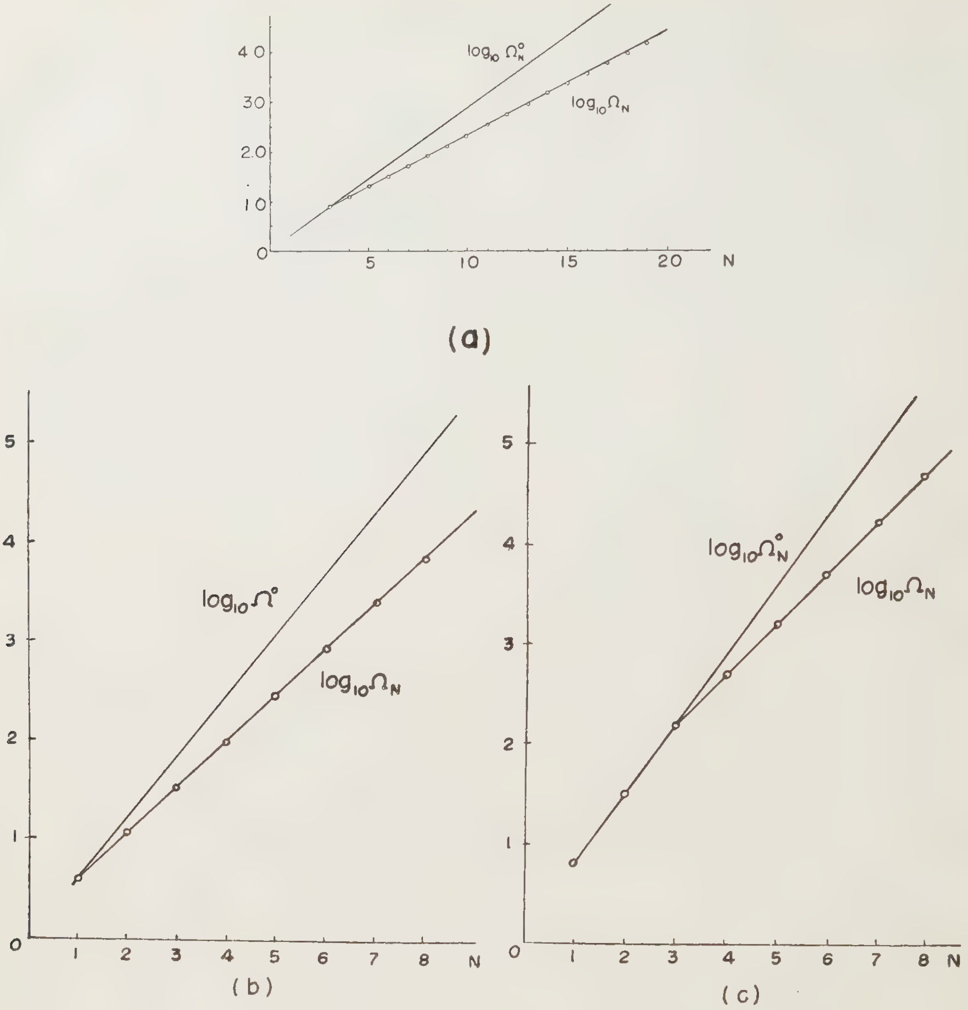

(a)

(b)

(c)

Fig. 3.

can be solved and we obtain the results

$$\Omega_N=3.578\times1.618^N \tag{5a}$$

$$\Omega_N=1.743\times2.836^N \tag{5b}$$

$$\Omega_N=1.743\times3.791^N \tag{5c}$$

where (5a), (5b) and (5c) correspond to the cases (a), (b) and (c) mentioned in the earlier part of this section. The agreement of these results with our data means that in our relatively short lattice chains volume effects of higher order are negligible.

§ 4. Distribution of End-to-end Distances

As is well known, in the case of the ideal chain, the probability distribution of the end-to-end distances of two-dimensional square lattice chains with a bond angle 90° is given by the Bernoulli distribution;

$$P^0{}_N(R)=\sum_{x^2+y^2=R^2}\frac{N_x!}{\{\frac{1}{2}(N_x+x)!\}\{\frac{1}{2}(N_x-x)!\}}\times\frac{N_y!}{\{\frac{1}{2}(N_y+y)!\}\{\frac{1}{2}(N_y-y)!\}} \tag{6}$$

where N_x and N_y represent the number of bonds in x and y directions respectively, and then $N_x+N_y=N$, and the bond length is assumed to be unity. When the bond numbers N_x and N_y are sufficiently large the distribution function (6) can be approximated by $4\pi R^2$ times the Gaussian distribution. In Fig. 4 the distribution function (6) is shown. For other two types of lattice chains (b) and (c), the similar expressions can be obtained in the ideal case.

In each of our cards the coordinates of the end point and the probability of that configu-

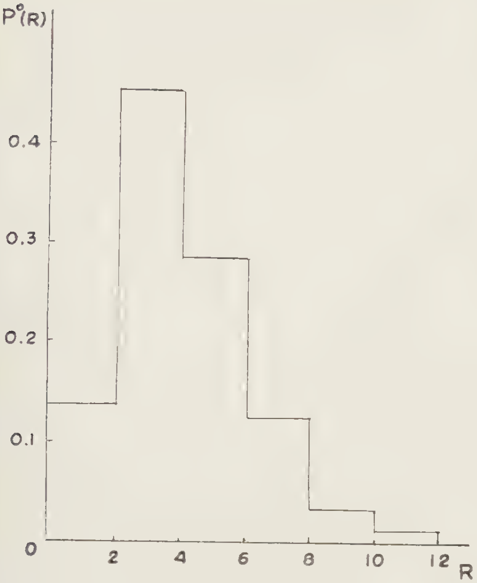

(N = 17)

Fig. 4.

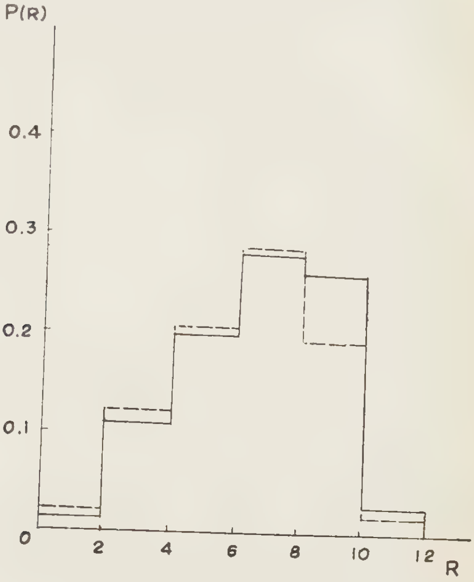

(a) (N = 17)

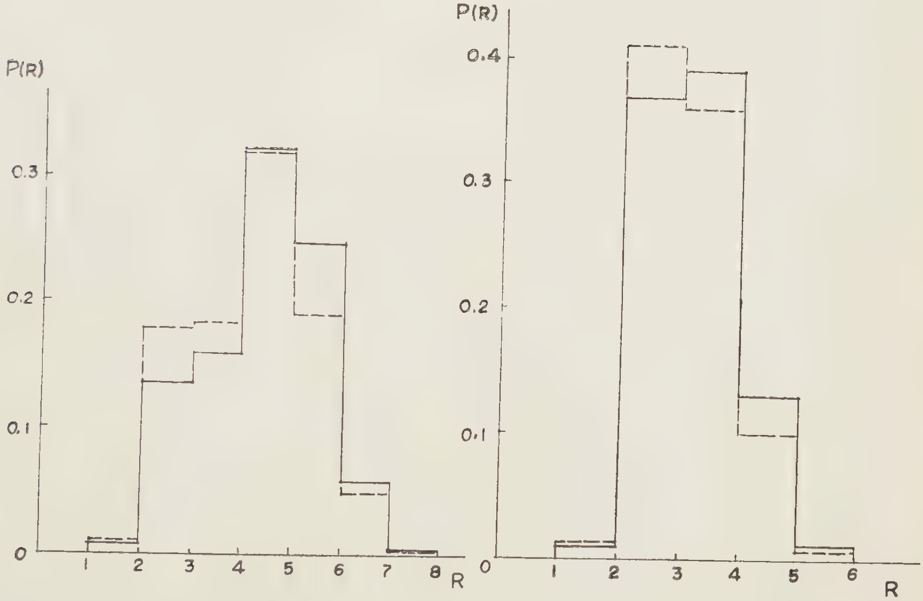

(b) N = 8 (c) N = 8

Fig. 5.

ration calculated by means of production type are indicated. By counting these cards we can find directly the probability distribution for both types of chains, real and production type, which are schematically shown in Fig. 5 (a), 5 (b) and 5 (c) respectively for the chains of types (a), (b) and (c). In these figures the solid line represents the case of real type and the broken line corresponds to the case of production type. Comparing the figures 4 and 5 (a), it is seen that these two curves have nearly the same form which differs essentially from that of Gaussian distribution of ideal chain. However, in detail, these two curves differ from each other and in the case of production type smaller values

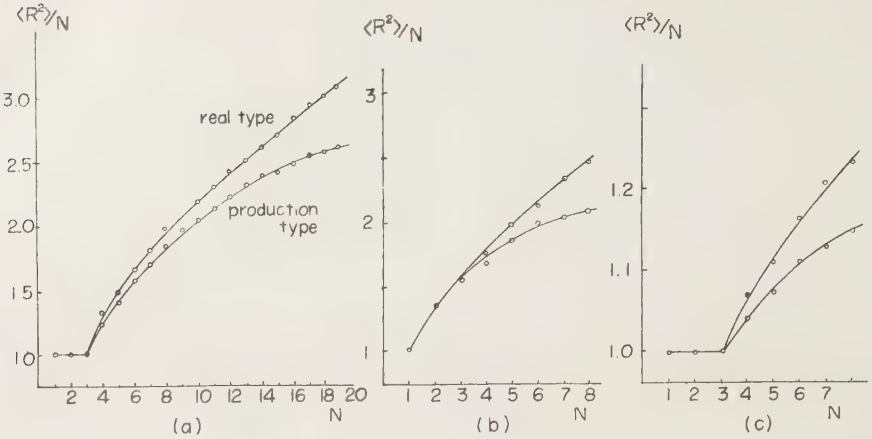

Fig. 6.

of end-to-end distances are preferable compared with the case of real type. This feature is easily recognized if we remember the manner of evaluation of the probability in the case of production type, which was stated in § 2, namely the smaller the end-to-end distance is, the more bonds are restricted to go to one direction and so the more factors 1 enter into the probability of such configurations.

Consequently it may be doubtful to represent the volume effects of the chain molecules only through the change of effective length of the chain elements, and the essential improvement of distribution function may be necessary.

§ 5. Mean Square End-to-end Distances

We have already obtained the probability distribution function of the end-to-end distance in the last section, then with the use of these data we can evaluate the mean square end-to-end distances in each case. The results are shown in Fig. 6 (a), (b) and (c). From Fig. 6 it becomes clear that the mean square end-to-end distance in the case of real type is always larger than that of production type, so that even if the value of $\langle R^2_N\rangle/N$ converges as $N\to\infty$ in the case of production type as stated by Hermans, the convergence of that of real type can not be asserted.

By our theoretical investigations of pearl necklace model, the mean square end-to-end distance is given by

$$\langle R^2_N\rangle = Na^2\left[1+\frac{1}{2}N\left(\frac{b}{a}\right)^3+\cdots\right] \quad (7)$$

in two-dimensional case, contrary to the equation (1) in three-dimensional case. However, these theoretical results give only the upper bound of N dependence, so that if the exact results are obtained in future, exact N dependence of $\langle R^2_N\rangle/N$ for large value of N would appear in the region between constant and $\sqrt{N}$ in three-dimensional case and in the region between $\sqrt{N}$ and N in two-dimensional case.

§ 6. Distribution of the Chain Elements

Lastly we shall present two data about the distribution of the bonds (or segments) which are examined using two-dimensional square lattice chain with bond angle 90° and bond number $N=17$.

(i) *distribution of bonds from one end of chain*

Let h_j be the distance of the end point of j-th bond from one end of the chain which consists of $N=17$ bonds. We examined the distribution of the distance h in such a way as follows. Concentric circles of the radii 2, 4, 6, 8, 10 and 12 whose center is at an end of the chain are written on our cards and the total number of the end points of bonds involved in each domain which is divided by these circles are computed for all possible configurations. The results are tabulated in Table II.

(ii) *mean square distance of bonds from the center of mass*

It is somewhat cumbersome to evaluate completely the mean square distance of bonds from the center of mass using all possible configurations. We adopted the method of random sampling in which about one-tenth of

Table II.

h	0~2	2~4	4~6	6~8	8~10	10~12	12~	total
number of bonds	3780	8054	7405	4286	1436	52	1	25014
probability	0.151	0.322	0.296	0.171	0.058	0.002	—	1

Table III.

s	0~1	1~2	2~3	3~4	4~5	5~6
probability	0.118	0.313	0.302	0.186	0.077	0.004

configurations are randomly picked up from each class of possible configurations which are divided into seven classes by the end-to-end distance i.e. $R=0\sim2$, $2\sim4, \cdots$, $12\sim14$. We computed the mean square end-to-end distance of this sample, and we obtained $\langle R^2\rangle=48.81$ which agrees with the exact value sufficiently well and also this sample gives almost the same distribution of distance h with exact one.

The probability distribution of the distance of bonds from the center of mass s is shown in Table III, and the mean square distance $\langle s^2\rangle=6.58$ contrary to that of ideal chain $\langle s^2\rangle=\langle R^2\rangle/6=2.33$, and for the ratio $\langle R^2\rangle/\langle s^2\rangle$ we obtain the value 7.41 from our data.

References

1) E. Teramoto: Busseiron Kenkyu (in Japanese) **39** (1951) 1, **40** (1951) 18, **41** (1951) 14.
M. Yamamoto: Busseiron Kenkyu **44** (1951) 36.
E. Teramoto: *Proceedihgs of the International Conference of Theoretical Physics Kyoto and Tokyo, September* (1953) 410.

2) R. J. Rubin: J. Chem. Phys. **20** (1952) 1940.
T. B. Grimley: J. Chem. Phys. **21** (1953) 185.
F. Bueche: J. Chem. Phys. **21** (1953) 205.
H. M. James: J. Chem. Phys. **21** (1953) 1628.
B. H. Zimm, W. H. Stockmayer and M. Fixman: J. Chem. Phys. **21** (1953) 1716.
N. Saito: J. Phys. Soc. Japan **9** (1954) 780.

3) J. J. Hermans, M. S. Klamkin and R. Ullman: J. Chem. Phys. **20** (1952) 1360.

4) F. T. Wall, L. A. Hiller and D. J. Wheeler: J. Chem. Phys. **22** (1954) 1036.
F. T. Wall, L. A. Hiller and W. F. Atchison: J. Chem. Phys. **23** (1955) 913.
M. N. Rosenbluth and A. W. Rosenbluth: J. Chem. Phys. **23** (1955) 356.

Journal of the Physical Society of Japan Vol. 10, No. 11, November, 1955

The Mechanism of Internal Friction due to the Motion of the Dislocation

By Tokutaro HIRONE, Nobuhiko KUNITOMI

Research Institute for Iron, Steel and Other Metals,
Tohoku University, Sendai, Japan

and Masajiro ABE

Faculty of Liberal Arts and Science, Yamagata University,
Yamagata, Japan

(Received June 24, 1955)

The mechanism of internal friction due to the motion of dislocation was studied from the measurement on the variation of internal friction with cold-work. For copper, internal friction increases with the initial cold-work and decreases after showing a maximum. Since the features do not depend on the frequency used in the experiment at room temperatures, the internal friction due to dislocations is concluded to be originated from the static hysteresis which is proposed by Nowick.

§ 1. Introduction

It has hitherto been known that the origins which give rise to internal friction may be classified into the following two categories[1]. The one is the viscous mechanism and the other is the non-viscous one. In the former case, internal friction originates from the relaxation between stress and strain as a consequence of the appearance of dissipation terms such as the first time derivatives of stress and strain in the equation of motion of the substances. Generally, this type of internal friction is characterized by amplitude independence and frequency dependence. For instance, the mechanism which is called anelasticity is a typical example of this case. On the other hand, internal friction is not accompanied by the stress-strain relaxation in the non-viscous case. It is attributed to the formation of hysteresis loop in the static stress-strain diagram. Since this mechanism is not a relaxation, it is independent of vibrational frequency but dependent on strain amplitude. For instance, internal friction due to magnetomechanical hysteresis in ferromagnetic substances belongs to this category.

It has been known from a number of theoretical and experimental studies that internal friction in single crystals is associated with the motion of dislocations. At present, however, two different interpretations on the mechanism of internal friction due to the motion of dislocations have been considered, corresponding to the two mechanisms described above.

The first is that proposed by Koehler[2] assuming the viscous motion of pinned dislocation, and the second is that proposed by Read[3] and Nowick[4], assuming the appearance of a static hysteresis loop in the stress-strain curve which arises from the motion of dislocation. Since these two theories have been able to explain respective experimental results without any contradiction, it is difficult to conclude clearly at present which of them is valid. Therefore, the authors have intended to solve this problem by measuring the internal friction on metal single crystals.

§ 2. Theoretical Conclusions Predicted from Viscous and Non-viscous Motion of Dislocation

Since it has been shown experimentally that internal friction is strikingly structure sensitive, it is difficult to give a physical meaning to its absolute value[4]. Therefore, in order to interpret experimental results theoretically, it is necessary to measure the internal friction as a function of some physical parameter and compare the results with the relation predicted theoretically. Generally, amplitude, frequency and temperature are used as such parameters, and for special substances, magnetization, degree of precipitation, degree of order, etc. are used according to the purposes. Since we are now concerned with the investigation of the motion of dislocation, the degree of cold-work was used as the parameter as it can be related directly to the number of dislocations.

Variation of internal friction with the degree of cold-work has been obtained theoretically by Koehler and Weertman[5] for the case of viscous mechanism. According to them, the equation of motion for a unit length of dislocation can be written as

$$M\frac{d^2x}{dt^2}+B\frac{dx}{dt}+(GN+G_0)x=F\cos\omega t \qquad (1)$$

where M is the effective mass of dislocation per unit length, $B\frac{dx}{dt}$ is the dissipative force per unit length, $F\cos\omega t$ is the applied force on the dislocation, G_0x is the restoring force of pinned dislocation, GNx is the restoring force due to the interaction of other dislocation, N is the number of dislocation per unit volume, and x is the average displacement of the dislocation loop from the equilibrium position. Solving Eq. (1) and taking into account the condition $G\gg M\omega^2$, which has been obtained by using the effective mass M introduced by Frank[6], one finds that internal friction $\varDelta$ is

$$\varDelta=\frac{(\pi/16)Ea^2NB\omega}{(G_0+GN)^2+B^2\omega^2} \qquad (2)$$

where E is the Young's modulus and a the interatomic distance. It has been found from this equation that the internal friction vanishes, when N is equal to zero, and that it rises with increasing N until it reaches a maximum and then decreases again. The maximum value of internal friction is

$$\varDelta_m=\frac{\pi Ea^2N_mB\omega}{32(GG_0N_m+G^2N_m^2)} \qquad (3)$$

where N_m is the dislocation density at maximum internal friction, and is given by the equation

$$GN_m^2=G_0^2+B^2\omega^2 \qquad (4)$$

It should be noticed from Eq. (3) and (4) that both $\varDelta_m$ and N_m increase monotonously with frequency at which they are measured but are independent of amplitude.

In the following, we shall investigate the behavior of internal friction for the static hysteresis mechanism. Since internal friction is not accompanied by relaxation in this mechanism, the equation of motion of dislocation for equilibrium state may be used. Suppose that the force acting on a dislocation under applied stress be denoted by F, and the restoring force be the same as in the viscous case, then we get the equation

$$F=(G_0+GN)x' \qquad (5)$$

where x' is the displacement corresponding to x in the preceeding case. According to experimental result of Read, Nowick and others, internal friction of metal single crystals may be represented by the equation

$$\varDelta=A+Bx^2 \qquad (6)$$

where A and B are constants varying from specimen to specimen. Since the internal friction of the substance is presumed to be caused by dislocations, an equation similar to (6),

$$\varDelta'=A'+B'x^2 \qquad (7)$$

is applicable for internal friction of a dislocation, where A' and B' are constants corresponding to A and B in Eq. (6), respectively. Substituting Eq. (5) into (7), internal friction arising from motion of a dislocation is given by the eqation

$$\varDelta'=A'+\frac{B'F^2}{(G_0+GN)^2} \qquad (8)$$

Thus the total internal friction is given by

$$\varDelta=A'N+\frac{B'F^2N}{(G_0+GN)^2} \qquad (9)$$

The first term in this equation increases monotonously with N, and the second term is a function which reaches a maximum value when N is equal to G_0/G. It should be noted from Eq. (9) that internal friction is independent of frequency but depends on amplitude. Since the internal friction for both viscous and non-viscous mechanisms are shown to vary similarly with respect to cold-work, the mechanism of internal friction cannot be determind from the measurement on the variation of internal friction by cold-work. For this purpose, it is desirable to measure the dependence of internal friction on other physical variables, for example, amplitude or frequency. Many experimental investigators[3][4] have shown that internal friction of metal single crystals increases linearly with the square of amplitude so long as the amplitude used is small. This fact can be explained quantitatively for the non-viscous mechanism by making proper assumptions as to the shape of the static hysteresis curve. For the viscous case, a qualitative explanation can be given by assuming that the pinned dislocation was released from the pinned position with increasing strain amplitude, in other words, by assuming that G_0 in Eq. (1) decreases with strain. On the other hand, it follows from the preceeding considerations that internal friction is independent of frequency for the non-viscous mechanism, while, it varies with frequency for the viscous mechanism. It is obvious from Eq. (3) in the last section that Δ_m increases linearly with the frequency in the viscous case, since the condition $G \gg B\omega$ seems to be valid in the frequency range at which measurements are carried out. In addition to the above viscous mechanism proposed by Koehler and Weertman, another mechanism in which the thermoelastic effect is assumed has been proposed by Eshelby[7]. In this case, internal friction will have a maximum at a frequency predicted by Zener's theory[8]. Therefore, from the fact described above, one can distinguish between viscous and non-viscous mechanisms by investigating the frequency dependence of internal friction. In order to determine the preferential mechanism from the frequency dependence of internal friction, it is desirable to cover a wide frequency range as possible. Generally, three modes of vibration, namely, longitudinal, transversal and torsional vibrations are used for the measurement of internal friction. Each of them covers a frequency range of about 10^4 to 10^5 cps., 10^2 to 10^3 cps., and 10^{-1} to 10^0 cps., respectively. Hence, in order to cover a wide frequency range from 10^{-1} to 10^5 cps., it will be necessary to compare the experimental results obtained from the three different modes of vibration with each other. Many investigations[3][5][9] have been made by using longitudinal vibration, and the experimental result of internal friction for torsional vibration will be published in the other paper[10]. Hence the authors performed measurements by using transversal vibration which remains uninvestigated.

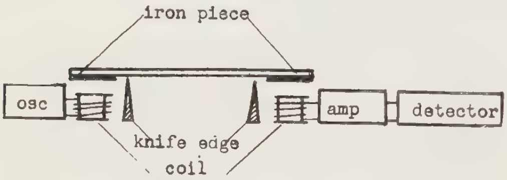

Fig. 1. Schematic diagram of the apparatus for transversal vibration method of measurement of internal friction.

§ 3. Specimens and Experimental Procedure

Specimens of single crystals of aluminum and copper used in this investigation were made by Bridgman's method from 99.99% Al and 99.9% Cu. These single crystals are narrow thin plates whose lengths, widths and thicknesses extend over 15 to 20 centimetres, 8 to 11 milimetres, and 1 to 2 milimetres respectively.

The measurement of internal friction were performed by an apparatus similar to Zener's[11] and is illustrated schematically in Fig. 1. The specimen was supported at two nodes of resonant vibration on knife edges, and small iron pieces attached at both ends of the specimen. Two coils, one of which was used to drive vibration and another to receive it, were set under the iron pieces. The former was connected with an oscillator in order to exite the specimen electromagnetically, and the latter was connected with an electronic voltmeter proceded by an amplifier by which the amplitude of mechanical vibration was received and observed. We measured the resonance curve by using fundamental vibration, the frequency of which extends over 200 to 400 cps., and calculated Q^{-1} from the following equation

$$Q^{-1} = \frac{\omega_2 - \omega_1}{\omega_r}$$

where ω_r is the resonant angular frequency of the specimen, and $\omega_2 - \omega_1$ is the width of the resonance curve at half maximum. We adopted Q^{-1} as a measure of internal friction.

To obtain sufficient sensitivity, the distance between the iron pieces and coils were kept as small as possible. We, then, performed the preliminary measurement in vacuum in order to estimate the order of magnitude of background internal friction resulting from the viscosity of air. Internal friction of the aluminum specimen No. 1, which was non cold-worked, decreased to 6.1×10^{-3} in vacuum of about 10^{-4} mm Hg, while it was 6.3×10^{-3} in atomospheric pressure. This implies that the contribution from the air damping effect is of the order of 10^{-4}. Since this amount was small compared with expected variation with cold-work, the measurements were made always in air for simplicity.

§ 4. Experimental Results

The variation of internal friction with cold-work were measured for the single crystals aluminium and copper. The degree of cold-work is expressed in terms of the rate of elongation, namely the percentage ratio of the amount of elongation divided by the original length of the specimen.

(1) *Aluminum*

Specimen No. 2 was annealed at about 350°C for 16 hours before the measurement of internal friction, while specimen No. 1 was not annealed. Each specimen was kept at room temperature for about 24 hours after every cold-work and recovery of internal friction at room temperature was measured every hour. Under the assumption that the recovery takes place exponentially, the experimental curves of recovery were calculated by the least square method. A typical curve, which is for the case of 4.0 percent cold-work of specimen No. 1, is shown in Fig. 2. In some cases, experimental values lie in the calculated exponential curve as in this case, while others exhibit considerable deviation. Although the exponential law is not always valid for all cases, it can be concluded that remarkable recovery is observed after cold-work.

The variation of internal friction with respect to the degree of cold-work is shown in Fig. 3. The values of internal friction plotted here correspond to those at 300 minutes after clod-work for specimen No. 1, and those at 200 minutes for specimen No. 2. The stress* versus elongation curves are shown in Fig. 4. Although the absolute magitudes are not identical, nearly the same feature are found for different specimens. Namely, internal friction of aluminum single crystals increases rapidly with the initial cold-work, and decreases after a sharp maximum, then increases again slowly with further cold-work. The maximum values of internal friction are 1.74×10^{-2} and 1.15×10^{-2} for the specimen No. 1 and No. 2 and the degree of cold-work corresponding to them are 2.0% and 1.9%, respectively. One cause of the discrepancy of the two specimens with regard to the maximum value of internal friction is attributed to the difference of the strain amplitude used for

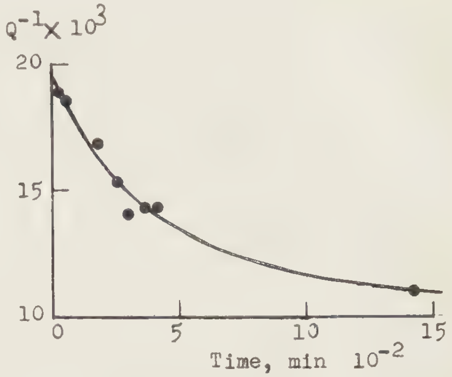

Fig. 2. A typical exponential curve calculated by the least square method showing the recovery of internal friction at room temperature for aluminum single crystals.

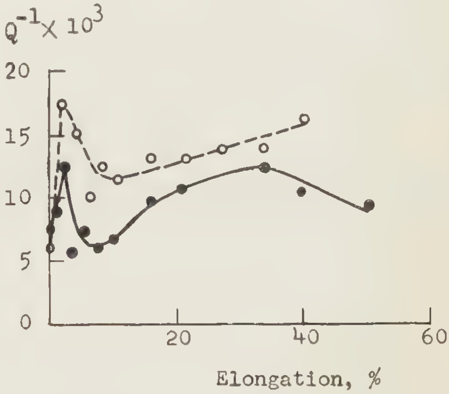

Fig. 3. Internal friction versus degree of cold-work curves for two aluminum single crystals.

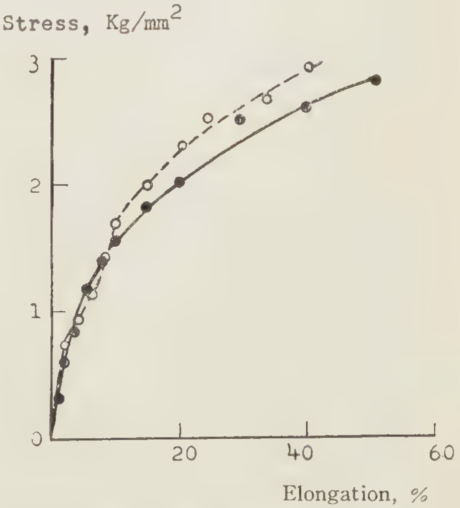

Fig. 4. Stress versus elongation curves for two aluminum single crystals.

---

* In the calculation of the stress, the decrease of cross section of the specimen with elongation was not taken into account in all cases.

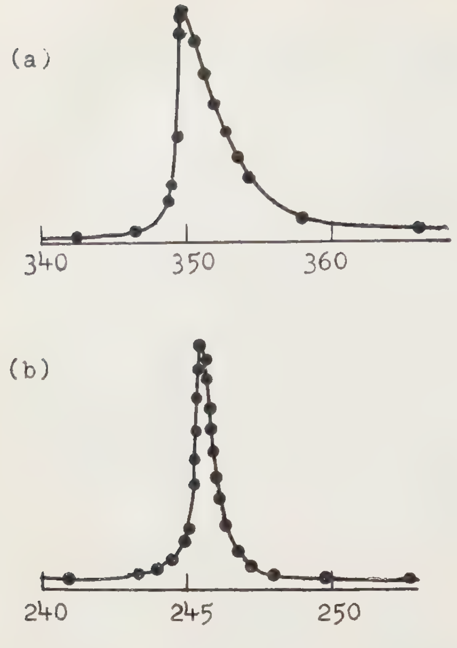

Fig. 5. Typical resonance curves strongly unsymmetrical and nearly symmetrical respectively.

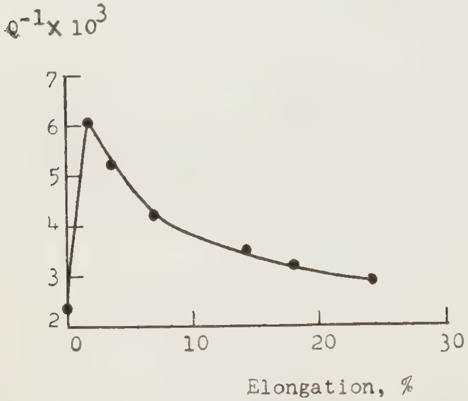

Fig. 6. Internal friction versus degree of cold-work curve for a copper single crystal.

both measurements. Their maximum values measured by microscopic method were about 8×10^{-6} for the specimen No. 1 and about 4×10^{-6} for No. 2, respectively. The strain amplitude was maintained at nearly the same value in all measurements for the same specimen. Although the amplitude dependence of internal friction was not investigated quantitively, it seems probable that the values of internal friction obtained here lie in the range where the internal friction depends on amplitude as is expected from the fact that the magnitude of strain amplitude used for the measurement is relatively large and the observed resonance curves are more or less asymmetrical. As a typical example of strongly asymmetrical resonance curves, the resonance curve for the non-cold-worked aluminum specimen No. 1 is shown in Fig. 5 (a).

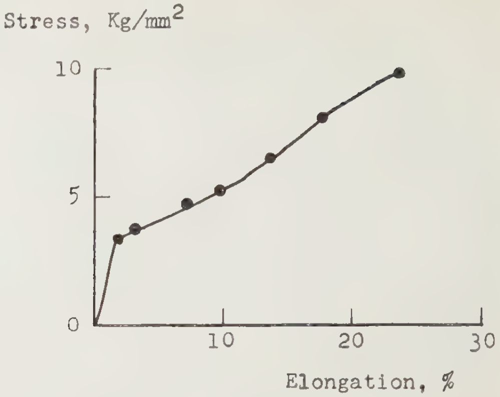

Fig. 7. Stress versus elongation curve for a copper single crystal.

(2) *Copper*

The specimen was annealed at 640°C for about 15 minutes, and etched by dilute aqua regia before measurements. The recovery effect at room temperature was measured continually over a duration of about 5 hours. However, no appreciable effect was found within this duration in contrast to the case of aluminum. The maximum strain amplitude used for the measurement was about 2×10^{-6}. Since the observed resonace curves are more symmetrical than the case of aluminum, it can be concluded that the amplitude dependence of this system is less than the latter, but it cannot be determined whether it is caused by the essential difference between copper and aluminum or by the difference of the amplitude employed.

The internal friction versus degree of cold-work curve is shown in Fig. 6. Because the recovery at room temperature was very small, the mean value of the measured values for 5 hours were plotted. The stress* versus elongation curve is shown in Fig 7. It was found that the internal friction of copper single crystal increases rapidly with increasing degree of cold-work, making maximum at 1.8 percent elongation. This maximum value

---

* See the foot note in p.

Table I.

	Longitudinal vibration	Transversal vibration	Torsional vibration
The degree of cold-work at which internal friction makes a maximum	1∼10% elongation	1.8% elongation	
The maximum value of internal friction	$3\sim10\times10^{-3}$	6×10^{-3}	$4\sim5\times10^{-3}$

of internal friction is 6.3×10^{-3}. After the maximum, it decreases rapidly as the cold-work increases, until it reaches a fairly constant value which is above the initial value.

§ 5. Discussion

Hasiguti and Hirai[9] have measured the dependence of internal friction with cold-work for single crystals of copper and aluminum by longitudinal vibration of about 20 kcps., and one of the present author[10] has made a similar experiment using torsional vibration at about 1 cps. Therefore, it is possible to determine the frequency dependece of the initial friction in the range 10^{-1} to 10^{5} cps. from the results of the above two experiments and the present one. Firstly, comparison was made for the case of copper. It was found that the internal friction shows a similar qualitative behavior with respect to the degree of cold-work in this frequency range, that is, in every case it makes a maximuim by the initial cold-work, then decreases again with increasing degree of cold-work and tends to approach a final value. Qualitatively this behavior is expected from the theoretical equations (2) or (9). In Eq. (9) which is applicable to the static hysterisis mechanism, internal friction contains a term which increass linearly with the dislocation density N, whereas such a behavior is not observed in the measurements. One might interpret this result as due to the fact that the 1st term of Eq. (9) is small compared with the 2nd term. The experimental features are also well explained Eq. (2) as was shown by Koehler and Weertman. We then compare the frequency dependence of two quantities, namely the degree of cold-work at which internal friction makes a maximum and the corresponding maximum value of internal friction Δ_m, in order to determine a more adequate mechanism to explain the measured results. The values are shown in Table I. The absolute value of cold-work corresponding to the maximum internal friction cannot be determined directly from the values in Table I, because it depends on the orientation of the crystallographic axis and on the type of applied cold-work. It should be noted, however, that maximum internal friction occurs for all cases by a slight cold-work. On the other hand, maximum internal friction Δ_m are well in accord with each other quantitatively in all cases. Consequently, it may be concluded that as far as we are concerned with copper single crystal, the variation of internal friction with cold-work will be independent on the frequency employed in the frequency range 10^{-1} to 10^{5} cps. which covers torsional, transversal and longitudinal vibrations. According to the preceeding theoretical consideration, it is expected that the maximum value of internal friction Δ_m must increase linearly with increasing degree of cold-work in the viscous mechanism; contrariwise, both the degree of cold-work at which the internal friction makes a maximum and the corresponding maximum value must be essentially independent on frequency in the static hysterisis mechanism. Hence, it may be concluded, that the mechanism of static hysterisis will be preferable as the energy dissipation mechanism due to dislocation.

Next, similar comparisons will be made for aluminum single crystals. In three measurements, the internal friction versus degree of cold-work curves have a common feature that internal friction increases rapidly and makes a maximum at the earlier degree of cold-work. This fact can be explained quite well by both equations (2) and (9). However, the further increase at high degree of cold-work would be explained more favorably by means of Eq. (8), since it contains the first term which increases linearly with dislocation density. On the other hand, the internal friction versus degree of cold-work curves obtained by torsional vibration bears little resemblance to the one mentioned above.

Although the curves make respective maxima at the earlier degree of cold-work, the height is so small that it can be neglected compared with the further increse at heavier cold-work. The qualitative behavior of this case is that internal friction increases parabolically with the degree of cold-work. Such a behavior, as mentioned above, can be explained qualitatively to some extent by Eq. (8) in the case of static hysterisis mechanism. However, it is difficult to explain this behavior with Eq. (2) in the case of viscous mechanism. Furthermore, it should be noted that, in contrast with the case of copper single crystal, the internal friction is dependent on the frequency employed in the case of aluminum single crystal. This conclusion is inconsistent with which one would expect from the essential features of the mechanism of static hysterisis. Therefore, in the case of aluminum, it seems to be difficult to interpret the behavior of internal friction as due to only the motion of free or pinned dislocation. Rather it would be more reasonable to attribute it to the motion of any imperfection other than free or pinned dislocation such as vacancy, or strongly coupled dislocations, or viscous motion of any kind like grain boundary migration.

It should be noted, in conclusion, that the mechanism of internal friction depends on the frequency or temperature used in the measurement. The static hysteresis mechanism discussed in this paper to interpret the origin of internal friction due to the motion of dislocation is only applicable to the measurement near room temperature and to the frequency range from 1 cps. to 10^5 cps. Anelastic internal friction attributed to the heat flow between upper and lower sides of slip plane is considered to occur. Actually, Bordoni[12] has observed appreciable internal friction peak at the temperature below the boiling point of liquid air by using the frequency of about 10∼50 kcps., which is considered to be due to an anelastic effect. And, internal friction due to the motion of dislocation will vanish at higher frequency range where the movement of dislocation cannot follow the variation of applied stress. However, static hysteresis loss is the most probable mechanism, because it occurs in the frequency and temperature range where the usual experiments are carried out.

References

1) A. S. Nowick: *Progress in Metal Physics* (Interscience Publishers, Inc., New York, 1953), Vol. 4, p. 1.
2) J. S. Koehler: *Imperfections in nearly perfect crystals* (John Wiley and Sono Inc., New York, 1952) p. 197.
3) T. A. Read: Phys. Rev. **58** (1940) 371.
4) A. S. Nowick: Phys. Rev. **80** (1950) 249.
5) J. Weertman and J. S. Koehler: J. Appl. Phys. **24** (1953) 624.
6) F. C. Frank: Proc. Phys. Soc., London (1948) p. 46.
7) J. D. Eshelby: Proc. Roy. Soc. **A 197** (1949) 396.
8) C. Zener: *Elasticity and Anelasticity of Metals*, Chicago 1948.
9) R. R. Hasiguti and T. Hirai: J. Appl. Phys. **22**)1951) 1084.
10) N. Kunitomi and K. Satō: J. Phys. Soc. Japan (to be published).
11) C. Zener, D. van Winkle and H. Nielsen: Trans. AIME **147** (1942) 98.
12) P. G. Bordoni: J. Acous. Soc. Am. **26** (1954) 495.

JOURNAL OF THE PHYSICAL SOCIETY OF JAPAN Vol. 10, No. 11, NOVEMBER, 1955

Diffusion of Silver in Silver-Zinc and Silver-Cadmium Alloys

By Tokutaro HIRONE*, Motoharu KIMURA**,
Toshio KITAGAKI**, Nobuhiko KUNITOMI*
and Yosimitsu SUGITA**,***

Tohoku University, Sendai

(Received June 30, 1955)

Diffusivity of Ag^{110} in AgZn and AgCd alloys containing about 30% Zn or Cd was measured by means of surface counting. The results show that the silver atoms diffuse most rapidly in the lattice of AgZn and that the diffusivity of silver in AgCd is still higher than that in silver itself. These facts are interpreted by considering that the cohesive energy of the metallic lattice is affected by the addition of the impurity atoms not only due to the screening effect of the valence electrons but also due to the change of the repulsive interaction of closed shells.

§ 1. Introduction

Remarkable progress has been made in the investigations of atomic diffusion mechanism in metals and alloys. This fact is mainly attributed to the development of the experimental techniques in which radioactive isotopes are utilized as tracers. By this method, most reliable diffusion constant can be obtained than any other method. Especially, it enables us to measure the self-diffusion coefficient which has not yet been obtained without isotopes excepting few cases using nuclear magnetic resonance[1][2]. On the other hand, the chemical diffusion constant has been measured by the other methods, namely, Kirkendall effect method[3], and anelastic method[4]. However, the values obtained by these method differ slightly with each other in spite of that each given a kind of diffusion coefficient which relates to the transposition probability of constituent atoms in alloy. And, the relations between these have not yet been known, hitherto. Since the study of chemical diffusion is an interesting problem, it is worth while to make the relations experimentally clear in order to increase the experimental results which are available for the theoretical considerations.

In this paper, the diffusivities of silver atoms in f.c.c. solid solution of silver-zinc and silver-cadmium system containing 30% zinc or cadmium have been measured by using radio-active isotope Ag^{110}. It is interesting to compare these values with those obtained for the same materials by Kirkendall effect measurement[5] and anelastic measurement[6][7]. However, we do not concern it in this paper and remains it for the following papers which will be published in near future.

§ 2. Method of Measurement and Self-Diffusion of Silver

It have been reported by Smith, Jaumot and Arné that the lathe-sectioning method[8]* is most accurate to determine diffusion coefficient by using radio-active isotope. In this experiment, however, surface-counting method[9] was used conveniently, because this method gives fairly accurate values without using any special apparatus. Since the purpose of this work is not to determine the accurate values of activation enthalpy and frequency factor, but to obtain the approximate value for the comparison of the other measurements, this method was considered to be sufficiently useful. In order to ascertain the accuracy of the measurement, the self-diffusion of silver was observed preliminary. The specimens was cut from high purity (99.99%) silver in the shape of square disk of 10 mm in edge length and 5 mm in thickness. Radio-active Ag^{110} was electrolytically plated on one side of the specimen surface in the thickness of 10 Å. In order to reduce the loss of radio-active silver during the diffusion anneal, the two specimens were combined in "plated face-to-face" position, packed with thin silver foil and placed in the sealed off quartz tube in which argon gas is filled. After the annealing, the radio-activity from the plated surface decreases because the radiation of diffused active silver is absorbed by the specimen material itself, and the decreasing rate of radio-activity is expressed by the equation

---

* Research Institute for Iron, Steel and Other Metals, Tohoku University, Sendai, Japan.

** Department of Physics, Faculty of Science, Tohoku University, Sendai, Japan.

*** Now in Hitachi Co. Hitachi, Japan.

$$F=e^{z}[1-p(z)] \tag{1}$$

where

$$p(z)=\frac{2}{\sqrt{\pi}}\int_{0}^{\sqrt{z}} e^{-y^2}dy \tag{2}$$

$$z=\mu Dt \tag{3}$$

In these equations μ is the absorption coefficient of the radiation from Ag^{110} by the specimen, t is the time of diffusion anneal and D is the diffusion coefficients. Hence, we can estimate the value of D from the observed values of, F, μ and t from Eqs. (1), (2) and (3). In the actual cases, the natural decay of the radio-activity of silver may give error to the value of F. Then, the activity of the standard specimens, which have the same size, same material and on which the radioactive silver is plated in the same condition as the actual specimen, are observed in the course of the measurement. The corrected values of F is thus obtained by comparing the observed change of radioactivity during the diffusion anneal with the natural decrease of the standard specimen. The value of the absorption coefficient μ is determined from the observed decrease of the radioactivity through the thin foil of the specimen material having known thickness. The absorption curve for silver is shown in Fig. 1. In this figure, the abscissa show the thickness of the silver foils through which the radioactivity of Ag^{110} was counted and the ordinate shows the logarithm of variation rate of the counting. As is shown, this curve is approximately straight, so the absorption coefficient is evaluated by least mean square method as $\mu=211$ /cm from the equation

$$F=1-e^{-\mu x} \tag{4}$$

The diffusion coefficient of self-diffusion silver was measured at three different temperatures by using thus obtained F and μ. The results are shown in Fig. 2, in which those obtained by other investigators[10][11][12] are also plotted. It is obvious from the figure that the observed values of D are not so much different from those observed by others who used the lathe-sectioning method, then it might be concluded that the accuracy is satisfactory for the purpose of the present work.

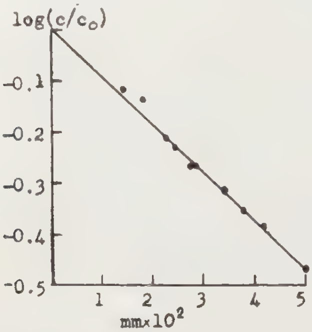

Fig. 1. Absorption of the radioactivity of Ag^{110} by silver.

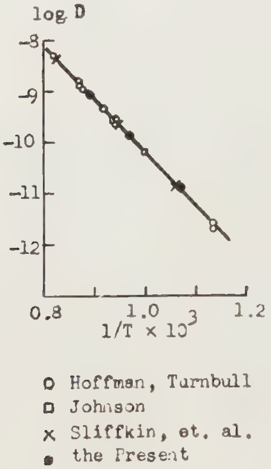

Fig. 2. Self-diffusion coefficient of silver.

§ 3. Experimental Results and Discussions

The diffusivity of silver in AgZn and AgCd alloys are measured by the same method as described in the last section. As both specimens contain about 30 atomic percent zinc and cadmium, (29.4 atomic % zinc in AgZn, 31.9 atomic % cadmium in AgCd) these have face-centered cubic structure. Since the vapor pressure of zinc and cadmium is considerably high in the temperature range of diffusion anneal, the specimens were annealed in the sealed tubes as in the case of silver. By this method, evaporation of zinc and cadmium becomes less than any other method of annealing. The observed absorption curve and the diffusivity of silver into these materials are shown in Fig. 3 and 4, respectively. In both cases, the diffusivity is higher and the activation energy is lower than the corresponding values of silver self-diffusion. These features do not contradict with the previous observations that the atoms in the impure lattice have higher diffusivity than in the pure lattice,$^{13)}$ and with the conclusions predicted from Lazarus' theory$^{14)}$, that the solute zinc or cadmium in silver lattice would diminish the cohesive energy and would make the diffusion of atoms easier than in the pure lattice. Unfortunately, the present results cannot be interpreted quantitatively by his theory directly, because it is based on the Thomas-Fermi's free electron models and should not be applied to the case of high impurity concentration like the present.

It is evident from Fig. 4, that the observed results approximately satisfy the classical law of rate process that the probability of atomic jump is in proportion to the expontial of the minus reciprocal of the absolute temperature. Therefore experimental formula could be expressed as

$$D=0.09\exp(-36.000/RT)\mathrm{cm}^2/\mathrm{sec} \quad \text{for AgZn}$$

$$D=10.0\exp(-46.000/RT)\mathrm{cm}^2/\mathrm{sec} \quad \text{for AgCd}$$

Since the accuracy of the measurement is not so high, the numerical values of the frequency factor and the activation enthalpy do not have high reliability. However, the each measured point is considered to be satisfactorily reliable that the comparison with the results obtained by Kirkendall and anelastic experiments. The work concerning these problem will be published nearly.

As is shown in Fig. 4, the diffusivity of Ag into AgZn lattice is appreciably higher than that into AgCd lattice, but this fact cannot be explained by Lazarus' theory. According to him, the variation of the diffusion constant due to impure atoms is influenced only by the difference of the number of valence electrons between solute and solvent atoms. In the present case, the number of valence electrons in silver is one and those in zinc and in cadmium are both two per an atom. Hence, no difference is expected between AgZn and AgCd systems from his theory, if the concentration of the solute atoms is the same for both cases. The second factor which is considered to influence the diffusion constant in the alloy is the difference of the radius of closed shell between solute and solvent atoms. In actual, ionic radius of zinc atom is much smaller than that of cadmium and silver, while the interatomic distance varies not so much by the addition of zinc or cadmium into silver. Then, it is concluded that the activation energy for the jump of atoms is smaller in AgZn because closed shell repulsion energy is smaller. Although the quantitative description of the effect of the difference of the atomic rudius remains a subject for the future investigation, the observed results can be explained qualitatively.

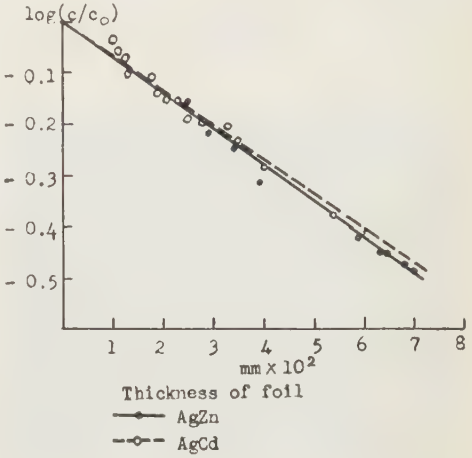

Fig. 3. Absorption of the radioactivity of Ag^{110} by AgZn and AgCd.

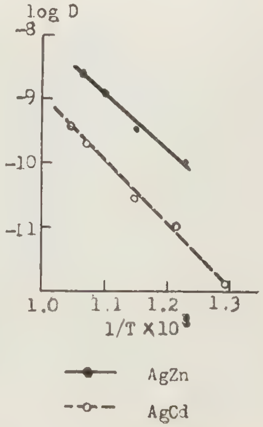

Fig. 4. Diffusion coefficient of Ag^{110} in AgZn and AgCd alloys.

It should be noted, in conclusion, that the

---

* from the suggestion of C. T. Tomizuka.

present investigation is greatly contributed by the assistance of Messers T. Nakamura, K. Masuhara, M. Sakamoto and Miss K. Edamoto who investigated this problem with the present authors as the graduation experiment during their undergraduate course of physics in Tohoku University. The present authors express their sincere thanks to them for their eager and kind assistances for the present investigation.

References

1) R. E. Nordberg, C. P. Plichter: Phys. Rev., **38** (1951) 1074.
2) E. F. W. Seymour: Proc. Phys. Soc. **66A** (1953) 85.
3) see for example, R. W. Balluffi, L. L. Seigle: J. App. Phys. **25** (1954) 607.
4) C. Zener: *Elasticity and Anelasticity of Metals* (The University of Chicago Press, Chicago, 1948).
5) N. Kunitomi and J. Mizuno: to be published.
6) A. S. Nowick: Phys. Rev. **88** (1952) 925.
7) N. Kunitomi, J. Mizuno, K. Sato: to be published.

JOURNAL OF THE PHYSICAL SOCIETY OF JAPAN Vol. 10, No. 11, NOVEMBER, 1955

Some Characters of the Soap Bubble Raft in a Vibrating State

By Einosuke FUKUSHIMA*
Department of Physics, Tokyo Metropolitan University, Tokyo
and Akiya OOKAWA*
Department of Physics and Chemistry, Gakushuin University, Mejiro, Tokyo

(Read October 30, 1954; Received July 9, 1955)

The bubble raft is set in a vibrating state in order to approximate the real crystal in thermal vibration more precisely by the model. The exciting vibration of 90 *c/sec* is transmitted to the bubble raft through the sustaining liquid. In the vibrating state, it is observed that the bubble raft expands uniformly until a critical state is reached, where the regular alignment is destroyed abruptly. By means of the lattice expansion, a formula is proposed defining a reduced temperature of the bubble raft corresponding to each input power of vibration. The diffuseness of the irregularity characteristic of the lattice imperfections, such as the vacancy, the vacancy group, the interstitial and the dislocation, is observed to increase in general under vibration. In the case of the vacancy group, it can be detected the stacking faults characteristic to the bubble raft.

Some preliminary discussions are attached as to the cause of the raft expansion and of the diffused lattice imperfections, the characteristics of the disordered state at the critical point, and the geometrical mechanism of formation of the stacking faults by means of the imperfect dislocations.

§ 1. Introduction

The bubble raft model of a crystalline solid introduced by W. L. Bragg and the others$^{1)}$ has contributed much to the study of the dislocation, the grain boundary$^{2)}$ and the recrystallization. However, the bubble raft model as it stands has substantial drawbacks in two respects, the two-dimensionality and the missing thermal agitation against the real crystal. In the latter respect, the model is estimated to correspond to the real crystal at very low temperature. One must accordingly be careful in relating the observed behaviours of the bubble raft to the experimental facts of the real crystal.

---

* Research member of the Kobayashi Institute of Physical Research, Kokubunji, Tokyo.

It is desirable under the circumstances to make observations on the behaviour of the bubble raft in a state somehow proximate to the real state accompanied with the thermal agitation*. For the purpose, the bubble raft was set under mechanical vibration and we could then detect behaviours different from those in the static state. Here is reported on the raft expansion, the diffused vacancy group and the dislocations in the vibrating state. On the behaviours of the grain boundaries in the vibrating state, it will be reported later.

§ 2. Experimental Method

A supersonic wave transmitted through the sustaining liquid was unsuccessful in the issue to set the floating bubble raft in vibration. Rather a vibration of much lower frequency was transmitted through the liquid successfully.

The experimental apparatus used is shown schematically in Fig. 1. The basin C containing the soap solution is brassmade except the iron-made baseplate of 1.5 *mm* thickness. The iron plate is set in vibration by the fixed electromagnet M driven by alternating current. The audio frequency oscillator is of range 35–18,000 *c/sec*, but the vibration of higher frequency (higher than 250 *c/sec*) is unavailable in the basin, due to the high mechanical impedance of the thick baseplate. Between 30–250 *c/sec*, the set has resonances at 60 and 120 *c/sec*. To avoid the complicating effects of fluctuating frequency, the constant frequency of 90 *c/sec* is used provisionaly throughout the present experiment. It can be detected by the Askania portable oscillograph analysis, that the vibrating mode of the baseplate driven at a fixed frequency of the oscillator contains unnegligible components of higher harmonics.

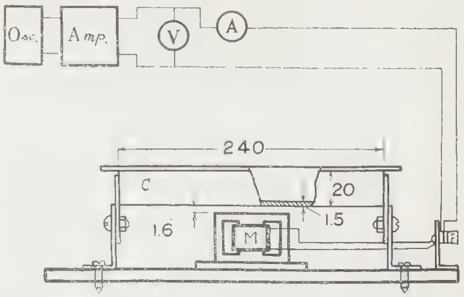

Fig. 1. Experimental apparatus to set the bubble raft floating on the soap solution in a vibrating state.

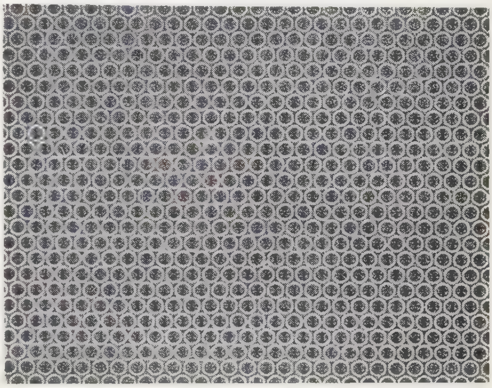

Fig. 2. The bubble raft in the static state ($d=1.0\,mm$). d is the diameter of the bubble.

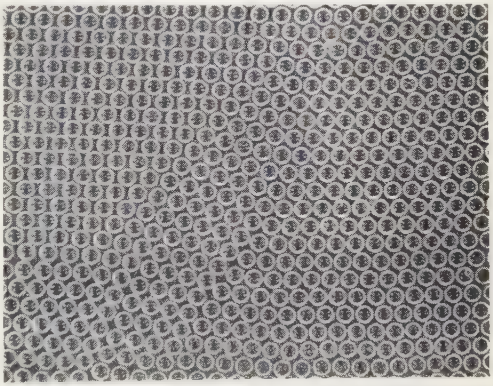

Fig. 3. The bubble raft in the critical vibrating state ($d=1.0\,mm$).

It is evident that, as to the frequency of vibration as well as to the frequency spectrum, the bubble raft excited by the present method is yet far from the real crystal under thermal vibration. But the raft, looking rather spacious between the constituent bubbles when at rest, looks the more closely packed with increasing the input power of the exciting current and we can really detect an expansion of the bubble raft under vibration. The observed raft expansion induced by the mechanical vibration may be marked as a characteristic corresponding to the thermal

---

* It was a problem of much interest to many attendants at the Nikko Symposium on Crystal Plasticity and Dislocations, 1953.

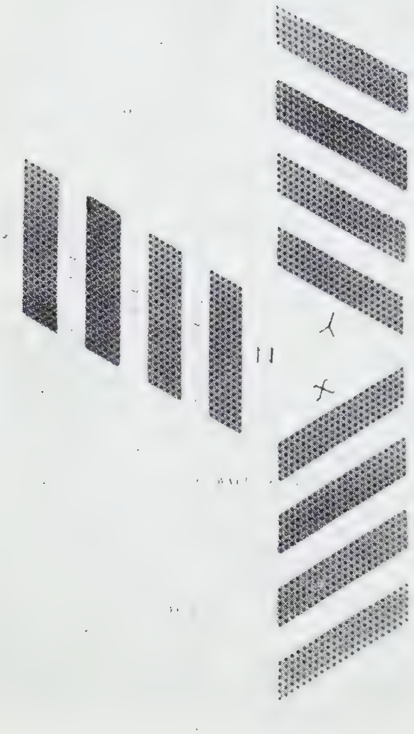

Fig. 4. An example showing the raft expansion in three lattice directions.

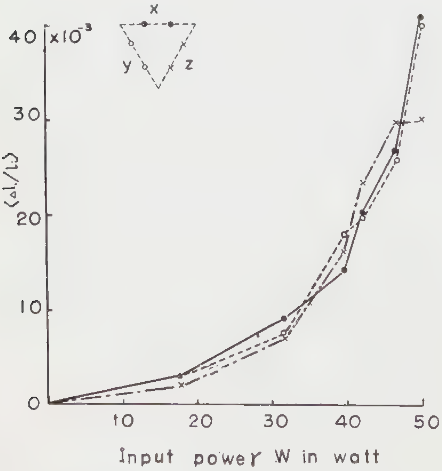

Fig. 5. The mean lattice expansion in each of the three lattice directions against the input power.

expansion of the real crystal. Thus we may presume the increased proximity between the real crystal under thermal vibration and the bubble raft model excited by the present method.

§ 3. Raft Expansion

Single crystalline bubble raft of free boundary, nearly rectangular or elliptic in shape, is made by the usual method and then we increase the input power W of exciting current driving the electromagnet. The bubble raft is photographed at each input power, exposure time being 1/25–1/50 *sec*. The expanding deformation of the raft properly set is in general not accompanied by the complexing factors, such as the shearing mode, the inhomogeneity and the anisotropy. But when a critical input power W_m is reached, the long range order of the bubble arrangement is destroyed abruptly. Figs. 2 and 3 represent the bubble raft in the static and in the critical state, respectively, where in the latter the characteristic wavy distortion of the bubble line is remarkable. The critical input power, where the disintegration of the long range regular pattern takes place can be determined fairly precisely. We propose to correlate this critical point of the bubble raft to the melting point of the real crystal.

After the photographs were enlarged under a standard condition, the raft dimensions were measured along three lattice directions, $(01\bar{1})$, $(\bar{1}01)$ and $(1\bar{1}0)$. An example of the raft expansion is shown in Fig. 4 along each lattice direction, where the innermost photographs are in the static state and the outgoing ones are in order of increasing input power. The length $l_i+\Delta l_i$ ($i=x$, y and z) of 30 to 10 bubbles, l_i being the length in the static state, is measured with respect to the enlarged photographs at several locations of the raft. The linear lattice expansion $\Delta l_i/l_i$ is nearly constant, notwithstanding the varied number of bubbles, 30 to 10, nor the varied location in the raft, thus verifying the homogeneity of the raft expansion.

The mean expansion $\langle \Delta l_i/l_i \rangle$ in each direction is plotted against the input power in Fig. 5. It can be seen that the raft expansion is nearly isotropic. For further use, we define the average of $\langle \Delta l_i/l_i \rangle$ over the three directions, denoting it by $\langle \Delta l/l \rangle$.

The measured input power W_m where the raft disintegrates was not constant under a seemingly constant condition. One of the most serious causes hereto was detected to be the varied temperature of the sustaining soap solution due to loss heating of the iron baseplate. To take refuge from this inconvenient circumstances, the average expansion $\langle \Delta l/l \rangle$ is plotted against the input power ratio W/W_m, and we have as its issue a unique relation between the two variables (see Fig. 6.) The experimental conditions for the three series are given in Table 1. As to Fig. 6 and Table 1, we may rely on a unique relation between $\langle \Delta l/l \rangle$ and W/W_m, notwithstanding the fluctuating W_m in different series. Plotting $\log_{10} \langle \Delta l/l \rangle$ against W/W_m, we have the curve A in Fig. 7. Here we propose a linear relation between the variables

$$\log_{10}\langle \Delta l/l \rangle = -3.192 + 1.731\, W/W_m\,, \quad (3\cdot 1)$$

thus obtaining an experimental formula

$$\langle \Delta l/l \rangle = 34.6\times 10^{-3} \exp[-3.96(1-W/W_m)]\,. \quad (3\cdot 2)$$

Now, it may be not whithout merit to have a reduced temperature scale associated with the vibrating raft at each input power. With the present experimental set, however, it remains yet unknown the functional relation between the energy of the raft itself and the input power exciting the electromagnet. On the other hand, the vibration applied to the bubble raft by the present procedure is apparently far from simulating the thermal vibration in the real crystal. Under the circumstances, as a mere tentative measure of correspondence, the reduced temperature T is defined by means of the raft expansion $\langle \Delta l/l \rangle$, taking account of the experimental formula (2) and an assumed linear expansion formula

$$\langle \Delta l/l \rangle = \alpha T\,. \quad (3\cdot 3)$$

From Eqs. (3·2) and (3·3), we have

$$\alpha T = 34.6\times 10^{-3} \exp[-3.96(1-W/W_m)]\,.$$

The constant α is determined by setting the reduced temperature T for W_m equal to the actual melting temperature T_m of the real crystal, to which the bubble raft under investigation is to correspond. If the bubble raft is to correspond to copper, we set $T=1350°K$ for $W/W_m=1$, the melting temperature of *Cu*, obtaining the linear expansion coefficient

$$\alpha = 0.255\times 10^{-4} \quad (3\cdot 4)$$

Table I.

Series	Diameter of bubble (mm)	Raft dimension (mm²)	Melting watt W_m	Refering	
				Number of bubbles	Number of locations
I	1.2	63 × 52 (rectangular)	43.2	30	5
II	1.2	72 × 53 (elliptic)	50	30 10	5 9
III	1.0	63 × 52 (elliptic)	32.8	10	15

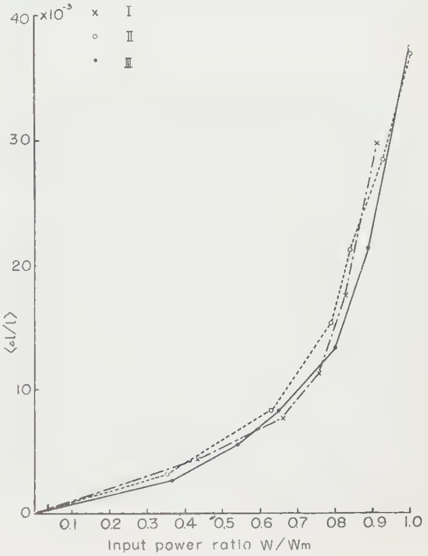

Fig. 6. The lattice expansion averaged over the three lattice directions against the input power ratio. W_m is the input power at the critical point.

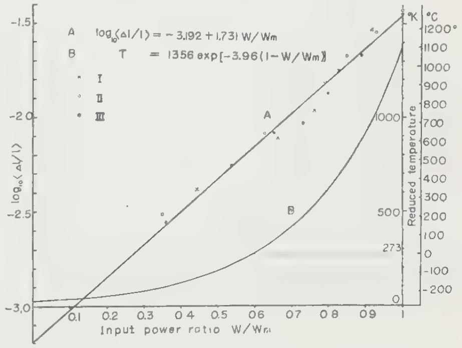

Fig. 7. Curve A; The logarithmic lattice expansion against the input power ratio. Curve B; The reduced temperature corresponding to each input power ratio.

The correspondence formula

$$T = 1356 \exp[-3.96(1-W/W_m)] \quad (3\cdot 5)$$

is plotted in Fig. 7, curve B. Thus we can estimate the temperature, where the corresponding real crystal, *Cu* in our case, is to be associated to each vibrating bubble raft under investigation. It may be noteworthy

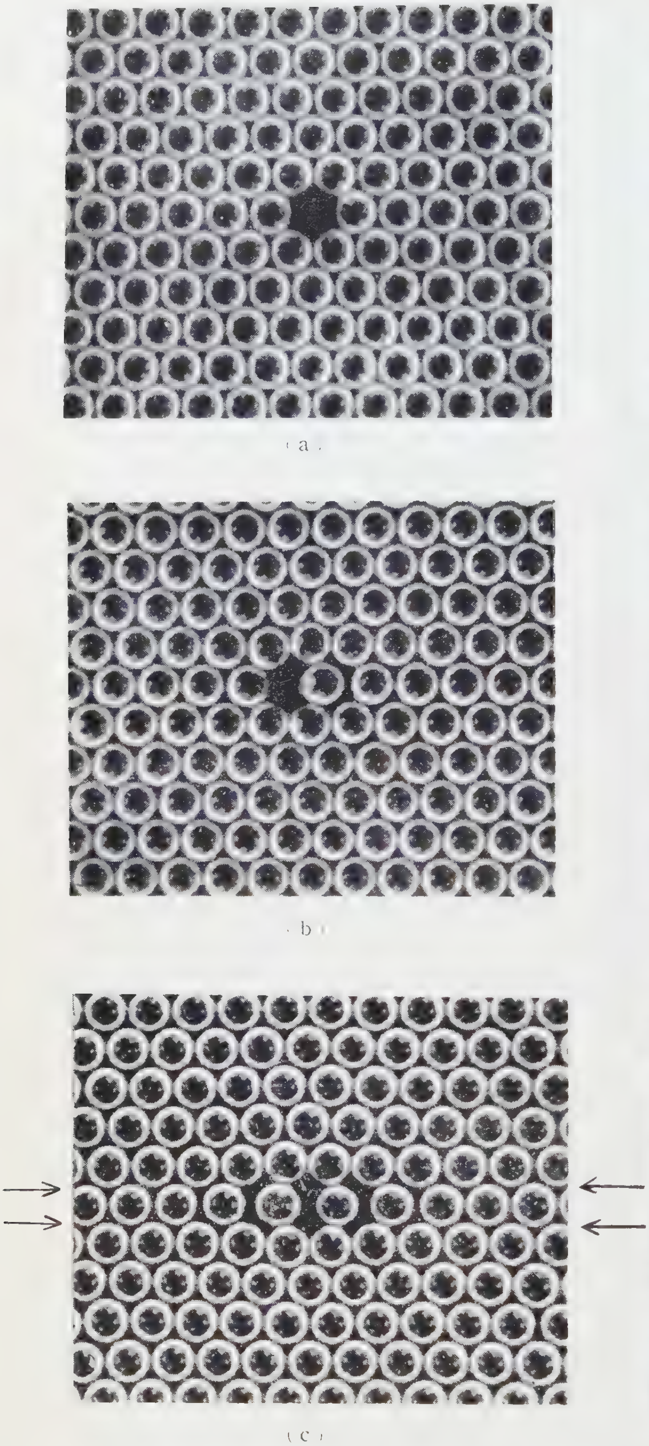

Fig. 8. Single vacancy ($d=0.9\,mm$). (a) the initial and the final state; (b) the state at about 1000°C; (c) the state just below the melting point. The arrows show the glide lines of the dislocations.

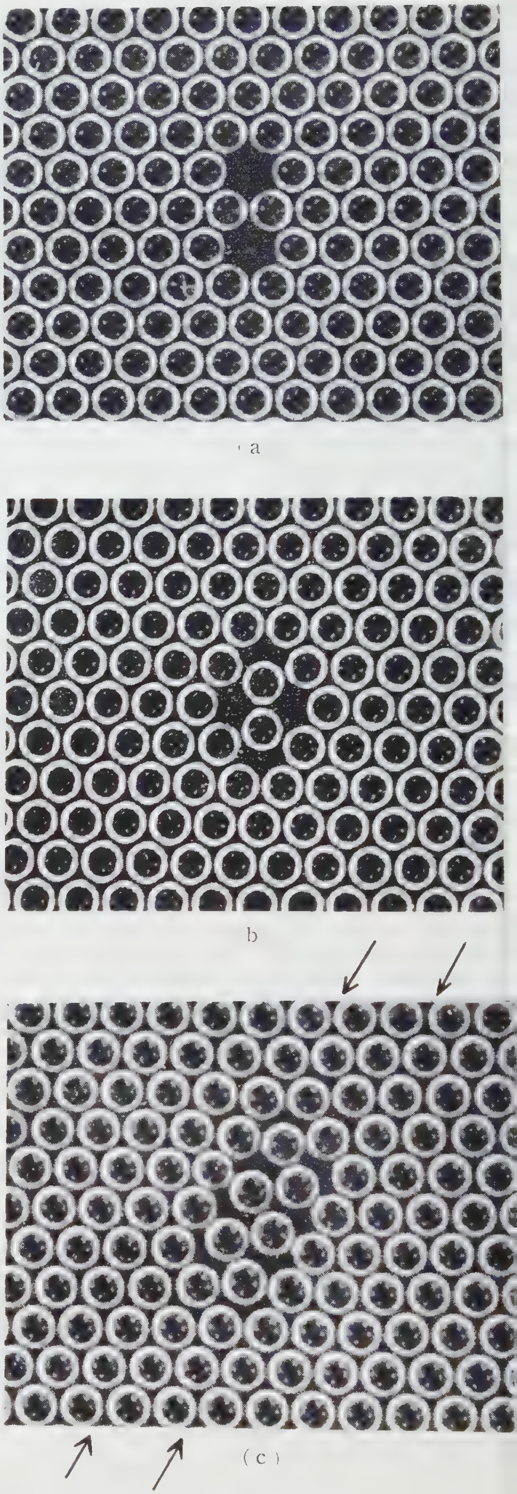

Fig. 9. Two vacancies ($d=0.9\,mm$). (a) the initial state; (b) the final state at rest; (c) the state at about 200°C. The arrows show the glide lines of the dislocations.

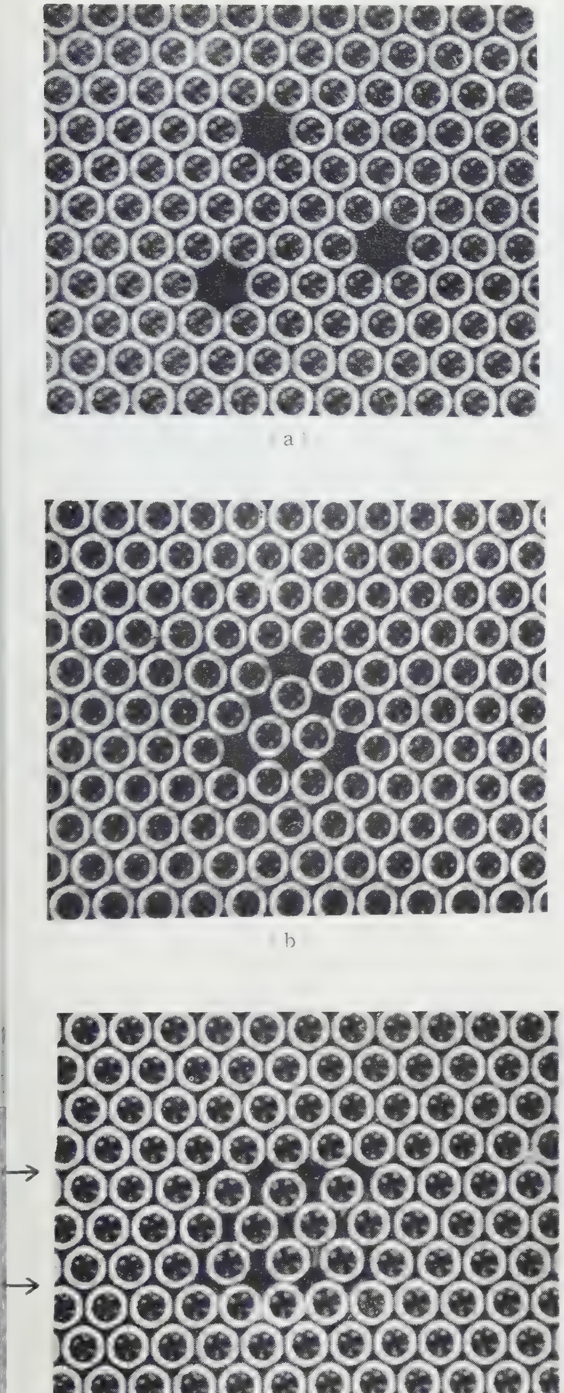

(a)

(b)

(c)

Fig. 10. Three vacancies ($d=0.9\,mm$). (a) the initial state; (b) the final state at rest; (c) the state at about 200°C. The arrows show the glide lines of the dislocations.

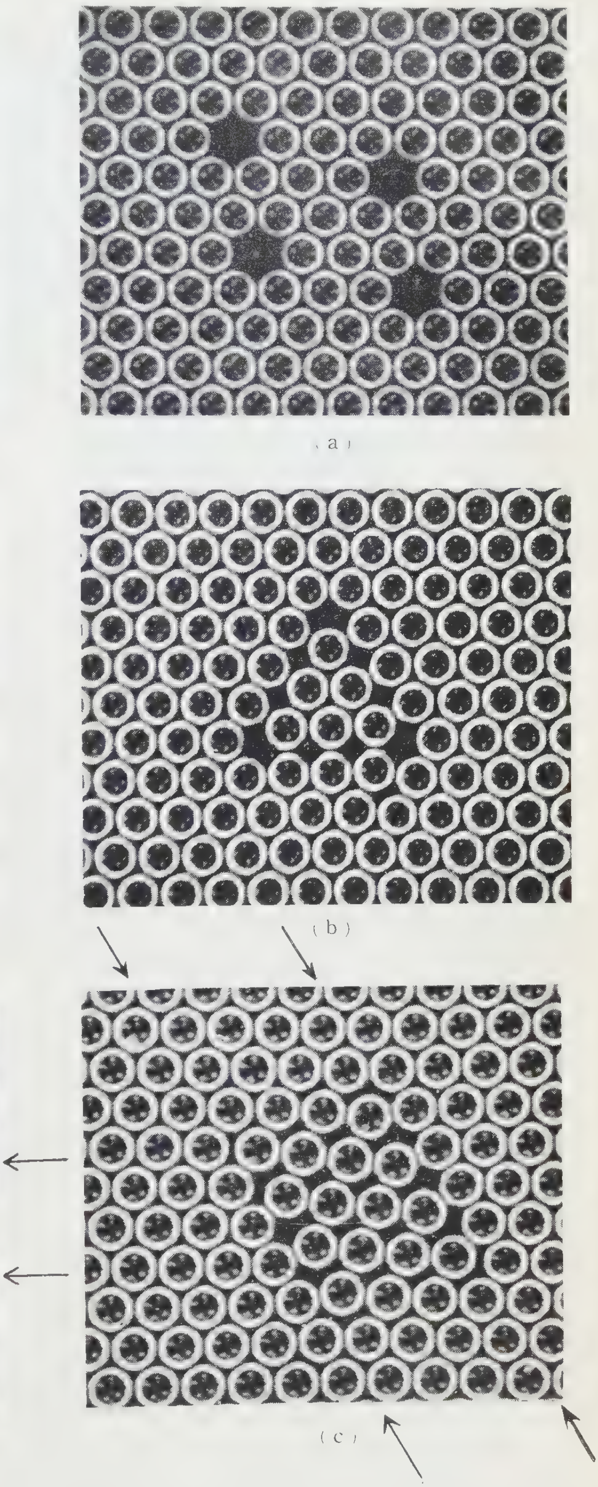

(a)

(b)

(c)

Fig. 11. Four vacancies ($d=0.9\,mm$). (a) the initial state; (b) the final state at rest; (c) the state at about 200°C. The arrows show the glide lines of the dislocations.

that the value of the linear expansion coefficient α of the bubble raft is in order of magnitude proximate to that of the real crystal copper (0.200×10^{-4} at 1000°C.)

In the followings, by means of the formula (5), we have the convenience of estimating the temperature T, where the behaviours in the real crystal should have resemblances to the observed behaviours in the bubble raft at each specified input power ratio W/W_m.

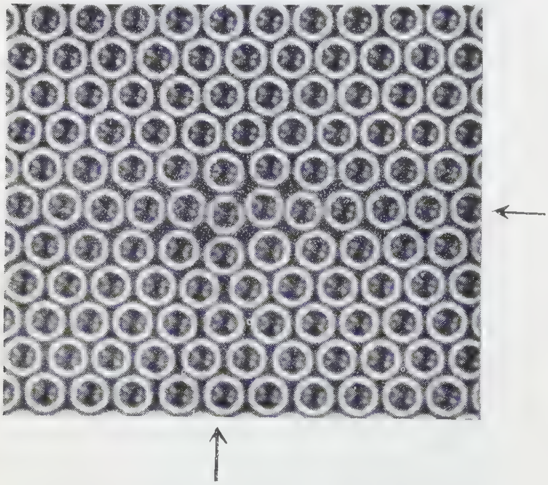

(a)

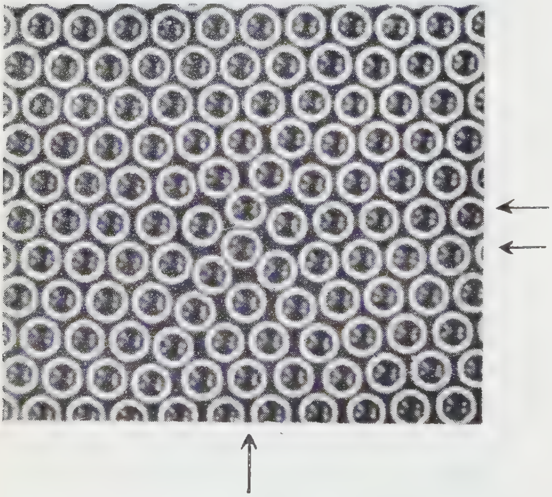

(b)

Fig. 12. An interstitial bubble ($d=1.0\,mm$). The deviation from the normal site is marked at the crossing points of the arrows.

§4. Lattice Imperfections of Bubble Raft in Vibrating State

The lattice imperfections of the bubble raft in vibrating state are observed to display characteristics different from those observed in the static state. In the following, some characteristic properties are described as to the vacancies, the interstitial and the dislocations. As to the grain boundaries, it will be reported later.

(i) *Vacancy.*

(a) *Single vacancy.*

A single vacancy transforms itself by increasing input power in order as shown in Fig. 8 *a*, *b*, and *c*, resuming the state *a* reversibly when at rest. Sharing of vacancy by the more bubbles with increasing the power is characteristic, but the direction of diffuseness is seemingly set by chance. The state *a* is stable until nearly the melting point.

(b) *Vacancy pair.*

As to two vacancies in close neighbourhood, the vacancy pair at the initial state, Fig. 9*a*, is transformed through the state *b* to the state *c* at the reduced temperature of about 450°C, resuming the state *b* when at rest. The state *b* is transformed to the state *c* at lower reduced temperature of about 200°C. The artificial initial state *a* is, so to speak, unattainable by the thermal process. As is the case with the single vacancy, the sharing of vacancy by the more bubbles in the vibrating state is remarkable but the isotropy of the diffuseness is hard to realize.

(c) *Three and four vacancies.*

In each case of Figs. 10 and 11, starting from the initial state *a*, the imperfections are transformed through *b* to *c* in process of increasing the input power, resuming finally the state *b* at rest. Again the sharing of vacancy by the more bubbles is remarkable at elevated temperatures but the anisotropy of diffuseness is hard to avoid.

It is noteworthy that, whereas the state *b* at lower temperature has a stacking fault of triangular shape of variable bubble length, the state *c* at higher temperature represents rather a dislocation pair on glide lines separated by variable bubble length with their dilatation sides in common.

(ii) *Interstitial.*

A single interstitial bubble is shown in Fig. 12*a* and *b*. For a remark, while in the state *a* at the reduced temperature of about 770°C the deviation form the regular lattice site is con-

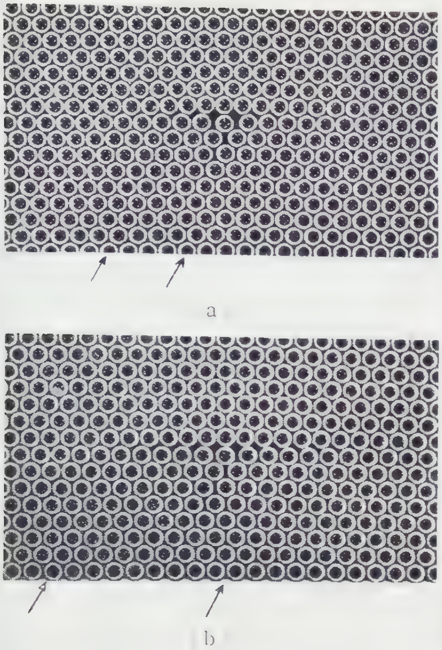

Fig. 13. Single dislocation ($d=0.9\,mm$). The dislocation width is indicated by the two arrows. (a) the state at rest; (b) the state at about 880°C.

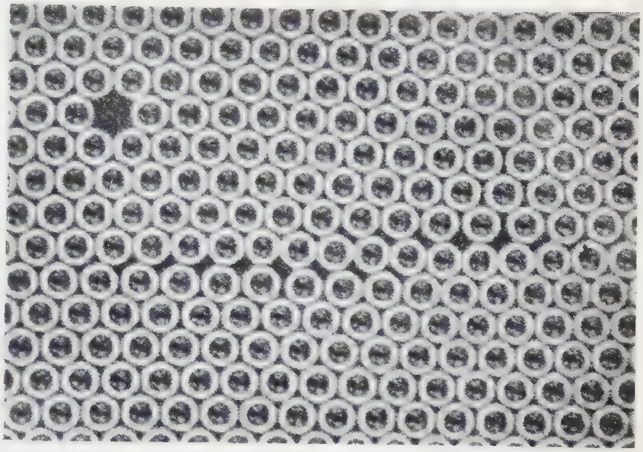

Fig. 14. Pair dislocations with their compression sides in common at about 350°C ($d=1.0\,mm$).

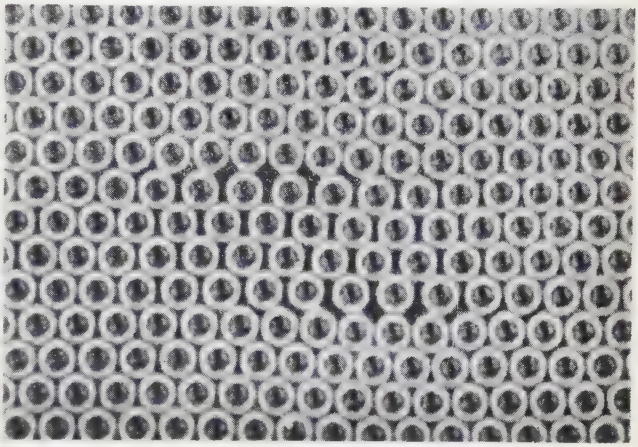

Fig. 15. Pair dislocations with their dilatation sides in common at about 350°C ($d=1.0\,mm$).

centrated on a single bubble, in the state *b* near the melting point the most remarkable deviation is shared by neighbouring two bubbles.

(iii) *Dislocation.*

(a) *Single dislocation.*

The general trend, that the lattice irregularity is shared by increasing number of bubbles with increasing the vibration intensity, is displayed in the case of the dislocation in its increasing width. The dislocation width of about 5 bubble length at rest, Fig. 13*a*, increases to about 10 bubble length at the reduced temperature of about 880°C, Fig. 13*b*.

(b) *Pair dislocations.*

Pair dislocations on parallel glide lines under vibration is shown in Figs. 14 and 15. The dislocations in Fig. 14 have their compression sides in common along single bubble line, thus amounting in net issue to a single interstitial bubble, and the dislocations in Fig. 15 have their dilatation sides in common along four bubble lines, thus amounting in net to four vacancies. In any case, however, the characteristic as the dislocation imperfection are undisputably clear, being in sharp contrast to those shown in Figs. 12*a* and 11*b*, respectively.

§ 5. Discussions

(i) *On the raft expansion in vibrating state.*

As the sharpness of the periphery of each bubble in the vibrating state is almost the same as that in the static state, the bubbles oscillate substantially in normal direction to their extension, the surface of the sustaining liquid. To explain the raft expansion due to this transversal vibration, we shall for the present put aside the complicating factors such as the normal modes of the bubble raft and the matching between its characteristic modes and the exciting vibration. We shall accordingly approximate each bubble by an independent linear oscillator with the characteristic frequency ν and the minimum potential $\mathcal{E}$, both depending on the two-dimensional extension S of the total raft composed of N bubbles.

The number of the available states of an oscillator, not exceeding a given energy $e-\mathcal{E}$, is proportional to the phase integral $\iint dq\,dp$ extended over $\{p^2+(2\pi m\nu)^2q^2\}/2m\leq e-\mathcal{E}$. With the proportionality constant $1/h$, it is given by $(e-\mathcal{E})/h\nu$ and the energy of the i-th bubble can be written as $e_i=\mathcal{E}+n_ih\nu$, where the n_i may be assumed to take a large positive integral value. The total energy E of the raft is therefore

$$E=\sum_{i=1}^{N}(\mathcal{E}+n_ih\nu)\,. \tag{5.1}$$

The number of configuration of the total raft for given total energy E is given by

$$C=(M+N-1)!/M!(N-1)! \tag{5.2}$$

where, refering to Eq. (5.1),

$$M=\sum_{i=1}^{N}n_i=(E-N\mathcal{E})/h\nu\,. \tag{5.3}$$

The raft in vibrating state is observed in the most probable state corresponding to the maximum number of configuration. As the number of configuration C is a monotonous increasing function of M, we have, maximizing the M of Eq. (5.3) with respect to the extension S of the raft, the condition

$$N\frac{d\mathcal{E}}{dS}h\nu+(E-N\mathcal{E})h\frac{d\nu}{dS}=0\,. \tag{5.4}$$

Expanding $d\mathcal{E}/dS$ about S_0, that minimizes the potential energy $\mathcal{E}$, it follows

$$\frac{d\mathcal{E}}{dS}=\left(\frac{d\mathcal{E}}{dS}\right)_0+\left(\frac{d^2\mathcal{E}}{dS^2}\right)_0(S-S_0)=\frac{1}{\kappa_0S_0}(S-S_0)\,, \tag{5.5}$$

κ_0 being the compressibility at S_0. Differentiation of Eq. (5.4) with respect to E, with Eq. (5.5) for $d\mathcal{E}/dS$, gives

$$\frac{dS}{dE}=-N\kappa_0\frac{d\log\nu}{d\log S}\,. \tag{5.6}$$

As the characteristic frequency ν of each bubble is presumably a decreasing function of the raft extension S, we can expect, according to Eq. (5.6), the raft to expand with increasing its total energy E.

(ii) *On the diffused imperfections in vibrating state.*

We have noted many examples in § 4 showing that the irregularity characteristic to each type of the lattice imperfections, such as the vacancy, the vacancy group, the interstitial and the dislocation, is shared in the vibrating state by the more bubbles than those in the static state. It can easily be foreseen that the bubble at an irregular lattice site has its potential energy greater and the characteristic frequency less than that of the bubble at a regular lattice site. The general trend of increasing diffuseness of the characteristic irregularity in the vibrating state can then be interpreted qualitatively, on the same line as the preceding discussion on the raft expansion, to the effect that the local number of configuration is more favoured by the locally decreasing characteristic frequency, in spite of the unfavourable increasing potential energy there. In thermodynamical language, one might speak of the bubble raft in vibrating state realized in the state of minimum free energy, not in the state of minimum potential energy.

(iii) *On the disordered state at the critical point.*

As to the disordered state at the critical point, shown in Fig. 3, it is of little value to speculate on the transformation process from the same elementary stand-point as those in the above discussions, because of the expected predominance of the cooperative interactions between the constituent bubbles. We want instead to depicture some characteristics discriminating the disordered state from the static state.

The short range order is preserved in the sense that the bubbles are packed in hexagonal alignment over separate extension. But the long range order is destroyed, the respective lattice directions being tilted at respective boundary lines. The lines B_1B_1, B_2B_2 and B_3B_3 in Fig. 16, the reprint of Fig. 3, shows the tilt boundary lines. These tilt boundaries, especially the line B_2B_2, are not accompanied with dislocations nor with the holes, which are indispensable as the constituent elements of the tilt boundary separating undistorted crystal grains. This discrepancy is compensated here by the elastic distortion of the neighbouring raft grains, which is evident from the distorted triangles of lattice points in Fig. 16. From the general viewpoint in section (i) and (ii) that the range of lattice imperfections is increased at the higher temperature, one might say that at the critical temperature the far reaching elastic distortion within each grain is rather favoured to the localized lattice imperfections on the boundary such as the dislocations and the holes.

(iv) *On the stacking fault*

The bubbles constituting the central triangle in Figs. 10*b* and 11*b* are in regular hexagonal alignment in themselves but are in disalignment with the surrounding mother raft. Refering to Fig. 17, they are in *b*-sites relative to the mother raft in *a*-sites, thus resulting in the boundary line of two-dimensional stacking fault. Several examples of this type of faults was detected by W. L. Bragg and J. F. Nye³⁾, leaving the mechanism of formation unrevealed. In the present stage of the dislocation theory, we can easily understand, at least, the geometrical mechanism of formation.

In order to visualize the geometrical mechanism of transformation between the state *b* of stacking fault and the state *c* of paired dislocations in these figures, it is convenient to introduce the dislocation reaction involving the imperfect dislocations symbolized by

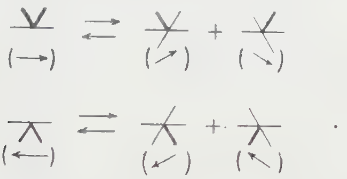

The glide line, the extra-half plane and the Burgers' vector characterizing each dislocation are represented in the symbol by the fine full line, the bold half line and the underlying arrow, respectively. The imperfect dislocations, standing on the right hand side, can glide on any one of the two glide lines but they issue in the wake of their travel to the stacking fault between the grain in *a*-sites and the grain in *b*-sites. Some examples are shown in Fig. 18, where the perfect dislocation D dissociates into two imperfect dislocations, A and B, with the stacking fault between. This is the analogue to the so-called extended dislocation⁴⁾.

Starting from the state in Fig. 18*p*, the paired dislocations D and D′ can dissociate into two imperfect dislocations, A and B, and

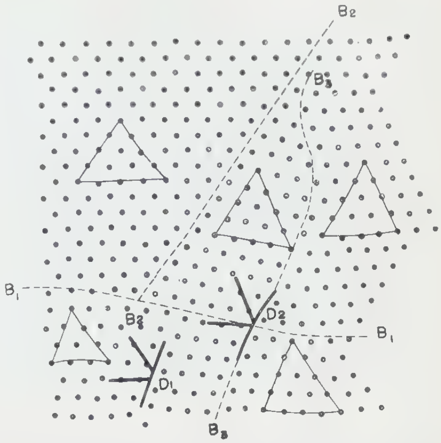

Fig. 16. Characteristic disalignment of bubbles at the critical state (see Fig. 3).

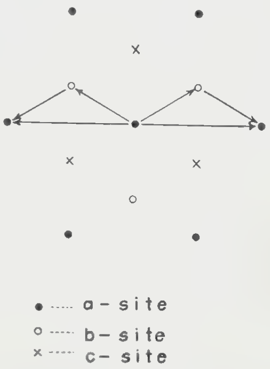

Fig. 17. Three types of the lattice sites in plane hexagonal bubble array.

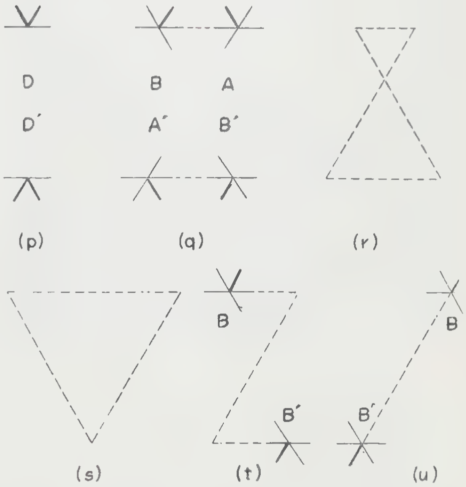

Fig. 18. Some of the possible dislocation reactions involving imperfect dislocations and the accompanied stacking faults.

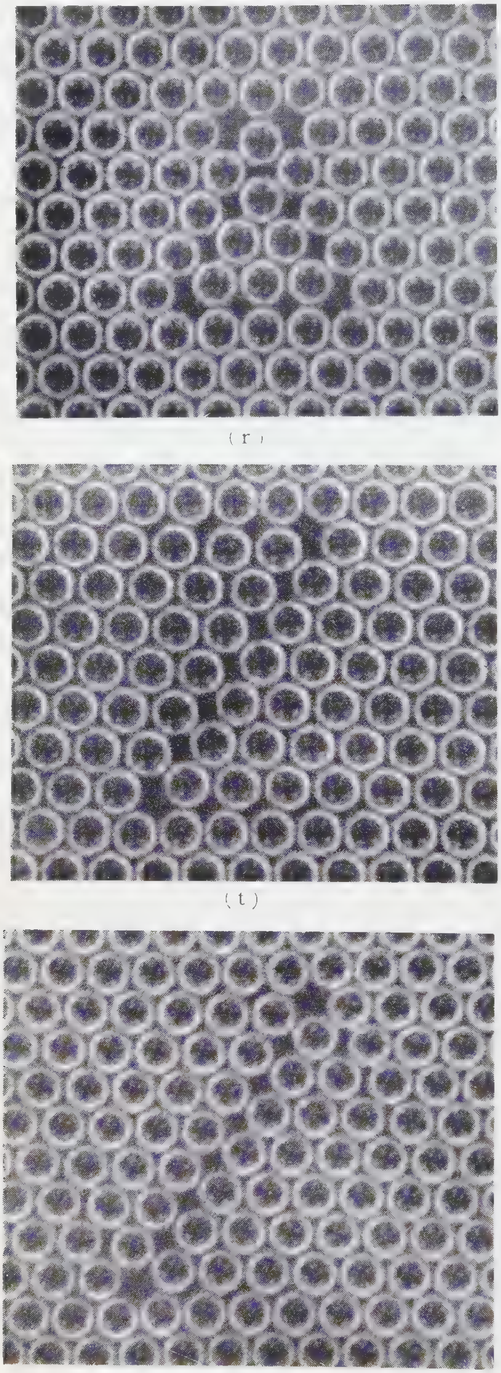
(r)
(t)
(u)

Fig. 19. Some examples of the stacking faults in the bubble raft at rest.

A′ and B′, respectively (see Fig. 18*q*), while the new pair of dislocations, A and A′, and B and B′, respectively, can switch onto the new glide lines to annihilate each other under favourable condition, to result in the stacking fault in the state of Fig. 18*r*. This type of the stacking fault is detected in the bubble raft shown in Fig. 19*r*. If only the dislocation D dissociates, we can expect the stacking fault in the state of Fig. 18*s*, which corresponds to Figs. 10*b* and 11*b*.

We can also expect the stacking faults with surviving imperfect dislocations. Starting from the state of Fig. 18*q*, we have the stacking fault in the state *t* as the result of pairwise annihilation of the imperfect dislocations A and A′, and the stacking fault in the state *u* as the result of further shifting of the remaining imperfect dislocations B and B′. Both types of the stacking faults are detected in the bubble raft shown in Figs. 19*t* and *u*, respectively. As to the latter type, it is noteworthy that this type of the stacking fault can be expected as the issue of coalescence of precipitated vacancies⁵⁾, but that the constituent imperfect dislocations can not glide without the stacking fault accompanying in its wake⁶⁾.

The interactions as well as the transformations between the lattice imperfections are expected to be of much interest in processes such as the diffusion, the order-disorder transformation and the allotropic transformation. In the respect, the bubble raft in the vibrating state displays remarkable characteristics, such as the increased diffuseness of the lattice imperfections in general and the predominant role of the imperfect dislocations.

After the geometrical mechanism of transformation is clarified, however, we must proceed onto the problem on the relative stability between the relevant states and then onto the problem on the rate process of transformation between the states. In the present stage of our investigation, we can not decide conclusively on these points. Yet, at any rate, we can not neglect the undeniable effect of the mechanical vibration of the bubble raft simulating the thermal vibration of the real crystal.

The authors are indebted to Mr. M. Yoshimura for the kind cowork in setting the vibration apparatus and to Mr. T. Zempô for the earnest experimental assistance throughout the present work. This work was supported by the Scientific Research Fund granted by the Ministry of Education.

References

1) W. L. Bragg and J. F. Nye: Proc. Roy. Soc. **A190** (1947) 474.
W. L. Bragg and W. M. Lomer: ibid. **A196** (1949) 171.
W. M. Lomer: ibid. **A196** (1949) 196; Proc. Camb. Phil. Soc. **45** (1949) 660.
2) W. M. Lomer and J. F. Nye: Proc. Roy. Soc. **A212** (1952) 576.
E. Fukushima and A. Ookawa: J. Phys. Soc. Japan **8** (1953) 609; **9** (1954) 44.
3) W. L. Bragg and J. F. Nye: Proc. Roy. Soc. **A190** (1947) 474.
4) R. D. Heidenreich and W. Shockley: *Bristol Conference on Strength of Solids* (1947) 57.
5) F. Seitz: Phys. Rev. **79** (1950) 890; Advances in Physics **1** (1952) 43.
6) F. C. Frank: Proc. Phys. Soc. London **A62** (1949) 202.

JOURNAL OF THE PHYSICAL SOCIETY OF JAPAN Vol. 10, No. 11, NOVEMBER, 1955

Some Observations on Dislocations in Copper Crystals

By Hideji SUZUKI

The Research Institute for Iron, Steel and Other Metals,
Tohoku University, Sendai

(Received August 1, 1955)

Well-developed octahedral {111} and cubic {100} faces have been obtained in recrystallized copper by annealing the material at a temperature close to the melting point. Monatomic steps on both octahedral and cube surfaces, which were caused by the presence of dislocations and their motion, are visible through the decoration by oxide particles formed in the course of cooling. Arrays of dislocations in sub-boundaries, random migration of each dislocation, the migration of dislocation groups in sub-boundaries, evaporation spirals are observed. Analysis of the structure of sub-boundaries in terms of constituent dislocations seems to support the main idea of the theory of dislocation network put forward by T. Suzuki and the present author.

§ 1. Introduction

Forty and Frank1) have succeeded in revealing the monatomic growth and slip steps on well-developed cube and octahedral faces of silver crystals, which were grown from the vapour. The heights of these monatomic steps are about 2A, and are of course out of resolving power of an optical microscope as well as an electron microscope. The detection of monatomic steps was greatly assisted by the remarkable phenomenon of 'decoration' of the edges of monolayers.

The observation by Forty and Frank afforded very important contributions to the theory of dislocation, i.e. informations concerning the distribution of dislocation, behaviours of each dislocation, etc.. The crystals in their observation, however, were grown from vapour, which might be very perfect in comparison with those employed usually in the studies of plastic deformation. Of particular interest are the dislocations left behind the recrystallization and their behaviours.

The positions of dislocations in metal crystals are also revealed in the other methods, such as, chemical etch2), thermal etch or oxidation3). Informations obtained from these observations, together with those obtained from the monatomic steps in habit surfaces will improve the basis of the dislocation theory of real crystals.

This article describes the observation on the monatomic steps in the well-developed octahedral {111} and cube {100} faces of recrystallized copper. The distribution of dislocations in these crystals, motion of each dislocation, migration of sub-boundaries are also discussed.

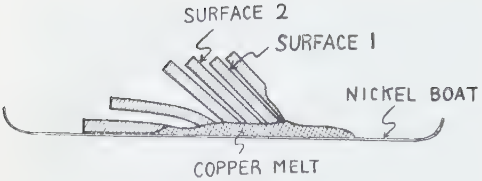

Fig. 1. The arrangement of annealed copper blocks.

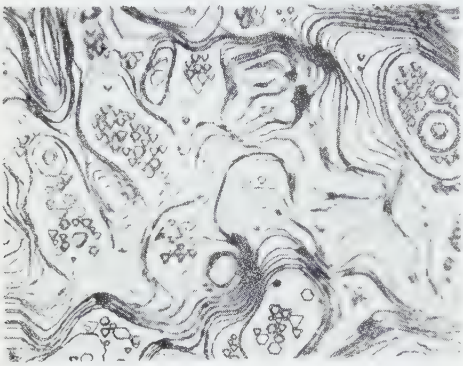

Fig. 2. Surface nearly parallel to a {111} face, after high temperature annealing. ×350

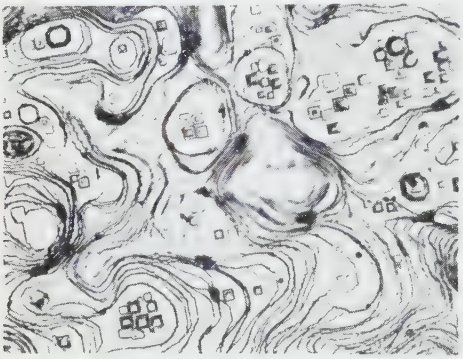

Fig. 3. Surface nearly parallel to a {100} face, after high temperature annealing. ×350

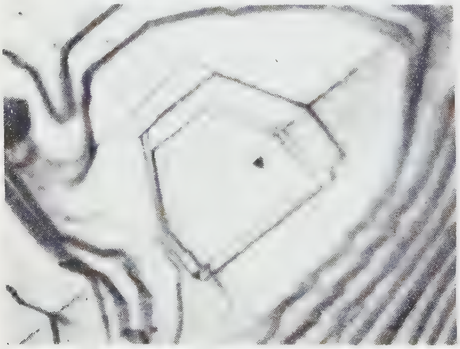

Eig. 4. Surface structure in the vicinity of coherent twin boundary. ×1,500

§2. Development of octahedral and cube faces by high temperature annealing

In order to detect the edges of monolayers of atoms on a close-packed atomic planes, the surfaces for the observation must be true to the appropriate plane to within only a few seconds of arc and it is difficult in practice to produce such suface on bulk metals, which were subjected to known deformation or heat treatment, by usual polishing techniques. Meanwhile, it was fourtunately found that the octahedral and cube faces develope on copper crystals which were annealed at a temperature very close to the melting point as follows.

When several cold worked copper blocks (99.98% copper) of a ring shape of 20 mm in inner diameter, 30 mm in outer diameter and 3 mm in thickness were heated to a temperature close to the melting point for about 3 hours in low vacuum (about 10^{-3} mm Hg), on account of accident in automatic controller, the furnace was heated beyond the melting point, so some outer parts of copper blocks melted and the molton material dripped in the bottom of the boat. (Fig. 1) The true temperature of the copper crystal was not measured, but it was estimated that any part of blocks was heated to a temperature within 0.001°C to the melting point if the melting took place at an ideally definite temperature and if the heat transfer through the evaporation or condensation of copper was neglected. It is, therefore, reasonable to suppose that any copper crystals was heated to a temperature within 0.1°C to the melting point. After this heat treatment it was found that {111} or {100} faces developed on the free surface associated with steps of about 0.5μ high. One can observe the exact {111} or {100} faces extending over several tens microns, even if the angle between a habit face and the average crystal surface is so large as a few degrees as shown in Figs. 2 and 3. The triangular or square pits on octahedral or cube faces may be related to dislocations respectively, but any convincible evidence has not been obtained.

Fig. 4 shows the neighbourhood of a coherent twin boundary, where the octahedral face developed in one crystal and the cube face in the twin related crystal. The step-line pattern in one face continues through the twin inter-

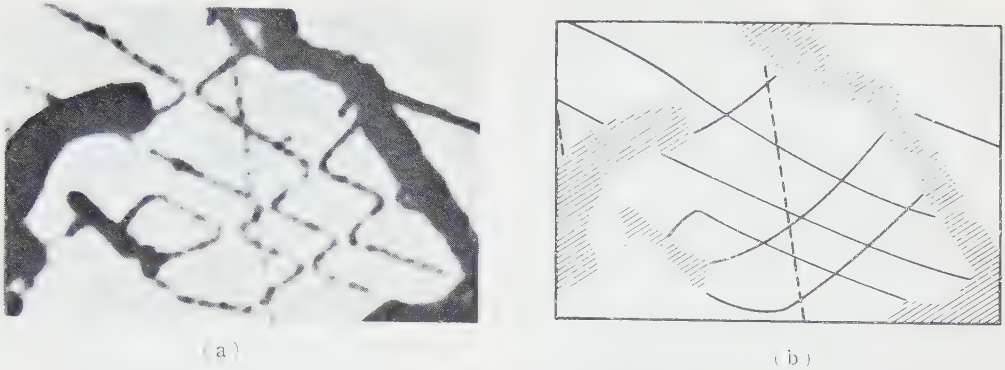
(a) (b)

Fig. 5. Distortion of step-line pattern due to atom migration. (a) Observed step-line pattern, (b) Initial step-line pattern before the atom migration takes place. ×5,700

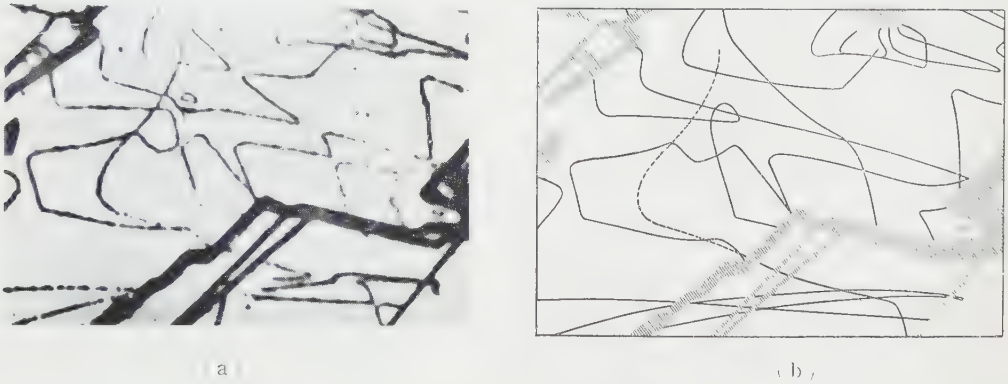
(a) (b)

Fig. 6. As Fig. 5. ×2,400

face as already mentioned by Forty and Frank[1] in their observation on the growth surface of silver.

§ 3. Decoration of Monatomic steps

By examination of the surface of the above mentioned crystals at high magnification, it was observed that the monatomic steps on octahedral face was decorated by arrays of oxide particles as shown in Fig. 5a and 6a. The evidence for the formation of these oxide particles along the monatomic steps in the octahedral faces is as follows. As already pointed out in the interpretation of growth patterns[1)4)] when two step-lines cross each other (Fig. 7a), the pattern becomes distorted by migration of atoms to remove sharp corners (Fig. 7b), if the heights of the both steps are equal to each other. The pattern shown in Fig. 5a might be produced from the step-line pattern shown by the solid curves in Fig. 5b, after the atom migration mentioned above. The hatching in the figure represents large steps or oxide particles irrespective to the elementary step-lines. The pattern in Fig. 6a

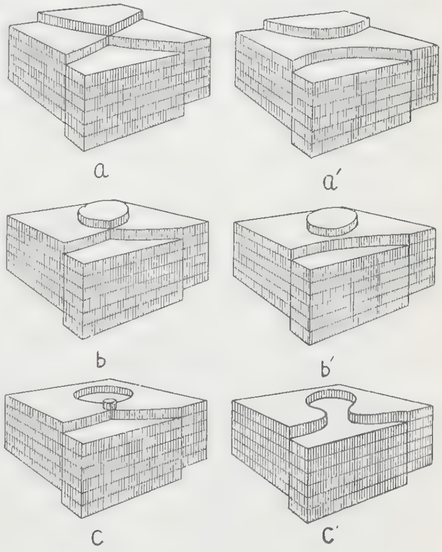

Fig. 7. Schematic representation of distortion of step-line patterns due to atom migration.

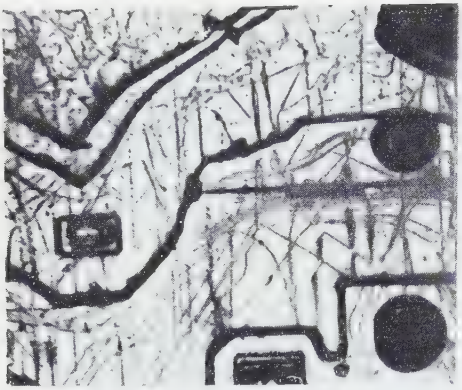

Fig. 8. Step-line patterns in a {100} face. ×2,000

is more complicated than in Fig. 5a but if the distortions of step-line patterns shown in Figs. 7b, b′ and c, c′ took place, the initial step-line pattern might be shown in Fig. 5b, where the dashed line represents the step-line produced after the atom migration was ceased. One could hardly find another interpretation for the patterns in Figs. 5a and 6a, so it may be reasonable to conclude that the heights of the majority of steps represented by thin curves are equal to each other. Since the step heights could not be detected by optical microscope using phase-contrast illumination, the height of each step should necessarily be less than 20A. It is, therefore, convincingly concluded that most of the thin curves indicate the monatomic steps. The decoration of steps in cube faces is not very perfect compared with that in octahedral faces as shown in Fig. 8. The distortion of step-line pattern took place in Fig. 8, so the thin curves in this figure may also represent monatomic steps.

Forty⁵⁾, Forty and Frank¹⁾ have succeeded in revealing the monatomic steps in some metals through the tarnish by 'Plasticine' at room temperature. The surface of copper are also decorated by oxide particles after exposing the crystal to atmosphere for a few months, but the decoration was very imperfect compared with those during high temperature oxidation.

§ 4. Dislocations in Sub-boundaries

Figs. 9 to 11 show step-line patterns on octahedral faces caused by dislocations in sub-boundaries, Fig. 9 is a typical example of straight sub-boundary composed of an array of dislocations. Fig. 10 shows an example of triple junction of sub-boundaries.

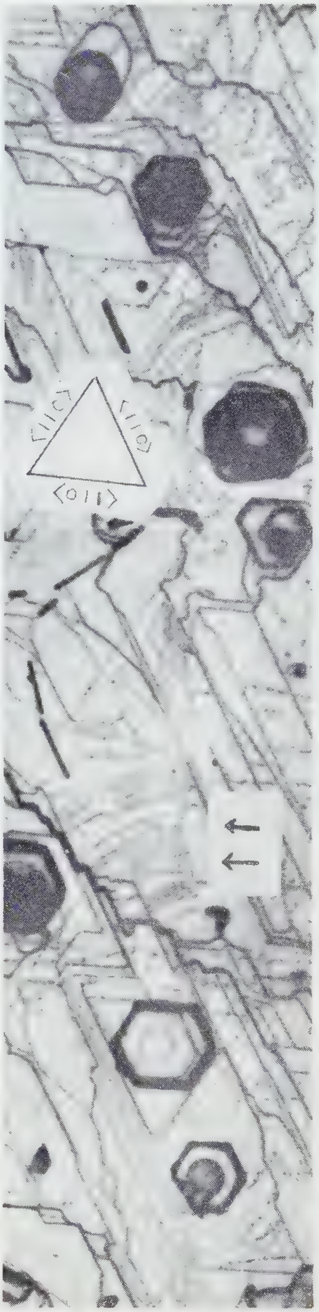

Fig. 9. Straight sub-boundary, ×1,500. Note the arrows, the pattern in these regions indicate that each dislocation has the same normal component of Burgers vector to the surface.

The most simple sub-boundary is a tilt boundary consisted of parallel edge dislocations with the same Burgers vector. Sub-boundaries of this type are parallel to {110} planes. Since a dislocation is associated with a monatomic step on the observed surface only when the Burgers vector of dislocation is not parallel to the surface, about a half number of dislocations cannot be visible in an octahedral face. The intersections of the observed surface with {110} tilt boundaries of visible dislocation arrays are parallel to ⟨110⟩. Fig. 11 shows perhaphs a sub-boundary of this type. But it must be noted that step-lines in Fig. 11 continue through the large steps. This indicates that the step-lines were caused by the migration of constituent dislocations of the sub-boundary.

According to the systematic observation over whole area of a few crystal grains with the surface nearly parallel to {111} faces, the sub-boundaries belonging to ⟨110⟩ directions in the surface were rather rare compared with those in the other directions. Further, the sub-boundaries in the former directions always reveal the trace of migration as in Fig. 11. The stable sub-boundaries, which do not show appreciable trace of migration, are not parallel to ⟨110⟩. Since the intersections of the sub-boundaries parallel to {100} or {111} with the octahedral face are parallel to ⟨110⟩, it is concluded that the sub-boundaries parallel to the above-mentioned planes are rather rare in recrystallized copper and that these sub-boundaries are less stable than the other type of sub-boundaries.

On the other hand according to the theory of dislocation networks put forward by T. Suzuki and the present author[6], the stable configuration of dislocation networks, which can remain after recrystallization, is a honeycomb structure composed of {112} plane networks as shown in Fig. 12. The components of Burgers vector of individual dislocation

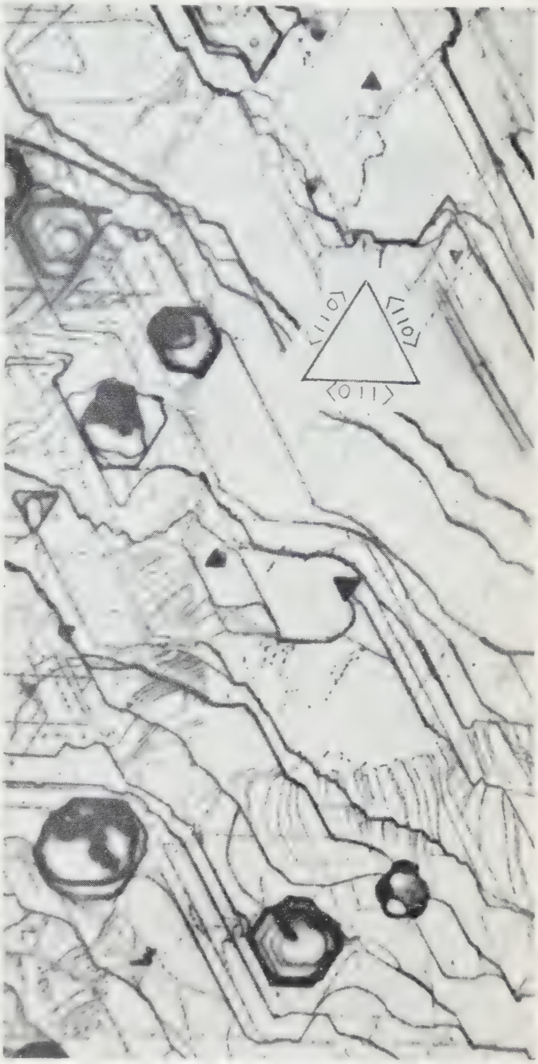

Eig. 10. Triple junction of sub-boundaries. ×1,500

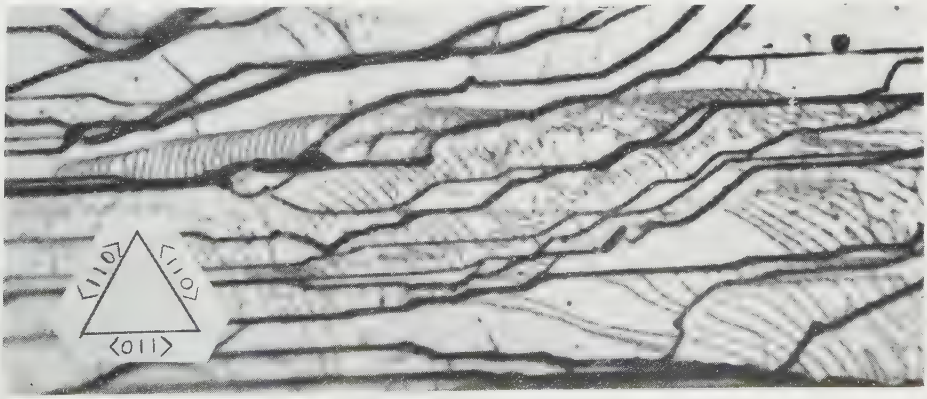

Fig. 11. Sub-boundary thought to be parallel to a {110} plane. ×2,400

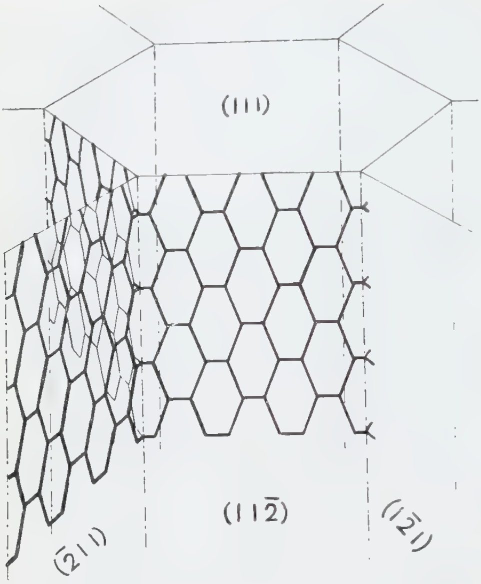

Fig. 12. Honeycomb structure composed of {112} plane networks.

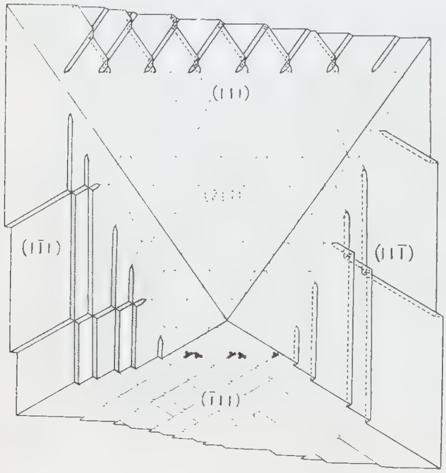

Fig. 13. Schematic representation of step-line formation in octahedral planes by the (211) dislocation network.

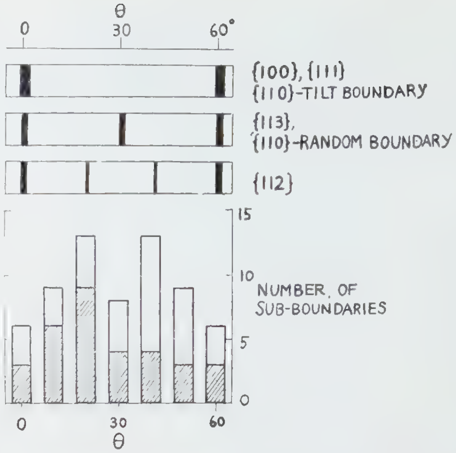

Fig. 14. Frequency finding sub-bounbaries in a range of direction in an octahedral face.

elements normal to octahedral faces are seen in Fig. 13. A plane network, for example, parallel to (211) causes step-lines on six octahedral faces parallel to (111), (1$\bar{1}$1) and (1$\bar{1}$1), but not any step-line on ($\bar{1}$11) face. When the (211) dislocation network is observed in (1$\bar{1}$1) or (11$\bar{1}$) face, the directions in the surface make an angle of 19°06′ with one of ⟨110⟩ directions in the surface, and when the (111) face was abserved the network is parallel to one of ⟨110⟩ directions. This network in the vicinity of (111) free surface, however, is very unstable, because the network meets with the surface at an angle of 19°28′, while the angle between (211) and (1$\bar{1}$1) or (11$\bar{1}$) is 61°52′.

In Fig. 14 the frequency finding the direction of sub-boundaries in a region of orientation from θ to $\theta+\delta\theta$ is plotted against θ, where $\delta\theta$ is 10°. The height of hatched region of the figure respresents the number of sub-boundaries counted for the angle from one of ⟨110⟩ directions, and the total height of the figure represents the number disregarding the sign of the angle. The upper of Fig. 14 shows the calculated direction of sub-boundaries parallel to some simple crystallographic planes. It seems, therefore, to be reasonable to suppose that the sub-boundaries are nearly parallel to {112} planes. Further considerations on the structure of sub-boundaries shall be found in § 7.

§ 5. Migrations of Dislocations

It must be noted that the monatomic steps in Fig. 5a and 6a are not parallel to the intersections of definite crystal planes with those observation surfaces, and that these monatomic steps are produced as a result of migration of individual dislocations. Some of irregular motion of dislocations are also shown in Figs. 15 to 18. The traces of dislocations drawn in Figs. 15b, 16b, 17b and 18b could not be obtained uniquely from corresponding step-line patterns, but may be accepted as plausible figures. These figures are also useful for the check of height of steps, and it may be seen that the majority of the step-lines are of monatomic height and

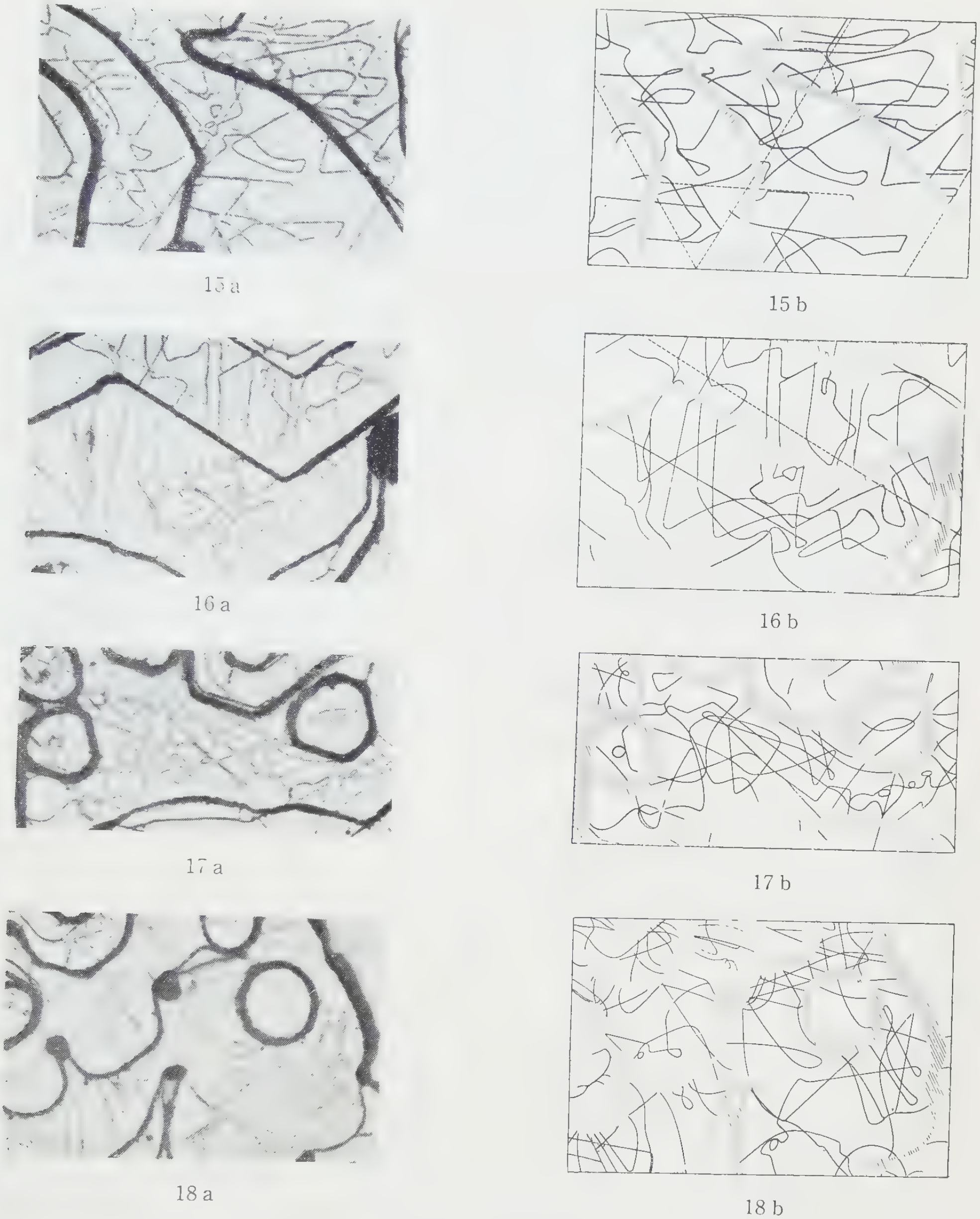

15 a 15 b

16 a 16 b

17 a 17 b

18 a 18 b

Fig. 15~18. Migration of dislocations. a; Observed step-line pattern, b; Trace of migration of dislocations derived from a. ×1,500

the rest are of the twice or thrice. The step-line pattern in Fig. 19 is so complex as to be impossible to reproduce the trace of dislocations uniquely. In spite of these distinct evidences of random motion of dislocation, it must be emphasized that the dislocations in copper crystal can hardly climb out from its slip plane under ordinary conditions, because the crystals examined here were annealed at an unusually high temperature perhaphs within 0.1°C of the melting point.

The mode of migration of dislocations may be classified into some classes, such as the shaking of the head (Fig. 20), the migration over long distance (Figs. 21 and 22), the migration of a group of dislocations in a small region (Fig. 23), and the migration of group of dislocations over a long distance (Figs. 24 and 25).

It was very rarely found that a dislocation shakes its head around a fixed position as in Fig. 20, while the shaking motion frequently

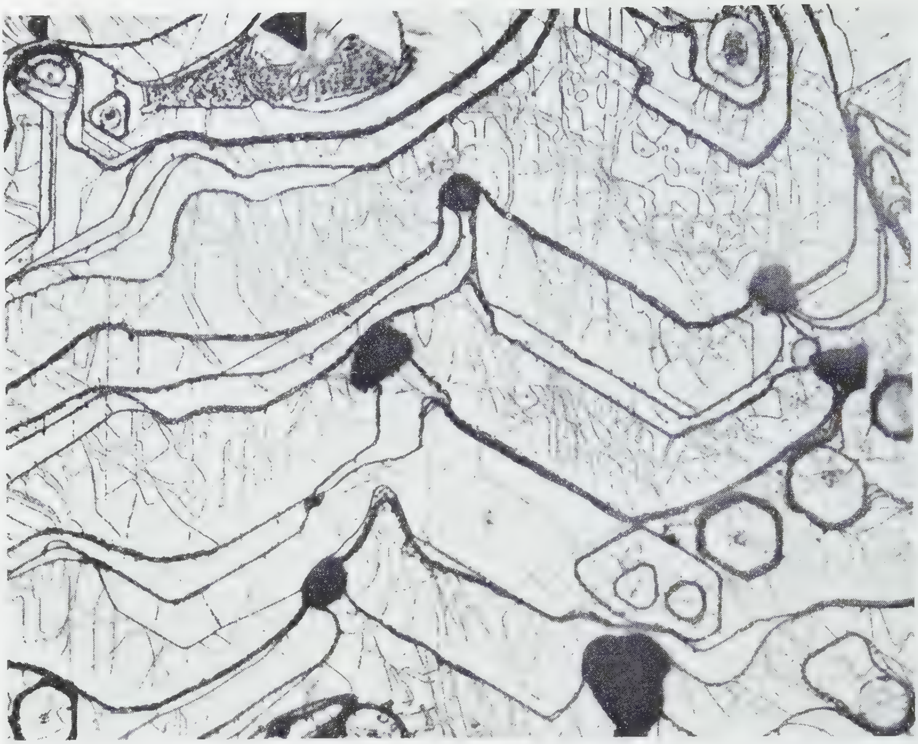

Fig. 19. Random motion of dislocations. ×1,200

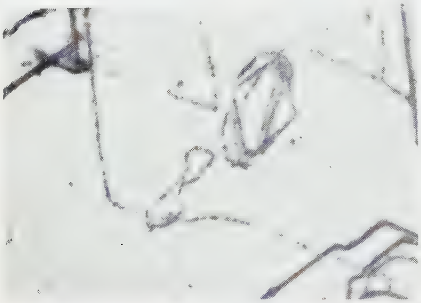

Fig. 20. Shaking motion of a dislocation head. ×2,400.

took place during the migration over long distance and resulted in many closed step-lines as already shown in Figs. 15 to 19. These patterns suggest that a part of a dislocation in the vicinity of free surface is more mobile than that in the interior of the crystal. It seems, therefore, to be reasonable to suppose that a part of the driving force making an isolated dislocation to migrate may be supplied from oxidation process at the monatomic step as Frank⁷⁾ employed in his theory on whisker formation.

The migration distance of each dislocation was usually of the order of 0.1 mm. A dislocation could not usually pass through a sub-boundary as shown in Figs. 9 and 10. These observations imply that the spacing between neighbouring sub-boundaries are usually of the order of 0.1 mm, which is considerably wider than that between large steps in the surface.

The migration patterns of dislocation groups as shown in Figs. 23, 24, 25 and 26 indicate that the interactions between individual dislocations could not be explained in terms of their elastic stress field, on account of the following reason. In Fig. 25, for example, the dislocations change their migrating direction by about 120 degrees abruptly. If these dislocations were nearly edge type, their motions are climb rather than glide, then these dislocations would spread out over far wider region than these figures because the repulsive force between them is stronger than the force acting on each dislocation due to an applied stress of the order of 500 $g\,mm^{-2}$. In the case of parallel screw dislocations, the rate of spreading out is fairly greater than in the case of edge dislocations. In this way the migration of dislocation groups shown in Figs. 23, 24, 25, and 26 may be regarded as an evidence indicating that there are stronger coupling between dislocations

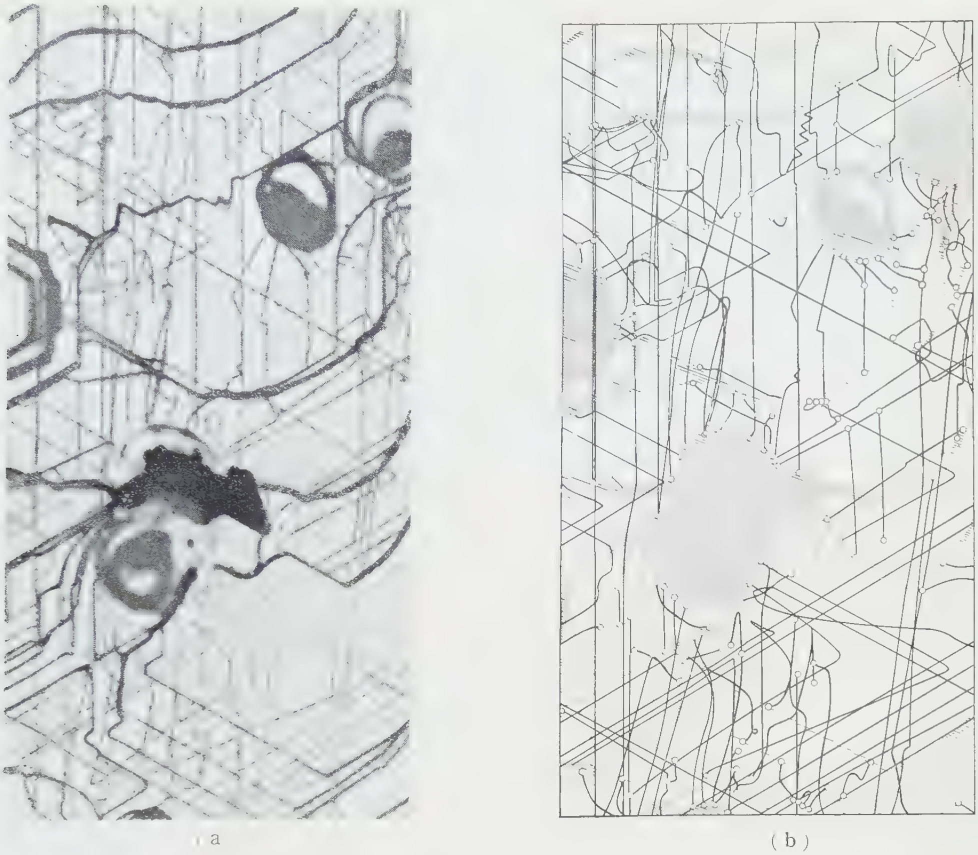

Fig. 21. Long distance migration of dislocations. (a) Observed step-line pattern. (b) Trace of migration of individual dislocations, an open circle represents the end point of each step. ×1,500

than elastic interaction. It is, therefore, reasonable to conclude that these groups of dislocations construct dislocation networks.

The step-line pattern in Fig. 23 indicates that dislocations in a network move rather randomly around a stationary position of its centre of gravity. Fig. 24 shows the straight migration of dislocation network, while Fig. 25 shows an abrupt change in the migration direction. These patterns in Figs. 24 and 25 seem to show the process of release of dislocations in the crystal through the migration of plane dislocation networks.

Fig. 26 shows the instability of a subboundary which is parallel to ⟨110⟩ direction in the observing octahedral face. The subboundary might have been on the line between two arrows in the figure before the migration. The pattern in the lower half seems to represent the step-lines associated with the initial position of dislocations in the subboundary, while the pattern in the upper half may be the trace of release of these dislocations. The instability of this type of subboundary is also seen from Fig. 11.

§ 6. Evaporation patterns

Figs. 2 to 26 show the crystal surface 1 in Fig. 1, which was faced to another block of copper, so that the evaporation rate of atoms is rather small compared with their surface migration rate. Hence there are not found any spiral patterns caused by evaporation, which might be the same with the growth except the direction of step.

The surface exposed to rather a wide space of vacuum, however, reveals a kind of spiral pattern. Fig. 27a to 30a show the micrographs on the surface 2 using normal illumination, while Figs. 27b to 30b are those using phase-contrast illumination of the same area with the corresponding micrographs, respectively. The patterns in these figures are not entirely the same with those obtained for the growth,

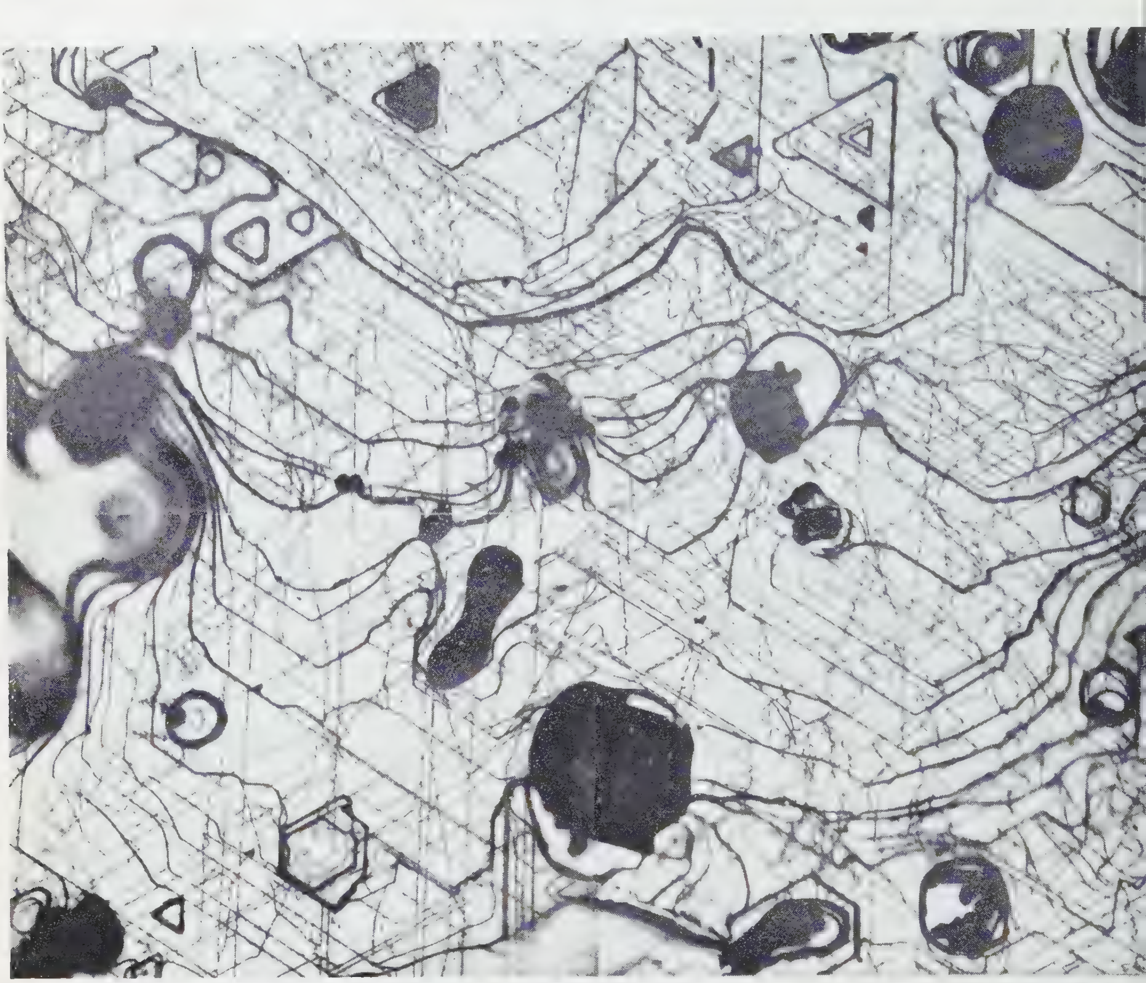

Fig. 22. Long distance migration of dislocations. ×1,200

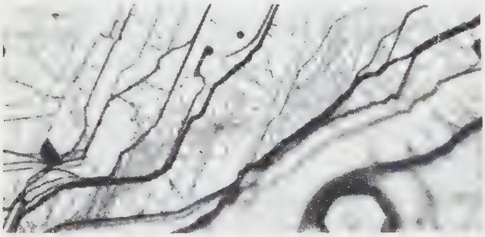

Fig. 23. Random migration of dislocation network around the stationary position of its centre of of gravity. ×1,200

but the difference between them may attributed to the tendency of the uniting of monatomic steps in this case.

The micrographs using phase-contrast illumination can detect the step heights, if several elementary steps are united into one. This observation seems also to support the conclusion that the elementary step is of monatomic height.

It is striking that the rotating direction of each spiral is the same with each other in a region of about 0.1 mm in diameter. The rotation is left handed in the whole region of Fig. 27, while Fig. 28 shows the boundary between two regions of right and left handed rotation. This fact indicates that the component of Burgers vector of a dislocation normal to the surface is the same with each other in a region over about 0.1 mm, i.e. a regular dislocation network has an extension of the order of this magnitude.

Fig. 29 indicates the evaporation pattern caused by a pair of dislocation groups with the components of Burgers vectors normal to the surface opposite to each other. Fig. 30 is the evaporation pattern initiated from dislocations in sub-boundaries.

§ 7. Distribution of Dislocations

As already mentioned in § 4 the long and straight sub-boundaries are formed preferen-

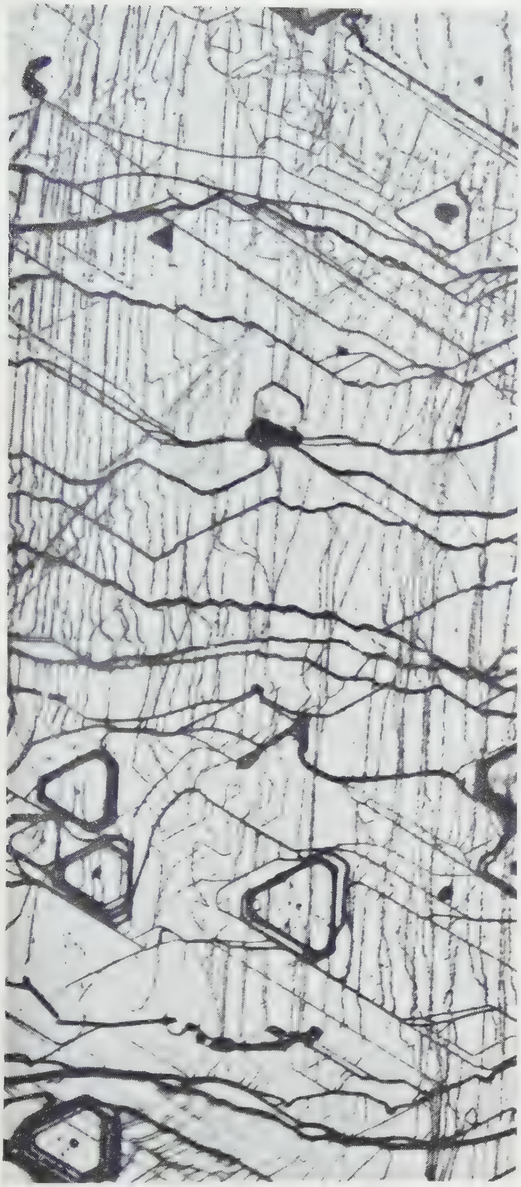

Fig. 24. Long distance migration of dislocation networks. ×1,500

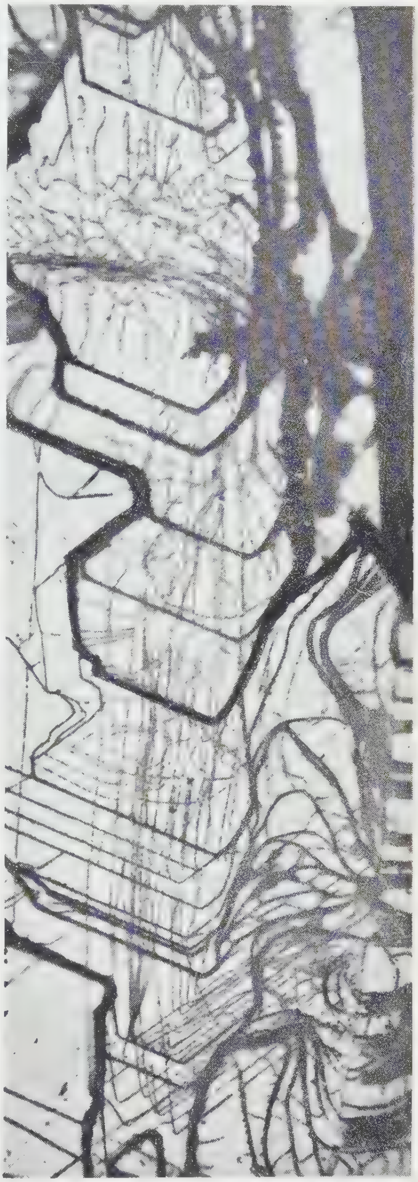

Fig. 25. Long distance migration of dislocation networks. Note the abrupt change of the migration direction. ×1,500

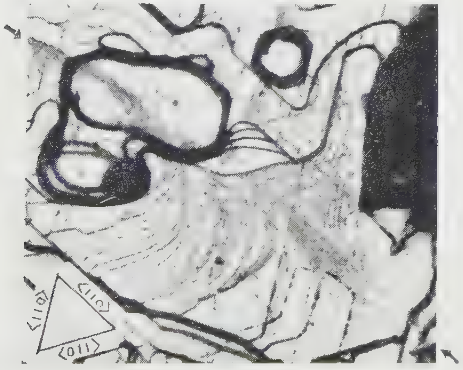

←Fig. 26. Migration of dislocation network, which is thought to be parallel to {110} face. The sub-boundary might be on the line between two arrows in the figure before the migration. ×1,800

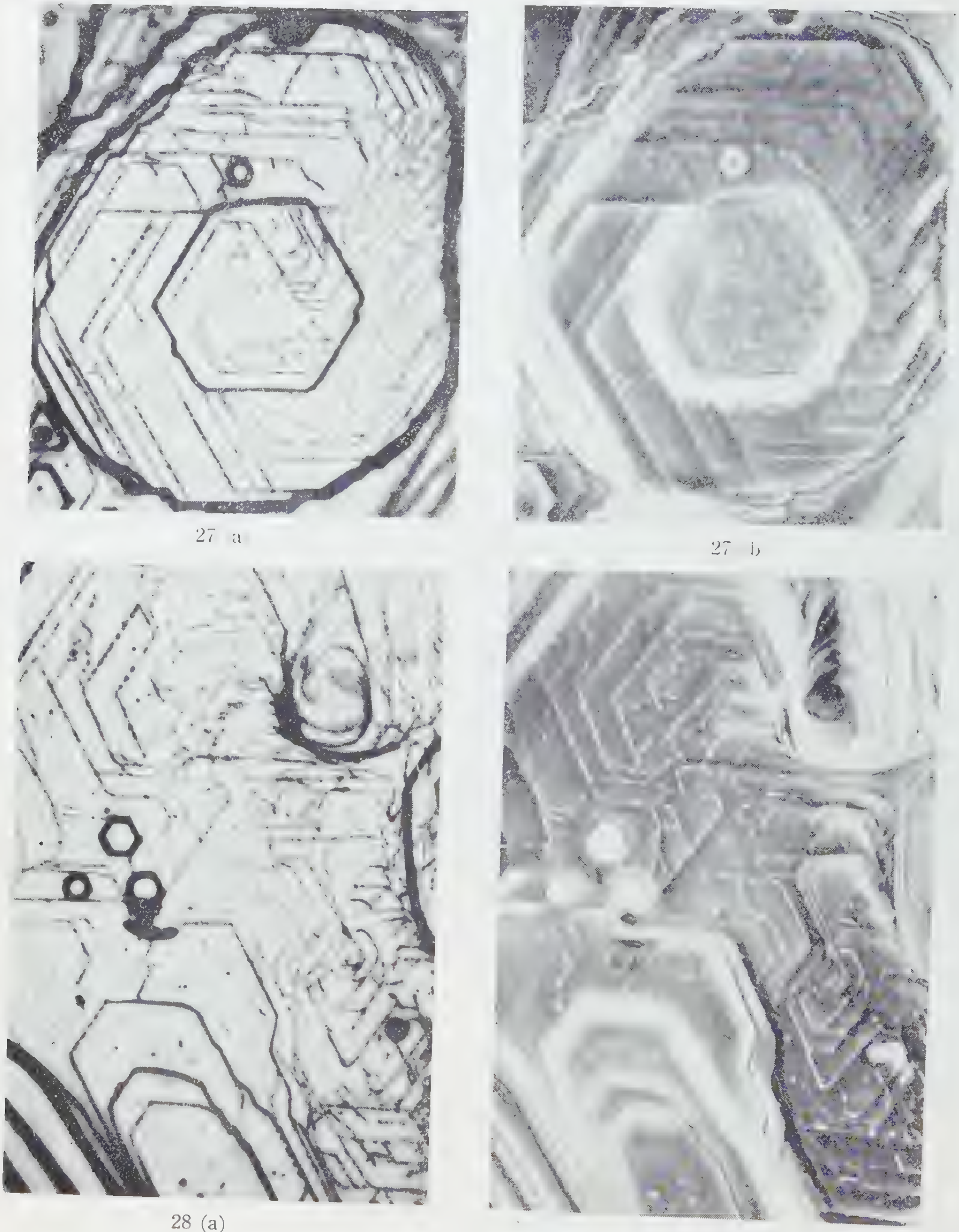

27 (a) 27 (b)

28 (a) 28 (b)

Figs. 27 and 28. Evaporation pattern on octahedral face. (a) Normal illumination. (b) Phase-contrast illumination. ×1,500

tially parallel to {112} faces. This may also be an evidence that the dislocations in sub-boundaries form networks, because it is difficult to find any reason for preferential direction of a sub-boundary, which consists of a grid of parallel dislocations, except {110}. The faces {112} are just the direction of the dislocation networks, predicted by T. Suzuki and the present author, having the longest life time.

The next problem arising from the observation is the spacing of dislocations in a sub-boundary, which is about 0.5 to 1μ in Figs. 9 and 10. These values of spacing are too small

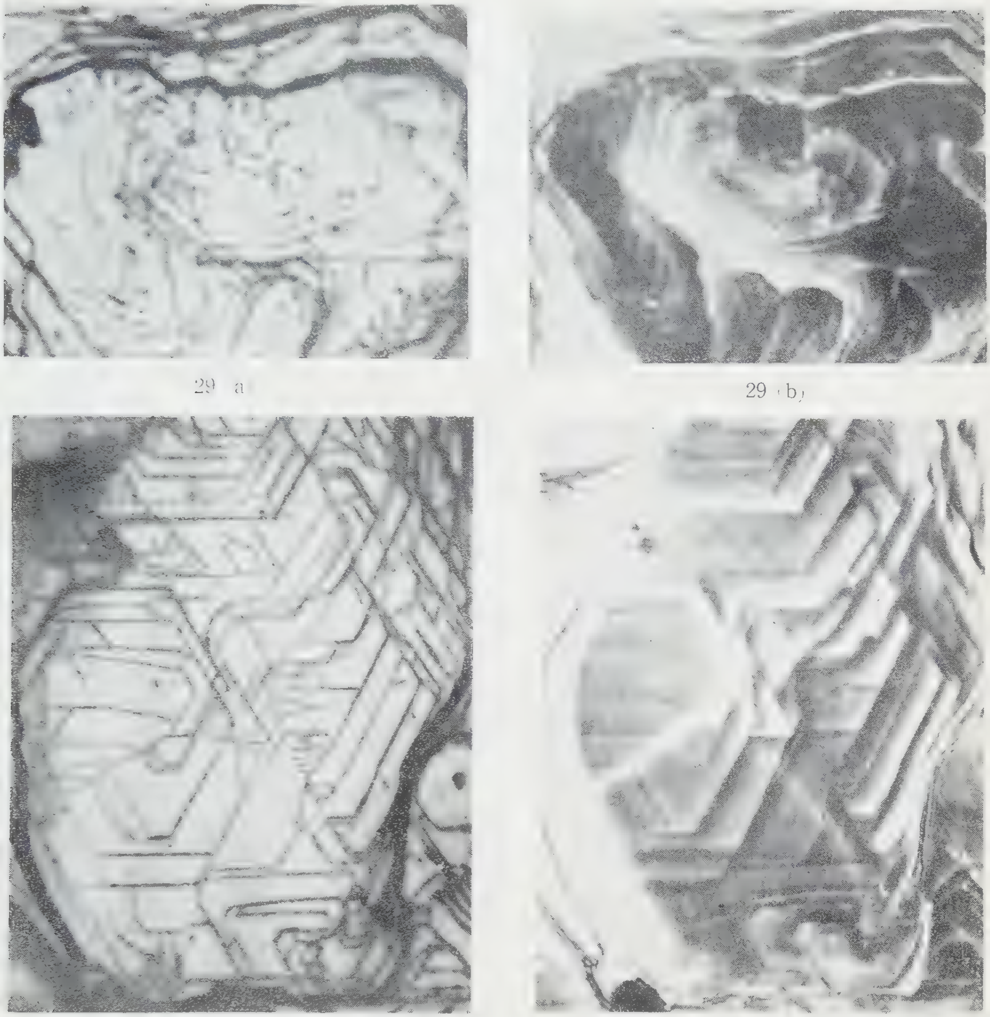

29 (a) 29 (b) 30 (a) 30 (b)

Figs. 29 and 30. Evaporation pattern on octahedral face. (a) Normal illumination. (b) Phase-contrast illumination. (Fig. 29 ×2,600. Fig. 30 ×1,500)

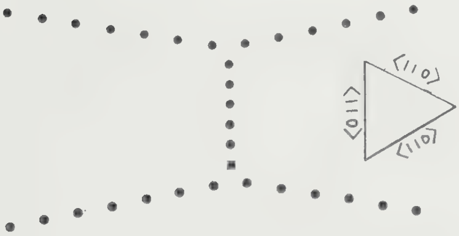

Fig. 31. Honeycomb structue of plane networks observed on an octahedral face.

to be accounted for by the theory of dislocation networks. Meanwhile the spacing between these sub-boundaries is too large to be expected from the theory.

T. Suzuki and the author have proposed a space structure of plane dislocation networks, which are parallel to {112} faces forming triple junctions along ⟨111⟩ direction, resulting in a honeycomb structure as already shown in Fig. 12. If dislocation networks are formed as just the theory predicted, the dislocation should arrange as the pattern in Fig. 31 in an octahedral plane. This type of triple junction, however, has not been found as yet among about fifteen triple junctions.

On the other hand it was frequently observed that these sub-boundaries migrate as a whole (Figs. 24 and 25). This observation suggests that the patterns in Figs. 9 and 10 are not those just after the recrystallization, but those resulted after the release or unification of dislocation networks. Then the above mentioned discrepancy between the theory and the observation might be explained as follows.

The {112} plane networks intersecting the surface at an angle about 19° tend to be swept out from the surface on account of the failure of mechanical balance in tension of the dislocation networks. The remaining networks are then united into a plane network to release the self energy. There may be thus only one plane network having a small mesh size and extending over long distance in the place of a regular honeycomb structure of plane networks at least in the vicinity of the free surface.

Though this explanation may interprete the whole observations, but one cannot be confident, because we have not been observed that the honeycomb structure of plane networks developed in a recrystallized pure metals.

The density of dislocations is also an important quantity characterizing the imperfections in crystals. If the Burgers vectors are not prefered to a special direction with respect to the orientation of the free surface, half number of dislocations can be observed in an octahedral face. The density of dislocations is then about 4×10^6 lines cm^{-2} in the surfaces without evaporation spirals, and it is about 2×10^7 lines cm^{-2} in the surface of rapid evaporation. The difference between these two values is too large to be neglected. It is easily supposed that a dislocation in the surface of rapid evaporation cannot migrate freely, because the dislocation is locked in the evaporation centre, while a dislocation in the surface of slow evaporation moves rather freely as shown in Figs. 15 to 26 and may annihilate meeting with an opposite dislocation, or combining with another. It must also be remembered that the dislocations at the large step of the surface could not be detected. The number of localized dislocations at the large steps may be neglected when each dislocation could not migrate freely. The density of dislocations in the surface of rapid evaporation, therefore, seems to be more faithful to that of the interior than in the surfaces of no evaporation spirals. The dislocation density 2×10^7 lines cm^{-2} is considerably greater than that observed by Forty and Frank1) and estimated by T. Suzuki and the author6), and is of the order of the other investigators8). This subject requires further examinations.

§ 8. Summary of Observations

Octahedral and cube faces develope on the surfaces of copper during high temperature annealing. Monatomic steps on these faces, caused by migration of dislocations and evaporation can be detected by ordinary microscope when they are decorated by oxide particles formed during cooling. Dislocations move randomly leaving complex traces. Dislocations in networks can also migrate. Dislocations construct usually a very straight sub-boundary. Most of the sub-boundaries are regarded to be parallel to {112} faces which were predicted as the plane of dislocation networks. Sub-boundaries which may be regarded as the tilt type sub-boundaries parallel to {110} faces are scarcely observed, and even those observed were unstable revealing distinct traces of migration.

The traces of migration of dislocations are observed. The non-crystallographic migrations were predominant at high temperatures. The migration of dislocation group indicates the existence of strong coupling between migrating dislocations, which cannot be explained in terms of elastic interaction between parallel dislocations, but in terms of line tension of dislocations in networks.

In the surface of rapid evaporation, spiral patterns are observed. The rotating directions of spirals are the same with each other in a region extending over about 0.1 mm.

The density of dislocations is of the order of 4×10^6 lines cm^{-2} in the surface where the evaporation spirals are not observed and is about 2×10^7 lines cm^{-2} in the surface of rapid evaporation. The latter number of dislocations may be more appropriate than the former to the real density of dislocations in the crystal.

The author wishes to express his hearty thanks to Professor Sakae Takeuchi for his interest and support.

References

1) A. J. Forty and F. C. Frank: Proc. Roy. Soc. **A217** (1953) 262.
2) see for example, A. J. Forty: Advances in Physics **3** (1954) 1.
P. A. Jacquet: Acta Met. **2** (1954) 752; 771.
S. Amelinckx: Acta Met. **2** (1954) 848.

3) A. A. Hendrickson and E. S. Machlin: Acta Met. **3** (1955) 64.
4) L. J. Griffin: Phil. Mag. **43** (1952) 827.
5) A. J. Forty: Phil. Mag. **43** (1952) 481; 949.
6) T. Suzuki and H. Suzuki: Sci. Rep. RITU **A6** (1954) 573.
7) F. C. Frank: Phil. Mag. **44** (1953) 854.
8) A. H. Cottrell: *Dislocations and Plastic Flow in Crystals*, (Oxford, 1953) 99.
P. Gay, P. B. Hirsch and A. Kelly: Acta Met. **1** (1953) 315.
A. Seeger: Z. Natureforschg. **9a** (1954) 758.

JOURNAL OF THE PHYSICAL SOCIETY OF JAPAN Vol. 10, No. 11, NOVEMBER, 1955

Aging Process in Quenched Aluminium-Zinc Solid Solutions

By Ken-ichi HIRANO

Department of Physics, Tokyo Institute of Technology,
Oh-okayama, Meguroku, Tokyo

(Received August 8, 1955)

Aging process in quenched Al–Zn solid solutions has been studied in the same manner as in the Al–Ag system. Specific-heat versus temperature curves have been obtained on the alloys after various aging treatments. Isothermal aging curves of electrical resistance have been also examined. In accordance with previous results on Al–Ag (J. Phys. Soc. Japan, **8**, 1953, 603; ibid. **10**, 1955, 23; ibid. **10**, 1955, 454.), Al–Mg–Zn (J. Phys. Soc. Japan **10**, 1955, 187.) and Al–Cu (in preparation), the present results reveal that the two independent reactions take place during the aging; they may be attributed respectively to the formation of Guinier-Preston zone and the precipitation of the new phase.

§ 1. Introduction

Studies of aging mechanism in Al–Ag, Al–Mg–Zn and Al–Cu alloys have distinguished between the low-temperature aging and the high-temperature aging[1]. During low-temperature aging, segregation of solute atoms to preferred planes of the matrix lattice, Guinier-Preston zones (G–P zones), are built up which are shown to be neither the nucleus of the precipitate nor the transition precipitate. Although still in the speculative stage, the new concept[2] of the origin of G–P zones is based on the possibility of an interaction between the solute atoms and lattice defects in the crystal. For example, both disc-shaped agrregates of vacancies and stacking faults surrounded by sessile dislocations may be formed by agglomeration of quenched-in excess vacancies to which the solute atoms diffuse. On the other hand, the major reactions during the high-temperature aging are the nucleation and growth of the transition or equilibrium precipitate.

In our previous papers[3]–[6] it has been shown that the property changes during the aging can be interpreted fairly well in terms of independent contributions from G–P zone and precipitate.

As for the Al–Zn system, Dehlinger first suggested in his discussion[7] on the resutls of the electrical resistance measurements of Meyer[8] on 80 wt. % Zn alloy that two independent reactions, characterized by the low- and the high-temperature aging, occur. Guinier[9] has carried out the X-ray examination by his small angle scatter method and shown that spherical zinc rich regions form in the matrix lattice during the low-temperature aging. However, Geisler, Barrett and Mehl[10] showed that coherent platelets form in the early stages of precipitation and these grow with time but break away from the matrix before they are thick enough to diffract X-ray as three-dimensional gratings: they did not distinguish between the low- and the high-temperature aging.

Therefore a further investigation has been made to find the relation between the low-

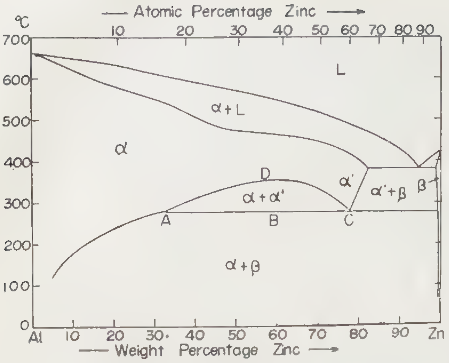
— Atomic Percentage Zinc →
10 20 30 40 50 60 70 80 90
°C
700
600
500
400
300
200
100
0
L
α+L
α
D
α'
α+α'
α'+β
β
A
B
C
α+β
Al 10 20 30 40 50 60 70 80 90 Zn
— Weight Percentage Zinc →

Fig. 1. Phase Diagram of Al–Zn System.

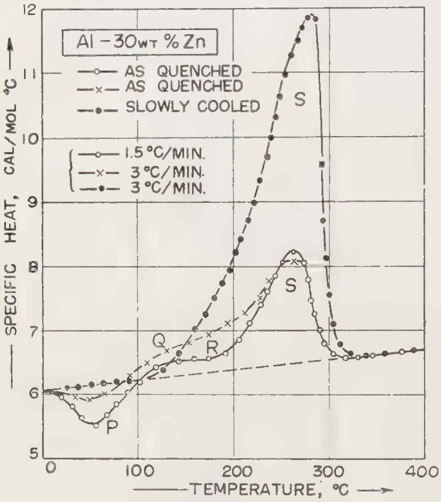

Fig. 2. Specific-heat/Temperature Curves of Al–30 wt. % Zn Alloy, As-Quenched and Slowly Cooled.

and the high-temperature aging. This has been carried out in the same manner as our earlier work on Al–Ag alloys and the results on both alloys have been used for discussion.

§ 2. Experimental Procedure

Alloys containing 20, 30, 40, 50, and 60 weight per cent of zinc were made from 99.99 per cent Al with distilled Zn, 99.99 per cent pure supplied from Mitsui Mining and Smelting Co. Weighed metals were melted in graphite crucible. After casting in an iron mold, the ingots were homogenized at 400°C for more than 200 hours.

The specimens for the specific-heat measurement were closed hollow cylinders having the external dimension; 2 cm in diameter and 3 cm in length. The electrical resistance specimens were square bars produced by cold rolling, 0.2 cm in both width and thickness and 8 cm in length.

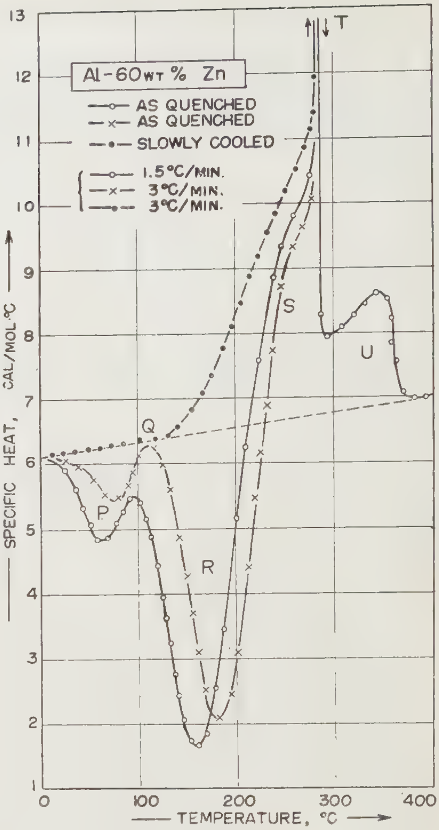

Fig. 3. Specific-heat/Temperature Curves of Al–60 wt. % Zn Alloy, As-Quenched and Slowly Cooled.

The methods for both the measurement of the specific-heat and that of the electrical resistance were the same as described in our previous papers$^{3)-6)}$.

All specimens were solution heat treated at 450°C which is in the single phase region in the equilibrium phase diagram as shown in Fig. 1, for 20 hours, after which they were rapidly quenched in a mixture of water and ice.

The aging treatments were conducted in air in an electrical furnace.

§ 3. Specific-heat/Temperature Curves

1. As-Quenched and Slowly Cooled Alloys

Figs. 2 and 3 represent the specific-heat /temperature curves (S–T curves) which were obtained with 30 and 60 wt. per cent zinc alloys respectively on reheating immediately after quenching. Two curves corresponding to different heating rates for the measurement, 1.5°C and 3°C per minute, are shown for both alloys. S–T curves on slowly cooled alloys, obtained by cooling from 450°C at the rate of 4°C per hour, are also shown in Figs. 2 and 3. Using the *Cp* values of pure Al and Zn, the specific-heat of the alloys have been calculated by Kopp-Neumann's rule and are given in Figs. 2 and 3 by dashed lines. These should be identical with the S–T curves of the alloys in which no change in atomic configuration occurs during heating.

Qualitatively similar curves to those in Fig. 2 were obtained with 20 wt. per cent zinc alloy and to those in Fig. 3 were obtained with 40 and 50 wt. per cent zinc alloys.

It will be noted that the S–T curves of as-quenched alloys show that energy is evolved at two temperature ranges, 0°∼100°C and 130°∼250°C, denoted by **P** and **R** respectively. This behaviour may be comparable with that observed in the S–T curves of as-quenched Al–Ag alloys, typical curve of which is shown in Fig. 4, obtained by the author with an alloy containing 50 wt. per cent silver, after quenching from 540°C, heating rate for the measurement was 2°C per minute.

Further, although not large as in the Al–Ag alloy, an absorption of heat denoted by **Q**, was detected at the temperature range between **P** and **R**.

As has been shown in the case of the Al–Ag alloys, the initial heat evolution **P** may be attributed to the formation of G–P zones during heating, and the dispersion of which by further heating may cause the heat absorption **Q**. The apparent smallness of **Q** in the present alloys seems to be due to the superposition of a heat evolution, **R**, on it. The second heat evolution, **R**, attaining a maximum at about 200°C, should be due to the precipitation of the new phase. Both **P** and **R** increase with decreasing heating rate; a similar fact has been observed also in the Al–Ag alloys.

In Fig. 2, at the temperature range of S, the apparent specific-heat rises rapidly and then diminishes approaching the dashed line at 310°C, indicating that complete solution of the precipitate has taken place.

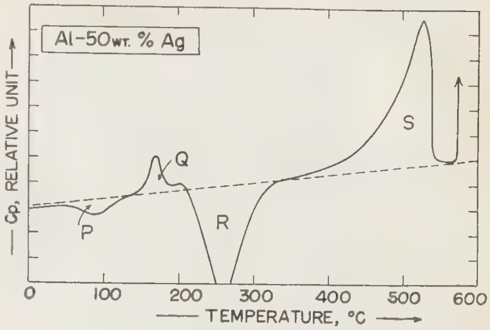

Fig. 4. Specific-heat/Temperature Curve of Al–50 wt. % Ag Alloy, As–Quenched.

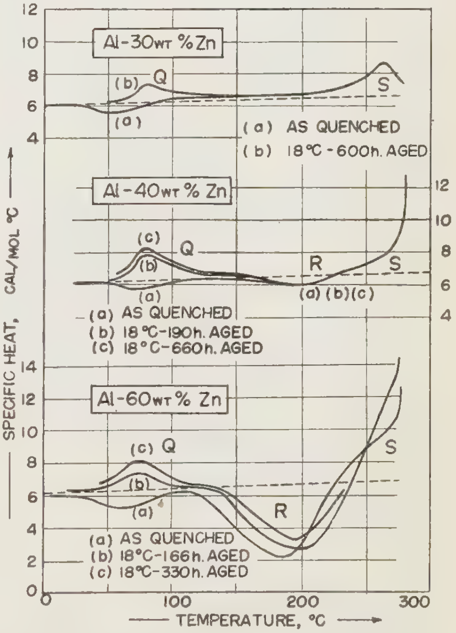

Fig. 5. Specific-heat/Temperature Curves of Al–Zn Alloys, Room Temperature Aged.

With slowly cooled alloys, neither **P**, **Q**, nor **R** could be detected, but cosiderable heat absorption corresponding to **S** was observed. With the alloys of higher zinc concentration, additional heat absorptions, denoted by **T** and **U** were observed as shown in Fig. 3. As may be seen from the equilibrium phase diagram (Fig. 1), **T** is the heat absorption required for the eutectoid reaction,

$$\alpha+\beta \rightarrow \alpha+\alpha' ,$$

which occurs when temperature rises across the eutectoid horizontal, **ABC** in Fig. 1, and **U** is required for the solid solution reaction,

$$\alpha+\alpha' \rightarrow \alpha ,$$

which occurs when temperature rises across the two phase boundary, **ADC**. The temperature of the eutectoid horizontal reported by the previous workers is somewhat variable; 275°C after Fink and Willey[12], 280°C after

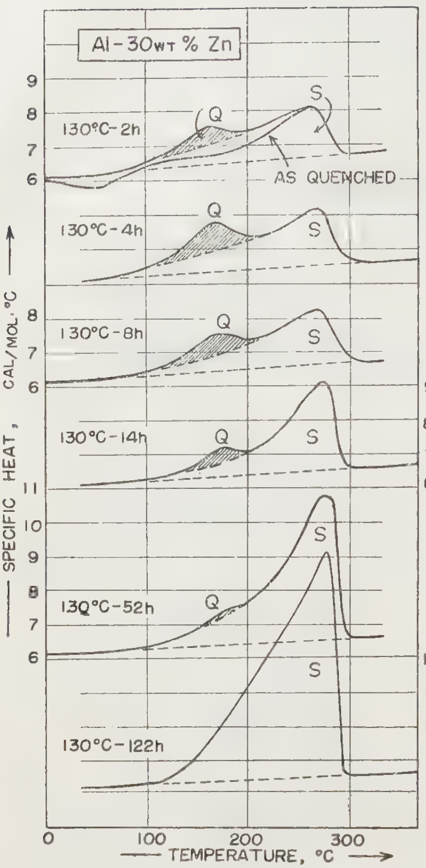

Fig. 6. Specific-heat/Temperature Curves of Al-30 wt. % Zn Alloy, 130°C-Aged.

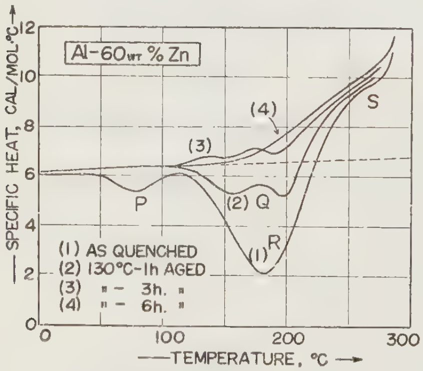

Fig. 7. Specific-heat/Temperature Curves of Al-60 wt. % Zn Alloy, 130°C-Aged.

Schmid and Wassermann[13], 283°C after Morinaga[14], 277°C after Borelius and Larsson[15]. However in the present experiment, the heat absorption **T** occurs at the range, 282°~285°C.

2. Room Temperature Aging

Fig. 5 shows the S-T curves for the alloys aged at room temperature for different periods. The heat absorption denoted by **Q** was observed at the range 50°~150°C, attaining its maximum at 70°C; this should be attributed to the re-solution of G-P zone formed by the room temperature aging. It may be noted that in all alloys **Q** occurs at the same temperature range independently of zinc concentration.

With 30 and 40 wt. per cent zinc alloys, it was observed that the room temperature aging did not affect the shape of the S-T curve at the range of **R**, so no difference between the S-T curve of as-quenched alloys and that of the room temperature aged alloys were detected, except the range of **Q**. This may indicate that precipitation of β phase does not set in appreciably during the room temperature aging in these alloys. On the other hand, in 50 and 60 wt. per cent zinc alloys, the room temperature aging affected the shape of the S-T curves at higher temperature range (**R** and **S**) which seems to be due to existence of small quantity of precipitate.

Comparison of the shape of **R** and **S** of the aged alloys with that of as-quenched alloys may give some information on appearance of transition precipitate, β' phase coherent with the matrix lattice, preceding the final β phase precipitate which is noncoherent with the matrix lattice. From this point of view, comparison of the results on 60 wt. per cent zinc alloy in Fig. 5 with those of the micrographic and X-ray study should be interesting.

3. 130°C-Aging

Figs. 6 and 7 show a number of S-T curves obtained on 30 and 60 wt. per cent zinc alloys respectively after aging at 130°C. The general behaviour of Fig. 6 is very similar to that obtained by Al-Zn-Mg system recorded in our previous paper[6].

As in the case of the room temperature aging, the S-T curves are again characterized by the fact that there are two heat absorption peaks, **Q** and **S**, which may be attributed to the re-solution of G-P zone and β phase respectively. The temperature range of **Q** is 120°~220°C, which is higher than that in Fig. 3; from this it will be predicted that G-P zone formed by 130°C-aging is more stable than that resulting from room temperature aging.

The heat absorption **Q** increased with increasing aging time until about 4 hours, beyond which it decreased and finally disappeared. No trace of **Q** could be detected in the curve obtained after 122 hours of the aging. Disappearance of **Q** at the later stage of the aging may be interpreted in the same manner as have been shown in our previous papers on the Al-Ag4) and Al-Mg-Zn5) alloys, where we have taken into account the relation between the stability of G-P zone and solute atom concentration in the matrix.

In contrast with the behaviour of **Q**, the heat absorption **S** increased with aging time and reached a final value when the β phase had precipitated completely. The shape of S-T curve of the over aged alloy coincides with that of the slowly cooled alloy shown in Fig. 2.

S-T curves in Fig. 7 have somewhat complex shape; temperature range of the heat absorption **Q** is superimposed on the heat evolution **R**. But the occurrence of **Q** is clearly detectable at an earlier stage of the aging.

It will be noticed that the temperature T_G where the heat absorption **Q** attains its maximum, is independent of zinc concentration but markedly dependent of the aging temperature. From the S-T curves of the alloy aged at various temperature, aging temperature dependence of T_G has been examined, the result is shown in Fig. 8, where linear relation between them may be seen. Since T_G can be regarded as a measure of the stability of the G-P zone, Fig. 8 indicates that the stability of the G-P zone increases linearly with the aging temperature. For comparison, the results obtained on the Al-$MgZn_2$5) and Al-$Al_2Mg_3Zn_3$5) systems are also shown in Fig. 8. It appears that the stability of the G-P zone increases by existence of magnesium atoms. It seems that the G-P zone containing Mg atoms may be a different type from that free from Mg atoms.

The temperature T_β, where the heat absorption **S** attains its maximum, may be regarded as a measure for the stability of β phase. It was confirmed that T_β of the slowly cooled alloy or over aged alloy coincides with the temperature of the two phase boundary in the equilibrium phase diagram.

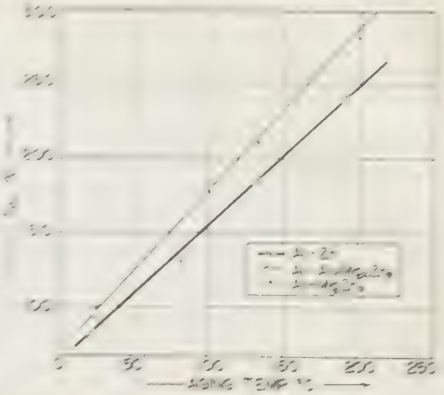

Fig. 8. Aging-Temperature Dependence of T_G.

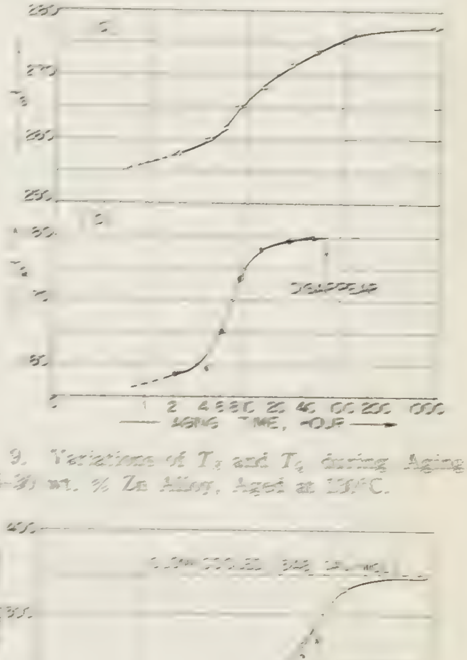

Fig. 9. Variations of T_β and T_G during Aging. Al-30 wt. % Zn Alloy, Aged at 130°C.

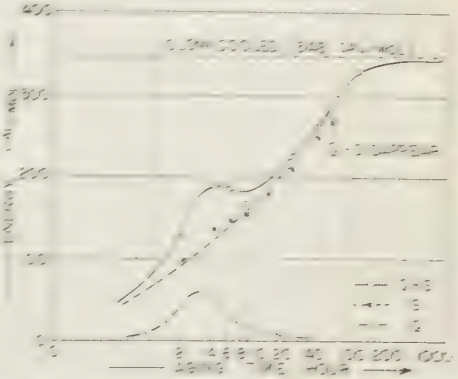

Fig. 10. Variation of Absorbed Energy during Aging. Al-30 wt. % Zn Alloy, Aged at 130°C.

Variations of T_G and T_β during aging are illustrated in Fig. 9 for the 130°C-aging of 30 per cent zinc alloy. Both T_G and T_β show tendency to saturation after the aging for 40 hours and 200 hours respectively.

To examine the change of the internal energy of the alloy during aging, the heat absorbed during the measurement of S-T curve, which corresponds to the area enclosed between the S–T curve and the dashed line in Fig. 6, is plotted against the aging time, thus leading to Fig. 10. The curve shows an intermediate maximum at about 4 hours. The value for slowly cooled alloy, 348 cal./mol., is also shown by dashed line for comparison. The curve seems to be constructed from two parts as shown by dashed and chain curves, denoted by **Q** and **S** respectively. **Q** comes from the heat absorption due to the re-solution of the G–P zone, and **S** comes from the heat abroption due to re-solution of β phase; the same heats as **Q** and **S** respectively must have been evolved during the aging.

§ 4. Electrical Resistance Measurements

1. Heating Curve (ρ–T curve)

In Fig. 11 electrical resistance versus temperature curves (ρ–T curves) are presented for 30 per cent zinc alloy. The heating rate for the measurements was about 2°C per minute.

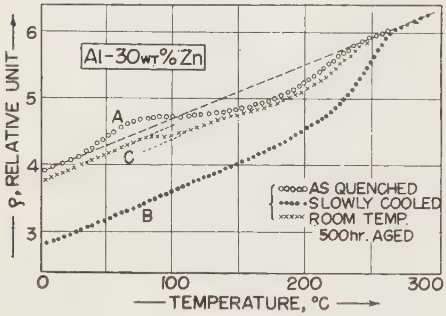

Fig. 11. Electrical Resistance/Temperature Curves of Al–30 wt. % Zn Alloy.

The curve denoted by **A**, given by open circles was obtained on freshly quenched alloy. The curve **B** given by solid circles was obtained on slowly cooled alloy, which may represent the values of equilibrium state at each temperature. The value given by dashed line which is the extrapolated line of the high temperature part of the curves **A** and **B**, should be taken as the value of supersaturated state.

As may be readily seen from Fig. 1, the curves **A** and **B** coincide each other at the temperature range above the solvus curve, where only α phase is stable to exist, while at the temperature range below the solvus curve, B phase can coexist with α matrix lattice of lower zinc concentration, so the value of equilibrium state is lower than that of supersaturated state.

The curves obtained with 60 per cent zinc alloy have more complex form than that in Fig. 11 as at the temperature range heigher than the two phase boundary, additional changes occur corresponding to the additional heat absorption **T** and **U** respectively as shown in Fig. 3.

The curve denoted by **C** drawn by crosses in Fig. 11 was obtained by the alloy aged at room temperature after quenching. It may be seen that the room temperature aging cause increase of the electrical resistivity and re-solution of G–P zone formed during room temperature aging on heating causes decreasing of it at the temperature range corresponding to the heat absorption **Q** in the S–T curves. To see more clearly the behaviour of the ρ–T curves in comparison with the S–T curves, we have derived $d\rho/dT$ versus temperature curves from the ρ–T curves obtained on the alloys of different zinc concentration and subjected various aging treatments. The result revealed that general shape of $d\rho/dT$ versus temperature curves is comparable with the corresponding S–T curves. It was seen commonly in all curves that the maximum in $d\rho/dT-T$ curve corresponds to the minimum **P** in the S–T curve (heat evolution **P**); this suggests that the formation of the G–P zone causes increasing of the electrical resistivity. The same phenomena were also observed with Al–$Al_2Mg_3Zn_3$[6] and Al–$MgZn_2$[16] systems.

2. Isothermal Aging Curve

The changes in the electrical resistivity on the aging of the 30 per cent zinc alloy at 70° and 100°C are shown in Fig. 12 as a function of aging time. Both curves have a slight intermediate maximum at an early part after some gradual decrease. The curves may be explained by two superimposed reactions attributted respectively to formation of G–P zone and precipitation of the new phase. As may be seen from the ρ–T curve, formation of G–P zone results in increasing in the electrical resistance, while the new phase precipitation results in decreasing of it, no doubt, due to depletion of the matrix in zinc. Thus schematic feature of intergration of above two reactions contributing to the change in resistivity is supposed as shown in Fig. 13. The curve of Al–Ag systems obtained previously[4]) is also presented in Fig. 13 for comparison. The apparent shape of observed curves for Al–Zn alloy is somewhat similar to those for Al–Ag alloy, but important difference lies in the contribution arising from the G–P zone. In contrast with a decrease due to G–P zone in Al–Ag alloy, increase occurs in Al–Zn alloy.

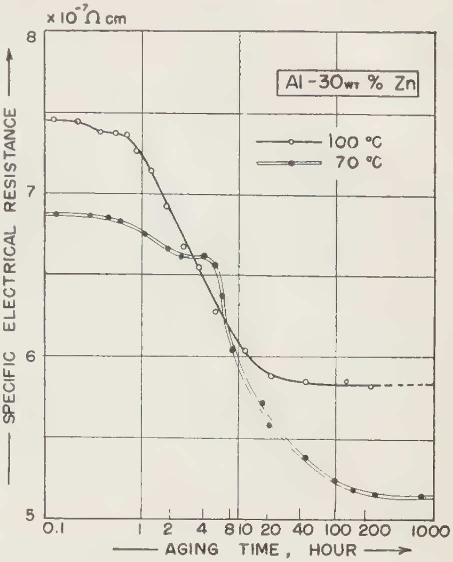

Fig. 12. Isothermal Aging Curves of Electrical Resistance. Al–30 wt. % Zn Alloy, Aged at 70° and 100°C.

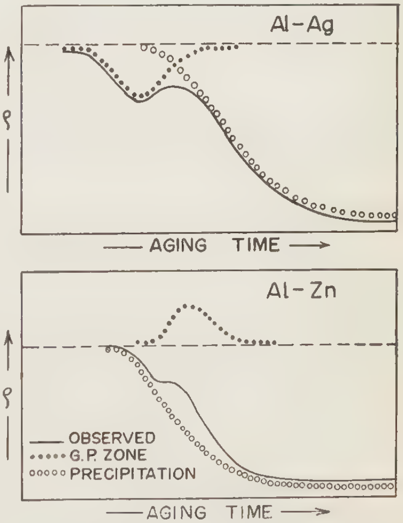

Fig. 13. Integration of Two Reacticns Contributing to Changes in Electrical Resistance during Aging.

§5. Discussion

Although the X-ray technique of Guinier gave an evidence of the formation of G–P zone on the alloys aged at low temperature, it did not answer to the question of whether G–P zone was allotropic nucleus of the precipitate or whether it was independent of the precipitate. The present results seem to indicate that the formation of G–P zone is foreign to the new phase precipitation. As shown in Fig. 6, variation of the energy **Q** due to G–P zone appears to be independent of that of the energy **S** due to the precipitate, and further in Fig. 9, the stability of G–P zone represented by T_Q and the stability of the precipitate, T_S, appear to vary with aging time independently of each other. These as well as that the electrical resistance increases due to G–P zone contrary to decrease due to the new phase precipitate, may be taken as evidences of independent formation of G–P zone and the new phase.

Since our proposed mechnism of the low temperature aging in this system is attributed to the chemical interaction of the solute zinc atoms with stacking faults in the matrix lattice, further experimental confirmation by the X-ray technique of the existence of stacking faults is desirable. Relation between our G–P zone and Guinier's spherical clusters is not obvious.

Further the work on quench-annealed pure aluminium may given some information on the possibility of stacking fault formation quenched-in excess vacancies. At this point it may be noted that measurements of the specific-heat on quench-annealed superpure Al and Cu metals have been carried out by the present author[17]), and the results on the metals annealed at 130°C after quenching from 600°C show occurrence of a heat absorption between 200° and 350°C in both metals, which seems to be the energy required to decompose stacking faults in the lattice, detailed account on this experiment will be published elsewhere.

Grain-boundary precipitation in this alloy has been examined by Geisler, Barrett and Mehl[10]), and preferred precipitation at grain-boundaries has been reported. But we could not detect the effect of the grain size on the temperature T_Q and the heat absorption **Q**, so grain-boundary can not cause a singnificant difference in the process of the G-P zone formation.

Acknowledgements

The author desires to express his thanks to Professor Y. Takagi and Mr. H. Maniwa for their helpful discussions during the course of this work, and thanks to Dr. H. K. Hardy (U.K. Atomic Energy Authority, England) for his kindness to peruse the manuscript of this paper and give useful suggestions. The author's thanks are also due to Dr. U. Nishioka and Mr. H. Sakai of the Mitsui Mining and Smelting Co. for supplying the high purity metals.

References

1) K. Hirano: J. Japan Inst. Metals **19** (1955) 136.
2) K. Hirano, Y. Takagi and H. Maniwa: J. Phys. Soc. Japan **10** (1955) 587.
3) K. Hirano: ibid. **8** (1953) 603.
4) K. Hirano and H. Sakai: ibid. **10** (1955) 23.
5) K. Tanaka, H. Abe and K. Hirano: ibid. **10** (1955) 454.
6) K. Hirano and Y. Takagi: ibid. **10** (1955) 187.
7) U. Dehlinger: Z. Metallkde. **29** (1937) 401.
8) H. Meyer: Z. Phys. **76** (1932) 268.
9) A. Guinier: Metaux et Corrosion **18** (1943) 209.
10) A. H. Geisler, C. S. Barrett and R. F. Mehl: Trans. AIME. **152** (1943) 201.
11) G. V. Raynor: Annoted Equilibrium Diagram Series, No. 1, Inst. Metals, London, 1943.
12) W. L. Fink and L. A. Willey: Trans. AIME. **122** (1935) 244.
13) E. Schmid and G. Wassermann: Z. Metallkde. **28** (1936) 159.
14) T. Morinaga: J. Japan Inst. Metals **3** (1939) 216.
15) G. Borelius and L. E. Larsson: Arkiv. f. mat. astr. o. fysik **35A** (1948) No. 13.
16) K. Hirano and Y. Takagi: J. Phys. Soc. Japan, will be published.
17) K. Hirano, H. Maniwa and Y. Takagi: ibid. will be published.

JOURNAL OF THE PHYSICAL SOCIETY OF JAPAN Vol. 10, No. 11, NOVEMBER, 1955

Density Analysis of Glass in Transformation Range

By Eizō KANAI
Research Laboratory, Asahi Glass Company Ltd., Yokohama, Japan
and Takesi SATOH
Physics Department, Defense Academy, Yokosuka, Japan

(Received July 12, 1955)

Analysing the transformation phenomena of glass, we emphasize that the fundamental irreversible change is caused by the network deformation. Further, we note that the rate equation of the network deformation plays the essential role in the stabilization process of glass and that this equation can be assumed in a simple form with the use of the network temperature which represents the state of network configuration. Next, we apply above equation to the analysis of the density data by Daragan and show that the activation energy of the rate mechanism is dependent upon the network temperature in accordance with the theory and its numerical value is nearly equal to the activation energy of viscosity.

§1. Introduction

The transformation phenomena of glass are now understood as follows. The normal glass has the unique equilibrium state at each temperature in the glassy range. When held at a certain temperature in this region, glass finally reaches the equilibrium state irrespective of its past history. However, the time needed in this stabilization process is strongly dependent upon temperature. Hence, in the temperature range where above time is comparable to our usual time scale of observation, glass shows various abnormal changes. The phenomena associated with these changes are generally called transformation phenomena.

Abnormal changes appear in density, heat capacity and most physical quantities of glass. They are, of course, not independent from each other, but related through the inner mechanism. So, it is important to search the place where the fundamental mechanism proceeds. For example, Tool[1]) considered the change of internal structure and Douglas and Jones[2]) discussed the behaviour of configuration change. On the other hand, we recognized the essential mechanism to lie in the disappearance and reappearance of one degree of freedom of internal motion of glass, as previously reported[3]).

Roughly speaking, glass has two modes of motion. One of them is network deformation and the other is vibration around the instantaneous network configuration. The network deformation is essentially a rate process and takes place very easily in liquid state, but is practically forbidden in solid state. Freezing or releasing of the network deformation gives characteristic influences to each of the physical quantities and results in abnormal changes.

From the above standpoint, our next step is to find how to represent the network deformation. For this purpose it is con venient to take up the physical quantities which can be divided into two components corresponding to the above two modes of motion. We selected the inner energy of the system as one of those quantities. Namely,

$$E=E_{\mathrm{net}}+E_{\mathrm{vib}}\ ,$$

where E_{net} and E_{vib} represent the network energy and the vibrational energy of the system, respectively. This circumstance is similar to the quantum theory of molecule which treats the energy of a molecule as the sum of electronic energy, vibrational energy and rotational energy.

Here we are mainly interested in the network energy E_{net}. Exactly speaking, E_{net} is a complex function of the network configuration. But we introduced one parameter τ with the dimension of temperature (network temperature), by the use of the equilibrium relation between E_{net} and the temperature T, and considered τ as the measure of the network deformation, as T is considered as the measure of the thermal vibration. At the present stage of physics of glassy state, reduction of complex glass structure to one parameter is inevitable to some extent as seen in the works of Tool[1]) (fictive temperature) and Davies and Jones[4]) (order parameter). But it is to be noted that reasonableness of these simplifications must be checked by experiments.

By the use of τ with the usual state variables, it becomes possible to discuss the behavior of the system thermodynamically. If we confine our interests to the conditions near equilibrium, the discussion is rigorous as shown by Davies and Jones[4]). However we often treat the states far from equilibrium. In these conditions also, we can constitute a thermodynamical theory with aid of some experimental facts as given in the previous paper I*.

Above all, the irreversible entropy increment dS_{irr} is given as follows,

$$dS_{\mathrm{irr}}=(C_p-C_p{}^*)((1/\tau-1/T)d\tau\geq 0\ .$$

In other words, τ must tend to T spontaneously and this $\tau\to T$ reaction exactly represents the process of the transformation phenomena of glass.

The rate equation of the $\tau\to T$ reaction cannot be derived from the thermodynamical discussion, so long as we are interested in the irreversible processes far from equilibrium. So, we deduced the rate equation from the kinetic standpoint in the paper I, and obtained the following equation:

$$\frac{d\tau}{dt}=\kappa(T-\tau)\ , \tag{1}$$

where $T-\tau$ is the measure of the deviation from equilibrium and driving force of the $\tau\to T$ reaction. Then, κ is the rate constant of this reaction which is represented, in most cases, as follows,

$$\kappa=A\exp(-B/T)\ , \tag{2}$$

where B is the activation energy of the process in question and is generally a function of τ and T.

The functional form of B has not been determined by above theory. But experiments including Lillie's [5] show

---

* Independency of $C_p{}^*$ of past history was confirmed by our later experiment in the case of usual soda-lime-silica glass.

$$\frac{dB}{d\tau}<0 .$$

In other words, the hotter the system is internally, the larger the mobility for network deformation is. Hence we assumed the simplest relation,

$$B=B_0-B_1\tau , \qquad (3)$$

where B_0 and B_1 are approximately constant. Thus, the rate equation becomes as follows,

$$\frac{d\tau}{dt}=A(T-\tau)\exp[(B_1\tau-B_0)/T] . \qquad (4)$$

Here we note that B_0 is the activation energy for network deformation in equilibrium condition, because in that case

$$A\exp[(B_1T-B_0)/T]=Ae^{B_1}\exp(-B_0/T) .$$

So, B_0 should be compared with activation energy of viscosity data for stabilized glass.

In the paper I, we checked the theory with experiments of thermal expansion[1] and refractive index[6]. But the latter has been proved to be inadequate, since the specific refraction receives stabilizing change[7]. Hence in order to check the theory with more direct data, we adopted the density measurement by Daragan[8]. Results will be given in subsequent sections.

§ 2. Data of Variation of Density with Time

The experimental data which we cite here were given by Boris Daragan[8]. The glass used as samples was designated to be Extra-white Boussoi's glass. This glass has the following chemical composition:

	Weight %
SiO_2	72.00
Na_2O	14
CaO	12
MgO	0.10
Al_2O_3	1.00
Fe_2O_3	0.05
SO_3	0.55
Total	99.70

According to this table, it is seen that the glass is very close to ordinary soda-lime-silica glass used for production of sheet or plate glass. The characteristic thermal properties of the glass are also tabulated as follows:

linear coefficient of thermal expansion	(0°–200°C)	87×10^{-7} °C^{-1}
〃 〃	(0°–300°C)	92×10^{-7} °C^{-1}
〃 〃	(0°–400°C)	96×10^{-7} °C^{-1}
transformation point		550°C
softening point		580°C

To give an outline of Daragan's experimental procedure, he puts a certain number of sample into a furnace with a constant temperature, and then takes off them one by one, to quench immediately to room temperature. Densities of quenched samples at room temperature are observed by means of Preston's sink-float apparatus with an accuracy of ±0.0001 g/cm³. The procedure is performed at various holding temperatures of the furnace, which are held constant within ±0.5°C during experiment.

Varying the holding temperatures from 650°C to 490°C, the variations of density with progress of time are obtained. A typical curve at 500°C is illustrated in Fig. 1. As seen from these curves, the samples used are undoubtedly chilled ones. By theoretical consideration it is also shown that the network temperature τ is higher than the actual temperature T in the present case. Among these we will use only a set of three data at 510°C, 500°C and 490°C, because others at higher temperatures are not sufficient to be analyzed in detail, especially in the early stage of the experiment. The values of equilibrium density at various temperatures obtained from extrapolation are also given.

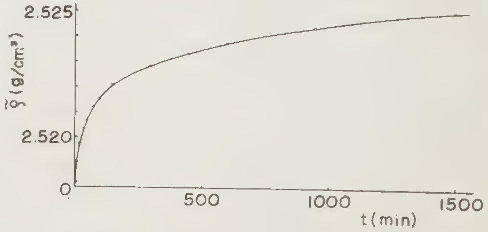

Fig. 1. Typical curve of saturation of density to equilibrium.

For application of our theory to these changes, it is necessary to know numerical values of cubic coefficients of thermal expansion, β and β^*. More strictly speaking, it is rather the value of difference $\Delta\beta=\beta-\beta^*$ that we need for analysis. The thermal expansion coefficient in the frozen condition, β^*, is obtained directly from the value of α^* referred to above. On the other hand the thermal expansion coefficient in the equilibrium condition, β, at higher temperatures is able to be evaluated from the gradient of the graph of equilibrium density versus the holding temperature (Fig. 2.) The obtained value of the difference $\Delta\beta$ is 5.6×10^{-5} °C^{-1}.

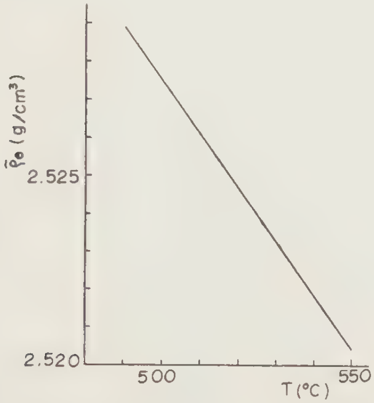

Fig. 2. Equilibrium density versus temperature.

§ 3. Theoretical Analysis

We can express the equation of state of glass in terms of density ρ as follows:

$$\rho(T,\tau)=\rho(T_0)[1-\beta^*(T-T_0)-\Delta\beta(\tau-T_0)]\,. \quad (5)$$

Or, if we designate the quenched density by $\tilde{\rho}$,

$$\tilde{\rho}=\rho(T_0)[1-\beta^*(T_r-T_0)-\Delta\beta(\tau-T_0)]\,, \quad (6)$$

where T_r represents the room temperature. Further, when the equilibrium quenched density is written as $\tilde{\rho}_e$,

$$\tilde{\rho}_e=\rho(T_0)[1-\beta^*(T_r-T_0)-\Delta\beta(T-T_0)]\,. \quad (7)$$

Hence

$$\tilde{\rho}_e-\tilde{\rho}=\Delta\beta(\tau-T)\rho(T_0)\,.$$

Or

$$\tau-T=\frac{1}{\Delta\beta}\frac{\tilde{\rho}_e-\tilde{\rho}}{\tilde{\rho}_e}\,. \quad (8)$$

With this relation and the measured density values, we can derive the time variation of the network temperature τ at each experimental temperature T.

Then, taking the logarithmus of eq. (8) and differentiating it with time t, we have

$$R\equiv-\frac{d}{dt}ln(\tau-T)=\frac{1}{T-\tau}\frac{d\tau}{dt}\,,$$

where it is evident that R can also be evaluated at each t or at each τ.

If we take here the rate equation (4) as the simplest assumption, the above equation can be transformed as follows,

$$R=A\exp[(B_1\tau-B_0)/T]\,.$$

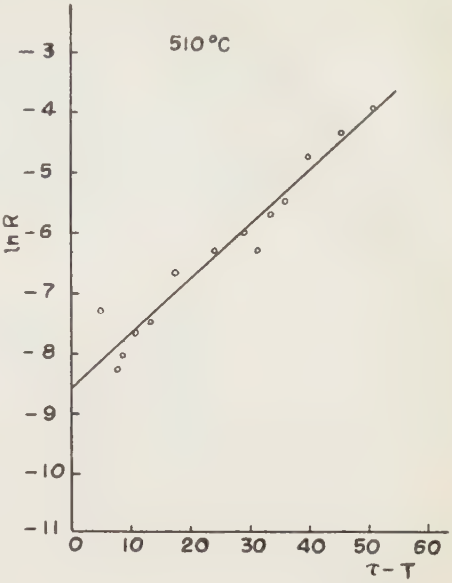

Fig. 3. lnR versus $(\tau-T)$ at 510°C.

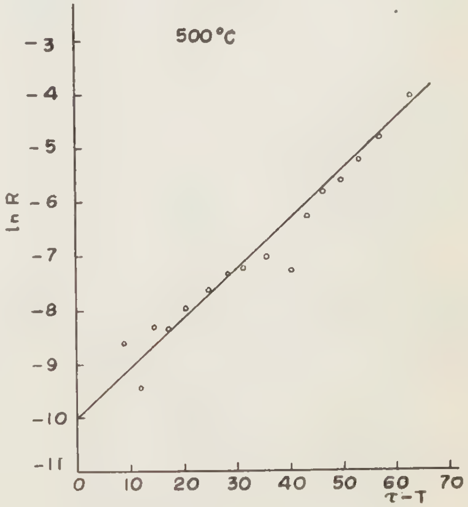

Fig. 4. lnR versus $(\tau-T)$ at 500°C.

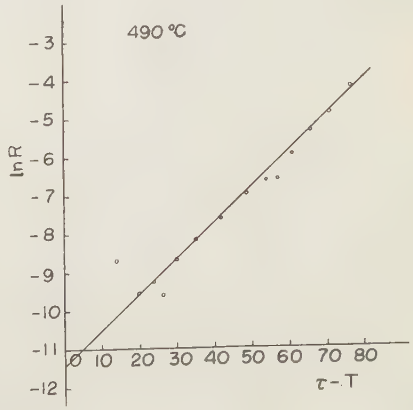

Fig. 5 lnR versus $(\tau-T)$ at 490°C.

Hence
$$lnR=lnA-\frac{B_0}{T}+\frac{B_1}{T}\tau\,. \qquad (9)$$

If the above simple rate equation is reasonable, we can expect the linear relation between lnR and τ.

This point is satisfied, at least approximately, as seen in Fig. 3 to Fig. 5*.

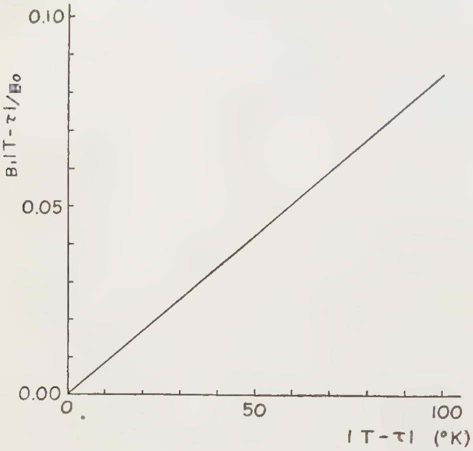

Fig. 6. $B_1|T-\tau|/B_0$ versus $|T-\tau|$.

From the tangent of each curve we can get value B_1/T as follows,

temperature	B_1/T	B_1
510°C	0.092	72.0
500	0.093	71.9
490	0.094	71.7

That is, B_1 may be taken as 72. Further, $(lnA+B_1)-B_0/T$ is obtained from intercept of each curve to $\tau=T$ axis, as shown in the next table.

temperature	$lnA+B_1-\frac{B_0}{T}$
510°C	−8.60
500	−10.00
490	−11.45

B_0 is easily calculated from these values and becomes as follows,

$$B_0=85\times10^3\ ^\circ K$$
$$=170\ Kcal/Mol\,. \qquad (10)$$

§4. Discussion and Conclusion

The density analysis described in the last section shows that Daragan's data can be explained by our theory. Moreover, the obtained activation energy (B_0) is nearly equal to that in the viscous flow of stabilized glass. This fact supports our basic idea that the fundamental process in transformation phenomena consists in network deformation, because the viscous flow and the stabilizing process have the network deformation in common, although the former is caused by external stress and the latter proceeds spontaneously. The fact also clarifies the meaning of the transformation range which is usually defined by the use of viscosity values.

The τ dependence of the activation energy B is the essential feature of the glass discussed here. In consequence of

$$A\exp(-B/T)=A'\exp[-\{B_0+B_1(T-\tau)\}/T]\,,$$

$B_1|T-\tau|/B_0$ represents the measure of the non-Maxwellian behavior in the present system. So far as it is negligibly small, we can expect the success of the theory of one relaxation time. As shown in Fig. 6, the non-Maxwellian character seems to be of a considerable extent. Of course, the simultaneous actions of many Maxwellian mechanisms can explain the present process as reported in the comments of Condon[9]. Without more detailed data, it is not clear which we should adopt, one non-Maxwellian mechanism or many Maxwellian mechanisms. But we would emphasize that non-Maxwellian character is a general feature in the system far from equilibrium.

Strictly speaking, there may be some points which cannot be explained by our theory. Ritland[10] has shown the inadequacy of simple theories in the case of borosilicate glasses and introduced the term proportional to $|T-\tau|^2$ in the equation of $\tau\rightarrow T$ reaction.

If similar inadequacy should be found in soda-lime-silica glasses, it would be necessary to revise the theory. And how to revise it presents the next problem of study.

References

1) A. Q. Tool: J. Am. Ceram. Soc. **29** (1946) 240.
2) R. W. Douglas and G. A. Jones: J. Soc. Glass Techn. **32** (1948) 309.
3) E. Kanai and T. Satoh: J. Phys. Soc. Japan **9** (1954) 417. This paper will be cited as I.
4) R. O. Davies and G. O. Jones: Proc. Roy. Soc. **217** (1953) 26.
5) H. R. Lillie: J. Am. Ceram. Soc. **16** (1933) 619.
6) P. W. Collyer: J. Am. Ceram. Soc. **30** (1947) 338.
7) N. M. Brandt: J. Am. Ceram. Soc. **34** (1951) 332. N. J. Kreidl and R. A. Weidel: ibid. **35** (1952) 198.
8) B. Daragan: Glass Ind. **33** (1952) 69.
9) E. U. Condon: Glass Ind. **33** (1952) 307.
10) H. N. Ritland: J. Am. Ceram. Soc. **37** (1954) 370.

---

* In these figures, the time differentiation was not calculated graphically, but derived directly from the adjacent measured values.

JOURNAL OF THE PHYSICAL SOCIETY OF JAPAN Vol. 10, No. 11, NOVEMBER, 1955

On the Nature of Silent Electric Discharge

By Kanji HONDA

Department of Physics, Tokyo University

and Yoshihide NAITO

Department of Chemistry, Tokyo Metropolitan University

(Received July 25, 1955)

The current pulses produced by the silent electric discharge of an ozonizer tube were measured by a cathoderay oscillograph as well as by a milliammeter with filter and rectifier, and from comparison of these two series of results, the following conclusions were attained.

(1) The wave form of each pulse consists of two parts, the peak rush of current at the head and the smooth tail following the former. There is a reason to infer that the rushing part is due to electrons and the smooth part to positive ions produced by electrons in the space.

(2) The measured average value of the rushing current is just one half of the total current, hence the electron current must be equal to the ion current.

(3) If we assume that the discharge dies away at the stage of electron avalanche, the calculation does not agree with the observation. On the other hand, if we assume the discharge develops at least up to the stage of streamer, the observed results can be well explained.

§ 1. Introduction

Many studies about silent electric discharge[1], for example, studies of electric characteristics[2-4], of chemical reaction[1,5-8], of the effect of irradiation[9,10], and studies concerned with the breakdown of ozonizers[11,12], have already been published. The mechanism of this discharge, however, has not yet been clearly explained.

The authors obtained from the measurements of pulse currents and some calculations thereof the result that the discharge develops into the streamer or more, and never stops at the stage of electron avalanche.

Further experiments with other gases, other pressure ranges, and other discharge tubes, are now in progress.

§ 2. Experimental

1). *Discharge tube*

The discharge tube used is a Siemens' glass ozonizer shown in Fig. 1. Dried atmospheric air was passed through the discharge space with a constant flow rate, and A.C. potential of 2–10 kV and 50 c/s was applied between the $CuSO_4$ solution contained in the inner tube and tin foil E pasted on the outer tube.

2). *Observation of current wave form*

The observed wave forms of the current which flows through the discharge tube are shown in Fig. 2 with corresponding measuring circuits. Fig. 2–a shows the case in which the sweep time of the Braun-tube-oscillograph is 1/50 sec. Fig. 2–b shows the individual pulse observed with relatively short sweep time of about 5×10^{-4} sec, and with stray capacity C_0 as small as possible. At the time A, discharge starts so abruptly that the build

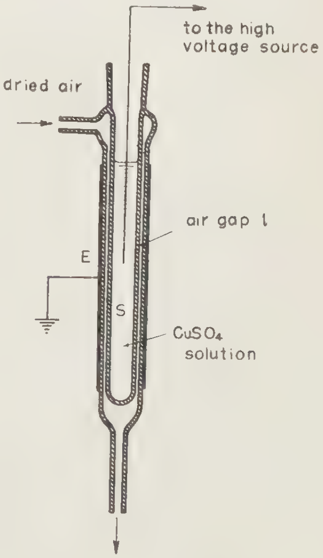

Fig. 1. Discharge tube.

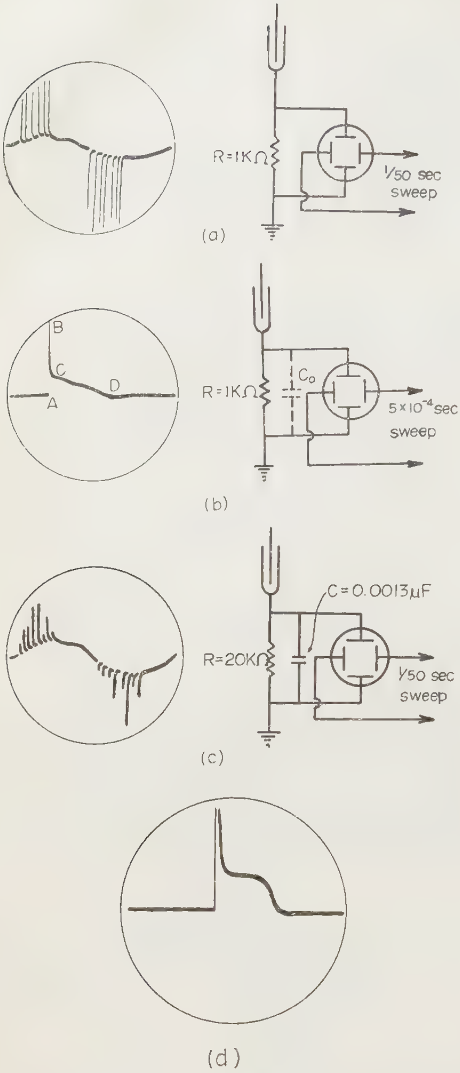

Fig. 2. Oscillograms and concerning circuits.

up of the pulse can not be observed. The decay path BC appeares faint and narrow, and the crest of the pulse lies far beyond the screen which is 120 mm in diameter. (The peak of current is larger than 120 mA.) The frequency analysis of discharge current enables us to estimate the width of this pulse to be about 10^{-6} sec. CD part that follows hereafter has far longer decay time of about 2×10^{-4} sec and suggests its different nature from the former peak current.

Fig. 2–c shows the case in which some capacitance was inserted so as to suppress the peak of pulse. Under this condition, the top of the pulse becomes so clear that the hight of which can be easily measured.

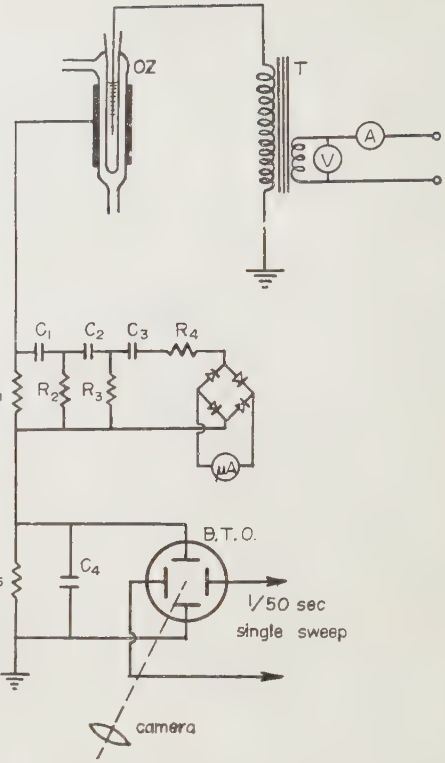

Fig. 3. Measuring circuit.

3). *Current measurement in two different methods*

The current was measured with the circuit showed in Fig. 3. The resistances R_1–R_4 and condencers C_1–C_3 together act as a filter, and stop the charging current of 50 c/s from flowing into the milliammeter circuit. Hence it gives the mean of the gas discharge current only, irrespective of the polarity of A.C. potential by the aid of rectifiers. (The current is divided uniformly to R_1–R_4, hence the current measured must be multiplied by factor four.)

The Braun-tube-oscillograph circuit is connected in series with this circuit. The pulse current charges up the capacity C_4 in a moment to certain voltage V, which thereafter decays gradually with the time-constant of 2.6×10^{-5} sec of the R_5C_4 parallel circuit. This R_5C_4 circuit acts, however, as simple resistance for a pulse current longer than 10^{-4} sec. Hence the potential V is rather chiefly due to the first peak rush than the tail part.

The voltage V, therefore, relates to the total charge q of a peak rush by the equation

$$V=q/C_4\ ,$$

and each pulse in Fig. 2–c has the height of

$$h=kV=kq/C_4\ , \tag{1}$$

where k is the voltage sensitivity of the Braun-tube. Accordingly we can calculate the mean current i_e of only the rush current part from the summation of pulse heights of Fig. 2–c in one second by the following equation

$$i_e=\frac{C_4}{k}\sum h\ . \tag{2}$$

To obtain $\sum h$, we photographed the oscillogram of Fig. 2–c three times for each condition, and summarized the h's over one cycle (1/50 sec) in each photogram, and after averaging them, multiplied the value by the factor 50. The voltage sensitivity of the Braun-tube was 0.5 mm/V.

Fig. 4 represents the experimental results showing that at every applied potential the mean current obtained by Eq. (2) is just the half of the reading of the milliammeter.

§ 3. Discussion

Several authors have already shown the wave form of the pulses in silent electric discharge[3,4,9]. Most of them have simple wave form of the order of 10^{-4} sec with no current peak. Since the current peak AB of Fig. 2–b does not appear unless RC_0 in Fig. 2–b is small enough, the authors wonder if the wave forms refered might have not been distorted by circult conditions.

Now we will consider the origin of the two parts of a pulse. One of the authors[13] has shown that in the begining of the needle corona discharge in air, there appear pulses having a particular sharp peak at the head accompanying flat tail part as shown in Fig. 2–d, and explained the wave form as follows: "In course of increasing the applied potential, streamer starts when the self-maintaining condition is attained electrostatically its current rush thus producing the head peak of pulse. But the space charge created by the streamer suppresses and stops the discharge immediately. Then the space charge of ions remaining in the air gap is swept to the cathode causing the flat part of the current to appear."

In the case of silent discharge, the discharge gap is bounded by glass surfaces. The electric charge produced by breakdown accumulates on the glass surfaces and reduces the field intensity of the gap, so that discharge is quenched out. We may then assume the mechanism of silent discharge analogous to that of corona initiation. Thus, the authors adopt for the silent electric discharge in dried atmospheric air the following mechanism: "When the discharge starts at any point of the gap, electron avalanches grow up to a streamer. The electrons reach the anode side glass and accumulate there. This accumulation of charge reduces the field intensity of the air gap, and stops the discharge. This behaviour of electrons corresponds to the first rush time 10^{-6} sec of the pulse. Afterwards, the slow positive ions are swept to the cathode side and this corresponds to the tail width of pulse of 10^{-4} sec."

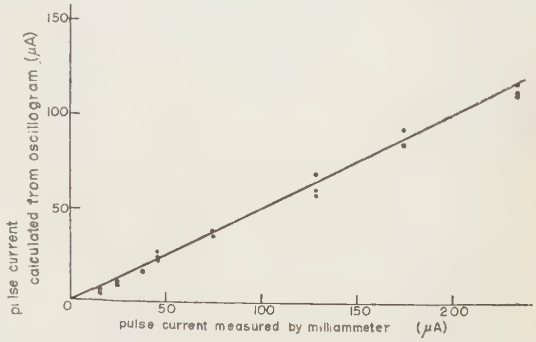

Fig. 4. Relation between two kinds of current.

According to this mechanism, ABC part of the pulse in Fig. 2–b represents the electron current of streamer, and hence it is possible to calculate the mean electron current by the method described in § 2–3.

On the other hand, since the mean total current containing both electron and ion current, i.e., AB CD in Fig. 2–b, can be measured by the combination of filter, rectifier and milliammeter, it is possible to obtain the ratio of ion to electron current. The experimental result of Fig. 4 shows that the electron current is just one half of the total current, and hence electron current and ion current are equal.

Next, we will show that the discharge can never stop in avalanche-stage, but must be growing up to streamer-stage.

The starting applied potential of the used discharge tube was 5kV (r.m.s. value). Subtructing the potential drop across the glass dielectrics, and converting from r.m.s. to peak value, the net starting potential of the air gap is found to be 5.6 kV. (The thickness of the air gap is 1.5 mm, that of the glass dielectrics 1.5 mm × 2, and dielectric constant of the glass c.a. 7) In this case, the α/p, αl and $e^{\alpha l}$ at the starting instant are respectively

$$\alpha/p = 0.054^{14)}$$
$$\alpha l = 6.2$$
$$e^{\alpha l} = 186,$$

where α is the ionozation coefficient of electron collision in cm^{-1}, l the air gap thickness in cm, and p the gas pressure in mmHg.

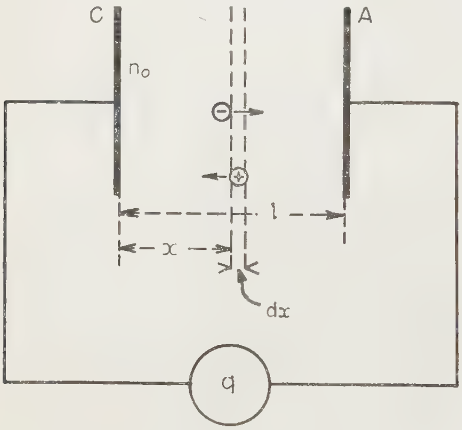

Fig. 5.

Now we calculate the ratio of ion current to electron current in case only electron avalanche would occur. One electron which starts from cathode and travels to anode with velocity v_e as is shown in Fig. 5 induces in external circuit a current

$$i_e = \frac{ev_e}{l} .$$

The total charge induced in the external circuit by the electrons in the avalanche is

$$q_e = \int_0^l \frac{ev_e}{l} n_0 e^{\alpha x} \frac{dx}{v_e} = \frac{en_0}{\alpha l}(e^{\alpha l} - 1) , \qquad (3)$$

where n_0 is the initial electron from cathode. The positive ions produced by the electron avalanche induce current in the external circuit, when swept to the cathode. The total charge of this current is

$$q_i = \int_0^l \frac{ev_i}{l}(n_0 e^{\alpha x})\alpha dx \frac{x}{v_i}$$
$$= \frac{en_0}{\alpha l}(\alpha l e^{\alpha l} - e^{\alpha l} + 1) . \qquad (4)$$

The ratio of ion to electron charge of avalanche is therefore

$$q_i/q_e = \frac{\alpha l e^{\alpha l}}{e^{\alpha l} - 1} - 1 , \qquad (5)$$

and, using our value of $\alpha l = 6.2$,

$$q_i/q_e = 5.2 .$$

This shows that, if the discharge were only the electron avalanche, the ratio of ion to electron current should be 5.2. This value is not essentially altered even when the avalanche started midway between electrodes.

The observed ratio of these two currents is just 1 as shown, and this proves that the silent electric discharge can not be the state of avalanche. And if we assume that the discharge developes to the state of streamer or further, and almost uniform ionization occures through its path, then a simple calculation shows immediately the equalness of the ion and electron currents.

One of the authors[6)] has found that the thin filamentary discharge of silent electric discharge in the air gap of separation 0.9 mm has a diameter about 2 mm, and the charge about 0.5×10^{-9} coulomb. Accordingly the volume of discharge column is about 2.8×10^{-3} cm^3, and the charge density, assumed to be distributed uniformely in the discharge column, is about 10^{12} electrons and ions per 1 cm^3. This value is large enough for plasma, and supports the above discussion.

§ 4. Conclusion

In careful observation of the current pulses of silent electric discharge, it was found that the pulse consists of two parts, i.e., the head sharp peak of 10^{-6} sec and the following smooth tail of 10^{-4} sec.

An interpretation was offered that the former peak is the electron current, and the tail part the ion current.

Adequate measurments showed that the ion current is equal to the electron current.

Some calculation led to the conclusion that the discharge does not stop at the state of electron avalanche, but developes into the streamer or further.

References

1) G. Glockler and S. C. Lind: *"The Electrochemistry of Gases and other Dielectrics."* John Wiley and Sons, Inc., New York (1939).

2) T. C. Manley: Trans. Electrochem. Soc. **84** (1943) 83.
3) S. Fuji and N. Takemura: Bul. Electrotech. Lab. (Japan) **14** (1950) 283.
4) Y. Inuishi: Electrotech. Papers (Japan) **2** (1950) 13.
5) M. Suzuki: Proc. Japan Acad. **26** (1950) 20.
6) M. Suzuki and Y. Naito: ibid. **28** (1952) 469.
7) K. Ouchi and T. Takamatsu: J. Electrochem. Soc. Japan **21** (1953) 376.
8) B. Kovaliv and E. Briner: Hel. Chim. Acta. **36** (1953) 275.
9) W. L. Harries and A. von Engel: Proc. Phys. Soc. **B64** (1951) 916.
10) V. Venkateswarlu and N. A. Ramaiah: J. Phys. Soc. Japan **9** (1954) 225.
11) A. E. W. Austen and W. Hackett: J. Inst. Elec. Engrs. **91 I** (1944) 298.
12) T. Takemura and R. Sugita: Bul. Electrotech. Lab. **15** (1951) 30.
13) K. Honda and Y. Terada: Electrotech. Papers (Japan) **1** (1949) 162.
14) L. B. Loeb: "*Fundamental Processes of Electrical Discharge in Gases.*" John Wiley and Sons, Inc., New York, (1939) pp. 345.

JOURNAL OF THE PHYSICAL SOCIETY OF JAPAN Vol. 10, No. 11, NOVEMBER, 1955

A Derivation of Guderley-Barish's Solution for the Sonic Flow on the Basis of the Thin-wing Expansion Method

By Kinzo HIDA

Department of Applied Physics, Faculty of Engineering,
Naniwa University

(Received July 4, 1955)

It is shown that Guderley and Barish's asymptotic solution for the sonic flow, which is valid far from the body, can also be derived on the basis of the thin-wing expansion method as extended by Imai.

Although Imai's formula cannot be applied to axisymmetrical cases, yet the first term of the asymptotic solution in these cases can be obtained as well by means of usual formula based on the linear theory.

§1. Introduction and Summary

Recently, Imai¹⁾ extended the similarity rule for a transonic flow due to von Kármán so as to hold in a wider range than the original one.

Assuming that the velocity perturbation due to the presence of an obstacle is everywhere small and, unlike the usual method of thin-wing expansion, retaining the terms up to the second order of disturbances, he obtained a new fundamental equation for two-dimensional flows, upon which his extended similarity law is based.

This equation, which bridges a gap between "Prandtl-Glauert's theory" and "von Kármán's transonic theory", enables us to obtain successive solutions with respect to some parameter and it may be expected that the similar procedure remains to be valid even for the sonic flow.

In this paper it will be shown that this is surely the case. To make the discussions irrespective of the individual form of an obstacle, we consider the sonic flow only at a great distance from a body. For this case, Guderley and Barish²⁾ gave the asymptotic solution in the physical plane, and to a derivation of their solution by applying Imai's formula the present paper is directed.

Usually, we require that the complex velocity potential is one-valued and continuous throughout the field of flow, but this condition does not hold in the case under consideration because one or a few shock waves will necessarily appear in the field of flow. Hence, an alternative condition is to be required such that the disturbed velocity remains finite throughout the field of flow.

All analyses are developed in the physical plane and the complex quantities are conveniently used. It follows from straightforward calculations that the successsive terms of Guderley-Barish's solution can be obtained one by one in each step of approximation.

Although Imai's formula cannot be used in axisymmetrical cases, yet, as long as the first term is concerned, the usual method of thin-wing expansion is still of use.

Necessary changes in boundary conditions are the same as before. However, some redundant terms appear already in the second approximation and in what follows we shall give only the solution to the first approximation.

§ 2. Guderley and Barish's Asymptotic Solution

Guderley and his collaborators have found a fruitful hunting-ground in researches for the sonic flow and have elucidated many important natures of this special flow field. Especially, the asymptotic behaviour of the field far from a body was discussed in collaboration with Barish.

Assuming that the deviation of the flow from a uniform sonic flow is small, they put the velocity potential Φ in the form:

$$\Phi=a_*(x+\varphi)\,, \tag{2.1}$$

where a_* is the critical sonic speed and x is the coordinate parallel to the direction of the uniform free-stream. Thus, φ is the velocity potential for perturbation.

According to the similarity law for transonic flow, this potential φ is governed by the Tricomi equation and Guderley and Barish obtained a solution of the form:

$$\varphi=y^{3n-2}f(\chi)\,, \tag{2.2}$$

with

$$\chi=(\gamma+1)^{-1/3}xy^{-n}\,, \tag{2.3}$$

where y in conjunction with x forms the rectangular coordinates and γ denotes the adiabatic index of a gas concerned. The constant n was determined by the conditions that the flow field is symmetrical with respect to the x-axis and is regular from infinity upstream to the limiting Mach wave, and it was found that $n=4/5$ for two-dimensional cases and $n=4/7$ for axisymmetrical cases.

Furthermore, they constructed the asymptotic solution for larger positive values of χ as follows:

$$f(\chi)=\chi^{\alpha}\sum_{\lambda=0}^{\infty}B_{\lambda}\chi^{(\alpha-3)\lambda}\,. \tag{2.4}$$

Here, α is a constant to be taken as 1/2 for two-dimensional cases and as $-1/2$ for axisymmetrical cases, and the numerical coefficients B_λ's are as shown in Table I. Unfortunately, Guderley and Barish's original paper contains some errors in B_2 as well as in subsequent B_λ's for axisymmetrical cases.

§ 3. Two-dimensional Flows

For convenience, we shall first summarize the extended formula due to Imai for the complex velocity potential.

Let Φ and Ψ be the velocity potential and the stream function respectively and define ϕ and ψ as follows:

$$\Phi=U(x+\phi)\,,\quad \Psi=U(y+\psi)\,, \tag{3.1}$$

where U is the velocity of a free-stream at infinity and therefore both ϕ and ψ refer to the perturbation. It is to be noted that if U tends to a_*, the first equation of (3.1) is reduced to Eq. (2.1) and ϕ becomes identical with φ.

Defining a parameter μ in terms of the Mach number at infinity M_∞ as:

$$\mu=\sqrt{1-M_\infty^2}\,, \tag{3.2}$$

and putting

$$\left.\begin{aligned} G&=\phi+i\psi/\mu\,,\\ \zeta&=\xi+i\eta=x+i\mu y\,, \end{aligned}\right\} \tag{3.3}$$

we have the fundamental equation for determining the complex velocity potential G in terms of the complex coordinate ζ and its conjugate complex $\bar{\zeta}$ in the form:

$$\frac{\partial G}{\partial\bar{\zeta}}=\beta\left(\frac{\partial G}{\partial\zeta}+\frac{\partial G}{\partial\bar{\zeta}}+\frac{\partial\bar{G}}{\partial\zeta}+\frac{\partial\bar{G}}{\partial\bar{\zeta}}\right)^2, \tag{3.4}$$

where

$$\beta=\frac{M_\infty^2}{4}\left(1+\frac{\gamma+1}{4}\frac{M_\infty^2}{1-M_\infty^2}\right). \tag{3.5}$$

This equation is due to Imai and is used in the subsequent works.

We notice first that when the free-stream Mach number M_∞ approaches unity, (3.5) is reduced to the form:

$$\beta=\frac{\gamma+1}{16\mu^2}+O(1)\,. \tag{3.6}$$

Now, we assume that G is expanded in an infinite series as:

$$G=G_1+G_2+G_3+G_4+\cdots\,. \tag{3.7}$$

Here $G_1, G_2, G_3, G_4, \cdots$ are quantities of the order $O(r\varepsilon)$, $O(r\varepsilon^2)$, $O(r\varepsilon^3)$, $O(r\varepsilon^4), \cdots$ respectively, where $r=\sqrt{x^2+y^2}$ and ε is a certain small quantity.

Substituting (3.7) into Eq. (3.4) and equating the same order terms on both sides, we have

$$\begin{aligned}
&\frac{\partial G_1}{\partial \bar{\zeta}}=0 , \\
&\frac{\partial G_2}{\partial \bar{\zeta}}=\beta\left(\frac{\partial G_1}{\partial \zeta}+\frac{\partial G_1}{\partial \bar{\zeta}}+\frac{\partial \bar{G}_1}{\partial \zeta}+\frac{\partial \bar{G}_1}{\partial \bar{\zeta}}\right)^2 , \\
&\frac{\partial G_3}{\partial \bar{\zeta}}=2\beta\left(\frac{\partial G_1}{\partial \zeta}+\frac{\partial G_1}{\partial \bar{\zeta}}+\frac{\partial \bar{G}_1}{\partial \zeta}+\frac{\partial \bar{G}_1}{\partial \bar{\zeta}}\right)\left(\frac{\partial G_2}{\partial \zeta}+\frac{\partial G_2}{\partial \bar{\zeta}}+\frac{\partial \bar{G}_2}{\partial \zeta}+\frac{\partial \bar{G}_2}{\partial \bar{\zeta}}\right) , \\
&\frac{\partial G_4}{\partial \bar{\zeta}}=\beta\left(\frac{\partial G_2}{\partial \zeta}+\frac{\partial G_2}{\partial \bar{\zeta}}+\frac{\partial \bar{G}_2}{\partial \zeta}+\frac{\partial \bar{G}_2}{\partial \bar{\zeta}}\right)^2 \\
&\qquad +2\beta\left(\frac{\partial G_1}{\partial \zeta}+\frac{\partial G_1}{\partial \bar{\zeta}}+\frac{\partial \bar{G}_1}{\partial \zeta}+\frac{\partial \bar{G}_1}{\partial \bar{\zeta}}\right)\left(\frac{\partial G_3}{\partial \zeta}+\frac{\partial G_3}{\partial \bar{\zeta}}+\frac{\partial \bar{G}_3}{\partial \zeta}+\frac{\partial \bar{G}_3}{\partial \bar{\zeta}}\right) .
\end{aligned} \tag{3.8}$$

The first equation is easily integrated, giving

$$G_1=g_1(\zeta) , \tag{3.9}$$

where g_1 is an arbitrary regular function of ζ only.

In usual applications of the method of thin-wing expansion, we impose, besides the boundary condition on the surface of a body, two more conditions as follows:

(i) $\partial G/\partial \zeta \to 0$ (as $\zeta \to \infty$) ,

(ii) $\partial G/\partial \zeta$ should be one-valued and continuous throughout the field of flow.

But, in a nearly sonic flow the second condition does no longer hold owing to the appearance of one or a few shock waves, and consequently we shall take an alternative condition:

(ii′) $\partial G/\partial \zeta$ should be finite throughout the field of flow even when the Mach number M_∞ approaches unity.

Conditions (i) and (ii′) are not yet sufficient, because they cannot determine the arbitrary function $g_1(\zeta)$ in Eq. (3.9).

Considerations to find this function reasonably lead back eventually to a series of Guderley's investigations, and are not a principal concern in this paper. Hence, with Eqs. (2.2), (2.3), (2.4) in mind, we shall take the supplementary condition as follows:

(iii) $$G_1=g_1(\zeta)=k\sqrt{\zeta} , \tag{3.10}$$

where k is an arbitrary constant. Though k may assume a complex number in general, it should be real in order to assure the symmetrical flow pattern, as is the case in this paper.

Remembering that we have assumed $G_1=O(r\varepsilon)$, we have

$$O(\varepsilon)=O(r^{-1/2}) ,$$

hence

$$G_2=O(1),\quad G_3=O(r^{-1/2}),\quad G_4=O(r^{-1}),\cdots . \tag{3.11}$$

Substituting (3.10) in the right-hand side of the second equation in (3.8) and then integrating, we find

$$G_2=\frac{k^2\beta}{4}\left(\frac{\zeta}{\zeta}+4\sqrt{\frac{\bar{\zeta}}{\zeta}}+\log \bar{\zeta}\right)+g_2(\zeta) , \tag{3.12}$$

$g_2(\zeta)$ being a certain analytic function of ζ to be determined later.

In order to obtain the velocity potential, we shall put the complex coordinate ζ in the form:

$$\zeta=te^{i\vartheta} . \tag{3.13}$$

As is easily seen from the comparison between (3.13) and (3.3), t and ϑ are connected with the Cartesian coordinates (x, y) by the relations:

$$t=x+O(\mu^2) ,\quad \vartheta=\mu\frac{y}{x}+O(\mu^3) , \tag{3.14}$$

which are useful especially in a transonic region.

Separating the real parts on both sides of Eq. (3.12) and making the substitution (3.13) for ζ and $\bar{\zeta}$, we have

$$\begin{aligned}
\phi_2=\Re(G_2)&=\frac{k^2\beta}{4}(\cos 2\vartheta+4\cos\vartheta+\log t)+\Re(g_2) \\
&=\frac{k^2\beta}{4}\{5-4\vartheta^2+O(\vartheta^4)+\log t\}+\Re(g_2) .
\end{aligned}$$

The condition (ii′), together with (3.6) and

(3.14), imposes the following condition on the function g_2:

$$\Re(g_2)+\frac{k^2\beta}{4}(5+\log t)=0\ ,$$

which, with consideration for the conditions (3.11), determines immediately the complementary function g_2 in the form:

$$g_2=-\frac{k^2\beta}{4}(5+\log\zeta)\ . \tag{3.15}$$

Thus, the second order solution is given by the formula:

$$G_2=\frac{k^2\beta}{4}\left(\frac{\bar\zeta}{\zeta}+4\sqrt{\frac{\bar\zeta}{\zeta}}+\log\frac{\bar\zeta}{\zeta}-5\right), \tag{13.6}$$

and the velocity potential for the sonic flow, φ_2, is easily obtained as well, namely:

$$\varphi_2=[\Re(G_2)]_{\mu=0}=-k^2\frac{\gamma+1}{16}\frac{y^2}{x^2}\ .$$

If the variable χ as defined in (2.3) is introduced, then this expression is rewritten in the form:

$$\varphi_2=-k^2\frac{(\gamma+1)^{1/3}}{16}(y^{2/5}\chi^{1/2})(\chi^{-5/2})\ ,$$

while Eq. (3.10) is reduced to

$$\varphi_1=k\sqrt{x}=k(\gamma+1)^{1/6}(y^{2/5}\chi^{1/2})\ .$$

With the abbreviation

$$\mathrm{B}_0=k(\gamma+1)^{1/6}$$

both equations take the forms:

$$\varphi_1=B_0(y^{2/5}\chi^{1/2})\ \text{and}\ \varphi_2=-\frac{B_0^{\,2}}{16}(y^{2/5}\chi^{1/2})\chi^{-5/2}\ ,$$

and, as will be easily confirmed from (2.4) and Table I, these expressions are surely identical with the corresponding terms in the expression (2.2).

The third term can be obtained in a similar way.

Raplacing G_2 on the right-hand side of the third equation in (3.8) by the expression (3.16), and then integrating the resulting equation with respect to $\bar\zeta$, we have

$$G_3=\frac{k^3\beta^2}{4}\left\{-\frac{\bar\zeta^2}{2\zeta^{5/2}}-2\frac{\bar\zeta^{3/2}}{\zeta^2}-\frac{\bar\zeta}{\zeta^{3/2}}+10\frac{\bar\zeta^{1/2}}{\zeta}\right.$$
$$\left.+5\frac{\log\bar\zeta}{\zeta^{1/2}}+2\frac{1}{\bar\zeta^{1/2}}+3\frac{\zeta^{1/2}}{\bar\zeta}+\frac{2}{3}\frac{\zeta}{\bar\zeta^{3/2}}\right\}+g_3(\zeta)\ . \tag{3.17}$$

The real part of this expression gives the third order term in the velocity potential and we have

$$\phi_3=\frac{k^3\beta^2}{4}\frac{1}{\sqrt{t}}\left\{-\frac{1}{2}\cos\frac{9}{2}\vartheta-2\cos\frac{7}{2}\vartheta\right.$$
$$-\frac{1}{3}\cos\frac{5}{2}\vartheta+13\cos\frac{3}{2}\vartheta+2\cos\frac{1}{2}\vartheta$$
$$\left.+5\left(\cos\frac{\vartheta}{2}\log t-\vartheta\sin\frac{\vartheta}{2}\right)\right\}+\Re(g_3)$$
$$=\frac{k^3\beta^2}{4}\frac{1}{\sqrt{t}}\left\{\frac{73}{6}+\frac{47}{48}\vartheta^2-\frac{43175}{2304}\vartheta^4+O(\vartheta^6)\right.$$
$$\left.+5\cos\frac{\vartheta}{2}\log t\right\}+\Re(g_3)\ .$$

Proceeding in the same way as before, we can find that the complementary function g_3 should be taken in the form:

$$g_3=-\frac{k^3\beta^2}{4}\left(\frac{73}{6}+5\log\zeta\right)\zeta^{-1/2}\ .$$

Thus, we have the final result for φ_3 as follows:

$$\varphi_3=[\phi_3]_{\mu=0}=-\frac{7}{384}(\gamma+1)^2\frac{k^3}{\sqrt{x}}\frac{y^4}{x^4}\ ,$$

which can be written, after some reductions, in an alternative form as:

$$\varphi_3=B_2(y^{2/5}\chi^{1/2})\chi^{-5}\ .$$

As should have beed expected, the numerical coefficient B_2 has the same value as given in Table 1.

Table I.

Two-dimensional cases	Axisymmetrical cases
$B_1=-(1/16)B_0^2$	$B_1=-(3/32)B_0^2$
$B_2=-(7/384)B_0^3$	$B_2=\ (39/512)B_0^3$
$B_3=-(5/512)B_0^4$	$B_3=-(405/4096)B_0^4$
$B_4=-(221/32768)B_0^5$	$B_4=(83835/524288)B_0^5$

It is to be noted that the suitable selection of complementary function g_3 enables us to eliminate both terms of the order ϑ^0 and ϑ^2 simultaneously.

Fourth and higher terms may also be obtained in like manner. Here, with the omission of analyses, we show the result only for the fourth approximation:

$$G_4=\frac{k^4\beta^3}{16}\left[\left\{10\frac{\bar\zeta}{\zeta^2}+20\frac{\bar\zeta^{1/2}}{\zeta^{3/2}}-120\frac{1}{\zeta}+20\frac{1}{\zeta^{1/2}\bar\zeta^{1/2}}\right.\right.$$
$$\left.+10\frac{1}{\bar\zeta}\right\}\log\frac{\zeta}{\bar\zeta}+2\frac{\bar\zeta^3}{\zeta^4}+10\frac{\bar\zeta^{5/2}}{\zeta^{7/2}}+8\frac{\bar\zeta^2}{\zeta^3}$$
$$-52\frac{\bar\zeta^{3/2}}{\zeta^{5/2}}-72\frac{\bar\zeta}{\zeta^2}+146\frac{\bar\zeta^{1/2}}{\zeta^{3/2}}-146\frac{1}{\zeta^{1/2}\bar\zeta^{1/2}}$$
$$\left.+72\frac{1}{\bar\zeta}+52\frac{\zeta^{1/2}}{\bar\zeta^{3/2}}-8\frac{\zeta}{\bar\zeta^2}-10\frac{\zeta^{3/2}}{\bar\zeta^{5/2}}-2\frac{\zeta^2}{\bar\zeta^3}\right], \tag{3.18}$$

and

$$\varphi_1=-\frac{5}{512}(\gamma+1)^{7/3}\frac{k^4}{x}\frac{y^6}{x^6}=B_3(y^{2/5}\chi^{1/2})\chi^{-15/2}\ .$$

In this case, the complementary function g_4 was chosen so as to make all terms up to the order ϑ^4 vanish.

§ 4. Axisymmetrical Flows

For want of an analogous formula to Eq. (3.4) in axisymmetrical cases, we must resort to another method of analysis.

We assume first that the perturbation velocity potential as defined in (3.1) can be further expanded in a series as:

$$\phi=\phi_1+\phi_2+\cdots\ , \tag{4.1}$$

where $\phi_1, \phi_2, \cdots$ are the small quantities of the order $O(r\mathcal{E})$, $O(r\mathcal{E}^2), \cdots$ respectively, and $\mathcal{E}$ denotes a small number as before, while r is the distance in three-dimensional space from the origin to any point.

Let us take the Cartesian coordinates x, y, z such that the x-axis coincides with the line of symmetry. Further, we define the reduced coordinates in the forms:

$$\xi=x\ ,\qquad \eta=\mu y\ ,\qquad \zeta=\mu z\ , \tag{4.2}$$

with

$$\mu=\sqrt{1-M_\infty{}^2}\ . \tag{4.3}$$

Then, the fundamental equations for ϕ_1 and ϕ_2 reduce respectively to the following forms:

$$\left.\begin{aligned}&\varDelta_\mu\phi_1=0\ ,\\&\varDelta_\mu\phi_2=M_\infty{}^2(\lambda\phi_{1\xi}{}^2+\phi_{1\eta}{}^2+\phi_{1\zeta}{}^2)_\xi\ ,\end{aligned}\right\} \tag{4.4}$$

where

$$\left.\begin{aligned}&\varDelta_\mu\equiv\frac{\partial^2}{\partial\xi^2}+\frac{\partial^2}{\partial\eta^2}+\frac{\partial^2}{\partial\zeta^2}\ ,\\&\lambda=1+\frac{\gamma+1}{2\mu^2}M_\infty{}^2\ .\end{aligned}\right\} \tag{4.5}$$

These reductions are the same as used by Hasimoto[3)] in his paper; "On the Asymptotic Behaviour of Three-dimensional Compressible Flow Field at a Great Distance from a Body, I".

As in two-dimensional cases, we assume that the velocity potential ϕ is subject to the following three boundary conditions:

(i) $\phi_\xi\to0,\ \phi_\eta\to0,\ \phi_\zeta\to0$, as $x\to\infty$,

(ii) $\phi_\xi,\ \phi_\eta,\ \phi_\zeta$ should remain to be finite even at $M_\infty=1$,

(iii) $\phi_1=O(1/\sqrt{x})$ as $x\to\infty$.

The third condition, which is necessary to settle the solution, is derived from (2.2), (2.3) and (2.4).

Bearing in mind that we have assumed $\phi_1=O(r\mathcal{E})$ and $\phi_2=O(r\mathcal{E}^2)$, we find that

$$\mathcal{E}=O(r^{-3/2})\ ,$$

and hence

$$\phi_2=O(r^{-2})\ . \tag{4.6}$$

Now, we shall show how the correct expression for ϕ_2 can be derived from Eq. (4.4) subject to the above boundary conditions.

Since the axisymmetrical cases are exculsively considered, the polar coordinates (R, Θ) in the reduced meridian plane are preferable to the Cartesian coordinates (ξ, ρ), where ρ denotes the radial distance of any point from the axis. These two systems of coordinates are connected by the relations:

$$\left.\begin{aligned}\xi&=R\cos\Theta\ ,\\\rho=\sqrt{\eta^2+\zeta^2}&=R\sin\Theta\ .\end{aligned}\right\} \tag{4.7}$$

With the boundary condition (iii) in mind, we shall take the solution of the first equation of (4.4) in the form:

$$\phi_1=kR^{-1/2}P_{-1/2}(\cos\Theta)\ , \tag{4.8}$$

where P_ν is Legendre's spherical function of ν-th order.

Substitution of this expression into the second equation of (4.4) gives

$$\begin{aligned}\varDelta_\mu\phi_2=-k^2M_\infty{}^2R^{-4}\Big\{&\frac{3}{4}\lambda P_{1/2}(\cos\Theta)P_{3/2}(\cos\Theta)\\&+\sin^2\Theta P'_{1/2}(\cos\Theta)P'_{3/2}(\cos\Theta)\Big\}\ .\end{aligned} \tag{4.9}$$

As the right-hand members of Eq. (4.9) can be expressed as a power series in $\sin^2\Theta$, Eq. (4.9) is written in the reduced form:

$$\varDelta_\mu\phi_2=-\frac{3}{4}M_\infty{}^2\lambda k^2R^{-4}\{1+O(\sin^2\Theta)\}\ .$$

But, as will be proved in the next section, the differential equation:

$$\varDelta_\mu\phi_2=R^{-4}\sin^{2n}\Theta\ ,\quad (n\text{: positive integer}) \tag{4.10}$$

has its particular solution in the form:

$$\phi_2=CR^{-2}\left\{1-\frac{\Theta^2}{2}+O(\Theta^4)\right\}\ , \tag{4.11}$$

C being a certain numerical constant.

As is well known, the homogeneous equation arisen from Eq. (4.10) is satisfied by the harmonic function: $R^{-2}P_1(\cos\Theta)$, which has also the same expression as Eq. (4.11).

Thus, taking into account the requirement (4.6), we have finally the solution of Eq. (4.10) in the form:

$$\phi_2 = -\frac{3}{4} M_\infty^2 \lambda k^2 R^{-2} \left\{ \frac{1}{2} + A\left(1 - \frac{\Theta^2}{2}\right) + O(\Theta^4) \right\} , \tag{4.12}$$

where A is a constant to be determined so as to satisfy the boundary condition (ii).

To this end, it is sufficient to notice, by (4.2), (4.5) and (4.7), that when M_∞ tends to unity, we have

$$\left. \begin{aligned} \lambda &= \frac{\gamma+1}{2\mu^2} + O(1) , \\ R^2 &= x^2 + O(\mu^2) , \\ \Theta^2 &= \mu^2 \frac{\tilde{\omega}^2}{x^2} + O(\mu^4) , \end{aligned} \right\} \tag{4.13}$$

with

$$\tilde{\omega}^2 = y^2 + z^2 = \rho^2/\mu^2 .$$

Substitution of these expressions into (4.12) shows immediately that A is to be taken as $-1/2$. Hence, the velocity potential for the sonic flow is ultimately given by

$$\varphi_2 = [\phi_2]_{\mu=0} = -\frac{3}{32}(\gamma+1)k^2 x^{-4} \tilde{\omega}^2 . \tag{4.14}$$

In axisymmetrical cases, χ as defined in (2.3) takes the form:

$$\chi = -(\gamma+1)^{-1/3} x \tilde{\omega}^{-4/7} . \tag{4.15}$$

Therefore, the expression for φ_2 can be written in an alternative form as:

$$\varphi_2 = -\frac{3}{32}(\gamma+1)^{-1/3} k^2 (\tilde{\omega}^{-2/7} \chi^{-1/2}) \chi^{-7/2} ,$$

and also we have from (4.8) the similar result for φ_1 as:

$$\varphi_1 = [\phi_1]_{\mu=0} = k x^{-1/2} = k(\gamma+1)^{-1/6} (\tilde{\omega}^{-2/7} \chi^{-1/2}) .$$

Comparing these expressions with (2.4), we have

$$B_0 = (\gamma+1)^{-1/6} k ,$$

$$B_1 = -\frac{3}{32}(\gamma+1)^{-1/3} k^2 = -\frac{3}{32} B_0^2 ,$$

the latter of which is surely coincident with the value as given in Table I.

§ 5. Proof of (4.11)

Putting

$$\cos^2 \Theta = z ,$$

we can rewrite Eq. (4.10) in the form:

$$\Delta_\mu \phi_2 = R^{-4}(1-z^2)^n, \quad (n\text{: positive integer}). \tag{5.1}$$

By virtue of the well-known Poisson's formula, a particular solution of this equation is given by

$$\phi_2(R, z) = -\frac{1}{2} \sum_{m=1}^{\infty} \left[\int_0^\infty dR_1 R_1^{-2} \frac{R_<^{2m}}{R_>^{2m+1}} \times \int_{-1}^{1} dz_1 (1-z_1^2)^n P_{2m}(z_1) \right] P_{2m}(z) , \tag{5.2}$$

where $R_<$ and $R_>$ denote the smaller and the larger quantities of R and R_1 respectively.

Performing the integration with respect to R_1 and taking into account the well-known formula:

$$P_{2m}(z) = F\left(2m+1, -2m; 1; \frac{1-z}{2}\right) = 1 - \frac{m(2m+1)}{2} \Theta^2 + O(\Theta^4) ,$$

we have

$$\phi_2 = -\frac{1}{2R^2} \sum_{m=0}^{\infty} \frac{4m+1}{(2m-1)(2m+2)} I(m, n) + \frac{\Theta^2}{4R^2} \sum_{m=0}^{n} \frac{(4m+1)m(2m+1)}{(2m-1)(2m+2)} I(m, n) + O(\Theta^4) , \tag{5.3}$$

with

$$I(m, n) = \int_{-1}^{1} (1-z_1^2)^n P_{2m}(z_1) dz_1 . \tag{5.4}$$

Now, we shall notice the following relation:

$$S_1 - S_2 = \frac{1}{2} \int_{-1}^{1} (1-z_1^2)^n \sum_{m=0}^{n} (4m+1) P_{2m}(z_1) dz_1 , \tag{5.5}$$

with

$$\left. \begin{aligned} S_1 &= \sum_{m=0}^{n} \frac{(4m+1)m(2m+1)}{(2m-1)(2m+2)} I(m, n) , \\ S_2 &= \sum_{m=0}^{n} \frac{(4m+1)}{(2m-1)(2m+2)} I(m, n) . \end{aligned} \right\} \tag{5.6}$$

Owing to the recurrence formula for Legendre's polynomials, the finite series standing in the integrand of (5.5) reduces to a single term, namely:

$$\sum_{m=0}^{n} (4m+1) P_{2m}(z_1) = \sum_{m=0}^{n} \{ P'_{2m+1}(z_1) - P'_{2m-1}(z_1) \} = P'_{2n+1}(z_1) .$$

Substituting this in (5.5) and integrating by parts, we have finally the relation:

$$S_1 - S_2 = n \int_{-1}^{1} (1-z_1^2)^{n-1} z_1 P_{2n+1}(z_1) dz_1 . \tag{5.7}$$

Since $(1-z_1^2)^{n-1} z_1$ is the polynomial of $(2n-1)$-th order, it follows from the orthogonality of Legendre's polynomials that the definite integral on the right-hand side vanishes identically.

Therefore, if we define a numerical constant

A_n as

$$A_n = S_1 = S_2 \,,$$

which depends on n only, then the expression (5.3) for ϕ_2 is reduced to the form:

$$\phi_2 = -\frac{A_n}{2R^2}\left\{1 - \frac{\Theta^2}{2} + O(\Theta^4)\right\} .$$

It will readily be seen that this is certainly identical with the expression (4.11).

In conclusion, the writer wishes to express his cordial thanks to Professor S. Tomotika for his help and encouragement throughout this work.

References

1) I. Imai: Journ. Phys. Soc. Japan **8** (1953) 537.
2) G. Guderley and D. T. Barish: Journ. Aeron. Sci. **20** (1953) 491.
3) H. Hasimoto: Journ. Phys. Soc. Japan **6** (1951) 383.

Short Notes

J. Phys. Soc. Japan **10** (1955) 1018

Decrement of Blast Wave

By Akira Sakurai
Tokyo Electrical Engineering College

(Received September 9, 1955)

In a recent extensive numerical study on the spherical blast wave generated by a point source, H. H. Goldstine and J. von Neumann[1] has described the decrement of the shock-front strength in terms of n which is defined as

$$p-1=AR^{-n},$$

where p is the ratio of the pressure at the shock-front to the undisturbed pressure, R is the distance between the centre and the shock-front and A is a constant. n is expected to be slowly varying and is tabulated in their paper as a function of p.

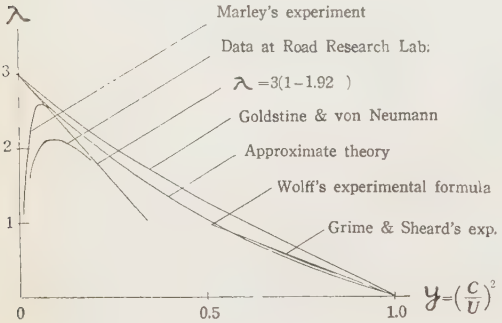

It is interesting for us to compare their value of n with the author's former results[2] about the same problem. Our previous definition of decrement expressed by λ in the papers[2] is, however, somewhat different from theirs, i.e.,

$$\lambda=\frac{1}{y}\frac{dy}{dR}=-\frac{2R}{U}\frac{dU}{dR},$$

where U is the shock-front velocity, $y=(C/U)^2$ and C is the sound velocity of the undisturbed gas. The relation between λ and n is easily obtained, if we utilize the Rankine-Hugoniot condition:

$$p=\frac{2\gamma}{\gamma+1}\left(\frac{U}{C}\right)^2-\frac{\gamma-1}{\gamma+1} \quad \text{or} \quad y=\left(1+\frac{\gamma+1}{2\gamma}p\right)^{-1}, \qquad (1)$$

thus

$$\lambda=p\left(p+\frac{2\gamma}{\gamma+1}\right)^{-1}n. \qquad (2)$$

Values of λ obtained from (1) and (2) using the values of n on the table in Goldstine and Neumann's paper, where γ was taken as 1.4, are plotted in the following figure and compared with the author's previous result[2]:

$$\lambda=3(1-1.92y+O(y^2)).$$

For the sake of comparison, we also give a result obtained from an approximate method[3] as well as results[2] deduced from the available experimental data.

It will be worth while to note that the description of the decrement in terms of n or λ is considered to be useful for both experimental and theoretical studies, because any kinds of explosions can be expressed in a single diagram as in the present figure.

References

1) H. H. Goldstine and J. von Neumann: Comm. Pure. and Appl. Math. **8** (1955) 327.
2) A. Sakurai: J. Phys. Soc. Japan **8** (1953) 662; **9** (1954) 256.
3) A. Sakurai: Res. Rep. of Tokyo Elect. Eng. College **3** (1955) (in Japanese).

J. Phys. Soc. Japan **10** (1955) 1018~1019

Observations of Dislocations along Grain Boundaries in Germanium Crystals

By Jun'ichi Okada
Matsuda Research Laboratory, Tokyo-Shibaura Electric Co., Kawasaki-city, Japan

(Received September 3, 1955)

In the course of a study of the dislocations in germanium crystals by means of the etching process, some results were obtained which verify the properties of dislocations along the small-angle-of-misfit grain boundaries. The crystals were grown by pulling in the ⟨100⟩ direction, and {100} surfaces perpendicular to the growth direction were etched about 5 min. by CP-4 solution.

Most of the boundaries could be resolved into separated etch-pits extended in ⟨110⟩ directions. The number of dislocations or their spacing D along a simple tilt boundary can be determined from a measurement of the orientation difference $\theta=b/D$, where b is the length of the Burgers vector of each dislocation. This relation has been verified by Vogel et al[1] by comparing D with θ obtained from the X-ray experiment. However, in some cases, the verification of this formula is possible, even though the angle θ is not measured directly.[2] This could be done in the following way by use of more general relations which hold for a simple cubic lattice.

(1) When ρ is the density of dislocations in a symmetrical boundary, the density ρ' of the asymmetrical boundary making an angle ϕ with the direction of the symmetrical one should be

$$\rho' = \rho(\sin\phi + \cos\phi)\ .$$

Fig. 1 shows an example of this case, and measurements give:

Boundary	ϕ	$\rho'_{obs.}$*	$\rho_{calc.}$
AB	~ 0°	34	34
BC	65°	48	36

* Number of etch-pits per 100 μ.

Values of $\rho_{calc.}$ for AB and BC boundaries show a good agreement.

(2) When three (in general asymmetrical) pure tilt boundaries meet, the following relation should hold:

$$\sum_{i=1}^{3} \frac{\rho_i'}{\sin\phi_i + \cos\phi_i} = 0$$

where ρ_i' are the dislocation densities and ϕ_i the angles of the boundary with the direction of the symmetrical one. Especially, when three boundaries are all symmetrical, the relation

$$\rho_1 + \rho_2 = \rho_3 \qquad (\rho_1,\ \rho_2 < \rho_3)$$

should hold. An example of this case is shown in Fig. 2 and measurements give:

Boundary	$\rho_{obs.}$	$D(\mu)$	$\theta_{calc.}$ (sec)
AP	28.0	3.6	22.9
BP	13.5	7.4	11.1
CP	13.5	7.4	11.1

The relation

$$\rho_{AP} = \rho_{BP} + \rho_{CP} \qquad (\theta_{AP} = \theta_{BP} + \theta_{CP})$$

is satisfied within the accuracy of the measurements.

(3) When the symmetrical or nearly symmetrical boundaries make "veining" structure and only three boundaries meet at its nodes, the density relation equivalent to Kirchhoff's law for electrical currents should hold. An example of this case is shown in Fig. 3 (a) and measurements give Fig. 3 (b). The results are satisfactory except for the inaccuracy at the part AB (the density of this part is expected to be 15).

These observations suggest that a one-to-one correspondency between etch-pits and edge dislocations exists so far as the grain boundaries are concerned. And this fact may permit us to conclude that the etch-pits distributed at random, also, are in edge orientation.

Similar observations on other surfaces are now in progress.

The author thanks Mr. Y. Uemura for his helpful discussions and Messrs. M. Takabayashi and T. Kobayashi for their kindness of preparing the samples.

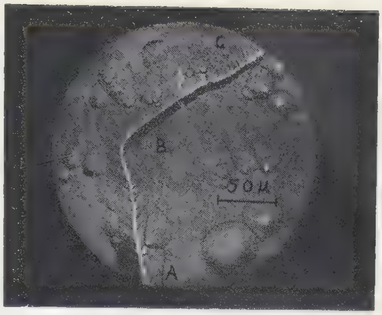

Fig. 1. Curved boundary. $\phi = 65°$

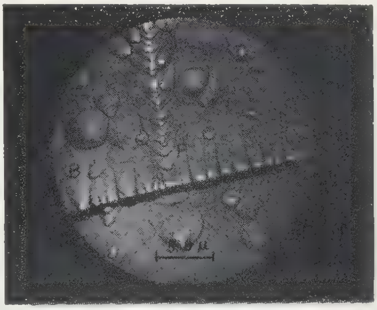

Fig. 2. Branching point of three symmetrical boundaries.

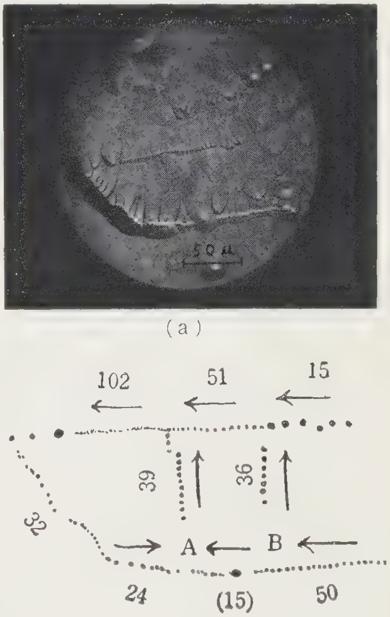

(a)

(b)

Fig. 3. The "veining" structure. Numbers in (b) indicate the dislocation densities.

References

1) F. L. Vogel, W. G. Pfann, H. E. Correy and E. E. Thomas: Phys. Rev. **90** (1953) 489 (L).
2) S. Amelinckx: Act. Met. **2** (1954) 848.

J. Phys. Soc. Japan **10** (1955) 1020~1022

On the Coupled Dislocations along a Grain Boundary

By Yasutada Uemura

Matsuda Research Laboratory, Tokyo-Shibaura Electric Co., Kawasaki-city, Japan

(Received September 3, 1955)

Recently J. J. Oberly[1] and J. Okada[2] obtained interesting patterns of coupled dislocatisns along a grain boundary in Ge-crystals. These patterns are observed in the {100} surface etched by means of the CP-4 solution, and the array of dislocations have the <110> direction. (Figs. 1, 2)

In order to investigate the origin of forces which determine the arrangement of these patterns, we try to estimate the separation of the doublets, triplets and quartets of the etched pits along the boundary using the simple models of pure edge dislocations in an isotropic elastic medium. The simple examples are shown in Table 1. The equations represent the condition to balance the forces of interaction between the dislocations along the slip plane.[3] In these equations, ξ means the distance of a dislocation from the boundary measured in the unit of length which shows the interval of dislocations on the array, and the functions $S(\xi)$, $C(\xi)$, and $R(s)$ are defined as follows:

$$S(\xi)=\pi^2\xi^2\sinh^{-2}\pi\xi$$
$$C(\xi)=\pi^2\xi^2\cosh^{-2}\pi\xi$$
$$R(s)=s^2(s^2-1)(s^2+1)^{-2}$$

By solving these equations graphically, we obtain the separations tabulated in Table 1.

To compare the results of the calculations with the actual patterns in Fig. 1 and Fig. 2, we further try to calculate in the same way the separations of the models shown in Fig. 3 and Fig. 4, which have a better fit of arrangement along the boundary than the models in Table 1. The calculated value for the Okada's doublet gives the separation of 0.95. On the other hand, the experiment shows the value of 1.0 or 1.1. In the cese of Oberly's pattern, the condition of balancing gives a set of three equations involving the three variables, and their roots ξ_1, ξ_2 and ξ_3 are obtained by using the self-consistent method graphically. The results are shown in Fig. 4.

The results of these estimations suggest that the main origin of forces which determine the separation of these coupled dislocations is the simple elastic interaction between edge dislocations. The fundamental assumptions used in these rough evaluations are as follows:

(A) The all edge dislocations observed in the pattern have the same Burgers vectors which are perpendicular to the surface of the grain boundary.

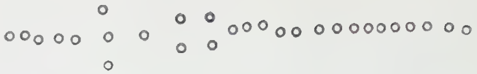

Fig. 1. Etched pattern reproduced from Oberly's paper.

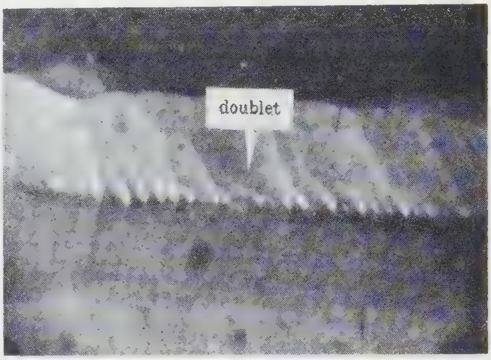

Fig. 2. Doublet structure of etched pits along a boundary observed by Okada in this laboratory.

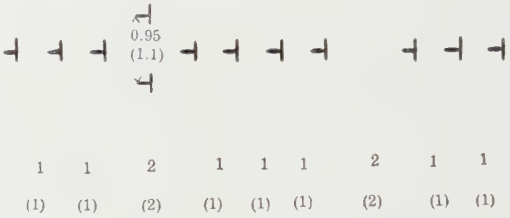

Fig. 3. A model of the Okada's doublet. The underlying numbers indicate the ratio of intervals in the array. The separation is given in the figure. Those in parenthesis are the experimental values corresponding to Fig. 2.

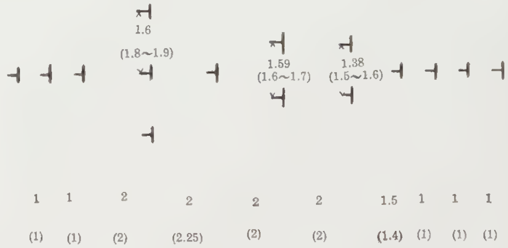

Fig. 4. A model of the Oberly's pattern. The numbers indicate the ratio of intervals in the array. The calculated separations are given in the figure. Those in parenthesis are the experimental values corresponding to Fig. 1.

(B) The arrangement along the boundary is mainly determined by the condition that the small angle of misfit near the coupled dislocations is not so different from that in the regular array.

(C) The crystal anisotropy of the interaction force is neglected.

(D) There is no other appreciable stress field than the interaction forces considered here.

Table I.

	Models	Equations	Separations
D.A.	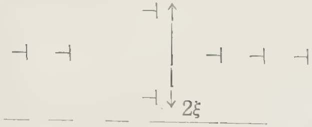	$\frac{1}{\xi}\left[-C(\xi)-2R(2\xi)+\frac{1}{2}\right]=0$	2ξ 1.16
D.B.	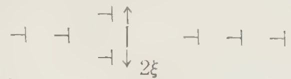	$\frac{1}{\xi}\left[S(\xi)-R(\xi)-\frac{1}{2}\right]=0$	2ξ 1.14
T.A.	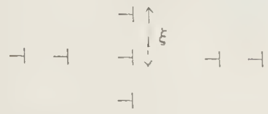	$\frac{1}{\xi}\left[S(\xi)-2R(\xi)+\frac{1}{2}\right]=0$	ξ 1.48
T.B.	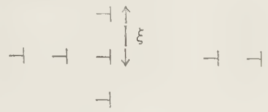	$\frac{1}{\xi}\left[S(\xi)-R(\xi)-R\left(\frac{\xi}{2}\right)+\frac{1}{2}\right]=0$	ξ 2.04
Q.A.	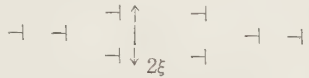	$\frac{1}{\xi}\left[-C(\xi)-2R(2\xi)-R\left(\frac{2}{3}\xi\right)-R\left(\frac{2}{5}\xi\right)+\frac{1}{2}R(\xi)+\frac{1}{2}\right]=0$	2ξ 1.52
Q.B.	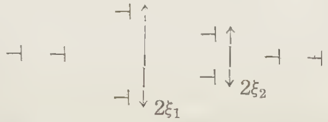	$\left\{\begin{array}{l}\frac{1}{\xi_1}\left[S(\xi_1)-2R(\xi_1)-R\left(\frac{\xi_1}{2}\right)-\frac{1}{2}\right]+\frac{1}{\xi_1+\xi_2}R\left(\frac{\xi_1+\xi_2}{2}\right)+\frac{1}{\xi_1-\xi_2}R\left(\frac{\xi_1-\xi_2}{2}\right)=0\\ \frac{1}{\xi_2}\left[S(\xi_2)-R(\xi_2)-R\left(\frac{\xi_2}{2}\right)-R\left(\frac{\xi_2}{3}\right)-\frac{1}{2}\right]+\frac{1}{\xi_1+\xi_2}R\left(\frac{\xi_1+\xi_2}{2}\right)+\frac{1}{\xi_2-\xi_1}R\left(\frac{\xi_2-\xi_1}{2}\right)=0\end{array}\right.$	$2\xi_1$ 1.34 $2\xi_2$ 1.22

The experimental results obtained by J. Okada[2] suggest that the assumptions (A) and (B) seem to be satisfied in the case of the dislocations having the ⟨100⟩ direction observed in the Ge-crystals grown in this direction.

Detailed discussions including those on the effects of the crystal anisotropy and the impurity atoms will be reported in this Journal. The author thanks Messrs. J. Okada, M. Takabayashi and T. Kobayashi for their valuable information on the experimental works.

References

1) J. J. Oberly: J. of Metals **6** (1954) 1026.
2) J. Okada: J. Phys. Soc. Japan **10** (1955) 1018.
3) for example Nabarrow: Adv. in Physics **1** (1952) 271.

Note added in proof

The recent calculations including the effect of anisotropy show the separation 1.07 of the doublet in Fig. 3, 1.80 of the triplet in Fig. 4, 1.72 and 1.54 of the quartet in Fig. 4. The agreement with observed values is fairly good.

J. Phys. Soc. Japan **10** (1955) 1022

The Angular Distribution of α-Particles from the Reaction $^{19}F(p\alpha)^{16}O^{*}(\pi)^{16}O$

By Akira Isoya, Kazuo Goto
and Teruo Momota

Department of Physics, Faculty of Science,
University of Tokyo

(Received May 26, 1955)

The angular distributions of α-particles from the reaction $^{19}F(p\alpha)^{16}O^{*}(\pi)^{16}O$ [1)†] have been measured by using a Van de Graaff generator. Detection of these α-particles (α_{π}) is not so simple, because the cross section of this reaction are small compared with those of other groups of α-particles (α_1, α_2, α_3), which are emitted by the reaction

$$^{19}F(p\alpha)^{16}O^{*}(\gamma)^{16}O,$$

and, moreover, the energy of α_{π} is very close to that of α_1. Although α_1, α_2, and α_3 have resonance characteristics quite different from those of α_{π}, their intensities are not negligible even at the resonances of α_{π}. In order to discriminate α_{π} from the other groups of α-particles, we made use of nuclear pair electrons which were emitted successively, that is, only those α-particles in coincidence with the electrons were counted. The direction of emission of pair electrons will not be correlated with that of α_{π} and uniformly distributed, because the de-excitation of the pair emitting state of ^{13}O (the 1st excited state) is believed to be a $O-O$ transition.

Four Geiger-Müller counters, which were connected parallel, and a proportional counter were used to detect electrons and α-particles respectively. (Fig. 1.) The proportional counter was mounted on a rotatable disc and could be set at any angles against the direction of the incident proton beam, while the Geiger-Müller counters were set at a fixed position. The proportional counter was filled with pure hydrogen gas to a low pressure, which seemed to make the counter fairly immune to paralysis under a strong flux of protons scattered from the target. In order to obtain good discrimination between α-particles and scattered protons, we placed a mica absorber in front of the window of the proportional counter to reduce the energy of α-particles so that they might be almost stopped in the counter gas, while scattered protons might go through with less energy loss. Thus we could make the pulse of α-particles eight times as high as that of protons. The Geiger-Müller counters were of cylindrical type. The wall was made of Al of 0.4 mm thickness. It was thin enough to make the counting efficiency for γ-rays which followed α_1, α_2, and α_3, as low as 0.001 per reaction so that coincidence counts between them might be negligible, and on the other hand it was thick enough to absorb soft X-rays emitted from the target.

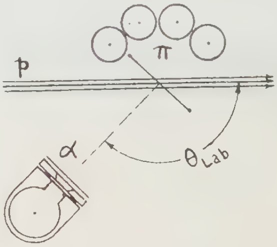

Fig. 1.

Besides the precautions mentioned above, the target was made as light as possible to reduce the amount of scattered protons and X-rays. The target used was AlF_3 evaporated onto a thin film of SiO of about 10 $\mu g\,cm^{-2}$ in thickness.[2)] This target was stable under the proton bombardment of a few μA per cm^2.

The energy of proton beam was kept constant within an accuracy of 0.5%. The thickness of the target was about 1 kev at the proton energy of 843 kev. The resolving time of the coincidence circuit was 0.42 μ sec.

We report here the result of the measurement on the angular distribution of α_{π} at the 843 kev resonance.

$$\frac{N_{tc}(\theta)}{N_{\beta}} \infty W(\theta) = 1 + 0.47 \cos\theta - 0.30 \cos^2\theta - 0.014 \cos^3\theta + 0.59 \cos^4\theta$$

where $N_{tc}(\theta)$ denotes the coincidence count corrected for accidental coincidences, and N_{β} the count of Geiger-Müller counters.

The results of the experiment being carried on now, and the analysis of the data will soon be published in this journal.

The authors wish to thank the members of Van de Graaff group at the University of Tokyo for their cooperation.

References

1) Chao, Tallestrup, Fowler and Lauritzen: Phys. Rev. **79** (1950) 108.
2) C. A. Sawyer: Rev. Sci. Instr. **23** (1952) 604.

† As to the definition of symbols α_{π}, α_0, α_1, etc. see ref. 1).

J. Phys. Soc. Japan **10** (1955) 1023~1024

Influence of Magnetic Field on the Precipitation Process of Ferromagnetic Phase in Cu-Co Alloy

By Tadayasu Mitui and Syôhei Miyahara
Department of Physics, Faculty of Science, University of Hokkaido, Sapporo, Japan

(Received August 5, 1955)

The evidence of the shape effect proposed by L. Néel1) has been fully examined experimentally by R. D. Heidenreich and E. A. Nesbitt2)3) for the Alnico V, the permanent magnet of precipitate alloy. However, the evidence of the directional order proposed by Néel4)5) *et al.*6)7)8) has not yet been examined experimentally. We have investigated an influence of a magnetic field on a process of precipitation of a ferromagnetic phase for the purpose of establishing the limit of application of the both mechanisms. We have taken the alloy of copper including ca. 2 weight % of cobalt as the most appropriate specimen. Measurements were made on the specimens that were prepared by quenching in a water after solid solution heat treatment and by the isothermal tempering in magnetic field at 750°C which is the temperature most effective to the magnetic heat treatment as we previously reported.9)10) The torsion method was used for measuring the magnetic anisotropy with disk-shaped polycrystalline specimen in a uniform magnetic field of 10000 Oe.

The experimental results are as follows:

(1) For a specimen tempered 20.0 hr. isothermally at 750°C without a field and successively tempered 4.0 hr. at 750°C with the field of 1000 Oe, the obtained value of the uniaxial magnetic anisotropy is ca. 10^2 ergs/cm^3, and this is smaller than the value 4×10^3 ergs/cm^3 of the specimen which is tempered 4.0 hr. isothermally under the field of 1000 Oe. at 750°C, as shown in Fig. 1.

(2) For the cold-worked specimen of solid solution, after being tempered 4.0 hr. isothermally under the field of 1000 Oe. 750°C, the torque value obtained is ca. 10^4 ergs/cm^3 and that of no cold-worked specimen is 4×10^3 ergs/cm^3.

(3) The specimen, which is tempered for 4.0 hr. isothermally with the field of 2000 Oe. at 750°C, shows the twofold rotational symmetry. On the other hand the specimen, which is tempered for 4.0 hr. isothermally with the field in a direction and then tempered as same manner in other direction orthogonal to the former, shows a fourfold symmetry, as shown in Fig. 2.

The results (1) and (2) mean that the magnetic field is effective to the initial stage of precipitation, and the result (3) cannot be fully explained by the anisotropy of directional order. Thus, it has been clarified that the origin of the uniaxial anisotropy would be decided by the directional distribution of precipitates which were obtained by magnetic field treatment and so the shape effect proposed by Néel would be more resposible than the directional order for the magnetic treatment of the precipitate alloys. Full report will be published soon elsewhere.

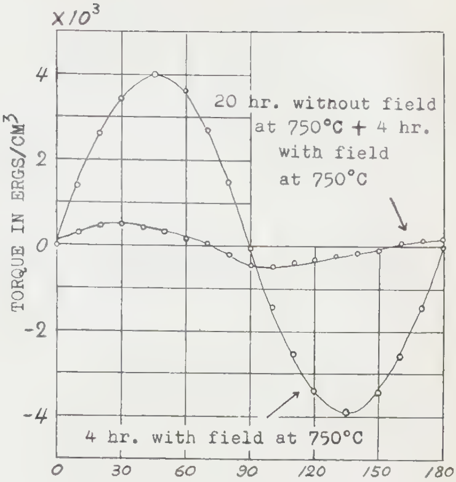

Fig. 1. Angle of field in Degrees.

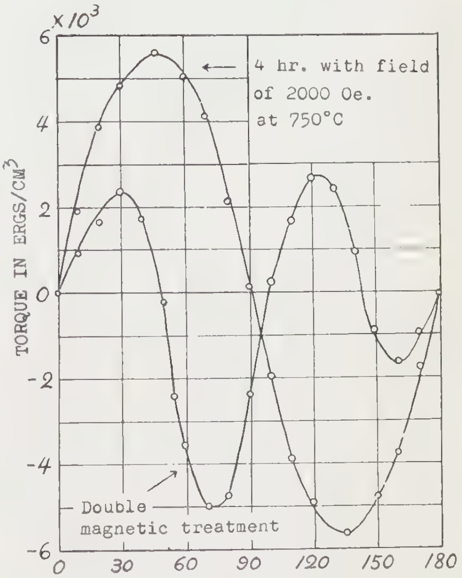

Fig. 2. Angle of field in degrees.

References

1) L. Néel: Compt. rend. **225** (1947) 109.
2) R. D. Heidenreich and E. A. Nesbitt: J. App. Phys. **23** (1952) 352.
3) E. A. Nesbitt and R. D. Heidenreich: J. App. Phys. **23** (1952) 366.
4) L. Néel: Compt. rend. **237** (1953) 1613.

5) L. Néel: J. Physique et Rad. **15** (1954) 225.
6) S. Chikazumi: J. Phys. Soc. Japan **5** (1950) 333.
7) S. Taniguchi and M. Yamamoto: Sci. Rep. RITU **A6** (1954) 330.
8) S. Taniguchi: Sci. Rep. RITU **A7** (1955) 269.
9) S. Miyahara and T. Mitui: J. Phys. Soc. Japan **7** (1952) 536.
10) S. Miyahara and T. Mitui: J. Fac. Sci. Hokkaido Univ. **4** (1953) 275.

J. PHYS. SOC. JAPAN **10** (1955) 1024~1025

Fibrous Growth of $NaClO_3$ on Single Crystal

By Norio KATO

Kobayasi Institute of Physical Research,
Kokubunji, Tokyo

(Received September 19, 1955)

Works on fibrous growth of alkali-halides[1][2] and of metals[3] have been published by several authors. The present author reports herein on his study of the fibrous growth of $NaClO_3$ on single crystals.

Single crystals of $NaClO_3$ were prepared by the evaporation method, keeping the saturated solution at 30±1°C. Each crystal was grown from a seed crystal which was placed between two parallel glass plates. All the crystals thus prepared were bounded by {100}-planes. They were picked out from the solution and kept in a desiccator of volume ca. 10^4 cc with $CaCl_2$ as the desiccating agent. After an induction period of from 30 minutes to 2 hours, with the naked eye numerous fibers were recognized on the crystals. The growth of the fibers ended within 3 to 12 hours. When the crystals were grown very slowly, their surfaces were flat as cleavage and on such surfaces the fibers rarely grew. When the crystals were grown rapidly with an increase of crystal volume of about 1 cc per day, white striations and steps appeared on the surface along ⟨100⟩-direction. Fibers usually started from these striations and steps. No fibrous growth took place when crystals were dried rapidly in a vacuum. If the vacuum dried crystals were immersed again in water and then kept in the desiccator, fibrous growth resulted. It is sure that moisture around the crystal is an important condition for the fibrous growth.

Since in the present experiment the fibrous growth occured on single crystals, the direction of the fibrous axis relative to the base crystals could be easily studied. The direction changed according to the temperature, as given in Table I. Two examples of the fibers are shown in photograph 1. The thickness of the fibers was 10–20 μ for ⟨100⟩-fibers and 1–5 μ for ⟨111⟩-fibers. While lengths were usually 1–10 mm, several were found longer than 15 mm. The fibrous crystals were never perfectly straight but deflections of small angles were observed by the naked eye. Frequently there was observed large angle deflection, as shown in photograph 2. Each stem forming the large angle was usually crystallographically equivalent. Successive observations on such deflected fibers confirmed that the growth took place at the fiber tip.

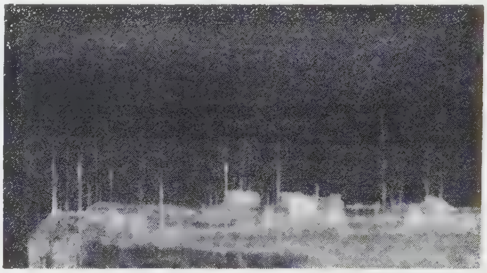
(a) ⟨100⟩-fibre grown at 15°C.

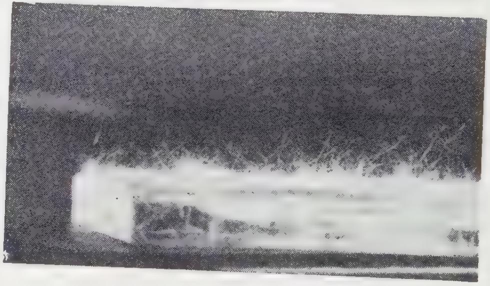
(b) ⟨111⟩-fibre grown at 35°C.

Photo. 1. (×3)

Photo. 2. Deflection of large angle in ⟨100⟩-fibre. (×10)

An X-ray examination of a ⟨100⟩-fiber (Table I) revealed that the fiber has the same crystal structure as the bulk crystal of $NaClO_3$ and has the same orientation as the base crystal. It was revealed, moreover, that the fiber used in the X-ray examination consisted of crystallites each of which was about 0.5 mm, every neighboring two crystallites forming an angle of about 1 degree.

In the present $NaClO_3$ fibre, it is sure that the growth takes place at the tip not at the bottom and that there must be moisture around crystal for the fibrous growth. Then it is most probable that, as suggested for NaCl by Gyulai[2], $NaClO_3$ molecules arrive at the tip of the fibre by diffusion through an adhesive layer of the solution on the crystal. It is not yet clear, however, why the rapid growth takes place at the tip and not on the stem of the fibre.

The author wishes to thank Mr. H. Nagasaki at Hitachi Central Research Laboratory who kindly allowed the author to use X-ray tube with a rotating anode.

Table I. Relations between the growth direction and temperature.

Temperature	Growth direction
10°~20°C	<100>
25°C	<100>,<111> and <110> (rare)
30°~60°C	<111> and more complex directions (rare)
above 60°C	No growth

The growth directions are referred to the base crystal.

References

1) H. A. Fells and J. B. Firth: Proc. Roy. Soc. London **112A** (1926) 468.
H. Tauber and I. S. Kleiner: J. Am. Chem. Soc. **54** (1932) 2392.
W. S. Hinegardner: J. Am. Chem. Soc. **55** (1933) 1461.
2) Z. Gyulai; Z. f. Phys. **125** (1948) 1; *ibid* **138** (1954) 317.
3) K. G. Compton, A. Mendizza and S. M. Arnold: Corrosion **7** (1951) 327.
G. W. Sears: Acta. Metal. **1** (1953) 457.

J. PHYS. SOC, JAPAN **10** (1955) 1025~1026

On the Magnetic Ageing of Pure Iron (II)

By Mitsuru ASANUMA and Sinji OGAWA*
Institute of Physics, Hokkaido University

(Received September 7, 1955)

In our previous paper[1] it was clarified that the origin from which the magnetic initial susceptibility of commercial pure iron was decreased by tempering at about 130°C was not FeS in iron as Y. Shimizu[2] pointed out, but very small amounts of nitrogen and carbon, and that the influence of nitrogen was dominant. But whether free nitrogen and carbon affect strongly the decrease of the initial susceptibility, or nitride and carbide are the essential origin of it was not clarified, and then has been investigated about these points.

After the specimen, a wire of commercial pure iron, is purified of carbon and nitrogen by annealing in a wet hydrogen atmosphere, 0.0065 wt % nitrogen was dissolved into the specimen, and then the ageing was investigated by the measurement of internal friction at 140°C. This result is shown in Fig. 1. And by the slope of the curve in this this figure, the parameter n is determined in the equation[3]

$$q=1-\exp[-Kt^n],$$

which shows the behavior of the growth of precipitates. Where q is the fraction transformed (in terms of Q^{-1}, $q=(Q_0^{-1}-Q_f^{-1})/(Q^{-1}-Q_f^{-1})$, Q_0^{-1}: initial Q^{-1} value, Q_f^{-1}: final Q^{-1} value. Q^{-1} corresponds to the concentration of the solute.), t is a growth time, and K is a constant which depends on the activation energy. According to our result, the first stage, from 0 to about 10 minutes, is not certain to be or not, because of the low

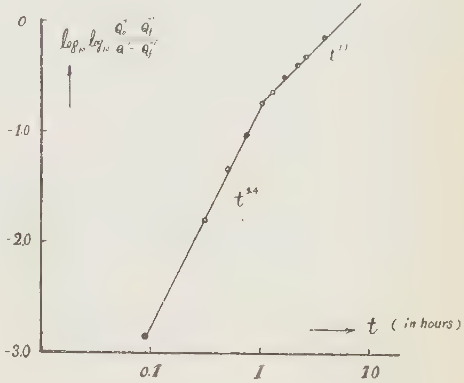

Fig. 1. $\log_{10}\log_{10}\dfrac{Q_0^{-1}-Q_f^{-1}}{Q^{-1}-Q_f^{-1}}$ *vs* $\log t$ curve. The nitrogen contents of this specimen is 0.0065 wt %. From the slope of this curve n is determined. The ageing temperature is 140°C.

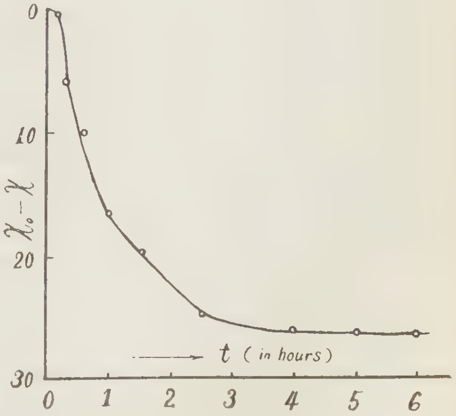

Fig. 2. The decrease of initial susceptibility *vs* ageing time. The ageing temperature is 140°C. The nitrogen contents of this specimen is 0.0060 wt %.

relative accuracy of measured value in this range, but if it is, its n would be about 2/3.[4] In the second stage, $n=2.4$ ($\doteqdot 5/2$) and in the third stage, $n=1.1$.

As Zenner[5] pointed out, $n=2.4$ ($\doteqdot 5/2$) means that the precipitates will have disk-like shape. That is, the intermediate phase $Fe_{16}N_2$ will precipitate in this stage and then Fe_4N follows it. These results are in agreement with those of C. Wert.[6]

The ageing of the magnetic initial susceptibility of the specimen which contains the same amount of nitrogen as that used to measure the ageing of internal friction is shown in Fig. 2. From Figs. 1 and 2, the followings are understood: even if there exists a stage of $n=2/3$ which means a formation of Cottrell atmosphere, the change of magnetic initial susceptibility corresponding to this stage is not observable. The precipitation which was proportional to $t^{5/2}$, that is, intermediate phase $Fe_{16}N_2$ have completely precipitated during an hour after the ageing treatment has begun, while in the same period, the decrease of the magnetic initial susceptibility is about three-fifth of total amount of it.

From these facts, it is concluded that the intermediate phase $Fe_{16}N_2$ which precipitated out in a disk-like shape is rather dominantly responsible for the decrease of the magnetic initial susceptibility and Fe_4N have also more or less influence on it, but the segregation of the nitrogen and the carbon to the dislocations would not affect it.

The details of this work will be published in another paper.

References

1) M. Asanuma and S. Ogawa: J. Phys. Soc. Japan **10** (1955) 161.
2) Y. Shimizu: Jour Japan Inst. Met. **5** (1941) 175 (in Japanese).
3) H. K. Hardy and T. J. Heal: Report on Precipitation (Progress in Metal Physics Vol. 5)
4) Cottrell and Bilby: Proc. Phys. Soc. A. **62** (1949) 49.
5) C. Zener: J. Appl. Phys. **20** (1949) 950.
6) C. Wert: Act. Metal. **2** (1954) 361.

* Now at the Research Institute of Applied Electricity, Hokkaido University.

J. Phys. Soc. Japan **10** (1950) 1026~1027

Electron Diffraction on Supercooled Gold

By Tadasu Suzuki

Institute of Physics, College of General Education, University of Tokyo

(Received August 29, 1955)

During a study of the liquid state of gold, a structure which seemed to correspond to a supercooled state of gold was detected by means of the transmission method of electron diffraction.

A thin gold foil beaten out to a thickness of about 800 Å was bridged over between two gold wires, and was directly heated with a direct current passed through itself, the wires serving as electrodes. The distance between the wires was about 2 m.m. and the breadth of the gold foil was several m.m. Heating current of about 0.5 Amp. was enough to melt the foil. When the foil melted, it was severed at its middle, and subsequently the flow of current stops, resulting in a sudden cooling of the foil.

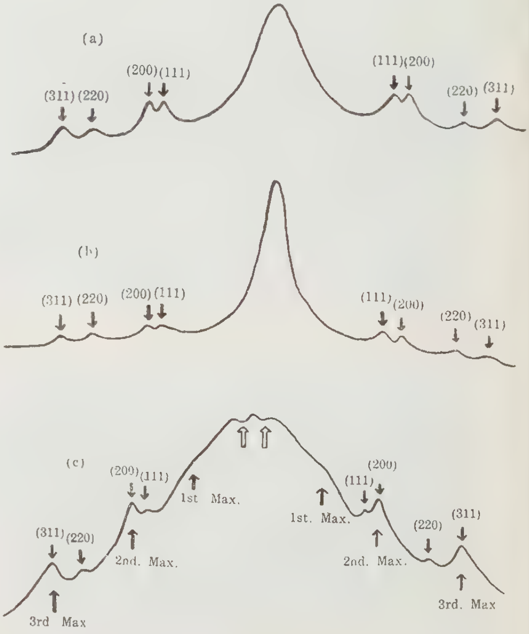

Fig. 1. The microphotometer records of the diffraction pattern from thin gold foil. (a) at a room temperature, (b) at a high temperature, (c) when the foil have melted.

Diffraction photographs were taken corresponding to various stages of heating, namely (a) at a room temperature, (b) at a high temperature shortly before melting and (c) at about the moment when the foil had melted. Microphotometer records of these photographs are shown in Fig. 1. Every photograph was taken with approximately the same exposure time.

In the stage (b) when compared with that of (a), the intensity of the diffraction lines is lower while the background is increased being due to the thermal vibration of the gold atoms. State (c) is remarkable as three halos are seen superposed on the ring patterns from the f.c.c. lattice of gold. The ring patterns have nearly the same sharpness as those patterns of the state (a) at a room temperature and the two rings (420) and (331) are clearly resolved.* The first halo inside of the (111) ring nearly agrees with the halo described by Nonaka and Kohra on a polished gold layer.¹⁾ By examining the original photograph, it is recognized that the intensity maxima of the second and the third diffuse halos nearly coinside with the (200) and (311) rings respectively. Although on the microphotometer records each pair of the corresponding rings and halos coalesce into a monotoneous peak, their distinction is clear on the original photograph. The positions of these three halos agree with those observed in an experiment on polished layer of gold by Kuriyama, Kohra and Takagi.²⁾ It is also interesting that in the immediate neighbourhood of the central spot there appear an intensity minimum (shown in Fig. 1 (c) by the large arrows), which is not due to the solarization of the photographic plate by strong insident beems. The similar minimum has been also observed by Kuriyama, Kohra and Takagi²⁾ in some of the transmission photographs from polished gold layers.

It is not clear that the state (c) correspond either to the liquid state or to the supercooled state. However, considering that the melting of the foil occurs almost instanteneously, it is reasonably presumed that the state (c) is the supercooled state. The similarity of the present halos to those from a polished gold layer shows that the atomic arrangement in the supercooled state is similar to that in the polished layer.

The sample used in the present work contains Ag and Cu as impurities, but their weight proportions, 2% and 0.8% respectively, are not sufficient to separate a new phase of alloys. The three diffuse halos and the small angle scattering seem to be not due to the impurities but rather to a particular arrangement of the gold atoms.³⁾ Although the experimental procedure is very simple, it was difficult to reproduce the state (c). Further studies are now in progress.

In conclusion the writer expresses his hearty thanks to Assistant Professor S. Takagi for his kind discussions and valuable criticisms throughout this experiment and also to Assistant Professor J. Matsuura for the analysis of the sample.

References

1) Nonaka and Kohra: J. Phys. Soc. Japan **9** (1954) 512.
2) Kuriyama, Kohra and Takagi: to be published.
3) cf. Blin and Guinier: Compt. Rend. **233** (1951) 1288.

---

* These ring patterns show a preferred orientation with (100) plane parallel to the surface of the sample, but this seems to be not directly related to the phenomenon dealt with in this paper.

Errata

On the Spectral Distribution of Infrared-Stimulated Phosphorescence of Pb-activated ZnS-Type Phosphors

By Sumitada ASANO

J. Phys. Soc. Japan **10** (1955) 903～905

Page	Column	Line		(should be read)
903	right	foot-note *	partialy	partially
904	left	6	mole %	weight %
〃	〃	Fig. 1.	monochiomator	monochromator
〃	〃	26	wavelength	wave-length
〃	right	9	forein	foreign
905	right	References 1)	**64** (1954)	**23** (1954)

PROGRESS OF THEORETICAL PHYSICS

(Founded by H. Yukawa in 1946)

Published for the

Research Institute for Fundamental Physics
The Physical Society of Japan

Progress of Theoretical Physics Vol. 13, No. 5, May 1955

Elementary Theory of Quantum-Mechanical Collective Motion of Particles, I .... Sin-itiro TOMONAGA..467
Elementary Theory of Quantum-Mechanical Collective Motion of Particles, II .... Sin-itiro TOMONAGA..482
Adiabatic Process and the Stationary State........ Hajime TANAKA..497
On the Theories of Higher Derivative and Non-Local Couplings, I ... Tosiya TANIUTI..505
On Bound Λ° Particles........ Ken-ichi ONO..522
On Interactions among Ions of a $BaTiO_3$ Crystal and on its 180° and 90° Type Domain Boundaries .... Wataru Kinase..529
Clebsch-Gordan Coefficients for $j_2=5/2$ .... Reiko SAITO and Masato MORITA..540
Remarks on Quantum Hydrodynamics .... Hirosi ITO..543

Letters to the Editor:

Self-Energy of Slow Polaron and Variational Method........ E. HAGA..555
On the Foundation of the Unified Nuclear Model, II........ T. MARUMORI and E. YAMADA..557
The Orbit-Orbit Interaction........ S. YANAGAWA..559

Progress of Theoretical Physics Vol. 13, No. 6, June 1955

On the Theory of Thermal Conductivity of Monovalent Metals ...... Tadao KASUYA..561
Phase Transition of Husimi-Temperley Model of Imperfect Gas..Shigetoshi KATSURA..571
On the Solution of Γ's for a Type of Non-Symmetric Tensor Field $g_{\mu\nu}$........ N. N. GHOSH..587
On the Intermediate Coupling Theory of Pseudoscalar Field and a Nucleon .... Daisuke ITO, Yoneji MIYAMOTO and Yukihiko WATANABE..594
On the Analysis for the Proper fiield of a Nucleon .... Yukihika WATANABE..603
Products of Improper Operators and the Renormalization Problem of Quantum Field Theory........ Werner GÜTTINGER..612

Letters to the Editor:

Quantum Hydrodynamics for a Charged Non-Viscous Fluid.... N. MIKOSHIBA..627
Quantum-Statistical Mechanics of Electron-Phonon System.... T. MATSUBARA..628
A General Theory of Meissner Effect........ T. MATSUBARA..631
Contents and Index to Volume 13 .... i-viii

Price $ 1.25 per copy
$ 15.00 per year (postage inclusive)
Annual dues for foreign members (individual subscribers)
$ 12.00 (postage inclusive)
" for foreign members of the Physical Society of Japan
$ 10.00 (postage inclusive)

Application for members, subscriptions and orders for back mumbers should be sent, directly or through book-dealers, to

The Publication Office
in
Yukawa Hall, Kyoto University, Kyoto, Japan

JOURNAL OF THE PHYSICAL SOCIETY OF JAPAN Vol. 10, No. 12, DECEMBER, 1955

Orbit-orbit Interactions in Atomic l^n Configurations

By Sadaaki YANAGAWA

*Department of Applied Physics, Faculty of Engineering,
University of Tokyo, Tokyo*

(Received August 22, 1955)

An simplified expression for the orbit-orbit interactions in terms of scalar products of tensor operators is derived for l^n configurations by use of the method of Racah. Main contribution of the interactions is given in the form $-\beta L(L+1)$, β being a positive constant.

Analyses are made for $4p^2$ and $5p^4$ configurations of *Ge*I, *As*II and *Te*I by taking the effects of the orbit-orbit interactions into account. The agreement between theoretical and experimental values of terms are satisfactory for *Ge*I and *As*II.

§ 1. Introduction

It is well known that in the isoelectronic sequences of $2p^2$ and $2p^4$ configurations the theoretical values of terms calculated by taking into account the self spin-orbit interactions as well as the electro-static interactions are not sufficient to explain the experimental data. The theoretical ratio of ${}^1S-{}^1D/{}^1D-{}^3P$ is 3/2, while the experimental value is nearly equal to 1 in these spectra. The disagreement between theoretical and experimental values can be explained if we take the configuration interactions into consideration, by virtue of which the theoretical position of ${}^1S$ level is depressed.

On the contrary in the spectra of $4p^2$ and $5p^4$ configurations of *Ge*I, *As*II and *Te*I etc. the intervals between ${}^1S$ and ${}^1D$ are considerably large, so that the calculated levels for ${}^1S$ are lower, and for ${}^1D$ are higher than each corresponding experimental levels.* The deviation of the calculated values from the observed ones (cal.—obs.), the mean deviation $\triangle$ and the values of ζ are given on the row (a) of Table I→IV. Such a situation can not be explained by the same idea because the effect of the configuration interactions pushes down the theoretical values for ${}^1S$ level and causes still larger discrepances. For our case, however, the effects of configuration interactions may be negligible because the levels of higher configurations with which original configuration can mix, do not localize in the neighbourhood of p^2 or p^4 levels. Therefore one is lead to assume a certain correction term giving rise to an opposite effect which depends on the orbital quantum number L. In the following we shall assume that the negative correction term has the form $-\beta L(L+1)$, $\beta>0$. Such an expression can be derived from the orbit-orbit interactions involved in Breit's Hamiltonian.

It has been pointed out by Trees[1] that the addition of a positive correction of the form $\alpha L(L+1)$ improves the agreement between theoretical and experimental values for $3d^5$ and $3d^6$ configurations of *Fe* III and *Mn*II. The proportional factor α is found to be the order of from 70 to 90 cm^{-1} in these spectra. Racah[2] has shown that this correction in d^n configurations arises from interactions of d^n with $d^{n-2}l^2$ and $d^{n-2}ll'$ configurations, in which two electrons are excited from the original one. Our assumption, however, is different from theirs not only in the sign of the correction term but also on its theoretical basis.

§ 2. Calculation and Comparison with Experiments

As will be shown in § 3 the orbit-orbit interactions between the two electrons i and j can be reduces to the following simple form for equivalent l-electrons;

$$H_{ij}=-\sum_{k\geqq 1}\frac{2}{2l+3}(2l+1)(2l-k+1)(2l+k+2)\times(l\|\boldsymbol{C}^{(k)}\|l+1)^2M^{(k-1)}(\boldsymbol{u}_i^{(k)}\cdot\boldsymbol{u}_j^{(k)})\,. \qquad (1)$$

$\boldsymbol{u}^{(k)}$ is a unit tensor operator of rank k, $\boldsymbol{C}^{(k)}$ a spherical harmonic operator of order k, both defined by Racah, and $M^{(k)}$ a radial integral defined by

$$M^{(k)}=\frac{\alpha^2}{4}\iint_{r_2>r_1} R_{nl}{}^2(r_1)R_{nl}(r_2)^2\frac{r_1{}^k}{r_2{}^{k+3}}dr_1dr_2\ , \qquad (2)$$

where α denotes the fine structure constant. In the summation over k all the even terms disappear and there remains first l terms of odd character and only l independent integrals $M^{(0)}, M^{(2)}, \cdots, M^{(2l-2)}$, will appear as parameters of the orbit-orbit interactions.

It is easily verified that the term for $k=1$ summed over all pairs of n electrons gives the result $-2M^{(0)}L(L+1)$ plus term independent of L. Though in the following we restrict ourselves to the case of p-electrons so that there appears no term with $k>1$, it is generally shown that they are small quantities of higher order and practically negligible even for $l\geqq 2$.

Thus it follows that the main contribution from the orbit-orbit interactions is given by $-2M^{(0)}L(L+1)$, the absolute value of which increases with the orbital quantum number L. In p^2 or p^4 configuration, for instance, it gives $-12\,M^{(0)}$ for ^1D and $-4M^{(0)}$ for ^3P respectively.

In these circumstances, analyses have been made in this paper for the term values of $4p^2$ and $5\,p^4$ of *Ge*I, *As*II and *Te*I, taking account of the orbit-orbit correction term as well as the electro-static and self spin-orbit interactions. We have four parameters to be determined to fit the experimental data, that is, F_0, F_2 for the electro-static energies, ζ for the self spin-orbit and $M^{(0)}$ for the orbit-orbit energies, while five observed values, i.e. one for each level of ^1D and ^1S, and three for the levels of ^3P are available. Thus we have determined the most reasonable values of these parameters from five equations. The values of parameters and the deviation of the calculated values from experimental data are gathered on the row (b) of Table I→V. Mean deviation is reduced from 28.7 to 6.7 cm^{-1} for *Ge*I and from 68.5 to 5.3 cm^{-1} for *As*II. The agreement of the calculated and experimental values has become excellent in these isoelectronic sequences. For *Te*I the mean deviation is 145 cm^{-1} and the quantitative agreement is not so satisfactory, but it is interesting to observe that the inversion of $^3P_1$ and $^3P_0$ level can be explained by adding this correction.

Table I. *Ge*I (in cm^{-1} *units*)

	$^1S_0$	$^1D_2$	$^3P_2$	$^3P_1$	$^3P_0$	
obs.	16367.14	7125.26	1409.90	557.10	0.0	
(*a*)	−15.6	+51.0	−21.4	− 2.8	0.0	(Δ=28.7)
(*b*)	+ 2.3	− 4.4	+ 6.8	+10.6	0.0	(Δ=6.7)
(*c*)	0.0	+29.3	− 8.7	+43.3	0.0	(Δ=26.5)

Table II. *As*II (in cm^{-1} *units*)

	$^1S_0$	$^1D_2$	$^3P_2$	$^3P_1$	$^3P_0$	
obs.	22593	10093	2540	1061	0.0	
(*a*)	−45.2	+111.6	−61.5	−22.4	0.0	(Δ=68.5)
(*b*)	+ 1.5	+ 1.5	0.0	+10.4	0.0	(Δ=5.3)
(*c*)	0.0	+ 79.3	−34.3	+93.6	0.0	(Δ=63.6)

Table III. *Te*I (in cm^{-1} *units*)

	$^1S_0$	$^1D_2$	$^3P_1$	$^3P_0$	$^3P_2$	
obs.	23199	10558.6	4751.0	4706.7	0.0	
(*a*)	− 14	+359.4	− 69	+ 76.3	0.0	(Δ=187)
(*b*)	−215	+ 10	+129	+164	0.0	(Δ=145)

Table IV. ζ (in cm^{-1} *units*)

	*Ge*I	*As*II	*Te*I
(*a*)	906	1612	3923
(*b*)	925.1	1653	4042
(*c*)	967.5	1751	

Table V. M^0 (in cm^{-1} *units*)

	*Ge*I	*As*II	*Te*I
(*b*)	8.2	17.6	38.4
(*c*)	5.6	12.9	

The spin-spin as well as the mutual spin-orbit interactions[3][4][5] for l^n configurations are expressed in terms of the same parameters $M^{(k)}$ as the orbit-orbit interactions. As is well known these interactions have appreciable effects on the multiplet splittings of the levels. So far we have neglected these two interactions, but it is to be desired to recalculate including all these interactions. The results thus obtained are on the row (c) of the Tables. For *Ge*I and *As*II, $M^{(0)}$ is 5.6 and 12.9 cm^{-1}, ζ is 968 and 1751 cm^{-1} respectively. The values of parameters do not vary so much, but mean deviation increases as much as 26.5 and 63.6 cm^{-1}. Though the results are not so satisfactory, the increace of mean deviation is principally caused by the somewhat large shift of $^3P_1$ level alone and other calculated levels have not large deviations. So far the author believes, this discrepancy may be taken off if we take into account configuration interactions. From this fact we can regard that $-\beta L(L+1)$ correction term plays a significant role in our cases and main contribution to this term is due to the orbit-orbit interactions considered here.

§ 3. Derivation of the Formula

The Hamiltonian for the orbit-orbit interactions between two electrons 1 and 2 has the form

$$H_{12}=\frac{\alpha^2}{2}\left[\frac{1}{r_{12}}(\nabla_1\cdot\nabla_2)+\frac{1}{2}\frac{1}{r_{12}^3}\{(\boldsymbol{r}_{12}\cdot\nabla_1)(\boldsymbol{r}_{12}\cdot\nabla_2)+(\boldsymbol{r}_{21}\cdot\nabla_2)(\boldsymbol{r}_{21}\cdot\nabla_1)\}+\frac{1}{2r_{12}^3}(\boldsymbol{r}_{12}\cdot\boldsymbol{\nabla}_1-\boldsymbol{\nabla}_2)\right], \tag{1}$$

where $\boldsymbol{r}_{12}=\boldsymbol{r}_1-\boldsymbol{r}_2,(r_{12}=|\boldsymbol{r}_{12}|)$ is a radius vector drawn from electron 2 to electron 1, ∇_i a gradient vector operator which operates on the coordinates of the i-th electron only, α the fine structure constant.

By use of the well known expansion theorem

$$\frac{1}{r_{12}}=\sum_{k=0}^{\infty}(-)^k a_k(2k+1)^{1/2}[\boldsymbol{C}_1^{(k)}\times\boldsymbol{C}_2^{(k)}]^{(0)} \tag{2}$$

with $a_k=r_<^k/r_>^{k+1}$,
the first term in (1) can be written as

$$\frac{1}{r_{12}}(\nabla_1\cdot\nabla_2)=\sum_{k=0}^{\infty}(-)^{k-1}a_k\sum_{\xi}(2\xi+1)^{1/2}[\boldsymbol{U}_1^{(\xi)}\times\boldsymbol{U}_2^{(\xi)}]^{(0)}, \tag{3}$$

where the summation should be taken over three values of ξ; $k, k\pm1$. $\boldsymbol{U}^{(\xi)}$ is an irreducible tensor operator of rank ξ derived from two tensors $\boldsymbol{C}^{(k)}$ and ∇, of which component is given by

$$U_\rho^{(\xi)}=[\boldsymbol{C}^{(k)}\times\nabla]_\rho^{(\xi)}\equiv\sum_{q,\sigma}C_q^{(k)}\nabla_\sigma(kq1\sigma|k1\xi\rho), \tag{4}$$

where $(j_1m_1j_2m_2|j_1j_2jm)$ is the Wigner coefficient.

Now we shall compute terms in the braces in (1), which can be transformed into

$$\frac{1}{r_{12}^3}\{(\boldsymbol{r}_{12}\cdot\nabla_1)(\boldsymbol{r}_1\cdot\nabla_2)-(\boldsymbol{r}_{12}\cdot\boldsymbol{\nabla}_1)(\boldsymbol{r}_2\cdot\boldsymbol{\nabla}_2)\}$$
$$+\text{ terms interchanged in 1 and 2.} \tag{5}$$

The following miscellaneous formulae are useful for the reduction of (5). They can easily be proved and are given without proof.

$$\frac{1}{r_{12}^3}(\boldsymbol{r}_{12}\cdot\boldsymbol{\nabla}_1)=\sum_{k,K,\sigma}(-)^{\sigma+k+1}\left(\frac{2K+1}{3}\right)^{1/2}(k010|k1K0)(D_1^{k[K]}a_k)[C_1^{(k)}\times C_2^{(k)}]_\sigma^{(1)}\nabla_{1,-\sigma};$$
$$K=k\pm1, \tag{6, a}$$
$$(\boldsymbol{r}_1\cdot\nabla_2)=\sum_q(-)^q r_1C_1^{(1)},_q\nabla_{2,-q}, \tag{6, b}$$

and

$$\nabla_{1,-\sigma}(\boldsymbol{r}_1\cdot\nabla_2)=\sum_{q,L,M}(-)^q(1q1-\sigma|11LM)\times(1010|11L0)C_{1,M}^{(L)}\times(D_1^{1[L]}r_1)\nabla_{2,-q}+\sum_q(-)^q r_1C_1^{(1)},_q\nabla_{1,-\sigma}\nabla_{2,-q};$$
$$L=2,0. \tag{6, c}$$

$\boldsymbol{D}^{k[k+1]}$ and $\boldsymbol{D}^{k[k-1]}$ in these expressions operate on radial functions only and are defined by

$$\boldsymbol{D}^{k[k+1]}=\frac{\partial}{\partial r}-\frac{k}{r}\quad\text{and}\quad\boldsymbol{D}^{k[k-1]}=\frac{\partial}{\partial r}+\frac{(k+1)}{r}.$$

With the aids of equation (6, a), (6, b) and (6, c) the first term of (5) can be expressed as

$$\frac{1}{r_{12}^3}(\boldsymbol{r}_{12}\cdot\nabla_1)(\boldsymbol{r}_1\cdot\nabla_2)=\sum_{k,\xi}(-)^{k+\xi+1}(2\xi+1)^{1/2}\times[\boldsymbol{T}_1^{(\xi)}\times\boldsymbol{U}_2^{(\xi)}]^{(0)}+\sum_{k,\eta}(-)^\eta(2\eta+1)^{1/2}[\boldsymbol{V}_1^{(\eta)}\times\boldsymbol{U}_2^{(\eta)}]^{(0)}, \tag{7}$$

and for the second term we have

$$-\frac{1}{r_{12}^3}(\boldsymbol{r}_{12}\cdot\nabla_1)(\boldsymbol{r}_2\cdot\nabla_2)=\sum_k\sqrt{3}\,[\boldsymbol{X}_1^{(k)}\times\boldsymbol{Y}_2^{(k)}]^{(0)}. \tag{8}$$

Here the operators $\boldsymbol{T}^{(\xi)}$, $\boldsymbol{V}^{(\eta)}$, $\boldsymbol{X}^{(k)}$ and $\boldsymbol{Y}^{(k)}$ are defined by

$$\boldsymbol{T}_1^{(\xi)}=\sum_{K,L}(-)^K[(2K+1)(2L+1)]^{1/2}(k010|k1K0)\times(1010|11L0)W(KkL1:1\xi)\times(\boldsymbol{D}_1^{k[K]}a_k)(\boldsymbol{D}_1^{1[L]}r_1)[\boldsymbol{C}_1^{(K)}\times\boldsymbol{C}_1^{(L)}]^{(\xi)}, \tag{9, a}$$

$$\boldsymbol{V}_1^{(\eta)}=\sum_{K,\xi}[(2K+1)(2\xi+1)]^{1/2}(k010|k1K0)\times W(Kk\xi\eta:11)\times(\boldsymbol{D}_1^{k[K]}a_k)r_1[[\boldsymbol{C}_1^{(K)}\times\boldsymbol{C}_1^{(1)}]^{(\xi)}\times\nabla_1]^{(\eta)}, \tag{9, b}$$

$$\boldsymbol{X}_1^{(k)}=\sum_K(-)^{1-K}(2K+1)^{1/2}(k010|k1K0)\times(\boldsymbol{D}_1^{k[K]}a_k)[\boldsymbol{C}_1^{(K)}\times\boldsymbol{\nabla}_1]^{(k)}, \tag{9, c}$$

and

$$\boldsymbol{Y}_1^{(k)}=\sum_\xi(-)^{k+1-\xi}\left[\frac{2\xi+1}{3(2k+1)}\right]^{1/2}r_1\times[[\boldsymbol{C}_1^{(k)}\times\boldsymbol{C}_1^{(1)}]^{(\xi)}\times\nabla_1]^{(k)}. \tag{9, d}$$

$W(abcd:ef)$ is a Racah coefficient.
The first and second sum in (6, c) corresponds

to the first and second term on the right-handed side of the equation (7) respectively. The derivation of (8) is simple because ∇_1 does not operate on the factor $(\boldsymbol{r}_2 \cdot \nabla_2)$

The third term in (1) can also be shown to be expressed in terms of the scalar product of $\boldsymbol{X}_1^{(k)}$ and $\boldsymbol{C}_2^{(k)}$ as follows,

$$\frac{1}{r_{12}^3}(\boldsymbol{r}_{12} \cdot \nabla_1 - \nabla_2) = \sum_k [\boldsymbol{X}_1^{(k)} \times \boldsymbol{C}_2^{(k)}]^{(0)}$$
$$+ \text{ term interchanged 1 and 2 .} \quad (10)$$

Further reductions of (3), (7), (8) and (10) for l^n configurations are carried out by making use of Racah method of tensor operators. After somewhat tedious calculations we obtained the final result (1) in § 2) for the orbit-orbit interactions.

In conclusion, the author wishes to express his hearty thanks to Professors T. Inui and and A. Amemiya of Department of Applied Physics, and T. Yamanouchi of Department of Physics for their encouragements, and also to Dr. T. Ishidzu and Y. Tanabe for their valuable discussions.

References

1) R. E. Trees: Phys. Rev. **83** (1951) 756, **84** (1951) 1089.
2) G. Racah: Phys. Rev. **85** (1952) 381.
3) R. E. Trees: Phys. Rev. **82** (1951) 683.
4) H. H. Marvin: Phys. Rev. **71** (1947) 102.
5) H. Horie: Prog. Theor. Phys. **10** (1953) 296.
* Experimental data are taken from Tables of National Bureau of Standards, and Atomic Energy States of Bacher Goudsmit.

JOURNAL OF THE PHYSICAL SOCIETY OF JAPAN Vol. 10, No. 12, DECEMBER, 1955

Studies of High Polymers by Radioactive Method I
Self-Diffusion of Ions in Ion Exchangers

By Shintaro SUGAI and Jiro FURUICHI

Physics Department, Faculty of Science, Hokkaido University
Sapporo, Japan

(Received June 27, 1955)

In order to study kinetic exchange reaction and self-diffusion of ions in ion exchangers, the rate of ion exchange was measured by radioactive tracer method similar to that employed by A. Langer and Pitts' general theory of radioactive ion exchange was applied, with the focus of attention on the rate determining factor of reaction in each case, to analyse the results. When concentrated external solution is utilized, diffusion of cation in cation exchangers and diffusion of anion in anion exchangers was suggested to be the controlling factor, whereas in the case of the use of dilute external solution, the rate of exchange is probably controlled by surface diffusion. In the former case, diffusion coefficients, activation energy of diffusion, and activation entropy of diffusion were calculated, and from the results obtained, the mechanism of diffusion in the exchange resins was discussed.

§ I. Introduction

Ion exchangers have, as well known, a wide scope in technical application. And since certain exchangers appear to be prototypes of naturally occurring ion exchange bodies such as protein, cell membrance, etc., careful studies of their permutation by various ions will be of general significance. On the other hand, theoretically speaking, ion exchanger is a kind of polyelectrolyte, then the studies of exchange reaction between exchange resin and external aqueous solution seems to shed light on the structure of polyelectrolyte solution.

Recently, numerous authors have published literatures on exchange rate in exchanger resins with attempts on obtaining complete information on such phenomenon. However, since their results do not always coincide, it would be difficult to say that the mechanism concerning the exchange reaction in ion exchange resins is of simple nature.

In order to obtain additional and conclusive information on the above descrived circumstances, the self exchange of ions in ion exchangers was measured by the radioactive tracer method, since observation of self exchange of ions in ion exchangers is considered to be the most simple and effective method in studying the exchange mechanism. In the present studies, the authors have attempted to determine the rate controlling factor of reaction under various conditions.

Published literature on ion exchange in exchangers has consisted of: (*a*) those contributions[1)][2)] in which the exchange velocity was thought to be governed by a chemical rate mechanism based on the law of mass action, and (*b*) those[3)][4)] wherein diffusional processes were considered to be rate controlling. However, an increasing weight of evidence[5)] favors the view that diffusion is the more usual mechanism. Ionic diffusion may be either of three types, or a mixture thereof: (*a*) slow diffusion in the solid particles, (*b*) diffusion in interface layers between external aqueous solution and solid exchangers, and (*c*) fast diffusion in external liquid phase.

L.W.Holm[6)] has recently analysed the exchange phenomenon using the theoretical results concerning the heat transfer problem by S. Paterson[7)]. The reason being that if the resin consists of spherical particles of equal diameters and diffusion inside the resins is considered as the sole rate determining process, the problem is analogous to the heat transfer case. And then Holm has pointed out that diffusion in film layer is rate determining in the case of the exchange of Na ions between Na saturated Dowex–50 and 0.01 M sodium chloride aqueous solution, while diffusion in the resin is rate determining in the case of Sm ions between Sm saturated Dowex-50 and 0.045 M samalium nitrate aqueous solution.

Similarly, G. E. Boyd and B. A. Soldano[8)][9)] have, using the Paterson's theory, studied the exchange rate under various conditions, with results from which similar conclusions to that of Holm may be drawn. However, they have considered that solid diffusion is more essential than the film diffusion.

C. N. Merriam, Jr. *et al*[10)] measured the exchange rate, by so called dynamic method, using flowing external solution containing the proper tracer. Their results seem to indicate that the rate determining process is a mixture of film diffusion and solid diffusion in the case of exchange of Na ions between Na saturated Amberlite XE79 and 0.197 M sodium chloride aqueous solution.

In the present studies, by an application of a static method similar to Langer's[11)], the exchange phenomena were observed, and the results were analysed by Pitts' general theory of radioactive ion exchange[12)], which was originally formulated to explain Langer's results.

§ 2. Theoreticals

When a certain cation exchanger is shaken for a sufficient length of time with AB type ionic aqueous solution under exchange active condition and is slightly washed with water during the process, it may be considered that it is a concentrated polyelectrolyte solution in which A ions are also considerably in mobile state.

Firstly, supposing that the above descrived resins are shaken with the same concentration of AB type ionic aqueous solution, in which a part of A ions is radioactive, a simple example in discussing the exchange phenomena in exchangers can be obtained, if morever it is assumed that all of exchange resins are spherical and have the same diameter r_0. When the resins are shaken with different concentration of AB type solution, the circumstances are slightly complex, but the principal mechanism of exchange is the same.

Put $C(t)$ as the concentration of radioactive ions in the external solution at time t after beginning of experiment. Naturally $C(O)$ will be proportional to the total amount of radioactive material present. And it will be supposed that at the termination of experiment ($t=\infty$) the radioactive ions are distributed between the solution and the resins in such a way that homogenous distribution is attained. Put, also, the concentration of radioactive ions at r from the center in the resin $c(r, t)$, the volume of the resins V_p; hence

$$V_p=(4\pi/3)nr^3$$

where n denotes the number of the resins. The volume of the external solution is expreesed as V.

(1) The Case in Which Solid Diffusion Is Rate Determining

At any moment during the reaction, the surface layer is assumed to be in equiblium with the solution in this case, so that

$C(t) = c(r_0, t)$ (concentration of inactive ions in solution/ concentration of inactive ions in surface layers)

Now, the actual number of radioactive ions in the whole system is only a very small fraction of all the ions present, and thus the ratio in the above bracket is probably constant throughout the reaction.

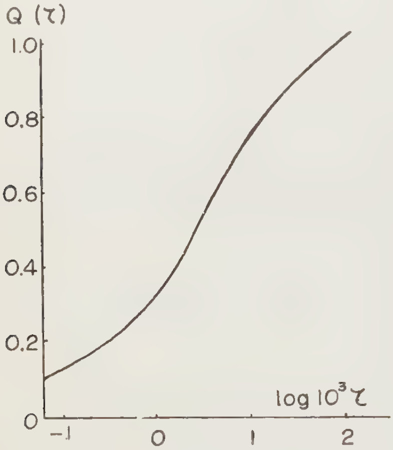

Fig. 1. Theoretical calculation of $Q(\tau)$ as a function of τ.

We may therefore write

$$C(t)=f\,c(r_0, t) \qquad (1)$$

where f is a constant. The fact that the total amount of radioactive substance in the system is constant throughout the course of reaction gives the equation;

$$VC(t)+4\pi n\int_0^{r_0} r^2c(r, t)dr=VC(\mathrm{o}) \qquad (2)$$

Equation (1) and (2) is, in fact, the boundary condition of diffusion equation;

$$\partial c(r, t)/\partial t=D(\partial^2c/\partial r^2+2/r(\partial c/\partial r)) \qquad (3)$$

where D is the diffusion coefficient in the resin.

According to E. Pitts, the solution of the above equation can be obtained under special condition as following;

$$\tau=Dt/r_0^2<0.1 \qquad (4)$$

In §3, it will be pointed out that the condition (4) is satisfied in the present studies. Instead of showing the solution $C(t)$ directly, a measure of exchange reaction $Q(t)$ as shown below is indicated as a function of τ in Fig. 1);

$$Q(t)=(C(O)-C(t))/(C(O)-C(\infty)) \qquad (5)$$

The value of τ corresponding to a certain value of Q observed in the experiment at time t is then determined using Fig. 1).

Supposing that the exchange is proceeding by this type of mechanism, it follows that if $\log t$ is plotted against $\log \tau$, a straight line of slope unity should be found, since from (4)

$$\log\tau=\log t+\log D/r_0^2 \qquad (6)$$

And from equation (6), in this case, the diffusion coefficient in the resins D can be calculated.

(2) The Case in Which Surface Diffusion Is Rate Determining

In this case, it can be imagined that the mobility of the ions within the resins is sufficiently high to maintain a uniform concentration throughout the interior, and that the rate of exchange depends only on the number crossing the solid-liquid interface, then $c(r, t)$ introduced in case (**1**) is a function of t alone. It is reasonable to suppose that the number of ions leaving the sphere may be $\alpha c(t)$, where α is a constant concerning the surface area of the sphere. Likewise, the number entering the sphere may be written $\alpha c(t)/\eta$, where η is another constant.

Hence we may write

$$V_0dc/dt=\alpha C(t)/\eta-\alpha c(t)$$

in which V_0 is the volume of a sphere.

Introducing σ as below, the above equation becomes;

$$\sigma=\alpha/V_0$$

$$dc/dt=\sigma(C(t)/\eta-c(t)) \qquad (7)$$

The equation expressing conservation of radioactive material is;

$$VC(t)+(4\pi/3)nr_0^3c(t)=VC(O) \qquad (8)$$

The solution of equation (7) and (8) and the usual initial conditions are therefore required.

Neglecting the detailed process of solving the above equation, the solution in accordance with E. Pitts is;

$$P(t)=1-Q(t)=\exp[-(\sigma+\lambda)t] \qquad (9)$$

where

$$\lambda=V_0\sigma/V$$

Therefore, in this case, $\log P$ should be a linear function of t.

§ 3. Experimentals

Measurements were conducted using the commercial exchangers Dowex-50 (cation exchanger) and Amberlite IRA-410 (anion exchanger), which are both considerably spherical as shown in Fig. 2). These are fractionated carefully, and any defectives were removed under a microscope. Dowex-50 (Na type) was, at first, converted to the hydrogen form with a large excess of $5N$ hydrochloric acid, and then washed continuously for a sufficiently long time with $1.0M$ calcium chloride aqueous solution after rinsing with distilled water. The diameter of these resins saturated with calcium chloride solution was measured under a microscope, and was obrerved to be larger than that of dry form due to the swelling effect. Approximately 15 ml. of the above described exchanger was transferred to a flask (volume 100 ml.), and the self exchange reaction was initiated by adding 40 ml. of radioactive calcium chloride aqueous solution with the same temperature to the flask.

0.1 ml. of the radioactive external solution was then withdrawn from the flask at determined times, and radioactivity was measured by G-M counter after drying the active solution in standard vessels.

The error following such experimental processes is negligible, and hardly exceedes the square root of radioactive count as shown in Table I. However, another important defect in experimental processing exists in the present case; namely the amount of external solution gradually decreasing in the process of measurement.

A. Langer measured the ion exchange phenomena by similar method to that employed by authors. He withdrew a certain amount of solution at definite time, and observed its radioactivity using liquid counter and requiring approximately 5 min., upon which the solution was returned to the flask. It may be said that as the amount of withdrawn solution is small, the order of experimental error in the present studies is similar to that in Langer's process.

Therefore an external solution with strong radioactivity had to be used in authors' case. In fact, activity in solution used is *ca* 5000 count/min./ml.

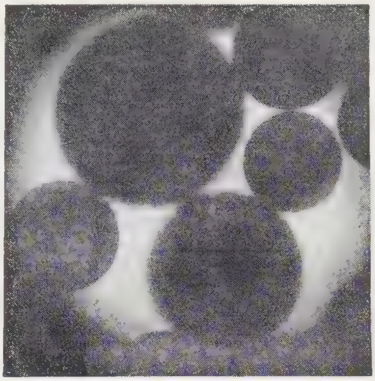

Fig. 2. Microphotograph of spherical exchange aesins Dowex-50.

Table I. An example of radioactivity measurement of solution containing tracer in the present method.

runs	count N /20 sec/0.1 ml	$N-N_{av}$
1	147	8
2	134	5
3	135	4
4	139	0
N_{av}	139	
$(N_{av})^{1/2}$	12	

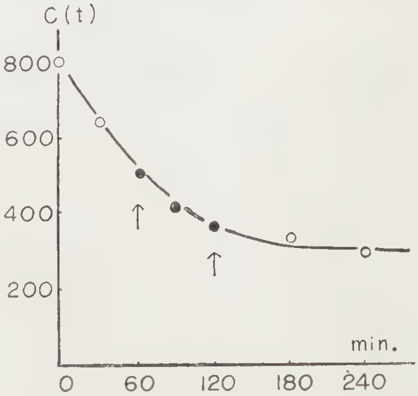

Fig. 3. Stirring effect of external solution in a certain case of self exchange. External solution is stirred between 60 min and 120 min after beginning of experiment.

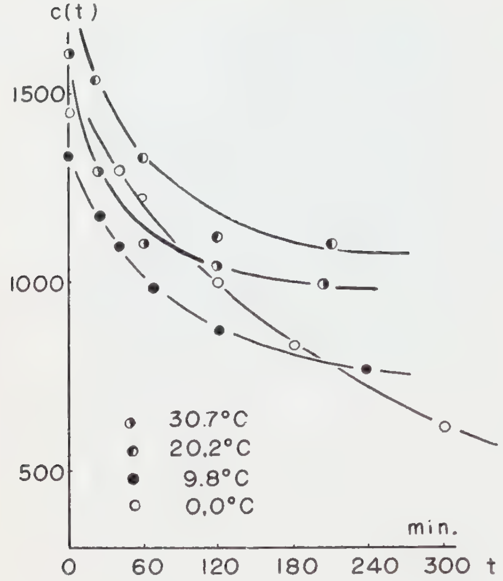

Fig. 4. Radioactivity variation of external calcium chloride aqueous solution in the case of sels exchange of Ca ions in Dowex-50.

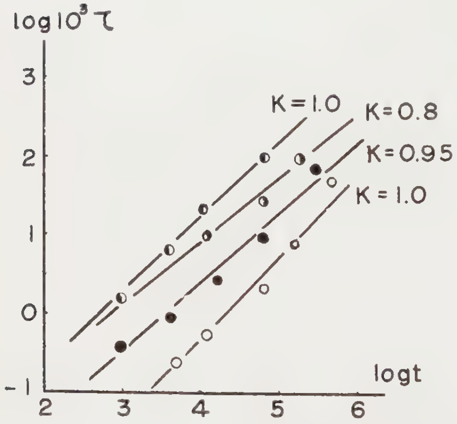

Fig. 5. The relation between log τ and log t in the case shown in Fig. 4.

As for the anion exchanger Amberlite IRA-410, the self exchange rate of Cl ions was measured in the same way using 1.0M sodium chloride aqueous solution.

The temperature was held within ±0.2°C by water bath. Stirring of the external radioactive solution was not important in this process as shown in Fig. 3). From a practically point of view, this would mean that diffusion of ions in liquid phase is not to be considered as important in determining the exchange rate.

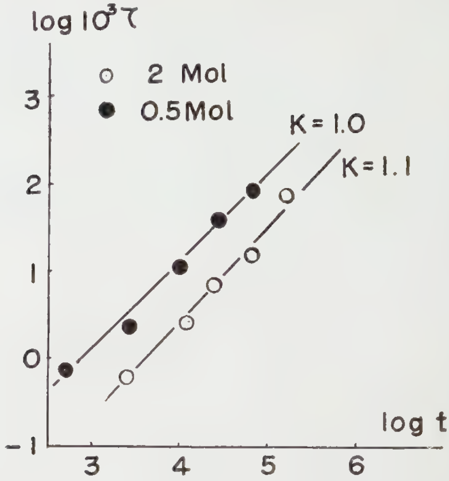

Fig. 6. The cases when external solutions, concentration of which are not 1.0 M, are used.

Table II. The relation between exchange duration t and $Q(t)$ or log τ in the case of the use of 1.0 M calcium chloride aqueous solution at various temperature (Size of Dowex-50 used 30 ~40 mesh.).

T °C	t min	$Q(t)$	log $(10^3\tau)$
30.7	20	0.46	0.22
	60	0.77	1.00
	120	0.88	1.45
	200	0.96	2.00
20.2	20	0.49	0.25
	40	0.69	0.80
	60	0.86	1.35
	120	0.98	2.00
9.8	20	0.26	−0.42
	40	0.40	−0.05
	70	0.59	0.45
	120	0.78	0.95
	240	0.97	1.90
1.0	40	0.21	−0.65
	60	0.28	−0.30
	120	0.52	0.35
	180	0.74	0.90
	305	0.96	1.85

§ 4. Experimental Results and Discussions

(1) The Rate Determining Factor of the Self Exchange of Ca Ions in Dowex-50 in the Case of the Use of the Concentrated External Solution

Firstly, the relation between the exchange duration and radioactivity of external solution (Ca^{45}, β-ray, 0.25 Mev., half-life 180 days) is shown in Fig. 4) in the case of the use of

Dowex-50 saturated with Ca ions and 1.0*M* calcium chloride aqueous solution.

From these results, $Q(t)$ and $\log\tau$ are calculated, which are indicated in Table II. Checking the solid diffusion condition (6) in these cases, $\log\tau$ are plotted as a function of $\log t$ in Fig. 5).

It is clear that in all cases, the rate determining factor seems to be the diffusion in the resin.

Table III. The relation between t and $Q(t)$ or $\log\tau$ in the case of the use of concentrated calcium chloride aqueous solution, concentration of which is not 1.0 *M* (Size of Dowex-50 used is 20～30 mesh.).

Conc. Mol	T °C	t min	$Q(t)$	$\log(10^3\tau)$
2	10.8	30	0.30	−0.20
		60	0.56	0.40
		80	0.70	0.80
		120	0.81	1.20
		180	0.94	1.90
0.5	12.5	15	0.36	−0.10
		30	0.54	0.38
		60	0.77	1.04
		80	0.89	1.60
		120	0.94	1.90

Table IV. The relation when the dilute calcium chloride aqueous solution is utilized (Size of Dowex-50 is 40～50 mesh.).

conc. Mol	T °C	t sec	$Q(t)$	$\log(10^3\tau)$	$P(t)$
0.05	10.0	15	0.20	−0.68	0.80
		30	0.29	−0.24	0.71
		45	0.38	0.04	0.62
		85	0.59	0.48	0.41
		155	0.81	1.20	0.19
0.008	11.0	15	0.20	−0.72	0.80
		30	0.45	−0.20	0.55
		60	0.62	0.50	0.38
		90	0.78	1.06	0.20

However, at 30.2°C, the value of slope k is a little smaller than unity, since the accuracy of temperature was probably less accurate than that in other cases.

Next, self exchange of Ca ions between Dowex-50 shaken for a sufficient length of time with 1.0*M*, calcium chloride aqueous solution, and extenal radioactive calcium chloride aqueous solution, concentration not being 1.0*M* are observed. The results in these cases are indicated in Fig. 6) and Table III. Although the mechanism of diffusion is, of course, more complex than in the case of the use of 1.0 *M* solution due to permutation of counter ions[13]), the rate determining factor seems also to be the diffusion in the resins.

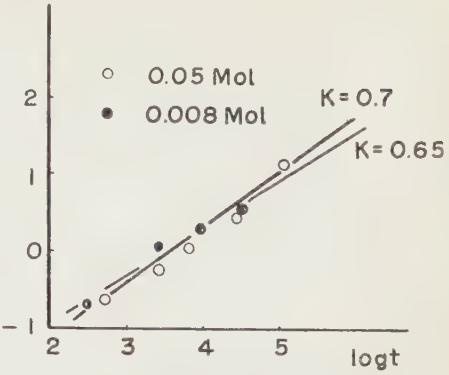

Fig. 7. The results when the dilute externel solution is used.

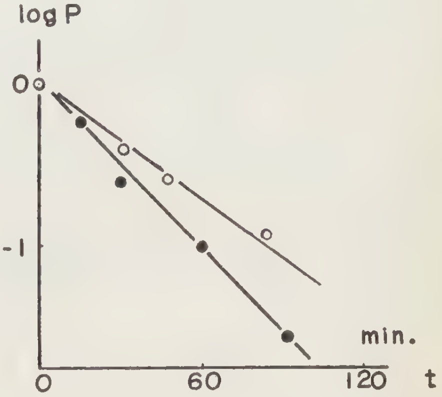

Fig. 8. Checking of surface diffusion condition in the case shown in Fig. 7.

(2) The Rate Determining Factor When Dilute External Solution is Used

0.05 *M* and 0.008 *M* solution of calcium chloride aqueous solution were used as the external radioactive solution in this case. The results are indicated in Table IV. Checking the solid diffusion condition (6), the value of k are both smaller than unity as shown in Fig. 7). Plotting $\log P$ as a function of t, surface diffusion condition (7) seems to be satisfied in these cases as shown in Fig. 8). Therefore, the rate of exchange is probably controlled by the surface phenomena.

L.W. Holm has observed that the rate controlling factor is the diffusion in the resins in the case of self exchange of Sm ions between samalium saturated Dowex-50 and 0.045*M* samalium nitrate aqueous solution.

However, since the valence of Ca ions is different from that of Sm ions, the results in this case cannot be compared with the results obtained by Holm.

Critical value of concentration of calcium chloride aqueous solution transiting from case (**1**) to case (**2**) are not ascertained, however the value is approximately at 0.1*M* in the present case.

(3) Diffusion Coefficient, Activation Energy and Activation Entropy of Diffusion When 1.0 *M* External Solution is Used

Self diffusion coefficient of Ca ions in Ca saturated Dowex-50 are calculated from the results in Fig. 5), and are indicated in Table V. In it activation energy E_{act} and term concerning activation entropy Δs are computed using the well known Eyring's formulae[14]);

Table V. Diffusion coefficient, activation energy of diffusion and activation entropy of diffusion in Dowex-50.

Ion	T °C	D^* 10^{-8}cm²/sec	E_{act} kcal/Mol	$d(e\Delta S/R)^{1/2}$ 10^{-8}cm/sec
Ca	1.0	1.2	8.5	8.17
	9.8	1.7		
	20.2	5.3		
	30.7	5.8		
Zr	25.0	3.38	8.2	5.1
Zn	25.0	2.89	7.8	3.1

* These values are a little larger than those reported previously by authors[15]), since variation of resins diameters due to the swelling are considered in the present studies.

$$D = D_0 \exp(-E_{act}/RT)$$

$$D_0 = ed^2(kT/h)\exp(\Delta S/R)$$

where symbols have the usual meaning.

According to Boyd *et al*, self diffusion coefficient of Sr and Zn ions in Dowex-50 are respectively 3.38×10^{-8}cm²/sec, and 2.89×10^{-8} cm²/sec at 25°C. As for Holm's results, self diffusion coefficient of Ca ions in Dowex-50 is approximately to $10^{-4}r_0^2$ at 25°C, where r_0 is the radius of the resins. Assuming that r_0 is 0.025 cm, the self diffusion coefficient of Ca ions is 6.3×10^{-8}cm²/sec.

These values agree considerably with diffusion coefficient of Ca ions in Dowex-50 at 20.2°C in the present studies.

On the other hand, activation energy of diffusion is only slightly larger than that in the case of Sr ions or Zn ions in Dowex-50 by Boyd *et al*, whereas activation entropy obtained by authors is comparatively larger than their results as shown in Table V.

The large value of ΔS is likely to be taken as an indication of a complex mechanism of diffusion in exchanger in this case.

However, since activation energy is not so large, it seems that diffusion of Ca ions in Dowex-50 is also, as pointed out by Boyd *et al*, similar to that in ordinary concentrated aqueous electrolyte solution, and large ΔS is probably due to the large size of Ca ions. Now, since diffusion coefficients can be obtained in some cases, condition (4) must be checked. Assuming r_0 is 0.03 cm, t is 100 sec, and D is $5\cdot10^{-8}$cm²/sec,

$$\tau = Dt/r_0^2 = 5\times10^{-8}\times10^2/9\times10^{-4} = 5\times10^{-3} < 0.1$$

Therefore Pitts' assumption is satisfied fully in this case.

(4) Diffusion of Cl Ions in Amberlite IRA 410

As in the cases of (**1**) and (**3**), the self diffusion of Cl ions in Cl saturated Amberlite IRA-410 was measured using 1.0 *M* sodium chloride aqueous solution as the radioactive external solution.

The results are shown in Fig. 9) and Fig. 10). In this case, it is apparent that the rate determining factor of reaction is the diffusion in the resins. Diffusion coefficients *etc.* are indicated in Table VI. Activation energy and activation entropy are not so large as compared with results obtained by Boyd *et al* as shown in Table VI.

Table VI. The self diffusion measurement of Cl ions in anion exchangers.

exchanger	T °C	D 10^{-8}cm² /sec	E_{act} kcal/Mol	$d(e\Delta S/R)^{1/2}$ 10^{-8} cm/sec
Amberlite IRA-410	3.8	1.0	8.0	4.5
	12.5	1.3		
	23.1	2.5		
Dowex–2			6.8	4.3

Therefore, strong interaction between ion and ion or ion and solvent are not considered in the present case.

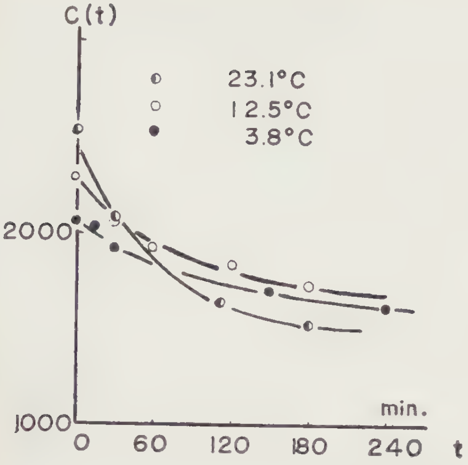

Fig. 9. Self exchange of Cl ions in Amberlite IRH-410.

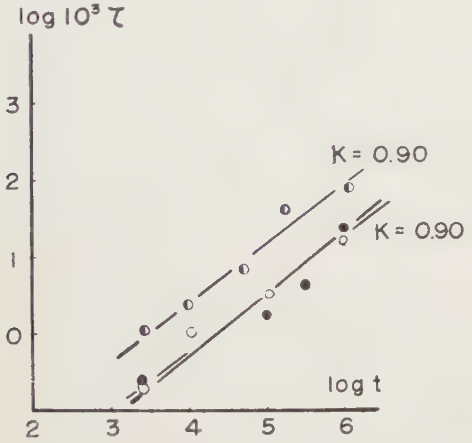

Fig. 10. Solid diffusion condition in the case shown in Fig. 9.

(5) The Exchange Reaction between OH Ions in Amberlite IRA 400 and Cl Ions in Hydrochloric Acid

Lastly, the most complex case was dealt with. The spherical resins Amberlite IRA-400 (anion exchanger) was shaken for a sufficient length of time with 0.5 M sodium hydroxide aqueous solution and was been in an active state of anion exchange. The above was placed in hydrochloric acid (0.5 M) containing radioactive Cl ions (β-ray, 0.66 Mev., half life 10^6 years) and the permutation of Cl ions in the resins was measured. The method of analysis is identical to that in the case of self diffusion measurement. The result is indicated in Fig. 11) and Fig. 12). And in this case the reaction is assumed to be controlled by diffusion in the resins.

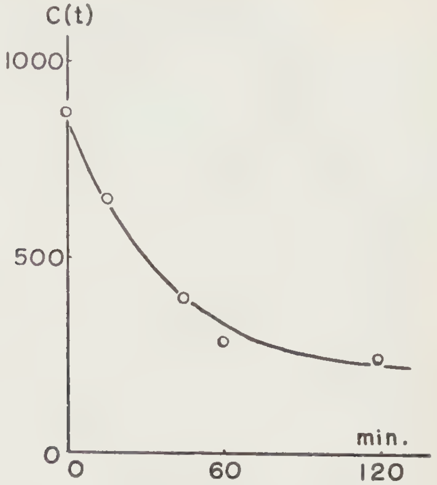

Fig. 11. Exchange between OH ions in Amberlite IRA400 and Cl ions in external hydrochloric acid.

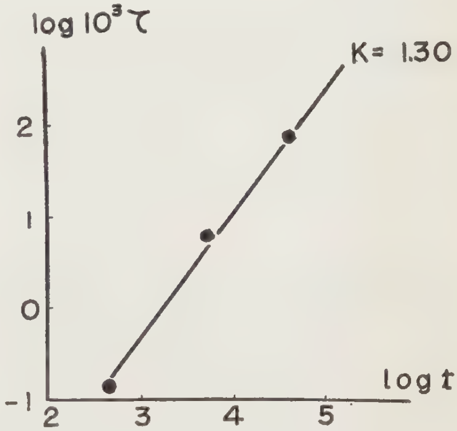

Fig. 12. The relation between log τ and log t in the case shown in Fig. 11.

However, it should be noted that diffusion in the resins, in this case, is not simple diffusion of Cl ions, but is rather in a complex state and actually may be noted as an average state of diffusion of Cl ions and OH ions, and if the proper assumption is used, the values of these diffusion coefficients are the same6).

Calculating from the results in Fig. 12), diffusion coefficient is approximately 2×10^{-8} cm^2/sec.

As described above, the rate of exchange is determined by the surface phenomena when dilute external solution is utilized.

However, if external solution is of a high concentration, diffusion of ions in the resins is of great importance in estimating the exchange rate. In the latter cases, ion-ion interaction or ion-solvent interaction is probably, considering the values of activation energy and activation entropy of diffusion, so small that the movement of ions is similar, in the process of diffusion, to that in ordinary concentrated aqueous electrolyte solution.

§ 5. Acknowledgement

The authors wish to express their hearty thanks to Mr. Yoshida for his assistance and advice in regards to this work. They are exceedingly grateful for the financial aids of the Ministry of Education of Japan, which has enabled them to conduct this research.

References

1) F. C. Nachod and W. Wood: J. A. C. S. **66** (1944) 1380.
2) W. Juda and M. Carron: J. A. C. S. **70** (1948) 3295.
3) G. E. Boyd, A. W. Adamson and L. S. Myers, Jr.: J. A. C. S. **69** (1947) 2836.
4) T. R. E. Kressman and J. A. Kitchener: Trans. Farad. Soc. Diss. **7** (1949) 90.
5) J. J. Grossman and A. W. Adamson: J. Phys. Chem. **56** (1952) 97.
6) L. W. Holm: J. Chem. Phys. **22** (1954) 1132.
7) S. Paterson: Proc. Phys. Soc. **59** (1947) 50.
8) G. E. Boyd and B. A. Soldano: J. A. C. S. **75** (1953) 6091.
9) B. A. Soldano and G. E. Boyd: J. A. C. S. **75** (1953) 6099.
10) C. N. Merriam, Jr., R. W. Southworth and H. C. Thomas: J. Chem. Phys. **20** (1952) 1842.
11) A. Langer: J. Chem. Phys. **10** (1942) 321.
12) E. Pitts: J. Chem. Phys. **22** (1954) 56.
13) G. E. Boyd and B. A. Soldano: J. A. C. S. **75** (1953) 6105.
14) H. Eyring: J. Chem. Phys. **4** (1936) 283.
15) S. Sugai and J. Furuichi: J. Chem. Phys. **23** (1955) 1181.

JOURNAL OF THE PHYSICAL SOCIETY OF JAPAN Vol. 10, No. 12, DECEMBER, 1955

The Cross-Chain Configuration and a New Type of Phase Transformation in Solid Long Chain Acid Amides

By Tosio SAKURAI

Institute of Science and Technology, University of Tokyo

(Received July 16, 1955)

From the X-ray investigation on the single crystal of long chain acid amides of even carbon number from C=10 to 18, three phases are found to exist. Phase A in palmitic, myristic, and capric acid amides has the unusual crossed chain configuration similar to that found in potassium soaps. In phase B, found in palmitic and stearic acid amides, and phase C, in stearamide under a special condition, chains are parallel as in the ordinary long chain compounds. All phases seem to be stable at room temperature, but phase A of palmitic amide transforms irreversibly into phase B by heating. But the basal plane is almost unchanged during the transformation.

§ 1. Introduction

In ordinary normal long chain compounds, in spite of their wide variaties, some of their properties are determined mainly by their long hydrocarbon chains. For example, their melting point increases at first rapidly with their chain length and then tends to saturate gradualy[1]. Their long chains, which are straight in form, are packed in layers, and as the result, two main strong Debye rings appear nearly at constant spacings in the powder pattern, irrespective of the chemical nature of the compounds. But in acid amides, it is well known that their melting point is almost constant with varying carbon numbers, and their powder patterns seem to be rather

Table I. Melting points and phases of amides.

Name	C no.	Melting points			Phases	
		observed	lit*	Wurz et al.	from liq.	sol.
Stearamide	18	107.1 °C	109.7 °C		B	B, C
Palmitamide	16	104.2	107.0		B	A
Myristamide	14	103.4	105.1	(94–95) °C	A	A
Lauramide	12	102.5	102.4	(97–99)		
Capramide	10	97.5	98.5	99	A	A

* These values differ considerably from literature to literature, the value in the Table refers to "Fatty Acids." by K. S. Markley, Interscience publishers, inc., New York (1947).

abnormal compared with other compounds[2][3]. These properties suggest that the camparatively strong hydrogen bonds between end groups may affect the whole molecular configurations to a considerable amount.

In this paper, the results of the X-ray investigation on the acid amides of carbon number from 10 to 18 are reported. Although the complete structure analysis is not yet performed, carbon chain configuration is determined, and a new type of phase transformotion is found, in which the crossed melocules change into parallel configuration.

§ 2. Experimental Procedure

2. a. *Apparatus*

A modified form the Ehrenberg, Spear type fine focus X-ray tube[4] is used. This tube was especially suitable for the preliminary stage of investigation when only small single crystals can be obtained.

Photographs are taken by the conventional single crystal rotation camera, and also by a Bouman type moving film camera[5][6]. The latter is designed to rotate the goniometer and the film separately with two synchronous motors in order to avoid the complex gear system. As the result, film holder can be moved comparatively freely and D (the distance between the film and the sample) and ν (cone angle) can be reduced to 1 cm. and 22.5° respectively. (For notation, see reference (6)). Both D and ν are smaller compared with the ordinary design, the result of which the larger Bragg angle and the smaller central blind area are allowed. A drawback from this small ν value is the elongation of the diffracted spot due to larger inclination of the beam with the film surface. An elongated spot of the long spacing compound sometimes intersects with neighbouring spots. But this does not cause any fear of mis-indexing, provided that the crystal setting is correctly adjusted. In spite of this elengation, the estimation of the relative intensity does not need any special correction, because every spot has the same obliquity. When necessary, the intensity is estimated visually with 4 series of films with different times of exposure. Lorentz and polarization factors are estimated easily from the chart, like that of the Amoros[7].

2. b. *The sample and the phase*

Even number amides from $C=10$ to 18 are investigated. Palmitic and stearic acid amides are of Kahlbaum's pure. Capric, lauric and myristic acid amides are synthesized from the corresponding commercial pure acid by the method essentially the same with that described by Wurz and Sharpless[3]. Whole amides are first recrystallized from benzol in order to separate the trace of free acid, then several times from methanol. Their melting points are shown in Table I.

After various attempts to get single crystals, at least three phases are found at room temperature depending on the carbon number and the condition of the formation. These relations are also tabulated in Table 1.

A well developed single crystal of capramide is easily obtained from methonol solution. Although very small crystals of myristamide and the phase A of palmitamides are easily obtained from the methonol or acetic acid solutions, several trials were necessary before well developed crystals are obtained. Rapid crystallization gives very small single crystals, but too slow crystallization gives voluminous

Table II. Crystallographic data.

No. of carbon atoms	Phase	Space group	a	b	c $\sin\beta$ or d_{001} for phase B	β
16	A	$P2_1/a$	9.931±0.016Å	5.541 ±0.012Å	31.517±0.028Å	105°
14	A	〃	9.896±0.035	5.616 ±0.004	27.858±0.020	106°
12					24.546±0.017	
10	A	$P2_1/a$	9.845±0.027	5.580 ±0.004	20.576±0.013	104°
18	B	P_1		5.772 ±0.025	30.160±0.040	
16	B	P_1		5.518 ±0.044	32.470±0.044	
18	C	$P2_1/a$	8.765±0.020	4.2807±0.0043	50.133±0.035	90°

but imperfect crystals. A method which seems to be successful is to evaporate the solutions with moderate speed in the thermostat, the temperature of which is kept constant at a little above the room temperature. Phase B single crystals are more difficult to be obtained. In palmitamide, this phase is obtained only from its own liquid by cooling, while in stearamide from both solutions and liquids. A small single crystal must be carefully separated from the cluster. C phase of stearamide was obtained in a special case from very slowly evaporating acetic acid solution. This condition, however, has not been able to reproduced. In lauramide, the crystal suitable for the X-ray investigations is very difficult to be obtained. Crystals thus obtained have, in general, a needle like shape, or sometimes the form of a thin strip, the longest direction of which being the monoclinic axis in case of A and C phases.

§ 3. Crystallographic Data

Phase A is monoclinic. No systematic extinction of the general (hkl) reflections occurred, but the presence of ($h0l$) reflections only with h even and ($0k0$) reflections only with k even uniquely determines the space group $P2_1/a$. The unit cell contains 4 molecules.

Phase B is triclinic. From the nature of the molecule, the space group is supposed to be $P\bar{1}$.

Phase C is monoclinic and the space group is $P2_1/a$ too.

Crystallographic data are summarized in Table II.

§ 4. Molecular Configuration

4. a. *Phase A*

Long spacing of phase A of different carbon number obeys a linear relation $d_{001}=PN+Q$, where N is the carbon number and PQ are constants. It is noted that these values are fairly different from the previously reported values of Wurz and Sharpless[3], but agree better with those given by Yoshida and Kurokawa[8], which is quite independent from ours. These are shown in Table III. These discrepancies from Wurz's results may occur from the effect of impurity in their sample, because the melting point of their sample included in Table I is considerably lower than ours.

Table III. Long spacings.

No. of carbon atoms	Phase	Author	Yoshida, Kurokawa	Wurz, Sharpless
18	B	36.16 Å	36.1 Å	
16	B	32.47	32.6	
16	A	31.52	30.6	
14	A	27.86	27.7	31.0 Å
12		24.55	24.3	25.7
10	A	20.58	20.6	21.2

From Table II we obtain

$$P=1.823\pm0.002$$

and $$Q=2.343\pm0.030\,, \quad \text{for phase A.}$$

As d_{001} is the spacing of a layer made up from double molecules, P corresponds to the increment of this spacing per two carbon atoms. Assuming a C–C bond length of 1.54 Å., and the $\mathrm{C}\diagup\overset{\mathrm{C}}{}\diagdown\mathrm{C}$ angle to be tetrahedral, distance of carbon atoms along the length of the molecule is 2.52 Å. Therefore angle of tilt τ between the chain axis and the (001) plane can be obtained approximately from the relation

$$2.52\sin\tau=1.82, \quad \text{whence} \quad \tau=46 \text{ degree.}$$

Now a very powerful method for the study of long chain compound is developed by V. Vand[9)10)11)]. As is pointed out by him, periodic configuration of CH_2 groups in a molecule can be described as a subcell much smaller than the main cell. In this case, structure factor F_h can be expressed as

$$F_h = F_h^0 + LF_h \exp(2\pi i x_m h)$$

where F_h^0 is the contribution from non-subcell atoms, L being the Laue type function depending on the period of CH_2 groups in a molecule and x_m the vector from the main cell origin to the centre of the block of subcells. As is easily seen, outstanding strong spots will appear near the maximum of L.

Fig 1 (a) and (b) show the Bouman photographs of the phase A, projected along the b axis. As the ratio of subcell constants and the main cell constants is not an integer, a maximum of L does not necessarilly correspond to a main cell spot, but to several main cell spots near the maximum of L. Spots indicated by the mark ↑ in Fig. 1 (a) represent these main cell spots. The distridution of these spots around the L maximum is affected by both the phase factor x_m and the contribution from non-subcell atoms. As these contributions are difficult to estimate at a first step, the subcell constants are estimated by least square methods from these main cell spots. The configuration of the hydrocarbon chain is thus easily known before the complete structure analysis.

In this way, angle of reciprocal sublattice β_s^* is determined to be 72°. β_s^* is the projection of the angle of titl τ on the (010) plane and as β_s^* is severely different from τ (which is about 46°) the molecule must tilt with this plane.

On the other hand, general positions for the space group $P2_1/a$ are

(a)	x,	y,	z;
(b)	$-x$,	$-y$,	$-z$;
(c)	$\frac{1}{2}+x$,	$\frac{1}{2}-y$,	z;
(d)	$\frac{1}{2}-x$,	$\frac{1}{2}+y$,	$-z$:

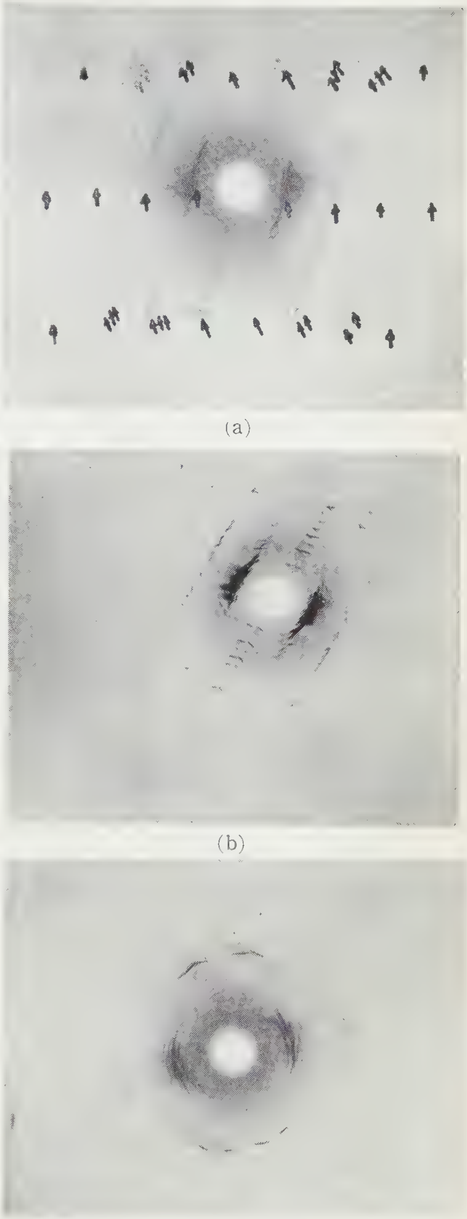
(a)

(b)

(c)

Fig. 1. (a) Palmitamide. Phase A. ($h0l$) reflexion. Spots indicated by the mark ↑ represent strong main cell spots near the maximum of L.
(b) Capramide. Phase A. ($h0l$) reflevion.
(c) Palmitamide. Phase B. ($h0l$) reflexion.

Therefore if a molecule is represented by a set of coordinates (a), second molecule (b) is centrosymmetrical with (a). The third molecule (c) is obtained by reflecting (a) with respect to the glide mirror plane parallel to (010). (d) is centrosymmetrical with (c).

Now suppose the molecule (a) tilt with the plane (010), another molecule (c) must tilt with the same plane with the same angle, *but in the opposite direiction.* Therefore, they cannot to parallel with each other but form a criss-cross configuration as is found in K soaps[12)13)].

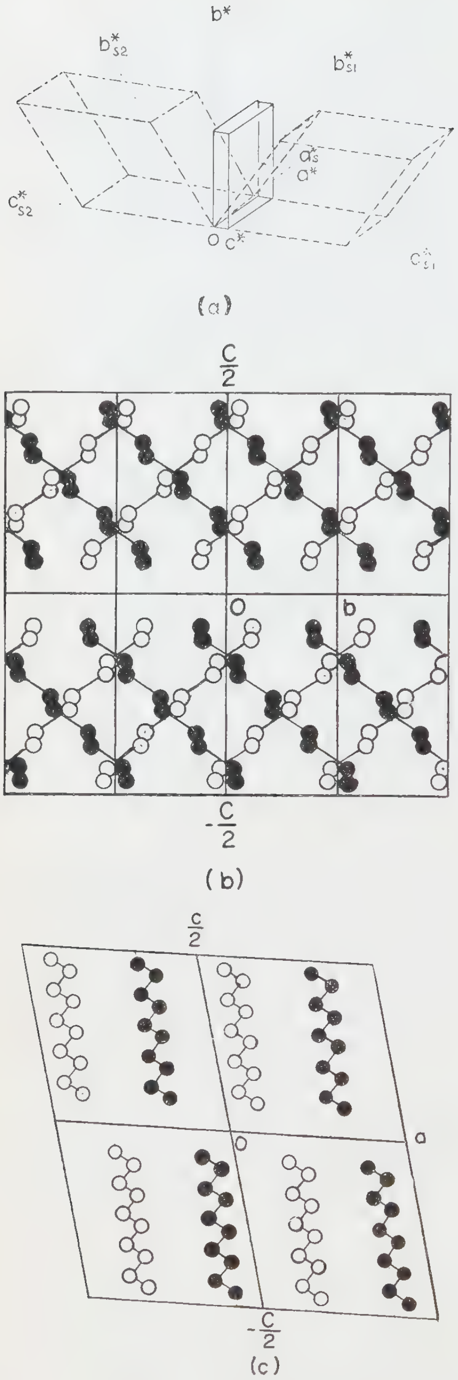

Fig. 2. (a) Relation between the main cell and the subcell, in the reciprocal space.
Suffix s_1 and s_2 indicate the axes reffered to the two kinds of subcells respectively.
(b)(c) Schematic configuration of the hydrocarbon chain.
(b); projection along the a axis.
(c); 〃 b 〃.
black and white circles represent atoms belong to different block of subcells.

As the centrosymmetrical subcell cannot be distinguished in the reciprocal space, the reciprocal subcell spots are separated into two groups, each of them corresponding to the (a), (b) molecules and (c), (d) molecules. These relations are clearly visualized from three dimensional distribution of subcell spots. Figure 2 show the relation between the main cell and the subcell in reciprocal space, together with the schematic configuration of the carbon chain. End group is ommitted in Fig. 2 (b) and (c), because its position is not determined yet.

It is worth to notice that main Debye rings of the powder pattern are not (200) and (110) as in ordinary parallel chain configuration, but group of lines near (200) and (01*l*) on which planes the chain axes being situated in this case. *l* is 6, 5 and 4 for palmitamide, myristamide and capramide respectively.

Subcell constants are summarized in Table IV. Those in phase A and B are triclinic.

Table IV. Subcell constants.

No. of carbon atoms	Phase	a_s	b_s	c_s	α_s	β_s	γ_s
16	A	9.93	5.54	2.69	135	103	90
14	A	9.90	5.62	2.71	134	102	90
10	A	9.85	5.58	2.70	133	102	~90
16	B	9.96	5.52	2.58	112	128	90
18	C	8.77	4.28	2.57	90	90	90

There are close similarities between subcell structures of palmitic, myristic and capric acid amides. Not only the subcell constants and subcell structure factors, but also the intensity distribution of the main cell around the subcell point are very much the same. (c.f. Fig. 1 (a) and (b)) Therefore packing scheme of the molecule are nearly alike in phase A of amides having different carbon numbers.

The projection of the subcell structure along the b_s axis is calculated by Fourier synthesis, the result of which is shown in Figure 3 and Table V. Fig. 3 represents the projection on the (010) plane of the main cell. In the calculation, only carbon atoms are considerd. Atomic structure factor is taken from Bragg' "Crystalline State", the temperature factor B is taken to be 3.4×10^{-16} cm². The reliability index *R* is 24%. No attempt is made to refine te parameter, because the intensity of the sub-cell can only be obtained by extrapolation and exact results cannot be expected. It can still be said that the plane of the carbon chain is likely to be parallel to the $(010)_s$, suffix *s* indicating the index of the plane refered to subcell.

4. b. *Phase B*

Phase B is triclinic. Chain is parallel as in the ordinary case. For the purpose of comparison with phase A, non-primitive subcell constants instead of primitive one is shown in Table IV. As the good single crystal is difficult to obtain, lattice constants are less trustworthy than in phase A. A Boumen photograph is show is Fig. 1 (c).

4. c. *Phase C*

Phase C is monoclinic, but $\beta=\beta_s=90°$ which means the molecule is perpendicular to the basal plane. It is found by S. Yoshida[8] that when acetic acid solution of palmitamide and stearamide is slowly evaporated on the glass plate, the molecule stands perpendicularly to the basal plane. Therefore, it may be concluded that under very particular condition, paraffin like structure appear, which is supposed to be mainly determined by the interaction between carbon chains.

4. d. *Discussion of the structure*

In subcell structure, most striking fact is the extraordinary large value of c_s, in phase A, which corresponds to the distance between alternating carbon atoms. If ordinary tetrahedral angle and C–C bond length 1.54 Å is assumed, this distance must be about 2.52 Å. In ordinary hydrocarbon chains, although it differs from compound to compound, even the longest value found in soaps does not exceed 2.61 Å[14]. Even if the comparatively large errors in the estimation of the subcell constant is considered, the mean value 2.70 is remarkably too large, while in phases B and C, c_s is within the range of ordinary values. It might be suggested that, in the crossed configuration, unfavourable packing of the CH_2 groups causes the strong van der Waals repulsion to deform the bond angle. If all bond lengths and angles are assumed to be equal, these values are roughly calculated from Fig. 3. The C–C bond length is about 1.55 Å and the $C\overset{C}{\diagup\;\diagdown}C$ angle is about 121°.

In ordinary hydrocarbons, the vertical cross section of a molecule decreases slightly with increasing corbon numbers[15], while in *K*–soaps it remains practically constant[16]. In phase A of amides, it seems to decrease with increasing carbon number as in the case in Na or Ag soaps[15]. The detailed structure analysis seems to be essential in order to clarify these points further. This is now in proceeding.

Table V. Subcell structure factor. (H O L)

H	L	F_c	$\|F_0\|$
0	1	−1.8	2.8
2	1	−2.9	2.8
2	0	7.3	6.2
2	1	0.4	0.8
4	1	−2.4	2.2
4	0	1.7	1.2
4	1	2.4	2.8
6	1	−1.1	1.0
6	0	−1.7	0.8
8	1	0.1	w
8	0	−1.9	1.2
8	1	1.7	2.4
10	0	−1.5	0.4

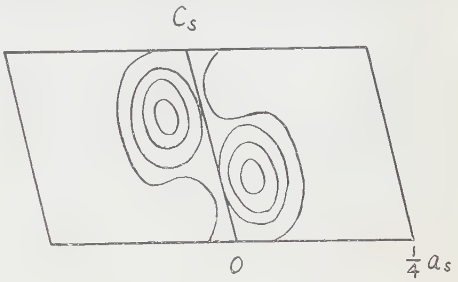

Fig. 3. Fourier projection on the $(010)_s$ plane.

Mean value of the angle of tilt τ in phase A is about 41° and that in phase B is 44°. Briefly speaking, phase A and B are very much the same in character with each other. Phase A may be considered to be composed of two B like lattices, each of them situated in glide mirror position of the other.

§ 6. Phase Transformation

5. a. *The nature of the transformation*

In previous report[17], a transformation deduced from the specific heat measurement was described in both stearamide and palmitamides. This transformation occurs reversibly. When phase B is heated, Debye rings are found to change rapidly but continuously above these transformation points. This high temperature phase is named B′. The detailed investigation of the temperature dependency of powder pattern is performed by Yoshida and Kurokawa independently$^{18)}$.

But when phase A of palmitamide is heated, the phase transformation occurs at about 80°C. This transformation is irreversible, and original A phase is not regained after cooling. The resulting phase is B. When this transformation is observed under the polarizing microscope with crossed nichols during heating, no appreciable change is observed till the transformation occurs. At the transformation point, a small spot of different colour appears and then immediately spreads over the whole crystal. After the transformation, the crystal is no longer single. (Fig. 4). In stearamide, only B–B′ transformation is found, no transformation being found in myristamide and other lower members. In the present stage of experiment, the temperature of Bouman camera cannot be controlled, therefore single crystal investigation of B–B′ transformation has not been attemted. (This is now under planning.) But as A–B transformation is irreversible, it is investigated from the displacement of the reciprocal cell before and after the transformation.

The Bouman photograph of a single crystal of phase A is taken first, then the crystal is heated above the A–B transformation point. After cooled to the room temperature again, another photograph is taken, with the same relative orientation of the film and the crystal.

Here, the original single crystal of phase A is destroyed and Debye rings appear. There appears, however, the single crystal spots of phase B. Important fact is that the direction of the c^* axis is conserved througout the transformation. Other single crystal spots corresponding to the superposition of two kinds of phase B spots, symmetrically situated about c^* axis. (c.f. Fig. 1 (c)). This means that although the resulting B phase is not a single crystal as a whole, the ab basal plane is nearly conserved and the c axis belongs to any one of the four equivalent directions corresponding to this basal plane with almost equal probabilities.

Concerning to the terminal amide groups, it is reported that C–N bond posseses considerable double bond character and each O atom accepts two hydrogen bonds$^{19)}$. Therefore, it may naturally be expected that in this case end groups are connected with each

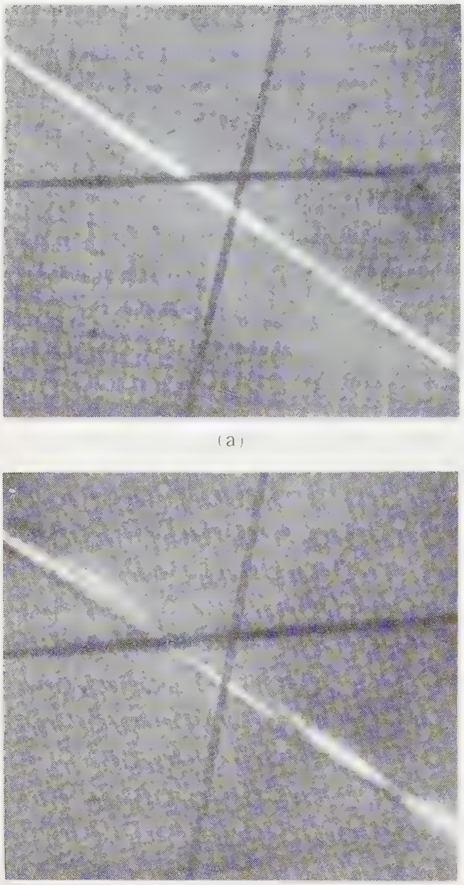
(a)
(b)

Fig. 4. Palmitamide. Observation under the polarizing microscope.
(a) Before transformation.
(b) After transformation.
A single crystal (white band) shown in (a) is no longer single in (b).

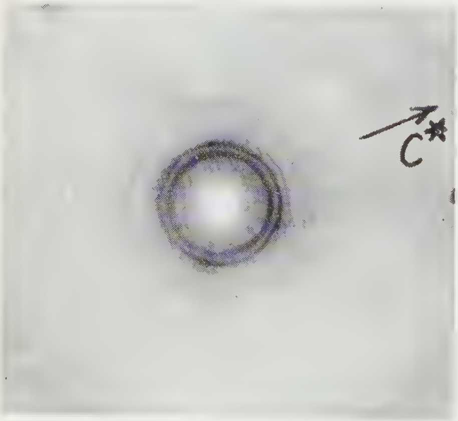

Fig. 5. Palmitamide. After the transformation.

other through strong hydrogen bonds forming a network, and the transformation from cross to parallel form does not affect this strong network greatly.

5. b. *Comparison with the transformation in soaps*

It seems to be interesting to compare the above mentioned transformation with that of the potassium soap. The potassium soap is the only other known example of crossed chain configuration, and the phase transformation of which was investigated by Lomer[16),]

From powder photographs, he recognized following three distinct phases. Phase A has the crossed chain configuration and the space group is $P2_1/a$. Phase B is triclinic. Phase C is monoclinic and the space group is suggested to be $P2_1/a$. Although nothing is mentioned by the original author about the chain configuration in phase C, the monoclinic angle and the angle of tilt of the chain is determined to be 92° and 55°30′ respectively. Therefore from the analogy of amides, it is suggested that the chain is parallel in phase B and is crossed in phase C.

Table VI. Comparison of the transformation.

K-soap.		Amide.	
No. of carbon atoms	Phases Low temp. High temp.	No. of carbon atoms	Phases Low temp. High temp.
4	A×		
6	A×	10	A×
8	A× ⇄ C×	12	
10	A× ⇄ C×	14	A×
12	B// → C× ↑ A× ← C×	16	A× →B′// B//⇄B′//
14	B// ⇄ C×	18	B//⇄B′//
16	B// ⇄ C×		
18	B// ⇄ C×		

K–soaps of carbon number 4 to 10, crystallize from alcohol into phase A, while those from 12 to 18 crystallize into phase B. With the only exception of butyrate and caprate, all of them transform to phase C on heating. These relations are shown in Table VI. Symbols × and // repreesnt the crossed chain and the parallel chain configuration respectively.

Phase B of potassium laurate which crystallizes from alcohol, transforms into phase C. But this phase C transforms on coolling into phase A, which reverts slowly during a period of months to the original phase B. At first glance, this resembles to that in palmitamide. But in soaps every high temperature phase may have crossed chain and types of transformation on heating is

× to × in lower member

and // to × in higher member

while in amides high temperature phase has parallel chain and types of transformation on heating is

× to // in palmitamide

and // to // in palmitamide and stearamide.

From these results, it may be concluded that when the crystal has strongly interacting end groups, the energy difference between the crossed and parallel chain per CH_2 group is small compared with the energy of the end groups. Therefore, especially when the chain is short, the structure favourable for the stable end group configuration occurs. In some cases this corresponds to the cross chain configuration. In such cases, as the chain becomes longer the parallel chain structure which is favourable for the carbon chain and unfavourable for the end group, upsets the crossed chain configuration. Carbon number 12 for the potassium soap and 16 for the amide just correspond to the transient position, where both structures have almost the same free energy and × to // transformation is realized. It may be of further interest to clarify the problem how such large displacements of long hydrocarbon chain can really occur in the solid state. The specific heat measurement seems to be highly desirable in this connection.

§ 6. Summary

From X-ray observation, the following results are obtained.

(1) Phase A of amides has unusual crossed chain configuration.

(2) 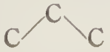 bond angle in the chain is deformed remarkably ih phase A.

(3) A subcell structure of phase A resembles to that of the parallel chain phase B.

(4) During the A–B′ transformation in palmitic amide, basal plane is left almost unchanged.

(5) The possibility of similar type of transformation is suggested in potassium soap.

§ 7. Acknowledgements

The author express his sincere thanks to Prof. Y. Kakiuchi for his kind guidance and encouragement especially in the long period of preliminary work, Prof. S. Yoshida and Mr. S. Kurokawa of Gakushuin university for their permission to cite their data before their publication, Mr. H. Hasegawa of this institute for his advice in the preparation of the sample, Mr. R. Shishikura of this laboratory for his assistance in the construction of the X-ray tube, and Mr. K. Tsuji and Mr. Z. Aoyama of the workshop of this institute for their skill in the construction of the Bouman Camera.

References

1) For example, V. Daniel: Advances in Phys. **2** (1953) 450.
2) Y. Kakiuchi: Sci. Pap. Inst. Phys. Chem. Res. **40** (1943) 189.
3) D. H. Wurz and N. E. Sharpless: Anal. Chem. **21** (1949) 1446.
4) W. Ehrenberg and W. E. Spear: Proc. Phys. Soc. **B64** (1951) 67.
5) W. F. De Jong, J. Bouman and J. J. De Lange: Physica **5** (1938) 188.
6) M. J. Buerger: *X-ray Crystallograph* (1942). J. Wiley and Sons.
7) J. L. Amoros: Pub. Ana. Real Socie. Espa. Fisi. Quin. **A** Fisica. **47** (1951) 161.
8) S. Yoshida and S. Kurokawa: Bull Chem. Soc. Japan **28** (1955) to be published soon.
9) V. Vand: Acta Cryst. **4** (1951) 104.
10) V. Vand and I. P. Bell. Acta Cryst. **4** (1951) 465.
11) H. Lipson and W. Cochran: *The determination of Crystal stractures.* (1953) G. Bell and Sons. Ltd. London, p. 132.
12) V. Vand, T. R. Lomer and A. Lang: Acta Cryst. **2** (1949) 214.
13) T. R. Lomer: Acta Cryst. **5** (1952) 14.
14) V. Vand, W. M. Morley and T. R. Lomer: Acta Cryst. **4** (1951) 324.
15) V. Vand and J. H. de Boer: Koninkl. Nederland. Akad. Wetenshap., Proc. **50** (1947) 991.
16) T. R. Lomer: Acta Cryst. **5** (1952) 11.
17) T. Sakurai: Rep. Inst. Sci. Tech. Univ. Tokyo **4** (1950) 1.
18) J. Ladell and B. Post: Acta Cryst. **7** (1954) 559.

JOURNAL OF THE PHYSICAL SOCIETY OF JAPAN Vol. 10, No. 12, DECEMBER, 1955

A New Dielectric Dispersion in Long-chain Normal Primary Alcohol of Probable Carbon Number 32 at Lower Temperature Phase

By Toshiaki TAKAMATSU
Scientific Research Institute

(Received August 12, 1955)

Certain normal long-chain alcohols are well known for their anomalous dielectric properties in higher temperature phase, which are often attributed to molecular rotation in the crystal lattice.

In the present article are described the experiments on the anomalous dielectric dispersion of long-chain normal primary alcohol of probable carbon number 32, extracted from Carnauba wax.

The higher temperature phase (68°–86°C) has quite the same dielectric behaviour which is already known in hexadecyl and octadecyl alcohol. But on the other hand, in lower temperature phase a new dispersion of Debye type was observed. The relaxation time seems to have a certain distribution, and the activation energy estimated from relaxation time versus inverse absolute temperature curve is 26.4 Kcal/mol. The dispersion is considered to be due to the reorientation of O–H group as a result of the restricted rotation or twisting of the molecule.

§ 1. Introduction

Certain normal higher long-chain alcohols are well known for their anomalous dielectric properties which are attributed to molecular rotation around their long axis[1)2)3)]. In this case it was assumed that a proton of one alcohol molecules transfers to another molecule. The proton thus transferred was thought to be carried to the next molecule, through the rotation of the molecule, thus resulting in the proton conduction, which in turn contributes to the anomalous dielectric behaviours[4)]. In the following, the dielectric behaviours of normal primary long-chain alcohols extracted from Carnauba wax is discussed. The similar anomaly as has been found in hexadecyl or octadecyl alcohol was observed at the temperature a little below its melting point. However, another anomaly was found at lower temperature phase, in which the molecular rotation is believed to be prohibited. *The apparent dispersion was noticed in this region, and it was concluded that the dispersion was of Debye type with distributed relaxation time.*

Table I.

(1) Physical constants		Chemical constants		
			obs.	cal.
melting point	87.0°C	acid value	0.0	0.0
solidifying point	86.0° -85.5°C	sap. value	0.0	0.0
		acetyl value	124	110.4

(2) Ultimate analysis (experimental error ±0.3%)

weight percentage of the element		Calculation			
		$C_{30}H_{62}O$	$C_{32}H_{66}O$	$C_{34}H_{70}O$	$C_{36}H_{74}O$
C%	82.52	82.11	82.31	82.50	82.60
H%	14.20	14.25	14.25	14.25	14.25
O%	3.28	3.65	3.44	3.25	3.15

§ 2. Preparation of the Sample

A good quantity of Carnauba wax (yellowish, first grade) was smashed and pulverized, and then washed with hot methanol using Soxlets extractor. This process eliminates the free alcohols, acids and resinous substances. After washing by hot methanol, insoluble part of the wax was fully saponified with excess amount of potassium hydrate-methanol solution. Then the saponified components were extracted with chloroform by Soxlets extractor. After evaporating chloroform off, the residue was washed out repeatedly with hot water and soap and free alkali ions were thus removed. After repeated recrystallization

Table II.

long spacing	Norelco		Photograph		Estimated value assuming Wilson and Ott's data					
					$C_{30}H_{62}O$		$C_{32}H_{66}O$		$C_{34}H_{70}O$	
(001)	2θ	d(Å)	2θ	d(Å)	2θ	d(Å)	2θ	d(Å)	2θ	d(Å)
	° ′		° ′		° ′		° ′		° ′	
001					1 6	80.1	1 2	85.3	58	90.4
002	2 4	42.5	2 0	44.4	2 12	40.05	2 4	42.7	1 58	45.2
003	3 6	28.4	3 5	28.6	3 18	26.7	3 6	28.4	2 56	30.15
004	4 6	21.5	4 2	21.9	4 24	20.02	4 8	21.32	3 54	22.6
005	5 12	16.95	5 8	17.2	5 30	16.02	5 10	17.06	4 52	18.09
006	6 12	14.3			6 34	13.36	6 12	14.21	5 50	15.07
007	7 10	12.0			7 40	11.45	7 14	12.18	6 50	12.91
008	8 6	10.8			8 48	10.02	8 16	10.67	7 48	11.30

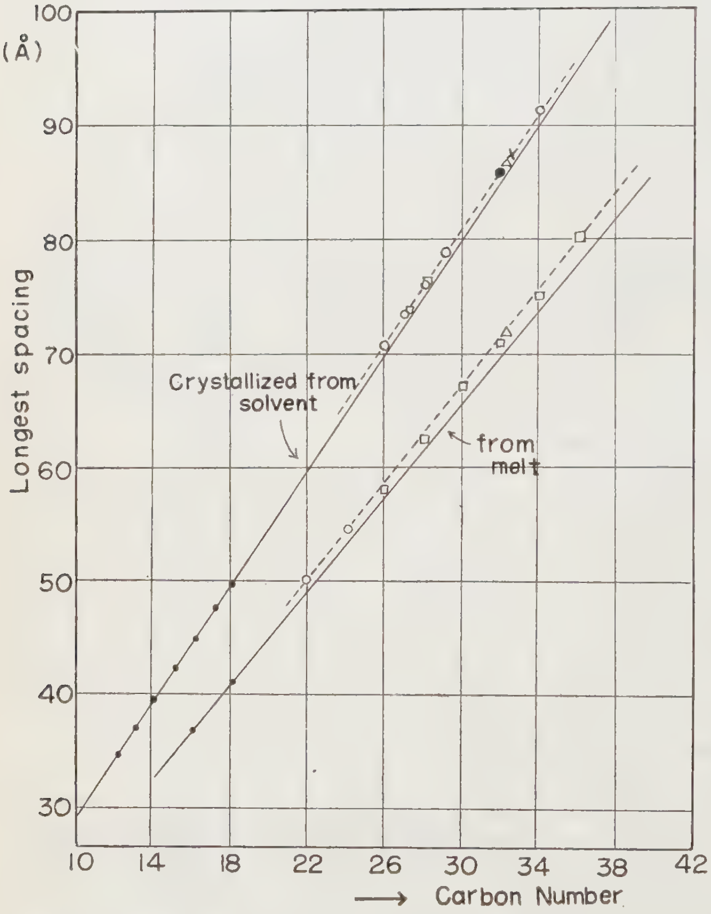

Fig. 1. Longest spacing for the carbon number.
● : Wilson and Ott.[5] ○: Francis, Collins and Piper.[6]
□: Piper, Chibnall and Williams.[7]
experimental data ●: norelco, △: Yoshida, ×: the auther.

from benzol solution, we obtained pure alcohol. It was further recrystallized from ligroin until its melting point of the sample was not affected by further recrystallization.

§ 3. Physical and Chemical Constants of the Sample

In Table, I, is shown the various physical as well as chemical constants together with the result of the chemical analysis.

Solubility for organic solvent;

Soluble in several hot organic solvent such as benzol, ligroin, ethyl ether and so on.

§ 4. Estimation of the Carbon Number

From the result of the ultimate analysis, the carbon number of this alcohol is deter- mined to be 32–34. the experimental error being taken into consideration. The X-ray analysis was also attempted for the determination of carbon chain length. As it was difficult to obtain a good single crystal, powder photograph was taken, using Cu-Kα radiation (λ=1.537 Å. U).

Long and short spacings of the sample were determined, the result of which is shown in Table II, together with the Norelco spectrometer data. The relation between long spacings and carb on number of normal higher alcohol was closely discussed by Wilson and Ott[5]. Their results are plotted in the curve in Fig. 1, ordinate and abscissa being the long spacing and carbon number respectively. Our results are also plotted in the same figure. As is easily recognized from the figure, the most probable carbon number of our sample seems to be 32[6][7]. Recently Prof. Yoshida in Gakushuin University have measured the long spacing of the same sample, which results are also shown in the above figure. His result seems to justify our conclusion.

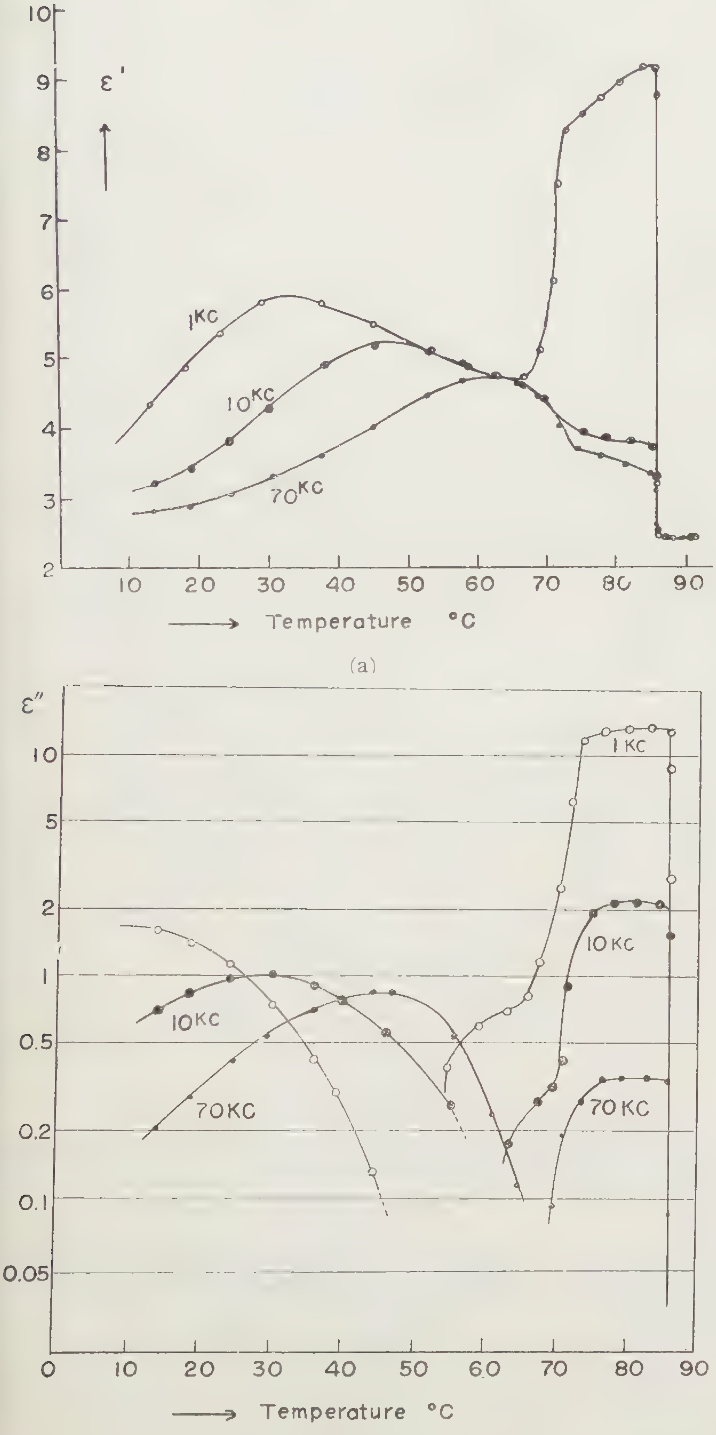

(a)

(b)

Fig. 2. (a) Dielectric constant versus temperature curve for the sample.
(b) Dielectric loss (ε'') versus temperature cnrve.

§ 5. Dielectric Properties

(a) *Experimental procedure*

In order to avoid the effect of volatile solvent or of water, the sample were previously melted and fully outgassed in vacua. Then the melted sample was put into a parallel plate condenser, the detail of which was described in the previous literature[4]. Temperature of the sample was measured by means of a previously calibrated *Cu*-Constantan thermojunction with covering glass tubes which was immersed directly into the sample. The dielectric constants ε' and loss ε'' were measured at various frequencies from 0.3 to 100 kilocycles within the temperature range from 3°C to 110°C by conventional substitution bridge method. The average rate of warming and cooling was about 0.2°C per minute. Several runs were tried for the same sample, and we found a satisfactory reproducibility.

(b) *Experimental results*

The variation of ε' and ε'' of the sample with temperature and frequency is shown graphically in Fig. 2(a), (b). and Fig. 3(a), (b). Abscissa indicates temperature and frequency, and ordinate shows ε', ε'' respectively. From these results we may clarify two distinct region of dielectric dispersion, namely higher temperature region from 68°C to 86°C and lower one from 0°C to 60°C, which will be described separately in the following.

(c) *Discussions*

(1) Higher temperature region (68°–86°C)

The behaviour of our sample in this temperature region was much the same with hexadecyl and octadecyl alcohols. It was already proposed that the proton-transfer-and-molecular-rotation mechanism is responsible for the dielectric anomaly[8]. Although there may exist much ambiguities concerning the detailed mechanism of high dielectric constant, it is agreed between authors that the anomaly is closely connected with molecular rotation around the long chain axis[1)4)]. It is at any rate of much interest that *a longer chain of alcohol of carbon number higher than 30 has also a rotational transformation.* Recently, Mr. Shishikura[9] in the Institute of Science and Technology, University of Tokyo has measured the specific heat of the same sample, and found a sharp peak at 73°C. The rise of the dielectric constant is seen exactly at the temperature corresponding to the specific heat anomaly starts.

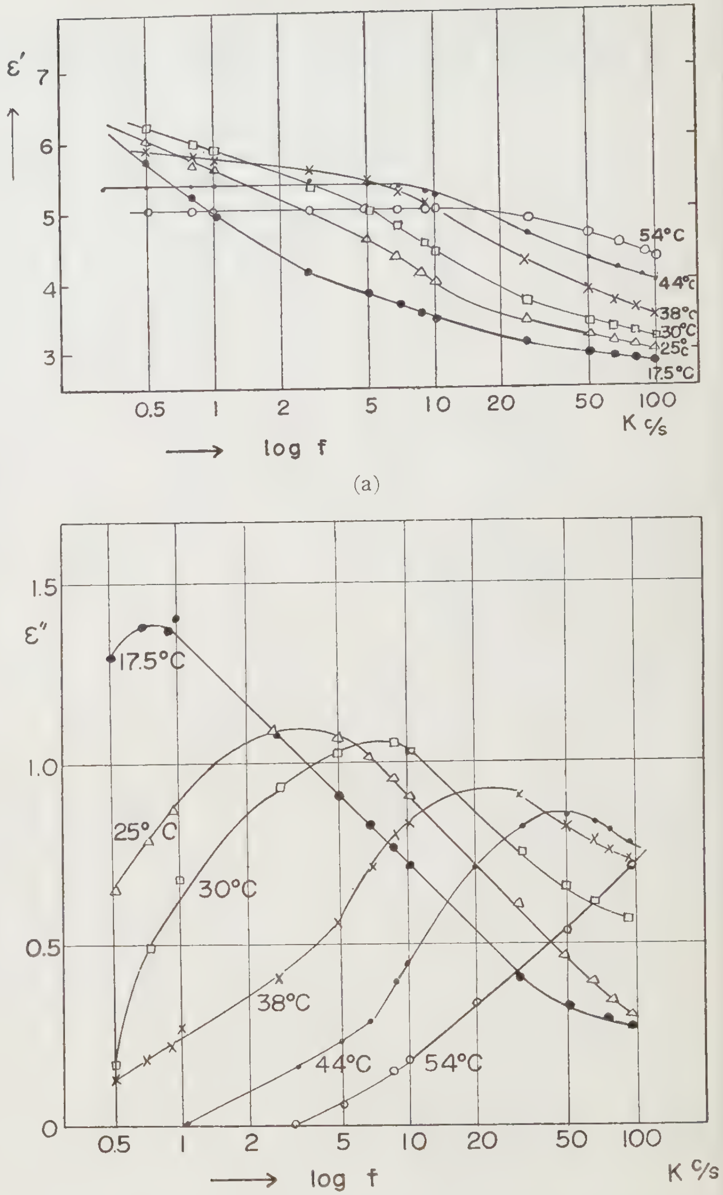

(a)

(b)

Fig. 3. Dielectric constant (ε') and its loss (ε'') versus logarithmic scale of frequency at lower temperature phase (0°–60°C).

(2) *Lower temperature phase* (0°–60°C)

In this temperature region, we have found another type of anomalous dispersion with the former case. We have never observed such a dispersion in alcohol of shorter chain length, that is in hexadecyl and octadecyl alcohols. It might be suspected that some impurities, for instance homologous alcohols or some other polar substances, may cause such an anomaly. However, the repeated recrystallization from ligroin *did not* result in any considerable change in dielectric property. Therefore, we believe it is not due to impurities, but to *a characteristic properties of the sample itself.* The effect of long chain impurities often resultsin hysteresis. If the alcohols of different carbon number are contained in the crystal, the lattice may be somewhat distorted and molecules having random orientation return to their original position with some difficulties even at lower temperatures, and this may in turn prevent the lattice distortion to be removed easily. In our dielectric measurements, no remarkable hysteresis was observed, showing

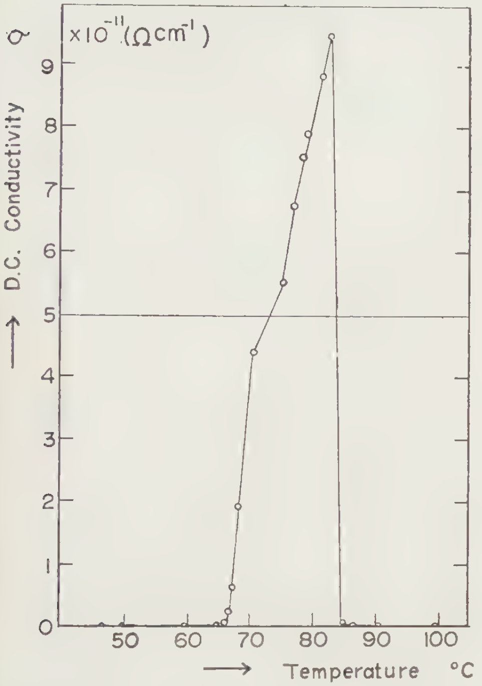

Fig. 4. D. C. Conductivity of the sample.

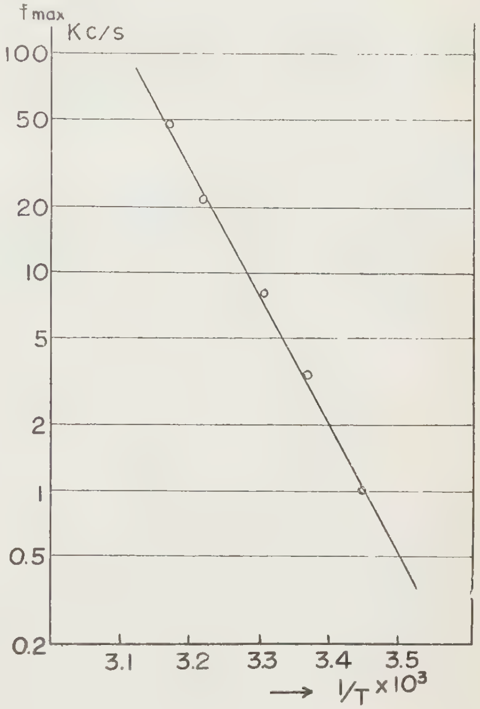

Fig. 6. Plots of logarithmic scale of frequency maximan versus inverse absolute temperature.

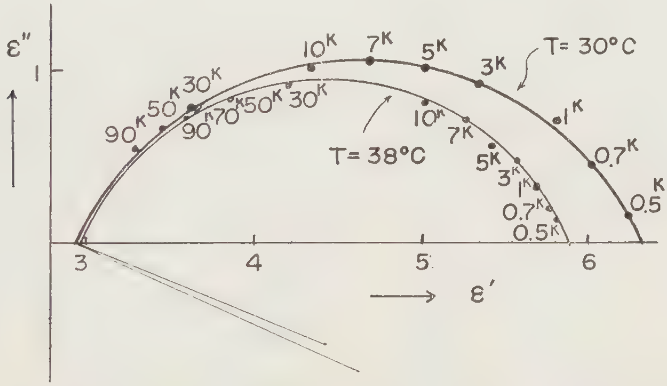

Fig. 5. Complex dielectric constants of higher long chain normal alcohol.

that the purity of our sample was sufficiently high. In ε' versus temperature curve, the peak for higher frequency shifted to the higher temperature side, and even at 100 kc/s, we could still recognize a clear peak. On the contrary, in higher temperature phase, we could not observe a peak at 100 kc/s, which shows that the relaxation time in lower temperature phase is *smaller* than that in higher temperature phase. For the purpose of studying the nature of the dispersion, we have plotted a Cole-Cole[10] diagram. A plot of ε' vs ε'' for different frequencies at a given temperature showed a circular arc with its center a little below ε' axis, showing a considerable distribution in relaxation time (Fig. 5.)

The relaxation time τ for each temperature was estimated as the inverse of the frequency corresponding to the maximum value of ε''. τ is plotted against the inverse of the absolute temperature T in Fig. 6. The activation energy was found to be 26.4 kcal/mol, from the slope of this $\tau - 1/T$ curve.

It is almost certain that the present dispersion is not due to molecular rotation, because the rotation is believed to be prohibited in low temperature phase. The dispersion still must be due to a certain kind of motion of O–H redicals which are the only polar groups in the crystal. It was already suggested that the twisting mode of vibration is already excited in the lower temperature phase, and it is responsible for the cooperative nature of the rotational transition[11]. Therefore, there is a good reason to ascribe the temperature dependent dielectric polarizability to the motion of O–H radicals, *as the result of the twisting of alcohol molecule.* Another possibility of rotation of O–H radical with fixed aliphatic chain is highly inconceivable, and must be ruled out since the recent nuclear magnetic resonance data obtained by Mr. Komatsu[12] in the Institute of Science and Technology, University of Tokyo showed the motional narrowing of the proton resonance line, which suggest the motion of not only O–H radicals, but also the aliphatic chain itself, supporting our views on twisting motion of the molecules.

Acknowledgements

The author wishes to express his sincere gratitude for kind encouragements given by Dr. K. Shinohara, chief of the laboratory. His thanks are also due to Prof. Y. Kakiuchi, of the Institute of Science and Technology, University of Tokyo, for his valuable instructions and discussions, and to Mr. T. Shimamoto for his instructions and his giving facilities in chemical treatments. He also wishes to thank Dr. M. Nakahira of Oyama laboratory, Prof. S. Yoshida of the Gakusyuin University and Mr. T. Sakurai of the Institute of Science and Technology, University of Tokyo, for their aids in X-ray investigations.

References

1) C. Baker and C. P. Smyth: J. Am. Chem. Soc. **60** (1938) 1229.
2) K. Higashi and M. Kubo: Sci. Pap. I. R. C. R. **36** (1939) 286.
3) J. D. Hoffman and C. P. Smyth: J. Am. Chem. Soc. **71** (1949) 431.
4) Y. Kakiuchi, H. Komatsu and S. Kyoya: J. Phys. Soc. Japan **6** (1951) 321.
5) P. A. Wilson and E. Ott: J. Chem. Phys. **2** (1934) 231.
6) F. Francis, F. J. E. Collins and S. H. Piper: Proc. Roy. Soc. **158 A** (1937) 691.
7) S. H. Piper, A. C. Chibnall and E. F. Williams: The Biochem. Jour. **28** (1934) 2175.
8) Y. Kakiuchi: "*Molecular Structure and Related Problems*" Monograph series Res. Inst. App. Elect. **4** (1954) 75.
9) R. Shishikura: J. Phys. Soc. Japan to be published.
10) K. S. Cole and R. H. Cole: J. Chem. Phys. **9** (1941) 341.
11) Y. Kakiuchi: J. Phys. Soc. Japan **6** (1951) 313.
12) H. Komatsu: J. Phys. Soc. Japan to be published.

JOURNAL OF THE PHYSICAL SOCIETY OF JAPAN Vol. 10, No. 12, DECEMBER, 1955

Selective Oxidation of Silver-Magnesium Alloys in Water Vapor

By Masaki HIRASHIMA

Research Laboratory, Tokyo-Shibaura Electric Co., Kawasaki City

(Received August 25, 1955)

A simple method is described for measuring low rates of selective oxidation of Ag-Mg alloys at elevated temperatures when water vapor is used as oxidizing agent. It is found that the MgO layer builds up on the surface of the alloy according to a parabolic law over a range of the water vapor pressure from 7×10^{-3} to 6×10^{-2} mm Hg, and the oxide growth begins to follow a linear law rather than a parabolic law at a pressure of 1 mm Hg. In the region where the parabolic law holds, the growth of the oxide layer seems to be controlled by the diffusion of Mg through the layer. 20.7 kcal/mol is obtained as the activation energy of diffusion. Applying the transition state theory of gas-metal reaction, as developed by Gulbransen, the diffusion constant of Mg through the oxide layer is given by $D\ (\mathrm{cm^2/sec}) = 2.17\times10^{-9}\exp(-20{,}700/RT)$.

§ 1. Introduction

In 1954 P. Rappaport of RCA Laboratories published a paper[1)] on methods of processing Ag-Mg secondary emitters. The results obtained by him are of very practical importance, but the oxidation mechanism was not pursued extensively. During the study of activation of Ag-Mg alloys as a secondary-electron emitting material, the mechanism of selective oxidation of the alloys was investigated, with the object of gaining a further understanding of the properties of the oxide layers applied to the secondary electron emitter. As Rappaport's experiments showed that far smoother and more compact oxide layers were obtained with water vapor than with oxygen as an oxidizing agent, water vapor at various pressures was employed as the oxidizing atmosphere throughout the present investigation.

The dissociation pressures of Ag_2O and MgO are greatly different from each other, as shown in Fig. 1[2)]. Therefore, when the alloy is subjected to heat treatment in an oxidizing atmosphere at a favorable pressure, only the MgO layer is specifically formed on the surface of the alloy[3)4)]. The secondary electron emission from this alloy depends on the formation of a MgO film on its surface[1)3)5)6)7)], and it is desirable to obtain a surface as compact and smooth as possible.

According to Leontis and Rhines' experiments on high-temperature oxidation rates of magnesium in oxygen atmosphere[8)], the rate of oxidation follows a linear law, in conformity with the generality first put forward by Pilling and Bedworth[9)]. The so-called Pilling-Bedworth's rule states that the non-protective oxidation characteristic is predicted from the fact that MgO occupies less space than does the metal destroyed in producing it (volume ratio=0.81)[10)], wherefore the oxide layer can not cover the underlying metal so completely as to exclude direct access to the atmosphere. Scheil[11)] argued that linear oxidation is common to all cases where the reaction occurs at the oxide-metal interface.

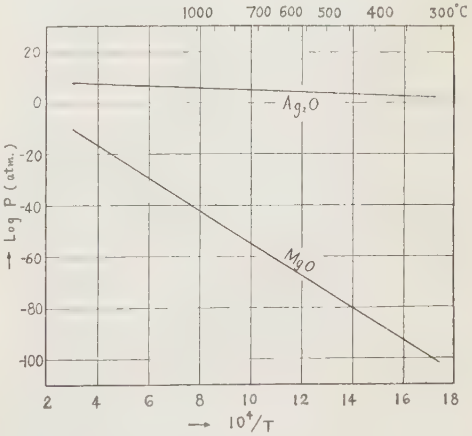

Fig. 1. Dissociation pressures of Ag_2O and MgO (Kawakami).

On the other hand, it was reported by Gulbransen[12)] that all the metals and alloys form protective films under certain conditions. Magnesium forms a protective film for the oxidizing conditions of 450°C and 0.20 cm

O_2; above this temperature the film is not protective to further oxidation.

In many studies on high-temperature oxidation of metals a method of measuring the weight increase of samples by means of a kind of calibrated microbalance has frequently been applied. However, the construction and manipulation of the microbalance seems to need refined techniques.

The experimental method described in this paper enables measurements of very low rates of oxidation to be made with a somewhat higher accuracy than has been attained by the microbalance method, and seems to give more deeper insight in the nature of very thin film oxidation. In earlier short notes some results of measurements are described[13]). These measurements have now been refined and extended and will be described more fully in this paper.

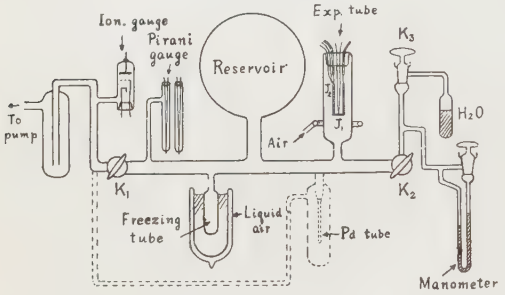

Fig. 2. Schematic view of apparatus for measuring the oxidation rates of Ag-Mg alloys.

§ 2. Experimental Procedure

2.1. *Principle of Measurement*

When a Ag-Mg alloy sample is heated in an atmosphere of water vapor, only the Mg component is oxidized according to the following chemical reaction, accompanied by the evolution of hydrogen:

$$H_2O + Mg \rightarrow MgO + H_2$$

As the dissociation pressure of MgO is extremely low (Fig. 1), the reaction in the reverse direction can hardly occur under ordinary conditions. After oxidation for some time interval, water vapor and hydrogen coexist in the reaction chamber, and we may be able to measure the pressure of hydrogen by a calibrated Pirani gauge allowing the water vapor to freeze. With the knowledge of the chamber volume, we can determine the number of the hydrogen molecules evolved from a unit area of the alloy surface; hence, the number of the oxygen atoms captured per unit area of the surface and the weight increase can be calculated. If the MgO film thus formed is protective and compact, the thickness of the film can be calculated to the first approximation, by use of the known lattice constant or density of MgO. From these results laws of oxidation may be determined.

2.2. *Apparatus and Procedure*

A schematic diagram of the apparatus used in the present investigation is shown in Fig. 2. The source of water vapor is well-degassed distilled water. It is immersed in liquid air, and then is again degassed on the vacuum pump. The pressure of water vapor in the reaction chamber is maintained nearly constant during the experiments by fitting a large reservoir. The pressure of water vapor is read on a manometer containing oil of very low vapor pressure for the higher pressure range; lower pressures are measured by a Pirani gauge, calibrated for hydrogen, oxygen, air and water vapor.

The experimental tube contains a ribbon-shaped Ag-Mg sample about 0.1 mm in thickness and 2 mm in width, and its temperature is controlled by an electric current passed through it. The temperatures at the center and at one end are measured respectively by the thermojunctions J_1 and J_2, made of very thin nickel and tungsten wires. To obtain a uniform temperature distribution, and to avoid end effect, the diameter of the nickel leads in contact with the Ag-Mg ribbon is kept very thin. The Ag-Mg ribbons were cut from rolled sheets of the same lot containing magnesium about 2.5 per cent in weight. The alloy was prepared by melting silver analyzing 99.96 per cent of Ag with no more than 0.003 Fe, 0.011 Cu and a trace of Au in a graphite crucible in the hydrogen atmosphere of dew point about −30°C, and then quickly thrusting a piece of Mg containing 0.008 Zn, traces of Al and Mn, and a minute quantity of Si as impurities beneath the surface of the melt; the mixture was stirred a little, and then allowed to cool.

The alloy specimen was cleaned by abrasion with levigated chromic oxide on wet cloth, washed in water, rinsed in benzene, followed

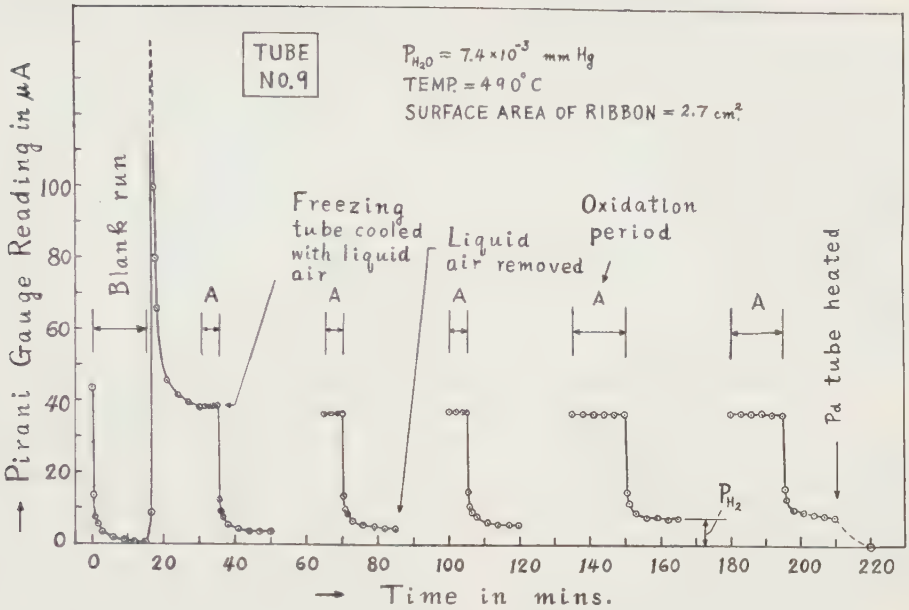

Fig. 3. An example of oxidation runs of Ag-Mg ribbon in water vapor atmosphere.

by a rinse in methanol.

After evacuating and degassing the apparatus, the Ag-Mg ribbon sample is also degassed at about 600°C, with utmost precaution so as to avoid the oxidation of the sample. Since, as a result of heating of the sample, a quantity of magnesium is noticed to evaporate onto the glass wall of the tube, the glass wall was cooled from outside by an air blast in order to minimize the reaction of magnesium with water vapor during the experiments.

When the degassing was complete, the tap K_1 is closed, and a small quantity of water vapor is admitted by opening the tap K_3 into the reaction chamber at a desired pressure. After a blank run was made to check the Pirani gauge reading, the temperature of the sample is raised quickly to a desired value and kept constant for a prescribed period until the passage of the heating current is stopped. The appendage (freezer) is then cooled by liquid air; water vapor is freezed, and the gas which remained uncondensed is read from the Pirani gauge. The fact that the remaining gas is actually hydrogen evolved from the decomposition of water vapor was proved as follows: when the palladium tube shown by dotted lines in the figure was subjected to high-frequency heating, while the appendage was kept immersed in liquid air, the Pirani gauge reading decreased almost to zero. The palladium tube was cut off from the apparatus in subsequent measurements. A typical example of such oxidation runs is shown by the curves in Fig. 3.

§ 3. Sources of Error and Preliminary Experiments

It was proved by Langmuir [14] that there is no measurable adsorption of hydrogen by glass even at liquid air temperature. It was confirmed by the following experiment that the same holds true also for glass covered with water molecules.

After the reaction chamber was filled with water vapor at a pressure of about 5×10^{-2}mm Hg on evacuating the chamber to vacuum of the order of 10^{-6}mm Hg, the appendage was cooled by liquid air, allowing water vapor to condense into it; then a small quantity of hydrogen was introduced from outside of the chamber through a palladium tube which was specially attached to it and was subjected to high-frequency heating. Then, the Pirani gauge reading increased with the admission of hydrogen, but it showed no noticeable decay characteristic of adsorption phenomena, indicating that there is no measurable adsorption of hydrogen by the glass wall covered with water molecules.

We can conceive that experimental errors might come from the following effects: (i) an evolution of hydrogen due to the reaction of nickel leads with water vapor; (ii) leakage of air through the taps into the reaction chamber from outside; and (iii) an evolution of hydrogen due to the reaction of water vapor with the magnesium film deposited on the glass wall of the experimental tube during the degassing process of the Ag-Mg ribbon.

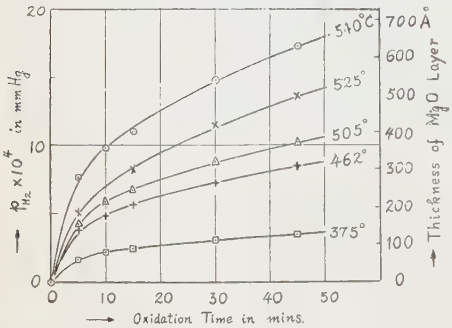

Fig. 4. Oxidation curves of Ag-Mg alloys in 6×10^{-2}mm water vapor.

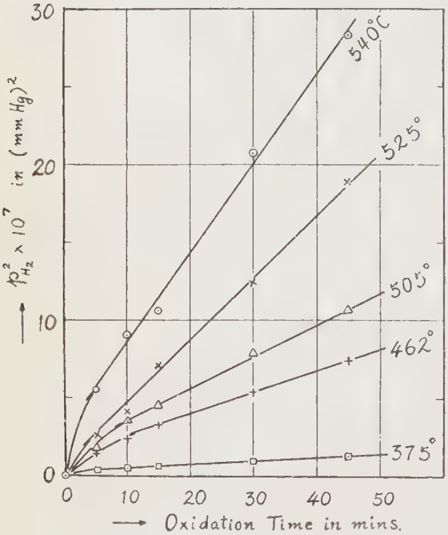

Fig. 5. Parabolic plot of oxidation of Ag-Mg alloys in 6×10^{-2} mm water vapor.

In order to estimate the errors due to the above-mentioned causes (i) and (ii), an oxidation experiment was carried out with a tube whose construction was similar to the experimental tube but with the difference that the Ag-Mg ribbon was replaced by a pure silver ribbon. In a measurement performed at 460°C in water vapor at 5×10^{-3}mm pressure, the pressure rise due to evolved hydrogen and leaked air was not higher than about 1.5×10^{-4}mm Hg after an oxidation time of 45 minutes. Since the surface area of the silver ribbon is 3 cm^2, this corresponds to a pressure of about 5×10^{-5}mm Hg. per unit area of the ribbon. The process (iii) seems to be not important in our experiments, for a preliminary experiment conducted at room temperature (17.5°C) for 60 minutes showed the pressure rise, which might be due to evolved hydrogen and leaked air, of the order of only 1.5×10^{-4} mm Hg. at the highest. The influence of absorption of hydrogen by the magnesium film can be neglected still more.

Thus, the errors in our experiments arising from these sources may be estimated roughly to be of the order of 10 per cent.

The surface area of the Ag-Mg ribbons was calculated from their dimensions, to the first approximation, neglecting roughness of the surface.

The error due to non-uniform temperature distribution along the Ag-Mg ribbon is minimized by taking a weighted mean instead of the simple arithmetical mean between the center and the end temperatures.

Effect of pressure of evolved hydrogen upon the oxidation rates of the alloys is negligible, for, as mentioned above, the chemical reaction in the reverse direction can hardly occur under ordinary circumstances. This was checked by an experiment.

§ 4. Experimental Results

From oxidation experiments carried out under conditions of various water vapor pressures, 7×10^{-3}, 6×10^{-2} and 1 mm Hg. respectively and Ag-Mg ribbon temperatures ranging from about 350° to 550°C, a great number of curves such as shown in Fig. 3 were obtained. The results are summerized as follows:

i) *Oxidation in 6×10^{-2} mm water vapor*

In Fig. 4 the values of pressure of hydrogen evolved from a unit area of the Ag-Mg samples and reduced to the values at 0°C are plotted against the oxidation time, with the temperature of the ribbons being taken as a parameter.

If the square of the pressure is plotted against the time, a family of straight lines is obtained as shown in Fig. 5. It is seen that

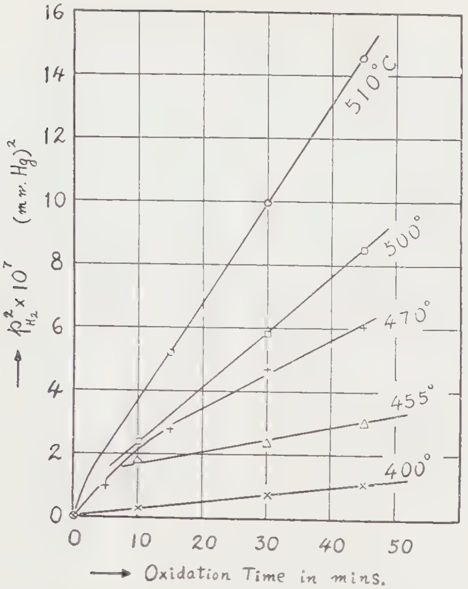

Fig. 6. Parabolic plot of oxidation of Ag-Mg alloys in 7×10^{-3} mm water vapor.

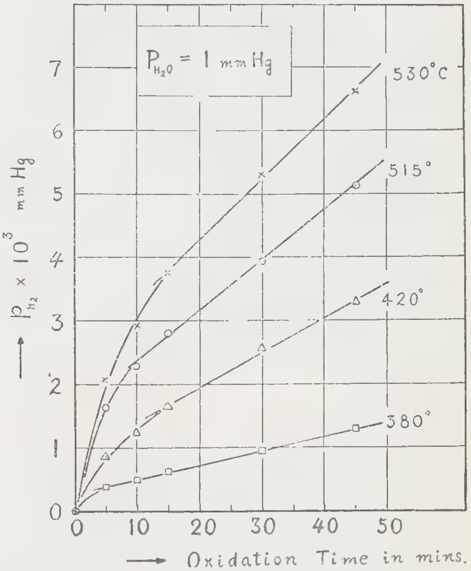

Fig. 7. Oxidation curves of Ag-Mg alloys in 1 mm water vapor.

the observations lie sufficiently closely on straight lines to leave little doubt that the build-up of the oxide layers satisfactorily follows the parabolic law, within the limits of experimental error. Deviations from the parabolic law occur only in the intial stages.

ii) *Oxidation in* 7×10^{-3}*mm water vapor*

For the oxidation in water vapor atmosphere at a pressure of about 7×10^{-3}mm Hg a similar linear relation holds between the square of the pressure of hydrogen evolved and the oxidation time, as shown in Fig. 6. In this case also the parabolic law holds for the build-up of the MgO layers except in the initial stages.

iii) *Oxidation in 1 mm water vapor.*

When the Ag-Mg samples are oxidized in water vapor at a pressure of 1 mm Hg, the build-up of the oxide layers does not follow the parabolic law, but is likely to follow more closely the linear law, as shown in Figs. 7 and 8; only in the initial stages the curves run nearly parabolic within the limits of experimental error.

iv) *Dependency of the oxidation rates on water vapor pressure*

It is important to know the effect of water vapor pressure upon the oxidation rate, in order to obtain the information as to which process, surface reaction or diffusion, plays the dominant role in the oxidation. As shown

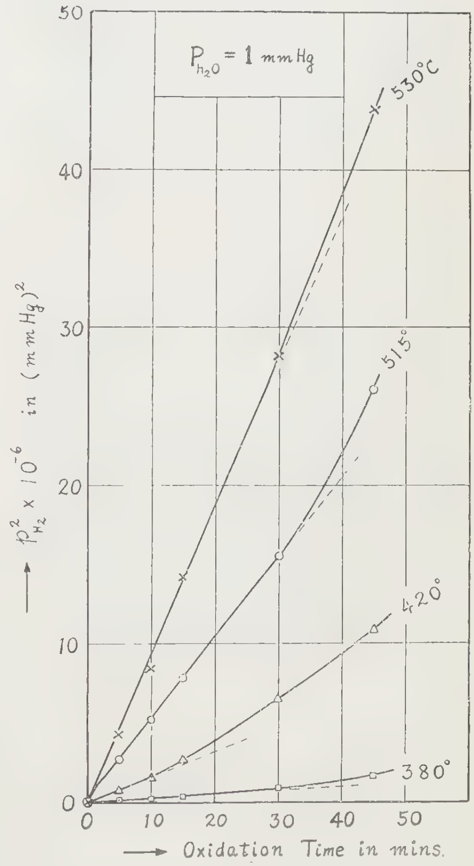

Fig. 8. Deviations from parabolic law of oxidation of Ag-Mg alloys in 1 mm water vapor.

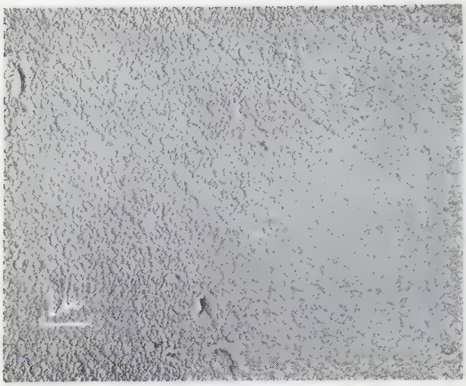

Photo. I. Electron micrograph of Ag-Mg alloy surface oxidized at 450°C for 60 minutes in 7×10^{-3} mm water vapor.

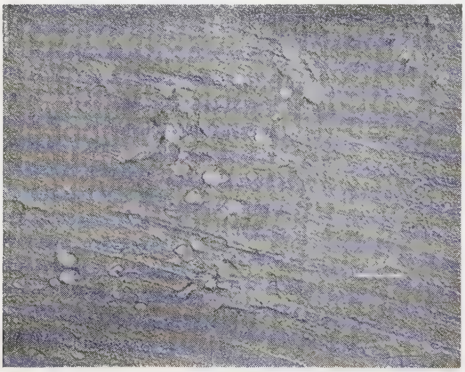

Photo. II. Electron micrograph of Ag-Mg alloy surface oxidized at 455°C for 45 minutes in 6×10^{-2} mm water vapor.

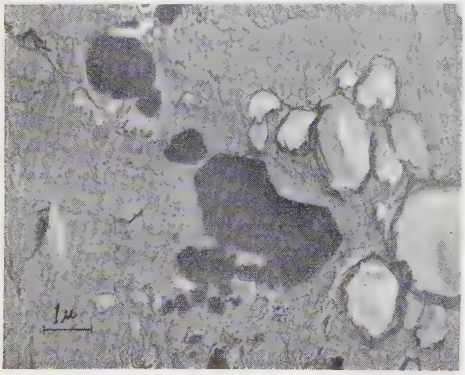

Photo. III. Electron micrograph of Ag-Mg alloy surface oxidized at 450°C for 45 minutes in 1 mm water vapor.

in Fig. 9, the oxidation rates seem to be almost independent of water vapor pressure within the pressure range of 1×10^{-1} to 7×10^{-3} mm Hg. This fact seems to imply that the rate-determining process is diffusion rather than surface reaction. This figure reveals also that the oxidation at 1 mm Hg pressure is governed by a quite different law.

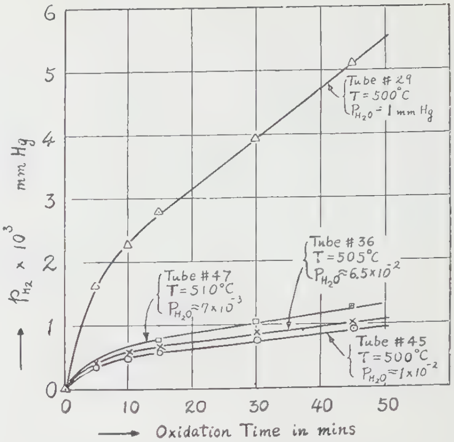

Fig. 9. Dependency of oxidation rates on water vapor pressure.

Electron microscopic study of the films indicated that the films built up under conditions for which the parabolic law holds (Photos. I and II) have far smoother appearances than those oxidized in the region where the linear law holds (Photo. III). In Photo. II it is noticed that MgO crystals begin to grow up, and fairly large crystals of MgO are clearly seen in Photo. III.

§ 5. Parabolic Oxidation and Diffusion Problem

In the region where the parabolic law holds the pressure of hydrogen, p_{H_2}, evolved per unit area of the Ag-Mg sample and reduced to the value at 0°C may be given as a function of the time of oxidation, t, in the next form:

$$p_{H_2}{}^2 = k_p t + c_1 \tag{1}$$

where c_1 is a constant and k_p is the parabolic rate constant. If the logarithm of k_p, the slope of the curves of Figs. 5 and 6, is plotted against the reciprocal of the absolute temperature $1/T$, a straight line is obtained as shown in Fig. 10. The activation energy Q of the rate-determining process, which is considered to be the diffusion of magnesium ions through the MgO layers, is calculated from the slope of the line to be 20.7 kcal/mol.

On the other hand, the number of hydrogen molecules, n, in $V\,\mathrm{cm}^3$ at 0°C and p_{H_2} mm Hg. is given by

$$n=3.56\times10^{16}\,p_{H_2}\,V=1.96\times10^{20}p_{H_2} \quad (2)$$

since the volume of the whole reaction chamber, V, in the present case is equal to 5.5×10^3 cm³. The oxygen atoms which have been decomposed from water vapor and captured by magnesium atoms per unit area to form MgO must be equal to n. The parabolic relation given by Eq. (1) may be represented in terms of the weight gain, $W(g/\text{cm}^2)$, as follows:

$$W^2=k_p't+c_2 \quad (3)$$

where $k_p'=2.71\times10^{-5}k_p$ and c_2 is a constant.

It has been generally agreed that parabolic thickening often occurs when the film substance is a semiconductor, as a result of lattice defects associated with a departure from the stoichiometric composition. Such defects make possible the outward diffusion of metallic cations and electrons, which meeting oxygen at the outer surface, build up additional layers of oxide. The facts that films grow outwards have been made clear by a number of experiments carried out by the use of radioactive isotopes in recent years[15]. The outward diffusion of magnesium atoms (or more likely ions) through the oxide layer may also be considered more probable on account of smaller radius of magnesium ion than oxygen ion, and electron micrographs of MgO layers seem likely to indicate the outward growth of the oxide layers. The activation energy of diffusion of oxygen through silver was given by Johnson and Larose[16] as 45.2 kcal/mol. The smaller value, 20.7 kcal/mol, obtained from the curve of Fig. 10 in our experiments also indicates that the outward diffusion of magnesium is more probable than the inward diffusion of oxygen. However, this may not be the case when the partial pressure of oxygen becomes extremely high, as shown by the experiments of Rappaport[1]. Although further evidences are required before we may come to a conclusion, radioactive isotopes of magnesium having half-value periods suitable for this purpose are unfortunately not found at the present time[17].

The parabolic law given by Eq. (1) or (3) assumes that every magnesium cation diffusing outwards from the metallic phase through the oxide film, finds an adsorbed oxygen atom waiting its arrival to convert it to oxide. However, if the water vapor pressure is low, the rate of oxidation may be insufficient to compete with the rate of the diffusion of magnesium, and some of the magnesium atoms diffused to the surface may evaporate without forming oxide. Therefore, deviations from the parabolic law are expected in the initial stages when the surface of the alloy is covered by the oxide layer insufficiently.

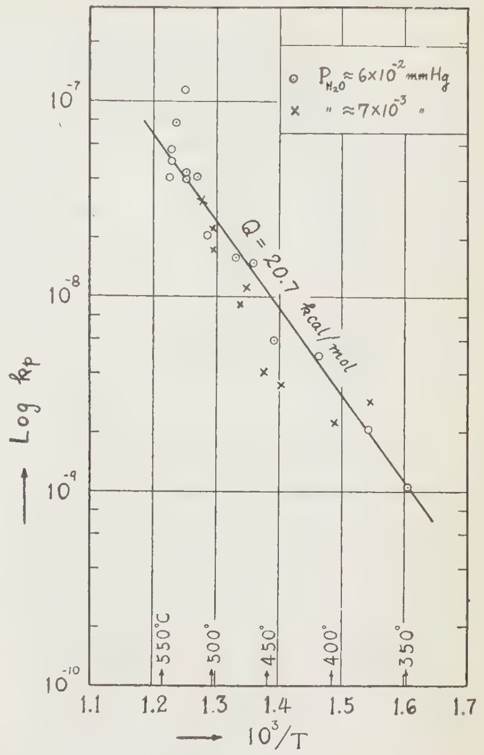

Fig. 10. Parabolic oxidation rate constant vs. $1/T$ plot.

§ 6. Thickness of MgO Layer

The fact that the MgO film builds up according to the parabolic law suggests that the formed oxide layer may be fairly compact without appreciable cracks. This point is open to some questions from an inspection of Photo. II, but this photograph shows that the surface is far more compact than that shown in Photo. III, obtained in the region where the linear law begins to hold. The crystal structure of MgO is NaCl type with $a_0=4.2$Å, and the number of oxygen atoms contained in a unit volume is about 5.4×10^{22}. The thickness of MgO layer ξ is given with a rough approximation by

$$\xi(\text{cm})\approx1.96\times10^{20}\,p_{H_2}/5.4\times10^{22} =3.64\times10^{-3}p_{H_2} \quad (4)$$

Table I.

T °C	k_p (mm Hg)²/sec	k_p' * (g/cm²)²/sec	Q cal/mol	D_0 cm²/sec	ΔS cal/mol/°C
350	1.75×10^{-11}	4.75×10^{-16}	20,700	2.12×10^{-9}	−32.12
400	$6.0\ \times10^{-11}$	1.63×10^{-15}	20,700	2.08×10^{-9}	−32.27
450	1.72×10^{-10}	4.67×10^{-15}	20,700	2.59×10^{-9}	−32.41
500	4.33×10^{-10}	1.17×10^{-14}	20,700	2.07×10^{-9}	−32.54
550	9.67×10^{-10}	2.62×10^{-14}	20,700	2.01×10^{-9}	−32.67
			Mean:	2.17×10^{-9}	−32.40

* k_p' should be multiplied by 0.486 in order to convert the unit from (g/cm²)²/sec to (cm³/cm²)²/sec since the weight gain of 1 gram corresponds to the volume increase of MgO of 0.697 cm³.

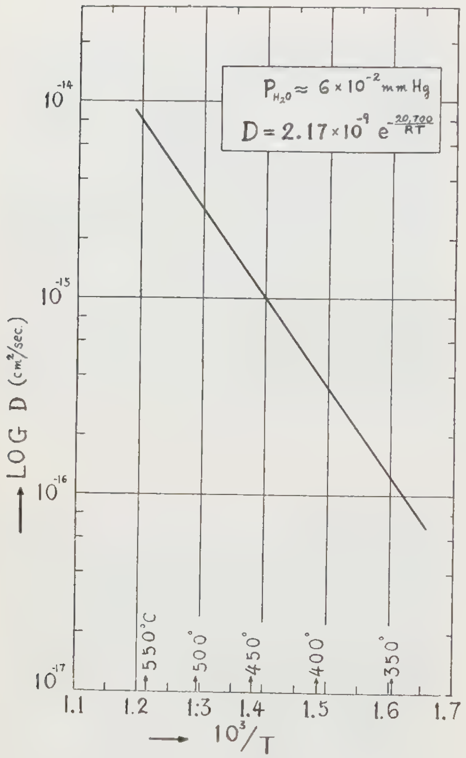

Fig. 11. Diffusion constant vs. $1/T$.

The thickness calculated from Eq. (4) is denoted on the right-hand side of Fig. 4. It should be noted, however, that it was almost inevitable for the Ag-Mg alloy samples to be oxidized during glass-working or degassing stage, although visual observation was not able to detect the existence of the oxide films. The true thickness of the oxide film will be somewhat larger than that given by Eq. (4) by at least 50Å or more.

§7. Diffusion Constant of Mg through MgO Layer

The fact that the MgO film builds up according to the parabolic law in spite of the volume contraction on oxidation, suggests that the thin film of MgO is subject to a strong stress, giving rise to a distortion or defects of the MgO lattice facilitating the passage of the magnesium atoms or ions. If we assume that the rate of diffussion of magnesium through the underlying alloy is sufficiently faster than that in the oxide, and the concentration of magnesium immediately below the interface is maintained substantially constant, the oxidation rate will be determined almost entirely by the diffusion of magnesium through the oxide layer. The rate of diffusion is then simply determined by the difference in the magnesium concentration at the metal-oxide interface and at the outer surface of the oxide. where it is substantially zero since the magnesium atoms or ions combine with the oxygen atoms or ions to form MgO as soon as the former arrive at the gas-oxide interface

Gulbransen[18][19] has applied the theory of chemical reactions and diffusion processes developed by Eyring to the problem of gas metal reactions, in particular the oxidation process. The parabolic rate constant k_p' and the frequency factor D_0 are given by the following equations:

$$k_p' = \frac{2kT}{h}\lambda^2 \exp[\Delta S/R]\cdot\exp[-Q/RT] \quad (5$$

$$D_0 = \frac{k_p'}{2\exp[-Q/RT]} \quad (6$$

where k is the Boltzmann's constant, h th Planck's constant, R the gas constant, λ th interatomic distance ($\sim a_0$), ΔS the entropy o activation, and Q the energy of activation. The values of ΔS and D_0 calculated from Eqs. (5) and (6) together with the observed values of k_p' and Q are tabulated in Table I. In Fig. 11 the diffusion constant, calculated from $D=D_0 \exp(-Q/RT)$, is plotted against $1/T$.

According to the oxidation theory put forward by Cabrera and Mott[20] the activation energy of diffusion through oxide layers should be equal to $\frac{1}{2}(W_i+\phi)+U$, where W_i is the energy required to remove an ion from its position in the surface layer of the underlying metal into an interstitial position of the oxide, ϕ the energy required to remove an electron from the metal into the conduction band of the oxide, and U the activation energy for movement between two equilibrium positions of the defects. Comparing this with our experimental result (0.9 eV), a very small value of the formation energy $(W_i+\phi)$ results, in contradiction to the value 4∼6 eV calculated by Yamashita and Kurosawa[21]. The properties of thin films of MgO may be considered to be quite different from those of bulk MgO.

§ 8. Linear Oxidation

At water vapor pressure of 1 mm Hg the oxidation rate of Ag-Mg alloy appears to follow the linear law as follows:

$$p_{H_2}=k_l t+c_3 \tag{7}$$

where k_l is the linear rate constant and c_3 is a constant. If the logarithm of the slope of the linear portion of the curves shown in Fig. 7 is plotted against $1/T$, a straight line should be obtained, and the slope of the line would give the activation energy of the rate-determining process. However, the linear rate constants obtained from Fig. 7 do not fit to a straight line. This is perhaps due to (1) the oxidation time in our case is too short to warrant the extrapolation of the linear portions of the curves to be the actual oxidation rates for prolonged oxidation; (2) the constancy of the concentration of magnesium just beneath the oxide layer will be more violated than in the case of parabolic oxidation due to the rapid growth of the oxide layer. Anyhow, the factor limiting the reaction rate in the linear oxidation may be the reaction of oxygen and magnesium at the oxide-metal interface rather than the diffusion of magnesium through the oxide layer as suggested by Leontis and Rhines[8] in the case of oxidation of magnesium. As mentioned before, the thin film of MgO will undergo a distortion of the lattice; as the oxide film becomes thicker, a certain critical thickness will be reached where cracks begin to yield[22]. Water molecules may be able to penetrate through these cracks without appreciable resistance, and reach the oxide-metal interface, resulting in a formation of MgO.

Acknowledgment

The author wishes to express his deepest appreciation to Dr. N. Saito, to whom he is indebted for many illuminating discussions of this subject. Many thanks are also due to Dr. E.A. Gulbransen of Research Laboratories, Westinghouse Electric Corporation, for his kind and pertinent comments. He also wishes to acknowledge with thanks the assistance of Mr. H. Yakoh for electron microscopy; Mr. S. Satoh for various phases of the experimental work; Mr. M. Taniguchi who carried out some of the experiments; and members of Metallurgical Engineering Section for preparation of Ag-Mg alloys.

References

1) P. Rappaport: J. Appl. Phys. **25** (1954) 288.
2) M. Kawakami: *Physics and Chemistry of Metals* (Sankaido, Tokyo, 1946), Vol. 1, p. 245 (in Japanese).
3) T. Tokumitsu and K. Takeya: J.I.E.E. Japan **9** (1944) 481 (in Japanese).
4) C. Wagner: J. Electrochem. Soc. **99** (1952) 369.
5) V. K. Zworykin, J. E. Ruedy and E. W. Pike: J. Appl. Phys. **12** (1941) 696.
6) K. Ono, A. Kondo and K. Ikegami: Res. Rep. Elect. Commun. Lab., Tokyo, No. 17 (July, 1951) (in Japanese).
7) S. Yoshida: J. Appl. Phys. Japan **19** (1950) 107 (in Japanese).
8) T. E. Leontis and F. N. Rhines: Trans. Am. Inst. Mining Met. Engrs. **166** (1946) 265.
9) N. B. Pilling and R. E. Bedworth: J. Inst. Met. London **29** (1923) 529.
10) O. Kubaschewski and B. E. Hopkins: *Oxidation of Metals and Alloys* (Butterworth's Scientific Publications, London, 1953).
11) E. Scheil: Z. Metallkunde **29** (1937) 209.
12) E. A. Gulbransen: Trans. Electrochem. Soc. **87** (1945) 463; **91** (1947) 573.
13) M. Hirashima *et al*: Convention Record of I.E.E. Japan, (3), p. 480 (May, 1953); (3), p.

557 (October, 1954); (3), p. 684 (May, 1955).
14) I. Langmuir: J. Am. Chem. Soc. **XL** (1918) 1361.
15) For example, G. W. Castellan and W. J. Moore: J. Chem. Phys. **17** (1949) 41.
16) C. J. Smithells: *Gases and Metals* (London, 1937).
17) J. M. Hollander, I. Perlman and G. T. Seaborg: Rev. Mod. Phys. **25** (1953) 469.
18) E. A. Gulbransen: Trans. Electrochem. Soc. **83** (1943) 301.
19) E. A. Gulbransen: Annals New York Acad. Sci. **58** (1954) 830.
20) N. Cabrera and N. F. Mott: Rep. Prog. Phys. **12** (1948-1949) 163.
21) J. Yamashita and T. Kurosawa: J. Phys. Soc. Japan **9** (1954) 944.
22) U. R. Evans: Trans. Electrochem. Soc. **91** (1947) 547.

JOURNAL OF THE PHYSICAL SOCIETY OF JAPAN Vol. 10, No. 12, DECEMBER, 1955

Studies on the Explosion Mechanism of Electric Blasting Caps by Ultra-High-Speed Grid Framing Camera

By Tsuneyoshi UYEMURA and Teruo MORISHIGE

Institute of Industrial Science, University of Tokyo
Institute of Science and Technology, University of Tokyo

(Received August 22, 1955)

The process of explosive fracture of the non-luminous subject has been distinctly photographed by the grid-type ultra-high-speed camera with the use of synchronized flash lighting. A description is given briefly of the equipment used and of some experimental results derived from the resulting photographs.

§ 1. Equipment Used

For the investigation of self-luminous detonation and shock waves, M. Sultanoff introduced a 10^8 frames per second camera in 1950[1)2)3)], and we undertook the making a camera of such a type with the idea that the device might similarly find application to studies on the explosive fracture of non-luminous materials by means of synchronized electric discharge flash tubes. The equipment, therefore, consists of such units as the camera, the electric flash source and synchronizing circuit (Fig. 1).

The optical system of the camera is quite simple as shown in Fig. 1. The first lens is used to image the event on the grid. The combined event-grid is then focused by the second lens, whose image, after being reflected on the rotating mirror, falls on the film plane. The photograph obtained in this way is a fixed space varying time record, which is suited for studying the phenomena.

Since lenses with large apertures and long focal lengths are suitable, a f/3.5; 250 mm first lens and a f/3.5; 300 mm second lens are used. If the magnification from the grid to the film plane is set for 1:1, the negatives or contact printed positives can be viewed by placing the grid directly over them.

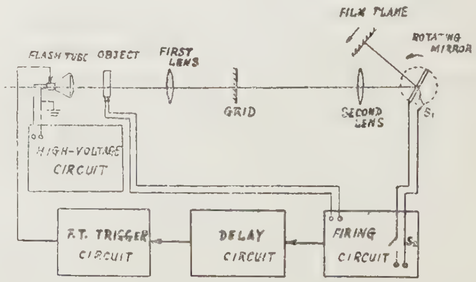

Fig. 1. Simplified diagram of synchronizing circuit.

Several grids with slits 0.01 mm and 0.0025 mm wide, cut at 0.4 mm, 1 mm, 2 mm, 5 mm and 10 mm intervals, have been tested depending on the size and the nature of the subjects.

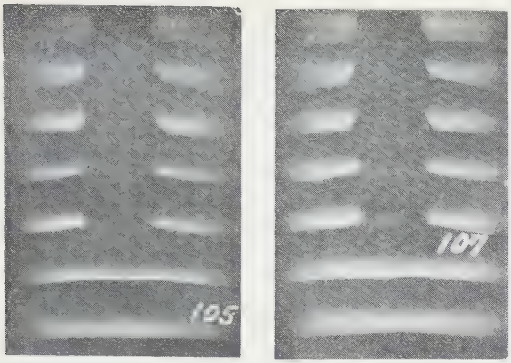

(a) (b)

Fig. 2. Resulting photographs of the blasting caps (filled will 0.4 gr. DDNP) in the process of exploding. Framing rate 3×10^7 frames per second.

The rotational speed of the reflecting mirror being used can be varied up to 20,000 RPM. With the combination of a rotational speed of 12,000 RPM and optical arm 380 mm, an image speed of about 1,000 meters per second on the film plane is easily obtainable.

The photographs shown in this paper were obtained by using of the Kodak Linograph Shellburst 35 mm Film (ASA 200).

On shorting the grid of the thyratron Type TX920 in the firing circuit to ground, a sudden flow of the current occurs through the tube, and fires the electric blasting cap. The initiation of the operation is determined by the proper pre-setting of a contacter attached to the rotating mirror. In order to avoid undesired scatter of the initiation of exploding, it is necessary to prepare electric blasting caps for the proper delay time (0.5-0.8 msec) within 0.1 msec scattering.

Triggering of the flash tube, a G.E. Type FT-220, is effected by the application of a fast-rising voltage obtained from the secondary of an ignition coil to a third electrode of the tube. The duration of the flash varies from 1/5,000 to 1/30,000 second corresponding to the capacitance of the energy storage capacitors of 10 to 60 microfarads.

The synchronizing operation of the flash with the phenomenon to be studied is made using a delay circuit with a range of 0.1 to 12.5 msec in steps of 0.01 msec.

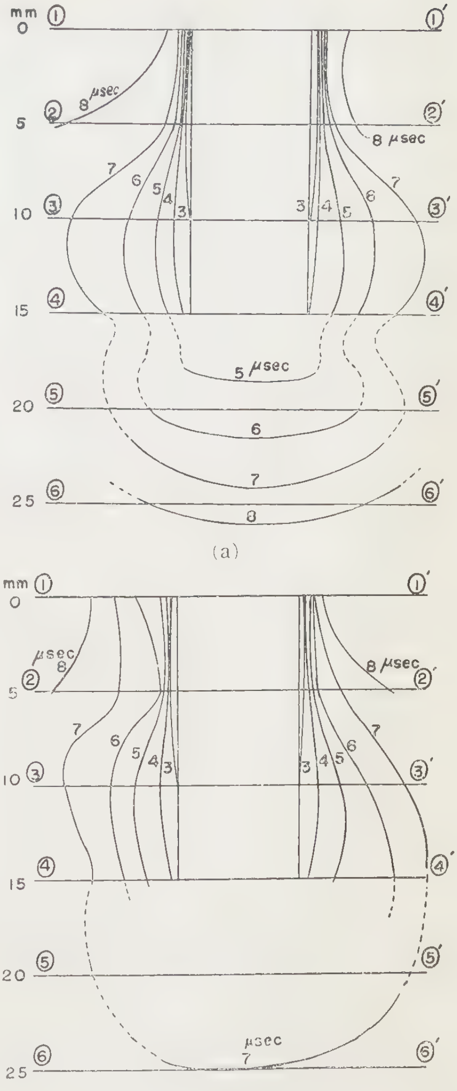

(a)

(b)

Fig. 3. (a) A plot of the process of exploding every 1.0 μ sec. (derived from Fig. 2 (a)).
(b) A plot of the process of exploding every 1.0 μ sec. (derived from Fig. 2 (b)).

§ 2. Experimental Results

Specially prepared electric blasting caps with the proper delay time and scattering, as stated above, were fired. Those were metal cylinders (alloy of copper and zinc in small amounts) of 17–35 mm length, 6.5–6.8 in diameter and 0.3 mm thick, filled with 0.2 to 1.0 gr. of explosives (DDNP). The pictures were taken at framing rates of $2 \times 10^7 - 3 \times 10^7$ frames per second, using a grid with slits 0.01 mm wide, cut at 5 mm intervals.

It has been possible, by examining the pictures obtained, to make clear the exploding process in which the blasting cap is deformed inelastically and the explosion products are propagated rapidly through the cracks.

Figures 2a and 2b show the resulting photographs of the blasting caps (filled with 0.4 gr. explosives DDNP) in the process of exploding, taken at the rate of 3×10^7 frames per second. In such cases as Figure 2a or 2b, where the framing rates (i.e. the sweeping velocities of the images across the film plane) are high enough, it will be noted that the flow of explosion products has been recorded as streaks that run slantwise to the sweeping direction of the image. The velocities of expansion of the explosion products, therefore, can be readily determined from these trails.

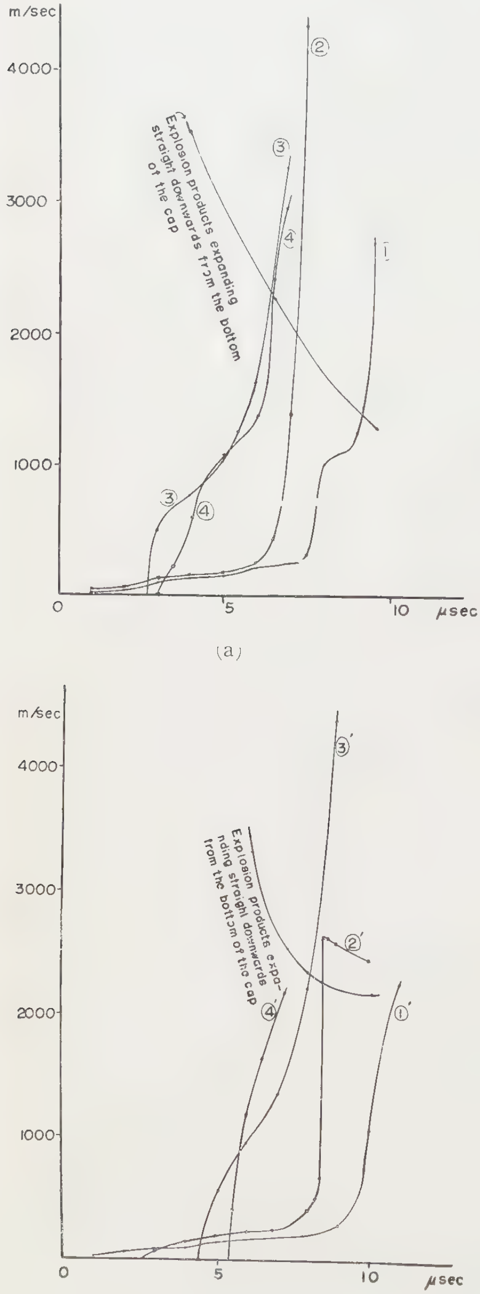

(a)

(b)

Fig. 4. (a) Velocity-time curves for explosion products expanding radially at the points ①-④ indicated in Fig. 3 (a), and straight downwards from the bottom.
(b) Velocity-time curves for explosion products expanding radially at the points ①'-④' indicated in Fig. 3 (b), and straight downwards from the bottom.

Figures 3a and 3b, obtained from both Figures 2a and 2b, show the cylinders in the process of exploding every 1.0 microsecond. In either case, the curves indicate the facts that in the process of the radial expansion of the cylinder, the deformation did not always take place symmetrically, and that the bottom were broken along the circumference and blew off the gas downwards at high speeds (in excess of 3,000 m/sec).

Figures 4a and 4b, derived from Figures 2a and 2b respectively, show velocity-time curves for explosion products expanding straight downwards from the bottom of the caps, and radially at points (1)-(4) along the cylinder as indicated in the figures. It will be noticed in Figure 2a or 2b, above shown, that the trails of explosion products differ slightly with one another, i.e., some are nearly straight from the starting points, some are curved initially and turn into straight lines half-way. This is due to the fact that these trails are the resulting pictures which present all the explosion products together in the process of exploding. The break points which can be seen in the pictures, therefore, correspond to the transition points of these products. Hence, it should be possible to assume that, in Figures 4a and 4b, the range up to 100-200 m/sec indicates the velocities of the (relatively) slowly expanding cylinder, the range from approximately 200 to 1,000 m/sec indicates the half-burnt particles during the flight, while the range exceeding 1,000 m/sec indicates the gas propagation.

It is also clear, by examining the starting positions of the velocity-time curves, that the blasting cap goes through the process of explosion in which it expands radially first with the shock pressure but, in a moment, it is broken at the bottom and begins to blow off the explosion gas.

§ 3. Conclusions

It has been demonstrated that the non-luminous subject (i.e., the copper cylinder) can be photographed in the process of explosive fracture which takes place within a few microseconds, and that the explosion gas propagated at velocities exceeding 4,000 m/sec can also be recorded on the film with the 1:1 magnification.

In this experiment, being given above, the phenomena accompanying the explosion of electric blasting caps were studied. It is proper, however, to regard the experiment as the one that could make clear, to some extent, the fracture mechnism of the metal cylinder under explosive attack. And this indicates that, with synchronized flash lighting, the grid-type camera as an effective research tool may find additional applications to studies on phenomena accompanying the explosive fracture of non-luminous materials. And it is now intended to make further studies of the explosive fracture of the tubing generally (i.e., metal, glass, plastics and etc.). It is hoped that a more detailed report on these topics can be given at a later date.

The authors wish to express their thanks to Professor Sukenori Yamamoto, Faculty of Engineering, University of Tokyo; and Professor Moriso Hirata, Faculty of Science, University of Tokyo; for valuable suggestions and encouragements through the progress of this experiment, and to Mr. Eiichi Kobayashi of Chuo University, Mr. Tamotsu Ono of University of Tokyo for their assistance.

References

1) M. Sultanoff: Rev. Sci. Inst. **21** (1950) 653-656.
2) M. Sultanoff: Jour. SMPTE **55** (1950) 158-166.
3) M. Sultanoff: Jour. SMPTE **60** (1953) 145-165.

JOURNAL OF THE PHYSICAL SOCIETY OF JAPAN Vol. 10, No. 12, DECEMBER, 1955

Oscillographic Studies of Joshi Effect and Secondary Processes in a Low Frequency Electric Discharge

By B. D. KHOSLA and N. A. RAMAIAH
Faculty of Science, University of Delhi, Delhi, India

(Received January 24, 1955)

Low frequency (50 cycles/sec) electric discharge in iodine vapour with glass electrodes was investigated by a cathode ray oscillograph. The rms value of the conductivity was contributed chiefly by two types of pulses, the electron avalanches of which were produced by secondary electrons originating from the cathode and the gas phase. The secondary process concerned with the liberation of electrons from the cathode due to positive ionic bombardment thereon appeared significant for the onset of the discharge under investigation. The maintenance of the discharge seemed primarily due to photo-ionization of the gas particles in the homogeneous phase. External radiation inhibited the secondary emission from the cathode to give negative Joshi effect, and enhanced that from the gas phase to produce positive Joshi effect; it, however, did not alter the field gradient in the system.

§ 1. Introduction

It has been reported in the previous communication[1] that the rms value of the current i passing through a discharge tube containing an electronegative gas or vapour and excited by alternating fields, is affected markedly by external radiation even in the visible range[2][3][4]. The change in i, usually referred to as Joshi effect (Δi), is positive ($+\Delta i$) or negative ($-\Delta i$) depending upon the experimental conditions especially the applied field X. Thus, while the positive effect $+\Delta i$ is observed in a narrow potential region below the breakdown value (X_s), $-\Delta i$ is detected invariably at $X \gg X_s$. This

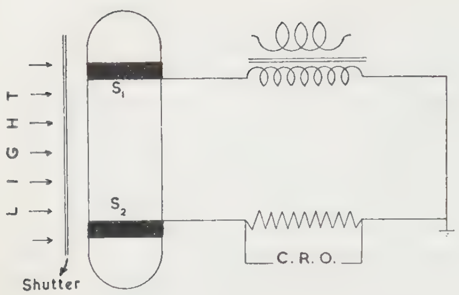

Fig. 1. Experimental set up for the studies of Joshi Effect in low frequency electric discharge.

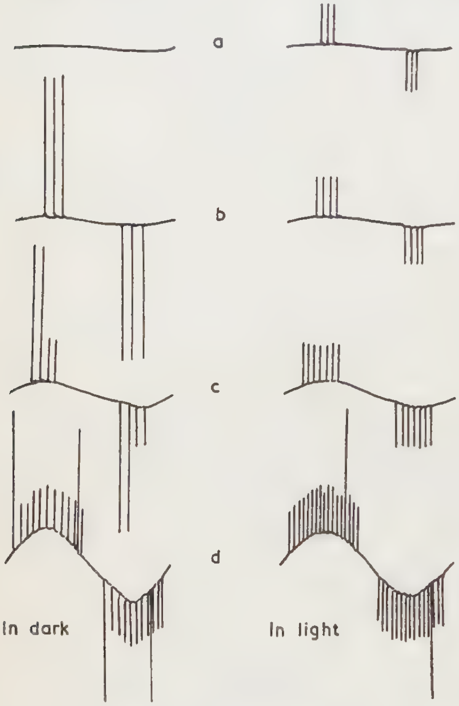

Fig. 2. Oscillograms representing the current structure in a low frequency electric discharge at varied fields: X=600 (a), X=650 (b), X=700 (c) and X=750 (d) volts/cm.
The electrode separation=2 cm was kept constant for a-d; X therefore, refers directly to the applied potential measured in volts (rms); $p_{\mathrm{I}_2}=0.45$ mm Hg.

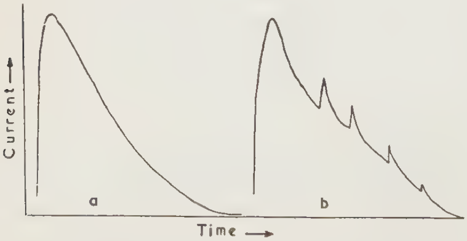

Fig. 3. Nature of a pulse in a low frequency electric discharge.
a: At electrode separation=2 cm.
b: At electrode separation=8 cm.

photo-variation, chiefly the decrease ($-\Delta i$), of i, cannot be anticipated from general theoretical considerations of photo- and thermo-electric effects[5], and appears to be of interest in view of the findings of Loeb[5], Townsend[7] and others indicating that external radiation is an indispensable factor for the inception of a discharge.

It is an established fact that the discharge current i in a system is primarily controlled by the well known secondary processes and the electron avalanches created thereby[6]. In order to understand the mechanism for the production of $\pm\Delta i$, it is of marked significance to study the influence of external radiation on these secondary processes which govern the magnitude of i. When this last is investigated by a cathode ray oscillograph, it is manifested in the form of certain *current pulses*[8]. The mechanism of the production of pulses in low frequency electric discharge chiefly with dielectric glass electrodes has been developed recently by Harries and von Engel[9] and others[10]. Detailed studies, now reported in this communication, on the nature and occurrence of these pulses in iodine vapour elucidated the varied secondary processes responsible for them and the influence thereon of irradiation giving $\pm\Delta i$.

§ 2. Experimental Arrangement

The experimental arrangement employed was essentially the same as described in earlier communications[1][11][12]. It consisted of cylindrical glass vessels containing pure iodine vapour at a desired pressure. They were fitted with external sleeve electrodes (S_1 and S_2, Fig. 1) and excited by 50 cycle potentials. The current was investigated by an oscillograph.

§ 3. Results and Discussion

Fig. 2 gives a typical series of oscillograms representing the current pulses in a low frequency electric discharge at varied applied fields (X) and the effect thereon of external radiation from a 200 watt bulb. It was noticed that on every half cycle of the current trace were produced some transient pulses.

§ 3.1 Nature of a Pulse

By suitable adjustment of the controls, by increasing the sweep frequency of the time base, of the oscillograph, the composition of a single pulse could be studied. It appeared generally in the form of a critically damped wave (Fig. 3a), consisting of a steep rise, followed by a slow decay, in the current trace. It may be pointed out that in the interpretation of any result obtained in these studies with alternating fields, the authors consider the features occurring in one half cycle of the alternating potential especially under simple enough conditions such as in the absence of space charge due to accumulation of positive ions, known to complicate the circumstances; and assume that the features which are established to be true in the case of dc discharges, are operative, save circumstances where the results are quite apparent to indicate the difference between the dc and ac discharges.

A pulse is generally defined by Korff$^{13)}$ as the potential drop of the anode. The electrons constituting an electron avalanche deposit themselves on the anode or the positively charged surface in an appreciably short interval of time; the fall in the corresponding potential is manifested in the form of a steep rise in the current trace (Fig. 3). This rise in the current trace is herein referred to as the *current pulse* and is a measure of the potential drop of the anode. The later phase of the pulse is attributed to the recovery of the anode potential to its normal value due to the increase of the applied field and also the deposition on the cathode of the positive ions produced in the avalanches. The total pulse time as computed by the oscillographic measurements was of the order of 200μ sec, indicating thereby that the repetition frequency of these pulses was roughly of the order of a few kilocycles per sec. As pointed out earlier$^{14)}$, this is similar to that of Trichel pulses$^{15)}$ noticed in negative corona produced with unidirectional fields.

At large electrode separations (>6 cm), however, the later phase of the current trace of a pulse acquired usually the form of a damped wave (see Fig. 3b); in this, the declining part of the pulse was irregular in nature. The mechanism for this needs further investigation.

§ 3.2. Different Types of Pulses and Their Origin

The oscillograms in Fig. 2 show that under ordinary conditions, there occurred two types of pulses: (*a*) longer and (*b*) shorter pulses. Their absolute amplitude in microamperes, which is of no significance for the matter under consideration, could be measured with the oscillograph; and was variant with electrode separation and gas pressure. Besides the diference in their amplitudes, the pulses, *a* and *b*, as will be shown below, are of different origin. It may be added that in the studies of the production of current pulses in low frequency electric discharge in chlorine, Harries and von Engel could not, however, find any distinction in the pulses observed on an oscillogragh. This might be due to the large pressures employed in their experiments. Number of other workers in this field using discharge tubes containing H_2O, H_2, etc. at low pressures observed essentially the same distinctive behaviour of these pulses *a* and *b*; their nomenclature was, however, different$^{10)16)17)}$. The authors' reference to *a* and *b* as longer and shorter pulses is obvious from the difference in their amplitudes; apart from this, there is no specific reason for this terminology.

The amplitude of the pulse is determined by the number of charged particles (electrons) arriving at the anode and the distributed capacity and other electrical factors attached to the system$^{13)}$. That is, the larger the number of electrons produced in an avalanche created by any secondary process and deposited on the anode, the larger is the height or the amplitude of a pulse. The following are known to be the different secondary mechanism for the liberation of electrons which under fields yield avalanches:

(A) In the gas phase:
  (i) Ionization and excitation by electron impact,
  (ii) ionization by positive ions,
  (iii) photo-ionization in the gas phase, and
  (iv) action of metastables in the gas phase.
(b) At the cathode:
  (i) Impact of electrons,
  (ii) positive ionic bombardment,
  (iii) photo-electric effects,
  (iv) effect of metastable atoms, and
  (v) field currents.

The relative significance of these processes responsible for the maintenance of any discharge, has been well discussed by Loeb[6][18] and others. Of these, the process (A i) is generally referred to as Townsend's α mechanism, which is primary for the development of electron avalanches. Further, for a discharge with metallic electrodes and normal, other than inert, gases, the processes (A ii), (A iii), (B ii) and (B iii) are of marked importance; these are hereafter referred to as β, ζ, γ and δ processes respectively, in accord with the general notation employed[19]. It may be added that for long time the process β viz. ionization in the gas phase by positive ionic impact, is assumed to be of no considerable value for the onset of the spark discharge; recent information[19][20], however, shows that the β process is also a significant one.

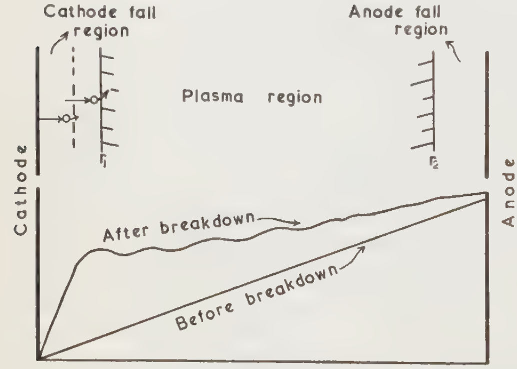

Fig. 4. Approximate representation of plasma region in a Low frequency electric discharge.

Let us consider first the secondary electrons produced in the gas phase especially in the neighbourhood of the cathode by any process say β or ζ; these acquire energy under fields and start ionization of the gas particles by inelastic collisions roughly from a point (say r_1, Fig. 4) away from the cathode. The production of electrons takes place exponentially; the number of electrons generated by every secondary electron is given roughly by $exp(\alpha d)$, where α is the coefficient representing the number of ionizing collisions in 1 cm path, and d, the electrode separation[9]. The ion multiplication occurs upto a point r_2 (Fig. 4) at one free path distance before the anode[6]. The region between r_1 and r_2 may be considered as the plasma region of the low frequency electric discharge; in this, the concentration of positive ions is approximately equal to that of the electrons, since the creation of one electron is accompanied by the production of one positive ion; double ionization, viz. ionization of positive ions, is not possible under the *low* fields employed. It may be noted that the potential gradient in the system is represented in Fig. 4 as uniform and linearly variant with distance before breakdown, and as non-uniform and variant differently after breakdown. That is, after the development of electron avalanches, the system is filled momentarily with electrons and positive ions; of these, electrons go fast to the anode, while positive ions move slowly in the form of a heavy space charge* towards the cathode. "These permeate the Crookes dark space and produce a powerful potential drop"[15], usually known as the cathode fall. The potential gradient in the system after the Faraday dark space i.e. in the positive column or what may be termed as the plasma region, rises to take on a constant practically linear slope (not shown in Fig. 4) in an unstriated discharge or differently as shown in Fig. 4 in a striated discharge[6]. These features exist as long as the ions remain in the discharge space. When once these are swept off and when no avalanche formation takes place, the potential variation becomes simple and linear ('before breakdown,' Fig. 4). The plasma region arises only when avalanches are produced; shortly afterwards, when the ions are swept off, the region *vanishes* in the sense that in the space between r_1 and r_2, the characteristics of the plasma region cannot be observed. Further, the width of the plasma region, controlled by experimental conditions such as electrode separation, gas pressure, etc. governs the number of electrons generated in an avalanche developed by one secondary electron produced by β or ζ. Ionization by electron impact between the cathode and the point r_1 is not excluded, and occurs by the electrons released from the cathode by any possible mechanism such as γ or δ, that is, due to the bombardment on the cathode by positive ions or photons. If the energy E of an electron in the metallic cathode acquired by γ or δ process is greater than the work function of the surface then the electron is liberated from the cathode (vide infra, for difference in E with dielectric glass electrodes). The released cathodic electron is having a more favorable circumstance than the electron produced in the gas phase by β or ζ process; the former travels before r_1 a longer distance and therefore, produces one or more further electrons (depending upon the width of the plasma region) before it reaches the point r_1.

---

* It may be pointed out that the space charge due to the slow moving positive ions referred to here, is distinct from the one possible to exist in discharges with alternating fields (cf. § 3.1). These *momentary* space charges causing a change in the potential distribution in the system (Fig. 4) are inevitable consequences of the development of avalanches and the movement of ions. In § 3.1, an altogether different circumstance has been cited: With alternating potentials, electrons and positive ions will be produced at the peak value of the breakdown voltage;[9] as the field declines, these will be swept out gradually: electrons will be removed first and then the slow moving positive ions. If the electrode separation and the frequency of the alternating field are small, the positive ions will be swept out completely from the system. For longer gaps and for larger frequencies like 20 kilocycles/sec used by Rukema[33] with metallic spheres, 2-10 megacycles/sec employed by Subrahmanyam and Ramaiah[34] with glass electrodes, etc., the positiye ions cannot cross the gap during the quarter cycle; a few positive ions remain in the space; these will build up gradually a space charge which is known to complicate the circumstances leading to usually low breakdown potentials, etc.[35] In § 3.1, the authors referred to that these positive space charges possible to exist on account of the alternating nature of the applied field, were not taken into consideration in the whole of the present article, since in the present investigation low frequency (50∿) potentials and short gaps were employed.

From the above, it can be seen that the average number of electrons reaching the anode, which controls the amplitude or height of a pulse, depends upon the following:

(A) The *length* of the avalanche: the number of ionizing events in an avalanche created by a cathodic electron can be two or more times the electrons produced in an avalanche resulting from a secondary electron generated in the gas phase by β or ζ process; and

(B) The number of avalanches: If a large number of avalanches of event smaller length are created at one and the same instant, the total number of electrons reaching the anode may be set equal to or greater than the electrons contributed by a fewer number of avalanches of longer amplitude.

At the outset it may be admitted that there is no positive proof available to the authors to show that the pulse height is controlled by (A) or (B) or to fix that the number of avalanches in a pulse (long or short) is constant or otherwise. The following are, however, the experimental findings which offer only indirect evidence for the conclusion arrived at by the authors regarding the pulse heights or the origin of the two types of pulses:

(i) At the breakdown potential V_m where it is well-known that the secondary processes from the cathode become operative, only the longer pulses are produced ; below V_m where the secondary emission from the cathode does not take place, always shorter pulses are initiated by external radiation.

(ii) The breakdown potential and the suppression under light of the longer pulses are highly susceptible to changes in the electrode surface, while the initiation of the shorter pulses below V_m are unaffected by these changes.

(iii) Removal of adsorbed gases held on the electrode surface by van der Waals forces at elevated temperatures reduced appreciably the photo-sensitive nature of the longer pulses while the production under light of the shorter pulses was unaffected.

(iv) Suggestively enough, over a narrow potential region below V_m, irradiation of specially designed discharge tubes with thin walls by sources (ultraviolet, x-rays, α-rays, etc.) of different intensities could never produce a longer pulse but initiated only shorter ones.

It is assumed therefore, that the longer pulses (a) are due to the larger number of electrons in an avalanche created by the secondary electrons liberated from the cathode by γ or δ mechanism, while the shorter ones (b) are due to avalanches generated by β or ζ.

§ 3.21. The Secondary Mechanism for Longer Pulses (a)

As pointed out earlier, of the various processes responsible for the liberation of electrons from the cathode, those referring to the bombardment on the cathode by positive ions (γ) and photons (δ) are significant in discharge tubes with metallic electrodes; in what follows, an attempt is made to understand, whether γ or/and δ are also significant for electron liberation from dielectric glass electrodes such as those employed in the present investigation.

It is well known that in discharge tubes, with metallic electrodes the free electrons forming the Fermi gas constitute the secondary electrons from the cathode. The same is incomprehensible in the case of glass electrodes. On account of this and especially from the data on breakdown potentials in discharge tubes with glass electrodes containing adsorbed layers and with their absence, it is suggested[21] that gas particles in the adsorbed medium on the glass surface, constitute the source of secondary electrons in the systems under investigation. It is beyond doubt that there exist adsorbed layers of H_2O, etc. on glass surface[22][23]. In ideal cases (1), these adsorbed layers are removed by processes of degassing[22][24] prior to the introduction of the medium like iodine vapour, in which the studies are sought to be made. It may be added that in most of the experiments described on this phenomenon, no such process is reported to have been undertaken; these cases (2) therefore, involve a circumstance such as that there exist water vapour layers adsorbed on the surface and iodine vapour in the gas phase.* A gas atom adsorbed on the surface acquires energy in the process γ or δ, ionises and contributes to the secondary emission. Let V_{si} be the ionization potential of the adsorbed medium** and V_i, that of the gas phase. In case (1), i.e. where the pre-adsorbed water vapour layers are removed from the surface before the introduction into the system of iodine vapour, $V_{si} \approx V_i$; in other cases (2), $V_{si} \neq V_i$. Further, the energy E that an adsorbed gas particle should acquire during bombardment by positive ions or photons is therefore, given by

$$E > V_i + \phi \qquad \cdots \text{case 1}$$

$$E > V_{si} + \phi \qquad \cdots \text{case 2}$$

where ϕ is the *resultant* work function of the surface. If we consider the case (2) representative of the systems used by the majority of the workers, there exist on the electrode surface, layers of H_2O, the ionization potential of which is 12.56 eV and in the gas phase, iodine vapour ($V_i = 9.7$ eV).[13] Liberation of a secondary electron from the surface is possible when bombardment thereon by photons or positive ions with an energy greater than $12.56 + \phi$eV takes place. The existence of photons produced by excited iodine atoms especially with energy greater than 9.7 eV is not feasible; on the other hand, a positive ion can acquire any amount of energy depending upon the field gradiant; it follows therefore, that the positive ionic bombardment (γ) alone is responsible for the secondary emission from the cathode and the longer pulses observed in low frequency electric discharge with glass electrodes. The same conclusion can be arrived at for the case (1) also.

The process (δ) acquires significance in discharges with metallic electrodes, since the Fermi electrons, as pointed out above, form the secondary electrons; to liberate these last from the surface, it is enough if a photon possesses an energy greater than the work function of the surface, which is of the order of 4–6 eV;*** and is sufficiently lower than the ionization potential of the normal gases. It may be added that when inert gases like helium ($V_i = 24.46$), neon ($V_i = 21.74$ eV), etc. are employed, the process (δ) may also take a prominent role in the liberation of secondary electrons even in discharges with glass electrodes (case 2).

§ 3.22. The Secondary Mechanism for Shorter Pulses (*b*)

Of the possible mechanisms responsible for the generation of secondary electrons from the gas phase viz. β and ζ, photo-ionization of the gas particles in the neighbourhood of the cathode (ζ) as shown later is significant for the production of shorter pulses. It may be added that photo-ionization occurs not only in the neighbourhood of the cathode but also at various places in the discharge space. A photo-electron created in the middle of, say, the positive column or plasma region (Fig. 4) travels shorter distance when compared with the distance travelled by an electron generated in the neighbourhood of the cathode, say, between cathode and r_1 (Fig. 4). It follows therefore that the avalanche created by the former possesses electrons many times less than the electrons in the avalanche developed by a photo-electron produced in the space between cathode and r_1. It is for this rsason that the average number of electrons reaching the anode to constitute a short pulse is assumed to be contributed largely by the avalanches created by secondary electrons generated by photo-ionization of the gas particles in the neighbourhood of the cathode.

---

* The production of pulses *a* and *b* and the influence thereon, of parameters like applied field, etc. are not materially affected by this process of degassing; there are, however, a few changes observed: for example, the breakdown potential of the medium and the potential width of the photosensitive non-selfmaintained region were altered markedly by this process; for details, see ref. 21.

** The arguments put forward in this secion are not materially affected by a possible difference not known to the authors in the ionization potential of an atom adsorbed on the surface and of the same existing in the free state.

*** cf. Vick: Brit. Jour. Appl. Phys. Supplement 2 (1953).

§ 3.3. Influence of Applied Field on the Production of Pulses

The data in Fig. 2 show the marked influence on the production of pulses *a* and *b* or the secondary processes responsible therefor, of the applied field X. When this last was not large enough to cause the system to breakdown as a dielectric, the current trace under simple enough conditions such as in the absence of external radiation (Fig. 2a, in dark) was but sinusoidal without superimposition of any pulses. When X was increased to X_s, remarkably enough, only the longer pulses *a* could be noticed on every half cycle of the current trace (Fig. 2b). These were roughly of the same height indicating that the amount of the charge deposited on the anode or the number of avalanches necessary to constitute a pulse was sensibly the same[25]. This observation suggests that liberation of secondary electrons from the cathode by γ mechanism plays a prominent role in the onset of self-maintained ac discharge. Increase of X decreased the number of the longer pulses (*a*) and initiated the shorter pulses (b) which always occurred after one or a group of pulses *a*. It seems therefore, that when the alternating potential exceeds the breakdown value the γ mechanism initiates the discharge and leads to the production of favourable circumstances for the development of other secondary processes. For example, the photons produced in the course of the formation of the avalanches leading to pulses *a*, appeared to be absorbed by the gas particles to generate electrons which give rise to the shorter pulses *b*. It is of interest to consider the following in this connection: When the electrons created in one pulse (say a longer one) are deposited on the anode, the potential of this last drops down; this causes the field in the gas phase also to decrease. Then the applied field and therefore the field in the gas rise again until the later reaches the breakdown value (see Fig. 5) when another pulse occurs, and so on. In the time interval (t′, Fig. 5) between the instant at which the field drops down and the moment at which it rises to the breakdown value, the field in the gas is not sufficient to cause ionization by collision; the electrons produced by ionization of excited particles by the photons gererated in the avalanches of the longer pulse are of no avail for the generation of further electron avalanches. Shorter pulses cannot therefore, be produced in this time interval t′. However, at the end of the time t′ i.e. when the field in the gas approaches the breakdown value, the photons available as "reasonance quanta"[26] due to emission by one atom, reabsorption by another and so on, are effective in the production of shorter pulses. Further, the pulses were all of the same height. At much larger fields, the production of the longer pulses was inhibited appreciably; only one pulse of this type could be detected at the beginning of that phase of the alternating cycle at which and above, the voltage was enough to cause ionization by electron impact. This pulse persisted over a wide range of applied potentials. Under these conditions, the current trace was superimposed, over an appreciable part of it, by the pulses *b*; the

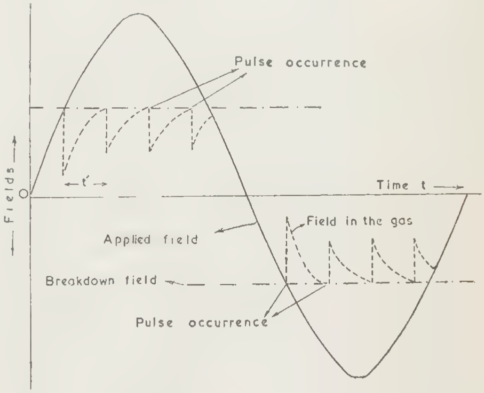

Fig. 5. Schematic representation of the variation of the field in the gas during the production of a pulse in a low frequency electric discharge.

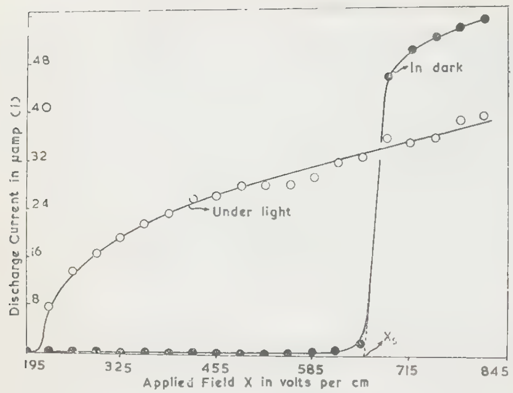

Fig. 6. Variation of the discharge current in dark and under light.

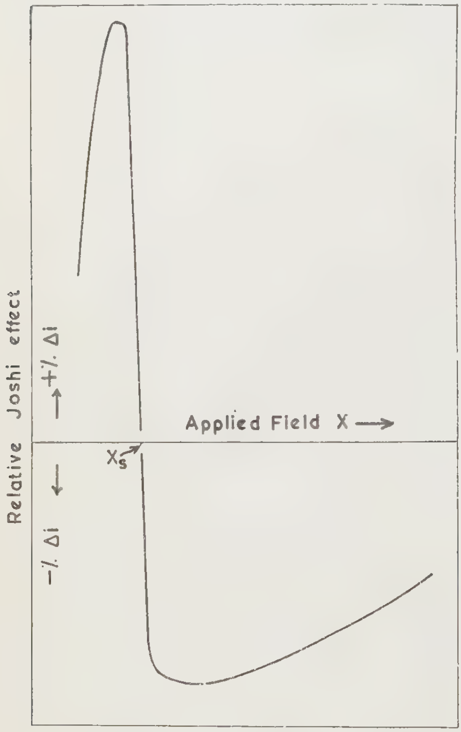

Fig. 7. Characteristic variation of Joshi effect with applied field.
(Relative effect % $\Delta i = 100\ \Delta i/i_D$ where i_D refers to the current in dark; the relative values viz. % Δi are usually plotted for facilities of comparison).

discharge at large fields appeared to be maintained completely by the secondary processes responsible for the shorter pulses. This observation suggested that photo-ionization in the gas phase was a significant mechanism for the (production of the shorter pulses (vide infra) and) maintenance of low frequency electric discharge in iodine vapour;[25] this feature brought out a distinction between low frequency discharge and that with dc potentials; it has been emphasised that the process ζ is insignificant for dc discharges especially in non-heterogenous gases[18].

The inhibitive influence on the longer pulses of the enhanced fields is apparently a characteristic feature of the low frequency electric discharge with glass electrodes; essentially similar data were recorded in chlorine by Harries and von Engel. These authors suggested that dissociation, by metastable atoms, of surface adsorbed molecules leads to the production of atoms or/and radicals with large electron affinity which inhibit the secondary electrons to be released from the cathode and therefore, the longer pulses.

At fields $X \gg X_s$, altogether a different type of pulses (*c*) has been noticed at the end of the half cycle representing the current trace (Fig. 2d). These had roughly the same amplitude as the pulses *a*. While the pulses *a* and *b* were produced regularly one after another, these pulses *c* found their place intermingled with the pulses *b*. Further, while the pulses *a* and *b* were affected by external radiation (vide infra), this last had little effect on *c*. The mechanism responsible for the production of pulses *c* needs further investigation.

§ 3.4. Influence of External Radiation: Joshi effect

The influence of external light on the two types of pulses (*a*) and (*b*) giving negative and positive effects respectively, is evident from the oscillograms in Fig. 2. A significant feature of these data is that at $X = X_s$, external light inhibited markedly the longer pulses, to give negative effect $-\Delta i$ viz. a decrease in the current *i* (cf. Fig. 6). This inhibition of pulses *a* was accompanied by the production of pulses *b*; this indicates the co-occurrence of positive and negative effects[27]. At one and the same instance, the inhibition of the longer pulses and the production of shorter pulses by external radiation, clearly points out that the pulses *a* and *b* are of different origin. When the rms value of *i* is measured, the resultant of positive and negative effects is observed; this invariably appeared as negative effect ($-\Delta i$) at $X \gg X_s$ (Fig. 7). Further, the negative effect attained characteristically its maximum value at the breakdown potential X_s (see Fig. 7)[26]. It was interesting to note that at fields $X>X_s$ (Fig. 2c) oscillograms under light contained only the shorter pulses *b*. Further, at $X\gg X_s$ (Fig. 2d), the one longer pulse *a* which occurred just at the beginning of that phase of the alternating potential sufficient to cause ionization by collision (vide supra), was suppressed by external light; this observation would indicate clearly the inhibitive influence of light on longer pulses *a* or the secondary mechanims responsible therefor viz. γ. That is, the action of light to give negative effect is to inhibit the secondary emission from the cathode[4)9)].

Irradiation initiated or/and increased the number of shorter pulses; these were of the same properties as of those produced in dark at $X>X_s$ (Fig. 2c). This favourable influence of radiation on the production of *b* suggests that of the various secondary processes occurring in the gase phase, β or ζ, the photoionization of the (pre-excited) gas particles (ζ) is fundamental for the occurrence of the pulses *b*[25] Essentially similar argument supports the deduction that of the two processes, γ and δ, responsible for liberation of electrons from the cathode and therefore, the production of longer pulses, the mechanism δ is not favourable; and γ is significant for the creation of the pulses *a* (vide supra).

The observation of photo-increase of the rms value of *i* (Fig. 6) and initiation under light of pulses (Fig. 2a) at fields $X<X_s$, was reported to be in agreement with Joshi's hypothesis[28] that $+\Delta i$ is due to uncaptured photo-electrons released from an adsorption-like layer formed under discharged on the electrode surface. Capture of an electron by an atom or a radical* is possible when the velocity of the electron is low. When this velocity increases, the probability of electron capture decreases; that is the population of uncaptured electrons increases. From the considerations put forward in this communication, electrons released from the cathode and unhindered, especially on account of their high velocity, by subsidiary processes, should lead to the production of the longer pulses *a* and not the shorter pulses *b* as observed under light (Fig. 2a). Further, with a constant light frequency, increase of applied field *X* from values below the breakdown potentials to those above it, will caused the velocity of the photo-electron to become larger and larger; this should reduce the probability of electron capture and lead to the production of more appreciable positive effect $+\Delta i$ at $X>X_s$ than that observed at $X<X_s$; however, at $X\gg X_s$, invariably negative effect $-\Delta i$ is detected (vide supra).

Harries and von Engel[9] and one of us (N. A.R.)[4] suggested simultaneously that the surface molecules held by van der Waal's forces dissociate under light to give rise to electronegative atoms or/and radicals; these last reduce the secondary emission from the cathode and therefore, the discharge current *i* to give $-\Delta i$; the positive effect $+\Delta i$ is due to photo-ionization of the pre-excited particles on or in the vicinity of the cathode[4]**. A significant observation of Harries and von Engel was that 'the pulse height did not change on irradiating only the centre of the discharge; on irradiating one wall only, the pulses were reduced every other half cycle viz. those pulses whose electron avalanches started from that wall[29]. This finding indicated that light inhibited the processes occurring at the cathode and responsible for the production of electron avalanches, i.e. the secondary emission. The observation[4)30)] from which Ramaiah could arrive at the above conclusion was that in degassed vessels, $-\Delta i$ characteristic of the system could be observed in less than ½ min and was independent of the predischarge interval which determined the Langmuir adsorption[4)30)]. In the light of experimental findings which indicate beyond doubt that the phenomenon $-\Delta i$ is primarily associated with the electrode surface[31], this observation leads to the conclusion that the other type of sorption viz. the instantaneous or van der Waal's adsorption is the chief seat of $-\Delta i$[30]. The preferential suppression of the longer pulses *a* and the creation of the shorter ones *b* by external light follow simply from this hypothesis.

§ 3.5. Effect of Irradiation and Field Gradient

Below the breakdown potentials i.e. at applied fields $X<X_s$, the field gradient F in the discharge space is linearly variant with the distance separating the two electrodes, cathode and anode in the type of discharge tubes employed by the present authors, and differently with a marked gradient near the wire in wire-in-cylinder type vessels used by other workers[32]. This potential distribution in the discharge space is of great importance in determining the magnitude of the current i: F controls the actual number of electrons produced in an avalanche due to an initiating electron generated by any secondary process, from the cathode or in the gas phase; that is, F determines the amplitude of the pulses a and b. It was instructive to consider from the data in Fig. 2 that at $X>X_s$, external light inhibited the longer pulses and produced larger number of shorter ones, remarkably enough, of the same height as of the shorter pulses appearing in dark (cf. Fig. 2c). That is, in the absence of external radiation, an electron formed in the gas phase by the process ζ acquires energy due to the field gradient and starts ionization by inelastic collisions after travelling a fixed distance away from the cathode (say from r_1, Fig. 4) in the field gradient. The number of electrons produced in the avalanche (s) which determines the height of the pulses b, is governed fundamentally by F. The observation that under light are initiated shorter pulses of the same height as of those produced in dark, suggests that the enhanced formation under light of initiating electrons causes ionization by impact roughly from the same point (r_1, Fig. 4) to give approximately the same number of electrons to constitute the increased number of shorter pulses. It could occur only when the field distribution between the cathode and anode, whatever manner it may be, was unaltered by the additional constraint viz. external radiation.

---

* Electron capture by molecules is negligible excepting in the case of oxygen (see ref. 6).

** Attempts to irradiate the gas phase near the cathode and the cathode separately were, however, unsuccessful on account of the diffusion of light in the body of the glass vessel.

§ 4. Conclusion

The following are the conclusions arrived at from the oscillographic data presented in this communication:

(1) For the onset of a low frequency electric discharge in glass vessels, liberation of electrons from the cathode by bombardment thereon of positive ions, is primarily significant; further, the secondary electrons originate from the gas layers adsorbed on the glass surface.

(2) The discharge is maintained chiefly by the secondary process involving the photo-ionization of the gas particles (ζ mechanism).

(3) External light inhibits the secondary emission from the cathode presumably due to the dissociation of the adsorbed molecules giving rise to electronegative atoms or/and radicals which capture the secondary electrons; this results in the production of negative Joshi effect. Further, external radiation enhances the secondary process involving the photo-ionization of the gas particles, to give the positive Joshi effect.

(4) The field distribution in the discharge space is varied little by external light.

References

1) Venkateswarlu and Ramaiah: Jour. Phys. Soc. (Japan) **9** (1954) 225.
2) Joshi: Proc. Ind. Sci. Cong., Chem. Sec. (1943).
3) Joshi and Deo: Nature **149** (1943) 561.
4) Ramaiah: Jour. Sci. Ind. Res. **10A** (1951) 182.
5) Ramaiah, Bhatawdekar and Subrahmanyam: Jour. Chem. Phy. **21** (1953) 1160.
6) Loeb: '*Fundamental Processes in Electric Discharge in Gases*' John Wiley, New York (1939).
7) Townsend: '*Electrons in Gases*' Huchison's Sci. and Techn. Publ. (1947).
8) Joshi: Nature **154** (1944) 147; cf. Saxena and Ramaiah: Jour. Chem. Phys. **20** (1952) 1342.
9) Harries and von Engel: Proc. Phys. Soc. **64B** (1951) 916.
10) Deb and Ghosh: Jour. Ind. Chem. Soc. **25** (1948) 449.
11) Subrahmanyam and Ramaiah: Zeit. f. Phys. **135** (1953) 274.
12) Dogra and Ramaiah: Jour. Sci. Ind. Res. **12B** (1953) 29.
13) Korff: '*Electrons and Nuclear Counters*', D. Van Nostrand Co. New York (1947).
14) Tiwary and Ramaiah: Jour. Sci. Ind. Res. **11B** (1952) 392.
15) cf. ref. 6, p. 567.
16) Khastgir and Setty: Proc. Phys. Soc. **65** (1952) 823.
17) Asolkar: Jour. Ind. Chem. Soc. **30** (1953) 234.
18) Loeb: Rev. Mod. Phys. **8** (1936) 267.
19) Llewellyn Jones and Parker: Nature **165** (1950) 960.
20) Bruce: Endeavour **13** (1954) 62.

21) Ramaiah: Jour. Sci. Ind. Res. **13B** (1954) 583.
22) Razouk and Salem: Jour. Phys. and Colloid Chem. **52** (1948) 1208.
23) Laidler: Jour. Phys. and Colloid Chem. **53** (1949) 713.
24) Manley: Proc. Phys. Soc. **36** (1924) 291.
25) Dogra, Bhatawdekar and Ramaiah: Proc. Phys. Soc. **66** (1953) 431.
Saxena, Bhatawdekar and Ramaiah: Jour. Chem. Phys. **21** (1953) 365.
26) Cf. ref. 9, p. 929.
27) Ramaiah: Jour. Phys. Chem. **56** (1952) 218.
28) Joshi: Curr. Sci. **16** (1947) 19.
29) Harries and von Engel: Jour. Chem. Phys. **19** (1951) 514.
30) Ramaiah: Jour. Chem. Phys. **22** (1954) 1507.
31) Ramaiah, Ratnam and Devi: Jour. Sci. Ind. Res. **11B** (1952) 524.
32) Rao and Sharma: Jour. Phys. and Colloid Chem. **53** (1949) 753; also ref. 12.
33) Rukema: Trans. Amer. Inst. Elect. Eng. **47** (1928) 38.
34) Subrahmanyam and Ramaiah: Zeit. f. Phys. **138** (1954) 151.
35) Cf. ref. 6, p. 551.

JOURNAL OF THE PHYSICAL SOCIETY OF JAPAN Vol. 10, No. 12, DECEMBER, 1955

Statistical Theory of Turbulence, III
Extension of Similarity Theory of Turbulence

By Yutaka SHIGEMITSU

Transportation Technical Research Institute, Tokyo

(Received July 23, 1955)

As the second stage of developments of our statistical theory of turbulence, extension of the initial-period similarity-law is attempted in order to give general explanations to distributions of turbulent quantity across the mean direction of flow, particularly in decaying and non-decaying shear turbulence. In (A), as the statistical hypothesis in our theory, we first give the Gaussian form to P-function. Then, as a simple theoretical result of the above extended similarity law, it can be proved that the distribution of an intermittency factor γ, introduced by A. A. Townsend in his study of turbulent wake, takes the form of Gaussian-integral function, which is surveyed further by experimental observations. In (B), by introducing the above result to our fundamental expressions of turbulent intensity, it is interpreted that in all the cases of shear turbulence $\boldsymbol{u}/\sqrt{\overline{\boldsymbol{u}^2}+\overline{\boldsymbol{v}^2}}$, $\overline{\boldsymbol{uv}}/\boldsymbol{uv}$ and $\boldsymbol{w}/\boldsymbol{u}$ have respective nearly constant values in the y-direction. These characters are investigated by experimental measurements. In (C), as the first step to study V_*-function in shear turbulent state, the problem of distortion of isotropic turbulence in a contracting stream is taken up. By rather qualitative hydrodynamical discussion on $\overline{V}_*$-function in the shearless turbulence with a non-uniform mean velocity, our fundamental formula in this case gives a result that $\boldsymbol{v}/\boldsymbol{u}=\overline{U}(x)/\overline{U}_0$, which is also checked in our measurements. In (D), by using all the results in (A) and (C) we derive theoretically the Reynolds-stress distribution across a symmetrical shear turbulence, which is the simplest shear turbulence and corresponds nearly to a free mixing flow. Mean velocity distribution is also determined by the Reynolds equations. They are compared with our experimental measurements.

§ 1. Introduction

In the previous paper, the condition of similarity preservation has been clarified based upon our statistical theory through all the types of turbulent flow. It is mentioned that the initial—period similarity-law in decaying turbulence or its extended non-decaying form gives an important idealized descriptions of the general turbulent phenomena. Previous discussions due to this similarity law have been related chiefly to decay or diffusion, namely to one-dimensional transient phenomena in the x-direction. But, we are usually interested also in the distribution of turbulent quantity in the y-direction, particularly in shear turbulence. In this paper, we shall attempt to develop the above-mentioned similarity law further so that we may interpret general turbulent states across the mean direction of flow.

As the character in the x-direction of P-function, whose functional form means the statistical foundation in our theory, the preservative condition expressed as (9.3) (II) is necessary and sufficient. We shall first give a more strict expression to $P_1(s, \theta; \eta)$ in shear turbulent state. As an experimental fact which is able to be interrelated to P-function in the simplest mathematical formula, we can take that of distribution of an intermitency factor γ which has been introduced by A. A. Townsend in the study of turbulent wake. It is the contents of (A) that detailed theoretical discussions on the functional form of P are made in comparison with experimental observations on the free-boundary phenomena of shear turblence.

Attending to many ovservations it may be recognized in every case of turbulence that the three components of velocity fluctuation have always the same order of intensity, independently of the position in the field of flow. It cannot be proved by the hydrodynamical equation of continuity. In (B), we interpret this fact through decaying and non-decaying shear turbulence, by introducing the result in (A) to the extended expression of turbulent intensity (10.1) or (17.3) (II).

As for $\bar{V}_*$-function in shear turbulence, we cannot now determine, because of mathematical difficulties, the exact functional form of $F_1'(s, \theta)$ by solving the hydrodynamical equations of motion. In the case of shearless turbulence with a non-uniform mean flow, however, the character of $F_1'(s, \theta)$ is easily related to the variation in every component of turbulent intensity, because we have a simple condition $P_1=1$. From this point of view, we treat in (C) the problem of distortion of isotropic turbulence in a contracting stream iniated by G. I. Taylor, by formulating $\bar{V}_*$-function based upon rather qualitative hydrodynamical considerations.

When the two functions $\bar{V}_*$ and P are determined, the Reynolds-stress distribution can be completely derived across the shear turbulence under the supposition of ideal state in the initial period. As the simplest case of shear turbulence, symmetrical decaying shear turbulence can be taken which correspnnds approximately to half jet or free mixing flow. In (D), we first give mathematical expressions to these functions depending upon the results in (A) and (C), and then we derive the Reylolds-stress distribution along the y-direction including that of the mean velocity.

A. Free-Boundary Phenomena of Shear Turbulence

§ 2. Determination of P-function

As a simple case of shear turbulence, the turbulent wake behind a single body will be considered. In the initial-period in which the vortex chaos motion of $\alpha=1$ is predominant, the centres of these vortices run in the field of flow irregularly broken from the regular arrangements of Kármán vortex street. In this case, however, these runnings have one mean path unlike the wake behind a grid, and the most probable locus of running can be pointed out. In these circumstrances, we assume that the probability density in the y-direction of loci of these centres obeys the Gauss distribution. This supposition can be formulated by using P-function which expresses their relative arrangement. To the previously introduced similarity assumption $P(s, \theta; x, y) = P_1(s, \theta; \eta)/S$, we will add such a more restricted condition that

$$P_1(s, \theta; \eta) = a_1 \exp\{-(\eta_1 - b_\eta)^2/\sigma^2\}) \quad (= P_1(\eta_1; \eta)) , \qquad (2.1)$$

where $\xi_1 = \sqrt{s} \cos\theta$ and $\eta_1 = \sqrt{s} \sin\theta$, a_1 is a constant determined by $\iint_D P dS = 1$, and the position of centre b_η is varied depending upon the ordinate η in the field of flown. The non-dimesional breadth σ is expressed in H/R_y and is taken to be constant, where H is the standard deviation of Gauss form.

We consider that (2.1) still holds in other decaying shear turbulence. In a non-decaying turbulence, (2.1) can also be adapted in every

P-function in a vortex chaos motion having the same production point. σ is considered to be not necessarily equal for all types of flow, but the functional form (2.1) can describe all sorts of vortex chaos motion. The shearless turbulence is a limiting case of $\sigma=\infty$, while the hydrodynamical non-stationary state is that of $\sigma=0$ (cf. Fig. 10 (I)).

§ 3. Distribution of Intermittency Factor

The existence of intermittency phenomena at free boundaries of turbulent wake was first found out by A. A. Townsend[1]. To investigate mean breadth of wake, he introduced the following intermittency factor

$$\gamma=\lim_{T\to\infty}(1-T_l/T)\,. \tag{3.1}$$

T_l is the summination of time intervals of so-called laminar state in total time T, which is determined as the parts having comparatively small velocity fluctuation with low frequency in oscillograph records. Because of the character of intermittency the above laminar parts can easily be pointed out in experiments, even if their intensities of velocity fluctuation are not zero. Many experimental measurements have indicated that the limiting value in (3.1) tends easily to a constant value and is distributed in the y-direction continuously in a fairly wide range.

As mentioned in § 8 (II), the existence of intermittency phenomena in shear turbulence has been interpreted as being attributed to the not completely irregular state in the loci of vortex centres in the field of flow. Namely, one time a vortex runs far from the centre of wake and then another vortex runs near it, and the locus of running change irregularly in time. In the initial period of decaying shear turbulence, deviation from the mean state can be neglected in the chaotic motion of $\alpha=1$ vortices and a definite mean velocity distribution $\bar{V}_*$ can be determined in D-domain. It is seen from the exact solution in § 9 (I) that in $\bar{V}_*=F_1'(s,\theta)G_1(t)$, $F_1'(s,\theta)$ tends to $1/r$ asymptotically far from the centre of D-domain, whose distribution in the y_1-direction may be as shown in Fig. 1. Then, far from the centre the velocity fluctuation caused by F_1' has small intensity and low frequency, and so the state may be called as laminar flow. Let $\eta_{1,c}$ be chosen on the η_1-axis not near the centre, so that it may correspond to a critical point to this laminar part. Near the boundary of wake, relative arrangement of the two functions P_1 and F_1' may be indicated in D-domain as shown in Fig. 1. Then, owing to the definition of P-function given in § 4 (I), the limiting value in (3.1) which expresses the ratio of laminar part, is equal to ratio of hatched area to the total one. The functional form of P_1 is given in (2.1). The relative position of $\eta_{1,c}$ to the centre of Gaussian curve b_η changes depending upon the position η in the field of flow. Then, the distribution of intermittency factor γ in the y-direction can be derived by integrating the Gauss function;

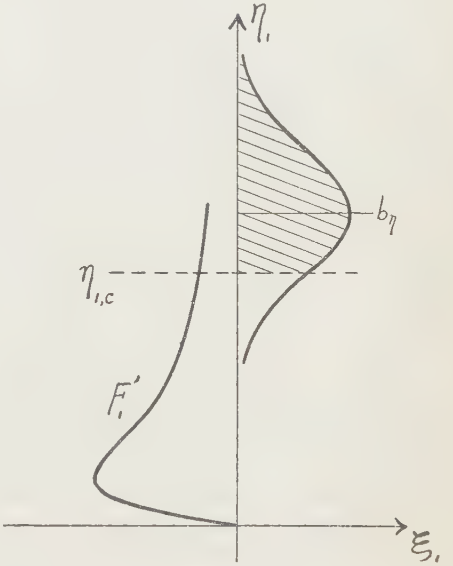

Fig. 1.

$$\gamma(\eta)=a_2\int_{\eta}^{\infty}\exp\{-(\eta-\bar{\eta})^2/\sigma^2\}d\eta\,, \tag{3.2}$$

where $\bar{\eta}$ is the non-dimensional ordinate of centre of Gaussian-integral form and a_2 is a constant to be determined by $\lim_{\eta\to\infty}\gamma(\eta)=1$.

The above expression is derived under the supposition of the initial-period similarity. Even in turbulent boundary layer, this character can be adapted at least in a group of vortices running not near the wall. Thus, the expression of Gaussian-integral form in γ-function will be found in all sorts of shear turbulence at their free boundaries to laminar flow.

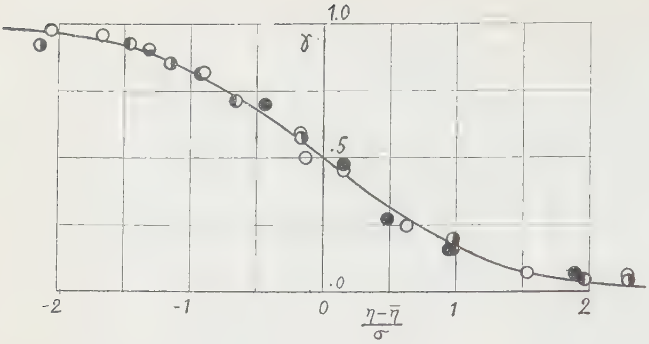

Fig. 2. Distribution of γ-function behind a circular cylinder. ○, ●, ◑, ◐ and ◒ are observed values at one section under variable undisturbed velocities of 3.07, 7.26, 10.85, 14.92 and 19.96 m/s. The position was 50.5 cm behind the cylinder whose diameter was 1.5 cm. The curve indicates Gaussian-integral form in (3.2).

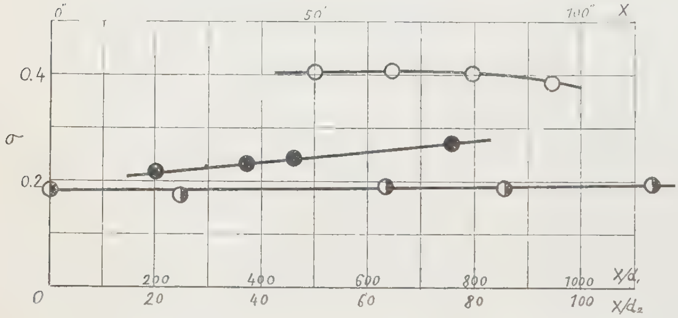

Fig. 3. Experimental results on the change of σ along the x-direction. ○, ● and ◑ are evaluated values respectively from the case of Townsend's two-dimensional wake, Corrsin's round jet and Corrsin's turbulent boundary layer along a flat plate. d_1 and d_2 are diameters of cylinder and tube, and in the boundary layer x is measured in inches. Those abscissae are measured from the apparent origin of wake, jet and boundary layer respectively.

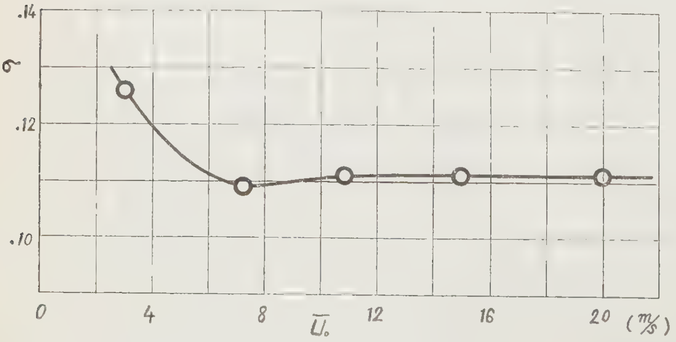

Fig. 4. Experimental result on the relation between σ and undisturbed velocity in a two-dimensional wake behind a circular cylinder. The states of measurements are the same as in Fig. 2.

§ 4. Experimental Investigations on Intermittency Phenomena

By Townsend's observation[1] on γ-function at several sections behind a circular cylinder under a constant velocity, it is seen that (3.2) agrees with these data favourably. Further, we made some measurements at one section behind a circular cylinder by changing the mean velocity. The distributions of γ to $(\eta-\bar{\eta})/\sigma$ are shown in Fig. 2. In a round jet and a turbulent boundary layer, S. Corrsin and others[2] presented plenty experimental results. It is important that all the experimental data can be expressed in the single theoretical curve of (3.2).

In the case of turbulence in a tube, an intermittency phenomenon cannot be detected by the hot-wire technique, because it has no free boundary to laminar flow. We consider, however, that the not completely irregular arrangements of vortex centres expressed as (2.1) still exist. It is suggested by several photographs of the flow patterns[3]. If detailed observations are made by taking photographs near the centre of tube, an irregular mixing between the vortex chaos motion produced at one wall and that produced at the opposite wall will be found. The relation of Gaussian-integral form in the generalized intermittency factor, which is defined not only between turbulent and laminar flows but also between two types of vortex chaos motions, may be found out. This generalized intermittency phonomena may be found also near the centre of turbulent wake behind a single body.

In (2.1) σ is taken to be constant. Under the state of initial-period similarity with a constant undisturbed velocity, R_y is proportional to the ordinate $\bar{Y}$ of the centre of Gaussian-integral form, and so the states of σ can be surveyed experimentally by taking $\sigma \backsim H/\bar{Y}$. In two-dimensional wake the change of σ along the x-direction is shown in Fig. 3, taken from Townsend's data[1]. For reference, the distributions evaluated from Corrsin's measurements[2] in a round jet and a turbulent boundary layer along a flat plate are also shown. It is seen from these results that our assumption of constancy of σ can be verified at least in the initial period of a given shear turbulent state. Further, we surveyed the relation between σ and undisturbed velocity $\bar{U}_0$ at one section behind a circular cylinder. The result is shown in Fig. 4, which indicates that except a narrow part of low speed σ does not change with $\bar{U}_0$. The exact determination of $\bar{Y}$ cannot be made in experiments like that of $\eta_{1,c}$ in the theory, and the above numerical value cannot be compared directly with Townsend's one. But, by the above experimental investigations, the following can be convinced; that the Gauss distribution in P-function indicates an essential point in the statistical mechanism of shear turbulent flow.

B. Proportionality in Turbulent Intensities

§ 5. Interrelation Between u- and v-intensity

The distribution of turbulent intensities will be considered across two-dimensional decaying shear turbulence. They are determined by the functions $C_{u^2}(\eta)$ etc. given in (10.1) (II). By introducing (2.1) they become

$$
\begin{aligned}
C_{u^2}(\eta) &= a_3\int_{\eta_{1,0}}^{\eta_{1,1}} P_1(\eta_1;\,\eta)\left\{\int_{\xi_{1,0}(\eta_1)}^{\xi_{1,1}(\eta_1)} F_1'^2(\xi_1,\,\eta_1)\,\mathcal{E}^2(\xi_1,\,\eta_1)\,d\xi_1\right\}d\eta_1 \\
C_{v^2}(\eta) &= a_3\int_{\eta_{1,0}}^{\eta_{1,1}} P_1(\eta_1,\,\eta)\left\{\int_{\xi_{1,0}(\eta_1)}^{\xi_{1,1}(\eta_1)} F_1'^2(\xi_1,\,\eta_1)(1-\mathcal{E}^2(\xi_1,\,\eta_1))d\xi_1\right\}d\eta_1 \qquad (5.1) \\
C_{\overline{uv}}(\eta) &= \pm a_3\int_{\eta_{1,0}}^{\eta_{1,1}} P_1(\eta_1;\,\eta)\left\{\int_{\xi_{1,0}(\eta_1)}^{\xi_{1,1}(\eta_1)} F_1'^2(\xi_1,\,\eta_1)\mathcal{E}(\xi_1,\,\eta_1)\sqrt{1-\mathcal{E}^2(\xi_1,\,\eta_1)}\,d\xi_1\right\}d\eta_1\,, \\
&\mathcal{E}(\xi_1,\,\eta_1)=\sin\theta\,, \qquad a_3=(4c^2\nu)\Big/\int_0^{2\pi} S_0(\theta)d\theta\,.
\end{aligned}
$$

$\xi_{1,0}(\eta)$, $\xi_{1,1}(\eta)$ and $\eta_{1,0}$, $\eta_{1,1}$ mean the boundary of D-domain.

In (5.1),

$$1 \geqq \mathcal{E}^2(\xi_1,\,\eta_1) \geqq 0$$

and so when we write

$$a_3\int_{\xi_{1,0}(\eta_1)}^{\xi_{1,1}(\eta_1)} F_1'^2(\xi_1,\,\eta_1)\mathcal{E}^2(\xi_1,\,\eta_1)d\xi_1 = \left\{a^3\int_{\xi_{1,0}(\eta_1)}^{\xi_{1,1}(\eta_1)} F_1'^2(\xi_1,\,\eta_1)d\xi_1\right\}\mathcal{E}'^2(\eta_1)\,,$$

it is easily proved that

$$1 > u_1 \geqq \mathcal{E}'^2(\eta_1) \geqq l_1 > 0\,,$$

where u_1 and l_1 are the upper and lower limit of $\mathcal{E}'^2(\eta)$. In the same manner, when we write

$$C_{u^2}(\eta) = \int_{\eta_{1,0}}^{\eta_{1,1}} P_1(\eta_1;\,\eta) f_1(\eta_1)\mathcal{E}'^2(\eta_1)d\eta_1 = f(\eta)\mathcal{E}_2{}^2(\eta)$$

where

$$
\begin{aligned}
f_1(\eta_1) &= a_3\int_{\xi_{1,0}(\eta_1)}^{\xi_{1,1}(\eta_1)} F_1'^2(\xi_1,\,\eta_1)d\xi_1 \\
f(\eta) &= \int_{\eta_{1,0}}^{\eta_{1,1}} P_1(\eta_1;\,\eta) f_1(\eta_1)d\eta_1\,, \qquad (5.2)
\end{aligned}
$$

such a relation

$$1 > u_1 > u_2 \geqq \mathcal{E}_2{}^2(\eta) \geqq l_2 > l_1 > 0 \qquad (5.3)$$

is derived. Namely, retaining the character (5.3) expressions of $\boldsymbol{u}$ and $\boldsymbol{v}$ can be transformed into

$$\boldsymbol{u}^2=f(\eta)\mathcal{E}_2{}^2(\eta)t^{-1}\ ,$$
$$\boldsymbol{v}^2=f(\eta)(l-\mathcal{E}_2{}^2(\eta))t^{-1}\ . \tag{5.4}$$

The functional form $P_1(\eta_1;\,\eta)$ does not change with the value of η as expressed in (2.1), and so the function $f(\eta)$ is seen by (5.2) to depend largely on that of $F_1'^2(\xi_1,\eta_1)$. But, it can be supposed by (5.3) that the value of $\mathcal{E}_2{}^2(\eta)$ does not change largely with η.

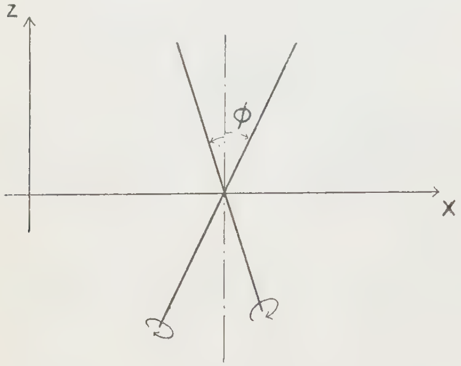

Fig. 5.

In the case of fully developed non-decaying turbulence the decaying term t^{-1} is integrated to be constant; (5.4) becomes (cf. (17.3) (II))

$$\boldsymbol{u}^2=\int_{-\infty}^{\xi} f_{\xi'}(\eta)\mathcal{E}^2{}_{\xi'}(\eta)t_{\xi'}^{-1}d\xi' \quad \text{etc.}$$

where (ξ,η) is the position of a fixed point in the field and the suffix ξ' indicates the position of production of vortices. They can be further transformed into

$$\boldsymbol{u}^2=f'(\eta)\mathcal{E}_2{}'^2(\eta)\ ,$$
$$\boldsymbol{v}^2=f'(\eta)(1-\mathcal{E}_2{}'^2(\eta))\ , \tag{5.4$'$}$$

where

$$f'(\eta)=\int_{-\infty}^{\xi} f_{\xi'}(\eta)t_{\xi'}^{-1}d\xi'\ . \tag{5.2$'$}$$

In this case, however, (5.3) comes to be more restricted as

$$1>u_1'>u_2'>u_3'\geqq\mathcal{E}_2{}'^2(\eta)\geqq l_3'>l_2'>l_1'>0\ . \tag{5.3$'$}$$

By (5.4) or (5.4′) we get

$$\boldsymbol{u}/\sqrt{\boldsymbol{u}^2+\boldsymbol{v}^2}=\mathcal{E}_2(\eta)\ . \tag{5.5}$$

Thus, by the above discussions it can be considered that in all sorts of shear turbulence (5.5) approaches a constant value across their flows. It is significant that in non-decaying turbulence it may take a value more close to a constant than in decaying shear turbulence.

As for u, v-correlation, it is also transformed form (5.1) into such an expression

$$\overline{\boldsymbol{uv}}=f(\eta)\mathcal{E}_1(\eta)\sqrt{1-\mathcal{E}_1{}^2(\eta)}t^{-1}\ , \tag{5.6}$$

where $f(\eta)$ is the same as given by (5.2), but different from $\mathcal{E}_2(\eta)$ the value of $\mathcal{E}_1(\eta)$ is restricted as

$$1>u_1>u_2\geqq\mathcal{E}_1(\eta)\geqq l_2>l_1>-1\ . \tag{5.7}$$

In non-decaying turbulence, (5.6) and (5.7) become

$$\overline{\boldsymbol{uv}}=f'(\eta)\mathcal{E}_1'(\eta)\sqrt{1-\mathcal{E}_1{}'^2(\eta)} \tag{5.6$'$}$$

and

$$1>u_1'>u_2'>u_3'\geqq\mathcal{E}_1'(\eta)\geqq l_3'>l_2'>l_1'>-1\ . \tag{5.7$'$}$$

Then the form of correlation coefficient becomes

$$\frac{\overline{\boldsymbol{uv}}}{\boldsymbol{uv}}=\frac{\mathcal{E}_1(\eta)\sqrt{1-\mathcal{E}_1{}^2(\eta)}}{\mathcal{E}_2(\eta)\sqrt{1-\mathcal{E}_2{}^2(\eta)}}\ , \tag{5.8}$$

The functional relation between $\mathcal{E}_1(\eta)$ and $\mathcal{E}_2(\eta)$ cannot be clarified unless exact evaluations of (5.2) and so forth are carried out. Nevertheless, it is seen by (5.8) that $\overline{\boldsymbol{uv}}/\boldsymbol{uv}$ may approach a constant value across shear turbulent flow, and it is also considered that such a tendency may be more conspicuous in non-decaying turbulence.

§ 6. Existence of *w*-fluctuation

By this time, our statistical studies on shear turbulence have been proceeded by taking two-dimensional vortex chaos motion for brevity. Many observations show, however, that a decaying or non-decaying shear turbulence has always w-component of velocity fluctuation even if its mean velocity distribution is two-dimentional.

We consider that when mean velocity field is two-dimensional in the x, y-plane, the vortex filaments of their chaotic motion are all parallel to the z, x-plane, but their directions are usually fluctuating about the z-direction with a symmetrical distribution function (cf. Fig. 5):

$$P_z(\phi)\ . \tag{6.1}$$

In the initial period of similarity, it is assumed, as mentioned in § 4 (II) referrring to the isotropic turbulence, that three-dimensional characters of vortex filaments—their elongation and culvature—can be neglected. Then, it is deduced that w-intensity is related quantitatively by (6.1) with $\boldsymbol{u}$-intensity, but owing to its symmetrical character there occurs no correlation between them. Our previous

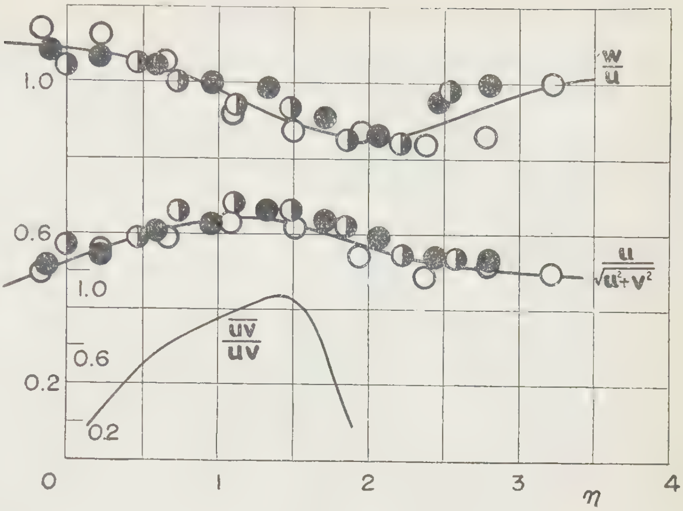

Fig. 6. Distributions of $u/\sqrt{u^2+v^2}$, w/u and $\overline{uv}/(uv)$ across the turbulent wake behind a circular cylinder. ○, ● and ◑ are evaluated values from Townsend's data at $x/d=91$, 180 and 725. η is defined by taking the half-width in mean velocity distributions and is measured from the centre of wake.

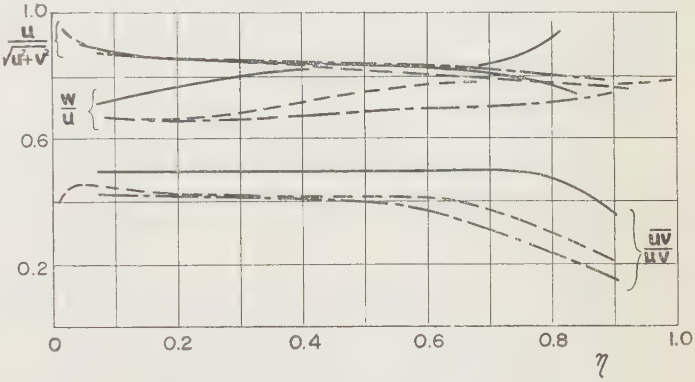

Fig. 7. Distributions of $u/\sqrt{u^2+v^2}$, w/u and $\overline{uv}/(uv)$ across non-decaying turbulent flows. The full lines, chain lines and broken lines represent experimental curves respectively in turbulent boundary layer along a flat plate, two-dimensional channel flow and pipe flow. η is defined using the thickness δ and the radii r.

studies of two-dimentional shear turbulence in Parts II and III have been made by taking (6.1) as the δ-function at $\phi=0$. When the functional form of $P_z(\phi)$ is taken to be similar in the whole field of flow, the functional relations in our previous studies still hold with somewhat different constant coefficients. In such a circumstance it is also derived that

$$w/u=\text{constant}. \qquad (6.2)$$

Depending upon the above discussion, the existence of w-intensity can be clarified. But it has no correlation with other velocity fluctuations and has little contribution to the mean velocity distribution. In the two-dimensional shear turbulence it is as yet essentially important to survey the interrelation between u- and v-fluctuation. By (6.2) it is also seen that (5.5) indicates the proportional character in

$$u/\sqrt{u^2+v^2+w^2} \quad \text{etc.}$$

§ 7. Comparison with Experimental Observation

As a typical decaying shear turbulence two-dimensional turbulent wake is taken up, where the distributions of (5.5), (6.2) and (5.8) are surveyed experimentally. According to Townsend's data[4)] behind a circular cylinder, the former two are seen to be roughly constant across the wake, which are shown in Fig. 6 evaluated from them. As for u, v-correlation coefficient, it is likely that it varies considerably as shown in the same figure. In the case of non-decaying turbulence, their distributions in turbulent boundary layer along a flat plate observed by Klevanoff[5)] and in two-dimensional channel flow by Laufer[6)] are shown in Fig. 7. For reference, Sandborn's data[7)] in pipe flow are compared. Theoretical results in previous sections are derived independently of the existence of pressure gradient along the x-direction. For instance, experimental results in turbulent boundary layer under a retarded main flow measured by Sandborn-Slogar[8)] and Schubauer-Klevanoff[9)] seem to support them favourably.

By the above comparisons our theoretical discussions may be verified. It is important that in non-decaying turbulence they are more supported than in decaying turbulence, as deduced in the theory.

C. Distortion of Isotropic Turbulence

§ 8. Velocity Distribution in a Deformed Vortex

It is known that the condition of isotropic turbulence cannot be adapted to an accelerated flow even if the value of shearing stress is zero[10]. As a physical foundation of the study in such a case of turbulence, deformation of vortex motion due to contracting or expanding stream has been taken. G.I. Taylor[11] studied the case of contracting stream by investigating characters of a flow pattern of regularly placed vortices. In order to retain the same regular flow pattern through contraction, the effect of contraction should be assumed to be very rapid. It is doubtful whether such an assumption may be adequate in a real turbulent state like a wind-tunnel contracting stream, and moreover by the study of this kind the value of $\overline{uv}$ cannot be proved to vanish. Recently G.K. Batchelor and I. Proudman[12] have refined this investigation by integrating over all the Fourier components. But the assumption of rapid distortion must be still retained and so the theoretical results are not supported by experimental verifications[13]. These studies correspond to treating of the state of B in Fig. 10 (I) which is considered in our study to be inappropriate as turbulent state.

In the case of our shearless turbulence, P is taken as constant in order to express the completely irregular arrangements of vortices in their chaotic states. Thus, if the mean vortex motion is given hydrodynamically in a non-uniform mean flow the states of turbulence can be determined. For brevity two-dimensional treatment will be given here. In the shearless turbulence, it is obvious that the condition of orthogonal trajectory holds between the mean stream and potential lines, and so from the Lagrangian point of view, some square part of fluid between two stream lines at $x=0$ takes a rectangular form at x if the effects of $d\bar{U}(x)/dx$ are neglected near these points. For the same reason, it may be said that every circular stream line of a vortex at $x=0$ changes uniformly into an ellipse at x. The effects of deformation on the velocity distribution will be estimated by neglecting viscosity as follows.

In the theory of potential flow in the Eulerian manner, it is well-known by the transformation $\zeta_1=\zeta+a^2/\zeta$ that the complex potential of a circular vortex $w(\zeta)=\dfrac{i\Gamma}{2\pi}\log\zeta$ with velocity components $\dfrac{d\xi}{dt}=\dfrac{\Gamma}{2\pi}\dfrac{\sin\theta}{r}$ and $\dfrac{d\eta}{dt}=\dfrac{-\Gamma}{2\pi}\dfrac{\cos\theta}{r}$ in the ζ-plane, becomes an allipse $\xi_1{}^2/(r+a^2/r)^2+\eta_1{}^2/(r-a^2/r)^2=1$ with

$$\frac{d\xi_1}{dt}=\frac{\Gamma}{2\pi}\frac{\sin\theta}{r}\frac{r^2(r^2+a^2)}{r^4+a^4-2r^2a^2\cos 2\theta}$$

and

$$\frac{d\eta_1}{dt}=\frac{-\Gamma}{2\pi}\frac{\cos\theta}{r}\frac{r^2(r^2-a^2)}{r^4+a^4-2r^2a^2\cos 2\theta}$$

in the ζ_1-plane. When λ^2 is taken as the ratio of two axes of deformation in the field of shearless turbulence, we have, by the condition of continuity,

$$\bar{U}(x)/\bar{U}_0=\lambda\ , \tag{8.1}$$

and the above elliptic form is determined by the condition

$$\frac{(r/a)^2+1}{(r/a)^2-1}=\lambda^2\ . \tag{8.2}$$

Then the velocity components expressed in the ζ-plane become those in the ζ_1-plane. But, observation of this field of flow will show that only one coordinate-system is required. When the unit of length in the ζ_1-plane is adjusted to that in the ζ-plane, the velocity components of circular and deformed vortices are expressed as follows;

$$u_0=\frac{\Gamma}{2\pi}\frac{\sin\theta}{r}\qquad v_0=\frac{-\Gamma}{2\pi}\frac{\cos\theta}{r}\ , \tag{8.3}$$

and

$$\begin{aligned} u_x&=\frac{\Gamma}{2\pi}\frac{\sin\theta}{r}\frac{r^4}{r^4+a^4-2r^2a^2\cos 2\theta}\ ,\\ v_x&=\frac{-\Gamma}{2\pi}\frac{\cos\theta}{r}\frac{r^4}{r^4+a^4-2r^2a^2\cos 2\theta}\ . \end{aligned} \tag{8.4}$$

It has been found that the vortex motion of $\alpha=1$ in the initial period has a character to tend to that of the potential flow as increasing distance from the centre. In this evaluation, let the velocity distribution of a deformed vortex of $\alpha=1$ expressed as

$$\begin{aligned} V_{*x}&=F_1(s)G_1(t)h(\theta,\lambda)\ ,\\ h(\theta,\lambda)&=r^4/(r^4+a^4-2r^2a^2\cos 2\theta), \end{aligned} \tag{8.5}$$

where the functional forms of $F_1(s)$ and $G_1(t)$ are the same as those in § 9 (I).

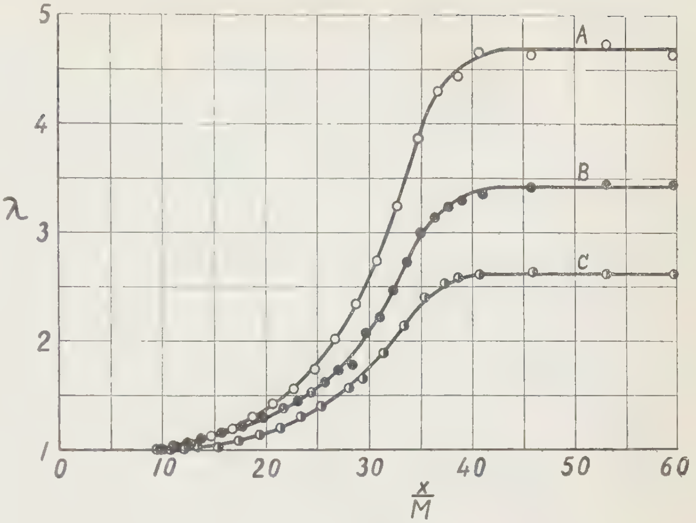

Fig. 8. Experimental curves of mean velocity distributions. M is the mesh length.

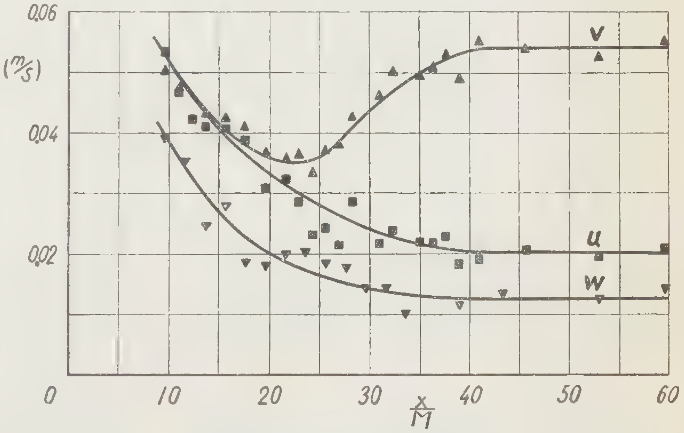

Fig. 9. Distribution of u-, v- and w-intensity of B-series.

§ 9. Deviation from the Isotropic Turbulence

It is shown that in the shearless turbulence $\overline{uv}=0$ but the u- and v-intensities are not necessarily equal to each other. In the initial period turbulent intensities are written as

$$u^2=(1/S)\iint_D F_1^2(s)G_1^2(t)\times h^2(\theta,\lambda)\sin^2\theta dS\,,\qquad(9.1)$$
$$v^2=(1/S)\iint_D F_1^2(s)G_1^2(t)\times h^2(\theta,\lambda)\cos^2\theta dS\,.$$

In this coordinate-system (r,θ), θ is elected to be equal to the angle between $\overline{V}_*$ and the y_1-axis in D-domain. As D-domain we take the following ellipse

$$\xi_0=r_0(1+a^2/r_0^2)\cos\theta\,,$$
$$\eta_0=r_0(1-a^2/r_0^2)\sin\theta\,,$$

where

$$\xi_0\eta_0=R^2\pi\,,\quad R^2/(4\nu t)=s_0\,,\quad(9.2)$$

(cf. (4.1) (II)). (9.1) has the two conditions of hydrodynamical and statistical similarity, and then the similarity law for the isotropic turbulence can be extended into this general case of shearless turbulence.

In § 8 the factor $h(\theta,\lambda)$ has been derived with neglect of the variation of $a(\lambda, r)$ and so in the above evaluation it will be as well neglected. Then

$$dS=\{(r^4+a^4-2r^2a^2\cos 2\theta)/r^4\}drrd\theta\,,$$

and so by taking (8.2) and (9.2) we have

$$\boldsymbol{u}^2=\{(c^2\nu)/(2s_0)\}\{(\lambda^2+1)/(2\lambda^2)\}\times\int_0^{((\lambda^2+1)^2/4\lambda^2)s_0}F_1^2(s)dst^{-1}\,,\qquad(9.3)$$
$$\boldsymbol{v}^2=\{(c^2\nu)/(2s_0)\}\{(\lambda^2+1)/2\}\times\int_0^{((\lambda^2+1)^2/4\lambda^2)s_0}F_1^2(s)dst^{-1}\,.$$

Namely, we get the following relation between mean velocity distribution and intensity of turbulence as

$$\boldsymbol{v}/\boldsymbol{u}=\overline{U}(x)/\overline{U}_0\,.\qquad(9.4)$$

(9.4) is one result of the generalized similarity law in the initial period in the case of non-uniform shearless turbulence.

To check (9.4) experimentally, we made a two-dimensional contracting stream behind a comb-like grid and measured u- and v-intensity along the centre line. Three series of measurements were made, and these velocity distributions are shown in Fig. 8 with marks A, B and C. To survey two-dimensionality in velocity fluctuations, an example of measurements of the three components of B-series is given in Fig. 9. Then the relation of $\boldsymbol{v}/\boldsymbol{u}$ and $\overline{U}(x)/\overline{U}_0$ was investigated. The whole results are shown in Fig. 10.

If three-dimensional discussions are made by introducing (6.1), the above theoretical result will be more improved to interpret the

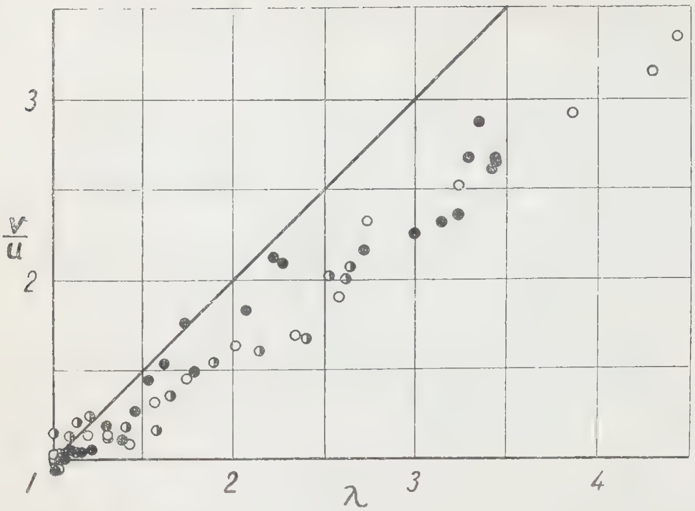

Fig. 10. Distribution of $\boldsymbol{v}/\boldsymbol{u}$ against $\overline{U}(x)/\overline{U}_0$. ○, ● and ◑ are the observed values respectively in A-, B- and C-series.

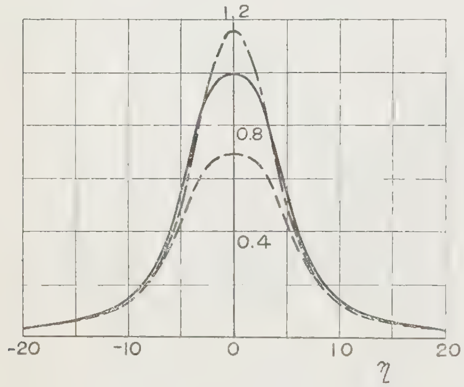

Fig. 11. Theoretical curves of relative distributions of $C_{u^2}(\eta)$ (full line), $C_{v^2}(\eta)$ (chain line) and $C_{\overline{uv}}(\eta)$ (broken line) across symmetrical shear turbulence.

experimental results. But, these observations will make it clear that the isotropic turbulence changes its state in a non-uniform flow, and the above theoretical discussions show, though approximately, the true aspects of a general shearless turbulent flow.

D. Symmetrical Shear Turbulence

§ 10. Distribution of Turbulent Intensities

As a simple decaying shear turbulence the following vortex chaos motion will be considered in which the vortices of $\alpha=1$ are produced at one point in the field of flow and carried in a not completely irregular arrangement. By the functional form of P expressed as (2.1), the state of flow in this case can be considered to be symmetrical across the x-axis. Even in this simplified vortex chaos motion an essential character of shear turbulence may be described. Approximately it corresponds to the half jet or free mixing flow. To determine the Reynolds-stress distribution across the mean flow, the functional form of $F_1'^2(\xi_1, \eta_1)$ in D-domain becomes very important as mentioned in § 5. Because of the difficulty of its theoretical derivation, however, the following rough evaluation will be made using the result in § 8.

In such a shear turbulence, a circular vortex motion is distorted by the difference of mean velocities in two main flows of upper and lower part. But, being different from the case of non-uniform shearless turbulence, this distortion is considered to be occurred obliquely in D-domain. In the initial period of our similarity law, their mean velocity function $\overline{V}_*=F_1'(\xi_1, \eta_1)G_1(t)$ is taken to be similar. As one example we take the case where mean circular vortex is change into elliptic form along the $\xi_1=\eta_1$ line in D-domain with a distortion ratio λ^2 of 2. Then, the function $F_1'(\xi_1, \eta_1)$ can be determined by (8.5). As the D-domain we take the range along $\xi_1=\eta_1$ line from $-\infty$ to ∞ with the breadth 2 in ξ_1, η_1-coordinate-system. In the Gaussian form of P-fuction introduced by (2.1), the non-dimensional parameter σ is taken here as 3 referring to experimental observations in § 4. Under the above circumstances the function $C_{u^2}(\eta)$ etc. in (5.1) can be evaluated completely excepting one parameter which concerns the initial condition of $\alpha=1$ vortex motion.

Through numerical calculations their relative curves were obtained. They are shown in Fig. 11. These results belong to only one example of calculation and have little theoretical meaning. But, it is deduced by inspecting also other measurements[14] that the above treatment based upon the initial-period similarity-law can interpret fundamental mechanism of shear turbulent flow.

§ 11. Mean Velocity Distribution

To determine mean velocity distribution across the shear turbulence the Reynolds equations become important. In this case of symmetrical shear turbulence, the mean stream function is written as

$$\psi = xF(\eta)\,,\quad \eta = y/x\,, \quad (11.1)$$

and the Reynolds equations are transformed into

$$F(\eta)\frac{d^2F(\eta)}{d\eta^2} = a_4\frac{dC_{\overline{uv}}(\eta)}{d\eta}\,, \quad (11.2)$$

where a_4 is a constant. When the curve of $C_{\overline{uv}}(\eta)$ given in § 10 is used, we can easily determine the function $\overline{U}(\eta)$ $(=F'(\eta))$ by integrating it.

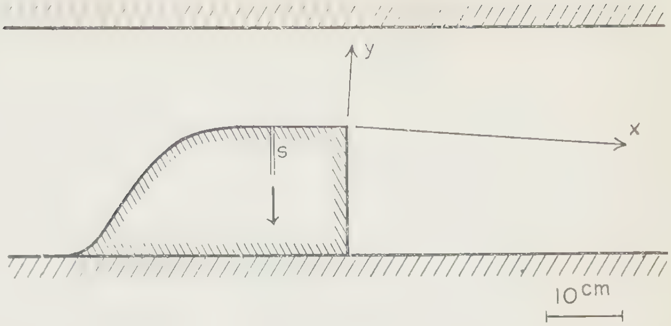

Fig. 12. Schematic diagram of experimental equipment to produce a free mixing turbulence. It was made in a rectangular test-section in a wind tunnel. S is a slit to suck the upward boundary layer.

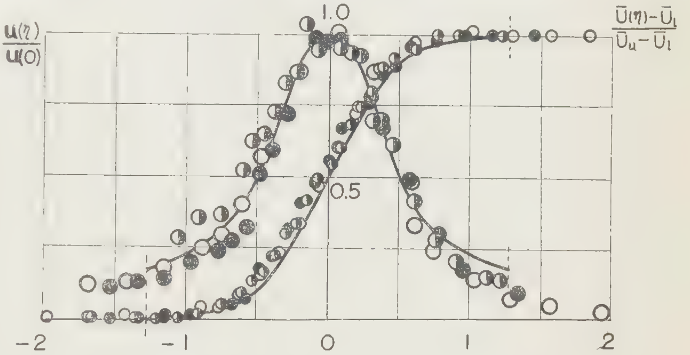

Fig. 13. Distribution of mean velocity (small marks) and u-intensity across the free mixing turbulent flow. $\overline{U}_u$ and $\overline{U}_l$ are mean velocities at upper and lower main flow. ○, ● and ◑ are observed values at $x=25.0$, 40.9 and 56.7 cm along the x-axis. The undisturbed velocity above the slit S was 18.7 m/s with u-intensity of 0.03 per cent. The curves are our theoretical results.

To examine these results experimentally, we made a free mixing stream by such an equipment as shown in Fig. 12. Distributions of mean velocity and u-intensity were measured at three sections along the x-axis. They are shown in Fig. 13, where η is defined in their mean velocity curves and it corresponds to (11.1) when the apparent origin coordinates is taken. In this figure, theoretical distribution of u-intensity given in Fig. 11 is drawn by adjusting the value of η, and the corresponding curve of $\overline{U}(\eta)$ is also inserted.

It is well known that such as exerimental curve of mean velocity distribution as above can be well predicted by transfer theory. It is proper by seeing the discussions in § 13 (II), that it does not differ largely from our result based upon the initial-period similarity-law. For the purpose of determining only mean velocity distribution, transfer theory is very useful even if it is powerless for the Reynolds-stress distribution. While, our statistical theory of turbulence has an important meaning in the point that it can include their theoretical foundations in our special case.

References

1) A. A. Townsend: Australian Journ. Sci. Res. A **2** (1949) 451.
2) S. Corrsin and A. L. Kistler: N.A.C.A. Tech. Note 3133 (1954).
3) Prandtl-Tietjens: Hydro- und Aeromechanik II (1931) Tafel 16.
4) A. A. Townsend: Proc. Roy. Soc. A **190** (1947) 551.
5) P. S. Klevanoff: N.A.C.A. Tech. Note 3178 (1954).
6) J. Laufer: N.A.C.A. Tech. Note 2133 (1950).
7) V. A. Sandborn: N.A.C.A. Tech. Note 3266 (1955).
8) V. A. Sandborn and R. J. Slogar: N.A.C.A. Tech. Note 3264 (1955).
9) G. B. Schubauer and P. S. Klevanoff: N.A.C.A. Tech. Note 2133 (1950).
10) S. Goldstein: Modern Developments in Fluid Dynamics (1938) § **78**.
11) G. I. Taylor: Z.A.M.M. **15** (1935) 91.
12) G. K. Batchelor and I. Proudman: Q.J.M.M. **7** (1954) 83.
13) A. A. Townsend: Q.J.M.M. **7** (1954) 104.
14) H. W. Liepmann and J. Laufer: N.A.C.A. Tech. Note 1257 (1947).
15) S. Goldstein: Modern Developments in Fluid Dynamics (1938) § **255**.

JOURNAL OF THE PHYSICAL SOCIETY OF JAPAN Vol. 10, No. 12, DECEMBER, 1955

The Application of Meksyn-Imai's Method to the Subsonic Flow past an Axisymmetric Body

By Ken-ichi KUSUKAWA

Department of Physics, Faculty of Science, Tokyo Metropolitan University

(Read November 2, 1954. Received August 15, 1955)

For the axisymmetric subsonic flow of a compressible fluid we shall develop an analogous procedure to Meksyn-Imai's method, which was offered for the two-dimensional irratational flow of a compressible fluid. And then it will be proved that the final results obtained in the two-dimensional case can also be immediately used in the present three-dimensional case.

Namely, the ratio of the velocity of a compressible fluid past an obstacle to that of an incompressible fluid past the same obstacle, denoted by (q/q_0), can be given by solving the following algebraic equation of fifth degree:

$$(q/q_0)=1+M_1^2(q/q_0)^3\left\{1-\frac{\gamma-1}{2}M_1^2\right\}K(\alpha,\beta)+M_1^4(q/q_0)^5L(\alpha,\beta)\,,$$

where M_1 and γ are respectively the Mach number of the main flow and the ratio of the specific heats, and K and L are functions determined merely by the form of the obstacle.

Also K and L can be related with the coefficients of the series of the M^2-expansion method as follows:

$$K=Q_1/q_0\,,$$

$$L=(Q_2/q_0)+\frac{\gamma-1}{2}(Q_1/q_0)-3(Q_1/q_0)^2\,,$$

where $$q=q_0+M_1^2Q_1+M_1^4Q_2+\cdots\,.$$

As an example the flow past a sphere is discussed.

§ 1. Introduction

The subsonic flow of a compressible fluid past an axisymmetric body, if it is very slender, can be easily dealt with by the linear theory, due originally to Prandtl[1] and Glauert[2]. However, this method does not give a good approximation for the flow past a moderately thick body. On the other hand, by using the successive approximations of the M^2-expansion method, due originally to Janzen[3] and Rayleigh[4], we can, in principle, approach the exact solution as closely as we want. In fact, this method is successfully used in the case of such low Mach numbers that even the first approximation can give a good result, but it is very laborious to obtain a good approximation in the case of high Mach numbers where we need to take many terms of M^2-expansion because of the convergence of the series becoming very slow.

Recently Meksyn[5] offered a new interesting method for dealing with the two-dimensional irrotational flow of a compressible fluid, which seems to be applicable to the flow past a thick obstacle for higher Mach numbers.

In Meksyn's paper, the fundamental equation for determining the velocity potential ϕ of a compressible fluid flow is reduced to the from:

$$\frac{\partial^2\phi}{\partial\alpha^2}+\frac{\partial^2\phi}{\partial\beta^2}=\frac{U_1^2}{2c^2}\left\{\frac{\partial\phi}{\partial\alpha}\frac{\partial q^2}{\partial\alpha}+\frac{\partial\phi}{\partial\beta}\frac{\partial q^2}{\partial\beta}\right\}, \tag{1.1}$$

where α and β are the velocity potential and the stream function of the corresponding incompressible flow respectively, U_1 is the velocity of the main flow, c is the local velocity of sound, and U_1q is the magnitude of local velocity of flow.

Remembering the term containing $\partial\phi/\partial\beta$ to be negligible in comparison with the term containing $\partial\phi/\partial\alpha$, and $\partial\phi/\partial\alpha$ to be a very slowly varying function, integration of (1.1) yields

$$\frac{q}{q_0}=1+M_1^2\left(\frac{q}{q_0}\right)^3\left\{1-\frac{\gamma-1}{2}M_1^2\right\}\cdot K(\alpha,\beta)+M_1^4\left(\frac{q}{q_0}\right)^5L(\alpha,\beta)\,, \tag{1.2}$$

where $U_1 q_0$ is the magnitude of local velocity of the corresponding incompressible fluid flow, M_1 is the Much number of the main flow, γ is the ratio of the specific heats, and $K(\alpha, \beta)$ and $L(\alpha, \beta)$ are functions determined merely by the form of an obstacle. It is remarked here that the functions $P(\alpha, \beta)$ and $Q(\alpha, \beta)$ in Meksyn's original paper are equivalent to our $8K(\alpha, \beta)$ and $32L(\alpha, \beta)$ respectively.

Imai[6] proved that K and L can be expressed by coefficients of the solution correct to the second approximation as obtained by the M^2-expansion method. Thus,

$$K(\alpha, \beta)=\frac{Q_1}{q_0},$$

$$L(\alpha, \beta)=\frac{Q_2}{q_0}+\frac{\gamma-1}{2}\left(\frac{Q_1}{q_0}\right)-3\left(\frac{Q_1}{q_0}\right)^2, \quad (1.3)$$

where $q=q_0+M_1^2 Q_1+M_1^4 Q_2+\cdots$.

By the use of (1.2) and (1.3), we can immediately obtain Meksyn's solution, provided the second approximation of the M^2-expansion method is known.

The order of approximation used in Meksyn-Imai's method is, in principle, quite the same as that of the second approximation of the M^2-expansion method. But, because of retaining the character of singularity at the point where the velocity is equal to the local velocity of sound, the result obtained by this method seems to be applicable even to the case of moderately high Mach numbers.

In this paper, we shall develop an analogous procedure for the axisymmetric subsonic flow, and it will be proved that the relations expressed by (1.2) and (1.3) can also be immediately used in the present three-dimensional case.

§ 2. Fundamental Equations

We shall take the cylindricel coordinates O-xy, where the x-axis is taken along the axis of revolution of the body, and y denotes the distanace from the axis. If we denote the velocity components along the x- and y-directions by u, v, and the density of the fluid by ρ, the axisymmetric irrotational flow of a compressible inviscid fluid is governed by the equations:

$$\frac{\partial}{\partial x}(\rho y u)+\frac{\partial}{\partial y}(\rho y v)=0, \quad (2.1)$$

$$\frac{\partial v}{\partial x}-\frac{\partial u}{\partial y}=0. \quad (2.2)$$

We now introduce the velocity potential ϕ satisfying (2.2) such that

$$\frac{\partial \phi}{\partial x}=\frac{u}{U_1}, \quad \frac{\partial \phi}{\partial y}=\frac{v}{U_1}, \quad (2.3)$$

where U_1 is the velocity of the main flow.

On the other hand, in the case of incompressible fluid flow, the velocity potential α and Stokes's stream function β can be introduced respectively such that

$$\frac{\partial \alpha}{\partial x}=\frac{u_0}{U_1}, \quad \frac{\partial \alpha}{\partial y}=\frac{v_0}{U_1}, \quad (2.4)$$

$$\frac{\partial \beta}{\partial y}=y\frac{u_0}{U_1}, \quad \frac{\partial \beta}{\partial x}=-y\frac{v_0}{U_1}, \quad (2.5)$$

It is of great importance to remark here that an obstacle being given, α and β can be determined as functions of variables x and y, and they are independent of the magnitude of the velocity of the main flow U_1.

For the purpose of obtaining the flow pattern of a compressible fluid flow past an obstacle, we shall start with obtaining the velocity potential α and Stokes's stream function β of an incompressible fluid flow past the same obstacle. Next, taking α and β instead of x and y as independent variables, we can obtain, from (2.1), (2.3), (2.4) and (2.5), the differential equation for determining the velocity potential:

$$\frac{\partial^2 \phi}{\partial \alpha^2}+y^2(\alpha, \beta)\frac{\partial^2 \phi}{\partial \beta^2}+\frac{1}{\rho}\frac{\partial \rho}{\partial \alpha}\frac{\partial \phi}{\partial \alpha}$$
$$+\frac{1}{\rho}\left(y\frac{\partial \rho}{\partial \beta}\right)\left(y\frac{\partial \phi}{\partial \beta}\right)+\frac{2u_0}{q_0^2}\left(\frac{\partial \phi}{\partial \beta}\right)=0, \quad (2.6)$$

with boundary conditions such that

$$\left.\begin{array}{l} \dfrac{\partial \phi}{\partial \beta}=0 \quad \text{on the surface} \\ \quad \text{of the obstacle (say } \beta=0\text{)}, \\ \dfrac{\partial \phi}{\partial \alpha}=1, \quad \dfrac{\partial \phi}{\partial \beta}=0, \text{ at infinity.} \end{array}\right\} \quad (2.7)$$

In Eq. (2.6), y is a definite function of independent variables α and β, which is obtained by solving the equations $\alpha=\alpha(x, y)$ and $\beta=\beta(x, y)$.

Remembering that for the undisturbed flow α and β are equal to x and $y^2/2$ respectively, $\partial\rho/\partial\alpha$ is of the same order of $y\partial\rho/\partial\beta$. And it is proved that $y\partial\phi/\partial\beta$ may be disregarded in comparison with $\partial\phi/\partial\alpha$ because of the following considerations:

(i) Both at infinity and on the surface of the obstacle, $y\partial\phi/\partial\beta$ vanishes.

(ii) Even at a distance from the obstacle, the difference between the slopes of stream lines in compressible and incompressible fluid flows is very small.

On the other hand, at the stagnation points ϕ becomes equal to α, and then $\partial\phi/\partial\beta$ vanishes. Therefore, in Eq. (2.6) the terms $\frac{2u_0}{q_0^2}\left(\frac{\partial\phi}{\partial\beta}\right)$ and $\frac{1}{\rho}\left(y\frac{\partial\rho}{\partial\beta}\right)\left(y\frac{\partial\phi}{\partial\beta}\right)$ can be neglected in comparison with the term

$$\frac{1}{\rho}\frac{\partial\rho}{\partial\alpha}\frac{\partial\phi}{\partial\alpha}\,.$$

Thus, finally Eq. (2.6) can be approximated very closely to

$$\frac{\partial^2\phi}{\partial\alpha^2}+y^2(\alpha,\beta)\frac{\partial^2\phi}{\partial\beta^2}+\frac{1}{\rho}\frac{\partial\rho}{\partial\alpha}\frac{\partial\phi}{\partial\alpha}=0\,. \tag{2.8}$$

Then, using Bernoulli's theorem:

$$\frac{c^2}{\rho}d\rho+\frac{1}{2}d(U_1q)^2=0\,, \tag{2.9}$$

where $c=(dp/d\rho)^{1/2}$ is the local speed of sound, and U_1q is the magnitude of local flow velocity, we obtain, from (2.8), the following equation:

$$\left.\begin{aligned}&\frac{\partial^2\phi}{\partial\alpha^2}+y^2(\alpha,\beta)\frac{\partial^2\phi}{\partial\beta^2}=\frac{U_1^2}{2c^2}\frac{\partial q^2}{\partial\alpha}\frac{\partial\phi}{\partial\alpha}\,,\\&c^2=c_2-\frac{\gamma-1}{2}(q^2-1)U_1^2\,,\end{aligned}\right\} \tag{2.10}$$

where c_1 is the velocity of sound in the main flow.

On the other hand, from (2.3), (2.4), and (2.5), we obtain

$$u=\frac{\partial\alpha}{\partial x}\frac{\partial\phi}{\partial\alpha}+\frac{\partial\beta}{\partial x}\frac{\partial\phi}{\partial\beta}=u_0\frac{\partial\phi}{\partial\alpha}-yv_0\frac{\partial\phi}{\partial\beta}\,,$$

$$v=\frac{\partial\alpha}{\partial y}\frac{\partial\phi}{\partial\alpha}+\frac{\partial\beta}{\partial y}\frac{\partial\phi}{\partial\beta}=v_0\frac{\partial\phi}{\partial\alpha}+yu_0\frac{\partial\phi}{\partial\beta}\,,$$

and therefore

$$U_1^2q^2=U_1^2q_0^2\left\{\left(\frac{\partial\phi}{\partial\alpha}\right)^2+y^2\left(\frac{\partial\phi}{\partial\beta}\right)^2\right\}\,, \tag{2.11}$$

where U_1q_0 is the magnitude of local flow velocity in the corresponding incompressible fluid flow.

Remembering $y\partial\phi/\partial\beta$ to be negligible in comparison with $\partial\phi/\partial\alpha$, Eq. (2.11) can be closely approximated to

$$q=q_0\left(\frac{\partial\phi}{\partial\alpha}\right)\,. \tag{2.12}$$

By the use of (2.12), Eq (2.10) becomes

$$\frac{\partial^2\phi}{\partial\alpha^2}+y^2(\alpha,\beta)\frac{\partial^2\phi}{\partial\beta^2}=\frac{M_1^2}{2}\left(\frac{\partial\phi}{\partial\alpha}\right)^3\frac{\partial q_0^2}{\partial\alpha}$$

$$+M_1^2\left(\frac{\partial\phi}{\partial\alpha}\right)^2q_0^2\frac{\partial^2\phi}{\partial\alpha^2}$$

$$+\frac{\gamma-1}{2}(q^2-1)M_1^2\left\{\frac{\partial^2\phi}{\partial\alpha^2}+y^2(\alpha,\beta)\frac{\partial^2\phi}{\partial\beta^2}\right\}\,, \tag{2.13}$$

where M_1 is the Mach number for the main flow.

It is of great interest to note that if the function $y(\alpha,\beta)$ is taken to be identically equal to unity, Eq. (2.13) degenerates formally to the equation for two-dimensional subsonic flow as introduced by Meksyn.

§ 3. Integration of Eq. (2.13)

Following the procedure for two-dimensional flow as developed by Meksyn, we shall solve Eq. (2.13) by succesive approximations starting from the incompressible solution. Since for incompressible flow $\partial\phi/\partial\alpha$ is constant, all terms on the right-hand side of (2.13) except the first vanish to the first approximation, whence denoting the function ϕ by ϕ_1 in this approximation, we obtain

$$\frac{\partial^2\phi_1}{\partial\alpha^2}+y^2(\alpha,\beta)\frac{\partial^2\phi_1}{\partial\beta^2}=\frac{M_1^2}{2}\left(\frac{\partial\phi_1}{\partial\alpha}\right)^3\frac{\partial q_0^2}{\partial\alpha}\,. \tag{3.1}$$

The function ϕ_1 must satisfy the conditions on the solid boundary and at infinity such that

$$\left.\begin{aligned}&\frac{\partial\phi_1}{\partial\beta}=0 \quad \text{on the surface of the obstacle (say } \beta=0)\\&\frac{\partial\phi_1}{\partial\alpha}=1\,,\quad \frac{\partial\phi_1}{\partial\beta}=0 \quad \text{at infinity.}\end{aligned}\right\} \qquad (3.2$$

We now make the assumption that for compressible flow $\partial\phi/\partial\alpha$ is a slowly varying function in comparison with $\partial q_0^2/\partial\alpha$, and that it can be treated as constant in the integration as well as in the differentiation. Thus setting

$$\phi_1=\alpha+\kappa(\alpha,\beta)M_1^2\left(\frac{\partial\phi_1}{\partial\alpha}\right)^3 \qquad (3.3$$

where $\kappa(\alpha,\beta)$ is a new dependent variable Eq.(3.1) and the boundary conditions (3.2 become respectively

$$\frac{\partial^2\kappa}{\partial\alpha^2}+y^2(\alpha,\beta)\frac{\partial^2\kappa}{\partial\beta^2}=\frac{1}{2}\frac{\partial q_0^2}{\partial\alpha}\,, \qquad (3.4$$

and

$$\left.\begin{aligned}&\frac{\partial\kappa}{\partial\beta}=0 && \text{at } \beta=0\,,\\ &\frac{\partial\kappa}{\partial\alpha}=0\,,\quad \frac{\partial\kappa}{\partial\beta}=0 && \text{at infinity.}\end{aligned}\right\}\tag{3.5}$$

The function κ may be obtained by adding a certain particular solution of (3.4) to an appropriate solution of the corresponding homogeneous differential equation such that

$$\frac{\partial^2\psi}{\partial\alpha^2}+y^2(\alpha,\beta)\frac{\partial^2\psi}{\partial\beta^2}=0\,.\tag{3.6}$$

Because of $y^2\geqq 0$, Eq. (3.6) is a differential equation of elliptic type. Thus, the above-mentioned problem is one of the well-known Neumann's problems, and the existence and the uniqueness of solution have already been assured by E. E. Levi, G. Giraud etc..

Remembering y^2 and $(1/2)(\partial q_0^2/\partial\alpha)$ to be determined merely by the form of the obstacle, the function κ is also determined by the form of the obstacle, the function κ is also determined by the form of the obstacle, independently of the Mach number M_1.

We now proceed to the second approximation. Differentiating (3.3) by α, we obtain

$$\frac{\partial\phi_1}{\partial\alpha}=1+K(\alpha,\beta)M_1^2\left(\frac{\partial\phi_1}{\partial\alpha}\right)^3,\tag{3.7}$$

where $K=\dfrac{\partial\kappa}{\partial\alpha}$.

Substituting (3.7) into the terms on the right-hand side of (2.13), we obtain

$$\frac{\partial^2\phi}{\partial\alpha^2}+y^2\frac{\partial^2\phi}{\partial\beta^2}=M_1^2\left(\frac{\partial\phi}{\partial\alpha}\right)^3\left\{1-\frac{\gamma-1}{2}M_1^2\right\}\left(\frac{1}{2}\frac{\partial q_0^2}{\partial\alpha}\right)+M_1^4\left(\frac{\partial\phi}{\partial\alpha}\right)^5 q_0^2\left\{\frac{\partial K}{\partial\alpha}+\frac{\gamma-1}{4}\frac{\partial q_0^2}{\partial\alpha}\right\},\tag{3.8}$$

where ϕ donotes now the second approximation.

The boundary conditions which ϕ has to satisfy, are

$$\left.\begin{aligned}&\frac{\partial\phi}{\partial\beta}=0 && \text{at } \beta=0\\ &\frac{\partial\phi}{\partial\alpha}=1\,,\quad \frac{\partial\phi}{\partial\beta}=0 && \text{at infinity.}\end{aligned}\right\}\tag{3.9}$$

Consequently the function ϕ may be expressed in the form:

$$\phi=\alpha+M_1^2\left(\frac{\partial\phi}{\partial\alpha}\right)^3\left\{1-\frac{\gamma-1}{2}M_1^2\right\}\kappa(\alpha,\beta)+M_1^4\left(\frac{\partial\phi}{\partial\alpha}\right)^5\lambda(\alpha,\beta)\,,\tag{3.10}$$

where the function κ is determined by (3.4) and (3.5), and λ is a function to be determined by the following differential equation:

$$\frac{\partial^2\lambda}{\partial\alpha^2}+y^2\frac{\partial^2\lambda}{\partial\beta^2}=q_0^2\left\{\frac{\partial K}{\partial\alpha}+\frac{\gamma-1}{4}\frac{\partial q_0^2}{\partial\alpha}\right\},\tag{3.11}$$

subject to the boundary conditions:

$$\left.\begin{aligned}&\frac{\partial\lambda}{\partial\beta}=0 && \text{at } \beta=0\,,\\ &\frac{\partial\lambda}{\partial\alpha}=0\,,\quad \frac{\partial\lambda}{\partial\beta}=0 && \text{at infinity.}\end{aligned}\right\}\tag{3.12}$$

Since the quantities on the right-hand side of (3.11) are determined merely by the form of the obstacle, the function λ can also be determined merely by the form of the obstacle as well as κ.

Differentiating (3.10) with respect to α, we obtain

$$\frac{\partial\phi}{\partial\alpha}=1+M_1^2\left(\frac{\partial\phi}{\partial\alpha}\right)^3\left\{1-\frac{\gamma-1}{2}M_1^2\right\}K(\alpha,\beta)+M_1^4\left(\frac{\partial\phi}{\partial\alpha}\right)^5 L(\alpha,\beta)\,,\tag{3.13}$$

where $K=\dfrac{\partial\kappa}{\partial\alpha}$, and $L=\dfrac{\partial\lambda}{\partial\alpha}$.

Combining (3.13) and (2.12), we obtain

$$\frac{q}{q_0}=1+M_1^2\left(\frac{q}{q_0}\right)^3\left\{1-\frac{\gamma-1}{2}M_1^2\right\}K(\alpha,\beta)+M_1^4\left(\frac{q}{q_0}\right)^5 L(\alpha,\beta)\,.\tag{3.14}$$

This final result has the same form as the equation expressed by (1.2), for the two-dimensional flow.

Following the procedure for two-dimensional flow as developed by Imai, K and L in Eq. (3.14) may be expressed by the coefficients of the solution obtained by the M^2-expansion method. By the use of the M^2-expansion method, the velocity q can be expanded into the M^2-power-series as:

$$q=q_0+M_1^2Q_1+M_1^4Q_2+\cdots , \qquad (3.15)$$

where q_0, Q_1, Q_2 etc. are functions dependent merely on the form of the obstacle.

Comparing the coefficients of M_1^2, M_1^4 etc. in both series given by (3.14) and (3.15), we can obtain

$$K=\frac{Q_1}{q_0},$$

$$L=\frac{Q_2}{q_0}+\frac{\gamma-1}{2}\left(\frac{Q_1}{q_0}\right)-3\left(\frac{Q_1}{q_0}\right)^2, \qquad (3.16)$$

which are the same as the relations for two-dimensional case.

§4. Numerical Example

For the purpose of obtaining the functions K and L from (3.16), we need to know the second approximation of the M^2-expansion method. For an axisymmetric flow, the flow past a sphere[7] seems to be only one case, for which the second approximation of the M^2-expansion method has hitherto been obtained. Thus for the flow past a sphere, we can immediately obtain K and L from Q_1 and Q_2, and therefore the velocity q from Eq. (3.14).

We have calculated the values of the ratio of the maximum velocity occurring at the end of a radius perpendicular to the main flow, by taking γ to be 1.4. The values thus calculated for $M=0.4$ and 0.5 are given in Table I, where are also shown for comparison the corresponding values obtained by the first and the second approximations of the M^2-expansion method. The values obtained by the present method seems to be very reasonable.

Table I.

Mach number	Incompressible flow	$O(M^2)$	$O(M^4)$	Present method
0.4	1.5000	1.5501	1.5592	1.5617
0.5	1.5000	1.5782	1.6005	1.6122

The writer wishes to express his heartiest gratitude to Professor I. Imai for his many useful suggestions and kind advice.

References

1) L. Prandtl: *Handbuch der Physik*, Band VII (1927) 340.
2) H. Glauert: Proc. Roy. Soc. **A118** (1927) 113.
3) O. Janzen: Phys. Zeits. **14** (1913) 639.
4) Lord Rayleigh: Phil. Mag. **32** (1916) 1.
5) D. Meksyn: Proc. Roy. Soc. **A220** (1953) 239.
6) I. Imai: Lectured at the 4th annual meeting of J.N.C.A.M. (1954).
7) K. Tamada: Proc. Phys.-Math. Soc. Japan **21** (1939) 743.

JOURNAL OF THE PHYSICAL SOCIETY OF JAPAN Vol. 10, No. 12, DECEMBER, 1955

On the Subsonic Flow of a Compressible Fluid past an Axisymmetric Moderately Thick Body

By Ken-ichi KUSUKAWA

Department of Physics, Faculty of Science,
Tokyo Metropolitan University

(Read May 8, 1955, Received August 15, 1955)

We shall take the cylindrical coordinates o-xy, where x-axis is taken along the axis of revolution and y denotes the distance from the axis. Introducing new variables the fundamental equations for compressible fluid flow in the hodograph space are reduced to a form similar to that for incompressible fluid flow. Thus the flow of an incompressible fluid past a profile P_0 corresponds to the flow of a compressible fluid past a profile P, where the coordinates (x, y) and (x_0, y_0) of the profiles P and P_0 are related by the equations:

$$dx=(Q/q)dx_0\ , \quad dy=(Q/q)dy_0\ ,$$

and q and Q denote the magnitudes of velocity at corresponding points on the surface of the profiles in compressible and incompressible flows. Also Q is a function of q defined as follows.

$$Q=\frac{2}{1+\mu}\left(\frac{1+a\mu}{1+a}\right)^{1/a} q(1-a^2q^2)^{1-a/2a}\ ,$$

$$\mu=(1-q^2/c^2)^{1/2}=\left(\frac{1-q^2}{1-a^2q^2}\right)^{1/2}, \qquad a^2=\frac{\gamma-1}{\gamma+1}\ ,$$

where c and γ denote respectively the local speed of sound and the ratio of the specific heats.

As examples the velocity distributions on the surface of a sphere and prolate spheroids with thickness ratio $t=0.9$ and 0.1 are calculated for various Mach numbers, and they are compared with the results obtained by the M^2-expansion method, Meksyn-Imai's method and the linear theory.

§ 1. Introduction

As is well known, the subsonic flow of a compressible fluid past an axisymmetric body can be dealt with by the M^2-expansion method, due originally to Janzen[1] and Rayleigh[2]. This method is successfully used in the case of such low Mach numbers that even the first approximation can give a good result, but it is very laborious to obtain a good approximation in the case of high Mach numbers where we need to take many terms of M^2-expansion because of the convergence of the series becoming very slow.

On the other hand, the linear theory, due originally to Prandtl[3] and Glauert[4], can be applied to the flow past a very slender obstacle. However, this method does not give a good approximation near the stagnation points where the perturbation velocity is not so small as to be negligible in comparison with the free stream velocity. In a previous paper[5], the present writer offered a new method which give a good approximation even near the stagnation points for the slender obstacle. In this method, the fundamental equation of compressible fluid flow in the hodograph space was expressed in a simple form by the use of new variables, based on the assumption that the angle of inclination of the velocity is very small. This simple equation was formally equal to the hodograph equation for incompressible fluid flow. The form of an obstacle in the compressible flow obtained from this correspondence was proved to be quite the same as that for the corresponding incompressible flow. Thus we could obtain very easily the velocity distribution over the surface of an axisymmetric slender body, provided that numerical tables of new variables are prepared.

In this paper, the above-mentioned simple method will be modified so as to be applicable even to the flow past a moderately thick obstacle.

The fundamental equations of compressible flow in the hodograph space will be expressed by the use of new variables similar to those introduced in the previous paper just cited. These equations will not take a simple form without any approximation, because of remaining of the terms involving the distance from the axis denoted by y, besides the velocity potential and Stokes's stream function as the dependent variables. As the first approximation we shall begin with taking the solution given by the method offered in the previous paper[5]. Substituting this first approximation for y in the fundamental equations, these equations for compressible fluid flow can be formally reduced to the hodograph equations for incompressible fluid flow. For any given profile in the physical space of incompressible fluid flow, the velocity on the surface of the profile may be assumed to be known theoretically or experimentally. Then, by the use of the above-mentioned correspondence of the fundamental equations in the hodograph space, we can obtain the velocity on the surface of the profile in the physical space of compressible fluid flow, which is given by a definite transformation from the profile in the physical space of incompressible fluid flow. For a very slender body, this difference between both shapes of profiles in compressible and incompressible flows being vanishingly small, the present method will be reduced to the simple method offered in the previous paper[5].

It will be of interest to mention here that an analogous procedure has been developed by Imai[6] for two-dimensional compressible flow, and it was reduced to the simple method[7], if the obstacle is assumed to be very slender.

§ 2. Fundamental Equations

We shall take the cylindrical coordinates 0-xy, where the x-axis is taken along the axis of revolution of the body and y denotes the distance from the axis. If we denote the velocity components along x- and y-directions by u, v and the density of the fluid by ρ, the axisymmetric irrotational flow of a compressible inviscid fluid is governed by the equations:

$$\frac{\partial}{\partial x}(\rho y u)+\frac{\partial}{\partial y}(\rho y v)=0\,, \qquad (2.1)$$

$$\frac{\partial v}{\partial x}-\frac{\partial u}{\partial y}=0\,. \qquad (2.2)$$

We shall introduce Stokes's stream function ψ, and the velocity potential φ satisfying (2.1) and (2.2) respectively such that

$$\rho y u=\partial\psi/\partial y\,, \qquad \rho y v=-\partial\psi/\partial x\,, \qquad (2.3)$$

$$u=\partial\varphi/\partial x\,, \qquad v=\partial\varphi/\partial y\,. \qquad (2.4)$$

Taking φ and ψ as independent variables instead of x and y, (2.1) and (2.2) become respectively

$$(u^2+v^2)\frac{\partial}{\partial\varphi}(\rho y)+\rho y\left(u\frac{\partial u}{\partial\varphi}+v\frac{\partial v}{\partial\varphi}\right)+\rho^2y^2\left(u\frac{\partial v}{\partial\psi}-v\frac{\partial u}{\partial\psi}\right)=0\,, \qquad (2.5)$$

$$u\frac{\partial v}{\partial\varphi}-v\frac{\partial u}{\partial\varphi}-\rho y\left(u\frac{\partial u}{\partial\psi}+v\frac{\partial v}{\partial\psi}\right)=0\,. \qquad (2.6)$$

If, instead of the velocity components u, v, we make use of the magnitude q and the angle of inclination θ of the velocity vector such that

$$u=q\cos\theta\,, \qquad v=q\sin\theta\,, \qquad (2.7)$$

the above two equations become respectively

$$q^2\frac{\partial}{\partial\varphi}(\rho y)+\rho y q\frac{\partial q}{\partial\varphi}+\rho^2y^2q^2\frac{\partial\theta}{\partial\psi}=0\,, \qquad (2.8)$$

$$q^2\frac{\partial\theta}{\partial\varphi}-\rho y q\frac{\partial q}{\partial\psi}=0\,. \qquad (2.9)$$

From (2.3) and (2.4), the total differentials of ψ and φ are respectively

$$d\psi=-\rho y v dx+\rho y u dy\,, \qquad (2.10)$$

$$d\varphi=u dx-v dy\,. \qquad (2.11)$$

Solving dx and dy from Eqs. (2.10) and (2.11), we obtain

$$dx=(\cos\theta/q)d\varphi-(\sin\theta/\rho y q)d\psi\,, \qquad (2.12)$$

$$dy=(\sin\theta/q)d\varphi+(\cos\theta/\rho y q)d\psi\,. \qquad (2.13)$$

Considering y to be a function of independent variables ψ and φ, we obtain from (2.13)

$$\partial y/\partial\varphi=\sin\theta/q \qquad (2.14)$$

Then, using (2.14) and Bernoulli's theorem:

$$(c^2/\rho)d\rho+q dq=0\,, \qquad (2.15)$$

where $c=(dp/d\rho)^{1/2}$ is the local speed of sound, we obtain, from (2.8), the following equation:

$$\frac{1}{q}\left(1-\frac{q^2}{c^2}\right)\frac{\partial q}{\partial\varphi}+\rho y\frac{\partial\theta}{\partial\psi}+\frac{\sin\theta}{yq}=0\,. \qquad (2.16)$$

If we introduce a new variable Q such that

$$dQ/Q=K^{1/2}dq/q\,, \qquad (2.17)$$

where

$$K=1-q^2/c^2\,,$$

then (2.9) and (2.16) become respectively

$$\frac{\partial\theta}{\partial\varphi}-\frac{\rho y}{K^{1/2}Q}\frac{\partial Q}{\partial\psi}=0\,, \tag{2.18}$$

$$\frac{1}{Q}\frac{\partial Q}{\partial\varphi}+\frac{\rho y}{K^{1/2}}\frac{\partial\theta}{\partial\psi}+\frac{\sin\theta}{K^{1/2}yq}=0\,. \tag{2.19}$$

Changing the dependent variables for the independent variables and vice versa, the above two equations become respectively

$$Q\left(\frac{Kq}{\rho Q}\right)\frac{\partial\psi}{\partial Q}-\left(\frac{K^{1/2}qy}{Q}\right)\frac{\partial\varphi}{\partial\theta}=0\,, \tag{2.20}$$

$$\left(\frac{Kq}{\rho Q}\right)\frac{\partial\psi}{\partial\theta}+\left(\frac{K^{1/2}qy}{Q}\right)Q\frac{\partial\varphi}{\partial Q}$$
$$+\frac{\sin\theta}{(K^{1/2}qy/Q)}\left(\frac{Kq}{\rho Q}\right)\left\{\frac{\partial\varphi}{\partial Q}\frac{\partial\phi}{\partial\theta}-\frac{\partial\psi}{\partial Q}\frac{\partial\varphi}{\partial\theta}\right\}=0\,. \tag{2.21}$$

Since Eqs. (2.20) and (2.21) involve the unknown function y besides φ and ψ, we need to consider one more equation for the purpose of solving the problem. However, in this paper we shall develop the following approximate treatment.

Assuming the obstacle to be very slender, it will be proved in § 3 that the functions $x(Q,\theta)$ and $y(Q.\theta)$ may be determined from the simple differential equations, based on the same assumption as that of the previous paper5). Taking this solution as the first approximation, and substituting it for y in Eqs. (2.20) and (2.21), we may obtain the second approximations of φ and ψ by solving these equations. Then this second approximation will be applicable even to a moderately thick obstacle.

§ 3. The Approximation for the Slender Obstacle

For the very slender body, θ itself and spatial derivatives of q, θ and ρ being all very small except in the vicinity of the stagnation points, we can obtain, from (2.1), (2.2), and (2.7), following simple equations:

$$\frac{\partial}{\partial x}(\rho q)+(\rho q)\frac{\partial\theta}{\partial y}+\frac{\rho q\theta}{y}=0\,, \tag{3.1}$$

$$q\frac{\partial\theta}{\partial x}-\frac{\partial q}{\partial y}=0\,. \tag{3.2}$$

These two equations were proved in the previous paper5) to be applicable even at the stagnation points, where θ is not always small.

By the use of Bernoulli's theorem (2.15), Eq. (3.1) becomes

$$\left(1-\frac{q^2}{c^2}\right)\frac{\partial q}{\partial x}+q\frac{\partial\theta}{\partial y}+\frac{q\theta}{y}=0\,. \tag{3.3}$$

Introducing the new variable Q determined by (2.17), Eqs. (3.2) and (3.3) become respectively

$$\frac{\partial\theta}{\partial x}-\frac{1}{K^{1/2}Q}\frac{\partial Q}{\partial y}=0\,, \tag{3.4}$$

$$\frac{1}{Q}\frac{\partial Q}{\partial x}+\frac{1}{K^{1/2}}\frac{\partial\theta}{\partial y}+\frac{\theta}{y}=0\,. \tag{3.5}$$

Then changing the dependent variables for the independent variables and vice versa, the above two equations become respectively

$$\frac{1}{Q}\left(\frac{K^{1/2}q}{Q}\right)\frac{\partial y}{\partial\theta}+\left(\frac{q}{Q}\right)\frac{\partial x}{\partial Q}$$
$$+\frac{\theta}{(K^{1/2}qy/Q)}\left(\frac{q}{Q}\right)\left(\frac{K^{1/2}q}{Q}\right)\left\{\frac{\partial x}{\partial Q}\frac{\partial y}{\partial\theta}\right.$$
$$\left.-\frac{\partial y}{\partial Q}\frac{\partial x}{\partial\theta}\right\}=0\,, \tag{3.6}$$

$$\left(\frac{K^{1/2}q}{Q}\right)\frac{\partial y}{\partial Q}-\frac{1}{Q}\left(\frac{q}{Q}\right)\frac{\partial x}{\partial\theta}=0\,. \tag{3.7}$$

Now, integrating (2.17), we obtain

$$\left.\begin{aligned}&Q=Cq(1-a^2q^2)^{(1-a)/2a}(1+a\mu)^{1/a}(1+\mu)^{-1}\\&\mu=(1-q^2/c^2)^{1/2}=(1-q^2)^{1/2}(1-a^2q^2)^{-1/2}\,,\\&a^2=(\gamma-1)(\gamma+1)^{-1}\,,\end{aligned}\right\} \tag{3.8}$$

where C is an arbitrary constant, which can be conveniently determined by the requirement that $Q\to q$ as $q\to 0$. We then have

$$C=2(1+a)^{-1/a}\,. \tag{3.9}$$

From this functional form of Q and the assumption that the obstacle is very slender, we discuss the orders of magnitudes of terms on the right-hand side of the following formulae:

$$\left.\begin{aligned}&\frac{\partial}{\partial Q}\left(\frac{qx}{Q}\right)=x\frac{\partial}{\partial Q}\left(\frac{q}{Q}\right)+\left(\frac{q}{Q}\right)\frac{\partial x}{\partial Q}\,,\\&\frac{\partial}{\partial Q}\left(\frac{K^{1/2}qy}{Q}\right)=y\frac{\partial}{\partial Q}\left(\frac{K^{1/2}q}{Q}\right)+\left(\frac{K^{1/2}q}{Q}\right)\frac{\partial y}{\partial Q}\,.\end{aligned}\right\} \tag{3.10}$$

To do this, we note that

(i) In the vicinity of the stagnation points, the terms $x(\partial/\partial Q)(q/Q)$ and $y(\partial/\partial Q)(K^{1/2}q/Q)$ can be neglected in comparison with other terms, since q/Q and $qK^{1/2}/Q$ can be expanded at the stagnation points into the form: $1+O(q^2)+O(q^4)+\cdots$

(ii) Except near the stagnation points, the flow of gas is nearly parallel to the x-axis, so that the terms involving $\partial x/\partial Q$ or $\partial y/\partial Q$ are very larger than other terms. Thus, as in the vicinity of stagnation points, $x(\partial/\partial Q)(q/Q)$ and $y(\partial/\partial Q)(K^{1/2}q/Q)$ can be neglected in comparison with other terms.

(iii) At a great distance from the obstacle, x and y may become very large. But making use of the relations:

$$\lim_{x\to\infty} x(\partial q/\partial x)=\lim_{x\to\infty} x(\partial Q/\partial x)=0 \quad \text{etc.},$$

$$\lim_{x\to\infty} \frac{\partial}{\partial Q}(q/Q)=\text{finite}\ ,$$

$$\lim_{x\to\infty} \frac{\partial}{\partial Q}(K^{1/2}q/Q)=\text{finite etc.},$$

it can be shown that the terms $(q/Q)(\partial x/\partial Q)$ and $(K^{1/2}q/Q)(\partial y/\partial Q)$ become infinity of the order higher than other terms.

Thus, finally in Eq (3.10), $(\partial/\partial Q)(qx/Q)$ and $(\partial/\partial Q)(K^{1/2}qy/Q)$ can be approximated very closely to $(q/Q)(\partial x/\partial Q)$ and $(K^{1/2}q/Q)(\partial y/\partial Q)$ respectively.

Then the fundamental equations (3.6) and (3.7) can be also approximated respectively to

$$\frac{1}{Q}\frac{\partial\eta}{\partial\theta}+\frac{\partial\xi}{\partial Q}+\frac{\theta}{\eta}\left\{\frac{\partial\xi}{\partial Q}\frac{\partial\eta}{\partial\theta}-\frac{\partial\eta}{\partial Q}\frac{\partial\xi}{\partial\theta}\right\}=0\ , \tag{3.11}$$

$$\frac{\partial\eta}{\partial Q}-\frac{1}{Q}\frac{\partial\xi}{\partial\theta}=0\ , \tag{3.12}$$

where

$$\xi=qx/Q, \text{ and } \qquad \eta=K^{1/2}qy/Q.$$

On the other hand, in the case of incompressible fluid flow, we have the equations which correspond respectively to Eqs. (3.1) and (3.2) for compressible fluid flow, namely:

$$\frac{\partial q_0}{\partial x_0}+q_0\frac{\partial\theta_0}{\partial y_0}+\frac{q_0\theta_0}{y_0}=0\ , \tag{3.13}$$

$$q_0\frac{\partial\theta_0}{\partial x_0}-\frac{\partial q_0}{\partial y_0}=0\ . \tag{3.14}$$

Changing the dependent variables for the independent variables and vice versa, (3.13) and (3.14) become respectively

$$\frac{1}{q_0}\left(\frac{\partial y_0}{\partial\theta_0}\right)+\frac{\partial x_0}{\partial q_0}+\frac{\theta_0}{y_0}\left\{\frac{\partial x_0}{\partial q_0}\frac{\partial y_0}{\partial\theta_0}-\frac{\partial y_0}{\partial q_0}\frac{\partial x_0}{\partial\theta_0}\right\}=0\ , \tag{3.15}$$

$$\frac{\partial y_0}{\partial q_0}-\frac{1}{q_0}\frac{\partial x_0}{\partial\theta_0}=0\ . \tag{3.16}$$

It is of great importance to note that these two equations are formally equal to the fundamental equations (3.11) and (3.12) for compressible fluid flow respectively. Thus, if we know an incompressible flow pattern expressed by $x_0(q_0, \theta_0)$, $y_0(q_0, \theta_0)$, we can immediately obtain a corresponding compressible flow pattern $x(q, \theta)$, $y(q, \theta)$; by making use of the following relations between the variables:

$$q_0=Q\ , \qquad \theta_0=\theta\ ,$$

$$x_0=\xi=qx/Q\ , \qquad y_0=\eta=K^{1/2}qy/Q\ , \tag{3.17}$$

where Q is given by the equation (3.8) together with (3.9).

It is of importance to mention here that in the case of tne flow past a slender obstacle the form of an obstacle in the compressible flow was proved in the previous paper[5] to be quite the same as that of the corresponding incompressible flow.

§ 4. The Approximate Solution of Eqs. (2.20) and (2.21)

Substituting the first approximation for the very slender obstacle expressed by (3.17) for y in Eqs. (2.20) and (2.21), we can obtain the following equations:

$$Q\left(\frac{Kq}{\rho Q}\right)\frac{\partial\psi}{\partial Q}-y_0(Q, \theta)\frac{\partial\varphi}{\partial\theta}=0\ , \tag{4.1}$$

$$\left(\frac{Kq}{\rho Q}\right)\frac{\partial\psi}{\partial\theta}+y_0(Q,\theta)Q\frac{\partial\varphi}{\partial Q} + \frac{\sin\theta}{y_0(Q, \theta)}\left(\frac{Kq}{\rho Q}\right)\left\{\frac{\partial\varphi}{\partial Q}\frac{\partial\psi}{\partial\theta}-\frac{\partial\psi}{\partial Q}\frac{\partial\varphi}{\partial\theta}\right\}=0\ , \tag{4.2}$$

where y_0 is the known function of the independent variables Q and θ.

We now discuss the orders of magnitudes of the terms on the right-hand side of the following formula:

$$\frac{\partial}{\partial Q}\left\{\left(\frac{Kq}{\rho Q}\right)\psi\right\}=\psi\frac{\partial}{\partial Q}\left(\frac{Kq}{\rho Q}\right)+\left(\frac{Kq}{\rho Q}\right)\frac{\partial\psi}{\partial Q}\ . \tag{4.3}$$

To do this we note that

(i) On the surface of the obstacle we may take $\psi=0$, and therefore near the obstacle the first term can be neglected in comparison with the second term.

(ii) For the flow at moderate distance from the obstacle, the velocity of gas does not vary so rapidly, and therefore $\partial\psi/\partial Q$ may become moderately large. Hence, the first term can be neglected in comparison with the second term.

(iii) At great distance from the obstacle, ψ may become very large because it is of the same order of magnitude as y^2.

But making use of the relations:

$$\lim_{\psi\to\infty} \psi \frac{\partial Q}{\partial \psi} = 0 \,,$$

$$\lim_{\psi\to\infty} \frac{\partial}{\partial Q}\left(\frac{Kq}{\rho Q}\right) = \text{finite}, \quad \lim_{\psi\to\infty} \frac{Kq}{\rho Q} = \text{finite}, \tag{4.4}$$

it can be shown that the second term becomes infinity of the order higher than the first term.

Thus, finally in Eq. (4.3), $(\partial/\partial Q)(Kq\psi/\rho Q)$ can be approximated very closely to $(Kq/\rho Q)(\partial\psi/\partial Q)$.

Then the fundamental equations (4.1) and (4.2) can be also approximated respectively to

$$Q\frac{\partial \omega}{\partial Q} - y_0(Q,\theta)\frac{\partial \varphi}{\partial \theta} = 0 \,, \tag{4.5}$$

$$\frac{\partial \omega}{\partial \theta} + y_0(Q,\theta)Q\frac{\partial \varphi}{\partial Q} + \frac{\sin\theta}{y_0(Q,\theta)}\left\{\frac{\partial \varphi}{\partial Q}\frac{\partial \omega}{\partial \theta} - \frac{\partial \omega}{\partial Q}\frac{\partial \varphi}{\partial \theta}\right\} = 0 \,, \tag{4.6}$$

where $\omega = (Kq/\rho Q)\psi$.

On the other hand, in the case of incompressible fluid flow, we have the equations which correspond respectively to Eqs. (2.9) and (2.16) for compressible fluid flow, namely:

$$q_0\frac{\partial \theta_0}{\partial \varphi_0} - \rho_0 y_0 \frac{\partial q_0}{\partial \psi_0} = 0 \,, \tag{4.7}$$

$$\frac{\partial q_0}{\partial \varphi_0} + \rho_0 y_0 q_0 \frac{\partial \theta_0}{\partial \psi_0} + \frac{\sin\theta_0}{y_0} = 0 \,, \tag{4.8}$$

where the density of incompressible fluid ρ_0 is taken to be equal to the density of compressible fluid at rest.

Taking conveniently this ρ_0 as the unit of density, and changing the dependent variables for the independent variables and vice versa, Eqs. (4.7) and (4.8) become respectively

$$q_0\frac{\partial \psi_0}{\partial q_0} - y_0(q_0,\theta_0)\frac{\partial \varphi_0}{\partial \theta_0} = 0 \,, \tag{4.9}$$

$$\frac{\partial \psi_0}{\partial \theta_0} + y_0 q_0 \frac{\partial \varphi_0}{\partial q_0} + \frac{\sin\theta_0}{y_0(q_0,\theta_0)}\left\{\frac{\partial \varphi_0}{\partial q_0}\frac{\partial \psi_0}{\partial \theta_0} - \frac{\partial \psi_0}{\partial q_0}\frac{\partial \varphi_0}{\partial \theta_0}\right\} = 0 \,. \tag{4.10}$$

Remembering that the function y_0 in the above two equations is quite the same as that in Eqs. (4.1) and (4.2), these equations (4.1) and (4.2) are formally equal to Eqs. (4.9) and (4.10) for incompressible fluid flow respectively.

Thus, if we know an incompressible flow pattern $\varphi_0(q_0,\theta_0)$, $\psi_0(q_0,\theta_0)$, we can immediately obtain a corresponding compressible flow pattern $\varphi(q,\theta)$, $\psi(q,\theta)$ by making use of the following relations between the variables:

$$\left.\begin{aligned} q_0 &= Q \,, & \theta_0 &= \theta \,, \\ \varphi_0 &= \varphi \,, & \psi_0 &= \omega = (Kq/\rho Q)\psi \,, \end{aligned}\right\} \tag{4,11}$$

where Q is given by (3.8) together with (3.9).

§ 5. Boundary Conditions

We now consider the relation between the boundaries of compressible and incompressible flows. According to (4.11) the meridian curve of the obstacle in an incompressible fluid expressed by $\psi_0 = 0$, corresponds to that in a compressible fluid expressed by $\psi = 0$.

On the profile for compressible fluid flow as expressed by $\psi = 0$, Eqs. (2.12) and (2.13) are respectively reduced to

$$dx = (\cos\theta/q)d\varphi \,, \tag{5.1}$$

$$dy = (\sin\theta/q)d\varphi \,. \tag{5.2}$$

In the case of incompressible fluid flow, we have the relation which correspond respectively to (5.1) and (5.2) for compressible fluid flow, namely:

$$dx_0 = (\cos\theta_0/q_0)d\varphi_0 \,, \tag{5.3}$$

$$dy_0 = (\sin\theta_0/q_0)d\varphi_0 \,. \tag{5.4}$$

Thus, by the use of (4.11), we can obtain the relations

$$dx = (Q/q)dx_0, \qquad dy = (Q/q)dy_0 \,, \tag{5.5}$$

which give the correspondence between the boundaries of compressible and incompressible flows.

For any given profile in the incompressible physical space the magnitude of the velocity $q_0(=Q)$ at a point of the surface may be assumed to be known theoretically or experimentally. Then the magnitude of velocity q at the corresponding point on the surface of an obstacle in the compressible physical space will be found with the aid of the relation (3.8). Next, by means of (5.5), the form of the profile for compressible fluid flow will be obtained by numerical or graphical integration.

For this purpose we can conveniently use the numerical tables for the relation (3.8) which has been given in Imai's papers[6][8].

It may be of interest to remark here that the relation between q and q_0 as expressed by (3.8) is quite the same as the corresponding relation for the two-dimensional flow introduced by Imai[6)7)], but that the relation between the boundaries of compressible and incompressible flows expressed by (5.5) is slightly different from the corresponding relation in the papers[6)7)].

§ 6. Numerical Examples

As an example of the flow past a slender obstacle—where the present method must give a good result—we shall investigate the flow past a prolate spheroid of thickness ratio $t=0.1$, and as examples of the flow past a moderately thick obstacle—even where the present method may be useful—the flow past a sphere and that past a prolate spheroid of thickness ratio $t=0.9$.

As is well known, the magnitude of velocity of incompressible flow on the surface of a prolate spheroid is expressed by

$$\left.\begin{aligned} q_0 &= Bq_{0\infty}\frac{\sin\theta}{\sqrt{1-e^2\cos^2\theta}}\,, \\ B &= e^2\Big/\left(1-\frac{1-e^2}{2e}\log\frac{1+e}{1-e}\right), \\ t &= c/a=\sqrt{1-e^2}\,, \\ x_0 &= a\cos\theta\,, \qquad y_0=c\sin\theta, \end{aligned}\right\} \tag{6.1}$$

where a, c and $q_{0\infty}$ are respectively the semi-major and semi-minor axes of the prolate spheroid and the free-stream velocity. Taking especially $t=1$ in Eq. (6.1), we can obtain the case of sphere.

Integrating (5.5), we obtain

$$x=a\int_0^{\pi/2}(Q\sin\theta/q)d\theta\,,\quad y=c\int_0^{\theta}(Q\cos\theta/q)d\theta\,, \tag{6.2}$$

where $Q=q_0$, and q will be found with the aid of Eq. (3.8).

The integration can be carried out by Simpson's rule, and it is sufficient to consider only 11 values of θ: $\theta_N=N\pi/20(N=0, 1,\cdots 10)$.

On the other hand, between the free-stream velocity q_∞ and the free-stream Mach number M in compressible flow, there exists the relation;

$$q_\infty{}^2=\frac{\frac{1}{2}(\gamma+1)M^2}{1+\frac{1}{2}(\gamma-1)M^2}\,. \tag{6.3}$$

Thus, for a given Mach number, starting from the incompressible flow velocity distribution on the surface of a certain prolate spheroid as given by (6.1), we can calculate, with the aid of (3.8) and (6.3), the velocity distribution of compressible flow on the surface of a nearly prolate spheroid slightly thicker than the former. In Table I, we shall give the several values of thickness ratio of nearly prolate spheroids, which are obtained by starting from the prolate spheroids of thickness ratio $t=0.1$, 0.9 and 1.0 in an incompressible fluid for several Mach numbers. Next, after a few trials, we can arrive at nearly prolate spheroids of thickness ratio t

Table of correspondence of the thickness ratio of a prolate spheroid in an incompressible fluid flow with that in a compressible fluid flow, where the former is denoted by T, the latter by t and M denotes the Mach number.

Table I.

M	T	t
0.4	1.0	1.0373
0.5	1.0	1.0454
0.4	0.9	0.9300
0.5	0.9	0.9572
0.7	0.1	0.1019
0.9	0.1	0.1046

Table II.

M	T	t
0.4	0.965	1.0
0.5	0.938	1.0
0.4	0.872	0.9
0.5	0.849	0.9
0.7	0.0981	0.1
0.9	0.0956	0.1

Table III.

Thickness ratio =0.900		Thickness ratio =0.900	
Mach number =0.4		Mach number =0.5	
θ_0	$(r_0-r)/r$	θ_0	$(r_0-r)/r$
0° 0′	0.00000	0° 0′	0.00000
9 17	0.00000	9 30	−0.00008
18 33	−0.00005	18 57	−0.00027
27 45	−0.00006	28 19	−0.00053
36 53	−0.00007	37 34	−0.00076
45 55	−0.00008	46 41	−0.00095
54 53	−0.00009	55 39	−0.00086
63 45	−0.00006	64 27	−0.00071
72 32	−0.00005	73 5	−0.00040
81 17	0.00000	81 35	−0.00013
90 0	0.00000	90 0	0.00000

Thickness ratio =0.100		Thickness ratio =0.100	
Mach number =0.7		Mach number =0.9	
θ_0	$(r_0-r)/r$	θ_0	$(r_0-r)/r$
0° 0′	0.00000	0° 0′	0.00000
9 25	0.00001	9 50	0.00002
18 23	0.00002	18 54	0.00004
27 19	0.00003	27 50	0.00007
36 15	0.00004	36 43	0.00009
45 12	0.00005	45 36	0.00011
54 9	0.00006	54 29	0.00012
63 7	0.00006	63 22	0.00013
72 5	0.00006	72 14	0.00013
81 2	0.00005	81 7	0.00010
90 0	0.00000	90 0	0.00000

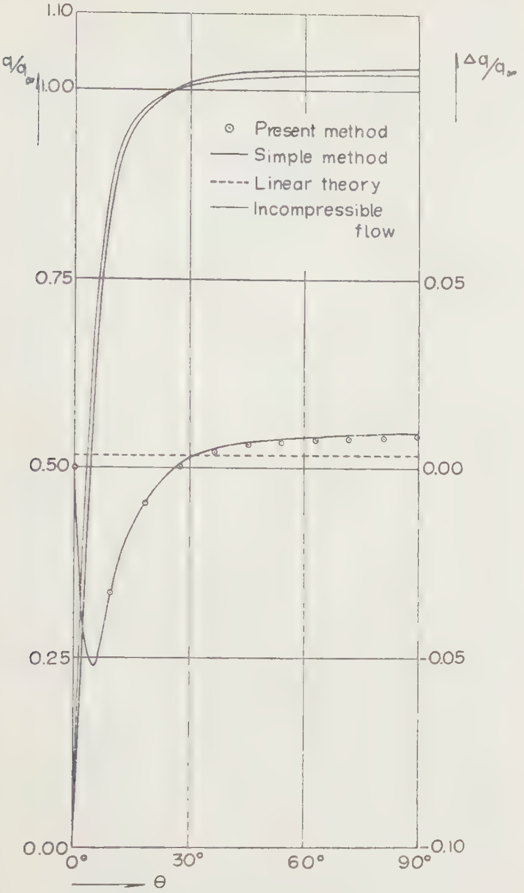

Fig. 1. Velocity distribution over a prolate spheroid of thickness ratio $t=0.1$ at $M=0.7$.

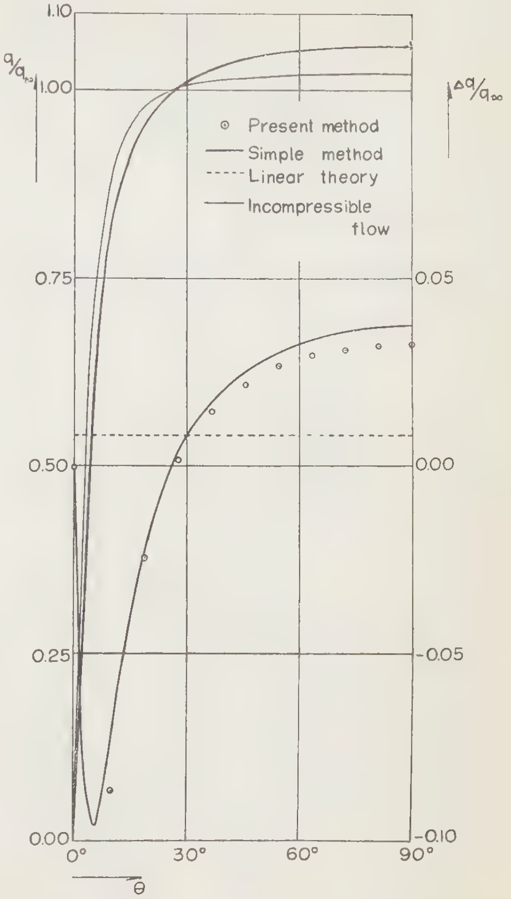

Fig. 2. Velocity distribution over a prolate spheroid of thickness ratio $t=0.1$ at $M=0.9$.

$=0.1$, 0.9 and 1.0 in a compressible fluid flow by starting from the corresponding prolate spheroids in the incompressible fluid flow of the certain values of thickness ratio, which are given in Table II.

We shall introduce the polar coordinates (r_0, θ_0) of the nearly prolate spheroid given by (6.2) such that

$$r_0=\sqrt{x^2+y^2}\,, \qquad \theta_0=\mathrm{Tan}^{-1}(y/x)\,. \qquad (6.4)$$

The semi-major and semi-minor axes of this nearly prolate spheroid being denoted by A and C, the true prolate spheroid with the same axes can be represented by

$$\left.\begin{array}{l} \xi=A\cos\theta_0, \qquad \eta=C\sin\theta_0, \\ \text{or } r=\sqrt{A^2\cos^2\theta_0+C^2\sin^2\theta_0} \end{array}\right\} \qquad (6.5)$$

For several cases, the values of $(r_0-r)/r$ as a function of θ_0 are given in Table III. Since these values are very small, the difference between the nearly and the corresponding true prolate spheroids can be safely disregarded.

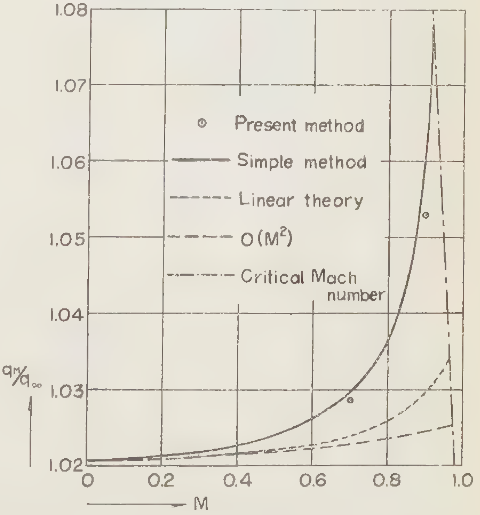

Fig. 3. Variation with the Mach number of the ratio of the maximum velocity occurring at the end of the minor axis of a prolate spheroid with thickness ratio $t=0.1$ to the free-stream velocity.

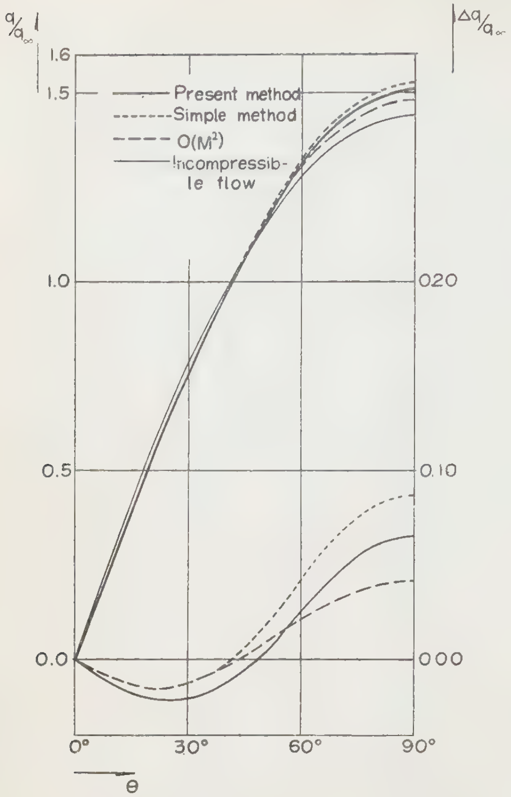

Fig. 4. Velocity distribution over a prolate spheroid of thickness ratio $t=0.9$ at $M=0.4$.

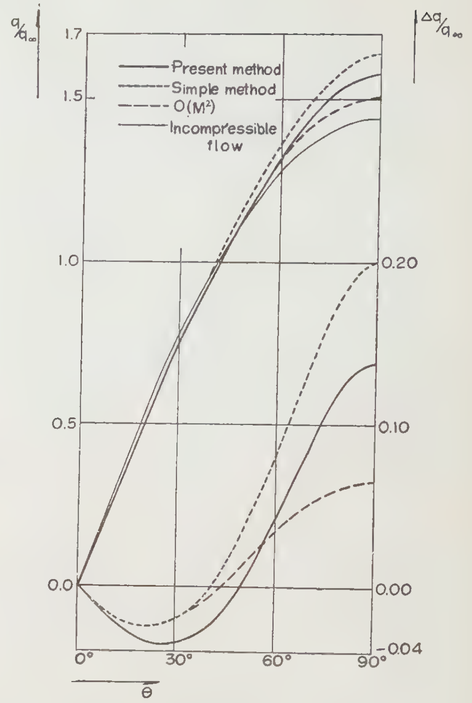

Fig. 5. Velocity distribution over a prolate spheroid of thickness ratio $t=0.9$ at $M=0.5$.

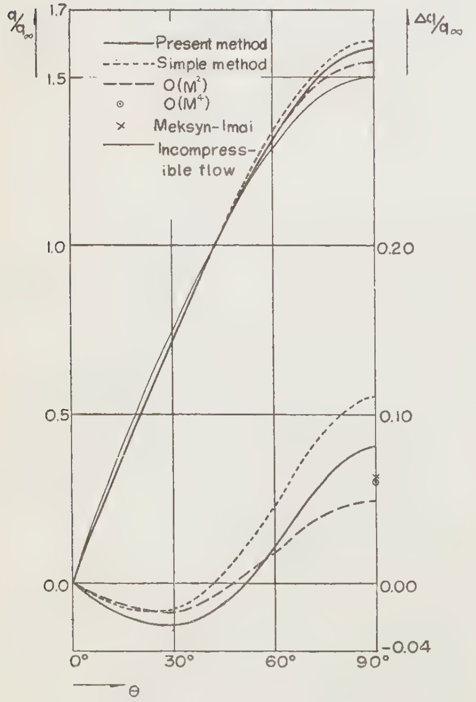

Fig. 6. Velocity distribution over a sphere at $M=0.4$.

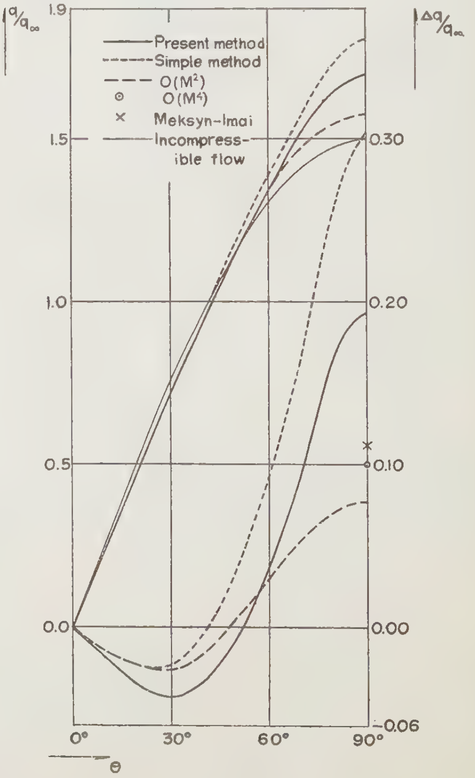

Fig. 7. Velocity distribution over a sphere at $M=0.5$.

The velocity distributions over a prolate spheroid of thickness ratio $t=0.1$ for $M=0.7$ and 0.9 are shown in Figs. 1 and 2, compared with the results obtained by the linear theory and the simple method[5]. The effect of compressibility on the velocity is represented by

$$\Delta q/q_\infty = q/q_\infty - q_0/q_{0\infty}\ ,$$

which is also shown in Fig. 1. and Fig. 2. For the same obstacle, the ratio of the maximum velocity occurring at the end of the minor axis to the free-stream velocity as a function of the Mach number, compared with the results obtained by the first approximation of the M^2-expansion method[9] the linear theory, and the simple method, are also shown in Fig. 3. In the case of such a small thickness ratio, the agreement between the results obtained by the present method and those obtained by the simplified theory[5], where the deformation of the profile was neglected, is fairly good, and this seems to show that the result obtained by the present method is very reliable.

The velocity distributions as well as $\Delta q/q_\infty$ over a prolate spheroid of thickness ratio $t=0.9$ and a sphere for $M=0.4$ and 0.5 are shown in Figs. 4, 5, 6 and 7. These results may be compared with those obtained by the M^2-expansion method[9][10] and Meksyn-Imai's method[11]. In the case of such a thick obstacle, the simple method gives only an absurd result. Even by the present method, the effect of compressibility seems to be somewhat overestimated. But the above-mentioned examples show us that the present method can be applied to the compressible flow past a moderately thick obstacle for moderately high Mach numbers.

The writer wishes to express his heartiest gratitude to Professor I. Imai for his many useful suggestions and kind advice.

References

1) O. Janzen: Phys. Zeits. **14** (1913) 639.
2) Lord Rayleigh: Phil. Mag. **32** (1916) 1.
3) L. Prandtl: Handbuch der Physik, Band VII (1927) 340.
4) H. Glauert: Proc. Roy. Soc. **A118** (1927) 113.
5) K. Kusukawa: Journ. Phys. Soc. Japan **9** (1954) 605.
6) I. Imai: Journ. Math. and Phys. **28** (1949) 173.
7) I. Imai: Journ. Phys. Soc. Japan **3** (1948) 352.
8) I. Imai and H. Hasimoto: Journ. Math. and Phys. **28** (1950) 205.
9) K. Hida: Journ. Phys. Soc. Japan **8** (1953) 257.
10) K. Tamada: Proc. Phys. Math. Soc. Japan **21** (1939) 743.
11) K. Kusukawa: Journ. Phys. Soc. Japan **10** (1955) 1088.

JOURNAL OF THE PHYSICAL SOCIETY OF JAPAN Vol. 10, No. 12, DECEMBER, 1955

On the Space Charge affected by the Magnetic Field

By Yoshio YASUOKA

Research Section, Nihon Musen K. K., Mitaka Tokyo

(Received July 18, 1955)

The characteristic phenomena of the dense space charge of electrons bound by the strong magnetic field are described. The electrons in the outermost sheath of electron cloud are considered to be scattered by mutual interaction and to have excess energies.

Calculation based on this view is in good agreement with experiment. It is especially noteworthy that when the anode voltage is raised to the proper value, this sheath is captured by the anode and certain unique oscillations are observed to occur. The frequencies of these oscillations very nearly coincide with those obtained from Langmuir's formula of plasma oscillation.

§ 1. Introduction

Many studies performed by other researchers so far on the motion of electrons in high vacuum under the influence of the magnetic field have made clear several phenomena related.

But almost all of them considered only the case when the density of the moving electrons was comparatively low, and hence the interaction between electrons was neglected. None of them treated the behaviour of electrons of high space charge density in the strong magnetic field.

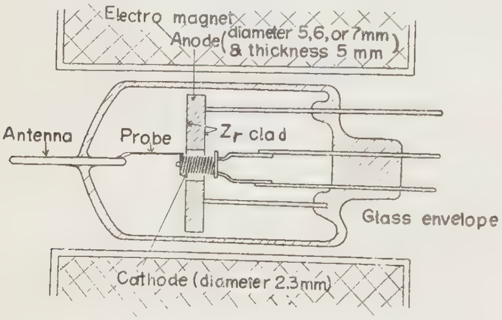

Fig. 1.

The characteristic phenomenon in the latter case is the generation of excess energy electrons which cause the back heating of the cathode and the anode dark current.

To make clear these phenomena, the author made special electron tubes to perform researches.

From the relations obtained between the back heating of the cathode and the anode dark current, it was concluded that the both should be caused by the same source, that is, the interacting electrons which appear in the outermost sheath of the space carge and have the excess energy.

The author made calculation about the back heating from this point of view and the results were in good agreement with experiment.

When the anode voltage is raised, this sheath is expected to be caught by the anode and in fact the back heating of the cathode disappeared and moreover certain unique oscillations were observed.

These oscillations are considered to be plasma oscillation, since the measured frequencies of these coincide with the values calculated from Langmuir's formula of plasma oscillation.

§ 2. Measurement Method of the Back Heating Power

One of the special tubes the author has made and used for experiments has the structure as shown in Fig. 1.

The anode is cut from copper block, and clad with *Zr* powder to be free from undersirable overheating and to prevent irregular oscillation.

The cathode consistes of direct-heating thoriated tungsten wire and is equipped with end plates at both ends.

The circuit used for the measurement is shown Fig. 2, and the back heating power is determined by measuring the corresponding variation of the cathode wire resistance.

The procedure is as follows:

First, we plot the relation between the

resistance value R of the cathode wire and the dissipated power W_H when there is no back heating, i.e. in the absence of the magnetic field. When there is back heating, we set the balance of the bridge in which the resistance value of the cathode wire is R' and the current passing through R' is I'.

Corresponding to $R=R'$, we take the point $W_H=W_H'$ on the curve. This point shows the balance of the bridge at the same value of the cathode wire resistance when there is no back heating.

When the resistances of the wire are the same, so are the temperatures of the wire, i.e. the total dissipated powers are the same.

Hence we can obtain the back heating power W_b by

$$W_b=W_H'-R'I'^2 \quad \text{with} \quad R'=\frac{R_1R_2}{R_v}\,.$$

In practice, we must take into account the effect of the anode current passing through the cathode wire, namely the following changes must be done:

$$I'^2 \to I'^2+I'i_a+1.3\,i_a^2$$

in the case of D.C. anode voltage,

or

$$I'^2 \to \left(I'+\frac{Di_a}{2}\right)^2+\frac{D}{3}\,i_a{}^2-\frac{D^2}{4}\,i_a{}^2$$

in the case of pulsed anode voltage

and

$$R' \to R'\left(\frac{1}{1+\sigma}\right)$$

where $\sigma=\pm\dfrac{Di_a}{2I'}$, D is the duty cycle and i_a the peak value of the anode current.

§ 3. Experimental Results

(i) *Measurement using pulsed anode voltage (qualitative observation).*

The use of the pulsed anode voltage is advantageous, because the mean input power and the back heating power are comparatively low, making easier the observation in the strong magnetic field and at the higher anode voltage. Fig. 3 shows the relation between the peak anode voltage and the back heating power.

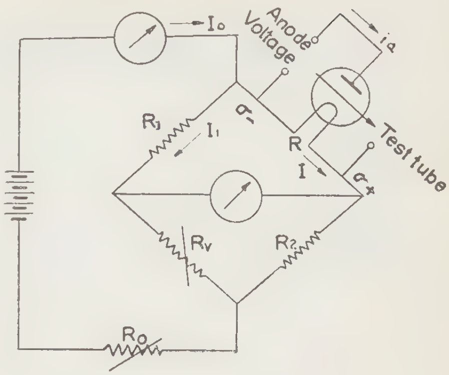

Fig. 2.

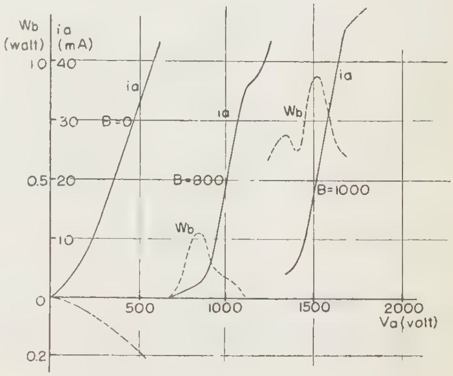

Fig. 3.

When there is no magnetic field, the tube operates simply as a diode, and the electron emission produces a cooling effect on the cathode and thus W_b is obtained negative to give a correct value $\phi=3.4\,V$ of the work function of thoriated tungsten. This is one of the evidences showing the reliability of the author's method.

In the presence of the magnetic field, the phenomena as follows:

It is observed that while the applied anode voltage is far below the cut-off, the anode current begins to flow, and increases rapidly with the anode voltage.

At the cut-off voltage, the anode current takes the value on Allis curve, and beyond that voltage the current asymptotically approaches Langmuir curve³⁾.

The back heating starts with the anode current and becomes considerable in power even far below the cut-off, and attains its maximum and then decreases, while the current still continues to increase. It is interpreted by supposing that the number of electrons directly flowing into the anode increase, and as a results the number of scattered electrons decreases, hence so does the back heating power. At the higher voltage, the cathode is rather cooled, just as in the absence of the magnetic field.

As is shown in Fig. 3, the back heating power increases with the increasing magnetic field.

In the very strong magnetic field, there appears the tendency of the back heating power having two maximum points.

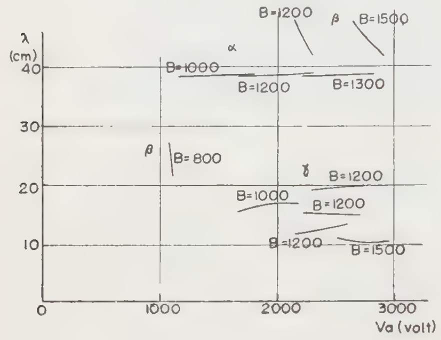

Fig. 4.

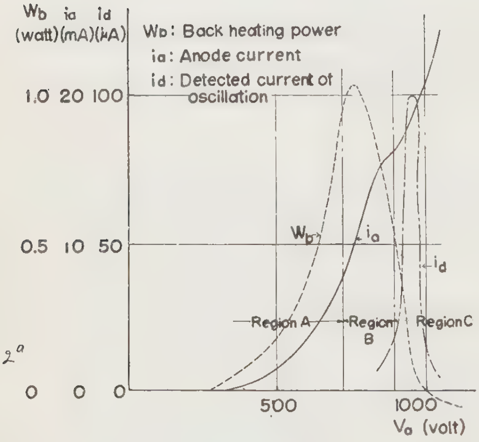

Fig. 5.

In the region of the decreasing back heating power, the different types of oscillation occur, which are detected by a crystal detector loosely coupled to the antenna which is connected with the probe inserted in the space between the anode and the cathode.

Fig. 4 shows the frequencies of these oscillations versus the anode voltage with the magnetic field as parameter.

As is shown in the figure, three types of oscillation are classfied as follows:

α-type. The frequency is independent of both the electric and the magnetic fields, and hence considered to be determined by a certain stray circuit. This oscillation is so weak and unstable, and only with some tubes this could be detected.

β-type. The frequency varies largely with the anode voltage. It is only sometimes that the oscillation of this type could be detected.

γ-type. The oscillation of this type is the most important of the three, being fairly intense, very stable and reproducible. The frequency depends almost only upon the magnetic field, varying little with the anode valtage.

(ii) *Measurement using D.C. anode voltage (quantitative observation)*

The measurement using pulsed anode voltage is not adequate for the quantitative observation, owing to the inaccurate values of duty cycle, the instantaneous anode current and the instantaneous anode voltage. The measurement using D.C. anode voltage was adopted, though the observation in the very strong magnetic field was impossible because of the large anode loss.

The typical result obtained is shown in Fig. 5, where the relationship between the anode current, the back heating power and the detected current of the oscillation is represented.

As is shown in Fig. 5, three regions A, B, and C of the back heating are classified for the description.

Region A. Both the back heating power and the anode current increase with the anode voltage, and their starting point is about 300 volt, in the magnetic field whose theoretical cut-off voltage is 1000 volt.

Region B. The back heating power attains its maximum and the anode current increases rather slowly.

Region C. The back heating power diminishes steeply after passing through its maximum, and the anode current again increases rapidly. The remarkable phenomena in this region is the gereration of a unique oscillation which has a considerably strong power.

§4. Calculation of the Back Heating Power

When there is no space charge, the electron orbit in the cylindrical magnetron is cycloidal as shown in Fig. 6 a, but the situation is quite different, when there is space charge.

On the assumption that each of electrons forming the space charge moves circulary as in Fig. 6 b, Brillouin derived the expressions;

$$V(r)=\frac{1}{8}\cdot\frac{e}{m}B^2r^2\left(1-\frac{r^2_c}{r^2}\right)^2 \qquad (1)$$

as the potential distribution, and hence

$$\rho(r)=-\frac{\mathcal{E}_0}{2}\frac{eB^2}{m}\left(1+\frac{r^4_c}{r^4}\right) \qquad (2)$$

as the space charge density, where e,m, B and r_c are electron charge, electron mass, magnetic field and the cathode radius respectively.

Linder⁷⁾, in 1938, proposed that the very dense space charge is formed by electrons near the cathode and the electron scattering occurs there by their mutual interaction, because the electron in the cylindrical magnetron performs cycloidal motion and can pass by the cathode many times with slow speed.

Reverdin⁹⁾, in 1951, measured the distribution of the space charge in the cylindrical magnetron by the method of electron optical mapping.

In Fig. 7, he gives his result shown by the curve-1, and also for comparison the curve-2 and-3 obtained respectively from Brillouin's expression (2) and from the calculation considering electron motion as cycloidal.

As easily seen, the practical space charge distribution is situated between curve-2 and -3. However, the space charge does not completely vanish at the cut-off radius but spreads beyond it and there occurs a marked maximum of space charge thereabout.

Thus, the electron scattering occurs both near the cathode and in the outermost sheath of the electron cloud. By comparing the energy of an electron scattered near the cathode with that of an electron scattered in the outermost sheath, it is reasonably concluded that the latter contributes much more to the back heating than the former. Hence, the author calculated the back heating power assuming that the anode dark current and the back heating are caused only by the electrons scattered in the outermost sheath.

As shown in Fig. 8, the space charge cloud is restricted between the cathode and the surface of the radius r_s which value depends on the electric and the magnetic fields.

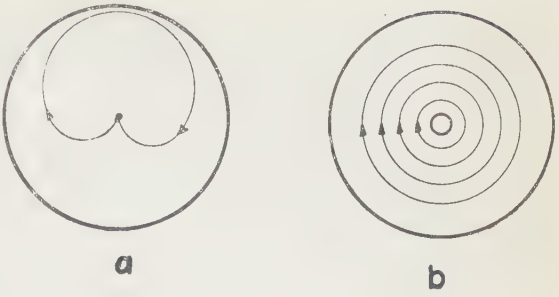

Fig. 6.

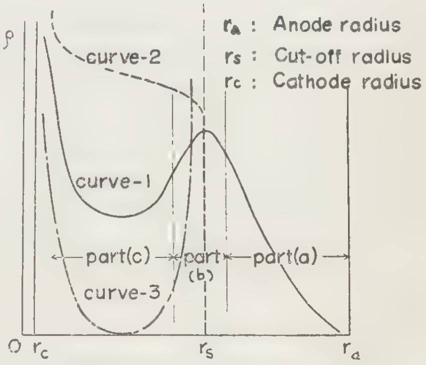

Fig. 7. (From Reverdin)

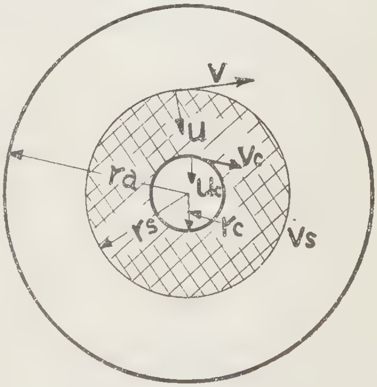

Fig. 8.

At r_s, the above mentioned outermost sheath is produced, and the orbital energy of electron is transformed into the energy of electron random motion, of which u and v denote radial (positive when directed to the cathode) and tangential velocity components respectively.

In the following the calculation is carried out on the assumption of the velocity distribution function of electron being Maxwellian:

$$f(u,v)=\frac{m}{2\pi kT}\,\mathcal{E}^{-(m(u^2+v^2))/2kT} \qquad (3)$$

where the axial velocity component is neglected, assuming a cylindrical magnetron of infinite length. And to the first approximation the influence of the magnetic field upon the motion of scattered electron is also neglected*). In fact its contribution to the back heating power is little.

The radial current density at r_s directed to the cathode is given by

$$I=Ne\int_0^\infty\int_{-\infty}^\infty uf(u,v)\,dvdu$$

$$=Ne\sqrt{\frac{kT}{2\pi m}}\ , \tag{4}$$

where N is the electron density at r_s.
If an electron starting at r_s with the velocity componets u and v arrieves at the cathode with u_c and v_c, the energy relation is

$$\frac{1}{2}m(u^2_c+v^2_c)=\frac{1}{2}m(u^2+v^2)-eV_s \tag{5}$$

and the momentum relation is

$$r_cv_c=r_sv\ , \tag{6}$$

where V_s is the potential at r_s against the cathode.

In order that the electron may arrive at the cathode, the condition $u>0$ and $u^2_c>0$ must be satisfied.

Putting

$$v_1=\frac{r_c}{\sqrt{r^2_s-r^2_c}}(u^2-2(e/m)V_s)^{1/2} \tag{7}$$

and

$$u_1=\left(\frac{2e}{m}V_s\right)^{1/2} \tag{8}$$

the above conditions become;

$$-v_1<v<v_1$$

and

$$u>v_1\ .$$

Then the total current flowing into the cahtode is expressed by

$$i_c=2\pi r_slNe\int_{u_1}^\infty\int_{-v_1}^{+v_1} uf(u,v)dvdu$$

$$=2\pi r_clI\varepsilon^{-(eV_s)/kT}\ , \tag{9}$$

where l is the anode thickness and cathode length.

The electrons which are not captured by the cathode come back to the outermost sheath as well as those newly emitted by the cathode get there and their energies are changed to those of electron random motion because the dense space charge existing there prevents the electrons' penetration.

Then the anode current is given by

$$i_a=2\pi lr_sI=2\pi lr_sNe\sqrt{\frac{kT}{2\pi m}} \tag{10}$$

and the back heating power by

$$W_b=2\pi r_slN\int_{u_1}^\infty\int_{-v_1}^{+v_1} u(\tfrac{1}{2}mu^2+\tfrac{1}{2}mv^2-eV_s)$$

$$\times f(u,v)dvdu\ . \tag{11}$$

Carrying out the integration in (11), the following expression is obtained;

$$W_b=3r_slNkT\sqrt{\pi}\cdot\varepsilon^{-(eVs)/kT}\left(\frac{kT}{2m}\right)^{1/2}\frac{r_c}{r_s} \tag{12}$$

(10) is rewritten:

$$r_slN=i_a\cdot\frac{1}{2\pi e\sqrt{\frac{kT}{2\pi m}}} \tag{13}$$

Substituting (13) into (12), we obtain:

$$W_b=\frac{3}{2}\cdot\frac{i_a}{e}\cdot\frac{r_c}{r_s}\cdot kT\cdot\varepsilon^{-(eVs)/kT}\ . \tag{14}$$

The electron temperature in the outermost sheath is determined by the relation;

$$NeV_s=\frac{3}{2}NkT\ , \tag{15}$$

which is derived by assuming that all the electron energies are changed to those of random motion.

Combination of (1) and (15) results in

$$W_b=\frac{1}{8}\frac{e}{m}r_cr_s\left(1-\frac{r^2_c}{r^2_s}\right)^2\varepsilon^{-3/2}B^2i_a\ . \tag{16}$$

Putting

$$c=\frac{1}{8}\frac{e}{m}\varepsilon^{-3/2}=4\cdot89\cdot10^9$$

and

$$f(r_s)=r_cr_s\left(1-\frac{r^2_c}{r^2_s}\right)^2.$$

(16) becomes

$$W_b=c\cdot f(r_s)\cdot i_a\cdot B^2\ . \tag{17}$$

In deriving this formula, the influence of the magnetic field upon the scattered electrons, the axial velocity component and the end effect have been left out of cosideration.

Corresponding to this neglect, it seems to to be reasonable to add the correction factor α_1. Then, finally the back heating power is given by:

---

* In the next paper, the author will report the case when this effect is taken into consideration.

$$W_b=\alpha_1\cdot c\cdot f(r_s)\cdot i_a B^2\,. \qquad (18)$$

In order to determine the dependency of r_s upon the anode voltage and the magnetic field, we proceed as follows.

The potential $V_1(r)$ for $r_a>r>r_s$ is given in the form of

$$V_1(r)=V_s+A\ln(r/r_s)$$

with an undetermined constant A.

$V_1(r)$ can be completely determined by joining this and the potential for $r_s>r>r_c$,

$$V_2(r)=\frac{1}{8}\frac{e}{m}r^2B^2\left(1-\frac{r_c^2}{r^2}\right)^2$$

smoothly at r_s, that is, putting

$$V_1(r_s)=V_2(r_s) \quad \text{and} \quad \left.\frac{dV_1}{dr}\right|_{r=r_s}=\left.\frac{dV_2}{dr}\right|_{r=r_s}.$$

By setting $r=r_a$ in V_1, the anode potential V_a is given by

$$V_a=\frac{1}{8}\frac{e}{m}B^2r_s^2\left[\left(1-\frac{r_c^2}{r_s^2}\right)^2 + 2\left(1-\frac{r_c^4}{r_s^4}\right)\ln\left(\frac{r_a}{r_s}\right)\right]=F(r_s)\cdot B^2\,. \qquad (19)$$

Utilizing this expression, we can determine the value r_s.

§ 5. Discussion

In the proceding sections, the author described the back heating by the scattered electrons and the unique oscillation which is considered to be plasma oscillation.

These phenomena can be explained by taking the space charge distribution as that of Reverdin shown by curve-1 in Fig. 7.

Because of the very high electron density in the part (b) of curve-1, the scattered electrons from this part form the space charge in the part (a). When the anode voltage is raised, the curve-1 moves toward the anode and is lifted upward as a whole.

In the following, the three regions A,B, and C given in Fig. 5 are separately decribed.

Region A.

In this region, the author observed the anode dark current which is considered to consist mainly of the flow of the electrons in the part (a). The formula of the back heating power is applicable in this region of its way of derivation. The correction factor α_1 is given as the ratio of the experimental value of the back heating power to the calculated, as in the following table.

V_a	α_1
680 Volt	1.95
617	2.11
560	2.33

in the magnetic field of 850 Gauss.

It will be shown in the next paper that when the influence of the magnetic field on the scattered electrons is taken into account, the value of α_1 approches to 1 and takes the values not scattered over this region.

Region B.

In this region, the part (b) comes to be situated very near the anode, with the anode voltage raised and accordingly both the density and the energy of the scattered electrons become largest, so the back heating power attains its maximum.

In Fig. 9, the magnetic field is plotted against the anode voltage giving the maximum back heating power. The relation between them is expressed experimentally by

$$V_a=KB^2$$

with K as a constant.

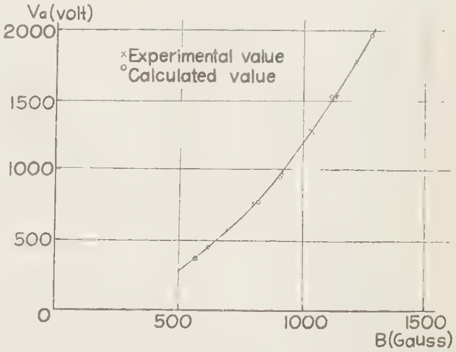

Fig. 9.

Comparing this with (19) in § 4, it follows that at the maximum back heating power, the radius of the outermost sheath must be a constant independent of the magnetic field, and can be determined graphically by using the measured values of V_a and B. This radius is denoted by r_m. With different anode radius r_a, the difference r_a-r_m was approximately constant as shown in the following:

r_a	r_m	r_a-r_m
2.5 mm	2.1 mm	0.4 mm
3.0	2.6	0.4
3.5	3.2	0.3

In Fig. 9, the calculated values with $r_m=2.6$

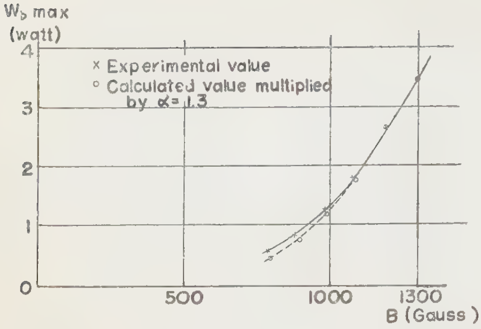

Fig. 10.

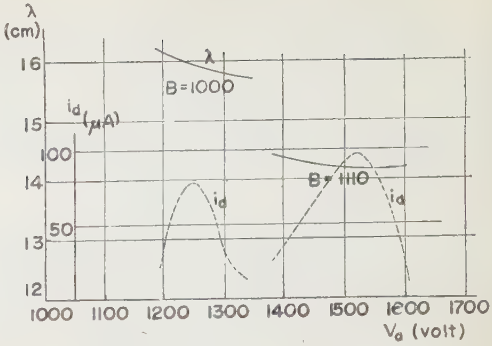

Fig. 11.

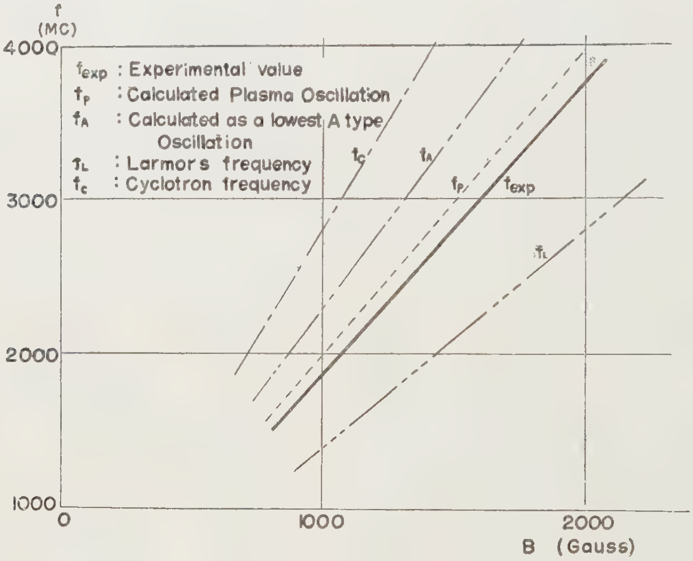

Fig. 12.

mm are added for comparison.

The second maximum of the back heating power, which appears in a very strong magnetic field (and accordingly with very high anode voltage) was observed when r_m was such that r_a-r_m=0.1 mm.

Fig. 10 shows the maximum back heating power versus the magnetic field. When multiplied by $\alpha_1=1.3$, the calculated values coincide precisely with the experimental values.

Region C.

In the measurement using the pulsed anode voltage, three types of oscillation α, β and γ were observed, as shown in Fig. 4.

In the measurement applying D. C. voltage to the anode, on the contrary, only γ-type oscillation appeared, as shown in Fig. 11. In this figure are shown both the frequency of γ-type oscillation and its detected current by a crystal detector against the anode voltage. The oscillation occurs within a certain range of the anode voltage when the magnetic field is given, and the frequency depends linearly upon the magnetic field and remains almost uninfluenced by the anode voltage so far as the oscillation is kept.

The result is given in Fig. 12. In the figure, f_{exp} denotes the experimental value and four kinds of calculated values f_p, f_A, f_L and f_C are plotted for comparison.

Here f_p is the value calculated by the formula;

$$f_p=\frac{1}{2\pi}\varepsilon^{1/2}\frac{e}{m}B\left(1+\frac{r^4_c}{r^4}\right)^{1/2},$$

which is obtained by substituting ρ from Brillouin's formula (2) in § 4 into Langmuir's expression of plasma oscillation,

$$f_p=\frac{1}{(2\pi)^2}\frac{e}{m}\frac{\rho}{\varepsilon_0}.$$

f_A is calculated according to the formula $\lambda_A=(13000/pB)$ with $p=1$ of A-type oscillation of magnetron.

f_L and f_c are respectively Larmor's and cyclotron frequencies.

As clearly seen, f_p represents f_{exp} exceedingly better than the other three f's.

In the region C, the part (b) of the curve-1 in Fig. 7 is captured completely by the anode and the number of scattered electrons becomes far less, and hence the back heating power decreses rapidly.

Thus it seems that the electron distribution becomes very like that of Brillouin, and the possibility of plasma oscillation grows.

The influence of the magnetic field upon the scattered electrons and the properties of the oscillation will be reported successively.

§ 6. Acknowledgement

The author wishes to thank Prof. I. Takahashi, Prof. S. Kojima, Prof. S. Okamura, Prof. S. Mito and Dr. S. Nakajima for their valuable advices and helpful discussions.

My thanks are also due to Mr. C. Shibata and Mr. N. Suehiro for their assistance.

References

1) G. B. Collins: *Microwave Magnetron*
2) K. R. Spangenberg: *Vacuum Tubes*
3) J. C. Slater: *Microwave Electronics*
4) W. Engbert: H.T.E.A. (1938)
5) R. L. Jepsen and M. W. Muller: J. Appl. Phys. **22** (1951)
6) L. Brillouin: Phys. Rev. **60** (1941) 385
7) E. G. Linder: Proc. I.R.E. **26** (1938) 346
8) L. Marton and S. H. Lachenbruch: J. Appl. Phys. **20** (1949) 1171
9) D. L. Reverdin: J. Appl. Phys. **22** (1951) 257
10) D. B. Langmuir: Phys. Rev. **28** (1926) 727
11) L. A. Harris: J. Appl. Phys. **23** (1952) 562
12) E. P. Gross: Phys. Rev. **82** (1951) 232

Short Notes

J. Phys. Soc. Japan **10** (1955) 1110

A Simple Method for the Visualization of Ultrasonic Fields

By Yasuo Torikai and Katsuo Negishi

Institute of Industrial Science, University of Tokyo, Chiba-City

(Read Oct. 19, 1953; Received Sept. 16, 1955)

Many methods have been developed for the visualization of ultrasonic fields, utilizing optical, thermal, mechanical or chemical effects of ultrasonic waves. Most of these methods, however, are limited in application because of requirements of optical accessibility, or of some special materials such as thermo-sensitive materials[1], phosphors[1][2][3] and starch plates[4].

In this note, a simple method is described using no special material except ordinary photographic paper and developer.

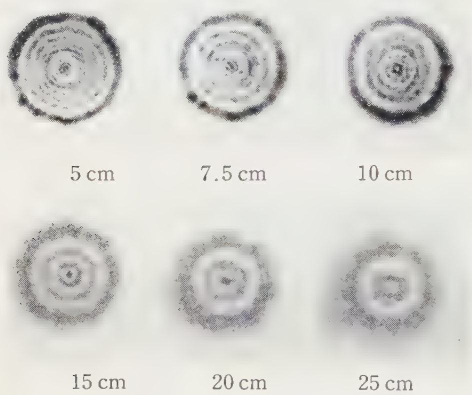

5 cm 7.5 cm 10 cm

15 cm 20 cm 25 cm

Fig. 1. Fresnel diffraction patterns of 3.3 cm diameter quartz transducer, frequency 7 MC. Distances from transducer are shown under each pattern.

A transducer was set in the tank filled with the dilute developer consisting of 1 part of Kodak D-19 and 10 parts of water. A sheet of photographic paper previously exposed to light uniformly was supported in the desired position by a suitable holder, and then irradiated ultrasonically. After 1 minute or so, the darkened pattern appeared gradually on the paper as the result of the accelerated development depending on the intensity distribution of the field. Then, the paper was removed and fixed in the usual manner.

In this method, the dark room is not necessary but all the procedures are allowed in any light room, and moreover, the permanent records can be taken directly. Any kind of photographic paper can be used and Kodak D-72 is also available instead of D-19.

Fig. 1 shows the Fresnel diffraction patterns of a circular quartz transducer at several distances from it. The diameter of the transducer is 3.3 cm and the frequency 7 MC. The tradsducer was driven by a self-exciting oscillator using a beam power tube, type 807, and the average intensity of the ultrasonic beam was estimated at 1 w/cm^2 or more.

The intensity alternation on the central axis and the number of the rings are in reasonable agreement with the diffraction theory.

References

1) P. J. Ernst and C. W. Hoffman: J.A.S.A. **24** (1952) 207.
2) H. Schreiber und W. Degner: Ann. Phys. **7** (1950) 275.
3) L. Pétermann: Helv. Phys. Acta **24** (1951) 596.
4) G. S. Bennett: J.A.S.A. **24** (1952) 470.

J. Phys. Soc. Japan **10** (1955) 1110~1111

Effects of the Dislocations on Minority Carrier Lifetime in Germanium

By Jun'ichi Okada

Matsuda Research Laboratory, Tokyo-Shibaura Electric Co., Kawasaki-city, Japan

(Received September 3, 1955)

The effects of the dislocations on minority carrier lifetime in germanium were studied. They have been reported already by several investigators,[1)-3)] but we tried more quantitative investigations on this problem.

Dislocations in or near the edge orientation act as a row of recombination centers. When the density of active recombination centers on a dislocation line is ρ and their cross section of recombination is σ, the rate of recombination per dislocation line is given by $v_T\sigma\rho$, where v_T is the thermal velocity of minority carriers.

The lifetime τ_d, due to the dislocations distributed at random, and the recombination velocity S, due to the dislocations along a lineage grain boundary, are defined simply by

$$\tau_d = 1/v_T\sigma\rho N_d$$

and

$$S = v_T\sigma\rho N_S$$

respectively, where N_d is the density of dislocations per cm^2 and N_S is the density of lineage boundary dislocations per cm. Then the measurements of τ_d and S with knowledge of N_d and N_S will give the same value of $\sigma\rho$, if there is no appreciable mutual interaction between the recombination centers along different dislocations.

We have tried to confirm the above relations in the following way.

Samples were the single crystals of n-type germanium of the resistivity about 2.5 Ω cm. (It is neceesary to use samples with the same resistivity, because ρ is considered to be a function of majority carrier density.) Dislocation density was measured by counting the number of etch-pits made by CP-4 etching.

Recombination velocity S of lineage boundary was determined by Vogel-Read-Lovell method,³⁾ and was 1.04×10^3 cm/sec for the boundary whose dislocation density N_S was 2.4×10^3/cm. This leads to $\sigma\rho=2.3\times10^{-8}$ cm.

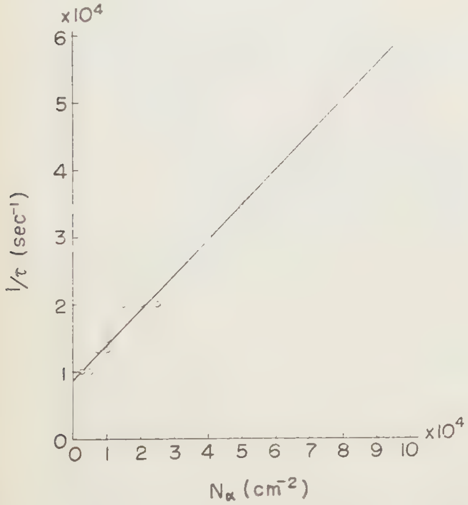

Fig. 1. Total lifetime *versus* dislocation density curve.

On the other hand, total lifetime τ was measured by Morton-Haynes method. The dislocation dependency of total lifetime is shown in Fig. 1. As readily seen, $1/\tau$ vs. N_d curve is linear. This shows that τ is given by

$$\frac{1}{\tau}=\frac{1}{\tau_b}+\frac{1}{\tau_d}$$

where τ_b is the body lifetime due to the recombination centers independent of dislocations. Then, τ_b can be determined by extrapolating the curve to $N_d=0$ and $\sigma\rho$ can be obtained from the slope of the curve. In this figure, $\tau_b=115\,\mu$s and $\sigma\rho=2.9\times10^{-8}$ cm were obtained. The latter must be compared with the value of $\sigma\rho$ determined from S. Their agreement is fairly good, but probably fortuitous. If we assume that recombination centers are the dangling bonds along the dislocation,⁴⁾ the value of ρ is about 6×10^5 cm^{-1}, and the cross section $\sigma\simeq4\times10^{-14}$ cm^2 is obtained. This seems to be a little larger than that of other recombination centers such as Cu or Ni,⁵⁾ but if each dislocation is surrounded by space charge, this value is not too unlikely.

Above results show also that the property of dislocations corresponding to etch-pits distributed at random are the same as that of the grain boundary dislocations, i.e. edge type.

The author thanks Mr. Y. Uemura for his valuable discussions.

References

1) G. L. Pearson, W. T. Read, Jr. and F. J. Morin: Phys. Rev. **93** (1954) 666.
2) S. S. Kulin and A. D. Kurtz: Act. Met. **2** (1954) 354.
3) F. L. Vogel, W. T. Read, L. C. Lovell: Phys. Rev. **94** (1954) 1791 (L).
4) W. T. Read, Jr.: Phil. Mag. **45** (1954) 775.
5) J. A. Burton, G. W. Hull, F. J. Morin and J. C. Severiens: J. Phys. Chem. **57** (1953) 853.

PROGRESS OF THEORETICAL PHYSICS

(Founded by H. Yukawa in 1946)

Published for the

Research Institute for Fundamental Physics
The Physical Society of Japan

Progress of Theoretical Physics Vol. 14, No. 2, August 1955

On the Gamma-Transition of Nuclei .... Mitsuo SANO .. 81
Nuclear Structure as Revealed by Elastic Excitation .... Clerk GOODMAN .. 95
Separation Energies and Nuclear Structures in Light Nuclei .... Takao TATI .. 107
The Cn(n; $2n$) Excitation Function and the Knock-out Process in Nuclear Reactions .... Ryuzo NAKASIMA and Ken KIKUCHI .. 126
On the Quenching of Molecular Rotation of Ortho-Hydrogen in Solid State .... Tuto NAKAMURA .. 135
On the Renormalization of Heisenberg Treatment .... Ichie WATANABE .. 151
Letters to the Editor:
  On the Wave Equation for Spin 1 in Hamiltonian Form .... I. FUJIWARA .. 166
  Note on the Lehmann's Modified Propagators .... K. HIIDA and M. SAWAMURA .. 167
  Magnetic Exchange Moment to Order eg^4 in Adiabatic Approximation .... S. HATANO .. 170
  On the Mass Reversal in the Quantized Field Theory .... T. OUCHI, K. SEMBA and M. YONEZAWA .. 172
Errata 174

Price $ 1.25 per copy
$ 15.00 per year (postage inclusive)
Annual dues for foreign members (individual subscribers)
$ 12.00 (postage inclusive)
〃 for foreign members of the Physical Society of Japan
$ 10.00 (postage inclusive)

Application for members, subscriptions and orders for back mumbers should be sent, directly or through book-dealers, to

The Publication Office
in
Yukawa Hall, Kyoto University, Kyoto, Japan

CONTENTS

(**Vol. 10**)

No. 1

Hiroshi FUJITA: Contribution to the Theory of Upper and Lower Bounds in Boundary Value Problems 1

Shūichi IIDA: Formation Energy of Superlattice in Ni_3Fe (III). Kinetics of the Superlattice at the Formation Stage with Long Range Order 9

Ken-ichi HIRANO and Hiroto SAKAI: On the Mechanism of Aging in Aluminium-Silver Alloys, II. Nature of the Guinier-Preston Zone 23

Otohiko NOMOTO: Molecular Sound Velocity and Molecular Compressibility of Organic Halogen Compounds 31

Tadatosi HIBI, Kyozaburo KAMBE and Goro HONJO: Interference Fringes in Electron Micrographs of Magnesium Oxide 35

Norio KATO: Integrated Intensities of the Diffracted and Transmitted X-rays due to Ideally Perfect Crystal 46

Takashi ITOH: Microwave Spectrum of $SPCl_3$, Theoretical 56

Kineo TSUKADA: Microwave Spectra of $SPCl_3$, Experimental 60

Hiromu WAKESHIMA: Development of Emulsions due to Self Nucleation 65

Ryozo YAMADA: On the Radio Wave Propagation in a Stratified Atmosphere 71

No. 2

Teinosuke KANDA: On the Halogen Nuclear Magnetic Resonance of Some Metal Halides I 85

Tetsuji NISHIKAWA and Koichi SHIMODA: Inversion Spectrum of Ammonia 89

J. KANAMORI, T. MORIYA, K. MOTIZUKI and T. NAGAMIYA: Methods of Calculating the Crystalline Electric Field 93

Takashi ITOH, Kimio OHNO and Hiroyuki YOSHIZUMI: Non-empirical Calculation of the Diamagnetic Anisotropy of Benzene 103

Shoichiro NOMURA and Shozo SAWADA: Dielectric Properties of Lead-Strontium Titanate 108

Shoichiro NOMURA: Dielectric Properties of Titanates Containg Sn^{4+} Ions I 112

Tyûsei AOI: The Steady Flow of Viscous Fluid past a Fixed Spheroidal Obstacle at Small Reynolds Numbers 119

Tyûsei AOI: On Spheroidal Functions 130

Hiromu WAKESHIMA: Spontaneous Condensation in a supersonic Flow of Humid Air .. 141

Eiichi FUKADA: Piezoelectricity of Wood 149

Kunio TERAO: Der Zündmechanismus im Dieselmotor (I) 154

No. 3

Toshio AZUMA: Beta-spectra of Ag110 and Sb124 167

Mitsuo MIWA: Excitation Function for the Reaction $^7Li(\gamma t)^4He$ up to 21 Mev 173

E. YAMAKA and K. SAWAMOTO: Electrical Conductivity and Thermo-electric Motive Force in MgO Single Crystal 176

Tamio SAKATA, Kimiko SAKATA and Kunihiko KIGOSHI: On the Resistivity and Crystal Structure of Binary Oxide of Nickel and Cobalt 179

Ken-ichi HIRANO and Yutaka TAKAGI: On the Precipitation Process in Aluminium-Zinc-Magnesium Alloys. Part I. $Al-Al_2Zn_3Mg_3$ System 187

Ken-ichi HIRANO, Hideyo MANIWA and Yutaka TAKAGI: Precipitation from Solid Solution of Lead in Magnesium 193

Sadao HOSHINO: Crystal Structure and Phase Transition of Some Metallic Halides (III). Structure Anomaly in α-Ag_2HgI_4 197

Takashi ITOH and Hiroyuki YOSHIZUMI: Application of the Alternant Orbital Method to Benzene 201

Takechiyo INOUE and Takehito TAKAHASHI: Vibrational Relaxation in Polyatomic Gas (Methane) 208

Tasaburô YAMAGUTI: On a Sodium Nitrate Polarization Prism and a Polarization Plate of a Scattering Type 219

Akira SAKURAI: The Flow due to Impulsive Motion of a Wedge and its Similarity to the Diffraction of Shock Waves 221
Isao OSHIDA: A New Graphical Solution of Ordinary Linear Differential Equation of the Second Order 228

No. 4

Goro FUJIOKA: The Lateral Distribution of Various Components in Extensive Air Showers at Sea Level 245
Taro KIHARA, Yukio MIDZUNO and Toshio SHIZUME: Virial Coefficients and Intermolecular Potential of Helium 249
Ryozi UYEDA: A Theory on Image Formation of Electron Microscope 256
Shoji KOJIMA, Kineo TSUKADA, Shizuko OGAWA, Akira SHIMAUCHI and Norio MATSUMIYA: On the Piezoelectric Lines at Sub-microwave Frequencies 265
Akio KOBAYASHI and Shinji KAWAJI: Adsorption and Surface Potential of Semiconductors. Part 1. Photo-enhanced Adsorption of Oxygen and Change of Contact Potential of ZnS Phosphors with Illumination 270
Akira SAKURAI: On Extraordinary Phenomena in a Non-linear Forced Oscillation 274
Hiroshi TSUJI: The Transformation Equations between One-and n-Dimensional Spectra in the n-Dimensional Isotropic Vector or Scalar Fluctuation Field 278
Yûkichi NOMURA and Shigetoshi KATSURA: Diffraction of Electromagnetic Waves by Circular Plate and Circular Hole 285
Kunio TERAO: Der Zündmechanismus im Dieselmotor (II) 304

No. 5

Shin-ichi KANEKO: A Calibration Measurement of Multiple Scattering of Slow μ-Mesons by the Constant Sagitta Method 325
Takeo HAYASHI, Mitsuhiro KAWAMURA and Atsushi AOKI: Directional Correlation of the Ti^{46} Gamma-Gamma Cascade 334
Kiyoshi MURAKAWA: Hyperfine Structure of the Spectrum of Mn I 336
Hiroshi FUJIWARA: Theoretical Study of Residual Resistance of Binary Alloys containing Foreign Atoms in small Concentration 339
Kozo KOMATSU: Theory of the Specific Heat of Graphite II 346
Enji UCHIDA and Hisamoto KONDOH: Magnetic Properties of FeTe 357
Toshio MISAWA: Emitter Efficiency of Junction Transistor 362
Takeo YOKOBORI: The Theory of Fatigue Fracture of Metals 368
Hiromu WAKESHIMA: Time Lag in the Self-Nucleation 374
Sohei KONDO: A Statistical-Mechanical Theory of Surface Tension of Curved Surface Layer I 381
Hisao TAKAYAMA and Koichi SHIMODA: Receiving Tubes with Very Small Grid Current 387
Kenji MITANI: The Direct Current associated with Microwave Gas Discharge between Coaxial Cylinders, IV 391
Hidenori HASIMOTO: Rayleigh's Problem for a Cylinder of Arbitrary Shape, II 397
Yorisaburo TAKAISI: The Forces on a Circular Cylinder moving with Low Speeds in a Semi-infinite Viscous Liquid bounded by a Plane Wall 407

No. 6

Yosiharu TORIZUKA, Yuzo KOJIMA, Tosihiko OKAMURA and Kozo KAMIRYO: The Zeeman Effect in Ammonia Microwave Spectra 417
Yasushige FUKANO: Variation in the Lattice Constant of Evaporated Potassium Chloride 420
Masakazu MARUTAKE and Takuro IKEDA: Elastic Properties of Lead Zirconate 424
Shiro OGAWA, Denjiro WATANABE and F. Eiichi FUJITA: On the Structure of Evaporated Thin Films of Metals 429
Junkichi NAKAI, Yoshio INUISHI and Yang TSUNG-CHE: On the Relations between Electron Emission, Conduction and Noise of Oxide-coated Cathodes 437
Tatsuya NIIMI: The Temperature Dependence of the Capacity of the Copper Oxide Rectifier 444
Kayako TANAKA, Hidetaro ABE and Ken-ichi HIRANO: On the Mechanism of Aging in Aluminium-Silver Alloys III. Variation of the Young's Modulus 454

M. SAWADA, K. TSUTSUMI, T. SHIRAIWA and M. OBASHI: On the Amorphous State of the Binary System of Nickel-Sulfur 459
M. SAWADA, K. TSUTSUMI, T. SHIRAIWA and M. OBASHI: On the Fine Structures of X-ray Absorption Spectra of Amorphous Substances........ 464
Hiroshi FUJIWARA and Takao ICHIKI: On Producing Thin Single Crystal Foils of Aluminium which have any Desired Crystallographic Orientations 468
Yutaka SHIGEMITSU: Statistical Theory of Turbulence I. Hypothesis of Vortex Chaos Motion........ 472
Saburô ASAKA: Application of the Thin-Wing-Expansion Method to the Flow of a Compressible Fluid past a Symmetrical Circular Arc Aerofoil 482

No. 7

Sōji KONO: Scintillation Spectrometer Studies on the Beta-activity of K^{40}........ 495
Shoji KOJIMA, Kineo TSUKADA and Yasushi HINAGA: Zeeman Splitting of Nuclear Quadrupole Resonance in Paradibromobenzene 498
Yoshimasa AOKI: Calculated Energy of A-O-A Type Molecules by Mulliken's Magic Formula 503
Morikazu TODA: On the Theory of Quantum Liquids. I. Surface Tension and Stress 512
Enji UCHIDA: Magnetic Properties of Cobalt Telluride........ 517
Sōshin CHIKAZUMI and Kenzō SUZUKI: On the Maze Domain of Silicon-Iron Crystal (I) 523
Atsuo NISHIOKA: Optical Observation of the First-Order Transition of Barium Titanate Single Crystal at the Curie Point 535
Tadao HORIE, Kazuo KAWABE, Masashi TACHIKI and Shozo SAWADA: Thermal Transition of Transparency in Ferroelectric Single Crystal of Barium Titanate 541
Sumiaki IBUKI and Seiichi YOSHIMATSU: Photoconductivity of Stibnite (Sb_2S_3) 549
Jitsuo TERADA: An X-Ray Study of Barium-Strontium-Calcium Triple Oxide 555
Junkichi NAKAI and Shogo NAKAMURA: Surface Treatment of Core Metal used for Oxide-coated Cathode........ 566
Kôichi ÔSHIMA: Shock Tube Study of the Flow past Circular-Arc Airfoils Using a Mach-Zehnder Interferometer 571
Hiroshi TSUJI: Experimental Studies on the Characteristics of Isotropic Turbulence behind Two Grids 578

No. 8

Isao MIURA, Tsuneo MATANO, Yoshio TOYODA and Takashi MURAYAMA: On the Extensive Air Showers Penetrating 10 cm of Lead Observed at 2,760 Meters above Sea Level........ 595
Shin-ichi KANEKO, Tadayoshi KUBOZOE, Moroe OKAZAKI and Masaomi TAKAHATA: Observations of Slow Particles and Stars in Nuclear Emulsions Exposed at 17 m.w.e. Underground 600
Jiro YAMASHITA and Tatumi KUROSAWA: The Theory of the Dielectric Constant of Ionic Crystals III 610
Kenjiro ASAI, Eiji YODA and Sueo YAMANAKA: On the Anomaly of the Dielectric Properties of n-Higher Alcohols........ 634
Hiroshi NIMURA: Anomalous Lattice Spacings Caused by Stacking Disorder........ 642
Masao SAWADA, Kenjiro TSUTSUMI, Toshio SHIRAIWA and Masayoshi OBASHI: On the Structure of the X-Ray Non-diagram Lines $K\beta_\eta$ for Elements from Cr(24) to Zn(30) 647
N. F. MOTT: A Theory of Fracture and Fatigue........ 650
A. J. FORTY and F. C. FRANK: The Interpretation of Etch Patterns on Aluminium.. 656
H. KANZAKI: On the Plasticity of Silver Bromide 663
J. S. KOEHLER: The Velocity of Dislocations 669
B. A. BILBY: The Migration of Solute Atoms to Dislocation Arrays 673
Frederick SEITZ: On the Theory of the Kirkendall Effect........ 679
Yorisaburo TAKAISI: The Drag on a Circular Cylinder moving with Low Speeds in a Viscous Liquid between Two Parallel Walls........ 685
Mitutosi KAWAGUTI: The Critical Reynolds Number for the Flow past a Sphere 695
Yûkichi NOMURA and Kôshun TAKAKU: On the Propagation of the Electromagnetic Waves in an Inhomogeneous Atmosphere 700

No. 9

Mitsuo SAKAI: Angular Correlation of Gamma Rays from Fe^{*56} 729
Shūji FUKUI, Takashi KITAMURA and Yojiro MURATA: On the Momentum Spectrum of μ-Mesons near Sea-Level at 24°N 735
Isao MIURA: On the Penetrating Showers Produced in Paraffin and Graphite 741
Kwai UMEDA and Shigehiro KOBAYASHI: Systematization of the Approximate Solutions of the Thomas-Fermi Equation 749
Kwai UMEDA and Yasuo TOMISHIMA: On the Influence of the Packing on the Atomic Scattering Factor Based on the Thomas-Fermi Theory 753
Shigehiro KOBAYASHI, late Takehiko MATSUKUMA, Sokichi NAGAI and Kwai UMEDA: Accurate Value of the Initial Slope of the Ordinary TF Function 759
Mario YOKOTA: A Note on the Paramagnetic Relaxation 762
Shūichi IIDA: Formation Energy of Superlattice in Ni_3Fe Part (IV) A Theoretical Treatment of Vacancy Migration and Disorder-order Transformation in Alloys.. 769
Shin-ya MIYATANI: On the Polarization of Silver Sulfide 786
Kazuo SUZUKI: X-ray Studies on the Structures of Solid Solutions NaCl-$CaCl_2$ II. Structures of {111} and {310} Plate-Zones 794
Osamu NAKADA: Theory of Viscoelasticity of Amorphous Polymers 804
Yaso'o MATUNOBU: Application of the Thin-Wing-Expansion Method to the Compressible Flow past a Kaplan Bump 814

No. 10

Masayoshi NINOMIYA: Rotational Analysis of the CrO Bands 829
Shoko CHIBA: The Magnetic Properties and Phase Diagram of Iron Tellurium System 837
Sōshin CHIKAZUMI and Tatsurō OOMURA: On the Origin of Magnetic Anisotropy Induced by Magnetic Annealing 842
Isao OSHIDA, Yuzuru OOSHIKA and Reikiti MIYASAKA: Proton Transfer in Hydrogen Bond and Its Participation in π-Electron Systems 849
Ikuro SHIMOSE: Equation of State for Vapor-Liquid-System 860
Yoshio URANO: An Equivalent Circuit of a Bolometer 864
Kinzo HIDA: On Some Singular Solutions of the Tricomi Equation relating to Transonic Flow 869
Kinzo HIDA: Asymptotic Behaviour of the Location of a Detached Shock Wave in a Nearly Sonic Flow 882
Yutaka SHIGEMITSU: Statistical Theory of Turbulence, II. Foundation of Similarity Theory of Turbulence 890

No. 11

Kiyoshi MURAKAWA: Hyperfine Structure of the Spectrum of Ruthenium Part III.... 919
Kiyoshi MURAKAWA: The Quadrupole Moment of La^{139} 927
Shoji KOJIMA, Akira SHIMAUCHI, Shigeo HAGIWARA and Yoshihito ABE: Observation of Nuclear Quadrupole Resonances with a Coaxial-cavity Spectrometer 930
Tadashi KISHIMOTO and Otohiko NOMOTO: Absorption of Ultrasonic Waves in Organic Liquids (III). Liquids with Negative Temperature Coefficient of Sound Absorption (b) o-Chlorophenol and Aniline 933
Yoji NAKAMURA: Residual Magnetization and Magnetostriction of Nickel Single Crystals 937
Wataru KINASE and Hidetoshi TAKAHASHI: Theory of Spontaneous Deformation of Barium Titanate 942
E. TERAMOTO, M. KURATA, R. CHÛJÔ, C. SUZUKI, K. TANI and T. KAJIKAWA: Statistical Properties of Lattice Chains 953
Tokutaro HIRONE, Nobuhiko KUNITOMI and Masajiro ABE: The Mechanism of Internal Friction due to the Motion of the Dislocation 960
Tokutaro HIRONE, Motoharu KIMURA, Toshio KITAGAKI, Nobuhiko KUNITOMI and Yosimitsu SUGITA: Diffusion of Silver in Silver-Zinc and Silver-Cadmium Alloys 967
Einosuke FUKUSHIMA and Akiya OOKAWA: Some Characters of the Soap Bubble Raft in a Vibrating State 970
Hideji SUZUKI: Some Observations on Dislocations in Copper Crystals 981

Ken-ichi HIRANO: Aging Process in Quenched Aluminium-Zinc Solid Solutions 995

Eizō KANAI and Takesi SATOH: Density Analysis of Glass in Transformation Range ..1002

Kanji HONDA and Yoshihide NAITO: On the Nature of Silent Electric Discharge 1007

Kinzo HIDA: A Derivation of Guderley-Barish's Solution for the Sonic Flow on the Basis of the Thin-wing Expansion Method 1011

No. 12

Sadaaki YANAGAWA: Orbit-orbit Interactions in Atomic l^n Configurations............1029

Shintaro SUGAI and Jiro FURUICHI: Studies of High Polymers by Radioactive Method I. Self Diffusion of Ions in Ion Exchangers............1032

Tosio SAKURAI: The Cross-Chain Configuration and a New Type of Phase Transformation in Solid Long Chain Acid Amides............1040

Toshiaki TAKAMATSU: A New Dielectric Dispersion in Long-Chain Normal Primary Alchohol of Probable Carbon Number 32 at Lower Temperature Phase 1049

Masaki HIRASHIMA: The Selective Oxidation of Silver-Magnesium Alloys in Water Vapor 1055

Tsuneyoshi UYEMURA and Teruo MORISHIGE: Studies on the Explosion Mechanism of Electric Blasting Caps by Ultra-High-Speed Grid Framing Camera 1064

B. D. KHOSLA and N. A. RAMAIAH: Oscillographic Studies of Joshi Effect and Secondary Processes in a Low Frequency Electric Discharge............1067

Yataka SHIGEMITSU: Statistical Theory of Turbulence, III Extension of Similarity Theory of Turbulence 1077

Ken-ichi KUSUKAWA: The Application of Meksyn-Imai's Method to the Subsonic Flow past an Axisymmetric Body............1088

Ken-ichi KUSUKAWA: On the Subsonic Flow of a Compressible Fluid past an Axisymmetric Moderately Thick Body 1093

Yoshio YASUOKA: On the Space Charge affected by the Magnetic Field............1102

SHORT NOTES

No. 1

Motozo KANEKO, Rokuro MURAI, Kei KISHI and Dai MORI: Study of the Second order Transition Temperature of High Polymer by the Photoelastic Method.......... 78

Atsuo NISHIOKA and Hiroshi OKAMOTO: Measurement of the Complex Permeability of Carbonyl Iron Powders at 4000 Mc/s 79

Kinzo HIDA: Supplementary Note to my Paper "An Approximate Study on the Detached Shock Wave in front of a Circular Cylinder and a Sphere" 79

Takuro TSUZUKU and Tsutomu KOMODA: Layer Growth of Artificial Graphite 81

No. 2

Mitsuru ASANUMA and Shinji OGAWA: On the Magnetic Ageing of Pure Iron........ 161

Hazimu KAWAMURA and Masami ONUKI: Drift Mobility of Conduction Electron in KCl 162

S. R. MOHANTY, T. S. NAGARJUNAN, R. SRINIVASAN and G. SRINIVASAN: Dependence on the Nature of the Electrode Surface of the Joshi Effect in Oxygen at Different Gas Pressures 163

Kiyoshi MIYAKE: Effect of Electron Bombardment on Secondary and Photo-electron Emission of Cesium antimonide............ 164

Yasuo KANAI and Katsuhisa FURUSYŌ: On the Hall Effect of P-type Germanium in the Near Intrinsic Range 165

No. 3

Jiro YAMAGUCHI, Tadao KANAZAWA, Toru MATOZAKI and Kazuji HIRAI: On the Blocking Layer of Selenium Rectifier (I) 233

Jiro YAMAGUCHI: On the Blocking Layer of Selenium Rectifier (II)............ 234

Ken-ichi NAKAMURA: Some Effects of Infrared Irradiation on ZnCdS Phosphors with Copper Activators 236

Chiyoe YAMANAKA and Tokuo SUITA: Electron Bombardment Conductivity in Alkali-halide Crystals I 238
Takeshi KOJIMA and Tetsuji NISHIKAWA: Microwave Spectrum of Methyl Mercaptan (I) 240
Tsunesaburo ASADA, Toshizo NAKAYA and Tetsuo MAMURO: Influence of External Radiation on an A-Hg Discharge Tube 241
Manabu HATTORI, Kazuo HISATAKE, Takasi MIKUMO and Teruo MOMOTA: Gamma Rays from the Reaction $^{27}\mathrm{Al}(p, \gamma)^{28}\mathrm{Si}$ 242

No. 4

Masao TOMURA and Eizo OTSUKA: Note on the Shift of Band Edge of Germanium with Temperature 313
Masayoshi SAKAMOTO: On the Threshold of the Exciton Band in BaO 314
Taro KIHARA and Shobu KANEKO: Confirmation of the Existence of a Helium Double-Molecule 314
Motoyosi SUGITA: The Metabolic Turnover and the Maintenance of the Low Entropy Level 316
I. OMURA, H. BABA and K. HIGASI: The Ionization Potentials of Some Conjugated Molecules 317
Mitsuo IDA: X-Ray Studies on Long Chain Compounds Solidified under an Alternating Electric Field 318
Kiyoshi MURAKAWA: Isotope Shift in Cd II λ 4415 319
Mitsuo MIWA and Katsumi KURIYAMA: Range-Energy Relation of Triton in the Nuclear Emulsion up to 10 Mev 320
Hiroshi WATANABE: Energy Analysis of Electron Diffraction Patterns 321

No. 5

Shigeya KUWABARA: Intensity Variations of Electron Diffraction Patterns from Metal Films of Various Thicknesses 416

No. 6

Seiichi YOSHIMATSU, Chikashi KANZAKI, Sumiaki IBUKI and Naomichi MURAI: Influence of Infrared Rays on the Photoconductivity of the Polycrystalline CdS .. 493
Inosuke SUMOTO: An Interesting Phenomenon Observed on Some Dielectrics 494

No. 7

Ken-ichi HIRANO, Yutaka TAKAGI and Hideyo MANIWA: Origin of Guinier-Preston Zones in Alloys 587
Yoshio INUISHI and Tokuo SUITA: The Effect of Mechanical Stress on Dielectric Breakdown of Alkali Halide Single Crystals 588
Yoshio INUISHI and Tokuo SUITA: Effects of Mechanical Stress in Dielectric Breakdown of Alkali-Halides II (Time Effect) 590
Shoji KOJIMA and Kineo TSUKADA: Fine Structure of Pure Quadrupole Spectrum in Iodine Crystal 591

No. 8

Ken-ichi NAKAMURA: Effects of Infrared on Emission of ZnS:Cu Phosphors 715
Kenjiro ASAI: On Chemical Change of n-Higher Alcohol Caused by the Influence of Strong Electric Field 716
Yasuo KANAI: On the Galvanomagnetic Effects in n-type Indium Antimonide........ 718
Yasuo KANAI: On the Inductive Part in the a.c. Characteristics of the Semiconductor Diodes 719
Ken-ichi HIRANO: Specific-Heat versus Temperature Curves of Aged Cu-Be Alloys .. 721
M. KIKUCHI and Y. TARUI: "Step" and "Oscillation" Phenomena in the Collector of A-type Transistors 722
Buichi KUBOTA and Chisato OKAZAKI: Multipolarization in the Hexagonal Barium Iron Oxide Magnets 723
Mikio YAMAMOTO: On an Empirical Formula for the Ferromagnetic Anisotropy Constant in Cubic Crystals 725

No. 9

Shigeyasu KODA and Taro TAKEYAMA: Interaction Between Slip Bands and Particles of Precipitate in an Aluminium Alloy 822
Yoshimoto NAKATA and Hiroshi FUJITA: On Upper and Lower Bounds of the Eigenvalues of a Free Plate 823
Shigehiro KOBAYASHI: Some Coefficients of the Series Expansion of the TFD Function 824
Kikusaburo OSADA: Ultraviolet Absorption Spectra of Uranium Glasses 825
Takeo KIKUCHI: The Thormoluminescence of Glasses 826
Akira SAKURAI: On Exact Solution of the Blast Wave Problem 827

No. 10

Ren SHISHIKURA: On the Specific Heat of Normal Solid Alcohol of Probable Carbon Number 32 903
Sumitada ASANO: On the Spectral Distribution of Infrared-Stimulated Phosphorescence of Pb-activated ZnS-Type Phosphors 903
Tadayasu MITUI: Effect of Directional Precipitation on Hardness in an Agehardened Alloy 905
Shūichi IIDA, Hisashi SEKIZAWA and Yoshimichi AIYAMA: Origin of the Uniaxial Anisotropy in Iron-Cobalt Ferrites 907
Hiroshi WATANABE: Energy Analysis of Kikuchi Lines 908
Ken-ichi HIRANO, Hideyo MANIWA and Yutaka TAKAGI: Specific-Heat Measurements on Quench-Annealed Al, Cu and α-phase Alloys of Cu 909
Susumu OKAZAKI and Hiroshi OKI: Noise in Germanium 910
Kiyoshi MIYAKE: Effect of Electron Bombardment on Secondary and Photoelectric Emission of Cesium-antimonide 912
Kiyoshi MIYAKE: Fatigue of Photoelectric Emission of Cesium-antimonide 913
Shin-ichi KANEKO, Tadayoshi KUBOZOE and Masaomi TAKAHATA: Intensities of Low Energy μ-Mesons and N-Component near Sea Level at 24°N 915

No. 11

Akira SAKURAI: Decrement of Blast Wave 1018
Jun'ichi OKADA: Observations of Dislocations along Grain Boundaries in Germanium Crystals 1018
Yasutada UEMURA: On the Coupled Dislocations along a Grain Boundary 1020
Akira ISOYA, Kazuo GOTO and Teruo MOMOTA: The Angular Distribution of α-Particles from the Reaction $^{19}F(p\alpha)^{16}O^*(\pi)^{16}O$ 1022
Tadayasu MITUI and Syôhei MIYAHARA: Influence of Magnetic Field on the Precipitation Process of Ferromagnetic Phase in Cu-Co Alloy 1023
Norio KATO: Fibrous Growth of $NaClO_3$ on Single Crystal 1024
Mitsuru ASANUMA and Sinji OGAWA: On the Magnetic Ageing of Pure Iron (II) 1025
Tadasu SUZUKI: Electron Diffraction on Supercooled Gold 1026

No. 12

Yasuo TORIKAI and Katsuo NEGISHI: A Simple Method for the Visualization of Ultrasonic Fields 1110
Jun'ichi OKADA: Effects of the Dislocations on Minority Carrier Lifetime in Germanium 1110

Arrata

Eiji HIRAHARA and Miyuki MURAKAMI: Hall Effect and Electrical Conductivity of Lead Selenide 83
Saburo ASAKA: Application of the Thin-Wing-Expansion Method to the Flow of a Compressible Fluid past a Symmetrical Circular Arc Aerofoil 593
Hiroshi FUJIWARA: Theoretical Study of Resistance of Binary Alloys Containing Foreign Atoms in small Concentration 727

Shoji KOJIMA, Kineo TSUKADA and Yasushi HINAGA: Zeeman Splitting of Nuclear Quadrupole Resonance in Paradibromobenzene 828
Yorisaburo TAKAISI: The Drag on a Circular Cylinder moving with Low Speeds in a Viscous Liquid between Two Parallel Walls 916
Kikusaburo OSADA: Ultraviolet Absorption Spectra of Uranium Glasses 917
Sumitada ASANO: On the Spectral Distribution of Infrared-Stimulated Phosphorescence of Pb-activated ZnS-Type Phosphors 1027

AUTHOR INDEX TO Vol. 10

ABE Hidetaro;
  K. TANAKA, ——— and K. Hirono: On the Mechanism of Aging in Aluminium-Silver Alloys III. Variation of the Young's Modulus 454
ABE Masajiro;
  T. HIRONE, N. KUNITOMI and ———: The Mechanism of Internal Friction due to the Motion of the Dislocation 960
ABE Yoshihito;
  S. KOJIMA, A. SHIMAUCHI, S. HAGIWARA and ———: Observation of Nuclear Quadrupole Resonances with a Coaxial-cavity Spectrometer 930
AIYAMA Yoshimichi;
  S. IIDA, H. SEKIZAWA and ———: Origin of the Uniaxial Anisotropy in Iron-Cobalt Ferrites 907
AOI Tyûsei: The Steady Flow of Viscous Fluid past a Fixed Spheroidal Obstacle at Small Reynolds Numbers 119
  ———: On Spheroidal Functions 130
AOKI Atsushi;
  T. HAYASHI, M. KAWAMURA and ———: Directional Correlation of the Ti^{46} Gamma-Gamma Cascade 334
AOKI Yoshimasa: Calculated Energy of A-O-A Type Molecules by Mulliken's Magic Formula 503
ASADA Tsunesaburo;
  ———, T. NAKAYA and T. MAMURO: Influence of External Radiation on an A-Hg Discharge Tube 241
ASAI Kenjiro;
  ———, E. YODA and S. YAMANAKA: On the Anomaly of the Dielectric Properties of *n*-Higher Alcohols 634
  ———: On Chemical Change of n-Higher Alcohol Caused by the Influence of Strong Electric Field 716
ASAKA Saburo: Application of tce Thin.Wing-Expansion Method to the Flow of a Compressible Fluid past a Symmetrical Circular Arc Aerofoil 482
  ———: (Errata) Application of the Thin-Wing-Expansion Method to the Flow of a Compressible Fluid past a Symmetrical Circular Arc Aerofoil 593
ASANO Sumitada: On the Spectral Distribution of Infrared-Stimulated Phosphorescence of Pb-activated Zn-S-Type Phosphors 903
ASANUMA Mitsuru;
  ——— and S. OGAWA: On the Magnetic Ageing of Pure Iron 161
  ——— and S. OGAWA: On the Magnetic Ageing of Pure Iron (II) 1025
  ———: (Errata) On the Spectral Distribution of Infrared-Stimulated Phosphorescence af Pb-activated ZnS-Type Phosphors 1027
AZUMA Toshio: Beta-spectra of Ag110 and Sb124 167
BABA H.;
  I. OMURA, ——— and K. HIGASI: The Ionization Potentials of Some Conjugated Molecules 317
BILBY B. A.: The Migration of Solute Atoms to Dislocation Arrays 673
CHIBA Shoko: The Magnetic Properties and Phase Diagram of Iron Tellurium System 837
CHIKAZUMI Sōshin;
  ——— and K. SUZUKI: On the Maze Domain of Silicon-Iron Crystal (I) 523
  ——— and T. OOMURA: On the Origin of Magnetic Anisotropy Induced by Magnetic Annealing 842
CHÛJÔ R.;
  E. TERAMOTO, M. KURATA, ———, C. SUZUKI, K. TANI and T. KAJIKAWA: Statistical Properties of Lattice Chains 953
FORTY A. J.;
  ——— and F. C. FRANK: The Interpretation of Etch Patterns on Aluminium 656
FRANK F. C.;
  A. J. FORTY and ———: The Interpretation of Etch Patterns on Aluminium 656

FUJIOKA Goro: The Lateral Distribution of Various Components in Extensive Air Showers at Sea Level 245

FUJITA F. Eiichi;
  S. OGAWA, D. WATANABE and ———: On the Structure of Evaporated Thin Films of Metals 429

FUJITA Hiroshi: Contribution to the Theory of Upper and Lower Bounds in Boundary Value Problems 1
  Y. NAKATA and ———: On Upper and Lower Bounds of the Eigenvalues of a Free Plate 823

FUJIWARA Hiroshi: Theoretical Study of Residual Resistance of Binary Alloys containing Foreign Atoms in small Concentration 339
  ——— and T. ICHIKI: On Producing Thin Single Crystal Foils of Alnminium which have any Desired Crystallographic Orientations 468
  : (Errata) Theoretical Study of Resistance of Binary Alloys Containing Foreign Atoms in small Concentration 727

FUKADA Eiichi: Piezoelectricity of Wood 149

FUKANO Yasushige: Variation in the Lattice Constant of Evaporated Potassium Chloride 420

FUKUI Shūji;
  ———, T. KITAMURA and Y. MURATA: On the Momentum Spectrum of μ-Mesons near Sea-Level at 24°N 735

FUKUSHIMA Einosuke;
  ——— and A. OOKAWA: Some Characters of the Soap Bubble Raft in a Vibrating State 970

FURUICHI Jiro;
  S. SUGITA and ———: Studies of High Polymers by Radioactive Method I —Self Diffusion of Ions in Ion Exchangers 1032

FURUSYŌ Katsuhisa;
  Y. KANAI and ———: On the Hall Effect of P-type Germanium in the Near Intrinsic Range 165

GOTO Kazuo;
  A. ISOYA, ——— and T. MOMOTA: The Angular Distribution of α-Particles from the Reaction $^{19}F(p\alpha)^{16}O^{*}(\pi)^{16}O$ 1022

HAGIWARA Shigeo;
  S. KOJIMA, A. SHIMAUCHI, ——— and Y. ABE: Observation of Nuclear Quadrupole Resonances with a Coaxial-cavity Spectrometer 930

HASIMOTO Hidenori: Rayleigh's Problem for a Cylinder of Arbitrary Shape, II 397

HATTORI Manabu;
  ———, K. HISATAKE, T. MIKUMO and T. MOMOTA: Gamma Rays from the Reaction ^{27}Al(p, γ)^{28}Si 242

HAYASHI Takeo;
  ———, M. KAWAMURA and A. AOKI: Directional Correlation of the Ti^{46} Gamma-Gamma Cascade 334

HIBI Tadatosi;
  ———, K. KAMBE and G. HONJO: Interference Fringes in Electron Micrographs of Magnesium Oxide 35

HIDA Kinzo: Supplementary Note to my Paper "An Approximate Study on the Detached Shock Wave in front of a Circular Cylinder and a Sphere" 79
  ———: On Some Singular Solutions of the Tricomi Equation relating to Transonic Flow 869
  ———: Asymptotic Behaviour of the Location of a Detached Shock Wave in a Nearly Sonic Flow 882
  ———: A Derivation of Guderley-Barish's Solution for the Sonic Flow on the Basis of the Thin-Wing Expansion Method 1011

HIGASI K.;
  I. OMURA, H. BABA and ———: The Ionization Potentials of Some Conjugated Molecules 317

HINAGA Yasushi;
  S. KOJIMA, K. TSUKADA and ———: Zeeman splitting of Nuclear Quadrupole Resonance in Paradibromobenzen 498
  S. KOJIMA, K. TSUKADA and ———: (Errata) Zeeman Splitting of Nuclear Quadrupole Resonance in Paradibromobenzene 828
HIRAHARA Eiji;
  ——— and M. MURAKAMI: (Errata) Hall Effect and Electrical Conductivity of Lead Selenide 83
HIRAI Kazuji;
  J. YAMAGUCHI, T. KANAZAWA, T. MATOZAKI and ———: On the Blocking Layer of Selenium Rectifier (I) 233
HIRANO Ken-ichi;
  ——— and H. SAKAI: On the Mechanism of Aging in Aluminium-Siver Alloys, II. Nature of the Guinier-Preston Zone 23
  ——— and Yutaka TAKAGI: On the Precipitation Process in Aluminium-Zinc-Magnesium Alloys. Part I. Al-$Al_2Zn_3Mg_3$ System 187
  ———, H. MANIWA and Y TAKAGI: Precipitation from Solid Solution of Lead in Magnesium 193
  K. TANAKA, H. ABE and ———: On the Mechanism of Aging in Aluminium-Silver Alloys III. Variation of the Young's Modulus 454
  ———, Y. TAKAGI and H. MANIWA: Origin of Guinier-Preston Zones in Alloys 587
  ———: Specific-Heat versus Temperature Curves of Aged Cu-Be Alloys 721
  ———, H. MANIWA and Y. TAKAGI: Specific-Heat Measurements on Quench-Annealed Al, Cu and α-phase Alloys of Cu 909
  ———: Aging Process in Quenched Aluminium-Zinc Solid Solutions 995
HIRASHIMA Masaki: Selective Oxidation of Silver-Magnesium Alloys in Water Vapor 1055
HIRONE Tokutaro;
  ———, N. KUNITOMI and M. ABE: The Mechanism of Internal Friction due to the Motion of the Dislocation 960
  ———, M. KIMURA, T. KITAGAKI, N. KUNITOMI and Y. SUGITA: Diffusion of Silver in Silver-Zinc and Silver-Cadmium Alloys 967
HISATAKE Kazuo;
  M. HATTORI, ———, T. MIKUMO and T. MOMOTA: Gamma Rays from the Reaction $^{27}Al(p, \gamma)^{28}Si$ 242
HONDA Kanji;
  ——— and Y. NAITO: On the Nature of Silent Electric Discharge 1007
HONJO Goro;
  T. HIBI, K. KAMBE and ———: Interference Fringes in Electron Micrographs of Magnesium Oxide 35
HORIE Tadao;
  ———, K. KAWABE, M. TACHIKI and S. SAWADA: Thermal Transition of Transparency in Ferrcelectric Single Crystal of Barium Titanate 541
HOSINO Sadao: Crystal Structure and Phase Transition of Some Metallic Halides (III). Structure Anomaly in α-Ag_2HgI_4 197
IBUKI Sumiaki;
  S. YOSHIMATSU, C. KANZAKI, ——— and N. MURAI: Influence of Infrared Rays on the Photoconductivity of the Polycrystalline CdS 493
  ——— and S. YOSHIMATSU: Photoconductivity of Stibnite (Sb_2S_3) 549
ICHIKI Takeo:
  H. FUJIWARA and ———: On Producing Thin Single Crystal Foils of Alluminium which have any Disired Crystallographic Orientations 468
IDA Mitsuo: X-Ray Studies on Long Chain Compounds Solidified under an Alternating Electric Field 318
IIDA Shūichi: Formation Energy of Superlattice in Ni_3Fe (III). Kinetics of the Superlattice at the Formation Stage with Long Range Order 9

: Formation Energy of Superlattice in Ni_3Fe Part (IV) A Theoretical Treatment of Vacancy Migration and Disorder-order Transformation in Alloys 769

-, H. SEKIZAWA and Y. AIYAMA: Origin of the Uniaxial Anisotropy in Iron-Cobalt Ferrites 907

IKEDA Takuro;

M. MARUTAKE and ———: Elastic Properties of Lead Zirconate 424

INOUE Takechiyo;

——— and T. TAKAHASHI: Vibrational Relaxation in Polyatomic Gas (Methane) 208

INUISHI Yoshio;

J. NAKAI, ——— and Y. TSUNG-CHE: On the Relations between Electron Emission, Conduction and Noise of Oxide-coated Cathodes 437

——— and T. SUITA: The Effect of Mechanical Stress on Dielectric Breakdown of Alkali-Halide Single Crystals 588

——— and T. SUITA: Effects of Mechanical Stress on Dielectric Breakdown of Alkali-Halides II (Time Effect) 590

ISOYA Akira;

—, K. GOTO and T. MOMOTA: The Angular Distribution of α-Particles from the Reaction $^{19}F(p\alpha)^{16}O^*(\pi)^{16}O$ 1022

ITOH Takashi: Microwave Spectrum of $SPCl_3$, Theoretical 56

———, K. OHNO and H. YOSHIZUMI: Non-empirical Calculation of the Diamagnetic Anisotropy of Benzene 103

——— and H. YOSHIZUMI: Application of the Alternant Orbital Method to Benzene 201

KAJIKAWA T.;

E. TERAMOTO, M. KURATA, R. CHÛJÔ, C. SUZUKI, K. TANI and ———: Statistical Properties of Lattice Chains 953

KAMBE Kyozaburo;

T. HIBI, ——— and Goro HONJO: Interference Fringes in Electron Micrographs of Magnesium Oxide 35

KAMIRYO Kozo;

Y. TORIZUKA, Y. KOZIMA, T. OKAMURA and ———: The Zeeman Effect in Ammonia Nicrowave Spectra 417

KANAI Eizo;

——— and T. SATOH: Density Analgsis of Glass in Transformation Range .. 1002

KANAI Yasuo;

——— and K. FURUSYO: On the Hall Effect of P-type Germanium in the Near Intrinsic Range 165

———: On the Galvanomagnetic Effect in n-type Indium Antimonide 718

———: On the Inductive Part in the a.c. Characteristics of the Semiconductor Diodes 719

KANAMORI J.;

, T. MORIYA, K. MOTIZUKI and T. NAGAMIYA: Methods of Calculating the Crystalline Electric Field 93

KANAZAWA Tadao;

J. YAMAGUCHI, ———, T. MATOZAKI and K. HIRAI: On the Blocking Layer of Selenium Rectifier (I) 233

KANDA Teinosuke: On the Halogen Nuclear Magnetic Resonance of Some Metal Halides I 85

KANEKO Motozo;

———, R. MURAI, K. KISHI and D. MORI: Study of the Second order Transition Temperature of High Polymer by the Photoelastic Method 78

KANEKO Shin-ichi: A Calibration Measurement of Multiple Scattering of Slow μ-Mesons by the Constant Sagitta Method 325

———, T. KUBOZOE, M. OKAZAKI and M. TAKAHATA: Observations of Slow Particles and Stars in Nuclear Emulsions Exposed at 17 m.w.e. Undergound 600

———, T. KUBOZOE and M. TAKAHATA: Intensities of Low Energy μ-Mesons and N-Component near Sea Level at 24°N 915

KANEKO Shobu;
T. KIHARA and ———: Confirmation of the Existence of a Helium Double-Molecule 314
KANZAKI Chikashi;
S. YOSHIMATSU, ———, S. IBUKI and N. MURAI: Influence of Infrared Rays on the Photoconductivity of the Polycrystalline CdS........ 493
KATO Norio: Integrated Intensities of the Diffracted and Transmited X-rays due to ideally Perfect Crystal 46
———: Fibrous Growth of $NaClO_3$ on Single Crystal........1024
KATSURA Shigetoshi:
Y. NOMURA and ———: Diffraction of Electromagnetic Waves by Circular Plate and Circular Hole........ 285
KANZAKI H.: On the Plasticity of Silver Bromide 663
KAWABE Kazuo;
T. HORIE, ———, M. TACHIKI and S. SAWADA: Thermal Transition of Transparency in Ferroelectric Single Crystal of Barium Titanate 541
KAWAGUTI Mitutosi: The Critical Reynolds Number for the Flow past a Sphere 695
KAWAJI Sinji;
A. KOBAYASHI and ———: Adsorption and Surface Potential of Semiconductors. Part 1. Photo-enhanced Adsorption of Oxygen and Change of Contact Potential of ZnS phosphors with Illumination 270
KAWAMURA Hazimu;
——— and M. ONUKI: Drift Mobility of Conduction Electron in KCl........ 162
KAWAMURA Mitsuhiro;
T. HAYASHI, ——— and A. AOKI: Directional Correlation of the Ti^{46} Gamma-Gamma Cascade 334
KHOSLA B. D.;
——— and N. A. RAMAIAH: Oscillographic Studies of Joshi Effect and Secondary Processes in a Law Frequency Electric Discharge........1067
KIGOSHI Kunihiko;
T. SAKATA, K. SAKATA and ———: On the Resistivity and Crystal Structure of Binary Oxide of Nickel and Cobalt........ 179
KIHARA Taro;
———, Y. MIDZUNO and T. SHIZUME: Virial Coefficients and Intermolecular Potential of Helium........ 249
——— and S. KANEKO: Confirmation of the Existence of a Helium Double-Molecule 314
KIKUCHI M.;
——— and Y. TARUI: "Step" and "Oscillation" Phenomena in the Collector of A-type Transistors........ 722
KIKUCHI Takeo: The Thormoluminescence of Glasses 826
KIMURA Motonobu;
T. HIRONE, ———, T. KITAGAKI, N. KUNITOMI and Y. SUGITA: Diffusion of Silver in Silver-Zinc and Silver-Cadmium Alloys........ 967
KINASE Wataru;
——— and H. TAKAHASHI: Theory of Spontaneous Deformation of Barium Titanate 942
KISHI Kei;
M. KANEKO, R. MURAI, ——— and D. NORI: Study of the Second order Transition Temperature of High Polymer by the Photoelastic Method...... 78
KISHIMOTO Tadashi;
——— and O. NOMOTO: Absorption of Ultrasonic Waves in Organic Liquids (III). Liquids with Negative Temperature Coefficient of Sound Absorption (b) o-Chlorophenol and Aniline 933
KITAGAKI Toshio;
T. HIRONE, M. KIMURA, ———, N. KUNITOMI and Y. SUGITA: Diffusion of Silver in Silver-Zinc and Silver-Cadmium Alloys 967

KITAMURA Takashi;
  S. FUKUI, ——— and Y. MURATA: On the Momentum Spectrum of μ-Mesons near Sea-Level at 24°N 735
KOBAYASHI Akio;
  — and S. KAWAJI: Adsorption and Surface Potential of Semiconductors. Part 1. Photo-enhanced Adsorption of Oxygen and Change of Contact Potential of ZnS Phosphors with Illumination 270
KOBAYASHI Shigehiro;
  K. UMEDA and ———: Systematization of the Approximate Solutions of the Thomas-Fermi Equation 749
  ———, late T. MATSUKUMA, S. NAGAI and K. UMDEA: Accurate Value of the Initial Slope of the Ordinary TF Function 759
  ———: Some Coefficients of the Series Expansion of the TFD Function 824
KODA Shigeyasu;
  — and T. TAKEYAMA: Interaction Between Slip Bands and Particles of Precipitate in an Aluminium Alloy 822
KOEHLER J. S.: The Velocity of Dislocations 669
KOJIMA Shoji;
  ——, K. TSUKADA, S. OGAWA, A. SHIMAUCHI and N. MATSUMIYA: On the Piezoelectric Lines at Sub-microwave Frequencies 265
  ———, K. TSUKADA and Y. HINAGA: Zeeman Splitting of Nuclear Quadrupole Resonance in Paradibromobenzene 498
  —— and K. TSUKADA: Fine Structure of Pure Quadrupole Spectrum in Iodine Crystal 591
  ———, K. TSUKADA and Y. HINAGA: (Errata) Zeeman Splitting of Nuclear Quadrupole Resonance in Paradibromo Benzene 828
  ———, A. SHIMAUCHI, S. HAGIWARA and Y. ABE: Observation of Nuclear Quadrupole Resonances with a Coaxial-cavity Spectrometer 930
KOJIMA Takeshi;
  ——— and T. NISHIKAWA: Microwave Spectrum of Methyl Mercaptan (I) .. 240
KOJIMA Yuzo;
  Y. TORIZUKA, ———, T. OKAMURA and K. KAMIRYO: The Zeeman Effect in Ammonia Microwave Spectra 417
KOMATSU Kozo: Theory of the Specific Heat of Graphite II 346
KOMODA Tsutomu;
  T. TSUZUKU and ———: Layer Growth of Artificial Graphite 81
KONDO Sohei: A Statistical-Mechanical Theory of Surface Tension of Curved Surface Layer I 381
KONDOH Hisamoto;
  E. UCHIDA and ———: Magnetic Properties of FeTe 357
KONO Sōji: Scintillation Spectrometer Studies on the Beta-activity of K^{40} 495
KUBOTA Buichi;
  ——— and C. OKAZAKI: Multipolarization in the Hexagonal Barium Iron Oxide Magnets 723
KUBOZOE Tadayoshi;
  S. KANEKO, ———, Moroe OKAZAKI and Masaomi TAKAHATA: Observations of Slow Particles and Stars in Nuclear Emulsions Exposed at 17 m.w.e. Underground 600
  S. KANEKO, ——— and M. TAKAHATA: Intensities of Low Energy μ-Mesons and N-Component near Sea Level at 24°N 915
KUNITOMI Nobuhiko;
  T. HIRONE, ——— and Masajiro ABE: The Mechanism of Internal Friction due to the Motion of the Dislocation 960
  T. HIRONE, M. KIMURA, T. KITAGAKI, ——— and Y. SUGITA: Diffusion of Silver in Silver-Zinc and Silver-Cadmium Alloys 967
KURIYAMA Katsumi;
  M. MIWA and ———: Range-Energy Relation of Triton in the Nuclear Emulsion up to 10 Mev 320

KUROSAWA Tatumi;
J. YAMASHITA and ———: The Theory of the Dielectric Constant of Ionic Crystals III 610
KUSUKAWA Ken-ichi: The Application of Meksyn-Imai's Method to the Subsonic Flow past an Axisymmetric Body 1088
———: On the Subsonic Flow of a Compressible Fluid past an Axisymmetric Moderately Thick Body 1093
KUWABARA Shigeya: Intensity Variations of Electron Diffraction Patterns from Metal Films of Various Thicknesses 416
MAMURO Tetsuo;
T. ASADA, T. NAKAYA and : Influence of External Radiation on an A-Hg Discharge Tube 241
MANIWA Hideyo;
K. HIRANO, and Y. TAKAGI: Precipitation from Solid Solution of Lead in Magnesium 193
K. HIRANO, Y. TAKAGI and ———: Origin of Guinier-Preston Zones in Alloys 587
K. HIRANO, ——— and Y. TAKAGI: Specific-Heat Measurements on Quench-Annealed Al, Cu and α-phase Alloys of Cu 909
MARUTAKE Masakazu;
——— and T. IKEDA: Elastic Properties of Lead Zirconate 424
MATANO Tsuneo;
I. MIURA, ———, Y. TOYODA and T. MURAYAMA: On the Extensive Air Showers Penetrating 10 cm of Lead Observed at 2,760 Meters above Sea Level 595
MATOZAKI Tôru;
J. YAMAGUCHI, T. KANAZAWA, ——— and K. HIRAI: On the Blocking Layer of Selenium Rectifier (I) 233
MATSUKUMA Takehiko (late);
S. KOBAYASHI, ———, S. NAGAI and K. UMEDA: Accurate Value of the Initial Slope of the Ordinary TF Function 759
MATSUMIYA Norio;
S. KOJIMA, K. TSUKADA, S. OGAWA, A. SHIMAUCHI and ———: On the Piezoelectric Lines at Sub-microwave Frequencies 265
MATUNOBU Yaso'o: Application of the Thin-Wing-Expansion Method to the Compressible Flow past a Kaplan Bump 814
MIDZUNO Yukio;
T. KIHARA, ——— and T. SHIZUME: Virial Coefficients and Intermolecular Potential of Helium 249
MIKUMO Takasi;
M. HATTORI, K. HISATAKE, ——— and T. MOMOTA: Gamma Rays from the Reaction ^{27}Al(p, γ)^{28}Si 242
MISAWA Toshio: Emitter Efficiency of Junction Transistor 362
MITANI Kenji: The Direct Current associated with Microwave Gas Discharge between Coaxial Cylinders, IV 391
MITUI Tadayasu: Effect of Directional Precipitation on Hardness in an Agehardened Alloy 905
——— and S. MIYAHARA: Influence of Magnetic Field on the Precipitation Process of Ferromagnetic Phase in Cu-Co Alloy 1023
MIURA Isao;
, T. MATANO, Y. TOYODA and T. MURAYAMA: On the Extensive Air Showers Penetrating 10 cm of Lead Observed at 2,760 Meters above Sea Level 595
———: On the Penetrating Showers Produced in Paraffin and Graphite 741
MIWA Mitsuo: Excitation Function for the Reaction ^{7}Li(γt)^{4}He up to 21 Mev 173
——— and K. KURIYAMA: Range-Energy Relation of Triton in the Nuclear Emulsion up to 10 Mev 320

MIYAHARA Shôhei;
  T. MITSUI and ———: Influence of Magnetic Field on the Precipitation Process of Ferromagnetic Phase in Cu–Co Alloy..........1023
MIYAKE Kiyoshi: Effect of Electron Bombardment on Secondary and Photo-electron Emission of Cesium antimonide.......... 164
  ———: Effect of Electron Bombardment on Secondary and Photoelectric Emission of Cesium-antimonide.......... 912
  : Fatigue of Photoelectric Emission of Cesium-antimonide.......... 913
MIYASAKA Reikiti;
  I. OSHIDA, Y. OOSHIKA and ———: Proton Transfer in Hydrogen Bond and Its Participation in π-Electron Systems.......... 849
MIYATANI Shin-ya: On the Polarization oi Silver Sulfide.......... 786
MOHANTY S. R.:
  ———, T. S. NAGARJUNAN, R. SRINIVASAN and G. SRINIVASAN: Dependence on the Nature of the Electrode Surface of the Joshi Effect in Oxygen at Different Gas Pressures.......... 163
MOMOTA Teruo;
  M. HATTORI, K. HISATAKE, T. MIKUMO and ———: Gamma Rays from the Reaction ${}^{27}\mathrm{Al}(p,\gamma){}^{28}\mathrm{Si}$.......... 242
  A. ISOYA, K. GOTO and ———: The Angular Distribution of α-Particle from the Reaction ${}^{19}F(p\alpha)^{16}O^{*}(\pi)^{16}O$..........1022
MORI Dai;
  M. KANEKO, R. MURAI, K. KISHI and ———: Study of the Second order Transition Temperature of High Polymer by the Photoelastic Method.......... 78
MORISHIGE Teruo;
  T. UYEMURA and ———: Studies on the Explosion Mechanisum of Electric Blasting Caps by Ultra-High-Speed Grid Framing Camera..........1064
MORIYA T.;
  J. KANAMORI, ———, K. MOTIZUKI and T. NAGAMIYA: Methods of Calculating the Crystalline Electric Field.......... 93
MOTIZUKI K.;
  J. KANAMORI, T. MORIYA, ——— and T. NAGAMIYA: Methods of Calculating the Crystalline Electric Field.......... 93
MOTT N. F.: A Theory of Fracture and Fatigue.......... 650
MURAI Naomichi;
  S. YOSHIMATSU, C. KANZAKI, J. IBUKI and ———: Influence of Infrared Rays on the Photoconductivity of the Polycrystalline CdS.......... 493
MURAI Rokuro;
  M. KANEKO, ———, K. KISHI and D. MORI: Study of the Second order Transition Temperature of High Polymer by the Photoelastic Method.......... 78
MURAKAMI Miyuki;
  E. HIRAHARA and ———: (Errata) Hall Effect and Electrical Conductivity of Lead Selenide.......... 83
MURAKAWA Kiyoshi: Isotope Shift in Cd II λ4415.......... 319
  ———: Hyperfine Structure of the Spectrum of Mn I.......... 336
  ———: Hyperfine Structure of the Spectrum of Ruthenium Part III.......... 919
  ———: The Quadrupole Moment of La^{139}.......... 927
MURATA M.
  E. TERAMOTO, ———, R. CHÛJÔ, C. SUZUKI, K. TANI and T. KAJIKAWA: Statistical Properties of Lattice Chains.......... 953
MURATA Yôjiro;
  S. FUKUI, T. KITAMURA and ———: On the Momentum Spectrum of μ-Mesons near Sea-Level at 24°N.......... 735
MURAYAMA Takashi;
  I. MIURA, T. MATANO, Y. TOYODA and ———: On the Extensive Air Showers Penetrating 10 cm of Lead Observed at 2,760 Meters above Sea Level.......... 595

NAGAI Sokichi;
  S. KOBAYASHI, late T. MATSUKUMA, ——— and K. UMEDA: Accurate Value of the Initial Slope of the Ordinary TF Function 759
NAGAMIYA T.
  J. KANAMORI, T. MORIYA, K. MOTIZUKI and ———: Methods of Calculating the Crystalline Electric Field 93
NAGARJUNAN T. S.;
  S. R. MOHANTY, ———, R. SRINIVASAN and G. SRINIVASAN: Dependence on the Nature of the Electrode Surface of the Joshi Effect in Oxygen at Different Gas Pressures 163
NAITO Yoshihide:
  K. HONDA and ———: On the Nature of Silent Electric Discharge 1007
NAKADA Osamu: Theory of Viscoelasticity of Amorphous Polymers 804
NAKAI Junkichi;
  ———, Y. INUISHI and Y. TSUNG-CHE: On the Relations between Electron Emission, Conduction and Noise of Oxide-coated Cathodes 437
  ——— and S. NAKAMURA: Surface Treatment of Core Metal used for Oxide-coated Cathode 566
NAKAMURA Ken-ichi: Some Effects of Infrared Irradiation on ZnCdS Phosphors with Copper Activators 236
  ———: Effects of Infrared on Emission of ZnS:Cu Phosphors 715
NAKAMURA Shōgo;
  J. NAKAI and ———: Surface Treatment of Core Metal used for Oxide-coated Cathode 566
NAKAMURA Yoji: Residual Magnetization and Magnetostriction of Nickel Single Crystals 937
NAKATA Yoshimoto;
  ——— and H. FUJITA: On Upper and Lower Bounds of the Eigenvalues of a Free Plate 823
NAKAYA Toshizo;
  T. ASADA, ——— and T. MAMURO: Influence of External Radiation on an A-Hg Discharge Tube 241
NEGISHI Katsuo:
  Y. TORIKAI and ———: A Simple Method for the Visualization of Ultrasonic Fields 1110
NIIMI Tatsuya: The Temperature Dependence of the Capacity of the Copper Oxide Rectifier 444
NIMURA Hiroshi: Anomalous Lattice Spacings Caused by Stacking Disorder 642
NINOMIYA Masayoshi: Rotational Analysis of the CrO Bands 829
NISHIKAWA Tetsuji;
  ——— and K. SHIMODA: Inversion Spectrum of Ammonia 89
  T. KOJIMA and ———: Microwave Spectrum of Methyl Mercapton (I) 240
NISHIOKA Atsuo;
  ——— and H. OKAMOTO: Measurement of the Complex Permeability of Carbonyl Iron Powders at 4000 Mc/s 79
  ———: Optical Observation of the First-Order Transition of Barium Titanate Single Crystal at the Curie Point 535
NOMOTO Otohiko: Molecular Sound Velocity and Molecular Compressibility of Organic Halogen Compounds 31
  T. KISHIMOTO and ———: Absorption of Ultrasonic Waves in Organic Liquids (III). Liquids with Negative Temperature Coefficient of Sound Absorption (b) o-Chlorophenol and Aniline 933
NOMURA Shoichiroand S. SAWADA: Dielectric Properties of Lead-Strontium Titanate.. 108
  ———: Dielectric Properties of Titanates Containg Sn^{4+} Ions I 112
NOMURA Yûkichi;
  ——— and S. KATSURA: Diffraction of Electromagnetic Waves by Circular Plate and Circular Hole 285

——— and K. TAKAKU: On the Propagation of the Electromagnetic Waves in an Inhomogeneous Atmosphere 700

OBASHI Masayoshi;
 M. SAWADA, K. TSUTSUMI, T. SHIRAIWA and ———: On the Amorphons State of the Binary System of Nickel-Sulfur........ 459
 M. SAWADA, K. TSUTSUMI, T. SHIRAIWA and ———: On the Fine Structures of X-ray Absorption Spectra of Amorphous Substances 464
 M. SAWADA, K. TSUTSUMI, T. SHIRAIWA and ———: On the Structure of the X-Ray Non-diagram Lines $K\beta_\eta$ for Elements from Cr(24) to Zn(30)...... 647

OGAWA Shinji;
 M. ASANUMA and ———: On the Magnetic Ageing of Pure Iron........ 161
 M. ASANUMA and ———: On the Magnetic Ageing of Pure Iron (II)........1025

OGAWA Shiro;
 ———, D. WATANABE and F. E. FUJITA: On the Structure of Evaporated Thin Films of Metals........ 429

OGAWA Shizuko;
 S. KOJIMA, K. TSUKADA, ———, A. SHIMAUCHI and N. MATSUMIYA: On the Piezoelectric Lines at Sub-microwave Frequencies........ 265

OHNO Kimio;
 T. ITOH, ——— and H. YOSHIZUMI: Nonempirical Calculation of the Diamagnetic Anisotropy of Benzene 103

OKADA Jun'ichi: Observations of Dislocations along Grain Boundaries in Germanium Crystals 1018
 ———: Effects of the Dislocation on Minority Carrier Lifetime in Germanium .1110

OKAMOTO Hiroshi;
 A. NISHIOKA and ———: Measurement of the Complex Permeability or Carbonyl Iron Powders at 4000 Mc/S........ 79

OKAMURA Tosihiko;
 Y. TORIZUKA, Y. KOJIMA, ——— and K. KAMIRYO: The Zeeman Effect in Ammonia Microwave Spectra........ 417

OKAZAKI Chisato;
 B. KUBOTA and ———: Multipolarization in the Hexagonal Barium Iron Oxide Magnets 723

OKAZAKI Susumu;
 ——— and H. OKI: Noise in Germanium 910

OKAZAKI Moroe;
 S. KANEKO, T. KUBOZOE, ——— and M. TAKAHATA: Observations of Slow Particles and Stars in Nuclear Emulsions Exposed at 17 m.w.e. Underground 600

OKI Hiroshi;
 S. OKAZAKI and ———: Noise in Germanium 910

OMURA I.;
 ———, H. BABA and K. HIGASI: The Ionization Potentials of Some Conjugated Molecules 317

ONUKI Masami;
 H. KAWAMURA and ———: Drift Mobility of Conduction Electron in KCl.... 162

OOKAWA Akiya;
 E. FUKUSHIMA and ———: Some Characters of the Soap Bubble Raft in a Vibrating State........ 970

OOMURA Tatsurô;
 S. CHIKAZUMI and ———: On the Origin of Mognetic Anisotropy Induced by Magnetic Annealing........ 842

OOSHIKA Yuzuru;
 I. OSHIDA, ——— and R. MIYASAKA: Proton Transfer in Hydrogen Bond and Its Participation in π-Electron Systems 849

OSADA Kikusaburo: Ultraviolet Absorption Spectra of Uranium Glasses 825
 ———: (Errata) Ultraviolet Absorption Spectra of Uranium Glasses........ 917

OSHIDA Isao: A New Graphical Solution of Ordinary Linear Differential Equation of the Second Order........ 228
 ———, Y. OOSHIKA and R. MIYASAKA: Proton Transfer in Hydrogen Bond and Its Participation in π-Electron Systems 849

ÔSHIMA Koichi: Shock Tube Study of the Flow past Circular-Arc Airfoils Using a Mach-Zehnder Interferometer 571

OTSUKA Eizo;
  M. TOMURA and ———: Note on the Shift of Band Edge of Germanium with Temperature 313

RAMAIAH N. A.;
  B. D. KHOSLA and ———: Oscillographic Studies of Joshi Effect and Secondary Processes in a Low Frequency Electric Discharge 1067

SAKAI Hiroto;
  K. HIRANO and ———: On the Mechanism of Aging in Aluminium-Silver Alloys, II. Nature of the Guinier-Preston Zone 23

SAKAI Mitsuo: Angular Correlation of Gamma Rays from Fe^{*56} 729

SAKAMOTO Masayoshi: On the Threshold of the Exciton Band in BaO 314

SAKATA Kimiko;
  T. SAKATA, ——— and K. KIGOSHI: On the Resistivity and Crystal Structure of Binary Oxide of Nickel and Cobalt 179

SAKATA Tamio, K. SAKATA and K. KIGOSHI: On the Resistivity and Crystal Structure of Binary Oxide of Nickel and Cobalt 179

SAKURAI Akira: The Flow due to Impulsive Motion of a Wedge and its Similarity to the Diffraction of Shock Waves 221
  ———: On Extraordinary Phenomena in a Non-linear Forced Oscillation 274
  ———: On Exact Solution of the Blast Wave Problem 827
  ———: Decrement of Blast Wave 1018

SAKURAI Tosio: The Cross-Chain Configuration and a New Type of Phase Transformation in Solid Long Chain Acid Amides 1040

SATOH Takesi;
  E. KANAI and ———: Density Analysis of Glass in Transformation Range..1002

SAWADA Masao;
  ———, K. TSUTSUMI, T. SHIRAIWA and M. OBASHI: On the Amorphous State of the Binary System of Nickel-Sulfur 459
  ———, K. TSUTSUMI, T. SHIRAIWA and M. OBASHI: On the Fine Structures of X-ray Absorption Spectra of Amorphous Substances 464
  ———, K. TSUTSUMI, T. SHIRAIWA and M. OBASHI: On the Structure of the X-Ray Non-diagram Lines $K\beta_\eta$ for Elements from Cr(24) to Zn(30)...... 647

SAWADA Shozo;
  S. NOMURA and ———: Dielectric Properties of Lead-Stroutium Titanate.... 108
  T. HORIE, K. KAWABE, M. TACHIKI and ———: Thermal Transition of Transparency in Ferroelectric Single Crystal of Barium Titante...... 541

SAWAMOTO K.;
  E. YAMAKA and ———: Electrical Conductivity and Thermo-electric Motive Force in MgO Single Crystal 176

SEITZ Frederick: On the Theory of the Kirkendall Effect 679

SEKIZAWA Hisashi;
  S. IIDA, ——— and Y. AIYAMA: Origin of the Unixial Anisotropy in Iron-Cobalt Ferrites 907

SHIGEMITSU Yutaka: Statistical Theory of Turbulence I. Hypothesis of Vortex Chaos Motion 472
  ———: Statistical Theory of Turbulence, II. Foundation of Similarity Theory of Turbulence 890
  ———: Statistical Theory of Turbulence, III. Extension of Similarity Theory of Turbulence 1077

SHIMAUCHI Akira;
  S. KOJIMA, K. TSUKADA, S. OGAWA, ——— and N. MATSUMIYA: On the Piezoelectric Lines at Sub-microwave Frequencies...... 265
  S. KOJIMA, ———, S. HAGIWARA and Y. ABE: Observation of Nuclear Quadrupole Resonances with a Coaxial-cavity Spectrometer...... 930

SHIMODA Koichi;
  T. NISHIKAWA and ———; Inversion Spectrum of Ammonia...... 85

TOYODA Yoshio;
I. MIURA, T. MATANO, ——— and T. MURAYAMA: On the Extensive Air Showers Penetrating 10 cm of Lead Observed at 2,760 Meters above Sea Level 595
TSUJI Hiroshi: The Transformation Equations between One- and n-Dimensional Spectra in the n-Dimensional Isotropic Vector or Scalar Fluctuation Field.......... 278
———: Experimental Studies on the Characteristics of Isotropic Turbulence behind Two Grids 578
TSUKADA Kineo: Microwave Spectra of $SPCl_3$, Experimental.......... 60
S. KOJIMA, ———, S. OGAWA, A. SHIMAUCHI and N. MATSUMIYA: On the Piezoelectric Lines at Sub-microwave Frequencies.......... 265
S. KOJIMA, ——— and Y. HINAGA: Zeeman Splitting of Nuclear Quadrupole Resonance in Paradibromobenzen 498
S. KOJIMA and ———: Fine Structure of Pure Quadrupole Spectrum in Iodine Crystal.......... 591
S. KOJIMA, ——— and Y. HINAGA: (Errata) Zeeman Splitting of Nuclear Quadrupole Resonance in Paradibromo Benzene 828
TSUNG-CHE Yang;
J. NAKAI, Y. INUISHI and ———: On the Relations between Electron Emission, Conduction and Noise of Oxide-coated Cathodes.......... 437
TSUTSUMI Kenjiro;
M. SAWADA, ———, T. SHIRAIWA and M. OBASHI: On the Amorphous State of the Binary System of Nickel-Sulfur 459
M. SAWADA, ———, T. SHIRAIWA and M. OBASHI: On the Fine Structures of X-ray Absorption Spectra of Amorphous Substances 464
M. SAWADA, ———, T. SHIRAIWA and M. OBASHI: On the Structure of the X-Ray Non-diagram Lines $K\beta_\eta$ for Elements from Cr(24) to Zn(30) 647
TSUZUKU Takurō;
——— and T. KOMODA: Layer Growth of Artificial Graphite 81
UCHIDA Enji;
——— and H. KONDOH: Magnetic Properties of FeTe.......... 357
———: Magnetic Properties of Cobalt Telluride.......... 517
UEMURA Yasutada: On the Coupled Dislocations along a Grain Boundary..........1020
UMEDA Kwai;
——— and S. KOBAYASHI: Systematization of the Approximate Solutions of the Thomas-Fermi Equation 749
——— and Y. TOMISHIMA: On the Influence of the Packing on the Atomic Scattering Factor Based on the Thomas-Fermi Theory.......... 753
S. KOBAYASHI, late T. MATSUKUMA, S. NAGAI and ———: Accurate Value of the Initial Slope of the Ordinary TF Function 759
URANO Yoshio: An Equivalent Circuit of a Bolometer 864
UYEDA Ryozi: A Theory on Image Formation Electron of Microscope 256
UYEMURA Tsuneyoshi;
——— and T. MORISHIGE: Studies on the Explosion Mechanisum of Electric Blasting Caps by Ultra-High-Speed Grid Framing Camera 1064
WAKESHIMA Hiromu: Development of Emulsions due to Self Nucleation 65
———: Spontaneous Condensation in a supersonic Flow of Humid Air 141
———: Time Lag in the Self-Nucleation.......... 374
WATANABE Denjiro;
S. OGAWA, ——— and F. FUJITA: On the Structure of Evaporated Thin Films of Metals.......... 429
WATANABE Hiroshi: Energy Analysis of Electron Diffraction Patterns 321
———: Energy Analysis of Kikuchi Lines 908
YAMADA Ryozo: On the Radio Wave Propagation in a Stratified Atmosphere.......... 71
YAMAGUCHI Jiro;
———, T. KANAZAWA, T. MATOZAKI and K. HIRAI: On the Blocking Layer of Selenium Rectifier (I) 233
———: On the Blocking Layer of Selenium Rectifier (II).......... 234

YAMAGUTI Tasaburô: On a Sodium Nitrate Polarization Prism and a Polarization Plate of a Scattering Type 219
YAMAKA E.;
——— and K. SAWAMOTO: Electrical Conductivity and Thermo-electric Motive Force in MgO Single Crystal 176
YAMAMOTO Mikio: On an Empirical Formula for the Ferromagnetic Anisotropy Constant in Cubic Crystals 725
YAMANAKA Chiyoe;
——— and T. SUITA: Electron Bombardment Conductivity in Alkalihalide Crystals I 238
YAMANAKA Sueo;
K. ASAI, F. YODA and ———: On the Anomaly of the Dielectric Properties of *n*-Higher Alcohols 634
YAMASHITA Jiro;
——— and T. KUROSAWA: The Theory of the Dielectric Constant of Ionic Crystals III 610
YANAGAWA Sadaaki: Orbit-orbit Interactions in Atomic l^n Configuration 1029
YASUOKA Yoshio: On the Space Charge affected by the Magnetic Field 1102
YODA Eiji;
K. ASAI, ——— and S. YAMANAKA: On the Anomaly of the Dielectric Properties of *n*-Higher Alcohols 634
YOKOBORI Takeo: The Theory of Fatigue Fracture of Metals 368
YOKOTA Mario: A Note on the Paramagnetic Relaxation 762
YOSHIMATSU Seiichi;
———, C. KANZAKI, S. IBUKI and N. MURAI: Influence of Infrared Rays on the Photoconductivity of the Polycrystalline CdS 493
S. IBUKI and ———: Photoconductivity of Stibuite (Sb_2S_3) 549
YOSHIZUMI Hiroyuki;
T. ITOH, K. OHNO and ———: Non-empirical Calculation of the Diamagnetic Anisotropy of Benzene 103
T. ITOH and ———: Application of the Alternant Orbital Method to Benzene 201